Bioconjugate Chemistry

Review

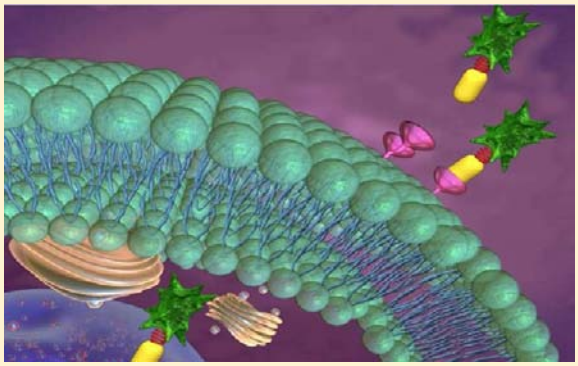
pubs.acs.org/bc

Engineering Folate–Drug Conjugates to Target Cancer: From Chemistry to Clinic

Iontcho R. Vlahov[†] and Christopher P. Leamon*[,‡]

Endocyte Inc., 3000 Kent Avenue, West Lafayette, Indiana 47906, United States

ABSTRACT: The folate receptor (FR) is a potentially useful biological target for the management of many human cancers. This membrane protein binds extracellular folates with very high affinity and, through an endocytic process, physically delivers them inside the cell for biological consumption. There are now many examples of how this physiological system can be exploited for the targeted delivery of biologically active molecules to cancer. In fact, strong preclinical as well as emerging clinical evidence exists showing how FR-positive cancers can be (i) anatomically identified using folate conjugates of radiodiagnostic imaging agents and (ii) effectively treated with companion folate-targeted chemotherapies. While the biological results are compelling, it is of equal importance to understand the conjugation chemistries that were developed to produce these active molecules. Therefore, this review will focus on the methods utilized to construct folate-based small-molecule drug conjugates (SMDCs), with particular attention focused on modular design, hydrophilic spacers, and self-immolative linkers.



INTRODUCTION

Since the birth of chemotherapy seven decades ago, during a time when aminopterin and nitrogen mustard "poisons" were systemically administered with the hopes of killing the tumor before the patient, variations of that same therapeutic strategy have continued, admittedly with some success, but always with significant toxic consequences. The concept of specifically directing, or "targeting" these poisons selectively to the diseased tissues did not escape the sharp minds of the founding fathers of chemotherapy. Rather, they simply did not have the means or scientific knowledge that is available today to pursue such approaches.

Homing to a life-threatening disease like cancer requires that an agent in circulation have the ability to recognize and bind to a unique trait expressed on that tissue. Although cancer tissue largely consists of "self" features, some differences are evident which can allow for exploitation, especially in the drug delivery setting. Thus, recombinant antibodies that recognize tumor-associated antigens have successfully been developed to treat various forms of human malignancies, such as trastuzumab, cetuximab, and rituximab.[1] Although it is not chemotherapy in the traditional sense, antibody therapy can elicit immune responses to fight the cancer. Furthermore, ground-breaking research has shown that potent chemotherapeutic molecules can be attached to these tumor-specific antibodies to form antibody–drug conjugates (ADC) that offer the added benefit of dropping off a chemical "bomb" on the cancer doorstep. This latter approach is actively being pursued by the pillars of biotechnology like Genentech, Seattle Genetics, and ImmunoGen. In fact, the Food and Drug Administration just recently approved Seattle Genetic's brentuximab vedotin (SGN-35), a conjugate comprising an anti-CD30 monoclonal antibody and monomethylauristatin E for the treatment of Hodgkin's lymphoma.[2] Clearly, cancer drug targeting is no longer a fantasy, but instead a realistic goal for future drug development.

In addition to antibodies, other tumor-selective ligands have been used to construct novel drug conjugates. For example, the vitamin folic acid (FA) displays high affinity for the folate receptor (FR), a glycosylphosphatidyinositol-linked membrane protein that captures its ligands from the extracellular milieu and transports them inside the cell via a nondestructive, recycling endosomal pathway.[3] Owing to the fact that its expression is largely absent from normal tissues, the FR is also a recognized tumor antigen/biomarker.[3] Because of this, diagnostic and therapeutic methods which exploit the FR's function have been developed to treat cancer (our laboratory pioneered this unique approach). Hence, molecular payloads that range in size from radionuclides to large DNA and liposomal constructs have successfully been delivered inside cancer cells via the FR pathway. As will be described below, one eminently related approach involves the attachment of FA to potent chemotherapeutic compounds to form small molecule drug conjugates, or SMDCs. To date, five FA-based SMDCs have been evaluated in clinical trials, including the most advanced agent, EC145 (vintafolide), which is currently being tested in a global phase 3 study in women with platinum-resistant ovarian cancer.

The purpose of this review is twofold: (i) to gain insight into the rational chemical design and synthesis of simple as well as complex FA-SMDCs, and (ii) to explore how subtle design changes impact pharmacological performance. The reader should be aware that much of what is presented relates to direct personal experience acquired by the authors over the past 13 years.

Received: October 12, 2011
Revised: May 30, 2012
Published: June 6, 2012

 © 2012 American Chemical Society dx.doi.org/10.1021/bc2005522 | *Bioconjugate Chem.* 2012, 23, 1357–1369

FOLATE RECEPTOR-MEDIATED DRUG TARGETING

FA (synonyms = folate, pteroyl-L-glutamic acid, vitamin B_9; see Figure 1) is itself not biologically active; rather, reduced

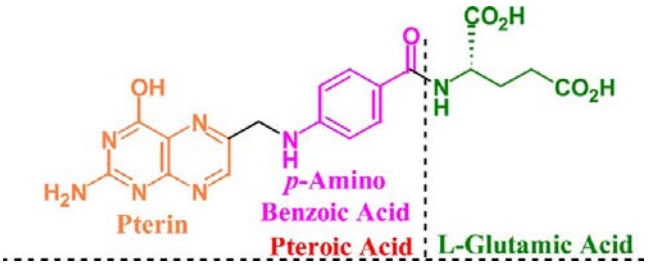


Figure 1. Chemical structure of the vitamin folic acid.

derivatives of this vitamin perform biological functions following its intestinal absorption and metabolism by dihydrofolate reductase in the liver.[4] Folates are needed within the cell to carry out one carbon methylation reactions as well as *de novo* synthesis of nucleotide bases (most notably thymine, but also purine bases). Therefore, folates are essential to the viability of normal, but especially proliferating, cells (including aggressively growing tumors).

Oxidized folates, such as FA, display the highest affinity for membrane-bound FR.[5] This property is preserved even when a drug payload is anchored to it to form a FA-SMDC.[6] As depicted in Figure 2, Step 1, a FA-SMDC extravasates from circulation to approach an FR-expressing tumor cell. From there, it readily binds to a FR (Step 2) and is brought inside the cell via an endocytosis process.[7] The FA-SMDC is now sequestered within an endosome where it encounters a mild drop in pH (due to resident proton pumps) to promote a conformational change in the FR, which subsequently enables the FA moiety of the SMDC to detach.[8] As will be described in detail below, biocleavable linkers placed within the SMDC construct are broken inside this endosomal compartment (Step 3) to release the intact, functionally active drug moiety of the SMDC which, in turn, diffuses out of the endosome to interact with its biological target (Step 4). At the same time, the FR protein recycles back to the plasma membrane where it can participate in additional rounds of internalization/drug delivery. In contrast, a ubiquitously expressed anion transporter, called the reduced folate carrier (RFC), can shuttle folate molecules directly inside the cell (see top right of Figure 2); however, FA-SMDCs are not substrates for the RFC,[9] and, consequently, acquisition of FA-SMDCs molecules within FR-negative normal cells is largely avoided. Biological activity mediated by FA-SMDCs is ultimately dependent on the successful release of the drug payload while inside the endosome. As will be discussed below, the selection of an appropriate linker system is of paramount importance for the construction of efficacious targeted compound.

DESIGN OF FA-SMDCS

In early attempts to target cytotoxic small molecules with folates, researchers focused mainly on the mere ability of the FR to sequester and then deliver FA-SMDCs inside tumor cells, thus ignoring structure−activity relationships in the payload and/or the importance of fine-tuning the release properties of the prepared conjugates. Consequently, results were of limited success.[10] Examples include chemotherapeutic agents that were covalently attached to FA or pteroic acid, such as bis(haloethyl) phosphoramidites,[11] PEG carboplatin,[12] a 10-mer conjugate of the thymidylate synthase inhibitor, 5-fluoro-2′-deoxyuridine-5′-*O*-monophosphate (FdUMP)[13] and paclitaxel.[14] However, the potencies of these rather stable constructs were not very high. On the basis of prior work showing that disulfide-containing linkers, when placed in between the FA ligand and a cytotoxic protein, yielded conjugates having superior activity against FR-positive cells relative to their "non-reducible" counterparts,[15] disulfide-containing SMDCs were constructed with molecules like maytansine,[16] desacetylvinblastine hydrazide (DAVLBH),[17] mitomycin C,[18] and the tubulysins.[19,20]

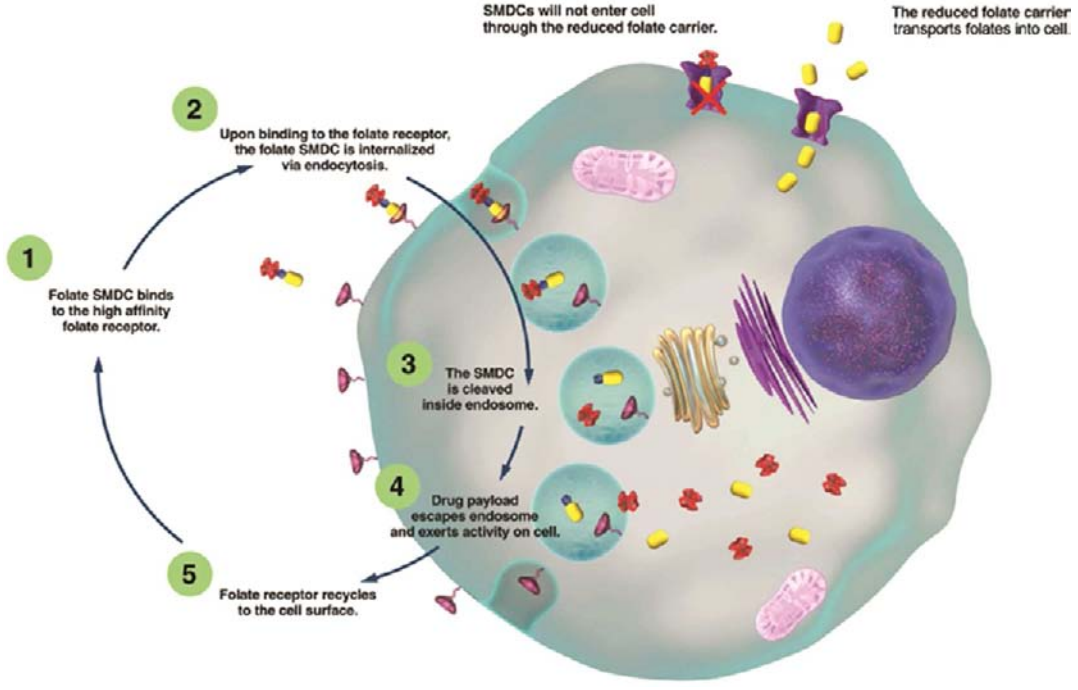


Figure 2. Schematic presentation of tumor cellular uptake of a FA-based SMDC by FR-mediated endocytosis. The SMDC consists of a folic acid moiety (shown as a yellow oval) and the drug payload (shown in red).

dx.doi.org/10.1021/bc2005522 | *Bioconjugate Chem.* 2012, 23, 1357−1369

Not surprisingly, each of these FA-SMDCs was found to be highly cytotoxic and specific for FR-expressing cells and/or tumor xenografts.

After years of intensive effort in this area of research, successful FA-SMDCs have been found to share several common characteristics. Outlined below is what our laboratory has observed to be useful Selection Criteria for producing active FA-SMDC lead compounds:

Highly potent drugs. The number of FRs on the surface of a given tumor cell is finite (typically in the 1−10 million copies/cell range[21]), and the FR recycling rate is on the order of 8−12 h.[22] Thus, there is both a lag time and a limit to the intracellular drug concentraton that can be achieved following a saturable exposure to a FA-SMDC. In fact, our laboratory has measured cytosolic concentrations of drug molecules in the 1−5 μM range (unpublished observations, Endocyte Inc.). Under such conditions, drug molecules with intrinsic IC_{50} values in the low nM range appear to be prerequisite for producing targeted cytotoxic activity.

Modifiable functional groups. Cytotoxic molecules must have a derivatizable "handle", such as $-NH_2$, −NH−, −OH, −SH, −CHO, R−C(O)−R′, or −COOH to allow for conjugation with FA.

Enhanced hydrophilicity. The lipophilicity of the vast majority of small-molecule chemotherapeutic compounds allows for their passive diffusion through cell membrane bilayers at random. FA-SMDCs with enhanced hydrophilicity (e.g., introducing a discrete number of charged residues; *vide infra*) will force these greasy molecules to exclusively enter FR-positive cells via FR-mediated endocytosis rather than indiscriminately into nontarget cells.

High stability. Conjugates must remain intact during systemic circulation to prevent drug exposure of normal cells. Serum stability of the FA-SMDC will allow for the carrying of a "payload" without disintegrating along the journey toward the tumor tissue. Ideally, FA-SMDCs should accumulate only at the tumor sites to saturate available FRs, and any excess should be cleared rapidly from the body in an intact form.

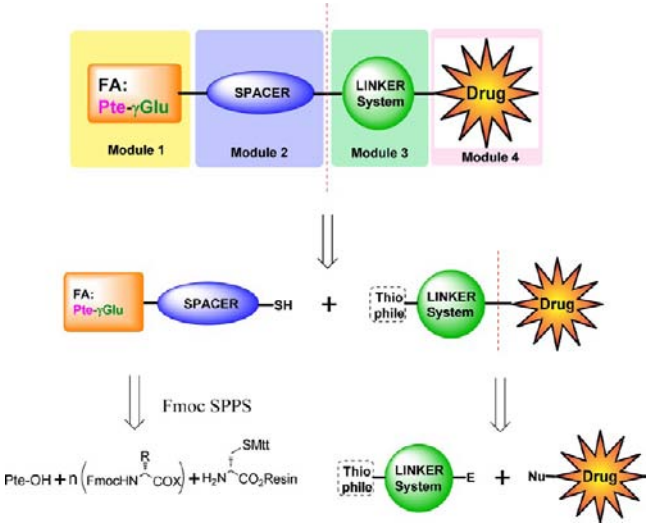
Releasable linkers. Most importantly, the activity of highly potent FA-SMDCs is closely dependent on an efficient cleavable linker system that is capable of releasing the active parent drug from the FA-SMDC at a predictable and reliable rate once inside the targeted cell. Two different trigger systems have been utilized to promote the programmed collapse of the linker system within the endosome. The most successful approach, a disulfide-bond-based linker system, takes advantage of the reducing power within the endosomal milieu.[23] The second approach, a pH-sensitive linker system, releases the active parent drug from its FA conjugate as the result of the drop in the pH in the endosome.[8] Studies have shown the pH values in endosomal compartments populated by monovalent FA conjugates to be around 6, whereas endosomes encapsulating multivalent folate conjugates have been found to have pH values as low as 5.0.[24,25] After release occurs by either of these two methods, highly lipophilic drugs cross the endosomal membrane and find their pharmacological target within the cytosol.

Low molecular weight. This property allows for better penetration of the FA-SMDC into solid tumor tissue with concomitant rapid systemic clearance. Typical FA-SMDC constructs are <2000 Da in size.

■ FA-SMDC CHEMISTRY

To meet the demand for expedient and efficient regioselective synthesis of releasable FA-SMDCs, and considering the requirements detailed above, our laboratory developed a modular synthetic approach for facile assembly of these complex molecules (see Scheme 1). The FA ligand serves as Module 1,

Scheme 1. Modular Design and *retro*-Synthetic Analysis of FA-SMDCs[a]

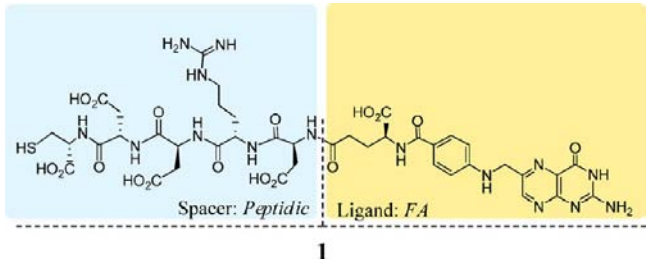


[a]Strategic disconnections depicted with red dotted lines. Abbreviations: Pte, pteroic acid; Glu, glutamic acid, Fmoc, fluorenylmethyloxycarbonyl, SPPS, solid-phase peptide synthesis. Note, a Glu residue is typically placed in the spacer position that lies adjacent to the Pte residue (to complete the FA molecule as shown).

while the active drug is represented as Module 4. The role of the spacer unit (Module 2) is twofold: (i) to properly position the ligand and drug cargo thereby preserving FR binding potential, and (ii) to provide the desired hydrophilicity to the overall construct. Juxtaposed between the spacer and the drug modules lies a cleavable linker system, represented as Module 3.

The presented *retro*-synthetic analysis is a roadmap for expedient assembly of FA-SMDCs. As indicated by the double-lined arrows, strategic disconnection transformed the final construct into two key synthon units: a FA-Spacer, which is terminated by a thiol group, and a thiophilic Linker−Drug derivative.

FA-SMDCs Containing Disulfide-Based Linker Systems and Peptide-Based Spacer Units. A commonly used FA-Spacer unit used in our laboratory is based on a simple peptidic extension of FA that terminates in a cysteine (Cys) residue. Thus, FA-Spacer unit **1** (structure as shown in Figure 3) is synthesized



1

Figure 3. Peptidic FA-Spacer unit **1**.

using standard fluorenylmethyloxycarbonyl-based solid-phase peptide synthesis techniques (Fmoc SPPS) on a Cys-loaded polymeric support.[26] Aspartic acid (Asp) and arginine (Arg) residues are added to the peptide to improve the overall water-solubility of the final SMDC construct. Importantly, the Cys thiol group serves as the attachment site for a cleavable linker system.

Self-Immolative Linker System Based on a 1,2-Elimination Mechanism. To facilitate the coupling process, we developed

dx.doi.org/10.1021/bc2005522 | *Bioconjugate Chem.* 2012, 23, 1357−1369

novel thiophilic heterobifunctional cross-linker **2** to incorporate disulfide linker systems into our SMDCs (Scheme 2).[26] Activated carbonate **2** has been found to react under mild conditions with many *N*- and *O*-nucleophiles, and as a result can be applied in the synthesis of a wide variety of drug conjugates. For example, **2** was utilized to link FA to highly potent drugs, such as the microtubule destabilizing agent DAVLBH **3**, a semisynthetic derivative of the *Vinca* alkaloid, vinblastine. Hydrazide **3** was treated with **2** and diisopropylethylamine (DIPEA) to yield 2-(vinblastinyl)hydrazine-carboxylic acid 2-pyridyldithioethyl ester **4**. To a solution of **1** in aqueous solution (pH = 6.5), under argon, was added a solution of **4** in THF, providing the SMDC referred to as EC145,[17] within 15 min.

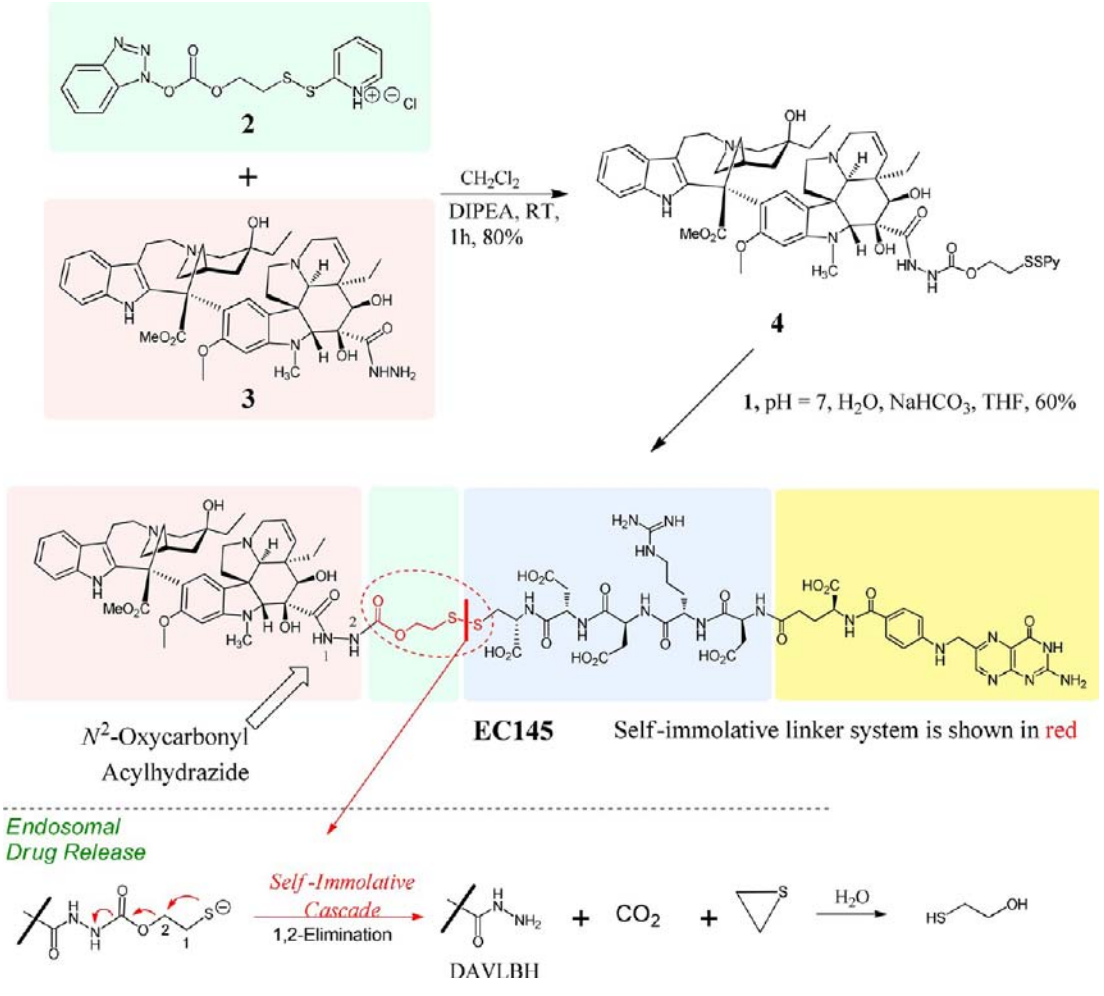
The endosomal milieu favors reduction of disulfide bonds,[23] and these conditions can be mimicked in a test tube. Accordingly, chemical release of parent drug **3** from the conjugate was accomplished by treating a 1 mM solution of EC145 in phosphate-buffered saline (PBS), pH = 7.4, with 20 mM of the reducing agent L-glutathione (GSH) at 37 °C. Complete cleavage of the disulfide bond with concomitant release of the FA-Spacer **1** and the highly unstable intermediate **A** occurred within 6 h ($t_{1/2}$ = 1 h; see Scheme 3). Electronic rearrangement in **A** resulted in self-fragmentation of the remnant linker. Formation of the free drug **3** was also confirmed by LCMS. Similar release profiles were also obtained with other reducing compounds, including (2*S*,3*S*)-dithiothreitol (DTT), which as expected, cleaved EC145 even faster than GSH ($t_{1/2}$ = 5 min). In contrast, EC145 was found to remain stable in PBS, pH = 7.4 at 37 °C for more than 24 h in the absence of a reducing agent.

Several representative conjugates utilizing FA-spacer **1** have been prepared by our group,[27] or in collaboration with scientists at Bristol-Myers Squibb Co,[28] ImmunoGen Inc.,[29] and the P.S. Low group at Purdue University[30] (see Figure 4). However, SMDCs which lack a spacer region (and therefore have limited hydrophilicity/water solubility) have been synthesized as well, including FA-paclitaxel and FA-daunomycin.[31] Similarly, Suzuki et al. synthesized a FA conjugate of the histone deacetylase (HDAC) inhibitor NCH-31.[32]

The preclinical pharmacology for many FA-SMDCs revealed persistent antitumor effect against FR-positive tumors against multiple animal models.[19,29,33,34] For example, EC145 was found to produce marked antitumor effect against well-established, subcutaneous FR-positive tumor xenografts using well-tolerated regimens. Thus, using a brief three times per week, two-week regimen, 100% of mice bearing well-established subcutaneous xenografts experienced full remissions (i.e., cures) under conditions that did not produce significant weight loss or normal tissue degeneration.[33]

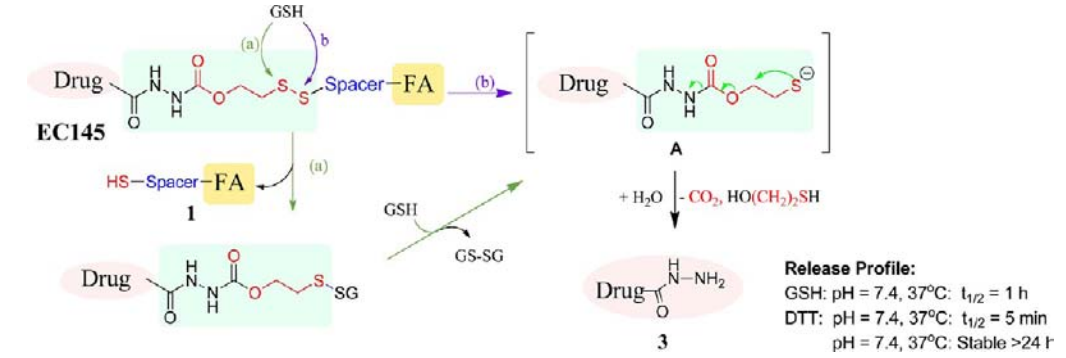
EC145 also represents the first FA-SMDC to be clinically tested.[35] Since 2006, one phase 1 safety study, two single-agent phase 2 studies (for refractory ovarian cancer and nonsmall cell lung cancer), and a randomized phase 2 study of EC145 in combination with pegylated

Scheme 2. Expedient Synthesis of EC145, a FA-SMDC Possessing a Disulfide-Based Self-Immolative Linker System



dx.doi.org/10.1021/bc2005522 | *Bioconjugate Chem.* 2012, 23, 1357–1369

Scheme 3. Release study of the Self-Immolative Disulfide-Based Linker System in the FA-Drug Conjugate in a Reductive Environment[a]



[a]A thiol group of a reducing agent can attack either of the two sulfur atoms in the linker system resulting in two distinguished pathways (a) or (b).

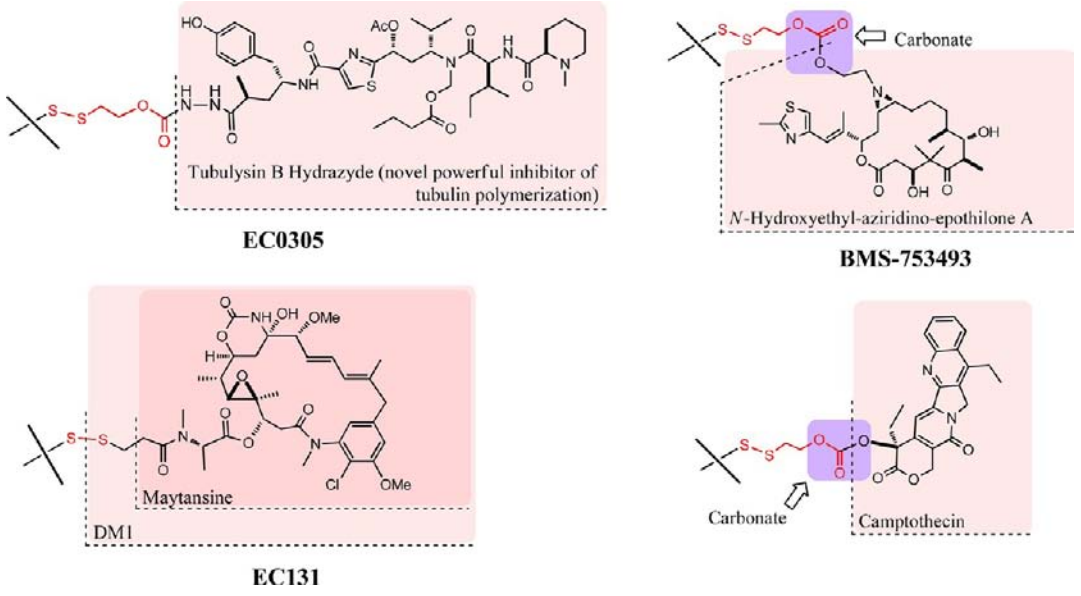


Figure 4. Chemical structures of representative FA–Drug conjugates utilizing the peptidic FA–Spacer **1** and possessing a disulfide-based linker system.

liposomal doxorubicin in platinum-resistant ovarian cancer patients (PRESCEDENT trial) have been completed.[35–38] On the basis of encouraging results observed in PRESCEDENT, where progression-free survival in the intent-to-treat population approximately doubled over the control arm (p = 0.031) without significant increase in toxicity, a global phase 3 study called PROCEED was recently initiated to confirm the phase 2 results. Such clinical signals reinforce the potential for targeting aggressively growing tumors with SMDC constructs.

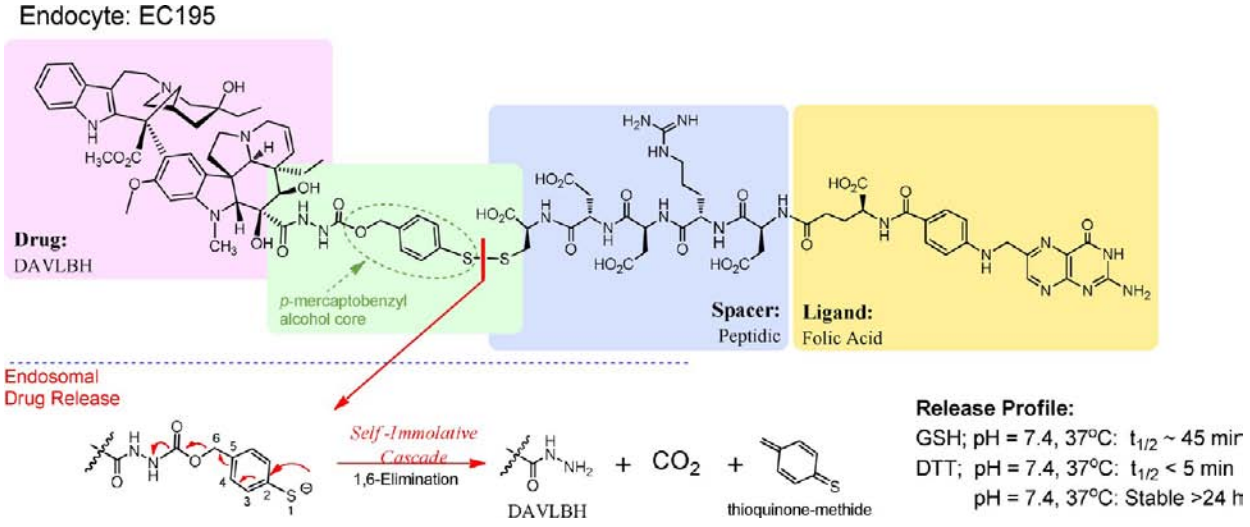
Self-Immolative Linker System Based on 1,6-Elimination Mechanism. Subsequent efforts have been focused on the drug release behavior of modified self-immolative linker systems. On the basis of modulation of the electronic influences, a DAVLBH-containing compound constructed of a *para*-mercaptobenzylalcohol core integrated into a disulfide trigger (EC195; Endocyte Inc.) was predicted to undergo thioquinone-methide-based 1,6-elimination (see Scheme 4). Release profiles of such SMDCs will be different compared to analogues with a mercaptoethanol core and relying on reduction-initiated episulfide-based 1,2-elimination reaction. Likewise, we found that such fine-tuning of these structural properties affected the kinetics of self-fragmentation, giving a slightly faster release rate of parent drug.[39] Overall, the thioquinone-methide elimination approach can be applied as an alternative tool in designing self-immolative linkers for release of active drug in an aqueous environment. Assembling constructs with this linker system required more elaborated synthetic protocols than the preparation of conjugates which make use of 1,2-elimination release.

Introducing Steric Hindrance in Disulfide-Based Linker Systems. Disulfide-based linkers have proven to be useful for many drug delivery applications, especially when one exploits an endocytosis delivery route.[40] However, sera contain a variety of free thiol-containing compounds (e.g., GSH, homocysteine, cysteine, albumin, and so forth) that can potentially attack the S–S bond within a conjugate's linker, especially if the agent remains in circulation for long periods of time. In fact, the latter point has been exemplified when early-generation ADCs constructed with unprotected disulfide-containing linkers were found to be unstable and to release free drug in the bloodstream.[41] Compared to ADCs, FA-SMDCs are eliminated much more quickly from circulation with half-lives ($t_{1/2}$) of ~26 min,[42] and virtually no free drug has been accurately measured in sera samples from EC145-treated patients.[42] Nonetheless, it is of interest to understand the stability properties of FA-SMDCs constructed with simple disulfides (like in EC145) versus sterically hindered counterparts.

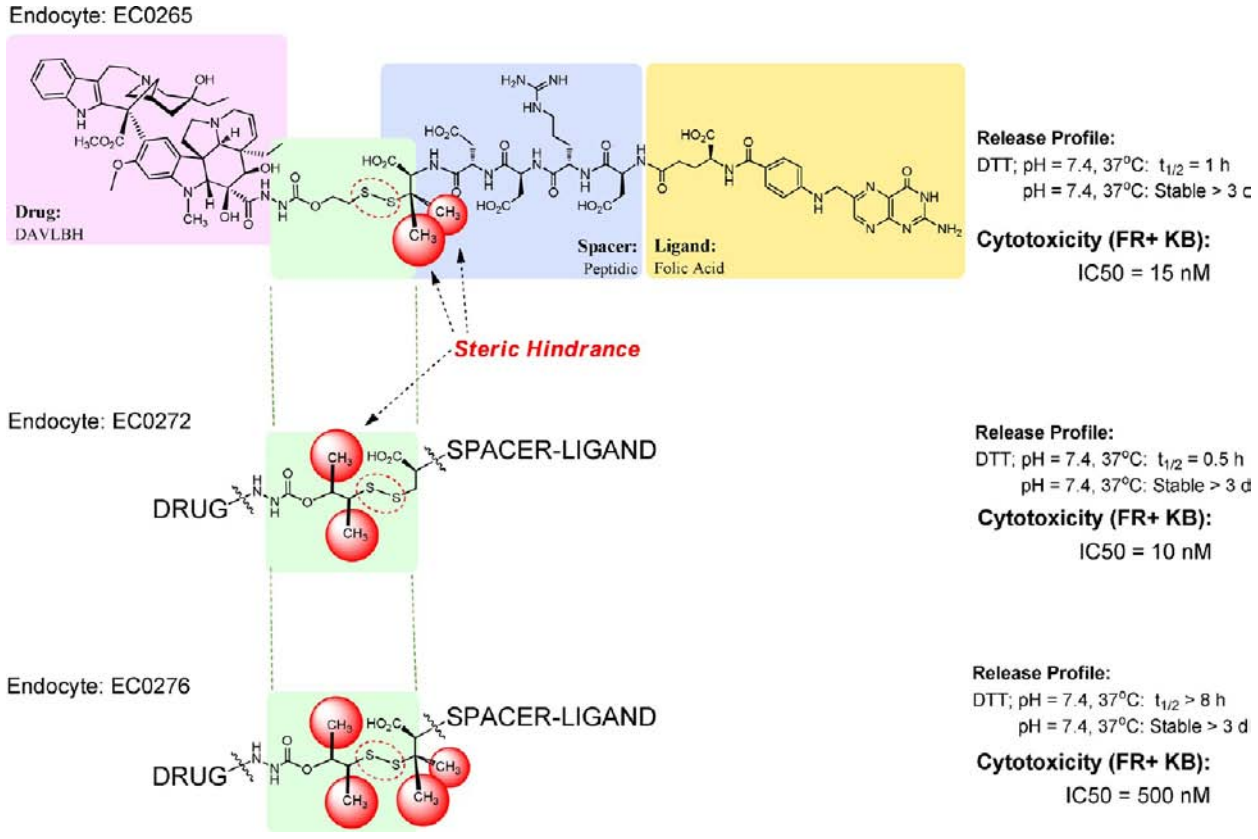
Mechanistically, nucleophilic substitution by an external thiol group on the disulfide moiety is the first step in both of the self-immolative

dx.doi.org/10.1021/bc2005522 | *Bioconjugate Chem.* 2012, 23, 1357–1369

Scheme 4. Self-Immolative Linker System Based on Thioquinone-Methide 1,6-Elimination



Scheme 5. Influence of Steric Hindrance on Parent Drug Release and Cytotoxicity of the Conjugates[a]



[a] *In vitro* cytotoxicity for each FA-SMDC was evaluated using human FR-positive KB cells according to standard pulse/chase conditions as reported elsewhere.[46]

cascades depicted above, and it strictly follows an S_N2 mechanism. This reaction is known to involve an attack by the HS-nucleophile on a trajectory opposite that of the S−S bond.[43,44] Any branching on the carbon atoms surrounding the disulfide site will intensify the steric hindrance by sheer physical obstruction to the action of the nucleophile. As a result, the rate of disulfide cleavage in the linker system will decrease with increasing steric blockage. Considering this, we constructed three SMDCs by introducing methyl groups (the red balls depicted in Scheme 5) around the S−S bond while keeping the ligand, the spacer, and the drug the same as in EC145 (Vlahov et al., manuscript in preparation).

All three of the FA-SMDCs shown in Scheme 5 (0.5 mM solutions in PBS, pH 7.4), where treated with 8 mM solution of DTT at 37 °C, and advancement of DAVLBH drug release was followed by LCMS. The results showed that introducing two methyl substituents next to one of the S-atoms (e.g., EC0265; Endocyte Inc.) extend the $t_{1/2}$ of the conjugate to 1 h in the presence of DTT. Placing single methyl groups on each carbon

dx.doi.org/10.1021/bc2005522 | *Bioconjugate Chem.* 2012, 23, 1357−1369

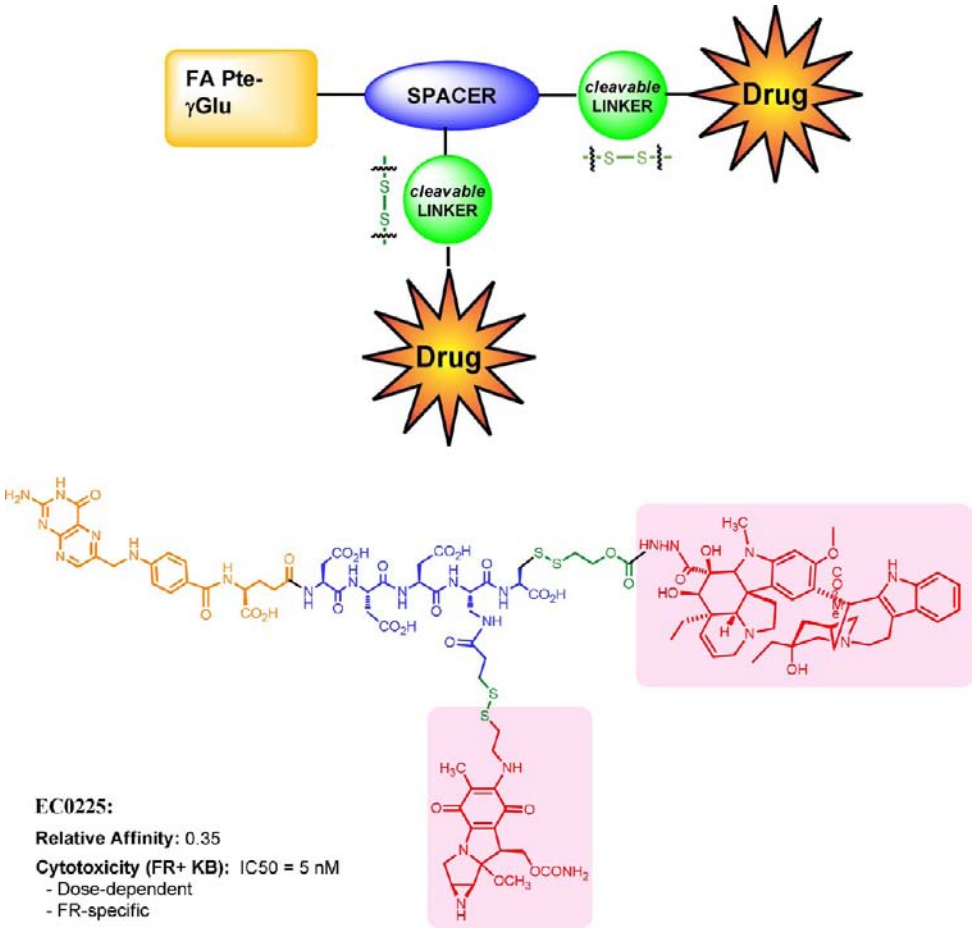


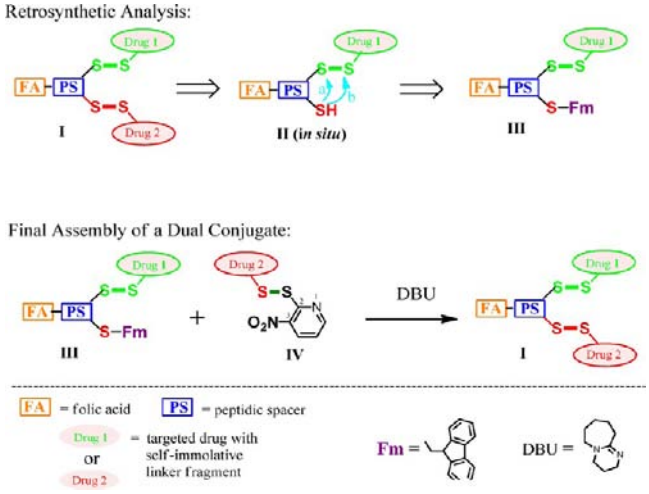
Figure 5. DAVLBH- and MMC-containing FA-based SMDC. *In vitro* cytotoxicity for each FA-SMDC was evaluated using human FR-positive KB cells according to standard pulse/chase conditions as reported elsewhere.[46]

atom in the self-immolative region of the linker system (e.g., EC0272; Endocyte Inc.) resulted in a somewhat lesser decrease of the release rate ($t_{1/2}$ = 0.5 h). On the contrary, the sterically very demanding situation with four methyl groups surrounding the disulfide bond (e.g., EC0276) extended the half-life of the conjugate to more than 8 h. When tested for cytotoxicity against FR+ cells *in vitro*, the concentrations needed to kill half of the cell population (IC_{50} value) for the dimethyl linker analogues, EC0265 and EC0272, were nearly the same; furthermore, they were comparable to the 9 nM IC_{50} of EC145.[17] In contrast, the IC_{50} of the tetramethyl linker-containing EC0276 agent was ~50-fold higher. Collectively, these data suggest that steric hindrance near the disulfide can slow down the rate of linker cleavage which, in turn, may increase the overall stability of the SMDC and simultaneously reduce their potency.

Synthesis of Releasable Dual-Drug SMDCs: Introduction of a Second Unsymmetrical Disulfide Bond. A logical extension of FA-SMDC design involved a novel synthetic strategy aimed to tether multiple drugs to the same FA ligand. However, this approach presented the challenge for generating a second disulfide bond into a molecular framework harboring already one disulfide-based linker system. An expedient solution of such synthetic problem would result in a methodology that ensures the delivery and release of multiple cargos (parent drugs, reporter molecules, and so forth) in targeted cells. As shown in Figure 5, synthetic efforts from our laboratory resulted in the synthesis of EC0225, the first FA-SMDC produced which contained two different biologically active agents: Drug 1 = DAVLBH, and Drug-2 = the highly chemically sensitive alkylating agent, mitomycin C (MMC).[45] Both drug cargos are covalently attached to a FA-Spacer unit *via* independent disulfide-based release systems.

As indicated in the *retro*-synthetic analysis (see Scheme 6), the key precursor to the final construct **I** (a simplified representation of the dual drug SMDC, EC0225) is the thiol-containing disulfide conjugate **II**. Molecules such as **II**, which possess a disulfide bond as

Scheme 6. Assembly Concept for Consecutive Introduction of Unsymmetrical Disulfide Bonds



dx.doi.org/10.1021/bc2005522 | *Bioconjugate Chem.* 2012, 23, 1357–1369

well as a free thiol functionality, are highly reactive and unstable in that they are prone to rearrangement and intramolecular cyclization (see Scheme 6; blue arrows a and b). An elegant solution to this challenging stability-related problem involved a synthetic route in which **II** was generated *in situ* from the stable *S*-protected monoconjugate **III**. Trapping the thiol group of **II** with a Drug 2-containing, disulfide-forming synthon **IV** resulted in the desired dual drug conjugate **I**. Importantly, monoconjugate **III** was synthesized using the same conjugation techniques as described for EC145 above.

When evaluated for activity *in vitro*, EC0225 was found to retain high affinity for FR-positive cells, and it produced potent dose-responsive activity. EC0225 further proved to be very active against syngeneic and xenograft tumor models, with curative activity occurring with the administration of exceptionally well-tolerated regimens.[46] Animals bearing well-established human tumor xenografts were consistently found to respond fully to EC0225 therapy when using dosing regimens that were approximately 3-fold less intensive compared to that required for EC145 (to produce similar responses). EC0225 is currently being evaluated in a phase 1 clinical trial for chemo-refractory cancer patients.

Carbohydrate-Based Spacers Designed to Control Toxicity Profiles of FA-SMDCs. The dose-limiting toxicity for EC145 in a phase 1 clinical trial was found to be constipation.[42] Since (i) EC145 remains intact while in circulation[42] and (ii) very low to nondetectable levels of the FR are found in hepatic tissue,[21] it was suspected that non-FR related liver clearance, with subsequent metabolic release of free DAVLBH, may have been (in part) responsible for producing the observed gastrointestinal toxicity. A novel, chemistry-based approach was later developed to substantially decrease the hepatobiliary route of clearance of free DAVLBH without affecting the targeted antitumor activity of SMDC.[47] Here, selective replacement of some of the amino acids in the spacer region with structurally optimized carbohydrate segments resulted in SMDCs that were equipotent, but less toxic than EC145. Notably, our laboratory's first-generation carbohydrate-containing FA-spacer units (see Scheme 7) were designed to be bifunctional, containing alternately repeating acidic (Asp) and saccharo-amino acid residues, thus providing high water solubility of the final SMDC under physiological conditions. This unit was assembled using standard Fmoc SPPS techniques.

The structural design of the saccharo-amino acid was of crucial importance to the successful execution of a simple and high-yielding SPPS protocol. The selected approach relied on a ring-opened carbohydrate chain rather than a cyclic pyranoside or furanoside unit, since the latter are of limited use for simplified SPPS-based protocols due to (i) the requirement of tedious protecting/deprotecting strategies, (ii) utilization of sensitive glycosyl donors, and (iii) the generation of diastereomeric glycosidic linkages. Therefore, we designed and synthesized uniformly protected 2-amino-2-deoxy-glyconic acid derivative **5** (Scheme 7) that is orthogonally stable to SPPS.

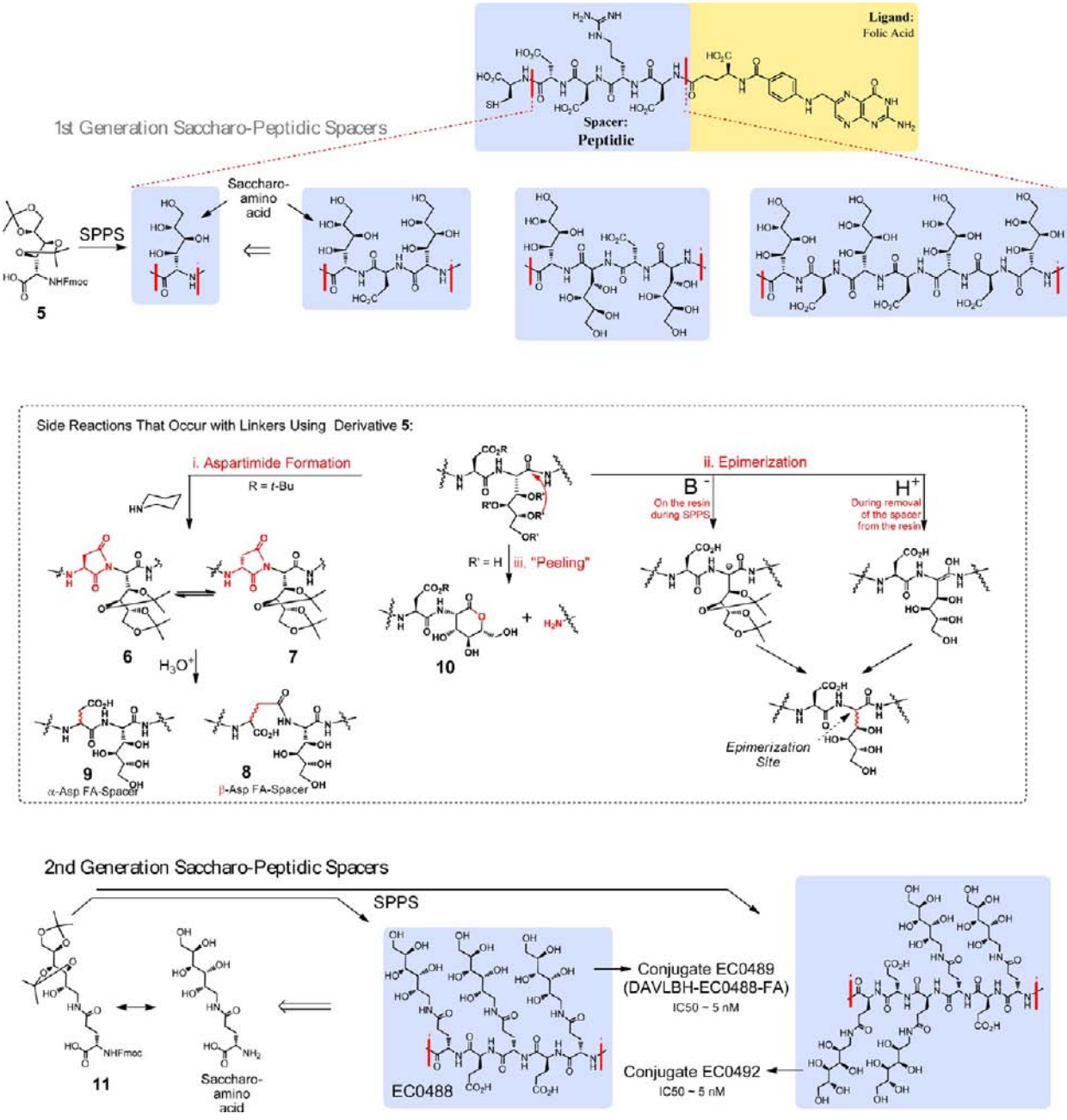
According to LCMS analysis, the synthesis of any particular FA-spacer unit using **5** and Asp residues resulted in a reaction mixture profile displaying a major peak and several satellite peaks with very close retention times. All possessed molecular masses identical to that expected for the desired structure. An additional peak was also observed having a mass that was suggestive of the FA-spacer molecule lacking the *C*-terminal Cys. These results were attributed to three major problems (see dotted frame, Scheme 7), all related to the molecular architecture of the first-generation saccharo-peptidic spacers: First, Aspartimide formation is a frequently encountered side reaction affecting Asp residues during Fmoc SPPS. In the presence of a strong base such as piperidine, used to remove the Fmoc group, the α-amide nitrogen atom attacks the carbonyl group of the β-carboxy side-chain resulting in ring-closure with loss of the ester protecting group. Aspartimides of type **6** are susceptible to base-catalyzed epimerization to **7**, and both of these species easily experience ring-opening with predominant formation of β-aspartyl peptide chain **8** in the presence of water. Desired α-Asp FA-spacer **9**, and all epimerized and β-rearranged counter partners, possess identical masses and elute closely or coelute with the desired α-isomer on HPLC. In our first-generation Spacer design, the peptide sequence possessed multiple sites for potential aspartimide formation making this problem even more serious. Therefore, we exchanged all aspartic acid residues for glutamic acids. To our surprise, there were still peaks in the LCMS with identical masses and close retention times. That they exhibited different fragmentation patterns in the mass spectrum brought us to the indirect conclusion that, most likely, we were not dealing only with rotameric forms, but instead with some other sort of closely related structural isomers. Second, in compounds of type **9** or in its isopropylidene-protected precursors, the protons attached to C-2-atoms in the saccharo-amino acid moieties are sufficiently acidic to readily undergo epimerizarion under the strong basic and/or acidic reaction conditions of SPPS protocols. Third, "peeling" of the *C*-terminal Cys is a side reaction initiated by 5- and/or 6-membered ring-closure, resulting in energetically stabilized lactone forms (e.g., **10**). Apparently, in our first generation design of the saccharo-amino acid we ignored this not-so-obvious problem, and suitably positioned a hydroxyl group in the carbohydrate chain that attacked the carboxy amide bond of *C*-terminal Cys and formed lactones.

To address and avoid the epimerization and peeling issues, we redesigned the structure of our saccharo-amino acid monomer by connecting (via an amide bond) two epimerization-inert modules, namely, glutamic acid and glucamine. Each possesses C−H bonds that are not inherently prone to configuration changes. Also, in the new resulting FA-Spacer unit, named EC0488, all hydroxyl groups in the glucamine module are more than seven atoms away from the amide bond which connects the saccharo-amino acid and the *C*-terminal Cys, thus suppressing lactone formation and the resulting peeling effect. The new diisopropylidene- and Fmoc-protected saccharo-amino acid **11** is orthogonally stable to the reaction conditions used in classical Fmoc SPPS protocols. Therefore, treatment of EC0488 with **4** under the same conditions as described for the synthesis of EC145 (see Scheme 3) resulted in the novel conjugate, EC0489.[48]

Release of DAVLBH from EC0489 was also studied (see Figure 6). Hence, a 1 mM solution of EC0489 in PBS, pH 7.4, was treated with 40 equiv of dithiothreitol (DTT) at room temperature. The HPLC profile (UV detection at 280 nm) showed complete cleavage of the disulfide bond with concomitant release of EC0488 (the FA-Spacer unit) within 15 min. At this early time point, DAVLBH exists as its free form (B) and with remnants of the linker still attached (A). However, over the next four hours, the remaining linker remnants experienced complete self-fragmentation, thus leaving only EC0488 and DAVLBH in solution.

In tumor-bearing mice, EC0489 was found to be equipotent, but less toxic than its non-saccharo-peptide-containing counterpart, EC145. As reported, both compounds could reproducibly cure tumor-bearing mice, but EC0489 differed from EC145 with

Scheme 7. Chemistry behind Novel Carbohydrate-Based Spacers



(i) a shorter elimination half-life, (ii) ~70% decrease in bile clearance, (iii) a 4-fold increase in urinary excretion, and (iv) improved tolerability in rodents.[48] The combination of these improvements justified the initiation of phase 1 clinical trials where it was determined that EC0489 could be dosed at levels that exceeded EC145's MTD by ~70%, which reflected the translational benefits to this new chemical approach.

Application of pH-Responsive Linker Systems for Synthesis of FA-SMDCs. A second approach sought to release a parent drug from a FA-SMDC was one that exploited the naturally lowered pH found within the endosomal milieu.[49] While conceptually straightforward, this approach requires a linker system that remains relatively stable at physiological pH, but not at mildly acidic pH levels (e.g., pH 5 to 6). Several examples are provided below, relative of course to FA-SMDCs.

Hydrolytically Labile Acyl Hydrazone Linkers. The concept of using a pH-sensitive linker system in FR-targeted drug delivery was first demonstrated with the design and synthesis of EC140, a FA-DAVLBH conjugate containing the acyl hydrazone linker functionality.[50] In general, based on the delocalization of their π-electrons, hydrazones are hydrolytically much more stable than imines. Therefore, an electron withdrawing group (e.g., an acyl) has to be placed into hydrazone systems in order to control electron delocalization and moderate their overall hydrolytic stability. As a result, these molecular constructs can find application in the design of releasable drug conjugates. Acyl hydrazones are easily prepared from aldehydes, ketones, and acyl hydrazides under mild conditions.

Synthesis of the acyl hydrazone conjugate, EC140, was accomplished in two steps, as presented in Scheme 8. In this linker design, we selected the commercially available and

dx.doi.org/10.1021/bc2005522 | Bioconjugate Chem. 2012, 23, 1357–1369

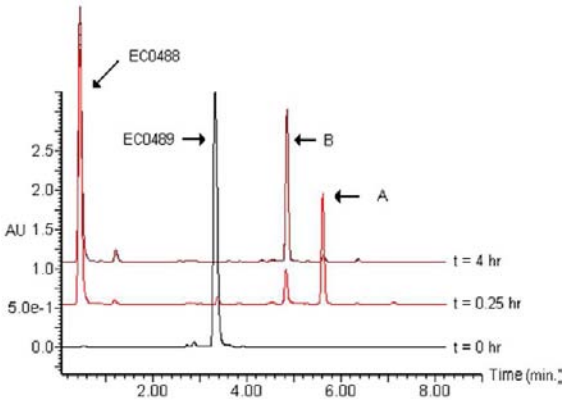


Figure 6. HPLC profile (280 nm) of the treatment of EC0489 with DTT at t = 0 h, 0.25 h, and 4 h. Peak A represents DAVLBH–$COOCH_2CH_2S^-$, whereas B is the released parent drug DAVLBH.

heterobifunctional molecule, 4-maleimido benzophenone **12**, as the key building block. Treatment of **3** with an equimolar amount of **12** resulted in the desired vinblastenyl acyl hydrazide **13**. Subsequently, the thiol moiety of the FA-Spacer unit **1** was reacted with the maleimide end of **13**, thus providing the N^1-acyl hydrazone-linked conjugate. Drug release studies were performed in pH 5.0 and pH 7.4 buffers at 37 °C. It was observed that, at the lower pH, the hydrazone bond in EC140 was cleaved with a hydrolysis rate of $t_{1/2} \approx 5.5$ h. In contrast, at pH 7.4 the rate was found to be 4 times slower ($t_{1/2} \approx 22$ h).

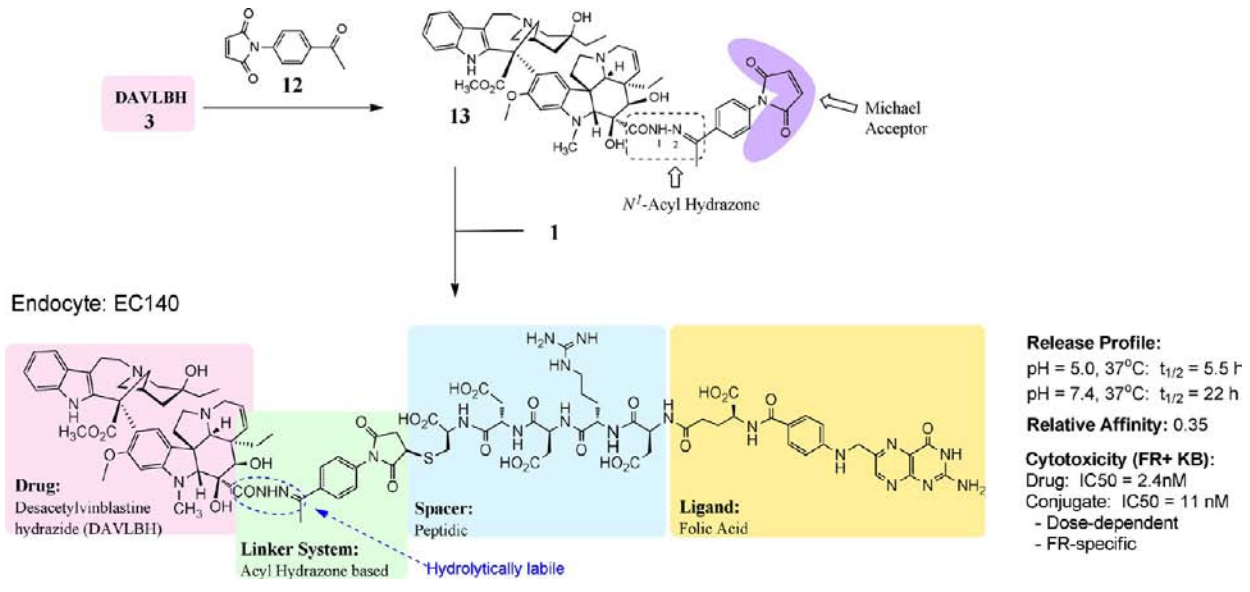
Like EC145, EC140 displayed high affinity for FR+ cells, and it produced specific, dose-responsive activity *in vitro*. However, in comparative *in vivo* efficacy tests, the disulfide-containing EC145 was found to be more active and better tolerated than its acyl hydrazone-containing counterpart, EC140.[50]

pH-Sensitive p-Alkoxybenzylidene-Acetal-Based Linker System. As shown in Scheme 9, unsymmetrical ring-open *p*-alkoxybenzylidene acetals belong to the arylmethylene acetal family. This rarely used functionality is an excellent candidate for development of pH-sensitive linker systems, and it has an important advantage over other acetals. The electron-donating effect of the *p*-alkoxy substituent in the aromatic ring (depicted with solid blue arrows) increases the acetal's sensitivity toward hydrolysis under mild acidic conditions. The intermediary *p*-alkoxybenzyloxonium cation is electronically stabilized, consequently ensuing enhanced hydrolytic lability of the linker system.

The parent drug, *N*-hydroxyethylvindesine **14**, is easily accessible from **3** after treatment with nitric acid to the respective acylazide, followed by its reaction with hydroxyethylamine. The key linker fragment **17** was synthesized starting from *p*-hydroxyethoxybenzaldehyde **15**. In brief, the hydroxyl group in **15** was converted to an azide. Dimethoxyacetal introduction and azide reduction resulted in aminoacetal derivative **16**. Maleimido transfer and treatment with methylorthoformate/acetyl chloride provided *in situ* the very reactive chloro-methoxy-benzyl derivative **17**. Nucleophilic substitution of the chloride by the primary hydroxyl group of **14** resulted in Drug–Linker unit **18**. The maleimido moiety in **18** served as an excellent Michael acceptor and reacted smoothly with the thiol group in the FA-Spacer unit **1**, thus furnishing the synthesis of EC193 (Endocyte, Inc.) as a mixture of diastereoisomers.

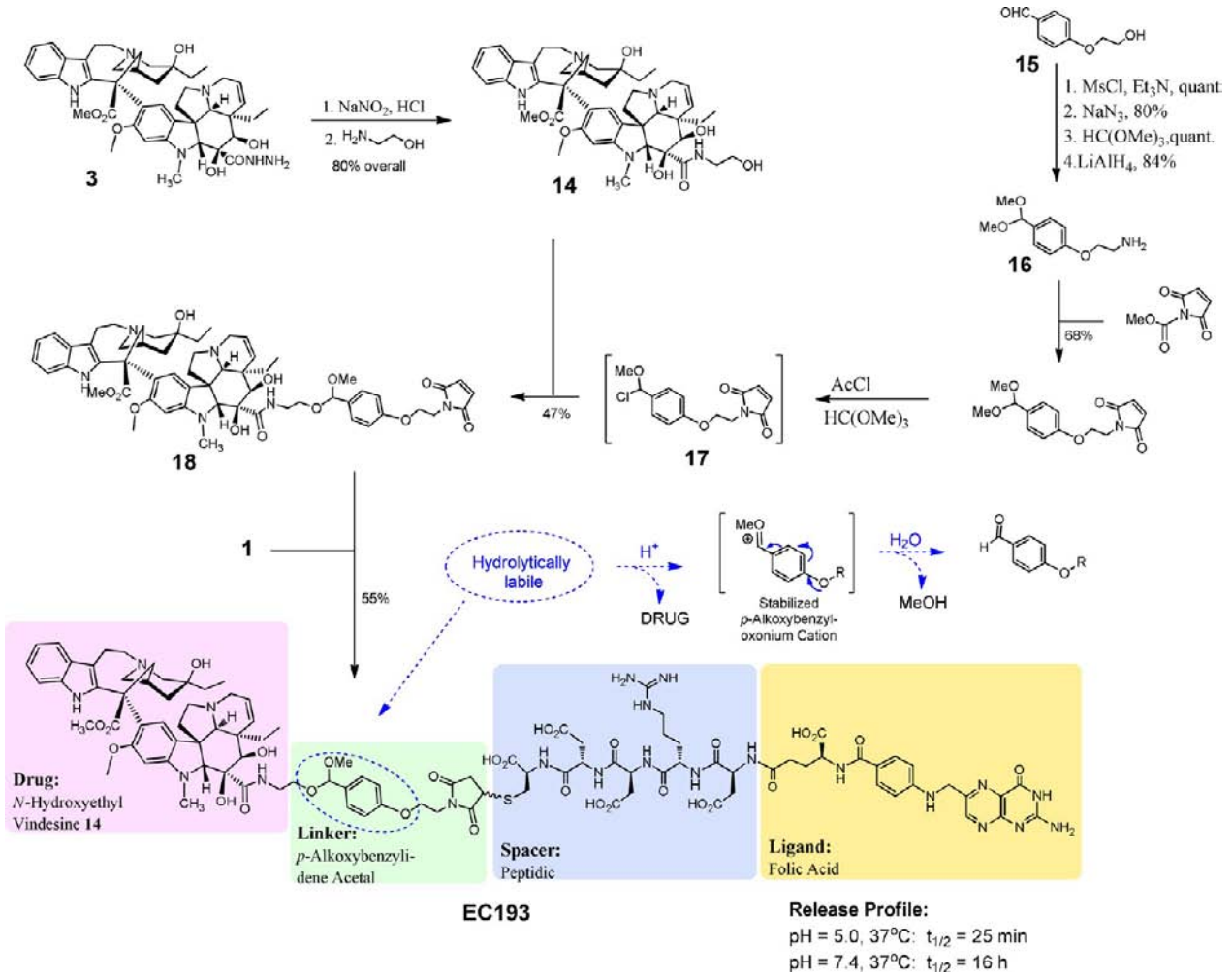
Chemically, EC193 exhibits remarkable drug release capacity at 37 °C. The *p*-alkoxybenzylideneacetal system in EC193 was cleaved at pH = 5.0 with a hydrolysis rate of $t_{1/2}$ = 25 min. In contrast, at pH 7.4 the rate was found to be $t_{1/2} \approx 16$ h. Surprisingly though, EC193 proved to be inactive *in vitro* (unpublished data; Endocyte Inc.). Perhaps a plausible reason for this finding is that the parent drug **14** is 8-fold less cytotoxic than DAVLBH in KB cells (IC_{50} = 16 nM vs IC_{50} = 2 nM, respectively). Another possible explanation can be related to observation made by Low et al. that "endosomal compartments visited by monovalent folate conjugates experience pH values only as low as 6.2".[24,51] This value is 1 order of magnitude higher than previously reported endosomal pH values of ~5.0.[8] Thus, under such circumstances, FA-SMDCs possessing *acid-sensitive* linker systems and, entering the cell via FR-mediated endocytosis, may have only limited capability and potential to release their parent drug at biologically meaningful rates.

Scheme 8. Synthesis of the pH-Sensitive Acyl Hydrazone-Based Conjugate EC140



dx.doi.org/10.1021/bc2005522 | *Bioconjugate Chem.* 2012, 23, 1357–1369

Scheme 9. Synthesis of EC193, a FA-Conjugate Possessing Unsymmetrical *p*-Alkoxybenzylidene Acetal in the Linker System



■ CONCLUDING REMARKS

When it emerged in 1991, the use of FA as a high-affinity ligand to deliver pharmacologically active agents to diseased cells was viewed as a provocative concept.[52] Today, following hundreds of publications and scores of diagnostic and therapeutic examples, "folate targeting" is now an accepted, clinically valuable approach used for drug delivery. Thus, a review of useful and (especially) applied chemistry for preparing FA-SMDCs appeared timely.

FA is small in size (molecular weight = 441), which certainly has its advantages for promoting deep penetration of attached drug cargo molecules into solid tumors.[33] However, simple attachment of FA to a typical lipophilic drug (e.g., *Vinca* alkaloids, taxanes, and so forth) will usually not yield a water-soluble FA-SMDC; furthermore, the drug cargo must be released from FA before it can escape the endosomal compartment. Therefore, a modular design for producing FA-SMDCs was presented in this review along with a series of synthetic examples. Linker chemistries have consistently proven to be important for targeted activity. Among the many linkers exemplified in drug delivery literature, disulfide- and acyl hydrazone-based linkers favor controlled drug release from FA within the endosomal milieu, with the former being the preferred tool.[17] In addition, as shown above, the disulfide linker can be modified to tailor the kinetics of drug release by adding steric hindrance near the sulfur atoms. Notably, no examples of FA-SMDCs constructed with releasable peptidic-based linkers (i.e., enzymatic substrates) were included in this review. Such constructs have been made by the authors, but they were all found to be inactive, presumably because the FR does not appreciably access the degradative lysosomal compartments while transiting through the recycling endosomal route.[53] However, we do not wish to completely discount such an approach because it is likely that the recycling endosome contains resident proteases whose catalytic functions can eventually be exploited for drug delivery purposes.

In conclusion, the chemistry examples presented above were all related to FA-SMDCs. However, based on our modular design concept, it should be apparent that FA can be substituted with alternative ligands; in fact, this has already been exemplified using small-molecular-weight ligands that target prostate-specific antigen (a biomarker expressed on prostate cancer).[54] In an era of creating targeted medicines, we will undoubtedly find that choosing the right combination of disease-specific ligands and self-immolative linker chemistries will be critical for success.

■ AUTHOR INFORMATION

Corresponding Author

*E-mail: chrisleamon@endocyte.com. Phone: 1-765-463-7175. Fax: 1-765-463-9271.

Notes

The authors declare no competing financial interest.

dx.doi.org/10.1021/bc2005522 | *Bioconjugate Chem.* 2012, 23, 1357–1369

■ ACKNOWLEDGMENTS

The authors wish to thank P. S. Low, P. R. Ellis, and the entire research staff at Endocyte Inc.

■ REFERENCES

(1) Oldham, R. K., and Dillman, R. O. (2008) Monoclonal antibodies in cancer therapy: 25 years of progress. *J. Clin. Oncol. 26*, 1774−7.
(2) Younes, A., Bartlett, N. L., Leonard, J. P., Kennedy, D. A., Lynch, C. M., Sievers, E. L., and Forero-Torres, A. (2010) Brentuximab vedotin (SGN-35) for relapsed CD30-positive lymphomas. *New Engl. J. Med. 363*, 1812−1821.
(3) Leamon, C. P. (2008) Folate-targeted drug strategies for the treatment of cancer. *Curr. Opin. Invest. Drugs 9*, 1277−86.
(4) Bailey SW, A. J. (2009) The extremely slow and variable activity of dihydrofolate reductase in human liver and its implications for high folic acid intake. *Proc. Natl. Acad. Sci. U. S. A. 106*, 15424−15429.
(5) Westerhof, G. R., Schornagel, J. H., Kathmann, I., Jackman, A. L., Rosowsky, A., Forsch, R. A., Hynes, J. B., Boyle, F. T., Peters, G. J., Pinedo, H. M., and Jansen, G. (1995) Carrier- and receptor-mediated transport of folate antagonists targeting folate-dependent enzymes: Correlates of molecular structure and biological activity. *Mol. Pharmacol. 48*, 459−471.
(6) Leamon, C. P., You, F., Santhapuram, H. K., Fan, M., and Vlahov, I. R. (2009) Properties influencing the relative binding affinity of pteroate derivatives and drug conjugates thereof to the folate receptor. *Pharm. Res. 26*, 1315−23.
(7) Leamon, C. P., and Low, P. S. (1993) Membrane folate-binding proteins are responsible for folate- protein conjugate endocytosis into cultured cells. *Biochem. J. 291*, 855−860.
(8) Lee, R. J., Wang, S., and Low, P. S. (1996) Measurement of endosome pH following folate receptor-mediated endocytosis. *Biochim. Biophys. Acta 1312*, 237−42.
(9) Leamon, C. P., and Jackman, A. L. (2008) Exploitation of the Folate Receptor in the Management of Cancer and Inflammatory Disease, in *Vitamins and Hormones* (Litwack, G., Ed.) pp 203−233.
(10) Leamon, C. P., and Reddy, J. A. (2004) Folate-targeted chemotherapy. *Adv. Drug Delivery Rev. 56*, 1127−1141.
(11) Steinberg, G., and Borch, R. F. (2001) Synthesis and evaluation of pteroic acid-conjugated nitroheterocyclic phosphoramidates as folate receptor-targeted alkylating agents. *J. Med. Chem. 44*, 69−73.
(12) Aronov, O., Horowitz, A. T., Gabizon, A., and Gibson, D. (2003) Folate-targeted PEG as a potential carrier for Carboplatin analogs. Synthesis and in vitro studies. *Bioconjugate Chem. 14*, 563−74.
(13) Liu, J. Q., Kolar, C., Lawson, T. A., and Gmeiner, W. H. (2001) Targeted drug delivery to chemoresistant cells: Folic acid derivatization of FdUMP[10] enhances cytotoxicity toward 5-FU-resistant human colorectal tumor cells. *J. Org. Chem. 66*, 5655−5663.
(14) Lee, J. W., Lu, J. Y., Low, P. S., and Fuchs, P. L. (2002) Synthesis and evaluation of taxol-folic acid conjugates as targeted antineoplastics. *Bioorg. Med. Chem. 10*, 2397−414.
(15) Leamon, C. P., Pastan, I., and Low, P. S. (1993) Cytotoxicity of folate-pseudomonas exotoxin conjugates toward tumor cells. *J. Biol. Chem. 268*, 24847−24854.
(16) Ladino, C. A., Chari, R. V. J., Bourret, L. A., Kedersha, N. L., and Goldmacher, V. S. (1997) Folate-maytansinoids: Target-selective drugs of low molecular weight. *Int. J. Cancer 73*, 859−864.
(17) Leamon, C. P., Reddy, J. A., Vlahov, I. R., Westrick, E., Parker, N., Nicoson, J. S., and Vetzel, M. (2007) Comparative preclinical activity of the folate-targeted Vinca alkaloid conjugates EC140 and EC145. *Int. J. Cancer 121*, 1585−92.
(18) Leamon, C. P. (2003) Folate-targeted chemotherapy: In vitro and in vivo activity of EC72. In *Proceedings of the American Association for Cancer Research 44*, Abstract # 2627, page 600.
(19) Leamon, C. P., Reddy, J. A., Vetzel, M., Dorton, R., Westrick, E., Parker, N., Wang, Y., and Vlahov, I. (2008) Folate targeting enables durable and specific antitumor responses from a therapeutically null tubulysin B analogue. *Cancer Res. 68*, 9839−44.
(20) Reddy, J. A., Dorton, R., Dawson, A., Vetzel, M., Parker, N., Nicoson, J. S., Westrick, E., Klein, P. J., Wang, Y., Vlahov, I. R., and Leamon, C. P. (2009) In vivo structural activity and optimization studies of folate-tubulysin conjugates. *Mol. Pharm. 6*, 1518−25.
(21) Parker, N., Turk, M. J., Westrick, E., Lewis, J. D., Low, P. S., and Leamon, C. P. (2005) Folate receptor expression in carcinomas and normal tissues determined by a quantitative radioligand binding assay. *Anal. Biochem. 338*, 284−93.
(22) Paulos, C. M., Reddy, J. A., Leamon, C. P., Turk, M. J., and Low, P. S. (2004) Ligand binding and kinetics of folate receptor recycling in vivo: impact on receptor-mediated drug delivery. *Mol. Pharmacol. 66*, 1406−14.
(23) Yang, J., Chen, H., Vlahov, I. R., Cheng, J. X., and Low, P. S. (2006) Evaluation of disulfide reduction during receptor-mediated endocytosis using fluorescence resonance energy transfer imaging. *Proc. Natl. Acad. Sci. U. S. A. 103*, 13872−13877.
(24) Yang, J., Chen, H., Vlahov, I. R., Cheng, J. X., and Low, P. S. (2007) Characterization of the pH of folate receptor-containing endosomes and the rate of hydrolysis of internalized acid-labile folate-drug conjugates. *J. Pharmacol. Exp. Ther. 321*, 462−8.
(25) Lee, R. J., Wang, S., Turk, M. J., and Low, P. S. (1998) The effects of pH and intraliposomal buffer strength on the rate of liposome content release and intracellular drug delivery. *Biosci. Rep. 18*, 69−78.
(26) Vlahov, I. R., Santhapuram, H. K., Kleindl, P. J., Howard, S. J., Stanford, K. M., and Leamon, C. P. (2006) Design and regioselective synthesis of a new generation of targeted chemotherapeutics. Part 1: EC145, a folic acid conjugate of desacetylvinblastine monohydrazide. *Bioorg. Med. Chem. Lett. 16*, 5093−6.
(27) Vlahov, I. R., Wang, Y., Kleindl, P. J., and Leamon, C. P. (2008) Design and regioselective synthesis of a new generation of targeted chemotherapeutics. Part II: Folic acid conjugates of tubulysins and their hydrazides. *Bioorg. Med. Chem. Lett. 18*, 4558−61.
(28) Vlahov, I. R., Vite, G. D., Kleindl, P. J., Wang, Y., Santhapuram, H. K., You, F., Howard, S. J., Kim, S. H., Lee, F. F., and Leamon, C. P. (2010) Regioselective synthesis of folate receptor-targeted agents derived from epothilone analogs and folic acid. *Bioorg. Med. Chem. Lett. 20*, 4578−81.
(29) Reddy, J. A., Westrick, E., Santhapuram, H. K., Howard, S. J., Miller, M. L., Vetzel, M., Vlahov, I., Chari, R. V., Goldmacher, V. S., and Leamon, C. P. (2007) Folate Receptor-specific antitumor activity of EC131, a folate-maytansinoid conjugate. *Cancer Res. 67*, 6376−82.
(30) Henne, W. A., Doorneweerd, D. D., Hilgenbrink, A. R., Kularatne, S. A., and Low, P. S. (2006) Synthesis and activity of a folate peptide camptothecin prodrug. *Bioorg. Med. Chem. Lett. 16*, 5350−5.
(31) Satyam, A. (2008) Design and synthesis of releasable folate-drug conjugates using a novel heterobifunctional disulfide-containing linker. *Bioorg. Med. Chem. Lett. 18*, 3196−3199.
(32) Suzuki, T., Hisakawa, S., Itoh, Y., Suzuki, N., Takahashi, K., Kawahata, M., Yamaguchi, K., Nakagawa, H., and Miyata, N. (2007) Design, synthesis, and biological activity of folate receptor-targeted prodrugs of thiolate histone deacetylase inhibitors. *Bioorg. Med. Chem. Lett. 17*, 4208−12.
(33) Reddy, J. A., Dorton, R., Westrick, E., Dawson, A., Smith, T., Xu, L. C., Vetzel, M., Kleindl, P., Vlahov, I. R., and Leamon, C. P. (2007) Preclinical evaluation of EC145, a folate-vinca alkaloid conjugate. *Cancer Res. 67*, 4434−42.
(34) Covello, K. L., Flefleh, C., Menard, K., Wiebesiek, A., Mcglinchey, K., Wen, M. L., Westhouse, R., Reddy, J. A., Vlahov, I. R., Hunt, J., Rose, W., Leamon, C. P., Vite, G., and Lee, F. (2008) in *Proceedings of the 99th Annual Meeting of AACR*, San Diego, CA.
(35) Sausville, E., LoRusso, P., Quinn, M., Forman, K., Leamon, C., Morganstern, D., Bever, S., and Messmann, R. (2007) A phase I study of EC145 administered weeks 1 and 3 of a 4-week cycle in patients with refractory solid tumors. *Proc. Am. Soc. Clin. Oncol. 25*, 2577.
(36) Naumann, R. W., and Coleman, R. L. (2011) Management strategies for recurrent platinum-resistant ovarian cancer. *Drugs 71*, 1397−412.
(37) Naumann, R. W., Morris, R., Harb, W., Micha, J., Sutton, G., Dinh, T., Mcintyre, J., Patel, R., Davidson, J., Hu, E., and Messmann, R. (2009)

in *16th International Meeting European Society Gynecological Oncology*, Abstract 1181.
(38) Symanowski, J. T., Maurer, A. H., Naumann, R. W., Shah, N. P., Morgenstern, D., and Messmann, R. A. *J. Clin. Oncol.*2010, *28* (15) Suppl. Abstr. 5034.
(39) Vlahov, I. R., Leamon, C. P., Parker, M., Howard, S., Santhapuram, H., Satyam, A., and Reddy, J. (2009) Vitamin receptor binding drug delivery conjugates. U.S. Patent 7,601,332 B2.
(40) Leamon, C. P., and Low, P. S. (2005) Receptor-Mediated Drug Delivery, in *Drug Delivery: Principles and Applications* (Wang, B., Siahaan, T., and Soltero, R. A., Eds.) pp 167−183, Hoboken.
(41) Ducry, L., and Stump, B. (2009) Antibody−drug conjugates: linking cytotoxic payloads to monoclonal antibodies. *Bioconjugate Chem. 21*, 5−13.
(42) Li, J., Sausville, E. A., Klein, P. J., Morgenstern, D., Leamon, C. P., Messmann, R. A., and LoRusso, P. (2009) Clinical pharmacokinetics and exposure-toxicity relationship of a folate-Vinca alkaloid conjugate EC145 in cancer patients. *J. Clin. Pharmacol. 49*, 1467−76.
(43) Oae, S. (1977) *Organic Chemistry of Sulfur*, Plenum, New York.
(44) Oae, S. (1985) *Historical development of sulphur bonding: A view of an experimental organosulphur chemist*, Elsevier, New York.
(45) Vlahov, I. R., Santhapuram, H. K., Wang, Y., Kleindl, P. J., You, F., Howard, S. J., Westrick, E., Reddy, J. A., and Leamon, C. P. (2007) An assembly concept for the consecutive introduction of unsymmetrical disulfide bonds: synthesis of a releasable multidrug conjugate of folic acid. *J. Org. Chem. 72*, 5968−72.
(46) Leamon, C. P., Reddy, J. A., Vlahov, I. R., Westrick, E., Dawson, A., Dorton, R., Vetzel, M., Santhapuram, H. K., and Wang, Y. (2007) Preclinical antitumor activity of a novel folate-targeted dual drug conjugate. *Mol. Pharm. 4*, 659−67.
(47) Vlahov, I. R., Santhapuram, H. K., You, F., Wang, Y., Kleindl, P. J., Hahn, S. J., Vaughn, J. F., Reno, D. S., and Leamon, C. P. (2010) Carbohydrate-based synthetic approach to control toxicity profiles of folate-drug conjugates. *J. Org. Chem. 75*, 3685−91.
(48) Leamon, C. P., Reddy, J. A., Klein, P. J., Vlahov, I. R., Dorton, R., Bloomfield, A., Nelson, M., Westrick, E., Parker, N., Bruna, K., Vetzel, M., Gehrke, M., Nicoson, J. S., Messmann, R. A., LoRusso, P. M., and Sausville, E. A. (2011) Reducing undesirable hepatic clearance of a tumor-targeted vinca alkaloid via novel saccharopeptidic modifications. *J. Pharmacol. Exp. Ther. 336*, 336−43.
(49) Kamen, B. A., Smith, A. K., and Anderson, R. G. W. (1991) The folate receptor works in tandem with a probenecid-sensitive carrier in MA104 cells in vitro. *J. Clin. Invest. 87*, 1442−1449.
(50) Leamon, C. P., Reddy, J. A., Vlahov, I. R., Kleindl, P. J., Vetzel, M., and Westrick, E. (2006) Synthesis and biological evaluation of EC140: A novel folate-targeted vinca alkaloid conjugate. *Bioconjugate Chem. 17*, 1226−32.
(51) Low, P. S., Henne, W. A., and Doorneweerd, D. D. (2008) Discovery and development of folic-acid-based receptor targeting for imaging and therapy of cancer and inflammatory diseases. *Acc. Chem. Res. 41*, 120−9.
(52) Leamon, C. P., and Low, P. S. (1991) Delivery of macromolecules into living cells: a method that exploits folate receptor endocytosis. *Proc. Natl. Acad. Sci. U.S.A. 88*, 5572−5576.
(53) Turek, J. J., Leamon, C. P., and Low, P. S. (1993) Endocytosis of folate-protein conjugates: ultrastructural localization in KB cells. *J. Cell Sci. 106* (Pt 1), 423−30.
(54) Kularatne, S. A., Venkatesh, C., Santhapuram, H. K., Wang, K., Vaitilingam, B., Henne, W. A., and Low, P. S. (2010) Synthesis and biological analysis of prostate-specific membrane antigen-targeted anticancer prodrugs. *J. Med. Chem. 53*, 7767−77.

Bioconjugate Chemistry

Communication

pubs.acs.org/bc

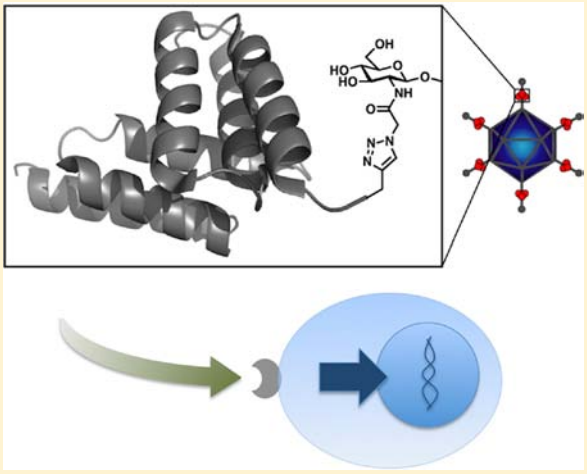
Altering Adenoviral Tropism via Click Modification with ErbB Specific Ligands

Yoon Hyeun Oum[†] and Isaac S. Carrico*[,†,‡]

[†]Department of Chemistry and [‡]Institute of Chemical Biology and Drug Discovery, State University of New York at Stony Brook, Stony Brook, New York 11794-3400, United States

Supporting Information

ABSTRACT: Methods for targeting oncolytic viruses can increase efficacy and accelerate development. Genetic engineering, the predominant method for changing vector tropism, is limited in scope and often represents the bottleneck for vector development. Metabolic incorporation of an unnatural azido sugar, *O*-GlcNAz, at a specific site on the adenoviral surface allows chemoselective attachment of affibodies for Her2 or EGF receptors. Modification with these high-affinity, high-selectivity proteins is straightforward and readily generalizable, demonstrates minimal impact on virus physiology, and affords significant increases in gene delivery to cancer cells. As a result, this method has significant potential to increase the efficacy of next-generation viral vectors.



Oncolytic adenoviruses (Ads) present compelling non-traditional methods for cancer therapy.[1,2] These viruses are designed to preferentially replicate in cancer cells, an effect driven through deletion of viral genes necessary for apoptosis suppression or by placing essential genes under the control of a tumor specific promoters, termed transcriptional targeting.[3,4] Replication within tumor cells leads to virus mediated cytolysis and release of progeny viruses. Potentially, these particles can spread throughout the tumor tissue causing extensive damage. Unfortunately, transcriptional targeting has not provided adequate levels of tumor selectivity.[3,4] In an effort to increase both efficiency and specificity, transcriptionally targeted vectors have been engineered to display ligands for cancer-associated cell surface receptors.[5,6] However, the ability to change viral tropism based on surface-displayed ligands, transductional targeting, is difficult, as standard protein modification approaches are often limited by the complex biology of mammalian viruses.

Three main strategies have been developed for transductional targeting, genetic modification of virus structural proteins, chemical modification of intact viral particles, or the creation of noncovalent virion/ligand complexes. Despite the significant losses in either particle production or infectivity that are typically associated with genetic insertion of targeting ligands, genetics remains the most prevalent form of transductional targeting.[7−9] In well-developed vectors like adenovirus, hot spots for genetic manipulation have been identified allowing the insertion of peptides without significant impact on viral fitness.[10] However, even at well-characterized sites, impact on viral fitness is generally a function of the size and physical properties of the insert. In order to move beyond these general restrictions, a number of laboratories have developed both chemical and noncovalent modification approaches. The former methodology typically takes advantage of surface exposed lysines for poly(ethylene glycol) modification, which generates particles that are both efficiently "detargeted" and shielded from immune recognition.[11,12] Such "stealth" vectors can be armed with targeting moieties, but lysine acylation precludes precise control and can lead to reduced infectivity.[13,14] Alternatively, bridging molecules composed of an Ad binding domain and a targeting domain have been used to create noncovalent targeted Ad complexes. In such a way, antibodies bearing targeting motifs can both "detarget" and retarget in tandem, but *in vivo* stability remains a significant question. Avidin-bridged complexes have higher affinity and provide more flexibility but require the genetic introduction of biotin accepting peptides.[15,16]

Recently, we reported a two-step labeling process that allows highly selective modification of adenoviruses with a wide variety of functionality and demonstrates no impact on viral fitness.[17] Viral particles produced in the presence of an azidosugar precursor, *N*-azidoacetylgalactosamine (Ac_4GalNAz), bear an *O*-GlcNAz at Ser109 of the fiber protein, which is normally

Received: September 7, 2011
Revised: May 24, 2012
Published: June 9, 2012

ACS Publications © 2012 American Chemical Society

dx.doi.org/10.1021/bc200477z | *Bioconjugate Chem.* 2012, 23, 1370−1376

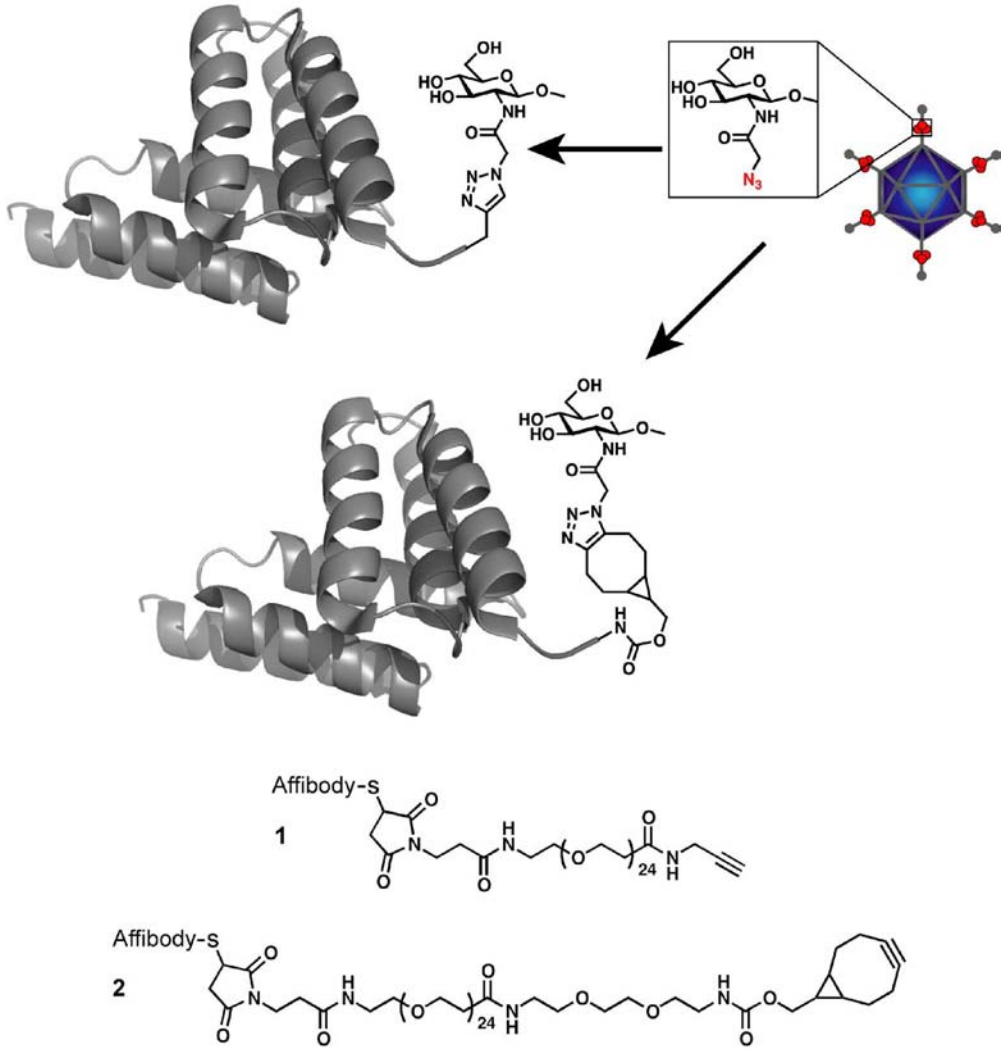


Figure 1. Cartoon illustrating affibody modification of *O*-GlcNAz enabled Ad via either Cu(I)- or strain-promoted click chemistry.

post-translationally modified with a single *O*-linked GlcNAc residue. Installed azides serve as handles for further chemoselective modification via the Staudinger, Cu (I), or strain promoted "click" chemistries, which allow for highly selective modification with small molecules or peptides.[18−20] A derivative of this two-step method also allows for modification through an azide or alkyne bearing unnatural amino acid, azidohomoalanine, or homopropargylglycine.[21,22]

In this study, we use this two-step labeling procedure to alter the tropism of adenoviral vectors by appending affibodies selective for either Her2 (ErbB2) or EGFR (ErbB1). Both receptors are validated, high-value targets for cancer targeting.[23−25] Affibody modification does not significantly impact particle aggregation or stability. Further, infection of a panel of cancer cells with modified Ad demonstrates significant increases in gene delivery that parallel known receptor availability. This work demonstrates the ease, speed, and utility of chemoselective modification of adenoviruses with engineered antibody domains, which is expected to encourage the development of next-generation therapeutic vectors.

O-GlcNAz enabled viruses were produced by standard Ad protocol with one exception: 50 μM Ac_4GalNAz was added to the media of Ad producer cells. Infection, production, and purification were in all other ways identical to published protocol.[17] *O*-GlcNAz enabled Ad exposed to fluorescent Cu(I)-promoted click reagents demonstrate ∼22 dye molecules per viral particle.[17] This number is consistent with *O*-GlcNAc occupancy at Ser109 (∼50%; 36 sites/particle),[26] indicating that both metabolic and chemical labeling are exceedingly efficient. Notably, treatment of these viruses with a glycosidase known to cleave *O*-GlcNAz abrogates chemical labeling, indicating that *O*-GlcNAz is the site for all click modification and that the reaction is exceedingly specific.[17]

As Cu(I)-promoted click chemistry is fast, robust, and easy to access, we initially used this chemistry to produce affibody-modified particles. In order to access "click" chemistry competent affibodies, we created affibodies bearing a poly(ethylene glycol) alkyne linker (PEG_{24}-CCH) **1** (Figure 1). Commercial affibodies with one available cysteine (Abcam) were modified with maleimide-PEG_{24}-CCH. The maleimide was obtained via reaction of commercially available maleimide-PEG_{24}-NHS with propargyl amine (Scheme S1; Supporting Information). While the ubiquity of Cu(I)-promoted click chemistry makes it easily accessible, particularly to the biological laboratories, cytotoxic Cu(I) is notoriously difficult to remove from the resultant conjugates. As an alternative, we explored the potential of strain promoted click chemistry.

dx.doi.org/10.1021/bc200477z | *Bioconjugate Chem.* 2012, 23, 1370−1376

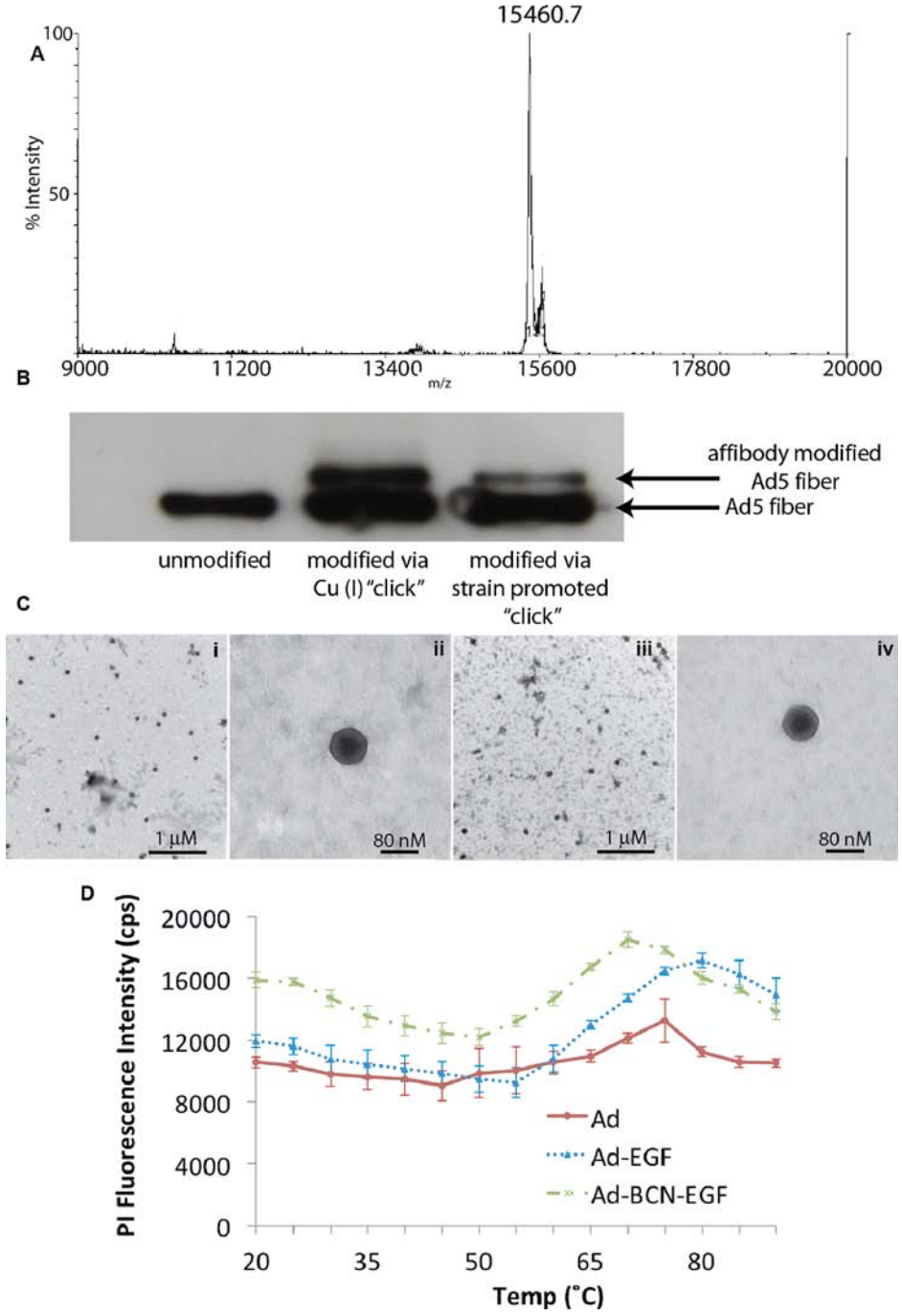


Figure 2. Characterization of affi-PEG-Ad conjugates. (a) MALDI-TOF analysis of HPLC purified affiEGFR-BCN. Calculated mass $[M+H]^+$, 15 456 Da; observed mass, 15 461 Da. (b) Western blot with α-fiber (Ad5) antibody; intact virus (left), affibody conjugated Ad through Cu (I) mediated "click" chemistry (middle), and affibody conjugated Ad through strain promoted "click" chemistry (right). (c) TEM comparison of unmodified Ad particle dispersion (i) and size (ii) to that of affiEGFR-CCH modified particles (iii and iv). ~15 μL of purified virus stock was placed on 400 mesh Formvar-coated copper grids for 1 min, fixed with 2% EM grade glutaraldehyde for 1 min, and then counter stained with 2% phosphotungstic acid for 30 s. (d) Thermal stability assays of particles modified with either Cu(I)- or strain-promoted click. Fluorescence spectra (excitation at 535 nm, emission scan from 550 to 650 nm, λ_{max} = 613, slit widths of 6 nm) of propidium iodide (7.5 μM) were collected at the viral concentration of 6.5 × 10^{10} particles/mL in 5 °C increments from 20 to 90 °C employing a QuantaMaster spectrofluorometer (Photon Technology International, Inc.).

While strain-promoted reagents have been difficult to access in the past, new syntheses have made this set of reactions both faster and more accessible. Further, a few strained alkyne reagents have recently become commercially available (Jena Bioscience).[27,28] We synthesized the precursor amino-bicyclononyne (BCN) derivative (Scheme S2; Supporting Information) via the literature procedure.[29] To quantify the efficiency of strain-promoted "click" modification, azide-labeled viruses were exposed to a tetramethyl rhodamine BCN reagent. Chemical modification with this reagent allowed comparison of this fluorescently labeled sample, with quantified particle number, to a known tetramethyl rhodamine standard (Figures S5 and S6; Supporting Information). Fluorescent gel scanning analysis revealed exclusive modification of a single protein with

dx.doi.org/10.1021/bc200477z | Bioconjugate Chem. 2012, 23, 1370−1376

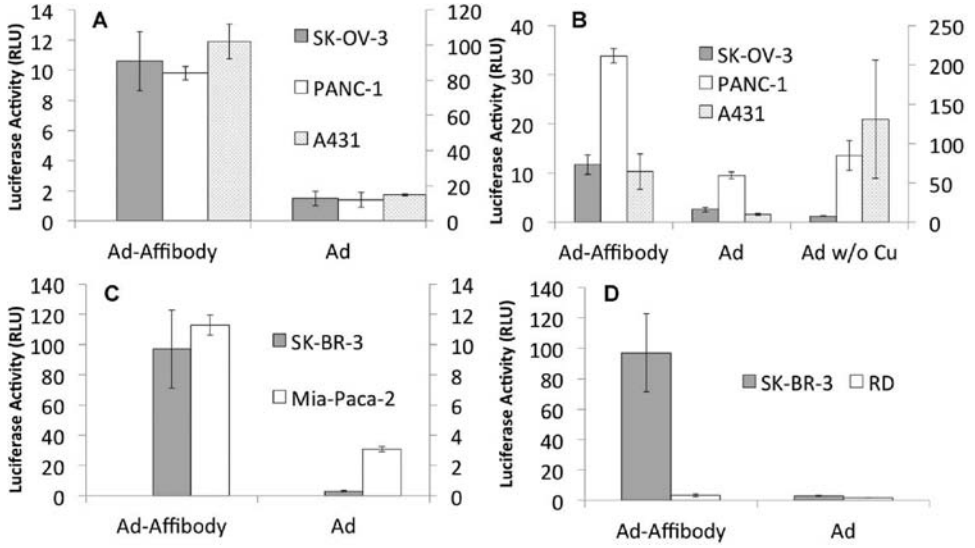


Figure 3. Affibody modification of AdLUC allows improved infection of cancer cells. Cells (A431, PANC-1, MIA PaCa-2, RD, SK-OV-3, SK-BR-3, and RD) were seeded in 96-well black and clear bottom plates at a density of 1×10^4 cells/well, 1 day before infection. Monolayer cells were washed with PBS and incubated in inhibition buffer ([Ad12 knob] $\approx$ 20 μM in PBS with 2% serum) for 1 h at 37 °C. Virus stock was added to the inhibition buffer at a multiplicity of infection (MOI) of 1000 and incubated at 37 °C. After 1 h, cell growth media were added and cells were incubated at 37 °C. Twenty-four hours post infection, the expression levels of luciferase transgene were determined by a photometer with the luciferase assay kit (Bright-Glo, Promega). (a) Comparison of gene delivery capabilities of affiEGFR-PEG-CCH modified and unmodified Ad. (b) Effects of Cu(I) on gene delivery with affiEGFR-PEG-CCH modified particles. (c) Gene delivery with affiHER2-PEG-CCH modified and unmodified Ad to cells expressing high levels of Her2. (d) Comparison of Her2 mediated gene delivery in cells with high (SK-BR-3) and low (RD) Her2 levels.

MW consistent with that of the fiber protein. Quantification demonstrated ~9 modifications per viral particle under standard conditions used for BCN labeling. Notably, the natural residue, GlcNAc, is present at ~20 residues per particle (50–60% occupancy of Ser109).[26] In previous studies, we determined that the metabolic replacement of *O*-GlcNAc with the azido surrogate, *O*-GlcNAz, was essentially complete. This indicates that the efficiency of strain-promoted modification was ~45% of that obtained for Cu(I)-promoted modification, which is consistent with previous bioconjugation studies.[18]

BCN-NH_2 was conjugated to maleimide-PEG_{24}-NHS to afford maleimide-PEG_{24}-BCN, which was conjugated to the EGFR selective affibody **2** via modification of the reduced *n*-terminal cysteine (Figure 1). Analysis of the HPLC purified constructs demonstrated masses that corresponded well with the theoretical values (Figure 2A and Figures S1 and S2; Supporting Information). Cu(I)-mediated modification *O*-GlcNAz enabled Ad was accomplished by exposure to the affibody-CCH under conditions previously optimized for bioconjugation (1 mM CuBr; 3 mM bathophenanthroline disulfonate; 100 μM alkyne; RT).[20,30] In an effort to reduce the amount of copper in the final viral preparation, a Cu(I)-specific chelator, bathocuproinedisulfonate, was added prior to desalting via size exclusion (Centri-Sep 400; Princeton separations) and virus quantitation by PicoGreen assay-(Quant-iT; Invitrogen). Modification of *O*-GlcNAz enabled Ad with affiEGFR-BCN was achieved via incubation with 100 μM of the strained alkyne at room temperature for 16 h (PBS; pH = 7.4). After removal of excess affibody reagents via desalting spin column, viruses were stored at 4 °C for up to 2 weeks. In order to more directly assess anti-EGFR affibody attachment to Ad viral particles, via either Cu(I)- or strain-promoted click chemistry, antifiber Western blotting was used. The results (Figure 2B) demonstrate the appearance of a new band above that of the native fiber, which is consistent with the conjugation of a small protein. Further, Cu(I)-mediated conjugation produces a significantly more intense band than the strain-promoted reaction, consistent with our assessment of the relative conjugation efficiencies.

To assess the physical impact of affibody modification, viral particles were characterized for changes in size, oligomerization, and thermal stability. TEM was used to assess both changes in size and oligomerization state.[31,32] TEM of affiEGFR-CCH, affiEGFR-BCN modified particles revealed discrete, uniform, and well-dispersed particles that measured ~90 nm in diameter (Figure 2C and Figure S3; Supporting Information). Both were indistinguishable from unmodified particles indicating that both oligomerization state and apparent size were largely unaffected by modification, which is unsurprising given the modification density and relatively small size of affibodies (~30 Å).[31,32] To further gauge the impact of modification on viral physiology, we sought to assess differences in stability of the resultant particles. A standard assay for Ad thermal stability requires the addition of propidium iodide, a DNA binding fluorophore that is nonfluorescent prior to intercalation. As a result, heating Ad samples at neutral pH in the presence of propidium iodide yields an increase in fluorescence upon capsid breakdown.[33–35] We compared thermal degradation of three viral particles, completely unmodified Ad, Ad modified with affiEGFR-PEG-CCH, and Ad modified with affiEGFR-PEG-BCN. Comparison of T2 transitions, the major structural transition for adenovirus thermal degradation, revealed that unmodified Ad (T2 = 67 °C), affiEGFR-PEG-CCH modified Ad (T2 = 65 °C), and affiEGFR-PEG-BCN modified Ad (T2 = 62 °C) (Figure 2D) have similar stabilities and are comparable to literature values for unmodified particles.[33]

In order to examine affibody-dependent increased infection of cancer cells, modified Ad5 particles were screened against a panel of well-established cancer lines for gene delivery. As these cells have different basal levels of the primary receptor for

dx.doi.org/10.1021/bc200477z | *Bioconjugate Chem.* 2012, 23, 1370–1376

adenovirus, coxsackie adenovirus receptor (CAR) background infection is highly variable. To mitigate this background, a truncated soluble form of the fiber protein, which serves as the ligand for the primary adenovirus receptor (coxsackie adenovirus receptor), was added to the medium prior to infection with modified Ad particles. This soluble knob domain is readily overexpressed in *E. coli* and derived from a different serotype adenovirus, Ad12.[36,37] However, the Ad12 knob has high sequence homology to the Ad5 knob (46% identity) and binds to the same region of CAR.

Ad5 bearing a luciferase transgene (AdLUC) and modified with affiEGFR-PEG-CCH via Cu(I)-promoted click was screened against three cancer lines known to express high levels of EGFR (A431; SK-OV-3; PANC-1) in the presence of 20 μM soluble Ad12 knob. After 24 h, cells were lysed and luciferase activity was measured. For these experiments, virus produced in the absence of azido sugar was used as a control. Apart from omission of the azido sugar, all other processing was identical, including purification, exposure to click reagents, and removal of these reagents. In all cases, a ~7-fold increase in gene delivery was observed with affibody-modified particles in comparison to unmodified particles (Figure 3A). As an additional control, copper was omitted from the coupling solution. In the context of both SK-OV-3 and PANC-1 cells, affibody-modified virus demonstrated higher levels of gene delivery than either negative control (-Ac_4GalNAz or -Cu(I)/-Ac_4GalNAz) (Figure 3B). However, A431 cells demonstrated much higher error, and the level of gene delivery for affibody-modified viruses was slightly less than virion not exposed to copper. This may be due to differences in copper sensitivity of the different cell lines used. In the context of these experiments, the effect of copper is complicated due to partial oxidation of Cu(I) to Cu(II) in solution.

AffiEGFR-PEG-BCN modified Ad screened against the same cell lines demonstrated more modest changes in gene delivery to SK-OV-3 and A431, and similar levels with PANC-1 cells (Figure S7; Supporting Information), which is consistent with lower modification efficiency obtained with strain-promoted "click" reactions. Completely untreated AdLUC and GlcNAz enabled AdLUC modified with BCN reagent without the affibody (maleimide-PEG-BCN), run as additional negative controls, demonstrated essentially equal signal to the −Ac_4GalNAz controls (Figure S7; Supporting Information).

Infectivity assays for affiHer2-PEG-CCH modified AdLUC were run in a manner identical to that described for affiEGFR-PEG-CCH modified Ad. These targeted viruses were screened against cells with high Her2 (MIA PaCa-2; SK-BR-3) and low Her2 (RD) levels (Figure 3C,D). Low Her2 cells demonstrated negligible increase in gene delivery over background, whereas the high Her2 cells demonstrated ~7 (MIA PaCa-2) and ~100 (SK-BR-3) -fold increases in gene expression. Although no difference in receptor-dependent targeting was seen for cells expressing different levels of EGFR, the differences in receptor levels were modest (A431 and SK-OV-3; ~820 000/cell and ~140 000/cell, respectively).[38] In contrast, Her2 targeted Ad demonstrated significant differences in gene delivery dependent on cell type, commensurate with receptor density that varies much more widely (SK-BR-3 and MIA PaCa-2; ~1 800 000/cell and ~21 000/cell, respectively).[38] Notably, in the absence of knob inhibition, SK-BR-3 cells infected with Her2-modified Ad demonstrated a ~2-fold increase in gene delivery over unmodified Ad, which indicates affibody-mediated cell entry can be even more efficient than the natural process (Figure S8; Supporting Information).

In summary, we have demonstrated that adenoviruses bearing metabolically incorporated *O*-GlcNAz moieties can be modified and targeted using affibody capable click reagents. Notably, this targeting strategy is exceedingly straightforward, requiring only minor modifications of Ad production protocol and click capable reagents. Enhancement with affibody or other antibody equivalents allows a high-specificity approach to target essentially any cell surface receptors. Modification via either Cu(I)- or strain-promoted click yield particles with similar stability and aggregation state to unmodified particles. Targeting studies indicate substantial (~100-fold) to modest (~3-fold) increases in infectivity dependent on both the nature of the cell line and the method of virus modification. These results are consistent with previous studies of affibody targeting and biomolecular modification. The remarkable ease of implementation and broad availability of click reagents make this technique readily accessible. Adenovirus was chosen for this study because it is a leading vector for gene delivery, oncolytic therapy, and vaccine development. However, this targeting strategy can be applied toward the majority of viral particles bearing surface-exposed glycans. In addition, with the recent modification of mammalian viruses via unnatural amino acids, we would expect that this approach could also be extended to the large number of viral particles that are not glycosylated.

■ ASSOCIATED CONTENT

Supporting Information

Details of azido sugar substrates, BCN-TAMRA and targeting molecule synthesis, cell culture conditions, adenovirus production and purification as well as experimental details of labeling, detection, characterization, and targeting of modified viruses. The material is available free of charge via the Internet at http://pubs.acs.org.

■ AUTHOR INFORMATION

Corresponding Author

*E-mail: Isaac.carrico@stonybrook.edu. Phone: 631-632-7935. Fax: 631-632-7960.

Notes

The authors declare no competing financial interest.

■ ACKNOWLEDGMENTS

We would like to thank Dr. Toni Kohler of the SBU proteomics facility for help with mass spectrometry and Dr. Susan Horn of the Central Microscopy Imaging Center for help with TEM imaging. We would to thank Prof. Paul Freimuth and Prof. Patrick Hearing for the generous donation of the Ad fiber expression system and antifiber antibody, respectively. We would also like to thank Lakshmi Rajaram for helpful editing. We are grateful to Prof. Nicole Sampson and Prof. Elizabeth M. Boon for assistance with instrumentation. Funding support for this work was provided by the NSF (CBET-0846259).

■ ABBREVIATIONS

GlcNAc, *N*-acetylglucosamine; GlcNAz, *N*-azidoacetylglucosamine; Ac_4GalNAz, peracetylated *N*-azidoacetylgalactosamine; PEG, polyethylene glycol; affiEGFR-CCH, EGFR selective affibody with a PEG propargyl amine linker; affiHer2-CCH, Her2 selective affibody with a PEG propargyl amine linker;

affiEGFR-BCN, EGFR selective affibody with a PEG bicyclononyne linker.

REFERENCES

(1) Shashkova, E. V., May, S. M., and Barry, M. A. (2009) Characterization of human adenovirus serotypes 5, 6, 11, and 35 as anticancer agents. *Virol. J. 394*, 311−320.

(2) Yamamoto, M., and Curiel, D. T. (2009) Current issues and future directions of oncolytic adenoviruses. *Mol. Ther. 18*, 243−250.

(3) Hogg, R. T., Thorpe, P., and Gerard, R. D. (2011) Retargeting adenoviral vectors to improve gene transfer into tumors. *Cancer Gene Ther. 18*, 275−287.

(4) Hernandez-Alcoceba, R. (2011) Recent advances in oncolytic virus design. *Clin. Translat. Oncol. 13*, 229−239.

(5) Waehler, R., Russell, S. J., and Curiel, D. T. (2007) Engineering targeted viral vectors for gene therapy. *Nat. Rev. Genet. 8*, 573−587.

(6) Hedley, S., Chen, J., Mountz, J., Li, J., Curiel, D., Korokhov, N., and Kovesdi, I. (2006) Targeted and shielded adenovectors for cancer therapy. *Cancer Immunol. Immunother. 55*, 1412−1419.

(7) Magnusson, M. K. H., S.S., Henning, P., Boulanger, P., and Lindholm, L. (2002) Genetic retargeting of adenovirus vectors: functionality of targeting ligands and their influence on virus viability. *J. Gene Med. 4*, 356−370.

(8) Henning, P., Lundgren, E., Carlsson, M., Frykholm, K., Johannisson, J., Magnusson, M. K., Tang, E., Franqueville, L., Hong, S. S., Lindholm, L., and Boulanger, P. (2006) Adenovirus type 5 fiber knob domain has a critical role in fiber protein synthesis and encapsidation. *J. Gen. Virol. 87*, 3151−3160.

(9) Matthews, Q. L., Yang, P., Wu, Q., Belousova, N., Rivera, A. A., Stoff-Khalili, M. A., Waehler, R., Hsu, H. C., Li, Z., Li, J., Mountz, J. D., Wu, H. J., and Curiel, D. T. (2008) Optimization of capsid-incorporated antigens for a novel adenovirus vaccine approach. *Virol. J. 5*.

(10) Belousova, N., Krendelchtchikova, V., Curiel, D. T., and Krasnykh, V. (2002) Modulation of adenovirus vector tropism via incorporation of polypeptide ligands into the fiber protein. *J. Virol. 76*, 8621−8631.

(11) Kreppel, F., Gackowski, J., Schmidt, E., and Stefan, K. (2005) Combined genetic and chemical capsid modifications enable flexible and efficient de- and retargeting of adenovirus vectors. *Mol. Ther. 12*, 107−117.

(12) Kreppel, F., and Kochanek, S. (2007) Modification of adenovirus gene transfer vectors with synthetic polymers: a scientific review and technical guide. *Mol. Ther. 16*, 16−29.

(13) Kreppel, F., Gackowski, J., Schmidt, E., and Kochanek, S. (2005) Combined genetic and chemical capsid modifications enable flexible and efficient de- and retargeting of adenovirus vectors. *Mol. Ther. 12*, 107−117.

(14) Kreppel, F., and Kochanek, S. (2008) Modification of adenovirus gene transfer vectors with synthetic polymers: A scientific review and technical guide. *Mol. Ther. 16*, 16−29.

(15) Campos, S. K., Parrott, M. B., and Barry, M. A. (2004) Avidin-based targeting and purification of a protein ix-modified, metabolically biotinylated adenoviral vector. *Mol. Ther. 9*, 942−954.

(16) Pereboeva, L., Komarova, S., Roth, J., Ponnazhagan, S., and Curiel, D. T. (2007) Targeting EGFR with metabolically biotinylated fiber-mosaic adenovirus. *Gene Ther. 14*, 627−637.

(17) Banerjee, P. S., Ostapchuk, P., Hearing, P., and Carrico, I. (2010) Chemoselective attachment of small molecule effector functionality to human adenoviruses facilitates gene delivery to cancer cells. *J. Am. Chem. Soc. 132*, 13615−13617.

(18) Agard, N. J., Baskin, J. M., Prescher, J. A., Lo, A., and Bertozzi, C. R. (2006) A comparative study of bioorthogonal reactions with azides. *ACS Chem. Biol. 1*, 644−648.

(19) Bruckman, M. A., Kaur, G., Lee, L. A., Xie, F., Sepulveda, J., Breitenkamp, R., Zhang, X., Joralemon, M., Russell, T. P., Emrick, T., and Wang, Q. (2008) Surface modification of tobacco mosaic virus with "click" chemistry. *ChemBioChem 9*, 519−523.

(20) Hong, V., Presolski, S., Ma, C., and Finn, M. (2009) Analysis and optimization of copper-catalyzed azide−alkyne cycloaddition for bioconjugation. *Angew. Chem., Int. Ed. Engl. 48*, 9879−9883.

(21) Banerjee, P. S., Ostapchuk, P., Hearing, P., and Carrico, I. S. (2011) Unnatural amino acid incorporation onto adenoviral (Ad) coat proteins facilitates chemoselective modification and retargeting of Ad type 5 vectors. *J. Virol. 85*, 7546−7554.

(22) Banerjee, P. S., Zuniga, E. S., Ojima, I., and Carrico, I. S. (2011) Targeted and armed oncolytic adenovirus via chemoselective modification. *Bioorg. Med. Chem. Lett. 29*, 4985−4988.

(23) Dreux, A. C., Lamb, D. J., Modjtahedi, H., and Ferns, G. A. A. (2006) The epidermal growth factor receptors and their family of ligands: Their putative role in atherogenesis. *Atherosclerosis 186*, 38−53.

(24) Belousova, N., Mikheeva, G., Gelovani, J., and Krasnykh, V. (2008) Modification of adenovirus capsid with a designed protein ligand yields a gene vector targeted to a major molecular marker of cancer. *J. Virol. 82*, 630−637.

(25) Magnusson, M. K., Henning, P., Myhre, S., Wikman, M., Uil, T. G., Friedman, M., Andersson, K. M. E., Hong, S. S., Hoeben, R. C., Habib, N. A., Stahl, S., Boulanger, P., and Lindholm, L. (2007) Adenovirus 5 vector genetically re-targeted by an affibody molecule with specificity for tumor antigen HER2/neu. *Cancer Gene Ther. 14*, 468−479.

(26) Cauet, G., Strub, J. M., Leize, E., Wagner, E., Van Dorsselaer, A., and Lusky, M. (2005) Identification of the glycosylation site of the adenovirus type 5 fiber protein. *Biochemistry 44*, 5453−5460.

(27) Ning, X. H., Guo, J., Wolfert, M. A., and Boons, G. J. (2008) Visualizing metabolically labeled glycoconjugates of living cells by copper-free and fast huisgen cycloadditions. *Angew. Chem., Int. Ed. Engl. 47*, 2253−2255.

(28) Debets, M. F., van Berkel, S. S., Schoffelen, S., Rutjes, F., van Hest, J. C. M., and van Delft, F. L. (2010) Aza-dibenzocyclooctynes for fast and efficient enzyme PEGylation via copper-free (3 + 2) cycloaddition. *Chem. Commun. 46*, 97−99.

(29) Dommerholt, J., Schmidt, S., Temming, R., Hendriks, L. J. A., Rutjes, F., van Hest, J. C. M., Lefeber, D. J., Friedl, P., and van Delft, F. L. (2010) Readily accessible bicyclononynes for bioorthogonal labeling and three-dimensional imaging of living cells. *Angew. Chem., Int. Ed. Engl. 49*, 9422−9425.

(30) Hong, V., Steinmetz, N. F., Manchester, M., and Finn, M. G. (2010) Labeling live cells by copper-catalyzed alkyne-azide click chemistry. *Bioconjugate Chem. 21*, 1912−1916.

(31) Chen, H. (2007) Comparative observation of the recombinant adeno-associated virus 2 using transmission electron microscopy and atomic force microscopy. *Microsc. Microanal. 13*, 384−389.

(32) Rexroad, J., Wiethoff, C. M., Green, A. P., Kierstead, T. D., Scott, M. O., and Middaugh, C. R. (2003) Structural stability of adenovirus type 5. *J. Pharm. Sci. 92*, 665−678.

(33) Rexroad, J., Martin, T. T., McNeilly, D., Godwin, S., and Middaugh, C. R. (2006) Thermal stability of adenovirus type 2 as a function of pH. *J. Pharm. Sci. 95*, 1469−1479.

(34) He, F., Joshi, S. B., Moore, D. S., Shinogle, H. E., Ohtake, S., Lechuga-Ballesteros, D., Martin, R. A., Truong-Le, V. L., and Middaugh, C. R. (2010) Using spectroscopic and microscopic methods to probe the structural stability of human adenovirus type 4. *Human Vaccines 6*, 202−211.

(35) Rexroad, J., Evans, R. K., and Middaugh, C. R. (2006) Effect of pH and ionic strength on the physical stability of adenovirus type 5. *J. Pharm. Sci. 95*, 237−247.

(36) Awasthi, V., Meinken, G., Springer, K., Srivastava, S. C., and Freimuth, P. (2004) Biodistribution of radioiodinated adenovirus fiber protein knob domain after intravenous injection in mice. *J. Virol. 78*, 6431−6438.

(37) Freimuth, P., Springer, K., Berard, C., Hainfeld, N., Bewley, M., and Flanagan, J. (1999) Coxsackievirus and adenovirus receptor amino-terminal immunoglobulin V-related domain binds adenovirus type 2 and fiber knob from adenovirus type 12. *J. Virol. 73*, 1392−1398.

(38) Gaborit, N., Larbouret, C., Vallaghe, J., Peyrusson, F., Bascoul-Mollevi, C., Crapez, E., Azria, D., Chardes, T., Poul, M. A., Mathis, G., Bazin, H., and Pelegrin, A. (2011) Time-resolved fluorescence resonance energy transfer (TR-FRET) to analyze the disruption of EGFR/HER2 dimers: a new method to evaluate the efficiency of targeted therapy using monoclonal antibodies. *J. Biol. Chem. 286*, 11337−45.

Bioconjugate Chemistry

Communication

pubs.acs.org/bc

PEGylation and Biodistribution of an anti-MUC1 Aptamer in MCF-7 Tumor-Bearing Mice

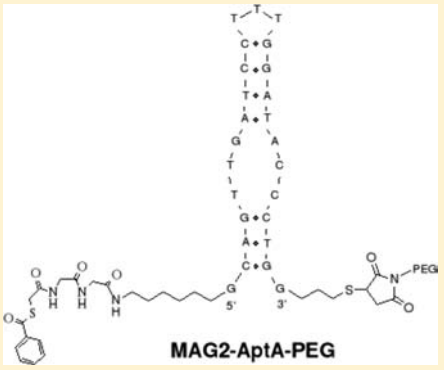
Chiara Da Pieve,*[,†] Elaine Blackshaw,[‡] Sotiris Missailidis,[†] and Alan C. Perkins[‡]

[†]Department of Chemistry and Analytical Sciences, The Open University, MK7 6AA Milton Keynes, United Kingdom

[‡]Academic Medical Physics, School of Clinical Sciences, University of Nottingham, NG7 2UH Nottingham, United Kingdom

Supporting Information

ABSTRACT: Aptamers are characterized by a rapid renal clearance leading to a short *in vivo* circulating half-life. In order to use aptamers as anticancer therapeutic agents, their exposure time to the tumor has to be enhanced via increasing residency in the bloodstream. A way to achieve this goal is by conjugating the aptamer to poly(ethylene glycol) (PEG). Herein, we present the conjugation of a bifunctionalized anti-MUC1 aptamer (NH_2-AptA-SR) with the ^{99m}Tc coordinating moiety MAG2 and either a conventional branched PEG or the comb-shaped PolyPEG via a two-step synthesis. The isolated products were radiolabeled with ^{99m}Tc and their biodistribution and tumor-targeting properties in MCF-7 tumor bearing mice were analyzed and compared.



Due to their ease of synthesis, high target specificity, and versatile pharmacokinetic properties, aptamers are becoming a highly promising new class of medicines. Aptamers have shown great potential for novel targeted diagnostic and therapeutic applications since they can effectively deliver cytotoxic agents or radionuclides to the targeted tissue or organ.[1−3] Radiolabeled aptamers are suitable for imaging applications due to their polyanionic nature and their small size and molecular weight (8−15 kDa), which are key properties leading to good tumor penetration, rapid tissue uptake, and rapid blood clearance. However, the fast systemic clearance is not an ideal characteristic when designing aptamer-based therapeutics. This would result in suboptimal exposure of the target to the agent and thus in the necessity to administer very high, or frequent, doses of the active substance to obtain a significant clinical effect.

Previously, an aptamer (AptA, Figure 1) against the immunogenic epitope of the unglycosylated protein core of MUC-1 was selected,[4−6] labeled with ^{99m}Tc, and injected in MCF-7 xenografts.[7,8] The biodistribution data showed that most of the activity was cleared from the system by 3 h post injection, preventing the aptamer from adequately accessing the tumor. The conjugation of molecules subject to rapid renal clearance to synthetic polymers such as poly(ethylene glycol) (PEG) is a method frequently used to increase their *in vivo* half-life.[9−11] Moreover, it has been found that PEGylated aptamers show a significantly higher uptake by the targeted tissue than their unconjugated form.[12,13]

The preparation of PEGylated aptamers for use as radiopharmaceuticals should be simple and high-yielding. Hicke et al. synthesized PEGylated TTA1 aptamers to be labeled with ^{99m}Tc by conjugating the 5′ amino modified

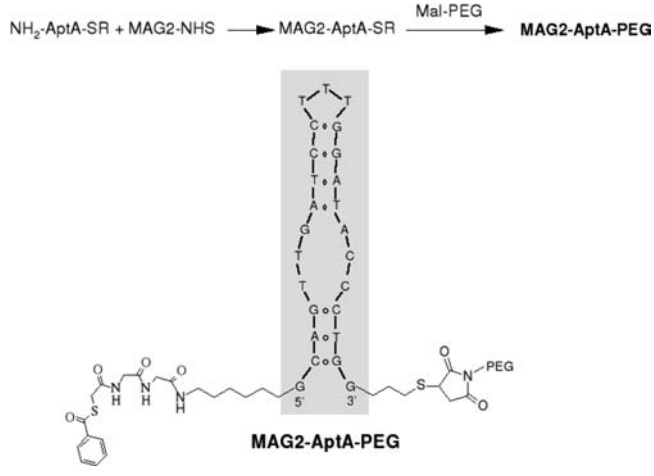


Figure 1. General structure MAG2-AptA-PEGs (bottom)[6] and the synthetic strategy followed for their preparation (top). The structure and sequence of the 25mer AptA has been highlighted in gray.

aptamers to the technetium chelator MAG2 and PEG via an *N*-hydroxysuccinimide (NHS) activated lysine linker.[12]

Although few biodistribution studies of aptamers conjugated to conventional PEG have been reported in the literature,[11−16] no *in vivo* studies using the novel PolyPEG have been carried out. In this work, we report an alternative two-step synthesis using a bifunctionalized AptA having a 5′ aminohexyl and a 3′

Received: March 15, 2012
Revised: June 11, 2012
Published: June 18, 2012

 © 2012 American Chemical Society

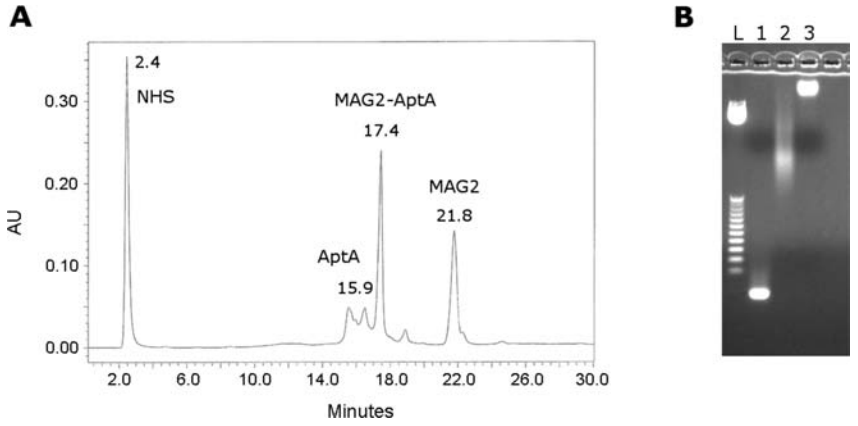


Figure 2. (A) RP-HPLC chromatogram of MAG2-AptA-SR reaction mixture. The peak at 2.4 min is NHS. Unconjugated MAG2 elutes at 21.8 min. The peak at 15.9 min is uncoupled NH_2-AptA-SR. The product (MAG2-AptA-SR) elutes at 17.4 min. (B) 3% Agarose gel of the MAG2-AptA-PEG conjugates. Lines: L, 25 base pair ladder; 1, NH_2-AptA-SR; 2, MAG2-AptA-PolyPEG17; 3, MAG2-AptA-BrPEG20.

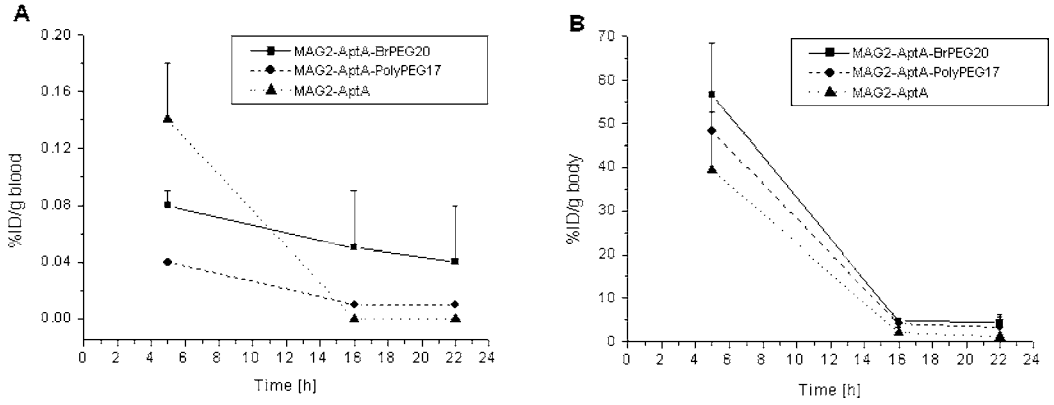


Figure 3. Clearances of radioactivity from blood (A) and body (B) of ^{99m}Tc-labeled MAG2-AptA, MAG2-AptA-BrPEG20, and MAG2-AptA-PolyPEG17 in MCF7 tumor-bearing mice. Data are mean %ID/g ± SD (Table S1 and S2).

thiol modification (NH_2AptASR). The synthesis consisted of the coupling reaction of the aptamer to MAG2 through the 5′ amino end followed by the conjugation to either maleimide-functionalized branched PEG20 kDa (BrPEG20) or Poly-PEG17 kDa (PolyPEG17) through the 3′ thiol end.[17] The isolated products (MAG2-AptA-BrPEG20 and MAG2-AptA-Poly17) were radiolabeled with ^{99m}Tc and their biodistribution and retention in MCF-7 tumor bearing mice were analyzed and compared. PolyPEG has been shown to possess interesting properties, such as low viscosity,[18] compared to conventional linear PEG.

The two-step synthesis of MAG2-AptA-PEGs is shown in Figure 1. Initially, the bifunctionalized aptamer (NH_2-AptA-SR) was reacted with NHS activated S-Benzoyl-MAG2 (MAG2-NHS). The reaction was monitored by reverse-phase high-performance liquid chromatography (RP-HPLC). The chromatogram (Figure 2A) showed a new peak eluting at 17.4 min, while the unconjugated NH_2-AptA-SR eluted at 15.9 min. The coupling yield was >70%. The isolated product (MAG2-AptA-SR) was then conjugated, via a maleimide−thiol reaction, to maleimide-functionalized BrPEG20 and PolyPEG17 using immobilized tris-[2-carboxy-ethyl]phosphine hydrochloride to reduce the disulfide bond on the aptamer. The products, MAG2-AptA-PolyPEG17 and MAG2-AptA-BrPEG20, were isolated by anion exchange HPLC, as previously described,[17] and analyzed by gel electrophoresis (Figure 2B). The shift of the PEGylated aptamer to higher molecular weights confirmed the conjugation. The MAG2-AptA-PEGs were labeled with ^{99m}Tc and the complexes were separated from unreacted pertechnetate and other small molecular weight impurities by ultrafiltration using 10 kDa MWCO filters. The radiochemical purity was monitored by ITLC using butanone as eluent. The isolated ^{99m}TcMAG2-AptA-PEGs had a retention factor (R_f) of 0, while free pertechnetate, present only in the discarded washings, had a R_f = 0.9.

An alternative two-step synthetic route, consisting of the reaction of NH_2-AptA-SR with the synthetic polymers followed by the coupling to MAG2-NHS, was not successful (see Supporting Information).

Table S1 and Figures S2−S5 give an overview of the tissue distribution in MCF-7 tumor-bearing mice of the ^{99m}Tc-labeled MAG2-AptA-PolyPEG17 and MAG2-AptA-BrPEG20 at 5, 16, and 22 h post injection. The previously reported biodistribution data of un-PEGylated MAG2-AptA[8] were used as comparison. As expected, the blood and body clearances of the aptamer were reduced by PEGylation (Figure 3). The body clearance data showed that more than 60% of the un-PEGylated aptamer was excreted after 5 h. In contrast, the excretion was ca. 43% and 51% in the case of MAG2-AptA-BrPEG20 and MAG2-AptA-PolyPEG17, respectively. Near-complete elimination (ca. 98%) of the un-PEGylated aptamer was observed after 16 h. As expected, the PEGylated aptamers resided longer in the body since ca. 95% of the activity was excreted after 16 h reaching 96−97% after 22 h. The aptamer conjugated to PolyPEG17,

dx.doi.org/10.1021/bc300128r | Bioconjugate Chem. 2012, 23, 1377−1381

having a molecular weight (MW) of 17 000 Da and a comb shape, was cleared from the blood (Figure 3A) and the body (Figure 3B) more quickly then the conventional branched PEG20, which has a comparable MW (20 000 Da), but a more rigid and linear shape, suggesting that both clearances were influenced by the molecular size, hydrodynamic volume, and structure of PEG.

As shown in Figure 4, the tumor uptake of MAG2-AptA was the highest at 5 h post injection (0.12%) showing a tumor-to-blood ratio of only 0.85 (Table S2). The aptamer was then rapidly washed out from the tumor resulting in an uptake of 0.01% at 22 h p.i. (Figure 5C). Similarly, the PEGylated aptamers showed the highest tumor retention at 5 h p.i. However, their uptake was significantly below the one of the un-PEGylated aptamer. In time, the activity was released from the tumor although less rapidly than the un-PEGylated aptamer (Figure 5). The PolyPEG-aptamer conjugate showed higher tumor-to-blood ratios than the conventional PEG conjugate (Figure 5D), but the values were always ≤2 (Table S2).

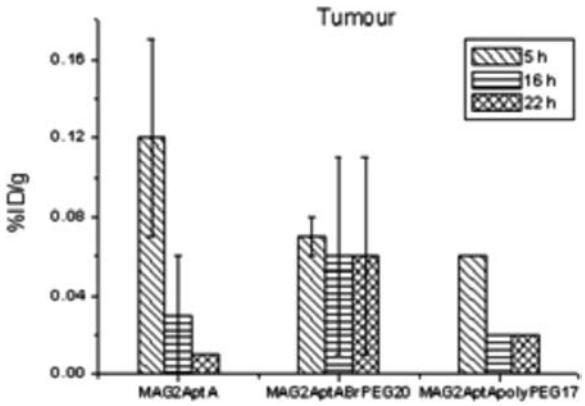


Figure 4. Tumor uptake after injection of ^{99m}Tc-labeled MAG2-AptA, MAG2-AptA-BrPEG20, and MAG2-AptA-PolyPEG17 at 5, 16, and 22 h p.i.

Previous *in vitro* studies showed that the conjugation of the aptamer to either MAG2 or branched PEG 20 kDa or PolyPEG17 kDa has no significant influence upon the binding affinity of AptA for its isolated target.[8,17] The lower tumor uptake could be caused by a decreased ability of the aptamer to penetrate the target tissue due to its increased molecular weight and hydrodynamic volume after conjugation to PEG.

As already mentioned, the residence times of aptamers in the body were increased by PEGylation. The level of radioactivity in the whole-body tissues was higher for MAG2-AptA-BrPEG20 than for the PolyPEG conjugate (Table S3). Table 1 shows the distribution of the activity in the nontarget organs involved in the metabolism and removal of the aptamer from the body as a percentage of the whole-body activity. After 5 h, in the case of the un-PEGylated aptamer, the residual activity is mainly in the small (52.1%) and large (22.94%) intestine indicating hepatobiliary excretion. This clearance pattern was determined by the chelator (MAG2).[12,19,20]

In the animals dosed with PEGylated aptamers, almost all the radioactivity (84−90%) was accumulated in the large intestine indicating an extensive and rapid clearance through the hepatobiliary system.

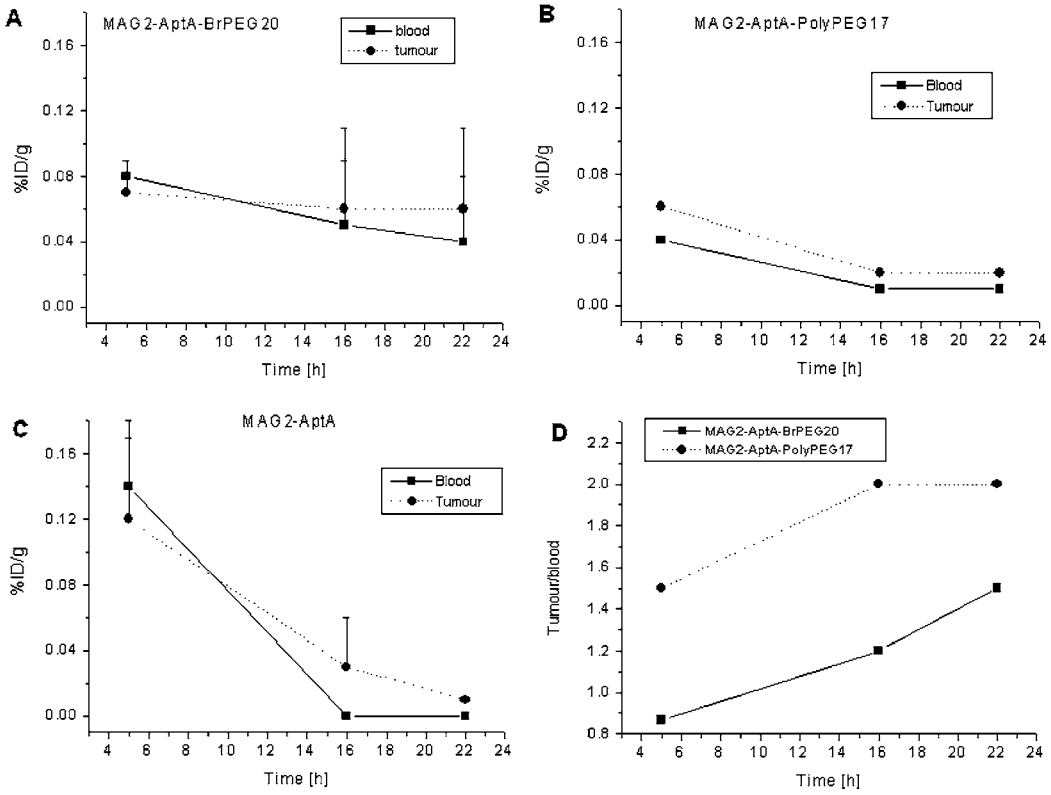


Figure 5. Tumor uptake of ^{99m}Tc-labeled MAG2-AptA-BrPEG20 (A), MAG2-AptA-PolyPEG17 (B), and MAG2-AptA (C) in MCF-7 xenograft-bearing mice at 5, 16, and 22 h p.i. Tumor-to-blood ratios (D), after injection of ^{99m}Tc-labeled MAG2-AptA-BrPEG20 and MAG2-AptA-PolyPEG17, vs time.

dx.doi.org/10.1021/bc300128r | *Bioconjugate Chem.* 2012, 23, 1377−1381

Table 1. Distribution of Radioactivity in the Excreting Organs and in Blood of MCF7 Xenograft-Bearing Mice (n = 3)[a]

		relative activity [%]		
tissue	time [h]	MAG2-AptA	MAG2-AptA-BrPEG20	MAG2-AptA-PolyPEG17
Kidney	5	1.16 (±0.93)	0.46 (±0.06)	0.51 (±0.04)*
	16	2.43 (±1.09)	4.78 (±1.67)	3.12 (±0.18)
	22	3.24 (±1.92)	4.97 (±2.41)	10.09 (±9.72)
Liver	5	2.57 (±0.69)	0.41 (±0.05)	0.33 (±0.00)*
	16	12.10 (±19.01)	2.74 (±3.19)	1.53 (±0.23)
	22	2.28 (±2.74)	4.12 (±2.18)	3.08 (±1.84)
S. Int.	5	52.10 (±31.04)	2.68 (±2.07)	1.74 (±0.86)*
	16	3.87 (±1.03)	5.14 (±1.68)	8.43 (±3.58)
	22	11.80 (±10.86)	4.91 (±2.52)	3.30 (±0.98)
L. Int.	5	22.94 (±36.87)	90.36 (±1.76)	84.46 (±11.52)*
	16	50.92 (±22.91)	39.91 (±8.57)	56.41 (±9.52)
	22	44.87 (±30.19)	44.27 (±10.70)	49.40 (±17.13)
Blood	5	0.37 (±0.17)	0.14 (±0.00)	0.08 (±0.00)*
	16	0.24 (±0.41)	1.06 (±0.71)	0.24 (±0.05)
	22	0.00 (±0.00)	1.01 (±0.49)	0.41 (±0.24)

[a]The values are relative to the whole-body radioactivity content at 5, 16 and 22 h p.i. (±SD, *n = 2).

Both PEGylated aptamers exhibit a higher bone accumulation than the un-PEGylated aptamer. The reason for this is unclear, but may be related to uptake of the conjugates by bone marrow cells due to some properties associated with PEG rather than with the aptamer itself.

The bifunctionalized AptA (NH_2-AptA-SR) has been conjugated, via a high-yielding two-step synthesis, to the ^{99m}Tc coordinating moiety MAG2 and to two kinds of PEG (BrPEG20 and PolyPEG17) having comparable molecular weights but completely different structures (linear and "comb-like", respectively).

We found that the blood and body clearances of the aptamer were reduced by PEGylation and were influenced by the synthetic polymer architecture. Consequently, the concentrations in the whole body tissues were higher in the mice dosed with PEGylated aptamers than in the animals dosed with the un-PEGylated aptamer.

In contrast to other studies previously reported in the literature,[12,13] in our case the conjugation to PEG did not promote the tumor uptake of the aptamer. The biodistribution data, in contrast to the previously performed *in vitro* studies,[17] showed that the synthetic polymer has some effect on the binding affinity of the aptamer for its target. At 5 h p.i., the tumor uptakes of the PEGylated aptamer (0.07 ± 0.01% and 0.06 ± 0.00%) were in fact lower than the already quite modest uptake (0.12 ± 0.05%) of the unPEGylated aptamer. In all cases, after 22 h, the activity was more or less rapidly washed out from the tumor. The low uptake of the unPEGylated and PEGylated aptamer could possibly be due to a relatively weak affinity of this aptamer for its target (K_D = 13.6 nM; see Materials and Methods in Supporting Information) combined to a fast and intense clearance (renal and hepatobiliary). In this study, the aptamer was therefore not able to reach and bind to the target and subsequently be internalized by the cancer cells in significant amounts. In order to further develop either an imaging or a therapeutic agent, the affinity of this anti-MUC1 aptamer (AptA) for its target needs to be improved.

■ ASSOCIATED CONTENT

Supporting Information

Materials and methods, an alternative synthetic route for MAG2-AptA-PEG, HPLC conditions, biodistribution tables and graphs, and γ scintigraphic images. This material is available free of charge via the Internet at http://pubs.acs.org

■ AUTHOR INFORMATION

Corresponding Author

*Phone: +44 1908653010, Fax: +44 1908858327. E-mail: c.dapieve@open.ac.uk or chiaradapi@googlemail.com.

Notes

The authors declare no competing financial interest.

■ ACKNOWLEDGMENTS

The authors would like thank Richard Palmer and Warwick Effect Polymers Ltd., and Andrew McKenzie and his staff (Cancer Studies, Nottingham University Hospital).

■ REFERENCES

(1) Tavitian, B. (2006) In vivo imaging with oligonucleotides for diagnosis and drug development. *Gut 52*, 40−47.
(2) Mayer, G., and Jenne, A. (2004) Aptamers in research and drug development. *Biodrugs 18*, 351−359.
(3) Cerchia, L., Hamm, J., Libri, D., Tavitian, B., and de Franciscis, V. (2002) Nucleic acid aptamers in cancer medicine. *FEBS Lett. 528*, 12−16.
(4) Ferreira, C. S. M., Matthews, C. S., and Missailidis, S. (2006) DNA aptamers that bind to MUC1 tumour marker: design and characterization of MUC1-binding single-stranded DNA aptamers. *Tumor Biol. 27*, 289−301.
(5) Ferreira, C. S. M., Papamichael, K., Guilbault, G., Schwarzacher, T., Gariepy, J., and Missailidis, S. (2008) DNA aptamers against the MUC1 tumour marker: design of aptamer-antibody sandwich ELISA for the early diagnosis of epithelial tumours. *Anal. Bioanal. Chem. 390*, 1039−1050.
(6) Baouendi, M., Cognet, J. A. H., Ferreira, C. S. M., Missailidis, S., Coutant, J., Piotto, M., Hantz, E., and Hervé du Penhoat, C. (2012) Solution structure of a truncated anti-MUC1 DNA aptamer determined by mesoscale modeling and NMR. *FEBS J. 279*, 479−490.
(7) Borbas, K. E., Ferreira, C. S. M., Perkins, A., Bruce, J. I., and Missailidis, S. (2007) Design and synthesis of mono- and multimeric targeted radiopharmaceuticals based on novel cyclen ligands coupled to anti-MUC1 aptamers for the diagnostic imaging and targeted radiotherapy of cancer. *Bioconjugate Chem. 18*, 1205−1212.
(8) Da Pieve, C., Perkins, A. C., and Missailidis, S. (2009) Anti-MUC1 aptamers: radiolabelling with ^{99m}Tc and biodistribution in MCF7 tumour bearing mice. *Nucl. Med. Biol. 36*, 703−710.
(9) Bailon, P., and Berthold, W. (1998) Polyethylene glycol-conjugated pharmaceutical proteins. *Pharm. Sci. Technol. Today 1*, 352−356.
(10) Duncan, R. (2003) The dawning era of polymer therapeutics. *Nat. Rev. Drug Discovery 2*, 347−360.
(11) Ng, E. W. M., Shima, D. T., Calias, P., Cunningham, E. T. J., Guyer, D. R., and Adamis, A. P. (2006) Pegaptanib, a targeted anti-VEGF aptamer for ocular vascular disease. *Nat. Rev. Drug Discovery 5*, 123−132.
(12) Hicke, B. J., Stephens, A. W., Gould, T., Chang, Y.-F., Lynott, K., Heil, J., Borkowski, S., Hilger, C.-S., Cook, G., Warren, S., and Schmidt, P. (2006) Tumor targeting by an aptamer. *J. Nucl. Med. 47*, 668−678.
(13) Boomer, R. M., Lewis, S. D., Healy, J. M., Kurz, M., Wilson, C., and McCauley, T. G. (2005) Conjugation to polyethylene glycol polymer promotes aptamer biodistribution to healthy and inflamed tissues. *Oligonucleotides 15*, 183−195.

(14) Ostendorf, T., Kunter, U., Grone, H. J., Bahlmann, F., Kawaki, H., Shimizu, F., Koch, K. M., Janjic, N., and Floege, J. (2001) Specific antagonism of PDGF prevents renal scarring in experimental glomerulonephritis. *J. Am. Soc. Nephrol. 12*, 909−918.
(15) Cosmi, B. (2009) ARC-1779, a PEGylated aptamer antagonist of von Willebrand factor for potential use as an anticoagulant or antithrombotic agent. *Curr. Opin. Mol. Ther. 11*, 322−328.
(16) Healy, J. M., Lewis, S. D., Kurz, M., Boomer, R. M., Thompson, K. M., Wilson, C., and McCauley, T. G. (2004) Pharmacokinetics and biodistribution of novel aptamer compositions. *Pharm. Res. 21*, 2234−2246.
(17) Da Pieve, C., Williams, P., Haddleton, D. M., Palmer, R. M. J., and Missailidis, S. (2010) Modification of thiol functionalized aptamers by conjugation of synthetic polymers. *Bioconjugate Chem. 21*, 169−174.
(18) Ryan, S. M., Mantovani, G., Wang, X., Haddleton, D. M., and Brayden, D. J. (2008) Advances in PEGylation of important biothech molecules: delivery aspects. *Expert Opin. Drug Delivery 5*, 371−383.
(19) Hjelstuen, O. K., By, B. C., Cleynhens, B., Ormstad, H. M., Roald, T. E., Tønnesen, H. H., Bremer, P. O., and Verbruggen, A. M. (1999) Comparative evaluation of ^{99m}Tc-MAG2-Oligodeoxynucleotides with phosphodiester or phosphorothioate backbones:preparation, stability and biodistribution. *J. Labelled Cpd. Radiopharm. 42*, 737−760.
(20) Zhang, Y.-M., Liu, N., Zhu, Z.-H., Rusckowski, M., and Hnatowich, D. J. (2000) Influence of different chelators (HYNIC, MAG3 and DTPA) on tumor cell accumulation and mouse biodistribution of technetium-99m labeled to antisense DNA. *Eur. J. Nucl. Med. 27*, 1700−1707.

Bioconjugate Chemistry

Communication

pubs.acs.org/bc

Site-Specific One-Pot Dual Labeling of DNA by Orthogonal Cycloaddition Chemistry

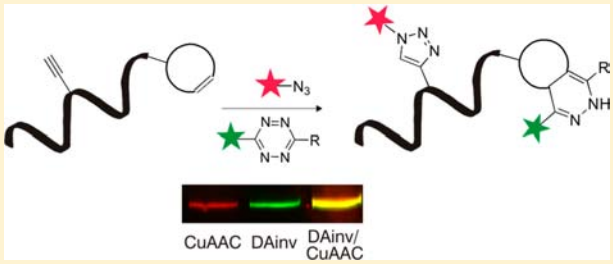
Juliane Schoch,[†] Markus Staudt,[†] Ayan Samanta,[†] Manfred Wiessler,[‡] and Andres Jäschke*[,†]

[†]Institute of Pharmacy and Molecular Biotechnology, Heidelberg University, 69120 Heidelberg, Germany

[‡]German Cancer Research Center, Division of Medical Physics in Oncology E020, 69120 Heidelberg, Germany

Supporting Information

ABSTRACT: Bioorthogonal reactions are of high interest in biosciences as they allow the introduction of fluorescent dyes, affinity tags, or other unnatural moieties into biomolecules. The site-specific attachment of two or more different labels is particularly demanding and typically requires laborious multistep syntheses. Here, we report that the most popular cycloaddition in bioconjugation, the copper-catalyzed azide−alkyne click reaction (CuAAC), is fully orthogonal to the inverse electron-demand Diels−Alder reaction (DAinv). We demonstrate that both bioorthogonal reactions can be conducted concurrently in a one-pot reaction by just mixing all components. Orthogonality has been established even for highly reactive *trans*-cyclooctene-based dienophiles (with rate constants up to 380 000 M^{-1} s^{-1}). These properties allow for the convenient site-specific one-step preparation of oligonucleotide FRET probes and related reporters needed in cellular biology and biophysical chemistry.



Labeling of oligonucleotides with fluorophores or affinity tags is of utmost importance in nanotechnology and modern life sciences. In particular, the site-specific introduction of multiple, spectrally different fluorophores is crucial for structure−function studies of biopolymers by bulk or single-molecule fluorescence spectroscopy and also for the development of DNA probes for imaging purposes.[1] While a number of non-nucleosidic modifications can be easily introduced during solid-phase DNA synthesis by phosphoramidite chemistry,[2,3] the harsh reaction conditions restrict the variety of modifications that can be inserted. Therefore, postsynthetic labeling strategies have received considerable attention, as they work under milder conditions and furthermore allow the screening over a range of labels in a short time as one phosphoramidite serves as precursor for all different labels that need to be introduced. Nevertheless, conventional postsynthetic labeling protocols suffer from low yield, prolonged reaction time and often require a high concentration of the biomolecule in combination with a huge excess of the coupling partner.[4] In contrast, bioorthogonal click reactions are very attractive for this purpose, as they work in aqueous solution under mild conditions and often with quantitative yields.[5−9] Among these reactions, the copper-catalyzed (CuAAC)[10−13] and strain-promoted azide−alkyne click reactions (SPAAC)[14,15] found widest application in the past few years. As azides are rather unstable under the conditions of phosphoramidite solid-phase synthesis, the chemical incorporation of "clickable" moieties into oligonucleotides has been focused on alkyne-carrying phosphoramidites, followed by postsynthetic labeling with azide-derivatives.[16,17] Recently, the successful synthesis of azide-modified RNA-oligonucleotides was reported by using either phosphotriester chemistry[18,19] or two-step procedures where a precursor is postsynthetically converted to the azide.[20] Another recently upcoming bioorthogonal labeling approach is based on the inverse electron-demand Diels−Alder (DAinv) reaction.[21−23] We have previously exploited this strategy for the site-specific labeling of DNA[24] and RNA.[25] This cycloaddition proceeds rapidly, without transition metals, and allows efficient functionalization of oligonucleotides at room temperature.

The selective coupling of two (or more) different labels to specific positions of an oligonucleotide is even more challenging than introducing a single modification. Using cycloaddition chemistry, this goal has been achieved on different routes: in stepwise processes, in which two different conjugation reactions are carried out successively with intervening purification,[26] or in which protecting groups must be removed between successive coupling steps in order to direct the reactivity.[27] Another approach is the ligation of individually synthesized singly modified fragments.[28] These sequential approaches, however, are time-consuming as well as laborious, and often result in low overall yields. Ideally, site-specific double-modification would be performed concurrently in a one-pot reaction without protection or intervening purification. This goal, however, requires the two different coupling chemistries not only to be bioorthogonal (no side reactions with the functional groups present in the oligonucleotide), but also mutually orthogonal so that no cross-reactivity

Received: April 3, 2012
Revised: May 30, 2012
Published: June 19, 2012

ACS Publications © 2012 American Chemical Society

dx.doi.org/10.1021/bc300181n | *Bioconjugate Chem.* 2012, 23, 1382−1386

occurs.[29,30] To our knowledge, no such systems are known for DNA and RNA modification.

Herein, we report the successful combination of CuAAC and DAinv for simultaneous site-specific double-labeling of DNA oligonucleotides in a true one-pot reaction (Figure 1). Both

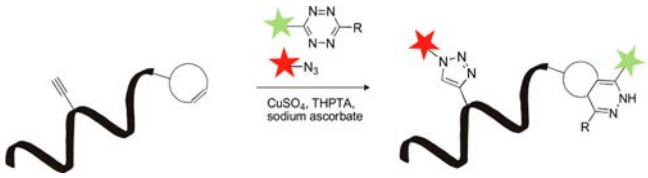


Figure 1. Double modification of a DNA oligonucleotide by simultaneous DAinv and CuAAC reaction.

CuAAC[16,17,31] and DAinv[24] reactions have been previously described to be bioorthogonal to DNA. We assumed that they could also be mutually orthogonal as alkynes that are reactive in CuAAC reactions should have low reactivity in DAinv cycloadditions due to their low HOMO energy.[32] To explore this possibility, we first evaluated three different dienophiles for their use in DAinv modification on DNA by determination of rate constants, followed by investigation of possible cross- and side-reactivity, in combination with CuAAC using different techniques ranging from tandem mass spectrometry (MS/MS) for shorter oligonucleotides to restriction digestion and polyacrylamide gel electrophoretic analysis on longer oligonucleotides. Finally, we carried out one-pot dual labeling on doubly modified oligonucleotides of different sizes and analyzed the reaction mixtures, whereupon all experiments indicated DAinv and CuAAC to be mutually orthogonal.

While our previous work used norbornene dienophiles, their moderate reactivity in DAinv reactions (second-order rate constant k_2 = 20 ± 2 M^{-1} s^{-1}) required prolonged reaction times (1 h) and caused nonquantitative reaction yields.[24,25] Meanwhile, *trans*-cyclooctene (TCO)-based dienophiles had been reported to react much more rapidly.[33] We therefore synthesized three different TCO-based alcohols as dienophilic moieties, namely, two diastereomers of (*E*)-cyclooct-4-enol and the cyclopropyl-appendent compound *endo*-(*E*)-bicyclo [6.1.0]non-4-en-9-yl methanol,[21,33] and converted them into phosphoramidites **PA1**-**PA3** using standard procedures. These phosphoramidites were then used to incorporate a single dienophile at the 5′-terminus of oligonucleotides ODN**1a**−**3a** (Figure 2). This required the use of *tert*-butylhydroperoxide as an oxidizer, as the standard aqueous iodine oxidizer led to quantitative degradation of the TCO moieties.

The second-order rate constants of the DAinv reactions with dansyl-tetrazine were determined in a stopped-flow apparatus exploiting the fluorogenic property of these cycloadditions. The values obtained for oligonucleotide ODN**1a** (k_2 = 26 000 ± 600 M^{-1} s^{-1}), ODN**2a** (k_2 = 83 000 ± 3500 M^{-1} s^{-1}), and ODN**3a** (k_2 = 380 000 ± 10 000 M^{-1} s^{-1}) indicate the high reactivity of TCO (factor 1200−19 000, compared to norbornene), which is in agreement with reported data for reaction of tetrazines with *trans*-cyclooctenols.[33,34] The same analysis was applied to an alkyne-only modified oligonucleotide, ODN**4**, where no reaction with dansyl-tetrazine was observed (Supporting Information, Figure S3−S5). Even after incubation of ODN**4** with dansyl-tetrazine for 48 h at room temperature and subsequent LC-MS analysis, no DAinv product of the alkyne was detectable. These data suggest a difference in reactivity of

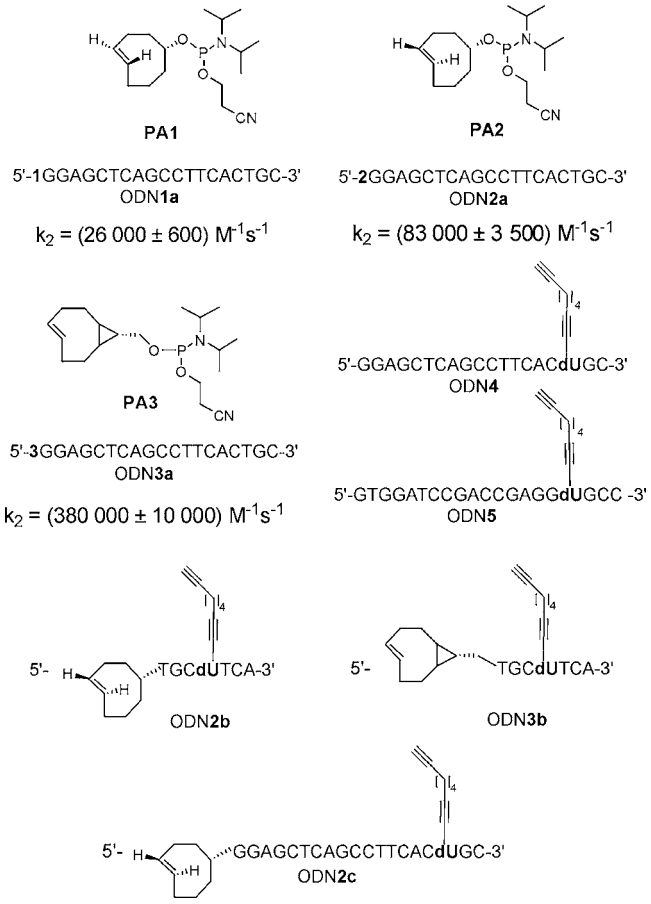


Figure 2. Dienophile-modified phosphoramidites **PA1**−**PA3** and synthesized oligonucleotides ODN**1a**−**5** with corresponding rate constants of ODN**1a**−**3a** in the DAinv reaction.

at least 8 orders of magnitude between TCO-based dienophiles and terminal alkynes.

Encouraged by these results, doubly modified oligonucleotides carrying both an alkyne and a dienophile, ODN**2b** and ODN**3b**, were synthesized in which one of the two most reactive dienophiles **2** and **3** was introduced at the 5′-end, while the alkynyl residue was attached to an internal position (Figure 2). The possibility to carry out the two cycloaddition reactions concurrently was examined by MS and LC-MS/MS analysis of crude one-pot concurrent DAinv/CuAAC reaction mixtures. High-resolution mass spectrometry served to identify the doubly labeled products, while orthogonality of the two cycloadditions was analyzed by fragmentation of the product signals using tandem mass spectrometry (MS/MS). The fragmentation schemes were then compared with the ones obtained for the nonreacted oligonucleotide ODN**2b** (Figure 3a), and with those from individual DAinv or CuAAC reactions (Figure 3b,c). When only the DAinv reaction was performed (by reacting the DNA with dansyl-tetrazine, Figure 3b), the dienophile-containing signals (green circles) disappeared, new signals with masses of DAinv products appeared (green stars), while the alkyne-only fragments (red circles) remained unchanged. On the other hand, when only the CuAAC was carried out (by incubation with Alexafluor-594 azide, $CuSO_4$, THPTA, and sodium ascorbate), the fragmentation scheme (Figure 3c) showed the disappearance of the alkyne signals (red circles) and the appearance of CuAAC product peaks (red stars), while the dienophile-related signals (green circles)

dx.doi.org/10.1021/bc300181n | *Bioconjugate Chem.* 2012, 23, 1382−1386

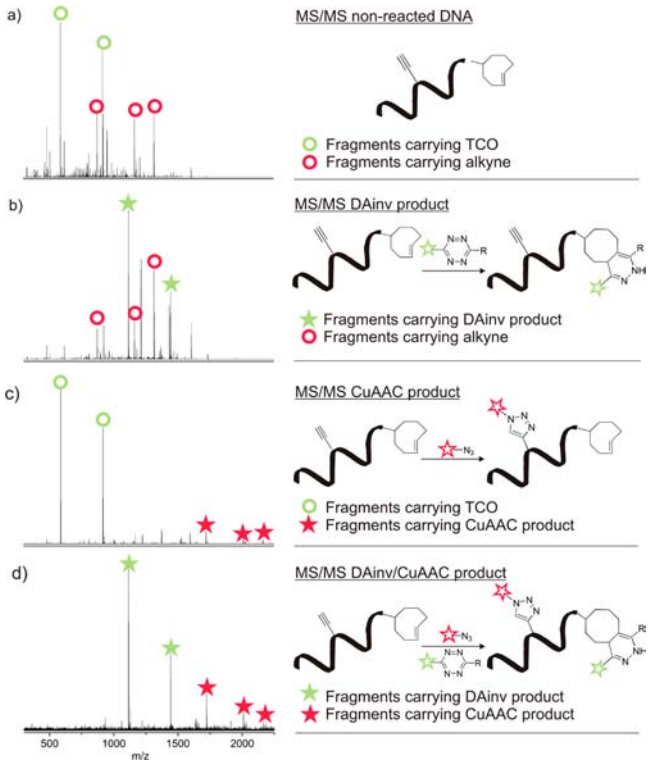


Figure 3. (a) MS/MS spectrum of nonreacted heptamer oligonucleotide ODN**2b**, (b) MS/MS spectrum of DAinv product of ODN**2b**, (c) MS/MS spectrum of CuAAC product of ODN**2b**, (d) MS/MS spectrum of simultaneous DAinv/CuAAC reaction on ODN**2b**.

remained unchanged. Importantly, neither the primary mass spectra nor the MS/MS spectra indicated the presence of multiply or wrongly functionalized fragments that would indicate cross-reactivity. These results demonstrate the selectivity of the two cycloaddition reactions for their intended functional groups. When both reactions were run simultaneously (by incubation of the oligonucleotide with Alexafluor-594 azide, $CuSO_4$, THPTA, sodium ascorbate, and dansyl-tetrazine), the mass signals of the dienophile- (green circles) as well as alkynyl-containing fragments (red circles) disappeared, while the DAinv (green star) and CuAAC product (red star) peaks appeared (Figure 3d). An identical MS/MS analysis was conducted for DAinv, CuAAC, and simultaneous DAinv/CuAAC on ODN**3b** where similar fragmentation schemes were obtained. (For MS spectra, LC traces, and analysis of MS and MS/MS spectra, see Supporting Information). These results demonstrate that—even when run simultaneously in a one-pot reaction—both reactions are orthogonal to each other, whereas the reactivity of the DAinv can be tuned by the choice of the dienophile.

To further analyze the labeling efficiency and orthogonality of the two reactions, we applied the one-pot double labeling reaction to a 19mer oligonucleotide carrying dienophile **2** and an alkyne moiety, ODN**2c** (Figure 2), bearing a restriction cleavage site in between the alkyne and TCO substitutions. After labeling, the oligonucleotide was hybridized to its complementary strand and restriction digested to yield a 5mer that was expected to contain exclusively the DAinv product and a 14mer that should be CuAAC product only. HPLC analysis in comparison with a restriction digest of the nonreacted oligonucleotide ODN**2c** showed the quantitative disappearance of the two unmodified oligonucleotide fragments, and the appearance of new product peaks (Supporting Information Figure S20). The mass spectrum of the combined product fractions confirmed the formation of the DAinv-functionalized 5mer and the CuAAC-functionalized 14mer, while there were no traces of the two hypothetical products, namely, CuAAC-functionalized 5mer and DAinv-functionalized 14mer, resulting from cross-reactivity of the two dienophiles (Figure 4).

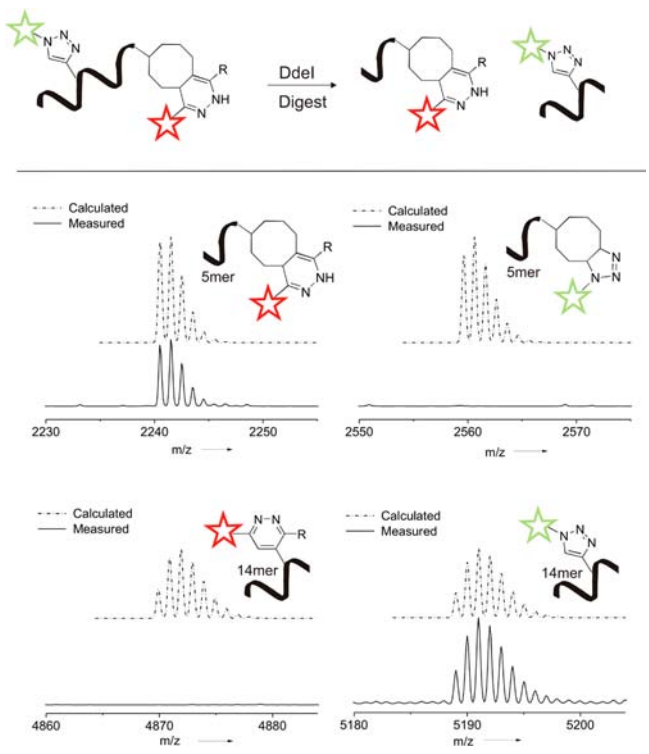


Figure 4. Calculated (dotted line) and measured (straight line) MS spectra of DAinv and CuAAC products of doubly labeled ODN**2b** after restriction digestion (DdeI restriction endonuclease).

After having demonstrated the orthogonality and efficiency of the labeling protocol, we in a next step applied this protocol to the preparative synthesis of a doubly labeled oligonucleotide. Varying amounts of ODN**2c** (162 pmole to 1.62 nmole) were subjected to the concurrent DAinv/CuAAC reaction, and the crude reaction mixture was purified on a denaturing polyacrylamide gel, followed by isopropanol precipitation. This protocol afforded the pure doubly labeled oligonucleotide in isolated yields of ~33% and amounts sufficient for typical biophysical experiments (Supporting Information Figure S21).

This approach opens up the possibility to label long, biologically relevant oligonucleotides simultaneously with different fluorophores as required for structural studies, e.g., by FRET spectroscopy. As proof-of-principle for the applicability to longer oligonucleotides, a TCO- and alkyne-modified 233mer oligonucleotide was amplified by PCR using singly modified primers ODN**1a**−**3a** (for DAinv, forward primer) and ODN**5** (for CuAAC, reverse primer). The PCR product was then subjected to either individual DAinv and CuAAC reactions, or to a simultaneous one-pot DAinv/CuAAC reaction using TAMRA-tetrazine and Cy5 azide. After polyacrylamide gel electrophoretic separation of the reaction mixtures, the gels were subjected to fluorescence imaging. The TAMRA scan (excitation 532 nm) revealed all products of a

dx.doi.org/10.1021/bc300181n | *Bioconjugate Chem.* 2012, 23, 1382−1386

reaction with tetrazine, while all azide-derived products were visualized in the Cy5 scan (excitation 633 nm, Figure 5). For

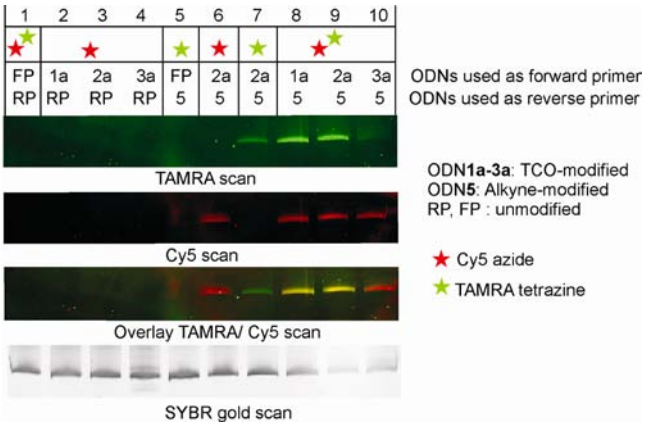


Figure 5. 15% Denaturing polyacrylamide gel of DAinv/CuAAC labeling reaction on an alkyne/TCO-modified ds233mer PCR-product: (1) negative control incubating nonmodified PCR product with dansyl-tetrazine, Cy5 azide, THPTA, $CuSO_4$, and sodium ascorbate; (2–4) CuAAC on TCO-modified PCR products; (5) DAinv on alkyne-modified PCR product; (6) CuAAC on doubly modified PCR product of ODN**2a**; (7) DAinv on doubly modified PCR product of ODN**2a**; (8–10) concurrent DAinv/CuAAC on doubly modified PCR products of ODN**1a**–**3a**. FP and RP are unmodified oligonucleotides having the same nucleotide sequence as ODN**1a**–**3a** and ODN**5**, respectively.

the PCR product based on ODN**3a**, no DAinv reaction product was observed (Figure 5, lane 10), likely due to decomposition of the highly reactive bicyclo[6.1.0]nonenyl ring system during multiple heating cycles to 98 °C. In contrast, the cyclooctenol-based dienophiles withstand such treatment without problems and CuAAC as well as DAinv products could be detected (Figure 5, lanes 6–9). For doubly labeled PCR products of primers ODN**1a** and ODN**2a**, the bands in both scans overlapped exactly, indicating attachment of both dyes to the same macromolecular species (Figure 5, lanes 8–9). We again checked for cross-reactivity by incubating the TCO-only modified PCR product with a 500-fold excess of Cy5 azide, $CuSO_4$, THPTA, and sodium ascorbate, and also the alkyne-only PCR product with a 10-fold excess of TAMRA-tetrazine. The absolute absence of any faint green or red band in these control experiments even after 1 h of reaction time unambiguously demonstrates the selectivity and orthogonality of these cycloadditions toward oligonucleotide functionalization (Figure 5, lanes 2–5).

Very recently, Karver et al. reported the orthogonality of the DAinv reaction and the strain-promoted alkyne–azide cycloaddition (SPAAC), and the application of this methodology to cell-surface labeling.[29] As strained alkynes are known to react as dienophiles in DAinv reactions,[35] this approach required fine-tuning of reactivities by the careful choice of reactants, and the authors settled for a less reactive tetrazine in combination with the highly reactive TCO (k_2 = 210 M^{-1} s^{-1}), for which they observed excellent orthogonality to the azide/dibenzocyclooctyne system. In our system, no compromise in tetrazine reactivity was necessary to achieve orthogonality of the cycloadditions, leading to rate constants of up to 380 000 M^{-1} s^{-1} for the DAinv reaction. This allows completion of the reaction within seconds even at low micromolar concentration of both biomolecule and labeling reagent. In contrast to the DAinv/SPAAC system, we could not observe any side reaction, such as the reaction of the azide with the alkene or the coupling of the tetrazine with the alkyne. To our knowledge, the DAinv reaction with the TCO reactants described here is—by several orders of magnitude—the fastest bioorthogonal modification reaction ever reported for nucleic acids. Future efforts will now be directed to increase the rate of the CuAAC reaction, too. We expect that the combination of CuAAC and DAinv will find broad application in biochemistry, polymer science, and nanotechnology. The commercial availability of a wide range of azide derivatives for conjugation—from dyes, amino acids, sugars, nucleotides to whole peptide tags or solid matrices—combined with the current rapid development of conjugatable tetrazine derivatives will facilitate the one-step synthesis of a broad array of double-functionalized biomolecules. While the requirement for copper ions hinders applications inside living cells, this does not present a problem for many other biological applications, from *in vitro* studies to fixed-cell labeling and cell-surface labeling.[36,37]

■ ASSOCIATED CONTENT

Supporting Information

Experimental details and analysis of MS/MS spectra. This material is available free of charge via the Internet at http://pubs.acs.org.

■ AUTHOR INFORMATION

Corresponding Author

*Tel: (+49) 6221-54 4851; Fax: (+49) 6221-5464 30; E-mail: jaeschke@uni-hd.de.

Notes

The authors declare no competing financial interest.

■ ACKNOWLEDGMENTS

This work was supported by the Deutsche Forschungsgemeinschaft (Grant # Ja 794/3). The authors thank Dr. Murat Sünbül for providing TAMRA.

■ REFERENCES

(1) Juskowiak, B. (2011) Nucleic acid-based fluorescent probes and their analytical potential. *Anal. Bioanal. Chem. 399*, 3157–76.
(2) Beaucage, S. L. (1993) Oligodeoxyribonucleotides synthesis. Phosphoramidite approach. *Methods Mol. Biol. 20*, 33–61.
(3) Lönnberg, H. (2009) Solid-phase synthesis of oligonucleotide conjugates useful for delivery and targeting of potential nucleic acid therapeutics. *Bioconjugate Chem. 20*, 1065–94.
(4) Hermanson, G. T. (1996) Bioconjugate Techniques, Academic Press, San Diego.
(5) Best, M. D. (2009) Click chemistry and bioorthogonal reactions: unprecedented selectivity in the labeling of biological molecules. *Biochemistry 48*, 6571–84.
(6) Debets, M. F., van Berkel, S. S., Dommerholt, J., Dirks, A. T., Rutjes, F. P., and van Delft, F. L. (2011) Bioconjugation with strained alkenes and alkynes. *Acc. Chem. Res. 44*, 805–15.
(7) Kohn, M., and Breinbauer, R. (2004) The Staudinger ligation-a gift to chemical biology. *Angew. Chem., Int. Ed. 43*, 3106–16.
(8) Lim, R. K., and Lin, Q. (2010) Bioorthogonal chemistry: recent progress and future directions. *Chem. Commun. (Camb.) 46*, 1589–600.
(9) Weisbrod, S. H., and Marx, A. (2008) Novel strategies for the site-specific covalent labelling of nucleic acids. *Chem. Commun. (Camb.)*, 5675–85.
(10) El-Sagheer, A. H., and Brown, T. (2011) Click chemistry with DNA. *Chem. Soc. Rev. 39*, 1388–405.

(11) Gierlich, J., Burley, G. A., Gramlich, P. M., Hammond, D. M., and Carell, T. (2006) Click chemistry as a reliable method for the high-density postsynthetic functionalization of alkyne-modified DNA. *Org. Lett. 8*, 3639−42.
(12) Kolb, H. C., Finn, M. G., and Sharpless, K. B. (2001) Click chemistry: diverse chemical function from a few good reactions. *Angew. Chem., Int. Ed. 40*, 2004−2021.
(13) Tornoe, C. W., Christensen, C., and Meldal, M. (2002) Peptidotriazoles on solid phase: [1,2,3]-triazoles by regiospecific copper(i)-catalyzed 1,3-dipolar cycloadditions of terminal alkynes to azides. *J. Org. Chem. 67*, 3057−64.
(14) Jewett, J. C., and Bertozzi, C. R. (2010) Cu-free click cycloaddition reactions in chemical biology. *Chem. Soc. Rev. 39*, 1272−9.
(15) Marks, I. S., Kang, J. S., Jones, B. T., Landmark, K. J., Cleland, A. J., and Taton, T. A. (2011) Strain-promoted "click" chemistry for terminal labeling of DNA. *Bioconjugate Chem. 22*, 1259−63.
(16) Gramlich, P. M., Wirges, C. T., Manetto, A., and Carell, T. (2008) Postsynthetic DNA modification through the copper-catalyzed azide-alkyne cycloaddition reaction. *Angew. Chem., Int. Ed. 47*, 8350−8.
(17) Seela, F., and Sirivolu, V. R. (2006) DNA containing side chains with terminal triple bonds: Base-pair stability and functionalization of alkynylated pyrimidines and 7-deazapurines. *Chem. Biodivers. 3*, 509−14.
(18) Aigner, M., Hartl, M., Fauster, K., Steger, J., Bister, K., and Micura, R. (2011) Chemical synthesis of site-specifically 2′-azido-modified RNA and potential applications for bioconjugation and RNA interference. *ChemBioChem 12*, 47−51.
(19) Fauster, K., Hartl, M., Santner, T., Aigner, M., Kreutz, C., Bister, K., Ennifar, E., and Micura, R. (2012) 2 ′-Azido RNA, a versatile tool for chemical biology: synthesis, X-ray structure, siRNA applications, click labeling. *ACS Chem. Biol. 7*, 581−589.
(20) Gerowska, M., Hall, L., Richardson, J., Shelbourne, M., and Brown, T. (2012) Efficient reverse click labeling of azide oligonucleotides with multiple alkynyl Cy-Dyes applied to the synthesis of HyBeacon probes for genetic analysis. *Tetrahedron 68*, 857−864.
(21) Blackman, M. L., Royzen, M., and Fox, J. M. (2008) Tetrazine ligation: fast bioconjugation based on inverse-electron-demand Diels-Alder reactivity. *J. Am. Chem. Soc. 130*, 13518−9.
(22) Devaraj, N. K., and Weissleder, R. (2011) Biomedical applications of tetrazine cycloadditions. *Acc. Chem. Res. 44*, 816−27.
(23) Wiessler, M., Waldeck, W., Kliem, C., Pipkorn, R., and Braun, K. (2009) The Diels-Alder-reaction with inverse-electron-demand, a very efficient versatile click-reaction concept for proper ligation of variable molecular partners. *Int. J. Med. Sci. 7*, 19−28.
(24) Schoch, J., Wiessler, M., and Jäschke, A. (2010) Post-synthetic modification of DNA by inverse-electron-demand Diels-Alder reaction. *J. Am. Chem. Soc. 132*, 8846−7.
(25) Schoch, J., Ameta, S., and Jäschke, A. (2011) Inverse electron-demand Diels-Alder reactions for the selective and efficient labeling of RNA. *Chem. Commun. (Camb.) 47*, 12536−7.
(26) Gutsmiedl, K., Fazio, D., and Carell, T. (2010) High-density DNA functionalization by a combination of Cu-catalyzed and Cu-free click chemistry. *Chem.—Eur. J. 16*, 6877−83.
(27) Gramlich, P. M., Warncke, S., Gierlich, J., and Carell, T. (2008) Click-click-click: single to triple modification of DNA. *Angew. Chem., Int. Ed. 47*, 3442−4.
(28) Paredes, E., Evans, M., and Das, S. R. (2011) RNA labeling, conjugation and ligation. *Methods 54*, 251−9.
(29) Karver, M. R., Weissleder, R., and Hilderbrand, S. A. (2012) Bioorthogonal reaction pairs enable simultaneous, selective, multi-target imaging. *Angew. Chem., Int. Ed. 51*, 920−2.
(30) Sletten, E. M., and Bertozzi, C. R. (2011) A bioorthogonal quadricyclane ligation. *J. Am. Chem. Soc. 133*, 17570−3.
(31) Kocalka, P., El-Sagheer, A. H., and Brown, T. (2008) Rapid and efficient DNA strand cross-linking by click chemistry. *ChemBioChem 9*, 1280−5.
(32) Thalhammer, F., Wallfahrer, U., and Sauer, J. (1990) Reaktivität einfacher offenkettiger und cyclischer Dienophile bei Diels-Alder-Reaktionen mit inversem Elektronenbedarf. *Tetrahedron Lett. 31*, 6851−6854.
(33) Taylor, M. T., Blackman, M. L., Dmitrenko, O., and Fox, J. M. (2011) Design and synthesis of highly reactive dienophiles for the tetrazine-trans-cyclooctene ligation. *J. Am. Chem. Soc. 133*, 9646−9.
(34) Karver, M. R., Weissleder, R., and Hilderbrand, S. A. (2011) Synthesis and evaluation of a series of 1,2,4,5-tetrazines for bioorthogonal conjugation. *Bioconjugate Chem. 22*, 2263−70.
(35) Chen, W., Wang, D., Dai, C., Hamelberg, D., and Wang, B. (2012) Clicking 1,2,4,5-tetrazine and cyclooctynes with tunable reaction rates. *Chem. Commun. (Camb.) 48*, 1736−8.
(36) Hong, V., Steinmetz, N. F., Manchester, M., and Finn, M. G. (2010) Labeling live cells by copper-catalyzed alkyne--azide click chemistry. *Bioconjugate Chem. 21*, 1912−6.
(37) Soriano Del Amo, D., Wang, W., Jiang, H., Besanceney, C., Yan, A. C., Levy, M., Liu, Y., Marlow, F. L., and Wu, P. (2010) Biocompatible copper(I) catalysts for in vivo imaging of glycans. *J. Am. Chem. Soc. 132*, 16893−9.

Bioconjugate Chemistry

Communication

pubs.acs.org/bc

Conformational Modulation of in Vitro Activity of Cyclic RGD Peptides via Aziridine Aldehyde-Driven Macrocyclization Chemistry

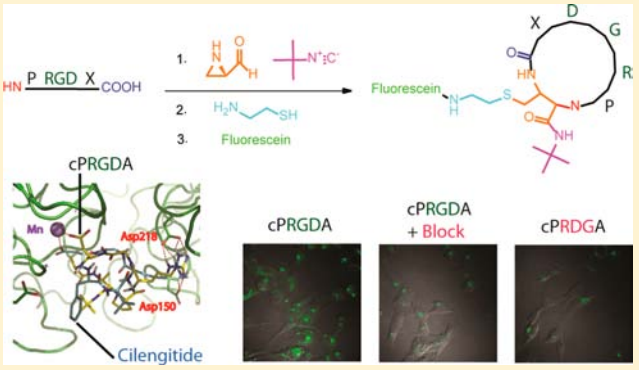
Áron Roxin,[§,†] Juan Chen,[†] Conor C. G. Scully,[‡] Benjamin H. Rotstein,[‡] Andrei K. Yudin,*[,‡] and Gang Zheng*[,§,†]

[§]Department of Pharmaceutical Sciences and [‡]Department of Chemistry, University of Toronto, Toronto, Ontario, Canada

[†]Ontario Cancer Institute and Princess Margaret Hospital, University Health Network, Toronto, Ontario, Canada

Supporting Information

ABSTRACT: Here, we demonstrate a conjugation strategy whereby cyclic RGD-containing macrocycles are prepared using aziridine aldehydes, isocyanides, and linear peptides, followed by conjugation to a cysteamine linker. Our method involves site-selective aziridine ring-opening with the nucleophilic sulfhydryl group of cysteamine. Fluorescein was then efficiently conjugated to the primary amine of cysteamine by NHS-chemistry. This strategy may be expanded to provide easy access to a wide variety of fluorescent dyes or radiometal chelators. Modeling studies showed that aziridine aldehyde cyclization chemistry stabilized the RGD motif into the required bioactive conformation and that this cyclization chemistry modulated the geometry of macrocycles of different residue lengths. In vitro studies showed that cPRGDA and cPRGDAA both selectively bound to $\alpha_V\beta_3$-overexpressing U87 glioblastoma cells, and that cPRGDA had a better binding affinity compared to cPRGDAA. The improved binding affinity of cPRGDA was attributed to the fixed Pro-C$^{\alpha}$-Asp-C$^{\alpha}$ distance surrounding the stabilized RGD motif in cPRGDA.



INTRODUCTION

Research into peptides targeting biomarkers associated with cancer actively pursues the creation of cyclic peptides that display specific biological activity and that can be functionalized for targeted imaging or therapy. A recent cyclization method developed in our laboratories employs amphoteric aziridine aldehydes and isocyanides to cyclize linear peptides through a rerouted Ugi reaction.[1] Aziridine aldehyde-driven cyclization proceeds rapidly, giving high yields at higher concentrations than is possible for conventional peptide cyclizations. This original procedure reported the conjugation of a thiolated coumarin fluorophore after cyclization and has since been refined to include several functional inputs. For instance, in addition to postcyclization fluorophore labeling, macrocycles have been labeled with a solvatochromic naphthalimide isocyanide during cyclization.[2] Most recently, novel thioester isocyanide reagents were developed with the goal of subsequent macrocycle−peptide ligation to access cycle-tail peptide scaffolds.[3] We sought to expand these recent conjugation strategies by developing a versatile modification chemistry whereby the conjugation of a wide variety of fluorophores, radiometal chelators, and other biological entities could be achieved.

Conventional amide-cyclized peptides often require additional lysine, cysteine, or glutamate residues to support side chain-selective conjugations. However, conjugations through these additional residues may hinder binding of the biologically relevant peptide regions[4−6] and often require cumbersome protection/deprotections protocols.[7−10] A method that enables one to constrain a linear epitope of interest into a macrocycle, while offering an exocyclic handle that can be modified at a late stage of synthesis without perturbing the desired conformation of the molecule,[11] is highly desirable. Here, we show a novel modification strategy wherein the thiol of cysteamine nucleophilically attacks aziridine aldehyde-cyclized macrocycles, resulting in aziridine ring-opening. Fluorescein was then conjugated to the macrocycles through the primary amine of cysteamine using *N*-hydroxysuccinimide (NHS)-chemistry (Scheme 1). This strategy removes the necessity of incorporating superfluous residues and allows the conjugation of a variety of biological entities containing carboxylic acid, isothiocyanate (ITC), or NHS functionalities by well-established amide coupling.

Arg-Gly-Asp (RGD)-containing peptides were chosen as a model for our investigations. The RGD motif is known to bind to the $\alpha_V\beta_3$ integrin receptor, which is overexpressed by several types of cancers and by tumor neovasculature.[12−15] To obtain biologically active RGD motifs, computer models of RGD-

Received: May 1, 2012
Revised: June 7, 2012
Published: June 18, 2012

ACS Publications © 2012 American Chemical Society

Scheme 1. General Strategy for Synthesizing the Fluorescein-Labeled Aziridine Aldehyde-Cyclized RGD Macrocycles

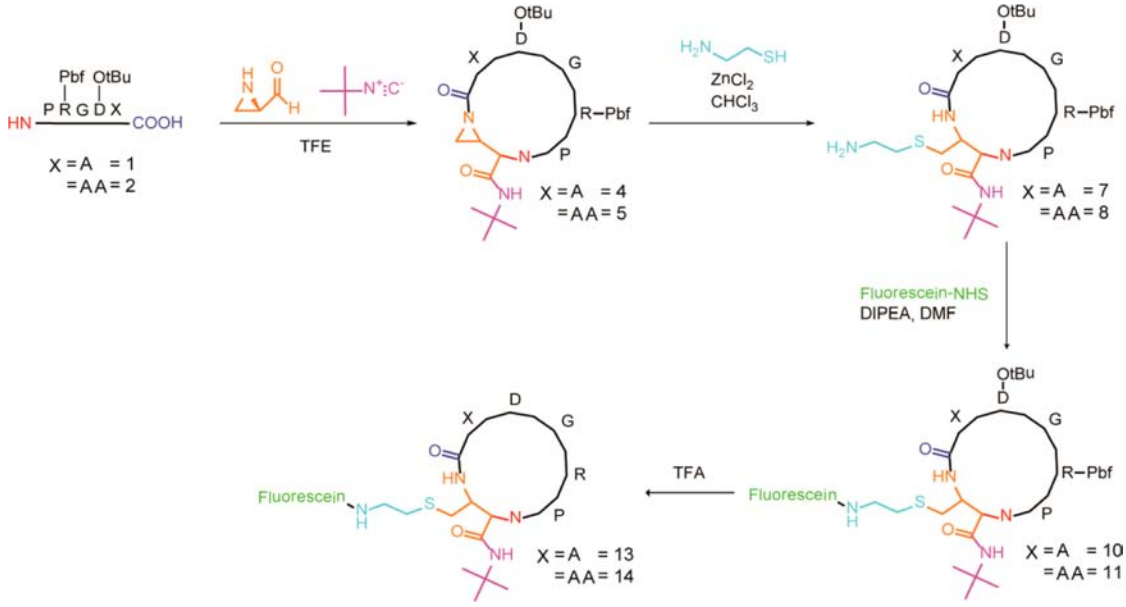
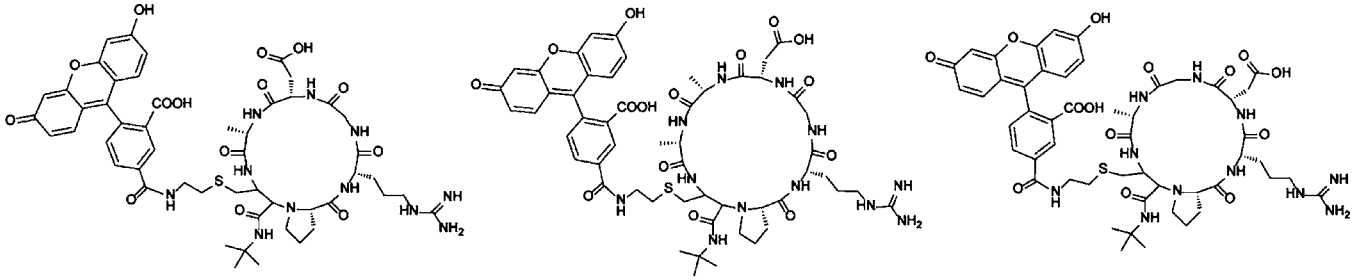


Chart 1. Novel Fluorescein-Labeled Macrocycles cPRGDA (13), cPRGDAA (14), and cPRDGA (15)



based aziridine aldehyde-cyclized pentapeptide and hexapeptide macrocycles were constructed in an attempt to recapitulate the observed backbone geometry from solution phase and crystallographic studies of potent integrin binding peptides. Docked conformations of promising RGD macrocycles and the $\alpha_V\beta_3$ integrin receptor were examined to investigate if these RGD macrocycles could attain binding geometries that were similar to the known high-affinity ligand cRGDf(N-Me)V (Cilengitide).[16−18] We proposed that if our RGD macrocycles could stabilize the RGD motif in a bioactive conformation similar to that of cRGDf(N-Me)V, then these peptides would be suitable for in vitro $\alpha_V\beta_3$ integrin-binding. Linear RGD-containing peptides were cyclized and labeled with fluorescein to experimentally validate the biological activity of the proposed functional macrocycles (Chart 1). Cell adhesion assays compared the binding affinity of the pentapeptide cPRGDA (**13**) and the hexapeptide cPRGDAA (**14**) to investigate how the geometry of these peptides correlated to their binding affinity for the $\alpha_V\beta_3$ integrin receptor of U87 glioblastoma cells. Confocal microscopy was then used to further investigate if these fluorescein-labeled macrocycles could specifically target the $\alpha_V\beta_3$ integrin receptor of U87 cells for in vitro cancer imaging. Our study provides a guide to experimentally verify the biological activity and specificity of our constrained RGD macrocycles proposed by computational geometry-based modeling that can be extended for screening other biologically active receptor-targeting motifs.

EXPERIMENTAL PROCEDURES

Chemicals. Organic solvents were purchased from Fisher Scientific and Sigma Aldrich. Amino acids and resins were purchased from Nova Biochem. Cysteamine, zinc chloride, L-serine, triphenyl phosphene (PPh_3), diisopropyl azodicarboxylate (DIAD), diisobutylaluminum hydride (DIBAL), *tert*-butyl isocyanide, and crystal violet were purchased from Sigma Aldrich. Fluorescein-NHS was purchased from Thermo Scientific. The chelator 1,4,7,10-tetraazacyclododecane-1,4,7-tris(*t*-butyl acetate)-10-acetate mono-succinimide ester (DOTA-NHS) was purchased from Macrocyclics. Pyropheophorbide-succinimide ester (Pyro-NHS) was synthesized following a previously published procedure.[19]

General Methods. Proton NMR was performed using a Bruker Ultrashield 400 Plus 400 MHz NMR. Mass spectrometry was performed using an Agilent Technologies 6130 Mass Spectrometer. The identity and purity of all peptide derivatives were assessed using a Waters 2695 HPLC with a Waters Delta Pak C18, 5 μm 3.9 × 150 mm column under reverse-phase conditions (0−100% acetonitrile in 0.1% TFA over 15 min at 0.8 mL/minute) while monitoring with a Waters 2996 photodiode array detector and a Waters Micromass ZQ mass spectrometer. Macrocycles were purified using a Waters Prep LC System with an Agilent 300SB-C3, 5 μm 9.4 × 250 mm column under reverse-phase conditions (0−100% acetonitrile in 0.1% TFA over 40 min at 3.0 mL/minute)

dx.doi.org/10.1021/bc300239a | *Bioconjugate Chem.* 2012, 23, 1387−1395

while monitoring with a Waters 2487 Dual λ absorbance detector set to 254, 300, 411, or 441 nm. Peptide derivatives were quantified spectrophotometrically by measuring the absorbance of Fmoc ((1:4) piperidine: DMF) or fluorescein (0.1 M NaOH) using a Varian 50 Bio UV−visible spectrophotometer. Binding affinity assays measured absorbance values using a Molecular Devices Spectra Max M5 plate reader. Confocal experiments were analyzed with an Olympus FV1000 laser confocal scanning microscope.

Synthesis of Unsubstituted Aziridine-Aldehyde (18). The unsubstituted aziridine-aldehyde (**18**) was synthesized as previously reported in our lab.[1,20] Briefly, 10 g (95 mmol) of L-serine was esterified to a serine propyl ester HCl salt (**16**) using 200 mL 1-propanol and 7.7 mL (106 mmol) $SOCl_2$. This reaction yielded 16.77 g (91.2 mmol) of precursor (96% yield). The identity was confirmed with ^{1}H NMR. ^{1}H NMR ($CDCl_3$, 400 MHz): δ 0.90 (t, J = 7.4 Hz, 3H), 1.62 (m, 2H), 3.51 (t, J = 4.1 Hz, 1H), 3.68 (dd, J = 10.9, 5.5 Hz, 1H), 3.76 (dd, J = 10.7, 4.0 Hz, 1H), 4.05 (t, J = 6.6 Hz, 2H).

The HCl salt (**16**) was converted to the free base (13.37 g or 90.9 mmol) using NH_4OH. A Mitsonobu reaction was performed using 23.85 g (90.9 mmol) of PPh_3 and 17.96 mL (90.9 mmol) of DIAD in anhydrous DCM at −10 °C for 3 h and at room temperature for 18 h. The workup required Et_2O precipitation to remove the white PPh_3O byproduct and a Kugelrohr apparatus (heated to 86 °C) to distill the aziridine propyl ester (**17**). This gave a 4.44 g (34.4 mmol) sample of this precursor (38% yield). The identity was confirmed with ^{1}H NMR. ^{1}H NMR ($CDCl_3$, 400 MHz): δ 0.92 (t, J = 7.4 Hz, 3H), 1.22 (m, 3H), 1.65 (m, 2H), 1.82 (d, J = 4.6 Hz, 1H), 1.96 (s, 1H), 2.49 (s, 1H), 4.08 (m, 2H).

The aziridine propyl ester (**17**) (2.0 g or 15.5 mmol) was reduced with 38.8 mL (38.8 mmol) of DIBAL (1.0 M in toluene) at −78 °C for 4.5 h. The reaction was quenched using MeOH after 2 h. Gelation was initiated with sat. $Na_2SO_{4\ (aq)}$ after 1 h and 45 min. The gel was filtered and washed with MeOH to give 532 mg (7.44 mmol) of the unsubstituted aziridine aldehyde dimer (**18**) (48% yield). Mass spectrometry was used to identify the product (ESI-MS: 143.1 (M+1) m/z). TLC was performed using acetonitrile/water (4:1) and showed an R_f = 0.4 (lit. R_f = 0.32).[1,20] $KMnO_4$ staining did not reveal any byproducts.

Manual Linear Peptide Synthesis. The linear peptides PRGDA (**1**), PRGDAA (**2**), PRDGA (**3**), PRGDK (**19**), and RGD (**20**) were synthesized on the solid-phase with 2-chlorotrityl chloride resin (loading ∼1.5 mmol/g) using standard Fmoc-chemistry. The amino acids Arg, Asp, and Lys had side chains protected by Pbf, OtBu, and Boc, respectively. Amide coupling of Fmoc-protected amino acids (3 equiv) was achieved after 2 h using HBTU (3 equiv) in (1:1) DCM/DMF containing 5% DIPEA (v/v). Resin capping was performed using 1-acetylimidazole (3 equiv) in a solution of (1:1) DCM/DMF containing 5% (v/v) DIPEA. Peptides were cleaved from the resin using (1:2:97) TFA/TIS/DCM after 2 h. Peptides were synthesized on a 250−550 μmol scale.

Aziridine-Driven Cyclization. The peptides PR(Pbf)GD(OtBu)A (**1**), PR(Pbf)GD(OtBu)AA (**2**), and PR(Pbf)D(OtBu)GA (**3**) were cleaved from the 2-chlorotrityl chloride resin as described and the N-terminal Fmoc was removed using standard piperidine cleavage. The peptides were precipitated from a minimal volume of DMF using cold Et_2O seven times. These peptides (10 μmol) were cyclized by the aziridine aldehyde-driven reaction[1,20] using 2.5 equiv of the unsubstituted aziridine-aldehyde dimer (**18**) and 3.5 equiv of *tert*-butyl isocyanide in TFE. The progress of cyclization reactions were assessed using HPLC-MS monitoring by integrating UV−vis spectra scanned at 254 nm. After 17−19 h, these cyclization reactions produced the desired macrocycles containing aziridine rings with the sequences PR(Pbf)GD(OtBu)A (**4**), PR(Pbf)GD(OtBu)AA (**5**), and PR(Pbf)D(OtBu)GA (**6**) where yields were estimated at ∼47%, ∼38%, and ∼43%, respectively. Mass spectrometry showed the production of **4** (ESI-MS: 960 (M+1) m/z), **5** (ESI-MS: 1031 (M+1) m/z), and **6** (ESI-MS: 960 (M+1) m/z). The reaction mixtures were precipitated using Et_2O. The crude mixtures were dried with a speed-vac and were stored at −20 °C.

Aziridine Ring-Opening with Cysteamine. The reaction crudes from the previous aziridine aldehyde-driven cyclization were dissolved in $CHCl_3$. Cysteamine was dissolved in DMSO to make a 3 mg/μL stock solution, while zinc chloride was dissolved in (95:5) $CHCl_3$/DMF to make a 0.1 mg/μL stock solution. Cysteamine and zinc chloride was added to the $CHCl_3$ solution containing the peptide crude. The molar ratio of peptide/cysteamine/zinc chloride was 1:3:1. The progress of this aziridine ring-opening reaction was assessed using HPLC-MS monitoring as described. Once the starting material was consumed, the reaction mixture was dried using a speed-vac. The crude was dissolved in a minimal volume of DMSO and was purified using a prep-HPLC. This gave the cysteamine-modified macrocycles with the sequences PR(Pbf)GD(OtBu)A (**7**), PR(Pbf)GD(OtBu)AA (**8**), and PR(Pbf)D(OtBu)GA (**9**) with yields of ∼23%, ∼33%, and ∼5%, respectively. The identity and purity of each product was confirmed using HPLC-MS (Figure S1, S2, and S3). Mass spectrometry showed the isolation of **7** (ESI-MS: 1037 (M+1) m/z), **8** (ESI-MS: 1108 (M+1) m/z), and **9** (ESI-MS: 1037 (M+1) m/z).

Amide Cyclization. The linear PR(Pbf)GD(OtBu)K(Boc) peptide (**19**) was cleaved from the 2-chlorotrityl chloride resin and the Fmoc-protecting group was removed as described. The NH-PR(Pbf)GD(OtBu)K(Boc)-COOH peptide (15 μmol) was cyclized using HBTU (1 equiv) and HOBt (1 equiv) while dissolved in 25 mL of DMF (1.76 mM) with 2.3% DIPEA (v/v). Reaction progress was monitored with HPLC-MS as described. The starting material was consumed within 20 h. The solution was aliquoted to 1.5 mL Eppendorf tubes and dried with a speed-vac. The dried product (**21**) was precipitated with DMF and Et_2O as described and dried with a speed-vac. The identity and purity of the product was confirmed using HPLC-MS (Figure S4). Mass spectrometry showed the product **21** (ESI-MS: 963 (M+1) m/z).

Fluorescein Conjugation. Fluorescein-NHS (1.5 equiv) was conjugated to the cysteamine-modified macrocycles in DMF containing 4% DIPEA (v/v) within 30 min. This reaction gave the side-chain protected fluorescein labeled macrocycles with the sequences PR(Pbf)GD(OtBu)A (**10**), PR(Pbf)GD(OtBu)AA (**11**), and PR(Pbf)D(OtBu)GA (**12**). ESI-MS(+) showed the production of **10** (ESI-MS: 1395 (M+1) m/z), **11** (ESI-MS: 1466 (M+1) m/z), and **12** (ESI-MS: 1395 (M+1) m/z). The Pbf and OtBu protecting groups were removed using TFA for 2 h. This side-chain deprotection step gave the final fluorescein-labeled macrocycles cPRGDA (**13**), cPRGDAA (**14**), and cPRDGA (**15**). These solutions were precipitated with Et_2O and purified using a prep-HPLC using the described method while detecting products with the 254 and 441 nm absorbance channels. HPLC-MS was used to determine the purity (>95% pure) and to confirm the identity

of each product (Figure S5, S6, and S7). Mass spectrometry showed the isolation of **13** (ESI-MS: 1087 (M+1) m/z), **14** (ESI-MS: 1158 (M+1) m/z), and **15** (ESI-MS: 1087 (M+1) m/z). The peptides were then quantified spectrophotometrically.

The Pbf, OtBu, and Boc protecting groups were removed from amide-cyclized PR(Pbf)GD(OtBu)K(Boc) peptide (**21**) using (95:5) TFA/DCM after 2 h. The production of the side-chain deprotected amide-cyclized PRGDK (**22**) was confirmed by mass spectrometry (ESI-MS: found 550 m/z). Fluorescein-NHS (1.3 equiv) was conjugated to the ε-NH_2 of Lys residue of the macrocycle (**22**) (7.5 μmol) in DMF containing 2.5% DIPEA (v/v) within 30 min. This solution was precipitated with Et_2O and purified using a prep-HPLC using the described method while detecting product with the 254 and 441 nm absorbance channels. HPLC-MS was used to determine the purity (>95% pure) and to confirm the identity of this fluorescein-labeled cyclic peptide amide-cPRGDK (**23**) (Figure S8). Mass spectrometry showed the isolation of amide-cPRGDK (**23**) (ESI-MS: 913 (M+1) m/z). The peptide was then quantified spectrophotometrically.

DOTA Conjugation. DOTA-NHS (3.3 equiv) was conjugated to the side-chain protected cysteamine-modified PR(Pbf)GD(OtBu)A macrocycle (**7**) (0.2 μmol or 1 equiv) in 50 μL of DMF containing 6% DIPEA (v/v) within 1 h. The crude was purified by prep-HPLC as described while detecting the product using a 254 nm absorbance channel. HPLC-MS was used to determine the purity (>90% pure) and to confirm the identity of the product (Figure S9). Mass spectrometry showed the production of cPRGDA-DOTA (**24**) (ESI-MS: 1423 (M^+) m/z).

Pyropheophorbide *a* Conjugation. Pyro-NHS (2 equiv)[19] was conjugated to the side chain-protected cysteamine-modified cPR(Pbf)GD(OtBu)A (**7**) (0.4 μmol or 1 equiv) in 70 μL of DMF containing 4% DIPEA (v/v) within 2 h. The crude was purified by prep-HPLC as described while detecting the product using 254 and 411 nm absorbance channels. HPLC-MS was used to determine the purity (>95% pure) and to confirm the identity of the product (Figure S10). Mass spectrometry showed the production of cPRGDA-Pyro (**25**) (ESI-MS: 1553 (M^+) m/z).

Computer Modeling. The cPRGDA (**13**) and cPRGDAA (**14**) peptides, as well as the amide-cPRGDK (**23**) peptide, were modeled using the Monte Carlo Multiple Minima (MCMM) algorithms implemented in *Macromodel*[21] using the OPLS2005 force field[22] and a Generalized-Born/Surface-Area (GB/SA) water model.[23] During this simulation, torsion angles of the macrocycles were varied randomly using a Monte Carlo procedure[24] and the conformational states were selected based on the Metropolis algorithm[25] according to the Boltzmann probabilities for each state based on its internal energy. We performed 1 000 000 steps of Monte Carlo sampling using 100 steps per each rotatable bond with retention of unique conformers. A 21 kJ/mol energy window was applied to discard high-energy conformers and we used a 0.5 Å maximum atom deviation cutoff to discard redundant conformers. An average structure was calculated for each peptide from their respective conformer families using *Macromodel*. Docking of cPRGDA, the N^{ε}-lysine-acetylated amide-cPRGDK and the highly studied cRGDf(N-Me)V peptide with the extracellular $\alpha_V\beta_3$ integrin protein (PDB entry 1L5G)[26] was performed using *Glide 5.7* (Schrodinger Inc.). The average ligand conformations used in the docking studies were obtained from the conformational search detailed above.

Binding Affinity. U87 glioblastoma cells were cultured in Corning 75 cm^2 flasks in MEM containing 10% FBS. Cells were allowed to reach ~70% confluence and were treated with trypsin containing EDTA for 15 min. The U87 cells (5×10^4 cells/well) were coincubated with various concentrations of the fluorescein-labeled cyclic peptides cPRGDA (**13**), cPRGDAA (**14**), cPRDGA (**15**), and amide-cPRGDK (**23**) (0−20 μM) on human vitronectin-coated 96-well plates (R&D Systems, Minneapolis, MN, USA) for 1 h at 37 °C. After washing, U87 cells were stained with 0.5% (v/v) crystal violet. The wells were washed and the absorbencies were measured at 627 nm in 0.1 M HCl using a plate reader.[27] IC_{50} values were calculated using Graph-Pad *PRISM* by a log(inhibitor) vs response three parameter nonlinear regression from $x-y$ scatter plots (bottom constraint at 18) of all normalized values from 3 independent experiments.

Confocal Microscopy. The U87 glioblastoma cells served as a positive cell line for the $\alpha_V\beta_3$ integrin receptor, while HT-29 colon cancer cells served as a negative cell line since these express low levels of the human $\alpha_V\beta_3$ integrin receptor.[28] U87 cells and HT-29 cells were cultured in Corning 75 cm^2 flasks in MEM and DMEM media, respectively, containing 10% FBS. Cells were allowed to reach ~70% confluence and were treated with trypsin containing EDTA for 15 min. Cells (3×10^4 cells/well) were transferred to 8-well Lab-Tek 155411 #1.0 borosilicate plates and were incubated with 10 μM solutions of fluorescein-labeled cPRGDA (**13**) and cPRGDAA (**14**) (0.5% v/v DMSO in media) for 2 h at 37 °C. The fluorescein-labeled cPRDGA scramble peptide (**15**) was used as a negative control, while the fluorescein-labeled amide-cPRGDK peptide (**23**) served as a positive control. The targeting specificity of cPRGDA and cPRGDAA was investigated by blocking the $\alpha_V\beta_3$ integrin receptor of U87 cells with a 50-fold molar excess of the linear RGD peptide (**20**). Laser confocal scanning microscopy was then performed with excitation wavelength of 488 nm using 5% laser power, PMT voltage of 760 V, and 120 μM pinhole diameter.

RESULTS

Aziridine Ring-Opening and Fluorophore/Chelator Conjugation. The general synthetic strategy included four distinct steps: (1) aziridine aldehyde-driven cyclization of linear peptides, (2) aziridine ring-opening by a heterobifunctional linker, (3) dye conjugation, and (4) full deprotection of amino acid side chains. The linear peptides with the sequences PR(Pbf)GD(OtBu)A, PR(Pbf)GD(OtBu)AA, and PR(Pbf)D-(OtBu)GA were successfully cyclized by our recently reported aziridine aldehyde-driven cyclization chemistry. Cysteamine was attached to these macrocycles by zinc chloride-catalyzed aziridine ring-opening. The cysteamine-modified macrocycles (**7**, **8**, and **9**) were then conjugated to fluorescein-NHS using DIPEA in DMF in 30 min (**10**, **11**, and **12**). The side-chain protecting groups were then removed using TFA to produce cPRGDA (**13**), cPRGDAA (**14**), and cPRDGA (**15**). We also extended the exocylic conjugation of the cysteamine-modified macrocycles to other reporters. The radiometal chelator DOTA was efficiently conjugated to the free amine of cysteamine on the macrocycle PR(Pbf)GD(OtBu)A (**7**) using NHS-chemistry (**24**). The multimodal fluorescent dye, photosensitizer, and radiometal chelator pyropheophorbide *a* was similarly con-

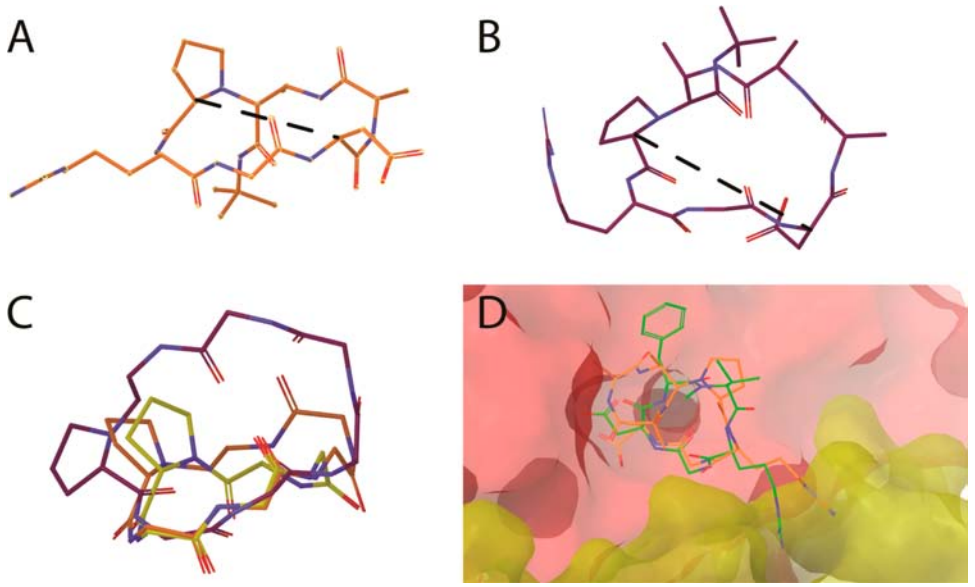


Figure 1. 3D models of (A) cPRGDA (orange) and (B) cPRGDAA (purple) separately showing Pro-C$^{\alpha}$–Asp-C$^{\alpha}$ vectors and (C) overlaid with amide-cPRGDK (yellow). The cPRGDA peptide (orange) was overlaid with cRGDf(N-Me)V (green) in a docked configuration with the $\alpha_V\beta_3$ protein to illustrate structural similarity at the RGD-motif.

jugated to the free amine of cysteamine on the macrocycle PR(Pbf)GD(OtBu)A (**7**) using NHS-chemistry (**25**).

Computer Modeling. *Macromodel* was used to generate conformational ensembles of cPRGDA (**13**), cPRGDAA (**14**), and amide-cPRGDK (**23**). The average conformations of cPRGDA (Figure 1A), cPRGDAA (Figure 1B), and the amide-cPRGDK were analyzed to investigate suitability for binding to the $\alpha_V\beta_3$ integrin receptor. A preliminary study indicated that the pentapeptides, cPRGDA and amide-cPRGDK, preferred a backbone conformation that overlaid well with the RGD motif of cRGDf(N-Me)V (bound to the extracellular $\alpha_V\beta_3$ integrin protein (PDB: 1L5G)[26]) (Figure 1D), while the hexapeptide cPRGDAA showed significant backbone deviation in this area (Figure 1C). Conformational searches generated between 233 and 368 conformers for each of these macrocycles from which the mean Pro-C$^{\alpha}$–Asp-C$^{\alpha}$ distances within cyclic peptides cPRGDA, cPRGDAA, and amide-cPRGDK (Table 1) were

Table 1. Calculated Pro-C$^{\alpha}$–Asp-C$^{\alpha}$ Distances of Macrocycles Using Averaged Conformer Geometries

peptide	Pro-C$^{\alpha}$–Asp-C$^{\alpha}$ distance (Å)	N^a
amide-cPRGDK	5.24 ± 0.15	368
cPRGDA	6.11 ± 0.17	264
cPRGDAA	8.37 ± 0.24	233

[a]Number of generated conformers.

calculated. Both cPRGDA and cPRGDAA contain a γ-turn-like backbone conformation similar to cRGDf(N-Me)V at the RGD motif (Arg-C$^{\alpha}$–Asp-C$^{\alpha}$ < 7 Å). However, the cycle topology is significantly different when the residue preceding the RGD motif is included in the backbone comparison. The Val-C$^{\alpha}$-Asp-C$^{\alpha}$ distance was measured at 6.9 Å in the crystal structure of cRGDf(N-Me)V which is similar to the distance calculated for Pro-C$^{\alpha}$–Asp-C$^{\alpha}$ in cPRGDA (6.1 Å). The Pro-C$^{\alpha}$–Asp-C$^{\alpha}$ distance in cPRGDK is shorter (5.2 Å) and is much longer in cPRGDAA (8.7 Å). This suggests that differing peptide backbone topology could account for the enhanced binding of the RGD-motif of cPRGDA to the $\alpha_V\beta_3$ integrin binding site compared to the larger cPRGDAA.

Ligand docking to the extracellular $\alpha_V\beta_3$ integrin protein showed that cPRGDA and the N$^{\varepsilon}$-acetyl-lysine analogue of amide-cPRGDK possessed similar stabilizing binding interactions to cRGDf(N-Me)V from the crystal structure. The Lys residue of amide-cPRGDK (**22**) was N$^{\varepsilon}$-acetylated in its docking study to mimic the presence of fluorescein in amide-cPRGDK (**23**). It was found that cPRGDA and cRGDf(N-Me)V docked to the $\alpha_V\beta_3$ integrin protein through their respective Arg residues to Asp150 and Asp218 of $\alpha_V\beta_3$ and through their Asp residues to Mn1 (Figure 2A). The N$^{\varepsilon}$-acetyl-

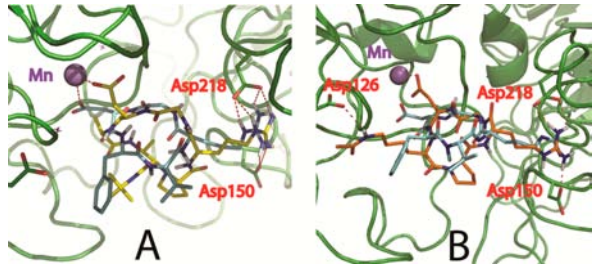


Figure 2. 3D modeling showing the comparative docking interactions of (A) cPRGDA (yellow) and cRGDf(N-Me)V (blue) and (B) amide-cPRGDK (orange) and cRGDf(N-Me)V (blue) with the extracellular binding regions of the $\alpha_V\beta_3$ integrin receptor.

lysine of the amide-cPRGDK analogue formed contacts to the same residues and also to Asp126 through the amide proton of the N$^{\varepsilon}$-acetyl-lysine residue (Figure 2B). Heavy atom distances between the respective docking regions of the $\alpha_V\beta_3$ integrin protein to cPRGDA, amide-cPRGDK, and cRGDf(N-Me)V were calculated (Table 2). These measurements showed that, while cPRGDA and cRGDf(N-Me)V used all three nitrogen atoms of their respective Arg residues for optimal binding to Asp150 and Asp218, the binding mode of the Arg of amide-cPRGDK is inferior. This observed binding mode uses two of

dx.doi.org/10.1021/bc300239a | *Bioconjugate Chem.* 2012, 23, 1387–1395

Table 2. Calculated Heavy Atom Distances between Macrocycles and the Extracellular Binding Regions of the $\alpha_V\beta_3$ Integrin Receptor

peptide	ligand atom	receptor atom	heavy atom distance (Å)
cPRGDA	Asp-OD	Mn1	2.1
	Arg-NE	D218-OD1	3.1
	Arg-NZ1	D218-OD2	3.1
	Arg-NZ2	D150-OD	3.2
amide-cPRGDK	Asp-OD	Mn1	2.1
	Arg-NZ1	D218-OD1	3.1
	Arg-NZ1	D218-OD2	2.9
	Arg-NZ2	D150-OD	3.0
	Ac-Lys-NZ	D126-OD	3.6
cRGDf(N-Me)V	Asp-OD	Mn1	2.7
	Arg-NE	D218-OD1	2.9
	Arg-NZ1	D218-OD2	2.8
	Arg-NZ2	D150-OD	3.3

its three available nitrogen atoms to bind to the dual aspartate motif of the integrin.

Binding Affinity. With computational insights in hand, the binding affinity of each fluorescein-labeled RGD-macrocycle for the $\alpha_V\beta_3$ integrin receptor was investigated experimentally using competitive cell adhesion assays. The peptide concentration-dependent displacement of U87 cell adherence from vitronectin-coated wells was used to calculate the respective IC_{50} values for fluorescein-labeled macrocycles cPRGDA (**13**), cPRGDAA (**14**), and amide-cPRGDK (**23**). The IC_{50} value of these RGD-containing macrocycles was on the same order (low μM) as previously reported amide-cyclized RGD sequences analyzed by this competitive cell adhesion method (Table 3).[27]

Table 3. Cell Adhesion Competition Assay Summary of IC_{50} Values of Fluorescein-Labeled Macrocycles

peptide	log IC_{50}[a] (M)	SE[b] (log M)	IC_{50}[c] (μM)
amide-cPRGDK	−5.114	±0.2	7.7
cPRGDA	−5.381	±0.2	4.2*
cPRGDAA	−4.955	±0.06	11.11*
cPRDGA	n.d.[d]	n.d.[d]	-

[a]Calculated in Graph-Pad *PRISM* using a log(inhibitor) vs response, three parameter nonlinear regression from an $x-y$ scatter plot (bottom constraint at 18) of all normalized values from 3 independent experiments. [b]Standard error calculated for log IC_{50} presented as log of molar concentrations. [c]Transformed from log IC_{50}. [d]n.d., Not determined. *Significantly different using a two-tailed unpaired t test ($p < 0.05$).

Though cRGDf(N-Me)V was not tested in this study, a review by Rüegg et al. reported that Cilengitide displays a similar $\alpha_V\beta_3$ integrin binding affinity (IC_{50} ~1 μM) to displace $\alpha_V\beta_3$ integrin-expressing cells from adhering to vitronectin.[29] The IC_{50} of cPRGDA (4.2 μM) was significantly lower compared to cPRGDAA (11.1 μM, $p < 0.05$) (Table 3). These differential IC_{50} values were attributed to modulated geometries as a result of peptide length and the presence of the constrained RGD motif in cPRGDA. It was also found that there was no significant difference in the IC_{50} of cPRGDA compared to amide-cPRGDK.

Confocal Microscopy. Confocal microscopy investigated the specific binding of the fluorescein-labeled cPRGDA (**13**) and cPRGDAA (**14**) peptides to the human $\alpha_V\beta_3$ integrin receptor of U87 glioblastoma cells. These studies showed that cPRGDA, cPRGDAA, and the amide-cPRGDK (**23**) each bound to U87 cells (Figure 3A,C,D) but none bound to HT-29 cells (Figure 3G,I,J). The cPRDGA scramble control (**15**) showed nonspecific binding to U87 cells (Figure 3B) but not to HT-29 cells (Figure 3H). The targeting specificity of cPRGDA and cPRGDAA was investigated by blocking the $\alpha_V\beta_3$ integrin receptor of U87 cells with a 50-fold molar excess of the linear RGD peptide (**20**). This blocking reduced specific $\alpha_V\beta_3$ integrin binding for both RGD-containing macrocycles, but the remaining fluorescence signals suggested additional nonspecific binding (Figure 3E,F).

DISCUSSION

The aziridine aldehyde-driven cyclization method has been successfully developed to synthesize functional $\alpha_V\beta_3$ integrin-targeting fluorescein-labeled macrocycles. We were able to show that increasing the peptide length (from five to six residues) and switching the Gly and Asp residues in the middle of the sequence did not affect the aziridine aldehyde-driven cyclization reaction. We used a simple zinc chloride salt to catalyze the sulfhydryl-driven aziridine ring-opening of the exocyclic unsubstituted aziridine handle of our macrocycles by the heterobifunctional linker cysteamine. The versatility of this synthetic strategy was illustrated by conjugating the common radiometal chelator DOTA and the multimodal fluorescent dye/radiometal chelator/photosensitizer pyropheophorbide *a* using NHS-chemistry. This conjugation could be easily adapted to a wide variety of other fluorescent dyes, radiometal chelators, or extended linkers using conventional amide-coupling, the described NHS-chemistry, or by analogous ITC-chemistry.

Aziridine aldehyde-driven macrocyclization reactions showed clear advantages over conventional end-to-end amide cyclization. The former reactions were performed at a much higher

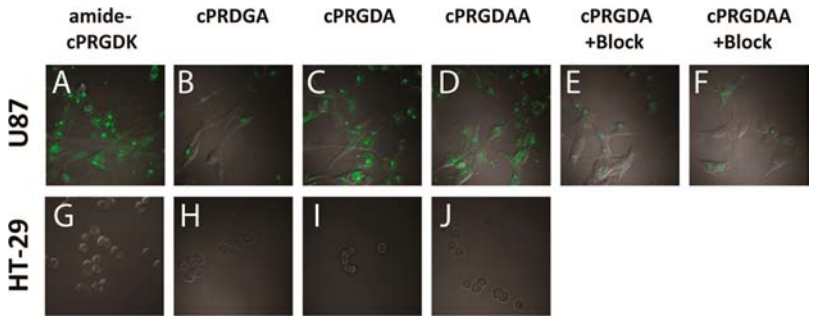


Figure 3. Confocal microscopy fluorescence images merged with DIC showing the differential binding of fluorescein-labeled macrocycles to U87 ($\alpha_V\beta_3$ +) (A–F) and HT-29 ($\alpha_V\beta_3$ −) cells (G–J).

dx.doi.org/10.1021/bc300239a | *Bioconjugate Chem.* 2012, 23, 1387–1395

concentration (50 mM in TFE) wherein no noticeable polymerization was observed. The amide cyclization required high dilution (0.6 mM in DMF) to ensure that amide coupling was predominantly due to intramolecular bonding of the free N- and C-termini within each monomeric linear PRGDK peptide.[30] In addition, the conventional amide cyclization reactions require an additional amino acid to provide a thiol, carboxylic acid, or primary amine for subsequent functional group conjugations. These amino acids should be specially protected and selectively deprotected for functional group conjugation.[7−10] On the contrary; the aziridine aldehyde-driven macrocyclization offers a free amine for conjugation once cysteamine has become bonded to the macrocycle by aziridine ring-opening. We are thereby able to avoid the challenges of protection/deprotection often required after amide cyclization. Finally, after the aziridine ring-opening of the aziridine aldehyde-cyclized macrocycles, the space between the binding motif of the macrocycle and the conjugation site may have allowed the desired receptor binding to proceed without imposing significant steric hindrance.

Analysis of the X-ray crystal structure of integrin-bound cRGDf(N-Me)V shows a significant difference between it and the solution-phase structure proposed by Kessler et al.[26] Cyclic pentapeptides with (LDLDL) relative stereochemistry often adopt a βII′/γ turn architecture in solution. In the case of cRGDf(N-Me)V, Gly occupies the i+1 position of the γ turn while D-Phe occupies the i+1 position of the βII′ turn. The X-ray crystal structure of integrin-bound cRGDf(N-Me)V shows that the γ turn is maintained in the bound state, with a 6.4 Å separation between the Arg and Asp α carbons and a 8.7 Å distance separating the Arg and Asp β carbons. cPRGDA docked to $\alpha_V\beta_3$ and shows that it adopts the same γ turn conformation as the docked cRGDf(N-Me)V, which is critical for the polar side chains of Arg and Asp to engage in receptor binding. The Arg-Asp intercarbon (C^α and C^β) distances of cPRGDA were similar to those of cRGDf(N-Me)V where the Arg-Asp (C^α-C^α) distance is 6.0 Å and the Arg-Asp (C^β-C^β) distance is 8.7 Å. Kessler et al. have shown that the identity of the remaining residues in the peptide are important for structural rigidity, but due to the fact that residues not in the RGD motif do not make contact with the integrin surface, ample room exists to splice different residues and functional handles into the macrocycle sequence,[31] hence the observed binding affinity for cPRGDA.

Computer modeling data showed that cPRGDA contained a similar backbone conformation at the RGD motif to cRGDf(N-Me)V, while cPRGDAA differs significantly. This suggested that the stabilized RGD motif within cPRGDA would contribute to a better binding affinity for the $\alpha_V\beta_3$ integrin receptor compared to cPRGDAA. Competitive cell adhesion assays experimentally showed that the IC_{50} of cPRGDA for $\alpha_V\beta_3$ integrin-overexpressing U87 glioblastoma cells was significantly lower compared to cPRGDAA. This may be explained by the backbone shape and macrocycle ring size differences between the two peptides. It is possible that other RGD-containing pentapeptide sequences cyclized by the aziridine aldehyde-driven reaction may also contain this desired turn at the RGD motif. Nevertheless, confocal analysis showed that both the fluorescein-labeled cPRGDA and cPRGDAA macrocycles could successfully bind to U87 cells for in vitro fluorescence cancer imaging while avoiding binding to HT-29 cells that express low levels of the $\alpha_V\beta_3$ integrin receptor.

The amide-cPRGDK also fulfills the α carbon requirement for a γ-turn-like structure, having a distance of 4.6 Å between the Arg and Asp α carbons. However, the β carbons are much closer than in either PRGDA or cRGDf(N-Me)V where a distance of 7.2 Å separates them. This means that the backbone dihedral angles are significantly different for amide-cPRGDK, which could contribute to a reduction in affinity compared to cRGDf(N-Me)V despite its similar ring size.

Computational docking studies identified the binding mode of cPRGDA and the N^ε-acetyl-lysine analogue of amide-cPRGDK with the extracellular $\alpha_V\beta_3$ integrin receptor. The Lys of amide-cPRGDK was acetylated to mimic the hindrance imposed by fluorescein at the Lys residue in amide-cPRGDK (**23**). We found that both macrocycles interacted with the Asp150 and Asp218 residues of the protein through their respective Arg residues, much the same as cRGDf(N-Me)V. Interestingly, amide-cPRGDK only used two of its three available Arg nitrogen atoms to bind to Asp150 and Asp218, while cPRGDA and cRGDf(N-Me)V used all three nitrogen atoms of their respective Arg residues for optimal integrin binding. In addition, the N^ε-acetyl-lysine residue of amide-cPRGDK interacted with Asp126. Therefore, it was not obvious which binding interaction would have the greatest contribution to the binding affinity of cPRGDA and amide-cPRGDK. Competitive cell adhesion assays experimentally showed that the IC_{50} of cPRGDA for U87 cells was not significantly different compared to amide-cPRGDK. This suggests that the aforementioned difference observed in the described docking studies compensated to create geometries that allowed similar in vitro binding to the $\alpha_V\beta_3$ integrin receptor on U87 cells.

The chemical structures of the cPRGDA, cPRGDAA, and cPRDGA macrocycles are inherently different from analogous peptide macrocycles generated through backbone amide coupling. The aziridine aldehyde-driven cyclization and the subsequent aziridine ring-opening reaction result in the formation of an sp^3-hybridized carbon atom at the non-amino acid portion of the macrocycles. The described geometric and binding affinity comparisons between cPRGDA and amide-cPRGDK are similar to the investigations published by Geyer et al. in 1994.[32] They developed the cyclic peptide cRGDfψ-[CH_2−NH]V that contained a reduced amide bond that imposed geometric differences when compared to the parent cRGDfV, whereas with cRGDfψ[CH_2−NH]V, they found that a β-turn forms between the Val and Asp residues (a γ turn lies between Arg and Asp in potent RGD cyclic peptides). They also found that the structural perturbation caused by the introduction of a reduced amide bond into a cyclic RGD peptide caused a significant drop in activity. This suggests that RGD macrocycles containing only amide bonds would stabilize geometries that result in superior $\alpha_V\beta_3$ integrin binding affinities compared to analogues that do not contain a fully amide-bonded backbone. Interestingly, the binding affinity of cPRGDA to the $\alpha_V\beta_3$ integrin receptor was not significantly different compared to amide-cPRGDK. Though the amino acid residues of cPRGDA and amide-cPRGDK were not identical, it could be inferred that the sp^3 carbon-containing macrocycles generated through aziridine aldehyde-driven cyclization and subsequent aziridine ring-opening may not hinder the binding affinity of cyclic RGD sequences to the same extent as the aforementioned study when compared to analogues that contain only amide bonds.

We have shown that the aziridine aldehyde-driven cyclization modulated the geometry of similar five- and six-membered

RGD macrocycles and was responsible for tuning the binding affinity of cPRGDA and cPRGDAA for the $\alpha_V\beta_3$ integrin receptor on U87 cancer cells. It is possible that the geometry-modulating ability of this macrocyclization reaction can create other RGD-based macrocycles that have varying binding affinities and also varying specificities to different integrin subtypes that are also overexpressed by cancers. This geometry-modulating ability could also be extended to other cancer biomarker-targeting peptide sequences. Using our current modification strategy, these new potential macrocycles could then be conjugated to a variety of functionalities for additional imaging and therapeutic applications.

CONCLUSION

We have created a versatile strategy for conjugating a common fluorescent dye to RGD-containing $\alpha_V\beta_3$ integrin receptor-targeting macrocycles which were cyclized by the aziridine aldehyde-driven reaction. This same general method was used to conjugate the commonly used radiometal chelator DOTA and the multifunctional porphyrin pyropheophorbide to a novel RGD-containing macrocycle to display the versatility of our conjugation strategy. Computer modeling studies showed that the aziridine aldehyde-driven cyclization modulated the geometry of similar five and six amino acid-containing RGD macrocycles. This cyclization chemistry was responsible for stabilizing a γ turn at the RGD motif of cPRGDA. Though each fluorescein-labeled RGD-containing peptide specifically targeted the $\alpha_V\beta_3$ integrin receptor of U87 glioblastoma cells in vitro, it is likely that a stabilized γ turn and the significantly shorter Pro-C^{α}-Asp-C^{α} distance were responsible for improving the binding affinity of cPRGDA compared to cPRGDAA. Future studies should continue using pentapeptides to constrain the RGD motif into an active conformation and replace the C-terminal Ala with other natural or synthetic L- or D-amino acid residues to further improve $\alpha_V\beta_3$ integrin binding or possibly to selectively target different integrin subtypes. Additional studies could use the aziridine aldehyde-driven cyclization chemistry to modulate the geometry of other cancer biomarker-targeting sequences and utilize the described modification strategy for a variety of cancer imaging and therapeutic applications.

ASSOCIATED CONTENT

Supporting Information

HPLC-MS characterization spectra for all the modified macrocycles. This material is available free of charge via the Internet at http://pubs.acs.org.

AUTHOR INFORMATION

Corresponding Author

*Prof. Andrei K. Yudin: Tel. 416-946-5042; E-mail: ayudin@chem.utoronto.ca. Prof. Gang Zheng: Tel. 416-581-7666, Fax 416-581-7667, E-mail: gang.zheng@uhnres.utoronto.ca.

Notes

The authors declare no competing financial interest.

ACKNOWLEDGMENTS

G.Z. and A.Y. thanks NSERC and CIHR for financial support of this project. Support from Princess Margaret Hospital Foundation is also acknowledged.

REFERENCES

(1) Hili, R., Rai, V., and Yudin, A. K. (2010) Macrocyclization of linear peptides enabled by amphoteric molecules. *J. Am. Chem. Soc. 132*, 2889−2891.
(2) Rotstein, B. H., Mourtada, R., Kelley, S. O., and Yudin, A. K. (2011) Solvatochromic reagents for multicomponent reactions and their utility in the development of cell-permeable macrocyclic peptide vectors. *Chem.—Eur. J. 17* (44), 12257−12261.
(3) Rotstein, B. H., Winternheimer, D. J., Yin, L. M., Deber, C. M., and Yudin, A. K. (2012) Thioester-isocyanides: versatile reagents for the synthesis of cycle-tail peptides. *Chem. Commun. 48* (31), 3775−3777.
(4) Zhang, Q.-J., Lindquist, Y., Levitsky, V., and Masucci, M. G. (1996) Solvent exposed side chains of peptides bound to HLA A*1101 have similar effects on the reactivity of alloantibodies and specific TCR. *Int. Immunol. 8* (6), 927−938.
(5) Zhang, X., Xiong, Z., Wu, Y., Cai, W., Tseng, J. R., Gambhir, S. S., and Chen, X. (2006) Quantitative PET imaging of tumor integrin $\alpha_V\beta_3$ expression with ^{18}F-FRGD2. *J. Nucl. Med. 47*, 113−121.
(6) Ratcliffe, K. E., Fraser, H. M., Sellar, R., Rivier, J., and Millar, R. P. (2006) Bifunctional gonadotropin-releasing hormone antagonist-progesterone analogs with increased efficacy and duration of action. *Endocrinology 147* (1), 571−579.
(7) Isidro-Llobet, A., Álvarez, M., and Albericio, F. (2009) Amino acid-protecting groups. *Chem. Rev. 109*, 2455−2504.
(8) Kopple, K. D. (1972) Synthesis of cyclic peptides. *J. Pharm. Sci. 61* (9), 1345−1356.
(9) Harris, K. M., Flemer, S., Jr., and Hondal, R. J. (2007) Studies on deprotection of cysteine and selenocysteine side-chain protecting groups. *J. Pept. Sci. 13*, 81−93.
(10) Guzmán, F., Barberis, S., and Illanes, A. (2007) Peptide synthesis: Chemical or enzymatic. *Electron. J. Biotechnol. 10* (2), 279−314.
(11) Ye, T., and Chen, X. (2011) Integrin targeting for tumor optical imaging. *Theranostics 1*, 102−126.
(12) Ruoslahti, E. (1996) RGD and other recognition sequences for integrins. *Annu. Rev. Cell Dev. Biol. 12*, 697−715.
(13) Montet, X., Montet-Abou, K., Reynolds, F., Weissleder, R., and Josephson, L. (2006) Nanoparticle imaging of integrins on tumor cells. *Neoplasia 8* (3), 214−222.
(14) Liu, Z., Wang, F., and Chen, X. (2008) Integrin $\alpha_V\beta_3$-targeted cancer therapy. *Drug Dev. Res. 69*, 329−339.
(15) Zhou, Y., Chakraborty, S., and Liu, S. (2011) Radiolabeled cyclic RGD peptides as radiotracers for imaging tumors and thrombosis by SPECT. *Theranostics 1*, 58−82.
(16) Dechantsreiter, M. A., Planker, E., Mathä, B., Lohof, E., Hölzemann, G., Jonczyk, A., Goodman, S. L., and Kessler, H. (1999) *N*-Methylated cyclic RGD peptides as highly active and selective $\alpha_V\beta_3$ integrin antagonists. *J. Med. Chem. 42*, 3033−3040.
(17) Gilbert, M. R., Kuhn, J., Lamborn, K. R., Lieberman, F., Wen, P. Y., Mehta, M., Cloughesy, T., Lassman, A. B., DeAngelis, L. M., Chang, S., and Prados, M. (2012) Cilengitide in patients with recurrent glioblastoma: the results of NABTC 03−02, a phase II trial with measures of treatment delivery. *J. Neuro-Oncol. 106* (1), 147−153.
(18) Hariharan, S., Gustafson, D., Holden, S., McConkey, D., Davis, D., Morrow, M., Basche, M., Gore, L., Zang, C., O'Bryant, C. L., Baron, A., Gallemann, D., Colevas, D., and Eckhardt, S. G. (2007) Assessment of the biological and pharmacological effects of the $\alpha_V\beta_3$ and $\alpha_V\beta_5$ integrin receptor antagonist, cilengitide (EMD 121974), in patients with advanced solid tumors. *Ann. Oncol. 18*, 1400−1407.
(19) Zhang, M., Zhang, Z., Blessington, D., Li, H., Busch, T. M., Madrak, V., Miles, J., Chance, B., Glickson, J. D., and Zheng, G. (2003) Pyropheophorbide 2-deoxyglucosamide: A new photosensitizer targeting glucose transporters. *Bioconjugate Chem. 14*, 709−714.
(20) Rotstein, B. H., Rai, V., Hili, R., and Yudin, A. K. (2010) Synthesis of peptide macrocycles using unprotected amino aldehydes. *Nat. Prot. 5* (11), 1813−1822.
(21) Mohamadi, F., Richard, N. G. J., Guida, W. C., Liskamp, R., Lipton, M., Caufield, C., Chang, G., Hendrickson, T., and Still, W. C.

(1990) MacroModel - an Integrated software system for modeling organic and bioorganic molecules using molecular mechanics. *J. Comput. Chem. 11* (4), 440−467.
(22) Jorgensen, W. L., and Tirado-Rives, J. (2005) Potential energy functions for atomic-level simulations of water and organic and biomolecular systems. *Proc. Natl. Acad. Sci. U.S.A. 102* (19), 6665−6670.
(23) Tsui, V., and D., A. (2001) Case, theory and applications of the generalized Born solvation model in macromolecular simulations. *Biopolymers 56* (4), 275−291.
(24) Hastings, W. K. (1970) Monte-Carlo sampling methods using Markov chains and their applications. *Biometrika 57*, 97−109.
(25) Metropolis, N., Rosenbluth, A. W., Rosenbluth, M. N., Teller, A. H., and Teller, E. (1953) Equations of state calculations by fast computing machines. *J. Chem. Phys. 21* (6), 1087−1092.
(26) Xiong, J. P., Stehle, T., Zhang, R., Joachimiak, A., Frech, M., Goodman, S. L., and Arnaout, M. A. (2002) Crystal structure of the extracellular segment of integrin $\alpha_v\beta_3$ in complex with an Arg-Gly-Asp ligand. *Science 296*, 151−155.
(27) Wang, W., Wu, Q., Pasuelo, M., McMurray, J. S., and Li, C. (2005) Probing for integrin $\alpha_v\beta_3$ binding of RGD peptides using fluorescence polarization. *Bioconjugate Chem. 16*, 729−734.
(28) Liu, Z., Jia, B., Shi, J., Jin, X., Zhao, H., Li, F., Liu, S., and Wang, F. (2010) Tumor uptake of the RGD dimeric probe 99mTc-G3−2P4-RGD2 is correlated with integrin $\alpha_v\beta_3$ expressed on both tumor cells and neovasculature. *Bioconjugate Chem. 21*, 548−555.
(29) Rüegg, C., Hasmim, M., Lejeune, F. J., and Alghisi, G. C. (2006) Antiangiogenic peptides and proteins: From experimental tools to clinical drugs. *Biochim. Biophys. Acta 1765*, 155−177.
(30) Davies, J. S. (2003) The cyclization of peptides and depsipeptides. *J. Pept. Sci. 9*, 471−501.
(31) Pfaff, M., Tanglemann, K., Müller, B., Gurrath, M., Müller, G., Kessler, H., Timpl, R., and Engel, J. (1994) Selective recognition of cyclic RGD peptides of NMR defined conformation by $\alpha_{IIb}\beta_3$, $\alpha_v\beta_3$, and $\alpha_5\beta_1$ integrins. *J. Biol. Chem. 269* (32), 20232−20238.
(32) Geyer, A., Müller, G., and Kessler, H. (1994) Conformational analysis of a cyclic RGD peptide containing a ψ[CH2-NH] bond: A positional shift in backbone structure caused by a single dipeptide mimetic. *J. Am. Chem. Soc. 116*, 7735−7743.

Bioconjugate Chemistry

Article

pubs.acs.org/bc

Enzymatic Deglutathionylation to Generate Interleukin-4 Cysteine Muteins with Free Thiol

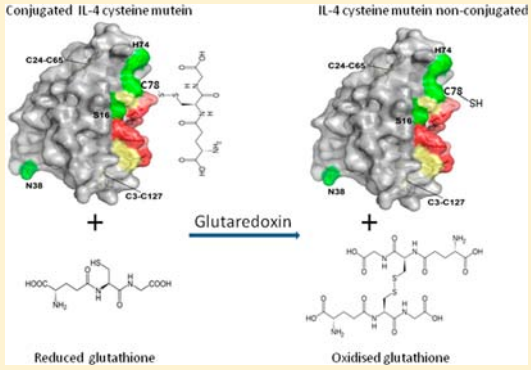
Viswanadham Duppatla,*[,†] Maja Gjorgjevikj,[†] Werner Schmitz,[†] Mathias Kottmair,[‡] Thomas D. Mueller,[‡] and Walter Sebald[†]

[†]Lehrstuhl für Physiologische Chemie II, Theodor-Boveri-Institut für Biowissenschaften (Biozentrum) der Universität Würzburg, Würzburg, Germany

[‡]Lehrstuhl für Botanik I-Molekulare Pflanzenphysiologie und Biophysik, Julius-von-Sachs-Institut für Biowissenschaften (Biozentrum) der Universität Würzburg, Würzburg, Germany

Supporting Information

ABSTRACT: Interleukin-4 (IL-4) is a prototypical regulator protein of the immune system that is crucial for the pathogenesis and maintenance of asthma and other atopic diseases. It, together with IL-13, uses the IL-4 receptor α chain (IL-4Rα) to signal into immune and other cells. An IL-4 mutein acting as a dual IL-4/IL-13 receptor antagonist is in clinical development. Here, it is described how IL-4 muteins containing a single engineered cysteine with a free thiol can be prepared and used for site-specific chemical modification. The muteins were initially expressed in *E. coli*, refolded, and purified, but not in a fully reduced nonconjugated form. Attempts to reduce the cysteine chemically failed because the native disulfide bonds of IL-4 were also reduced under similar conditions. Therefore, an enzymatic procedure was developed to reduce glutathionylated IL-4 cysteine muteins employing glutaredoxin and reduced glutathione. Cysteine muteins engineered at four different positions around the IL-4Rα binding site were enzymatically reduced at different rates. All muteins were prepared with free thiol in reasonable yield and were modified by *N*-ethylmaleimide (NEM) or maleimido-PEG. The effect on IL-4Rα binding of cysteine substitution and of the site-specific modification by glutathione, *N*-ethylmaleimide (NEM), or a branched 2.36 kDa poly(ethylene glycol) (PEG) will be discussed.



INTRODUCTION

Human Interleukin-4 (IL-4) is a differentiation factor of T- and B-lymphocytes and many other cells, such as eosinophiles, mast cells, endothelial cells, and fibroblasts.[1,2] IL-4 is particularly involved in the sensitization to allergens, in IgE synthesis, and, together with IL-13, in late-phase inflammatory reactions during allergies, eczema/atopic dermatitis, and asthma.[3] Some tumor cells use IL-4 as a survival factor to escape apoptosis.[4]

IL-4 signals through two types of single-span transmembrane receptors.[5,6] In type I, an IL-4 receptor α chain (IL-4Rα) is assembled with a common γ chain (γ_c); in type II, IL4-Rα is assembled with an IL-13 receptor α1 chain (IL-13Rα1). Type II is also used as the lone receptor by IL-13. Due to the role of IL-4 and IL-13 in the onset and progression of allergies and asthma, IL-4Rα has become a highly promising drug target, since it mediates both IL-4 and IL-13 responses.[7] An IL-4 double mutein containing amino acid substitutions R121D and Y124D (also known as IL4DM, Bay 16−9996, Pitrakinra, AER 001) with disrupted binding epitopes for γ_c and IL-13α1 is a high-affinity antagonist inhibiting IL-4 and IL-13 signals mediated by IL-4Rα.[8,9] It proved to be quite effective in a recent clinical trial for eosinophilic asthma.[10,11]

IL-4 is a secreted glycoprotein belonging to the short four-helix bundle cytokine family.[12] The crystal structures of the binary and ternary complexes of IL-4 with the ectodomains of the receptor chains have been determined.[13,14] The structure of the protein interfaces, together with a mutational and interaction analysis, shows that the high-affinity interaction between IL-4 and IL-4Rα is derived from a mosaic of three binding clusters.[6]

IL-4 contains three disulfide bonds but no free cysteine. It is therefore an attractive protein to introduce a cysteine residue singly at defined positions for subsequent site-specific chemical modifications. Protein tethering has been proposed to employ single cysteine muteins for the screening of low-affinity binding molecules.[15,16] Site-specific PEGylation of single cysteine is a well-established method for modifying the properties and application of proteins (see, for instance, refs 17−19), in particular, for enhancing protein solubility and serum lifetime in vivo. A PEGylated form of IL-4DM is in clinical development for the treatment of eczema.[20] Site-specific PEGylation at

Received: August 15, 2011
Revised: June 1, 2012
Published: June 9, 2012

ACS Publications © 2012 American Chemical Society

dx.doi.org/10.1021/bc2004389 | *Bioconjugate Chem.* 2012, 23, 1396−1405

specific engineered cysteine residues of human IL-4 wild-type or antagonistic muteins has been demonstrated (U.S. Patent 7,785,580).

Coupling of disulfide- or maleimide-activated compounds to a cysteine of a protein is highly specific but requires a free thiol group. Engineered single cysteines of recombinant proteins produced by refolding after bacterial expression, or by secretion from transfected insect or animal cells, are often not completely reduced and therefore not at all or only partially reactive (see, for instance, ref 21). The present study explores the possibility of generating IL-4 muteins with an unpaired cysteine residue. Several trials failed to obtain muteins with a fully unpaired cysteine during in vitro refolding. Thus, muteins with fully glutathione-conjugated cysteine were generated, and an attempt was then made to reduce the disulfide blocked cysteine with chemical or enzymatic approaches for subsequent site-specific chemical modification, including PEGylation. Surprisingly, the three internal disulfide bonds of IL-4 could not withstand a chemical reduction. An enzymatic reduction using glutaredoxin, however, allowed the preparation of IL-4 cysteine muteins with a entirely free thiol.

EXPERIMENTAL PROCEDURES

Chemicals. *E. coli* glutaredoxin (GRX-01) was obtained from IMCO (Sweden), glutathione from Fluka, NADPH and yeast glutathione reductase (GR) from Sigma (St. Louis, MO, USA). TMS(PEG)$_{12}$ [(Methyl-PEG$_{12}$)$_3$-PEG$_4$-Maleimide, MW 2360.75] was purchased from Thermo Scientific, Dreieich, Germany.

Preparation of IL-4 Proteins (Wild Type and Cysteine Muteins). The cDNA of IL-4 cysteine muteins was generated by recombinant PCR employing the mutagenesis primers compiled in SI Table S-1. The cDNA encoding mature human IL-4 (UniProtKB/Swissprot P05112) plus an N-terminal methionine were inserted into plasmid pQKA (a modified version of the pQE-80 Qiagen expression plasmid) and transformed into expression host *E. coli* BLR(DE3) (EMD4Biosciences). Bacteria were grown in LB medium plus Kanamycin (25 μg mL^{-1}) on a rotatory shaker at 37 °C to early exponential phase and IL-4 protein expression was then induced by addition of 1 mM isopropyl-thiogalactopyranoside (IPTG) for 3 h. The sedimented bacteria were suspended in 20 volumes STE buffer (0.325 M sucrose, 10 mM Tris-HCl pH 8.0, 1 mM EDTA), and then 1 mM DTT and hen egg lysozyme (final concentration 75 μg mL^{-1}) was added. The cells were lysed by sonication (150 W Bandelin Sonopuls HD3200) with the cell suspension cooled on ice. The sediment was resuspended and sonicated as above. The insoluble fraction ("inclusion bodies") was separated by centrifugation and washed once with STE buffer plus 1 mM DTT and once with STE buffer, 1% Triton X-100, and 1 mM DTT. The final sediment was kept frozen at temperatures −20 °C.

The IL-4 protein was extracted from the inclusion bodies using a solution containing 6 M guanidinium hydrochloride (GuCl), 0.1 M TrisHCl, pH 8.0, and 1 mM DTT (10 volumes per gm wet weight). For refolding of the IL-4, the clarified protein extract was diluted 25-fold with ice-cold refolding buffer (1 M arginine, 50 mM Tris-HCl, pH 8.0, 5 mM EDTA, 5 mM glutathione (oxidized form), 2 mM glutathione (reduced form)) and kept at 4 °C for three days.

The solution was dialyzed twice against 10 volumes of PBS (150 mM sodium chloride, 10 mM sodium phosphate, pH 7.4) at 4 °C for 12 to 18 h. For purification of the refolded IL-4 protein, the pH of the dialyzed refolding solution was adjusted to 5.0 by adding 0.01 volumes of 4 M ammonium acetate pH 5.0. The slightly turbid solution was clarified by centrifugation, and the supernatant was loaded on 10 mL CM-Sepharose FastFlow resin (up to 1 L refolding solution) that was equilibrated with 25 mM ammonium acetate pH 5.0. The IL-4 protein was eluted via a step gradient using 2 × 10 mL buffer containing between 0.5 and 1.5 M sodium chloride. Combined protein-containing fractions were concentrated to 5 mL via ultrafiltration (cutoff 3 kDa). The clarified protein solution was then loaded onto a C4 reversed-phase HPLC column (Vydac 12.5 mL column volume) equilibrated with 0.1% trifluoroacetic acid (TFA). The IL-4 was eluted from the reversed-phase C4 resin by applying a gradient from 0.1% TFA to acetonitrile with an increase from 20% to 80% acetonitrile in 60 min at a flow rate of 0.8 mL min^{-1}. Natively folded IL-4 eluting as the major peak at 25−30% acetonitrile was freeze−dried and stored in aliquots at −20 °C until further use.

Analytical refolding experiments with the IL-4 muteins S16C or N38C were performed at analytical scale with 1 mL GuCl extract following the procedure detailed above, with the only exception that the glutathione redox couple was substituted by 5 mM concentrations of glutathione, cysteamine, β-mercaptoethanol, or thioglycolate.

Chemical Reduction of IL-4 Proteins. IL-4 muteins containing an engineered cysteine residue were dissolved in PE7 buffer (0.1 M potassium phosphate pH 7.0, 2 mM EDTA) at 50 μM concentration and incubated with 50, 100, or 150 μM dithiothreitol (DTT) at 20 °C for 24 h. Then, 0.01 volume of 100 mM TMS(PEG)12 dissolved in DMSO was added for 30 min. The PEGylation reaction was halted by adding 0.02 volume of 250 mM glutathione (reduced form). After mixing with an equal volume of 2 × SDS sample buffer, 5 or 10 μL were submitted to SDS PAGE analysis.

Reaction with *N*-Ethylmaleimide or TMS(PEG)12. Reaction at prepararative scale was performed at a 3-fold molar excess in PE7 buffer (0.1 M potassium phosphate pH 7.0, 2 mM EDTA) at 20 °C for 30 min. The solution was mixed with 0.1% TFA to a final volume of 5 mL and loaded on a C4 revered-phase HPLC column (Vydac 214TP54, 250 × 4.6 mm) equilibrated with 0.1% TFA. The modified protein was purified by applying an acetonitrile gradient running from 20% to 80% acetonitrile in 60 min and using a flow rate of 0.8 mL min^{-1}. Protein-containing fractions were pooled and freeze−dried. The conjugated IL-4 protein was dissolved in water at concentrations of about 100 μM and stored at −20 °C until further use.

Enzymatic Reduction of IL-4 Cysteine Muteins with GRX1 from *E. coli*. The final reaction conditions were 100 mM potassium phosphate, pH 7.0, 2 mM EDTA, 6 μg mL^{-1} glutathione reductase, 0.2 mM NADPH, 0.5 mM glutathione (reduced form), and 50 μM IL-4 protein. The redox reaction was started by adding 0.01 volume of a 300 μM glutaredoxin solution prepared according to the manufacturer's recommendation. The progress of the reaction was monitored by the oxidation of NADPH, which can be measured by the decrease in the extinction at 340 nm. After 30 min, 0.025 volume of 4 M ammonium acetate pH 5.0 was added. The reaction mixture was immediately loaded on a 1 mL SOURCE 15S column (GE Healthcare) equilibrated with 25 mM ammonium acetate pH 5.0. The IL-4 protein was eluted via a salt gradient increasing from 0.5 to 1.5 M sodium chloride in 60 min at a flow rate of 0.5 mL min^{-1}. The protein-containing fractions from the ion exchange chromatography step (containing about 0.75 M NaCl) were immediately loaded onto a

C4 reversed-phase HPLC column (Vydac 214TP54, 250 × 4.6 mm) equilibrated with 0.1% TFA for further purification. The IL-4 protein was eluted via a gradient increasing from 20% to 80% acetonitrile in 60 min at a flow rate of 0.8 mL min^{-1}. IL-4 protein containing fractions were pooled, freeze−dried, and dissolved in water at a final concentration of about 100 μM.

Electrospray Ionization Mass Spectrometry Analysis (ESI-MS). ESI-MS was performed using an APEX-II FT-ICR (Bruker Daltonic GmbH, Bremen) equipped with a 7.4 T magnet and an Apollo ESI ion source in positive mode. The proteins were desalted by C4 reversed-phase HPLC (see above) and then were dissolved in methanol/water/acetic acid (49.5/49.5/1) to yield a sample concentration ranging between 1 and 5 μM. The sample was injected using a Hamilton syringe at a speed of 2 μL per minute with a capillary voltage of 360 mV. Detection range was typically set to 300−3000 m/z in initial measurements. The detection range was then optimized to the signal-containing area. An accumulation of 256 scans was combined at a resolution of 256 K.

For evaluation, the mass spectra were deconvolved to the single protonated ion mode using the Bruker *Xmas* software. The most intense isotope signal was selected for mass determination.

Surface Plasmon Resonance (SPR) Interaction Analysis. Biosensor experiments were carried out employing a BIAcore 2000 system (GE Healthcare, Freiburg, Germany) at 25 °C and a flow rate of 50 μL min^{-1} in HBS150 running buffer (10 mM 4-(2-hydroxyethyl)-1-piperazine ethanesulfonic acid, pH 7.4, 150 mM sodium chloride, 3.4 mM EDTA, 0.005% surfactant polyoxyethylene sorbitan P20) with a data collection rate of 2.5 Hz. A CM5 biosensor chip (GE Healthcare Freiburg, Germany) was first coated with streptavidin (coating density about 2000 RU, with 1 RU = 1 pg mm^{-2}) in all four flow cells, and subsequently, the biotinylated ectodomain of IL-4Rα was immobilized on the streptavidin matrix in flow cell 2 up to 80 RU.[22] To account for bulk face effects, a control experiment acquired from flow cell 1 (which contained only streptavidin but no IL-4Rα) was subtracted from all measurement flow cells. The rate constant for dissociation (k_d) and for association (k_a) were evaluated using the *BIAevaluation* software v 2.1.2. The apparent equilibrium binding constant K_D was calculated from the rate constants using the equation $K_D = k_d/k_a$. The interaction with IL-4Rα was measured at one IL-4 concentration only (10 nM), since the main interest of the present study was a comparison of the various IL-4 analogues. Accordingly, no "correct" constants have been deteremined, but only "apparent" kinetic and equilibrium constants. Mean values with standard deviations of 30% for k_d and 20% for k_a were deduced from two to four independent measurements.

Protein Analysis. Protein concentrations of purified IL-4 proteins were determined by measuring a UV absorption spectrum between 250 and 320 nm. The molar extinction coefficient was calculated from the amino acid sequence using the ProtParam tool and used to determine the protein concentration according to the law of Lambert−Beer (molar extinction coefficient $\sum_{278}$ = 8900 M^{-1} cm^{-1}). SDS-polyacrylamide gel electrophoresis (SDS-PAGE) was performed using a 12% polyacrylamide gel as described previously.[23] In some experiments, precast polyacrylamide gels (4−20% polyacrylamide; Thermo Scientific) were used. Protein samples for SDS PAGE analysis were diluted 2- to 5-fold with sample buffer plus 50 mM DTT (for analysis under reducing conditions) or without reducing agent (gel under nonreducing conditions to determine disulfide bonding). The gels were stained with Coomassie Blue R-250 for 1 h and destained overnight. Molecular weight standards phosphorylase b (M_r 97 000), albumin bovine serum (M_r 66 000), ovalbumin (M_r 45 000), carbonic anhydrase (M_r 29 000), trypsin inhibitor soybean (M_r 20 100), and α-lactalbumin (M_r 14 400) were obtained from GE Healthcare (Freiburg, Germany). In some experiments, prestained size standards (PageRuler Prestained Protein Ladder; Thermo Scientific) were used.

RESULTS

Preparation of IL-4 Cysteine Muteins (S16C, N38C, H74C, Q78C, R81C). Cysteine residues were introduced at IL-4 positions localized at the periphery of the binding epitope for the IL-4 receptor alpha chain (IL4Rα) as shown in the space-filling model of IL-4 in Figure 1. The IL-4 N38C variant was prepared as a control, since Asn38 is located far away from the IL4Rα binding epitope. Asn38 is glycosylated in native IL-4.

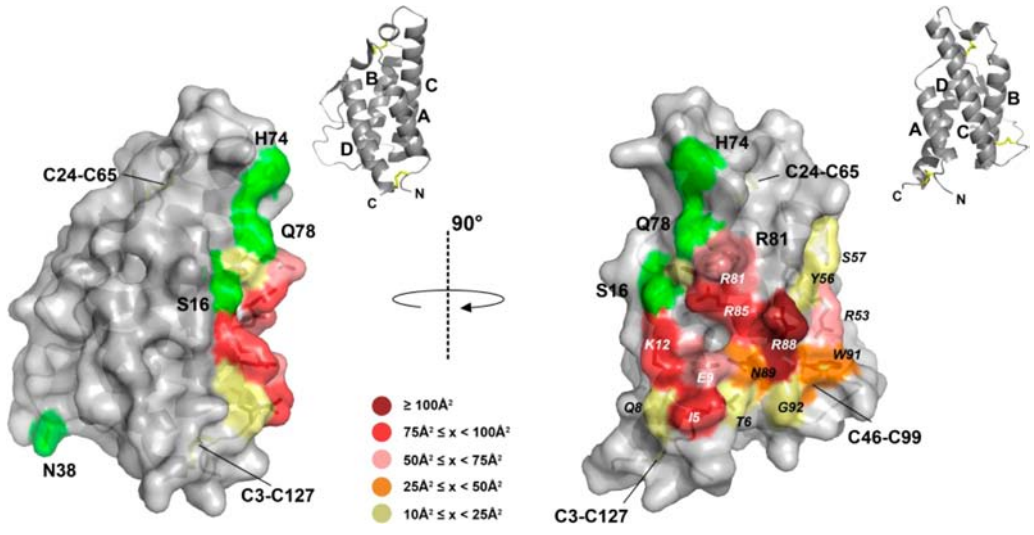


Figure 1. Sites S16, N38, H74, Q78, and R81 chosen for engineering an unpaired cysteine residue into human IL-4 are indicated in green. The area of IL-4 surface residues buried in contact with IL-4Rα (PDB entry 1IAR, chain A) (marked in italic) are color-coded as indicated in the displayed scheme. Small ribbon panels on the upper right indicate the orientation of IL-4. Positions of the native disulfide bonds are marked.

Table 1. Mass Spectrometry Analysis of Refolding Experiments of IL-4 S16C Mutein in the Presence of Different Thiol Compounds[a]

	unmodified			modified with thiol compound		
	molecular mass [Da]		[%]	molecular mass [Da]		[%]
IL4 protein	theoretical	observed	relative amount	theoretical	observed	relative amount
S16C SH	15104.708	15105.704	100	n.d.	n.d.	n.d.
S16C GS	15104.708	15105.047	10	15409.775	15409.956	90
S16C ME	15104.708	15104.997	20	15181.713	15181.889	80
S16C CA	15104.708	15104.938	43	15179.722	15180.924	57
S16C TG	15104.708	15104.997	7	15194.685	15195.908	93

[a]Observed and theoretical mass of IL-4 S16C refolded in the presence of different thiol compounds was derived from the mass spectrometry analysis shown in Figure S-1. For comparison, enzymatically reduced IL4S16C is included as S16C SH (compare in Figure 8). Abbreviations are GS for glutathione, ME for β-mercaptoethanol, CA for cysteamine, and TG for thioglycolate.

The recombinant proteins were solubilized from inclusion bodies in the presence of guanidinium chloride. For refolding, the solution was 25-fold diluted in a refolding medium yielding a protein concentration of 50 to 100 μg per mL. The 1.2 M guanidinium chloride employed for refolding in the original procedure (see, for instance, refs 24,25) was substituted by 1 M arginine, since consistently higher yields of the refolded IL-4 protein were obtained.

In the absence of any thiol compound or redox couple, the refolding was poor (data not shown). In the example presented in Table 1 and Figure S-1, the IL-4S16C protein was refolded in the presence of 5 mM β-mercaptoethanol, cysteamine, thioglycolate, or glutathione with the presumption to obtain the mutein with a free thiol. However, mass spectrometry of the purified proteins revealed that the thiol group of the additional unpaired cysteine was only partially free, and for the most part, disulfide bonded with the reducing agent (Table 1, Figure S-1A). Similar refolding experiments with the IL-4N38C protein yielded only mutein with mixed disulfides but not with free thiol group (Figure S-1B). The evaluated mass values are in accordance with the assumption that the three native disulfide bonds are formed. The mixed disulfide bond involving the assumed unpaired cysteine was likely formed by dissolved oxygen, since no special precautions were followed to keep the solutions anaerobic. However, even under these only minimally oxidizing conditions, it was not possible to keep the engineered cysteine completely in the nonconjugated form, suggesting that the redox potentials of the disulfide bonds present in the native IL-4 and in the conjugated thiol compounds are not vastly different. This conclusion holds for the S16C and N38C muteins, which show large differences in the rate of enzymatic reduction of the mixed disulfide with glutathione (see below).

As an alternative approach, the ratio of reduced and oxidized form of the thiol compound employed during refolding was changed systematically in order to obtain a completely conjugated mutein. In the presence of 2 mM reduced and 5 mM oxidized glutathione, all mutant proteins were refolded and prepared in good yield (2−3 mg per gram wet weight of *E. coli* cells) and the engineered cysteine was completely disulfide bonded to glutathione (see below). These fully modified IL-4 cysteine muteins then served as starting material for the chemical and enzymatic deglutathionylation trials.

Glutathione Modification of IL-4 Muteins. Mass spectrometry of the purified IL-4 muteins (Table S-2 and Figure 2) showed one major protein species with the respective molecular weight consistent with the IL-4 mutein protein plus one glutathione moiety lacking the two hydrogen atoms of the two thiol groups. Nonconjugated mutant proteins could not be detected or were present in only vanishing amounts. For the wild-type IL-4 (IL4WT) exclusively, the species with a molecular weight of the unmodified protein could be observed. This suggests that in the muteins the glutathione is disulfide-bonded to the engineered cysteine residue. Varying amounts of minor species seen in the spectra represent mono-oxygenated (plus 16 Da) and dehydrated/deaminated (minus 18 Da) proteins. In some preparations, N-terminal residues methionine or methionine plus the succeeding histidine residue had been removed by post-translational processing. No protein species possibly representing dimerized IL-4 molecules were detected.

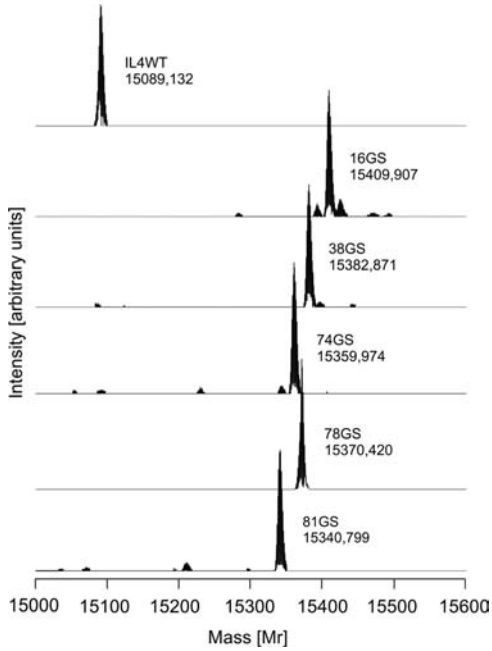


Figure 2. Mass spectrometry of the purified glutathionylated IL-4 proteins (wild-type IL-4 (IL4WT), 16GS, 38GS, 74GS, 78GS, and 81GS). The molecular masses deduced from the deconvoluted spectra are consistent with the molecular weights of the respective IL-4 mutein plus one glutathione moiety added and two hydrogens subtracted (derived from the oxidation of the two thiol groups) (see Table S-2).

Surface plasmon resonance (SPR) interaction analysis employing immobilized IL4Rα ectodomain[22] showed that the glutathione-conjugated IL-4 cysteine proteins still bound efficiently to the receptor, thereby indicating that the sites of the engineered cysteine residues do not abrogate receptor binding (Table 2 and Figure 3A). Compared to wild type IL-4, the association rate constant k_a was reduced about 2-fold in

dx.doi.org/10.1021/bc2004389 | *Bioconjugate Chem.* 2012, 23, 1396−1405

Table 2. Kinetic Parameters Deduced from SPR Analysis for the Receptor Interaction of IL-4 Analogues[a]

IL-4 proteins	k_d [s^{-1}] × 10^3	k_a [$M^{-1}s^{-1}$] × 10^{-6}	K_D (=k_d/k_a) [pM]
IL4WT	1.5	19.0	78
16GS	2.9	8.4	350
16SH	1.3	20.0	67
16NEM	1.4	16.0	70
16PEG	1.1	7.0	160
IL4WT	1.3	15.0	90
38GS	1.3	8.0	170
38SH	1.5	11.0	130
38NEM	1.6	15.0	110
38PEG	1.6	10.0	160
IL4WT	1.7	13.0	130
74GS	1.4	7.8	170
74SH	1.3	5.0	270
74NEM	1.9	13.0	140
74PEG	1.5	8.1	180
IL4WT	0.9	14.0	62
78GS	2.4	8.7	280
78SH	2.2	13.0	170
78NEM	2.5	13.0	180
78PEG	2.4	7.5	340
IL4WT	1.2	14.0	80
81GS	10.0	1.8	5700
81SH	2.9	7.9	400
81NEM	4.1	9.1	450
81PEG	4.2	1.6	2600

[a]The rate constants for dissociation (k_d) and association (k_a) were derived from sensorgrams as shown in Figure 3.

16GS, 38GS, 74GS and 78GS analogues and 8-fold in 81GS. The dissociation rate constant k_d was similar in wild-type IL-4, 38GS, and 74GS, about two times faster in 16GS and 78GS, and 6-fold faster in 81GS.

Chemical Reduction of Glutathione-Modified IL-4 Analogues. In previous experiments employing bone morphogenetic protein (BMP), 2 cysteine muteins[27] disulfide-bonded glutathione could be removed by dithiothreitol (DTT) treatment without reducing any of the seven native disulfide bonds. In contrast, trials to remove the IL-4 conjugated glutathione with various chemical compounds without destroying the IL-4 protein were not successful.

In one set of experiments, the IL4 muteins 16GS and 38GS were incubated with DTT at molar ratios of 1:1 (50:50 μM) to 1:3 (50:150 μM). Free thiol groups were then identified by MA-PEGylation and subsequent SDS PAGE analysis (Figure 4).

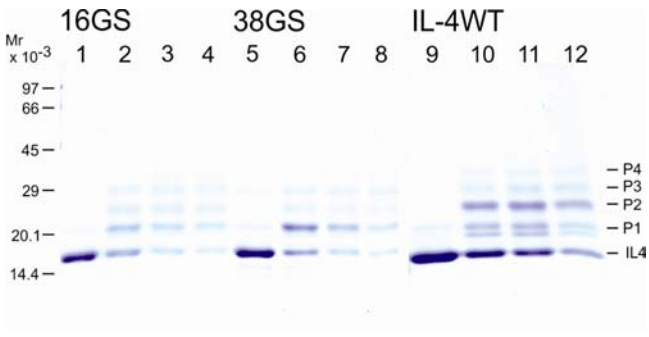


Figure 4. Chemical reduction of 50 μM IL-4 proteins. 16GS (lanes 1–4), 38GS (lanes 5–8), and wild-type IL-4 (lanes 9–12) with DTT at concentration of 50 μM (lanes 2, 6, and 10), 100 μM (lanes 3, 7, and 11), and 150 μM (lanes 4, 8, and 12). The controls without DTT reduction are shown in lanes 1, 5, and 9. After chemical reduction, proteins were maleimide-PEGylated and analyzed by SDS PAGE on 12% gels. P1 denotes the migration of monopegylated IL-4. Multipegylated IL-4 species are tentatively marked P2, P3, and P4. The same aliquot of the reaction mixture containing 1.9 μg IL-4 protein was loaded on each lane.

Upon reaction of equimolar concentrations of DTT and the glutathionylated IL-4 mutein, an indiscriminative reduction of multiple disulfide bonds was observed. Protein bands probably representing mono- and multi-PEGylated species were detected in addition to the original glutathionylated protein, indicating that the engineered cysteine was reduced in parallel with the native disulfide bonds. The intensity of the stained protein bands decreases in the DTT reduced samples more than expected when the same amount of protein is distributed among progressively increasing number of species. It was noticed that upon reduction the solution of the IL-4 proteins became turbid. This aggregated material apparently was not dissolved by the SDS sample buffer and therefore was not recovered in the stained gels. When 38GS was reacted with equimolar amounts of DTT, a somewhat higher percentage of mono-PEGylated protein could be seen compared to the 16GS mutein, suggesting a higher reactivity of the glutathionylated Cys38. When wild-type IL-4 was used as a major species, di-PEGylated protein was formed. The dose-dependent reduction of 74GS, 78GS, and 81GS with DTT showed that multipegylated species have formed beside the monopegylated

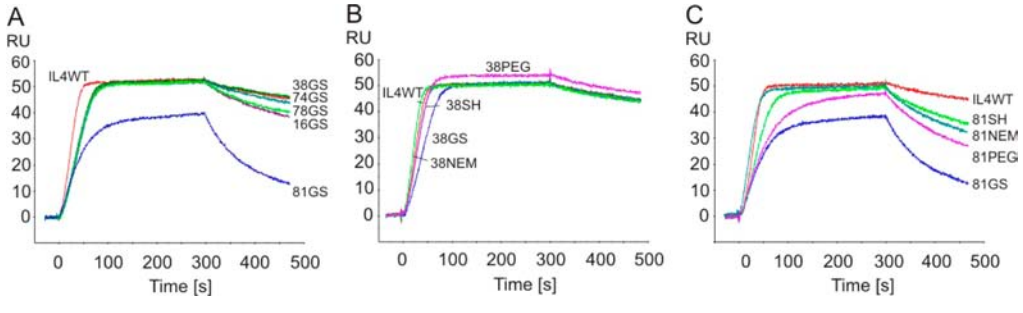


Figure 3. Surface plasmon resonance (SPR) analysis of the interaction of IL-4 proteins with IL-4Rα ectodomain which was immobilized on a CM5 biosensor chip. Perfusion with IL4 protein at concentration of 10 nM starts at time point 0 s for a duration of 300 s after which the biosensor is again perfused with buffer to measure dissociation started at time 300 s. (A) Interaction of IL4WT and glutathionylated IL4 muteins (16GS, 38GS, 74GS, 78GS, 81GS), (B) IL4WT and modified IL4S38C analogues (38GS, 38SH, 38NEM, 38PEG), (C) IL4WT and modified IL4R81C analogues (81GS, 81SH, 81NEM, 81PEG). Calculation of the kinetic rate constants and equilibrium binding constants are shown in Tables 2 and S-3.

dx.doi.org/10.1021/bc2004389 | Bioconjugate Chem. 2012, 23, 1396–1405

mutein even at the lowest DTT concentration of 50 μM. Some nonpegylated, meaning nonreduced, protein has remained (Figure S-2) (because gradient gels with a higher resolution have been used, a more complex protein pattern can be seen in Figures S-2 and S-3 than in Figure 4).

When the reduction of the six GS analogues was analyzed after different time periods (0, 2, 6, 12 h) at a concentration of 150 μM DTT; also, no window for a preferential reduction of the mixed disulfide could be detected (Figure S-3). Progressively less protein was recovered on the stained gels after longer time periods of reduction. The 74GS protein was reduced most rapidly among the analyzed proteins. Some preferential appearance of the monopegylated N38C and 78GS analogues was seen after 6 h, probably due to a faster reduction of the mixed disulfide, compared to the other analogues. Comparable results were obtained for the dose-dependent reduction with tris(2-carboxyethyl)phosphine (TCEP).

In order to see if DTT reduces a particular disulfide bond of IL-4, a second set of experiments was performed. IL4 wild-type was reduced with a 3-fold molar excess of DTT and subsequently modified by *N*-ethylmaleimide (NEM). Di-NEM IL-4 was isolated as the major reaction product. Peptides obtained after proteolytic cleavage of the di-NEM adducts with the endopeptidases Trypsin and GluC were analyzed by mass spectrometry (see ref 27). Under the conditions used here, the NEM label was distributed among several cysteines of the IL-4 protein involved in several of the native disulfide bonds (data not shown). This strongly suggests that there is no disulfide bond more sensitive to DTT reduction than the others.

Together, these results demonstrate that human IL-4 contains disulfide bonds that are susceptible to chemical reduction under quite mild conditions. The disulfide bond between conjugated glutathione and the IL-4 cysteine mutein is reduced at the same concentration range of DTT and at a similar rate as the native disulfide bonds. Variation of the reaction conditions, such as using different pH between 7.0 and 8.5, altering the temperature (4 or 20 °C), employing different buffer composition (high ionic strength, using arginine as chaperone), or using different reducing agents (glutathione, 2-aminothiophenol, β-mercaptoethanol, cysteamine, thioglycolate), did not yield a higher selectivity (data not shown). Thus, it seems to be difficult if not impossible to deglutathionylate these proteins by chemical reduction without disrupting the native disulfide bonds.

Enzymatic Deglutathionylation of IL-4 Cysteine Muteins with Glutaredoxin. Glutaredoxin[28,29] can catalyze the deglutathionylation of proteins in the presence of reduced glutathione. In an assay employing *E. coli* glutaredoxin-1,[28] the glutathione that becomes oxidized during the reaction is reduced by NADPH and yeast glutathione reductase. This assay allows observation of the deglutathionylation by the decline in the extinction at 340 nm, as shown in Figure 5. Initial trials using buffer conditions at pH 8 showed that the protein solution became turbid during the reaction, most likely due to aggregation of the reduced IL4 mutein. Incubation at pH 7 alleviated this problem. Furthermore, some reducing activity was also observed for wild-type IL-4, suggesting that the enzymatic reduction was not completely specific for the glutathione bond, and also that some of the native disulfide bonds were slowly reduced under these conditions. This unwanted side reaction could be attenuated by running the enzymatic reaction at pH 7.0 and using low concentration (0.5 mM) of reduced glutathione.

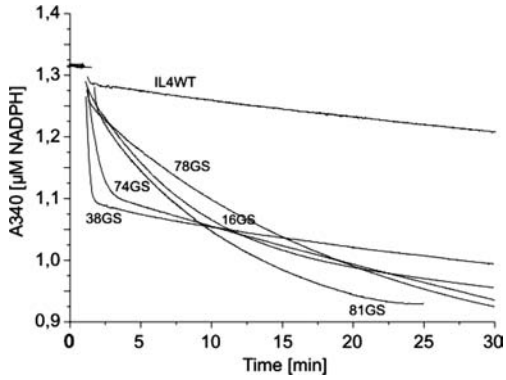


Figure 5. Enzymatic deglutathionylation of IL-4 proteins using the enzyme glutaredoxin (*E. coli* GRX-1). The NADPH-dependent reduction of GS-modified IL-4 cysteine muteins was recorded after addition of glutaredoxin by the decline in the extinction at 340 nm through the conversion of NADPH to $NADP^+$.

Interestingly, the rate of glutaredoxin-mediated deglutathionylation differs among the different cysteine muteins. The rate of reduction was fast for 38GS and 74GS and slow for 16GS, 78GS, and 81GS. The early decline of the reduction rate seen for 38GS and 74GS could be fitted to a monoexponential decrease with half-life of 18 s (38GS) and 55 s (74GS). For the other IL-4 analogues, a monoexponential decline over the whole time period with half-lives of 10 min (16GS, 81GS) and 20 min (78GS) was obtained. The second slower phase of reduction of 38GS showed a similar reduction rate, as observed in the reduction of wild-type IL-4, and it was slightly faster for 74GS. The clear differences in the reaction rate of the enzymatic reduction pointed to a different accessibility and/or mobility of the S−S conjugated glutathione in the different IL-4 muteins.

The very slow reduction of the wild-type IL-4 suggested that even glutaredoxin mediated some reduction of the native disulfide bonds. This possibility was further explored by determining free thiol groups at different time points of the reaction by MA-PEGylation. Reaction products obtained after 2.5−30 min were analyzed by SDS PAGE (Figure 6).

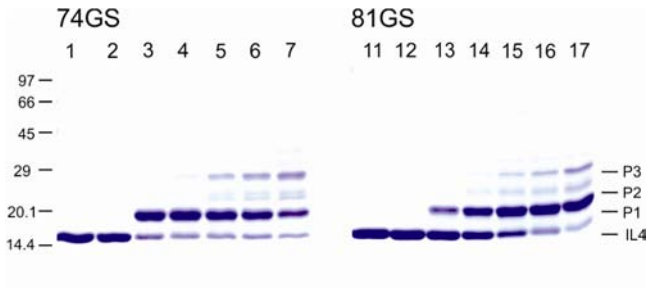


Figure 6. Reaction kinetics of GRX-mediated reduction of 74GS (left) and 81GS (right) are monitored by maleimide-PEGylation at 0, 2.5, 5, 10, 15, 20, and 30 min time points and subsequent SDS PAGE analysis.

The mono-PEGylated IL-4 H74C reached peak levels after 2.5−5 min, and the amount of this product then declined at the expense of small amounts of tri- and multi-PEGylated species. The mono-PEGylated R81C accumulated until 20−30 min reaction time, and toward the later time points, multi-PEGylated species became apparent as minor bands. These

dx.doi.org/10.1021/bc2004389 | *Bioconjugate Chem.* 2012, 23, 1396−1405

Table 3. Mass Spectrometry Analysis of Enzymatically Reduced IL-4 Cysteine Muteins[a]

	unmodified			unmodified	glutathione-modified
	molecular mass [Da]			relative amount [%]	
IL4 protein	theoretical	observed	difference		
IL4WT	15088.731	15089.132	0.401	100	0
S16C	15104.708	15105.704	0.996	100	0
N38C	15077.697	15077.653	−0.044	100	0
H74C	15054.681	15055.788	1.107	100	0
Q78C	15063.681	15063.562	−0.119	96	4
R81C	15035.639	15035.672	0.033	100	0

[a]Spectra as compiled in Figure 7 were evaluated.

results showed that some unspecific reduction of the native disulfide bonds had occurred and corroborated the above kinetic data measured by NADPH oxidation. Thus, in future experiments the reaction time must be optimized for each cysteine mutein to minimize incomplete and unspecific reduction. It must be noted that even after 30 min reaction time a small amount of unmodified mutein remained (see Discussion).

The enzymatically reduced mutant proteins were purified using reversed-phase HPLC with a final yield of 40−60%. Mass spectrometry analysis revealed (Table 3, Figure 7) that all

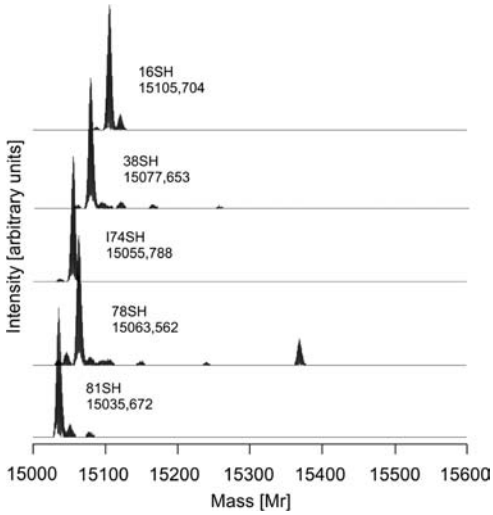


Figure 7. Mass spectrometry analysis of the enzymatically (glutaredoxin) reduced IL-4 muteins.

muteins were devoid of conjugated glutathione with the exception of IL-4 Q78C, where a small amount (4%) of the 78GS analogue could be detected. SDS PAGE analysis in the presence and absence of DTT showed that more than 95% of the enzymatically reduced proteins existed in the monomeric form. In addition, small and variable amounts of dimeric protein were observed for some muteins (Figure S-2).

***N*-Ethylmaleimide- and PEG-Labeling of IL-4 Cysteine Muteins.** The conjugation of the reduced IL-4 cysteine analogues with *N*-ethylmaleimide proved to be highly selective. Under the applied conditions, only the mono-NEM conjugate of the IL-4 mutein proteins could be detected by mass spectrometry analysis (Figure S-3, Table S-4). Di- or multi-NEM conjugates and nonconjugated IL-4 proteins were absent. Mass spectrometry analysis of peptides obtained by proteolytic digestion of the NEM-labeled IL-4 indeed confirmed that the NEM-label could only be detected in peptides containing the engineered cysteine (data not shown; see ref 27) and was thus specific for the single free cysteine in each mutein.

After reaction with branched MA-PEG, mono-PEGylated analogues were purified and were contaminated with only minor amounts of unmodified protein (Figure 8). This pattern

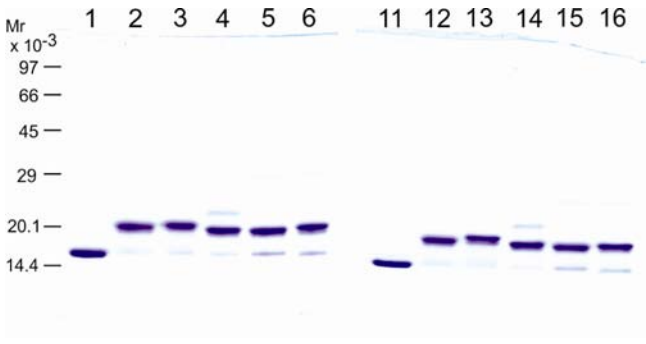


Figure 8. SDS PAGE analysis of PEGylated IL-4 cysteine muteins under reducing (lanes 2−6) and nonreducing (lanes 12−16) conditions. Lanes 1,11, wild-type IL-4; 2,12, 16PEG; 3,13, 38PEG; 4,14, 74PEG; 5,15, 78PEG; 6,16, 81PEG.

was no different when the proteins were analyzed under reducing or nonreducing conditions, making it unlikely that the lack of PEGylation resulted from disulfide-mediated dimer formation of the reduced proteins. A small amount of di-PEGylated protein was seen with the IL-4 H74C mutein, possibly due to over-reduction. The slightly different electrophoretic mobility, for instance, of the reduced and nonreduced 38PEG analogue remains unexplained at this time. One might speculate that the attached PEG in 38PEG exists in a more open or flexible state that might impede the mobility in the SDS gel.

The receptor binding properties of the modified IL-4 analogues were compared with those of wild-type IL-4 and the unmodified analogues by in vitro SPR interaction analysis, using the immobilized ectodomain of IL-4Rα (see Table 2, Figure 3B,C). The quite large variations of the data such as seen, for instance, in the multiple experiments with wild-type IL-4 are explained by the fact that the kinetic constants for the interaction of IL-4 and IL-4Rα are at the limits of resolution of the employed Biacore 2000 system.[22] Accordingly, the calculated apparent dissociation constants of, for instance, the 38SH and 38NEM analogues did not differ significantly from the wild-type IL-4. The 5-fold decrease in affinity observed with 81SH resulted mainly from an increased dissociation rate constant k_d. The more than 2-fold lower on-rate constant determined for 74SH could possibly result from a partial inactivation due to over-reduction (see Discussion). The NEM

modification was well-tolerated without affecting the receptor binding affinity significantly in 16NEM, 38NEM, and 74NEM. With 78NEM and 81NEM, the affinity was decreased to a similar degree as for the free thiol analogues. PEGylation of the thiol group resulted in a marginal decrease in affinity for IL-4Rα with the 16PEG, 38PEG, and 74PEG analogues. 81PEG showed a strongly reduced affinity for IL-4Rα due to a moderately increased dissociation rate and a strongly reduced association rate indicating some steric hindrance effect of PEG moiety attached to the thiol group when in close proximity to the receptor binding epitope (see Figure 1).

DISCUSSION

Many secreted proteins, such as cytokines or immunoglobulins, are devoid of unpaired reactive cysteines and contain only internal disulfide bonds. The engineering of cysteines into such proteins offers attractive possibilities for thiol-based site-directed modifications. However, the production of cysteine muteins with a reactive free cysteine can pose serious technical problems, since, during recombinant expression and refolding of cysteine muteins, regularly mixed disulfides and protein aggregates are formed. These have to be reduced before the thiol can be efficiently modified with thiol-specific chemical compounds.

Several proteins, such as GSF, erythropoietin, BMP-2, immunoglobulin fragments, and others, have been described as containing native disulfide bonds which survive incubation with an excess of strong reducing agents like DTT or TCEP[17−19,30−32] (see also U.S. Patent 7,855,275). Surprisingly, as described in the present article, with human IL-4 it is not trivial to first generate cysteine muteins with nonconjugated, meaning non-disulfide-bonded, thiol groups that can then be modified. Chemical reduction of IL-4 cleaved both the native and the engineered disulfides in parallel. Both disulfide species exhibited a comparable reactivity under a variety of conditions, impeding site-specific reaction conditions.

This indiscriminate reduction points to an unusually high reactivity of the native disulfide bonds of IL-4 that might be attributed to various causes. First, some of the three disulfide bonds of IL-4 might contribute little to conformational stability. As a consequence, the redox potential might be increased. Functional analysis indeed showed that two of the three native disulfide bonds of IL-4 (Cys3-Cys127, Cys24-Cys65) can be disrupted mutationally by a substitution of the cysteine with threonine, while preserving the biological activity.[33] The disulfide bond between Cys46 and Cys99, however, appeared to be crucial for the structure and/or function of IL-4. This suggested that the conformational stability conferred by the three disulfide bonds differs, which was also shown by analyzing IL-4 stability using NMR techniques.[34] Second, a disulfide bond might be easily accessible to a reducing agent in solution. An analysis of the accessibility of the three individual disulfide bonds present in IL-4 using structural data from X-ray or NMR data[12] shows that, of the three native disulfides, cys3-cys127 is highly accessible in the protein crystal (accessible surface area 32.1 Å^2; PDB entry 2B8U), while Cys46- Cys99 is highly accessible in the protein in solution (accessible surface area 27.0 Å^2; PDB entry 1ITM). Possibly IL-4 can adopt different conformations with different accessibility of disulfide bonds. A large exposed surface area of a disulfide has been shown to greatly accelerate chemical reduction by DTT.[35,36] Third, a high mobility/flexibility might diminish the stability of a disulfide bond. A comparison of the temperature sensitivity of the backbone and side chain atoms of the six cysteine residues in wild-type IL-4 (PDB entry 2B8U) shows very little variation.[24] The atoms of the disulfide bridge between Cys46 and Cys99 show elevated B-factors; however, their values are still lower compared to atoms directly located at the protein's surface and less than 1.5-fold larger than the B-factors of the atoms of the two other disulfide bonds. This little difference in crystallographic disorder is also confirmed by NMR relaxation data of wild type IL-4.[37] All three native disulfide bonds of IL-4 are located in regions with lowered order parameter S^2 and the long helix-connecting loops also showing slower motions leading to line broadening of NMR signals of residues close to the disulfide bonds Cys24-Cys65 and Cys46-Cys99. In summary, the available evidence suggests that the three native disulfide bonds of IL-4 are in a similar structural environment and can exhibit a similar accessibility to the surface-exposed engineered cysteine residue.

Preliminary data further suggest that during DTT reduction of IL-4 no preferential pathway for reductive unfolding exists. After reaction with a 3-fold molar excess of DTT and subsequent modification with NEM, no preferential labeling of a cysteine pair normally forming a native disulfide bond could be detected in the di-NEM IL-4 species.

In our study, the three native disulfide bonds were readily formed during refolding of bacterially produced IL-4 under different conditions and using different redox compounds.[38] Additionally, the engineered cysteine became conjugated to a variable extent with the thiol compound present in the refolding solution (see also ref 16). With a sacrifice of yield, it is possible to submit the resulting protein mixture containing the free and the conjugated cysteinyl side chain to modification, for instance, PEGylation. Afterward, the modified protein must be purified, which often requires sophisticated isolation techniques to separate the different species, which differ only in the modified moiety attached to the engineered cysteine residue. Therefore, the present experiments offer a different approach to generation of IL-4 cysteine muteins with a nonconjugated free thiol group. The IL-4 protein is refolded under conditions leading to the formation of the native disulfides and a complete disulfide conjugation for the engineered cysteine residue with the tripeptide glutathione. The glutathione is subsequently removed enzymatically with high specificity by means of glutaredoxin.[28] The IL-4 cysteine mutein containing the free thiol can then be easily isolated with good yield.

The enzymatic rates for the removal of the glutathione differed approximately 50-fold among the five IL-4 cysteine muteins investigated here. The highest rate was observed for 38GS. Position 38 is located in one of the large overhand β-strands connecting helices A and B (see ref 6). Asn38 occurring normally at this position is N-glycosylated in the native protein, indicating that the side chain is readily accessible from the bulk phase. Remarkably, the side chains of Asn38 have high temperature factors (B values) in the crystal structure and are highly disordered in the NMR solution structure, and they are therefore probably highly flexible.[12] 74GS is also reduced at a high rate, about 4 times more slowly than 38GS. Position 74 is located at the N-terminal start of helix C in a segment that is not present, for instance, in murine IL-4, and is thus probably dispensable for the functional activity. This indicates that the rate of enzymatic reduction is very dependent on the accessibility of the mixed disulfide, and it has been demonstrated that in peptides the reduction of conjugated glutathione by GRX is sensitive to the environment.[39,40]

In this study, the preparative reduction by means of *E. coli* glutaredoxin-1 was allowed to proceed for 30 min. This

reaction time was too short for 78GS, which was not completely reduced. Under the same conditions, the reaction time was too long for 74GS, which was "over-reduced" and contained some IL-4 protein reduced at the native disulfides. The latter contaminants then had to be separated later after NEM or PEG-modification using reversed-phase HPLC. This demonstrates that in future experiments the reaction time must be optimized separately for each cysteine mutein. Invariably, a small amount of nonconjugated mutein remained at the end of the incubation period. Possibly, the affinity of glutaredoxin for the IL-4 mutein is too low to catalyze the reduction at low mutein concentration. The GS mutein reduction might also be out-competed by the unspecific reduction of the internal disulfide bonds. Remarkably, the 74GS analogue which was over-reduced enzymatically in the present experiments also showed a high susceptibility of native disulfide bonds by DTT. This suggests that depending on the location the engineered cysteine can destabilize the conformation of IL-4.

Site-specific modification offers a chemical method to study the interaction of IL-4 with the IL-4Rα receptor chain. While the cysteine substitution per se yielded a similar effect on affinity as the previously described alanine substitution,[25] the conjugation with the tripeptide glutathione or MA-PEG resulted in additional effects. N-Ethylmaleimide conjugation did not produce major changes in affinity compared to the free thiol form. Conjugated glutathione had the same or larger effects than conjugating poly(ethylene glycol) (branched PEG, M_r 2360) at a position near to or within the receptor binding epitope, suggesting that both steric requirements and charge are important factors influencing receptor binding. When comparing the positions of the engineered cysteine residues in the structure of IL-4 bound to the IL4Rα ectodomain, the affinity declines with the distance of the engineered cysteine from the IL4Rα binding epitope. The most distant glutathione label at positions 38 and 74 caused a marginal less than 2-fold decrease in the affinity; glutathione labels at positions 16 and 78 are at the periphery of the epitope and led to a 2- to 3-fold increased K_D; glutathione attached to the engineered cysteine at position 81 leads to the modification of a minor binding determinant, Arg81, which is partially buried in the contact and engaged in a salt bridge to receptor Asp66,[13] thus resulting in an almost 50-fold reduction of its binding affinity to IL4Rα. IL-4 exhibits an unusually high rate of association with IL-4Rα (k_a = 1.5 × 10^7 M^{-1} s^{-1}).[22] Ligand and receptor exhibit a high charge complementarity leading to electrostatic steering during association.[26] Concordantly, in previous mutational analysis the removal of one positive charge in IL-4 resulted in a 1.3- to 2-fold reduction in the association rate constant. Thus, the additional negative charge introduced by the glutathione in the mixed disulfide might account for the 2-fold reduced association rate. The glutathione tripeptide attached to the cysteine at position 81 in 81GS will also impose some steric hindrance thereby altering the rate of dissociation and association.

In future experiments, the present collection of IL-4 cysteine muteins with a single free thiol will be exploited to find the optimal attachment site for fluorescent dyes and other labels. Obviously, it is of prime importance that the conjugated compound is disturbing IL-4 receptor binding as little as possible. Above all, the IL-4 cysteine muteins will be used for the screening of chemical libraries by the tethering approach, which is proposed to identify compounds also binding with low affinity.[15,41] The goal is to find chemical compounds binding to the IL-4 interface for IL-4Rα, thereby interfering with the interaction of IL-4 and IL-4Rα.

■ ASSOCIATED CONTENT

Supporting Information

Figure S-1 shows mass spectrometry analysis of IL-4S16C and IL4N38C mutein refolded in the presence of 5 mM glutathione, β-mercaptoethanol, cysteamine, or thioglycolate. Figure S-2 shows SDS PAGE analysis of reduction of IL-4 muteins 74GS, 78GS, and 81GS. Figure S-3 shows time course of IL-4 wild-type and IL-4 GS analogues reduction. Figure S-4 shows SDS PAGE analysis of nonconjugated IL-4 cysteine muteins under reducing and nonreducing conditions. Figure S-5 shows mass spectrometry analysis of NEM labeled IL-4 cysteine muteins. Table S-1 shows primers used for mutagenesis of IL-4 cDNA. Table S-2 mass spectrometry analysis of purified glutathione-modified IL-4 cysteine muteins. Table S-3 shows mass spectrometry analysis of purified NEM-labeled IL-4 cysteine analogues. This material is available free of charge via the Internet at http://pubs.acs.org.

■ AUTHOR INFORMATION

Corresponding Author

*E-mail: viswa@live.de. Phone: +49-931-3180767. Fax: +49-931-3184113.

Notes

The authors declare no competing financial interest.

■ ACKNOWLEDGMENTS

The authors thank N. Seher and A. Schaaf for excellent technical assistance and Markos Pechlivanis for both a critical reading of the manuscript and his invaluable input in our many discussions. This project was supported by the EU Marie Curie IAPP research fund FOLDAPPI and the Deutsche Forschungsgemeinschaft (DFG), SFB 487 TP B2.

■ ABBREVIATIONS:

Nomenclature of the IL-4 analogues, The number gives the position of the engineered cystein in the IL-4 mutein and the ending indicates non-conjugated thiol (SH), conjugated GS, NEM, and PEG; PEG, poly (ethylene glycol); MA, maleimide; MA-PEG, maleimido-PEG; NEM, *N*-ethyl-maleimide; GS, glutathione.

■ REFERENCES

(1) Paul, W. E. (1991) Interleukin-4: a prototypic immunoregulatory lymphokine. *Blood 77*, 1859−70.

(2) Paul, W. E., and Seder, R. A. (1994) Lymphocyte responses and cytokines. *Cell 76*, 241−51.

(3) Kuperman, D. A., and Schleimer, R. P. (2008) Interleukin-4, interleukin-13, signal transducer and activator of transcription factor 6, and allergic asthma. *Curr. Mol. Med. 8*, 384−92.

(4) Li, Z., Jiang, J., Wang, Z., Zhang, J., Xiao, M., Wang, C., Lu, Y., and Qin, Z. (2008) Endogenous interleukin-4 promotes tumor development by increasing tumor cell resistance to apoptosis. *Cancer Res. 68*, 8687−94.

(5) Kelly-Welch, A. E., Hanson, E. M., Boothby, M. R., and Keegan, A. D. (2003) Interleukin-4 and interleukin-13 signaling connections maps. *Science 300*, 1527−8.

(6) Mueller, T. D., Zhang, J. L., Sebald, W., and Duschl, A. (2002) Structure, binding, and antagonists in the IL-4/IL-13 receptor system. *Biochim. Biophys. Acta 1592*, 237−50.

(7) Borish, L. (2010) IL-4 and IL-13 dual antagonism: a promising approach to the dilemma of generating effective asthma biotherapeutics. *Am. J. Respir. Crit. Care Med. 181*, 769−70.

(8) Kruse, N., Tony, H. P., and Sebald, W. (1992) Conversion of human interleukin-4 into a high affinity antagonist by a single amino acid replacement. *EMBO J. 11*, 3237−44.
(9) Tony, H. P., Shen, B. J., Reusch, P., and Sebald, W. (1994) Design of human interleukin-4 antagonists inhibiting interleukin-4-dependent and interleukin-13-dependent responses in T-cells and B-cells with high efficiency. *Eur. J. Biochem. 225*, 659−65.
(10) Burmeister Getz, E., Fisher, D. M., and Fuller, R. (2009) Human pharmacokinetics/pharmacodynamics of an interleukin-4 and interleukin-13 dual antagonist in asthma. *J. Clin. Pharmacol. 49*, 1025−36.
(11) Wenzel, S., Wilbraham, D., Fuller, R., Getz, E. B., and Longphre, M. (2007) Effect of an interleukin-4 variant on late phase asthmatic response to allergen challenge in asthmatic patients: results of two phase 2a studies. *Lancet 370*, 1422−31.
(12) Smith, L. J., Redfield, C., Smith, R. A., Dobson, C. M., Clore, G. M., Gronenborn, A. M., Walter, M. R., Naganbushan, T. L., and Wlodawer, A. (1994) Comparison of four independently determined structures of human recombinant interleukin-4. *Nat. Struct. Biol. 1*, 301−10.
(13) Hage, T., Sebald, W., and Reinemer, P. (1999) Crystal structure of the interleukin-4/receptor alpha chain complex reveals a mosaic binding interface. *Cell 97*, 271−81.
(14) LaPorte, S. L., Juo, Z. S., Vaclavikova, J., Colf, L. A., Qi, X., Heller, N. M., Keegan, A. D., and Garcia, K. C. (2008) Molecular and structural basis of cytokine receptor pleiotropy in the interleukin-4/13 system. *Cell 132*, 259−72.
(15) Erlanson, D. A., Wells, J. A., and Braisted, A. C. (2004) Tethering: fragment-based drug discovery. *Annu. Rev. Biophys. Biomol. Struct. 33*, 199−223.
(16) Tóth, G., Mukhyala, K., and Wells, J. A. (2007) Computational approach to site-directed ligand discovery. *Proteins 68*, 551−60.
(17) Doherty, D. H., Rosendahl, M. S., Smith, D. J., Hughes, J. M., Chlipala, E. A., and Cox, G. N. (2005) Site-specific PEGylation of engineered cysteine analogues of recombinant human granulocyte-macrophage colony-stimulating factor. *Bioconjugate Chem. 16*, 1291−8.
(18) Kubetzko, S., Sarkar, C. A., and Plückthun, A. (2005) Protein PEGylation decreases observed target association rates via a dual blocking mechanism. *Mol. Pharmacol. 68*, 1439−54.
(19) Rosendahl, M. S., Doherty, D. H., Smith, D. J., Carlson, S. J., Chlipala, E. A., and Cox, G. N. (2005) A long-acting, highly potent interferon alpha-2 conjugate created using site-specific PEGylation. *Bioconjugate Chem. 16*, 200−7.
(20) Antoniu, S. A. (2010) Pitrakinra, a dual IL-4/IL-13 antagonist for the potential treatment of asthma and eczema. *Curr. Opin. Investig. Drugs 11*, 1286−94.
(21) Hyde, J., Braisted, A. C., Randal, M., and Arkin, M. R. (2003) Discovery and characterization of cooperative ligand binding in the adaptive region of interleukin-2. *Biochemistry 42*, 6475−83.
(22) Shen, B. J., Hage, T., and Sebald, W. (1996) Global and local determinants for the kinetics of interleukin-4/interleukin-4 receptor alpha chain interaction. A biosensor study employing recombinant interleukin-4-binding protein. *Eur. J. Biochem. 240*, 252−61.
(23) Laemmli, U. K. (1970) Cleavage of structural proteins during the assembly of the head of bacteriophage T4. *Nature 227*, 680−5.
(24) Kraich, M., Klein, M., Patino, E., Harrer, H., Nickel, J., Sebald, W., and Mueller, T. D. (2006) A modular interface of IL-4 allows for scalable affinity without affecting specificity for the IL-4 receptor. *BMC Biol. 4*, 13.
(25) Kruse, N., Shen, B. J., Arnold, S., Tony, H. P., Müller, T., and Sebald, W. (1993) Two distinct functional sites of human interleukin 4 are identified by variants impaired in either receptor binding or receptor activation. *EMBO J. 12*, 5121−9.
(26) Demchuk, E., Mueller, T., Oschkinat, H., Sebald, W., and Wade, R. C. (1994) Receptor binding properties of four-helix-bundle growth factors deduced from electrostatic analysis. *Protein Sci. 3*, 920−35.
(27) Hu, J., Duppatla, V., Harth, S., Schmitz, W., and Sebald, W. (2010) Site-specific PEGylation of bone morphogenetic protein-2 cysteine analogues. *Bioconjugate Chem. 21*, 1762−72.
(28) Björnberg, O., and Holmgren, A. (1991) Characterization of homogeneous recombinant glutaredoxin from Escherichia coli: purification from an inducible lambda PL expression system and properties of a novel elongated form. *Protein Expr. Purif. 2*, 287−95.
(29) Bushweller, J. H., Billeter, M., Holmgren, A., and Wüthrich, K. (1994) The nuclear magnetic resonance solution structure of the mixed disulfide between Escherichia coli glutaredoxin(C14S) and glutathione. *J. Mol. Biol. 235*, 1585−97.
(30) Cox, G. N., Rosendahl, M. S., Chlipala, E. A., Smith, D. J., Carlson, S. J., and Doherty, D. H. (2007) A long-acting, mono-PEGylated human growth hormone analog is a potent stimulator of weight gain and bone growth in hypophysectomized rats. *Endocrinology 148*, 1590−7.
(31) Long, D. L., Doherty, D. H., Eisenberg, S. P., Smith, D. J., Rosendahl, M. S., Christensen, K. R., Edwards, D. P., Chlipala, E. A., and Cox, G. N. (2006) Design of homogeneous, monopegylated erythropoietin analogs with preserved in vitro bioactivity. *Exp. Hematol. 34*, 697−704.
(32) Tolmachev, V., Xu, H., Wållberg, H., Ahlgren, S., Hjertman, M., Sjöberg, A., Sandström, M., Abrahmsén, L., Brechbiel, M. W., and Orlova, A. (2008) Evaluation of a maleimido derivative of CHX-A″ DTPA for site-specific labeling of affibody molecules. *Bioconjugate Chem. 19*, 1579−87.
(33) Kruse, N., Lehrnbecher, T., and Sebald, W. (1991) Site-directed mutagenesis reveals the importance of disulfide bridges and aromatic residues for structure and proliferative activity of human interleukin-4. *FEBS Lett. 286*, 58−60.
(34) Vaz, D. C., Rodrigues, J. R., Sebald, W., Dobson, C. M., and Brito, R. M. (2006) Enthalpic and entropic contributions mediate the role of disulfide bonds on the conformational stability of interleukin-4. *Protein Sci. 15*, 33−44.
(35) Narayan, M., Xu, G., Ripoll, D. R., Zhai, H., Breuker, K., Wanjalla, C., Leung, H. J., Navon, A., Welker, E., McLafferty, F. W., and Scheraga, H. A. (2004) Dissimilarity in the reductive unfolding pathways of two ribonuclease homologues. *J. Mol. Biol. 338*, 795−809.
(36) Wedemeyer, W. J., Welker, E., Narayan, M., and Scheraga, H. A. (2000) Disulfide bonds and protein folding. *Biochemistry 39*, 7032.
(37) Redfield, C., Boyd, J., Smith, L. J., Smith, R. A., and Dobson, C. M. (1992) Loop mobility in a four-helix-bundle protein: 15N NMR relaxation measurements on human interleukin-4. *Biochemistry 31*, 10431−7.
(38) Millis, K. K., Weaver, K. H., and Rabenstein, D. L. (1993) Oxidation-Reduction Potential of Glutathione. *J. Org. Chem. 58*, 4144−4146.
(39) Elgán, T. H., Planson, A. G., Beckwith, J., Güntert, P., and Berndt, K. D. (2010) Determinants of activity in glutaredoxins: an in vitro evolved Grx1-like variant of Escherichia coli Grx3. *Biochem. J. 430*, 487−95.
(40) Peltoniemi, M. J., Karala, A. R., Jurvansuu, J. K., Kinnula, V. L., and Ruddock, L. W. (2006) Insights into deglutathionylation reactions. Different intermediates in the glutaredoxin and protein disulfide isomerase catalyzed reactions are defined by the gamma-linkage present in glutathione. *J. Biol. Chem. 281*, 33107−14.
(41) Erlanson, D. A., Braisted, A. C., Raphael, D. R., Randal, M., Stroud, R. M., Gordon, E. M., and Wells, J. A. (2000) Site-directed ligand discovery. *Proc. Natl. Acad. Sci. U. S. A. 97*, 9367−72.

Bioconjugate Chemistry

Article

pubs.acs.org/bc

Engineering of *Aerococcus viridans* L-Lactate Oxidase for Site-Specific PEGylation: Characterization and Selective Bioorthogonal Modification of a S218C Mutant

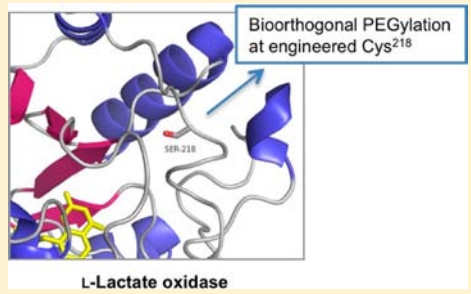
Birgit Unterweger,[†] Thomas Stoisser,[†] Stefan Leitgeb,[†] Ruth Birner-Grünberger,[‡] and Bernd Nidetzky*[,†]

[†]Research Center Pharmaceutical Engineering, and Institute of Biotechnology and Biochemical Engineering, Graz University of Technology, Petersgasse 12, A-8010 Graz, Austria

[‡]Institute of Pathology and Center for Medical Research, Medical University of Graz, Stiftingtalstraße 24, A-8010 Graz, Austria

Supporting Information

ABSTRACT: A defined bioconjugate of *Aerococcus viridans* L-lactate oxidase and poly(ethylene glycol) 5000 was prepared and characterized in its structural and functional properties in comparison to the unmodified enzyme. Because the L-lactate oxidase in the native form does not contain cysteines, we introduced a new site for chemical modification via thiol chemistry by substituting the presumably surface-exposed serine-218, a nonconserved residue in the amino acid sequence, with cysteine. The resulting S218C mutant was isolated from *Escherichia coli* and shown in kinetic assays to be similarly (i.e., about half as) active as the native enzyme, thus validating the structure-guided design of the mutation. Using maleimide-activated methoxypoly(ethylene glycol) 5000 in about 10-fold molar excess over protein, the S218C mutant was converted in high yield (94%) into PEGylated derivative, while the native enzyme was totally unreactive under equivalent conditions. PEGylation caused only a relatively small decrease (30%) in the specific activity of the S218C mutant, and it did not change the protein stability. PEGylation went along with enhancement of the apparent size of the homotetrameric L-lactate oxidase in gel permeation chromatography, from 170 kDa to 250 kDa. The protein hydrodynamic diameter determined by dynamic light scattering increased from 11.9 nm in unmodified S218C mutant to 16.4 nm in the PEGylated form. Site-selective PEGylation of the mutated L-lactate oxidase, using orthogonal maleimide−thiol coupling, could therefore facilitate incorporation of the enzyme into biosensors currently employed for determination of blood L-lactate levels, and it could also support different applications of the enzyme in applied biocatalysis.



INTRODUCTION

Covalent grafting of poly(ethylene glycol) chains on proteins, in short, "PEGylation", is a powerful technique to optimize the structure and function of a given protein for a destined application.[1−4] One major use of PEGylation is in the development of protein biopharmaceuticals for human therapy where PEGylated proteins often display longer in vivo circulating half-lives than the native (unPEGylated) counterparts.[5] PEGylation has also been used widely in the preparation of apt molecular sensors for diagnostic assays.[6−9] Moreover, it has been employed to enhance activity and stability of enzymes, particularly for biocatalysis in nonaqueous solvents.[3,10−12] Recent studies emphasize another interesting effect of PEGylation that is in fine-tuning of protein interactions with surfaces.[13,14] PEGylated lysozyme, for example, showed attenuated adsorption and aggregation on solid surfaces as compared to the unconjugated protein.[14] In addition, PEGylation increased the reversibility of adsorption of lysozyme on solid supports.[14]

PEG−protein conjugates are often prepared by reaction of the protein with PEG molecules having amine-reactive end-groups.[4] Because it is typical for most proteins to contain a variety of internal amine groups from lysine residues in addition to the N-terminal amine, the resulting PEGylation is normally quite heterogeneous in the number and placement of the PEG chains. Heterogeneity in the structure may hinder the biological activity, and separation of the individual PEGylated forms is usually not practical.[4] It is therefore important to generate well-defined PEG−protein conjugates, and site-selective derivatization is probably the best way to obtain such biomolecules.[2,4,15,16] Cysteine residues are often the targets for site-specific modification using thiol chemistry.[2,17−20] Proteins lacking a cysteine in their native structure can be genetically engineered to incorporate one or more cysteines in specific positions, which are usually chosen away from the protein functional site to minimize possible interference of chemical modification with the biological activity. Even though the literature gives a few examples of site-specific PEGylation of proteins at newly introduced cysteines,[21−23] it is also clear from these studies that the overall approach remains a difficult

Received: January 2, 2012
Revised: May 11, 2012
Published: May 31, 2012

ACS Publications © 2012 American Chemical Society

dx.doi.org/10.1021/bc2006847 | *Bioconjugate Chem.* 2012, 23, 1406−1414

challenge that necessitates useful coordination of protein design with cysteine-directed conjugation.

L-Lactate oxidase (EC 1.13.12.4; LOX) is a flavin mononucleotide (FMN)-dependent enzyme that catalyzes oxidation of L-lactate into pyruvate.[24] O_2 serves as the terminal electron acceptor of the enzymatic reaction that gives H_2O_2 as its second product. LOX has its major uses in medical analytics where the enzyme is applied widely as biological transducer of different biosensors and test strips.[25−27] LOX from the bacterium *Aerococcus viridans* has been well-characterized biochemically,[24] and a high-resolution crystal structure has been determined for this homotetrameric enzyme.[28,29] Each subunit of about 41 kDa size contains one FMN that is bound noncovalently. The *A. viridans* LOX does not contain cysteine residues. Here, a potentially useful concept of bioconjugation by design is proposed for this LOX that exploits cysteine-directed chemical modification of a mutated LOX (having residue Ser^{218} replaced by Cys; S218C mutant) with PEG molecule containing maleimide end-group. The modification is shown to proceed selectively and in quantitative yields. About 30% of original biological activity of the wild-type enzyme is retained in PEGylated S218C mutant.

The enzymatically active part of the lactate biosensor is usually a thin solid film in which the used LOX is immobilized through the combined physical effects of adsorption to and entrapment within the matrix materials.[30−32] Of note, the often irreversible adsorption to the film can result in substantial activity loss, and controlled PEGylation of the enzyme might help preventing it (see ref 14 for the case of lysozyme). In the absence of covalent fixation, strength of retention of the enzyme in the matrix can present another problem. Even though chemical cross-linking with a bifunctional reagent such as glutardialdehyde presents a possible solution, there are the clear disadvantages that the cross-linking very often results in large losses of the enzyme activity, and homogeneous distribution of the cross-linked, sometimes partly insoluble enzyme in the matrix can become a serious issue.[33] A method providing controlled size enhancement for the soluble LOX would facilitate stable embedment of the enzyme in the sensor matrix, and it should additionally be compatible with the currently used immobilization procedures. It might also have favorable effects on enzyme adsorption on the biosensor film (considering ref 14). Nonselective (random) PEGylation was previously applied to a maltose biosensor[6] as well as glucose oxidase,[7,8] and the resulting bioconjugates showed useful properties for sensor development. The results presented herein open up the possibility to provide selectively PEGylated LOX for biosensor applications. Other applications of the enzyme in applied biocatalysis[34,35] could also benefit from the reported developments.

EXPERIMENTAL PROCEDURES

Materials. Monomethoxypoly(ethylene glycol) maleimide (mPEG-mal) 5000, L-(+)-lactic acid, (*S*)-2-hydroxybutyric acid, and (*S*)-2-hydroxyisocaproic acid in the highest available purity, 3,3-dimethylglutaric acid, 4-aminoantipyrine, peroxidase from horseradish, *N*,*N*-dimethylaniline, and dodecylbenzenesulfonic acid were all obtained from Sigma Aldrich. Lyophilized wild-type LOX from *Aerococcus viridans* (WT) was a gift of Roche Diagnostics GmbH. Enzyme was stored at −25 °C until further use. The plasmid pLO-1, which harbored the LOX gene, was kindly provided by Dr. T. Meier (Roche).

Molecular Cloning and Site-Directed Mutagenesis. Mutations leading to substitution of Ser^{218} by Cys were introduced by a two-stage polymerase chain reaction, using a protocol from the literature.[36] Briefly, two separate primer extension reactions were carried out in which pLO-1 was used as the template and one of the two mutagenic oligonucleotide primers was also present. The two primers were 5′-GGTGCTTGCAAACAAAAAATCTCACCAAGA-GA-TATTG-3′ (termed S218Cfw; melting point: 61.3 °C), and 5′-TTGTTTGCAAGCACCGTAGAT-ATTGTTTAATGACA-TACC-3′ (termed S218Crev; melting point: 61.3 °C). DNA was amplified by Pfu DNA Polymerase (Promega) using the following conditions: heat denaturation at 95 °C for 1 min; 4 elongation cycles, each consisting of 95 °C for 50 s, 59 °C for 50 s, and 68 °C for 10 min; final extension at 68 °C for 7 min, and cooling at 4 °C. The two separate PCR mixtures were combined in a volume ratio of 1:1, and another PCR was performed under the conditions above, but with a total repeat of 18 cycles. Template DNA was digested with *Dpn*I at 37 °C for 1 h. Plasmid DNA was transformed into electrocompetent *E. coli* BL21 (DE3) cells. After regeneration, the cells were cultured overnight at 37 °C on LB-amp plates (1% peptone, 0.5% yeast extract, 0.5% NaCl, 1.8% agar supplemented with 100 μg/mL ampicillin). Only transformants carrying plasmids with the mutation of interest verified by DNA sequencing were used for further steps.

Production of S218C Mutant. *Escherichia coli* BL21 (DE3) was grown overnight as starter culture in medium containing 5.5 g/L glucose monohydrate, 10 g/L peptone, 5 g/L yeast extract, 5 g/L NaCl, 1 g/L NH_4Cl, 0.25 g/L $MgSO_4$ monohydrate, 3 g/L K_2HPO_4, 6 g/L KH_2PO_4, 2 mg/L thiamine, 115 mg/L ampicillin, 4 mg/L $FeSO_4$ heptahydrate, 1 mg/L $MnSO_4$ monohydrate, 0.4 mg/L $CoCl_2$, 0.15 mg/L $CuSO_4$ pentahydrate, 0.1 mg/L H_3BO_3, 0.2 mg/L $ZnSO_4$ heptahydrate, 0.2 mg/L Na_2MoO_4 dihydrate, and 0.4 mg/L $AlCl_3$. About 100 μL poly(propylene glycol) was added per L medium. The main culture was prepared from the same medium except that a 4-fold higher amount of glucose monohydrate was used. It was inoculated to an OD_{600} of 0.5. Cultivation was performed in B. Braun Biotech International BiostatC, Type CT5−2 bioreactor. Temperature, stirring, pH, and oxygen partial pressure were controlled and adjusted automatically. The pH was controlled at pH 7.0 using 2 M KOH and 1 M H_3PO_4; the pO_2 was fixed to a minimum of 40%. The cells were grown at 37 °C before induction. At an OD_{600} of about 2, isopropyl β-D-1-thiogalactopyranoside was added to a final concentration of 0.25 mM. Upon induction, the cells were cultured at 30 °C. When the level of glucose had decreased to a level <1 g/L (Diabur Test 5000, Roche Diagnostics), the cells were harvested by centrifugation. About 33 g wet cell mass/L was obtained. The cell pellet was suspended in 50 mM potassium phosphate buffer, pH 7.0, and stored at −25 °C.

Protein Purification. All steps were performed in 50 mM potassium phosphate buffer, pH 7.0. Cells were disrupted in a French press, and the crude extract was obtained by centrifugation. Protein was precipitated in the presence of 1.5 M $(NH_4)_2SO_4$ at 4 °C, and precipitate was removed by centrifugation. The S218C mutant remaining in the supernatant was further purified by hydrophobic interaction chromatography using a Phenyl Sepharose 6 Fast Flow (High Sub) column (GE Healthcare Life Sciences; 64 mL) and the Äkta FPLC system (Amersham Biosciences). The protein

dx.doi.org/10.1021/bc2006847 | *Bioconjugate Chem.* 2012, 23, 1406−1414

(about 100 mg in total) was loaded on the column equilibrated with buffer and eluted at 25 °C with a linearly decreasing gradient of $(NH_4)_2SO_4$. The flow rate was 5 mL/min, and eluted protein was detected at 280 nm. Fractions containing LOX activity were pooled. Purity was checked with SDS-PAGE, using PhastGel Gradient 8−25 (GE Healthcare Life Sciences) gels and the Pharmacia High Speed Electrophoresis System (Pharmacia Biotech). Enzyme solution was then desalted by repeated cycles of concentration and dilution using concentrator tubes (Vivaspin 20, 10 kDa cutoff, Vivascience AG) and stored in 50 mM potassium phosphate buffer, pH 7.0, at −25 °C until further use.

Assays. LOX activity was measured using a peroxidase-coupled spectrophotometric assay (Sigma) in which the H_2O_2 produced in the LOX reaction is further reacted with peroxidase in the presence of 4-aminoanipyrine and *N*,*N*-dimethylaniline to give a quinonediimine dye that is detected. About 5 to 10 μL of enzyme appropriately diluted in 50 mM potassium phosphate buffer, pH 7.0, was added to a solution containing 40 mM 3,3-dimethylglutaric acid, 2.5 units peroxidase, 1.5 mM 4-aminoantipyrine, 50 mM L-(+)-lactic acid, and 0.04% (v/v) *N*,*N*-dimethylaniline in a total volume of 0.5 mL. The pH of the solution was pH 6.5. After a reaction time of between 10 and 20 min at 37 °C, 1 mL of 0.25% (w/v) dodecylbenzenesulfonic acid was added to stop the reaction. The produced quinonediimine dye was measured spetrophotometrically at 565 nm with a Varian Cary 50 Bio UV−visible spectrophotometer at 25 °C.

Protein concentrations were measured according to the Bradford protein quantification assay (Roti-Quant, Carl Roth GmbH + Co KG) using BSA as reference. Note: the commercial preparation of LOX was not used for calibration of the protein assay. The enzyme is a solid powder that contains various substances other than target enzyme. Calibration based on solid mass is therefore not possible.

PEGylation. PEGylation was done according to a procedure adopted from the literature.[20] Briefly, the purified S218C mutant (8 μM) was incubated in the presence of different molar excesses of mPEG-mal 5000 in 50 mM potassium phosphate buffer, pH 7.0, at 4 °C for up to 7 h under gentle agitation (300 rpm; Eppendorf Thermomixer). The molar ratio of mPEG-mal 5000 to protein was varied in several steps in the range 1−12.5. Samples were taken and processed after 2, 4, and 7 h. To remove residual mPEG-mal 5000, repeated ultrafiltration with Vivaspin 6 centrifugal concentrator tubes (10 kDa cutoff, Vivascience AG) was performed. The PEGylated S218C mutant was used immediately for further characterization. The wild-type enzyme was treated in exactly the same manner for reference. To determine if residual free PEG that was not removed by the ultrafiltration could affect the measured enzyme activities, we performed controls in which PEG 4000 was added to the assays. The PEG 4000 was used in 12.5-fold molar excess over protein (WT; S218C mutant).

Mass Spectrometry. MALDI-TOF (time-of-flight)-MS measurements were performed on a Bruker Ultraflextreme instrument. Protein solutions (2.4 mg/mL PEGylated enzyme; 7.2 mg/mL unPEGylated enzyme) in 50 mM potassium phosphate buffer (pH 7.0) were diluted in 50% acetonitrile and 0.1% trifluoroacetic acid 1:5 (v/v). They were mixed 1:1 (v/v) with a suspension of 5 mg super-DHB matrix (Sigma; 9:1 mixture of 2,5-dihydroxybenzoic acid and 2-hydroxy-5-methoxybenzoic acid) in 50 μL acetonitrile and 50 μL 0.1% trifluoroacetic acid. One microliter was spotted onto an 800 μm Bruker MTP Anchorchip and left to dry. Full MS spectra were obtained in positive linear mode after external calibration using an appropriate protein standard (10−70 kDa) in the mass/charge range from 550 to 73 000 by summarizing 9000 laser shots.

Internal sequence information of PEGylated LOX as confirmed by the detected mass shifts in MALDI-TOF analysis was received from LC-MS/MS. Details of the experimental protocol are given in the Supporting Information. The LC-MS/MS data were analyzed by searching the amino acid sequence of LOX of *Aerococcus viridans* (NCBI accession number ZP_06807595), with *Mascot 2.2* (MatrixScience) contained in a database including known contaminants such as the enzymes used for digestion and human keratins. PEGylation with 110 and 111 monomeric units (the two most abundant masses of PEG 5000) was included as variable modification at Cys or the protein N-terminus next to carbamidomethylation on Cys as variable modification. A maximum false discovery rate of 5% using decoy database search, an ion score cutoff of 20, and a minimum of 2 identified peptides was chosen as identification criteria.

Absorbance Spectroscopy. UV−vis absorbance spectra were recorded with a Varian Cary 50 Bio UV−visible Spectrophotometer in quartz cuvettes (Hellma GmbH & Co. KG) of 10 mm light path. About 0.1 mM enzyme in potassium phosphate buffer, pH 7.0, was scanned at 25 °C, and the values were corrected for blank readings. Determination of enzyme-bound cofactor was done by spectrophotometric quantification of free FMN at 445 nm. A molar extinction coefficient of 12500 M^{-1} cm^{-1} was assumed, and the FMN was released from the enzyme (typically about 25 μM) by treatment with trifluoroacetic acid.[37]

Kinetic Analysis. Initial rates of enzymatic oxidation of L-(+)-lactic acid or an alternative α-hydroxy acid substrate were obtained at pH 6.5 and 37 °C. A 50 mM potassium phosphate buffer was used. The substrate concentration was varied, typically at 10 different levels in the range 0.1−50 mM. The rates were recorded using the peroxidase-coupled spectrophotometric assay. Kinetic constants (K_M, V_{max}) were obtained from nonlinear fit of the Michaelis−Menten equation to the measured data using *Sigma Plot*. Turnover numbers (k_{cat}) were calculated from V_{max} using the relationship, $k_{cat} = V_{max}/E$ where E is the molar enzyme concentration. E was determined from the protein concentration assuming a molecular mass of 41 kDa for the enzyme subunit.

Stability of Enzyme Activity. Irreversible inactivation at 37 °C was measured. The enzyme (WT, PEGylated, or unmodified S218C mutant) was incubated in a concentration of 0.2−0.4 μM in 40 mM HEPES buffer (pH 8.1) containing 150 mM NaCl. An Eppendorf Thermomixer was used for temperature control and slight agitation. Samples were taken at different times, and residual enzyme activity was measured. Enzyme half-life times were determined by fitting an exponential decay function to the experimental time course.

Protein Conformational Stability. Differential scanning fluorimetry was used. This was performed with a Bio-Rad C1000 Thermocycler RT-PCR machine (CFX96 system) applying a general protocol reported elsewhere.[38] Experiments were done in 50 mM potassium phosphate buffer (pH 7.0) using 2−10 μM enzyme (WT, PEGylated or unmodified S218C mutant). SYPRO Orange (Invitrogen) was used as fluorescence probe. It was diluted 100-fold from the commercial stock solution (in dimethylsulfoxide) using

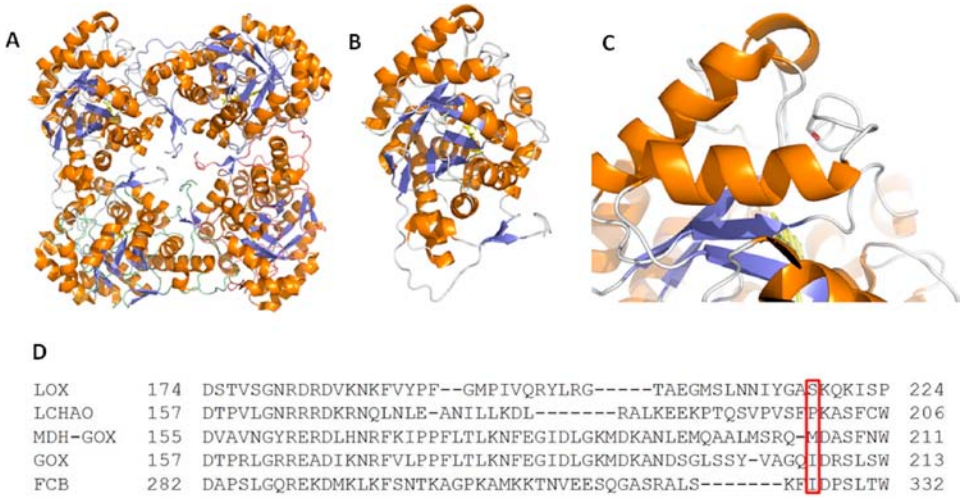


Figure 1. Structure of *A. viridans* LOX and selection of Ser[218] as site for site-directed substitution with cysteine and subsequent PEGylation via thiol chemistry: (A) the functional LOX homotetramer; (B) overall fold of monomer A of LOX; (C) loop 4 region with Ser[218] rendered as stick representation in CPK coloring. Structural data was from PDB-file 2DU2. Graphical representations were done in *Pymol 0.99*. Orange color represents helix regions, blue the sheet regions. The cofactor FMN is shown in stick representation in yellow. (D) Structure-based sequence alignment of the loop 4 between members of the family of α-hydroxy acid oxidases. LOX, L-lactate oxidase from *Aerococcus viridans*; LCHAO, rat kidney long-chain α-hydroxy acid oxidase; MDH-GOX, soluble chimeric mutant form of L-mandelate dehydrogenase from *Pseudomonas putida*, where parts of loop 4 were substituted by a corresponding GOX sequence part. GOX, glycolate oxidase from *Spinacia oleracea*; FCB, flavocytochrome *b*2 from *Saccharomyces cerevisiae*. The alignment was adapted from the literature.[28]

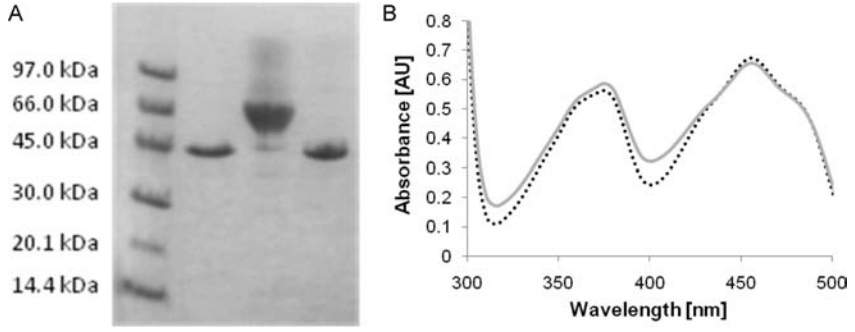


Figure 2. PEGylation of purified S218C mutant monitored by SDS-PAGE (A) and comparison of the visible absorbance spectrum of the mutated LOX with that of the wild-type enzyme. Panel A: lane 1, molecular mass markers; lane 2, unmodified WT; lane 3, PEGylated S218C; lane 4, WT LOX incubated under PEGylation conditions; about 10 μg protein was applied on each lane. Panel B: WT (broken black line) and S218C (full light gray line). Spectra were recorded at an enzyme concentration of 0.1 mM in 50 mM potassium phosphate buffer, pH 7.0, at 25 °C. The enzyme molarity was calculated from the protein concentration, determined with the Bradford dye binding assay using BSA as reference. A molecular mass of 41 kDa was assumed. AU, arbitrary units.

phosphate buffer (50 mM; pH 7.0). Excitation and emission filters for SYPRO Orange were at 465 and 610 nm, respectively. Reactions were carried out in 96-well format using 25 μL of total reaction volume each. Bio-Rad thin-wall PCR plates were used. Temperature was raised at 0.5 °C/min from 25 to 95 °C, and fluorescence intensity was measured every 0.5 °C. Fluorescence intensity increases when due to unfolding at elevated temperature hydrophobic surfaces are exposed in the protein, and SYPRO Orange binds to them. A control containing 25 μM of each free FMN and wild-type enzyme was carried out in the absence of SYPRO Orange. Boltzmann sigmoid was used for data fitting, yielding a temperature of inflection of the transition curve (T_i), as shown in Figures S1 of Supporting Information. The T_i value is used here to characterize the conformational stabilities of the different protein preparations used. Reported T_i values are means of eight independent experiments.

Dynamic Light Scattering. Nanosizer ZS (Malvern) was used for measurement of particle size distribution. All samples (WT, S218C in PEGylated and unmodified form) were analyzed in triplicate. Protein concentrations of 1 mg/mL (24 μM) were used. Proteins were dissolved in 50 mM potassium phosphate buffer (pH 7.0). The total volume of sample analyzed was 800 μL. A DTS0012 disposable sizing cuvette was used. A temperature of 25 °C was applied, and the measurement time was 60 s. Samples were analyzed at a backscattering angle of 173°. The size distribution was automatically evaluated by the program *Zetasizer* v 6.30. Mean value and standard deviation were calculated out of the three independent measurements using the peak with the main intensity.

RESULTS AND DISCUSSION

Preparation of the S218C Mutant. The LOX from *A. viridans* that does not contain cysteines in its wild-type form

dx.doi.org/10.1021/bc2006847 | *Bioconjugate Chem.* 2012, 23, 1406–1414

was mutated at position 218 (Figure 1) where a possibly sufficiently accessible Ser is positioned on the surface of the structure of the native protein. Ser^{218} is situated on a loop that has been reported to be highly flexible in LOX,[28] as well as in related flavoenzymes of the α-hydroxyacid oxidase family.[39−41] The relevant loop was seen to be disordered in several crystal structures, suggesting that Ser^{218} of *A. viridans* LOX may not adopt a single defined structural position. In the crystal structure of wild-type LOX,[28] the inward-directed side-chain of Ser^{218} would not be optimally available for reaction. However, conformational flexibility of the loop harboring Ser^{218} was thought to be conducive to the intended site-directed protein modification. To further explain the choice of the mutation site, we must also emphasize that the native structure of the enzyme should be perturbed as little as possible by the site-specific substitution of a serine by cysteine. Candidate serine residues from highly conserved regions of the protein (e.g., the fully exposed Ser^{163}) were therefore not considered. Moreover, using Ser^{218}, the site for covalent attachment of a PEG molecule was considered to be sufficiently far away from the enzyme active site, as indicated by the FMN cofactor in the structure, to prevent interference with LOX function after derivatization of Cys^{218}. The resulting S218C mutant was obtained by expression in *E. coli*, and we show successful modification of the isolated mutant with mPEG-mal 5000.

Mutations in the native LOX gene (GenBank accession number: D50611.1) resulting in site-directed substitution of Ser^{218} by Cys were introduced by a two-stage PCR employing a suitable pair of oligonucleotide primers. The mutated gene was verified by sequencing and placed into plasmid vector pLO-1 that provided target gene expression under control of the *tac* promotor. Enzyme production was done in *E. coli* BL21 (DE3) using controlled cultivation conditions in a 5 L stirred bioreactor. The S218C mutant was obtained in apparent electrophoretic homogeneity (Figure 2A) by using a two-step purification consisting of ammonium sulfate precipitation of non-LOX protein from *E. coli* cell extract followed by hydrophobic interaction chromatography. Table 1 shows a summary of the purification. Figure S2 (panel A) in the Supporting Information displays the protein elution profile during hydrophobic interaction chromatography. Figure S2 (panel B) shows the different steps of the purification documented by SDS-PAGE. Note that a final step of desalting by repeated ultrafiltration, removing any residual $(NH_4)_2SO_4$ from the elution buffer, was important to recover mutated enzyme in a high specific activity and with good storage stability. Figure S2 shows that contaminating proteins of low molecular mass were removed by appropriate fraction collection during HIC. From a comparison of the specific activity of the S218C mutant in the *E. coli* cell extract and the specific activity of the purified enzyme, we can estimate that the mutant was expressed to a level of 12% (=15/90 × 100) of total intracellular protein. The mutated LOX was recovered in an overall yield of 27%. About 50 mg of purified enzyme was obtained from each liter of medium from the bioreactor.

Table 1. Purification of the S218C Mutant[a]

purification step	specific activity [U/mg]	activity recovery [%]	total protein [mg] and activity [U]
Crude cell extract	15	100	1003/15000
$(NH_4)_2SO_4$ precipitation	24	89	564/13254
HIC pool 1	56	8	21/1193
HIC pool 2, after desalting	90 (±5)	27	45/4022

[a]Data are based on the processing of 30 g wet biomass. HIC column chromatography was performed in 10 runs. Two pools denoted 1 and 2 were obtained. Pool 2 was used for further experiment.s.

Characterization of the S218C Mutant. The specific activity of the mutated LOX was measured with a standard peroxidase-coupled assay (Sigma) using 50 mM L-lactate as substrate. A value of 90 (±10) units/mg was obtained. By way of comparison, the specific activity of wild-type LOX produced and purified in exactly the same way as the mutant was about 200 (±25) U/mg. The commercial preparation of the wild-type enzyme (Roche Diagnostics) displayed identical specific activity (~200 U/mg). Additionally, the commercial enzyme appeared to be essentially pure by the criterion of migration as single protein band in SDS-PAGE, as shown in the Supporting Information (Figure S2B). Therefore and because of convenient availability, we used the commercial LOX as a reference for the characterization of the S218C mutant. A more detailed kinetic comparison of the enzymes used in this study is shown later in Table 1.

Figure 2B shows an overlay of the visible absorbance spectra of S218C mutant and wild-type LOX, both recorded at an exactly comparable protein concentration. Each spectrum contains two prominent bands with wavelengths of maximum absorption at around 375 and 455 nm that are highly characteristic of the FMN cofactor in its oxidized form. The spectrum of the mutant was nearly superimposable on the reference spectrum, suggesting that binding of FMN to LOX was essentially unaffected by the site-directed substitution of Ser^{218}. The result also implies that catalytic constants for the two enzymes can be compared with the assumption of a similar occupancy of their respective FMN binding site. The saturation of both proteins with their FMN cofactor was determined to be close to 100% (WT: 0.98; S218C: 0.95).

PEGylation of the S218C Mutant. Different molar ratios of enzyme and mPEG-mal 5000 were tested for bioconjugate formation, and a 12.5-fold molar surplus of mPEG-mal 5000 was found to give exhaustive modification of the S218C mutant, as demonstrated by SDS-PAGE and MALDI-TOF MS. Figure 2A shows that the apparent molecular mass of wild-type LOX had not been affected by incubation with mPEG-mal 5000, suggesting the absence of PEGylation, as expected. The S218C mutant by contrast displayed a clear shift in apparent mass to a higher value due to the PEGylation reaction, indicating that derivatization of the mutated LOX had taken place. The absence of a prominent protein band corresponding to the unmodified mutant in the sample analyzed implies that the chemical modification of the S218C mutant had proceeded to near-completion under the conditions used. MS analysis of the S218C mutant prior to and after incubation with mPEG-mal 5000 gave more detailed information about the process of PEGylation. Figure 3 shows that the underivatized enzyme, which displayed the expected molecular mass of 41 kDa, had disappeared almost entirely from the protein sample after the PEGylation reaction, corroborating the results of SDS PAGE (Figure 2A). Two new macromolecular species were formed in the reaction, and they were present in different amounts. The by-far abundant species displayed a mass of 46 kDa, consistent with the notion that the unmodified S218C mutant had acquired the extra mass of +5 kDa resulting from attachment of one mPEG-mal 5000 to the protein at Cys^{218}. The second mass

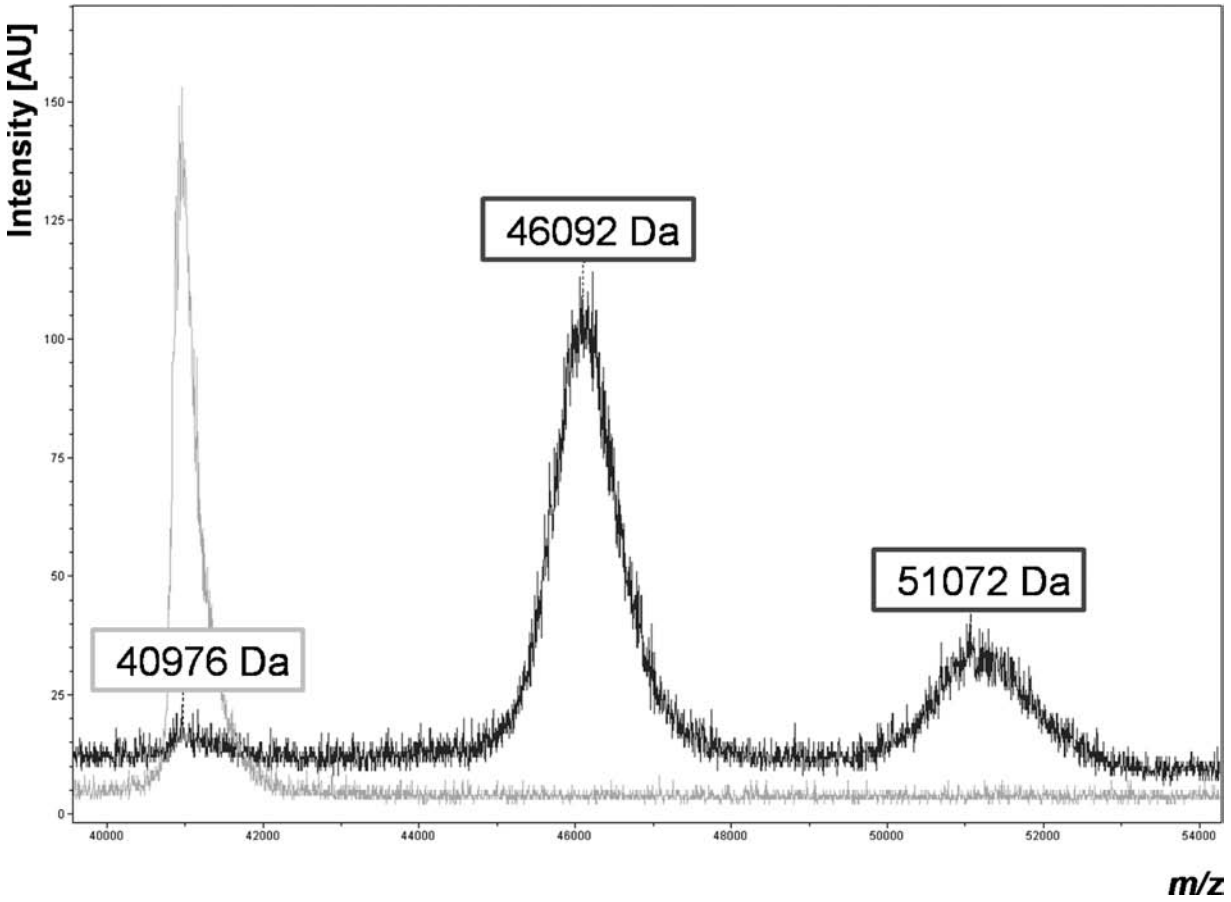


Figure 3. PEGylation of S218C mutant monitored by MS. Peaks at the indicated masses around 41 kDa, 46 kDa, and 51 kDa, respectively, represent unPEGylated (light gray line), monoPEGylated, and doubly PEGylated (dark gray line) S218C forms. AU, arbitrary units.

peak of 51 kDa could have originated from a double modification of the mutant. Assuming that the PEGylation(s) did not interfere with ionization of the protein, we estimated the relative quantities by integration of the peaks in Figure 3, which were determined to be 6% unmodified protein, 77% mono-, and 17% di-PEGylated protein.

Overall high sequence coverage was achieved by LC-MS/MS for all digested protein samples. For the PEGylated protein, 867 peptides were matched with combined 98% sequence coverage and a score of 29 407 for the 6 digests. The N-terminus was covered with 11 unmodified peptides. The Cys was covered with only 2 carbamidomethylated peptides. For the original protein without PEGylation, 735 peptides with combined sequence coverage of 97% and a score of 23 932 of the 6 digests were matched to the protein. The N-terminus was covered with 13 peptides, the Cys with 2 carbamidomethylated peptides. Detection of the PEGylation sites by this approach may have failed due to insufficient cleavage of the enzymes close to the site(s) of modification and/or the high mass of the modification, which may have hindered efficient fragmentation by collision induced dissociation. However, the aggregate data on the chemical modification of the S218C mutant (Figures 2A and 3) plus the absence detectable modification in the wild-type enzyme leave relatively little doubt that Cys^{218} is in fact the major site of derivatization by mPEG-mal 5000.

The high efficiency of PEGylation of the S218C mutant is worth noting. Modification with mPEG-mal 5000 of engineered cysteines in other proteins was incomplete, even when large molar excesses (≥20-fold) of reagent over target protein were employed.[17−23] The yields often did not exceed values around 50%, implying the need to separate the PEGylated protein from the unmodified form. Derivatization of the S218C mutant proceeded to near-completion. However, double PEGylation of the S218C mutant might be an issue.

To examine enlargement of the hydrodynamic volume of the S218C mutant resulting from PEGylation, we performed gel filtration analysis using conditions in which direct interaction of protein and PEG with the chromatographic material should have been minimized. The elution profiles of the PEGylated and underivatized forms of the mutant are superimposed in Figure 4. The results are clear in showing a marked size enhancement for the PEGylated enzyme. The elution volume for the main peak corresponded to an apparent molecular mass of approximately 250 kDa that can be compared to a native molecular mass for the homotetramer of about 170 kDa. We also analyzed our protein samples by dynamic light scattering. The WT displayed a hydrodynamic diameter of 11.67 ± 0.46 nm. The S218C mutant showed essentially the same hydrodynamic diameter (11.88 ± 0.86 nm). The PEGylated mutant was substantially larger; its hydrodynamic diameter was determined to be 16.38 ± 3.09 nm. The measurement did not detect peaks of smaller size, suggesting that PEGylation did not trigger dissociation of the protein subunits in the functional enzyme tetramer.

Functional Properties of PEGylated and unPEGylated Forms of the S218C Mutant. To obtain more detailed information about functional consequences of the site-directed replacement of Ser^{218} by Cys and of the modification by

dx.doi.org/10.1021/bc2006847 | *Bioconjugate Chem.* 2012, 23, 1406−1414

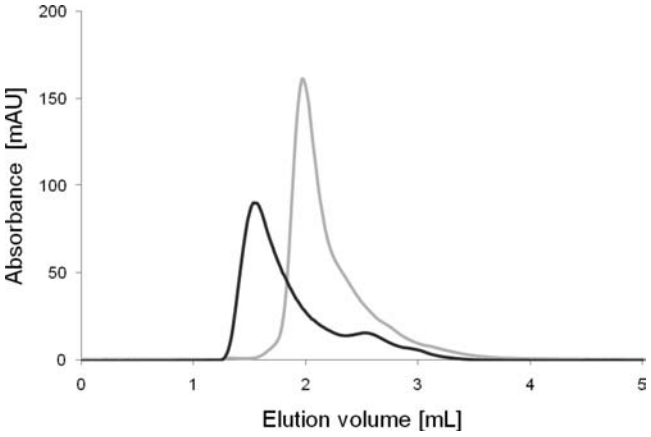


Figure 4. Gel filtration analysis for S218C mutant and the PEGylated derivative thereof. 50 μL of PEGylated (full dark gray line) and unPEGylated forms (full light gray line) of the S218C mutant (3 mg/mL) were loaded on a Superdex 200 column (GE Healthcare Life Sciences) and eluted isocratically at 25 °C with 50 mM potassium phosphate buffer, pH 7.0, containing 150 mM NaCl. The flow rate was 0.5 mL/min, and detection was at 280 nm. mAU, arbitrary units.

mPEG-mal 5000, we carried out a steady-state kinetic characterization of the S218C mutant in both unmodified and PEGylated forms. Table 2 summarizes the results, showing

Table 2. Kinetic Characterization of PEGylated and Unmodified forms of S218C for Reaction with L-(+)-Lactic Acid[a]

enzyme	specific activity [U/mg]	k_{cat} [s^{-1}]	K_M [mM]	k_{cat}/K_M [$(s\ mM)^{-1}$]
Wild-type LOX	204 (±10)	140 (±1)	0.83 (±0.03)	167
S218C mutant	90 (±5)	62 (±2)	1.0 (±0.10)	61
PEGylated S218C	62 (±4)	43 (±3)	1.0 (±0.10)	42

[a] k_{cat} ($=V_{max}/E$) was calculated from maximum initial rates (V_{max}) with the molar enzyme concentration (E) used. Standard deviation on specific activity is from five independent experiments. Standard deviations on kinetic parameters are from nonlinear fits of data with the Michaelis-Menten equation.

kinetic parameters for the two preparations of the mutant along with kinetic parameters for the wild-type enzyme. Experimental data are shown in Figures S3 of Supporting Information. The mutation resulted in a 2.7-fold loss in catalytic efficiency for reaction with L-lactate (k_{cat}/K_M). This loss can be ascribed almost exclusively to a decrease in turnover number (k_{cat}) caused by the mutation. Apparent substrate binding (K_M) was only slightly affected in the mutant as compared to WT. When compared to its unmodified counterpart, the PEGylated mutant displayed a relatively small loss in k_{cat}/K_M (by about 30%), again resulting from a corresponding decrease in k_{cat}. The PEGylated mutant was about one-fourth as efficient (k_{cat}/K_M) as the wild-type enzyme. Note: we determined that free PEG that might have remained in the PEGylated enzyme preparation due to incomplete removal of unreacted mPEG-mal 5000 after the modification is very unlikely to have affected the activity of PEGylated S218C mutant in any way. There was no significant (≤2%) effect of added PEG4000 (12.5-fold molar excess over protein present) on the specific activity of WT and S218C mutant.

We further tested two other α-hydroxy acids (*S*-2-hydroxybutyric acid, *S*-2-hydroxyisocaproic acid) that serve as relatively slow alternative substrates of the wild-type LOX ($k_{cat} \leq 1.4\ s^{-1}$). Table S1 in Supporting Information shows the results. It is interesting that both unmodified ($1.8\ s^{-1}$) and PEGylated S218C mutant ($1.6\ s^{-1}$) displayed a higher k_{cat} for reaction with *S*-2-hydroxybutyric acid than wild-type LOX. However, the K_M for *S*-2-hydroxybutyric acid (~4 mM) was about 10 times higher in these enzymes as compared to the wild-type LOX. In k_{cat}/K_M terms, therefore, the wild-type LOX ($3.2\ mM^{-1}\ s^{-1}$) was still an 8-fold better catalyst for conversion of *S*-2-hydroxybutyric acid than the two forms of the S218C mutant. Using *S*-2-isocaproic acid as substrate, kinetic consequences of replacing Ser^{218} by Cys and of modifying Cys^{218} with mPEG-mal 5000 were markedly different from those observed in the reaction with *S*-2-hydroxybutyric acid. The k_{cat} of the mutated enzymes was decreased more substantially (up to 4-fold) than the K_M was increased in comparison to the wild-type enzyme ($k_{cat} = 1.1\ s^{-1}$; $K_M = 0.43$ mM). The unmodified S218C mutant even showed a lower K_M for *S*-2-isocaproic acid (0.26 mM) than the wild-type enzyme. Substrate specificity of LOX was therefore changed somewhat as a result of both point mutation of Ser^{218} and PEGylation of Cys^{218}.

We also examined the stability of the S218C mutant, unmodified and PEGylated, measuring irreversible loss of activity during incubation at 37 °C. Figure 5 shows that the

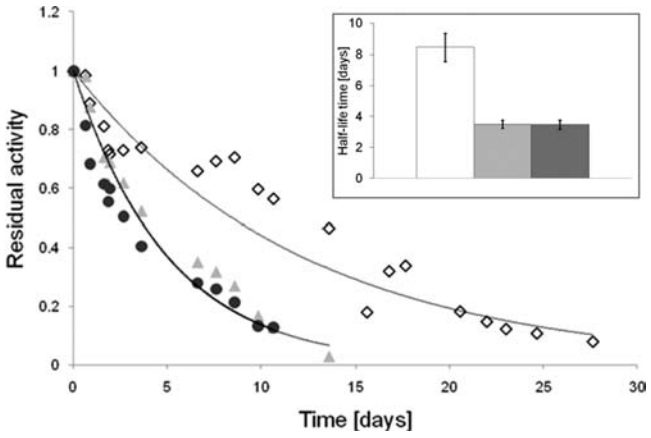


Figure 5. Inactivation time courses for S218C mutant (light gray triangles) and the PEGylated derivative (dark gray circles) thereof are shown in comparison to wild-type LOX (white diamonds). Residual activity is expressed as a fraction of the starting activity. The inset shows half-life times calculated from the data assuming pseudo-first-order decay of activity, shown as lines in the main panel. WT (white bar), S218C (light gray bar), PEGylated S218C (dark gray bar). Incubations were done in 40 mM HEPES buffer, pH 8.1, containing 150 mM NaCl. The temperature was 37 °C. The enzyme concentration was 0.4 μM.

unmodified mutant was inactivated somewhat faster than the wild-type enzyme, manifested in a decrease in half-life time by a factor of about 2.5. Stability of the S218C mutant was unchanged after PEGylation, implying that the PEGylation itself did not deteriorate the stability of enzyme activity. This is worth remarking because it is quite difficult to predict the effect of PEGylation on the stability of a protein. In hemoglobin, for example, multiple-site PEGylation resulted in dissociation of the native protein homotetramer.[42] Differential scanning

dx.doi.org/10.1021/bc2006847 | Bioconjugate Chem. 2012, 23, 1406–1414

fluorimetry was used here to obtain a relevant parameter of overall conformational stability of the different LOX samples used. Unfolding of WT at high temperature was characterized by a T_i value of 69.5 ± 0.5 °C. The T_i values for S218C (70.0 ± 0.5 °C) and the PEGylated mutant (68.0 ± 0.5 °C) were very similar to the T_i of WT. PEGylated S218C may show a slightly reduced conformational stability as compared to the two unmodified proteins; however, any stability loss after PEGylation was clearly small. Lowering of the half-life time in S218C mutant as compared to WT was not reflected in the T_i values. However, it is not uncommon that different assays of stability give different results.

In conclusion, we have achieved the intended specific modification of LOX using a bioconjugation approach in solution that was based on introduction of a single Cys at position 218, identified through structure-guided selection, and Cys-directed modification with mPEG-mal 5000. Marked loss of activity and/or stability is a problem often encountered in the preparation of enzyme bioconjugates, especially when random multisite PEGylation is applied.[1−4] Replacement of Ser^{218} by Cys and PEGylation of Cys^{218} also decreased the catalytic efficiency of LOX for reaction with L-lactate (4-fold overall) and abated resistance of the enzyme to inactivation at 37 °C (2.5-fold). However, the S218C mutant was still sufficiently active to be considered a useful biocatalyst. Importantly, the final PEGylation proceeded with very good yield in a selective modification reaction. The PEGylated form of the LOX could thus be an interesting new candidate enzyme for evaluation in lactate biosensors.[8,25−27,30−33] It was shown for glucose oxidase that PEGylation brought about significant enhancement of the performance of the enzyme embedded in a carbon paste-based electrode.[8] The availability of a defined PEG-LOX bioconjugate now enables similar questions to be addressed for LOX. Position Cys^{218} presents an interesting site for further diversification of LOX bionconjugates (e.g., in situ polymerization[43]) and optimization for the various known applications of the enzyme.[34,35] Cys^{218} could be used to attach redox mediators to the protein with the aim of facilitating direct ("wired") electron transfer between the redox-active FMN cofactor and an electrode. The location of Cys^{218} in the structure seems suitable for this purpose, and a recent study of glucose oxidase has elegantly demonstrated the use of gold nanoparticle conjugation to an engineered cysteine to achieve this effect.[44]

■ ASSOCIATED CONTENT

Supporting Information

Table S1 summarizes kinetic parameters of wild-type enzyme, the S218C mutant, and the PEGylated form of the mutant for α-hydroxyacid substrates other than L-lactate; Figure S1 shows determination of T_i values for temperature-dependent protein denaturation using differential scanning fluorimetry data. Figure S2 shows elution of the S218C mutant in hydrophobic interaction chromatography (panel A) and a SDS polyacrylamide gel documenting the different steps of the purification (panel B). Figure S3 shows Michaelis−Menten plots of data used for determination of kinetic parameters for reaction with L-lactate. Detailed protocol of LC-MS/MS analysis is provided. This material is available free of charge via the Internet at http://pubs.acs.org.

■ AUTHOR INFORMATION

Corresponding Author

*Telephone: +43-316-873-8400; fax: +43-316-873-8434; e-mail: bernd.nidetzky@tugraz.at.

Notes

The authors declare no competing financial interest.

■ ACKNOWLEDGMENTS

This work was supported by FFG, Land Steiermark, Steirische Wirtschaftsförderung (SFG) and Roche Diagnostics GmbH (Graz, Austria). We thank Dr. Bernhard Schaffar, Dr. Christoph Ritter and Dr. Thomas Meier (Roche Diagnostics) for helpful discussion. Assistance of Karin Longus and Daniela Rainer (Institute of Biotechnology and Biochemical Engineering) in the production of the S218C mutant is gratefully acknowledged.

■ ABBREVIATIONS

FMN, flavin mononucleotide; LOX, L-lactate oxidase; mPEG-mal 5000, methoxypoly(ethylene glycol) 5000; PEG, poly(ethylene glycol); WT, wild-type

■ REFERENCES

(1) Pasut, G., and and Veronese, F. M. (2012) State of the art in PEGylation: The great versatility after 40 years of research. *J. Controlled Release*, in press (dx.doi.org/10.1016/j.jconrel.2011.10.037)

(2) Jevsevar, S., Kunstelj, M., and Porekar, V. G. (2010) PEGylation of therapeutic proteins. *Biotechnol. J. 5*, 113−128.

(3) Matsushima, A., Kodera, Y., Hiroto, M., Nishimura, H., and Inada, Y. (1996) Bioconjugates of proteins and polyethylene glycol: potent tools in biotechnological processes. *J. Mol. Cat. B: Enzymatic 2*, 1−17.

(4) Fee, C. J., and Van Alstine, J. M. (2006) PEG-proteins: Reaction engineering and separation issues. *Chem. Eng. Sci. 61*, 924−939.

(5) Veronese, F. M. (2011) Peptide and protein PEGylation: a review of problems and solutions. *Biomaterials 22*, 405−417.

(6) Dattelbaum, A. M., Baker, G. A., Fox, J. M., Iyers, S., and Dattelbaum, J. D. (2009) PEGylation of a maltose biosensor promotes enhanced signal response when immobilised in a silica sol-gel. *Bioconjugate Chem. 20*, 2381−2384.

(7) Doretti, L., Ferrara, D., Gattolin, P., Lora, S., Schiavon, F., and Veronese, F. M. (1998) PEG-modified glucose oxidase immobilized on a PVA cryogel membrane for amperometric biosensor applications. *Talanta 45*, 891−898.

(8) Mizutani, F., Yabuki, S., and Iijima, S. (1995) Amperometric glucose-sensing electrode based on carbon paste containing poly(ethylene glycol)-modified glucose oxidase and cobalt octaethoxyphthalocyanine. *Anal. Chim. Acta 300*, 59−64.

(9) Allard, L., Cheynet, V., Oriol, G., Gervasi, G., Imbert-Laurenceau, E., Mandrand, B., Delair, T., and Mallet, F. (2004) Antigenicity of recombinant proteins after regioselective immobilization onto polyanhydride-based copolymers. *Bioconjugate Chem. 15*, 458−466.

(10) Rodriguez-Martinez, J. A., Rivera-Rivera, I., and Griebenow, K. (2011) Prevention of benzyl alcohol-induced aggregation of chymotrypsinogen by PEGylation. *J. Pharm. Pharmacol. 63*, 800−805.

(11) Castillo, B., Sola, R. J., Ferrer, A., Barletta, G., and Griebenow, K. (2008) Effect of PEG modification on subtilisin Carlsberg activity, enantioselectivity, and structural dynamics in 1,4-dioxane. *Biotechnol. Bioeng. 99*, 9−17.

(12) Lopez-Cruz, J. I., Viniegra-Gonzalez, G., and Hernandez-Arana, A. (2006) Thermostability of native and pegylated *Myceliophthora thermophila* laccase in aqueous and mixed solvents. *Bioconjugate Chem. 17*, 1093−1098.

(13) Daly, S. M., Przybycien, T. M., and Tilton, R. M. (2007) Aggregation of lysozyme and poly(ethylene glycol)-modified lysozyme after adsorption to silica. *Colloids Surf., B: Biointerfaces 57*, 81−88.

(14) Pai, S. S., Przybycien, T. M., and Tilton, R. M. (2010) Protein PEGylation attenuates adsorption and aggregation on a negatively charged and moderately hydrophobic polymer surface. *Langmuir 26*, 18231−18238.
(15) Popp, M. W., Dougant, S. K., Chuang, T.-Y., Spooner, E., and Ploegh, H. L. (2011) Sortase-catalyzed transformation that improve the properties of cytokines. *Proc. Natl. Acad. Sci. U.S.A. 108*, 3169−3174.
(16) Rossi, E. A., Goldenberg, D. M., and Chang, C.-H. K. (2011) The Dock-and-Lock method combines recombinant engineering with site-specific covalent conjugation to generate multifunctional structures. *Bioconjugate Chem. 23*, 309−323.
(17) Veronese, F. M., Mero, A., Caboi, F., Sergi, M., Marongiu, C., and Pasut, G. (2007) Site-specific pegylation of G-CSF by reversible denaturation. *Bioconjugate Chem. 18*, 1824−1830.
(18) Manujula, B. N., Tsai, A., Upadhya, R., Perumalsamy, K., Smith, P. K., Malavalli, A., Vandegriff, K., Winslow, R. M., Intaglietta, M., Prabhakaran, M., Friedman, J. M., and Acharya, A. S. (2003) Site-specific PEGylation of hemoglobin at Cys-93(β): correlation between the colligative properties of the PEGylated protein and the length of the conjugated PEG chain. *Bioconjugate Chem. 14*, 464−472.
(19) Balan, S., Choi, J.-w., Godwin, A., Teo, I., Laborde, C. M., Heidelberger, S., Zloh, M., Shaunak, S., and Brocchini, S. (2007) Site-specific PEGylation of protein disulfide bonds using a three-carbon bridge. *Bioconjugate Chem. 18*, 61−76.
(20) Slavica, A., Dib, I., and Nidetzky, B. (2007) Selective modification of surface-exposed thiol groups in *Trigonopsis variabilis* D-amino acid oxidase using poly(ethylene glycol) maleimide and its effect on activity and stability of the enzyme. *Biotechnol. Bioeng. 96*, 9−17.
(21) Doherty, D. H., Rosendahl, M. S., Smith, D. J., Hughes, J. M., Chlipala, E. A., and Cox, G. N. (2005) Site-specific PEGylation of engineered cysteine analogues of recombinant human granulocyte-macrophage colony-stimulating factor. *Bioconjugate Chem. 16*, 1291−1298.
(22) Hu, J., Duppatla, V., Harth, S., Schmitz, W., and Sebald, W. (2010) Site-specific PEGylation of bone morphogenetic protein-2 cysteine analogues. *Bioconjugate Chem. 21*, 1762−1772.
(23) Lamppa, J. W., Ackerman, M. E., Lai, J. I., Scanlon, T. C., and Griswold, K. E. (2011) Genetically engineered alginate lyase-PEG conjugates exhibit enhanced catalytic function and reduced immunoreactivity. *PLoS ONE 6*, e17042.
(24) Maeda-Yorita, K., Aki, K., Sagai, H., Misaki, H., and Massey, V. (1995) L-Lactate oxidase and L-lactate monooxygenase: mechanistic variations on a common structural theme. *Biochimie 77*, 631−642.
(25) Minagawa, H., Nakayama, N., Matsumoto, T., and Ito, N. (1998) Development of long life lactate sensor using thermostable mutant lactate oxidase. *Biosens. Bioelectron. 13*, 313−318.
(26) Wang, J., and Chen, Q. (1994) Enzyme microelectrode array strips for glucose and lactate. *Anal. Chem. 66*, 1007−1011.
(27) Romero, M. R., Ahumada, F., Garay, F., and Baruzzi, A. M. (2010) Amperometric biosensor for direct blood lactate detection. *Anal. Chem. 82*, 5568−5572.
(28) Furuichi, M., Suzuki, N., Dhakshnamoorthy, B., Minagawa, H., Yamagishi, R., Watanabe, Y., Goto, Y., Kaneko, H., Yoshida, Y., Yagi, H., Waga, I., Kumar, P. K., and Mizuno, H. (2008) X-ray structures of *Aerococcus viridans* lactate oxidase and its complex with D-lactate at pH 4.5 show an α-hydroxyacid oxidation mechanism. *J. Mol. Biol. 378*, 436−446.
(29) Li, S. J., Umena, Y., Yorita, K., Matsuoka, T., Kita, A., Fukui, K., and Morimoto, Y. (2007) Crystallographic study on the interaction of L-lactate oxidase with pyruvate at 1.9 Ångstrom resolution. *Biochem. Biophys. Res. Commun. 358*, 1002−1007.
(30) Patel, N. G., Erlenkötter, A., Cammann, K., and Chemnitius, G.-C. (2000) Fabrication and characterization of disposable type lactate oxidase sensors for dairy products and clinical analysis. *Sens. Actuators, B: Chem. 67*, 134−141.
(31) Zanina, V. P., López de Mishimaa, B., and Solísb, V. (2010) An amperometric biosensor based on lactate oxidase immobilized in laponite−chitosan hydrogel on a glassy carbon electrode. Application to the analysis of L-lactate in food samples. *Sens. Actuators, B: Chem. 155*, 75−80.
(32) Park, B. W., Yoon, D. Y., and Kim, D. S. (2010) Recent progress in bio-sensing techniques with encapsulated enzymes. *Biosens. Bioelectron. 26*, 1−10.
(33) Romero, M. R., Garay, F., and Baruzzi, A. M. (2008) Design and optimization of a lactate amperometric biosensor based on lactate oxidase cross-linked with polymeric matrixes. *Sens. Actuators, B: Chem. 131*, 590−595.
(34) Oikawa, T., Mukoyama, S., and Soda, K. (2001) Chemo-enzymatic D-enantiomerization of DL-lactate. *Biotechnol. Bioeng. 73*, 80−82.
(35) Soda, K., Oikawa, T., and Yokoigawa, K. (2001) One-pot chemo-enzymatic enantiomerization of racemates. *J. Mol. Catal. B: Enzymatic 11*, 149−153.
(36) Wang, W., and Malcom, B. A. (1999) Two-stage PCR protocol allowing introduction of multiple mutations, deletions and insertions using QuikChange Site-Directed Mutagenesis. *Biotechniques 26*, 680−682.
(37) Munro, A. W., and Noble, M. A. (1999) Fluorescence analysis of flavoproteins. *Methods Mol. Biol.* (Chapman, S. K., and Reid, G. A., Eds.) pp 25−48, Vol. *131* Flavoprotein Protocols, Humana Press, Totowa, NJ.
(38) Niesen, F. H., Berglund, H., and Vedadi, M. (2007) The use of differential scanning fluorimetry to detect ligand interactions that promote protein stability. *Nat. Protoc. 2*, 2212−21.
(39) Cunane, L. M., Barton, J. D., Chen, Z. W., Diêp Lê, K. H., Amar, D., Lederer, F., and Mathews, F. S. (2005) Crystal structure analysis of recombinant rat kidney long chain hydroxy acid oxidase. *Biochemistry 44*, 1521−1531.
(40) Xia, Z. X., and Mathews, F. S. (1990) Molecular structure of flavocytochrome b2 at 2.4 Å resolution. J. *Mol. Biol. 212*, 837−863.
(41) Sukumar, N., Xu, Y., Gatti, D. L., Mitra, B., and Mathews, F. S. (2001) Structure of an active soluble mutant of the membrane-associated (S)-mandelate dehydrogenase. *Biochemistry 40*, 9870−9878.
(42) Caccia, D., Ronda, L., Frassi, R., Perella, M., Del Favero, E., Bruno, S., Pioselli, B., Abbruzzetti, S., Viappiani, C., and Mozzarelli, A. (2009) PEGylation promotes hemoglobin tetramer dissociation. *Bioconjugate Chem. 20*, 1356−1366.
(43) Heredia, K. L., Bontempo, D., Ly, T., Byers, J. T., Halstenberg, S., and Maynard, H. D. (2005) In situ preparation of protein −, ‚smart" polymer conjugates with retention of bioactivity. *J. Am. Chem. Soc. 127*, 16955−16960.
(44) Holland, J. T., Lau, C., Brozik, S., Atanassov, P., and Banta, S. (2011) Engineering of glucose oxidase for direct electron transfer via site-specific gold nanoparticle conjugation. *J. Am. Chem. Soc. 133*, 19262−19265.

Bioconjugate Chemistry

Article

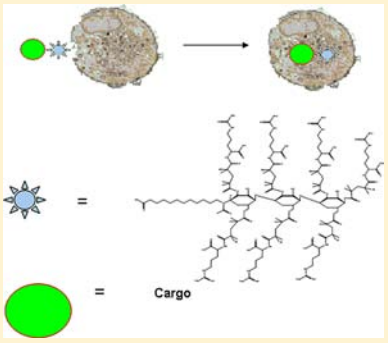
pubs.acs.org/bc

Star-Like Oligo-Arginyl-Maltotriosyl Derivatives as Novel Cell-Penetrating Enhancers for the Intracellular Delivery of Colloidal Therapeutic Systems

Sara Bersani, Stefano Salmaso, Francesca Mastrotto, Elena Ravazzolo, Alessandra Semenzato, and Paolo Caliceti*

Deprtament of Pharmaceutical and Pharmacological Sciences, University of Padova, Via F. Marzolo, 5 35131 Padova, Italy

ABSTRACT: A novel nonpeptide, multiarmed oligo-arginyl derivative was engineered as a cell-penetration enhancer for the delivery of bioactive macromolecules and colloidal drug systems. Hepta-arginyl-maltotriosylamido-*N*-acetyl-dodecanoyl acid (Arg_7-Malt-$NAcC_{12}$ acid) was synthesized through a carefully designed multistep chemical protocol, as follows: (1) maltotriose derivatization with 12-amino-dodecanoic acid and acetylation of the free amino group; (2) esterification of the maltotriosyl hydroxyl groups with 2-bromo-isobutyryl bromide; and (3) synthesis of star-like oligomer bearing multiple copies of arginine moieties under atom transfer radical polymerization (ATRP) conditions. The intermediates and final product were characterized by ^{1}H NMR, IR, mass spectrometry, colorimetric assays, and elemental analysis. Cytotoxicity studies on the final polymeric material showed that this novel cell-penetrating enhancer does not have significant toxic effects on MCF-7 and MC3T3-E1 cell lines. The IC_{50} was greater than 100 μM with both cell lines, while the polyethylenimine with similar average molecular mass (M_n) that was used as a reference showed an IC_{50} of 30 and 40 μM, for MCF-7 and MC3T3-E1, respectively. The biological properties of the novel bioconjugate were investigated using a fluorescein-labeled bovine serum albumin (FITC-BSA) as a hydrophilic cargo model. MCF-7 and MC3T3-E1 cells were incubated for 60 min with the Arg_7-Malt-$NAcC_{12}$-conjugated FITC-BSA [$(Arg_7$-Malt-$NAcC_{12})_2$-FITC-BSA] or FITC-BSA, and the intracellular fluorescence level was analyzed by spectrofluorimetric analysis of cell lysate, cytofluorimetry, and confocal microscopy. The fluorescence of the lysate of MCF-7 and MC3T3-E1 cells that were incubated with $(Arg_7$-Malt-$NAcC_{12})_2$-FITC-BSA at 37 °C was approximately 4.5 times higher than the fluorescence obtained with cells incubated with FITC-BSA. At 4 °C, the cell uptake of $(Arg_7$-Malt-$NAcC_{12})_2$-FITC-BSA was only 2 times higher than that of FITC-BSA. Cytofluorimetric studies showed that, after $(Arg_7$-Malt-$NAcC_{12})_2$-FITC-BSA treatment, over 80% of MCF-7 cells and over 95% of MC3T3-E1 cells displayed enhanced fluorescence. Confocal investigations showed punctuated fluorescence within the cytosol in both cell lines, indicating that $(Arg_7$-Malt-$NAcC_{12})_2$-FITC-BSA was confined to endosomes, with no fluorescence observed in the nucleus.



INTRODUCTION

The impermeable nature of large hydrophilic structures to biological barriers is one of the primary causes for the poor absorption and inefficient intracellular delivery of proteins, oligonucleotides, and colloidal supramolecular systems. Poor transmembrane permeability strongly limits the development of efficient, nonparenteral formulations, and the intracellular delivery of bioactive macromolecules and colloidal therapeutic systems, such as polymer conjugates and nanoparticles.[1] The development of technologies that enable low-membrane-permeability therapeutics to effectively penetrate biological membranes is currently one of the greatest challenges in pharmaceutical development.[2]

Recently, small regions of proteins, termed protein transduction domains (PTDs) or cell-penetrating peptides (CPPs), have been demonstrated to possess cell-penetrating properties that can be exploited to enhance the performance of colloidal therapeutics.[3−6]

CPPs include Tat (trans-activator of transcription)-derived peptides, signal sequence-derived peptides, and synthetic or chimeric peptides. Most of the recognized CPPs contain cationic, amphiphilic, or hydrophobic functions that promote cell surface interaction and translocation.

Tat-derived peptides have been demonstrated to be very efficient penetrating agents. Synthetic peptides have been designed to mimic the HIV-1 Tat structure, an 86-amino-acid nuclear transcription-activating protein comprising three functional domains. The region responsible for cell uptake and nuclear import contains 6 arginine and 2 lysine residues within a short linear sequence, and the amino acids are in random conformation.[7]

The presence of short peptide sequences containing basic residues, such as arginines and lysines, is a structural requisite to enabling cell-penetrating activity and nucleus translocation of these oligo amino acids.[8,9] Accordingly, model peptides that contain repeat motifs or poly residues, such as homopolymers

Received: January 3, 2012
Revised: May 4, 2012
Published: June 18, 2012

 © 2012 American Chemical Society dx.doi.org/10.1021/bc200666u | *Bioconjugate Chem.* 2012, 23, 1415−1425

of arginine, have been synthesized and investigated. Studies have demonstrated that their internalization efficiency depends on the length of the peptide backbone. Stretches of six (R6) to eight (R8) arginine residues showed the highest cytoplasmic internalization ability.[10]

The exact mechanism by which cell translocation occurs is still a matter of debate, as either passive or active pathways, or receptor- or absorptive-mediated endocytosis, have been proposed. In addition, the correlation between the structural features of these peptides and the cell uptake behavior is still under investigation.[11,12]

Although many aspects of CPP activity have not been fully elucidated, and a number of contrasting data have been generated, it is anticipated that these molecules will have a broad relevance in the pharmaceutical and medical fields, and they may find applications either for enhancing transmucosal absorption, mostly for nasal and intestinal delivery, or for intracellular drug delivery and targeting.[13,14] Covalent linkages or simple physical interactions of CPPs have been demonstrated to promote the cell entry of a variety of hydrophilic compounds ranging from small molecules to plasmid DNA and oligonucleotides,[15,16] peptides,[17,18] proteins,[19−21] nanocarriers, such as liposomes and micelles,[22] and quantum dots.[23,24] Nevertheless, many studies have highlighted pitfalls in using CPPs in drug delivery, including poor cell uptake, unspecific cell delivery, inconvenient *in vivo* performance, low stability, and intrinsic biological activity. Therefore, the use of these molecules in combination with colloidal therapeutic systems may result in ineffective systems and/or entail risks of toxicity.[25]

These drawbacks could be overcome by designing novel nonpeptide molecules with cell-penetrating activity. These novel structures could display higher stability and lower toxicity compared to CPPs and may be devoid of intrinsic biological activity. Recently, high-molecular-weight polymers bearing oligo-Arg as pendant functions have been demonstrated to enhance the nasal absorption of insulin.[26] Oligo-Lys and oligo-Arg hydrophobic-core polysaccharide dendrons have been investigated for the oral delivery of heparin.[27] A novel class of Arg-rich dendrimers has been successfully developed for the conjugation and delivery of PNA705 splice-redirecting oligonucleotides,[28] while a myristoylated hendecaarginine derivative has been found to possess promising cell-penetration properties for pharmaceutical applications.[29]

Intrigued by the evidence that nonpeptide cell-penetrating enhancers may be advantageously exploited for drug delivery, we designed a novel class of cell-penetrating enhancers with unusual star-like structures that can be covalently or physically combined with colloidal therapeutic systems to promote their cellular uptake. The new enhancers were designed with regard to the oligo-Arg structure of the Tat-penetrating domain 49−57 and the evidence that the guanidinium headgroup of Arg are crucial for cellular uptake due to their interactions with membrane phospholipids.[30] Guanidinium-rich structures, in fact, undergo cell translocation three times faster than the transduction domain of Tat, as their insertion into lipid bilayers produces local membrane distortion leading to transient pore formation on the membranes.[31]

In this paper, we report an efficient, multistep protocol for the synthesis of a novel nonlinear multi-Arg-armed molecule starting from a short oligosaccharide. The cell-penetration properties of the multiarmed derivative were investigated using fluorescein-labeled bovine serum albumin as a hydrophilic cargo model. The cell-penetration studies were performed using two cell lines and fluorescence spectroscopy, flow cytofluorimetry, and confocal microscopy.

MATERIALS AND METHODS

Maltotriose [*O*-α-D-glucopyranosyl-(1,4)-*O*-α-D-glucopyranosyl-(1,4)- α-D-glucopyranose], 12-amino-dodecanoic acid, acetic anhydride, 2-bromo-isobutyryl bromide, triethylamine, ascorbic acid, 1-ethyl-3-(3-dimethylaminopropyl) carbodiimide hydrochloride (EDC), polyethylenimine (PEI, 1.8 kDa Mn), fetal bovine serum (FBS), RPMI-1640 medium, Dulbecco's modified essential medium (D-MEM), penicillin (10 000 IU/mL)−streptomycin (10 mg/mL)−amphotericin B (25 μg/mL) stabilized solution, L-glutamine (200 mM), Dulbecco's phosphate buffered saline (DPBS), trypsin−EDTA solution (2.5 w/v %), and 3-(4,5-dimethylthiazol-2-yl)-2,5-diphenyltetrazolium bromide (MTT) were purchased from Sigma-Aldrich (St. Louis, MO, USA). L-Arginine hydrochloride was furnished by SERVA Electrophoresis (Heidelberg, Germany). Fluorescein isothiocyanate (FITC), 2-picolyl hydrochloride, 2-picolylamine, copper(I) bromide (CuBr), bovine serum albumin−fraction V (BSA), Triton X-100, and paraformaldehyde were purchased from Fluka (Buchs SG, Switzerland). Vectashield Mounting Medium with DAPI was from Vector Laboratories (Peterborough, UK). All other reagents were obtained from Fluka Analytical or Sigma-Aldrich. The solvents of analytical or HPLC grade were furnished by Carlo Erba (Milan, Italy), VWR International (Lutterworth, UK), and Sigma-Aldrich (St. Louis, MO, USA). Cell culture plates and flask, 96-well flat bottomed microassay plate and chambered slides were purchased from BD Falcon (BD Bioscience, NJ, USA).

Synthesis of Maltotriosylamido-*N*-Acetyl-Dodecanoic Acid (Malt-NAcC_{12} acid). 12-Amino-dodecanoic acid (1.0 g, 4.6 mmol) was dissolved in 15 mL of methanol/acetic acid (95:5 vol/vol). The solution was maintained at 60 °C, and 1.2 g of maltotriose (2.4 mmol) was added. After 24 h, 7.5 mL of acetic anhydride (79.4 mmol) was added, and the resulting solution was stirred for 96 h at room temperature. The volume was reduced to ca. 4 mL under vacuum, and then 3 mL of 30% ammonia aqueous solution was added. After 12 h, the solvent was removed under reduced pressure, and the crude product was redissolved in 3 mL of methanol and added dropwise to 200 mL of diethyl ether. The precipitate was collected by filtration and desiccated under vacuum. The recovered product mass was 1.2 g. The product was analyzed by RP-HPLC using a Luna C18 column (250 × 4.6 mm, Phenomenex, Torrance, CA, USA) eluted with a gradient of H_2O/0.05% trifluoroacetic acid (A) and acetonitrile/0.05% trifluoroacetic acid (B) (0−3 min 10% B, 3−27 min from 10% to 80% B). The UV detector was set at 220 nm. The product was also characterized by elemental analysis, mass spectrometry (ESI-MS; ESI-TOF Applied Biosystems Mariner Foster City, CA, USA), ^{1}H NMR (AMX 300 MHz, Bruker Spectrospin, Fallanden, Switzerland), and FT-IR (FT-IR 1600, Perkin-Elmer, Norwalk, CT, USA).

RP-HPLC (C18): 16.3 min retention time. Elemental analysis: C, 51.2%; H, 7.9%; N, 1.7% (O, 39.2%) [calcd for Malt-NAcC_{12} acid ($C_{32}H_{57}NO_{18}$): C, 51.7%; H, 7.7%; N, 1.8% (O, 39.8%)]. ESI-MS [m/z]: 742.34 $(M\text{-}H^+)^{1-}$ [calcd for $C_{32}H_{57}NO_{18}$: 743.36]. ^{1}H NMR (D_2O): δ ppm 5.40 (d, J = 3.3 Hz, 2H, anomeric), 5.23 (d, J = 3.8 Hz, 1H, anomeric), 4.20−3.60 (m, 18H - sugar region), 3.55 (t, J = 9.3 Hz, 2H, λ-CH_2−), 2.33 (t, J = 7.2 Hz, 2H, α-CH_2−), 2.18 (s, 3H, CH_3−CO−), 1.59 (bm, 4H, ι-CH_2− and β-CH_2− of alkyl chain), 1.29 (bs,

14H, $-CH_2-$ of alkyl chain). NMR signals were indicated as singlet (s), broad singlet,[32] doublet (d), triplet (t), multiplet (m), and broad multiplet (bm); coupling constants of peak multiplicities (J) have been expressed in Hz. FT-IR (KBr): ν (cm^{-1}) 3396 (OH), 2929 (CH), 1717 (CO−OH), 1612 (acetyl CO−N).

Synthesis of Hepta(2-bromoisobutyryl)-Maltotriosylamido-*N*-Acetyl-Dodecanoic Acid (BrIsoBut$_7$-Malt-NAcC$_{12}$ acid). Hepta(2-bromoisobutyryl)-maltotriosylamido-*N*-acetyl-dodecanoic acid (BrIsoBut$_7$-Malt-NAcC$_{12}$ acid) was synthesized according to a modified procedure reported in the literature.[33] Briefly, 1.0 g of Malt-NAcC$_{12}$ acid (1.35 mmol) was suspended in 20 mL of anhydrous chloroform containing triethylamine (3.7 mL, 26.7 mmol). The suspension was cooled to 0 °C, and 2-bromo-isobutyryl bromide (3.3 mL, 26.7 mmol) was added over 30 min. The solution was stirred for 72 h. The mixture was filtered, and the organic solution was washed three times with 30 mL of cold water, three times with 20 mL of 0.1 N NaOH, and again three times with 30 mL of cold water. The organic phase was then dried over anhydrous Na_2SO_4, filtered, and concentrated under reduced pressure. The resulting red−brown solid was dissolved in 5 mL of acetone and added to 100 mL of cold water under vigorous stirring. Acetone was removed under reduced pressure, and the aqueous suspension was lyophilized. The crude product (1.47 g) was analyzed by elemental analysis, ^{1}H NMR, and FT-IR.

Elemental analysis: C, 40.8%; H, 5.1%; N, 1.0%; Br, 30.4% (O, 22.7%) [calcd for BrIsoBut$_7$-Malt-NAcC$_{12}$ acid ($C_{60}H_{92}Br_7N_1O_{25}$): C, 40.3%; H, 5.2%; N, 0.8%; Br, 31.3% (O, 22.4%)]. ^{1}H NMR ($CDCl_3$): δ ppm 4.60−3.30 (m, 18H sugar region), 3.29 (m, 2H, λ-CH_2-), 2.15 (m, 2H, α-CH_2-), 1.96 (bs, 42H, CH_3), 1.94 (s, 3H, CH_3-COO-), 1.59 (m, 4H, ι-CH_2- and β-CH_2- of alkyl chain), 1.33−1.22 (bm, 14H, $-CH_2-$ of alkyl chain). FT-IR: ν (cm^{-1}) 3437 (OH), 2932 (CH), 1743 (isobutyryl CO-O), 1619 (acetyl CO-N).

Synthesis of Arginine-Methacryloylamide (Arg-methacryloylamide). Arginine-methacryloylamide (Arg-methacryloylamide) was synthesized according to a procedure described in literature.[34] Arginine hydrochloride (2.1 g, 10 mmol) was dissolved in 20 mL of saturated $NaHCO_3$ solution and was then cooled to 0 °C. Next, 970 μL of methacryloyl chloride (10 mmol) was added dropwise under vigorous stirring. After 1 h, the pH of the mixture was adjusted to 1 with hydrochloric acid, and the solution was saturated with sodium chloride, filtered, washed three times with 30 mL of ethyl acetate, and finally extracted three times with 20 mL of a 1:1 vol/vol mixture of ethyl acetate/isopropanol. The ethyl acetate/isopropanol fractions were pooled, concentrated under reduced pressure, and filtered. The resulting colorless oil was added to 50 mL of water, and the resulting solution was freeze−dried. The mass of the final product was 2.4 g. The product was analyzed by ESI-MS, ^{1}H NMR, and FT-IR.

ESI-MS [m/z]: 243.13 ($M+H^+$) [calcd for Arg-methacryloylamide ($C_{10}H_{18}N_4O_3$): 242.14]. ^{1}H NMR (D_2O): δ ppm 5.69 (s, 1H, HHC=C), 5.47 (s, 1H, HHC=C), 4.41 (dd, J = 9.2, 5.1 Hz, 1H, α-CH), 3.20 (t, J = 6.8, 2H, δ-CH_2), 1.91 (s, 3H, CH_3), 1.85−1.72 (m, 2H, γ-CH_2), 1.72−1.58 (m, 2H, β-CH_2). FT-IR (KBr): ν (cm^{-1}) 3368 (OH), 3150 ($NHC(NH_2)_2^+$), 1654 (C=C, C=O, and C=N), 1528 (CNH_2 or CNH_3^+).

The purity of the compound was assessed by the integration of the ^{1}H NMR triplet at 3.20 ppm compared with methacryloyl singlets at 5.69 and 5.47 ppm (99%).

Synthesis of Tris[(2-pyridyl)methyl]amine (TPMA). Tris[(2-pyridyl)methyl]amine (TPMA) was prepared according to a modified protocol described in the literature.[32] First, 2-picolyl chloride (10.0 g, 61.0 mmol) was dissolved in 25 mL of distilled water, and the mixture was cooled to 0 °C and added to 12 mL of 5 N NaOH. This solution was then added to 2-(aminomethyl)pyridine (3.2 mL, 30.5 mmol) and 50 mL of dichloromethane. The reaction mixture was allowed to reach room temperature under vigorous stirring and the pH was maintained at 9.5 by the addition of 5.0 N NaOH. After 48 h, the organic phase was washed three times with 20 mL of 2.5 N NaOH and then dried with anhydrous Na_2SO_4 and filtered. The organic solvent was removed under reduced pressure. TPMA was recovered by extracting the resulting waxy, red−brown residue three times with 25 mL of boiling petroleum ether. The volatiles were removed under vacuum to afford the desired TPMA ligand. The mass of the final product was 5.6 g.

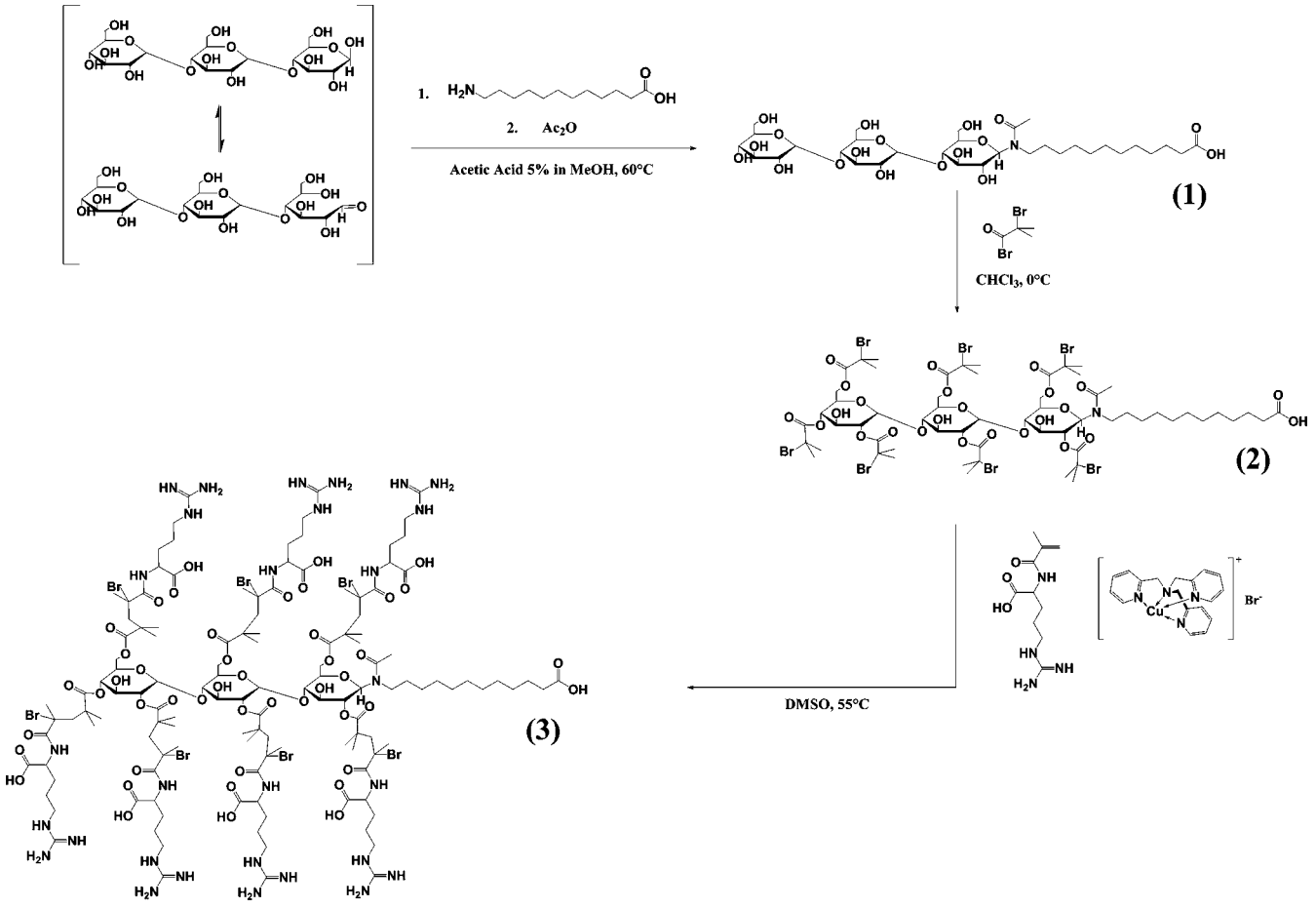
ESI-MS [m/z]: 291.15 $(M+H^+)^{1+}$ and 313.14 $(M+Na^+)^{1+}$ [calcd for TPMA ($C_{18}H_{18}N_4$): 290.15]. ^{1}H NMR ($CDCl_3$): δ ppm 8.53 (d, J = 4.2 Hz, 3H, H-α), 7.65 (t, J = 7.6 Hz, 3H, H-$\beta\delta$), 7.6 (d, 3H, H-$\beta\delta$), 7.1 (t, 3H, H-γ), 3.9 (s, 6H, $-CH_2-$).

Synthesis of Hepta-Arginyl-Maltotriosylamido-*N*-Acetyl-Dodecanoic Acid (Arg$_7$-Malt-NAcC$_{12}$ acid). TPMA (1.31 g, 4.5 mmol), CuBr (0.65 g, 4.5 mmol), and ascorbic acid (7.9 mg, 0.045 mmol) were dissolved in 5 mL of DMSO that had been previously purged with nitrogen. This solution was then added to 8.5 mL of 0.18 mg/mL Arg-methacryloylamide solution (6.3 mmol) in DMSO while stirring at 55 °C. Next, the solution was added to 3 mL of 0.27 mg/mL BrIsoBut$_7$-Malt-NAcC$_{12}$ acid (0.45 mmol) in DMSO. The reaction mixture was maintained under an atmosphere of nitrogen for 12 h and then was exposed to air. Next, the solution was added dropwise to 200 mL of an ice-cold 1:1 acetone/diethyl ether mixture containing 1% acetic acid. The precipitate was desiccated under reduced pressure, redissolved in 5 mL of warm methanol, and reprecipitated by the addition of the resulting solution into 200 mL of the acetone/diethyl ether/acetic acid mixture. Using this procedure, we obtained 1.54 g (98% product yield) of Arg$_7$-Malt-NAcC$_{12}$ acid. The arginine content in the final product was quantified by Sakaguchi assay.[35] The experimental data were plotted on a calibration curve obtained with standard solutions of 0−0.6 μM guanidinium content ($y = 7.3955x - 0.0386$, $R^2 = 0.99$). The final product was also analyzed by elemental analysis, FT-IR, and ^{1}H NMR (D_2O).

Elemental analysis: found C, 39.3%; H, 5.9%; N, 10.0%; Br, 28.1% (O, 16.7%); [calcd for Arg$_7$-Malt-NAcC$_{12}$ acid HBr salt ($C_{130}H_{218}Br_7N_{29}O_{46}$·7HBr): C, 38.6%; H, 5.6%; N, 10.0%; Br, 27.6% (O, 18.2%)]. FT-IR: ν (cm^{-1}) 3373 and 3182 [$NHC(NH_2)_2^+$], 2938 (CH), 1735 (C=O), 1657 (C=N).

Conjugation of Arg$_7$-Malt-NAcC$_{12}$ Acid to Fluorescein-Labeled Bovine Serum Albumin. Bovine serum albumin (BSA, 10 mg, 0.15 μmol) was dissolved in 250 μL of 0.1 M borate buffer, pH 8.3, and then added to 58 μL of a 10 mg/mL solution of FITC (0.15 μmol) in DMSO. The protein solution was left at room temperature under mild stirring for 1 h and then was added to 5.0 μL of ethanolamine (5 mg, 80 μmoles). The FITC-labeled protein (BSA-FITC) was purified by fast protein liquid chromatography (FPLC) using a Superose 12 gel-filtration column (Amersham-Pharmacia Biotech, Uppsala, Sweden) and was isocratically eluted with 0.5 mL/min of 100 mM phosphate buffer, pH 7.0. The fractions containing the fluorescent protein were pooled, lyophilized, and analyzed by

Scheme 1. Synthesis of Oligo-Arginyl-*N*-Acetyl-Maltotriosylamido-Dodecanoic Acid (Arg_7-Malt-$NAcC_{12}$ acid)[a]



[a](1) Maltotriose derivatization with 12-amino-dodecanoic acid; (2) esterification of the maltotriosyl hydroxyl groups with 2-bromoisobutyryl bromide; (3) Arg-mathacryloylamide conjugation by ATRP reaction.

RP-HPLC using a Jupiter C4 column (250 × 4.6 mm, Phenomenex, Torrance, CA, USA) eluted with a gradient of H_2O/0.05% trifluoroacetic acid (A) and acetonitrile/0.05% trifluoroacetic acid (B) (0−3 min 5% B, 3−23 min from 5% to 55% B). The UV detector was set at 280 nm. The bioconjugation degree (number of FITC molecules per BSA molecule) was assessed by spectrophotometric determination of FITC at 494 nm ($Abs_{0.1\%\ p/v}$ = 184.9), and the protein was detected at 280 nm {$Abs_{0.1\%\ p/v}$ = 0.667; [BSA] = [$Abs_{280\ nm}$ − ($Abs_{494\ nm}$. 0.30)]/0.667}.

Following this, 100 μL of a solution of 5.5 mg/mL Arg_7-Malt-$NAcC_{12}$ acid (0.16 μmol) in DMSO was added to 1 mL of water containing 0.12 mg/mL EDC (0.63 μmol). After 30 min, the solution was added to 1.0 mL of 5.2 mg/mL FITC-BSA (0.08 μmol) in 0.1 M 2-(*N*-morpholino)ethane sulfonic acid, pH 4.6. The reaction mixture was stirred overnight and then ultrafiltered using an Amicon System equipped with a 10 kDa cutoff Ultrafree-CL membrane (Millipore Amicon, Bedford, MA, USA). The bioconjugate was finally purified by ion exchange chromatography using a TSK-GEL Chelate-5PW column eluted with a gradient of (A) 20 mM phosphate buffer, 0.1 M NaCl, pH 6.5; and (B) 20 mM phosphate buffer, 0.7 M NaCl, pH 6.5. The elution profile was analyzed online by UV at 280 nm and by fluorescence (λ_{ex} 494 nm; λ_{em} 520 nm). The peak detected by UV and fluorescence [(Arg_7-Malt-$NAcC_{12}$)$_2$-FITC-BSA] was collected, concentrated by ultrafiltration, and analyzed by RP-HPLC, as reported above. The number of Arg_7-Malt-$NAcC_{12}$ moieties per FITC-BSA molecule was determined by a Sakaguchi assay, using FITC-BSA as reference.

Cell Lines and Culture. The human MCF-7 breast adenocarcinoma and murine MC3T3-E1 embryonic fibroblast cell lines were grown in RPMI 1640 and DMEM medium, respectively, and supplemented with a mixture of 10% heat-inactivated fetal bovine serum (FBS), 1% L-glutamine, and a 1% penicillin−streptomycin−amphotericin B mixture. All cells were maintained at 37 °C in a humidified 5% CO_2 atmosphere and split every 2−3 days.

Cytotoxicity Assay. MCF-7 and MC3T3-E1 cells were plated in 96-well flat-bottomed microassay plates (1 × 10^4 cells/well) and grown for 24 h. After complete adhesion, Arg_7-Malt-$NAcC_{12}$ acid or polyethylenimine (PEI) was added to the culture media at increasing concentrations from 0 to 100 μM. The cells were incubated for 24 h at 37 °C, and then the medium was discarded by aspiration and replaced with 100 μL of fresh medium. The cells were grown for a further 48 h. Next, 20 μL of a 5 mg/mL solution of 3-(4,5-dimethylthiazol-2-yl)-2,5-diphenyltetrazolium bromide (MTT) in 20 mM phosphate buffer and 0.15 M NaCl, pH 7.2, was added to each well. After 4 h, the MTT-containing medium was removed and 200 μL of DMSO was added to each well to dissolve the formazan crystals formed by live cells.[36] The plates were gently shaken for 30 min and the absorbance was measured at 570 nm. The cell viability

was expressed as a percent viability of treated cells with untreated cells used as a control.

Fluorescence Analysis. MCF-7 and MC3T3-E1 cells were seeded in 12-well plates (5×10^5 cells/well). After 48 h (90% confluence), the medium was removed and the cells were incubated with FITC-BSA or $(Arg_7\text{-Malt-NAcC}_{12})_2$-FITC-BSA (0.2 μM in culture medium supplemented with 10% FBS) at 37 or 4 °C. After 60 min, the medium was removed and the cells were washed three times with DPBS and lysed in 1 mL of 0.1% Triton X-100 solution. The plates were gently shaken for 2 h and the lysates were centrifuged at 12 000 rpm (10 625 g) for 5 min. The fluorescence intensity was measured at 520 nm by a FP-6500 Jasco Fluorescence Spectrophotometer (Kyoto, Japan) using 0.1% Triton X-100 as the blank. A similar procedure was carried out with unseeded plates to quantify the fluorescence intensity of the background. The relative fluorescence (fluorescence/cell number) was calculated by determining the cell number on the basis of the BCA protein assay (Pierce, Celbio, Pero, Italy). The optical density (O.D.) data at 570 nm were plotted on a standard curve (O.D. values vs cells/mL; $y = 10^{-6}\,x + 0.024$, $R^2 = 0.996$).

Fluorescence-Activated Cell Sorting (FACS) Analysis. MCF-7 and MC3T3-E1 cells were seeded in six-well plates (1×10^6 cells/well, 1.8 mL culture medium/well). After 48 h, the medium was removed and the cells were washed with 1.8 mL of DPBS and incubated with FITC-BSA or $(Arg_7\text{-Malt-NAcC}_{12})_2$-FITC-BSA (0.2 μM in culture medium supplied with 10% FBS), as described above. After 60 min of incubation at 37 °C, the cells were washed three times with DPBS and treated for 2 min with trypsin/EDTA. Trypsin-treated cells were recovered by centrifugation at 1500 rpm (166 g) for 2 min and were washed twice with DPBS. The cells were fixed with 1% (w/v) paraformaldehyde in phosphate buffer and stored overnight at 4 °C, protected from light. Afterward, the cell samples (100 000 cells in average count) were analyzed by a FACSCalibur flow cytometer using the *CellQuest* software package (BD Bioscience, Heidelberg, Germany) and then gated using forward vs side scatter to exclude debris and dead cells.

Confocal Microscopy. MCF-7 and MC3T3-E1 cells were plated on four-well chamber slides at a density of 1×10^5 cells per chamber and incubated at 37 °C in a humidified 5% CO_2 atmosphere. After 24 h of adhesion, the cells were incubated with FITC-BSA or $(Arg_7\text{-Malt-NAcC}_{12})_2$-FITC-BSA (0.2 μM in culture medium supplemented with 10% FBS), as described above. After 60 min incubation at 37 °C, the cells were thoroughly washed with DPBS and fixed with 1% (w/v) paraformaldehyde in phosphate buffer for 1 h at 4 °C. Afterward, the fixed cells were rinsed twice with DPBS, and the samples were mounted with Vectashield containing 1.5 μg/mL DAPI and kept at 4 °C. The cells were protected from light until microscopic examination. Confocal imaging was performed using a Leica TCS SP5 confocal laser-scanning microscope (Leica Microsystems, Mannheim, Germany) equipped with a Leica HCX PL APO 63×/1.40 oil immersion objective. The blue argon laser was set at 351 nm (blue) and 488 nm[9] to produce the excitation wavelengths for DAPI and fluorescein, respectively.

RESULTS

Synthesis and Characterization of Hepta-Arginyl-*N*-Acetyl-Maltotriosylamido-Dodecanoic Acid (Arg_7-Malt-$NAcC_{12}$ acid). The synthesis of hepta-arginyl-*N*-acetyl-maltotriosylamido-dodecanoic acid (Arg_7-Malt-$NAcC_{12}$ acid) was carried out according to a three-step procedure described in Scheme 1: (1) synthesis of maltotriosylamido-dodecanoic acid (Malt-C_{12} acid) and *N*-acetylation of the amino group of Malt-C_{12} acid (Malt-$NAcC_{12}$ acid); (2) synthesis of hepta-(2-bromoisobutyryl)-*N*-acetyl-maltotriosylamido-dodecanoic acid ($BrIsoBut_7$-Malt-$NAcC_{12}$ acid); (3) synthesis of hepta-arginyl-*N*-acetyl-maltotriosylamido-dodecanoic acid (Arg_7-Malt-$NAcC_{12}$ acid).

The synthesis of Malt-C_{12} acid was carried out through the reaction of the amino group of 12-amino-dodecanoic acid with the reducible anomeric carbon of maltotriose. The resulting amino group was stabilized by acetylation at the nitrogen to avoid the detachment of the 12-amino-dodecanoic acid residue. The synthesis and purification process yielded an approximate 70% molar yield (Malt-C_{12} acid/maltotriose, mol/mol %). The HPLC analysis of Malt-C_{12} acid showed a single sharp peak, which indicated that the product was pure. The chemical composition of the conjugate was confirmed by elemental analysis, FT-IR, ^{1}H NMR, and ESI-MS (see Materials and Methods). FT-IR showed the presence of characteristic signals corresponding to the hydroxyl groups of the maltotriosyl residue, C−H bonds and the terminal carboxyl group of the alkyl moiety and the acetyl functionality. The ^{1}H NMR showed the presence of typical signals of Malt-$NAcC_{12}$ acid. Mass spectrometry analysis showed the correspondence of the final product mass with the expected value. These results confirmed the chemical identity of the monoacetylated conjugate.

The carbohydrate hydroxyl groups of Malt-$NAcC_{12}$ acid were esterified with 2-bromo-isobutyryl bromide to obtain a multiarmed oligosaccharide initiator for ATRP reaction. The FT-IR analysis showed the nearly complete disappearance of the glycosidic OH signal at 3437 cm^{-1}, which indicates the extensive functionalization of the hydroxyl groups with 2-bromo-isobutyryl bromide. The intensity of the signals of the acetyl and alkyl terminating carbonyl groups at 1741 and 1619 cm^{-1} were unaffected by the conjugation reaction. The ^{1}H NMR showed the presence of the typical signals corresponding to the oligo-2-bromoisobutyryl derivative (see Materials and Methods). The elemental analysis showed that the composition of the multiarmed initiator corresponded to $BrIsoBut_7$-Malt-$NAcC_{12}$ acid indicating that 7 out of the 10 available hydroxyl groups were modified with 2-bromo-isobutyryl-bromide. On the basis of these data, the calculated molecular weight of the novel bioconjugate was 3482 Da. The synthesis of $BrIsoBut_7$-Malt-$NAcC_{12}$ acid resulted in approximately 60% product yield [$BrIsoBut_7$-Malt-$NAcC_{12}$ acid/Malt-$NAcC_{12}$ acid, mol/mol %].

The conjugation of the arginyl residues to the $BrIsoBut_7$-Malt-$NAcC_{12}$ acid was carried out under ATRP conditions using arginine-methacryloylamide (Arg-methacryloylamide) as the monomer and tris[(2-pyridyl)methyl]amine (TPMA) as the ligand for $Cu(I)^+$. Both Arg-methacryloylamide and TPMA were prepared with high product yields, 99% and 64%, respectively, and in high purity.

The reaction was carried out under an atmosphere of nitrogen to avoid the catalyst inactivation by oxidation of Cu(I) to Cu(II). The reaction also used a 2:1 molar excess of Arg-methacryloylamide with respect to the 2-bromo-isobutyryl residues to obtain complete 2-bromo-isobutyryl derivatization. The ^{1}H NMR spectrum of the purified final product (Figure 1A) was complex, but did show the presence of the triplet at 3.35 ppm (J = 6.8 Hz) corresponding to the δ-CH_2 of arginyl moieties. The two singlets at 5.69 and 5.47 ppm, corresponding to the methacrylic functionality, were also absent, confirming

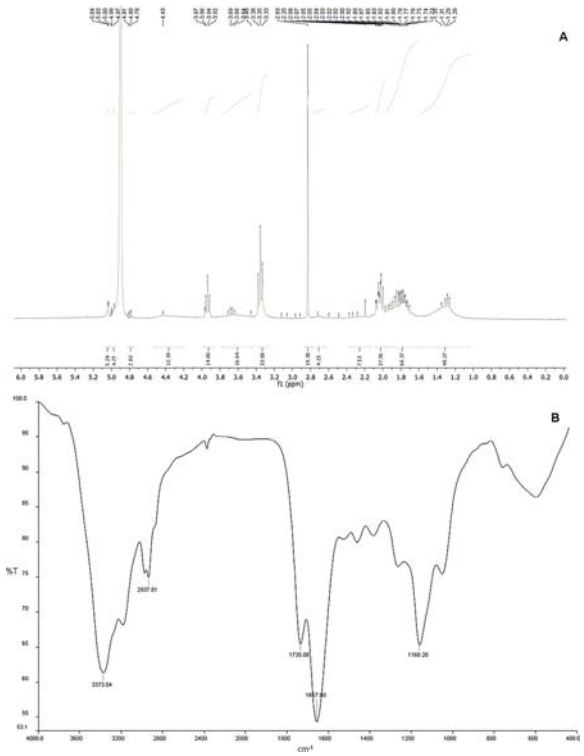


Figure 1. ^{1}H NMR spectrum (A) and IR spectrum (B) of hepta-arginyl-*N*-acetyl-maltotriosylamido-undecanoyl acid (Arg_7-Malt-$NAcC_{12}$ acid).

the absence of unreacted monomer. The IR spectrum (Figure 1B) confirmed the presence of the guanidine functions. These data indicated the conjugation of the Arg-methacryloylamide to the oligosaccharide structure, and elemental analysis suggested the hepta-arginyl derivative. This result was confirmed by the colorimetric determination of the arginyl groups by the Sakaguchi assay.

Cytotoxicity Assay. The cytotoxicity of Arg_7-Malt-$NAcC_{12}$ acid was investigated by incubation for 24 h in the presence of MCF-7 and MC3T3-E1 cells. A comparative cell viability assay was carried out using polyethylenimine (PEI) with a similar average molecular weight of Arg_7-Malt-$NAcC_{12}$ acid.

The cytotoxicity profiles reported in Figure 2 show that the Arg_7-Malt-$NAcC_{12}$ acid has a very low toxicity toward both of the examined cell lines compared to PEI. The IC_{50} measured for PEI was 40 and 30 μM for MCF-7 and MC3T3-E1, respectively, while for the Arg_7-Malt-$NAcC_{12}$ acid, the obtained IC_{50} with both cell lines was higher than 100 μM.

Preparation of Hepta-Arginyl-*N*-Acetyl-Maltotriosylamido-Dodecanoyl-FITC-BSA [$(Arg_7$-Malt-$NAcC_{12})_2$-FITC-BSA]. Bovine serum albumin (BSA, 66 kDa, isoelectric point 4.7) was used as a cargo model to assess the ability of Arg_7-Malt-$NAcC_{12}$ acid to act as an intracellular carrier for hydrophilic macromolecules.

The conjugation of Arg_7-Malt-$NAcC_{12}$ acid to fluorescein-labeled BSA (FITC-BSA) (Scheme 2) was carried out by EDC-mediated condensation. The chromatographic and spectroscopic analyses of the purified product showed the conjugation of FITC-BSA to Arg_7-Malt-$NAcC_{12}$ acid. The Sakaguchi assay showed that the Arg_7-Malt-$NAcC_{12}$ acid-derivatized FITC-BSA contained a mean of two Arg_7-Malt-$NAcC_{12}$ moieties per FITC-BSA molecule, yielding $(Arg_7$-Malt-$NAcC_{12})_2$-FITC-BSA.

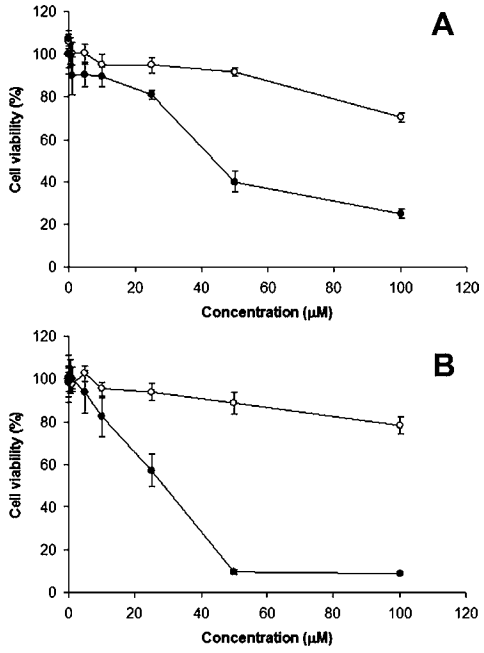


Figure 2. Cytotoxicity profiles obtained by MCF-7 (A) and MC3T3-E1 (B) incubation with increasing concentrations of polyethylenimine (●) and hepta-arginyl-*N*-acetyl-maltotriosylamido-dodecanoic acid (○). The mean values and standard deviations were calculated on the basis of values obtained from six experiments.

Fluorimetric Assays. *In vitro* studies were undertaken to evaluate the ability of Arg_7-Malt-$NAcC_{12}$ acid to transport hydrophilic macromolecules into cells. MCF-7 and MC3T3-E1 cells were incubated with FITC-BSA or $(Arg_7$-Malt-$NAcC_{12})_2$-FITC-BSA, and the protein uptake was evaluated by spectrofluorimetric analysis, flow cytometry, and confocal microscopy.

Since studies reported in the literature showed that tumor cells, namely, MCF-7 cells, can internalize serum proteins including serm albumin,[37,38] FITC-BSA was used as control.

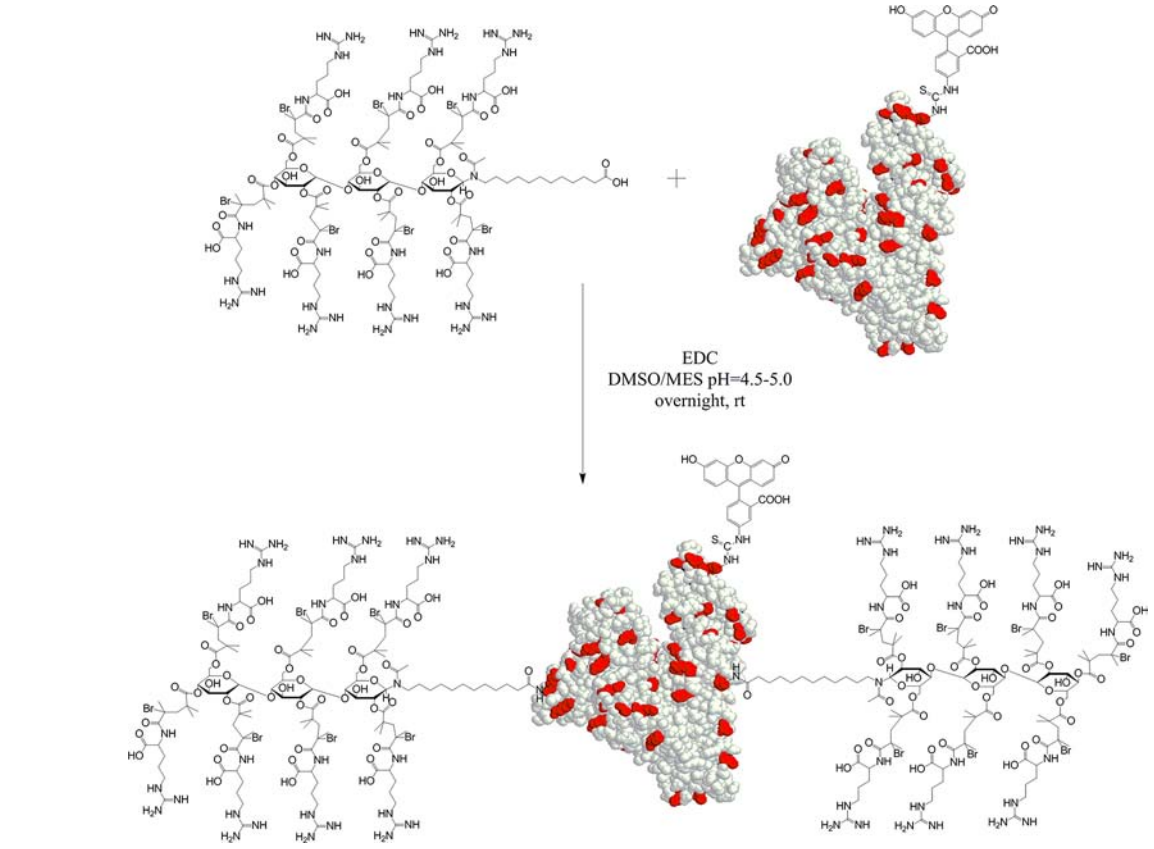
Before the fluorimetric analyses, the cells were extensively washed with buffer to eliminate the FITC-BSA or $(Arg_7$-Malt-$NAcC_{12})_2$-FITC-BSA that was not taken up by the cells.

Spectrofluorimetric Analysis. The cell-associated relative fluorescence (RF) was examined after MCF-7 and MC3T3-E1 incubation at 37 and 4 °C with FITC-BSA and $(Arg_7$-Malt-$NAcC_{12})_2$-FITC-BSA and cell lysis with Triton X/100. To compare the results obtained under different conditions, the relative fluorescence (RI) values were normalized to 10^6 cells.

Figure 3 reports the RF obtained by cell incubation at 37 °C with buffer (self-fluorescence), FITC-BSA, and $(Arg_7$-Malt-$NAcC_{12})_2$-FITC-BSA. The RF associated with the MCF-7 and MC3T3-E1 cells incubated with FITC-BSA was in agreement with the evidence reported in the literature that serum albumin can be taken up by tumor cells.[37,38] The fluorescence intensity values obtained by MCF-7 and MC3T3-E1 cell incubation with $(Arg_7$-Malt-$NAcC_{12})_2$-FITC-BSA were approximately 4.5 times higher than those obtained with FITC-BSA-treated cells.

Figure 4 shows the RF values obtained by MCF-7 and MC3T3-E1 incubation with buffer, FITC-BSA, and $(Arg_7$-Malt-$NAcC_{12})_2$-FITC-BSA at 4 °C. The basal cell RF of untreated MCF-7 and MC3T3-E1 cells was similar to that obtained at 37°, while the RF obtained with FITC-BSA and $(Arg_7$-Malt-$NAcC_{12})_2$-FITC-BSA was significantly lower. The incubation with FITC-BSA resulted in an approximate 2-fold RF increase

Scheme 2. Synthesis of Fluorescent Hepta-Arginyl-*N*-Acetyl-Maltotriosylamido-Undecanoyl-BSA [$(Arg_7$-Malt-$NAcC_{12})_2$-FITC-BSA]



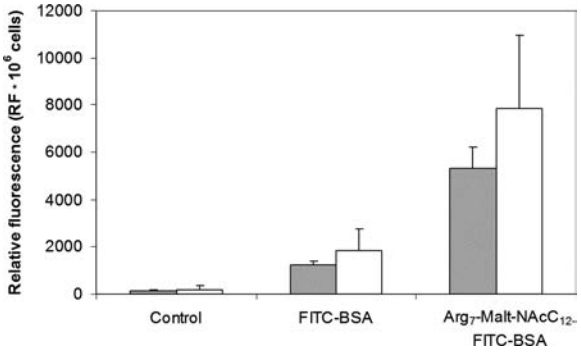


Figure 3. Relative fluorescence of lysated MCF-7 cells (white) and MC3T3-E1 cells (gray) incubated at 37 °C with buffer (control), FITC-BSA, and hepta-arginyl-N-acetyl-maltotriosylamido-dodecanoyl-FITC-BSA. The mean values and standard deviations were calculated on the basis of values obtained from five experiments.

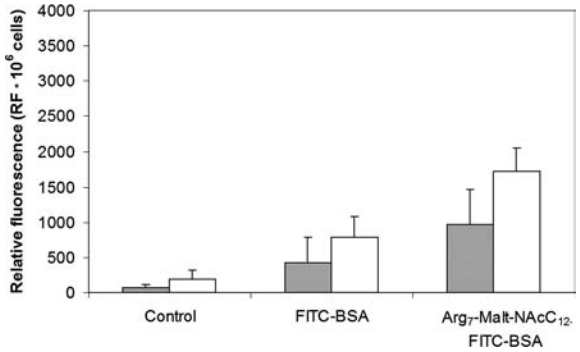


Figure 4. Relative fluorescence of lysated MCF-7 cells (white) and MC3T3-E1 cells (gray) incubated at 4 °C with buffer (control), FITC-BSA, and hepta-arginyl-N-acetyl-maltotriosylamido-dodecanoyl-FITC-BSA. The mean values and standard deviations were calculated on the basis of values obtained from five experiments.

compared to the basal cell RF, and the RF of MCF-7 and MC3T3-E1 cells incubated with $(Arg_7$-Malt-$NAcC_{12})_2$-FITC-BSA was 2 times higher than that obtained with the cells incubated with FITC-BSA.

Flow Cytometry Analysis. Figure 5 reports the dot plots of side scatter (SSC-H) vs fluorescence intensity (FL1-H) obtained by fluorescence-activated cell sorting. The plots reported in panels A2 and B2 show that the percentage of FITC-BSA-treated MCF-7 and MC3T3-E1 cells with higher fluorescence were lower than 8% and 11%, respectively, compared to the untreated cells (panels A1 and B1). The dot plots reported in panels A3 and B3 show that the incubation with $(Arg_7$-Malt-$NAcC_{12})_2$-FITC-BSA significantly increases the cell-associated fluorescence. Over 85% and 95% of the $(Arg_7$-Malt-$NAcC_{12})_2$-FITC-BSA treated MCF-7 and MC3T3-E1 cells, respectively, displayed higher fluorescence compared to the self-fluorescence of untreated cells.

Confocal Microscopy. The confocal images obtained with MCF-7 and MC3T3-E1 cells incubated with FITC-BSA and $(Arg_7$-Malt-$NAcC_{12})_2$-FITC-BSA are reported in Figures 6 and 7, respectively. Figures 6A and 7A report the images obtained after 60 min cell incubation at 37 °C, while Figures 6B and 7B report the images obtained after cell incubation at 4 °C. In order to evidence the fluorescence of $(Arg_7$-Malt-$NAcC_{12})_2$-

dx.doi.org/10.1021/bc200666u | *Bioconjugate Chem.* 2012, 23, 1415–1425

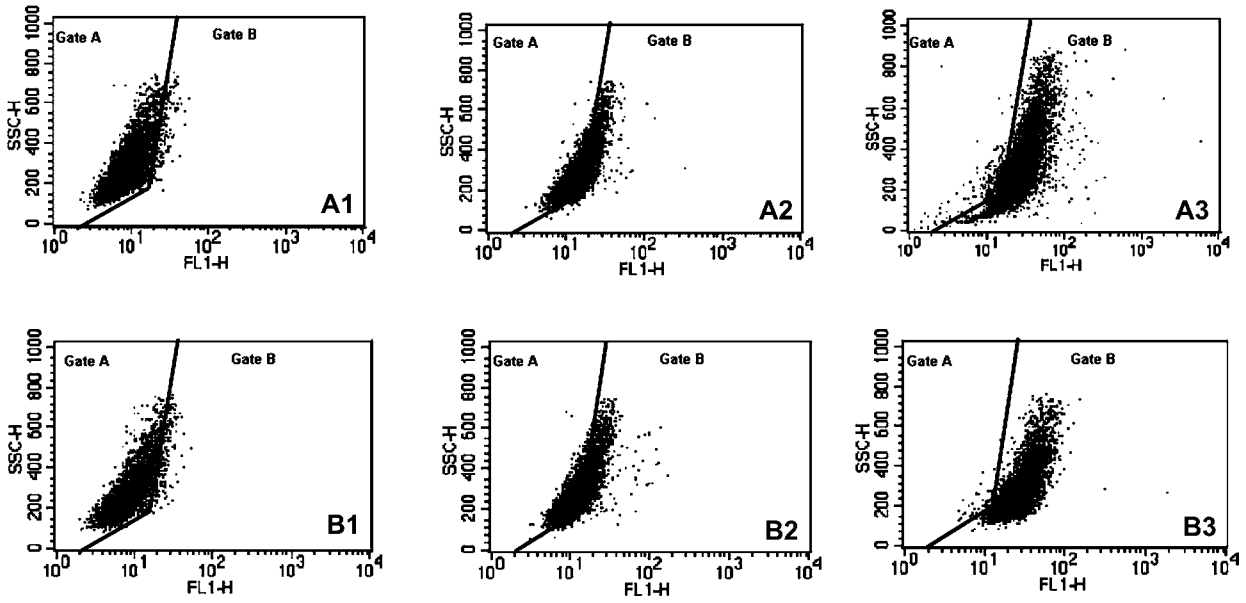


Figure 5. Side scatter (SSC-H) versus fluorescence (FL1-H) plots obtained by flow-activated cytometry sorting analysis of MCF-7 (A) and MC3T3-E1 (B) cells after incubation with plain buffer (A1 and B1), FITC-BSA (A2 and B2), and hepta-arginyl-*N*-acetyl-maltotriosylamido-dodecanoyl-FITC-BSA (A3 and B3).

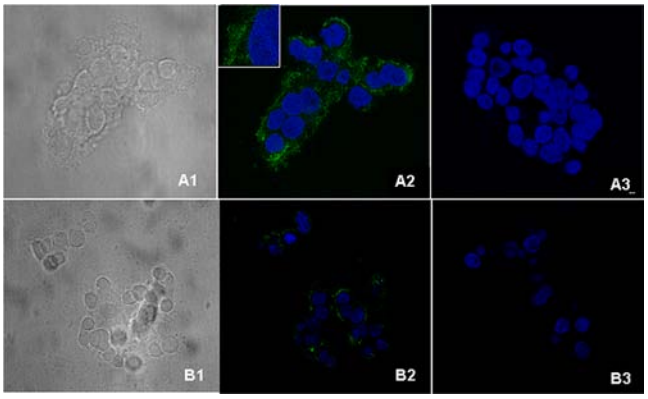


Figure 6. Confocal microscopy images (63×) obtained with MCF-7 incubated for 60 min with (A) $(Arg_7\text{-Malt-NAcC}_{12})_2$-FITC-BSA at 37 °C (A1, transmission image; A2, reflection image) and FITC-BSA (A3); (B) $(Arg_7\text{-Malt-NAcC}_{12})_2$-FITC-BSA at 4 °C (B1, transmission image; B2, reflection image) and FITC-BSA (B3). The green fluorescence obtained with FITC-BSA was set as basal level.

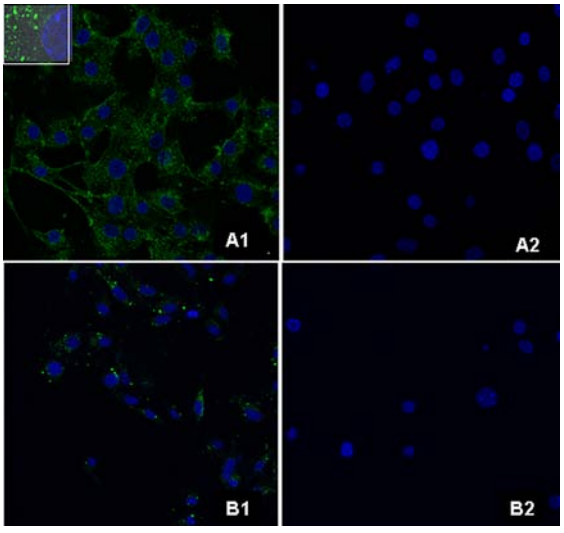


Figure 7. Confocal microscopy images (63×) obtained with MC3T3-E1 incubated for 60 min with (A) $(Arg_7\text{-Malt-NAcC}_{12})_2$-FITC-BSA at 37 °C (A1) and FITC-BSA (A3); (B) $(Arg_7\text{-Malt-NAcC}_{12})_2$-FITC-BSA at 4 °C (B1) and FITC-BSA (B3). The green fluorescence obtained with FITC-BSA was set as basal level.

FITC-BSA internalized by the cells. the fluorescence of FITC-BSA treated MCF-7 (Figure 6A3,B3) and MC3T3-E1 cells (and Figure 7A2,B2) has been set as basal level. Therefore, the images obtained with the control cells (Figures 6A3,B3 and 7A2,B2) show the intense blue fluorescence corresponding to DAPI-stained nuclei only. The images obtained with $(Arg_7\text{-Malt-NAcC}_{12})_2$-FITC-BSA-treated MCF-7 (Figure 6A2,B2) and MC3T3-E1 cells (Figure 7A1,B1) show intense green fluorescence in the cytosol. The inset of Figures 6A2 and 7A1 show the punctuated fluorescence distribution in the cytosol. The images obtained with cells incubated at 4 °C (Figures 6B and 7B) show that $(Arg_7\text{-Malt-NAcC}_{12})_2$-FITC-BSA is taken up by the cells at a lower extent. This qualitative result confirms the data obtained by spectrofluorimetry and FACS. Finally, green fluorescence was never found in the nuclei.

DISCUSSION

The nonlinear oligo-arginyl cell-penetrating enhancer $Arg_7\text{-Malt-NAcC}_{12}$ acid was designed for conjugation to large systems, namely, proteins, oligonucleotides, or colloidal drug carriers, to promote their cell entry. The nonconventional architecture of this bioconjugate was obtained by introducing arginyl moieties, which are the key functions of the cell-penetrating 49−57 Tat, to a core anchoring structure. The synthesis protocol was originally designed to obtain a series of derivatives with a nonpeptidic structure containing a variable number of Arg functions attached to an anchoring structure that could perform as a cell-penetration enhancer.

Maltotriose was selected as the anchoring molecule. The hydroxyl groups of this molecule can provide for multiple

derivatizations with arginyl residues through simple chemical protocols to obtain a nonpeptide, star-like construct. In addition, the peculiar reactivity of the reducible anomeric carbon of maltotriose toward amines can be exploited to introduce functional groups, namely, −COOH, $-NH_2$, −SH, and so forth, for conjugation to macromolecules or supramolecular drug delivery systems.

According to the chemical features of maltotriose, the anomeric carbon of the oligosaccharide was functionalized with linear alkyl chains of 12-amino-dodecanoic acid, and the resulting amino group was stabilized by N-acetylation. Spectrophotometric and elemental analysis showed that the acetylation reaction involved only the amino group of the conjugate, while the hydroxyl functions of maltotriose were not acetylated and remained available for the following modification steps.

The conjugation of arginine functions to Malt-$NAcC_{12}$ acid was carried out under ATRP conditions, a technique that yields macromolecular products with defined composition under controlled reaction conditions.[39,40] Accordingly, Malt-$NAcC_{12}$ acid was first converted into a multiarmed initiator by reaction with 2-bromo-isobutyryl bromide. The acid was then reacted in the presence of Arg-methacryloylamide, using TPMA/Cu(I)Br as the catalytic system.

The incomplete maltotriose hydroxyl substitution with 2-bromo-isobutyryl bromide (7 out of the 10 available OH) that occurred despite the use of excess 2-bromo-isobutyryl bromide/Malt-$NAcC_{12}$ acid molar ratios may be ascribed to steric hindrance that prevents the 2-bromo-isobutyryl-bromide from reacting with the two vicinal hydroxyl groups of the oligosaccharide.

Under ATRP conditions, 7 Arg-methacryloylamido moieties were attached to the $BrIsoBut_7$-Malt-$NAcC_{12}$. Preliminary studies showed that the derivatization of maltotriose bearing two and four 2-bromo-isobutyryl functions resulted in the maximal conjugation of two and four Arg-methacryolylamido moieties, respectively (data not shown). These results seem to suggest that, under the operative conditions, the 2-bromo-isobutyryl-bromide groups are completely functionalized with one Arg-methacryloylamido moiety. Indeed, even the use of high molar ratios of Arg-methacryloylamide/$BrIsoBut_7$-Malt-$NAcC_{12}$ (14:1 and 21:1) did not yield higher Arg-methacryloylamido functionalization. Therefore, for bioconjugates bearing short Arg-methacryloylamido chains, the Arg-methacryloylamide oligomerization could not be obtained. In this regard, studies reported in the literature have demonstrated that the inefficient polymerization of (meth)acrylamide monomers may be ascribed to various phenomena, including catalyst deactivation by the amido groups and the strong bond between the (meth)acrylamide units and the bromide atom.[41,42]

The bioconjugate containing 7 Arg residues that is described in the present study displays composition analogies with cell-penetration peptides, such as the 49−57 Tat domain and oligoarginine peptides. Therefore, it was considered a good candidate as a penetration enhancer for further biological investigations.

Cell culture studies showed that the novel nonlinear hepta-arginyl derivative does not exhibit significant cytotoxicity, which is a requisite for a new product that is expected to undergo intracellular localization. The high IC_{50} (>100 μM) and the fact that only a limited amount of enhancer may be required for promoting the cell translocation of colloidal formulations suggest that this product is potentially safe for pharmaceutical applications. However, since the nonlinear hepta-arginyl derivative has been designed for conjugation to macromolecules or supramolecular drug vehicles, the short- and long-term toxicity of each colloidal bioconjugate containing the star-like oligo-arginyl-maltotriosyl derivative must be investigated in detail.

The most common way to confirm the cell-penetrating efficiency of different CPPs has been through labeling with fluorophores, such as fluorescein or rhodamine. Therefore, the cell-penetrating properties of the Arg_7-Malt-$NAcC_{12}$ derivative were evaluated using BSA as a cargo molecule labeled with fluorescein isothiocyanate (FITC).

The spectrofluorimetric analyses, fluorescence activated cell sorting, and confocal microscopy showed that, as with other Arg rich macromolecules described in the literature,[43] Arg_7-Malt-$NAcC_{12}$ can bestow promising cell-penetration properties on macromolecular bioconjugates.

The quantitative fluorescence studies and the cytofluorimetric analyses showed that both the MC3T3-E1 and the MCF-7 cell lines underwent $(Arg_7$-Malt-$NAcC_{12})_2$-FITC-BSA uptake. The slight differences observed between the MC3T3-E1 and the MCF-7 cells appear to indicate that the translocation process may depend on surface cell-specific properties, such as specific membrane biological activity or membrane composition.

Confocal microscopy confirmed the cell uptake of $(Arg_7$-Malt-$NAcC_{12})_2$-FITC-BSA. The punctuated fluorescence distribution in the cytosol obtained with the cells treated with $(Arg_7$-Malt-$NAcC_{12})_2$-FITC-BSA and the lack of fluorescence in the nucleus indicate that the cell uptake of $(Arg_7$-Malt-$NAcC_{12})_2$-FITC-BSA was limited to the cytoplasm compartment. This result is in agreement with the data reported in the literature, which showed that branching membrane translocational peptides promote gene delivery in the cytoplasm, but not in the nucleus.[44]

The cell trafficking of arginine-rich CPPs is still controversial. The cell uptake of cargo-CCPs has been found to occur according to mechanisms and kinetics that depend on the chemical nature of the cell-penetrating function and assay conditions, namely, temperature, pH, cargo-CCP dose, and so forth.[45] The arginine-rich CPPs were found to destabilize the plasma membrane, creating transient pores for cellular penetration that resulted in cytosol or nucleus localization without organelle confinement. Nevertheless, the confocal results obtained with the cells incubated with $(Arg_7$-Malt-$NAcC_{12})_2$-FITC-BSA indicate that active mechanisms may be involved in or contribute to the cell uptake of the bioconjugate. The punctuated fluorescence obtained by the confocal analysis of cells incubated with $(Arg_7$-Malt-$NAcC_{12})_2$-FITC-BSA at 37 °C seems, in fact, to corroborate the hypothesis that the star-like penetration enhancer promotes the macromolecular cargo uptake by endocytosis or macropinocytosis.[46] This hypothesis is also confirmed by the data obtained at 4 °C. Under these conditions, the active cell uptake is minimized and the cell translocation of $(Arg_7$-Malt-$NAcC_{12})_2$-FITC-BSA was significantly lower than that obtained at 37 °C. However, the lower FITC-BSA uptake observed at 4 °C compared to that obtained at 37 °C may be ascribed to the temperature-related permeability impairment of the cell membrane. Therefore, the lower cell uptake of $(Arg_7$-Malt-$NAcC_{12})_2$-FITC-BSA at 4 °C could be related to both the inhibition of the active

translocation and the lower passive diffusion due to decreased membrane permeability.

The combined biological data emphasize the complexity of the cell uptake process that is mediated by the novel penetrating agent. Currently, studies have been undertaken to elucidate the cellular mechanisms involved in the translocation of Arg_7-Malt-$NAcC_{12}$ functions. These studies are aimed at comparatively examining the cell-penetrating properties of the corona-like derivative and linear TAT-like sequences. Additional investigations will also be performed using different cell lines and experimental conditions, namely, time, pH, and temperature.

CONCLUSIONS

The results reported in the present work show that a novel class of cell-penetration enhancers with unusual chemical structures can be easily obtained via simple and reproducible synthetic steps. In principle, the proposed chemical synthesis protocol is flexible and can be properly managed to obtain products that, by virtue of their unconventional structural properties, open new possibilities in drug delivery.

A wide array of cell-penetration enhancers can be obtained by slight modifications of the main structure of these enhancers to provide for their conjugation or physical combination with a variety of therapeutic systems. These molecules can be designed for conjugation to proteins or polymer therapeutics, or for surface decoration of liposomes or nanoparticles. The cationic features and the penetration-enhancing properties of the star-like oligo-arginyl can also be exploited for oligonucleotide, namely, siRNA, or gene delivery.

Finally, a combination of residues, such as histidines and cysteines, that have been found to possess endosomolytic properties or short peptides that increase the gene expression of DNAs, can be introduced within the core structure.

AUTHOR INFORMATION

Corresponding Author

*E-mail: paolo.caliceti@unipd.it; phone +39 049 8275695; fax +39 049 8275366.

Notes

The authors declare no competing financial interest.

REFERENCES

(1) Amidon, G. L., Lennernäs, H., Shah, V. P., and Crison, J. R. (1995) A theoretical basis for a biopharmaceutic drug classification: the correlation of in vitro drug product dissolution and in vivo bioavailability. *Pharm. Res. 12*, 413−420.

(2) Williams, A. C., and Barry, B. W. (2004) Penetration enhancers. *Adv. Drug Delivery Rev. 56*, 603−618.

(3) Wadia, J. S., and Dowdy, S. F. (2002) Protein transduction technology. *Curr. Opin. Biotechnol. 13*, 52−56.

(4) Stewart, K. M., Horton, K. L., and Kelley, S. O. (2008) Cell-penetrating peptides as delivery vehicles for biology and medicine. *Org. Biomol. Chem. 6*, 2242−2255.

(5) Fonseca, S. B., Pereira, M. P., and Kelley, S. O. (2009) Recent advances in the use of cell-penetrating peptides for medical and biological applications. *Adv. Drug Delivery Rev. 61*, 953−964.

(6) Tung, C.-H., and Weissleder, R. (2003) Arginine containing peptides as delivery vectors. *Adv. Drug Delivery Rev. 55*, 281−294.

(7) Jeyapaul, J., Reddy, M. R., and Khan, S. A. (1990) Activity of synthetic tat peptides in human immunodeficiency virus type 1 long terminal repeat-promoted transcription in a cell-free system. *Proc. Natl. Acad. Sci. U.S.A. 87*, 7030−4.

(8) Kalderon, D., Roberts, B. L., Richardson, W. D., and Smith, A. E. (1984) A short amino acid sequence able to specify nuclear location. *Cell 39*, 499−509.

(9) Green, M., and Loewenstein, P. M. (1988) Autonomous functional domains of chemically synthesized human immunodeficiency virus tat trans-activator protein. *Cell 55*, 1179−1188.

(10) Futaki, S., Suzuki, T., Ohashi, W., Yagami, T., Tanaka, S., Ueda, K., and Sugiura, Y. (2001) Arginine-rich Peptides. *J. Biol. Chem. 276*, 5836−5840.

(11) Futaki, S. (2006) Oligoarginine vectors for intracellular delivery: Design and cellular-uptake mechanisms. *Pept. Sci. 84*, 241−249.

(12) Patel, L., Zaro, J., and Shen, W.-C. (2007) Cell penetrating peptides: intracellular pathways and pharmaceutical perspectives. *Pharm. Res. 24*, 1977−1992.

(13) Wagstaff, K. M., and Jans, D. A. (2006) Protein transduction: cell penetrating peptides and their therapeutic applications. *Curr. Med. Chem. 13*, 1371−87.

(14) Okuyama, M., Laman, H., Kingsbury, S. R., Visintin, C., Leo, E., Eward, K. L., Stoeber, K., Boshoff, C., Williams, G. H., and Selwood, D. L. (2007) Small-molecule mimics of an [alpha]-helix for efficient transport of proteins into cells. *Nat. Meth. 4*, 153−159.

(15) Fisher, A. A., Ye, D., Sergueev, D. S., Fisher, M. H., Shaw, B. R., and Juliano, R. L. (2002) Evaluating the specificity of antisense oligonucleotide conjugates. *J. Biol. Chem. 277*, 22980−22984.

(16) Veldhoen, S., Laufer, S., and Restle, T. (2008) Recent developments in peptide-based nucleic acid delivery. *Int. J. Mol. Sci. 9*, 1276−1320.

(17) Dostmann, W. R. G., Taylor, M. S., Nickl, C. K., Brayden, J. E., Frank, R., and Tegge, W. J. (2000) Highly specific, membrane-permeant peptide blockers of cgmp-dependent protein kinase iα inhibit no-induced cerebral dilation. *Proc. Natl. Acad. Sci. U.S.A. 97*, 14772−14777.

(18) Bonny, C., Oberson, A., Negri, S., Sauser, C., and Schorderet, D. F. (2001) Cell-permeable peptide inhibitors of JNK. *Diabetes 50*, 77−82.

(19) Patsch, C., and Edenhofer, F. (2007) , *Conditional Mutagenesis by Cell-Permeable Proteins: Potential Limitations and Prospects Conditional Mutagenesis: An Approach to Disease Models* (Feil, R., and Metzger, D., Eds.) pp 203−232, Springer, Berlin.

(20) Säälik, P., Elmquist, A., Hansen, M., Padari, K., Saar, K., Viht, K., Langel, Ü., and Pooga, M. (2004) Protein cargo delivery properties of cell-penetrating peptides. a comparative study. *Bioconjugate Chem. 15*, 1246−1253.

(21) Albarran, B., To, R., and Stayton, P. S. (2005) A TAT−streptavidin fusion protein directs uptake of biotinylated cargo into mammalian cells. *Protein Eng., Des. Sel. 18*, 147−152.

(22) Torchilin, V. P. (2008) Tat peptide-mediated intracellular delivery of pharmaceutical nanocarriers. *Adv. Drug Delivery Rev. 60*, 548−558.

(23) Medintz, I. L., Pons, T., Delehanty, J. B., Susumu, K., Brunel, F. M., Dawson, P. E., and Mattoussi, H. (2008) Intracellular delivery of quantum dot−protein cargos mediated by cell penetrating peptides. *Bioconjugate Chem. 19*, 1785−1795.

(24) Liu, B. R., Huang, Y.-w., Winiarz, J. G., Chiang, H.-J., and Lee, H.-J. (2011) Intracellular delivery of quantum dots mediated by a histidine- and arginine-rich HR9 cell-penetrating peptide through the direct membrane translocation mechanism. *Biomaterials 32*, 3520−3537.

(25) Tréhin, R., and Merkle, H. P. (2004) Chances and pitfalls of cell penetrating peptides for cellular drug delivery. *Eur. J. Pharm. Biopharm. 58*, 209−223.

(26) Sakuma, S., Suita, M., Masaoka, Y., Kataoka, M., Nakajima, N., Shinkai, N., Yamauchi, H., Hiwatari, K.-i., Tachikawa, H., Kimura, R., and Yamashita, S. (2010) Oligoarginine-linked polymers as a new class of penetration enhancers. *J. Controlled Release 148*, 187−196.

(27) Hayes, P. Y., Ross, B. P., Thomas, B. G., and Toth, I. (2006) Polycationic lipophilic-core dendrons as penetration enhancers for the oral administration of low molecular weight heparin. *Bioorg. Med. Chem. 14*, 143−152.

(28) Saleh, A. F., Arzumanov, A., Abes, R., Owen, D., Lebleu, B., and Gait, M. J. (2010) Synthesis and splice-redirecting activity of branched, arginine-rich peptide dendrimer conjugates of peptide nucleic acid oligonucleotides. *Bioconjugate Chem. 21*, 1902−1911.
(29) Lee, J. S., and Tung, C.-H. (2010) Lipo-oligoarginines as effective delivery vectors to promote cellular uptake. *Mol. BioSyst. 6*, 2049−2055.
(30) Pantos, A., Tsogas, I., and Paleos, C. M. (2008) Guanidinium group: A versatile moiety inducing transport and multicompartmentalization in complementary membranes. *Biochim. Biophys. Acta 1778*, 811−823.
(31) Wender, P. A., Mitchell, D. J., Pattabiraman, K., Pelkey, E. T., Steinman, L., and Rothbard, J. B. (2000) The design, synthesis, and evaluation of molecules that enable or enhance cellular uptake: Peptoid molecular transporters. *Proc.Natl. Acad. Sci. U. S. A. 97*, 13003−13008.
(32) Tyeklar, Z., Jacobson, R. R., Wei, N., Murthy, N. N., Zubieta, J., and Karlin, K. D. (1993) Reversible reaction of dioxygen (and carbon monoxide) with a copper(I) complex. X-ray structures of relevant mononuclear Cu(I) precursor adducts and the trans-(.mu.-1,2-peroxo)dicopper(II) product. *J. Am. Chem. Soc. 115*, 2677−2689.
(33) Stenzel-Rosenbaum, M. H., Davis, T. P., Chen, V., and Fane, A. G. (2001) Synthesis of poly(styrene) star polymers grown from sucrose, glucose, and cyclodextrin cores via living radical polymerization mediated by a half-metallocene iron carbonyl complex. *Macromolecules 34*, 5433−5438.
(34) Otiai, M., Hattori, T., Kitada, Y., Kuroda, H., Oyobikawa, M., Ichinomiya, S. Novel compound, polymer prepared from the compound, and composition comprising the polymer. European Patent 1156031, September 17, 2008.
(35) Sakaguchi, S. (1925) A new color reaction of protein and arginine. *J. Biochem. 5*, 25−31.
(36) Tim, M. (1983) Rapid colorimetric assay for cellular growth and survival: Application to proliferation and cytotoxicity assays. *J. Immunol. Methods 65*, 55−63.
(37) Uriel, J., Poupon, M. F., and Geuskens, M. (1983) Alphafoetoprotein uptake by cloned cell lines derived from a nickel-induced rat rhabdomyosarcoma. *Br. J. Cancer 48*, 261−9.
(38) Uriel, J., Failly-Crepin, C., Villacampa, M. J., Pineiro, A., and Geuskens, M. (1984) Incorporation of alphafetoprotein by the MCF-7 human breast cancer cell line. *Tumour Biol. 5*, 41−51.
(39) Wang, J.-S., and Matyjaszewski, K. (1995) Controlled/"living" radical polymerization. halogen atom transfer radical polymerization promoted by a Cu(I)/Cu(II) redox process. *Macromolecules 28*, 7901−7910.
(40) Kato, M., Kamigaito, M., Sawamoto, M., and Higashimura, T. (1995) Polymerization of methyl methacrylate with the carbon tetrachloride/dichlorotris- (triphenylphosphine)ruthenium(II)/methylaluminum bis(2,6-di-tert-butylphenoxide) initiating system: possibility of living radical polymerization. *Macromolecules 28*, 1721−1723.
(41) Rademacher, J. T., Baum, M., Pallack, M. E., Brittain, W. J., and Simonsick, W. J. (1999) Atom transfer radical polymerization of N,N-dimethylacrylamide. *Macromolecules 33*, 284−288.
(42) Teodorescu, M., and Matyjaszewski, K. (2000) Controlled polymerization of (meth)acrylamides by atom transfer radical polymerization. *Macromol. Rapid Commun. 21*, 190−194.
(43) Madani, F., Lindberg, S. Langel, U., Futaki, S., Gräslund, A. (2011) Mechanisms of cellular uptake of cell-penetrating peptides. *J. Biophys.*, 414729.
(44) Huang, K., Voss, B., Kumar, D., Hamm, H. E., and Harth, E. (2007) Dendritic molecular transporters provide control of delivery to intracellular compartments. *Bioconjugate Chem. 18*, 403−409.
(45) El-andaloussi, S., Järver, P., Johansson, H. J., and Langel, Ü. (2007) Cargo-dependent cytotoxicity and delivery efficacy of cell-penetrating peptides: a comparative study. *Biochem. J. 407*, 285−292.
(46) Nakase, I., Niwa, M., Takeuchi, T., Sonomura, K., Kawabata, N., Koike, Y., Takehashi, M., Tanaka, S., Ueda, K., Simpson, J. C., Jones, A. T., Sugiura, Y., and Futaki, S. (2004) Cellular uptake of arginine-rich peptides: roles for macropinocytosis and actin rearrangement. *Mol. Ther. 10*, 1011−1022.

Bioconjugate Chemistry

Article

pubs.acs.org/bc

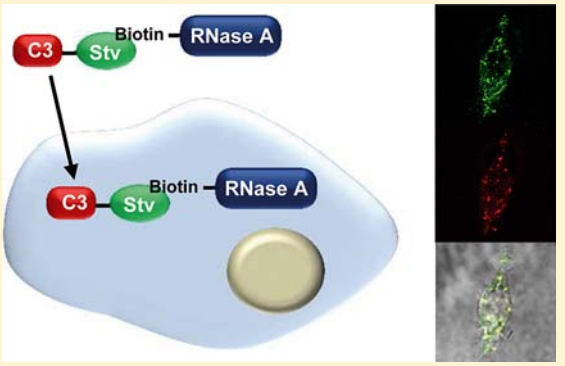
Streptavidin-Conjugated C3 Protein Mediates the Delivery of Mono-Biotinylated RNAse A into Macrophages

Maren Lillich,[‡] Xi Chen,[§] Tanja Weil,[§] Holger Barth,*[,‡] and Jörg Fahrer*[,†,‡]

[‡]Institute of Pharmacology and Toxicology, University of Ulm Medical Center, Albert-Einstein-Allee 11, D-89081 Ulm, Germany

[§]Institute of Organic Chemistry III, University of Ulm, Albert-Einstein-Allee 11, D-89081 Ulm, Germany

ABSTRACT: The C3 toxin produced by *Clostridium botulinum* (C3bot) catalyzes the mono-ADP-ribosylation of the small GTPases Rho A, B and C, resulting in their inactivation. Recently, a specific endocytotic uptake mechanism of C3bot was identified in macrophages and myeloid leukemia cells. Here, we present a novel delivery system based upon a mutant C3bot devoid of ADP-ribosylation activity (C3Mut) and wild-type streptavidin (Stv). The C3Mut moiety mediates endocytosis into macrophages, whereas Stv functions as an adaptor protein for attaching biotinylated molecules to facilitate their subsequent internalization. First, a bioconjugate consisting of recombinant C3Mut and Stv was generated via a thioether linkage that tightly interacted with biotinylated bovine serum albumin as demonstrated by dot blot analysis. We then showed the internalization of C3Mut-Stv into J774A.1 macrophages by confocal microscopy and observed translocation into the cytosol using cell fractionation. The C3Mut-Stv bioconjugate did not affect cell viability. Next, we prepared mono-biotinylated RNase A, which was attached to the C3Mut-Stv transporter, and demonstrated its C3Mut-Stv-mediated delivery into the cytosol of J774A.1 cells. Finally, C3Mut-Stv also promoted the efficient uptake of mono-biotinylated lysozyme into J774A.1 cells, highlighting its versatility. This study intriguingly demonstrates the use of the novel C3Mut-Stv delivery system for protein transduction and may provide a basis for future applications, in particular, of cytotoxic RNase A mutants.



INTRODUCTION

The C3-protein secreted by *Clostridium botulinum* (C3bot) belongs to the family of C3-like transferases that selectively catalyze the ADP-ribosylation of the small GTP-binding proteins RhoA, B, and C.[1] Modification of these Rho GTPases by ADP-ribose results in their inactivation due to enhanced sequestration by RhoGDI in the cytoplasm and impaired interaction with Rho-GEF.[2,3] Subsequently, Rho-mediated signaling is abolished and cellular processes governed by Rho such as control of the actin cytoskeleton are disturbed. One hallmark of Rho inactivation by C3 ADP-ribosyltransferases is a morphological change induced by a drastic rearrangement of the actin cytoskeleton.[4−6] As Rho proteins are also master regulators of other cellular functions including cell cycle progression and cell migration, C3 transferases have been widely used as pharmacological tools to study Rho-mediated signaling cascades.[7] Furthermore, C3bot was shown to stimulate neuronal outgrowth,[8] and more recently, a C3bot-derived peptide was reported to promote the recovery after spinal cord injury by increased neuronal growth.[9] In general, C3 proteins are internalized poorly into eukaryotic cells, most probably via unspecific pinocytosis, and have been considered as exoenzymes for a long time; no transport domain has been identified so far in C3-like ADP-ribosyltransferases. However, an efficient uptake of C3bot into macrophages and monocytes has been demonstrated recently.[10] The uptake mechanism has not yet been completely elucidated, but there is strong evidence for a specific entry pathway of C3bot via acidified endosomal compartments.[10]

Streptomyces avidinii produces streptavidin, a tetrameric protein, which is characterized mainly by its extraordinarily high affinity for biotin (K_D = 10^{-15} M). Each streptavidin subunit forms an antiparallel β-barrel structure which is exceptionally stable even if exposed to heat, high or low pH, denaturants, or proteases.[11] Due to its unique features, streptavidin as well as the related avidin from chicken egg white have been widely used in biochemical and pharmaceutical applications.[12] Pharmaceutical applications comprise avidin-fused monoclonal antibodies directed against cell surface receptors such as the human insulin receptor for targeted drug delivery.[13] Conjugation of streptavidin to a monoclonal antibody directed against the transferrin receptor allowed the targeting of biotinylated siRNA to rat glial cells after intravenous application.[14] In addition, biotinylated saporin, a plant-derived toxin that inactivates ribosomes, was successfully delivered into cancer cells using an anti-transferrin receptor−avidin fusion protein and was shown to potently induce cytotoxicity.[15] Growth factors such as TGF-alpha have also

Received: January 29, 2012
Revised: May 23, 2012
Published: June 9, 2012

 © 2012 American Chemical Society

been used as streptavidin fusion proteins to promote the uptake of biotin-labeled DNA into cells via the EGF receptor.[16] Furthermore, streptavidin fused to importin-β promoted the transport of biotinylated DNA into the nucleus after microinjection into the cytoplasm of cells.[17] Recently, we generated a novel delivery system based upon the binary C2 toxin of *C. botulinum* and streptavidin.[18] The C2-streptavidin transporter allowed the specific uptake of small biotinylated compounds into various mammalian cell lines.[18,19] Interestingly, a C3bot mutant is available that is devoid of ADP-ribosylation[20] and is efficiently internalized into macrophages allowing the generation of a molecular Trojan horse for drug delivery.[21]

RNase A is a small (14 kDa) bovine pancreatic ribonuclease that exhibits endonuclease activity catalyzing the cleavage of single-stranded RNA.[22] RNase A displays high thermal stability,[23] can be completely refolded after denaturation,[24] and is commercially available in huge amounts. Interestingly, RNase A is internalized poorly into mammalian cells,[25] which renders it an attractive model cargo protein for cellular delivery systems. Native RNase A is not cytotoxic in mammalian cells due to inactivation by ribonuclease inhibitor (RI) protein that binds with femtomolar affinity to RNase A.[26]

The present study builds on the uptake of an inactive C3 mutant (C3Mut) linked to wild-type-streptavidin (Stv) to deliver biotinylated ligands into macrophage-like cells. The synthesized C3Mut-Stv bioconjugate exhibits strong biotin binding and is internalized into J774A.1 macrophage-like cells without affecting cell viability. Importantly, we demonstrate the C3Mut-Stv-mediated uptake of macromolecules into the cytosol of J774A.1 cells using both RNase A and lysozyme, which carry single biotin groups at their N-terminus, as protein cargos.

EXPERIMENTAL PROCEDURES

Material. Cell culture medium and fetal calf serum (FCS) were obtained from Invitrogen (Karlsruhe, Germany). Cell culture dishes and plates were bought from TPP (Trasadingen, Switzerland). Trypsin and digitonin were purchased from Sigma-Aldrich (Munich, Germany). Streptavidin and Sulfo-SMCC were from Pierce (Rockford, USA). Page Ruler prestained Protein Ladder was obtained from Fermentas (St. Leon-Rot, Germany). Streptavidin-POD and staurosporine were purchased from Roche (Mannheim, Germany). Immobilon Western Chemiluminescent HRP Substrate was obtained from Millipore (Schwalbach, Germany). Biotin−fluorescein was obtained from Sigma (Deisenhofen, Germany) and fluorophor-coupled secondary antibodies were from Invitrogen (Karlsruhe, Germany). DyLight649-NHS was bought from Pierce (Rockford, USA). Biotin-LC-NHS was received from Sigma-Aldrich (Deisenhofen, Germany). Ribonuclease A (RNase A) and lysozyme were obtained from MP Biomedicals (Illkirch, France) and Sigma (Deisenhofen, Germany), respectively. 10× phosphate buffered saline was purchased from first BASE (Singapore). Monomeric Avidin Kit for affinity chromatography and Sephadex G-15 for gel filtration were from Pierce (Rockford, USA) and Sigma-Aldrich (Deisenhofen, Germany), respectively. BCA assay kit for protein concentration determination was obtained from Merck Biosciences (Darmstadt, German) and absorbance was recorded by a BioTEK Synergy 4 Microplate Reader (Bad Friedrichshall, Germany). All MALDI-ToF-MS spectra of protein samples were recorded on Applied Biosystems 4700 Proteomics Analyzer 88 using sinapinic acid solution as matrix. Baker's yeast ribonucleic acid was purchased from Sigma-Aldrich (Deisenhofen, Germany). SYBR Safe DNA gel stain was obtained from Invitrogen (Karlsruhe, Germany). Tris base and EDTA were purchased from first BASE (Singapore). 384-Well black microtiter plates for RNase A activity assay and sterile 96-well plates were received from Greiner Bio-One (Frickenhausen, Germany) and Nunc Surface (Roskilde, Denmark), respectively.

Purification of Mutant C3bot Protein. The enzymatically inactive C3bot mutant E174Q (C3Mut) was overexpressed as GST-tagged fusion protein as described previously.[10] Briefly, *E. coli* BL21 transformed with pGEX-2T-GL-C3Mut were grown in LB-medium to an optical density of 0.6−0.8. Isopropyl-β-D-thiogalactopyranoside (IPTG) was added to induce protein expression, and the culture was incubated at 29 °C for further 20 h. Cells were pelleted by centrifugation for 10 min at 4 °C at 4400 *g*. The pellet was resuspended in lysis buffer containing 1% Triton X-100 and sonicated. Cellular debris was pelleted (17 000 *g*, 15 min, 4 °C), and the supernatant was incubated with glutathione agarose beads (Macherey Nagel, Düren, Germany) for 20 h at 4 °C. Subsequently, the beads were washed several times and then incubated with thrombin (20 NIH units/L culture) for 1 h to remove the GST-tag. Glutathione beads were pelleted by centrifugation for 30 s at 10 000 *g* at 4 °C, and the supernatant containing C3Mut protein was incubated with benzamidin sepharose beads (GE Healthcare, Uppsala, Sweden) to remove thrombin. Isolated C3Mut was checked for purity by SDS-PAGE followed by Coomassie staining.

Bioconjugation of C3Mut and Streptavidin. C3Mut protein in borate buffer containing 2 mM EDTA, pH 8.0, was incubated with 5-fold molar excess of 2-iminothiolane (Sigma, Deisenhofen, Germany) for 90 min at 25 °C. Thiolation efficiency was then monitored using Ellman's reagent.[27] Briefly, 12.5 μL of the protein solution were incubated with Ellman's reagent (4 mg/mL in buffer containing 100 mM Na_2HPO_4 and 1 mM EDTA, pH 8.0) for 15 min at RT. Absorbance was measured at 405 nm, and the number of thiol groups was determined by comparison with a standard curve. Wild-type streptavidin (Pierce, Rockford, USA) was dissolved in buffer containing 50 mM NaH_2PO_4, 2 mM EDTA (pH 7.2), and activated for 30 min at 25 °C using a 10-fold molar excess of Sulfo-SMCC (Pierce, Rockford, USA) dissolved in DMF. Afterward, nonreacted 2-iminothiolane and Sulfo-SMCC, respectively, were removed by desalting spin columns (Bio-Rad, Munich, Germany). Equal amounts of both activated proteins were then incubated together for 2 h at 25 °C. The coupling reaction was then monitored by SDS-PAGE and Western Blot analysis using anti-C3- and antistreptavidin antibodies.

SDS-PAGE and Immunoblot Analysis. Proteins were separated by SDS-PAGE and subsequently transferred to a nitrocellulose membrane (Whatman, Dassel, Germany). 5% nonfat dry milk in PBS containing Tween-20 (0.1%, PBS-T) was used to block the membrane for 1 h at room temperature (RT). Subsequently, the membrane was probed with the respective primary antibody diluted in PBS-T for 1 h at RT. After washing the membrane 3 times with PBS-T, it was incubated with the appropriate secondary antibody coupled to horseradish peroxidase for 1 h (1:2500 in PBS-T). After further washing steps, proteins were detected using enhanced chemiluminescence.

Dot Blot Analysis. Decreasing amounts of biotinylated and native BSA, RNase A, or lysozyme were vacuum-aspirated onto

a nitrocellulose membrane using a dot-blot manifold (Bio-Rad, Munich, Germany). The membrane was then stained with Ponceau S and blocked with 5% nonfat dry milk in PBS-T for 1 h. Subsequently, the membrane was incubated with C3Mut-Stv conjugate (5 μg/mL in PBS-T) or C3Mut (5 μg/mL in PBS-T) for 1 h. After three washing steps in PBS-T, the membrane was incubated with a polyclonal anti-C3-antibody. Following additional washing steps in PBS-T, the membrane was incubated with peroxidase-coupled anti-rabbit−antibody. Bound proteins were finally detected using the ECL system. In addition, biotinylated proteins were detected with streptavidin−peroxidase.

Cell Culture and Cell Viability Assay. J774A.1 cells were cultured in DMEM containing 10% heat-inactivated FCS, L-glutamate (4 mM), penicillin (100 U/mL), and streptomycin (100 μg/mL) at 37 °C with 5% CO_2. Cells were scraped off and reseeded three times a week.

To check for possible cytotoxic effects of the C3Mut-streptavidin delivery system, cell viability was measured over a period of 48 h. To this end, J774A.1 cells were grown in 96-well plates and incubated with up to 16 μg/mL C3Mut−streptavidin bioconjugate. Staurosporine, a strong inducer of apoptosis, was used as a positive control. Cell viability was then determined with Cell Titer 96 Aqueous One Solution Proliferation Assay (Promega, Mannheim, Germany) according to the manufacturer's instructions.

Confocal Microscopy of C3Mut-Stv Uptake. J774A.1 cells grown on coverslips were incubated for 4 h with C3Mut-Stv (8 μg/mL) that was conjugated to biotin−fluorescein. Furthermore, cells were treated with C3Mut/biotin−fluorescein or biotin−fluorescein. Subsequently, the medium was removed and cells were washed twice with PBS. After fixation with 4% PFA and permeabilization by 0.4% Triton X-100, the cells were blocked in 5% nonfat dry milk in PBS-T. To stain early endosomes, cells were then treated with an anti-EEA1-antibody (1:250), washed with PBS, and incubated with an Alexa-647-coupled secondary antibody (1:400). Finally, cells were mounted on microscope slides with Prolong Gold Antifade Solution (Invitrogen, Karlsruhe, Germany) and analyzed by confocal microscopy using a LSM510 Meta confocal system connected to a Zeiss Axiovert 200 M microscope (Zeiss, Oberkochen, Germany). Z-Stack images were acquired in optical sections of 1 μm and processed with *ImageJ* (NIH, USA).

Digitonin-Based Cell Fractionation. Cell fractionation of J774A.1 macrophages was performed as described earlier.[18,28] Briefly, cells were seeded in 12-well plates and incubated with C3Mut or C3Mut-Stv for the time points indicated. The medium was then removed and cells were washed 3 times with PBS. Subsequently, the cells were permeabilized by incubation with digitonin (20 μg/mL in PBS) for 5 min at RT. Cells were incubated for additional 25 min on ice to obtain the cytosolic supernatant. Afterward, the supernatant was collected carefully and the extracted cells were scraped off. Both fractions were subjected to SDS-PAGE followed by Western Blot analysis. C3Mut-Stv was detected using an anti-C3-antibody. To confirm equal protein amounts, the cytosolic marker protein Hsp90 was probed using a monoclonal anti-Hsp90 antibody (Santa Cruz, Heidelberg, Germany). The endosomal protein EEA1 was visualized by a polyclonal antibody (Acris, Herford, Germany) to check for cross-contamination of the cytosol with endosomal vesicles.

Preparation of Mono-Biotinylated RNase A. Mono-biotinylated RNase A was prepared based on a procedure reported very recently.[29] A single Biotin-LC (biotinamidohexanoyl) group was introduced at the side chain of Lys 1 residue of RNase A via an amide bond, thus yielding Biotin-LC-(K1)RNase A. The corresponding MALDI-ToF-MS spectrum is depicted in Figure 5 revealing that monofunctionalized RNase A was obtained. The location of the biotin substituent has been identified via the $LCMS^2$-XIC method. The protein concentration of mono-biotinylated RNase was determined by BCA assay as described by the manufacturer.

Conjugation of DyLight 649 Fluorophore to Mono-Biotinylated RNase A. 50 μg of DyLight 649 (49.5 nmol) was added to 250 μL of mono-biotinylated RNase A solution (250 μg, 17.5 nmol) in PBS buffer (0.1 M, pH 7.2) and incubated at RT overnight. Thereafter, the labeled protein was desalted via gel filtration using Sephadex G-15 gel and successful labeling was confirmed by MALDI-ToF-MS analysis. According to the mass spectrum, about 2−3 chromophores were attached to mono-biotinylated RNase A, yielding a clear blue solution. MALDI-ToF-MS (SA): m/z 15716 (dual labeled), m/z 16547 (triple labeled).

In Vitro RNase A Activity Test. The enzymatic activity of native and modified RNase A was assessed using yeast RNA (yRNA), which forms a fluorescent complex in the presence of SYBR dye. RNase A catalyzes the cleavage of yRNA to ribonucleotides, resulting in the release of free SYBR dye and a concomitant drop in fluorescence, which is proportional to the RNase A activity.

The in vitro assay was performed in a sterile 384-well plate under light exclusion. Briefly, 10 μL of SYBR dye (10× in TE buffer pH 8.0) was transferred into each well and supplemented with 50 μL TE buffer (blank) or native RNase A (100 ng/mL), mono-biotinylated RNase A (100 ng/mL), C3Mut-Stv (400 ng/mL), and C3Mut-Stv/mono-biotinylated RNase A complex (400 ng/mL and 100 ng/mL), respectively. Subsequently, 40 μL of freshly prepared yRNA substrate (100 μg/mL) was added into each well. The relative fluorescence units (RFU) of the samples were then monitored for 7 min in a BioTEK Synergy 4 Microplate Reader (excitation 485 nm; emission 535 nm).

C3Mut-Stv-Mediated Internalization of Mono-Biotinylated RNase A. Internalization of mono-biotinylated RNase A (B-RNase A) was analyzed with confocal microscopy. To this end, J774A.1 cells seeded on coverslips were treated with 8 μg/mL C3Mut-Stv and 4 μg/mL DyLight649-labeled B-RNase A or each protein alone for 4 h. Afterward, cells were fixed, permeabilized, and processed as described above. C3Mut-Stv was visualized using an anti-C3-antibody (1:5000) in conjunction with an anti-rabbit-IgG-Alexa488 (1:400). Finally, confocal images were recorded in 1 μm sections.

To analyze the intracellular localization of B-RNase A in more detail, digitonin-based cell fractionation was used. J774A.1 cells grown in 12-well plates were treated with 4 μg/mL C3Mut-Stv, 2 μg/mL B-RNase A, or both proteins for up to 24 h. Control cells were left untreated. Afterward, cells were washed and digitonin-based cell fractionation was performed as described before. Recovered fractions were then subjected to SDS-PAGE followed by Western Blot analysis. Internalized B-RNase A was detected using Streptavidin-POD and enhanced chemoluminescence. In addition, the C3Mut-Stv transporter was visualized using an anti-C3-antibody. Equal protein loading was confirmed by an anti-Hsp90-immunoblot, and the absence

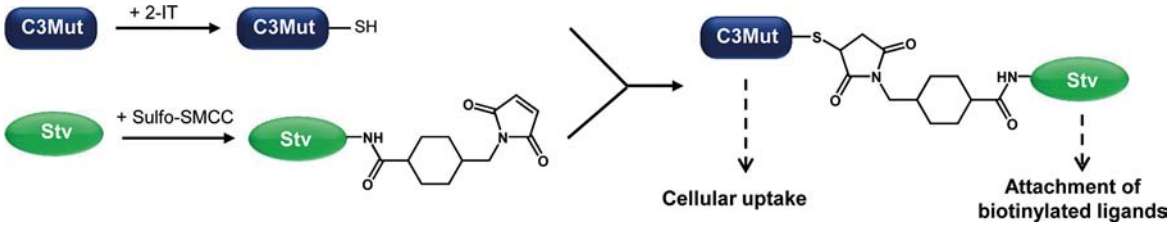


Figure 1. Generation of C3Mut−streptavidin bioconjugate and functional properties. C3Mut protein was treated with 2-iminothiolane to introduce sulfhydryl groups. Wild-type streptavidin (Stv) was maleimide-activated with sulfo-SMCC. Subsequently, activated proteins were incubated together to yield the C3Mut-Stv bioconjugate. The C3Mut domain facilitates cellular uptake, while Stv provides a versatile platform for the attachment of biotinylated ligands such as proteins or siRNA.

of endosomal vesicles in the cytosolic fractions was confirmed using an anti-EEA1-antibody.

To quantify the cytosolic internalization, the signal intensity of B-RNase A in the cytosolic fractions was determined by *Adobe Photoshop CS3* software, corrected for background using untreated control cells and evaluated by *GraphPad Prism 4* software.

Preparation and C3Mut-Stv-Mediated Internalization of Mono-Biotinylated Lysozyme. Site-selective mono-biotinylation of lysozyme was performed as described very recently.[29] A single Biotin-LC group was attached to the side chain of Lys 1 via an amide bond, resulting in Biotin-LC-(K1) lysozyme. N-Terminal monofunctionalization of lysozyme was confirmed by MALDI-ToF-MS and nanoLC-MS^2 analysis.[29] The protein concentration of mono-biotinylated lysozyme was determined by BCA assay. Internalization of mono-biotinylated lysozyme into J774A.1 macrophages was monitored by digitonin-based cell fractionation as described above for B-RNase A.

Reproducibility of the Experiments and Statistics. All experiments were performed independently at least twice. Results from representative experiments are shown in the figures. Values ($n \geq 3$) are calculated as mean ± standard error of the mean (SEM) using *GraphPad Prism 4* Software.

RESULTS

Generation and Characterization of the C3Mut−Streptavidin Bioconjugate. To generate the novel transport system, we have selected an enzymatically inactive mutant of C3bot—C3botE174Q—which lacks ADP-ribosyltransferase activity, but is internalized into target cells comparable to wild-type C3bot. This mutant C3 protein (C3Mut) was chemically linked to wild-type streptavidin (Stv), which provides a platform for biotin binding (Figure 1). Therefore, thiol groups were introduced into C3Mut, while Stv was activated using the amine-reactive linker Sulfo-SMCC. Equal amounts of activated proteins were then incubated to allow bioconjugation via a stable thioether linkage. The coupling reaction was analyzed by immunoblotting and showed the formation of multiple C3Mut−Stv coupling products of varying molecular weight (Figure 2A). Interestingly, Stv was efficiently converted into bioconjugate molecules, whereas a substantial amount of free C3Mut was detected after the reaction. However, further attempts to optimize the coupling procedure, e.g. increasing the stoichiometry of Stv versus C3Mut, increasing thiolation of C3Mut, or application of a long amine-reactive PEG-linker to minimize steric hindrance, did not result in a higher yield of bioconjugate molecules.

Subsequently, the C3Mut−Stv bioconjugate was characterized regarding its biotin-binding ability. Dot Blot analysis was performed, in which biotinylated and non-biotinylated bovine serum albumin (BSA) was vacuum aspirated onto a nitrocellulose membrane in decreasing amounts. The efficiency of the blotting was monitored with Ponceau S staining of the

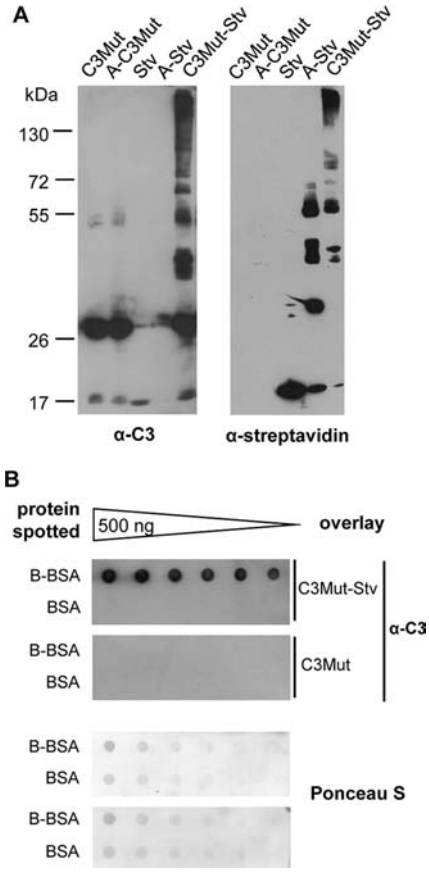


Figure 2. Analysis of C3Mut−streptavidin conjugate. (A) Immunoblot analysis of the resulting bioconjugation products. Detection with anti-C3-antibody and anti-streptavidin-antibody, respectively, showed the formation of C3Mut−streptavidin bioconjugates with different molecular weight. (B) C3Mut−streptavidin specifically binds to biotin-labeled BSA in vitro. Biotinylated BSA (B-BSA) and non-biotinylated BSA were vacuum-aspirated onto a nitrocellulose membrane using a dot-blot manifold (500, 250, 125, 63, 31, and 16 ng of each protein). The membrane was blocked and afterward incubated with either C3Mut-streptavidin (5 μg/mL, upper panel) or native C3Mut (5 μg/mL, lower panel). Bound C3Mut(-streptavidin) was detected using a C3-antibody. Binding is only observed for C3Mut−streptavidin conjugate but not for native C3Mut protein, and is specific for biotinylated BSA. Ponceau S staining at the bottom shows the membranes spotted with BSA and biotinylated BSA.

dx.doi.org/10.1021/bc300041z | *Bioconjugate Chem.* 2012, 23, 1426−1436

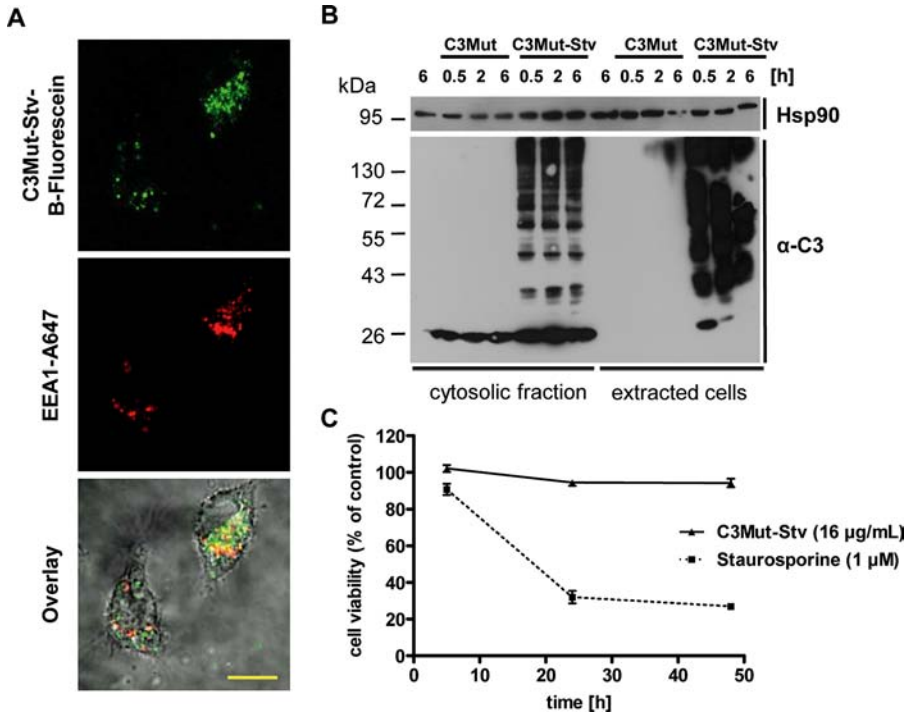


Figure 3. Internalization of C3Mut−streptavidin into the cytosol of J774A.1 cells without affecting cell viability. (A) Uptake of C3Mut−Stv into macrophages using immunofluorescence analysis. J774A.1 cells seeded on coverslips were treated with 8 μg/mL of C3Mut−Stv conjugated with biotin−fluorescein. After 4 h of incubation, cells were fixed and stained with an EEA1-antibody to visualize early endosomes. *Z*-Stack images were acquired by confocal microscopy in 1 μm sections and processed by *ImageJ*. Representative single optical sections thereof are displayed. Scale bar: 10 μm. (B) C3Mut−Stv bioconjugate is translocated into the cytosol of J774A.1 cells. Cells were incubated with C3Mut (1 μg/mL) or C3Mut−streptavidin (12 μg/mL), respectively, for up to 6 h. Subsequently, cell fractionation was performed and fractions were subjected to SDS-Page followed by Western Blot analysis with a C3-antibody. Equal amounts of proteins were confirmed by an anti-Hsp90 immunoblot. (C) Treatment of J774A.1 cells with C3Mut−Stv exerts no cytotoxic effect. J774A.1 cells were seeded into 96 well plates and treated with C3Mut−Stv (16 μg/mL) or staurosporine (1 μM). After 5, 24, and 48 h, cell viability was measured using MTS cell proliferation assay. Data are given as mean ± SEM, $n = 2$ (each experiment performed in triplicate).

membrane (Figure 2B). The membrane was blocked and then incubated with C3Mut−Stv. After extensive washing steps, bound C3Mut−Stv was visualized using an anti-C3-antibody. As expected, C3Mut−Stv binds to biotinylated BSA in a concentration-dependent manner, but not to non-biotinylated BSA. Importantly, native C3Mut protein binds neither biotinylated nor non-biotinylated BSA (Figure 2B).

C3Mut−Stv was also capable of binding an end-biotinylated oligonucleotide with high affinity as assessed by an electrophoretic mobility shift assay in solution (data not shown). Notably, a huge excess of C3Mut did not bind the biotinylated oligonucleotide, underscoring the binding specificity.

Taken together, the C3Mut−Stv bioconjugate interacts with biotinylated macromolecules such as proteins and oligonucleotides in vitro, which is crucial for further cell-based delivery studies.

C3Mut−Stv is Internalized into J774A.1 Macrophages without Affecting Cell Viability. First, we used confocal laser-scanning microscopy to study the uptake of C3Mut−Stv into J774A.1 macrophages. Cells were grown on coverslips and were treated with C3Mut−Stv labeled with biotin−fluorescein (BF) for 4 h. Thereafter, cells were thoroughly washed, fixed, and stained for EEA1, a specific marker for early endosomes.[30] Strikingly, the BF-conjugated C3Mut−Stv was clearly detectable in the cytoplasm of J774A.1 cells and displayed perinuclear staining (Figure 3A, upper panel). In addition, C3Mut−Stv showed some overlap with early endosomal vesicles as attested by the yellow dots in the merged channel (Figure 3A, lower panel). Confocal microscopy using an anti-C3 antibody revealed the same cytoplasmic distribution of C3Mut−Stv (data not shown). It is important to note that BF was not observed in J774A.1 cells without C3Mut−Stv. As expected, neither native C3Mut nor wt-Stv promoted the internalization of BF (data not shown).

To analyze the internalization of C3Mut−Stv in more detail, J774A.1 cells were incubated for up to 6 h with C3Mut−Stv and native C3Mut, respectively. Thereafter, digitonin-based cell fractionation was performed as described previously[19,28] to monitor the cytosolic delivery of the C3Mut−Stv bioconjugate. Both the cytosolic fraction and the extracted cells were subjected to SDS-PAGE followed by Western Blot analysis. Using an anti-C3-antibody, C3Mut as well as C3Mut−Stv were detected in the cytosolic fraction already after 30 min of incubation, and protein levels in the cytosol remained stable up to 6 h, which is in agreement with previous studies on the uptake kinetics of native C3 protein.[10] However, we observed a strong decrease of the bioconjugate in the cytosol after 24 h, most likely due to protein degradation (data not shown and Figure 5B). As expected, high amounts of C3Mut−Stv were detected in extracted cells corresponding to membrane-bound or vesicular internalized bioconjugate (Figure 3B). Comparable protein amounts and successful cytosol preparation were confirmed with an immunoblot against cytosolic Hsp90, which was found in both fractions likewise. The endosomal marker protein EEA1[30] was visualized only in extracted cells, excluding contaminations of the cytosolic fraction with

dx.doi.org/10.1021/bc300041z | *Bioconjugate Chem.* 2012, 23, 1426−1436

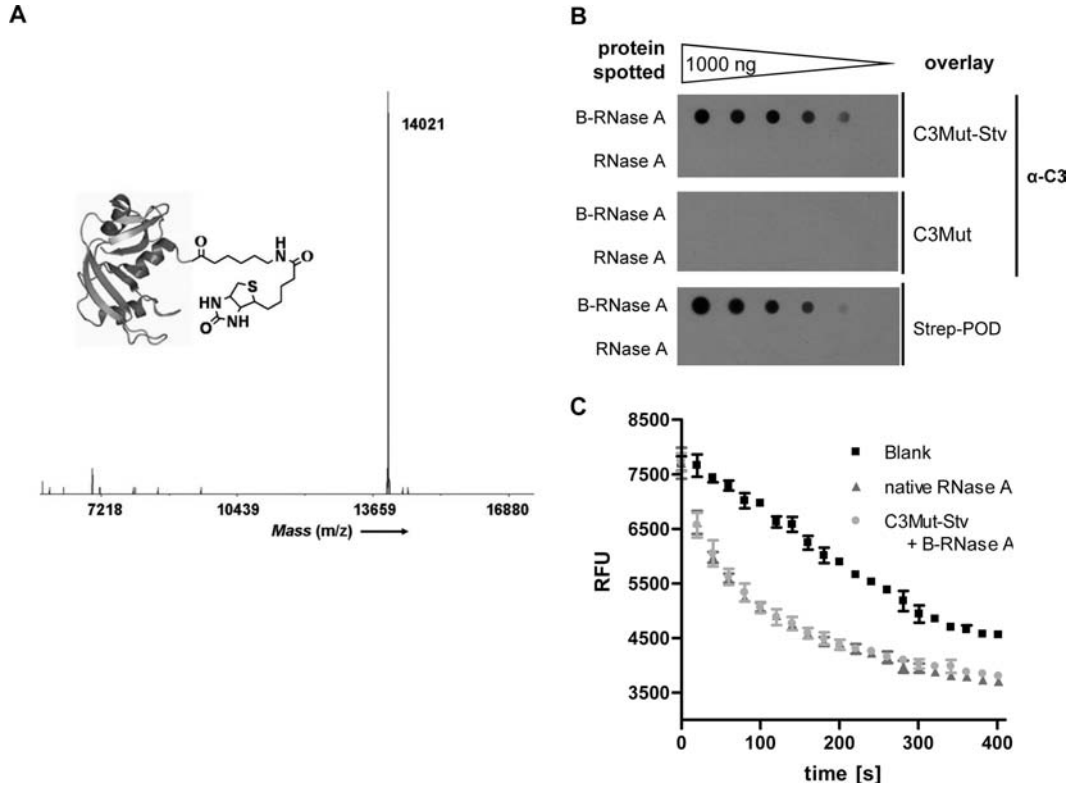


Figure 4. Characterization of Biotin-LC-(K1)RNase A. (A) MALDI-ToF MS spectrum of Biotin-LC-(K1)RNase A. Biotin-LC-(K1)RNase A displays a peak at m/z 14 021 $[M+H]^+$ in the recorded MS spectrum. The increase in molecular weight from native RNase A to mono-biotinylated RNase A (339.5 Da) exactly matches the molecular weight of the Biotin-LC moiety. B. C3Mut−Stv binds to Biotin-LC-(K1)RNase A with high affinity. Mono-biotinylated RNase A (b-RNase A) and native RNase A were vacuum-aspirated onto a nitrocellulose membrane in decreasing amounts. After blocking, the membrane was incubated with either C3Mut−Stv (5 μg/mL, upper panel) or native C3Mut (5 μg/mL, middle panel). Bound C3Mut(-Stv) was detected using a C3-antibody and revealed a strong and specific interaction of the C3Mut−Stv conjugate with mono-biotinylated RNase A. In addition, biotin-modified RNase A was detected with a streptavidin−peroxidase conjugate (lower panel). (C) Mono-biotinylated RNase A retains its functional activity upon binding to C3Mut−Stv. Enzymatic degradation of substrate RNA was determined in the presence of SYBR dye and measured as decay in fluorescence.

endosomal vesicles (data not shown). It should also be mentioned that C3Mut−Stv was detectable in CHO-K1 fibroblasts (data not shown), which has not been observed for C3Mut in previous studies.[10]

To exclude cytotoxic effects of the novel transport system, cell viability was measured in J774A.1 cells after treatment with C3Mut−Stv. Staurosporine was applied as a positive control, which strongly induces apoptosis by inhibiting protein kinases. Cells incubated with up to 16 μg/mL C3Mut−Stv showed no reduction in cell viability compared to untreated cells for up to 48 h, whereas the viability in staurosporine-challenged cells was decreased to 25% after 24 h (Figure 3C).

Collectively, we demonstrated the internalization of C3Mut−Stv into the cytosol of J774A.1 macrophages without affecting cell viability over a period of 48 h.

Generation and Characterization of Mono-Biotinylated RNase A. Mono-biotinylated RNase A serves as an attractive model protein due to the availability of a single biotin group at a precisely defined position (K1), which was introduced via a procedure developed very recently,[29] as well as its high homology with clinically relevant RNase variants such as Onconase.[31] The structure of the prepared Biotin-LC-(K1)RNase A was determined by MALDI-ToF (Figure 4A), and the position of the biotin substituent was identified via the LCMS^2-XIC method (data not shown). Subsequently, a dot blot analysis was performed, in which mono-biotinylated RNase A and native RNase A were spotted onto a nitrocellulose membrane. After blocking, the membrane was incubated with C3Mut−Stv and binding was revealed by immunoblot detection using a polyclonal C3 antibody. C3Mut−Stv showed a concentration-dependent binding to Biotin-LC-(K1)RNase, whereas no interaction was observed with native RNase A (Figure 4B, upper panel). As an important negative control, spotted proteins were also probed with C3Mut that did bind neither to native RNase A nor to mono-biotinylated RNase A (Figure 4B, middle panel). In addition, the biotin moiety of the synthesized Biotin-LC-(K1)RNase A was also detected with a streptavidin−peroxidase conjugate (Figure 4B, lower panel). Next, we analyzed the influence of the C3Mut−Stv transporter on the enzymatic activity of biotin-substituted RNase A upon preincubation of both components, since tight interaction with C3Mut−Stv may affect RNA substrate accessibility and degradation. The enzymatic activity of Biotin-LC-(K1)RNase bound to C3Mut−Stv was assessed using a functional in vitro assay. Here, yeast RNA (yRNA) forms a fluorescent complex with the SYBR dye and serves as substrate. Degradation of yRNA leads to the release of the SYBR dye, which is nonfluorescent in its free form, resulting in decay of the fluorescence. As a control, the reactions were performed in TE buffer and revealed autohydrolysis of yRNA over time (Figure 4C, squares). In contrast, the addition of both native RNase A (triangles) and Biotin-LC-(K1)RNase A (data not shown)

dx.doi.org/10.1021/bc300041z | Bioconjugate Chem. 2012, 23, 1426−1436

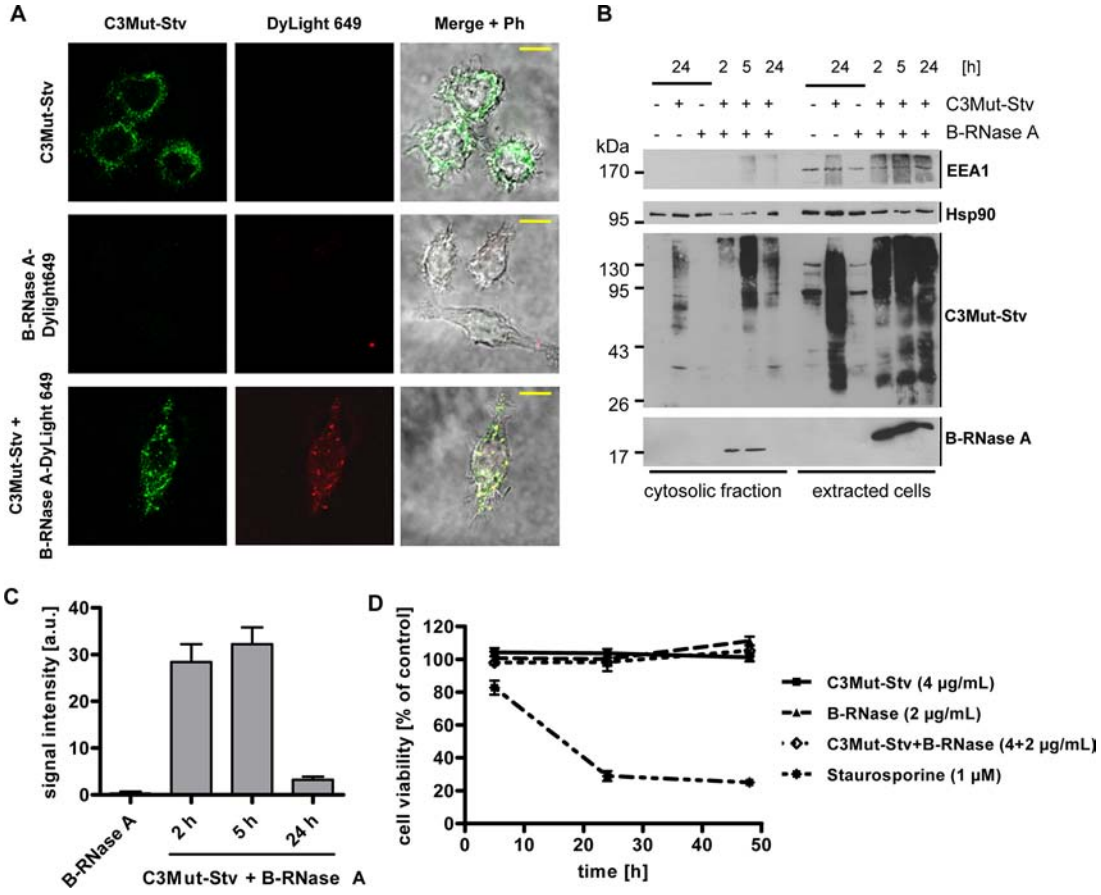


Figure 5. C3Mut−streptavidin-dependent delivery of mono-biotinylated RNase A into J774A.1 cells. (A) J774A.1 cells were treated with C3Mut−streptavidin (8 μg/mL), mono-biotinylated RNase A-DyLight649 (4 μg/mL), or both proteins. After 4 h, cells were fixed and C3Mut−streptavidin was visualized using C3-antibody. Finally, *z*-stack images were recorded by confocal microscopy with an optical section of 1 μm and processed with *ImageJ*. Representative single optical sections thereof are shown. Scale bar: 10 μm. Ph = phase contrast. (B) Mono-biotinylated RNase A (B-RNase A) is taken up into the cytosol of J774A.1 cells. Macrophages were treated with C3Mut−streptavidin (4 μg/mL), B-RNase A (2 μg/mL), or both proteins for up to 24 h. Subsequently, cell fractionation was performed and samples were subjected to SDS-PAGE and Western Blot analysis. C3Mut−streptavidin and B-RNase A were visualized using a C3-antibody and streptavidin-POD, respectively. Equal protein amounts were confirmed by Hsp90-immunoblot. EEA1 was detected as marker for early endosomes. (C) Quantification of B-RNase A uptake into the cytosol of J774A.1 cells. Intensity of B-RNase A signal in cytosolic fractions was determined using *Adobe Photoshop CS3* software. Signal intensity is given as mean ± SEM of three independent experiments (a.u., arbitrary units). (D) Influence of C3Mut−Stv-mediated uptake of B-RNase A on J774A.1 cells. Cells were seeded on 96-well plates and treated for 5, 24, or 48 h with C3Mut−Stv, B-RNase A, or both proteins. As a positive control, staurosporine was used to induce apoptosis. Cell viability was determined using MTS cell proliferation assay. Data are given as mean ± SEM, n = 3 (each experiment performed in triplicate).

resulted in a fast drop of the fluorescence intensity of the yRNA-SYBR complex due to RNA degradation. Importantly, Biotin-LC-(K1)RNase A attached to the C3Mut−Stv transporter (circles) causes a similar decay of the fluorescence intensity as native RNase A, indicating that the complex retained its functional activity in vitro.

C3Mut−Stv Promotes the Internalization of Mono-Biotinylated RNase A into J774A.1 Cells. To monitor the uptake of Biotin-LC-(K1)RNase A into J774A.1 cells by the C3Mut−Stv transporter, laser-scanning microscopy was performed. Cells seeded on coverslips were treated with DyLight649-labeled Biotin-LC-(K1)RNase alone or together with C3Mut−Stv. Subsequently, cells were fixed, permeabilized, and incubated with an anti-C3-antibody followed by an Alexa488-coupled secondary antibody. Negligible amounts of Biotin-LC-(K1)RNase A-DyLight649 were detectable in the macrophages in the absence of the transporter (Figure 5A, middle panel). In turn, the C3Mut−Stv delivery system strongly promoted the uptake of Biotin-LC-(K1)RNase A-DyLight649 into J774A.1 cells, which displayed almost complete colocalization with the C3Mut−Stv transporter as visualized by the yellow staining in the merge channel (Figure 5A, bottom panel). Due to the high biotin-binding affinity of the C3Mut−Stv bioconjugate, the cargo molecule should not be released, but remains attached to the transporter inside the cell.

To study the intracellular localization of mono-biotinylated RNase A in more detail, digitonin-based cell fractionation was used. J774A.1 cells were incubated with C3Mut−Stv complexed to Biotin-LC-(K1)RNase A for up to 24 h. As controls, cells were left untreated or incubated only with the single components. Cell fractionation was then performed to obtain the cytosol and extracted cells. Both fractions were subjected to SDS-PAGE followed by immunoblot analysis (Figure 5B). The majority of Biotin-LC-(K1)RNase A was detected in extracted cells, but was also found in the cytosol of J774A.1 cells (Figure 5B). Biotin-LC-(K1)RNase A accumulated in the cytosol after 5 h and disappeared after 24 h, most likely due to protein

dx.doi.org/10.1021/bc300041z | *Bioconjugate Chem.* 2012, 23, 1426−1436

degradation, which is further illustrated by quantification of three independent time course experiments (Figure 5C). This paralleled the uptake kinetics of the C3Mut−Stv transporter that colocalized with Biotin-LC-(K1)RNase A to a large extent as shown above by confocal microscopy. It should also be noted that the early endosomal marker EEA1 was visualized exclusively in extracted cells, ruling out a putative contamination of the cytosol with early endosomal vesicles (Figure 5B). Equal protein amounts were confirmed by immunoblot detection of the cytosolic protein Hsp90. Importantly, Biotin-LC-(K1)RNase A was not internalized into J774A.1 cells in the absence of C3Mut−Stv, highlighting the specificity of the C3Mut−Stv-mediated delivery. Internalization of Biotin-LC-(K1)RNase A into J774A.1 cells did not influence cell viability over a period of 48 h as measured by MTS assay (Figure 5D). This finding was anticipated due to the known inactivation of wild-type RNase A by its highly potent inhibitor protein RI that is abundantly expressed in mammalian cells.[26]

C3Mut−Stv Facilitates the Delivery of Mono-Biotinylated Lysozyme into J774A.1 Cells. To establish the novel C3Mut−Stv delivery vehicle for a more general purpose, we used the protein lysozyme from hen egg white. At first, lysozyme was site-selectively labeled with biotin as outlined very recently,[29] yielding Biotin-LC-(K1)-lysozyme. The structure was confirmed by MALDI-ToF-MS and subsequent nano-LC-MS^2 analysis (data not shown). Next, the specific high-affinity binding of C3Mut−Stv to immobilized mono-biotinylated lysozyme was shown by dot blot analysis (Figure 6A), which is instrumental for subsequent uptake studies. Finally, we were able to demonstrate the C3Mut−Stv-dependent uptake of Biotin-LC-(K1)-lysozyme into J774A.1 cells. Five hours after treatment, mono-biotinylated lysozyme was detected in extracted J774A.1 cells and, to a lower extent, in the cytosol obtained after cell fractionation (Figure 6B). It is noteworthy that streptavidin on its own does not facilitate the uptake of Biotin-LC-(K1)-lysozyme into the cytosol of J774A.1 cells. Furthermore, the endosomal marker protein EEA1 was observed only in extract cells, indicating successful separation of endosomal compartments and the cytosol.

In summary, the novel C3Mut−Stv delivery system mediated the specific uptake of both mono-biotinylated RNase A and lysozyme into the cytosol of J774A.1 macrophage-like cells.

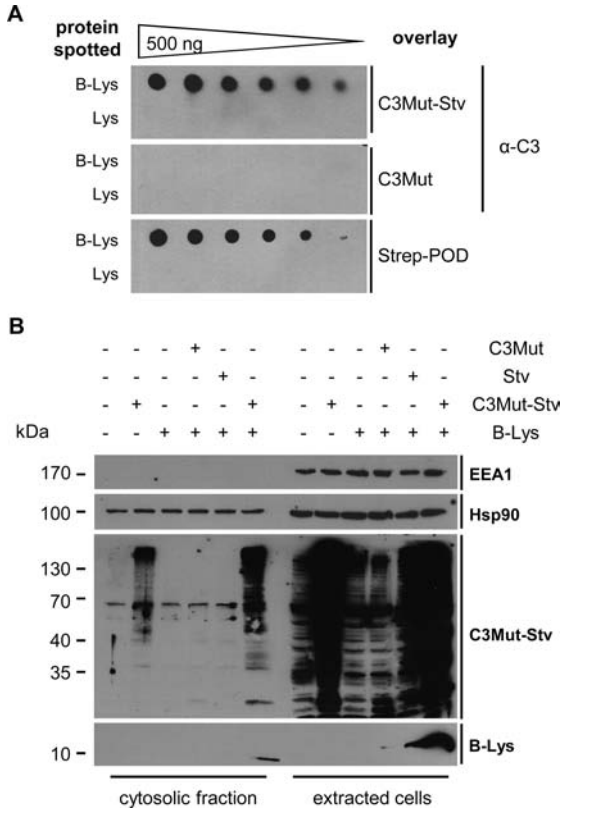


Figure 6. C3Mut−Stv interacts with biotinylated lysozyme (B-Lys) and promotes its internalization into J774A.1 cells. (A) C3Mut−Stv binds specifically to B-Lys. B-Lys and native lysozyme (Lys) were vacuum-aspirated onto nitrocellulose membrane in decreasing concentrations (500, 250, 125, 62.5, 31.3, and 15.7 ng). After blocking of the membrane, overlay with C3Mut−Stv or uncoupled C3Mut (5 μg/mL each) was performed. Bound protein was detected using a C3-antibody and the ECL system, revealing a specific binding of the bioconjugate C3Mut−Stv to B-Lys. (B) C3Mut−Stv promotes the internalization of B-Lys into the cytosol of J774A.1 macrophages. C3Mut, Stv, or C3Mut−Stv (4 μg/mL each) was preincubated with B-Lys (2 μg/mL) for 30 min at room temperature. Proteins were then added to J774A.1 cells grown in 12-well plates and further incubated for 5 h. Control cells were treated with PBS, C3Mut−Stv (4 μg/mL), or B-Lys (2 μg/mL) alone. Subsequently, digitonin-based cell fractionation was performed, and the fractions obtained were subjected to SDS-PAGE and Western Blot. B-Lys was visualized using streptavidin−POD, while the bioconjugate was detected using anti-C3-antibody. Equal protein loading was confirmed with Hsp90 immunostaining. Detection of EEA1 was used to exclude endosomal contamination of the cytosolic fraction.

DISCUSSION

Owing to their unique features such as efficient and specific cellular uptake, bacterial protein toxins are of growing interest in the field of drug delivery,[32] which led to the development of cellular delivery vehicles based upon the clostridial C2 toxin and diphtheria toxin.[18,33] In the present study, we have engineered a C3bot-derived transport system by covalent linkage of wt-streptavidin (wt-Stv) to the enzymatically inactive C3Mut protein. Wt-Stv is commercially available and recombinant C3Mut protein can be purified at huge amounts after expression in *E. coli*. The bioconjugate obtained was heterogeneous, comprising several species of varying molecular weight and still contained free C3Mut protein, which could interfere with the subsequent entry of C3Mut−Stv into cells. Nevertheless, we observed efficient intracellular uptake of C3Mut−Stv in the presence of nonreacted C3Mut (Figures 3 and 5). Owing to its homogeneity and site-directed character, genetic engineering of a C3Mut−Stv fusion protein would offer some advantages over the bioconjugation procedure reported herein. However, genetic fusions in general are more time-consuming and, in case of C3 protein, have to be performed under elevated biological safety level S2. We have very recently succeeded in the construction of a genetic fusion protein that displays comparable biochemical and cell-biological features as the C3Mut−Stv bioconjugate (H. Christow, unpublished results). The bioconjugate prepared was functionally active in vitro with regard to biotin binding as attested by its high-affinity interaction with immobilized biotin-labeled BSA and a biotinylated oligonucleotide in solution. The strong interaction of wt-Stv and its biotinylated ligands is crucial for complex stability in vivo and has also enabled the use of streptavidin for pretargeting of cancer cells in radioimmunotherapy.[34] In addition, we could demonstrate an efficient uptake of the C3Mut−Stv conjugate into J774A.1 cells where it translocated

dx.doi.org/10.1021/bc300041z | Bioconjugate Chem. 2012, 23, 1426−1436

into the cytosol. As mentioned above, C3Mut−Stv internalization was also detectable in CHO-K1 cells (data not shown), which is in contrast to native C3 protein that is predominantly internalized into macrophages/monocytes.[10] This change in cell-type selectivity could arise from the covalent bioconjugation to streptavidin molecules, influencing the interaction with cell surface proteins. Streptavidin was reported to harbor an RYD sequence that is similar to the RGD motif of fibronectin involved in cell adhesion.[35] It is conceivable that the chemical engineering used herein may have modulated the cell surface binding properties of the C3Mut-coupled streptavidin. On the other hand, streptavidin on its own does not facilitate the internalization of biotinyated (macro)molecules into J774A.1 cells as confirmed above. This altered cell-type selectivity may broaden the general applicability of the bioconjugate and allows addressing other cell types of interest. Furthermore, the C3Mut−Stv transporter did not affect cell viability, which is in accordance with other streptavidin-based delivery vehicles.[18,36]

We then used Biotin-LC-(K1)RNase A as protein cargo to analyze the internalization of biomacromolecules. To this end, RNase A was mono-biotinylated at the N-terminal Lys residue by site-directed chemistry, not affecting its ribonuclease activity. This specific labeling is very important, since modification of other Lys residues, in particular, Lys41, can strongly reduce its activity.[37] Mono-biotinylation of RNase A is also beneficial with regard to complex formation with C3Mut−Stv, since high degrees of biotin modification could favor aggregation. In addition, C3Mut−Stv did not affect the degradation of RNA catalyzed by Biotin-LC-(K1)RNase A as demonstrated above by an in vitro RNase A activity assay. Biotin-LC-(K1)RNase A was then successfully delivered into J774A.1 macrophages using the C3Mut−Stv delivery system. Immunoblot analysis revealed partial translocation into the cytosol of J774A.1 cells after cell fractionation. To further increase the cytosolic translocation of RNase A, it is conceivable to use pH-responsive polymers co-complexed with C3Mut−Stv that disrupt endosomal membranes upon acidification.[38,39] In line with this, the cytosolic release of RNase A could be promoted by endosome-disruptive peptides such as the HA2 peptide derived from influenza virus.[40] Future studies may also involve cleavable biotin linkers with disulfide bonds that undergo reduction in the intracellular environment, leading to the release of the cargo molecule.[41]

Native RNase A used in the present study is a good model cargo protein for delivery studies, but is known not to be cytotoxic in mammalian cells, which was also confirmed by our delivery studies using biotin-substituted native RNase A (Figure 5D). This is attributable to the presence of ribonuclease inhibitor (RI) protein which was found at micromolar concentrations in the cytosol of all mammalian cells studied so far[26] and binds with femtomolar affinity to RNase A,[42] resulting in its inactivation. Hence, RNase A variants with a reduced binding to RI and related ribonucleases such as onconase that does not interact with RI are of great interest in tumor therapy.[31,43] On the basis of the findings presented herein, the promising C3Mut−Stv delivery strategy could be transferred to mono-biotinylated cytotoxic RNase A mutants such as G88R-RNase A that evades RI binding and inhibits cell proliferation.[44] Enhanced cellular uptake of these mutants mediated by the C3Mut−Stv delivery system should potentiate their cytotoxic effect, which would be of great clinical relevance in tumor therapy.

The novel C3Mut−Stv delivery system described in this study is a versatile tool for the efficient cytosolic internalization of biotin-labeled macromolecules into macrophages as exemplified by the use of Biotin-LC-(K1)RNase A. Moreover, the established delivery system is not restricted to transduction of mono-biotinylated RNase A, but also efficiently promoted the uptake of biotin-labeled lysozyme into J774A.1 cells, suggesting a more general applicability. This approach should also prove to be useful for the internalization of biotin-labeled siRNA to silence gene expression. This is supported by a study of Xia and co-workers that demonstrated the efficient siRNA-mediated knockdown of target gene expression by means of biotin−streptavidin technology.[45] Another promising application for C3Mut−Stv represents the delivery of peptides spanning BH3-domains into malignant leukocytes to induce mitochondrial apoptosis via cytochrome *c* release.[46] This is illustrated by the finding that a cell-permeable Bax peptide was able to trigger apoptosis in cancer cells.[47]

Collectively, we have generated a novel delivery vehicle consisting of clostridial C3 protein and streptavidin that directs the uptake of biotin-labeled molecules into macrophages. Moreover, we demonstrated the C3Mut-Stv-mediated internalization of mono-biotinylated RNase A into the cytosol of J774A.1 cells, providing a framework for future applications of cytotoxic RNase A variants to kill cancer cells.

AUTHOR INFORMATION

Corresponding Author

*Dr. Holger Barth: Tel. +49-731-50065503; Fax +49-731-50065502; E-mail holger.barth@uni-ulm.de. Dr. Jörg Fahrer: Tel. +49-6131-179218; Fax +49-6131-230506; E-mail fahrer@uni-mainz.de.

Present Address

[†]Institute of Toxicology, University Medical Center Mainz, Obere Zahlbacher Str. 67, D-55131 Mainz, Germany.

Notes

The authors declare no competing financial interest.

ACKNOWLEDGMENTS

We are grateful to Dr. Angelika Rück, ILM, University of Ulm, Germany, for kindly providing the confocal microscope facility and to Ulrike Binder for excellent technical assistance. This work was funded by grant of the Medical Faculty, University of Ulm (Bausteinprojekt L.SBN.0060 to J.F.) and supported by the International Graduate School in Molecular Medicine Ulm.

REFERENCES

(1) Vogelsgesang, M., Pautsch, A., and Aktories, K. (2007) C3 exoenzymes, novel insights into structure and action of Rho-ADP-ribosylating toxins. *Naunyn Schmiedebergs Arch. Pharmacol. 374*, 347−60.

(2) Genth, H., Gerhard, R., Maeda, A., Amano, M., Kaibuchi, K., Aktories, K., and Just, I. (2003) Entrapment of Rho ADP-ribosylated by Clostridium botulinum C3 exoenzyme in the Rho-guanine nucleotide dissociation inhibitor-1 complex. *J. Biol. Chem. 278*, 28523−7.

(3) Sehr, P., Joseph, G., Genth, H., Just, I., Pick, E., and Aktories, K. (1998) Glucosylation and ADP ribosylation of rho proteins: effects on nucleotide binding, GTPase activity, and effector coupling. *Biochemistry 37*, 5296−304.

(4) Aepfelbacher, M., Essler, M., Huber, E., Czech, A., and Weber, P. C. (1996) Rho is a negative regulator of human monocyte spreading. *J. Immunol. 157*, 5070−5.

(5) Chardin, P., Boquet, P., Madaule, P., Popoff, M. R., Rubin, E. J., and Gill, D. M. (1989) The mammalian G protein rhoC is ADP-ribosylated by Clostridium botulinum exoenzyme C3 and affects actin microfilaments in Vero cells. *EMBO J. 8*, 1087−92.
(6) Ridley, A. J., and Hall, A. (1992) The small GTP-binding protein rho regulates the assembly of focal adhesions and actin stress fibers in response to growth factors. *Cell 70*, 389−99.
(7) Aktories, K., Wilde, C., and Vogelsgesang, M. (2004) Rho-modifying C3-like ADP-ribosyltransferases. *Rev. Physiol. Biochem. Pharmacol. 152*, 1−22.
(8) Ahnert-Hilger, G., Holtje, M., Grosse, G., Pickert, G., Mucke, C., Nixdorf-Bergweiler, B., Boquet, P., Hofmann, F., and Just, I. (2004) Differential effects of Rho GTPases on axonal and dendritic development in hippocampal neurones. *J. Neurochem. 90*, 9−18.
(9) Boato, F., Hendrix, S., Huelsenbeck, S. C., Hofmann, F., Grosse, G., Djalali, S., Klimaschewski, L., Auer, M., Just, I., Ahnert-Hilger, G., and Holtje, M. (2010) C3 peptide enhances recovery from spinal cord injury by improved regenerative growth of descending fiber tracts. *J. Cell Sci. 123*, 1652−62.
(10) Fahrer, J., Kuban, J., Heine, K., Rupps, G., Kaiser, E., Felder, E., Benz, R., and Barth, H. (2010) Selective and specific internalization of clostridial C3 ADP-ribosyltransferases into macrophages and monocytes. *Cell Microbiol. 12*, 233−47.
(11) Laitinen, O. H., Hytonen, V. P., Nordlund, H. R., and Kulomaa, M. S. (2006) Genetically engineered avidins and streptavidins. *Cell. Mol. Life Sci. 63*, 2992−3017.
(12) Laitinen, O. H., Nordlund, H. R., Hytonen, V. P., and Kulomaa, M. S. (2007) Brave new (strept)avidins in biotechnology. *Trends Biotechnol. 25*, 269−77.
(13) Boado, R. J., Zhang, Y., Zhang, Y., Xia, C. F., Wang, Y., and Pardridge, W. M. (2008) Genetic engineering, expression, and activity of a chimeric monoclonal antibody-avidin fusion protein for receptor-mediated delivery of biotinylated drugs in humans. *Bioconjugate Chem. 19*, 731−9.
(14) Xia, C. F., Zhang, Y., Zhang, Y., Boado, R. J., and Pardridge, W. M. (2007) Intravenous siRNA of brain cancer with receptor targeting and avidin-biotin technology. *Pharm. Res. 24*, 2309−16.
(15) Daniels, T. R., Ng, P. P., Delgado, T., Lynch, M. R., Schiller, G., Helguera, G., and Penichet, M. L. (2007) Conjugation of an anti transferrin receptor IgG3-avidin fusion protein with biotinylated saporin results in significant enhancement of its cytotoxicity against malignant hematopoietic cells. *Mol. Cancer Ther. 6*, 2995−3008.
(16) Garcia-Espana, A., Biria, S., Malumbres, M., Levin, B., Meruelo, D., and Pellicer, A. (1999) Targeted gene transfer system using a streptavidin-transforming growth factor-alpha chimeric protein. *DNA Cell Biol. 18*, 743−9.
(17) Nagasaki, T., Kawazu, T., Tachibana, T., Tamagaki, S., and Shinkai, S. (2005) Enhanced nuclear import and transfection efficiency of plasmid DNA using streptavidin-fused importin-beta. *J. Controlled Release 103*, 199−207.
(18) Fahrer, J., Plunien, R., Binder, U., Langer, T., Seliger, H., and Barth, H. (2010) Genetically engineered clostridial C2 toxin as a novel delivery system for living mammalian cells. *Bioconjugate Chem. 21*, 130−9.
(19) Fahrer, J., Rieger, J., van Zandbergen, G., and Barth, H. (2010) The C2-streptavidin delivery system promotes the uptake of biotinylated molecules in macrophages and T-leukemia cells. *Biol. Chem. 391*, 1315−25.
(20) Saito, Y., Nemoto, Y., Ishizaki, T., Watanabe, N., Morii, N., and Narumiya, S. (1995) Identification of Glu173 as the critical amino acid residue for the ADP-ribosyltransferase activity of Clostridium botulinum C3 exoenzyme. *FEBS Lett. 371*, 105−9.
(21) Pardridge, W. M. (2002) Drug and gene targeting to the brain with molecular Trojan horses. *Nat. Rev. Drug Discovery 1*, 131−9.
(22) Raines, R. T. (1998) Ribonuclease A. *Chem. Rev. 98*, 1045−1066.
(23) Klink, T. A., Woycechowsky, K. J., Taylor, K. M., and Raines, R. T. (2000) Contribution of disulfide bonds to the conformational stability and catalytic activity of ribonuclease A. *Eur. J. Biochem. 267*, 566−72.
(24) Anfinsen, C. B. (1973) Principles that govern the folding of protein chains. *Science 181*, 223−30.
(25) Leich, F., Stohr, N., Rietz, A., Ulbrich-Hofmann, R., and Arnold, U. (2007) Endocytotic internalization as a crucial factor for the cytotoxicity of ribonucleases. *J. Biol. Chem. 282*, 27640−6.
(26) Haigis, M. C., Kurten, E. L., and Raines, R. T. (2003) Ribonuclease inhibitor as an intracellular sentry. *Nucleic Acids Res. 31*, 1024−32.
(27) Yoshikawa, T., and Pardridge, W. M. (1992) Biotin delivery to brain with a covalent conjugate of avidin and a monoclonal antibody to the transferrin receptor. *J. Pharmacol. Exp. Ther. 263*, 897−903.
(28) Sorensen, V., Zhen, Y., Zakrzewska, M., Haugsten, E. M., Walchli, S., Nilsen, T., Olsnes, S., and Wiedlocha, A. (2008) Phosphorylation of fibroblast growth factor (FGF) receptor 1 at Ser777 by p38 mitogen-activated protein kinase regulates translocation of exogenous FGF1 to the cytosol and nucleus. *Mol. Cell. Biol. 28*, 4129−41.
(29) Chen, X., Muthoosamy, K., Pfisterer, A., Neumann, B., and Weil, T. (2012) Site-selective lysine modification of native proteins and peptides via kinetically controlled labeling. *Bioconjugate Chem. 23*, 500−8.
(30) Simonsen, A., Lippe, R., Christoforidis, S., Gaullier, J. M., Brech, A., Callaghan, J., Toh, B. H., Murphy, C., Zerial, M., and Stenmark, H. (1998) EEA1 links PI(3)K function to Rab5 regulation of endosome fusion. *Nature 394*, 494−8.
(31) Arnold, U. (2008) Aspects of the cytotoxic action of ribonucleases. *Curr. Pharm. Biotechnol. 9*, 161−8.
(32) Barth, H., and Stiles, B. G. (2008) Binary actin-ADP-ribosylating toxins and their use as molecular Trojan horses for drug delivery into eukaryotic cells. *Curr. Med. Chem. 15*, 459−69.
(33) Kakimoto, S., Hamada, T., Komatsu, Y., Takagi, M., Tanabe, T., Azuma, H., Shinkai, S., and Nagasaki, T. (2009) The conjugation of diphtheria toxin T domain to poly(ethylenimine) based vectors for enhanced endosomal escape during gene transfection. *Biomaterials 30*, 402−8.
(34) Sato, N., Hassan, R., Axworthy, D. B., Wong, K. J., Yu, S., Theodore, L. J., Lin, Y., Park, L., Brechbiel, M. W., Pastan, I., Paik, C. H., and Carrasquillo, J. A. (2005) Pretargeted radioimmunotherapy of mesothelin-expressing cancer using a tetravalent single-chain Fv-streptavidin fusion protein. *J. Nucl. Med. 46*, 1201−9.
(35) Alon, R., Bayer, E. A., and Wilchek, M. (1990) Streptavidin contains an RYD sequence which mimics the RGD receptor domain of fibronectin. *Biochem. Biophys. Res. Commun. 170*, 1236−41.
(36) Fahrer, J., Funk, J., Lillich, M., and Barth, H. (2011) Internalization of biotinylated compounds into cancer cells is promoted by a molecular Trojan horse based upon core streptavidin and clostridial C2 toxin. *Naunyn Schmiedebergs Arch. Pharmacol. 383*, 263−73.
(37) Rutkoski, T. J., Kink, J. A., Strong, L. E., Schilling, C. I., and Raines, R. T. (2010) Antitumor activity of ribonuclease multimers created by site-specific covalent tethering. *Bioconjugate Chem. 21*, 1691−702.
(38) Murthy, N., Robichaud, J. R., Tirrell, D. A., Stayton, P. S., and Hoffman, A. S. (1999) The design and synthesis of polymers for eukaryotic membrane disruption. *J. Controlled Release 61*, 137−43.
(39) Pack, D. W., Hoffman, A. S., Pun, S., and Stayton, P. S. (2005) Design and development of polymers for gene delivery. *Nat. Rev. Drug Discovery 4*, 581−93.
(40) Nakase, I., Kobayashi, S., and Futaki, S. (2010) Endosome-disruptive peptides for improving cytosolic delivery of bioactive macromolecules. *Biopolymers 94*, 763−70.
(41) Chu, T. C., Twu, K. Y., Ellington, A. D., and Levy, M. (2006) Aptamer mediated siRNA delivery. *Nucleic Acids Res. 34*, e73.
(42) Lee, F. S., Shapiro, R., and Vallee, B. L. (1989) Tight-binding inhibition of angiogenin and ribonuclease A by placental ribonuclease inhibitor. *Biochemistry 28*, 225−30.

(43) Leland, P. A., and Raines, R. T. (2001) Cancer chemotherapy--ribonucleases to the rescue. *Chem. Biol. 8*, 405−13.
(44) Leland, P. A., Schultz, L. W., Kim, B. M., and Raines, R. T. (1998) Ribonuclease A variants with potent cytotoxic activity. *Proc. Natl. Acad. Sci. U. S. A. 95*, 10407−12.
(45) Xia, C. F., Boado, R. J., and Pardridge, W. M. (2009) Antibody-mediated targeting of siRNA via the human insulin receptor using avidin-biotin technology. *Mol. Pharm. 6*, 747−51.
(46) Letai, A., Bassik, M. C., Walensky, L. D., Sorcinelli, M. D., Weiler, S., and Korsmeyer, S. J. (2002) Distinct BH3 domains either sensitize or activate mitochondrial apoptosis, serving as prototype cancer therapeutics. *Cancer Cell 2*, 183−92.
(47) Li, R., Boehm, A. L., Miranda, M. B., Shangary, S., Grandis, J. R., and Johnson, D. E. (2007) Targeting antiapoptotic Bcl-2 family members with cell-permeable BH3 peptides induces apoptosis signaling and death in head and neck squamous cell carcinoma cells. *Neoplasia 9*, 801−11.

Bioconjugate Chemistry

Article

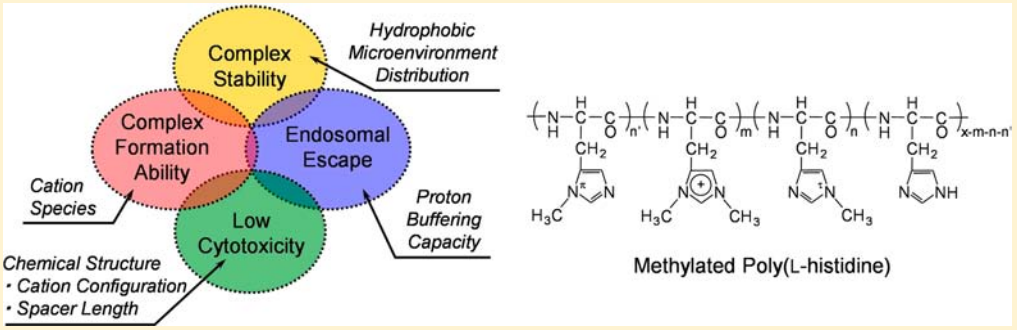
pubs.acs.org/bc

Synthesis and Characterization of Methylated Poly(L-histidine) To Control the Stability of Its siRNA Polyion Complexes for RNAi

Shoichiro Asayama,* Takao Kumagai, and Hiroyoshi Kawakami

Department of Applied Chemistry, Tokyo Metropolitan University, 1-1 Minami-Osawa, Hachioji, Tokyo 192-0397, Japan

Supporting Information



ABSTRACT: Poly(L-histidine) (PLH) with dimethylimidazole groups has been synthesized as a pH-sensitive polypeptide to control the stability of its small interfering RNA (siRNA) polyion complexes for RNA interference (RNAi). The resulting methylated PLH (PLH-Me) was water-soluble despite deprotonation of the imidazole groups at physiological pH, as determined by acid−base titration and solution turbidity measurement. Agarose gel retardation assay proved that the quaternary dimethylimidazole groups worked as cationic groups to retain siRNA. The stability of the PLH-Me/siRNA complexes has depended on the content of hydrophobic groups, that is, τ/π-methylimidazole groups as well as deprotonated imidazole groups. PLH-Me exhibited no significant cytotoxicity despite the existence of cationic dimethylimidazole groups. By use of PLH-Me as a pH-sensitive siRNA carrier, the PLH-Me/siRNA complexes mediated efficient siRNA delivery attributed to the dimethylimidazole groups, and the gene silencing depended on the content balance among dimethyl, τ/π-methyl, and unmodified imidazole groups. These results suggest that PLH-Me controls the stability of siRNA polyion complexes by enhancing noncytotoxic siRNA delivery by optimizing the content balance of dimethyl, τ/π-methyl, and unmodified imidazole groups.

INTRODUCTION

Small interfering RNA (siRNA) has drawn much attention because of its specific and effective gene silencing action on the expression of a specific target protein in a posttranscriptional mRNA level.[1,2] The siRNA composed of a double-strand RNA with 21 nucleotide base pairs specifically degrades a target mRNA with the help of a RNA induced silencing complex (RISC), resulting in the inhibition of the synthesis of the target protein. In siRNA delivery systems, the formation of polycation/siRNA polyion complexes is a key factor for new design of efficient delivery.[3−5]

Because siRNA has a short structure compared to plasmid DNA, the polyion complexes between siRNA and oppositely charged polycations lack stability under physiological conditions. Therefore, stabilization of the polycation/siRNA polyion complexes is essential for successful siRNA delivery, whereas the polyion complexes are required to release siRNA for its gene silencing effect in the cytoplasm after endosomal escape. For fulfillment of the above inconsistent properties, many efforts to design and chemical modification of polycations have been reported.[6−13]

Furthermore, the polycations modified with the histidine or other moieties containing an imidazole group have the ability to escape from an endosome by a proton sponge mechanism.[14−19] The imidazole heterocycles displaying a pK_a of ∼6 possess a buffering capacity in endosomal pH, inducing membrane destabilization after their protonation. The resulting imidazole groups are therefore considered to facilitate the release of the polycation/siRNA complexes to cytosol.

We have already reported carboxymethyl poly(L-histidine) as a pH-sensitive polypeptide to enhance polyplex gene delivery.[20] The resulting carboxymethyl poly(L-histidine) possesses dicarboxymethyl, τ/π-carboxymethyl, and unmodified imidazole groups. Moreover, we have already reported alkylated poly(1-vinylimidazole) to control of the stability of the polyion complexes by the length and density of the alkylated imidazole groups, where the methylimidazole groups form the most stable polyion complexes with the highest gene expression.[21]

Received: January 31, 2012
Revised: June 9, 2012
Published: June 10, 2012

ACS Publications © 2012 American Chemical Society

dx.doi.org/10.1021/bc300044r | *Bioconjugate Chem.* 2012, 23, 1437−1442

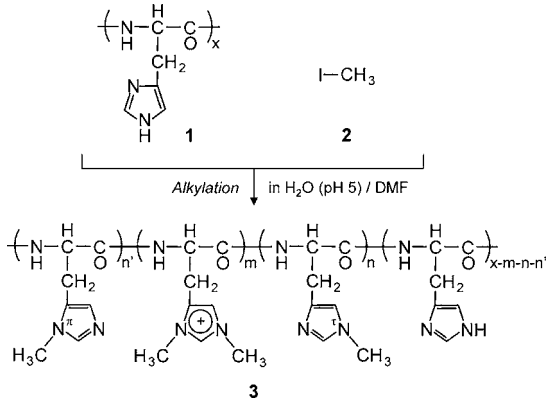
The above background has led us to synthesize the poly(L-histidine) with dimethylimidazole, τ/π-methyl, and unmodified imidazole groups, that is, methylated poly(L-histidine), as a new pH-sensitive polypeptide to control the stability of its siRNA polyion complexes for efficient RNA interference (RNAi). The control of the siRNA polyion complex stability for efficient RNAi by the content balance among dimethyl, τ/π-methyl, and unmodified imidazole groups has no precedent, to the best of our knowledge. Consequently, the pH-sensitive methylated poly(L-histidine), that is, PLH-Me, to control the stability of siRNA polyion complexes is expected to mediate efficient gene silencing by optimizing the content balance among dimethyl, τ/π-methyl, and unmodified imidazole groups in the polypeptide backbone.

EXPERIMENTAL PROCEDURES

Materials. Poly(L-histidine) (PLH) hydrochloride ($M_w \geq 5000$), poly(L-lysine) (PLL) hydrobromide (M_w, 4000–15000), and poly(ethylenimine) (PEI) solution ($M_w \approx 750000$) were purchased from Sigma-Aldrich Co. LLC. Iodomethane was purchased from Kanto Chemical Co., Inc. (Tokyo, Japan). Synthetic siRNA for luciferase GL3 was obtained from Gene Design Inc. (Osaka, Japan), and the sequence was CUUACGCUGAGUACUUCGA (19-mer) for sense and UCGAAGUACUCAGCGUAAG (19-mer) for antisense with dTdT-overhang at two terminal ends. The scrambled siRNA for a negative control was also from Gene Design Inc. and the sequence was UUCUCAGAACGUGUCACGU (19-mer) for sense and ACGUGACACGUUCUGAGAA (19-mer) for antisense with dTdT-overhang. All other chemicals of a special grade were used without further purification.

Synthesis of PLH-Me. A typical procedure is as follows (Scheme 1): PLH hydrochloride (**1**) (50 mg) was dissolved in

Scheme 1. Synthesis of Methylated Poly(L-histidine)



4 mL of water, which was brought to pH 5 by the addition of 1 M NaOH. To the resulting PLH solution was added the iodomethane (**2**) (100 μL) dissolved in 2 mL of *N*,*N*-dimethylformamide (DMF). The reaction mixture was incubated at 40 °C for 24 h. After the incubation, the iodomethane (**2**) (100 μL) dissolved in 2 mL of DMF was added to the reaction mixture again. For further modification, the iodomethane (**2**) (100 μL) in 2 mL of DMF was repeatedly (four times or six times) added to the reaction mixture, around pH 6. The resulting reaction mixture was further incubated at 40 °C for 24 h, followed by the dialysis against distilled water using a Spectra/Por 7 membrane (molecular weight cutoff of 10^3). The resulting polypeptide (**3**) was obtained by freeze-drying.

Gel Filtration Chromatography (GFC). GFC was carried out using a JASCO PU-980 pumping system (Tokyo, Japan) at a flow rate of 1.0 mL/min with a Shodex OHpak SB-804 HQ column (Showa Denko K.K., Tokyo, Japan). The aqueous solution containing 0.5 M CH_3COOH and 0.3 M Na_2SO_4 was used as a mobile phase. An amount of 100 μL of 1 mg/mL sample was injected into the column. Eluate was detected by a refractive index detector (RI-1530, JASCO). Calibration was made with polyethylene glycol standards.

^{1}H NMR Spectroscopy. Each polypeptide (3 mg) was dissolved in 700 μL of D_2O (99.8 atom % deuterium; Acros, NJ). The ^{1}H NMR spectra (400 MHz) were obtained by a JEOL JNM-AL400 spectrometer (Tokyo, Japan).

Amino Acid Analysis. Each polypeptide (1 mg) was dissolved in 500 μL of 6 M HCl and hydrolyzed at 110 °C for 24 h. The hydrolysate was diluted to 3 mL with water. The 100 μL of the diluted hydrolysate was then dried, followed by the addition of 800 μL of 0.2 M sodium citrate buffer (pH 2.2). After filtration (0.45 μm), the resulting samples were injected into an ion-exchange column (Hitach High-Technologies Co., Tokyo, Japan) with sodium citrate buffer (pH 3.2–4.9) as a mobile phase. The elution was gradually carried out with changing pH at a flow rate of 0.4 mL/min and was analyzed by the ninhydrin method.

Acid–Base Titration and Turbidity Measurement of PLH-Me. To 1.5 mL of an aqueous solution of the polypeptide (3 mg/mL) was added a 0.5 M HCl solution, and the acidic polypeptide solution (pH 2) was titrated with a 0.5 M NaOH solution. The pH value was checked with a pH meter (model F-52T, Horiba, Kyoto, Japan). The titration was carried out by the stepwise addition of 0.5 M NaOH and stopped at pH 12. The turbidity of the solution during the titration was measured by monitoring the absorbance at 500 nm with a spectrophotometer (model V-660, JASCO, Tokyo, Japan).

Agarose Gel Retardation Assay. The PLH-Me and siRNA were mixed in 50 mM sodium phosphate buffer (pH 7.4) at various polypeptide/DNA ratios (positive/negative = 0–32) as follows: The siRNA stock solution (1.93 μL) was diluted with the phosphate buffer (pH 7.4). To the resulting siRNA solution was added a stock solution of the polypeptide (1–4 μL) at various polypeptide/siRNA ratios. The final volume of the mixture was adjusted to 13.5 μL. After 5 min of incubation at room temperature, 13.5 μL of each sample (corresponding to 500 ng of siRNA) was mixed with a loading buffer (1.5 μL) and loaded onto a 1% agarose gel containing 1 μg/mL ethidium bromide (EtBr). Gel electrophoresis was run at room temperature in 50 mM sodium phosphate buffer (pH 7.4) at 50 V for 15 min. The siRNA bands were visualized under UV irradiation. In the case of assay for the stability of the PLH-Me/siRNA complexes, gel electrophoresis was run in the presence of dextran sulfate (1–6 mM as sulfate group) incubated with each sample at room temperature for 10 min.

Cell Viability Assay. HepG2 cells (a gift from the Japan Health Sciences Foundation), human hepatoma cell line, were cultured in tissue culture flasks containing Dulbecco's modified Eagle's medium supplemented with 10% heat-inactivated fetal bovine serum (FBS). The cells were seeded at 1×10^4 cells/well in a 96-well plate and incubated overnight at 37 °C in a 5% CO_2 incubator. The cells were treated with each polymer (0–400 μg/mL) and incubated for 48 h at 37 °C. By further

dx.doi.org/10.1021/bc300044r | Bioconjugate Chem. 2012, 23, 1437–1442

incubation for 4 h, the cell viability was measured using the Alamar Blue assay[22] in triplicate.

RNA Interference. In a typical 96-well plate experiment, 1 × 10^4 cells/well HepG2 cells were transfected in Dulbecco's modified Eagle's medium supplemented with 10% heat-inactivated FBS by the addition of 15 μL of PBS (−) containing 200 ng of plasmid DNA encoding the modified firefly luciferase (pGL3-Control Vector, from Promega Co.) and complexed with PEI. After 1 day of incubation, the medium containing PEI/pGL3 complexes was removed and the cells were thoroughly washed twice with the medium supplemented with 10% FBS. PLH-Me/siRNA complexes were prepared by mixing various amounts (1−10 μL) of PLH-Me stock solutions in PBS (−) with anti-luciferase GL3 siRNA or nonspecific scrambled control siRNA solutions (195 ng in 5.25 μL) to obtain various positive/negative ratios in a final volume of 105 μL (per 7 wells), followed by 5 min of incubation at room temperature. Then an amount of 15 μL (per 1 well) of the resulting PLH-Me/siRNA complexes was added to the above washed cells to obtain a final siRNA concentration of 100 nM. After 2 days of incubation without washing, the cells were subjected to the luciferase assay (Promega kit) according to the manufacturer's instruction. Luciferase activities were normalized by protein concentrations and are presented as relative light unit (RLU). Protein concentrations were determined by BCA protein assay kit (Pierce) according to the manufacturer's instruction.

RESULTS AND DISCUSSION

Synthesis of PLH-Me. To synthesize methylated poly(L-histidine), as shown in Scheme 1, poly(L-histidine) hydrochloride (**1**) was reacted with iodomethane (**2**) to obtain quaternary imidazole groups, that is, cationic dimethylimidazole groups. The GFC profile of the resulting polypeptides (**3**) indicated that the number-average molecular weight (M_n) of the resulting polypeptide (**3**) was about 1.2 × 10^4. The ^{1}H NMR spectrum of the resulting polypeptides (**3**) showed the characteristic signals of both poly(L-histidine) backbone [β-methylene (δ 2.6−3.0 ppm), α-methine (δ 4.3−4.6 ppm), and imidazole (δ 6.6−7.1, 7.3−7.8, and 8.4−8.5 ppm)] and methyl groups (δ 3.3−3.7 ppm) (Figure S-1A, Supporting Information). However, the amount of dimethyl histidine, τ-methyl isomer, and π-methyl isomer, respectively, is unclear, so that amino acid analysis was carried out. From the chromatograms, the content of dimethyl histidine is estimated to be 25 mol % (τ-methyl, 16 mol %; π-methyl, 17 mol %), 68 mol % (τ-methyl, 16 mol %; π-methyl, 8 mol %), and 87 mol % (τ-methyl, 7 mol %; π-methyl, 4 mol %) (Figure S-1B, Supporting Information). Thus, we have synthesized various poly(L-histidine) biomacromolecules with cationic dimethylimidazole groups, that is, "PLH-Me." Namely, we call the PLH with 25, 68, and 87 mol % dimethyl hitidine PLH-Me(25), PLH-Me(68), and PLH-Me(87), respectively.

pH-Dependent Behavior of PLH-Me in Water. To examine the ionic properties of the remaining imidazole groups, we carried out the acid−base titration of the resulting PLH-Me solution, as shown in Figure 1A. The imidazole protons of the PLH-Me were gently dissociated around pH 6 so that the pK_a of the PLH-Me is considered to be around 6. The proton dissociation profile approximately depended on the content of dimethylimidazole groups. Namely, the PLH-Me(25) exhibited larger capacity of proton buffering around pH 6 because the PLH-Me(25) had more unmodified imidazole groups with a

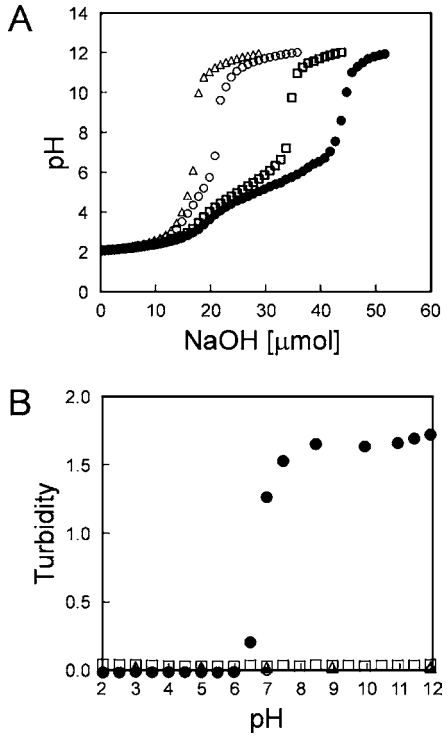


Figure 1. (A) Acid−base titration curves of PLH-Me: (●) PLH-Me(0); (□) PLH-Me(25); (○) PLH-Me(68); (△) PLH-Me(87). Acidic polypeptide solutions (3 mg/mL) were titrated with the stepwise addition of 0.5 M NaOH. (B) Effect of pH on the solubility of the PLH-Me in water (3 mg/mL): (●) PLH-Me(0); (□) PLH-Me(25); (○) PLH-Me(68); (△) PLH-Me(87). The turbidity was measured by monitoring the absorbance at 500 nm of the polypeptide aqueous solution during the acid−base titration.

pK_a of ∼6. On the other hand, almost no proton buffering of the PLH-Me(87) was observed around pH 6, owing to almost complete modification of imidazole groups to form quaternary dimethylimidazole groups. From these titration results, the following positive/negative charge ratio of PLH-Me/siRNA complexes will be estimated as a ratio of the quaternary dimethylimidazole groups of PLH-Me to the phosphate groups of siRNA at pH 7.4.

The solution behavior of the PLH-Me, as shown in Figure 1B, is totally different from that of the PLH, that is, PLH-Me(0). The PLH-Me(0) exhibits precipitation above pH 6.0 owing to the deprotonation of the imidazole groups of the PLH-Me(0); namely, the PLH-Me(0) is not water-soluble. Therefore, the PLH-Me(0) is not available as siRNA carrier. On the other hand, the aqueous solution of the PLH-Me(25) exhibited no significant turbidity above pH 6 in spite of the deprotonation of unmodified imidazole groups (Figure 1A). The introduction of the cationic dimethylimidazole groups, therefore, improves the water solubility of the PLH at physiological pH.

Complex Formation between PLH-Me and siRNA. We examined whether the PLH-Me formed the polyion complexes with siRNA by agarose gel electrophoresis (Figure 2). The complete retardation of siRNA was observed at a positive/negative charge ratio of 32. However, under experimental conditions, significant free siRNA was observed in spite of the mixing at a positive/negative charge ratio of 2. Under same experimental conditions, instead of siRNA, no free DNA was observed at a positive/negative charge ratio of 1 (results not

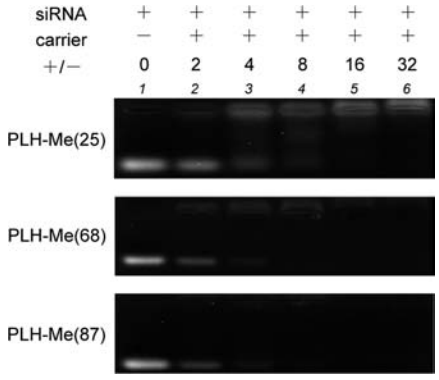


Figure 2. Analysis of the formation of the complexes between PLH-Me and siRNA by agarose gel electrophoresis, showing the interaction of each PLH-Me (carrier) with siRNA at pH 7.4: lane 1, siRNA alone; lanes 2–6, PLH-Me/siRNA mixtures at different charge ratios relative to dimethylimidazole groups of PLH-Me per phosphate group of siRNA (+/− = 2 (lane 2), 4 (lane 3), 8 (lane 4), 16 (lane 5), or 32 (lane 6)).

shown). Therefore, these results are consistent with less formation of the PLH-Me/siRNA polyion complexes because of the lower molecular weight of siRNA, compared with DNA.

Stability of PLH-Me/siRNA Complexes. To examine further the stability of the PLH-Me/siRNA complexes, we attempted to release siRNA from the polyion complexes by competitive exchange with other polyanions.[23] For effective RNA interference (RNAi), the release of siRNA should not happen outside the target cell, whereas that must occur somewhere inside to allow binding of the RNAi machinery. In biological fluids, the proteins borne by various anionic polysaccharides circulate. As an extreme case, dextran sulfate was used as a polyanion; namely, the agarose gel electrophoresis was carried out after the PLH-Me/siRNA complexes at a positive/negative charge ratio of 32 were incubated with dextran sulfates. The results are shown in Figure 3. As the concentration of the dextran sulfate increased, the siRNA increasingly migrated (lanes 6–8) in the case of the PLH-Me(87)/siRNA complexes. Furthermore, the siRNA complexes was hard to migrate in the case of the PLH-Me(68)/siRNA complexes, as compared with the PLH-Me(87)/siRNA complexes. On the other hand, in the case of the PLH-Me(25)/siRNA complexes, few siRNA migrated even in the presence of the higher concentration of the dextran sulfate (lane 8). These results suggest that the PLH-Me(87)/siRNA complexes easily released the siRNA by exposure to polyanions and that the PLH-Me(25)/siRNA complexes stably retained the siRNA. Moreover, when we determined the particle size and ζ potential of PLH-Me/siRNA complexes (Table S-1, Supporting Information), a significant value was obtained in the only case of the PLH-Me(25)/siRNA complexes. This is probably caused by adequate content of methyl (τ-methyl and π-methyl) imidazole groups as hydrophobic moiety to stabilize the electrostatic interaction between siRNA and dimethylimidazole groups of the PLH-Me. In this study, the stability of polycation/siRNA complexes has depended on the content of hydrophobic groups, that is, methylimidazole groups as well as deprotonated imidazole groups, in the polycation, promising unique design of polycation/siRNA complexes. We have therefore considered that the PLH-Me(25)/siRNA complexes have the ability to retain the siRNA stably outside the target cell for RNAi.

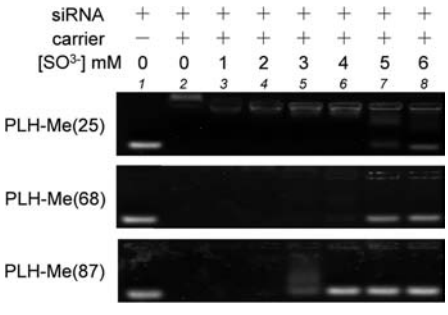


Figure 3. Release of siRNA from PLH-Me/siRNA complexes by dextran sulfates (DS) as assessed by agarose gel electrophoresis: lane 1, siRNA alone; lane 2, 0 mM; lane 3, 1 mM; lane 4, 2 mM; lane 5, 3 mM; lane 6, 4 mM; lane 7, 5 mM; lane 8, 6 mM. The siRNA mixtures with each PLH-Me (carrier) at a positive/negative charge ratio of 32 were incubated for 10 min at room temperature in the presence (lanes 3–8) or absence (lane 2) of DS (1–6 mM as sulfate group), followed by loading to the gel.

Cytotoxicity of PLH-Me/siRNA Complexes. Cytotoxicity of a siRNA carrier is an important factor for clinical applications. After the endosomal escape of siRNA mediated by the free polycations that has been internalized at the same time as the siRNA polyion complexes, in general, free polycations also exist solely during the release of siRNA from the polyion complexes. Furthermore, the overall cytotoxicity of free polycations is higher than that of the corresponding complexes. Accordingly, we chose the cytotoxicity assay of the free polycations to give a worst case estimation of the interaction of the polycations with cells rather than that of the polyion complexes with siRNA. As shown in Figure 4, we

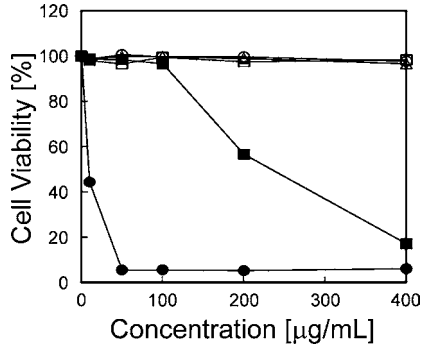


Figure 4. Effect of PLH-Me on the viability of HepG2 cells after 48 h incubation: (□) PLH-Me(25); (○) PLH-Me(68); (△) PLH-Me(87); (■) PLL; (●) PEI. Symbols and error bars represent the mean and standard deviation of the measurements made in triplicate wells.

therefore examined the effect of the PLH-Me on the cell viability. The viability of HepG2 hepatoma cells did not significantly decrease when all PLH-Me was added up to the concentration of 400 μg/mL, which was higher than the RNAi conditions. Consequently, it is worth noting that the PLH-Me exhibited no apparent cytotoxicity in spite of the content of the cationic dimethylimidazole groups. On the other hand, little viability was observed when the control PEI with higher molecular weight ($M_n \approx 60000$) was added up to 50 μg/mL. The control cationic polypeptide PLL ($M_n = 1.0 \times 10^4$) with the almost same molecular weight of the PLH-Me exhibited significant cytotoxicity at 200 μg/mL. In view of a positive charge concentration, the cytotoxic concentration of both PEI

and PLL was also lower than that of PLH-Me (Figure S-2, Supporting Information). These results suggest that the PLH-Me polypeptide with dimethylimidazole groups promises to be a noncytotoxic siRNA carrier; namely, dimethylimidazole groups are considered to be noncytotoxic cationic species.

RNAi by PLH-Me/siRNA Complexes. As a result of no apparent cytotoxicity, we further examined the RNAi mediated by the PLH-Me/siRNA complexes in view of the content of dimethylimidazole groups. As shown in Figure 5 (also see Figure S-3, Supporting Information), the PLH-Me polycations with different content of dimethylimidazole groups were used for the siRNA complex formation. No gene silencing efficacy was observed at any positive/negative charge ratio when we used the siRNA complexes with the PLH-Me(87). In the case of the PLH-Me(68), on the other hand, the siRNA complexes mediated little gene silencing at a positive/negative charge ratio of 32. The PLH-Me(25)/siRNA complexes mediated significant gene silencing (65%) at a positive/negative charge ratio of 32 without cytotoxicity (70 μg/mL, see Figure 4). Although the control PEI/siRNA complexes mediated remarkable gene silencing (98%) at a positive/negative charge ratio of 32,[24] cytotoxicity was observed under the experimental conditions (11 μg/mL, see Figure 4). Therefore, the resulting RNAi may be partially due to the cytotoxic property of PEI. These results suggest that the content of the dimethylimidazole groups in the PLH-Me was an important factor for RNAi. The PLH-Me(25)/siRNA complexes exhibited the most stable retention of siRNA in the PLH-Me at a positive/negative charge ratio of 32 (Figure 3), due to the hydrophobic groups (τ/π-methylimidazole groups as well as deprotonated imidazole groups). Furthermore, it can be said that the PLH-Me(25)/siRNA complexes maintain the stable retention of siRNA in the presence of 10% serum (Figure 5). For efficient gene silencing, the endosomal escape of siRNA, caused by the protonation of imidazole groups, is also necessary. Our preliminary study of the intracellular trafficking of the PLH-Me(25)/siRNA complexes by observation with a confocal laser scanning microscope shows that the PLH-Me(25) enhanced the cellular uptake and endosomal escape of siRNA for efficient RNAi (Figure S-4, Supporting Information). Taking these results into account, the dimethylimidazole groups are essential and unique functional groups in the PLH-Me for efficient siRNA delivery. Furthermore, the content balance among dimethyl, τ/π-methyl, and unmodified imidazole groups is considered to be important for efficient gene silencing by siRNA.

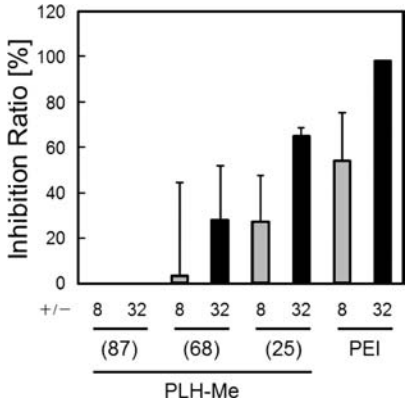


Figure 5. Luciferase gene knockdown by PLH-Me/siRNA complexes. The PLH-Me polypeptides with different contents of the dimethyl histidine were formed with siRNA at a positive/negative charge ratio of 8 (gray bars) or 32 (black bars). PEI was used as a positive control. The data were represented as inhibition ratio of siRNA for luciferase GL3 to scrambled siRNA. In particular, the PLH-Me(25)/siRNA complexes at a positive/negative charge ratio of 32 are statistically different, $p < 0.005$ using t-test. Symbols and error bars represent the mean and standard deviation of the measurements made in triplicate wells.

CONCLUSION

We have synthesized the unique pH-sensitive polypeptide PLH-Me and evaluated the physicochemical and biochemical properties of the siRNA carrier to control the stability of its siRNA polyion complexes for RNAi. The resulting PLH-Me was water-soluble in spite of the deprotonation of the imidazole groups at physiological pH. The PLH-Me/siRNA complex formation was mediated by the quaternary dimethylimidazole groups working as cationic groups to retain siRNA. The stability of the PLH-Me/siRNA complexes has depended on the content of hydrophobic groups, that is, τ/π-methylimidazole groups as well as deprotonated imidazole groups. The PLH-Me exhibited no significant cytotoxicity in spite of the existence of cationic dimethylimidazole groups. By use of PLH-Me as a pH-sensitive siRNA carrier, the PLH-Me/siRNA complexes mediated efficient siRNA delivery attributed to the dimethylimidazole groups, and the gene silencing depended on the content balance among dimethyl, τ/π-methyl, and unmodified imidazole groups. Consequently, the PLH-Me to control the stability of siRNA polyion complexes enhanced the noncytotoxic siRNA delivery by the optimized content of dimethyl, τ/π-methyl, and unmodified imidazole groups. The control of the polycation/siRNA complexes properties by varying the content balance of the methylation of the imidazole groups of pH-sensitive poly(L-hisitidine) biomacromolecules is expected to offer a unique design for siRNA delivery systems.

ASSOCIATED CONTENT

Supporting Information

Representative ^{1}H NMR spectrum of the PLH-Me; chromatograms (amino acid analysis) of the various PLH-Me polypeptides; particle size and ζ potential of PLH-Me/siRNA complexes; effect of PLH-Me on the viability of HepG2 cells; luciferase gene knockdown (inhibition ratio as the % of the untreated cells) by PLH-Me/siRNA complexes; confocal laser scanning microscope images showing intracellular trafficking of the PLH-Me/siRNA complexes. This material is available free of charge via the Internet at http://pubs.acs.org.

AUTHOR INFORMATION

Corresponding Author

*Telephone: +81-42-677-1111, extension 4976. Fax: +81-42-677-2821. E-mail: asayama-shoichiro@tmu.ac.jp.

Notes

The authors declare no competing financial interest.

ACKNOWLEDGMENTS

We are grateful to Professor Yukihiko Aramaki, Associate Professor Yoichi Negishi, and Assistant Professor Yoko Endo-Takahashi of the Tokyo University of Pharmacy and Life Sciences for use the confocal laser scanning microscope with their helpful assistance.

REFERENCES

(1) Michael, T. M., and Phillip, A. S. (2002) Gene silencing in mammals by small interfering RNAs. *Nat. Rev. Genet. 3*, 737−747.

(2) Marques, J. T., and Williams, B. R. (2006) A structural basis for discriminating between self and nonself double-stranded RNAs in mammalian cells. *Nat. Biotechnol. 24*, 559−565.

(3) Fukushima, S., Miyata, K., Nishiyama, N., Yamasaki, Y., and Kataoka, K. (2005) PEGylated polyplex micelles from triblock catiomers with spatially ordered layering of condensed pDNA and buffering units for enhanced intracellular gene delivery. *J. Am. Chem. Soc. 127*, 2810−2811.

(4) Zugates, G. T., Anderson, D. G., Little, S. R., Lowhorn, I. E. B., and Ranger, R. (2006) Synthesis of poly(β-amino ester)s with thiol-reactive side chains for DNA delivery. *J. Am. Chem. Soc. 128*, 12726−12734.

(5) Liu, Y., and Reineke, T. M. (2007) Poly(glycoamidoamine)s for gene delivery. Structural effects on cellular internalization, buffering capacity, and gene expression. *Bioconjugate Chem. 18*, 19−30.

(6) Itaka, K., Kanayama, N., Nishiyama, N., Jang, W. D., Yamasaki, Y., Nakamura, K., Kawaguchi, H., and Kataoka, K. (2004) Supramolecular nanocarrier of siRNA from PEG-based block catiomer carrying diamine side chain with distinctive pK_a directed to enhance intracellular gene silencing. *J. Am. Chem. Soc. 126*, 13612−13613.

(7) Read, M. L., Singh, S., Ahmed, Z., Stevenson, M., Briggs, S. S., Oupicky, D., Barrett, L. B., Spice, R., Kendall, M., Berry, M., Preece, J. A., Logan, A., and Seymour, L. W. (2005) A versatile reducible polycation-based system for efficient delivery of a broad range of nucleic acids. *Nucleic Acids Res. 33*, e86.

(8) Heidel, J. D., Yu, Z., Liu, J. Y., Rele, S. M., Liang, Y., Zeidan, R. K., Kornbrust, D. J., and Davis, M. E. (2007) Administration in non-human primates of escalating intravenous doses of targeted nanoparticles containing ribonucleotide reductase subunit M2 siRNA. *Proc. Natl. Acad. Sci. U.S.A. 104*, 5715−5721.

(9) Meyer, M., Philipp, A., Oskuee, R., Schmidt, C., and Wagner, E. (2008) Breathing life into polycations: functionalization with pH-responsive endosomolytic peptides and polyethylene glycol enables siRNA delivery. *J. Am. Chem. Soc. 130*, 3272−3273.

(10) Matsumoto, S., Christie, R. J., Nishiyama, N., Miyata, K., Ishii, A., Oba, M., Koyama, H., Yamasaki, Y., and Kataoka, K. (2009) Environment-responsive block copolymer micelles with a disulfide cross-linked core for enhanced siRNA delivery. *Biomacromolecules 10*, 119−127.

(11) Eguchi, A., Meade, B. R., Chang, Y. C., Fredrickson, C. T., Willert, K., Puri, N., and Dowdy, S. F. (2009) Efficient siRNA delivery into primary cells by a peptide transduction domain-dsRNA binding domain fusion protein. *Nat. Biotechnol. 27*, 567−571.

(12) Kim, H. J., Ishii, A., Miyata, K., Lee, Y., Wu, S., Oba, M., Nishiyama, N., and Kataoka, K. (2010) Introduction of stearoyl moieties into a biocompatible cationic polyaspartamide derivative, PAsp(DET), with endosomal escaping function for enhanced siRNA-mediated gene knockdown. *J. Controlled Release 145*, 141−148.

(13) Takemoto, H., Ishii, A., Miyata, K., Nakanishi., M., Oba, M., Ishii, T., Yamasaki, Y., Nishiyama, N., and Kataoka, K. (2010) Polyion complex stability and gene silencing efficiency with a siRNA-grafted polymer delivery system. *Biomaterials 31*, 8097−8105.

(14) Midoux, P., and Monsigny, M. (1999) Efficient gene transfer by histidylated polylysine/pDNA complexes. *Bioconjugate Chem. 10*, 406−411.

(15) Kim, T. H., Ihm, J. E., Choi, Y. J., Nah, J. W., and Cho, C. S. (2003) Efficient gene delivery by urocanic acid-modified chitosan. *J. Controlled Release 93*, 389−402.

(16) Park, J. S., Han, T. H., Lee, K. Y., Han, S. S., Hwang, J. J., Moon, D. H., Kim, S. Y., and Cho, Y. W. (2006) *N*-Acetyl histidine conjugated glycol chitosan self-assembled nanoparticles for intracytoplasmic delivery of drugs: endocytosis, exocytosis and drug release. *J. Controlled Release 115*, 37−45.

(17) Mishra, S., Heidel, J. D., Webster, P., and Davis, M. E. (2006) Imidazole groups on a linear, cyclodextrin-containing polycation produce enhanced gene delivery via multiple processes. *J. Controlled Release 116*, 179−192.

(18) Swami, A., Aggarwal, A., Pathak, A., Patnaik, S., Kumar, P., Singh, Y., and Gupta, K. C. (2007) Imidazolyl-PEI modified nanoparticles for enhanced gene delivery. *Int. J. Pharm. 335*, 180−192.

(19) Asayama, S., Sekine, T., Kawakami, H., and Nagaoka, S. (2007) Design of aminated poly(1-vinylimidazole) for a new pH-sensitive polycation to enhance cell-specific gene delivery. *Bioconjugate Chem. 18*, 1662−1667.

(20) Asayama, S., Sudo, M., Nagaoka, S., and Kawakami, H. (2008) Carboxymethyl poly(L-histidine) as a new pH-sensitive polypeptide to enhance polyplex gene delivery. *Mol. Pharmaceutics 5*, 898−901.

(21) Asayama, S., Hakamatani, T., and Kawakami, H. (2010) Synthesis and characterization of alkylated poly(1-vinylimidazole) to control the stability of its DNA polyion complexes for gene delivery. *Bioconjugate Chem. 21*, 646−652.

(22) Unsworth, J. M., Rose, F. R. A. J., Wright, E., Scotchford, C. A., and Shakesheff, K. M. (2003) Seeding cells into needled felt scaffolds for tissue engineering applications. *J. Biomed. Mater. Res. 53*, 617−620.

(23) Chittimalla, C., Zammut-Italiano, L., Zuber, G., and Behr, J. P. (2005) Monomolecular DNA nanoparticles for intravenous delivery of genes. *J. Am. Chem. Soc. 127*, 11436−11441.

(24) Boussif, O., Lezoualc'h, F., Zanta, M. A, Mergny, M. D., Scherman, D., Demeneix, B., and Behr, J. P. (1995) A versatile vector for gene and oligonucleotide transfer into cells in culture and in vivo: polyethylenimine. *Proc. Natl. Acad. Sci. U.S.A. 92*, 7297−7301.

Bioconjugate Chemistry

Article

pubs.acs.org/bc

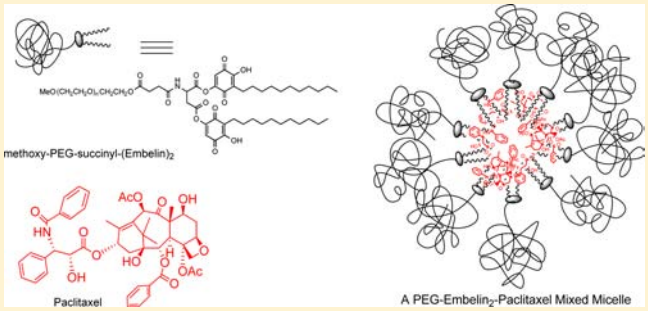
PEG-Derivatized Embelin as a Dual Functional Carrier for the Delivery of Paclitaxel

Yixian Huang,[#,†,‡] Jianqin Lu,[#,†,‡] Xiang Gao,[†,‡] Jiang Li,[†,‡] Wenchen Zhao,[‡] Ming Sun,[§] Donna Beer Stolz,[§] Raman Venkataramanan,[‡] Lisa Cencia Rohan,[‡,∥] and Song Li*[,†,‡]

[†]Center for Pharmacogenetics, [‡]Department of Pharmaceutical Sciences, School of Pharmacy; [§]Department of Cell Biology and Physiology, School of Medicine; [∥]Magee Women's Research Institute, University of Pittsburgh, Pittsburgh, Pennsylvania 15261, United States

Supporting Information

ABSTRACT: Embelin, identified primarily from the *Embelia ribes* plant, has been shown to be a natural small molecule inhibitor of X-linked inhibitor of apoptosis protein (XIAP). It is also a potent inhibitor of NF-κB activation, which makes it a potentially effective suppressor of tumor cell survival, proliferation, invasion, angiogenesis, and inflammation. However, embelin itself is insoluble in water, which makes it unsuitable for in vivo applications. In this work, we developed a novel micelle system through conjugating embelin to a hydrophilic polymer, poly(ethylene glycol) 3500 ($PEG_{3.5K}$) through an aspartic acid bridge. The $PEG_{3.5k}$-$embelin_2$ ($PEG_{3.5k}$-EB_2) conjugate readily forms micelles in aqueous solutions with a CMC of 0.0205 mg/mL. Furthermore, $PEG_{3.5k}$-EB_2 micelles effectively solubilize paclitaxel (PTX), a model hydrophobic drug used in this study. Both drug-free and drug-loaded micelles were small in size (20−30 nm) with low polydispersity indexes. In vitro cytotoxicity studies with several tumor cell lines showed that $PEG_{3.5k}$-EB_2 is comparable to embelin in antitumor activity and synergizes with PTX at much lower doses. Our results suggest that PEG-derivatized embelin may represent a novel and dual-functional carrier to facilitate the in vivo applications of poorly water-soluble anticancer drugs such as PTX.



INTRODUCTION

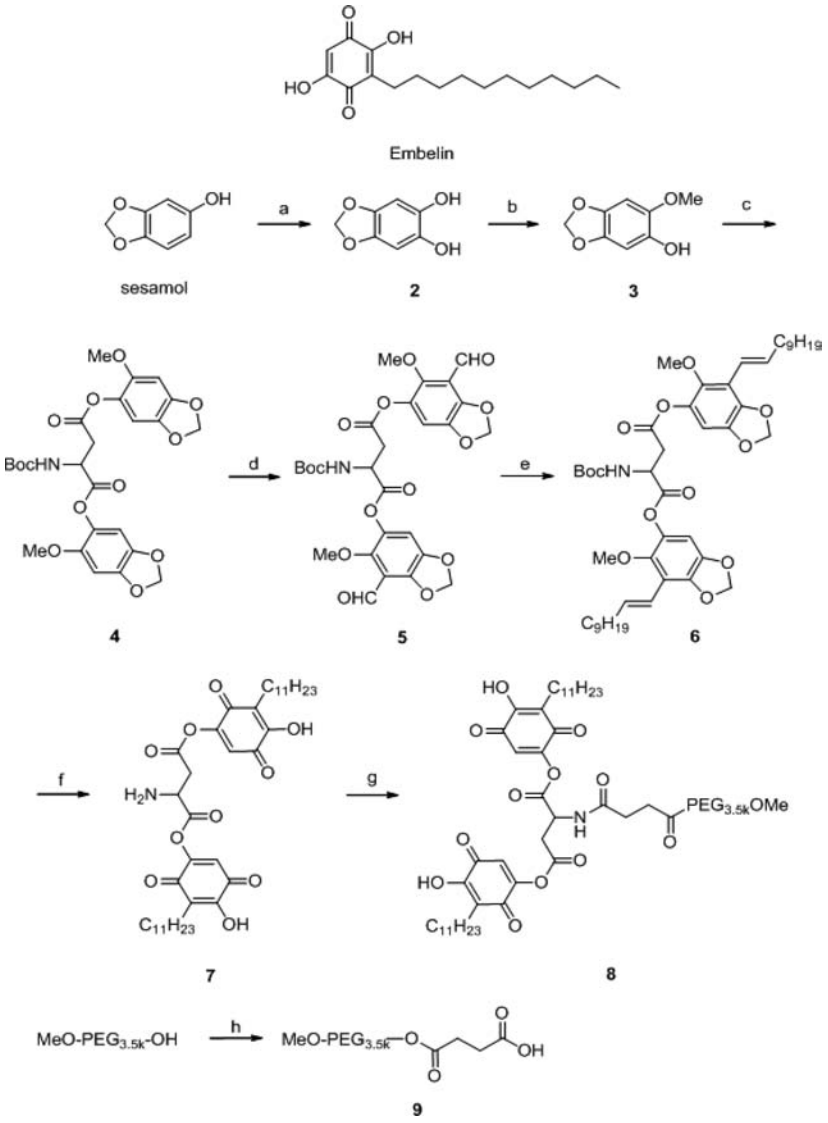
Low water solubility, high protein binding, and relatively short half-life are major problems in clinical applications of many potent anticancer drugs such as paclitaxel (PTX).[1,2] Currently, a variety of drug delivery systems such as liposomes, dendrimers, microcapsules, and polymeric micelles have been developed to address these problems and further to promote sustained, controlled, and targeted delivery of poorly water-soluble anticancer drugs.[3] Of all these delivery systems, polymeric micelles have gained considerable attention as a versatile nanomedicine platform due to their technical ease, high biocompatibility, and high efficiency in drug delivery.[4,5] Polymer micelles have been demonstrated to improve the aqueous solubility of chemotherapeutic agents and prolong their in vivo half-lives, owing to the steric hindrance provided by a hydrophilic shell.[4,5] Moreover, compared with other delivery systems, micelles show advantages in passive tumor targeting through the leaky vasculature via the enhanced permeability and retention (EPR) effect due to their small size ranging from 10 to 100 nm.[6,7] Favorable drug biodistribution and improved therapeutic index can be achieved by using the micelle delivery system.[3,4] However, most of the polymeric systems use "inert" excipients that lack therapeutic activity. The presence of large amounts of carrier materials not only adds to the cost, but also imposes additional safety issues.[8]

One of the most sophisticated designs of drug delivery systems is that in which the components forming the carriers can also have therapeutic effects. The carrier materials may be capable of counteracting the side effects caused by the loaded anticancer drugs.[9] Also, it is possible that the carrier may collaborate with the loaded drug to achieve synergistic effects to better treat the tumor.[5] However, the strategy of using highly water-insoluble drugs themselves as the hydrophobic region of polymeric micelles is rarely reported. One example is the pegylated vitamin E, D-α-tocopheryl poly(ethylene glycol) succinate (Vitamin E TPGS or TPGS).[10−12] Vitamin E shows antitumor activity against a number of types of cancers through various mechanisms such as induction of apoptosis, inhibition of tumor cell proliferation and differentiation, suppression of nuclear factor-kappa B (NF-κB) activation, and so forth.[13,14] The pegylated vitamin E is a highly water-soluble amphiphilic molecule comprising a lipophilic alkyl tail and a hydrophilic polar head portion. In addition to its antitumor activity, it is

Received: February 2, 2012
Revised: June 4, 2012
Published: June 9, 2012

ACS Publications © 2012 American Chemical Society

Scheme 1. Synthesis of $PEG_{3.5K}$-EB_2[a]



[a]Conditions: (a) water, Fremy's salt, KH_2PO_4, 5 min; $Na_2S_2O_4$, 30 min; (b) water, Mel NaOH: l h; (c) Boc-Aspartic acid DCC, DMAP, CH_2Cl_2, overnight; (d) MeCN, DMF, $POCl_3$; (e) THF, LiHMDS 2 M in THF, decyltriphenylphosphonium bromide, 2 h (f) (1) MeOH, H_2, Pd/C; (2) MeCN, CAN; (3) dioxane, HCl, 2 h; (g) CH_2Cl_2, DCC, DMAP, **9**; overnight; (h) succinic anhydride, DMAP, CH_2Cl_2, 2 days.

effective in solubilizing various hydrophobic drugs such as PTX. Synergistic actions between the TPGS-based carrier and delivered anticancer agents have been reported.[5]

In this study, we report the development of PEG-derivatized embelin as another novel and dual-functional carrier for delivery of poorly water-soluble anticancer drugs. Embelin is a naturally occurring alkyl-substituted hydroxyl benzoquinone compound and a major constituent of *Embelia ribes* BURM. It has been shown to possess antidiabetic, anti-inflammatory, and hepatoprotective activities.[15−17] Embelin also shows antitumor activity in various types of cancers.[15,18−21] One major mechanism involves the inhibition of the activity of X-linked inhibitor of apoptosis protein (XIAP).[22] XIAP is overexpressed in various types of cancers cells, particularly drug-resistant cancer cells, and inhibition of XIAP has been explored as a new approach for the treatment of cancers.[23,24] XIAP plays a minimal role in normal cells, and therefore, embelin shows significantly less toxicity on normal cells. Embelin also downregulates the expression of survivin, XIAP, IAP1/2, TRAF1, cFLIP, Bcl-2, and Bcl-x_L through the inhibition of NF-κB activation.[25] Embelin is poorly water-soluble, and PEG modification was originally explored by us as an approach to increase its solubility. Interestingly, PEG-derivatized embelin forms micelles that are highly efficient in solubilizing other compounds such as PTX. Preparation of PEG-derivatized embelin can be readily achieved with commercially available embelin. In addition, we have developed an efficient synthesis strategy to prepare PEG−embelin conjugate. Our in vitro studies showed that PEG−embelin has similar activity to free embelin with IC_{50} in the low micromolar range. More importantly, PEG−embelin synergizes with PTX at much lower doses (~nM) in a number of cancer cell lines tested.

EXPERIMENTAL PROCEDURES

Materials. Paclitaxel (98%) was purchased from AK Scientific. Inc. (CA, USA). 2,5-Dihydroxy-3-undecyl-1,4-benzoquinone (embelin 98%) was purchased from 3B Scientific Corporation (IL, USA). Dulbecco's phosphate buffered saline

dx.doi.org/10.1021/bc3000468 | *Bioconjugate Chem.* 2012, 23, 1443−1451

(DPBS) was purchased from Lonza (MD, USA). Methoxy-$PEG_{3,500}$-OH, dimethyl sulfoxide (DMSO), 3-(4,5-dimethylthiazol-2-yl)-2,5-diphenyl tetrazolium bromide (MTT), trypsin-EDTA solution, Triton X-100, and Dulbecco's Modified Eagle's Medium (DMEM) were all purchased from Sigma-Aldrich (MO, USA). Fetal bovine serum (FBS) was purchased from Gibco Life Technologies (AG, Switzerland). Penicillin–streptomycin solution was from Invitrogen (NY, USA). All solvents used in this study were HPLC grade.

Cell Culture. DU145 and PC3 are two androgen-independent human prostate cancer cell lines. MDA-MB-231 is a human breast adenocarcinoma cell line. 4T1 is a mouse metastatic breast cancer cell line. All cell lines were cultured in DMEM containing 10% FBS and 1% penicillin–streptomycin in a humidified environment at 37 °C with 5% CO_2.

Synthesis of $PEG_{3.5K}$-Embelin$_2$ ($PEG_{3.5K}$-EB_2). Scheme 1 shows the synthesis sequence of $PEG_{3.5K}$-EB_2 conjugate. Synthesis of the intermediates and structural characterizations are detailed below.

Compound **2**: Sesamol (1.52 g, 24 mmol) in 30 mL of methanol was added to a rapidly stirred solution of Fremy's salt (7.96 g, 30 mmol) and 5.49 g (40 mmol) of KH_2PO_4 in 400 mL water at 5 °C. The color of the solution changed from light brown to bright yellow within 5 min. The mixture was stirred for another 30 min and then extracted with 4 × 40 mL of ethyl acetate. The ethyl acetate phase was treated with a solution of $Na_2S_2O_4$ (9.0 g, 52 mmol) in water (30 mL), and the yellow color changed to a colorless solution. The organic layer was acidified with HCl (1 N), extracted with ethyl acetate (3 × 30 mL), washed with water (20 mL), dried with anhydrous $MgSO_4$, and concentrated to give 1.1 g (65%) of **2** as a light pink solid. ^{1}H NMR($(CD_3)_2CO$): δ 7.49 (s, 2H), 6.45 (s, 2H), 5.79 (s, 2H).

Compound **3**: A solution of **2** (1.54 g, 10 mmol) in water (30 mL) was treated with NaOH (0.4 g, 10 mmol) while the flask was kept in an ice bath. The reaction mixture was stirred for 15 min after which MeI (1.41 g, 10 mmol) was added dropwise. The reaction mixture was then heated under reflux for 1 h, allowed to cool down to room temperature, and the solvent was removed via a rotary evaporator. The crude product was purified by flash chromatography with silica gel (ethyl acetate:petroleum ether, 1:5) and pure **3** was obtained as an amber oil with a yield of 99% (1.68 g). ^{1}H NMR($CDCl_3$): δ 6.11 (m, 2H), 5.88 (s, 2H), 5.35 (s, 1H), 3.72 (s, 3H).

Compound **4**: To a solution of *N*-(*tert*-butoxycarbonyl)-L-aspartic acid (Boc-Asp-OH) (2.33 g, 10 mmol) in CH_2Cl_2 (40 mL) was added dicyclohexylcarbodiimide (DCC) (6.2 g, 30 mmol), 4-dimethyamineopyridine (DMAP) (0.61 g, 5 mmol), and compound **3** (3.36 g, 20 mmol) at room temperature. The reaction mixture was stirred overnight at room temperature. After the reaction was completed, 100 mL Et_2O was added to the mixture. The mixture was filtered to remove the insoluble DCU byproduct and the organic phase of the filtrate was concentrated under vacuum. The resulting residue was purified by silica gel flash chromatography (MeOH:CH_2Cl_2, 1:10) to give pure **4** as an oil in 62% yield (3.31 g). ^{1}H NMR ($CDCl_3$): δ 6.11 (m, 4H), 5.88 (m, 4H), 5.40 (m, 1H), 4.65 (m, 1H), 3.74 (s, 3H), 3.72 (s, 3H), 2.88 (m, 1H), 2.64 (m, 1H), 1.42 (s, 9H). ESI-MS m/z 534.2 ($[M+H]^+$).

Compound **5**: To a solution of **4** (5.33 g, 10 mmol) in acetonitrile (MeCN, 10 mL) at 0–5 °C, dry dimethylformamide (DMF) (0.73 g, 10 mmol) and $POCl_3$ (1.78 g, 11 mmol) were added with constant stirring over 0.5 h. The salt formed was filtered, washed with cold MeCN, dissolved in 20 mL of water, heated at 50 °C for 0.5 h, and then cooled. The mixture was extracted with 3 × 40 mL of CH_2Cl_2, and the combined organic phase was washed with brine, dried over anhydrous Na_2SO_4, and concentrated in vacuum. The crude residue was purified by silica gel flash chromatography (MeOH:CH_2Cl_2, 1:10) to give pure **5** as an oil in 80% yield (4.82 g). ^{1}H NMR ($CDCl_3$): δ 10.21 (s, 1H), 10.18 (s, 1H), 6.65 (m, 2H), 5.92 (m, 4H), 5.37 (m, 1H), 4.51 (m, 1H), 3.75 (s, 3H), 3.72 (s, 3H), 2.85 (m, 1H), 2.60 (m, 1H), 1.40 (s, 9H). ESI-MS m/z 590.5 ($[M+H]^+$).

Compound **6**: A solution of sodium bis(trimethylsilyl)amide (12 mL, 2 M solution in THF) was added dropwise to a stirred solution of decanyltriphenylphosphonium bromide (9.67 g, 20 mmol) in 40 mL THF at room temperature. The resulting mixture was stirred for 30 min at room temperature and then cooled to −78 °C. To this mixture was added compound **5** (6.03 g, 10 mmol). The reaction mixture was stirred for 2 h at −78 °C and then warmed up to room temperature. The reaction mixture was quenched with saturated solution of NH_4Cl, extracted with ethyl acetate. The combined organic layer was washed with brine, dried over anhydrous Na_2SO_4, and concentrated in vacuum. The crude residue was purified by silica gel flash chromatography (MeOH:CH_2Cl_2, 1:10) to give pure **6** as an oil in 90% yield. ^{1}H NMR ($CDCl_3$): δ 6.48 (m, 2H), 6.39 (m, 2H), 6.02 (m, 2H), 5.86 (m, 4H), 5.35 (m, 1H), 4.53 (m, 1H), 3.75 (s, 3H), 3.72 (s, 3H), 2.83 (m, 1H), 2.61 (m, 1H), 2.15 (m, 4H), 1.40 (s, 9H), 1.29 (m, 28H), 0.91 (m, 6H). ESI-MS m/z 838.4 ($[M+H]^+$).

Compound **7**: The double bond in compound **6** (8.37 g, 10 mmol) was saturated by catalytic hydrogenolysis with Pd/C (10%, 500 mg) under H_2 (1 atm) in a methanol solution (50 mL) at room temperature for 2 h. The solution was filtered to remove Pd/C and concentrated under vacuum. The resulting product was then dissolved in the solution of 10 mL of water, 10 mL MeCN, and 20 mmol CAN (ammonium ceric nitrate) (10.96 g). The mixture was cooled to 0 °C and stirred for another 2 h. MeCN was then removed via evaporation under reduced pressure, 100 mL CH_2Cl_2 was added to the remaining aqueous solution. The organic phase was washed with brine and then concentrated under vacuum. 10 mL dioxane and 10 mL HCl were then added to the residue. The mixture was stirred at room temperature for 24 h. The reaction mixture was quenched with saturated solution of $NaHCO_3$ and extracted with ethyl acetate. The organic layer was washed with brine, dried over anhydrous Na_2SO_4, and concentrated under vacuum. The crude product was purified by silica gel flash chromatography (MeOH:CH_2Cl_2, 1:10) to give pure **7** as an oil in 42% yield (2.89 g). ^{1}H NMR($CDCl_3$): δ 8.16 (m, 2H), 6.75 (m, 2H), 5.35 (m, 2H), 4.53 (m, 1H), 2.85 (m, 1H), 2.60 (m, 1H), 2.43 (m, 4H), 1.25 (m, 36H), 0.89 (m, 6H). ESI-HRMS calcd for $C_{38}H_{55}NO_{10}Na$ ($[M+Na]^+$) 708.4766, found 708.4747.

Compound **8**: A solution of MeO-$PEG_{3.5k}$-CO_2H (3.5 g, 1 mmol) in CH_2Cl_2 (5 mL) was treated with DCC (0.41 g, 2 mmol), DMAP (0.12 g, 1 mmol), and compound **7** (689 mg, 1 mmol) at room temperature. The reaction mixture was stirred overnight. After the reaction was completed, 100 mL of Et_2O was added and the mixture was filtered and concentrated under vacuum. The resulting residue was purified by silica gel flash chromatography (MeOH:CH_2Cl_2, 1:10) to give pure **8** ($PEG_{3.5K}$-EB_2) as a wax solid in ~50% yield (2.1 g). ^{1}H NMR ($CDCl_3$): δ 8.14 (m, 2H), 6.72 (m, 2H), 5.57 (m, 1H),

dx.doi.org/10.1021/bc3000468 | *Bioconjugate Chem.* 2012, 23, 1443–1451

4.98 (m, 1H), 3.35 (s, 3H), 2.60 (m, 10H), 1.25 (m, 36H), 0.89 (m, 6H).

Formation of Micelles. PTX-solubilized micelles were prepared by the following method. PTX (10 mM in chloroform) was added to $PEG_{3.5K}$-EB_2 (10 mM in chloroform) with various carrier/drug ratios. The organic solvent was first removed by nitrogen flow to form a thin film of drug/carrier mixture. The film was further dried under high vacuum for 2 h to remove any traces of remaining solvent. Drug-loaded micelles were formed by suspending the film in DPBS. The drug-free micelles were similarly prepared as described above.

Measurement of Size and Zeta Potential. Zetasizer (Zetasizer Nano ZS instrument, Malvern, Worcedtershire, UK) was used to measure the particle size and zeta potential of drug-free and drug-loaded micelles. Micelles were stored at 4 °C, and the samples were tested for changes in particle size and size distribution.

Determination of PTX Loading Efficiency. PTX-solubilized micelles were prepared at an input PTX concentration of 1.07, 2.14, and 3.21 mg/mL, respectively. Aliquots of samples were filtered through 0.45 μm PVDF syringe filter. PTX in the filtered and nonfiltered micelles was extracted using methanol and measured by high-performance liquid chromatography (HPLC, Waters). A reverse phase column (C18) was employed. The detection was performed by using UV detector at 227 nm, 70% methanol as a mobile phase, flow rate at 1.0 mL/min. Drug loading capacity (DLC) and drug loading efficiency (DLE) were calculated according to the following formula:

$$\mathrm{DLC}(\%) = [\text{weight of drug used}/(\text{weight of polymer} + \text{drug used})] \times 100\%$$

$$\mathrm{DLE}(\%) = (\text{weight of loaded drug}/\text{weight of input drug}) \times 100\%$$

Determination of the Critical Micelle Concentration (CMC). The CMC of $PEG_{3.5K}$-EB_2 was determined by employing pyrene as a fluorescence probe.[26] A drug-free micelle solution in DPBS (2.5 mg/mL) was prepared via solvent evaporation method. A series of 2-fold dilutions was then made with $PEG_{3.5K}$-EB_2 concentrations ranging from 7.63×10^{-5} to 2.5 mg/mL. At the same time, aliquots of 50 μL of 4.8×10^{-6} M pyrene in chloroform were added into 15 separate vials. The chloroform was first removed by nitrogen flow to form a thin film. The film was further dried under high vacuum for 2 h to remove any traces of remaining solvent. Then, the preprepared micelle solutions (400 μL in DPBS) of varying $PEG_{3.5K}$-EB_2 concentrations were added to the pyrene film to obtain a final pyrene concentration of 6×10^{-7} M for each vial. The solutions were kept on a shaker at 37 °C for 24 h to reach equilibrium before fluorescence measurement. The fluorescence intensity of samples was measured at the excitation wavelength of 334 nm and emission wavelength of 390 nm by Synergy H1 Hybrid Multi-Mode Microplate Reader (Winooski, VT). The CMC is determined from the threshold concentration, where the sharp increase in pyrene fluorescence intensity is observed.

Transmission Electron Microscope (TEM). The morphology of micelles was observed on a Jeol 1011 transmission electron microscope (TEM). The aqueous micelle solution (1.0 mg/mL) was added onto copper grids coated with Formvar, and then stained with 1% uranyl acetate. The sample processing and imaging were performed at room temperature.

Hemolysis Assay. Fresh blood samples were collected through cardiac puncture from rats. Ten milliliters of blood was added with EDTA-Na_2 immediately to prevent coagulation. Red blood cells (RBCs) were separated from plasma by centrifugation at 1500 rpm for 10 min at 4 °C. The RBCs were washed three times with 30 mL ice-cold DPBS. RBCs were then diluted to 2% w/v with ice-cold DPBS and utilized immediately for the hemolysis assay. One milliliter of diluted RBC suspension was treated with various concentrations (0.2 and 1.0 mg/mL) of $PEG_{3.5k}$-EB_2 and PEI, respectively, and then incubated at 37 °C in an incubator shaker for 4 h. The samples were centrifuged at 1500 rpm for 10 min at 4 °C, and 100 μL of supernatant from each sample was transferred into a 96-well plate. The release of hemoglobin was determined by the absorbance at 540 nm using a microplate reader. RBCs treated with Triton X-100 (2%) and DPBS were considered as the positive and negative controls, respectively. Hemoglobin release was calculated as $(OD_{sample} - OD_{negative\ control})/(OD_{positive\ control} - OD_{negative\ control}) \times 100\%$.

In Vitro Cell Cytotoxicity. DU145 (2000 cells/well), PC-3 (5000 cells/well), MDA-MB-231 (2000 cells/well), or 4T1 (1000 cells/well) were seeded in 96-well plates followed by 24 h of incubation in DMEM with 10% FBS and 1% streptomycin–penicillin. Then, various concentrations of PTX (dissolved in DMSO or formulated in $PEG_{3.5K}$-EB_2 micelles) were added in quadruplicate and cells were incubated for 72 h. 20 μL of 3-(4, 5-dimethylthiazol-2-yl)-2,5-diphenyltetrazolium-bromide (MTT) in PBS (5 mg/mL) was added and cells were further incubated for 4 h. The medium in the plates was removed and MTT formazan was solubilized by DMSO. The absorbance was measured by microplate reader with wavelength at 550 nm and reference wavelength at 630 nm. Untreated groups were used as controls. Cell viability was calculated as $[(OD_{treat} - OD_{blank})/(OD_{control} - OD_{blank}) \times 100\%]$.

RESULTS

Synthesis of $PEG_{3.5K}$-EB_2 Conjugates. We have developed a strategy to synthesize $PEG_{3.5K}$-EB_2 conjugate in which two molecules of embelin were coupled to one molecule of PEG via a linker of aspartic acid. This is modified from the scheme reported by Wang's group[27] for the total synthesis of embelin. This involves the synthesis of benzoquinone followed by coupling to carboxyl groups of aspartic acid. Undecyl side chains were then installed onto each of the two benzoquinone rings. Finally, PEG was coupled to aspartic acid-EB_2 through the deprotected amino group. HPLC shows that the purity of the final product ($PEG_{3.5K}$-EB_2) is 94% (Figure S1). ^{1}H NMR spectrum of $PEG_{3.5K}$-EB_2 shows signals at 3.63 ppm attributable to the methylene protons of PEG, the embelin proton signals at 8.14 and 6.72 ppm, and the carbon chain singles at 1.05–1.25 ppm. The aspartate signals were identified at 5.57, 4.98, and 2.60 ppm (Figure S2). The molecular weight of the $PEG_{3.5K}$-EB_2 conjugate from MALDI-TOF MS (4197) is very similar to the theoretical value (4203) (Figure S3). These results suggest successful synthesis of $PEG_{3.5K}$-EB_2 conjugate.

Biophysical Characterization of Micelles. Micelles were readily prepared from $PEG_{3.5K}$-EB_2 conjugate via solvent evaporation method. $PEG_{3.5K}$-EB_2 conjugate can be dissolved in water at concentration up to 750 mg/mL (data not shown). Dynamic light scattering (DLS) measurements showed that these micelles had hydrodynamic sizes around 22 nm at the

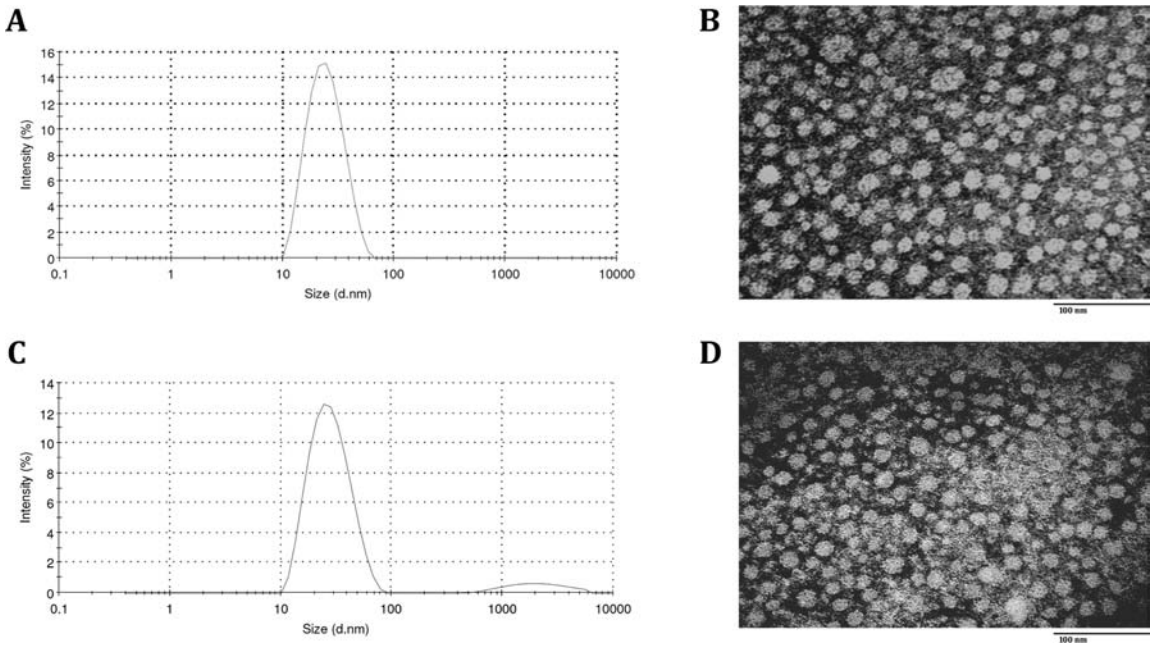


Figure 1. Particle size distribution of $PEG_{3.5K}$-EB_2 (A) and PTX-loaded $PEG_{3.5K}$-EB_2 (C). TEM images of self-assembled micelles of $PEG_{3.5K}$-EB_2 (B) and PTX-loaded $PEG_{3.5K}$-EB_2 (D). The spherical micelles with the diameter of around 20 nm were observed. The drug loading level was 1 mg/mL (PTX) in $PEG_{3.5K}$-EB_2.

concentration of 20 mg/mL (Figure 1A), which shall ensure efficient passive targeting to the solid tumors.

PTX, a potent hydrophobic anticancer agent, was readily loaded into $PEG_{3.5K}$-EB_2 micelles. Figure 1C shows the DLS size measurement of PTX-loaded $PEG_{3.5K}$-EB_2 micelles at a drug concentration of 1 mg/mL. There were minor changes in sizes when PTX was loaded into micelles at a carrier/drug ratio of 7.5/1 (m/m).

Figure 1B,D shows the TEM images of drug-free and PTX-loaded micelles after staining with 1% uranyl acetate. Spherical particles of uniform size were observed for both drug-free and PTX-loaded micelles. The sizes of the micelles observed under TEM are consistent with those measured by DLS.

Table 1 shows the sizes of PTX-loaded micelles at different carrier/drug molar ratios. PTX-loaded $PEG_{3.5K}$-EB_2 micelles had relatively large size (~143 nm) at a carrier/drug ratio of 2.5: 1 (m/m) and the particles were stable for less than 1 day. Increasing the input molar ratio of $PEG_{3.5K}$-EB_2/PTX led to gradual decrease in the size of PTX-loaded micelles. At the molar ratio of 7.5/1, the size of the PTX-loaded micelles was similar to that of drug-free micelles.

Table 1. DLS Analysis of the Sizes of Free and Drug-Loaded $PEG_{3.5K}$-EB_2 Micelles[a]

micelles	molar ratio	size[b] (nm)	PDI[c]
$PEG_{3.5K}$-EB_2	—	22.8 ± 0.3	0.09
$PEG_{3.5K}$-EB_2:PTX[d]	2.5:1	143 ± 17	0.23
$PEG_{3.5K}$-EB_2:PTX	5:1	58.7 ± 0.5	0.32
$PEG_{3.5K}$-EB_2:PTX	7.5:1	27.5 ± 0.2	0.23

[a]PTX concentration in micelle was kept at 1 mg/mL. Blank micelle concentration was 20 mg/mL. Values repotted are the mean ± SD for triplicate samples. [b]Measured by dynamic light scattering particle sizer (Zetasizer). [c]PDI = polydispersity index. [d]PTX = paclitaxel.

Drug Loading Efficiency (DLE). DLE of PTX-loaded micelles were determined by HPLC and the results are shown in Table 2. DLE was as high as 79.89% when PTX was formulated in $PEG_{3.5K}$-EB_2 micelles at a carrier/PTX input ratio of 2.5/1 (m/m) and PTX concentration of 1.07 mg/mL. Increasing the carrier/PTX input ratios led to further increase in DLE. $PEG_{3.5K}$-EB_2/PTX formed the most stable particles at a carrier/drug ratio of 7.5/1. At this ratio, PTX was quantitatively formulated in the $PEG_{3.5K}$-EB_2 micelles when the PTX concentration was less than 2.14 mg/mL. Increasing the PTX concentration to 3.21 mg/mL led to a slight decrease in DLE (81.3%). The surface charges of PTX-loaded $PEG_{3.5K}$-EB_2 micelles were close to neutral (+1.89 to −2.64) for all particles examined.

Table 2. Physicochemical Characterization of PTX-Loaded $PPEG_{3.5K}$-EB_2 Micelles[a]

$PEG_{3.5K}$-EB_2:PTX (m/m)	concentration of PTX in micelles (mg/mL)	DLC[b] (%)	DLE[c] (%)	zeta[d] (mV)
2.5:1	1.07	7.51	79.9	1.58 ± 0.37
5:1	1.07	3.90	96.7	1.89 ± 0.08
7.5:1	1.07	2.63	98.6	−1.52 ± 0.20
	2.14	2.63	97.5	−1.29 ± 0.19
	3.21	2.63	81.3	−2.64 ± 0.43

[a]Values reported are the means ± SD for triplicate samples. [b]DLC = drug loading capacity. [c]DLE = drug loading efficiency. [d]Measured by dynamic light scattering particle sizer (Zetasizer).

CMC Measurements. Figure 2 shows the results of CMC measurements using pyrene as a fluorescence probe. Upon incorporation into the micelles, the fluorescence intensity of pyrene increases substantially at the concentration of micelles above the CMC.[28] On the basis of the partition of the pyrene, the CMC of $PEG_{3.5K}$-EB_2 could be obtained by plotting the fluorescence intensity versus logarithm concentration of the polymer. The CMC of $PEG_{3.5K}$-EB_2 was determined from the crossover point at the low concentration range. The CMC of

dx.doi.org/10.1021/bc3000468 | Bioconjugate Chem. 2012, 23, 1443−1451

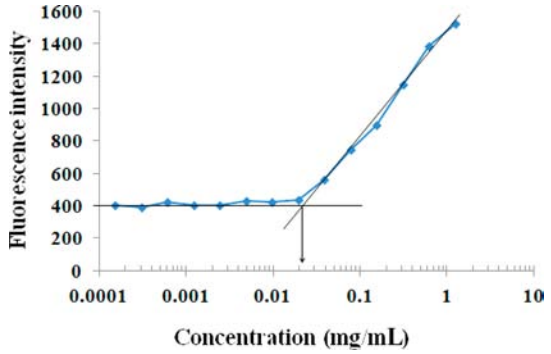


Figure 2. CMC measurement of the $PEG_{3.5K}$-EB_2 micelles using pyrene as a hydrophobic fluorescence probe. The fluorescence intensity of pyrene was collected at the excitation wavelength of 334 nm and the emission wavelength of 390 nm. The fluorescence intensity was plotted as a function of logarithmic concentration of $PEG_{3.5K}$-EB_2 micelles, [pyrene] = 6×10^{-7} mol/L. Values reported are the means ± SD for triplicate samples.

the $PEG_{3.5K}$-EB_2 conjugate is 4.9 μM, which is similar to most reported micellar delivery systems.

Hemolysis Study. One of the safety concerns for polymeric micelle systems is the hemolytic activity. To address this issue, the hemolytic activity of drug-free $PEG_{3.5K}$-EB_2 micelles was examined and compared to a strong detergent Triton X-100 and polyethylenimine (PEI), a cationic polymer known to have significant hemolytic effect.[29] As shown in Figure 3, PEI

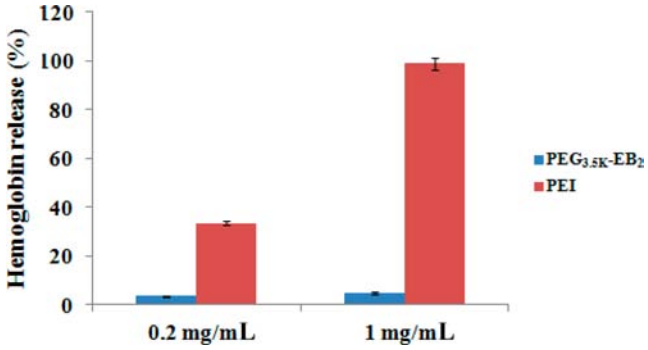


Figure 3. In vitro hemolysis assay of $PEG_{3.5K}$-EB_2 compared with PEL Both $PEG_{3.5K}$-EB_2 and PEI with two different concentrations [0.2, 1 mg/mL) were incubated with rat red blood cells (RBCs) for 4 h at 37 °C in an incubator shaker. The degree of RBCs lysis was measured spectrophotometrically (λ = 540 nm) according to the release of hemoglobin in process (2% Triton X-100 and DPBS were used as a positive and negative control, respectively). Values reported are the means ± SD for triplicate samples.

induced hemolysis in a dose-dependent manner. In contrast, no observable hemolytic activities (<5%) were found for $PEG_{3.5K}$-EB_2 micelles, suggesting the excellent safety of our new delivery system.

In Vitro Cytotoxicity. Figure 4 shows the cytotoxicity of $PEG_{3.5K}$-EB_2 in comparison with free embelin (dissolved in DMSO) in 3 cancer cell lines tested including murine breast cancer cells 4T1, and two human prostate cancer cell lines PC3 and DU145. $PEG_{3.5K}$-EB_2 was comparable to free embelin in antitumor activity in all 3 cancer cell lines with IC_{50} in the low micromolar range.

Figure 5A compares the cytotoxicity of free PTX (in DMSO) to that of $PEG_{3.5K}$-EB_2-formulated PTX (5/1, m/m) in MDA-MB-231 cells. Drug-free $PEG_{3.5K}$-EB_2 did not cause any cytotoxicity to MDA-MB-231 cells due to its relatively low concentrations used in this study. Free PTX exhibited cytotoxicity on MDA-MB-231 cells in a dose-dependent manner. However, formulation of PTX in $PEG_{3.5K}$-EB_2 micelles resulted in a significant increase in the cytotoxicity. Similar results were found with three other cancer cell lines (Figure 5B–D). Table 3 summarizes the IC_{50} of free PTX and $PEG_{3.5K}$-EB_2-formulated PTX in the four different cancer cell lines. Depending on the cell lines, the IC_{50} was decreased by 1.5- to 8.7-fold when PTX was formulated in $PEG_{3.5K}$-EB_2 micelles.

DISCUSSION

We have developed a new delivery system that consists of an embelin-based hydrophobic domain and a PEG hydrophilic segment. The $PEG_{3.5K}$-EB_2 conjugate readily forms micelles in aqueous solutions. More importantly, hydrophobic drugs such as PTX can be loaded into $PEG_{3.5K}$-EB_2 micelles.

Various polymeric micelle systems have been reported. Most micellar systems consist of a hydrophobic core that does not have any potential therapeutic effect.[30] In addition, the metabolites of the hydrophobic segments might contribute to some undesired effects, such as inflammation and systemic toxicity.[30,31] The $PEG_{3.5K}$-EB_2 conjugate developed in this study represents a dual-functional delivery system that may overcome these limitations. Embelin is a natural product that demonstrates various biological effects including antitumor activity.[15] Embelin also shows excellent safety profiles in animals.[32] Thus, PEG-derivatized embelin may be an attractive delivery system to achieve synergistic activity with anticancer agents while minimizing the carrier-associated toxicity. PEG–embelin conjugates can be synthesized via direct coupling of embelin to PEG via an ester linkage. However, such synthesis is likely to yield a mixture of products with PEG randomly linked to the different hydroxyl groups in the benzene ring. We have developed a strategy to generate $PEG_{3.5K}$-EB_2 conjugate via total synthesis (Scheme 1). This method was modified from a scheme reported by Wang's group for total synthesis of embelin.[27] Our synthesis ensures generation of a structurally well-defined conjugate in which PEG is attached to 1-OH group in the quinone ring. Most of the steps give good yields, and the synthesis of PEG–embelin conjugate involves a similar number of steps and cost as that of embelin alone.[27]

$PEG_{3.5K}$-EB_2 conjugate forms small-sized micelles (20–30 nm), and loading of PTX did not significantly affect the size of the micelles. It was generally believed that particles in the size range 100–200 nm can effectively penetrate solid tumors via an EPR effect.[6] A recent study from Lam's group compared the passive targeting of nanoparticles of different sizes in a subcutaneous model of human ovarian cancer xenograft. It was shown that particles with a size of 154 nm were significantly taken up by liver and lungs with limited accumulation at tumor sites. In contrast, particles with respective size of 17 and 64 nm were much more effective in passive targeting to the solid tumor.[33] Cabral and colleagues compared the targeting efficiency of polymeric micelles of different sizes (30, 50, 70, and 100 nm) in both highly and poorly permeable tumors. While all of the tested polymer micelles penetrated highly permeable tumors in mice, only the 30 nm micelles could penetrate poorly permeable pancreatic tumors to achieve an antitumor effect.[34] The small size of our new micelle system suggests its potential for effective tumor

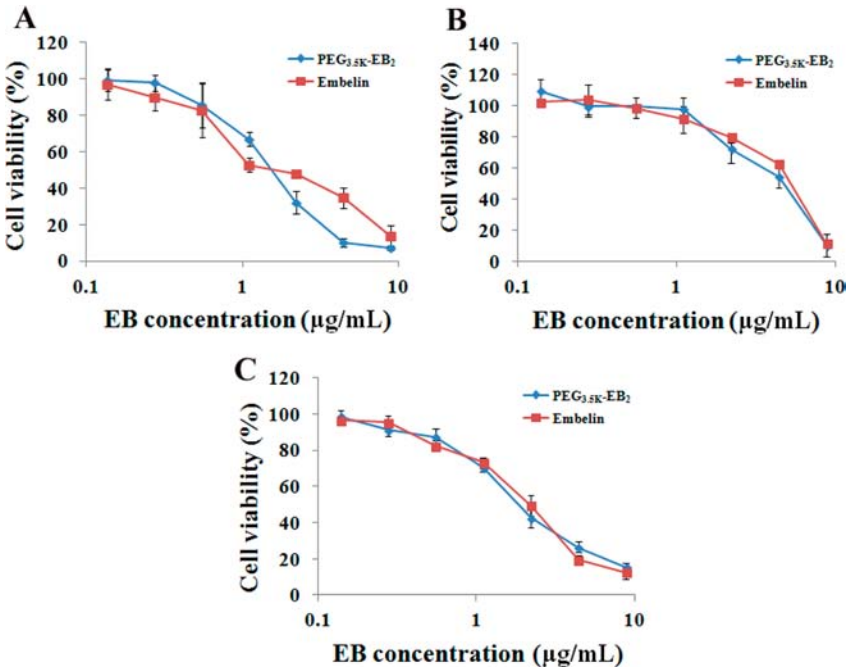


Figure 4. Cytotoxicity of free EB and $PEG_{3.5K}$-EB_2 against the 4T1 mouse breast cancer cell line (A) and two androgen-independent human prostate cancer cell lines PC-3 (B) and DU145 (C). Cells were treated by free EB or $PEG_{3.5K}$-EB_2 for 72 h under the equivalent concentrations of EB. Cytotoxicity was determined by MTT assay.

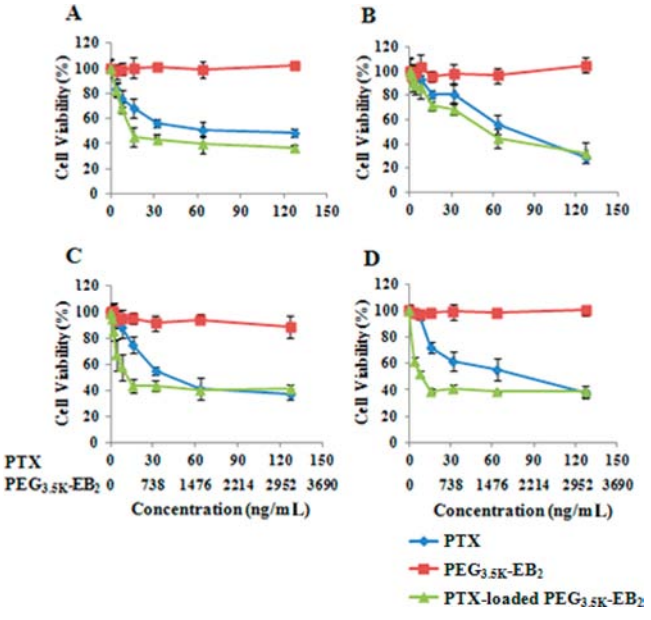


Figure 5. Cytotoxicity of free PTX, free $PEG_{3.5K}$-EB_2, and PTX-loaded $PEG_{3.5K}$-EB_2 (1/5, m/m) nanoparticles against the MDA-MB-231 human breast cancer cell line (A), the 4T1 mouse breast cancer cell line (B), and two androgen-independent human prostate cancer cell lines PC-3 (C) and DU145 (D). Cells were treated with free or formulated PTX for 72 h and cytotoxicity was determined by MTT assay.

targeting in vivo, which is currently being evaluated in our laboratory.

In vitro cytotoxicity with several cancer cell lines showed that $PEG_{3.5K}$-EB_2 is comparable to free embelin in antitumor activity with IC_{50} in the low micromolar range. More importantly, $PEG_{3.5K}$-EB_2 synergizes with PTX in antitumor activity at much lower concentrations (~nM) in all 4 cancer cell lines tested.

Table 3. IC_{50} of PTX and PTX-Loaded $PEG_{3.5K}$-EB_2 (1/5, m/m) after 72 h Incubation with Different Cancer Cell Lines

	IC_{50}[a] (ng/mL)			
	MDA-MB-231	4T1	PC-3	DU145
PTX-loaded $PEG_{3.5K}$-EB_2	13.5	51	12.7	8.9
PTX	65	73	42.3	78

[a]The concentration of a drug that is required for 50% inhibition in vitro.

The $PEG_{3.5K}$-EB_2-mediated cytotoxicity is unlikely attributed to its surface activity, as $PEG_{3.5K}$-EB_2 showed minimal hemolytic activity even at mM concentrations (Figure 3). Embelin is coupled to PEG via a cleavable ester linkage. It is likely that embelin is released from the conjugate following intracellular delivery and executes the antitumor effect by itself or synergizes with PTX in antitumor activity. These data are consistent with the observation that free embelin synergizes with PTX at subeffective doses (Figure S4). More studies are needed to better understand the mechanism by which the $PEG_{3.5K}$-EB_2-based delivery system synergizes with PTX in vitro.

It should be noted that $PEG_{3.5K}$-EB_2 conjugate only represents a model micelle to demonstrate the utility of PEG-derivatized embelin as a dual functional delivery system for hydrophobic anticancer drugs. Considering the flexibility of our synthesis scheme, more studies on structure–activity relationship (SAR) can be designed to further improve this new delivery system. These include optimization of the molar ratio of PEG/embelin in the conjugates, the length and structure of the acyl chain in the embelin, and the molecular weight of PEG. Recently, embelin derivatives with improved affinity toward XIAP have been developed.[27] The utility of these new derivatives as drug carriers can also be examined and compared to native embelin. Finally, promising candidates identified from these studies need to be further evaluated in vivo. These studies are currently ongoing in our laboratory.

dx.doi.org/10.1021/bc3000468 | Bioconjugate Chem. 2012, 23, 1443–1451

■ ASSOCIATED CONTENT

Supporting Information

HPLC trace, ^{1}H NMR spectra, and MALDI-TOF of $PEG_{3.5K}$-EB_2, and the cytotoxicity of embelin, PTX, and the combination of embelin and PTX against human prostate cancer cells DU145. This material is available free of charge via the Internet at http://pubs.acs.org.

■ AUTHOR INFORMATION

Corresponding Author

*Tel: 412-383-7976. Fax: 412-648-1664. E-mail: sol4@pitt.edu.

Author Contributions

#Authors contributed equally to this work.

Notes

The authors declare no competing financial interest.

■ ACKNOWLEDGMENTS

This work was supported in part by NIH grants R21CA128415 and R21CA155983, and a DOD grant BC09603. We would like to thank Dr. Gong Chen at Penn State University for critical reading of this manuscript.

■ REFERENCES

(1) Paál, K., Müller, J., and Hegedûs, L. (2001) High affinity binding of paclitaxel to human serum albumin. *Eur. J. Biochem. 268*, 2187−2191.

(2) Xie, Z., Guan, H., Chen, X., Lu, C., Chen, L., Hu, X., Shi, Q., and Jing, X. (2007) A novel polymer-paclitaxel conjugate based on amphiphilic triblock copolymer. *J. Controlled Release 117*, 210−216.

(3) Torchilin, V. P. (2007) Micellar nanocarriers: pharmaceutical perspectives. *Pharm. Res. 24*, 1−16.

(4) Sutton, D., Nasongkla, N., Blanco, E., and Gao, J. (2007) Functionalized micellar systems for cancer targeted drug delivery. *Pharm. Res. 24*, 1029−1046.

(5) Mi, Y., Liu, Y., and Feng, S. S. (2011) Formulation of docetaxel by folic acid-conjugated D-a-tocopheryl polyethylene glycol succinate 2000 (Vitamin E $TPGS_{2k}$) micelles for targeted and synergistic chemotherapy. *Biomaterials 32*, 4058−4066.

(6) Matsumura, Y., and Maeda, H. (1986) A new concept for macromolecular therapeutics in cancer chemotherapy: mechanism of tumouritropic accumulation of proteins and the antitumour agent smancs. *Cancer Res. 46*, 6387−6392.

(7) Gao, Z., Lukyanov, A. N., Singhal, A., and Torchilin, V. P. (2002) Diacyllipid-polymer micelles as nanocarriers for poorly soluble anticancer drugs. *Nano Lett. 2*, 979−982.

(8) Croy, S. R., and Kwon, G. S. (2006) Polymeric micelles for drug delivery. *Curr. Pharm. Des. 12*, 4669−4684.

(9) Dong, Y., and Feng, S. S. (2005) Poly(d,l-lactide-co-glycolide)/montmorillonite nanoparticles for oral delivery of anticancer drugs. *Biomaterials 30*, 6068−6076.

(10) Zhang, Z., and Feng, S. S. (2006) Nanoparticles of poly(lactide)/vitamin E TPGS copolymer for cancer chemotherapy: synthesis, formulation, characterization and in vitro drug release. *Biomaterials 27*, 262−270.

(11) Zhang, Z., Lee, S. H., Gan, C. W., and Feng, S. S. (2008) In vitro and in vivo investigation on PLA-TPGS nanoparticles for controlled and sustained small molecule chemotherapy. *Pharm. Res. 8*, 1925−1935.

(12) Prashant, C., Dipak, M, Yang, C. T., Chuang, K. H., Jun, D., and Feng, S. S. (2010) Superparamagnetic iron oxide--loaded poly(lactic acid)-D-alpha-tocopherol polyethylene glycol 1000 succinate copolymer nanoparticles as MRI contrast agent. *Biomaterials 31*, 5588−5597.

(13) Ji, X., Wang, Z., Geamanu, A., Sarkar, F. H., and Gupta, S. V. (2011) Inhibition of cell growth and induction of apoptosis in non-small cell lung cancer cells by delta-tocotrienol is associated with notch-1 down-regulation. *J. Cell. Biochem. 112*, 2773−2783.

(14) Husain, K., Francois, R. A., Yamauchi, T., Perez, M., Sebti, S. M., and Malafa, M. P. (2011) Vitamin E δ-Tocotrienol augments the antitumor activity of gemcitabine and suppresses constitutive NF-κB activation in pancreatic cancer. *Mol. Cancer Ther. 10*, 2363−2372.

(15) Chitra, M., Sukumar, E., Suja, V., and Devi, C. S. (1994) Antitumor, anti-inflammatory and analgesic property of embelin, a plant product. *Chemotherapy 40*, 109−113.

(16) Bhandari, U., Jain, N., and Pillai, K. K. (2007) Further studies on antioxidant potential and protection of pancreatic beta-cells by Embelia ribes in experimental diabetes. *Exp. Diabetes Res. 2007*, 15803−15808.

(17) Singh, D., Singh, R., Singh, P., and Gupta, R. S. (2009) Effect of embelin on lipid peroxidation and free radical scavenging activity against liver damage in rats. *Basic Clin. Pharmacol. Toxicol. 105*, 243−248.

(18) Danquah, M., Li, F., Duke, C. B., Miller, D. D., and Mahato, R. I. (2009) Micellar delivery of bicalutamide and embelin for treating prostate cancer. *Pharm. Res. 26*, 2081−2092.

(19) Sreepriya, M., and Bali, G. (2005) Chemopreventive effects of embelin and curcumin against N-nitrosodiethylamine/phenobarbital-induced hepatocarcinogenesis in Wistar rats. *Fitoterapia 76*, 549−555.

(20) Dai, Y., Qiao, L., Chan, K. W., Yang, M., Ye, J., Ma, J., Zou, B., Gu, Q., Wang, J., Pang, R., Lan, H. Y., and Wong, B. C. (2009) Peroxisome proliferator-activated receptor-gamma contributes to the inhibitory effects of Embelin on colon carcinogenesis. *Cancer Res. 69*, 4776−4783.

(21) Heo, J. Y., Kim, H. J., Kim, S. M., Park, K. R., Park, S. Y., Kim, S. W., Nam, D., Jang, H. J., Lee, S. G., Ahn, K. S., Kim, S. H., Shim, B. S., Choi, S. H., and Ahn, K. S. (2011) Embelin suppresses STAT3 signaling, proliferation, and survival of multiple myeloma via the protein tyrosine phosphatase PTEN. *Cancer Lett. 308*, 71−80.

(22) Nikolovska-Coleska, Z., Xu, L., Hu, Z., Tomita, Y., Li, P., Roller, P. P., Wang, R., Fang, X., Guo, R., Zhang, M., Lippman, M. E., Yang, D., and Wang, S. (2004) Discovery of embelin as a cell-permeable, small-molecular weight inhibitor of XIAP through structure-based computational screening of a traditional herbal medicine three-dimensional structure database. *J. Med. Chem. 47*, 2430−2440.

(23) Tamm, I., Kornblau, S. M., Segall, H., Krajewski, S., Welsh, K., Kitada, S., Scudiero, D. A., Tudor, G., Qui, Y. H., Monks, A., Andreeff, M., and Reed, J. C. (2000) Expression and prognostic significance of IAP-family genes in human cancers and myeloid leukemias. *Clin. Cancer Res. 6*, 1796−1803.

(24) Holcik, M., Gibson, H., and Korneluk, R. G. (2001) XIAP: apoptotic brake and promising therapeutic target. *Apoptosis 6*, 253−261.

(25) Ahn, K. S., Sethi, G., and Aggarwal, B. B. (2007) Embelin, an inhibitor of X chromosome-linked inhibitor-of-apoptosis protein, blocks nuclear factor-kappaB (NF-kappaB) signaling pathway leading to suppression of NF-kappaB-regulated antiapoptotic and metastatic gene products. *Mol. Pharmacol. 71*, 209−219.

(26) La, S. B., Okano, T., and Kataoka, K. (1996) Preparation and characterization of the micelle-forming polymeric drug indomethacin-incorporated poly(ethylene oxide)-poly(beta-benzyl L-aspartate) block copolymer micelles. *J. Pharm. Sci. 85*, 85−90.

(27) Chen, J., Nikolovska-Coleska, Z., Wang, G., Qiu, S., and Wang, S. (2006) Design, synthesis, and characterization of new embelin derivatives as potent inhibitors of X-linked inhibitor of apoptosis protein. *Bioorg. Med. Chem. Lett. 16*, 5805−5808.

(28) Kabanov, A. V., Nazarova, I. R., Astafieva, I. V., Batrakova, E. V., Alakhov, V. Y., Yaroslavov, A. A., and Kabanov, V. A. (1995) Micelle formation and solubilization of fluorescent probes in poly-(oxyethylene-b-oxypropylene-b-oxyethylene) solutions. *Macromolecules 28*, 2303−2314.

(29) Reul, R., Nguyen, J., and Kissel, T. (2009) Amine-modified hyperbranched polyesters as non-toxic, biodegradable gene delivery systems. *Biomaterials 30*, 5815−5824.

(30) Li, G., Liu, J., Pang, Y., Wang, R., Mao, L., Yan, D., Zhu, X., and Sun, J. (2011) Polymeric micelles with water-insoluble drug as

hydrophobic moiety for drug delivery. *Biomacromolecules 12*, 2016−2026.
(31) Tang, N., Du, G., Wang, N., Liu, C., Hang, H., and Liang, W. (2007) Improving penetration in tumors with nanoassemblies of phospholipids and doxorubicin. *J. Natl. Cancer Inst. 99*, 1004−1015.
(32) Kumar, G, K., Dhamotharan, R., Kulkarni, N. M., Honnegowda, S., and Murugesan, S. (2011) Embelin ameliorates dextran sodium sulfate-induced colitis in mice. *Int. Immunopharmacol. 11*, 724−731.
(33) Luo, J., Xiao, K., Li, Y., Lee, J. S., Shi, L., Tan, Y. H., Xing, L., Cheng, R. H., Liu, G. Y., and Lam, K. S. (2010) Well-defined, size-tunable, multifunctional micelles for efficient paclitaxel delivery for cancer treatment. *Bioconjugate Chem. 21*, 1216−1224.
(34) Cabral, H., Matsumoto, Y., Mizuno, K., Chen, Q., Murakami, M., Kimura, M., Terada, Y., Kano, M. R., Miyazono, K., Uesaka, M., Nishiyama, N., and Kataoka, K. (2011) Accumulation of sub-100 nm polymeric micelles in poorly permeable tumours depends on size. *Nat. Nanotechnol. 6*, 815−823.

Bioconjugate Chemistry

Article

pubs.acs.org/bc

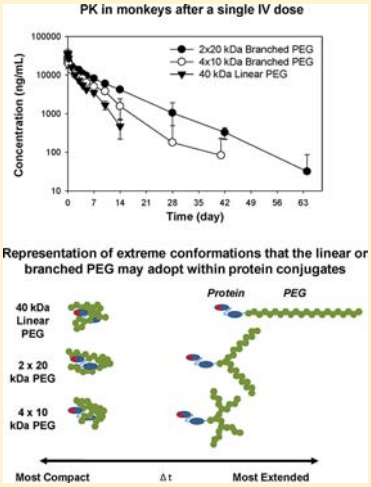
Pharmacokinetic, Biodistribution, and Biophysical Profiles of TNF Nanobodies Conjugated to Linear or Branched Poly(ethylene glycol)

Yulia Vugmeyster,*[,†] Clifford A. Entrican,[‡] Alison P. Joyce,[†] Rosemary F. Lawrence-Henderson,[†] Beth A. Leary,[†] Christopher S. Mahoney,[‡] Himakshi K. Patel,[‡] Stephen W. Raso,[‡] Stephane H. Olland,[∥] Martin Hegen,[§] and Xin Xu[†,#]

[†]Department of Pharmacokinetics, Dynamics, and Metabolism and [‡]Department of Analytical Research & Development, Pfizer Inc., Andover, Massachusetts, United States

[§]Department of Immunology and Autoimmunity and [∥]Department of Global Biotherapeutics Technologies, Pfizer Inc., Cambridge, Massachusetts, United States

ABSTRACT: Covalent attachment of poly(ethylene glycol) (PEG) to therapeutic proteins has been used to prolong *in vivo* exposure of therapeutic proteins. We have examined pharmacokinetic, biodistribution, and biophysical profiles of three different tumor necrosis factor alpha (TNF) Nanobody−40 kDa PEG conjugates: linear 1 × 40 KDa, branched 2 × 20 kDa, and 4 × 10 kDa conjugates. In accord with earlier reports, the superior PK profile was observed for the branched versus linear PEG conjugates, while all three conjugates had similar potency in a cell-based assay. Our results also indicate that (i) a superior PK profile of branched versus linear PEGs is likely to hold across species, (ii) for a given PEG size, the extent of PEG branching affects the PK profile, and (iii) tissue penetration may differ between linear and branched PEG conjugates in a tissue-specific manner. Biophysical analysis (R_g/R_h ratio) demonstrated that among the three protein−PEG conjugates the linear PEG conjugate had the most extended time-average conformation and the most exposed surface charges. We hypothesized that these biophysical characteristics of the linear PEG conjugate accounts for relatively less optimal masking of sites involved in elimination of the PEGylated Nanobodies (e.g., intracellular uptake and proteolysis), leading to lower *in vivo* exposure compared to the branched PEG conjugates. However, additional studies are needed to test this hypothesis.



INTRODUCTION

Covalent attachment of poly(ethylene glycol) (PEG) to therapeutic proteins has been used to extend the half-life and prolong *in vivo* exposure of therapeutic proteins.[1] The pharmacokinetic (PK) and pharmacodynamic (PD) profiles of a PEGylated protein can be affected by a number of factors, such as the site of PEG attachment, the molecular weight (MW) of the PEG used, the number of PEG molecules attached to a protein, and the stability of the protein−PEG bond (reviewed in refs 1−4). While more comprehensive analyses on the effect of bound PEG conjugate on protein structure remain to be conducted, most of the current data indicate that the secondary protein structure is unchanged upon PEG attachment.[5−7] In addition, it appears that the structural properties, such as hydrodynamic volume, of the protein−PEG conjugate in aqueous solutions are dominated by the structural properties of the PEG.[8]

For both the protein−PEG conjugate and the free PEG, MW of PEG molecule and/or the combined MW of the protein−PEG conjugate have been shown to have a significant impact on the PK profile and the major route of elimination.[9,10] Several mechanisms are likely to contribute to the effect of PEGylation on PK profiles of therapeutic proteins: reduction in renal clearance through increased overall MW, masking of the proteolytic sites on the therapeutic protein, and reduction of intracellular uptake (and subsequent intracellular proteolysis/catabolism) by masking recognition sites for specific and nonspecific processes (reviewed in refs 2−4). The ^{125}I-labeled PEG molecules with MW below 20 kDa (with no attached protein moiety) have been shown to be cleared primarily through the kidney.[9] For ^{125}I-labeled PEG molecules with MW above 20 kDa, the contribution of renal filtration decreases and the contribution of biliary excretion increases, and above a MW of ∼50 kDa, hepatobiliary clearance is the major route of elimination, with increase in ^{125}I-PEG uptake by liver Kupffer cells.[9,10]

Both the linear and the branched PEGs have been used to improve circulating half-lives of therapeutic proteins (reviewed in refs 3,4). Several case studies describe improved exposure (AUC) and circulating half-lives for a branched protein−PEG conjugate compared to a linear PEG conjugate of the same or similar total PEG MW in single dose mouse or rabbit PK studies.[11,12] It remains to be established whether the differences in PK profiles for branched versus linear protein−PEG

Received: February 9, 2012
Revised: May 29, 2012
Published: June 25, 2012

 © 2012 American Chemical Society

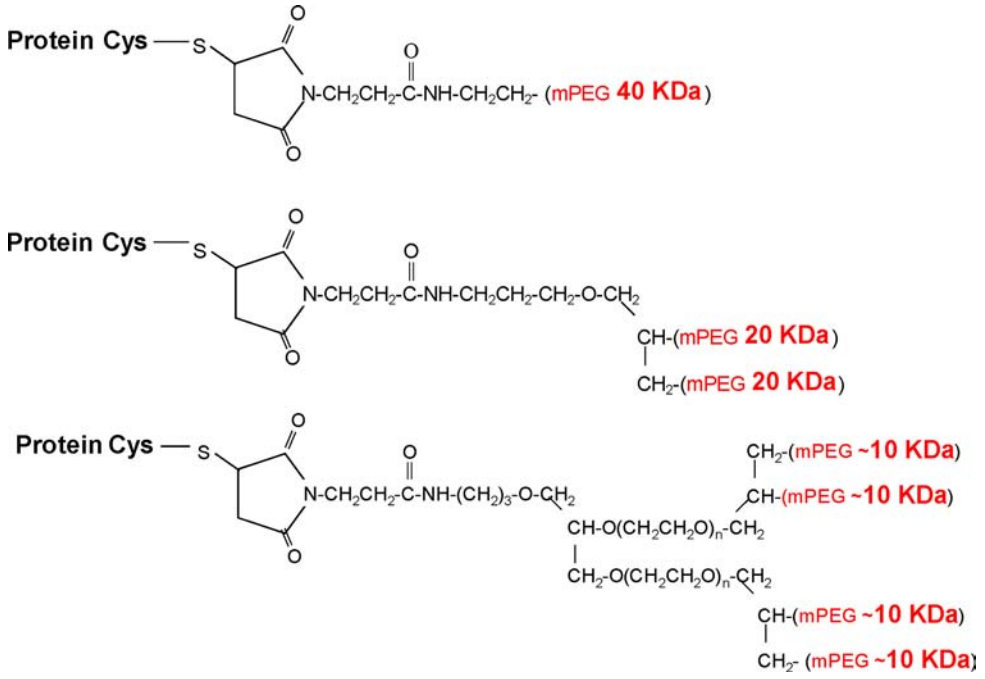


Figure 1. Structures for TNF Nanobody PEG conjugates. The C-terminal cysteine of the TNF Nanobody was conjugated to linear 1 × 40 kDa (A), branched 2 × 20 kDa (B), or branched 4 × 10 kDa (C) methoxy-poly(ethylene glycol) (mPEG)-malemide.

conjugates is a consistent phenomenon that holds across the different types of proteins and different PEG sizes/types and degree of branching, as well as across species including primates. In addition, differences in biodistribution for a linear versus branched protein−PEG conjugate remains to be examined.

The possible cause for these differences in PK profiles between the linear and branched PEG conjugates of the same MW is disputed. Proposed explanations include differences in hydrodynamic volume (for the protein−PEGs conjugates of MW both below and well above the postulated glomerular filtration cutoff); differences in conformational flexibility leading to difference in diffusion rates through the membrane pore; masking of the protein surface resulting in a reduced proteolysis rate; and differences in clearance by the immune system.[12−14] It is likely that the size/type of PEG conjugate, as well as protein moiety of the conjugate and the site of conjugation, would contribute to a certain set of characteristics that could result in different PK profiles for branched versus linear PEGs. Likewise, the optimal degree of branching for different types/sizes of PEGs remains to be examined and also likely varies for different therapeutic proteins.

In this study, we compare PK profiles of 1 × 40 kDa linear, 2 × 20 kDa branched, and 4 × 10 kDa branched protein−PEG conjugates in mice, rats, and cynomolgus monkeys and the biophysical characteristics of these protein−PEG conjugates. We also assess biodistribution of the linear versus branched PEG conjugates in mice.

The protein moiety used for this study is a bivalent antihuman tumor necrosis factor alpha (TNF) Nanobody (protein molar mass of ~27 kDa) that cross-reacts with cynomolgus monkey but not mouse or rat TNF.[15] The TNF Nanobody−PEG conjugates are being considered as possible agents to treat autoimmune disorders, such as rheumatoid arthritis (RA).[16] The target contribution to the disposition of these biotherapeutics in normal subjects is likely to be minimal at the dose levels examined and, thus, PK optimization efforts were focused on the PEG moiety.

EXPERIMENTAL PROCEDURES

Test Articles. TNF Nanobody, a 27 kDa protein comprising of two anti-human TNF specific humanized llama V_{HH} domains, was produced at Pfizer, Inc. using stable Chinese hamster ovary (CHO) cell lines.[15] The engineered C-terminal cysteine of the TNF Nanobody was conjugated to the branched 2 × 20 kDa, branched 4 × 10 kDa, or linear 1 × 40 kDa methoxy-poly(ethylene glycol) (mPEG)-malemide (abbreviated as "PEG"; obtained from NOF American Corporation (White Plains, New York); Figure 1). Specifically, after protein A affinity chromatography the engineered cysteine of the purified protein was uncapped with a 10 mM DTT treatment. A buffer exchange by G-25 Sephadex gel filtration removed the reducing agent, and the protein was then immediately PEGylated with a 2−10-fold molar excess of maleimide activated PEG for 1 h at 25 °C. The pH of the crude reaction mix was adjusted down below the pI of the protein and the mixture was loaded on a cation exchange column. After developing a linear NaCl gradient and eluting the PEGylated Nanobody, it was further purified by size exclusion chromatography in PBS. The fractions of over 99% purity were pooled and concentrated via Amicon Stirred Cell (10 kD MWCO, PES).

After PEGylation, all materials predominantly consisted of the TNF Nanobody covalently linked to a single 40 kDa PEG. Depending on the preparation, the main peak (representing the PEGylated Nanobody) ranged from 86.8% to 99%, determined by size exclusion HPLC; 83.3−96.8% determined by capillary electrophoresis-sodium dodecyl sulfate; and 77.0−98.3% determined by reverse-phase HPLC with low level of high and low molecular weight species (data not shown). Under physiological conditions (37 °C), no cleavage of PEG moiety from the conjugate was detected.

Bioactivity. U937 cells (a human monocyte cell, ATCC, 1.875×10^5 cells/mL in 96-well plate resuspended in the assay media) were incubated for 2 h at 37 °C, 5%CO_2 with 1 ng/mL TNFα (R&D Systems) in the presence of a TNF inhibitor (in a dilution series from 9 to 0.3 ng/mL). The assay media used for the bioassay was RPMI (no phenol red) supplemented with 10% fetal bovine serum, 2% penicillin/streptomycin, 2 mM L-glutamine, 25 mM Hepes buffer, 1 mM sodium pyruvate, and 0.25% glucose. The apoptotic activity was measured by the Caspase-Glo 3/7 luminescence assay, with modifications to the manufacturer's instructions (Promega). This assay measures caspase-3/7 activities which occur early in apoptosis. The luminescent data were fitted with a four-parameter logistic equation (Microsoft *Excel* software) to estimate IC_{50}, and the bioactivity (IC_{50} relative to that of the PEGylated reference material) was calculated for each protein−PEG conjugate and unPEGylated protein.

Iodination Procedure and Preparation of ^{125}I-Labeled Dosing Solutions. Iodination was performed by the IODOBEADS method according to manufacturer's instructions (Pierce, Rockford, IL), using ∼0.2 mg of PEGylated proteins and 2 mCi of 125-iodine (Perkin-Elmer; Waltham, MA). A dosing solution was prepared by mixing unlabeled test article, a trace amount of ^{125}I-labeled test article, and the formulation buffer. Dosing solutions were characterized by gamma-counting of trichloroacetic acid-precipitable radioactivity and gel electrophoresis, as previously described.[17] In rat PK studies, the specific activity of radiolabeled proteins ranged from 37 to 62 μCi/mg (with <4.2% free iodine), and the final protein concentration was 1 mg/mL. In mouse biodistribution studies, the specific activity ranged from 771 to 807 μCi/mg (with <3.8% free iodine), and the final protein concentration was 0.075 mg/mL.

Animals. Mice (male B6CBAF1/J) and rats (male Sprague−Dawley with two jugular vein catheters) were obtained from Jackson Laboratory (Bar Harbor, ME) and Taconic Farms (Germantown, NY), respectively. Adult male cynomolgus monkeys (with no prior exposure to human proteins) were housed at Pfizer, Inc. (Pearl River, NY or Chazy, NY). Animals used in PK studies were not fasted. The Pfizer (formerly Wyeth) Animal Care and Use Committee approved all aspects of animal studies.

PK Study Design. Test articles (unlabeled for mice and monkeys and ^{125}I-labeled for rats) were administered as a single IV bolus dose into the tail vein, jugular vein via catheter, or saphenous vein for mice, rats, and monkeys, respectively. Rats were given water containing KI (20 mM) for 3 days prior to dosing. The dose was based on the most recent body weights prior to dosing. The dosing volume was 4−5 mL/kg for mice and 1 mL/kg for rats and monkeys in formulation buffer containing 10 mM L-histidine, 5% sucrose, pH 6.0. For PK studies, nonserial sampling was used for mice (n = 3 per time point), and serial sampling was used for rat (n = 5−7 per test article, as specified in Table 3) and monkeys (n = 3 per test article). Serum samples for determination of test article concentrations were collected during the 5 min to 14 day period in mice, 5 min to 24 day period in rats, and 5 min to 56−62 day period in monkeys (as specified in Table 4).

Biodistribution Study Design. Mice were given water containing KI (20 mM) for 3 days prior to dosing, and the dosing solution was administered as a single IV bolus dose into the tail vein (at a volume of 3 mL/kg to result in a 0.3 mg/kg dosage). After a whole body perfusion with heparinized (25 U/mL) PBS, tissue (fat, heart, kidney, liver, lung, muscle, skin, spleen, and stomach) and serum samples were taken at 1, 24, 48, 168 h (7 day) postdose (n = 12 for 168 h and n = 8 for other time points). Additional serum samples were taken via retro-orbital bleeding at 5 min, 6 h, and 72 h. Urine was collected over the 7 day period. Tissue weights and total urine volumes were recorded for each sample.

Determination of Test Article Concentrations. When ^{125}I-labeled test articles were used (rat PK and mouse biodistribution studies), radioactive equivalent (RE) concentrations in serum and tissues were determined by gamma-counting based on trichloroacetic acid precipitable and total counts, respectively, as described previously.[17] Total and trichloroacetic acid precipitable urine counts were also determined, using a previously described approach.[17] In mouse and monkey PK studies, serum concentrations were determined using enzyme linked immunosorbent assays (ELISA). A test article was captured by biotinylated TNF and was detected with a rabbit polyclonal anti-serum that recognizes the protein portion of the PEGylated TNF Nanobody. The goat anti-rabbit immunoglobulin horseradish peroxidase and the enzyme substrate, 3′,5,5′-tetramethylbenzidine were used for the colorimetric readout at 450 nm. Sample concentrations were determined by interpolation from a calibration curve that was fit using a four-parameter logistic equation (*Softmax Pro* v 4.3.1, Molecular Devices, and *Watson LIMS* v 7.0.0.01, Thermo Electron Corporation). The lower limit of quantitation ranged from ∼49 to 83 ng/mL.

PK Calculations. PK parameters were calculated based on individual animal concentrations for rats and monkeys and sparse sampling method for mice using noncompartmental analysis (*WinNonlin* software, Pharsight, Inc., St. Louis, MO; model 201 for serum and model 200 for tissues). The area under the serum concentration versus time curve (AUC) was calculated using the linear trapezoidal method. The slope of the apparent terminal phase was estimated by log−linear regression using at least 3 data points, and the terminal rate constant (λ) was derived from the slope. $AUC_{0\text{-}\infty}$ was estimated as the sum of the $AUC_{0\text{-last}}$ (where t = last is the time of the last measurable concentration) and C_{last}/λ. The apparent terminal half-life ($t_{1/2}$) was calculated as $0.693/\lambda$.

Statistical Analyses. All statistical analyses were conducted using *Prism 5* software package (GraphPad Software, Inc.), and $p < 0.05$ was assumed for statistical significance. For PK studies (three test articles), analyses were performed using ANOVA with Dunnett's post test, with the linear 1 × 40 kDa PEG group as the control. Specifically, for rat and monkey PK studies, the mean $AUC_{0\text{-}\infty}$, $AUC_{0\text{-}\infty}$/Dose, CL, Vd_{ss}, and $t_{1/2}$ values were analyzed, while for mouse PK studies (sparse sampling), only mean AUC_{last} values were analyzed. For mouse biodistribution studies (2 test articles, sparse sampling), the statistical analyses of mean serum and tissues $AUC_{0-168\ h}$ values were performed using unpaired t test.

Cation Exchange High Performance Liquid Chromatography. Prior to cation exchange−HPLC analysis, the protein concentration of each material was adjusted to 1.0 mg/mL with formulation buffer; 10 μL was injected onto a Dionex ProPac WCX-10 column using a Waters Alliance 2690 system. Mobile phase A was 10 mM ammonium formate, pH 4.0. Mobile phase B was 10 mM ammonium formate, 500 mM sodium chloride, pH 4.0. Protein was eluted at a flow rate of 0.75 mL/min with a linear gradient of sodium chloride (0−40% B in 40 min). Absorbance at 280 nm was monitored.

Size Exclusion High Performance Liquid Chromatography with Multi-Angle Light Scattering (SEC-MALS). Size and conformational analysis was completed using SEC-MALS. All samples were analyzed using a Waters Alliance 2695 separations module. Size and mass were determined from data measured by a Waters 2489 UV absorbance detector, Wyatt Technologies, Inc. HELEOS II multiangle light scattering detector and a Wyatt Technologies, Inc. rEX differential refractometer. The MALS detector was equipped with an in-line quasi-elastic light-scattering (QELS) detector, also from Wyatt Technologies Inc. The samples were fractionated by a Superose 6 10/300 GL size-exclusion column from GE Healthcare (PN: 17−5172−01) in a mobile phase consisting of 20 mM sodium phosphate, 400 mM sodium chloride, pH 7.2, filtered with a 0.02 μm cellulose acetate filter.

Determination of Molar Mass, Hydrodynamic Radii (R_h), and Root Mean Squared Radii (rms or R_g). All molar mass and rms radii were calculated from the MALS data using *ASTRA V* v 5.3.4.14 (Wyatt Technologies, Inc.). The protein conjugate analysis was performed using an application embedded in the *ASTRA* software. The hydrodynamic radii were determined from data obtained from the quasi-elastic light-scattering detector and calculated with an autocorrelater function embedded in the *ASTRA* software.

RESULTS

Bioactivity. All three conjugates and the unPEGylated protein had ≥92% bioactivity, relative to the reference material in the cell-based bioassay (Table 1), suggesting that the PEGylation did not alter the activity of the protein.

Table 1. Biological Activity of PEGylated TNF Nanobodies in the Cell-Based Assay[a]

Ccnstruct	% activity
TNF Nanobody (not PEGylated)	100
TNF Nanobody_branched 2 × 20 kDa PEG	95
TNF Nanobody_branched 4 × 10 kDa PEG	92
TNF Nanobody_linear 1 × 40 kDa PEG	108

[a]U937 cells were incubated for 2 h with TNF in the presence of a TNF Nanobody. The TNF-induced apoptosis was measured by the Caspase-Glo 3/7 luminescence assay (Promega) and the IC_{50} was determined. The bioactivity (IC_{50}) of all the PEG−conjugates and un-PEGylated protein are presented relative to that of the PEGylated reference material. Data show mean of 2 experiments for each test article.

Serum Pharmacokinetics. Serum PK profiles of TNF Nanobody_branched 2 × 20 kDa PEG, TNF Nanobody_branched 4 × 10 kDa PEG, and TNF Nanobody_linear 1 × 40 kDa PEG constructs were examined in B6CBAF1/J mice, Sprague−Dawley rats, and cynomolgus monkeys following a single IV administration of 2 or 3 mg/kg (based on protein content). Serum concentrations were determined using either specific ELISA (mice and monkeys) or gamma-counting (rats).

In all three species examined, the branched 2 × 20 kDa PEG construct had significantly higher exposure (AUC) compared to the linear 1 × 40 kDa PEG construct ($p < 0.05$) (Figure 2 and Tables 2−4). Specifically, the relative increase in mean dose-normalized $AUC_{0-\infty}$ for the branched 2 × 20 kDa PEG construct relative to the linear 1 × 40 kDa PEG construct was ∼94%, 102%, and 136% in mice, rats, and monkeys, respectively. Accordingly, the total body clearance (CL) of the branched 2 × 20 kDa PEG construct was lower and elimination half-life ($t_{1/2}$) of the branched 2 × 20 kDa PEG appeared longer compared to the linear 1 × 40 kDa PEG construct. Specifically, the relative decrease in mean CL value for the branched 2 × 20 kDa PEG construct was ∼48%, 50%, and 66% in mice, rats, and monkeys, respectively, and the relative increase in mean $t_{1/2}$ values was 43%, 26%, and 54% in mice, rats, and monkeys, respectively.

The branched 4 × 10 kDa PEG construct also had higher mean serum $AUC_{0-\infty}$ and lower CL, compared to the linear 1 × 40 kDa PEG construct in rats and monkeys, but not in mice (Tables 2−4). In rats and monkeys, the magnitude of change in PK parameters for the branched 4 × 10 kDa PEG construct relative to the linear construct were less pronounced (43−51% increase in $AUC_{0-\infty}$ and 35−45% decrease in CL), compared to those for the branched 2 × 20 kDa PEG construct.

Biodistribution. Biodistribution of TNF Nanobody_branched 2 × 20 kDa PEG and TNF Nanobody_linear 1 × 40 kDa PEG constructs were examined over 7 days (168 h) in B6CBAF1/J mice following a single IV dose of 0.3 mg/kg (based on protein content) of ^{125}I-labeled test articles. Radioactive equivalent (RE) serum and tissue concentrations were determined using gamma-counting, serum, and tissue exposures ($AUC_{0-168\ h}$), and tissue-to-serum (T/S) AUC ratios were calculated.

Similar to the observation in the earlier study in B6CBAF1/J mice with nonradiolabeled PEG conjugates, the branched 2 × 20 kDa PEG construct had ∼80% higher $AUC_{0-168\ h}$ ($p < 0.05$), compared to the linear 1 × 40 kDa construct (Figure 3). The branched construct also had significantly higher exposures in some but not all tissues examined (Figure 3). Specifically, the increase in $AUC_{0-168\ h}$ for the branched 2 × 20 kDa PEG construct relative to the linear 1 × 40 kDa PEG construct was 72%, 115%, 43%, 55%, and 80% in heart, lung, muscle, skin, and stomach, respectively. T/S AUC ratios (Table 5) and T/S concentration ratios (data not shown) were approximately similar between the two constructs for these tissues.

In contrast to serum, heart, lung, muscle, skin, and stomach, the $AUC_{0-168\ h}$ in fat, kidney, liver, and spleen were similar for the two constructs, leading to lower T/S AUC ratios (Table 5) and T/S concentration ratios (data not shown) for the branched 2 × 20 kDa PEG construct.

For both constructs, approximately 60% of total administered radioactivity was excreted in urine within 1 week (168 h) after dosing, with most of the radioactivity excreted in urine (approximately 70%) attributed to free iodine or small degradants.

Biophysical Analyses. To investigate potential reasons for differential PK profiles of three TNF Nanobody−40 kDa PEG conjugates, additional biophysical analyses were conducted.

The cation exchange-HPLC was performed to monitor the charge heterogeneity of the three constructs. The representative chromatographic profiles are presented in Figure 4. A significant amount of charge heterogeneity was observed for all PEGylated TNF Nanobody conjugates. The main peak of the linear PEG conjugate eluted at a later retention time when compared to the two branched conjugates (2 × 20 kDa and 4 × 10 kDa), suggesting that the linear conjugate has more exposed positive charges on the surface compared to the branched conjugates. The retention time of the main peak for the two branched conjugates (2 × 20 kDa and 4 × 10 kDa) was similar. By comparison, the unconjugated protein eluted much later

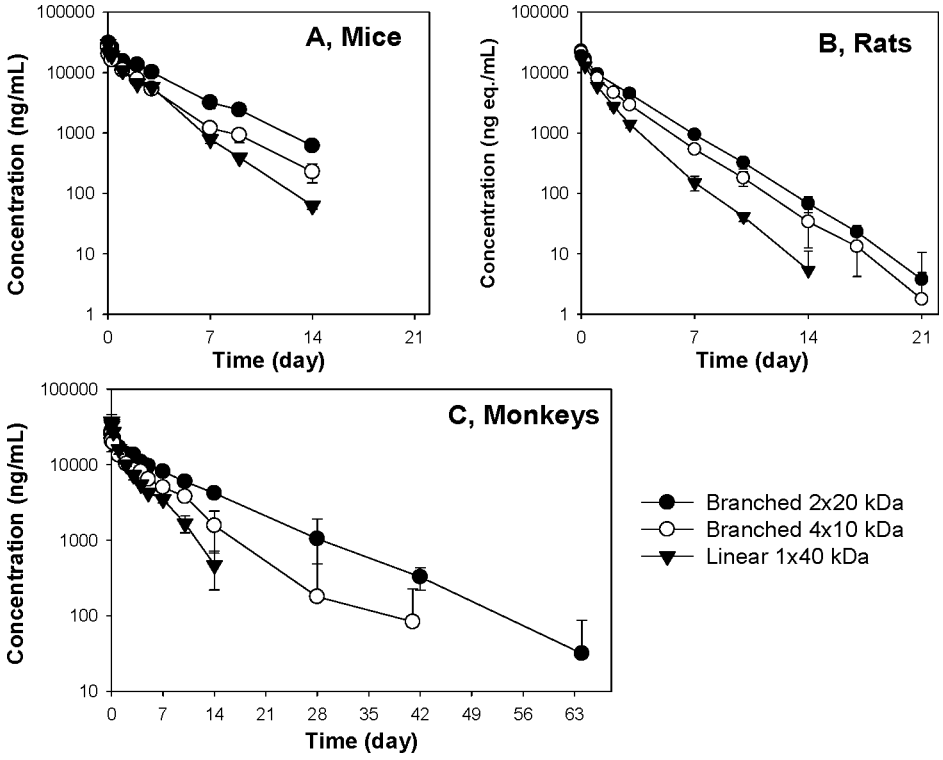


Figure 2. Mean (±SD) dose-normalized serum concentrations of PEGylated TNF Nanobodies after a single IV dose to mice, rats, or cynomolgus monkeys. TNF Nanobody_2 × 20 kDa PEG (filled circles), TNF Nanobody_4 × 10 kDa PEG (open circles), or TNF Nanobody_1 × 40 kDa PEG (filled triangles) were administered a single IV bolus dose to B6CBAF1/J mice (A: 2 mg/kg for the 2 × 20 kDa PEG conjugate and 3 mg/kg for the other two conjugates); Sprague–Dawley rats (B: 2 mg/kg), or cynomolgus monkeys (C: 3 mg/kg). For the mouse and monkey PK studies (A and C), unlabeled test articles were used, while for the rat PK studies (B), ^{125}I-labeled test articles were used. Nonserial sampling was used for mice (n = 3 per time point), and serial sampling was used for rat (n = 5–7 per compound) and monkeys (n = 3 per compound). Serum concentrations were determined by the specific immunoassays (mice and monkeys; in ng/mL) or gamma-counting (rats; in ng equiv/mL). In-life duration was 14, 24, and 56–62 days for mice, rats, and monkeys, respectively. Individual animal concentration values below the lower limit of quantitation were treated as zero for the calculations of the mean and SD. Data show mean (±SD) dose-normalized concentrations at each time point (i.e., for 1 mg/kg dose). Data points at which serum concentrations were below the lower limit of quantitation for all animals (mean of zero) are not shown on the logarithmic scale.

Table 2. Pharmacokinetic Parameters of PEGylated TNF Nanobodies after a Single IV Dose to B6CBAF1/J Mice[a]

construct	dose (mg/kg)	$C_{5\ min}$ (μg/mL)	$AUC_{0-\infty}$/dose (μg·h/mL)/(mg/kg)	AUC_{last}/dose (μg·h/mL)/(mg/kg)	CL (mL/h/kg)	Vd_{ss} (mL/kg)	$t_{1/2}$ (h)
TNF Nanobody_branched 2 × 20 kDa PEG	2	55	2179	2121 ± 61*	0.46	40	66
TNF Nanobody_branched 4 × 10 kDa PEG	3	80	1193	1174 ± 23	0.84	58	56
TNF Nanobody_linear 1 × 40 kDa PEG	3	89	1126	1122 ± 22	0.89	46	46

[a]Male B6CBAF1/J mice were administered a single IV bolus dose of the indicated test article. Serum samples were taken at 5 min to 14 days post dose once from each mouse (n = 3 per time point), and serum concentrations were determined by the specific ELISA. PK parameters were determined by noncompartmental analysis using the sparse sampling method and statistical analysis of AUC_{last}/dose values was performed using ANOVA with Dunnett's post test, with the linear 1 × 40 PEG group as the control. Star (*) indicates statistically significant differences (p < 0.05) relative to the linear PEG group.

than all of the PEGylated conjugates tested, indicating it has even greater positive surface charge density. The theoretical isoelectric point of the unconjugated protein is greater than 9; therefore, the protein is predicted to have a net positive charge in the cation exchange running buffers, which are at pH 4.0.

Size and mass distributions were determined using size exclusion-HPLC with MALS monitored by UV absorbance, differential refractometry (dRI), and online quasi-elastic light-scattering. Since the PEG on the TNF Nanobody–PEG conjugates does not absorb at 280 nm, it is possible to determine the distributions of protein and PEG in the conjugate using SEC-MALS with UV and dRI detection. The calculated protein and PEG mass distributions were consistent with each other for all 3 conjugates (Table 6 and Figure 5a,b).

The branched 4 × 10 kDa PEG conjugate had a noticeably later elution volume on the SEC-MALS than the branched 2 × 20 kDa and linear 1 × 40 kDa PEG conjugates, indicating that the branched 4 × 10 kDa PEG conjugate is hydrodynamically smaller compared to the other two conjugates (Figure 5a). The smaller hydrodynamic radius (R_h, defined as the radius of a sphere with the same diffusion coefficient as the sample being measured) of the 4 × 10 kDa branched PEG conjugate was

dx.doi.org/10.1021/bc300066a | Bioconjugate Chem. 2012, 23, 1452–1462

Table 3. Pharmacokinetic Parameters (mean ± SD) of ^{125}I-Labeled PEGylated TNF Nanobodies after a Single IV Dose to Sprague-Dawley Rats[a]

construct	dose (mg/kg)	$C_{5\ min}$ (μg equiv/mL)	$AUC_{0-\infty}$ (μg equiv·h/mL)	$AUC_{0-\infty}$/dose (μg equiv·h/mL)/ (mg/kg)	CL (mL/h/kg)	Vd_{ss} (mL/kg)	$t_{1/2}$ (h)
TNF Nanobody_branched 2 × 20 kDa PEG	2	46 ± 4.9	2025 ± 214	1013 ± 107	1.0 ± 0.12*	53 ± 5.5*	44 ± 3.5
TNF Nanobody_branched 4 × 10 kDa PEG	2	44 ± 2.2	1514 ± 78*	757 ± 39*	1.3 ± 0.07*	63 ± 4.1	42 ± 8.2
TNF Nanobody_linear 1 × 40 kDa PEG	2	39 ± 2.6	1001 ± 62	500 ± 31	2.0 ± 0.13	65 ± 2.2	35 ± 5.7

[a]Male Sprague−Dawley rats were given a single IV bolus dose of the indicated ^{125}I-labeled test article, serum samples were taken at 5 min to 24 days post dose, and radioactive equivalent (RE) concentrations in serum were determined by gamma-counting. PK parameters were calculated for each individual animal (n = 7 for 2 × 20 and 4 × 10 kDa PEG constructs and n = 5 for the 1 × 40 kDa PEG construct) by noncompartmental analysis. Statistical analyses of $AUC_{0-\infty}$, $AUC_{0-\infty}$/Dose, CL, Vd_{ss}, and $t_{1/2}$ values were performed using ANOVA with Dunnett's post test, with the linear 1 × 40 kDa PEG group as the control. Star (*) indicates statistically significant differences relative to the linear PEG ($p < 0.05$).

Table 4. Pharmacokinetic Parameters (mean ± SD) of PEGylated TNF Nanobodies after a Single IV Dose to Cynomolgus Monkeys[a]

construct	dose (mg/kg)	$C_{5\ min}$ (μg/mL)	$AUC_{0-\infty}$ (μg·h/mL)	$AUC_{0-\infty}$/dose (μg·h/mL)/ (mg/kg)	CL (mL/h/kg)	Vd_{ss} (mL/kg)	$t_{1/2}$ (h)
TNF Nanobody_branched 2 × 20 kDa PEG	3	82 ± 6.4	13293 ± 820*	4431 ± 273*	0.23 ± 0.01*	57 ± 4.8*	188 ± 19*
TNF Nanobody_branched 4 × 10 kDa PEG	3	76 ± 3.2	8055 ± 736*	2685 ± 245*	0.37 ± 0.03*	79 ± 12	153 ± 30*
TNF Nanobody_linear 1 × 40 kDa PEG	3	111 ± 26	5637 ± 263	1879 ± 88	0.67 ± 0.10	78 ± 13	122 ± 12

[a]Male cynomolgus monkeys were administered a single IV bolus dose of the indicated test article, serum samples were taken at 5 min to 62, 57, and 56 days for the 2 × 20, 4 × 10, and 1 × 40 kDa PEG constructs, respectively, and serum concentrations were determined by ELISA. PK parameters were calculated for each individual animal (n = 3 per construct) by noncompartmental analysis. Data points with the sharp concentration drop were not used for PK calculations (for one of the 3 monkey dosed with the 2 × 20 kDa PEG construct). Statistical analyses of $AUC_{0-\infty}$, $AUC_{0-\infty}$/Dose, CL, Vd_{ss}, and $t_{1/2}$ values were performed using ANOVA with Dunnett's post test, with the linear 1 × 40 kDa PEG group as the control. *Star indicates statistically significant differences relative to the linear PEG group ($p < 0.05$).

confirmed by quasi-elastic light-scattering measurements (Table 6 and Figure 5c).

Using the angular dependency of the scattered light measured by MALS, the distribution of root mean squared (rms) radii can be determined. The rms radius (also referred to as radius of gyration, R_g) is a measurement of the root-mean-square distance that all parts of the molecule are from the center of its mass at any given time and provides information about the average volume a molecule occupies. Both the branched 2 × 20 kDa and the branched 4 × 10 kDa PEG conjugates had smaller R_g (rms radii) than the linear PEG conjugate (Table 6 and Figure 5d).

Finally, conformational information can be obtained by calculating the rms/R_h (R_g/R_h) ratio: the larger the value of the ratio, the more elongated or extended the molecule is. The rms/R_h ratio was 1.77, 1.45, and 1.37 for the linear 1 × 40 kDa PEG, branched 2 × 20 kDa, and branched 4 × 10 kDa PEG conjugates, respectively, indicating that the conjugate with the linear 1 × 40 kDa PEG had a more extended time-averaged conformation than the more compact conjugates containing the branched PEGs (Table 6). It should be noted that the size exclusion-HPLC method used to analyze the PEGylated conjugates is not suitable for side-by-side analysis of the unconjugated proteins.

DISCUSSION

In this report, PK and biodistribution profiles of TNF Nanobody (~27 kDa protein) conjugated at the engineered C-terminal cysteine to the 1 × 40 kDa linear, 2 × 20 kDa branched, or 4 × 10 kDa branched PEG in various species were compared and the biophysical characteristics of the protein−PEG conjugates were assessed.

Following a single IV dose to mice, rats, or monkeys, TNF Nanobody 2 × 20 kDa PEG construct had higher mean serum dose-normalized AUC (94−136%), lower CL (48−66%), and longer serum $t_{1/2}$ (26−54%) compared to the corresponding values for the TNF Nanobody_linear 1 × 40 kDa PEG construct. Conjugation of the branched 4 × 10 kDa PEG instead of linear 1 × 40 kDa PEG to TNF Nanobody also resulted in higher mean serum dose-normalized AUC and lower CL in rats and monkeys (but not in mice); however, the differences were less pronounced compared to those observed between the branched 2 × 20 kDa PEG conjugate and linear 1 × 40 kDa PEG conjugate. These results are in agreement with the previous reports in rabbits (in which the PK profiles of anti-IL-8 Fab′ conjugated to either the linear 40 kDa or branched 2 × 20 kDa PEG was examined[11]) and mice (in which PK profile of asparaginase conjugated to either the linear 10 kDa or branched 10 kDa PEG was assessed[12]).

Biodistribution studies indicated that following a single IV dose of ^{125}I-labeled PEGylated constructs to mice, TNF Nanobody_branched 2 × 20 kDa PEG construct had significantly higher exposure ($AUC_{0-168\ h}$) compared to the TNF Nanobody_linear 1 × 40 kDa PEG in serum and in some but not all tissue examined (4 × 10 kDa PEG conjugate was not used in biodistribution studies). Tissues that had different exposures to the linear 1 × 40 kDa and the branched 2 × 20 kDa PEG conjugates were heart, lung, muscle, skin, and stomach, with the mean increase in AUC for the branched construct ranging from 43% to 115%. In contrast, the mean

dx.doi.org/10.1021/bc300066a | Bioconjugate Chem. 2012, 23, 1452−1462

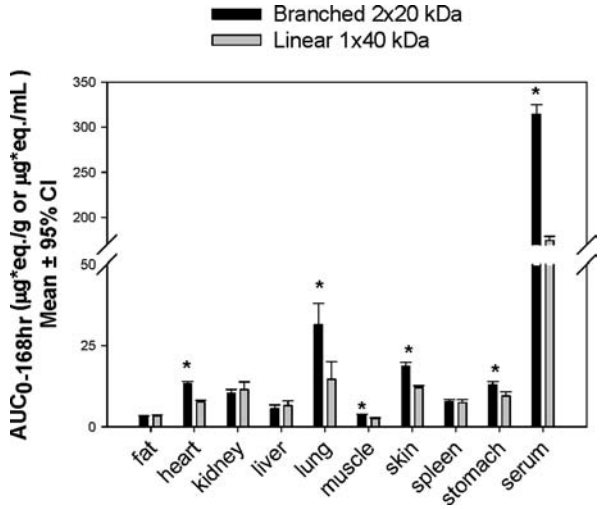


Figure 3. Mean tissue and serum exposures ($AUC_{0-168\ h}$) of ^{125}I-labeled PEGylated TNF Nanobodies after a single 0.3 mg/kg IV dose to mice. B6CBAF1/J mice were administered a single 0.3 mg/kg IV bolus dose of ^{125}I-labeled TNF Nanobody_branched 2 × 20 kDa PEG (black bars) or TNF Nanobody_linear 40 kDa PEG (gray bars). Serum and tissue samples (n = 8−12 per time point) were collected over the 7 days (168 h), and radioactive equivalent (RE) concentrations in tissue and serum were determined by gamma-counting, as described in the text. $AUC_{0-168\ h}$ (area under the concentration−time curve from time 0 to 168 h) in serum (in μg equiv·h/mL) and in each tissue (μg equiv·h/g) were determined by noncompartmental analysis using the sparse sampling method, and the 95% confidence interval (95% CI, the error bars on the graph) was calculated using the standard error of the mean. Star (*) indicates statistically significant difference ($p < 0.05$) in $AUC_{0-168\ h}$ between the two constructs.

Table 5. Tissue-to-Serum (T/S) AUC Ratios of ^{125}I-Labeled PEGylated TNF Nanobodies after a Single 0.3 mg/kg IV Dose to B6CBAF1/J Mice[a]

tissue	TNF Nanobody_branched 2 × 20 kDa PEG	TNF Nanobody_linear 1 × 40 kDa PEG
fat	0.01	0.02
heart	0.04	0.04
kidney	0.03	0.07
liver	0.02	0.04
lung	0.10	0.08
muscle	0.01	0.01
skin	0.06	0.07
spleen	0.02	0.04
stomach	0.04	0.05

[a]B6CBAF1/J mice were administered a single 0.3 mg/kg IV bolus dose of ^{125}I-labeled TNF Nanobody_branched 2 × 20 kDa PEG or TNF Nanobody_linear 40 kDa PEG. Serum and tissue samples (n = 8−12 per time point) were collected over the 7 days (168 h), and radioactive equivalent (RE) concentrations in tissue and serum were determined by gamma-counting, as described in the text. $AUC_{0-168\ h}$ for serum (in μg·equiv/mL) and each tissue (μg·equiv/g) were determined by noncompartmental analysis using the sparse sampling method and the tissue-to-serum (T/S) AUC ratios ($AUC_{0-168\ h,\ tissue}$/$AUC_{0-168\ h,\ serum}$) was calculated. Note, that because of the nonserial sampling design and sparse sampling method for AUC estimation, it is only possible to obtain standard deviations and conduct statistical analyses for the AUC values themselves (as shown in Figure 3) but not for the AUC ratios.

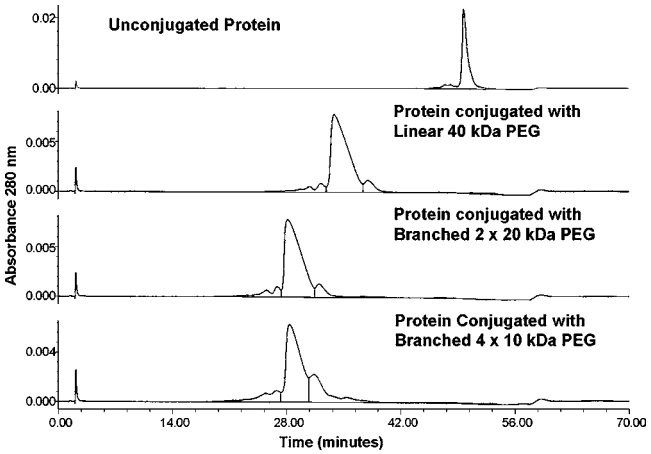


Figure 4. Cation exchange high-performance liquid chromatography (profiles of PEGylated TNF Nanobodies). The protein concentration of each material was adjusted to 1.0 mg/mL with formulation buffer and 10 μL was injected onto a Dionex ProPac WCX-10 column. Mobile phase A was 10 mM ammonium formate, pH 4.0. Mobile phase B was 10 mM ammonium formate, 500 mM sodium chloride, pH 4.0. Protein conjugates were eluted at a flow rate of 0.75 mL/min with a linear gradient of sodium chloride (0−40% B in 40 min). Absorbance at 280 nm was monitored.

$AUC_{0-168\ h}$ in fat, kidney, liver, and spleen were similar for the two PEGylated constructs.

Thus, our case study on PEGylated TNF Nanobodies implies that (i) a superior PK profile of branched versus linear PEG−protein conjugates is likely to hold across species; (ii) for a given PEG size, the extent of PEG branching affects the PK profile, with the 2 × 20 kDa PEG conjugate having a superior PK profile compared to the 4 × 10 kDa conjugate in this particular example; and (iii) tissue penetration might differ between the linear and branched PEG conjugates in a tissue-specific manner.

The observation that PK differences between the various protein−PEG conjugates is likely to hold across species, supporting the use of rodent models to screen/rank PEGylated protein construct in early lead development. However, the actual magnitude of differences in a given PK parameter may not be assumed to hold across rodent and primates.

While the elimination pathways of the PEGylated TNF Nanobodies have not been determined, it is likely that similar to other therapeutic proteins that are above the renal filtration cutoff, the main elimination route for PEGylated TNF Nanobodies is degradation by proteolysis and catabolism into amino acids throughout the body.[2,18,19] The evidence that PEGylated TNF Nanobodies are degraded *in vivo* comes from the observation that in mouse radiolabeled studies approximately 60% of total administered radioactivity was excreted in urine within 1 week (168 h) after dosing (in line with observed serum PK profiles), with most of the urine counts attributed to free iodine or small degradants. In contrast to PEGylated Nanobodies, nanobodies without a half-life extension moiety are usually below the renal filtration cutoff, have a short half-life (of less than 2 h), and are largely cleared by the kidneys;[20,21] although the disposition of the specific unconjugated TNF Nanobody used in this case study was not directly examined. The kinetics and mechanistic details of proteolytic elimination/catabolism of large therapeutic proteins are poorly understood, although they are likely to occur at various sites in the body, and in general, there are minimal to no predictive in vitro

Table 6. Calculated Weight Averaged Mass and Sizes of PEGylated TNF Nanobodies from SEC-MALS and QELS Analysis

	total molar mass (kDa)	PEG molar mass (kDa)	protein molar mass (kDa)	rms (R_g) radius (mm)	R_h radius (mm)	rms/R_h
TNF Nanobody_linear 1 × 40 kDa PEG	64.86	39.01	25.85	9.9	5.6	1.77
TNF Nanobody_branched 2 × 20 kDa PEG	64.54	38.97	25.57	8.0	5.5	1.45
TNF Nanobody_branched 4 × 10 kDa PEG	61.78	36.29	25.49	7.0	5.1	1.37

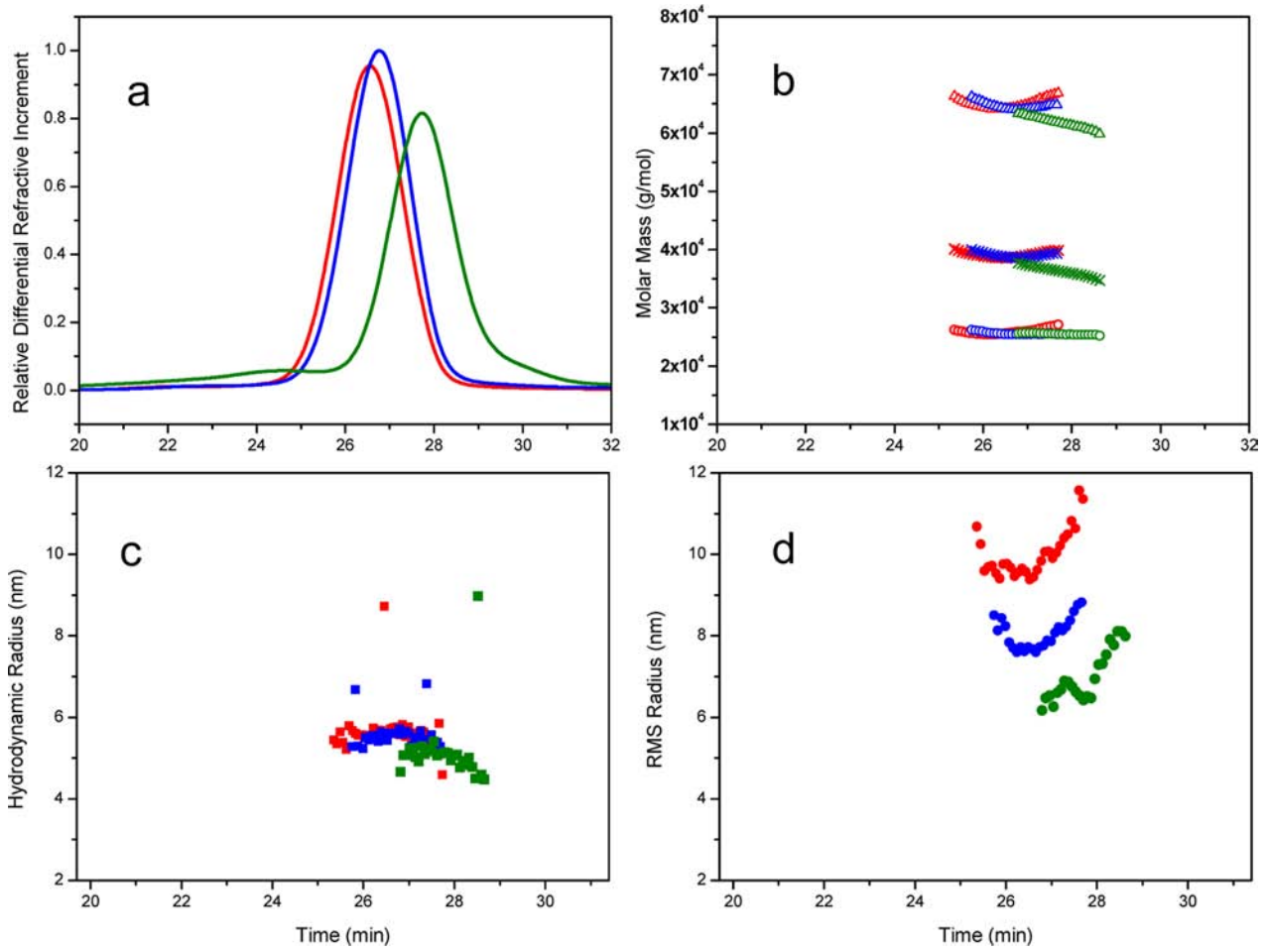


Figure 5. SEC-MALS profiles of PEGylated TNF Nanobodies. TNF Nanobody_2 × 20 kDa PEG (blue line and symbols), TNF Nanobody_4 × 10 kDa PEG (green line and symbols), or TNF Nanobody_1 × 40 kDa PEG (red line and symbols) were diluted to 2.0 mg/mL and 100 μL of each sample was injected over a Superose 6 column heated to 30 °C. The dRI SEC profiles for the above-mentioned PEG conjugates are overlaid in part a. Part b shows total mass (open triangles), PEG mass (x), and protein mass (open circles) for all the conjugates, determined using MALS in conjunction with UV and dRI detectors. Part c shows hydrodynamic radius measured by in-line QELS. Part d is an overlay of the measured rms radius for the different conjugates determined by MALS. All sizes were calculated using *ASTRA V* v 5.3.4.14 data analysis software from Wyatt Technologies.

systems to study these processes.[19,22] In the case of PEGylated TNF Nanobodies, proteolysis likely occurs intracellularly in the lysosomes throughout the body, as well to some extent in blood and the interstitial fluids. Intracellular uptake is likely to occur in the tissues containing cells of the reticuloendothelial system (RES; e.g., macrophages, monocytes and Kupffer cells in the liver, spleen, kidneys, lymph nodes, and lungs), as well as in endothelial cells of perfused organs. Similar to other large therapeutic proteins, PEGylated TNF Nanobodies likely are taken into the cells by both the nonspecific and receptor-mediated mechanisms. For example, hepatocytes have receptors for both glycosylated and nonglycosylated proteins, while epithelial cells more efficiently internalize negatively charged proteins. PEGylation is thought to reduce the intracellular catabolism by several mechanisms, including masking of charge and recognition sites for the specific uptake receptors, as well as protection from the proteolysis inside the lysosome.[2,18,19]

Biophysical analyses of the three TNF Nanobody−40 kDa PEG conjugates were conducted in order to investigate potential reasons for differential PK profiles of these constructs. These analyses included cation exchange-HPLC, which is a measure of surface charge coverage, and R_g/R_h ratio, which is measure of proximity of the PEG moiety to the protein moiety. Specifically, R_h (hydrodynamic radius, radius of a sphere with the same diffusion coefficient as sample) and R_g (rms radii, a measurement of the root-mean-square distance that all parts of

dx.doi.org/10.1021/bc300066a | *Bioconjugate Chem.* 2012, 23, 1452−1462

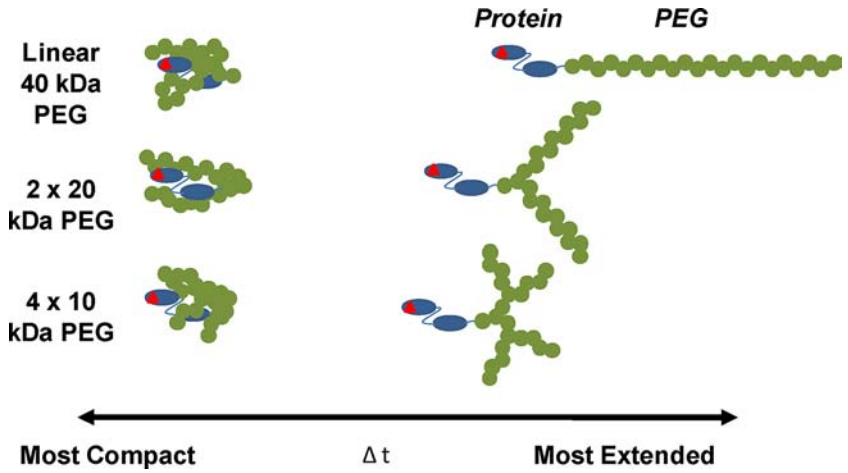


Figure 6. Representation of extreme conformations that the linear or branched PEG may adopt within protein conjugates. This figure illustrates the model in which the shape of a TNF Nanobody–PEG conjugate is a time-averaged distribution (indicated by "Δt") between the most compact and extended conformations. In this model, PEG and the protein moieties, although interacting, maintain their independent characteristics, relative to the corresponding unconjugated domains. The more compact conformation (theoretical extremes shown in the left side), wherein the PEG wraps around the protein creating a protective shell, is proposed as a mechanism for prolonged exposure. Biophysical analyses described in the text suggest that among the three protein–PEG conjugates, the linear PEG conjugate has the most extended time-average conformation, such that the PEG moiety is the least proximal to the protein moiety, and therefore provides the least extent of PK optimization. Triangle represents a putative proteolytic site or a site involved in the cellular uptake, which may be masked more efficiently by the 2 × 20 kDa PEG compared to the 4 × 10 kDa PEG, such that the 2 × 20 kDa PEG is the most efficient for PK optimization of this specific TNF Nanobody.

the molecule are from the center of its mass at any given time) values were obtained by SEC-MALS and quasi-elastic light-scattering and provided conformational information on the three types of PEG conjugates. A given PEG conjugate is likely to assume many conformational states between the most compact and fully extended/elongated (Figure 6); within this distribution of conformational states, some will be more highly favored than others. R_g/R_h ratio is a measure of the time-averaged conformational state for each conjugate, with elongated conjugates displaying R_g/R_h ratios of >1.

Earlier studies indicate that the PEG moiety within a protein–PEG conjugate assumes a conformation similar to that of the unconjugated PEG.[8,13,23,24] In addition, most of the current data indicate that the secondary protein structure is unchanged upon PEG attachment.[5−7] Our data are likewise supportive of a model in which the PEG and the protein moieties, although interacting, maintain their independent characteristics. For example, the presence of the 2 × 20 kDa PEG had little or no effect on the protein structure itself, as determined by near- and far-UV circular dichroism and differential scanning calorimetry (data not shown). Similar observations have been made for other proteins, protected by covalent PEGylation.[8,24,25] In addition, similar to other protein–PEG conjugates, the hydrodynamic properties of the TNF Nanobody–PEG conjugates are similar to those of the unconjugated PEG (data not shown). Considering that a random-coiled PEG is highly extended, the depiction on the right side of Figure 6 may be a more populated state than the fully compact theoretical extreme. Caliceti and Veronese proposed the hypothesis of enhanced protein protection from "umbrella-like" branched PEG molecules.[2] The more compact conformation (theoretical extremes shown in the left side of Figure 6), wherein the PEG wraps around the protein creating a protective shell, had been proposed as a mechanism for prolonged plasma half-life.[26] Even without direct PEG–protein contact, the extended arms of the PEG can mask the protein surface from proteases, cellular uptake, and other clearance pathways.

The R_g/R_h ratio (Table 6) indicated that the conjugate with the linear 1 × 40 kDa PEG had a more extended time-averaged conformation (ratio of 1.77) than the branched 2 × 20 kDa or 4 × 10 kDa PEG conjugates (ratios of 1.45 and 1.37, respectively), suggesting that branched PEGs are, on average, more proximal to the protein moiety compared to the linear PEG. These data are in good agreement with cation exchange-HPLC profiles (Figure 4), which indicated that apparent charge was different between the linear and the two branched PEG conjugates. Specifically, cation exchange-HPLC elution profile of the linear PEG conjugate was shifted toward that of the unconjugated protein, in line with the model in which the proximity of PEG to the protein affects the apparent surface charge of the protein. Thus, a possible explanation for the better PK profile of branched versus linear PEGs is the higher proximity of PEG to the protein moiety, resulting in higher extent of masking of sites involved in intracellular uptake and/or proteolytic sites by branched PEGs.[27] However, additional experimental data are needed to support this hypothesis. The alternative explanations for the difference in pharmacokinetics of linear versus branched PEG conjugates of the same MW include (i) differences in hydrodynamic volumes, (ii) differences in conformational flexibility between the linear versus branched PEGs leading to difference in diffusion rates through the kidney membrane pores, and (iii) difference in clearance by the immune system of the different PEG conjugates.

The reason for the differences in PK profiles between the branched 2 × 20 kDa and 4 × 10 kDa PEG conjugates remains to be understood. Both the cation exchange HPLC (Figure 4) and the R_g/R_h ratio analysis (Table 6) showed similar apparent surface charge and average PEG proximity between the two branched conjugates, respectively. Therefore, if the differences in PK profiles between the two branched PEG conjugates are related to masking of cellular uptake/proteolytic sites, then these masking differences may be site-specific, such that for the

specific example of TNF Nanobody protein moiety and 40 kDa PEG described here, the two-branched PEG appeared to provide a more optimal balance of "protective umbrella" coverage superior PK advantage compared to the four-branched PEG conjugate (illustrated in Figure 6 by different coverage of a specific putative site important for catabolic elimination). It should also be noted that the higher degree of heterogeneity in MW of 4 × 10 kDa PEG compared to 2 × 20 kDa PEG conjugate (Figure 5a) could be contributing to the differences in PK profiles between the conjugates. However, it is unlikely to be the sole reason for the differences, based on magnitude of differences in mean exposures (AUC). Additional hypotheses mentioned in the preceding paragraph as alternative explanations to the differences in PK profiles between the linear and branched PEG conjugates may also be relevant when considering the PK differences between the branched PEG conjugates with different degrees of branching. For example, it is possible that the 2 × 20 kDa PEG is more effective in reducing the kidney elimination compared to 4 × 10 kDa PEG, especially considering that the 4 × 10 kDa PEG conjugate had the smallest R_h and R_g among the three protein−PEG conjugates tested.

The mechanistic explanation on the observed differences in tissue distribution parameters for the TNF Nanobodies conjugated to the 40 kDa linear PEG versus 2 × 20 kDa branched PEG likewise remains to be established. As mentioned above, the R_g/R_h ratio analysis suggested that the conjugate with the linear PEG had a more extended time-averaged conformation than the branched PEG, perhaps resulting in differential accessibility to certain tissues. However, additional studies are needed to systematically examine the differences in tissue distribution for protein−PEG conjugates of various degrees of branching and mechanistic bases behind those differences.

In summary, we have examined pharmacokinetic, biodistribution, and biophysical profiles of three different TNF Nanobody−40 kDa PEG conjugates that varied in the degree of PEG branching: linear 1 × 40 kDa, branched 2 × 20 kDa, and 4 × 10 kDa PEGs. While all three conjugates had similar potency in a cell-based assay, differences in PK and biodistribution profiles were observed, such that 2 × 20 kDa PEG conjugate had the highest *in vivo* exposure in all species tested. On the basis of the R_g/R_h ratio analysis and other biophysical data, as well as previously published reports, we propose that the extent of PEG proximity and available PEG surface area determine the optimal extent of proteolytic masking and/or masking of recognition sites for intracellular uptake and impact PK profiles of different PEG conjugates, such that in this particular case study 2 × 20 kDa conjugation resulted in optimal extent of masking of these sites. Further studies are needed to understand the mechanistic basis of differences in disposition profiles of protein−PEG conjugates of the same MW but different degree of branching.

AUTHOR INFORMATION

Corresponding Author

*Telephone: 978-247-1404. E-mail: yulia.vugmeyster@pfizer.com.

Present Address

#Center for Translational Therapeutics, National Institutes of Health, Rockville, MD, USA.

Notes

The authors declare the following competing financial interest(s): All authors are current or former employees of Pfizer, Inc.

ACKNOWLEDGMENTS

We thank Michel Awwad, David Wensel, Jason Fernandez, and Pam Szklut for their valuable discussions and support of this study.

ABBREVIATIONS

PEG, poly(ethylene glycol); PK, pharmacokinetics; $C_{5\ min}$, concentration at 5 min, the first sampling time point after IV administration; CL, total body clearance based on serum concentration; Vd_{ss}, volume of distribution at steady-state; $t_{1/2}$, elimination half-life; $AUC_{0-\infty}$, area under the concentration−time curve from time 0 to infinity; AUC_{last}, area under the concentration−time curve from time 0 up to sampling time at which a quantifiable concentration is found; TNF, tumor necrosis factor alpha; HPLC, high performance liquid chromatography; RE, radioactive equivalent; ELISA, enzyme linked immunosorbent assay; MALS, multi angle light scattering; SEC-MALS, size exclusion HPLC with MALS; R_h, hydrodynamic radii. root mean squared radii or radius of gyration (rms or R_g, respectively).

REFERENCES

(1) Pasut, G., Veronese, F. M. (2012) State of the art in PEGylation: The great versatility achieved after forty years of research. *J. Controlled Release 161*, 461−472.

(2) Caliceti, P., and Veronese, F. M. (2003) Pharmacokinetic and biodistribution properties of poly(ethylene glycol)-protein conjugates. *Adv. Drug Delivery Rev. 55*, 1261−1277.

(3) Fishburn, C. S. (2008) The pharmacology of PEGylation: balancing PD with PK to generate novel therapeutics. *J. Pharm. Sci. 97*, 4167−4183.

(4) Harris, J. M., and Chess, R. B. (2003) Effect of pegylation on pharmaceuticals. *Nat. Rev. Drug Discovery 2*, 214−221.

(5) Digilio, G., Barbero, L., Bracco, C., Corpillo, D., Esposito, P., Piquet, G., Traversa, S., and Aime, S. (2003) NMR structure of two novel polyethylene glycol conjugates of the human growth hormone-releasing factor, hGRF(1−29)-NH2. *J. Am. Chem. Soc. 125*, 3458−3470.

(6) Greenwald, R. B. (2002) Poly(ethylene glycol) anticancer drug delivery systems. *P. R. Health Sci. J. 21*, 113−121.

(7) Hinds, K. D., and Kim, S. W. (2002) Effects of PEG conjugation on insulin properties. *Adv. Drug Delivery Rev. 54*, 505−530.

(8) Lu, Y., Harding, S. E., Turner, A., Smith, B., Athwal, D. S., Grossmann, J. G., Davis, K. G., and Rowe, A. J. (2008) Effect of PEGylation on the solution conformation of antibody fragments. *J. Pharm. Sci. 97*, 2062−2079.

(9) Yamaoka, T., Tabata, Y., and Ikada, Y. (1994) Distribution and tissue uptake of poly(ethylene glycol) with different molecular weights after intravenous administration to mice. *J. Pharm. Sci. 83*, 601−606.

(10) Yamaoka, T., Tabata, Y., and Ikada, Y. (1995) Comparison of body distribution of poly(vinyl alcohol) with other water-soluble polymers after intravenous administration. *J. Pharm. Pharmacol. 47*, 479−486.

(11) Leong, S. R., DeForge, L., Presta, L., Gonzalez, T., Fan, A., Reichert, M., Chuntharapai, A., Kim, K. J., Tumas, D. B., Lee, W. P., Gribling, P., Snedecor, B., Chen, H., Hsei, V., Schoenhoff, M., Hale, V., Deveney, J., Koumenis, I., Shahrokh, Z., McKay, P., Galan, W., Wagner, B., Narindray, D., Hebert, C., and Zapata, G. (2001) Adapting pharmacokinetic properties of a humanized anti-interleukin-8 antibody for therapeutic applications using site-specific pegylation. *Cytokine 16*, 106−119.

(12) Veronese, F. M., Caliceti, P., and Schiavon, O. (1997) Branched and linear poly(ethylene glycol): Influence of the polymer structure on enzymological, pharmacokinetic, and immunological properties of protein conjugates. *Bioact. Compat. Polym. 12*, 196−207.
(13) Fee, C. J. (2007) Size comparison between proteins PEGylated with branched and linear poly(ethylene glycol) molecules. *Biotechnol. Bioeng. 98*, 725−731.
(14) Monfardini, C., Schiavon, O., Caliceti, P., Morpurgo, M., Harris, J. M., and Veronese, F. M. (1995) A branched monomethoxypoly-(ethylene glycol) for protein modification. *Bioconjugate Chem. 6*, 62−69.
(15) Hegen, M., Olland, S. H., Vugmeyster, Y., and Xu, X. (2012) Modified single domain antigen binding molecules and uses thereof. (USPTO, Ed.) Wyeth LLC, Madison NJ, USA.
(16) Coppieters, K., Dreier, T., Silence, K., de Haard, H., Lauwereys, M., Casteels, P., Beirnaert, E., Jonckheere, H., Van de Wiele, C., Staelens, L., Hostens, J., Revets, H., Remaut, E., D., V, and Rottiers, P. (2006) Formatted anti-tumor necrosis factor alpha VHH proteins derived from camelids show superior potency and targeting to inflamed joints in a murine model of collagen-induced arthritis. *Arthritis Rheum. 54*, 1856−1866.
(17) Vugmeyster, Y., DeFranco, D., Szklut, P., Wang, Q., and Xu, X. (2010) Biodistribution of [125I]-labeled therapeutic proteins: application in protein drug development beyond oncology. *J. Pharm. Sci. 99*, 1028−1045.
(18) Veronese, F. M. (2009) *PEGylated Protein Drugs: Basic Science and Clinical Applications*, Birkhäuser, Basel, Switzerland.
(19) Vugmeyster, Y., Xu, X., Theil, F. P., Khawli, L. A., and L. M., W. (2012) Pharmacokinetics and Toxicology of Therapeutic Proteins: Advances and Challenges. *World J. Biol. Chem. 3*, 73−92.
(20) Cortez-Retamozo, V., Lauwereys, M., Hassanzadeh, Gh, G., Gobert, M., Conrath, K., Muyldermans, S., De Baetselier, P., and Revets, H. (2002) Efficient tumor targeting by single-domain antibody fragments of camels. *Int. J. Cancer. 98*, 456−462.
(21) Gainkam, L. O., Huang, L., Caveliers, V., Keyaerts, M., Hernot, S., Vaneycken, I., Vanhove, C., Revets, H., De Baetselier, P., and Lahoutte, T. (2008) Comparison of the biodistribution and tumor targeting of two 99mTc-labeled anti-EGFR nanobodies in mice, using pinhole SPECT/micro-CT. *J. Nucl. Med. 49*, 788−795.
(22) Wang, W., Wang, E. Q., and Balthasar, J. P. (2008) Monoclonal antibody pharmacokinetics and pharmacodynamics. *Clin. Pharmacol. Ther. 84*, 548−558.
(23) Fee, C. J., and Van Alstine, J. M. (2004) Prediction of the viscosity radius and the size exclusion chromatography behavior of PEGylated proteins. *Bioconjugate Chem. 15*, 1304−1313.
(24) Pai, S. S., Tilton, R. D., and Przybycien, T. M. (2009) Poly(ethylene glycol)-modified proteins: implications for poly(lactide-co-glycolide)-based microsphere delivery. *AAPS J. 11*, 88−98.
(25) Ragi, C., Sedaghat-Herati, M. R., Ouameur, A. A., and Tajmir-Riahi, H. A. (2005) The effects of poly(ethylene glycol) on the solution structure of human serum albumin. *Biopolymers 78*, 231−236.
(26) Greenwald, R. B., Choe, Y. H., McGuire, J., and Conover, C. D. (2003) Effective drug delivery by PEGylated drug conjugates. *Adv. Drug Delivery Rev. 55*, 217−250.
(27) Caserman, S., Kusterle, M., Kunstelj, M., Milunovic, T., Schiefermeier, M., Jevsevar, S., and Porekar, V. G. (2009) Correlations between in vitro potency of polyethylene glycol-protein conjugates and their chromatographic behavior. *Anal. Biochem. 389*, 27−31.

Bioconjugate Chemistry

Article

pubs.acs.org/bc

Open-Sandwich Molecular Imprinting: Making a Recognition Matrix with Antigen-Imprinted Antibody Fragments

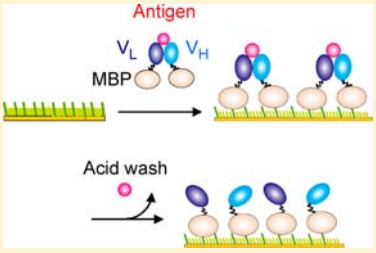
Koichi Minami,[†] Masaki Ihara,[‡,∥] Shou Kuroda,[§] Hirohiko Tsuzuki,[†] and Hiroshi Ueda*[,§,‡]

[†]Frontier Core-Technology Laboratories, FUJIFILM Corporation, Kaisei-Machi, Ashigarakami-Gun, Kanagawa, Japan

[‡]Department of Bioengineering and [§]Department of Chemistry and Biotechnology, School of Engineering, The University of Tokyo, Tokyo, Japan

Supporting Information

ABSTRACT: A novel antibody−polymer conjugation method termed open-sandwich molecular imprinting (OS-MIP) has been proposed to produce a specific recognition matrix in the presence of a target antigen. The resultant carboxymethyldextran matrix conjugated with two separate antibody variable region fragments imprinted with the cognate antigen showed higher antigen-binding capacity than non-imprinted ones and was successfully used to sensitively monitor multiple antigen binding/desorption events by a surface plasmon resonance biosensor. Furthermore, when each fragment was labeled with different fluorophores before conjugation, the fluorescence signals of the matrix made by OS-MIP clearly showed an antigen concentration dependent increase in Förster resonance energy transfer between the two dyes. By using a combination of various methods for detecting interaction, OS-MIP will be a useful platform for detecting various targets from small molecules to proteins with high sensitivity and specificity.



INTRODUCTION

In analytical fields such as immunodiagnostics and environmental analysis, technological demands are mounting for quick and accurate methodologies for identifying various molecules, ranging from small organic compounds to larger proteins. To address these needs, development of a compact and robust analytical device that affords real-time sensing is essential. Although powerful analytical instruments such as GC/MS and LC/MS/MS already exist in the market, due to their size, they are far from being suitable for *in situ* use for point-of-care tests. Besides these, alternative methods such as ELISA utilizing antigen−antibody reactions are compatible with miniaturized portable apparatuses. However, with these methods, collected samples must be carefully analyzed by experts, which makes real-time monitoring and/or simultaneous concurrent measurements difficult.

As a means to implement rapid and specific detection of various analytes *in situ*, molecular imprinting has been proposed for decades.[1] Although conventional molecularly imprinted polymers (MIP) have been able to recognize and rapidly separate small analytes by template-assisted polymerization, strong and specific recognition of larger proteins in aqueous solution has been elusive[2,3] without the help of natural antibodies.[4] However, even with the help of antibodies, a conventional method utilizing an antibody−lectin pair in an MIP matrix to detect a glycoprotein CEA can only emit a small and slow signal on the basis of gel shrinkage,[5] and it is unclear whether the method can be applied to the detection of other (smaller or larger) antigens.

As an alternative, we propose a novel method for making a reaction matrix, which we call open sandwich molecular imprinting (OS-MIP). OS-MIP enables specific recognition, as well as real-time detection of various targets in a small reaction volume. Instead of using whole antibody molecules, we used isolated antigen recognition domains of antibodies V_H and V_L. On the basis of the nature of these domains, where the association between them is weak in the absence of antigen but markedly strengthened by a specific antigen, many targets, not only proteins but also various small molecules, were specifically detected with a high degree of sensitivity in a noncompetitive manner (open sandwich immunoassay, OS-IA).[6,7] We attempted to apply this phenomenon to make a novel matrix of protein (antibody fragments)-carboxymethyl (CM)-dextran polymer conjugate for the detection and sensing of various molecules *in situ*.

EXPERIMENTAL SECTION

Cloning of anti-HEL Gene. Two mice were immunized with 1 mg/mL hen egg lysozyme (HEL) in Freund's complete adjuvant five times in two week intervals, and sacrificed to obtain the spleen 3 days after the last immunization. Total RNA was extracted from the spleen using Isogen (Nippon Gene, Toyama, Japan) and used for RT-PCR to amplify V_H and V_L cDNAs. The primers used for amplifying variable region sequences are based on Thomas Grunwald and Greg Winter, "Primer set for generation of highly diversified mouse phage display libraries", MRC Centre for Protein Engineering, Cambridge, UK (2000). The V_H and V_L genes were inserted

Received: February 16, 2012
Revised: May 26, 2012
Published: June 5, 2012

ACS Publications © 2012 American Chemical Society

dx.doi.org/10.1021/bc3000782 | Bioconjugate Chem. 2012, 23, 1463−1469

to phagemid pIT2 [8] to make a single-chain Fv (scFv) library, and an antigen-specific scFv-encoding vector pIT2-LxE16 was selected by phage display, the detail of which will be described elsewhere.

Construction of Vectors. An expression vector pET-MBPp-V_H(HEL)-His10 encoding a MBP-V_H(HEL)-His_{10} protein, in which *E. coli* maltose binding protein (MBP) and a His-tag containing ten histidine residues (His_{10}) are, respectively, fused to N- and C-termini of anti-hen egg lysozyme (HEL) V_H, was constructed by using the pET-MBPp-V_L(BPA)-His6 encoding V_L of an anti-bisphenol A antibody[9] tagged with MBP and six histidine residues at its N- and C-termini, respectively. To replace a His_6 tag of pET-MBPp-V_L(BPA)-His6 with a His_{10} tag, PCR product amplified with primers, 5′-AAAAAAAGCGGCCGCGGAG*CATCA-TCACCATCACCACCACCACCACCAC*TGAGATCCGG-3′ (underlined: *Not*I site; italicized: His_{10} sequence) and 5′-CCAATGCTTAATCAGTGA-3′ using pET-MBPp-His6 as the template was digested with *Not*I and *Sca*I, and inserted between *Not*I and *Sca*I sites of pET-MBPp-V_L(BPA)-His6, yielding pET-MBPp-V_L(BPA)-His10. PCR amplification of the V_H(HEL) gene fragment was performed by using pIT2-LxE16 encoding an scFv gene for anti-HEL antibody as a template, with primers 5′-CTTTCTATGCGGCCCAGCCGGCCATGGCCGAK-GTSVAGCTTCAGGAGTC-3′ (underlined: *Sfi*I site) and 5′-AAAAAAGCGGCCGCGCTCGAGACGGTGACCGTGG-3′ (underlined: *Not*I site). The V_H(HEL) fragment was digested with *Not*I and *Sfi*I, and ligated to pET-MBPp-V_L(BPA)-His10 digested with the same enzymes, obtaining pET-MBPp-V_H(HEL)-His10. An expression vector pET-MBPp-V_L(HEL)-His10 encoding a MBP-V_L(HEL)-His_{10} protein was constructed similarly to pET-MBPp-V_H(HEL)-His10, except that V_L(HEL) gene fragment was amplified using pIT2-LxE16 with primers AAAAAAGGCCCAGCCGGCCATGGCGTCG-ACGGATATTTGATGAC (underlined: *Sfi*I site) and TTTCTCGTGCGGCCGCACGTTTTATTTCCAACTTTG (underlined: *Not*I site) instead of V_H(HEL) fragment.

Preparation of MBP-V_H and MBP-V_L Proteins. *E. coli* OverExpress C41(DE3) cells were transformed with either pET-MBPp-VH(HEL)-His10 or pET-MBPp-VL(HEL)-His10, and single colonies were used to inoculate 4 mL of LB medium containing 100 μg/mL ampicillin and 0.1% glucose and cultured overnight at 30 °C. Four milliliters of the small-scale culture was used to inoculate 800 mL of LB medium containing 100 μg/mL ampicillin, and cultured at 30 °C. When an OD_{600} of the culture reached 0.5, isopropyl-β-thiogalactopyranoside (IPTG) was added up to 500 μM and further cultured overnight at 30 °C. The bacterial culture was then separated into supernatants and pellets of *E. coli* by centrifugation. The protein was independently collected from the supernatants by ammonium sulfate precipitation and from the pellet by ultrasonication of bacterial cells. From the supernatant, 344 g of ammonium sulfate was added to about 800 mL of the culture supernatant and the mixture was stirred overnight at 4 °C. Subsequently, the protein was collected by centrifugation and the pellet was suspended in 30 mL of Talon buffer (50 mM sodium phosphate, 300 mM NaCl, pH 7.0). From the pellet, the pellet was suspended in 30 mL of Talon buffer and then subjected to ultrasonication, followed by centrifugation, to collect a supernatant. The supernatant was dialyzed against Talon buffer. Each protein collected in Talon buffer was applied to a column (ϕ16 mm × 15 mm) filled with Talon affinity resin (Clontech Laboratories, Inc., Mountain View, CA). Subsequently, the resin was washed with the Talon buffer, and then Elution buffer (Talon buffer containing 500 mM imidazole) was added to elute the protein. The purified protein was confirmed by SDS-PAGE. The buffer of the eluate was changed to HBS-N (10 mM HEPES, 150 mM NaCl, pH 7.4), and then glycerol was added at a final concentration of 16%. The obtained solution was stored at −80 °C. MBP-V_H(BGP)-His_6 and MBP-V_L(BGP)-His_6 proteins were prepared as described previously.[10]

Preparation of V_H(HEL) and V_L(HEL) Proteins. To 1 mL of the purified MBP-V_H(HEL)-His_{10} or MBP-V_L(HEL)-His_{10} solution (in HBS-N, ∼1000 μg/mL), 20 units of Genenase (New England Biolabs, Inc., Ipswich, MA) was added to digest the linker containing HY sequence. The mixture was allowed to react at 25 °C for 5 h. After the reaction, the protein was purified with Talon affinity resin as above, and the buffer of the eluate was changed to HBS-N.

Preparation of the scFv(HEL) Protein. *E. coli* HB2151 strain was transformed with pIT2-LxE16 plasmid and the resulting single colony was used to inoculate 4 mL of LB medium containing 100 μg/mL ampicillin and 0.1% glucose. After overnight cultivation at 30 °C, the culture was added to 800 mL of LB medium containing 100 μg/mL ampicillin, and cultured at 30 °C until OD_{600} reached 0.5−0.6. Then, IPTG was added up to 400 μM and further cultured at 16 °C for 16 h. The bacteria were removed by centrifugation, and the protein was recovered from the supernatant and purified as described above.

Open-Sandwich Molecular Imprinting (OS-MIP). To perform imprinting of V_H/V_L with corresponding antigen before conjugation with CM-dextran (CMD) polymer, ∼10 μM each of V_H and V_L fused with or without MBP as prepared above were mixed with 0.1−1.0 mol equiv antigen in HBS-N at 25 °C for 3 h. Thereafter, the conjugation/immobilization reaction was performed as below.

Immobilization of Antibody Fragments and Evaluation of Antigen Binding Activity by SPR Biosensor. To immobilize and evaluate the binding activity of antibody fragments, SPR biosensor Biacore 3000 (GE Healthcare, Tokyo, Japan) was used. The proteins (diluted to ∼200 μg/mL in 10 mM NaOAc, pH 4.5) were immobilized onto a sensor chip CM5 (GE Healthcare) by amine coupling according to manufacturer's recommendations. Briefly, CM dextran in the sensor chip was activated by the 1:1 mixture of 0.4 M 1-ethyl-3-(3-dimethylaminopropyl)-carbodiimide and 0.1 M *N*-hydroxysuccinimide in water for up to 7 min, and after brief washing with HBS-N, it was treated with the proteins for 7 min, before deactivation of excess reactive groups by 1 M ethanolamine−HCl, pH 8.5, for 7 min and washing with 10 mM glycine−HCl, pH 1.5, for 1 min. Afterward, either hen egg lysozyme or osteocalcin C-terminal peptide in HBS-N was added to the flowcells as an antigen at 25 °C at 10 μL/min, and its binding and dissociation kinetics (10 min each) were monitored. The RU value obtained with a control flowcell without immobilized protein was subtracted to determine specific binding.

To monitor repeated bindings, the flowcells after reaction with antigen in HBS-N for 10 min and dissociation in HBS-N for 10 min were serially washed for 1 min each with 10 mM glycine−HCl, pH 1.5, and 10 mM NaOH. The cycles were repeated, and the maximum increases in RU were recorded. During the measurement, the sensor chip surface was kept wet with HBS-N, while during longer storage periods, it was kept

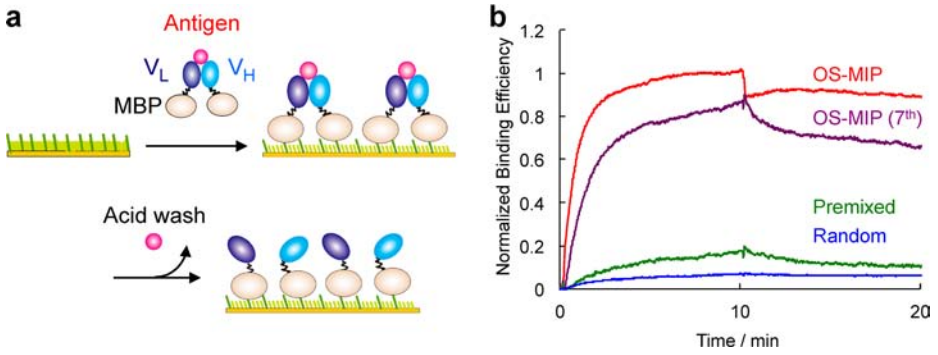


Figure 1. OS-MIP. (a) Scheme of OS-MIP. (b) SPR sensorgrams obtained for the flowcells immobilized with MBP-fused V_H and V_L fragments by the methods shown. HEL (100 nM) in HBS-N was introduced from 0 to 10 min, and dissociation in HBS-N was monitored. The sensorgrams obtained with OS-MIP (red and magenta for the first and the seventh run, respectively) are compared with those for premixed (green) and randomly immobilized (blue) surfaces.

dry at 4 °C. To calculate K_d values, *BIAevaluation 4.1* software (GE Healthcare) was used.

Thermodynamic Parameters. To derive entropic and enthalpic parameters of each antibody fragment and their mixture, SPR analysis was performed at four different temperatures (15−45 °C) using BIAcore T100 (GE Healthcare). The proteins were immobilized on a Series S sensor chip CM5 (GE Healthcare) and used for kinetic analyses as described above. The relationship between the calculated K_d value and temperature was used to derive ΔG and ΔH values using the *BIAevaluation* software.

Fluorescence Labeling. Fluorescence labeling of each antibody fragment was performed with one of the following succinimide esters: Alexa Fluor 555 (Molecular probes), Alexa Fluor 647 (Molecular probes), or HiLyte Fluor 555 (Anaspec). The antibody fragment (~0.8 mg/mL in 10 mM sodium phosphate, pH 7.0) was mixed with an appropriate amount of dye-succinimide in HBS-N and rotated at 25 °C for 30 min. The mixture was separated from free dye by gel-filtration. The *F*/*P* ratio of the protein was calculated by spectroscopy according to the manufacturer, which was controlled to fall between 1 and 2. The labeled proteins were stored at 4 °C.

Immobilization to a CMD-Modified Glass Plate. To immobilize antibody fragments onto a glass surface to enable optical observation, a Biacore 3000 surface prep unit (GE Healthcare) and CMD-modified glass slide were employed. An alkaline-treated glass slide (Matsunami Glass Co.) was washed in an ultrasonic acetone bath with ddH_2O and treated with UV/O_3 cleaner to clean its surface. The plate was then immersed once in 3-aminopropylethoxysilane and baked at 120 °C for 1 h.

A 1% CMD (M_w: 1000 k, Meito Sangyo, Aichi, Japan) solution in ddH_2O was mixed with 1 vol 5 mM 1-ethyl-3-(3-dmiethylaminopropyl)carbodiimide (EDC)-HCl, and the mixture was applied to the glass slide above, spin-coated, and incubated at 25 °C. The plate was sequentially washed with 100 mM NaOH and ddH_2O to produce a CMD-modified glass slide. The CMD-glass slide was placed on the Biacore 3000 surface prep unit, and the fluorescence-labeled antibody fragments were immobilized as above. The plate was washed serially with 10 mM glycine-HCl, pH 1.5, and 10 mM NaOH and used for FRET measurement.

FRET Measurement. Sample solution with or without antigen was applied to the CMD-glass slide immobilized with labeled antibody fragments, and incubated for 1−10 min at 25 °C. The slide was washed with HBS-N and dried briefly with an air-spray. The fluorescence intensities at 570 and 675 nm were measured with a fluorescence image analyzer (FLA-8000, Fuji Film) at an excitation wavelength of 532 nm. The FRET efficiency was calculated as (F_A/F_D), The antigen dependency of (F_A/F_D) was calculated as $\Delta(F_A/F_D) \times 100$ (%), where the (F_A/F_D) just before antigen addition was subtracted to obtain $\Delta(F_A/F_D)$. Three measurements for each matrix with two different ligand densities (375 and 627 pg/mm^2 for OS-MIP, and 396 and 648 pg/mm^2 for premixed condition) were performed. After each measurement, the slide was washed with 10 mM glycine−HCl, pH 1.5, for 1 min for regeneration. The limit of detection was determined as the antigen concentration that gives $\Delta(F_A/F_D)$ higher than its 3 SD.

For real-time fluorescence measurement, the fluorescence time course upon the addition of sample solution to the CMD-slide was monitored by a photomultiplier tube H5784−02 (Hamamatsu Photonics, Hamamatsu, Japan), equipped with a 667 nm band-pass filter, with excitation provided by an LD-excited green solid-state laser (λ = 532 nm). The time course of fluorescence intensities after injection of either HBS-N alone or 1 μM HEL in HBS-N was monitored to derive the fluorescence ratio of the two samples.

RESULTS AND DISCUSSION

Fabrication of OS-MIP. The scheme of OS-MIP is shown in Figure 1a. Many antibody variable regions (Fv = V_H + V_L) devoid of corresponding constant regions retain a property whereby they are more stable in the presence of antigen than in its absence (open sandwich principle).[6] We ventured to utilize this property for making a functional antibody−polymer conjugate that can specifically capture antigen only when the matrix is imprinted with antigen during the conjugation reaction. In other words, when a Fv−polymer conjugate is made in the presence of antigen, a high proportion of the two variable region fragments V_H and V_L would be immobilized as a functional complex. However, when the same conjugate is made in the absence of antigen, the proportion of functional V_H/V_L complex would be considerably low, leading to nonfunctional conjugate without full antigen-binding capability. To make the proposed matrix, first we obtained the genes for antibody variable region fragments V_H and V_L that specifically recognize hen egg lysozyme (HEL) from immunized mice. We successfully obtained the genes, which showed high homologies (88% and 94% amino acid identity in V_H and V_L, respectively) to corresponding genes from a known anti-HEL antibody

dx.doi.org/10.1021/bc3000782 | *Bioconjugate Chem.* 2012, 23, 1463−1469

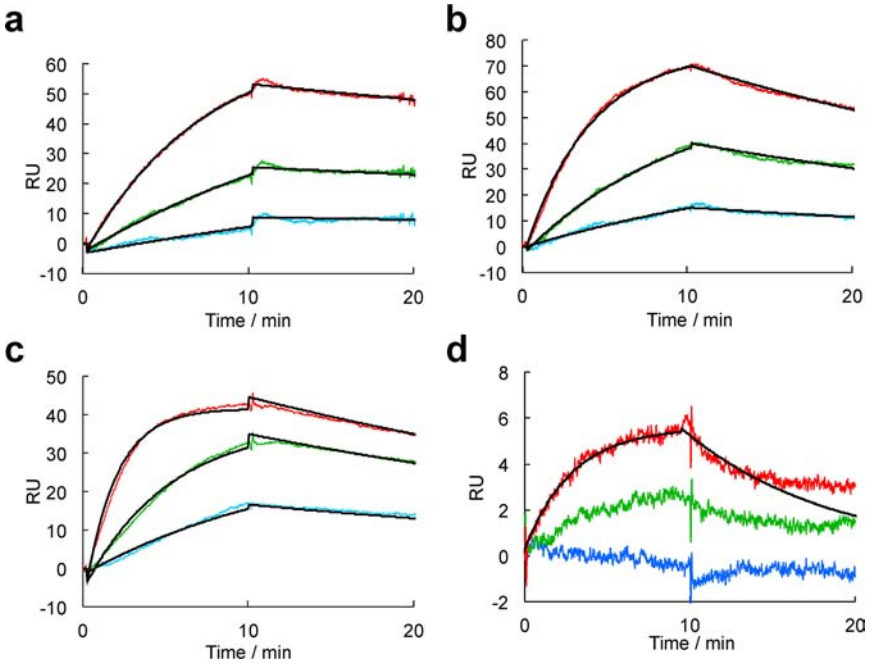


Figure 2. SPR sensorgram for the OS-MIP complex immobilized with anti-HEL (a) MBP-V_H/MBP-V_L (b) MBP-V_H/V_L, and (c) V_H/V_L. Blue, green, and red lines show signals with 3, 10, and 30 nM HEL, respectively, with fitted curves. (d) The same for anti-BGP MBP-fused Fv immobilized by OS-MIP. Blue, green, and red lines show signals with 1, 10, and 100 nM BGP-C7, respectively.

HyHEL-10.[11] From our previous results, [6] it was probable that the Fv (=V_H + V_L) also showed antigen-dependent stabilization.

Therefore, the obtained genes were used to prepare fusion proteins with maltose binding protein (MBP), and these fusion proteins were then used for chemical conjugation with CM dextran immobilized on a CM5 surface plasmon resonance (SPR) sensor chip by amine coupling. We used MBP as a fusion partner because we expected its stabilizing effect as a molecular chaperon.[12] However, it was found later that MBP is not essential in OS-MIP itself (see below). We used the following three conditions: (i) V_H and V_L were conjugated serially ("random" in Figure 1b); (ii) both proteins were premixed and conjugated (premixed); and (iii) both proteins were premixed with template (HEL) before conjugation (OS-MIP). When the sensor matrices after conjugation were acid-washed and evaluated for their HEL binding responses with the Biacore 3000 SPR biosensor, the matrix immobilized with the Fv mixed with template showed a markedly higher HEL binding response than the former two matrices prepared without template (Figure 1b). Compared with the matrices made under random and premixed conditions, the matrix made by OS-MIP showed a 14- and 5.7-fold higher maximum resonance unit, respectively. In addition, when this matrix was subjected to six antigen binding/acid-wash cycles and subjected to the same measurement, the response showed only a slight (14.3%) decrease, indicating its practical reusability.

SPR Analysis of OS-MIP. We further characterized the nature of the matrix made by a template-assisted conjugation by SPR-based kinetic and thermodynamic analyses. As controls, we prepared V_H and V_L fragments devoid of the MBP moiety, as well as the single chain Fv fragment (scFv), in which the V_H and V_L fragments are connected by a flexible $(G_4S)_3$ linker. As shown in Figure 2a–c, the matrices made with three combinations of variable region fragments (MBP-V_H/MBP-V_L, MBP-V_H/V_L, and V_H/V_L) in the presence of template HEL showed similar SPR responses to the analyte HEL. When these data as well as those for scFv were subjected to global fitting kinetic analysis, it was found that the association rate (k_{on}) of the interaction was significantly increased (up to 4.1-fold) when the ligands were each devoid of MBP. The resultant equilibrium dissociation constant K_d was as low as 1.4 nM, which was similar to that of scFv (Table 1). From this result, it was revealed that the MBP moiety is not essential for creating specific recognition matrix by OS-MIP. Considering the molecular weights for MBP-V_H (MBP-V_L) and V_H (V_L) of ~60 k and ~15 k, respectively, this result suggests sufficient mobility of the ligands made by OS-MIP upon binding with the analyte, implying ligand-dependent association of V_H/V_L as depicted in Figure 1a.

Table 1. Thermodynamic Parameters Obtained for the Interaction between Antigen HEL and the Ligands

ligand	MBP-V_H/MBP-V_L	MBP-V_H/V_L	V_H/V_L	scFv (V_H-V_L)
k_{on} (10^4/Ms)	6.7	13	28	38
k_{off} (10^{-4} s^{-1})	2.2	4.7	4.1	3.5
K_d (nM)	3.3	3.7	1.4	0.94
ΔH (kJ/mol)	−128	−132	−117	−170
ΔS (J/K·mol)	−260	−260	−240	−380

Thermodynamic Analysis of OS-MIP. To further analyze the nature of these matrices, we obtained thermodynamic parameters ΔH and ΔS by the SPR analysis with Biacore T100 at four different temperatures. As shown in Table 1, while the derived ΔH and ΔS values for matrices made by OS-MIP remain essentially the same (−125.7 ± 7.8 kJ/mol for ΔH, 253.3 ± 11.5 J/K·mol for ΔS) irrespective of tethered MBP, the absolute values were considerably smaller than those obtained for the scFv (−170 kJ/mol and −380 J/K·mol, respectively). The smaller entropy loss of OS-MIP suggests a higher degree of

dx.doi.org/10.1021/bc3000782 | Bioconjugate Chem. 2012, 23, 1463–1469

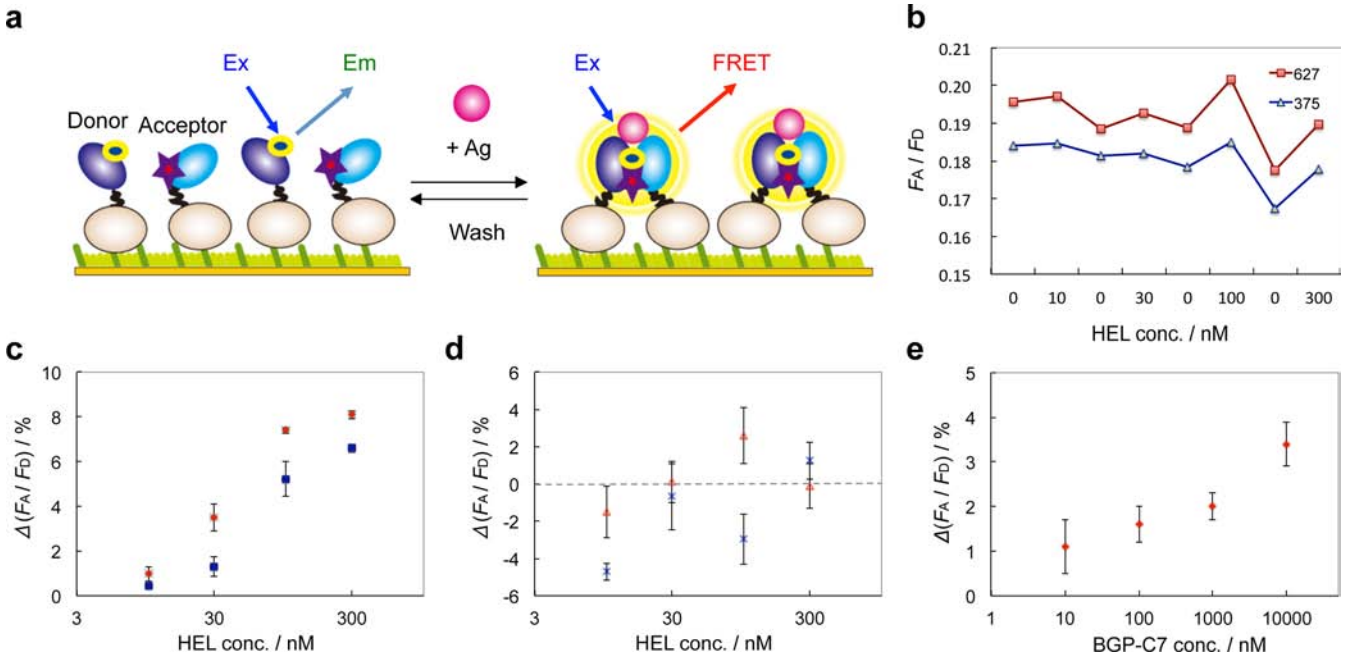


Figure 3. OS-MIP-based antigen sensor: (a) scheme; (b) example of raw data used to derive $\Delta(F_A/F_D)$ for immobilized anti-HEL Abs (Alexa555-MBP-V_H and Alexa647-MBP-V_L) made by OS-MIP at indicated ligand density (pg/mm^2); (c) dose−responses for HEL detection. Incubation time with antigen solution was 1 min (blue) or 10 min (red). The antigen-dependent change in F_A/F_D, taken as an index for FRET is shown. Average of six measurements (three each for two different amounts of immobilized ligand) with 1 SD is shown. (d) Results obtained with the matrix made under the premixed condition are shown as in (c) with open symbols. (e) Result for BGP detection with HiLyte555-MBP-V_L and Alexa647-MBP-V_H. The incubation time with antigen BGP-C7 was 10 min.

V_H/V_L prearrangement attained by OS-MIP than scFv, in which V_H and V_L fragments are connected by a flexible linker. Again, the apparent absence of the effect of MBP on ΔH and ΔS is considered to reflect the minor role of MBP in OS-MIP.

Application to Anti-Peptide Antibody. To assess the generality of the OS-MIP approach, we prepared the corresponding antibody fusion proteins derived of another antibody that recognizes the C-terminal fragment of human osteocalcin (bone gla protein, BGP).[13] BGP is known as a marker for bone metabolism and also suspected for its roles in insulin regulation[14] and male fertility.[15] Upon the binding of BGP or its C-terminal peptide, the Fv of this antibody is markedly stabilized. The matrix containing MBP-fused V_H/V_L was made in the presence of the BGP C-terminal peptide BGP-C7 (MW: 894) and measured for its antigen-binding response with an SPR biosensor as above (Figure 2d). In spite of lower signal due to lower molecular weight of the analyte, dose-dependent binding was surely observed with a calculated K_D of 4.68×10^{-8} M. On the contrary, we could not observe significant antigen binding when the antibody fusion proteins were immobilized in the absence of BGP peptide (data not shown). From these results, we concluded that the OS-MIP approach for making a specific recognition matrix has a generality in terms of applicable antigen−antibody pairs.

Application to FRET-Based Biosensor. To take advantage of the strong and specific binding of the matrix made by OS-MIP, we next examined its possibility as a fluorescence-based optical biosensor. Generally, Förster resonance energy transfer (FRET) is a useful technique to monitor intermolecular interaction in solution, and it has been successfully applied to detect many interactions in a small volume, such as an intracellular environment where bound per free (B/F) separation is impossible.[16,17] However, while FRET has also been proven useful to monitor the conformational change of proteins, it has been considered difficult to detect the interaction between immobilized molecules. To this end, we labeled the MBP-fused V_H and V_L fragments of anti-HEL antibody with fluorochromes Alexa555 and Alexa647, respectively, by amine coupling and used them for OS-MIP prepared similarly on a transparent glass slide. We expected that the CM dextran-tethered Alexa555-V_H and Alexa647-V_L would work, respectively, as a donor and an acceptor of FRET, which should be strengthened by the bridging antigen (Figure 3a).

When the two matrices with different ligand densities were made and tested for their antigen binding by SPR, a similar, albeit several-fold increase in K_d, antigen-binding affinity to that made with nonlabeled proteins was observed (Table S1, SI Figure S1a). Next, for fluorescence measurement, OS-MIP matrix was made on a glass slide and measured for the emission intensity ratio of two fluorochromes upon illumination of green laser (532 nm). To determine the antigen dose−response, the fluorescence intensity at the two wavelengths (F_D and F_A for 570 and 675 nm, respectively) was determined before and after antigen addition, and the change in their ratio (F_A/F_D) was taken as the signal. During these measurements, the same surfaces with two different ligand densities were regenerated by an acid wash and used repeatedly for each measurement (Figure 3b). As a result, the obtained HEL dose-dependency of the signal $\Delta(F_A/F_D)$ clearly showed a low limit of detection (LOD) of 30 nM HEL for 1 min incubation, and as low as 10 nM LOD for 10 min incubation (Figure 3c). It is worth noting that the intermeasurements error of $\Delta(F_A/F_D)$ was within ±5% when detected at 10 min, showing similar performance to SPR measurements. As a control, when the matrices were made similarly but without antigen (the "premixed" condition), the

dx.doi.org/10.1021/bc3000782 | Bioconjugate Chem. 2012, 23, 1463−1469

obtained signal did not show reliable antigen dependency (Figure 3d).

Furthermore, detection of the BGP peptide was attempted using the OS-MIP matrix made with fluorescence-labeled MBP-fused anti-BGP antibody fragments. The SPR results showed similar antigen-binding kinetics of the HiLyte555-labeled MBP-V_L/Alexa647-labeled MBP-V_H mixture to those obtained with nonlabeled proteins (SI Table S1, SI Figure S1b). The dose–response relationship of the OS-MIP matrix made on a glass slide for FRET measurement showed a good correlation with an LOD of 100 nM BGP-C7 within 10 min (Figure 3e).

Taken together, these data clearly show the practical utility of FRET-based antigen sensors made by OS-MIP. The obtained response is fast and reproducible. Moreover, such non-competitive and label-free antigen detection by FRET signal *in situ* would be hard to achieve by using conventional monoclonal antibody-based matrices, partly due to the lack of suitable fluorochrome pair with large (>100 Å) Förster distance R_0, which should be large enough if one wants to detect a sandwich complex made of two full-sized antibodies bridged by a typical protein antigen.

When the FRET response attained here is not enough and one wishes higher response in this OS-MIP based sensor, use of fluorochrome pairs giving more efficient FRET, such as those with Europium chelate,[18] and/or use of a more reliable fluorolabeling method such as position specific labeling during *in vitro* translation[19] will further increase the intensity and reproducibility of obtained FRET response.

Real-Time FRET Detection with OS-MIP. We also tried real-time detection of FRET-derived fluorescence using an OS-MIP matrix imprinted by HEL. With the use of anti-HEL HiLyte555-labeled MBP-V_L and Alexa647-labeled MBP-V_H fragments together with a handmade monitoring device (SI Figure S2), we were able to observe a significant time-dependent change in fluorescence intensity (SI Figure S3). Compared with the control sample without antigen, we could see a clear FRET-derived signal increase for the sample containing 1 μM HEL, which peaked within 10 min of HEL injection.

CONCLUSION

We combined the OS immunoassay concept with that of MIP, thus proposing a novel antibody-based recognition matrix that can be imprinted by a target antigen. Unlike conventional MIP, available targets include not only small molecules such as peptide but also larger proteins. Moreover, we successfully extended this concept to SPR- and FRET-based biosensors, and the affinity and sensitivity attained with the sensor were in the $\sim 10^8$/M range, which well exceeds that of most conventional MIP-based systems. Especially, the results of the FRET-based sensors suggest that they can detect different antigens *in situ* as a real-time fluorescence signal, which is hard to achieve with conventional antibody-based matrix. By utilizing the OS principle, the present strategy will be applicable to the detection of a range of antigens from proteins to small chemicals, probably on a protein chip in an arrayed format. The antibody V_H/V_L fragments have a merit that they can be immobilized at higher density than full-size antibodies to attain higher signal, and those obtained from synthetic phage-display libraries will enable detection of various targets even if they are toxic to immunized animals.[20] Furthermore, affinity maturation of antibody fragments is readily available by using phage display technology, if further enhancement of detection sensitivity is needed.[21] Hence, this method will be a strong analytical tool, possibly implemented as a portable and easy-to-use real-time analyzer, provided with a fertile library of available antibody reagents and sensitive sensing devices.

ASSOCIATED CONTENT

Supporting Information

A table for characterization of immobilized ligands, and supporting figures for FRET experiments. This material is available free of charge via the Internet at http://pubs.acs.org.

AUTHOR INFORMATION

Corresponding Author

*E-mail: hueda@chembio.t.u-tokyo.ac.jp, Tel/Fax: 81-3-5841-7362.

Present Address

[‖]Department of Bioscience and Biotechnology, Faculty of Agriculture, Shinshu University, Nagano, Japan.

Notes

The authors declare no competing financial interest.

ACKNOWLEDGMENTS

This work was done as a work of the donated chair "Biorecognition Molecular Technology, Fuji Film". We thank K. Kataoka, K. Ishihara, and T. Nagamune in Center for Nanobio Integration, UT for their valuable suggestions. We also thank T. Shinoda for allowing the use of anti-BGP antibody gene. We in debt M. Yoshida in UT, T. Adachi, S. Ohtsuka, Y. Takeuchi, and M. Ikeda in Frontier Core-Technology Laboratories, Fujifilm, M. Kawakami and S. Kimura in Lifescience Laboratories, Fujifilm for their experimental help. This work is partly supported by Grant-in-Aid for Scientific Research, JSPS, Japan, and by the Global COE Program for Chemistry Innovation, MEXT, Japan.

ABBREVIATIONS

BGP, bone gla protein (osteocalcin); ELISA, enzyme-linked immunoadsorbent assay; FRET, Förster resonance energy transfer; HEL, hen egg lysozyme; MBP, maltose-binding protein; MIP, molecularly imprinted polymers; OS-MIP, open-sandwich molecular imprinting; SPR, surface plasmon resonance; V_H, antibody heavy chain variable region; V_L, antibody light chain variable region.

REFERENCES

(1) Haupt, K. (2003) Imprinted polymers-tailor-made mimics of antibodies and receptors. *Chem. Commun. (Camb.)*, 171–178.

(2) Ge, Y., and Turner, A. P. (2008) Too large to fit? Recent developments in macromolecular imprinting. *Trends Biotechnol. 26*, 218–224.

(3) Janiak, D. S., and Kofinas, P. (2007) Molecular imprinting of peptides and proteins in aqueous media. *Anal. Bioanal. Chem. 389*, 399–404.

(4) Takeuchi, T., and Hishiya, T. (2008) Molecular imprinting of proteins emerging as a tool for protein recognition. *Org. Biomol. Chem. 6*, 2459–2467.

(5) Miyata, T., Jige, M., Nakaminami, T., and Uragami, T. (2006) Tumor marker-responsive behavior of gels prepared by biomolecular imprinting. *Proc. Natl. Acad. Sci. U.S.A. 103*, 1190–1193.

(6) Ueda, H., Tsumoto, K., Kubota, K., Suzuki, E., Nagamune, T., Nishimura, H., Schueler, P. A., Winter, G., Kumagai, I., and Mahoney, W. C. (1996) Open sandwich ELISA: A novel immunoassay based on

the interchain interaction of antibody variable region. *Nat. Biotechnol. 14*, 1714−1718.
(7) Ueda, H. (2002) Open sandwich immunoassay: a novel immunoassay approach based on the interchain interaction of an antibody variable region. *J. Biosci. Bioeng. 94*, 614−619.
(8) de Wildt, R. M., Mundy, C. R., Gorick, B. D., and Tomlinson, I. M. (2000) Antibody arrays for high throughput screening of antibody-antigen interactions. *Nat. Biotechnol. 18*, 989−994.
(9) Nishi, K., Takai, M., Morimune, K., and Ohkawa, H. (2003) Molecular and immunochemical characteristics of monoclonal and recombinant antibodies specific to Bisphenol A. *Biosci. Biotechnol. Biochem. 67*, 1358−1367.
(10) Ihara, M., Yoshikawa, A., Wu, Y., Takahashi, H., Mawatari, K., Shimura, K., Sato, K., Kitamori, T., and Ueda, H. (2010) Micro OS-ELISA: Rapid noncompetitive detection of a small biomarker peptide by open-sandwich enzyme-linked immunosorbent assay (OS-ELISA) integrated into microfluidic device. *Lab. Chip 10*, 92−100.
(11) Newman, M. A., Mainhart, C. R., Mallett, C. P., Lavoie, T. B., and Smith-Gill, S. J. (1992) Patterns of antibody specificity during the BALB/c immune response to hen eggwhite lysozyme. *J. Immunol. 149*, 3260−3272.
(12) Bach, H., Mazor, Y., Shaky, S., Shoham-Lev, A., Berdichevsky, Y., Gutnick, D. L., and Benhar, I. (2001) *Escherichia coli* maltose-binding protein as a molecular chaperone for recombinant intracellular cytoplasmic single-chain antibodies. *J. Mol. Biol. 312*, 79−93.
(13) Lim, S.-L., Ichinose, H., Shinoda, T., and Ueda, H. (2007) Noncompetitive detection of low molecular weight peptides by open sandwich immunoassay. *Anal. Chem. 79*, 6193−6200.
(14) Lee, N. K., Sowa, H., Hinoi, E., Ferron, M., Ahn, J. D., Confavreux, C., Dacquin, R., Mee, P. J., McKee, M. D., Jung, D. Y., Zhang, Z., Kim, J. K., Mauvais-Jarvis, F., Ducy, P., and Karsenty, G. (2007) Endocrine regulation of energy metabolism by the skeleton. *Cell 130*, 456−469.
(15) Oury, F., Sumara, G., Sumara, O., Ferron, M., Chang, H., Smith, C. E., Hermo, L., Suarez, S., Roth, B. L., Ducy, P., and Karsenty, G. (2011) Endocrine regulation of male fertility by the skeleton. *Cell 144*, 796−809.
(16) Miyawaki, A. (2003) Visualization of the spatial and temporal dynamics of intracellular signaling. *Dev. Cell 4*, 295−305.
(17) Wu, P., and Brand, L. (1994) Resonance energy transfer: Methods and applications. *Anal. Biochem. 218*, 1−13.
(18) Selvin, P. R., and Hearst, J. E. (1994) Luminescence energy transfer using a terbium chelate: improvements on fluorescence energy transfer. *Proc. Natl. Acad. Sci. U. S. A. 91*, 10024−10028.
(19) Hohsaka, T., Kajihara, D., Ashizuka, Y., Murakami, H., and Sisido, M. (1999) Efficient incorporation of nonnatural amino acids with large aromatic groups into streptavidin in in vitro protein synthesizing systems. *J. Am. Chem. Soc. 121*, 34−40.
(20) Strachan, G., McElhiney, J., Drever, M. R., McIntosh, F., Lawton, L. A., and Porter, A. J. R. (2002) Rapid selection of anti-hapten antibodies isolated from synthetic and semi-synthetic antibody phage display libraries expressed in Escherichia coli. *FEMS Microbiol. Lett. 210*, 257−261.
(21) Iwai, H., Oztürk, B., Ihara, M., and Ueda, H. (2010) Antibody affinity maturation *in vitro* using unconjugated peptide antigen. *Protein Eng. Des. Sel. 23*, 185−193.

Bioconjugate Chemistry

Article

pubs.acs.org/bc

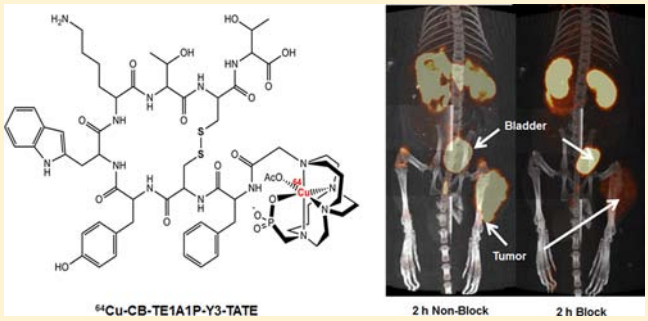
Preparation and Biological Evaluation of ^{64}Cu Labeled Tyr^3-Octreotate Using a Phosphonic Acid-Based Cross-Bridged Macrocyclic Chelator

Yunjun Guo,[†,‡] Riccardo Ferdani,[†] and Carolyn J. Anderson*[,†,‡,§,∥]

[†]Mallinckrodt Institute of Radiology, [‡]Department of Chemistry, and [§]Department of Biochemistry & Molecular Physics, Washington University, St. Louis, Missouri, United States

[∥]Department of Radiology, University of Pittsburgh, Pittsburgh, Pennsylvania, United States

ABSTRACT: Somatostatin receptors (SSTr) are overexpressed in a wide range of neuroendocrine tumors, making them excellent targets for nuclear imaging and therapy, and radiolabeled somatostatin analogues have been investigated for positron emission tomography imaging and radionuclide therapy of SSTr-positive tumors, especially of the subtype-2 (SSTr2). The aim of this study was to develop a somatostatin analogue, Tyr^3-octreotate (Y3-TATE), conjugated to a novel cross-bridged macrocyclic chelator, 11-carboxymethyl-1,4,8,11-tetraazabicyclo[6.6.2]hexadecane-4-methanephosphonic acid (CB-TE1A1P). Unlike traditional cross-bridged macrocycles, such as 4,11-bis(carboxymethyl)-1,4,8,11-tetraazabicyclo[6.6.2]hexadecane (CB-TE2A), CB-TE1A1P-Y3-TATE was radiolabeled with ^{64}Cu in high purity and high specific activity using mild conditions. Saturation binding assays revealed that ^{64}Cu-CB-TE1A1P-Y3-TATE had comparable binding affinity but bound to more binding sites in AR42J rat pancreatic tumor cell membranes than ^{64}Cu-CB-TE2A-Y3-TATE. Both radiopharmaceuticals showed comparable uptake in SSTr2 positive tissues in AR42J tumor-bearing rats. ^{64}Cu-CB-TE1A1P-Y3-TATE demonstrated improved blood clearance compared to ^{64}Cu-CB-TE2A-Y3-TATE, as the tumor/blood ratios of ^{64}Cu-CB-TE1A1P-Y3-TATE were shown to be significantly higher than those of ^{64}Cu-CB-TE2A-Y3-TATE at 4 and 24 h postinjection. ^{64}Cu-CB-TE1A1P-Y3-TATE, in spite of a relatively high kidney uptake, accumulated less in nontarget organs such as liver, lung, and bone. Small animal PET/CT imaging of ^{64}Cu-CB-TE1A1P-Y3-TATE in AR42J tumor bearing rats validated significant uptake and good contrast in the tumor. This study suggests that CB-TE1A1P is a promising bifunctional chelator for ^{64}Cu-labeled for Y3-TATE, owing to high binding affinity and target tissue uptake, the ability to radiolabel the agent at lower temperatures, and improved tumor/nontarget organ ratios over ^{64}Cu-CB-TE2A-Y3-TATE.



INTRODUCTION

Copper-64 ($T_{1/2}$ = 12.7 h) is an attractive radiometal for positron emission tomography, as it decays by β^+ at 656 keV (17.8% abundance), which provides high-quality PET images at relatively low radiation dose to patients and radiochemistry personnel. Moreover, ^{64}Cu is a promising therapeutic radiometal owing to its emission of β^- at 573 keV (39.6% abundance). Thus, ^{64}Cu holds great promise for combined cancer imaging and targeted radiotherapy.[1] We previously reported that the cross-bridged macrocycle 4,11-bis(carboxymethyl)-1,4,8,11-tetraazabicyclo[6.6.2]hexadecane (CB-TE2A) was a superior bifunctional chelator for ^{64}Cu compared with 1,4,8,11-tetraazacyclotetradecane-1,4,8,11-tetraacetic acid (TETA) and 1,4,7,10-tetraazacyclododecane-1,4,7,10-tetraacetic acid (DOTA) due to the exceptional kinetic inertness of its Cu (II) complexes.[2] CB-TE2A stably chelated ^{64}Cu *in vivo* and significantly reduced the amount of ^{64}Cu being transchelated to superoxide dismutase in the liver.[3−5] The advantage could be retained after CB-TE2A was conjugated to the somatostatin analogue Y3-TATE, as ^{64}Cu-CB-TE2A-Y3-TATE demonstrated improved tumor uptake, as well as liver and blood clearance compared to ^{64}Cu-TETA-Y3-TATE, resulting in higher tumor to tissue ratios.[6] Though CB-TE2A is a very promising bifunctional chelator for ^{64}Cu, a significant disadvantage is that it cannot be applied in radiolabeling antibodies or other heat-sensitive compounds, due to the fact that radiolabeling with ^{64}Cu requires heating to 95 °C for at least 1 h.

It has been reported that the metal-binding kinetics of cyclam-derived macrocycles can be accelerated by substituting the carboxylate pendant arms with phosphonate pendant arms.[7] The thermodynamic stability of the Cu(II) complexes of certain phosphonate chelators was proven to be favorable compared to their acetate analogues.[8] The radiochemistry and biodistribution of a diphosphonate cross-bridged macrocycle, 1,4,8,11-tetraazabicyclo[6.6.2]hexadecane-4,11-bismethanephosphonic

Received: February 24, 2012
Revised: May 24, 2012
Published: June 5, 2012

 © 2012 American Chemical Society

acid (CB-TE2P) labeled with ^{64}Cu, was recently communicated.[7] Although CB-TE2P could be radiolabeled with ^{64}Cu at room temperature, there were challenges in conjugating the diphosphonate to primary amine side chains of peptides. Ferdani et al. recently reported the synthesis and ^{64}Cu radiolabeling of a monocarboxylate monophosphonate chelator, CB-TE1A1P (11-carboxymethyl-1,4,8,11-tetraazabicyclo[6.6.2]hexadecane-4-methanephosphonic acid).[9] ^{64}Cu-CB-TE1A1P can be prepared at room temperature and was shown to have high *in vivo* stability in normal rats.

We report here the synthesis of CB-TE1A1P conjugated to the somatostatin analogue Y3-TATE radiolabeled with ^{64}Cu for PET imaging and targeted radiotherapy for SSTr2 positive tumors. SSTr2-positive rat pancreatic AR42J cells and tumor-bearing rats are used to evaluate the *in vitro* and *in vivo* behavior of ^{64}Cu-CB-TE1A1P-Y3-TATE. The biological behavior of ^{64}Cu-CB-TE1A1P-Y3-TATE is compared to previously published data with ^{64}Cu-CB-TE2A-Y3-TATE.[12]

MATERIALS AND METHODS

Copper-64 was produced on a CS-15 biomedical cyclotron at Washington University School of Medicine as previously described.[10] Unless specified, all chemicals were purchased from Sigma-Aldrich Chemical Co. (St. Louis, MO). Aqueous solutions were prepared using ultrapure water (resistivity, 18 mΩ). The peptide Y3-TATE was purchased from CS Bio (Madera, CA) and Tianma Pharma (Sichuan, China). Analytical and semipreparative reversed-phase high-performance liquid chromatography (HPLC) was performed on a Waters 600E (Milford, MA) chromatography system with a Waters 991 photodiode array detector and an Ortec model 661 (EG&G Instruments, Oak Ridge, TN) radioactivity detector. Non-radioactive HPLC samples were analyzed on an analytical C18 column (Vydac, Deerfield, IL) and purified on a semipreparative C18 column (Waters, Milford, MA). Radiochemistry reaction progress and purity were monitored on a rocket C18 column (Alltima, Deerfield, IL). The mobile phase was H_2O (0.1% TFA; solvent A) and acetonitrile (0.1% TFA; solvent B). Radioactive samples were counted using an automated well-type γ-counter (8000; Beckman, Irvine, CA) or a β-plate reader (1450 Micro Beta; Perkin-Elmer, Waltham, MA). The PET data were acquired using an Inveon small animal PET/CT scanner (Siemens Medical Solutions; Knoxville, TN). Electrospray mass spectrometry was accomplished using a Waters Micromass ZQ (Milford, MA).

Animal Model. Male Lewis rats (age, 21 d; weight, 40−50 g) were purchased from Charles River Laboratories (Boston, MA) and handled according to the procedures outlined by the Washington University Animal Studies Committee. AR42J pancreatic tumors were implanted into the hind limbs by serial passage as previously described and were allowed to grow 10−14 d.[6]

Synthesis of CB-TE1A1P-Y3-TATE. The conjugation of Y3-TATE to CB-TE1A1P was performed based on the method by Sprague et al.[6] side-chain protected Y3-TATE on resin (50.3 mg, 6.2 μmol of Y3-TATE peptide) was washed sequentially with dichloromethane (DCM) (2 × 3 mL), methanol (2 × 3 mL), and DCM (2 × 3 mL), and dried under vacuum. The resin was swollen in DCM (3 mL) for 45 min and washed with DMF (3 mL) several times. To a solution of CB-TE1A1P (32.2 mg, 85 μmol) in DMF (1.5 mL) and DMSO (1 mL), DIC (20.4 mg, 161 μmol), and DIEA (37.1 mg, 288 μmol) was added. The mixture was stirred for 25 min before being added to the peptide resin. After end-to-end rotation at room temperature for 10 d, the resin was filtered, washed with DCM (3 × 3 mL) to remove residual DMF, and dried under vacuum. The peptide conjugate was cleaved from the resin by stirring with a mixture of TFA/water/thioanisol/phenol (85:5:5:5) for 4 h followed by precipitation in cold *t*-butyl methyl ether. HPLC purification of CB-TE1A1P-Y3-TATE was performed on a semipreparative C18 column (10 × 250 mm, 10 μm; Alltima) using two solvent systems with the gradient elution method at a flow rate of 3 mL/min. Solvent A was 0.1% TFA in water, and solvent B was 0.1% TFA in acetonitrile. The elution method started with a linear gradient from 90% to 80% A over 10 min, followed by 80% to 70% A over 10 min, and from 70% to 40% over 3 min. The elution profile was monitored by UV absorbance at 254 nm.

Purified CB-TE1A1P-Y3-TATE (~7% yield) was obtained as a white powder after lyophilization in water/acetonitrile mixture. The compound was characterized by analytical HPLC and electrospray mass spectroscopy. Calculated mass for $C_{64}H_{92}N_{14}O_{16}P_1S_2$ = 1409.6 (ESI + MS) *m/z* (% relative intensity, ion), $(M+H)^+$ = 1409.1399, $(M+2H)^{2+}$ = 705.0614, and $(M+3H)^{3+}$ = 470.3873.

Radiochemistry of ^{64}Cu-CB-TE1A1P-Y3-TATE. Radiolabeling of CB-TE1A1P-Y3-TATE with ^{64}Cu was achieved by reacting 1−1.5 mCi (37−55.5 MBq) of ^{64}Cu with 1 μg (7.09 × 10^{-4} μmol) of CB-TE1A1P-Y3-TATE in 100 μL of 0.1 M ammonium acetate (pH 8.0). The reaction was incubated for various times at 95 °C, 40 °C or room temperature. Radiochemical purity was determined by radio-HPLC with a rocket C18 column (7 × 53 mm, 3 μm; Alltima). For reactions of less than 95% purity, ethylenediaminetetraacetic acid (EDTA) and a C-18 SepPak Light cartridge (Waters) were used to remove nonchelated ^{64}Cu as described by Wadas et al.[11] Briefly, buffered EDTA was added to chelate free ^{64}Cu and the mixed solution was then loaded onto a SepPak cartridge (Waters, Milford, MA). After washing the SepPak cartridge with 5 mL water, eluting with absolute ethanol containing 5% acetic acid recovered 70−80% of the labeled peptide. The radiopharmaceutical was evaporated and rediluted in buffer or saline before being used for further cell or animal studies.

***In Vitro* Binding Affinity.** The affinity of ^{64}Cu-CB-TE1A1P-Y3-TATE for SSTr2 was determined by a saturation binding assay based on previously published methods.[12] AR42J cell membrane preparations were diluted in binding buffer [0.1% bovine serum albumin, 50 mM Tris-HCl (pH 7.4), 5.0 mmol/L $MgCl_2$, 0.5 μg/mL aprotinin, 200 μg/mL bacitracin, 10 μg/mL leupeptin, and 10 μg/mL pepstatin A], and 20 μg of membrane was added to each well of a 96-well filtration plate (Multiscreen Durapore; Millipore; Billerica, MA). Membranes were incubated with increasing concentrations of ^{64}Cu-CB-TE1A1P-Y3-TATE for 2 h at room temperature. Nonspecific binding was determined by saturating receptors with excess Y3-TATE. Upon reaching equilibrium, unbound radioactivity was filtered, and the membranes were washed twice with 200 μL binding buffer. Bound radioactivity was measured with a liquid scintillation and luminescence plate reader (1450 Microbeta; Perkin-Elmer; Waltham, MA). Total binding sites (B_{max}) and binding affinity (K_d) were determined by a nonlinear regression fit of bound peptides per milligram of protein versus concentration of radioligand using GraphPad Prism v 5.0 (San Diego, CA).

Cellular Internalization. AR42J cells were seeded in 6-well plates and cultured with DMEM medium supplemented with 20% fetal bovine serum and 0.1% gentamicin (3 mL/well) at 37

°C in a humidified atmosphere containing 5% CO_2 until 90% confluence was reached. Cells were incubated with 4 nM ^{64}Cu-CB-TE1A1P-Y3-TATE (37 MBq/μg), with or without the addition of excess Y3-TATE (2 μg/well) to block nonspecific internalization. At each time point, the surface-bound fractions were collected as previously described.[13] Internalized activity was collected by lysing the cells with 0.5% SDS. Total protein content in the cell lysates was determined by BCA protein assay (Pierce Biotechnology; Rockford, IL). Surface-bound and internalized fractions were expressed as the percentage of administered activity per milligram of protein.

***In Vivo* Biodistribution.** The biodistribution studies were carried out as previously described.[14] ^{64}Cu-CB-TE1A1P-Y3-TATE (0.74 MBq, 20 ng in 150 μL) was injected into AR42J tumor-bearing male Lewis rats (5 weeks old) via tail vein. At 1, 4, and 24 h after injection, rats were sacrificed and selected organs were taken, weighed, and counted on a γ counter (Beckman 8000; Irvine, CA). A blocking study was also conducted to examine the specificity of *in vivo* uptake where ^{64}Cu-CB-TE1A1P-Y3-TATE (0.74 MBq, 20 ng in 150 μL) was coinjected with 200 μg of Y3-TATE into AR42J tumor-bearing male Lewis rats (5 weeks old) via tail vein. Tissue uptake was measured at 4 h after injection.

Small Animal PET/CT Imaging. AR42J tumor-bearing male Lewis rats (5 weeks old) were injected with ^{64}Cu-CB-TE1A1P-Y3-TATE (7.4 MBq, 200 ng in 150 μL). At 2 h after injection, rats were anesthetized with 1−2% isoflurane and imaged. A blocking study was conducted in two AR42J tumor-bearing male Lewis rats (5 weeks old) by coinjecting ^{64}Cu-CB-TE1A1P-Y3-TATE (7.4 MBq, 200 ng in 150 μL) with 200 μg of Y3-TATE. The blocking group was also imaged at 2 h postinjection. Tumor standard uptake values (SUV) were generated by measuring regions of interest from PET/CT images and calculated with the formula: SUV = [*n*Ci/mL] × [animal weight (g)]/injected dose [*n*Ci].

Statistical Methods. All of the data are presented as mean ± standard error. To determine statistical significance, two-tailed unpaired *t*-tests were performed using GraphPad Prism, with $p < 0.05$ considered statistically significant.

RESULTS

Synthesis of CB-TE1A1P-Y3-TATE. The chemical structure of CB-TE1A1P-Y3-TATE is shown in Figure 1A. The carboxylic group of CB-TE1A1P first reacts with dicyclohexylcarbodiimide to form an *O*-acylisourea or an intermolecular acid anhydride. Both activated intermediates then react with *N*-terminal amino groups of the peptides on solid support to produce amide linkages. The presence of phosphoramidates was not observed, indicating that the phosphonic group of CB-TE1A1P does not form stable conjugates with peptides. Previous studies have shown that the reaction between phosphonic groups and amines can occur, but the products hydrolyze and are stable only under strongly basic conditions.[15,16] We postulate that the hydrolysis of phosphoramidates leads to a lowered conjugation yield (~7%) and necessitates HPLC purification to separate desired carboxylate-conjugated species from the unconjugated Y3-TATE peptide. The yield can be further improved by more cycles of HPLC purification, if needed.

Radiochemistry of ^{64}Cu-CB-TE1A1P-Y3-TATE. As shown in Figure 1B, radiolabeling of CB-TE1A1P-Y3-TATE with ^{64}Cu in 0.1 M NH_4OAc (pH 8.0) at room temperature resulted in ~60% labeling efficiency after 1 h, while raising the temperature to 40 °C increased the radiochemical yield to over 90%. Heating

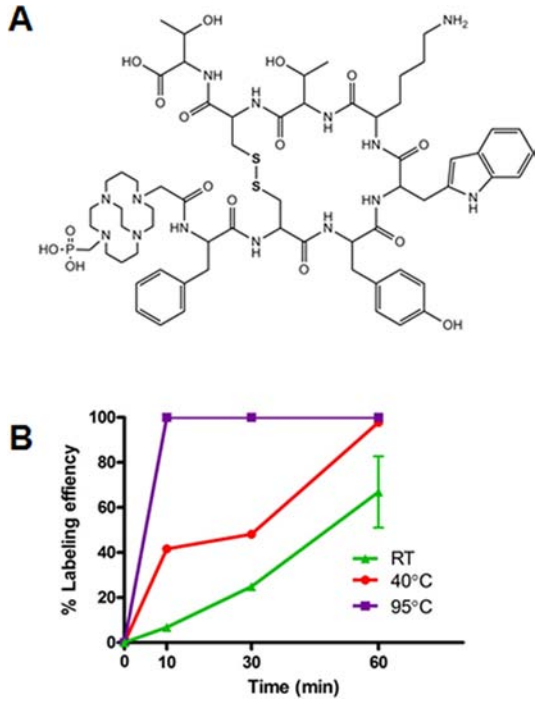


Figure 1. Chemical structure of CB-TE1A1P-Y3-TATE (A). Labeling efficiency of CBTE1A1P-Y3-TATE with ^{64}Cu in in 0.1 M NH_4OAc (pH 8.0) at different temperatures (B).

to 95 °C reduced the reaction time to less than 10 min with a labeling efficiency over 95% and improved specific activity from 1 mCi/μg to 1.5 mCi/μg. The radiochemical purity of ^{64}Cu-CB-TE1A1P-Y3-TATE was validated by radio-HPLC on a rocket C18 column.

***In Vitro* Binding Affinity.** Saturation binding assays were performed with AR42J cell membranes bearing SSTr2 based on previously described methods (Figure 2A).[15] The total number of binding sites (B_{max}) for ^{64}Cu-CB-TE1A1P-Y3-TATE was 3410 ± 220 fmol/mg, which is 1.5−3-fold higher than that observed for ^{64}Cu-CB-TE2A-Y3-TATE (B_{max} = 1090−2100 fmol/mg).[6] The K_d for ^{64}Cu-CB-TE1A1P-Y3-TATE was 1.8 ± 0.5 nM, suggesting that the CB-TE1A1P and CB-TE2A conjugates (K_d of ^{64}Cu-CB-TE2A-Y3-TATE = 1.7 nM) have similar binding affinities for SSTr2 in AR42J membranes.

Cellular Internalization. Internalization studies of ^{64}Cu-CB-TE1A1P-Y3-TATE were also performed with AR42J cells based on previously described methods (Figure 2B).[20] All data are presented as the percentage of administrated radioactivity per milligram of protein. Rapid early stage internalization was observed for ^{64}Cu-CB-TE1A1P-Y3-TATE during the initial 30 min, which was followed by two slower phases at 60 and 120 min. The amount of radiotracer internalized reached 34 ± 0.4% by 240 min. Specific receptor-mediated internalization could be readily blocked by an excess of Y3-TATE in the medium. The surface-bound fraction of radiotracer was also collected and quantified. The amount of ^{64}Cu-CB-TE1A1P-Y3-TATE bound to the cell surface reached 5.2 ± 0.03% within the first 15 min, and increased slightly over the next 225 min. Surface-bound activity was blocked with excess Y3-TATE in the culture medium.

***In Vivo* Biodistribution.** The biodistribution study of ^{64}Cu-CB-TE1A1P-Y3-TATE was conducted in 42-day-old AR42J tumor-bearing male Lewis rats (Figure 3). The data are compared to previously published data with ^{64}Cu-CB-TE2A-

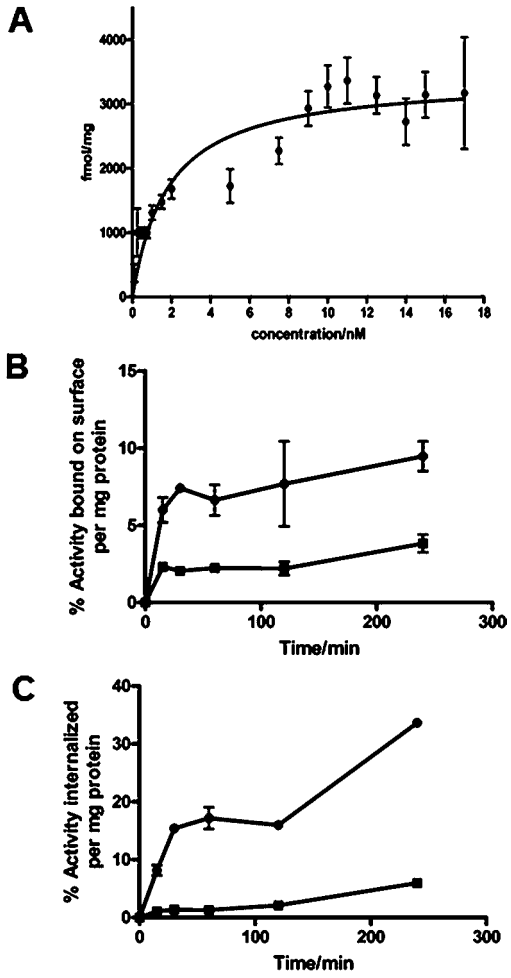


Figure 2. *In vitro* binding affinity of ^{64}Cu-CB-TE1A1P-Y3-TATE for SSTr2 was determined by a saturation binding assay in AR42J rat pancreatic tumor cell membranes (n = 3 for each data point; mean value ± SE) (A). Internalization studies of ^{64}Cu-CB-TE1A1P-Y3-TATE were conducted in AR42J whole cells. Radioactivity bound on cell surface (B) and internalized (C) were determined. Specific uptake was blocked by addition of 2 μg Y3-TATE to the incubation media (^{64}Cu-CB-TE1A1P-Y3-TATE; blocked ^{64}Cu-CB-TE1A1P-Y3-TATE; n = 3 for each data point; mean value ± SE).

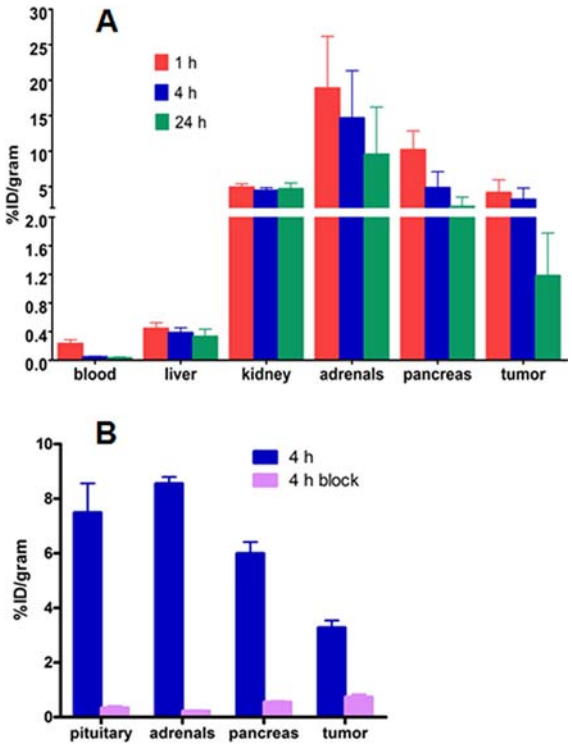


Figure 3. Biodistribution of ^{64}Cu-CB-TE1A1P-Y3-TATE was conducted in AR42J tumor-bearing male lewis rats (A). A separate blocking study (B) was performed to confirm the specificity of ^{64}Cu-CB-TE1A1P-Y3-TATE for SSTr2. Data are presented as percent injected dose per gram (n = 3−5 for each data point; bars ± SE).

Y3-TATE.[12] Both ^{64}Cu-CB-TE1A1P-Y3-TATE and ^{64}Cu-CB-TE2A-Y3-TATE demonstrated rapid blood clearance at 1 h (0.2 ± 0.05 vs 0.2 ± 0.01%ID/g for ^{64}Cu-CB-TE1A1P-Y3-TATE and ^{64}Cu-CB-TE2A-Y3-TATE, respectively). By 24 h, ^{64}Cu-CB-TE1A1P-Y3-TATE cleared from the blood to 14.6% of the 1 h ^{64}Cu activity, compared to 26.3% for ^{64}Cu-CB-TE2A-Y3-TATE. At 1 h, liver uptake of ^{64}Cu-CB-TE2A-Y3-TATE was significantly higher than of ^{64}Cu-CB-TE1A1P-Y3-TATE (p < 0.03). However, there was higher uptake of ^{64}Cu-CB-TE1A1P-Y3-TATE in the kidneys at every time point compared to ^{64}Cu-CB-TE2A-Y3-TATE (p < 0.0001). From 1 to 24 h, 75% of the ^{64}Cu-CB-TE1A1P-Y3-TATE activity was cleared from liver, whereas less than 10% was excreted from the kidneys. The ^{64}Cu-CB-TE2A-Y3-TATE activity in the liver and kidneys fell by 36% and 50% at 24 h, respectively.

Lower accumulation of ^{64}Cu activity in other nontarget organs was observed for the ^{64}Cu labeled CB-TE1A1P conjugate as compared to CB-TE2A. Bone uptake at every time point was significantly higher for ^{64}Cu-CB-TE2A-Y3-TATE than for ^{64}Cu-CB-TE1A1P-Y3-TATE (p < 0.03). In addition, there was about 3-fold greater activity in the lung for ^{64}Cu-CB-TE2A-Y3-TATE than for ^{64}Cu-CB-TE1A1P-Y3-TATE at 1 h after injection (p = 0.001), increasing to 5.6 times greater at 4 h (p < 0.0001). Activity levels in the lung were reduced by 76% and 85% of the 1 h activity for ^{64}Cu-CB-TE1A1P-Y3-TATE and ^{64}Cu-CB-TE2A-Y3-TATE at 24 h, respectively, resulting in comparable uptake for the two radiopharmaceuticals.

The amount of activity associated with SSTr2 positive tumor and pancreas was also quantified. Initially at 1 h, ^{64}Cu uptake in pancreas was high for both ^{64}Cu-CB-TE1A1P-Y3-TATE and ^{64}Cu-CB-TE2A-Y3-TATE (CB-TE1A1P = 10.2 ± 2.7% ID/g, CB-TE2A = 5.7 ± 0.4 ID/g); however, clearance appeared to be quite efficient as 79% and 85% of the 1 h activity had been cleared by 24 h, respectively. In addition, more ^{64}Cu accumulation in the pancreas was observed for ^{64}Cu-CB-TE1A1P-Y3-TATE than for ^{64}Cu-CB-TE2A-Y3-TATE at both 1 and 4 h after administration of radiopharmaceuticals ($p \leq 0.01$). Both ^{64}Cu-labeled conjugates were retained in the tumor for at least 4 h, as no significant change of tumor uptake was observed from 1 to 4 h. The two radiopharmaceuticals cleared from the tumor at a similar rate over time (72% of ^{64}Cu-CB-TE1A1P-Y3-TATE and 69% of ^{64}Cu-CB-TE2A-Y3-TATE from 1 to 24 h). Tumor to blood ratios for ^{64}Cu-CB-TE1A1P-Y3-TATE were 76 ± 20 and 33 ± 7 at 4 and 24 h, respectively, and 44 ± 10 and 20 ± 4, respectively, for ^{64}Cu-CB-TE2A-Y3-TATE ($p \leq 0.01$) (Figure 4). Similarly, the tumor to muscle ratio for ^{64}Cu-CB-TE1A1P-Y3-TATE was significantly higher than for ^{64}Cu-CB-TE2A-Y3-TATE at both 4 h (CB-TE1A1P = 178 ± 56, CB-TE2A = 77 ± 16; p < 0.01) and 24 h (CB-TE1A1P = 112 ± 10, CB-TE2A = 47 ± 18, p < 0.0001).

dx.doi.org/10.1021/bc300092n | *Bioconjugate Chem.* 2012, 23, 1470−1477

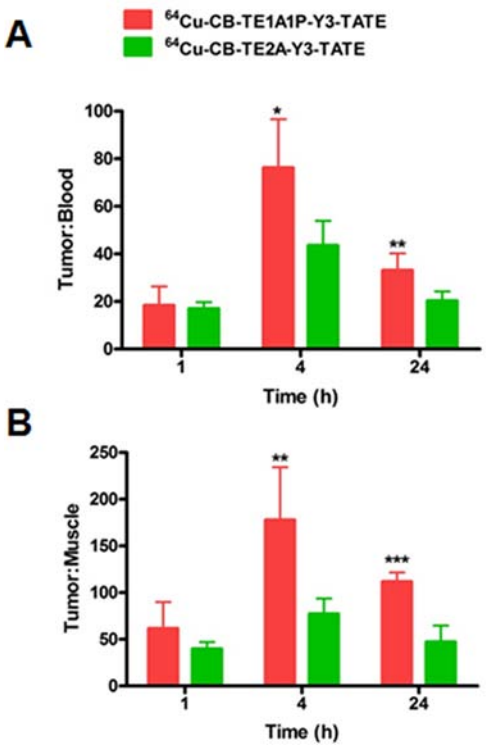


Figure 4. Comparison of tumor/blood (A) and tumor/muscle (B) ratios of ^{64}Cu-CB-TE1A1P-Y3-TATE and ^{64}Cu-CBTE2A-Y3-TATE[11] at 1, 4, and 24 h postinjection in AR42J pancreatic tumor-bearing male lewis rats (*p < 0.05, **p < 0.01, ***p < 0.001).

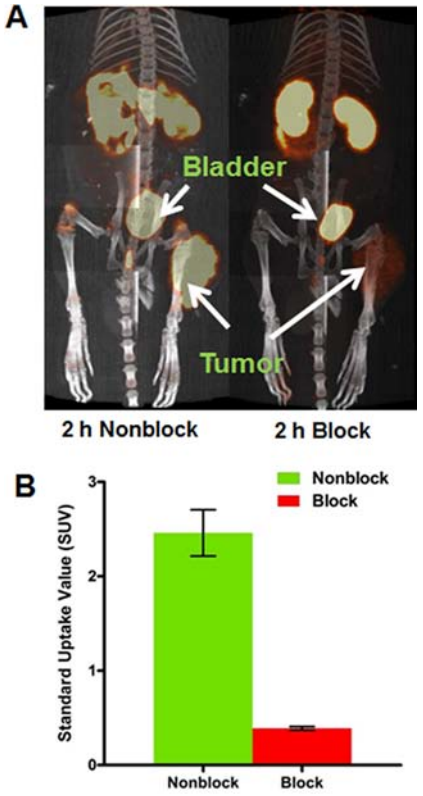


Figure 5. Small animal PET/CT projection images of AR42J tumor bearing rats at 2 h postinjection of ^{64}Cu-CBTE1A1P-Y3-TATE, with or without 24 h preinjection of excess amount of Y3-TATE (A). PET/CT image at 2 h after administration of ^{64}Cu-CB-TE1A1P-Y3-TATE (B). Standard uptake values (SUV) were calculated by measuring the activity in regions of interest from PET images of AR42J pancreatic tumor bearing Lewis rats (n = 2; bars ± SE; p = 0.007).

A separate blocking study was performed at 4 h after injection for ^{64}Cu-CB-TE1A1P-Y3-TATE by coinjecting cold peptide Y3-TATE (Figure 3A). Injection of Y3-TATE increased the kidney uptake from 1.9 ± 0.03%ID/g to 2.4 ± 0.2%ID/g. This observation is in agreement with previous studies of ^{64}Cu-labeled somatostatin analogues and may be due to the increase in bioavailability of radioactive compounds when excess cold peptide blocks receptor-mediated uptake. All SSTr2 expressing tissues showed at least 90% reduction in ^{64}Cu uptake when blocked with Y3-TATE (pituitary, 7.5 ± 1.1%ID/g; pituitary blocked, 0.3 ± 0.07%ID/g; adrenals, 8.6 ± 0.2%ID/g; adrenals blocked, 0.2 ± 0.02%ID/g; pancreas 6.0 ± 0.1%ID/g; pancreas blocked, 0.6 ± 0.04%ID/g). Tumor uptake of ^{64}Cu-CB-TE1A1P-Y3-TATE was reduced from 3.3 ± 0.3%ID/g to 0.7 ± 0.09%ID/g (p < 0.0001), demonstrating that this novel radiopharmaceutical specifically targets SSTr2.

Small Animal PET/CT Imaging. Figure 5 shows the small animal PET/CT projection images of AR42J tumor-bearing male Lewis rats. As early as 2 h after administration of ^{64}Cu-CB-TE1A1P-Y3-TATE, the tumor was clearly visible in PET image with an average SUV of 2.5 ± 0.2. The coinjection of cold Y3-TATE resulted in a significant reduction in the tumor signal, and the average tumor SUV fell to 0.4 ± 0.02. On the basis of SUV analysis, 85% of the tumor uptake was effectively blocked by coinjecting excess cold peptide (p = 0.007). This further confirms the specificity of ^{64}Cu-CB-TE1A1P-Y3-TATE to SSTr2 and reveals a low level of nonspecific binding. Prominent uptake was observed in the bladder and kidneys of all animals, which was primarily due to the fact that renal clearance was the major excretion route for small peptide radiopharmaceuticals. Excess Y3-TATE also blocked uptake in the bone. This finding correlates with the results from previously performed biodistribution experiments (data not shown).

■ DISCUSSION

CB-TE2A has been reported as a promising chelator for ^{64}Cu radiopharmaceuticals owing to its remarkable kinetic inertness.[2,6,17] However, the requirement of harsh labeling conditions has precluded its applications in heat-sensitive targeting vectors. Methanephosphonic acid ($-CH_2-PO(OH)_2$) groups were introduced into macrocyclic chelators to improve thermodynamic and kinetic stability.[7,18,19] Unlike previously reported cross-bridged cyclam chelators, CB-TE1A1P readily forms ^{64}Cu complexes at room temperature under no-carrier-added conditions. This advantage of CB-TE1A1P over CB-TE2A is mostly preserved after conjugation to Y3-TATE. Radiolabeling of CB-TE1A1P-Y3-TATE with ^{64}Cu reached 98% at 40 °C after 60 min without the need of further purification, while more rigorous conditions (95 °C, 1 h) are necessary for labeling CB-TE2A-Y3-TATE. CB-TE1A1P-Y3-TATE is the first cross-bridged chelator–peptide conjugate that can be labeled with ^{64}Cu at 40 °C. We anticipate that expanding the length of the covalent linkage between the CB-TE1A1P and the Y3-TATE peptide will enhance facile radiolabeling, which is particularly important for radiolabeling proteins and monoclonal antibodies.

^{64}Cu-CB-TE1A1P-Y3-TATE and ^{64}Cu-CB-TE2A-Y3-TATE have similar binding affinities as for SSTr2, but the total binding sites on AR42J membranes is greater for the CB-TE1A1P

dx.doi.org/10.1021/bc300092n | Bioconjugate Chem. 2012, 23, 1470–1477

conjugate than for the CB-TE2A conjugate. Reubi et al. have demonstrated that relatively small changes in a radiolabeled peptide, such as changing the chelator, can markedly change the SSTr binding profile of the somatostatin analogues.[20] In fact, the difference in the B_{max} value between ^{64}Cu-labeled CB-TE1A1P- and CB-TE2A-Y3-TATE conjugates (3410 ± 220 vs 1090−2100 fmol/mg) is much less dramatic than that between CB-TE2A and TETA (B_{max} = 192 fmol/mg).[6] The structural change from Cu(II)-TETA to Cu(II)-CB-TE2A is significant, as the two oxygen donors from carboxylate groups adapt axial positions in the pseudo-octahedral geometry of Cu(II)-TETA, but the two oxygens are in the plane of the Cu(II)-CB-TE2A complex.[21−23] The X-ray structure of Cu(II)-CB-TE1A1P reveals a full six-coordinate distorted octahedral N_4O_2 envelopment of the cation with Jahn−Teller elongation along the O(1)−Cu(1)−N(2) axis, which is very similar to the structure of Cu(II)-CB-TE2A.[19] Thus, the relatively small yet significant increase in B_{max} may be attributed to the minor structural alteration and stabilization of the Cu(II)-CB-TE1A1P chelate in the lipid-rich environment of the receptor.

Assays were performed to determine the extent of radiopharmaceutical internalization of ^{64}Cu-CB-TE1A1P-Y3-TATE in AR42J rat pancreatic carcinoma cells. Rapid internalization was observed for the initial 30 min, followed by a static period from 30 to 120 min. Another active internalizing period occurred after 120 min and was sustained through 240 min. These observations are consistent with a previous report that somatostatin agonists and the SSTr2 receptor are predominantly recycled after receptor-mediated endocytosis rather than being routed to lysosomes for degradation.[24] After the initial 30 min of rapid internalization, most receptors that are bound to the radiopharmaceutical have been internalized and few receptors are available on the cell surface to internalize more radioligands. The recycling of SSTr2 receptors from the cell cytosol to the surface takes place between 30 and 120 min after the administration of radiopharmaceutical, which explains the static period and a subsequent round of active endocytosis after 120 min. Internalization of ^{64}Cu-CB-TE1A1P-Y3-TATE was blocked by excess cold Y3-TATE, validating that this is a receptor-mediated process.

Comparison of *in vivo* behaviors between ^{64}Cu-CB-TE1A1P-Y3-TATE and ^{64}Cu-CB-TE2A-Y3-TATE[12] was made in AR42J tumor-bearing male Lewis rats. To facilitate comparison, the same amounts of radiopharmaceuticals, both mass- and activity-wise, were administrated in both biodistribution studies. The two radiopharmaceuticals demonstrated substantial uptake in SSTr2 positive tissues and AR42J tumors. The uptake was significantly reduced by coinjection of cold Y3-TATE as a blocking agent, demonstrating that the interaction between the radiotracers and the organs is a specific receptor-mediated process *in vivo*. Comparable tumor uptake values were observed at every time point. In addition, they were cleared from the tumors at similar rates, which is correlated with the fact that ^{64}Cu-CB-TE1A1P-Y3-TATE has similar binding affinity to ^{64}Cu-CB-TE2A-Y3-TATE for SSTr2 in AR42J tumor membranes.

There was greater accumulation of ^{64}Cu-CB-TE2A-Y3-TATE in the liver than ^{64}Cu-CB-TE1A1P-Y3-TATE at 1 h post-injection, which may be attributed to charge differences of the two conjugates. Cu(II)-CB-TE2A-Y3-TATE has a net charge of +2 on the entire conjugate, while Cu(II)-CB-TE1A1P-Y3-TATE is +1 due to the one extra negative charge of the methanephosphonate arm. Jones-Wilson et al. reported that positively charged cyclam and Et-cyclam had higher accumulation in the liver of normal rats.[25] On the basis of several studies that had been conducted to investigate the effect of charge on kidney uptake of radiolabeled peptides,[3,25,26] renal retention of radioactivity was typically greatest for positively charged peptide conjugates and lowest for negatively charged ones. We observed increased renal retention for ^{64}Cu-CB-TE1A1P-Y3-TATE compared to ^{64}Cu-CB-TE2A-Y3-TATE, suggesting that more factors than charge should be considered when one is predicting the *in vivo* performance of a radiopharmaceutical. Sun et al. examined the *in vivo* behaviors of a series of ^{64}Cu-labeled methanephosphonate tetraaza macrocyclic ligands (DO2P, DO3P, and DOTP).[8] Their results suggested that the renal retention of the Cu(II) complexes increased as the number of methanephosphonate groups increased, regardless of the extra negative charges from phosphonic acid moieties.

The results from animal studies stand in contrast to those from *in vitro* stability tests. An acid inertness study of Cu(II)-CB-TE1A1P in 5 M HCl at 90 °C gave a half-life of 6.8 h,[9] which indicates significantly less stability under these conditions than Cu(II)-CB-TE2A (half-life = 154 h).[22] This discrepancy can be explained by the possibility that conjugation of CB-TE1A1P to Y3-TATE improves the stability of Cu-CB-TE1A1P complex, or that the acid stability studies are not highly accurate for predicting *in vivo* behavior.

Recently, Fani et al. reported the evaluation of two novel ^{64}Cu-labeled somatostatin antagonists, ^{64}Cu-CB-TE2A-LM3 and ^{64}Cu-NODAGA-LM3,[27] and demonstrated a strong dependence of the affinity and pharmacokinetics of the radiolabeled somatostatin antagonists on the chelators. Similar to our observations with CB-TE2A and CB-TE1A1P, they observed a significant improvement of tumor-to-normal-tissue ratios with a NOTA-based chelator, NODAGA, compared to CB-TE2A, which was attributed to the neutral charge and higher hydrophilicity of ^{64}Cu-NODAGA-LM3. In addition, they indicated that the antagonist LM3 was more sensitive to N-terminal modification than somatostatin agonists. At 4 and 24 h postinjection in human embryonic kidney (HEK)-sst2 tumor bearing nude mice, the liver uptake of ^{64}Cu-CB-TE2A-LM3 was 3−4-fold higher than ^{64}Cu-NODAGA-LM3, and the kidney uptake of ^{64}Cu-CB-TE2A-LM3 was over 5-fold higher than ^{64}Cu-NODAGA-LM3. Using the agonist Y3-TATE as our targeting peptide for SSTr2 in AR42J tumor-bearing rats, we also observed decreased liver uptake of ^{64}Cu-CB-TE1A1P-Y3-TATE compared to ^{64}Cu-CB-TE2A-Y3-TATE at 1 h postinjection, although this was significantly less than Fani et al.'s observations with LM3. Moreover, we observed unexpectedly higher kidney uptake of ^{64}Cu-CB-TE1A1P-Y3-TATE than ^{64}Cu-CB-TE2A-Y3-TATE at all time points postinjection. The advantages of CB-TE1A1P to CB-TE2A may be amplified by conjugation of CB-TE1A1P to somatostatin antagonists. Interestingly, CB-TE2A performed better than NODAGA when compared as RGD conjugates,[28] confirming that the target tissue and nontarget organ uptake is dependent on both the chelator and the targeting peptide.

CONCLUSIONS

In summary, a novel PET radiopharmaceutical, ^{64}Cu-CB-TE1A1P-Y3-TATE, has been successfully synthesized and evaluated *in vitro* and for imaging SSTr2 positive tumors in an AR42J tumor-bearing rat model. The data suggest that CB-TE1A1P is a promising bifunctional chelator for ^{64}Cu, owing to the improved tumor-to-blood and tumor-to-muscle ratios, as well as excellent tumor detection by PET. Integration of a methanephosphonate group to the cross-bridged macrocyclic

chelator results in much milder labeling conditions and higher specific activity. These results demonstrate the promise of CB-TE1A1P as a chelator for stably complexing ^{64}Cu for a wide variety of biological applications, including proteins such as monoclonal antibodies. Additionally, the ^{64}Cu-labeled CB-TE1A1P-Y3-TATE conjugate shows improved biodistribution compared to ^{64}Cu-CB-TE2A-Y3-TATE.

AUTHOR INFORMATION

Corresponding Author

*Phone: 412-624-6887. E-mail: andersoncj@upmc.edu.

Notes

The authors declare no competing financial interest.

ACKNOWLEDGMENTS

The authors gratefully acknowledge Christopher Sherman for performing the biodistribution studies and Dexing Zeng for assistance with compound characterization. This research was supported by NIH/NCI 5 R01 CA 093375 (CJA) and DOE DE-FG02-08ER64671 (Integrated Research Training Program of Excellence in Radiochemistry awarded to Michael J. Welch supporting YG).

REFERENCES

(1) Eiblmaier, M., Andrews, R., Laforest, R., Rogers, B. E., and Anderson, C. J. (2007) Nuclear uptake and dosimetry of ^{64}Cu-labeled chelator somatostatin conjugates in an SSTr2-transfected human tumor cell line. *J. Nucl. Med. 48*, 1390−1396.

(2) Sun, X., Wuest, M., Weisman, G. R., Wong, E. H., Reed, D. P., Boswell, C. A., Motekaitis, R., Martell, A. E., Welch, M. J., and Anderson, C. J. (2002) Radiolabeling and *in vivo* behavior of copper-64-labeled cross-bridged cyclam ligands. *J. Med. Chem. 45*, 469−477.

(3) Bass, L. A., Wang, M., Welch, M. J., and Anderson, C. J. (2000) In vivo transchelation of copper-64 from TETA-octreotide to superoxide dismutase in rat liver. *Bioconjugate Chem. 11*, 527−532.

(4) Boswell, C. A., McQuade, P., Weisman, G. R., Wong, E. H., and Anderson, C. J. (2005) Optimization of labeling and metabolite analysis of copper-64-labeled azamacrocyclic chelators by radio-LC-MS. *Nucl. Med. Biol. 32*, 29−38.

(5) Rogers, B. E., Anderson, C. J., Connett, J. M., Guo, L. W., Edwards, W. B., Sherman, E. L., Zinn, K. R., and Welch, M. J. (1996) Comparison of four bifunctional chelates for radiolabeling monoclonal antibodies with copper radioisotopes: biodistribution and metabolism. *Bioconjugate Chem. 7*, 511−522.

(6) Sprague, J. E., Peng, Y., Sun, X., Weisman, G. R., Wong, E. H., Achilefu, S., and Anderson, C. J. (2004) Preparation and biological evaluation of copper-64-labeled tyr3-octreotate using a cross-bridged macrocyclic chelator. *Clin. Cancer Res. 10*, 8674−8682.

(7) Stigers, D. J., Ferdani, R., Weisman, G. R., Wong, E. H., Anderson, C. J., Golen, J. A., Moore, C., and Rheingold, A. L. (2010) A new phosphonate pendant-armed cross-bridged tetraamine chelator accelerates copper(ii) binding for radiopharmaceutical applications. *Dalton Trans. 39*, 1699−1701.

(8) Sun, X., Wuest, M., Kovacs, Z., Sherry, A. D., Motekaitis, R., Wang, Z., Martell, A. E., Welch, M. J., and Anderson, C. J. (2003) In vivo behavior of copper-64-labeled methanephosphonate tetraaza macrocyclic ligands. *J. Biol. Inorg. Chem. 8*, 217−225.

(9) Ferdani, R., Stigers, D. J., Fiamengo, A. L., Wei, L., Li, B. T., Golen, J. A., Rheingold, A. L., Weisman, G. R., Wong, E. H., and Anderson, C. J. (2012) Synthesis, Cu(ii) complexation, ^{64}Cu-labeling and biological evaluation of cross-bridged cyclam chelators with phosphonate pendant arms. *Dalton Trans. 41*, 1938−1950.

(10) McCarthy, D. W., Shefer, R. E., Klinkowstein, R. E., Bass, L. A., Margeneau, W. H., Cutler, C. S., Anderson, C. J., and Welch, M. J. (1997) Efficient production of high specific activity ^{64}Cu using a biomedical cyclotron. *Nucl. Med. Biol. 24*, 35−43.

(11) Wadas, T. J., and Anderson, C. J. (2006) Radiolabeling of TETA- and CB-TE2A-conjugated peptides with copper-64. *Nat. Protoc. 1*, 3062−3068.

(12) Wadas, T. J., Eiblmaier, M., Zheleznyak, A., Sherman, C. D., Ferdani, R., Liang, K., Achilefu, S., and Anderson, C. J. (2008) Preparation and biological evaluation of ^{64}Cu-CB-TE2A-sst2-ANT, a somatostatin antagonist for PET imaging of somatostatin receptor-positive tumors. *J. Nucl. Med. 49*, 1819−1827.

(13) Wang, M., Caruano, A. L., Lewis, M. R., Meyer, L. A., VanderWaal, R. P., and Anderson, C. J. (2003) Subcellular localization of radiolabeled somatostatin analogues: implications for targeted radiotherapy of cancer. *Cancer Res. 63*, 6864−6869.

(14) Lewis, J. S., Srinivasan, A., Schmidt, M. A., and Anderson, C. J. (1999) In vitro and in vivo evaluation of ^{64}Cu-TETA-Tyr3-octreotate. A new somatostatin analog with improved target tissue uptake. *Nucl. Med. Biol. 26*, 267−273.

(15) Mucha, A., Grembecka, J., Cierpicki, T., and Kafarski, P. (2003) Hydrolysis of the phosphonamidate bond in phosphono dipeptide analogues - The influence of the nature of the N-terminal functional group. *Eur. J. Org. Chem.*, 4797−4803.

(16) Mucha, A., Kunert, A., Grembecka, J., Pawelczak, M., and Kafarski, P. (2006) A phosphonamidate containing aromatic N-terminal amino group as inhibitor of leucine aminopeptidase - design, synthesis and stability. *Eur. J. Med. Chem. 41*, 768−772.

(17) Boswell, C. A., Sun, X., Niu, W., Weisman, G. R., Wong, E. H., Rheingold, A. L., and Anderson, C. J. (2004) Comparative in vivo stability of copper-64-labeled cross-bridged and conventional tetraaza-macrocyclic complexes. *J. Med. Chem. 47*, 1465−1474.

(18) Lukes, I., Kotek, J., Vojtisek, P., and Hermann, P. (2001) Complexes of tetraazacycles bearing methylphosphinic/phosphonic acid pendant arms with copper(II), zinc(II) and lanthanides(III). A comparison with their acetic acid analogues. *Coordin. Chem. Rev. 216*, 287−312.

(19) Svobodova, I., Lubal, P., Plutnar, J., Havlickova, J., Kotek, J., Hermann, P., and Lukes, I. (2006) Thermodynamic, kinetic and solid-state study of divalent metal complexes of 1,4,8,11-tetraazacyclotetradecane (cyclam) bearing two trans (1,8-)methylphosphonic acid pendant arms. *Dalton Trans. 43*, 5184−5197.

(20) Reubi, J. C., Schar, J. C., Waser, B., Wenger, S., Heppeler, A., Schmitt, J. S., and Macke, H. R. (2000) Affinity profiles for human somatostatin receptor subtypes SST1-SST5 of somatostatin radiotracers selected for scintigraphic and radiotherapeutic use. *Eur. J. Nucl. Med. 27*, 273−282.

(21) Anderson, C. J., Jones, L. A., Bass, L. A., Sherman, E. L., McCarthy, D. W., Cutler, P. D., Lanahan, M. V., Cristel, M. E., Lewis, J. S., and Schwarz, S. W. (1998) Radiotherapy, toxicity and dosimetry of copper-64-TETA-octreotide in tumor-bearing rats. *J. Nucl. Med. 39*, 1944−1951.

(22) Wadas, T. J., Wong, E. H., Weisman, G. R., and Anderson, C. J. (2010) Coordinating radiometals of copper, gallium, indium, yttrium, and zirconium for PET and SPECT imaging of disease. *Chem. Rev. 110*, 2858−2902.

(23) Wong., E. H., Weisman, G. R., Hill, D. C., Reed, D. P., Rogers, M. E., Condon, J. S., Fagan, M. A., Calabrese., J. C., Lam, K. C., Guzei, I. A., and Rheingold, A. L. (2000) Synthesis and characterization of cross-bridged cyclams and pendant-armed derivatives and structural studies of their copper(II) complexes. *J. Am. Chem. Soc. 122*, 10561−10572.

(24) Koenig, J. A., Kaur, R., Dodgeon, I., Edwardson, J. M., and Humphrey, P. P. (1998) Fates of endocytosed somatostatin sst2 receptors and associated agonists. *Biochem. J. 336* (Pt 2), 291−298.

(25) Jones-Wilson, T. M., Deal, K. A., Anderson, C. J., McCarthy, D. W., Kovacs, Z., Motekaitis, R. J., Sherry, A. D., Martell, A. E., and Welch, M. J. (1999) The in vivo behavior of copper-64-labeled azamacrocyclic complexes. *Nucl. Med. Biol. 25*, 523−530.

(26) Akizawa, H., Arano, Y., Mifune, M., Iwado, A., Saito, Y., Mukai, T., Uehara, T., Ono, M., Fujioka, Y., Ogawa, K., Kiso, Y., and Saji, H. (2001) Effect of molecular charges on renal uptake of ^{111}In-DTPA-conjugated peptides. *Nucl. Med. Biol. 28*, 761−768.

(27) Fani, M., Del Pozzo, L., Abiraj, K., Mansi, R., Tamma, M. L., Cescato, R., Waser, B., Weber, W. A., Reubi, J. C., and Maecke, H. R. (2011) PET of somatostatin receptor-positive tumors using ^{64}Cu- and ^{68}Ga-somatostatin antagonists: the chelate makes the difference. *J. Nucl. Med. 52*, 1110−1118.

(28) Dumont, R. A., Deininger, F., Haubner, R., Maecke, H. R., Weber, W. A., and Fani, M. (2011) Novel ^{64}Cu- and ^{68}Ga-labeled RGD conjugates show improved PET imaging of alpha$_v$beta$_3$ integrin expression and facile radiosynthesis. *J. Nucl. Med. 52*, 1276−84.

Bioconjugate Chemistry

Article

pubs.acs.org/bc

M13 Bacteriophage Display Framework That Allows Sortase-Mediated Modification of Surface-Accessible Phage Proteins

Gaelen T. Hess,[†,‡] Juan J. Cragnolini,[§] Maximilian W. Popp,[§] Mark A. Allen,[†,∥] Stephanie K. Dougan,[§] Eric Spooner,[§] Hidde L. Ploegh,*[,§,⊥] Angela M. Belcher,*[,†,∥,#] and Carla P. Guimaraes*[,§]

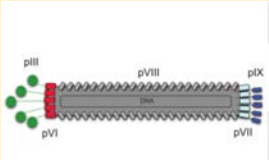
[†]The David H. Koch Institute for Integrative Cancer Research, [∥]Department of Materials Science and Engineering, [⊥]Department of Biology, and [#]Department of Biological Engineering, Massachusetts Institute of Technology, Cambridge, Massachusetts 02139, United States

[‡]Biophysics Program, Harvard University, Cambridge, Massachusetts 02138, United States

[§]Whitehead Institute for Biomedical Research, Cambridge, Massachusetts 02142, United States

Supporting Information

ABSTRACT: We exploit bacterial sortases to attach a variety of moieties to the capsid proteins of M13 bacteriophage. We show that pIII, pIX, and pVIII can be functionalized with entities ranging from small molecules (e.g., fluorophores, biotin) to correctly folded proteins (e.g., GFP, antibodies, streptavidin) in a site-specific manner, and with yields that surpass those of any reported using phage display technology. A case in point is modification of pVIII. While a phage vector limits the size of the insert into pVIII to a few amino acids, a phagemid system limits the number of copies actually displayed at the surface of M13. Using sortase-based reactions, a 100-fold increase in the efficiency of display of GFP onto pVIII is achieved. Taking advantage of orthogonal sortases, we can simultaneously target two distinct capsid proteins in the same phage particle and maintain excellent specificity of labeling. As demonstrated in this work, this is a simple and effective method for creating a variety of structures, thus expanding the use of M13 for materials science applications and as a biological tool.



Minor Capsid Proteins

capsid protein	probe	efficiency
pIII	Biotin	68 ± 9%
pIII	GFP	56 ± 2%
pIX	Biotin	73 ± 2%
pIX	GFP	74 ± 1%

Major Capsid Protein

capsid protein	probe	optimal packing	copy number/phage using sortase	literature
pVIII	Biotin	2700	1350 ± 90	400–700
pVIII	GFP	385	91 ± 20	<1

INTRODUCTION

M13 bacteriophage has a cylindrical shape with a length of 880 nm and a diameter of 6 nm. It encapsulates a single-strand genome that encodes five different capsid proteins (Figure 1A). The body of the phage is composed of 2700 copies of pVIII, the major capsid protein. At one end of the virus, there are ∼5 copies of both pIII and pVI proteins, and at the other end, there are ∼5 copies of both pVII and pIX proteins.[1]

The capsid proteins of M13 bacteriophage have been used to express combinatorial peptide libraries or protein variants (ranging from single domains to antibodies) to screen for target ligands in a process known as phage display.[2] This technique has not only enabled identification of peptides with affinity for biological targets such as proteins, cells, and tissues,[3−6] but also allowed the identification of biomolecules that bind inorganics.[7,8] These molecules, when expressed on the M13 capsid proteins, can serve as scaffolds for nanowires, structures, and devices.[9−13] Functionalization of a virion capsid such as M13 is currently accomplished using chemical and/or genetic approaches.[14,15] However both strategies have limitations. Chemical conjugations are convenient and versatile, but they label motifs found on multiple M13 capsid proteins and oftentimes require nonphysiological pH and reducing conditions that compromise the activity of the molecule that is being attached or of the moieties already displayed on other capsid proteins.[14]

Genetic engineering of phage allows the encoded protein/peptide to be displayed precisely,[13,16] but it has intrinsic restrictions. Two classes of vectors are available for genetic phage display: phagemid and phage. A phagemid allows expression of large fusions with any of the five M13 phage capsid proteins, but these fusions are incorporated at low efficiency.[17−21] In a phage vector, the M13 bacteriophage genome is modified directly. As a result, every copy of the recombinant capsid protein incorporated into the virus displays the modified protein. However, this strategy does not support display of large moieties.[22−24] pVIII allows the display of a larger number of recombinant molecules per phage particle, but it also has the strictest size limitation in phage vector display. pVIII peptide libraries are mostly limited to sizes of up to 10 amino acids, as phage with longer insertions rarely assemble.[25,26] Insertions of 6−20 amino acids onto pVIII are possible using phagemid, but their display is inefficient with fewer than 25% of the copies of pVIII containing the desired fusion product.[20] Incorporation of proteins is even less efficient on pVIII: a 23 kDa protein is displayed, on average, on less than a single copy of the pVIII fusion per phage particle using a phagemid vector.[18] Phage display methods on the pVIII have

Received: March 15, 2012
Revised: June 12, 2012
Published: July 3, 2012

ACS Publications © 2012 American Chemical Society

dx.doi.org/10.1021/bc300130z | *Bioconjugate Chem.* 2012, 23, 1478−1487

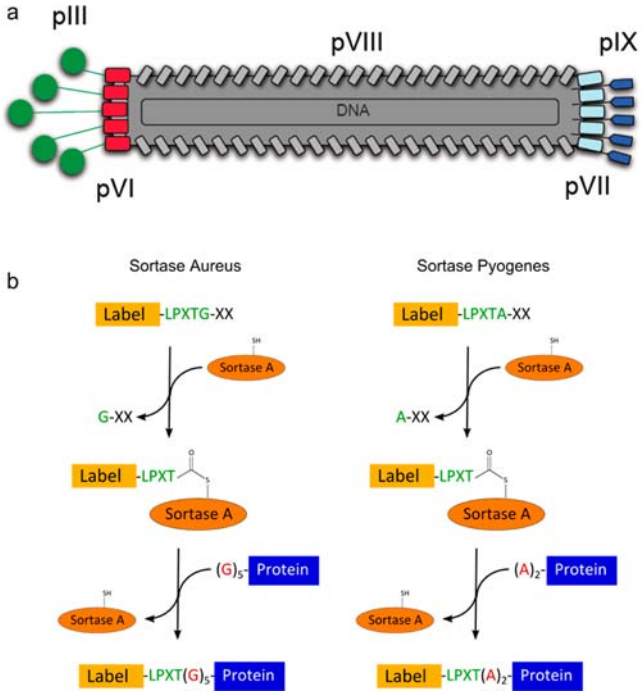


Figure 1. M13 bacteriophage structure and sortase-based reaction schemes. M13 bacteriophage is composed of five capsid proteins. pVIII is the major capsid protein with ~2700 copies in each phage particle. The pVII (light blue) and pIX (blue) are located at one end and start the assembly process, while pIII (green) and pVI (red) are at the other end and cap the phage. Note: the image is not to scale (a). Schematic representation of the mechanism of chemo-enzymatic labeling mediated by *Staphylococcus aureus* ($SrtA_{aureus}$-left) or *Streptococcus pyogenes* ($SrtA_{pyogenes}$-right) (b).

been able to increase the binding affinity of phage displaying a moiety,[23] but the displayed copy number of the moiety has not been determined. Large moieties of at least 23 kDa have been genetically fused to all four minor capsid proteins using a phagemid vector,[22,27,28] but only pIII has been extensively used in the phage vector system.[29] However, viability of the resultant phage fusions does not guarantee that the recombinant peptide/protein of interest displays its native structure. Both the environment where phage assembles and the phage coat protein to which the protein of interest is fused may interfere with proper folding.[30] This is particularly critical for enzymes and antibodies, as they might not be functional when incorporated into the phage structure.

To expand the versatility of M13 as a display platform, we devised a strategy based on sortase-mediated chemo-enzymatic reactions to covalently attach a variety of moieties to the N-terminus of pIII, pIX, and pVIII. We obtained a vast improvement over the published data in the copy number of displayed peptides and proteins, particularly on pVIII.

Sortase A enzymes allow modification of proteins by enzymatic ligation with a wide range of functional groups (including biotin, fluorophores, and other proteins) at the C-terminus, N-terminus, or both termini of the protein of interest.[31−35] The widely used sortase A from *Staphylococcus aureus* ($SrtA_{aureus}$) recognizes substrates that contain an LPXTG sequence,[36−38] whereas sortase A from *Streptococcus pyogenes* ($SrtA_{pyogenes}$) recognizes substrates with an LPXTA motif.[33,39] The sortase enzymes cleave between the threonine and glycine or alanine residue, respectively, to yield a covalent acyl-enzyme intermediate that is resolved by nucleophilic attack of a suitably exposed amine, namely, oligoglycine or oligoalanine-containing peptides[39] in the case of $SrtA_{aureus}$ or $SrtA_{pyogenes}$, respectively (Figure 1B). Using these two orthogonal sortase A enzymes,[33] we established conditions to site-specifically attach two different moieties onto two capsid proteins in a single phage particle.

The sortase labeling method has several advantages over genetic and chemical methods. First, the reaction is site-specific, as none of the coat proteins naturally display the required motifs to participate in sortase-mediated reactions. Second, these motifs are small and, therefore, can be easily inserted into the phage genome, maximizing the number of potential attachment sites. Third, a protein to be displayed on phage by means of sortase can be properly folded separate from the assembly of phage. The site-specific nature of the reaction fixes the orientation of the displayed protein. Fourth, the reactions are performed under physiological conditions. Fifth, sortase reactions afford attachment of a wide range of molecules, including those that cannot be genetically encoded such as fluorophores and biotin.

This work establishes the component parts to build phage structures that have new material and biological applications. We provide two examples: the creation of a new lampbrush structure by fusing different phage particles through pIII/pVIII and a fluorescently labeled phage containing a cell-targeting moiety to stain and to FACS sort cells.

EXPERIMENTAL PROCEDURES

Generation of the M13 Phage Constructs. The oligonucleotides used to design the different phage constructs are compiled in SI Table S1. The G_5-pIII phage was engineered by inserting the G5pIIIC and G5pIIINC annealed oligonucleotides into the M13KE vector (New England Biolabs), previously digested with *Eag*I and *Acc*65I restriction enzymes. To construct the A_2G_4-pVIII phage, the M13SK vector[40] was digested with *Pst*I and *Bam*HI restriction enzymes and the A2G4pVIIIC and A2G4pVIIINC annealed oligonucleotides were inserted. To engineer the G_5HA-pIX construct, the 983 vector was used. This vector was created by refactoring the M13SK vector so the pIX and pVII genes are not overlapping. Upon digestion of this vector with *Sfi*I, the annealed G5HApIXC and G5HApIXNC oligonucleotides were inserted. The G_5-pIII-A_2-pVIII phage construct was created using a modified M13SK vector,[40] which has a DSPHTELP sequence on pVIII and a biotin acceptor peptide (GLQDIFEAQ-KIEWHE) on pIII. Five N-terminal glycines were added to pIII following the above strategy described for G_5-pIII phage. The resultant vector was then modified at the N-terminus of pVIII using the QuikChange II site-directed mutagenesis kit (Stratagene) and the pVIIIAADSPH oligonucleotide pair. All the generated phage vectors were transformed into the XL-1 Blue bacterial strain, plated in agar top on LB agar plates containing 1 mM IPTG, 40 μg/mL X-Gal, and 30 μg/mL tetracycline. Plaques were selected, and DNA was isolated and sequenced to check for the insertion.

For phage amplification, the *E. coli* strain ER2738 (New England Biolabs) in LB media supplemented with 30 μg/mL tetracycline, was infected with phage for at least 12 h at 37 °C. The cultures were centrifuged at 12 000*g* for 20 min and the phage was precipitated from the supernatant at 4 °C with the addition of 1/5 of the supernatant volume of 20% PEG8000/2.5 M NaCl solution. Upon centrifugation at 13 500*g* for 20 min, the pellet was resuspended in 25 mM Tris, 150 mM NaCl,

dx.doi.org/10.1021/bc300130z | *Bioconjugate Chem.* 2012, 23, 1478−1487

pH 7.0−7.4 (TBS). For further purification, this resuspension was subjected to two rounds of centrifugation/precipitation. The final phage concentration averaged between 10^{13}−10^{14} plaque forming units (pfu) per mL as determined by UV−vis spectrometry.[41]

Sortase-Mediated Reactions. $SrtA_{pyogenes}$ and $SrtA_{aureus}$ were expressed and purified as described.[33,42] Sortase reactions were performed as indicated in the figures. A typical sortase reaction with $SrtA_{aureus}$ included 200 nM phage, 50 μM $SrtA_{aureus}$, and 50 μM substrate for small peptides or 20 μM for proteins. The reactions were incubated for 3 h at 37 °C (for small peptides) or at room temperature (for proteins) in TBS with 10 mM $CaCl_2$. $SrtA_{pyogenes}$-mediated reactions included 8 nM phage, 50 μM $SrtA_{pyogenes}$, and 20 μM substrate, incubated for 3 h at 37 °C in TBS. Where indicated, phage was purified by PEG 8000/NaCl precipitation after diluting the reactions with TBS such that the substrate concentration was below 600 nM.

For the flow cytometry experiments, the G_5-pIII-A_2-pVIII phage construct was labeled with K(TAMRA)-LPETAA on pVIII. The resultant labeled phage was purified by PEG8000/NaCl precipitation, resuspended in TBS, and split into three parts. One part remained unlabeled, and the other two were labeled with either VHH7.LPETG or anti-GFP.LPETG on pIII. As assessed by the anti-pIII antibody, a yield of 2.5 antibody molecules per virion was achieved in both cases.

The yield of the sortase-mediated biotinylation reactions was determined using biotinylated GFP as a standard. This was prepared labeling GFP—comprising a LPETG at its C-terminus—with a biotin group using $SrtA_{aureus}$ (GFP.LPETGGGK(biotin)).[42] Known amounts of the purified GFP.LPETGGGK(biotin) standard and varying volumes of the phage labeling reactions were loaded onto the same SDS-PAGE gel and analyzed by immunoblot using streptavidin-HRP (GE Healthcare). The signal obtained in the phage labeling reactions was compared with the signal derived from the GFP.LPETGGGK(biotin) calibration curve allowing us to infer the amount of phage protein labeled in the reaction. To calculate the labeling efficiency, the amount of labeled protein was divided by the amount of total phage protein loaded into the gel. The phage concentration was determined by UV−vis spectrometry and it was assumed that there were 2700 copies of pVIII, 5 copies of pIII, and 5 copies of pIX per phage particle.

To determine the yield of GFP-pVIII phage labeling, unincorporated GFP and sortase was removed from phage by PEG8000/NaCl precipitation. Varying volumes of GFP-pVIII phage and known amounts of GFP were loaded onto the same SDS-PAGE gel and analyzed by immunoblot using an anti-GFP-HRP antibody (Santa Cruz Biotechnology). The signal of the GFP-pVIII fusion protein was compared to the signal of the GFP calibration curve as described for the biotinylation reactions. For GFP-pIII and GFP-pIX labeling, the signal of the fusion protein was compared to the input amount of pIII or pIX as detected by anti-pIII (New England Biolabs) or anti-HA (Roche) antibodies, respectively. For GFP-pIII, the input signal consisted of only intact pIII molecules and lower molecular weight anti-pIII reactive proteins were not included. These proteins can be attributed to proteolyzed pIII.[43] Because the anti-pIII antibody recognizes the C-terminus of the protein, these fragments cannot be labeled using $SrtA_{aureus}$. In all cases, the blots were scanned and densitometric analysis was performed using the *ImageJ* program (National Institutes of Health). The labeling yield was averaged over three independent reactions with three aliquots from each reaction analyzed. The standard deviation of the reactions was calculated from the averages of the three independent reactions.

Dynamic Light Scattering (DLS). DLS measurements were obtained with a Beckman Delsa-Nano C Particle Analyzer (Beckman Coulter Inc.). Phage mixtures were diluted to ~10^{11} pfu/mL in 1 mL of water and loaded into a cuvette. Samples from each experiment were measured in triplicate and the results were averaged by cumulant analysis. Autocorrelation functions were used as a direct comparison of aggregation, because aggregates have a slower Brownian motion causing the signal correlation to be delayed to longer relaxation times.

Atomic Force Microscopy (AFM). Phage preparations were diluted to a concentration of ~10^{11} pfu/mL, and 100 μL of this mixture were deposited on a freshly cleaved mica disk. AFM images were taken on a Nanoscope IV (Digital Instruments) in air using tapping mode. The tips had spring constants of 20−100 N/m driven near their resonant frequency of 200−400 kHz (MikroMasch). Scan rates were approximately 1 Hz. Images were leveled using a first-order plane fit to remove sample tilt.

Flow Cytometry Analysis. C57BL/6 mice were purchased from Jackson Laboratories. Animals were housed at the Whitehead Institute for Biomedical Research and were maintained according to guidelines approved by the Massachusetts Institute of Technology (MIT) Committee on Animal Care.

Lymph nodes were isolated from 6 to 8-week-old C57BL/6 mice and crushed through a 40 μM cell strainer. Cells were washed once with PBS, resuspended at 2 × 10^7 cells per mL, aliquoted at ~1 × 10^6 cells per sample, and incubated with staining agents in 5% milk in PBS for 1 h at room temperature. 10^{11} VHH7 molecules and 10^{11} anti-GFP molecules either directly conjugated to TAMRA using $SrtA_{aureus}$ or covalently attached to phage (5 × 10^{10} phage particles of VHH7-G_5-pIII-TAMRA-A_2-pVIII or anti-GFP-G_5-pIII-TAMRA-A_2-pVIII; see Sortase-Mediated Reactions section) were incubated with the cells. The same amount of nontargeted fluorescent phage particles (i.e., G_5-pIII-TAMRA-A_2-pVIII) was used as a negative control. B cells were stained with Pacific Blue antimouse B220 (BD Pharmingen, clone RA3−6B2). Upon staining, the cells were centrifuged at 170*g* for 5 min, washed with PBS three times, and resuspended in 500 μL of PBS. Flow cytometry was performed using a FACSAria (BD). 100 000 events were collected for each sample.

Miscellaneous. Expression and purification of GFP.LPETG.His_6 and GFP.LPETA.His_6 were performed as described.[33] Identification, characterization, expression, and purification of VHH7.LPETG.His_6 will be published elsewhere. Streptavidin was cloned as a streptavidin.LPETG.HAtag.His_6 fusion protein using the template Addgene 20860,[44] and expressed as a soluble tetrameric streptavidin.[45] Purification was performed following the same protocol used for GFP.[33] Sortase reactions were analyzed on 4−12% Bis-Tris SDS-PAGE gels with MES running buffer except for SI Figure S4, which was analyzed on a 12% Laemmli SDS-PAGE gel.

The K(biotin)-LPETGG, K(biotin)-LPETAA, K(TAMRA)-LPETAA, and GGGK(biotin) peptides were obtained from the Swanson Biotechnology Center. For mass spectrometry, the protein bands of interest were excised, subjected to protease digestion, and analyzed by electrospray ionization tandem mass spectrometry (MS/MS). Fluorescent gel images were obtained using a variable mode imager (Typhoon 9200; GE Healthcare).

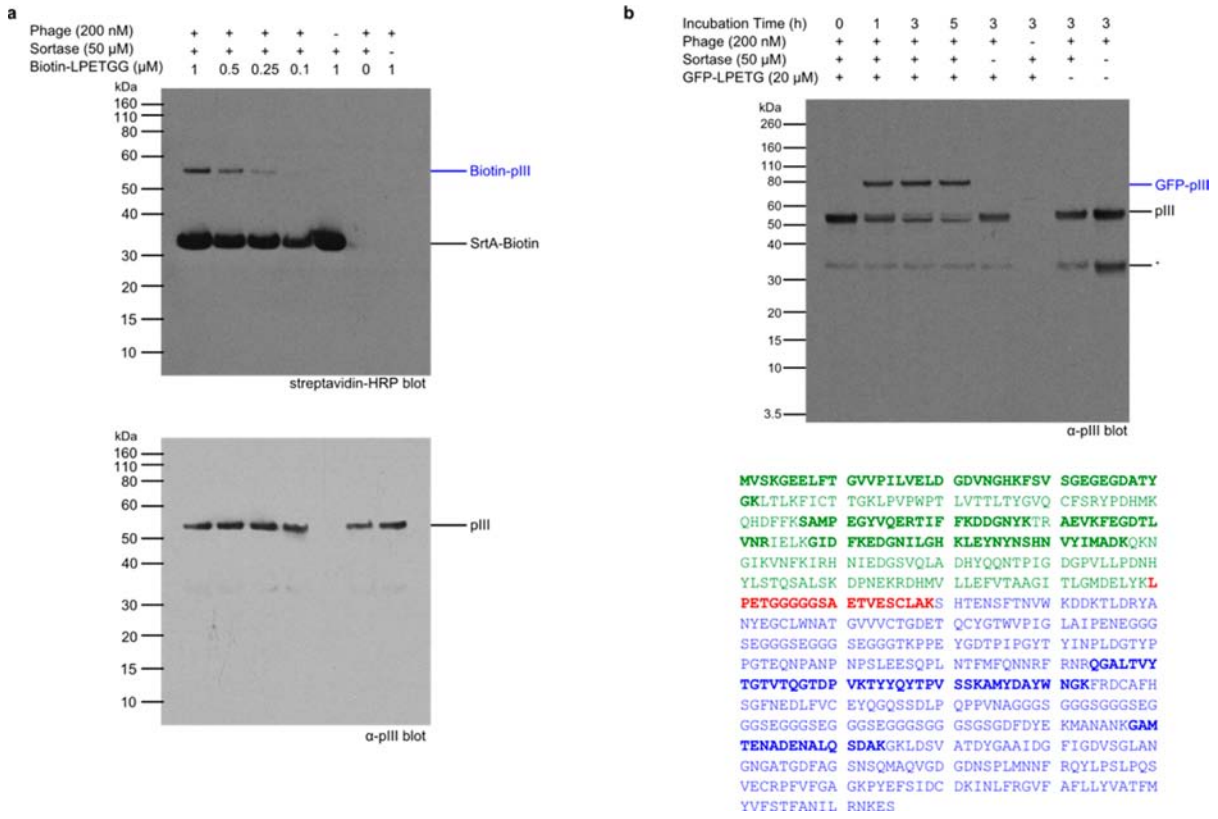


Figure 2. pIII labeling. G_5-pIII modified phage (there are five copies of pIII/phage particle) was incubated with $SrtA_{aureus}$ and K(biotin)-LPETGG peptide (a), or GFP-LPETG (b), for 3 h at 37 °C or room temperature, respectively. The reactions were monitored by SDS-PAGE under reducing conditions followed by immunoblotting using streptavidin-HRP (a, top panel) or an anti-pIII antibody (a, bottom panel and b). The molecular weight markers are shown on the left. The unidentified anti-pIII reactive protein (*) is most probably a proteolytic fragment of pIII. The identity of the GFP-pIII fusion product was determined by mass spectrometry. The amino acid sequences of pIII and GFP are shown in blue and green, respectively. The peptides identified are highlighted in bold. The tryptic peptide comprising the GFP C-terminus, followed by the $SrtA_{aureus}$ cleavage site, fused to the N-terminal glycines of pIII is shown in red.

RESULTS

N-Terminal Labeling of pIII Using $SrtA_{aureus}$. pIII has been the most extensively explored of the M13 capsid proteins in phage display because of the flexibility and accessibility of its N-terminus.[46] Thus, we introduced five glycines at the N-terminus of pIII (G_5-pIII phage) and used $SrtA_{aureus}$ to covalently attach a K(biotin)-LPETGG peptide (Figure 2A). The biotin moiety allowed us to monitor the reaction by immunoblot analysis using streptavidin-HRP. Only when sortase, G_5-pIII phage, and the peptide are incubated together did we detect a 55 kDa streptavidin and anti-pIII reactive protein band (Figure 2A). The reaction was specific: no other phage proteins were biotinylated. After 3 h at 37 °C, we achieved a yield of 68 ± 9% labeling using 50 μM peptide, 50 μM $SrtA_{aureus}$, 200 nM G_5-pIII phage, and 10 mM $CaCl_2$. The efficiency of the reaction was calculated using densitometric analysis of immunoblots where we compared the signal of the biotinylated pIII to biotinylated GFP standards of known concentration. The amount of biotinylated pIII was then divided by the amount of pIII molecules loaded onto the gel, as determined by UV−vis spectrometry. The quantification was repeated for three independent reactions with three samples analyzed for each reaction. The method of quantification is described in further detail in the Experimental Procedures section.

To determine whether sortase could be exploited to attach prefolded proteins onto pIII, we used GFP containing an LPETG motif at its C-terminus as a substrate. The reaction was analyzed by immunoblot using an anti-pIII antibody (Figure 2B). Upon completion of the reaction, a mobility shift of pIII to the ~80 kDa region, corresponding to the GFP-pIII fusion product, was detected. The identity of this material was confirmed by mass spectrometry (Figure 2B and SI Figure S1). After 3 h at room temperature, we achieved a yield of 56 ± 2% labeling using 20 μM GFP-LPETG, 50 μM $SrtA_{aureus}$, 200 nM G_5-pIII phage, and 10 mM $CaCl_2$. The reaction was quantified by densitometry comparing the signal of pIII-GFP to the signal of the intact pIII input loaded into the reaction.

N-Terminal Labeling of pIX Using $SrtA_{aureus}$. Because the C-terminus of pIX is buried in the phage structure and therefore unavailable for labeling,[47] we attempted to label its N-terminus. However, this region of the protein is not as accessible as in pIII and our first attempts at labeling a phage construct displaying five glycines at the N-terminus of pIX using sortase failed (data not shown). To increase accessibility of the five glycines, the N-terminus of pIX was extended with an HA tag, a useful handle for detection, as no pIX-specific antibodies are available. This G_5HA-pIX phage construct was labeled with the K(biotin)-LPETGG peptide and the reactions were analyzed by immunoblot using streptavidin-HRP and an anti-HA antibody. A 5 kDa polypeptide, reactive with both streptavidin and anti-HA, was seen only in the complete reaction (Figure 3A). We achieved a yield of 73 ± 2% using 50 μM peptide, 50 μM $SrtA_{aureus}$, 200 nM G_5HA-pIX phage, and

dx.doi.org/10.1021/bc300130z | Bioconjugate Chem. 2012, 23, 1478−1487

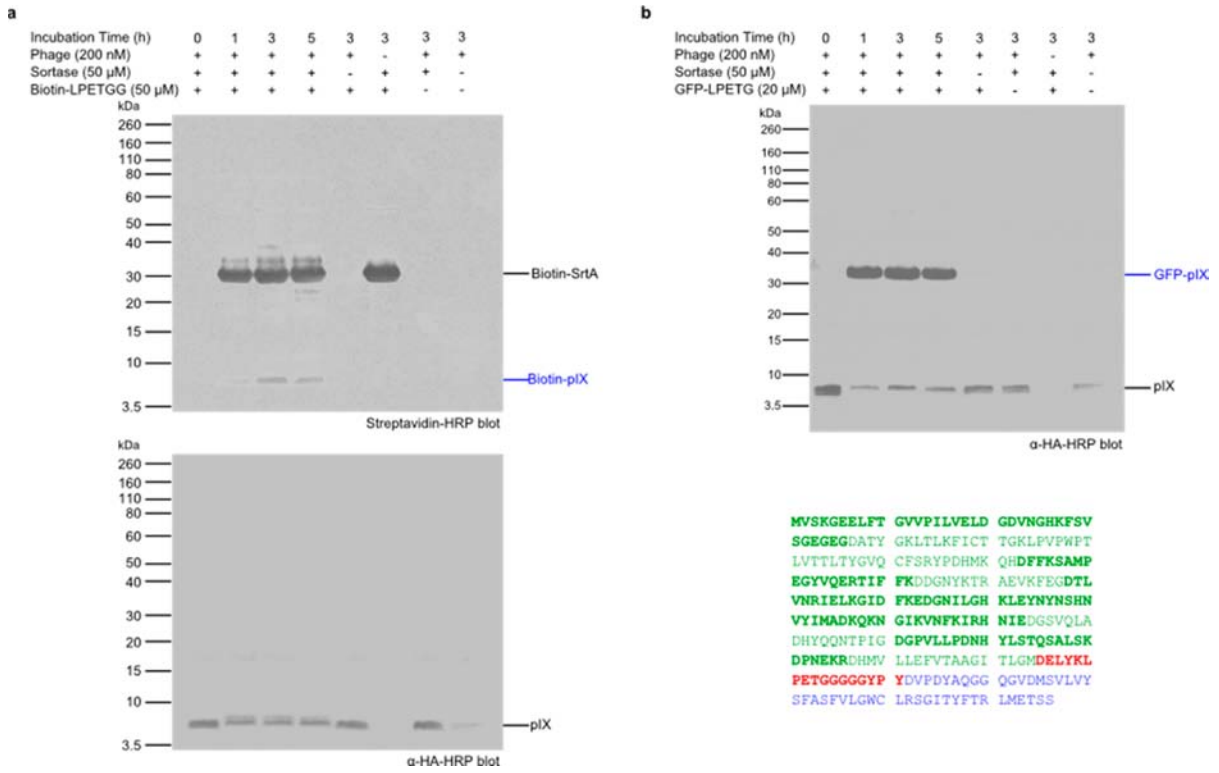


Figure 3. pIX labeling. G_5HA-pIX modified phage (there are five copies of pIX/phage particle) was incubated with $SrtA_{aureus}$ and K(biotin)-LPETGG peptide (a), or GFP-LPETG (b), at 37 °C and room temperature, respectively, for the times indicated. The reactions were monitored by SDS-PAGE under reducing conditions followed by immunoblotting using streptavidin-HRP (a, top panel) or an anti-HA antibody (a, bottom panel and b). The molecular weight markers are shown on the left. The identity of the GFP-pIX fusion product was determined by mass spectrometry. The amino acid sequences of pIX and GFP are shown in blue and green, respectively. The peptides identified are highlighted in bold. The AspN digestion-resultant peptide comprising the GFP C-terminus, followed by the $SrtA_{aureus}$ cleavage site, fused to the N-terminal glycines of pIX is shown in red.

10 mM $CaCl_2$ upon incubation at 37 °C for 3 h. A similar efficiency was attained when attaching GFP to pIX: 74 ± 1% of pIX was labeled when 20 μM GFP-LPETG, 50 μM $SrtA_{aureus}$, 200nM G_5HA-pIX phage, and 10 mM $CaCl_2$ were incubated for 3 h at room temperature. A 35 kDa anti-HA reactive polypeptide—consistent with the molecular mass of the GFP-pIX fusion protein—was detected only in the complete reaction, and its identity was confirmed by mass spectrometry (Figure 3B and SI Figure S2).

N-Terminal Labeling of pVIII Using $SrtA_{pyogenes}$. In the course of phage biogenesis, the N-terminus of pVIII is proteolytically cleaved, resulting in the display of an N-terminal alanine.[41] We took advantage of this feature and exploited $SrtA_{pyogenes}$ to label pVIII. Also, the ability of using two orthogonal sortase enzymes ($SrtA_{pyogenes}$ for pVIII and $SrtA_{aureus}$ for pIII and pIX labeling) would further enable dual labeling of the same phage particle.

To be used as a nucleophile in $SrtA_{pyogenes}$-mediated reactions, pVIII requires display of two N-terminal alanines. Thus, the N-terminus of the mature form of pVIII was modified to AAGGGG (A_2G_4-pVIII phage). The glycines were introduced to extend the N-terminus of pVIII away from the body of the phage, thus improving the accessibility of the Ala-Ala motif for participation in the sortase reaction. Using $SrtA_{pyogenes}$ and a K(biotin)-LPETAA substrate peptide, we showed robust labeling of pVIII based on an immunoblot using streptavidin-HRP (Figure 4A). Only when A_2G_4-pVIII phage, $SrtA_{pyogenes}$, and the peptide were mixed together did we detect a biotinylated 10 kDa protein, consistent with the size of pVIII. The labeling reaction was site-specific, as no other proteins can be detected in the blot. We obtained a yield of 50 ± 3% labeled pVIII when reactions were performed at 37 °C for 3 h with 20 μM peptide, 50 μM $SrtA_{pyogenes}$, and 8nM A_2G_4-pVIII phage. This translated to 1350 ± 90 biotin molecules on average per phage particle.

Phage assembly either limits the size of the modifications displayed on pVIII to a few residues when using a phage vector or limits the number of labels attached to pVIII when using a phagemid vector.[20] In this context, the sortase-labeling strategy is an obvious alternative to overcome such limitations. Using 20 μM GFP containing a LPETA motif at its C-terminus, 50 μM $SrtA_{pyogenes}$, and 8 nM A_2G_4-pVIII phage, we were able to attach 91 ± 20 GFP molecules on average per phage particle upon incubation at 37 °C for 3 h (Figure 4B). The identity of the 35 kDa anti-GFP reactive protein, consistent with the size of a GFP-pVIII fusion protein, was confirmed by mass spectrometry (Figure 4B and SI Figure S3). As estimated by nearest-neighbor packing (described in Supporting Information), a single virion can accommodate 385 copies of GFP on its surface. Thus, using the sortase-mediated reaction, we obtained a yield of ~25% of estimated maximum packing.

Building End-to-Body Phage Structures. The ability to site-specifically label the M13 capsid proteins provides the opportunity to create novel multiphage structures, which may provide scaffolds for new materials and devices. One such structure (Figure 5A) relies on tight binding of the ends of several phage particles (via either pIII or pIX) to the body of another single phage (onto pVIII). However, direct covalent

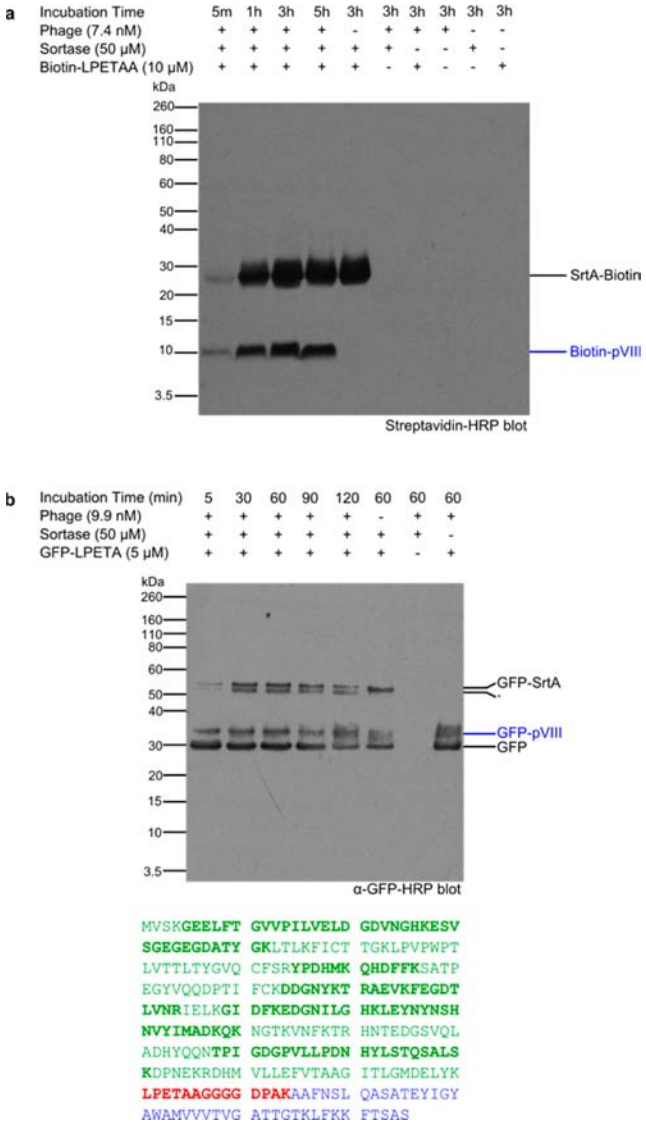


Figure 4. pVIII labeling. A_2G_4-pVIII modified phage (there are 2700 copies of pVIII/phage particle) was incubated with $SrtA_{pyogenes}$ and K(biotin)-LPETAA peptide (a), or GFP-LPETA (b), at 37 °C for the times indicated in the figure. The reactions were monitored by SDS-PAGE under reducing conditions followed by immunoblotting using streptavidin-HRP (a) or an anti-GFP antibody (b). The molecular weight markers are shown on the left. The unidentified anti-GFP reactive protein (*) is attributed to proteolyzed GFP forming an intermediate with $SrtA_{pyogenes}$. The identity of the GFP-pVIII fusion product was determined by mass spectrometry. The amino acid sequences of pVIII and GFP are shown in blue and green, respectively. The peptides identified are highlighted in bold. The tryptic peptide comprising the GFP C-terminus, followed by the $SrtA_{pyogenes}$ cleavage site, fused to the N-terminal alanines of pVIII is shown in red.

attachment between two phage proteins is not possible using sortase as we were unable to label the C-terminus of pIII, pIX, or pVIII (data not shown). This issue was solved by attaching streptavidin to pIII, biotin to pVIII, and then mixing the two preparations.

Streptavidin, modified to contain a C-terminal LPETG motif in each of its monomers, was attached to the G_5-pIII phage using $SrtA_{aureus}$. The samples were boiled, loaded onto an SDS-PAGE gel, and analyzed by immunoblot using an anti-pIII antibody. A 90 kDa polypeptide, consistent with the size of pIII fused to a streptavidin monomer, was seen only when all the reaction components were mixed together (SI Figure S4). The streptavidin-pIII phage was purified from sortase and free streptavidin by PEG/NaCl precipitation. Dynamic light scattering (DLS) was performed in order to monitor dispersity and aggregation. The normalized autocorrelation function (ACF) of streptavidin-pIII phage showed an exponential decay consistent with monodisperse populations (Figure 5B). This was confirmed by atomic force microscopy (AFM) that showed individual virions, indicating that only a single phage particle was attached per streptavidin tetramer (SI Figure S5). Biotin was conjugated to pVIII using the K(biotin)-LPETAA peptide and $SrtA_{pyogenes}$ as described above. The biotinylated phage was purified by PEG/NaCl precipitation to remove free peptide and the sortase-acyl intermediate. The biotinylated phage was observed as individual phage particles by AFM and the ACF showed an exponential decay, again indicating a monodisperse population (Figure 5B and SI Figure S5).

The streptavidin-pIII phage and the biotin-pVIII phage were mixed at a 5:1 molar ratio and incubated at room temperature for 15 min. Analysis of these samples by DLS showed an increase of the hydrodynamic diameter for the lampbrush phage mixture (700 nm) when compared to streptavidin-pIII (516 nm) and biotin-pVIII (204 nm) phage preparations. When the two types of phage were mixed, the ACF (Figure 5B) shows a rising shoulder at longer relaxation times, indicating a polydisperse population. The longer relaxation times observed in the shoulder represent structures larger than single phage. These larger structures were observed by AFM (Figure 5C and SI Figure S5). Linkages between the end of one phage and the body of another phage were observed when streptavidin-pIII and biotin-pVIII are mixed. These linkages were not detected when the individual phages were visualized by AFM (SI Figure S5).

Site-Specific Labeling of Two Capsid Proteins in the Same Phage Particle. The two orthogonal sortases used to label different capsid proteins offer the possibility to attach different moieties to the body (using $SrtA_{pyogenes}$) and to the end of phage (using $SrtA_{aureus}$) within the same virion. In such a strategy, either pIII or pIX could be labeled with $SrtA_{aureus}$ orthogonally to the pVIII, so as a proof-of-concept, a phage variant that contains a double alanine at the N-terminus of pVIII and the pentaglycine motif at the N-terminus of pIII was generated (this construct is referred to as G_5-pIII-A_2-pVIII). Conditions were optimized to label each of these proteins in a site-specific manner. Because such dual-labeled phage could be a useful tool to sort cells by FACS (see below and Discussion section), we provide here the proof-of-concept by labeling the body of phage with a fluorophore and the tip of phage with a cell-targeting moiety.

pVIII was labeled with a K(TAMRA)-LPETAA peptide and purified using PEG/NaCl precipitation to remove free peptide and sortase (Figure 6A). A fluorescent 10 kDa protein, corresponding to pVIII, was the only polypeptide detected in the complete reaction. This confirmed successful labeling and site-specificity of $SrtA_{pyogenes}$. The pIII of this fluorescent phage was then incubated with $SrtA_{aureus}$ and a 15 kDa single domain antibody, VHH7, modified with a C-terminal LPETG motif. VHH7 recognizes murine Class II MHC products (the development and expression of VHH7 will be described elsewhere). Attachment of VHH7 to pIII was monitored by immunoblot using an anti-pIII antibody (Figure 6B). Comparing the signal intensities of VHH7-pIII 90 kDa

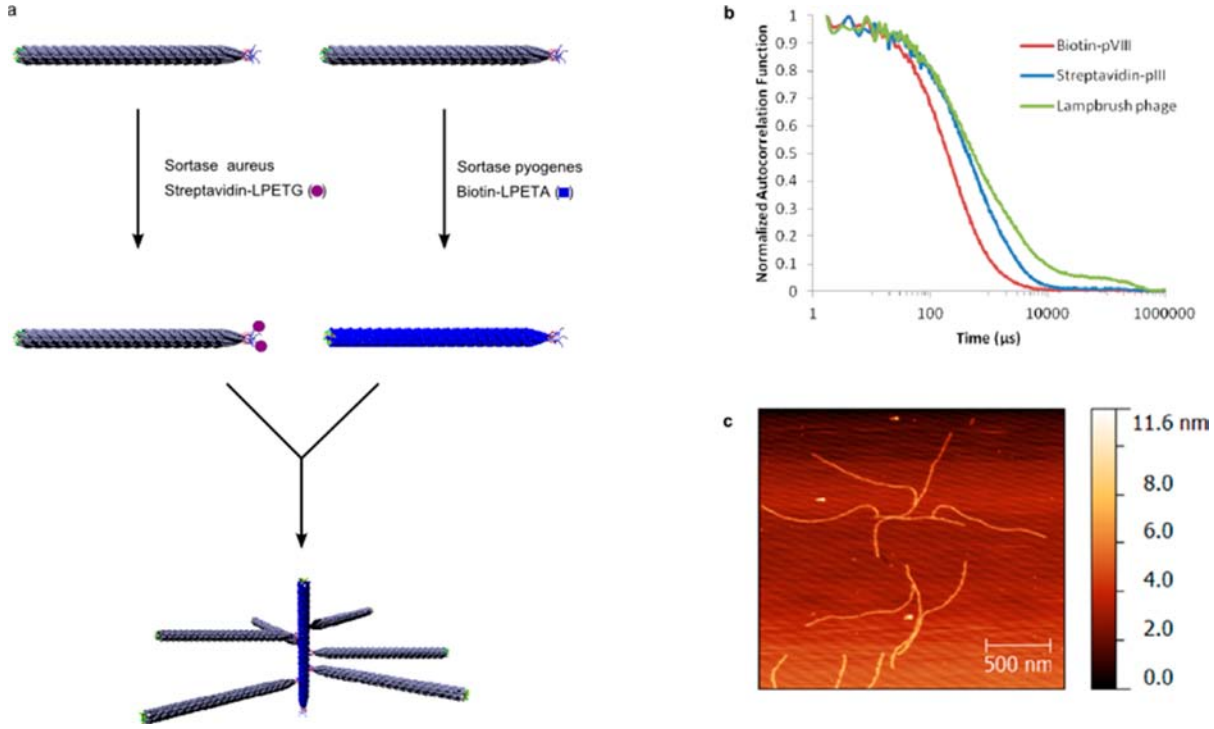


Figure 5. Creation of a multiphage structure. Schematic representation of the strategy used to build a lampbrush structure (a). Upon labeling of the N-terminus of pIII with streptavidin and of the N-terminus of pVIII with biotin using sortase-mediated reactions, the phage were mixed (see Experimental Procedures section for details). The resulting product was visualized by dynamic light scattering (b) and by atomic force microscopy (c).

polypeptide and of pIII, we estimated that on average 2−3 VHH7 molecules are attached per phage particle, a number similar to what can be obtained when screening phagemid libraries of pIII fusions by panning.[48,49]

Flow Cytometry Experiments Using Fluorescent Phage. Fluorescent phage has been used for targeted staining *in vivo*[50,51] as well as flow cytometry experiments.[52] However, these have been performed with short peptide phage display libraries. The ability to label phage with a large number of fluorophores that are site-specifically attached to pVIII is a tool useful for selecting phage of interest from phage display libraries of large moieties (such as antibodies) by fluorescence. With libraries of this type, less specific labeling methods can alter the displayed moiety. To provide proof-of-concept that fluorescent phage can be used for this purpose, we tested the ability of the dual-labeled phage—containing TAMRA fluorophore sortagged onto pVIII and VHH7 onto pIII—to stain B cells. As a negative control, we used a fluorescent phage containing an anti-GFP VHH attached to pIII.[53] An average yield of 2.5 antibodies per phage virion was achieved for both VHH7 and anti-GFP VHH as determined by densitometric analysis.

Mouse lymphocytes obtained from lymph nodes were stained for B cells using a fluorescent Pacific Blue antimouse B220 antibody and incubated with phage-VHH7, phage-anti-GFP, or nontargeted phage. All phage preparations were similarly labeled with TAMRA on pVIII. After removal of unbound materials by washing, cells were subjected to flow cytometry (Figure 6C). When stained with phage-VHH7, we detected an increase in cells double positive for TAMRA and the B cell marker compared to nonspecific staining with phage-anti-GFP or nontargeted phage. Staining of cells with phage-VHH7 was vastly superior to VHH7 directly conjugated to TAMRA, as only a few double positive cells were detected when incubated with an equivalent amount of the latter (Figure 6C).

■ DISCUSSION

We show that sortase-mediated reactions overcome many of the limitations of current methods to functionalize M13 capsid proteins. The main body and both ends of the viral capsid can be functionalized with substituents that cannot be encoded genetically (such as biotin and fluorophores), and we can also install properly folded and assembled proteins (such as GFP and streptavidin) in a manner that could easily be extended to oligomeric proteins as well.

One of the major challenges has been the modification of the major capsid protein pVIII. Using sortase, labeling efficiencies were greater than those obtained genetically (Table 1). In the past, biotinylated phage has been produced by display of the biotin acceptor peptide (BAP),[54] a 15-amino-acid sequence. Peptides similar in size have been displayed at no more than 400−700 copies per phage, with the efficiency being sequence-dependent.[20] Here, we attach 1350 biotin molecules on average per phage particle, a great improvement in the display of a small molecule. Moreover, because the peptide substrate for sortase can be modified with peptides, proteins, fluorophores, and so forth,[31−35] phage can be decorated with a wide range of substituents. As far as display of proteins is concerned, proteins similar in size to GFP have been incorporated at fewer than one copy per phage on pVIII using a phagemid system.[18] Using sortase, we display ∼90 GFP molecules on average per phage particle.

For the pIII and pIX proteins, we show that every phage can be labeled with multiple copies of the desired peptide/protein (Table 1). An advantage of using sortase to covalently attach

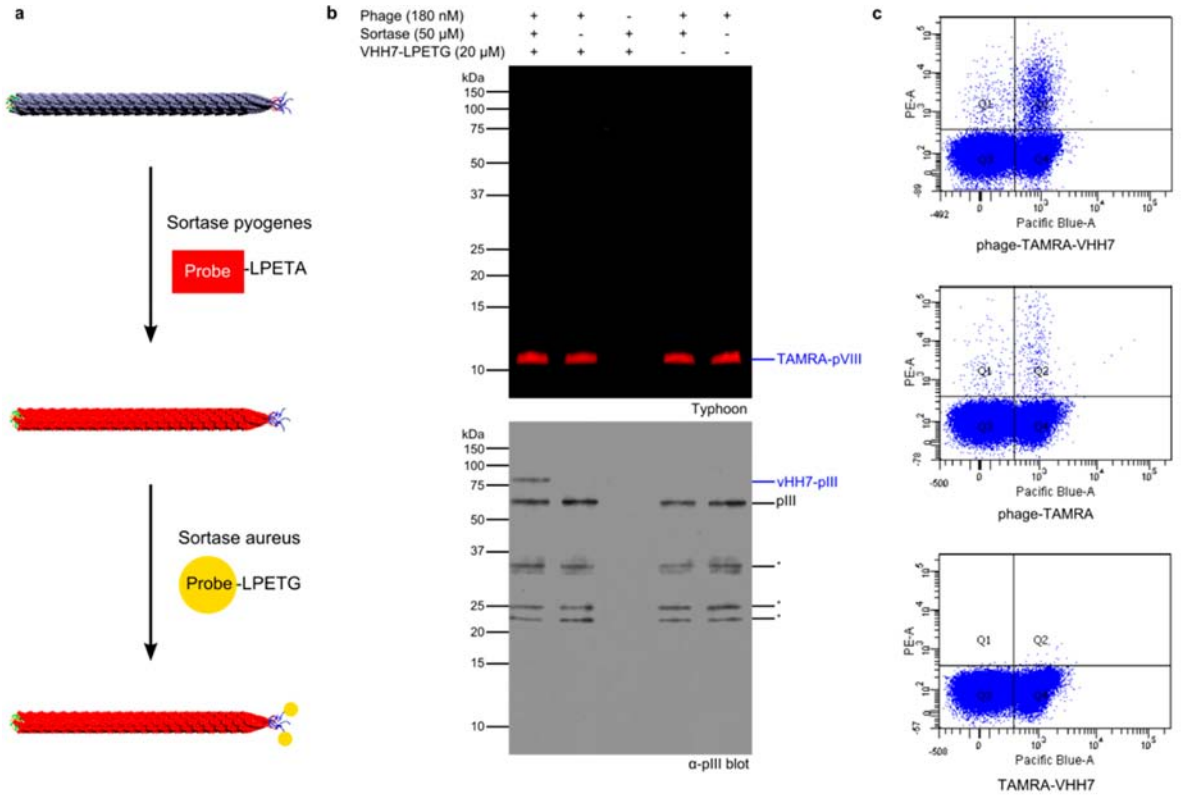


Figure 6. Dual labeling of phage using orthogonal $SrtA_{pyogenes}$ and $SrtA_{aureus}$. Schematic representation of the strategy used to couple two different moieties to two different capsid proteins (a). Labeling of pVIII with a K(TAMRA)-LPETAA peptide mediated by $SrtA_{pyogenes}$ was followed by labeling of pIII with a single domain antibody directed to Class II MHC as a cell targeting moiety and $SrtA_{aureus}$ (see Experimental Procedures for details). The final product was analyzed by fluorescent scanning imaging to visualize labeling of pVIII, followed by immunoblotting using an anti-pIII antibody to monitor the efficiency of labeling (b). There are five copies of pIII/phage particle. The asterisks indicate unidentified anti-pIII reactive proteins, which probably correspond to proteolytic fragments of pIII. Binding of the dual-labeled phage to lymphocytic Class II MHC+ cells was observed by flow cytometry (c). C57BL/6 mouse lymph node cells were stained for B220 together with the dual-labeled phage (phage-TAMRA-VHH7), TAMRA-labeled phage (no cell targeting motif, phage-TAMRA), or anti-Class II MHC directly conjugated to TAMRA (TAMRA-VHH7). B220 signal is on the x-axis; TAMRA signal is on the y-axis.

Table 1. Labeling Efficiency for Each of the Phage Coat Proteins Using Sortase

Minor Capsid Proteins				
capsid protein		probe		efficiency
pIII		Biotin		68 ± 9%
pIII		GFP		56 ± 2%
pIX		Biotin		73 ± 2%
pIX		GFP		74 ± 1%
Major Capsid Protein				
capsid protein	probe	optimal packing	copy number/phage using sortase	literature
pVIII	Biotin	2700	1350 ± 90	400−700
pVIII	GFP	385	91 ± 20	<1

proteins to phage over genetically engineering pIII directly is that it ensures display of the correct quaternary structure of the protein. This can be inferred from our experiments using streptavidin. The mixing of two phage particles, one containing streptavidin on pIII and the other containing biotin on pVIII, results in a novel and complex phage structure. This shows that the streptavidin structure displayed on phage remains fully active and binds biotin.

Sortase enzymes in combination with the streptavidin−biotin pair[45] or in conjunction with click-chemistry can generate novel structures. The ability of patterning and aligning materials on phage or of increasing its surface area is important for the development of new materials. For example, the lampbrush phage structure generated here (Figure 5) may find application in light-sensitive processes where phage branching off the stem could be functionalized to act as antennae to capture light.[55]

In addition to N-terminal labeling of single capsid proteins, two capsid proteins were labeled site-specifically on a single phage particle using two orthogonal sortases. This could be explored for panning of antibody libraries displayed on pIII. Due to the exquisite site-specificity of sortase, fluorescent peptides can be added to pVIII without modification of the moiety displayed at pIII. Fluorescent labeling by other chemistries does not easily afford such specificity, especially when displaying a large moiety, such as an antibody fragment. The sensitivity of detection should increase when a phage particle contains many fluorophore groups on pVIII. This is indeed what we observe in our flow cytometry experiments, showing that this strategy greatly enhances the sensitivity of detection. Increased sensitivity would be instrumental in the context of a future panning strategy for detection of rare binding events, whether due to low concentration of the target or due to low phage concentration.

Modification of pIII and pIX by sortase will be useful first and foremost for material applications, where the physical

dx.doi.org/10.1021/bc300130z | Bioconjugate Chem. 2012, 23, 1478−1487

properties of phage and not its utility as a library vector are of prime concern. Fluorescent modification of pVIII is compatible with the construction and screening of libraries created using pIII genetic fusions. In this case, the site-specificity and yield of the sortase reaction allow the generation of libraries that can be screened directly by fluorescence. Thus, the versatility of the sortase-based labeling strategy described here will enable development of a wide array of tools, expanding the use of phage either for the creation of new materials or for new biological applications.

■ ASSOCIATED CONTENT

Supporting Information

List of peptides identified by mass spectrometry of GFP-pIII, GFP-pIX, and GFP-pVIII proteins; immunoblot analysis of streptavidin-pIII labeling; atomic force microscopy images of lampbrush phage, streptavidin-pIII phage, and biotin-pVIII phage; table of oligonucleotides used in phage engineering; and method for estimating the number of GFPs that can be packed on the surface of phage. This material is available free of charge via the Internet at http://pubs.acs.org.

■ AUTHOR INFORMATION

Corresponding Author

*Hidde L. Ploegh/Carla P. Guimaraes, Whitehead Institute for Biomedical Research, 9 Cambridge Center, Cambridge, MA 02142; Phone (617) 324-2031, Fax (617) 452-3566, e-mail: ploegh@wi.mit.edu/guimarae@wi.mit.edu. Angela M. Belcher, Massachusetts Institute of Technology, 77 Massachusetts Avenue, Room 76-561, Cambridge, MA 02139; phone (617) 252 1163; e-mail: belcher@mit.edu.

Notes

The authors declare no competing financial interest.

■ ACKNOWLEDGMENTS

We thank Ana Avalos and Lee Kim Swee for help with FACS acquisition and to Debadyuti Ghosh and Nimrod Heldman for helpful discussions. This work was supported by the Institute for Collaborative Biotechnologies through grant W911NF-09-0001 from the U.S. Army Research Office. The content of the information does not necessarily reflect the position or the policy of the Government, and no official endorsement should be inferred. J.J.C. is grateful for a fellowship from The International Human Frontier Science Program Organization.

■ ABBREVIATIONS

ACF,autocorrelation function; AFM,atomic force microscopy; BAP,biotin acceptor peptide; DLS,dynamic light scattering; FACS,fluorescence-activated cell sorting; GFP,green fluorescent protein; HA,hemagglutinin; HRP,horseradish peroxidase; IPTG,isopropyl β-D-1-thiogalactopyranoside; LB,Luria broth; MHC,major histocompatibility complex; PBS,phosphate buffer saline; PEG,poly(ethylene glycol); pfu,plaque forming units; SDS-PAGE,sodium dodecyl sulfate polyacrylamide gel electrophoresis; $SrtA_{aureus}$,sortase A from *Staphylococcus aureus*; $SrtA_{pyogenes}$,sortase A from *Streptococcus pyogenes*; TBS,Tris buffered saline; TAMRA,tetramethylrhodamine; VHH,camelid heavy-chain antibody; X-gal,5-bromo-4-chloro-indolyl-β-D-galactopyranoside.

■ REFERENCES

(1) Sidhu, S. S. (2001) Engineering M13 for phage display. *Biomol. Eng. 18*, 57−63.
(2) Bratkovic, T. (2010) Progress in phage display: evolution of the technique and its application. *Cell. Mol. Life. Sci. 67*, 749−67.
(3) Burritt, J. B., Quinn, M. T., Jutila, M. A., Bond, C. W., and Jesaitis, A. J. (1995) Topological mapping of neutrophil cytochrome b epitopes with phage-display libraries. *J. Biol. Chem. 270*, 16974−80.
(4) Barry, M. A., Dower, W. J., and Johnston, S. A. (1996) Toward cell-targeting gene therapy vectors: selection of cell-binding peptides from random peptide-presenting phage libraries. *Nat. Med. 2*, 299−305.
(5) Jaye, D. L., Nolte, F. S., Mazzucchelli, L., Geigerman, C., Akyildiz, A., and Parkos, C. A. (2003) Use of real-time polymerase chain reaction to identify cell- and tissue-type-selective peptides by phage display. *Am. J. Pathol. 162*, 1419−29.
(6) Mazzucchelli, L., Burritt, J. B., Jesaitis, A. J., Nusrat, A., Liang, T. W., Gewirtz, A. T., Schnell, F. J., and Parkos, C. A. (1999) Cell-specific peptide binding by human neutrophils. *Blood 93*, 1738−48.
(7) Whaley, S. R., English, D. S., Hu, E. L., Barbara, P. F., and Belcher, A. M. (2000) Selection of peptides with semiconductor binding specificity for directed nanocrystal assembly. *Nature 405*, 665−8.
(8) Udit, A. K., Hollingsworth, W., and Choi, K. (2010) Metal- and metallocycle-binding sites engineered into polyvalent virus-like scaffolds. *Bioconjugate Chem. 21*, 399−404.
(9) Mao, C., Flynn, C. E., Hayhurst, A., Sweeney, R., Qi, J., Georgiou, G., Iverson, B., and Belcher, A. M. (2003) Viral assembly of oriented quantum dot nanowires. *Proc. Natl. Acad. Sci. U.S.A. 100*, 6946−51.
(10) Mao, C., Solis, D. J., Reiss, B. D., Kottmann, S. T., Sweeney, R. Y., Hayhurst, A., Georgiou, G., Iverson, B., and Belcher, A. M. (2004) Virus-based toolkit for the directed synthesis of magnetic and semiconducting nanowires. *Science 303*, 213−7.
(11) Nam, K. T., Kim, D. W., Yoo, P. J., Chiang, C. Y., Meethong, N., Hammond, P. T., Chiang, Y. M., and Belcher, A. M. (2006) Virus-enabled synthesis and assembly of nanowires for lithium ion battery electrodes. *Science 312*, 885−8.
(12) Nam, Y. S., Magyar, A. P., Lee, D., Kim, J. W., Yun, D. S., Park, H., Pollom, T. S., Jr., Weitz, D. A., and Belcher, A. M. (2010) Biologically templated photocatalytic nanostructures for sustained light-driven water oxidation. *Nat. Nanotechnol. 5*, 340−4.
(13) Dang, X., Yi, H., Ham, M. H., Qi, J., Yun, D. S., Ladewski, R., Strano, M. S., Hammond, P. T., and Belcher, A. M. (2011) Virus-templated self-assembled single-walled carbon nanotubes for highly efficient electron collection in photovoltaic devices. *Nat. Nanotechnol. 6*, 377−84.
(14) Ng, S., Jafari, M. R., and Derda, R. (2011) Bacteriophages and viruses as a support for organic synthesis and combinatorial chemistry. *ACS Chem. Biol. 7*, 123−38.
(15) Kaltgrad, E., O'Reilly, M. K., Liao, L., Han, S., Paulson, J. C., and Finn, M. G. (2008) On-virus construction of polyvalent glycan ligands for cell-surface receptors. *J. Am. Chem. Soc. 130*, 4578−9.
(16) Lee, Y. J., Yi, H., Kim, W. J., Kang, K., Yun, D. S., Strano, M. S., Ceder, G., and Belcher, A. M. (2009) Fabricating genetically engineered high-power lithium-ion batteries using multiple virus genes. *Science 324*, 1051−5.
(17) Bianchi, E., Folgori, A., Wallace, A., Nicotra, M., Acali, S., Phalipon, A., Barbato, G., Bazzo, R., Cortese, R., Felici, F., et al. (1995) A conformationally homogeneous combinatorial peptide library. *J. Mol. Biol. 247*, 154−60.
(18) Corey, D. R., Shiau, A. K., Yang, Q., Janowski, B. A., and Craik, C. S. (1993) Trypsin display on the surface of bacteriophage. *Gene 128*, 129−34.
(19) Kang, A. S., Barbas, C. F., Janda, K. D., Benkovic, S. J., and Lerner, R. A. (1991) Linkage of recognition and replication functions by assembling combinatorial antibody Fab libraries along phage surfaces. *Proc. Natl. Acad. Sci. U.S.A. 88*, 4363−6.
(20) Malik, P., Terry, T. D., Gowda, L. R., Langara, A., Petukhov, S. A., Symmons, M. F., Welsh, L. C., Marvin, D. A., and Perham, R. N.

(1996) Role of capsid structure and membrane protein processing in determining the size and copy number of peptides displayed on the major coat protein of filamentous bacteriophage. *J. Mol. Biol. 260*, 9–21.
(21) Markland, W., Roberts, B. L., Saxena, M. J., Guterman, S. K., and Ladner, R. C. (1991) Design, construction and function of a multicopy display vector using fusions to the major coat protein of bacteriophage M13. *Gene 109*, 13–9.
(22) Bass, S., Greene, R., and Wells, J. A. (1990) Hormone phage: an enrichment method for variant proteins with altered binding properties. *Proteins 8*, 309–14.
(23) Sidhu, S. S., Weiss, G. A., and Wells, J. A. (2000) High copy display of large proteins on phage for functional selections. *J. Mol. Biol. 296*, 487–95.
(24) Kretzschmar, T., and Geiser, M. (1995) Evaluation of antibodies fused to minor coat protein III and major coat protein VIII of bacteriophage M13. *Gene 155*, 61–5.
(25) Greenwood, J., Willis, A. E., and Perham, R. N. (1991) Multiple display of foreign peptides on a filamentous bacteriophage. Peptides from Plasmodium falciparum circumsporozoite protein as antigens. *J. Mol. Biol. 220*, 821–7.
(26) Iannolo, G., Minenkova, O., Petruzzelli, R., and Cesareni, G. (1995) Modifying filamentous phage capsid: limits in the size of the major capsid protein. *J. Mol. Biol. 248*, 835–44.
(27) Gao, C., Mao, S., Lo, C. H., Wirsching, P., Lerner, R. A., and Janda, K. D. (1999) Making artificial antibodies: a format for phage display of combinatorial heterodimeric arrays. *Proc. Natl. Acad. Sci. U.S.A. 96*, 6025–30.
(28) Jespers, L. S., Messens, J. H., De Keyser, A., Eeckhout, D., Van den Brande, I., Gansemans, Y. G., Lauwereys, M. J., Vlasuk, G. P., and Stanssens, P. E. (1995) Surface expression and ligand-based selection of cDNAs fused to filamentous phage gene VI. *Biotechnology 13*, 378–82.
(29) Georgieva, Y., and Konthur, Z. (2011) Design and screening of M13 phage display cDNA libraries. *Molecules 16*, 1667–81.
(30) Zozulya, S., Lioubin, M., Hill, R. J., Abram, C., and Gishizky, M. L. (1999) Mapping signal transduction pathways by phage display. *Nat. Biotechnol. 17*, 1193–8.
(31) Guimaraes, C. P., Carette, J. E., Varadarajan, M., Antos, J., Popp, M. W., Spooner, E., Brummelkamp, T. R., and Ploegh, H. L. (2011) Identification of host cell factors required for intoxication through use of modified cholera toxin. *J. Cell Biol. 195*, 751–64.
(32) Popp, M. W., Dougan, S. K., Chuang, T. Y., Spooner, E., and Ploegh, H. L. (2011) Sortase-catalyzed transformations that improve the properties of cytokines. *Proc. Natl. Acad. Sci. U.S.A. 108*, 3169–74.
(33) Antos, J. M., Chew, G. L., Guimaraes, C. P., Yoder, N. C., Grotenbreg, G. M., Popp, M. W., and Ploegh, H. L. (2009) Site-specific N- and C-terminal labeling of a single polypeptide using sortases of different specificity. *J. Am. Chem. Soc. 131*, 10800–1.
(34) Antos, J. M., Miller, G. M., Grotenbreg, G. M., and Ploegh, H. L. (2008) Lipid modification of proteins through sortase-catalyzed transpeptidation. *J. Am. Chem. Soc. 130*, 16338–43.
(35) Popp, M. W., Antos, J. M., Grotenbreg, G. M., Spooner, E., and Ploegh, H. L. (2007) Sortagging: a versatile method for protein labeling. *Nat. Chem. Biol. 3*, 707–8.
(36) Ton-That, H., Liu, G., Mazmanian, S. K., Faull, K. F., and Schneewind, O. (1999) Purification and characterization of sortase, the transpeptidase that cleaves surface proteins of Staphylococcus aureus at the LPXTG motif. *Proc. Natl. Acad. Sci. U.S.A. 96*, 12424–9.
(37) Ton-That, H., Mazmanian, S. K., Faull, K. F., and Schneewind, O. (2000) Anchoring of surface proteins to the cell wall of Staphylococcus aureus. Sortase catalyzed in vitro transpeptidation reaction using LPXTG peptide and NH(2)-Gly(3) substrates. *J. Biol. Chem. 275*, 9876–81.
(38) Popp, M. W., and Ploegh, H. L. (2011) Making and breaking peptide bonds: protein engineering using sortase. *Angew. Chem., Int. Ed. Engl. 50*, 5024–32.
(39) Race, P. R., Bentley, M. L., Melvin, J. A., Crow, A., Hughes, R. K., Smith, W. D., Sessions, R. B., Kehoe, M. A., McCafferty, D. G., and Banfield, M. J. (2009) Crystal structure of Streptococcus pyogenes sortase A: implications for sortase mechanism. *J. Biol. Chem. 284*, 6924–33.
(40) Petrenko, V. A., Smith, G. P., Gong, X., and Quinn, T. (1996) A library of organic landscapes on filamentous phage. *Protein Eng. 9*, 797–801.
(41) Barbas, C. F., Burton, D. R., Scott, J. K., and Silverman, G. J. (2001) *Phage Display: A Laboratory Manual*, Cold Spring Harbor Laboratory Press, Cold Spring Harbor, NY.
(42) Popp, M. W., Antos, J. M., and Ploegh, H. L. (2009) Site-specific protein labeling via sortase-mediated transpeptidation. *Current Protocols in Protein Science*; Wiley Interscience, USA; Chapter 15, Unit 15 3.
(43) Lee, C. V., Sidhu, S. S., and Fuh, G. (2004) Bivalent antibody phage display mimics natural immunoglobulin. *J. Immunol. Methods 284*, 119–32.
(44) Howarth, M., Chinnapen, D. J., Gerrow, K., Dorrestein, P. C., Grandy, M. R., Kelleher, N. L., El-Husseini, A., and Ting, A. Y. (2006) A monovalent streptavidin with a single femtomolar biotin binding site. *Nat. Methods 3*, 267–73.
(45) Matsumoto, T., Sawamoto, S., Sakamoto, T., Tanaka, T., Fukuda, H., and Kondo, A. (2011) Site-specific tetrameric streptavidin-protein conjugation using sortase A. *J. Biotechnol. 152*, 37–42.
(46) Lubkowski, J., Hennecke, F., Pluckthun, A., and Wlodawer, A. (1998) The structural basis of phage display elucidated by the crystal structure of the N-terminal domains of g3p. *Nat. Struct. Biol. 5*, 140–7.
(47) Makowski, L. (1992) Terminating a macromolecular helix. Structural model for the minor proteins of bacteriophage M13. *J. Mol. Biol. 228*, 885–92.
(48) O'Connell, D., Becerril, B., Roy-Burman, A., Daws, M., and Marks, J. D. (2002) Phage versus phagemid libraries for generation of human monoclonal antibodies. *J. Mol. Biol. 321*, 49–56.
(49) Rondot, S., Koch, J., Breitling, F., and Dubel, S. (2001) A helper phage to improve single-chain antibody presentation in phage display. *Nat. Biotechnol. 19*, 75–8.
(50) Kelly, K. A., Setlur, S. R., Ross, R., Anbazhagan, R., Waterman, P., Rubin, M. A., and Weissleder, R. (2008) Detection of early prostate cancer using a hepsin-targeted imaging agent. *Cancer Res. 68*, 2286–91.
(51) Kelly, K. A., Waterman, P., and Weissleder, R. (2006) In vivo imaging of molecularly targeted phage. *Neoplasia 8*, 1011–8.
(52) Jaye, D. L., Geigerman, C. M., Fuller, R. E., Akyildiz, A., and Parkos, C. A. (2004) Direct fluorochrome labeling of phage display library clones for studying binding specificities: applications in flow cytometry and fluorescence microscopy. *J. Immunol. Methods 295*, 119–27.
(53) Kirchhofer, A., Helma, J., Schmidthals, K., Frauer, C., Cui, S., Karcher, A., Pellis, M., Muyldermans, S., Casas-Delucchi, C. S., Cardoso, M. C., Leonhardt, H., Hopfner, K. P., and Rothbauer, U. (2010) Modulation of protein properties in living cells using nanobodies. *Nat. Struct. Mol. Biol. 17*, 133–8.
(54) Schatz, P. J. (1993) Use of peptide libraries to map the substrate specificity of a peptide-modifying enzyme: a 13 residue consensus peptide specifies biotinylation in Escherichia coli. *Biotechnology 11*, 1138–43.
(55) Nam, Y. S., Shin, T., Park, H., Magyar, A. P., Choi, K., Fantner, G., Nelson, K. A., and Belcher, A. M. (2010) Virus-templated assembly of porphyrins into light-harvesting nanoantennae. *J. Am. Chem. Soc. 132*, 1462–3.

Bioconjugate Chemistry

Article

pubs.acs.org/bc

Site-Specific Attachment of a Protein to a Carbon Nanotube End without Loss of Protein Function

Shige H. Yoshimura,*[,†,⊥] Shahbaz Khan,[‡,⊥] Satoshi Ohno,[§] Takashi Yokogawa,[§] Kazuya Nishikawa,[§] Takamitsu Hosoya,[∥] Hiroyuki Maruyama,[‡] Yoshikazu Nakayama,[‡,⊥] and Kunio Takeyasu[†,⊥]

[†]Graduate School of Biostudies, Kyoto University, Yoshida-konoe-cho, Sakyo-ku, Kyoto, 606-8501, Japan

[‡]Graduate School of Engineering, Osaka University, 2-1 Yamadaoka, Suita, 565-0871, Japan

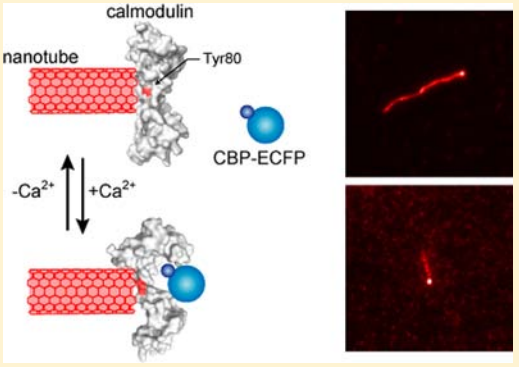
[§]Faculty of Engineering, Gifu University, 1-1 Yanagido, Gifu, 501-1193, Japan

[∥]Graduate School of Biomedical Science, Tokyo Medical and Dental University, 2-3-10 Kanda-surugadai, Chiyoda-ku, Tokyo, 101-0062, Japan

[⊥]CREST, Japan Science and Technology Agency, 4-1-8 Honcho, Kawaguchi, 332-0012, Japan

Supporting Information

ABSTRACT: Establishing a nanobiohybrid device largely relies on the availability of various bioconjugation procedures which allow coupling of biomolecules and inorganic materials. Especially, site-specific coupling of a protein to nanomaterials is highly useful and significant, since it can avoid adversely affecting the protein's function. In this study, we demonstrated a covalent coupling of a protein of interest to the end of carbon nanotubes without affecting protein's function. A modified Staudinger-Bertozzi ligation was utilized to couple a carbon nanotube end with an azide group which is site-specifically incorporated into a protein of interest. We demonstrated that Ca^{2+}-sensor protein, calmodulin, can be attached to the end of the nanotubes without affecting the ability to bind to the substrate in a calcium-dependent manner. This procedure can be applied not only to nanotubes, but also to other nanomaterials, and therefore provides a fundamental technique for well-controlled protein conjugation.



INTRODUCTION

A number of single-molecule-based measurement and manipulation techniques have made enormous contributions to biological and chemical sciences over the last 20 years.[1−3] The information derived from a single-molecule event is useful in elucidating the molecular mechanisms of biological reactions. In these techniques, biomolecules such as DNA or proteins are attached to larger substrates such as micrometer beads or silicon surfaces. In a single-molecule force measurement using optical tweezers, proteins and DNAs are attached to micrometer beads made of latex or other materials,[4−6] and in the case of atomic force microscopy, molecules are attached to a large probe made of silicon or silicon nitride.[7,8] In most cases, a single substrate can carry a vast number of molecules on the surface, and the device measures or captures only a single event that happens to only one of the molecules bound to the substrate surface. Therefore, the result obtained from each single measurement may vary if the molecular species attached to the substrate are heterogeneous, or if the manner of attachment is not uniform. These effects of heterogeneous events can be accounted for by statistical analysis; however, when the number of molecules in the measurement system is very small, molecular heterogeneity has a significant impact on the accuracy of the measurement.

When examining the function of a protein using a single-molecule system, it is important to take into consideration how the protein molecules are to be attached to the substrate. In cases in which the protein is directly adsorbed onto the substrate surface, the portion of the protein in contact with the surface is enzymatically inactive, since access to the active site is spatially hindered. Alternatively, proteins can be anchored to the substrate via a flexible polymer chain such as poly(ethylene glycol) or DNA.[8] Even in such cases, however, the point of attachment (amino acid) with the polymer may affect access of the protein's substrate. Thus, the orientation of a protein molecule on the substrate surface is a critical consideration, especially when protein−protein or protein−substrate interactions are to be analyzed.

Carbon nanotubes (CNTs) have revolutionized material sciences and the development of biosensors because of their biocompatibility and chemical inertness. A variety of biological molecules (proteins, carbohydrates, DNA, etc.) have been conjugated to carbon nanotubes for use in biosensors and other devices.[9−11] In many cases, biomolecules were attached to the

Received: March 15, 2012
Revised: May 31, 2012
Published: June 13, 2012

ACS Publications © 2012 American Chemical Society

dx.doi.org/10.1021/bc300131w | Bioconjugate Chem. 2012, 23, 1488−1493

sidewall of the CNT via either noncovalent or covalent bonding. Noncovalent couplings are typically based on hydrophobic interactions between a CNT and a biomolecule (or hydrophobic moieties, such as pyrene, that are attached to the biomolecule).[11,12] This type of method, due to its simplicity, has been used extensively in field-effect transistor (FET)-based sensor devices.[10,13,14] Nonspecific adsorption on CNTs is an interesting phenomenon, but represents a relatively less controllable mode of attaching molecules to CNTs. Covalent couplings include chemical cross-linking between an oxidized CNT (carboxylic acid) and a biomolecule. Oxidation of a CNT (either by acid treatment or heating in air) produces carboxylic groups at the nanotube ends (as well as defect sites on the sidewalls),[15−17] and has been used to attach molecules of interest to the ends of CNTs.[16,18] Because of its small diameter, the end of a CNT is a good target site for trapping a small number of protein molecules, and therefore can be used for single-molecule measurements. However, even in such cases, it is difficult to control the attachment site within the protein because of the lack of suitable protein engineering techniques. Therefore, a procedure for covalently attaching a protein of interest to CNTs in a desired position and orientation is important and necessary for establishing new bioconjugation systems. In the previous study, we reported that a modified Staudinger-Bertozzi reaction can be used to covalently couple CNTs and azide groups in a protein.[19] In this report, we utilized this reaction scheme to site-specifically attach a protein of interest to the end of a CNT without affecting the protein's enzymatic function.

EXPERIMENTAL PROCEDURES

Proteins. The cDNA encoding calmodulin carrying an amber mutation at residue 80 was prepared as described previously.[20] The cDNA fragment encoding mouse importin α (a.a. 1−133) was amplified using PCR and subcloned into the pIVEX vector (Roche Applied Science). The codon corresponding to Phe54 or Phe124 was substituted with an amber codon (TAG) using PCR with mutated oligonucleotides. *In vitro* transcription and translation were carried out as described previously.[20,21] Briefly, the suppressor $tRNA^{Tyr}_{(CUA)}$ was synthesized in *E. coli* cells from the plasmid carrying the yeast amber suppressor tRNA gene, and then purified using ion exchange chromatography (DEAE-sepharose, GE Healthcare). The transcription/translation-coupled reaction (50 μL) contained 50 mM HEPES-KOH (pH 7.5), 7.7 mM $Mg(OAc)_2$, 27.5 mM NH_4OAc, 200 mM KOAc, 1.7 mM DTT, 1.25 mM ATP, 0.83 mM GTP, UTP, and CTP, 80 mM creatine phosphate, 0.21 mg/mL creatine kinase, 0.1 mg/mL T7 RNA polymerase, 4% poly(ethylene glycol) (average MW 8000 Da), 3.4 A_{260} units/mL *E. coli* tRNA mix, 30% *E. coli* cell extract, 80 μM tyrosine, 200 μM each of 19 amino acids (excluding tyrosine) (Peptide Institute Inc.), 500 μM 3-azidotyrosine (Watanabe Chemical Industries Ltd.), 0.17 mg/mL tyrosyl-tRNA synthetase mutant (TyrRS Y43G), 0.2 A_{260} units/mL yeast suppressor $tRNA^{Tyr}_{(CUA)}$, and 0.02 mg/mL template DNA. Synthesized protein was purified using Ni-NTA resin (Qiagen) for importin α fragment or phenyl sepharose CL-4B (GE Healthcare) for calmodulin. To confirm the incorporation of azidotyrosine, synthesized protein was reacted with a rhodamine-conjugated triarylphosphine derivative (3-diphenylphosphino-4-(methoxycarbonyl) benzamide), separated by SDS-PAGE, and the gel was imaged using a fluoroimager. The construction of ECFP-fused calmodulin-binding peptide was described previously.[20] The fusion protein was expressed in bacteria and purified using Ni-NTA resin (Qiagen) according to the manufacturer's protocol.

Coupling of Azide Proteins to CNTs and Observation Using Fluorescence Microscopy. SWNTs synthesized using the chemical vapor deposition (CVD) method (Nanocyl s.a.) were oxidized as described in the previous study[22] and dispersed in ultrapure water using ultrasonication. CDI-activated Tween 20 was then added to a final concentration of 10%. The nanotubes were washed with 50 mM sodium borate (pH 7.5) to remove excess Tween 20 and then incubated with a fluorophore carrying an amino group (Texas Red hydrazide or BODIPY FL-hydrazide, Invitrogen) at 25 °C for 4 h. Excess fluorophore was removed either by passing the solution through a gel filtration column (Micro Bio-Spin 6, Bio Rad) or by repeated centrifugation and redissolution. The fluorescent-labeled oxidized nanotubes were reacted with ethylenediamine (2.5 mg/mL) and EDC (2.5 mg/mL) in 50 mM borate buffer (pH 7.5) for 20 min at 20 °C. After removal of free cross-linkers, the nanotubes were incubated with a NHS-coupled triarylphosphine derivative (3-diphenylphosphino-4-(methoxycarbonyl) benzoic acid *N*-hydroxysuccimide ester) (47 μM) at 20 °C for 60 min, and subsequently with purified calmodulin with or without azidotyrosine at position 80 (56 nM). The nanotubes were then incubated with purified ECFP carrying calmodulin peptide (1 μM) in the presence or absence of 5 μM $CaCl_2$. The sample was observed on a conventional fluorescence microscope (IX71, Olympus) equipped with an EM-CCD camera (Hamamatsu Photonics) and fluorescence filter sets.

Expression and Purification of VLPs. Expression vectors for rotavirus GFP-ΔVP2 and VP6 were kind gifts from Dr. Didier Poncet (Laboratoire de Virologie Moléculaire et Structurale, France). The DNA region encoding GFP was replaced by a DNA fragment encoding ECFP, which was amplified from ECFP-C1 vector using PCR. The plasmid (ECFP-ΔVP2 and VP6 in pFastBac1) was introduced into *E. coli* DH10Bac (Invitrogen) to produce a bacmid. Sf9 cells were transfected with the purified bacmid (ECFP-ΔVP2 or VP6) and the virus was harvested. The Sf9 cells were simultaneously infected with these two different viruses (ECFP-ΔVP2 and VP6) and VLPs were purified as described previously.[23] Briefly, the cells were lysed with Triton X-100 and the cell debris was removed by passage through a 0.2 μm filter. Virus-like particles were concentrated using an ultrafiltration membrane (300 000 MWCO, Amicon). Purified VLPs were observed using the same microscopic settings as were used for the observation of CNTs (see above). The fluorescence intensity of VLPs was quantified using image-analysis software (*MetaMorph*, Molecular Imaging).

RESULTS AND DISCUSSION

Amino Acid-Specific Incorporation of an Azide Group into a Protein of Interest. The azide group is a chemically useful reactive group, but it does not exist in natural proteins.[24−26] We employed an azide group to site-specifically attach a protein of interest to the end of a CNT. Amino acid-specific incorporation of azidotyrosine (Figure 1a) into the protein of interest was achieved using a previously reported procedure.[20] Briefly, a cDNA encoding the protein of interest was mutated such that the codon for the target amino acid was replaced by the amber codon (TAG) (Figure 1b). Using this cDNA as a template, transcription and translation were carried

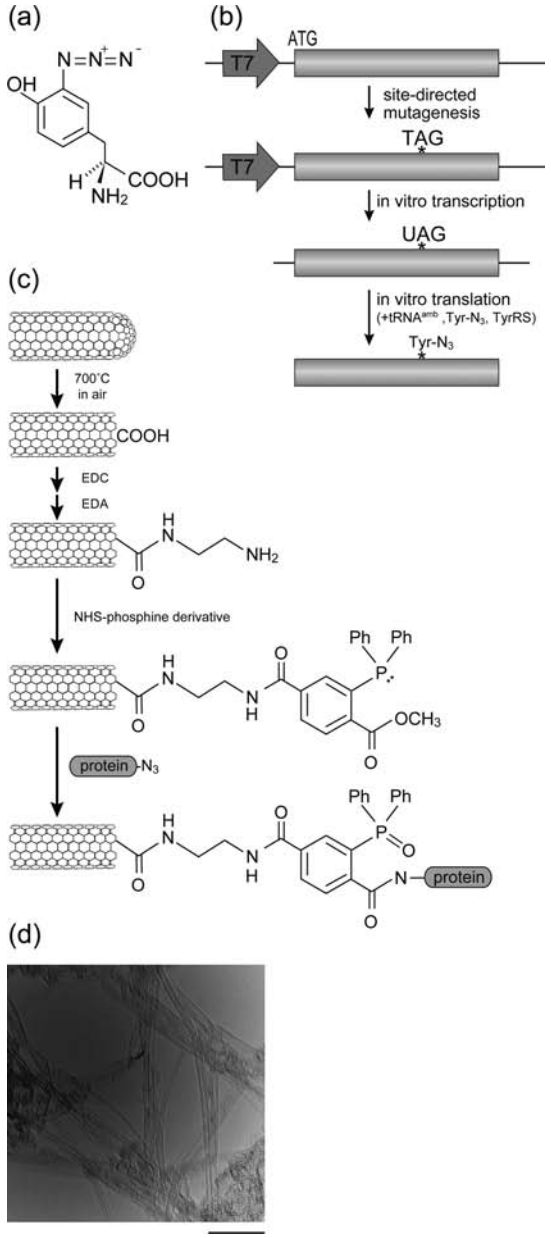


Figure 1. Reaction scheme for the site-specific coupling of a protein to the tip of a nanotube. (a) Structure of azidotyrosine. (b) Schematic illustration of amino acid specific incorporation of azidotyrosine into the protein of interest. The details of the procedure are described in the text and in the Experimental Procedures section. (c) Reaction scheme for coupling an azido-containing protein to the end of the CNT. The details of the reaction are described in the main text. (d) Transmission electron micrograph of CNTs utilized in this study. Most of the nanotubes (>95%) are single-walled. We utilized mild oxidation process to avoid the damage to the sidewall of the CNT. Because of this oxidation procedure, not all of the nanotube ends were oxidized and opened. Scale bar: 50 nm.

out *in vitro*. The translation reaction mixture contained a suppressor tRNA carrying a CUA anticodon, azidotyrosine (Figure 1b), and the corresponding aminoacyl-tRNA synthetase, so that the azidotyrosine could be incorporated specifically into the position of the TAG codon (see Experimental Procedures section for the detailed procedure). The reaction scheme for the covalent coupling of an azide group to the end of the nanotube is depicted in Figure 1c. The end of the nanotube was first oxidized to produce carboxylic acid group(s),[22] which then reacted with EDC and ethylenediamine to generate amino group(s) at the end. The coupling of the amino group with the azide group incorporated into the protein was achieved using a modified Staudinger-Bertozzi ligation,[27,28] which utilizes an NHS-coupled triarylphosphine derivative (Figure 1c). The Staudinger reaction is highly specific for azide groups and therefore does not normally occur on CNT surfaces. In a previous study, an azido-carrying molecule (sugar) was specifically attached to acid-treated CNTs via a carbodiimide (DCC/HOBt).[17] Our modified reaction scheme includes Staudinger-Bertozzi ligation as the final step of the conjugation, which catalyzes formation of the linkage between an amino group on the CNT and an azide group on the protein (Figure 1c). This reaction scheme was validated by a simple experimental system utilizing quantum dots (Supporting Information, Figure S1), as well as in our previous report.[19]

Calmodulin Functions at the End of a Carbon Nanotube. We applied the procedure described above to attach calmodulin to the end of a CNT and monitor enzymatic function. Calmodulin is a ubiquitous calcium-binding protein (K_D = 0.5−5 (nM)) that regulates the activities of a variety of cellular enzymes. It undergoes a conformational change when bound to Ca^{2+}, which then facilitates the interaction with the substrate (Figure 2a).

We prepared full-length calmodulin carrying azidotyrosine at position 80 using the procedure described above. Tyr80 is not directly involved in the interaction with the substrate (Figure 2a). Biochemical analysis demonstrated that calmodulin containing azidotyrosine at position 80 retains Ca^{2+}- and substrate-binding properties comparable to those of the wild-type protein (K_D ~10 nM).[20] Azido-calmodulin was attached to the end of the CNT using the procedure described in Figure 1c (see also Experimental Procedures). CNTs (Figure 1d) were oxidized in the air to produce carboxyl groups at the ends.[22] We employed mild oxidation condition in order to minimize damage to the sidewalls of the CNTs.[22] The oxidized CNTs were mixed with fluorophore-coupled detergent (Tween 20-Texas Red) to enable observation under fluorescence microscopy,[29] and then reacted with EDC and ethylenediamine (EDA) to produce amino groups. Finally, the CNTs were incubated with the NHS-coupled phosphine derivative, after which they were ready for reaction with the azide group. The successful attachment of azido-calmodulin to the CNT was monitored by observing the binding and unbinding of ECFP-fused calmodulin-binding peptide (ECFP-CBP). To obtain maximum binding efficiency, a saturating amount of the substrate (1 μM) was added to the nanotube/calmodulin hybrid. In the presence of 5 μM Ca^{2+} in the observation buffer, an ECFP signal was observed mainly at the ends of the CNTs (Figure 2b, arrowheads). Some of the CNTs carried the ECFP signal at both ends, but others had signal at only one end, because under our mild oxidation process, not all of the CNT ends were oxidized and some of them still remained as closed ends judging from electron micrographs. In total, approximately 17% of the CNTs in the observation fields had an ECFP signal on at least one end (Figure 2c). Additional images are shown in Figure S2, Supporting Information. The ECFP signal was also detected on the sidewall of the CNT, but with very low frequency (approximately 2% of the total nanotubes) (Figure 2b, asterisk). This was probably due to the production of carboxyl groups not only at the ends of the CNT during the

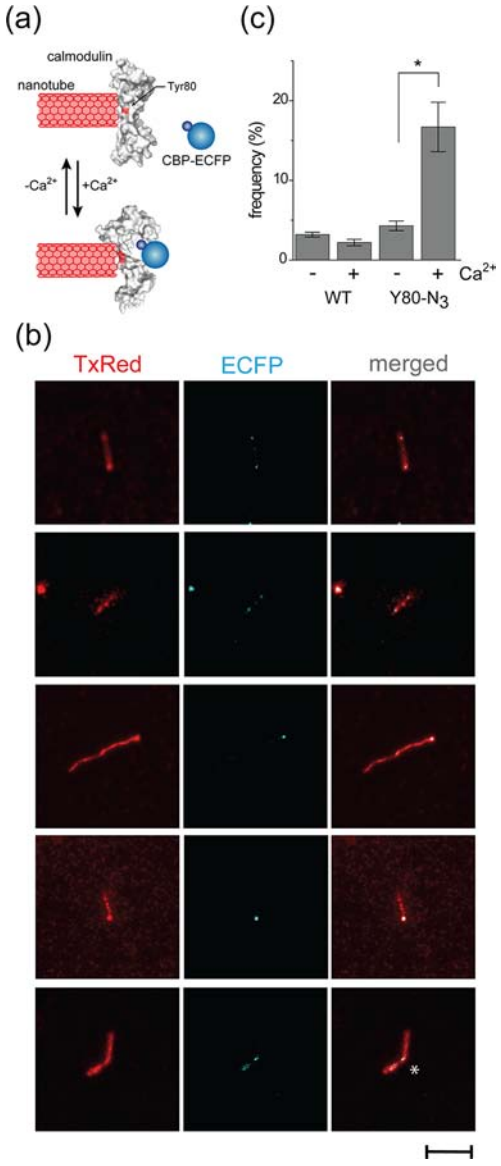


Figure 2. Site-specific attachment of calmodulin to the CNT end without affecting the interaction with its substrate peptide. (a) Schematic representation of the experimental system. Purified calmodulin carrying azidotyrosine at position 80 was covalently attached to a TxRed-labeled oxidized nanotube via the Staudinger-Bertozzi ligation. The function of attached calmodulin was examined under a fluorescence microscope by monitoring the binding of calmodulin-binding peptide (CBP) fused with ECFP (ECFP-CBP) in the presence or absence of Ca^{2+}. (b) Fluorescence images of CNTs and ECFP-CBP. A TxRed-labeled nanotube and ECFP-CBP were imaged using the appropriate filter sets (excitation, BP400−440 nm; dichroic mirror, 455 nm; emission, LP475 nm for ECFP; and excitation, BP545−580 nm; dichroic mirror, 600 nm; emission, LP610 nm for TxRed). Arrows indicate bound ECFP at the end of the nanotube, and asterisk (*) indicates ECFP signal on the sidewall. Scale bar: 5 μm. (c) Ca^{2+}-dependent binding of the substrate to calmodulin at the nanotube end. The experiment described in (b) was performed in the absence of Ca^{2+}. As a negative control, wild-type calmodulin (lacking an azide group) was used instead of azido-containing calmodulin. CNTs carrying a signal on at least one end were counted and are represented as a percentage of all the nanotubes in the image. The error bar indicates the standard deviation of more than three independent experiments. Asterisk indicates a significant difference ($P < 0.001$) as determined using a t-test.

oxidation process, but also on its sidewall, even though our oxidation process was mild.

In the absence of Ca^{2+}, in contrast, the frequency of detecting ECFP signals on the CNTs was drastically reduced (<4%). When the same experiment was performed with wild-type calmodulin (without an azide group), almost no ECFP signal was detected on the nanotubes in both the presence and absence of Ca^{2+} (Figure 2c), demonstrating the specificity of the Staudinger-Bertozzi ligation.

Quantifying the Number of Proteins at the End of the Nanotube. The intensity of the ECFP fluorescence at the CNT end was quantified in order to estimate the number of bound ECFP molecules utilizing virus-like particles (VLPs) of rotaviruses as described previously[23,30,31] (Figure 3). The expression of ECFP-fused VP2 protein together with normal VP6 in insect cells (Sf9) results in the formation of the empty VLP, which contains exactly 120 molecules of ECFP-VP2. These VLPs were purified from the cells and used as a standard to calibrate the ECFP fluorescence signal under a fluorescence microscope (Figure 3a).

Quantitative fluorescence imaging of both ECFP-VLPs and calmodulin-bound CNTs demonstrated that the number of ECFP-CBPs at the end of a single CNT varied from 5 to 58 (Figure 3b). Approximately half of the CNT ends had less than 20 ECFP molecules, with 5 ECFP molecules representing the fewest. This is a reasonable result considering that the diameter of the CNTs utilized in this study ranged between 5 and 15 nm (Figure 1d) and could therefore spatially accommodate 3−9 molecules of calmodulin at an open end (the hydrodynamic diameter of a calmodulin molecule is approximately 5.0 nm),[32] although there are more reactive carbon atoms at the end (Figure 3c). Furthermore, a single calmodulin molecule contains 2 substrate binding sites. In the presence of an excess amount of the substrate (in our experimental condition, 1 μM of ECFP-CBP), both of the binding sites are supposed to be occupied by the substrates. Considering all these factors, the number of possible binding sites for ECFP-CBP could be less than 18. The result shown in Figure 3b is in good agreement with this estimation, although it has a wider distribution in the histogram. The large distribution of ECFP signal at the CNT ends might have been due to aggregation of calmodulin and/or CBP-ECFP molecules at the end of the CNT, or existence of multiwalled CNTs. The electron micrograph demonstrated that approximately 5% of the CNTs utilized here were multiwalled.

■ CONCLUSIONS

We demonstrated successful attachment of a protein of interest (calmodulin) to the termini of CNTs without affecting enzymatic function (calcium-dependent substrate-binding). The attachment point using our method is specific to the end of the CNT. In the current experiment, due to the size (diameter) of the nanotubes utilized, the number of protein molecules bound to the end of each nanotube was greater than one. As the diameter of the nanotube increases, the number of bound protein molecules also increases. Therefore, we can control the number of molecules by controlling the size of the nanotube end. We have established a method to sharpen the tip of a CNT by introducing excess current, which produces a tip diameter of less than 5 nm. Using this sharpened CNT in conjunction with a selective oxidation procedure, it will be possible to trap a single protein at the CNT end. These techniques may be particularly useful in cases in which a small number of molecules are to be examined. For instance, we are

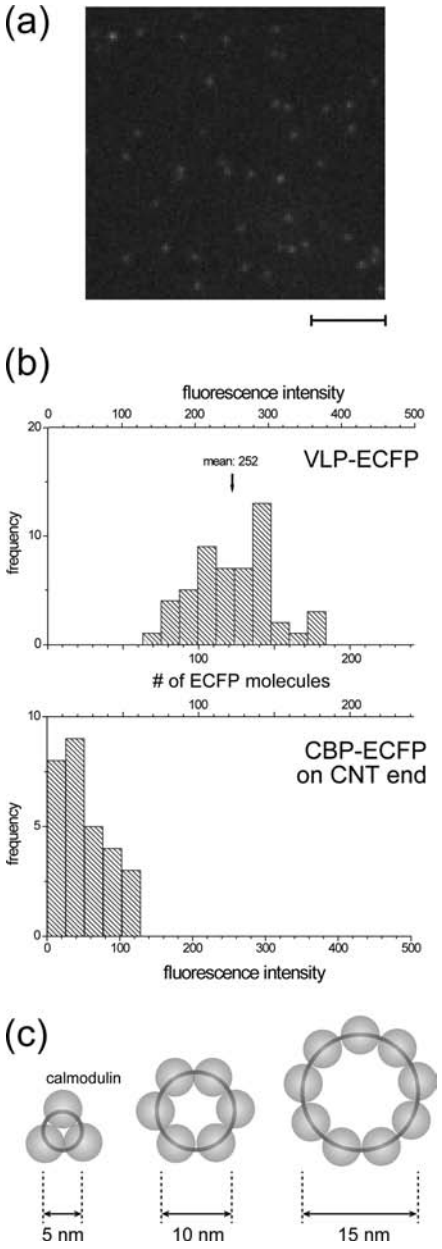


Figure 3. Estimating the number of ECFP molecules in fluorescence images. (a) Fluorescence image of purified VLPs (excitation, BP400–440 nm; dichroic mirror, 455 nm; emission, LP475 nm). The purification of VLPs is described in the Experimental Procedures section. Scale bar: 5 μm. (b) Quantification of ECFP fluorescence spots from VLPs (top panel) and the ends of CNTs (bottom panel). Since a single VLP contains 120 molecules of ECFP-VP2, the number of ECFP-CBP molecules in a single fluorescent spot at a CNT end (NCBP) can be calculated using the following equation: $N_{CBP} = I_{CBP}/(I_{VLP}/120)$ where I_{CBP} represents the fluorescence intensity of a single ECFP spot at the CNT end and I_{VLP} represents the average intensity of a single VLP (252 ± 21.8, mean ± S.D.) under identical imaging conditions. Both the integrated fluorescence intensity and the calculated number of ECFP molecules are indicated on the *x*-axis. (c) The diameter of a CNT and the number of calmodulin molecules at the CNT end. Maximum numbers of calmodulin molecules (5 nm hydrodynamic diameter) are arranged at the ends of 5-, 10-, and 15-nm-diameter single-walled CNTs.

currently applying this method to single-molecule force measurements (manuscript in preparation). The well-controlled attachment of a protein of interest to the end of the CNT probe can provide accurate kinetic information regarding enzyme–ligand interactions. Furthermore, our procedure will be useful in electronic characterization and detection of various biological molecules. Nanotubes and other carbon materials have been utilized to measure electronic properties of ion channels, pumps, and receptors, and to modulate the functions of these enzymes and even neuronal cells.[33−35] Since interactions between ligands and enzymes are sensitive to the orientation of both the ligand and the receptor, our procedure allows for more precise construction of CNT–protein hybrid devices. The integration of protein engineering techniques with advances in the various nanomaterial sciences will contribute greatly to biomaterial sciences and the development of biosensor technologies.

■ ASSOCIATED CONTENT

Ⓢ Supporting Information

Site-specific incorporation of azidotyrosine in the protein of interest and attachment to quantum dots are shown in Figure S1. Fluorescence images of CNT/calmodulin/ECFP-CBP complexes are shown in Figure S2. This material is available free of charge via the Internet at http://pubs.acs.org.

■ AUTHOR INFORMATION

Corresponding Author

*Tel & Fax: +81-75-753-7906. E-mail: yoshimura@lif.kyoto-u.ac.jp.

Notes

The authors declare no competing financial interest.

■ ACKNOWLEDGMENTS

Plasmids for rotavirus VP2 and VP6 were kind gifts from Dr. Didier Poncet (Laboratoire de Virologie Moléculaire et Structurale, France). cDNA encoding calmodulin was kindly provided by Nobuhiro Hayashi (Tokyo Institute of Technology, Japan). This work was supported by the Japan Science and Technology Agency (Core Research for Evolutional Science and Technology (CREST) program).

■ ABBREVIATIONS

CNT, carbon nanotube; CaM, calmodulin; Tx-Red, Texas Red; NHS, *N*-hydroxysuccinimide; CDI, 1,1′-carbonyldiimidazole; EDC, 1-ethyl-3-(3-dimethylaminopropyl) carbodiimide; EDA, ethylenediamine; PBS, phosphate buffered saline; GST, glutathione *S*-transferase; Tween 20, polyoxyethylene sorbitan monolaurate; ECFP, enhanced cyan fluorescent protein; aaRS, aminoacyl-tRNA synthetase; SDS, sodium dodecyl sulfate; PAGE, polyacrylamide gel electrophoresis; CBB, Coomassie Brilliant Blue; DTT, dithiothreitol; TMR, tetramethylrhodamine; VLP, virus-like particle

■ REFERENCES

(1) Zlatanova, J., and Leuba, S. H. (2002) Stretching and imaging single DNA molecules and chromatin. *J. Muscle Res. Cell Motil. 23*, 377–395.

(2) Leuba, S. H., Wheeler, T. B., Cheng, C. M., LeDuc, P. R., Fernandez-Sierra, M., and Quinones, E. (2009) Structure and dynamics of single DNA molecules manipulated by magnetic tweezers and or flow. *Methods 47*, 214–222.

(3) Moffitt, J. R., Chemla, Y. R., Smith, S. B., and Bustamante, C. (2008) Recent advances in optical tweezers. *Annu. Rev. Biochem. 77*, 205–228.

(4) Bennink, M. L., Leuba, S. H., Leno, G. H., Zlatanova, J., de Grooth, B. G., and Greve, J. (2001) Unfolding individual nucleosomes by stretching single chromatin fibers with optical tweezers. *Nat. Struct. Biol. 8*, 606−610.
(5) Wen, J. D., Lancaster, L., Hodges, C., Zeri, A. C., Yoshimura, S. H., Noller, H. F., Bustamante, C., and Tinoco, I. (2008) Following translation by single ribosomes one codon at a time. *Nature 452*, 598−603.
(6) Galburt, E. A., Grill, S. W., Wiedmann, A., Lubkowska, L., Choy, J., Nogales, E., Kashlev, M., and Bustamante, C. (2007) Backtracking determines the force sensitivity of RNAP II in a factor-dependent manner. *Nature 446*, 820−823.
(7) Ebner, A., Wildling, L., Kamruzzahan, A. S. M., Rankl, C., Wruss, J., Hahn, C. D., Holzl, M., Zhu, R., Kienberger, F., Blaas, D., Hinterdorfer, P., and Gruber, H. J. (2007) A new, simple method for linking of antibodies to atomic force microscopy tips. *Bioconjugate Chem. 18*, 1176−1184.
(8) Hinterdorfer, P., and Dufrene, Y. F. (2006) Detection and localization of single molecular recognition events using atomic force microscopy. *Nat. Methods 3*, 347−355.
(9) Star, A., Tu, E., Niemann, J., Gabriel, J. C., Joiner, C. S., and Valcke, C. (2006) Label-free detection of DNA hybridization using carbon nanotube network field-effect transistors. *Proc. Natl. Acad. Sci. U. S. A. 103*, 921−926.
(10) Chen, R. J., Choi, H. C., Bangsaruntip, S., Yenilmez, E., Tang, X., Wang, Q., Chang, Y. L., and Dai, H. (2004) An investigation of the mechanisms of electronic sensing of protein adsorption on carbon nanotube devices. *J. Am. Chem. Soc. 126*, 1563−1568.
(11) Besteman, K., Lee, J., Wiertz, F. G. M., Heering, H. A., and Dekker, C. (2003) Enzyme-coated carbon nantubes as single-molecule biosensors. *Nano Lett. 3*, 727−730.
(12) Chen, R. J., Zhang, Y., Wang, D., and Dai, H. (2001) Noncovalent sidewall functionalization of single-walled carbon nanotubes for protein immobilization. *J. Am. Chem. Soc. 123*, 3838−3839.
(13) Star, A., Gabriel, J. P., Bradley, K., and Grner, G. (2003) Electronic detection of specific protein binding using nanotube FET devices. *Nano Lett. 3*, 459−463.
(14) Kauffman, D. R., and Star, A. (2008) Electronically monitoring biological interactions with carbon nanotube field-effect transistors. *Chem. Soc. Rev. 37*, 1197−1206.
(15) Diao, P., Liu, Z., Wu, B., Nan, X., Zhang, J., and Wie, Z. (2002) Chemically assembled single-wall carbon nanotubes and their electrochemistry. *Chem. Phys. Chem. 3*, 898−901.
(16) Patolsky, F., Weizmann, Y., and Willner, I. (2004) Long-range electrical contacting of redox enzymes by SWCNT connectors. *Angew. Chem., Int. Ed. Engl. 43*, 2113−2117.
(17) Hong, S. Y., Tobias, G., Ballesteros, B., Oualid, F. E., Errey, J. C., Doores, K. J., Kirkland, A. I., Nellist, P. D., Green, M. L. H., and Davis, B. J. (2007) Atomic-scale detection of organic molecules coupled to single-walled carbon nanotubes. *J. Am. Chem. Soc. 129*, 10966−10967.
(18) Wong, S. S., Joselevich, E., Woolley, A. T., Cheung, C. L., and Lieber, C. M. (1998) Covalently functionalized nanotubes as nanometre-sized probes in chemistry and biology. *Nature 394*, 52−55.
(19) Maruyama, H., Yoshimura, S. H., Ohno, S., Nishikawa, K., and Nakayama, Y. (2012) Covalent attachment of a specific site of a protein molecule on a carbon nanotube tip. *J. Appl. Phys. 111*, 074701.
(20) Ohno, S., Matsui, M., Yokogawa, T., Nakamura, M., Hosoya, T., Hiramatsu, T., Suzuki, M., Hayashi, N., and Nishikawa, K. (2007) Site-selective post-translational modification of proteins using an unnatural amino acid, 3-azidotyrosine. *J. Biochem. 141*, 335−343.
(21) Yokogawa, T., Ohno, S., and Nishikawa, K. (2010) Incorporation of 3-azidotyrosine into proteins through engineering yeast tyrosyl-tRNA synthetase and its application to site-selective protein modification. *Methods Mol. Biol. 607*, 227−242.
(22) Maruyama, H., Yoshimura, S. H., Akita, S., Nagataki, A., and Nakayama, Y. (2007) Covalent attachment of protein to the tip of a multiwalled carbon nanotube without sidewall decoration. *J. Appl. Phys. 102*, 094701.
(23) Charpilienne, A., Nejmeddine, M., Berois, M., Parez, N., Neumann, E., Hewat, E., Trugnan, G., and Cohen, J. (2001) Individual rotavirus-like particles containing 120 molecules of fluorescent protein are visible in living cells. *J. Biol. Chem. 276*, 29361−29367.
(24) Abe, M., Ohno, S., Yokogawa, T., Nakanishi, T., Arisaka, F., Hosoya, T., Hiramatsu, T., Suzuki, M., Ogasawara, T., Sawasaki, T., Nishikawa, K., Kitamura, M., Hori, H., and Endo, Y. (2007) Detection of structural changes in a cofactor binding protein by using a wheat germ cell-free protein synthesis system coupled with unnatural amino acid probing. *Proteins 67*, 643−652.
(25) Coudijzer, K., and Joniau, M. (1990) 3-azido-L-tyrosine as a photoinhibitor of tubulin:tyrosine ligase. Role of thiol groups. *FEBS Lett. 268*, 95−98.
(26) Kiick, K. L., Saxon, E., Tirrell, D. A., and Bertozzi, C. R. (2002) Incorporation of azides into recombinant proteins for chemoselective modification by the Staudinger ligation. *Proc. Natl. Acad. Sci. U. S. A. 99*, 19−24.
(27) Saxon, E. (2000) Cell Surface Engineering by a Modified Staudinger Reaction. *Science 287*, 2007−2010.
(28) van Berkel, S. S., van Eldijk, M. B., and van Hest, J. C. (2011) Staudinger ligation as a method for bioconjugation. *Angew. Chem., Int. Ed. Engl. 50*, 8806−8827.
(29) Yoshimura, S. H., Khan, S., Maruyama, H., Nakayama, Y., and Takeyasu, K. (2011) Fluorescence labeling of carbon nanotubes and visualization of a nanotube-protein hybrid under fluorescence microscope. *Biomacromolecules 12*, 1200−1204.
(30) Dundr, M., McNally, J. G., Cohen, J., and Misteli, T. (2002) Quantitation of GFP-fusion proteins in single living cells. *J. Struct. Biol. 140*, 92−99.
(31) Rabut, G., Doye, V., and Ellenberg, J. (2004) Mapping the dynamic organization of the nuclear pore complex inside single living cells. *Nat. Cell Biol. 6*, 1114−1121.
(32) Papish, A. L., Tari, L. W., and Vogel, H. J. (2002) Dynamic light scattering study of calmodulin-target peptide complexes. *Biophys. J. 83*, 1455−1464.
(33) Huang, S. C., Artyukhin, A. B., Misra, N., Martinez, J. A., Stroeve, P. A., Grigoropoulos, C. P., Ju, J. W., and Noy, A. (2010) Carbon nanotube transistor controlled by a biological ion pump gate. *Nano Lett. 10*, 1812−1816.
(34) Malarkey, E. B., and Parpura, V. (2007) Applications of carbon nanotubes in neurobiology. *Neurodegener. Dis. 4*, 292−299.
(35) Park, K. H., Chhowalla, M., Iqbal, Z., and Sesti, F. (2003) Single-walled carbon nanotubes are a new class of ion channel blockers. *J. Biol. Chem. 278*, 50212−50216.

Bioconjugate Chemistry

Technical Note

pubs.acs.org/bc

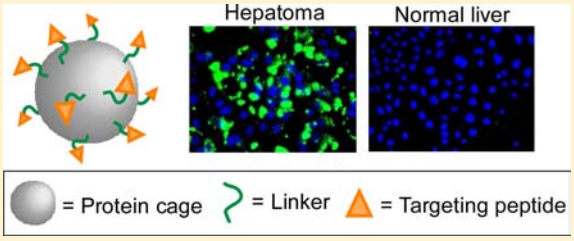
Development of Human Hepatocellular Carcinoma Cell-Targeted Protein Cages

Riki Toita,[†,⊥] Masaharu Murata,*[,†,‡,∥] Shigekazu Tabata,[‡] Kana Abe,[∥] Sayoko Narahara,[†] Jing Shu Piao,[‡] Jeong-Hun Kang,[#] and Makoto Hashizume[†,‡,∥]

[†]Innovation Center for Medical Redox Navigation, [‡]Department of Advanced Medical Initiatives, Faculty of Medical Sciences, and [∥]Center for Advanced Medical Innovation, Kyushu University, 3-1-1 Maidashi, Higashi-ku, Fukuoka 812-8582, Japan

[#]Department of Biomedical Engineering, National Cerebral and Cardiovascular Center Research Institute, 5-7-1 Fujishirodai, Suita, Osaka 565-8565, Japan

ABSTRACT: We described herein a human hepatocellular carcinoma (HCC) cell-targeted protein cage for which the HCC-binding peptide termed SP94 was modified at the surface of a naturally occurred heat shock protein (Hsp) cage. Six types of HCC-targeted Hsp cages were chemically synthesized using two types of heterobifunctional linker ($SM(PEG)_n$) with different lengths and two types of SP94 peptide, which contained a unique Cys residue at the N- or C-terminus of the peptide. These Hsp cages were characterized using matrix-assisted laser desorption/ionization-time-of-flight mass spectrometry (MALDI-ToF MS) analyses, sodium dodecylsulfate–polyacrylamide gel electrophoresis (SDS-PAGE) analyses, and dynamic light scattering (DLS) measurement. Fluorescence microscopic observations revealed that all the engineered protein cages bind selectively to HCC cells but not to the other cell lines tested (including normal liver cell). Moreover, the number of SP94 peptides on Hsp cages, conjugation site of SP94 peptide, and linker length between a Hsp cage and a SP94 peptide had important effects upon the binding of engineered Hsp cages to HCC cells. An engineered Hsp cage conjugated to the N-terminus of SP94 peptide via a longer linker molecule and containing high SP94 peptide levels showed greater binding toward HCC cells. Surprisingly, through optimization of these three factors, up to 10-fold greater affinity toward HCC cells was achieved. These results are critically important not only for the development of HCC cell-targeting devices using SP94 peptide, but also to create other cell-targeting materials that utilize other peptide ligands.



INTRODUCTION

Hepatocellular carcinoma (HCC) is one of the most common types of malignant tumors worldwide. It is the fifth leading cause of cancer death, and is associated with a relatively low prevalence of survival at 5 years.[1] Systemic chemotherapies have been thought to be the most promising strategies for patients with HCC.[2−4] However, many of these conventional chemotherapies have not been shown to improve survival, primarily because HCC is highly resistant against such chemotherapies.[2−4] In addition, many conventional antitumor agents do not selectively kill HCC cells, which can lead to undesirable side effects.[3] Many researchers have therefore attempted to develop tumor-selective carriers (e.g., polymers, liposomes, proteins) for drug delivery system (DDS) based mainly on active targeting strategies (e.g., folic acid, peptide ligands, and antibody-modification with carriers).[5−7]

Recently, a short peptide ligand termed SP94 (peptide sequence: SFSIIHTPILPL) was discovered by using an *in vivo* phase display technique, and was shown to bind selectively to various types of HCC cells.[8] Moreover, SP94-displayed liposome-containing chemotherapeutic agents exhibited much higher affinity toward various types of HCC cells compared with normal cells (including normal hepatocytes, endothelial cells, and immune cells) and killed HCC cells.[9] Thus, SP94 peptide could be useful as a HCC cell-targeted ligand and can be available for developing HCC-targeted DDS. In general, compared with antibodies, peptide ligands have advantages such as easier synthesis, lower expense, and lower immunogenesis. However, the effects of peptide conjugation methodologies (e.g., peptide content, site of peptide conjugation, and effect of linker length between peptide and carriers on affinity of engineered carriers toward HCC cells) have not been thoroughly investigated, even though these factors will be very important for the development of effective drug carriers.

In this study, we described a human HCC-targeted nanoparticle, which was chemically modified SP94 peptides at the exterior of the nanoparticle (Figure 1A). As a model nanoparticle, we focused on small heat shock protein 16.5 (Hsp), a naturally occurring protein in *Methanococcus jannaschii*, which forms a "cage" structure through self-assembly of 24 subunit proteins (i.e., outer size and inner size are 12 and 6.5 nm, respectively) (Figure 1A).[10] Hsp is attractive as a biomedical tool for delivery of therapeutics, imaging device, and sensing material due to its biocompatibility, monodispersed

Received: January 13, 2012
Revised: April 10, 2012
Published: May 23, 2012

 © 2012 American Chemical Society dx.doi.org/10.1021/bc300015f | *Bioconjugate Chem.* 2012, 23, 1494−1501

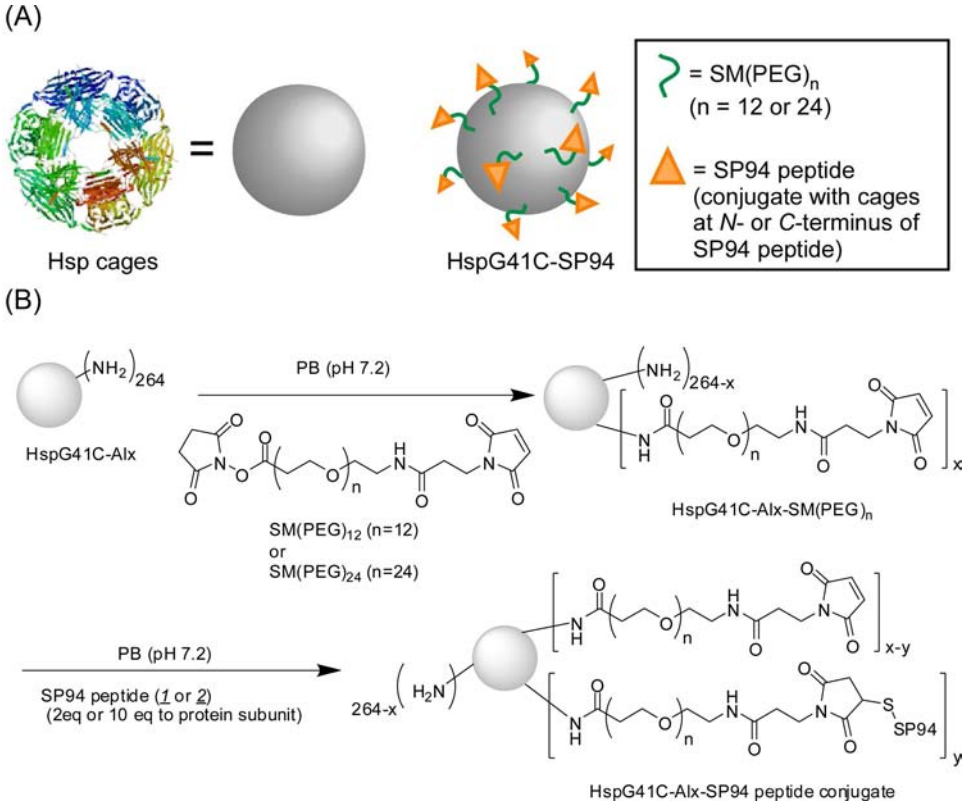


Figure 1. (A) SP94-modified Hsp cage (schematic). An Hsp cage consisted of 24 protein subunits with a molecular weight of 16.5 kDa, and formed a hollow-shaped structure. (B) Synthetic scheme of HspG41C−SP94 peptide conjugates.

formation, robust structure, easy acquisition from *Escherichia coli*, and easy functionalization through chemical and genetic strategies.[11−20] However, Hsp does not have sufficient specificity for cells or tissues, which is a major obstacle to its application as a drug carrier or imaging device. Therefore, providing specificity toward certain cells or tissues for Hsp is very important for disease treatment and diagnostic imaging.

We first synthesized six types of engineered "protein cages" which were different in (i) SP94 peptide contents, (ii) conjugation site of SP94 peptide, and (iii) linker length between an Hsp cage and an SP94 peptide. Synthesized Hsp cage-SP94 peptide conjugates were analyzed using matrix-assisted laser desorption/ionization−time-of-flight mass spectrometry (MALDI-ToF MS) analyses, sodium dodecylsulfate−polyacrylamide gel electrophoresis (SDS-PAGE) analyses, and dynamic light scattering (DLS) measurement. Observation of fluorescence microscopic images revealed that all of the engineered Hsp cages bind selectively to human HCC cells (HepG2 and Huh-7 cells) but not to other cell lines including human cervical carcinoma (HeLa) cells and rat normal hepatocyte (RLN-8). Interestingly, the level of binding to HCC cells of engineered protein cages was changed appreciably according to (i) peptide content, (ii) conjugation site of peptide, and (iii) linker length. These results provide useful information to enhance cellular uptake of peptide ligand-fabricated nanoparticles by simply changing chemical conjugation strategy of peptide ligands.

■ EXPERIMENTAL PROCEDURES

Expression and Purification of HspG41C Cages. The pET21a(+) vector-encoded HspG41C mutant in which Gly residue at position 41 of wild-type Hsp was substituted with a Cys residue was prepared by polymerase chain reaction (PCR)-mediated mutagenesis using the appropriate primers. The success of mutagenesis was confirmed by DNA sequencing. HspG41C mutant protein was expressed from *E. coli*, and was purified using anion exchange chromatography and size exclusion chromatography (SEC). BL21 Gold(DE3) (Novagene, Tokyo, Japan) was used as a strain for HspG41C.

E. coli containing the pET21a(+) plasmid vector were grown in 2 × YT medium containing 100 μg/mL of ampicillin at 37 °C. When the optical density (OD) at 600 nm of the culture medium reached between 0.5 and 0.6, expression of a recombinant protein was induced with 1 mM of isopropyl-β-D-thiogalactopyranoside (IPTG) (Wako Pure Chemical Ind. Ltd., Osaka, Japan) for 4 h at 37 °C. After collection by centrifugation, cells were suspended in 25 mM KH_2PO_4 solution (containing 1 mM ethylenediamine tetraacetic acid (EDTA) and 2 mM dithiothreitol (DTT), pH 7.0) and stored at −80 °C until purification. Cell suspensions were sonicated to disrupt the cell membrane. Cell lysate solutions were then centrifuged at 15 000 rpm for 30 min at 4 °C and then supernant collected. Proteins were purified using a HiLoad 26/10 QSepharose HP anion exchange column (GE Healthcare, Buckinghamshire, UK) and a SEC column (TSKgel G3000SW; Tosoh, Tokyo, Japan). Purification was confirmed by 15% SDS-PAGE analyses.

Synthesis of Alexa488-Modified HspG41C (HspG41C-Alx). For modification of fluorophores on the interior of HspG41C, HspG41C (2.5 mg, 152 nmol Cys residues) was reacted with Alexa-Fluor 488 C_5-maleimide (0.13 mg, 182 nmol) (Invitrogen, Carlsbad, CA, USA) in 0.1 M phosphate buffer (PB; pH 7.2) for 2 h at room temperature. The reactant was further incubated for 20 h at 4 °C. Unreacted Alexa-Fluor

dx.doi.org/10.1021/bc300015f | *Bioconjugate Chem.* 2012, 23, 1494−1501

488 C_5-maleimide was removed by ultrafiltration using Amicon Ultra Centrifugal Filters with MWCO 100 000 (Millipore, Tokyo, Japan). The success of Alexa488 modification to HspG41C was confirmed using MALDI-ToF MS analyses. Modified amounts of Alexa488 in HspG41C-Alx cages were calculated from absorbance data of Alexa488 (ε_{495} = 73 000 cm^{-1} M^{-1}).

Synthesis of SP94 Peptide-Modified HspG41C-Alx. To introduce maleimide groups to Hsp cages, heterobifunctional poly(ethylene glycol) linkers possessing succinimidyl and maleimide groups at the end of linkers (SM(PEG)$_n$; n = 12 or 24) (Thermo Scientific, Kanagawa, Japan) were used. HspG41C-Alx was modified with SM(PEG)$_n$ (50× excess of the protein monomer) through amide bonds in PB (0.1 M, pH 7.2) for 2 h at room temperature, followed by removal of unreacted SM(PEG)$_n$ by ultrafiltration as described above to obtain HspG41C-Alx-SM(PEG)$_n$-containing maleimide groups.

For modification of SP94 peptide, two types of SP94 peptides containing a Cys residue at the N-terminus or C-terminus were prepared; sequences of peptides **1** and **2** were Ac-CGGSFSIIHTPILPL-NH_2 and Ac-SFSIIHTPILPLGGC-NH_2, respectively (the underline indicates the SP94 peptide sequence). HspG41C-Alx-SM(PEG)$_n$ and SP94 peptides (2 or 10 equiv to protein monomer) were dissolved in PB (0.1 M, pH 7.2) and stirred for 6 h at room temperature, and allowed to stand for 20 h at 4 °C. The mixture was purified by ultrafiltration as described above.

MALDI-ToF MS Analyses. Measurement of the molecular weight of PEG-modified HspG41C cages was performed by MALDI-ToF MS analysis using Autoflex Speed (Bruker Daltonics Inc., Billerica, MA, USA), and sinapinic acid (Bruker Daltonic Inc.) was used as a matrix.

SDS-PAGE Analysis. SDS-PAGE was performed using 15% SDS-PAGE gel (Wako Pure Chemical. Ind.). Sample bands were imaged by the fluorescence of Alexa488 bound to each protein cage using a Typhoon FLA9000 Biomolecular Imager (GE Healthcare). Fluorescence images were analyzed using ImageQuant TL (GE Healthcare). Modified amounts of SM(PEG)$_n$ and SP94 peptides in Hsp cages were determined from band intensity of SDS-PAGE analysis as described in previous stuides.[16,21] Briefly, band fluorescence intensities of each modified Hsp cage were measured quantitatively using ImageQuant TL, and then contents of SM(PEG)$_n$ and SP94 peptides were calculated from the fluorescence intensity ratios of each band.

Measurement of the Size of SP94-Modified HspG41C Cages by DLS. All samples and buffer solutions were filtered using Ultrafree-MC with pore sizes of 0.22 μm (Millipore, Tokyo, Japan) before DLS measurement. Sizes of protein cages (0.1 mg/mL) were measured thrice using a Zeta-Sizer Nano ZS Analyzer (Malvern, UK) at the detection angles of 173° and temperature of 25 °C. The 633 nm wavelength from a He−Ne laser was used as an incident beam.

Cell Culture. Human HCC (Huh-7 and HepG2), human cervical carcinoma HeLa, and rat normal liver cell RLN-8 cells were cultured in the appropriate medium containing 10% fetal bovine serum (FBS), 100 U/mL penicillin, 100 μg/mL streptomycin, and 0.25 μg/mL amphotericin-B (all from Gibco, NY, USA) in a humidified atmosphere of 5% CO_2 and 95% air at 37 °C. Dulbecco's modified Eagle's medium (DMEM) was used for cultivation of Huh-7 and HepG2 cells, Eagle's minimal essential medium (EMEM) containing nonessential amino acids for HeLa cells and minimal essential medium α (MEMα) for RLN-8 cells (all from Wako) were used.

Fluorescence Microscopic Observation. Cells were seeded on 96-well culture plates with an initial cell density of 10 000/well and cultured for 1 day in 100 μL of the appropriate medium containing 10% FBS. Final concentrations of Hsp cages were adjusted to 40 nM (1 μM of subunit protein) by Opti-MEM (Gibco) and 100 μL of diluted Hsp cages was added to the each well. After incubation for 24 h, the medium was changed to fresh Opti-MEM containing 5 μg/mL of Hoechst 33342 (Dojindo, Kumamoto, Japan) and incubated for 1 h. Fluorescence images were obtained using the fluorescence microscope BZ-9000 (Keyence, Osaka, Japan). For blocking the binding of Hsp cages to target receptors, excessive amounts of free SP94 peptides (100 μM) were added to cells with Hsp cages.

Fluorescence Measurement of Cellular Uptake of HspG41C-SM(PEG)$_n$-SP94 Peptide Conjugates. Huh-7 and HepG2 cells were harvested on 96-well plates with an initial cell density of 10 000/well, and cultured for 1 day. Fifty microliters of each protein cage diluted with Opti-MEM (4 nM) were added to each well. After incubation for 24 h, cells were rinsed twice with phosphate-buffered saline (PBS)(−) and then lysed in 100 μL of buffer (pH 7.5, 20 mM Tris-HCl, 2 mM EDTA, and 0.05% Triton-X 100). Lysate solutions were replaced on black-bottomed 96-well plates, and the fluorescence intensity of each sample measured using a Microplate Reader (ARVO MX 1420; Perkin-Elmer Inc., Waltham, MA, USA).

Cell Viability Assay after Adding Free SP94 Peptides to Huh-7 Cells. Huh-7 cells were harvested on 96-well plates at an initial cell density of 10 000 cells/well and grown overnight at 37 °C overnight. After adding SP94 peptides (3−300 μM) dissolved in Opti-MEM to cells, the cells were incubated at 37 °C for 24 h. Cell viability was measured using a CellTiter-Glo luminescent cell viability assay kit (Promega, Madinson, WI, USA) according to the manufacture's protocol. Luminescence intensity was measured using a Microplate Reader (ARVO MX 1420; Perkin-Elmer Inc., Waltham, MA, USA).

Fluorescence Microscopic Observation of Subcellular Localization of HspG41C-SM(PEG)$_n$-SP94 Peptide Conjugates. Huh-7 cells were harvested on 48-well plates at initial density of 10 000 cells/well and grown overnight at 37 °C overnight. After adding HspG41C-SM(PEG)$_n$-SP94 peptide conjugates (40 nM) to cells, the cells were incubated at 37 °C for 24 or 48 h. Acidic organelles and nuclei were stained by LysoTracker Red DND-99 (Invitrogen, Carlsbad, CA, USA) and Hoechst 33342 (Dojindo), respectively. Fluorescence images were obtained using the fluorescence microscope BZ-9000 (Keyence, Osaka, Japan).

■ RESULTS AND DISCUSSION

Synthesis and Characterization of HCC Targeted Peptide- and Fluorophore-Modified HspG41C Cages. The synthetic scheme of HspG41C-Alx-SP94 is described in Figure 1B. HspG41C was labeled with Alexa488-maleimide at the interior of HspG41C cages via thioether bonds between a unique Cys residue of HspG41C and a maleimide group of Alexa488 (HspG41C-Alx). Binding of Alexa488 to HspG41C was identified by MALDI-ToF MS analyses (Figure 2A). From absorbance of Alexa488 at 495 nm (ε_{495} = 73 000 cm^{-1} M^{-1}), we estimated that 22 molecules of Alexa488 were modified with each HspG41C-Alx cage (0.93 molecules/monomer protein).

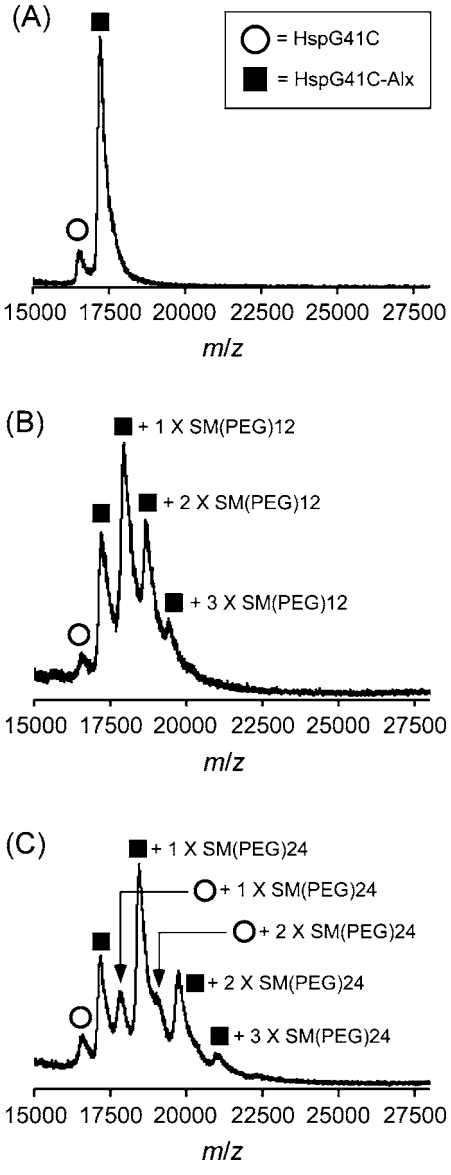


Figure 2. MALDI-ToF MS analyses of (A) HspG41C-Alx, (B) HspG41C-Alx-SM(PEG)$_{12}$, and (C) HspG41C-Alx-SM(PEG)$_{24}$. Open circles and filled squares indicate HspG41C- and HspG41C-derived peaks, respectively. Theoretical molecular weight of HspG41C and HspG41C-Alx were 16498 g/mol and 17219 g/mol, respectively. Net mass addition through conjugation of one SM(PEG)$_{12}$ and one SM(PEG)$_{24}$ molecule with protein cages were 750 g/mol and 1279 g/mol, respectively.

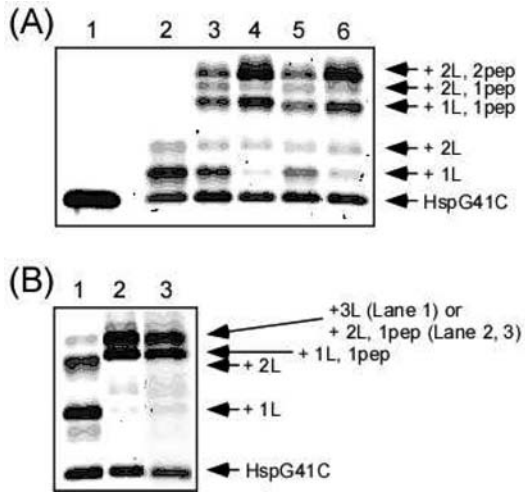


Figure 3. SDS-PAGE analyses of HspG41C−SP94-peptide conjugates. (A) HspG41C-Alx-SM(PEG)$_{12}$−SP94 peptide conjugates. Lane 1, HspG41C-Alx; lane 2, HspG41C-Alx-SM(PEG)$_{12}$; lane 3, 12-N(1); lane 4, 12-N(2); lane 5, 12-C(1); and lane 6, 12-C(2). (B) HspG41C-Alx-SM(PEG)$_{24}$−SP94 peptide conjugates. Lane 1, HspG41C-Alx-SM(PEG)$_{24}$; lane 2, 24-N(1); and lane 3, 24-C(1). Each band was imaged by fluorescence from Alexa488 conjugated with protein cages. "L" and "pep" indicate SM(PEG)$_n$ linker and SP94 peptide, respectively.

To introduce the maleimide groups into HspG41C-Alx, heterobifunctional linkers (SM(PEG)$_{12}$ or SM(PEG)$_{24}$) that possessed NHS ester and maleimide groups at either side of the linkers were conjugated to HspG41C-Alx thorough amide bonds to obtain HspG41C-Alx-SM(PEG)$_n$. MALDI-ToF MS analyses showed that 1−3 molecules of the linker were bound to HspG41C-Alx-SM(PEG)$_n$ (Figure 2B,C). Moreover, these corresponding bands were observed from SDS-PAGE analysis (Figure 3). SDS-PAGE analyses revealed that, on average, 23 ± 2 molecules of SM(PEG)$_{12}$ and 23 ± 3 molecules of SM(PEG)$_{24}$ were bound to HspG41C-Alx-SM(PEG)$_{12}$ and HspG41C-Alx-SM(PEG)$_{24}$, respectively (Figure 3).

To conjugate SP94 peptides into HspG41C-Alx-SM(PEG)$_n$, two SP94 peptide derivatives containing a Cys residue at the N-terminus or the C-terminus of the original SP94 peptide sequences were prepared, i.e., peptide **1** and peptide **2** possessed a Cys residue at the N-terminus and the C-terminus of the original SP94 peptide sequences, respectively. Peptide **1** or **2** was modified with HspG41C-Alx-SM(PEG)$_n$ through a Michael addition reaction between a thiol group of a SP94 peptide derivative and maleimide groups of HspG41C-Alx-SM(PEG)$_n$. SDS-PAGE analyses revealed that peptides **1** and **2** were successfully modified with HspG41C-Alx-SM(PEG)$_{12}$ because three new bands corresponding to HspG41C-Alx-SM(PEG)$_{12}$ bound to one or two SP94 peptide molecules per protein monomer were observed (lanes 3−6) (Figure 3A). Moreover, one SP94 peptide per protein monomer could conjugate into HspG41C-Alx-SM(PEG)$_{24}$ (Figure 3B). Average SP94 peptide contents in each HspG41C-Alx-SM(PEG)$_n$ were determined from SDS-PAGE analyses (Figure 3) and are summarized in Table 1.

Size Measurements of Linker- and Peptide-Modified HspG41C. Sizes of HspG41C conjugates in PBS were measured by DLS analyses. HspG41C is known to form a cage structure with a diameter of 12 nm.[10] As shown in Figure 4A, HspG41C used in the present study also showed a comparable size. After conjugation of SM(PEG)$_n$ linkers to HspG41C, the size distribution peak of HspG41C-SM(PEG)$_n$ was slightly shifted to a larger size when compared with that of HspG41C. However, both of HspG41C-SM(PEG)$_n$ did not form any large aggregates (>100 nm) (Figure 4A, inset).

As shown in Figure 4B, the size distribution peak of all HspG41C-SM(PEG)$_{12}$-SP94 peptide conjugates are slightly shifted to a larger size when compared with that of their precursor (HspG41C-SM(PEG)$_{12}$). Same trends were detected from the system of HspG41C-SM(PEG)$_{24}$-SP94 peptide conjugates (Figure 4C). On the other hand, all of the HspG41C-SM(PEG)$_n$-SP94 peptide conjugates did not show any large aggregate formations (>100 nm) (Figure 4B,C, inset).

Table 1. Characterization of HspG41C-SP94 Peptide Conjugates Used in This Study

sample[a]	peptide number/cage[b]	conjugated peptide[c]
12-N(1)	12 ± 2	**1**
12-N(2)	23 ± 2	**1**
12-C(1)	13 ± 2	**2**
12-C(2)	22 ± 3	**2**
24-N(1)	15 ± 2	**1**
24-C(1)	16 ± 1	**2**

[a]Numbers 12 and 24 indicate HspG41C-SP94 peptide conjugates using HspG41C-Alx-SM(PEG)$_{12}$ and HspG41C-Alx-SM(PEG)$_{24}$ as the precursors, respectively. N and C mean SP94 peptides containing a Cys residue at the N-terminus and C-terminus, respectively. Furthermore, parenthesized number 1 and 2 exhibit the addition of 2 and 10 equiv of SP94 peptides to HspG41C-Alx-SM(PEG)$_n$, respectively, when synthesizing them. [b]SP94 peptide contents of each cage were calculated from the results of SDS-PAGE analyses. Data are means ± SD of three independent experiments. [c]Sequences of peptides **1** and **2** were Ac-CGGSFSIIHTPILPL-NH$_2$ and Ac-SFSIIHTPILPLGGC-NH$_2$, respectively.

These results showed that the cage structure of HspG41C was sufficiently robust for chemical modification of target peptides.

Fluorescence Microscopic Observation of Cellular Binding of HspG41C-SM(PEG)$_n$-SP94 Peptide Conjugates toward Various Kinds of Cell Lines. To verify if HspG41C-SM(PEG)$_n$-SP94 peptide conjugates could bind selectively to HCC cells, Alexa488-labeled conjugates were added to human HCC cell lines (Huh-7 and HepG2), HeLa and RLN-8, and binding of conjugates to cells was then detected using a fluorescence microscope. When Alexa488-labeled HspG41C-SM(PEG)$_n$-SP94 peptide conjugates were added to Huh-7 and HepG2 cells, green fluorescence was observed, indicating that all conjugates could bind the human HCC-derived cell lines (Figure 5A). However, of the number of protein cages bound to HCC cells changed appreciably according to (i) SP94 peptide content, (ii) conjugation site of the SP94 peptide, and (iii) linker length, which will be discussed later. In contrast to HCC-derived cells, obvious green fluorescence was not detected after addition of Alexa488-labeled HspG41C-SM(PEG)$_n$-SP94 peptide conjugates to the other cell lines (HeLa and RLN-8 cells). These results showed that HspG41C-SM(PEG)$_n$-SP94 peptide conjugates could bind selectively to human HCC-derived cell lines.

Influence of SP94 Peptide Content in HspG41C-SM(PEG)$_n$-SP94 Peptide Conjugates on Cellular Binding. To clarify whether SP94 peptide content in HspG41C-SM(PEG)$_n$-SP94 peptide conjugates affected cellular binding, the fluorescence intensity of cellular lysates was compared 24 h after the addition of Alexa-labeled conjugates to HepG2 and Huh-7cells. When 12-N(2) (23 peptides/cage) and 12-N(1) (12 peptides/cage), both of which were modified SP94 peptides at the N-terminus of SP94 peptides, were added to HepG2 cells, 12-N(2) showed 3.9× higher fluorescence intensity than 12-N(1) (Figure 5B). Moreover, 2.7× higher fluorescence intensity from 12-C(2) (22 peptides/cage) was observed when compared with that from 12-C(1) (13 peptides/cage) (Figure 5B). Similarly, an increase in SP94 peptide content in conjugates increased fluorescence intensity in Huh-7 cells, but their variances (~1.5× higher) in Huh-7 cells were slightly lower than those in HepG2 cells (Figure 5C). Similarly, one study reported that SP94 peptide-displayed liposomes increased their binding to HCC cells with increasing

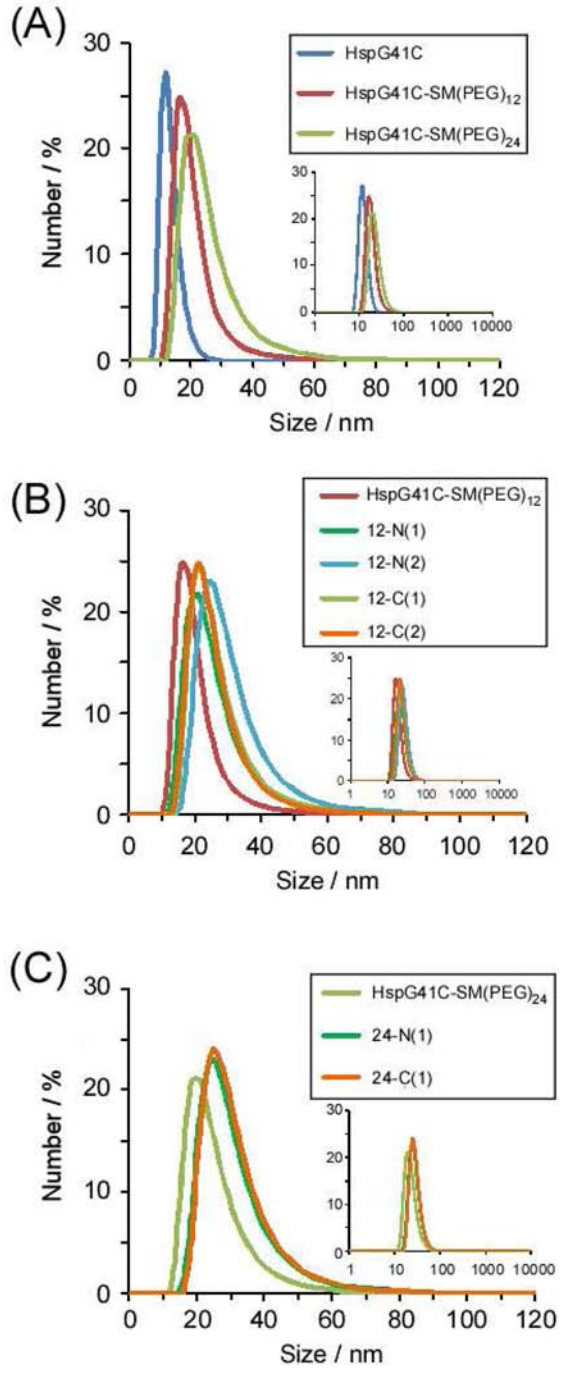


Figure 4. Size distributions of (A) HspG41C-SM(PEG)$_n$, (B) HspG41C-SM(PEG)$_{12}$-SP94 peptide conjugates, and (C) HspG41C-SM(PEG)$_{24}$-SP94 peptide conjugates determined by DLS. Measurements were undertaken at least twice, and the results showed almost identical size distributions.

SP94 peptide numbers on liposomes.[9] Therefore, we concluded that an increase in SP94 peptide levels in conjugates could increase the binding of conjugates toward HCC cells due to the multivalent interaction of conjugates.

Influence of SP94 Peptide Conjugation Site (N- or C-Terminus) in Conjugates upon Cellular Binding. One study suggested that the C-terminal region of SP94 peptide is essential for the binding of HCC cells (SFSIIHTPILPL; consensus sequence shown in under-lined segment).[8] Thus, we investigated whether the SP94 peptide conjugation site on

dx.doi.org/10.1021/bc300015f | Bioconjugate Chem. 2012, 23, 1494−1501

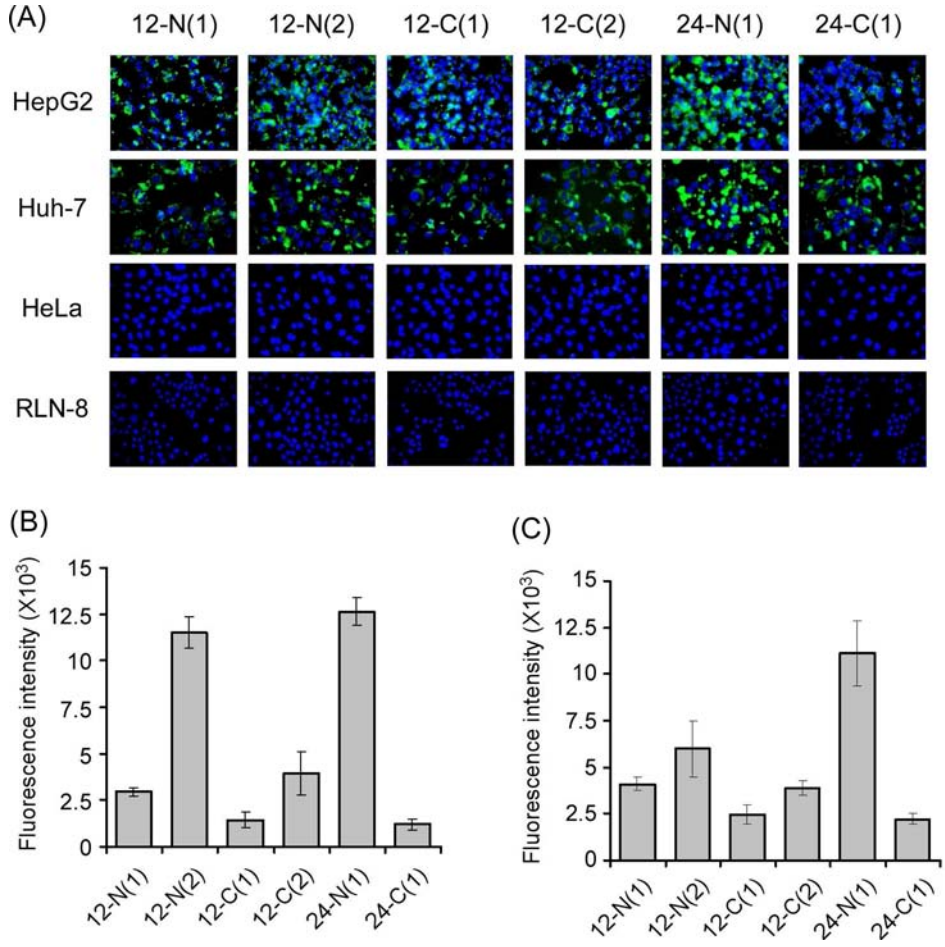


Figure 5. (A) Fluorescence microscopic observation of the uptake of each HspG41C-SM(PEG)$_n$−SP94. Images were obtained 24 h after addition of 40 nM of HspG41C-SM(PEG)$_n$−SP94. Green (Alexa488) and blue (Hoechst 33342) colors indicate HspG41C-SM(PEG)$_n$−SP94 and the nucleus, respectively. Experiments were undertaken at least thrice. Fluorescence intensity in (B) HepG2 and (C) Huh-7 cells after addition of each HspG41C-SM(PEG)$_n$−SP94. Twenty-four hours after the addition of 4 nM of protein cages, cells were lysed in lysis buffer (20 mM Tris-HCl, 2 mM EDTA, and 0.05% Triton-X 100 at pH 7.4), and the fluorescence intensity of lysate solution measured using a microplate reader. Data are means ± SD of three independent experiments.

protein cages (i.e., N- or C-terminal of SP94 peptide) could the affect affinity of SP94-modified cages toward HCC cells using each conjugate, which had identical peptide content and linker length, but a different SP94 peptide conjugation site. Protein cages modified by the N-terminal of SP94 peptide (12-N(1), 12-N(2), and 24-N(1)) showed 2−11× higher fluorescence intensity in HepG2 cells compared with those on the C-terminal of SP94 peptide (12-C(1), 12-C(2), and 24-C(1)) (i.e., 2.1× for 12-N(1) vs 12-C(1), 2.9× for 12-N(2) vs 12-C(2), and 11× for 24-N(1) vs 24-C(1)) (Figure 5B). Similar results were observed in Huh-7 cells (Figure 5C). These results strongly suggested that, with respect to cell binding, the SP94 peptide bound to a protein cage at the N-terminus of peptides was superior to that at the C-terminus of peptides in cell binding because C-terminal region of SP94 peptide is indispensable to its binding to HCC cells.

Influence of Linker Length between Protein Cage and SP94 Peptide upon Cellular Binding. To investigate the effect of linker length between cages and SP94 peptides upon the affinity of engineered cages against HCC cells, the fluorescence intensity of HCC cells was measured after addition of 12-N(1) and 24-N(1) with different numbers of SP94 peptide to HCC cells. The 24-N(1) containing longer linkers showed 4.3× higher fluorescence intensity than 12-N(1) in HepG2 cells (Figure 5B). Similarly, a 2.7× higher fluorescence intensity in Huh-7 cells was detected from 24-N(1) compared with 12-N(1) (Figure 5C). These results suggested that a SP94-modified cage through a longer linker was superior in binding to HCC cells, because a longer linker is more flexible, which can make binding of cages to cells easier. Interestingly, 12-C(1) and 24-C(1) exhibited almost comparable fluorescence intensity after their addition into HCC cells. This observation suggested that linker length affects affinity of cages toward HCC cell only when SP94 peptide is modified with protein cages at N-terminus.

Cellular Uptake Mechanisms and Subcellular Localization of HspG41C-SM(PEG)$_n$-SP94 Peptide Conjugates. To verify cellular uptake mechanisms of HspG41C-SM(PEG)-SP94 peptide conjugates, Alexa-modified SP94-Hsp cages (40 nM of 12-N(1) or 24-N(1)) were transfected into Huh-7 cells with excessive amounts of free SP94 peptides (100 μM). Free SP94 peptides showed no effect on the viability of Huh-7 cells at concentrations of <300 μM (Figure 6A). As shown in Figure 5A, 12-N(1) and 24-N(1) were effectively taken up by Huh-7 cells, but their uptakes were dramatically reduced after adding excessive amounts of free SP94 peptides that block the binding of 12-N(1) and 24-N(1) to target receptors (Figure 6B). These

dx.doi.org/10.1021/bc300015f | Bioconjugate Chem. 2012, 23, 1494−1501

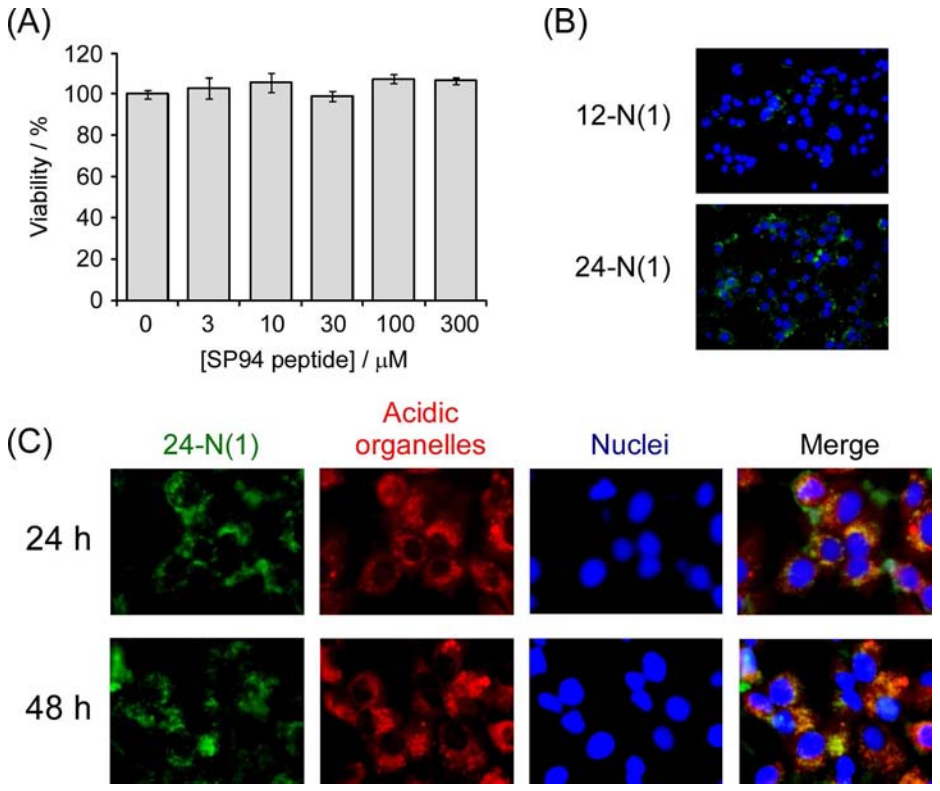


Figure 6. (A) Cytotoxicity of free SP94 peptides toward Huh-7 cells. Data are means ± SEM of three independent experiments. (B) Uptake of HspG41C-SM(PEG)$_n$-SP94 (40 nM) by Huh-7 cells after adding excessive amounts of free SP94 peptides (100 μM). (C) Subcellular localization of 24-N(1) in Huh-7 cells. Acidic organelles (red) and nuclei (blue) were stained by LysoTracker-Red and Hoechst 33342, respectively. Overlapping of 24-N(1) with acidic organelles resulted in yellow fluorescence in the merged pictures.

results show that 12-N(1) and 24-N(1) are taken up by Huh-7 cells through receptor-mediated endocytosis.

Intracellular localization of HspG41C-SM(PEG)$_n$-SP94 peptide conjugates (24-N(1)) was examined using a fluorescence microscopy. Cellular acidic organelles (endosomes/lysosomes) and nuclei were stained by LysoTracker-Red and Hoechst 33342, respectively. Twenty-four hours after adding 24-N(1) conjugates (green) to Huh-7 cells, most of them localized in acidic organelles (red), which was shown in yellow fluorescence in the merged pictures. Furthermore, the 24-N(1) conjugates were still localized in acidic organelles even at 48 h post-transfection (Figure 6C).

■ CONCLUSION

We synthesized an SP94 peptide-modified protein cage (HspG41C-SM(PEG)$_n$-SP94) that could bind selectively to HCC-derived cell lines. An increase in SP94 peptide contents in engineered cages elevated the affinity of cages to HCC cells (especially HepG2 cells). In addition, protein cages modified by the N-terminus of SP94 peptides showed higher cellular uptake than those modified by the C-terminus. Moreover, an increase in linker length between protein cages and SP94 peptide increased the affinity of conjugates to HCC cells. Collectively, a protein cage modified by the N-terminus of SP94 peptide through a longer linker molecule and containing high SP94 peptide levels showed the most effective binding toward HCC cells. These observations could be helpful for developing DDS carriers and imaging systems based on the targeting of peptide ligands. Furthermore, an SP94 peptide-modified Hsp cage will be an effective DDS carriers and imaging device toward HCC cells.

■ AUTHOR INFORMATION

Corresponding Author

*Tel: +81-92-642-6251. Fax: +81-92-642-6252. E-mail: m-murata@dem.med.kyushu-u.ac.jp.

Present Address

$^{\perp}$Department of Applied Chemistry, Graduate School of Engineering, Osaka University, 2−1 Yamadaoka, Suita, Osaka 565−0871, Japan.

Notes

The authors declare no competing financial interest.

■ ACKNOWLEDGMENTS

This work was supported financially by a Health Labour Sciences Research Grant (Research on Publicly Essential Drugs and Medical Devices) from the Ministry of Health Labour and Welfare of Japan, and Grant-in-Aid for Scientific Research (no. 21300190, no. 23650288) from the Ministry of Education, Culture, Sports, Science and Technology of Japan, and Grant-in-Aid for Research Activity Start-up (no. 23800045) from the MEXT of Japan.

■ REFERENCES

(1) Siegel, R., Ward, E., Brawley, O., and Jemal, A. (2011) Cancer statics, 2011: the impact of eliminating socioeconomic and radical disparities on premature cancer deaths. *CA Cancer J. Clin. 61*, 212−236.

(2) Llovet, J. M., and Bruix, J. (2008) Molecular targeted therapies in hepatocellular carcinoma. *Hepatology 48*, 1312−1327.

(3) Thomas, M. (2009) Molecular targeted therapy for hepatocellular carcinoma. *J. Gastroenterol. 44*, 136−141.

(4) Finn, R. S. (2010) Development of molecularly targeted therapies in hepatocellular carcinoma: where do we go now? *Clin. Cancer Res. 16*, 390−397.
(5) Byrne, J. D., Betancourt, T., and Brannon-Peppas, L. (2008) Active targeting schemes for nanoparticle systems in cancer therapeutics. *Adv. Drug Delivery Rev. 60*, 1615−1626.
(6) Shimoda, A., Sawada, S., and Akiyoshi, K. (2011) Cell specific peptide conjugated polysaccharide nanogels for protein delivery. *Macromol. Biosci. 11*, 882−888.
(7) Allen, T. M. (2002) Ligand-targeted therapeutics in anticancer therapy. *Nat. Rev. Cancer 2*, 750−763.
(8) Lo, A., Lin, C. T., and Wu, H. C. (2008) Hepatocellular carcinoma cell-specific peptide ligand for targeted drug delivery. *Mol. Cancer Ther. 7*, 579−589.
(9) Ashley, C. E., Carnes, E. C., Phillips, G. K., Padilla, D., Durfee, P. N., Brown, P. A., Hanna, T. N., Liu, J., Phillips, B., Carter, M. B., Carroll, N. J., Jiang, X., Dunphy, D. R., William, C. L., Petsev, D. N., Evans, D. G., Parikh, A. N., Chackerian, B., Wharton, W., Peabody, D. S., and Brinker, C. J. (2011) The targeted delivery of multicomponent cargos to cancer cells by nanoporous particles-supported lipid bilayers. *Nat. Mater. 10*, 389−397.
(10) Kim, K. K., Kim, R., and Kim, S. H. (1998) Crystal structure of a small heat-shock protein. *Nature 394*, 595−599.
(11) Flenniken, M. L., Liepold, L. O., Crowley, B. E., Willits, D. A., Young, M. J., and Douglas, T. (2005) Selective attachment and release of a chemotherapeutic agent from the interior of a protein cage architecture. *Chem. Commun.*, 447−449.
(12) Varpness, Z., Suci, P. A., Ensign, D., Young, M. J., and Douglas, T. (2009) Photosensitizer efficiency in genetically modified protein cage architectures. *Chem. Commun.*, 3726−3728.
(13) Liepold, L. O., Abedin, M. J., Buckhouse, E. D., Frank, J. A., Young, M. J., and Douglas, T. (2009) Supramolecular protein cage composite MR contrast agents with extremely efficient relaxivity properties. *Nano Lett. 9*, 4520−4526.
(14) Uchida, M., Kosuge, H., Terashima, M., Willits, D. A., Liepold, L. O., Young, M. J., McConnell, M. V., and Douglas, T. (2011) Protein cage nanoparticles bearing the LyP-1 peptide for enhanced imaging of macrophage-rich vascular lesions. *ACS Nano 5*, 2493−2502.
(15) Choi, S. H., Kwon, I. C., Hwang, K. Y., Kim, I. S., and Ahn, H. J. (2011) Small heat shock protein as a multifunctional scaffold: integrated tumor targeting and caspase imaging within a single cage. *Biomacromolecules 12*, 3099−3106.
(16) Sao, K., Murata, M., Umezaki, K., Fujisaki, Y., Mori, T., Niidome, T., Katayama, Y., and Hashizume, M. (2009) Molecular design of protein-based nanocapsules for stimulus-responsive characteristics. *Bioorg. Med. Chem. 17*, 85−93.
(17) Sao, K., Murata, M., Fujisaki, Y., Umezaki, K., Mori, T., Niidome, T., Katayama, Y., and Hashizume, M. (2009) A novel protease activity assay using a protease-responsive chaperone protein. *Biochem. Biophys. Res. Commun. 383*, 293−297.
(18) Flenniken, M. L., Willits, D. A., Brumfield, S., Young, M. J., and Douglas, T. (2003) The small heat shock protein cage from *Methanococcus jannaschii* is a versatile nanoscale platform for genetic and chemical modification. *Nano Lett. 3*, 1573−1576.
(19) Flenniken, M. L., Willits, D. A., Harmsen, A. L., Liepold, L. O., Harmsen, A. G., Young, M. J., and Douglas, T. (2006) Melanoma and lymphocyte cell-specific targeting incorporated into a heat shock protein cage architecture. *Chem. Biol. 13*, 161−170.
(20) Flenniken, M. L., Uchida, M., Liepold, L. O., Kang, S., Young, M. J., and Douglas, T. (2009) A library of protein cage architectures as nanomaterials. *Curr. Top. Microbiol. Immunol. 327*, 71−93.
(21) Kovacs, E. W., Hooker, J. M., Romanini, D. W., Holder, P. G., Berry, K. E., and Francis, M. B. (2007) Dual-surface-modified bacteriophage MS2 as an ideal scaffold for a viral capsid-based drug delivery system. *Bioconjugate Chem. 18*, 1140−1147.

Bioconjugate Chemistry

Communication

pubs.acs.org/bc

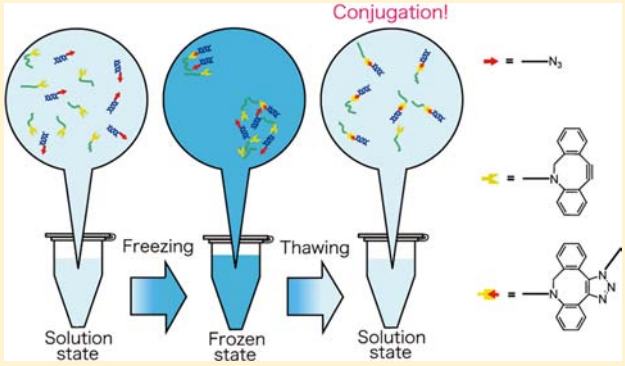
Accelerated Polymer–Polymer Click Conjugation by Freeze–Thaw Treatment

Hiroyasu Takemoto,[†] Kanjiro Miyata,[‡] Takehiko Ishii,[§] Shota Hattori,[§] Shigehito Osawa,[†] Nobuhiro Nishiyama,[‡] and Kazunori Kataoka*[,†,‡,§,∥]

[†]Department of Materials Engineering and [§]Department of Bioengineering, Graduate School of Engineering, [‡]Center for Disease Biology and Integrative Medicine, Graduate School of Medicine, and [∥]Center for NanoBio Integration, The University of Tokyo, 7-3-1 Hongo, Bunkyo-ku, Tokyo 113-8656, Japan

Supporting Information

ABSTRACT: Herein, we report a unique technique to accelerate polymer–SNA conjugation based on copper-free click chemistry: gradual freeze–thawing of the reaction solution substantially increases the conjugation rate possibly because of the reactant concentration at the microenvironment scale. This technique was applied to the conjugation between a small interfering RNA (siRNA) and PEG in an aqueous buffer at/below room temperature.



The Huisgen cycloaddition of azides and alkynes that enables hetero linking under mild conditions using Cu(I) as a catalyst is one of the most popular reactions within click chemistry.[1,2] Recently, this conjugation reaction has been extended to a copper-free condition by utilizing a strained cyclooctyne structure (copper-free click chemistry),[3,4] which is preferable for the modification of biomolecules because of less toxic metal-free conditions.[3] However, the reaction rate in polymer–polymer conjugation is considerably slower than that in low molecular weight compounds, and thus, a longer reaction period is required for higher conjugation ratios. This limitation could sometimes be problematic for conjugation of fragile biomacromolecules, such as small nucleic acids (SNAs), as they are likely denatured or degraded during the reaction. Therefore, further improvements are necessary to perform the accelerated conjugation reaction with biomacromolecules.

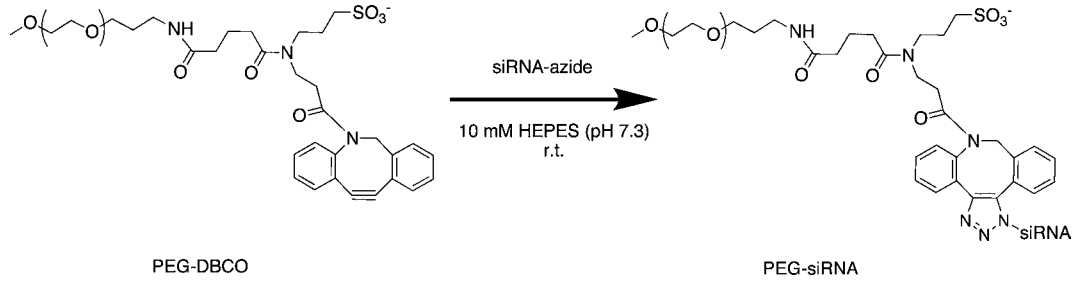
Polymer–SNA conjugates are one of the promising formulations of biomacromolecular conjunction because of their potential utility in diverse therapeutic and diagnostic applications.[5−10] Indeed, conjugation of SNA to biologically inert poly(ethylene glycol) (PEG), PEGylation, is highly beneficial for reducing immunogenicity, enhancing stability against nucleases, and avoiding rapid renal clearance due to the steric hindrance of PEG and increased molecular weight.[11−14] Also, conjugation of SNA to a functional polymer has allowed further functionalization, such as enhanced cell penetration, fluorescent detection, and nuclear localization.[11,15−17] Thereby, based on the fact that SNAs are water-soluble, and also, in the double-stranded case, dehybridized at high temperature, efficient conjugation methods with aqueous solutions at low temperature are intensely desired for the facile preparation of polymer–SNA conjugates.

Herein, we report a unique technique to accelerate a polymer–SNA conjugation based on copper-free click chemistry: gradual freeze–thawing of the reaction solution substantially increases the conjugation rate possibly because of the reactant concentration at the microenvironment scale. This technique was applied to the conjugation between a small interfering RNA (siRNA) and PEG in an aqueous buffer at/below room temperature. Note that siRNA has been greatly focused as a potential nucleic acid drug that induces the potent sequence-specific gene silencing in the cell cytoplasm, known as RNA interference.[18] Toward copper-free click chemistry, a strained alkyne group was introduced into the distal end of PEG ($M_w \cong 12\,000$) to obtain PEG-DBCO (Supporting Information Scheme S1 and Figure S1). Azide-modified siRNA ($M_w \cong 13\,600$) (siRNA-azide) and PEG-DBCO (2 equiv to siRNA-azide) were mixed and reacted in 10 mM HEPES buffer (pH 7.3) at room temperature (Scheme 1). The reaction solution was analyzed by size exclusion chromatography (SEC) and UV absorbance was detected at 254 nm (Figure 1a). The conjugation ratio of siRNA-azide with PEG-DBCO was calculated from the peak intensity ratio of PEG-conjugated siRNA (PEG-siRNA) to siRNA-based molecules (PEG-siRNA and siRNA-azide). The SEC analyses revealed that the conjugation ratios were 1.6% and 21.9% for 1 and 10 h incubation, respectively. In contrast, when these reaction

Received: April 3, 2012
Published: July 2, 2012

ACS Publications © 2012 American Chemical Society

Scheme 1. Synthetic Scheme of PEG-siRNA through the Conjugation between PEG-DBCO and siRNA-azide



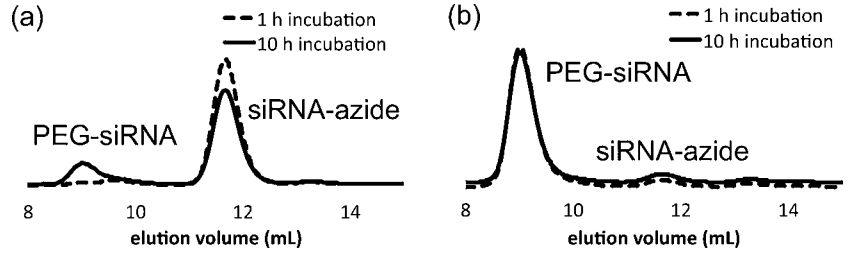


Figure 1. SEC charts of reaction solution after 1 or 10 h incubation at room temperature (15 μM siRNA-azide). (a) Reaction solution without freeze–thaw treatment. (b) Reaction solution after the freeze–thaw treatment (freeze: overnight at −30 °C; thaw: 1 h at 4 °C).

solutions were frozen overnight at −30 °C and subsequently thawed at 4 °C, the conjugation ratios drastically increased up to approximately 95% (Figure 1b). Figure 2 summarizes the

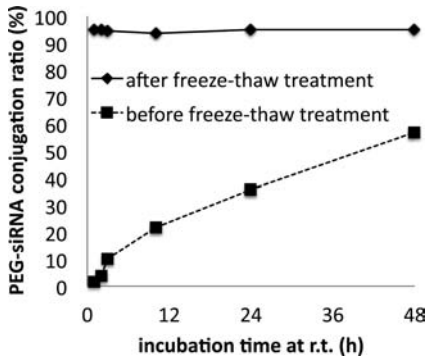


Figure 2. PEG-siRNA conjugation ratios before and after freeze–thaw treatment (freeze: overnight at −30 °C; thaw: 1 h at 4 °C) (15 μM siRNA-azide in the reaction solution). PEG-DBCO and siRNA-azide reacted at room temperature for the indicated periods. Next, the reaction solutions were analyzed by SEC without freeze–thawing or were freeze–thawed prior to the SEC analysis.

conjugation ratios of the reaction solutions at varying incubation times at room temperature. Without freeze–thaw treatment, the conjugation ratio obtained was 56.8% even for 48 h reaction. In striking contrast, freeze–thawing after 1 h incubation resulted in a conjugation ratio of 95.0%, indicating that freeze–thawing the reaction solutions allows the conjugation ratio to jump up.

To gain further insight into this accelerated polymer–polymer click conjugation, freeze–thawing temperatures were varied at −30 and −80 °C for freezing and 4, 20, and 42 °C for thawing (Table 1). Freezing at −30 °C resulted in a conjugation ratio of approximately 80%, while the freezing at −80 °C resulted in a conjugation ratio of approximately 10% indicating that the freezing temperature is apparently critical for accelerated conjugation. This freezing temperature dependency

Table 1. Effect of Freezing and Thawing Temperatures on PEG-siRNA Conjugation Ratios[a]

	thawing temperature		
freezing temperature	4 °C	20 °C	42 °C
−30 °C	85.6%	85.4%	77.1%
−80 °C	10.5%	9.6%	10.0%

[a]siRNA-azide concentration: 7.5 μM, incubation time at room temperature: 1 h.

supposes that the accelerated click conjugation is ascribed to the generation of a highly reactive, solute-enriched microenvironment in the reaction solution. Compared to the lower temperature (−80 °C), the higher freezing temperature (−30 °C) will enable crystallization of the solvent molecules as well as slower freezing of the reaction solution. The solvent crystallization can more effectively exclude the solute molecules, resulting in a phase separation that generates a solute-rich phase toward less enthalpy.[19,20] The thawing temperatures of the reaction solution were also effective in the reaction solution frozen at −30 °C: thawing at 4 and 20 °C resulted in a conjugation ratio of 85%, and thawing at 42 °C resulted in a ratio of 77%. The lower temperatures (4 and 20 °C) will enable slower thawing of the reaction solution, probably resulting in longer duration of the solute-rich phase.[21] In contrast, thawing temperatures were not effective in the reaction solution frozen at −80 °C, presumably because of a lower degree of phase separation in the original solution, which was frozen rapidly.

To examine the validity of the solute-rich phase effect (or the phase separation effect) on the accelerated conjugation, siRNA-azide concentrations were varied from 0.536 μM to 53.6 μM with PEG-DBCO concentrations fixed at 2 equiv to siRNA-azide (Figure 3). Without the freeze–thaw treatment, 2.14 μM siRNA-azide resulted in a conjugation ratio of 7.1%, while 53.6 μM siRNA-azide resulted in a ratio of 56.9%. This result indicates that higher concentrations of the reactants result in higher conjugation ratios probably because of the increased collision opportunities between the reactants in the reaction

dx.doi.org/10.1021/bc300182y | Bioconjugate Chem. 2012, 23, 1503–1506

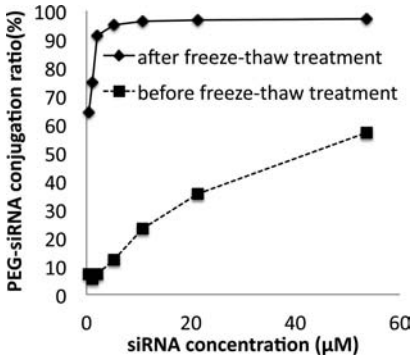


Figure 3. Effect of siRNA-azide concentration on PEG-siRNA conjugation ratios. The reaction solution was subjected to 24 h incubation at room temperature. PEG-DBCO and siRNA-azide were reacted at indicated siRNA-azide concentrations with 2 equiv of PEG-DBCO to siRNA-azide. The reaction solutions were analyzed by SEC without the freeze−thawing treatment (freeze: overnight at −30 °C; thaw: 1 h at 4 °C) prior to the SEC analysis.

solution. Similarly, the conjugation ratio after freeze−thawing increased as the siRNA-azide concentration increased especially at the lower range (<2.14 μM), which is consistent with the solute-rich phase effect.

In general, the freeze−thaw process/cycle is not preferable for biomacromolecules, including siRNA, because it might denature their structures, resulting in lack of biological (or therapeutic) activities. Thus, to examine whether the biological activity of siRNA was maintained after the freeze−thawing conjugation, the obtained PEG-siRNA was subjected to the gene silencing assay in cultured cells. PEG-siRNA and unconjugated siRNA as a control were complexed with lipofectamine RNAi MAX and then transfected to a human cervical cancer cell stably expressing luciferase (HeLa-Luc). siLuc was a target sequence for the luciferase gene, and siScramble was a control sequence to confirm the sequence-specific gene silencing effect. Figure 4a clearly shows that PEG-siLuc lipoplex induced strong gene silencing (>90%), whereas PEG-siScramble lipoplex did not, similar to unconjugated siRNA lipoplex. Furthermore, the cellular viability, which was estimated using Cell Counting Kit-8 in a condition similar to the gene silencing assay, reveals that the PEG-siRNA lipoplex induced no significant cytotoxicity (Figure 4b). These results indicate that the PEG-siRNA obtained by the freeze−thaw treatment maintains sequence-specific gene silencing ability compared to the original siRNA without associated cytotoxicity.

As shown, the unique technique, i.e., the gradual freeze−thawing of the reaction solution, demonstrated dramatic acceleration of the click conjugation between PEG-DBCO and siRNA-azide. Slower freezing of the reaction solution at −30 °C probably resulted in the phase separation of the solute-rich phase and solute-poor phase. The solute-rich phase is a highly reactive environment that accelerates the conjugation reaction. Also, slower thawing of the reaction solution at 4 or 20 °C probably allows a longer duration of the solute-rich phase for further acceleration of the reaction. Thus, both freezing and thawing temperatures are critical for the accelerated reaction. This technique may be useful for the conjugation reaction of diverse biomacromolecules, especially in the case where products or reactants are not tolerant of long reaction period and/or high temperature.

■ ASSOCIATED CONTENT

Ⓢ Supporting Information

Experimental procedures, a Supporting Figure, and a Supporting Scheme. This material is available free of charge via the Internet at http://pubs.acs.org.

■ AUTHOR INFORMATION

Corresponding Author

*Tel: +81 −3-5841-7138. FAX: +81 −3-5841-7139. E-mail: kataoka@bmw.t.u-tokyo.ac.jp.

Notes

The authors declare no competing financial interest.

■ ACKNOWLEDGMENTS

This research was supported financially by the Funding Program for World-Leading Innovative R&D on Science and Technology (FIRST) from the Japan Society for the Promotion of Science (JSPS). H. Takemoto thanks the Japan Society for the Promotion of Science (JSPS) Research Fellowships for Young Scientists.

■ REFERENCES

(1) Kolb, H. C., Finn, M. G., and Sharpless, K. B. (2001) Click chemistry: diverse chemical function from a few good reactions. *Angew. Chem., Int. Ed. 40*, 2004−2021.

(2) Lutz, J. F. (2007) 1,3-Dipolar cycloadditions of azides and alkynes: a universal ligation tool in polymer and materials science. *Angew. Chem., Int. Ed. 46*, 1018−1025.

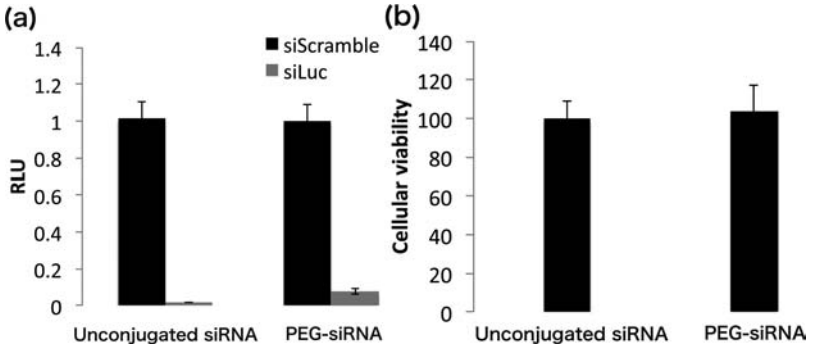


Figure 4. Relative luminescence unit (RLU) (a) and cellular viability (b) of cultured HeLa-Luc cells after treatment of lipoplexes prepared with PEG-siRNA (1 h incubation at room temperature, freezing at −30 °C and thawing at 4 °C) or unconjugated siRNA (siRNA concentration: 20 nM, incubation time: 48 h).

(3) Jewetta, J. C., and Bertozzi, C. R. (2010) Cu-free click cycloaddition reactions in chemical biology. *Chem. Soc. Rev. 39*, 1272−1279.
(4) Debets, M. F., Berkel, S. S., Schoffelen, S., Rutjes, F. P. J. T., Hest, J. C. M., and Delft, F. L. (2010) Aza-dibenzocyclooctynes for fast and efficient enzyme PEGylation via copper-free (3 + 2) cycloaddition. *Chem. Commun. 46*, 97−99.
(5) Crooke, S. T. (2004) Progress in antisense technology. *Annu. Rev. Med. 55*, 61−95.
(6) Watts, J. K., Deleavey, G. F., and Damha, M. J. (2008) Chemically modified siRNA: tools and applications. *Drug Discovery Today 13*, 842−855.
(7) Kurreck, J. (2009) RNA interference: from basic research to therapeutic applications. *Angew. Chem., Int. Ed. 48*, 1378−1398.
(8) Bell, N. M., and Micklefield, J. (2009) Chemical modification of oligonucleotides for therapeutic, bioanalytical and other applications. *ChemBioChem 10*, 2691−2703.
(9) Soontornworajit, B., and Wang, Y. (2011) Nucleic acid aptamers for clinical diagnosis: cell detection and molecular imaging. *Anal. Bioanal. Chem. 399*, 1591−1599.
(10) Kole, R., Krainer, A. R., and Altman, S. (2011) RNA therapeutics: beyond RNA interference and antisense oligonucleotides. *Nat. Rev. Drug Discovery 11*, 125−140.
(11) Singh, Y., Murat, P., and Defrancq, E. (2010) Recent developments in oligonucleotide conjugation. *Chem. Soc. Rev. 39*, 2054−2070.
(12) Lee, S. H., Mok, H., and Park, T. G. (2011) Di- and triblock siRNA-PEG copolymers: PEG density effect of polyelectrolyte complexes on cellular uptake and gene silencing efficiency. *Macromol. Biosci. 11*, 410−418.
(13) Rozema, D. B., Lewis, D. L., Wakefield, D. H., Wong, S. C., Klein, J. J., Roesch, P. L., Bertin, S. L., Reppen, T. W., Chu, O., Blokhin, A. V., Hagstrom, J. E., and Wolff, J. A. (2007) Dynamic polyconjugates for targeted in vivo delivery of siRNA to hepatocytes. *Proc. Natl. Acad. Sci. U. S. A. 104*, 12982−12987.
(14) Oishi, M., Nagasaki, Y., Itaka, K., Nishiyama, N., and Kataoka, K. (2005) Lactosylated poly(ethylene glycol)-siRNA conjugate through acid-labile beta-thiopropionate linkage to construct pH-sensitive polyion complex micelles achieving enhanced gene silencing in hepatoma cells. *J. Am. Chem. Soc. 127*, 1624−1625.
(15) Jeong, J. H., Mok, H., Oh, Y. K., and Park, T. G. (2008) siRNA conjugate delivery systems. *Bioconjugate Chem 20*, 5−14.
(16) Jung, J., Solanki, A., Memoli, K. A., Kamei, K., Kim, H., Drahl, M. A., Williams, L. J., Tseng, H. R., and Lee, K. B. (2009) Selective inhibition of human brain tumor cells through multifunctional quantum-dot-based siRNA delivery. *Angew. Chem., Int. Ed. 48*, 1−6.
(17) Takemoto, H., Ishii, A., Miyata, K., Nakanishi, M., Oba, M., Ishii, T., Yamasaki, Y., Nishiyama, N., and Kataoka, K. (2010) Polyion complex stability and gene silencing efficiency with a siRNA-grafted polymer delivery system. *Biomaterials 31*, 8097−8105.
(18) Elbashir, S. M., Harborth, J., Lendeckel, W., Yalcin, A., Weber, K., and Tuschl, T. (2001) Duplexes of 21-nucleotide RNAs mediate RNA interference in cultured mammalian cells. *Nature 411*, 494−498.
(19) Worster, M. G., and Wettlaufer, J. S. (1997) Natural convection, solute trapping, and channel formation during solidification of saltwater. *J. Phys. Chem. B 101*, 6132−6136.
(20) Izutsu, K., and Kojima, S. (2000) Freeze-concentration separates proteins and polymer excipients into different amorphous phases. *Pharm. Res. 17*, 1316−1322.
(21) Wettlaufer, J. S. (1999) Impurity effects in the premelting of ice. *Phys. Rev. Lett. 82*, 2516−2519.

Bioconjugate Chemistry

Communication

pubs.acs.org/bc

Antiandrogen Gold Nanoparticles Dual-Target and Overcome Treatment Resistance in Hormone-Insensitive Prostate Cancer Cells

Erik C. Dreaden,[†,‡,¶] Berkley E. Gryder,[§,¶] Lauren A. Austin,[†] Brice A. Tene Defo,[§] Steven C. Hayden,[†] Min Pi,[∥] L. Darryl Quarles,[∥] Adegboyega K. Oyelere,[*,§] and Mostafa A. El-Sayed[*,†]

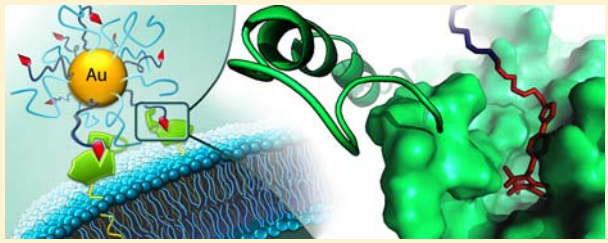
[†]Department of Chemistry and Biochemistry, Georgia Institute of Technology, 901 Atlantic Drive NW, Atlanta, Georgia 30332-0400, United States

[§]Parker H. Petit Institute for Bioengineering and Biosciences, Department of Chemistry and Biochemistry, Georgia Institute of Technology, 315 Ferst Drive NW, Atlanta, Georgia 30332-0230, United States

[∥]Department of Medicine, University of Tennessee Health Science Center, 19 South Manassas Street, Memphis, Tennessee 38163, United States

Supporting Information

ABSTRACT: Prostate cancer is the most commonly diagnosed cancer among men in the developed countries.[1] One in six males in the U.S.[2] and one in nine males in the U.K.[3] will develop the disease at some point during their lifetime. Despite advances in prostate cancer screening, more than a quarter of a million men die from the disease every year[1] due primarily to treatment-resistance and metastasis. Colloidal nanotechnologies can provide tremendous enhancements to existing targeting/treatment strategies for prostate cancer to which malignant cells are less sensitive. Here, we show that antiandrogen gold nanoparticles—multivalent analogues of antiandrogens currently used in clinical therapy for prostate cancer—selectively engage two distinct receptors, androgen receptor (AR), a target for the treatment of prostate cancer, as well as a novel G-protein coupled receptor, GPRC6A, that is also upregulated in prostate cancer. These nanoparticles selectively accumulated in hormone-insensitive and chemotherapy-resistant prostate cancer cells, bound androgen receptor with multivalent affinity, and exhibited greatly enhanced drug potency versus monovalent antiandrogens currently in clinical use. Further, antiandrogen gold nanoparticles selectively stimulated GPRC6A with multivalent affinity, demonstrating that the delivery of nanoscale antiandrogens can also be facilitated by the transmembrane receptor in order to realize increasingly selective, increasingly potent therapy for treatment-resistant prostate cancers.



Androgen deprivation therapy (ADT) is currently recommended for the treatment of advanced/metastatic prostate cancer.[4] Nonsteroidal antiandrogens such as flutamide (Eulexin), bicalutamide (Casodex), and nilutamide (Nilandron) are some of the most commonly prescribed ADT drugs and diminish androgenic effects by competitively inhibiting androgen−androgen receptor binding associated with prostate cancer growth, division, and survival. While most advanced or metastatic prostate cancers initially respond well to ADT, malignant cells that survive 2−3 years will typically enter an antiandrogen-resistant[5] (i.e., castration-resistant) state and subsequently exhibit chemotherapy resistance as well.[6] Without further intervention, median survival following this period is just 18−24 months. Increasingly selective and potent drugs are urgently needed to treat these prostate cancers.

Nanoscale drug conjugates can provide improved targeting selectivity for prostate cancer treatments via multivalent ligand display (augmented affinity and avidity) and size-dependent passive accumulation;[7] they can also realize increasing potency through high drug loading capacity and enhanced intracellular transport rates (endocytosis versus passive diffusion).[8] Langer, Farokhzad, and Lippard have shown that PLGA nanoparticles targeted with aptamers toward prostate-specific membrane antigen can deliver platinum prodrug chemotherapeutics to prostate cancer cells with substantially greater drug potency than untargeted carriers or cisplatin alone.[9,10] Folate-targeted lipid nanoparticles have also been applied in gene therapy[11] and RNA interference[12] for prostate cancer in vivo. Katti and Kannan have shown that gold nanoparticles targeted with bombesin peptides directed toward gastrin-releasing peptide receptor (overexpressed on prostate cancer cells) selectively target prostate cancer cells in vitro/vivo with multivalent affinity and can provide enhanced contrast for X-ray computed tomography (CT) imaging.[13] Neoadjuvant administration of gold nanoparticles has been further shown to sensitize prostate cancer cells toward external beam radiation therapy[14] and to facilitate in vivo laser photothermal ablation therapy in animal models of prostate cancer.[15]

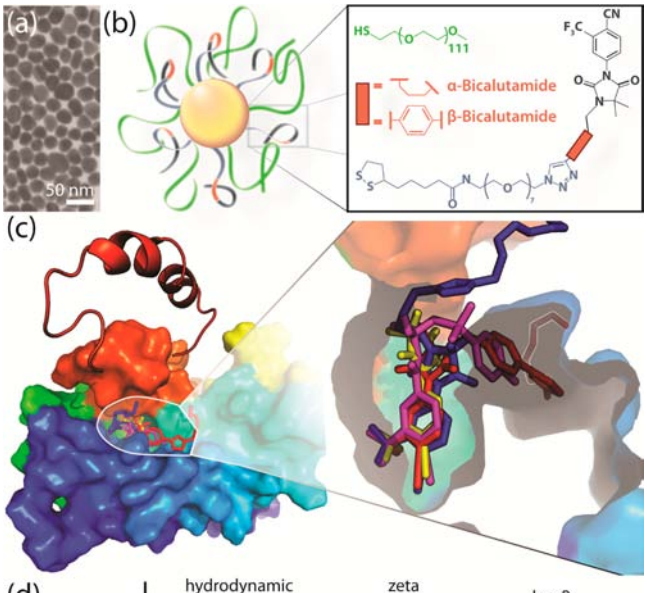
Received: March 25, 2012
Revised: June 25, 2012
Published: July 9, 2012

ACS Publications © 2012 American Chemical Society

dx.doi.org/10.1021/bc300158k | *Bioconjugate Chem.* 2012, 23, 1507−1512

We hypothesized that derivatives of commercially available antiandrogen chemotherapeutics could serve as combined targeting *and* therapeutic agents for tissue-selective drug delivery of nanoscale drug carriers to prostate cancers expressing *membrane* androgen receptor[16,17] *and/or* a recently deorphaned androgen-sensing G protein-coupled receptor, GPRC6A,[18] involved in increased prostate cancer risk, growth, and poor survival. We found that antiandrogen gold nanoparticles selectively target and engage both androgen receptor and GPRC6A with multivalent affinity and facilitate cell death in antiandrogen treatment-resistant prostate cancer cells at substantially lower concentrations than their corresponding free drugs. Per ligand, antiandrogen gold nanoparticles bound androgen receptor with affinity 5−11-times greater than free antiandrogens and, per particle, bound androgen receptor with affinity superior to *endogenous* androgens, providing opportunities for further increased treatment efficacy via drug coconjugation, laser photothermal ablation, radiotherapy sensitization, and imaging-based treatment guidance/monitoring.[8,19]

Gold nanoparticles (AuNPs, 29 ± 4 nm diameter; Figure 1a) were synthesized by Turkevich/Frens reduction of chloroauric acid and conjugated with a mixed self-assembled monolayer of 5% thiol PEGylated antiandrogen and 95% thiolated poly(ethylene glycol) stabilizer (PEG-SH, 5 kDa). Antiandrogen ligands used in these studies were employed to reflect structural homology between antiandrogens in clinical use with α- and β-Bicalutamide (α-Bic, β-Bic; Figure 1a) both bearing an aromatic α-anilide ring characteristic of flutamide, bicalutamide, and nilutamide, as well as a five-membered imidazolidinedione ring characteristic of nilutamide and the H-bonded structure of bicalutamide and/or the active metabolite of flutamide. β-Bic contains an additional β-aromatic ring characteristic of bicalutamide which binds the hydrophobic pocket formed by helix 12 residues on androgen receptor and confers it enhanced potency[20] (Figure 1b). Antiandrogen ligands were synthesized by Cu(I)-catalyzed Huisgen cycloaddition (i.e., click, azide−alkyne coupling) with PEGylated lipoic acid. Thiol anchoring groups were used to enable stable Au surface bond formation, and PEG stabilizer/spacer groups were employed to sterically stabilize the subsequent nanoparticle constructs in physiological media and to resist protein adsorption and/or diminish immunogenic response. α-Bic- and β-Bic-AuNPs contained $(2.25 \pm 0.02) \times 10^3$ and $(1.56 \pm 0.08) \times 10^3$ antiandrogen ligands per particle, respectively (see Supporting Information for detailed experimental methods; Scheme S1, Figure S1).



(d)

	hydrodynamic diameter (nm)	zeta potential (mV)	log *P*
PEG-AuNPs	49 ± 1	-17.2 ± 0.9	-1.5 ± 0.3
α-Bic-AuNPs	50 ± 1	-13.7 ± 0.6	-1.45 ± 0.2
β-Bic-AuNPs	50 ± 1	-4.3 ± 0.4	-0.27 ± 0.03

Figure 1. Multivalent antiandrogen gold nanoparticles for the treatment of castration-resistant prostate cancer. (a) Electron micrographs of the as-synthesized 29 ± 4 nm diameter gold nanoparticles. (b) Illustration of the antiandrogen nanoconjugates with receptor binding groups shown in gray/red. (c) Molecular docking of the antiandrogen ligands with androgen receptor showing outward orientation of the thiol PEGylated nanoparticle linker groups and maintenance of contact points within the androgen receptor binding pocket by the bicalutamide ligand (β-Bic, red) and its β ring-deficient analogue (α-Bic, blue), as compared to their precursor drugs bicalutamide (magenta) and its nilutamide analogue (yellow). (d) Physiochemical properties of the antiandrogen gold nanoparticles.

α-Bic and β-Bic AuNPs were found to be 50 ± 1 nm in hydrodynamic diameter, which recent studies by Chan and coworkers indicate to the be within the optimal size range for both tumor accumulation and cellular internalization of AuNPs[21,22] (Figure 1d). PEGylated control nanoparticles were found to be 49 ± 1 nm. The octanol/water partition coefficient of α-Bic- and β-Bic-AuNPs was found to be −1.4 ± 0.2 and −0.27 ± 0.03, respectively, both below that expected from an intravenously administered drug (1.92) with acceptable pharmacokinetics.[23]

Molecular docking of the antiandrogen ligands with androgen receptor (AR) show that the contact points of their parent drugs within the AR binding pocket are maintained by the ligands and that their thiol PEGylated linker groups face outward to enable accessibility by nanoparticle-bound ligands (Figure 1c).[24] Receptor binding competition with radiolabeled androgen (Figure 2a) shows that the AR binding inhibition constant (K_i) of α-Bic and β-Bic is enhanced 11- and 5.4-fold per drug molecule, respectively, when displayed as a multivalent construct, with total nanoparticle AR binding affinity exceeding that of its endogenous hormone dihydroxytestosterone (DHT, 0.28−2 nM v 0.16−0.24 nM nanoparticles)[20,25] and yielding, to the best of our knowledge, the highest reported nanoparticle K_i for a nonsteroidal antiandrogen (Figure 2a inset, Figure 2b). Free α-Bic- and β-Bic bound AR with affinities comparable to those previously reported for bicalutamide.[26] Because membrane AR (mAR) binds antibodies[16] and endogenous androgens[27] for intracellular AR, and because antiandrogens can diminish the effects of androgenic mAR stimulation,[28] these data suggest that antiandrogen gold nanoparticles can selectively target mAR which is preferentially overexpressed by human prostate cancer cells and whose expression levels correlate with poor prognosis (Gleason score)[29] and total AR levels[16] found in 80−90% of all prostate cancers.[30]

GPRC6A[31] is a membrane-associated C family G protein-coupled receptor recently discovered[32] through genomic homology search. We have previously shown that GPRC6A senses androgens and is a positive regulator of testosterone and a negative regulator of estrogen production in mice;[18] its expression was also found to contribute to prostate cancer growth, malignancy, and poor survival in animal models of prostate cancer.[18] Polymorphism at the *GPRC6A* gene locus was recently associated with significantly altered susceptibility

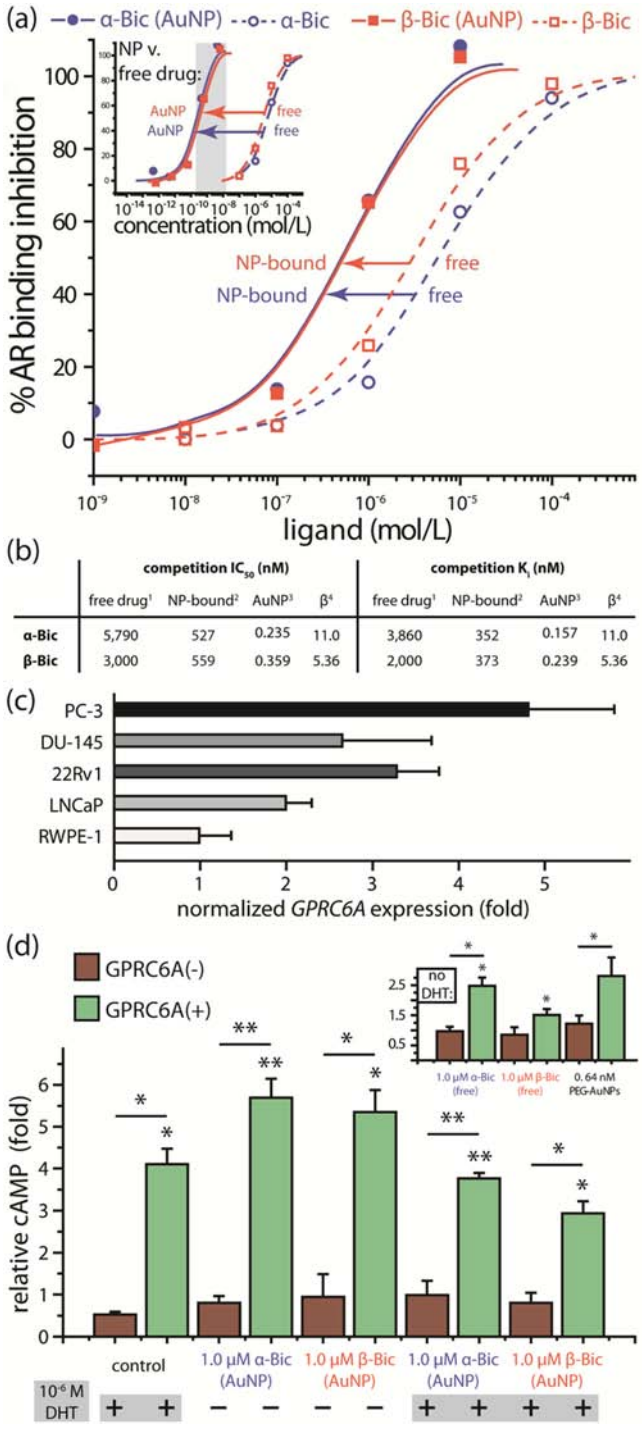


Figure 2. Antiandrogen gold nanoparticles selectively engage androgen receptor (AR) and G protein-coupled receptor GPRC6A targets. (a) AR binding competition between radiolabeled androgen and nanoparticle-bound antiandrogens (solid) or free antiandrogens (dashed) showing multivalency-enhanced AR binding affinity (K_i) from the nanoparticle constructs. Nanoparticle-bound antiandrogens displaced [^{3}H]androgen from AR with 5.4−11-fold greater per-ligand affinity than an equivalent concentration of free antiandrogens. Inset, Nanoparticle and free drug concentrations. (b) Half-maximal inhibitory concentration (IC_{50}) and binding inhibition constant (K_i) for free[1] and nanoparticle-bound[2] antiandrogens, nanoparticles[3], and their corresponding (per-drug-molecule) multivalency-enhanced values (β^4). (c) Upregulated GPRC6A mRNA expression levels measured from various prostate cancer cell lines relative to nonmalignant RWPE-1 prostate cells (see Supporting Information). (d) Androgen-competitive downstream production of cyclic adenosine monophosphate (cAMP) second messenger accumulated in response to overnight stimulation of GPRC6A signal transduction by α-Bic- and β-Bic-AuNPs in an AR$^-$/GPRC6A$^-$ and AR$^-$/GPRC6A+ transfected cell line. Inset: Fold-change in GPRC6A signal transduction (cAMP accumulation) in response to GPRC6A stimulation by nanoparticle-equivalent concentrations of free α-Bic/β-Bic and PEGylated control nanoparticles showing significantly lower GPRC6A engagement/stimulation by free α-Bic (2.3-fold, P = 0.003), β-Bic (3.5-fold, P = 0.03), and PEGylated gold nanoparticles (2.0-fold v α-Bic-AuNPs, P = 0.06; 1.9-fold v β-Bic-AuNPs, P = 0.15) relative to their respective particle constructs. cAMP levels from PEG-AuNPs were comparable to those observed from DHT-abrogated α-Bic/β-Bic-AuNPs indicating antiandrogen ligand-enhanced GPRC6A engagement. Note that GPRC6A is a promiscuous receptor for androgenic ligands and that the cell lines in (d) are AR null. DHT, dihydrotestosterone. Grayscale area in (a) denotes the lower and upper limits previously reported for AR's endogenous high-affinity ligand, dihydrotestosterone (DHT). Error bars represent SEM. P for individual values relative to untreated controls or as indicated; *P < 0.05, **P < 0.01.

to prostate cancer in a genome-wide association study among Japanese men ($P = 1.6 \times 10^{-12}$).[18,33] Here, we found that *GPRC6A* overexpression strongly correlates malignant phenotype across several prostate cell lines (Figure 2c). Although Pi et al. recently found that androgens selectively stimulate GPRC6A and subsequently promote prostate cancer cell growth,[34] we hypothesized that high-affinity antiandrogens and multivalent antiandrogen gold nanoparticles may similarly engage GPRC6A, albeit with subsequently diminished cell growth (vide supra) rather than agonist-induced proliferation. Downstream production of the second messenger, cyclic adenosine monophosphate (cAMP), accumulated in response to stimulated GPRC6A signal transduction, was assessed using an established AR$^-$/GPRC6A$^-$ and AR$^-$/GPRC6A$^+$ transfected cell line (see Supporting Information).[34] α-Bic- and β-Bic-AuNPs significantly stimulated GPRC6A in an androgen-competitive manner (Figure 2d), eliciting cAMP production at low micromolar ligand (sub-nanomolar AuNP) concentrations. GPRC6A stimulation by α-Bic- and β-Bic-AuNPs was 2.0- and 1.9-fold greater than that by an equivalent or greater concentration of PEGylated-AuNPs (P = 0.06 and 0.15, respectively) and was 2.3- and 3.5-fold greater than their nanoparticle-equivalent concentrations of free antiandrogen ligands (P = 0.003 and 0.03, respectively) (Figure 2d inset). GPRC6A stimulation by PEG-AuNPs was nearly equivalent to that observed from testosterone-abrogated α-Bic- and β-Bic-AuNPs, indicating GPRC6A ligand-enhanced activity from antiandrogen-AuNPs. Together, these data show that antiandrogen gold nanoparticles can selectively engage GPRC6A with multivalent affinity and can do so in a manner *independent* of AR/mAR expression (Figure 2d).

Binding/uptake selectivity of the antiandrogen gold nanoparticles was assessed in a membrane-AR$^+$ and GPRC6A$^+$ prostate carcinoma cell line[27] whose response to chemotherapy and antiandrogen therapy reflects that of castration-resistant prostate cancer,[6] DU-145 (Figure 3a). Fluorescently labeled

dx.doi.org/10.1021/bc300158k | *Bioconjugate Chem.* 2012, 23, 1507−1512

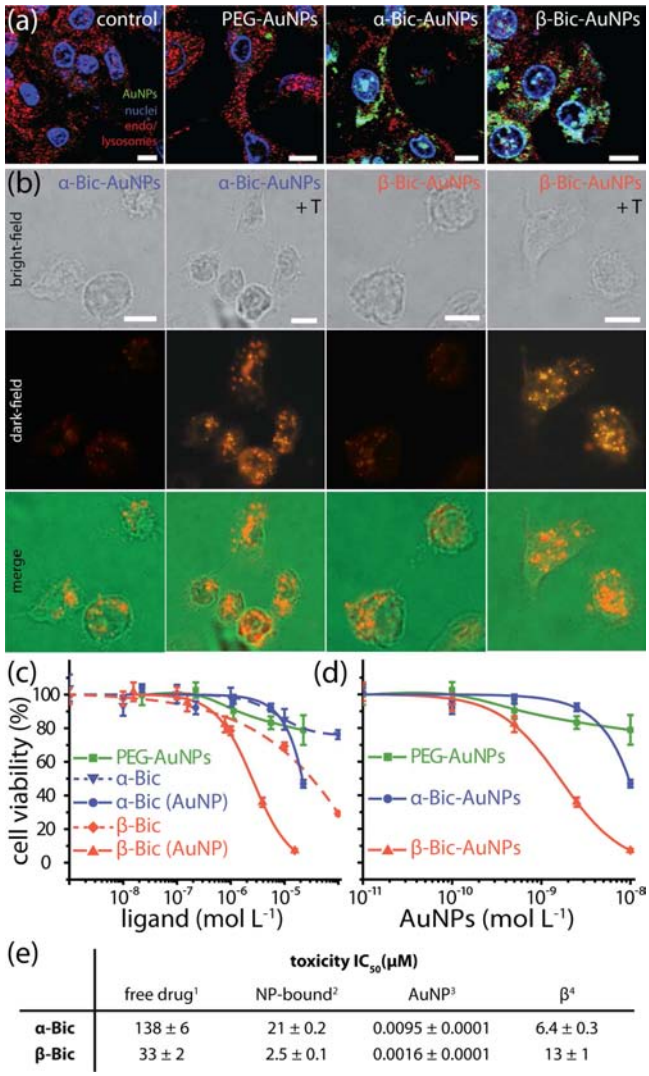


Figure 3. Antiandrogen gold nanoparticles selectively accumulate in chemotherapy- and antiandrogen-resistant prostate cancer cells expressing membrane-androgen receptor (mAR) and G protein-coupled receptor GPRC6A and induce cell death with multivalency-enhanced drug potency. (a) Confocal fluorescence images of selective antiandrogen nanoparticle intracellular localization (green) in mAR +/GPRC6A+ DU-145 prostate cancer cells. Endo/lysosomes were labeled with dextran (red) and nuclei were stained with DAPI (blue). (b) Optical dark-field scattering microscopy of DU-145 cells showing augmented antiandrogen gold nanoparticle accumulation in response to androgen-stimulated mAR-upregulation by testosterone (T, 10^{-6} M). Note that images in (a) and (b) were obtained using different instruments. (c) Dose-dependent cell viability (%) of antiandrogen treatment-resistant DU-145 prostate cancer cells incubated with free antiandrogens and ligand-equivalent concentrations of antiandrogen gold nanoparticles (24 h). (d) Total nanoparticle concentrations represented in c. (e) Figures of merit for cytotoxicity of the free drug[1], nanoparticle-bound ligand[2], and multivalent nanoparticle[3], as well as the multivalency enhancement factor β^4 exhibiting 6.4- and 13-fold enhanced potency per drug molecule. Scale bars represent 10 μm. Error bars represent SD.

antiandrogen gold nanoparticles exhibited high intracellular accumulation in DU-145 cells and localized in a manner similar to that reported for AR,[35] while PEGylated nanoparticles exhibited no significant accumulation. Uptake and localization patterns of both targeted and untargeted nanoparticles in an AR null[36] squamous cell carcinoma cell line showed only nonspecific cell surface binding (Supporting Information Figure S2). We hypothesized that androgen-stimulated upregulation of AR in DU-145,[37] and correspondingly increased mAR expression,[16] may augment antiandrogen nanoparticle accumulation in prostate cancer cells. Particle uptake/localization was imaged using cardioid immersion optical dark-field scattering microscopy which can achieve sensitivity orders of magnitude higher than conventional fluorescence-based methods.[8,19] Testosterone (T, 10^{-6} M) stimulation of DU-145 had no effect on PEGylated nanoparticle accumulation (Supporting Information Figure S3), but significantly increased α-Bic- and β-Bic-AuNP accumulation. These findings are consistent with previous reports demonstrating 1.5−2-fold upregulation of androgen receptor expression following testosterone stimulation in DU-145[37] and concomitant increases in membrane-AR traslocation[16] (Figure 3b). These imaging data show that antiandrogen gold nanoparticles selectively accumulate in antiandrogen treatment-resistant $AR^+/GPRC6A^+$ prostate cancer cells and can also do so in an AR-/mAR-*dependent* manner.

Cytotoxicity of the antiandrogen nanoparticles and their ligands to chemotherapy- and antiandrogen-resistant[6] $mAR^+/GPRC6A^+$ DU-145 prostate carcinoma cells was investigated by tetrazolium assay (24 h, see Supporting Information). AuNP-bound α-Bic- and β-Bic induced half-maximal cytotoxicity (IC_{50}) at 21 and 2.5 μM ligand concentrations, respectively, exhibiting per-molecule potency 6.4- and 13-fold greater than their corresponding free drugs, respectively (Figure 3c−e). Free α-Bic- and β-Bic cytotoxicity was comparable to that previously reported for bicalutamide and OH-flutamide with DU-145,[38] while nanoparticle-equivalent concentrations of PEGylated gold nanoparticles exhibited no significant toxicity over therapeutically relevant antiandrogen-AuNP concentrations. Unlike androgenic GPRC6A agonists, which we have previously shown induce cell proliferation,[34] antiandrogen-AuNPs stimulate GPRC6A while diminishing cell proliferation (Figure 3c−e) and also maintaining antagonist activity toward androgen receptor (Figure 2a,b). Together, these data correlate selective AR and GPRC6A engagement (vide infra) with enhanced drug potency and cell death by antiandrogen gold nanoparticles.

In summary, we found that antiandrogen gold nanoparticles selectively engaged two distinct receptors involved in prostate cancer growth and progression. These particles selectively accumulated in castration- and chemotherapy-resistant prostate cancer cells, induced cell death at nanomolar particle concentrations, and enhanced the potency of antiandrogens currently in clinical use by roughly 1 order of magnitude. Further, antiandrogen gold nanoparticles antagonized androgen receptor with multivalent affinity and selectively engaged a newly discovered transmembrane G-protein coupled receptor, GPRC6A, involved in prostate carcinogenesis and disease risk. These platforms provide opportunities for increasingly potent and selective therapy for treatment-resistant prostate cancers and may exhibit further enhanced therapeutic efficacy via drug coconjugation, image-based treatment guidance/monitoring, concurrent laser photothermal ablation therapy, and/or high-Z enhanced radiotherapy.

■ ASSOCIATED CONTENT

Supporting Information

Antiandrogen ligand synthesis; nanoparticle synthesis, conjugation, and characterization; docking methods, cell culture/in

vitro analysis, radioligand binding, *GPRC6A* expression/stimulation, and imaging methods. This material is available free of charge via the Internet at http://pubs.acs.org.

AUTHOR INFORMATION

Corresponding Author

*Prof. Mostafa A. El-Sayed: E-mail melsayed@gatech.edu. Prof. Adegboyega K. Oyelere: E-mail aoyelere@gatech.edu.

Present Address

‡The David H. Koch Institute for Integrative Cancer Research, Massachusetts Institute of Technology, 77 Massachusetts Avenue, Cambridge, Massachusetts 02139, United States.

Author Contributions

¶These authors contributed equally to this work.

Notes

The authors declare the following competing financial interest(s): L.D.Q. is a consultant to Amgen, KAI Pharmaceuticals and Shire; he has also been a paid speaker for Amgen.

ACKNOWLEDGMENTS

This work was supported by the U.S. National Institutes of Health (1U01CA151802-01, MAE; R01CA131217, AKO; R01-AR37308, LDQ). The authors also thank Dr. Jian Hui Wu for providing the apo homology model of AR.

ABBREVIATIONS

α-Bic, α-Bicalutamide ligand; β-Bic, β-Bicalutamide ligand; ADT, androgen deprivation therapy; AR, androgen receptor; AuNP, gold nanoparticle; cAMP, cyclic adenosine monophosphate; DAPI, 4′,6-diamidino-2-phenylindole; DHT, dihydrotestosterone; IC_{50}, half maximal concentration; mAR, membrane androgen receptor; PEG, poly(ethylene glycol); T, testosterone

REFERENCES

(1) Ferlay, J., Shin, H.-R., Bray, F., Forman, D., Mathers, C., and Parkin, D. M. (2010) Estimates of worldwide burden of cancer in 2008: GLOBOCAN 2008. *Int. J. Cancer 127*, 2893−2917.

(2) Siegel, R., Ward, E., Brawley, O., and Jemal, A. (2011) Cancer statistics. *CA Cancer J. Clin. 61*, 212−236.

(3) Statistics on the risk of developing cancer, *Cancer Research UK*, accessed 7 December, 2011, http://info.cancerresearchuk.org/cancerstats/incidence/risk/.

(4) Chen, Y., Clegg, N. J., and Scher, H. I. (2009) Anti-androgens and androgen-depleting therapies in prostate cancer: new agents for an established target. *Lancet Oncol. 10*, 981−991.

(5) Attar, R. M., Takimoto, C. H., and Gottardis, M. M. (2009) Castration-resistant prostate cancer: locking up the molecular escape routes. *Clin. Cancer Res. 15*, 3251−3255.

(6) Borsellino, N., Belldegrun, A., and Bonavida, B. (1995) Endogenous interleukin 6 is a resistance factor for cis-diamminedichloroplatinum and etoposide-mediated cytotoxicity of human prostate carcinoma cell lines. *Cancer Res. 55*, 4633−4639.

(7) Dreaden, E. C., Mwakwari, S. C., Sodji, Q. H., Oyelere, A. K., and El-Sayed, M. A. (2009) Tamoxifen-poly(ethylene glycol)-thiol gold nanoparticle conjugates: enhanced potency and selective delivery for breast cancer treatment. *Bioconjugate Chem. 20*, 2247−2253.

(8) Dreaden, E. C., Alkilany, A. M., Huang, X., Murphy, C. J., and El-Sayed, M. A. (2012) The golden age: gold nanoparticles for biomedicine. *Chem. Soc. Rev. 41*, 2740−2779.

(9) Dhar, S., Gu, F. X., Langer, R., Farokhzad, O. C., and Lippard, S. J. (2008) Targeted delivery of cisplatin to prostate cancer cells by aptamer functionalized Pt(IV) prodrug-PLGA−PEG nanoparticles. *Proc. Natl. Acad. Sci. U.S.A. 105*, 17356−17361.

(10) Dhar, S., Kolishetti, N., Lippard, S. J., and Farokhzad, O. C. (2011) Targeted delivery of a cisplatin prodrug for safer and more effective prostate cancer therapy in vivo. *Proc. Natl. Acad. Sci. U.S.A.,*.

(11) Hattori, Y., and Maitani, Y. (2005) Folate-linked nanoparticle-mediated suicide gene therapy in human prostate cancer and nasopharyngeal cancer with herpes simplex virus thymidine kinase. *Cancer Gene Ther. 12*, 796−809.

(12) Xue, H.-Y., and Wong, H.-L. (2011) Solid lipid−PEI hybrid nanocarrier: an integrated approach to provide extended, targeted, and safer siRNA therapy of prostate cancer in an all-in-one manner. *ACS Nano 5*, 7034−7047.

(13) Chanda, N., Kattumuri, V., Shukla, R., Zambre, A., Katti, K., Upendran, A., Kulkarni, R. R., Kan, P., Fent, G. M., Casteel, S. W., Smith, C. J., Boote, E., Robertson, J. D., Cutler, C., Lever, J. R., Katti, K. V., and Kannan, R. (2010) Bombesin functionalized gold nanoparticles show in vitro and in vivo cancer receptor specificity. *Proc. Natl. Acad. Sci. U.S.A. 107*, 8760−8765.

(14) Roa, W., Zhang, X., Guo, L., Shaw, A., Hu, X., Xiong, Y., Gulavita, S., Patel, S., Sun, X., Chen, J., Moore, R., and Xing, J. Z. (2009) Gold nanoparticle sensitize radiotherapy of prostate cancer cells by regulation of the cell cycle. *Nanotechnology 20*, 375101.

(15) Stern, J. M., Stanfield, J., Kabbani, W., Hsieh, J.-T., and Cadeddu, J. A. (2008) Selective prostate cancer thermal ablation with laser activated gold nanoshells. *J. Urol. 179*, 748−753.

(16) Pedram, A., Razandi, M., Sainson, R. C. A., Kim, J. K., Hughes, C. C., and Levin, E. R. (2007) A conserved mechanism for steroid receptor translocation to the plasma membrane. *J. Biol. Chem. 282*, 22278−22288.

(17) Hatzoglou, A., Kampa, M., Kogia, C., Charalampopoulos, I., Theodoropoulos, P. A., Anezinis, P., Dambaki, C., Papakonstanti, E. A., Stathopoulos, E. N., Stournaras, C., Gravanis, A., and Castanas, E. (2005) Membrane androgen receptor activation induces apoptotic regression of human prostate cancer cells in vitro and in vivo. *J. Clin. Endocrinol. Metab. 90*, 893−903.

(18) Pi, M., and Quarles, L. D. (2011) GPRC6A regulates prostate cancer progression. *Prostate 72*, 399−409.

(19) Dreaden, E. C., Mackey, M. A., Huang, X., Kang, B., and El-Sayed, M. A. (2011) Beating cancer in multiple ways using nanogold. *Chem. Soc. Rev. 40*, 3391−3404.

(20) Bohl, C. E., Gao, W., Miller, D. D., Bell, C. E., and Dalton, J. T. (2005) Structural basis for antagonism and resistance of bicalutamide in prostate cancer. *Proc. Natl. Acad. Sci. U.S.A. 102*, 6201−6206.

(21) Jiang, W., Kim, B. Y. S., Rutka, J. T., and Chan, W. C. W. (2008) Nanoparticle-mediated cellular response is size-dependent. *Nat. Nanotechnol. 3*, 145−150.

(22) Perrault, S. D., Walkey, C., Jennings, T., Fischer, H. C., and Chan, W. C. W. (2009) Mediating tumor targeting efficiency of nanoparticles through design. *Nano Lett. 9*, 1909−1915.

(23) Obach, R. S., Lombardo, F., and Waters, N. J. (2008) Trend analysis of a database of intravenous pharmacokinetic parameters in humans for 670 drug compounds. *Drug Metab. Dispos. 36*, 1385−1405.

(24) Zhou, J., Liu, B., Geng, G., and Wu, J. H. (2010) Study of the impact of the T877A mutation on ligand-induced helix-12 positioning of the androgen receptor resulted in design and synthesis of novel antiandrogens. *Proteins 78*, 623−637.

(25) He, Y., Yin, D., Perera, M., Kirkovsky, L., Stourman, N., Li, W., Dalton, J. T., and Miller, D. D. (2002) Novel nonsteroidal ligands with high binding affinity and potent functional activity for the androgen receptor. *Eur. J. Med. Chem. 37*, 619−634.

(26) Kirkovsky, L., Mukherjee, A., Yin, D., Dalton, J. T., and Miller, D. D. (2000) Chiral nonsteroidal affinity ligands for the androgen receptor. 1. Bicalutamide analogues bearing electrophilic groups in the B aromatic ring1. *J. Med. Chem. 43*, 581−590.

(27) Papadopoulou, N., Charalampopoulos, I., Anagnostopoulou, V., Konstantinidis, G., Foller, M., Gravanis, A., Alevizopoulos, K., Lang, F., Stournaras, C. (2008) Membrane androgen receptor activation triggers down-regulation of PI-3K/Akt/NF-kappaB activity and induces apoptotic responses via Bad, FasL and caspase-3 in DU145 prostate cancer cells. *Mol. Cancer 7*.

(28) Gu, S., Papadopoulou, N., Gehring, E.-M., Nasir, O., Dimas, K., Bhavsar, S., Föller, M., Alevizopoulos, K., Lang, F., and Stournaras, C. (2009) Functional membrane androgen receptors in colon tumors trigger pro-apoptotic responses in vitro and reduce drastically tumor incidence in vivo. *Mol. Cancer 8*, 1−14.
(29) Kampa, M., Kogia, C., Theodoropoulos, P. A., Anezinis, P., Charalampopoulos, I., Papakonstanti, E. A., Stathopoulos, E. N., Hatzoglou, A., Stournaras, C., Gravanis, A., and Castanas, E. (2006) Activation of membrane androgen receptors potentiates the antiproliferative effects of paclitaxel on human prostate cancer cells. *Mol. Cancer Ther. 5*, 1342−1351.
(30) Heinlein, C. A., and Chang, C. (2004) Androgen receptor in prostate cancer. *Endocr. Rev. 25*, 276−308.
(31) Schuh-Huerta, S. M., and Pera, R. A. R. (2011) Reproductive biology: Bone returns the favour. *Nature 472*, 46−47.
(32) Wellendorph, P., and Bräuner-Osborne, H. (2004) Molecular cloning, expression, and sequence analysis of GPRC6A, a novel family C G-protein-coupled receptor. *Gene 335*, 37−46.
(33) Takata, R., Akamatsu, S., Kubo, M., Takahashi, A., Hosono, N., Kawaguchi, T., Tsunoda, T., Inazawa, J., Kamatani, N., Ogawa, O., Fujioka, T., Nakamura, Y., and Nakagawa, H. (2010) Genome-wide association study identifies five new susceptibility loci for prostate cancer in the Japanese population. *Nat. Genet. 42*, 751−754.
(34) Pi, M., Parrill, A. L., and Quarles, L. D. (2010) GPRC6A mediates the non-genomic effects of steroids. *J. Biol. Chem. 285*, 39953−39964.
(35) Whitaker, H. C., Hanrahan, S., Totty, N., Gamble, S. C., Waxman, J., Cato, A. C. B., Hurst, H. C., and Bevan, C. L. (2004) Androgen receptor is targeted to distinct subcellular compartments in response to different therapeutic antiandrogens. *Clin. Cancer Res. 10*, 7392−7401.
(36) Virolainen, E., Vanharanta, R., and Carey, T. E. (1984) Steroid hormone receptors in human squamous carcinoma cell lines. *Int. J. Cancer 33*, 19−25.
(37) Alimirah, F., Chen, J., Basrawala, Z., Xin, H., and Choubey, D. (2006) DU-145 and PC-3 human prostate cancer cell lines express androgen receptor: Implications for the androgen receptor functions and regulation. *FEBS Lett. 580*, 2294−2300.
(38) Kreis, W., Budman, D. R., and Calabro, A. (2001) A reexamination of PSC 833 (Valspodar) as a cytotoxic agent and in combination with anticancer agents. *Cancer Chemother. Pharmacol. 47*, 78−82.

Bioconjugate Chemistry

Article

pubs.acs.org/bc

Design and Synthesis of Multifunctional Gold Nanoparticles Bearing Tumor-Associated Glycopeptide Antigens as Potential Cancer Vaccines

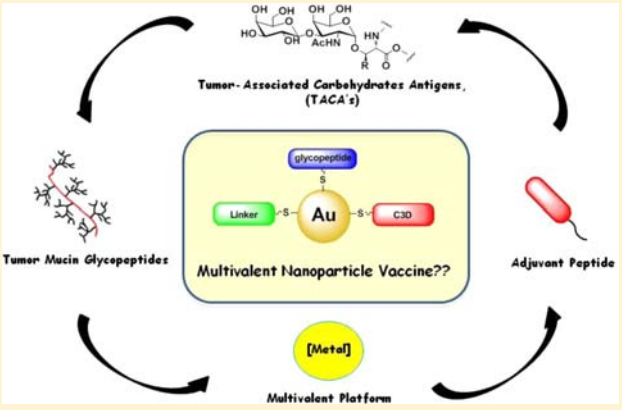
Raymond P. Brinãs,[†] Andreas Sundgren,[†,#] Padmini Sahoo,[‡] Susan Morey,[‡] Kate Rittenhouse-Olson,[‡] Greg E. Wilding,[§] Wei Deng,[§] and Joseph J. Barchi, Jr.*[,†]

[†]Chemical Biology Laboratory, Center for Cancer Research, National Cancer Institute, Frederick National Laboratory for Cancer Research, Frederick, Maryland 21702, United States

[‡]Department of Biotechnical and Clinical Laboratory Sciences, and [§]Department of Biostatistics, School of Public Health and Health Professions, University of Buffalo, Buffalo, New York 14214, United States

Supporting Information

ABSTRACT: The development of vaccines against specific types of cancers will offer new modalities for therapeutic intervention. Here, we describe the synthesis of a novel vaccine construction prepared from spherical gold nanoparticles of 3−5 nm core diameters. The particles were coated with both the tumor-associated glycopeptides antigens containing the cell-surface mucin MUC4 with Thomsen Friedenreich (TF) antigen attached at different sites and a 28-residue peptide from the complement derived protein C3d to act as a B-cell activating "molecular adjuvant". The synthesis entailed solid-phase glycopeptide synthesis, design of appropriate linkers, and attachment chemistry of the various molecules to the particles. Attachment to the gold surface was mediated by a novel thiol-containing 33 atom linker which was further modified to be included as a third "spacer" component in the synthesis of several three-component vaccine platforms. Groups of mice were vaccinated either with one of the nanoplatform constructs or with control particles without antigen coating. Evaluation of sera from the immunized animals in enzyme immunoassays (EIA) against each glycopeptide antigen showed a small but statistically significant immune response with production of both IgM and IgG isotypes. Vaccines with one carbohydrate antigen (B, C, and E) gave more robust responses than the one with two contiguous disaccharides (D), and vaccine E with a TF antigen attached to threonine at the 10th position of the peptide was selected for IgG over IgM suggesting isotype switching. The data suggested that this platform may be a viable delivery system for tumor-associated glycopeptide antigens.



INTRODUCTION

Tumor-associated carbohydrate antigens[1] (TACA's) are aberrantly expressed glycan chains on cell surface proteins and lipids specific to various tumor subtypes. They arise from the modified expression of various glycoprocessing enzymes in tumors leading to structures that are otherwise rarely observed in the "normal" cell phenotype. Both N- and O-linked glycans, the two major forms of carbohydrate post-translational protein modifications, are modified in specific ways: N-linked (attached to asparagines) glycans become more branched and extended, while O-linked (attached to serine/threonine) are truncated and prematurely sialylated. These modifications lead to a variety of cellular consequences within the tumor, including modified cell adhesion, enhanced aggression, and metastasis.[2] In addition, the shortened O-linked glycans linked to cell surface proteins called mucins expose underlying peptide sequences that are masked by heavily clustered glycosylation in normal tissue. This presentation of new sugar chains and amino acid motifs elicits a tumor type-specific immune response against these "non-self" structures.[3] Hence, a variety of studies in the past 20 years have attempted to use TACA's as immunogens for active immunity against different tumors.[4−13] In addition, passive therapy with antibodies directed toward TACA structures such as the Tn[14] and TF[15] antigens also have demonstrated therapeutic potential via inhibition of tumor cell-specific adhesion events.

More importantly, a judicious combination of both the TACA saccharide and the underlying peptide sequence should more accurately present the true antigen to the immune system in a vaccine preparation. Several TACA-containing glycopep-

Received: November 15, 2011
Revised: May 28, 2012
Published: July 19, 2012

 © 2012 American Chemical Society

tides have been employed in vaccines and immunotherapeutic applications against various tumors.[8,10−12,16−33] The majority of these glycopeptides are synthetic in origin, as it is difficult to isolate homogeneous glycosylated protein fragments from cell or tissue preparations. The immune response to these antigens is highly dependent on the chemistry that is used to prepare the vaccine: Differences can be seen with different linkers, carrier proteins, multivalent scaffolds, and antigen conformations. Thus, each construct needs to be evaluated on a case-by-case basis and compared with regard to proper presentation of antigen and efficacy in eliciting a response.

We have been interested in employing metal nanoparticles as scaffolds for multivalent presentation of sugars and glycopeptides for various applications.[34−36] In particular, gold nanoparticles (AuNPs) are useful inasmuch as they are easily prepared, present a high degree of multivalency, and their size range is easily controllable.[37] Several biological applications of carbohydrate-coated gold "glyconanoparticles" (GNP) have been published which attest to the validation of using this simple and highly nontoxic platform.[38] Several years ago, we reasoned that these platforms may be used as carriers of tumor antigens and hence as possible novel vaccine constructs. Since then, one article has been published on the synthesis of a potential vaccine using carbohydrate-coated gold nanoparticles.[39] Here, we present the synthesis of several new gold nanoparticle-based glycopeptide constructions as possible "carriers" for TACA's and TACA-conjugated glycopeptides. The peptide sequences are from MUC4, a biomarker mucin for pancreatic adenocarcinomas[40] and hence a valid starting target for vaccine development.

■ EXPERIMENTAL SECTION

General Methods. Chemicals were purchased from Sigma−Aldrich (Milwaukee, WI) and used without further purification. $HAuCl_4 \cdot H_2O$ was purchased from Strem Chemicals. The H-Gly-ClTrt resin was purchased from Novabiochem (Darmstadt, Germany). Flash column chromatography (FCC) was performed using RediSep silica columns on a CombiFlash Companion employing solvent polarity gradient (dichloromethane→methanol). Preparative reversed-phase HPLC was performed using Phenomenex Columbus column (C18, 5 μ, 0.100 Å) employing gradient elutions of varying percent of water to organic modifier (solvent A: 0.1% TFA/H_2O; solvent B: 0.1% TFA/acetonitrile). Analytical reversed-phase chromatography was done using a Phenomenex Gemini column (C18, 5 μ, 110 Å, 150 mm × 4.6 mm) with similar gradients. NMR spectra were recorded on a Varian Inova 400 instrument with residual $CHCl_3$ (7.26 ppm) as the internal standard at frequencies of 399.74 MHz for ^{1}H and 100.51 MHz for ^{13}C. High-resolution mass spectra were performed by Mass Spectrometry Facility at University of California, Riverside.

TEM Measurements. Transmission electron micrograph samples were prepared by placing an aqueous solution (~2 μL) of the AuNP's on the grid with a carbon-coated support film that was previously treated with glow discharge. The excess liquid was blotted with a filter paper, allowed to dry, and rinsed with distilled water twice. TEM images were taken using a Hitachi H7650 TEM (Tokyo, Japan) operating at 80 kV with a 2k × 2k CCD camera (AMT, Danvers, MA). The sizes of Au NPs were analyzed using the camera's measurement software (AMT).

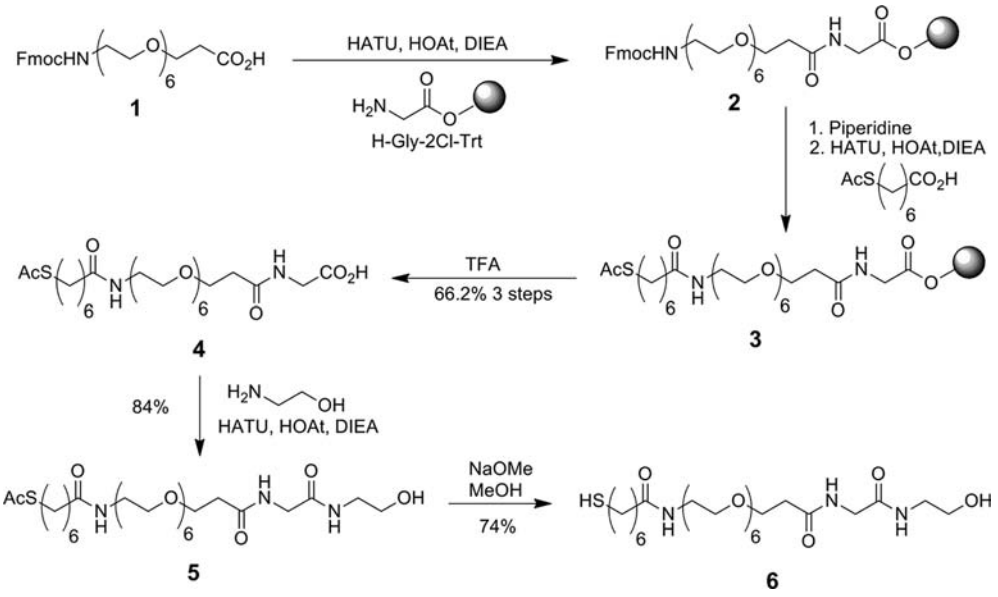
DLS Measurements. Dynamic light scattering measurements were performed on a DynaPro Tytan instrument equipped with a Temperature-Controlled MicroSampler (Wyatt Technology Corp., Santa Barbara, CA) at a laser wavelength of 830 nm, scattering angle of 90°, in a 12 μL quartz cuvette at 23 °C. Each measurement consisted of sixty 10 s acquisitions. All samples were centrifuged before measurement. To obtain the hydrodynamic radii (R_h) and percentage polydispersity, the intensity autocorrelation functions were fitted with a proprietary non-negative least-squares algorithm by *Dynamics 7.0.3* software (Wyatt Technology Corp., Santa Barbara, CA).

Zeta Potential Measurements. A Malvern Zetasizer Nano ZS instrument was used to measure zeta potential at 25 °C for all samples. Stock samples were diluted 10-fold in 10 mM NaCl and loaded into prerinsed folded capillary cells for measurements. Sample pH was measured before each measurement. An applied voltage of 150 V was used and a minimum of three measurements were made per sample (see Supporting Information for additional descriptions).

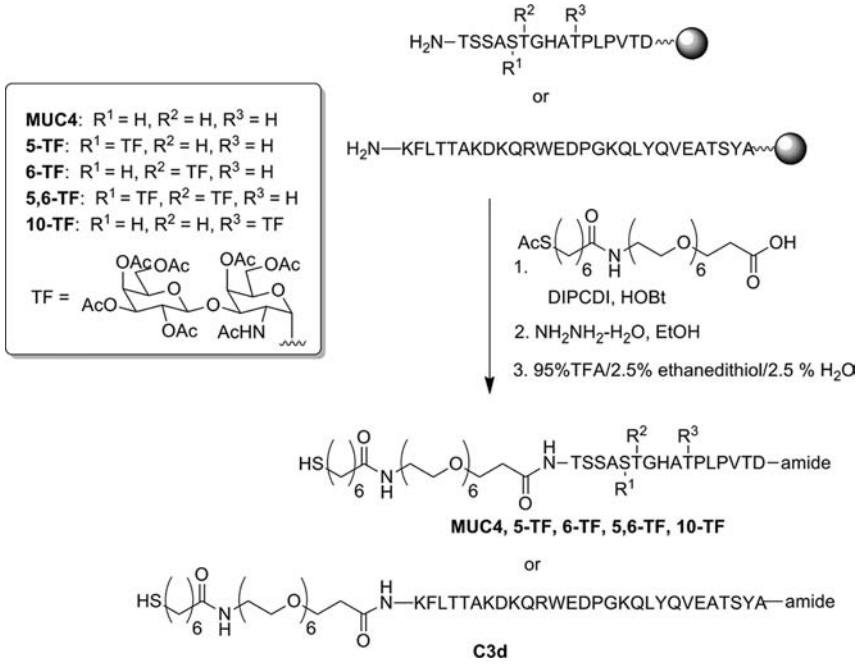
Synthesis. *N*-(2-(2-Hydroxyethylamino)-2-oxoethyl)-1-(7-mercaptoheptanamido)-3,6,9,12,15,18-hexaoxaheni-cosan-21-amide (6). The hydroxyl linker **6** via the intermediate acid **4** was synthesized by a slightly modified version of our previous synthesis[41] as follows: To a well-stirred solution of the commercially available (PolyPeptides, San Diego, CA) Fmoc-21-amino-4,7,10,13,16,19-hexaoxaheneicosanoic acid (**1**, 200 mg, 0.347 mmol) in dry DMF (1.74 mL) was added HOAt (47.2 mg, 0.347 mmol). After 5 min of stirring, HATU (132 mg, 0.347 mmol) was added and the reaction mixture was stirred for 15 min. H-Gly-2Cl-TrT resin (434 mg of 0.404 mmol/g, 0.175 mmol) was added to the activated acid mixture, followed by diisopropylethylamine (DIEA, 121 μL, 0.694 mmol). After 2 h, the reaction was filtered, and the resin was washed 5× with DMF. Any remaining amino groups were capped with a 2-Chloro CBz group by reaction with *N*-(2-chlorobenzyloxycarbonyloxy)succinimide (Z-(2Cl)-OSu, 394 mg in 2.8 mL, 1:1 DMF-DCM). The excess capping reagent solution was filtered, and the resin was washed again with DMF (5×). On the basis of the Fmoc-group cleavage of a small amount of the resin, the yield of the intermediate **2** was found to be 74%. Resin 2 (470 mg, 0.274 mmol/g, 0.129 mmol) was deprotected with 4 mL of 20% piperidine in DMF for 1 h at r.t. The mixture was filtered, and the resin was washed with DMF (5×). 7-(Acetylthio)heptanoic acid (31.6 mg, 0.155 mmol) was mixed with HOAt (21 mg, 0.155 mmol) in DMF (0.8 mL). HATU (59 mg, 0.155 mmol) was added, and the mixture was stirred for 5 min. The mixture was added to the deprotected resin, DIEA (54 μL, 40 mg, 0.310 mmol) was added, and the mixture was allowed to react for 2 h. The resulting resin **3** was filtered, washed with DMF (5×), DCM (2×), and diethyl ether (2×) and dried under vacuum. This resin **3** (104 mg, 0.159 mg) was cleaved with TFA/thioanisole/water/phenol/EDT (82.5:5:5:5:2.5) for 2 h at r.t. The solvent was evaporated to dryness, and the residue was collected, dissolved in water, and lyophilized overnight. The crude product was purified by reversed-phase HPLC (A:B, 20% to 50% over 32.7 min) to give the pure **4** in 66.2% yield (51 mg). Compounds **5** and **6** were subsequently prepared according to our previously published procedures. Characterization data of all compounds were in good agreement with the published results.[41]

General Procedure for the Synthesis of the Thiolated Peptides. Peptides were prepared by Fmoc chemistry on a Liberty Microwave Peptide synthesizer (CEM corp., North Carolina, USA). The glycoamino acids (threonine or serine

Scheme 1. Synthesis of the Linker with Modifications from Previous Preparations



Scheme 2. Final Synthesis of Glycopeptides Precursors for GNP Preparations



with an α-O-linked peracetylated Thomsen-Friedenreich disaccharide and Fmoc-protected amino group, TF-Ser, TF-Thr) were either prepared as described[42] or purchased from Sussex Research (Ontario, Canada). The general protocol using the microwave-assisted peptide synthesis is as follows: (1) 0.100 mmol of the resin (Rink amide resin with the first Fmoc-protected amino acid, ~0.35 meq/g substitution) was loaded into the synthesizer. (2) A two-step deprotection sequence was performed; step 1 involved treatment with 20% piperidine in DMF (containing 0.1 M HOBt) for 30 s at 75 °C (25 W maximum) followed by step 2, which was treatment with a second portion of 20% piperidine in DMF (containing 0.1 M HOBt) for 3 min at 75 °C (25 W). (3) Coupling reactions were carried out by reacting the resin with 4-fold excess of the next amino acid in the presence of HBTU/DIEA for 2 min at 75 °C (25 W). Deprotection (step 2) and coupling (step 3) were repeated until the desired peptide sequence was complete. The Fmoc-protected peptide on the resin was then manually deprotected using 20% piperidine in DMF for 1 h at r.t. in order to couple with either the glycoamino acid or the linker **4** to form the desired peptide. The coupling of each glycoamino acid (1.1 equiv) to the peptide was done manually by activation with HATU (1.1 equiv) and HOAt (1.1 equiv) for 5 min followed by reaction at 25 °C for 2 h in the presence of DIPEA (2.2 equiv). Coupling of the linker **4** with the peptides or glycopeptides on the resin was done by standard DIPCDI/HOBt conditions (see Schemes 1 and 2). Briefly, linker **4** was dissolved in DMF, and then HOBt and DIPCDI were added. The resulting mixture was agitated for 30 min at r.t. and added to the resin. After 5–6 h of agitation, another portion of HOBt

dx.doi.org/10.1021/bc200606s | *Bioconjugate Chem.* 2012, 23, 1513–1523

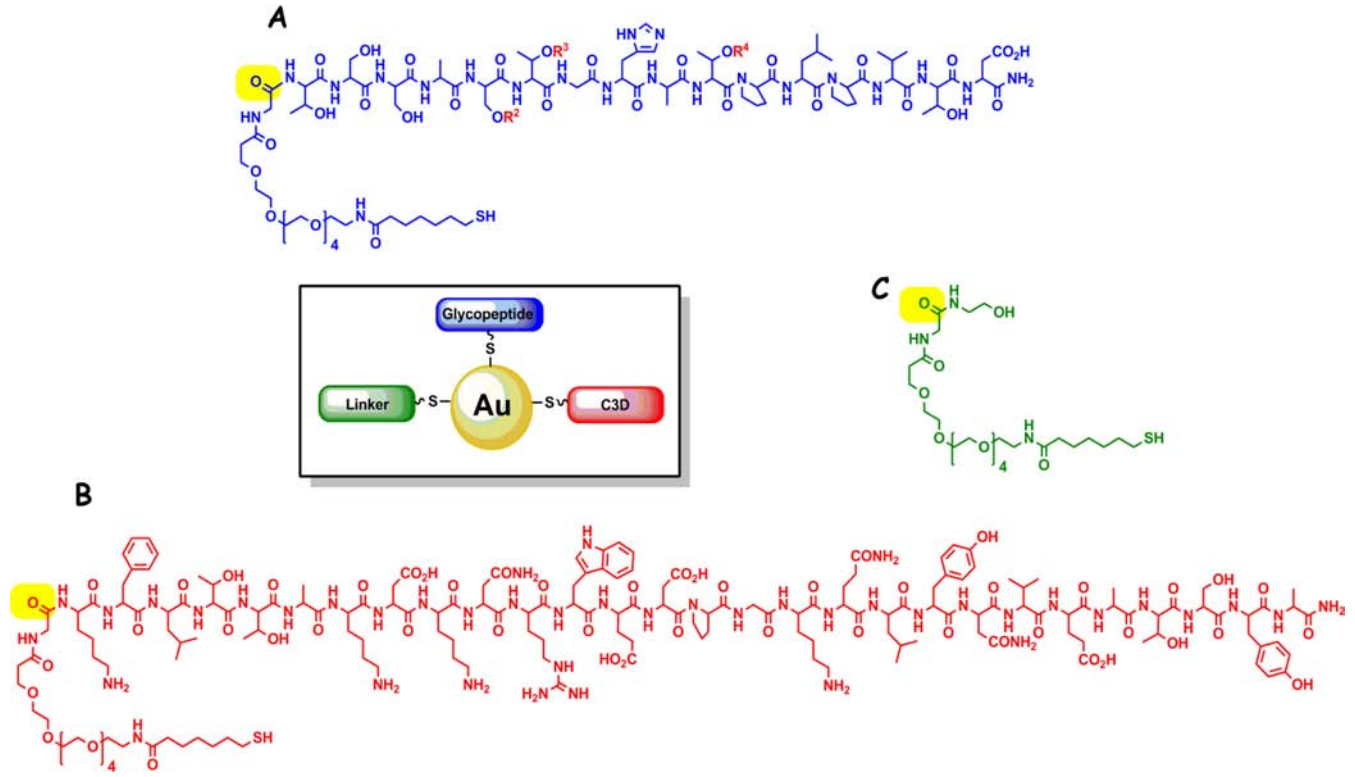


Figure 1. AuNP vaccine design (center). (A) MUC4 glycopeptides conjugated to the carbonyl highlighted in yellow of the linker shown in (C). R^2–R^4 indicate residues that are glycosylated. (B) C3d 28 residue peptide (P28) conjugated to the linker. The linker in (C) is shown modified with the addition of terminal hydroxyl group to maintain bioavailability and reduce density. The ratio of each thiol used in the construction of AuNPs was **A**:**B**:**C** = 1:1:3.

(5 equiv) and DIPCDI (5 equiv) was added. The mixture was agitated for an additional 18 h. The resin was isolated, washed with DMF (5×) and ethanol (2×), and treated with 10% hydrazine hydrate in EtOH for 18 h. After removal of the hydrazine hydrate solution, the resin was washed with ethanol, DMF, and ethyl ether. The resin was dried under vacuum and then treated with the cleavage mixture (2.5% 1,2-ethanedithiol/2.5% water/95% TFA) for 2 h. Precipitation of the peptides was done by pouring the TFA solution into a flask containing ice-cold ether. The precipitates were collected by centrifugation. The residue was purified by HPLC (water/acetonitrile gradient, each containing 0.1% TFA) to give the desired peptide as a white, fluffy solid.

HS-Linker-KFLTTAKDKQRWEDPGKQLYQVEATSYA (C3d). This compound was synthesized in 20% yield (32 mg). RP-HPLC (water/acetonitrile gradient, 15–45%, 20 min): R_t = 13.3 min. HRMS–ESI (m/z): M^+ calcd for $C_{171}H_{270}N_{42}O_{54}S$, 3807.9388; found: 3807.9241.

HS-Linker-TSSAS(Galβ1→3GalNAcα)TGHATPLPVTD (5-TF). This compound was synthesized in 22% yield (22 mg) RP-HPLC (water/acetonitrile gradient, 15–45%, 20 min): R_t = 11.77 min. HRMS–ESI (m/z): M^+ calcd for $C_{102}H_{172}N_{22}O_{44}S$, 2441.1613; found: 2441.1589.

HS-Linker-TSSAS(Galβ1→3GalNAcα)T(Galβ1→3GalNAcα)GHATPLPVTD (5,6-TF). This compound was synthesized in 22% yield (25 mg) RP-HPLC (water/acetonitrile gradient, 15–45%, 20 min): R_t = 11.40 min. HRMS–ESI (m/z): M^+ calcd for $C_{116}H_{195}N_{23}O_{54}S$, 2806.2935; found: 2806.2981.

General Procedure for the Synthesis of Gold Nanoparticles. To a flask containing water (10 mL/total μmol thiol) was added an aqueous solution of the thiols (1:1:3 molar ratio glycopeptide/C3d/hydroxyl-linker) and 58 mM $HAuCl_4$ (2.75 equiv). The pale yellow solution was cooled to 0 °C, and an aqueous solution of $NaBH_4$ (1 mL/total μmol thiol) was added over 10 min. The resulting solution was stirred for 2 h at 0 °C and then for 16 at r.t. The mixture was concentrated and washed with water (2×) using Centriplus ultrafiltration tubes (MWCO 30 kDa). The retentate was lyophilized to give the desired Au NPs as dark purple solids.

Mice Immunizations and Blood Sampling. Vaccination studies were performed in 3-week-old female Balb/c mice. Groups of 20 mice were each were vaccinated with one of the six GNP's A–F shown in Figure 2 along with a seventh group that was treated with PBS alone as a control. Mice were immunized subcutaneously with their respective GNP antigen, and serum samples were obtained preimmunization and at 2, 4, 6, and 12 week time periods. Serum samples from the mice were obtained using submandibular bleeding prior to immunization and two weeks following each injection. All animal protocols were approved by the institutional animal care and use committee and animals were housed in an ALAC accredited animal facility. The marginal model was used to make pairwise comparisons between test groups and control groups and between different times within each test group to determine statistically significant differences in IgG and IgM titers at significance level α = 0.05.

Enzyme Immunoassay. Enzyme-linked immunosorbent assays were performed with the mouse serum samples from different time points against the glycopeptide conjugates used for coating the gold nanoparticles. Immulon HB High-Binding EIA 96-well plates were coated with optimized concentration of

1.25 μg/mL of each respective glycopeptide conjugate (Scheme 2) and washed four times with 1× TBS-Brij wash buffer. Mouse sera (100 μL of at 1:100 dilution) were added and IgG and IgM were detected by antimouse IgG/alkaline phosphatase or antimouse IgM/horseradish peroxidase systems, respectively, according to the manufacturer's protocol. The TF antigen-binding monoclonal antibody JAA-F11[15] (1 mg/mL Stock Solution) was used as a positive control and 1×-PBS Buffer as a negative control.

Statistical Analysis. The marginal model was used to make pairwise comparisons between test groups and control groups and between different times within each test group to determine statistically significant differences in IgG and IgM titers at significance level, $\alpha = 0.05$.[43] Error bars for EIA assays for the seven sets of 20 mice were calculated with this method and reported as standard error from the mean, which is the standard deviation divided by the square root of the sample size: $SD/\sqrt{n}$.

RESULTS AND DISCUSSION

Particle Design. Our design is illustrated in Figure 1. Small diameter AuNPs can be coated with various molecular entities in the same reaction by performing the self-assembly in the presence of multiple auro-philic reactants. Thiols are commonly used to conjugate to a metallic gold surface due to the affinity of sulfur for gold. Thus, using a variation of the Brust-type procedure,[44,45] GNP vaccine constructs can be prepared in one pot by reduction of gold salts with sodium borohydride in the presence of different thiols. The reductant serves to both reduce the gold to Au(0) and keep the thiols present in their reduced state for binding to the gold.

Choice of Ligands. The choice of ligands was made based on several criteria. First, the aforementioned importance of aberrant mucin expression and O-linked glycosylation in tumor progression is well-established. We reasoned also that neither the carbohydrate nor peptide sequence alone would be sufficient for a potent immune response (vide supra). Mucin extracellular domains consist of large strings of tandem repeat peptide sequences of between 16 and 22 amino acids, decorated with large numbers of O-linked carbohydrate chains that occur in "clusters". Hence, we used specific glycopeptides from the mucin tandem repeating unit as antigens to attach to gold. There have been a host of immunological studies with MUC1, a mucin found aberrantly expressed on many prostate and breast tumor lines.[28] However, there has been mounting evidence that another mucin, MUC4, is also a valid biomarker, especially for pancreatic carcinomas.[40] The Kunz group has synthesized several MUC4-based glycopeptides containing various TACAs and T-cell epitopes conjugated together chemically as potential single-component vaccines.[27,46−49] Thus, we chose to follow a similar path and prepare MUC4 glycopeptides with covalently attached TF disaccharides as potential antigens. We chose TF as the carbohydrate antigen since this disaccharide is rarely displayed in normal tissue and its presence has been related to enhanced aggression and metastasis of many solid tumors.[15,50] The use of nanoparticles as a delivery vehicle offers the opportunity to present antigens, potential T-helper peptides, and adjuvants within one entity in a multivalent fashion. In addition, although AuNP cores have been implicated in a small number of studies as harboring some immunostmulant activity in vivo,[51] this core will not present both B-and T-cell epitopes as is the case with many of the various carrier proteins that are used for conjugate vaccines, such as KLH and BSA.

Since carbohydrate antigens are T-cell independent, the standard protocol for vaccine design includes conjugation to a large carrier protein such as KLH or alternatively to small peptides such as the PADRE[52] sequence to elicit T-helper cell production for sustained immunological memory and antibody class switching. Our design concentrated on a B-cell immune response, and this dictated our choice of "molecular adjuvant" to add to the system. One of these "adjuvants" used in polysaccharide-based vaccines is the final degradation product of the third component of complement or C3d.[53] C3d binds CR2/CD21 on B-cells enhancing cell activation and, through simultaneous interaction of antigen with B-cell surface immunoglobulin, activates various pathways that crosstalk to reduce the amount of antigen needed for activation and enhance antigen uptake and presentation. The CR2/CD21 binding epitope of C3d was mapped to a 28-residue peptide that was shown by surface plasmon resonance to bind to CR2/CD21 and elicit similar immune responses as full-length C3d.[54] In addition, immunization with C3d-conjugated antigen can also increase antibody titers and Th1/Th2 cytokine production in CR2/CD21 knockout mice, suggesting an alternative mechanism of immune stimulation in this system.[55] In this study, it was shown that other peptide regions of C3d can turn on a T-cell mediated response in the absence of CR2/CD21. The versatility of this peptide adjuvant suggested that C3d was a judicious choice to include in our design. We concentrated initially on the 28-residue CR2/CD21-binding motif. The third component of our particle was the linker used to attach the other units to the gold surface. This provided an interstitial random "spacer" to reduce the density of the antigen/adjuvant molecules for better molecular recognition. We designed this conjugate to be "naked" at the terminus that normally displays a biologically active entity (e.g., peptide, glycopeptides,C3d) but to present a common functional group, in our case a free hydroxyl, to maintain water solubility.

Synthesis. The synthesis of the hydroxyl-terminated thiol linker (C in Figure 1) followed a modified version of the procedure by our group.[41] Notable differences from our previous synthesis were as follows: (1) the first three steps were performed on the solid phase, and (2) the coupling agents used for peptide bond formation between the various linker segments were 2-(7-Aza-1*H*-benzotriazole-1-yl)-1,1,3,3-tetramethyluronium hexafluorophosphate (HATU)/1-Hydroxy-7-azabenzotriazole (HOAt) in place of DIPCDI/HOBt. These two changes combined to increase yields and efficiency in all reactions. The HATU/HOAt chemistry was used primarily to reduce the reaction times for the amide couplings to only about 2 h versus 18 h needed for the DIPCDI-mediated coupling. The remaining reactions were similar to those in ref 50 (see Scheme 1).

Peptide/glycopeptide synthesis proceeded under mostly standard conditions, i.e., using Fmoc chemistry on Rink amide resins. Serine and threonine glycoamino acids bearing a single TF antigen (Galβ1−3GalNAc-α-O-Ser/Thr) were either prepared as previously described[42] or purchased commercially (see Experimental Section) and used for incorporation of the TF antigen into the growing peptide chain. In the case of the unglycosylated MUC4 peptide and one with TF antigen at the 10th position (10-TF), the amino acids were coupled using a microwave-assisted peptide synthesizer (CEM Corp.) with HBTU\DIEA coupling chemistry. In spite

of these conditions, coupling of the glycoamino acid to the nascent peptide did not occur for the synthesis of the 10-TF construct E. Instead, performing the coupling reaction manually with only a very slight excess of the glycoamino acid and using a more reactive coupling reagent (HATU) furnished the desired glycopeptide in modest yields. This position is notoriously refractory to efficient coupling, as the preceding amino acid is proline, where the combination of a secondary amino group and the steric bulk of the protected TF disaccharide conspire to slow down the reaction. The 28 residue C3d peptide fragment was prepared in a similar fashion (Scheme 2).

Deprotection of the amino termini of the peptides on the Rink amide resin provided points of attachment for the thiol-terminated linker **4**. The reaction sequence for this is shown in Scheme 2. After employing the DIPCDI/HOBt coupling condition, the coupling of linker to the peptides on resin afforded the thiol-terminated acetylated glycopeptides which were deprotected both on the sugar hydroxyl groups and the thioacetate on resin by treatment with hydrazine hydrate. Cleavage from the resin and HPLC purification afforded the final glycopeptides-linker-thiol units in yields ranging from 11% to 63%.

The AuNP vaccine constructs were synthesized from various glycopeptides, **C3d**, and the hydroxyl-terminated linker **6** via the sodium borohydride reduction of chloroauric acid in the presence of the thiols. The molar ratio of the thiols used in the synthesis was 1:1:3 (**MUC4** peptide/glycopeptide):(C3d peptide):(linker **6**). Previous work by our group and others has shown that a higher ratio of interstitial linker molecules favors better size distribution and ligand recognition.[41] Also, this may confer better presentation of the glycopeptides and the C3d peptide to the receptors since steric crowding is minimal. Six constructs (A–F) with varying antigens were prepared using the aforementioned procedure (Figure 2). These constructs were very stable in solution and could be stored at 4 °C for months. Samples could be lyophilized and reconstituted several times with no sign of precipitation or flocculation.

Characterization. UV–vis spectra of each nanoconstruct showed typical plasmon band absorption at ~520 nm with extinction coefficients consistent with particles in this size regime (Supporting Information). TEM measurements showed the average core size of each nanoparticle. The sizes of the Au core ranged primarily from 2.40 to 4.5 nm with two of the constructs (A and F) slightly larger (6.98 and 9.0 nm). This was somewhat curious since both of these constructs contained no carbohydrate modifications. Construct F gave the highest coefficient of variation (CV) (40%), followed by construct A (30%), and compared with the much more reasonable values for constructs B–E (18.8–22.7%). Dynamic light scattering experiments showed polydispersity measurements ranging from 21% to 55%. Although the range is broad and the maximum is somewhat high, the autocorrelation functions of each measurement were consistent with polydispersity within a very narrow size range (see data tables and histograms in Supporting Information). Interestingly, all of the constructs bearing a TF-containing glycopeptide exhibited good CV values and a size range of 2.40 to 4.7 nm. At present, it is not known why GNP's A and F seemed to be inferior to B–E regarding uniformity and polydispersity. However, one possibility is that the covalently attached sugars prevent interparticle stacking by blocking nonspecific binding of peptide chains on opposing GNP's, a phenomenon that may occur readily in construct A. What remains a mystery are the relatively poor results obtained for construct F, which contains solely the linker as a ligand. A possible explanation is the lack of charge on these particles and the presence of a hydroxyl group that may hydrogen bond via water bridges among different particles. We previously observed this behavior when using a similar strategy for particle preparation: Various thio-linker/$HAuCl_4$ molar ratios to prepare simple particles using compound **5** produced particles of unacceptable quality and uniformity with noticeable aggregation (Sundgren and Barchi, unpublished).

Coverage estimates for gold nanoparticles coated with a single ligand are relatively straightforward.[56] Typical analytical techniques such as thermogravimetric and elemental analyses are usually appropriate for determining the surface coverage of these types of constructs. Others have used very specific and sophisticated methods such as spectroscopy of fluorescently labeled ligands,[57] PCR methods for DNA ligands,[58] and X-ray crystallography.[59] However, when passivating ligands are derived from several different molecular families, the estimates become much more complex. This is because most of the analytical tools are designed for single-component species. Analysis of mixed-ligand AuNPs requires differential analysis of each molecular family, which could entail laborious separation steps. There are only a few examples in the literature demonstrating the analysis of mixed-ligand AuNPs. Murray and co-workers made efficient use of ESI mass spectrometry,[60] but this method is limited to the analysis of very small AuNP cores (25 to 38 Au atoms). Another method is by selectively labeling the target ligand on AuNP with a fluorophore and then decomposing the AuNP into fluorophore-labeled "free" ligands, which can be subsequently analyzed by fluorescence spectroscopy. This method may not accurately estimate the ligands because of several factors such as the ease with which the flourophore–ligand reaction occurs and/or steric factors.[61] This method is also only applicable to a specific type of functional group on the ligands.

Due to the lack of a general and robust method for determining the coverage of mixed-ligand AuNPs and also because of the complexity of the structure of our glycopeptide ligands (i.e., presence of a wide range of functional groups), an estimation based on the size of the AuNP core would be appropriate. This type of estimation has been used previously by Penades and co-workers in determining the approximate number of carbohydrate ligands on AuNPs in the only other study where particles of this nature were prepared.[39] An estimate of ligand coverage was based on calculations of surface gold atoms and starting concentrations of reactants. We have performed a similar analysis and find differential coverage based on the TEM-determined core size and theoretical analysis of the number of surface atoms that can be occupied as comprehensively examined by Hostetler et al.[62] and Lewis et al.[63] We assumed that the initial ratio of the ligands used to prepare the AuNPs was the same as the ratio present on the nanoparticles. Table 1 lists the estimates for each ligand on the series of AuNPs prepared. More robust methods are desperately needed for quantitative determination of coverage by ligands of any molecular family, and we are working on methods to perform this analysis (to be reported elsewhere).

Zeta potential measurements were performed on each of the constructs and are shown in Table 2. The graph from the raw data are shown in Figure S18. Construct A with no sugar is the most negative at nearly −25 mV, and the values tend toward more positive potentials as sugars are added to the mucin

Table 1. Calculated Number of Antigens and C3d Molecules Based on the TEM Core Size of the Constructs

construct	core diameter (nm)	core radius (nm)	percent coverage[a]	number of surface atoms[b]	number of thiolate chains[c]	antigen or C3d number[d]
A	4.82	2.41	42%	1238	520	104
B	4.70	2.35	42%	1177	494	99
C	3.35	1.68	46%	602	277	55
D	3.28	1.64	46%	573	264	53
E	2.40	1.20	50%	307	154	31
F	9.02	4.51	~33%	4335	1431	-

[a]Based on the calculated percent coverage from ref 56. The value for construct F is the theoretical coverage for large clusters. [b]The values were calculated using the equations in ref 62. [c]Obtained by multiplying the number of surface atoms with the percent coverage. [d]Based on the molar ratio of antigen to C3d to linker during the synthesis, which is 1:1:3.

Table 2. Zeta Potential of Vaccine Constructs

vaccine #	pH	zeta potential, mV[a]
A	6.3	−24.9 (1.4)
B	6.8	−21.7 (1.0)
C	6.7	−18.4 (2.5)
D	6.9	−13.6 (3.1)
E	7.0	−15.6 (0.8)
F	7.3	−17.4 (0.8)

[a]All measurements were 0.2 mg/mL, in 10 mM NaCl, 25 °C. Results are based on an average of three measurements and the values in parentheses represents the standard error.

peptide. Given the complexity of our system, it is difficult to predict the exact mechanism for the change in zeta potential, but the data suggest that the MUC4 peptide/glycopeptides and C3d adsorb to the particle surface with different aptitudes during self-assembly. The MUC4 sequence contains one aspartate, while C3d has four aspartates and five basic residues (four lysines and one arginine). With the hydroxyl linker being neutral, a 1:1 addition of each peptide would have a net zero charge, suggesting that adsorption of the more electropositive C3d may exceed that of MUC4 as the mucin sequence is glycosylated; the diglycosylated construct D being the most "electropositive" of the six particles. There are many other factors involved in the zeta potential of each system such as van der Waals interactions and steric compression. However, the intriguing results may offer qualitative clues into the ligand capacity of multicomponent AuNP mixtures.

Vaccinations and Analysis of Antisera. All gold particles described here were used to vaccinate mice, and their sera were evaluated for binding to the individual antigens that were coated on the particles. Groups of 20 mice each were vaccinated with all 6 GNP's A–F shown in Figure 2 along with a seventh group that was treated with PBS alone as a control (Figure 2G). Construct F, which is simply GNP's with the linker unit attached and no glycopeptides nor adjuvant, can be considered as a "control" group. However, since the chemical linkers of many synthetic vaccine constructions have been shown to be immunogenic, it also served as an important vaccine conjugate to identify *in vivo* responses generated to the linker alone. Figure 3 shows the enzyme immunoassay (EIA) results with relative responses of both IgM and IgG in the sera of mice before (preimmune) and 12 weeks after vaccinations of

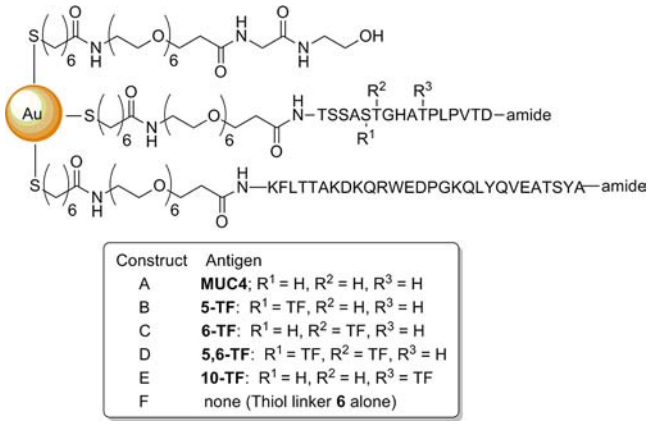


Figure 2. Structures of the six AuNP-based vaccine constructs prepared in the text.

representative constructs B–E. All particle vaccines bearing the TF antigen (B–E) gave small but statistically significant antibody responses (both IgG and IgM) from mice injected subcutaneously at 50 μM particle concentration with boosts every two weeks for 12 weeks. Postimmunization responses were significantly higher than prevaccination responses for all four particles, against all conjugates that were tested. Most antisera bound not only to their respective immunogens, but also with the free peptide and to the linker molecules (self-glycopeptide, unglycosylated MUC4 peptide and linker alone, Figure 3); however, the greatest responses were to the self-antigen. Antigens with single TF substitutions at positions 5 or 6 in the MUC4 repeating unit showed almost equal IgM and IgG production, whereas the glycopeptide with a single TF threonine-substitution at position 10 seemed to select for IgG (Figure 3D). Clustering the TF antigen on positions 5 and 6 suppressed the response.

Statistical significance calculated with the marginal mode model[43] ($P < 0.05$) was achieved for several responses. A listing of each of these measurements is shown in Table 3. It is apparent that the peptide sequence generates a significant response as all AuNPs with vaccine components (A–E) reacted with MUC4 with statistical significance. Group D, with two contiguous TF disaccharides, was the only vaccine construct that did not reach significance for IgG generation when tested against its self-structure and the unglycosylated peptide. Neither of the control groups reached any statistical significance to any of the tested molecules in the assays.

The work described here is still preliminary but highly encouraging. Many features of the TF antigen make it an ideal vaccine epitope:[64] (1) It is found almost exclusively on carcinomas and not normal tissue.[65] (2) In human with cancer, those with lower amounts of anti-TF-antigen antibodies have poorer prognoses than those with low circulating levels. (3) TF-antigen has a defined and distinct role in metastatic spread of various tumor types,[50,66] and thus, active or passive anti-TF therapy could have positive consequences on both tumor growth and metastatic spread as well as overall survival. There have been a host of vaccines prepared based on the TF antigen and many have had positive effects.[64] However, none of these therapeutic strategies has found its way to a clinical setting. In order to progress to a more translationally relevant therapy, finding the proper vaccine vehicle (carrier) to display antigen in the most biologically relevant presentation while choosing the best antigens and stimulatory molecules will be key to

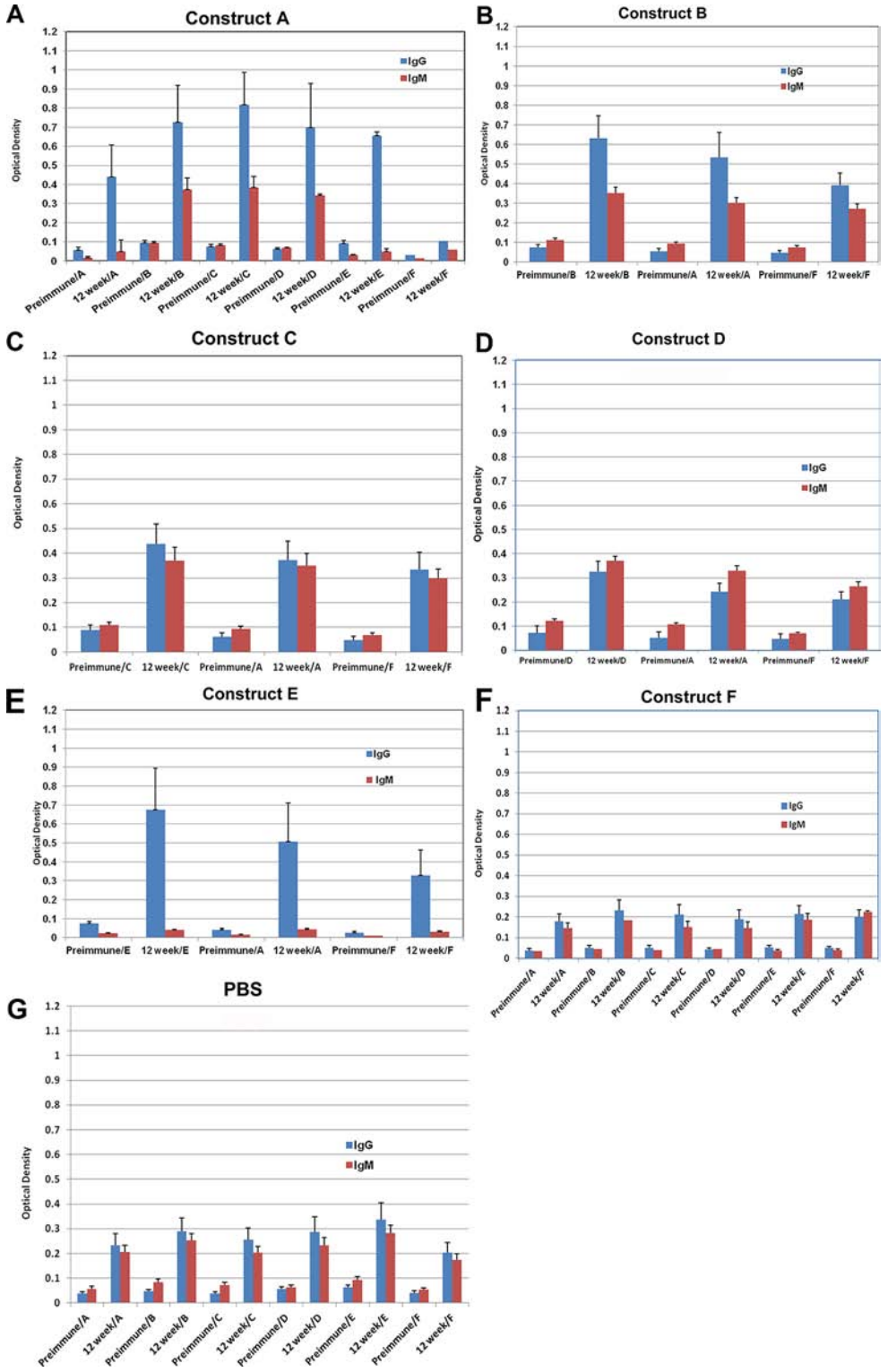


Figure 3. EIA graphs of sera from mice vaccinated with (A) construct **A** (MUC4); (B) construct **B** (5-TF); (C) construct **C** (6-TF); (D) construct **D** (5,6-TF); (E) construct **E** (10-TF); (F) Construct **F** (linker alone); and (G) PBS. The graphs are divided into sets of bars where red represents IgM responses and blue represents IgG response. Preimmune bleeds are in alternate columns followed by responses after 12 weeks to either self-peptide, unglycosylated MUC4 peptide or linker alone for constructs B, C, D, and E. For vaccination with the unglycosylated MUC4 peptide (A), linker alone (F) and PBS (G) responses at preimmune and 12-week stages are shown for all constructs.

producing a high-quality immune response with proper specificity and potency. For this reason, a variety of options need to be explored, and nanoparticle carriers are reasonable choices for reasons already discussed. We have prepared various presentations of the TF antigen on gold particles and have tested some of these in mice for immune responses (Barchi and Rittenhouse-Olson, unpublished); however, the constructions described here with the C3d molecular adjuvant were the only

dx.doi.org/10.1021/bc200606s | *Bioconjugate Chem.* 2012, 23, 1513–1523

Table 3. Summary of Statistically Significant Immune Responses to AuNP Vaccinations

	molecule tested against					
	Self Glycopeptide[a]		MUC4 Peptide[b]		Self-and MUC4 Peptide[c]	
group sera tested	IgG (Pre/ 12wk)[c]	IgM (Pre/ 12wk)	IgG (Pre/ 12wk)	IgM (Pre/ 12wk)	IgG Self-vs MUC-4	IgM Self-vs MUC-4
Group A	ND	ND	+	+	ND	NVD
Group B	+	+	+	+	+	+
Group C	+	+	+	+	+	+
Group D	–	+	–	+	+	+
Group E	+	+	+	+	+	+
Group F*	–	–	–	–	–	–
Group G*	–	–	–	–	–	–

[a]These columns show responses when each construct was tested against the glycopeptides of groups B, C, D, and E. A "+" sign indicates statistical significance between sera from mice collected preimmunization and after 12 weeks with $P \leq 0.05$. [b]Sera from each group were tested against the unglycosylated peptide. Sera from mice vaccinated with all (glyco)peptide-coated AuNPs (A–E) reacted with MUC4 peptide sequence and were statistically significant. [c]These two columns show that reaction of a specific group sera to the "self" glycopeptides was significantly greater than reaction with the unglycosylated MUC4 peptide for both IgG and IgM. NA = Not determined.

ones that gave measurable and statistically significant responses. The provocative differential response of the various structures bodes well for future studies using similar platforms with second-generation epitopes and nanoplatforms. These studies are currently in progress and will be reported in due course.

CONCLUSIONS

Several putative glycopeptide antigens were coated onto gold with a molecular adjuvant in defined densities, resulting in particles that could act as both immunogens and immune system stimulants. The preparation of these fully synthetic GNP constructs encompassed (1) design of appropriate immunogens, (2) choice of molecular adjuvant, and (3) design of robust linker. Synthesis of the particles proceeded without incident to afford multifunctional GNP's. Characterization showed that some constructs were more polydispersed than others, with the linker-coated "control" particles interestingly being the least homogeneous. This is in contrast to our previous particles where shorter linkers were actually the least polydispersed among GNP's with various saccharides.[34] Constructs were prepared with the antigen, molecular adjuvant, and interstitial linker coated in a 1:1:3 ratio, and there was evidence of differential coating. A response in mice was generated to each glycopeptide antigen with statistical significance; this is one of the first reports of an immune response generated to an immunogen coated on gold without the use of additional adjuvants admixed with the vaccine preparation. Further development to enhance the uniformity and immunogenicity of the particles is in progress. These initial data suggest that glycopeptides-bearing nanoparticles have the potential to be part of the repertoire of anticancer vaccine modalities that may have distinct and intriguing therapeutic utility. Details of the comprehensive biological evaluation of these novel particles will be reported in separate publications.

ASSOCIATED CONTENT

Supporting Information

UV–vis spectra of all AuNP constructs, DLS histograms with polydispersity measurements, zeta potential graphs, ^{1}H NMR spectra of all synthetic molecules and AuNP's, and transmission electron microscopy images of AuNP's. This material is available free of charge via the Internet at http://pubs.acs.org.

AUTHOR INFORMATION

Corresponding Author

*E-mail: barchi@helix.nih.gov; 301-846-5905 (VOICE); 301-846-6033 (FAX).

Present Address

[#]Norwegian Medicines Agency Sven Oftedals vei 8, N-0950 Oslo, Norway +47 22 89 77 00 (V) + 47 22 89 77 99 (FAX). E-mail: Andreas.Sundgren@legemiddelverket.no; website www.legemiddelverket.no.

Notes

The authors declare no competing financial interest.

ACKNOWLEDGMENTS

The authors wish to acknowledge Sergey Tarasov and Marzena Dyba of the Biophysics Resource, Structural Biophysics Laboratory, Frederick National Laboratories for Cancer Research for help in obtaining DLS data, and Kunio Nagashima of the Electron Microscopy Laboratory, Advanced Technology Program, Frederick National Laboratories for Cancer Research for TEM images. The intramural Research Program of the Center for Cancer Research, National Cancer Institute is acknowledged for financial support.

REFERENCES

(1) Hakomori, S. I. (1989) Aberrant glycosylation in tumors and tumor-associated carbohydrate antigens. *Adv. Cancer Res. 52*, 257–331.

(2) Dennis, J. W., Granovsky, M., and Warren, C. E. (1999) Glycoprotein glycosylation and cancer progression. *Biochim. Biophys. Acta 1473*, 21–34.

(3) Hanisch, F. A. (2001) O-glycosylation of the mucin type. *Biol. Chem. 382*, 143–149.

(4) Xu, Y. F., Sette, A., Sidney, J., Gendler, S. J., and Franco, A. (2005) Tumor-associated carbohydrate antigens: A possible avenue for cancer prevention. *Immunol. Cell Biol. 83*, 440–448.

(5) Newsom-Davis, T. E., Wang, D., Steinman, L., Chen, P. F. T., Wang, L. X., Simon, A. K., and Screaton, G. R. (2009) Enhanced immune recognition of cryptic glycan markers in human tumors. *Cancer Res. 69*, 2018–2025.

(6) Brockhausen, I. (2003) Glycodynamics of mucin biosynthesis in gastrointestinal tumor cells. *Glycobiol. Med. 535*, 163–188.

(7) Indar, A., Maxwell-Armstrong, C. A., Durrant, L. G., Carmichael, J., and Scholefield, J. H. (2002) Current concepts in immunotherapy for the treatment of colorectal cancer. *Journal of the Royal College of Surgeons of Edinburgh 47*, 458–474.

(8) Cipolla, L., Peri, F., and Airoldi, C. (2008) Glycoconjugates in cancer therapy. *Anti-Cancer Agents Med. Chem. 8*, 92–121.

(9) Slovin, S. F., Ragupathi, G., Musselli, C., Fernandez, C., Diani, M., Verbel, D., Danishefsky, S., Livingston, P., and Scher, H. I. (2005) Thomsen-Friedenreich (TF) antigen as a target for prostate cancer vaccine: clinical trial results with TF cluster (c)-KLH plus QS21 conjugate vaccine in patients with biochemically relapsed prostate cancer. *Cancer Immunol. Immunother. 54*, 694–702.

(10) Lo-Man, R., Vichier-Guerre, S., Perraut, R., Deriaud, E., Huteau, V., BenMohamed, L., Diop, O. M., Livingston, P. O., Bay, S., and Leclerc, C. (2004) A fully synthetic therapeutic vaccine candidate targeting carcinoma-associated Tn carbohydrate antigen induces

tumor-specific antibodies in nonhuman primates. *Cancer Res. 64*, 4987−4994.
(11) Buskas, T., Ingale, S., and Boons, G. J. (2005) Towards a fully synthetic carbohydrate-based anticancer vaccine: Synthesis and immunological evaluation of a lipidated glycopeptide containing the tumor-associated Tn antigen. *Angew. Chem., Int. Ed. 44*, 5985−5988.
(12) Ingale, S., AWolfert, M., Gaekwad, J., Buskas, T., and Boons, G. J. (2007) Robust immune responses elicited by a fully synthetic three-component vaccine. *Nat. Chem. Biol. 3*, 663−667.
(13) Buskas, T., Thompson, P., and Boons, G. J. (2009) Immunotherapy for cancer: synthetic carbohydrate-based vaccines. *Chem. Commun.*, 5335−5349.
(14) Danussi, C., Coslovi, A., Campa, C., Mucignat, M. T., Spessotto, P., Uggeri, F., Paoletti, S., and Colombatti, A. (2009) A newly generated functional antibody identifies Tn antigen as a novel determinant in the cancer cell-lymphatic endothelium interaction. *Glycobiology 19*, 1056−1067.
(15) Heimburg, J., Yan, J., Morey, S., Glinskii, O. V., Huxley, V. H., Wild, L., Klick, R., Roy, R., Glinsky, V. V., and Rittenhouse-Olson, K. (2006) Inhibition of spontaneous breast cancer metastasis by anti-Thomsen-Friedenreich antigen monoclonal antibody JAA-F11. *Neoplasia 8*, 939−948.
(16) Koganty, R. R., Reddish, M. A., and Longenecker, B. M. (1996) Glycopeptide- and carbohydrate-based synthetic vaccines for the immunotherapy of cancer. *Drug Discovery Today 1*, 190−198.
(17) Bay, S., LoMan, R., Osinaga, E., Nakada, H., Leclerc, C., and Cantacuzene, D. (1997) Preparation of a multiple antigen glycopeptide (MAG) carrying the Tn antigen - A possible approach to a synthetic carbohydrate vaccine. *J. Pept. Res. 49*, 620−625.
(18) Kuduk, S. D., Schwarz, J. B., Chen, X. T., Glunz, P. W., Sames, D., Ragupathi, G., Livingston, P. O., and Danishefsky, S. J. (1998) Synthetic and immunological studies on clustered modes of mucin-related Tn and TF O-linked antigens: The preparation of a glycopeptide-based vaccine for clinical trials against prostate cancer. *J. Am. Chem. Soc. 120*, 12474−12485.
(19) Hilaire, P. M. S., Cipolla, L., Franco, A., Tedebark, U., Tilly, D. A., and Meldal, M. (1999) Synthesis of T-antigen-containing glycopeptides as potential cancer vaccines. *J. Chem. Soc., Perkin Trans. 1*, 3559−3564.
(20) Vichier-Guerre, S., Lo-Man, R., Bay, S., Deriaud, E., Nakada, H., Leclerc, C., and Cantacuzene, D. (2000) Short synthetic glycopeptides successfully induce antibody responses to carcinoma-associated Tn antigen. *J. Pept. Res. 55*, 173−180.
(21) Kudryashov, V., Glunz, P. W., Williams, L. J., Hintermann, S., Danishefsky, S. J., and Lloyd, K. O. (2001) Toward optimized carbohydrate-based anticancer vaccines: Epitope clustering, carrier structure, and adjuvant all influence antibody responses to Lewis(y) conjugates in mice. *Proc. Natl. Acad. Sci. U.S.A. 98*, 3264−3269.
(22) Kunz, H. (2003) Synthetic glycopeptides for the development of tumour-selective vaccines. *J. Pept. Sci. 9*, 563−573.
(23) Vichier-Guerre, S., Lo-Man, R., BenMohamed, L., Deriaud, E., Kovats, S., Leclerc, C., and Bay, S. (2003) Induction of carbohydrate specific antibodies in HLA-DR transgenic mice by a synthetic glycopeptide: a potential anti cancer vaccine for human use. *J. Pept. Res. 62*, 117−124.
(24) Xu, Y. F., Gendler, S. J., and Franco, A. (2004) Designer glycopeptides for cytotoxic T cell-based elimination of carcinomas. *J. Exp. Med. 199*, 707−716.
(25) Vichier-Guerre, S., Lo-Man, R., Huteau, V., Deriaud, E., Leclerc, C., and Bay, S. (2004) Synthesis and immunological evaluation of an antitumor neoglycopeptide vaccine bearing a novel homoserine Tn antigen. *Bioorg. Med. Chem. Lett. 14*, 3567−3570.
(26) Dziadek, S., Kowalczyk, D., and Kunz, H. (2005) Synthetic vaccines consisting of tumor-associated MUC1 glycopeptide antigens and bovine serum albumin. *Angew. Chem., Int. Ed. 44*, 7624−7630.
(27) Dziadek, S., Hobel, A., Schmitt, E., and Kunz, H. (2005) A fully synthetic vaccine consisting of a tumor-associated glycopeptide antigen and a T-Cell epitope for the induction of a highly specific humoral immune response. *Angew. Chem., Int. Ed. 44*, 7630−7635.
(28) Liakatos, A., and Kunz, H. (2007) Synthetic glycopeptides for the development of cancer vaccines. *Curr. Opin. Mol. Ther. 9*, 35−44.
(29) Niederhafner, P., Reinis, M., Sebestik, J., and Jezek, J. (2008) Glycopeptide dendrimers, Part III - a review: Use of glycopeptide dendrimers in immunotherapy and diagnosis of cancer and viral diseases. *J. Pept. Sci. 14*, 556−587.
(30) Westerlind, U., Hobel, A., Gaidzik, N., Schmitt, E., and Kunz, H. (2008) Synthetic vaccines consisting of tumor-associated MUC1 glycopeptide antigens and a T-cell epitope for the induction of a highly specific humoral immune response. *Angew. Chem., Int. Ed. 47*, 7551−7556.
(31) Zhu, J. L., Wan, Q., Ragupathi, G., George, C. M., Livingston, P. O., and Danishefsky, S. J. (2009) Biologics through chemistry: total synthesis of a proposed dual-acting vaccine targeting ovarian cancer orchestration of oligosaccharide and polypeptide domains. *J. Am. Chem. Soc. 131*, 4151−4158.
(32) Ryan, S. O., Vlad, A. M., Islam, K., Gariepy, J., and Finn, O. J. (2009) Tumor-associated MUC1 glycopeptide epitopes are not subject to self-tolerance and improve responses to MUC1 peptide epitopes in MUC1 transgenic mice. *Biol. Chem. 390*, 611−618.
(33) Brooks, C. L., Schietinger, A., Borisova, S. N., Kufer, P., Okon, M., Hirama, T., MacKenzie, C. R., Wang, L. X., Schreiber, H., and Evans, S. V. (2010) Antibody recognition of a unique tumor-specific glycopeptide antigen. *Proc. Natl. Acad. Sci. U.S.A. 107*, 10056−10061.
(34) Svarovsky, S. A., Szekely, Z., and Barchi, J. J. (2005) Synthesis of gold nanoparticles bearing the Thomsen-Friedenreich disaccharide: a new multivalent presentation of an important tumor antigen. *Tetrahedron-Asymmetry 16*, 587−598.
(35) Barchi, J. J. (2005) Carbohydrate nanoscience: A new realm for biochemical and therapeutic applications. *Abstr. Pap. Am. Chem. Soc. 229*, U254−U254.
(36) Sundgren, A., and Barchi, J. J. (2008) Varied presentation of the Thomsen-Friedenreich disaccharide tumor-associated carbohydrate antigen on gold nanoparticles. *Carbohydr. Res. 343*, 1594−1604.
(37) De la Fuente, J. M., and Penades, S. (2006) Glyconanoparticles: Types, synthesis and applications in glycoscience, biomedicine and material science. *Biochim. Biophys. Acta 1760*, 636−651.
(38) Goodman, C. M., McCusker, C. D., Yilmaz, T., and Rotello, V. M. (2004) Toxicity of gold nanoparticles functionalized with cationic and anionic side chains. *Bioconjugate Chem. 15*, 897−900.
(39) Ojeda, R., de Paz, J. L., Barrientos, A. G., Martin-Lomas, M., and Penades, S. (2007) Preparation of multifunctional glyconanoparticles as a platform for potential carbohydrate-based anticancer vaccines. *Carbohydr. Res. 342*, 448−459.
(40) Moniaux, N., Andrianifahanana, M., Brand, R. E., and Batra, S. K. (2004) Multiple roles of mucins in pancreatic cancer, a lethal and challenging malignancy. *Br. J. Cancer 91*, 1633−1638.
(41) Sundgren, A., and Barchi, J. (2008) *Carbohydr. Res. 343*, 1594−1604.
(42) Svarovsky, S. A., and Barchi, J. J. (2003) Highly efficient preparation of tumor antigen-containing glycopeptide building blocks from novel pentenyl glycosides. *Carbohydr. Res. 338*, 1925−1935.
(43) Heagerty, P. J., and Zeger, S. L. (2000) Marginalized multilevel models and likelihood inference. *Stat. Sci. 15*, 1−19.
(44) Brust, M., Walker, M., Bethell, D., Schiffrin, D. J., and Whyman, R. (1994) Synthesis of thiol-derivatized gold nanoparticles in a 2-phase liquid-liquid system. *J. Chem. Soc., Chem. Commun.*, 801−802.
(45) Brust, M., Fink, J., Bethell, D., Schiffrin, D. J., and Kiely, C. (1995) Synthesis and reactions of functionalized gold nanoparticles. *J. Chem. Soc., Chem. Commun.*, 1655−1656.
(46) Brocke, C., and Kunz, H. (2003) Synthetic glycopeptides of the tandem repeat sequence of the epithelial mucin MUC4 with tumour-associated carbohydrate antigens. *Synlett*, 2052−2056.
(47) Dziadek, S., Brocke, C., and Kunz, H. (2004) Biomimetic synthesis of the tumor-associated (2,3)-sialyl-T antigen and its incorporation into glycopeptide antigens from the mucins MUC1 and MUC4. *Chem.—Eur. J. 10*, 4150−4162.

(48) Brocke, C., and Kunz, H. (2004) Synthetic tumor-associated glycopeptide antigens from the tandem repeat sequence of the epithelial mucin MUC4. *Synthesis-Stuttgart*, 525−542.
(49) Becker, T., Kaiser, A., and Kunz, H. (2009) Synthesis of dendrimeric tumor-associated mucin-type glycopeptide antigens. *Synthesis-Stuttgart*, 1113−1122.
(50) Glinsky, V. V., Glinsky, G. V., Rittenhouse-Olson, K., Huflejt, M. E., Glinskii, O. V., Deutscher, S. L., and Quinn, T. P. (2001) The role of Thomsen-Friedenreich antigen in adhesion of human breast and prostate cancer cells to the endothelium. *Cancer Res. 61*, 4851−4857.
(51) Zolnik, B. S., Gonzalez-Fernandez, A., Sadrieh, N., and Dobrovolskaia, M. A. (2010) Minireview: nanoparticles and the immune system. *Endocrinology 151*, 458−465.
(52) Alexander, J., del Guercio, M. F., Maewal, A., Qiao, L., Fikes, J., Chesnut, R. W., Paulson, J., Bundle, D. R., DeFrees, S., and Sette, A. (2000) Linear PADRE T helper epitope and carbohydrate B cell epitope conjugates induce specific high titer IgG antibody responses. *J. Immunol. 164*, 1625−1633.
(53) Toapanta, F. R., and Ross, T. M. (2006) Complement-mediated activation of the adaptive immune responses - Role of C3d in linking the innate and adaptive immunity. *Immunol. Res. 36*, 197−210.
(54) Sarrias, M. R., Franchini, S., Canziani, G., Argyropoulos, E., Moore, W. T., Sahu, A., and Lambris, J. D. (2001) Kinetic analysis of the interactions of complement receptor 2 (CR2, CD21) with its ligands C3d, iC3b, and the EBV glycoprotein gp350/220. *J. Immunol. 167*, 1490−1499.
(55) Knopf, P. M., Rivera, D. S., Hai, S. H., McMurry, J., Martin, W., and De Groot, A. S. (2008) Novel function of complement C3d as an autologous helper T-cell target. *Immunol. Cell Biol. 86*, 221−225.
(56) Srinivasan, B., and Huang, X. F. (2008) Functionalization of magnetic nanoparticles with organic molecules: Loading level determination and evaluation of linker length effect on immobilization. *Chirality 20*, 265−277.
(57) Demers, L. M., Mirkin, C. A., Mucic, R. C., Reynolds, R. A., Letsinger, R. L., Elghanian, R., and Viswanadham, G. (2000) A fluorescence-based method for determining the surface coverage and hybridization efficiency of thiol-capped oligonucleotides bound to gold thin films and nanoparticles. *Anal. Chem. 72*, 5535−5541.
(58) Pease, L. F., Tsai, D. H., Zangmeister, R. A., Zachariah, M. R., and Tarlov, M. J. (2007) Quantifying the surface coverage of conjugate molecules on functionalized nanoparticles. *J. Phys. Chem. C 111*, 17155−17157.
(59) Heaven, M. W., Dass, A., White, P. S., Holt, K. M., and Murray, R. W. (2008) Crystal structure of the gold nanoparticle [N(C8H17)(4)][Au-25(SCH2CH2Ph)(18)]. *J. Am. Chem. Soc. 130*, 3754+.
(60) Tracy, J. B., Kalyuzhny, G., Crowe, M. C., Balasubramanian, R., Choi, J. P., and Murray, R. W. (2007) Poly(ethylene glycol) ligands for high-resolution nanoparticle mass spectrometry. *J. Am. Chem. Soc. 129*, 6706−6707.
(61) Maus, L., Spatz, J. P., and Fiammengo, R. (2009) Quantification and reactivity of functional groups in the ligand shell of PEGylated gold nanoparticles via a fluorescence-based assay. *Langmuir 25*, 7910−7917.
(62) Hostetler, M. J., Wingate, J. E., Zhong, C. J., Harris, J. E., Vachet, R. W., Clark, M. R., Londono, J. D., Green, S. J., Stokes, J. J., Wignall, G. D., Glish, G. L., Porter, M. D., Evans, N. D., and Murray, R. W. (1998) Alkanethiolate gold cluster molecules with core diameters from 1.5 to 5.2 nm: Core and monolayer properties as a function of core size. *Langmuir 14*, 17−30.
(63) Lewis, D. J., Day, T. M., MacPherson, J. V., and Pikramenou, Z. (2006) Luminescent nanobeads: attachment of surface reactive Eu(III) complexes to gold nanoparticles. *Chem. Commun.*, 1433−1435.
(64) Almogren, A., Abdullah, J., Ghapure, K., Ferguson, K., Glinsky, V. V., and Rittenhouse-Olson, K. (2012) Anti-Thomsen-Friedenreich-Ag (anti-TF-Ag) potential for cancer therapy. *Front. Biosci. (Schol. Ed.) 4*, 840−863.
(65) Springer, G. F. (1995) T and Tn pancarcinoma markers - autoantigenic adhesion molecules in pathogenesis, prebiopsy carcinoma-detection, and long-term breast-carcinoma immunotherapy. *Crit. Rev. Oncogenesis 6*, 57−85.
(66) Yu, L. G. (2007) The oncofetal Thomsen-Friedenreich carbohydrate antigen in cancer progression. *Glycoconjugate J. 24*, 411−420.

Bioconjugate Chemistry

Article

pubs.acs.org/bc

Glycoengineering Approach to Half-Life Extension of Recombinant Biotherapeutics

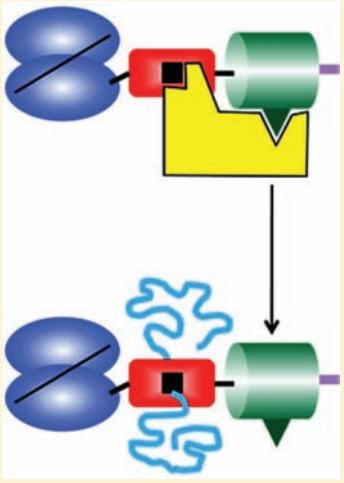
Chen Chen,[†,#] Antony Constantinou,[†,#] Kerry A. Chester,[‡] Bijal Vyas,[†] Kevin Canis,[†] Stuart M. Haslam,[†] Anne Dell,[†] Agamemnon A. Epenetos,[†] and Mahendra P. Deonarain*[,†]

[†]Department of Life Sciences, Faculty of Natural Sciences, Imperial College London, Exhibition Road, London, United Kingdom, SW7 2AZ

[‡]UCL Cancer Institute, Paul O'Gorman Building, 72 Huntley Street, London, United Kingdom, WC1E 6BT

Supporting Information

ABSTRACT: The potential for protein-engineered biotherapeutics is enormous, but pharmacokinetic modulation is a major challenge. Manipulating pharmacokinetics, biodistribution, and bioavailability of small peptide/protein units such as antibody fragments is a major pharmaceutical ambition, illustrated by the many chemical conjugation and recombinant fusion approaches being developed. We describe a recombinant approach that leads to successful incorporation of polysialic acid, PSA for the first time, onto a therapeutically valuable protein. This was achieved by protein engineering of the PSA carrier domain of NCAM onto single-chain Fv antibody fragments (one directed against noninternalizing carcinoembryonic antigen-CEA and one against internalizing human epidermal growth factor receptor-2-HER2). This created novel polysialylated antibody fragments with desired pharmacokinetics. Production was achieved in human embryonic kidney cells engineered to express human polysialyltransferase, and the recombinant, glycosylated product was successfully fractionated by ion-exchange chromatography. Polysialylation was verified by glycosidase digestion and mass spectrometry, which showed the correct glycan structures and PSA chain length similar to that of native NCAM. Binding was demonstrated by ELISA and surface plasmon resonance and on live cells by flow cytometry and confocal immunofluorescence. Unexpectedly, polysialylation inhibited receptor-mediated endocytosis of the anti-HER2 scFv. Recombinant polysialylation led to an estimated 3-fold increase in hydrodynamic radius, comparable to PEGylation, leading to an almost 30-fold increase in blood half-life and a similar increase in blood exposure. This increase in bioavailability led to a 12-fold increase in tumor uptake by 24 h. In summary, recombinant polysialylation of antibody fragments in our system is a novel and feasible approach applicable for pharmacokinetic modulation, and may have wider applications.



INTRODUCTION

The clinical and commercial success of therapeutic antibodies has led to a proliferation of alternative formats[1] and non-antibody alternative scaffolds.[2] This has been driven, in part, by the limitations of whole immunoglobulin in some targeted applications. Their relatively large size and poor tumor vascularization impedes tissue penetration.[3,4] Furthermore, in immuno-compromised patients and within the immuno-suppressed microenvironment of the tumor the Fc effector/recruitment function of whole antibodies becomes largely redundant.[5] Finally, the Fc domain can cross-react with normal tissues, which can also lead to unwanted side effects, particularly when cytotoxin-loaded antibodies are used. Binding ligands devoid of Fc-regions such as nanobodies, scFvs, anticalins, and DARPins are being developed.[1,2] Being smaller, they are capable of more rapid tissue penetration but clear from the system rapidly thus decreasing the therapeutic window. There is a need for noninvasive technologies to increase small protein half-life, without the disadvantages associated with the Fc-domain.

Polymer conjugation using poly(ethylene glycol) (PEGylation) has been one of the most successful approaches to increasing protein serum half-life. PEG is a neutral polymer that can bind water molecules, forming an "aqueous cloud" around the protein.[6,7] This gives the conjugate a larger hydrodynamic volume compared to its true molecular weight, affecting its pharmacokinetics and pharmacodynamics in the body. Increasing protein size to above 60−70 kDa (or around 50 Å in diameter) excludes it from glomerular filtration and maintains its bioavailability.[8] In addition to its size, the protein surface is modified and biological epitopes are shielded from potential immune responses or degradation.[6−8]

However, the use of synthetic nonbiodegradable polymers has raised concerns. The primary reason for this is the discovery that, when PEG is used for chronic conditions, PEGylated peptides or byproducts have been reported to

Received: November 17, 2011
Revised: June 2, 2012
Published: June 9, 2012

ACS Publications © 2012 American Chemical Society

dx.doi.org/10.1021/bc200624a | Bioconjugate Chem. 2012, 23, 1524−1533

accumulate in tissues and cause unforeseen toxic effects (e.g., kidney cells vacuolizaton[9]) and/or generate an immune response.[10] As such, a new generation of biodegradable biopolymers are now being investigated as candidates to supersede PEG technology by addressing these concerns. These technologies include HEPylation (heparosan polymer), HESylation (hydroxyethyl starch[7]), and the most extensively studied, polysialylation (polysialic acid). Polysialic acid (PSA) is a highly hydrophilic and negatively charged biopolymer that is extensively found in nature. On pathogenic bacteria, PSA (columinic acid) is a capsular virulence factor and is involved in protecting against phagocytosis and immune clearance.[11] PSA has similar properties to PEG, including the ability to associate with 5−10 times its mass of water increasing its hydrodynamic volume, hiding immunogenic epitopes, and increasing overall conjugate solubility and stability.[12−14] These properties have led to commercialized use of chemically linked PSA,[15] and early clinical data have shown that polysialylated erythropoietin is well-tolerated in patients.[12]

We have recently examined the chemical conjugation of PSA onto antibody fragments, showing that their systemic half-life and bioavailabilty can be significantly increased while maintaining better tumor/blood ratios than whole immunoglobulins.[12−14] However, limitations such as loss of antibody binding, long processing times, and poor conjugate yields were observed.

In humans, PSA is found predominantly on NCAM where it has a role in lubricating interactions and cell migration and promoting the plasticity of neuronal cells in early brain development.[16] We hypothesized that a recombinant human-based approach to heterologous protein polysialylation would have many biotechnological advantages over chemical approaches (e.g., retention of function and product yields). This could lead to the target therapeutic being made in its final form with no further manipulations necessary in a fully human form. Although glyco-engineering of biotechnologically important proteins is an advanced and evolving field, with applications ranging from increased potency[17] to longer half-life,[18] there was no existing means to recombinantly attach PSA onto heterologous proteins. Therefore, we set out to develop such a technology based on NCAM which is naturally polysialylated and shares homology with antibody immunoglobulin domains.

EXPERIMENTAL SECTION

Reagents. N-A1 (CEA subdomain which bears the epitope for MFE-23) was expressed from *Pichia pastoris* and purified by IMAC.[19] Recombinant HER2 (hErbB2/Fc) was from R&D system Ltd. All standard antibodies were from Sigma, but specific clones were as follows: Anti-NCAM (CD56, mouse monoclonal clone 123C3 recognizing NCAM epitope between exons 11−13, first fibronectin type-III, FN1, Abcam); Anti-PSA (rat monoclonal IgM clone-12F8, recognizing the polysialic acid on NCAM, with sialic acid residue number >7, BD Pharmingen); Endo-Neuraminidase (Endo-N from Phage K1 0.7, recognizing α2−8 linked sialyl residues, requiring a minimum of 5 sialyl residues for activity (Abcys)); Acetylneuraminyl hydrolase (Exo-N, *Clostridium perfringens* α2−3,α2−6 sialidase, New England Biolabs); N-Glycosidase F (PNGase F- *Flavobacterium meningosepticum* amidase that cleaves between the innermost GlcNAc and asparagine residues of high mannose, hybrid, and complex oligosaccharides from glycoproteins; New England Biolabs). Healthy female BALB/c nude mice (6−8 weeks old) were from Harlan UK and all in vivo work was carried out under Home Office Project License: 70/6982 under Dr. Deonarain, Imperial College London.

Cell Transfections, Selections, and Expression. HEK cell transfections were done using Fugene HD (Roche) in serum-free DMEM media using 3×10^6 cells in 10 cm tissue-culture dishes and 10 μg/40 μL of Fugene HD. Double transfection was achieved by mixing both plasmid DNA (10 μg each) and 80 μL of Fugene HD. For stable cell selection, cells were washed with PBS, trypsinized, and reseeded in complete DMEM media with Zeocin (1 mg/mL) or G418 sulfate solution (1 mg/mL). The surviving transfected cells formed monoclonal cell colonies, which were expanded and maintained in 0.25 mg/mL antibiotic. Selected colonies on the plate were picked by trypsin-soaked 5 mm sterilized paper and transferred into a 24-well plate where they were expanded and stored. Recombinant protein-expressing cells were grown in Freestyle-293 expression medium, supplemented with 4 mM L-glutamine. Valproic acid (1 mM) was included in the culture media to enhance polysialyl-transferase (PST) enzyme expression as suggested by previous researchers.[20] Clones were identified by protein expression level using dot-blots and ELISAs.

Prior to HEK293 cells, initial experiments were carried out in a rat neuronal cell line (NB2a) which was expected to express high levels of polysialylated NCAM. However, none of the derived clones displayed significant polysialylation. Successful polysialylation was also achieved in CHO and HeLa cells coexpressing PST.

Enzyme-Linked Immunosorbent Assay (ELISA). Antigens were immobilized on the surface of 96-well Nunc immunosorb plates overnight at 4 °C in Tris-buffered saline-TBS, pH 7.8 (100 ng/well for biotinylated N-A1 and hErbB2-Fc). Biotinylation was carried out at a minimal 1:1 ratio using SulphoNHS-LC-LC-Biotin (Pierce). All incubations were carried out in PBS+3% Marvel milk protein and all washes in PBS+0.01% Tween-20 followed by PBS. All binding incubations were at 37 °C for at least 1 h. For biotinylated antigens, plates were precoated in 20 μg/mL avidin. A serial dilution of samples (scFvs or scFv fusion proteins) was prepared with a typical range between 5000 and 0.05 nM in triplicate. Detection was achieved using the relevant horseradish peroxidase conjugated secondary antibodies. Development was with BM Blue POD substrate. Absorbance at 450 nm was measured on a Spectramax 340pc plate reader. The equilibrium dissociation constant (K_D) determinations were fitted, using *Sigmaplot* v 11, to a standard three-parameter sigmoid curve.

Surface Plasmon Resonance. Real-time binding analysis of MFE23 scFv and its fusions was performed on a BIAcore 3000 instrument. The running buffer was 100 mM Tris buffer pH 7.4 containing 300 mM NaCl, 0.005% P20 surfactant, and 0.005% sodium azide. All experiments were carried out using double referencing. A streptavidin (SA) sensor chip was immobilized with 700−900 resonance units (RU) of biotinylated N-A1. For kinetic measurement experiments, a serial dilution containing a concentration range of 50 to 0.4 nM of each MFE23-based fusion protein sample was prepared in the running buffer. The standard kinetic wizard was used including blank buffer injections. Regeneration was with 10 mM HCl for 60 s. Evaluation of the kinetic data was with the *BIAevalution* software (v 4.1) employing a global fit to the 1:1 (Langmuir) binding model correcting for spikes and bulk shifts.

Chromatography. Cobalt metal affinity resin (TALON) run in TBS was used to purify the proteins with 2 mL TALON

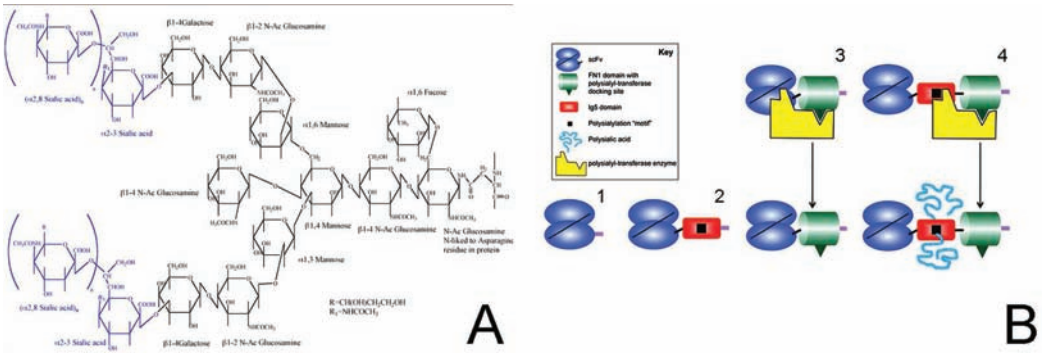


Figure 1. Schematic illustration of PSA fusion protein structures. (A) Glycan structure of the polysialylated core on NCAM Ig5 for reference. (B) Cartoon illustrations of the fusion proteins with the scFv-Iq5-FN1 protein attaining recombinant polysialylation (blue line) after enzymic processing (scheme 4). The controls cannot achieve polysialylation (schemes 1−3).

resin was used for 500 mL dialyzed cell culture medium. Protein was eluted in cold 200 mM imidazole in TBS. Further purification of proteins with different degrees of polymerization (DP) after IMAC purification was achieved by anion exchange chromatography based on the negative charge nature of sialic acid. A 1 mL AcroSep Chromatography column with strong anion exchanger Q-Ceramic HyperD F was used connected to a BIO-RAD BioLogic DuoFlow liquid chromatography system with QuadTec UV−vis detector for simultaneous wavelengths monitoring. Tris buffer (100 mM, pH 7.0) was used as the chromatography buffer with a NaCl step elution. Low salt (0.1 M NaCl) buffer eluted the non-PSA containing scFv-Ig5-FN1, whereas 0.2 M NaCl eluted low-PSA containing proteins. A long wash was used to remove all of these species before a high salt (1 M NaCl) wash eluted the highly polysialylated scFv fusion protein. Pure proteins were analyses by SDS-PAGE and quantified by Nanodrop using extinction coefficients of 97 750 M^{-1} cm^{-1}, which was determined from the protein amino acid sequence using ProtParam on the ExPASy Server (http://www.expasy.ch/tools/protparam.html). Size exclusion chromatography (SEC) was used for the determination of protein apparent hydrodynamic volume. HiLoad Superdex-200 prep grade column (MW range 10−600 kDa, bed volume 120 mL) was used on a BIO-RAD BioLogic DuoFlow system with Quadtec. The running buffer was TBS at 1 mL/min.

Glycosidase Treatments. Typically, excess amounts of each were used to hydrolyze the oligosaccharides from the various proteins (less than 10 μg, incubated overnight incubation at 37 °C). For Endo-Neuraminidase, 2 units of the enzyme was used in PBS buffer. For Exo-N, 25 units was used with 1×G1 Reaction Buffer (50 mM sodium citrate, pH 6.0). Before PNGase F hydrolysis, proteins were denatured with 1× "Glycoprotein denaturing buffer" (which contains a final concentration of 0.5% SDS and 40 mM DTT) in a total volume of 10 μL at 100 °C for 10 min. Together with the addition of 1% NP-40 and 1× G7 Reaction Buffer (50 mM sodium phosphate, pH 7.5), 20 units of PNGase F was used.

Confocal Laser Scanning Immunofluorescent Microscopy. Confocal laser scanning microscopy (CLSM) was used for tracking live cell (LS174T-CEA expressing and SKOV3-HEr2 expressing) surface antigen binding and internalization processes. Secondary antibodies, such as anti-*myc*, anti-6×His, anti-FN1, or anti-PSA antibodies were used. Full details are described in the Supporting Information.

MALDI-TOF Mass Spectrometry Analyses. Carboxymethylated tryptic fragments were prepared and purified. The glycans were released by PNGase F digest and extracted using a Sep-pak C_{18} reverse-phase column. Aliquots of purified native oligosaccharides were spotted onto a MALDI TOF-MS target and allowed to dry. The dried samples were lactonized by addition of 1 μL of a 0.1% *ortho*-phosphoric acid solution. Lactonized samples were dissolved in 1 μL of the ATT matrix (20 mg/mL 6-aza-2-thiothymine in 50:50 acetonitrile/50 mM ammonium citrate) and allowed to dry. Matrix assisted laser desorption ionization/time of flight (MALDI-TOF) MS analyses were performed using a Voyager DE-STR (Applied Biosystems) mass spectrometer in the linear negative mode with delayed extraction. For the N-glycan cores and PSA, aliquots of native N- and O-linked oligosaccharide samples were subjected to digestion by endoneuraminidase. Permethylated glycans were extracted in chloroform and washed several times with dH_2O, prior to a C_{18} purification step of the derivatized glycans. Permethylated glycans were dissolved in 10 μL of 1:1 methanol/water. One μL was mixed with 1 μL of the DHB matrix (10 mg/mL of 2,5-dihydroxybenzoic acid in 50:50 methanol/water) and was spotted onto a MALDI-TOF/TOF plate and allowed to dry under vacuum. MS and MS/MS analyses were performed using a 4800 MALDI TOF/TOF mass spectrometer (Applied Biosytems) in the reflectron positive mode with delayed extraction. In MS/MS mode, the collision energy was set to 1 kV and argon was used as collision gas. The instrument was calibrated using [Glu1]-fibrinopeptide G human as external calibrant. All data were acquired using the 4000 Series Explorer Instrument Control Software and were processed using Data Explorer MS processing software. Full technical details and conditions are described in the Supporting Information.

Mouse Pharmacokinetic and Biodistribution Studies. Protein samples were dialyzed PBS buffer prior to iodination. Pierce Pre-Coated Iodination tubes were used to radio-iodinate the protein samples. Direct iodination was carried out inside the tubes according to the manufacturer's protocol, but this led to overiodination and oxidation of the PSA. A more gentle iodination was carried out by removing the activated ^{125}I and radiolabeling in a clean tube, To stop the reaction, 50 μL of scavenging buffer (10 mg/mL tyrosine) in PBS was added. All samples were dialyzed into PBS were sterilized through a 0.2 μm PES syringe filter before injecting to the mice. Up to 200 μL (~10 μg) of each radiolabeled fusion protein was injected intravenously into the mouse tail vein. For blood pharmacokinetic studies, groups of 4−6 BALB/c mice were used for each protein sample test. At the appropriate time points after

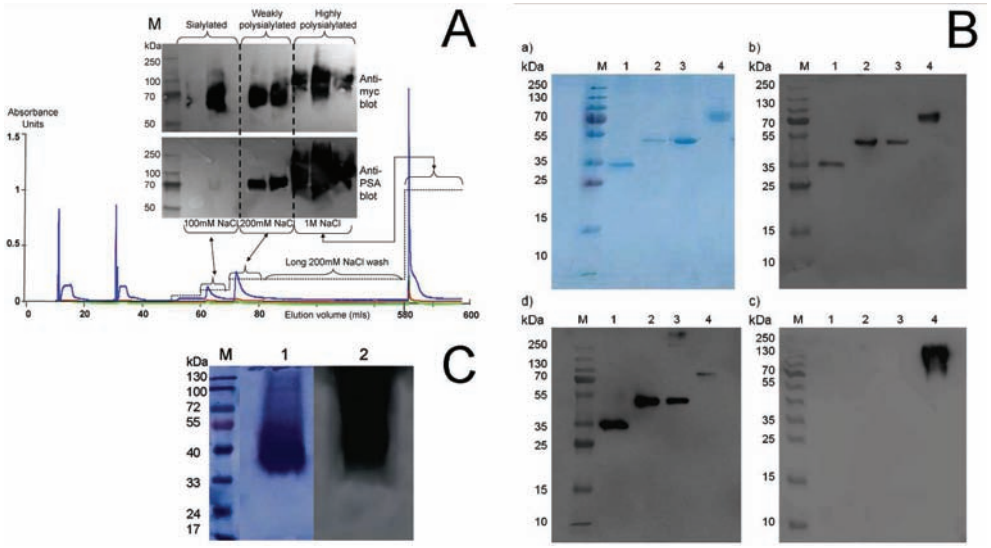


Figure 2. Production and purification of scFv-NCAM fusion proteins. (A) Chromatogram trace of the purification of various polysialylated species based on degree of negative charge, using increasing NaCl steps to elute proteins. Inset is an antimyc blot (to detect entire protein) and an anti-PSA blot (to detect polysialylated protein) showing that the 1 M NaCl buffer eluted the highly polysialylated protein. Around 70% of the applied material eluted as highly polysialylated. (B) SDS-PAGE (a, Coomassie-stained) and Western blotting (b, anti-Myc; c, anti-MFE23; and d, anti-PSA) all confirmed that the correct full-length proteins had been produced and isolated bearing the correct molecular weight. The polysialylated protein appeared as a more diffuse band, especially when detected with the anti-PSA antibody which detects longer chains of PSA. The SDS-PAGE (and calculated) molecular weights were as follows: Lane 1, scFv 28 kDa (29.2 kDa); Lane 2, scFv-FN1 48 kDa (43.7 kDa); Lane 3, scFv-Ig5 49 kDa (44.3 kDa); Lane 4, scFv-Iq5-FN1 75 kDa (53.6 kDa + (0.29 × PSA DP). (C) An 11 kDa bacterial PSA, chemically attached to a scFv, is shown for comparison showing a greater range of heterogeneity.

injection, a cut was made in the mouse tail tip, and 20 μL of blood was taken from each mouse by using microhematocrit capillary tubes. Blood radioactivity was determined by gamma counting and values converted to percentage of injected dose per gram of tissue. For analyzing the in vivo blood clearance, pharmacokinetics data were fitted to the two-compartmental intravenous model of clearance, which takes into account the biexponential clearance pattern of systemic molecules. Tumor and normal tissue uptake was determined in groups of 4 mice culled at two time points using proteins radiolabeled as above injected into BALB/c nude mice bearing subcutaneously implanted LS174T tumors.[14] All tissues were weighed and counted and the uptake expressed as the percentage per gram tissue of injected sample.

RESULTS

Construction and Production of scFv-NCAM Based Fusion Proteins. Colley and co-workers have described substantial and elegant research mapping out the important features of NCAM polysialylation.[21,22] They discovered that the N-linked core glycosylation motif on the fifth immunoglobulin (Ig5) domain was the acceptor for sialic acid polymerization[21,22] (Figure 1a), which was catalyzed by polysialyltransferase enzymes docking onto the juxtaposed first fibronectin (FN1) domain, which lies C-terminal to the five immunoglobulin domains of the polymeric glycoprotein.[22] We proposed that the Ig5 domain could be used as a carrier for PSA on alternative proteins, such as antibody fragments. We constructed a series of anticarcinoembryonic antigen[23] single-chain Fv-fusion proteins (Supporting Information Figure 1 and Figure 1b) to test this idea and transfected the DNA constructs into human embryonic kidney (HEK293) cells which were already transgenically expressing a human polysialyltransferase enzyme, PST/ST8SiaIV[24] (STX/ST8SiaII[24] also gave similar results; not shown). Individual clones expressing recombinant proteins of all types were selected, cultured, and screened for binding activity by ELISA. All clones were screened for binding with anti-His_6 or antimyc secondary antibodies. ScFv-fusion clones that were designed to be polysialylated (polysialylated scFv: scFv-Ig5-FN1) were additionally screened with an anti-PSA antibody which detects PSA chain lengths (degree of polymerization, DP) of greater than 5 sialic acid units.[25] Positive clones were identified, expanded, adapted to serum-free media, and purified by metal affinity chromatography. Polysialylated scFvs were further purified to separate non-PSA, low-PSA, and high-PSA glycoforms by anion exchange chromatography (Figure 2a). No carry-over of contaminants such as autopolysialylated polysialyltransferase enzymes was seen.

Full protein chemical and glycosylation characterization was confirmed by Western blotting (Figure 2b) demonstrating scFv polysialylation and full-length protein production (Figure 2b). All proteins were expressed and purified well (yields were around 2−5 mg/L cell culture) and migrated as expected on SDS-PAGE (Figure 2b). The polysialylated scFv displayed a polydisperse migration pattern (around 70 kDa) confirming various degrees of polysialylation. SDS-PAGE, although indicative of molecular weight, is likely to be misleading due to the steric hindrance of PSA influencing migration. The polysialylated scFv dispersity was lower than chemically produced polysialylated antibodies as judged by immunoblotting (Figure 2c) indicating a higher-quality, better polysialylated product.

Characterization of the Glycans on scFv-NCAM-Based Fusion Proteins. Glycosidase treatment was used to verify that various glyco-species were present (Figure 3a). Three scFv glyco-isoforms differing by the degree of polysialylation showed corresponding band shifts by different sialic acid hydrolyzing

dx.doi.org/10.1021/bc200624a | Bioconjugate Chem. 2012, 23, 1524−1533

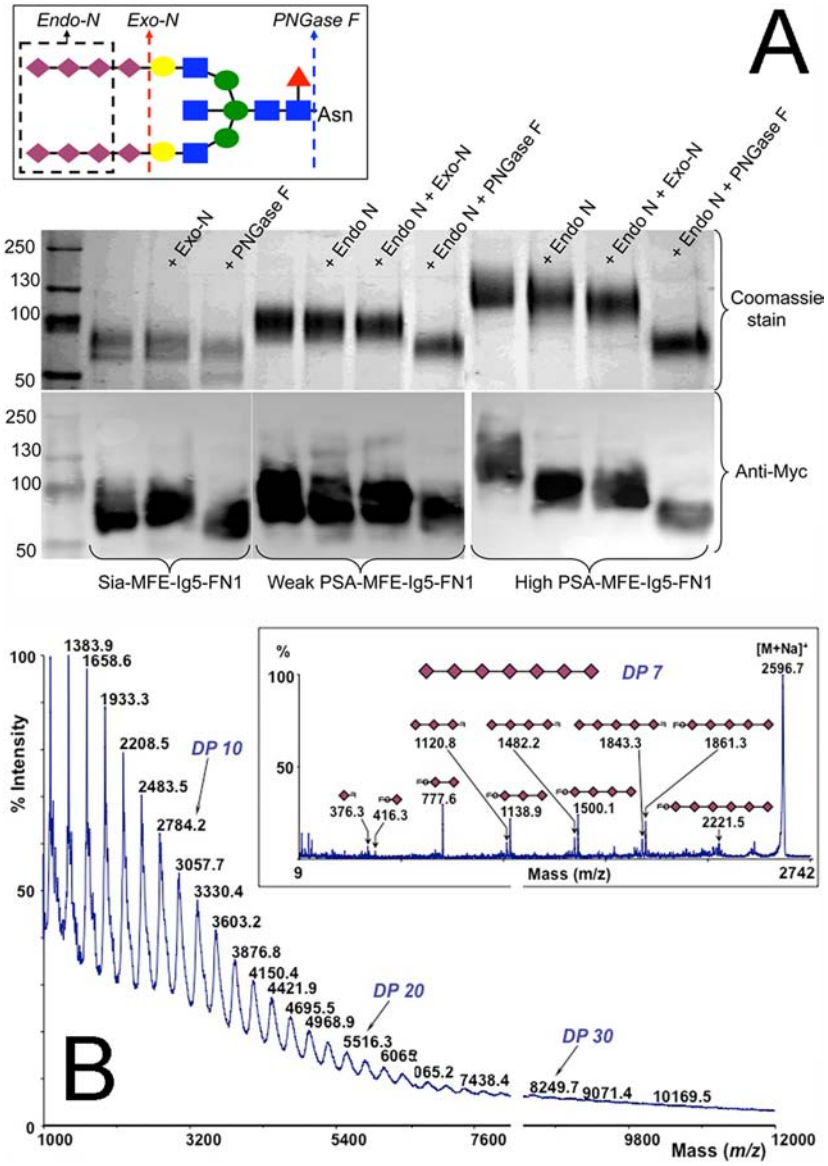


Figure 3. Glycosylation characterization of the scFv-NCAM fusion proteins. (A) Glycosylation status of the scFv-fusion proteins was verified by exo-N (which cleaves 2,3- or 2,6-linked sialic acids), endo-N (which cleaves 2,8- or 2,9-linked sialic acids) and PNGase F (which cleaves the entire N-linked glycan core). Protein band shifts were revealed by both Coomassie staining and anti-Myc immunoblotting. The Endo-N treatment results in a significant shift in molecular weight for the highly polysialylated scFv only. (B) Characterization of PSA levels were determined by MALDI-TOF mass spectrometry. N-Glycans released from the scFv-Iq5-FN1 protein by PNGase F digestion were lactonized prior to analyses. The linear negative ion mode MS spectrum shows the detection of a population of 273 Da unit oligomers corresponding to lactonized neuraminic acid chains up to about 35 residues long. In order to confirm the nature of these oligomers, the PSA extensions were digested by an endoneuraminidase followed by permethylation and analyses by MS/MS. The resulting reflectron positive mode MALDI-TOF/TOF MS/MS spectrum (inset) provides a diagnostic fragmentation pattern undoubtedly confirming the nature of the neuraminic acid chains.

glycosidases and eventually reached the same molecular weight level after N-glycan removal. Conventional mass spectrometry glycomics was able to determine the core N-glycosylation (Supporting Information Figure 2). However, the distribution of the oligo-sialylation status was not determinable. The degree of terminal polysialylation of the highly polysialylated scFv was also not possible by conventional techniques. A modification of the procedure reported by Galuska[26] was carried out utilizing PSA lactonization to stabilize the labile sugars during MALDI-TOF mass spectrometry. Analyses of N-glycans released from the polysialylated scFv by PNGase F digestion were performed in the linear negative ion mode (Figure 3b). A heterogeneous population oligomers comprising lactonized sialic acid units (273 Da) was detected up to about 35 residues long, confirming the high polysialylation level of the scFv glycoprotein. In addition, treatment of the native glycans by endoneuraminidase followed by permethylation and MS and MS/MS analyses on a MALDI-TOF/TOF instrument confirmed the presence of a linear oligomer of sialic acids and revealed the nature of the N-glycan cores (Figure 3b and Supporting Information Figure 2). In contrast, the same analyses undertaken on the post PNGase F fraction focusing on potential O-glycans did not provide any signals, showing that polysialylation, very similar to the level found on human NCAM,[26] occurs only on N-glycans of the scFv.

dx.doi.org/10.1021/bc200624a | *Bioconjugate Chem.* 2012, 23, 1524–1533

Table 1. Binding Constants of the Various MFE-23 Based scFv-NCAM Fusion Proteins[a]

scFv sample	ELISA K_d (nM)	SPR K_d (nM)	SPR k_{on} (M^{-1} s^{-1})	SPR k_{off} (s^{-1})
scFv	4.3 ± 0.6	5.7	(6.3 ± 0.2) × 10^4	(3.6 ± 0.2) × 10^{-4}
scFv-Ig5	9.4 ± 1.9	ND	ND	ND
scFv-FN1	17.5 ± 3.9	ND	ND	ND
scFv-Ig5-FN1(Sia)	13.9 ± 1.5	7.4	(4.7 ± 0.6) × 10^4	(3.5 ± 0.4) × 10^{-4}
scFv-Ig5-FN1(low-PSA)	8.3 ± 0.7	6.1	(9.2 ± 0.4) × 10^4	(5.6 ± 0.5) × 10^{-4}
scFv-Ig5-FN1(high-PSA, CM3)	6.0 ± 0.6	13.8	(2.1 ± 0.3) × 10^4	(2.9 ± 0.1) × 10^{-4}
scFv-Ig5-FN1(high-PSA, CM5)	5.9 ± 0.5	141	(3.9 ± 0.3) × 10^3	(5.5 ± 0.9) × 10^{-4}

[a]Equilibrium dissociation constants determined by ELISA on immobilized NA1 antigen and kinetic constants/equilibrium dissociation constants determined by BIACore SPR on low-dextran, CM3 chip-immobilized NA1 antigen. The SPR data was modeled to a 1:1 Langmuir binding equation which resulted in a good fit with χ^2 values all less than 5% of R_{max}. The anti-CEA K_d values determined by ELISA were all consistent with the published affinity of the MFE23 scFv (4 nM).[34] The K_d value determined by SPR correlated with the ELISA data, but diffusion effects were seen when using a more dense and charged CM5 surface. This resulted in a lower association rate and hence K_d. ND-Not determined.

Antigen Binding Characterization. The various scFv-fusion proteins were tested for both binding function by ELISA and surface plasmon resonance (SPR) kinetic analyses (Table 1). ELISA binding studies showed that the affinities as measured by equilibrium dissociation constants were similar (K_d = 3−10 nM), suggesting little or no detrimental effect due to the fusion domains and resulting glycosylation (Table 1). This was consistent with our previous work with C-terminal chemically conjugated PSA.[14] BIAcore SPR using a low-density matrix surface gave similar affinities and component on- and off-rates (Table 1). However, a noticeable decrease in association rate of the polysialylated species was observed when using a high-density carboxy-methyl dextran/antigen matrix, suggesting some biophysical interactions (see Discussion).

Cell Binding Studies. With the "front end" (antigen binding) and "back end" (effector function-polysialylation) characterized, we tested the ability of the various scFv derivatives to bind to live cells in vitro and its behavior in vivo. To make a comparison, we additionally made a series of similar fusion proteins with an anti-HER2 internalizing scFv, C6.5.[27] This was expressed/purified and characterized in the same way as the anti-CEA MFE23 scFv proteins. Live cell binding was determined by confocal immunofluorescent microscopy on antigen-expressing and antigen-negative cell lines. The anti-CEA based scFv-NCAM fusion proteins all bound to CEA-expressing LS174T cells with no significant binding to antigen negative KB cells (Supporting Information Figure 3). A similar observation was made using flow cytometry, where all the anti-CEA scFv-NCAM fusion proteins bound similarly to LS174T cells, with negligible binding to KB cells (Supporting Information Figure 4). Anti-PSA antibody successfully detected the polysialylated scFv only. These observations also support the previous findings of Constantinou et al. using chemically conjugated PSA[14] where we observed a lack of nonspecific binding to normal tissues in vivo. Interestingly, the anti-HER2 based polysialylated fusion protein was able to bind but not internalize to any significant level at 37 °C. This was in contrast to the nonpolysialylated anti-HER2 scFv (Figure 4). This suggested that polysialylation, in some instances, could interfere with internalization.

Hydrodynamic Volume, Pharmacokinetic and Tumor Uptake Effects. The low and high levels of polysialylation resulted in an increased hydrodynamic volume as determined by size-exclusion chromatography (Supporting Information Figure 5). This confirmed that the PSA sugars were functioning as a water-retaining biopolymer. The highly polysialylated scFv had an apparent molecular weight of over 700 kDa. Compared to BSA (hydrodynamic diameter of around 35 Å, molecular weight of 66 kDa), which migrates true to its molecular weight by SEC,[28] the highly polysialylated scFv was estimated to have a radius of up to 78 Å, an almost 3-fold increase compared to that predicted for the nonpolysialylated proteins. This is clearly above the renal exclusion limit[29] and comparable to the effects of protein PEGylation.[6] This increase in hydrodynamic volume and consequently increased apparent mass led to an increase in blood half-life in vivo (Figure 5a; Table 2). This pharmacokinetic modulatory function led to a moderate increase in distribution half-life ($t_{1/2}$ α), a 29.6-fold increase in blood elimination half-life ($t_{1/2}$ β) and thus a 28.8-fold increase in overall blood bioavailability. The longer half-life in the blood allowed greater tumor exposure resulting in 19.5% injected dose/gram tissue being taken up by the tumor by 6 h and 21.4% by 24 h, a 7-fold and 12-fold increase, respectively (Figure 5b). Concomitantly, there were higher levels in polysialylated scFv in all the other organs, but there was no suggestion of nonspecific cross reactivity. As expected and also seen for chemically polysialylated scFvs, the tumor/blood ratios were lower due to the longer presence of the proteins in blood. Therefore, the achieved recombinant polysialylation technology was able to extend the half-life of an antibody fragment as well as chemical polysialylation and approaching PEGylation.

DISCUSSION

In many technological applications, recombinant approaches supersede chemical methods due to the direct and simplified systems used. However, the commercial value of chemical polysialylation or PEGylation has driven its development to be a highly efficient and established process. A direct comparison showed that, for the recombinant polysialylation, protein yields were on average 5 mg/L/day, representing a yield of at least 50% of the expressed material (10 mg/L). This is substantially higher than the 1 mg obtained from a 10% yielding chemical process (10 mg starting material) in our hands.[14] The polysialylated scFv dispersity was lower than chemically produced polysialylated antibodies as judged by immunoblotting, indicating a better polysialylated product. Recombinant protein could be isolated within a day from expression, compared to 2−3 days for a chemical approach.[14]

This reduced association rate "phenomenon" observed on a BIACore chip surface was explored by Pluckthun's group[30] investigating the binding of PEGylated scFvs by SPR. They similarly observed reduced association rates, which they attributed to the SPR system rather than an actual reduction

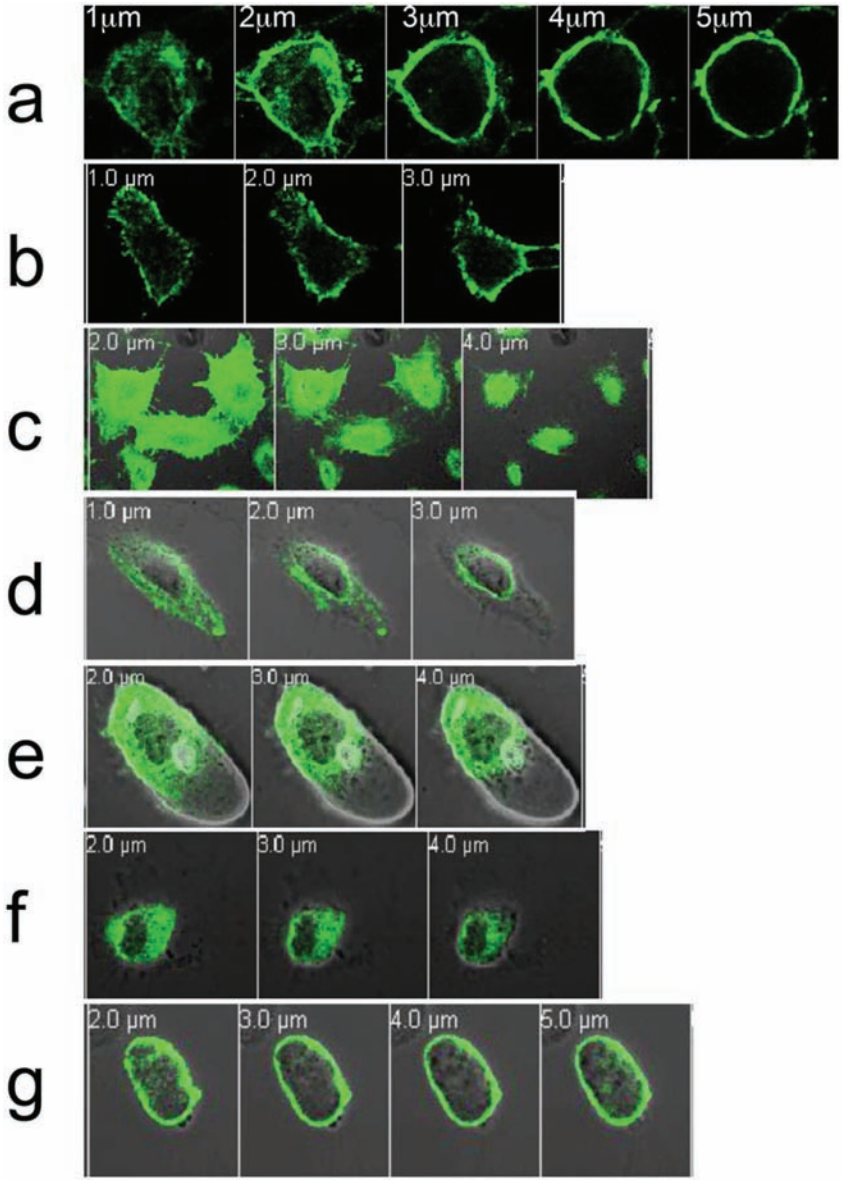


Figure 4. Internalization properties scFv-NCAM fusion proteins. A comparison of the binding and internalization properties of anti-CEA and anti-HER2 based scFv-Iq5-FN1 fusion proteins: (a) anti-CEA scFv-Iq5-FN1(PSA) on LS174T cells at 37 °C, (b) anti-HER2 IqG on SKOV3 cells at 4 °C, (c) anti-HER2 IgG on SKOV3 cells at 37 °C, (d) anti-HER2 scFv on SKOV3 cells at 37 °C, (e) anti-HER2 scFv-FN1 on SKOV3 cells at 37 °C, (f) anti-HER2 scFv-Iq5-FN1(Low PSA) on SKOV3 cells at 37 °C, (g) anti- HER2 scFv-Iq5-FN1(high PSA) on SKOV3 cells at 37 °C. Panels (a) and (b) show cell surface binding with little significant internalization, whereas panel (c) shows complete and significant internalization. Panels (d) to (f) show lower levels of internalization, whereas the highly polysialylated scFv (panel g) shows cell surface only binding comparable to (a) and (b).

of affinity. The large hydrodynamic volume of PEG (and here, PSA) could impede scFv-antigen association by sterically blocking epitopes/paratopes, slowing diffusion, or, potentially significant for PSA, negative dextran surface−PSA repulsion.[30] This finding also supports the biophysical data suggesting increased hydrodynamic volume, but it may have implications for the type of application best suited to such charged polymer−conjugates.

The increased hydrodynamic volume achieved using the recombinant polysialylation technology was able to extend the half-life of an antibody fragment more effectively than the chemical polysialylation methods used previously in our laboratory. Here, a 10- to 15-fold increase in half-life/bioavailability is seen with a 11 kDa PSA chain),[14] whereas the recombinantly applied PSA chain appears to be around 5−8 kDa. It is possible that the recombinantly applied PSA is longer and underestimated by the mass spectrometry due to the difficulty and complexities in obtaining a spectrum. It is clear that the PSA chain is the major determining factor in modulating the half-life. The increase in protein molecular weight (around 24 kDa) did not seem to affect the half-life as seen in the blood clearance studies. It is possible that there were minor effects due to the changes in protein pI which were not investigated. One should consider the possibility of refining the NCAM fusion proteins to possess the minimal protein sequences needed to achieve recombinant polysialylation. This would require a lot of protein design, but toward this we attempted to engineer a protease cleavage site between the Ig5

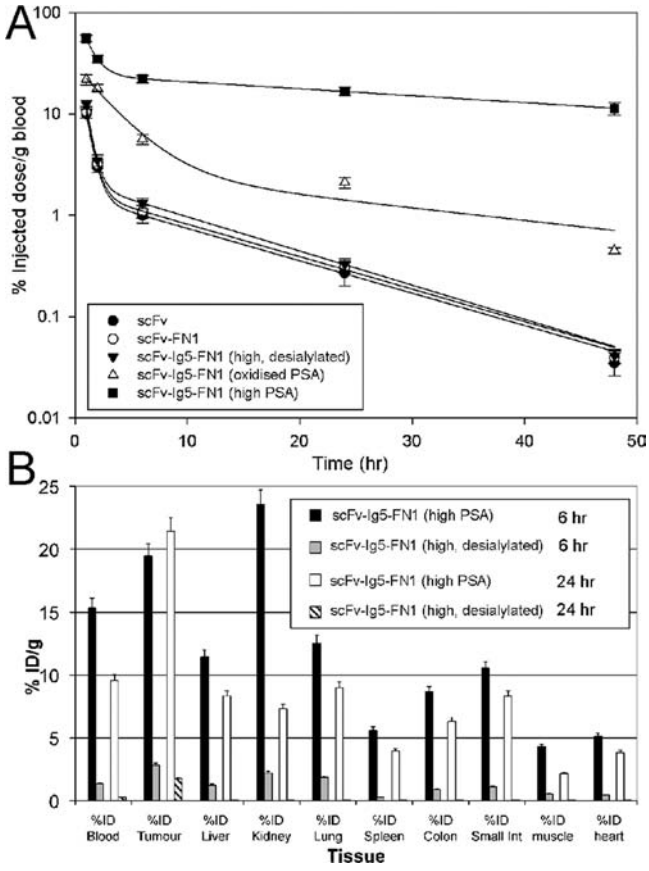


Figure 5. Blood pharmacokinetic analyses. Blood pharmacokinetic analyses. (a) Pharmacokinetic analyses of selected scFv-NCAM fusion proteins in BALB/c mice. Blood levels were monitored over time for radiolabeled polysialylated and nonpolysialylated scFvs The scFvs ± FN1 domain had near-identical pharmacokinetic profiles (rapid clearance). The highly polysialylated scFv demonstrated a slow blood equilibrium (α-) phase and a slow (β-) elimination phase, properties which were lost upon enzymic desialylation. The low-level polysialylated scFv, a result of periodate oxidation, showed intermediate pharmacokinetic properties. See Table 2 for pharmacokinetic constants. (b) Bar graph (±SEM) of mean tumor and normal organ uptake at two selected time points (6 h and 24 h) for scFv-Iq5-FN1 (high PSA) and scFv-Iq5-FN1 (desialylated) fusion proteins.

and FN1 domains to remove the FN1 docking domain once it had performed its function. This subtle sequence change led to unexpected but significantly reduced polysialylation and structural changes (data not shown). This supports the observations by Colley et al.[22] relating to the key structural features required for enzyme recognition and NCAM polysialylation.

The longer half-life led to a similar increase in tumor uptake as observed before with chemical polysialylation.[14] However, this was a model system to exemplify the technology, and tumor localization may not be the best use for this technology due to poor specificity ratios and a lack of understanding of other factors such as tumor perfusion. The antibody blocking of soluble growth factors is likely to benefit from this type of half-life extension.

Our previous work with fluorescent dye conjugates of C6.5 scFv showed that these conjugates were able to successfully internalize[31] whereas the same polysialyated scFv was unable to enter cells. It is possible that the increased hydrodynamic volume resulted in a steric effect which physically blocks

Table 2. Pharmacokinetic Characterization of Selected MFE-23 Based scFv-NCAM Fusion Proteins[a]

scFv sample	$t_{1/2}\alpha$ (h)	$t_{1/2}\beta$ (h)	$t_{1/2}\beta$ fold-change	AUC (% h/g)	AUC fold-change
scFv	0.353 ± 0.07	4.78 ± 1.1	1	30.86	1
scFv-FN1	0.383 ± 0.09	4.58 ± 1.5	1	31.26	0.9
scFv-Ig5-FN1 (High-PSA) *desialylated*	0.301 ± 0.19	2.66 ± 0.4	0.6	25.79	0.7
scFv-Ig5-FN1 (high-PSA)	1.474 ± 2.32	78.75 ± 7.3	29.6	890.14	28.8
scFv-Ig5-FN1 (high-PSA) *oxidized*	2.19 ± 0.12	24.75 ± 2.1	5.2	132.43	4.3

[a]Radiolabeled proteins were injected IV (t=0 h) and blood sampled at 1, 2, 6, 24, and 48 h post injection. The percentage of the injected dose per gram of blood was determined, plotted, and modeled to a bi-exponential decay equation to estimate the clearance pharmacokinetic parameters. The plots were also integrated to estimate the total blood exposure (bioavailability) for t = 0 to t = 48 h. Polysialylated scFv had a significantly slower blood clearance and correspondingly higher bioavailability (as measured by area under the curve-AUC of dose vs time).

receptor dimerization and hence internalization. Normally, size is not a limitation to internalization since 750 kDa IgMs can internalize. The other possible mechanism is that the high negative charge makes it unfavorable to internalize. Similar observations have been made in the nanoparticle research field. For example, the biodegradable poly(ethylene glycol-*graft*-methyl methacrylate) polymer designed for drug release was found to internalize less effectively when the zeta potential was more negative.[32] Further experiments are needed to explore this observation further, but this observation points to alternative ways to inhibit receptor function.

This technology, suitably developed, could result in a simple fusion tag that will extend the half-life of antibody fragments or any pharmaceutically important protein. This is a powerful approach with immense potential: The highly hydrophilic and negatively charged structure could have a better pharmacokinetic effect than PEG due to repulsion from the negatively charged glomeruli membranes.[29] This same structure could also act as a nanoparticle framework for use as a scaffold for conjugating a variety of additional effectors. Further work is needed to understand how internalization is prevented, but this opens up intriguing and novel ways to antagonize receptor-mediated signaling. Yet to be explored would be the ability of sialic acids to confer anti-inflammatory effects.[33] The next step is to apply recombinant polysialylation to a therapeutic model, such as TNFα or VEGFα antagonists, and more detailed studies regarding the microdistribution of such highly charged species within target tissues is needed.

Recombinant polysialylation represents an attractive alternative to the Fc-domain of immunoglobulins, which may be less useful in effector recruitment within the immuno-suppressed microenvironment of the tumor.[3] Additionally, the Fc domain can cross-react with normal tissues, leading to unwanted side effects. Hence, our work adds to the recently described peptide-based approaches of homoamino acid polymers (HAPylation[34]), the improved derivative, Pro-Ala-Ser (PASylation, being developed by the company called XL-protein), and the hydrophilic unstructured sequence called XTEN.[35] Sialic acids, we believe, present additional benefits already outlined. Given

dx.doi.org/10.1021/bc200624a | *Bioconjugate Chem.* 2012, 23, 1524−1533

the growth and antibody fragments with some entering advanced clinical trials,[36] and other binding ligands, recombinant polysialylation could be a valuable technology.

CONCLUSIONS

This technology, suitably developed, could result in a simple fusion tag that will extend the half-life of antibody fragments. It is proposed that the recombinant attachment of PSA onto heterologous proteins would offer versatility in the modulation and enhancement of the pharmacokinetics of therapeutically useful proteins and demonstrates a new capability of transferring post-translational modifications to heterologous proteins.

ASSOCIATED CONTENT

Supporting Information

Additional figures. This material is available free of charge via the Internet at http://pubs.acs.org.

AUTHOR INFORMATION

Corresponding Author

*E-mail: m.deonarain@imperial.ac.uk.

Author Contributions

#Both authors contributed equally to the work.

Notes

The authors declare no competing financial interest.

ACKNOWLEDGMENTS

We thank Daniel Wells from the CBS unit for excellent technical assistance and Imperial College for funding. We wish to thank Prof. K. Colley for polysialyltransferase clones and useful comments on the manuscript, Dr. J. Saffell for guidance and NCAM clones, and Dr. J. Silva for technical help. This work was also supported by the Biotechnology and Biological Sciences Research Council (BBSRC), studentship 01/A2/C/07249 (to A.C. and M.P.D.), grant BBF0083091 (to A.D. and S.M.H.) and by the British Heart Foundation (FS/06/069/21490).

REFERENCES

(1) Holliger, P., and Hudson, P. J. (2005) Engineered antibody fragments and the rise of single domains. *Nat. Biotechnol. 23*, 1126−36.

(2) Gebauer, M., and Skerra, A. (2009) Engineered protein scaffolds as next-generation antibody therapeutics. *Curr. Opin. Chem. Biol. 13*, 245−55.

(3) Fukumura, D., and Jain, R. K. (2007) Tumor microenvironment abnormalities: causes, consequences, and strategies to normalize. *J. Cell Biochem. 101*, 937−49.

(4) Graff, C. P., and Wittrup, K. D. (2003) Theoretical analysis of antibody targeting of tumor spheroids: importance of dosage for penetration, and affinity for retention. *Cancer Res. 63*, 1288−96.

(5) Dougan, M., and Dranoff, G. (2009) The immune response to tumors. In *Current Protocols in Immunology*, Chapter 20, Unit 20.11, John Wiley & Sons, New Jersey.

(6) Jevsevar, S., Kunstelj, M., and Porekar, V. G. (2010) PEGylation of therapeutic proteins. *Biotechnol. J. 5*, 113−28.

(7) Chen, C., Constantinou, A., and Deonarain, M. (2011) Modulating antibody pharmacokinetics using hydrophilic polymers. *Expert Opin. Drug Delivery 8*, 221−36.

(8) Deen, W. M., Bohrer, M. P., and Brenner, B. M. (1979) Macromolecule transport across glomerular capillaries: application of pore theory. *Kidney Int. 16*, 353−65.

(9) Gaberc-Porekar, V., Zore, I., Podobnik, B., and Menart, V. (2008) Obstacles and pitfalls in the PEGylation of therapeutic proteins. *Curr. Opin. Drug Discovery Devel. 11*, 242−50.

(10) Armstrong, J. K., Hempel, G., Koling, S., Chan, L. S., Fisher, T., Meiselman, H. J., and Garratty, G. (2007) Antibody against poly(ethylene glycol) adversely affects PEG-asparaginase therapy in acute lymphoblastic leukemia patients. *Cancer 110*, 103−11.

(11) Muhlenhoff, M., Eckhardt, M., and Gerardy-Schahn, R. (1998) Polysialic acid: three-dimensional structure, biosynthesis and function. *Curr. Opin. Struct. Biol. 8*, 558−64.

(12) Constantinou, A., Chen, C., and Deonarain, M. P. (2012) Polysialic acid and polysialylation to modulate antibody pharmacokinetics. In *in Pharmacokinetic modulation of therapeutic proteins* (Kontermann, R, Ed) Wiley, London (in press).

(13) Constantinou, A., Epenetos, A. A., Hreczuk-Hirst, D., Jain, S., and Deonarain, M. P. (2008) Modulation of antibody pharmacokinetics by chemical polysialylation. *Bioconjugate Chem 19*, 643−50.

(14) Constantinou, A., Epenetos, A. A., Hreczuk-Hirst, D., Jain, S., Wright, M., Chester, K. A., and Deonarain, M. P. (2009) Site-specific polysialylation of an antitumor single-chain Fv fragment. *Bioconjugate Chem. 20*, 924−31.

(15) Fernandes, A. I., and Gregoriadis, G. (1997) Polysialylated asparaginase: preparation, activity and pharmacokinetics. *Biochim. Biophys. Acta 1341*, 26−34.

(16) Mühlenhoff, M., Oltmann-Norden, I., Weinhold, B., Hildebrandt, H., and Gerardy-Schahn, R. (2009) Brain development needs sugar: the role of polysialic acid in controlling NCAM functions. *Biol Chem. 390*, 567−74.

(17) Umaña, P., Jean-Mairet, J., Moudry, R., Amstutz, H., and Bailey, J. E. (1999) Engineered glycoforms of an antineuroblastoma IgG1 with optimized antibody-dependent cellular cytotoxic activity. *Nat. Biotechnol. 17*, 176−80.

(18) Elliott, S., Lorenzini, T., Asher, S., Aoki, K., Brankow, D., Buck, L., Busse, L., Chang, D., Fuller, J., Grant, J., Hernday, N., Hokum, M., Hu, S., Knudten, A., Levin, N., Komorowski, R., Martin, F., Navarro, R., Osslund, T., Rogers, G., Roger,s, N., Trail, G., and Egrie, J. (2003) Enhancement of therapeutic protein in vivo activities through glycoengineering. *Nat. Biotechnol. 21*, 414−21.

(19) Sainz-Pastor, N., Tolner, B., Huhalov, A., Kogelberg, H., Lee, Y. C., Zhu, D., Begent, R. H., and Chester, K. A. (2006) Deglycosylation to obtain stable and homogeneous Pichia pastoris-expressed N-A1 domains of carcinoembryonic antigen. *Int. J. Biol. Macromol. 39*, 141−50.

(20) Beecken, W. D., Engl, T., Ogbomo, H., Relja, B., Cinatl, J., Bereiter-Hahn, J., Oppermann, E., Jonas, D., and Blaheta, R. A. (2005) Valproic acid modulates NCAM polysialylation and polysialyltransferase mRNA expression in human tumor cells. *Int. Immunopharmacol. 5*, 757−69.

(21) Nelson, R. W., Bates, P. A., and Rutishauser, U. (1995) Protein determinants for specific polysialylation of the neural cell adhesion molecule. *J. Biol. Chem. 270*, 17171−9.

(22) Colley, K. J. (2010) Structural basis for the polysialylation of the neural cell adhesion molecule. *Adv. Exp. Med. Biol. 663*, 111−26.

(23) Begent, R. H., Verhaar, M. J., Chester, K. A., Casey, J. L., Green, A. J., Napier, M. P., Hope-Stone, L. D., Cushen, N., Keep, P. A., Johnson, C. J., Hawkins, R. E., Hilson, A. J., and Robson, L. (1996) Clinical evidence of efficient tumor targeting based on single-chain Fv antibody selected from a combinatorial library. *Nat. Med. 2*, 979−84.

(24) Foley, D. A., Swartzentruber, K. G., and Colley, K. J. (2009) Identification of sequences in the polysialyltransferases ST8Sia II and ST8Sia IV that are required for the protein-specific polysialylation of the neural cell adhesion molecule, NCAM. *J. Biol. Chem. 284*, 15505−16.

(25) Perera, A. D., Lagenaur, C. F., and Plant, T. M. (1993) Postnatal expression of polysialic acid-neural cell adhesion molecule in the hypothalamus of the male rhesus monkey (*Macaca mulatta*). *Endocrinology 133*, 2729−35.

(26) Galuska, S. P., Geyer, R., Mühlenhoff, M., and Geyer, H (2007) Characterization of oligo- and polysialic acids by MALDI-TOF-MS. *Anal. Chem. 79*, 7161−9.
(27) Schier, R., Bye, J., Apell, G., McCall, A., Adams, G. P., Malmqvist, M., Weiner, L. M., and Marks, J. D. (1996) Isolation of high-affinity monomeric human anti-c-erbB-2 single chain Fv using affinity-driven selection. *J. Mol. Biol. 255*, 28−43.
(28) Müller, D., Karle, A., Meissburger, B., Höfig, I., Stork, R., and Kontermann, R. E. (2007) Improved pharmacokinetics of recombinant bispecific antibody molecules by fusion to human serum albumin. *J. Biol. Chem. 288*, 12650−60.
(29) Deen, W. M., Lazzara, M. J., and Myers, B. D. (2001) Structural determinants of glomerular permeability. *Am. J. Physiol. Renal Physiol. 281*, 579−96.
(30) Kubetzko, S., Sarkar, C. A., and Plückthun, A. (2005) Protein PEGylation decreases observed target association rates via a dual blocking mechanism. *Mol. Pharmacol. 68*, 1439−54.
(31) Kuimova, M. K., Bhatti, M., Deonarain, M., Yahioglu, G., Levitt, J. A., Stamati, I., Suhling, K., and Phillips, D. (2007) Fluorescence characterisation of multiply-loaded anti-HER2 single chain Fv-photosensitizer conjugates suitable for photodynamic therapy. *Photochem. Photobiol. Sci. 6*, 933−9.
(32) Scheler, S., Kitzan, M., and Fahr, A. (2011) Cellular uptake and degradation behaviour of biodegradable poly(ethylene glycol-graft-methyl methacrylate) nanoparticles crosslinked with dimethacryloyl hydroxylamine. *Int. J. Pharm. 403*, 207−18.
(33) Anthony, R. M., and Ravetch, J. V. (2010) A novel role for the IgG Fc glycan: the anti-inflammatory activity of sialylated IgG Fcs. *J. Clin. Immunol. 30* (Suppl 1), S9−14.
(34) Schlapschy, M., Theobald, I., Mack, H., Schottelius, M., Wester, H. J., and Skerra, A. (2007) Fusion of a recombinant antibody fragment with a homo-amino-acid polymer: effects on biophysical properties and prolonged plasma half-life. *Protein Eng. Des. Sel. 20*, 273−84.
(35) Schellenberger, V., Wang, C. W., Geething, N. C., Spink, B. J., Campbell, A., To, W., Scholle, M. D., Yin, Y., Yao, Y., Bogin, O., Cleland, J. L., Silverman, J., and Stemmer, W. P. (2009) A recombinant polypeptide extends the in vivo half-life of peptides and proteins in a tunable manner. *Nat. Biotechnol. 27*, 1186−90.
(36) Nelson, A. L., and Reichert, J. M. (2009) Development trends for therapeutic antibody fragments. *Nat. Biotechnol. 27*, 331−7.

Bioconjugate Chemistry

Article

pubs.acs.org/bc

Synthesis of a Library of Fucosylated Glycoclusters and Determination of their Binding toward *Pseudomonas aeruginosa* Lectin B (PA-IIL) Using a DNA-Based Carbohydrate Microarray

Béatrice Gerland,[†] Alice Goudot,[‡] Gwladys Pourceau,[†] Albert Meyer,[†] Vincent Dugas,[§] Samy Cecioni,[∥] Sébastien Vidal,[∥] Eliane Souteyrand,[‡] Jean-Jacques Vasseur,[†] Yann Chevolot,*[,‡] and François Morvan*[,†]

[†]Institut des Biomolécules Max Mousseron (IBMM), UMR 5247 CNRS—Université Montpellier 1—Université Montpellier 2, Place Eugène Bataillon, CC1704, 34095 Montpellier Cedex 5, France

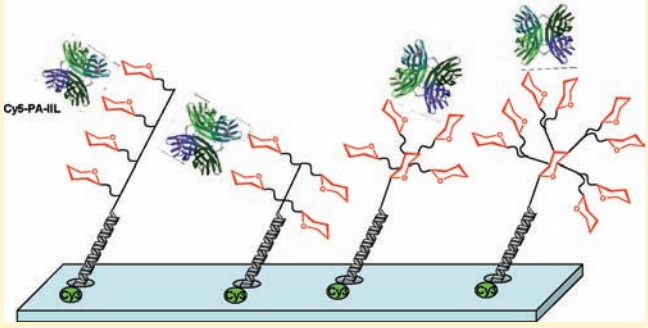
[‡]Institut des Nanotechnologies de Lyon (INL), UMR 5270 CNRS, Ecole Centrale de Lyon, 36 Avenue Guy de Collongue, 69134 Ecully Cedex, France

[§]Laboratoire des Sciences Analytiques, UMR 5180 CNRS, Université Claude Bernard Lyon 1, 43 Boulevard du 11 Novembre 1918, 69622 Villeurbanne Cedex, France

[∥]Institut de Chimie et Biochimie Moléculaires et Supramoléculaires (ICBMS), Laboratoire de Chimie Organique 2—Glycochimie, UMR 5246 CNRS, Université Claude Bernard Lyon 1, 43 Boulevard du 11 Novembre 1918, 69622 Villeurbanne, France

Supporting Information

ABSTRACT: *Pseudomonas aeruginosa* (PA) is a Gram negative opportunistic pathogen and is the major pathogen encounter in the cystic fibrosis (CF) lung airways. It often leads to chronic respiratory infection despite aggressive antibiotic therapy due to the emergence of resistant strains and to the formation of biofilm. The lectin PA-IIL (LecB) is a fucose-specific lectin from PA suspected to be involved in host recognition/adhesion and in biofilm formation. Thus, it can be foreseen as a potential therapeutic target. Herein, 16 fucosylated glycoclusters with antenna-like, linear, or crown-like spatial arrangements were synthesized using a combination of DNA solid-phase synthesis and alkyne azide 1,3-dipolar cycloaddition (CuAAC). Their binding properties toward PA-IIL were then evaluated based on DNA directed immobilization (DDI) carbohydrate microarray. Our results suggested that the antenna-like scaffold was preferred to linear or crown-like glycoclusters. Among the crown-like carbohydrate centered fucosylated glycoclusters, mannose-based core was better than glucose- and galactose-based ones. The influence of the linker arm was also evaluated, and long linkers between fucoses and the core led to a slight better binding than the short ones.



INTRODUCTION

Carbohydrate−lectin interactions play an important role in several biological processes such as cell−cell communication, inflammation, innate system, and infections by pathogens (i.e., viruses or bacteria).[1−4] *Pseudomonas aeruginosa* (PA) is the causative agent of lung infections and the major cause of morbidity and mortality among cystic fibrosis patients but also among patients hospitalized in intensive care units. PA expresses two soluble lectins, PA-IL (LecA) and PA-IIL (LecB). PA-IIL has been proposed to be implicated in host recognition and adhesion and also in biofilm formation.[5,6] This tetrameric lectin presents four carbohydrate recognition domains and binds L-fucose with micromolar affinity.[7] It is more or less a two-tilted cobblestone-shaped protein leading to a tetrahedral spatial distribution with a distance of 40 Å between two carbohydrate binding sites.[8]

This lectin has become an attractive target for therapeutics, and several groups have developed new glycomimetics with high affinity for PA-IIL. Thus, it is claimed that they may compete with host glycans and hence could inhibit the adhesion of the bacteria. Indeed, carbohydrates and their mimetics could be developed as antiadhesive drugs[17,18] against pathogens as an alternative to antibiotics. Because antiadhesive drugs do not affect the viability of bacteria,[6,9−16] it is rather improbable that bacteria will develop a resistance to such drugs.

As the lectin avidity is relatively low when only one carbohydrate residue is involved, Nature uses a cluster effect where several weak interactions yield to a higher affinity than the sum of individual interactions.[4,19−21] The design of

Received: November 28, 2011
Revised: June 20, 2012
Published: July 16, 2012

ACS Publications © 2012 American Chemical Society

dx.doi.org/10.1021/bc2006434 | *Bioconjugate Chem.* 2012, 23, 1534−1547

glycoclusters has been extensively investigated to discover synthetic glycomimetics able to show high avidity for lectins.[22]

Herein, 16 different fucosylated glycomimetics exhibiting from one to eight fucose residues were synthesized with antenna-like, linear (or comb-like), or crown-like spatial arrangements.[23] Next, their binding properties toward PA-IIL were determined using DDI-based carbohydrate microarray.[24,25] DNA directed immobilization (DDI)[26,27] uses DNA/DNA hybridization between an immobilized single-stranded oligonucleotide at the surface of a solid (DNA chip) and a DNA tagged molecule. In our case, fucosylated glycoclusters carry a DNA tag for their DDI immobilization as well as a Cy3 fluorescent dye as an immobilization quality control reporter. Binding properties of the lectin to the designed glycoclusters were measured using Alexa-647 labeled PA-IIL.

EXPERIMENTAL PROCEDURES

General Procedure for the Elongation by Hydrogenophosphonate Chemistry. Elongation was performed on a DNA synthesizer (ABI 394) using a *H*-phosphonate chemistry cycle starting from a 1,3-propanediol solid support **7** (1 μmol). The detritylation step was performed with 2.5% DCA in CH_2Cl_2 for 35 s. Then dimethanolcyclohexane (DMCH) *H*-phosphonate monoester **9** (60 mM in anhydrous CH_3CN/C_5H_5N 1:1 v/v) and pivaloyl chloride as activator (200 mM in anhydrous CH_3CN/C_5H_5N 1:1 v/v) were passed six times through the column alternatively for 5 s, (30 molar excess). The cycle was repeated as required to afford **12a−d**.

General Procedure for the Elongation Mixing Hydrogenophosphonate and Phosphoramidite Chemistries. The solid-supported hydrogenophosphonate diester scaffold **12m** was synthesized at the 1 μmol scale on a DNA synthesizer (ABI 394). First, *H*-phosphonate monoester **9** was coupled as described above. Then, the DMCH phosphoramidite **11**[28] (0.09 M in anhydrous CH_3CN) was introduced using a phosphoramidite chemistry cycle with benzylmercaptotetrazole as activator (0.3 M in anhydrous CH_3CN) with a 120 s coupling time. No capping step was performed to avoid *O*-acylation. Oxidation was performed with a solution of *t*BuOOH (1.1 M in anhydrous CH_2Cl_2) for 60 s to avoid the oxidation of *H*-phosphonate diester. Detritylation was performed with 2.5% DCA in CH_2Cl_2 for 35 s. The last two *H*-phosphonate monoesters **9** were coupled using the *H*-phosphonate chemistry cycle, affording **12m**.

General Procedure for Amidative Oxidation. The solid-supported *H*-phosphonate diesters scaffolds **12a−12d** and **12m** (1 μmol) were treated back and forth using two syringes with 2 mL of a solution of 10% of propargylamine in CCl_4/C_5H_5N (1:1 v/v) for 30 min. The CPG beads were washed with C_5H_5N (2 × 2 mL) and CH_3CN (3 × 2 mL) and then dried by flushing with argon.

General Procedure for Elongation of DNA Sequences and Labeling with Cy3. The DNA sequences were synthesized on the solid-supported scaffolds at the 1 μmol scale on a DNA synthesizer (ABI 394) by standard phosphoramidite chemistry. For the coupling step, benzylmercaptotetrazole was used as activator (0.3 M in anhydrous CH_3CN), and commercially available nucleosides phosphoramidites (0.09 M in anhydrous CH_3CN) were introduced with a 20 s coupling time and Cy3 amidite (0.06 M in anhydrous CH_3CN) with a 180 s coupling time. The capping step was performed with acetic anhydride using commercial solution (Cap A, Ac_2O/pyridine/THF, 10:10:80; Cap B, 10% *N*-methylimidazole in THF) for 15 s. Each oxidation was performed for 15 s. Detritylation was performed with 2.5% DCA in CH_2Cl_2 for 35 s.

Immobilization on Azide Solid Support 4 of 1-*O*-Propargyl Hexoses 15a−c by Cu(I)-Catalyzed Alkyne Azide 1,3-Dipolar Cycloaddition. An aqueous solution of 1-*O*-propargyl hexose (α-mannose **15a**, β-galactose **15b**, β-glucose **15c**) (100 mM, 175 μL), freshly prepared aqueous solutions of $CuSO_4$ (100 mM, 14 μL) and sodium ascorbate (500 mM, 14 μL), water (147 μL), and MeOH (350 μL) were added to 3.5 μmol of azide solid support **4**. The resulting mixture was treated in a sealed tube with a microwave synthesizer at 60 °C for 45 min (premixing time: 30 s). The temperature was monitored with an internal infrared probe. The solution was removed, and CPG beads were washed with H_2O (3 × 2 mL), MeOH (3 × 2 mL), and CH_3CN (3 × 2 mL), and dried, affording **16a−c**.

Immobilization on Alkyne Solid Support 1 of 3-Azidopropyl-α-D-mannopyranoside 24 by Cu(I)-Catalyzed Alkyne Azide 1,3-Dipolar Cycloaddition. A solution of 3-azidopropyl-α-D-mannopyranoside **24** (100 mM in MeOH, 300 μL), freshly prepared aqueous solution of $CuSO_4$ (100 mM, 24 μL), and sodium ascorbate (500 mM, 24 μL), water (552 μL), and MeOH (300 μL) were added to 6 μmol of alkyne solid support **1**. The tube containing the resulting suspension was sealed and placed in an oil bath at 60 °C for 1 h. After the reaction, the solution was removed, and the CPG beads were washed with H_2O (3 × 2 mL), MeOH (3 × 2 mL), and CH_3CN (3 × 2 mL), and dried, affording **25**.

General Procedure for Introduction of Pent-4-ynyl, Bis-pent-4-ynyl, Bromohexyl, or 3,6-Dioxanon-8-yn-1-yl Phosphoramidites on Mannose, Glucose, or Galactose Hydroxyls of 16a−16c or 25. Solid-supported hexose derivatives **16a−16c** or **25** (1 μmol scale) were treated by phosphoramidite chemistry, on a DNA synthesizer, with pentyn-4-yl phosphoramidite **17**, 6-bromohexyl phosphoramidite **22**, or 3,6-dioxanon-8-yn-1-yl phosphoramidite **26**. Only coupling and oxidation steps were performed. For the coupling step, benzylmercaptotetrazole was used as activator (0.3 M in anhydrous CH_3CN), and phosphoramidite **17**, **22**, or **26** (0.2 M in anhydrous CH_3CN) was introduced three times (120 μmol) with a 180 s coupling time. Oxidation was performed with commercial solution of iodide (0.1 M I_2, THF/pyridine/water 90:5:5) for 15 s.

General Procedure for Azidation. The solid-supported oligonucleotides bearing the tetrabromohexyl hexoses (1 μmol) were treated with a solution of TMG-N_3 (31.6 mg, 200 equiv) and NaI (30 mg, 200 equiv) in DMF (1 mL) for 1 h at 65 °C. The beads were washed with DMF (3 × 2 mL), H_2O (3 × 2 mL) and CH_3CN (3 × 2 mL) and then dried by flushing with argon.

General Procedure for Deprotection of Solid-Supported Oligonucleotides. The CPG beads bearing modified oligonucleotides were transferred to a 4 mL screw top vial and treated with 2 mL of concentrated aqueous ammonia for 15 h at room temperature and warmed to 55 °C for 2 h. For each compound, the supernatants were withdrawn and evaporated to dryness. Residues were dissolved in water.

General Procedure for CuAAC Reaction. *Procedure for Introduction of Azide L-Fucose Derivative* ***3***. To a solution of 5′-fluorescent-3′-alkyne oligonucleotide **2**, **14a−14d**, **14m**, **18a−18c**, **20**, and **27** (100 nmol in 100 μL of H_2O) were

dx.doi.org/10.1021/bc2006434 | Bioconjugate Chem. 2012, 23, 1534−1547

added 8-azido-3,6-dioxaocta-1-yl 2,3,4-tri-*O*-acetyl-L-fucopyranoside **3** (3 equiv per alkyne function, 100 mM in MeOH), 1 mg of Cu(0) nanopowder, triethylammonium acetate buffer 0.1 M, pH 7.7 (25 μL), water, and MeOH to obtain a final volume of 250 μL (water MeOH, 1:1 v/v). The tube containing the resulting preparation was sealed and placed in a microwave synthesizer Initiator from Biotage with a 30 s premixing time at 60 °C for the indicated time (see Table S1 in Supporting Information).

Procedure for Introduction of 1-O-propargyl-L-Fucose ***6***. To a solution of 5′-fluorescent-3′-azide oligonucleotide **5** and **23a−23c** (100 nmol in 100 μL of H_2O) were added 1-*O*-propargyl 2,3,4-tri-*O*-acetyl-L-fucopyranoside **6** (3 or 5 equiv per azide function, 100 mM in MeOH), 1 mg of Cu(0) nanopowder, triethylammonium acetate buffer 0.1 M, pH 7.7 (25 μL), water, and MeOH to obtain a final volume of 250 μL (water MeOH, 1:1 v/v). The tube containing the resulting preparation was sealed and placed in a oil bath with magnetic stirring at 60 °C for the indicated time (see Table S1 in Supporting Information).

Workup of CuAAC Reactions and HPLC Purifications. EDTA (400 μL) was added to the mixtures, and after centrifugation, the supernatants were withdrawn to eliminate Cu(0) and were desalted by size-exclusion chromatography on NAP10. After evaporation, the 5′-fluorescent 3′-acetyl-glycomimetic oligonucleotides were dissolved in water and purified by reversed-phase preparative HPLC. Pure compounds were treated with concentrated aqueous ammonia (3 mL) for 2 h at room temperature to remove acetyl groups and evaporated to dryness (purity >97%). Final compounds were purified again by reversed-phase preparative HPLC using a linear gradient from 8% to 32% of acetonitrile in TEAAc buffer pH 7 over 20 min. Residues were dissolved in water for subsequent analyses (see Supporting Information).

Bis-(pent-4-ynyl) N,N-diisopropyl phosphoramidite ***19***. To a solution of anhydrous 4-pentyn-1-ol (5.4 mmol, 500 μL) and anhydrous Et_3N (6 mmol, 826 μL) in dry CH_2Cl_2 (5 mL), stirring at 0 °C under argon, was added a solution of diisopropylphosphorodichloridite (2 mmol, 550 mg) in dry CH_2Cl_2 (5 mL). The resulting mixture was stirred for 4 h at room temperature, diluted with CH_2Cl_2 (100 mL), filtered to remove triethylammonium chloride salt, and washed with $NaHCO_3$ (1 × 150 mL). The organic layer was dried (Na_2SO_4), filtered, and evaporated to dryness. The crude product was purified by silica gel column chromatography (0−50% CH_2CL_2 in cyclohexane containing 10% triethylamine) to afford the title compound (500 mg, 83%) as clear oil. TLC R_f: 0.60 (cyclohexane/AcOEt/Et_3N: 5:4:1, v/v/v). ^{1}H NMR (CD_3CN, 300 MHz): δ 1.18 (d, 12H, J = 6.8 Hz, 4 × CH_3), 1.73−1.82 (m, 4H, 2 × $CH_2\underline{CH_2}CH_2$), 2.16−2.19 (t, 2H, J = 2.6 Hz 2 × CCH), 2.29 (dt, 4H, J_d = 2.6 Hz, J_t = 7.1 Hz, 2 × $CH_2\underline{CH_2}CCH$), 3.54−3.77 (m, 6H, 2 × O−CH_2, 2 × $\underline{CH}Me_2$). ^{13}C NMR ($CDCl_3$, 300 MHz): δ 14.2, 23.6, 29.8, 42.3, 61.2, 68.6, 83.5. ^{31}P NMR (CD_3CN): δ 146.25 ppm. HRMS ESI+ m/z $[M + H]^+$ for $C_{16}H_{29}O_2NP$ calcd 298.1915, found 298.1936.

3,6-Dioxanon-8-yn-1-ol. 3,6-Dioxanon-8-yn-1-ol was synthesized by a slightly modified procedure.[29] Bis(2-hydroxyethyl)ether (1.19 g, 14.1 mmol) and sodium hydride (471 mg, 11.8 mmol) were dissolved in anhydrous DMF (80 mL), and the mixture was stirred at 0 °C for 30 min. Then propargyl bromide (1.30 mL, 11.8 mmol) was added dropwise, and the resulting mixture was stirred for 6 h at rt. Methanol (5 mL) was added, and the mixture was evaporated under reduced pressure and the residue dissolved in ethyl acetate (40 mL). The organic layer was washed with saturated ammonium chloride (40 mL), the aqueous layer was extracted with ethyl acetate (2 × 20 mL), and the combined organic layers were evaporated under vacuum. The dry residue was purified via silica gel column chromatography (eluting with *c*-C_6H_{12}:EtOAc 7:3 to 2:8) to give 3,6-dioxanon-8-yn-1-ol (1.15 g, 67%) as a clear oil. ^{1}H NMR (300 MHz, $CDCl_3$): δ = 4.15 (2 H, d, J = 2.4 Hz, CH_2-CCH), 3.74−3.49 (8 H, m, CH_2), 2.38 (1 H, t, J = 2.4 Hz, HCC−). LRMS (ESI+): for $C_7H_{16}NO_3$ $[M + NH_4]^+$ calcd 162.1, found 162.1.

O-2-Cyanoethyl-O′-(3,6-dioxanon-8-ynyl)-N,N-diisopropyl-phosphoramidite ***26***. 2-Cyanoethyl-*N*,*N*-diisopropylchlorophosphoramidite (500 mg, 2.11 mmol) was added to a solution of 3,6-dioxanon-8-yn-1-ol (253 mg, 1.76 mmol), 4 Å molecular sieves and *N*,*N*′-diisopropylethylamine (DIEA) (489 μL, 2.81 mmol) in anhydrous dichloromethane (20 mL). The resulting mixture was stirred at room temperature for 5 h 30, 1 mL of H_2O was added, and then the solution was diluted with CH_2Cl_2 (15 mL). The organic layer was washed with an aqueous saturated $NaHCO_3$ solution (30 mL). The resulting aqueous layer was then extracted with CH_2Cl_2 (2 × 30 mL). The organics were collected, washed with brine (30 mL), and dried ($MgSO_4$), filtered, and evaporated. The dry residue was purified via silica gel column chromatography (eluting with *c*-C_6H_{12}:EtOAc: 8:2:0.5 to 0:10:0.5) to give the title compound **26** (379 mg, 63%) as a clear oil. R_f: 0.51 (*c*-C_6H_{12}/AcOEt/Et_3N 6:4:0.1). ^{1}H NMR (200 MHz, $CDCl_3$): δ 4.14 (d, J = 2.4 Hz, 2 H, CH_2-CCH), 3.87−3.45 (m, 12 H, 3 × $CH_2C\underline{H_2}O$, $C\underline{H_2}OP$, 2 × CH(*i*Pr), $C\underline{H_2}CH_2C{\equiv}N$), 2.59 (t, J = 6.6 Hz, 2 H, $CH_2C\underline{H_2}C{\equiv}N$), 2.36 (t, J = 2.4 Hz, 1 H, $\underline{H}C{\equiv}C-$), 1.11 (dd, J = 2.0, 6.8 Hz, 12 H, *i*Pr_2). ^{13}C NMR (300 MHz, $CDCl_3$) δ 117.7 ($\underline{C}{\equiv}N$), 79.7 ($\underline{C}{\equiv}CH$), 74.5 ($C{\equiv}\underline{C}H$), 71.3, 71.2, 70.4, 69.2 ($\underline{C}H_2\underline{C}H_2O\underline{C}H_2\underline{C}H_2$), 62.7, 62.5 ($C\underline{C}H_2O$), 58.7, 58.4 ($PO\underline{C}H_2CH_2C{\equiv}N$), 43.2, 43.0 ($N\underline{C}Me_2$), 24.7, 24.6, 24.6, 24.3 (2 × $C(\underline{C}H_3)2$), 20.4, 20.3 ($POCH_2\underline{C}H_2C{\equiv}N$). ^{31}P NMR (121 MHz, $CDCl_3$):δ 148.5.

Fabrication of Microarrays. *Fabrication of Microstructured Slides*. Photolithography and wet etching process were employed for the fabrication microreactors onto flat glass slides. Theses methods are detailed elsewhere.[30,31]

Silanization of the Glass Slides. Borosilicate glass slides (Schott) featured 52 round microreactors (2 mm diameter, 65−100 μm deep with less than 1% variation in depth for one etching lot) with a volume below 1 μL. They were functionalized according to the protocol developed by Dugas et al.[32,33] In brief, after piranha treatment, the slides were heated under dry nitrogen at 150 °C for 2 h. Next, dry pentane and *tert*-butyl-11-(dimethylamino)silylundecanoate were added at room temperature. After 2 h of incubation, the pentane was evaporated and the slides were heated at 150 °C overnight. Functionalized slides were obtained after washing in THF and rinsing in water. The ester function was converted into the corresponding acid using formic acid for 7 h at room temperature. Acid group bearing slides were activated for amine coupling with *N*-hydroxysuccinimide (0.1 M) and di(isopropyl) carbodiimide (0.1 M) in dry THF, overnight at room temperature. The slides were rinsed in THF and dichloromethane.

Immobilization of Amino-Modified Oligonucleotides. 3′-Amino-modified oligonucleotides were purchased from Eurogentec. Two sequences were used: S1: 5′-GTG AGC CCA

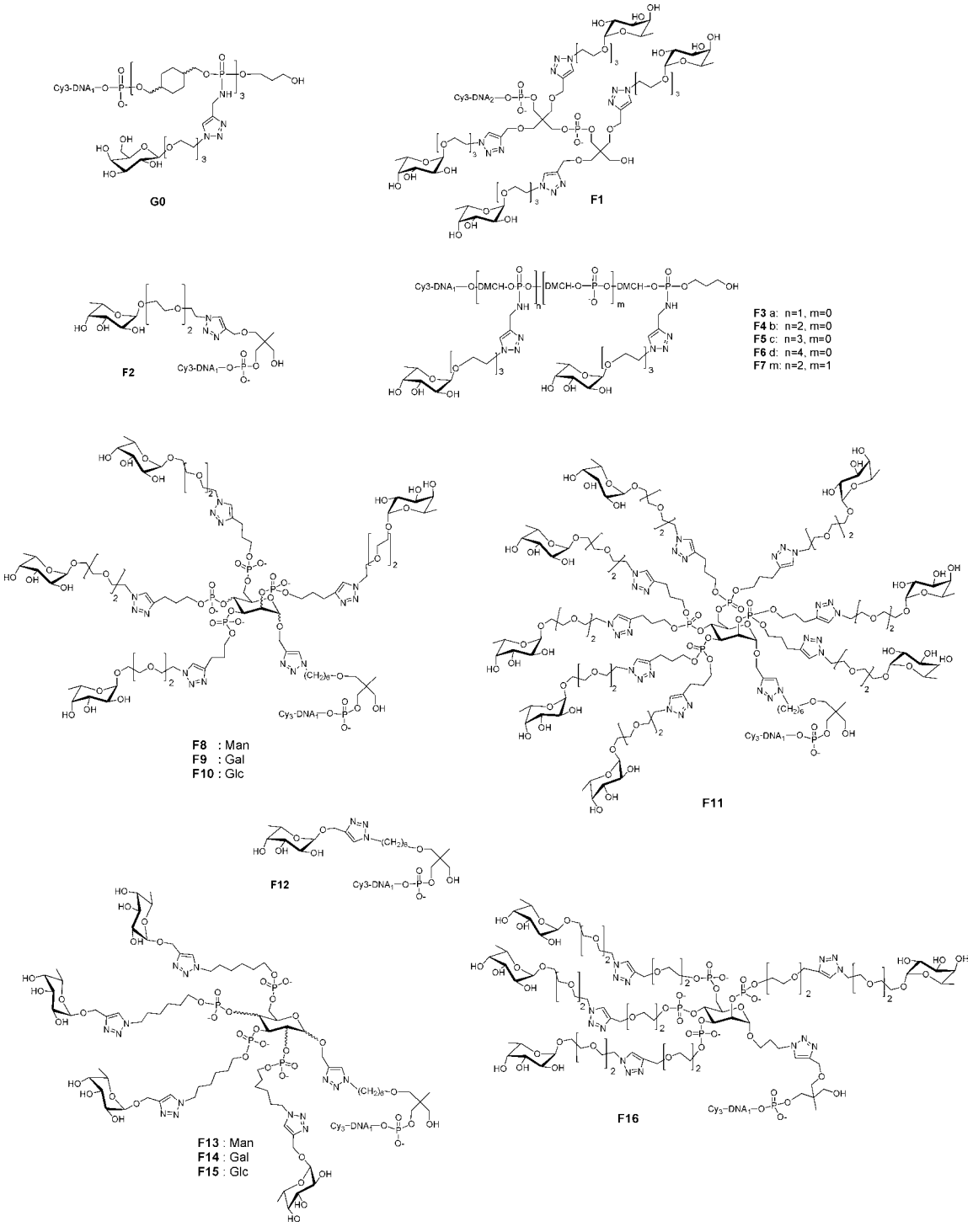


Figure 1. Structures of the linear dimethylcyclohexane-tri-β-D-galactomimetic **G0** and the fucomimetics **F1**−**F16**.

GAG GCA GGG-5CH_2)$_7$-NH_2 and S2: 5′-GCT AAT CCA ACG CGG GCC AAT CCT T-(CH_2)$_7$-NH_2. One μL of the desired sequence (S1 or S2) at 25 μM in PBS 10× (pH 8.5) were deposited at the bottom of the corresponding well. The substitution reaction was performed overnight at room temperature in a water saturated atmosphere, and then water was allowed slowly to evaporate. Sequential washing of the slides was performed with SDS (0.1%) at 70 °C for 30 min and deionized water.

Blocking. After ssDNA immobilization, all slides were blocked with bovine serum albumin (BSA). Blocking was performed with BSA 4% solution in PBS 1× (pH 7.4) at 37 °C for 2 h. The washing steps were: 3 × 3 min in PBS-Tween 20 (0.05%) followed by 3 × 3 min in PBS 1×, and finally the glasses were rinsed with deionized water before being dried by centrifugation.

Hybridization of the Glycoconjugates on DNA Array. First, 1 μL of a solution of each glycoconjugate bearing a DNA tag at 1 μM in PBS 1× (pH 7.4) were placed at the bottom of the corresponding well and allowed to hybridize overnight at room temperature in a water vapor saturated chamber. Then the samples were washed in saline−sodium citrate 2× (SSC 2X),

dx.doi.org/10.1021/bc2006434 | *Bioconjugate Chem.* 2012, 23, 1534−1547

SDS (0.1%) at 51 °C for 1 min, followed by SSC 2X at room temperature for an additional 5 min, and finally rinsed with deionized water before being dried by centrifugation.

Blocking. After hybridization, all slides were blocked again with bovine serum albumin (BSA). Blocking was performed with BSA 4% solution in PBS 1× (pH 7.4) at 37 °C for 1 h. Same washing steps: 3 × 3 min in PBS-Tween 20 (0.05%), followed by 3 × 3 min in PBS 1×, and briefly rinsed with deionized water before dried by centrifugation.

Alexa-647 Labeling of PA-IIL Lectin. PA-IIL lectin was labeled with Alexa Fluor 647 microscale protein labeling kit (A30009) from Invitrogen. In brief, 100 μL of a 1 mg/mL solution of PA-IIL (MW: 47 kDa, PA-IIL was kindly provided by Dr. Anne Imberty, CERMAV, Grenoble) diluted in PBS 1× (pH 7.4) was mixed with 10 μL of 1 M sodium bicarbonate (pH 8.3). Separately, 10 μL of water was added to the vial of Alexa Fluor 647 succinimidyl ester in order to have a reactive dye stock solution at 7.94 nmol/μL. The appropriate volume of reactive dye solution was transferred into the reaction tube containing the pH-adjusted protein. Reaction mixture was mixed for 15 min at room temperature before purification on a spin column (gel resin container) in order to separate the labeled protein from unreacted dye. Lectin concentration and the dye to lectin ratio were estimated by optical density (nanodrop) reading the absorbance at 281 and 650 nm. PA-IIL concentration was estimated to be 3.86 μM bearing an average of 0.49 dyes per PA-IIL.

Probing Microarrays. *On Chip Biological Recognition.* First, 1 μL of a solution in PBS 1× containing labeled lectin diluted (final concentration 0.12 μM), $CaCl_2$ (final concentration 5 μM), and BSA 20% (final concentration 2%) was placed at the bottom of each well. Then slides were incubated at 37 °C in a water vapor saturated chamber for 3 h. The washing steps are: PBS-Tween 20 (0.02%), 5 min at 4 °C, then briefly in deionized water.

IC_{50} Measurement Assay. For IC_{50} experiments, fucose was added to the solution of labeled PA-IIL at different final concentrations (from 0 to 50000 μM maximum of fucose as represented below). Each solution (1 μL) was placed at the bottom of each well and incubated at 37 °C in a water vapor saturated chamber for 3 h. The slides were then washed in PBS-Tween 20 (0.02%) for 5 min at 4 °C and finally rinsed with deionized water before being dried by centrifugation.

Fluorescence Scanning. Slides were scanned with the Microarray scanner, GenePix 4100A software package (Axon Instruments; λ_{ex} 532/635 nm and λ_{em} 575/670 nm). The fluorescence signal of each conjugate was determined as the average of the mean fluorescence signal of four spots.

RESULTS AND DISCUSSION

We have previously reported a family of galactomimetics with different spatial arrangements, i.e., linear, antenna-like, or crown-like (calixarene core)[24,34] and different electrostatic behaviors (i.e., neutral, positively, or negatively charged).[35] Their binding to galactose-binding lectins (i.e., RCA120 and PA-IL) was highly dependent on the architecture of the glycomimetics, and the influence of valency proved less important. Herein, we have synthesized a series of 16 new fucosylated derivatives in order to identify new glycomimetics presenting high affinity for PA-IIL. Each of these glycoclusters was labeled with a Cy3-DNA sequence for their immobilization on a DNA microarray through DNA directed immobilization (DDI) for a rapid screening of their binding to PA-IIL.[27]

The 16 different fucomimetics **F1**−**F16** exhibiting from one to eight α-L-fucose residues were synthesized through the introduction of alkyne or azide functions in several scaffolds by means of phosphoramidite or *H*-phosphonate chemistries in combination with the copper catalyzed alkyne azide 1,3-dipolar cycloaddition (CuAAC reaction).[36,37] This strategy allows for the multiple conjugations of oligonucleotide-like structures with azido-functionalized or alkynylated carbohydrate derivatives. For this study, we used a linear dimethanolcyclohexane (DMCH) trigalactosylated glycocluster **G0** as a negative control (Figure 1) in order to demonstrate the absence of nonspecific interactions of the lectin PA-IIL.[24] The antenna-like fucomimetic **F1** with a bis-pentaerythrityl (Pe) scaffold and four residues was previously reported by us (Figure 1).[25] For the linear glycomimetics **F3**−**F7**, with a DMCH scaffold, two to five fucose residues were introduced to evaluate the effect of valency on their affinity for PA-IIL. For the carbohydrate-centered fucosylated clusters (crown-like structures) **F8**−**F11** and **F13**−**F16**, a hexose core was used with three different configurations using mannose, galactose, or glucose residues. Four fucose residues were introduced on each carbohydrate core with different linkers to evaluate the effects of both the spatial orientation and the nature of the linker. Among them, a mannosyl-centered octa-fucosylated glycocluster **F11** was synthesized to evaluate the effect of an increased valency from tetravalent to octavalent.

Three linker lengths were evaluated with 13, 17, or 21 atoms between the alcohol functions of the hexose platform and the *exo*-anomeric oxygen atom of the fucose moiety for **F8**−**F11** and **F13**−**F16** (Figure 2). Furthermore, glycoclusters **F13**−**F15**

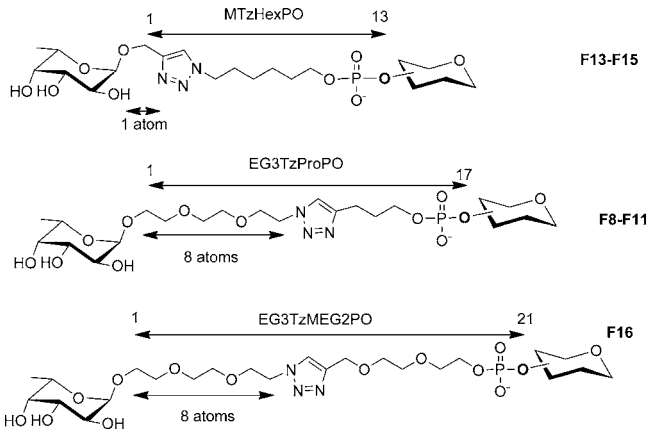
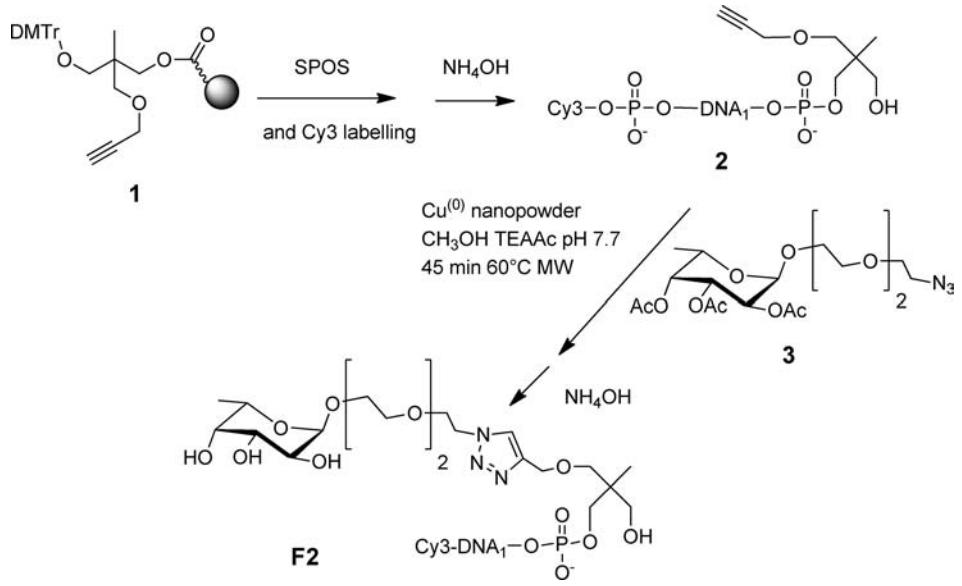


Figure 2. Structures of linkers used for the construction of glycoclusters **F8**−**F11**, **F13**−**F16**, and distances between L-fucose and triazole ring estimated in number of atoms. MTzHexPO: Methylene triazole hexyl phosphodiester, $EG_3TzProPO$: triethylene glycol triazole propyl phosphodiester, EG_3TzMEG_2PO: triethylene glycol triazole methylene diethylene glycol phosphodiester.

display a triazole aromatic ring (MTz) at one atom distance from the fucose moiety (with a methylene bridge) while the triazole ring is located much further away at eight atoms distance (EG_3Tz) for the other glycoclusters. It has been reported that *p*-nitrophenyl α-L-fucoside displays a better affinity than L-fucose, probably to a π−π stacking interaction of the phenyl ring with aromatic residues of the lectin.[7] The present library of glycoclusters will provide insights on the influence of an aromatic moiety in close vicinity to the fucose epitope on the affinity for the PA-IIL lectin. Finally, two

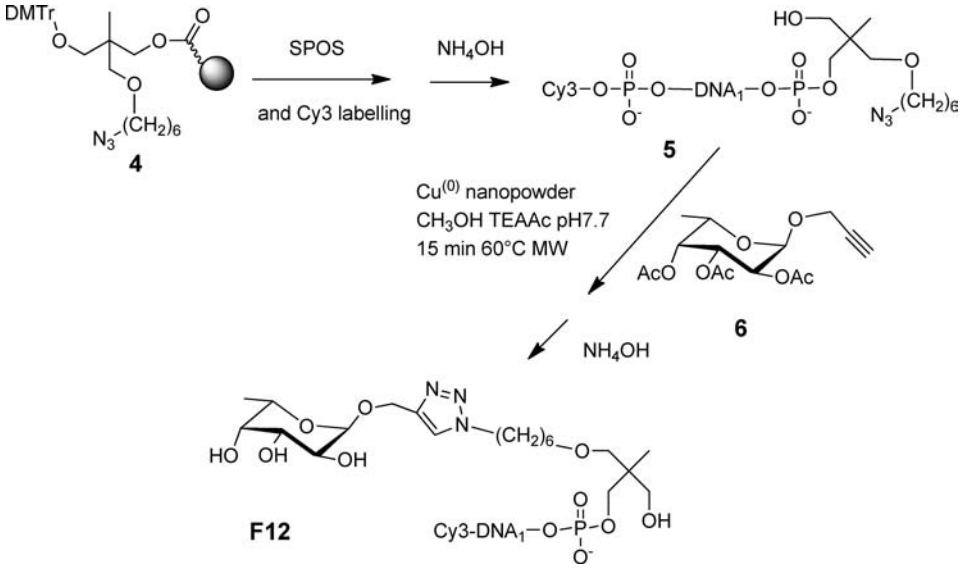
dx.doi.org/10.1021/bc2006434 | *Bioconjugate Chem.* 2012, 23, 1534−1547

Scheme 1. Synthesis of the Monovalent Fucosylated Conjugate F2[a]



[a]SPOS: solid phase oligonucleotide synthesis: (1) 0.09 M phosphoramidite derivative in dry CH_3CN + 0.3 M benzylthiotetrazole in dry CH_3CN; (2) Ac_2O, *N*-methyl-imidazole, 2,6-lutidine; (3) 0.1 M I_2 THF/H_2O/pyridine; (4) 2.5% dichloroacetic acid in CH_2Cl_2.

Scheme 2. Synthesis of the Monovalent Fucosylated Oligonucleotide Conjugate F12



monovalent constructions **F2** and **F12** with only one fucose residue but with different linkers were prepared as control for the evaluation of the multivalency effect (Schemes 1 and 2).

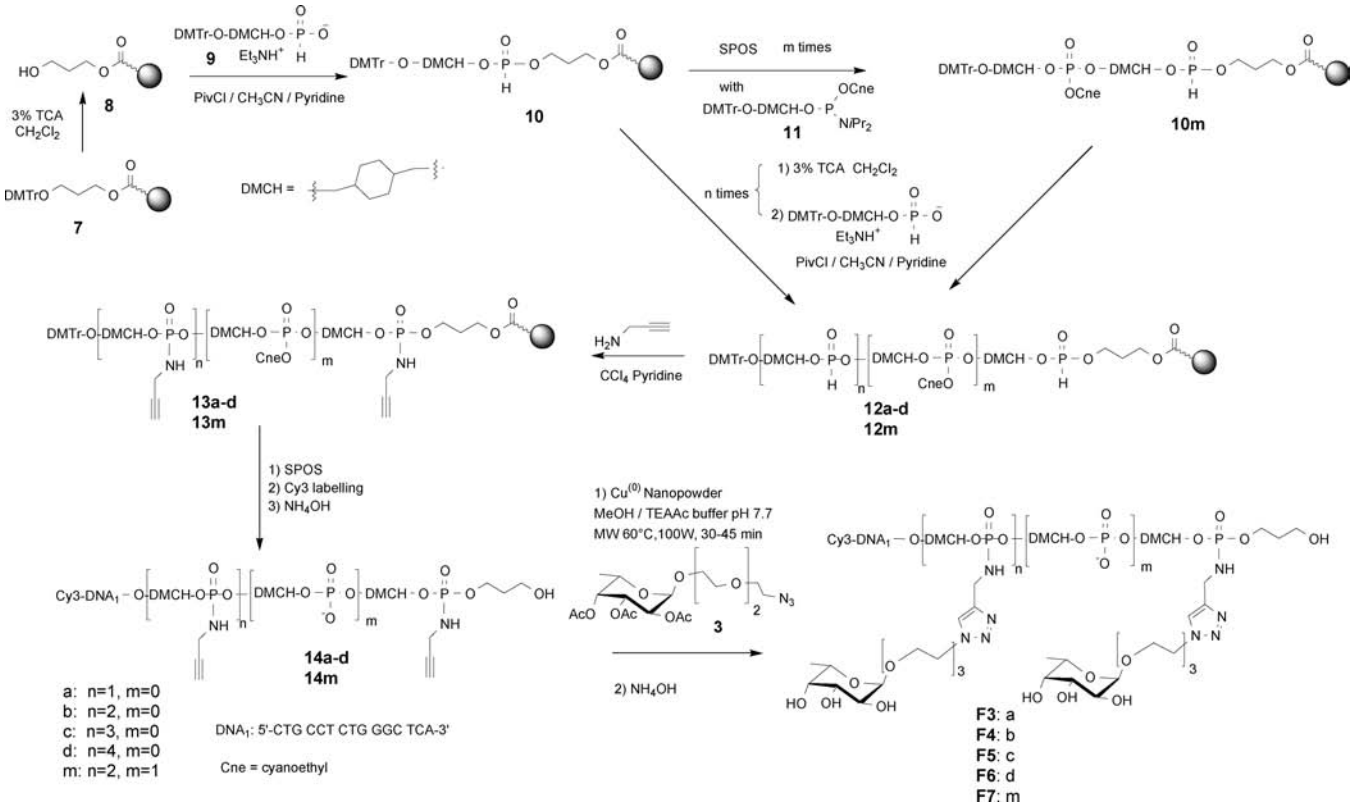
Synthesis of Monovalent Fucosylated Oligonucleotide Conjugates F2 and F12. A monovalent fucosylated oligonucleotide conjugate with a triethyleneglycoltriazole (EG_3Tz) linker was synthesized starting from the propargylated solid support **1**[38] on which the oligonucleotide sequence was assembled and then labeled with Cy3 fluorescent dye using standard phosphoramidite chemistry on a DNA synthesizer (Scheme 1). After treatment with concentrated ammonia for deprotection and release from the solid support, the resulting 5′-Cy3 oligonucleotide with a 3′-alkyne function **2** was conjugated with the 8-azido-3,6-dioxaocta-1-yl 2,3,4-tri-*O*-acetyl-α-L-fucopyranoside **3**[12] by CuAAC using Cu(0) nanopowder[39] in a mixture of methanol and TEAAc buffer under microwave assistance.[40] After centrifugation, the supernatant was desalted by size-exclusion chromatography (SEC). The resulting acetylated conjugate was treated with ammonia, providing the monovalent fucosylated conjugate **F2** after purification by HPLC.

The monovalent fucosylated oligonucleotide conjugate **F12** with a methylene triazole (MTz) linker was synthesized similarly starting from the azidohexyl solid support **4**[41] on which the oligonucleotide was elongated then labeled with Cy3 and subsequently deprotected with ammonia (Scheme 2). The resulting 3′-azide oligonucleotide **5** was conjugated with propargyl 2,3,4-tri-*O*-acetyl-α-L-fucopyranoside **6**,[42] affording the monovalent conjugate **F12** after ammonia treatment and HPLC purification.

Synthesis of Linear DMCH Fucosylated Glycoclusters F3–F7. The linear fucosylated oligonucleotide conjugates were

dx.doi.org/10.1021/bc2006434 | *Bioconjugate Chem.* 2012, 23, 1534–1547

Scheme 3. Synthesis of Linear DMCH Fucosylated Glycoclusters F3−F7



synthesized using *H*-phosphonate chemistry combined with amidative oxidation to introduce the alkyne functions as previously reported (Scheme 3).[40] The oligonucleotide was then elongated and labeled with Cy3 by phosphoramidite chemistry (Scheme 3). After treatment with ammonia to release the conjugate from the solid support and deprotect the polyalkyne oligonucleotide conjugate, the fucose moieties were introduced in solution by CuAAC reaction as described for monovalent glycomimetics. Starting from the 1,3-propanediol solid-support **7**, deprotection of the dimethoxytrityl group afforded alcohol **8**. Two, three, four, or five DMCH *H*-phosphonate monoesters **9** were then introduced, affording four different scaffolds **12a−12d** with two to five *H*-phosphonate diesters. Amidative oxidation[43] of the *H*-phosphonate linkages by carbon tetrachloride in the presence of propargylamine led to multialkynylated scaffolds **13a−13d**, which were then elongated by phosphoramidite chemistry and labeled with Cy3. The 5′-Cy3−3′-polyalkyne oligonucleotides **14a−14d** were obtained in solution after deprotection by ammonia treatment. Each modified oligonucleotide was conjugated with the azido functionalized fucose derivative **3** by CuAAC reaction using Cu(0) nanopowder[39] as described earlier. Acetyl groups were hydrolyzed by ammonia treatment, and the conjugates were purified by C18 reverse phase HPLC.

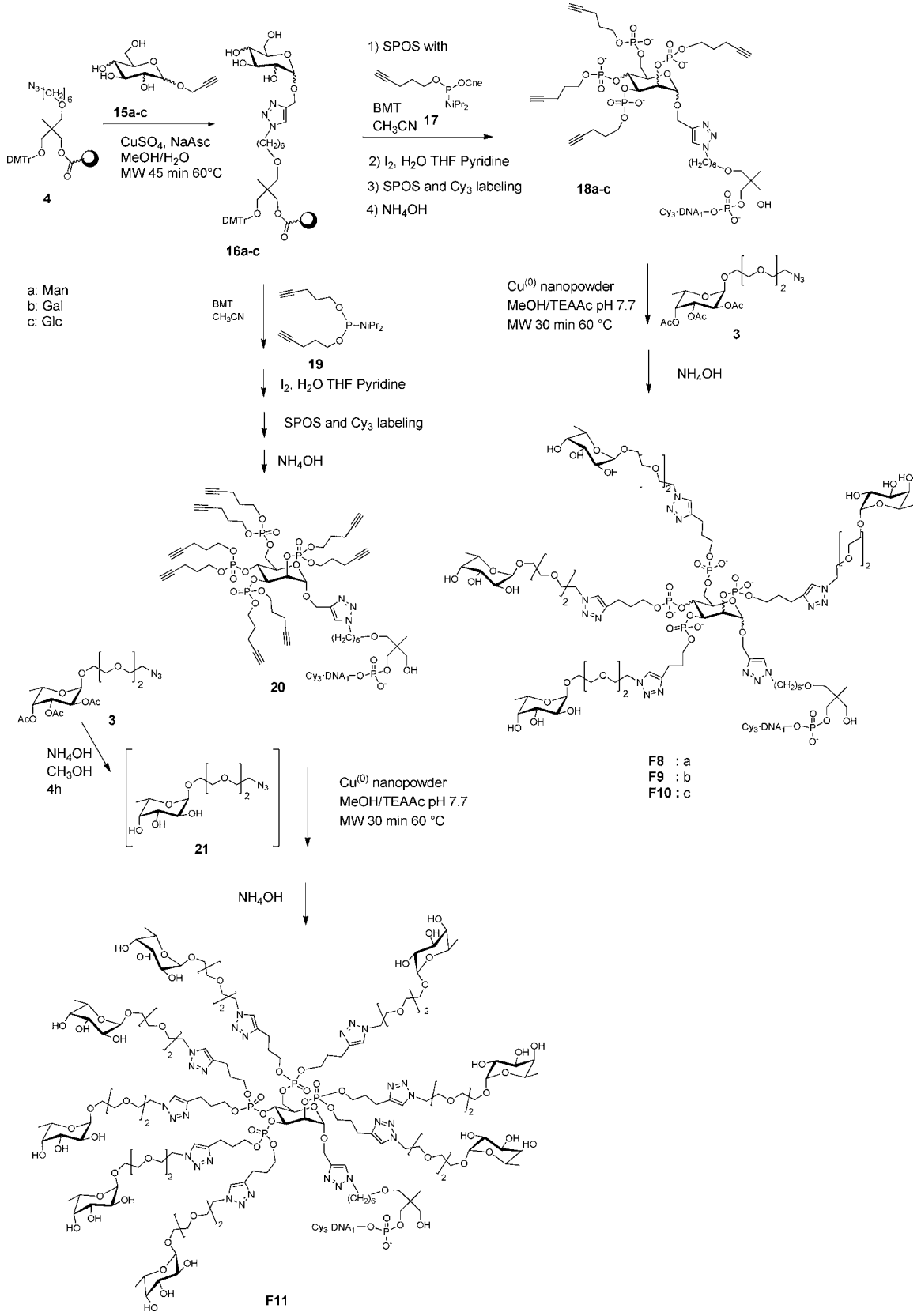
Among the linear fucosylated glycoclusters, a trifucosylated conjugate with a second DMCH linker between two fucose residues was synthesized to evaluate the impact of the distance between fucose residues on its affinity toward PA-IIL. Hence, after the incorporation of the first *H*-phosphonate DMCH **9** to afford **10**, an additional phosphoramidite DMCH building block **11** was introduced by phosphoramidite chemistry using *tert*-butylhydroperoxide as an oxidizing agent to avoid the oxidation of the *H*-phosphonate diester moiety present in compound **10m**.[44,45] Then, the synthesis was continued through *H*-phosphonate chemistry for the two subsequent coupling cycles, providing **12m** followed by the amidative oxidation with CCl_4/propargylamine (leading to **13m**), DNA elongation, and Cy3 labeling (leading to **14m**). After ammonia deprotection, the three fucose residues were introduced in solution by CuAAC reaction, affording the desired trifucosylated glycocluster **F7**.

*Synthesis of Crown-Like Fucosylated Oligonucleotide Conjugates **F8−F11**, and **F13−F16**.* The tetra- and octavalent crown-like fucosylated glycoclusters were synthesized according to the strategy recently reported,[39] starting from an azido-functionalized solid support **4**[41] on which propargyl α-D-mannopyranoside **15a**,[46] propargyl β-D-galactopyranoside **15b**,[47] or propargyl β-D-glucopyranoside **15c**[47] was immobilized by CuAAC with copper sulfate and sodium ascorbate under microwave assistance (Scheme 4), affording the corresponding solid-supported hexose-based platforms **16a−16c**, respectively. Then, four pent-4-ynyl chains were coupled on the four hydroxyls of the solid supported hexoses **16a−16c** using the pent-4-ynyl phosphoramidite **17** on a DNA synthesizer followed by the oligonucleotide elongation and Cy3 labeling. After an ammonia treatment, the resulting 5′-Cy3-oligonucleotides with a tetra-alkynylated hexose moiety **18a−18c** were conjugated by CuAAC with azido-functionalized α-L-fucose **3** as described above to give the fucosylated glycoclusters **F8−F10** with the EG_3Tz linker.

The octavalent glycocluster **F11** was synthesized on a mannose platform **16a** on which eight alkyne functions were introduced using the bis-pent-4-ynyl phosphoramidite **19** conjugated with each alcohol of the mannose residue by phosphoramidite chemistry (Scheme 4). Compound **19** was prepared by reaction between pent-4-yn-1-ol and diisopropy-

dx.doi.org/10.1021/bc2006434 | *Bioconjugate Chem.* 2012, 23, 1534−1547

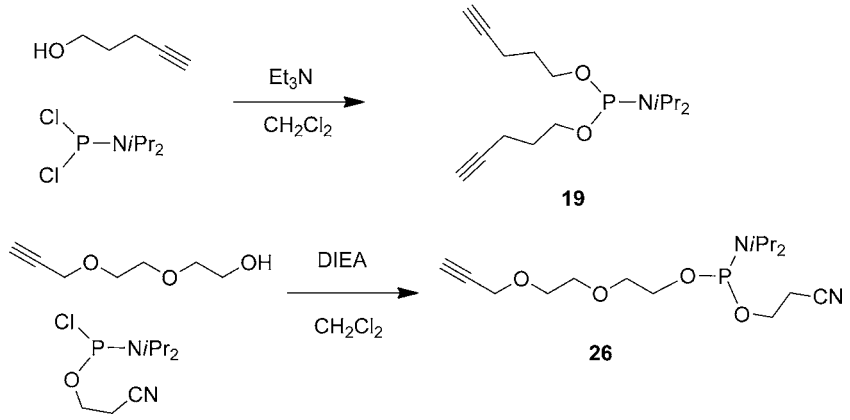
Scheme 4. Crown-Like Tetra-fucosylated Glycoclusters Based on Mannose F8, Galactose F9, and Glucose F10 Cores and Octa-fucoylated Glycocluster Based on Mannose Core F11 with EG_3Tz Linkers



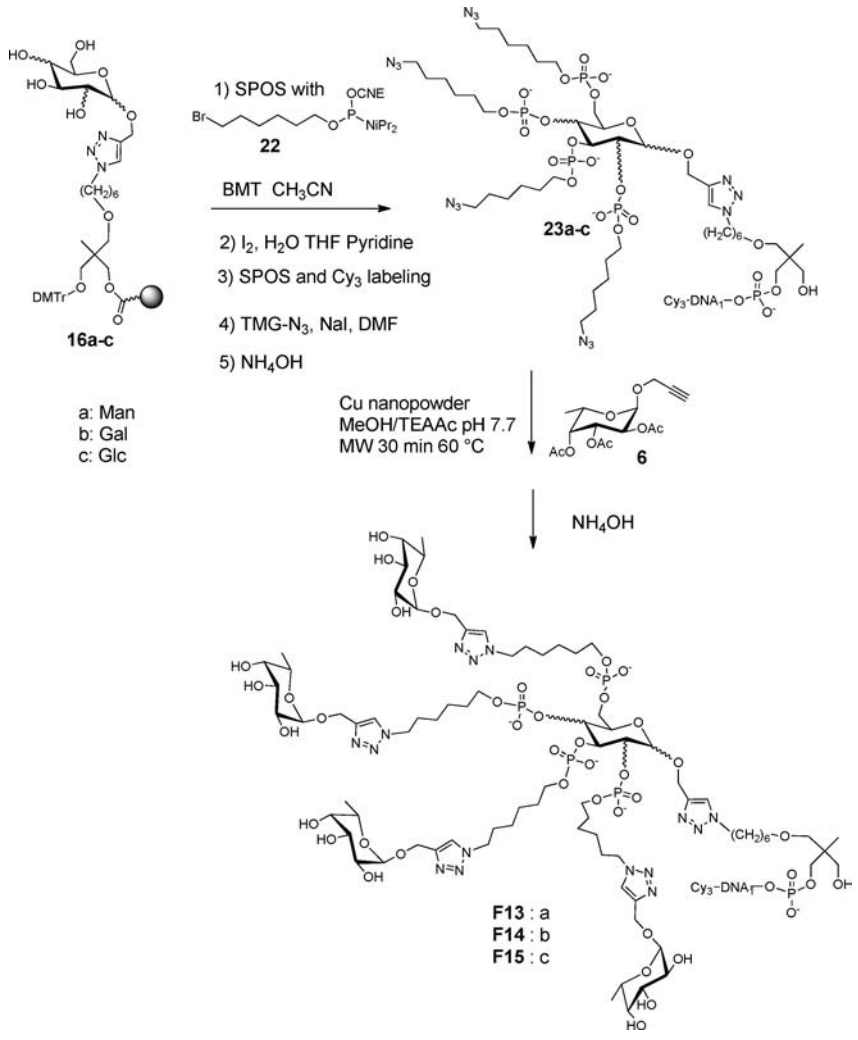
lamino phosphorodichloride in the presence of triethylamine in dichloromethane (Scheme 5). The oligonucleotide was then elongated and labeled with Cy3. The ammonia treatment led to the intermediate **20**, which was conjugated with the azido-functionalized fucose derivative **3**. However, our first attempts to introduce the eight fucose residues **3** in TEAAc buffer and

dx.doi.org/10.1021/bc2006434 | *Bioconjugate Chem.* 2012, 23, 1534−1547

Scheme 5. Synthesis of the Bis-pent-4-ynyl Phosphoramidite 19 and 3,6-Dioxanon-8-yn-1-yl 2-Cyanoethyl *N*,*N*-Diisopropyl Phosphoramidite 26



Scheme 6. Crown-Like Tetra-fucosylated Glycoclusters on Mannose F13, Galactose F14, and Glucose F15 Cores with MTz Linkers

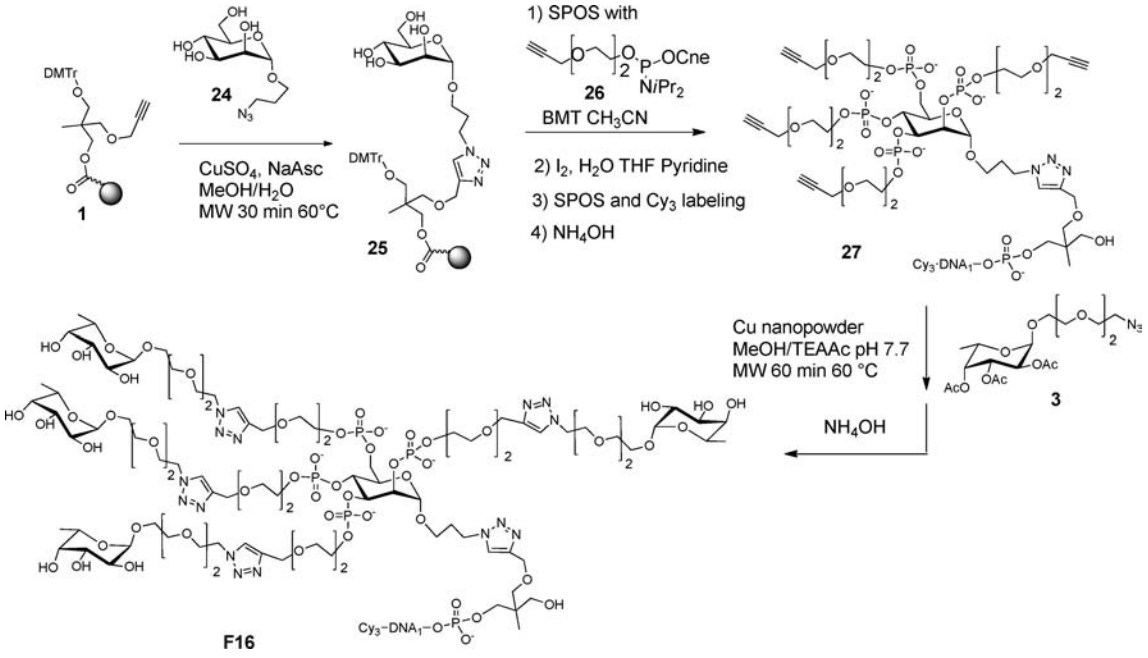


methanol gave an incomplete reaction. The solubility of the intermediates most probably decreased due to the introduction of nonpolar residues during the progress of the successive CuAAC conjugations. To overcome this limitation, the acetyl groups of **3** were hydrolyzed with aqueous ammonia, affording **21**, which was directly used after evaporation and dissolution in water/methanol. The eight conjugations with **21** could be performed smoothly in TEAAc buffer and methanol (3:1, v/v) using Cu(0). The resulting 3′-mannose-centered octa-L-fucose 5′-Cy3-oligonucleotide conjugate **F11** was purified by HPLC.

The fucosylated mimetics with MTz linkers were prepared starting from the hexose-based solid supported platforms **16a**–

dx.doi.org/10.1021/bc2006434 | *Bioconjugate Chem.* 2012, 23, 1534–1547

Scheme 7. Crown-Like Tetra-fucosylated Glycocluster Based on a Mannose Core F16 with EG_3TzMEG_2PO Linkers



16c on which the 6-bromohexyl phosphoramidite **22**[38,48] was conjugated on each alcohol function, and the oligonucleotide was then elongated and labeled with Cy3 (Scheme 6). The four bromine atoms were then substituted with azides by means of tetramethylguanidine azide ($TMGN_3$), and the Cy3-oligonucleotides **23a**−**23c** with the tetra-6-azidohexyl platforms were obtained in solution after ammonia treatment. The fucose moieties were introduced using the propargyl derivative **6**[42] by CuAAC reaction as described above using Cu(0) nanopowder and microwaves. The resulting acetylated fucosylated glycoclusters were purified by HPLC and deprotected by ammonia, affording glycoclusters **F13**−**F15** incorporating MTz linkers.

A fucosylated glycocluster based on a mannose core with a longer linker (EG_3TzMEG_2PO) was also synthesized to evaluate the impact of the linker length on the affinity for the PA-IIL lectin (Figure 2). The phosphoramidite **26** with a longer alkyne linker was prepared from 3,6-dioxanon-8-yn-1-ol[29] by reaction with the *N*,*N*-diisopropylcyanoethyl chlorophosphoramidite in presence of *N*,*N*-diisopropylethylamine in dry dichloromethane (Scheme 5). The solid-supported mannose platform **25** was prepared by CuAAC reaction between the propargylated solid support **1** and the 3-azido-prop-1-yl α-D-mannopyranoside **24**[49] using $CuSO_4$ and sodium ascorbate in methanol and water under microwave assistance (Scheme 7). The long linker phosphoramidite **26** was then introduced, followed by the oligonucleotide elongation and labeling. After ammonia treatment, the Cy3-oligonucleotide mannose with four long alkyne linkers **27** was conjugated with fucosylated azide **3** and purified by HPLC. The fucosylated glycocluster **F16** was obtained after deacetylation by ammonia.

Binding Assays Using a Carbohydrate Microarray. The DNA microarray was prepared by covalent immobilization of a 3′-amino-oligonucleotide by reaction on NHS ester modified glass slides divided in microwells. The carbohydrate−oligonucleotide conjugates **G0** and **F1**−**F16** with their complementary Cy3-oligonucleotide tag were then immobilized in each microwell through DNA/DNA duplex formation. After washing, Alexa-647 labeled PA-IIL lectin was then incubated in each well for binding to the glycoclusters. After washing, the fucomimetic/PA-IIL interaction was visualized by fluorescence scanning.

Immobilization was controlled by fluorescence scanning at 537 nm (excitation) due to the presence of Cy3, allowing the control of the relative surface densities of the immobilized glycomimetics **G0** and **F1**−**F16** in the absence of Alexa-647−PA-IIL.[24,50] The variation of the average Cy3 fluorescence signals (from four repetitions) between fucomimetics was within 6−7% except for fucomimetics **F1**, **F2**, **F13**, and **F16**, where the observed signal deviated by 9%, 12%, 33%, and 19%, respectively. The lectin/glycomimetic interaction was visualized after incubation with Alexa-647 labeled PA-IIL and fluorescence scanning at 635 nm (excitation). The corresponding Alexa-647 signal observed upon interaction with the labeled lectin was normalized based on the Cy3 fluorescence signal.

This qualitative information was complemented with quantitative IC_{50} values measured by incubation of the PA-IIL lectin with an increasing concentration of L-fucose used as a reference ligand of this lectin, therefore, the higher the binding of PA-IIL for the fucomimetic, the higher the concentration of L-fucose required to obtain a 50% reduction of the Alexa-647 fluorescence signal. Hence, the higher the IC_{50} value, the higher the binding of the fucomimetic for the lectin.[50]

The fluorescence intensity of Alexa-647 signal for the 17 glycomimetics (**G0** and **F1**−**F16**) was measured by direct fluorescence scanning (Figure 3). The very low fluorescence intensity observed for the galactosylated glycomimetic **G0** demonstrated the absence of nonspecific binding of PA-IIL to the carbohydrate microarray surface. As previously reported, direct fluorescence scanning is qualitative and a more precise binding efficacy is obtained by determination of IC_{50} values.[34,50]

The monovalent fucosides **F2** and **F12** displayed a similar fluorescence signal around 15000 au lower than all other multivalent fucomimetics. This result shows that the presence of the triazole ring in vicinity to the anomeric center of the L-fucose has no or very little positive influence on the binding to PA-IIL.

dx.doi.org/10.1021/bc2006434 | *Bioconjugate Chem.* 2012, 23, 1534−1547

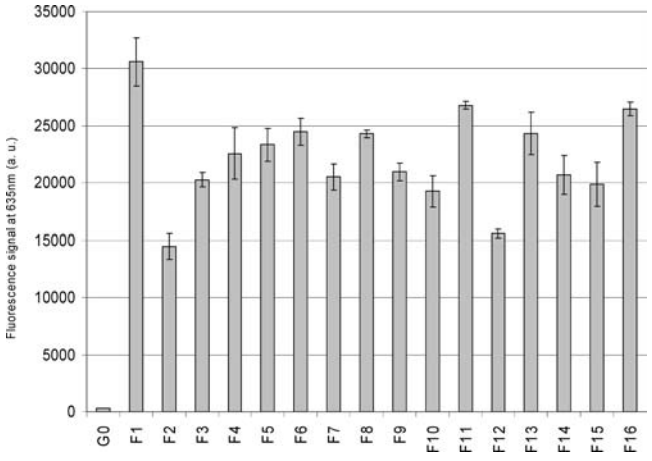


Figure 3. Binding of Alexa-647−PA-IIL to the glycomimetics evaluated by a carbohydrate microarray.

PA-IIL is a tetrameric lectin exhibiting four carbohydrate binding domains.[8] **F1**, **F5**, **F8**−**F10**, and **F13**−**F16** exhibit four fucose residues in antenna-like (**F1**), linear (**F5**), or crown-like arrangements (**F8**−**F10** and **F13**−**F16**) (Table 1). Among the carbohydrate-centered fucomimetics (crown-like arrangement), three different carbohydrate cores were tested: mannose (**F8**, **F13**, and **F16**), galactose (**F9** and **F14**), and glucose (**F10** and **F15**). For these crown-like fucomimetics, three different linkers (MtzHexPO, EG_3TzProPO, and EG_3TzMEG_2PO, Figure 2) were also tested to study the influence of the distance between the fucose and triazole group (1 or 8 atoms) as well as the distance between the fucose residues and the hydroxyl of the carbohydrate core (13, 17, or 21 atoms, Figure 2).

The fluorescence signals observed were above 30000 au for **F1**, near 25000 au for **F5**, **F13**, and **F16**, and near 20000 au for **F9**, **F10**, **F14**, and **F15** (Figure 3). This data suggested that the antenna-like topology (Pe) was preferred by PA-IIL than the linear or the crown-like arrangements. These observations were further confirmed by IC_{50} measurements where the fucomimetics competed with an increasing concentration of L-fucose. Glycomimetics **F1**, **F5**, and **F8** exhibiting the same linker displayed IC_{50} values of 15, 5, and 11 μM, respectively.

Independently from the nature of the linker, the fluorescence signals on crown-like fucomimetics were higher for mannose-centered fucomimetics compared to galactose- or glucose-centered glycoclusters. These results were further corroborated by IC_{50} measurements on the carbohydrate microarray. Glycomimetics **F8**, **F9**, and **F10** displayed IC_{50} values of 11, 1, and 2 μM, respectively, confirming that mannose-centered molecules displayed a better binding than glucose- and galactose-centered fucomimetics while the glucose and galactose cores led to similar properties. In addition, the linear pentavalent fucomimetics **F6** and the mannose crown-like fucomimetics (**F8** and **F13**) displayed a similar binding.

Glycomimetics **F8**, **F13**, and **F16** are mannose-centered fucomimetics bearing MtzHexPO, EG_3TzProPO, and EG_3TzMEG_2PO linkers, respectively. The fluorescence signals measured were similar for the two first linkers used but with a slight increase for the latter and longer linker. This result corroborates the data obtained for the monofucomimetics **F2** and **F12**, showing that the presence of the triazole close to fucose has little to no influence on the binding to PA-IIL. In addition, the increased length of the linker from 13 to 17 atoms led to the same binding, while a linker of 21 atoms was found

Table 1. Characteristic of Glycomimetics Derivatives and IC_{50} Values

	glyco cluster															
	G0	**F1**	**F2**	**F3**	**F4**	**F5**	**F6**	**F7**	**F8**	**F9**	**F10**	**F11**	**F12**	**F13**	**F14**	**F15**	**F16**
Nb of residues	3	4	1	2	3	4	5	3	4	4	4	8	1	4	4	4	4
IC_{50} [a] (μM fuc)	n.d	15	0.2	2	3	5	8	nd	11	1	2	16	nd	7	nd	nd	14
relative potency	nd	75	1	10	15	25	40	nd	55	5	10	80	nd	35	nd	nd	70
relative potency per fucose residues	nd	18.8	1	5	5	6.3	8	nd	13.8	1.25	2.5	10	na	8.8	nd	nd	17.5
spatial arrangement	linear	antenna	mono			linear				crown-like			mono	crown-like			
scaffold	DMCH	Pe				DMCH			Man	Gal	Glc	Man		Man	Gal	Glc	Man
linker	EG_3TzPro		EG_3Tz			EG_3TzPro				EG_3TzPro				MTzHex			EG_3TzMEG_2

[a] IC_{50} values were determined as the concentration of L-fucose required to decrease the Alexa-647-PA-IIL fluorescence signal of 50%. nd: not determined.

dx.doi.org/10.1021/bc2006434 | *Bioconjugate Chem.* 2012, 23, 1534−1547

slightly better. Similar trends were observed for **F9**/**F14** and **F10**/**F15**, the crown-like fucomimetics bearing the EG_3TzProPO/MTzHexPO linkers with a galactose- and glucose-based core, respectively. Determination of IC_{50} values gave a confirmation of these results. The mannose crown-like fucomimetics **F13**, **F8**, and **F16**, exhibiting increasing length of linker with 13, 17, and 21 atoms, respectively, displayed an increasing relative potency of 8.8, 13.8, and 17.5, respectively, showing the beneficial effect of a longer linker on the binding (Figure 4).

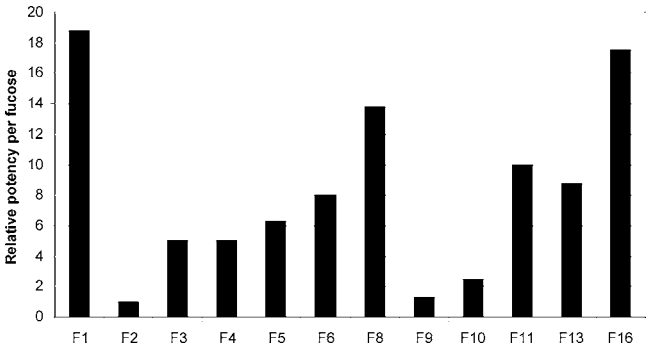


Figure 4. Relative potency per fucose of some fucomimetics.

The influence of the number of carbohydrates was then studied by increasing the number of fucose residues from 2 to 5 for linear fucomimetics (**F3**−**F6**). The fluorescence signal increased from 20270 au to 24460 au, matching the increasing number of fucose epitopes. Likewise, the relative potency per fucose residues was slightly increased for fucomimetics **F3**−**F6** (from 5 to 8, Table 1, Figure 4). The spacing between fucose residues was also studied for three fucoses bearing glycomimetics (**F4** and **F7**), but no significant difference in the fluorescence signal could be observed (Figure 3). On the basis of the relative potency values, the pentavalent fucomimetic **F6** displayed the best binding of the linear ones but lower than the antenna-like tetravalent fucomimetic **F1** and the mannose crown-like fucomimetics (**F8**, **F13**, and **F16**) whatever their linker.

Similarly to comb-like fucomimetics, the binding of PA-IIL was improved by increasing to eight the number of fucose residues at the periphery of a mannose-centered glycomimetics (**F11** vs **F8**). The IC_{50} values measured for **F8** and **F11** were 11 and 16 μM, respectively, showing a better binding for the **F11** but a lower potency per fucose residue (13.8 and 10 for **F8** and **F11**, respectively, Figure 4).

The binding properties toward PA-IIL of divalent and trivalent glycoclusters bearing the Lewis a trisaccharide (Le^a) as epitopes were studied by enzyme linked lectin assay (ELLA) and by isothermal titration microcalorimetry (ITC) by Roy et al.[11] The fucosylated glycoclusters were assembled on linear or aromatic platforms by Cu(I) alkyne−azide 1,3-dipolar cycloaddition (CuAAC). The triazole group did not favor or hampered the interaction between the lectin and the clusters. The distance between the fucose residues in their extended conformation was estimated by molecular modeling of 22−41 Å. Their results showed that the molecules interacted with only one binding site within the same lectin. No influence of the length of the spacer was observed, maybe because the length and structure of the linker did not allow the interaction of glycoclusters with two binding sites on the same tetramer in a chelate binding mode. In another recent study, Reymond et al.[6] studied the interaction of PA-IIL with fucosylated peptide-based dendrimers. The best ligand identified in this study displayed its fucose residues separated by 7 amino acids. Similarly, molecular modeling demonstrated that the glycodendrimer was too small to interact in a chelate binding mode.

In the present study, the relative potency per fucose residues remained similar for mannose centered fucomimetics **F8** and **F11**, slightly increased as a function of fucose residues for linear fucomimetics **F3**−**F6**, and displayed a neat increase for the mannose centered fucomimetics **F13**, **F8**, and **F16** according to the increase length of the linker. However, the distance between the fucose residues is expected to be in the same range as those of the glycoclusters from Roy or Reymond laboratories. Therefore, similarly to these two precedent studies, the distance between each fucose epitope in our glycoclusters was not sufficient to bind two distinct binding sites on the same lectin tetramer, preventing a chelate effect to occur.

CONCLUSION

The binding affinity of 16 fucomimetics for PA-IIL using minute amounts (few picomoles) of glycoclusters could be rapidly and efficiently screened using a carbohydrate microarray. According to our results, both monofucose derivatives (**F2** and **F12**) displayed a lower binding affinity for PA-IIL than all the other oligofucomimetics, showing the local concentration effect of glycoclusters on binding. The best binding properties were observed for the antenna-like fucomimetic **F1** bearing four residues and for the mannose-centered fucomimetics **F16** and **F11** bearing four and eight fucosyl residues, respectively. Among the carbohydrate-centered fucomimetics exhibiting four residues (**F8**−**F10** and **F13**−**F16**), the mannose core showed the best binding (**F8**, **F13** and **F16**) and a better effect was observed with the longer linker (**F16**). The linear fucomimetics showed an increase of binding correlated with the number of residues.

Our results suggested that our fucomimetics were not able to bind more than one site per lectin resulting, no chelate effect was observed.. The increase bindings most probably were the result of increased fucose local concentration for linear fucomimetics **F3**−**F6**, while the increase of binding for the mannose-centered fucomimetics **F8**, **F13**, and **F16** may be due to additional interactions or to steric stabilization, preventing the approach of free fucose

From all studied glycomimetics, the present study allowed us to select two fucomimetics, **F1** and **F16**, bearing four fucose moieties exhibiting the best binding affinity for PA-IIL (relative potency per fucose around 18). Work is in progress to synthesize fucomimetics with longer linker with the expectation to bind two PA-IIL sites within the same lectin in order to obtain chelate effect. Furthermore, **F1** and **F16** without the DNA sequence will be synthesized at a higher scale for biophysical and biological studies.

ASSOCIATED CONTENT

Supporting Information

General procedures, HPLC data of fucomimetics, NMR data of compounds **19** and **26**. This material is available free of charge via the Internet at http://pubs.acs.org.

dx.doi.org/10.1021/bc2006434 | *Bioconjugate Chem.* 2012, 23, 1534−1547

AUTHOR INFORMATION

Corresponding Author

*For F.M.: phone, +33/467 144 961; fax, +33/467 042 029; E-mail morvan@univ-montp2.fr. For Y.C.: phone, +33/472 186 240; fax, +33/4 78 43 35 93; E-mail, yann.chevolot@ec-lyon.fr.

Notes

The authors declare no competing financial interest.

ACKNOWLEDGMENTS

This work was financially supported by ANR-08-BLAN-0114-01, Lyon Biopole, and Vaincre la Mucoviscidose. G.P. thanks the CNRS and the Région Languedoc–Roussillon for the award of a research studentship. F.M. is from Inserm. Programme Cible 2010 "region Rhône-Alpes" is acknowledged.

REFERENCES

(1) Bertozzi, C. R., and Kiessling, L. L. (2001) Chemical glycobiology. *Science 291*, 2357–2364.

(2) Seeberger, P. H., and Werz, D. B. (2007) Synthesis and medical applications of oligosaccharides. *Nature 446*, 1046–1051.

(3) Varki, A. (1993) Biological Roles of Oligosaccharides—All of the Theories Are Correct. *Glycobiology 3*, 97–130.

(4) Lee, Y. C., and Lee, R. T. (1995) Carbohydrate–Protein Interactions: Basis of Glycobiology. *Acc. Chem. Res. 28*, 321–327.

(5) Imberty, A., Wimmerova, M., Mitchell, E. P., and Gilboa-Garber, N. (2004) Structures of the lectins from *Pseudomonas aeruginosa*: insights into the molecular basis for host glycan recognition. *Microb. Infect. 6*, 221–228.

(6) Johansson, E. M. V., Crusz, S. A., Kolomiets, E., Buts, L., Kadam, R. U., Cacciarini, M., Bartels, K. M., Diggle, S. P., Camara, M., Williams, P., Loris, R., Nativi, C., Rosenau, F., Jaeger, K. E., Darbre, T., and Reymond, J. L. (2008) Inhibition and Dispersion of Pseudomonas aeruginosa Biofilms by Glycopeptide Dendrimers Targeting the Fucose-Specific Lectin LecB. *Chem. Biol. 15*, 1249–1257.

(7) Mitchell, E. P., Sabin, C., Snajdrova, L., Pokorna, M., Perret, S., Gautier, C., Hofr, C., Gilboa-Garber, N., Koca, J., Wimmerova, M., and Imberty, A. (2005) High affinity fucose binding of *Pseudomonas aeruginosa* lectin PA-IIL: 1.0 angstrom resolution crystal structure of the complex combined with thermodynamics and computational chemistry approaches. *Proteins 58*, 735–746.

(8) Gilboa-Garber, N., Katcoff, D. J., and Garber, N. C. (2000) Identification and characterization of *Pseudomonas aeruginosa* PA-IIL lectin gene and protein compared to PA-IL. *FEMS Immunol. Med. Microbiol. 29*, 53–57.

(9) Deguise, I., Lagnoux, D., and Roy, R. (2007) Synthesis of glycodendrimers containing both fucoside and galactoside residues and their binding properties to PA-IL and PA-IIL lectins from *Pseudomonas aeruginosa*. *New J. Chem. 31*, 1321–1331.

(10) Johansson, E. M. V., Kolomiets, E., Rosenau, F., Jaeger, K. E., Darbre, T., and Reymond, J. L. (2007) Combinatorial variation of branching length and multivalency in a large (390 625 member) glycopeptide dendrimer library: ligands for fucose-specific lectins. *New J. Chem. 31*, 1291–1299.

(11) Marotte, K., Eville, C. P., Sabin, C., Pymbock, M. M., Imberty, A., and Roy, R. (2007) Synthesis and binding properties of divalent and trivalent clusters of the Lewis a disaccharide moiety to *Pseudomonas aeruginosa* lectin PA-IIL. *Org. Biomol. Chem. 5*, 2953–2961.

(12) Morvan, F., Meyer, A., Jochum, A., Sabin, C., Chevolot, Y., Imberty, A., Praly, J. P., Vasseur, J. J., Souteyrand, E., and Vidal, S. (2007) Fucosylated pentaerythrityl phosphodiester oligomers (PePOs): automated synthesis of DNA-based glycoclusters and binding to *Pseudomonas aeruginosa* lectin (PA-IIL). *Bioconjugate Chem. 18*, 1637–1643.

(13) Kolomiets, E., Swiderska, M. A., Kadam, R. U., Johansson, E. M. V., Jaeger, K. E., Darbre, T., and Reymond, J. L. (2009) Glycopeptide Dendrimers with High Affinity for the Fucose-Binding Lectin LecB from *Pseudomonas aeruginosa*. *ChemMedChem 4*, 562–569.

(14) Andreini, M., Anderluh, M., Audfray, A., Bernardi, A., and Imberty, A. (2010) Monovalent and bivalent *N*-fucosyl amides as high affinity ligands for *Pseudomonas aeruginosa* PA-IIL lectin. *Carbohydr. Res. 345*, 1400–1407.

(15) Johansson, E. M. V., Kadam, R. U., Rispoli, G., Crusz, S. A., Bartels, K. M., Diggle, S. P., Camara, M., Williams, P., Jaeger, K. E., Darbre, T., and Reymond, J. L. (2011) Inhibition of *Pseudomonas aeruginosa* biofilms with a glycopeptide dendrimer containing D-amino acids. *MedChemComm 2*, 418–420.

(16) Consoli, G. M. L., Granata, G., Cafiso, V., Stefani, S., and Geraci, C. (2011) Multivalent calixarene-based C-fucosyl derivative: a new *Pseudomonas aeruginosa* biofilm inhibitor. *Tetrahedron Lett. 52*, 5831–5834.

(17) Sharon, N. (2006) Carbohydrates as future anti-adhesion drugs for infectious diseases. *Biochim. Biophys. Acta 1760*, 527–537.

(18) Pieters, R. J. (2007) Intervention with bacterial adhesion by multivalent carbohydrates. *Med. Res. Rev. 27*, 796–816.

(19) Lee, R., T., Lee, Y., C. (1994) Neoglycoconjugates: Preparation and Applications. In *Enhanced Biochemical Affinities of Multivalent Neoglycoconjugates* (Lee, R., T., Lee, Y., C., Eds.) pp 23–50, Academic Press, San Diego.

(20) Lis, H., and Sharon, N. (1998) Lectins: Carbohydrate-Specific Proteins That Mediate Cellular Recognition. *Chem. Rev. 98*, 637–674.

(21) Lundquist, J. J., and Toone, E. J. (2002) The cluster glycoside effect. *Chem. Rev. 102*, 555–578.

(22) Chabre, Y. M., and Roy, R. (2010) Design and Creativity in Synthesis of Multivalent Neoglycoconjugates. *Adv. Carbohydr. Chem. Biochem. 63*, 165–393.

(23) Obviously, the final topology of the glycoclusters in solution is much more complex due to flexible scaffolds and arms.

(24) Chevolot, Y., Bouillon, C., Vidal, S., Morvan, F., Meyer, A., Cloarec, J. P., Jochum, A., Praly, J. P., Vasseur, J. J., and Souteyrand, E. (2007) DNA-based carbohydrate biochips: a platform for surface glyco-engineering. *Angew. Chem., Int. Ed. 46*, 2398–2402.

(25) Zhang, J., Pourceau, G., Meyer, A., Vidal, S., Praly, J. P., Souteyrand, E., Vasseur, J. J., Morvan, F., and Chevolot, Y. (2009) Specific recognition of lectins by oligonucleotide glycoconjugates and sorting on a DNA microarray. *Chem. Commun.*, 6795–6797.

(26) Niemeyer, C. M., Boldt, L., Ceyhan, B., and Blohm, D. (1999) DNA-directed immobilization: efficient, reversible, and site-selective surface binding of proteins by means of covalent DNA–streptavidin conjugates. *Anal. Biochem. 268*, 54–63.

(27) Wacker, R., and Niemeyer, C. M. (2004) DDI-mu FIA—a readily configurable microarray-fluorescence immunoassay based on DNA-directed immobilization of proteins. *ChemBioChem 5*, 453–459.

(28) Pourceau, G., Chevolot, Y., Goudot, A., Giroux, F., Meyer, A., Moulès, V., Lina, B., Cecioni, S., Vidal, S., Yu, H., Chen, X., Ferraris, O., Praly, J. P., Souteyrand, E., Vasseur, J. J., and Morvan, F. (2011) Measurement of enzymatic activity and specificity of human and avian influenza neuraminidases from whole virus by glycoarray and MALDI-TOF mass spectrometry. *ChemBioChem 12*, 2071–2080.

(29) Diot, J., Garcia-Moreno, M. I., Gouin, S. G., Mellet, C. O., Haupt, K., and Kovensky, J. (2009) Multivalent iminosugars to modulate affinity and selectivity for glycosidases. *Org. Biomol. Chem. 7*, 357–363.

(30) Mazurczyk, R., Khoury, G. E., Dugas, V., Hannes, B., Laurenceau, E., Cabrera, M., Krawczyk, S., Souteyrand, E., Cloarec, J. P., and Chevolot, Y. (2008) Low-cost, fast prototyping method of fabrication of the microreactor devices in soda-lime glass. *Sens. Actuators, B 128*, 552–559.

(31) Vieillard, J., Mazurczyk, R., Morin, C., Hannes, B., Chevolot, Y., Desbène, P.-L., and Krawczyk, S. (2007) Application of microfluidic chip with integrated optics for electrophoretic separations of proteins. *J. Chromatogr., B 845*, 218–225.

(32) Dugas, V., and Chevalier, Y. (2003) Surface hydroxylation and silane grafting on fumed and thermal silica. *J. Colloid Interface Sci. 264*, 354–361.

(33) Dugas, V., Depret, G., Chevalier, B., Nesme, X., and Souteyrand, E. (2004) Immobilization of single-stranded DNA fragments to solid surfaces and their repeatable specific hybridization: covalent binding or adsorption? *Sens. Actuators, B 101*, 112−121.
(34) Moni, L., Pourceau, G., Zhang, J., Meyer, A., Vidal, S., Souteyrand, E., Dondoni, A., Morvan, F., Chevolot, Y., Vasseur, J. J., and Marra, A. (2009) Design of Triazole-Tethered Glycoclusters Exhibiting Three Different Spatial Arrangements and Comparative Study of their Affinities towards PA-IL and RCA 120 by Using a DNA-Based Glycoarray. *ChemBioChem 10*, 1369−1378.
(35) Chevolot, Y., Zhang, J., Meyer, A., Goudot, A., Rouanet, S., Vidal, S., Pourceau, G., Cloarec, J. P., Praly, J. P., Souteyrand, E., Vasseur, J. J., and Morvan, F. (2011) Multiplexed binding determination of seven glycoconjugates for *Pseudomonas aeruginosa* lectin I (PA-IL) using a DNA-based carbohydrate microarray. *Chem. Commun. 47*, 8826−8828.
(36) Rostovtsev, V. V., Green, L. G., Fokin, V. V., and Sharpless, K. B. (2002) A Stepwise Huisgen Cycloaddition Process: Copper(I)-Catalyzed Regioselective "Ligation" of Azides and Terminal Alkynes. *Angew. Chem., Int. Ed. 41*, 2596−2599.
(37) Tornoe, C. W., Christensen, C., and Meldal, M. (2002) Peptidotriazoles on solid phase: [1,2,3]-triazoles by regiospecific copper(I)-catalyzed 1,3-dipolar cycloadditions of terminal alkynes to azides. *J. Org. Chem. 67*, 3057−3064.
(38) Lietard, J., Meyer, A., Vasseur, J. J., and Morvan, F. (2008) New strategies for cyclization and bicyclization of oligonucleotides by click chemistry assisted by microwaves. *J. Org. Chem. 73*, 191−200.
(39) Pourceau, G., Meyer, A., Chevolot, Y., Souteyrand, E., Vasseur, J. J., and Morvan, F. (2010) Oligonucleotide Carbohydrate-Centered Galactosyl Cluster Conjugates Synthesized by Click and Phosphoramidite Chemistries. *Bioconjugate Chem. 21*, 1520−1529.
(40) Bouillon, C., Meyer, A., Vidal, S., Jochum, A., Chevolot, Y., Cloarec, J. P., Praly, J. P., Vasseur, J. J., and Morvan, F. (2006) Microwave assisted "click" chemistry for the synthesis of multiple labeled-carbohydrate oligonucleotides on solid support. *J. Org. Chem. 71*, 4700−4702.
(41) Pourceau, G., Meyer, A., Vasseur, J. J., and Morvan, F. (2009) Azide Solid Support for 3′-Conjugation of Oligonucleotides and Their Circularization by Click Chemistry. *J. Org. Chem. 74*, 6837−6842.
(42) Roy, B., and Mukhopadhyay, B. (2007) Sulfuric acid immobilized on silica: an excellent catalyst for Fischer type glycosylation. *Tetrahedron Lett. 48*, 3783−3787.
(43) Atherton, F. R., Openshaw, H. T., and Todd, A. R. (1945) Studies on Phosphorylation 0.2. The Reaction of Dialkyl Phosphites with Polyhalogen Compounds in Presence of Bases—A New Method for the Phosphorylation of Amines. *J. Chem. Soc.*, 660−663.
(44) Peyrottes, S., Vasseur, J. J., Imbach, J. L., and Rayner, B. (1996) Oligodeoxynucleoside Phosphoramidates (P-NH2)—Synthesis and Thermal Stability of Duplexes With DNAand RNA Targets. *Nucleic Acids Res. 24*, 1841−1848.
(45) Bologna, J. C., Morvan, F., and Imbach, J. L. (1999) The prooligonucleotide approach: synthesis of mixed phosphodiester and SATE phosphotriester prooligonucleotides using H-phosphonate and phosphoramidite chemistries. *Eur. J. Org. Chem.*, 2353−2358.
(46) Hasegawa, T., Numata, M., Okumura, S., Kimura, T., Sakurai, K., and Shinkai, S. (2007) Carbohydrate-appended curdlans as a new family of glycoclusters with binding properties both for a polynucleotide and lectins. *Org. Biomol. Chem. 5* (15), 2404−2412.
(47) Mereyala, H. B., and Gurrala, S. R. (1998) A highly diastereoselective, practical synthesis of allyl, propargyl 2,3,4,6-tetra-*O*-acetyl-beta-D-gluco, beta-D-galactopyranosides and allyl, propargyl heptaacetyl-beta-D-lactosides. *Carbohydr. Res. 307*, 351−354.
(48) Lietard, J., Meyer, A., Vasseur, J. J., and Morvan, F. (2007) An efficient reagent for 5 ′-azido oligonucleotide synthesis. *Tetrahedron Lett. 48*, 8795−8798.
(49) Joosten, J. A. F., Loimaranta, V., Appeldoorn, C. C. M., Haataja, S., El Maate, F. A., Liskamp, R. M. J., Finne, J., and Pieters, R. J. (2004) Inhibition of *Streptococcus suis* adhesion by dendritic galabiose compounds at low nanomolar concentration. *J. Med. Chem. 47*, 6499−6508.
(50) Zhang, J., Pourceau, G., Meyer, A., Vidal, S., Praly, J.-P., Souteyrand, E., Vasseur, J.-J., Morvan, F., and Chevolot, Y. (2009) DNA-directed immobilisation of glycomimetics for glycoarrays application: comparison with covalent immobilisation, and development of an on-chip IC50 measurement assay. *Biosens. Bioelectron. 24*, 2515−2521.

Bioconjugate Chemistry

Article

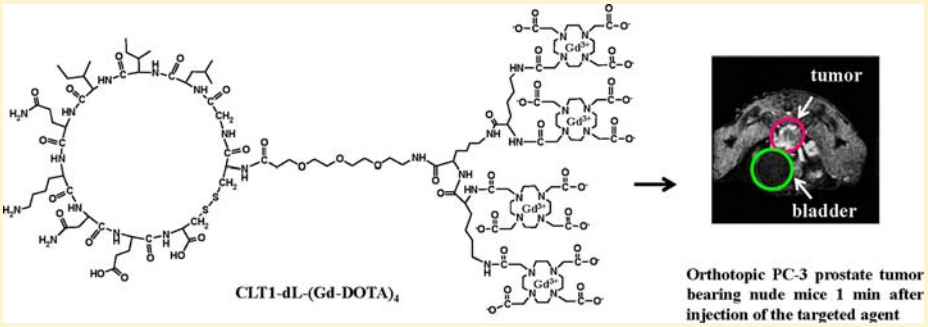
pubs.acs.org/bc

Synthesis and Evaluation of a Peptide Targeted Small Molecular Gd-DOTA Monoamide Conjugate for MR Molecular Imaging of Prostate Cancer

Xueming Wu,[†] Susan M. Burden-Gulley,[‡] Guan-Ping Yu,[†] Mingqian Tan,[†] Daniel Lindner,[§] Susann M. Brady-Kalnay,[‡] and Zheng-Rong Lu*,[†]

[†]Department of Biomedical Engineering, and [‡]Department of Molecular Biology and Microbiology, School of Medicine, Case Western Reserve University, Cleveland, Ohio 44106, United States

[§]Department of Translational Hematology & Oncology Research, Cleveland Clinic, Cleveland, Ohio 44195, United States



ABSTRACT: Tumor extracellular matrix has an abundance of cancer related proteins that can be used as biomarkers for cancer molecular imaging. Innovative design and development of safe and effective targeted contrast agents to these biomarkers would allow effective MR cancer molecular imaging with high spatial resolution. In this study, we synthesized a low molecular weight CLT1 peptide targeted Gd(III) chelate CLT1-dL-$(Gd\text{-}DOTA)_4$ specific to clotted plasma proteins in tumor stroma for cancer MR molecular imaging. CLT1-dL-$(Gd\text{-}DOTA)_4$ was synthesized by conjugating four Gd-DOTA monoamide chelates to a CLT1 peptide via generation 1 lysine dendrimer. The T_1 relaxivity of CLT1-dL-$(Gd\text{-}DOTA)_4$ was 40.4 mM^{-1} s^{-1} per molecule (10.1 mM^{-1} s^{-1} per Gd) at 37 °C and 1.5 T. Fluorescence imaging showed high binding specificity of CLT1 to orthotopic PC3 prostate tumor in mice. The contrast agent resulted in improved tumor contrast enhancement in male athymic nude mice bearing orthotopic PC3 prostate tumor xenograft at a dose of 0.03 mmol Gd/kg. The peptide targeted MRI contrast agent is promising for high-resolution MR molecular imaging of prostate tumor.

INTRODUCTION

Early accurate detection and diagnosis of malignant tumors enable more effective cancer treatment at an earlier stage, resulting in improved survival rate and quality of the life of cancer patients.[1] Effective imaging of cancer-related molecular targets is of great significance to improve the accuracy of earlier cancer detection and diagnosis. Molecular imaging has been proven successful for accurate cancer detection and rapid assessment of therapeutic efficacy with highly sensitive imaging modalities, including PET and SPECT.[2−6] However, these imaging modalities cannot provide high-resolution images of anatomic structures and are often combined with other anatomic imaging modalities, e.g., CT and MRI, to correlate molecular imaging with structural imaging for accurate diagnosis.[7−10]

Magnetic resonance imaging (MRI) is a powerful clinical imaging modality with high spatial resolution and no ionization radiation. MRI provides both anatomical and physiological information of soft tissues.[11,12] Contrast enhanced MRI can produce high-resolution image contrast between diseased tissue and normal tissue. Currently, no targeted contrast agent is available for clinical MR cancer molecular imaging. Innovative design and development of targeted MRI contrast agents would greatly advance the application of MR cancer molecular imaging. Significant efforts have been made on developing targeted contrast agents for MR imaging of the biomarkers expressed on the surface of cancer cells. Due to relatively low sensitivity of MRI and low concentration of these biomarkers, it is a challenge to generate sufficient contrast enhancement for effective MR molecular imaging using small molecular targeted contrast agents.[13,14] In order to obtain sufficient enhancement, various delivery systems such as liposomes, nanoparticles, and polymer conjugates with a high payload of paramagnetic Gd(III) chelates have been prepared to increase local concentration of contrast agents at the target sites.[15−22] Although these delivery systems are able to generate significant tumor enhancement in animal models, their large sizes result in slow and incomplete elimination from the

Received: January 12, 2012
Revised: July 10, 2012
Published: July 19, 2012

 © 2012 American Chemical Society

body, resulting in prolonged accumulation of toxic Gd(III) ions that can cause serious safety concerns and prevent further clinical development.[23−26] Recently, some studies have shown that the limitations of MRI for molecular imaging can be overcome by selecting proper molecular biomarkers with high local expression in the lesion tissues and using small molecular agents that can be readily excreted.[27−35] The key feature of these agents is that they target molecular markers abundantly present in the diseased tissues with little presence in normal tissues. A sufficient amount of contrast agents can bind to these targets, resulting in sufficient contrast enhancement for effective MR molecular imaging. Since their size is smaller than the renal filtration threshold, unbound contrast agents can readily be excreted from the body with reduced background noise.

Malignant tumors have a unique microenvironment that contains a meshwork of clotted proteins in the tumor stroma, but no such meshwork is detectable in normal tissues.[36−40] The protein clots are formed by plasma proteins that leak into the extravascular space in tumors, presumably due to tumor angiogenesis and vascular hyperpermeability. We hypothesized that clotted plasma proteins in tumor stroma could be a viable target for MR cancer molecular imaging. Their abundance in the tumor stroma allows the binding of sufficient low molecular weight targeted contrast agents to generate MRI detectable contrast enhancement for effective cancer molecular imaging. Ruoslahti's group recently reported two cyclic peptides CGLIIQKNEC (CLT1) and CNAGESSKNC (CLT2) bound specifically to the clotted plasma proteins (fibrin−fibronectin complexes) formed in tumor stroma.[39] We have recently demonstrated that CLT1-(DTPA-Gd) was effective in generating sufficient contrast enhancement for MR cancer molecular imaging in different tumor models, including MDA-MB-231 breast cancer and HT29 colon cancer.[41,42] Although Gd-DTPA and its derivatives have been used in clinical practice, the linear Gd(III) chelates suffer from low kinetic stability against transmetalation with endogenous metal ions.[43,44]

Macrocyclic Gd(III) chelates have high thermodynamic and kinetic stability with no transmetalation with endogenous metal ions.[43−46] In this study, we designed and synthesized a new low molecular weight CLT1 targeted contrast agent based on a highly stable macrocyclic Gd(III) chelate, Gd-DOTA. The new CLT1 targeted contrast agent CLT1-dL-$(Gd\text{-}DOTA)_4$ had 4 Gd-DOTA monoamide chelates conjugated to a CLT1 molecule via a generation 1 lysine dendrimer. A corresponding scrambled CLT1 targeted agent was synthesized and used as a nontargeted control agent. The tumor specificity of CLT1 was determined in an orthotopic xenograft PC3 prostate tumor model in male athymic nude mice using fluorescence imaging. The effectiveness of CLT1-dL-$(Gd\text{-}DOTA)_4$ for MR molecular imaging of the prostate tumor was determined in the same tumor model.

MATERIALS AND METHODS

1,4,7,10-Tetraazacyclododecane-1,4,7-tris-*tert*-butyl acetate-10-acetic acid [DOTA-tris(*t*-Bu)] was purchased from TCI America (Portland, OR, USA). Benzotriazol-1-yl-oxytripyrrolidinophosphonium hexafluorophosphate (PyBOP), 1-hydroxybenzotriazole hydrate (HOBt), and 2-(1*H*-benzotriazol-1-yl)-1,1,3,3-tetramethyl uronium hexafluorophosphate (HBTU) were purchased from Nova Biochem (Darmstadt, Germany). Fmoc-protected amino acids and Fmoc-12-amino-4,7,10-trioxadodecanoic acid (Fmoc-NH-PEG-COOH, MW = 443.5) were purchased from EMD Chemicals Inc. (Gibbstown, NJ, USA). Anhydrous *N*,*N*-diisopropylethylamine (DIPEA), dichloromethane (DCM), and *N*,*N*-dimethylformamide (DMF) were purchased from Alfa Aesar (Ward Hill, MA, USA). Trifluoroacetic acid (TFA) was purchased from ACROS Organics (Morris Plains, NJ, USA). Thallium(III) trifluoroacetate and triisobutylsilane (TIS) were purchased from Sigma-Aldrich Corp. (St. Louis, MO, USA). Texas Red, succinimidyl ester, single isomer (T20175) was purchased from Invitrogen (Eugene, Oregon, USA). All reagents were used without further purification.

Synthesis of Cyclic Peptide CLT1 (CGLIIQKNEC). Peptide CLT1 was synthesized using standard solid-phase peptide synthesis from Fmoc-protected amino acids on a 2-chlorotrityl chloride resin. 2-Chlorotrityl chloride resin (1.27 g, 2.0 mmol, loading rate = 1.58 mmol Cl/g) was suspended and swollen in anhydrous dichloromethane (DCM) (20 mL) and shaken for 1 h in an ISOLUTE column. The resin was then filtered and washed with anhydrous DCM (20 mL), and anhydrous dimethylformamide (DMF, 20 mL). Fmoc-Cys(Acm)-OH (414 mg, 1.0 mmol) was dissolved in DMF (10 mL) and added to the resin. *N*,*N*-Diisopropylethylamine (DIPEA, 800 μL) was added and the suspension was shaken for 2 h. The resin was then filtered and washed with DCM/DMF three times. The resin was further shaken with methanol/DIPEA (20 mL/800 μL) for 20 min to block the remaining active chloride on the resin. After washing with DCM/DMF, the Fmoc protecting group was removed with 20% piperidine in DMF (5 min × 3, 20 mL/each). This procedure was repeated in the following order: Fmoc-Glu(O*t*Bu)-OH, Fmoc-Asn(Trt)-OH, Fmoc-Lys(Boc)-OH, Fmoc-Gln-(Trt)-OH, Fmoc-Ile-OH, Fmoc-Ile-OH, Fmoc-Leu-OH, Fmoc-Gly-OH, Fmoc-Cys(Acm)-OH. Each Fmoc deprotection and amino acid coupling step was followed by a Kaiser's test on resin. The resin in each reaction cycle was extensively washed with DCM/DMF and dried under reduced pressure before proceeding to the next step. After adding final amino acid, on-resin cyclization of the linear peptide was carried out with thallium(III) trifluoroacetate (1.09 g, 2.0 mmol, 2 equiv) in DMF (20 mL) at 0 °C for 2 h, followed by extensively washing with DMF/DCM. A sample of the dry resin was treated with a cocktail of trifluoroacetic acid (TFA), water, and triisobutylsilane (TIS) (2 mL, 95/2.5/2.5) and shaken for 1 h at room temperature to remove the protection groups and to cut the peptide from the resin. The filtered solution was dropped to cold ethyl ether (50 mL). The solid product was collected by centrifugation and washed with ether 4 times to give compound CLT1, which was characterized by MALDI-TOF [(m/z, $[M+H]^+$): 1118.82 (obsd.), 1118.33 (calcd.)].

Synthesis of CLT1-dL-$(DOTA)_4$. After on-resin cyclization, PEG and lysine were sequentially conjugated to the N-terminus of CLT1 peptide (1.0 mmol) on resin by reacting with Fmoc-NH-PEG-COOH (3.0 mmol), Fmoc-Lys(Fmoc)-OH (3.0 mmol), and then another batch of Fmoc-Lys(Fmoc)-OH (6 mmol). After removal of Fmoc, DOTA-tris(t-Bu) (4.58 g, 8.0 mmol, 2 equiv to each amino group) was reacted with the four free amines from the lysine dendrimer on the resin surface for 2 h. Finally, the product was deprotected and cleaved from the resin by treating with a cocktail of trifluoroacetic acid, water, and triisobutylsilane (20 mL, 95/2.5/2.5) and shaken for 8 h at room temperature. The resin was removed by filtration and washed with TFA. Combined filtrates were added dropwise to cold ethyl ether (200 mL). The precipitated crude product was centrifuged, washed with ethyl ether 4 times, and dried under vacuum to give a colorless solid (1.99 g, 61% yield). The crude product was then purified by preparative HPLC on an Agilent 1100 HPLC system equipped with a ZORBAX 300SB-C18 PrepHT column. The gradient of HPLC was 0−40% solvent B (0.1% TFA in

acetonitrile) in solvent A (0.1% TFA aqueous solution) for 20 min and 40−90% solvent B in solvent A for 10 min. The purified product CLT1-dL-$(DOTA)_4$ was characterized by MALDI-TOF [(m/z, $[M+H]^+$): 3251.62 (obsd.), 3251.68 (calcd.)].

Synthesis of CLT1-dL-$(Gd\text{-}DOTA)_4$. CLT1-dL-$(DOTA)_4$ (250 mg, 0.077 mmol) was dissolved in DI water (15 mL), and the pH was adjusted to 6 using 1 M NaOH. $Gd(OAc)_3{\cdot}4H_2O$ (472 mg, 0.462 mmol, 1.5 equiv to DOTA monoamide) was added in portions to the solution, while maintaining the pH at 6 using 1 M NaOH. The reaction was stirred for 48 h at room temperature. The excess of $Gd(OAc)_3$ was used to ensure complete chelation. Residual Gd(III) was complexed with ethylenediaminetetraacetic acid (EDTA) (90 mg, 0.31 mmol), and the crude product was then purified by Sephadex G-10 column to give final product CLT1-dL-$(Gd\text{-}DOTA)_4$ (169 mg, 57%). CLT1-dL-$(Gd\text{-}DOTA)_4$ was characterized by MALDI-TOF [(m/z, $[M+H]^+$): 3869.85 (obsd.), 3869.53 (calcd.)].

Synthesis of Scrambled CLT1-dL-$(Gd\text{-}DOTA)_4$. A scrambled CLT1 (CIEGNKIQLC, sCLT1) Gd-DOTA monoamide conjugate sCLT1-dL-$(Gd\text{-}DOTA)_4$ was synthesized using the similar procedure as CLT1-dL-$(Gd\text{-}DOTA)_4$. sCLT1-dL-$(Gd\text{-}DOTA)_4$ was characterized by MALDI-TOF [(m/z, $[M+H]^+$): 3869.10 (obsd.), 3869.63 (calcd.)].

Synthesis of CLT1-Texas Red (TR) and Scrambled sCLT1-TR Conjugates. The peptides CLT1 and sCLT1 were first synthesized using standard solid-phase peptide chemistry as described above. Fluorescence dye Texas Red (2 mg) was then conjugated to the peptides on resin (10 mg) in the presence of coupling agents. After cleavage from the resin with an acidic cocktail of TFA/water/TIS (95:2.5:2.5), the products CLT1-TR and sCLT1-TR were purified by preparative HPLC using the same separation protocol as above. Molecular weight of the conjugates was determined by MALDI-TOF [(m/z, $[M+H]^+$): 2023.05 (obsd.), 2023.41 (calcd.); (m/z, $[M+Na]^+$): 2045.61 (obsd.), 2045.41 (calcd.)]. sCLT1-TR conjugate was similarly prepared. sCLT1-TR was also characterized by MALDI-TOF [(m/z, $[M+H]^+$): 2022.75 (obsd.); (m/z, $[M+Na]^+$): 2045.89 (obsd.)].

Characterization of Purified Compounds. The Gd(III) content was measured by inductively coupled plasma-optical emission spectroscopy (ICP-OES Optima 3100XL, Perkin-Elmer, Norwalk, CT). Matrix-assisted laser desorption/ionization time-of-flight (MALDI-TOF) mass spectra were acquired on a MALDI-TOF mass spectrometer (AutoflexTM Speed, Bruker) in a linear mode with 2,5-dihydroxybenzoic acid (2,5-DHB) as a matrix. Relaxation times of the aqueous solution of the contrast agents of CLT1-dL-$(Gd\text{-}DOTA)_4$ and sCLT1-dL-$(Gd\text{-}DOTA)_4$ with different concentrations were measured at 60 MHz (1.5 T) using a Bruker minispec relaxometer at 37 °C. T_1 was measured with an inversion−recovery pulse sequence. T_2 was measured using a Carr-Purcell-Meiboom-Gill sequence with 500 echoes collected. The T_1 and T_2 relaxivities of the agents were calculated from the slopes of the plots of $1/T_1$ and $1/T_2$ versus the Gd concentrations.

Animal Model with Orthotopic PC3 Prostate Tumor. Male NIH athymic nude mice (4−5 weeks old) were maintained at the Athymic Animal Core Facility at Case Western Reserve University according to an animal protocol approved by the CWRU Institutional Animal Care and Use Committee. PC3 prostate cancer cells with constitutive expression of green fluorescence protein (GFP) were cultured in RPMI medium supplemented with 5% fetal bovine serum and penicillin/streptomycin/fungizone, harvested by trypsinization and resuspended at density of 2.5×10^4 cells per 1.0 μL PBS. The mice were anesthetized and a small incision was made through the skin and peritoneum along the lower midline for about 1 cm. The prostate dorsal lobes were gently exteriorized and stabilized. The suspension of PC3-GFP cells in PBS (20 μL) was injected into the prostate with a 30-gauge needle. Finally, the incision was closed with wound autoclip.[47]

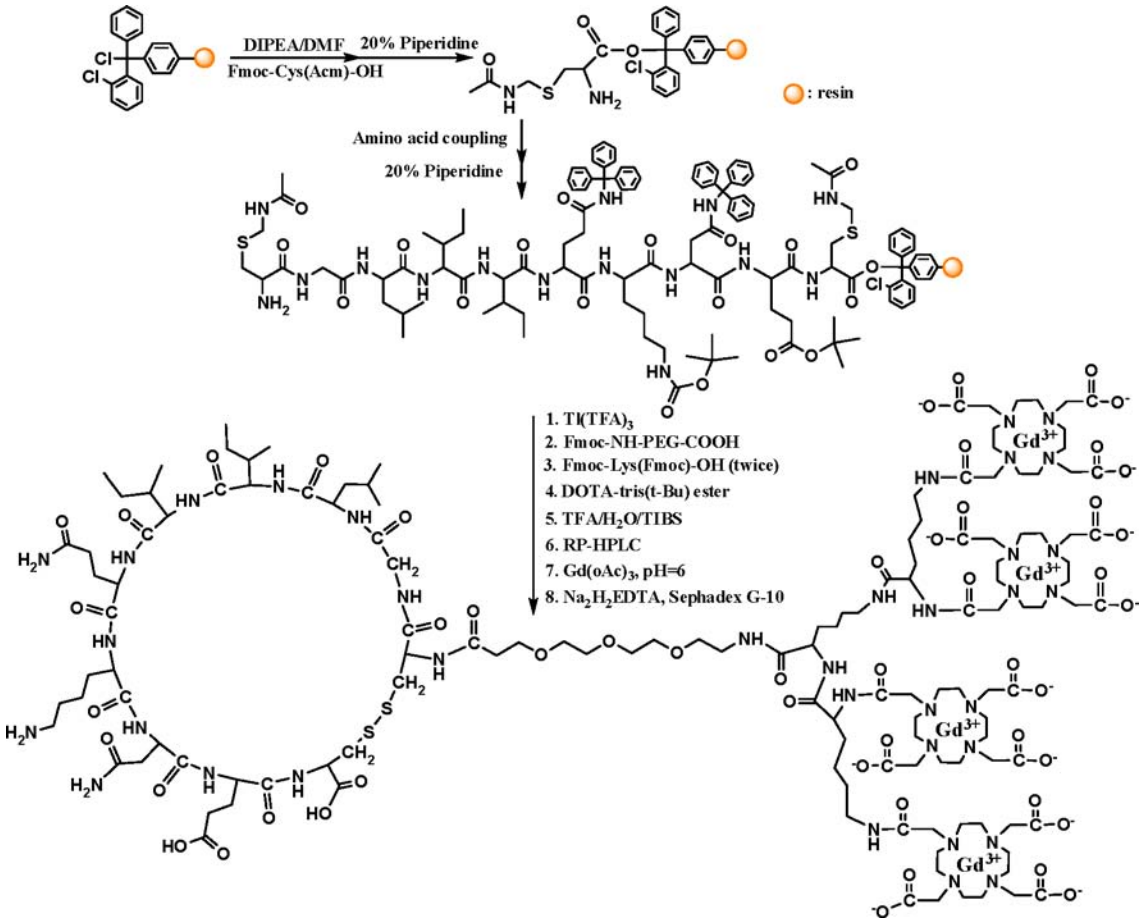
Tumor Binding Specificity of the Peptides. Before injection of the peptide probes, GFP fluorescence images with live mice were acquired to verify the tumor presence. Texas Red labeled peptides were intravenously injected to the tumor bearing mice at a dose of 10 nmol/mouse. After 2 h, the mice were sacrificed, and the tumors and major organs were collected and imaged immediately on a Maestro fluorescence imager. GFP fluorescence images were obtained using green light filters (excitation: 444−490 nm; emission: 515 nm long-pass filter; acquisition settings: 500−720 in 10 nm steps) and red light filters for Texas Red labeled probes (excitation: 576−621 nm; emission: 635 nm long-pass filter; acquisition settings: 630−800 in 10 nm steps). Exposure time was 10 ms for GFP and 150 ms for Texas Red.

Histology Studies. Immediately after measurement of whole tissue fluorescence imaging, tumor tissues were collected and cryosectioned into 5 μm slices. After rinsing with PBS, 1 drop of UltraCruzmounting medium (sc-24941, Santa Cruz Biotechnology, Inc., Santa Cruz, CA, USA) containing 4′,6-diamidino-2-phenylindole (DAPI) was mounted and imaged immediately on an Olympus FV1000 confocal laser scanning microscope.

MR Tumor Molecular Imaging. The MRI study was performed on a Bruker Biospec 7 T MRI scanner (Bruker Corp., Billerica, MA, USA) with a volume radio frequency (RF) coil. Mice were anesthetized with a 2% isoflurane−oxygen mixture in an isoflurane induction chamber. A tail vein of mouse was catheterized with a 30 gauge needle connected with a 2.5-m-long tubing filled with heparinized saline. The animal was then placed into the magnet and kept under inhalation anesthesia with 1.5% isoflurane−oxygen via a nose cone. A respiratory sensor connected to a monitoring system (SA Instruments, Stony Brook, NY) was placed on the abdomen to monitor rate and depth of respiration. The body temperature was maintained at 37 °C by blowing hot air into the magnet through a feedback control system. A group of 6 mice was used for each agent. Sagittal section images were acquired with a localizing sequence to identify the tumor location, followed by a 2D T_1-weighted gradient fat suppression sequence before injection. After preinjection baseline MR image acquisition, the targeted agent or control agent was injected at a dose of 0.03 mmol of Gd/kg by flushing with 200 μL of saline. T_1-weighted 2D axial images were then acquired at different time points after the injection for up to 30 min. Parameters of the 2D T_1-weighted gradient echo sequence were TR/TE = 151.2/1.9 ms, FOV = 3.0 cm, slice thickness = 1.2 mm, slice number = 20, average = 1, flip angle = 80°, matrix = 128 × 128. In order to acquire the images of the tumor and kidneys, 20 slices were acquired to cover the whole tumor and the kidneys. MR images of the kidneys were also acquired at 48 h after injection.

Image Processing and Analysis. Image analysis was performed using Bruker *ParaVision 4.0* imaging software. Regions of interest (ROIs) were drawn over the whole tumor and the kidneys in the two-dimensional imaging plane and average signal intensity was measured. Tumor or kidney contrast enhancement (ΔSNR) was calculated as postcontrast SNR increase over precontrast SNR using the following equation: $\Delta SNR = (S_t/\sigma_t) - (S_0/\sigma_0)$, where S_0 and S_t denoted the signal in

Scheme 1. Synthesis of CLT1-dL-(Gd-DOTA)$_4$



the tumor or the kidneys before and after contrast, σ_0 and σ_t were the standard deviation of noise measured from the background air before and after contrast. The p values were calculated using the Student's two-tailed t-test, assuming statistical significance at $p < 0.05$.

Biodistribution Study. The mice from the MRI study were sacrificed by cervical dislocation at 48 h postinjection. The organ and tissue samples, including the heart, liver, spleen, lung, kidneys, brain, skin, muscle, femur, and tumor were collected and weighed. The tissue samples were then cut into small pieces and mixed with ultrapure nitric acid (1.0 mL, 70%, EMD, Gibbstown, NJ). The tissue samples were liquefied for 1 week, and the solution was transferred to a centrifuge tube and centrifuged at 14 000 rpm for 5 min. The supernatant (0.2 mL) was diluted 10 times with deionized water and further centrifuged at 14 000 rpm for 5 min. The Gd(III) concentration in the supernatant solution was measured by ICP-OES. The average Gd(III) content in each organ or tissue was calculated from the measured Gd(III). The Gd content was calculated as the percentage of injected dose per gram of organ/tissues (% ID/g).

RESULTS

Synthesis and Characterization. The synthesis of CLT1 peptide targeted Gd-DOTA monoamide conjugate, CLT1-dL-(Gd-DOTA)$_4$, is described in Scheme 1. A generation 1 lysine dendrimer was used to increase the molar ratio of Gd-DOTA monoamide to the peptide in the targeted contrast agent for effective targeted contrast enhancement. The small size of G1 lysine dendrimer would allow the unbound contrast agent to rapidly excrete from the body via renal filtration. The lysine dendrimer also had a neutral core, which could minimize charge-associated nonspecific tissue uptake. The conjugation of multiple Gd-DOTA monoamide chelates to each CLT1 peptide resulted in a final product with good water solubility. The peptide and lysine dendrimer were connected via a short PEG linker to avoid steric hindrance for target binding. sCLT1 (CIEGNKIQLC) was used to prepare the nontargeted control agent. sCLT1-dL-(Gd-DOTA)$_4$ was similarly synthesized as described in Scheme 1. The final products were characterized by MALDI-TOF mass spectrometry (Figure 1), ICP-OES, and Bruker minispec relaxometer. Figure 2 shows the plots of the T_1 and T_2 water proton relaxation rates versus the concentrations of CLT1-dL-(Gd-DOTA)$_4$ and sCLT1-dL-(Gd-DOTA)$_4$ at 1.5 T (60 MHz), 37 °C. The physicochemical parameters of the contrast agents are listed in Table 1. Both targeted and scrambled agents had similar relaxivity. At 1.5 T, the T_1 relaxivity per gadolinium of CLT1-dL-(Gd-DOTA)$_4$ in pH 7.4 PBS was about 3 times higher than that of Gd-DOTA.[48] Synthesis of CLT1-TR and sCLT1-TR was confirmed by MALDI-TOF mass spectrometry.

Tumor Binding Specificity of CLT1 Peptide. Figure 3A,B shows the bright field images and fluorescence images of tumors and major organs that were collected from mice injected with CLT1-TR and sCLT1-TR fluorescence probes. The GFP expressing tumors showed strong green fluorescence. Texas Red labeled CLT1 demonstrated strong binding to tumor, while the nonspecific scrambled peptide resulted in little tumor binding. Both peptides showed little binding to the normal organs and tissues. Figure 3C shows red fluorescence intensity

dx.doi.org/10.1021/bc300009t | Bioconjugate Chem. 2012, 23, 1548−1556

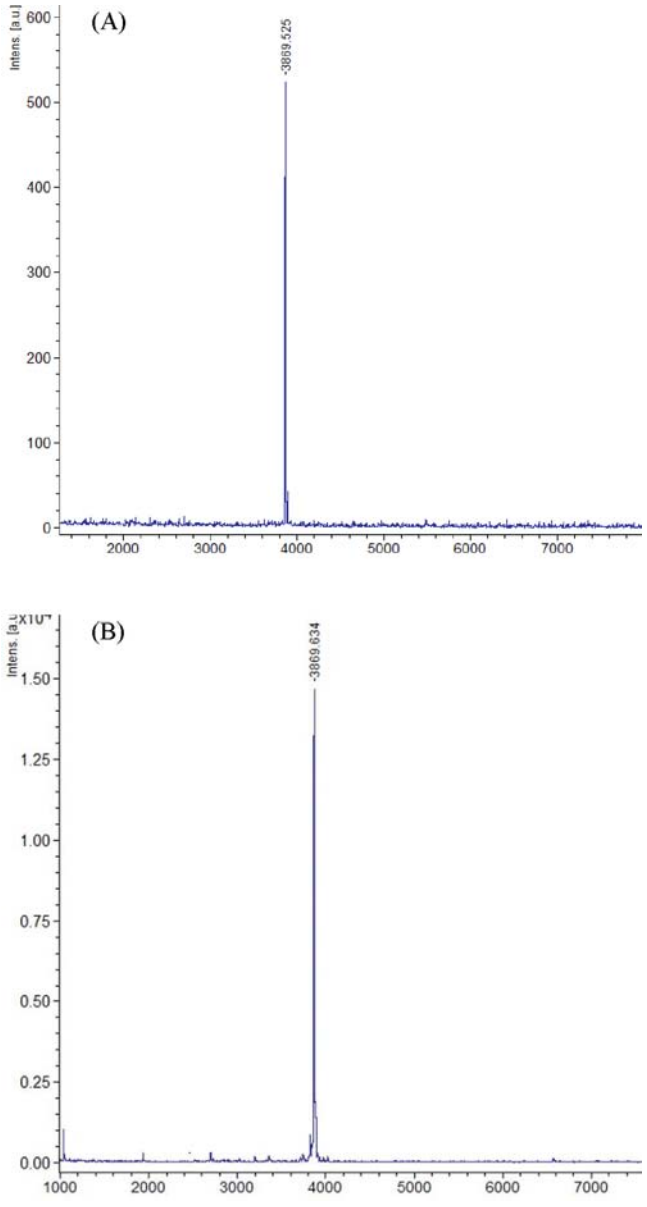


Figure 1. MALDI-TOF mass spectra of CLT1-dL-(Gd-DOTA)$_4$ (A) and sCLT1-dL-(Gd-DOTA)$_4$ (B).

extracted from the orthotopic prostate tumors of the mice injected with CLT1-TR and sCLT1-TR. The targeted CLT1-TR showed 5.7 times higher binding to the tumor tissue than nontargeted sCLT1-TR.

Figure 4 shows the microscopic fluorescence images of the tumor sections from these mice injected with CLT1-TR and sCLT1-TR. Blue fluorescence was from DAPI bound to the DNA in cell nuclei. Both tumor sections showed strong green fluorescence from GFP. Strong red fluorescence of Texas Red was shown in the tumor section obtained from the mice injected with CLT1-TR, while no fluorescence was essentially detected in tumor section from the mice injected with sCLT1-TR. The merged low-resolution fluorescent images (yellow color) exhibited good correlation of the green fluorescence from the tumor cells to the red fluorescence from CLT1-TR in the vicinity of the cells, indicating strong binding of the probe to viable tumor regions after intravenous administration.

MR Tumor Molecular Imaging with CLT1-dL-(Gd-DOTA)$_4$. Figure 5 shows the representative 2D axial T_1-weighted gradient echo tumor images of the mice bearing orthotopic human PC3 prostate tumor before and after injection of CLT1-dL-(Gd-DOTA)$_4$ and sCLT1-dL-(Gd-DOTA)$_4$ at a dose of 0.03 mmol-Gd/kg. The targeted agent resulted in greater and longer enhancement in tumor tissue compared to nontargeted scrambled agents. Contrast enhancement in the urinary bladder gradually increased over time, indicating that the unbound contrast agents were excreted via renal filtration. Quantitative signal analysis revealed that the targeted agent produced more significant signal enhancement in the tumor tissue than the control agent ($p < 0.05$) up to 30 min. CLT1-dL-(Gd-DOTA)$_4$ resulted in approximately 110% more signal enhancement than sCLT1-dL-(Gd-DOTA)$_4$ in the tumor tissue at 1 min postinjection. The signal enhancement gradually decreased over time and about 60% more signal enhancement was still observed for the targeted agent than the control agent at 30 min postinjection.

Figure 6B shows the contrast enhancement in the kidneys up to 48 h after injection of the agents. Both agents showed similar dynamic kidney enhancement patterns, whereby strong contrast enhancement was observed at early time points after injection, followed by a rapid signal decrease, indicating rapid washout of the agents in the kidneys. Little enhancement was observed in the kidneys at 48 h after injection.

Biodistribution in Mice. Figure 7 shows the biodistribution of Gd(III) in the major organs and tissues, including the femur, heart, kidneys, liver, lung, muscle, and spleen of mice 48 h after receiving CLT1-dL-(DOTA-Gd)$_4$ and sCLT1-dL-(DOTA-Gd)$_4$ at a dose of 0.03 mmol-Gd/kg. The Gd retention of both agents was comparable ($p > 0.05$) in the main normal organs and tissues,

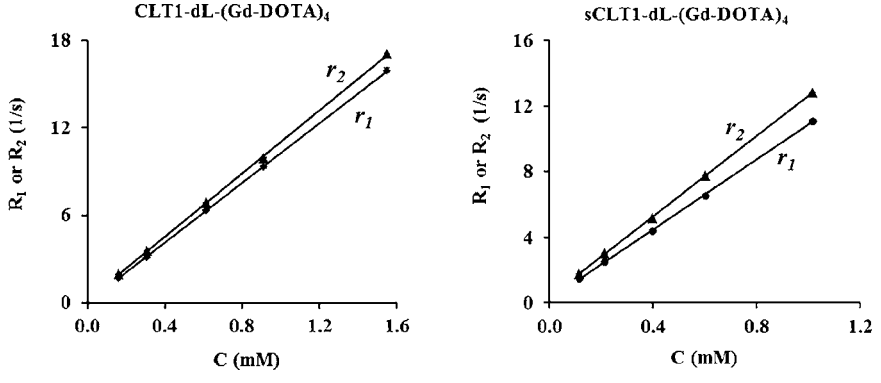


Figure 2. Plots of $1/T_1$ (R_1) and $1/T_2$ (R_2) versus the concentration of the contrast agents CLT1-dL-(Gd-DOTA)$_4$ and sCLT1-dL-(Gd-DOTA)$_4$.

dx.doi.org/10.1021/bc300009t | *Bioconjugate Chem.* 2012, 23, 1548−1556

Table 1. Physicochemical Properties of the Targeted and Scrambled MRI Contrast Agents

	r_1 ($mM^{-1}.s^{-1}$)		r_2 ($mM^{-1}.s^{-1}$)		
	per Gd	per molecule	per Gd	per molecule	Gd content (mmol-Gd/g)
CLT1-dL-$(Gd\text{-}DOTA)_4$	10.1 ± 1.0	40.4 ± 3.0	13.0 ± 3.1	52.0 ± 9.6	1.05 ± 0.10
sCLT1-dL-$(Gd\text{-}DOTA)_4$	11.5 ± 1.4	46.0 ± 5.0	12.4 ± 0.3	49.6 ± 1.3	0.97 ± 0.08
Gd-DOTA	2.9[a]	2.9[a]	3.2[a]	3.2[a]	-

[a]Relaxivities for Gd-DOTA in water at 37 °C are from ref 48.

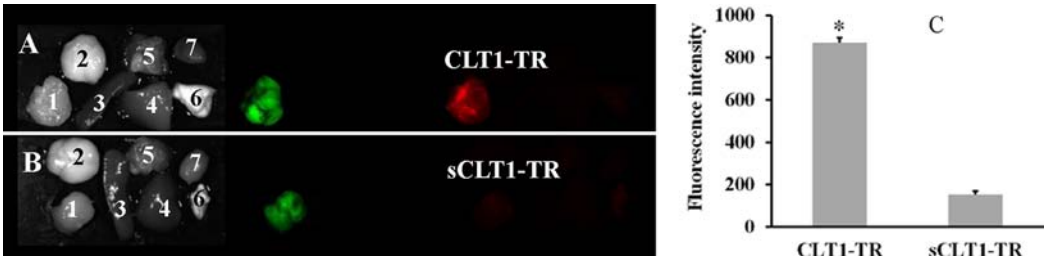


Figure 3. Tumor binding of CLT1-TR (A) and sCLT1-TR (B) in athymic nude mice bearing orthotopic PC3-GFP prostate tumor 2 h after intravenous injection at a dose of 10 nmol/mouse. CLT1-TR resulted in 5.7 times higher red fluorescence intensity in the tumor than sCLT1-TR (C, $n = 3$, * $p < 0.05$). 1, tumor; 2, brain; 3, spleen; 4, liver; 5, muscle; 6, lung; 7, heart.

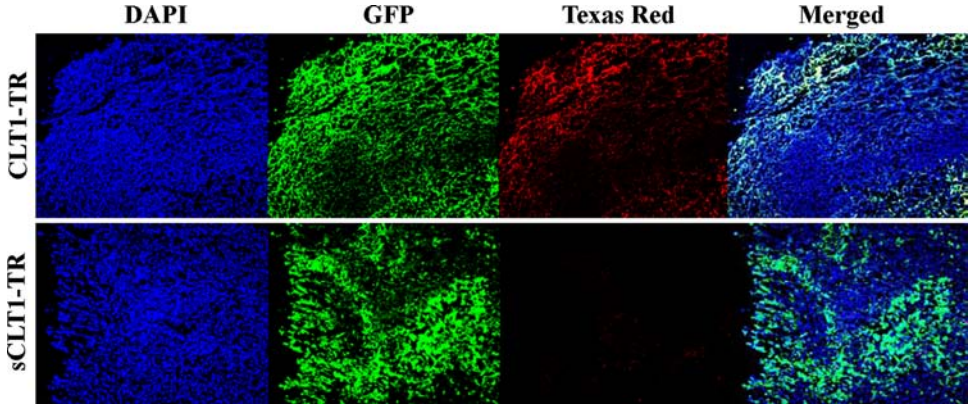


Figure 4. Histological analysis of tumor tissue injected with CLT1-TR or sCLT1-TR at a dose of 10 nmol/mouse.

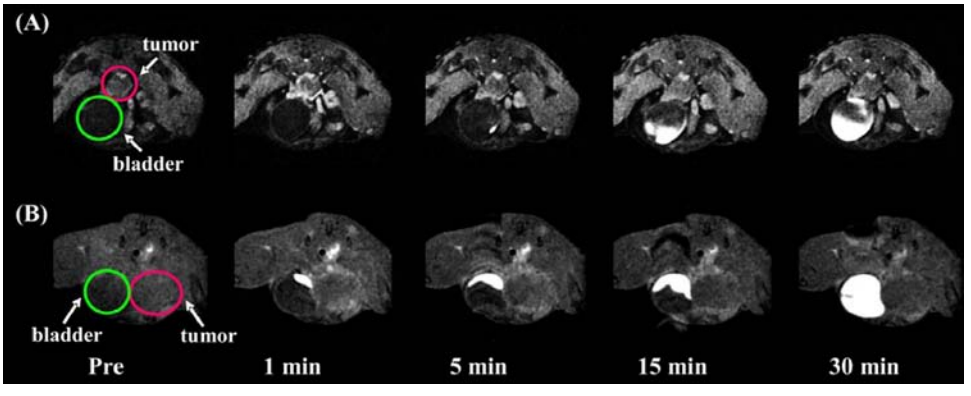


Figure 5. Representative T_1-weighted axial 2D gradient images of orthotopic PC-3 human prostate tumor before and after intravenous injection of CLT1-dL-$(Gd\text{-}DOTA)_4$ (A) and sCLT1-dL-$(Gd\text{-}DOTA)_4$ (B) at 0.03 mmol Gd/kg in nu/nu mice. Tumor labeled with red circle and bladder labeled with green circle.

except kidneys, femur, and tumor ($p < 0.05$) at 48 h after the injection. Approximately 0.5%, 0.8%, and 1.3% of injected targeted CLT1-dL-$(DOTA\text{-}Gd)_4$ per gram of tissue was measured in the liver, spleen, and kidneys, while very little (less than 0.1%) or no Gd was measured in other tissues and organs.

DISCUSSION

Currently, nuclear medicine is routinely used for cancer molecular imaging in clinical practice. Dual imaging modalities are often needed to coregister molecular imaging with anatomical imaging due to the poor spatial resolution of nuclear medicine. It would be ideal to use a single imaging modality for

dx.doi.org/10.1021/bc300009t | Bioconjugate Chem. 2012, 23, 1548−1556

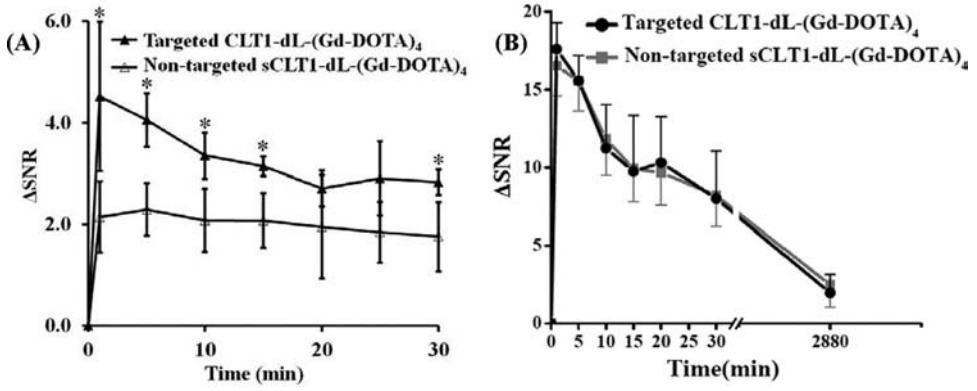


Figure 6. Contrast enhancement (ΔSNR) in the tumor (A) and kidneys (B) produced by CLT1-dL-$(Gd\text{-}DOTA)_4$ and sCLT1-dL-$(Gd\text{-}DOTA)_4$ at 0.03 mmol-Gd/kg in nu/nu nude with athymic mice ($n = 6$) bearing orthotopic human prostate tumor. * $p < 0.05$.

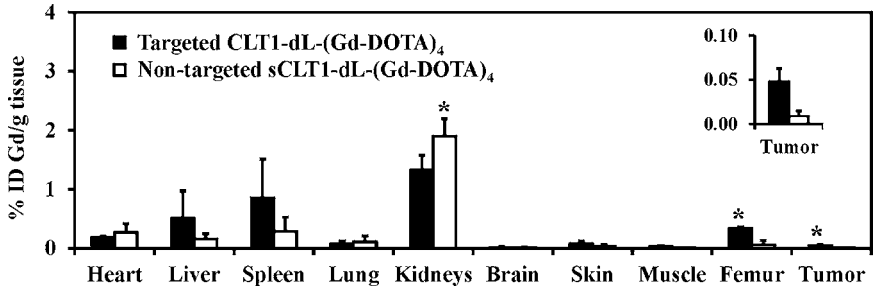


Figure 7. Biodistribution of gadolinium in the major organs and tissues of mice at 48 h after intravenous injection of CLT1-dL-$(Gd\text{-}DOTA)_4$ and sCLT1-dL-$(Gd\text{-}DOTA)_4$ at a dose of 0.03 mmol-Gd/kg in nu/nu athymic mice ($n = 4$) bearing orthotopic human prostate tumor (* $p < 0.05$).

effective molecular and anatomic imaging to reduce unnecessary exposure to ionizing radiation, as well as the cost of the diagnosis. MRI is advantageous due to its high spatial resolution of soft tissues and the absence of ionizing radiation. The key for effective clinical MR cancer molecular imaging is the design and development of safe, effective targeted MRI contrast agents. This study has shown that it is possible to achieve effective MR cancer molecular imaging by utilizing a small molecule targeted contrast agent that binds properly selected molecular targets. Small size of the targeted MRI contrast agents is critical to allow the unbound targeted agents to rapidly excrete from the body via renal filtration and to minimize potential toxic side effects associated with Gd(III) based contrast agents. Tumor stroma have abundant local expression of cancer-related proteins, which could be suitable biomarkers for effective MR cancer molecular imaging. Their abundant expression in tumor stroma allows the binding of sufficient small molecule Gd(III) based contrast agents to generate robust contrast enhancement and to overcome the low sensitivity of MRI. Both thermodynamic and kinetic stability of the Gd(III) chelates should be considered in the design of new targeted agents to avoid the release of free Gd(III) ions and potential toxic side effects.

Previous studies have shown that the CLT1 peptide specifically bound to clotted plasma proteins, fibrin−fibronectin complexes, that are abundantly expressed in the stroma of many different tumors, including Lewis lung carcinoma,[38,39] MDA-MB-231 breast cancer, and HT29 colon cancer.[41,42,49] In this study, we further verified the specific binding of CLT1 peptide to the orthotopic prostate PC-3 tumor tissue using in vivo fluorescence imaging. The peptide was highly specific to prostate tumor tissue and with little nonspecific binding to normal tissues.

Numerous studies have demonstrated that macrocyclic chelate Gd-DOTA and its derivatives have higher kinetic stability than Gd-DPTA against transmetalation with endogenous metal ions, particularly Zn^{2+} ions.[44−46] CLT1-dL-$(Gd\text{-}DOTA)_4$ should have high kinetic stability compared to previously reported linear CLT1-(Gd-DTPA) conjugate.[41] The conjugation of multiple Gd-DOTA chelates to each CLT1 improved the water solubility of the peptide and the final product. The small molecule CLT1-dL-$(Gd\text{-}DOTA)_4$ generated significant contrast enhancement at a reduced dose of 0.03 mmol/kg. The tumor contrast enhancement was comparable to our previously reported CLT1 targeted nanoglobular contrast agents at the same dose.[50] The results indicate that MRI with the small molecule targeted contrast agent is effective for high-resolution anatomic and molecular imaging of the abundant cancer-related biomarkers in tumor stroma. Our previous study showed that the tumor enhancement with CLT1 peptide targeted contrast agent CLT1-(Gd-DTPA) was reduced after the coinjection of free CLT1 peptide, indicating that the free peptide competitively recognizes the same binding site within tumor tissue as the CLT1 peptide targeted contrast agent.[41] Due to the abundance of clotted plasma proteins in the tumor stroma, sufficient targeted contrast agents can bind to the molecular target. Consequently, the targeted agent overcomes the relatively low sensitivity of contrast enhanced MRI, resulting in improved contrast enhancement for effective cancer molecular imaging at a reduced dose. MR molecular imaging of the clotted plasma proteins is advantageous over nuclear medicine for the same molecular targets because of its high anatomical resolution and the absence of ionizing radiation. Furthermore, no dual imaging modalities are needed to coregister molecular imaging with anatomic imaging.

As compared to macromolecules, the small peptide targeted contrast agent has a small size and can readily diffuse into tumor tissues for effective cancer molecular imaging. The small size also allows unbound contrast agents to be excreted from the body

via renal filtration to reduce background signal and minimize the accumulation of Gd(III) chelates in the body. Complete elimination of the Gd(III) based MRI contrast agents from the body is critical for minimizing the safety concerns related to their slow excretion. According to a previous report,[51] peptides may generally be reabsorbed by renal tubular cells. Here, the contrast enhanced MRI study showed that the targeted contrast agent excreted rapidly through the kidneys into the urinary bladder. The kidneys had strong contrast enhancement at early time points after injection, and the enhancement gradually decreased over time (Figure 6B), while strong contrast enhancement was observed in the urinary bladder within 15 min after injection of both agents (Figure 5). The results indicated that the peptide targeted agent could be readily excreted through the kidneys with minimal renal accumulation. The biodistribution studies also showed that the agent had minimal Gd retention in the main organs and tissues 2 days after injection, much lower than our previously reported high-generation nanoglobular targeted MRI contrast agent.[49] CLT1-dL-$(Gd\text{-}DOTA)_4$ showed promising properties for safe and effective cancer molecular imaging. Nevertheless, comprehensive toxicological evaluations are also required before further development of the agent for clinical cancer molecular imaging with MRI.

In summary, this study has validated the feasibility of CLT1 targeted small molecular contrast agent containing highly stable macrocyclic Gd(III) chelates for effective MR molecular imaging of biomarkers in the stroma of prostate tumor. The peptide-targeted contrast agent has shown a great potential for accurate and earlier detection of small malignant tumors with contrast-enhanced MRI. MR cancer molecular imaging with the targeted agent also has the potential for cancer grading and prognosis.

AUTHOR INFORMATION

Corresponding Author

*E-mail: zxl125@case.edu.

Notes

The authors declare no competing financial interest.

ACKNOWLEDGMENTS

This work is supported in part by the NIH R01 CA097465. This material is based upon work supported by the National Science Foundation under Grant No. MRI-0821515 (for the purchase of the MALDI-TOF/TOF). We highly appreciate Dr. Wen Li and Dr. Vikas Gulani for MRI protocol test and setup, and Ms. Yvonne Parker for her assistance on tumor implantation.

REFERENCES

(1) Vlastos, G., and Verkooijen, H. M. (2007) Minimally invasive approaches for diagnosis and treatment of early-stage breast cancer. *Oncologist 12*, 1−10.

(2) Gelovani, J. G. (2008) Molecular imaging of epidermal growth factor receptor expression-activity at the kinase level in tumors with positron emission tomography. *Cancer Metastasis Rev. 27*, 645−53.

(3) Piwnica-Worms, D, Kesarwala, A. H., Pichler, A., Prior, J. L., and Sharma, V. (2006) Single photon emission computed tomography and positron emission tomography imaging of multi-drug resistant P-glycoprotein–monitoring a transport activity important in cancer, blood-brain barrier function and Alzheimer's disease. *Neuroimaging Clin. N. Am. 16*, 575−89.

(4) Hayashi, M., Murakami, K., Oyama, T., Domeki, Y., Hagiwara, S., Katsumata, D., and Sunagawa, M. (2008) PET/CT supports breast cancer diagnosis and treatment. *Breast Cancer. 15*, 224−230.

(5) Saga, T., Koizumi, M., Furukawa, T., Yoshikawa, K., and Fujibayashi, Y. (2009) Molecular imaging of cancer: evaluating characters of individual cancer by PET/SPECT imaging. *Cancer Sci. 100*, 375−81.

(6) Oude Munnink, T. H., Nagengast, W. B., Brouwers, A. H., Schroder, C. P., Hospers, G. A., Lub-de Hooge, M. N., van der Wall, E., van Diest, P. J., and de Vries, E. G. (2009) Molecular imaging of breast cancer. *Breast 18* (Suppl 3), S66−73.

(7) Pan, T., and Mawlawi, O. (2008) PET/CT in radiation oncology. *Med. Phys. 35*, 4955−4966.

(8) Lucignani, G. (2008) PET-MRI synergy in molecular, functional and anatomical cancer imaging. *Eur. J. Nucl. Med. Mol. Imaging 35*, 1550−1553.

(9) Maurer, A. H. (2008) Combined imaging modalities: PET/CT and SPECT/CT. *Health Phys. 95*, 571−576.

(10) Lijowski, M., Caruthers, S., Hu, G., Zhang, H., Scott, M. J., Williams, T., Erpelding, T., Schmieder, A. H., Kiefer, G., Gulyas, G., Athey, P. S., Gaffney, P. J., Wickline, S. A., and Lanza, G. M. (2009) High sensitivity: high-resolution SPECT-CT/MR molecular imaging of angiogenesis in the Vx2 model. *Invest. Radiol. 44*, 15−22.

(11) Haacke, E. M., Brown, R. W., Thompson, M. R., and Venkatesan, R. (1999) *Magnetic Resonance Imaging Physical Principles and Sequence Design*, John Wiley & Sons, Inc., New York.

(12) Brown, M. A., and Semelka, R. C. (2003) *MRI Basic Principles and Applications*, 3rd ed., John Wiley & Sons, Inc., Hoboken, NJ.

(13) Artemov, D. (2003) Molecular magnetic resonance imaging with targeted contrast agents. *J. Cell. Biochem. 90*, 518−524.

(14) Kalber, T. L., Kamaly, N., So, P. W., Pugh, J. A., Bunch, J., McLeod, C. W., Jorgensen, M. R., Miller, A. D., and Bell, J. D. (2011) A low molecular weight folate receptor targeted contrast agent for magnetic resonance tumor imaging. *Mol. Imaging Biol. 13*, 653−562.

(15) Unger, E. C., Totty, W. G., Neufeld, D. M., Otsuka, F. L., Muephy, W. A., Welch, M. S., Connett, J. M., and Philpott, G. W. (1985) Magnetic resonance imaging using gadolinium labeled monoclonal antibody. *Invest. Radiol. 20*, 693−700.

(16) Schmieder, A. H., Winter, P. M., Caruthers, S. D., Harris, T. D., Williams, T. A., Allen, J. S., Lacy, E. K., Zhang, H., Scott, M. J., Hu, G., Robertson, J. D., Wickline, S. A., and Lanza, G. M. (2005) Molecular MR imaging of melanoma angiogenesis with alphanubeta3-targeted paramagnetic nanoparticles. *Magn. Reson. Med. 53*, 621−7.

(17) Mulder, W. J., Strilkers, G. J., Griffioen, A. W., van Bloois, L., Molema, G., Storm, G., Koning, G. A., and Nicolay, K. (2004) A liposomal system for contrast-enhanced magnetic resonance imaging of molecular targets. *Bioconjugate Chem. 15*, 799−806.

(18) Lipinski, M. J., Amirbekian, V., Frias, J. C., Aguinaldo, J. G., Mani, V., Briley-Saebo, K. C., Fuster, V., Fallon, J. T., Fisher, E. A., and Fayad, Z. A. (2006) MRI to detect atherosclerosis with gadolinium-containing immunomicelles targeting the macrophage scavenger receptor. *Magn. Reson. Med. 56*, 601−10.

(19) Lanza, G. M., Winter, P. M., Caruthers, S. D., Morawski, A. M., Schmieder, A. H., Crowder, K. C., and Wickline, S. A. (2004) Magnetic resonance molecular imaging with nanoparticles. *J. Nucl. Cardiol. 11*, 733−743.

(20) Anderson, S. A., Rader, R. K., Westlin, W. F., Null, C., Jackson, D., Lanza, G. M., Wickline, S. A., and Kotyk, J. J. (2000) Magnetic resonance contrast enhancement of neovasculature with alpha(v)beta(3)-targeted nanoparticles. *Magn. Reson. Med. 44*, 433−439.

(21) Amirbekian, V., Lipinski, M. J., Briley-Saebo, K. C., Amirbekian, S., Aguinaldo, J. G., Weinreb, D. B., Vucic, E., Frias, J. C., Hyafil, F., Mani, V., Fisher, E. A., and Fayad, Z. A. (2007) Detecting and assessing macrophages in vivo to evaluate atherosclerosis noninvasively using molecular MRI. *Proc. Natl. Acad. Sci. U.S.A. 104*, 961−966.

(22) Mulder, W. J., Strijkers, G. J., Habets, J. W., Bleeker, E. J., van der Schaft, D. W., Storm, G., Koning, G. A., Griffioen, A. W., and Nicolay, K. (2005) MR molecular imaging and fluorescence microscopy for identification of activated tumor endothelium using a bimodal lipidic nanoparticle. *FASEB J. 19*, 2008−10.

(23) Franano, F. N., Edwards, W. B., Welch, M. J., Brechbiel, M. W., Gansow, O. A., and Duncan, J. R. (1995) Biodistribution and metabolism of targeted and nontargeted protein-chelate-gadolinium

complexes: evidence for gadolinium dissociation in vitro and *in vivo*. *Magn. Reson. Imaging 13*, 201−214.
(24) Wang, S. J., Brechbiel, M., and Wiener, E. C. (2003) Characteristics of a new MRI contrast agent prepared from polypropyleneimine dendrimers, generation 2. *Invest. Radiol. 38*, 662−668.
(25) Bryant, L. H., Jr, Jordan, E. K., Bulte, J. W., Herynek, V., and Frank, J. A. (2002) Pharmacokinetics of a high-generation dendrimer-Gd-DOTA. *Acad. Radiol. 9* (S1), S29−33.
(26) Helbich, T. H., Gossman, A., Mareski, P. A., Raduchel, B., Roberts, T. P., Shames, D. M., Muhler, M., Turetschek, K., and Brasch, R. C. (2000) A new polysaccharide macromolecular contrast agent for MR imaging: biodistribution and imaging characteristics. *J. Magn. Reson. Imaging 11*, 694−701.
(27) Burtea, C., Laurent, S., Murariu, O., Rattat, D., Toubeau, G., Verbruggen, A., Vansthertem, D., Vander, E. L., and Muller, R. N. (2008) Molecular imaging of $\alpha_v\beta_3$ integrin expression in atherosclerotic plaques with a mimetic of RGD peptide grafted to Gd-DTPA. *Cardiovasc. Res. 78*, 148−157.
(28) Botnar, R. M., Buecker, A., Wiethoff, A. J., Parsons, E. C., Katoh, M., Jr, Katsimaglis, G., Weisskoff, R. M., Lauffer, R. B., Graham, P. B., Gunther, R. W., Manning, W. J., and Spuentrup, E. (2004) In vivo magnetic resonance imaging of coronary thrombosis using a fibrin-binding molecular magnetic resonance contrast agent. *Circulation 110*, 1463−1466.
(29) Spuentrup, E., Katoh, M., Wiethoff, A. J., Parsons, E. C., Jr, Botnar, R. M, Mahnken, A. H., Gunther, R. W., and Buecker, A. (2005) Molecular magnetic resonance imaging of pulmonary emboli with a fibrin-specific contrast agent. *Am. J. Respir. Crit. Care Med. 172*, 494−500.
(30) Overoye-Chan, K., Koerner, S., Looby, R. J., Kolodziej, A. F., Zech, S. G., Deng, Q., Chasse, J. M., McMurry, T. J., and Caravan, P. (2008) EP-2104R: a fibrin-specific gadolinium-Based MRI contrast agent for detection of thrombus. *J. Am. Chem. Soc. 130*, 6025−6039.
(31) Spuentrup, E., Botnar, R. M., Wiethoff, A. J., Ibrahim, T., Kelle, S., Katoh, M., Ozgun, M., Nagel, E., Vymazal, J., Graham, P. B., Gunther, R. W., and Maintz, D. (2008) MR imaging of thrombi using EP-2104R, a fibrin-specific contrast agent: initial results in patients. *Eur. Radiol. 18*, 1995−2005.
(32) Spuentrup, E., Ruhl, K. M., Botnar, R. M., Wiethoff, A. J., Buhl, A., Jacques, V., Greenfield, M. T., Krombach, G. A., Gunther, R. W., Vangel, M. G., and Caravan, P. (2009) Molecular magnetic resonance imaging of myocardial perfusion with EP-3600, a collagen-specific contrast agent: initial feasibility study in a swine model. *Circulation 119*, 1768−1775.
(33) Caravan, P., Das, B., Dumas, S., Epstein, F. H., Helm, P. A., Jacques, V., Koerner, S., Kolodziej, A., Shen, L., Sun, W. C., and Zhang, Z. (2007) Collagen-targeted MRI contrast agent for molecular imaging of fibrosis. *Angew. Chem., Int. Ed. Engl. 46*, 8171−8173.
(34) Amirbekian, V., Aguinaldo, J. G., Amirbekian, S., Hyafil, F., Vucic, E., Sirol, M., Weinreb, D. B., Le Greneur, S., Lancelot, E., Corot, C., Fisher, E. A., Galis, Z. S., and Fayad, Z. A. (2009) Atherosclerosis and matrix metalloproteinases: experimental molecular MR imaging in vivo. *Radiology 251*, 429−438.
(35) Boutry, S., Burtea, C., Laurent, S., Toubeau, G., Vander Elst, L., and Muller, R. N. (2005) Magnetic resonance imaging of inflammation with a specific selectin-targeted contrast agent. *Magn. Reson. Med. 53*, 800−807.
(36) Abe, K., Shoji, M., Chen, J., Bierhaus, A., Danave, I., Micko, C., Casper, K., Dillhay, D. L., Nawroth, P. P., and Rickles, F. R. (1999) Regulation of vascular endothelial growth factor production and angiogenesis by the cytoplasmic tail of tissue factor. *Proc. Natl. Acad. Sci. U.S.A. 96*, 8663−8668.
(37) Zhang, J., Ding, J., Zhang, X., Shao, X., and Hao, Z. (2005) Regulation of vascular endothelial growth factor (VEGF) production and angiogenesis by tissue Factor (TF) in SGC-7901 gastric cancer cells. *Cancer Biol. Ther. 4*, 769−772.
(38) Ruoslahti, E. (2002) Specialization of tumour vasculature. *Nat. Rev. Cancer. 2*, 83−90.
(39) Pilch, J., Brown, D. M., Komatsu, M., Jarvinen, T. A., Yang, M., Peters, D., Hoffman, R. M., and Ruoslahti, E. (2006) Peptides selected for binding to clotted plasma accumulate in tumor stroma and wounds. *Proc. Natl. Acad. Sci. U.S.A. 103*, 2800−2804.
(40) Simberg, D., Duza, T., Park, J. H., Essler, M., Pilch, J., Zhang, L., Derfus, A. M., Yang, M., Hoffman, R. M., Bhatia, S., Sailor, M. J., and Ruoslahti, E. (2007) Biomimetic amplification of nanoparticle homing to tumors. *Proc. Natl. Acad. Sci. U.S.A. 104*, 932−936.
(41) Ye, F., Wu, X., Jeong, E. K., Jia, Z., Yang, T., Parker, D., and Lu, Z.-R. (2008) A peptide targeted contrast agent specific to fibrin-fibronectin complexes for cancer molecular imaging with MRI. *Bioconjugate Chem. 19*, 2300−2303.
(42) Ye, F., Jeong, E. K., Parker, D., and Lu, Z.-R. (2011) Evaluation of CLT1-(Gd-DTPA) for MR molecular imaging in a mouse breast cancer model. *Chin. J. Magn. Reson. Imaging 2*, 325−330.
(43) Idée, J. M., Port, M., Metdina, C., Lancelot, E., Fayoux, E., Ballet, S., and Corot, C. (2008) Possible involvement of gadolinium chelates in the pathophysiology of nephrogenic systemic fibrosis: a critical review. *Toxicology 248*, 77−88.
(44) Idée, J. M., Port, M., Raynal, I., Schaefer, M., Le Greneur, S., and Corot, C. (2006) Clinical and biological consequences of transmetallation induced by contrast agents for magnetic resonance imaging: a review. *Fundam. Clin. Pharmacol. 20*, 563−576.
(45) White, G. W., Gibby, W. A., and Tweedle, M. F. (2006) Comparison of Gd(DTPA-BMA) (Omniscan) versus Gd(HP-DO3A) (ProHance) relative to gadolinium retention in human bone tissue by inductively coupled plasma mass spectroscopy. *Invest. Radiol. 41*, 272−8.
(46) Wu, X., Zong, Y., Ye, Z., and Lu, Z.-R. (2010) Stability and biodistribution of a biodegradable macromolecular MRI contrast agent Gd-DTPA cystamine copolymers (GDCC) in rats. *Pharm. Res. 27*, 1390−1397.
(47) Burden-Gulley, S. M., Gates, T. J., Burgoyn, A. M., Cutte,r, J. L., Lodowski, D. T., Robinson, S., Sloan, A. E., Miller, R. H., Basilion, J. P., and Brady-Kalnay, S. M. (2010) A novel molecular diagnostic of glioblastomas: detection of an extracellular fragment of protein tyrosine phosphatase mu. *Neoplasia 12*, 305−316.
(48) Rohrer, M., Bauer, H., Mintorovitch, J., Requardt, M., and Weinmann, H. J. (2005) Comparison of magnetic properties of MRI contrast media solutions at different magnetic field strengths. *Invest. Radiol. 40*, 715−724.
(49) Tan, M., Wu, X., Jeong, E. K., Chen, Q., and Lu, Z.-R. (2010) Peptide-targeted Nanoglobular Gd-DOTA monoamide conjugates for magnetic resonance cancer molecular imaging. *Biomacromolecules 11*, 754−761.
(50) Tan, M., Burden-Gulley, S., Li, W., Wu, X., Lindner, D., Brady-Kalnay, S., and Lu, Z.-R. (2012) MR molecular imaging of prostate cancer with a peptide-targeted contrast agent in a mouse orthotopic prostate cancer model. *Pharm. Res. 29*, 953−60.
(51) DeNardo, S. J., O'Donnell, R. T., and DeNardo, G. L. (1996) Potential use of amino acid cocktails to reduce renal tubular reabsorption of radioconjugates. *J. Nucl. Med. 37*, 837−8.

Bioconjugate Chemistry

Article

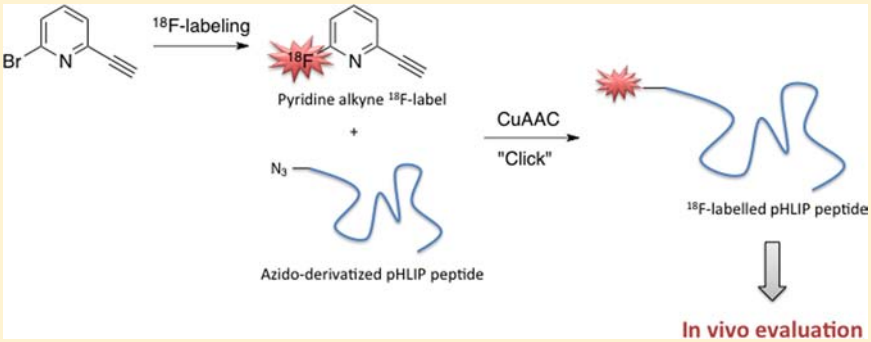
pubs.acs.org/bc

Efficient ^{18}F-Labeling of Large 37-Amino-Acid pHLIP Peptide Analogues and Their Biological Evaluation

Pierre Daumar,[†,§] Cindy A. Wanger-Baumann,[†,§] NagaVaraKishore Pillarsetty,[†] Laura Fabrizio,[†] Sean D. Carlin,[†] Oleg A. Andreev,[‖] Yana K. Reshetnyak,[‖] and Jason S. Lewis*[,†,‡]

[†]Department of Radiology and the [‡]Program in Molecular Pharmacology and Chemistry, Memorial Sloan-Kettering Cancer Center, New York, New York 10065, United States

[‖]Physics Department, University of Rhode Island, Kingston, Rhode Island 02881, United States



ABSTRACT: Solid tumors often develop an acidic microenvironment, which plays a critical role in tumor progression and is associated with increased level of invasion and metastasis. The 37-residue pH (low) insertion peptide (pHLIP) is under study as an imaging platform because of its unique ability to insert into cell membranes at a low extracellular pH (pH_e < 7). Labeling of peptides with [^{18}F]-fluorine is usually performed via prosthetic groups using chemoselective coupling reactions. One of the most successful procedures involves the alkyne−azide copper(I) catalyzed cycloaddition (CuAAC). However, none of the known "click" methods have been applied to peptides as large as pHLIP. We designed a novel prosthetic group and extended the use of the CuAAC "click chemistry" for the simple and efficient ^{18}F-labeling of large peptides. For the evaluation of this labeling approach, a D-amino acid analogue of WT-pHLIP and an L-amino acid control peptide K-pHLIP, both functionalized at the N-terminus with 6-azidohexanoic acid, were used. The novel 6-[^{18}F]fluoro-2-ethynylpyridine prosthetic group, was obtained via nucleophilic substitution on the corresponding bromo-precursor after 10 min at 130 °C with a radiochemical yield of 27.5 ± 6.6% (decay corrected) with high radiochemical purity ≥98%. The subsequent Cu^{I}-catalyzed "click" reaction with the azido functionalized pHLIP peptides was quantitative within 5 min at 70 °C in a mixture of water and ethanol using Cu-acetate and sodium L-ascorbate. [^{18}F]-D-WT-pHLIP and [^{18}F]-L-K-pHLIP were obtained with total radiochemical yields of 5−20% after HPLC purification. The total reaction time was 85 min including formulation. *In vitro* stability tests revealed high stability of the [^{18}F]-D-WT-pHLIP in human and mouse plasma after 120 min, with the parent tracer remaining intact at 65% and 85%, respectively. PET imaging and biodistribution studies in LNCaP and PC-3 xenografted mice with the [^{18}F]-D-WT-pHLIP and the negative control [^{18}F]-L-K-pHLIP revealed pH-dependent tumor retention. This reliable and efficient protocol promises to be useful for the ^{18}F-labeling of large peptides such as pHLIP and will accelerate the evaluation of numerous [^{18}F]-pHLIP analogues as potential PET tracers.

INTRODUCTION

Positron emission tomography (PET) is a noninvasive functional *in vivo* imaging modality, commonly used in tumor diagnosis. Tremendous effort has been made toward the development of additional efficient and widely applicable PET tracers, given the limitations of [^{18}F]-FDG, for the targeting of a large variety of cancers. However, the development of a universal tumor targeting PET tracer is limited due to tumor heterogeneity and differences within the tumor environment.[1] Therefore, targeting a physiological anomaly present in most cancers seems very promising for the development of a widely applicable diagnostic agent in oncology. The acidity of the tumor microenvironment is one of such anomalies, which plays a significant role in progression and is often associated with increased invasion and metastasis.[2] It is present in 90% of tumor microenvironments and is therefore considered a promising environmental marker for targeting.[3,4]

A 37-residue peptide discovered in 1997 by Hunt et al.[5] was recently shown to display unique pH-dependent properties: the pH Low Insertion Peptide (WT-pHLIP, NH_2-ACEQNPIY-WARYADWLFTTPLLLLDLALLVDADEGTG-CO_2H) is

Received: January 16, 2012
Revised: June 15, 2012
Published: July 12, 2012

 © 2012 American Chemical Society

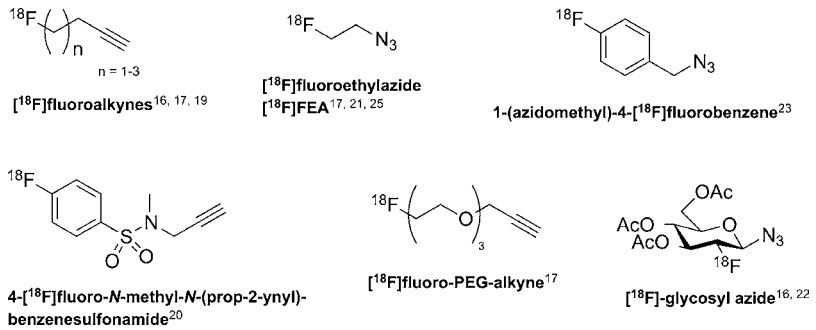


Figure 1. Examples of [^{18}F]-labeled prosthetic groups for the CuAAC "click" reaction with functionalized peptides and proteins.

soluble in aqueous solution at physiological pH and shows transient interaction with cell membranes in tissues with neutral extracellular pH (pH_e). In tissues with an acidic pH_e, Asp/Glu residues of pHLIP are protonated, which increases the overall hydrophobicity of the peptide and affinity to the cell membrane. As a result, pHLIP inserts and translocates itself through the phospholipid bilayer that is the cellular membrane.[6] This insertion involves a change in the peptide conformation to a α-helix, the N-terminus remaining in the extracellular space, while the C-terminus reaches the intracellular lumen.

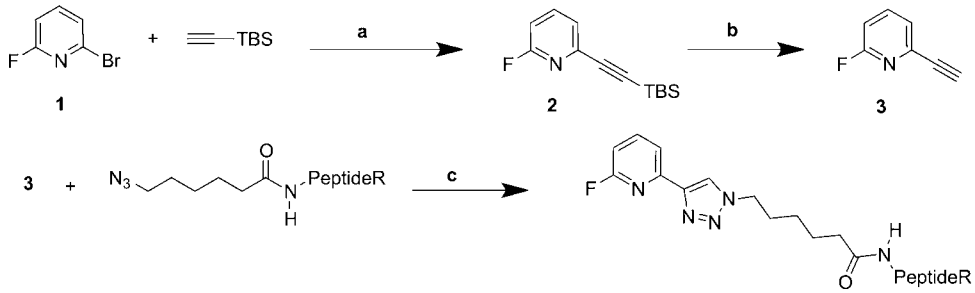
The pHLIP peptide was recognized as a potentially useful platform for tissue acidity imaging, and therefore, its potential application as a universal tool in oncology was envisaged.[7] We successfully demonstrated that fluorescent pHLIP could be used to detect tissue acidity and target tumors in mice.[8] In an extension to the study, ^{64}Cu-labeled pHLIP was evaluated for its suitability as a PET tumor imaging agent. The novel tracer displayed good imaging characteristics with the highest level of radioactivity accumulation in LNCaP tumor being reached 1 h after administration, but some demetalation[9] and a significant retention of activity in the GI tract were also observed.

Fluorine-18 is the most common PET nuclide due to its favorable physical properties (low positron energy, pure positron decay, and 110 min half-life), availability, and dosimetry.[10,11] Therefore, the ^{18}F-nuclide was considered the ideal nonmetal-based alternative for the PET-labeling of pHLIP and its analogues. However, the ^{18}F-labeling of large peptides such as WT-pHLIP (molecular weight (MW) > 4000 Da) still remains challenging because nucleophilic substitution with [^{18}F]-fluoride requires harsh basic conditions and cannot be performed directly on peptides.[12] As a result, numerous approaches to label peptides with ^{18}F were developed, including bioconjugation with prosthetic groups like *N*-succinimidyl-4-[^{18}F]fluorobenzoate ([^{18}F]SFB) or *p*-nitrophenyl-2-[^{18}F]-fluoropropionate ([^{18}F]NFP),[13] or more recent methodologies involving Al^{18}F chelation[14] or the "less conventional" use of organosilicon-based fluoride acceptor.[15] Among the recent chemoselective ^{18}F-labeling strategies involving indirect labeling by means of [^{18}F]-prosthetic groups, the popular alkyne−azide copper(I) catalyzed cycloaddition (CuAAC) "click" reaction, where the coupling of an azide and an alkyne leads to the formation of a triazole ring, appeared well-suited for our purpose. It has been shown to be widely applicable and efficient for the labeling of peptides, mostly requiring a two-step synthetic approach. The success of this strategy and its wide range of application led to the development of a large variety of ^{18}F-labeled prosthetic groups as exemplified in Figure 1 and recently reviewed.[16,17] Thus, the one-step radiolabeling of suitable precursors followed by cycloaddition of the resulting ^{18}F-bearing alkyne prosthetic groups with azido-functionalized peptides of interest was shown to result in total RCYs of 20−75% (d. c.).[18−20] The corresponding radiosyntheses utilizing an ^{18}F-labeled azido prosthetic group and an alkyne-functionalized peptide were shown to be equally efficient.[21−23]

With regard to the radiochemistry, however, only a few of the common ^{18}F-labeled prosthetic groups like 1-(azidomethyl)-4-[^{18}F]-fluorobenzene[24] or 4-[^{18}F]fluoro-*N*-methyl-*N*-(prop-2-ynyl)-benzenesulfonamide[20] are UV-detectable. A common disadvantage of [^{18}F]-fluoroalkynes or azides is also their high volatility, which can be technically challenging.[13,18,19,21,25] Finally, the preparation of [^{18}F]-glycosylazides or azidomethyl-[^{18}F]-benzenes, for example, involves more than one step and is therefore more laborious.[22] Besides the inherent difficulties of a prosthetic group radiosynthesis, to the best of our knowledge, only Hausner et al. have demonstrated an efficient ^{18}F-radiolabeling of peptides with a high molecular weight (MW > 2000 Da), commenting on the increasing challenge to label peptides with increasing complexity and size.[13] Ramenda et al. have reported the ^{18}F-radiolabeling of azide-functionalized human serum albumin but noted that the introduction of azide residues into HSA and subsequent radiolabeling via click chemistry significantly altered the structural and functional integrity of HSA.[20] More recently, in an eloquent approach, Gill et al. have demonstrated the utility of maleimide functionalized alkyne in labeling antibodies with [^{18}F]-fluorine via a click approach.[26] However, the presence of cysteine and lysine residues in the pHLIP amino acid sequence makes this approach unrealistic in our case, as it is necessary to limit the number of derivatization sites to one in order to preserve the unique pHLIP properties. Therefore, it appears that further efficient ^{18}F-labeling procedures are necessary for the development of a successful and widely applicable [^{18}F]-pHLIP derivative.

Herein, we report on the use of a novel ^{18}F-labeled prosthetic group for the efficient two-step "click" radiolabeling of azido-hexanoic acid derivatized pHLIP involving a UV-detectable prosthetic group. The ultimate aim of this study was to evaluate the novel prosthetic group for its universal utilization in [^{18}F]-peptide chemistry. Therefore, the reaction conditions were investigated with two different peptides: D-WT-pHLIP (all amino acids have D-configuration) and L-K-pHLIP (all amino acids have L-configuration), which has exactly the same sequence as WT-pHLIP, but two aspartic acid residues have been replaced with lysines. These aspartic acid residues are present in the transmembrane part after insertion and are critical for pH-dependent behavior. Therefore, L-K-pHLIP lacks pH-dependent behavior and was used as a negative control in our study.[6,27,28] *In vitro* stability of the [^{18}F]-D-WT-pHLIP in both human and murine plasma was also examined.

Scheme 1. Synthetic Route Yielding the Non-Radiolabeled Reference Compounds 3 to 5



Reagents and conditions: (a) $Pd(PPh_3)_4$, CuI, Et_3N, DMF, RT, 24 h; (b) THF, TBAF, 1 h, RT; (c) H_2O, ACN, EtOH, Cu-acetate × 5 H_2O, sodium L-ascorbate, 48-70 h, RT.

Finally, PET imaging and biodistribution studies were performed in order to determine the *in vivo* properties of the novel [^{18}F]-pHLIP conjugates in LNCaP and PC-3 tumor xenografts bearing mice.

MATERIALS AND METHODS

General Methods. All chemicals and solvents were purchased from Sigma-Aldrich, Anichem or Fluka and were used without further purification unless specifically stated otherwise. All peptide starting materials were purchased from C S Bio Co. (Menlo Park, CA, USA). Ultrapure water was used in this work (>18 MΩ cm^{-1} at 20 °C, Milli-Q, Millipore, Billerica, MA, USA). All instruments were maintained and calibrated regularly according to quality control procedures as previously reported. Thin layer chromatography performed on precoated silica gel 60 F245 aluminum sheets suitable for UV detection of compounds was used for monitoring the reactions. Radioactivity measurements were performed with a Capintec CRC1243 Dose Calibrator (Capintec, Ramsay, NJ, USA). Precise quantification of low radioactivity samples was achieved with a Perkin-Elmer (Waltham, MA, USA) Automatic Wizard2 Gamma Counter. Nuclear magnetic resonance spectra were recorded on a Bruker AVIII 500.13 MHz spectrometer with an internal standard from solvent signals. Chemical shifts are given in parts per million (ppm) relative to tetramethylsilane (0.00 ppm). Values of the coupling constant, *J*, are given in hertz (Hz). The following abbreviations are used for the description of ^{1}H NMR and ^{13}C NMR spectra: singlet (s), doublet (d), doublet of doublets (dd), triplet (t), quartet (q). The chemical shifts of complex multiplets are given as the range of their occurrence. Low resolution mass spectra (LRMS) were recorded with a Waters Acquity UPLC with electrospray ionization SQ detector (ESI). High resolution mass spectra (HRMS) were recorded with a Waters LCT Premier system (ESI) and MALDI TOF analysis was performed on a Bruker Ultraflex TOF/TOF MALDI tandem TOF mass spectrometer. Quality control and purification of the final products in order to confirm the purity ≥95% of the radioactive intermediates and final products were achieved by analytical or semipreparative high-performance liquid chromatography (HPLC). All HPLC experiments were performed on a Shimadzu HPLC system equipped with a Flow Count PIN diode radiodetector from BioScan, a DGU-20A degasser, two LC-20AB pumps, and SPD-M20A photodiode array detector and a SPD-M20A autosampler using reverse-phase columns: (1) semipreparative, Luna 5 μm C18, 100 Å, 250 × 10 mm, (Phenomenex, Torrance, CA); (2) analytical, Luna 5 μm C18, 100 Å, 250 × 4.6 mm, (Phenomenex, Torrance, CA); (3) semipreparative, Nova-Pak 6 μm C18, 60 Å, 300 × 7.8 mm, (Waters, Milford, MA). Different gradient solvent systems were applied: (A) 20−80% MeCN in water in the presence of 0.1% trifluoroacetic acid (TFA) in 20 min with a flow of 5 mL/min; (B) 20−80% MeCN in water with 0.1% TFA in 20 min with a flow of 1.5 mL/min; (C) 5−40% EtOH in water in 5 min, 40% EtOH in water from 5 to 15 min with a flow rate of 3 mL/min.

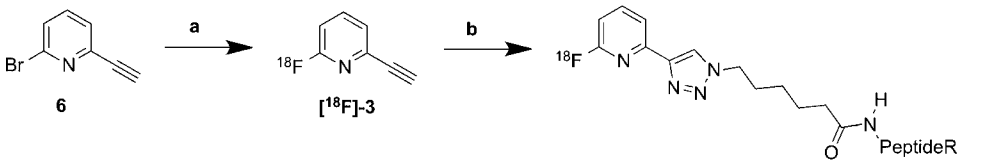
Chemistry. Syntheses of cold reference compounds **2** to **5** are presented in Scheme 1.

*2-((tert-Butyldimethylsilyl)ethynyl)-6-fluoropyridine (**2**).* To a degassed solution of *tert*-butyl(ethynyl)dimethylsilane (190 mg, 1.30 mmol) in triethylamine (Et_3N, 0.6 mL) and DMF (2 mL) was added CuI (50 mg, 0.26 mmol). To a second degassed solution of 2-bromo-6-fluoropyridine (200 mg, 1.10 mmol) in DMF (4 mL) was added $Pd(PPh_3)_4$ (15 mg, 0.013 mmol). Both mixtures were stirred for 5 min and then combined and allowed to react at RT for 24 h before saturated aqueous NH_4Cl (7 mL) was added. The resulting solution was then extracted with diethyl ether (Et_2O, 3 × 20 mL). The combined organic layers were washed with water (2 × 20 mL) and brine (20 mL) before drying over Na_2SO_4. Careful evaporation resulted in a brown oily residue. Purification by silica gel column chromatography utilizing pentane/Et_2O (95:5) gave **2** (105 mg, 40%) as a colorless oil that formed white crystals at 4 °C. R_f = 0.8 (pentane/ethyl acetate; 9:1). ^{1}H NMR (500 MHz, $CDCl_3$): δ 7.71 (q, *J* = 7.7 Hz, 1H), 7.33 (d, *J* = 6.5 Hz, 1H), 6.88 (dd, *J* = 1.3, 2.5 Hz, 1H), 0.99 (s, 9H), 0.20 (s, 6H). ^{13}C NMR (500 MHz, $CDCl_3$): 162.9 (d, *J* = 241.2 Hz), 141.0 (d, *J* = 12.7 Hz), 125.0 (d, *J* = 3.9 Hz), 124.8 (d, *J* = 54.2 Hz), 109.6 (d, *J* = 36.9 Hz), 102.9, 95.0, 26.1, 16.7, 1.0. ^{19}F NMR (500 MHz, $CDCl_3$): δ −65.17. MS *m*/*z*: 236.21 (M + H)$^+$.

*2-Ethynyl-6-fluoropyridine (**3**).* To a solution of **2** (30 mg, 0.12 mmol) in dry tetrahydrofuran (THF, 2.5 mL) was added tetrabutylammonium fluoride (TBAF) trihydrate (120 mg, 0.38 mmol). After stirring the reaction mixture for one hour at RT, water (10 mL) was added. This mixture in water/THF (4:1) was used without further purification for the synthesis of the fluorinated reference peptides. For analytical purposes, compound **3** was purified by semipreparative HPLC using column 1 and the gradient solvent system A. The retention time of compound **3** was 11.2 min. Due to the volatility of the product and the small scale of the synthesis, concentration of

dx.doi.org/10.1021/bc3000222 | *Bioconjugate Chem.* 2012, 23, 1557−1566

Scheme 2. Radiosynthesis Yielding Radiolabeled Products [^{18}F]-3 to [^{18}F]-5



[^{18}F]-4; PeptideR = D-WT-pHLIP (37 amino acids)
[^{18}F]-5; PeptideR = K-pHLIP (37 amino acids)

Reagents and conditions: (a) K[^{18}F]F-Kryptofix 222, DMSO, 130 °C, 10 min; (b) H_2O, EtOH, Cu-acetate × 5 H_2O, sodium L-ascorbate, azidohexanoic acid derivatised peptide, 70 - 80 °C, 5 - 10 min.

the product was achieved using a C18 light cartridge (Waters) preconditioned with 5 mL of EtOH, followed by 5 mL of water. The combined fractions were diluted with water and passed over the cartridge. Pure product **3** was eluted with $CDCl_3$. ^{1}H NMR (500 MHz, $CDCl_3$): δ 7.76 (q, J = 7.8 Hz, 1H), 7.38 (d, J = 7.6 Hz, 1H), 6.94 (dd, J = 2.7, 2.9 Hz, 1H), 3.19 (s, 1H). ^{13}C NMR (500 MHz, $CDCl_3$): δ 162.9 (d, J = 237.8 Hz), 141.2 (d, J = 7.2 Hz), 125.4 (d, J = 96.3 Hz), 125.0 (d, J = 36.9 Hz), 110.2 (d, J = 36.8 Hz), 81.3, 78.3. ^{19}F NMR (500 MHz, $CDCl_3$): δ −65.30. MS m/z 121.89 $(M + H)^+$. HRMS calcd for C_7H_5NF, 122.0407; found, 122.0406.

6-(4-(6-Fluoropyridin-2-yl)-1H-1,2,3-triazol-1-yl)hexanoyl-D-WT-pHLIP (Fpyrtriazolo-D-WT-pHLIP, 4). 100 μL (0.01 mmol) of a freshly prepared solution of Cu(II) acetate (18 mg/mL) and 200 μL (0.02 mmol) of a fresh (+)-sodium L-ascorbate solution (20 mg/mL) in water were mixed in a sealed vial under argon. To the yellow mixture was added a solution of azidohexanoyl-D-WTpHLIP ($N_3(CH_2)_5$CONH-ACEQNPIY-WARYADWLFTTPLLLLDLALLVDADEGTG-CO_2H) in EtOH (5 mg in 300 μL, 0.0012 mmol). Further addition of 2.7 mL of the solution of **3** (0.025 mmol) in water/THF (4:1) was followed by stirring of the reaction mixture at RT for 70 h before MeCN (3 mL) and water (3 mL) were added. The product was purified using semipreparative HPLC (column 1, solvent gradient system A): two conformational isomers (**4a**, **4b**) of Fpyrtriazolo-D-WTpHLIP were obtained with t_{R1} = 18.7 min and t_{R2} = 20.1 min, respectively. HPLC analysis indicated that the overall chemical purity of the compound **4** (**4a** + **4b**) is >98%. Calculated mono-isotopic mass for Fpyrtriazolo-D-WTpHLIP ($C_{206}H_{301}FN_{48}O_{58}S$): 4426.18. **4a**: found, MS (MALDI) m/z = 4426.65, **4b**: found, MS (MALDI) m/z = 4426.56.

6-(4-(6-Fluoropyridin-2-yl)-1H-1,2,3-triazol-1-yl)hexanoyl-L-K-pHLIP (Fpyrtriazolo-L-K-pHLIP, 5). This compound was prepared in an analogous way to compound **4**. The mixture containing the azidohexanoyl-L-K-pHLIP ($N_3(CH_2)_5$CONH-ACEQNPIYWARYAKWLFTTPLLLLKLALLVDADEGTG-CO_2H, 7.7 mg, 1.18 μmol) was stirred at RT for 48 h. Purification of the product was achieved by semipreparative HPLC on column 1 using the gradient solvent system A: t_R = 15.7 min; 99% purity. Calculated monoisotopic mass for peptide **5** ($C_{210}H_{315}FN_{50}O_{54}S$): 4452.31; found, MS (MALDI) m/z = 4452.724.

Radiochemistry. Radiosyntheses of [^{18}F]-**3** to [^{18}F]-**5** are presented in Scheme 2.

Radiosynthesis of [^{18}F]-3. [^{18}F]-fluoride (1480−2220 MBq) was obtained via the ^{18}O(p,n)^{18}F reaction of 11-MeV protons in an EBCO TR-19/9 cyclotron using enriched ^{18}O-water. QMA light cartridges (Waters) preconditioned with 0.5 M K_2CO_3 (5 mL) and water (5 mL) were used for trapping of $^{18}F^-$ from the aqueous solution. In order to elute $^{18}F^-$ from the cartridge into a sealed 5 mL reaction vial, 1 mL of Kryptofix K_{222} solution (Kryptofix K_{222}, 2.5 mg; K_2CO_3, 0.5 mg in MeCN/water (3:1)) was slowly passed through the cartridge. The solvents were evaporated at 110 °C under vacuum in the presence of slight inflow of argon gas. After addition of MeCN (1 mL), azeotropic drying was achieved under vacuum and with a slight argon inflow. For the complete removal of water traces, the procedure was repeated twice. A solution of the corresponding precursor **6** (Anichem), 1.5−2 mg in 200 μL of dry DMSO, was added to the Kryptofix complex and the reaction mixture was heated at 130 °C for 10 min before 1 mL of water and 0.4 mL of MeCN were added (total injection volume 1.6 mL). Purification by semipreparative HPLC was carried out using the reversed-phase column 3 with the gradient solvent system C: the product was eluted with the same retention time as the cold standard **3**: t_R = 9.2 min. Under the conditions used, the bromo precursor **6** has a retention time of 10.8 min. Identification of [^{18}F]-**3** was achieved by coinjection with the reference **3** on the reversed-phase column 1 and the solvent system A: t_R = 10.2 min (Figure 2A).

Radiosynthesis of [^{18}F]-4. Stock solutions of copper(II) acetate (18 mg/mL) and (+)-sodium L-ascorbate (20 mg/mL), respectively, were freshly prepared. A v-shaped 4 mL HPLC vial (MT-IT, Prominence, Shimadzu) was equipped with a stir bar, sealed, and set under argon before 30 μL of the Cu(II) acetate solution and 60 μL of the (+)-sodium L-ascorbate solution were mixed. The prosthetic group [^{18}F]-**3** (150−500 MBq) was directly collected from the HPLC into the prepared 4 mL HPLC vial (V = 1.2−1.6 mL). A solution of azidohexanoyl-D-WT-pHLIP ($N_3(CH_2)_5$CONH-ACEQNPIYWARYADWLF-TTPLLLLDLALLVDADEGTG-CO_2H, 1 mg, 0.2 μmol) in EtOH (150 μL) was added and the mixture was heated at 70 °C for 5−10 min. After addition of MeCN (100 μL), purification of the product was achieved using semipreparative HPLC on reversed-phase column 1 with solvent system A (total injection volume 1.5−2.0 mL). Two main radioactive peaks were eluted with the same retention time as the cold reference compounds **4a** and **4b** that are conformational isomers. HPLC analysis indicated that the overall radiochemical purity of the compound **4** (**4a** + **4b**) was >98%. The radiolabeled peptide could not be isolated from the peptide starting material, resulting in lowered apparent specific activity. Only [^{18}F]-**4a**, obtained in MeCN/water (3:1, 0.1% TFA), was used for *in vivo* evaluation. After dilution with 7 mL of water, the solution was passed over a C18 light Sep Pak cartridge (Waters), preconditioned with 5 mL of EtOH followed by 5 mL of water. The cartridge was washed with further 3 mL of water in order to remove traces of MeCN and TFA, and the trapped [^{18}F]-D-WT-pHLIP ([^{18}F]-**4a**) was eluted with 0.5−1 mL of EtOH. Identification of [^{18}F]-**4a** was achieved by comparison of the retention time with the cold reference compound **4** eluted with identical retention time

dx.doi.org/10.1021/bc3000222 | Bioconjugate Chem. 2012, 23, 1557−1566

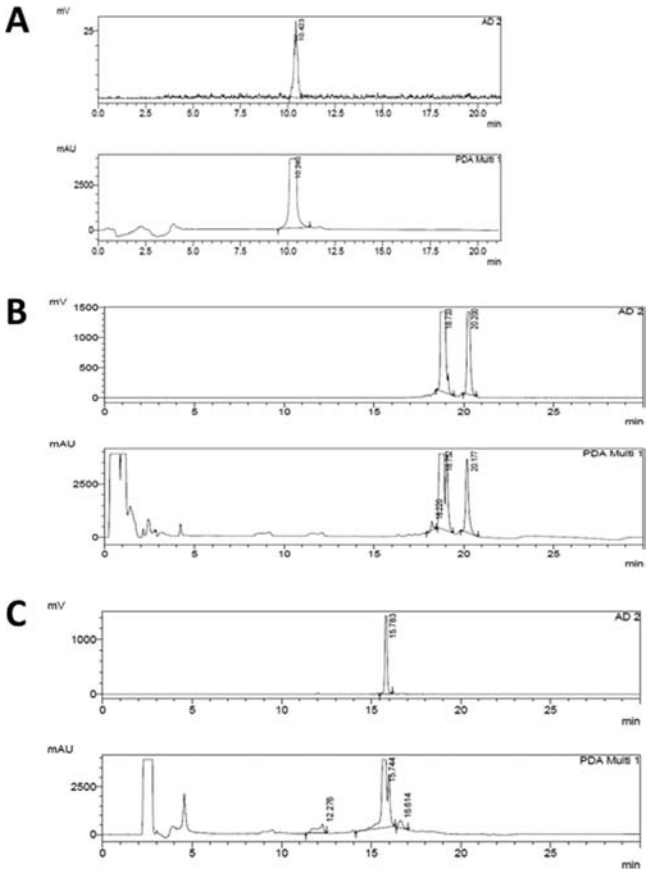


Figure 2. HPLC chromatograms with radio and UV-traces (UV traces were recorded at 254 nm and retention times are given with respect to the radiotrace): (A) coinjection of compound **3** and [^{18}F]-**3** with t_R = 10.4 min on column 1; (B) purification of [^{18}F]-**4a** and -**4b** after 5 min at 70 °C with t_R = 18.7 min and t_R = 20.2 min, respectively; (C) purification of [^{18}F]-**5** after 5 min reaction at 70 °C (t_R = 15.8 min). HPLC chromatograms were recorded utilizing column 1 applying elution conditions A.

under the same HPLC conditions but injecting only 50 μL of the collected solution for analysis. After evaporation of the solvent under vacuum and a slight argon inflow, which was completed within 6−8 min, the product was formulated in saline with 3% ethanol for injection.

*Radiosynthesis of [^{18}F]-**5**.* The radiosynthesis and purification were achieved in an analogous way to [^{18}F]-**4**. For the formulation of an injectable solution of [^{18}F]-**5**, a cartridge purification step was performed as described above. The product was eluted with 1.5 mL of acidified EtOH containing 0.02% 2 N HCl and the solvent was removed under vacuum and a slight argon inflow. [^{18}F]-**5** was formulated in phosphate buffer for injection after addition of 50 μL of 0.1 N NaOH for neutralization. Identification of [^{18}F]-**5** was achieved by comparison of the retention time with the cold reference compound **5** eluted with identical retention time under the same HPLC conditions.

Determination of the Lipophilicity of [^{18}F]-4 and [^{18}F]-5 ($logD_{pH7.4}$). As described by Wilson et al.[29] for the shake flask method, phosphate buffer (pH 7.4) saturated octanol (500 μL) and octanol saturated phosphate buffer (500 μL) were added to a microcentrifuge tube (1.5 mL, Eppendorf). Following the addition of 10 μL of the radiotracer solution (approximately 37 kBq), the samples were first vortexed and then shaken for 15 min. For phase separation, the samples were centrifuged at 2348 rcf for 5 min. 50 μL aliquots of each layer were withdrawn carefully from each phase and pipetted into microcentrifuge tubes (Eppendorf) for measurement of the distribution of the activity with a gamma-counter (Wizard,[2] Perkin-Elmer). The experiment was performed in quintuplicate.

***In Vitro* Stability test.** For the determination of the *in vitro* stability of ^{18}F-labeled pHLIP analogues, 20 μL aliquots of the model peptide [^{18}F]-D-WT-pHLIP ([^{18}F]-**4**) in EtOH were added to both human and murine plasma (380 μL) and incubated at 37 °C. After 60 and 120 min, aliquots of 180 μL were removed and added to an equal amount of MeCN for precipitation of the present proteins. After 5 min of centrifugation (21 130 rcf), 4 °C), the supernatant was analyzed under semipreparative HPLC conditions as described for the purification of the radiolabeled peptides.

Tumor Cell Culture. Human prostate cancer cell lines LNCaP and PC-3 from the American Tissue Culture Collection (ATCC, Manassas, VA, USA) were cultured in a 5% CO_2 atmosphere at 37 °C. LNCaP cells were cultured in RPMI 1640 medium containing 10% fetal calf serum (FCS), 2 mM L-glutamine, 1 mM sodium pyruvate, 4.5 g/L glucose, 1.5 g/L sodium bicarbonate, and 100 U/mL of penicillin and streptomycin. PC-3 cell were cultured in F-12 Kaighn's medium containing 10% FCS, 2 mM L-glutamine, 1.5 g/L sodium bicarbonate, and 100 U/mL of penicillin and streptomycin. Cells were trypsinized in the absence of magnesium or calcium ions using a cocktail of 0.25% trypsin and 0.53 mM EDTA in Hank's buffered salt solution.

LNCaP and PC-3 Tumor Xenografts. Male athymic mice (NCRNU-M, 20−25 g) were obtained from Taconic Farms, Inc. (Hudson, NY, USA) and were kept in the MSKCC vivarium for one week before any experimental handling was performed. The animals were allowed free access to water and food, and all animal care and experimental procedures were approved by the Institutional Animal Care and Use Committee (IACUC). LNCaP and PC-3 tumor xenografts were induced on the right and the left shoulder of each mouse, respectively, by subcutaneous injection of the corresponding cell suspension in Matrigel (BD, Collaborative Biomedical Products, Inc., Bedford, MA, USA) and media (1:1) containing (5.0×10^6)−10^7cells (viability >90%) per injection (200 μL). All procedures were carried out under anesthesia (1.5% isoflurane). Because of the slow rate of growth of the LNCaP tumors, these tumors were implanted 14 days prior to the PC-3 tumor implantation to have similarly sized tumors for the imaging and biodistribution studies. Palpable tumors of similar size developed after 4 to 5 weeks after the initial tumor xenograft induction.

Small-Animal PET Imaging Studies. PET imaging studies were conducted on a microPET Focus 120 rodent scanner (Concorde Microsystems). Dual tumor bearing mice (n = 4) with LNCaP tumor (right shoulder, V = 100−200 mm^3) and PC-3 (left shoulder, V = 100−200 mm^3) were administered [^{18}F]-**4** [160−170 μCi (5.9−6.3 MBq)] in 200 μL formulated solution (3% EtOH in saline) and control peptide [^{18}F]-**5** [260 μCi (9.8 MBq)] in 200 μL formulated solution (phosphate buffered saline) via tail vein injection. Approximately 3 min prior to the PET scan, mice were anesthetized by inhalation of 2% isoflurane (Baxter Healthcare, Deerfield, IL, USA)/ oxygen gas mixture and placed on the bed of the scanner, while anesthesia was maintained using 1.5% isoflurane/gas mixture. PET data for each mouse were recorded via a 15 min static acquisition 2 and

dx.doi.org/10.1021/bc3000222 | *Bioconjugate Chem.* 2012, 23, 1557−1566

4 h post injection (p.i.). For the static images, a minimum of 20 million coincident events were detected.

An energy window of 350−700 keV and a coincidence timing window of 6 ns were used. Data were sorted into two-dimensional histograms by Fourier rebinning, and transverse images were reconstructed by filtered back-projection into a 128 × 128 × 63 (0.72 × 0.72 × 1.3 mm^3) matrix. The images were normalized to correct for nonuniformity of response of the PET, dead-time count losses, positron branching ratio, and physical decay to the time of injection, but no attenuation, scatter, or partial-volume averaging correction was applied. The measured reconstructed spatial resolution for the Focus 120 is approximately 1.6 mm in full width at half-maximum at the center of the field of view. The counting rates in the reconstructed images were converted to percent of injected dose per weight (%ID/g) by use of a system calibration factor derived from the imaging of a mouse-sized water-equivalent phantom containing ^{18}F. Images were evaluated by region-of-interest (ROI) analysis using *ASIPro VM* software (Concorde Microsystems).

Combined Histological/Autoradiographic Analysis. After the completion of the last imaging session, vascular perfusion marker Hoechst 33342 (15 mg/kg in 0.2 mL of sterile saline) was administered via the tail vein catheter. Series of contiguous fresh-frozen tumor sections of 10 μm thickness were cut and exposed to a phosphor-imaging plate (Fujifilm BAS-MS2325, Fuji Photo Film, Japan) for an appropriate length of time at −20 °C. Digital images of radioactivity distribution at 50 μm resolution were obtained. The same sections were subsequently used for immunofluorescence imaging of Hoechst 33342, and finally stained with H&E. Autoradiographic and histological images were registered using Adobe *Photoshop CS3* software.

Post-Mortem Biodistribution Studies. Dual tumor-bearing mice (LNCaP and PC-3 tumors) were randomized before the experiment. Only mice with palpable tumors (V = 0.5−1.5 cm^3) were utilized. In order to investigate the biodistribution of radioactivity upon [^{18}F]-D-WT-pHLIP ([^{18}F]-**4**) injection, the tracer [~39 μCi (1.4 MBq), 15 nmol, 150−250 μL] was administered intravenously to the mice (n = 4 per time point, 16−24 g). Four mice were euthanized at 2 and 4 h post injection (p.i.), respectively. The blood was collected immediately followed by quick removal of the tumors. The lung, liver, heart, kidneys, spleen, bone, muscle, stomach, small intestines (SI), large intestines (LI), and testes were taken as well. The individual tumors and further organs were weighed and the radioactivity in each sample was measured in the gamma counter. Activity concentrations were calculated as percentage injected dose per tissue weight (%ID/g wet tissue).

As a negative control, a formulated solution of [^{18}F]-**5** [55 μCi (2 MBq), 3.5 nmol)] was administered to a further group of dual tumor bearing mice (n = 4, 19−22 g). These mice were euthanized at 2 h p. i. and biodistribution performed as above.

RESULTS AND DISCUSSION

Recently, the CuAAC "click reaction" has attracted increasing interest for the ^{18}F-labeling of peptides, mainly because of the recent development of novel [^{18}F]-prosthetic groups and efficient protocols for this type of chemistry.[16,17,30] However, the feasibility of such methods for the synthesis of large [^{18}F]-peptides (MW > 2000 Da) has yet to be proven. Indeed, the preparation of an ^{18}F-labeled $\alpha_v\beta_6$ specific 20 amino acids peptide by Hausner et al. in 2008 is the only successful report,[13] which demonstrates the challenge of labeling large peptides efficiently without affecting their integrity.

We experienced numerous difficulties during our first attempts to synthesize ^{18}F-labeled WT-pHLIP via CuAAC using a previously described [^{18}F]fluoro-PEG-alkyne. Indeed, even though such a prosthetic group has been used successfully for the radiolabeling of RGD constructs,[18] no "click coupling" with azido-derivatized pHLIP analogues was observed in the standard CuAAC conditions that we used (Cu(II) acetate/(+)-sodium L-ascorbate in H_2O/CH_3CN 1:1). We were therefore interested in the development of a novel fluorinated prosthetic group and a corresponding synthetic procedure (Scheme 1), suitable for the radiolabeling of large peptides. We chose fluoropyridinealkyne **3** because of the commercial availability of the corresponding bromo-precursor **6**, its UV-detectability, and the fact that 2-[^{18}F]fluoropyridines were shown to display high *in vivo* stability.[31] Moreover, the small size of **3** was expected to have a very limited impact on the pharmacokinetic of peptides as large as pHLIP.

Radiochemistry. [^{18}F]-**3** was prepared in one step by nucleophilic fluorination of the corresponding bromo precursor **6** (Scheme 2) using Kryptofix and K_2CO_3. Optimized conditions (DMSO, 10 min, 130 °C) led to [^{18}F]-**3** in RCYs of 27.5 ± 6.6% (n = 11) decay-corrected (d.c.), with conversion rates between 70% and 90%. This high labeling efficacy was not translated into higher RCYs because a loss of radioactivity was systematically observed during the transfer to the HPLC, presumably due to the volatility of [^{18}F]-**3**. Although a distillation-based purification might allow for higher yields, like those obtained with volatile [^{18}F]fluoroalkynes prosthetic groups,[19] it would also introduce MeCN, which in our case was not favorable for the subsequent "click" reaction. Instead, technical improvements or pH adjustments could potentially minimize the effect of the pyridine alkyne volatility issue. Our HPLC purification has a principal advantage to afford [^{18}F]-**3** in high radiochemical purity (RCP > 98%, Figure 2A) in a mixture of ethanol and water, which appeared to be a perfectly suitable solvent system for the CuAAC with pHLIP. Indeed, full incorporation of [^{18}F]-**3** was achieved within 10 min at 70 °C as demonstrated by the HPLC chromatograms in Figure 2B,C, where no unreacted material [^{18}F]-**3** was detected.

The two peaks observed in Figure 2B are due to acidic HPLC conditions, which promotes the formation of two pH-dependent conformational isomers (**4a** and **4b**). When either of the peaks was collected separately and reinjected, we observed two peaks in HPLC indicating that these are same chemical species. This fact has also been confirmed by HPLC-MS. No dimerization of peptide (through cysteine-cysteine disulfide linkage) was observed. It is also interesting to note that conformational isomers were only observed in the case of WT-pHLIP (Figure 2B), which reflects the non-acidity-dependent behavior of K-pHLIP (Figure 2C). Figure 2 also reveals that the radiolabeled peptides [^{18}F]-**4** and [^{18}F]-**5** could not be separated from the azido-derivatized starting materials. Consequently, the apparent specific activities were low (0.1−1 GBq/μmol), which should not question the use of [^{18}F]-pHLIP as an efficient PET tracer anyway. Indeed, given the mechanism of pHLIP insertion across the cell membrane, the number of insertion sites is theoretically unlimited wherever an acidic microenvironment is present,[7] as opposed to receptor-based targeting systems.[32]

Considering the size and the complexity of the [^{18}F]-pHLIP analogues, the detailed radiochemical data obtained with

Table 1. Analytical Data Determined for Radiolabeled Peptides [^{18}F]-4a, [^{18}F]-4b (n = 4), and [^{18}F]-5 (n = 3) after Semipreparative HPLC Purification

	RCP [%]	total RCY [%]	specific activity (EOS) [GBq/μmol]	total preparation time [min]	$\log D_{pH7.4}$
[^{18}F]-D-WT-pHLIP ([^{18}F]-**4a**)	≥95	13.6 ± 6.0	0.1−1.0	85	−0.70 ± 0.04
[^{18}F]-D-WT-pHLIP ([^{18}F]-**4b**)	−	13.6 ± 6.0	−	85	−0.70 ± 0.20
[^{18}F]-L-K-pHLIP ([^{18}F]-**5**)	≥98	5−13	0.1−0.8	85	−1.30 ± 0.03

[^{18}F]-**4** and [^{18}F]-**5** (Table 1) show the high efficacy of our novel strategy using [^{18}F]-**3**. Total RCYs of up to 20% could be achieved with respect to the starting amount of [^{18}F]-fluoride activity in a short synthesis time (≤85 min) and in one step, whereas several of the UV-detectable prosthetic groups that were used for peptide labeling were produced after multistep radiosyntheses.[22,23,33] The total radiochemical yields also reflect that some radioactivity was lost during the transfers and on the HPLC, which leads to reduced overall yields. In our preparative HPLC conditions, we never observed any unreacted [^{18}F]-**3** or other byproducts in the reaction. Although better yields were reported with small-sized peptides,[16] the CuAAC for was never achieved in such high yields with large peptides. By comparison, Hausner et al. radiolabeled a 20-amino-acid peptide via "click" reaction in yields below 10%.[13] Finally, our novel ^{18}F-labeling protocol was performed with low amounts of copper, and a minimum of 1 mg peptide starting material was necessary to achieve complete incorporation of [^{18}F]-**3**, which is in line with previously reported ^{18}F-"click" reactions on larger peptides.[13]

For the characterization of the novel ^{18}F-labeled pHLIP analogues, a $\log D_{pH7.4}$ determination was carried out (Table 1). [^{18}F]-**4a** and [^{18}F]-**4b** eluted from the HPLC system with different retention times and relative lipophilicity, exhibited the same $\log D_{pH7.4}$ of −0.7 presumably due to isomerization and formation of the same equilibrium state at pH 7.4. [^{18}F]-**5** was eluted from the HPLC system with shorter retention time, and it accordingly displayed a $\log D_{pH7.4}$ of −1.30 ± 0.03. It is well accepted that most of the [^{18}F]-prosthetic groups (Figure 1) lead to more lipophilic ^{18}F-labeled peptides, especially as the "click" approach involves the formation of a lipophilic triazole ring, often considered a surrogate for the amide bond.[16,34] Although a similar effect is expected with the use of [^{18}F]-**3**, the small size of the prosthetic group and the triazole ring should only have a limited impact on the pharmacological properties of future investigated peptides.

The stability of the [^{18}F]-prosthetic group in the [^{18}F]-peptide construct is important in terms of clearance and metabolism. In particular, *in vivo* radio-defluorination is easily detectable because of the related bone uptake of radioactivity.[32] Therefore, [^{18}F]-**4a**, as a prominent pHLIP analogue, was first subjected to an *in vitro* stability test in human and murine plasma at 37 °C. The tracer displayed good stability: after 60 min, 80% and 100% of the parent tracer remained intact in human and murine plasma, respectively; 65% and 85% were still present after 120 min. The degradation products were more hydrophilic and displayed retention times (t_R) suggesting potential peptide fragments. [^{18}F]-Fluoride is very hydrophilic and an elution from the HPLC column within the first 3 min is expected. However, no radioactive peaks were detected during the first 10 min. The fact that peptides derived from D-amino acids were shown to display higher *in vivo* stability,[35,36] and the good *in vitro* stability of the D-WT-pHLIP analogue, [^{18}F]-**4a**, encouraged the *in vivo* evaluation of the novel peptide tracers.

PET Imaging Studies. In order to prove the ability of [^{18}F]-**4a** to target acidity, we chose two prostate carcinoma tumor models, LNCaP and PC-3. Indeed, as determined by magnetic resonance, Vavere et al. reported a significantly more acidic average pH_e for LNCaP tumors when compared with the PC-3 tumors.[9] Therefore, we were hopeful that this difference could be observed with PET following [^{18}F]-**4a** administration.

As a matter of fact, the LNCaP tumor could be clearly visualized at both time points (Figure 3) and exhibited a

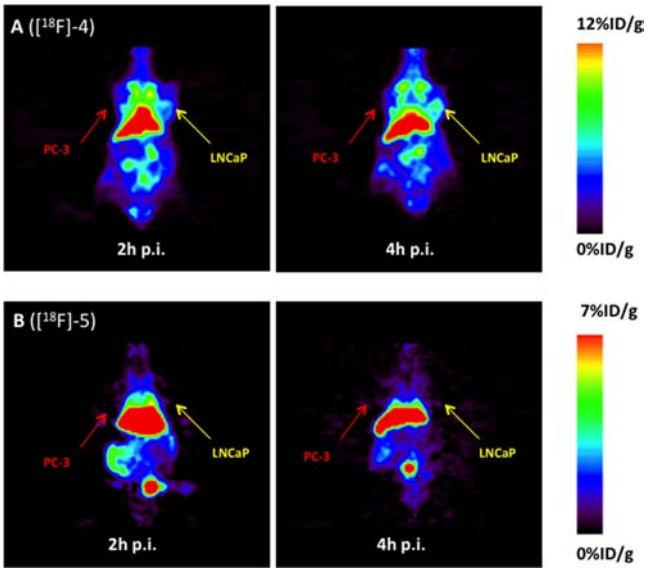


Figure 3. Representative coronal PET images of mice bearing LNCaP (right) and PC-3 (left) tumors injected with [^{18}F]-**4** (A) and [^{18}F]-**5** (B).

radioactivity accumulation of 8.3 ± 1.5 and 8.5 ± 1.3%ID/g at 2 and 4 h p. i., respectively. The PC-3 tumor showed lower radioactivity accumulation of 4.2 ± 0.4 to 5.4 ± 0.5%ID/g at 2 and 4 h p.i, respectively, and was poorly visualized. The lower uptake is a good indication for the successful application of the pHLIP principle for PET imaging of acidic tumors. Another indication for the specificity of the pHLIP was the lack of any tumor accumulation observed with the negative control peptide [^{18}F]-K-pHLIP (Figure 3).

The MR studies reported by Vavere et al. determined the total volume average pH_e in the tumors, but the heterogeneity of the tumor microenvironment suggests the formation of acidic and nonacidic areas in tumors. Accordingly, the PET images acquired after [^{18}F]-**4a** administration displayed a heterogeneous distribution of the tracer in the tumor since hot spots within the LNCaP tumor could be visualized, indicating the specific enrichment of pHLIP analogues in acidic regions. Therefore, following PET imaging at 4 h p. i., tumors were excised, sectioned, and evaluated by digital autoradiography for ^{18}F-distribution. This distribution was subsequently compared to the distribution of the vascular

dx.doi.org/10.1021/bc3000222 | Bioconjugate Chem. 2012, 23, 1557−1566

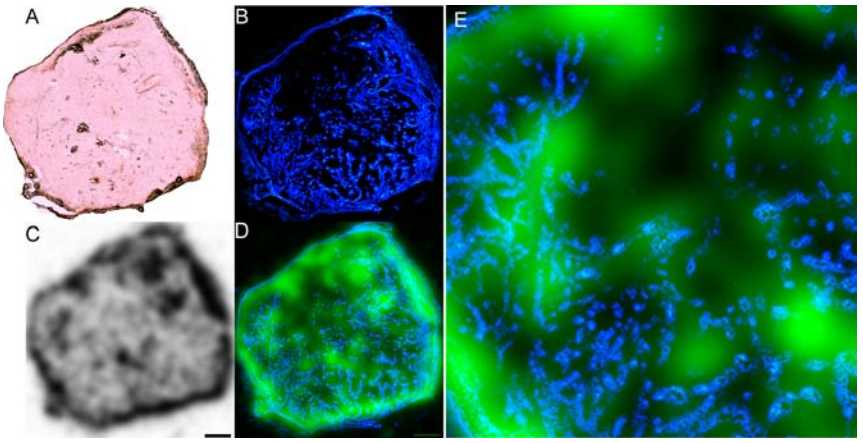


Figure 4. Combined histological/autoradiographic analysis obtained after [^{18}F]-**4** injection (4 h p. i.). Data from a single 10 μm frozen section obtained from a LNCaP tumor. H&E staining (panel A), the vascular perfusion marker Hoechst 33342 (blue, panel B) and autoradiograph of radioactivity distribution (panel C) are shown. Panel D shows co-registration of autoradiograph (pseudocolor green) overlaid with Hoechst 33342 (blue). Panel E contains a high-magnification region from the image shown in Panel D. Scale bar = 1 mm.

perfusion marker Hoechst 33342 using the same section. A clear pattern of higher ^{18}F uptake in tumor regions lacking vascular perfusion was observed (Figure 4). Previous studies have shown that tumor regions with low vascular perfusion are associated with low pO_2 and anaerobic glycolysis, resulting in lactate accumulation and reduced pH.[37] The accumulation of [^{18}F]-**4a** in tumor regions lacking vascular perfusion is consistent with the proposed mechanism of pHLIP accumulation, and corroborates the specificity underlying the heterogeneous tumor distribution observed in the PET imaging.

For both tracers, the PET images exhibited the highest radioactivity concentrations in the liver indicating that [^{18}F]-**4a** and [^{18}F]-**5** are mainly excreted via the hepatobiliary system. Little radioactivity accumulation was detected in the bone in all PET imaging studies performed with the [^{18}F]-pHLIP radiotracer that were radiolabeled using our novel [^{18}F]-labeling protocol, pointing to a high *in vivo* stability of the [^{18}F]-prosthetic groups. The high activity observed in the liver might preclude the use of the tracer for imaging tumors near the liver.

Biodistribution. Biodistribution studies were performed with [^{18}F]-**4a** and [^{18}F]-**5** in mice with dual PC-3 (left) and LNCaP (right) tumors on the shoulders. On the basis of our preliminary imaging studies, we chose the 2 and 4 h time points for the biodistribution study. Figure 5 shows the distribution of radioactivity in mice of [^{18}F]-**4a** at 2 and 4 h p.i. and of [^{18}F]-**5** at 2 h. For [^{18}F]-**4a**, the highest accumulation of radioactivity in LNCaP tumors was observed at 4 h p.i.. The uptake in PC-3 tumors was much lower at both time points. At 4 h p.i., LNCaP tumors had uptake of 8.0 ± 0.7%ID/g as compared to PC-3 tumors which had uptake 5.3 ± 0.7%ID/g. These results are in line with our earlier publication[9] with [^{64}Cu]-DOTA-pHLIP (all L-amino acids) and with PET imaging studies.

The highest accumulation of radioactivity at both time points was detected in the liver (32.5 ± 4.3%ID/g and 34.9 ± 5.8% ID/g at 2 and 4 h p. i., respectively), followed by the kidneys. As expected, with large hydrophobic peptides the blood clearance was slow. [^{64}Cu]-pHLIP shows highest accumulation in LNCaP tumors at 1 h p.i. (4.5 ± 1.7%ID/g) and highest tumor-to-blood ratio at 24 h p.i.[9]

The tumor-to-tissue ratios for [^{18}F]-**4a** and [^{18}F]-**5** are shown in Table 2. The tumor (LNCaP)-to-liver and the tumor

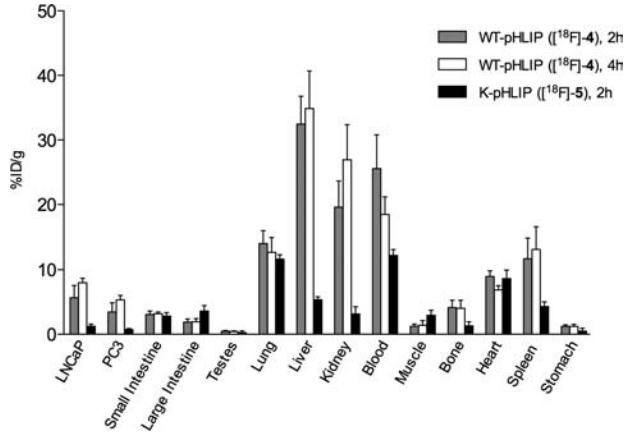


Figure 5. Biodistribution of [^{18}F]-**4** and [^{18}F]-**5** at 2 and 4 h p.i. with uptake values expressed as %ID/g.

Table 2. LNCaP Tumor-to-Tissue Ratios Determined upon Biodistribution Studies with the Tracers Administered to Tumor Bearing Mice

tumor-to-tissue ratio	[^{18}F]-**4** 2 h p. i.	[^{18}F]-**4** 4 h p. i.	[^{18}F]-**5** 2 h p. i.
tumor/blood	0.2	0.4	0.1
tumor/muscle	4.5	5.7	0.4
tumor/liver	0.2	0.2	0.2
tumor/kidney	0.3	0.3	0.4

(LNCaP)-to-kidney ratios are 0.2 and 0.3, respectively, at both 2 and 4 h. From our limited biodistribution studies, it is difficult to differentiate between excretory and metabolic factors contributing to these high values. As shown in Table 2, the negative control peptide [^{18}F]-**5** exhibits similar ratios in liver and kidney. It can be hypothesized that the activity in these organs is due to excretion rather than metabolism. The tumor-to-muscle ratio of 4.5 measured at 2 h p.i. with [^{18}F]-**4a** in comparison to 0.4 with [^{18}F]-**5** demonstrates that we are specifically targeting the tumor with [^{18}F]-**4a** and is not a result of nonspecific accumulation. The tumor-to-muscle ratio is even higher at 4 h p.i. with a value of 5.7. These studies clearly demonstrate that this click approach with prosthetic group **3** has no negative impact on the biological properties of pHLIP. Additionally, higher %ID/g values in LNCaP tumors as

dx.doi.org/10.1021/bc3000222 | *Bioconjugate Chem.* 2012, 23, 1557−1566

compared to the PC-3 tumor indicate that the accumulation of the tracer reflects acidity of the tissue.

[^{18}F]-pyridines labeled at ortho-position to the nitrogen have been reported to be stable against *in vivo* defluorination.[31] However, we observe some bone uptake with [^{18}F]-**5** (1.31 ± 0.63%ID/g) and [^{18}F]-**4a** (4.14 ± 1.12%ID/g) 2 h p.i. In comparison, [^{18}F]-fluoropentyne-based prosthetic group shows very minimal bone uptake (0.39%ID/g at 1 h p.i.). In our case, it is unclear whether the uptake is the result of defluorination or specific accumulation, because the two peptides radiolabeled with the same prosthetic group show different bone uptake values.

CONCLUSION

We have extended the use of the CuAAC "click chemistry" to the development of 2-ethynyl-6-[^{18}F]fluoropyridine as a new prosthetic group suitable for the ^{18}F-labeling of large peptides. This approach should be widely applicable and was shown to be efficient for the radiolabeling of pHLIP analogues with a molecular weight over 4000 Da. Two ^{18}F-labeled analogues were injected in mice in order to acquire the first *in vivo* [^{18}F]-pHLIP data. The WT-pHLIP construct showed good *in vitro* stability, and only mild *in vivo* defluorination was observed in both cases. A milestone in the development of an ^{18}F-labeled pHLIP tumor imaging agent was achieved, as the use of [^{18}F]-**3** will allow for fast production and evaluation of second-generation pHLIP analogues, designed for higher accumulation in the tumors and faster clearance from nontarget tissues.

AUTHOR INFORMATION

Corresponding Author

*Tel: 1-646-888-3038. Fax: 1-646-422-0408. E-mail: lewisj2@mskcc.org.

Author Contributions

§These authors contributed equally to this work.

Grant Support

Funded in part by the NIH/NCI R01CA138468 (JSL) and the Office of Science (BER) - U.S. Department of Energy (Award DE-SC0002456; JSL). Technical services provided by the MSKCC Small-Animal Imaging Core Facility were supported in part by NIH grants R24-CA83084 and P30-CA08748.

Notes

The authors declare no competing financial interest.

ACKNOWLEDGMENTS

Funded in part by the NIH/NCI R01CA138468 (JSL) and the Office of Science (BER) - U.S. Department of Energy (Award DE-SC0002456; JSL). Technical services provided by the MSKCC Small-Animal Imaging Core Facility were supported in part by NIH grants R24-CA83084 and P30-CA08748. Special thanks to Valerie Longo, Vadim Divilov, Kuntalkumar Sevak, and Nicholas Ramos for technical support, Calvin Lom and Howard Sheh from the MSKCC Radiochemistry-Cyclotron Core, and George Sukenick from the MSKCC Nuclear Magnetic Resonance (Analytical).

REFERENCES

(1) Bild, A. H., Potti, A., and Nevins, J. R. (2006) Linking oncogenic pathways with therapeutic opportunities. *Nat. Rev. Cancer 6* (9), 735–741.

(2) Gillies, R. J. (2001) Causes and consequences of hypoxia and acidity in tumors. Novartis Foundation symposium. *Trends Mol. Med. 7* (2), 47–49.

(3) Cairns, R., Papandreou, I., and Denko, N. (2006) Overcoming physiologic barriers to cancer treatment by molecularly targeting the tumor microenvironment. *Molecular Cancer Research: MCR 4* (2), 61–70.

(4) Sakamoto, S., Ryan, A. J., and Kyprianou, N. (2008) Targeting vasculature in urologic tumors: mechanistic and therapeutic significance. *J. Cell. Biochem. 103* (3), 691–708.

(5) Hunt, J. F., Rath, P., Rothschild, K. J., and Engelman, D. M. (1997) Spontaneous, pH-dependent membrane insertion of a transbilayer alpha-helix. *Biochemistry 36* (49), 15177–15192.

(6) Reshetnyak, Y. K., Andreev, O. A., Lehnert, U., and Engelman, D. M. (2006) Translocation of molecules into cells by pH-dependent insertion of a transmembrane helix. *Proc. Natl. Acad. Sci. U.S.A. 103* (17), 6460–6465.

(7) Andreev, O. A., Dupuy, A. D., Segala, M., Sandugu, S., Serra, D. A., Chichester, C. O., Engelman, D. M., and Reshetnyak, Y. K. (2007) Mechanism and uses of a membrane peptide that targets tumors and other acidic tissues in vivo. *Proc. Natl. Acad. Sci. U.S.A. 104* (19), 7893–7898.

(8) Reshetnyak, Y. K., Yao, L., Zheng, S., Kuznetsov, S., Engelman, D. M., and Andreev, O. A. (2011) Measuring tumor aggressiveness and targeting metastatic lesions with fluorescent pHLIP. *Mol. Imaging Biol. 13* (6), 1146–1156.

(9) Vavere, A. L., Biddlecombe, G. B., Spees, W. M., Garbow, J. R., Wijesinghe, D., Andreev, O. A., Engelman, D. M., Reshetnyak, Y. K., and Lewis, J. S. (2009) A novel technology for the imaging of acidic prostate tumors by positron emission tomography. *Cancer Res. 69* (10), 4510–4516.

(10) Ametamey, S. M., Honer, M., and Schubiger, P. A. (2008) Molecular imaging with PET. *Chem. Rev. 108* (5), 1501–1516.

(11) Okarvi, S. M. (2001) Recent progress in fluorine-18 labelled peptide radiopharmaceuticals. *European J. Nucl. Med. 28* (7), 929–938.

(12) Olberg, D. E., and Hjelstuen, O. K. (2010) Labeling Strategies of Peptides with ^{18}F for Positron Emission Tomography. *Curr. Top. Med. Chem. 10* (16), 1669–1679.

(13) Hausner, S. H., Marik, J., Gagnon, M. K. J., and Sutcliffe, J. L. (2008) In Vivo Positron Emission Tomography (PET) Imaging with an $\alpha v\beta 6$ Specific Peptide Radiolabeled using ^{18}F-"Click" Chemistry: Evaluation and Comparison with the Corresponding 4-[^{18}F]-Fluorobenzoyl- and 2-[^{18}F]Fluoropropionyl-Peptides. *J. Med. Chem. 51* (19), 5901–5904.

(14) McBride, W. J., D'Souza, C. A., Sharkey, R. M., Karacay, H., Rossi, E. A., Chang, C. H., and Goldenberg, D. M. (2010) Improved ^{18}F Labeling of Peptides with a Fluoride-Aluminum-Chelate Complex. *Bioconjugate Chem. 21* (7), 1331–1340.

(15) Schirrmacher, R., Bradtmoller, G., Schirrmacher, E., Thews, O., Tillmanns, J., Siessmeier, T., Buchholz, H. G., Bartenstein, P., Waengler, B., Niemeyer, C. M., and Jurkschat, K. (2006) F-18-labeling of peptides by means of an organosilicon-based fluoride acceptor. *Angew. Chem., Int. Ed. 45* (36), 6047–6050.

(16) Glaser, M., and Robins, E. G. (2009) 'Click labelling' in PET radiochemistry. *J. Labelled Compd. Radiopharm. 52* (9–10), 407–414.

(17) Mamat, C., Ramenda, T., and Wuest, F. R. (2009) Recent Applications of Click Chemistry for the Synthesis of Radiotracers for Molecular Imaging. *Mini-Rev. Org. Chem. 6* (1), 21–34.

(18) Li, Z.-B., Wu, Z., Chen, K., Chin, F. T., and Chen, X. (2007) Click Chemistry for ^{18}F-Labeling of RGD Peptides and microPET Imaging of Tumor Integrin $\alpha v\beta 3$ Expression. *Bioconjugate Chem. 18* (6), 1987–1994.

(19) Marik, J., and Sutcliffe, J. L. (2006) Click for PET: rapid preparation of [^{18}F]fluoropeptides using CuI catalyzed 1,3-dipolar cycloaddition. *Tetrahedron Lett. 47* (37), 6681–6684.

(20) Ramenda, T., Kniess, T., Bergmann, R., Steinbach, J., and Wuest, F. (2009) Radiolabelling of proteins with fluorine-18 via click chemistry. *Chem. Commun. (Camb.) 48*, 7521–7523.

(21) Glaser, M., and Årstad, E. (2007) "Click labeling" with 2-[^{18}F]fluoroethylazide for positron emission tomography. *Bioconjugate Chem. 18* (3), 989−993.
(22) Maschauer, S., Einsiedel, J., Haubner, R., Hocke, C., Ocker, M., Hübner, H., Kuwert, T., Gmeiner, P., and Prante, O. (2010) Labeling and glycosylation of peptides using click chemistry: a general approach to ^{18}F-glycopeptides as effective imaging probes for positron emission tomography. *Angew. Chem., Int. Ed. 49* (5), 976−979.
(23) Thonon, D., Kech, C. c., Paris, J. r. m., Lemaire, C., and Luxen, A. (2009) New strategy for the preparation of clickable peptides and labeling with 1-(azidomethyl)-4-[^{18}F]-fluorobenzene for PET. *Bioconjugate Chem. 20* (4), 817−823.
(24) Thonon, D., Paris, J., Kech, C., Lemaire, C., and Luxen, A. (2009) Peptide click labeling with 1-(azidomethyl)-4-[^{18}F]-fluorobenzene and solid phase synthesis of reference compounds. *J. Labelled Compd. Radiopharm. 52*, S26−S26.
(25) Iddon, L., Leyton, J., Indrevoll, B., Glaser, M., Robins, E. G., George, A. J. T., Cuthbertson, A., Luthra, S. K., and Aboagye, E. O. (2011) Synthesis and in vitro evaluation of [^{18}F]fluoroethyl triazole labelled [Tyr3]octreotate analogues using click chemistry. *Bioorg. Med. Chem. Lett. 21* (10), 3122−3127.
(26) Gill, H. S., Tinianow, J. N., Ogasawara, A., Flores, J. E., Vanderbilt, A. N., Raab, H., Scheer, J. M., Vandlen, R., Williams, S. P., and Marik, J. (2009) A modular platform for the rapid site-specific radiolabeling of proteins with ^{18}F exemplified by quantitative positron emission tomography of human epidermal growth factor receptor 2. *J. Med. Chem. 52* (19), 5816−5825.
(27) Reshetnyak, Y. K., Andreev, O. A., Segala, M., Markin, V. S., and Engelman, D. M. (2008) Energetics of peptide (pHLIP) binding to and folding across a lipid bilayer membrane. *Proc. Natl. Acad. Sci. U.S.A. 105* (40), 15340−15345.
(28) Reshetnyak, Y. K., Segala, M., Andreev, O. A., and Engelman, D. M. (2007) A monomeric membrane peptide that lives in three worlds: In solution, attached to, and inserted across lipid bilayers. *Biophys. J. 93* (7), 2363−2372.
(29) Wilson, A. A., Jin, L., Garcia, A., DaSilva, J. N., and Houle, S. (2001) An admonition when measuring the lipophilicity of radiotracers using counting techniques. *Appl. Radiat. Isot. 54* (2), 203−208.
(30) Schirrmacher, R., Wangler, C., and Schirrmacher, E. (2007) Recent developments and trends in ^{18}F-radiochemistry: syntheses and applications. *Mini-Rev Org. Chem. 4* (4), 317−329.
(31) Dolle, F. (2007) [^{18}F]fluoropyridines: From conventional radiotracers to the labeling of macromolecules such as proteins and oligonucleotides. *Ernst Schering Research Foundation Workshop 62*, 113−157.
(32) Burns, H. D., Hamill, T. G., Eng, W., Francis, B., Fioravanti, C., and Gibson, R. E. (1999) Positron emission tomography neuroreceptor imaging as a tool in drug discovery, research and development. *Curr. Opin. Chem. Biol. 3* (4), 388−394.
(33) Ramenda, T., Bergmann, R., and Wuest, F. (2007) Synthesis of F-18-labeled neurotensin(8−13) via copper-mediated 1,3-dipolar [3 + 2] cycloaddition reaction. *Lett. Drug Des. Discovery 4* (4), 279−285.
(34) Demko, Z. P., and Sharpless, K. B. (2002) A click chemistry approach to tetrazoles by Huisgen 1,3-dipolar cycloaddition: Synthesis of 5-sulfonyl tetrazoles from azides and sulfonyl cyanides. *Angew. Chem., Int. Ed. 41* (12), 2110−2113.
(35) Miller, S. M., Simon, R. J., Ng, S., Zuckermann, R. N., Kerr, J. M., and Moos, W. H. (1995) Comparison of the proteolytic susceptibilities of homologous L-amino-acid, D-amino-acid, and *N*-substituted glycine peptide and peptoid oligomers. *Drug Dev. Res. 35* (1), 20−32.
(36) Wade, D., Boman, A., Wahlin, B., Drain, C. M., Andreu, D., Boman, H. G., and Merrifield, R. B. (1990) All-D amino acid-containing channel-forming antibiotic peptides. *Proc. Natl. Acad. Sci. U.S.A. 87* (12), 4761−4765.
(37) Yaromina, A., Quennet, V., Zips, D., Meyer, S., Shakirin, G., Walenta, S., Mueller-Klieser, W., and Baumann, M. (2009) Co-localisation of hypoxia and perfusion markers with parameters of glucose metabolism in human squamous cell carcinoma (hSCC) xenografts. *Int. J. Radiat. Biol. 85* (11), 972−98.

Bioconjugate Chemistry

Article

pubs.acs.org/bc

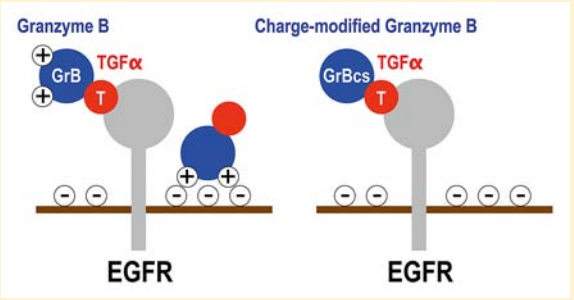
Surface Charge-Modification Prevents Sequestration and Enhances Tumor-Cell Specificity of a Recombinant Granzyme B–TGFα Fusion Protein

Robert A. Jabulowsky, Pranav Oberoi, Hayat Bähr-Mahmud, Benjamin Dälken, and Winfried S. Wels*

Chemotherapeutisches Forschungsinstitut Georg-Speyer-Haus, Paul-Ehrlich-Str. 42-44, 60596 Frankfurt am Main, Germany

Supporting Information

ABSTRACT: The serine protease granzyme B (GrB) plays an important role in the immune defense mediated by cytotoxic lymphocytes. Recombinant derivatives of this pro-apoptotic protein fused to tumor-targeting ligands hold promise for cancer therapy, but their applicability may be limited by promiscuous binding to nontarget tissues via electrostatic interactions. Here, we investigated cell binding and specific cytotoxicity of chimeric molecules consisting of wild-type or surface-charge-modified human GrB and the natural EGFR ligand TGFα for tumor targeting. We mutated two cationic heparin-binding motifs responsible for electrostatic interactions of GrB with cell surface structures, and genetically fused the resulting GrBcs derivative to TGFα for expression in the yeast *Pichia pastoris*. Purified GrBcs-TGFα (GrBcs-T) and a corresponding fusion protein employing wild-type GrB (GrB-T) displayed similar enzymatic activity and targeted cytotoxicity against EGFR-overexpressing breast carcinoma cells in the presence of an endosomolytic reagent. However, unspecific binding of the modified GrBcs-T variant to EGFR-negative cells was dramatically reduced, preventing the sequestration by nontarget cells in mixed cell cultures and increasing tumor-cell specificity. Likewise, modification of the GrB domain alleviated unspecific extracellular effects such as cell detachment indicative of extracellular matrix degradation. Our data demonstrate improved selectivity and functionality of surface-charge-modified GrBcs, suggesting this strategy as a general approach for the development of optimized GrB fusion proteins for therapeutic applications.



INTRODUCTION

Cancer cells are frequently insensitive to apoptotic stimuli due to deregulation of apoptotic cell death pathways. Targeted delivery of a potent apoptosis inducer into such cells that can concurrently activate multiple targets within the apoptotic cascade may effectively overcome apoptosis resistance and selectively induce cancer cell death. One such strategy with therapeutic potential is based on recombinant granzyme B (GrB) fused to tumor-targeting ligands.[1,2] These chimeric molecules structurally and functionally reflect immunotoxins,[3,4] but in contrast to the latter, they employ an effector domain of human origin. This can be expected to result in lower immunogenicity and circumvent complications frequently observed with classical immunotoxins due to their toxin domain of plant or bacterial origin.[5]

The serine protease GrB plays an important role in the immune defense against virus-infected and transformed cells.[6] It is naturally produced by cytotoxic T lymphocytes and NK cells, where it resides together with other granzymes in cytotoxic granules. Upon target cell recognition and induction of degranulation, GrB is released in a directed fashion into the immunological synapse formed between effector and target cells. Following cellular uptake aided by the pore-forming protein perforin, GrB rapidly induces target cell apoptosis via caspase-dependent and caspase-independent mechanisms.[7] Recombinant human GrB and GrB–ligand fusion proteins have been successfully produced in bacterial, yeast, and mammalian expression systems,[8−10] and have been shown to retain potent cell-death inducing activity upon targeted delivery into tumor cells.[11−14] Nevertheless, while natural GrB is released complexed with the negatively charged chondroitin sulfate proteoglycan serglycin that shields its positively charged surface,[15,16] the applicability of recombinant GrB derivatives may be limited by promiscuous binding of uncomplexed GrB to negatively charged cell surface proteoglycans via electrostatic interactions.[17−19] Two major heparin-binding motifs, RKAKRTR (residues 116 to 122; GrB numbering) and KKTMKR (residues 241 to 246) were identified on GrB surface loops, both electrostatically interacting with glucosaminoglycans on the cell surface. Exchange of basic amino acid residues within these sites with neutral alanines diminished cell binding and endocytosis, but also disturbed perforin-assisted cytotoxicity.[17]

Here, we investigated intrinsic and ligand-mediated cell binding, and *in vitro* antitumoral activity of recombinant proteins employing wild-type or surface-charge-modified

Received: February 9, 2012
Revised: June 11, 2012
Published: July 3, 2012

ACS Publications © 2012 American Chemical Society

dx.doi.org/10.1021/bc3000657 | *Bioconjugate Chem.* 2012, 23, 1567−1576

human GrB fused to the natural epidermal growth factor receptor (EGFR) ligand transforming growth factor α (TGFα). EGFR overexpression has been found in many tumors of epithelial origin, and has been shown to contribute to cellular transformation.[20] Due to its accessibility from the extracellular space, this tumor-associated surface antigen is an attractive therapeutic target for monoclonal antibodies and other targeted reagents.[3,21] We mutated the two cationic heparin-binding motifs responsible for nonselective electrostatic interactions of GrB with cell surface structures, and fused the resulting GrBcs derivative to TGFα for expression in the yeast *Pichia pastoris*. Purified GrBcs-TGFα (GrBcs-T) and a corresponding TGFα fusion protein employing wild-type GrB (GrB-T) displayed similar enzymatic activity and targeted cytotoxicity against EGFR-overexpressing breast carcinoma cells. However, unspecific binding of the modified GrBcs-T variant to EGFR-negative cells was dramatically reduced, preventing the sequestration by nontarget cells in mixed cell cultures seen for GrB-T, and increasing tumor-cell specificity.

EXPERIMENTAL PROCEDURES

Cells and Culture Conditions. Human MDA-MB468 and MDA-MB453 breast carcinoma, HeLa cervix carcinoma, and LN-18 glioblastoma cells (all ATCC, Manassas, VA) were cultured in DMEM (Lonza, Köln, Germany) supplemented with 10% heat-inactivated FBS, 2 mM L-glutamine, 100 U/mL penicillin, 100 μg/mL streptomycin.

Construction of Granzyme B Expression Vectors. Plasmids pPIC9-GrB and pPIC9-GrB-T for expression of mature human wild-type GrB and the GrB−TGFα fusion protein GrB-T in the yeast *Pichia pastoris* were described previously.[8,13] The surface-charge-modified GrB variant GrBcs was generated by stepwise replacement of codons encoding amino acid residues R116, R120, R122, K241, K242, K245, and R246 (GrB numbering) within cationic sites of GrB[17] with codons encoding alanine residues by PCR-based site-directed mutagenesis using human GrB cDNA as a template. The resulting GrBcs PCR product was fused to a sequence encoding a Myc- and a hexa-histidine-tag, and subcloned as an *Xho*I-*Not*I fragment into the yeast vector pPIC9 (Invitrogen, Karlsruhe, Germany), resulting in plasmid pPIC9-GrBcs. A fusion gene encoding the GrBcs domain followed by a $(Gly_4Ser)_4$ linker, an internal hexa-histidine-tag, the EGFR ligand TGFα,[22] and C-terminal Myc- and hexa-histidine-tags was assembled *in silico*, synthesized in codon-optimized form for expression in *Pichia pastoris* (GeneArt, Regensburg, Germany), and subcloned as an *Xho*I-*Not*I fragment into the vector pPIC9, resulting in plasmid pPIC9-GrBcs-T.

Expression and Purification of Recombinant Proteins. Recombinant human GrB, GrBcs, GrB-T, and GrBcs-T were expressed in *Pichia pastoris* and purified from culture supernatants basically as described.[13] Briefly, *Pichia pastoris* GS115 cells (Invitrogen) were transformed with pPIC9 expression plasmids by electroporation, and positive clones were selected following the manufacturer's recommendations. For large-scale protein expression, single colonies were grown in 80 mL YPD medium (Invitrogen) for 2 days at 28 °C. For induction of expression, cultures were diluted to an OD_{600} of 1 to 2 in buffered methanol complex medium (pH 6) containing 2% methanol (v/v), and incubated for another 3 to 4 days at 28 °C with addition of methanol every 24 h. Supernatants containing recombinant proteins were harvested by centrifugation, adjusted to pH 8, filtered, and applied to a Ni-NTA superflow column (Qiagen, Hilden, Germany). Specifically bound proteins were eluted with 250 mM imidazole, 1 M NaCl in PBS (pH 8). Protein fractions containing GrB derivatives were identified by SDS-PAGE and immunoblotting with GrB-specific monoclonal antibody (mAb) 2C5 (Santa Cruz Biotechnology, Heidelberg, Germany), pooled, dialyzed against PBS (pH 7.4), concentrated, and stored until use at −80 °C. Native human GrB purified from NK cells was purchased from Enzo Life Sciences (Lörrach, Germany).

GrB Activity Assays. Enzymatic activity of recombinant GrB proteins was analyzed using the synthetic GrB substrate Ac-IETD-pNA (Alexis, Grünberg, Germany) as described.[9] Purified proteins were incubated with reaction buffer (10 mM Hepes pH 7.4, 140 mM NaCl, 2.5 mM $CaCl_2$) and 200 μM Ac-IETD-pNA in a total volume of 100 μL per sample in 96-well plates. Triplicate samples were incubated for 3 h at 37 °C, and substrate cleavage was quantified by measuring the absorbance (A) at 405 nm (corrected for background by subtracting A490) with a microplate reader (Molecular Devices, Ismaning, Germany). Buffered substrate solution without recombinant proteins served as blank. GrB dependence of cleavage was confirmed by preincubation of recombinant proteins with 400 μM of GrB-specific peptide aldehyde inhibitor Ac-IETD-CHO (Alexis) for 15 min at room temperature prior to the addition of peptide substrate.

Binding Analysis. Expression of EGFR on the surface of tumor cells was investigated by flow cytometry. Trypsinized MDA-MB468 and MDA-MB453 cells (2.5 to 5 × 10^5) were incubated with antihuman EGFR antibody R-1 (Santa Cruz Biotechnology) for 30 min at 4 °C, followed by phycoerythrin (PE)-conjugated goat antimouse IgG secondary antibody (Jackson ImmunoResearch, West Grove, PA, USA). For flow cytometric analysis of binding of recombinant GrB proteins to the surface of tumor cells, trypsinized MDA-MB468 and MDA-MB453 cells (2.5 to 5 × 10^5) were incubated with up to 0.5 μg of purified GrB proteins for 30 min at 4 °C. Unbound proteins were removed, cells were washed, and bound proteins were detected with 20 μg/mL of Alexa Fluor 647-conjugated antihuman GrB antibody (BD Biosciences, Heidelberg, Germany). Fluorescence of cells was analyzed using FACSCalibur and FACSCanto II flow cytometers, and *CELLQuest Pro* and *FACSDiva* software, respectively (BD Biosciences). To investigate the contribution of the positively charged GrB domain to intrinsic cell binding, GrB proteins were incubated with an 18-fold molar excess of heparin (Ratiopharm, Ulm, Germany) for up to 60 min at room temperature before cell-binding analysis. For analysis of binding of GrB-T and GrBcs-T to mixed cell populations, first 4 × 10^6 washed EGFR-positive MDA-MB468 cells were labeled with 4 μL calcein violet AM stock solution (Molecular Probes, Invitrogen, Karlsruhe, Germany) for 1 h at 4 °C and washed twice with RPMI medium. Then, the labeled cells were mixed with unlabeled EGFR-negative MDA-MB453 cells prior to incubation with the GrB fusion proteins and analysis of binding by flow cytometry as described above.

Confocal Laser Scanning Microscopy. Cells were grown overnight on coverslips coated with poly(L-lysine) (Sigma-Aldrich, Taufkirchen, Germany), and then treated with 2.5 μg/mL (62.5 nM) of recombinant GrB proteins for 60 min at 4 °C. Cells were washed, fixed with 4% paraformaldehyde in PBS for 20 min at room temperature, and incubated with 1 μg/mL of GrB-specific mAb 2C5 in PBS, 3% BSA, followed by Alexa Fluor 488-conjugated donkey antimouse IgG (Molecular

Probes). Nucleic acids were counterstained with TO-PRO-3 (Invitrogen). Samples were then analyzed with a Leica TCS SL laser scanning microscope (Leica Mikrosysteme, Bensheim, Germany).

Cell Viability Assays. Cytotoxicity of GrB and GrB fusion proteins was analyzed in WST-1 cell viability assays (Roche Diagnostics, Mannheim, Germany) following the manufacturer's recommendations. Cells were seeded in 96-well plates at a density of 1.5×10^4 cells/well in triplicates, and incubated for 14 to 48 h at 37 °C with varying concentrations of purified GrB proteins in the presence or absence of 50 μM chloroquine. After addition of WST-1 reagent for 4 h, the relative number of viable cells in comparison to cells grown without recombinant GrB proteins was determined by measuring the absorbance (A) at 450 nm (corrected for background by subtracting A690).

To compete binding of GrBcs-T to EGFR, cells were preincubated with a 23-fold molar excess of anti-EGFR antibody cetuximab[23] for 30 min at 4 °C prior to the addition of recombinant protein and determination of cytotoxicity. To evaluate sequestration of EGFR-specific GrB-T and GrBcs-T fusion proteins by nontarget cells, EGFR-negative MDA-MB453 cells were seeded in 96-well plates at a density of 1×10^5 cells/well and incubated in triplicate with 2.5 nM (100 ng/mL) of purified GrB fusion proteins for 4 h at 37 °C. Supernatants containing unbound proteins were collected, and analyzed for specific cytotoxicity toward EGFR-positive MDA-MB468 cells in the presence of 50 μM chloroquine as described above.

Analysis of Granzyme B-Induced Cell Detachment. HeLa cells were seeded in 96-well plates at a density of 1×10^4 cells/well and allowed to adhere for 24 h. Cells were then treated for 24 h at 37 °C with different concentrations of purified GrB proteins, or GrB proteins preincubated for 30 min at room temperature with an 18-fold molar excess of heparin. Control cells were treated with PBS or 1 μM staurosporine. Morphological changes of cells were analyzed after 24 h by light microscopy using a Nikon ECLIPSE TE3000 inverted microscope (Nikon, Düsseldorf, Germany) at 200× magnification. To quantify cell detachment, nonadherent cells were removed by washing once with PBS, and the relative number of remaining attached cells was determined in WST-1 cell viability assays as described above.

Statistical Analysis. Differences between values were evaluated using the two-tailed unpaired Student's t test. P values <0.05 were considered significant. Statistical calculations were done using *Prism* 5 software (GraphPad Software, La Jolla, CA).

RESULTS

Cell Binding and Cytotoxic Activity of the Granzyme B Fusion Protein GrB-T. The chimeric fusion protein GrB-T consists of human granzyme B (GrB) (amino acid residues 21–247) genetically fused via a flexible linker to transforming growth factor-α (TGFα), a peptide ligand specific for epidermal growth factor receptor (EGFR).[13] Recombinant GrB-T was produced as a secreted protein in *Pichia pastoris* transformed with expression plasmid pPIC9-GrB-T, which encodes GrB-T under the control of the methanol-inducible alcohol oxidase *AOX*1 promoter (Figure 1A). Release of GrB-T into the culture supernatant is mediated by the α-factor signal peptide from *Saccharomyces cerevisiae*, which is cleaved off during secretion, thereby generating the N-terminus of mature GrB.[9,13]

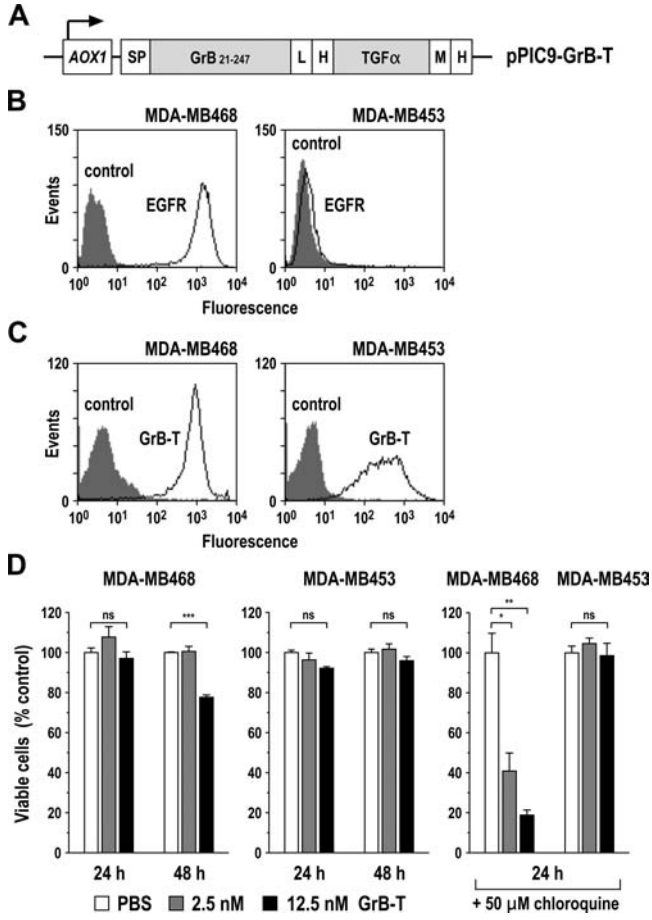


Figure 1. Cell binding and cytotoxicity of the recombinant Granzyme B–TGFα fusion protein GrB-T. (A) Construct pPIC9-GrB-T for expression of GrB-T in the yeast *Pichia pastoris*. *AOX*1, methanol-inducible alcohol oxidase I promoter; SP, α-factor signal peptide; GrB_{21-247}, cDNA encoding mature human GrB (amino acids 21–247); L, linker and H, polyhistidine tags; TGFα, cDNA encoding mature human transforming growth factor α; M, Myc tag. (B) Expression of EGFR on the surface of MDA-MB468 and MDA-MB453 breast carcinoma cells was determined by flow cytometry with EGFR-specific R-1 antibody (open areas). Cells treated only with phycoerythrin-conjugated secondary antibody served as controls (shaded areas). (C) Binding of purified GrB-T to MDA-MB468 and MDA-MB453 breast carcinoma cells was determined with Alexa Fluor 647-conjugated GrB-specific antibody (open areas). Control cells were treated with GrB-specific antibody in the absence of GrB-T protein (shaded areas). (D) To determine cytotoxic activity, EGFR-positive MDA-MB468 (left panel) and EGFR-negative MDA-MB453 cells (middle panel) were incubated with 2.5 or 12.5 nM of purified GrB-T. In a parallel experiment, MDA-MB468 and MDA-MB453 cells were treated with purified GrB-T in the presence of 50 μM of the endosomolytic reagent chloroquine (right panel). Control cells were treated with PBS. After 24 or 48 h as indicated, the relative number of viable cells was determined in WST-1 assays. Mean values ± SEM are shown (n = 3). ***, $P < 0.001$; **, $P < 0.01$; *, $P < 0.05$; ns, $P > 0.05$.

Cell binding of GrB-T purified from yeast culture supernatants was investigated by flow cytometry using human MDA-MB468 and MDA-MB453 breast cancer cells. While MDA-MB468 cells express high levels of EGFR, MDA-MB453 cells are EGFR-negative (Figure 1B). As expected, we observed strong binding of GrB-T to EGFR-expressing MDA-MB468 cells utilizing fluorochrome-labeled GrB-specific antibody for direct detection of surface-bound protein (Figure 1C, left

dx.doi.org/10.1021/bc3000657 | Bioconjugate Chem. 2012, 23, 1567–1576

panel). However, considerable binding of GrB-T to EGFR-negative MDA-MB453 cells was also found (Figure 1C, right panel). Similar binding to both cell lines was also observed for recombinant wild-type GrB and native GrB purified from NK cells (see Supporting Information Figure S1). Preincubation of untargeted GrB with heparin markedly reduced cell binding, suggesting the previously reported interaction of cationic residues within the GrB domain with negatively charged structures on the cell surface as the underlying mechanism.[17,19]

Even at high concentrations, intrinsic cell binding of recombinant and purified native GrB did not result in cell killing (see Supporting Information Figure S2). To investigate cytotoxicity of EGFR-targeted GrB-T, MDA-MB468, and MDA-MB453 cells were treated with 2.5 or 12.5 nM of purified fusion protein for 24 or 48 h. While prolonged incubation of the EGFR-positive cells with high concentrations of GrB-T resulted in significant cell killing in comparison to PBS-treated controls (Figure 1D, left panel), no reduction in cell viability was observed upon treatment of the EGFR-negative cells (Figure 1D, middle panel). Addition of chloroquine as an endosomolytic activity strongly enhanced target cell-specific cytotoxicity of GrB-T,[13] facilitating marked and concentration-dependent killing of MDA-MB468, but not MDA-MB453 cells already upon short exposure to the fusion protein (Figure 1D, right panel).

These data demonstrate an ability of GrB-T to bind to cells irrespective of the presence of the TGFα receptor EGFR. However, cell killing activity was restricted to EGFR-expressing cells, indicating that cell binding via electrostatic interactions is not sufficient to mediate routing of the protein to intracellular GrB substrates.

Expression and Functional Characterization of a Surface-Charge-Modified Granzyme B Derivative. To reduce intrinsic cell binding of the GrB domain, we replaced seven positively charged amino acid residues within two cationic clusters on the surface of GrB by alanine residues following the strategy reported by Bird et al.[17] (Figure 2A). Upon expression in *Pichia pastoris* and purification from culture supernatants, the identity of this mutant GrBcs derivative was confirmed by immunoblot analysis with GrB-specific antibody. Recombinant wild-type GrB was included for comparison (Figure 2B). GrB expressed in *Pichia pastoris* in secreted form is glycosylated.[8] This resulted in a higher apparent molecular mass for GrB and GrBcs than calculated from the amino acid sequence (38 versus 29 kDa). Modification of residues on the surface of GrB had no effect on enzymatic activity of the protein. GrBcs and wild-type GrB cleaved the GrB-specific peptide substrate Ac-IETD-pNA equally well, and enzymatic activity of both proteins was abolished upon preincubation with the peptide aldehyde inhibitor Ac-IETD-CHO (Figure 2C). Flow cytometric analysis with fluorochrome-labeled GrB-specific antibody revealed a marked reduction in the binding of untargeted GrBcs to MDA-MB468 and MDA-MB453 cells when compared to wild-type GrB (Figure 2D). Quantification of flow cytometric data demonstrated reduction of binding of GrBcs to 1.2% of that of GrB in the case of MDA-MB468 cells, and to 2.8% of that of GrB in the case of MDA-MB453 cells (see Supporting Information Table S1).

Generation and Functional Characterization of EGFR-Specific Fusion Protein GrBcs-T. Next, we generated an EGFR-targeted GrBcs fusion protein by replacing wild-type GrB cDNA in the pPIC9-GrB-T vector (see Figure 1A) with the mutant GrBcs sequence. The modified GrBcs-T protein

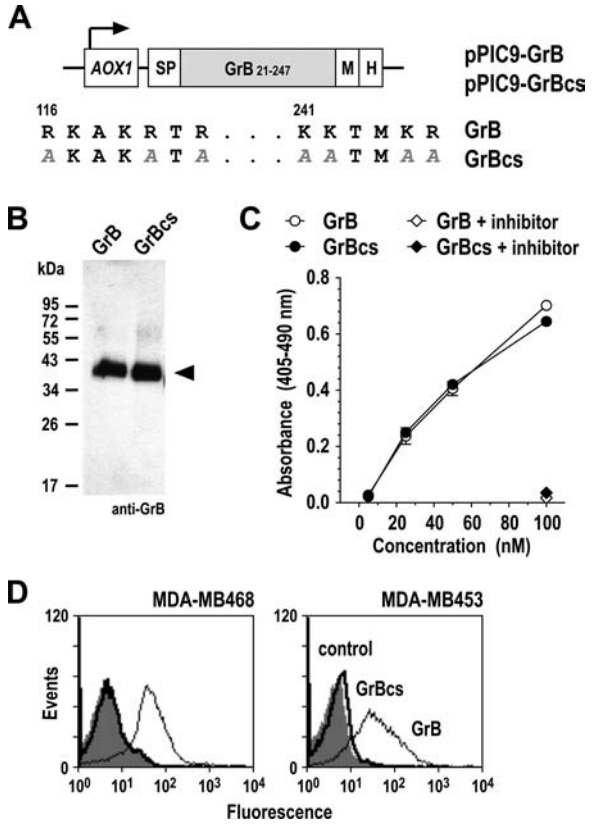


Figure 2. Expression and functional characterization of wild-type and surface-charge-modified Granzyme B. (A) Constructs pPIC9-GrB and pPIC9-GrBcs for expression of human wild-type GrB and the GrBcs mutant protein in the yeast *Pichia pastoris*. In GrBcs, amino acid residues R116, R120, R122, K241, K242, K245, and R246 within cationic sites are replaced by alanine residues (lower panel). *AOX*1, methanol-inducible alcohol oxidase I promoter; SP, α-factor signal peptide; GrB_{21-247}, cDNA encoding mature human GrB or mutant GrBcs (amino acids 21−247); M, Myc tag; H, polyhistidine tag. (B) GrB and GrBcs proteins were purified from yeast culture supernatants by Ni^{2+}-affinity chromatography. Eluate fractions were analyzed by SDS-PAGE and immunoblotting with GrB-specific antibody followed by horseradish-peroxidase-coupled secondary antibody and chemiluminescent detection. (C) To determine enzymatic activity, GrB-specific peptide substrate Ac-IETD-pNA was incubated with the indicated concentrations of purified GrB (open circle) or GrBcs proteins (filled circle) for 3 h. Cleavage of substrate was determined by measuring the absorbance at 405 nm. GrB dependence of cleavage was confirmed by preincubation of recombinant proteins with 400 μM of GrB-specific peptide aldehyde inhibitor Ac-IETD-CHO (open and filled diamonds). Mean values ± SEM are shown (n = 3). (D) Binding of purified GrB (regular line) and GrBcs (bold line) proteins to MDA-MB468 and MDA-MB453 breast carcinoma cells was determined by flow cytometry with Alexa Fluor 647 conjugated GrB-specific antibody (open areas). Control cells were treated with GrB-specific antibody in the absence of GrB proteins (shaded areas).

was expressed in *Pichia pastoris*, purified from culture supernatants, and analyzed in comparison to GrB-T by immunoblot analysis with GrB-specific antibody (Figure 3A). Both proteins exhibited an apparent molecular mass of approximately 40 kDa. Subsequently, enzymatic activity of GrBcs-T was investigated in colorimetric cleavage assays using Ac-IETD-pNA as a GrB-specific peptide substrate. Like in the case of untargeted GrBcs, the activity of the targeted GrBcs-T variant was indistinguishable from that of the corresponding

dx.doi.org/10.1021/bc3000657 | *Bioconjugate Chem.* 2012, 23, 1567−1576

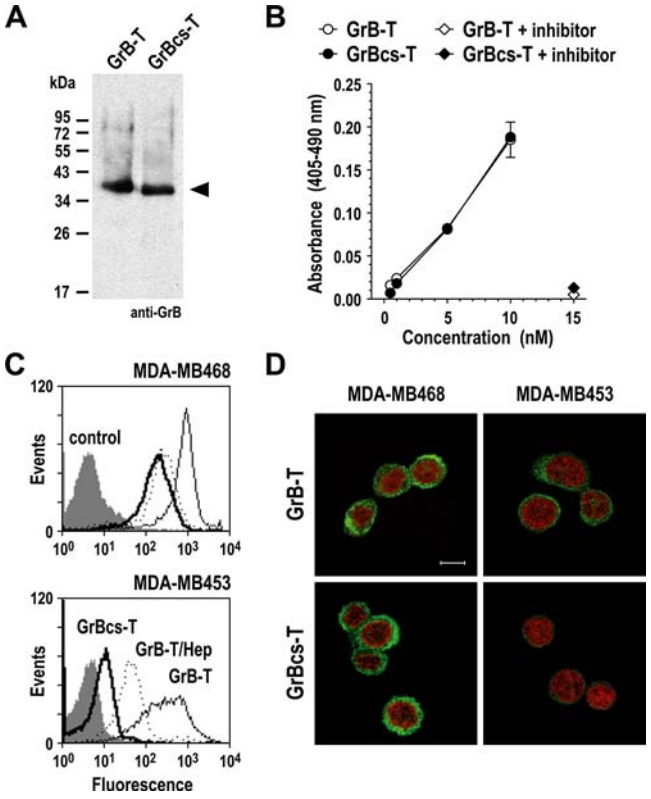


Figure 3. Expression, enzymatic activity, and cell binding of surface-charge-modified Granzyme B - TGFα fusion protein GrBcs-T. (A) GrB-T and GrBcs-T proteins were purified by Ni^{2+}-affinity chromatography from culture supernatants of *Pichia pastoris* cells carrying pPIC9-GrB-T or pPIC9-GrBcs-T vectors. Eluate fractions were analyzed by SDS-PAGE and immunoblotting with GrB-specific antibody followed by horseradish-peroxidase-coupled secondary antibody and chemiluminescent detection. (B) Enzymatic activity of purified GrB-T (open circle) or GrBcs-T proteins (filled circle) was determined with synthetic GrB substrate Ac-IETD-pNA as described in the legend of Figure 2. GrB dependence of cleavage was confirmed by preincubation of recombinant proteins with 400 μM of GrB-specific inhibitor Ac-IETD-CHO (open and filled diamonds). Mean values ± SEM are shown (n = 3). (C) Binding of purified GrB-T (regular line), GrB-T preincubated with heparin (dotted line) and GrBcs-T (bold line) proteins to MDA-MB468 and MDA-MB453 cells was determined by flow cytometry with Alexa Fluor 647 conjugated GrB-specific antibody (open areas). Control cells were treated with GrB-specific antibody in the absence of GrB proteins (shaded areas). Data for GrB-T are the same as in Figure 1C and shown here for comparison. (D) Binding of GrB-T and GrBcs-T to the surface of MDA-MB468 and MDA-MB453 cells was also analyzed by confocal laser scanning microscopy with GrBspecific antibody followed by Alexa Fluor 488 conjugated secondary antibody (green). Nucleic acids were counterstained with TO-PRO-3 (red). Merged images are shown. Size bar: 10 μm.

GrB-T protein, and specifically inhibited by preincubation with Ac-IETD-CHO (Figure 3B).

In flow cytometric analysis with fluorochrome-labeled GrB-specific antibody, GrBcs-T displayed strong binding to EGFR-positive MDA-MB468 cells, but only minimal remaining binding to EGFR-negative MDA-MB453 cells (Figure 3C). While preincubation of unmodified GrB-T with heparin also decreased intrinsic GrB-mediated binding to MDA-MB453 cells, replacement of positively charged amino acid residues within the GrB domain was more effective, resulting in a stronger reduction of GrBcs-T binding to cells that do not express EGFR (Figure 3C, lower panel; see also Supporting Information Table S2). Interestingly, in comparison to GrB-T we observed weaker binding of GrBcs-T to EGFR-expressing cells (Figure 3C, upper panel; see also Supporting Information Table S2). This suggests that, in addition to TGFα–EGFR interactions, also in the case of cognate target cells, electrostatic interactions via the GrB domain contribute to cell binding. In an independent experiment, binding of GrB-T and GrBcs-T to the surface of MDA-MB468 and MDA-MB453 cells was analyzed by confocal laser scanning microscopy. Thereby, strong binding of both proteins to EGFR-positive cells was observed (Figure 3D, left panels). However, while unmodified GrB-T also displayed significant binding to the surface of the EGFR-negative cells, this was not the case for GrBcs-T (Figure 3D, right panels).

To investigate the potential influence of the mutations introduced into the effector domain on cytotoxic activity of GrBcs-T, MDA-MB468 and MDA-MB453 cells were treated for 14 h with increasing concentrations of the fusion protein in the presence of chloroquine. Cells treated with unmodified GrB-T were included for comparison. Incubation of the EGFR-positive cells with GrBcs-T or GrB-T resulted in effective and concentration-dependent cell killing in comparison to PBS-treated controls (Figure 4A, left panel). While GrBcs-T appeared slightly more active than GrB-T in these experiments (IC_{50} values of 125 versus 225 pM), this difference was statistically not significant ($P > 0.05$). No reduction in cell viability was observed upon treatment of the EGFR-negative cells with increasing concentrations of GrBcs-T or GrB-T (Figure 4A, right panel). Also, human LN-18 glioblastoma and HeLa cervix carcinoma cells that express more moderate EGFR levels than MDA-MB468 cells were killed equally well by GrBcs-T and GrB-T (see Supporting Information Figure S3). However, due to the lower amount of target receptor available on the cell surface this required higher concentrations of GrB fusion proteins and prolonged exposure of the cells. Specificity of target cell killing was confirmed by competition of GrBcs-T binding to EGFR with anti-EGFR antibody cetuximab, which blocks ligand binding to the receptor.[23] While in this experiment in the absence of competitor treatment of MDA-MB468 cells with 2.5 nM of GrBcs-T resulted in 66% of cell killing, cytotoxicity was reduced to 26% in the presence of a 23-fold molar excess of cetuximab (Figure 4B). In contrast, anti-ErbB2 antibody trastuzumab included as a control had no significant effect on GrBcs-T activity (62% of cell killing). In addition to specific target cell recognition via the TGFα domain, cytotoxic activity of GrBcs-T was also dependent on enzymatic activity of the GrB domain. Preincubation of GrBcs-T with the peptide aldehyde inhibitor Ac-IETD-CHO abolished cytotoxic activity of the fusion protein against MDA-MB468 cells (Figure 4C).

These results demonstrate that surface-charge-modified GrBcs can functionally replace wild-type GrB in the context of a tumor-specific fusion protein. While intrinsic cell binding of GrBcs-T via electrostatic interactions was markedly reduced in comparison to GrB-T, this did not affect specific binding to EGFR-expressing cells via the TGFα domain, resulting in potent targeted cytotoxicity.

Sequestration of GrB-T and GrBcs-T by Binding to Non-Target Cells. Fusion of GrB to a target-cell-specific ligand such as TGFα should enable selective recognition and elimination of tumor cells by the chimeric molecule while not

dx.doi.org/10.1021/bc3000657 | *Bioconjugate Chem.* 2012, 23, 1567–1576

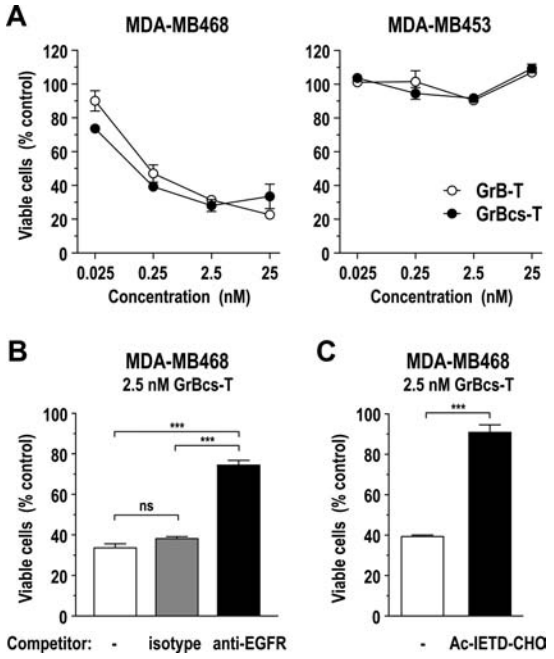


Figure 4. Cytotoxic activity of surface-charge-modified Granzyme B–TGFα fusion protein GrBcs-T. (A) EGFR-positive MDA-MB468 (left panel) and EGFR-negative MDA-MB453 cells (right panel) were treated with the indicated concentrations of purified GrB-T (open circles) or GrBcs-T protein (filled circles) in the presence of 50 μM of the endosomolytic reagent chloroquine. Control cells were treated with PBS. After 14 h, the relative number of viable cells was determined in WST-1 assays. (B) To compete binding of GrBcs-T to EGFR, MDA-MB468 cells were preincubated with a 23-fold molar excess of anti-EGFR antibody cetuximab prior to the addition of 2.5 nM of purified protein and determination of cytotoxicity as described above (filled bar). Control cells were treated with GrBcs-T in the absence of competitor (open bar), or preincubated with isotype-matched anti-ErbB2 antibody trastuzumab before addition of GrBcs-T (shaded bar). (C) Dependence of cell killing on GrB activity was investigated by preincubation of GrBcs-T with 400 μM of GrB-specific inhibitor Ac-IETD-CHO before addition to MDA-MB468 cells (filled bar). Control cells were treated with GrBcs-T in the absence of inhibitor (open bar). For all experiments, mean values ± SEM are shown (n = 3). ***, $P < 0.001$; ns, $P > 0.05$.

affecting target antigen-negative bystander cells. As a model system to investigate the selectivity of GrB-T and GrBcs-T in mixed cell populations, we performed flow cytometric cell binding analyses with GrB-specific antibody using mixtures of MDA-MB468 and MDA-MB453 cells. To distinguish between the two cell lines, prior to the experiment MDA-MB468 cells were fluorescently labeled with calcein violet AM. While in 1:1 mixed cell populations GrB-T displayed similar binding to EGFR-positive and EGFR-negative cells, this was not the case for GrBcs-T, which selectively bound only to EGFR-positive MDA-MB468 cells (Figure 5A). Similar results were also obtained with 5:1 and 10:1 mixtures, where EGFR-negative cells were in excess (data not shown).

Next, we investigated the effect of sequestration by nontarget cells on selective cytotoxicity of GrB-T and GrBcs-T. MDA-MB453 cells were incubated with equal amounts of the fusion proteins for 4 h, before culture supernatants containing unbound GrB-T and GrBcs-T proteins were collected, and added for 14 h to MDA-MB468 cells in the presence of chloroquine (Figure 5B, left panel). Preincubation of GrB-T with EGFR-negative cells significantly reduced the amount of free protein and selective cytotoxicity against EGFR-positive cells (Figure 5B, right panel). This was not the case for GrBcs-T, which upon prior contact with MDA-MB453 cells remained in solution, and subsequently killed MDA-MB468 cells to a comparable degree as purified GrBcs-T not preadsorbed to MDA-MB453 cells.

Extracellular Effects of GrBcs-T. In addition to its apoptosis-inducing activity upon cleavage of intracellular substrates, granzyme B can also process components of the extracellular matrix.[24] To investigate potential differences in the extracellular activities of wild-type GrB and GrBcs derivatives, we employed human HeLa cervix carcinoma cells as a model. These cells undergo morphological changes upon degradation of their extracellular matrix by GrB,[8] but were not sensitive to the apoptosis-inducing effects of GrB-T or GrBcs-T in the absence of chloroquine (data not shown). Cultures of adherent HeLa cells were treated for 24 h with increasing concentrations of GrB, GrBcs, GrB-T, or GrBcs-T without addition of an endosomolytic activity, before cellular morphology was analyzed by light microscopy (Figure 6A). While low concentrations of GrB proteins had no visible effects (Figure 6B and data not shown), at higher GrB or GrB-T concentrations HeLa cells rounded up and partially lost contact to the culture dish (Figure 6A, middle panels). Nevertheless, we did not observe membrane blebbing, cellular fragmentation or other characteristics of apoptotic morphology, which were seen in staurosporine-treated cells. In contrast to GrB and GrB-T, treatment of HeLa cells with GrBcs or GrBcs-T had no visible effects (Figure 6A, right panels), resulting in cellular morphology very similar to that of PBS-treated controls. Similar results were obtained upon treatment of MDA-MB453 cells with GrBcs and GrBcs-T (data not shown). The marked reduction in the extracellular activity of the GrBcs derivatives was confirmed by quantification of cells still attached to the culture dish after prolonged exposure to GrB proteins (Figure 6B). While exposure to GrB and GrB-T resulted in a concentration-dependent loss of adherent cells, GrBcs and GrBcs-T induced only minimal cell detachment. This was also the case upon pretreatment of GrB and GrB-T with heparin, indicating that electrostatic interactions of the GrB domain also play a role for the extracellular proteolytic activity of GrB and GrB fusion proteins.

■ DISCUSSION

Targeted delivery of pro-apoptotic proteins to tumor cells represents a promising strategy to induce selective tumor cell death.[25] We and others have described prototypic granzyme B fusion proteins that carry natural peptide ligands or antibody fragments specific for tumor-associated surface antigens for cell binding.[11−14,26] After uptake, such molecules cleaved natural GrB substrates within the target cells, and rapidly induced programmed cell death with kinetics similar to that of GrB/perforin-mediated cell killing by cytotoxic lymphocytes.[13] Targeted GrB derivatives so far have employed an active fragment of the wild-type enzyme. Hence, in addition to specific and high-affinity binding mediated by their heterologous targeting ligands, such molecules likely retained the GrB-intrinsic ability to also interact with natural GrB binding sites present on the surface of cells[17−19] and components of extracellular matrix.[24,27] Here, we have functionally characterized recombinant GrB-TGFα fusion proteins either harboring the wild-type enzyme (GrB-T) or a variant where the two cationic heparin-binding motifs of GrB were mutated (GrBcs-

dx.doi.org/10.1021/bc3000657 | Bioconjugate Chem. 2012, 23, 1567−1576

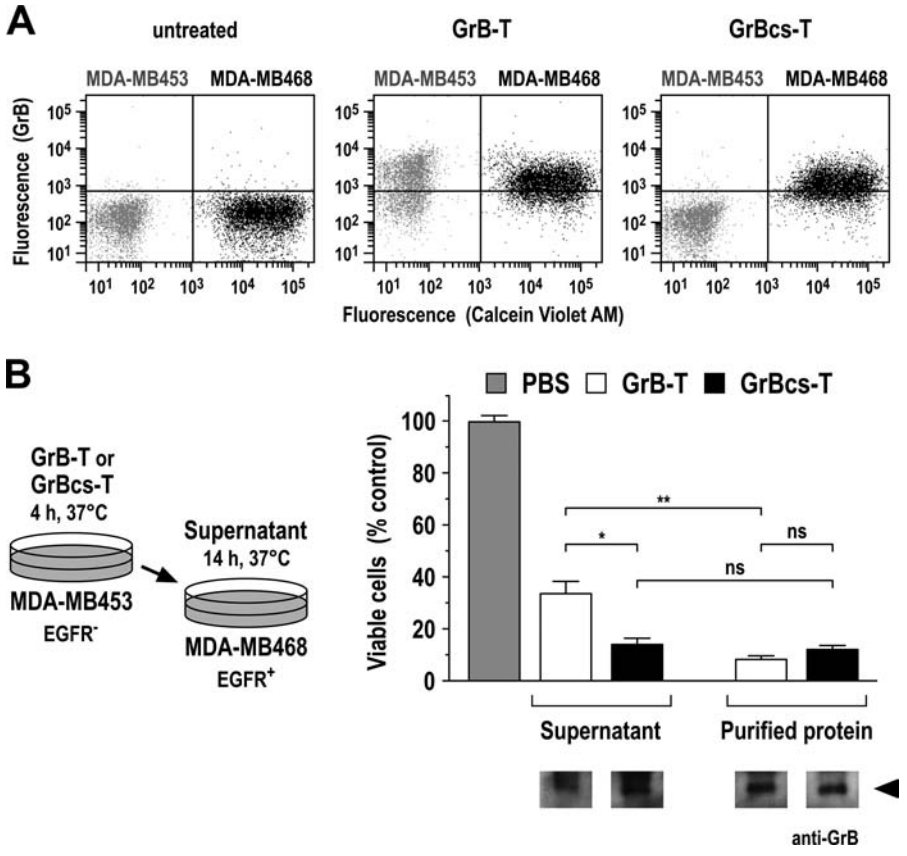


Figure 5. Differential binding of GrB-T and GrBcs-T to EGFR-negative cells. (A) EGFR-positive MDA-MB468 cells (black) were fluorescently labeled with calcein violet AM and mixed at a 1:1 ratio with unlabeled EGFR-negative MDA-MB453 cells (gray) prior to incubation with GrB-T (middle panel) or GrBcs-T fusion proteins (right panel) and analysis of binding with Alexa Fluor 647 conjugated GrB-specific antibody by flow cytometry. Control cells were treated with GrB-specific antibody in the absence of GrB fusion proteins (left panel). (B) Sequestration of GrB fusion proteins by binding to nontarget cells was analyzed by incubation of EGFR-negative MDA-MB453 cells with 2.5 nM of purified fusion proteins for 4 h. Then, EGFR-positive MDA-MB468 cells were treated for 14 h with MDA-MB453 culture supernatants containing unbound GrB-T (open bars) or GrBcs-T (filled bars) proteins in the presence of 50 μM chloroquine before determination of the relative number of viable MDA-MB468 cells in WST-1 assays. Control cells were treated with PBS (shaded bar) or purified proteins without prior adsorption to MDA-MB453 cells as indicated. The relative amounts of GrB fusion proteins in the samples was analyzed by immunoblotting with GrB-specific antibody followed by horseradish-peroxidase-coupled secondary antibody and chemiluminescent detection. Mean values ± SEM are shown (n = 3). **, $P < 0.01$; *, $P < 0.05$; ns, $P > 0.05$.

T). In the presence of an endosomolytic activity, GrBcs-T retained the high and specific cytotoxicity of GrB-T toward EGFR-expressing targets. However, sequestration by promiscuous binding to EGFR-negative cells as observed for GrB-T was greatly diminished, resulting in increased availability of the modified GrBcs-T molecule for specific cell killing.

With a calculated pI of ~10 GrB is a highly basic protein, which enables binding to glucosaminoglycans and other negatively charged structures such as gangliosides, sulfated lipids, and phospholipid head groups on the surface of different cell types.[17,19,28] Bird and colleagues identified two cationic sequence loops RKAKRTR (residues 116 to 122; GrB numbering) and KKTMKR (residues 241 to 246) within GrB that electrostatically interact with heparan-sulfate-containing molecules.[17] Mutation of these sequences resulted in diminished binding to the plasma membrane and suppression of subsequent endocytosis. More recently, residues K133 and K137 were also implicated in nonselective cell binding of GrB.[28] Following the strategy described by Bird et al., we generated a surface-charge-modified GrB derivative.[17] This recombinant GrBcs molecule displayed markedly reduced binding to cells derived from epithelial tissues, but retained enzymatic activity when expressed in yeast on its own or fused to the natural EGFR ligand TGFα.

To determine the consequences of GrB-mediated intrinsic cell binding for selectivity of a targeted GrB fusion protein, binding of GrBcs-T and GrB-T to EGFR-overexpressing human MDA-MB468 and EGFR-negative MDA-MB453 breast carcinoma cells was investigated utilizing directly fluorochrome-labeled anti-GrB antibody for detection of cell-bound fusion proteins. This detection system proved much more sensitive than indirect detection with an anti-Myc tag antibody that we employed previously.[13] We observed strong binding of GrB-T to MDA-MB468 cells, but also considerable binding to EGFR-negative control cells. Preincubation of GrB-T with heparin markedly reduced cell binding, suggesting interaction of cationic residues within the GrB domain with negatively charged structures on the cell surface as the underlying mechanism.[17,19,28] In contrast, modified GrBcs-T displayed strong binding only to EGFR-positive MDA-MB468 cells. Interestingly, this binding of GrBcs-T to EGFR-expressing cells was less pronounced than observed for GrB-T. Masking of the positive surface charge of GrB-T by heparin also reduced binding to MDA-MB468 cells, suggesting a general contribu-

dx.doi.org/10.1021/bc3000657 | Bioconjugate Chem. 2012, 23, 1567−1576

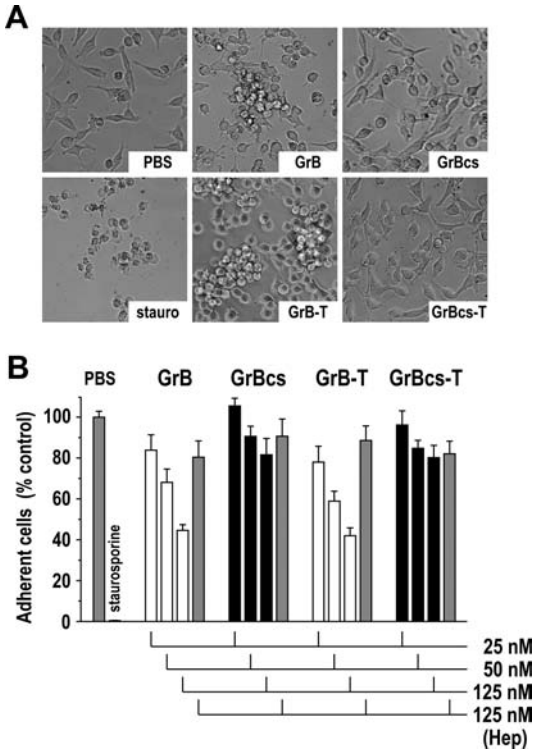


Figure 6. Morphological changes and cell detachment induced by recombinant GrB proteins. Human HeLa cervix carcinoma cells were treated for 24 h with 25, 50, or 125 nM of GrB proteins, or 125 nM of proteins preincubated with heparin. Control cells were treated with PBS or 1 μM staurosporine. (A) Morphology of cells treated with 125 nM of GrB, GrBcs, GrB-T or GrBcs-T, PBS, or staurosporine as indicated. Representative microscopic fields at 200× magnification are shown. (B) To quantify cell detachment, nonadherent cells were removed by washing with PBS, and the relative number of remaining attached cells was determined in WST-1 cell viability assays as indicated. Mean values ± SEM are shown (n = 9).

tion of electrostatic interactions via the GrB domain to cell binding of GrB-T that is independent from TGFα–EGFR interactions. Importantly, GrB-mediated cell binding did not affect cytotoxic activity, which was very similar for GrB-T and GrBcs-T and restricted to EGFR-expressing target cells, thereby correlating with the amount of target receptor on the cell surface. Hence, promiscuous charge-mediated cell binding of the GrB-T fusion protein alone did not mediate access to GrB substrates in intracellular compartments and induction of apoptosis, even when the endosomolytic reagent chloroquine was present.[8,13] Chloroquine accumulates in acidic compartments such as late endosomes and lysosomes, where it interferes with the pH equilibrium, leading to osmotic rupture of the vesicles.[29] While GrB fusion proteins taken up via binding to growth factor receptors such as EGFR are routed to chloroquine-sensitive endosomes,[13] this is not the case for GrB bound via electrostatic interactions, which is transported to neutral vesicles insensitive to the endosomolytic reagent.[8]

Promiscuous binding of targeted GrB to the surface of cells did not result in nonspecific cytotoxicity, but could limit the amount of protein available for specific tumor cell killing. In binding experiments with mixed populations of EGFR-positive and EGFR-negative cells, GrB-T interacted with both cell types to a similar extent, while GrBcs-T exclusively bound to cells expressing the tumor-associated antigen. Consequently, preincubation of GrB-T with EGFR-negative cells significantly reduced the amount of free protein and selective cytotoxicity against EGFR-positive cells. This was not the case for GrBcs-T, which upon prior contact with MDA-MB453 control cells remained in solution, and subsequently killed MDA-MB468 tumor cells to a comparable degree as purified GrBcs-T not preadsorbed to cells. Hence, modification of the GrB domain in GrBcs-T prevented the sequestration by nontarget cells seen for GrB-T, and increased tumor-cell specificity. This will likely be important for *in vivo* applications, where unmodified GrB fusion proteins could be trapped to a large extent by nontarget tissues before reaching the site of the tumor. Experiments are underway to scale up protein production for the investigation of differential effects of GrB-T and GrBcs-T in *in vivo* models.

In addition to its apoptosis-inducing activity within cells, GrB can also process components of the extracellular matrix,[24,27] which may be important for tissue remodeling in the course of an ongoing immune reaction. However, excessive extracellular activity of GrB has been linked to pathophysiological conditions such as rheumatoid arthritis[30,31] and atherosclerosis,[32,33] and may complicate application of large doses of recombinant GrB proteins for therapeutic purposes. We analyzed morphological changes and cell detachment in the presence of GrB-T and GrBcs-T to assess potential differences in the extracellular activities of the fusion proteins. While exposure to GrB-T or untargeted GrB resulted in a concentration-dependent loss of adherent cells, GrBcs-T and GrBcs induced only minimal cell detachment. This confirms that electrostatic interactions also play a role for the extracellular proteolytic activity of GrB and GrB fusion proteins, which can be controlled by surface charge modification as in the case of unspecific cell binding.

Taken together, our data demonstrate that surface charge modification of the GrB domain reduces promiscuous binding of a targeted GrB fusion protein and alleviates unwanted extracellular effects without interfering with enzymatic activity and ligand-mediated tumor cell recognition. Reduced sequestration by nontarget cells enhanced availability of the GrBcs-T molecule for tumor cell binding, resulting in increased specific cytotoxicity. Hence, this strategy may serve as a general approach for the development of optimized immunotoxin-like GrB fusion proteins for therapeutic applications.

■ ASSOCIATED CONTENT

Ⓢ Supporting Information

Supplementary Figure S1 presents data on the cell binding of recombinant and native GrB, Supplementary Figure S2 presents data on the cytotoxicity of untargeted GrB, Supplementary Table S1 compares cell binding of GrB and GrBcs, Supplementary Table S2 compares cell binding of GrB-T and GrBcs-T fusion proteins, and Supplementary Figure S3 presents data on targeted cytotoxicity of GrB-T and GrBcs-T toward cells with moderate EGFR expression. This material is available free of charge via the Internet at http://pubs.acs.org.

■ AUTHOR INFORMATION

Corresponding Author

*Telephone: +49-69-63395-188. Telefax: +49-69-63395-189. E-mail: wels@em.uni-frankfurt.de.

Notes

The authors declare no competing financial interest.

■ ACKNOWLEDGMENTS

This work was supported in part by Deutsche Forschungsgemeinschaft (DFG) grant WE 2589/2-1 and DFG Graduiertenkolleg GRK1172, and institutional funds of the Georg-Speyer-Haus. The Georg-Speyer-Haus is funded jointly by the German Federal Ministry of Health (BMG) and the Ministry of Higher Education, Research and the Arts of the State of Hessen (HMWK). We thank Dr. Christian Brendel, Georg-Speyer-Haus, for help with CLSM analysis, and Drs. Kurt Schönfeld and Martin Zörnig, Georg-Speyer-Haus, for helpful suggestions.

■ REFERENCES

(1) Rosenblum, M. G., and Barth, S. (2009) Development of novel, highly cytotoxic fusion constructs containing granzyme B: unique mechanisms and functions. *Curr. Pharm. Des. 15*, 2676−2692.

(2) Kurschus, F. C., and Jenne, D. E. (2010) Delivery and therapeutic potential of human granzyme B. *Immunol. Rev. 235*, 159−171.

(3) Wels, W., Biburger, M., Müller, T., Dälken, B., Giesübel, U., Tonn, T., and Uherek, C. (2004) Recombinant immunotoxins and retargeted killer cells: employing engineered antibody fragments for tumor-specific targeting of cytotoxic effectors. *Cancer Immunol. Immunother. 53*, 217−226.

(4) FitzGerald, D. J., Wayne, A. S., Kreitman, R. J., and Pastan, I. (2011) Treatment of hematologic malignancies with immunotoxins and antibody-drug conjugates. *Cancer Res. 71*, 6300−6309.

(5) von Minckwitz, G., Harder, S., Hövelmann, S., Jäger, E., Al-Batran, S. E., Loibl, S., Atmaca, A., Cimpoiasu, C., Neumann, A., Abera, A., Knuth, A., Kaufmann, M., Jäger, D., and Wels, W. S. (2005) Phase I clinical study of the recombinant antibody-toxin scFv(FRP5)-ETA specific for the ErbB2/HER2 receptor in patients with advanced solid malignomas. *Breast Cancer Res. 7*, R617−R626.

(6) Cullen, S. P., Brunet, M., and Martin, S. J. (2010) Granzymes in cancer and immunity. *Cell Death Differ. 17*, 616−623.

(7) Afonina, I. S., Cullen, S. P., and Martin, S. J. (2010) Cytotoxic and non-cytotoxic roles of the CTL/NK protease granzyme B. *Immunol. Rev. 235*, 105−116.

(8) Giesübel, U., Dälken, B., Mahmud, H., and Wels, W. S. (2006) Cell binding, internalization and cytotoxic activity of human granzyme B expressed in the yeast Pichia pastoris. *Biochem. J. 394*, 563−573.

(9) Dälken, B., Jabulowsky, R. A., Oberoi, P., Benhar, I., and Wels, W. S. (2010) Maltose-binding protein enhances secretion of recombinant human granzyme B accompanied by in vivo processing of a precursor MBP fusion protein. *PLoS One 5*, e14404.

(10) Gehrmann, M., Doss, B. T., Wagner, M., Zettlitz, K. A., Kontermann, R. E., Foulds, G., Pockley, A. G., and Multhoff, G. (2011) A novel expression and purification system for the production of enzymatic and biologically active human granzyme B. *J. Immunol. Methods 371*, 8−17.

(11) Liu, Y., Cheung, L. H., Thorpe, P., and Rosenblum, M. G. (2003) Mechanistic studies of a novel human fusion toxin composed of vascular endothelial growth factor (VEGF)121 and the serine protease granzyme B: directed apoptotic events in vascular endothelial cells. *Mol. Cancer Ther. 2*, 949−959.

(12) Kurschus, F. C., Kleinschmidt, M., Fellows, E., Dornmair, K., Rudolph, R., Lilie, H., and Jenne, D. E. (2004) Killing of target cells by redirected granzyme B in the absence of perforin. *FEBS Lett. 562*, 87−92.

(13) Dälken, B., Giesübel, U., Knauer, S. K., and Wels, W. S. (2006) Targeted induction of apoptosis by chimeric granzyme B fusion proteins carrying antibody and growth factor domains for cell recognition. *Cell Death Differ. 13*, 576−585.

(14) Stahnke, B., Thepen, T., Stöcker, M., Rosinke, R., Jost, E., Fischer, R., Tur, M. K., and Barth, S. (2008) Granzyme B-H22(scFv), a human immunotoxin targeting CD64 in acute myeloid leukemia of monocytic subtypes. *Mol. Cancer Ther. 7*, 2924−2932.

(15) Metkar, S. S., Wang, B., Aguilar-Santelises, M., Raja, S. M., Uhlin-Hansen, L., Podack, E., Trapani, J. A., and Froelich, C. J. (2002) Cytotoxic cell granule-mediated apoptosis: perforin delivers granzyme B-serglycin complexes into target cells without plasma membrane pore formation. *Immunity 16*, 417−428.

(16) Raja, S. M., Metkar, S. S., Höning, S., Wang, B., Russin, W. A., Pipalia, N. H., Menaa, C., Belting, M., Cao, X., Dressel, R., and Froelich, C. J. (2005) A novel mechanism for protein delivery: granzyme B undergoes electrostatic exchange from serglycin to target cells. *J. Biol. Chem. 280*, 20752−20761.

(17) Bird, C. H., Sun, J., Ung, K., Karambalis, D., Whisstock, J. C., Trapani, J. A., and Bird, P. I. (2005) Cationic sites on granzyme B contribute to cytotoxicity by promoting its uptake into target cells. *Mol. Cell. Biol. 25*, 7854−7867.

(18) Kurschus, F. C., Bruno, R., Fellows, E., Falk, C. S., and Jenne, D. E. (2005) Membrane receptors are not required to deliver granzyme B during killer cell attack. *Blood 105*, 2049−2058.

(19) Shi, L., Keefe, D., Durand, E., Feng, H., Zhang, D., and Lieberman, J. (2005) Granzyme B binds to target cells mostly by charge and must be added at the same time as perforin to trigger apoptosis. *J. Immunol. 174*, 5456−5461.

(20) Hynes, N. E., and MacDonald, G. (2009) ErbB receptors and signaling pathways in cancer. *Curr. Opin. Cell Biol. 21*, 177−184.

(21) Groner, B., Hartmann, C., and Wels, W. (2004) Therapeutic antibodies. *Curr. Mol. Med. 4*, 539−547.

(22) Schmidt, M., Vakalopoulou, E., Schneider, D. W., and Wels, W. (1997) Construction and functional characterization of scFv(14E1)-ETA - a novel, highly potent antibody-toxin specific for the EGF receptor. *Br. J. Cancer 75*, 1575−1584.

(23) Mendelsohn, J., and Baselga, J. (2000) The EGF receptor family as targets for cancer therapy. *Oncogene 19*, 6550−6565.

(24) Boivin, W. A., Cooper, D. M., Hiebert, P. R., and Granville, D. J. (2009) Intracellular versus extracellular granzyme B in immunity and disease: challenging the dogma. *Lab. Invest. 89*, 1195−1220.

(25) Mahmud, H., Dälken, B., and Wels, W. S. (2009) Induction of programmed cell death in ErbB2/HER2-expressing cancer cells by targeted delivery of apoptosis-inducing factor. *Mol. Cancer Ther. 8*, 1526−1535.

(26) Liu, Y., Zhang, W., Niu, T., Cheung, L. H., Munshi, A., Meyn, R. E., and Rosenblum, M. G. (2006) Targeted apoptosis activation with GrB/scFvMEL modulates melanoma growth, metastatic spread, chemosensitivity, and radiosensitivity. *Neoplasia 8*, 125−135.

(27) Buzza, M. S., Zamurs, L., Sun, J., Bird, C. H., Smith, A. I., Trapani, J. A., Froelich, C. J., Nice, E. C., and Bird, P. I. (2005) Extracellular matrix remodeling by human granzyme B via cleavage of vitronectin, fibronectin, and laminin. *J. Biol. Chem. 280*, 23549−23558.

(28) Kurschus, F. C., Fellows, E., Stegmann, E., and Jenne, D. E. (2008) Granzyme B delivery via perforin is restricted by size, but not by heparan sulfate-dependent endocytosis. *Proc. Natl. Acad. Sci. U. S. A. 105*, 13799−13804.

(29) Zenke, M., Steinlein, P., Wagner, E., Cotten, M., Beug, H., and Birnstiel, M. L. (1990) Receptor-mediated endocytosis of transferrin-polycation conjugates: an efficient way to introduce DNA into hematopoietic cells. *Proc. Natl. Acad. Sci. U. S. A. 87*, 3655−3659.

(30) Tak, P. P., Spaeny-Dekking, L., Kraan, M. C., Breedveld, F. C., Froelich, C. J., and Hack, C. E. (1999) The levels of soluble granzyme A and B are elevated in plasma and synovial fluid of patients with rheumatoid arthritis (RA). *Clin. Exp. Immunol. 116*, 366−370.

(31) Ronday, H. K., van der Laan, W. H., Tak, P. P., de Roos, J. A., Bank, R. A., TeKoppele, J. M., Froelich, C. J., Hack, C. E., Hogendoorn, P. C., Breedveld, F. C., and Verheijen, J. H. (2001) Human granzyme B mediates cartilage proteoglycan degradation and is expressed at the invasive front of the synovium in rheumatoid arthritis. *Rheumatology (Oxford) 40*, 55−61.

(32) Skjelland, M., Michelsen, A. E., Krohg-Sorensen, K., Tennoe, B., Dahl, A., Bakke, S., Brosstad, F., Damas, J. K., Russell, D., Halvorsen, B., and Aukrust, P. (2007) Plasma levels of granzyme B are increased in patients with lipid-rich carotid plaques as determined by echogenicity. *Atherosclerosis 195*, e142−146.

(33) Saito, Y., Kondo, H., and Hojo, Y. (2011) Granzyme B as a novel factor involved in cardiovascular diseases. *J. Cardiol.* *57*, 141−147.

Bioconjugate Chemistry

Article

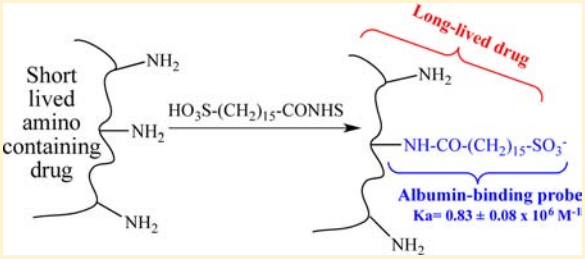
pubs.acs.org/bc

Newly Designed Modifier Prolongs the Action of Short-Lived Peptides and Proteins by Allowing Their Binding to Serum Albumin

Yoram Shechter,*[,†] Keren Sasson,[†] Vered Lev-Goldman,[‡] Sara Rubinraut,[‡] Menachem Rubinstein,[§] and Mati Fridkin*[,‡]

[†]Departments of Biological Chemistry, [‡]Organic Chemistry and [§]Molecular Genetics, The Weizmann Institute of Science, Rehovot, 76100, Israel

ABSTRACT: We found that human serum albumin (HSA) contains a single binding domain for derivatives of long-chain fatty acid (LCFA)-like molecules in which the carboxylate is replaced by sulfonate. Accordingly, we have synthesized 16-sulfo-hexadecanoic acid-*N*-hydroxysuccinimide ester [HO_3S-$(CH_2)_{15}$-CONHS], an agent that reacts selectively with the amino side chains of peptides and proteins. A macromolecule containing a single 16-sulfohexadecanoate moiety associating with albumin with a K_a value of 0.83 ± 0.08 × 10^6 M^{-1}, a sufficient affinity to extend the actions in vivo of such short-lived peptides and proteins. Subcutaneous administration of insulin-NHCO-$(CH_2)_{15}$-SO_3^- into mice facilitated a glucose-lowering effect 4.3 times in duration and 6.6 times in area under the curve (AUC) as compared to an in vitro equipotent amount of Zn^{2+}-free insulin. Similarly, subcutaneous and intravenous administration of exendin-4-NHCO-$(CH_2)_{15}$-SO_3^- to mice yielded prolonged and stable reduction in glucose level, 5−9-fold longer than that of exendin-4. Also, a single subcutaneous administration of human interferon-α2-[NH-CO-$(CH_2)_{15}$-SO_3^-]$_3$ to mice yielded circulating antiviral activity over a period of 40 h. In conclusion, a simple, hydrophilic reagent has been engineered, synthesized, and studied. Its linkage to peptides and proteins in a monomodified fashion yielded hydrophilic, prolonged acting derivatives, due to their acquired ability to associate with serum albumin after administration.



INTRODUCTION

Extending the actions of short-lived peptide/protein drugs can be accomplished by endowing them with affinity to serum albumin. This has been achieved by the covalent linking of ligands that bind albumin such as long-chain fatty acids (LCFA) or bile acids.[1−5] This leads to significant elevation in the hydrophobic character of those peptide/protein derivatives and a modest elevation in their affinity toward serum albumin. Bile acids have low association affinity to albumin[6] and have considerably lower affinity after linkage to a peptide or a protein. Long-chain fatty acids (LCFA) associate tightly with albumin, but negligibly if covalently linked via their carboxylate moiety.[7] These findings were the impetus for designing insulin-detemir and insulin degludec, two human insulin derivatives in which an LCFA-like probe was integrated into the insulin molecule.[1,2,8] In both cases, Thr^{B30} was removed to obtain a free carboxylate anion, in close vicinity to the long methylene chain located on lysine^{B29}.

In this study, we examined the option of engineering a new version of reagents containing an albumin binding probe, which combines the following features: (i) specificity to the α or ε amino side-chain moieties thereby permitting linkage to essentially any peptide or a protein; (ii) preservation of high affinity to albumin, following linkage to a peptide or a protein, in a monomodified fashion; and (iii) minimization of increased hydrophobicity and potential antigenicity of the resultant derivatives.[9,10]

LCFAs such as palmitic acid [H_3C-$(CH_2)_{14}$-COOH] associate tightly with albumin.[7,11] Here, we wished to investigate whether the carboxylate anion, at the end of the methylene-chain, can be replaced with the highly hydrophilic sulfonate anion [-$(CH_2)_n$-SO_3^-] to generate considerably more hydrophilic peptide/protein derivatives. A key question to be answered was whether a methylene chain, ending with a sulfonate anion, would maintain the efficacy of LCFA to associate with albumin, and would retain sufficient affinity after linkage to a peptide or a protein to prolong significantly conjugate stability and residence time in vivo. We present here our studies in this direction.

EXPERIMENTAL SECTION

Materials. *Human (Zn^{+2}-free) insulin* was donated by Novo Nordisk, Bagsvalrd, Denmark or by Biotechnology General (Rehovot, Israel).

Insulin-detemir, a Novo Nordisk product, was extensively dialyzed against 0.01 M $NaHCO_3$ and stored at 7 °C until use. The concentration of this derivative was determined by its absorbance at 279 nm (ε_{279} = 5800) and/or by acid hydrolyzing an aliquot (in 6 M HCl for 22 h at 110 °C) followed by quantitative amino acid analysis.

Received: February 20, 2012
Revised: May 21, 2012
Published: July 3, 2012

 © 2012 American Chemical Society

D-[U-^{14}C] glucose (4−7 mCi/mol) was obtained from Du Pont-NEN (Boston, Ma).

Type 1 collagenase (134 U/mg) was purchased from Worthington (Freehold, NY).

Exendin-4 (HGEGTFTSDLSKQMEEEAVRLFIEWLKNGGPSSGAPPPS-NH_2) was synthesized by the solid-phase method using a multiple peptide synthesizer, AMS 422 (Abimed Analyzer Technik, GmbH). IFNα2 was prepared as described in detail by Piehler and Schreiber.[12]

11-Mercaptoundecanoic acid and 16-mercaptohexadecanoic acid were purchased from Aldrich (Saint-Louis, MO). All other materials used in this study were of analytical grade.

Chemical Syntheses. *HO_3S-$(CH_2)_{15}$-COOH* was prepared by performic acid oxidation of 16-mercaptohexadecanoic acid. The latter compound (432 mg, 1.5 mmol) was suspended in 14 mL formic acid. Hydrogen peroxide (1.0 mL) was then added (5.86 mmol), and the reaction was carried out for 14 h at 25 °C. Formic acid and residual H_2O_2 were removed by evaporation. The product obtained was suspended in H_2O and lyophilized. This procedure was repeated 3 times. The calculated mass of HO_3S-$(CH_2)_{15}$-COOH is 336.4858 Da. Found ESMS M = 335.16 Da. The product was obtained in 94% yield.

HO_3S-$(CH_2)_{10}$-COOH was prepared by performic acid oxidation of 11-mercaptoundecanoic acid under the same synthesizing conditions applied above. The calculated mass of HO_3S-$(CH_2)_{10}$-COOH is 266.3518 Da. Found ESMS M = 264.96 Da.

Synthesis of HO_3S-$(CH_2)_{15}$-CONHS. This was carried out in 1.0 mL DMF containing 34 mg HO_3S-$(CH_2)_{15}$-COOH (0.1 mmol) and 38 mg of *N*-hydroxysuccinimide (0.3 mmol). *N*-Ethyldiisopropylamine (DIPEA) (5.2 μL) was then added to obtain a DIPEA concentration of 30 mM. Solid EDC (40 mg) were next added (0.2 mmol). The reaction was carried out at 25 °C with stirring over a period of 2 h. Hydrochloric acid (3 mL, 0.02 M) was then added, and the precipitated product was dialyzed overnight against 0.01 M HCl at 7 °C to dialyze out DMF, DIPEA, EDC, and NHS, which did not participate in the coupling procedure. The suspended product thus obtained was lyophilized. The calculated mass of HO_3S-$(CH_2)_{15}$-CONHS is 433.559 Da. Found ESMS M = 432.18 Da.

Synthesis of HO_3S-$(CH_2)_{10}$-CONHS. This procedure was carried out under the same synthesizing conditions applied for HO_3S-$(CH_2)_{15}$-CONHS, starting from HO_3S-$(CH_2)_{10}$-COOH. The calculated mass is 363.425 Da. Found ESMS M = 362.05 Da.

Preparation of PEG_{40}-NH-$(CH_2)_3$-NH_2. PEG_{40}-OSu (m-PEG_2-N-hydroxysuccinimide ester, Shearwater product) was dissolved at a concentration of 20 mg/mL in 0.1 M $NaHCO_3$, containing 1 M of 1.3 diaminopropane dihydrochloride (Aldrich). The reaction was carried out for 1 h at 25 °C. The product was extensively dialyzed against H_2O, lyophilized and kept at 7 °C until use.

Preparation of PEG_{40}-$(NH_2)_2$. PEG_{40}-OSu (Batch Nof, Sunbright, GL2−400TS) was dissolved at a concentration of 20 mg/mL in an aqueous solution of 0.5 M L-glutamic acid in 0.1 M $NaHCO_3$ (pH 8.5). Reaction was carried out for 2 h at 0 °C. The product thus obtained [PEG_{40}-Glu-$(COOH)_2$] was dialyzed overnight against H_2O, lyophilized, and dissolved in 0.5 M dicystamine-diHCl in H_2O (pH 6.0). Solid EDC was then added (10 mg; 100 molar excess over PEG_{40}-Glu-$(COOH)_2$), and the reaction was carried out for 2 h at 25 °C. The product thus obtained was dialyzed extensively against H_2O and lyophilized.

Preparation of PEG_{40}-NHCO-$(CH_2)_{15,10}$-SO_3^-] and PEG_{40}-[NH-$(CH_2)_{15}$-SO_3^-]$_2$. PEG_{40}-NH_2 or PEG_{40}-$(NH_2)_2$ (10 mg/mL of each in 0.1 M $NaHCO_3$) were treated with 20 molar excess of ^-O_3S-$(CH_2)_{10}$ CONHS or ^-O_3S-$(CH_2)_{15}$ CONHS (predissolved in 0.1 mL DMF) for 2 h at 25 °C, followed by dialysis for 24 h against 0.01 M Na_2CO_3 (pH = 10.3) and 24 h against H_2O and then lyophilized. The products thus obtained were TNBS negative, indicating that the amino side chains were fully derivatized.

Preparation of Monomodified Exendin-4 [Exendin-4-NHCO-$(CH_2)_{15}$-SO_3^-]. Exendin-4 (4.2 mg, 1 μmol) dissolved in 0.1 M Hepes buffer, pH 7.4. ^-O_3S-$(CH_2)_{15}$-CONHS (2.2 mg, 5 μmol dissolved in 30 μL DMF) was then added and the reaction was carried out for 3 h with stirring at 0 °C. The reaction mixture was then dialyzed to remove low-molecular-weight materials and the remaining protein function was lyophilized. Monomodified derivative of exendin-4 linked to ∼CO-$(CH_2)_{15}$-SO_3^- was purified from unreacted exendin-4 and from residual bismodified derivative using semipreperative HPLC on RP-4 column. The derivative was obtained in an overall yield of 34 ± 3%. It migrates on an analytical HPLC column as a single symmetric peak with an R_t value of 9.22 ± 0.04 min. Native exendin-4 migrates under the same running conditions with an R_t value of 8.2 ± 0.1 min. The calculated mass of Exendin-4-NHCO-$(CH_2)_{15}$-SO_3H is 4505 Da, found by ESMS-analysis, M = 4504.44 ± 0.77 Da.

Preparation of Monomodified Insulin [Insulin-NHCO-$(CH_2)_{15}$-SO_3^-]. To a stirred solution of Zn^{2+}-free insulin (29 mg in 4.8 mL 0.1 M Hepes buffer, pH 7.4, 5 μmol) was added 6.5 mg ^-O_3S-$(CH_2)_{15}$-CONHS dissolved in 0.2 mL DMF (3 molar excess over insulin). The reaction was carried out for 4 h at 0 °C, dialyzed extensively against H_2O, and lyophilized. Monomodified derivative of insulin linked to ∼CO-$(CH_2)_{15}$-SO_3^- was obtained in 29 ± 2% yield following removal of unreacted and bismodified insulin by semipreparative HPLC, using RP-4 column.

Preparation of IFNα2-[NHCO-$(CH_2)_{15}$-SO_3^-]$_3$. IFNα2 (0.5 μmol/mL) in 0.1 M Hepes buffer (pH = 7.4) was treated with 8 molar excess of ^-O_3S-$(CH_2)_{15}$-CONHS (1.73 mg, 4 μmol, dissolved in 40 μL DMF). The reaction was carried out for 1 h with stirring at 0 °C. The product was extensively dialyzed overnight against 0.01 M Na_2CO_3 and then for an additional 12 h against H_2O, and lyophilized. This derivative contains 3.1 ± 0.3 mol HO_3S-$(CH_2)_{15}$-CO∼ per mole IFNα2 as determined by quantitating the remaining amino side chains of this derivative with TNBS. IFNα2-[NHCO-$(CH_2)_{15}$-SO_3^-]$_3$ has 20 ± 4% of the antiviral potency of the native cytokine as judged by its potency to protect human WISH cells from vesicular stomatitis virus (VSV) induced cytopathic effects in vitro. An $I.C._{.50}$ value of 1.5 ± 0.2 pM was obtained for this derivative.

Chemophysical Procedures. *Ultraviolet spectra* were obtained by a Beckman DU 7500 spectrophotometer in 1-cm path length UV cuvettes. Mass spectra were determined using ESMS technique (Bruker-Reflex-Reflectron model and VG-platform-II electrospray single-quadrupole mass spectrometer).

HPLC analyses were performed using a Spectra-Physics SP8800 liquid chromatography system equipped with an Applied Biosystems 757 variable wavelength absorbance detector and a Spectra-SYSTEM P2000 liquid chromatography system equipped with a Spectra-SYSTEM AS100 autosampler and a Spectra-SYSTEM UV1000, all controlled by a ThermoQuest chromatography data system (ThermoQuest Inc., San Jose, CA). The column effluents were monitored by UV absorbance at 220 nm.

Analytical reverse-phase HPLC was performed using a prepacked Chromolith column (4.6 × 100 mm, Merck, Darmstadt, Germany). The column was eluted with a binary gradient of 10−100% solution B over 10 min with a flow rate of 3

mL/min (solution A was 0.1% trifluoroacetic acid in H_2O and solution B was 0.1% trifluoroacetic acid in acetonitrile:H_2O; 3:1, v/v).

Preparative separations were performed with prepacked Vydac RP-18 or RP-4 columns (250 × 22 mm). The column was eluted with 10−100% solution B over 60 min (12 mL/min).

Isothermal scanning calorimetry measurements were performed with ITC200 microcalorimeter (Micro Cal LLC, Northampton, MA 01060, USA). Experimental details were carried out according to the ITC200 microcalorimeter users' manual with the modifications specified in the legend of Figure 2.

Biological Procedures. Rat adipocytes were prepared from fat pads of male Wistar rats (100−200 g) by collagenase digestion.[13]

Lipogenesis (during which [U−^{14}C] glucose was incorporated into lipids) was carried out by the procedure of Moody et.al.[14] The fat pads of three rats were cut into small pieces with scissors and suspended in 3 mL of KRB-buffer (0.7% BSA) or in 3 mL of KRP-buffer (0.7% BSA) (pH 7.4). KRB Krebs Ringer bicarbonate buffer consists of the following: NaCl, 110 mM; $NaHCO_3$, 25 mM; KCl, 5 mM; KH_2PO_4, 1.2 mM; $CaCl_2$, 1.3 mM; $MgSO_4$, 1.3 mM. KRP buffer consists of Hepes, 10 mM; NaCl, 120 mM; KCl, 5.2 mM; $CaCl_2$, 1.4 mM; $MgSO_4$, 1.2 mM; and NaH_2PO_4/Na_2HPO_4, 25 mM, containing collagenase, 1 mg/mL. The digestion was performed in a 25 mL flexible plastic bottle under an atmosphere of carbogen (95% O_2, 5% CO_2) for 40 min at 37 °C with vigorous shaking. Five milliliters of buffer was then added, and the cells were squeezed through a mesh screen. The cells were then allowed to stand for several minutes (in a 15 mL plastic test tube at room temperature, floating) and the buffer underneath was removed. This procedure (suspension, floating, and removal of buffer underneath) is repeated three times. The fat cell suspensions (3×10^5 cells/mL) were divided into plastic vials (0.5 mL per vial) and incubated for 60 min at 37 °C under an atmosphere of 95% O_2, 5% CO_2, with 0.2 mM [U−^{14}C]glucose, in either the presence or absence of insulin (100 ng/mL) and its derivatives. The reaction was terminated by adding toluene-based scintillation fluid (1.0 mL per vial) and the extracted lipids were counted. Insulin-stimulated lipogenesis was 4- to 5-fold higher than basal; basal ∼2000 c.p.m. per 3×10^5 cells/h; $V_{insulin}$ 8000−10 000 cpm per 3×10^5 cells/h.

Blood glucose levels were determined at varying time points following administration of insulin, exendin-4, and their derivatives in blood aliquots taken from the tail vein. Glucose analyzer (Beckman Instruments Fullerton, CA) was used. Groups consisted of six mice each. Data are presented as means ± SE.

Antiviral activity. Antiviral activity of IFNα2, its derivatives, and serum samples containing IFNα2 was determined by the capacity of the cytokine to protect human amnion WISH cells against vesicular stomatitis virus (VSV)-induced cytopathic effects.[15] WISH cells (4.5×10^5 cells/ml) were seeded in a 96-well plate (100 μL/well) and incubated with 2-fold serial dilutions of IFNα2, its derivative, or serum samples, measuring the absorbance of crystal violet stained cells in an ELISA plate. In this assay, native IFNα2 shows 50% protection of VSV-induced WISH cells at a concentration of 0.3 ± 0.04 pM (5.8 ± 0.75 pg/mL).

RESULTS

Engineering and Synthesizing Sulfonyl-Containing Albumin Binding Probes for the Covalent Attachment to Peptides and Proteins. Derivatives resembling LCFAs that contain a C-terminal sulfonate rather than a carboxylate anion are not available commercially. We therefore converted 11-mercapto-undecanoic acid [HOOC-$(CH_2)_{10}$-SH] and 16-mercaptohexadecanoic acid [HOOC-$(CH_2)_{15}$-SH] to the corresponding sulfonated derivatives using performic acid oxidation (Experimental Section and a schematic illustration in Figure 1A). Those were subsequently turned into the active

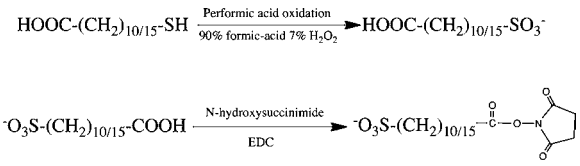


Figure 1. Schematic illustration of the synthesis and the structure of 11-sulfo-undecanoic-*N*-hydroxysuccinimide [HO_3S-$(CH_2)_{10}$-CONHS] and of 16-sulfohexa-decanoic-*N*-hydroxysuccinimide [HO_3S-$(CH_2)_{15}$-CONHS].

esters by linking *N*-hydroxysuccinimide to their carboxylate moieties (Figure 1B). The structures of the intermediates and the final products were validated by mass spectroscopy. Both compounds, ^-O_3S-$(CH_2)_{10}$-CONHS and ^-O_3S-$(CH_2)_{15}$-CONHS, were obtained in >80% overall yields.

Associating Affinity of Macromolecules Containing ∼∼ $(CH_2)_{10}$-SO_3^- and ∼∼ $(CH_2)_{15}$-SO_3^- with Human Serum Albumin. Figure 2 shows the associating affinities of macromolecules containing a single or a pair of covalently linked ∼OC-$(CH_2)_{10/15}$-SO_3^- toward HSA using isothermal scanning calorimetry.[16] As a model for a macromolecule, we used a poly(ethylene glycol) chain of 40 kDa. PEG_{40}-NH-CO-$(CH_2)_{10}$-SO_3^- and PEG_{40}-NH-CO-$(CH_2)_{15}$-SO_3^- associate with HSA. The K_a values observed for these macromolecules were 0.195 ± 0.0274 and 0.829 ± 0.0821 × 10^6 M^{-1}, respectively (Figure 2A,B). PEG_{40} containing a pair of the longer moieties showed a K_a value of 0.803 ± 0.0495 × 10^6 M^{-1} (Figure 2C). Thus, a methylene chain composed of C10 or C15 atoms ending with a C-terminal sulfonate anion, which has been linked to a macromolecule, binds to HSA with K_a values in the range of 0.2−0.8 × 10^6 M^{-1}.

Chemical and Biological Features of Insulin-NHCO-$(CH_2)_{15}$-SO_3^-. Table 1 summarizes the characteristic features of the HPLC-purified insulin derivative relevant to this study. Insulin-NHCO-$(CH_2)_{15}$-SO_3H is a monomodified derivative having molecular weight of 6124.98 ± 0.27 Da (calculated value is 6126 Da), as verified by mass spectroscopy. The derivative is soluble in aqueous buffers (pH 7.5−8.0) at a concentration of >10 mg/mL. It has the absorbance of the native hormone (ε_{279} = 5800). Insulin-NHCO-$(CH_2)_{15}$-SO_3^- emerged as a symmetric peak on analytical HPLC column with R_t = 7.97 ± 0.04 min (Figure 3). It activates lipogenesis in rat adipocytes at about 20% the efficacy of insulin, yielding a half-maximal effect (ED_{50}) at a concentration of 0.5 ± 0.5 nM (summarized in Table 1).

HPLC purified insulin-NHCO-$(CH_2)_{15}$-SO_3^- is derivatized exclusively on the α-amino moiety of PheB1, as determined from N-terminal protein sequence analysis of this derivative (Figure 4, and summarized in Table 1). The sequence obtained was Gly-Ileu-Val-Glu, identical to that of the A-chain of human insulin.

Insulin-NHCO-$(CH_2)_{15}$-SO_3^- is Relatively Hydrophilic. Figure 5 shows the retention times (R_t values) of insulin, insulin-NHCO-$(CH_2)_{15}$-SO_3^-, and insulin-detemir loaded on analytical-HPLC-chromolith R.P-18e column. This approach of hydrophobic chromatography yields an estimate of the overall

dx.doi.org/10.1021/bc3000854 | *Bioconjugate Chem.* 2012, 23, 1577−1586

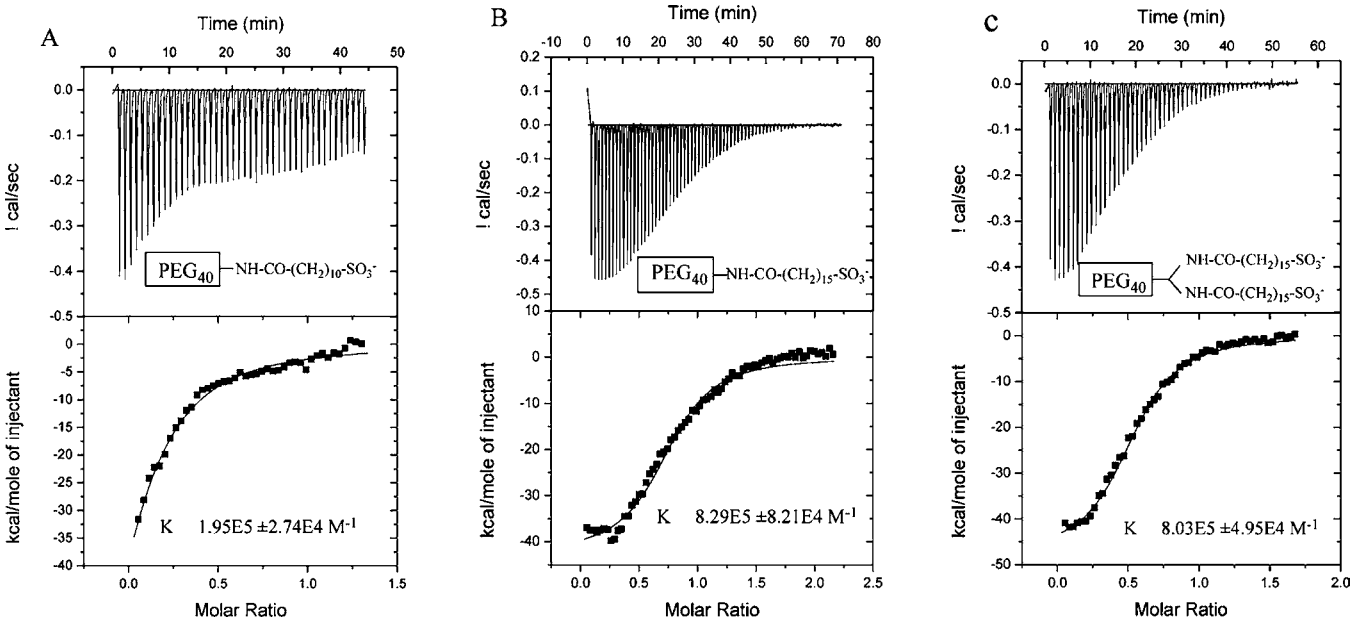


Figure 2. Simulating binding isotherms for the association of PEG_{40}-NHCO-$(CH_2)_{10}$-SO_3^-, PEG_{40}-NHCO-$(CH_2)_{15}$-SO_3^-, and PEG_{40}-[NHCO-$(CH_2)_{10}$-$SO_3^-]_2$ with human serum albumin as determined by ITC-200. The raw data were obtained for 50 injections each of 0.3 μL at intervals of 1 min. The sample cell contained the ligands at a concentration of 20 μM, and the injection syringe contained 400 μM HSA. Both components dissolved in 0.1 M Hepes buffer, pH 7.4. The experiments were conducted at 23 °C.

Table 1. Chemical and Biological Features of HPLC-Purified Insulin-NHCO-$(CH_2)_{15}$-SO_3^-

characteristic	Ins-NHCO-$(CH_2)_{15}$-SO_3^-
amino acid composition	identical to insulin
absorbance at 279 nm[a]	ε_{279} = 5800, identical to insulin
analytical HPLC; a single peak, retention time (R_t)	7.97 ± 0.04 min[b]
mass spectroscopy (electrospray ionization)	
calcd (m/z)	6126 Da[c]
found ES−	6124.98 ± 0.27 Da
found ES+	6126.82 ± 0.50 Da
solubility in aqueous buffer (pH 7.5−8.0)	> 10 mg/mL
lipogenic potency in rat adipocytes	ED_{50} = 0.5 ± 0.03 nM (~20%)[d]
site of derivatization	amino side chain of Phe[B1][e]

[a]Derivative with known absorbance at 279 nm was quantitated by hydrolyzing an aliquot in 6 N HCl (110 °C, 22 h). [b]Under the same running conditions, insulin elutes with R_t = 7.30 ± 0.01 min. [c]Calculated mass is the molecular weight of human insulin (5807 Da) combined with that of ~~OC-$(CH_2)_{15}$-SO_3H which amounted to 319 Da. [d]In this assay, insulin stimulates lipogenesis 4−5 times above basal level, with ED_{50} value of 0.1 ± 0.02 nM (0.58 ± 0.06 ng/mL). [e]Determined by N-terminal protein sequence analysis (Figure 4).

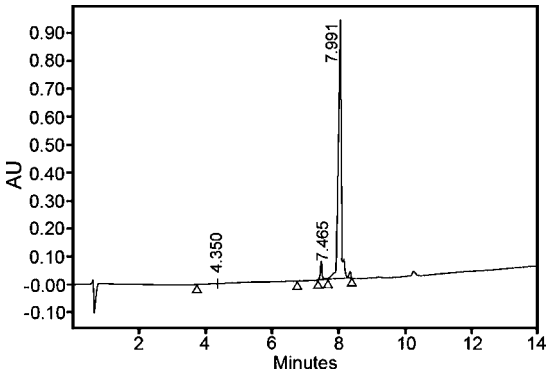


Figure 3. HPLC analysis of purified insulin-NHCO-$(CH_2)_{15}$-SO_3^-. The derivative (30 μg) was loaded onto a chromolith Rp-18e (100 mm × 4 mm) column and run with a linear gradient from 0% to 100% solution A (0.1% TFA) to solution B (acetonitrile−H_2O 75:25 in 0.1% TFA) over 10 min and then 4 min in solution B at a rate of 3 mL/min. The effluent was monitored at 220 nm.

lipophilicity of peptides analogues.[17] Insulin, insulin-NHCO-$(CH_2)_{15}$-SO_3^-, and insulin-detemir emerged from the column with R_t values of 7.31, 7.94, and 9.10 min, respectively. Thus, Insulin-NHCO-$(CH_2)_{15}$-SO_3^- is quite hydrophilic in nature. This is particularly valid in comparison to insulin-detemir. The latter derivative contains a single C-14 fatty acid chain covalently linked to lysine B^{29}.[18]

Glucose Lowering Pattern of Insulin-NH-CO-$(CH_2)_{15}$-SO_3^-. In Figure 6, we compared the glucose-lowering pattern obtained after a single subcutaneous administration of insulin-NH-CO-$(CH_2)_{15}$-SO_3^- to that of Zn^{2+}- free insulin. Since insulin-NH-CO-$(CH_2)_{15}$-SO_3^- has ~20% the potency of insulin to stimulate lipogenesis in vitro (Table 1), a dose of 0.65 nmol/mouse was compared to a dose of 0.13 nmol/mouse of the native hormone. Insulin-NHCO-$(CH_2)_{15}$-SO_3^- showed a prolonged glucose lowering pattern ($t_{1/2}$ = 3 ± 0.4 h), 4.3 times in duration and 6.6 times the area under the curve (AUC) of that manifested by administering an equipotent amount of Zn^{2+}-free insulin as determined by the in vitro assay. It should be noted, however, that AUC is not a sufficient parameter for determining glucodynamic potency of insulin and derivatives in vivo.[19] Additional measurements, such as glucose-clamps,[20,21] are to be applied in the future as well.

High-Bioavailability of Insulin-NHCO-$(CH_2)_{15}$-SO_3^- Following Subcutaneous Administration. To evaluate if there is any reduction in the diffusion rate of Insulin-NHCO-$(CH_2)_{15}$-SO_3^- from the subcutis to the circulatory system, in Figure 7 we have compared the glucose-lowering pattern of intravenous versus subcutaneous administered Insulin-NHCO-$(CH_2)_{15}$-SO_3^- to that of Zn^{2+}-free insulin (Figure 7A,B). The areas

dx.doi.org/10.1021/bc3000854 | Bioconjugate Chem. 2012, 23, 1577−1586

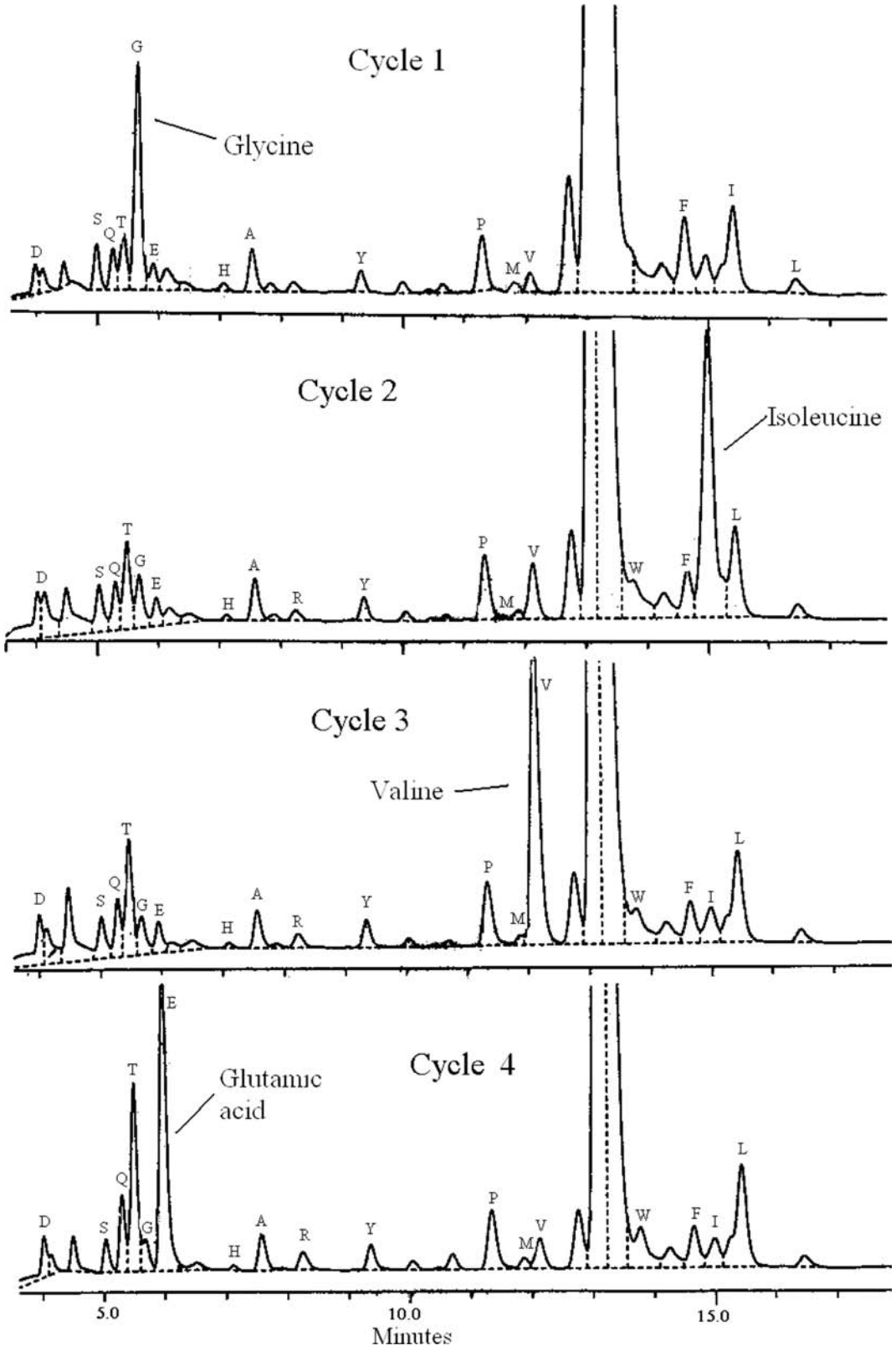


Figure 4. Insulin-NHCO-$(CH_2)_{15}$-SO_3^- is derivatized exclusively at the α-amino group of phenylalanine B^1. HPLC purified Insulin-NHCO-$(CH_2)_{15}$-SO_3^- (190 pmol) was subjected to four cycles of N-terminal protein sequence analysis. The sequence obtained was Gly-Isoleu-Val-Glu, corresponding to the A-chain N-terminal portion of human insulin. Sequence analysis of native insulin yields as well Phe-Val-Asn-Glu on cycles 1 to 4, respectively (not shown).

under the curves (AUC) were integrated (Figure 7C). The AUC of subcutaneous administered Zn^{2+}-free insulin and of Insulin-NHCO-$(CH_2)_{15}$-SO_3^- exceeded by 1.23 ± 0.06 and 1.43 ± 0.1 times those obtained following intravenous administrations (Figure 7C).

dx.doi.org/10.1021/bc3000854 | *Bioconjugate Chem.* 2012, 23, 1577−1586

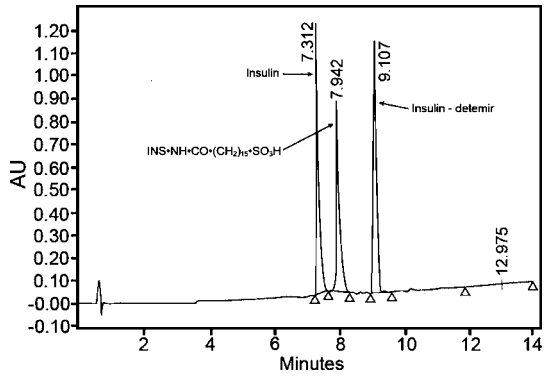


Figure 5. Relative hydrophilicity of insulin-NH-$(CH_2)_{15}$-SO_3^- as determined by hydrophobic chromatography. A mixture of Zn^{2+}-free insulin, HPLC-purified monomodified insulin-NHCO-$(CH_2)_{15}$-SO_3^-, and insulin-detemir (40 μg each) were loaded on to a chromolith Rp-18e (100 mm × 4 mm) column and run under the same running conditions specified in detail in the legend to Figure 3.

Exendin-4-NHCO-$(CH_2)_{15}$-SO_3^- Facilitates Prolonged Glucose-Lowering Effect in CD1 Mice Following Subcutaneous Administration. Figure 8 shows the glucose-lowering profile of subcutaneously administered native exendin-4 and of HPLC-purified exendin-4-NHCO-$(CH_2)_{15}$-SO_3^-, both administered at a dose of 0.25 nmol/CD1 mice. Previously, we reported that in this strain of mice the action of this glucagon-like peptide-1 agonist resembled the pharmacodynamic pattern obtained in db/db mice. Also, as has been observed in Type II diabetic patients, circulating BGL at any dosage of exendin-4 injected never falls below a threshold level, which in CD1 mice amounted to 70 ± 7 mg/dl.[22,23]

Following subcutaneous administration of Exendin-4-NHCO-$(CH_2)_{15}$-SO_3^- glucose level fell to 70 ± 5 mg/dl and remained at low level over a period of ~24 h, before slowly returning to the level of the saline-injected CD1 mice. The half-life of the glucose lowering response was 32 ± 2 h, which is 5.5 times longer than that obtained by the same dose of the native hormone. The AUC of subcutaneously administered exendin-4-NHCO-$(CH_2)_{15}$-SO_3H exceeded 7 ± 0.1 times that obtained by a similar subcutaneously administered dose of the native hormone (Figure 8).

Glucose Lowering Pattern of Exendin-4-NHCO-$(CH_2)_{15}$-SO_3^- Following Intravenous Administration. The prolonged-acting feature of subcutaneous administered Ex-4-NHCO-$(CH_2)_{15}$-SO_3^- may be partly due to association with albumin present in the subcutaneous interstitial fluid, and therefore, this derivative may have slower, more prolonged rate of diffusion from the subcutis to the circulatory system. In Figure 9, we bypassed the subcutaneous compartment by administering Exendin-4 and Exendin-4-NHCO-$(CH_2)_{15}$-SO_3^- intravenously. Intravenously administered Ex-4-NHCO-$(CH_2)_{15}$-SO_3^- yielded a prolonged glucose-lowering pattern having a $t_{1/2}$ value of 28 ± 2 h, exceeding that of exendin-4 by 9−10-fold (Figure 9). BGL was still low 48 h after administration, which was the last time point measured. Thus, the prolonged-acting feature of Ex-4-NHCO-$(CH_2)_{15}$-SO_3^- appears to be predominantly the outcome of its association with circulating serum albumin.

IFNα2-[NH-CO-$(CH_2)_{15}$-SO_3^-]$_3$ is a Long-Lived Species in Vivo. Either native or the tris-modified IFNα2 derivative were administered at equal antiviral units to mice by a single

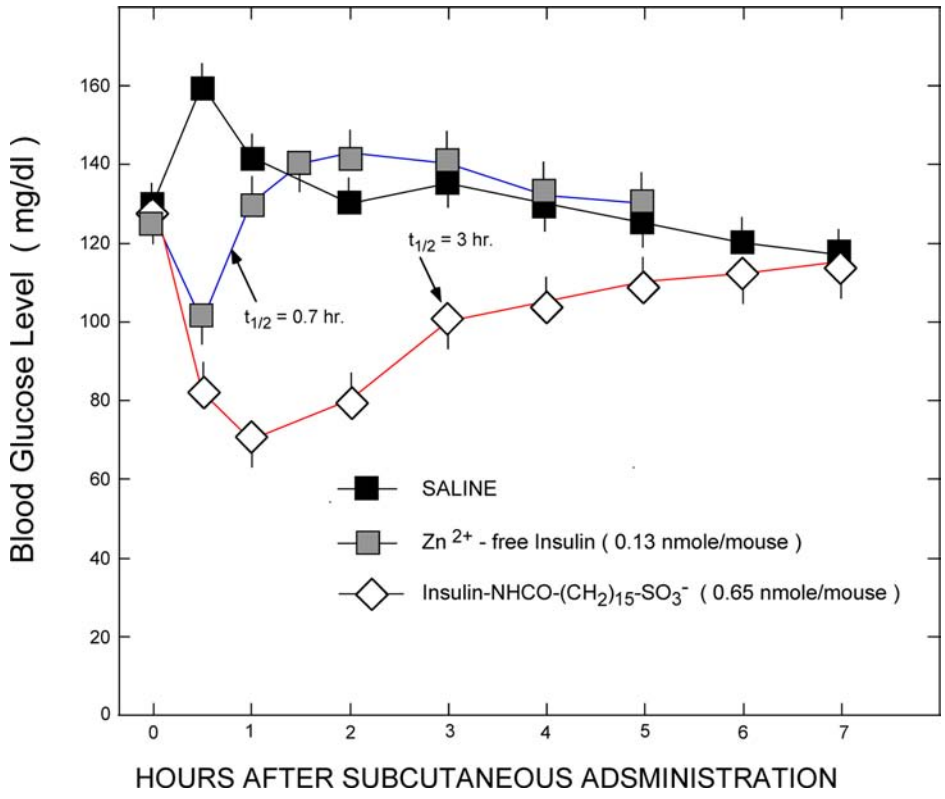


Figure 6. Circulating glucose levels in mice following a single subcutaneous administration of insulin-NHCO-$(CH_2)_{15}$-SO_3^-. CD1-mice were injected subcutaneously with saline (0.2 mL/mouse), Zn^{2+}-free insulin (0.13 nmol/mouse in 0.2 mL saline), or with insulin-NHCO-$(CH_2)_{15}$-SO_3^- (0.65 nmol/mouse in 0.2 mL saline). Blood glucose levels were determined at the indicated time points. Each point is the arithmetic mean of n = 6 mice ± SE.

dx.doi.org/10.1021/bc3000854 | Bioconjugate Chem. 2012, 23, 1577−1586

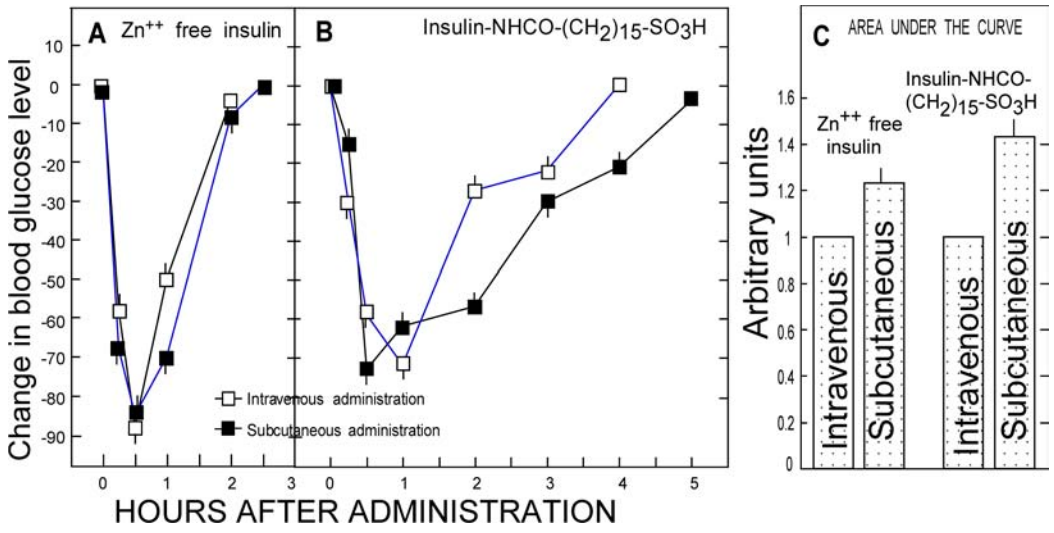


Figure 7. Intravenous versus subcutaneous glucose lowering patterns of Insulin-NHCO-$(CH_2)_{15}$-SO_3^-. Comparison to Zn^{2+}-free insulin. Groups of CD1-mice (n = 6 per group) have received intravenously or subcutaneously Zn^{2+}-free insulin (0.35 nmol/mouse, A) or Insulin-NHCO-$(CH_2)_{15}$-SO_3^- (1.3 nmol/mouse, B). Circulating glucose levels were then monitored. Results are expressed as percent decrease in plasma glucose concentrations relative to those found in the saline-treated groups, measured at the same time point during the day. (C) AUC values integrated from (A) and (B).

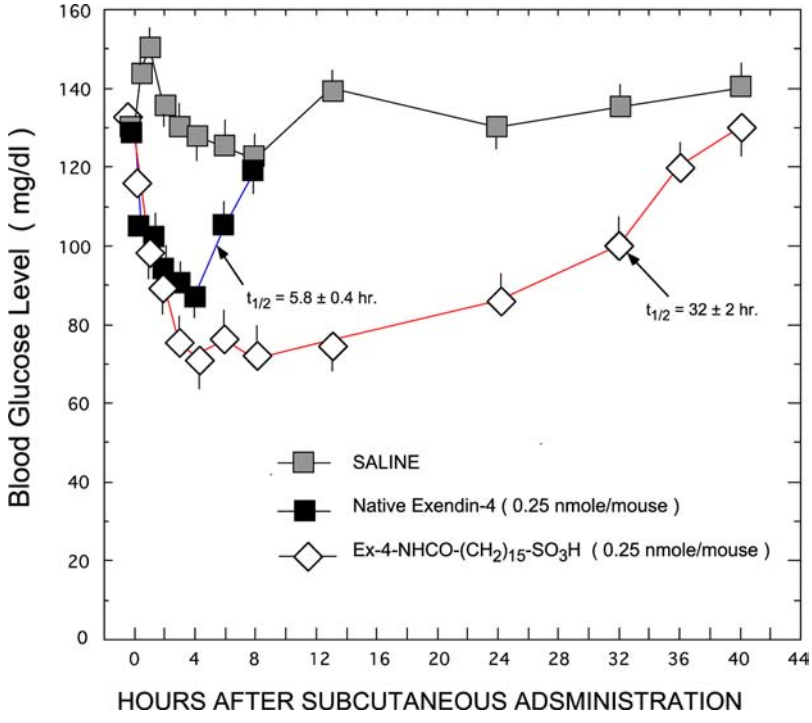


Figure 8. Glucose lowering pattern of Exendin-4-NHCO-$(CH_2)_{15}$-SO_3^- following a single subcutaneous administration to CD1-mice. Three groups of CD1-mice (n = 6 per group) underwent one subcutaneous administration of saline, native exendin-4 (0.25 nmol/mouse), or exendin-4-NHCO-$(CH_2)_{15}$-SO_3^- (0.25 nmol/mouse). Circulating glucose levels were monitored at the time points indicated. Each point is the arithmetic mean of n = 6 mice ± SE.

subcutaneous injection. Figure 10 shows the concentration of IFNα2 activity in the circulatory system of these mice. The circulating levels of native IFNα2 activity reached a plateau at 1 h, declining with a half-life of 2.5 ± 03 h. No detectable levels of antiviral activity were observed 10 h after administration (limit of detection is 100 IU/mL; Figure 10A and inset). Following administration of the tris-modified IFNα2-derivative, circulating IFNα2 activity was gradually elevated over a period of 2 h, suggesting the association of this derivative with subcutis albumin. The antiviral activity of the modified IFNα2 persisted much longer than that of the native IFNα2, exhibiting a half-life of 6.5 ± 0.4 h (Figure 10B). Antiviral activity at a concentration sufficient to fully suppress viral infection (≥100 IU/mL) was present in the mouse circulation for over 40 h (Figure 10B, and inset).

DISCUSSION

In this study, we aimed to design new reagents containing albumin-binding probes capable of converting short-lived peptide/protein drugs into long-lived species in vivo. We have

dx.doi.org/10.1021/bc3000854 | Bioconjugate Chem. 2012, 23, 1577−1586

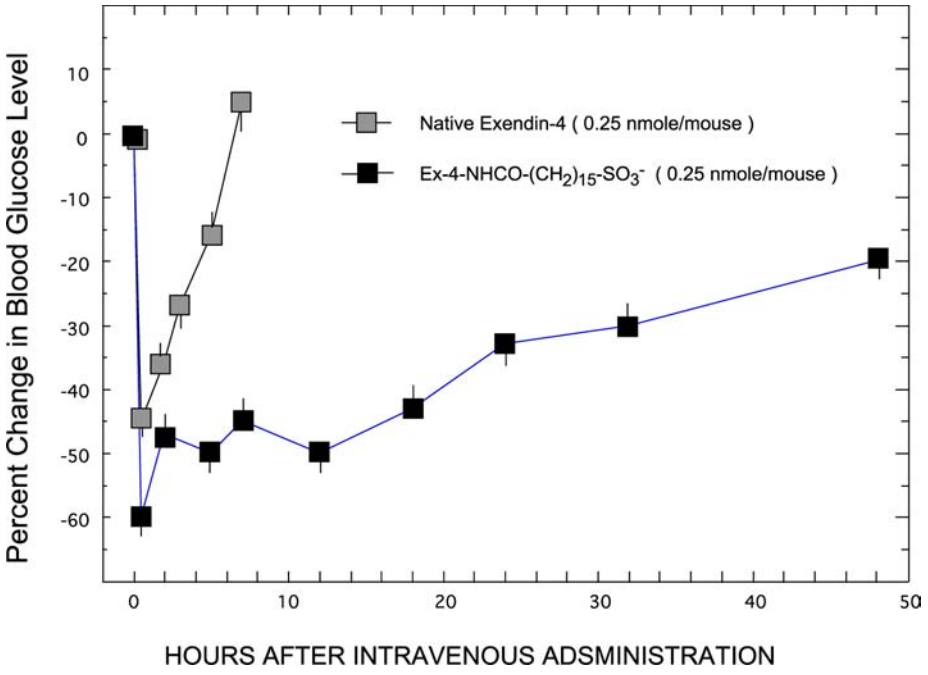


Figure 9. Glucose lowering pattern of Exendin-4-NHCO-$(CH_2)_{15}$-SO_3^- following a single intravenous administration to CD1-mice. Three groups of CD1-mice ($n = 6$ per group) underwent one intravenous administration of saline, native exendin-4 (0.25 nmol/mouse), or exendin-4-NHCO-$(CH_2)_{15}$-SO_3^- (0.25 nmol/mouse). Circulating glucose levels were then monitored. Results are expressed as percent decrease in plasma glucose concentration in the group treated with exendin-4 or Exendin-4-NHCO-$(CH_2)_{15}$-SO_3^-, relative to that found in the saline treated group, measured at the same time point during the day.

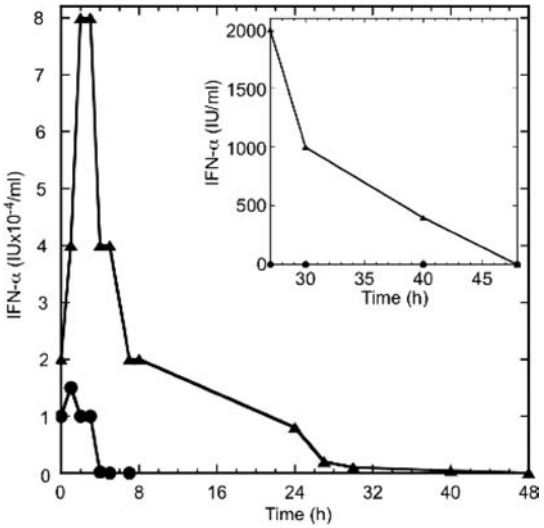


Figure 10. Subcutaneously administered IFNα2-[NH-CO-$(CH_2)_{15}$-SO_3^-]$_3$ in mice facilitates prolonged circulating antiviral activity. Mice received subcutaneously 10 μg of native IFNα2 (circles) or 50 μg of IFNα2-[NH-CO-$(CH_2)_{15}$-SO_3^-]$_3$ (triangles). At time-0 (3 min after administration), and at later time points, three mice were sacrificed and serum IFNα was determined by the antiviral activity assay. Each value is the arithmetic mean of three mice.

searched for molecules containing neither ring structures nor bulky elements that are hydrophilic in nature and preserve sufficient affinity to albumin after covalent attachment of one such probe to a peptide or a protein.

By analogy to LCFA, we hypothesized that a long methylene chain, containing no double bonds, would be an appropriate spacer element.[24] In order to significantly elevate hydrophilicity, we tested whether the carboxylate anion could be replaced by a sulfonate anion. The latter is highly hydrophilic, but the absence of LCFA-like sulfonated derivatives prevented the option of determining albumin association. Notably, sulfonate is a highly hydrated anion, surrounded by several molecules of water, and its molecular radius significantly exceeds that of the carboxylate anion.[25,26]

We have converted 11-mercaptoundecanoic acid [HOOC-$(CH_2)_{10}$-SH] and 16-mercaptohexadecanoic acid [HOOC-$(CH_2)_{15}$-SH] to the corresponding LCFA-like sulfonated derivatives by performic acid oxidation (Figure 1A). The products were obtained in high yield in spite of the negligible solubility of the parent molecules in formic acid (experimental procedure). Those were turned into active esters by linking *N*-hydroxysuccinimide to the carboxylate moieties using EDC (Figure 2B), thereby turning them into reagents that react selectively with amino side chain moieties of peptides and proteins.

Initially, we linked those derivatives to PEG_{40}-NH_2 in a monomodified fashion and investigated the association with HSA using isothermal scanning calorimetry. Both PEG_{40}-NHCO-$(CH_2)_{10}$-SO_3^- and PEG_{40}-NHCO-$(CH_2)_{15}$-SO_3^- do associate with HSA; the shorter version yielded a K_a value of 0.195×10^6 M^{-1} and the longer version had a K_a value of 0.829×10^6 M^{-1} (Figure 2A,B). Thus, HSA has a binding domain for LCFA-like sulfonated molecules as well. There was no increase in affinity toward HSA applying PEG_{40} containing two such probes [PEG_{40}-$(NHCO\text{-}(CH_2)_{15}\text{-}SO_3^-)_2$] (Figure 2C), suggesting that HSA contains a single binding domain for a sulfonated LCFA-like molecule if the given spacing allows a bivalent type of association with this carrier protein.

As observed here, the covalent introduction of a single ~OC-$(CH_2)_{15}$-SO_3^- moiety to PEG molecule of 40 kDa yielded a macromolecule that associates with HSA with a K_a of 0.829×10^6 M^{-1} (Figure 2A). This value exceeds by about 4.3 times the

dx.doi.org/10.1021/bc3000854 | *Bioconjugate Chem.* 2012, 23, 1577−1586

documented affinity of insulin-detemir to this carrier protein.[18] We therefore envisioned that such associating affinity would be sufficient to significantly extend the actions of short-lived peptides and proteins in vivo. Indeed, derivatives of insulin and exendin-4 containing a single such probe are long-lived in vivo. The glucose-lowering effect of insulin was increased about 4.3-fold and that of exendin-4 about 5−10-fold (Figures 6−9). Thus, HO_3S-$(CH_2)_{15}$-CONHS is a simple, hydrophilic reagent, containing no ring nor hydrophobic elements, which turns short-lived peptide drugs into long-lived species in vivo. Conjugates are expected therefore to be neither toxic nor immunogenic.

It should be noted that this approach is restricted to peptides and proteins, which do not significantly lose their biological/therapeutic activity upon introduction of this probe to the drug molecule. Proteins in general can undergo a considerable degree of lysine modifications before being substantially inactivated, and this is valid also to monomodified derivatives of insulin and exendin-4.[4,5,27] However, this may not be the case for low-molecular-weight drugs such as amino acid derivatives, catecholamines, and aminoglycosides. With this drug category, a strategy of introducing a slowly hydrolyzable albumin-binding probe, previously developed in our laboratories, is recommended.[28]

Previously, we found that we can covalently link up to seven bulky groups to the amino side chains of IFNα2 with relatively little loss in its antiviral potency.[29] In view of that, we studied here an IFNα2-derivative containing three covalently linked~OC-$(CH_2)_{15}$-SO_3^- moieties per one IFNα2 molecule. This tris-modified derivative showed an IC_{50} value of 1.5 pM, representing 20% of the native antiviral potency. Such derivatization yielded a dramatically prolonged pharmacodynamic profile in mice (Figure 10B). Since albumin has a single binding domain for a protein-linked ~CO-$(CH_2)_{15}$-SO_3^- residue (Figure 2), we currently study whether this tris-modified IFNα2 derivative can accommodate more than one molecule of albumin and whether such a complex displays a further increase in residence time in vivo.

Finally, we stress that modification with HO_3S-$(CH_2)_{15}$-CONHS can be simply applied as the last step of solid-phase peptide synthesis, linking it selectively to the α-amino side-chain, prior to deprotecting the lysine moieties. This approach can turn any peptide that can therapeutically tolerate an additional molecule at its N-terminal position into an albumin binding species, with prolonged residence time in vivo, as well as resistance to degradation by serum amino peptidases.

AUTHOR INFORMATION

Corresponding Author

*Y. S.: Tel. 972-8-9344530, Fax 972-8-9344118; e-mail: yoram.shechter@weizmann.ac.il. M. F.: Tel. 972-8-9342505, Fax 972-8-9344142; e-mail: mati.fridkin@weizmann.ac.il.

Notes

The authors declare no competing financial interest.

ACKNOWLEDGMENTS

Y.S. is the incumbent of the C.H. Hollenberg Chair in Metabolic and Diabetes Research established by the friends and associates of Dr. C. H. Hollenberg of Toronto, Canada. M.F. is the Lester Pearson Professor of Protein Chemistry. M.R. is the Edna & Maurice Weiss Professor of Cytokine Research.

ABBREVIATIONS USED

HSA, human serum albumin; HPLC, high-performance liquid chromatography; HO_3S-$(CH_2)_{10}$-COOH, 11-sulfo undecanoic acid; HO_3S-$(CH_2)_{15}$-COOH, 16-sulfo hexadecanoic acid; HO_3S-$(CH_2)_{10}$-CONHS, 11-sulfo undecanoic-*N*-hydroxysuccinimide ester; HO_3S-$(CH_2)_{15}$-CONHS, 16-sulfo hexadecanoic-*N*-hydroxysuccinimide ester; EDC, 1-ethyl-3-(3-dimethylaminopropyl) carbodiimide; ESMS, electrospray single quadrupole mass spectroscopy; DMF, dimethylforamide; NHS, *N*-hydroxysuccinimide; AUC, area under the curve; BGL, blood glucose level; LCFA, long-chain fatty acid; Ex-4-NH-CO-$(CH_2)_{15}$-SO_3^-, monomodified exendin-4 containing -$CO(CH_2)_{15}$-SO_3^- moiety; Ins-NH-$CO(CH_2)_{15}$-SO_3^-, monomodified insulin containing -$CO(CH_2)_{15}$-SO_3^- moiety; IFNα2, interferon-α2; IFNα2-$[NHCO(CH_2)_{15}$-$SO_3^-]_3$, interferon-α2 containing 3 mol/mol of -$CO(CH_2)_{15}$-SO_3^-; PEG, poly(ethylene glycol); PEG_{40}-NH-$CO(CH_2)_{10}$-SO_3^-, poly(ethylene glycol) chain of 40 kDa containing a moiety of -$CO(CH_2)_{10}$-SO_3^-; PEG_{40}-NH-CO-$(CH_2)_{15}$-SO_3^-, poly(ethylene glycol) chain of 40 kDa containing a moiety of -$CO(CH_2)_{15}$-SO_3^-; PEG_{40}-$[NH$-$CO(CH_2)_{15}$-$SO_3^-]_2$, PEG chain of 40 kDa containing two moieties of -$CO(CH_2)_{15}$-SO_3^-; ITC, isothermal scanning calorimetry; TNBS, trinitrobenzenesulfonic acid

REFERENCES

(1) Kurtzhals, P., Havelund, S., Jonassen, I., Kiehr, B., Larsen, U. D., Ribel, U., and Markussen, J. (1995) Albumin binding of insulins acylated with fatty acids: characterization of the ligand-protein interaction and correlation between binding affinity and timing of the insulin effect in vivo. *Biochem. J. 312* (Pt 3), 725−31.

(2) Jonassen, I., Havelund, S., Ribel, U., Plum, A., Loftager, M., Hoeg-Jensen, T., Volund, A., and Markussen, J. (2006) Biochemical and physiological properties of a novel series of long-acting insulin analogs obtained by acylation with cholic acid derivatives. *Pharm. Res. 23*, 49−55.

(3) Rolin, B., Larsen, M. O., Gotfredsen, C. F., Deacon, C. F., Carr, R. D., Wilken, M., and Knudsen, L. B. (2002) The long-acting GLP-1 derivative NN2211 ameliorates glycemia and increases beta-cell mass in diabetic mice. *Am. J. Physiol. Endocrinol. Metab. 283*, E745−52.

(4) Son, S., Chae, S. Y., Kim, C. W., Choi, Y. G., Jung, S. Y., Lee, S., and Lee, K. C. (2009) Preparation and structural, biochemical, and pharmaceutical characterizations of bile acid-modified long-acting exendin-4 derivatives. *J. Med. Chem. 52*, 6889−96.

(5) Chae, S. Y., Choi, Y. G., Son, S., Jung, S. Y., Lee, D. S., and Lee, K. C. (2010) The fatty acid conjugated exendin-4 analogs for type 2 antidiabetic therapeutics. *J. Controlled Release 144*, 10−6.

(6) Roda, A., Cappelleri, G., Aldini, R., Roda, E., and Barbara, L. (1982) Quantitative aspects of the interaction of bile acids with human serum albumin. *J. Lipid. Res. 23*, 490−5.

(7) Peters, T. J. (1996) The albumin molecule: its structure and chemical properties, , In *All about albumin, Biochemistry, Genetics and Medical Applications*, pp 24−54, Academic Press, Inc., San Diego, CA.

(8) Jonassen, I., Havelund, S., Hoeg-Jensen, T., Steensgaard, D. B., Wahlund, P. O., and Ribel, U. (2012) Design of the novel protraction mechanism of insulin degludec, an ultra-long-acting basal insulin. *Pharm. Res.*, DOI: 10.1007/s11095-012-0739-z.

(9) Aoki, T., Iskandar, S., Yoshida, T., Takahashi, K., and Hattori, M. (2006) Reduced immunogenicity of β-lactoglobulin by conjugating with chitosan. *Biosci. Biotechnol. Biochem. 70*, 2349−2356.

(10) Goodman, L., and Gilman, A. (1995) *The Pharmacological Basis of Therapeutic*, Mc Graw-Hill, New York.

(11) Carter, D. C., and Ho, J. X. (1994) Structure of serum albumin. *Adv. Protein Chem. 45*, 153−203.

(12) Piehler, J., and Schreiber, G. (1999) Biophysical analysis of the interaction of human ifnar2 expressed in E. coli with IFNalpha2. *J. Mol. Biol. 289*, 57−67.

(13) Rodbell, M. (1964) Metabolism of isolated fat cells. I. Effects of hormones on glucose metabolism and lipolysis. *J. Biol. Chem. 239*, 375–80.
(14) Moody, A. J., Stan, M. A., Stan, M., and Gliemann, J. (1974) A simple free fat cell bioassay for insulin. *Horm. Metab. Res. 6*, 12–6.
(15) Rubinstein, S., Familletti, P. C., and Pestka, S. (1981) Convenient assay for interferons. *J. Virol. 37*, 755–8.
(16) Chaires, J. B. (2008) Calorimetry and thermodynamics in drug design. *Annu. Rev. Biophys. 37*, 135–51.
(17) Shechter, Y., Heldman, E., Sasson, K., Bachar, T., Popova, M., and Fridkin, M. (2010) Delivery of neuropeptide from the periphery to the brain: studies with enkephalin. *ACS Chem. Neurosci. 1*, 399–406.
(18) Markussen, J., Havelund, S., Kurtzhals, P., Andersen, A. S., Halstrom, J., Hasselager, E., Larsen, U. D., Ribel, U., Schaffer, L., Vad, K., and Jonassen, I. (1996) Soluble, fatty acid acylated insulins bind to albumin and show protracted action in pigs. *Diabetologia 39*, 281–8.
(19) Wartburg, L. (2007) What's Glucose Clamp, Anyway? http://www.diabeteshealth.com/read/2007/11/06/5500/ehats-a-glucose-clamp-anyway/.
(20) DeFronzo, R. A., Tobin, J. D., and Andres, R. (1979) Glucose clamp technique: a method for quantifying insulin secretion and resistance. *Am. J. Physiol. 237*, E214–23.
(21) Hompesch, M., and Rave, K. (2008) An analysis of how to measure glucose during glucose clamps: are glucose meters ready for research? *J. Diabetes Sci. Technol. 2*, 896–8.
(22) Shechter, Y., Tsubery, H., and Fridkin, M. (2003) [2-Sulfo-9-fluorenylmethoxycarbonyl]$_3$-exendin-4-a long-acting glucose-lowering prodrug. *Biochem. Biophys. Res. Commun. 305*, 386–91.
(23) Tsubery, H., Mironchik, M., Fridkin, M., and Shechter, Y. (2004) Prolonging the action of protein and peptide drugs by a novel approach of reversible polyethylene glycol modification. *J. Biol. Chem. 279*, 38118–24.
(24) Richieri, G. V., Anel, A., and Kleinfeld, A. M. (1993) Interactions of long-chain fatty acids and albumin: determination of free fatty acid levels using the fluorescent probe ADIFAB. *Biochemistry 32*, 7574–80.
(25) Arora, S. K. (1971) The crystal and molecular structure of 4-methyl sulfonic acid (p-toluenesulfonic acid) monohydrate, C7H8SO3−.H3O+, an oxonium salt. *Acta Crystallogr., Sect. B 27*, 1293–1298.
(26) Wyckoff, R. (1966) *Crystal Structure*, Vol. *6*, Wiley, New York.
(27) Blundell, T. L., Dodson, G. G., Hodgkin, D. A., and Mercola, D. A. (1972) Insulin: the structure in the crystal and its reflection in chemistry and biology. *Adv. Protein Chem. 26*, 279–403.
(28) Sasson, K., Marcus, Y., Lev-Goldman, V., Rubinraut, S., Fridkin, M., and Shechter, Y. (2010) Engineering prolonged-acting prodrugs employing an albumin-binding probe that undergoes slow hydrolysis at physiological conditions. *J. Controlled Release 142*, 214–20.
(29) Shechter, Y., Preciado-Patt, L., Schreiber, G., and Fridkin, M. (2001) Prolonging the half-life of human interferon-alpha 2 in circulation: Design, preparation, and analysis of (2-sulfo-9-fluorenylmethoxycarbonyl)$_7$-interferon-alpha 2. *Proc. Natl. Acad. Sci. U. S. A. 98*, 1212–7.

Bioconjugate Chemistry

Article

pubs.acs.org/bc

Use of Biotinylated Chitosan for Substrate-Mediated Gene Delivery

Wei-Wen Hu,*[,†] Wun-Jheng Syu,[†] Wen-Yih Chen,[†,‡] Ruoh-Chyu Ruaan,[†,§] Yu-Che Cheng,[§,∥] Chih-Cheng Chien,[§,∥,⊥,#] Chuan Li,[¶] Chih-Ang Chung,[¶] and Chia-Wen Tsao[¶]

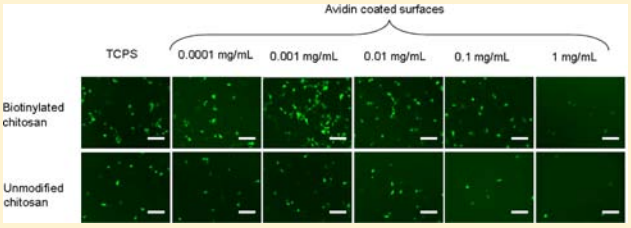
[†]Department of Chemical and Materials Engineering, [‡]Center for Dynamical Biomarkers and Translational Medicine, [§]Institute of Biomedical Engineering, and [¶]Department of Mechanical Engineering, National Central University, Jhongli City, Taiwan

[∥]Department of Medical Research, Cathay General Hospital, Taipei, Taiwan

[⊥]School of Medicine, Fu Jen Catholic University, Taipei, Taiwan

[#]Department of Anesthesiology, Sijhih Cathay General Hospital, Sijhih City, Taipei, Taiwan

ABSTRACT: To improve transfection efficiency of nonviral vectors, biotinylated chitosan was applied to complex with DNA in different N/P ratios. The morphologies and the sizes of formed nanoparticles were suitable for cell uptake. The biotinylation decreased the surface charges of nanoparticles and hence reduced the cytotoxicity. The loading capacities of chitosan were slightly decreased with the increase of biotinylation, but most of the DNA molecules were still complexed. Using different avidin-coated surfaces, the interaction between biotinylated nanoparticles to the substrate may be manipulated. The *in vitro* transfection results demonstrated that biotinylated nanoparticles may be bound to avidin coated surfaces, and the transfection efficiencies were thus increased. Through regulating the N/P ratio, biotinylation levels, and surface avidin, the gene delivery can be optimized. Compared to the nonmodified chitosan, biotinylated nanoparticles on biomaterial surfaces can increase their chances to contact adhered cells. This spatially controlled gene delivery improved the gene transfer efficiency of nonviral vectors and could be broadly applied to different biomaterial scaffolds for tissue engineering applications.



INTRODUCTION

Regenerative gene therapy is a promising strategy for tissue engineering in which therapeutic genes can be delivered to express biological signals to guide tissue repair.[1] Both viral and nonviral vectors can be used for gene transfer. Viral vectors have been applied due to their excellent transduction efficiency. However, the risks of immunogenic response, host reaction, and insertion-caused mutation restrict their application for clinical treatment.[2] In contrast, nonviral vectors, such as cationic polymer and liposome, are synthetic polymer materials which may encapsulate or complex DNA for transportation through the cell membrane. Such vehicles are desired because of their relative safety, low immunogenicity and toxicity, ease of administration and manufacture, as well as lack of DNA size limitation.[3]

Chitosan is a polysaccharide material derived from crustacean shells and composed of *N*-acetyl-D-glucosamine and D-glucosamine monomers linked by β-(1,4) glycosidic bonds. It has been broadly applied for pharmaceutical and drug delivery because of its nontoxicity and tissue compatibility.[4−7] In addition, there are abundant amines in chitosan chains because it is synthesized by deacetylation of chitin. Therefore, chitosan can condense DNA and is a suitable carrier for gene delivery. It also has been reported that chitosan can be applied for siRNA delivery for gene silencing application.[8,9] In addition, chitosan is one of few agents which can be administrated through the oral route for gene transfer.[10] Compared to other frequently used polycationic vectors, such as poly(L-lysine) (PLL) and polyethyleneimine (PEI), chitosan has a relatively low charge density.[11] This property not only enhances the biocompatibility of chitosan, but also reduces its gene transfer ability.[12,13] Different strategies have been developed to improve the transfection efficiency of chitosan. For example, chitosan has been grafted with PEI,[14,15] PLL,[16] or spermine [17] to increase its amine density; however, the grafted pendants may increase the toxicity. Because amino groups of chitosan can be easily reacted for conjugation, different modifications have been developed to improve gene delivery. Cell penetrating peptides (CPP) have been conjugated to chitosan to improve gene internalization efficiency.[18−20] PEGylation and folate modification have been applied to chitosan to improve the water solubility and the specificity of transportation to tumor cells.[21] Chitosan has also been modified with nucleus localization signal (NLS) to increase its nucleus transportation.[22,23] Furthermore, chitosan has been biotinylated to bind different ligands on the outer layer of a polymer/DNA complex for targeting delivery.[24] These results suggested that bioconjugation is accessible to improve and control gene delivery pathway of chitosan.

Substrate-mediated delivery is a useful way to enhance gene transfer efficiency by concentrating gene vehicles on bio-

Received: March 13, 2012
Revised: June 27, 2012
Published: July 9, 2012

 © 2012 American Chemical Society dx.doi.org/10.1021/bc300121y | *Bioconjugate Chem.* 2012, 23, 1587−1599

materials. For example, physical adhesion or chemical conjugation has been applied to localize or immobilize viral vectors on material surfaces.[25,26] These strategies demonstrated that gene delivery can be controlled to *in situ* transduce cells on scaffolds. Because adhered cells can easily contact gene vectors on material surfaces, gene transfer may thus be improved. Consequently, different studies of substrate-mediated delivery have been performed to chitosan. For example, chitosan has been coated on hydroxyapatite nanoparticles to increase its precipitation to the substrate for gene delivery.[27] Layer-by-layer assembly has also been applied to incorporate chitosan/DNA nanoparticles into multilayers with hyaluronic acid (HA) on biomaterial surfaces.[28] Such polyelectrolyte multilayer may further transfect mesenchymal stem cells for differentiation.[29] In addition, chitosan/DNA nanoparticles have been directly coated on stent surfaces for localizing and prolonging transgene expression *in vivo*.[30] These results demonstrate that spatially controlled delivery should improve transfection efficiency of chitosan.

The biotin−avidin interaction is known to be the strongest noncovalent bond.[31] They are highly specific, commercially available, and can be easily linked to different molecules by conjugation. Consequently, we would like to combine bioconjugation and substrate-mediate delivery to improve the transfection ability of chitosan. Chitosan was biotinylated before complexing with DNA, and the formed nanoparticles were immobilized on biomaterial surfaces using biotin−avidin interaction. Although biotin has high specificity to avidin for spatial control, too strong biotin−avidin interaction may retard gene delivery.[32] Therefore, chitosan molecules were biotinylated at different levels to adjust the density of binding ligands. These biotin-modified chitosan molecules were complexed with DNA as nanoparticles in different ratios, and then were immobilized on surfaces coated with different amounts of avidin. By changing the ratio of biotin and avidin moieties on nanoparticles and material surfaces, respectively, the binding forces could be delicately adjusted to stably maintain gene vehicles for cell internalization.

MATERIALS AND METHODS

Plasmid DNA Preparation. Plasmid DNA, pCMV-$\beta$and pEGFP-C3 (Clontech, Mountain View, CA, USA), were used as reporter genes for *in vitro* study. They were cloned and amplified in *Escherichia coli* DH5α. The amplified plasmid DNA was isolated by sodium hydroxide and then was precipitated by PEG purification. Finally, restriction enzyme mapping, polymerase chain reaction (PCR) detection, and DNA sequencing were performed to determine the quality of purified plasmid DNA.

Preparation of Chitosan-DNA Complexes. Chitosans with molecular weight of 10 kDa was purchased from Charming & Beauty Co. (Taiwan). Chitosan and DNA were both dissolved in 20 mM sodium acetate buffer, and the final pH 5.0 was adjusted by 0.2 N NaOH. To control the charge ratio between chitosan and DNA, chitosan was used to complex with DNA in different ratios of amino groups to phosphate groups (N/P ratios). The concentration of DNA was fixed to 0.05 g/L, and the concentrations of chitosan varied according to the required N/P ratios. Equal volumes of both solutions were mixed together and vortexed for 10 s, and were then incubated at room temperature for 30 min before experiments.

Biotinylation of Chitosan. To immobilize chitosan vehicles on material surfaces using biotin−avidin interaction, SulfoNHS-LC-Biotin (Pierce, Rockford, IL, USA) was applied to biotinylate chitosan molecules. Different molar ratios of SulfoNHS-LC-Biotin to amine groups of chitosan from 0.01 to 1 were used for modification, which were denoted as B0.01 to B1 in the following description. First, SulfoNHS-LC-Biotin was dissolved in PBS, and then was reacted with chitosan for 3 h at room temperature. Unreacted SulfoNHS-LC-Biotin molecules were removed by dialysis, and the level of biotinylation was quantified by HABA (2-(4-hydroxyazobenzene) benzoic acid, HABA) assay.[26] Briefly, the HABA solution was prepared by adding 6 μmol of HABA and 5 mg of avidin to 10 mL of PBS, which had an absorption at wavelength of 500 nm.[33] This absorption decreased proportionally when biotin was added due to high affinity of biotin to avidin. The changes of OD 500 nm before and after adding biotinylated chitosan were compared to determine the grafted biotin on chitosan molecules. The conjugation efficiencies were defined as the molar ratios of SulfoNHS-LC-Biotin molecules added in the reaction to the biotin moieties grafted on chitosan molecules.

Physical Properties of Chitosan-DNA Complexes. To determine the zeta potentials and the size distribution of nanoparticles, dynamic light scattering (DLS) analysis was performed using Zetasizer Nano ZS (Malvern, Worcestershire, UK). The size distribution was measured by photon correlation spectroscopy at a 173° scattering angle. Three measurements were performed for each sample to confirm that the record was reliable, and the mean hydrodynamic diameter was generated by cumulative analysis. The zeta potential was performed by laser Doppler anemometry. The samples were placed in a disposable capillary cell, and the electrophoretic mobility was measured to determine the zeta potential of nanoparticles.

Complexation Efficiency of Chitosan to DNA. The loading capacity of chitosan to DNA was analyed by ethidium bromide (EtBr) displacement assay and gel retardation assay. About EtBr displacement assay, DNA was dissolved in 20 mM sodium acetate buffer (pH = 5.0) with final concentration of 0.05 mg/mL and was mixed with EtBr (DNA base:EtBr (mol) = 200:1). The EtBr/DNA solution was mixed with equal volume of biotinylated chitosan and then was vortexed for 10 s. After 30 min incubation at room temperature, 100 μL samples were placed in 96-well microplates and measured by fluorescence spectroscopy (Synergy H1m, Biotek, Winooski, VT, USA). The excitation and emission wavelengths were 511 and 603 nm, respectively. For gel retardation assay, nanoparticles were loaded in 1% agarose gels to perform electrophoresis at 100 V for 40 min and were stained by EtBr.

Integrity Assay of DNA/Chitosan Nanoparticles. The protection efficiency of chitosan to complexed DNA was evaluated by deoxyribonuclease I (DNase I) digestion assay. Nanoparticles (20 μL) were mixed with 5 μL of DNase I (Sigma-Aldrich, St. Louis, MO, USA) and were incubated at 37 °C for 30 min. To terminate the activity of DNase I, 10 μL of 0.2 M EDTA was added and was heated to 68 °C for 15 min. Furthermore, to release the complexed DNA from nanoparticles, 1 μL of chitosanase (Merck, Germany) was added to nanoparticles at 37 °C for 1 h. Finally, the sample was loaded to 1% agarose for electrophoresis analysis.

***In Vitro* Studies for Transfection.** Both pCMV-β and pEGFP-C3 were delivered in this study. Chitosan with different levels of biotinylation was used to complex with 0.8 μg of pCMV-β DNA in different N/P ratios for gene delivery. Human embryonic kidney cell line (HEK-293T) was used to evaluate gene transfer efficiency. Nanoparticles were loaded to

96-well multiplates for 2 h before cell seeding. The transfection medium was DMEM with 10% FBS (pH = 6.5), which was replaced by normal culture medium (DMEM with 10% FBS, pH = 7.0) after 20 h.[34] The transgene efficiency was evaluated after 48 h of transfection. For pCMV-β delivery, the gene expression was quantified by the activity of β-galactosidase. Medium was removed and 40 μL of 0.25 M Tris-HCl was added following freeze/thaw cycles to lyze cells. Then, 20 μL of cell lysis was reacted with *ortho*-nitrophenyl-β-D-galactopyranoside (ONPG) for substrate analysis. To normalize the ONPG results, the other 20 μL of sample was used for protein quantification by BCA kit (Pierce, Rockford, IL, USA). The expression of pEGFP-C3 was determined by fluorescent microscopy (Eclipse Ti−U, Nikon, Japan).

Preparation of Avidin-Coated Surfaces. Avidin (Pierce) was dissolved in PBS in different concentrations, and was added in 96-well ELISA plates (Corning, Lowell, MA, USA) at volume of 100 μL per well. After overnight incubation at 4 °C, well surfaces were washed by PBS and then were used to immobilize biotinylated nanoparticles. To determine levels of avidin coated on the surfaces, alkaline phosphatase (biotin-AP; Pierce) was used to illustrate the avidin binding sites. Botin-AP was diluted in PBS and was added to the plates at volume of 100 μL/well for 1 h. After three washes in PBST, the surfaces were developed by 100 μL of *p*-nitrophenyl phosphate (pNPP) substrate for 20 min before being read spectrophotometrically at OD 405 nm.

Cytotoxicity and Relative Viability Analysis of Biotinylated Nanoparticles. To investigate the extent to which nonviral vectors affected cell physiology during transfection, 3-(4,5-dimethylthiazol-2-yl)-5-(3-carboxymethoxyphenyl)-2-(4-sulfophenyl)-2*H*-tetrazolium (MTS) and lactate dehydrogenase (LDH) assays were performed to determine relative cell viability and relative cytotoxicity, respectively. After 48 h of transfection, 20 μL of CellTiter 96 AQueous kit (Promega, Madison, WI, USA) was added per well and incubated at 37 °C for 1 h, then read spectrophotometrically at wavelength of 490 nm. The LDH assay was performed by LDH kit (CytoTox 96 Nonradioactive Cytotoxicity assay, Promega), then the sample analyzed spectrophotometrically at a wavelength of 490 nm.

RESULTS

Biotinylation of Chitosan. To specifically immobilize chitosan/DNA nanoparticles on material surfaces, biotin moieties were conjugated to amine groups of chitosan using biotinylation reagent, SulfoNHS-LC-biotin. Different molar ratios of SulfoNHS-LC-Biotin to amine groups of chitosan from 0.01 to 1 were used to control the level of biotinylation, and were denoted as B0.01 to B1. The conjugation efficiencies were evaluated by HABA assays (Figure 1). Although the conjugation efficiencies decreased with the increase of the concentrations of Sulfo-NHS-LC-biotin (from 57% to 12%), the levels of biotinylation increased with the number of moles of Sulfo-NHS-LC-biotin (from 0.302 to 5.230 biotin moieties per chitosan molecules). These results suggest that the molar ratio of biotin to chitosan could be adjusted by simply controlling the concentration of biotinylation reagent.

Physical Properties of Biotinylated Chitosan/DNA Complex Nanoparticles. Chitosan with different levels of biotinylation was used to complex with DNA in different N/P ratios. Their zeta potentials and sizes were analyzed to determine the surface charges and the diameter distribution, respectively. Increasing the N/P ratio raised the zeta potential

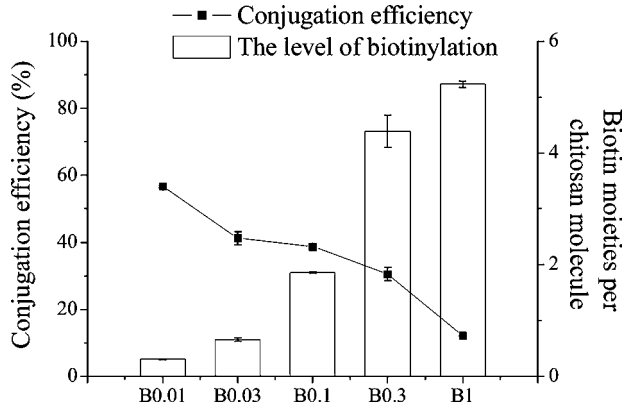


Figure 1. Biotinylation of chitosan using different concentrations of SulfoNHS-LC-biotin. Chitosan was biotinylated in different mole ratios of SulfoNHS-LC-biotin to amine moieties of chitosan. The conjugation efficiency (line) was defined as the number of moles of SulfoNHS-LC-biotin to the grafted biotin moieties on chitosan molecules, which was measured by HABA assay. The level of biotinylation was also compared, which was the average number of biotin moieties grafted per chitosan molecule (bar).

of chitosan/DNA complexes due to there being more chitosan molecules per nanoparticle (Figure 2a). Except DNA, which has negative zeta potential due to its phosphate groups, all chitosan/DNA groups demonstrated positive surface charge and that the zeta potentials were between 20 and 35 mV, indicating that these nanoparticles should be able to be applied for gene delivery. The zeta potential of nanoparticles decreased with the increasing level of biotinylation, suggesting that the conjugation of biotin moieties reduced amine groups of chitosan molecules, thus leading to declining positive charge of nanoparticle surfaces (Figure 2b). Interestingly, the B0 group was always the group with highest zeta potential except for the N/P ratio of 30 (Figure 2b). This may be because biotin moieties shielded the charge interaction between chitosan and DNA, and hence, more chitosan molecules were required to adhere on the surface of nanoparticles, which resulted in higher zeta potentials of biotinylated chitosan groups than that of the nonmodified group (B0) at N/P = 30.

The size distribution was determined by DLS analysis. Naked DNA had a diameter of 67.0 nm, and all of the nanoparticles demonstrated larger diameters than that of the naked DNA. For the nonmodified group (B0), nanoparticle sizes increased with the increase of N/P ratio (Figure 2c). It may be because using more chitosan increased the amount of chitosan molecules per nanoparticle, hence enlarging the nanoparticles. However, this trend was not significant for the biotinylated chitosan groups. Most of the particle sizes were between 66.8 and 109.8 nm. Only the B1 group at N/P ratio of 2 exhibited an unusually large particle size (578 nm), which also demonstrated a cloudy appearance. It was consistent with its weak zeta potential that aggregation may occur without forming stable nanoparticles.

To confirm the size distribution analysis by DLS, scanning electron microscopy (SEM) was also performed. Different chitosan groups from B0 to B1 were used to complex with DNA at N/P ratio of 10 (Figure 3). The SEM result suggested that the sizes of the B0, B0.01, B0.03, B0.1, B0.3, and B1 groups were in the range 50−90 nm, 70−80 nm, 40−100 nm, 40−100 nm, 70−100 nm, and 70−90 nm, respectively. These results were consistent with the results of DLS analysis (B0, 88.9 nm;

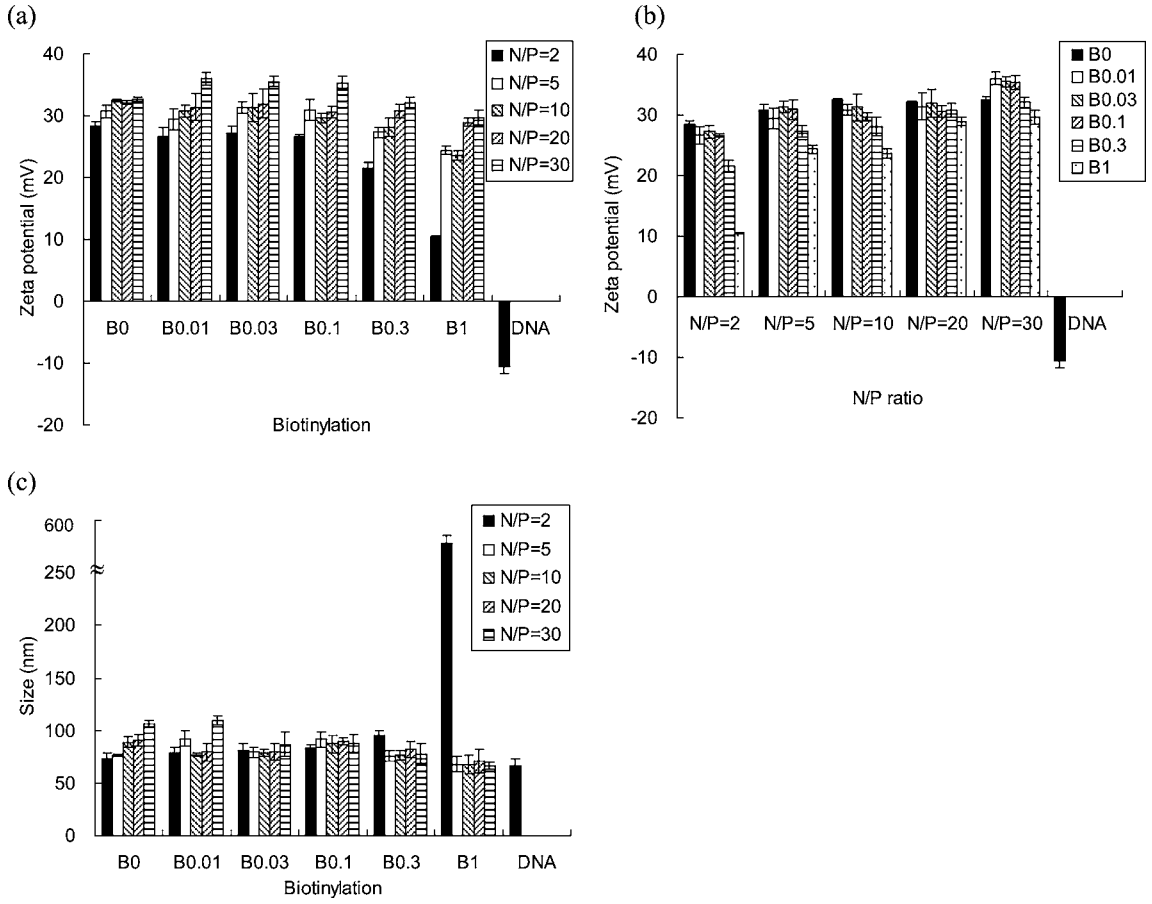


Figure 2. Dynamic light scattering assay for determining the surface charges and size distributions of nanoparticles. The zeta potentials of chitosan/DNA nanoparticles were compared in different (a) N/P ratios and (b) biotinylations. (c) Their sizes were also determined. The control group DNA was naked DNA only.

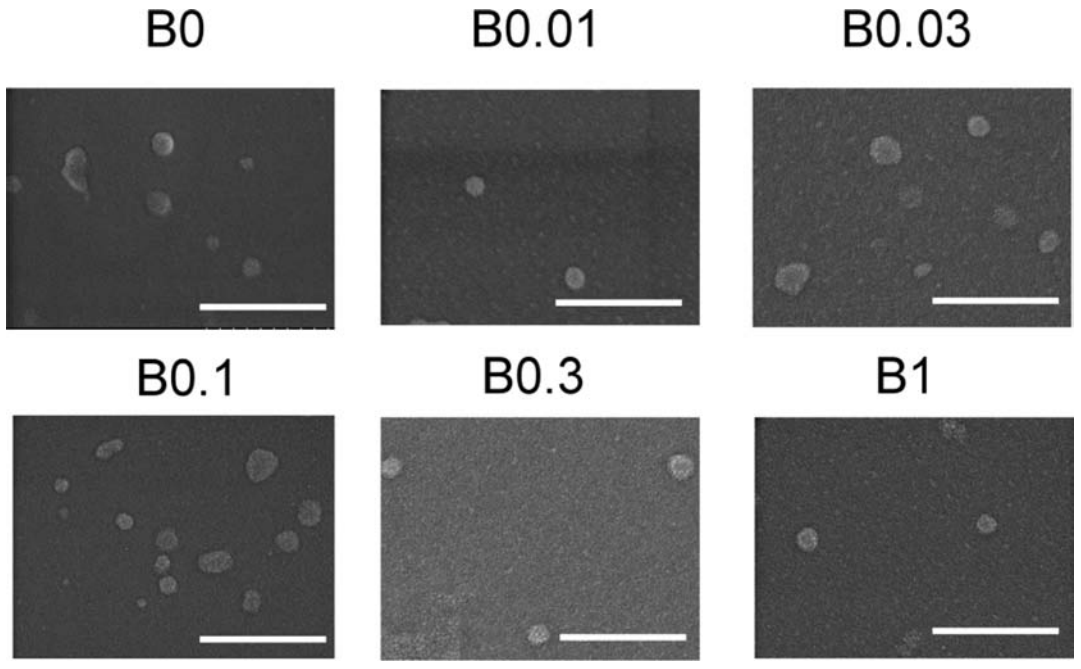


Figure 3. Scanning electron microscopy images of biotinylated chitosan/DNA nanoaprticles. Chitosans with different biotinylations were used to complex with DNA in N/P ratio of 10. The nanoparticles formed were illustrated by SEM to determine their morphologies and size distribution. The scale bar in each picture was 500 nm.

dx.doi.org/10.1021/bc300121y | *Bioconjugate Chem.* 2012, 23, 1587−1599

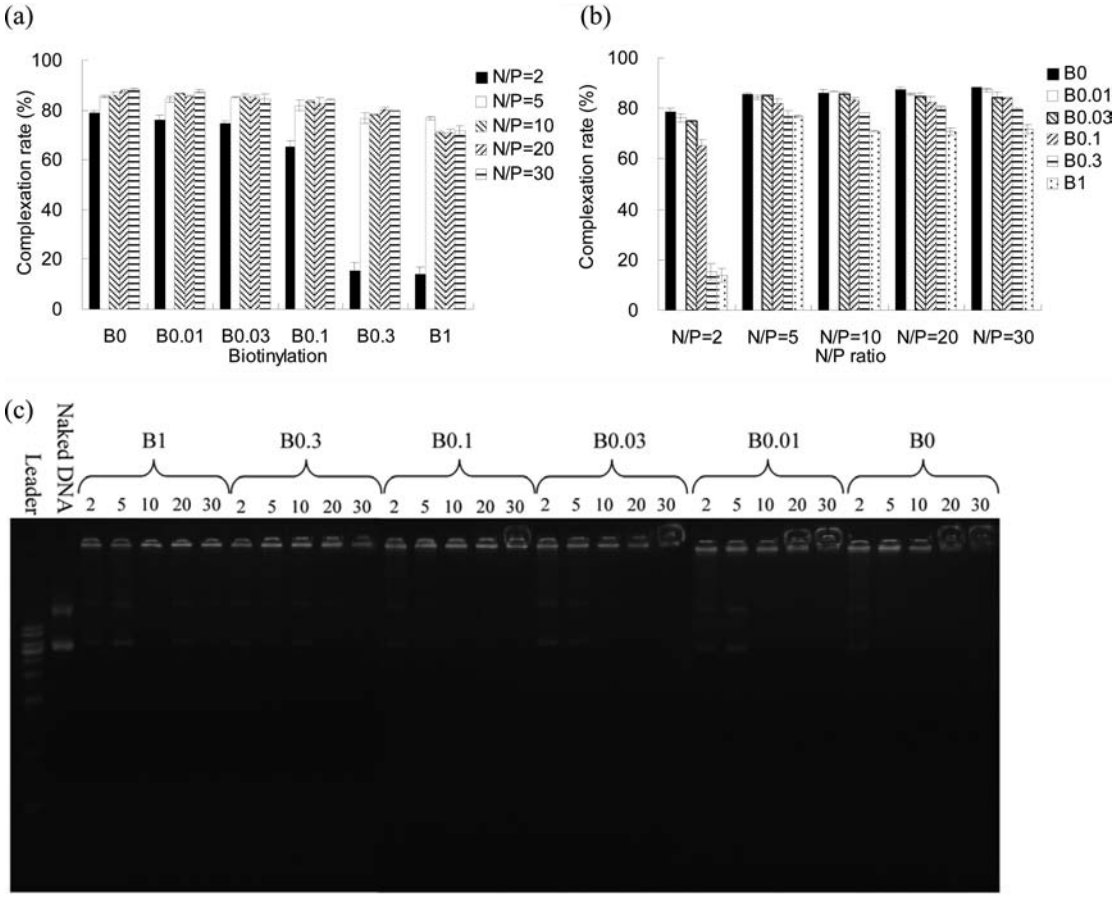


Figure 4. Complexation efficiency of biotinylated chitosan. DNA was stained by EtBr before complexing with chitosan. The intensity of fluorescence was compared before and after nanoparticle formation to determine the complexation efficiency of chitosan at different (a) N/P ratios and (b) biotinylation. (c) Chitosan with different biotinylation was complexed with DNA at different N/P ratios, and was loaded to agarose gel for electrophoresis analysis.

B0.01, 76.7 nm; B0.03, 78.5 nm; B0.1, 87.0 nm; B0.3, 76.0 nm; and B1, 67.5 nm) (Figure 2c). It suggested that DLS results were reliable. In addition, chitosan with or without biotinylation can complex with DNA to display a spherical appearance, suggesting that nanoparticle formation should be accessible after biotin modification.

Effect of Biotinylation on the Complexation Efficiency of Chitosan to DNA. Ethidium bromide (EtBr) is a compound which can intercalate between the base pairs of the DNA double helix, and the DNA-EtBr complex shows high fluorescence activity.[35] When DNA was bound by the cationic polymer, EtBr would be expelled from the DNA-EtBr complex.[36,37] Therefore, the DNA loaded by chitosan led to a decrease in fluorescence. The complexation rates of nanoparticles varied with the N/P ratios and the levels of biotinylation. Higher N/P ratio groups had more chitosan to adsorb DNA, and thus caused better complexation efficiency (Figure 4a). Most of the groups had lower complexation rates when the N/P ratio was 2, and there were almost no significant differences in loading capacities at N/P ratios higher than 5, indicating that the chitosan molecules at this ratio should be saturated for complex formation. On the other hand, the biotinylation used up positive amines and hence reduced the attracting force to DNA, causing lower complexation efficiency (Figure 4b). Most of the complexation rates can be higher than 65% except the groups of N/P = 2 and biotinylation ratios of 0.3 and 1, which only had complexation rates less than 20%. This suggested that high biotinylation may retard the electrostatic affinity of chitosan to DNA, and this phenomenon was more obvious when the chitosan molecules were insufficient.

Gel retardation assay was also analyzed to confirm the results of chitosan complexation efficiencies (Figure 4c). Chitosan/DNA nanoparticles were formed and loaded to agarose gels to perform electrophoresis. Because the negatively charged DNA was shielded by chitosan, only unloaded DNA may move down in the electrical field and be separated from the complex. Therefore, nanoparticles formed from chitosan/DNA complex were retained in the loading wells. For the nonmodified B0 group, there was some free DNA at N/P ratio of 2, suggesting that chitosan molecules were insufficient to complex DNA. In contrast, DNA was completely loaded when N/P ratio was higher than 2. The bands in the well even moved in the opposite direction to the free DNA when N/P ratio was larger than 10. This should be because free chitosan molecules may become entangled with nanoparticles so that their positive charges eventually moved DNA/chitosan complexes to the cathode. The results of the B0.01 to B0.1 groups were similar to those of the B0 group except that some released DNA was found at N/P ratio of 5, suggesting that biotinylation should reduce the charge density, which further reduced the stability of complex to maintain DNA in the well. The diffusion of nanoparticles to the cathode occurred only at N/P ratio of 30 for the B0.1 group. It should be because the increasing

dx.doi.org/10.1021/bc300121y | *Bioconjugate Chem.* 2012, 23, 1587−1599

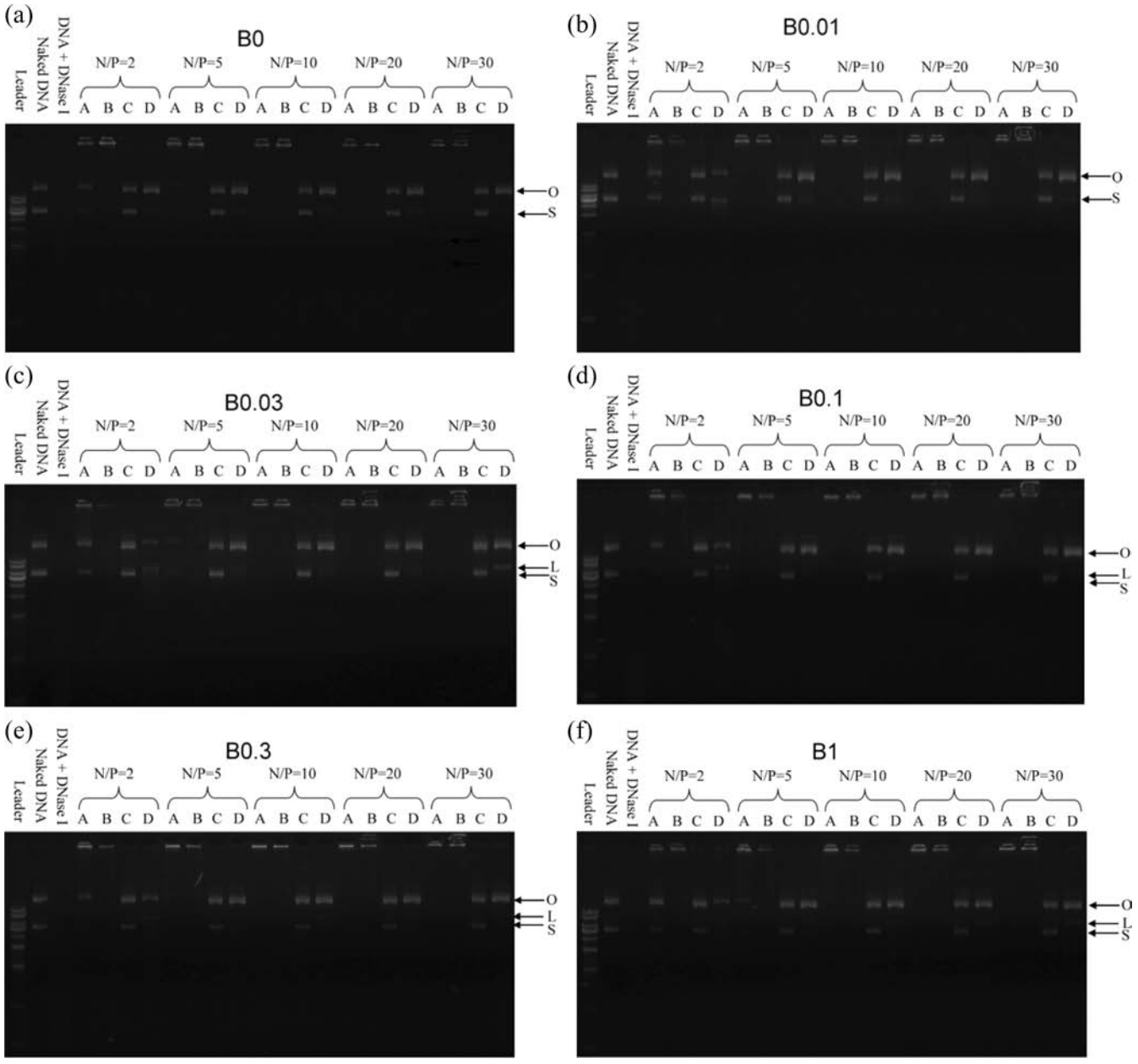


Figure 5. Protection Assay of Biotinylated Chitosan to DNA. Chitosan with biotinylation of (a) B0; (b) B0.01; (c) B0.03; (d) B0.1; (e) B0.3; (f) B1 was complexed with DNA in various N/P ratios. Different treatments were performed before electrophoresis analysis: (A) nontreatment; (B) nanoparticles treated with DNase I for 30 min and then inactivated; (C) nanoparticles treated with chitosanase; (D) nanoparticles treated with DNase I for 30 min, inactivated, and then treated with chitosanase. The labels at the right sides of the gels were to indicate DNA in open-circular (O), linear (L), or supercoiled (S) forms.

biotinylation decreased the charge density, and thus, the driving forces of positive chitosan molecules to move nanoparticles to the cathode were reduced. As the level of biotinylation increased to B0.3, there was no diffusion of nanoparticles to the cathode, and some free DNA was found when the N/P ratio was less than 30. The loading efficiency of the B1 group further declined so that free DNA was found even when the N/P ratio was 30.

Protection Assay of Botinylated Chitosan to DNA. DNA loaded to chitosan carrier can be shielded from enzymatic digestion.[38] However, because biotinylation used up amine groups of chitosan, it probably affected the protection ability of nanoparticles for *in vivo* application. Therefore, a protection assessment was applied using DNase I digestion to determine the extent to which the complexed DNA may be attacked.[39,40] Chitosan molecules with different levels of biotinylation were complexed with DNA at various N/P ratios. These nanoparticles were treated four different ways and then were analyzed by electrophoresis (Figure 5). Nanoparticles in the A treatment were the nontreated groups; the B treatment was the nanoparticles treated with DNase I for 30 min and then inactivated. The C treatment was the nanoparticles only treated with chitosanase, and the D treatment was the nanoparticles treated with DNase I for 30 min, which were inactivated and then treated with chitosanase. The A treatment was used to illustrate nonloaded free DNA. The B treatment was used to determine if DNase I may destroy the construction of nanoparticles. The C treatment was used to release the loaded

DNA, and the D treatment was used to confirm the integrity of the loaded DNA after the DNase I treatment.

For the nonmodified B0 group, only DNA was released at the N/P ratio of 2 (Figure 5a). The B treatment demonstrated that only the released free DNA was digested by DNase I, whereas the brightness of the DNA/chitosan complex staying in the loading well was almost identical to it in the A treatment. The D treatment results indicated that DNase I digestion made the composition of DNA within the nanoparticles a little different from DNA directly released by chitosanase in the C treatment. The band of supercoiled DNA was slightly reduced, but the band of the open circular DNA was increased. However, the total amounts of these two bands in these two treatments were almost equal, and linear DNA was not found in all N/P ratios. Compared to open circular DNA, supercoiled DNA has a complicated conformation, which may inhibit chitosan from completely warping DNA around. Therefore, DNase I may react with the unprotected part of the DNA/chitosan complex to relax DNA to an open circular form. However, the conformation of circular DNA is looser than in the supercoiled form, which made the adsorption of chitosan easier than with supercoiled DNA, and thus the protection of chitosan was able to avoid further digestion.

There was a similar trend of the B0.01 group to the nonmodified chitosan (Figure 5b). Only N/P ratio less than 10 displayed free DNA release, which was digested by DNase I, and the biotinylated chitosan may protect circular plasmid DNA from DNase I digestion. However, the integrity of nanoparticles became reduced when the biotinylation increased. The bands of supercoiled DNA disappeared after DNase I treatment for B0.03−B1 groups, which was seen along with the appearance of linear DNA bands (Figure 5c−f). These results suggest that increasing biotinylation may reduce the electrostatic forces between DNA and chitosan; the wrapped polycation was not strong enough to protect DNA from enzymatic digestion.

Biocompatibility of Biotinylated Chitosan/DNA Nanoparticles. To ensure that the biotinylation does not negatively affect the physiology of the tranfected cells, it is necessary to determine the biocompatibilities of nanoparticles. Two assessments, LDH and MTS assays, were applied to evaluate cytotoxicity and cell viability, respectively.

For the LDH assay, there were no obvious trends of cytotoxicity for different N/P ratios and biotinylations; all of the nanoparticles exhibited relative cytotoxicities between 70% and 130% (Figure 6a). In contrast, the Lipofectamine group caused severe cell death that the relative cytoxicity was 2.5 times more than that of the untreated group. These results suggested that chitosan was a biocompatible material which is suitable for gene delivery application, and the biotinylation did not increase cytotoxicity to the transfected cells.

In the MTS assay, the cells treated with naked DNA were used as a control group, for which the viability was defined as 100%. The absorbance of experimental groups at 490 nm was compared to that of the control group to determine the relative viability, and the Lipofectamine 2000 transfection was used as the positive group (Figure 6b). For the nonmodified B0 group, the cellular viabilities decreased with the increasing N/P ratios. This should be because the increase of chitosan molecules increased positive charges, which interfered with cell physiology through the interaction/disruption of cellular organelles including mitochondria.[41] Similar trends were found at the B0.01 and B0.03 groups, suggesting that the low level of

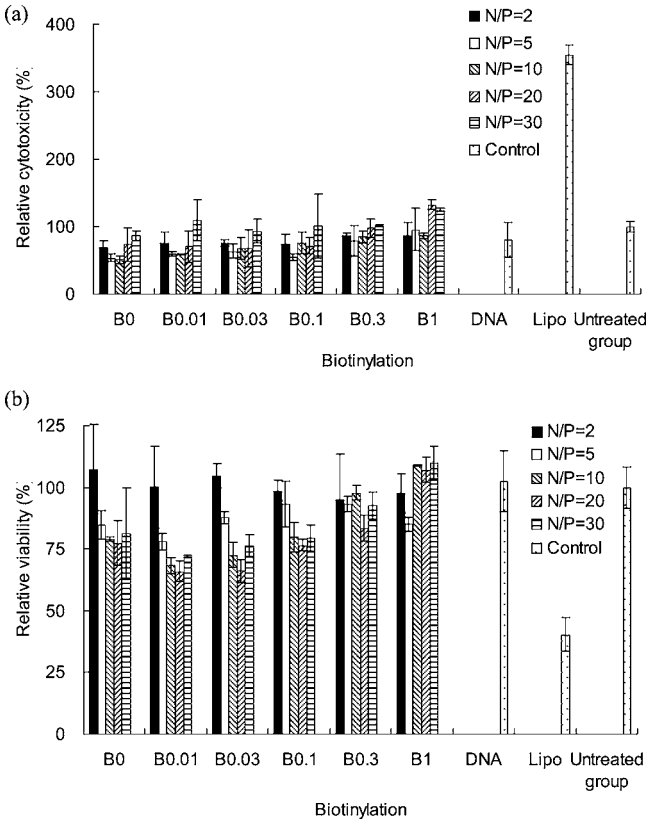


Figure 6. Biocompatibility of biotinylated nanoparticles. Nanoparticles formed by chitosan with different biotinylation in different N/P ratios were applied to transfect HEK 293T cells for 2 days. (a) The relative cytotoxicity of nanoparticles was evaluated by the LDH assay. (b) The relative viability of trasnfected cells was determined by the MTS assay. These spectrometric results were normalized by comparing with the untreated group. Lipofectamine 2000 (Lipo) was used as the positive control in both analyses.

biotinylation did not affect the cellular bioactivity. However, the viabilities of the high N/P ratios were improved when the level of biotinylation was higher than B0.03. There were no significant differences of bioactivity between different N/P ratios for the B0.3 and B1 groups; almost all of the viabilities were close to 100%. Our zeta potential results have demonstrated that the biotinylation used up amines and thus decreased the positive charges (Figure 2b). Therefore, the interference of charge with organelles may thus be reduced, which rescues cells from the cytotoxicity of the polycation.

Transfection Efficiency of Biotinylated Chitosan/DNA Nanoparticles. Chitosan with different levels of biotinylation was complexed with DNA at different N/P ratios to examine the transfection ability of these nanoparticles on tissue culture polystyrene (TCPS) (Figure 7a). For the nonmodified B0 group, the N/P ratio of 5 exhibited highest LacZ gene expression. When the level of biotinylation increased to B0.1, the N/P ratio of the best transfection shifted to 10. The zeta potential results indicated that the positive charges were reduced with the increase of biotinylation (Figure 2b), and thus the electrostatic forces between DNA and chitosan were weakened so that more chitosan molecules were required to increase the charge density for transfection. In addition, the increasing biotinylation improved transfection ability of nanoparticles (Figure 7a). It should be relative to the increasing viability that biotinylation may reduce the damage caused by

dx.doi.org/10.1021/bc300121y | Bioconjugate Chem. 2012, 23, 1587−1599

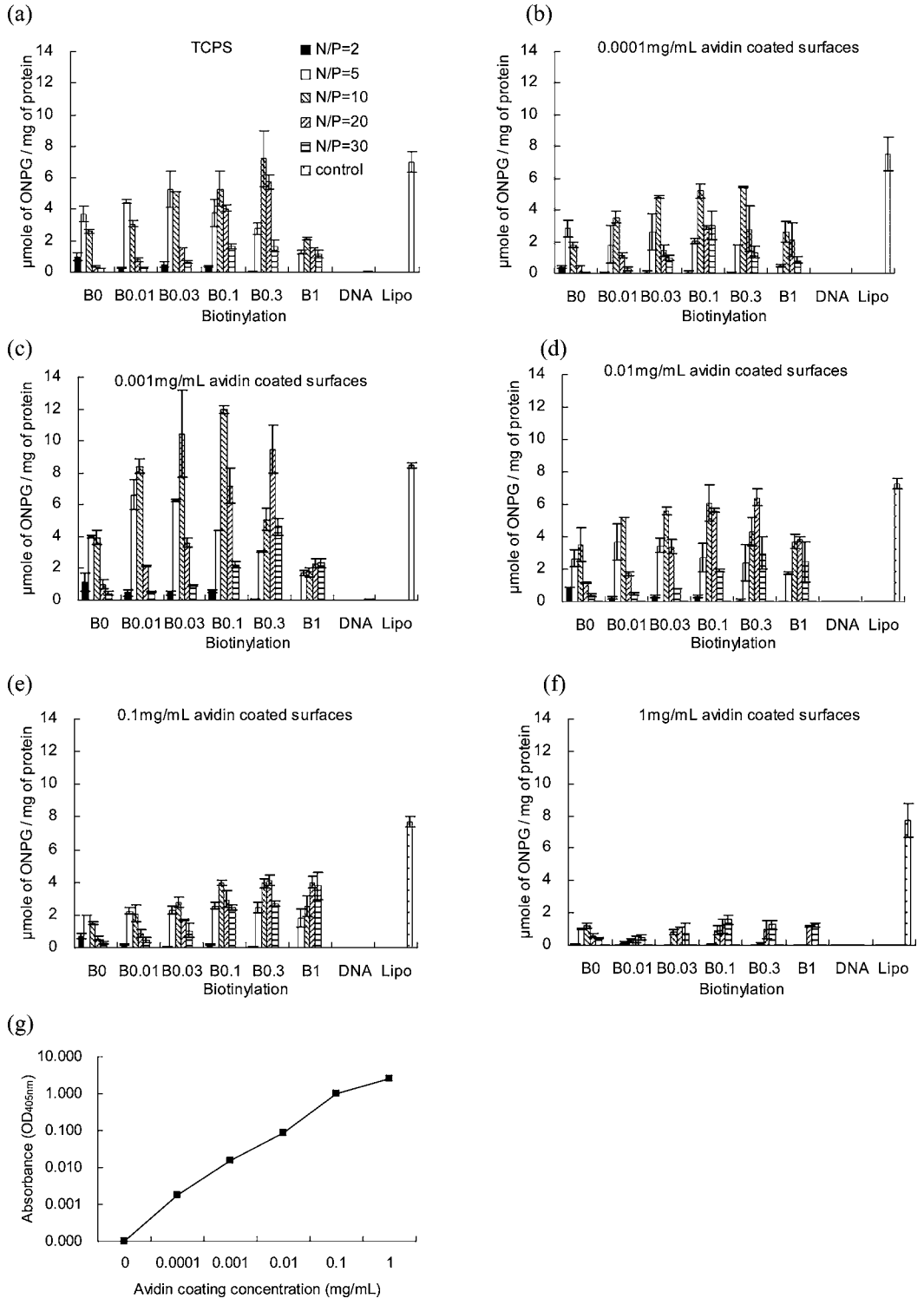


Figure 7. *In vitro* transfection efficiency of biotinylated chitosan/DNA nanoparticles. Nanoparticles formed by chitosan with different biotinylation at different N/P ratios were applied to transfect HEK 293T cells for 2 days on (a) TCPS or surfaces coated with avidin solution of concentrations of (b) 0.0001 mg/mL, (c) 0.001 mg/mL, (d) 0.01 mg/mL, (e) 0.1 mg/mL, and (f) 1 mg/mL. The expression of β-galactosidase was determined by ONPG substrate, which was normalized by total protein amount. Naked DNA (DNA) only was used as the negative control group, and the Lipofectamine 2000 (Lipo) delivery was used as the positive control group. (g) Coated avidin on multiple plates was analyzed by biotin-AP labeling, which was developed by substrate pNPP and was read spectrophotometrically at OD405.

the positive charges and thus enhance the cellular activity, which facilitated the expression of the transgene (Figure 6b). However, when the biotinylation increased to B1, the transfection efficiency was reduced. The complexation experiments demonstrated that the loading capacity of DNA at the B1 group was significantly lower than that of the other groups, which may thus reduce the transfection efficiency (Figure 4b).

***In Vitro* Transfection Regulated by Biotin/Avidin Interaction.** Because the biotinylated nanoparticles demonstrated a successful transfection, these groups were applied to

dx.doi.org/10.1021/bc300121y | *Bioconjugate Chem.* 2012, 23, 1587−1599

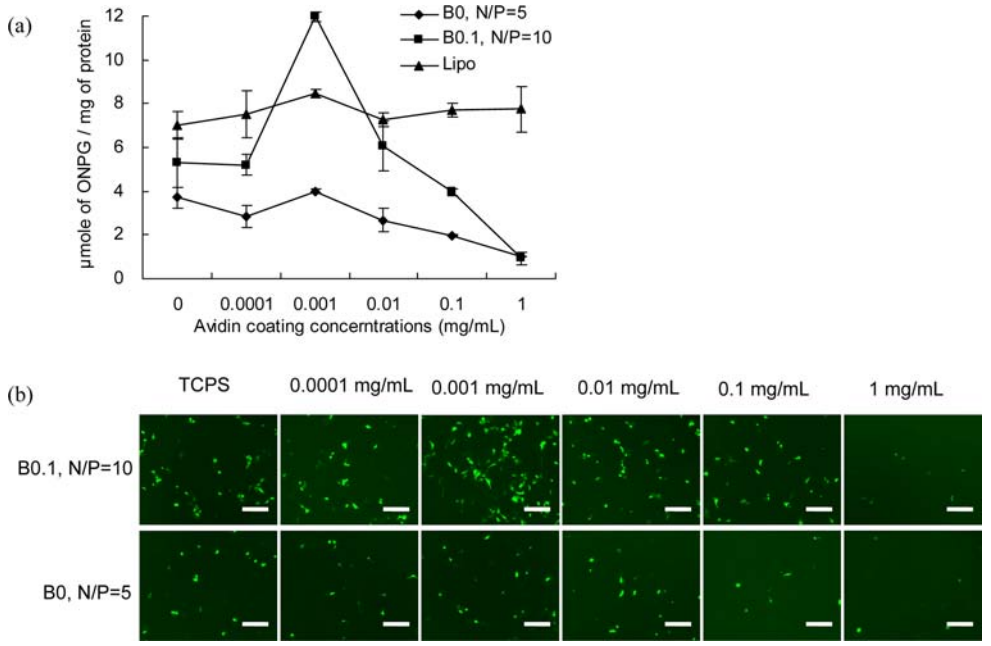


Figure 8. Transfection efficiencies of biotinylated chitosan on avidin-coated surfaces. Nanoparticles formed by biotinylated chitosan (B0.1, N/P = 10, square) and nonmodified chitosan (B0, N/P = 5, diamond) were used to transfect HEK 293T cells on surfaces coated with different concentrations of avidin. (a) Plasmid pCMV-β was delivered, and the expression of β-galactosidase was determined by ONPG substrate, which was normalized by total protein amount. The Lipofectamine 2000 (Lipo) delivery was used as the positive control group (triangle). (b) Plasmid pEGFP-C3 was delivered and the expression of eGFP was evaluated by fluorescent microscopy (scale bar = 200 μm).

avidin-modified surfaces to determine if biotin−avidin interaction may facilitate substrate-mediated gene delivery. To regulate the binding forces of avidin to biotinylated chitosan/DNA nanoparticles, different concentrations of avidin were used for coating on ELISA plates from 0.0001 to 1 mg/mL. Biotin-AP was used to evaluate the binding sites of coated avidin on the plates. The absorbance of 405 nm revealed that the surface-coated avidin was increased with increasing concentrations of avidin (Figure 7g). For the lowest avidin-coated surface (0.0001 mg/mL), the transfection efficiencies were slightly reduced in comparison to the results at TCPS only (Figure 7a,b). Because the ELISA plates were not suitable for cell attachment and growth, the tough environment may negatively affect cell transfection. In addition, the best N/P ratios were shifted from 5 to 10 for B0.01 and B0.03 groups compared to that in TCPS (Figure 7a,b). It may be because nanoparticles with N/P ratio of 10 had more biotin moieties than that of 5, and thus more biotinylated particles were maintained on surfaces with even a low level of coated avidin to facilitate transfection.

When the level of avidin coating increased to 0.001 mg/mL, the transfection efficiencies were highly improved (Figure 7c). The ONPG result of the best transfection group (B0.1) was 11.97 μmol/mg of protein, which was double that at TCPS (5.31 μmol of ONPG/mg of protein) (Figure 7a,c), suggesting that biotin modification may increase retention of nanoparticles on the substrate and thus improve transfection efficiencies. In addition, the B0.3 group exhibited a reduced transfection at the N/P ratio of 10, while expression was improved when the N/P ratio increased to 20. This should be because B0.3 had more biotin moieties, and thus the binding affinities became large, which retarded the cell uptake. In contrast, when the N/P ratio shifted to 20, more free biotinylated chitosan molecules existed in the system which may compete with biotinylated nanoparticles for the binding sites of surface avidin. Consequently, the binding affinity of nanoparticles to the surfaces was thus reduced, which may further enhance the uptake of cell to gene.

As the avidin coating increased to 0.01 mg/mL, the transfection results were not as good as those at the 0.001 mg/mL avidin-coated surface (Figure 7d), which may be because the high density of avidin provided more biotin binding sites, thus hindering nanoparticle release for transfection. Interestingly, the transfection of the B1 group was better than that at surfaces with lower avidin coating. Because the B1 groups had a loose interaction between DNA and biotinylated chitosan, DNA may release from nanoparticles and complex with free biotinylated chitosan molecules in the solution for cell transfection, which thus rescued the difficulty due to too-strong biotin−avidin interaction. When the avidin coating kept increasing to 0.1 mg/mL, the high affinity of avidin to biotinylated nanoparticles obstructed gene transfer so that the transfection efficiencies were negatively affected (Figure 7e). The trend was more obvious when the coating concentration increased to 1 mg/mL so that almost all of the groups exhibited an extremely low level of transgene expression (Figure 7f).

The transfection results on different surfaces indicated that biotinylation indeed enhanced the transfection efficiency, and the best formula was at B0.1 with N/P of 10 (Figure 7). To systemically determine the effect of biotinylation to gene delivery, the transfection efficiencies of biotinylated nanoparticles, nonmodified nanoparticles, and the positive group (Lipofectamine 2000) were compared on different avidin-coated surfaces (Figure 8a). The results demonstrated that biotinylated groups always have better transfection than nonmodified groups, which may result in higher bioactivity of biotinylated chitosan (Figure 6b). The best transfection result of biotinylated nanoparticles was at 0.001 g/mL of avidin coating concentration in which the expressed β-galactosidase resulted in 12 μmol of ONPG converted per mg of protein, which was almost 3 times more than that of the nonmodified

dx.doi.org/10.1021/bc300121y | *Bioconjugate Chem.* 2012, 23, 1587−1599

group, suggesting that specifically immobilized nanoparticles may increase the chance to contact adhered cells and enhance gene delivery. However, higher coated avidin caused stronger binding affinity, which further diminished the transfection ability of biotinylated nanoparticles. The transfection efficiencies of nonmodified nanoparticles were also reduced when they were applied to surfaces with high concentration of coated avidin (0.1 and 1 mg/mL), which may result in nonspecific binding of a high level of surface protein. Although the transfection of both biotinylated and nonmodified nanoparticles were highly affected by the surfaces, there was no difference to the Lipofectamine group. This should contribute to their different transfection mechanisms in which Lipofectamine 2000 is a liposomal transfection reagent, while chitosan/DNA complexes are nanoparticles fabricated by electrostatic forces. Therefore, liposomes may be released from the substrate even if partial molecules of it are adsorbed on the surface. The integrity of the liposome may recover easily and thus still have the ability for transfection. Another plasmid DNA, pEGFP-C3, encoding enhanced green fluorescent protein (eGFP) was also applied to compare their delivery by modified and nonmodified nanoparticles on different avidin-coated surfaces and TCPS (Figure 8b). The green fluorescence expression of transfected cells illustrated similar trends to the pCMV-β results, suggesting that our developed method should be able to be applied to different plasmid DNA.

Previous experiments were based on 0.8 μg of pCMV-β delivery. To investigate the extent to which the biotinylation method may improve transfection, different dosages of DNA were applied for cell transfection. The expression of β-galactosidase was dose dependent on the amount of DNA, and the expressions were saturated when the DNA amounts were 0.8 and 1.6 μg for the nonmodified and biotinylated nanoparticles, respectively (Figure 9). Compared to the nonmodified nanoparticle (B0, N/P = 5 at TCPS), which may only achieve the expression of 3 μmol of ONPG/mg of protein, biotinylated nanoparticles (B0.1, N/P = 10 at 0.001 mg/mL avidin) demonstrated an excellent transfection efficiency so that the expression level was almost 6 times higher than that of the nonmodified group when the DNA was 1.6 μg. These results suggest that our biotinylation method could significantly enhance gene delivery compared to the conventional method, so the drawback of low transfection efficiency of chitosan should thus be improved.

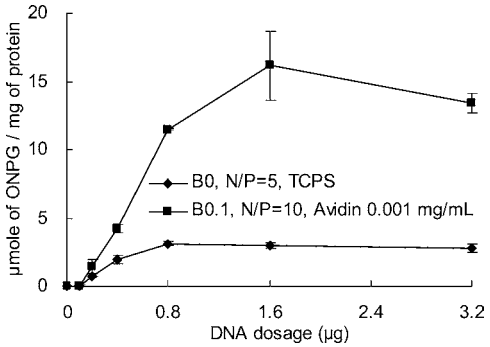


Figure 9. Dosage effect on transfection efficiencies of biotinylated chitosan on avidin-coated surfaces. Nanoparticles formed by biotinylated chitosan with different amount of DNA (B0.1 and N/P = 10) were used to transfect HEK 293T cells on surfaces coated with avidin solutions of 0.001 mg/mL for 2 days (square). The expression of β-galactosidase was determined by ONPG substrate, which was normalized by total protein amount. The corresponding transfection results were compared with that of nonmodified chitosan (B0, N/P = 5) on TCPS (diamond).

DISCUSSION

Chitosan is a frequently used nonviral vector. Compared to other polycationic vectors, chitosan exhibits better biocompatibility with lower transfection ability. Therefore, in this study we developed substrate-mediated gene delivery to enhance the delivery efficiency of chitosan.

Because the surface charge densities of nanoparticles may affect the efficiencies of gene delivery,[42] DLS analysis was performed to determine the zeta potential and the size distribution of biotinylated chitosan/DNA complex. Previous studies have indicated that the size of the nanoparticles may significantly determine their transfection ability because of the process of endocytosis.[43] For example, a diameter of PLL/DNA complex less than 100 nm is suitable for gene delivery.[44] Regarding chitosan, the appropriate size and surface charge for transfection vary with studies; however, all of them indicate that chitosan/DNA nanoparticles with sizes between 50 and 200 nm and zeta potentials between 15 and 37 mV should be suitable for gene delivery.[38,45,46] In our study, the surface charges were increased with the N/P ratio and decreased with the level of biotinylation (Figure 2a,b). Except for the B1 group with N/P of 2, all of the biotinylated nanoparticles demonstrate a positive zeta potential between 20 and 35 mV. In addition, the sizes of formed nanoparticles were between 66.8 and 109.8 nm. These results suggest that our developed biotinyalted nanoparticles are proper for gene transfer.

To determine if the loading capacities of chitosan to DNA are affected by biotinylation, two experiments have been performed: the fluorescent dye displacement assay and the gel retardation assay. Compared to the results of the fluorescent dye displacement, relatively low complexation efficiencies were demonstrated in the gel retardation experiment (Figure 4). The EtBr assay is based on reduction of fluorescence due to the dye exclusion from DNA during complex formation. In contrast, gel retardation is to apply the resistance of the agarose gel during electrophoresis. Because the biotinylation may reduce the interaction between chitosan and DNA, DNA may be extracted in the electrical field from loosely composed nanoparticles in which the positive charges were not strong enough to maintain DNA within the loading wells.

The protection abilities of chitosan with and without modification to DNA were analyzed by DNase I digestion assay. Our results demonstrate that the complexed DNA in nonmodified chitosan was partially digested so that the intensity of the supercoiled form was reduced, while that of the open circular form was increased (Figure 5a). The damage caused by enzyme attack increases with increase of biotinylation (Figure 5c–f). Chitosan with molecular weight of 10 kDa was applied in this study because lower molecular weight usually demonstrated better transfection ability and thus was frequently used for gene delivery application.[47−49] However, some studies have indicated that the protection ability of chitosan to DNA may be reduced with decreasing molecular weight. Huang et al. indicated that chitosan may completely shield DNA when its molecular weight greater than 48 kDa.[39] Their results demonstrated that chitosan with molecular weight of 17 kDa was partially degraded by DNase I, and was completely degraded for chitosan with molecular weight of 10 kDa.

Douglas et al. also suggested that chitosan with molecular weight of 10 kDa may not protect DNA from enzymatic attack.[50] Therefore, it is not surprising that complexed DNA may not be perfectly shielded in our results, and biotinylation may further reduce the protection ability of chitosan.

The biocompatibilities of nanoparticles were evaluated by MTS and LDH assay. Our results suggest that the level of LDH was low in all groups, suggesting that the cytotoxicity should not an important concern in this study (Figure 6a). For nonmodified chitosan, the MTS results of transfected cells was reduced with the increase of the N/P ratio (Figure 6b). However, the biotinylation may compensate the decrease of bioactivity at high N/P ratios. This may be because biotinylation diminished amine groups and thus weakened the charge density of chitosan molecules. Similar results have been found for biotinylated PEI which was bioconjugated with avidin for gene delivery.[51] Compared to nonmodified PEI, the cytotoxicity of biotinylated PEI demonstrated lower cytotoxicity due to lower surface charges. These results suggest that reducing positive charges of polycations should be beneficial to cell survival rates.

To enhance gene delivery of chitosan, we developed chitosan biotinylation to tether nanoparticles on biomaterial surfaces for substrate mediated delivery. Previous studies suggest that gene vehicles may thus be concentrated to facilitate gene transfer.[52,53] For example, DNA has been complexed with cationic polymers or lipids and was fixed on surface-coated fetal bovine serum (FBS), which demonstrated better transfection efficiency than bolus delivery.[54] However, nonspecific binding forces may lead DNA to diffuse from target sites and elicit unwanted systemic transfection and immune response.[55] Our previous studies suggested that the biotin−avidin interaction for viral vector immobilization may not only enhance cell transduction efficiency, but also spatially control gene delivery at the target sites.[26,56] Therefore, in this study we intended to apply this strategy to improve the poor transfection ability of chitosan.

Comparing the transfection ability of nanoparticles on TCPS, biotinylation reduced the charge density of chitosan, and thus, more chitosan molecules were necessary for transfection (Figure 7a). Interestingly, biotinylated chitosan demonstrated superior transfection efficiency. This may be because the biotinylation reduced the positive charges of chitosan. Decreasing the charge density of the polycations may reduce their damage to organelles.[41] Other studies also indicated that the stable interaction between chitosan and DNA may preclude the translation of the transgene.[45] The transfection efficacy of chitosans is governed by the interaction strength between the chitosan vector and the DNA in the polyplex.[57] Alatorre-Meda et al. have compared the transfection ability of chitosan with different molecular weights and assembly conditions.[58] Their results suggested that the weaker DNA−chitosan binding resulted in higher transfection efficiency. Incorporating anionic polymers, such as alginate, is another frequently used strategy to mediate the stability of the complex so the negative charged polyanion may compete with DNA and the electrostatic interaction between DNA and chitosan should thus be regulated.[50] About chitosan modification, histidine has been applied to modify chitosan, and the complex with DNA demonstrated an improvement to enhance endosomal escape, which eventually improved the gene delivery.[59] Our gel retardation experiment indicated that the biotinylation treatment may weaken the interaction between DNA and chitosan, so that loaded DNA may thus escape from chitosan (Figure 4c). These results suggested that biotinylation should loosen the chitosan/DNA complex and thus improve the transduction efficiencies.

By controlling the coating of avidin as well as the N/P ratio and the biotinylation levels of chitosan/DNA complex, we may regulate the affinity of surfaces to nanoparticles. Through appropriate ratio, the transfection efficiency was significantly improved (Figure 7c). The optimal N/P ratio was increased with the increase of biotinylation. In this study, we did not remove free biotinylated chitosan, because a DNA/polycation complex only is not sufficient for gene delivery. Sabine Boeckle et al. have compared the transfection ability between purified and nonpurified PEI/DNA complexes.[60] Their results indicated that the gene delivery of purified nanoparticles was inefficient; however, the transfection can be rescued by providing free PEI. It may be because the free PEI molecules aid in releasing polyplexes from the endosomes.[61] Excess free polycations may induce a proton sponge effect to facilitate endosomal escape and gene expression.[62] In addition, our results indicated that free biotinylated chitosan may occupy binding sites and hence regulate the binding affinity between nanoparticles and biomaterials.

■ CONCLUSION

In this study, we improved the transfection efficiency of nonviral vectors using substrate-mediated delivery. Biotinylation of chitosan can successfully complex with DNA and the formed nanoparticles have proper surface charges and size for gene delivery. The biotinylated nanoparticles provide good complexation efficiency and may protect DNA to a certain extent. In addition, the cytotoxicity of chitosan may be reduced by the biotinylation, which further increases the cell activity and transgene expression. Through appropriate biotin−avidin interaction, the transfection efficiency can be highly increased. These results suggest that this gene delivery may improve the transfection ability of nonviral vectors, and this approach should be able to be applied to various biomaterial surfaces for tissue engineering applications.

■ AUTHOR INFORMATION

Corresponding Author

*Tel.: +886 3 422 7151 Ex 34243. Fax: +886 3 422 5258. E-mail address: huweiwen@cc.ncu.edu.tw.

Notes

The authors declare no competing financial interest.

■ ACKNOWLEDGMENTS

This research was supported by the grant of NSC 98-2218-E-008-009 from the National Science Council of Taiwan, and 99CGH-NCU-A2 from the National Central University and Cathy General Hospital Joint Research Center.

■ REFERENCES

(1) Franceschi, R. T., Wang, D., Krebsbach, P. H., and Rutherford, R. B. (2000) Gene therapy for bone formation: In vitro and in vivo osteogenic activity of an adenovirus expressing BMP7. *J. Cell. Biochem.* 78, 476−486.

(2) Jullig, M., Zhang, W. V., and Stott, N. S. (2004) Gene therapy in orthopaedic surgery: the current status. *Anz. J. Surg.* 74, 46−54.

(3) Pfeifer, A., and Verma, I. M. (2001) Gene therapy: Promises and problems. *Annual Review of Genomics and Human Genetics* 2, 177−211.

(4) Hu, W. W., Lang, M. W., and Krebsbach, P. H. (2009) Digoxigenin modification of adenovirus to spatially control gene delivery from chitosan surfaces. *J. Controlled Release 135*, 250−258.
(5) Illum, L. (1998) Chitosan and its use as a pharmaceutical excipient. *Pharm. Res. 15*, 1326−1331.
(6) Oungbho, K., and Müller, B. W. (1997) Chitosan sponges as sustained release drug carriers. *Int. J. Pharm. 156*, 229−237.
(7) Rao, S. B., and Sharma, C. P. (1997) Use of chitosan as a biomaterial: Studies on its safety and hemostatic potential. *J. Biomed. Mater. Res. 34*, 21−28.
(8) Katas, H., and Alpar, H. O. (2006) Development and characterisation of chitosan nanoparticles for siRNA delivery. *J. Controlled Release 115*, 216−225.
(9) Mao, S. R., Sun, W., and Kissel, T. (2010) Chitosan-based formulations for delivery of DNA and siRNA. *Adv. Drug Delivery Rev. 62*, 12−27.
(10) Kai, E., and Ochiya, T. (2004) A method for oral DNA delivery with N-acetylated chitosan. *Pharm. Res. 21*, 838−843.
(11) Denuziere, A., Ferrier, D., and Domard, A. (1996) Chitosan-chondroitin sulfate and chitosan-hyaluronate polyelectrolyte complexes. Physico-chemical aspects. *Carbohydr. Polym. 29*, 317−323.
(12) Lai, W. F., and Lin, M. C. M. (2009) Nucleic acid delivery with chitosan and its derivatives. *J. Controlled Release 134*, 158−168.
(13) Sarkar, K., Srivastava, R., Chatterji, U., and Kundu, P. P. (2011) Evaluation of chitosan and their self-assembled nanoparticles with pDNA for the application in gene therapy. *J. Appl. Polym. Sci. 121*, 2239−2249.
(14) Wang, X., Yao, J., Zhou, J. P., Lu, Y., and Wang, W. (2010) Synthesis and evaluation of chitosan-graft-polyethylenimine as a gene vector. *Pharmazie 65*, 572−579.
(15) Li, Z. T., Guo, J., Zhang, J. S., Zhao, Y. P., Lv, L., Ding, C., and Zhang, X. Z. (2010) Chitosan-graft-polyethylenimine with improved properties as a potential gene vector. *Carbohydr. Polym. 80*, 254−259.
(16) Yu, H. J., Deng, C., Tian, H. Y., Lu, T. C., Chen, X. S., and Jing, X. B. (2011) Chemo-physical and biological evaluation of poly(l-lysine)-grafted chitosan copolymers used for highly efficient gene delivery. *Macromol. Biosci. 11*, 352−361.
(17) Jiang, H. L., Lim, H. T., Kim, Y. K., Arote, R., Shin, J. Y., Kwon, J. T., Kim, J. E., Kim, J. H., Kim, D., Chae, C., Nah, J. W., Choi, Y. J., Cho, C. S., and Cho, M. H. (2011) Chitosan-graft-spermine as a gene carrier in vitro and in vivo. *Eur. J. Pharm. Biopharm. 77*, 36−42.
(18) Zhai, X. Y., Sun, P., Luo, Y. F., Ma, C. N., Xu, J., and Liu, W. G. (2011) Guanidinylation: a simple way to fabricate cell penetrating peptide analogue-modified chitosan vector for enhanced gene delivery. *J. Appl. Polym. Sci. 121*, 3569−3578.
(19) Zhang, H. L., Zhu, D. W., Song, L. P., Liu, L. X., Dong, X., Liu, Z. B., and Leng, X. G. (2011) Arginine conjugation affects the endocytic pathways of chitosan/DNA nanoparticles. *J. Biomed. Mater. Res., Part A 98A*, 296−302.
(20) Zhao, X. L., Li, Z. Y., Liu, W. G., Lam, W., Sun, P., Kao, R. Y. T., Luk, K. D. K., and Lu, W. W. (2011) Octaarginine-modified chitosan as a nonviral gene delivery vector: properties and in vitro transfection efficiency. *J. Nanopart. Res. 13*, 693−702.
(21) Chan, P., Kurisawa, M., Chung, J. E., and Yang, Y. Y. (2007) Synthesis and characterization of chitosan-g-poly(ethylene glycol)-folate as a non-viral carrier for tumor-targeted gene delivery. *Biomaterials 28*, 540−549.
(22) Zhao, R. L., Sun, B., Liu, T. Y., Liu, Y., Zhou, S. M., Zuo, A. J., and Liang, D. C. (2011) Optimize nuclear localization and intra-nucleus disassociation of the exogene for facilitating transfection efficacy of the chitosan. *Int. J. Pharm. 413*, 254−259.
(23) Opanasopit, P., Rojanarata, T., Apirakaramwong, A., Ngawhirunpat, T., and Ruktanonchai, U. (2009) Nuclear localization signal peptides enhance transfection efficiency of chitosan/DNA complexes. *Int. J. Pharm. 382*, 291−295.
(24) Chung, Y. C., Chang, F. H., Wei, M. F., and Young, T. H. (2010) A variable gene delivery carrier-biotinylated chitosan/polyethyleneimine. *Biomed. Mater. 5*, 1−8.
(25) Hu, W. W., Wang, Z., Hollister, S. J., and Krebsbach, P. H. (2007) Localized viral vector delivery to enhance in situ regenerative gene therapy. *Gene Ther. 14*, 891−901.
(26) Hu, W. W., Lang, M. W., and Krebsbach, P. H. (2008) Development of adenovirus immobilization strategies for in situ gene therapy. *J. Gene. Med. 10*, 1102−1112.
(27) Wang, J. W., Chen, C. Y., and Kuo, Y. M. (2011) Preparation and characterization of chitosan-coated hydroxyapatite nanoparticles as a promising non-viral vector for gene delivery. *J. Appl. Polym. Sci. 121*, 3531−3540.
(28) Lin, Q. K., Ren, K. F., and Ji, J. (2009) Hyaluronic acid and chitosan-DNA complex multilayered thin film as surface-mediated nonviral gene delivery system. *Colloids Surf., B: Biointerfaces 74*, 298−303.
(29) Hu, Y., Cai, K. Y., Luo, Z., Zhang, R., Yang, L., Deng, L. H., and Jandt, K. D. (2009) Surface mediated in situ differentiation of mesenchymal stem cells on gene-functionalized titanium films fabricated by layer-by-layer technique. *Biomaterials 30*, 3626−3635.
(30) Zhu, D. W., Jin, X., Leng, X. G., Wang, H., Bao, J. B., Liu, W. G., Yao, K. D., and Song, C. X. (2010) Local gene delivery via endovascular stents coated with dodecylated chitosan-plasmid DNA nanoparticles. *Int. J. Nanomed. 5*, 1095−1102.
(31) Green, N. M. (1963) Avidin. 1. The use of (14-C)biotin for kinetic studies and for assay. *Biochem. J. 89*, 585−91.
(32) Segura, T., Volk, M. J., and Shea, L. D. (2003) Substrate-mediated DNA delivery: role of the cationic polymer structure and extent of modification. *J. Controlled Release 93*, 69−84.
(33) Livnah, O., Bayer, E. A., Wilchek, M., and Sussman, J. L. (1993) The structure of the complex between avidin and the dye, 2-(4′-hydroxyazobenzene) benzoic acid (HABA). *FEBS Lett. 328*, 165−168.
(34) Buschmann, M. D., Lavertu, M., Methot, S., and Tran-Khanh, N. (2006) High efficiency gene transfer using chitosan/DNA nanoparticles with specific combinations of molecular weight and degree of deacetylation. *Biomaterials 27*, 4815−4824.
(35) LePecq, J. B., and Paoletti, C. (1967) A fluorescent complex between ethidium bromide and nucleic acids. Physical-chemical characterization. *J. Mol. Biol. 27*, 87−106.
(36) Izumrudov, V. A., Zhiryakova, M. V., and Kudaibergenov, S. E. (1999) Controllable stability of DNA-containing polyelectrolyte complexes in water-salt solutions. *Biopolymers 52*, 94−108.
(37) Seymour, L. W., Parker, A. L., Oupicky, D., and Dash, P. R. (2002) Methodologies for monitoring, nanoparticle formation by self-assembly of DNA with poly(L-lysine). *Anal. Biochem. 302*, 75−80.
(38) Mao, H. Q., Roy, K., Troung-Le, V. L., Janes, K. A., Lin, K. Y., Wang, Y., August, J. T., and Leong, K. W. (2001) Chitosan-DNA nanoparticles as gene carriers: synthesis, characterization and transfection efficiency. *J. Controlled Release 70*, 399−421.
(39) Huang, M., Fong, C. W., Khor, E., and Lim, L. Y. (2005) Transfection efficiency of chitosan vectors: Effect of polymer molecular weight and degree of deacetylation. *J. Controlled Release 106*, 391−406.
(40) Yang, S. J., Chang, S. M., Tsai, K. C., Chen, W. S., Lin, F. H., and Shieh, M. J. (2010) Effect of chitosan-alginate nanoparticles and ultrasound on the efficiency of gene transfection of human cancer cells. *J. Gene Med. 12*, 168−79.
(41) Hunter, A. C., and Moghimi, S. M. (2010) Cationic carriers of genetic material and cell death: a mitochondrial tale. *Biochim. Biophys. Acta 1797*, 1203−9.
(42) Ghosn, B., Kasturi, S. P., and Roy, K. (2008) Enhancing polysaccharide-mediated delivery of nucleic acids through functionalization with secondary and tertiary amines. *Curr. Top. Med. Chem. 8*, 331−340.
(43) Rejman, J., Oberle, V., Zuhorn, I. S., and Hoekstra, D. (2004) Size-dependent internalization of particles via the pathways of clathrin- and caveolae-mediated endocytosis. *Biochem. J. 377*, 159−169.
(44) Wagner, E., Cotten, M., Foisner, R., and Birnstiel, M. L. (1991) Transferrin polycation DNA complexes - the effect of polycations on the structure of the complex and DNA delivery to cells. *Proc. Natl. Acad. Sci. U.S.A. 88*, 4255−4259.

(45) MacLaughlin, F. C., Mumper, R. J., Wang, J. J., Tagliaferri, J. M., Gill, I., Hinchcliffe, M., and Rolland, A. P. (1998) Chitosan and depolymerized chitosan oligomers as condensing carriers for in vivo plasmid delivery. *J. Controlled Release 56*, 259−272.
(46) Erbacher, P., Zou, S. M., Bettinger, T., Steffan, A. M., and Remy, J. S. (1998) Chitosan-based vector/DNA complexes for gene delivery: Biophysical characteristics and transfection ability. *Pharm. Res. 15*, 1332−1339.
(47) Lavertu, M., Methot, S., Tran-Khanh, N., and Buschmann, M. D. (2006) High efficiency gene transfer using chitosan/DNA nanoparticles with specific combinations of molecular weight and degree of deacetylation. *Biomaterials 27*, 4815−4824.
(48) Lee, M., Nah, J. W., Kwon, Y., Koh, J. J., Ko, K. S., and Kim, S. W. (2001) Water-soluble and low molecular weight chitosan-based plasmid DNA delivery. *Pharm. Res. 18*, 427−431.
(49) Nimesh, S., Thibault, M. M., Lavertu, M., and Buschmann, M. D. (2010) Enhanced gene delivery mediated by low molecular weight chitosan/DNA complexes: effect of pH and serum. *Mol. Biotechnol. 46*, 182−196.
(50) Douglas, K. L., Piecirillo, C. A., and Tabrizian, M. (2006) Effects of alginate inclusion on the vector properties of chitosan-based nanoparticles. *J. Controlled Release 115*, 354−361.
(51) Zeng, X., Sun, Y. X., Zhang, X. Z., Cheng, S. X., and Zhuo, R. X. (2009) A potential targeting gene vector based on biotinylated polyethyleneimine/avidin bioconjugates. *Pharm. Res. 26*, 1931−1941.
(52) Wang, C. H. K., and Pun, S. H. (2011) Substrate-mediated nucleic acid delivery from self-assembled monolayers. *Trends Biotechnol. 29*, 119−126.
(53) Pannier, A. K., and Shea, L. D. (2004) Controlled release systems for DNA delivery. *Mol. Ther. 10*, 19−26.
(54) Bengali, Z., Pannier, A. K., Segura, T., Anderson, B. C., Jang, J. H., Mustoe, T. A., and Shea, L. D. (2005) Gene delivery through cell culture substrate adsorbed DNA complexes. *Biotechnol. Bioeng. 90*, 290−302.
(55) Herweijer, H., and Wolff, J. A. (2003) Progress and prospects: naked DNA gene transfer and therapy. *Gene Ther. 10*, 453−458.
(56) Hu, W. W., Elkasabi, Y., Chen, H. Y., Zhang, Y., Lahann, J., Hollister, S. J., and Krebsbach, P. H. (2009) The use of reactive polymer coatings to facilitate gene delivery from poly(ε-caprolactone) scaffolds. *Biomaterials 30*, 5785−5792.
(57) Strand, S. P., Lelu, S., Reitan, N. K., Davies, C. D., Artursson, P., and Varum, K. M. (2010) Molecular design of chitosan gene delivery systems with an optimized balance between polyplex stability and polyplex unpacking. *Biomaterials 31*, 975−987.
(58) Alatorre-Meda, M., Taboada, P., Hardl, F., Wagner, T., Freis, M., and Rodriguez, J. R. (2011) The influence of chitosan valence on the complexation and transfection of DNA The weaker the DNA-chitosan binding the higher the transfection efficiency. *Colloids Surf., B: Biointerfaces 82*, 54−62.
(59) Chang, K. L., Higuchi, Y., Kawakami, S., Yamashita, F., and Hashida, M. (2010) Efficient gene transfection by histidine-modified chitosan through enhancement of endosomal escape. *Bioconjugate Chem. 21*, 1087−1095.
(60) Boeckle, S., von Gersdorff, K., van der Piepen, S., Culmsee, C., Wagner, E., and Ogris, M. (2004) Purification of polyethylenimine polyplexes highlights the role of free polycations in gene transfer. *J. Gene. Med. 6*, 1102−1111.
(61) Kichler, A., Leborgne, C., Coeytaux, E., and Danos, O. (2001) Polyethylenimine-mediated gene delivery: a mechanistic study. *J. Gene. Med. 3*, 135−144.
(62) Thibault, M., Astolfi, M., Tran-Khanh, N., Lavertu, M., Darras, V., Merzouki, A., and Buschmann, M. D. (2011) Excess polycation mediates efficient chitosan-based gene transfer by promoting lysosomal release of the polyplexes. *Biomaterials 32*, 4639−4646.

Bioconjugate Chemistry

Article

pubs.acs.org/bc

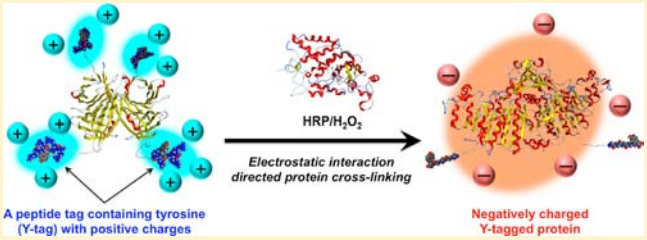
Control of a Tyrosyl Radical Mediated Protein Cross-Linking Reaction by Electrostatic Interaction

Kosuke Minamihata,[†] Masahiro Goto,[†,§] and Noriho Kamiya*[,†,§]

[†]Department of Applied Chemistry, Graduate School of Engineering, and [§]Center for Future Chemistry,Kyushu University

Supporting Information

ABSTRACT: Herein, we demonstrate the control of protein heteroconjugation via a tyrosyl coupling reaction by using electrostatic interaction. Aspartic acid and arginine were introduced to a tyrosine containing peptide tag (Y-tag) to provide electrostatic charge. Designed negatively or positively charged Y-tags were tethered to the C-terminus of *Escherichia coli* alkaline phosphatase (BAP) and streptavidin (SA), and these model proteins were subjected to horseradish peroxidase (HRP) treatment. The negatively charged Y-tags showed low reactivity due to repulsive interactions between the Y-tags with the negatively charged BAP and SA. In contrast, the positively charged Y-tags showed high reactivity, indicating that the electrostatic interaction between Y-tags and proteins significantly affects the tyrosyl radical mediated protein cross-linking. From the heteroconjugation reaction of BAP and SA, the SA with the positively charged Y-tags exhibited favorable cross-linking toward negatively charged BAP, and the BAP-SA conjugates prepared from BAP with GY-tag (GGGGY) and SA with RYR-tag (RRYRR) had the best performance on a biotin-coated microplate. Encompassing the reactive tyrosine residue with arginine residues reduced the reactivity against HRP, enabling the modulation of cross-linking reaction rates with BAP-GY. Thus, by introducing a proper electrostatic interaction to Y-tags, it is possible to kinetically control the heteroconjugation behavior of proteins, thereby maximizing the functions of protein heteroconjugates.



INTRODUCTION

The protein−protein heteroconjugation reaction is one of the principal techniques in biotechnology, enabling the generation of new biomaterials that have distinct functions of the building block proteins.[1−4] The heteroconjugation has to be well-controlled to maximize the function of the resulting heteroconjugates and also to avoid the loss of function. Therefore, techniques that provide controlled protein−protein heteroconjugation are of great importance, and many heteroconjugation methods have been utilized including the leucine zipper,[5] production of fusion proteins, [6] and protein ligation using intein,[7,8] while new heteroconjugation methods are still being developed.[9−11]

One of the most promising ways to achieve a controlled heteroconjugation reaction is the use of enzymatic reactions.[12] With the high substrate specificity of enzymes, the cross-linking of proteins can be oriented to a desired position in a target protein. Also, the cross-linking can be carried out under mild conditions, minimizing the loss of protein function. The enzymes that have been extensively used for the purpose of protein heteroconjugation reactions are transglutaminase (TGase)[13] and sortase A (SrtA).[14,15] There are other candidates that can be used for protein−protein heteroconjugation, such as hAGT,[16] PFTase,[17] and PPTase;[18] yet, these enzymes require introduction of small chemical substrates to target proteins. TGase and SrtA require only short peptidyl substrates, usually less than 20 amino acids; therefore when combined with genetic modification of the target protein, the use of TGase and SrtA has become a reliable technique to achieve protein heteroconjugation.

Following these established enzymatic modification methods, we have reported a protein heteroconjugation reaction using the horseradish peroxidase (HRP) mediated oxidative tyrosine-coupling reaction.[4] As described in the previous report, a peptide tag containing tyrosine residues (Y-tag: the sequence of GGGGY, which is abbreviated as GY-tag in this report) was genetically introduced at the C-terminus of *Escherichia coli* alkaline phosphatase (BAP) and streptavidin (SA) derived from *Streptomyces avidinii*. Both the GY-tagged BAP and SA became reactive to the enzymatic reaction of HRP, and a high cross-linked BAP-SA heteroconjugate via the Y-tag was obtained. However, since the protein heteroconjugation reaction was based on a homocoupling reaction of tyrosyl radicals, it was difficult to control the conjugation efficiency between BAP and SA. Stewart and co-workers demonstrated the control of a tyrosyl radical homocoupling reaction by using a hexahistidine-Ni^{2+} complex, in which a cross-linkage forms between the proximally positioned tyrosine residues of the complex to yield a protein dimer.[19] Another possible way to control the tyrosine-coupling reaction could be the use of a leucine zipper,[5,20] which has been intensively exploited for artificial protein dimerization. The Fos and Jun families of eukaryotic transcription factors

Received: March 18, 2012
Revised: July 5, 2012
Published: July 20, 2012

ACS Publications © 2012 American Chemical Society

dx.doi.org/10.1021/bc300137s | *Bioconjugate Chem.* 2012, 23, 1600−1609

form a heterodimer,[21] yet they can also homodimerize, which might cause aggregation when the leucine zipper is appended to proteins which originally form oligomers.

Herein, we explored the control of the HRP-mediated protein heteroconjugation by introducing electric charges on the Y-tags. The electrostatic interaction between positive and negative charges clearly shows both attractive and repulsive forces between charges; therefore, the use of such interactions for conducting heteroconjugation is ideal. In addition, since the tyrosine-coupling reaction takes place through the formation of tyrosyl radicals, which have a very short lifetime, it can be expected that, if the attractive or repulsive interaction affects the accession of tyrosyl radicals, it will result in a significant difference in the cross-linking behavior. This was suggested from our previous study, where the negatively charged BAP possessing GY-tag was capable of co-cross-linking with the positively charged lysozyme, but it showed no reactivity against the negatively charged ovalbumin (OVA) or bovine serum albumin (BSA).[22] Aspartic acid (Asp, D) and arginine (Arg, R) were used to electrostatically charge the Y-tags. The Y-tag sequences of DDDDY, DDYDD, RRRRY, and RRYRR, which are abbreviated as DY-tag, DYD-tag, RY-tag, and RYR-tag, respectively, were appended to the C-terminus of BAP and SA. We anticipated that the positive and negative charges of these Y-tags would hamper the self-cross-linking reaction while facilitating the heterocross-linking reaction between the oppositely charged Y-tags. The BAP mutants and SA mutants tagged with electrostatically charged Y-tags were treated by HRP, and the possibility of controlling the tyrosyl radical coupling reaction by electrostatic interaction was investigated.

EXPERIMENTAL PROCEDURES

Materials and Instruments. The wild-type BAP (WT-BAP) and SA (WT-SA) and GY-tagged BAP (BAP-GY) and SA (SA-GY) were prepared according to our previous reports.[4,22] HRP-type VI (250−330 units/mg solid using pyrogallol), albumin from chicken egg white grade V (OVA), and ribonuclease A from bovine pancreas (RNase A) were purchased from Sigma Aldrich Co. Hydrogen peroxide solution (30 wt %), lysozyme from chicken egg white, and albumin from bovine serum, cohn fraction V, pH 7.0 (BSA), were purchased from Wako Pure Chemical Industries, Ltd. (Osaka, Japan). EGFP(Y237F) was prepared from the gene coding wild-type EGFP with an N-terminal His_6-tag. The mutation was introduced by site-directed mutagenesis using a KOD-Plus-Mutagenesis Kit (Toyobo Co., Ltd. Life Science Department Osaka, Japan), and the expression and the purification of EGFP(Y237F) were done as previously reported.[23] All other reagents were purchased and used as received. Prepacked columns including a Ni-NTA column (His-Trap HP column 5 mL), an anion-exchange column (HiTrap DEAE FF 5 mL), a cation exchange column (HiTrap SP HP 1 mL), and a desalting column (PD-10) were purchased from GE Healthcare Bio-Sciences. A size-exclusion chromatography column was constructed by packing the XK16 column with Superdex 200 prep grade that were both purchased from GE Healthcare Bio-Sciences. All of the chromatography experiments for the purification of BAPs and SAs were conducted on a BioLogic DuoFlow Chromatography System (Bio-Rad Laboratories, Inc.).

Preparation of BAPs and SAs Possessing Negatively or Positively Charged Y-tags. The expression genes for BAP mutants were prepared from the expression plasmid of BAP-GY (pET22b+ with gene coding BAP-GY in between its *Bam*HI and *Xho*I sites). The gene coding the GY-tag and thrombin cleavage sequence (LVPRGSGGGGY) in the plasmid were substituted with genes coding an additional linker sequence and the positively or negatively charged Y-tags by site-directed mutagenesis using a KOD-Plus-Mutagenesis Kit as follows: DY-tag (LVPRGSGGGSDDDDY), DYD-tag (LVPRGSGGGS-DDYDD), RY-tag (LVPRGSGGGSRRRRY), and RYR-tag (LVPRGSGGGSRRYRR). The BAPs possessing these Y-tags are abbreviated as BAP-DY, BAP-DYD, BAP-RY, and BAP-RYR, respectively. The additional linker sequence was added to ensure the thrombin recognition of the Y-tags.

The constructed expression plasmids for BAP-DY, BAP-DYD, BAP-RY, and BAP-RYR were transformed into *E. coli* BL21 (DE3), and the general expression and purification process for these BAP mutants were carried out as in our previous report,[22] except in the purification step for BAP-RY and BAP-RYR using the anion exchange column, the pH value of the binding and the washing buffer was changed to 9.0. The BAP mutants were then purified using a SEC column equilibrated with the SEC mobile phase (10 mM Tris-HCl, pH 8.0, 150 mM NaCl), and finally desalted into 10 mM Tris-HCl (pH 8.0) on a PD-10 column.

The expression genes for SA mutants were prepared from the expression plasmid for SA-GY (pET22b+ with gene coding SA-GY in between its *Nde*I and *Hind*III sites). The gene coding the GY-tag (GGGGY) in the plasmid was substituted to genes coding the DY-tag (DDDDY), DYD-tag (DDYDD), RY-tag (RRRRY), or RYR-tag (RRYRR) by site-directed mutagenesis. The SAs possessing these Y-tags are abbreviated as SA-DY, SA-DYD, SA-RY, and SA-RYR, respectively. The expression of these SA mutants was conducted using *E. coli* BL21 (DE3). The general expression and purification process of SA mutants was carried out as our previous report[4] except the purification step was carried using an ion exchange column. For the purification of SA-RY and SA-RYR, a minor change in the procedure was made in the purification step using a cation exchange column due to the additional positive charges. The SA-RY and the SA-RYR were eluted from the column using a salt gradient of up to 75% of elution buffer (100 mM succinic acid, 10 mM EDTA, 1 M NaCl, pH 4.4). For SA-DY and SA-DYD, instead of using a cation exchange column, the SAs were purified using an anion exchange column and the purification condition for these SAs with the negatively charged Y-tags was the same as for the BAPs. The concentrations of BAPs and SAs were determined by a BCA assay with BSA as the standard. The purities of the prepared proteins were evaluated by SDS-PAGE analysis.

Evaluation of the Effect of Negative and Positive Charges on Y-tags. The reactivity of newly prepared DY-tag, DYD-tag, RY-tag, and RYR-tag against HRP treatment was tested by treating BAP and SA mutants solely by HRP. BAP or SA and HRP were dissolved into 10 mM Tris-HCl (pH8.0) at a final concentration of 0.2 mg/mL and 0.1 mg/mL, respectively and H_2O_2 was then added to the solution 5 times every 10 min at a final concentration of 50 μM at 37 °C. The sample solution was incubated overnight at 37 °C and analyzed by SDS-PAGE analysis.

To analyze whether the negative and positive charges on the Y-tags work to control the protein heteroconjugation, the SA mutants and various negatively charged proteins were treated together by HRP. The model conjugation partners for SA were EGFP(Y237F), OVA, and BSA. The EGFP(Y237F) was used because in our previous report, it was shown that the wild-type

EGFP cross-linked by itself upon HRP treatment probably due to the tyrosine residue at its penultimate C-terminal position.[22] SA mutants, model proteins, and HRP were mixed together in 10 mM Tris-HCl (pH 8.0) at final concentrations of 0.2 mg/mL, 0.2 mg/mL, and 0.1 mg/mL, respectively. The heteroconjugation reaction was conducted by adding H_2O_2 in the same manner as described above, and the sample solutions were analyzed by SDS-PAGE. In addition, the BAP mutants were treated by HRP with the positively charged proteins, lysozyme and RNase A. The heteroconjugation reaction condition for BAP mutants and the model proteins was the same as for the heteroconjugation reaction between the SA mutants and various proteins described above. The samples were analyzed by SDS-PAGE analysis. SA mutants were not employed in this experiment, because SAs and the positively charged proteins have similar molecular weights, thus making it difficult to follow the cross-linking behavior by SDS-PAGE analysis.

Heteroconjugation Reaction of BAP Mutants and SA Mutants. BAP mutants and SA mutants were treated together by HRP to examine the possibility of controlling the cross-linking between BAP and SA by the tethered positive or negative charges on the Y-tags. BAP and SA were dissolved into 10 mM Tris-HCl (pH 8.0) at a final concentration of ~7 μM each, which is equivalent to 0.35 mg/mL and 0.1 mg/mL, respectively. The heteroconjugation reaction was initiated by adding H_2O_2 5 times every 10 min at a final concentration of 50 μM. The sample solutions were analyzed by SDS-PAGE and native-PAGE analyses. Prior to native-PAGE analyses, biotin-4-fluorescein was added to the sample solutions at a final concentration of 50 μM and incubated for 1 h at 4 °C.

Measurement of the Enzymatic Activities of BAP-SA Conjugates. After the heteroconjugation reaction described above, the sample solutions were diluted 10-fold by 10 mM Tris-HCl (pH 8.0), and 10 μL aliquots of the diluted solutions were dispensed into the wells of a 96-well microplate. To measure the BAP enzymatic activities of the BAP-SA conjugates, 190 μL of 1 mM *p*-nitrophenylphosphate (*p*-NPP)/1 M Tris-HCl (pH 8.0) solution was added to each well, and the change in absorbance at 410 nm, derived from the formation of *p*-nitrophenol (*p*-NP) from *p*-NPP by BAP enzymatic activity, was monitored for 10 min at 37 °C. The enzymatic activities of untreated BAPs were also measured in the same manner and the obtained values were used to calculate the relative activity of each BAP-SA conjugate. To convert the enzymatic activity values measured on the microplate into unit/mg, the specific activities of untreated BAPs were measured using a UV−vis spectrometer in the following manner. Ten microliters of 0.1 mg/mL BAP solution was mixed with 990 μL of 1 mM *p*-NPP/1 M Tris-HCl (pH 8.0) in a UV quartz cell. The change in absorbance at 410 nm was monitored for 3 min at 25 °C. One unit of BAP enzymatic activity was defined as the activity that catalyzes the dephosphorization reaction of 1 μmol of *p*-NPP in 1 min where the *p*-NP absorbance coefficient of 16 900 M^{-1} cm^{-1} was employed to calculate the unit value.

Fluorescence Measurement of Dityrosine. The reactivities of the RY-tag and RYR-tag against HRP treatment was evaluated by measuring the fluorescence intensity increase at 420 nm derived from dityrosine formation. The fluorescence measurement was carried out on a Perkin-Elmer LS55. Either SA-RY or SA-RYR and HRP were dissolved into 10 mM Tris-HCl (pH 8.0) at a final concentration of 0.2 mg/mL and 0.1 mg/mL, respectively, in a total volume of 400 μL. The solution was placed into a quartz cell for fluorescence measurement (cell volume of 400 μL), and a portion of a 500 μM H_2O_2 solution was mixed into the solution to a final concentration of 50 μM to conduct the HRP treatment on the proteins. As soon as the reaction was started, the time-driven fluorescence measurement at 420 nm was initiated and the intensity was monitored for 3 min at 25 °C (excitation light wavelength of 315 nm, a sharp-cut filter at 350 nm, both excitation and fluorescence slits of 10 nm).

Investigation of the Function of the BAP-SA Conjugates on a Biotin-Coated Plate. BAP (0.2 mg/mL) and SA (0.2 mg/mL) were co-cross-linked by HRP treatment (0.1 mg/mL of HRP and 50 μM H_2O_2). After HRP treatment, the sample solutions were diluted using 10 mM Tris-HCl (pH 8.0) to a concentration of 0.5 unit/mL and 125 mM of NaCl was added. One hundred microliters of each BAP-SA conjugate solution was added to a well of a biotin-coated plate (Pierce Biotin Coated Clear 8-Well Strip Plates) preliminarily washed with TBS three times and then incubated for 30 min at 25 °C for immobilization. The wells were washed with TBS three times to remove unbound proteins. BAP enzymatic activity of the immobilized BAP-SA conjugates was measured by adding 200 μL of 1 mM *p*-NPP/1 M Tris-HCl (pH 8.0) to each well and the increase in the absorbance at 410 nm was monitored for 10 min at 37 °C.

Two-Step Conjugation Reaction of BAP and SA. The BAP-SA conjugates were prepared by a two-step conjugation reaction. In the first step, H_2O_2 was added to a solution containing BAP and HRP twice at 37 °C to conduct the homoconjugation reaction of BAP. In the second step, additional HRP and SA were added to the solution and H_2O_2 was added two more times to carry out the heteroconjugation reaction. The final concentration of BAP, SA, and HRP was 0.2 mg/mL and that of H_2O_2 was 50 μM. HRP was added twice because HRP may have been inactivated by H_2O_2 in the first step. The function of the BAP-SA conjugates prepared by the two-step conjugation reaction was evaluated by immobilizing the conjugates on the biotin-coated plate as described earlier.

Investigation of Effect of Conjugation pH on the Function of BAP-SA Conjugates. The BAP-SA conjugates were prepared at various pH conditions from pH 5.0 to 9.0. Acetate buffer was used for the condition of pH 5.0. For pH 6.0 and 7.0, phosphatase buffer was used and Tris-HCl buffer was used to prepare the conditions of pH 8.0 and 9.0. All of the buffer concentrations were 50 mM. The preparation of BAP-SA conjugate was conducted the same as the one-step process described earlier. After conjugation reaction, all of the sample solutions were dialyzed against 10 mM Tris-HCl (pH 8.0) for 24 h at 4 °C using Slide-A-Lyzer Mini Dialysis Unit (7000 MWCO). The function of the BAP-SA conjugates prepared at different pH conditions was evaluated by immobilizing the conjugates on the biotin-coated plate as described earlier.

RESULTS AND DISCUSSION

Reactivity of the Negatively or Positively Charged Y-tags against HRP Treatment. It has been demonstrated by our previous work that the GY-tag, a very flexible peptide sequence consisting of GGGGY, is efficiently recognized by HRP resulting in the conjugation of the GY-tagged proteins to each other. In contrast, DY-tag, DYD-tag, RY-tag, and RYR-tag are much more sterically hindered at the tyrosine residue

reaction site and also have strong negative or positive charges; therefore, it seemed that the tyrosine residues in these tags were much less likely to be recognized by HRP. Figure 1 shows the result of the SDS-PAGE analysis of BAP mutants and SA mutants after HRP treatment.

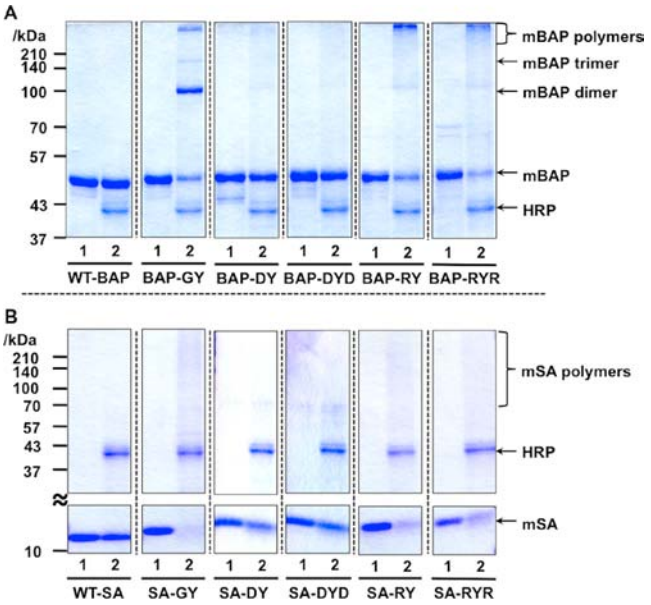


Figure 1. SDS-PAGE analyses of the homoconjugation reaction of BAP mutants (A) and SA mutants (B). Lane 1: SA or BAP; Lane 2: SA or BAP with the addition of HRP and H_2O_2.

As shown in lane 2 for each protein, RY- and RYR-tagged BAP and SA were cross-linked upon HRP treatment resulting in the disappearance of bands for mBAP and mSA. Thus, despite the surrounding positive charges and steric hindrance caused by arginine, the tyrosine residue in either RY-tag or RYR-tag can be recognized by HRP. The homoconjugation reaction of BAP-GY primarily produced a mBAP dimer as visualized by SDS-PAGE analysis (lane 2 for BAP-GY). Interestingly, from the results shown in lanes 2 for the BAPs with the positively charged Y-tags (BAP-RY and BAP-RYR), almost no mBAP dimer was observed after HRP treatment and the band intensity for the mBAP polymers significantly increased compared with BAP-GY. The difference of cross-linking behavior between BAP-GY and BAP-RY or BAP-RYR suggests that BAP-RY and BAP-RYR cross-linked via some of their intrinsic tyrosine residues. BAP itself has a relatively low pI value, ~4.5,[24] so the BAP surface charges are strongly negative under the reaction conditions at pH 8.0. Meanwhile, RY- and RYR-tags have positive charges within a small region. Therefore, RY- and RYR-tags electrostatically interacted with BAP itself and cross-linked with the intrinsic tyrosine residues on BAP, resulting in complex conjugates which appeared as polymers on SDS-PAGE. In contrast, in the case of SA, we could not see a clear difference in reactivity between the positively charged Y-tags and GY-tag, all resulting in the formation of broad, blurred bands of mSA polymer. This is probably because SA has several intrinsic tyrosine residues that are largely exposed on its surface which can react with GY-tag.[4]

DY- and DYD-tagged BAP and SA showed much lower reactivity compared with other mutants against HRP treatment

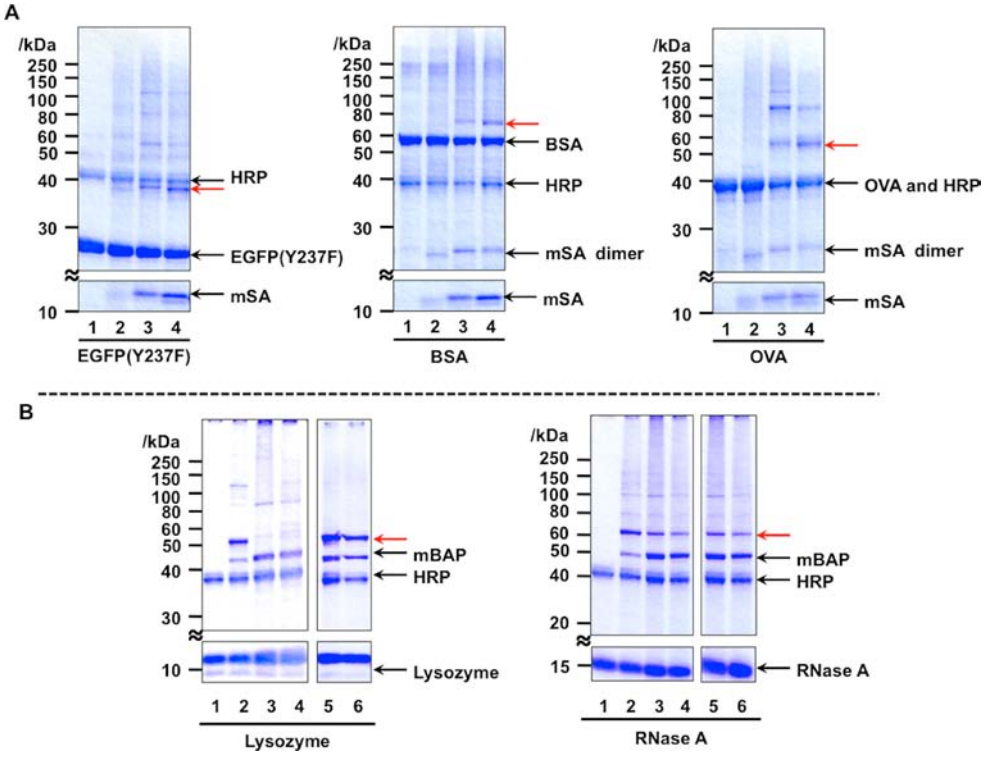


Figure 2. SDS-PAGE analyses of the heteroconjugation reaction of negatively charged proteins with SA mutants (A) and positively charged proteins with BAP mutants (B). All lanes: HRP and H_2O_2 were added. Lane 1: each protein; Lane 2: each protein with the addition of GY-tagged SA or BAP; Lane 3: each protein with the addition of RY-tagged SA or BAP; Lane 4: each protein with the addition of RYR-tagged SA or BAP; Lane 5: each protein with the addition of BAP-DY; Lane 6: each protein with the addition of BAP-DYD. The red arrows indicate bands corresponding to heteroconjugates of each protein with mSA or mBAP.

dx.doi.org/10.1021/bc300137s | *Bioconjugate Chem.* 2012, 23, 1600–1609

Table 1. Properties of Proteins Used in this Study[a]

proteins	M.W.	pI	Tyr	self-cross-linking upon HRP treatment
WT-BAP	48 809.48[b]	4.5[24]	11	ND
BAP-GY	49 810.59[b]	5.73[b]	12	High (cross-linking is selective at GY-tag)
BAP-DY or -DYD	50 300.97[b]	5.44[b]	12	Low (inhibited by electrostatic repulsion)
BAP-RY or -RYR	50 465.37[b]	6.06[b]	12	High (intrinsic Tyr residues are involved)
WT-SA	13 402.62[b]	5−6[32]	6	Low (Y72 is recognized by HRP[4])
SA-GY	13 794.00[b]	6.04[b]	7	High (intrinsic Tyr residues are involved)
SA-DY or -DYD	14 026.15[b]	4.74[b]	7	Low (inhibited by electrostatic repulsion)
SA-RY or -RYR	14 190.54[b]	9.34[b]	7	High (intrinsic Tyr residues are involved)
EGFP(Y237F)	27 879.52[b]	4.6−5.4[25]	10	ND
BSA	67 kDa	4.6[26]	20	ND
OVA	45 kDa	4.6[27]	10	ND
Lysozyme	14 kDa	9.3[28]	3	ND
RNase A	14 kDa	9.6[29]	6	ND
HRP	44 kDa	9.4[33]	5[c]	ND

[a]M.W.: molecular weight of monomer; ND: not detected; Tyr: number of tyrosine residues in a single polypeptide chain. [b]Calculated values using a web tool, Compute pI/M_w, on ExPASy server at http://web.expasy.org/compute_pi/. [c]Based on the sequence of HRP C1A (PDB:1H58).

as observed by the intact bands for mBAP and mSA after HRP treatment. Since the number of carbons in the side chain of aspartic acid is smaller than that of arginine, the effect of the steric hindrance on HRP recognition of the tyrosine residue can be excluded as a possible reason for the low reactivity. Alternatively, it is possible that the negative charges hampered the HRP recognition. The reactivity of DY-tag and DYD-tag will be discussed further in subsequent sections.

Heteroconjugation Reaction of BAP and SA Mutants with Various Proteins. Next, to further investigate the cross-linking behavior of reactive RY- and RYR-tags, heteroconjugation reactions of SA-RY and SA-RYR with negatively charged proteins, EGFP(Y237F) (pI: 4.6−5.4),[25] BSA (pI: 4.6),[26] and OVA (pI: 4.6),[27] were conducted, and the results of SDS-PAGE analyses are shown in Figure 2. In lanes 3 and 4 for each protein in Figure 2A, bands corresponding to the heteroconjugates of mSA with each protein emerged after HRP treatment. The corresponding bands were not observed in lanes 2 for BSA and OVA, where the band for co-cross-linked SA-GY was identified. EGFP(Y237F) has several tyrosine residues that are largely exposed on its surface; therefore, it formed heteroconjugates with SA-GY. However, the band intensity of the heteroconjugate was weaker than that observed in lanes 3 and 4. Taken together with the results of the homoconjugation reaction of BAP-RY and BAP-RYR (Figure 1A), it can be concluded that the protein heteroconjugation reaction was directed to the negatively charged proteins by the positively charged RY-tag and RYR-tag.

Furthermore, RY- and RYR-tagged BAP mutants were treated by HRP in the presence of the positively charged proteins lysozyme (pI: 9.3)[28] and RNase A (pI: 9.6), [29] to determine the reactivity of RY- and RYR-tags against positively charged proteins. Also, BAP-DY and BAP-DYD were employed in this experiment to identify whether the low reactivity of the negatively charged Y-tags against HRP treatment was because the negative charges inhibit the recognition of HRP or the negative charges repel each other, hence hampering the cross-linking of tyrosyl radicals. As shown in lane 2, the BAP-GY cross-linked with the lysozyme after HRP treatment because of some exposed tyrosine residues on lysozyme and the electrostatic interaction between positively charged lysozyme and negatively charged BAP itself, resulting in a band for the mBAP-lysozyme conjugate at around 50 kDa. In contrast, corresponding bands for the heteroconjugates were not clearly observed in lanes 3 and 4 for lysozyme where BAP-RY and BAP-RYR were co-cross-linked, respectively. These results indicate that the positive charges on the RY- and RYR-tags inhibited the approach of the Y-tag to the positively charged lysozyme. RNase A co-cross-linked with all of the BAP mutants, resulting in a band for the heteroconjugate at around 60 kDa (lanes 2, 3, and 4 for RNase A in Figure 2B). Yet, the intensity of the bands decreased in BAP-RY and BAP-RYR compared with BAP-GY, suggesting the inhibitive effect of cross-linking with RNase A. The positive charge of the RNase A is concentrated mainly on the surface of its RNA binding site while the remainder is not so highly positively charged (PDB ID: 2AAS). In contrast, the positive charges are widely distributed on the whole surface of lysozyme (PDB ID: 1LYS). We assumed that the differences in the charge distribution on the protein surface between RNase A and lysozyme caused the differences in the cross-linking behaviors.

Intriguingly, as shown from the results of lanes 5 and 6 for both lysozyme and RNase A, BAP-DY and BAP-DYD were co-cross-linked with these positively charged proteins with considerably high efficiency compared with BAP-GY (lane 2). When the DY- and DYD-tagged BAP and SA were treated by HRP alone, almost no self-cross-linked products were observed. Thus, it can be concluded that, in the homoconjugation reaction of DY- and DYD-tagged BAPs and SAs, the DY- and DYD-tags were indeed recognized by HRP in the solution, but they repelled each other, and the negatively charged BAP and SA resulting in suppression of the self-cross-linking. It was also interesting to understand how the activated DY- and DYD-tags act under conditions where there is no cross-linking partner. It is possible that the activated negatively charged Y-tags are repaired by the reaction with superoxide, [30] which can be generated by the alternative catalytic cycle of HRP.[31] They may also react with proteinaceous impurities in the reaction mixture, which is suggested by the formation of very weak broad bands in the high-molecular-weight region in lanes 2 for BAP-DY and BAP-DYD in Figure 1; however, further study is needed to clarify this point.

The properties of all of the proteins used in this study are summarized in Table 1. From the results obtained, it was clearly shown that the negative and positive charges on the Y-tags definitely alter the cross-linking behavior of Y-tagged proteins,

and it was largely affected by the charge on the protein surfaces. Since the model proteins studied here, BAP and SA, are both negatively charged under the reaction conditions of pH 8.0 (pI values for BAP and SA are 4.5 and 5−6,[32] respectively), the RY- and RYR-tags resulted in random self-cross-linking of BAP or SA upon HRP treatment, but they inhibited the co-cross-linking of BAP against positively charged proteins. The negative charges on the DY- and DYD-tags almost completely suppressed the self-cross-linking of BAP and SA, but the BAP with the negatively charged Y-tags showed co-cross-linking ability against positively charged proteins. From these results, two conclusions were drawn. One is that the RY- and RYR-tags were mainly cross-linked to the intrinsic tyrosine residues of BAP and SA, not to the tyrosine residue in the RY- and RYR-tags. Second is that, if the RY- and RYR-tags were tethered to positively charged proteins, they might show reactivity as low as that of the DY- and DYD-tags obtained in this study.

One interesting fact is that the electrostatic interaction between HRP and those positively or negatively charged Y-tags showed no apparent effect on the cross-linking of Y-tagged proteins. The exact pI value of HRP used in this study is not clear since HRP exists as a group of isozymes. However, the pI value for one of the major isozymes, HRP C1, was reported to be 9.4,[33] and also, the HRP passes through an anion-exchange column equilibrated with a buffer of pH 8.0;[22] it can be predicted that the HRP used in this study was positively charged in the reaction condition. Even though HRP is positively charged, the DY- and the DYD-tagged proteins showed no reactivity against HRP. The inertness of HRP against Y-tag mediated protein cross-linking is probably due to the glycosylation on HRP, by which sugar chains might act like shields against the radical species that HRP generates. Also, the positively charged Y-tags were efficiently recognized by positively charged HRP. This result indicates that the electrostatic repulsion may not dominate the substrate recognition of HRP.

The results showed that the cross-linking of Y-tagged proteins was significantly affected by the electrostatic interaction between substrate proteins. This can be explained as follows. The HRP mediated protein cross-linking reaction using Y-tags is initiated by formation of tyrosyl radicals. As the tyrosyl radicals have a short lifetime, the subtle repulsive or attractive interaction between Y-tags and proteins showed major impact on the tyrosyl radical coupling reaction. That is to say, the cross-linking of Y-tagged proteins was controlled by the spatial-temporal manner in which tyrosyl radical accession is regulated by the electrostatic interaction.

Heteroconjugation Reaction between BAP Mutants and SA Mutants. Next, BAP mutants and SA mutants were co-cross-linked with each other to investigate the cross-linking properties between electrostatically charged Y-tags. The representative results of the SDS-PAGE and native-PAGE analyses for the heteroconjugation reaction between WT-BAP, BAP-GY, BAP-DYD, or BAP-RYR and the SA mutants are shown in Figure 3 (see Figure S1 and Figure S2 in the Supporting Information for more results).

From lanes 3 and 4 for BAP-GY in Figure 3A, where SA-RY and SA-RYR were co-cross-linked, respectively, the band intensity of the mBAP dimer at 100 kDa significantly decreased while the band intensity of the polymers increased, compared with lane 1 where SA-GY was co-cross-linked. The differences in the resulting bands were caused by the following reason (Figure 4). The BAP-GY cross-links by itself through its GY-tag

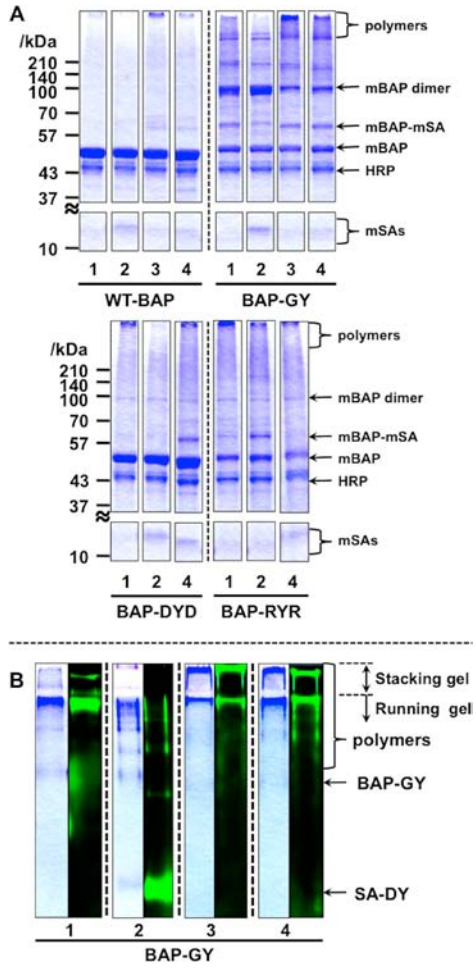


Figure 3. SDS-PAGE analyses (A) and native-PAGE analyses (B) of the heteroconjugation reaction of BAP-GY with SA mutants. All lanes: HRP and H_2O_2 were added; Lane 1: BAP with the addition of SA-GY; Lane 2: BAP with the addition of SA-DY; Lane 3: BAP with the addition of SA-RY; Lane 4: BAP with the addition of SA-RYR. In the native-PAGE analysis, SA was visualized by biotin-4-fluorescein (right of each picture).

mostly in a linear form,[22] which appears as mBAP dimers in SDS-PAGE analysis (lane 2 for BAP-GY in Figure 1A and Figure 4A). Meanwhile, the positively charged Y-tags are capable of cross-linking with the intrinsic tyrosine residues of BAP, resulting in mBAP polymers (lane 2 for BAP-RY and BAP-RYR in Figure 1A and as depicted in Figure 4B). Also, in lanes 3 and 4 in Figure 3B, where SA-RY and SA-RYR were cross-linked with BAP-GY, a portion of the resultant BAP-SA conjugates barely entered the stacking gel, while most of the (BAP-GY)-(SA-GY) heteroconjugate penetrated through the stacking gel. The results obtained here indicate that the SAs with positively charged Y-tags directed the cross-linking of SAs toward negatively charged BAP-GY and favorably cross-linked not only with the GY-tag, but also with the intrinsic tyrosine residues, yielding less mBAP dimer and more mBAP-mSA polymers (Figure 4C). BAP possesses three tyrosine residues that are located near the protein surface and are suspected to be the cross-linking site with the positively charged Y-tags (Figure S3 in the Supporting Information). Meanwhile, SA has several largely exposed tyrosine residues, which can be cross-linked even with the GY-tag. In the heteroconjugation reaction between BAP-GY and SA with positively charged Y-tags, the

dx.doi.org/10.1021/bc300137s | Bioconjugate Chem. 2012, 23, 1600−1609

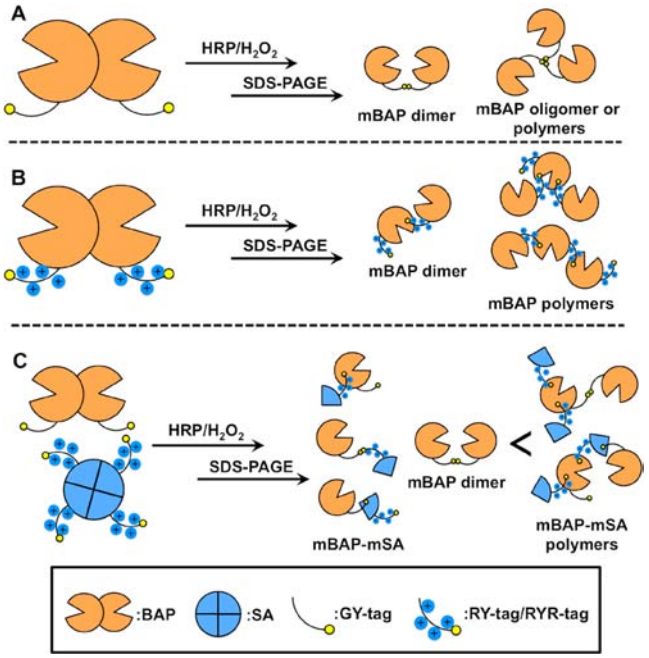


Figure 4. Schematic illustration of the possible forms of cross-linked BAP and SA. (A) Self-cross-linking of BAP-GY. (B) Self-cross-linking of BAP-RY or BAP-RYR. (C) Co-cross-linking of BAP-GY with SA-RY or SA-RYR. Only representative forms of cross-linking are illustrated.

intrinsic tyrosine residues of BAP are involved in cross-linking with the positively charged Y-tags. In such conditions, both BAP and SA have multiple cross-linking sites in each polypeptide, leading to formation of highly complex heteroconjugates (Figure 4C). This can be supported by the results in lanes 3 and 4 for WT-BAP in Figure 3A, where SA-RY and SA-RYR were capable of cross-linking with WT-BAP, resulting in mBAP-mSA bands around 60 kDa. In comparison with the combination of BAP-GY and SA-GY, the overall BAP-GY cross-linking yield was increased when BAP-GY and SA-RYR was co-cross-linked (Figure S4 in the Supporting Information). This result also supports the favorable cross-linking formation of RYR-tag with BAP. In addition, when WT-BAP was co-cross-linked with the SAs with positively charged Y-tags, precipitates were formed in the solution after HRP treatment. Precipitates were not observed for BAP-GY, suggesting that the GY-tag is actively involved in cross-linking with the RY- or RYR-tag to prevent the intrinsic tyrosine residues of BAP from cross-linking.

In Figure 3A, lane 2, as shown for BAP-GY with the addition of SA-DY, in spite of the presence of reactive BAP-GY in the system, the mSA band remained and the profiles of the resulting bands of conjugates are almost same as that of WT-SA (Figure S1 and Figure S2 in the Supporting Information), suggesting that the negative charges on the DY-tag repelled the SAs from BAP. When SAs with negatively charged Y-tags were co-cross-linked with BAP-RY or BAP-RYR, the negative charges worked to direct the cross-linking of SAs toward BAP, resulting in the formation of bands for mBAP-mSA as observed in SDS-PAGE analysis (lane 2 for BAP-RYR in Figure 3A). Similar results were obtained when the SAs with positive Y-tags and BAPs with negative Y-tags were co-cross-linked (lane 4 for BAP-DYD in Figure 3A). From these results, it was concluded that the charges on the Y-tags interact not only with the charges of the protein surfaces but also with the charges on the Y-tags.

Enzymatic Activities of BAP-SA Conjugates. To investigate the effect of the cross-linking using the SAs with positively charged Y-tags, the BAP enzymatic activities of the BAP-SA conjugate were measured after the heteroconjugation reaction. WT-BAP heteroconjugates co-cross-linked with SA-RY and SA-RYR formed precipitates after HRP treatment; therefore, measurement of the enzymatic activity of these heteroconjugates was not possible. The results for the (WT-BAP)-(SA-GY) conjugates and (BAP-GY)-SA conjugates are shown in Figure 5. All of the BAP-SA conjugates retained more

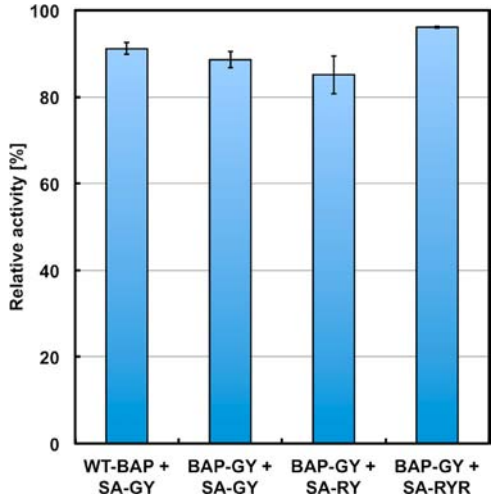


Figure 5. Enzymatic activity of BAP-SA conjugates. The enzymatic activities of untreated WT-BAP and BAP-GY were defined as 100% of the relative activity of each BAP.

than 80% of their enzymatic activities. The negative effect of co-cross-linking with positively charged Y-tags on the enzymatic activity was alleviated for the BAP-GY heteroconjugates. By comparison, the heteroconjugation reaction of RY- or RYR-tagged BAPs with SA mutants significantly decreased their enzymatic activities by about 40%, probably because of intramolecular cross-linking of the RY- and RYR-tags onto BAP's intrinsic tyrosine residues (Figure S6 in the Supporting Information). When the SA-DY and SA-DYDs were co-cross-linked, the reduction in the enzymatic activity of BAP-RY and BAP-RYR was relatively small, although the overall heteroconjugation efficiency was not high, probably due to intramolecular cross-linking of BAPs with positively charged Y-tags (Figure S2 in the Supporting Information). In Figure 3B, it is clearly seen that the BAP-GY was highly cross-linked to form extremely complex heteroconjugates with SAs with retaining the biotin binding ability. It is amazing that even in such a complex highly cross-linked form, the (BAP-GY)-SA conjugates substantially retained the BAP enzymatic activity, demonstrating the advantage of tethering the GY-tags to BAP.

Kinetically Controlled Tyrosine Radical Coupling Reaction. The reactivities of RY- and RYR-tags were evaluated by measuring the dityrosine fluorescence change upon HRP treatment (Figure 6). The fluorescence intensity for SA-RY increased rapidly, implying that the formation of dityrosine was completed within a short time period. The fluorescence intensity of SA-RYR increased slowly within the time period of measurement. Since the tyrosine residue in the RYR-tag is encompassed by positively charged arginines, the steric hindrance and the effect of the positive charges on the tyrosine

dx.doi.org/10.1021/bc300137s | Bioconjugate Chem. 2012, 23, 1600−1609

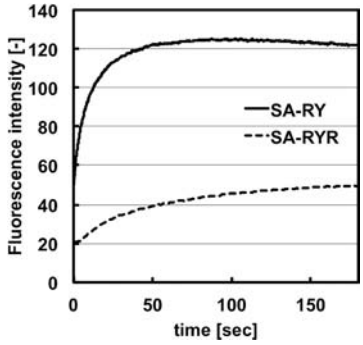


Figure 6. Time-driven measurements of fluorescence intensity of dityrosine at 420 nm.

residue are maximized. Therefore, the recognition of the tyrosine residue by HRP is inhibited, resulting in slow dityrosine formation. The results suggested that heteroconjugation can be kinetically controlled.

When focusing on the molar ratio of the protein components of BAP-SA conjugates, the heteroconjugates which contain a higher ratio of BAP to SA are likely to perform well for the purposes of detecting a biotin moiety immobilized on a solid surface. To control the conjugation ratio between $(BAP)_n$ and $(SA)_m$ as $n > m$, we attempted to kinetically control the BAP-SA heteroconjugation using BAP-GY and either SA-GY or SAs with positively charged Y-tags. The characteristics of heteroconjugates obtained under different conditions were compared by BAP enzymatic activity on a biotin-coated plate (Figure 7).

The BAP-SA conjugates prepared using SA-RY or SA-RYR showed higher enzymatic activity than the (BAP-GY)-(SA-GY) conjugate (Figure 7A). In particular, (BAP-GY)-(SA-RYR) performed the best in this experiment, increasing the BAP enzyme activity by 40% of the conjugate using SA-GY. The BAP enzymatic activities of all samples were adjusted to 0.5 U/mL before immobilizing the BAP-SA conjugate on the biotin-coated plate, and the BAP enzymatic activity of each (BAP-GY)-SA conjugate measured in the solution state was essentially identical (Figure 5). Hence, the variations in the BAP enzymatic activities measured on the plate represent the differences in the BAP-SA conjugation ratio. The GY-tag gives BAP the ability to intermolecularly cross-link through the Y-tag while minimizing the unfavorable intramolecular cross-linking between the GY-tag and the intrinsic tyrosine residues. The RYR-tag shows slow reactivity upon HRP treatment providing more opportunities for BAP-GY to yield $(BAP-GY)_n$ homoconjugates,[22] and it also shows favorable cross-linking formation toward negatively charged BAP-GY due to its positive charges. As a result, the combination of BAP-GY and SA-RYR worked well to obtain the $(BAP-GY)_n$-$(SA-RYR)_m$ conjugate of which $n > m$. The results described herein indicated that, by introducing the GY-tag to BAP and the RYR-tags to SA, the heteroconjugation reaction between BAP and SA was kinetically controlled.

To test this idea further, we performed a two-step conjugation reaction where BAP-GY was first pretreated by HRP to form $(BAP-GY)_n$ homoconjugates, then SAs were co-cross-linked toward $(BAP-GY)_n$. Figure 7B clearly illustrates the advantage of SA-RY and SA-RYR over SA-GY, as the conjugation partner for BAP-GY. The BAP-SA conjugate prepared by using SA-RY and SA-RYR showed about double and triple activity of the conjugate of SA-GY, respectively, and notably, the (BAP-GY)-(SA-RYR) conjugate showed quite

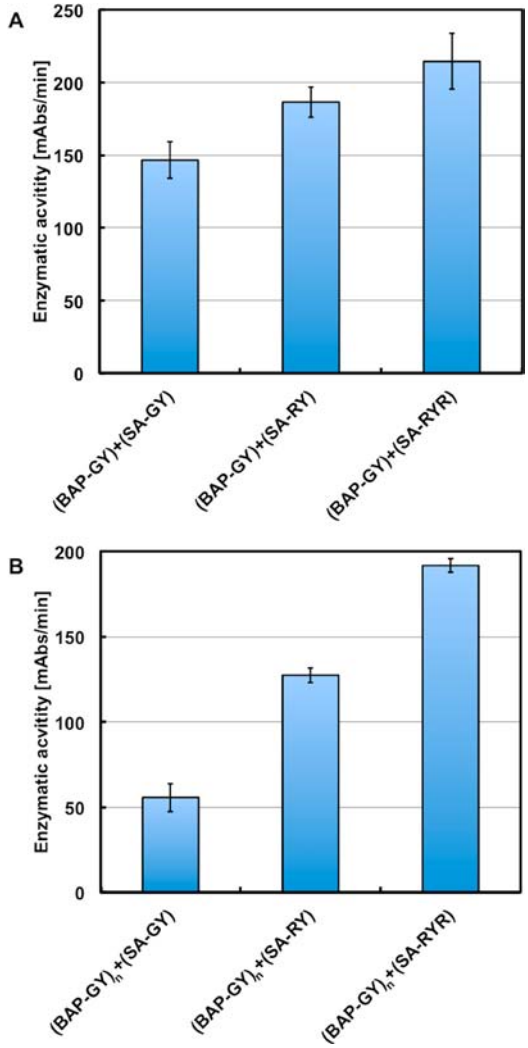


Figure 7. Enzymatic activity of the BAP-SA conjugates on a biotin-coated plate. (A) BAP-SA conjugates prepared by one-step conjugation reaction; (B) BAP-SA conjugates prepared by two-step conjugation reaction.

similar enzymatic activity to that prepared by the single step. In the reaction system, many types of cross-linking are taking place such as intramolecular cross-linking of Y-tags or Y-tags with intrinsic tyrosine residues and intermolecular cross-linking between $(BAP-GY)_n$-$(BAP-GY)_n$, $(BAP-GY)_n$-SA, and SA-SA. It can be considered that the intermolecular cross-linking between $(BAP-GY)_n$ and SA competes directly with the cross-linking between SA-SA, since the cross-linking between $(BAP-GY)_n$-$(BAP-GY)_n$ seems negligible due to the low concentration of $(BAP-GY)_n$. In Figure 7B, the SAs with positively charged Y-tags had better enzymatic activity than the SA-GY in the two-step conjugation, indicating that the RY- and RYR-tags have a higher tendency to cross-link with $(BAP-GY)_n$ than the GY-tag. The SA-RYR showed higher performance than the SA-RY because the self-cross-linking rate of the RYR-tag is lower than that of RY-tag (Figure 6), indicating less SA-SA cross-linking.

Last, the effect of the conjugation pH on the activity of BAP-SA conjugates was evaluated. The BAP-SA conjugates were prepared with different pairs of BAP and SA mutants at different pH, and the enzymatic activity was measured after immobilization on the biotin-coated plate (Figure 8). The BAP-

dx.doi.org/10.1021/bc300137s | Bioconjugate Chem. 2012, 23, 1600−1609

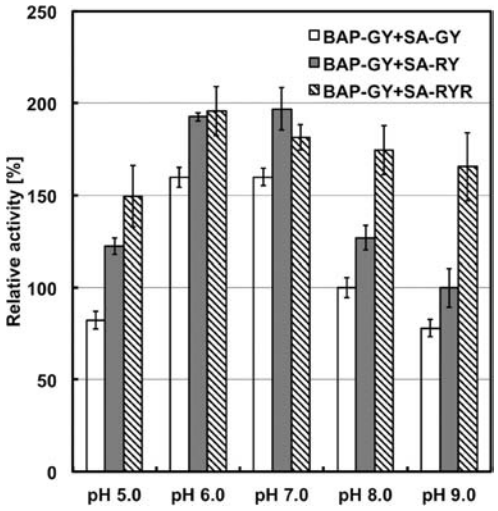


Figure 8. Effect of the conjugation pH on the function of BAP-SA conjugates on a biotin-coated plate. The measured activity of (BAP-GY)-(SA-GY) conjugate prepared at pH 8.0 was defined as 100%. pH 5.0: acetate buffer; pH 6.0 and pH 7.0: phosphate buffer; pH 8.0 and pH 9.0: Tris-HCl buffer.

SA conjugates prepared at pH 6.0 and 7.0 showed high enzymatic activity for all combinations of BAP and SA. Since the pI value of SA is close to neutral, the repulsive interaction between BAP-GY and SA-GY is minimized at pH 6.0 and 7.0, resulting a higher cross-linking efficiency compared with higher pH conditions where SA-GY is negatively charged. The advantages of positive charges on RY-tag and RYR-tag over GY-tag still can be observed at these pH conditions, probably because the positive charges on Y-tag act to hamper the self-cross-linking of SA mutants while facilitating the cross-linking toward negatively charged BAP-GY. In addition, HRP has its optimal condition at pH 6.0−6.5; therefore, the Y-tags were efficiently activated by HRP at this pH range. At pH 5.0, the activity of all of BAP-SA conjugates was decreased, probably due to lower HRP activity. Intriguingly, the (BAP-GY)-(SA-RYR) conjugates prepared at the conjugation pH values of 8.0 and 9.0 showed high activity, as well as at pH 6.0 and 7.0. The other BAP-SA conjugates decreased the activity on the plate at pH 8.0 and 9.0. The conjugation pH independency of (BAP-GY)-(SA-RYR) conjugate can be explained by the reduced tyrosine radical formation rate of RYR-tag.

From the results obtained here, it can be concluded that, in the tyrosyl radical mediated protein cross-linking reaction, both the rate of tyrosyl radical formation and the coupling reaction rate are important to the heteroconjugation. The position of tyrosine residue in the Y-tag affects the tyrosyl radical formation, i.e., HRP recognition. The positive and negative charges on Y-tags affect mainly the tyrosyl radical coupling reaction, i.e., the reaction takes place after HRP recognition. For comparison, in the enzyme-mediated protein heteroconjugation catalyzed by MTG or SrtA,[13−15] The cross-linking process is strictly regulated by substrates recognition by these enzymes, and the cross-linking efficiency is mostly dependent on whether the peptide sequence is suitable or not. Therefore, it can be said that controlling the protein coupling reaction by using such electrostatic interaction is unique to the tyrosyl radical-mediated protein cross-linking. The insights obtained in this study will be helpful for further application of the protein cross-linking method using Y-tag and HRP.

In conclusion, by controlling the intramolecular and intermolecular cross-linking rates by means of tethering appropriate electrostatic interactions onto the Y-tags and also optimizing the Y-tag sequence, it is possible to kinetically control the heteroconjugation reactions of distinct proteins via a tyrosine radical-coupling reaction to maximize a specific functionality of the protein heteroconjugates.

CONCLUSION

The cross-linking of electrostatically charged Y-tags was strongly dependent on the charges of the protein surfaces. The DY- and DYD-tags showed a considerably high cross-linking efficiency against positively charged protein, while the DY- and DYD-tagged BAP and SA were almost inactive in terms of self-cross-linking. In contrast, the RY- and RYR-tagged BAP and SA were efficiently self-cross-linked and also co-cross-linked with negatively charged proteins. In the heteroconjugation reaction of BAP and SA, SAs possessing positively charged Y-tags favorably co-cross-linked with negatively charged BAP with GY-tag. The GY-tag on BAP had high self-cross-linking ability while retaining BAP's enzymatic activity. When comparing the reactivity of RY- and RYR-tags, the RYR-tag formed dityrosine pairs slower than the RY-tag. Taking all the results into consideration, it was concluded that the BAP-SA conjugation pair which had the best performance on the biotin-coated plate was BAP-GY and SA-RYR. The (BAP-GY)-(SA-RYR) conjugate showed higher enzymatic activity on a biotin-coated plate compared with its counterpart, the (BAP-GY)-(SA-GY) conjugate. From our results, it can be concluded that by introducing very simple electrostatic interactions between protein and Y-tags and by optimizing the HRP recognition reactivity of Y-tag it was possible to kinetically control the heteroconjugation of proteins via a tyrosyl-radical coupling reaction.

ASSOCIATED CONTENT

Supporting Information

Heteroconjugation reaction between BAP mutants and SA mutants. The intrinsic tyrosine residues of BAP and SA, which are suspected to be involved in cross-linking. Study of cross-linking efficiency of BAP in the heteroconjugation reaction between BAP and SA. Thrombin treatment reaction on BAP-SA conjugates. The enzymatic activity of BAP-RY and BAP-RYR after heteroconjugation reaction with SA mutants. This material is available free of charge via the Internet at http://pubs.acs.org.

AUTHOR INFORMATION

Corresponding Author

*Phone: +81-92-802-2806. FAX: +81-92-802-2810. E-mail: nori_kamiya@mail.cstm.kyushu-u.ac.jp.

Notes

The authors declare no competing financial interest.

ACKNOWLEDGMENTS

This work was supported in part by a Grant-in-Aid for the Global COE program, "Science for Future Molecular Systems" from the Ministry of Education, Culture, Sports, Science and Technology of Japan. K.M. was supported by Research Fellowships of the Japan Society for the Promotion of Science (JSPS) for Young Scientists.

■ ABBREVIATIONS

BAP, bacterial alkaline phosphatase; BSA, bovine serum albumin; EDTA, ethylenediaminetetraacetic acid; EGFP, enhanced green fluorescent protein; SA, streptavidin; NPP, nitrophenylphosphate; HRP, horseradish peroxidase; m, monomeric; NP, nitrophenol; OVA, ovalbumin; RNase, ribonuclease; SEC, size-exclusion chromatography; SDS-PAGE, sodium dodecyl sulfate poly acrylamide gel electrophoresis; Tris, tris(hydroxymethyl)aminomethane

■ REFERENCES

(1) Shah, D., and Shen, W.-C. (1996) Transcellular delivery of an insulin-transferrin conjugate in enterocyte-like caco-2 cells. *J. Pharm. Sci. 85*, 1306−1311.

(2) Giepmans, B. N. G., Adams, S. R., Ellisman, M. H., and Tsien, R. Y. (2006) The Fluorescent toolbox for assessing protein location and function. *Science 312*, 217−224.

(3) Hirakawa, H., and Nagamune, T. (2010) Molecular assembly of P450 with ferredoxin and ferredoxin reductase by fusion to PCNA. *ChemBioChem 11*, 1517−1520.

(4) Minamihata, K., Goto, M., and Kamiya, N. (2011) Protein heteroconjugation by the peroxidase-catalyzed tyrosine coupling reaction. *Bioconjugate Chem. 22*, 2332−2338.

(5) Kostelny, S. A., Cole, M. S., and Tso, J. Y. (1992) Formation of a bispecific antibody by the use of leucine zippers. *J. Immunol. 148*, 1547−1553.

(6) Newman, R. H., Fosbrink, M. D., and Zhang, J. (2011) Genetically encodable fluorescent biosensors for tracking signaling dynamics in living cells. *Chem. Rev. 111*, 3614−3666.

(7) Guo, C., Li, Z., Shi, Y., Xu, M., Wise, J. G., Trommer, W. E., and Yuan, J. (2004) Intein-mediated fusion expression, high efficient refolding, and one-step purification of gelonin toxin. *Protein Expr. Purif. 37*, 361−367.

(8) Hackenberger, C. P. R., Chen, M. M., and Imperiali, B. (2006) Expression of N-terminal Cys-protein fragments using an intein refolding strategy. *Bioorg. Med. Chem. 14*, 5043−5048.

(9) Bundy, B. C., and Swartz, J. R. (2010) Site-specific incorporation of *p*-propargyloxyphenylalanine in a cell-free environment for direct protein-protein click conjugation. *Bioconjugate Chem. 21*, 255−263.

(10) Xiao, J., Hamilton, B. S., and Tolbert, T. J. (2010) Synthesis of N-terminally linked protein and peptide dimers by native chemical ligation. *Bioconjugate Chem. 21*, 1943−7.

(11) Ferrari, E., Soloviev, M., Niranjan, D., Arsenault, J., Gu, C., Vallis, Y., O'Brien, J., and Davletov, B. (2012) Assembly of protein building blocks using a short synthetic peptide. *Bioconjugate Chem. 23*, 479−484, DOI: 10.1021/bc2005208.

(12) Sunbul, M., and Yin, J. (2009) Site specific protein labeling by enzymatic posttranslational modification. *Org. Biomol. Chem. 7*, 3361−3371.

(13) Tanaka, T., Kamiya, N., and Nagamune, T. (2004) Peptidyl linkers for protein heterodimerization catalyzed by microbial transglutaminase. *Bioconjugate Chem. 15*, 491−497.

(14) Yamamoto, T., and Nagamune, T. (2009) Expansion of the sortase-mediated labeling method for site-specific N-terminal labeling of cell surface proteins on living cells. *Chem. Commun.*, 1022−1024.

(15) Parthasarathy, R., Subramanian, S., and Boder, E. T. (2007) Sortase A as a novel molecular "stapler" for sequence-specific protein conjugation. *Bioconjugate Chem. 18*, 469−476.

(16) Keppler, A., Gendreizig, S., Gronemeyer, T., Pick, H., Vogel, H., and Johnsson, K. (2003) A general method for the covalent labeling of fusion proteins with small molecules *in vivo*. *Nat. Biotechnol. 21*, 86−89.

(17) Gauchet, C., Labadie, G. R., and Poulter, C. D. (2006) Regio- and chemoselective covalent immobilization of proteins through unnatural amino acids. *J. Am. Chem. Soc. 128*, 9274−9275.

(18) Wong, L. S., Thirlway, J., and Micklefield, J. (2008) Direct site-selective covalent protein immobilization catalyzed by a phosphopantetheinyl transferase. *J. Am. Chem. Soc. 130*, 12456−12464.

(19) Stayner, R. S., Min, D.-J., Kiser, P. F., and Stewart, R. J. (2005) Site-specific cross-linking of proteins through tyrosine hexahistidine tags. *Bioconjugate Chem. 16*, 1617−1623.

(20) Rieker, J. D., and Hu, J. C. (2000) Molecular applications of fusions to leucine zippers. *Methods Enzymol. 328*, 282−296.

(21) Glover, J. N. M., and Harrison, S. C. (1995) Crystal structure of the heterodimeric bZIP transcription factor c-Fos-c-Jun bound to DNA. *Nature 373*, 257−261.

(22) Minamihata, K., Goto, M., and Kamiya, N. (2011) Site-specific protein cross-linking by peroxidase-catalyzed activation of a tyrosine-containing peptide tag. *Bioconjugate Chem. 22*, 74−81.

(23) Tanaka, Y., Doi, S., Kamiya, N., Kawata, N., Kamiya, S., Nakama, K., and Goto, M. (2008) A chemically modified glass surface that facilitates transglutaminase-mediated protein immobilization. *Biotechnol. Lett. 30*, 1025−1029.

(24) Garen, A., and Levinthal, C. (1960) A fine-structure genetic and chemical study of the enzyme alkaline phosphatase of *E. coli*. *Biochim. Biophys. Acta 38*, 470−483.

(25) Penna, T. C. V., Ishii, M., Cholewa, O., and De Souza, L. C. (2004) Thermal characteristics of recombinant green fluorescent protein (GFPuv) extracted from *Escherichia coli*. *Lett. Appl. Microbiol. 38*, 135−139.

(26) Chaiyasut, C., and Tsuda, T. (2001) Isoelectric points estimation of proteins by electroosmotic flow: pH relationship using physically adsorbed proteins on silica gel. *Chromatography 22*, 91−95.

(27) Holen, E., and Elsayed, S. (1990) Characterization of four major allergens of hen-egg white by IEF/-SDS-PAGE combined with electrophoretic transfer and IgE-immunoautoradiography. *Int. Arch. Allergy Immunol. 91*, 136−141.

(28) Alderton, G., Ward, W. H., and Febold, H. L. (1945) Isolation of lysozyme from egg white. *J. Biol. Chem. 157*, 43−58.

(29) Anderson, E. A., and Alberty, R. A. (1948) Homogeneity and the electrophoretic behavior of some proteins. II. Reversible spreading and steady-state boundary criteria. *J. Phys. Chem. 52*, 1345−1364.

(30) Hunter, E. P. L., Desrosiers, M. F., and Simic, M. G. (1989) The effect of oxygen, antioxidants, and superoxide radical on tyrosine phenoxyl radical dimerization. *Free Radical Biol. Med. 6*, 581−585.

(31) Arnao, M. B., Acosta, M., del Río, J. A., Varón, R., and García-Cánovas, F. (1990) A kinetic study on the suicide inactivation of peroxidase by hydrogen peroxide. *Biochim. Biophys. Acta 1041*, 43−47.

(32) Diamandis, E. P., and Christopoulos, T. K. (1991) The biotin-(strept)avidin system: principles and applications in biotechnology. *Clin. Chem. 37*, 625−636.

(33) Aibara, S., Yamashita, H., Mori, E., Kato, M., and Morita, Y. (1982) Isolation and characterization of five neutral isoenzymes of horseradish peroxidase. *J. Biochem. 92*, 531−539.

Bioconjugate Chemistry

Article

pubs.acs.org/bc

Design, Synthesis, and Biological Evaluation of Novel cRGD–Paclitaxel Conjugates for Integrin-Assisted Drug Delivery

Michael Pilkington-Miksa,[†] Daniela Arosio,[‡] Lucia Battistini,[§] Laura Belvisi,[#] Marilenia De Matteo,[†] Francesca Vasile,[†] Paola Burreddu,[∥] Paola Carta,[▲] Gloria Rassu,[∥] Paola Perego,[⊥] Nives Carenini,[⊥] Franco Zunino,[⊥] Michelandrea De Cesare,[⊥] Vittoria Castiglioni,[□,¶] Eugenio Scanziani,[□,¶] Carlo Scolastico,[†] Giovanni Casiraghi,[§] Franca Zanardi,*[,§] and Leonardo Manzoni*[,‡]

[†]Centro Interdipartimentale Studi Biomolecolari e Applicazioni Industriali, Università degli Studi di Milano, Via Fantoli 16/15, I-20138 Milano, Italy

[‡]Istituto di Scienze e Tecnologie Molecolari, Consiglio Nazionale delle Ricerche, Via Golgi 19, I-20133 Milano, Italy

[§]Dipartimento Farmaceutico, Università degli Studi di Parma, Parco Area delle Scienze 27A, I-43124 Parma, Italy

[#]Dipartimento di Chimica Organica e Industriale, Università degli Studi di Milano, Via Venezian 21, I-20133 Milano, Italy

[∥]Istituto di Chimica Biomolecolare, Consiglio Nazionale delle Ricerche, Traversa La Crucca 3, I-07100 Li Punti, Sassari, Italy

[▲]Porto Conte Ricerche Srl, I-07041 Tramariglio Alghero, Sassari, Italy

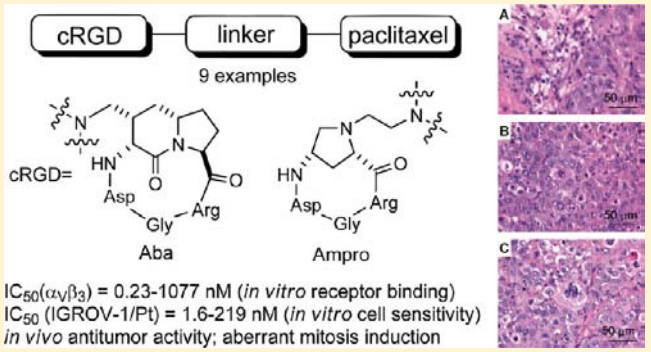
[⊥]Dipartimento di Oncologia Sperimentale e Medicina Molecolare, Fondazione IRCCS Istituto Nazionale Tumori, Via Amadeo 42, I-20133 Milano, Italy

[□]Dipartimento di Patologia Animale, Igiene e Sanità Pubblica Veterinaria (DIPAV), Facoltà di Medicina Veterinaria, Università degli Studi di Milano, Via Celoria 10, I-20133 Milano, Italy

[¶]Mouse and Animal Pathology Laboratory, Fondazione Filarete, Viale Ortles 22/4, I-20139 Milano, Italy

Supporting Information

ABSTRACT: The efficacy of taxane-based antitumor therapy is limited by several drawbacks which result in a poor therapeutic index. Thus, the development of approaches that favor selective delivery of taxane drugs (e.g., paclitaxel, PTX) to the disease area represents a truly challenging goal. On the basis of the strategic role of integrins in tumor cell survival and tumor progression, as well as on integrin expression in tumors, novel molecular conjugates were prepared where PTX is covalently attached to either cyclic AbaRGD (Azabicycloalkane-RGD) or AmproRGD (Aminoproline-RGD) integrin-recognizing matrices via structurally diverse connections. Receptor-binding assays indicated satisfactory-to-excellent $\alpha_V\beta_3$ binding capabilities for most conjugates, while *in vitro* growth inhibition assays on a panel of human tumor cell lines revealed outstanding cell sensitivity values. Among the nine conjugate ensemble, derivative **21**, bearing a robust triazole ring connected to ethylene glycol units by an amide function and showing excellent cell sensitivity properties, was selected for *in vivo* studies in an ovarian carcinoma model xenografted in immunodeficient mice. Remarkable antitumor activity was attained, superior to that of PTX itself, which was associated with a marked induction of aberrant mitoses, consistent with the mechanism of action of spindle poisons. Overall, the novel cRGD-PTX conjugates disclosed here represent promising candidates for further advancement in the domain of targeted antitumor therapy.



INTRODUCTION

The curative potential of clinically available antitumor agents is limited by a number of factors which may include tumor-related factors (e.g., activation of drug resistance mechanisms by tumor cells), drug-related factors (e.g., inadequate intratumor concentration of the drug), tumor microenvironment interactions (e.g., hypoxia, microvesicle release), and individual features of the patients (i.e., genetic polymorphisms).[1] Thus, an impressive effort is still required in an attempt to optimize the use of available drugs, in particular, cytotoxic agents. Impressive advances in the molecular and biological characterization of human tumors have led to the identification of specific alterations exploitable for tumor targeting. In this context, strong interest for integrins has recently emerged.[2] Various

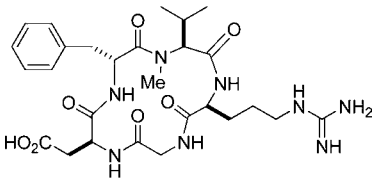
Received: April 5, 2012
Revised: May 21, 2012
Published: July 9, 2012

 © 2012 American Chemical Society

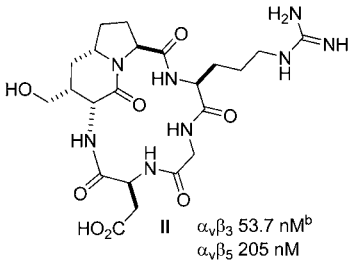
studies have indicated that integrins promote cell attachment and migration on the surrounding extracellular matrix and mediate cell interactions during several pathological processes.[2] Indeed, the available evidence supports a role for integrins in proliferation, migration, and survival of tumor cells, as well as in additional processes that favor tumor progression such as angiogenesis and inflammation.[2] In particular, specific integrin receptors, i.e., the $\alpha_V\beta_3$ and $\alpha_V\beta_5$ families, have been elected as compelling molecular indicators of tumor angiogenesis and tumor progression, invasion, and metastasis, since they are overexpressed on proliferating endothelial cells as well as on various tumor cells including breast,[3,4] glioma,[5] melanoma,[6,7] prostate,[8] and ovarian carcinoma.[9]

A large number of specific, highly potent $\alpha_V\beta_3$- and $\alpha_V\beta_5$-addressed small molecule ligands have been designed and implemented so far, which contain or mimic the key receptor-recognizing RGD (Arg-Gly-Asp) tripeptide motif;[10,11] these include the landmark cyclic pentapeptide c(RGDf[N-Me]V) (Cilengitide, **I**)[12] (Chart 1), the azabicycloalkane-based cyclic RGD semipeptide **II** (AbaRGD),[13] and the 4-aminoproline-based cyclic RGD semipeptide **III** (AmproRGD).[14]

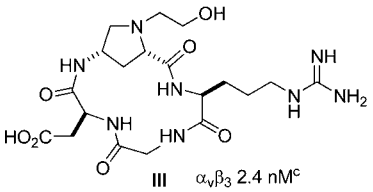
Chart 1High-Affinity $\alpha_V\beta_3$-Targeting Cyclic RGD Ligands[a]



I $\alpha_V\beta_3$ 0.6 nM[a]



II $\alpha_V\beta_3$ 53.7 nM[b]
$\alpha_V\beta_5$ 205 nM



III $\alpha_V\beta_3$ 2.4 nM[c]
$\alpha_V\beta_5$ 38 nM

[a]Ref 12. [b]Ref 13. [c]Ref 14.

Apart from the preeminent use of small-molecule integrin antagonists as antiangiogenic and antitumor agents per se,[10,11,15−18] such motifs may be exploited with even more success as *active targeting tools*, provided that appropriate cytotoxic and/or imaging cargos are consigned to them.[10,19−21] Since the pioneering work by Arap and Pasqualini,[22] where effective delivery of the antitumor agent doxorubicin to human breast cancer xenografts in nude mice was given in charge of a small RGD-doxo conjugate, several reports have appeared concerning the synthesis and biology of actively targeted therapeutics where the RGD-homing function is coupled to the effector moiety under the shape of either conventional covalent conjugates[10,20−29] or nanosized molecular/supramolecular entities.[10,20,21,30−34] Among the chemotherapeutics which were incorporated in these RGD-conjugates, the microtubule-interfering agent paclitaxel (PTX, **1**, Scheme 1) has often been selected, in an attempt to overcome the inherent drawbacks such as low aqueous solubility, short half-life, poor bioavailability, and systemic toxicity—all features resulting in a poor therapeutic index. The use of paclitaxel is of specific interest in this approach, because taxanes are known to have anti-angiogenic effects.[35] Quite surprisingly, however, the broad spectrum of tumor-addressing integrin ligands to be exploited in conjugated entities was limited to linear RGD-embedded peptides or no more than a couple of cyclic peptide candidates, namely, c(RGDfK), c(RGDyK), or E-[c(RGDfK)$_2$], which represent the conjugable versions of Cilengitide.[10,27−29]

In the structural design of novel, potentially bioactive conjugates, the judicious calibration of both the targeting device and the appropriate linker is crucial for the successful delivery of a given cytotoxic drug. Along this line, we present here nine novel molecular conjugates where the common PTX cytotoxic cargo is covalently attached to either cyclic AbaRGD or AmproRGD integrin-recognizing matrices via structurally diverse connections. Preeminent goals of the study were as follows: (1) to assay the feasibility of the chemistry involved by means of simple and efficient conjugation reactions under gentle and faithful conditions; (2) to assess the structural integrity/purity of the targets; (3) to evaluate by biological tests in vitro the mutual influence of the Aba/AmproRGD, PTX, and linker modules on the $\alpha_V\beta_3/\alpha_V\beta_5$ targeting capabilities, solubility, and tumor cell sensitivity; and (4) to assay via in vivo biological studies the antitumor activity of a selected candidate in order to gain insight into possible structural amendments and future development of the proposed conjugates.

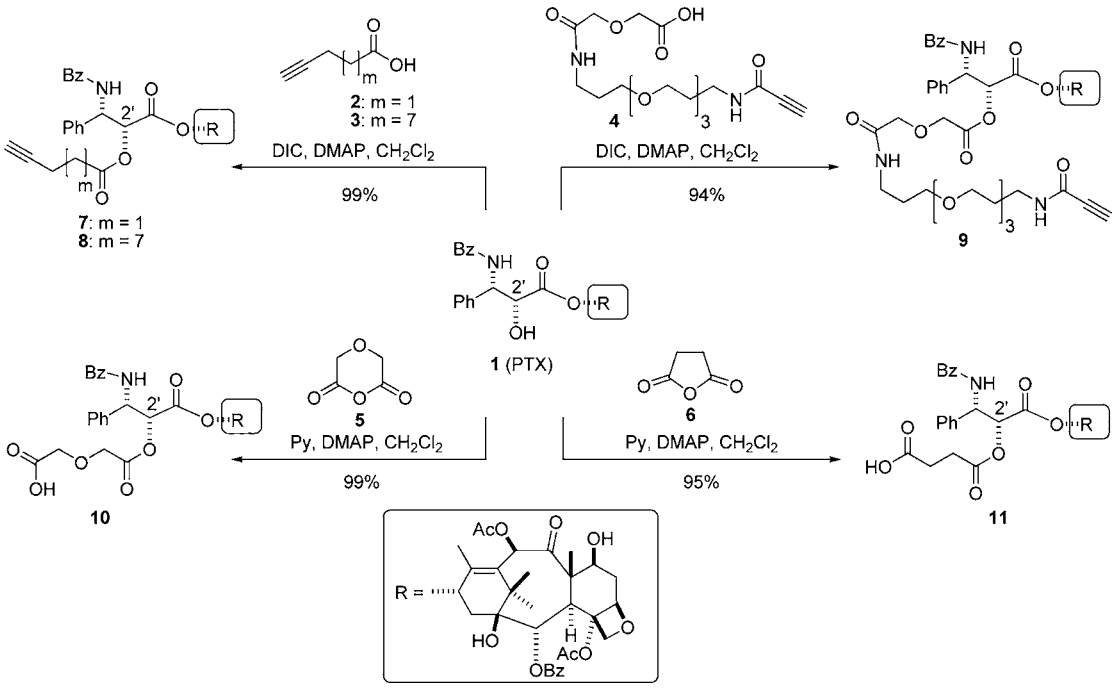
EXPERIMENTAL PROCEDURES

Chemistry. *General.* All chemicals and solvents were of reagent grade and were used without further purification. Solvents were dried by standard procedures and reactions requiring anhydrous conditions were performed under nitrogen or argon atmosphere. ^{1}H and ^{13}C NMR spectra were recorded at 300 K on Bruker AVANCE-400 or Bruker AVANCE-600 MHz spectrometers. Chemical shifts δ are expressed in ppm relative to internal Me_4Si as the standard reference. Mass spectra were obtained with an ESI apparatus Bruker Esquire 3000 plus. Thin-layer chromatography (TLC) was carried out with precoated Merck F_{254} silica-gel plates. Flash chromatography (FC) was carried out with Macherey-Nagel silica gel 60 (230−400 mesh). Reverse-phase column chromatography was carried out with the Biotage SP1 or SP4 systems using the Biotage 25+M C_{18} cartridges. Unless otherwise stated, semipreparative HPLC was carried out on a Waters SymmetryPrep C_{18}-7 μm 7.8 × 300 mm column or a Waters Atlantis C_{18} OBD 5 μm 19 mm × 10 cm or a Supelco Ascentis RPAmide 5 μm 21.1 mm × 15 cm; gradient from 100% H_2O (+ 0.1% TFA) to 75% H_2O (+ 0.1% TFA)/25% MeCN (+ 0.1% TFA) over 30 min.

Representative Procedure A. Preparation of C2′ Paclitaxel Ester 7. To Paclitaxel **1** (PTX, 50 mg, 0.059 mmol, 1.0 equiv), 4-pentynoic acid **2** (6.32 mg, 0.0644 mmol, 1.1 equiv), and a catalytic quantity of *N,N*-dimethylaminopyridine (DMAP) in

dx.doi.org/10.1021/bc300164t | *Bioconjugate Chem.* 2012, 23, 1610−1622

Scheme 1. Synthesis of Activated Taxane Modules 7−11



dry dichloromethane (1.0 mL), diisopropylcarbodiimide (DIC, 13.6 μL, 11.08 mg, 0.088 mmol, 1.5 equiv) was added. The resulting solution was left to stir under argon at room temperature for 20 h. The reaction mixture was then concentrated in vacuo to give a yellow solid. This was purified by reverse-phase chromatography eluting with water and acetonitrile to give a white solid in 99% yield. For characterization data of compound **7**, see Supporting Information.

Compounds **8** and **9** were obtained following the above procedure as white solid in 99% and 94% yield, respectively.

*Paclitaxel Ester **8**.* The title compound was obtained from Paclitaxel **1** and undec-10-ynoic acid **3** following representative procedure A. After reverse-phase chromatography, compound **8** was recovered as a white solid in 99% yield. For characterization data of compound **8**, see Supporting Information.

*Paclitaxel Ester **9**.* The title compound was obtained from Paclitaxel **1** and alkyne linker **4** (preparation reported in the Supporting Information) following representative procedure A. After reverse-phase chromatography, compound **9** was recovered as a white solid in 94% yield. For characterization data of compound **9**, see Supporting Information.

*Representative Procedure B. Preparation of C2′ Paclitaxel Ester **10**.* To PTX **1** (50 mg, 0.059 mmol, 1.0 equiv) and diglycolic anhydride **5** (8.6 mg, 0.074 mmol, 1.25 equiv) in dry dichloromethane (1.0 mL), pyridine (0.474 mL, 463 mg, 5.855 mmol, 100 equiv) and a catalytic quantity of DMAP were added. The resulting solution was left to stir under argon for 3 h at 0 °C and then left to warm to room temperature. After 20 h, the reaction mixture was concentrated in vacuo; the resulting solid was dissolved in water/acetonitrile/acetic acid (3 mL, 1:1:1) and purified by reverse-phase chromatography eluting with water and acetonitrile to give a white solid in 99% yield. For characterization data of compound **10**, see Supporting Information.

*Paclitaxel Ester **11**.* The title compound was obtained from PTX **1** and succinic anhydride **6** following representative procedure B. After reverse-phase chromatography, compound **11** was recovered as a white solid in 95% yield. For characterization data of compound **11**, see Supporting Information.

*Preparation of Cyclic AbaRGD (Compounds **12** and **13**) and AmproRGD (Compounds **14**−**16** and **18**) Modules.* Cyclic AbaRGD compounds **12** and **13** were prepared according to a reported procedure.[13] Cyclic AmproRGD compounds **14**−**16** were prepared according to a reported procedure.[14]

*Compound **18**.* Azidopeptide **14** (280 mg, 0.55 mmol, 2.2 equiv) and dialkyne **17**[36] (93 mg, 0.25 mmol, 1.0 equiv), dissolved in 20 mL of *tert*-butanol/water (1:1), were sequentially treated with 0.3 M solution of copper(II) acetate (333 μL, 0.1 mmol, 0.4 equiv) and 0.9 M solution of sodium L-ascorbate (222 μL, 0.2 mmol, 0.8 equiv). The resulting heterogeneous mixture was sonicated for 1 h and then stirred at room temperature for additional 4 h. After reaction completion, the mixture was lyophilized and the residue was purified by flash chromatography (EtOAc/MeOH, 85:15 to 75:25) affording a protected dimeric peptide (250 mg, 72%) as a glassy solid. This protected intermediate (250 mg, 0.18 mmol, 1.0 equiv) was treated with a solution of TFA/TIS/water 95:2.5:2.5 (16 mL) at room temperature. After 5 h, the solvent was evaporated under vacuum and the residue dissolved in water (15 mL) and thoroughly washed with Et_2O (4×). The aqueous phase was concentrated under vacuum furnishing 240 mg (95%) of dimeric amine **18** as a trifluoroacetate salt, which was used as such in the following coupling step. For characterization data of compound **18**, see Supporting Information.

*Representative Procedure C. Preparation of Triazolyl-Linked Conjugate **19**.* To azido-cRGD compound **12** (33.8 mg, 0.059 mmol, 1.0 equiv) and PTX ester **7** (54.7 mg, 0.059 mmol, 1.0 equiv) in *tert*-butanol/water (6:4, 3 mL) was added 0.9 M sodium L-ascorbate (28.39 μL, 0.026 mmol, 0.4 equiv). To this solution was then added 0.3 M copper(II) acetate (42.6 μL, 0.013 mmol, 0.2 equiv) and the resulting mixture was left to

dx.doi.org/10.1021/bc300164t | *Bioconjugate Chem.* 2012, 23, 1610−1622

stir at room temperature and monitored by LC-MS. When the reaction reached completion (2−4 h), the solution was frozen in liquid nitrogen and then freeze−dried. The solid recovered from freeze−drying was purified by RP-HPLC eluting with water + 0.1% formic acid and acetonitrile + 0.1% formic acid. The purified product was then freeze−dried to give a white solid in 75% yield. For characterization data of compound **19**, see Supporting Information.

*Triazolyl-Linked Conjugate **20**.* The title compound was obtained from azido-cRGD **12** and PTX ester **8** following representative procedure C. After RP-HPLC purification, compound **20** was recovered as a white solid in 59% yield. For characterization data of compound **20**, see Supporting Information.

*Triazolyl-Linked Conjugate **21**.* The title compound was obtained from azido-cRGD **12** and PTX ester **9** following representative procedure C. After RP-HPLC purification, compound **21** was recovered as a white solid in 46% yield. For characterization data of compound **21**, see Supporting Information.

*Triazolyl-Linked Conjugate **22**.* The title compound was obtained from azido-cRGD **14** and PTX ester **7** following representative procedure C. After RP-HPLC purification, compound **22** was recovered as a white solid in 57% yield. For characterization data of compound **22**, see Supporting Information.

*Triazolyl-Linked Conjugate **23**.* The title compound was obtained from azido-cRGD **15** and PTX ester **7** following representative procedure C. After RP-HPLC purification, compound **23** was recovered as a white solid in 48% yield. For characterization data of compound **23**, see Supporting Information.

*Representative Procedure D. Preparation of Amide-Linked Conjugate **24**.* To PTX-ester **10** (122 mg, 0.126 mmol, 1.0 equiv) and *N*-hydroxysulfosuccinimide sodium salt (34.1 mg, 0.157 mmol, 1.25 equiv) in dry *N,N*-dimethylformamide (DMF, 4.0 mL) was added diisopropylcarbodiimide (DIC, 29.2 μL, 23.8 mg, 0.188 mmol, 1.5 equiv). The resulting mixture was left to stir under argon at room temperature for 24 h. The reaction was then concentrated in vacuo to give an off-white solid. To this solid was added amino-cRGD **13** (108 mg, 0.126 mmol, 1.0 equiv) in acetonitrile (2.0 mL) and pH 7.0 phosphate buffer (PBS, 0.5 M, 1.0 mL), and the resulting mixture was rapidly cooled to 0 °C and then sonicated to favor dissolution. The reaction mixture was then left to stir at 0 °C for 10 h after which time it was allowed to warm to room temperature. After 18 h stirring, dioxane/water (1:1, 10 mL) was added and the resulting solution was freeze−dried. The solid recovered from freeze−drying was purified by RP-HPLC eluting with water + 0.1% formic acid and acetonitrile + 0.1% formic acid. The purified product was then freeze−dried to give a white solid in 43% yield.

Compounds **25**−**27** were obtained following the above procedure as white solid in 45%, 40%, and 62%, respectively.

*Amide-Linked Conjugate **25**.* The title compound was obtained from amino-cRGD **16** and PTX ester **10** following representative procedure D. After RP-HPLC purification, compound **25** was recovered as a white solid in 45% yield. For characterization data of compound **25**, see Supporting Information.

*Amide-Linked Conjugate **26**.* The title compound was obtained from amino-cRGD **18** and PTX ester **10** following representative procedure D. After RP-HPLC purification, compound **26** was recovered as a white solid in 40% yield. For characterization data of compound **26**, see Supporting Information.

*Amide-Linked Conjugate **27**.* The title compound was obtained from amino-cRGD **13** and PTX ester **11** following representative procedure D. After RP-HPLC purification, compound **27** was recovered as a white solid in 62% yield. For characterization data of compound **27**, see Supporting Information.

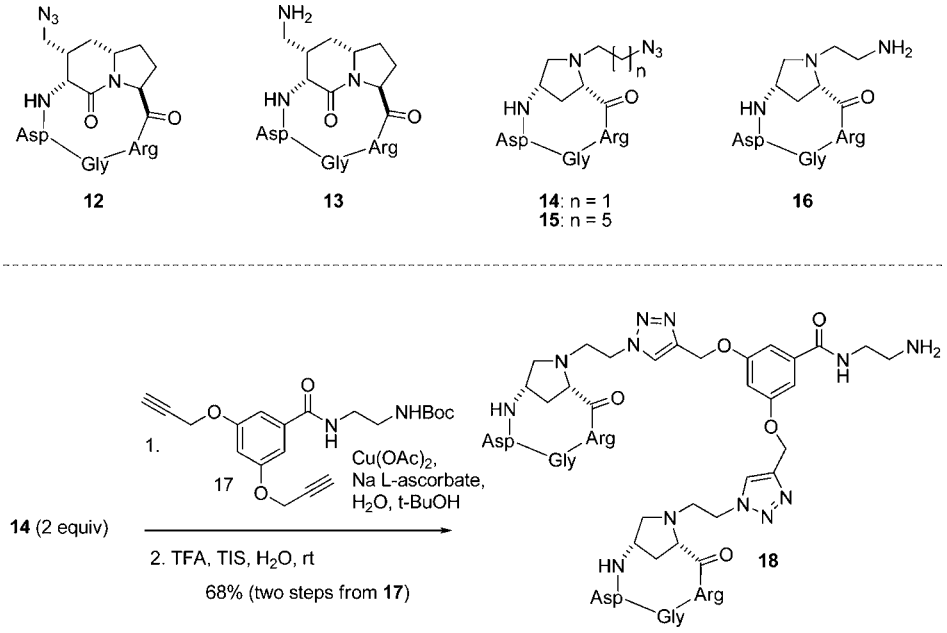
Biology. *Solid-Phase Receptor Binding Assay.* Purified $\alpha_v\beta_3$ and $\alpha_v\beta_5$ receptors (Chemicon International, Inc., Temecula, CA, USA) were diluted to 0.5 μg/mL in coating buffer containing 20 mM Tris-HCl (pH 7.4), 150 mM NaCl, 1 mM $MnCl_2$, 2 mM $CaCl_2$, and 1 mM $MgCl_2$. An aliquot of diluted receptors (100 μL/well) was added to 96-well microtiter plates (NUNC MW 96F Medisorp Straight) and incubated overnight at 4 °C. The plates were then incubated with blocking solution (coating buffer plus 1% bovine serum albumin) for an additional 2 h at room temperature to block nonspecific binding, followed by 3 h incubation at room temperature with various concentrations (10^{-5}−10^{-12} M) of test compounds in the presence of biotinylated vitronectin (1 μg/mL). Biotinylation was performed using an EZ-Link Sulfo-NHS-Biotinylation kit (Pierce, Rockford, IL, USA). After washing, the plates were incubated for 1 h at room temperature with biotinylated streptavidin−peroxidase complex (Amersham Biosciences, Uppsala, Sweden) followed by 30 min incubation with 100 μL/well Substrate Reagent Solution (R&D Systems, Minneapolis, MN) before stopping the reaction with the addition of 50 μL/well 2 N H_2SO_4. Absorbance at 415 nm was read in a SynergyTM HT Multi-Detection Microplate Reader (BioTek Instruments, Inc.). Each data point represents the average of triplicate wells; data analysis was carried out by nonlinear regression analysis with *GraphPad Prism 5.0* software. Each experiment was repeated in triplicate.

Drugs. For in vitro studies, PTX and compounds under investigation were dissolved in dimethylsulfoxide (DMSO) and then added to culture medium. DMSO concentration in medium never exceeded 0.5%. For in vivo studies, PTX was dissolved in a mixture of ethanol and cremophor ELP (50 + 50%) and kept at 4 °C. At treatment, the drug was diluted in 90% of cold saline after magnetic stirring and administered i.v. keeping the vial in ice. Compound **21** was dissolved and administered like PTX at room temperature.

Cell Lines and Growth Conditions. The human ovarian carcinoma IGROV-1 cell line,[37] the cisplatin-resistant IGROV-1/Pt1 subline[38] and the human large cell lung H460 carcinoma cell line (ATCC, HTB-177) were cultured in RPMI-1640 medium; the human osteosarcoma U2-OS cell line (ATCC, HTB-96) was grown in McCoy's 5A medium. Medium was supplemented with 10% fetal calf serum.

Cell Sensitivity to Drugs. The cell sensitivity to antitumor agents was measured by using the growth-inhibition assay based on cell counting. Cells were seeded in duplicates into 6-well plates and exposed to drug 24 h later. The compounds were dissolved in DMSO at 3.3 mM. Before cell treatment, the compounds were further diluted in DMSO. Five microliters of 200× solutions were used for treating cells in a volume of 1 mL of culture medium. The final DMSO concentration was not toxic. After 72 h of drug incubation, cells were harvested for counting with a cell counter. IC_{50} is defined as the drug concentration producing 50% decrease of cell growth. At least three independent experiments were performed.

Scheme 2. Structures of Monomeric AbaRGD and AmproRGD Modules 12−16 and Synthesis of Dimeric AmproRGD Module 18



Analysis of Integrin Levels. The expression of integrins was measured by flow cytometry, following optimization of antibody concentration. Exponentially growing cells were harvested and incubated for 30 min at 4 °C with anti-human $\alpha_v\beta_3$ or $\alpha_v\beta_5$ antibodies or isotypic controls (Millipore, Temecula, CA; Chemicon International). Cells were then washed and samples were immediately used for flow cytometric analysis (FACScan, Becton-Dickinson). Integrin levels were expressed as the ratio between the mean fluorescence intensity obtained in cells incubated with anti-integrin antibodies and that of cells incubated with isotypic control (Table 2).

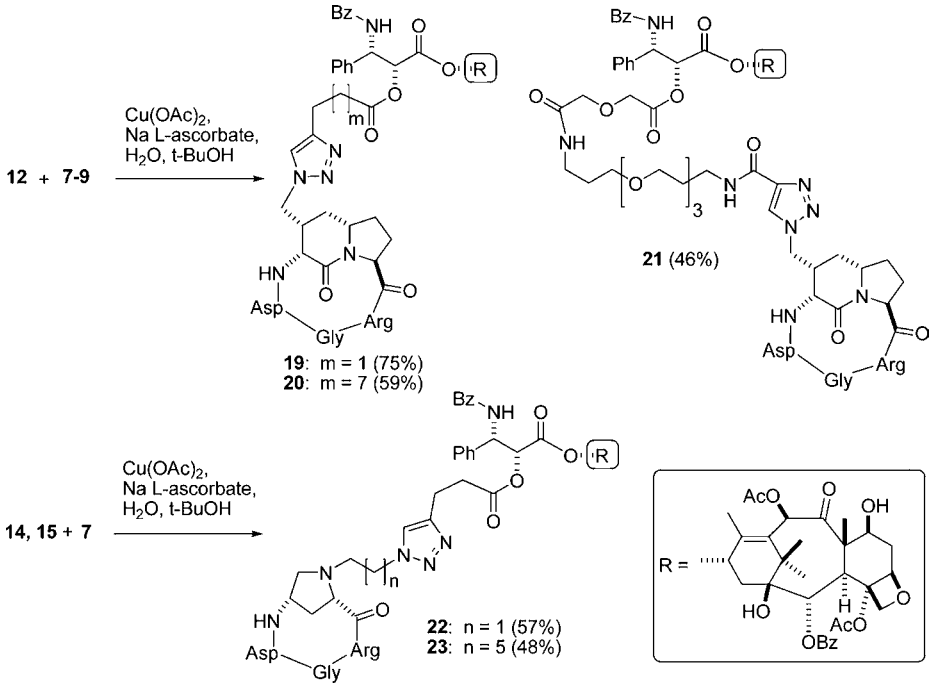
Antitumor Activity Studies. All experiments of antitumor activity were carried out using female athymic Swiss nude mice, 8−10 weeks old (Charles River, Calco, Italy). Mice were maintained in laminar flow rooms keeping temperature and humidity constant. Mice had free access to food and water. Experiments were approved by the Ethics Committee for Animal Experimentation of the Istituto Nazionale Tumori of Milan according to institutional guidelines. The IGROV-1/Pt1 human tumor xenograft derived from cultures of the ovarian carcinoma cell line[38] was used. Exponentially growing cells were s.c. injected into the right flank of athymic nude mice, and the tumor line was achieved by serial s.c. passages of fragments of regrowing tumors into healthy mice. Groups of five mice bearing bilateral s.c. tumors were employed. Tumor fragments were implanted on day 0 and tumor growth was followed by biweekly measurements of tumor diameters with a Vernier caliper. Tumor volume (TV) was calculated according to the formula: TV (mm^3) = $d^2 \times D/2$ where d and D are the shortest and the longest diameter, respectively. Drugs were delivered i.v. into the lateral tail vein using a 26G needle equipped syringe. Drugs were administered in a volume of 10 mL/kg of body weight every 4 days for 4 times (q4d × 4). Treatment started three days after tumor implant, when tumors were just palpable. The efficacy of the drug treatment was assessed as tumor volume inhibition percentage (TVI%) in treated versus control mice, calculated as follows: TVI% = 100 − (mean TV treated/mean TV control × 100) and log cell kill, evaluated by the formula: LCK = $(T - C)/(3.32 \times DT)$, where T and C are the times (days) to reach a tumor volume in treated and control mice, respectively, and DT is the doubling time of control tumors. Tumor DT (days) was obtained from semilog best-fit curves of mean tumor volumes in untreated control mice plotted against time. The toxicity of the drug treatment was determined as body weight loss and lethal toxicity. Student's t test (two-tailed) was used for statistical comparison of tumor volumes in mice.

Immunohistochemistry. Tumor xenografts and adjacent tissues were excised and formalin fixed and paraffin embedded. Four micrometer sections from each tumor xenograft were routinely stained with Hematoxylin-Eosin (HE) and evaluated under a light microscope. Mitoses were evaluated in 3 randomly selected 400× fields within the bulk of the xenograft, avoiding areas of necrosis and hemorrhage. The total number of mitoses and the mean value for each sample were evaluated. Furthermore, mitoses were differentiated as "normal" and "aberrant", the latter class characterized by both small, condensed hyperchromatic nuclei and large cells composed of nuclear envelope around individual clusters of mis-segregated chromosomes (mitotic catastrophe), and the ratio between these two classes was evaluated. The analysis of mitoses was performed in a blind fashion. Statistical analysis of the obtained data was carried out with the Kruskal−Wallis test followed by Dunn's multiple comparison test using *GraphPad Prism* (GraphPad Software, Inc.).

RESULTS

Chemistry. In engineering versatile, covalent connections of the building modules (PTX, RGD-semipeptide, and linker), mainly two requisites had to be satisfied. First, these linkages had to be easy to make and robust enough to guarantee the structural integrity of the whole construct until contacting and entering the cell compartment in such a way to fully exploit the specific targeting capabilities and the target-mediated cell internalization elicited by the RGD moiety. Second, connection to PTX, chosen at its C2′−OH position, has to be scissile

Scheme 3. Synthesis of Triazolyl-Linked Paclitaxel-AbaRGD and Paclitaxel-AmproRGD Conjugates 19−23



(hopefully inside the cell) to allow complete exercise of the cytotoxic function.[39] Accordingly, either a triazole-forming Hüisgen 1,3-dipolar cycloaddition reaction ("click reaction")[40] or popular amide conjugation was judged a viable solution, considering their intrinsic robustness, easy execution, and compatibility of the experimental conditions with the exposed functional groups within the moieties.

Synthesis of Activated Taxane Modules. The first step in the synthesis of the conjugates involved preparation of various C2′-esters of PTX **7**−**11** (Scheme 1) bearing either alkyne or carboxylic acid terminating moieties for subsequent triazolyl/amide conjugation. For **7**−**9**, two commercially available, diversely sized alkynoic acids **2** and **3**, along with an ad hoc prepared short PEG acid **4** (for preparation, see Supporting Information), were regioselectively coupled to PTX at the free C2′-position. Standard DIC/DMAP chemistry in dichloromethane was effective for preparing the corresponding esters **7**−**9** in 94−99% isolated yields. Notably, no parasite esterification at the unprotected C7-hydroxyl of the taxane was observed. For carboxylic acids **10** and **11**, two commercially available cyclic acid anhydrides, namely, glycolic anhydride **5** and succinic anhydride **6**, were used and coupled to the cytotoxic drug **1** without any byproducts under conventional esterification conditions.

Synthesis of Cyclic AbaRGD and AmproRGD Modules. As disclosed above, a key point of innovation of the present work with respect to the reported studies in the field is the selection of the $\alpha_V\beta_3$-integrin targeting unit. A first class of integrin ligands (compounds **12** and **13** in Scheme 2) features a fifteen-membered cyclopentapeptide where a 5,6-fused azabicycloalkane (Aba) amino acid moiety is tethered to the amino/acid terminals of the Arg-Gly-Asp tripeptide sequence. A second, different category of integrin ligands is represented by compounds **14**, **15**, **16**, and **18** (Scheme 2), all characterized by a fourteen-membered cyclotetrapeptide where a 4-aminoproline scaffold (Ampro) is grafted onto the Arg-Gly-Asp moiety. Structurally related to the known, high-affinity ligands **II** and **III** (Chart 1), these RGD peptides have the notable presence of exocyclic free azide or amine functional groups prone to conjugation with external partners.

Compounds **12**−**16** were synthesized from the respective amino acid building blocks in 30−44% yields, as reported.[13,14]

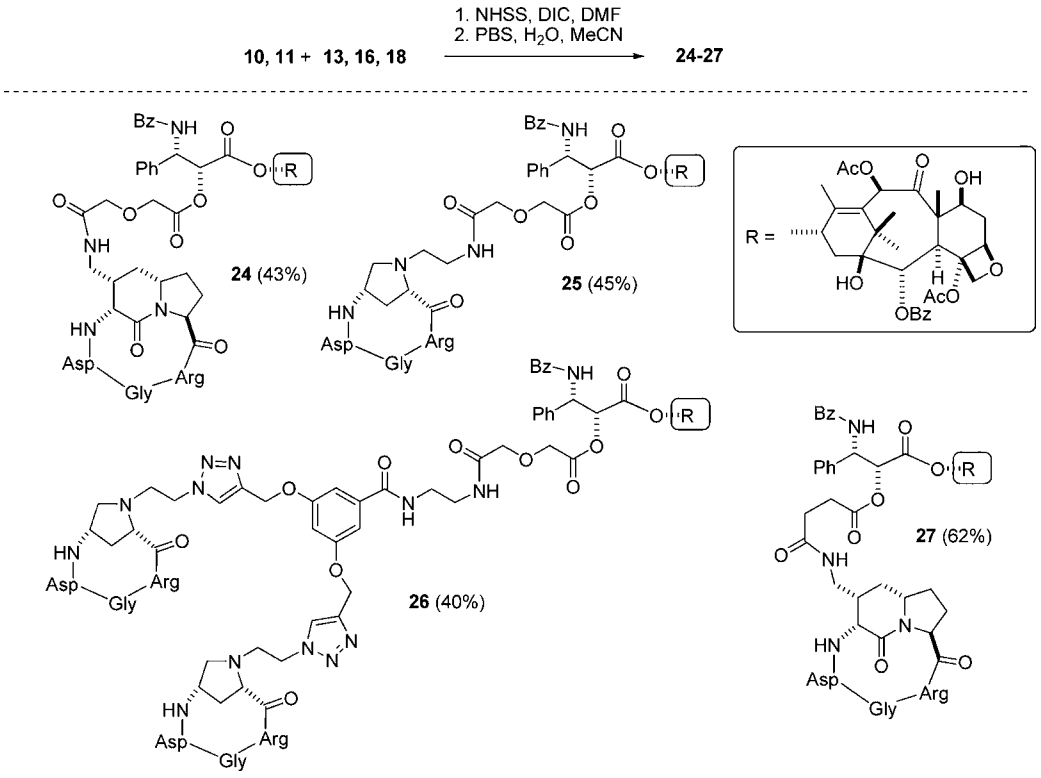
Another point of interest was the multipresentation of the ligands, since it is known that in many cases close correlation exists between the "RGD-valency" of the construct and the targeting capability enhancement.[41−43] To this end, compound **18** was built, where a rigid phenolic core is twofold linked to the AmproRGD unit through robust triazolyl connections, while leaving a free amino function ready for further conjugation. Thus, ad hoc-prepared bis-alkyne **17**, in turn obtained from 3,5-dihydroxy methyl benzoate and 1,2-diaminoethane according to a reported procedure,[36] was reacted with azide **14** (2 mol equiv) under copper-catalyzed Hüisgen 1,3-dipolar cycloaddition conditions[40] to furnish, after acidic removal of the Boc protection, dimeric amine **18** in 68% yield for the two steps.

Of note, RGD-cyclopeptides **12**−**16** and **18** were recovered as fully deprotected, >95% pure, and homogeneous materials as trifluoroacetate salts after semipreparative HPLC and proved completely water-soluble (25 °C, pH 7).

Synthesis of Triazolyl-Linked Paclitaxel-AbaRGD and Paclitaxel-AmproRGD Conjugates. With alkyne-ending taxane esters **7**−**9** and azide-terminating cycloRGD-peptides **12**, **14**, and **15** in hand, the next task was to couple these modules to create the projected triazolyl-linked conjugates. The regioselective copper-catalyzed Hüisgen 1,3-dipolar cycloaddition between an azide and a terminal alkyne, often referred to as "click reaction",[40] has been reported to proceed in very good yields in *t*-butanol/water, a solvent mixture that appeared ideal for dissolution of both lipophilic PTX and water-soluble cyclopeptides. Thus, the "click" reactions of completely deprotected azides **12**, **14**, or **15** with taxane alkynes **7**, **8**, or **9** proceeded fairly rapidly giving the corresponding triazolyl conjugates **19**−**23** in 46−75% yields (Scheme 3).

dx.doi.org/10.1021/bc300164t | *Bioconjugate Chem.* 2012, 23, 1610−1622

Scheme 4. Synthesis of Amide-Linked Paclitaxel-AbaRGD and Paclitaxel-AmproRGD Conjugates 24−27



Structurally speaking, these conjugates differed from each other by the nature of the integrin-ligand moiety (e.g., AbaRGD **19**−**21** vs AmproRGD **22**−**23**), by the distance of the taxane unit from the triazole (e.g., **19** vs **20** vs **21**) and by the distance of the RGD unit from the triazole (e.g., **22** vs **23**).

Synthesis of Amide-Linked Paclitaxel-AbaRGD and Paclitaxel-AmproRGD Conjugates. For the amide coupling between primary amine RGD ligands of types **13**, **16**, and **18** and carboxylic acid taxanes **10** and **11**, we had to face and solve some inherent, exquisitely chemical problems such as (1) the use of solvent mixtures compatible with both reacting partners; (2) the minimization of undesired side reactions between the free functional groups of the cyclopeptide and the taxane moiety, which is normally susceptible to attacks from nucleophiles; (3) the annihilation of the possibly competitive acylation at the RGD guanidinium group; and (4) acceleration of the amidation reaction as compared to unwanted competitive hydrolytic paths.

Following indications given by Staros[44] and Anjaneyulu,[45] optimum conditions were found using the carbodiimide DIC and *N*-hydroxysulfosuccinimide (NHSS) activating couple in organic−aqueous media at nearly neutral pH at low temperature. In practice, as outlined in Scheme 4, DMF solutions of carboxylic acids **10** or **11** were reacted with DIC and NHSS to furnish the corresponding hydrophilic *N*-hydroxysulfosuccinimidyl ester intermediates. Subsequent addition of the amine component (**13**, **16**, or **18**) in a pH 7.0 phosphate buffered water/acetonitrile (1:1) solvent mixture at 0 °C ensured preparation of the respective amide conjugates **24**−**27** in 40−62% yields.

From a structural viewpoint, amides **24** and **25** share a common diglycolic ester link but differ from each other in their targeting RGD unit, while compound **26** is the dimeric version of its counterpart **25**. Finally, compounds **24** and **27** exhibit a common AbaRGD unit linked to the taxane by different diglycolic vs succinic acid spacers.

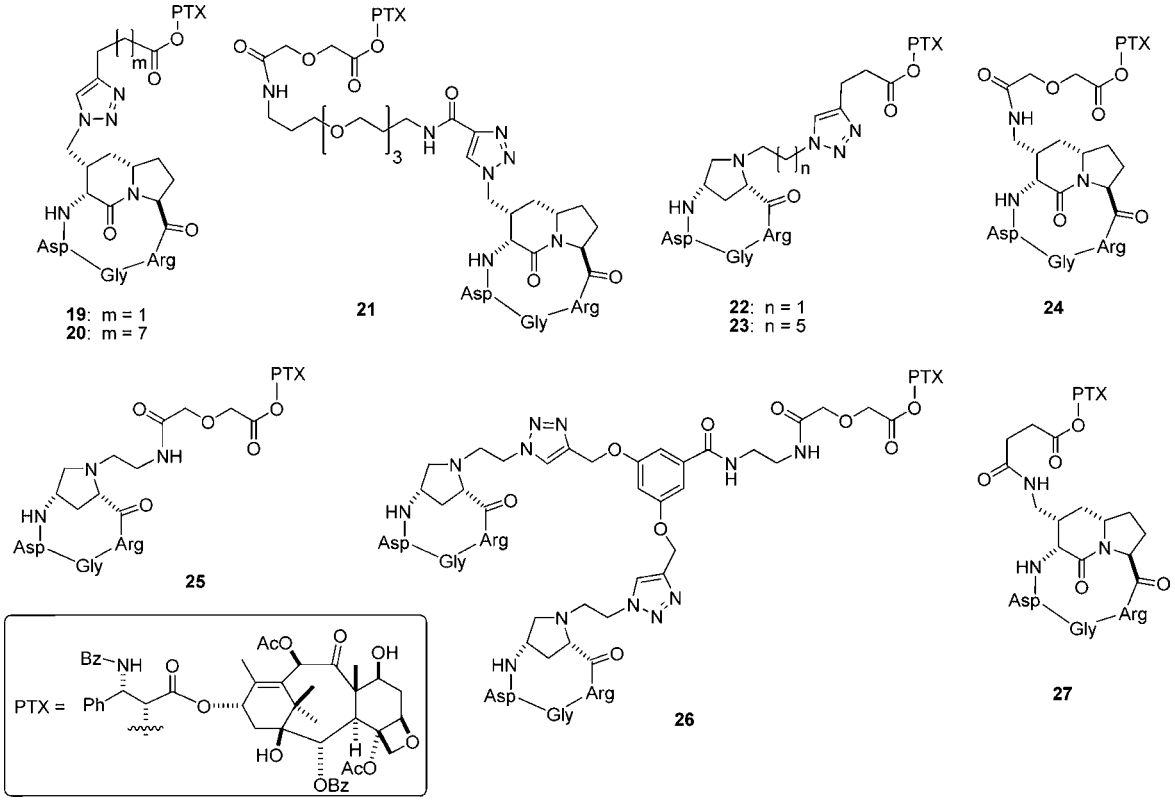
Biology. *Receptor Binding Assay.* The ability of the nine PTX-AbaRGD and PTX-AmproRGD conjugates **19**−**27** to bind to human, isolated $\alpha_V\beta_3$ and $\alpha_V\beta_5$ integrin receptors in vitro was evaluated by competitive displacement assays using biotinylated vitronectin (Table 1). To better estimate the impact of taxane-linker conjugation on the binding capability of the RGD portions, the data were compared to those of unconjugated parent RGD counterparts **12**−**16** and to known high-affinity binders c(RGDfV), Aba-based compound **II**, and Ampro-based derivative **III** (see Chart 1).

Triazolyl conjugates **19**−**23** showed variable results. In particular, AbaRGD derivatives exhibited some decrease (8-fold for **19** and 7-fold for **21**) or complete abrogation (for **20**) of $\alpha_V\beta_3$-binding affinity with respect to the parent azide counterpart **12**, while AmproRGD compounds **22** and **23** showed substantially unaltered, if not improved, one-digit nanomolar affinity and $\alpha_V\beta_3/\alpha_V\beta_5$ selectivity (as compared to azides **14** and **15**).

For diglycolic amide-linked conjugates **24** and **25**, a nanomolar binding capability was observed in both cases: the former displayed a 30-fold IC_{50} decrease with untouched $\alpha_V\beta_3/\alpha_V\beta_5$ selectivity as compared to the parent compound **13**, while the latter exhibited a comparable IC_{50} value and 4-fold increased $\alpha_V\beta_3/\alpha_V\beta_5$ selectivity as compared to the parent compound **16**. Succinic ester-linked Aba-conjugate **27** exhibited dual affinity for both receptors similar to triazolyl derivative **19**; compound **26**, bearing a 2-fold AmproRGD repeat, showed notable 0.23 nM $\alpha_V\beta_3$ binding capability, in line with the behavior observed for similar multimeric presentations.[14,41−43] In this case, again, remarkable selectivity amplification was observed.

dx.doi.org/10.1021/bc300164t | *Bioconjugate Chem.* 2012, 23, 1610−1622

Table 1. Solid-Phase Receptor Binding Assay[a]



compound	IC_{50} (nM) ± SD	
	$\alpha_V\beta_3$	$\alpha_V\beta_5$
19	266 ± 75	330 ± 54
20	$>10^{-5}$	$>10^{-5}$
21	220.0 ± 13.2	805 ± 309
22	4.3 ± 1.6	187 ± 65
23	2.3 ± 2.0	82 ± 16
24	35.6 ± 9.7	344 ± 196
25	8.9 ± 0.9	1909 ± 351
26	0.23 ± 0.012	725.0 ± 234.4
27	237 ± 89	219 ± 51
12	32.6 ± 15.7	98.3 ± 51.4
13	1077 ± 624	11300 ± 1480
14	6.0 ± 1.5	1208 ± 373
15	6.4 ± 2.4	38 ± 20
16	6.1 ± 1.6	315 ± 137
c(RGDfV)	3.2 ± 1.3	7.5 ± 4.8
II	53.7 ± 17.3	205 ± 33.5
III	2.4 ± 1.0	38 ± 11
vitronectin	47.1 ± 10.0	13.7 ± 6.2

[a] IC_{50} values were calculated as the concentration of compound required for 50% inhibition of biotinylated vitronectin binding to human, isolated $\alpha_V\beta_3$ and $\alpha_V\beta_5$ integrin receptors. High-affinity integrin binders c(RGDfV), **II** and **III**, were used as positive controls.

Overall, the presence of a common taxane unit and chemically different linkers covalently attached to the integrin-recognizing RGD units led to appreciable results, with satisfactory to excellent $\alpha_V\beta_3$ binding capabilities (in the 266−0.23 nM range) which were not generally compromized by the added cargo. It appears that interposition of a flexible chain (e.g., ethylene) between the RGD moiety and the linker is favorable for affinity (e.g., **22**, **23**, **25**, and **26**); also, the presence of the amide-attached diglycolic unit seems to be beneficial to the overall binding capability (e.g., **24**, **25**, and **26**). As a sole exception, compound **20** exhibited a completely annihilated binding affinity, possibly due to the presence of a long, flexible hydrocarbon linker chain, which would allow folding of the cytotoxic unit onto the RGD portion, thereby suppressing its integrin recognizing capability.

In Vitro Cell Sensitivity Assays. The ability of PTX conjugates **19**−**27** to inhibit growth of tumor cells was assessed using a growth inhibition assay (72 h exposure) in which the effect of free PTX **1** was also examined. Cell sensitivity to the different conjugates was evaluated using cell lines characterized

dx.doi.org/10.1021/bc300164t | *Bioconjugate Chem.* 2012, 23, 1610−1622

by a variable expression of $\alpha_v\beta_3$ and $\alpha_v\beta_5$ integrins. In U2-OS cells, the basal expression of $\alpha_v\beta_5$ was more marked than that of all other cell systems, whereas the cell line displaying the highest level of expression of $\alpha_v\beta_3$ was the cisplatin-resistant IGROV-1/Pt1 subline (Table 2). For this reason, the IGROV-1/Pt1 cell model was employed for subsequent in vivo studies. As detailed in Table 3, all conjugate compounds **19**−**27** showed an antiproliferative effect which varies from low nanomolar to micromolar IC_{50} values, indirectly supporting a possible cleavage and release of the PTX drug from the conjugate in the 72 h exposure time.[39] Triazolyl-linked compound **20**, which does not possess appreciable binding affinity toward the $\alpha_V\beta_3/\alpha_V\beta_5$ integrins, may be regarded as a nondirecting control; the IC_{50} values of **20** are the highest in the series along all tested tumor cell lines supporting the belief of a close correlation between overall antiproliferative activity and $\alpha_V\beta_3/\alpha_V\beta_5$ recognition capability. Residual, poor activity could be ascribed to aspecific delivery of the drug. Compound **19**, a shortened homologue of **20**, is endowed with improved targeting ability, and accordingly, the IC_{50} values appear appreciably improved, though still far from action of the free drug. Derivative **21**, which presents a robust triazole ring connected to ethylene glycol units by an amide function, shows flattened, low-nanomolar IC_{50} values that are comparable, if not superior, to those of free PTX; and this could be imputable either to excellent active targeting and $\alpha_V\beta_3$-mediated internalization or, simply, to premature and complete release of the cytotoxic cargo during the 72 h exposure. For robust triazolyl compounds **22** and **23**, displaying very good in vitro $\alpha_V\beta_3$ affinity, the cell sensitivity of the different cell lines was variable, reaching in some cases interesting results. Conjugates **24** and **25**, bearing diglycolic amide linkers, show nonflattened one-to-two-digit nanomolar IC_{50} values for all cell lines; interestingly enough, treatment with compound **24** inhibited proliferation of ovarian carcinoma IGROV-1 cells at a lower IC_{50} as compared to free PTX (1.04 nM vs 23.4 nM) and this could be due to an additive cytotoxic effect deriving from both PTX and the RGD unit itself. Compound **26**, bearing two RGDs per PTX, represents a dimeric version of **25** and displays superior in vitro $\alpha_v\beta_3$-targeting capabilities. Accordingly, **26** shows a 2-fold cytotoxic activity as compared to **25**, supporting the hypothesis of active directioning and $\alpha_V\beta_3$-mediated endocytosis. Unconjugated integrin ligands **13** and **16** do not show any sign of cytotoxicity in the present assay.

Table 2. Cytofluorimetric Analysis of $\alpha_V\beta_3$ and $\alpha_V\beta_5$ Levels in Cell Lines of Different Tumor Types

	relative mean fluorescence intensity[a]	
cell line	$\alpha_V\beta_3$	$\alpha_V\beta_5$
H460	1.1 ± 0.5	3.36 ± 1.1
U2-OS	2.43 ± 0.3	27.3 ± 1.4
IGROV-1	2.70 ± 0.6	4.33 ± 1.7
IGROV-1/Pt1	13.27 ± 4.9	2.8 ± 0.3

[a]The value is the ratio between mean fluorescence intensity of cells incubated with primary antibody and that of cells incubated with isotypic control.

In Vivo Antitumor Activity. Due to the good growth inhibition capability (slightly improved in comparison to PTX) displayed in vitro by compound **21**, it was selected to be further examined for in vivo studies. When mice were xenografted s.c. with IGROV-1/Pt1, a significant inhibition of tumor growth was observed following **21** administration. The compound was administered i.v. (36 mg/kg) every 4 days for 4 times. Under these conditions, the TVI (tumor volume inhibition) was 98% (Figure 1, Table 4, $P < 0.05$ vs PTX-treated mice). PTX used at the same treatment conditions displayed a lower antitumor effect. An improved antitumor activity of **21** was also indicated by the LCK (log cell kill) value.

Histological analysis highlighted an exceedingly higher number of mitoses in the group treated with compound **21**, compared to other groups (Figure 2). The majority of the mitoses observed in the group treated with compound **21** and in the group treated with PTX were aberrant, an observation consistent with the mechanism of action of the drug.[46−48] Examples are provided in Figure 3.

DISCUSSION

In the present study, we report the synthesis and biological evaluation of nine PTX conjugates characterized by structural novelty due to Aba-based or Ampro-based RGD moieties which are joined as C2′ PTX esters through variable triazolyl- or amide-connecting moieties. A number of molecules for which

Table 3. Cell Sensitivity of Cells with Variable Expression of Integrins to cRGD Ligand Conjugates[a]

	IC_{50} (nM) ± SD			
compound	U2-OS[b]	IGROV-1[c]	IGROV-1/Pt1[d]	H460[e]
19	107 ± 27	541 ± 334	140 ± 53	58 ± 27
20	244 ± 20	2870 ± 822	219 ± 63	236 ± 79
21	2.0 ± 1.1	1.6 ± 0.9	1.6 ± 1.1	9.5 ± 2.2
22	nd	277 ± 180.1	11.7 ± 6.2	nd
23	28.0 ± 6.7	333.4 ± 200	73.3 ± 6.7	nd
24	10.1 ± 3.3	1.04 ± 0.47	10.1 ± 4.7	13.1 ± 2.7
25	nd	43.1 ± 6.8	3.4 ± 2.4	nd
26	nd	28.0 ± 2.2	1.6 ± 0.5	nd
27	6.36 ± 0.18	81.0 ± 6.8	5.8 ± 0.5	6.9 ± 1.4
PTX	3.4 ± 0.5	23.4 ± 8.2	2.2 ± 0.8	5.4 ± 1.3
13	>4000	22 300	>30 000	>4000
16	>50 200	>16 700	>16 700	nd

[a]Cell sensitivity was evaluated by growth inhibition assays based on cell counting after 72 h exposure. IC_{50} is defined as the drug concentration inhibiting cell growth by 50%. [b]Human osteosarcoma. [c]Human ovarian adenocarcinoma. [d]Cisplatin resistant human ovarian adenocarcinoma. [e]Human large cell lung carcinoma.

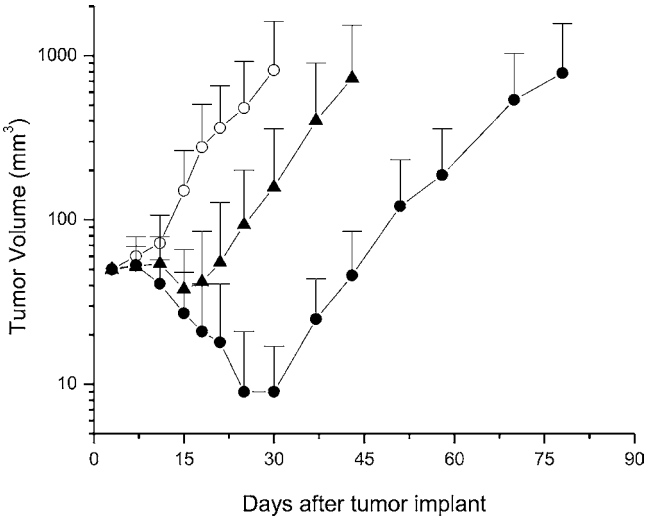


Figure 1. Antitumor activity studies of compound **21**. Efficacy of i.v. **21** (●) and paclitaxel (▲) administered at 36 mg/kg every fourth day four times on the ovarian carcinoma IGROV-1/Pt1 xenografted s.c. in athymic nude mice. Solvent was injected for the control group (○). Each point represents the mean tumor volume from 9 to 11 tumors. Bars represent SD.

Table 4. Efficacy of i.v. 21 and PTX (36 mg/kg q4d×4) on the Ovarian Carcinoma IGROV-1/Pt1 Xenografted s.c. in Athymic Nude Mice

compound	TVI%[a]	LCK[b]	BWL%[c]	Tox[d]
21	98	2	7	0/5
PTX	81	0.7	5	0/5

[a]Tumor volume inhibition % in treated over control mice assessed 7 days after last treatment. [b]Gross $\log_{10}$ cell kill to reach 700 mm^3 of tumor volume. [c]Body weight loss % induced by treatment; the highest change is reported. [d]Dead/treated mice.

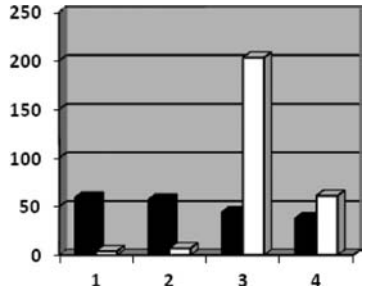


Figure 2. Comparison between normal (■) and aberrant (□) mitoses in different groups of treatment. Mitoses were evaluated in 3 randomly selected 400× fields using quadruplicate samples. The reported numbers correspond to the total number of normal/aberrant mitoses in analyzed group **1**, control group; **2**, group treated with ligand **13**; **3**, group treated with compound **21**; **4**, group treated with PTX. Group treated with compound **21** has the highest number of mitoses and in the meanwhile the highest number of aberrant mitoses ($p < 0.05$).

conjugation did not negatively influence binding to integrins was obtained. Such molecules were also endowed with marked cytotoxic activity in the range of that observed for PTX. In fact, cell sensitivity assays toward $\alpha_V\beta_3/\alpha_V\beta_5$-overexpressing human tumor cell lines support that PTX preserves or improves its cytotoxic activity when delivered through the covalent conjugates **19**–**27**, thus indirectly supporting its release as a free drug.[39] Whether it is prematurely released outside the cell

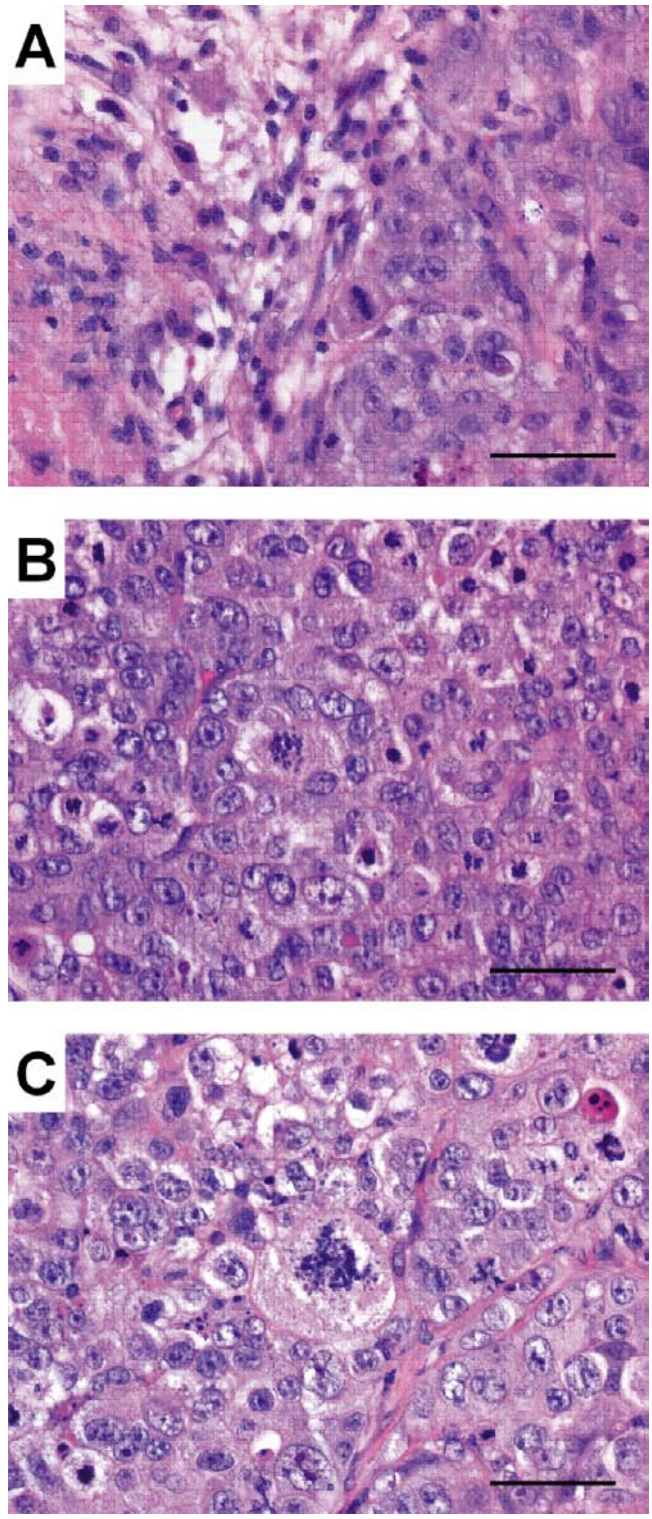


Figure 3. Randomly selected fields of (A) G1 sample, characterized by up to two "normal" mitoses (hematoxylin and eosin; Bar, 50 μm); (B) sample from mice treated with compound **21**. Note the central aberrant mitosis, characterized by mis-segregated chromosomes within a nuclear envelope (mitotic catastrophe), surrounded by a large number of small condensed hyperchromatin nuclei, both examples of "atypical" mitoses (hematoxylin and eosin; Bar, 50 μm); (C) G4 sample. In the center, there is an aberrant mitosis, characterized by mis-segregated chromosomes surrounded by a nuclear envelope (mitotic catastrophe) (hematoxylin and eosin; Bar, 50 μm).

dx.doi.org/10.1021/bc300164t | *Bioconjugate Chem.* 2012, 23, 1610–1622

and subsequently internalized through cell membrane diffusion or it is actively targeted and released inside the cell following integrin-mediated endocytosis, it is hard to definitely conclude here. Observation of nonflattened and nonhomogeneous data in the tested assay (with exception of compound **21**), which are closely related to the corresponding affinity toward the receptors, favors the second hypothesis.

Though the details of the release process remain to be defined, it would seem likely that the PTX-AbaRGD and PTX-AmproRGD junction is a well-done marriage where the partners, more than simply tolerant, cooperate with each other.

Last, during in vivo assays performed on compound **21**, outstanding control of tumor growth (TVI 98% for **21** vs 81% for PTX at 25 day) in a model overexpressing $\alpha_V\beta_3$ was achieved at well-tolerated doses of the conjugate (36 mg/kg). This result is even more impressive if we consider that the effective amount of PTX administered to the animals treated with compound **21** is 17 mg/kg (the MW being almost double). Since tumors from mice treated with compound **21** had the highest number of mitoses and the major part of them were atypical, it can be speculated that neoplastic cells treated with compound **21** enter mitosis but fail to replicate and incur in mitotic arrest, as already described in the current literature for "spindle poisons" such as PTX. As mentioned in the Introduction, a few studies exist where cyclopeptide RGD moieties—namely, dimeric E-[c(RGDfK)$_2$] or E-[c-(RGDyK)$_2$]—were covalently conjugated to PTX in its 2′-OH position through a succinate spacer.[27−29] In a first contribution, Chen and Neamati[28] tested their PTX-RGD construct against metastatic breast cancer cells (MDA-MB-438) showing a cell proliferation inhibition comparable to that observed for paclitaxel and a slightly decreased integrin binding affinity with respect to the unconjugated counterpart. In vivo and ex vivo data of the same conjugate were reported shortly afterward[29] and its antitumor therapeutic effect compared to simple PTX/RGD combinations. In this case, although the tritiated conjugate showed higher tumor uptake and longer retention of PTX in the MDA-MB-438 tumor than PTX alone, the absolute tumor uptake value was still rather low. The E-[c(RGDfK)$_2$]-PTX conjugate was also evaluated by Satchi-Fainaro and Kratz et al.[27] demonstrating that in a standard 72 h assay it inhibited the proliferation of HUVECs in a similar manner as free PTX (IC_{50} 0.4 nM) suggesting complete hydrolysis of the succinate ester under the tested conditions. Furthermore, in vivo studies in a OVCAR-3 xenograft model demonstrated no antitumor efficacy.

Here, the connection of robust semipeptidic and highly $\alpha_V\beta_3$-selective RGD ligands to PTX through chemically diverse tethers gave rise to constitutionally and geometrically diverse conjugate products whose varied physical and chemical properties were anticipated to significantly impact the biological response. Indeed, the diversified, yet interesting in vitro cytotoxic activity as well as the outstanding in vivo antitumor response obtained in this work seem unique in the field; and this strengthens the notion that the Aba- and Ampro-based RGD semipeptides may be conveniently added in the list of the integrin-targeting moieties for the construction of effective and selective antitumor and anti-angiogenesis agents.

CONCLUSION

The study focused on the synthesis and biological evaluation of nine PTX-conjugates compounds **19**−**27**, whose structural novelty is represented by Aba-based or Ampro-based RGD moieties which are joined as C2′ PTX esters through variable triazolyl- or amide-connecting moieties. The main goals of the work have been accomplished. The synthesis proved viable and faithful, efficiently furnishing the nine conjugates in 38−74% yields from the taxane and respective RGD starting modules. Purification and complete structural characterization of the final products guaranteed reliability during subsequent biological tests. Preservation of high in vitro $\alpha_V\beta_3$-receptor affinity observed for almost all conjugate candidates in the series as compared to free RGD-counterparts demonstrated that the cytotoxic cargo and/or the linker unit may comfortably coexist with the RGD moiety without damaging the exquisite $\alpha_V\beta_3$-selective targeting capability. In vitro growth inhibition assays on a panel of $\alpha_V\beta_3/\alpha_V\beta_5$-overexpressing human tumor cell lines showed remarkable cytotoxic activity. Finally, in vivo evaluation of conjugate **21** confirmed the effectiveness of this compound to inhibit tumor growth, displaying an enhanced activity in comparison to that of free Paclitaxel. This result is further strengthened by the fact that the effective quantity of Paclitaxel administered to the animals treated with compound **21** is almost half the given doses.

Favorable indications of the present work incite further investigations (e.g., evaluation of metabolic stability, toxicity, and actual drug release localization) to be performed on selected candidates in order to gain insight into optimal structural compromise between selective targeting ability, in-cell drug release capability, and overall solubility/permeability in human tissues.

ASSOCIATED CONTENT

Supporting Information

Characterization data, HPLC traces, and copies of ^{1}H NMR spectra of RGD conjugates. This material is available free of charge via the Internet at http://pubs.acs.org.

AUTHOR INFORMATION

Corresponding Author

*Leonardo Manzoni: Tel. (+39) 02 50314064, Fax (+39) 02 50314072, e-mail: leonardo.manzoni@istm.cnr.it. Franca Zanardi: Tel. (+39) 0521 905067, Fax (+39) 0521 905006, e-mail: franca.zanardi@unipr.it.

Notes

The authors declare no competing financial interest.

ACKNOWLEDGMENTS

This work was supported by Associazione Italiana per la Ricerca sul Cancro (Milano, Italy), Ministero dell'Istruzione, dell'Università e della Ricerca (MIUR, PRIN 2008), and Fondazione Banco di Sardegna. Thanks are due to the Centro Interdipartimentale Misure "G. Casnati" (Università degli Studi di Parma) for instrumental facilities, and to "Regione Autonoma della Sardegna" for research fellowships to P.B. and P.C. (PO Sardegna FSE 2007-2013, L.R. 7/2007 "Promozione della ricerca scientifica e dell'innovazione tecnologica in Sardegna").

REFERENCES

(1) Cossa, G., Gatti, L., Zunino, F., and Perego, P. (2009) Strategies to improve the efficacy of platinum compounds. *Curr. Med. Chem. 16*, 2355−2365.

(2) Desgrosellier, J. S., and Cheresh, D. A. (2010) Integrins in cancer: biological implications and therapeutic opportunities. *Nat. Rev. Cancer 10*, 9−22.

(3) Harms, J. F., Welch, D. R., Samant, R. S., Shevde, L. A., Miele, M. E., Babu, G. R., Goldberg, S. F., Gilman, V. R., Sosnowski, D. M., Campo, D. A., Gay, C. V., Budgeon, L. R., Mercer, R., Jewell, J., Mastro, A. M., Donahue, H. J., Erin, N., Debies, M. T., Meehan, W. J., Jones, A. L., Mbalaviele, G., Nickols, A., Christensen, N. D., Melly, R., Beck, L. N., Kent, J., Rader, R. K., Kotyk, J. J., Pagel, M. D., Westlin, W. F., and Griggs, D. W. (2004) A small molecule antagonist of the alpha(v)beta3 integrin suppresses MDA-MB-435 skeletal metastasis. *Clin. Exp. Metastasis 21*, 119−128.

(4) Vellon, L., Menendez, J. A., and Lupu, R. (2006) A bidirectional ″alpha(v)beta(3) integrin-ERK1/ERK2MAPK″ connection regulates the proliferation of breast cancer cells. *Mol. Carcinog. 45*, 795−804.

(5) Gingras, M. C., Roussel, E., Bruner, J. M., Branch, C. D., and Moser, R. P. (1995) Comparison of cell adhesion molecule expression between glioblastoma multiforme and autologous normal brain tissue. *J. Neuroimmunol. 57*, 143−153.

(6) Albelda, S. M., Mette, S. A., Elder, D. E., Stewart, R., Damjanovich, L., Herlyn, M., and Buck, C. A. (1990) Integrin distribution in malignant melanoma: association of the beta3 subunit with tumor progression. *Cancer Res. 50*, 6757−6764.

(7) Dang, D., Bamburg, J. R., and Ramos, D. M. (2006) Alphavbeta3 integrin and cofilin modulate K1735 melanoma cell invasion. *Exp. Cell Res. 312*, 468−477.

(8) Cooper, C. R., Chay, C. H., and Pienta, K. J. (2002) The role of alpha(v)beta(3) in prostate cancer progression. *Neoplasia 4*, 191−194.

(9) Hapke, S., Kessler, H., Luber, B., Benge, A., Hutzler, P., Hofler, H., Schmitt, M., and Reuning, U. (2003) Ovarian cancer cell proliferation and motility is induced by engagement of integrin alpha(v)beta3/vitronectin interaction. *Biol. Chem. 384*, 1073−1083.

(10) Auzzas, L., Zanardi, F., Battistini, L., Burreddu, P., Carta, P., Rassu, G., Curti, C., and Casiraghi, G. (2010) Targeting $\alpha_V\beta_3$ integrin: design and applications of mono- and multifunctional RGD-based peptides and semipeptides. *Curr. Med. Chem. 17*, 1255−1299.

(11) Paolillo, M., Russo, M. A., Serra, M., Colombo, L., and Schinelli, S. (2009) Small molecule integrin antagonists in cancer therapy. *Mini-Rev. Med. Chem. 9*, 1439−1446.

(12) Dechantsreiter, M. A., Planker, E., Matha, B., Lohof, E., Holzemann, G., Jonczyk, A., Goodmann, S. L., and Kessler, H. (1999) *N*-Methylated cyclic RGD peptides as highly active and selective $\alpha_V\beta_3$ integrin antagonist. *J. Med. Chem. 42*, 3033−3040.

(13) Manzoni, L., Belvisi, L., Arosio, D., Civera, M., Pilkington-Miksa, M., Potenza, D., Caprini, A., Araldi, E. M. V., Monferini, E., Mancino, M., Podestà, F., and Scolastico, C. (2009) Cyclic RGD-containing functionalized azabicycloalkane peptides as potent integrin antagonists for tumor targeting. *ChemMedChem 4*, 615−632.

(14) Battistini, L., Burreddu, P., Carta, P., Rassu, G., Auzzas, L., Curti, C., Zanardi, F., Manzoni, L., Araldi, E. M. V., Scolastico, C., and Casiraghi, G. (2009) 4-Aminoproline-based arginine-glycine-aspartate integrin binders with exposed ligation points: practical in-solution synthesis, conjugation and binding affinity evaluation. *Org. Biomol. Chem. 7*, 4924−4935.

(15) Liu, Z., Wang, F., and Chen, X. (2008) Integrin $\alpha_V\beta_3$-targeted cancer therapy. *Drug Dev. Res. 69*, 329−339.

(16) Stupp, R., and Ruegg, C. (2007) Integrin inhibitors reaching the clinic. *J. Clin. Oncol. 25*, 1637−1638.

(17) Reardon, D. A., Fink, K. L., Mikkelsen, T., Cloughesy, T. F., O'Neill, A., Plotkin, S., Glantz, M., Ravin, P., Raizer, J. J., Rich, K. M., Schiff, D., Shapiro, W. R., Burdette-Radoux, S., Dropcho, E. J., Wittemer, S. M., Nippgen, J., Picard, M., and Nabors, B. L. (2008) Randomized phase II study of cilengitide, an integrin-targeting arginine-glycine-aspartic acid peptide, in recurrent glioblastoma multiforme. *J. Clin. Oncol. 26*, 5610−5617.

(18) MacDonald, T. J., Stewart, C. F., Kocak, M., Goldman, S., Ellenbogen, R. G., Phillips, P., Lafond, D., Young Poussaint, T., Kieran, M. W., Boyett, J. M., and Kun, L. E. (2008) Phase I clinical trial of Cilengitide in children with refractory brain tumors: pediatric brain tumor consortium study PBTC-012. *J. Clin. Oncol. 26*, 919−924.

(19) Schottelius, M., Laufer, B., Kessler, H., and Wester, H.-J. (2009) Ligands for mapping $\alpha_V\beta_3$-integrin expression *in vivo*. *Acc. Chem. Res. 42*, 969−980.

(20) Garanger, E., Boturyn, D., and Dumy, P. (2007) Tumor targeting with RGD peptide ligands − Design of new molecular conjugates for imaging and therapy of cancers. *Anti Cancer Agents Med. Chem. 7*, 552−558.

(21) Temming, K., Schiffelers, R. M., Molema, G., and Kok, R. J. (2005) RGD-Based strategies for selective delivery of therapeutics and imaging agents to the tumor vasculature. *Drug Resistance Updates 8*, 381−402.

(22) Arap, W., Pasqualini, R., and Ruoslahti, E. (1998) Cancer treatment by targeted drug delivery to tumor vasculature in a mouse model. *Science 279*, 377−380.

(23) Liu, Y., Bajjuri, K. M., Liu, C., and Sinha, S. C. (2012) Targeting cell surface alpha(v)beta(3,5) integrins increases therapeutic efficacies of a legumain protease-activated auristatin prodrug. *Mol. Pharm. 9*, 168−175.

(24) Dufort, S., Sancey, L., Hurbin, A., Foillard, S., Boturyn, D., Dumy, P., and Coll, J.-L. (2011) Targeted delivery of a proapoptotic peptide to tumors *in vivo*. *J. Drug Targeting 19*, 582−588.

(25) Dal Pozzo, A., Esposito, E., Ni, M., Muzi, L., Pisano, C., Bucci, F., Vesci, L., Castorina, M., and Penco, S. (2010) Conjugates of a novel 7-substituted camptothecin with RGD-peptides as $\alpha_V\beta_3$ integrin ligands: an approach to tumor-targeted therapy. *Bioconjugate Chem. 21*, 1956−1967.

(26) Braun, K., Wiessler, M., Pipkorn, R., Ehemann, V., Bäuerle, T., Fleischhacker, H., Müller, G., Lorenz, P., and Waldeck, W. (2010) A cyclic-RGD-BioShuttle functionalized with TMZ by DAR_{inv} "Click Chemistry" targeted to $\alpha_V\beta_3$ integrin for therapy. *Int. J. Med. Sci. 7*, 326−339.

(27) Ryppa, C., Mann-Steinberg, H., Biniossek, M. L., Satchi-Fainaro, R., and Kratz, F. (2009) *In vitro* and *in vivo* evaluation of a paclitaxel conjugate with the divalent peptide E-[c(RGDfK)$_2$] that targets integrin $\alpha_V\beta_3$. *Int. J. Pharm. 368*, 89−97.

(28) Chen, X., Plasencia, C., Hou, Y., and Neamati, N. (2005) Synthesis and biological evaluation of dimeric RGD peptide-paclitaxel conjugate as a model for integrin-targeted drug delivery. *J. Med. Chem. 48*, 1098−1106. (corrigendum (2005) *J. Med. Chem. 48*, 5874).

(29) Cao, Q., Li, Z.-B., Chen, K., Wu, Z., He, L., Neamati, N., and Chen, X. (2008) Evaluation of biodistribution and anti-tumor effect of a dimeric RGD peptide-paclitaxel conjugate in mice with breast cancer. *Eur. J. Nucl. Med. Mol. Imaging 35*, 1489−1498.

(30) Arosio, D., Casagrande, C., and Manzoni, L. (2012) Integrin-mediated drug delivery in cancer and cardiovascular diseases with peptide-functionalized nanoparticles. *Curr. Med. Chem. 19*, 3128−3151.

(31) Zhan, C., Meng, Q., Li, Q., Feng, L., Zhu, J., and Lu, W. (2012) Cyclic RGD−Polyethylene Glycol−Polyethylenimine for Intracranial Glioblastoma-Targeted Gene Delivery. *Chem. Asian J. 7*, 91−96.

(32) Yao, H.-J., Ju, R.-J., Wang, X.-X., Zhang, Y., Li, R.-J., Yu, Y., Zhang, L., and Lu, W.-L. (2011) The antitumor efficacy of functional paclitaxel nanomicelles in treating resistant breast cancers by oral delivery. *Biomaterials 32*, 3285−3302.

(33) Eldar-Boock, A., Miller, K., Sanchis, J., Lupu, R., Vicent, M. J., and Satchi-Fainaro, R. (2011) Integrin-assisted drug delivery of nano-scaled polymer therapeutics bearing paclitaxel. *Biomaterials 32*, 3862−3874.

(34) Austin, L. A., Kang, B., Yen, C.-W., and El-Sayed, M. A. (2011) Nuclear targeted silver nanospheres perturb the cancer cell cycle differently than those of nanogold. *Bioconjugate Chem. 22*, 2324−2331.

(35) Ubezio, P., Garofalo, A., Borsotti, P., Cassis, L., Riccardi, E., Scanziani, E., Eccles, S. A., Bani, M. R., and Giavazzi, R. (2006) The vascular targeting property of paclitaxel is enhanced by SU6668, a receptor tyrosine kinase inhibitor, causing apoptosis of endothelial cells and inhibition of angiogenesis. *Clin. Cancer Res. 12*, 1839−1849.

(36) Dijkgraaf, I., Rijnders, A. Y., Soede, A., Dechesne, A. C., van Esse, G. W., Brouwer, A. J., Corstens, F. H. M., Boerman, O. C., Rijkers, D. T. S., and Liskamp, R. M. (2007) Synthesis of DOTA-

conjugated multivalent cyclic-RGD peptide dendrimers via 1,3-dipolar cycloaddition and their biological evaluation: implications for tumor targeting and tumor imaging purposes. *Org. Biomol. Chem. 5*, 935−944.
(37) Benard, J., Da Silva, J., De Blois, M. C., Boyer, P., Duvillard, P., Chiric, E., and Riou, G. (1985) Characterization of a human ovarian adenocarcinoma line, IGROV1, in tissue culture and in nude mice. *Cancer Res. 45*, 4970−4979.
(38) Perego, P., Giarola, M., Righetti, S. C., Supino, R., Caserini, C., Delia, D., Pierotti, M. A., Miyashita, T., Reed, J. C., and Zunino, F. (1996) Association between cisplatin resistance and mutation of p53 gene and reduced bax expression in ovarian carcinoma cell systems. *Cancer Res. 56*, 556−562.
(39) Kingston, D. G. (2000) Recent advances in the chemistry of taxol. *J. Nat. Prod. 63*, 726−734.
(40) Himo, F., Lovell, T., Hilgraf, R., Rostovtsev, V. V., Noodleman, L., Sharpless, K. B., and Fokin, V. V. (2005) Copper(I)-catalyzed synthesis of azoles. DFT study predicts unprecedented reactivity and intermediates. *J. Am. Chem. Soc. 127*, 210−216.
(41) Wester, H. J., and Kessler, H. (2005) Molecular targeting with peptides or peptide-polymer conjugates: just a question of size? *J. Nucl. Med. 46*, 1940−1945.
(42) Sancey, L., Garanger, E., Foillard, S., Schoehn, G., Hurbin, A., Albiges-Rizo, C., Boturyn, D., Souchier, C., Grichine, A., Dumy, P., and Coll, J.-L. (2009) Clustering and internalization of integrin $\alpha_V\beta_3$ with a tetrameric RGD-synthetic peptide. *Mol. Ther. 17*, 837−843.
(43) Liu, S., Hsieh, W.-Y., Jiang, Y., Kim, Y.-S., Sreerama, S. G., Chen, X., Jia, B., and Wang, F. (2007) Evaluation of a ^{99m}Tc-labeled cyclic RGD tetramer for non invasive imaging integrin $\alpha_V\beta_3$-positive breast cancer. *Bioconjugate Chem. 18*, 438−446.
(44) Staros, J. V. (1982) *N*-Hydroxysulfosuccinimide active esters: bis(*N*-hydroxysulfosuccinimide) esters of two dicarboxylic acids are hydrophilic, membrane-impermeant, protein cross-linkers. *Biochemistry 21*, 3950−3955.
(45) Anjaneyulu, P. S. R., and Staros, J. V. (1987) Reactions of *N*-hydroxysulfosuccinimide active esters. *Int. J. Pept. Protein Res. 30*, 117−124.
(46) Matson, D. R., and Stukenberg, P. T. (2011) Spindle poisons and cell fate: a tale of two pathways. *Mol. Interv. 11*, 141−150.
(47) Portugal, J., Mandilla, S., and Bataller, M. (2010) Mechanisms of drug-induced mitotic catastrophe in cancer cells. *Curr. Pharm. Des. 16*, 69−78.
(48) Roninson, I. B., Broude, E. V., and Chang, B. D. (2001) If not apoptosis, then what? Treatment-induced senescence and mitotic catastrophe in tumor cells. *Drug Res. Updates 4*, 303−313.

Bioconjugate Chemistry

Article

pubs.acs.org/bc

Comparative Studies of the Cellular Uptake, Subcellular Localization, and Cytotoxic and Phototoxic Antitumor Properties of Ruthenium(II)–Porphyrin Conjugates with Different Linkers

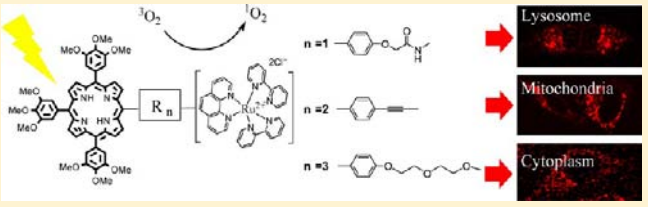
Jing-Xiang Zhang,[†,#] Jun-Wei Zhou,[§,#] Chi-Fai Chan,[†,#] Terrence Chi-Kong Lau,*[,§] Daniel W. J. Kwong,[†] Hoi-Lam Tam,[‡] Nai-Ki Mak,[∥] Ka-Leung Wong,*[,†] and Wai-Kwok Wong*[,†]

[†]Department of Chemistry, [‡]Department of Physics, and [∥]Department of Biology, Hong Kong Baptist University, Kowloon Tong, Hong Kong SAR

[§]Department of Biology and Chemistry, City University of Hong Kong, Tat Chee Avenue, Kowloon Tong, Hong Kong SAR

Supporting Information

ABSTRACT: Six water-soluble free-base porphyrin-Ru(II) conjugates, **1**–**3**, and Zn(II) porphyrin-Ru(II) conjugates, **4**–**6**, with different linkers between the hydrophobic porphyrin moiety and the hydrophilic Ru(II)-polypyridyl complex, have been synthesized. The linear and two-photon-induced photophysical properties of these conjugates were measured and evaluated for their potential application as dual in vitro imaging and photodynamic therapeutic (PDT) agents. Conjugates **1**–**3**, with their high luminescence and singlet oxygen quantum yields, were selected for further study of their cellular uptake, subcellular localization, and cytotoxic and photocytotoxic (under linear and two-photon excitation) properties using HeLa cells. Conjugate **2**, with its hydrophobic phenylethynyl linker, was shown to be highly promising for further development as a bifunctional probe for two-photon (NIR) induced PDT and in vitro imaging. Cellular uptake and subcellular localization properties were shown to be crucial to its PDT efficacy.



INTRODUCTION

Photodynamic therapy (PDT) has recently emerged as a promising alternative therapy against cancer, with several PDT agents approved and used clinically in the past two decades.[1−3] In PDT, three key elements are required: a photosensitizer (PS), which when excited by light of an appropriate wavelength, converts molecular oxygen in tissues to the cytotoxic singlet oxygen ($^1O_2$).[4−13] A porphyrin-based compound, shown to accumulate preferentially in solid tumors, was the first PDT agent approved by the U.S. Food and Drug Administration as a noninvasive antitumor treatment modality.[14−16] Ruthenium and organoruthenium complexes have also been shown to be effective chemotherapeutic agents against a variety of cancer cells.[17−21] Recently, several hydrophilic Ru(II)-porphyrin conjugates were synthesized and reported to have potent cytotoxic, as well as phototoxic activities toward tumors.[22,23] The IC_{50} values of these conjugates obtained under photoirradiation (λ_{irr} = 590−700 nm) were found to be lower by 1 order of magnitude than those obtained in the dark. However, the strongest absorptions of these Ru(II) conjugates were at ca. 420 nm, with less than 3% of their maximum absorption intensities found in the tissue-transparent region (>650 nm). To overcome this problem, we have designed some Ru(II)-porphyrin conjugates with substantial absorption under two-photon excitation at $\lambda_{ex} \geq 800$ nm.[22−24] In these conjugates, the linkage of the Ru(II)-polypyridyl complex, a charge-transfer moiety, to the tetraphenylporphyrin raised its two-photon absorption (TPA) cross section, σ^2, from <20 GM to 178 GM, permitting their potential use as TPA-PDT agents against solid tumors. Furthermore, these conjugates became luminescent upon visible/near-infrared excitation in vitro, thus enabling their development as bifunctional tumor imaging and PDT agents.[25,26] Nonetheless, to be an efficacious photochemotherapeutic agent, its cellular uptake and subcellular localization properties are important parameters to consider as well.[27]

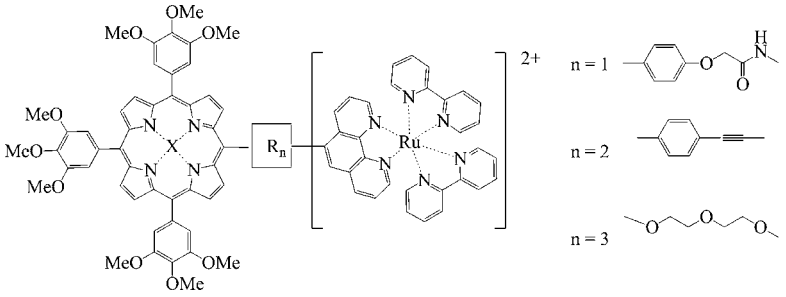
In this work, we report the synthesis of six amphiphilic Ru(II) appended porphyrins (**1**, **2**, **3**) and Zn(II) porphyrins (**4**, **5**, **6**) using linkers with different physicochemical (e.g., hydrophobic, electronic) properties and compare their luminescent (via linear and two-photon excitations), cellular uptake, subcellular localization, and (dark) cytotoxic and photocytotoxic properties in order to determine the optimal linker properties in these Ru(II)-porphyrin conjugates for TPA-PDT application.

EXPERIMENTAL SECTION (MATERIALS AND METHODS)

Synthesis of Compounds 1 to 6. All analytical-grade solvents were dried by standard procedures, distilled, and

Received: April 10, 2012
Revised: May 23, 2012
Published: July 9, 2012

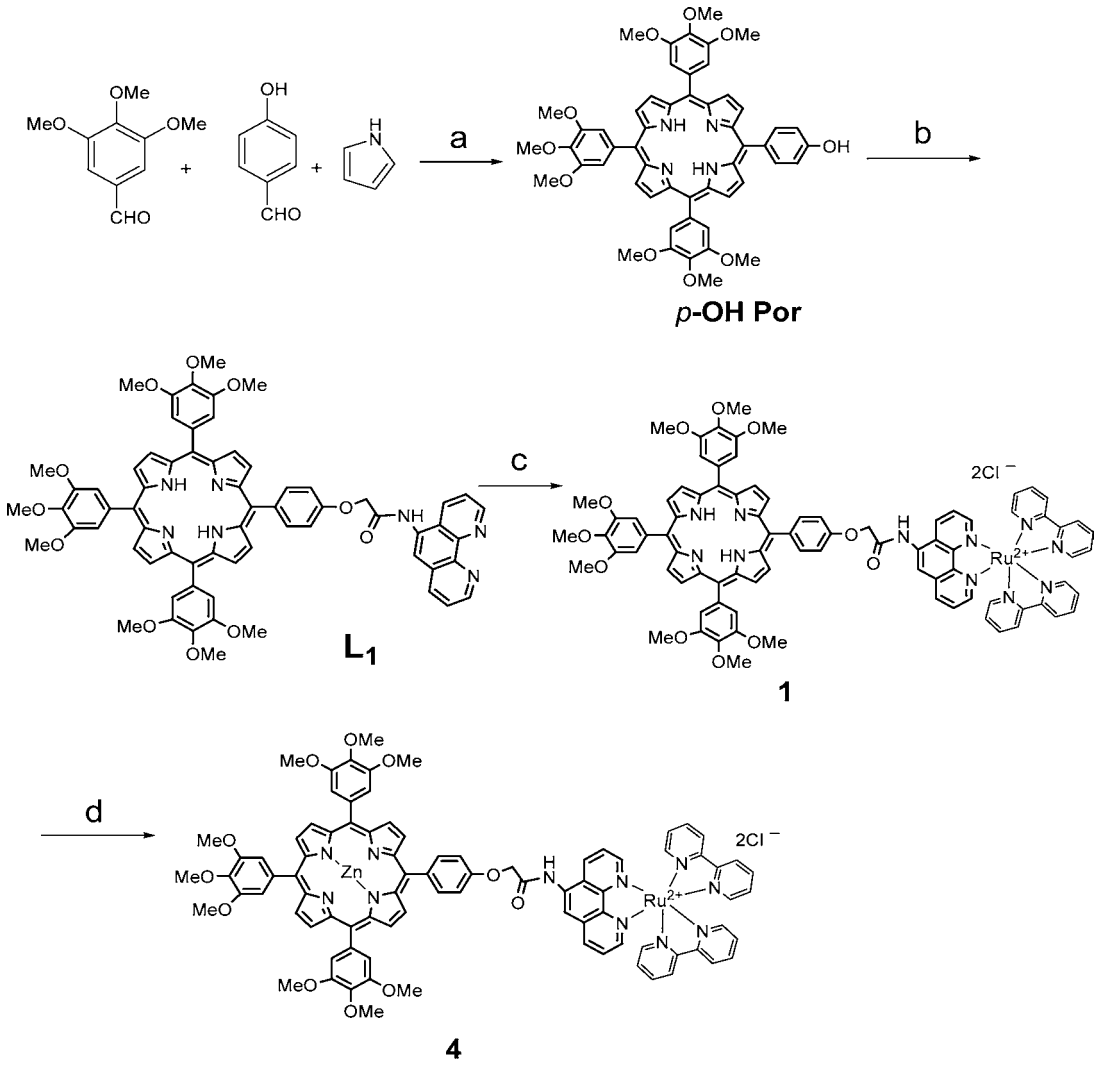
 © 2012 American Chemical Society



Compound	R_n	X
1	n = 1	$2H^+$
2	n = 2	$2H^+$
3	n = 3	$2H^+$
4	n = 1	Zn^{2+}
5	n = 2	Zn^{2+}
6	n = 3	Zn^{2+}

Figure 1. Schematic structures of ruthenium-porphyrin conjugates **1**−**6**.

Scheme 1. Synthetic Route for Conjugates 1 and 4[a]



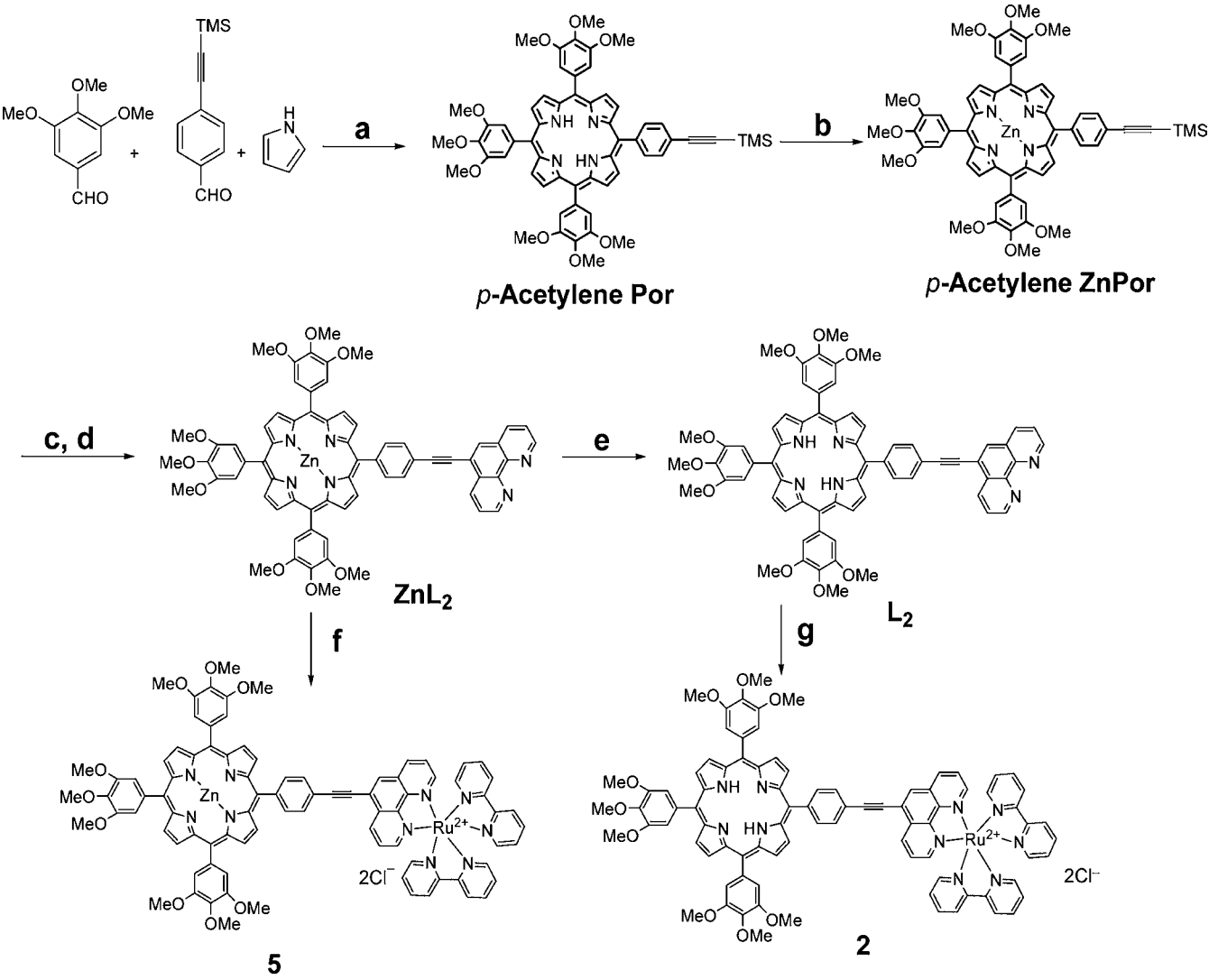
[a]Reactions and conditions: (a) propionic acid, 140 °C, 15%; (b) $BrCH_2CONH$-phen, Cs_2CO_3, DMF, 80 °C, 42%; (c) *cis*-$Ru(bpy)_2Cl_2$, THF/ethanol, 81%; (d) $Zn(OAc)_2{\cdot}2H_2O$, MeOH, 98%.

deaerated before use. NMR spectra were recorded on a Bruker Ultrashield 400 plus NMR spectrometer. The ^1H NMR chemical shifts were referenced to tetramethylsilane, TMS (d = 0.00). High-resolution mass spectra were obtained on a Bruker Autoflex MALDI−TOF mass spectrometer. IR spectra were recorded on Nicolet Magna 550 Series II. Preparations of cis-$Ru(bpy)_2Cl_2$,[28] 5-bromo-1,10-phenanthroline,[29] and di-(ethylene glycol) di-*p*-toluenesulfonate[30] were performed according to literature procedures. The synthetic routes of compounds **1**−**6** are listed in Schemes 1, 2, and 3.

*5,10,15-Tris(3′,4′,5′-trimethoxylphenyl)-20-(4′-hydoxylphenyl)-21H,23H-porphyrin (**p-OH Por**).* A solution of pyrrole (4.556 g, 0.068 mol) in 100 mL of propionic acid was added dropwise into a solution of 3,4,5-trimethoxylbenzaldehyde (10.00 g, 0.051 mol) and 4-hydroxylbenzaldehyde (2.075 g, 0.017 mol) in 300 mL of propionic acid at 120 °C. When it is completed, the temperature was raised up to 140 °C. After

dx.doi.org/10.1021/bc300201h | *Bioconjugate Chem.* 2012, 23, 1623−1638

Scheme 2. Synthetic Route for Conjugates 2 and 5.[b]



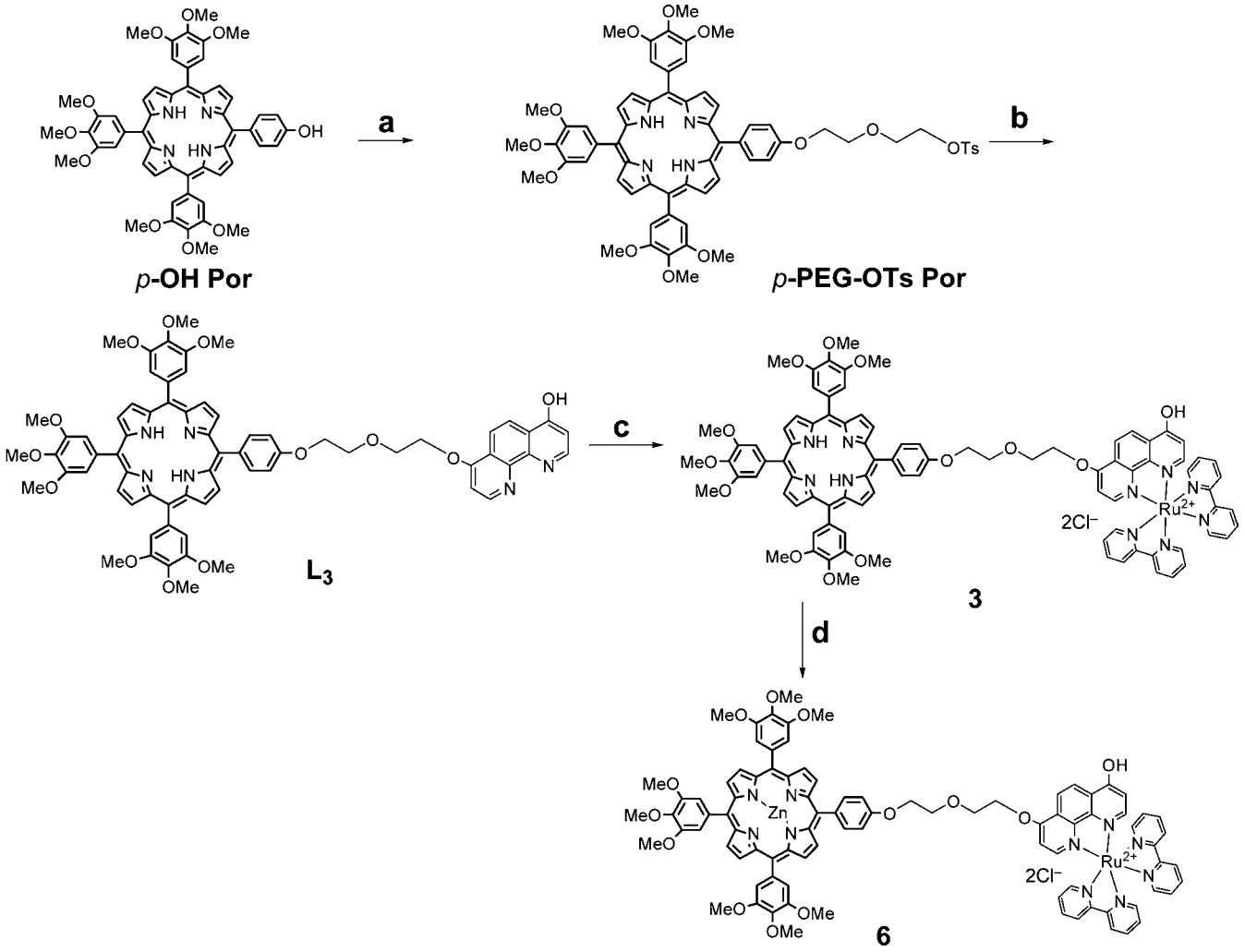
[b]Reactions and conditions: (a) propionic acid, 140 °C, 18%; (b) $Zn(OAc)_2 \cdot 2H_2O$, $CHCl_3$, MeOH, 97%; (c) TBAF, THF; (d) $Pd(PPh_3)_4$, CuI, THF, diisopropylamine, 5-bromo-1,10-phen, 51% (two steps); (e) HCl, CH_2Cl_2, RT, 90%; (f) *cis*-$Ru(bpy)_2Cl_2$, THF/ethanol, 85%; (g) *cis*-$Ru(bpy)_2Cl_2$, THF/ethanol, 81%.

refluxing for 3 h, the propionic acid was distillated out under reduced pressure until about 80 mL solution was left. Then, 100 mL of ethanol was added into the flask and the solution was cooled overnight in the refrigerator. The precipitate was filtered out and washed with ethanol for several times. The product (2.297 g, 0.003 mol) was obtained in the second band as a purple solid after column chromatography ($CHCl_3$ as eluent), yield 15%. UV−visible ($CHCl_3$), λ_{abs}/nm (log ε) 422 (5.56), 518 (4.35), 553 (3.86), 592 (3.80), 648 (3.75). IR (KBr), ν/cm^{-1}: 2925 (s), 2847 (w), 1576 (s), 1495 (s), 1460 (s), 1401 (s), 1356 (s), 1245 (s), 1168 (m), 1119 (s), 996 (m), 972 (w), 918 (s), 792 (m), 730 (m), 587 (m). ^{1}H NMR ($CDCl_3$) δ −2.79 (s, 2H), 3.96 (s, 18H), 4.18 (s, 9H), 5.30 (s, 1H), 7.22 (d, 2H, J = 8.6 Hz), 7.46 (d, 6H, J = 1.6 Hz), 8.07 (d, 2H, J = 8.4 Hz), 8.88 (d, 2H, J = 4.7 Hz), 8.94 (d, 6H, J = 4.7 Hz). HRMS (MALDI-TOF) ([M]$^+$, m/z): Calcd for $C_{53}H_{48}N_4O_{10}$, 900.9; Found for [M+H]$^+$, 901.3.

*Amide-Linked Porphyrin-Phen (**L$_1$**).* 2-Bromo-*N*-(1,10-phenanthrolin-5-yl) acetamide (421 mg, 1.332 mmol) and Cs_2CO_3 (64 mg, 0.333 mmol) were added into a solution of ***p*-OH Por** (200 mg, 0.222 mmol) in anhydrous DMF (10 mL). The solution was stirred for 24 h at 80 °C, and then the solvent was removed; the residue was extracted with $CHCl_3$ and washed with water. The organic solvent was collected and removed under reduced pressure. The crude product was purified by column chromatography ($CHCl_3$/MeOH (v/v) = 30:1); yield: 106 mg, 42%. UV−visible ($CHCl_3$), λ_{abs}/nm (log ε) 422 (5.51), 518 (4.30), 553 (3.87), 592 (3.70), 651 (3.68). IR (KBr), ν/cm^{-1}: 2917 (s), 2843 (w), 1699 (m), 1576 (s), 1499 (s), 1458 (s), 1401 (s), 1356 (m), 1233 (s), 1180 (m), 1119 (s), 1004 (m), 967 (w), 927 (m), 792 (s), 730 (m), 628 (w), 583 (w). ^{1}H NMR ($CDCl_3$) δ −2.76 (s, 2H), 3.98 (s, 18H), 4.19 (s, 9H), 5.16 (s, 2H), 7.48 (d, 6H, J = 2.0 Hz), 7.52 (d, 2H, J = 8.2 Hz), 7.69−7.72 (m, 1H), 7.80−7.84 (m, 1H), 8.27 (d, 2H, J = 8.4 Hz), 8.33−8.35 (dd, 1H, J = 1.6 Hz, 8.1 Hz), 8.44−8.46 (dd, 1H, J = 1.5 Hz, 8.4 Hz), 8.57 (s, 1H), 8.88 (d, 2H, J = 4.7 Hz), 8.98 (s, 6H), 9.14 (s, 1H), 9.20−9.22 (dd, 1H, J = 1.7 Hz, 4.4 Hz), 9.32 (dd, 1H, J = 1.7 Hz, 4.1 Hz). HRMS (MALDI-TOF) ([M]$^+$): Calcd for $C_{67}H_{57}N_7O_{11}$, 1136.2; Found for [M]$^+$, 1136.4.

dx.doi.org/10.1021/bc300201h | *Bioconjugate Chem.* 2012, 23, 1623−1638

Scheme 3. Synthetic Route for Conjugates 3 and 6[c]



[c]Reactions and conditions: (a) Di(ethylene glycol) di-*p*-toluenesulfonate, K_2CO_3, DMF, 55%; (b) 4,7-diol-1,10-phen, NaH, DMF, 30%; (c) *cis*-$Ru(bpy)_2Cl_2$, acetic acid, reflux, 56%; (d) $Zn(OAc)_2{\cdot}2H_2O$, MeOH, 88%.

Amide-Linked [(Porphyrin-Phen)Ru(bpy)$_2$][Cl]$_2$ (1). Porphyrin ligand L_1 (50 mg, 0.044 mmol) and cis-$Ru(bpy)_2Cl_2$ (85 mg, 0.176 mmol) were added into a solution of 15 mL THF and 15 mL ethanol, and then the solution was bubbled with N_2 for a few minutes, and the reaction temperature was set to 85 °C. After refluxing 15 h, the solvent was removed under vacuum and the residue was chromatographed on Al_2O_3 several times, the eluent in turn is $CHCl_3$, ($CHCl_3$:MeOH (v/v) = 12:1), yield 58 mg, 81%. UV−visible ($CHCl_3$), λ_{abs}/nm (log ε) 288 (4.91), 424 (5.58), 517 (4.29), 554 (3.98), 592 (3.79), 646 (3.65). IR (KBr), ν/cm^{-1}: 2925 (m), 2819 (w), 1580 (s), 1540 (m), 1499 (s), 1466 (s), 1405 (s), 1356 (m), 1233 (s), 1176 (m), 1119 (s), 1004 (m), 976 (m), 932 (m), 845 (w), 800 (m), 763 (m), 726 (m), 566 (m). ^{1}H NMR (d_6-DMSO) δ −2.91 (s, 2H), 3,89 (s, 18H), 3.99 (s, 9H), 5.39 (s, 2H), 7.36−7.40 (m, 2H), 7.50 (m, 8H), 7.58−7.62 (m, 4H), 7.84−7.89 (m, 3H), 7.94−7.98 (m, 1H), 8.06−8.14 (m, 3H), 8.16−8.23 (m, 5H), 8.78 (s, 1H), 8.82−8.91 (m, 7H), 8.94 (s, 6H), 9.18 (m, 1H), 11.31 (s, 1H). HRMS (MALDI−TOF) ([M−2Cl]$^+$, m/z): Calcd for $[C_{87}H_{73}N_{11}O_{11}Ru]^+$, 1549.6; Found for [M−2Cl]$^+$, 1549.4.

Amide-Linked [(Zn-porphyrin-Phen)Ru(bpy)$_2$][Cl]$_2$ (4). **1** (30 mg, 0.0185 mmol) was treated with $Zn(OAc)_2{\cdot}2H_2O$ (5 mg, 0.022 mmol) in 20 mL of methanol at 65 °C for 3 h. The crude product was washed with water and then dried in vacuum. The pure product was obtained by flash chromatography on Al_2O_3, yield: 31 mg, 98%. UV−visible ($CHCl_3$), λ_{abs}/nm (log ε) 288 (4.94), 431 (5.67), 560 (4.28), 603 (4.32). IR (KBr), ν/cm^{-1}: 2917 (s), 2847 (w), 1593 (m), 1580 (s), 1540 (m), 1507 (s), 1458 (s), 1409 (s), 1343 (s), 1237 (s), 1176 (m), 1123 (s), 996 (m), 943 (m), 800 (m), 763 (m), 722 (m), 620 (m). ^{1}HNMR (d_6-DMSO) δ 3.90 (s, 18H), 4.00 (s, 9H), 5.33 (s, 2H), 7.35−7.38 (m, 2H), 7.43 (d, 6H, J = 6.2 Hz), 7.52 (d, 2H, J = 8.5 Hz), 7.58−7.63 (m, 4H), 7.83−7.88 (m, 3H), 7.94−7.99 (m, 1H), 8.06−8.15 (m, 5H), 8.19−8.24 (m, 3H), 8.75 (s, 1H), 8.79−8.87 (m, 7H), 8.89 (d, 6H, J = 4.4 Hz), 9.05 (d, 1H, J = 8.5 Hz), 11.06 (s, 1H). HRMS (MALDI−TOF) ([M−2Cl]$^+$, m/z): Calcd for $[C_{87}H_{71}N_{11}O_{11}RuZn]^+$, 1613.4; Found for [M−2Cl]$^+$, 1612.1.

5,10,15-Tris(3′,4′,5′-trimethoxylphenyl)-20-[4′-(2″-trimethylsilylethyl)phenyl]-21H,23H-porphyrin (p-Acetylene Por). A solution of pyrrole (3.646 g, 0.054 mol) in propionic acid (100 mL) was added dropwise into a solution of 3,4,5-trimethoxylbenzaldehyde (8.00 g, 0.041 mol) and 4-[2′-(trimethylsilyl)ethynyl]benzaldehyde (2.748 g, 0.014 mol) in propionic acid (300 mL) at 120 °C. When it was completed,

dx.doi.org/10.1021/bc300201h | *Bioconjugate Chem.* 2012, 23, 1623−1638

the temperature was raised up to 140 °C. After refluxing for 3 h, the propionic acid was distilled out completely under reduced pressure. The residue was dissolved in $CHCl_3$ and filtered through a short silica gel column and then the filtrate was washed with water. The crude product was purified by column chromatography using $CHCl_3$ as eluent. Purple solid was obtained. Yield: 2.400 g, 18%. UV−visible ($CHCl_3$), λ_{abs}/nm (log ε) 422 (5.65), 516 (4.31), 553 (3.90), 591 (3.83), 648 (3.81). IR (KBr), ν/cm^{-1}: 2925 (s), 2823 (m), 1576 (s), 1499 (s), 1470 (s), 1405 (s), 1352 (s), 1225 (s), 1176 (m), 1123 (s), 1017 (m), 967 (w), 918 (m), 861 (m), 792 (m), 730 (m), 653 (w), 567 (w). ^{1}H NMR ($CDCl_3$) δ −2.80 (s, 2H), 0.38 (s, 9H), 9.36 (s, 18H), 4.18 (s, 9H), 7.45 (s, 6H), 7.86 (d, 2H, J = 8.2 Hz), 8.16 (d, 2H, J = 8.3 Hz), 8.91 (d, 2H, J = 4.7 Hz), 9.08 (m, 6H). HRMS (MALDI-TOF) ([M]$^+$, m/z): Calcd for $C_{58}H_{56}N_4O_9Si$, 981.2; Found for [M]$^+$, 981.2.

*5,10,15-Tris(3′,4′,5′-trimethoxylphenyl)-20-[4′-[2″-(trimethylsilyl)ethynyl]-phenyl]-21H,23H porphyrinato zinc-(II) (**p-Acetylene ZnPor**).* $Zn(OAc)_2{\cdot}2H_2O$ (107 mg, 0.490 mmol) and porphyrin ***p*-Acetylene Por** (400 mg, 0.408 mmol) were dissolved in a mixture of $CHCl_3$ and MeOH, and the reaction was maintained at 60 °C for 3 h. The solvent was removed and the residue was purified on a silica gel using $CHCl_3$ as eluent to give **7** as purple solid. Yield: 413 mg, 97%. ^{1}H NMR ($CDCl_3$) 0.39 (s, 9H), δ 3.92 (s, 18H), 4.12 (s, 9H), 7.45 (s, 6H), 7.86 (d, 2H, J = 8.1 Hz), 8.07 (d, 2H, J = 8.0 Hz), 8.93 (d, 2H, J = 4.7 Hz), 9.07 (m, 6H).

*Phenylacetylene-Linked Zinc-Porphyrin-Phen (**ZnL$_2$**).* ***p*-Acetylene ZnPor** (380 mg, 0.364 mmol) was dissolved in anhydrous CH_2Cl_2 in N_2 atmosphere, TBAF solution (400 μL, 1 M in THF) was injected into the CH_2Cl_2 solution and the resultant solution was stirred at room temperature for 30 min. The reaction solution was filtered by flash chromatography and the deprotected ethynyl-zinc-porphyrin was dried in vacuum. 5-Bromo-1,10-phenanthrolin (62.8 mg, 0.242 mmol) and then 20 mL of anhydrous THF was added in the above flask. The Sonogashira coupling reaction was administered in N_2 atmosphere using $Pd(PPh_3)_4$ (28 mg, 0.024 mmol) and CuI (2.3 mg, 0.012 mmol) as catalysts and diisopropylamine (6 mL) as base. The reaction mixture was heated at 45 °C for 8 h. The solvent was removed and the residue was purified on silica gel using $CHCl_3$/MeOH (v/v = 20:1) as eluent, yield 142 mg, 51%. UV−visible ($CHCl_3$), λ_{abs}/nm (log ε) 278 (4.20), 426 (5.58), 553 (4.30), 595 (3.95). IR (KBr), ν/cm^{-1}: 2921 (s), 2851 (w), 1617 (s), 1576 (s), 1556 (m), 1535 (w), 1503 (s), 1458 (s), 1405 (s), 1348 (s), 1237 (s), 1127 (s), 992 (m), 935 (w), 796 (m), 718 (m), 669 (m), 567 (s). ^{1}H NMR ($CDCl_3$) δ 3.97 (s, 18H), 4.19 (s, 9H), 7.49 (d, 6H, J = 1.7 Hz), 7.68−7.71 (m, 1H), 7.81−7.88 (m, 1H), 8.08 (d, 2H, J = 8.1 Hz), 8.27 (s, 1H), 8.29−8.31 (m, 3H), 8.97 (d, 2H, J = 4.7 Hz), 9.04−9.08 (m, 7H), 9.18 (d, 1H, J = 3.6 Hz), 9.25 (d, 1H, J = 2.8 Hz). HRMS (MALDI−TOF) ([M]$^+$, m/z): Calcd for $C_{67}H_{52}N_6O_9Zn$, 1148.3; Found for [M+H]$^+$, 1149.3.

*Phenylacetylene-Linked Porphyrin-Phen (**L$_2$**).* Demetalation of **ZnL$_2$** was achieved by dissolving **ZnL$_2$** (60 mg, 0.052 mmol) in a mixture of concentrated HCl (2 mL) and CH_2Cl_2 (10 mL). After stirring for 1 h, the solvent was washed by water and the organic phase was neutralized by $NaHCO_3$. The solvent was dried by sodium sulfate and removed under reduced vacuum. Purification was done on silica gel to give purple−red solid of **L$_2$**. Yield: 51 mg, 90%. UV−visible ($CHCl_3$), λ_{abs}/nm (log ε) 282 (4.18), 424 (5.57), 518 (4.27), 554 (3.83), 592 (3.83), 648 (3.76). IR (KBr), ν/cm^{-1}: 2913 (s), 2855 (w), 1638 (s), 1613 (s), 1580 (s), 1511 (m), 1454 (m), 1405 (w), 1356 (m), 1241 (s), 1119 (s), 1070 (w), 1004 (w), 927 (s), 804 (m), 726 (w), 665 (w), 575 (w). ^{1}H NMR ($CDCl_3$) δ −2.75 (s, 2H), 3.98 (d, 18H, J = 4.2 Hz), 4.18 (d, 9H, J = 4.2 Hz), 7.49 (m, 6H), 7.69 (m, 1H), 7.84 (m, 1H), 8.10 (m, 2H), 8.27 (d, 1H, J = 3.4 Hz), 8.30 (m, 3H), 8.91 (d, 2H, J = 4.4 Hz), 8.99−9.06 (m, 7H), 9.22−9.26 (m, 1H), 9.29−9.33 (m, 1H). HRMS (MALDI−TOF) ([M]$^+$, m/z): Calcd for $C_{67}H_{54}N_6O_9$, 1086.4; Found for [M+H]$^+$, 1087.4.

*Phenylacetylene-Linked [(Zinc-Porphyrin-Phen)Ru(bpy)$_2$][Cl]$_2$ (**5**).* Zinc-porphyrin ligand **ZnL$_2$** (50 mg, 0.044 mmol) and cis-$Ru(bpy)_2Cl_2$ (63 mg, 0.131 mmol) were added in a mixture of THF (15 mL) and ethanol (15 mL). The solution was then bubbled with N_2 for a few minutes, and heated to 85 °C. After refluxing 15 h, the solvent was removed under vacuum and the residue was chromatographed on Al_2O_3 several times, and the eluent in turn was $CHCl_3$, ($CHCl_3$:MeOH (v/v) = 12:1). Yield: 60 mg, 85%. UV−visible ($CHCl_3$), λ_{abs}/nm (log ε) 288 (4.92), 431 (5.55), 562 (4.46), 606 (4.31). IR (KBr), ν/cm^{-1}: 2921 (s), 2843 (w), 1625 (s), 1572 (s), 1482 (m), 1462 (s), 1405 (s), 1348 (s), 1229 (s), 1115 (s), 1061 (w), 988 (s), 935 (m), 792 (w), 763 (m), 722 (m), 543 (m). ^{1}H NMR (d_6-DMSO) δ 3.91 (d, 18H, J = 11.7 Hz), 4.06 (d, 9H, J = 10.6 Hz), 7.37−7.40 (m, 2H), 7.51 (d, 6H, J = 4.8 Hz), 7.57−7.61 (m, 2H), 7.74−7.79 (m, 4H), 7.83−7.87 (m, 1H), 7.91 (d, 2H, J = 7.2 Hz), 7.95−7.99 (m, 3H), 8.08−8.12 (m, 2H), 8.18−8.24 (m, 3H), 8.31 (d, 1H, J = 5.1 Hz), 8.61 (s, 1H), 8.65−8.68 (m, 3H), 8.73−8.79 (m, 4H), 8.89 (d, 2H, J = 4.7 Hz), 8.94−8.97 (m, 4H), 9.15 (d, 1H, J = 8.4 Hz). HRMS (MALDI-TOF) ([M−2Cl]$^+$, m/z): Calcd for $C_{87}H_{68}N_{10}O_9RuZn$, 1563.9; Found for [M−2Cl]$^+$, 1563.2; [M−2Cl−bpy]$^+$, 1408.1.

*Phenylacetylene-Linked [(Porphyrin-Phen)Ru(bpy)$_2$][Cl]$_2$ (**2**).* Porphyrin ligand **L$_2$** (50 mg, 0.046 mmol) and cis-$Ru(bpy)_2Cl_2$ (67 mg, 0.138 mmol) were dissolved in a mixture of THF (15 mL) and ethanol (15 mL). The solution was then bubbled with N_2 for a few minutes before heating to 85 °C. After refluxing 15 h, the solvent was removed under vacuum and the residue was chromatographed on Al_2O_3 several times; the eluent in turn was $CHCl_3$ ($CHCl_3$:MeOH (v/v) = 12:1). Yield: 58 mg, 81%. UV−visible ($CHCl_3$), λ_{abs}/nm (log ε) 288 (4.66), 425 (5.33), 517 (4.12), 554 (3.91), 593 (3.72), 646 (3.66). IR (KBr), ν/cm^{-1}: 2925 (s), 2843 (w), 1643 (s), 1609 (s), 1576 (w), 1503 (m), 1450 (m), 1405 (s), 1380 (m), 1237 (w), 1119 (s), 993 (m), 800 (m), 767 (w), 661 (w), 561 (m). ^{1}H NMR (d_6-DMSO) δ −2.98 (s, 2H), 3.82 (s, 18H), 3.91 (s, 9H), 7.32−7.37 (m, 2H), 7.45 (d, 6H, J = 7.8 Hz), 7.54−7.57 (m, 2H), 7.61 (d, 2H, J = 5.4 Hz), 7.80 (s, 2H), 7.88−7.91 (m, 1H), 7.99−8.03 (m, 1H), 8.06−8.11 (m, 2H), 8.13−8.21 (m, 6H), 8.31 (d, 2H, J = 8.0 Hz), 8.81−8.93 (m, 14H), 9.21 (d, 1H, J = 8.6 Hz). HRMS (MALDI-TOF) ([M−2Cl]$^+$, m/z): Calcd for $C_{87}H_{70}N_{10}O_9Ru$, 1500.6; Found for [M−2Cl]$^+$, 1500.4; [M−2Cl +DHB]$^+$, 1653.3.

*1-[4-[5,10,15-Tris(3,4,5-trimethoxylphenyl)-20-porphyrin-yl]-phenoxy]-5-(p-tolylsulfonyloxy)ethoxy-ethane (**p-PEG-OTs Por**).* Di(ethylene glycol) di-*p*-toluenesulfonate (345 mg, 0.832 mmol) and porphyrin ***p*-OH Por** (300 mg, 0.332 mmol) were dissolved in anhydrous DMF (10 mL), and then K_2CO_3 (68 mg, 0.498 mmol) was added into the solution. The reaction solution was heated at 65 °C for 24 h. DMF was removed and the residue was washed with water several times and extracted with CH_2Cl_2. The organic phase was collected and purified on silica gel to give ***p*-PEG-OTs Por** as purple solid. Yield: 208 mg, 55%. UV−visible ($CHCl_3$), λ_{abs}/nm (log ε) 422 (5.68), 518

dx.doi.org/10.1021/bc300201h | Bioconjugate Chem. 2012, 23, 1623−1638

(4.41), 553 (3.87), 592 (3.87), 648 (3.80). IR (KBr), ν/cm^{-1}: 2921 (s), 2847 (w), 1707 (s), 1646 (w), 1597 (s), 1580 (s), 1495 (s), 1462 (m), 1413 (s), 1352 (s), 1327 (s), 1233 (s), 1172 (s), 1131 (s), 1000 (m), 923 (m), 812 (m), 763 (m), 661 (m), 555 (m). ^{1}H NMR ($CDCl_3$) δ −2.78 (s, 2H), 2.45 (s, 3H), 3.92 (m, 2H), 3.97 (s, 18H), 4.15 (m, 2H), 4.17 (s, 9H), 4.31 (m, 2H), 4.37 (m, 2H), 7.30 (d, 2H, J = 8.7 Hz), 7.47 (d, 6H, J = 1.5 Hz), 7.78 (d, 2H, J = 8.3 Hz), 7.86 (d, 2H, J = 8.3 Hz), 8.11 (d, 2H, J = 8.4 Hz), 8.87 (d, 2H, J = 4.7 Hz), 8.94 (d, 6H, J = 5.3 Hz). HRMS (MALDI−TOF) ([M]$^+$, m/z): Calcd for $C_{64}H_{62}N_4O_{14}S$, 1143.2; Found for [M]$^+$, 1143.4.

*Ethoxyethane-Linked Porphyrin-Phen (**L$_3$**).* 1,10-Phenanthroline-4,7-diol (74 mg, 0.350 mmol) was dissolved in 5 mL anhydrous DMF, and then NaH (17 mg, 0.7 mmol) was added to the solution. The solution was stirred for 20 min, then a DMF solution of porphyrin ***p*-PEG-OTs Por** (200 mg, 0.175 mmol) was added dropwise into the reaction mixture. The reaction temperature was maintained at 50 °C for 8 h. DMF was removed and CH_2Cl_2 was added. The unreacted 1,10-phenanthroline-4,7-diol was filtered out and the organic phase was washed by water for several times. The product was purified on silica gel with the mixed solvent ($CHCl_3$/MeOH (v/v) = 25:1) as eluent. Yield: 62 mg, 30%. UV−visible ($CHCl_3$), λ_{abs}/nm (log ε) 330 (4.30), 422 (5.72), 516 (4.43), 554 (3.89), 591 (3.88), 648 (3.80). IR (KBr), ν/cm^{-1}: 2917 (s), 2847 (w), 1625 (m), 1580 (s), 1499 (s), 1458 (s), 1405 (s), 1352 (m), 1303 (w), 1282 (w), 1233 (s), 1168 (m), 1119 (s), 1049 (m), 1004 (m), 967 (m), 914 (w), 792 (s), 628 (w), 555 (m). ^{1}H NMR ($CDCl_3$) δ −2.78 (s, 2H), 3.96 (s, 18H), 4.18 (s, 9H), 4.21 (m, 2H), 4.27 (m, 2H), 4.48 (m, 2H), 4.54 (m, 2H), 6.48 (d, 1H, J = 7.3 Hz), 7.03 (d, 1H, J = 5.2 Hz), 7.29 (d, 2H, J = 8.5 Hz), 7.46 (s, 6H), 7.73 (m, 1H), 8.08−8.14 (m, 3H), 8.37 (d, 1H, J = 9.0 Hz), 8.75 (d, 1H, J = 5.2 Hz), 8.84 (d, 2H, J = 4.6 Hz), 8.92−8.95 (m, 6H), 10.41 (s, 1H). HRMS (MALDI−TOF) ([M]$^+$, m/z): Calcd for $C_{69}H_{62}N_6O_{13}$, 1183.2; Found for [M]$^+$, 1183.4.

*Ethoxyethane-Linked [{Porphyrin-(5-hydroxyl-Phen)Ru(bpy)$_2$}][Cl]$_2$ (**3**).* Porphyrin ligand $\mathbf{L}_3$ (50 mg, 0.042 mmol) and cis-Ru(bpy)$_2$Cl$_2$ (61 mg, 0.127 mmol) were added to acetic acid (10 mL). Then, the reaction solution was refluxed under N_2 atmosphere for 3 h. The solvent was removed under vacuum and the residue was chromatographed on Al_2O_3 several times; the eluents in turn were ($CHCl_3$:MeOH (v/v) = 20:1), ($CHCl_3$:MeOH (v/v) = 10:1). Yield: 39 mg, 56%. UV−visible ($CHCl_3$), λ_{abs}/nm (log ε) 288 (4.71), 424 (5.48), 517 (4.30), 554 (3.98), 592 (3.97), 646 (3.71). IR (KBr), ν/cm^{-1}: 2921 (s), 2847 (m), 1629 (s), 1576 (m), 1508 (m), 1462 (s), 1404 (s), 1343 (m), 1282 (w), 1231 (s), 1131 (s), 1119 (s), 1053 (m), 1010 (m), 955 (w), 759 (s), 628 (w), 555 (m). ^{1}H NMR (d_6-DMSO) δ −2.92 (s, 2H), 3.89 (d, 18H, J = 2.0 Hz), 3.99 (d, 9H, J = 2.6 Hz), 4.09−4.12 (m, 4H), 4.44−4.51 (m, 4H), 6.14 (d, 1H, J = 6.8 Hz), 6.74 (d, 1H, J = 6.8 Hz), 7.26 (d, 1H, J = 6.3 Hz), 7.37−7.45 (m, 5H), 7.47−7.51 (m, 8H), 7.58 (d, 1H, J = 6.1 Hz), 7.77 (d, 1H, J = 5.7 Hz), 7.81−7.84 (m, 2H), 7.87−7.91 (m, 2H), 7.96−8.03 (m, 2H), 8.05−8.12 (m, 4H), 8.27−8.30 (m, 1H), 8.70−8.80 (m, 6H), 8.93−8.96 (m, 6H). HRMS (MALDI-TOF) ([M−2Cl]$^+$, m/z): Calcd for $C_{89}H_{78}N_{10}O_{13}Ru$, 1596.7; Found for [M−2Cl]$^+$, 1596.4.

*Ethoxyethane-Linked [{Zn-porphyrin-(5-hydroxyl-Phen)}Ru(bpy)$_2$][Cl]$_2$ (**6**).* Ethoxyethane-linked [{porphyrin-(5-hydroxyl-Phen)}Ru(bpy)$_2$][Cl]$_2$ (**3**) (18 mg, 0.011 mmol) was treated with Zn(OAc)$_2$·2H$_2$O (3 mg, 0.013 mmol) in methanol (20 mL) at 65 °C for 3 h. The crude product was washed with water and then dried under vacuum. The pure product was obtained by column chromatography on Al_2O_3 ($CHCl_3$:MeOH (v/v) = 10:1 as eluent). Yield: 16 mg, 88%. UV−visible ($CHCl_3$), λ_{abs}/nm (log ε) 288 (4.72), 431 (5.64), 562 (4.28), 600 (4.01). IR (KBr), ν/cm^{-1}: 2921 (s), 2847 (w), 1625 (s), 1576 (m), 1503 (m), 1454 (s), 1405 (s), 1343 (m), 1282 (w), 1229 (s), 1131 (s), 1119 (s), 1053 (m), 1004 (m), 967 (w), 759 (s), 628 (w), 555 (m). ^{1}H NMR (d_6-DMSO) δ 3.83 (d, 18H, J = 2.5 Hz), 3.93 (d, 9H, J = 2.2 Hz), 4.03−4.07 (m, 4H), 4.39−4.46 (m, 4H), 6.00 (d, 1H, J = 6.8 Hz), 6.64 (d, 1H, J = 6.8 Hz), 7.24 (d, 1H, J = 6.4 Hz), 7.28−7.35 (m, 3H), 7.36−7.39 (m, 7H), 7.42−7.46 (m, 3H), 7.52 (d, 1H, J = 6.2 Hz), 7.72 (d, 1H, J = 5.8 Hz), 7.76−7.78 (m, 2H), 7.80−7.83 (m, 2H), 7.93−7.98 (m, 4H), 8.01−8.06 (m, 2H), 8.14 (d, 1H, J = 9.0 Hz), 8.68−8.76 (m, 6H), 8.83−8.86 (m, 6H). HRMS (MALDI−TOF) ([M−2Cl]$^+$, m/z): Calcd for [$C_{89}H_{76}N_{10}O_{13}RuZn$]$^+$, 1660.1; Found for [M−2Cl−H]$^+$, 1658.9.

Linear-Induced Photophysical Properties. UV−visible absorption spectra in the spectral range 200−1100 nm were recorded by an HP UV-8453 spectrophotometer. Single-photon luminescence spectra were recorded using an Edinburgh Instrument FLS920 combined fluorescence lifetime and steady state spectrophotometer that was equipped with a visible to near-infraed-sensitive photomultiplier by in-nitrogen flow-cooled housing. The spectra were corrected for detector response and stray background light phosphorescence. The emission quantum yields of all the compounds were measured by a demountable 142 mm (inner) diameter barium sulfide-coated integrating sphere supplied with two access ports in Edinburgh Instrument FLS920. pH titrations of porphyrin-Ru homometallic complexes **1**−**3** were performed on 10 μM (DMSO) samples dissolved in aqueous solution whose pH was adjusted by small addition of 1 M NaOH or HCl.

Two-Photon Induced Emission and Two-Photon Absorption Cross-Section Measurement. Two-photon absorption spectra of **1**−**6** were measured at 850 nm by the open-aperture Z-scan method[31] using 100 fs laser pulses with a peak power of 276 GW cm^{-2} from an optical parametric amplifier operating at a 1 kHz repetition rate generated from a Ti:Sapphire regenerative amplifier system. The laser beam was split into two parts by a beam splitter. One was monitored by a photodiode (D1) as the incident intensity reference, I_0, and the other beam was detected by the photodiode (D2) as the transmitted intensity. After passing through a lens with f = 20 cm, the laser beam was focused and passed through a quartz cell. The position of the sample cell, z, was moved along the laser-beam direction (z axis) by a computer-controlled translatable table so that the local power density within the sample cell could be changed under the constant incident intensity laser power level. Finally, the transmitted intensity from the sample cell was detected by the photodiode D2 interfaced to a computer for signal acquisition and averaging. Each transmitted intensity data represent an average of over 100 measurements. Assuming a Gaussian beam profile, the nonlinear absorption coefficient β can be obtained by curve fitting to the observed open-aperture traces, $T(z)$, with eq 1

$$T(z) = 1 - \frac{\beta I_0 (1 - e^{-\alpha_0 \mathcal{L}})}{2a_0[1 + (z/z_0)]^2} \quad (1)$$

where a_0 is the linear absorption coefficient, l is the sample length (1 mm quartz cell), and z_0 is the diffraction length of the incident beam.

After obtaining the nonlinear absorption coefficient β, the two-photon absorption cross section σ_2 of the sample molecule (in units of GM, where 1 GM = 10^{-50} cm^4 s photon^{-1}) can be calculated using eq 2

$$\sigma_2 = \frac{1000\beta h v}{N_A d} \quad (2)$$

where N_A is the Avogadro constant, d is the concentration of the sample compound in solution, h is the Planck constant, and v is the frequency of the incident laser beam.

Singlet Oxygen Quantum Yield Measurement. Singlet oxygen was detected directly by its phosphorescence emission at 1270 nm using an InGaAs detector on a PTI QM4 luminescence spectrometer. The singlet oxygen quantum yields (Φ_Δ) of the test compounds were determined in $CHCl_3$ by comparing the singlet oxygen emission intensity of the sample solution to that of a reference compound (H_2TPP, Φ_Δ = 0.55 in $CHCl_3$)[32] according to eq 3[33]

$$\Phi_\Delta^S = \Phi_\Delta^{REF} \times \left(\frac{n_S}{n_{REF}}\right)^2 \frac{G_\Delta^S}{G_\Delta^{REF}} \times \frac{A_{REF}}{A_S} \quad (3)$$

where Φ_Δ is the singlet oxygen quantum yield, G_Δ is the integrated emission intensity, A is the absorbance at the excitation wavelength, n is the refractive index of the solvent. Superscripts REF and S correspond to the reference and the sample, respectively. In all measurements, the $^1O_2$ emission spectra were obtained using an excitation with the absorbance set at 0.05 in order to minimize reabsorption of the emitted light.

Cell Culture. Human cervical carcinoma (HeLa) cells were maintained in an RMPI 1640 medium supplemented with 10% fetal bovine serum (FBS) and 1% penicillin and streptomycin in 5% CO_2. Culture medium in each dish was changed prior to exposure to the test compounds. Stock solutions of the test compounds (1 mM) were prepared in aqueous solution and stored in the dark at room temperature. These compounds, when used in the imaging and bioassay experiments involving cultured cells, were diluted with the corresponding culture media to appropriate concentrations.

Confocal Microscopic Imaging of Compounds 1−6. HeLa cells (1×10^5) were seeded onto coverslip in 35 mm culture dishes for overnight. The cells were initially incubated with compounds **1**−**6** (1 μM) for 30 min in the dark. For colocalization experiments, the cells were then washed and stained with 100 nM mitochondria-specific probe Mito Tracker Green FM dye M7514 or lysosome-specific probe Lyso Tracker Green DND-26 L7526, for 30 min. The emitted fluorescent signals of tested compounds and the organelle-specific probes were examined using the Leica SP5 (upright configuration) confocal microscope equipped with argon laser, HeCd laser and a femtosecond-pulsed Ti:Sapphire laser (Libra II, Coherent) inside the tissue culture chamber (5% CO_2, 37 °C). A 40× oil immersion objective and pinhole size of 110 μm was used for image capturing.

Flow Cytometric Cellular Uptake. HeLa cells cells (10^5 per sample) were seeded to 35 m Petri dish for overnight and then the cells were incubated with drugs at 2 mM for 1 and 6 h. Cells were trypsinized and washed with PBS for twice. The drug's uptakes by the HeLa cells were analyzed with flow cytometry. The cells were excited with 488 nm argon laser and emission was collected with FL-3 (equipped with 650 nm long pass filter) and 10000 events were analyzed.

Photocytotoxicity Assay. HeLa cells (2×10^4/well) were incubated in wells of a 96-well plate overnight. The cells were treated with **1**, **2**, and **3** for 6 h in the dark. The culture medium was then replaced with fresh medium and the cells were exposed to yellow light (1−4 J/cm^2) produced from a 400 W tungsten lamp fitted with a heat-isolation filter and a 500 nm long-pass filter. The fluence rate was 4 mW/cm^2. Cell viability was determined by the MTT reduction assay at 24 h post-PDT.[34] The cell monolayers were rinsed twice with phosphate-buffered saline (PBS) and then incubated with 250 μg/mL MTT solution at 37 °C for 3 h. The formazan crystal formed was dissolved in DMSO and the absorbance of dissolved formazan crystal at 540 and 690 nm was measured using a 96-well plate reader (ELx800 Absorbance Microplate Reader).

Two-Photon-Induced Confocal Microscopic Imaging of 1−3. HeLa cells (1×10^5) were seeded onto coverslip in 35-mm culture dishes overnight. The cells were initially incubated with **1**−**3** for 6 h in the dark. The two-photon-induced fluorescent signals of **1**−**3** were captured using the Leica SP5 (upright configuration) confocal microscope equipped with a femtosecond-pulsed Ti:Sapphire laser (Libra II, Coherent) inside the tissue culture chamber (5% CO_2, 37 °C). The excitation beam produced by the femtosecond laser, which was tunable from 680 to 1050 nm, was focused on the adherent cells through a 40× oil immersion objective. For the evaluation of effectiveness of photodynamic therapy, the time-lapse images (0−32 min, one laser shot per 8 min) were obtained with femtosecond laser excitation at 850 nm (laser power ∼8 mW).

RESULTS AND DISCUSSION

Synthesis and Characterization. (Scheme 1) The substitution reaction of 2-bromo-*N*-(1,10-phenanthrolin-5-yl)-acetamide and 5,10,15-tris(3,4,5-trimethoxylphenyl)-20-(4-hydoxylphenyl)-21*H*,23*H*-porphyrin (*p*-OH Por) in the presence of Cs_2CO_3 in DMF afforded the $\mathbf{L_1}$ porphyrin ligand with a yield of 42%. The identity of $\mathbf{L_1}$ was confirmed by ^{1}H NMR, in which the two internal NH pyrrole protons appeared as a sharp singlet at ca. −2.7 ppm, the two CH_2 protons appeared as a singlet at ca. 5.1 ppm, the seven protons of 1,10-phenanthroline occurred at ca. 8.2−8.5 ppm (4 protons) and 9.1−9.5 ppm (3 protons), respectively. High-resolution mass spectrum of $\mathbf{L_1}$ showed two peaks at m/z 1136.4, which corresponded to the to the peak $[M+H]^+$ (cf. calculated $[M]^+$, m/z 1135.4) and m/z 901, which corresponded to the loss of the 2-bromo-*N*-(1,10-phenanthrolin-5-yl)acetamide fragment. Ru(II) complexation was carried out with cis-Ru(bpy)$_2$Cl$_2$ in mixed solvent THF/CH_3CH_2OH (1:1), giving compound **1** with 81% yield. Metalation of the porphyrin in **1** with zinc acetate afforded compound **4** in good yield. Both **1** and **4** were characterized by ^{1}H NMR, HRMS, IR, and UV−vis spectroscopies. In their ^{1}H NMR spectra (Figure S1 and S3), the two internal NH pyrrole protons of **1** appeared as a relatively broad singlet at −2.9 ppm and the bipyridine protons in both **1** and **4** appeared as multiplets in the downfield region. The high-resolution mass spectra of **1** and **4** are given in Figures S2 and S4, respectively. Figure S2 shows a single peak at m/z 1549.4, which corresponds to the molecular ion peak of **1** (calculated $[M]^+$, m/z 1549.6), and Figure S4 shows a single peak at m/z 1612.1, which corresponds to the loss of a proton in either the pyrrole ring or the amide bond of **4** (calculated $[M]^+$, m/z 1613.4).

In Scheme 2, Sonogashira coupling reaction between *p*-acetylene-ZnPor and 5-bromo-1,10-phenanthroline under N_2 atmosphere afforded the zinc porphyrin, $\mathbf{ZnL_2}$, in moderate yield. Demetalation of $\mathbf{ZnL_2}$ in concentrated HCl solution gave the free base porphyrin, $\mathbf{L_2}$. ^{1}H NMR spectra of $\mathbf{L_2}$ and $\mathbf{ZnL_2}$ show the Phen proton signals at $\delta \approx 8.2-8.4$ ppm (4 protons) and 9.2−9.5 ppm (3 protons), respectively. High-resolution mass spectra of $\mathbf{L_2}$ and $\mathbf{ZnL_2}$ show their respective $[M+H]^+$ peaks at m/z 1087.4 (calculated $[M]^+$, m/z 1086.4) and m/z 1149.3 (calculated $[M]^+$, m/z 1148.3). Reaction of $\mathbf{L_2}$ and $\mathbf{ZnL_2}$ with cis-Ru(bpy)$_2$Cl$_2$ gave conjugates **2** and **5**, respectively, in good yields. These products were characterized by ^{1}H NMR, HRMS, IR, and UV−vis spectra. The ^{1}H NMR spectra (in d_6-DMSO) of **2** displayed slightly broader peaks and overlapping resonances for the bipyridine protons can be observed in the region 8.0−8.5 ppm. The two internal pyrrole NH protons also located in the upfield region ($\delta = -2.9$ ppm). High-resolution mass spectrum of **2** shows two peaks at m/z 1500.4 (M^+) and 1653.3 ($[M+DHB]^+$). ^{1}H NMR spectrum of **5** has a relatively well-resolved pattern, possibly because of its more symmetric structure. High-resolution mass spectrum of **5** also shows two peaks, one at m/z 1563.2 (M^+) and the other at m/z 1408.1 ($[M\text{-bipyridine}]^+$).

In Scheme 3, the reaction between *p*-OH Por and diethylene glycol di-*p*-toluenesulfonate in 1:1 ratio gave *p*-PEG-OTs Por as the main product. Reaction of *p*-PEG-OTs Por with 4,7-diol-1,10-phenanthroline in the ratio of 1:2 gave $\mathbf{L_3}$ with a relatively low yield, owing to the poor solubility of 4,7-diol-1,10-phenanthroline in the reaction media. The complexation of $\mathbf{L_3}$ with cis-Ru(bpy)$_2$Cl$_2$ gave **3**, which upon metalation with Zn(OAc)$_2$ afforded **6**. These final products, **3** and **6**, were also characterized by ^{1}H NMR, HRMS, IR, and UV−vis spectroscopies. ^{1}H NMR spectra of **3** and **6** are quite similar with well-resolved peaks. High-resolution mass spectra of both **3** and **6** show single peaks at m/z 1596.4 and 1658.9, which match favorably to the calculated m/z values of their respective molecular ions (for **3**, calculated $[M]^+$, m/z 1596.7; and for **6**, calculated $[M]^+$, m/z 1660.1).

Photophysical Properties. The objective of this work is to develop a dual probe capable of in vitro imaging and photodynamic therapeutic treatment. Herein, we report the relevant photophysical properties, which include both the linear and multiphoton-induced photophysical properties, singlet oxygen quantum yields, and so forth, of the porphyrin-Ru(II) conjugates synthesized.

UV−visible Absorption. The UV−vis absorption spectra of the six conjugates (**1** to **6**) were recorded in DMSO. Figure 2 shows the electronic spectra of free-base porphyrin-Ru(II) conjugates **1** to **3**, with the intense π to π^* transitions, the Soret band, and the four weak Q-bands of the porphyrin found at ∼300 nm, ∼430 nm, and 500−700 nm, respectively. Introduction of a Zn(II) ion to the porphyrin in conjugates **4** to **6**, resulted in small (a few nm) red shift of the Soret band and the number of Q bands were reduced from four to two. [35]

Linear (One-Photon) Emission Spectra. The emission spectra of the six Ru(II)-porphyrin conjugates, excited at 430 nm and measured in DMSO, are shown in Figure 3. The free-base porphyrin-Ru(II) conjugates, **1**, **2**, and **3**, show intense emission bands at ∼655 and ∼718 nm (Figure 3, upper panel). These two bands are assigned to the Q(0−0) and Q(0−1) transitions of the free-base porphyrins based on their emission wavelengths and lifetimes. The emission quantum yields of these conjugates, measured relative to the reference standard of

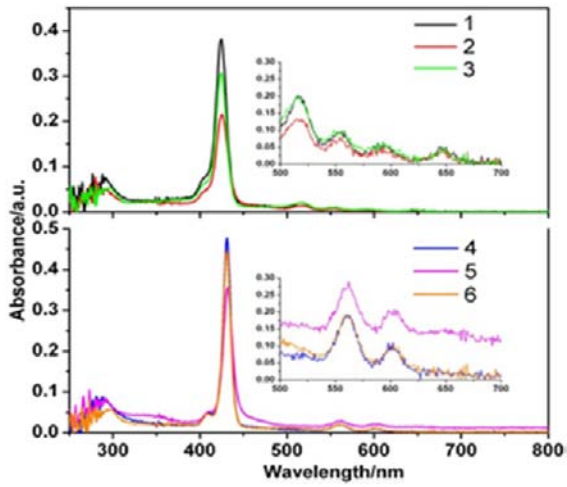


Figure 2. UV−vis absorption spectra of conjugates **1**−**3** (upper) and **4**−**6** (lower) in DMSO (1 μM). The inset shows the Q bands between 500 and 700 nm.

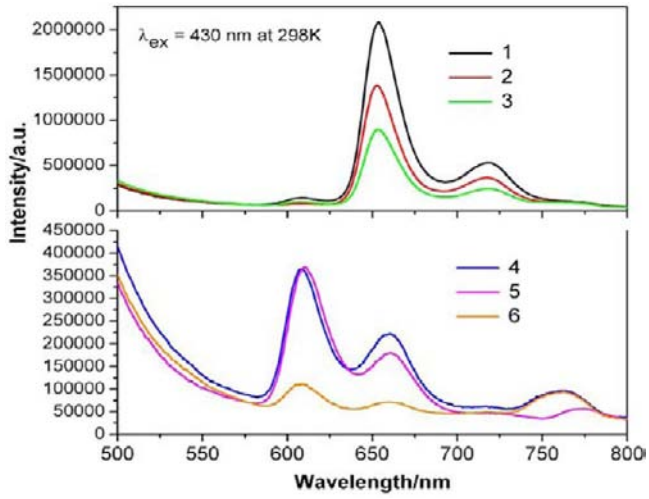


Figure 3. Emission spectra (λ_{ex} = 430 nm) of 1 μM of **1**−**3** (upper panel) and **4**−**6** (lower panel) measured in DMSO at 298 K.

5,10,15,20-tetrakis(4-methoxyphenyl)porphyrin,[36] are given in Table 1. From this table, it can be seen that the emission quantum yields of conjugates **1**, **2**, and **3** are strongly influenced by the length and conjugation of the linker between the porphyrin moiety and the Ru(bpy)$_2$(phen)$^{2+}$ complex. By elongating the linkage using an ethoxyethane group in **3**, we observed a dramatic reduction in the emission quantum yields from 5.30% (**1**) and 4.96% (**2**) to 1.93% (**3**). This result indicates that the observed porphyrin emissions are due to an energy transfer from the excited Ru(II)-polypyridyl moiety ($\lambda_{max}^{abs} \approx 450$ nm) to the porphyrin.

The Ru(II)−Zn(II) porphyrin conjugates, **4**, **5**, and **6**, give emission peaks at 610, 659, and 760 nm (Figure 3, lower panel) with the first two peaks assigned to the fluorescent emissions of the Zn(II) porphyrin. The 760 nm peak was assigned to the phosphorescence of the Zn(II) porphyrin.[37] The significant reduction in emission intensity observed in **6** is due to the longer ethoxyethane linkage between Ru(phen)(bpy)$_2^{2+}$ and Zn(II) porphyrin, making energy transfer between these two chromophores less efficient.

dx.doi.org/10.1021/bc300201h | *Bioconjugate Chem.* 2012, 23, 1623−1638

Table 1. Photophysical Properties of the Ru(II)-Porphyrin Conjugates 1 to 6

compound	λ_{Abs}/nm (log ε)	emission/nm (τ/ns)	$\Phi_{em}{}^{a}$/%	$\Phi_{\Delta}{}^{b}$/%	σ/GM
1	288(4.91), 424(5.58), 517(4.29), 554(3.98), 592(3.79), 646(3.65)	607(weak) 655(10.70), 718(8.78)	5.30	43	177
2	288(4.66), 425(5.33), 517(4.12), 554(3.91), 593 (3.72), 646(3.66)	607(weak) 654(11.6), 718(9.54)	4 90	58	168
3	288(4.71), 424(5.48), 517(4.30), 554(3.98), 592(3.97), 646(3.71)	607(weak) 653(4.23), 718(3.82)	1.93	38	144
4	288(4.94), 431(5.67). 560(4.28), 603(4.32)	610(10.50), 659(3.88) 760(weak)	0.58	52	172
5	288(4.92), 431(5.55), 562(4.46), 606(4.31)	610(3.74), 659(3.06) 760(weak)	0.30	73	228
6	288(4.72), 431(5.64), 562(4.28), 600(4.01)	610(3.04), 659(3.50) 770(weak)	0.16	45	106

[a]The emission quantum yields of **1** to **6** (λ_{em} = 550−800 nm, λ_{ex} = 430 nm). [b]The $^{1}O_{2}$ quantum yields of **1** to **6** (λ_{ex} = 430 nm). [c]Two-photon absorption cross sections of **1** to **6** (GM = 10^{-50} cm^{4} s photon^{-1} molecule^{-1}, λ_{ex} = 800 nm), with an average measurement uncertainty of ±23.5 GM.

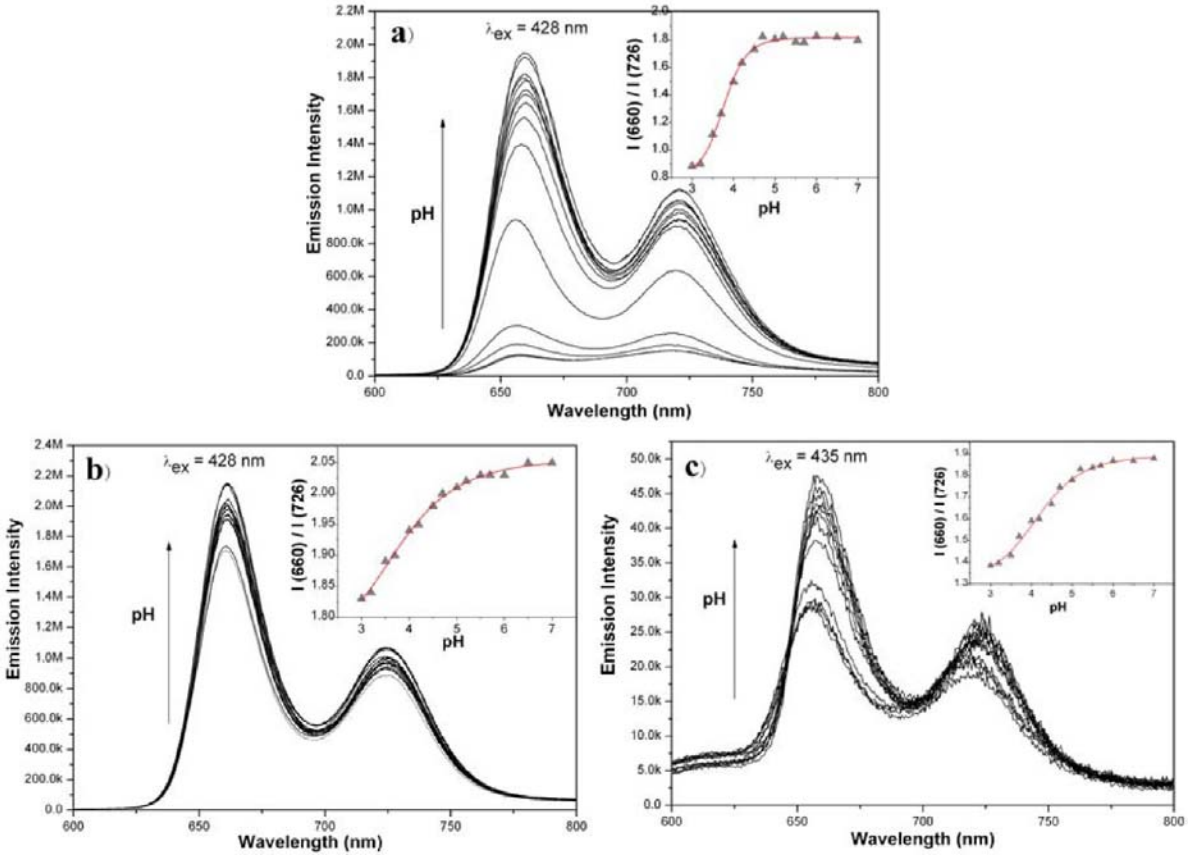


Figure 4. Emission spectral response of 10 μM of free-base porphyrin-Ru(II) conjugates **1** (a), **2** (b), and **3** (c) as a function of pH (pH = 3−7) measured in aqueous solution (295 K, <5% DMSO, λ_{ex} = 428 nm for **1** and **2**, 435 nm for **3**). Inset: Variation of the intensity ratio of the emission at 659 and 718 nm of **1**−**3** with pH in aqueous solution. The data were fitted with a sigmoidal function (shown as red curves) to give the following apparent pK_a values: 3.75 (7) for **1**, 3.26 (8) for **2**, and 4.39 (0) for **3**.

The emission spectra of the free-base porphyrin-Ru(II) (**1**, **2**, and **3**) and the Zn(II) porphyrin-Ru(II) (**4**, **5**, and **6**) series of conjugates are seen to be quite similar to those of the Ru(bpy)$_2$-(pyridylporphyrin)$_2$ hybrid (1:2) complexes synthesized and studied by Kon et al.[37] These authors showed that the excitation energy transfer mechanism in the Ru(II)-porphyrin conjugates corresponded to an energy transfer from the excited Ru(II) ^{1}MLCT state via its ^{3}MLCT state to the porphyrin B_1 singlet state. However, in Zn(II) porphyrin, the energy level of the porphyrin singlet state becomes destabilized, as shown by a blue shift of ca. 45 nm (~1126 cm^{-1}), resulting in the porphyrin singlet state of these conjugates being higher in energy than the Ru(II) ^{3}MLCT excited state. This led to a reverse energy transfer in conjugates **4**−**6**, where the energy migrates from the Soret-excited porphyrin to the Ru(II) chromophore. Even though this is not the first example of reverse energy transfer going from free-base porphyrin-Ru(II) to Zn(II) porphyrin-Ru(II) conjugates, the emission quantum yield variations among these two systems are obviously different compared to other systems in the literature.[38−40]

pH-Dependence Emission Change. It is well-known that the cellular uptake of an acidic organelle probe used to stain lysosomes as well as other acidic subcellular compartments, such as trans-Golgi vesicles, endosomes, and so forth,[41−45] is driven by the plasma membrane H^{+} gradient.[46−48] Free-base porphyrin (H_2P), with two imine nitrogens which can be protonated at low pH to give the mono-(H_3P^{+}) and dications (H_4P^{2+}), can potentially serve as an in vitro probe for the subcellular acidic organelles and compartments.

In principle, two distinct protonation reactions can occur on a free-base porphyrin, but the proton affinity of this macrocycle is generally represented by an averaged protonation constant,

dx.doi.org/10.1021/bc300201h | *Bioconjugate Chem.* 2012, 23, 1623−1638

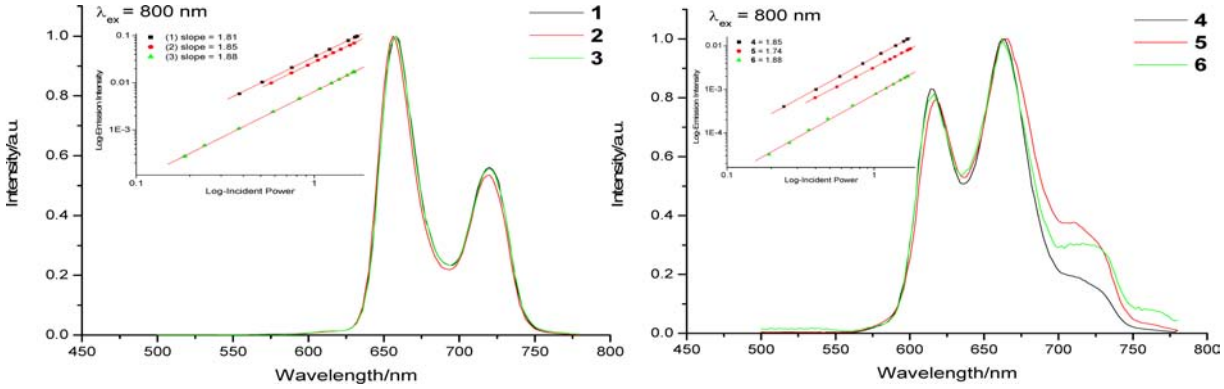


Figure 5. The two-photon induced emission spectra of conjugates **1**−**3** (left) and **4**−**6** (right) in aqueous DMSO (10 μM, λ_{ex} = 800 nm). Inset: Plots of the observed emission intensities (**1**−**3**, λ_{em} = 650 nm; **4**−**6**, λ_{em} = 610 nm) against the laser excitation (λ_{ex} = 800 nm) power used.

p*K*, as often only one p*K* value can be determined in pH titration experiments. The p*K* values measured for most water-soluble porphyrins were in the range 2−4[49] and were shown to depend on a complex interplay of the following factors: electronic effects of the substituents, the degrees of planarity and extended conjugation,[50−52] and the peripheral charges, which provide electrostatic shielding to the protonation site, surrounding the porphyrin.[53,54] In this work, we attempted to evaluate the potential application of the free-base porphyrin-Ru(II) conjugates, **1**−**3**, as probes for subcellular acidic compartments by studying their spectral changes under different pH conditions and measure their p*K* values.

Absorption spectra of the deprotonated (free-base) form of **1**−**3** in aqueous solution (pH = 10.0) showed their Soret bands at ∼428 nm (Figure S13) and the characteristic four-band pattern in the Q-band region, which is typical for tetraarylporphyrins. At pH 2, the fully protonated form of **1**−**3** (i.e., porphyrin dication) exhibited a red-shifted Soret band (λ_{max} ≈ 450 nm) with increased intensity and a single Q-band pattern (λ_{max} ≈ 665 nm) due to the higher symmetry of the porphyrin dication. The fluorescence spectra of **1**−**3** (Figure S14) also show clear changes upon protonation. The emission spectra of these free-base porphyrins show two well-defined peaks, a strong emission at 660 nm and a weak emission at 726 nm at pH 10. However, when fully protonated at pH 2 (i.e., dicationic form), only one broad emission band at around 715 nm was seen.

Figure 4 shows the emission spectral changes of the conjugates **1**−**3** in the pH range 3.0−7.0. The change in the fluorescence intensity ratio at 660 and 726 nm (I_{660}/I_{726}) for **1**−**3** from pH 3.0 to 7.0 is shown as insets in Figure 4 as well. The fluorescence intensity of these conjugates at 660 nm increases with increasing pH, corresponding to the conversion of the porphyrin from its dicationic form to the free-base form. Fitting the I_{660}/I_{726} vs pH curve (insets, Figure 4) with a Sigmoidal function of the Hasselbach equation[55] gave the following protonation constants p*K* for these conjugates: ∼3.75 (**1**), ∼3.26 (**2**), and ∼4.39 (**3**). At first glance, the relatively lower p*K* values in **1** and **2** can be explained in terms of the more extensive π-conjugation in these conjugates with conjugative linkers which decreases the porphyrin p*K* via delocalization of the core electron density and reduces the intrinsic basicity of the macrocycle.[50] However, the perpendicular orientation adopted by the phenyl ring in the linkers of **1** and **2** relative to the porphyrin ring does not seem to support a significant extension of π-conjugation beyond the macrocycle (vide infra). Thus, at this point we have no adequate explanation for the significantly lower p*K* values observed in **1** and **2** as compared to **3**.

$^1O_2$ Quantum Yield. To assess their potential application as PDT agents, the $^1O_2$ production yields of these Ru(II)-porphyrin conjugates were measured based on the phosphorescence intensities of the $^1O_2$ produced upon photoirradiation (at 430 nm) of these compounds. Figure S15 shows the $^1O_2$ phosphorescence spectra of the Ru(II)-porphyrin conjugates, **1**−**6**, together with tetraphenylporphyrin, H_2TPP, used as a reference, in $CHCl_3$. On the basis of the $^1O_2$ quantum yield of H_2TPP (Φ_Δ = 0.55 ± 0.11),[35] the relative Φ_Δ values of these conjugates are given in Table 1. Conjugates **2** and **5**, with their relative Φ_Δ estimated to be 0.58 ± 0.11 and 0.73 ± 0.11, respectively, exhibited the highest $^1O_2$ yields in their respective series of free-base and Zn(II) porphyrin-Ru(II) conjugates. A comparison of the trend of $^1O_2$ quantum yields with that of the emission quantum yields for the two series of conjugates (**1**−**3** and **4**−**6**) shows no apparent correlation, suggesting that the energy transfer pathways leading to emission and $^1O_2$ production are perhaps distinct. A more detailed investigation of these photophysical processes by transient absorption spectroscopy will be undertaken.

Two-Photon Induced Emission and Absorption. Photoexcitation in the near-infrared (NIR) region followed by luminescence at a shorter wavelength in the visible region is known as NIR-induced visible emission. This is a rather unusual process because apparently low-energy photons are "converted" to higher energy photons. This process is accomplished by the simultaneous absorption of two or three NIR photons via virtual intermediate states to produce a real excited state, which then returns to the ground state by the emission of a single photon in the visible region. The study of two- or three-photon induced emission processes on novel organic materials has received considerable attention recently because of potential applications in bioimaging and photodynamic therapy, optical data storage, and microfabrication.[56−58]

Figure 5 shows the emission spectra of a series of Ru(II)-porphyrin conjugates, **1**−**6**, in aqueous DMSO (0.4 mM) excited by near-infrared femtosecond laser (λ_{ex} = 800 nm). The emission spectral profiles (i.e., band shape, position, and width) obtained bear a close resemblance to the corresponding single-photon emission spectra (shown in Figure 3) of these conjugates. To confirm the involvement of two photons in the observed induced emission, the emission peak intensities of these conjugates were plotted against the incident laser

excitation power at 800 nm (inset of Figure 5). A slope of 1 in this plot would indicate that the emission resulted from one-photon absorption, whereas a slope of 2 is indicative of a two-photon absorption process. The slopes obtained for these conjugates in these plots (1.81 for **1**, 1.88 for **2**, 1.85 for **3**, 1.87 for **4**, 1.88 for **5**, 1.83 for **6**) clearly demonstrate the two-photon nature of their induced emissions.

Open-aperture *Z*-scan method (λ_{ex} = 800 nm) was used to measure their two-photon absorption properties of conjugates **1**−**6**. The Z-scan traces and the derived two-photon absorption cross sections, σ^2 (average uncertainty ±23.5 GM), of these conjugates are shown in Figure 6 and Table 1, respectively.

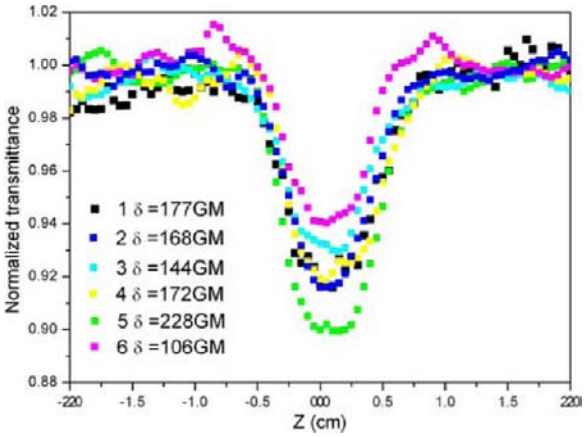


Figure 6. Open-aperture *Z*-scan traces of 0.4 mM of free-base porphyrin-Ru conjugates (**1**−**3**) and Zn(II) porphyrin-Ru conjugates (**4**−**6**) excited at 800 nm in DMSO. The average power of the laser beam was 0.271 mW.

The σ^2 value measured for conjugate **1** (177 ± 23.5 GM) was found to be virtually identical to that of a structurally very similar Ru(II)-porphyrin conjugate, Ru−P (178 ± 26.8 GM),[25] indicating that hydrophobic perturbation of the porphyrin substituent (3,4,5-trimethoxyphenyl in **1** vs phenyl in Ru−P) exerts no effect on the two-photon absorption cross section of these conjugates. Since σ^2 is strongly dependent on the π-conjugation length of a molecule, the lack of substantial enhancement in the σ^2 of conjugates **1** and **2** relative to **3** must be due to the perpendicular orientation of their *meso*-substituted phenyl linkers with respect to the porphyrin ring, which does not support extending the porphyrin π-conjugation to the polypyridyl ligand of the Ru(II) complex via the ethynyl and amide linkages. This interpretation is consistent with the substantially higher σ^2 value (555 GM) observed in a similar free-base porphyrin-Ru(phen)$(bpy)_2^{2+}$ conjugate connected through a β-ethynyl only linkage (i.e., no intervening phenyl ring).[32]

In Vitro Studies. On the basis of the observed photophysical properties (i.e., stronger emission and $^1O_2$ quantum efficiency) of the Ru(II)-porphyrin conjugates studied, the free-base porphyrin-Ru(II) conjugates, **1**, **2**, and **3**, appear to be more suitable for further investigation as potential dual probes for imaging and photodynamic therapy. The following in vitro experiments, i.e., flow cytometry for cellular uptake, MTT assay for cytotoxicity (dark and light), subcellular localization imaging, and two-photon PDT experiments, were carried out to evaluate the potential biological and clinical applications of these compounds.

Cellular Uptake. In the past decades, many luminescent transition metal complexes have been extensively studied for potential in vitro and in vivo applications. However, most research work have been devoted to the screening of these complexes for biological applications, with few studies focusing on the effects of a systematic variation of particular structural elements on particular in vitro and/or in vivo properties of these complexes.[60−62] Puckett et al.[63] measured and compared the cellular uptake, a crucial property for any bioprobe and drug molecule, of Ru(II) complexes with different polypyridyl ligands by human cervical carcinoma HeLa cells and investigated the underlying transport mechanism as well.[42] In this work, we examined the cellular uptake properties of these porphyrin-Ru(II) conjugates with different linkers by HeLa cells using flow cytometry. The results obtained are shown in Figure 7.

From Figure 7, conjugates **1** and **2**, with relatively hydrophobic linkers between the porphyrin and the Ru(II)-polypyridyl complex, are seen to be taken up by the HeLa cells much more efficiently than conjugate **3**, which contains a relatively more hydrophilic ethoxyethane linker. For **3**, the luminescence signal observed, which was indicative of the number of **3**-loaded cells, after 6 h of incubation, was even less than those observed after 1 h of incubation with **1** and **2**. Thus, even taking into account that **3** is ca. 2−3-fold less luminescent (i.e., lower Φ_{em}) than **1** and **2**, the data support the following order of cellular uptake rates: **1** ∼ **2** ≫ **3**.

Subcellular Localization. Localization of these porphyrin-Ru(II) conjugates (2 μM) within the HeLa cells after incubation for 6 h was examined by laser confocal microscopy

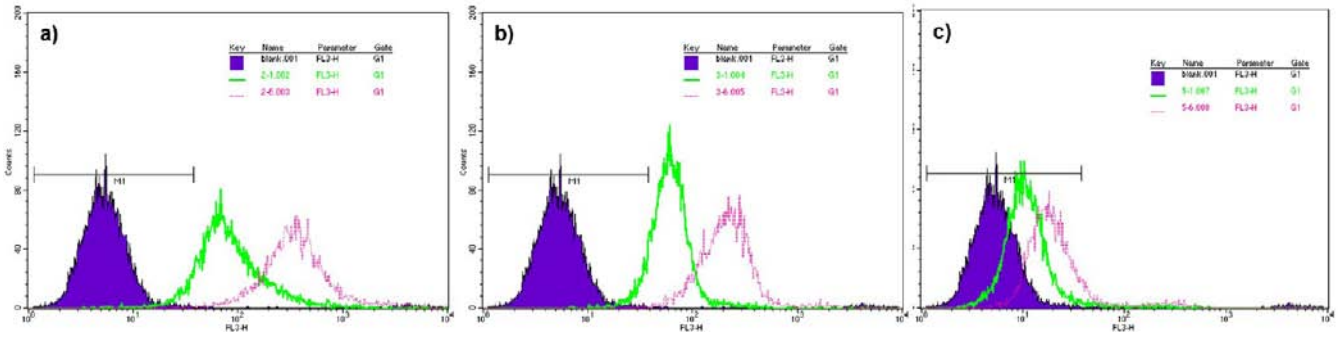


Figure 7. Flow cytometric analysis of the cellular uptakes of 2 μM of **1** (a), **2** (b), and **3** (c) by HeLa cells (10^5 cells per sample) after incubation for 1 h (green curve) and 6 h (pink curve) in dark. The luminescence signal (λ_{ex} = 488 nm) was collected using FL-2 channels equipped with a long pass filter (>650 nm). At least 10 000 events were counted. Live cells were differentiated by their low To-Pro-3 emission.

dx.doi.org/10.1021/bc300201h | *Bioconjugate Chem.* 2012, 23, 1623−1638

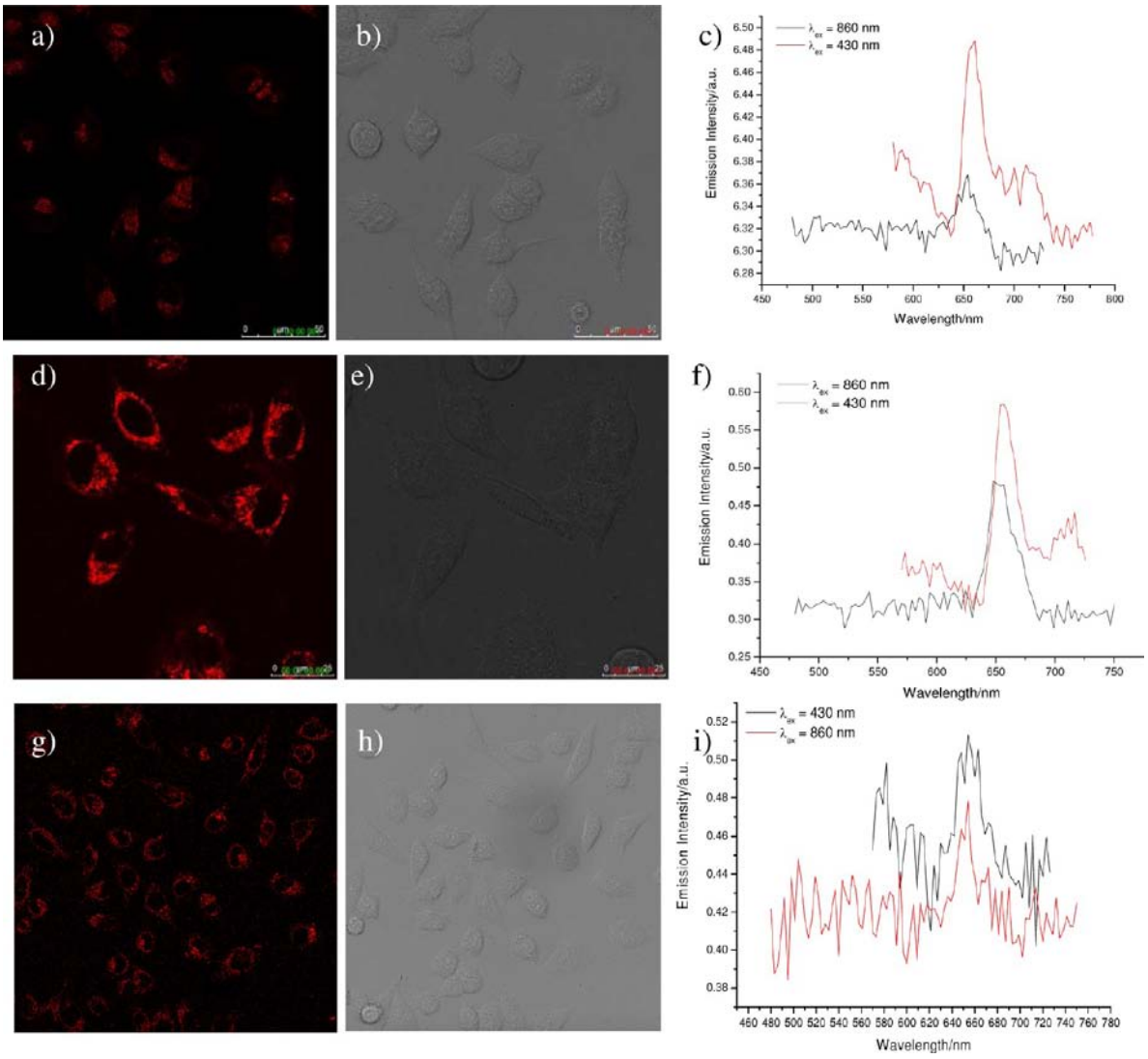


Figure 8. Confocal fluorescent microscopic images of the free-base porphyrin-Ru(II) conjugates **1** (a), **2** (d), and **3** (g) (dosed concentration = 2 μM, λ_{ex} = 860 nm, incubation time = 6 h), together with their corresponding bright-field images (**1** − b; **2** − e; **3** − h), linear (λ_{ex} = 430 nm) and two-photon induced (λ_{ex} = 860 nm) in vitro emission spectra in HeLa cells (resolution = 4 nm).

(Figure 8). Cells loaded with conjugates **1** (Figure 8a,b,c), **2** (Figure 8d,e,f), and **3** (Figure 8g,h,i) were excited by visible argon-ion (λ_{ex} = 432 nm, Figures S18 and S19) and near-infrared femtosecond lasers (λ_{ex} = 860 nm, Figure 8). The in vitro emission profiles of the three conjugates are similar under linear or two-photon excitation using the same dosed concentration and time duration.

The subcellular localizations of conjugates **1** and **2** were determined by costaining experiments using organelle-specific trackers. After 3 h of incubation, conjugate **1** showed specific localization in lysosomes (Figure S18), whereas conjugate **2** showed specific localization in mitochondria (Figure S19). Furthermore, when the in vitro luminescence of these conjugates was monitored hourly, 90% of the maximum luminescence (measured after 3 h) was observed after 2 h of incubation, showing a fairly rapid intracellular trafficking of these conjugates to their targeted organelles. As for conjugate **3**, it appeared to reside in the cytoplasm with no obvious organelle localization (Figure 8).

Dark Cytotoxicity and Photocytotoxicity. MTT assay was used to measure the cytotoxicity of conjugates **1**, **2**, and **3**.[37] The dose−response curves obtained by incubation of these conjugates in the dark at various concentrations ranging from 1 to 250 μM with HeLa cells are shown in Figure 9a. From these curves, the IC_{50} of **1**, **2**, and **3** were estimated to be 118, 175, and >250 μM, respectively. The lower cytotoxicity seen in **3** is presumably related to its lower cellular uptake rate by the cells.

The photocytotoxicity of conjugates **1**, **2**, and **3** was measured at 1 μM under varying light doses from 1.5 to 12.5 J/cm^2. The light dose−response curves obtained are shown in Figure 9b. Conjugate **2** showed the strongest photocytotoxicity (LD_{50} = 2 J/cm^2), followed by conjugate **1** (LD_{50} = 6.5 J/cm^2), with conjugate **3** showing the weakest photocytotoxicity (LD_{50} = 11.5 J/cm^2) toward HeLa cells. This trend does not seem to correlate with either the cellular uptake rates of these conjugates (**1** ∼ **2** ≫ **3**) or their $^1O_2$ quantum yields (Table 1, **1** ∼ **2** > **3**), but appears to correlate better with their subcellular localization properties. As **2** exhibits mitochondria-localizing property, its photoexcitation in this organelle produces $^1O_2$-mediated oxidative stress which can readily elicit apoptotic cell death. Since **1** is shown to localize in lysosomes, its photoexcitation in this organelle produces $^1O_2$ that can

dx.doi.org/10.1021/bc300201h | *Bioconjugate Chem.* 2012, 23, 1623−1638

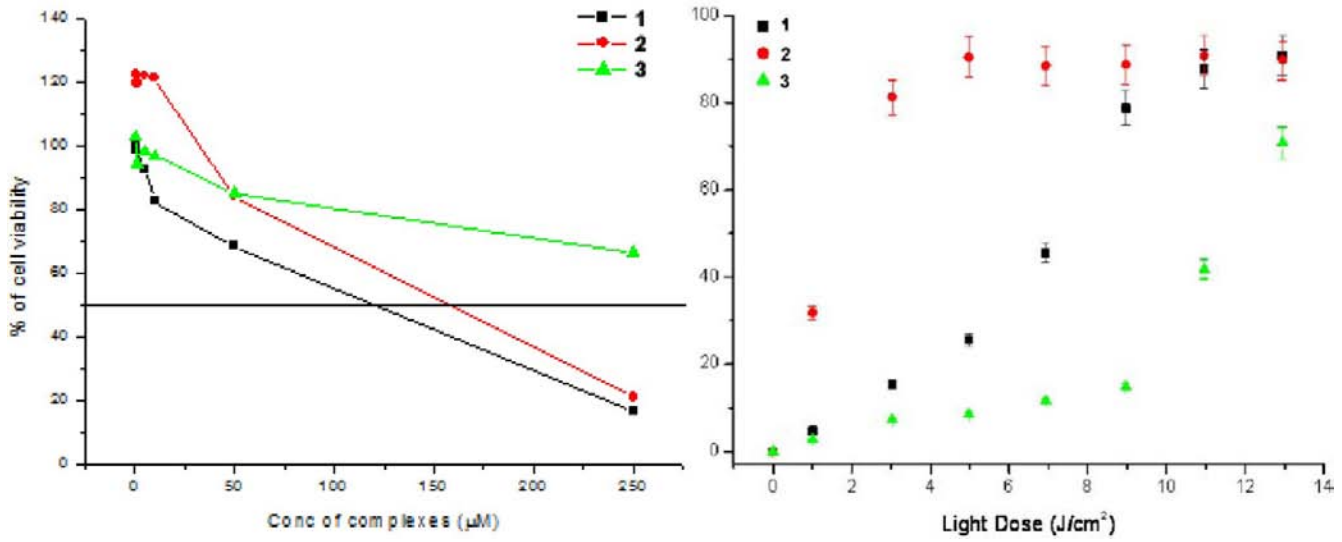


Figure 9. Dose−response curves of the dark cytotoxicity (left) and photocytotoxicity (right) of conjugates **1**, **2**, and **3**. Dark cytotoxicity curves were obtained using dosed concentration from 1 to 250 μM. Photocytotoxicity curves were obtained using 1 μM of conjugates and various light doses from 0 to 12.5 J/cm^2. MTT assay was carried out after incubation for 24 h. The results were expressed as the mean ± SD of three separate trials.

Table 2. Summary of the in Vitro Properties of the Free-Base Porphyrin-Ru(II) Conjugates 1, 2, and 3

	cytotoxicity (IC_{50})		cellular uptake			
compound	dark[a] (μM)	light[b] (J/cm^2)	flow cytometry[c] (1 h)	flow cytometry[c] (6 h)	subcellular localization	p*K*
1	118	6.5	80-fold	500-fold	lysosome	3.75
2	175	2	80-fold	500-fold	mitochondria	3.26
3	>250	11.5	10-fold	20-fold	cytoplasm	4.39

[a]Dark cytotoxicities (IC_{50}) of **1**, **2**, and **3** toward HeLa cells were determined from the dose−response curve obtained after 24 h incubation with various concentrations of the conjugates. [b]Photocytotoxicities of **1**, **2**, and **3** toward HeLa cells was determined using 1 μM of the conjugates under various light doses. MTT assay was performed on the HeLa cells after 24 h incubation. [c]The luminescence signal measured (relative to the control) was used as the parameter for comparing the cellular uptake rates of the conjugates.

damage the lysosomal membrane, causing the release of the lysosomal enzymes which leads to necrosis. Conjugate **3**, which is more hydrophilic, distributes in the cytoplasm. When photoexcited, **3** produces $^1O_2$ in the cytosol where a substantial $^1O_2$ population could become deactivated before inflicting damage on any vital subcellular targets to cause cell death. The results of the in vitro properties of these conjugates, **1**−**3**, toward HeLa cells, which include their cellular uptake, subcellular localization, and dark cytotoxicity and photocytotoxicity, are summarized in Table 2.

Two-Photon Induced Imaging and Cytotoxicities of 1, 2, and 3. HeLa cells were incubated with 5 μM of conjugates **1**, **2**, or **3** separately for 6 h. The cells were then excited at 850 nm, at which the three conjugates **1**, **2**, and **3** showed a two-photon absorption cross section of 177, 168, and 144 GM, respectively. The confocal images were captured at one laser shot per minute for a total of 32 min. Figure 10 shows the confocal images of these cells after two-photon laser irradiation for time t = 0, 8, 16, and 32 min. To demonstrate the potential use of conjugates **1**, **2**, and **3** as two-photon excited imaging agents, these conjugates stained HeLa cells were excited with a snap laser flash at 860 nm and the images were captured under a confocal microscope. A clear fluorescent image of the stained HeLa cells was obtained (Figure 10a,e,i). The fluorescence intensities of the **1**- and **2**-stained cells were greater than that of the **3**-stained cells. This observation is consistent with the flow cytometric analysis (Figure 7) that the intracellular concentrations of **1** and **2** are greater than **3**.

To further study the efficacy of these conjugates on two-photon induced cytotoxicity, the cells were continuously irradiated and the fluorescent images of the cells were captured at 8 (Figure 10b,f,j), 16 (Figure 10c,g,k), and 32 min (Figure 10d,h,l) after irradiation. After 2PA-PDT, the patterns of subcellular localization of conjugates **1** and **3** in the treated HeLa cells were similar to those of the control cells (Figure 10a,i). A significant nuclear localization of **2** (Figure 10f,g,h) was seen in cells at 8 to 32 min after irradiation. Cell shrinkage was also apparent at 16 to 32 min in the PDT-treated cells, indicating that conjugate **2**-mediated PDT could effectively damage the nuclear membrane and caused the cell death. The nuclear localization of **2** is probably due to a redistribution of **2** from the cytoplasm (presumably released from the damaged mitochondria during initial PDT) to the nucleus. In this short-term cell imaging study, conjugate **2**-mediated PDT is found to be more effective than **1** and **3** in triggering the cell death process. This result is also consistent with the result of conventional one-photon PDT-induced cell death assay as shown in Table 2.

CONCLUSION

Six water-soluble free-base porphyrin-Ru(II) conjugates, **1**−**3**, and Zn(II) porphyrin-Ru(II) conjugates, **4**−**6**, have been synthesized with satisfactory yields (>70%) and their potential development as dual in vitro imaging and photodynamic therapeutic agents investigated. Photoexcitation of conjugates **1**−**3** at 430 nm led to an energy transfer from the Ru(II)

dx.doi.org/10.1021/bc300201h | *Bioconjugate Chem.* 2012, 23, 1623−1638

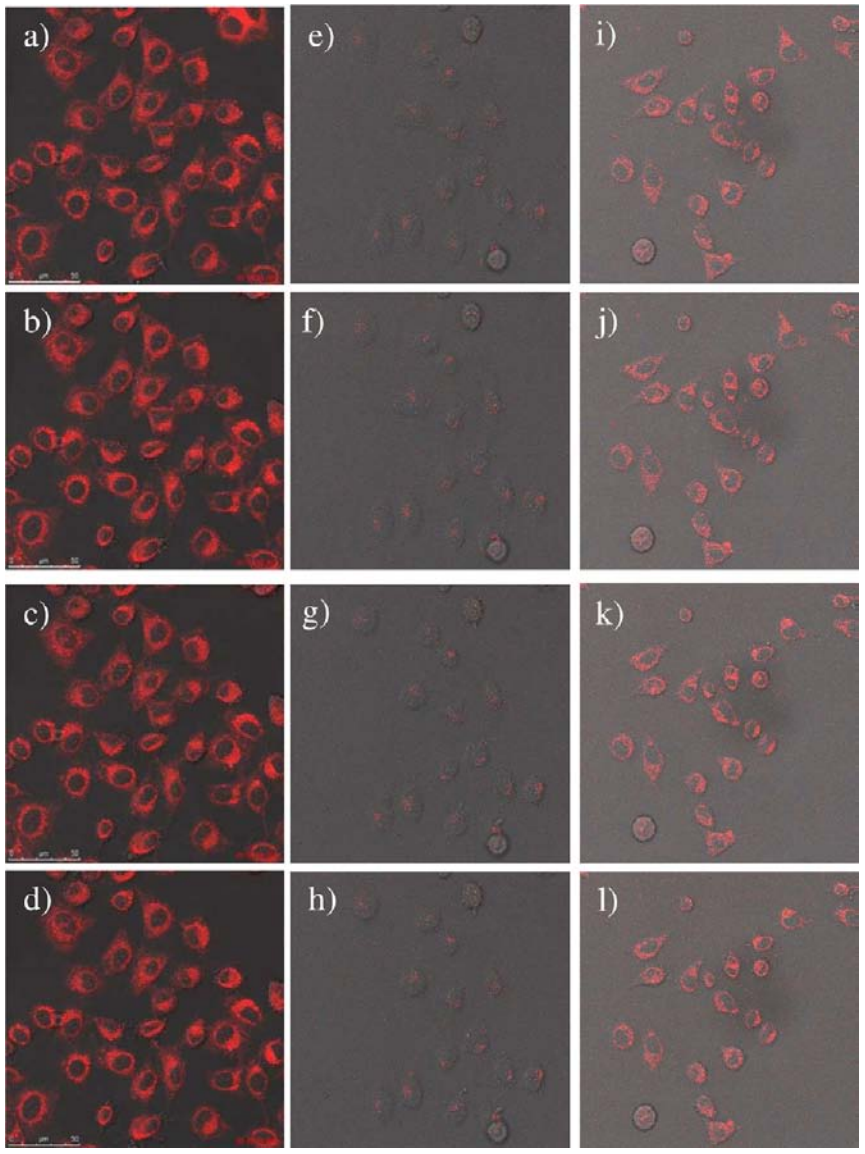


Figure 10. Confocal microscopic images of HeLa cells treated with 5 μM of **1** (a, b, c, d), **2** (e, f, g, h), and **3** (i, j, k, l) for 6 h. Top row: images obtained for **1** (left), **2** (middle), and **3** (right) -treated cells after one snap laser flash (to avoid $^1O_2$ generation) at 860 nm. Second row: images obtained after 8 min of laser irradiation. Third row: images obtained after 16 min of laser irradiation. Bottom row: images obtained after 32 min of laser irradiation.

^{1}MLCT excited state to the porphyrin singlet state, resulting in emissions at ca. 659 and 718 nm. In contrast, photoexcitation of the Zn(II) porphyrin-Ru(II) conjugates, **4**–**6**, at 430 nm resulted in an energy transfer from the Soret-excited porphyrin to the Ru(II) due to an increase in the singlet energy level of Zn(II) porphyrin to above that of the Ru(II) ^{3}MLCT state. The emission quantum yields of these conjugates, **4**–**6**, were ca. 10-fold lower than those of conjugates **1**–**3**. An obvious dependence of the energy transfer efficiency on the linker of these conjugates was noted (**1** ∼ **2** > **3** and **4** > **5** > **6**), with the efficiency reduced by 2–3-fold via the longer ethoxyethane linkage. All conjugates gave $^1O_2$ quantum yields (ranging from 0.73 to 0.38) adequate for potential application as PDT agents, with no obvious difference between conjugates with different linkers. The two-photon absorption cross sections, σ^2, of these conjugates ranged from 228 GM in **5** to 106 GM in **6**, with no expected enhancement from the "conjugative" phenylethynyl and phenylamide linkers. This observation is explained in terms of the perpendicular orientation adopted by the phenyl-containing linkers which does not support the extension of the porphyrin π-conjugation to the polypyridyl ligand of the Ru(II) complex.

The in vitro properties of conjugates **1**–**3** toward HeLa cells were further investigated as they gave higher emission and $^1O_2$ quantum yields. The IC_{50} measured for conjugates **1**, **2**, and **3** in the dark were 118, 175, and >250 μM, which is consistent with their cellular uptake properties with **1** ∼ **2** ≫ **3**, where **3**, which contained a more hydrophilic poly(ethylene glycol) linkage, was the least efficient in cell penetration. The photocytotoxicity of these conjugates, however, gave the following light dose dependence at 1 μM concentration: **2** (2 J/cm^2) > **1** (6.5 J/cm^2) > **3** (11.5 J/cm^2), which is explained by their respective subcellular localizations at the mitochondria, lysosomes and cytoplasm. These one-photon induced cytotoxicity data is consistent with the observed two-photon PDT data, which taken together strongly suggest the importance of

dx.doi.org/10.1021/bc300201h | *Bioconjugate Chem.* 2012, 23, 1623–1638

subcellular localization in affecting the in vitro PDT activity of a drug. Among the three porphyrin-Ru(II) conjugates studied, **2**, with its high emission quantum yield, low dark cytotoxicity, and high phototoxicity, is the most promising candidate for both in vitro imaging and PDT activity.

■ ASSOCIATED CONTENT

Supporting Information

Synthetic details, ^{1}HNMR spectra, HRMS spectra, $^1O_2$ phosphorescence spectra, comparative absorption and fluorescence spectra of the porphyrin-Ru(II) conjugates in free-base form (pH = 10.0) and dicationic form (pH = 2.0), luminescence decay curves of the six porphyrin-Ru(II) conjugates, costaining confocal microscopic images of **1** and **2**. This material is available free of charge via the Internet at http://pubs.acs.org.

■ AUTHOR INFORMATION

Corresponding Author

*E-mail: wkwong@hkbu.edu.hk, klwong@hkbu.edu.hk, chiklau@cityu.edu.hk. Fax: +852-3411-5862. Tel: +852-34117011. Tel: +852-34112370.

Author Contributions

#The first to third authors contributed equally as co-1st author.

Notes

The authors declare no competing financial interest.

■ ACKNOWLEDGMENTS

The work described in this paper was partially supported by grants from the Research Grants Council of the Hong Kong SAR, P.R. China (HKBU 202509 and HKBU 202210) and a starting grant from the Hong Kong Baptist University (KLW).

■ ABBREVIATIONS:

PDT, photodynamic therapy; TPA, two-photon absorption; NIR, near-infrared; phen, 1,10-phenanthroline; bpy, 2,2′-bipyridine.

■ REFERENCES

(1) Mack, J., and Kobayashi, N. (2011) Low symmetry phthalocyanines and their analogues. *Chem. Rev. 111*, 281−321.

(2) Biswas, S., Ahn, H.-Y., Bondar, M. V., and Belfield, K. D. (2011) Tetracene-doped anthracene nanowire arrays: preparation and doping effects. *Langumir 27*, 06374−06380.

(3) Zhao, Z., Chan, P.-S., Li, H., Wong, K.-L., Wong, R. N. S., Mak, N.-K., Zhang, J., Tam, H.-L., Wong, W.-Y., Kwong, D. W. J., and Wong, W.-K. (2012) Highly selective mitochondria-targeting amphiphilic silicon (IV) phthalocyanines with axially ligated rhodamine B for photodynamic therapy. *Inorg. Chem. 51*, 812−821.

(4) Hasan, T., Ortel, B., Moor, A. C. E., and Pogue, B. W. (2003) *Holland-Frei Cancer Medicine 6*, (Kufe, D. W., Pollock, R. E., Weichselbaum, R. R., Bast, R. C., Jr., Gansler, T. S., Holland, J. F., Frei, E., III, Eds.) pp 605−622, Decker, Hamilton.

(5) Triesscheijn, M., Bass, P., Schellens, J. H. M., and Stewart, F. A. (2006) Photodynamic therapy in oncology. *The Oncologist 11*, 1034−1044.

(6) Brown, S. B., Brown, E. A., and Walker, I. (2004) The present and future role of photodynamic therapy in cancer treatment. *Lancet. Oncol. 5*, 497−508.

(7) Dolmans, D. E. J. G. J., Fukumura, D., and Jain, R. K. (2003) Photodynamic therapy for cancer. *Nat. Rev. Cancer 3*, 380−387.

(8) Dougherty, T. J., Gomer, C. J., Henderson, B. W., Jori, G., Kessel, D., Korbelik, M., Moan, J., and Peng, Q. (1998) Photodynamic therapy. *J. Natl. Cancer Inst. 90*, 889−905.

(9) Castano, A. P., Demidova, T. N., and Hamblin, M. R. (2004) Mechanisms in photodynamic therapy: part one—photosensitizers, photochemistry and cellular localization. *Photodiagn. Photodynam. Ther. 1*, 279−293.

(10) Castano, A. P., Demidova, T. N., and Hamblin, M. R. (2005) Mechanisms in photodynamic therapy: Part three-Photosensitizer pharmacokinetics, biodistribution, tumor localization and modes of tumor destruction. *Photodiagn. Photodynam. Ther. 2*, 91−106.

(11) Plaetzer, K., Krammer, B., Berlanda, J., Berr, F., and Klesslich, T. (2009) Photophysics and photochemistry of photodynamic therapy: fundamental aspects. *Lasers Med. Sci. 24*, 259−268.

(12) Detty, M. R., Gibson, S. L., and Wagner, S. J. (2004) Current clinical and preclinical photosensitizers for use in photodynamic therapy. *J. Med. Chem. 47*, 3897−3915.

(13) Moan, J. (1990) Properties for optimal PDT sensitizers. *J. Photochem. Photobiol. B: Biol. 5*, 521−524.

(14) MacDonald, I. J., and Dougherty, J. (2001) Basic principles of photodynamic therapy. *J. Porphyrins Phthalocyanines 5*, 105−129.

(15) Vicente, M. G. (2001) Porphyrin-based sensitizers in the detection and treatment of cancer: recent progress. *Curr. Med. Chem.: Anti-cancer Agents 2*, 175−194.

(16) Schmitt, F., Govindaswamy, P., Süss-Fink, G., Ang, W. H., Dyson, P. J., Juillerat-Jeanneret, L., and Therrien, B. (2008) Ruthenium porphyrin compounds for photodynamic therapy of cancer. *J. Med. Chem. 51*, 1811−1816.

(17) Bergamo, A., Gaiddon, C., Schellens, J. H. M., Beijinen, J. H., and Sava, G. (2011) Approaching tumour therapy beyond platinum drugs: status of the art and perspectives of ruthenium drug candidates. *J. Inorg. Biochem. 106*, 90−99.

(18) Ang, W. H., Casini, A., Sava, G., and Dyson, P. J. (2011) Organometallic ruthenium-based antitumor compounds with novel modes of action. *J. Organomet. Chem. 696*, 989−998.

(19) Antonarakis, E. S., and Emadi, A. (2010) Ruthenium-based chemotherapeutics: are they ready for prime time? *Cancer Chemother. Pharmacol. 66*, 1−9.

(20) Suess-Fink, G. (2010) Arene ruthenium complexes as anticancer agents. *Dalton Trans. 39*, 1673−1688.

(21) Bruijnincx, P. C. A., and Sadler, P. J. (2009) Controlling platinum, ruthenium, and osmium reactivity for anticancer drug design. *Adv. Inorg. Chem. 61*, 1−62.

(22) Gianferrara, T., Bergamo, A., Bratsos, I., Milani, B., Spagnul, C., Sava, G., and Alessio, E. (2010) Ruthenium−porphyrin conjugates with cytotoxic and phototoxic antitumor activity. *J. Med. Chem. 53*, 4678−4690.

(23) Juzeniene, A., Peng, Q., and Moan, J. (2007) Milestones in the development of photodynamic therapy and fluorescence diagnosis. *Photochem. Photobiol. Sci. 6*, 1234−1245.

(24) Moan, J. J. (1990) On the diffusion length of singlet oxygen in cells and tissues. *Photochem. Photobiol. B: Biol. 6*, 343−344.

(25) Poon, C. T., Chan, P. S., Man, C., Jiang, F.-L., Wong, R. N. S., Mak, N. K., Kwong, D. W. J., Tsao, S. W., and Wong, W. K. (2010) An amphiphilic ruthenium(II)-polypyridyl appended porphyrin as potential bifunctional two-photon tumor-imaging and photodynamic therapeutic agent. *J. Inorg. Biochem. 104*, 62−70.

(26) Ke, H.-Z., Wang, H.-D., Wong, W. K., Mak, N. K., Kwong, D. W. J., Wong, K.-L., and Tam, H.-L. (2010) Responsive and mitochondria-specific ruthenium(II) complex for dual in vitro applications: two-photon (near-infrared) induced imaging and regioselective cell killing. *Chem. Commun. 46*, 6678−6680.

(27) Saha, S., Mallick, D., Majumdar, R., Roy, M. R., Dighe, R. D., Jemmis, E. R., and Chakravarty, A. (2011) Structure−activity relationship of photocytotoxic iron(III) complexes of modified dipyridophenazine ligands. *Inorg. Chem. 250*, 2975−2987.

(28) Sullivan, B. P., Salmon, D. J., and Meyer, T. J. (1978) Mixed phosphine 2,2′-bipyridine complexes of ruthenium. *Inorg. Chem. 17*, 3334−3341.

(29) Ziessel, R. (1996) General method for the preparation of alkyne-functionalized oligopyridine building blocks. *J. Org. Chem. 61*, 6535−6546.

(30) Faragher, R. J., and Schwan, A. L. (2008) New deuterated oligo(ethylene glycol) building blocks and their use in the preparation of surface active lipids possessing labeled hydrophilic tethers. *J. Org. Chem. 73*, 1371−1378.
(31) heik-Bahae, M., Said, A. A., Wei, T.-H., Hagan, D. J., and Van Stryland, E. W. (1990) Sensitive measurement of optical nonlinearities. *IEEE J. Quantum Electron. 26*, 760−769.
(32) Zhang, J, Wong, K.-L., Wong, W.-K., Mak, N.-K., Kwong, W. J. D., and Tam, H. L. (2011) Two-photon induced luminescence, singlet oxygen generation, cellular uptake and photocytotoxic properties of amphiphilic Ru(II) polypyridyl - porphyrin conjugates as potential bifunctional photodynamic therapeutic agents. *Org. Biomol. Chem. 50*, 5517−5525.
(33) Li, Y., Pritchett, T. M., Huang, J., Ke, M., Shao, P., and Sun, W. (2008) Photophysics and nonlinear absorption of peripheral-substituted zinc phthalocyanines. *J. Phys. Chem. A 112*, 7200−7207.
(34) Mak, N. K., Li, K. M., Leung, W. N., Wong, R. N., Huang, D. P., Lung, M. L., Lau, Y. K., and Chang, C. K. (2004) Involvement of both endoplasmic reticulum and mitochondria in photokilling of nasopharyngeal carcinoma cells by the photosensitizer Zn−BC−AM. *Biochem. Pharmacol. 68*, 2387−2396.
(35) Gouterman, M. (1978) *The Porphyrins: Physical Chemistry* (Dolphin, D., Ed.) p 1, Vol. *III*, Academic Press, New York.
(36) Lee, W. A., Graetzel, M., and Kalyanasundaram, K. (1984) Anomalous ortho effects in sterically hindered porphyrins: tetrakis(2,6-dimethylphenyl)porphyrin and its sulfonate derivative. *Chem. Phys. Lett. 107*, 308−313.
(37) Kon, H., Tsuge, K., Imamura, T., Sasaki, Y., Ishizaka, S., Kitamura, N., and Kato, M. (2008) Excitation energy flow control in $\{Ru(2,2'\text{-bipyridine})_2\}$-$\{pyridylporphyrin\}_2$ systems. *Dalton Trans. 12*, 1541−1543.
(38) Flamigni, L. (2001) Charge separation and energy transfer in multicomponent porphyrinic arrays. *Pure Appl. Chem. 3*, 421−424.
(39) Flamigni, L., Armaroli, N., Barigelletti, F., Balzani, V., Collin, J.-P., Dalbavie, J.-O., Heitz, V., and Sauvage, J.-P. (1997) Photoinduced processes in dyads made of a porphyrin unit and a ruthenium complex. *J. Phys. Chem. B 101*, 5936−5943.
(40) Collin, J.-P., Harriman, A., Heitz, V., Odobel, F., and Sauvage, J.-P. (1994) Photoinduced electron- and energy-transfer processes occurring within porphyrin-metal-bisterpyridyl conjugates. *J. Am. Chem. Soc. 116*, 5679−5690.
(41) Albertazzi, L., Storti, B., Marchetti, L., and Beltram, F. (2010) Delivery and subcellular targeting of dendrimer-based fluorescent pH sensors in living cells. *J. Am. Chem. Soc. 132*, 18158−18167.
(42) Wu, M. M., Llopis, J., Adams, S., McCaffery, J. M., Kulomaa, S. M., Machen, T. E., Moore, H.- P. H., and Tsien, R. Y. (2000) Organelle pH studies using targeted avidin and fluorescein-biotin. *Chem. Biol. 3*, 197−209.
(43) Ohkuma, S., and Poole, B. (1978) Fluorescence probe measurement of the intralysosomal pH in living cells and the perturbation of pH by various agents. *Proc. Natl. Acad. Sci. U.S.A. 75*, 3327−3331.
(44) Abiko, A., and Masamune, S. (1996) Synthesis of (+)-siphonarienone: Asymmetric alkylation using a chiral benzopyrano-isoxazolidine auxiliary. *Tetrahedron Lett. 37*, 1081−1084.
(45) Han, J., and Burgess, K. (2010) Fluorescent indicators for intracellular pH. *Chem. Rev. 110*, 2709−2728.
(46) Paroutis, P., Touret, N., and Grinstein, S. (2004) The pH of the secretory pathway: measurement, determinants, and regulation. *Physiology 19*, 207−215.
(47) Orij, R., Postmus, J., Ter Beek, A., Brul, S., and Smits, G. J. (2009) In vivo measurement of cytosolic and mitochondrial pH using a pH-sensitive GFP derivative in Saccharomyces cerevisiae reveals a relation between intracellular pH and growth. *Microbiology 155*, 268−278.
(48) Bagar, T., Altenbach, K., Read, N. D., and Benčina, M. (2009) Live-cell imaging and measurement of intracellular pH in filamentous fungi using a genetically encoded ratiometric probe. *Eukaryotic Cell 5*, 703−712.
(49) Hambright, P. (2000) Chemistry of water soluble porphyrins. In *The Porphyrin Handbook* (Kadish, K. M., Smith, K. M., and Guilard, R., Eds.) Chapter 18, Academic Press, New York.
(50) Finikova, O. S., Cheprakov, A. V., Carroll, P. J., Dalosto, S., and Vinogradov, S. A. (2002) Influence of nonplanarity and extended conjugation on porphyrin basicity. *Inorg. Chem. 41*, 6944−6946.
(51) Barkigia, K. M., Berber, M. D., Fajer, J., Medforth, C. J., Renner, M. W., and Smith, K. M. (1990) Nonplanar porphyrins. X-ray structures of (2,3,7,8,12,13,17,18-octaethyl- and -octamethyl-5,10,15,20-tetraphenylporphinato)zinc(II). *J. Am. Chem. Soc. 112*, 8851−8857.
(52) Takeda, J., Ohya, T., and Sato, M. (1992) A ferrochelatase transition-state model. Rapid incorporation of copper (II) into nonplanar dodecaphenylporphyrin. *Inorg. Chem. 31*, 2877−2880.
(53) Vinogradov, S. A., and Wilson, D. F. (2000) Electrostatic core shielding in dendritic polyglutamic porphyrins. *Chem.−Eur. J. 6*, 2456−2461.
(54) Kohata, K., Higashio, H., Yamaguchi, Y., Koketsu, M., and Odashima, T. (1994) Synthesis and characterization of new style of water-soluble glycosylated porphyrins as a spectrophotometric reagent for metal ions. *Bull. Chem. Soc. Jpn. 67*, 668−679.
(55) Finikova, O., Galkin, A., Rozhkov, V., Cordero, M., Hägerhäll, C., and Vinogradov, S. (2003) Porphyrin and tetrabenzoporphyrin dendrimers: tunable membrane-impermeable fluorescent pH nanosensors. *J. Am. Chem. Soc. 125*, 4882−4893.
(56) Valiotti, A., Adeyemo, A., Williams, R. F. X., Ricks, L., North, J., and Hambright, P. (1981) A water soluble "picket fence" porphyrin and its isomers. *J. Inorg. Nucl. Chem. 43*, 2653−2658.
(57) Tan, L.-S., Zheng, Q., and Prasad, P. N. (2008) Multiphoton absorbing materials: molecular designs, characterizations, and applications. *Chem. Rev. 108*, 1245−1330.
(58) Maiti, M., and Steer, R. P. (2009) Soret-excited ZnTPP quenched by electron transfer in chlorinated solvents? *Chem. Phys. Lett. 482*, 254−258.
(59) Zhang, J. X., Wong, K. L., Wong, W. K., Mak, N. K., Kwong, D. W. J., and Tam, H. L. (2011) Two-photon induced luminescence, singlet oxygen generation, cellular uptake and photocytotoxic properties of amphiphilic Ru(II) polypyridyl−porphyrin conjugates as potential bifunctional photodynamic therapeutic agents. *Org. Biomol. Chem. 9*, 6004−6010.
(60) Puckett, C. A., and Barton, J. K. (2007) Methods to explore cellular uptake of ruthenium complexes. *J. Am. Chem. Soc. 129*, 46−47.
(61) Gasser, G., Ott, I., and Metzler-Nolte, N. (2011) Organometallic anticancer compounds. *J. Med. Chem. 54*, 3−25.
(62) Gianferrara, T., Bratsos, I., Iengo, E., Milani, B., Oštrić, A., Spagnul, C., Zangrando, E., and Alessio, E. (2009) Synthetic strategies towards ruthenium−porphyrin conjugates for anticancer activity. *Dalton Trans. 48*, 10742−10756.
(63) Puckett, C. A., and Barton, J. K. (2008) Mechanism of cellular uptake of a ruthenium polypyridyl complex. *Biochemistry 47*, 11711−11716.

Bioconjugate Chemistry

Article

pubs.acs.org/bc

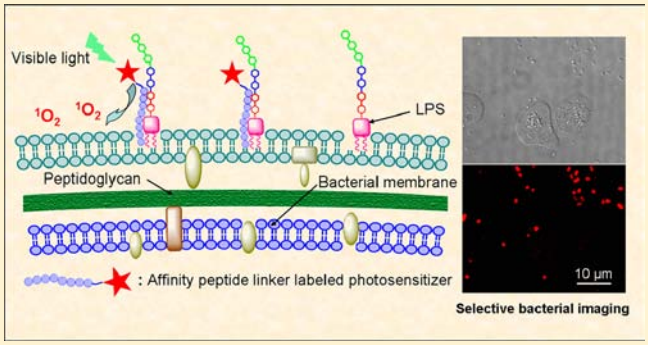
Lipopolysaccharide Neutralizing Peptide–Porphyrin Conjugates for Effective Photoinactivation and Intracellular Imaging of Gram-Negative Bacteria Strains

Fang Liu,[†] Annie Soh Yan Ni,[†] Yingjie Lim,[†] Harini Mohanram,[‡] S. Bhattacharjya,*[,‡] and Bengang Xing*[,†]

[†]Division of Chemistry & Biological Chemistry, School of Physical & Mathematical Sciences, and [‡]Division of Structural and Computational Biology, School of Biological Physical Sciences, Nanyang Technological University, Singapore 637371

Supporting Information

ABSTRACT: A simple and specific strategy based on the bioconjugation of a photosensitizer protophophyrin IX (PpIX) with a lipopolysaccharide (LPS) binding antimicrobial peptide YI13WF (YVLWKRKRKFCFI-Amide) has been developed for the effective fluorescent imaging and photodynamic inactivation of Gram-negative bacterial strains. The intracellular fluorescent imaging and photodynamic antimicrobial chemotherapy (PACT) studies supported our hypothesis that the PpIX-YI13WF conjugates could serve as efficient probes to image the bacterial strains and meanwhile indicated the potent activities against Gram-negative bacterial pathogens especially for those with antibiotics resistance when exposed to the white light irradiation. Compared to the monomeric PpIX-YI13WF conjugate, the dimeric conjugate indicated the stronger fluorescent imaging signals and higher photoinactivation toward the Gram-negative bacterial pathogens throughout the whole concentration range. In addition, the photodynamic bacterial inactivation also demonstrated more potent activity than the minimum inhibitory concentration (MIC) values of dimeric PpIX-YI13WF conjugate itself observed for *E. coli* DH5a (~4 times), *S. enterica* (~8 times), and other Gram-negative strains including antibiotic-resistant *E. coli* BL21 (~8 times) and *K. pneumoniae* (~16 times). Moreover, both fluorescent imaging and photoinactivation measurements also demonstrated that the dimeric PpIX-YI13WF conjugate could selectively recognize bacterial strains over mammalian cells and generate less photo damage to mammalian cells. We believed that the enhanced fluorescence and bacterial inactivation were probably attributed to the higher binding affinity between dimeric photosensitizer peptide conjugate and LPS components on the surface of bacterial strains, which were the results of efficient multivalent interactions.



INTRODUCTION

Since penicillin was first introduced into medical practice in the 1940's, a large number of various antibiotics have been developed to successfully inhibit bacterial infection diseases in clinics. However, increasing bacteria resistance to most of antibiotics has been extensively reported in medical treatment and has currently emerged as a serious threat to public health.[1−6] As such, there is an emergent need to design new types of antimicrobial agents and alternative treatment strategies that can effectively kill the bacterial strains with potent drug-resistant properties. One promising approach for microbiological inactivation is based on photodynamic antimicrobial chemotherapy (PACT), by which porphyrins or related compounds such as photofrin and foscan have been employed as photosensitizers (PS) to activate reactive oxygen species (ROS, e.g., singlet oxygen ($^1O_2$)) when exposed to room light with a suitable wavelength. The activated singlet oxygen species can be used as highly reactive oxidants and are capable of destroying the cell walls and membranes in close proximity, thus resulting in cell death.[7−13] In the process of PACT, the effective affinity of the photosensitizers on the surface of target bacterial cells would be crucial to enable the potent photoinactivation against bacterial strains. One possible antimicrobial strategy to minimize the side effects and enhance the potency of bacterial PACT inactivation is the utility of affinity ligands, which can selectively deliver the PSs to the targeted bacterial infection sites and lead to bacterial killing with minimum nonspecific drug accumulation.[14−16] So far, several affinity ligand conjugated photosensitizer complexes have been used to successfully inactivate a variety of antibiotic-resistant pathogens, especially for those methicillin-resistant *Staphylococcus aureus* (MRSA) and vancomycin-resistant *enterococci* (VRE).[17−25] However, most of the existing photosensitizer systems based on affinity ligands only exhibit efficient antimicrobial activity against Gram-positive strains rather than Gram-negative ones mostly due to the presence of a highly

Received: April 13, 2012
Revised: June 19, 2012
Published: July 9, 2012

 © 2012 American Chemical Society

organized outer bacterial membrane structure with a highly negatively charged lipid portion, which blocks the cellular attachment between PS and bacteria and thus intercepts $^1O_2$.[26] Although several affinity ligands based on nanoparticles[18] and water-soluble conjugated polymers[19,25] and polypeptides[20] have been recently developed to achieve close association of PSs to the Gram-negative bacterial strains and have indicated effective photoinactivation toward these strains, the development of simple and specific affinity ligand molecules that can selectively direct photosensitizers to the surface of Gram-negative bacteria pathogens is of great importance and remains the challenge in the antimicrobial studies, since the current approaches may indicate potential disadvantages including tedious sample treatment, nonspecific aggregation, possible immune response, or less cellular penetration.

Generally, Gram-negative bacteria are characterized by two distinct lipid membrane structures, one is an inner membrane consisted of glycerophospholipids and the other is an asymmetric bilayer outer membrane predominantly composed of a highly conserved and chemically unique lipopolysaccharide (LPS) moiety. The amphiphilic LPS contains one lipid A, a lipid fragment with six or seven fatty-acid-acylated chains, and a few hydrophilic polysaccharides components with negatively charged phosphate and carboxyl groups, which have been considered an efficient barrier to prevent bacterial pathogen strains from the permeability of antimicrobial molecules including hydrophobic antibiotics, surfactants, host-defense proteins, and peptides.[27−29] Apart from the function as the major constituent of the outer membrane of Gram-negative bacteria, LPS has also been considered as one of the most potent bacterial signal molecules that can strongly stimulate the host defenses to release proinflammatory mediators and often result in endotoxic shock or sepsis in intensive care units.[30−32] One promising strategy to inhibit septic shock will be the rational development of functional antimicrobial peptides, the ubiquitous arsenals of all living organisms, which would bind with LPS with a high affinity and significantly block the interactions between LPS and its recognition protein receptors. So far, extensive studies have been recently carried out to investigate the interactions of antimicrobial peptides toward LPS for their important roles in antibacterial activation, outer membrane perturbation, and LPS neutralization.[33−37]

In this study, we report a simple and effective dimeric peptide porphyrin binding system, by which a cationic antimicrobial peptide with the sequence of YVLWKRKRKFCFI-Amide (YI13WF) was chosen as a bacterial affinity ligand to link with a most commonly used porphyrin photosensitizer (PpIX). This new dimeric antimicrobial PpIX−peptide conjugate may indicate a unique advantage to selectively adhere to the surface of Gram-negative bacterial strains based on the enhanced multivalent/polyvalent interactions between disubstituted peptides and LPS moieties on bacterial strains, and thus serve as a promising fluorescent probe and potent photosensitizer for specific imaging and photodynamic inactivation of drug-resistant Gram-negative bacterial strains.

EXPERIMENTAL PROCEDURES

General. All the chemical reagents were purchased from Sigma Aldrich or Fluka. Commercially available reagents were used without further purification. The antimicrobial peptides were synthesized commercially by GL Biochem (Shanghai, China) and further purified by reverse-phase HPLC. All bacterial strains were from American Type Culture Collection (ATCC), USA. ^{1}H NMR spectra were recorded using either a Bruker 300 or 400 MHz spectrometer. Mass spectra (MS) were measured with a Thermo LCQ Deca XP Max for ESI. Analytical reverse-phase HPLC analysis was performed on a Shimadzu HPLC system using an Alltima C-18 (250 × 10 mm) column at a flow rate of 2.5 mL/min for preparation and a C-18 (250 × 4.6 mm) for analysis. Fluorescence emission spectra were performed on a Varian Cary eclipse Fluorescence spectrometer. UV absorption spectra were recorded in a 5 mm path quartz cell on a Beckman coulter DU 800 spectrometer. Photoirradiation experiments were performed at a fluence rate of 50 mW/cm^2 with a cool-light fiber optic illuminator provided by a 150 W OSRAM Quartz Halogen bulb (400−900 nm).

Synthesis. *N-Boc-Ethylenediamine* ***1***. Di-*tert*-butyldicarbonate (Boc_2O) (10.0 g, 46 mmol) was added into a mixture of ethylenediamine (10.0 mL, 150 mmol) and triethylamine (2 mL) in 20 mL of ethanol at 0 °C. The solution was stirred for 2 h at room temperature. The solvent was then removed using a rotator evaporator and the contents were redissolved in 20 mL of dichloromethane (DCM). The solution was subsequently extracted with 1.0 M acetic acid, and the pH of the aqueous layer was adjusted to pH 9−10 using 2.0 M sodium hydroxide (NaOH). Extraction was carried out with DCM (3 × 10 mL). **1** was collected by removing the solvent and used in the next step of the synthesis without further purification (9.6 g, 40%). ^{1}H NMR (300 MHz, $CDCl_3$): δ 1.40 (9H, s), 2.76 (2H, t, J = 5.85 Hz), 3.12 (2H, t, J= 5.70 Hz), 5.07 (1H, s). $C_7H_{16}N_2O_2$, ESI-MS: m/z 160.12 (calcd); 160.84 $[M+H]^+$, 320.78 $[2M+H]^+$ (found).

N-(2-[(t-Boc)amino]ethyl Maleimide ***2***. Maleic anhydride (400 mg, 1.66 mmol) in 35 mL of ethanol was added dropwise into a solution of **1** (1.2 equiv) and triethylamine in 30 mL of ethanol at 0 °C and stirred for 4 h. The solvent was removed and the contents were redissolved in 8 mL of acetic anhydride. Sodium acetate (1.0 equiv) was added and the solution was heated to 60−70 °C for 30 min then cooled to room temperature. Water was added to the solution and subsequent extraction was carried out with ethyl acetate. The organic layer was collected and washed with saturated sodium bicarbonate solution. After drying with anhydrous sodium sulfate, the organic layer was concentrated and purified with flash chromatography (EA/hexanes, 1:3) to give a white solid **2** (1.2 g, 82%). ^{1}H NMR (300 MHz, $CDCl_3$): δ 1.40 (9H, s), 3.32 (2H, d, J = 5.4 Hz), 3.65 (2H, t, J = 5.6 Hz), 4.73 (1H, s), 6.70 (2H, s). $C_{11}H_{16}N_2O_4$, ESI-MS: m/z 240.11 (calcd); 240.83 $[M+H]^+$ (found).

N-(2-Aminoethyl)maleimide Trifluoroacetate Salt ***3***. Compound **2** (1.0 g, 4.17 mmol) dissolved in 10 mL of DCM was added with trifluoroacetic acid (TFA) (5 mL) at 0 °C and stirred for 1 h. DCM was removed by evaporation and contents were redissolved in 3 mL of methanol. The desired product was precipitated with 50 mL of diethyl ether and used without further purification.

Monomeric PpIX-Maleimide Derivative ***4***. Protoporphyrin IX (PpIX) (50 mg, 0.09 mmol) and *N*-hydroxysuccinimide (HOSu) (9.2 mg, 0.08 mmol, 0.9 equiv) was dissolved in 8 mL of dimethyl formamide (DMF) at 0 °C and stirred for 10 min before the addition of 1-ethyl-3-(3-dimethyl-aminopropyl) carbodiimide hydrochloride (EDC.HCl) (20.4 mg, 0.117 mmol, 1.3 equiv). The reaction mixture was stirred at room temperature for 4 h. Compound **3** (20 mg, 0.08 mmol, 0.9 equiv) was then added and the system was left to stir for a

further 5 h at room temperature. The compound was purified by flash chromatography with eluent methanol/DCM = 1:20 to give a red solid product as mixture of two regioisomers (26.2 mg, 43%) . ^{1}H NMR (400 MHz, DMSO-d_6): δ 2.92 (2H, t, J = 7.6 Hz), 3.16−3.20 (4H, m), 3.44 (2H, t, J = 5.8 Hz), 3.61 (6H, m), 3.71 (6H, m), 4.27 (2H, t, J = 7.6 Hz), 4.35 (2H, t, J = 7.2 Hz), 6.23 (2H, d, J = 11.2 Hz), 6.47 (2H, dd, J_1 = 18.0 Hz, J_2 = 2.0 Hz), 6.86 (2H, s), 8.06 (1H, s), 8.48 (2H, dd, J_1 = 17.6 Hz, J_2 = 11.6 Hz), 10.20−10.25 (4H, m). $C_{40}H_{40}N_6O_5$, ESI-MS: m/z 684.31 (calcd); 685.48 $[M+H]^+$, 1368.80 $[2M+H]^+$ (found).

Dimeric PpIX-Maleimide Derivative ***5***. PpIX (20 mg, 0.036 mmol) and HOSu (9.2 mg, 0.079 mmol) was dissolved in 4 mL of DMF at 0 °C, EDC.HCl (15 mg, 0.079 mmol) was then added to the reaction mixture and allowed to stirred at room temperature for 4 h. Following the addition of compound **3** (20 mg, 0.079 mmol), the system was left to stir for another 5 h at room temperature. The compound was purified by flash chromatography with eluent methanol/DCM 1:50 to give a red solid product (20.9 mg, 73%). ^{1}H NMR (400 MHz, DMSO-d_6): δ 2.95 (4H, t, J =7.6 Hz), 3.19 (4H, t, J = 6.0 Hz), 3.43 (4H, t, J =5.6 Hz), 3.61 (3H, s), 3.64 (3H, s), 3.76 (3H, s), 3.77 (3H, s), 4.29 (4H, t, J =7.2 Hz), 6.24 (2H, d, J = 11.6 Hz), 6.47 (2H, dd, J_1 = 18.0 Hz, J_2 = 4.0 Hz,), 6.80 (4H, s), 8.14 (2H, t, J = 6.0 Hz,), 8.54 (3H, m), 10.21 (1H, s), 10.29 (2H, s), 10.38 (1H, s). $C_{46}H_{46}N_8O_6$, ESI-MS: m/z 806.35 (calcd); 807.49 $[M+H]^+$, 1613.92 $[2M+H]^+$ (found).

Monomeric PpIX−Peptide Conjugate ***6***. Compound **4** (1.1 mg, 1.6 μmol) and peptide YI13WF (2.8 mg, 1.6 μmol) in 200 μL of dimethylsulfoxide (DMSO) were added with 5 μL DMSO solution containing 10% diisopropylethylamine (DIPEA). The mixture was allowed to stir at room temperature overnight and then was added to 10 mL diethyl ether to give a red precipitate. This crude solid was purified by reverse-phase high performance liquid chromatography (HPLC) with eluting system consisting of A (water with 0.1% TFA) and B (acetonitrile with 0.1% TFA) under a linear gradient, monitored by UV absorbance at 280 and 400 nm. The linear gradient stretched over 43 min from t = 2 min at 70% solution A and 30% solution B to t = 45 min at 20% solution A and 80% solution B. The reaction yielded a deep red solid monomeric PpIX−peptide conjugate **6** (2.3 mg 56%) after lyophilization. ^{1}H NMR (400 MHz, DMSO-d_6): δ 0.66−0.80 (m), 0.96 (br s), 1.12 (s), 1.21−1.71 (overlapped), 1.84−1.92 (m), 2.25−2.36 (m), 2.65−2.75 (overlapped), 2.76−2.92 (m), 2.81−3.15 (m), 3.57 (dd, J_1 = 10.6 Hz, J_2 = 7.2 Hz), 3.69−3.71 (m), 3.89−3.96 (m), 4.12−4.30 (m), 4.47−4.55 (m), 6.15−6.19 (m), 6.41 (d, J = 17.6 Hz), 6.56 (d, J = 8.4 Hz), 6.87−6.98 (m), 7.00−7.20 (m), 7.24 (d, J = 8.0 Hz), 7.52−7.63 (m), 7.68−7.75 (br s), 7.82−7.94 (br s), 7.96−8.21 (m), 8.42−8.52 (m), 9.15 (br s), 10.19 (s), 10.23 (s), 10.25 (s), 10.32 (s),10.70 (s). $C_{128}H_{175}N_{29}O_{20}S$, ESI-MS: m/z 2471.33 (calcd); $m/2z$, 1236.53, $m/3z$ 825.11, $m/4z$ 619.18, $m/5z$, 495.69 (found).

Dimeric PpIX−Peptide Conjugate ***7***. Compound **5** (2.0 mg, 2.5 μmol) and peptide YI13WF (10 mg) (10.0 mg, 5.6 μmol) in 200 μL of dimethylsulfoxide (DMSO) was added with 5 μL of DMSO solution containing 10% diisopropylethylamine (DIPEA). The reaction was treated as described above and the crude products were purified by reverse-phase HPLC with the same eluting system as purification of the monomeric conjugate **6**. The reaction yielded a deep red solid **7** (5.3 mg, 48%) after lyophilization. ^{1}H NMR (400 MHz, DMSO-d_6): δ 0.65−0.80 (m), 0.95 (br s), 1.12−1.74 (overlapped), 1.84−1.92 (m), 2.25−2.36 (m), 2.70 (br s), 2.83−3.15 (overlapped), 3.60 (d, J = 10.8 Hz), 3.71 (d, J = 3.6 Hz), 3.86−3.95 (m), 4.12−4.31 (overlapped), 4.35−4.55 (overlapped), 6.17 (dd, J_1 = 11.8 Hz, J_2 = 6.0 Hz), 6.42 (dd, J_1 = 18.5 Hz, J_2 = 5.4 Hz), 6.85−7.35 (m), 7.52 (d, J = 8.0 Hz), 7.60 (d, J = 4.8 Hz), 7.80 (br s), 8.10 (br s), 8.05−8.15 (m), 8.20 (br s), 8.40−8.55 (m), 9.16 (s), 10.17 (s), 10.24 (s), 10.34 (s), 10.75 (s). $C_{222}H_{316}N_{54}O_{36}S_2$, ESI-MS: m/z 4380.41(calcd); $m/3z$ 1460.97, $m/4z$ 1096.29, $m/5z$ 877.34, $m/6z$ 731.43, $m/7z$ 627.18, $m/8z$ 549.09 (found).

General Spectroscopic Measurements. 1.0 mM stock solution (in DMSO) of PpIX, conjugate **6** and **7**, was diluted to 5.0 μM in DMSO. The UV−vis spectra were recorded using a Beckman coulter DU800 spectrometer. Wavelength Interval: 1.0 nm. Scan Speed: 1200 nm/min. Fluorescence spectroscopic studies were also performed using a Varian Cary Eclipse Fluorescence Spectrophotometer at the excitation wavelength of 504 nm.

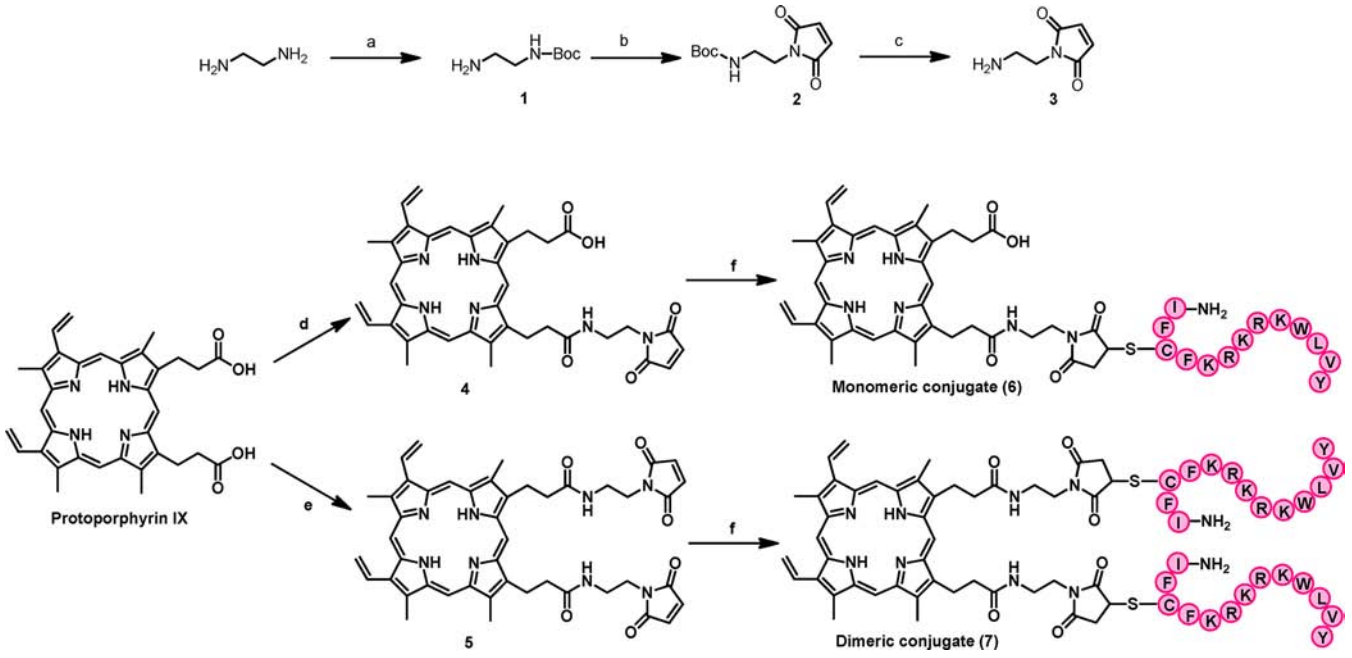
Bacterial and Cell Culture. Four Gram-negative bacteria strains: *E. coli* DH5a (ATCC 53868), *S. enterica* (ATCC 14028), and ampicillin-resistant bacterial strains *E. coli* BL21 (Amp^r *E. coli*) and *K. pneumoniae* (ATCC 700603) were used in this study. Luria−Bertani (LB) medium was used for all four bacterial strains tested in this study. A single colony from the stock LB agar plate was added to 3 mL of liquid medium, then was grown at 37 °C on a shaker incubator (200 rpm) overnight followed by a subculture until an OD_{600} of approximately 0.5−0.7 was reached.

Minimum Inhibitory Concentration (MIC) Test. Antimicrobial activities of the designed peptides were determined following a previously reported method with a light modification.[38] Briefly, 1.0 mL aliquots of bacterial strains cultured in LB solution were collected and centrifuged. The cell pellets were washed twice and resuspended in PBS (pH 7.2) at OD_{600} of 0.5, then further diluted to a final concentration of 2 × 10^5 cfu/mL. Aliquots of this suspension (25 μL) were placed into a 96-well plate. PpIX and its synthesized conjugates were diluted in 25 μL PBS and then added into the bacteria suspensions to give the desired concentration. After treating with compounds at 37 °C in the dark for 2 h, the cultures were then added to 50 μL of twice-LB solution and further incubated at 37 °C for 16 h. The wells containing the same number of cells but no compounds and the wells containing the same culture solution but without bacterial cells were set as control groups. The plate was then read using a 96-well plate reader at 600 nm. The MIC value was the lowest concentration of compound that prevented the growth of bacteria.

Bacterial Cell Imaging. Bacterial strains cultured overnight in Luria−Bertani (LB) solution were harvested and washed twice with sterile phosphate-buffered saline (PBS, pH 7.2). The washed cells were resuspended in PBS with an OD_{600} of 0.7, Then 100 μL aliquots were treated with 2 μM of compounds PpIX and these two PpIX−peptide conjugates. After incubation for 20 min in the dark at 37 °C, the cells were washed with PBS by centrifugation to remove the unbound compounds and then a drop of the suspension was immobilized on poly(L-lysine)-treated coverslips followed by covering with another coverslip. Fluorescent images were acquired with confocal laser microscope (Nikon Eclipse TE2000-E, CFI VC 100× oil immersed optics), using an excitation wavelength of 488 nm and a LP filter at 650 nm.

Quantification of bacterial cell staining was performed with *Image J* software v 1.44 (NIH) according to its standard manual. Statistic analysis was carried out using *Origin* v 8.0 software. Error bars reflect the standard error of the mean.

Scheme 1. Synthesis and Characterization of PpIX−Peptide Conjugates[a]



[a]Reagents and conditions: (a) Boc_2O, Et_3N, EtOH, 0 °C; (b) 1. Maleic anhydride, Et_3N, Et_2O, 0 °C; 2. Ac_2O, Na_2OAc, 60−70 °C; (c) TFA, DCM, 0 °C−rt; (d) and (e) HOSu, EDC·HCl, DMF, 0 °C−rt; (f) DIPEA, DMSO, rt.

Statistical significance (set at $P < 0.05$) was determined by Student's t test.

Selective Bacterial Cell Staining over Mammalian Cells. A mixture of live Jurkat T cells [$(0.5-1) \times 10^5$ cfu/mL] and bacteria (10^8 cfu/mL) in PBS (pH = 7.2) was incubated with 4 μM of dimeric PpIX−peptide conjugate 7 at 37 °C for 10 min. After being harvested by centrifugation (5 min at 500 g for Jurkat T cells and then 5 min at 3000 g for bacterial cells), the pellets of both mammalian and bacterial cells were mixed again in PBS, and 8 μL of the suspensions was added to a poly(L-lysine)-coated coverslip followed by slightly covering with another coverslip for immobilization. The images were taken as described above.

Photodynamic Inactivation against Bacterial Cells. Bacteria were grown and washed as imaging and MIC tests. From OD_{600} of 0.7 in PBS, the bacteria suspension was diluted to a final concentration of 2×10^8 cfu/mL. 60 μL aliquots of this suspension were mixed with the compounds (in 60 μL PBS) and then added into the wells of the 96-well plate made up the calculated concentration of compound (0, 0.25, 0.5, 1.0, or 2.0 μM). The plate was incubated in the dark at 37 °C for 20 min. Before irradiation, 20 μL aliquots from each well were pipeted out and further diluted to a series of sample concentrations from 10^7 cfu/mL to 10^4 cfu/mL. The remaining was exposed to a white light source for 2, 5, and 10 min, and then again, 20 μL aliquots from each well were diluted to the same series of concentrations after the specific light exposure time. Twenty-five microliter aliquots of each suspension of bacteria were subsequently plated onto LB agar plates then incubated at 37 °C overnight. The number of colony-forming units was counted after incubation and plotted onto a log scale.

Phototoxicity of Conjugate 7 toward Jurkat T Cells. The cell toxicity assay was performed using the Tox-8 assay (Sigma Aldrich) according to the manufacturer's instructions and the reported method.[39] In brief, Jurkat T cells were cultured in 96-well plates at a density of 2×10^4 cells/well, and then were incubated with the dimeric PpIX−peptide conjugate (7) with varying concentrations at 37 °C for 20 min. After incubation, the cells were exposed to a white light source for 10 min (30 J/cm^2), and then incubated for a further 24 h in the dark. As for the dark control assays, the plate was kept in the dark during the whole process. After removing the conjugate 7 containing medium by centrifugation, the cells were incubated with the Tox-8 reagent. After two hours' incubation, the absorbance was measured at the wavelength of 600 nm by a Tecan Infinite M200 microplate reader. The measurement at the wavelength of 690 nm was set as reference, which was subtracted from the 600 nm measurement later. The wells without cells but with Tox-8 reagent were used as controls. Each experiment was performed in quintuplicate.

RESULTS AND DISCUSSION

Chemistry and Spectroscopic Studies. Scheme 1 illustrated the synthetic pathway for the preparation of porphyrin and peptide derivatives. Typically, unlike the Gram-positive organisms, the cell wall of Gram-negative strains contains LPS in the outer membrane, which generally acts as a protective permeability barrier. The LPS component increases the negative charge in the cell wall, thus reducing the binding effect of many neutral and anion drugs. In our previous work, we described a series of de novo designed antimicrobial and anti-endotoxic peptides. These peptides selectively interacted with negatively charged lipids including LPS and adopted β-boomerang structures in LPS micelles.[40] As a mode of action, these peptides destabilized LPS structures and penetrated into the outer membrane of Gram-negative bacterial strains. In this study, we chose an analogue of the β-boomerang antimicrobial peptide YI13WF with the sequence of YVLWKRKRKFCFI-Amide as target ligand due to the higher affinity to neutralize LPS in Gram-negative bacterial membrane. The designed peptide sequence was prepared based on the standard solid-

dx.doi.org/10.1021/bc300203d | Bioconjugate Chem. 2012, 23, 1639−1647

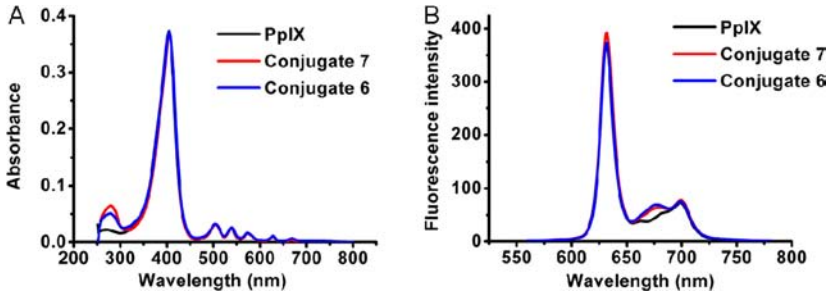


Figure 1. UV−vis absorption and fluorescent emission spectrum. (A) Absorption at concentration of 5.0 μM in DMSO; (B) emission spectrum excited at 504 nm at same concentration.

phase preparation through a commercial source. Considering a single cysteine residue in the peptide sequence, a thiol-reactive maleimide group was first introduced into the PpIX structure through ethylenediamine as the linkage to yield the maleimide-modified monomeric PpIX intermediates **4**, which could further react with the cysteine residue in the peptide sequence to afford the PpIX−peptide conjugate through the specific interaction between free thiol and maleimide group. A simple reverse-phase HPLC purification produced the monomeric PpIX-peptide derivative **6** with the yield of 56%. Similarly, the dimeric peptide adduct with PpIX moiety was also prepared in 48% yield by conjugating the bimaleimide PpIX intermediate **5** with excess YI13WF peptide sequence. The final products **6** and **7** were purified to >95% purity (Supporting Information Figure S1) by reverse-phase HPLC and further characterized by NMR and mass spectrometry (ESI-MS).

After obtaining the porphyrin−peptide derivatives, their photochemical properties were investigated by UV−vis absorption and fluorescence spectra. The spectroscopic characterization demonstrated that both the monomeric and dimeric PpIX-conjugates exhibited similar absorptions from 330 to 650 nm with an intense soret band near 400 nm and four Q-band peaks between 500 and 620 nm (Figure 1A). The emission spectra of monomeric and dimeric peptide PpIX−peptide conjugates are similar and showed no difference from those of PpIX molecule (Figure 1B). The results indicated that the peptide conjugation has no significant effect on the fluorescent properties of PpIX molecule. Moreover, the PpIX−peptide conjugates together with PpIX could also produce reactive oxygen species (e.g., singlet oxygen, etc.) when excited by white light irradiation, which were determined by the standard assay based on the specific probe of 9,10-anthracennediyl-bis(methylene) dimalonic acid (ABDA) reported previously (Supporting Information Figure S2).[19,21,22]

MIC Tests. The antibacterial studies were first carried out by investigating the minimum inhibitory concentration (MIC) of PpIX-peptide derivatives. In order to avoid the potential interferences of photoexcitation during the MIC tests, the MIC experiments were performed in the dark. In a typical study, four standard Gram-negative bacteria including *E. coli* DH5a (ATCC 53868), *S. enterica* (ATCC 14028), and ampicillin-resistant bacterial strains *E. coli* BL21 (Amp^r *E. coli*) and *K. pneumoniae* (ATCC 700603) were used as model organisms. As expected, the antimicrobial peptide sequence, YI13WF, demonstrated potent MIC activity against these Gram-negative bacterial strains mostly attributed to its stronger binding effect toward lipids exists at the outer membrane of Gram-negative bacteria.[29,40] Compared to the parent peptide sequence, monomeric PpIX-peptide derivative showed a similar trend to inhibit bacterial growth (Table 1), suggesting that conjugation of PpIX to the peptide would not affect the binding affinity between the antimicrobial peptide and LPS moieties on the bacterial membranes. Under the same assay conditions, the MIC value of dimeric PpIX-peptide against bacterial strains was found to be 4- to 8-fold less than that of YI13WF peptide or monomeric PpIX-YI13WF derivative, indicating that the greater potency of bacterial inactivation could be caused by the dimeric derivative. As control, similar antimicrobial activity was also evaluated by using the PpIX molecule alone (Table 1). The higher MIC value of PpIX clearly demonstrated the limited activity to inhibit the bacterial growth, which was consistent with the bacterial inactivation results reported previously.[17−26]

Table 1. MIC Values of PpIX, Free Peptide YI13WF, and PpIX-YI13WF Conjugates

	MIC (μM)			
	E. coli DH5a	*E. coli* BL-21	*K. pneumoniae*	*S. enterica*
Conjugate **7**	2	4	8	4
Conjugate **6**	8	32	32	32
YI13WF	8	32	32	~ 24
PpIX	>64	>64	>64	>64

Bacterial Imaging Studies. In order to verify the binding affinity of PpIX-peptide derivatives toward various Gram-negative bacterial strains, living cell imaging was conducted under a confocal microscope upon laser excitation of the Q-band absorbance of PpIX. In this study, the bacterial strains were incubated with PpIX−peptide conjugates as described in the experiment section. As show in Figure 2A, the bacterial strains incubated with PpIX itself did not show any obvious fluorescence. However, after incubation of the bacterial strains with PpIX−peptide conjugates, the confocal microscope indicated a significant fluorescent imaging of the bacterial cells stained with both dimeric and monomeric PpIX−peptide conjugates. In contrast to the monomeric conjugate **6** and free PpIX, the dimeric conjugate **7** exhibited stronger fluorescence, suggesting a higher binding ability of dimeric peptide conjugate toward the surface of bacterial strains. The different staining effects of the tested compounds were further quantified by measuring the fluorescence imaging intensity.[41] As shown in Figure 2B, fluorescence intensity from the monomeric PpIX-peptide stained cells is about 8 times greater than that of free PpIX stained cells, and such a difference would even increase up to about 20 times when the same bacterial strains were stained with dimeric PpIX−peptide conjugate, suggesting an even higher binding association between the dimeric peptide conjugate and Gram-negative bacteria. By contrast, the

dx.doi.org/10.1021/bc300203d | *Bioconjugate Chem.* 2012, 23, 1639−1647

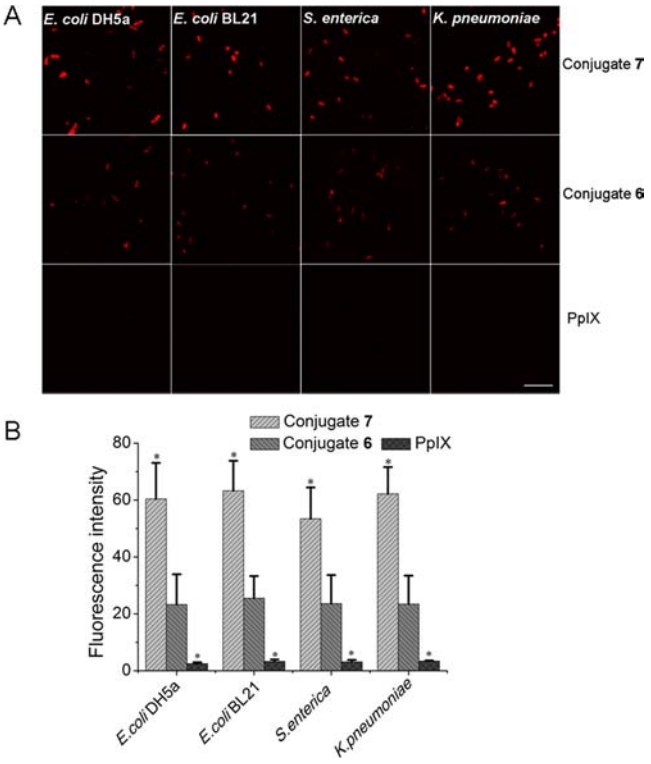


Figure 2. Fluorescent imaging of bacterial staining with PpIX and its derivatives. (A) The bacterial cells were treated with 2 μM compounds at room temperature for 10 min. Excitation wavelength was 488 nm, and fluorescence was detected using a long-pass filter at 650 nm. Scale bar = 10 μm. (B) Quantitative analysis of bacterial staining, mean ± S.E. * $P < 0.05$ versus the monomeric conjugate.

incubation of porphyrin itself with bacterial strains would not result in obvious fluorescence signals, mostly due to the weak binding affinity of porphyrin molecules with LPS moieties on the surface of Gram-negative bacteria. The living bacterial imaging and fluorescent intensity measurements clearly confirmed the hypothesis that antimicrobial peptide sequence YI13WF may act as affinity ligands for specific targeting the surface of Gram-negative bacterial strains. The enhanced bacterial imaging and bacterial MIC inactivation properties observed in the living cells treated with dimeric porphyrin–peptide conjugate may be attributable to the multivalent effects.[18,42−46]

Encouraged by the effective bacterial imaging results, the dimeric PpIX–peptide conjugate was further applied to investigate the possibility of selective recognition and imaging of bacterial strains over mammalian cells. As proof-of-concept, the Jurkat T cells were chosen and co-cultured with different Gram-negative bacteria such as Amp^r *E. coli* and *K. pneumonia*, respectively, and then incubated with dimeric PpIX–peptide conjugate at 37 °C for 10 min. The bacterial and cellular imaging measurements were acquired by using a confocal fluorescence microscope. As shown in Figure 3, for both mixtures of Jurkat T cells with Amp^r *E. coli* and Jurkat T cells with *K. pneumonia*, the significant red fluorescence could only be observed in bacteria, and there was no obvious fluorescence detected in Jurkat T cells (Figure 3 and Supporting Information Figure S4). The higher fluorescence observed in bacteria clearly indicated the ability of the dimeric PpIX–peptide conjugate to selectively recognize and image bacterial strains over mammalian cells. Generally, phosphatidylcholine (PC) and phosphatidylserine (PS) are commonly found lipid components located at the exoplasmic leaflet and inner leaflet of the plasma membrane of mammalian cells, respectively. Compared to the different phospholipids in the mammalian cell membranes, the major components of LPS located at the surface of Gram-negative bacterial strains would be the main reason to greatly contribute the selective recognition of dimeric PpIX–peptide conjugate to bacterial strains instead of mammalian cells.[37]

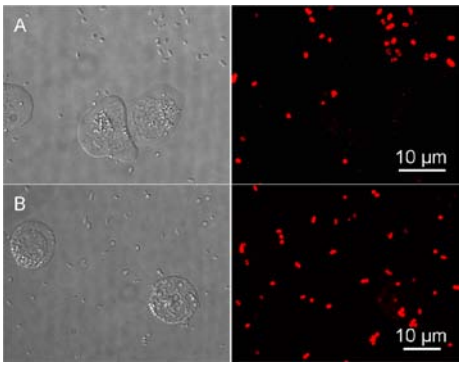


Figure 3. Fluorescent images of Jurkat T cells and two antibiotic-resistant Gram-negative bacteria: (A) *E. coli* BL21 and (B) *K. pneumoniae* incubated with conjugate 7 (4 μM). Left: bright field images, right: fluorescent images. The fluorescence of PpIX is highlighted in red.

Photodynamic Bacterial Inactivation Studies. To demonstrate that the PpIX-peptide derivatives are effective for the photodynamic inactivation of bacterial growth, the PACT treatment was conducted by exposure of Gram-negative strains with white light illumination in the presence of PpIX–peptide conjugates. Upon white light irradiation, the bacteria lethality was evaluated by counting the number of colony forming units (cfu) on the LB agar plate. It is found that both of the monomeric and dimeric PpIX–peptide conjugates displayed effective photoinactivation to the tested bacterial strains including those strains (e.g., ampicillin-resistant *E. coli* BL2l and *K. pneumoniae*) with drug resistance properties. In contrast to the monomeric PpIX–peptide conjugate, the dimeric one showed that higher antibacterial activity and more than 99% bacterial lethality (>2.0 $\log_{10}$ reduction) could be observed at only 0.5 μM after 30 J/cm^2 of light irradiation (Figure 4A,C), whereas the control studies without light irradiation only showed limited bacterial lethality. Under a fixed concentration (0.5 μM) of photosensitizers, these two PpIX–peptide conjugates also demonstrated even more significant bacterial reduction when higher doses of light irradiation were employed (Figure 4A,B). This photodynamic bacterial inactivation indicated more potent activity than the MIC values of dimeric PpIX–peptide conjugate observed for *E. coli* DH5a (~4 times) and *S. enterica* (~8 times) including other Gram-negative strains such as ampicillin-resistant *E. coli* BL21 (~8 times) and *K. pneumoniae* (~16 times). Moreover, the efficacy of bacterial photoinactivation was also found to be concentration-dependent, where the significant bacterial killing with more than 99.9% bacterial lethality (>3.0 $\log_{10}$ reduction) could still be easily obtained when photodynamic inactivation was conducted in the presence of higher concentrations of dimeric PpIX–peptide conjugate (Figure 4 and Supporting Information Figure S3). In contrast, the presence of free PpIX alone would not produce any detectable bacterial inactivation when the bacterial strains were treated with identical white light

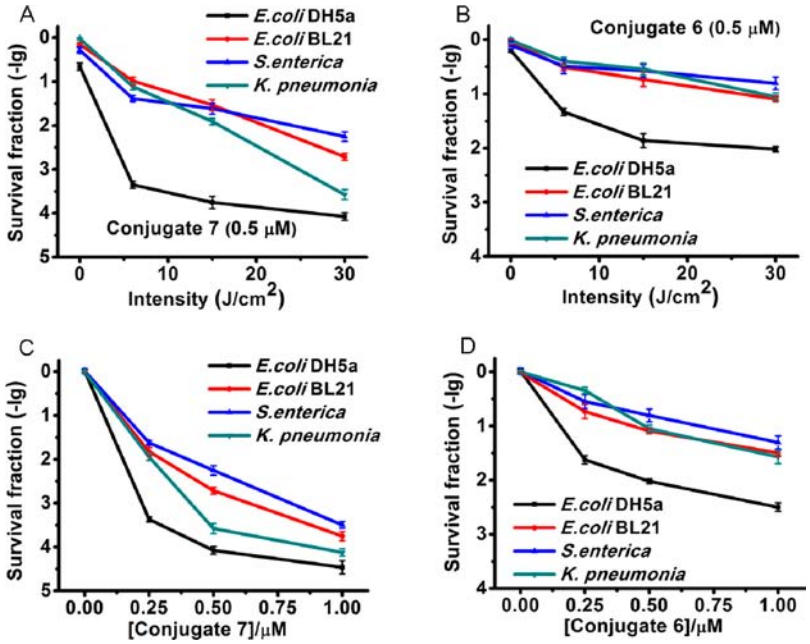


Figure 4. Bacterial photoinactivation with PpIX–peptide conjugates. (A and B) Dose effects in light-induced toxicity against bacterial cells at the fixed concentarion (0.5 μM) of PpIX–peptide conjugates **7** and **6**. (C and D) Survival curves of the bacterial cells treated with several concentrations of PpIX–peptide conjugates **7** and **6** at the fixed energy of irradiation (30 J/cm^2). *E. coli* DH5a (■), *E. coli* BL21 (●), *S. enterica* (▲), and *K. pneumoniae* (▼).

irradiation (Supporting Information Figure S3). A similar mammalian cell viability analysis toward Jurkat T cells with and without white light irradiation was also conducted by using Tox-8 assay. There were no significant mammalian cell viabilities changed with the increase of dimeric PpIX-peptide concentration and no obvious cytotoxicity detected for both the light irradiation and dark conditions (Supporting Information Figure S5). These results clearly supported our hypothesis that PpIX-conjugated dimeric peptide derivative could serve as an effective reagent to inactivate Gram-negative bacteria over mammalian cells, mostly owing to the higher binding affinity of the dimeric peptide sequence toward the LPS moieties on the surface of bacterial strains, which may lead to the locally high concentration of photosensitizers caused by the efficient polyvalent/multivalent interactions. The high concentration of dimeric porphyrin peptide conjugate accumulated at close proximity to the bacterial surface could thus constitute significant bacterial lethality upon exposure to some dose of light illumination.

■ CONCLUSIONS

In this work, we have successfully constructed a simple and specific strategy for effective fluorescent imaging and photodynamic inactivation of Gram-negative bacterial strains through the conjugation of photosensitizer protoporphyrin IX (PpIX) with two lipopolysaccharide (LPS) neutralizing peptide sequences: YI13WF (YVLWKRKRKFCFI-Amide). By taking advantage of the higher binding affinity of the peptide sequence toward the LPS components, the dimeric PpIX peptide conjugate can effectively deliver the photosensitizer to the surface of Gram-negative bacterial strains and thus enhance the local concentration through the effects of multivalency. Upon the white light illumination, the dimeric PpIX–peptide derivative indicated the potent activity against Gram-negative bacterial pathogens including those with drug-resistant properties, which is more active than the MIC values of YI13WF peptide and PpIX alone. Apart from the higher photodynamic antimicrobial application, the dimeric PpIX–peptide conjugate also displayed the promising function in real-time fluorescent imaging of living bacterial strains. Moreover, both fluorescent imaging and photoinactivation experiments also demonstrated that the dimeric PpIX-YI13WF conjugate could selectively target bacterial strains over mammalian cells and generate less damage to mammalian cells. The demonstrated strategy based on the dimeric lipids affinity peptide sequence derivative may provide the great possibility for further study of biological functions in Gram-negative bacterial strains under living settings. It may also supply the potential alternative for the effective inactivation of bacterial pathogens especially for those with drug-resistant properties.

■ ASSOCIATED CONTENT

Ⓢ Supporting Information

HPLC analysis of peptide conjugates, measurement of singlet oxygen generation, controlled bacterial and cellular photoinactivation, controlled bacterial and cellular fluorescent imaging, bacterial imaging and fluorescent intensity quantification, ^{1}H NMR for compounds **1**, **2**, **4**–**7**, and ESI-MS for compounds **6** and **7**. This material is available free of charge via the Internet at http://pubs.acs.org.

■ AUTHOR INFORMATION

Corresponding Author

*Xing Bengang: Phone 65-63168758, e-mail bengang@ntu.edu.sg. S. Bhattacharjya: Phone 65-63167997, e-mail surajit@ntu.edu.sg.

Notes

The authors declare no competing financial interest.

■ ACKNOWLEDGMENTS

This work was supported in part by Nanyang Technological University (NTU) Start-Up Grant and MOE/NTU Tier 1 Grant (RG 64/10) in Singapore.

■ ABBREVIATIONS:

PACT, photodynamic antimicrobial chemotherapy; HPLC, high-performance liquid chromatography; LPS, lipopolysaccharide; PpIX, protoporphyrin IX; MIC, minimum inhibitory concentration.

■ REFERENCES

(1) Walsh, C. T. (2003) *Antibiotics: actions, origins, and resistance*, pp 195−220, ASM Press, Washington, DC.
(2) Spencer, J., and Walsh, T. R. (2006) A new approach to the inhibition of metallo-beta-lactamases. *Angew. Chem., Int. Ed. 45*, 1022−1026.
(3) Fisher, J. F., Meroueh, S. O., and Mobashery, S. (2005) Bacterial resistance to beta-lactam antibiotics: compelling opportunism, compelling opportunity. *Chem. Rev. 105*, 395−424.
(4) Xing, B. G., Rao, J. H., and Liu, R. (2008) Novel beta-lactam antibiotic derivatives: their new applications as gene reporters, antitumor prodrugs, and enzyme inhibitors. *Mini-Rev. Med. Chem. 8*, 455−471.
(5) Maiti, S. N., Phillips, O. A., Micetich, R. G., and Livermore, D. M. (1998) Beta-lactamase inhibitors: agents to overcome bacterial resistance. *Curr. Med. Chem. 5*, 441−456.
(6) Jiang, T., Liu, R., Huang, X., Feng, H., Teo, W., and Xing, B. G. (2009) Colorimetric screening of bacterial enzyme activity and inhibition based on the aggregation of gold nanoparticles. *Chem. Commun. 15*, 1972−1974.
(7) Dolmans, D. E., Fukumura, D., and Jain, R. K. (2003) Photodynamic therapy for cancer. *Nat. Rev. Cancer 3*, 380−387.
(8) Detty, M. R., Gibson, S. L., and Wagner, S. J. (2004) Current clinical and preclinical photosensitizers for use in photodynamic therapy. *J. Med. Chem. 47*, 3897−3915.
(9) Castano, A. P., Mroz, P., and Hamblin, M. R. (2006) Photodynamic therapy and anti-tumour immunity. *Nat. Rev. Cancer 6*, 535−545.
(10) Wu, S., Chang, E., and Cheng, Z. (2011) Molecular probes for bioluminescence imaging. *Curr. Org. Synth. 8*, 488−497.
(11) Lovell, J. F., Liu, T. W., Chen, J., and Zheng, G. (2010) Activatable photosensitizers for imaging and therapy. *Chem. Rev. 110*, 2839−2857.
(12) Ragas, X., Copper, L. P., White, J. H., Nonell, S., and Flors, C. (2011) Quantification of photosensitized singlet oxygen production by a fluorescent protein. *ChemPhysChem 12*, 161−165.
(13) Shao, Q., and Xing, B. G. (2010) Photoactive molecules for applications in molecular imaging and cell biology. *Chem. Soc. Rev. 39*, 2835−2846.
(14) Philips, D. (2011) Toward targeted photodynamic therapy. *Pure Appl. Chem. 83*, 733−748.
(15) Celli, J. P., Spring, B. Q., Rizvi, I., Evans, C. L., Samkoe, K. S., Verma, S., Pogue, B. W., and Hasan, T. (2010) Imaging and photodynamic therapy: mechanisms, monitoring, and optimization. *Chem. Rev. 110*, 2795−2838.
(16) Wainwright, M. (1998) Photodynamic antimicrobial chemotherapy (PACT). *J. Antimicrob. Chemother. 42*, 13−28.
(17) Suci, P. A., Varpness, Z., Gillitzer, E., Douglas, T., and Young, M. (2007) Targeting and photodynamic killing of a microbial pathogen using protein cage architectures functionalized with a photosensitizer. *Langmuir 23*, 12280−12286.
(18) Strassert, C. A., Otter, M., Albuquerque, R. Q., Hone, A., Vida, Y., Maier, B., and De Cola, L. (2009) Photoactive hybrid nanomaterial for targeting, labeling, and killing antibiotic-resistant bacteria. *Angew. Chem., Int. Ed. 48*, 7928−7931.
(19) Xing, C. F., Xu, Q. L., Tang, H. W., Liu, L. B., and Wang, S. (2009) Conjugated polymer/porphyrin complexes for efficient energy transfer and improving light-activated antibacterial activity. *J. Am. Chem. Soc. 131*, 13117−13124.
(20) Gad, F., Zahra, T., Francis, K. P., Hasan, T., and Hamblin, M. R. (2004) Targeted photodynamic therapy of established soft-tissue infections in mice. *Photochem. Photobiol. Sci. 3*, 451−458.
(21) Xing, B. G., Jiang, T., Bi, W., Yang, Y., Li, L., Ma, M., Chang, C. K., Xu, B., and Yeow, E. K. L. (2011) Multifunctional divalent vancomycin: the fluorescent imaging and photodynamic antimicrobial properties for drug resistant bacteria. *Chem. Commun. 47*, 1601−1603.
(22) Shao, Q., and Xing, B. G. (2012) Enzyme responsive luminescent ruthenium (II) cephalosporin probe for intracellular imaging and photoinactivation of antibiotics resistant bacteria. *Chem. Commun. 48*, 1739−1741.
(23) Hope, C. K., Packer, S., Wilson, M., and Nair, S. P. (2009) The inability of a bacteriophage to infect Staphylococcus aureus does not prevent it from specifically delivering a photosensitizer to the bacterium enabling its lethal photosensitization. *J. Antimicrob. Chemother. 64*, 59−61.
(24) Perni, S., Prokopovich, P., Pratten, J., Parkin, I. P., and Wilson, M. (2011) Nanoparticles: their potential use in antibacterial photodynamic therapy. *Photochem. Photobiol. Sci. 10*, 712−720.
(25) Zhu, C., Yang, Q., Liu, L., Lv, F., Li, S., Yang, G., and Wang, S. (2011) Multifunctional cationic poly(p-phenylene vinylene) polyelectrolytes for selective recognition, imaging, and killing of bacteria over mamalian cells. *Adv. Mater. 23*, 4805−4810.
(26) Bonnett, R., Buckley, D. G., Burrow, T., Galia, A. B. B., Saville, B., and Songca, S. P. (1993) Photobactericidal materials based on porphyrins and phthalocyanines. *J. Mater. Chem. 3*, 323−324.
(27) Raetz, C. R., and Whitfield, C. (2002) Lipopolysaccharide endotoxins. *Annu. Rev. Biochem. 71*, 365−700.
(28) Hancock, R. E. (1997) The bacterial outer membrane as a drug barrier. *Trends. Microbiol. 5*, 37−42.
(29) Bhattacharjya, S. (2010) *De novo* designed lipopolysaccharide binding peptides: structure based development of antiendotoxic and antimicrobial drugs. *Curr. Med. Chem. 17*, 3080−3093.
(30) Beutler, B., and Rietschel, E. T. (2003) Innate immune sensing and its roots: the story of endotoxin. *Nat. Rev. Immunol. 3*, 169−176.
(31) Cohen, J. (2002) The immunopathogenesis of sepsis. *Nature 420*, 885−891.
(32) Hardaway, R. M. (2000) A review of septic shock. *Am. Surg. 66*, 22−29.
(33) Hancock, R. E., and Scott, M. G. (2000) The role of antimicrobial peptides in animal defenses. *Proc. Natl. Acad. Sci. U.S.A. 97*, 8856−8861.
(34) Dürr, U. H., Sudheendra, U. S., and Ramamoorthy, A. (2006) LL-37, the only human member of the cathelicidin family of antimicrobial peptides. *Biochem. Biophys. Acta 1758*, 1408−1425.
(35) Rosenfeld, Y., Papo, N., and Shai, Y. (2006) Endotoxin (lipopolysaccharide) neutralization by innate immunity host-defense peptides. *J. Biol. Chem. 281*, 1636−1643.
(36) Bourre, L., Giuntini, F., Eggleston, I. M., Mosse, C. A., Macrobert, A. J., and Wilson, M. (2010) Effective photoinactivation of Gram-positive and Gram-negative bacterial strains using an HIV-1 Tat peptide-porphyrin conjugate. *Photochem. Photobiol. Sci. 9*, 1613−1620.
(37) Zasloff, M. (2002) Antimicrobial peptides of multicellular organisms. *Nature 415*, 389−395.
(38) Zou, G., De Leeuw, E., Li, C., Pazgier, M., Li, C., Zeng, P., Lu, W.-Y., Lubkowski, J., and Lu, W. (2007) Toward understanding the cationicity of defensins. *J. Biol. Chem. 282*, 19653−19665.
(39) Liu, D. (1981) A rapid biochemical test for measuring chemical toxicity. *Bull. Environ. Contam. Toxicol. 26*, 145−149.
(40) Bhunia, A., Mohanram, H., Domadia, P. N., Torres, J., and Bhattacharjya, S. (2009) Designed β-boomerang antiendotoxic and antimicrobial peptides. *J. Biol. Chem. 284*, 21991−22004.
(41) Hamilton, N. (2009) Quantification and its application in fluorescent microiscopy imaging. *Traffic 10*, 951−961.

(42) Perni, S., Prokopovich, P., Pratten, J., Parkin, I. P., and Wilson, M. (2011) Nanoparticles: their potential use in antibacterial photodynamic therapy. *Photochem. Photobiol. Sci. 10*, 712−720.
(43) Bombelli, C., Bordi, F., Ferro, S., Giansanti, L., Jori, G., Mancini, G., Mazzuca, C., Monti, D., Ricchelli, F., Sennato, S., and Venanzi, M. (2008) New cationic liposomes as vehicles of m-tetrahydroxyphenylchlorin in photodynamic therapy of infectious diseases. *Mol. Pharmaceutics 5*, 672−679.
(44) Li, L. H., and Xu, B. (2005) Multivalent vancomycins and related antibiotics against infectious diseases. *Curr. Pharm. Des. 11*, 3111−3124.
(45) Liu, S. P., Zhou, L., Lakshminarayanan, R., and Beuerman, R. W. (2010) Multivalent antimicrobial peptides as therapeutics: design principles and structural diversities. *Int. J. Pept. Res. Ther. 16*, 199−213.
(46) Pieters, R. J., Arnusch, C. J., and Breukink, E. (2009) Membrane permeabilization by multivalent anti-microbial peptides. *Protein Pept. Lett. 16*, 736−742.

Bioconjugate Chemistry

Article

pubs.acs.org/bc

Site-Specific PEGylation of HR2 Peptides: Effects of PEG Conjugation Position and Chain Length on HIV-1 Membrane Fusion Inhibition and Proteolytic Degradation

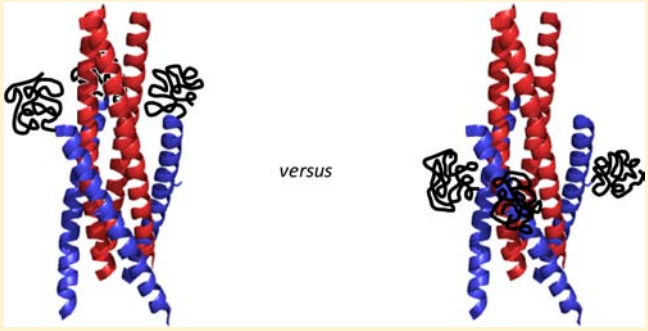
Maarten Danial,[‡] Tim H. H. van Dulmen,[‡] Joanna Aleksandrowicz,[†] Andy J. G. Pötgens,[†] and Harm-Anton Klok*,[‡]

[‡]École Polytechnique Fédérale de Lausanne, Institut des Matériaux and Institut des Sciences et Ingénierie Chimiques, Laboratoire des Polymères, Bâtiment MXD, 1015 Lausanne, Switzerland

[†]AplaGen GmbH, Arnold Sommerfeld-Ring 2, D-52499, Baesweiler, Germany

Supporting Information

ABSTRACT: Peptides derived from the HR1 or HR2 regions of the HIV-1 envelope glycoprotein gp41 have been shown to be effective inhibitors to prevent virus–host cell membrane fusion. These peptide drugs, however, suffer from relatively short plasma half-lives and are susceptible to enzymatic degradation. Modification of peptides/proteins with poly(ethylene glycol) (PEG) is a well-established strategy to overcome these limitations. This manuscript presents the results of a systematic study on the influence of the site of PEGylation of HR2-derived peptides, as well as of PEG molecular weight on the biological activity and proteolytic stability of these conjugates. Investigation of the fusion inhibitory efficacy of the conjugates in a model cell–cell based assay revealed a loss in activity for the PEGylated peptides as compared to the wild-type HR2-derived peptide. The loss of activity, however, can be minimized by controlling the site of PEGylation, more specifically, by introducing the PEG chain at one of the more central positions along the non-interacting α-helical surface of the peptides. The proteolytic stability of the PEG–peptide conjugates was assessed in a trypsin-based model assay, which revealed an up to 3.4-fold increase in degradation half-life that may help to compensate for the lower inhibitory efficacy of the PEG–peptide conjugates as compared to the wild-type peptide. The results of this study emphasize the power of site-specific PEGylation to improve the stability of peptide/protein drugs while minimizing adverse effects on biological activity.



INTRODUCTION

It has been estimated that 33 million people worldwide have been infected by the human immunodeficiency virus type 1 (HIV-1).[1] Despite being a pandemic, there is no cure against this virus that can lead to acquired immune deficiency syndrome (AIDS). Nevertheless, a number of drug therapies are available nowadays that can delay the onset of AIDS, which include entry/fusion inhibitors, reverse transcriptase inhibitors, protease inhibitors, and integrase inhibitors.[2] From these therapies, fusion and entry inhibitors are a particularly intriguing therapeutic option since these prohibit the virus from entering the cell. Moreover, the application of effective fusion/entry inhibitors may reduce the need for the conventional reverse transcriptase, integrase, and protease inhibitors. One such fusion inhibitor, T-20 (Fuzeon, Enfuvirtide), which was approved in 2003, is a peptide drug derived from the gp41 HR2 domain that competitively inhibits the fusion process between the viral and host cell membranes.[3−5]

While T-20 has been shown to be very effective in preventing virus–host cell membrane fusion and reducing viral loads in HIV-1-infected individuals,[6] it also suffers from the same drawbacks as other protein/peptide drugs, i.e., short plasma half-lives (~3.8 h)[6] and susceptibility to proteolytic degradation. This is nicely illustrated by the fact that treatment with T-20 requires two daily subcutaneous injections of 90 mg each in order to maintain an effective therapeutic concentration.[6] A widely used and effective strategy to increase the plasma half-life of protein/peptide drugs and prevent proteolytic degradation involves their modification with poly(ethylene glycol) (PEG).[7−11] Mono-PEGylation of interferon α-2a with a 40 kDa branched PEG derivative, for example, has been shown to result in a 70-fold increase in serum half-life and a 50-fold increase in mean plasma residence time.[12] Interestingly, the *in vitro* activity of the PEGylated protein was only 7% of that of the unmodified analogue, while a several-fold increase in *in vivo* activity was observed upon PEGylation.[12] In another example, site-specific PEGylation of erythropoiesis protein was found to

Received: April 22, 2012
Revised: June 22, 2012
Published: July 9, 2012

 © 2012 American Chemical Society

lead to a 2-fold increase in elimination half-life and mean residence time, while maintaining cell proliferation activity.[13]

Whereas early PEGylation strategies only provided little or no control over the degree and site of conjugation, a variety of approaches is available nowadays that allow access to well-defined PEG−peptide/protein conjugates where these parameters can be accurately controlled.[14,15] The ability to site-specifically modify peptides and proteins is of critical importance to generate biologically active PEG−peptide/protein conjugates.[16] Doherty et al., for example, prepared and PEGylated a library of 13 cysteine analogues of the granulocyte macrophage colony-stimulating factor (GM-CSF).[17] By targeting regions of the protein that are located away from the active sites, a variety of PEGylated GM-CSF analogues was obtained that possessed biological activities comparable to that of the wild-type protein. In another study, Salhanick et al. compared the biological activity of N- and C-terminal PEGylated glucose-dependent insulinotropic polypeptide (GIP).[18] Whereas N-terminal PEGylation essentially resulted in a complete loss of activity, C-terminal modification only modestly affected functional activity. Yamamoto et al. prepared and investigated the biological activity of a site-specifically mono-PEGylated variant of tumor necrosis factor-α (TNF-α).[19] Site-specific PEGylation was found to result in PEG−protein conjugates that possessed 80% of the activity of the unmodified wild-type TNF-α, whereas random PEGylation resulted in conjugates that only showed 10% residual activity.

One possible strategy to improve the pharmacokinetics and *in vivo* half-life of peptide-based HIV-1 fusion inhibitors involves the design of variants ("third-generation fusion inhibitors") that contain stabilizing intramolecular salt bridges or covalent bonds.[5] A second option is the use of protease-resistant D-peptide based inhibitors.[20] Site-specific polymer (or more specifically, poly(ethylene glycol) (PEG) modification) is a third possibility. Whereas site-specific polymer/PEG modification of proteins and peptides is well-established (*vide supra*), this strategy has only been explored to a limited extent to improve the stability and half-life of peptide-based HIV-1 fusion inhibitors. In a patent application, Bailon and Won describe the preparation and antiviral activity of two N-terminal PEGylated T20 variants, which were found to possess IC_{50} values that are approximately one order of magnitude higher as compared to the unmodified T20 peptide.[21] In a second patent, Bailon and Won describe the PEGylation at the N-terminus of a T20 peptide variant known as T1249.[22] The T1249−PEG20k conjugate was found to have 13.7−56.7-fold reduction in anti-HIV activity (IC_{50} = 0.041 to 0.170 μg/mL) relative to the unmodified T1249 peptide (IC_{50} = 0.003 μg/mL). Others have explored the conjugation of peptide-based HIV-1 fusion inhibitors to biological macromolecules in order to develop long-lasting conjugates.[23,24] Stoddart et al. studied the *in vitro* anti-HIV activity of human serum albumin conjugates of the C34 peptide fusion inhibitor, where the human serum albumin was covalently attached via a maleimide linker to the N- or C-terminus of the peptide.[23] The N-terminal human serum albumin conjugates showed only minor losses in anti-HIV activity ($IC_{50} \approx 2$ nM) relative to the C34 peptide (IC_{50} = 0.6 nM). Conversely, C-terminal human serum albumin−C34 conjugates showed an order of magnitude loss in antiviral activity (IC_{50} = 11.2 nM). The human serum albumin conjugated to the N-terminus of C34 was shown to take more than 96 h for complete renal elimination compared to ~10 h for the C34 peptide alone. In another example, Huet et al. reported the development of long-lasting T-20 variants, which were obtained by N-terminal modification of the peptide with an anti-thrombin-binding carrier pentasaccharide.[24] These saccharide−peptide conjugates were found to possess an elimination half-life of more than 10 h in rat plasma as compared to 2.8 h for the unmodified peptide. In the examples discussed above, however, no efforts were reported to systematically study and understand the effects of the site of polymer conjugation on the biological activity and stability of the fusion inhibitors. This manuscript describes the preparation of a library of PEGylated HR2 derivatives and systematically studies the influence of the site of PEGylation and PEG molecular weight on the biological activity and proteolytic stability of the conjugates. The fusion inhibitory efficacy of the polymer conjugates was studied using a model syncytia assay, whereas the proteolytic stability of the PEG−peptide conjugates was assessed in a trypsin-based model assay.

EXPERIMENTAL SECTION

Materials. Rink amide AM resin (mesh 200−400 with 0.61 mmol·g^{-1} loading), Fmoc-L-Ala-OH, Fmoc-L-Arg(Pbf)−OH, Fmoc-L-Asn(Trt)−OH, Fmoc-L-Asp(OtBu)−OH, Fmoc-L-Cys(Trt)−OH, Fmoc-L-Gln(Trt)−OH, Fmoc-L-Glu(OtBu)−OH, Fmoc-Gly-OH, Fmoc-L-His(Trt)−OH, Fmoc-L-Ile-OH, Fmoc-L-Leu-OH, Fmoc-L-Lys(Boc)−OH, Fmoc-L-Phe-OH, Fmoc-L-Ser(tBu)−OH, Fmoc-L-Thr(tBu)−OH, Fmoc-L-Trp(Boc)−OH, Fmoc-L-Tyr(tBu)−OH, and Fmoc-L-Val-OH, as well as hydroxybenzotriazole (HOBT) and 2-(6-chloro-1*H*-benzotriazole-1-yl)-1,1,3,3-tetramethylaminium hexafluorophosphate (HCTU), were all purchased from IRIS Biotech (Marktredwitz, Germany). Piperidine (99%), diisopropylethylamine (DIPEA, 99%), trypsin DPCC treated type XI from bovine pancreas, phenylmethanesulfonyl fluoride (PMSF), triethylamine (Et_3N, >99%), acryloyl chloride (97%), and phosphate buffered saline (PBS) sachets were purchased from Sigma-Aldrich (Buchs, Switzerland). Celltracker Green (CTgreen) and Celltracker Orange (CTorange) were obtained from Invitrogen, dissolved at 5 mM in DMSO and stored in aliquots at −20 °C in the dark. Dulbecco's PBS (containing 10 mM of sodium phosphate) and Hank's balanced salt solution (HBSS) were purchased from Invitrogen (Karlsruhe, Germany). *N*,*N*-dimethylformamide (DMF) and acetonitrile (HPLC grade) were obtained from VWR (Nyon, Switzerland). *N*-Methylpyrrolidone (NMP) and diethyl ether (Et_2O) were obtained from Schweizerhall (Basel, Switzerland).

Cell Lines. Chinese hamster ovarian (CHO-WT) cells that express the wild-type HIV-1 envelope glycoprotein gp120 were obtained through the AIDS Research and Reference Reagent Program, Division of AIDS, NIAID, NIH from Judith M. White.[25] To preserve the expression of the HIV-1 gp120 protein, CHO-WT cells were maintained in glutamine-deficient GMEM medium (a modification of MEM-alpha medium, PAN Biotech, Aidenbach, Germany) to which L-glutamic acid (final conc. 0.2942 g·L^{-1}), L-asparagine (final conc. 0.03020 g·L^{-1}), Na-pyruvate (final conc. 0.22 g·L^{-1}), and non-essential amino acids L-alanine (0.01782 g·L^{-1}), L-aspartic acid (final conc. 0.2662 g·L^{-1}), glycine (final conc. 0.01501 g·L^{-1}), L-proline (final conc. 0.06906 g·L^{-1}), and L-serine (0.02102 g·L^{-1}) (all from Sigma Aldrich, Taufkirchen, Germany) were added, together with 400 μM methionine sulfoximine (Sigma Aldrich, Schnelldorf, Germany), 1% penicillin/streptomycin, 1% amphotericin B, and 10% fetal calf serum (FCS, Sigma Aldrich). Adherent CHO-WT cells were passaged using

dx.doi.org/10.1021/bc3002248 | *Bioconjugate Chem.* 2012, 23, 1648−1660

trypsin/ethylene diamine tetraacetic acid (EDTA). SupT1 cells (containing the CD4 HIV receptor) and K562 cells (lacking CD4) were obtained from DSMZ (Braunschweig, Germany) and grown in suspension in Roswell Park Memorial Institute (RPMI) medium (Invitrogen, Karlsruhe, Germany) with 1% penicillin/streptomycin, 1% amphotericin B, and 10% FCS, as recommended by the supplier. All cell lines were passaged for a maximum of four weeks, at which point a new batch of cells was thawed and cultured.

Peptide Synthesis and Purification. All peptides were synthesized using a CEM Liberty automated microwave peptide synthesizer on a 0.25 mmol scale by Fmoc chemistry on a Rink amide AM resin (0.61 mmol·g^{-1} loading). Fmoc deprotection was achieved in two subsequent steps using 20% piperidine with 0.1 M HOBT in DMF (to reduce racemization[26]) for 1 min and subsequently 6 min using 56 W of microwave power at 75 ± 5 °C. After that, the resin was washed with five 10 mL portions of DMF and cooled to approximately 25 °C. A single 0.2 M (1 mmol, 5 mL) amino acid coupling for each residue of the sequence was performed with stock solutions of 0.5 M HOBT/HCTU in DMF (1 mmol, 2 mL) as the activator mixture and 2 M DIPEA in NMP (2 mmol, 1 mL) as the base. The final molar ratio with respect to the Rink amide AM resin for amino acid/activator/base during the reaction was 4:4:8 and the coupling reaction proceeded for 7 min using 24 W of microwave power at 60 ± 5 °C per the manufacturer's protocol.[26] After completion of the synthesis, the peptide was cleaved from the resin and deprotected using 10 mL of a mixture of trifluoroacetic acid (TFA), triisopropylsilane (TIS), and Milli-Q water (~18 MΩ cm, Millipore) in the volume ratio 95:2.5:2.5% for 3.5−4 h at room temperature.

All peptides were purified by preparative high-pressure liquid chromatography (HPLC) using a Waters 600 automated gradient controller pump module connected to a Waters prep degasser system. Sample elution was monitored by a Waters 2487 dual λ absorbance detector and peptides collected using a Waters fraction collector III. Purification was achieved with an Atlantis OBD C-18 reverse-phase column (5 μm, 30 × 150 mm, Waters) using water/TFA (0.1% TFA in water, Solvent A) and acetonitrile/TFA (0.1% TFA in acetonitrile, Solvent B) as the mobile phase. Elution was achieved at 20 mL/min by typically running gradients of 40−50% solvent B over 20 min. All peptides were purified to at least 95% by preparative HPLC and verified for purity by analytical HPLC using a monomeric C-18 column (5 μm, 4.6 × 150 mm, 238TP5415, Vydac). Fractions containing peptide were detected by UV absorbance at 220 and 280 nm. The molecular masses of the peptides were confirmed by electrospray ionization mass spectrometry (ESI-MS) or MALDI-TOF using α-cyano-4-hydroxycinnamic acid as the matrix as described below. All peptide samples were freeze−dried yielding a white powder.

Synthesis of Monomethoxy-PEG-Acrylates. Monomethoxy-PEG750-OH (mPEG−OH, 5.0 g, 6.7 mmol) was dried azeotropically in 50 mL dry toluene through rotary evaporation. After that, the resulting mPEG−OH melt was placed on ice and dissolved in 300 mL dry dichloromethane (DCM). After addition of Et_3N (1.86 mL, 2.0 equiv), acryloyl chloride (0.81 mL, 1.5 equiv) was added dropwise over a period of 30 min. The reaction was allowed to proceed with stirring overnight in the dark at room temperature under nitrogen. After that, the resulting pale yellow solution was extracted twice with 5% HCl, twice against 5% NaOH, once against saturated $NaHCO_3$, and once against brine. The DCM layer was collected and dried over $MgSO_4$, and the volume of the solution was reduced to approximately 5 mL using rotary evaporation. After addition of 80 mL of Et_2O and storage at −20 °C overnight, the desired mPEG was precipitated, isolated by filtration, and dried *in vacuo*. Yield: 42%; conversion OH to acrylate: 95% (from ^{1}H NMR analysis). ^{1}H NMR ($CDCl_3$, 400 MHz): 6.4 ppm (dd, 1H, C***H***$_2$CHOOCH$_2$CH$_2$−PEG chain), 6.1 (dd, 1H, CH$_2$C***H***OOCH$_2$CH$_2$−PEG chain), 5.8 ppm (dd, 1H, C***H***$_2$CHOOCH$_2$CH$_2$−PEG chain), 4.3 ppm (t, 2H, CH$_2$CHOOC***H***$_2$CH$_2$−PEG chain), 3.6 ppm (m, 68H, PEG chain protons), 3.3 ppm (s, 3H, methoxy).

The protocol outlined above was also used to prepare mPEG2000-acrylate from mPEG2000-OH. Yield: 77%; conversion OH to acrylate: 95% (from ^{1}H NMR analysis). ^{1}H NMR ($CDCl_3$, 400 MHz): 6.4 ppm (dd, 1H, C***H***$_2$CHOOCH$_2$CH$_2$−PEG chain), 5.8 ppm (dd, 1H, C***H***$_2$CHOOCH$_2$CH$_2$−PEG chain), 6.1 ppm (dd, 1H, CH$_2$C***H***OOCH$_2$CH$_2$−PEG chain), 4.3 ppm (t, 2H, CH$_2$CHOOC***H***$_2$CH$_2$−PEG chain), 3.6 ppm (m, 180H, PEG chain protons), 3.3 ppm (s, 3H, methoxy). ^{1}H NMR and MALDI-ToF mass spectra of mPEG750-acrylate and mPEG2000-acrylate are included in the Supporting Information (Figure S1 and Figure S2).

Peptide PEGylation. PEGylation was typically carried out with 1.60 μmol (approximately 8 mg) of peptide dissolved in 4 mL of a 10 mM sodium phosphate buffer (pH 7.4). Then, 40 μmol (25 equiv) of the dry mPEG-acrylate was added to the reaction mixture. The peptide-PEG750 and peptide-PEG2000 reaction mixtures were allowed to stir at room temperature in the dark for approximately 44−48 h. After that, the peptide-mPEG conjugates were purified with preparative RP-HPLC using a 20 min solvent gradient from 40/60% acetonitrile/water (with 0.1% TFA) to 50/50% acetonitrile/water (with 0.1% TFA). The conjugate fractions were freeze−dried and lyophilized to yield a white powder (yield: 60−90%). MALDI-ToF mass spectra of all synthesized conjugates are included in the Supporting Information (Figure S3 and Figure S4).

Matrix Assisted Laser Desorption Ionization−Time of Flight Mass Spectrometry (MALDI-ToF MS). MALDI-ToF MS was carried out on a Shimadzu Axima-CFR plus MALDI-ToF mass spectrometer operating in the linear mode in the 500−14 000 m/z range. For the characterization of the mPEG-OH and mPEG-acrylates, saturated dithranol matrix in dichloromethane (DCM) with 30 wt % sodium trifluoroacetate (Na TFA) was used. This was mixed in a 1:1 volume ratio with the mPEG-OH or mPEG-acrylate (1 mg·mL^{-1}) dissolved in DCM from which 1 μL was applied onto the plate. For analysis of the peptides and the mPEG-peptide conjugates, a 10 mg·mL^{-1} THF solution of α-cyano-4-hydroxycinnamic acid was used to prepare the matrix. The matrix solution was mixed in a 1:1 volume ratio with the mPEG-peptide conjugates dissolved in Milli-Q water (1 mg·mL^{-1}). The samples were placed on the MALDI-ToF plate and allowed to dry. Calibration was achieved using several references: Angiotensin II ([M+H$^+$] = 1045.54), adrenocorticotropic hormone$_{18-39}$ (ACTH$_{18-39}$) peptide fragment ([M+H$^+$] = 2464.20), and bovine insulin ([M+H$^+$] = 5729.61). Measurements were performed with a laser power of 45−65 (max. laser power: 180).

Circular Dichroism Spectroscopy. Circular dichroism (CD) spectroscopy measurements were performed on a JASCO-715 spectropolarimeter equipped with a water bath and a PTC-348WI Peltier temperature controller. All samples were dissolved at approximately 1 mg·mL^{-1} in 10 mM

phosphate buffered saline (PBS, pH 7.4) and then diluted to a working concentration of 20 μM. The concentration of the peptides was verified by UV−vis spectroscopy using the extinction coefficient of the peptides at 280 nm determined using the linear combination of extinction coefficients of tyrosine (1490 $M^{-1}\cdot cm^{-1}$) and tryptophan (5500 $M^{-1}\cdot cm^{-1}$).[27] Experiments were carried out in a 0.1 cm path length quartz cuvette in the range 260−200 nm. All CD spectra were corrected for the baseline of 10 mM PBS (pH 7.4) and converted to mean residue ellipticity (MRE). α-Helix contents were calculated as follows:

$$\alpha\text{-helix content} = [\theta]_{222}/[\theta]_{222}^{100\%} \quad (1)$$

where $[\theta]_{222}^{100\%}$ is the theoretical mean residue ellipticity of a peptide with n residues with 100% α-helix content as defined by[28]

$$[\theta]_{222}^{100\%} = -40000\cdot(1 - 4.6/n) \quad (2)$$

Analytical Ultracentrifugation. Sedimentation equilibrium experiments were performed on a Beckman Optima XL-I analytical ultracentrifuge (Beckman, Palo Alto, CA, USA) at 20 °C. Six-channel quartz cells were used with an An-60 titanium rotor. All samples were dissolved in 10 mM PBS, pH 7.4, to a working concentration of 20 μM (or 10 μM PEG conjugate with 10 μM N45). Samples were initially scanned at 5000 rpm to identify appropriate wavelengths for data collection. The cells were scanned using a step size of 0.001 cm, and the data points were averaged over 6 replicates. The samples were then scanned at 280 nm at 20 000 or 25 000 rpm until two equilibrium curves taken 6 h apart were perfectly superimposed. The solvent density (ρ = 1.00534 $g\cdot mL^{-1}$) and partial specific volume of the peptide was calculated using the program *SEDNTERP* ($\bar{\nu}$ = 0.7293 $mL\cdot g^{-1}$ for the WT peptide).[29] The partial specific volumes of the S15C-PEG750 and S15C-PEG2000 conjugates were calculated to be 0.7435 and 0.7584 $mL\cdot g^{-1}$, respectively, by a weighted average of specific volumes between the peptide and PEG (0.833 $mL\cdot g^{-1}$). The sedimentation equilibrium data were then fitted to several models to reflect the oligomeric state of the system using the *Sedphat* program[30] as has been described with similar peptides.[31] The data were fitted with a "single species of interacting system" model, which yields a molecular weight of the sample. For all samples, the molecular weights of the samples were deemed reliable when the residuals between the fit and the data points was random around zero.

Trypsin Degradation Assay. Solutions of bovine trypsin (2 μM) and the peptide or PEG−peptide conjugate (20 μM) in 10 mM PBS (pH 7.4) were freshly prepared at room temperature. The concentrations of the solutions were verified by UV−vis spectroscopy as described in the section on CD spectroscopy (*vide supra*). A 1 mL aliquot of trypsin solution was warmed to 37 °C for exactly 5 min, and 1 mL of peptide or PEG−peptide conjugation solution was subsequently added. To stop the degradation, 50 μL samples were taken from the reaction mixture and added to 50 μL of a freshly prepared solution containing 5% acetic acid with 5 mM PMSF. Peptide degradation was monitored by analytical reverse-phase HPLC using a C-18 monomeric column (S/N E950404−10−3, Vydac) and a gradient of 5−95% acetonitrile (with 0.1% TFA) against water (with 0.1% TFA) over 16 min for sample elution. Sample elution was monitored using a UV−vis detector set at 280 nm. The main peptide or PEG−peptide conjugate peak was integrated and analyzed relative to the peak area at t = 0 and its disappearance monitored over approximately 100 min. The relative peak area (A_t/A_0) was fitted with a first-order exponential decay

$$A_t = A_0 \exp(-kt) \quad (3)$$

where A_t is the area at a specific time, t, A_0 is the peak area at t = 0, and k is the rate constant from which the degradation half-life, $t_{1/2}$ can be defined as

$$t_{1/2} = \ln 2/k \quad (4)$$

Syncytia Assay. Twenty-four hours prior to commencing the assay, CHO-WT cells expressing the HIV-1 IIIB gp120 and gp41 proteins were seeded in GMEM and 10% FCS in 6-well plates with 2.5 × 10^5 cells at 2 mL/well.

On the day of the assay, approximately 6 × 10^5 SupT1 cells (or CD4-negative K652 cells as a negative control) were counted with a Neubauer chamber followed by 5 min centrifugation at 1500 rpm. The supernatant was removed and the cells were washed with approximately 5 mL RPMI medium and centrifuged once more at 1500 rpm for 5 min. After removal of the supernatant, the cells were washed in serum free RPMI and then incubated with 5 μM CTOrange dye, suspended in serum free RPMI medium, for 20 min at 37 °C. The cells were centrifuged at 1500 rpm and washed three times with 5 mL mixture of RPMI medium and 10% FCS followed by resuspension of the SupT1 (or K652) cells in 6 mL RPMI medium with 10% FCS. The wells containing CHO-WT cells were washed with 2 mL serum free GMEM followed by the addition of 2 mL CellTracker Green (5 μM, CTgreen) dye suspended in GMEM-SF medium and 20 min incubation at 37 °C. The cells were washed twice with 2 mL GMEM + 10% FCS after which 1 mL of peptide or PEG−peptide conjugate dissolved at a 2-fold higher concentration than desired for the assay was added to the wells with CHO-WT. The concentrations of the peptide and PEG−peptide conjugates in the solutions that were added to the well containing CHO-WT cells were determined by UV−vis spectrophotometry at 280 nm using the extinction coefficient determined from the linear combination of the molar extinction coefficients from tyrosine and tryptophan.[27]

To assess the membrane fusion inhibitory efficacy of the peptide and peptide conjugates, 1 mL (1 × 10^5 cells) CTOrange stained SupT1 (or K652) cells were added to the wells containing the CTgreen stained CHO-WT cells and the peptide or peptide−conjugate and subsequently incubated for 4 h at 37 °C. The nonadherent cells were removed and the wells were washed twice with 2 mL HBSS. Finally, the cells were fixed using ice-cold 70% methanol (kept at −20 °C) and incubated at 4 °C for 15 min. Subsequently, the methanol was removed and the wells were washed with HBSS medium. As a negative control, exactly the same protocol was followed for the preparation of the CD4 negative K652 cells. The K652 cells do not have the CD4 receptor and therefore do not fuse with CHO-WT cells to form syncytia. K652 cells were used as a control to prove that the formation of syncytia was due to fusion of membranes as a result of the CHO-WT envelope protein interaction with CD4 and not via another (unknown) mechanism.

The wells were analyzed using fluorescence microscopy monitoring the green channel and red channel. Cells were counted similarly as described by Muñoz-Barroso et al.[32] Briefly, fusion was quantified by counting the numbers of red

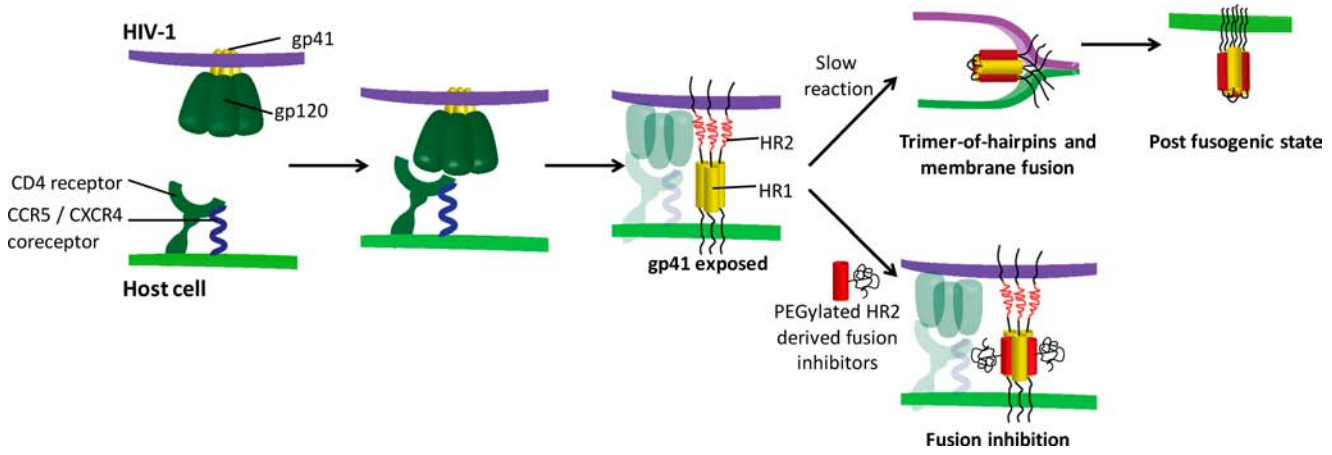


Figure 1. Schematic overview of the HIV-1–host cell membrane fusion process and its proposed inhibition by PEGylated HR2 derived fusion inhibitors.

Table 1. Sequences of the Peptide and Peptide–PEG Conjugates

Sample	*f c f c f c f c f*
WT	EWDREINN YTSLIHSLIEESQNQQEKNEQELLELDKWASLW
N terminus	CEWDREINN YTSLIHSLIEESQNQQEKNEQELLELDKWASLW
R4C	EWD**C**EINN YTSLIHSLIEESQNQQEKNEQELLELDKWASLW
S11C	EWDREINN YT**C**LIHSLIEESQNQQEKNEQELLELDKWASLW
S15C	EWDREINN YTSLIH**C**LIEESQNQQEKNEQELLELDKWASLW
E18C	EWDREINN YTSLIHSLI**C**ESQNQQEKNEQELLELDKWASLW
N22C	EWDREINN YTSLIHSLIEESQ**C**QQEKNEQELLELDKWASLW
Q29C	EWDREINN YTSLIHSLIEESQNQQEKNE**C**ELLELDKWASLW
C terminus	EWDREINN YTSLIHSLIEESQNQQEKNEQELLELDKWASLWC
S20C	EWDREINN YTSLIHSLIEE**C**QNQQEKNEQELLELDKWASLW

dx.doi.org/10.1021/bc3002248 | *Bioconjugate Chem.* 2012, 23, 1648–1660

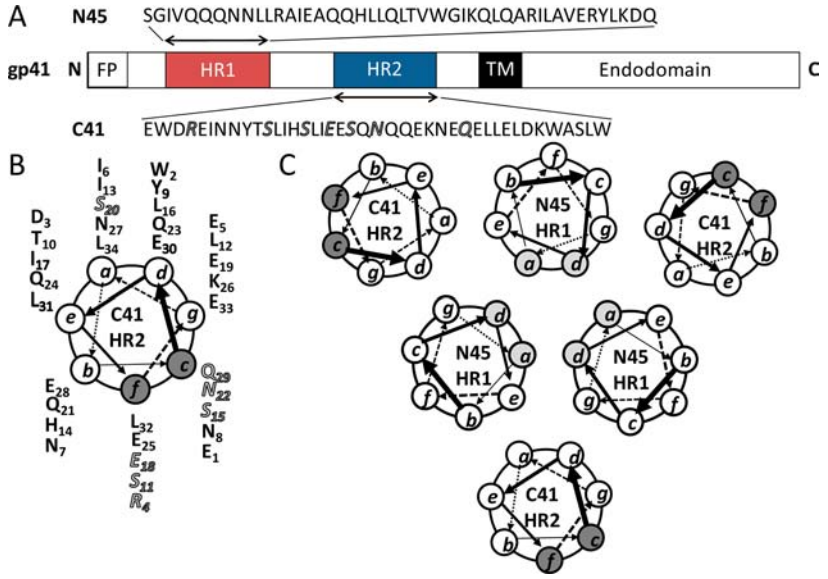


Figure 2. (A) Sequences of the HR1 derived peptide N45 and the HR2 derived peptide C41. (B) Helical wheel representation of the C41 peptide with residues mutated to cysteine highlighted in the *c* and *f* positions. (C) Helical wheel representation of the six-helix bundle formed by assembly of the 3 N45 and 3 C41 peptides. The sequences of the HR1 and HR2 domains are defined as published in ref 39, while the HR1 derived peptide sequence N45 is defined as published in ref 31.

(SupT1 derived) nuclei inside the syncytia relative to the number of nuclei inside the syncytia observed in the absence of peptide fusion inhibitor. Counting was facilitated using the cell counter plugin in *ImageJ* software.[33] This process was repeated for all peptide–PEG conjugates at concentrations between 0 and approximately 400 nM. The relative data were fitted with the following equation:

$$y = 1/(1 + [\text{peptide}]/\text{IC}_{50}) \quad (3)$$

where y is the normalized number of syncytia as a function of peptide concentration to deduce a concentration at which 50% of the syncytia are inhibited, IC_{50}. The standard error bars indicate variance of syncytia formation between three or more areas under the microscope from two independent assays.

RESULTS AND DISCUSSION

Conjugate Design and Synthesis. Fusion of the HIV-1 virus with a host cell proceeds via the formation of a six-helix bundle that has been identified as a trimer of antiparallel coiled-coil hairpins (Figure 1).[34,35] Formation of the fusion active trimer of hairpins starts with binding of the HIV-1 gp120 envelope glycoprotein, which is presented as trimers on the viral envelope, to a CD4 receptor and a CXCR4 or CCR5 coreceptor on the target cell.[34] This binding process induces a conformational change in gp120 and exposes gp41. Each gp41 protein contains two domains, HR1 and HR2, that each have the characteristic primary structural features of coiled coil forming peptides.[36] Successful HIV-1–host cell fusion involves intramolecular antiparallel heterodimerization of the HR1 and HR2 regions of all three gp41 glycoproteins that are present on the viral envelope.[35] Peptides derived from the HR1 and HR2 region have been successfully explored as competitive inhibitors to prevent the formation of the fusion active trimer of hairpins.[3,37,38]

To explore the PEGylation of these fusion inhibitors and, more specifically, study the effects of PEG molecular weight and site of conjugation on fusion inhibiting activity and proteolytic stability, a library of PEG–peptide conjugates based on the HR2 region of gp41 has been prepared (Table 1). To illustrate the rationale behind the synthesis of the PEGylated peptides listed in Table 1, Figure 2 presents the amino acid sequence of the HR2 region as well as helical wheel representations of a peptide derived from HR2 (C41, WT), both as a single helix and as part of the fusogenic six-helix bundle complex with the N45 peptide[31] derived from the HR1 region. The HR1 and HR2 regions are defined according to the heptad repeats as shown by Weissenhorn et al.[39] The design of the HR2 derived peptide C41 was based on the sequence of T-20[3] but with an extension at the N-terminal end to include the deep-pocket binding residues Trp-2 and Ile-6 that have been shown to increase antiviral potency,[40] while truncating the C-terminus of T-20, which is outside the heptad repeat region.[39] In addition to the N- and C-terminal amino acids of C41, residues 4, 11, 15, 18, 22, and 29, which are located at the *c* or *f* heptad position of the peptide, were targeted for PEGylation so as to minimize interference of the PEG chain with the formation of the six-helix bundle structure. To enable site-selective PEGylation, the appropriate residues in the wild-type HR2 sequence were replaced by cysteine. Selective N- and C-terminal PEGylation was achieved by extending the HR2 sequence with an additional cysteine residue at the desired chain end of the peptide. The sample names in Table 1 reflect these mutations and indicate the original amino acid in the HR2 sequence that was targeted, the position of this amino acid in the wild-type HR2 peptide, as well as the amino acid by which the wild-type residue was replaced (cysteine C in all cases). As negative controls, two conjugates (S20C) were prepared in which two different molecular weight PEGs were attached to the heptad position *a* of the HR2 peptide.

The PEGylated HR2 derivatives listed in Table 1 were prepared via a Michael-type addition reaction between an acrylate-modified monomethoxy poly(ethylene glycol) and the cysteine thiol group on the peptide (Supporting Information Scheme S1). The conjugates were purified and isolated by preparative HPLC and obtained in 60–90% yield. The PEG–peptide conjugates were characterized by MALDI-ToF mass

dx.doi.org/10.1021/bc3002248 | *Bioconjugate Chem.* 2012, 23, 1648–1660

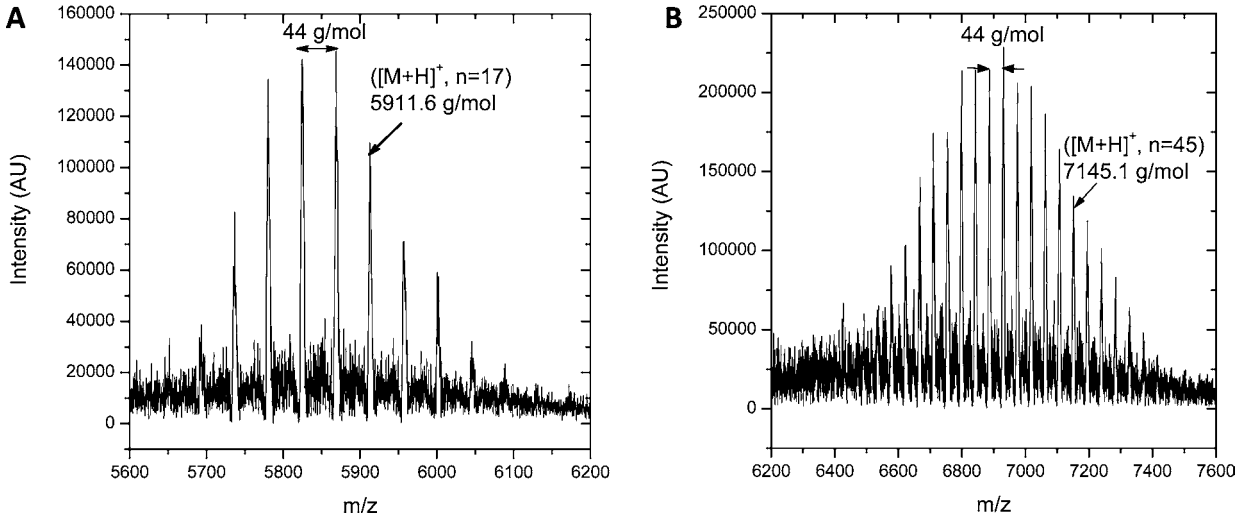


Figure 3. MALDI-ToF mass spectra of (A) the S15C-PEG750 and (B) the S15C-PEG2000 conjugates.

Table 2. Biophysical Characterization, Trypsin Degradation Half-Life ($t_{1/2}$), and Cell−Cell Fusion Inhibition Efficacy (IC_{50}) of the Peptides and Peptide−PEG Conjugates Investigated in This Study[a]

sample	MRE $-[\theta]_{222}$ (deg cm^2 dmol^{-1})	α-helical content (%)	N45:Sample $-[\theta]_{222}$ (deg cm^2 dmol^{-1})	N45:Sample α-helical content (%)	$t_{1/2}$ (min)	$t_{1/2}/t_{1/2,WT}$ (−)	IC_{50} (nM)
Wild type, WT	7700	22	28100	79	37.2	n. a.	1.5 ± 0.1
N-terminus	7100	20	17300	48	38.6	1.0	n.d.
N-terminus-PEG750	9300	26	23200	65	40.0	1.1	7.2 ± 0.7
N-terminus-PEG2000	9300	26	27500	77	79.3	2.1	11.2 ± 1.9
R4C	7000	20	23600	66	37.4	1.0	n.d.
R4C-PEG750	7900	22	24000	67	44.1	1.2	5.1 ± 1.1
R4C-PEG2000	8400	24	25800	72	67.4	1.8	8.7 ± 1.3
S11C	7800	22	18600	52	38.9	1.0	n.d.
S11C-PEG750	8100	23	22300	63	50.2	1.3	4.4 ± 0.8
S11C-PEG2000	7900	22	24700	69	91.0	2.4	4.9 ± 0.5
S15C	7400	21	16700	47	39.9	1.1	n.d.
S15C-PEG750	7700	22	22700	64	53.7	1.4	4.1 ± 1.0
S15C-PEG2000	8400	24	26100	73	82.4	2.2	5.0 ± 0.5
E18C	7700	22	18700	53	38.4	1.0	n.d.
E18C-PEG750	8100	23	23100	65	50.3	1.4	4.5 ± 1.0
E18C-PEG2000	7900	22	28300	79	81.3	2.2	4.9 ± 0.6
N22C	7900	22	22200	62	38.9	1.0	n.d.
N22C-PEG750	9400	26	22400	63	51.8	1.4	4.2 ± 0.9
N22C-PEG2000	8000	23	29100	82	80.7	2.2	5.1 ± 0.5
Q29C	7800	22	19700	55	38.6	1.0	n.d.
Q29C-PEG750	8200	23	21100	59	58.1	1.6	5.2 ± 0.8
Q29C-PEG2000	7000	20	27000	76	84.1	2.3	5.5 ± 0.5
C-terminus	7000	20	20700	58	39.0	1.0	n.d.
C-terminus-PEG750	9300	26	22500	63	81.2	2.2	10.9 ± 2.2
C-terminus-PEG2000	8700	25	23400	66	126.0	3.4	43.3 ± 14.8
S20C	7100	20	22000	62	38.6	1.0	n.d.
S20C-PEG750	8600	24	16300	46	42.0	1.1	>400
S20C-PEG2000	9500	27	16700	47	76.3	2.1	>400

[a]n.d. = not determined.

spectrometry. As a typical example, the MALDI-ToF mass spectra of S15C-PEG750 and S15C-PEG2000 are shown in Figure 3. The MALDI-ToF mass spectra for all other conjugates listed in Table 1 are included in the Supporting Information Figures S3 and S4. The mass spectra are characterized by a series of peaks that are spaced 44 Da apart, which corresponds to the mass of a single ethylene glycol repeat unit and reflects the chain length heterogeneity of the PEG chain. In Figure 3A,B, a representative peak is labeled with its respective mass that corresponds to the sum of the mass of the peptide and the mass of an integer number of ethylene glycol units (17 for PEG750 and 45 for PEG2000 in the spectra in Figure 3).

dx.doi.org/10.1021/bc3002248 | Bioconjugate Chem. 2012, 23, 1648−1660

Biophysical Characterization. The putative mode of action of the PEG−peptide conjugates listed in Table 1 involves binding to the complementary HR1 domain of the virus bound gp41 glycoprotein to form a six helix bundle (see Figure 1). To obtain first insight into the potential of the PEG−peptide conjugates to inhibit the formation of a fusogenic trimer of hairpins, the secondary structure and assembly behavior of the PEGylated peptides were studied with circular dichroism spectroscopy (CD) and analytical ultracentrifugation sedimentation equilibrium experiments. In these experiments, the N45 peptide was used to mimic the HR1 domain of the gp41 viral envelope protein (Figure 2).[31]

The results of the CD experiments are summarized in Table 2 and Figure 4. The CD spectra in Figure 4A and the mean molar residue ellipticities and helical contents listed in Table 2 indicate that neither the replacement of the selected residues in the wild-type C41 peptide by cysteine nor the PEGylation strongly affects the largely unordered secondary structure. In several cases for the PEGylated HR2 peptides, helical contents of 22−26% were determined, which are slightly increased as compared to the respective non-PEGylated peptide.

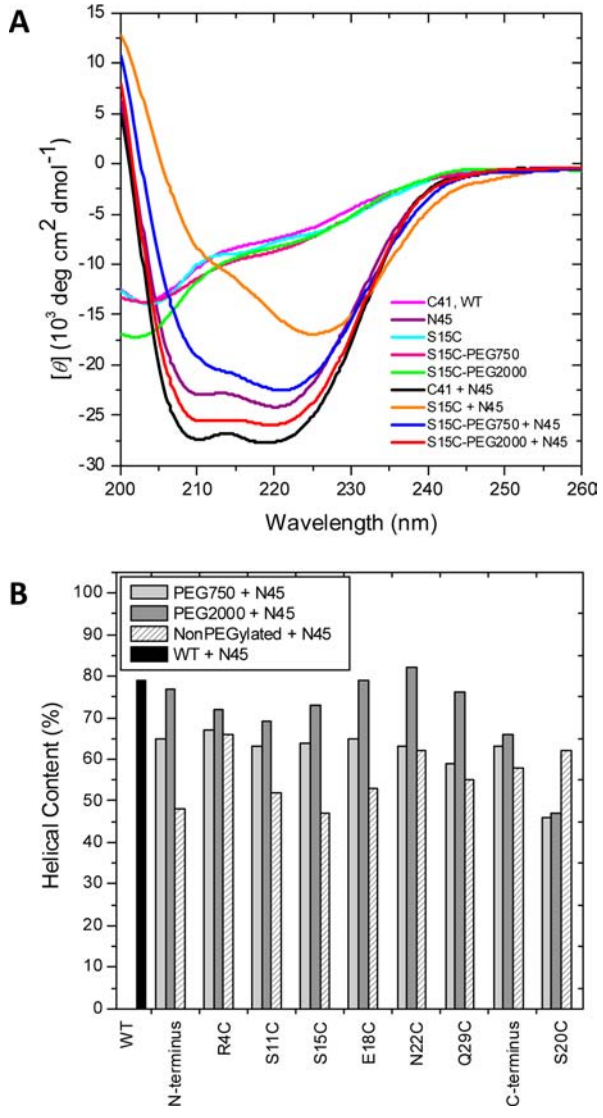


Figure 4. (A) CD spectra of the S15C non-PEGylated and PEG−peptide conjugates alone and in an equimolar mixture with N45. (B) Comparison of the helical contents of equimolar mixtures of wild-type, non-PEGylated peptides and PEG−peptide conjugates with N45.

Equimolar mixtures of the cysteine modified HR2 peptides and the N45 peptide afforded CD spectra that were indicative of α-helical structures but with $[\theta_{222}]/[\theta_{208}]$ values equal to ~0.78, which is lower than expected for a coiled coil. The α-helical contents that were determined for stoichiometric mixtures of the cysteine modified HR2 derivatives and N45 were lower than that of a stoichiometric mixture of the wild-type HR2 peptide (C41) and N45 indicating that the cysteine residue distorts the formation of the coiled coil superstructures. It is interesting to note that the S20C peptide, which contains a cysteine residue at an unfavorable *a* position of the heptad repeat, does not behave much differently from the other peptides which contain cysteine residues at positions that are anticipated to interfere less with coiled coil formation.

The PEGylated HR2 derivatives when mixed with an equimolar quantity of N45 produced CD spectra that are characteristic of coiled coil assemblies with relatively high α-helix contents (59−82%) and $[\theta_{222}]/[\theta_{208}]$ values of ~1. With the exception of the S20C derivatives, all of the investigated PEG−peptide samples showed higher α-helical contents in the presence of an equimolar amount of the N45 peptide as compared to a stoichiometric mixture of the corresponding non-PEGylated peptide and N45, which points toward a stabilizing effect of the PEG chain on the coiled coil assemblies. In all cases, the helical contents of the PEG2000 conjugates were higher than that of the PEG750 conjugates. The relatively low helical contents of the PEGylated S20C derivatives are in agreement with the conjugation site of this peptide and indicate that, as expected, PEGylation at the *a* position of the heptad repeat hampers "coiled coil" formation (*vide infra*).

To further assess the ability of the PEGylated peptides to form a six-helix bundle-type assembly in the presence of a stoichiometric amount of the HR1-derived N45 peptide, analytical ultracentrifugation experiments were carried out. As a typical example, Figure 5 shows the results of sedimentation equilibrium experiments that were performed on equimolar mixtures of the PEGylated S15C peptides and N45. Fitting of the data afforded molar masses of 32.8 kDa and 37.4 kDa for the PEG750 and PEG2000 based assemblies, which are within 3% of the expected masses of the corresponding six-helix bundles (33.4 kDa and 36.3 kDa for S15C-PEG750 and S15C-PEG2000, respectively). Sedimentation equilibrium experiments with the N- and C-terminally PEGylated HR2 peptide afforded molar masses of 32.3 kDa and 36.1 kDa for N-terminal-PEG750 and N-terminal-PEG2000 conjugates, respectively, and similarly 32.0 kDa and 35.9 kDa for C-terminal-PEG750 and C-terminal-PEG2000 conjugates, respectively. These molar masses agree well with expected molar masses of 33.7 kDa and 37.3 kDa for the C-/N-terminal-PEG750 and C-/N-terminal-PEG2000 conjugates, respectively (see Figure S5). Analytical ultracentrifugation studies of the S20C-PEG conjugates with N45 did not yield any sedimentation equilibrium curves, suggesting that the former did not form six-helix bundle structures. Taken together, the results from the CD and analytical ultracentrifugation experiments indicate that, with judicious control of the site of conjugation, PEGylation does not impair the self-assembly properties of the peptides.

Fusion Inhibition. To assess their membrane fusion inhibitory efficacy, the PEGylated HR2 peptides were investigated in a model cell−cell-based fusion assay, which involved an adherent Chinese Hamster Ovarian cell line

dx.doi.org/10.1021/bc3002248 | *Bioconjugate Chem.* 2012, 23, 1648−1660

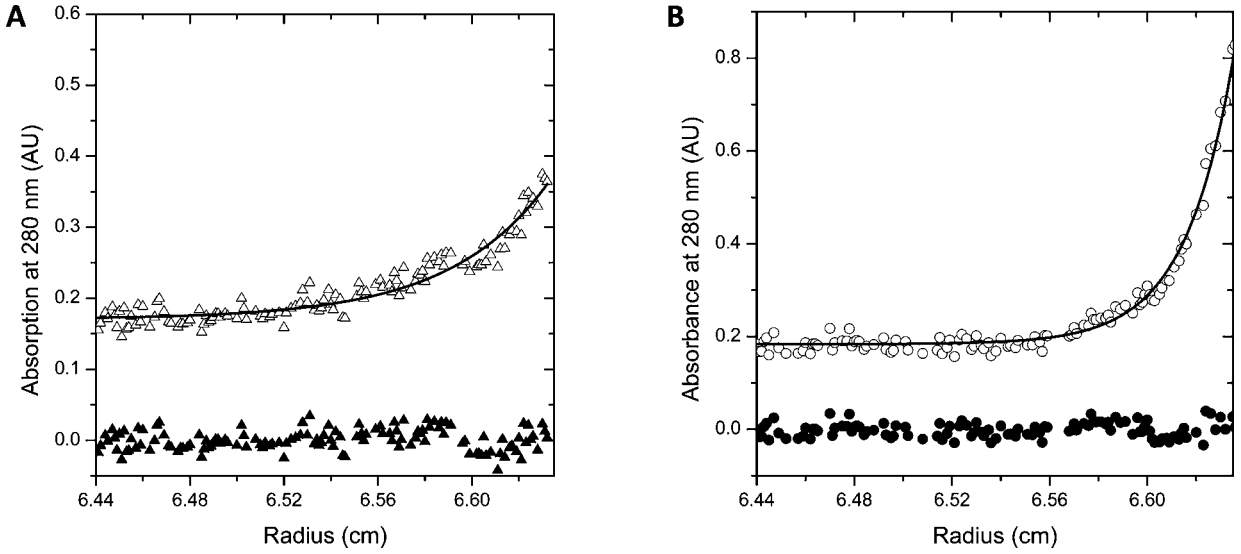


Figure 5. Results of sedimentation equilibrium experiments on equimolar mixtures of 10 μM N45 and 10 μM (A) S15C-PEG750 or (B) S15C-PEG2000 conjugates performed at 25 000 rpm over 24 h. The open symbols are the data points obtained from the sedimentation equilibrium experiment and the filled symbols are the residuals.

expressing the HIV-1 gp120 and gp41 surface proteins (CHO-WT)[25] and the CD4 positive SupT1[41] cell line. In the absence of a fusion inhibitor, addition of SupT1 cells to wells containing CHO-WT cells results in fusion of the cells, of which multiple fusion events lead to large cell-like structures with multiple nuclei known as syncytia.[25] To measure the fusion inhibitory efficacy of the PEGylated HR2 peptides, aliquots of the conjugates at concentrations ranging from 0 to 500 nM were added to a mixture of the CHO-WT and SupT1 cells and the number of syncytia counted after 4 h (SI Figure S6). From these experiments, dose–response curves, which represent the relative number of syncytia as a function of the concentration of the PEG–peptide conjugate, were obtained. As a representative example, the dose–response curves for three different conjugates are shown in Figure 6. Data for all the other conjugates are included in the Supporting Information (Figure S7). For each conjugate, the dose–response curve affords an IC_{50} value, which is used as a measure for the fusion inhibitory efficacy of that particular compound and represents the concentration of the PEG–peptide conjugate at which 50% of the relative number of syncytia were inhibited. The IC_{50} values for all PEG–peptide conjugates are included in Table 2 and also summarized in Figure 7.

With the exception of the S20C conjugates, the IC_{50} values determined for the PEGylated HR2 peptides varied between 4 and 40 nM. For the S20C-PEG750 and S20C-PEG2000 conjugates, IC_{50} values >400 nM were found. This is consistent with the low helical contents measured by CD and the lack of evidence of the formation of a six-helix bundle by analytical ultracentrifugation for these samples in the presence of an equimolar amount of the N45 peptide (*vide supra*). The results obtained with the S20C conjugates reflect the steric blocking of the unfavorably positioned PEG chains that prevent association of the HR2-derived peptide conjugates with the complementary HR1 domain of the gp41 protein on the CHO-WT cell surface. The data in Table 2 and Figure 7 indicate that PEGylation results in a decrease in the fusion inhibitory efficacy as compared to the wild-type peptide, but also demonstrate that the reduction in efficacy very much depends on the site of PEGylation. PEGylation at or near the N- or C-terminus is most unfavorable as evidenced from the IC_{50} values of the N-terminus, R4C, and C-terminus modified peptides. The IC_{50} values of the C-terminal-PEG750 and C-terminal-PEG2000 samples are significantly higher than those of the corresponding N-terminal PEGylated peptides. This may be related to the antiparallel orientation of the HR2 and HR1 peptides in the six-helix bundle structure,[42] which places the C-terminus of the HR2 peptide in closer proximity to the host cell membrane and makes the formation of this assembly, and thus fusion inhibition, more susceptible to the introduction of sterically demanding groups such as the PEG chains. These results also follow a similar trend obtained by Stoddart et al. with human serum albumin–C34 peptide conjugates, where conjugation of human serum albumin to the C-terminus of the C34 peptide resulted in an order-of-magnitude loss in efficacy relative to the unconjugated peptide and N-terminal conjugation.[23] Variation of the site of PEGylation from position 11, 15, 18, 22, or 29 in the HR2 sequence, in contrast, was not found to result in statistically significant variations in the IC_{50} values, irrespective of the PEG molecular weight. PEGylation at these positions resulted in IC_{50} values around 4.5 nM, which represents a 3-fold reduction in efficacy as compared to the wild-type, unmodified peptide. The only relatively moderate reduction in efficacy (in comparison to the N- and C-terminal PEGylated analogues) indicates that side chain as opposed to peptide chain end PEGylation imposes fewer steric constraints on the formation of the putative six-helix bundle structure and, as a consequence, fusion inhibition. The results of the fusion inhibition experiments emphasize that judicious choice of the site of PEGylation allows one to minimize detrimental steric effects that may impair the therapeutic efficacy of the PEG–peptide conjugates. Furthermore, slight losses in therapeutic efficacy may be compensated for by the increase in half-life of the HR2 peptides as has been observed with other PEGylated peptides and proteins (*vide infra*).[12,17,18,43]

Enzymatic Degradation. Since one of the major limitations of peptide/protein based drugs is their susceptibility to enzymatic degradation, a final series of model experiments was performed to study the influence of PEGylation on the degradation of the PEG–peptide conjugates. These experi-

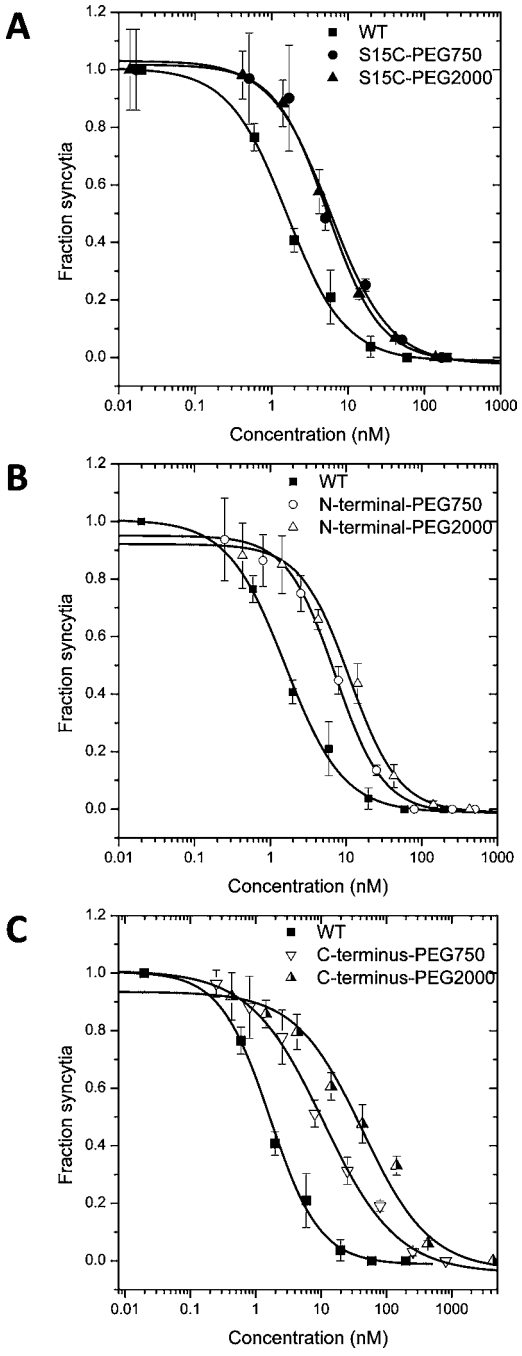


Figure 6. Dose–response curves obtained from the cell–cell fusion assay with (A) the S15C PEGylated, (B) the N-terminal PEGylated, and (C) the C-terminal PEGylated HR2 derived peptides. In each of the graphs, the dose–response curve of the wild-type HR2 derived peptide is included for comparison. If the error bars are not visible, they fall into the data point.

ments were carried out using the serine protease trypsin as a model enzyme. Trypsin was selected, as it is cheap and readily available and selectively cleaves amide bonds at the C-terminal side of positively charged lysine and arginine,[44] which facilitates the analysis of degradation products by analytical HPLC. Degradation experiments were performed over a time frame of approximately 100 min by incubating a 10 μM solution of the peptide or PEG–peptide conjugate with 1 μM trypsin. At regular time intervals, aliquots were taken and added to a solution containing the trypsin inhibitor phenylmethanesulfonyl fluoride in order to stop the degradation process. The aliquots were subsequently analyzed by reverse-phase HPLC. As a representative example, Figure 8A shows a series of HPLC chromatograms that were recorded on samples taken during the degradation of the wild-type peptide, C41. The chromatogram at t = 2 min shows a single peak (retention time = 14.2 min) corresponding to the intact wild-type peptide. With increasing incubation time, a second peak at a retention time of 13.1 min appears. Using electrospray ionization mass spectrometry, this peak was identified as being due to the N-terminal fragment WASLW-NH_2 (Figure 8B). The area of the main peak was determined via integration and plotted against time. As an example, Figure 8C shows the degradation profile of the wild-type peptide, as well as the S15C-PEG750 and S15C-PEG2000 conjugates. The resulting degradation curves were fitted with a single exponential decay, from which the trypsin degradation half-lives of the non-PEGylated and PEGylated peptides were determined. The degradation half-lives ($t_{1/2}$) of the wild-type peptide, the cysteine modified variants, and the PEG–peptide conjugates are summarized in Table 2 and Figure 9. The data illustrate that PEGylation is an effective strategy to increase the degradation half-life of the peptides. Whereas conjugation of a short PEG chain only leads to moderate improvements, the introduction of a longer PEG chain (PEG2000) increases the trypsin degradation half-life by a factor of 1.8–3.4. Analysis of the degradation half-lives as a function of the site of PEGylation in most cases only reveals minor variations and no real trends. The degradation half-lives of the PEG750 conjugates seem to gradually increase as the site of PEGylation shifts progressively closer to the C-terminus of the peptide, which may be due to the fact that trypsin cleaves at the C-terminal site of the targeted amide bond. The degradation half-lives of the C-terminus PEG750 and C-terminus PEG2000 conjugates, however, clearly stand out, for reasons which are unclear at the moment.

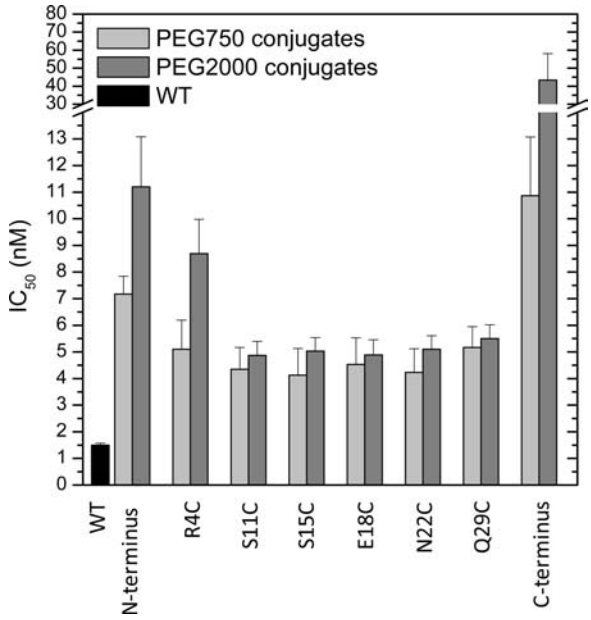


Figure 7. Comparison of the fusion inhibition efficacies of the PEG750 and PEG2000 peptide conjugates.

dx.doi.org/10.1021/bc3002248 | *Bioconjugate Chem.* 2012, 23, 1648–1660

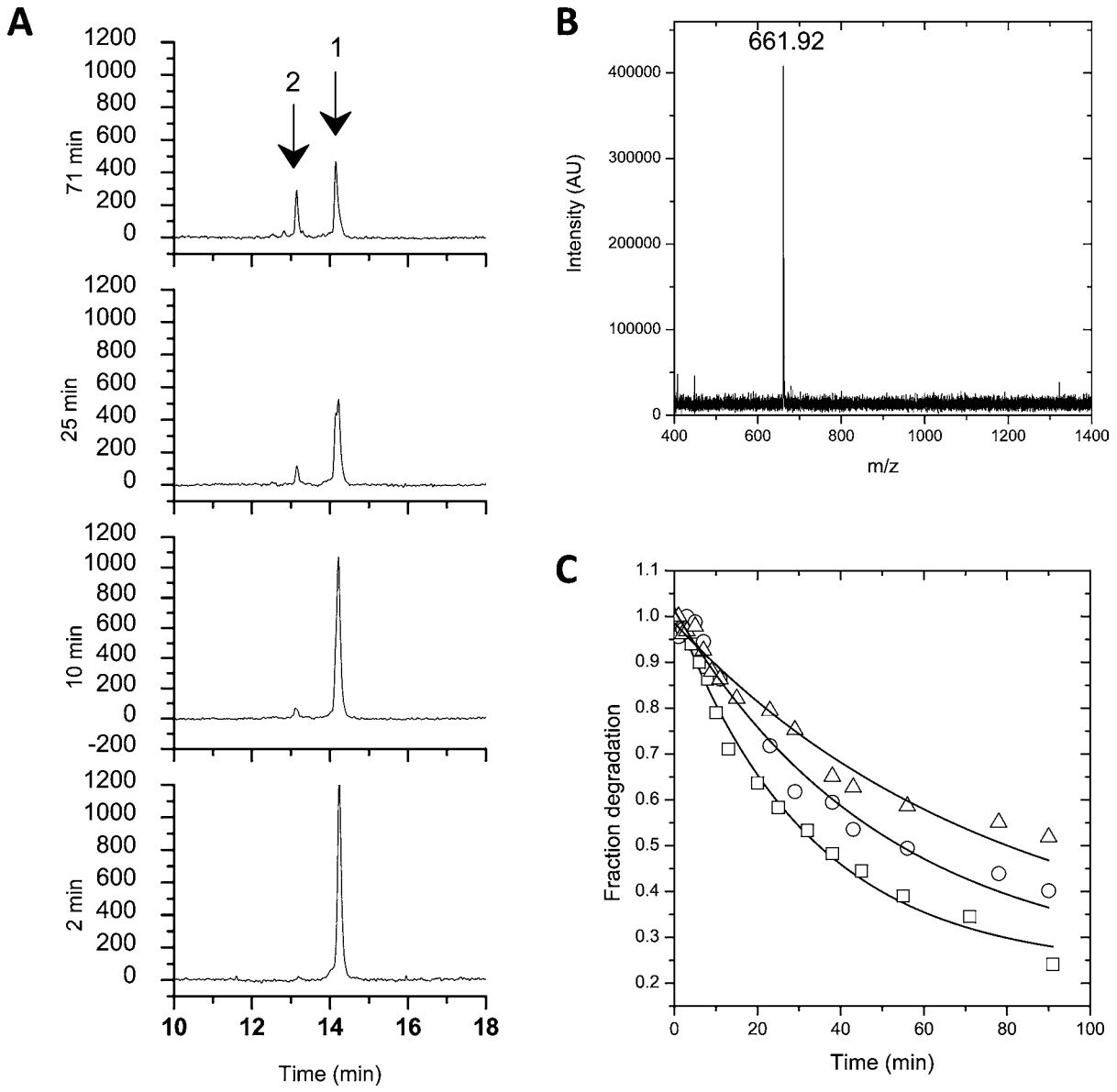


Figure 8. Enzymatic degradation of the wild-type peptide and the PEG-peptide conjugates. (A) Typical analytical reverse-phase HPLC chromatograms of wild-type peptide digests at 2, 10, 25, and 71 min. Peak 1 (retention time = 14.2 min) is the main peak that corresponds to the intact peptide and peak 2 (retention time = 13.1 min) refers to the fragment WASLW-NH_2. (B) The ESI mass spectrum of the isolated fragment peak 2. (C) Comparison of main peak areas as a function of time for the wild-type peptide (squares), S15C-PEG750 (circles), and S15C-PEG2000 conjugates (triangles).

■ CONCLUSIONS

This contribution has investigated the PEGylation of HIV-1 fusion inhibitors derived from the HR2 domain of the HIV-1 gp41 envelope glycoprotein. The specific aim of this study was to systematically investigate the influence of the site of PEGylation and PEG molecular weight on the biological activity and proteolytic stability of these peptides. The results of this study demonstrate that judicious choice of the site of conjugation enables access to PEGylated HR2 derivatives with only slightly reduced fusion inhibitory efficacies as compared to the non-PEGylated peptide, but with significantly improved proteolytic stabilities. PEGylation at positions *c* and *f* of the heptad repeat of the HR2 peptide places the PEG chain at the noninteracting surface of this peptide in its helical conformation. CD and analytical ultracentrifugation experiments demonstrated that these PEG-peptides form a six-helix bundle structure in the presence of an equimolar amount of a complementary HR1-derived peptide. Introducing the PEG chain at position *a* of the heptad repeat, which is located at the interacting interface of the helix, however, prevented the formation of the six-helix bundle structure. The fusion inhibition efficacy of the PEG−peptide conjugates was assessed in model cell−cell fusion experiments. Whereas conjugation of PEG2000 at the N- and C-terminus of the peptide resulted in a 7.5- and 29-fold reduction in fusion inhibitory efficacy, respectively, modification along the non-interacting helical surface of the peptide led only to a 3.3−5.8-fold reduction of efficacy as compared to the wild-type peptide. Similarly, conjugation of PEG750 to the N- and C-terminus resulted in a 4.8- and 7.3-fold reduction in efficacy, respectively, whereas side chain PEGylation only led to a 2.7−3.4-fold decrease in the fusion inhibitory efficacy. At the same time, however,

dx.doi.org/10.1021/bc3002248 | *Bioconjugate Chem.* 2012, 23, 1648−1660

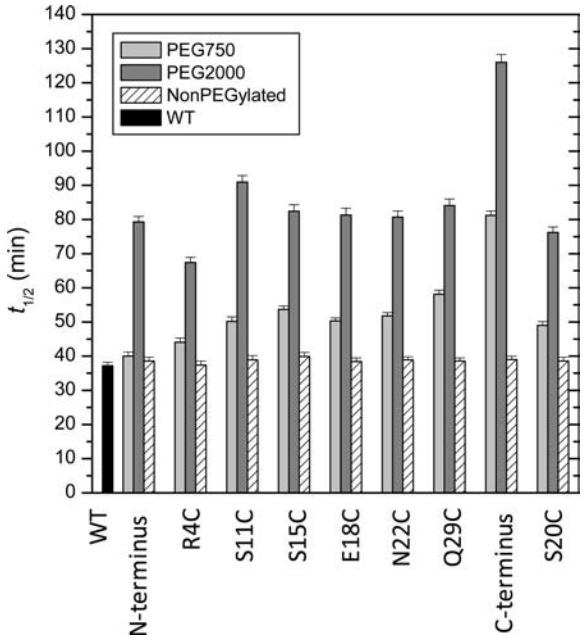


Figure 9. Comparison of the trypsin degradation half-lives of the wild-type peptide, the cysteine-modified variants, and the PEG−peptide conjugates. The error bars represent the error from the nonlinear fitting procedure.

modification of the peptides with PEG2000 led to a 1.8−3.4-fold increase in the trypsin degradation half-life. The results of this study emphasize the potential of site-specific PEGylation to modify therapeutic peptides and proteins and improve their stability, while minimizing adverse effects on bioactivity.

■ ASSOCIATED CONTENT

Ⓢ Supporting Information

Additional ^{1}H NMR and MALDI-ToF mass spectra of the PEG-acrylates and PEG-peptide conjugates, as well as analytical ultracentrifugation and cell−cell fusion inhibition micrographs and data. This material is available free of charge via the Internet at http://pubs.acs.org.

■ AUTHOR INFORMATION

Corresponding Author

*E-mail Address: Harm-Anton.Klok@epfl.ch.

Notes

The authors declare no competing financial interest.

■ ACKNOWLEDGMENTS

This work was supported by the European Commission, FP6 project 'NanoBioPharmaceutics' (NMP4-CT-2006-026723).

■ REFERENCES

(1) Cohen, J. (2007) New estimates scale back scope of HIV/AIDS epidemic. *Science 318*, 1360−1361.
(2) Mehellou, Y., and De Clercq, E. (2010) Twenty-six years of anti-HIV drug discovery: Where do we stand and where do we go? *J. Med. Chem. 53*, 521−538.
(3) Wild, C., Greenwell, T., and Matthews, T. (1993) A synthetic peptide from HIV-1 gp41 is a potent inhibitor of virus-mediated cell-cell fusion. *AIDS Res. Hum. Retroviruses 9*, 1051−1053.
(4) De Clercq, E. (2009) Anti-HIV drugs: 25 compounds approved within 25 years after the discovery of HIV. *Int. J. Antimicrob. Agents 33*, 307−320.
(5) Eggink, D., Berkhout, B., and Sanders, R. W. (2010) Inhibition of HIV-1 by fusion inhibitors. *Curr. Pharm. Des. 16*, 3716−3728.
(6) Fuzeon Product Information, http://www.fuzeon.com.
(7) Veronese, F. M. (2001) Peptide and protein PEGylation: A review of problems and solutions. *Biomaterials 22*, 405−417.
(8) Caliceti, P., and Veronese, F. M. (2003) Pharmacokinetic and biodistribution properties of poly(ethylene glycol)-protein conjugates. *Adv. Drug Delivery Rev. 55*, 1261−1277.
(9) Pasut, G., and Veronese, F. M. (2007) Polymer-drug conjugation, recent achievements and general strategies. *Prog. Polym. Sci. (Oxford, U.K.) 32*, 933−961.
(10) Klok, H.-A. (2009) Peptide/protein - synthetic polymer conjugates - Quo vadis. *Macromolecules 42*, 7990−8000.
(11) Caliceti, P., Salmaso, S., Walker, G., and Bernkop-Schnurch, A. (2004) Development and in vivo evaluation of an oral insulin-PEG delivery system. *Eur. J. Pharm. Sci. 22*, 315−323.
(12) Bailon, P., Palleroni, A., Schaffer, C. A., Spence, C. L., Fung, W. J., Porter, J. E., Ehrlich, G. K., Pan, W., Xu, Z. X., Modi, M. W., Farid, A., and Berthold, W. (2001) Rational design of a potent, long-lasting form of interferon: A 40 kDa branched polyethylene glycol-conjugated interferon α-2a for the treatment of hepatitis C. *Bioconjugate Chem. 12*, 195−202.
(13) Kochendoerfer, G. G., Chen, S. Y., Mao, F., Cressman, S., Traviglia, S., Shao, H., Hunter, C. L., Low, D. W., Cagle, E. N., Carnevali, M., Gueriguian, V., Keogh, P. J., Porter, H., Stratton, S. M., Con Wiedeke, M., Wilken, J., Tang, J., Levy, J. J., Miranda, L. P., Crnogorac, M. M., Kalbag, S., Botti, P., Schindler-Horvat, J., Savatski, L., Adamson, J. W., Kung, A., Kent, S. B. H., and Bradburne, J. A. (2003) Design and chemical synthesis of a homogeneous polymer-modified erythropoiesis protein. *Science 299*, 884−887.
(14) Roberts, M. J., Bentley, M. D., and Harris, J. M. (2002) Chemistry for peptide and protein PEGylation. *Adv. Drug Delivery Rev. 54*, 459−476.
(15) Gauthier, M. A., and Klok, H.-A. (2008) Peptide/protein-polymer conjugates: Synthetic strategies and design concepts. *Chem. Commun.*, 2591−2611.
(16) Bailon, P., and Won, C. Y. (2009) PEG-modified biopharmaceuticals. *Expert Opin. Drug Delivery 6*, 1−16.
(17) Doherty, D. H., Rosendahl, M. S., Smith, D. J., Hughes, J. M., Chlipala, E. A., and Cox, G. N. (2005) Site-specific PEGylation of engineered cysteine analogues of recombinant human granulocyte-macrophage colony-stimulating factor. *Bioconjugate Chem. 16*, 1291−1298.
(18) Salhanick, A. I., Clairmont, K. B., Buckholz, T. M., Pellegrino, C. M., Ha, S., and Lumb, K. J. (2005) Contribution of site-specific PEGylation to the dipeptidyl peptidase IV stability of glucose-dependent insulinotropic polypeptide. *Bioorg. Med. Chem. Lett. 15*, 4114−4117.
(19) Yamamoto, Y., Tsutsumi, Y., Yoshioka, Y., Nishibata, T., Kobayashi, K., Okamoto, T., Mukai, Y., Shimizu, T., Nakagawa, S., Nagata, S., and Mayumi, T. (2003) Site-specific pegylation of a lysine-deficient TNF-α with full bioactivity. *Nat. Biotechnol. 21*, 546−552.
(20) Welch, B. D., VanDemark, A. P., Heroux, A., Hill, C. P., and Kay, M. S. (2007) Potent D-peptide inhibitors of HIV-1 entry. *Proc. Natl. Acad. Sci. U.S.A. 104*, 16828−16833.
(21) Bailon, P. S., and Won, C.-Y. (2004) PEGylated T20 Polypeptide. WO/2004/013164.
(22) Bailon, P. S., and Won, C.-Y. (2004) PEGylated T1249 Polypeptide. WO/2004/013165.
(23) Stoddart, C. A., Nault, G., Galkina, S. A., Thibaudeau, K., Bakis, P., Bousquet-Gagnon, N., Robitaille, M., Bellomo, M., Paradis, V., Liscourt, P., Lobach, A., Rivard, M. È., Ptak, R. G., Mankowski, M. K., Bridon, D., and Quraishi, O. (2008) Albumin-conjugated C34 peptide HIV-1 fusion inhibitor: Equipotent to C34 and T-20 in vitro with sustained activity in SCID-HU THY/LIV mice. *J. Biol. Chem. 283*, 34045−34052.
(24) Huet, T., Kerbarh, O., Schols, D., Clayette, P., Gauchet, C., Dubreucq, G., Vincent, L., Bompais, H., Mazinghien, R., Querolle, O., Salvador, A., Lemoine, J., Lucidi, B., Balzarini, J., and Petitou, M.

(2010) Long-lasting enfuvirtide carrier pentasaccharide conjugates with potent anti-human immunodeficiency virus type 1 activity. *Antimicrob. Agents Chemother. 54*, 134−142.
(25) Weiss, C. D., and White, J. M. (1993) Characterization of stable Chinese hamster ovary cells expressing wild- type, secreted, and glycosylphosphatidylinositol-anchored human immunodeficiency virus type 1 envelope glycoprotein. *J. Virol. 67*, 7060−7066.
(26) Palasek, S. A., Cox, Z. J., and Collins, J. M. (2007) Limiting racemization and aspartimide formation in microwave-enhanced Fmoc solid phase peptide synthesis. *J. Pept. Sci. 13*, 143−148.
(27) Pace, C. N., Vajdos, F., Fee, L., Grimsley, G., and Gray, T. (1995) How to measure and predict the molar absorption coefficient of a protein. *Protein Sci. 4*, 2411−2423.
(28) Chen, Y. H., Yang, J. T., and Chau, K. H. (1974) Determination of the helix and β form of proteins in aqueous solution by circular dichroism. *Biochemistry 13*, 3350−3359.
(29) http://www.jphilo.mailway.com/download.htm.
(30) http://www.analyticalultracentrifugation.com/sedphat/sedphat.htm.
(31) Dwyer, J. J., Hasan, A., Wilson, K. L., White, J. M., Matthews, T. J., and Delmedico, M. K. (2003) The hydrophobic pocket contributes to the structural stability of the N-terminal coiled coil of HIV gp41 but is not required for six-helix bundle formation. *Biochemistry 42*, 4945−4953.
(32) Muñoz-Barroso, I., Durell, S., Sakaguchi, K., Appella, E., and Blumenthal, R. (1998) Dilation of the human immunodeficiency virus-1 envelope glycoprotein fusion pore revealed by the inhibitory action of a synthetic peptide from gp41. *J. Cell Biol. 140*, 315−323.
(33) http://rsbweb.nih.gov/ij/.
(34) Gallo, S. A., Finnegan, C. M., Viard, M., Raviv, Y., Dimitrov, A., Rawat, S. S., Puri, A., Durell, S., and Blumenthal, R. (2003) The HIV Env-mediated fusion reaction. *Biochim. Biophys. Acta 1614*, 36−50.
(35) Chan, D. C., and Kim, P. S. (1998) HIV entry and its inhibition. *Cell 93*, 681−684.
(36) Lu, M., Blacklow, S. C., and Kim, P. S. (1995) A trimeric structural domain of the HIV-1 transmembrane glycoprotein. *Nat. Struct. Biol. 2*, 1075−1082.
(37) Bianchi, E., Finotto, M., Ingallinella, P., Hrin, R., Carella, A. V., Hou, X. S., Schleif, W. A., Miller, M. D., Geleziunas, R., and Pessi, A. (2005) Covalent stabilization of coiled coils of the HIV gp41 N region yields extremely potent and broad inhibitors of viral infection. *Proc. Natl. Acad. Sci. U.S.A. 102*, 12903−12908.
(38) Eggink, D., Langedijk, J. P. M., Bonvin, A. M. J. J., Deng, Y., Lu, M., Berkhout, B., and Sanders, R. W. (2009) Detailed mechanistic insights into HIV-1 sensitivity to three generations of fusion inhibitors. *J. Biol. Chem. 284*, 26941−26950.
(39) Weissenhorn, W., Dessen, A., Harrison, S. C., Skehel, J. J., and Wiley, D. C. (1997) Atomic structure of the ectodomain from HIV-1 gp41. *Nature 387*, 426−430.
(40) Chan, D. C., Chutkowski, C. T., and Kim, P. S. (1998) Evidence that a prominent cavity in the coiled coil of HIV type 1 gp41 is an attractive drug target. *Proc. Natl. Acad. Sci. U.S.A. 95*, 15613−15617.
(41) Smith, S. D., Morgan, R., and Link, M. P. (1986) Cytogenetic and immunophenotypic analysis of cell lines established from patients with T cell leukemia/lymphoma. *Blood 67*, 650−656.
(42) Buzon, V., Natrajan, G., Schibli, D., Campelo, F., Kozlov, M. M., and Weissenhorn, W. (2010) Crystal structure of HIV-1 gp41 including both fusion peptide and membrane proximal external regions. *PLoS Pathog. 6*, e1000880.
(43) Rosendahl, M. S., Doherty, D. H., Smith, D. J., Carlson, S. J., Chlipala, E. A., and Cox, G. N. (2005) A long-acting, highly potent interferon α-2 conjugate created using site-specific PEGylation. *Bioconjugate Chem. 16*, 200−207.
(44) http://www.sigmaaldrich.com/life-science/metabolomics/enzyme-explorer/analytical-enzymes/trypsin.html.

Bioconjugate Chemistry

Article

pubs.acs.org/bc

Influence of DOTA Chelator Position on Biodistribution and Targeting Properties of ^{111}In-Labeled Synthetic Anti-HER2 Affibody Molecules

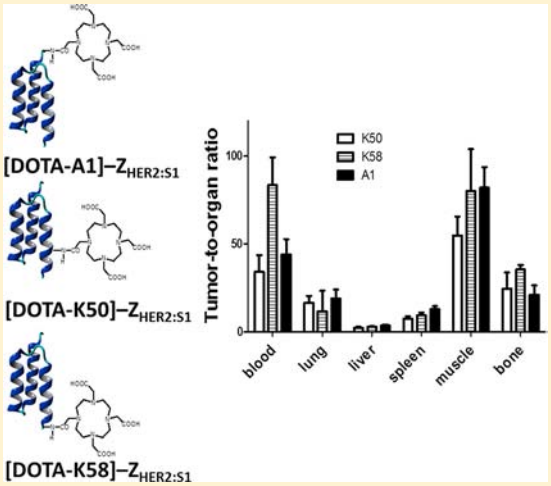
Anna Perols,[†] Hadis Honarvar,[‡] Joanna Strand,[‡] Ramkumar Selvaraju,[§] Anna Orlova,[§] Amelie Eriksson Karlström,[†] and Vladimir Tolmachev[‡,*]

[†]Division of Molecular Biotechnology, School of Biotechnology, KTH Royal Institute of Technology, Stockholm, Sweden

[‡]Unit of Biomedical Radiation Sciences, Rudbeck Laboratory, and [§]Preclinical PET Platform, Department of Medicinal Chemistry, Uppsala University, Sweden

Supporting Information

ABSTRACT: Affibody molecules are a class of affinity proteins. Their small size (7 kDa) in combination with the high (subnanomolar) affinity for a number of cancer-associated molecular targets makes them suitable for molecular imaging. Earlier studies demonstrated that the selection of radionuclide and chelator may substantially influence the tumor-targeting properties of affibody molecules. Moreover, the placement of chelators for labeling of affibody molecules with ^{99m}Tc at different positions in affibody molecules influenced both blood clearance rate and uptake in healthy tissues. This introduces an opportunity to improve the contrast of affibody-mediated imaging. In this comparative study, 1,4,7,10-tetraazacyclododecane-1,4,7,10-tetraacetic acid (DOTA) was conjugated to the synthetic affibody molecule $Z_{HER2:S1}$ at three different positions: DOTA-A1-$Z_{HER2:S1}$ (N-terminus), DOTA-K58-$Z_{HER2:S1}$ (C-terminus), and DOTA-K50-$Z_{HER2:S1}$ (middle of helix 3). The affinity for HER2 differed slightly among the variants and the K_D values were determined to be 133 pM, 107 pM and 94 pM for DOTA-A1-$Z_{HER2:S1}$, DOTA-K50-$Z_{HER2:S1}$, and DOTA-K58-$Z_{HER2:S1}$, respectively. $Z_{HER2:S1}$-K50-DOTA showed a slightly lower melting point (57 °C) compared to DOTA-A1-$Z_{HER2:S1}$ (64 °C) and DOTA-K58-$Z_{HER2:S1}$ (62 °C), but all variants showed good refolding properties after heat treatment. All conjugates were successfully labeled with ^{111}In resulting in a radiochemical yield of 99% with preserved binding capacity. In vitro specificity studies using SKOV-3 and LS174T cell lines showed that the binding of the radiolabeled compounds was HER2 receptor-mediated, which also was verified in vivo using BALB/C nu/nu mice with LS174T and Ramos lymphoma xenografts. The three conjugates all showed specific uptake in LS174T xenografts in nude mice, where DOTA-A1-$Z_{HER2:S1}$and DOTA-K58-$Z_{HER2:S1}$ showed the highest uptake. Overall, DOTA-K58-$Z_{HER2:S1}$ provided the highest tumor-to-blood ratio, which is important for a high-contrast imaging. In conclusion, the positioning of the DOTA chelator influences the cellular processing and the biodistribution pattern of radiolabeled affibody molecules, creating preconditions for imaging optimization.



INTRODUCTION

Human epidermal growth receptor type 2 (HER2) is a transmembrane protein which belongs to the ErbB family of receptor tyrosine kinases together with EGFR (HER1), HER3, and HER4. HER2 signaling occurs mainly by dimerization, either with other members of the HER family (heterodimerization) or at high expression levels with HER2 itself (homodimerization). Within the ErbB family, HER2 is the only receptor not having a known ligand.[1] The receptor constitutively adopts an active-like conformation prearranged for dimerization, making HER2 the preferred dimerization partner among the HER family members.[2] Amplified signaling due to overexpression of HER2 causes cell proliferation and suppression of apoptosis, providing a growth advantage to the malignant cells.[3] This overexpression of HER2 is a well-known biomarker in breast cancer[4,5] and is linked to poor prognosis.[6] It is also linked to other types of cancer such as prostate,[7,8] ovarian,[9] and colorectal cancer.[10] As a result of this association with the malignant behavior of cancer, HER2 has become an interesting target, both for development of HER2-targeting therapeutics and for specific diagnosis. Among the therapeutics directed to HER2-expressing tumors, the best known example is the HER2-binding antibody trastuzumab (Herceptin), which

Received: April 28, 2012
Revised: July 4, 2012
Published: July 8, 2012

 © 2012 American Chemical Society

has shown improved survival of treated patients in combination with first-line chemotherapy.[11]

Patient stratification using noninvasive methods for detection of molecular targets is a promising way to predict a therapeutic outcome and reduce unnecessary toxicities.[12] For example, therapies using the monoclonal antibody trastuzumab or the tyrosine kinase inhibitor lapatinib are both targeting HER2-expressing breast cancer; however, only 20% of breast cancer patients have HER2-overexpressing tumors.[4] Molecular imaging is a promising noninvasive method for investigating the expression of specific tumor-associated molecular therapeutic targets, such as HER2, EGFR, or variants of VEGFR.[13] This approach provides information about the molecular and functional properties of a tumor, in contrast to CT or MRI that give anatomical information. In addition, molecular imaging has a substantial advantage over biopsy-based methods, since it allows for repetitive evaluation for monitoring treatment response. Furthermore, the problems with tumor heterogeneity associated with analysis of biopsies can be avoided.[13] Radiolabeled antibodies targeting HER2 have been used for imaging of HER2-positive tumors.[13] However, the antibodies provide low imaging contrast and are suboptimal imaging agents due to limitations caused by the long circulation time, slow clearance from healthy tissues, and low tumor penetration rate.

An alternative to antibodies is smaller affinity proteins, which can be engineered for high affinity. Affibody molecules is a class of affinity proteins, which is derived from the immunoglobulin-binding protein A of *Staphylococcus aureus*.[15] The protein comprises 58 amino acids, which form a triple-helical bundle, with no internal disulfide bonds. Thirteen amino acids on helices 1 and 2 have been randomized for selection of new affinity binders, for example, targeting HER2, EGFR, HER3, IGF1R, or PDGFR beta.[14,16] The affibody molecule $Z_{HER2:342}$, with high affinity to the extracellular part of HER2 (K_D = 22 pM), has been generated by affinity maturation of a selected binder.[17] Because of the small size, it is possible to produce Affibody molecules by chemical synthesis, which enables site-specific introduction of functional groups using orthogonal protection strategies.[18] The small size, in combination with the high affinity, is a great advantage when using Affibody molecules for in vivo molecular imaging. Affibody molecules show faster clearance and better tissue penetration, which resulted in superior imaging contrast for the Affibody molecules when evaluated side-by-side to other HER2-imaging agents.[19,20]

Affibody molecules have successfully been labeled with different radionuclides.[21] It has been demonstrated in previous studies that labeling-associated modifications of the affibody molecule, such as modification of local charge or lipophilicity due to chelator incorporation, could alter the biodistribution pattern. For example, labeling with ^{99m}Tc using peptide-based chelators has shown that even single substitution of the chelating amino acids can alter the biodistribution pattern and shift the excretion from hepatobiliary to renal.[22] Differences in biodistribution of $[^{99m}Tc(CO)_3]^+$-labeled affibody molecules were also seen when the chelating hexahistidine moiety was transferred from the N-terminus to the C-terminus of the protein.[23] During the development of site-specific labeling for recombinant anti-HER2 affibody molecules, Ahlgren and co-workers have conjugated maleimido derivatives of DOTA chelator (MMA-DOTA) to a derivative of $Z_{HER2:342}$ having a C-terminal cysteine, $Z_{HER2:2395}$-C.[24] The targeting properties of the ^{111}In-[MMA-DOTA-C61]-$Z_{HER2:2395}$ affibody molecule were compared with the best available affibody-based imaging tracer, synthetic ^{111}In-DOTA-$Z_{HER2:342}$ having DOTA conjugated to N-terminal valine. Although the biodistribution profiles of both variants were similar, difference in organ uptake resulted in significant difference in tumor-to-spleen, tumor-to-colon, tumor-to-kidney, and tumor-to-bone ratios.[24] This indicated that the placement of the DOTA chelator in different positions on the affibody molecule could influence the biodistribution and targeting properties, which might be a way to maximize the tumor-to-organ ratios for this imaging agent. However, the constructs evaluated by Ahlgren and co-workers[24] differed in the production routes, in the chelator conjugation chemistry, and in the sequences of affibody proteins (six different amino acids). It was thus impossible to distinguish the influence of these factors from the influence of the chelator position.

To verify the hypothesis that DOTA positioning can be used for modification of targeting properties, a panel of derivatives of the HER2-binding affibody molecule has been synthesized. In the present study, DOTA was conjugated to position A1 (the N-terminus), position K58 (the C-terminus), or position K50 (located in the middle of helix 3) via amide bond. Thus, the proteins in the panel had the same sequence and were conjugated to the chelator in the same way. The binding, biodistribution, and targeting properties of these synthetic affibody molecules were evaluated.

MATERIALS AND METHODS

Material. Buffers, including 0.1 M phosphate buffered saline (PBS), pH 7.5, 0.2 M ammonium acetate, pH 5.5, and 0.2 M citric acid were prepared using common methods from chemicals supplied by Merck (Darmstadt, Germany). High-quality Milli-Q water (resistance higher than 18 MΩ cm) was used for preparing the solutions. Buffers, which were used for labeling, were purified from metal contamination using Chelex 100 resin (Bio-Rad Laboratories, Richmond, USA). [^{111}In]-indium chloride was purchased from Covidien (Hazelwood, U.S.) as a solution in 0.05 M hydrochloric acid. The yield and radiochemical purity of the labeled affibody constructs were analyzed using 150−771 Dark Green, Tec-Control Chromatography strips from Biodex Medical Systems (New York, U.S.). The accuracy of radio-ITLC analysis was cross-validated by SDS-PAGE. Ketalar [ketamine] (50 mg/mL, Pfizer, NY, USA), Rompun [xylazin] (20 mg/mL, Bayer, Leverkusen, Germany), and Heparin (5000 IE/mL, Leo Pharma, Copenhagen, Denmark) were obtained commercially.

Data on cellular uptake and biodistribution were analyzed by unpaired, two-tailed *t*-test using *GraphPad Prism* (v 4.00 for Windows GraphPad Software, San Diego, U.S.) in order to determine any significant differences ($P < 0.05$).

Synthesis of DOTA-Conjugated Affibody Molecules. A synthetic variant of the $Z_{HER2:342}$ affibody molecule, denoted $Z_{HER2:S1}$, with the sequence AEAKYAKEMRNAY-WEIALLPNLNNQQKRAFIRSLYDDPSQSANLLAEAKKLN-DAQAPK-amide was assembled on a 433A Peptide Synthesizer (Applied Biosystems, Foster City, CA) using Fmoc/tBu-chemistry in 0.1 mmol scale and Fmoc-rink amide resin with a substitution level of 0.39 mmol/g. Preparation of DOTA-A1-$Z_{HER2:S1}$ (PEP10415), has been described earlier.[25] Briefly, the chelator DOTA was conjugated to the deprotected N-terminus of $Z_{HER2:S1}$, prior to cleavage from solid support. For preparation of DOTA-K50-$Z_{HER2:S1}$ (PEP11301) and DOTA-K58-$Z_{HER2:S1}$ (PEP11302), an acid-labile side chain protecting

dx.doi.org/10.1021/bc3002369 | *Bioconjugate Chem.* 2012, 23, 1661−1670

group, the 4-methyltrityl (Mtt) group, was used for protection of either Lys^{50} or Lys^{58}. The Mtt group was removed by TFA/triisopropylsilane/DCM (1:5:94) treatment for 10 × 2 min. *tert*-Butyl-protected monoreactive DOTA chelator was manually conjugated to the free ε-amino group of lysine using DOTA (5 equiv), 2-(1*H*-7-azabenzotriazol-1-yl)-1,1,3,3-tetramethyluronium hexafluorophosphate (HATU) (5 equiv) and diisopropylethylamine (DIEA) (5 equiv) in NMP at RT overnight, which was repeated until the Ninhydrin test indicated complete conjugation. Removal of side-chain protecting groups and cleavage of the protein from the resin were performed in a single-step treatment for 3 h with TFA/triisopropylsilane/H_2O (95:2.5:2.5) for all variants. Proteins were extracted in *tert*-butyl methyl ether/water (50:50) three times before the water phase was filtered and lyophilized.

Purification and Characterization of DOTA-Conjugated Affibody Molecules. The crude synthetic product was analyzed using RP-HPLC (1200 series, Agilent). For purification, a semipreparative column, Reprosil Gold 10 × 250 mm, 5 μm particle size (Dr Maisch, Ammerbuch, Germany) was used with a flow rate of 3.5 mL/min and a gradient of 25−45% B (A: 0.1% TFA/H_2O and B: 0.1%TFA/CH_3CN) over 25 min. Purity analysis was performed with an analytical column, Zorbax CB300-C18 4.6 × 150 mm, 3.5 μm particle size (Agilent), with a flow rate of 1 min/mL using the same gradient as above. Verification of the correct products was performed by ESI-Q-TOF MS (Agilent).

Variable temperature measurements (VTM) were performed using a JASCO-810 instrument (Jasco, Tokyo, Japan), in order to determine the melting points for the variants. The DOTA-conjugated Affibody molecules were diluted to 0.5 mg/mL in 1 × PBS (pH 7.2) and analyzed in 1 mm quartz cuvette, with the temperature increased by 5 °C/min from 20 to 90 °C and detection at 221 nm. To verify proper refolding after heat treatment, circular dichroism spectra, ranging from 195 to 250 nm, were recorded before and after VTM and presented as the mean value of five accumulated scans.

For affinity determination of the DOTA-conjugated proteins, real-time biosensor analysis was performed on a Biacore 3000 instrument (GE Healthcare). The recombinant human extracellular domain of HER2 expressed as an Fc-fusion was diluted to 5 μg/mL in 10 mM NaOAc (pH 4.5), and immobilized on a dextran-coated CM5-chip. NHS/EDC were used for activation and after immobilization, unreacted groups were capped using ethanolamine. For reference, one flow cell was activated and deactivated without ligand immobilization. Pure conjugates were diluted in HBS-EP (10 mM HEPES, 150 mM NaCl, 3.4 mM EDTA, 0.05% Tween20, pH 7.2) to concentrations ranging from 0.31 nM to 10 nM and analyzed in duplicate. The concentrations of the proteins were determined by amino acid analysis (Amino Acid Analysis Centre, Uppsala, Sweden). The samples were allowed to interact with the sensor surface during a 5 min association phase followed by a dissociation phase of 10 min, before injection of a short pulse of 25 mM HCl to regenerate the surface. The *BIAevaluation 4.1* software was used for the kinetic analysis with a 1:1 Langmuir binding model.

Radiolabeling Chemistry and in Vitro Stability. The radioactivity was measured using an automated gamma-counter with a 3 in. NaI(Tl) detector (1480 WIZARD, Wallac OY, Turku, Finland). The data were corrected for background.

Before labeling, freeze−dried DOTA-A1-$Z_{HER2:S1}$, DOTA-K50-$Z_{HER2:S1}$, and DOTA-K58-$Z_{HER2:S1}$ were reconstituted in 0.2 M ammonium acetate, pH 5.5, to a concentration of 1 mg/mL. Aliquots containing 50 μg of each conjugate were stored frozen at −20 °C. For labeling, an aliquot of a conjugate was mixed with predetermined amounts of ^{111}In-chloride solution (ca. 35 MBq at calibration time). The reaction mixtures were incubated at 95 °C. At 10, 20, and 30 min after the start of the incubation, small aliquots (1.4 μL) of reaction mixtures were taken and analyzed by radio-ITLC eluted with 0.2 M citric acid and radiochemical purity was evaluated. In this system, labeled compounds remain at the application point, while free ^{111}In or ^{111}In-chelate migrates with the solvent front. To cross-validate the ITLC results, an SDS-PAGE analysis on 4−12% bis-tris gel (200 V constant) was performed. To evaluate stability of labeling, the ^{111}In-labeled conjugates were incubated with 500-fold excess of EDTA for 4 h at room temperature and then analyzed using ITLC.

Distribution of radioactivity along the thin layer chromatography strips and SDS-PAGE gels was measured on a Cyclotrone Storage Phosphor System and analyzed using the OptiQuant image analysis software (Perkin-Elmer, Wellesley, MA, USA).

In Vitro Studies. For cell studies, the HER2-expressing ovarian carcinoma SKOV-3, 1.6×10^6 HER2 receptors per cell, and colorectal carcinoma LS174T, 4×10^4 HER2 receptors per cell, cell lines (ATCC, purchased via LGC Promochem, Borås, Sweden) were used. The cell lines were cultured in RPMI medium (Flow Irvine, U.K.) supplemented with 10% fetal calf serum (Sigma, USA), 2 mM L-glutamine, and PEST (penicillin 100 IU/mL and 100 μg/mL streptomycin), all from Biokrom kg, Germany.

In vitro specificity test was performed according to the methods described earlier.[26] Briefly, a solution of ^{111}In-[DOTA-K50]-$Z_{HER2:S1}$ and ^{111}In-[DOTA-K58]-$Z_{HER2:S1}$ (1.99 ng/dish, 27 pM) was added to a set of six Petri dishes (ca. 5×10^5 cells in each). For blocking, an excess of nonlabeled recombinant $Z_{HER2:342}$ (1.99 μg/dish) was added 5 min before ^{111}In-labeled conjugates to saturate the receptors. The cells were incubated during one hour in a humidified incubator at 37 °C. Thereafter, the media was collected, the cells were detached by trypsin-EDTA solution (0.25% trypsin, 0.02% EDTA in buffer, Biochrom AG, Berlin, Germany), and the radioactivity in cells and media was measured to calculate percentage of cell-bound radioactivity.

A comparison of ^{111}In-[DOTA-A1]-$Z_{HER2:S1}$, ^{111}In-[DOTA-K50]-$Z_{HER2:S1}$, and ^{111}In-[DOTA-K58]-$Z_{HER2:S1}$ processing by SKOV-3 and LS174T cells was performed according to the method developed and validated by Wållberg and Orlova.[26] The cells (ca. 5×10^5 per dish) were incubated with the labeled compounds (1.99 ng/dish, 27 pM) at 37 °C, 5% CO_2. At predetermined time points (0.5, 1, 2, 3, 4, 8, and 24 h after incubation start), the medium from a set of three dishes was removed and the cells were washed with ice-cold serum-free medium. The cells were then treated with 0.5 mL 0.2 M glycine buffer containing 4 M urea, pH 2.5, for 5 min on ice. The acidic solution was collected, and the cells were washed additionally with 0.5 mL glycine buffer, which was collected and pooled with the first fraction. The radioactivity in the acid wash fractions was considered membrane-bound radioactivity. After addition of 0.5 mL 1 M NaOH, cells were incubated at 37 °C for 0.5 h before the alkali containing cell debris was collected. The cell dishes were washed with an additional 0.5 mL NaOH and the alkaline fractions were pooled. The radioactivity in the alkaline fractions was considered internalized. Percent of

Table 1. Biophysical Characterization of the DOTA Conjugates

variant	purity	theor. M_w (Da)	exp. M_w (Da)	k_a ($M^{-1}\cdot s^{-1}$)	k_d (s^{-1})	K_D (pM)	T_m (°C)
DOTA-A1-$Z_{HER2:S1}$	98%	7006.9	7007.1	4.8×10^6	6.4×10^{-4}	133	64
DOTA-K50-$Z_{HER2:S1}$	97%	7006.9	7007.3	7.2×10^6	7.7×10^{-4}	107	57
DOTA-K58-$Z_{HER2:S1}$	97%	7006.9	7007.0	7.9×10^6	7.4×10^{-4}	94	62

internalized radioactivity was calculated for each fraction at each time point.

In Vivo Studies. The animal experiments were planned and performed in accordance with the national regulation on laboratory animal protection. The animal study plans have been approved by the local Ethics Committee for Animal Research in Uppsala. BALB/C nu/nu mice bearing LS174T colorectal cancer and Ramos lymphoma (as a HER2-negative control) xenografts were used for comparative biodistribution studies. The mice were kept using standard sterile diet, bedding, and environment with free access to food and water. The mice were acclimatized for one week at the Rudbeck Laboratory animal facility before any experimental procedures. For tumor implantation, 5×10^6 LS174T or Ramos lymphoma cells in Matrigel (BD Bioscience) were implanted in right hind legs. Average tumor weight was 0.54 ± 0.36 g at the time of experiment. Average animal weight was 18.6 ± 0.9 g. The mice were randomized into groups of four. Animals were injected intravenously (tail vein) with 1 μg (30 kBq) of each labeled compound in 100 μL PBS. At four hours after injection, a mixture of Ketalar-Rompun (20 μL of solution per gram body weight; Ketalar: 10 mg/mL; Rompun: 1 mg/mL) was injected intraperitonealy, and the mice were euthanized by a heart puncture using a syringe, prewashed with diluted heparin (5000 IE/mL). Blood and lung, liver, spleen, kidneys, tumor, samples of muscle and bone, gastrointestinal tract (with its content), and remaining carcass were collected in preweighed plastic vials. Organs and tissue samples were weighed and measured for radioactivity using an automatic gamma counter. The tissue uptake values were calculated as percent injected activity per gram tissue (% ID/g), except for the gastrointestinal tract and the carcass, which were calculated as % ID per whole sample. The radioactivity in the gastrointestinal tract with its content was used as a measure of hepatobiliary excretion.

A set of additional animal studies with a different xenograft model were performed for the conjugate with the best properties, ^{111}In-[DOTA-K58]-$Z_{HER2:S1}$, to confirm its tumor-targeting and imaging capacity. For the biodistribution measurement, 10×10^6 SKOV-3 ovarian carcinoma cells were implanted in right hind legs of BALB/C nu/nu mice. Average tumor weight was 0.30 ± 0.11 g at the time of experiment, and the average animal weight was 18.1 ± 0.6 g. A group of four mice was injected intravenously (tail vein) with 1 μg (30 kBq) ^{111}In-[DOTA-K58]-$Z_{HER2:S1}$ in 100 μL PBS, and the biodistribution of the radioactivity was measured as described above.

One mouse was injected with 3 μg (5 MBq) ^{111}In-[DOTA-K58]-$Z_{HER2:S1}$. At four hours after injection, the animal was euthanized by overdosing of anesthesia, and the cadaver was used in a confirmatory imaging experiment. The SPECT/CT imaging experiment was performed using the Triumph Trimodality system (Gamma Medica, Inc., Northridge, USA), an integrated microSPECT/PET/CT hardware and software platform. A CT acquisition was carried out to place the body of the animal in the camera covering tumor, kidneys, and liver with the following parameters: field of view, 53.82 mm; magnification, 2.2; one projection and 512 frames for 2.13 min. SPECT acquisition was performed using two solid-state cadmium zinc telluride (CZT) cameras equipped with a five-pinhole collimator. The following acquisition parameters were used for SPECT: nongated; tomographic; field of view, 53.82 mm; 32 projections/1000 s. SPECT raw data was reconstructed by the *FLEX SPECT* software, which uses an ordered Subset Expectation Maximization (OSEM) iterative reconstruction algorithm. CT raw files were reconstructed by Filter Back Projection (FBP). SPECT and CT data were fused and analyzed in PMOD (PMOD Technologies Ltd., Zurich, Switzerland). For quantification of uptake, the volumes of interest (VOIs) were defined for tumor and contralateral leg on the CT image, and transferred to the SPECT image.

RESULTS

Design and Synthesis of the DOTA-Conjugated Tracers DOTA-A1-$Z_{HER2:S1}$, DOTA-K50-$Z_{HER2:S1}$, and DOTA-K58-$Z_{HER2:S1}$ Affibody Molecules. Conjugation of the DOTA chelator to the $Z_{HER2:S1}$ affibody molecule via peptide synthesis provided DOTA-A1-$Z_{HER2:S1}$, DOTA-K50-$Z_{HER2:S1}$, and DOTA-K58-$Z_{HER2:S1}$, which could be isolated in a final purity of over 97% (Table 1). The identity of all three variants was confirmed by mass spectrometry. According to the surface plasmon resonance measurements, the equilibrium dissociation constants (K_D) were 133 pM, 107 pM, and 94 pM for DOTA-A1-$Z_{HER2:S1}$, DOTA-K50-$Z_{HER2:S1}$, and DOTA-K58-$Z_{HER2:S1}$, respectively. The melting points for the proteins with DOTA conjugated to either the N- or C-terminus had similar values, 64 and 62 °C, respectively, whereas conjugation of DOTA to the side chain of Lys^{50} had a certain destabilizing effect on the structure, and decreased the thermal stability of the protein to 57 °C. However, CD analysis showed good refolding properties for all variants after heat treatment to 90 °C.

Labeling and Stability of DOTA-Conjugated $Z_{HER2:S1}$ Affibody Molecules with ^{111}In. Radiochemical yield of all three variants was more than 99% (specific radioactivity of 1.5 MBq/μg) after labeling at 95 °C in all incubation time points. The stability of all three labeled compounds was evaluated by challenge with a 500-fold molar excess of EDTA during 4 h, which demonstrated very high labeling stability (release of free ^{111}In of less than 1.5%). The radiochemical purity of the treated samples was 96.7 ± 0.43% (average ± SEM), while the purity of the untreated control was 98.1 ± 0.36%, i.e., the difference was within the accuracy of the analytical method. Results of the analysis were confirmed by radioSDS PAGE analysis (Figure 1).

In Vitro Studies. A binding specificity test showed that there was a significant decrease of binding of labeled compounds to the HER2 receptors after receptor presaturation by incubation with an access of nonlabeled $Z_{HER2:342}$ affibody molecules in both SKOV-3, and LS174T cell lines (Figure 2). This indicates that binding of all labeled compounds was HER2 receptor mediated. The level of cell associated radioactivity was lower for nonblocked LS174T than for SKOV-3 cell line,

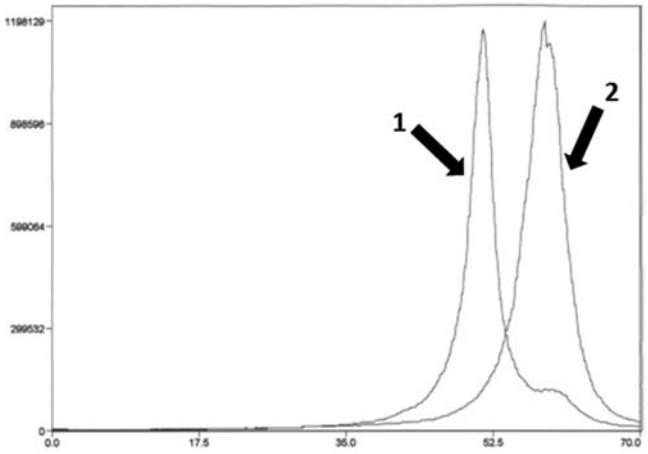


Figure 1. Representative SDS-PAGE analysis of the stability of ^{111}In-labeled Affibody molecules (^{111}In-[DOTA-K58]-$Z_{HER2:S1}$) in serum. (1) ^{111}In-[DOTA-K58]-$Z_{HER2:S1}$ incubated in a 500-fold molar excess of EDTA during 4 h; (2) ^{111}In-acetate used as a marker for low-molecular-weight compounds. The signal was measured as digital light units (DLU) is proportion to radioactivity in a given point of a lane in the SDS-PAGE gel.

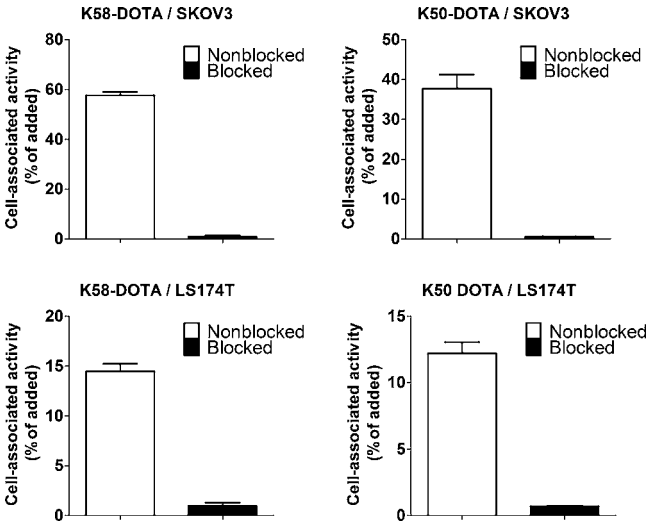


Figure 2. Binding specificity of ^{111}In-[DOTA-K50]-$Z_{HER2:S1}$, and ^{111}In-[DOTA-K58]-$Z_{HER2:S1}$ to HER2 expressing cell lines SKOV3 (upper row) and LS174T (lower row). Two groups of culture dishes containing test cells were incubated with 27 pM of radiolabeled conjugate. One group of culture dishes was pretreated with saturating amounts of nonlabeled $Z_{HER2:342}$. Cell-associated radioactivity was calculated as a percentage of total added radioactivity.

reflecting lower expression level of HER2 receptors. Specificity of ^{111}In-[DOTA-A1]-$Z_{HER2:S1}$ binding to HER2-expressing cells has been established earlier.[25]

The cellular processing of ^{111}In-[DOTA-A1]-$Z_{HER2:S1}$, ^{111}In-[DOTA-K50]-$Z_{HER2:S1}$, and ^{111}In-[DOTA-K58]-$Z_{HER2:S1}$ by HER2-expressing SKOV-3 cells are presented in Figure 3. All labeled compounds demonstrated a similar processing pattern, which is typical for $Z_{HER2:342}$ and its derivatives. Internalization rate of all three labeled compounds was slow, although internalized fractions increased continuously throughout the experiment. There was some variation between conjugates. After 24 h incubation, the internalization rate of ^{111}In-[DOTA-K58]-$Z_{HER2:S1}$ with 43.6 ± 0.3% was slightly higher than that of ^{111}In-[DOTA-A1]-$Z_{HER2:S1}$ and ^{111}In-[DOTA-K50]-$Z_{HER2:S1}$ with 31 ± 1% and 37 ± 4%, respectively.

The cellular processing of ^{111}In-[DOTA-A1]-$Z_{HER2:S1}$, ^{111}In-[DOTA-K50]-$Z_{HER2:S1}$, and ^{111}In-[DOTA-K58]-$Z_{HER2:S1}$ by HER2-expressing LS174T cells (presented in Figure 4) show a similar pattern to SKOV-3 cells. However, cell-associated radioactivity increased with a slower rate at early time points in comparison to that of SKOV-3 cells. After 24 h incubation, 35.7 ± 0.1%, 38.5 ± 1%, and 38.5 ± 1% of the cell-associated radioactivity was internalized for ^{111}In-[DOTA-A1]-$Z_{HER2:S1}$, ^{111}In-[DOTA-K50]-$Z_{HER2:S1}$, and ^{111}In-[DOTA-K58]-$Z_{HER2:S1}$, respectively.

In Vivo Studies. Data concerning targeting specificity of HER2-expressing LS174T xenografts in BALB/C nu/nu mice using ^{111}In-[DOTA-A1]-$Z_{HER2:S1}$, ^{111}In-[DOTA-K50]-$Z_{HER2:S1}$, and ^{111}In-[DOTA-K58]-$Z_{HER2:S1}$ are presented in Figure 5. In order to verify the HER2-specificity of ^{111}In-labeled affibody molecules, their biodistribution at 4 h p.i. was also studied in BALB/C nu/nu mice bearing HER2-negative Ramos lymphoma xenograft (Figure 4). The tumor uptake in HER2-positive xenografts was significantly higher than in HER2-negative, 9.65 ± 1.9 vs 0.17 ± 0.06%ID/g ($p < 0.0005$), 5.53 ± 0.91 vs 0.25 ± 0.02%ID/g ($p < 0.0001$), and 11.77 ± 1.94 vs 0.34 ± 0.06%ID/g ($p < 0.0001$), for ^{111}In-[DOTA-A1]-$Z_{HER2:S1}$, ^{111}In-[DOTA-K50]-$Z_{HER2:S1}$, and ^{111}In-[DOTA-K58]-$Z_{HER2:S1}$, respectively. This demonstrates specificity of HER2 targeting by all conjugates.

Comparison of ^{111}In-[DOTA-A1]-$Z_{HER2:S1}$, ^{111}In-[DOTA-K50]-$Z_{HER2:S1}$, and ^{111}In-[DOTA-K58]-$Z_{HER2:S1}$ biodistribution is presented in Figures 6 and 7 and Tables S1 and S2. All radiolabeled conjugates showed rapid clearance from blood and nonexcretory organs. The low radioactivity level in the gastrointestinal tract (with content) indicated that the hepatobiliary pathway played a minor role in the excretion of all radioconjugates. Predominantly renal clearance was accompanied by reabsorption in kidneys. There were apparent differences in the biodistribution of the radioconjugates ^{111}In-[DOTA-A1]-$Z_{HER2:S1}$, ^{111}In-[DOTA-K50]-$Z_{HER2:S1}$, and ^{111}In-[DOTA-K58]-$Z_{HER2:S1}$. For example, the radioactivity uptake of ^{111}In-[DOTA-K58]-$Z_{HER2:S1}$ in lung, liver, and spleen was significantly higher than uptake of two other variants. The bone uptake of ^{111}In-[DOTA-A1]-$Z_{HER2:S1}$was the highest. Tumor radioactivity accumulation of ^{111}In-[DOTA-K50]-$Z_{HER2:S1}$ was significantly lower than that of two other variants. The difference between tumor uptakes of ^{111}In-[DOTA-K58]-$Z_{HER2:S1}$ and ^{111}In-[DOTA-A1]-$Z_{HER2:S1}$ was not significant. Accordingly, high tumor uptake and rapid blood clearance of ^{111}In-[DOTA-K58]-$Z_{HER2:S1}$ resulted in significantly higher tumor-to-blood ratio (Figure 7). Low tumor uptake of ^{111}In-[DOTA-K50]-$Z_{HER2:S1}$ resulted in the lowest tumor-to-organ ratios.

The biodistribution of the conjugate with the best targeting properties, ^{111}In-[DOTA-K58]-$Z_{HER2:S1}$, was verified in an additional HER-expressing xenograft model based on the SKOV3 ovarian carcinoma cell line. Comparison between ^{111}In-[DOTA-K58]-$Z_{HER2:S1}$ biodistribution in mice bearing LS174T and SKOV3 xenografts is presented in Figure 8. The biodistribution data were in very good agreement. There was a significant difference ($p < 0.05$) in the tumor uptake between these two models: 16.3 ± 2.2%ID/g for SKOV3 tumors and 11.7 ± 1.9%ID/g for LS174T. There were also small but

dx.doi.org/10.1021/bc3002369 | Bioconjugate Chem. 2012, 23, 1661−1670

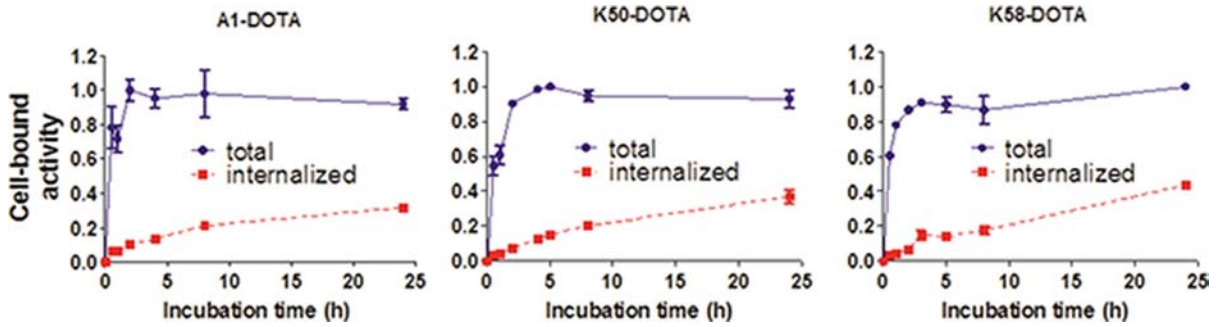


Figure 3. In vitro cellular processing of ^{111}In-[DOTA-A1]-$Z_{HER2:S1}$, ^{111}In-[DOTA-K50]-$Z_{HER2:S1}$, and ^{111}In-[DOTA-K58]-$Z_{HER2:S1}$ bound to SKOV-3 cells. Cells were incubated with the labeled compounds at 37 °C. Acid wash was used to determine the membrane-bound radioactivity. Cell-bound activity is normalized to the maximum uptake. Error bars might not be seen in some because they, in most cases, are smaller than the symbols.

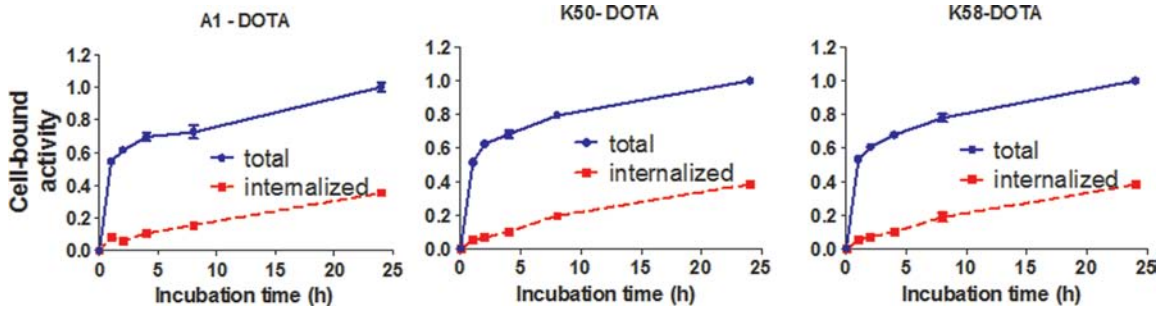


Figure 4. In vitro cellular processing of ^{111}In-[DOTA-A1]-$Z_{HER2:S1}$, ^{111}In-[DOTA-K50]-$Z_{HER2:S1}$, and ^{111}In-[DOTA-K58]-$Z_{HER2:S1}$ bound to LS174T (moderate HER2 expression) cells. Cells were incubated with the labeled compounds at 37 °C. Acid wash was used to determine the membrane-bound radioactivity. Cell-bound activity is normalized to the maximum uptake. Error bars might not be seen because they, in most cases, are smaller than the symbols.

significant differences in the liver and spleen uptake between the models.

MicroSPECT/CT imaging, performed 4 h pi (Figure 9), confirmed the results of the biodistribution experiments. ^{111}In-[DOTA-K58]-$Z_{HER2:S1}$ was capable of high-contrast imaging of the HER2-expressing xenograft. The tumor-to-contralateral leg ratio (calculated as a ratio between average concentrations in the VOIs defined by CT) was 8.2.

DISCUSSION

Affibody molecules represent a new class of affinity proteins capable of molecular recognition in vivo. Recently, a clinical study confirmed the feasibility of imaging of HER2-expressing metastases using ^{111}In- and ^{68}Ga-labeled affibody molecules.[27] Development of several affibody-based imaging agents for visualization of EGFR,[28] HER3,[29] IGF1R,[14] and PDGFRβ [30] has been reported. It is very likely that affibody molecules will evolve into a novel class of targeting agents for radionuclide molecular imaging. This prompts us to investigate different factors influencing the sensitivity of molecular imaging using affibody molecules. An important parameter here is the ratio of radioactivity concentrations between tumors and healthy tissues, as this ratio determines the imaging contrast. The labeling chemistry (i.e., the chemical and physicochemical properties of the radionuclide and the chelator/linker) is essential, as it can influence the binding affinity and cellular processing of an imaging agent, the cellular retention of a radionuclide, the biodistribution of a targeting peptide, and the excretion pathways of nonbound tracer and radiocatabolites.[31]

Earlier, we showed that the chemical nature of chelators coupled to the N-terminus of synthetic affibody molecules influences both biodistribution and blood clearance rate of ^{111}In-labeled proteins.[25] However, not only the composition of a chelator might influence the biodistribution and targeting properties of a targeting peptide, but also its position in the peptide. The position of a chelator in a peptide might influence the binding affinity, by affecting the interaction between the peptide and its molecular target. For example, coupling of DOTA chelators to the C-terminal end of a short α-MSH analogue [Nle^4,Asp^5,D-Phe^7]-α-MSH4−11 (NAPamide) via the ε-amino group of Lys^{11} instead of the N-terminal α-amino group increased the affinity almost 7-fold, from 1.37 to 0.21 nM.[32] Improved affinity translated to twice higher uptake of ^{111}In-DOTA-NAPamide in melanoma xenografts in mice. At the same time, the blood clearance rate was appreciably slower, 0.12 ± 0.01%ID/g at 4 h p.i. for ^{111}In-DOTA-NAPamide vs 0.03 ± 0.00%ID/g for the protein with DOTA at the N-terminus. Still, such a strong influence of the chelator positioning is not surprising for a short octapeptide, where the molecular weight of the chelator is comparable to the molecular weight of the polypeptide moiety. For the significantly larger affibody molecules, such an influence would be less expected. However, it has been shown that placement of a hexahistidine chelator moiety at either the C- or N-terminus of affibody molecules had a substantial effect on the biodistribution of $[^{99m}Tc(CO)_3]^+$-labeled affibody molecules.[23] It is noteworthy that the placement of the label at the C-terminus reduced hepatic uptake 2-fold, but increased blood radioactivity concentration 4-fold at 4 h pi. That study suggested that positioning of a lipophilic label can modify the biodistribution of affibody molecules.

dx.doi.org/10.1021/bc3002369 | Bioconjugate Chem. 2012, 23, 1661−1670

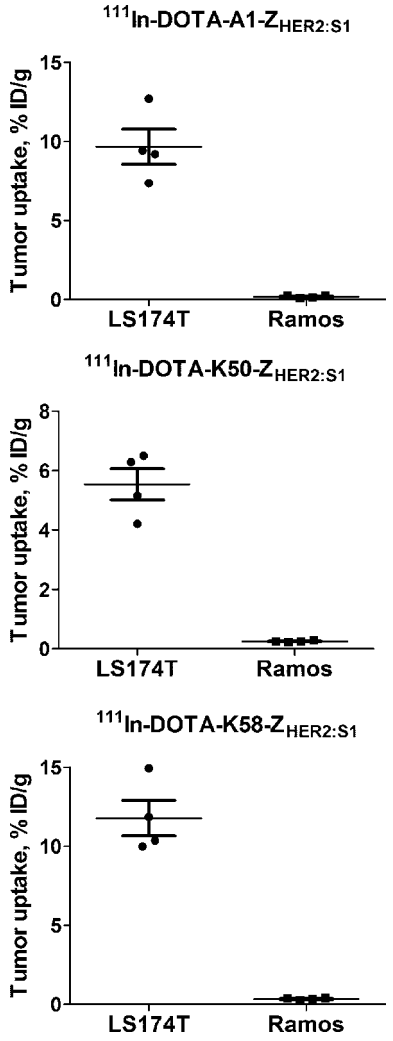


Figure 5. HER2-targeting specificity using ^{111}In-[DOTA-A1]-$Z_{HER2:S1}$, ^{111}In-[DOTA-K50]-$Z_{HER2:S1}$, and ^{111}In-[DOTA-K58]-$Z_{HER2:S1}$ in BALB/C nu/nu mice. The tumor uptake is expressed as %ID/g, Radioactivity uptake in HER2-positive LS174T xenografts was significantly ($p < 0.05$) higher than in HER2 negative Ramos xenografts.

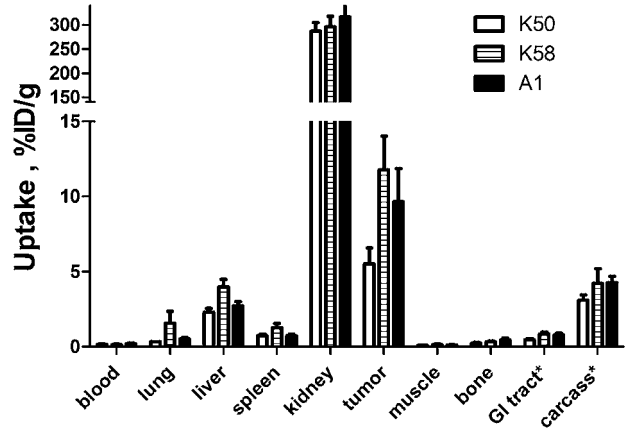


Figure 6. Comparative biodistribution of ^{111}In-[DOTA-A1]-$Z_{HER2:S1}$, ^{111}In-[DOTA-K50]-$Z_{HER2:S1}$, and ^{111}In-[DOTA-K58]-$Z_{HER2:S1}$ in BALB/C nu/nu mice bearing LS174T xenografts at 4 h after injection. The concentration of radioactivity is expressed as % ID/g, and presented as an average value from 4 animals ± standard deviation. Data for gastrointestinal tract (GI) with content and carcass are presented as % of injected radioactivity per whole sample.

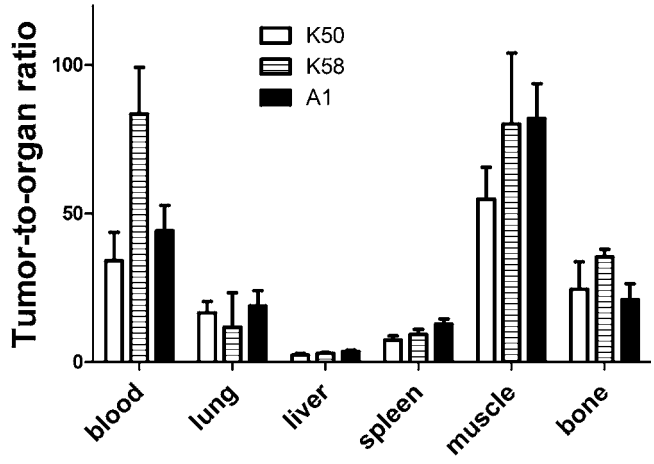


Figure 7. Comparison of tumor-to-organ ratios for ^{111}In-[DOTA-A1]-$Z_{HER2:S1}$, ^{111}In-[DOTA-K50]-$Z_{HER2:S1}$, and ^{111}In-[DOTA-K58]-$Z_{HER2:S1}$ in BALB/C nu/nu mice bearing LS174T xenografts at 4 h after injection.

In this study, we investigated the effect of placement of a hydrophilic DOTA chelator in different positions of an affibody molecule. The conjugation chemistry via formation of an amide bond with one of the carboxylic arms of DOTA was the same for all three tested variants. There was a slight influence of the chelator positioning on the affinity (Table 1), with the highest affinity found for [DOTA-K58]-$Z_{HER2:S1}$. The binding site of affibody molecules comprises amino acids at helices 1 and 2, close to the N-terminus.[17,33] NMR studies of a HER2-binding affibody molecule have shown that the N-terminal part of the protein displays a high degree of conformational dynamics,[33] suggesting that a chelator conjugated to the flexible N-terminus could affect the affibody binding site. In contrast, placement of the chelator at K58 (C-terminus), at the end of helix 3, provides a large distance between the chelator and the binding site, and it can be speculated that this positioning minimizes interference of the chelator with binding to a molecular target. However, the effect was quite modest, and the difference between the highest and the lowest dissociation constants was only 1.4-fold. There was a noticeable effect of the DOTA position on the melting point, suggesting a certain destabilizing effect of placement of DOTA at K50, i.e., in the middle of helix 3.

All three conjugates were successfully labeled with ^{111}In with high label stability and preserved binding capacity (Figure 2). A study using two different HER2-expressing cell lines suggested a rather small influence of the chelator position on the internalization rate (Figures 3 and 4). However, ^{111}In-[DOTA-K58]-$Z_{HER2:S1}$ still showed the highest degree of internalization in both SKOV-3 and LS174T cells.

In vivo, all conjugates could target HER2-expressing LS174T xenografts specifically (Figure 5). However, the tumor uptake of ^{111}In-[DOTA-K50]-$Z_{HER2:S1}$ was significantly lower than the uptake of the two other conjugates. This cannot be explained by lower bioavailability, as the blood concentration was similar for all variants. It might be that the destabilizing effect of the chelator coupled to helix 3 causes a substantial loss of binding capacity in vivo. The uptake of ^{111}In-[DOTA-K58]-$Z_{HER2:S1}$ was the highest in lung, liver, and spleen, but the blood concentration decreased more rapidly for this conjugate

dx.doi.org/10.1021/bc3002369 | Bioconjugate Chem. 2012, 23, 1661−1670

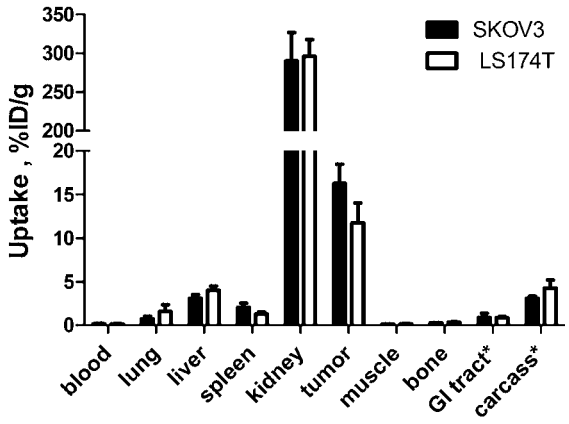


Figure 8. Comparative biodistribution of ^{111}In-[DOTA-K58]-$Z_{HER2:S1}$ in BALB/C nu/nu mice bearing LS174T and SKOV3 xenografts at 4 h after injection. The concentration of radioactivity is expressed as %ID/g, and presented as an average value from 4 animals ± standard deviation. Data for gastrointestinal tract (GI) with content and carcass are presented as % of injected radioactivity per whole sample.

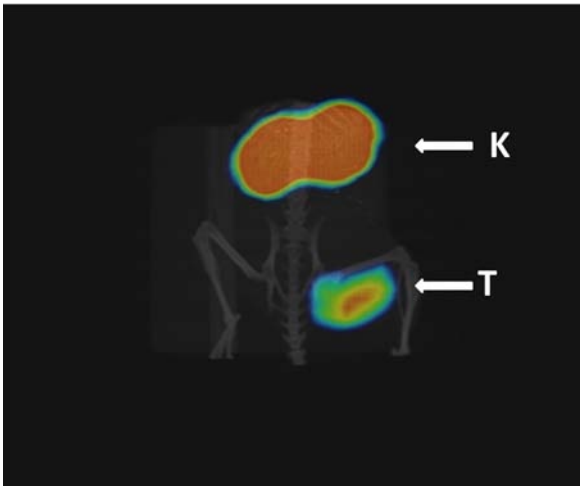


Figure 9. Imaging of HER2 expression in SKOV3 xenografts in BALB/C nu/nu mice using microSPECT/CT. Images were acquired 4 h after administration of the tracer. Arrows point at tumor (T) and kidneys (K).

compared to ^{111}In-[DOTA-A1]-$Z_{HER2:S1}$. Overall, ^{111}In-[DOTA-K58]-$Z_{HER2:S1}$ provided the highest tumor-to-blood and tumor-to-bone ratios, although the tumor-to-liver ratio was the lowest (Figure 7). As blood-borne radioactivity contributes to radioactivity in many organs and tissues, the highest tumor-to-blood ratio is an important argument for conjugation of DOTA to K58 in synthetic affibody molecules. Furthermore, ^{111}In-[DOTA-K58]-$Z_{HER2:S1}$, as the conjugate with the best in vivo targeting properties, was additionally evaluated in a second xenograft model based on SKOV-3 xenografts. The biodistribution data for both models were in a very good agreement (Figure 8). The higher uptake in SKOV3 xenografts can be explained by the appreciably higher expression of HER2 in this cell line. The small discordance between the models with respect to liver and spleen uptake of radioactivity might be due to certain physiological variability between the animal batches. Furthermore, an imaging study confirmed that ^{111}In-[DOTA-K58]-$Z_{HER2:S1}$ can image SKOV-3 xenografts with high contrast (Figure 9).

Earlier, a recombinant ^{111}In-[MMA-DOTA-C61]-$Z_{HER2:2395}$ affibody molecule having DOTA conjugated via maleimide to a C-terminal cysteine has been compared with ^{111}In-DOTA-$Z_{HER2:342}$ (with N-terminal DOTA).[24] In that study, ^{111}In-[MMA-DOTA-C61]-$Z_{HER2:2395}$ provided equal tumor-to-blood and tumor-to-liver ratios in comparison with ^{111}In-DOTA-$Z_{HER2:342}$, but higher tumor-to-spleen and tumor-to-bone ratios. In the present study, ^{111}In-[DOTA-K58]-$Z_{HER2:S1}$ had not only higher tumor-to-bone ratio compared to ^{111}In-[DOTA-A1]-$Z_{HER2:S1}$, but also higher tumor-to-blood ratio. However, the tumor-to-lung and tumor-to-spleen ratios were lower for ^{111}In-[DOTA-K58]-$Z_{HER2:S1}$. This might be an indication that not only the positioning of chelator, but also the chemistry of its conjugation to affibody molecules influences biodistribution and targeting properties. However, ^{111}In-[MMA-DOTA-C61]-$Z_{HER2:2395}$ and ^{111}In-[DOTA-K58]-$Z_{HER2:S1}$ differ not only in the way the chelator is conjugated, but also in the amino acid sequence (six different amino acids), which complicates the ability to draw conclusions.

We showed earlier that decreased N-terminal lipophilicity in affibody molecules can reduce hepatic uptake and hepatobiliary excretion of radioactivity.[23,22] This might further increase the sensitivity of imaging of hepatic metastases. On the basis of these results, it can be suggested that re-engineering of the affibody scaffold aiming to further increase the hydrophilicity of the N-terminus of affibody molecules might be desirable in the case of placement of a chelator at K58.

In conclusion, the results of this study suggest that optimization of the labeling chemistry has the potential to further increase the contrast of molecular imaging using affibody molecules. The positioning of the DOTA chelator influences the melting point, the cellular processing of an affibody molecule by cancer cells, and the biodistribution and targeting properties. This creates preconditions for further enhancement of the tumor-to-organ ratios, and thereby, sensitivity of molecular imaging. This is particularly important for visualization of small metastatic lesions, when the partial volume effect causes decrease of the imaging sensitivity.

■ ASSOCIATED CONTENT

Supporting Information

Tabulated data concerning biodistribution and tumor-to-organ ratios for ^{111}In-[DOTA-A_1]-$Z_{HER2:S1}$, ^{111}In-[DOTA-K_{50}]-$Z_{HER2:S1}$, and ^{111}In-[DOTA-K_{58}]-$Z_{HER2:S1}$ in female in BALB/C nu/nu mice bearing LS174T colorectal cancer xenografts 4 h after intravenous injection. This material is available free of charge via the Internet at http://pubs.acs.org.

■ AUTHOR INFORMATION

Corresponding Author

*Phone: +46 18 471 3414. Fax: + 46 18 471 3432. E-mail: vladimir.tolmachev@bms.uu.se.

Author Contributions

Anna Perols and Hadis Honarvar contributed equally to this study

Notes

The authors declare no competing financial interest.

■ ACKNOWLEDGMENTS

This study was supported by grants from the Swedish Cancer Society (Cancerfonden) and the Swedish Research Council (Vetenskapsrådet).

REFERENCES

(1) Yarden, Y., and Sliwkowski, M. X. (2001) Untangling the ErbB signalling network. *Nat. Rev. Mol. Cell Biol. 2*, 127−137.

(2) Graus-Porta, D., Beerli, R. R., Daly, J. M., and Hynes, N. E. (1997) ErbB-2, the preferred heterodimerization partner of all ErbB receptors, is a mediator of lateral signaling. *EMBO J. 16*, 1647−1655.

(3) Witton, C. J., Reeves, J. R., Going, J. J., Cooke, T. G., and Bartlett, J. M. (2003) Expression of the HER1−4 family of receptor tyrosine kinases in breast cancer. *J. Pathol. 200*, 290−297.

(4) Cobleigh, M. A., Vogel, C. L., Tripathy, D., Robert, N. J., Scholl, S., Fehrenbacher, L., Wolter, J. M., Paton, V., Shak, S., Lieberman, G., and Slamon, D. J. (1999) Multinational study of the efficacy and safety of humanized anti-HER2 monoclonal antibody in women who have HER2-overexpressing metastatic breast cancer that has progressed after chemotherapy for metastatic disease. *J. Clin. Oncol. 17*, 2639.

(5) Slamon, D. J., Godolphin, W., Jones, L. A., Holt, J. A., Wong, S. G., Keith, D. E., Levin, W. J., Stuart, S. G., Udove, J., Ullrich, A., et al. (1989) Studies of the HER-2/neu proto-oncogene in human breast and ovarian cancer. *Science 244*, 707−712.

(6) Yu, D., and Hung, M. C. (2000) Overexpression of ErbB2 in cancer and ErbB2-targeting strategies. *Oncogene 19*, 6115−6121.

(7) Craft, N., Shostak, Y., Carey, M., and Sawyers, C. L. (1999) A mechanism for hormone-independent prostate cancer through modulation of androgen receptor signaling by the HER-2/neu tyrosine kinase. *Nat. Med. 5*, 280−285.

(8) Morote, J., de Torres, I., Caceres, C., Vallejo, C., Schwartz, S., Jr., and Reventos, J. (1999) Prognostic value of immunohistochemical expression of the c-erbB-2 oncoprotein in metastasic prostate cancer. *Int. J. Cancer 84*, 421−425.

(9) Verri, E., Guglielmini, P., Puntoni, M., Perdelli, L., Papadia, A., Lorenzi, P., Rubagotti, A., Ragni, N., and Boccardo, F. (2005) HER2/neu oncoprotein overexpression in epithelial ovarian cancer: evaluation of its prevalence and prognostic significance. Clinical study. *Oncology 68*, 154−161.

(10) Carlsson, J. (2012) Potential for clinical radionuclide-based imaging and therapy of common cancers expressing EGFR-family receptors. *Tumour Biol.* [Online early access].

(11) Slamon, D. J., Leyland-Jones, B., Shak, S., Fuchs, H., Paton, V., Bajamonde, A., Fleming, T., Eiermann, W., Wolter, J., Pegram, M., Baselga, J., and Norton, L. (2001) Use of chemotherapy plus a monoclonal antibody against HER2 for metastatic breast cancer that overexpresses HER2. *N. Engl. J. Med. 344*, 783−792.

(12) Woodard, L. E., and Nimmagadda, S. (2011) CXCR4-based imaging agents. *J. Nucl. Med. 52*, 1665−1669.

(13) Tolmachev, V., Stone-Elander, S., and Orlova, A. (2010) Radiolabelled receptor-tyrosine-kinase targeting drugs for patient stratification and monitoring of therapy response: prospects and pitfalls. *Lancet Oncol. 11*, 992−1000.

(14) Tolmachev, V., Malmberg, J., Hofstrom, C., Abrahmsen, L., Bergman, T., Sjoberg, A., Sandstrom, M., Graslund, T., and Orlova, A. (2012) Imaging of insulinlike growth factor type 1 receptor in prostate cancer xenografts using the affibody molecule ^{111}In-DOTA-ZIGF1R:4551. *J. Nucl. Med. 53*, 90−97.

(15) Nygren, P. A. (2008) Alternative binding proteins: affibody binding proteins developed from a small three-helix bundle scaffold. *FEBS J. 275*, 2668−2676.

(16) Lofblom, J., Feldwisch, J., Tolmachev, V., Carlsson, J., Stahl, S., and Frejd, F. Y. (2010) Affibody molecules: engineered proteins for therapeutic, diagnostic and biotechnological applications. *FEBS Lett. 584*, 2670−2680.

(17) Orlova, A., Magnusson, M., Eriksson, T. L., Nilsson, M., Larsson, B., Hoiden-Guthenberg, I., Widstrom, C., Carlsson, J., Tolmachev, V., Stahl, S., and Nilsson, F. Y. (2006) Tumor imaging using a picomolar affinity HER2 binding affibody molecule. *Cancer Res. 66*, 4339−4348.

(18) Engfeldt, T., Renberg, B., Brumer, H., Nygren, P. A., and Karlstrom, A. E. (2005) Chemical synthesis of triple-labelled three-helix bundle binding proteins for specific fluorescent detection of unlabelled protein. *ChemBioChem 6*, 1043−1050.

(19) Orlova, A., Wallberg, H., Stone-Elander, S., and Tolmachev, V. (2009) On the selection of a tracer for PET imaging of HER2-expressing tumors: direct comparison of a 124I-labeled affibody molecule and trastuzumab in a murine xenograft model. *J. Nucl. Med. 50*, 417−425.

(20) Malmberg, J., Sandstrom, M., Wester, K., Tolmachev, V., and Orlova, A. (2011) Comparative biodistribution of imaging agents for in vivo molecular profiling of disseminated prostate cancer in mice bearing prostate cancer xenografts: focus on ^{111}In- and ^{125}I-labeled anti-HER2 humanized monoclonal trastuzumab and ABY-025 affibody. *Nucl. Med. Biol. 38*, 1093−1102.

(21) Ahlgren, S., and Tolmachev, V. (2010) Radionuclide molecular imaging using Affibody molecules. *Curr. Pharm. Biotechnol. 11*, 581−589.

(22) Engfeldt, T., Tran, T., Orlova, A., Widstrom, C., Feldwisch, J., Abrahmsen, L., Wennborg, A., Karlstrom, A. E., and Tolmachev, V. (2007) ^{99m}Tc-chelator engineering to improve tumour targeting properties of a HER2-specific Affibody molecule. *Eur. J. Nucl. Med. Mol. Imaging 34*, 1843−1853.

(23) Tolmachev, V., Hofstrom, C., Malmberg, J., Ahlgren, S., Hosseinimehr, S. J., Sandstrom, M., Abrahmsen, L., Orlova, A., and Graslund, T. (2010) HEHEHE-tagged affibody molecule may be purified by IMAC, is conveniently labeled with [(m)Tc(CO)](+), and shows improved biodistribution with reduced hepatic radioactivity accumulation. *Bioconjugate Chem. 21*, 2013−2022.

(24) Ahlgren, S., Orlova, A., Rosik, D., Sandström, M., Sjöberg, A., Baastrup, B., Widmark, O., Fant, G., Feldwisch, J., and Tolmachev, V. (2008) Evaluation of maleimide derivative of DOTA for site-specific labeling of recombinant Affibody molecules. *Bioconjugate Chem. 19*, 235−243.

(25) Malmberg, J., Perols, A., Varasteh, Z., Altai, M., Braun, A., Sandstrom, M., Garske, U., Tolmachev, V., Orlova, A., and Eriksson Karlstrom, A. (2012) Comparative evaluation of synthetic anti-HER2 Affibody molecules site-specifically labelled with (111)In using N-terminal DOTA, NOTA and NODAGA chelators in mice bearing prostate cancer xenografts. *Eur. J. Nucl. Med. Mol. Imaging 39*, 481−492.

(26) Wallberg, H., and Orlova, A. (2008) Slow internalization of anti-HER2 synthetic affibody monomer ^{111}In-DOTA-ZHER2:342-pep2: implications for development of labeled tracers. *Cancer Biother. Radiopharm. 23*, 435−442.

(27) Baum, R. P., Prasad, V., Muller, D., Schuchardt, C., Orlova, A., Wennborg, A., Tolmachev, V., and Feldwisch, J. (2010) Molecular imaging of HER2-expressing malignant tumors in breast cancer patients using synthetic ^{111}In- or ^{68}Ga-labeled affibody molecules. *J. Nucl. Med. 51*, 892−897.

(28) Tolmachev, V., Rosik, D., Wallberg, H., Sjoberg, A., Sandstrom, M., Hansson, M., Wennborg, A., and Orlova, A. (2010) Imaging of EGFR expression in murine xenografts using site-specifically labelled anti-EGFR ^{111}In-DOTA-Z EGFR:2377 Affibody molecule: aspect of the injected tracer amount. *Eur. J. Nucl. Med. Mol. Imaging 37*, 613−622.

(29) Kronqvist, N., Malm, M., Gostring, L., Gunneriusson, E., Nilsson, M., Hoiden Guthenberg, I., Gedda, L., Frejd, F. Y., Stahl, S., and Lofblom, J. (2011) Combining phage and staphylococcal surface display for generation of ErbB3-specific Affibody molecules. *Protein Eng. Des. Sel. 24*, 385−296.

(30) Lindborg, M., Cortez, E., Hoiden-Guthenberg, I., Gunneriusson, E., von Hage, E., Syud, F., Morrison, M., Abrahmsen, L., Herne, N., Pietras, K., and Frejd, F. Y. (2011) Engineered high-affinity affibody molecules targeting platelet-derived growth factor receptor beta in vivo. *J. Mol. Biol. 407*, 298−315.

(31) Tolmachev, V., and Orlova, A. (2010) Influence of labelling methods on biodistribution and imaging properties of radiolabelled peptides for visualisation of molecular therapeutic targets. *Curr. Med. Chem. 17*, 2636−2655.

(32) Froidevaux, S., Calame-Christe, M., Schuhmacher, J., Tanner, H., Saffrich, R., Henze, M., and Eberle, A. N. (2004) A gallium-labeled

DOTA-alpha-melanocyte- stimulating hormone analog for PET imaging of melanoma metastases. *J. Nucl. Med. 45*, 116−123.
(33) Eigenbrot, C., Ultsch, M., Dubnovitsky, A., Abrahmsén, L., and Härd, T. (2010) Structural basis for high-affinity HER2 receptor binding by an engineered protein. *Proc. Natl. Acad. Sci. U. S. A. 107*, 15039−15044.

Bioconjugate Chemistry

Article

pubs.acs.org/bc

Galactosyl Human Serum Albumin-NMP1 Conjugate: A Near Infrared (NIR)-Activatable Fluorescence Imaging Agent to Detect Peritoneal Ovarian Cancer Metastases

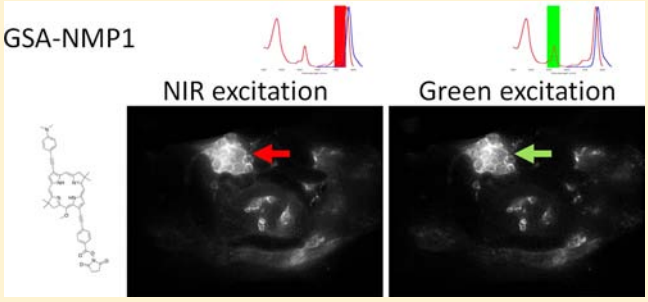
Vinita M. Alexander,[†] Kohei Sano,[†] Zhanqian Yu,[‡] Takahito Nakajima,[†] Peter L. Choyke,[†] Marcin Ptaszek,[‡] and Hisataka Kobayashi*[,†]

[†]Molecular Imaging Program, Center for Cancer Research, National Cancer Institute, National Institutes of Health, Bethesda, Maryland 20892, United States

[‡]Department of Chemistry and Biochemistry, University of Maryland Baltimore County, Baltimore, Maryland 21250, United States

Supporting Information

ABSTRACT: Patient survival depends on the completeness of resection of peritoneal ovarian cancer metastases (POCM), and therefore, it is important to develop methods to enhance detection. Previous probe designs based on activatable galactosyl human serum albumin (hGSA)−fluorophore pairs, which target lectin receptors expressed on POCM, have used only visible range dyes conjugated to hGSA. However, imaging probes emitting fluorescence in the NIR range are advantageous because NIR photons have deeper *in vivo* tissue penetration and result in lower background autofluorescence than those emitting in the visible range. A NIR-activatable hGSA fluorophore was synthesized using a bacteriochlorin-based dye, NMP1. NMP1 has two unique absorption peaks, one in the green range and the other in the NIR range, but emits at a NIR peak of 780 nm. NMP1, thus, has two different Stokes shifts that have the potential to allow imaging of POCM both at the peritoneal surface and just below it. hGSA was conjugated with 2 NMP1 molecules to create a self-quenching complex (hGSA-NMP1). The activation ratio of hGSA-NMP1 was measured by the fluorescence intensity before and after exposure to 10% SDS. The activation ratio of hGSA-NMP1 was ∼100-fold *in vitro*. Flow cytometry, fluorescence microscopy, and *in vivo* spectral fluorescence imaging were carried out to compare hGSA-NMP1 with hGSA-IR800 and hGSA-ICG (two always-on control agents with similar emission to NMP1) in terms of comparative fluorescence signal and the ability to detect POCM in mice models. The sensitivity and specificity of hGSA-NMP1 for POCM implant detection were determined by colocalizing NMP1 emission spectra with red fluorescent protein (RFP) expressed constitutively in SHIN3 tumor implants at different depths below the peritoneal surface. In vitro, SHIN3 cells were easily detectable after 3 h of incubation with hGSA-NMP1. *In vivo* submillimeter POCM foci were clearly detectable with spectral fluorescence imaging using hGSA-NMP1. Among 555 peritoneal lesions, hGSA-NMP, using NIR and green excitation light, respectively, detect 75% of all lesions and 91% of lesions ∼0.8 mm or greater in diameter. Few false positives were encountered. Nodules located at a depth below the small bowel surface were only depicted with hGSA-NMP1. We conclude that hGSA-NMP1 is useful in imaging peritoneal ovarian cancer metastases, located both superficially and deep in the abdominal cavity.



INTRODUCTION

Ovarian cancer is the second most common gynecologic cancer in the United States, with 21 650 estimated new cases in 2008; however, it is the most deadly gynecologic malignancy, resulting in 15 520 estimated annual deaths. Due to its nonspecific symptoms, the majority of patients (60−70%) present at an advanced stage, and peritoneal carcinomatosis with ascites is often the first presentation of ovarian malignancy.[1]

Long-term cure rates of ovarian cancer range between 20% and 30%, and the most important prognostic factors for patients are primary surgical outcome and patients' clinical response to postoperative platinum-based chemotherapy. However, attempts to detect peritoneal metastases using only the surgeon's unaided eye often results in persistent disease even after maximal debulking. Thus, improving the imaging and detection and, hence, resection of peritoneal metastases at the patient's first surgery could improve outcomes.

Fortunately, the uniquely large surface area and shallow depth of peritoneal ovarian cancer metastases (POCM) are well-suited to optical imaging, which could be easily incorporated into laparoscopic resections. Fluorescence imaging allows the detection of POCM at the surface of the peritoneum.[2] As a result, fluorescence imaging has been

Received: May 4, 2012
Revised: June 22, 2012
Published: July 16, 2012

 © 2012 American Chemical Society

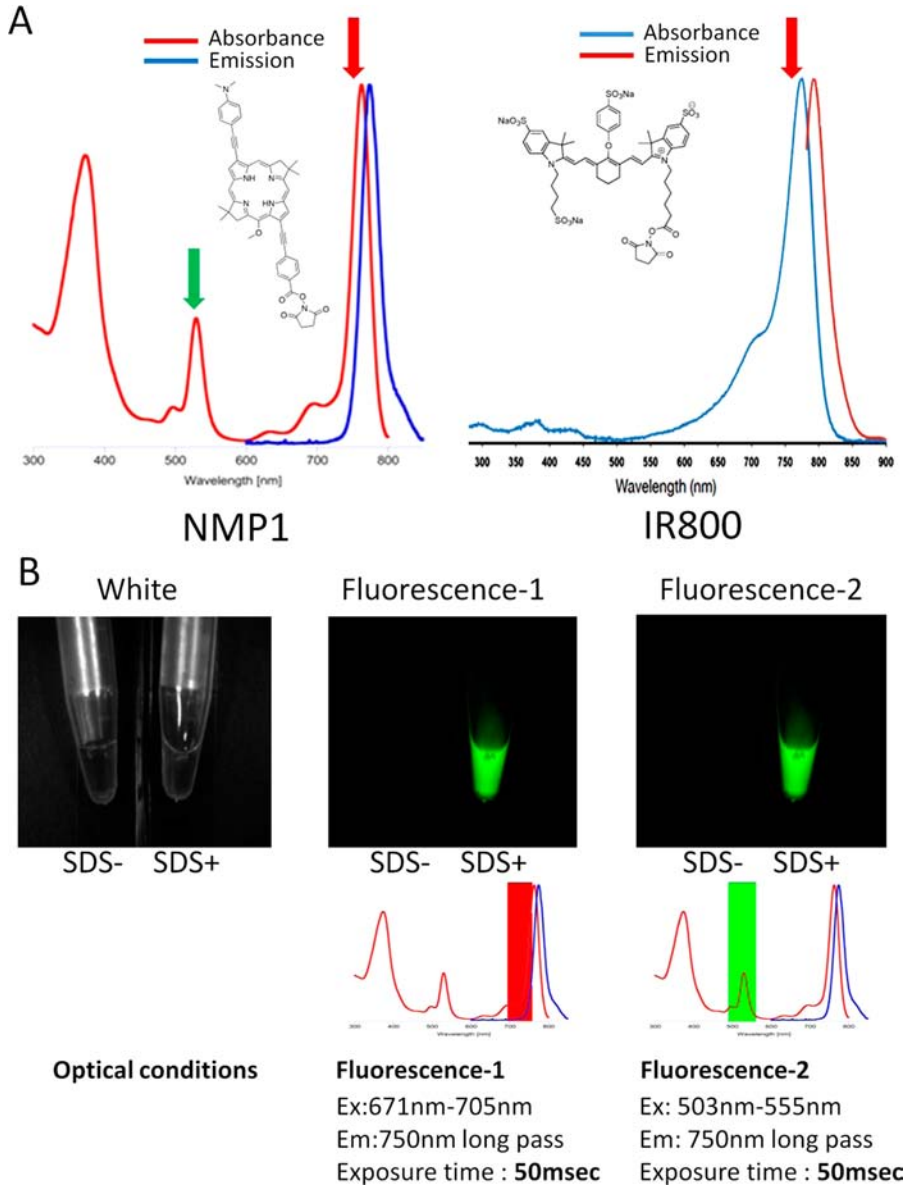


Figure 1. A. Structures and emission profiles of NMP1 and IR800 are shown. NMP1 has two available excitation peaks in green and NIR wavelengths. B. The fluorescence signals of hGSA-NMP1 with or without chemical activation by adding 1% SDS are shown. hGSA-NMP1 yields similar strength of NIR emission by exciting green or NIR light.

proposed as a practical means of guiding surgical resection. Additional advantages include the ability to quickly scan large surface areas with high resolution, its relatively low cost and portability, and its lack of ionizing radiation exposure.[3]

Although many candidate fluorescent imaging agents have been proposed, they usually suffer from one or more shortcomings. For instance, "always on" probes require a prolonged interval for the unbound but fluorescing probe to be cleared to enable sufficient tumor to background (TBR) ratios for visualization. Activatable probes can be imaged more quickly after injection and produce signal only at the tumor site yielding higher TBR. However, many previous probes have emitted light only in the visible range, thus limiting the depth at which POCM can be detected. This can be corrected by using fluorescence probes that emit in the NIR where tissue penetration is greater.

Galactosyl human serum albumin (hGSA) is a galactose-conjugated human protein that binds to lectin receptors on the surfaces of POCM. hGSA−fluorophore conjugates bind the β-D-galactose (a lectin) receptor on ovarian cancer cells at physiologic pH. Upon internalization, the hGSA−fluorophore conjugates are "dequenched," thus emitting light.[4−7] Activatable fluorophores that emit in the near-infrared range (NIR) are advantageous because they have deeper *in vivo* tissue penetration and yield lower background autofluorescence than those emitting in the visible range. The newly synthesized bacteriochlorin-based NIR dye, NMP1, has two unique absorption peaks [in the green (λ_1 = 530 nm) and NIR (λ_2 = 760 nm) wavelength ranges], with a single NIR emission peak of 780 nm (Figure 1A).[8] NMP1 has the potential to allow separate excitation of tumor nodules at the surface (green excitation) and at a depth below the surface (NIR excitation).

Herein, we describe our findings with an NIR-activatable hGSA-NMP1, and we compare it to two probes with similar emission wavelengths ("always-on" hGSA-ICG and hGSA-IR800 probes, with peak emission wavelengths of 830 nm and

800 nm, respectively)[9] to determine its advantages in detecting cancer foci.

MATERIALS AND METHODS

Synthesis, Chemical Activation, and Stability in Serum of hGSA−NMP1 Conjugate. The synthesis method of NMP1 has been published.[10] Briefly, bacteriochlorin possessing two phenylethynyl substituents was prepared by sequential functionalization of the corresponding dibromobacteriochlorin[11] with palladium-catalyzed Sonogashira reaction. The NHS ester was obtained by basic hydrolysis of the corresponding methyl ester (NaOH in MeOH/THF) and reaction of the resulting acid with *N*-hydroxysuccinimide, in the presence of EDCI and 4-(dimethylamino)pyridine in DMF. The final product was obtained in 96% yield, after purification with column chromatography.[10] Synthesis of hGSA was performed with direct amidation reaction with human serum albumin and β-galactosamine. The details of synthesis and characterization have been previously published.[12]

hGSA (0.25 mg, 3.5 nmol) and HSA were incubated with NMP1-NHS ester (27.5 μg, 35 nmol) in 0.1 M Na_2HPO_4 (pH 8.6) at room temperature for 1 h, followed by purification with a size exclusion column (PD-10; GE Healthcare, Piscataway, NJ). ICG-Sulfo-OSu (Dojindo Molecular Technologies, Rockville, MD) and IRDye 800CW (IR800; LI-COR Biosciences, Lincoln, NE) labeling of hGSA was also performed by reacting hGSA with ICG and IR800 at a ratio of 1:10 and 1:5, respectively, in the same manner as hGSA-NMP1. The concentrations of each dye were calculated by measuring the absorption with the UV−vis system (8453 Value UV−vis system; Agilent Technologies, Santa Clara, CA) to confirm the number of fluorophore molecules conjugated with each hGSA molecule. The protein concentration was also determined by measuring the absorption at 280 nm with a UV−vis system.

The quenching abilities of each conjugate were investigated by denaturing each with 1% SDS as described previously.[5] Briefly, the conjugates were incubated either with 1% SDS in PBS or PBS alone for 15 min at room temperature. The change in fluorescence intensity of NMP1 was investigated with an *in vivo* imaging system (Maestro, CRi Inc., Woburn, MA) using two distinct band-pass filters [(i) 671−705 nm; (ii) 503−555 nm] and one long-pass filter over 750 nm for excitation and emission light, respectively. The fluorescence signal intensity of ICG and IR800 was measured by using 710−760 nm excitation and 800 nm long-pass emission filters.

hGSA-NMP1 was added to mouse serum collected from female nude mice (National Cancer Institute Animal Production Facility, Frederick, MD), and the serum samples were incubated at 37 °C for 0, 1.5, and 3 h. After incubation, the change in fluorescence intensity was evaluated on the Maestro camera.

Cell Culture. The established ovarian cancer cell line, SHIN3, was used for *in vitro* fluorescence microscopy, flow cytometry, and *in vivo* optical imaging of POCM.[13] Cell lines were grown in RPMI 1640 medium (Invitrogen) containing 10% fetal bovine serum (Gibco), 0.03% L-glutamine at 37°C, 100 U/mL penicillin, and 100 μg/mL streptomycin in 5% CO_2.

Confirmation of Red Fluorescent Protein (DsRed2) Transfection in SHIN3 Cells. The red fluorescent protein (RFP DsRed2)-expressing plasmid (Clontech Laboratories) was previously transfected into the SHIN3 cell line and served as the standard of reference for cancer location.[3] Flow cytometry and fluorescence microscopy were carried out as described below to confirm continued successful expression of RFP in the SHIN3_DsRed cell line.

Fluorescence Microscopy. In order to study and compare the temporal sequence of intracellular fluorescence activation of hGSA-NMP1 with that of hGSA-ICG and hGSA-IR800, SHIN3 cells (2×10^4) were plated on a cover glass bottom culture well and incubated for 10 h. hGSA-NMP1, hGSA-ICG, hGSA-IR800, or no dye at all was added to the media at 1 μg/mL. For the blocking study, 100 μg of nonconjugated hGSA was added together with hGSA-NMP1. In order to confirm the continued successful expression of RFP in the SHIN3_DsRed cell line, 2×10^4 transfected cells were plated on a cover glass and also incubated for 10 h. The nontransfected SHIN3 cells were incubated with each dye for either 1.5 h or 3 h and then washed once with PBS. Fluorescence microscopy was carried out on an Olympus BX61 microscope (Olympus America, Inc.) for hGSA-NMP, hGSA-ICG, and hGSA-IR800 using the filters settings: excitation wavelength 672.5−747.5 nm and emission wavelength range 765−855 nm. For the SHIN3 cells transfected with RFP, a band-pass filter of 530−570 nm and one long-pass filter over 590 nm were used for excitation and emission light, respectively. Transmitted light differential interference contrast (DIC) images were obtained as well.

Animal Model of Peritoneal Metastatses. All procedures were carried out in compliance with the Guide for the Care and Use of Laboaratory Animal Resources (1996), the National Research Council, and approved by the local Animal Care and Use Committee. Intraperitoneal xenografts were established by i.p. injection of 2×10^6 SHIN3 cells suspended in 200 μL PBS into the peritoneum of female nude mice (National Cancer Institute Animal Production Facility, Frederick, MD). Imaging was performed at 14−21 days after injection of the cells.

***In Vivo* Spectral Fluorescence Imaging.** To compare the utility of hGSA-NMP1, hGSA-ICG, and hGSA-IR800 in detecting peritoneal tumor implants, aliquots of hGSA-NMP1 (25 μg), hGSA-ICG (25 μg), hGSA-IR800 (25 μg), or control HSA-NMP1 (25 μg) were suspended in 300 μL PBS and injected into the peritoneal cavities of tumor bearing female nude mice. For each sample, either 1.5 h or 3 h after i.p. injection of each probe, mice were euthanized by carbon dioxide inhalation. Several mice were allocated to each dye and corresponding time point group as follows: hGSA-NMP1 (n = 5 for 1.5 h; n = 15 for 3 h), hGSA-ICG (n = 5 for 1.5 h; n = 5 for 3 h), hGSA-IR800 (n = 5 for 1.5 h; n = 13 for 3 h), and HSA-NMP1 (n = 3 for 3 h). After euthanasia, the mouse abdominal wall was excised, and the abdominal cavity was exposed. Optical images of the whole abdomen were first obtained. Following this, the small bowel mesentery was extracted and close-up images were obtained. Spectral fluorescence images were acquired using the Maestro In-Vivo Imaging System. Two distinct band-pass filters [(i) 671−705 nm; (ii) 503−555 nm] and one long-pass filter over 750 nm were used for excitation and emission light, respectively. The tunable filter was automatically stepped in 10 nm increments from 650 to 950 nm for time course experiments, while the optical imaging camera captured images at each wavelength interval with constant exposure. The spectral fluorescence images consisting of autofluorescence spectra (from the small bowel, the black plate, and the mouse's skin) and the spectra specific to each probe were obtained. Using commercial software (*Maestro* software) and saved fluorescence spectra, the original spectral fluorescence images were unmixed to show

dx.doi.org/10.1021/bc3002419 | *Bioconjugate Chem.* 2012, 23, 1671−1679

the fluorescent signal unique to each injected probe and autofluorescence. To calculate the tumor-to-background ratio (TBR), two regions of interest (ROIs) were placed at the largest tumor and its adjacent intestine or mesenteric membrane (background) in an unmixed image, which was produced based on the respective spectra of fluorophores.

Phantom "Proof of Principle" Experiments. To evaluate the utility of hGSA-NMP1 in detecting implants located superficially and deep in the abdominal cavity, the abdominal walls of female nude mice were excised (n = 3). A "phantom" sample consisting of an Eppendorf tube wrapped in optical black lab tape leaving only the tip exposed, with approximately 20 μL of fully activated (with 1% SDS) hGSA-NMP1, was placed atop a piece of small intestine. Spectral fluorescent images were obtained using two distinct band-pass excitation filters [(i) green spectral range filter, 503−555 nm, and (ii) near-infrared spectral range filter, 671−705 nm] and one long-pass emission filter over 750 nm, as described above. Then, the phantom sample was placed beneath the same section of small intestine, and spectral fluorescent images were again obtained in both settings.

ImageJ software (National Institutes of Health) was used to subtract the spectral image obtained using the green spectral range band-pass filter (presumed to depict only surface fluorescence) from that obtained using the NIR-spectral range filter presumed to detect both surface and deeper fluorescence. The resulting images represented the fluorescence signal present at a shallow depth below the surface (~2 mm).

"Tumor Depth" Model. To compare the utility of hGSA-NMP1 and hGSA-IR800 in imaging peritoneal implants located both superficially and deep in the abdominal cavity, peritoneal xenografts were established 14 d after i.p. injection of SHIN3 cells (2×10^6) suspended in 200 μL PBS in female nude mice. At day 14, each mouse received either 25 ug of hGSA-NMP1 or hGSA-IR800 diluted in 300 μL PBS. Three hours later, the abdominal wall was excised, and a sub-diaphragmatic tumor nodule was removed (n = 13 for hGSA-NMP1, n = 9 for hGSA-IR800). A standard reference solution of hGSA-NMP1 or hGSA-IR800 was placed adjacent to the mouse. The extracted nodule was placed atop a piece of small intestine, and spectral fluorescent images were obtained using two distinct band-pass filters [(i) a green spectral range filter (503−555 nm) and (ii) a near-infrared spectral range filter (671−705 nm)] and one long-pass filter over 750 nm. The extracted nodule was then placed beneath the same section of small intestine, and spectral fluorescent images were again obtained.

The intensities between the two images obtained using the two different sets of band-pass filters were normalized based on standard reference solutions. The green spectral image (presumed to depict fluorescence only at the surface of the abdominal cavity) was subtracted from the NIR-spectral range filter (presumed to depict fluorescence at and below the surface of the abdominal cavity). The resulting images represent tumor nodules located at a shallow depth below the surface (thickness ~2 mm).

Assessment of the Sensitivity and Specificity of hGSA-NMP1 in the Detection of Peritoneal Metastases. To verify that there was no spectral overlap between NMP1 and DsRed, tumor models were established 14 d after i.p. injection of nontransfected SHIN3 cells (n = 8) and RFP-transfected SHIN3 cells (2×10^6) suspended in 200 μL PBS into female nude mice (n = 10). Mice with nontransfected SHIN3 tumors (n = 3) were injected with 25 μg of hGSA-NMP1 suspended in 300 μL PBS (n = 3) or 300 μL PBS alone (n = 5). Mice with RFP-transfected SHIN3 tumors were injected with 25 μg of hGSA-NMP1 suspended in 300 μL PBS (n = 5) or 300 μL PBS alone (n = 5). Three hours after injection of the dyes, spectral fluorescent images were obtained with the appropriate filter settings, and spectral unmixing demonstrated no overlap between NMP1 or DsRed fluorescence.

Sensitivity and specificity were determined by comparing sites of fluorescence from hGSA-NMP1 with sites of fluorescence from RFP-transfected SHIN3 tumors (n = 10). Three hours after i.p. injection of 25 μg of hGSA-NMP1, the mouse abdominal wall was excised and the small bowel mesentery extracted. A nonfluorescent optically black plate was placed under the extracted small bowel mesentery, and a ruler and reference solution (of either hGSA-NMP1 or hGSA-IR800) were placed adjacent to the specimen. Magnified *in vivo* spectral fluorescence imaging was performed using the Maestro In-Vivo Imaging System. In these experiments, the tunable filter was automatically stepped in 10 nm increments from 450 to 950 nm. To isolate the fluorescent signal from DsRed, an excitation filter of 503−555 nm and a long-pass filter over 580 nm were used. The detection size limit for the tumor implants was determined visually using an unmixed composite image.

The spectral fluorescence images were unmixed, and regions of interest (ROI) were assigned using automated software based on a predetermined threshold. All visible nodules with short axis diameters of ≥0.8 mm on RFP images were included based on the minimum ROI size. True positives for hGSA-NMP1 were defined as ROIs with average fluorescence intensity of >3 a.u., whereas true negatives for hGSA-NMP1 were defined as ROIs with average fluorescence intensity of <3 a.u. on the spectrally unmixed images. False positives for hGSA-NMP1 were defined as ROIs in which fluorescence was seen only on the NMP1 image and not the RFP image.

The sensitivity of hGSA-NMP1 for the detection of peritoneal cancer foci was defined as the number of foci positive for both hGSA-NMP1 and RFP divided by the number of foci positive for just RFP. In contrast, the specificity of hGSA-NMP1 was defined as the number of peritoneal foci negative for both RFP and hGSA-NMP1 divided by the number of peritoneal foci negative for RFP.

RESULTS

Optical Characteristics of hGSA−NMP1 Conjugate. The number of NMP1, ICG, and IR800 dyes conjugated with each hGSA molecule was 1.8 ± 0.3, 0.9 ± 0.3, 1.6 ± 0.4, respectively. The quenching capacities measured by adding 1% SDS to dye-conjugated antibody were >50-, 5-, and 2-fold for hGSA-NMP1, hGSA-ICG, and hGSA-IR800, respectively. No measurable dequenching of hGSA-NMP1 was observed in mouse serum at 37 °C for 3 h. As expected, hGSA-NMP1 yielded a single NIR emission peak after green or NIR excitation (Figure 1B).

Intracellular Activation of hGSA−NMP1 after Cellular Internalization. Microscopic images of the SHIN3 cells incubated with 1 μg/mL of hGSA-NMP1, hGSA-ICG, and hGSA-IR800 demonstrated diffuse and vague fluorescence but showed no clustering of signal in the cytoplasm 1.5 h after incubation with hGSA-NMP1; however, several large and intense clusters of fluorescence representing probe accumulation in lysosomes were seen 3 h after incubation with hGSA-NMP1 (Figure 2). Clear blocking of binding with excess hGSA

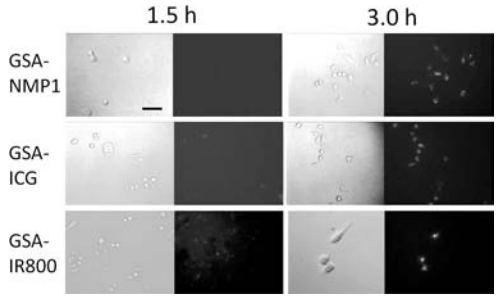


Figure 2. Sequential microscopic images of SHIN3 cells, which are incubated with 1 μM of activatable hGSA-NMP1, always on hGSA-IR800 and hGSA-ICG for 1.5 and 3 h, clearly show fluorescence signal in lysosomes only in cells with 3 h incubation (right column). However, each dye only minimally accumulated in SHIN3 cells at 1.5 h. Differential interference contrast and fluorescence images are shown. Scale bar represents 25 μm (original magnification 200×).

demonstrated the specific binding of hGSA to the β-D-galactose receptor (Supporting Information Figure 1A). These results suggest that hGSA-NMP1 is activated after internalization and lysosomal processing (Supporting Information Figure 1B), which leads to complete dequenching by 3 h.

hGSA-NMP1 Produces High *in Vivo* Tumor-to-Background Fluorescence. To determine the optimal timing for in vivo imaging and also to evaluate the feasibility of using hGSA-NMP1 for the detection of peritoneal metastases, spectral fluorescent images were obtained 1.5 h and 3 h after intraperitoneal injection of 25 μg of each dye into live nude mice.

One and a half hours after i.p. injection of hGSA-NMP1, hGSA-IR800, and hGSA-ICG, fluorescence imaging of the small bowel mesentery began to reveal peritoneal metastases with hGSA-NMP1 (Supporting Information Figure 2). However, by 3 h after i.p. injection, the fluorescence intensity of hGSA-NMP1 had increased leading to higher activation ratios. hGSA-IR800 and hGSA-ICG produced comparable signal after NIR excitation. However, images using hGSA-NMP1 with green excitation were sharper and there was less background than other images due to the longer Stokes shift (Figure 3A). HSA-NMP1 did not show specific accumulation in SHIN3 tumors (Supporting Information Figure 3). Submillimeter cancer foci were clearly detectable with close-up imaging of the small bowel mesentery (Figure 3B). The mean tumor-to-intestine ratios with green and NIR excitation light in the abdomen *in situ* was only 3.17 ± 2.02 and 2.95 ± 1.46 1.5 h after injection with hGSA-NMP1, respectively; but by 3 h, the tumor-to-intestine ratios increased to 22.21 ± 10.24 and 13.32 ± 8.27. Comparatively, the tumor-to-intestine ratios for hGSA-ICG and hGSA-IR800 in labeling of SHIN3 POCM in the abdomen *in situ* were much lower at 3.30 ±1.54 and 4.65 ± 2.01, respectively, after 1.5 h of incubation,. The tumor-to-intestine ratios for each of those dyes increased to 7.89 ± 4.70 and 3.93 ±1.90 3 h after injection, respectively. (see also Supporting Information Figure 2 and Table 1).

Phantom "Proof of Principle" Experiments. When the phantom sample was placed atop the small intestine, the resulting image clearly depicted the signal (Figure 4). However, when the phantom sample was placed below the small intestine, it was not visible in the green range but was clearly seen using the NIR filter set.

"Tumor Depth" Model. In the mice injected with hGSA-NMP1 (n = 13) in which a tumor nodule was placed atop the small intestine, the nodule was clearly visualized with either the green or NIR image (Figure 5). However, when the tumor nodule was placed below the small intestine, the lesion could only be detected with the NIR-Green subtraction image.

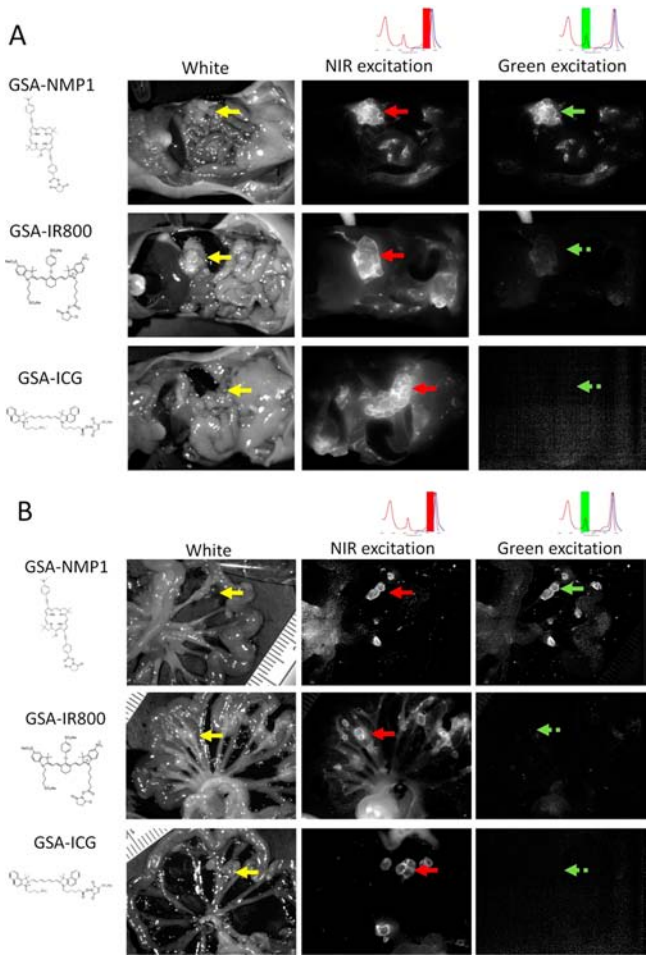


Figure 3. *In situ* spectral fluorescence images of abdomen (A) and mesenteric membrane (B) in mice bearing peritoneal SHIN3 ovarian cancer are shown. Images obtained with NIR excitation were comparable for the use of all three agents. However, images using hGSA-NMP1 with green excitation were sharper with less background than other images due to the longer Stokes shift (A, right column). No fluorescence is shown in mice injected hGSA-IR800 and hGSA-ICG with green excitation. Submillimeter cancer foci were clearly detectable with close-up imaging of the small bowel mesentery (B).

In contrast, in mice injected with hGSA-IR800 (n = 9) only the superficial implants were detected (Figure 5). The deeper tumor nodules were not visualized. Furthermore, since hGSA-IR800 lacks an absorption peak in the green spectrum, the original images acquired using the band-pass filter in the green spectral range depicted only blurry fluorescent signal.

Sensitivity and Specificity of hGSA-NMP1. Analysis of unmixed images showed no spectral overlap between hGSA-NMP1 and DsRed (Supporting Information Figure 4). The sensitivity and specificity of hGSA-NMP1 in detecting peritoneal cancer nodules were calculated and compared, using RFP-positive nodules as the reference for true positive tumors. A separate sensitivity and specificity was calculated for each of the hGSA-NMP1 dye's two unique absorption peaks and the corresponding optical filter settings.

dx.doi.org/10.1021/bc3002419 | *Bioconjugate Chem.* 2012, 23, 1671–1679

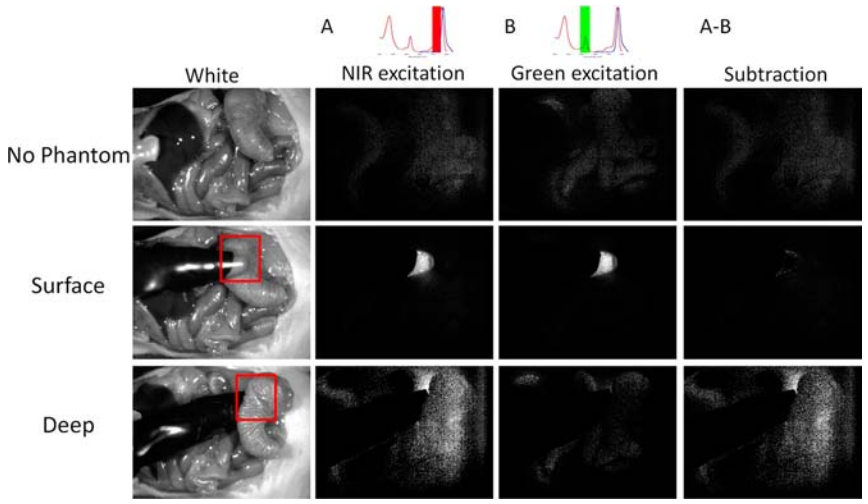


Figure 4. *In situ* spectral fluorescence images of non-tumor-bearing mice with a tube phantom of hGSA-NMP1 are shown. When the phantom sample was placed atop the small intestine, the resulting image clearly indicated that the fluorescent signal was located atop the small intestine. However, when the phantom sample was placed below the small intestine, the resulting image in the emission light was not visible in the green range but was clearly seen like a backlit image using the NIR filter set.

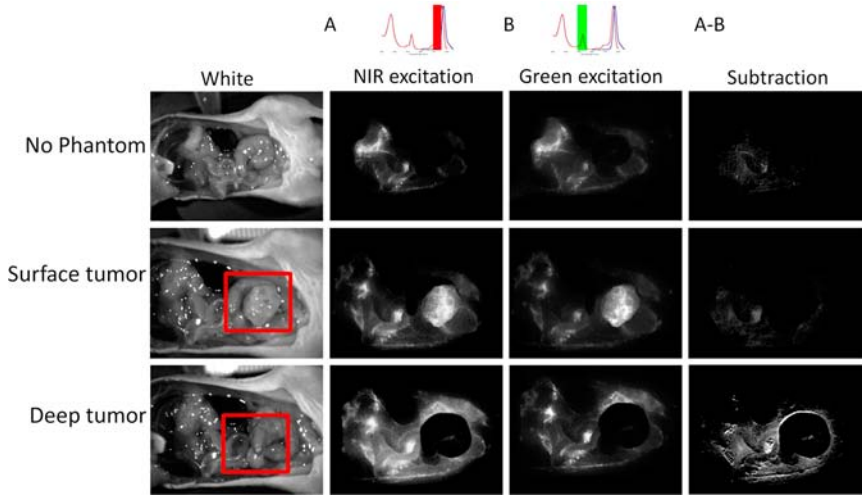


Figure 5. *In situ* spectral fluorescence images of peritoneal SHIN3-tumor bearing mice with a resected large tumor nodule containing hGSA-NMP1 are shown. In images in which a tumor nodule was placed atop the small intestine, the nodule was clearly visualized with either the green or NIR excitation light. However, when the tumor nodule was placed below the small intestine, the lesion could only be detected with the NIR-Green subtraction image shown like a backlight image. Since hGSA-IR800 lacks an absorption peak in the green spectrum, the original images acquired using the band-pass filter in the green spectral range depicted only a blurry fluorescent signal.

RFP-positive nodules were defined as having an average fluorescence intensity of >100 a.u. (scaled a.u./s) on images unmixed for the DsRed spectra (>3 a.u. on images unmixed for the hGSA-NMP1 spectra) (Figure 6). One hundred and eleven foci showed hGSA-NMP1 fluorescence among the 149 RFP-positive foci of ≥0.8 mm with the NIR images (λ_2 = 750 nm). Twenty foci showed hGSA-NMP1 fluorescence with intensity of >3 a.u. among the 237 RFP-negative foci. Thus, hGSA-NMP1 using NIR excitation light was found to have a sensitivity of 74.5% (111 of 149) and a specificity of 92% (217 out of 237).

In contrast, 135 foci showed hGSA-NMP1 fluorescence among the 149 RFP-positive foci of ≥0.8 mm with green images (λ_1 = 550 nm). Twenty foci were found to show hGSA-NMP1 fluorescence with intensity of >3 a.u. among the 237 RFP-negative foci. Thus, hGSA-NMP1 using green light excitation had a sensitivity of 91% (135 out of 149) and specificity of 92% (217 out of 237) in detecting peritoneal implants of ≥0.8 mm.

■ DISCUSSION

Improving the completeness of resection of POCM is likely to improve survival. The unaided human eye cannot detect small or hidden lesions, and therefore, POCM has been a target of research in optically enhanced surgery.

Many fluorescent agents and designs have been proposed for this task. These designs have evolved from the first nontargeted fluorophores, which nonspecifically leaked into abnormal areas, to newer targeted "always on" probes, which bind disease-specific molecular targets, and on to activatable "smart probes," which fluoresce only when binding to the targets. Early on, our laboratory explored targeting probes to POCM using the glycoprotein avidin, a ligand for lectins like the β-D-galactose receptor. Unfortunately, since avidin is a hen egg protein, its

dx.doi.org/10.1021/bc3002419 | *Bioconjugate Chem.* 2012, 23, 1671−1679

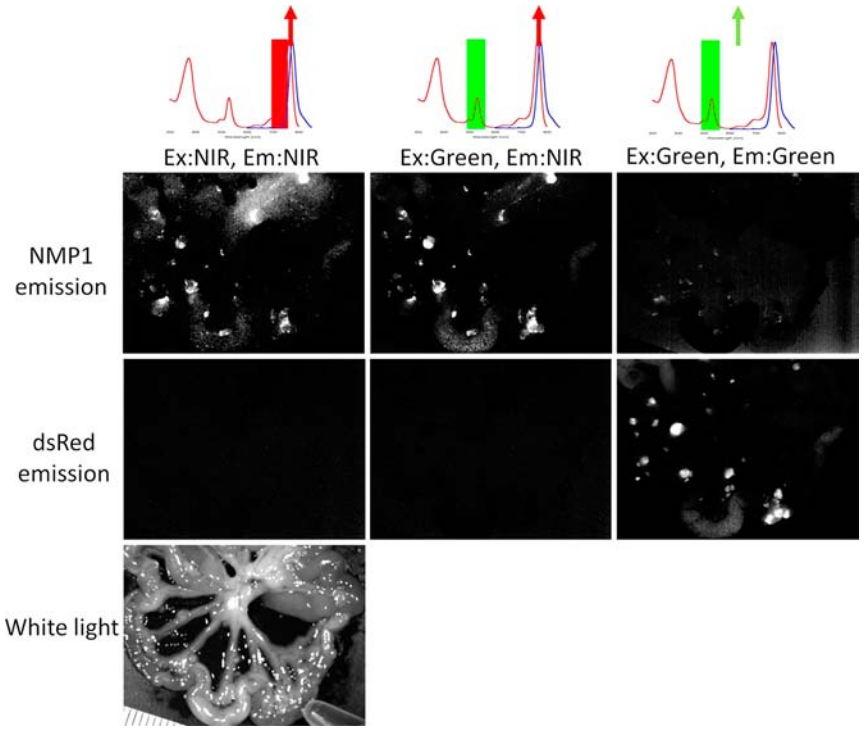


Figure 6. *In situ* spectral fluorescence images of the mesenteric membrane in mice bearing peritoneal SHIN3-dsRed ovarian cancer are shown. Fluorescence signals of NMP1 and RFP, which are shown separately in different spectrally resolved fluorescence images, are mostly coincident. Sensitivity and specificity of hGSA-NMP1 for detecting SHIN3-dsRed tumors of around 1 mm were calculated by examining 386 nodules.

immunogenicity precludes its clinical use. Seeking alternative lectin-targeted moieties, we subsequently conjugated green fluorescent dyes like rhodamine green to a non-immunogenic ligand to human using galactose-conjugated human albumins.[14] Here, we have reported on the newly synthesized bacteriochlorin-based NIR fluorescence agent, hGSA-NMP1, which has several favorable properties for optical imaging of POCM. The hGSA component is highly biocompatible and binds ovarian cancer with high specificity when administered intraperitoneally. Furthermore, the D-galactose receptor is an optimal target for other peritoneal metastases, since it is expressed in a wide range of cancers prone to metastases.[15] In addition, hGSA has already been used as a clinical diagnostic agent for measuring hepatic reserve in Japan.

The NMP1 component also demonstrates desirable features. Its two unique absorption peaks (one in the green and one in the NIR spectrum) have the potential to allow separate imaging of tumor nodules located both superficially and deeper in the abdominal cavity. Although we have covalently conjugated ICG with antibodies to successfully synthesize activatable imaging probes,[5] this chemistry did not work similarly with ICG and albumin-derivatives because ICG can noncovalently bind to albumin and yield brighter emission. IR800 is a hydrophilic variant of pentamethines, designed to resist quenching when conjugated with proteins due to reduced interaction with aromatic rings associated with hydrophobic amino acids. On the other hand, our lab has also synthesized other activatable imaging probes, but these were limited to emissions in the green range.[3] Therefore, activatable versions of hGSA probes, which emit NIR light, presented challenges. In this study, hGSA-NMP1 demonstrated activatable emission of NIR light with very high activation ratios (~100). By combining an "activatable" quenching mechanism with lectin-targeting in the design of hGSA-NMP1, we improved the TBR by minimizing background, and we also improved sensitivity and specificity for tumor foci using a highly fluorescent dye.

NMP1 has similar structure to a second-generation photosensitizer with photodynamic properties, and it has already entered phase I studies for the treatment of colorectal liver metastases.[16,17] Thus, beyond its diagnostic capabilities, hGSA-NMP1 and its derivatives have potential as phototherapeutic agents. Moreover, due to the high efficiency of NMP1, a relatively low dose of hGSA-NMP1 (25 μg), containing less than 1 μg of NMP1 (estimated adult human dose ~3 mg), is required to visualize POCM suggesting that this probe may have an acceptable toxicity profile for clinical use. For comparison, the typical adult dose of fluorescein 10% is 500 mg via intravenous administration.

A potential alternative will be the use of fluorescent proteins, which are excellent endogenous fluorescence emitters to be used for depicting various biological processes both *in vitro* and *in vivo*.[18,19] A recently reported alternative technology to this method is the tumor-specific imaging using telomerase promoter-regulated expression of fluorescent proteins, which are induced with the adenovirus-mediated gene transfection *in vivo*.[20,21] However, for the medical application, fluorescence proteins require virus-mediated *in vivo* gene transfection, which is unlikely to be permitted in humans at least in the short-term. In contrast, one concern of this hGSA-NMP1 probe for clinical translation is whether suitable equipment is available. Not only must such cameras be capable of imaging in the NIR, but they also must deliver near-real-time imaging. Recently, several major optical camera manufacturers introduced cameras that could potentially be introduced into operating rooms. With the proper equipment, fluorescence imaging could be safe, low cost, and highly efficient.[22,23]

A limitation of this and other optical fluorescence imaging probes is that even NIR light can only penetrate to a depth of a

dx.doi.org/10.1021/bc3002419 | *Bioconjugate Chem.* 2012, 23, 1671–1679

maximum of a few centimeters. The detection of deeper lesions is very blurred due to light scattering. However, most ovarian cancer metastases are at or near the surface and can be made more visible by moving bowel and mesentery out of the way so that it is closer to the camera. One concern relating to the detection of metastases at varied depths is that the apparent size of the peritoneal tumor nodule could appear larger than its actual size: an intensely fluorescing tiny mass buried deep in tissue could theoretically yield the same appearance as a larger tumor with lower fluorescence located closer to the surface. The correct size of the lesion would become clear as the lesion was resected and became closer to the surface.[24]

From the surgeon's perspective, the highly activatable characteristics of the hGSA-NMP1 probe can offer significant advantages by allowing more specific visualization enabling more complete surgical resection of surface implants using green excitation light that does not penetrate beyond the surface. Then, after resecting the visible surface tumor implants, NIR excitation could be used to detect deeper lesion utilizing the very high (~100-fold) activation ratio of hGSA-NMP1. The surgeon can then resect down to the subsurface lesion, whereupon excitation can be switched back to green so that these implants can be clearly visualized with high specificity and removed with fluorescence guidance.

In conclusion, we demonstrate that hGSA-NMP1 could be useful in diagnosing peritoneal ovarian cancer implants both at the surface and at a shallow depth in the abdominal cavity with high sensitivity and specificity. This probe binds specifically to the D-galactose receptor on ovarian cancer cells and is activated after internalization that generally requires 3 h for optimal results. The experience in animal models suggests that hGSA-NMP1 may be useful not only for implant detection during surgical resection of peritoneal metastases, but also for targeted phototherapy or drug delivery.

■ ASSOCIATED CONTENT

Supporting Information

Additional figures and data. This material is available free of charge via the Internet at http://pubs.acs.org.

■ AUTHOR INFORMATION

Corresponding Author

*Phone: 301-451-4220; Fax: 301-402-3191; E-mail: kobayash@mail.nih.gov.

Notes

The authors declare no competing financial interest.

■ ACKNOWLEDGMENTS

This research was supported by the Intramural Research Program of the National Institutes of Health, National Cancer Institute, Center for Cancer Research. M.P. thanks University of Maryland Baltimore County for financial support (start-up funds and SRAIS award).

■ REFERENCES

(1) Zivanovic, O., and Chi, D. S. (2008) Surgical resection and reconstruction for advanced and recurrent gynecologic malignancies. *Expert Rev. Obstet. Gynecol. 3*, 677−690.

(2) Kyriazi, S., Kaye, S. B., and deSouza, N. M. (2010) Imaging ovarian cancer and peritoneal metastases−current and emerging techniques. *Nat. Rev. Clin. Oncol. 7*, 381−393.

(3) Hama, Y., Urano, Y., Koyama, Y., Gunn, A. J., Choyke, P. L., and Kobayashi, H. (2007) A self-quenched galactosamine-serum albumin-rhodamineX conjugate: a "smart" fluorescent molecular imaging probe synthesized with clinically applicable material for detecting peritoneal ovarian cancer metastases. *Clin. Cancer Res. 13*, 6335−6343.

(4) Hama, Y., Urano, Y., Koyama, Y., Kamiya, M., Bernardo, M., Paik, R. S., Krishna, M. C., Choyke, P. L., and Kobayashi, H. (2006) In vivo spectral fluorescence imaging of submillimeter peritoneal cancer implants using a lectin-targeted optical agent. *Neoplasia 8*, 607−612.

(5) Ogawa, M., Kosaka, N., Choyke, P. L., and Kobayashi, H. (2009) In vivo molecular imaging of cancer with a quenching near-infrared fluorescent probe using conjugates of monoclonal antibodies and indocyanine green. *Cancer Res. 69*, 1268−1272.

(6) Ogawa, M., Kosaka, N., Urano, Y., Choyke, P. L., and Kobayashi, H. (2009) Activatable optical imaging probes with various fluorophore-quencher combinations. *SPIE Proc. 7190*, 7190−7190Z.

(7) Weissleder, R., Tung, C. H., Mahmood, U., and Bogdanov, A., Jr. (1999) In vivo imaging of tumors with protease-activated near-infrared fluorescent probes. *Nat. Biotechnol. 17*, 375−378.

(8) Kee, H. L., Nothdurft, R., Muthiah, C., Diers, J. R., Fan, D., Ptaszek, M., Bocian, D. F., Lindsey, J. S., Culver, J. P., and Holten, D. (2008) Examination of chlorin-bacteriochlorin energy-transfer dyads as prototypes for near-infrared molecular imaging probes. *Photochem. Photobiol. 84*, 1061−1072.

(9) Kosaka, N., Mitsunaga, M., Longmire, M. R., Choyke, P. L., and Kobayashi, H. (2011) Near infrared fluorescence-guided real-time endoscopic detection of peritoneal ovarian cancer nodules using intravenously injected indocyanine green. *Int. J. Cancer 129*, 1671−1677.

(10) Yu, Z., and Ptaszek, M. (2012) Selective functionalization of dibromobacteriochlorins leading to non-symmetrical derivatives. *Org. Lett.*, DOI: 10.1021/ol3015545.

(11) Krayer, M., Ptaszek, M., Kim, H.-J., Meneely, K. R., Fan, D., Secor, K., and Lindsey, J. S. (2010) Expanded scope of synthetic bacteriochlorins via improved acid catalysis conditions and diverse dihydrodipyrrin-acetals. *J. Org. Chem. 75*, 1016−1039.

(12) Regino, C. A., Ogawa, M., Alford, R., Wong, K. J., Kosaka, N., Williams, M., Feild, B. J., Takahashi, M., Choyke, P. L., and Kobayashi, H. (2010) Two-step synthesis of galactosylated human serum albumin as a targeted optical imaging agent for peritoneal carcinomatosis. *J. Med. Chem. 53*, 1579−1586.

(13) Imai, S., Kiyozuka, Y., Maeda, H., Noda, T., and Hosick, H. L. (1990) Establishment and characterization of a human ovarian serous cystadenocarcinoma cell line that produces the tumor markers CA-125 and tissue polypeptide antigen. *Oncology 47*, 177−184.

(14) Gunn, A. J., Hama, Y., Koyama, Y., Kohn, E. C., Choyke, P. L., and Kobayashi, H. (2007) Targeted optical fluorescence imaging of human ovarian adenocarcinoma using a galactosyl serum albumin-conjugated fluorophore. *Cancer Sci 98*, 1727−1733.

(15) Hama, Y., Urano, Y., Koyama, Y., Choyke, P. L., and Kobayashi, H. (2006) Targeted optical imaging of cancer cells using lectin-binding BODIPY conjugated avidin. *Biochem. Biophys. Res. Commun. 348*, 807−813.

(16) Damoiseau, X., Schuitmaker, H. J., Lagerberg, J. W., and Hoebeke, M. (2001) Increase of the photosensitizing efficiency of the Bacteriochlorin a by liposome-incorporation. *J. Photochem. Photobiol. B 60*, 50−60.

(17) Hopper, C. (2000) Photodynamic therapy: a clinical reality in the treatment of cancer. *Lancet Oncol. 1*, 212−219.

(18) Kishimoto, H., Aki, R., Urata, Y., Bouvet, M., Momiyama, M., Tanaka, N., Fujiwara, T., and Hoffman, R. M. (2011) Tumor-selective, adenoviral-mediated GFP genetic labeling of human cancer in the live mouse reports future recurrence after resection. *Cell Cycle 10*, 2737−2741.

(19) Kishimoto, H., Urata, Y., Tanaka, N., Fujiwara, T., and Hoffman, R. M. (2009) Selective metastatic tumor labeling with green fluorescent protein and killing by systemic administration of telomerase-dependent adenoviruses. *Mol. Cancer Ther. 8*, 3001−3008.

(20) Bouvet, M., and Hoffman, R. M. (2011) Glowing tumors make for better detection and resection. *Sci. Transl. Med. 3*, 110.

(21) Kishimoto, H., Zhao, M., Hayashi, K., Urata, Y., Tanaka, N., Fujiwara, T., Penman, S., and Hoffman, R. M. (2009) In vivo internal tumor illumination by telomerase-dependent adenoviral GFP for precise surgical navigation. *Proc. Natl. Acad. Sci. U. S. A. 106*, 14514−14517.
(22) Levenson, R. M., Lynch, D. T., Kobayashi, H., Backer, J. M., and Backer, M. V. (2008) Multiplexing with multispectral imaging: from mice to microscopy. *ILAR J. 49*, 78−88.
(23) Ntziachristos, V., Bremer, C., and Weissleder, R. (2003) Fluorescence imaging with near-infrared light: new technological advances that enable in vivo molecular imaging. *Eur. Radiol. 13*, 195−208.
(24) Boas, D. A., O'Leary, M. A., Chance, B., and Yodh, A. G. (1994) Scattering of diffuse photon density waves by spherical inhomogeneities within turbid media: analytic solution and applications. *Proc. Natl. Acad. Sci. USA 91*, 4887−4891.

Bioconjugate Chemistry

Article

pubs.acs.org/bc

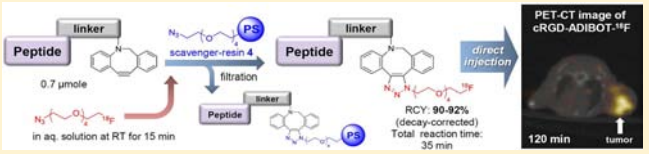
F-18 Labeling Protocol of Peptides Based on Chemically Orthogonal Strain-Promoted Cycloaddition under Physiologically Friendly Reaction Conditions

Kalme Sachin,[†] Vinod H. Jadhav,[†] Eun-Mi Kim,[†] Hye Lan Kim, Sang Bong Lee, Hwan-Jeong Jeong, Seok Tae Lim, Myung-Hee Sohn, and Dong Wook Kim*

Department of Nuclear Medicine, Cyclotron Research Center, Research Institute of Clinical Medicine, Chonbuk National University Medical School, Jeonju, Jeonbuk 561-712, Korea

Supporting Information

ABSTRACT: We introduce the high-throughput synthesis of various ^{18}F-labeled peptide tracers by a straightforward ^{18}F-labeling protocol based on a chemo-orthogonal strain-promoted alkyne azide cycloaddition (SPAAC) using aza-dibenzocyclooctyne-substituted peptides as precursors with ^{18}F-azide synthon to develop peptide based positron emission tomography (PET) molecular imaging probes. The SPAAC reaction and subsequent chemo-orthogonal purification reaction with azide resin proceeded quickly and selectively under physiologically friendly reaction conditions (i.e., toxic chemical reagents-free, aqueous medium, room temperature, and pH ≈7), and provided four ^{18}F-labeled tumor targetable bioactive peptides such as cyclic Arg-Gly-Asp (cRGD) peptide, bombesin (BBN), c-Met binding peptide (cMBP), and apoptosis targeting peptide (ApoPep) in high radiochemical yields as direct injectable solutions without any HPLC purification and/or formulation processes. *In vitro* binding assay and *in vivo* PET molecular imaging study using the ^{18}F-labeled cRGD peptide also demonstrated a successful application of our ^{18}F-labeling protocol.



1. INTRODUCTION

Positron emission tomography (PET) molecular imaging in living subjects provides exciting opportunities to understand fundamental biological processes, disease pathologies and pharmaceutical development.[1,2] Specific molecular imaging probes labeled with positron-emitting radioisotopes must be prepared to measure these processes with PET.[3,4] Among various radioisotopes, fluorine-18 is considered as an ideal positron-emitter due to its excellent chemical, physiological, and nuclear characteristics.[3−7] In this regard, the efficient application of rapid, simple, and reliable ^{18}F-labeling strategies is an extremely important topic to synthesize and obtain new radiopharmaceuticals for PET molecular imaging studies.[8,9]

The implementation of phase display and combinatorial chemistry technologies has allowed the development of novel and diverse peptide-based probes, which can specifically address molecular targets *in vivo* and be rapidly evolving radiolabeled bioactive peptides.[10] In particular, ^{18}F-labeled peptides have received much attention in the field of PET molecular imaging and diagnosis.[11] In general, the direct ^{18}F-labeling method by the radiofluorination with no-carrier-added (nca) for introducing a fluorine-18 into the bioactive peptide at specific sites requires harsh strong basic reaction conditions in organic media, which may not be suitable for these bioactive peptide molecules containing various sensitive functional groups.[12,13] As a result, diverse ^{18}F-labeled building blocks referred to as prosthetic groups as well as the conjugation methods between these prosthetic groups and peptides such as acylation, alkylation, amidation, and hydrazone formation with amino- or thiol- reactive groups, have been developed for the preparation of ^{18}F-labeled peptide based probes.[12,13] However, these established labeling protocols can frequently show synthetic limitations due to the short half-life of fluorine-18 ($t_{1/2}$ = 109.8 min), the denaturation of peptides by reactive reagents or organic media, the complicated synthesis procedure, or the time-consuming purification process, thereby providing relatively low radiochemical yields or/and low purities including low radiospecific activities.[12−14] Additionally, when performing the labeling reactions with ^{18}F-labeled synthon or [^{18}F]fluorine atom, which are usually produced in trace quantities with high radiospecific activity, the use of excess amounts of precursor should be required for a reasonable reaction time and radiochemical yield (RCY), and the resulting mixtures should be purified by high performance liquid chromatography (HPLC) to separate trace quantities of radioprobes from both non-labeled compounds and chemical reagents for increasing PET imaging quality and reducing the toxicity or the side-effects of these radioprobes.[3,4] Therefore, an ideal ^{18}F-labeled method should provide (1) a short reaction time and high RCY with a high purity including a high radiospecific activity; (2) proceed under mild reaction conditions (i.e., room temperature, pH 7, and aqueous medium) to prevent the denaturation of the biomolecules; and (3) make the procedure simple for easy handling and automatic production.

Received: May 4, 2012
Revised: June 20, 2012
Published: July 9, 2012

ACS Publications © 2012 American Chemical Society

dx.doi.org/10.1021/bc3002425 | *Bioconjugate Chem.* 2012, 23, 1680−1686

Recently, the copper(I)-catalyzed azide−alkyne [3 + 2] cycloaddition (CuAAC), which is the so-called "click reaction", has become an emerging method to ligate biomolecules with radioprosthetic groups for the synthesis of radiopharmaceuticals.[15−19] However, the possibility that the Cu(I) catalyst can bind to biomolecules, may lead to various problems, such as blocking or reducing the biological activity, as well as the rate of the CuAAC reaction, and the cytotoxicity by residual copper in products, in the synthetic process of radiolabeled biomolecules using the CuAAC conjugation method.[20−22] In a recent significant advance, an interesting copper-free "click chemistry" based on strain-promoted alkyne−azide cycloaddition (SPAAC) has been developed as a fast and bioorthogonal conjugation protocol for the biological application in live-cell imaging, radioisotope labeling, and surface modification.[23−31] In particular, dibenzocyclooctyne (DIBO) or aza-dibenzocyclooctyne (ADIBO) derivatives have shown good performance in this SPAAC reaction for these purposes (Figure 1).[32−35] In this article, we introduce a

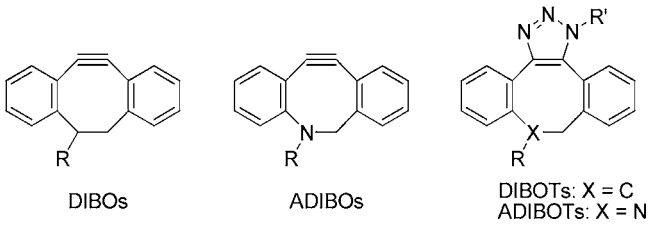


Figure 1. Strain-promoted compounds and their corresponding products by copper-free click reactions. DIBOs = dibenzocyclooctynes; ADIBO = aza-dibenzocyclooctynes; ADIBOT = aza-dibenzocycloocta-triazoles.

facile ^{18}F-labeling protocol based on a copper-free SPAAC reaction using the ADIBO peptide system with [^{18}F]fluoro-azide synthon to prepare ^{18}F-labeled peptide tracers, and this protocol exactly meets the above requirement.

2. EXPERIMENTAL SECTION

2.1. General. Unless otherwise noted, all reagents and solvents were commercially available. cRGDyK, C-Bombesin, and cMBP were purchased from PEPTRON Co. (South Korea), and ApoPep was purchased from FutureChem Co. (South Korea). Reaction progress was followed by TLC on 0.25 mm silica gel glass plates containing F-254 indicator. Visualization on TLC was monitored by UV light or a radio-TLC scanner. Flash chromatography was performed using 230−400 mesh silica gel (Merck KGaA). ^{1}H spectra were recorded on a 600 MHz spectrometer. Chemical shifts were reported in δ units (ppm) relative to tetramethylsilane, and coupling constants were reported in hertz. ^{13}C NMR spectra were acquired at 100 or 150 MHz. Low- and high-resolution electron impact (EI) or fast atom bombardment (FAB) mass spectra were obtained. [^{18}F]Fluoride ion was produced from a cyclotron (KIRAMS 13 MeV, South Korea) using the ^{18}O(p,n)^{18}F nuclear reaction with 13 MeV proton irradiation of an enriched [^{18}O]H_2O target. High performance liquid chromatography (HPLC) was performed with a spectra system (Thermo Scientific, Waltham, MA) using a semipreparative column (C18 silica gel, 10 μm, 10 × 250 mm) and an analytic column (C18 silica gel, 5 μm, 4.6 × 250 mm). The eluant was simultaneously monitored by a UV detector (215 and 254 nm) and a NaI(Tl) radioactivity detector. Radioactivity was measured in a dose calibrator.

2.2. Representative Procedure for the Preparation of [^{18}F]2. [^{18}F]fluoride was produced in a cyclotron by the ^{18}O(p, n)^{18}F reaction. A volume of 100−200 μL of [^{18}F]fluoride (1665 MBq) in water was added to a vacutainer containing n-Bu_4NHCO_3 (40% aq, 3.7 μL, 7.68 μmol). The azeotropic distillations were conducted with 200 μL aliquots of CH_3CN at 75 °C under a stream of nitrogen. A [^{18}F]fluoride displacement reaction of **14** (2.5 mg, 7.32 μmol) with n-Bu_4N[^{18}F]F in *tert*-amyl alcohol (500 μL) was carried out in a reaction vial at 100 °C for 20 min. After cooling to room temperature, the solvent was removed with a gentle stream of nitrogen. The crude compound was injected onto reverse-phase HPLC with acetonitrile (1 mL) and purified. The desired compound [^{18}F]**2** was collected from HPLC (t_R = 11.1 min; C18 silica gel, 10 μm, 4.6 × 250 mm; 0.1% TFA in H_2O/acetonitrile = 30:70 (v/v); 214 nm; 2 mL/min). Then 790 MBq of [^{18}F]**2** was obtained after evaporation under a stream of nitrogen in 63% decay-corrected radiochemical yield with high radiochemical purity (>99%). The total synthesis time was 45 min. For the identification of the radioactive-product, the collected HPLC fraction was coinjected with the nonradioactive **2**.

2.3. ADIBO Scavenger Azide-Resin 4. Pentaethylene glycolic azide **13** (3.3 g, 12.5 mmol) was added to a suspension of NaH (60% in mineral oil, 500 mg, 12.5 mmol) in dried THF at 0 °C, and stirred for 30 min at 0 °C. Merrifield resin (1.0 g, 2.5 mmol, 1% DVB, 2.5 mmol Cl/g) was then added to the reaction mixture, which was followed by the addition of tetrabutylammonium iodide (920 mg, 2.5 mmol). The reaction mixture was then stirred over 3 days at 25 °C. After filtration, the resin was washed repeatedly with THF, water, acetone, water, methanol, and finally with dichloromethane. After drying under high vacuum, 1.1 g of resin **4** was obtained and identified by solid state NMR and elemental analysis: ^{13}C NMR (solid state) δ 41 (aliphatic polystyrene skeleton), 51 (terminal azido methylene carbon), 71−74 (ether carbons), 120−150 (aromatic polystyrene skeleton). Anal. N, 4.7 (1.05 mmol of azide portion per gram).

2.4. Typical Procedure for the Preparation of cRGD-ADIBOT-^{18}F. To a solution of cRGD-ADIBO (1.0 mg, 0.77 μmol) in 0.1 mL of EtOH/water (1/1) was added a solution of [^{18}F]**2** (500 MBq) in 0.1 mL of EtOH/water (1/1). The reaction mixture was stirred at room temperature for 15 min. To remove nonreacted cRGD-ADIBO precursor, 50 mg of ADIBO-precursor−scavenger-resin **4** (1.05 mmol of azide portion/g) was added to the reaction mixture, and this heterogeneous solution was then stirred for approximately 20 min at room temperature. After the filtration and washing with PBS solution (2 × 0.5 mL), 368 MBq of cRGD-ADIBOT-^{18}F was obtained in 92% decay-corrected radiochemical yield (35 min total reaction time) as a direct injectable solution for animal PET image study. Both isomers of the triazole were collected and treated as one compound.

2.5. *In Vitro* Binding Assays. *In vitro* integrin $\alpha_v\beta_3$ binding affinity and specificity of cRGD-ADIBOT-F was assessed via a displacement cell-binding assay using ^{125}I-echistatin (μCi/well) as a radioligand. Experiments were performed on U87MG cells by a previously published method. For the integrin $\alpha_v\beta_3$ binding affinity assay, U87MG cells were seeded onto 96-well plates at 3 × 10^4 cells per well and incubated overnight at 37 °C. Serial dilutions of cRGD-ADIBOT-F and cRGDyk (corresponding to concentrations of 0.45 nM to 1.4 μM) were added to 96-well plates. The plates were then incubated for 0.5 h at 37 °C, washed, and dried, and 0.1 mL of 2 N NaOH solution was added to each

dx.doi.org/10.1021/bc3002425 | *Bioconjugate Chem.* 2012, 23, 1680−1686

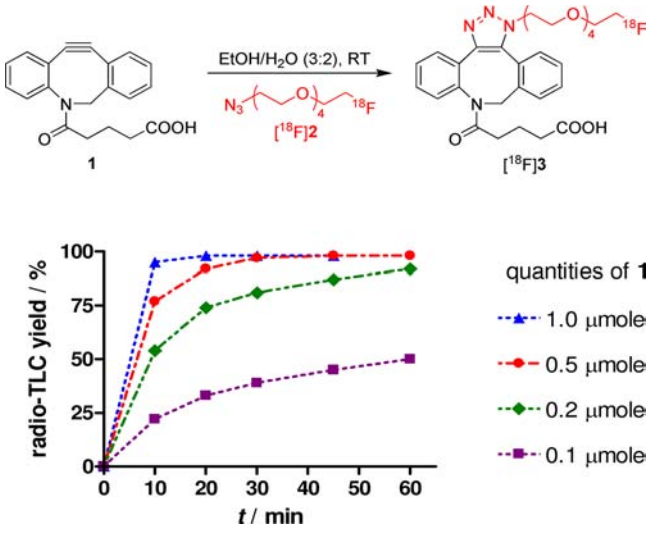


Figure 2. Copper-free strain-promoted alkyne azide cycloaddition (SPAAC) reaction of the model ADIBO compound **1** with [^{18}F]fluorohexaethylene glycolic azide ([^{18}F]**2**) based on levels of **1**.

well to facilitate cell lysis. The lysates were collected and counted in a gamma counter (Perkin-Elmer, USA). Binding affinities (IC_{50}) for both receptors were calculated by nonlinear regression analysis (sigmoidal dose response equation) using the GraphPad Prism 4.0 computer-fitting program (Graph-Pad Software, San Diego, CA, USA).

2.6. *In Vivo* MicroPET Imaging. All animal experiments were performed in compliance with the policies and procedures of Institutional Animal Care and Use Committee for animal treatment. Female athymic nude mice (4-wk, *nu/nu*) were obtained from Orient-Bio (Seoul, Korea). Mice were anesthetized by subcutaneous injection with a mixture of ketamine (50 mg/kg) and xylazine (10 mg/kg). After sedation, glioblastoma (U87MG) tumors were established by the subcutaneous injection in the right flank of 5×10^6 cells mixed with matrigel. The mice underwent PET/CT studies when the tumor volume reached 150−250 mm^3 (eq = length × W^2 × 0.5 4−5 wk after inoculation). PET and CT scans and image analyses were performed using a microPET/CT scanner (GE Healthcare). About 1.8−2.6 MBq of cRGD-ADIBOT-^{18}F was intravenously injected into each mouse under isoflurane anesthesia (1.5%). PET images were acquired at 10, 30, and 60 min, 2 and 3 h after postinjection. For each microPET scan, regions of interest (ROIs) were drawn over the tumor and muscle on decay-corrected whole-body images that were gained by 3D-OSEM iterative image reconstruction (Amira 3.1, GE Healthcare). For receptor-blocking experiments, nude mice bearing U87MG tumors were scanned after coinjection with cRGD-ADIBOT-^{18}F (1.8−2.6 MBq) and cRGDyk (10 mg/kg). The radioactivity concentration within the tumor or muscle was obtained from the mean value, and then these values were compared.

2.7. Biodistribution Study. Female BALB/c mice (n = 4, aged 4 weeks with 15 g) were obtained from Orient Bio, Inc. (Seoul, Korea). All animal experiments were performed according to the Institutional Animal Care and Use Committee for animal treatment of Chonbuk National University. U87MG tumor xenografted mice were subjected to the biodistribution study when the tumor reached in 0.7−1.0 cm. All mice received intravenous (i.v.) injections through the tail vein with approximately 1.11 MBq of cRGD-ADIBOT-^{18}F. At 120 min after the radiotracer injection, the animals were anesthetized and

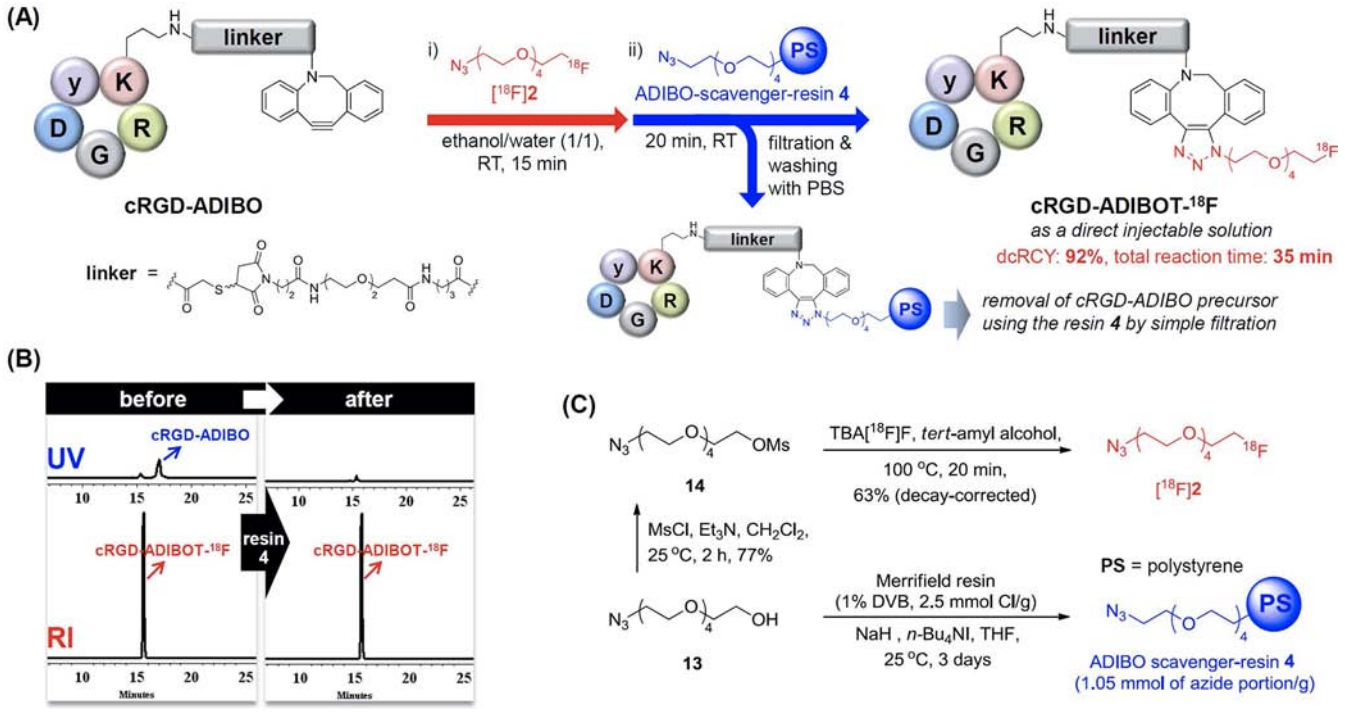


Figure 3. (A) Schematic procedure for the preparation of cRGD-ADIBOT-^{18}F with [^{18}F]**2** and subsequent chemo-orthogonal purification using a polystyrene-supported azide resin **4** as a ADIBO-precursor−scavenger. (B) HPLC chromatograms of the cRGD-ADIBOT-^{18}F reaction mixture before and after treatment with the ADIBO-precursor−scavenger-resin **4**. (C) Schematic procedure for the preparation of [^{18}F]fluoropentaethylene glycolic azide ([^{18}F]**2**) and ADIBO scavenger azide-resin **4**.

dx.doi.org/10.1021/bc3002425 | *Bioconjugate Chem.* 2012, 23, 1680−1686

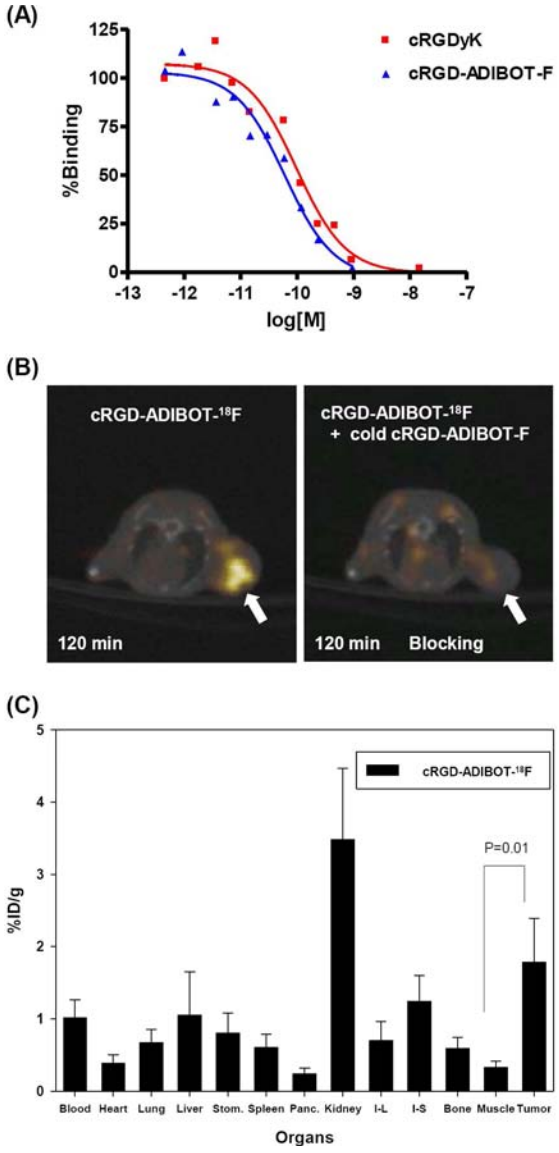


Figure 4. (A) Competitive binding assay of cRGD-ADIBOT-F in comparison with the nonmodified cRGDyK with ^{125}I-echistatin using U87MG cells. (B) *In vivo* evaluation of cRGD-ADIBOT-^{18}F; transaxial microPET-CT images of U87MG tumor bearing mice at 120 min postinjection of 1.8 MBq of cRGD-ADIBOT-^{18}F without and with (denoted as "blocking") a coinjection of nonradioactive cRGD-ADIBOT-F (10 mg/kg). Tumors are indicated by white arrows. (C) Biodistribution of cRGD- ADIBOT-^{18}F at 2 h. Data are expressed as normalized accumulation of activity in % ID/g ± SD (n = 4).

necropsied. Tissues were weighed and counted on a gamma counter. Uptake in each tissue was expressed as the percentage injected dose per gram of tissue (% ID/g). All experiments was repeated many times, and the results were presented as the mean ± standard deviation. A p-value of less than 0.05 was considered statistically significant.

3. RESULTS AND DISCUSSION

3.1. Model SPAAC Reactions Using a Simple ADIBO Precursor with ^{18}F-Labeled Synthon. Considering the highly bio- and chemo-orthogonal features of the SPAAC reaction, we attempted to find the minimal amount of ADIBO peptide precursor enabling a reasonable reaction time and a high RCY. For this purpose, we examined the SPAAC based conjugation reaction using different quantities (0.1−1.0 μmol) of a simple model ADIBO precursor compound **1** with a 481 MBq (specific radioactivity: 42 GBq/μmol) of [^{18}F]-fluoropentaethylene glycolic azide ([^{18}F]**2**, see Figure 3C) as a ^{18}F-labeled synthon at room temperature in aqueous solution (ethanol/water = 3/2) as shown in Figure 2. On a 1.0−0.5 μmol reaction scale of the ADIBO compound **1**, the SPAAC reactions were completed within a reasonable reaction time (15−30 min), affording the ^{18}F-labeled aza-dibenzocyclooctatriazole (ADIBOT) product ([^{18}F]**3**) in nearly quantitative RCYs. However, the use of <0.2 μmol of **1** required too a long reaction time in the same reaction. This finding inspired us to explore F-18 peptide labeling by copper-free click chemistry on a 1.0−0.5 μmol reaction scale under physiologically friendly reaction conditions.

3.2. Synthesis of F-18 Labeled cRGD Based on Chemo-Orthogonal SPAAC Reaction Protocol. From four tumor targetable bioactive peptides such as cyclic Arg-Gly-Asp (cRGD) peptide,[36,37] bombesin (BBN),[38−40] c-Met binding peptide (cMBP),[41,42] and apoptosis targeting peptide (ApoPep),[43] we prepared the corresponding ADIBO substituted peptides, cRGD-ADIBO, BBN-ADIBO, cMBP-ADIBO, and ApoPep-ADIBO, respectively, as chemically orthogonal reactive precursors (see Supporting Information). Figure 3A illustrated the preparation of the ^{18}F-labeled cRGD peptide (cRGD-ADIBOT-^{18}F). The SPAAC reaction of cRGD-ADIBO precursor (0.77 μmol) with [^{18}F]**2** in ethanol/water (1/1) solution was completed within 15 min, providing cRGD-ADIBOT-^{18}F quantitatively with excess of nonlabeled cRGD-ADIBO precursor. Considering a chemo-orthogonal scavenger-assisted separation concept to avoid HPLC purification process,[44] we prepared a polystyrene-supported azide resin (resin **4**, 1.05 mmol of azide portion per gram) as an ADIBO precursor scavenger (Figure 3C), and the subsequent treatment of this crude solution with the azide resin **4** for 20 min could allow the nonreacted cRGD-ADIBO precursor to be removed as shown in the HPLC analysis of the reaction mixture before and after treatment with the scavenger resin **4** (Figure 3B). After filtration and washing of the resin **4** with PBS solution, a cRGD-ADIBOT-^{18}F was produced within approximately 35 min total reaction time in a 92% decay-corrected RCY (dcRCY) with >98% of radiochemical purity as a direct injectable solution for an animal PET image study without any HPLC purification and formulation process by this F-18 labeling protocol.

3.3. *In Vitro* and *in Vivo* Evaluation of cRGD-ADIBOT-^{18}F. To verify that the incorporation of the ^{18}F-labeled ADIBOT prosthetic group into the peptide did not affect its biological behavior *in vitro*, the affinities of the nonradioactive standard cRGD-ADIBOT-F compound and the nonmodified corresponding peptide (cRGDyK) were determined for binding to integrin $\alpha_v\beta_3$ expressing U87MG cells in a competitive binding assay against ^{125}I-echistatin. Figure 4A showed that the modified cRGD-ADIBOT-F had a similar binding affinity with the nonmodified cRGDyK, suggesting that the attachment of the ^{18}F-labeled ADIBOT prosthetic group into the peptide had no effect on its specific binding. We also conducted an *in vivo* evaluation of cRGD-ADIBOT-^{18}F using the micro-PET-CT system. A transaxial image of a mouse bearing a U87MG tumor on the right front leg at 120 min postinjection of 1.8 MBq of cRGD-ADIBOT-^{18}F is shown in Figure 4B (left). The tumor was clearly visible with a high contrast to contralateral background. As shown in Figure 4B (right), uptake of a tumor coinjected with 10 mg/kg nonradioactive cRGD-ADIBOT-F was significantly lower than that in a nonblocked a mouse

dx.doi.org/10.1021/bc3002425 | *Bioconjugate Chem.* 2012, 23, 1680−1686

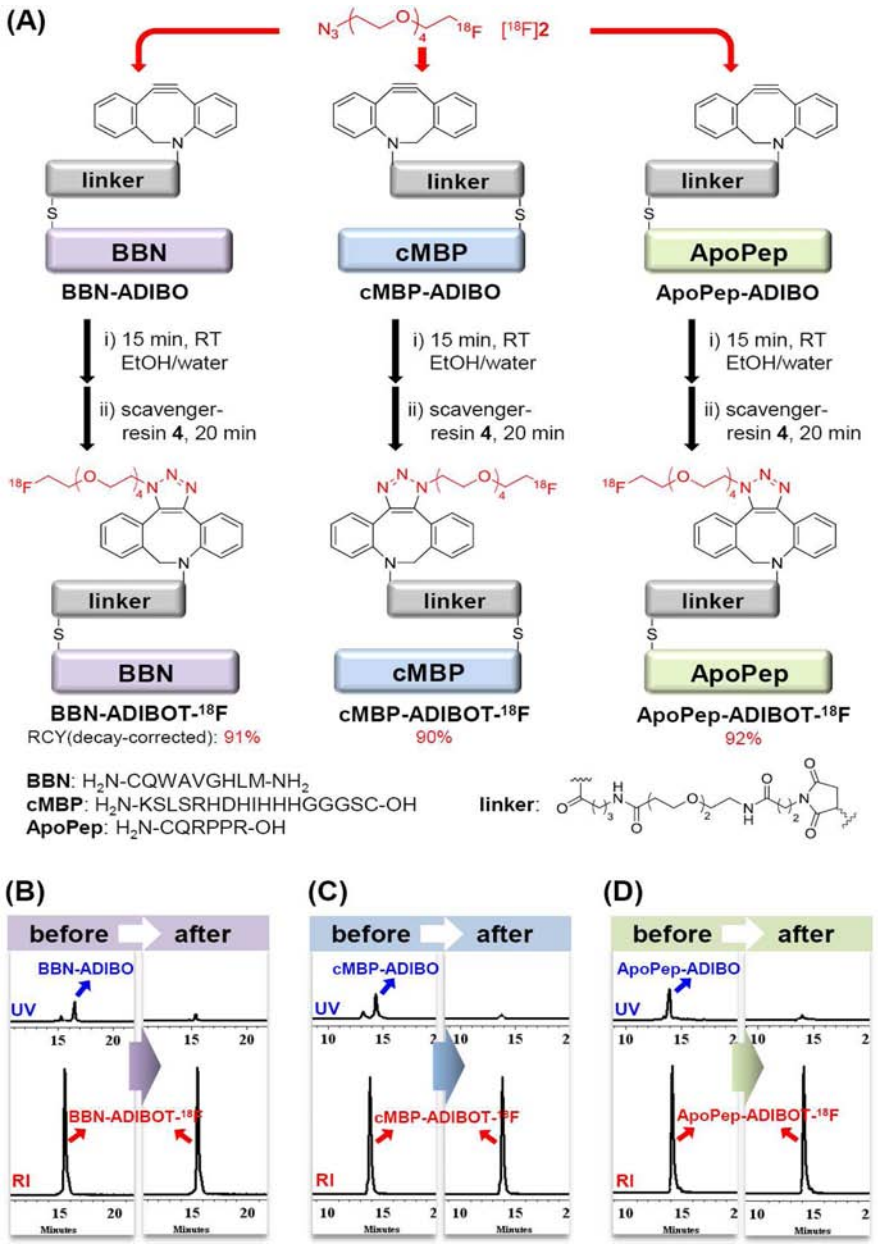


Figure 5. (A) Schematic high-throughput synthesis of BBN-ADIBOT-^{18}F, cMBP-ADIBOT-^{18}F, and ApoPep-ADIBOT-^{18}F. (B, C, and D) HPLC chromatograms of the BBN-ADIBOT-^{18}F (B), cMBP-ADIBOT-^{18}F (C), and ApoPep-ADIBOT-^{18}F (D) reaction mixtures before and after treatment with the ADIBO scavenger-resin **4**.

model. These *in vivo* studies demonstrated a successful specific visualization of integrin $\alpha_v\beta_3$ expression, indicating a high potential for our sequential F-18 labeling protocol in future PET imaging studies. Figure 4C showed the result of the biodistribution experiment. The tissue distribution studies showed that there was a significantly high uptake of cRGD-ADIBOT-^{18}F radiotracer in tumor−principal target tissues for integrin $\alpha_v\beta_3$ compared to nontarget tissues such as muscle.

3.4. High-Throughput Synthesis of ^{18}F-Labeled Peptides. To demonstrate that our strategy is generally applicable to other more complicated peptides, we carried out the SPAAC reactions with three ADIBO substituted peptide precursors, such as BBN-ADIBO, cMBP-ADIBO, and ApoPep-ADIBO, under the same reaction conditions as that described in Figure 3A for F-18 labeling. Figure 5A showed that, with [^{18}F]**2** from its one time production, three ^{18}F-labeled BBN (BBN-ADIBOT-^{18}F), cMBP (cMBP-ADIBOT-^{18}F), and ApoPep (ApoPep-ADIBOT-^{18}F) were obtained readily and simultaneously in excellent dcRCYs (90−92%) and radiochemical purities (>98%) within only a 35 min total reaction time by this copper-free SPAAC reaction and subsequent treatment of the azide-resin **4**. Figure 5B−D demonstrated the successful removal of all three unreacted ADIBO precursors from the corresponding reaction mixture solutions by the scavenger resin **4**. In particular, the ApoPep-ADIBOT-^{18}F tracer showed almost the same retention time as its precursor on the HPLC chromatogram (Figure 5D), which can make the separation of this tracer using a conventional HPLC system difficult or impossible, whereas the chemo-orthogonal scavenger method can provide a highly efficient and easy purification process even though the tracer has the same HPLC retention time as its precursor.

dx.doi.org/10.1021/bc3002425 | *Bioconjugate Chem.* 2012, 23, 1680−1686

4. CONCLUSIONS

In summary, we have described a tremendously efficient and straightforward ^{18}F-labeling protocol platform based on the highly chemo-orthogonal copper-free SPAAC reaction using the ADIBO peptide precursors with the ^{18}F-azide synthon for the high-throughput synthesis of ^{18}F-labeled peptide tracers. In this method, the SPAAC conjugation reaction and subsequent chemo-orthogonal treatment of the azide-resin proceeded quickly and selectively under physiologically friendly reaction conditions (i.e., toxic chemical reagents-free, aqueous medium, room temperature, and pH ≈7), and provided ^{18}F-labeled peptide tracers in high RCY as direct injectable solutions without any HPLC purification and formulation processes for the *in vivo* molecular imaging study. The successful application of our F-18 labeling protocol was also demonstrated by *in vitro* and *in vivo* studies on cRGD-ADIBOT-^{18}F. We believe that this is a very versatile protocol for numerous applications in the field of radiopharmaceutical science and molecular imaging. Further studies on the development of a more efficient protocol for automated production and application of *in vivo* PET molecular imaging studies using ^{18}F-labeled peptides prepared by this protocol are currently underway.

■ ASSOCIATED CONTENT

Ⓢ Supporting Information

Full experimental procedures and characterization data of all compounds. This material is available free of charge via the Internet at http://pubs.acs.org.

■ AUTHOR INFORMATION

Corresponding Author

*Tel: +82-63-250-2396. Fax: +82-63-255-1172. E-mail: kimdw@chonbuk.ac.kr.

Author Contributions

†These authors contributed equally to this work.

Notes

The authors declare no competing financial interest.

■ ACKNOWLEDGMENTS

This work was supported by the Nuclear Research & Development Program of the National Research Foundation of Korea (NRF) grant, funded by the Korean government (MEST) (grant code: 2011-0006322 and 2011-0030952), and the Conversing Research Center Program through the MEST (grant code: 2011K000705).

■ REFERENCES

(1) Phelps, M. E. (2000) Positron emission tomography provides molecular imaging of biological processes. *Proc. Natl. Acad. Sci. U.S.A. 97*, 9226−9233.

(2) Massoud, T. F., and Gambhir, S. S. (2003) Molecular imaging in living subjects: seeing fundamental biological processes in a new light. *Genes Dev. 17*, 545−580.

(3) Vallabhajosula, S. (2009) *Molecular Imaging: Radiopharmaceuticals for PET and SPECT*, 1st ed., pp 133−193, Springer, New York.

(4) Ametamey, S. M., Honer, M., and Schubiger, P. A. (2008) Molecular imaging with PET. *Chem. Rev. 108*, 1501−1516.

(5) Gambhir, S. S. (2002) Molecular imaging of cancer with positron emission tomography. *Nature Rev. 2*, 683−693.

(6) Schirrmacher, R., Wängler, C., and Schirrmacher, S. (2007) Recent developments and trends in F-18-radiochemistry: Syntheses and applications. *Mini-Rev. Org. Chem. 4*, 317−329.

(7) Kim, D. W., Jeong, H.-J., Lim, S. T., and Sohn, M.-H. (2010) Recent trends in the nucleophilic [^{18}F]-radiolabeling method with no-carrier-added [^{18}F]fluoride. *Nucl. Med. Mol. Imaging 44*, 25−32.

(8) Kim, D. W., Ahn, D.-S., Oh, Y.-H., Lee, S., Kil, H. S., Oh, S. J., Lee, S. J., Kim, J. S., Ryu, J. S., Moon, D. H., and Chi, D. Y. (2006) A new class of S_N2 reaction catalyzed by protic solvents: facile fluorination for isotopic labeling of diagnostic molecules. *J. Am. Chem. Soc. 128*, 16394−16397.

(9) Miller, P. W., Long, N. J., Vilar, R., and Gee, A. D. (2008) Synthesis of ^{11}C, ^{18}F, ^{15}O, and ^{13}N radiolabels for positron emission tomography. *Angew. Chem., Int. Ed. 47*, 8998−9033.

(10) Deutscher, S. L. (2010) Phage display in molecular imaging and diagnosis of cancer. *Chem. Rev. 110*, 3196−3211.

(11) Chen, K., and Conti, P. S. (2010) Target-specific delivery of peptide-based probes for PET imaging. *Adv. Drug Delivery Rev. 62*, 1005−1022.

(12) Okarvi, S. M. (2001) Recent progress in fluorine-18 labelled peptide radiopharmaceuticals. *Eur. J. Nucl. Med. 28*, 929−938.

(13) Wuest, F. (2005) Aspects of positron emission tomography radiochemistry as relevant for food chemistry. *Amino Acids 29*, 323−339.

(14) Lee, S., Xie, J., and Chen, X. (2010) Peptides and peptide hormones for molecular imaging and disease diagnosis. *Chem. Rev. 110*, 3087−3111.

(15) Kolb, H. C., Finn, M. G., and Sharpless, K. B. (2001) Click chemistry: diverse chemical function from a few good reactions. *Angew. Chem., Int. Ed. 40*, 2004−2021.

(16) Mamat, C., Ramenda, T., and Wuest, F. R. (2009) Application of click chemistry for the synthesis of radiotracers for molecular imaging. *Mini-Rev. Org. Chem. 6*, 21−34.

(17) Mindt, T. L., Struthers, H., Brans, L., Anguelov, T., Schweinsberg, C., Maes, V., Tourwé, D., and Schibli, R. (2006) "Click to chelate": synthesis and installation of metal chelates into biomolecules in a single step. *J. Am. Chem. Soc. 128*, 15096−15097.

(18) Thonon, D., Kech, C., Paris, J., Lemaire, C., and Luxen, A. (2009) New strategy for the preparation of clickable peptides and labeling with 1-(azidomethyl)-4-[^{18}F]-fluorobenzene for PET. *Bioconjugate Chem. 20*, 817−823.

(19) Maschauer, S., Einsiedel, J., Haubner, R., Hocke, C., Ocker, M., Hübner, H., Kuwert, T., Gmeiner, P., and Prante, O. (2010) Labeling and glycosylation of peptides using click chemistry: a general approach to ^{18}F-glycopeptides as effective imaging probes for positron emission tomography. *Angew. Chem., Int. Ed. 49*, 976−979.

(20) Baskin, J. M., Prescher, J. A., Laughlin, S. T., Agard, N. J., Chang, P. V., Miller, I. A., Lo, A., Codelli, J. A., and Bertozzi, C. R. (2007) Copper-free click chemistry for dynamic in vivo imaging. *Proc. Natl. Acad. Sci. U.S.A. 104*, 16793−16797.

(21) Lallana, E., Fernandez-Megia, E., and Riguera, R. (2009) Surpassing the use of copper in the click functionalization of polymeric nanostructures: a strain-promoted approach. *J. Am. Chem. Soc. 131*, 5748−5750.

(22) Kennedy, D. C., McKay, C. S., Legault, M. C. B., Danielson, D. C., Blake, J. A., Pegoraro, A. F., Stolow, A., Mester, Z., and Pezacki, J. P. (2011) Cellular consequences of copper complexes used to catalyze bioorthogonal click reactions. *J. Am. Chem. Soc. 133*, 17993−18001.

(23) Sletten, E. M., and Bertozzi, C. R. (2011) From mechanism to mouse: a tale of two bioorthogonal reactions. *Acc. Chem. Res. 44*, 666−676.

(24) Debets, M. F., van Berkel, S. S., Dommerholt, J., Dirks, A. J., Rutjes, F. P. J. T., and van Delft, F. L. (2011) *Acc. Chem. Res. 44*, 805−815.

(25) Jewett, J. C., and Bertozzi, C. R. (2010) Bioconjugation with strained alkenes and alkynes. *Chem. Soc. Rev. 39*, 1272−1279.

(26) Sletten, E. M., and Bertozzi, C. R. (2009) Bioorthogonal chemistry: fishing for selectivity in a sea of functionality. *Angew. Chem., Int. Ed. 48*, 6974−6998.

(27) Laughlin, S. T., Baskin, J. M., Amacher, S. L., and Bertozzi, C. R. (2008) In vivo imaging of membrane-associated glycans in developing zebrafish. *Science 320*, 664−667.

(28) Jewett, J. C., Sletten, E. M., and Bertozzi, C. R. (2010) Rapid Cu-free click chemistry with readily synthesized biarylazacyclooctynones. *J. Am. Chem. Soc. 132*, 3688−3690.
(29) Campbell-Verduyn, L. S., Mirfeizi, L., Schoonen, A. K., Dierckx, R. A., Elsinga, P. H., and Feringa, B. L. (2011) Strain-promoted copper-free "click" chemistry for ^{18}F radiolabeling of bombesin. *Angew. Chem., Int. Ed. 50*, 11117−11120.
(30) Carpenter, R. D., Hausner, S. H., and Sutcliffe, J. L. (2011) Copper-free click for PET: rapid 1,3-dipolar cycloadditions with a fluorine-18 cyclooctyne. *ACS Med. Chem. Lett. 2*, 885−889.
(31) Bouvet, V., Wuest, M., and Wuest, F. (2011) Copper-free click chemistry with the short-lived positron emitter fluorine-18. *Org. Biomol. Chem. 9*, 7393−7399.
(32) Ning, X., Guo, J., Wolfert, M. A., and Boons, G.-J. (2008) Visualizing metabolically labeled glycoconjugates of living cells by copper-free and fast huisgen cycloadditions. *Angew. Chem., Int. Ed. 47*, 2253−2255.
(33) Poloukhtine, A. A., Wolfert, M. A., Mbua, N. E., Boons, G.-J., and Popik, V. V. (2009) Selective labeling of living cells by a photo-triggered click reaction. *J. Am. Chem. Soc. 131*, 15769−15776.
(34) Debets, M. F., van Berkel, S. S., Schoffelen, S., Rutjes, F. P. J. T., van Hest, J. C. M., and van Delft, F. L. (2010) Aza-dibenzocyclooctynes for fast and efficient enzyme PEGylation via copper-free (3 + 2) cycloaddition. *Chem. Commun. 46*, 97−99.
(35) Varga, B. R., Kállay, M., Hegyi, K., Béni, S., and Kele, P. (2012) A non-fluorinated monobenzocyclooctyne for rapid copper-free click reactions. *Chem.—Eur. J. 18*, 822−828.
(36) Schottelius, M., Laufer, B., Kessler, H., and Wester, H.-J. (2009) Ligands for mapping alphavbeta3-integrin expression in vivo. *Acc. Chem. Res. 42*, 969−980.
(37) Li, Z.-B., Wu, Z., Chen, K., Chin, F. T., and Chen, X. (2007) Click chemistry for ^{18}F-labeling of RGD peptides and microPET imaging of tumor integrin $\alpha_v\beta_3$ expression. *Bioconjugate Chem. 18*, 1987−1994.
(38) Zhang, X., Cai, W., Cao, F., Schreibmann, E., Wu, Y., Wu, J. C., Xing, L., and Chen, X. (2006) ^{18}F-labeled bombesin analogs for targeting GRP receptor-expressing prostate cancer. *J. Nucl. Med. 47*, 492−501.
(39) Liu, Z., Yan, Y., Liu, S., Wang, F., and Chen, X. (2009) ^{18}F, ^{64}Cu, and ^{68}Ga Labeled RGD-bombesin heterodimeric peptides for PET imaging of breast cancer. *Bioconjugate Chem. 20*, 1016−1025.
(40) Höhne, A., Mu, L., Honer, M., Schubiger, P. A., Ametamey, S. M., Graham, K., Stellfeld, T., Borkowski, S., Berndorff, D., Klar, U., Voigtmann, U., Cyr, J. E., Friebe, M., Dinkelborg, L., and Srinivasan, A. (2008) Synthesis, ^{18}F-labeling, and in vitro and in vivo studies of bombesin peptides modified with silicon-based building blocks. *Bioconjugate Chem. 19*, 1871−1879.
(41) Kim, K., Hur, Y., Ryu, E. K., Rhim, J. H., Choi, C. Y., Baek, C. M., Lee, J. H., and Chung, J. (2007) A neutralizable epitope is induced on HGF upon its interaction with its receptor cMet. *Biochem. Biophys. Res. Commun. 354*, 115−121.
(42) Kim, E.-M., Joung, M.-H., Lee, C.-M., Jeong, H.-J., Lim, S. T., Sohn, M.-H., and Kim, D. W. (2010) Synthesis of Tc-99m labeled 1,2,3-triazole-4-yl c-met binding peptide as a potential c-met receptor kinase positive tumor imaging agent. *Bioorg. Med. Chem. Lett. 20*, 4240−4243.
(43) Wang, K., Purushotham, S., Lee, J.-Y., Na, M.-H., Park, H., Oh, S.-J., Park, R. -W., Park, J. Y., Lee, E., Cho, B. C., Song, M.-N., Baek, M.-C., Kwak, W., Yoo, J., Hoffman, A. S., Oh, Y.-K., Kim, I.-S., and Lee, B.-H. (2010) In vivo imaging of tumor apoptosis using histone H1-targeting peptide. *J. Controlled Release 148*, 283−291.
(44) Reiner, T., Keliher, E. J., Earley, S., Marinelli, B., and Weissleder, R. (2011) Synthesis and in vivo imaging of a ^{18}F-labeled PARP1 inhibitor using a chemically orthogonal scavenger-assisted high-performance method. *Angew. Chem., Int. Ed. 50*, 1922−1925.

Bioconjugate Chemistry

Article

pubs.acs.org/bc

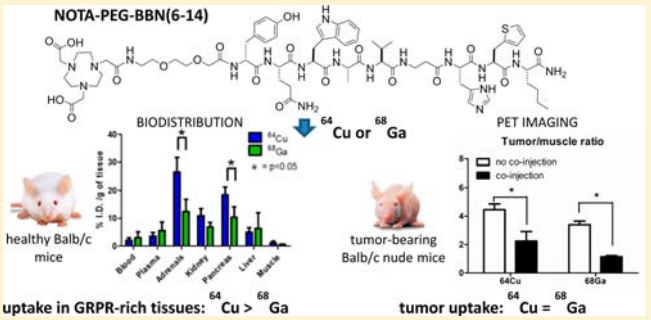
Novel Radiolabeled Peptides for Breast and Prostate Tumor PET Imaging: ^{64}Cu/and ^{68}Ga/NOTA-PEG-[D-Tyr^{6},βAla^{11},Thi^{13},Nle^{14}]BBN(6−14)

Patrick Fournier,[†] Véronique Dumulon-Perreault,[†] Samia Ait-Mohand,[†] Sébastien Tremblay,[†] François Bénard,[‡] Roger Lecomte,[†] and Brigitte Guérin*[,†]

[†]Centre d'imagerie moléculaire de Sherbrooke (CIMS), Centre Hospitalier Universitaire de Sherbrooke and, Department of Nuclear Medicine and Radiobiology, Université de Sherbrooke, 3001, 12th Avenue North, Sherbrooke, Quebec, Canada, J1H 5N4

[‡]BC Cancer Agency Research Centre, Vancouver, British Columbia, Canada

ABSTRACT: Bombesin (BBN)-based radiolabeled peptides exhibit promising properties for targeted imaging of gastrin-releasing peptide receptors (GRPR)-positive tumors. The aim of this study was to evaluate with positron emission tomography (PET) the pharmacokinetic and imaging properties of two novel BBN-based radiolabeled peptides, ^{64}Cu/and ^{68}Ga/NOTA-PEG-BBN(6−14), for diagnosis of breast and prostate cancers using small animal models. Competitive binding assays on T47D breast and PC3 prostate cancer cells showed that the affinity for GRPR depends on the complexed metal and can vary up to a factor of about 3; ^{64}Cu/NOTA-PEG-BBN(6−14) was found to have the lowest inhibition constant (1.60 ± 0.59 nM). ^{64}Cu/and ^{68}Ga/NOTA-PEG-BBN(6−14) presented similar cell uptake on T47D and PC3 cells and were stable *in vivo*. Biodistribution studies of radiolabeled peptides carried out in Balb/c and tumor-bearing Balb/c nude mice showed that ^{64}Cu/NOTA-PEG-BBN(6−14) presented higher GRPR-mediated uptake in pancreas and adrenal glands, but comparable PC3 tumor uptake as ^{68}Ga/NOTA-PEG-BBN(6−14). Finally, receptor-dependent responses were observed during blocking studies with unlabeled peptide in both biodistribution and small-animal PET imaging studies. Our results confirmed the dependence of the affinity and pharmacokinetics of BBN-based radiopeptides on the complexed radiometal. Interspecies differences between mouse and human GRPR binding properties were also noted in these preclinical studies. Considering their good imaging characteristics, both ^{64}Cu/NOTA-PEG-BBN(6−14) and ^{68}Ga/NOTA-PEG-BBN(6−14) are promising candidates for GRPR-targeted PET imaging of breast and prostate cancers.



INTRODUCTION

Prostate and breast cancers are, respectively, the most frequently diagnosed cancers for males and females in North America. One promising diagnostic approach is the utilization of target-specific radiolabeled peptides for positron emission tomography (PET) imaging of these cancers. Gastrin-releasing peptide (GRP) is a 27 amino acid peptide that displays a wide range of physiological effects, including gastric and pancreatic secretion, nervous system stimulation, smooth muscle contraction, blood pressure, and the regulation of cell growth in some malignant cell lines.[1,2] The presence of the gastrin-releasing peptide receptor (GRPR) has been documented in many cancers including prostate[3,4] and breast cancers.[5,6] GRPR is overexpressed in 84% of all human prostate cancers[4] and 65−70% of breast cancer carcinomas.[7] These receptors represent an interesting molecular target for radiolabeled bombesin analogues as diagnostic or radiotherapeutic agents for prostate and breast cancers.

Bombesin (BBN), a 14 amino acid potent GRPR agonist, is involved in regulating exocrine secretion, smooth muscle contraction, and gastrointestinal hormone release,[8] and is widely expressed in the central nervous system.[9] [D-Tyr^{6},βAla^{11},Thi^{13},Nle^{14}]BBN(6−14) [BBN(6−14)] is a potent modified BBN-based peptide that binds to GRPR with high affinity.[10] Various BBN analogues have already been labeled with radiometals and used for PET imaging of GRPR-positive tumors.[11−14] Indeed, the use of radiometal/chelator complexes for labeling is easy and convenient, and the most commonly used radiometals for PET imaging with peptides are ^{64}Cu and ^{68}Ga. ^{64}Cu has a mean positron energy of 0.66 MeV, similar to that of ^{18}F, and a half-life of 12.7 h. ^{68}Ga emits a high mean energy positron (1.90 MeV) and has a short half-life of 68 min.

Our laboratory has reported the synthesis and the characterization of DOTA (1,4,7,10-tetraazacyclododecane-*N*,*N*′,*N*″,*N*‴-tretraacetic acid) and NOTA (1,4,7-triazacyclononane-1,4,7-triacetic acid)-BBN derivatives and showed that

Received: May 4, 2012
Revised: June 19, 2012
Published: July 9, 2012

ACS Publications © 2012 American Chemical Society

the NOTA-BBN(6−14) had an inhibition constant value slightly lower than that of the DOTA-BBN(6−14) analogue.[15] NOTA is well-descibed for the efficient complexation properties of both ^{64}Cu and ^{68}Ga. Moreover, the resulting complexes showed high resistance to transmetalation reactions *in vivo*.[16,17] Liu et al. reported similar tumor uptake for their NOTA-heterodimer labeled with ^{64}Cu and ^{68}Ga.[18] On the other hand, Fani et al. observed higher affinity for ^{64}Cu/NODAGA-peptide (NOGADA being a chemically close triazacyclononane derivative of NOTA) compared to ^{68}Ga/NODAGA-peptide, but no significant difference in tumor uptake.[19] In this study, we report a direct comparison of a novel NOTA-PEG-BBN(6−14) peptide bearing either ^{64}Cu or ^{68}Ga in terms of labeling, stability, affinity, cellular uptake, biodistribution, and μPET imaging of breast and prostate tumors in order to fully compare the diagnostic properties of these peptides.

EXPERIMENTAL PROCEDURES

Peptide Synthesis. We recently reported the synthesis, characterization, and biological activity of the NOTA-BBN(6−14) peptide.[20] Briefly, using NovaSyn TGR resin, a 2-fold excess of Fmoc-protected amino acids over resin substitution rate was utilized for coupling. Fmoc-protected amino acids were activated for coupling with an equimolar amount of HATU (2-(1*H*-7-azabenzotriazol-1-yl)-1,1,3,3-tetramethyluronium hexa-fluorophosphate) and 2-fold excess of DIEA (diisopropylethylamine). Fmoc deprotection was performed in 20% piperidine in DMF. After peptide assembly, the NOTA moiety was synthesized manually on the solid phase under a mechanical agitation as described previously by our group.[15] The peptide was deprotected and cleaved from the support by treatment with a cocktail of TFA/H_2O/thioanisole (92:2:6, v/v/v) for 4 h at room temperature under mechanical agitation to yield the desired peptide. Purity of the crude peptide was verified by high performance liquid chromatography (HPLC) and its identity was confirmed by API 3000 LC/MS/MS.

Cell Culture. The human prostate cancer PC3 and human breast cancer T47D cell lines were, respectively, used in their 8th to 12th and 25th to 35th passages after receipt and were cultured in HAM'S/F-12 and RPMI 1640 medium, respectively supplemented with 2.5 mM glutamin, 100 U/mL penicillin, 100 μg/mL streptomycin, 100 ng/mL amphothericin B, and 10% fetal bovine serum. Cells were grown in a 5% CO_2 air atmosphere at 37 °C.

***In Vitro* Receptor-Binding.** Competition assays were performed on PC3 or T47D cells. The cells were cultured until near-confluence in 24-well plates and the medium was replaced with reaction medium (RPMI complemented with 2 mg/mL BSA, 4.8 mg/mL HEPES, 1 U/mL penicillin G and 1 μg/mL streptomycin). For the assay, equal volumes of radioactive and nonradioactive ligands were added. The concentration of [^{125}I-Tyr^4]bombesin (74 TBq/mmol; Perkin-Elmer Life Science Products, Boston, MA) was 10^{-12} M. Increasing concentrations (10^{-6} to 10^{-14} M) of the NOTA-BBN(6−14) peptide were added. The plates were incubated for 40 min at 37 °C with agitation. After the incubation, the reaction medium was removed and the cells were washed thrice with phostate-buffered saline (PBS) at room temperature. The cells were harvested and counted in a gamma counter (Cobra II autogamma counter, Packard, MN). Experiments were realized in triplicate. Data were analyzed with *GraphPad Prism 5* Software (GraphPad Software, San Diego, CA, USA) to determine the IC_{50}. Finally, the inhibition constant (K_i) was determined using Cheng and Pursoff's formula.[21] The K_d value for [^{125}I-Tyr4]bombesin has been determined previously from experiments performed under similar conditions and was found to be 1.5×10^{-10} M.[22]

Peptide Radiolabeling with ^{64}Cu and ^{68}Ga. Our EBCO TR-19 cyclotron facility provides ^{64}Cu isotope on a routine basis for research purposes, using a target system developed in collaboration with Advanced Cyclotron Systems Inc. (ACSI, Richmond, BC, CA). ^{64}Cu was prepared by the ^{64}Ni(p,n)^{64}Cu reaction using an enriched ^{64}Ni target electroplated on a rhodium disk.[23] [^{64}Cu]$CuCl_2$ was recovered from the target following the procedure of McCarthy et al.[24] and converted to [^{64}Cu]copper[II] acetate ([^{64}Cu]$Cu(OAc)_2$) by dissolving the [^{64}Cu]$CuCl_2$ in ammonium acetate (0.1 M; pH 5.5). Peptides were labeled with ^{64}Cu following conditions optimized in our laboratory.[15] Briefly, the peptide (5 μg) was dissolved in ammonium acetate buffer (0.1 M, pH 5.5) with [^{64}Cu]$Cu(OAc)_2$ (296−370 MBq; 8−10 mCi) in a total volume of 250−300 μL, and then, the resulting solution was incubated at 100 °C for 10 min. ^{68}Ga was obtained from a commercially available generator system (Eckert & Ziegler Isotope Products Inc.) and eluted and purified according to manufacturer's instructions. Peptide labeling was realized following the procedure described by Zhernosekov et al.[25] The peptide (3−5 μg) was dissolved in 500 μL of HEPES buffer (1 M, pH 4.0) in the presence of the concentrated and purified ^{68}Ga (222−370 MBq; 6−10 mCi) eluted from the resin (50 mg AG 50W-X8, 400 mesh) with 400 μL of the 97.7% acetone/0.05 N HCl solution. The mixture was incubated at 100 °C for 10 min. The labeled peptide was purified by HPLC using a C-18 column and a radiodetector. The amount of radiolabeled peptide was determined by the peak area of the tracer in the UV-chromatogram compared to the UV peak area of the standard unlabeled peptide. In all cases, starting materials and the radiolabeled peptide were separable. The radiolabeled peptide fraction was collected, evaporated, and counted in a Capintec Radioisotope Calibrator to calculate the specific activity of the product.

Stability Studies. Plasma and *in vivo* stability studies were realized as previously described by our group.[16] After peptide reconstitution in PBS, studies were carried out by incubating a fraction of the solution containing the radiolabeled peptide in mouse plasma for a period of 2 h for ^{68}Ga/peptide and 24 h for ^{64}Cu/peptide or by injecting 15−25 MBq (400−650 μCi; 100 μL) of the appropriate radiolabeled peptide to Balb/c mice (3 mice per peptide) and regular blood withdrawn. The stability was determined by radioTLC (C-18-coated plastic sheets) directly from plasma and blood samples without further handling; free metal and purified radiolabeled peptides were used as standards. The radioTLCs were eluted with 0.1 M sodium citrate buffer at pH 5.5 using an Instant Imager system for the radiodetection.

Cellular Uptake. Cellular uptake studies were realized in triplicate on T47D and PC3 cells in the presence of NOTA-PEG-BBN(6−14) labeled with ^{64}Cu or ^{68}Ga. First, PC3 or T47D cells were seeded in 12-well plates at a density of 2×10^5 cells per well 48 h prior to the experiment. Cells were incubated 15, 30, 60, or 90 min with 37 kBq (1 μCi; 50 μL) of radiolabeled peptide per well at 37 °C with agitation. Afterward, the medium was removed and the cells were washed thrice with PBS. The cells were harvested and counted in a gamma counter. The results were expressed as percentage of added dose retained per 10^5 cells (%AD/10^5cells).

dx.doi.org/10.1021/bc3002437 | *Bioconjugate Chem.* 2012, 23, 1687−1693

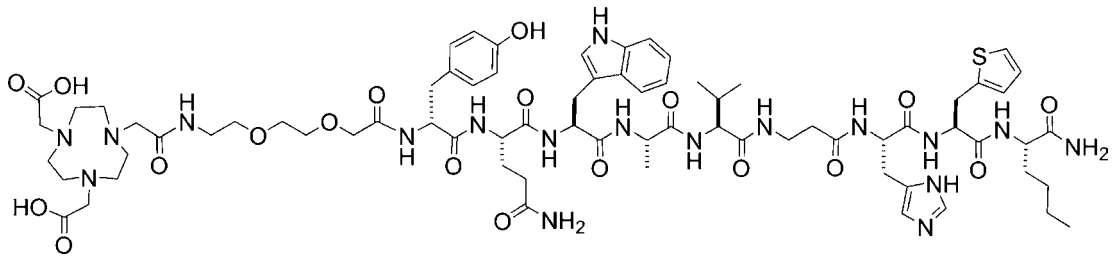


Figure 1. Amino acids sequence of NOTA-PEG-BBN(6−14).

Biodistribution Studies. All animal studies were conducted in compliance with the Canadian Council on Animal Care guidelines and with the approval of the Animal Care Committee of the Université de Sherbrooke. To determine the *in vivo* GRPR-targeting efficacy of labeled peptides, biodistribution was realized with a minimum of 3 mice for each time point. Mice were injected 370−740 kBq (10−20 μCi; 100 μL) of either ^{64}Cu/or ^{68}Ga/NOTA-PEG-BBN(6−14) via the caudal vein. The animals were euthanized by CO_2 inhalation at 30 min postinjection (p.i.). Organs of interest were then collected, weighed, and measured in a gamma-counter. The results were expressed as percentage of the injected dose per gram of tissue (%ID/g). Measurements with coinjection of 0.1 μmol of unlabeled peptide were performed to evaluate GRPR-dependent accumulation of the tracers. Biodistribution studies were conducted on Balb/c mice and tumor-bearing Balb/c nude mice. Balb/c nude mice were implanted with 10^7 PC3 or T47D tumors. Tumor cells were injected in 150 μL of Matrigel (BD Biosciences, CA, USA) and PBS (2:1). Tumors were given 3 or 5 weeks to grow to the size of 5 mm in diameter for PC3 and T47D, respectively. For T47D tumors, a 17β-Estradiol pellet, (1.7 mg/90-day release; Innovative Research of America, FL, USA), was placed under the skin of mice one week prior to tumor implantation.

PET Imaging. PET scans were performed using a LabPET8 (Gamma Medica Inc.) small animal scanner with an axial field of view of 7.5 cm. Xenografted Balb/c nude mice were injected with 3.7−7.4 MBq (100−200 μCi; 100 μL) of ^{64}Cu/or ^{68}Ga/NOTA-PEG-BBN(6−14) via the caudal vein under isoflurane anesthesia with a minimum of 3 mice for each tracer. Each animal had a 10 min static scan 30 min p.i. The images were reconstructed by a two-dimensional MLEM algorithm implementing an analytically derived system matrix.[26] Regions of interest (ROI) were traced for tumor, liver, kidney, and muscle, and the activity in each organ was measured at 30 min p.i. Co-injections of 0.1 μmol of unlabeled peptide were also realized to measure GRPR-dependent accumulation of the tracers.

RESULTS

Peptide Synthesis, Labeling with ^{64}Cu and ^{68}Ga, and Stability Studies. We recently reported the synthesis, characterization, and biological activity of ^{64}Cu/NOTA-PEG-BBN(6−14), a water-soluble GRPR-targeting peptide having a LogD value of −1.91 (Figure 1).[15] This peptide (MS calc: 1570; Found: 1571 (M+1)) was prepared with a yield of 38% based on the resin substitution rate and a purity of 99%. The labeling with the radiometals was straightforward. NOTA-PEG-BBN(6−14) was labeled at 100 °C for 10 min with ^{64}Cu and ^{68}Ga with labeling yields superior to 90% and specific activities of 88.1 ± 4.6 TBq/mmol and 60.5 ± 21.6 TBq/mmol, respectively. Both radiolabeled peptides were stable up to 2 and 24 h, respectively, in mouse circulation, as no trace of free ^{64}Cu or ^{68}Ga was detected by radioTLC. In previous work, we have demonstrated by radioHPLC that the absence of free ^{64}Cu and metabolites confirmed that the peptide itself was stable *in vivo* 1 h p.i.[20]

***In Vitro* Experiments.** NOTA-PEG-BBN(6−14) affinity was tested on two human cancer cell lines overexpressing GRPR: T47D breast cancer and PC3 prostate cancer cells. All inhibitory constants are summarized in Table 1. NOTA-PEG-BBN(6−14) presents an excellent affinity in the low nanomolar range on T47D (1.27 ± 0.95 nM) and PC3 (2.51 ± 1.54 nM) cells comparable to bombesin, a natural ligand for GRPR. The peptide was labeled with non-radioactive Cu(II) and Ga(III) in order to evaluate the change in affinity by addition of the metal in the chelator. The K_i values vary 3-fold between Cu(II)/ and Ga(III)/NOTA-PEG-BBN(6−14) on T47D cells. The complexation of Cu(II) to NOTA did not significantly alter the affinity of the peptide for GRPR (1.60 ± 0.59 nM), while a significantly lower affinity was observed for the Ga(III) complex (4.87 ± 1.27 nM) ($p < 0.05$). Cellular uptake of radiolabeled NOTA-PEG-BBN(6−14) was evaluated on T47D and PC3 cells. Results are presented in Figure 2. ^{64}Cu/and

Table 1. Affinities of NOTA-PEG-BBN(6-14) for GRPR on Breast and Prostate Cancer Cells

peptide	K_i GRPR	
	on T47D (nM)	on PC3 (nM)
Bombesin	0.76 ± 0.54	0.59 ± 0.32
NOTA-PEG-BBN(6−14)	1.27 ± 0.95	2.51 ± 1.54
Cu(II)/NOTA-PEG-BBN(6−14)	1.60 ± 0.59	---
Ga(III)/NOTA-PEG-BBN(6−14)	4.87 ± 1.27[a]	---

[a]Significantly higher inhibition constant than NOTA-PEG-BBN(6−14) and Cu(II)/NOTA-PEG-BBN(6−14) on T47D cells ($p < 0.05$).

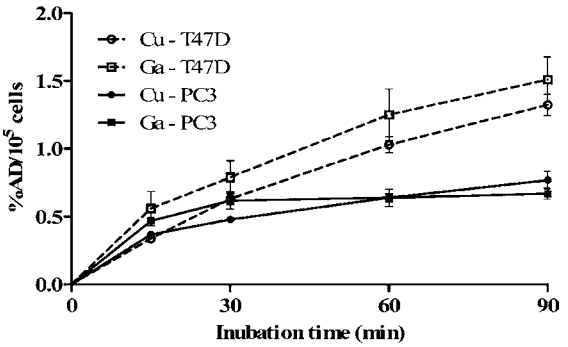


Figure 2. Cellular uptake of ^{64}Cu/and ^{68}Ga/NOTA-PEG-BBN(6−14) on T47D and PC3 cells.

dx.doi.org/10.1021/bc3002437 | *Bioconjugate Chem.* 2012, 23, 1687−1693

Table 2. Biodistributions of Healthy Female Balb/c Mice 30 min Post-Injection of ^{64}Cu/NOTA-PEG-BBN(6-14) or ^{68}Ga/NOTA-PEG-BBN(6-14) with or without Co-Injection of Non-Radioactive Peptide

	^{64}Cu/NOTA-PEG-BBN(6−14)						^{68}Ga/NOTA-PEG-BBN(6−14)					
organ	unblocked			blocked			unblocked			blocked		
blood	2.02	±	0.93	3.15	±	0.59	2.97	±	2.07	3.62	±	1.80
plasma	3.50	±	1.38	6.35	±	1.31	5.64	±	3.15	6.95	±	3.44
adrenals	26.61	±	5.03	4.34	±	2.14[b]	12.39	±	4.42[a]	4.05	±	2.60[b]
ovaries	5.37	±	4.06	7.79	±	6.83	2.21	±	1.54	5.58	±	3.79
uterus	7.15	±	3.26	5.45	±	1.96	1.98	±	1.40	3.97	±	1.75
fat	0.76	±	0.35	1.49	±	1.02	0.49	±	0.13	1.43	±	1.10
kidney	10.88	±	2.61	15.06	±	4.30	6.83	±	1.71	10.69	±	2.00
spleen	4.55	±	2.10	2.51	±	0.12	4.43	±	2.07	1.48	±	0.32
pancreas	18.39	±	2.90	3.12	±	0.07[b]	10.41	±	3.75[a]	2.65	±	1.38[b]
liver	4.97	±	1.69	11.39	±	8.33	6.29	±	5.70	3.59	±	0.98
heart	1.22	±	0.40	2.29	±	1.48	1.04	±	0.42	2.27	±	1.86
lungs	3.92	±	2.27	4.79	±	2.68	2.67	±	1.20	5.59	±	4.51
muscle	1.06	±	0.76	1.34	±	0.49	0.61	±	0.08	1.83	±	0.99
bone	0.73	±	0.20	1.21	±	1.15	0.90	±	0.46	1.48	±	1.28
brain	0.13	±	0.06	0.21	±	0.13	0.11	±	0.03	0.22	±	0.15

[a]Significantly lower than ^{64}Cu/NOTA-PEG-BBN(6−14) for the same organ ($p < 0.05$). [b]Co-injection significantly lowered the uptake for the same organ for the corresponding tracer ($p < 0.05$).

^{68}Ga/NOTA-PEG-BBN(6−14) exhibit relatively similar cellular uptake on both cell lines, with the gallium analogue showing, however, a slightly higher uptake than the copper analogue especially in the T47D cells. Cellular uptake results are all significantly higher on T47D when compared to the corresponding condition on PC3 cells after 60 min. At all time points, internalization of the peptides represented around 80% of the total cellular uptake (data not shown).

Biodistribution Studies. Biodistribution studies of ^{64}Cu/ and ^{68}Ga/NOTA-PEG-BBN(6−14) were carried out in Balb/c mice 30 min p.i. Results are summarized in Table 2. ^{64}Cu/and ^{68}Ga/NOTA-PEG-BBN(6−14) present similar biodistribution patterns with high uptake in the GRPR-rich tissues (pancreas and adrenal glands).[27] ^{64}Cu/NOTA-PEG-BBN(6−14) presents a significantly higher pancreas and adrenal gland uptake than ^{68}Ga/NOTA-PEG-BBN(6−14) ($p < 0.05$). In order to assess the GRPR-mediated accumulation of the tracers, biodistribution studies were repeated with coinjection of 0.1 μmol of unlabeled peptide. Co-injection of unlabeled NOTA-PEG-BBN(6−14) slightly increased the tracer levels in blood, kidneys, and muscle, as well as most other organs. Significant decreases in pancreas and adrenal gland uptake were observed for both ^{64}Cu/and ^{68}Ga/NOTA-PEG-BBN(6−14) indicating GRPR-mediated uptake in these organs ($p < 0.05$). Other measured organs presented low uptake and no significant difference between both tracers.

PET Imaging. Decay-corrected transaxial PET images of ^{64}Cu/and ^{68}Ga/NOTA-PEG-BBN(6−14) in PC3 and T47D tumor-bearing Balb/c nude mice are presented in Figure 3. From these images, ROI were traced for tumors, liver, kidney, and muscle. Quantitative PET image-derived uptake 30 min p.i. were determined for both tracers (Figure 4). PET-derived biodistribution indicated similar liver, muscle, PC3, and T47D uptake. However, higher kidney uptake was measured for ^{68}Ga-labeled peptide compared to ^{64}Cu-labeled peptide (Figure 4A). PET-derived uptake and biodistribution studies were compared, and results for tumors are presented in Figure 4B,C. PC3 and T47D tumors presented similar tumor uptake (Figure 4B) and tumor-to-muscle (T/M) ratio (Figure 4C). Liver, muscle,

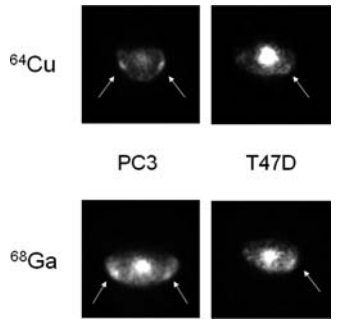


Figure 3. PC3 and T47D tumors transaxial PET images of ^{64}Cu/and ^{68}Ga/NOTA-PEG-BBN(6−14) 30 min p.i.

and PC3 tumors presented similar results with both methods. However, kidney uptakes are higher from PET-derived uptake, while T47D tumor uptake seems lower in the same conditions. In all conditions tested, both tracers presented comparable PC3 and T47D tumor uptake and tumor-to-muscle (T/M) ratio. Co-injections of unlabeled peptide were performed during PET imaging of PC3 tumor-bearing mice, and transaxial decay-corrected PET images are presented at Figure 5A. PC3 tumor uptake of ^{64}Cu/NOTA-PEG-BBN(6−14) was not different following coinjection. However, significant decreases in PC3 tumor uptake for ^{68}Ga-labeled peptide (Figure 5B) and in T/M ratio for both ^{64}Cu/and ^{68}Ga/NOTA-PEG-BBN(6−14) (Figure 5C) were observed.

DISCUSSION

In the present research, NOTA-PEG-BBN(6−14), a water-soluble GRPR-targeting peptide, was prepared entirely on solid-phase support following a method developed in our laboratory[15] with good yields and high purity. NOTA-PEG-BBN(6−14) presented an excellent GRPR affinity on human breast cancer cells (T47D) and human prostate cancer cells (PC3), which is comparable to natural BBN in the low nanomolar range. Furthermore, Cu(II)/NOTA-PEG-BBN(6−14) presented similar affinity to NOTA-PEG-BBN(6−14), while Ga(III)/NOTA-PEG-BBN(6−14) exhibited significantly

dx.doi.org/10.1021/bc3002437 | Bioconjugate Chem. 2012, 23, 1687−1693

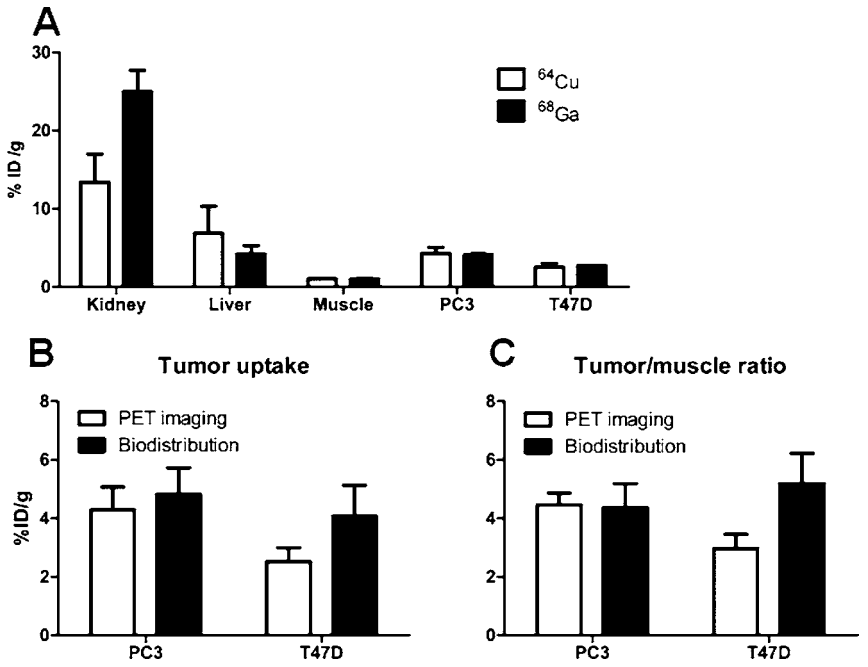


Figure 4. Comparative biodistribution, tumor uptake, and tumor-to-muscle ratio of PC3 and T47D tumor-bearing mice 30 min pi of ^{64}Cu/and ^{68}Ga/NOTA-PEG-BBN(6−14) by PET imaging and biodistribution. (A) PET-derived biodistribution of ^{64}Cu/and ^{68}Ga/NOTA-PEG-BBN(6−14); (B) tumor uptake of PC3 and T47D tumors by PET imaging and biodistribution for ^{64}Cu/NOTA-PEG-BBN(6−14); (C) tumor-to-muscle ratio of PC3 and T47D tumors measured by PET imaging and biodistributions for ^{64}Cu/NOTA-PEG-BBN(6−14).

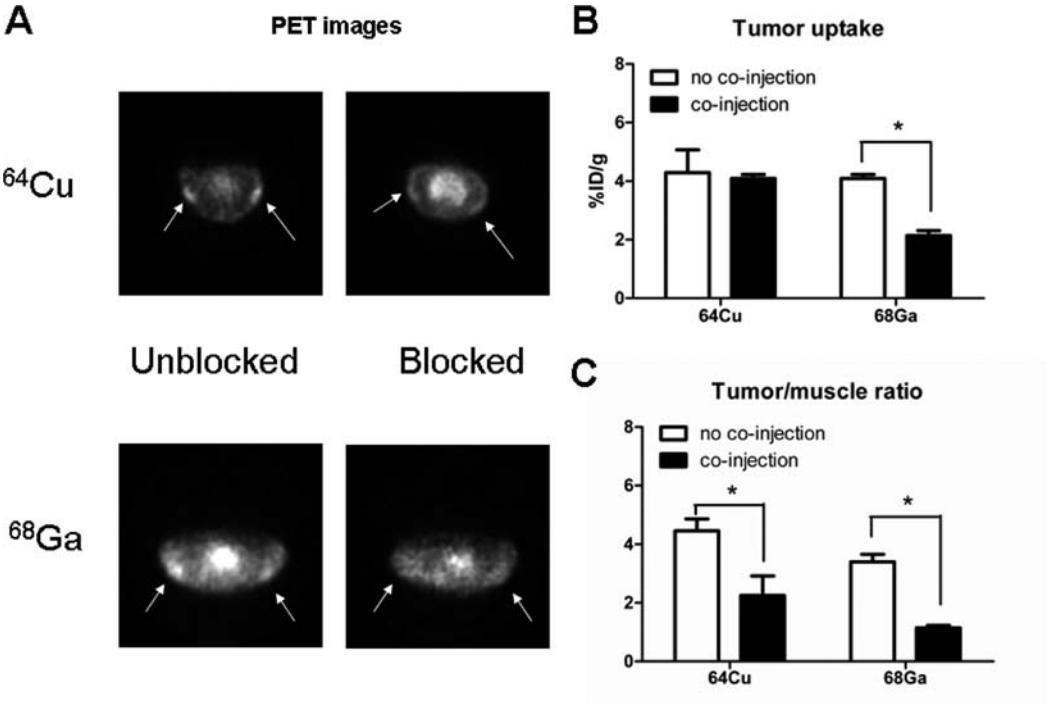


Figure 5. Comparative tumor uptake and tumor-to-muscle ratio of PC3 tumors 30 min pi of ^{64}Cu/and ^{68}Ga/NOTA-PEG-BBN(6−14) by PET imaging with or without coinjection of unlabeled peptide. (A) Transaxial PET images of PC3 tumor-bearing Balb/c nude mice of ^{64}Cu/ (top row) and ^{68}Ga/NOTA-PEG-BBN(6−14) (bottom row) with (right side) and without (left side) coinjection. (B) PET-derived tumor uptake of PC3 tumors of ^{64}Cu/and ^{68}Ga/NOTA-PEG-BBN(6−14) with or without coinjection. (C) PET-derived tumor-to-muscle ratio of PC3 tumors of ^{64}Cu/ and ^{68}Ga/NOTA-PEG-BBN(6−14) with or without coinjection. * = $p < 0.05$.

lowered affinity for human GRPR. We postulate that this alteration in affinity is caused by the difference in charge between Cu(II)/ and Ga(III)/NOTA-PEG-BBN(6−14). Cu-(II) forms a stable and neutral complex, whereas Ga(III) forms a stable, but positively charged complex with the NOTA chelator. We hypothesize that the counterion of this charge might interfere in the binding process of the peptide by causing steric hindrance diminishing the measured affinity. Lane et al. also observed that insertion of metal in the NOTA chelator could influence the affinity of the resulting peptide.[11] These

dx.doi.org/10.1021/bc3002437 | Bioconjugate Chem. 2012, 23, 1687−1693

observations stress the importance of considering the metal used for labeling in peptide affinity measurements. High yields and excellent specific activities were obtained following the labeling of NOTA-PEG-BBN(6−14) with ^{64}Cu and ^{68}Ga. No significant difference in specific activity between both labeled tracers was measured. Both ^{68}Ga/and ^{64}Cu/NOTA complexes were stable *in vivo* up to 2 h and 24 h, respectively, as determined by radioTLC. The stability of the peptide itself cannot be established by radioTLC because the peptide separation from its potential metabolites may be extremely difficult to distinguish using this method. Instead, the peptide stability was measured by radioHPLC for ^{64}Cu/NOTA-PEG-BBN(6−14) and showed that the tracer is stable up to 1 h *in vivo*, as no trace of free ^{64}Cu or metabolite was detected.[15] This result is consistent with radioTLC data. Cellular uptake of ^{64}Cu/and ^{68}Ga/NOTA-PEG-BBN(6−14) were evaluated on T47D and PC3 cells. No significant difference was observed between ^{64}Cu/and ^{68}Ga/NOTA-PEG-BBN(6−14) for both cell lines. Hence, the lower affinity for GRPR of ^{68}Ga/NOTA-PEG-BBN(6−14) did not seem to alter the observed cellular uptake, this peptide even having a higher uptake that its ^{64}Cu-labeled analogue. Following these results, we evaluated the impact of GRPR affinity *in vivo*.

To measure *in vivo* GRPR-targeting properties of both tracers, biodistribution and PET imaging studies were carried out. Biodistribution measurements in Balb/c mice showed a relatively similar uptake in non-GRPR-expressing tissue such as liver, kidneys, and muscle for both ^{64}Cu/and ^{68}Ga/NOTA-PEG-BBN(6−14), which indicates that both tracers have similar elimination pathways and clearance profiles. However, when comparing PET image-derived kidney uptake to values from biodistribution studies, we measured a higher uptake for both labeled peptides. These higher values might be from radiolabeled peptide still circulating in the organ during imaging, while during biodistribution studies, the organs are rinsed before measurement eliminating circulating compound. Furthermore, ^{68}Ga/NOTA-PEG-BBN(6−14) presented higher renal uptake than ^{64}Cu/NOTA-PEG-BBN(6−14). Since positively charged compounds are known to be retained in kidneys by reabsorption,[28] the difference observed could be explained by the positive charge of the ^{68}Ga/NOTA complex.

In our study, we observed significant uptake differences in pancreas and adrenal glands, but similar tumor uptake for both labeled peptides. Since pancreas, adrenal glands, and tumors are all GRPR-expressing tissues, similar uptake patterns in these organs were expected. However, while pancreas uptake is considered an indication of GRPR-targeting for tumor tracer development, many studies in nude mice bearing human tumor xerographs have also demonstrated that higher pancreas uptake does not match the higher tumor uptake due to GRPR interspecies differences.[11,28] Pancreas and adrenal glands express mice-specific GRPR, while human-specific GRPR are present on PC3 and T47D cells. Since all affinities were measured on human GRPR, it is hazardous to speculate on relative affinities of Cu(II)/ and Ga(III)/NOTA-PEG-BBN(6−14) for mice GRPR, as not enough data are available yet to explain these differences. Since *in vivo* GRPR-targeting is known to be highly dependent on GRPR affinity rather than internalization rate[28] and since Ga(III)/NOTA-PEG-BBN(6−14) presented lower GRPR-affinity on T47D cells, reduced *in vivo* tumor uptake was expected for this tracer. However, *in vitro* and *in vivo* breast and prostate tumor uptake were similar for both tracers. We hypothesize that the affinity for human GRPR of our novel BBN-based radiolabeled peptides, while being significantly different, is still in the low nanomolar range and might not be different enough to observe *in vitro* or *in vivo* GRPR-targeting differences at the tumor site. These results indicate that both tracers are promising probes that can be used as breast and prostate cancer diagnosis PET tracers.

CONCLUSION

We have developed two PET tracers targeting the gastrin-releasing peptide receptor (GRPR) and exhibiting excellent pharmacokinetic properties for *in vivo* imaging of breast and prostate cancer. Dependence of the affinity and pharmacokinetics of these radiopeptides on the complexed radiometal and interspecies differences between mice and men with respect to GRPR pharmacokinetics were clearly demonstrated in the preclinical studies herein reported.

AUTHOR INFORMATION

Corresponding Author

*Phone: (819) 820-6868 ext. 15285. Fax: (819) 829-3238. E-mail: Brigitte.Guerin2@USherbrooke.ca.

Notes

The authors declare no competing financial interest.

ACKNOWLEDGMENTS

B.G. and R.L. are members of the Centre de recherche clinique Étienne-Le Bel funded by the Fonds de Recherche en Santé du Québec. The work was financially supported by the Natural Sciences and Engineering Research Council of Canada (NSERC), the Canadian Institute of Health Research (CIHR grants MOP-86717 and MOP-89875), and the BC Leadership Chair in Functional Cancer Imaging. P.F. had support from graduate scholarships (CIHR 98147 and FRSQ 21116).

REFERENCES

(1) Reubi, J. C., Wenger, S., Schmuckli-Maurer, J., Schaer, J. C., and Gugger, M. (2002) Bombesin receptor subtypes in human cancers: detection with the universal radioligand (125)I-[D-Tyr(6), beta-Ala(11), Phe(13), Nle(14)] bombesin(6−14). *Clin. Cancer Res. 8*, 1139−1146.

(2) Albrecht, M., Doroszewicz, J., Gillen, S., Gomes, I., Wilhelm, B., Stief, T., and Aumüller, G. (2004) Proliferation of prostate cancer cells and activity of neutral endopeptidase is regulated by bombesin and IL-1beta with IL-1beta acting as a modulator of cellular differentiation. *Prostate 58*, 82−94.

(3) Reile, H., Armatis, P. E., and Schally, A. V. (1994) Characterization of high-affinity receptors for bombesin/gastrin releasing peptide on the human prostate cancer cell lines PC-3 and DU-145: internalization of receptor bound ^{125}I-(Tyr4) bombesin by tumor cells. *Prostate 25*, 29−38.

(4) Markwalder, R., and Reubi, J. C. (1999) Gastrin-releasing peptide receptors in the human prostate: relation to neoplastic transformation. *Cancer Res. 59*, 1152−1159.

(5) Pagani, A., Papotti, M., Sanfilippo, B., and Bussolati, G. (1991) Expression of the gastrin-releasing peptide gene in carcinomas of the breast. *Int. J. Cancer 47*, 371−375.

(6) Gugger, M., and Reubi, J. C. (1999) Gastrin-releasing peptide receptors in non-neoplastic and neoplastic human breast. *Am. J. Pathol. 155*, 2067−2076.

(7) Parry, J. J., Andrews, R., and Rogers, B. E. (2007) MicroPET imaging of breast cancer using radiolabeled bombesin analogs targeting the gastrin-releasing peptide receptor. *Breast Cancer Res. Treat. 101*, 175−183.

(8) Delle Fave, G., Annibale, B., De Magistris, L., Severi, C., Bruzzone, R., Puoti, M., Melchiorri, P., Torsoli, A., and Erspamer, V. (1985) Bombesin effects on human GI fonctions. *Peptides 6*, 113−116.
(9) Martinez, V., and Tache, Y. (2000) Bombesin in the brain-gut axis. *Peptides 21*, 1617−1625.
(10) Pradhan, T. K., Katsuno, T., Taylor, J. E., Kim, S. H., Ryan, R. R., Mantey, S. A., Donohue, P. J., Weber, H. C., Sainz, E., Battey, J. F., and Coy, D. H. (1998) Identification of a unique ligand which has high affinity for all four bombesin receptor subtypes. *Eur. J. Pharmacol. 343*, 275−287.
(11) Lane, S. R., Nanda, P., Rold, T. L., Sieckman, G. L., Figueroa, S. D., Hoffman, T. J., Jurisson, S. S., and Smith, C. J. (2010) Optimization, biological evaluation and microPET imaging of copper-64-labeled bombesin agonists, [^{64}Cu-NO2A-(X)-BBN(7−14)NH_2], in prostate tumor xenografted mouse model. *Nucl. Med. Biol. 37*, 751−761.
(12) Prasanphanich, A. F., Nanda, P. K., Rold, T. L., Ma, L., Lewis, M. R., Garrison, J. C., Hoffman, T. J., Sieckman, G. L., Figueroa, S. D., and Smith, C. J. (2007) [^{64}Cu-NOTA-8-Aoc-BBN(7−14)NH_2] targeting vector for positron-emission tomography imaging of gastrin-releasing peptide receptor-expressing tissues. *Proc. Natl. Acad. Sci. U. S. A. 104*, 12462−12467.
(13) Schuhmacher, J., Zhang, H., Doll, J., Maecke, H. R., Matys, R., Hauser, H., Henze, M., Haberkorn, U., and Eisenhut, M. (2005) GRP receptor-targeted PET of a rat pancreas carcinoma xenograft in nude mice with a ^{68}Ga-labeled Bombesin(6−14) analog. *J. Nucl. Med. 46*, 691−699.
(14) Chen, X., Park, R., Hou, Y., Tohme, M., Shahinian, A. H., Bading, J. R., and Conti, P. S. (2004) MicroPET and autoradiographic imaging of GRP receptor expression with ^{64}Cu-DOTA-[Lys^3]-Bombesin in human prostate adenocarcinoma xenografts. *J. Nucl. Med. 45*, 1390−1397.
(15) Guérin, B., Ait-Mohand, S., Tremblay, M.-C., Dumulon-Perreault, V., Fournier, P., and Bénard, F. (2010) Total solid-phase synthesis of NOTA-functionalized peptides for PET imaging. *Org. Lett. 12*, 280−283.
(16) Ait-Mohand, S., Fournier, P., Dumulon-Perreault, V., Keifer, G. E., Jurek, P., Ferreira, C. L., Bénard, F., and Guérin, B. (2011) Evaluation of ^{64}Cu-labeled bifonctional chelate-bombesin conjugates. *Bioconjugate Chem. 22*, 1729−1735.
(17) Ferreira, C. L., Lamsa, E., Woods, M., Duan, Y., Fernando, P., Bensimon, C., Kordos, M., Guenther, K., Jurek, P., and Keifer, G. E. (2010) Evaluation of bifunctional chelates for the development of gallium-based radiopharmaceuticals. *Bioconjugate Chem. 21*, 5361−5369.
(18) Liu, Z., Yan, Y., Liu, S., Wang, F., and Chen, X. (2009) (18)F, (64)Cu and (68)Ga labelled RGD-Bombesin heterodimeric peptides for PET imaging of breast cancer. *Bioconjugate Chem. 20*, 1016−1025.
(19) Fani, M., Del Pozzo, L., Abiraj, K., Mansi, R., Tamma, M. L., Cescato, R., Waser, B., Weber, W. A., Reubi, J. C., and Maecke, H. R. (2011) PET somatostatin receptor-positive tumors using ^{64}Cu- and ^{68}Ga-somatostatin antagonists: the chelate makes the difference. *J. Nucl. Med. 52*, 1110−1118.
(20) Fournier, P., Dumulon-Perreault, V., Ait-Mohand, S., Langlois, R., Bénard, F., Lecomte, R., and Guérin, B. (2012) Comparative study of ^{64}Cu/NOTA-[D-Tyr^6,beta-Ala^{11},Thi^{13},Nle^{14}]BBN(6−14) monomer and dimers for prostate cancer PET imaging. *Eur. J. Nucl. Med. Mol. Imaging Res. 2*, 8.
(21) Cheng, Y., and Prusoff, W. H. (1973) Relationship between the inhibition constant ([K_i]) and the concentration of inhibitor which causes 50% inhibition ([I_{50}]) of an enzymatic reaction. *Biochem. Pharmacol. 22*, 3099−3108.
(22) Aprikian, A. G., Han, K., Chevalier, S., Bazinet, M., and Viallet, J. (1996) Bombesin specifically induces intracellular calcium mobilization via gastrin-releasing peptide receptors in human prostate cancer cells. *J. Mol. Endocrinol. 16*, 297−306.
(23) Zeisler, S. K., Pavan, R. A., Orzechowski, J., Langlois, R., Rodrigue, S., and van Lier, J. E. (2003) Production of ^{64}Cu on the Sherbrooke TR-PET cyclotron. *J. Radioanal. Nucl. Chem. 257*, 175−177.
(24) McCarthy, D. W., Shefer, R. E., Klinkowstein, R. E., Bass, L. A., Margeneau, W. H., Cutler, C. S., Anderson, C. J., and Welch, M. J. (1997) Efficient production of high specific activity ^{64}Cu using a biomedical cyclotron. *Nucl. Med. Biol. 24*, 35−43.
(25) Zhernosekov, K. P., Filosofov, D. V., Baum, R. P., Aschoff, P., Bihl, H., Razbash, A. A., Jahn, M., Jennewein, M., and Rösch, F. (2007) Processing of generator-produced ^{68}Ga for medical application. *J. Nucl. Med. 48*, 1741−1748.
(26) Selivanov, V., Picard, Y., Cadorette, J., Rodrigue, S., and Lecomte, R. (2000) Detector response models for statistical iterative image reconstruction in high resolution PET. *IEEE Trans. Nucl. Sci. 47*, 1168−1175.
(27) Xiao, D., Wang, J., Hampton, L. L., and Weber, H. C. (2001) The human gastrin-releasing peptide receptor gene structure, its tissue expression and promoter. *Gene 264*, 95−103.
(28) Behr, T. M., Goldenberg, D. M., and Becker, W. (1998) Reducing the renal uptake of radiolabeld antibody fragment and peptides for diagnosis and therapy: present status, future prospects and limitations. *Eur. J. Nucl. Med. 25*, 201−212.

Bioconjugate Chemistry

Article

pubs.acs.org/bc

Tobacco Mosaic Virus as a New Carrier for Tumor Associated Carbohydrate Antigens

Zhaojun Yin,[†] Huong Giang Nguyen,[‡] Sudipa Chowdhury,[§] Philip Bentley,[†] Michael A. Bruckman,[‡] Adeline Miermont,[†] Jeffrey C. Gildersleeve,[§] Qian Wang,*[,‡] and Xuefei Huang*[,†]

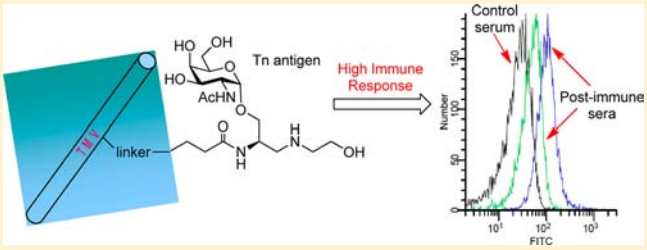
[†]Department of Chemistry, Chemistry Building, Room 426, 578 S. Shaw Lane, Michigan State University, East Lansing, Michigan 48824, United States

[‡]Department of Chemistry and Biochemistry, University of South Carolina, 631 Sumter Street, Columbia, South Carolina 29208, United States

[§]Chemical Biology Laboratory, Center for Cancer Research, National Cancer Institute-Frederick, 376 Boyles Street, Building 376, Room 208, Frederick, Maryland 21702, United States

Supporting Information

ABSTRACT: Tumor-associated carbohydrate antigens (TACAs) are being actively studied as targets for antitumor vaccine development. One serious challenge was the low immunogenecity of these antigens. Herein, we report the results of using the tobacco mosaic virus (TMV) capsid as a promising carrier of a weakly immunogenic TACA, the monomeric Tn antigen. The copper(I) catalyzed azide−alkyne cycloaddition reaction was highly efficient in covalently linking Tn onto the TMV capsid without resorting to a large excess of the Tn antigen. The location of Tn attachment turned out to be important. Tn introduced at the N terminus of TMV was immunosilent, while that attached to tyrosine 139 elicited strong immune responses. Both Tn specific IgG and IgM antibodies were generated as determined by enzyme-linked immunosorbent assay and a glycan microarray screening study. The production of high titers of IgG antibodies suggested that the TMV platform contained the requisite epitopes for helper T cells and was able to induce antibody isotype switching. The antibodies exhibited strong reactivities toward Tn antigen displayed in its native environment, i.e., cancer cell surface, thus highlighting the potential of TMV as a promising TACA carrier.



INTRODUCTION

Anticancer vaccines and immunotherapy are attractive approaches for cancer therapy. Recent FDA approval of Provenge has lent credence to the idea that an effective immune response induced against tumor associated antigens can benefit cancer treatment. Tumor cells are often characterized with aberrant glycosylation resulting in high levels of tumor associated carbohydrate antigens (TACAs) expressed on cell surfaces.[1−3] For example, while the Tn antigen (GalNAc-α-O-Ser/Thr)[4,5] is rarely found in normal tissues, it is expressed on the surface of a variety of cancer cells including breast,[6] colon,[7] and prostate cancer.[8] The Springer group reported that more than 90% primary invasive ductal breast cancer tissues expressed Tn, and the high level of Tn correlated significantly with shortened disease-free interval and increased tumor metastasis in patients.[9] Histochemical studies by Kawaguchi and co-workers showed that the atypical mucin 1 bearing the Tn antigen was involved in aggressive growth and lymphatic metastasis of primary breast cancers.[10] These observations strongly suggest the key role of Tn antigen in cancer development. Thus, Tn antigens, and TACAs in general, present excellent targets for the development of carbohydrate-based anticancer vaccines.[11,12]

One serious challenge in the development of carbohydrate-based anticancer vaccines is that TACAs are only weakly immunogenic because they are T-cell independent B cell antigens. Upon binding with TACAs through B cell receptors, B cells can secret antibodies against TACAs. However, these antibodies are the low-affinity IgM type, which typically only last for a short period of time. To elicit a long lasting immunomemory, high-affinity IgG antibodies need to be generated, which requires the coactivation of helper T (Th) cells to potentiate the maturation of B cells and to induce antibody isotype switching from IgM to IgG.[13] Thus, an immunogenic carrier containing the requisite epitopes for Th cells is required for an effective TACA based vaccine construct.

Due to the importance of the Tn antigen, many innovative studies have been performed to link Tn antigens with Th epitopes for anticancer vaccine studies. Livingston and co-workers conjugated Tn with a highly immunogenic carrier protein, keyhole limpet hemocyanine (KLH).[14] However, the Tn-KLH conjugate failed to elicit a humoral immune response

Received: May 4, 2012
Revised: June 18, 2012
Published: July 19, 2012

ACS Publications © 2012 American Chemical Society

presumably due to the weak immunogenicity of Tn. To overcome this obstacle, a Tn cluster composed of three consecutive Tn antigens was synthesized and subsequently linked to KLH.[14,15] With the increasing size of Tn antigen clusters, strong antibody responses were obtained.

Instead of employing a whole protein such as KLH to introduce Th epitopes, Lo-Man and co-workers used a single Th epitope derived from a poliovirus (PV).[16] They designed a fully synthetic multiple antigen glycopeptide (MAG) construct connecting the PV peptide and Tn antigen. Consistent with the results from the Livingston group, Tn trimer cluster conjugated to MAG-PV gave higher immune responses.[16−18] The Andreana group demonstrated that zwitterionic polysaccharide could also provide the necessary Th help to boost the immune response to covalently linked Tn antigen.[19] Other novel constructs include the self-adjuvanting multicomponent assemblies from the Dumy[20,21] and Boons groups,[22] the Calix[4]arene platform,[23] dendrimers,[24] as well as coconjugation of a xenoantigen such as rhamnose to boost the antibody response to Tn.[25]

Besides the requirement of Th epitopes, the manner TACAs are displayed in the vaccine construct can be crucial. B cells are known to be sensitive to the display pattern of B cell antigens.[26,27] While antigens displayed randomly often weakly activate B cells, the same antigens presented in a highly organized manner can elicit potent antibody responses.[28] This is attributed to the effective cross-linking of B cell receptors by the highly patterned antigens, thus inducing B cell maturation and isotype switching. The widely used carrier such as KLH is amorphous, which renders it impossible to control the display pattern of the antigen. In addition, the inherent glycans on native KLH[29] may compete with the desired TACA antigen for anticarbohydrate immune responses.[30]

Plant viruses or virus-like particles (VLPs) are becoming attractive platforms for displaying B cell epitopes.[31,32] VLPs often contain multiple copies of Th epitopes, which can facilitate the potent activation of Th cells. Furthermore, due to the simplicity of their genome, viruses use repetitive protein units to construct their capsids, which lead to highly organized structures on the surface. This can provide a highly ordered platform to display antigens, which in turn can potentially break B cell tolerance and generate strong immune responses.[28,33−37]

Given the aforementioned potential of VLPs, we become interested in examining a VLP, the tobacco mosaic virus (TMV), as the carrier for Tn antigen to elicit anti-Tn immune responses. The capsid of TMV is composed of 2130 copies of identical coat proteins, which self-assemble into a 300-nm-long rod.[38] Noninfectious to humans, TMV has been utilized to present peptide antigens through genetic engineering.[39] Fitchen and co-workers reported that a B-epitope peptide from murine zona pellucid inserted into TMV could break the immunotolerance and induce antigen specific antibodies.[40,41] Exogenous peptide antigens have been introduced to the N-terminus of the TMV coat protein,[42,43] which self-assembled into stable virion and led to a high antipeptide immune response. These results suggest that TMV contains the requisite Th epitopes for Th activation. TMV particles are stable in various harsh conditions, such as temperatures up to 60 °C, a wide range of pH values (2−10) and organic solvents (ethanol, methanol, and dimethyl sulfoxide), thus allowing chemical derivatizations without affecting the integrity of the particles.[44] Furthermore, kilogram quantities of TMV virion can be produced from infected leaves, which suggest the strong potential of TMV for large-scale clinical studies or production.

Herein, we report our results on engineering of TMV as a carrier for the monomeric Tn antigen and evaluation of the immunological effects of various TMV-Tn constructs. Our results demonstrated that the immunotolerance of Tn can be broken when delivered by the TMV carrier and the location of TMV modification is crucial for high immune responses.

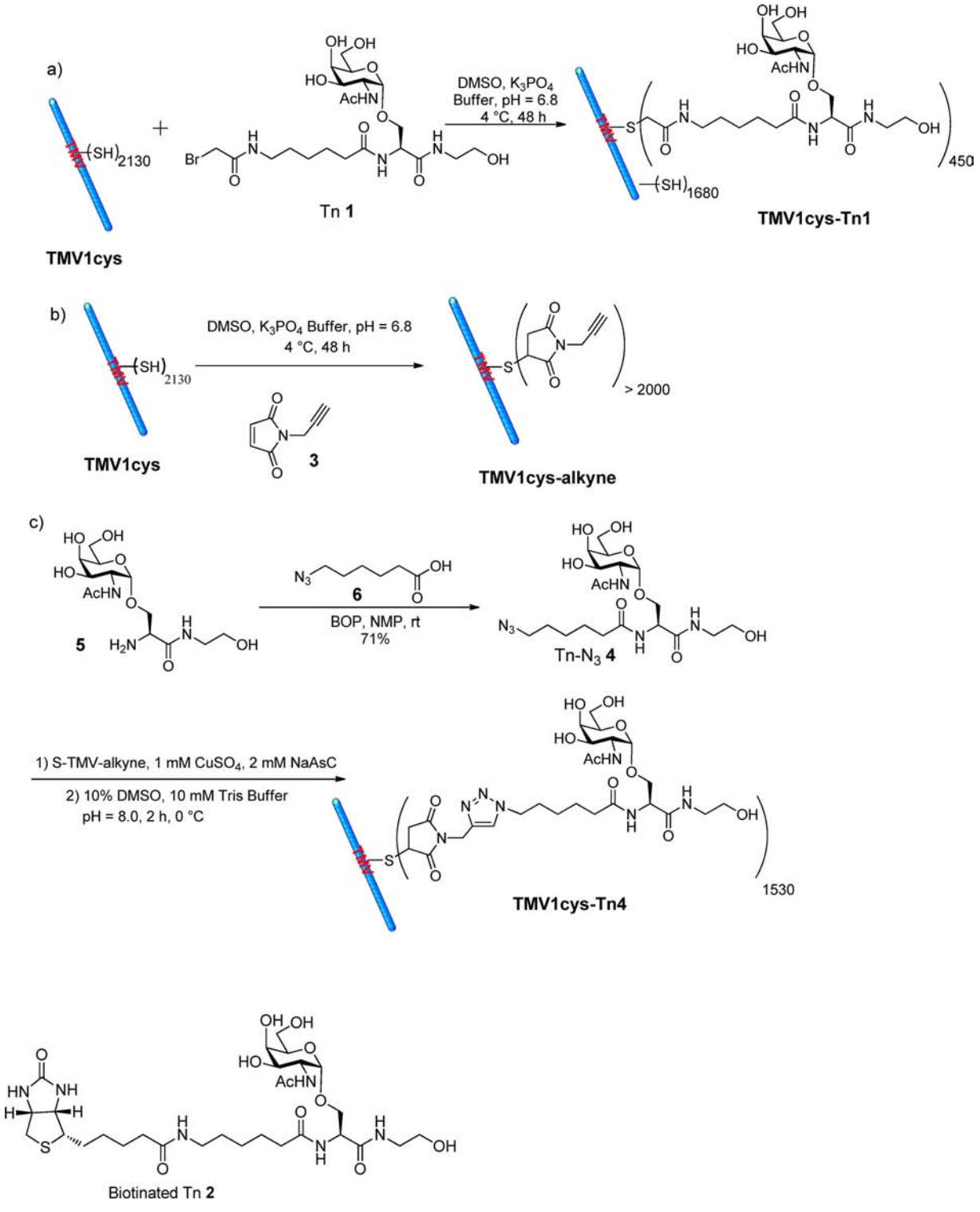
EXPERIMENTAL PROCEDURES

1. General Experimental Procedures and Methods. All chemicals were purchased from VWR and used as received. Dialysis tubing of 300 000 molecular weight cutoff (MWCO) was purchased from Spectrum Laboratories. TEM analyses were carried out by depositing 20 μL aliquots of each sample at a concentration of 0.1 mg/mL onto 100-mesh carbon-coated copper grids for 2 min. The grids were then stained with 20 μL of 2% uranyl acetate and viewed with a Hitachi H-8000 TEM electron microscope. For MALDI-TOF MS analysis, each sample was prepared by mixing the viral sample (0.1 mg/mL, 1 μL) with 9 μL of matrix solution (saturated sinapic acid in 70% acetonitrile, 0.1% trifluoroacetic acid). Using a Zip Tip, 1 μL of the mixture was spotted on a MALDI plate, air-dried, and analyzed by MALDI-TOF mass spectrometry (Bruker Daltonics Ultraflex ITOF/TOF).

2. General Procedures for Mouse Immunization. Pathogen-free C57BL/6 female mice age 6−10 weeks were obtained from Charles River and maintained in the University Laboratory Animal Resources facility of Michigan State University. All animal care procedures and experimental protocols have been approved by the Institutional Animal Care and Use Committee of Michigan State University. Groups of five C57BL/6 mice were injected subcutaneously under the scruff on day 0 with various TMV constructs as emulsions in complete Freund's adjuvant (0.1 mL, Fisher) or TiterMax Gold adjuvant (Sigma-Aldrich) for the TMV-Tyr-Tn studies. Boosters were given subcutaneously under the scruff on days 14 and 28 with the constructs as emulsions in incomplete Freund's adjuvant (0.1 mL) or TiterMax Gold adjuvant. Blood (∼0.2 mL/mouse) was collected from both groups of mice on days 0, 7, and 35. Sera from each group of mice were isolated and pooled. Human lymphoma Jurkat cells (kindly provided by Profs. Barbara Kaplan and Norbert Kaminski, Michigan State University) were cultured in RPMI 1640 supplemented with 10% FBS, 2 mM L-glutamine, 1 mM sodium pyruvate, minimal essential medium nonessential amino acid, 100 units/mL each of penicillin G, and streptomycin (all from Invitrogen).

3. General Procedures for ELISA and Competitive ELISA. A 96-well microtiter plate was first coated with a solution of Neutravidin in PBS buffer (8 μg/mL) and then incubated overnight at 4 °C. The plate was then washed four times with PBS/0.5% Tween-20 (PBST), followed by the addition of 1% (w/v) BSA in PBS to each well and incubation at room temperature for one hour. The plate was washed again with PBST and a solution of biotinylated Tn **2** (5 μg/mL) in 0.1% BSA in PBS was added. The plate was incubated for one hour at 37 °C. The plate was then washed, and mouse sera were added in a 1:3 serial dilution in 0.1% BSA/PBS. The plate was incubated for two hours at 37 °C and washed. A 1:2000 diluted horseradish peroxidase (HRP)-conjugated goat antimouse IgG+IgM, IgG, or IgM antibody (Jackson ImmunoResearch Laboratory IgG +IgM catalog #115−035−068, IgM #115−035−075, IgG #115−035−071) in 0.1% BSA/PBS was added to each well, respectively. The plate was incubated for one hour at 37 °C, washed, and a solution of 3,3′,5,5′-tetramethylbenzidine (TMB)

Scheme 1. Synthesis of (a) TMV1cys-Tn1, (b) TMV1cys-alkyne, and (c) TMV1cys-Tn4



was added. Color was allowed to develop for 20 min, and then a solution of 0.5 M H_2SO_4 was added to quench the reaction. The optical density was then measured at 450 nm. Each experiment was repeated at least four times, and the average of the quadruplicate was used to calculate the titer. Errors of each measurement were typically within 10%. Antibody titers were defined as the maximum-fold dilution resulting in 0.1 OD unit higher than average absorbance after greater than 100 000-fold of dilution.

For competitive ELISA, the same procedure was adapted with the only exception being that 0.1 M GalNAc was added to the serum prior to addition of the mouse sera to the ELISA plate.

RESULTS AND DISCUSSION

As the Tn antigen cannot be directly inserted into the TMV capsid, a reactive functional group needs to be available on TMV for bioconjugation. Although there are no lysine or cysteine residues exposed on the exterior surface of native TMV,[39] X-ray

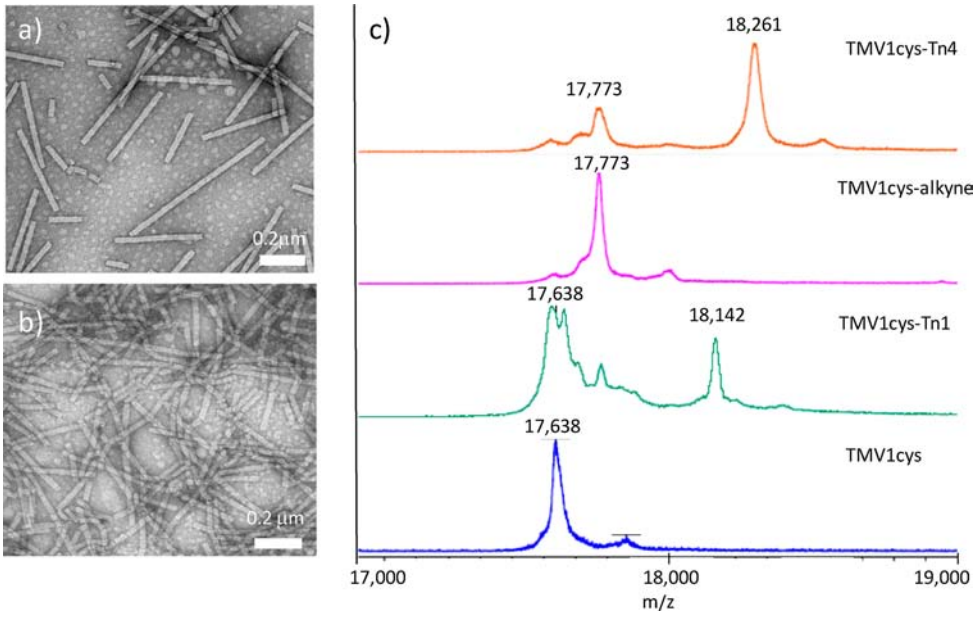


Figure 1. TEM images of (a) TMV1cys-Tn1 and (b) TMV1cys-Tn4 confirming that TMV was still intact after Tn conjugation. (c) MALDI-TOF MS spectra of the monomer units of TMV1cys, TMV1cys-Tn1, TMV1cys-alkyne, and TMV1cys-Tn4. The ion intensity ratio of the peaks corresponding to Tn functionalized monomer of TMV1cys-Tn1 (m/z = 18 142) and the underivatized monomer (m/z = 17 638) was 1: 4, suggesting approximately 450 of the possible 2330 Cys 3 sites were derivatized. Analogously, it was determined that on average 1530 Tn antigens were attached on each TMV1cys-Tn4 capsid.

structure of TMV revealed that the N-terminus, the C-terminus, and a loop between amino acid residues 55 and 60 of TMV were surface exposed.[45] Through mutagenesis, surface accessible cysteine or lysine residues have been introduced to the N-terminus of TMV coat protein to produce stable virions, which could be subsequently functionalized.[39,44,46−48] In our study, a cysteine mutant of TMV (TMV1cys),[46,48] which contains a cysteine residue inserted between Ser 2 and Tyr 3 of the TMV coat protein, was used for the conjugation with the Tn antigen. The bromoacetamide Tn derivative **1** (Tn **1**)[34] was conjugated to TMV1cys through a S_N2 displacement reaction with the Cys 3 residue (Scheme 1a). Due to the low reactivity of bromoacetamide toward thiols, an excess of Tn **1** (200 equiv per subunit) was utilized. The resulting TMV1cys-Tn1 was analyzed by transmission electron microscopy (TEM), which verified that the capsid remained intact (Figure 1a). MALDI-TOF MS analysis of TMV1cys-Tn1 showed a 1:4 ion intensity ratio of the peaks corresponding to the monomeric units of TMV1cys-Tn1 and TMV1cys (Figure 1b). Assuming similar ionization efficiencies of the Tn functionalized and unmodified monomers of coat proteins, we concluded that 20% of the capsid subunits were derivatized with Tn **1**. This suggested that approximately 450 Tn antigens were coupled onto TMV1cys out of the 2130 possible Cys 3 sites.

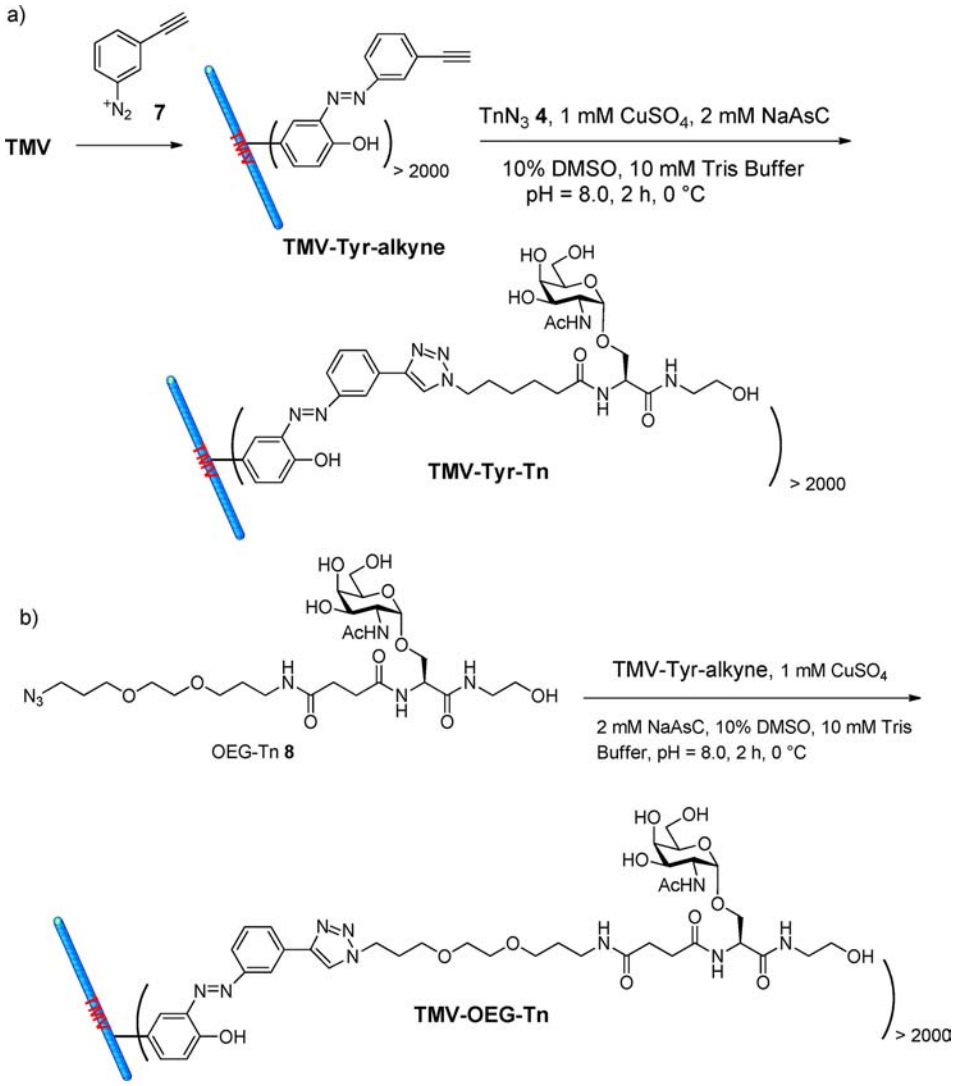
With TMV1cys-Tn1 in hand, immunological evaluations were carried out in C57BL/6 mice. Each mouse received a subcutaneous injection of TMV1cys-Tn1 (equivalent to 4 μg of Tn) together with the complete Freund's adjuvant. On days 14 and 28 after the initial injection, the same amounts of TMV1cys-Tn1 in the presence of incomplete Freund's adjuvant were given to the mice to boost the immune responses. Mice in the control group underwent the identical procedure except that native TMV was used to replace TMV1cys-Tn1. On day 35, blood was collected from each mouse and anti-Tn antibody titers from the sera were analyzed by enzyme-linked immunosorbent assay (ELISA) against biotinated Tn **2** immobilized on the ELISA plate. Negligible amounts of IgG or IgM antibodies were found in all sera at a 1600-fold serum dilution (denoted as 1/1600 dilution). As only about 20% of the TMV subunits in TMV1cys-Tn1 were functionalized with Tn, it was possible that the lack of immune responses resulted from the low Tn density on TMV1cys. Since the reactivity of bromoacetamide toward thiol was low, it was difficult to improve the Tn loading level by increasing the amount of Tn **1** for bioconjugation. This led us to examine alternative bioconjugation chemistry.

In the past decade, the copper(I) catalyzed azide−alkyne cycloaddition reaction (CuAAC) has become a powerful technique for biomacromolecule functionalization.[49,50] The biocompatible reaction conditions, simple purification procedures, wide functional group tolerance, and high conjugation yield render the CuAAC reaction a good tool for vaccine construction.

In order to take advantage of the CuAAC reaction, an alkyne group was introduced to TMV1cys by coupling with a maleimide containing bifunctional linker **3** (Scheme 1b). Only 5 equiv of maleimide alkyne **3** was needed to generate TMV1cys-alkyne in near-quantitative yield as verified by MALDI-TOF MS (Figure 1c). The azido bearing Tn **4** was prepared in 71% yield by amidation of glycosyl amino acid **5**[34] with azido carboxylic acid **6** (Scheme 1c). Unlike the maleimide and bromoacetamide Tn derivatives that were side reaction prone,[34] Tn-N_3 **4** was very stable and was much easier to purify. The Tn-N_3 **4** was conjugated to TMV1cys-alkyne under the standard CuAAC reaction condition in the presence of $CuSO_4$ and sodium ascorbate (NaAsC), with the structural integrity of the resulting TMV1cys-Tn4 proven by TEM (Figure 1b). The high reaction efficiencies were confirmed by MALDI-TOF MS (Figure 1c) with about 1530 Tn antigens displayed on one TMV capsid based on intensity analysis of the corresponding MS peaks. It should be noted that only 16 equiv of Tn-N_3 **4** per subunit protein was needed to achieve the observed 70% conjugation efficiency. This result highlights the power of CuAAC reaction for the site-directed functionalization of TMV.

dx.doi.org/10.1021/bc300244a | *Bioconjugate Chem.* 2012, 23, 1694−1703

Scheme 2. Synthesis of (a) TMV-Tyr-Tn and (b) TMV-OEG-Tn



The immunological properties of TMV1cys-Tn4 were evaluated in mice at two doses (1 μg and 4 μg Tn per mouse) with the Freund's adjuvant. To our disappointment, sera from both groups showed negligible amounts of IgG or IgM antibodies at 1/1600 dilution. Although peptide antigens inserted at the N-terminus of TMV could elicit strong immune responses,[43] our results suggested that, even with high loading of Tn, little immune response was generated against Tn linked close to the N-terminus of TMV. This is unlikely due to the disruption of Th cell epitope, since Cys 3 was inserted close to the N-terminus (between Ser 2 and Tyr 3). Although the exact reason for the low immune response is not clear, one possible explanation is that Tn displayed at the N terminus of TMV was not recognized by B cell receptors. This consideration led us to explore other locations for Tn conjugation.

Recently, Francis and others described that Tyr 139 of TMV could be modified to install various functionalities by diazonium coupling,[51,52] and this chemistry was examined for our vaccine construction. Tyr 139 was functionalized by treatment of TMV with the diazonium alkyne **7** to give TMV-Tyr-alkyne (Scheme 2a). Close to complete modification was achieved as evident from MALDI-TOF MS analysis, with the m/z ratio of the capsid shifting completely from 17 535 to 17 664 (Figure 2). TMV-Tyr-alkyne was then coupled to Tn-N_3 **4** via the CuAAC reaction. Even with just 5 equiv of Tn-N_3 **4**, more than 2000 copies of Tn antigens were successfully coupled to TMV surface as demonstrated by MALDI-TOF analysis of TMV-Tyr-Tn (Figure 2). TMV-Tyr-Tn was further characterized by TEM and UV−vis spectroscopy confirming the integrity of the virion (SI Figure S1).

The immunological responses against the TMV-Tyr-Tn construct were evaluated in C57BL/6 mice, by administering TMV-Tyr-Tn (20 μg Tn per mouse) subcutaneously with the Freund's adjuvant (CFA) followed by booster injections on days 14 and 28. Mice in the control group underwent the identical procedure using native TMV. Excitingly, significant amounts of anti-Tn antibodies were induced by TMV-Tyr-Tn on day 35 as compared to the control group (Figure 3a). Adjuvants can play important roles in directing immune responses. To test the effect of adjuvants, another common adjuvant TiterMax Gold was evaluated. The total antibody (IgG + IgM) titer in the Freund's adjuvant group (titer 2550) was five times higher than that from the TiterMax Gold group (titer 520), suggesting that the Freund's adjuvant was superior.

The triazole ring was believed to be immunogenic due to its aromatic and rigid structure. The unwanted anti-triazole linker

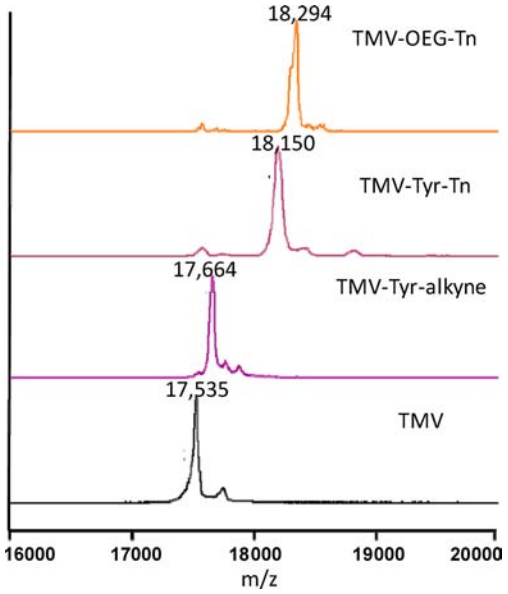


Figure 2. MALDI-TOF MS spectra of the monomer units of TMV, TMV-Tyr-alkyne, TMV-Tyr-Tn, and TMV-OEG-Tn. The near-complete MS shifts following each derivatization step suggested the high conversion in TMV functionalization.

response may suppress the immunoresponses against the desired epitopes. Since our ELISA was performed against Tn **2** lacking the triazole, the observed antibody titers were not against the triazole linker. Our results demonstrate that, in the presence of the triazole, antibody responses could still be generated against the weak carbohydrate antigen Tn.

In order to confirm the carbohydrate recognition specificity of the antibodies, a competitive ELISA procedure was developed by adding free GalNAc to the serum prior to serum incubation with the ELISA plate. As GalNAc is part of the Tn antigen, the free GalNAc should bind with Tn specific antibodies, thus reducing the number of antibodies available to bind with the plate. Indeed, addition of 0.1 M GalNAc for competitive ELISA significantly reduced anti-Tn antibody titers (Figure 3b). The inhibitory effect was more pronounced for the Freund's adjuvant group than the TiterMax Gold group.

For an effective vaccine, the generation of IgG is important. Subtyping the antibodies from the Freund's adjuvant group demonstrated that both IgG and IgM antibodies were produced with higher IgM titers than IgG (Figure 3c). The generation of IgG antibodies indicated that the TMV platform could stimulate activation of Th cells and isotype switching of antibodies.

The strong humoral responses induced by TMV-Tyr-Tn as compared to the ineffective TMV1cys-Tn construct highlighted the importance of the position where the antigen was introduced.[53] Tyr 139 allowed better access of the reagent to functionalize the viral capsid, which may also be more accessible for recognition by B cells.

A close examination of TMV structure revealed that Tyr 139 is located in a shallow groove on the external surface of TMV (Figure 4).[52] It is possible that the Tn antigen could be partially

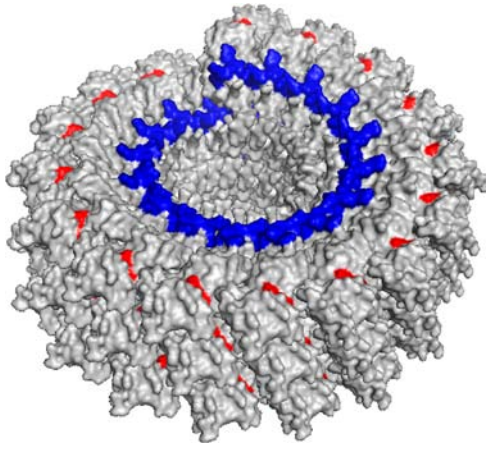


Figure 4. Cross section of a TMV capsid. The red-colored residue is Tyr 139, residing in a shallow groove. The genomic RNA is marked in blue.

buried in the groove. A longer linker between Tn and TMV could potentially extend the Tn antigen out of the groove and enhance B cell recognition. To test this, Tn antigen derivative **8** with an oligoethylene oxide (OEG) linker was conjugated to TMV-Tyr-alkyne through the CuAAC reaction (Scheme 2b). MALDI-TOF confirmed that close to complete alkyne functionalization and CuAAC reaction were achieved (Figure 2).

The immune responses to TMV-OEG-Tn were evaluated following the previously established prime and boost protocol with the Freund's adjuvant. To investigate the effect of vaccine dose on immune response, three groups of five mice received vaccine constructs corresponding to 1 μg, 4 μg, and 20 μg Tn antigen, respectively. As shown in Figure 5, all three groups generated significant antibodies compared to the control group immunized with TMV only. The 4 μg group led to the highest antibody titers, and high IgG titers were produced in the 4 μg and 20 μg groups (Figure 5b,c). The antibody responses to the 20 μg group were comparable to those elicited by the TMV-Tyr-Tn

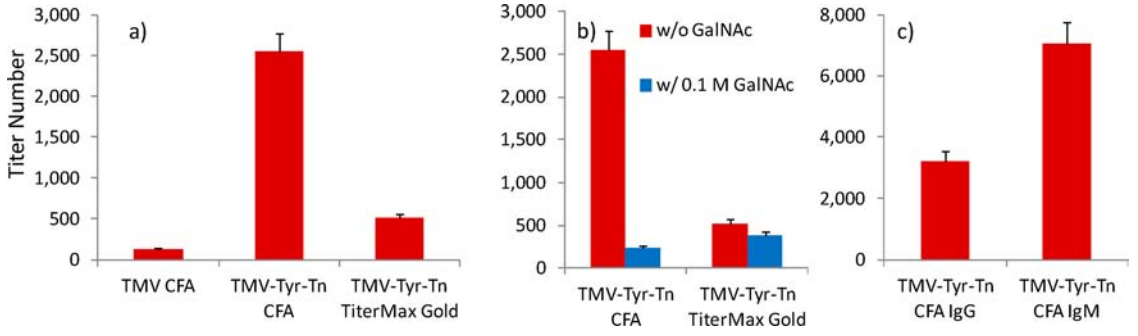


Figure 3. (a) ELISA titers of anti-Tn IgG + IgM antibodies for control group TMV, and TMV-Tyr-Tn (20 μg Tn) with either CFA or TiterMax Gold adjuvant; (b) ELISA titers of anti-Tn IgG + IgM antibodies generated by TMV-Tyr-Tn with either CFA or TiterMax Gold in the absence and presence of 0.1 M GalNAc; (c) ELISA titers of anti-Tn IgG and IgM antibodies.

dx.doi.org/10.1021/bc300244a | *Bioconjugate Chem.* 2012, 23, 1694−1703

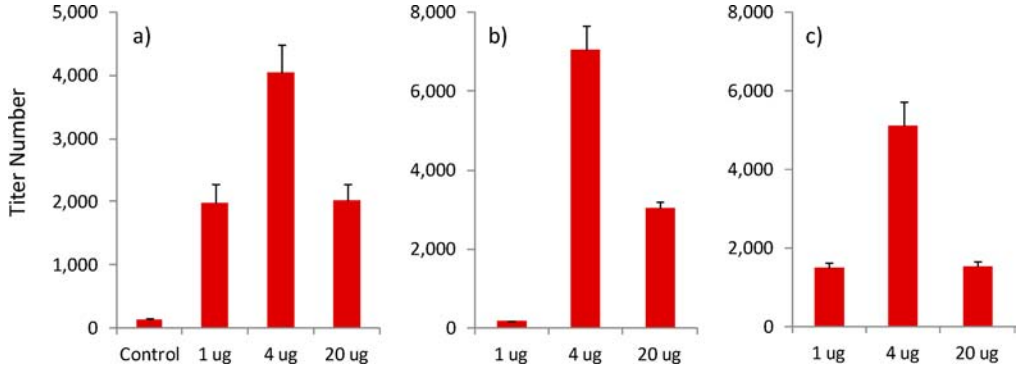


Figure 5. Anti-Tn ELISA titers of (a) IgG + IgM for TMV control group and TMV-OEG-Tn groups corresponding to 1 μg, 4 μg, and 20 μg Tn respectively; (b) IgG and (c) IgM of TMV-OEG-Tn groups corresponding to 1 μg, 4 μg, and 20 μg Tn, respectively.

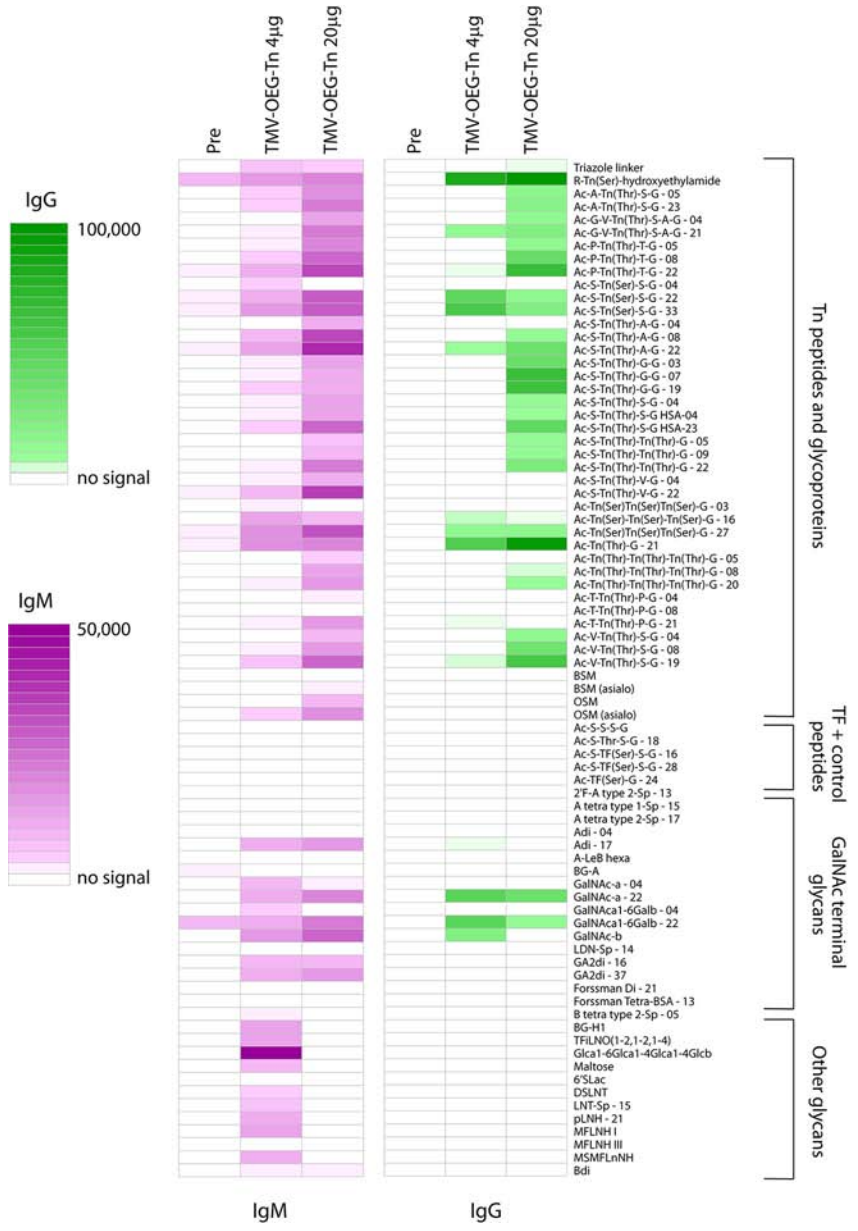


Figure 6. Microarray profiles comparing pre- and postimmune sera from mice immunized with TMV-OEG-Tn. Colored boxes correspond to the average fluorescence signal from duplicate experiments. IgM data is shown in magenta, and IgG data is shown in green. Glycans are attached to albumin prior to printing on the array surface. The numbers after the glycan abbreviation correspond to the average number of glycans per molecule of albumin (for example, Ac-A-Tn(Thr)-S-G-05 is a neoglycoprotein with an average of 5 Tn peptides per molecule of albumin). Selected array results are shown and full results can be found in the Supporting Information.

dx.doi.org/10.1021/bc300244a | *Bioconjugate Chem.* 2012, 23, 1694−1703

construct, indicating that the length of the linker between Tn and TMV did not have a significant role.

To further analyze the specificity of the induced antibodies, the sera from the 4 μg and 20 μg groups were screened at a dilution of 1:100 against a carbohydrate microarray, which is a powerful high-throughput method to rapidly establish carbohydrate binding specificities.[54−56] The microarray used in this study contained 329 array components, including a variety of *O*-linked glycopeptides, *N*-linked glycopeptides, glycolipids, and glycoproteins. After the array was incubated with sera and the unbound antibodies were washed off the slide, serum antibody binding to individual array components was detected using fluorescently labeled secondary antibodies.[54]

The 4 μg and 20 μg groups both produced significant IgM and IgG responses relative to the prevaccination sera (see Figure 6; for the full list of glycoconjugate structures on the microarray, see Table S1 in Supporting Information). The induced IgM and IgG bound to a variety of Tn peptides, along with some reactivity with a subset of other GalNAc-terminal glycans. Neither IgM nor IgG reacted with nonglycosylated peptides or TF-containing peptides, which possess an internal GalNAc (for example, see compound Ac-S-TF(Ser)-S-G), demonstrating that a nonreducing terminal GalNAc is critical for recognition. In general, induced IgG antibodies had better specificity than IgM antibodies. For example, the induced IgM antibodies reacted with the triazole linker and the GA2 disaccharide (GA2di, see Table S1 for structure), while the IgG antibodies did not show any appreciable binding to either of these array components.

While the overall patterns from the 4 and 20 μg groups were similar, the vaccine dose affected the antibody responses with the 20 μg group generally having higher levels of induced antibodies to various Tn antigen containing array components (Figure 6). The antibodies from the 20 μg group showed better reactivities toward Tn peptides with a GalNAc linked to a threonine. Of note, the 20 μg group also showed less cross-reactivity to glycans that are not part of a Tn peptide. While this was true for both IgM and IgG responses, the effect was more pronounced for IgMs. This is possibly because, with higher antigen dose, the immune response generated was more focused toward the desired antigen.

As both ELISA and microarray studies measure antibody binding against synthetic Tn antigens, it would be important to test antibody recognition of Tn antigens present in the native environment, i.e., cancer cell surface. It is known that Tn antigen is expressed on human leukemia Jurkat cells.[57,58] Upon incubation of Jurkat cells with the postimmune sera, a significant increase in binding to Jurkat cells was found (Figure 7), suggesting the antibodies were able to recognize Tn antigens displayed in its native configurations on tumor cell surface. Although the serum from the 4 μg group gave high titers of antibodies against Tn as determined by ELISA, the 20 μg group showed stronger reactivity with cancer cells presumably due to the higher affinities and/or broader reactivities toward Tn containing peptides by antibodies from the 20 μg group.

In conclusion, we have demonstrated that TMV is a promising platform to deliver TACAs. The location where antigen was immobilized had great influence on the ease of viral capsid functionalization as well as outcome of the immune responses. Even though Tn is a very weakly immunogenic tumor-associated carbohydrate antigen, when placed at strategic sites, strong humoral immune responses could be induced. High titers of IgG antibodies were elicited by the TMV-Tyr-Tn and TMV-OEG-Tn constructs, which recognized human tumor cells. Further studies are in progress to optimize this new platform for the development of TACA based anticancer vaccine.

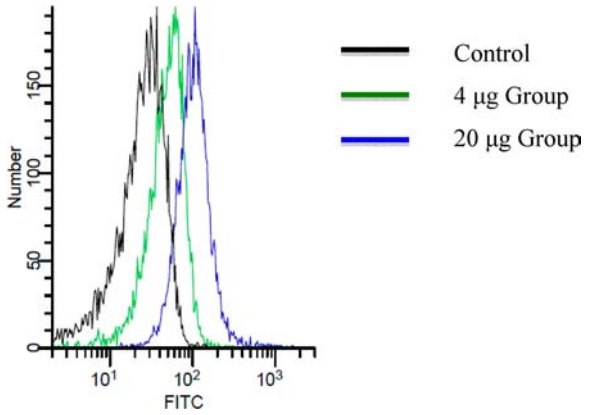


Figure 7. Fluorescence activated cell sorting analysis of IgG antibodies present in postimmune sera binding with Jurkat cells.

■ ASSOCIATED CONTENT

Supporting Information

Information on purification, characterization, and functionalization TMV, various TMV mutants, and TMV conjugates. Procedures for glycan microarray analysis and fluorescence activated cell sorting. This material is available free of charge via the Internet at http://pubs.acs.org.

■ AUTHOR INFORMATION

Corresponding Author

*E-mail addresses: wang263@mailbox.sc.edu (Q.W.); xuefei@chemistry.msu.edu (X.H.).

Notes

The authors declare no competing financial interest.

■ ACKNOWLEDGMENTS

The authors are indebted to Professor J. Culver (University of Maryland) for providing the mutant virus TMV1cys. We would like to thank the National Cancer Institute for generous financial support of our work (XH, R01CA149451-01A1), partial financial support from NSF (QW, CHE-0748690), the Alfred P. Sloan Scholarship (QW), and the Camille Dreyfus Teacher Scholar Award (QW). This work was supported in part by the intramural research program of the NIH, NCI.

■ ABBREVIATIONS:

CFA, Freund's adjuvant; CuAAC, copper(I) catalyzed azide−alkyne cycloaddition reaction; ELISA, enzyme-linked immunosorbent assay; KLH, keyhole limpet hemocyanine; MAG, multiple antigen glycopeptide; MALDI-TOF, matrix assisted laser desorption ionization − time-of-flight; MWCO, molecular weight cutoff; NaAsC, sodium ascorbate; PV, poliovirus; TACAs, tumor associated carbohydrate antigens; Th, helper T cells; TMV, tobacco mosaic virus; TMV1cys, a cysteine mutant of TMV; VLPs, virus like particles

■ REFERENCES

(1) Hakomori, S. (2001) Tumor-associated carbohydrate antigens defining tumor malignancy: basis for development of anti-cancer vaccines. *Adv. Exp. Med. Biol. 491*, 369−402.

(2) Danishefsky, S. J., and Allen, J. R. (2000) From the laboratory to the clinic: a retrospective on fully synthetic carbohydrate-based anticancer vaccines. *Angew. Chem. Int. Ed 39*, 836−863 and references cited therein.
(3) Hakomori, S., and Zhang, Y. (1997) Glycosphingolipid antigens and cancer therapy. *Chem. Biol. 4*, 97−104.
(4) Springer, G. F. (1984) T and Tn, general carcinoma autoantigens. *Science 224*, 1198−1206.
(5) Springer, G. F., Desai, P. R., Spencer, B. D., Tegtmeyer, H., Carlstedt, S. C., and Scanlon, E. F. (1995) T/Tn antigen vaccine is effective and safe in preventing recurrence of advanced breast carcinoma. *Cancer Detect. Prev. 19*, 374−380.
(6) Cazet, A., Julien, S., Bobowski, M., Burchell, J., and Delannoy, P. (2010) Tumour-associated carbohydrate antigens in breast cancer. *Breast Cancer Res. 12*, 204−216.
(7) Itzkowitz, S. H., Yuan, M., Montgomery, C. K., Kjeldsen, T., Takahashi, H. K., Bigbee, W. L., and Kim, Y. S. (1989) Expression of Tn, sialosyl-Tn, and T antigens in human colon cancer. *Cancer Res. 49*, 197−204.
(8) Li, Q., Anver, M. R., Butcher, D. O., and Gildersleeve, J. C. (2009) Resolving conflicting data on expression of the Tn antigen and implications for clinical trials with cancer vaccines. *Mol. Cancer Ther. 8*, 971−979.
(9) Wang, B.-L., Springer, G. F., and Carlstedt, S. C. (1997) Quantitative computerized image analysis of Tn and T (Thomsen−Friedenreich) epitopes in prognostication of human breast carcinoma. *J. Histochem. Cytochem. 45*, 1393−1400.
(10) Kawaguchi, T., Takazawa, H., Imai, S., Morimoto, J., Watanabe, T., Kanno, M., and Igarashi, S. (2006) Expression of vicia villosa agglutinin (VVA)-binding glycoprotein in primary breast Cancer cells in relation to lymphatic metastasis: is atypical MUC1 bearing Tn antigen a receptor of VVA? *Breast Cancer Res. Treat. 98*, 31−43.
(11) Yin, Z., and Huang, X. (2012) Recent development in carbohydrate based anticancer vaccines. *J. Carbohydr. Chem 31*, 143−186 and references cited therein.
(12) Freire, T., Bay, S., Vichier-Guerre, S., Lo-Man, R., and Leclerc, C. (2006) Carbohydrate antigens: synthesis aspects and immunological applications in cancer. *Mini-Rev. Med. Chem. 6*, 1357−1373.
(13) Goldsby, R. A., Kindt, T. J., and Osborne, B. A. (2000) *Kuby Immunology*, pp 461−464, Freeman, New York.
(14) Kagan, E., Ragupathi, G., Yi, S. S., Reis, C. A., Gildersleeve, J., Kahne, D., Clausen, H., Danishefsky, S. J., and Livingston, P. O. (2005) Comparison of antigen constructs and carrier molecules for augmenting the immunogenicity of the monosaccharide epithelial cancer antigen Tn. *Cancer Immunol. Immunother. 54*, 424−430.
(15) Slovin, S. F., Ragupathi, G., Musselli, C., Olkiewicz, K., Verbel, D., Kuduk, S. D., Schwarz, J. B., Sames, D., Danishefsky, S., Livingston, P. O., and Scher, H. I. (2003) Fully synthetic carbohydrate-based vaccines in biochemically relapsed prostate cancer: clinical trial results with α-N-acetylgalactosamine-O-serine/threonine conjugate vaccine. *J. Clin. Oncol. 21*, 4292−4298.
(16) Lo-Man, R., Bay, S., Vichier-Guerre, S., Deriaud, E., Cantacuzene, D., and Leclerc, C. (1999) A fully synthetic immunogen carrying a carcinoma-associated carbohydrate for active specific immunotherapy. *Cancer Res. 59*, 1520−1524.
(17) Lo-Man, R., Vichier-Guerre, S., Perraut, R., Deriaud, E., Huteau, V., BenMohamed, L., Diop, O. M., Livingston, P. O., Bay, S., and Leclerc, C. (2004) A fully synthetic therapeutic vaccine candidate targeting carcinoma-associated Tn carbohydrate antigen induces tumor-specific antibodies in nonhuman primates. *Cancer Res. 64*, 4987−4994.
(18) Lo-Man, R., Vichier-Guerre, S., Bay, S., Deriaud, E., Cantacuzene, D., and Leclerc, C. (2001) Anti-tumor immunity provided by a synthetic multiple antigenic glycopeptide displaying a Tri-Tn glycotope. *J. Immunol. 166*, 2849−2854.
(19) De Silva, R. A., Wang, Q., Chidley, T., Appulage, D. K., and Andreana, P. R. (2009) Immunological response from an entirely carbohydrate antigen: design of synthetic vaccines based on Tn-PS A1 conjugates. *J. Am. Chem. Soc. 131*, 9622−9623.
(20) Bettahi, I., Dasgupta, G., Renaudet, O., Chentoufi, A. A., Zhang, X., Carpenter, D., Yoon, S., Dumy, P., and BenMohamed, L. (2009) Antitumor activity of a self-adjuvanting glyco-lipopeptide vaccine bearing B Cell, CD4+ and CD8+ T cell epitopes. *Cancer Immunol. Immunother. 58*, 187−200.
(21) Renaudet, O., BenMohamed, L., Dasgupta, G., Bettahi, I., and Dumy, P. (2008) Towards a self-adjuvanting multivalent B and T cell epitope containing synthetic glycolipopeptide cancer vaccine. *ChemMedChem 3*, 737−741.
(22) Ingale, S., Wolfert, M. A., Buskas, T., and Boons, G.-J. (2009) Increasing the antigenicity of synthetic tumor-associated carbohydrate antigens by targeting toll-like receptors. *ChemBiochem 10*, 455−463 and references cited therein.
(23) Geraci, C., Consoli, G. M. L., Galante, E., Bousquet, E., Pappalardo, M., and Spadaro, A. (2008) Calix[4]arene decorated with four Tn antigen glycomimetic units and P3CS immunoadjuvant: synthesis, characterization, and anticancer immunological evaluation. *Bioconjugate Chem. 19*, 751−758.
(24) Vepřek, P., Hajdúch, M., Džubák, P., Kuklík, R., Poláková, J., and Bezouška, K. (2006) Comblike dendrimers containing Tn antigen modulate natural killing and induce the production of Tn specific antibodies. *J. Med. Chem. 49*, 6400−6407.
(25) Sarkar, S., Lombardo, S. A., Herner, D. N., Talan, R. S., Wall, K. A., and Sucheck, S. J. (2010) Synthesis of a single molecule L-rhamnose-containing three component vaccine and evaluation of antigenicity in the presence of anti-L-rhamnose antibodies. *J. Am. Chem. Soc. 132*, 17236−17246.
(26) Bachmann, M. F., and Zinkernagel, R. M. (1997) Neutralizing antiviral B cell responses. *Annu. Rev. Immunol. 15*, 235−270.
(27) Bachmann, M. F., Rohrer, U. H., Kundig, T. M., Burki, K., Hengartner, H., and Zinkernagel, R. M. (1993) The influence of antigen organization on B cell responsiveness. *Science 262*, 1448−1451.
(28) Denis, J., Majeau, N., Acosta-Ramirez, E., Savard, C., Bedard, M.-C., Simard, S., Lecours, K., Bolduc, M., Pare, C., Willems, B., Shoukry, N., Tessier, P., Lacasse, P., Lamarre, A., Lapointe, R., Lopez Macias, C., and Leclerc, D. (2007) Immunogenicity of papaya mosaic virus-like particles fused to a hepatitis C virus epitope: evidence for the critical function of multimerization. *Virology 363*, 59−68.
(29) Geyer, H., Wuhrer, M., Kurokawa, T., and Geyer, R. (2004) Characterization of keyhole limpet hemocyanin (KLH) glycans sharing a carbohydrate epitope with *Schistosoma mansoni* glycoconjugates. *Micron 35*, 105−106.
(30) Oyelaran, O., and Gildersleeve, J. C. (2010) Evaluation of human antibody responses to keyhole limpet hemocyanin (KLH) on a carbohydrate microarray. *Proteomics - Clin. Appl. 4*, 285−294.
(31) Chackerian, B. (2007) Virus-like particles-flexible platforms for vaccine development. *Expert Rev. Vaccines 6*, 381−390.
(32) Jennings, G. T., and Bachmann, M. F. (2007) Designing recombinant vaccines with viral properties: a rational approach to more effective vaccines. *Curr. Mol. Med. 7*, 143−155.
(33) Cornuz, J., Zwahlen, S., Jungi Walter, F., Osterwalder, J., Klingler, K., van Melle, G., Bangala, Y., Guessous, I., Muller, P., Willers, J., Maurer, P., Bachmann Martin, F., and Cerny, T. (2008) A vaccine against nicotine for smoking cessation: a randomized controlled trial. *PLoS ONE 3*, e2547.
(34) Miermont, A., Barnhill, H., Strable, E., Lu, X., Wall, K. A., Wang, Q., Finn, M. G., and Huang, X. (2008) Cowpea mosaic virus capsid: a promising carrier for the development of carbohydrate based antitumor vaccines. *Chem.—Eur. J. 14*, 4939−4947.
(35) Kaltgrad, E., Sen Gupta, S., Punna, S., Huang, C. Y., Chang, A., Wong, C. H., Finn, M. G., and Blixt, O. (2007) Anti-carbohydrate antibodies elicited by polyvalent display on a viral scaffold. *ChemBioChem 8*, 1455−1462.
(36) Chackerian, B., Rangel, M., Hunter, Z., and Peabody, D. S. (2006) Virus and virus-like particle-based immunogens for Alzheimer's disease induce antibody responses against amyloid-beta without concomitant T cell responses. *Vaccine 24*, 6321−31.
(37) Brennan, F. R., Jones, T. D., and Hamilton, W. D. O. (2001) Cowpea mosaic virus as a vaccine carrier of heterologous antigens. *Mol. Biotechnol. 17*, 15−26.

(38) Culver, J. N. (2002) Tobacco mosaic virus assembly and disassembly: determinants in pathogenicity and resistance. *Annu. Rev. Phytopathol. 40*, 287−308.
(39) McCormick, A. A., and Palmer, K. E. (2006) Genetically engineered tobacco mosaic virus as nanoparticle vaccines. *Expert Rev. Vaccines 7*, 33−41 and references cited therein..
(40) Koo, M., Bendahmane, M., Lettieri, G. A., Paoletti, A. D., Lane, T. E., Fitchen, J. H., Buchmeier, M. J., and Beachy, R. N. (1999) Protective immunity against murine hepatitis virus (MHV) induced by intranasal or subcutaneous administration of hybrids of tobacco mosaic virus that carries an MHV epitope. *Proc. Natl. Acad. Sci. U.S.A. 96*, 7774−7779.
(41) Fitchen, J., Beachy, R. N., and Hein, M. B. (1995) Plant virus expressing hybrid coat protein with added murine epitope elicits autoantibody response. *Vaccine 13*, 1051−1057.
(42) McCormick, A. A., Corbo, T. A., Wykoff-Clary, S., Nguyen, L. V., Smith, M. L., Palmer, K. E., and Pogue, G. P. (2006) TMV-peptide fusion vaccines induce cell-mediated immune responses and tumor protection in two murine models. *Vaccine 24*, 6414−6423.
(43) McCormick, A. A., Corbo, T. A., Wykoff-Clary, S., Palmer, K. E., and Pogue, G. P. (2006) Chemical conjugate TMV-peptide bivalent fusion vaccines improve cellular immunity and tumor protection. *Bioconjugate Chem. 17*, 1330−1338.
(44) Smith, M. L., Lindbo, J. A., Dillard-Telm, S., Brosio, P. M., Lasnik, A. B., McCormick, A. A., Nguyen, L. V., and Palmer, K. E. (2006) Modified tobacco mosaic virus particles as scaffolds for display of protein antigens for vaccine applications. *Virology 348*, 475−488.
(45) Namba, K., and Stubbs, G. (1986) Structure of tobacco mosaic virus at 3.6Å resolution: implications for assembly. *Science 231*, 1401−1406.
(46) Lewis, C. L., Lin, Y., Yang, C., Manocchi, A. K., Yuet, K. P., Doyle, P. S., and Yi, H. (2010) Microfluidic fabrication of hydrogel microparticles containing functionalized viral nanotemplates. *Langmuir 26*, 13436−13441.
(47) Yi, H., Nisar, S., Lee, S.-Y., Powers, M. A., Bentley, W. E., Payne, G. F., Ghodssi, R., Rubloff, G. W., Harris, M. T., and Culver, J. N. (2005) Patterned assembly of genetically modified viral nanotemplates via nucleic acid hybridization. *Nano Lett. 5*, 1931−1936.
(48) Lee, L. A., Nguyen, H. G., and Wang, Q. (2011) Altering the landscape of viruses and bionanoparticles. *Org. Biomol. Chem. 9*, 6189−6195.
(49) Gupta, S. S., Kuzelka, J., Singh, P., Lewis, W. G., Manchester, M., and Finn, M. G. (2005) Accelerated bioorthogonal conjugation: a practical method for the ligation of diverse functional molecules to a polyvalent virus scaffold. *Bioconjugate Chem. 16*, 1572−1579.
(50) Wang, Q., Chan, T. R., Hilgraf, R., Fokin, V. V., Sharpless, K. B., and Finn, M. G. (2003) Bioconjugation by copper(I)-catalyzed azide-alkyne [3 + 2] cycloaddition. *J. Am. Chem. Soc. 125*, 3192−3193.
(51) Schlick, T. L., Ding, Z., Kovacs, E. W., and Francis, M. B. (2005) Dual-surface modification of the tobacco mosaic virus. *J. Am. Chem. Soc. 127*, 3718−3723.
(52) Bruckman, M. A., Kaur, G., Lee, A., Xie, F., Sepulveda, J., Breitenkamp, R., Zhang, X., Joralemon, M., Russell, T. P., Emrick, T., and Wang, Q. (2008) Surface modification of tobacco mosaic virus with "Click" chemistry. *ChemBioChem 9*, 519−523.
(53) Schödel, F., Moriarty, A. M., Peterson, D. L., Zheng, J. A., Hughes, J. L., Will, H., Leturcq, D. J., McGee, J. S., and Milich, D. R. (1992) The position of heterologous epitopes inserted in hepatitis B virus core particles determines their immunogenicity. *J. Viology 66*, 106−114.
(54) Oyelaran, O., and Gildersleeve, J. C. (2009) Glycan arrays: recent advances and future challenges. *Curr. Opin. Chem. Biol. 13*, 406−413.
(55) Manimala, J. C., Roach, T. A., Li, Z., and Gildersleeve, J. C. (2006) High-throughput carbohydrate microarray analysis of 24 lectins. *Angew. Chem., Int. Ed. 45*, 3607−3610.
(56) Feizi, T., and Chai, W. (2004) Oligosaccharide microarrays to decipher the glyco code. *Nat. Rev. Mol. Cell Biol. 5*, 582−588.
(57) Inoue, M., Nakada, H., Tanaka, N., and Yamashina, I. (1994) Tn antigen is expressed on leukosialin from T-lymphoid cells. *Cancer Res. 54*, 85−88.
(58) Nakada, H., Inoue, M., Tanaka, N., Numata, Y., Kitagawa, H., Fukui, S., and Yamashina, I. (1991) Expression of the Tn antigen on T-lymphoid cell line Jurkat. *Biochem. Biophys. Res. Commun. 179*, 762−767.

Bioconjugate Chemistry

Article

pubs.acs.org/bc

Activatable Near-Infrared Fluorescent Probe for *In Vivo* Imaging of Fibroblast Activation Protein-alpha

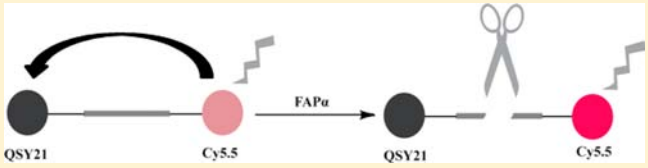
Jinbo Li,[†,‡] Kai Chen,[†] Hongguang Liu,[†] Kai Cheng,[†] Meng Yang,[†] Jiping Zhang,[§] Jonathan D. Cheng,[§] Yan Zhang,*[,‡] and Zhen Cheng*[,†]

[†]Molecular Imaging Program at Stanford (MIPS), Department of Radiology, and Bio-X Program, Canary Center at Stanford for Cancer Early Detection, Stanford University, Stanford, California, 94305-5344, United States

[‡]School of Chemistry and Chemical Engineering, Institute of Chemical Biology and Drug Innovation, Nanjing University, Nanjing 210093, China

[§]Department of Medical Oncology, Fox Chase Cancer Center, Philadelphia, Pennsylvania 19111, United States

ABSTRACT: Fibroblast activation protein-alpha (FAPα) is a cell surface glycoprotein which is selectively expressed by tumor-associated fibroblasts in malignant tumors but rarely on normal tissues. FAPα has also been reported to promote tumor growth and invasion and therefore has been of increasing interest as a promising target for designing tumor-targeted drugs and imaging agents. Although medicinal study on FAPα inhibitors has led to the discovery of many FAPα-targeting inhibitors including a drug candidate in a phase II clinical trial, the development of imaging probes to monitor the expression and activity of FAPα *in vivo* has largely lagged behind. Herein, we report an activatable near-infrared (NIR) fluorescent probe (ANP_{FAP}) for *in vivo* optical imaging of FAPα. The ANP_{FAP} consists of a NIR dye (Cy5.5) and a quencher dye (QSY21) which are linked together by a short peptide sequence (KGPGPNQC) specific for FAPα cleavage. Because of the efficient fluorescence resonance energy transfer (FRET) between Cy5.5 and QSY21 in ANP_{FAP}, high contrast on the NIR fluorescence signal can be achieved after the cleavage of the peptide sequence by FAPα both *in vitro* and *in vivo*. *In vitro* assay on ANP_{FAP} indicated the specificity of the probe to FAPα. The *in vivo* optical imaging using ANP_{FAP} showed fast tumor uptake as well as high tumor to background contrast on U87MG tumor models with FAPα expression, while much lower signal and tumor contrast were observed in the C6 tumor without FAPα expression, demonstrating the *in vivo* targeting specificity of the ANP_{FAP}. *Ex vivo* imaging also demonstrated ANP_{FAP} had high tumor uptake at 4 h post injection. Collectively, these results indicated that ANP_{FAP} could serve as a useful NIR optical probe for early detection of FAPα expressing tumors.



INTRODUCTION

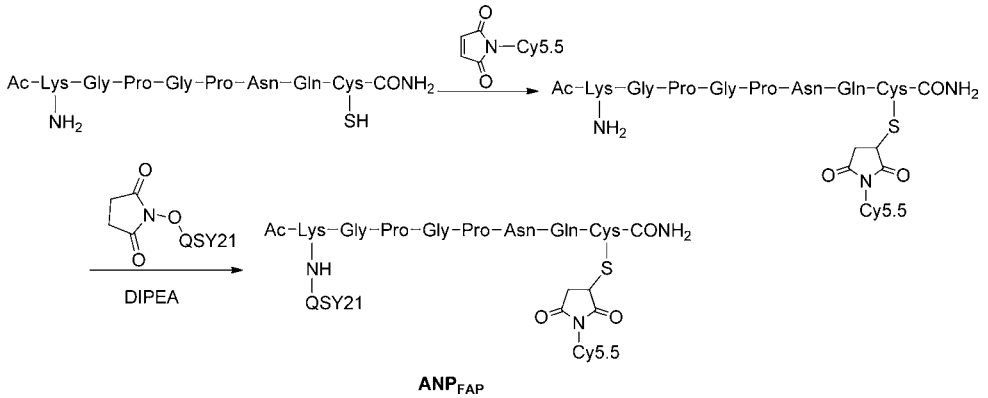
Fibroblast activation protein-α (FAPα) is a cell surface glycoprotein and a member of the serine protease family.[1] It has been found to be selectively produced by tumor-associated fibroblasts[2] and expressed in over 90% of malignant breast, colorectal, skin, and pancreatic tumors.[3] In contrast, most normal adult tissues do not have detectable FAP protein expression.[2] FAPα is also known as a biomarker of the cancer-associated fibroblasts (CAFs) in the stroma, which plays an important role in affecting the proliferation, invasion, and metastasis of cancer cells.[4−7] Besides, recent investigations have revealed that FAPα-expressing cells provide a nonredundant, immune-suppressive component of the tumor microenvironment.[8] Consequently, FAPα has been increasingly accepted and pursued as a promising tumor target for designing novel pharmaceuticals.[9] These efforts have led to the discovery of many small molecular FAPα inhibitors including Val-boroPro (Talabostat), which has been tested in a phase II clinical trial for treatment of patients with metastatic colorectal cancer.[10] Considering the important role of FAPα in tumor biology and cancer therapy, development of molecular probes for *in vivo* FAPα detection and quantification is thus of great importance. These probes could serve as noninvasive imaging tools for early detection of cancer, stratification of cancer patients for FAPα targeted therapy, monitoring treatment response, and even future theranostic applications.

In vivo optical imaging using near-infrared (NIR) fluorescent probes has been of great interest because of the relatively deep tissue penetration ability of NIR dyes as well as low tissue autofluorescence.[11−13] Activatable NIR probes that can generate a strong NIR fluorescence signal upon enzyme activation could further enhance the tumor to background signal ratio. Therefore, this type of probe has been considered a promising smart probe for early detection of small tumor lesions.[14] Many activatable NIR probes based on fluorescence resonance energy transfer (FRET) and targeting proteases including matrix metalloproteinases (MMPs),[15−19] cysteine proteases,[20−22] and caspase[23,24] have been successfully developed and widely explored in biomedical research. However, to the best of our knowledge, activatable NIR probes

Received: May 24, 2012
Revised: July 9, 2012
Published: July 19, 2012

 © 2012 American Chemical Society

Scheme 1. Chemical Strategy for Synthesis of ANP_{FAP}



ANP_{FAP}

for FAPα *in vivo* imaging have not been reported despite the great potential of FAPα in tumor theranostics.

The difficulty in the construction of activatable NIR probes specific for FAPα lies in the fact that FAPα shares the same peptide substrates for other postprolyl peptidases that are capable of cleaving the Pro-Xxx amino acid bond.[25] The most closely related prolyl peptidase family member of FAPα is the dipeptidyl peptidase-IV (DPPIV). The important substrate-binding domain and the key substrate-binding residues in FAPα and DPPIV are in very similar positions.[26] However, systematic structural and kinetic analysis of the substrate specificity of FAPα[27] and peptide substrate profiling revealed that FAPα possesses endopeptidase activity.[28] Then, peptide substrates such as Ac-GPGP-2SBPO[29] and Pyro-TSGPNQEQK(BHQ)[9] were found able to discriminate FAPα from DPPIV. Therefore, it is possible for us to develop novel activatable NIR probes which can be selectively activated by FAPα and consequently be used as *in vivo* optical imaging probes for FAPα.

Here, we report our work on the development of the novel activatable NIR probe for FAPα (ANP_{FAP}) and the successful application of the probe for *in vivo* imaging of tumor with FAPα expression. The FRET pair used in the probe is Cy5.5 and QSY21, which are linked by the peptide substrate (KGPGPNQC) specific for FAPα (Scheme 1). *In vitro* assay on the fluorescence activation by FAPα, DPPIV, and MMP-2 proteins indicated the specificity of the probe for FAPα. *In vivo* imaging using the probe on two tumor models with and without FAPα expression showed high contrast from the FAPα-positive tumor model and much lower contrast from the FAPα-negative tumor model. *Ex vivo* imaging further revealed the tissue distribution of the activated probe, which may provide important information on further modification and optimization of the probe for *in vivo* imaging.

MATERIALS AND METHODS

General. All N-Fmoc-protected amino acids and rink amide MBHA resin were purchased from CS Bio Company (Menlo Park, CA). Cy5.5-monomaleimide was purchased from GE Health Care (Piscataway, NJ). QSY21-NHS was purchased from Invitrogen (Carlsbad, CA). All other standard chemicals were purchased from Sigma-Aldrich Chemical Co. (St. Louis, MO). Recombinant FAPα and DPPIV were obtained from R&D systems (Minneapolis, MN); recombinant MMP-2 was purchased from EMD Millipore (Billerica, MA). The C6 and U87MG cells were obtained from American Type Tissue Culture Collection (Manassas, VA). Female athymic nude mice were purchased from Charles River Laboratories (Boston, MA).

The peptide Lys-Gly-Pro-Gly-Pro-Asn-Gln-Cys was synthesized on an automatic peptide synthesizer (CS Bio) using Fmoc-protected amino acids and rink amide MBHA resin. Reversed-phase high-performance liquid chromatography (RP-HPLC) was performed on a Dionex Ultimate 3000 HPLC system (Sunnyvale, CA) for analysis and preparation of peptides and bioconjugates. Both semipreparative (Vydac, Hesperia, CA, 218TP510-C18, 10 mm × 250 mm) and analytical (Dionex, Sunnyvale, CA, Acclaim120 C18, 4.6 mm × 250 mm) RP-HPLC columns were used. The mobile phase was solvent A, 0.1% trifluoroacetic acid (TFA)/H_2O, and solvent B, 0.1% TFA/acetonitrile. Matrix-assisted laser desorption/ionization time-of-flight mass spectrometry (MALDI-TOF-MS, Framingham, MA) was performed by Stanford Protein and Nucleic Acid Biotechnology Facility to verify the preparation of compounds. Absorption and emission spectra of ANP_{FAP} were measured on an Agilent UV−visible ChemStation (Agilent Technologies, Wilmington, DE) and an Inifite M1000 spectrofluorometer (Tecan, Austria), respectively. *In vivo* and *ex vivo* imaging were performed with an IVIS200 small animal imaging system (Caliper, Hopkinton, MA).

Synthesis of ANP_{FAP}. The crude peptide Lys-Gly-Pro-Gly-Pro-Asn-Gln-Cys on the resin was first acetylated by anhydrous acetic anhydride with hydroxybenzotriazole (HOBt)/*N*,*N*-diisopropylethylamine (DIPEA) in dimethylformamide (DMF). Ac-Lys-Gly-Pro-Gly-Pro-Asn-Gln-Cys was then cleaved from the resin by addition of a 92.5/2.5/2.5/2.5 (v/v) mixture of TFA/triisopropylsilane/ethanedithiol/water for 2 h at room temperature (RT) and then precipitated by cold anhydrous diethyl ether. The resulted peptide was dried and further purified by a preparative RP-HPLC. The flow rate was 4 mL/min, with the mobile phase starting from 95% solvent A and 5% solvent B (0−3 min) to 35% solvent A and 65% solvent B at 33 min. Fractions containing the product were collected and lyophilized. The target product was characterized by MALDI-TOF-MS and ready for use in the next step.

The purified peptide (450 μg) was then conjugated with Cy5.5-monomaleimide (300 μg) in 300 μL of phosphate buffered saline (PBS, 0.1 M, pH = 7.4) with a molar ratio of 2:1 for 2 h in the dark at RT. The Cy5.5-labeled peptide was purified by RP-HPLC using the same flow rate and gradient as that for the unmodified peptide listed above. The product was characterized by MALDI-TOF-MS and then used for the next step. Further conjugation with QSY21-NHS ester in dimethyl sulfoxide (DMSO) and 2% DIPEA (1.5 equiv of QSY21-NHS ester per equivalent of peptide) for 2 h resulted the final product, ANP_{FAP}. The probe was also purified by HPLC and

dx.doi.org/10.1021/bc300278r | *Bioconjugate Chem.* 2012, 23, 1704−1711

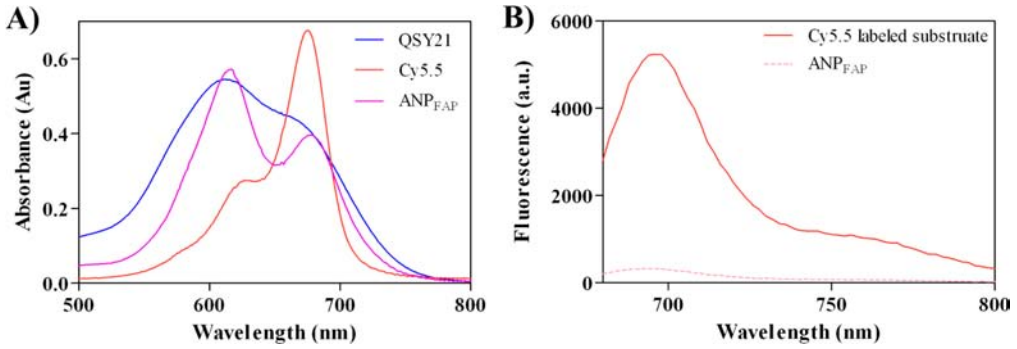


Figure 1. (A) Absorption spectrum of QSY21, Cy5.5, and ANP_{FAP}. (B) Fluorescence emission spectrum of Cy5.5 labeled substrate and ANP_{FAP}.

lyophilized using the same conditions. ANP_{FAP} was characterized by MALDI-TOF-MS and purity was confirmed by analytical RP-HPLC using the same gradient as the preparative runs.

***In Vitro* Assay of ANP_{FAP} Activation by FAPα.** ANP_{FAP} was dissolved in water as a stock solution with a concentration of 1 mM. For enzymatic assays, ANP_{FAP} was mixed with FAPα, DPPIV, or MMP-2 and diluted with PBS to a final concentration of 10 μM. Different concentrations of FAPα (0.25 μg/mL, 0.5 μg/mL, 1 μg/mL) were used for dose-dependent study and 1 μg/mL of DPPIV and MMP-2 was used to demonstrate the specificity of ANP_{FAP}. All the assays were performed in triplicate on a 96-well plate, and the emission spectra of ANP_{FAP} were recorded at 37 °C every 10 min on spectrofluorometer for 1 h. The excitation wavelength was set at 675 nm and the emission spectra were recorded from 680 to 800 nm. After 1 h incubation, samples were imaged immediately by the IVIS200 imaging system for phantom study.

Cell Culture and Animal Models. C6 and U87MG cells were cultured in DMEM medium (Gibco, Carlsbad, CA), supplemented with 10% fetal bovine serum (FBS) (Gibco, Carlsbad, CA) and 1% penicillin−streptomycin (Gibco, Carlsbad, CA). Cells were maintained in a humidified atmosphere of 5% CO_2 at 37 °C. C6 and U87MG tumor models were developed by subcutaneous injection of 3×10^6 and 5×10^6 cells, respectively, into the right shoulder of female athymic nude mice. Tumor-bearing mice were subjected to *in vivo* imaging studies when tumor volume reached 200−300 mm^3. All animal studies were performed according to the protocol approved by the Stanford University Administrative Panels on Laboratory Animal Care (APLAC).

Western Blot Analysis. The expression of FAPα in C6 and U87MG tumor tissues was analyzed by Western blot analysis with anti-FAPα monoclonal antibody. Tumors were collected right after the end of *in vivo* experiment and quickly frozen for preservation. Before protein extraction, tumors were weighed, homogenized, and lysed with M-PER mammalian protein extraction reagent (Thermo Fisher, Waltham, MA). After centrifugation, clear cell lysates were transferred to new tubes. The protein concentrations were determined by using Bradford reagent (Bio-Rad, Hercules, CA). The cell lysates (50 μg) were loaded onto NuPAGE 4−12% Bis-Tris Gel gel (Invitrogen, Carlsbad, CA) and transferred to Immun-blot PVDF membranes (Invitrogen, Carlsbad, CA). Anti-FAP monoclonal antibody was used at a 1:100 dilution. Anti-rabbit HRP conjugated secondary antibody was purchased from Thermo Fisher (Waltham,MA) and used at a 1:5000 dilution. Actin antibody (Abcam, Cambridge, MA) was used at 1:3000 to detect expression of actin as a control for protein loading. All immunoblots were analyzed by using the ECL detection system (Thermo Fisher, Waltham, MA).

***In Vivo* and *Ex Vivo* Imaging.** For *in vivo* imaging, C6 and U87MG tumor-bearing mice (n = 5 for each group) were injected intravenously via tail vein with 1 nmol of ANP_{FAP} in 150 μL of PBS. NIRF imaging was then performed with the IVIS200 small animal imaging system. To acquire fluorescence of ANP_{FAP} *in vivo*, Cy5.5 filter (excitation 615−665 nm; emission 695−770 nm) and Cy5.5 background filter (580−610 nm) were used. Identical illumination settings (lamp voltage, filters, f/stop, field of views, binning) were used for acquiring all images. Fluorescence images were taken at 0.5, 1, 2, 3, and 4 h post injection (p.i.) using a 2 s exposure time (f/stop = 1, binning = 4). Images were then analyzed using *Living Image* 3.2 software (Caliper, Hopkinton, MA). The Cy5.5 background filter image was subtracted from the Cy5.5 filter image and the fluorescence emission was normalized to photons per second per centimeter squared per steradian ($p/s/cm^2/sr$). For comparison of tumor contrast, mean fluorescence intensities of the tumor area (T) at the right foreleg of the animal and of the area (N) at the right flank (normal tissue) were calculated by the region-of-interest (ROI) function of *Living Image* software integrated with Igor (Wavemetrics, Lake Oswego, OR). Dividing T by N yielded the contrast between tumor tissue and normal tissue.

For *ex vivo* imaging, mice were sacrificed 4 h p.i. Tumor and other major tissues were dissected, rinsed with PBS, dried with tissue paper, and then put on black paper. The *ex vivo* images were acquired immediately using IVIS200 system with the same illumination setting as the *in vivo* imaging. Images were also processed with the same method as described above.

Statistical Analysis. All data are shown as mean ± SD (standard deviation). Difference between groups was assessed by Student's t test. Statistical significance was considered if P values are less than 0.05.

RESULTS

Design and Synthesis of the FAPα-Specific Probe. To design an optical probe suitable for *in vivo* imaging, the NIR dye Cy5.5 with maximum emission wavelength at 695 nm was selected to label the peptide substrate. Since the emission of Cy5.5 was known to be efficiently quenched by the dye QSY21,[30] QSY21 was chosen as the FRET pair with Cy5.5 to label the peptide substrate. The selection of the peptide sequence (GPGPNQ) was based on the reported specific FAPα substrate sequences which could be cleaved by FAPα but not DPPIV.[9,28,29] For efficient and site-specific labeling the peptide

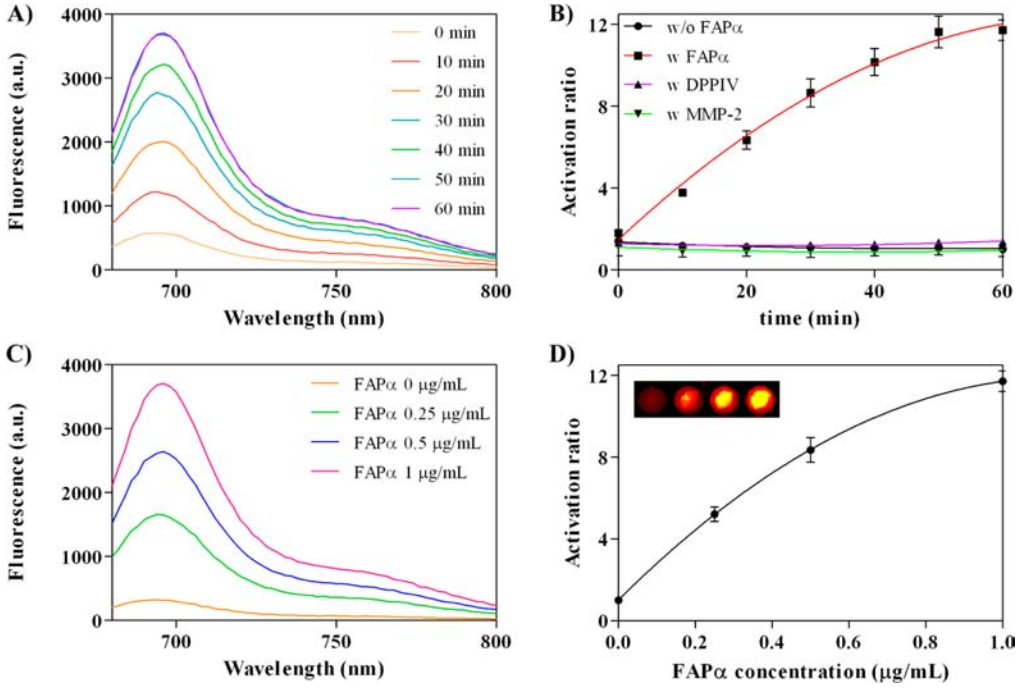


Figure 2. (A) Time-dependent fluorescence spectrum of 10 μM ANP_{FAP} with 1 μg/mL FAPα at 37 °C. (B) Time-dependent fluorescence change of 10 μM ANP_{FAP} without FAPα, with 1 μg/mL FAPα, 1 μg/mL DPPIV, or 1 μg/mL MMP-2. (C) FAPα concentration-dependent fluorescence spectrum of 10 μM ANP_{FAP} with different concentrations of FAPα after a 1 h incubation at 37 °C. (D) Fluorescence increase ratio of ANP_{FAP} in the presence of various concentrations of FAPα after a 1 h incubation. Insert: phantom study of activated ANP_{FAP}.

substrate with Cy5.5 and QSY21, a lysine residue with a free amine group on the side chain and a cysteine with a thiol group were inserted to the N and C terminal of the peptide, respectively. More specifically, Conjugation of the two dyes with the peptide substrate was easily realized through the reaction of the cysteine thiol group with the Cy5.5 maleimide and the lysine amine with QSY21 NHS ester in ~26% yield and >95% purity (Scheme 1). Successful conjugation of Cy5.5 and further modification with QSY21 were indicated by the peak with m/z at 1880.6 (calculated as 1879.6) and 2544.6 (calculated as 2544.9) on the MALDI-TOF-MS spectrum of the purified product, respectively. The UV spectra of Cy5.5, QSY21, and ANP_{FAP} were shown in Figure 1A. There were two significant absorption bands centered at 620 and 676 nm, respectively, for ANP_{FAP}. In addition, the strong fluorescent emission at ~695 nm of the substrate labeled with Cy5.5 alone was efficiently quenched by QSY21 as shown in the fluorescence spectrum of ANP_{FAP} (Figure 1B).

Sensitivity and Specificity of ANP_{FAP} to FAPα. Sensitivity of ANP_{FAP} to FAPα was first examined *in vitro*. Upon incubation with FAPα at 37 °C, ANP_{FAP} showed significant increase of the intensity of the fluorescence emission corresponding to that of Cy5.5. It indicated that the probe could be efficiently cleaved by FAPα to release the Cy5.5 labeled residue and split the FRET pair. Fluorescent spectra of ANP_{FAP} incubated with FAPα at different time points were collected as shown in Figure 2A. It showed that the activation of ANP_{FAP} was fast in kinetics, and an increase of 12-fold in fluorescence emission intensity at 695 nm could be achieved within 1 h. As a contrast, ANP_{FAP} which was not incubated with any enzyme showed no increase in fluorescence emission intensity. Besides, ANP_{FAP} incubated with the same amount of postprolyl peptidase DPPIV and MMP-2 did not show significant activation on fluorescent emission either (Figure 2B). These results clearly suggested that the activation of ANP_{FAP} was caused by the specific recognition and cleavage of the peptide substrate by FAPα.

Dose-dependent activation of the ANP_{FAP} was also observed when the probe was incubated with different concentrations of FAPα. Fluorescent spectra of ANP_{FAP} incubated with different amounts of FAPα at 37 °C for 1 h were recorded as shown in Figure 2C. The increase of the fluorescence intensity at 695 nm was significant upon titration of FAPα concentration from 0.25 μg/mL to 1 μg/mL (Figure 2D). Phantom study on the ANP_{FAP} incubated with FAPα at concentrations of 0, 0.25, 0.5, and 1 μg/mL also showed increased brightness of the probe (Figure 2D). The brightness of ANP_{FAP} under optical imaging corresponded well with the amount of FAPα presented within the target.

***In Vivo* Imaging.** After successfully validating the specificity and sensitivity of ANP_{FAP} *in vitro*, its potential for *in vivo* imaging was further investigated. For this purpose, the U87MG tumor model was developed because of the high expression of FAPα in U87MG tumor. To evaluate the specificity of ANP_{FAP} *in vivo*, another tumor model C6, which is not supposed to express FAPα, was also established. Expression of FAPα in these two tumor models was measured, and it was found that FAPα was highly expressed in U87MG tumors, while almost no detectable expression in C6 tumor (Figure 3).

On the basis of the expression of FAPα in these tumors, C6 and U87MG were used as negative and positive tumor models, respectively, for evaluation of the FAPα imaging ability of ANP_{FAP} *in vivo*. ANP_{FAP} was first injected into C6 and U87MG tumor-bearing mice through the tail vein. *In vivo* imaging was recorded over 4 h. Representative *in vivo* whole-body images of mice at different time points (0.5, 1, 2, 3, and 4 h) were shown in Figure 4A. Strong fluorescent signals in FAPα positive tumor U87MG were observed, while much lower fluorescent signals

dx.doi.org/10.1021/bc300278r | *Bioconjugate Chem.* 2012, 23, 1704–1711

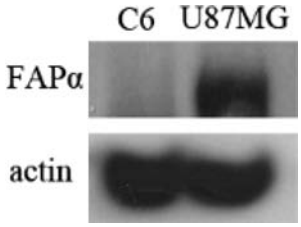


Figure 3. Western blot analysis of tumor tissue lysates.

were detected in FAPα negative tumor C6 in all the corresponding time points ($P < 0.05$). Early activation of ANP_{FAP} in U87MG tumor was observed at 0.5 h, and the fluorescent signals increased from 0.5 to 4 h p.i. Quantification analysis of fluorescent signals in tumors was calculated by drawing ROI, and the results were shown in Figure 4B. The fluorescence intensities of U87MG tumor increased after 0.5 h and reached maximum at 2 h p.i. and then remained unchanged, while fluorescence intensities of C6 tumor did not alter over the same time period. The fluorescence ratios between tumor and normal tissue were also calculated and shown in Figure 4C. The tumor-to-normal tissue ratios of U87MG increased rapidly from 0.5 h (2.218 ± 0.403) to 4 h (4.630 ± 0.728), suggesting accumulation of ANP_{FAP} in tumors. In contrast, tumor-to-normal tissue ratios of C6 remained constant at all time points, and these ratios were significantly lower than the corresponding ratios obtained from the U87MG tumor model, highlighting the *in vivo* targeting specificity of the ANP_{FAP}.

***Ex Vivo* Imaging.** To further confirm the *in vivo* imaging results and specific activation and accumulation of ANP_{FAP} in tumors, *ex vivo* imaging of tumors and other normal organs was performed after *in vivo* imaging finished. Representative *ex vivo* images of tumors and normal organs were shown in Figure 5A. Similarly to the *in vivo* imaging (Figure 4A), the U87MG tumor was much brighter than the C6 tumor ($P < 0.05$), which demonstrated successful activation of ANP_{FAP} by FAPα *in vivo*. Quantitative analysis of the fluorescent signals confirmed that activated ANP_{FAP} was mainly located in the U87MG tumor, but not in the FAPα negative tumor C6 (Figure 5B). Strong signals from stomachs of both U87MG and C6 tumor bearing mice were also observed, which were likely from the autofluorescence of remaining mouse chow. Last, it was noticed that the other major organs gave comparable signals (Figure 5B). The tumor-to-normal tissue signal ratios were also calculated (Figure 5C), and a significant difference of the ratios between U87MG and C6 was clearly viewed ($P < 0.05$). All these findings were consistent with the *in vivo* imaging results, demonstrating that ANP_{FAP} can be efficiently applied for *in vivo* imaging of FAPα.

DISCUSSION

Enzymes play important roles in many biological and physiological processes, and sometimes, they can serve as valid biomarkers for various diseases. Thus, imaging enzymes help to investigate enzyme function and even diagnose diseases. Unique catalytic activities of enzymes enable design of smart optical probes that can be turned on upon meeting with the enzyme target. The self-quenching probe, Ac-GPGP-2SBPO,

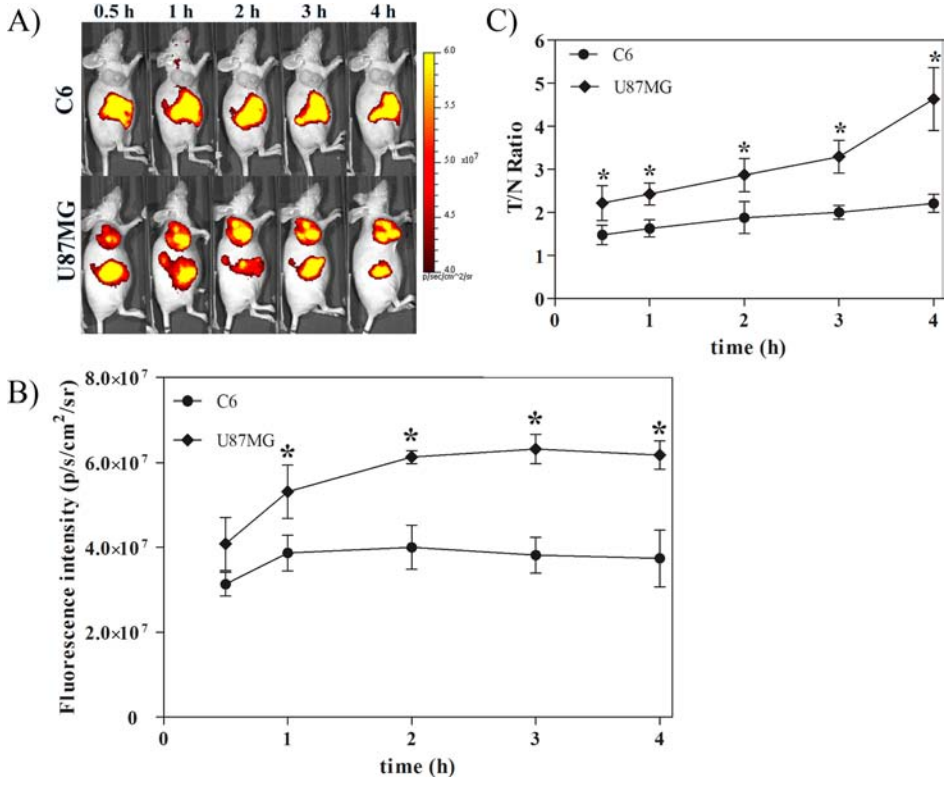


Figure 4. (A) *In vivo* fluorescent imaging of subcutaneous C6 and U87MG tumor-bearing mice at 0.5, 1, 2, 3, and 4 h post tail vein injection of ANP_{FAP} (1 nmol). (B) Fluorescence ROI analysis of tumor and muscle in mice bearing C6 and U87MG tumor from 0.5 to 4 h p.i. (C) ROI analysis of tumor-to-normal tissue ratios of ANP_{FAP} in mice bearing C6 and U87MG tumor from 0.5 to 4 h. Data are shown as mean ± SD ($n = 5$ per group), $^*P < 0.05$.

dx.doi.org/10.1021/bc300278r | *Bioconjugate Chem.* 2012, 23, 1704–1711

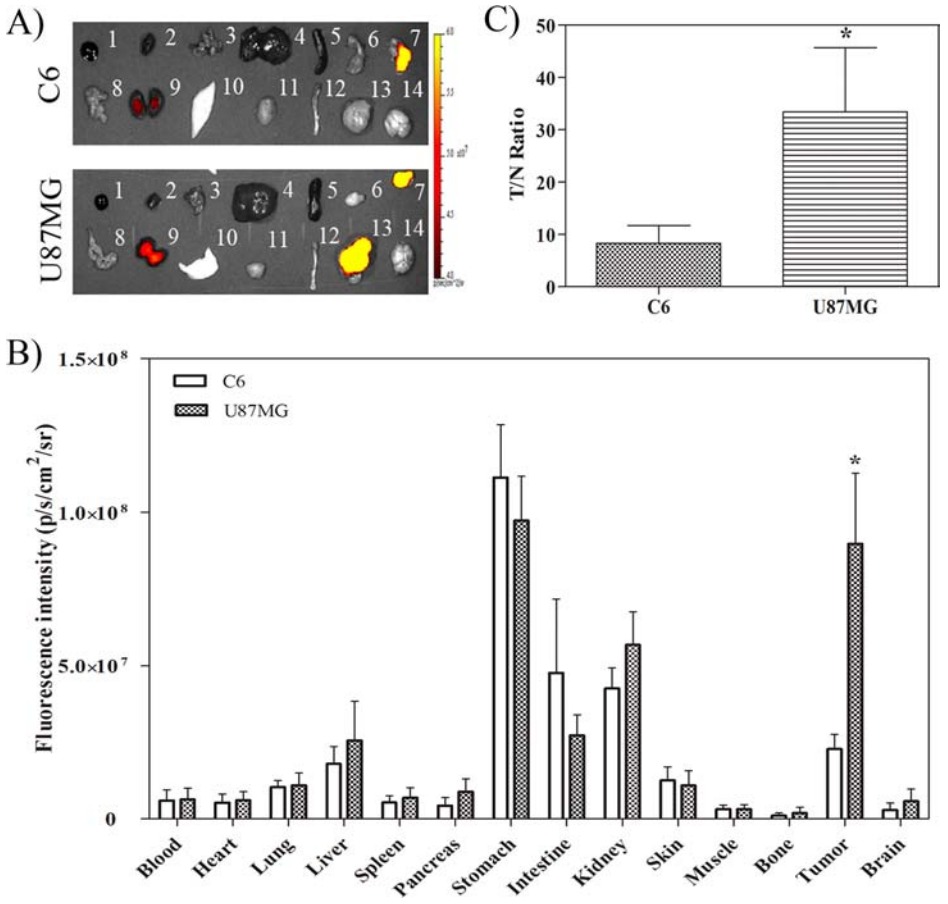


Figure 5. (A) *Ex vivo* imaging of tumor and normal tissue of C6 and U87MG mice after mice were sacrificed at 4 h post injection. The numeric label for each organ is as follows: 1, blood; 2, heart; 3, lung; 4, liver; 5, spleen; 6, pancreas; 7, stomach; 8, intestine; 9, kidney; 10, skin; 11, muscle; 12, bone; 13, tumor; 14, brain. (B) ROI analysis of fluorescent signals from tumors and normal tissues. (C) Tumor-to-normal tissue ratio of fluorescent intensities based on ROI analysis. Data are shown as mean ± SD (n = 5 per group), *P < 0.05.

demonstrates specificity to FAPα, and it could be activated in FAPα transfected cells.[29] The dual functional probe, Pyro-TSGPNQEQK(BHQ), developed by Zheng et al. can image FAPα and produce cytotoxicity simultaneously, by combination of pyropheophorbide α acid (Pyro) as a photosensitizer as well as a fluorophore whose fluorescence can be quenched by BHQ.[9] The specificity of these probes to FAPα indicates the importance of the peptide sequence used as a linker in the activatable probes.

Different from previous studies, a new specific peptide substrate was selected by us according to the reported substrates specific to FAPα.[9,28,29] Unlike Ac-GPGP-2SBPO,[29] which utilizes the strategy of self-quenching of the dye, ANP_{FAP} employs a quencher (QSY21) to make a NIR dye (Cy5.5) silent (Figure 1B), and the quenching efficiency was found to be 94%. In the enzymatic assay, ANP_{FAP} shows good sensitivity and selectivity toward FAPα (Figure 2). Approximately 12-fold fluorescence recovery of ANP_{FAP} can be achieved after incubation with 1 μg/mL of FAPα for 1 h (Figure 2B). Furthermore, for testing the specificity of ANP_{FAP}, DPPIV, which also belongs to the serine protease family and has 50% amino acid similarity to FAPα, was selected. Coupled expression of DPPIV and FAPα has been found in transformed astrocytic cells.[31] The difference of these two enzymes mainly lies in their catalytic activities. FAPα is a strict endopeptidase, while DPPIV is a strict exopeptidase.[25−28] On the basis of the high similarity between DPPIV and FAPα, DPPIV was chosen as a specificity control for investigating the specificity of ANP_{FAP}. When incubating ANP_{FAP} with 1 μg/mL of DPPIV, no activation of ANP_{FAP} can be observed (Figure 2C). Incubating ANP_{FAP} with another enzyme, MMP-2, also give similar results. Titration studies show nonlinear dose dependent activation of ANP_{FAP} toward FAPα (Figure 2D). One possible reason is that fluorescence recovery of ANP_{FAP} has reached maximum at 1 h incubation with a higher concentration of FAPα such as 1 μg/mL (Figure 2A), while fluorescence intensities of the probe incubating with smaller amounts of FAPα for 1 h may not have fully recovered. Collectively, these *in vitro* assays demonstrate that ANP_{FAP} is highly specific and sufficient to be used for further *in vivo* evaluation.

Recently, FAPα was found to be expressed in U87MG cells, making U87MG tumor model a good candidate for FAPα *in vivo* imaging.[31] The C6 tumor model which is FAPα negative was also generated as a control. Western blot results confirm that FAPα is indeed expressed in U87MG tumor but not in C6 tumor (Figure 3). Then, the ability of ANP_{FAP} for *in vivo* imaging was evaluated in these mice models through intravenous tail vein injection of the probe. Despite limited delivery efficiency of Pyro-TSGPNQEQK(BHQ) after systematic administration reported before,[9] ANP_{FAP} shows efficient accumulation in U87MG tumor but not in C6 tumor (Figure 4A). By quantitative analysis of fluorescence intensities in the U87MG tumor region, it can be seen that the signal increases from 0.5 to 2 h and reaches maximum at 2 h (Figure 4B),

dx.doi.org/10.1021/bc300278r | *Bioconjugate Chem.* 2012, 23, 1704−1711

indicating fast activation of the probe *in vivo*, and 2 h is a good imaging time for future applications of ANP_{FAP}. For C6 tumor, only a slight increase of the fluorescence intensities is observed from 0.5 to 1 h, which might be due to the influx of activated probes from blood into tumor through the enhanced permeability and retention effect. Nevertheless, the difference of fluorescence intensities between C6 tumor and U87MG tumor is significant ($P < 0.05$). It is worth noting that, since the probe is not actively targeted, it may have different levels of accumulations in two tumor models, which may make some contributions to the different fluorescence signals in tumors. Moreover, different from the absolute fluorescence intensities, tumor-to-normal tissue ratio of U87MG mice keeps increasing from 0.5 to 4 h (Figure 4C), suggesting a reduction of background signals all the time. *Ex vivo* imaging also shows a significant difference in tumor-to-normal tissue ratios between C6 tumor and U87MG tumor (Figure 5C), which is consistent with the *in vivo* results. All these results demonstrate the high specificity of ANP_{FAP} and its high potential for serving as an NIR probe to image FAPα *in vivo*.

Interestingly, signals from the mouse body were also observed. Though autofluorescence was subtracted using the appropriate function of IVIS system, some signals could still be caused by autofluorescence of mice. An alternative imaging system, *Maestro*, may help further improve the imaging quality by using spectral unmixing function. Another possible reason is that FAPα can also be secreted from tumors, and soluble forms of FAPα have been found in bovine serum.[32] Therefore, the soluble FAPα expressed in the blood or other tissues could cleave the probe to generate background signal. The *ex vivo* imaging study also confirms that, besides the high uptake of ANP_{FAP} in U87MG tumor, background signals can be seen in the liver, stomach, intestine, and kidney (Figure 5B). Specific activation of probes in tumor is really hard to achieve and represents a common hurdle for enzyme imaging using activatable probes in this field, our finding here is really not a surprise. As an example, for imaging MMPs, a relatively high uptake of MMP activatable probes in organs beside tumor has also been observed.[18,19] Regardless of the background signal, the encouraging thing is that we still can clearly visualize the target tumor. To further optimize the probe and overcome the production of nonspecific background signal, the activatable probes could be encapsulated in polymers for protection during the circulation while being released when reaching tumors.

It should be pointed out that some of the limitations of optical imaging techniques can also hinder the use of ANP_{FAP} *in vivo*. For example, it is very hard to get quantitative information about FAPα, and the optical signals sometimes are misleading, as they can be easily affected by many other factors such as depth of the probe presented *in vivo,* absorption and refraction of tissues, and so forth. To solve these problems, other imaging modalities such as positron emission tomography (PET) and magnetic resonance imaging (MRI) can be combined with fluorescence imaging. For example, MRI/NIRF activatable imaging of MMP-2 has been realized by loading Cy5.5 labeled MMP substrates onto iron oxide nanoparticles.[33] It is thus possible to use iron oxide nanoparticles to quench fluorescence of the Cy5.5 labeled peptide substrate of FAPα and to realize MR/NIRF imaging. An alternative strategy is to directly link ANP_{FAP} with iron oxide nanoparticles, and then dual modality imaging (NIRF/MRI) can be performed to image FAPα more efficiently. One example is that prequenched MT1-MMP probe was anchored to magnetic nanocrystals for molecular imaging of invasive cancer cells.[34] It is expected that this approach could be adapted to improve the imaging efficiency of ANP_{FAP}. Last, it is worth noting that the FRET based activatable probe itself could provide a target-dependent photoacoustic signal.[35] With the photoacoustic signal, FAPα expressing tumors could be visualized more easily and clearly. Therefore, while combining fluorescence imaging with other imaging modalities, ANP_{FAP} may serve as a more efficient probe for better understanding of the distribution and function of FAPα *in vivo*.

CONCLUSION

An FAPα specific NIRF probe ANP_{FAP}, which is composed of NIR dye Cy5.5, peptide substrate of FAPα, and a quencher QSY21, was designed and successfully synthesized. Fluorescent signals of ANP_{FAP} can be recovered in the presence of FAPα, while not by DPPIV or MMP-2, suggesting the high specificity of ANP_{FAP} toward FAPα. *In vivo* imaging studies further demonstrate that ANP_{FAP} can be activated rapidly in FAPα positive U87MG tumor but not in the negative C6 tumor. Overall, our study provides a new type of FAPα specific probe that can be used to image FAPα *in vivo* and to better understand the roles of FAPα *in vitro* and *in vivo*.

AUTHOR INFORMATION

Corresponding Author

*Zhen Cheng, Ph.D., MIPS: 650-723-7866 (V); 650-736-7925 (Fax); E-mail: zcheng@stanford.edu. Yan Zhang, Ph.D., Nanjing University, E-mail: njuzy@nju.edu.cn.

Notes

The authors declare no competing financial interest.

ACKNOWLEDGMENTS

This work was supported in part by National Cancer Institute (NCI) 5R01 CA119053 (ZC) and the National Basic Research Program of China (No. 2011CB935800). J. L. was supported by a fellowship from the Chinese Scholarship Council (CSC).

ABBREVIATIONS:

FAPα, fibroblast activation protein-alpha; NIR, near-infrared; FRET, fluorescence resonance energy transfer; p.i, post injection; HPLC, high-performance liquid chromatography; ROI, regions of interest

REFERENCES

(1) Rettig, W. J., Garin-Chesa, P., Beresford, H. R., Oettgen, H. F., Melamed, M. R., and Old, L. J. (1988) Cell-surface glycoproteins of human sarcomas: differential expression in normal and malignant tissues and cultured cells. *Proc. Natl. Acad. Sci. U. S. A. 85*, 3110−4.

(2) Scanlan, M. J., Raj, B. K., Calvo, B., Garin-Chesa, P., Sanz-Moncasi, M. P., Healey, J. H., Old, L. J., and Rettig, W. J. (1994) Molecular cloning of fibroblast activation protein alpha, a member of the serine protease family selectively expressed in stromal fibroblasts of epithelial cancers. *Proc. Natl. Acad. Sci. U. S. A. 91*, 5657−61.

(3) Garin-Chesa, P., Old, L. J., and Rettig, W. J. (1990) Cell surface glycoprotein of reactive stromal fibroblasts as a potential antibody target in human epithelial cancers. *Proc. Natl. Acad. Sci. U. S. A. 87*, 7235−9.

(4) Kalluri, R., and Zeisberg, M. (2006) Fibroblasts in cancer. *Nat. Rev. Cancer 6*, 392−401.

(5) Cheng, J. D., Dunbrack, R. L., Jr., Valianou, M., Rogatko, A., Alpaugh, R. K., and Weiner, L. M. (2002) Promotion of tumor growth by murine fibroblast activation protein, a serine protease, in an animal model. *Cancer Res. 62*, 4767−72.

(6) Huang, Y., Simms, A. E., Mazur, A., Wang, S., Leon, N. R., Jones, B., Aziz, N., and Kelly, T. (2011) Fibroblast activation protein-alpha promotes tumor growth and invasion of breast cancer cells through non-enzymatic functions. *Clin. Exp. Metastasis 28*, 567−79.
(7) Lee, H. O., Mullins, S. R., Franco-Barraza, J., Valianou, M., Cukierman, E., and Cheng, J. D. (2011) FAP-overexpressing fibroblasts produce an extracellular matrix that enhances invasive velocity and directionality of pancreatic cancer cells. *BMC Cancer 11*, 245.
(8) Kraman, M., Bambrough, P. J., Arnold, J. N., Roberts, E. W., Magiera, L., Jones, J. O., Gopinathan, A., Tuveson, D. A., and Fearon, D. T. (2010) Suppression of antitumor immunity by stromal cells expressing fibroblast activation protein-alpha. *Science 330*, 827−30.
(9) Lo, P. C., Chen, J., Stefflova, K., Warren, M. S., Navab, R., Bandarchi, B., Mullins, S., Tsao, M., Cheng, J. D., and Zheng, G. (2009) Photodynamic molecular beacon triggered by fibroblast activation protein on cancer-associated fibroblasts for diagnosis and treatment of epithelial cancers. *J. Med. Chem. 52*, 358−68.
(10) Narra, K., Mullins, S. R., Lee, H. O., Strzemkowski-Brun, B., Magalong, K., Christiansen, V. J., McKee, P. A., Egleston, B., Cohen, S. J., Weiner, L. M., Meropol, N. J., and Cheng, J. D. (2007) Phase II trial of single agent Val-boroPro (Talabostat) inhibiting Fibroblast Activation Protein in patients with metastatic colorectal cancer. *Cancer Biol. Ther. 6*, 1691−9.
(11) Petrovsky, A., Schellenberger, E., Josephson, L., Weissleder, R., and Bogdanov, A., Jr. (2003) Near-infrared fluorescent imaging of tumor apoptosis. *Cancer Res. 63*, 1936−42.
(12) Cheng, Z., Levi, J., Xiong, Z., Gheysens, O., Keren, S., Chen, X., and Gambhir, S. S. (2006) Near-infrared fluorescent deoxyglucose analogue for tumor optical imaging in cell culture and living mice. *Bioconjugate Chem. 17*, 662−9.
(13) Miao, Z., Ren, G., Liu, H., Jiang, L., and Cheng, Z. (2010) Cy5.5-labeled Affibody molecule for near-infrared fluorescent optical imaging of epidermal growth factor receptor positive tumors. *J. Biomed. Opt. 15*, 036007.
(14) Weissleder, R., Tung, C. H., Mahmood, U., and Bogdanov, A., Jr. (1999) In vivo imaging of tumors with protease-activated near-infrared fluorescent probes. *Nat. Biotechnol. 17*, 375−8.
(15) Pham, W., Choi, Y., Weissleder, R., and Tung, C. H. (2004) Developing a peptide-based near-infrared molecular probe for protease sensing. *Bioconjugate Chem. 15*, 1403−7.
(16) Chen, J., Tung, C. H., Allport, J. R., Chen, S., Weissleder, R., and Huang, P. L. (2005) Near-infrared fluorescent imaging of matrix metalloproteinase activity after myocardial infarction. *Circulation 111*, 1800−5.
(17) Yoon, S. M., Myung, S. J., Ye, B. D., Kim, I. W., Lee, N. G., Ryu, Y. M., Park, K., Kim, K., Kwon, I. C., Park, Y. S., Park, C. S., Moon, D. H., Kim do, H., Do, M. Y., Byeon, J. S., Yang, S. K., and Kim, J. H. (2010) Near-infrared fluorescence imaging using a protease-specific probe for the detection of colon tumors. *Gut Liver 4*, 488−97.
(18) Zhu, L., Xie, J., Swierczewska, M., Zhang, F., Quan, Q., Ma, Y., Fang, X., Kim, K., Lee, S., and Chen, X. (2011) Real-time video imaging of protease expression in vivo. *Theranostics 1*, 18−27.
(19) Zhu, L., Zhang, F., Ma, Y., Liu, G., Kim, K., Fang, X., Lee, S., and Chen, X. (2011) In vivo optical imaging of membrane-type matrix metalloproteinase (MT-MMP) activity. *Mol. Pharm. 8*, 2331−8.
(20) Jaffer, F. A., Kim, D. E., Quinti, L., Tung, C. H., Aikawa, E., Pande, A. N., Kohler, R. H., Shi, G. P., Libby, P., and Weissleder, R. (2007) Optical visualization of cathepsin K activity in atherosclerosis with a novel, protease-activatable fluorescence sensor. *Circulation 115*, 2292−8.
(21) Kim, D. E., Kim, J. Y., Schellingerhout, D., Shon, S. M., Jeong, S. W., Kim, E. J., and Kim, W. K. (2009) Molecular imaging of cathepsin B proteolytic enzyme activity reflects the inflammatory component of atherosclerotic pathology and can quantitatively demonstrate the antiatherosclerotic therapeutic effects of atorvastatin and glucosamine. *Mol. Imaging 8*, 291−301.
(22) Abd-Elgaliel, W. R., Cruz-Monserrate, Z., Logsdon, C. D., and Tung, C. H. (2011) Molecular imaging of Cathepsin E-positive tumors in mice using a novel protease-activatable fluorescent probe. *Mol. Biosyst. 7*, 3207−13.
(23) Bullok, K., and Piwnica-Worms, D. (2005) Synthesis and characterization of a small, membrane-permeant, caspase-activatable far-red fluorescent peptide for imaging apoptosis. *J. Med. Chem. 48*, 5404−7.
(24) Barnett, E. M., Zhang, X., Maxwell, D., Chang, Q., and Piwnica-Worms, D. (2009) Single-cell imaging of retinal ganglion cell apoptosis with a cell-penetrating, activatable peptide probe in an in vivo glaucoma model. *Proc. Natl. Acad. Sci. U. S. A. 106*, 9391−6.
(25) Park, J. E., Lenter, M. C., Zimmermann, R. N., Garin-Chesa, P., Old, L. J., and Rettig, W. J. (1999) Fibroblast activation protein, a dual specificity serine protease expressed in reactive human tumor stromal fibroblasts. *J. Biol. Chem. 274*, 36505−12.
(26) Edosada, C. Y., Quan, C., Wiesmann, C., Tran, T., Sutherlin, D., Reynolds, M., Elliott, J. M., Raab, H., Fairbrother, W., and Wolf, B. B. (2006) Selective inhibition of fibroblast activation protein protease based on dipeptide substrate specificity. *J. Biol. Chem. 281*, 7437−44.
(27) Aertgeerts, K., Levin, I., Shi, L., Snell, G. P., Jennings, A., Prasad, G. S., Zhang, Y., Kraus, M. L., Salakian, S., Sridhar, V., Wijnands, R., and Tennant, M. G. (2005) Structural and kinetic analysis of the substrate specificity of human fibroblast activation protein alpha. *J. Biol. Chem. 280*, 19441−4.
(28) Edosada, C. Y., Quan, C., Tran, T., Pham, V., Wiesmann, C., Fairbrother, W., and Wolf, B. B. (2006) Peptide substrate profiling defines fibroblast activation protein as an endopeptidase of strict Gly(2)-Pro(1)-cleaving specificity. *FEBS Lett. 580*, 1581−6.
(29) Lai, K. S., Ho, N. H., Cheng, J. D., and Tung, C. H. (2007) Selective fluorescence probes for dipeptidyl peptidase activity-fibroblast activation protein and dipeptidyl peptidase IV. *Bioconjugate Chem. 18*, 1246−50.
(30) Kong, Y., Yao, H., Ren, H., Subbian, S., Cirillo, S. L., Sacchettini, J. C., Rao, J., and Cirillo, J. D. (2010) Imaging tuberculosis with endogenous beta-lactamase reporter enzyme fluorescence in live mice. *Proc. Natl. Acad. Sci. U. S. A. 107*, 12239−44.
(31) Balaziova, E., Busek, P., Stremenova, J., Sromova, L., Krepela, E., Lizcova, L., and Sedo, A. (2011) Coupled expression of dipeptidyl peptidase-IV and fibroblast activation protein-alpha in transformed astrocytic cells. *Mol. Cell. Biochem. 354*, 283−9.
(32) Collins, P. J., McMahon, G., O'Brien, P., and O'Connor, B. (2004) Purification, identification and characterisation of seprase from bovine serum. *Int. J. Biochem. Cell Biol. 36*, 2320−33.
(33) Cha, E. J., Jang, E. S., Sun, I. C., Lee, I. J., Ko, J. H., Kim, Y. I., Kwon, I. C., Kim, K., and Ahn, C. H. (2011) Development of MRI/NIRF 'activatable' multimodal imaging probe based on iron oxide nanoparticles. *J. Controlled Release 155*, 152−8.
(34) Park, J., Yang, J., Lim, E. K., Kim, E., Choi, J., Ryu, J. K., Kim, N. H., Suh, J. S., Yook, J. I., Huh, Y. M., and Haam, S. (2012) Anchored proteinase-targetable optomagnetic nanoprobes for molecular imaging of invasive cancer cells. *Angew. Chem., Int. Ed. Engl. 51*, 945−8.
(35) Levi, J., Kothapalli, S. R., Ma, T. J., Hartman, K., Khuri-Yakub, B. T., and Gambhir, S. S. (2010) Design, synthesis, and imaging of an activatable photoacoustic probe. *J. Am. Chem. Soc. 132*, 11264−9.

Bioconjugate Chemistry

Technical Note

pubs.acs.org/bc

Simplified NaCl Based ^{68}Ga Concentration and Labeling Procedure for Rapid Synthesis of ^{68}Ga Radiopharmaceuticals in High Radiochemical Purity

Dirk Mueller,*[,†] Ingo Klette,[†] Richard P. Baum,[†] M. Gottschaldt,[‡] Michael K. Schultz,[¶] and Wouter A. P. Breeman[§]

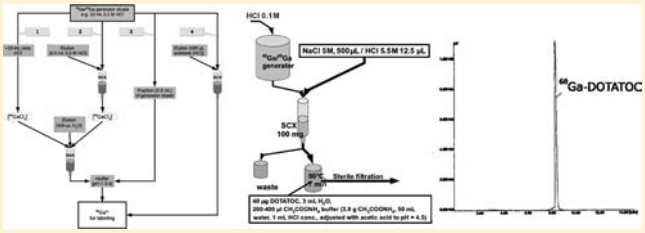
[†]Zentralklinik Bad Berka, Department of Nuclear Medicine/PET Center, 99437 Bad Berka, Germany

[‡]Friedrich Schiller University of Jena, Institute for Organic and Macromolecular Chemistry, Jena Center for Soft Matter (JCSM), 07743 Jena, Germany

[¶]University of Iowa, Departments of Radiology and Radiation Oncology (Free Radical Radiation Biology Program), ML B180, 500 Newton Road, Iowa City, Iowa 52242, United States

[§]Department of Nuclear Medicine, Erasmus MC Rotterdam, 's Gravendijkwal 230, 3015CE Rotterdam, The Netherlands

ABSTRACT: A simple sodium chloride (NaCl) based ^{68}Ga eluate concentration and labeling method that enables rapid, high-efficiency labeling of DOTA conjugated peptides in high radiochemical purity is described. The method utilizes relatively few reagents and comprises minimal procedural steps. It is particularly well-suited for routine automated synthesis of clinical radiopharmaceuticals. For the ^{68}Ga generator eluate concentration step, commercially available cation-exchange cartridges and ^{68}Ga generators were used. The ^{68}Ga generator eluate was collected by use of a strong cation exchange cartridge. 98% of the total activity of ^{68}Ga was then eluted from the cation exchange cartridge with 0.5 mL of 5 M NaCl solution containing a small amount of 5.5 M HCl. After buffering with ammonium acetate, the eluate was used directly for radiolabeling of DOTATOC and DOTATATE. The ^{68}Ga-labeled peptides were obtained in higher radiochemical purity compared to other commonly used procedures, with radiochemical yields greater than 80%. The presence of ^{68}Ge could not be detected in the final product. The new method obviates the need for organic solvents, which eliminates the required quality control of the final product by gas chromatography, thereby reducing postsynthesis analytical effort significantly. The ^{68}Ga-labeled products were used directly, with no subsequent purification steps, such as solid-phase extraction. The NaCl method was further evaluated using an automated fluid handling system and it routinely facilitates radiochemical yields in excess of 65% in less than 15 min, with radiochemical purity consistently greater than 99% for the preparation of ^{68}Ga-DOTATOC.



INTRODUCTION

PET imaging with ^{68}Ga-labeled compounds is of increasing interest in nuclear medicine worldwide. ^{68}Ga-labeled DOTA-peptides, such as DOTA-conjugated somatostatin analogues DOTATOC and DOTATATE, are particularly well suited for PET imaging of tumors expressing somatostatin receptors.[1−3] The synthesis of ^{68}Ga-based radiopharmaceuticals, in principle, can be performed on site, without the need for a medical cyclotron.[4] However, widespread use of ^{68}Ga-based radiopharmaceuticals in clinical practice has been limited due to concerns related to parent radionuclide ^{68}Ge breakthrough, concentration and purification of ^{68}Ga in advance of the radiolabeling step, and analytical requirements for quality control.[5] As generator technologies have matured to more consistently deliver high-purity ^{68}Ga over many months, the availability of highly adaptable postprocessing radiochemistry modules has also increased. These developments suggest a rich future for generator-produced ^{68}Ga as an attractive candidate for radiolabeling of not only peptides, but also other molecular targeting vectors such as bisphosphonates, amino acids, or carbohydrates.[6−9]

Although numerous methods for the elution of ^{68}Ga from the generator, its purification, and for labeling peptide radiopharmaceuticals with it have been advanced, these approaches are primarily based on four different ^{68}Ga eluate concentration and purification procedures (Figure 1).

Meyer et al. described a method for ^{68}Ga concentration and purification via an anion exchange column (Figure 1, route 1).[10] In this procedure, ^{68}Ga chloride from the ^{68}Ge/^{68}Ga generator eluate is converted into the gallate anion $[^{68}GaCl_4]^-$ by addition of concentrated HCl (final $[Cl^-] > 5$ M). $[^{68}GaCl_4]^-$ is then trapped on an anionic exchange cartridge and is subsequently eluted with a small volume of water into a buffer solution (containing, e.g., 4-(2-hydroxyethyl)-1-piperazineethanesulfonic

Received: March 11, 2012
Revised: June 25, 2012
Published: July 4, 2012

ACS Publications © 2012 American Chemical Society

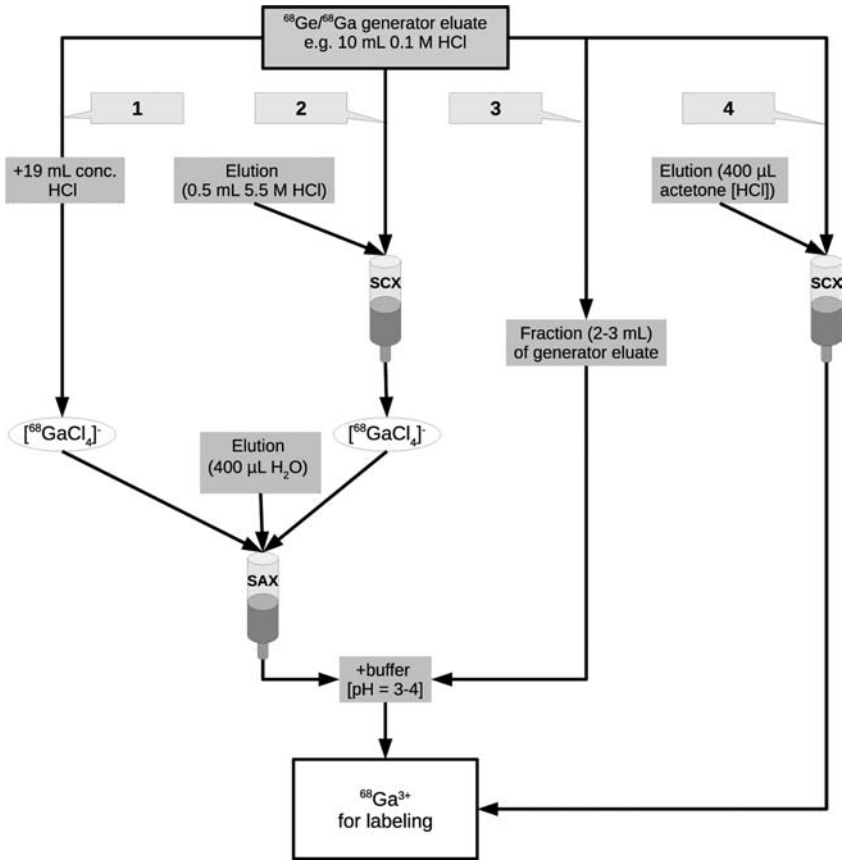


Figure 1. Schematic drawing of the currently mostly applied ^{68}Ge/^{68}Ga-generator eluate concentration methods prior to ^{68}Ga labeling reactions: SCX, strong cation exchanger; SAX, strong anion exchanger; 1, anionic eluate concentration; 2, combined cationic/anionic eluate concentration; 3, fractionated method; 4, cationic eluate concentration.

acid, HEPES) for the labeling step. After labeling, further purification steps are necessary in order to remove HEPES. In addition, ^{68}Ge that might still be present is removed by solid-phase extraction, while the final product is eluted with ethanol.

A second approach for the concentration of ^{68}Ga takes advantage of the occurrence of different gallium species (Ga^{3+} cations and anionic $[GaCl_4]^-$) depending on varying pH and chloride concentrations. In this procedure, ^{68}Ga is trapped on a strong cation exchange cartridge (SCX) and then converted to $[^{68}GaCl_4]^-$ and eluted with a small volume of 5.5 M HCl. In step two, the $[^{68}GaCl_4]^-$ is adsorbed on a strong anion exchange cartridge (SAX) and $^{68}Ga^{3+}$ is subsequently eluted with water (Figure 1, route 2). This concentration method is particularly well suited for the subsequent labeling of fragile peptides such as DOTA conjugated Affibody molecules (e.g., DOTA-$Z_{Her2:342\text{-}pep2}$).[11,12] Because of the high purity of the labeled peptide after the radiolabeling reaction step, a final purification step is usually not required. However, the method requires two cartridges.

A third approach to obtain ^{68}Ga-labeled peptides uses the generator eluate directly by a fractional elution of the ^{68}Ge/^{68}Ga-generator. In this method, the fraction with the highest volume activity is collected and buffered to an appropriate pH for radiolabeling (e.g., in HEPES).[13] While potentially effective, this method has the drawback that only a fraction of the eluted ^{68}Ga activity is used, which potentially reduces the achievable specific activity of the final product (Figure 1, route 3).

The fourth and most popular methodology currently used for the synthesis of ^{68}Ga-labeled compounds was described by Zhernosekov et al.,[14] which is based on a two-step approach. ^{68}Ga eluted from the generator in dilute HCl is trapped on a cation exchange resin, washed and eluted with two different hydrochloric acid/acetone solutions (Figure 1, route 4). The majority of acetone is removed during the radiolabeling step, which is carried out at 100 °C. To ensure that the final product is of sufficient radiochemical purity (>95%), the procedure includes a purification step using a solid-phase extraction. Although this method has proven to be effective and reliable, the disadvantage for routine clinical production is the use of organic solvents acetone and ethanol. The use of these organic solvents requires additional quality control testing of the final products that not only adds to the production effort for technical staff, but also requires purchase and maintenance of additional quality control instrumentation (e.g., gas chromatography equipment). Furthermore, the acetone-HCl-based solution may contain breakdown impurities (mesityloxide, 4-methyl-3-penten-2-on), which can be detected in the final products. Although these methods have been proven to deliver ^{68}Ga-labeled compounds in high radiochemical purity and specific activity, the increasing number of ^{68}Ga labeling procedures performed in our facilities prompted us to explore more rapid methods, with reduced quality control requirements and in which organic solvents could be removed from the preparation protocol. Thus, in this work, we report a new NaCl-based highly efficient ^{68}Ga eluate concentration and labeling procedure for DOTA conjugated peptides that is particularly well-suited for routine production and clinical use—and has the potential to be expanded to other ligands.

dx.doi.org/10.1021/bc300103t | *Bioconjugate Chem.* 2012, 23, 1712–1717

EXPERIMENTAL SECTION

All reagents were purchased from commercial sources and used as received. Cartridges used for separation are commercially available from Varian. For all experiments, a ^{68}Ga generator from Obninsk (Eckert & Ziegler Europe) or an IGG100 ^{68}Ga generator (Eckert & Ziegler Europe) were used. The total radioactivity used for the labeling reactions was between 1.6 and 2.0 GBq over a period of two months. The SCX cartridge (Varian, Bond Elut-SCX, 100 mg, 1 mL) was preconditioned with 1 mL 5.5 M HCl and 10 mL water prior to the elution step. For this investigation, the radiochemical purity was determined by HPLC using the following conditions: HPLC pump, Jasco PU-1580; quaternary gradient unit, Jasco LG-1580−04; radio detector, biostep IsoScan LC; multiwavelength detector, Jasco MD 1510; column, RP-18, LiChroCART 250−4, LiChrospher 100, RP-18 (5 μm). Radiochemical purity was also examined by routine radio-thin layer chromatography using ITLC-SG (Varian) (mobile phase: acetonitrile/water 1:1). The radiochemical yields are expressed as a percentage of total activity of ^{68}Ga from the generator eluates and are not decay-corrected.

Labeling of DOTA Conjugated Peptides Using the NaCl Based Method. The ^{68}Ga generators were eluted with a total of 10 mL of 0.1 M HCl. On a SCX cartridge, 99.9% of ^{68}Ga of the generator eluate was collected and subsequently eluted with minimal loss (1−2%) using a mixture of 12.5 μL of 5.5 M HCl and 500 μL of 5 M NaCl. This eluate was slowly added to a solution of 200−400 μL ammonium acetate buffer (1 M) and 40 μg of the DOTA conjugated peptide (DOTATOC or DOTATATE) in 3.0 mL of water. The acetate buffer solution was prepared using a mixture of 3.9 g ammonium acetate and 1 mL conc. HCl, diluted to 50 mL with water, and the pH was adjusted with glacial acetic acid to 4.5. When mixed, the final pH of the radiolabeling reaction mixture was determined to be 3.6 ± 0.3. The radiolabeling reaction was carried out at 90 °C for 7 min. Finally, the reaction mixture was neutralized with 2 mL of sterile sodium phosphate buffer (1 mmol/L Na^+, 0.6 mmol/L PO_4^{3-}, pH = 7.0; B. Braun, Melsungen AG, Germany) and can be diluted further for dose administration to any desired volume. Using this approach, radiochemical purity of >99% was routinely achieved for the labeled peptide as determined by radio HPLC. The radiochemical yield after sterile filtration was 80% ± 2% (manual method).

Automated Concentration and Labeling Procedure. DOTATOC was labeled on a Modular-Lab PharmTracer module (Eckert & Ziegler). The elution of the ^{68}Ga generators, the ^{68}Ga concentration step, and the subsequent elution of ^{68}Ga using NaCl/HCl were carried out similarly as described above. This eluate was slowly added into a solution of 350 μL ammonium acetate buffer (as mentioned above), 5 mg ascorbic acid, and 50 μg of the DOTA conjugated peptide (DOTATOC) in 3.0 mL of water. The final pH of the reaction mixture was determined to be 3.6 ± 0.3. After heating the solution (7 min at 90 °C), the ^{68}Ga chloride is quantitatively coupled to the DOTA moiety of the peptide conjugate. The reaction mixture was diluted with 2 mL of water and sterile-filtered. Radiochemical purity of >99% is routinely achieved as determined by radio HPLC. The radiochemical yield after sterile filtration was about 65%, which is comparable to the manual method using acetone/HCl. The final product was neutralized with 2 mL of sterile sodium phosphate buffer (1 mmol/L Na^+, 0.6 mmol/L PO_4^{3-}; B. Braun, Melsungen AG, Germany). The total duration of the automated synthesis was 14 min.

RESULTS AND DISCUSSION

The foundation for our initiatives is based on the supposition that ^{68}Ga adsorbed onto a silica-based SCX cation exchange cartridge should be elutable with a concentrated NaCl solution by conversion of adsorbed $^{68}Ga^{3+}$ to the $[^{68}GaCl_4]^-$ anion in the presence of a high concentration of chloride anions. In our initial experiments, it was found that 70% of the adsorbed ^{68}Ga activity can be eluted with 3 mL of 5 M NaCl solution from a SCX cartridge, which was preloaded with ^{68}Ga directly from the generator 0.1 M HCl eluate. Indeed, the eluate from the SCX column was examined by radio HPLC and the main peak at 2.2 min corresponds to the retention time for $[^{68}GaCl_4]^-$ established previously (Figure 2).[11,12,15] Due to the large elution volume, the

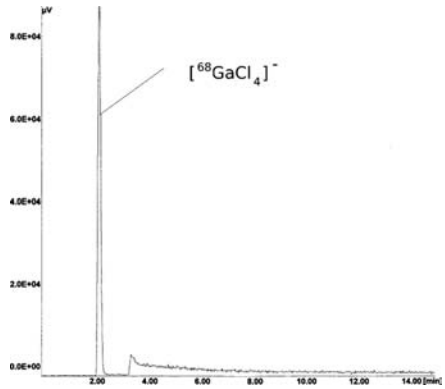


Figure 2. HPLC chromatogram of the SCX cartridge eluate in 5 M NaCl. HPLC: column: RP-18, LiChroCART 250−4, LiChrospher 100, RP-18 (5 μm); solvent A: acetonitrile solution in water (5%), 0.1% TFA; solvent B: 95% acetonitrile solution in water, 0.1% TFA; flow rate: 1.2 mL/min; gradient: from 0 to 2 min 100% A, 2−15 min to 100% B; main peak of $[^{68}GaCl_4]^-$ at 2.2 min.

obtained $[^{68}GaCl_4]^-$ had to be trapped on a SAX cartridge, but after elution with water, it could be directly used for the labeling of DOTATOC. Later, we found that, by addition of a minimum amount of HCl to the 5 M NaCl solution, the ^{68}Ga activity was almost quantitatively elutable directly from the SCX cartridge. In this way, the amount of HCl could be reduced in the final elution step. The optimal mixture was found to be 12.5 μL of 5.5 M HCl in 0.5 mL of 5 M NaCl solution. This eluate could be used directly for ^{68}Ga labeling of DOTA conjugated peptides in buffered reaction mixtures.

This new NaCl-based concentration and labeling procedure is a combination of a cationic trapping and an intermediate transformation of the absorbed $^{68}Ga^{3+}$ into $[^{68}GaCl_4]^-$ by elution with 5 M NaCl solution and re-transformation to $^{68}Ga^{3+}$ with the help of acetate buffer. Figure 3 shows the scheme of the complete procedure for the labeling of DOTATOC with ^{68}Ga.

It was found that ammonium acetate is suited for buffering the reaction solution to an optimal pH between 3 and 4.[16] The radiochemical and chemical purity of the sterile-filtered final product allows for direct use of the neutralized radiopharmaceutical without a subsequent purification step to remove unreacted ^{68}Ga. If ascorbic acid (5 mg) was added to the peptide/buffer solution before the labeling reaction, the ^{68}Ga-DOTATOC is stable for more than two half-lives. As shown in Figure 4A, radiolysis was not detectable by radio HPLC, even two hours after the labeling reaction. In contrast, even after a final purification step, the ^{68}Ga-labeled DOTATOC produced by the

dx.doi.org/10.1021/bc300103t | Bioconjugate Chem. 2012, 23, 1712−1717

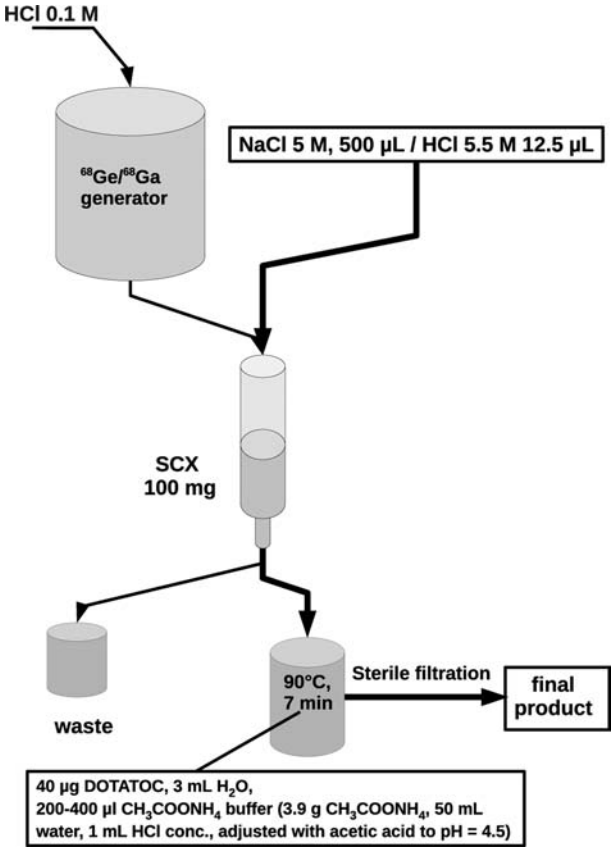


Figure 3. Schematic drawing of the NaCl-based labeling procedure.

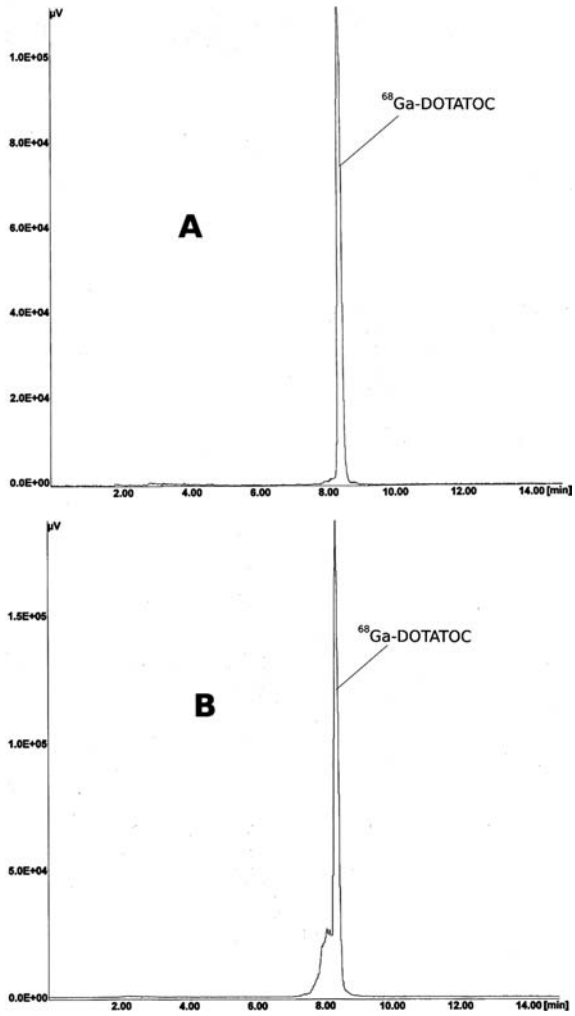


Figure 4. (A) Typical HPLC chromatogram of ^{68}Ga-DOTATOC using the NaCl-based labeling procedure, 2 h after synthesis. (B) Typical HPLC chromatogram of purified ^{68}Ga-DOTATOC using the acetone/HCl method immediately after synthesis; for HPLC conditions, see Figure 2.

acetone/HCl concentration procedure[14] had side products that can be detected by radio HPLC (Figure 4B).

For the labeling of DOTATATE using the HCl/acetone procedure, larger amounts of side products are frequently seen in the final solution most probably arising from unspecific partial hydrolysis or hydroxylation by radiolysis of the peptide residue (Figure 5B). A subsequent purification with the help of a solid-phase extraction would only separate the free ^{68}Ga. In these cases, the radiochemical purity of the final product can be lower than 90% and therefore will not be sufficient for clinical use. In contrast, the NaCl method described herein delivers the ^{68}Ga-DOTATATE in high radiochemical purity (with no apparent side products) as detected by radio HPLC (Figure 5A).

To further evaluate the new NaCl method for routine radiopharmaceutical production, the manual preparation was adapted for use with an automated fluid-handling system for labeling of DOTATOC (Table 1). For these experiments, a Modular-Lab PharmTracer automated fluid handling module (Eckert & Ziegler) was employed. The optimal radiolabeling conditions were found to be the use of 250−450 μL 1 M ammonium acetate buffer and 30−50 μg of DOTATOC with 3.0 mL of water. Additionally, by using the NaCl based method, the synthesis time could be significantly reduced (14 min) compared to the HCl/acetone method, thereby improving overall radiochemical yields (a radiochemical yield of 65% could be achieved).

After complete decay of ^{68}Ga ($t_{1/2}$ = 68 min), analysis by high-purity germanium detector revealed no evidence of parent radionuclide ^{68}Ge in the final products (i.e., no significant difference between background and sample spectrum), whether performed manually or by automated spectral analysis methods. The main ^{68}Ge breakthrough from the generator was not adsorbed on the SCX cartridge during the initial adsorption of ^{68}Ga and is therefore found in the SCX waste. A small amount of ^{68}Ge activity was retained on the cartridge, but was not eluted with the NaCl/HCl solution. These results are consistent with other published methods.[13]

With the success in adapting the new NaCl method for automated preparation of radiopharmaceuticals, we have used this preparation routinely in more than 300 automated runs for the production of ^{68}Ga-DOTATOC, which were applied for molecular imaging of more than 800 patients.

CONCLUSION

The use of 5 M NaCl solution containing a very low amount of HCl in the initial step for ^{68}Ga concentration leads to a greatly simplified concentration and labeling procedure for DOTA conjugated peptides. The one-step concentration method provides >98% of generator-based ^{68}Ga eluant for radiolabeling, and can be used directly for the radiolabeling reaction. A radiochemical purity greater than 99% was routinely achieved. Compared to the widely used acetone/HCl procedure, no peptide side products were observed by radio HPLC. In addition,

dx.doi.org/10.1021/bc300103t | *Bioconjugate Chem.* 2012, 23, 1712−1717

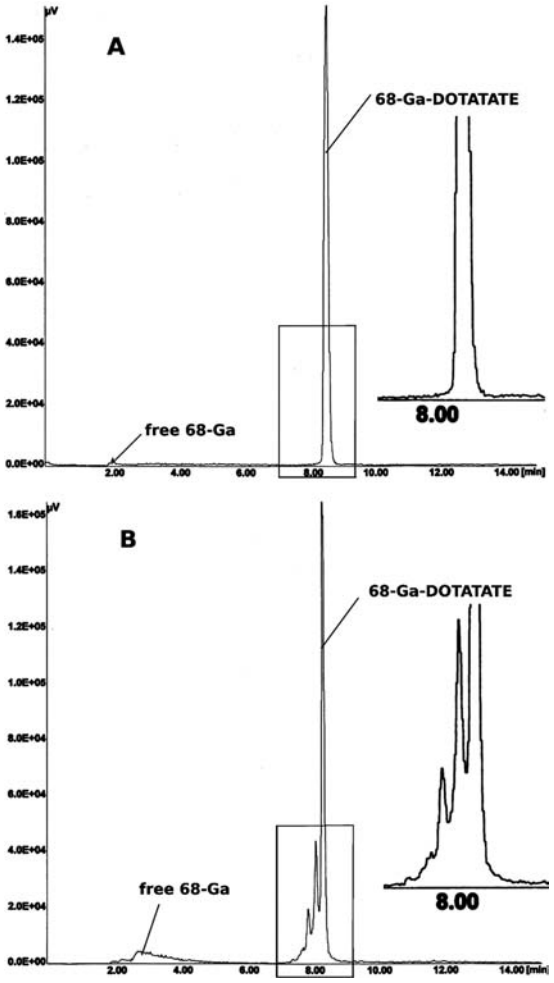


Figure 5. (A) Typical HPLC chromatogram of the final reaction mixture after ^{68}Ga-DOTATATE synthesis using the NaCl-based labeling procedure. (B) Typical HPLC chromatogram of the final reaction mixture after ^{68}Ga-DOTATATE synthesis using the acetone/HCl method; HPLC conditions similar to those described in Figure 2.

Table 1. Comparisons of Results from Automated Labeling Procedures Based on Cationic Exchange Cartridge Purification of ^{68}Ga[a]

			result ± SD	
parameter	test method	specification	method A	method B
peptide-bound ^{68}Ga (%)	ITLC	>90%	98 ± 1	99 ± 1
specific activity ($\frac{MBq}{nmol}$)	dose calibrator	>20	31 ± 4	45 ± 4
acetone (ppm)	gas chromatography	<5000	399 ± 64	n/a
ethanol (%)	gas chromatography	<10	5 ± 0	n/a
pH (reaction mixture)	pH-meter	3.0–4.3	n/a	3.6 ± 0.3
pH (final product)	pH-meter	4.5–8.5	6 ± 1	6.9 ± 0.3

[a]Eluent method A: acetone/HCl (n = 17). Eluent method B: NaCl/HCl (n = 5).

the method significantly reduces required analytical efforts for clinical production of radiopharmaceuticals by removing organic solvents, and enables the direct use of the final products for patient studies. The method was adapted to an automated synthesis module leading to a rapid preparation (14 min vs 32 min in our hands). Therefore, the described procedure makes ^{68}Ga-labeled compounds more easily accessible for institutions with less frequent production needs (and smaller quality control instrumentation budgets), as well as for routine preparations in centers with heavy production requirements via reduced analytical effort and more rapid production.

AUTHOR INFORMATION

Corresponding Author

*E-mail: dirk.mueller@zentralklinik.de.

Notes

The authors declare no competing financial interest.

REFERENCES

(1) Prasad, V., and Baum, R. P. (2010) Biodistribution of the Ga-68 labeled somatostatin analogue DOTA-NOC in patients with neuroendocrine tumors: characterization of uptake in normal organs and tumor lesions. *Q. J. Nucl. Med. Mol. Imaging 54*, 61–67.

(2) Baum, R. P., Prasad, V., Müller, D., Schuchardt, C., Orlova, A., Wennborg, A., Tolmachev, V., and Feldwisch, J. (2010) Molecular imaging of HER2-expressing malignant tumors in breast cancer patients using synthetic ^{111}In- or ^{68}Ga-labeled affibody molecules. *J. Nucl. Med. 51*, 892–897.

(3) Sainz-Esteban, A., Prasad, V., and Baum, R. P. (2010) Interesting image. Pancreatic neuroendocrine tumor with involvement of the inferior mesenteric vein diagnosed by Ga-68 DOTA-TATE PET/CT. *Clin. Nucl. Med. 35*, 40–41.

(4) Fani, M., Andre, J. P., and Maecke, H. R. (2008) ^{68}Ga-PET: a powerful generator-based alternative to cyclotron-based PET radiopharmaceuticals. *Contr. Media Mol. Imaging 3*, 67–77.

(5) Ballinger, J. R., and Solanki, K. K. (2011) What will be required to bring (68)Ga-labelled peptides into routine clinical use? *Nucl. Med. Commun. 32*, 1109–1112.

(6) Tolmachev, V., Altai, M., Sandström, M., Perols, A., Eriksson Karlström, A. H., Boschetti, F., and Orlova, A. (2011) Evaluation of a maleimido derivative of NOTA for site-specific labeling of Affibody molecules. *Bioconjugate Chem. 22*, 894–902.

(7) Fellner, M., Baum, R. P., Kubicek, V., Hermann, P., Lukes, I., Prasad, V., and Rösch, F. (2010) PET/CT imaging of osteoblastic bone metastases with ^{68}Ga-bisphosphonates: first human study. *Eur. J. Nucl. Med. Mol. Imaging 37*, 834.

(8) Riss, P. J., Burchardt, C., and Roesch, F. (2011) A methodical 68Ga-labelling study of DO2A-(butyl-l-tyrosine)2 with cation-exchanger post-processed ^{68}Ga: practical aspects of radiolabelling. *Contr. Media Mol. Imaging 6*, 492–498.

(9) Gottschaldt, M., Bohlender, C., Pospiech, A., Goerls, H., Walther, M., Mueller, D., Klette, I., Baum, R. P., and Schubert, U. S. (2009) In(III) and Ga(III) complexes of sugar substituted tripodal trisalicylidene imines: The first ^{68}Ga labelled sugar derivative. *Eur. J. Inorg. Chem.*, 4298–4307.

(10) Meyer, G. J., Mäcke, H., Schuhmacher, J., Knapp, W. H., and Hofmann, M. (2004) ^{68}Ga-labelled DOTA-derivatised peptide ligands. *Eur. J. Nucl. Med. Mol. Imaging 31*, 1097–1104.

(11) Müller, D., Klette, I., Wortmann, R., and Baum, R. P. (2006) Markierung von DOTA-Peptiden mit Gallium-68 für die nuklearmedizinische Routinediagnostik. *Nuklearmedizin 45*, A 88–89.

(12) Mueller, D., Klette, I., Gottschaldt, M., and Baum, R. P. (2009) Radiolabeling of fragile macroligands with Ga-68. *J. Labeled Compd. Radiopharm. 52*, S477.

(13) de Blois, E., Sze Chan, H., Naidoo, C., Prince, D., Krenning, E. P., and Breeman, W. A. (2011) Characteristics of SnO_2-based ^{68}Ge/^{68}Ga generator and aspects of radiolabelling DOTA-peptides. *Appl. Radiat. Isot. 69*, 308–315.

(14) Zhernosekov, K. P., Filosofov, D. V., Baum, R. P., Aschoff, P., Bihl, H., Razbash, A. A., Jahn, M., Jennewein, M., and Rösch, F. (2007)

Processing of generator produced ^{68}Ga for medical application. *J. Nucl. Med. 48*, 1741−1748.
(15) Müller, D., Klette, I., and Baum, R. P. (2011) The combined cationic-anionic purification of the ^{68}Ge/^{68}Ga generator eluate for the labeling of fragile peptides. *World J. Nucl. Med. 10*, 77−78.
(16) Breeman, W. A., de Jong, M., de Blois, E., Bernard, B. F., Konijnenberg, M., and Krenning, E. P. (2005) Radiolabelling DOTA-peptides with ^{68}Ga. *Eur. J. Nucl. Med. Mol. Imaging 32*, 478−485.

Bioconjugate Chemistry

Editorial

pubs.acs.org/bc

Tribute to Professor Michael John Welch (1939−2012)

Professor Michael Welch was a true pioneer in showing what a chemist can contribute to a Department of Radiology. Before he started his career at Washington University in 1967, there were no chemists developing new cyclotron-based imaging agents in radiology departments; Michael was an original, an innovator, and the person who has become a model for a basic scientist in a clinical department. Dr. Welch was trained as a physical chemist and radiochemist. He received his education at Cambridge University (BA 1961, MA 1965) and from Queen Mary College, University of London (PhD 1965) under Professor David Urch. After a postdoctoral stint with A.P. Wolf at Brookhaven National Laboratory, he moved to St. Louis where he spent 45 yrs pioneering new radioactive molecules for imaging human biology.

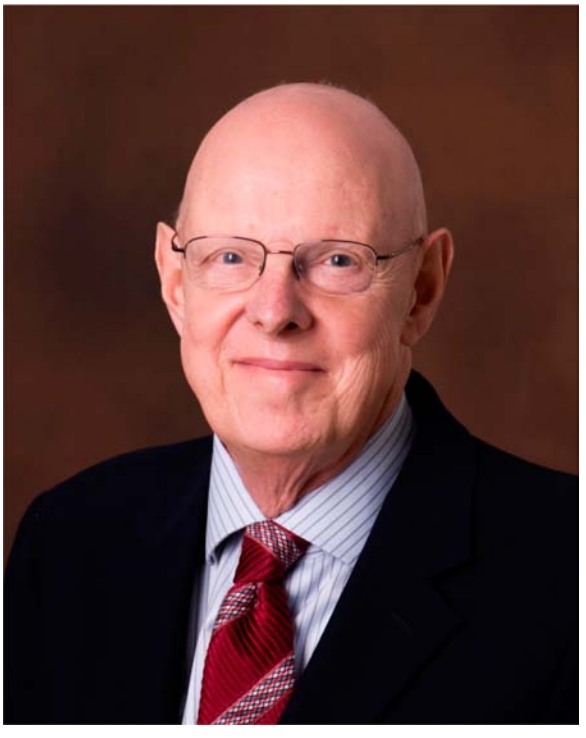
Over the course of his career, Mike mentored as graduate students, postdocs, and faculty colleagues over fifty of the leading scientists developing new radioactive imaging agents. Michael's trainees are today's leaders in industry and government as well as academia, and they can be found in every corner of the globe. Dr. Welch was an ambassador to the world; he traveled tirelessly, and he lectured extensively as an advocate for excellence in biomedical research. He served on numerous peer review committees for NIH, DOE, DOD, and other agencies in the United States and abroad. He had excellent instincts for selecting the best students and the best research proposals, and he provided sage scientific and strategic advice to investigators, science administrators, and policy makers alike.

Dr. Welch had a great passion for life, for his science, for his family, and for sports and music, and he never did anything halfway. He was an accomplished swimmer and captain of his high school team, an avid fan of English football, and he enjoyed sailing. He could be seen at sporting events for the collegiate and professional sports teams in the St. Louis area, and he took great pride in getting the best tickets to the most sought-after musical concerts. Michael was also a loving and nurturing father to two children, Colin and Lesley, and for several years, as a family activity, Dr. Welch raised and showed champion Norwegian Elk Hounds, often traveling on weekends with his children to shows throughout the Midwest.

Professor Welch's research accomplishments cannot be easily summarized. At the time of his death, his bibliography listed over 550 peer-reviewed papers and 73 book chapters, but this list will grow as work already in progress is published by his many collaborators. His early work involved very short-lived radionuclides to study human physiology at the Division of Radiation Sciences, Mallinckrodt Institute of Radiology, directed by Professor Michel Ter-Pogossian and with such distinguished colleagues as Professors Marcus Raichle, E. James Potchen, Barry Siegel, William Powers, and others. While his research started with imaging agents labeled with ^{18}F, ^{15}O, ^{13}N, and ^{11}C, he developed a long list of metal-labeled imaging agents, beginning with ^{113m}In. This list subsequently extended to isotopes of numerous metals and halogens. These imaging agents were used in a wide range of research, from basic human physiology to neuroscience, heart and lung diseases, diabetes and cancer, both diagnosis and therapy. He pioneered methods for labeling cells, as well as proteins, peptides, and small molecules for imaging, and his research with ^{77}Br-estradiol laid the foundation for PET radioligands used today to image receptors in vivo.

The list of honors bestowed on Dr. Welch is long and includes the Nuclear Applications award of ACS, essentially every award of the Society of Nuclear Medicine, of which he served as President in1984, and several named lectureships. He was elected to the Institute of Medicine in 1996. Perhaps the most personal tribute to his stature as a visionary scholar and educator was that Washington University flew the university flag at half-staff for three days after his passing.

Professor Welch is survived by his two children and five grandchildren and by his long-time companion, Mickey Clark. He was remembered fondly by numerous friends and colleagues, past and present, in a memorial service on the campus of Washington University on June 4, 2012. His family has established a foundation in his memory to support research and education in nuclear medicine: www.mjwelchfoundation.org.



Kenneth A. Krohn

Department of Radiology, University of Illinois, 1959 NE Pacific Street, Box 356004, Seattle, Washington 98195, United States

John A. Katzenellenbogen

Published: August 18, 2012

 © 2012 American Chemical Society dx.doi.org/10.1021/bc300336k | *Bioconjugate Chem.* 2012, 23, 1719−1720

Department of Chemistry, University of Washington, 600 S. Mathews Avenue, 461 RAL, Box 37-5 Urbana, Illinois 61801, United States

AUTHOR INFORMATION

Corresponding Authors

E-mail: jkatzene@illinois.edu. Phone: (217) 333-6310. Fax: (217) 333-7325.

E-mail: kkrohn@uw.edu. Phone: (206) 598-6245. Fax: (206) 598-4192.

Notes

The authors declare no competing financial interest.

Bioconjugate Chemistry

Communication

pubs.acs.org/bc

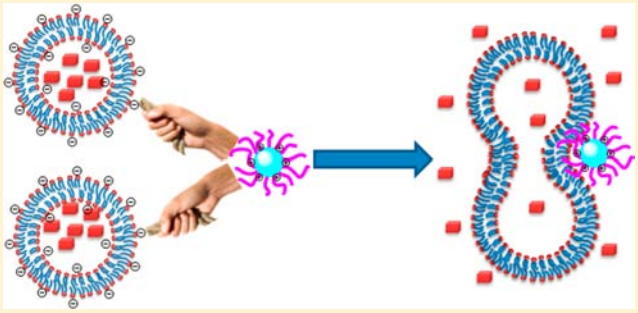
Tunable Fusion and Aggregation of Liposomes Triggered by Multifunctional Surface-Cross-Linked Micelles

Xueshu Li and Yan Zhao*

Department of Chemistry, Iowa State University, Ames, Iowa 50011-3111, United States

Supporting Information

ABSTRACT: Water-soluble organic nanoparticles were prepared by cross-linking the micelles of a tripropargylated cationic surfactant by a diazide cross-linker in the presence of Cu(I) catalysts. The nanoparticles were decorated with hydrophilic ligands of different lengths on the surface. By interacting with negatively charged liposomes through tunable electrostatic interactions, these nanoparticles induced fusion and leakage of large unilamellar vesicles (LUVs). Fusion or aggregation of the membranes was highly sensitive to the rigidity and phase structures of the membranes, enabling thermally gated fusion to occur within a very narrow window of temperature change.



Membrane fusion is a key step in many biological processes including fertilization, cell infection by enveloped viruses, and intracellular molecular trafficking.[1] For two lipid membranes to fuse, they have to overcome significant steric/electrostatic repulsion before merging with each other. Opening of aqueous fusion pores allows the two vesicles to connect their aqueous contents. Biological fusion is tightly regulated by specific fusion proteins.[1,2] Developing a detailed understanding of the fusion mechanism is of great fundamental and practical significance. Fusion inhibitors, for example, could become useful antiviral agents, and materials mimicking enveloped viruses in cell entry may be highly useful for the intracellular delivery of pharmaceuticals.

Synthetic fusogens are simplified small- or macromolecular systems capable of inducing membrane fusion in a controllable manner.[3] In addition to providing mechanistic insight into the fusion process, their ease of synthesis makes them promising candidates as drug delivery vehicles. Chemists have employed metal–ligand complexation,[4] reversible boronate ester bonds,[5,6] and DNA base-pairing[7,8] to overcome repulsive forces of membranes. Some researchers used bioinspired peptides for similar purposes.[9−13] Bong and co-workers in recent years reported a number of strategies to control fusion. Some of the interactions (e.g., vancomycin/D-Ala-D-Ala)[14,15] in their fusogens were adapted from biology and others (e.g., cyanuric acid–melamine)[16,17] were purely synthetic. The latter example was particularly intriguing because hydrogen-bonded systems are normally assumed to be ineffective for water-based applications.

Herein, we report easy-to-synthesize, water-soluble surface-cross-linked micelles (SCMs) that induce membrane fusion through tunable electrostatic interactions. The size of the SCM was critical to its activity. The electrostatically induced fusion was highly sensitive to the phase structure of the lipids, enabling thermally gated fusion within a very narrow window of temperature change.

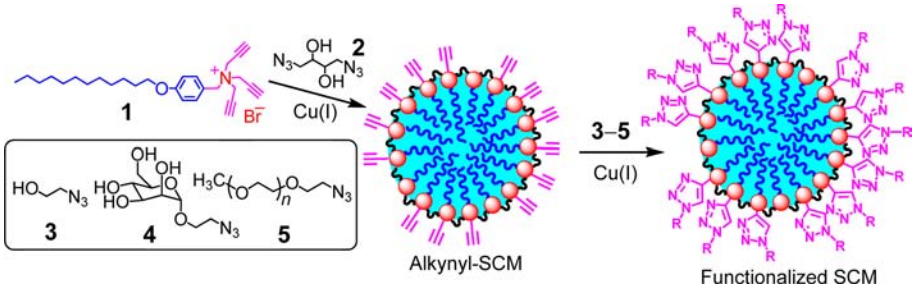
The synthesis of the SCMs was shown in Scheme 1. Briefly, 4-dodecyloxybenzyltripropargyl ammonium bromide (**1**) forms micelles with a dense layer of alkyne groups on the surface. The addition of 1 equiv of water-soluble cross-linker **2** and Cu(I) fixes the dynamic assemblies of surfactants into water-soluble nanoparticles with numerous residual alkyne groups on the surface. According to our previous study,[18] the majority of the surfactant molecules under such reaction conditions underwent two cycloaddition reactions and some reacted three times—fully in line with the high efficiency of the click reaction. Post-functionalization of the alkynyl-SCM was achieved readily by another round of click chemistry using various azide-functionalized compounds **3**−**5** in a one-pot reaction.

The hydrodynamic diameters of the hydroxyl-, mannose-, and PEG-functionalized SCMs were determined by DLS to be ca. 14, 20, and 150 nm, respectively (Figures 1−3S, Supporting Information). Similar materials were characterized by TEM previously and found to be spherical in shape.[18] To understand how these differently-sized particles interact with liposomes, we prepared large unimolecular vesicles (LUVs) containing carboxyfluorescein (CF) by the membrane extrusion method. The liposomes, ca. 120 nm after extrusion, were made of neutral POPC and 10 mol % anionic POPG. This formulation is frequently used in liposomal research and mimics the composition of bacterial membranes. The negative charges of the liposomes make them colloidally more stable. Moreover, the charges allow the liposomes to interact with the positively charged SCMs through Coulombic interactions.

Received: February 17, 2012
Revised: August 14, 2012
Published: August 24, 2012

 © 2012 American Chemical Society dx.doi.org/10.1021/bc300082b | *Bioconjugate Chem.* 2012, 23, 1721−1725

Scheme 1. Synthesis of Functionalized Surface-Cross-Linked Micelles (SCMs)



CF is a water-soluble fluorescent dye that displays self-quenching at high concentrations (>50 mM).[19] If the membranes are unaffected by SCMs, CF would stay within the liposomes and emit weakly due to self-quenching. If the SCMs cause any leakage of the liposomes, CF would escape, get diluted, and display enhanced emission. The percent leakage is generally calculated based on the complete release at the end of the assay triggered by a nonionic surfactant, 1% Triton X-100.

The leakage assay showed that all three SCMs were able to trigger the release of CF (Figure 1). SCM−OH (i.e., SCM functionalized by 2-azidoethanol **3**) was the most effective among all, triggering significant leakage at 0.1 μM of the (cross-linked) surfactant. Note that the CF leakage was nearly instantaneous at the addition of SCM−OH and exceeded 90% when the concentration of the cross-linked micelles reached 1.0 μM.

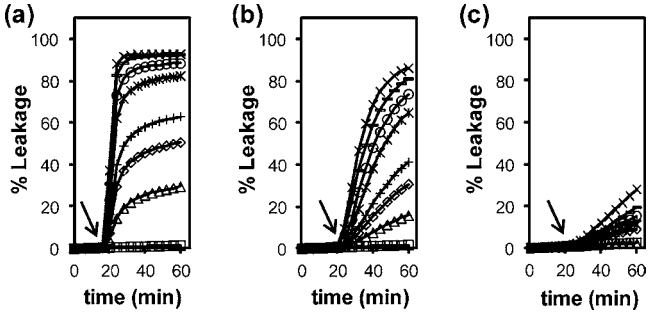


Figure 1. Percent CF leakage from POPC/POPG LUVs upon the addition of different concentrations of (a) SCM−OH, (b) SCM−mannose, and (c) SCM−PEG at 25 °C. The concentrations of the (cross-linked) surfactant in the SCMs were 0, 0.1, 0.2, 0.3, 0.5, 0.7, 1.0, and 1.5 μM from bottom to top. [phospholipids] = 2.9 μM. The concentration of CF was 50 mM within the LUVs. The arrow indicates the addition of SCM at 20 min.

Surface-functionalization overall reduced the potency of the SCMs. As the size of the surface groups increased from CH_2CH_2OH to mannose to PEG, CF leakage became noticeably slower (Figure 1b,c). For the PEGylated SCM, the leakage was less than 30% after 60 min even at the highest tested concentration.

Tunable electrostatic interactions between the SCMs and the liposomes were confirmed by zeta-potential measurements. As seen in Figure 4S, the POPC/POPG LUVs had a zeta-potential of −5.8 mV in the HEPES buffer, apparently due to the negatively charged POPG lipids. The SCMs were all positively charged, as expected. The zeta-potentials decreased with increasing length of the surface ligands, being 37.3, 32.3, and 18.0 for SCM−OH, SCM−mannose, and SCM−PEG, respectively.

A combination of lipid-mixing assay and DLS study shed light on the leakage mechanism. In the lipid-mixing assay, one batch of LUVs containing 1 mol % NBD- and rhodamine-functionalized lipids was mixed with another batch of unlabeled LUVs. If any process exists that causes membrane disintegration or fusion, the labels would be diluted, lowering the fluorescence resonance energy transfer (FRET) from NBD to rhodamine.[20] Indeed, significant fusion of the POPC/POPG membranes was induced by SCM−OH. The percent fusion of the membranes was over 60% when the concentration of the (cross-linked) surfactant in the SCM was 1.5 μM (Figure 2a). Because the percent CF leakage was about 90% at the same concentration of SCM (Figure 1a), membrane fusion was responsible for most, if not all, of the leakage.

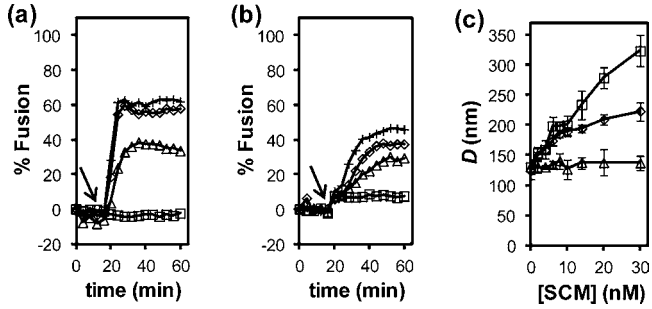


Figure 2. (a) Percent fusion of POPC/POPG LUVs triggered by (a) SCM−OH and (b) SCM−mannose at 25 °C. The concentrations of the (cross-linked) surfactant in the SCM were 0, 0.5, 1.0, and 1.5 μM from bottom to top. The arrow indicates the addition of SCM at 20 min. (c) DLS diameter of the liposomes after the addition of SCM−OH (□), SCM−mannose (◇), and SCM−PEG (Δ). [phospholipids] = 2.9 μM.

The mannose-functionalized SCM seemed to trigger the CF efflux by the same mechanism. At 1.5 μM of the (cross-linked) surfactant, the percent fusion was nearly 50% (Figure 2b), comparing favorably with the 85% CF leakage under the same condition (Figure 1b). Note that the CF leakage and membrane fusion had similar profiles. SCM−OH, in general, induced abrupt changes, whereas SCM−mannose was more gradual (compare the curves with >0.5 μM SCM in Figure 1a and b with those in Figure 2a and b). Bergstrand and co-workers found that liposome leakage sometimes proceeded more rapidly than lipid mixing, suggesting that liposomes could leak prior to aggregation and lipid rearrangement.[21] In our case, when the leakage and lipid mixing were normalized, it was clear that the two processes occurred simultaneously (Figure 5S). The nearly identical time responses observed in two different

dx.doi.org/10.1021/bc300082b | *Bioconjugate Chem.* 2012, 23, 1721−1725

assays strongly support that membrane fusion was responsible for the CF leakage.

Membrane fusion was also confirmed by DLS. As shown in Figure 2c, both SCM−OH (□) and SCM−mannose (◇) increased the size of the liposomes significantly, following a nearly linear relationship to the SCM concentration. Once again, the size increase was most significant with SCM−OH. It should be noted that no sedimentation or precipitation of liposomes was observed in our experiments.

SCM−PEG, on the other hand, behaved differently in every aspect. As shown earlier, it was quite ineffective at inducing CF leakage. The lipid-mixing assay showed negligible fusion (Figure 6S). DLS, in the meantime, revealed that the liposomes stayed unchanged in size upon the addition of the PEGylated SCMs (Figure 2c, Δ).

The above results may be understood from the tunable Coulombic interactions between the liposomes and the SCMs. Because the charges of an SCM come from the ammonium headgroups of the cross-linked surfactants, their locations on the SCM are fixed. Surface-functionalization adds nonionic hydrophilic ligands to the surface of the SCM nanoparticle. These ligands essentially represent an "insulating" layer when the SCMs adsorb unto the oppositely charged liposomes. A thicker insulating layer weakens the Columbic interactions, making the larger SCMs less capable of inducing CF leakage and membrane fusion. Because SCM−PEG caused neither fusion nor size change in the liposomes, the small extent of leakage in Figure 1c most likely comes from local destabilization of the membranes.

The smaller SCMs (SCM−OH and SCM−mannose) thus were able to overcome the repulsion forces between negatively charged liposomes quite effectively. We hypothesized that, even when liposomes were brought together by the SCMs, whether membrane fusion took place would still depend on other factors such as the rigidity of membranes. Membranes that deform easily should fuse more easily than those that are rigid.

To test the hypothesis, we studied the effects of the SCMs on DPPC/DPPG liposomes. The LUVs had a zeta-potential of −13.4 mV at 25 °C in the HEPES buffer (Figure 4S). The saturated lipids have a gel−liquid-crystalline transition temperature of 41 °C. The membranes, thus, should be quite rigid at room temperature. Indeed, no CF efflux was observed with any of the three SCMs at 25 °C (see Figure 3a for SCM−OH and Figure 7S for SCM−PEG). Interestingly, the lipid-mixing assay gave negative numbers for the membrane fusion (Figure 3b). In other words, instead of decreasing the FRET from NBD to rhodamine, the addition of the SCM−OH enhanced the energy transfer. This behavior normally takes place when liposomes aggregate without the membranes fusing together.[22] Under such a situation, the energy transfer within a labeled liposome remains effective and additional energy transfer occurs when multiple labeled liposomes come close—the Förster radius of the two fluorophores is ~5 nm.[20] Our DLS study confirmed the conclusion, showing a quick increase of the liposome size upon the addition of SCM−OH (Figure 3c, □). As expected from the electrostatic model, aggregation was less prominent with SCM−mannose (◇) and absent with SCM−PEG (Δ).

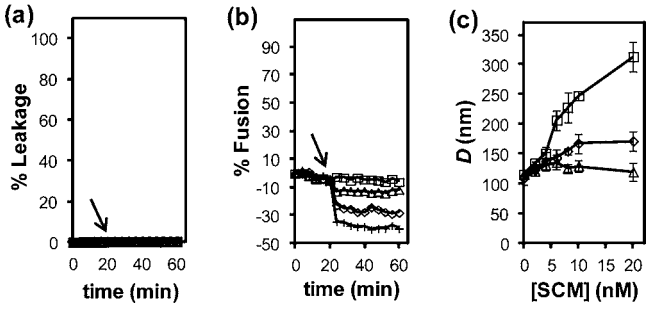


Figure 3. (a) Percent CF leakage from DPPC/DPPG LUVs upon the addition of different concentrations of SCM−OH at 25 °C. (b) Percent fusion of DPPC/DPPG LUVs triggered by SCM−OH at 25 °C. The concentrations of the (cross-linked) surfactant in the SCM were 0, 0.5, 1.0, and 1.5 μM from bottom to top. The arrow indicates the addition of SCM at 20 min. (c) DLS diameter of the DPPC/DPPG liposomes after the addition of SCM−OH (□), SCM−mannose (◇), and SCM−PEG (Δ) at 25 °C.

The above experiments demonstrated that rigid membranes are quite resistant to the electrostatically induced membrane fusion. The results are reasonable because fusion requires substantial reorganization of the membranes, which should be more difficult when lipid molecules have low mobility. The situation changed as soon as the membranes went into the liquid-crystalline state. As shown by Figure 4a, the nano-

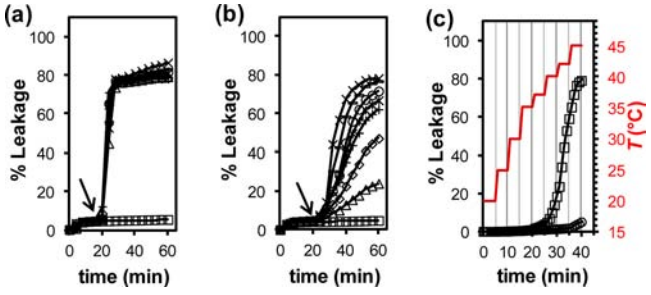


Figure 4. Percent leakage of CF from DPPC/DPPG LUVs upon the addition of different concentrations of (a) SCM−OH and (b) SCM−PEG at 42 °C The concentrations of the (cross-linked) surfactant in the SCM were 0, 0.1, 0.2, 0.3, 0.5, 0.7, 1.0, and 1.5 μM from bottom to top. The arrow indicates the addition of SCM at 20 min. The concentration of CF was 50 mM within the LUVs. (c) Percent CF leakage from DPPC/DPPG LUVs in the presence (□) and absence (◇) of 1.0 μM SCM−OH during temperature change. [phospholipids] = 2.9 μM.

particles became extremely potent. Most remarkably, even 0.1 μM of the (cross-linked) surfactant in SCM−OH was able to leak over 80% of the CF from the DPPC/DPPG LUVs at 42 °C, whereas the same could only be achieved at much higher levels of the SCMs for POPC/POPG LUVs (Figure 1a). Similar observations were made for the SCM−mannose (Figure 8S).

The dependence of leakage on the lipid phase was demonstrated most clearly by a temperature-controlled experiment, in which the sample was heated from 20 to 45 °C with step-changes every 5 min (Figure 4c, red). In the absence of the SCM, little CF efflux occurred from the DPPC/DPPG liposomes. With as little as 0.1 μM of the cross-linked surfactant in SCM−OH, the situation was enormously different. Almost no leakage occurred before 40 °C and the majority of all the leakage took place between 40 and 42 °C. Apparently, the aggregated [23] liposomes were able to resist the electrostatic stress right until the phase transition occurred.

The above results indicate that the saturated DPPC/DPPG membrane just above the phase-transition temperature was *far more sensitive* to the electrostatic stress than the monounsatu-

dx.doi.org/10.1021/bc300082b | *Bioconjugate Chem.* 2012, 23, 1721−1725

rated POPC/POPG. SCM−PEG showed the same trend. Low activity was observed with the PEGylated SCMs for POPC/POPG liposomes (Figure 1c). Although not as effective as SCM−OH and SCM−mannose, SCM−PEG induced significant leakage of CF at 42 °C for the saturated liposomes, most likely due to local destabilization of the membranes. Nearly 80% of CF was released by 1.5 μM of the (cross-linked) surfactant in the PEGylated SCM (Figure 4b).

The phase-transition temperature of POPC/POPG is −2 °C. At 25 °C, the membrane should be much more fluid-like than DPPC/DPPG at 42 °C right above the latter's phase-transition temperature. Permeability of membranes is known to increase at the phase-transition temperature due to coexisting gel and liquid-crystalline phases.[24−27] The higher permeability is considered to result from packing defects at the boundaries of solid−lipid phase boundaries. It should be emphasized that, under our experimental conditions, very little CF leakage occurred from DPPC/DPPG liposomes in the absence of the SCMs (Figure 4c, ◇). Thus, the temperature-triggered release in our case was caused by the vulnerability of the membranes with coexisting domains to the electrostatic stress. A separate study of ours demonstrated that, once the charge of the liposomes was reversed (to positive), membrane fusion disappeared completely.[28]

Quite likely, mobile lipids in the fluid phase can adjust easily to accommodate both the liposome−SCM electrostatic interactions and the hydrophobic interactions of the lipid tails. Near the phase-transition temperature, on the other hand, lipid rearrangement could only occur within the more mobile domains of liquid-crystalline phase, making it more difficult to relieve the electrostatic stress induced by the SCMs and affording higher leakage as a result.

The most attractive feature of the SCMs is their ease of synthesis and post-functionalization. Ligand attachment can accurately tune the thickness of the insulating layer on the SCM and, in turn, modulate the Coulombic interactions between the nanoparticles and the oppositely charged liposomes. Depending on the rigidity and phase structures of the membranes, well-regulated aggregation and fusion of membranes may result.

■ ASSOCIATED CONTENT

Ⓢ Supporting Information

Liposome preparation, liposome assays, and additional figures. This material is available free of charge via the Internet at http://pubs.acs.org.

■ AUTHOR INFORMATION

Corresponding Author

*Phone: 515-294-5845. Fax: 515-294-0105. E-mail: zhaoy@iastate.edu.

Notes

The authors declare no competing financial interest.

■ ACKNOWLEDGMENTS

We acknowledge NSF (DMR-1005515) for supporting the research.

■ REFERENCES

(1) Jahn, R., Lang, T., and Südhof, T. C. (2003) Membrane fusion. *Cell 112*, 519−533.

(2) Harrison, S. C. (2008) Viral membrane fusion. *Nat. Struct. Mol. Biol. 15*, 690−698.

(3) Marsden, H. R., Tomatsu, I., and Kros, A. (2011) Model systems for membrane fusion. *Chem. Soc. Rev. 40*, 1572−1585.

(4) Richard, A., Marchi-Artzner, V., Lalloz, M.-N., Brienne, M.-J., Artzner, F., Gulik-Krzywicki, T., Guedeau-Boudeville, M.-A., and Lehn, J.-M. (2004) Fusogenic supramolecular vesicle systems induced by metal ion binding to amphiphilic ligands. *Proc. Natl. Acad. Sci. U. S. A. 101*, 15279−15284.

(5) Kashiwada, A., Tsuboi, M., and Matsuda, K. (2009) Target-selective vesicle fusion induced by molecular recognition on lipid bilayers. *Chem. Commun.*, 695−697.

(6) Kashiwada, A., Tsuboi, M., Mizuno, T., Nagasaki, T., and Matsuda, K. (2009) Target-selective vesicle fusion system with pH-selectivity and responsiveness. *Soft Matter 5*, 4719−4725.

(7) Stengel, G., Zahn, R., and Hook, F. (2007) DNA-induced programmable fusion of phospholipid vesicles. *J. Am. Chem. Soc. 129*, 9584−9585.

(8) Chan, Y.-H. M., van Lengerich, B., and Boxer, S. G. (2009) Effects of linker sequences on vesicle fusion mediated by lipid-anchored DNA oligonucleotides. *Proc. Natl. Acad. Sci. U. S. A. 106*, 979−984.

(9) Parente, R. A., Nir, S., and Szoka, F. C. (1988) pH-Dependent fusion of phosphatidylcholine zmall esicles - Induction by a zynthetic amphipathic peptide. *J. Biol. Chem. 263*, 4724−4730.

(10) Puyal, C., Maurin, L., Miquel, G., Bienvenüe, A., and Philippot, J. (1994) Design of a short membrane-destabilizing peptide covalently bound to liposomes. *Biochim. Biophys. Acta, Biomembr. 1195*, 259−266.

(11) Lorin, A., Charloteaux, B., Fridmann-Sirkis, Y., Thomas, A., Shai, Y., and Brasseur, R. (2007) Mode of membrane interaction and fusogenic properties of a de novo transmembrane model peptide depend on the length of the hydrophobic core. *J. Biol. Chem. 282*, 18388−18396.

(12) Kashiwada, A., Matsuda, K., Mizuno, T., and Tanaka, T. (2008) Construction of a pH-responsive artificial membrane fusion system by using designed coiled-coil polypeptides. *Chem.—Eur. J. 14*, 7343−7350.

(13) Marsden, H. R., Elbers, N. A., Bomans, P. H. H., Sommerdijk, N. A. J. M., and Kros, A. (2009) A reduced SNARE model for membrane fusion. *Angew. Chem., Int. Ed. 48*, 2330−2333.

(14) Gong, Y., Luo, Y., and Bong, D. (2006) Membrane activation: selective vesicle rusion via small molecule recognition. *J. Am. Chem. Soc. 128*, 14430−14431.

(15) Gong, Y., Ma, M., Luo, Y., and Bong, D. (2008) Functional determinants of a synthetic vesicle fusion system. *J. Am. Chem. Soc. 130*, 6196−6205.

(16) Ma, M., Paredes, A., and Bong, D. (2008) Intra- and intermembrane pairwise molecular recognition between synthetic hydrogen-bonding phospholipids. *J. Am. Chem. Soc. 130*, 14456−14458.

(17) Ma, M., Gong, Y., and Bong, D. (2009) Lipid membrane adhesion and fusion driven by designed, minimally multivalent hydrogen-bonding lipids. *J. Am. Chem. Soc. 131*, 16919−16926.

(18) Zhang, S., and Zhao, Y. (2010) Facile synthesis of multivalent water-soluble organic nanoparticles via "surface clicking" of alkynylated surfactant micelles. *Macromolecules 43*, 4020−4022.

(19) New, R. R. C. (1990) *Liposomes: A Practical Approach*, IRL Press, Oxford.

(20) Struck, D. K., Hoekstra, D., and Pagano, R. E. (1981) Use of resonance energy-transfer to monitor membrane-fusion. *Biochemistry 20*, 4093−4099.

(21) Bergstrand, N., Arfvidsson, M. C., Kim, J.-M., Thompson, D. H., and Edwards, K. (2003) Interactions between pH-sensitive liposomes and model membranes. *Biophys. Chem. 104*, 361−379.

(22) Rafikova, E. R., Melikov, K., Ramos, C., Dye, L., and Chernomordik, L. V. (2009) Transmembrane protein-free membranes fuse into xenopus nuclear envelope and promote assembly of functional pores. *J. Biol. Chem. 284*, 29847−29859.

(23) According to Figures 3b and 4c.

(24) Papahadjopoulos, D., Jacobson, K., Nir, S., and Isac, T. (1973) Phase transitions in phospholipid vesicles. Fluorescence polarization

and permeability measurements concerning the effect of temperature and cholesterol. *Biochim. Biophys. Acta 311*, 330−48.
(25) Blok, M. C., van Deenen, L. L., and De Gier, J. (1976) Effect of the gel to liquid crystalline phase transition on the osmotic behaviour of phosphatidylcholine liposomes. *Biochim. Biophys. Acta 433*, 1−12.
(26) Clerc, S. G., and Thompson, T. E. (1995) Permeability of dimyristoyl phosphatidylcholine/dipalmitoyl phosphatidylcholine bilayer membranes with coexisting gel and liquid-crystalline phases. *Biophys. J. 68*, 2333−41.
(27) Mills, J. K., and Needham, D. (2005) Lysolipid incorporation in dipalmitoylphosphatidylcholine bilayer membranes enhances the ion permeability and drug release rates at the membrane phase transition. *Biochim. Biophys. Acta, Biomembr. 1716*, 77−96.
(28) Li, X., and Zhao, Y. (2012) Protection/deprotection of surface activity and its applications in the controlled release of liposomal contents. *Langmuir 28*, 4152−4159.

Bioconjugate Chemistry

Communication

pubs.acs.org/bc

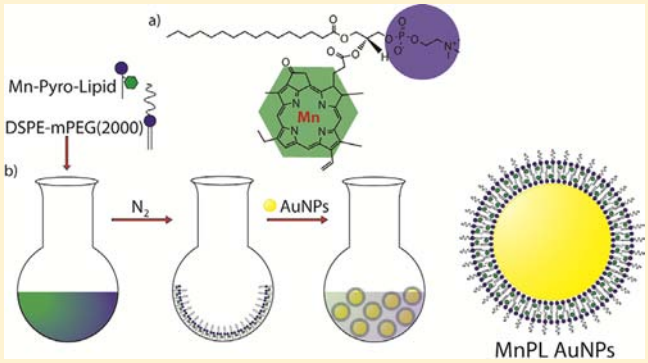
Porphyrin–Lipid Stabilized Gold Nanoparticles for Surface Enhanced Raman Scattering Based Imaging

Natalie C. M. Tam,[†,‡] Patrick Z. McVeigh,[†,§] Thomas D. MacDonald,[†,∥] Arash Farhadi,[†,§] Brian C. Wilson,[†,§] and Gang Zheng*[,†,‡,§,∥]

[†]Ontario Cancer Institute, Campbell Family Cancer Research Institute, and Techna Institute [‡]Institute of Biomaterials and Biomedical Engineering, [§]Department of Medical Biophysics, and [∥]Department of Pharmaceutical Sciences, University of Toronto, Toronto, Ontario, Canada

Supporting Information

ABSTRACT: A porphyrin–phospholipid conjugate with quenched fluorescence was utilized to serve as both the Raman dye and a stabilizing, biocompatible surface coating agent on gold nanoparticles. Through simple synthesis and validation with spectroscopy and confocal microscopy, we show that this porphyrin–lipid stabilized AuNP is a novel SERS probe capable of cellular imaging. To date, this is the first use of porphyrin as a Raman reporter molecule for SERS based imaging.



INTRODUCTION

Raman spectroscopy has translated from molecular analysis of chemicals to molecular imaging due to its capacity for molecular identification, photostability, and multiplexing capability.[1,2] In particular, surface enhanced Raman scattering (SERS) techniques based on metallic nanoparticles such as gold (AuNPs) have further advanced its utility for molecular diagnostic imaging by augmenting, by orders of magnitude, the intensity of the inelastically scattered photons, allowing ultrasensitive levels of detection.[1,3] With AuNPs, the SERS probes are inert, show low toxicity,[4] and can be functionalized with targeting moieties and tuned for near-infrared (NIR) wavelengths to facilitate in vivo imaging.[3,5]

Currently, gold nanostructures for SERS imaging and sensing have been based on chromophores adsorbed onto the metallic surface and subsequently encapsulated by various surface coatings to improve biocompatibility and stability. Such Raman dyes commonly contain symmetrical moieties, such as pyrrole or benzene rings, that have strong Raman-active modes due to the double bonds being highly polarizable.[6] Dyes are either selected for or modified to contain functional groups (e.g., thiol –SH) that allow for chemi- or physi-adsorption to metallic surfaces; however, they may have altered affinities in the presence of differing surrounding biological matrix,[7] likely from competing thiols or oxidation.[8] To date, several different classes of surface coating, namely, poly(ethylene glycol) (PEG) and silica, have produced stable SERS probes for in vitro and in vivo imaging.[3,5,9] Recently, our group designed Raman active phospholipid gold nanoparticles (RAP AuNPs), a biocompatible and versatile alternative that shows both structural and Raman signal stability, using phospholipid as a surface coating.[10] Although robust, RAP AuNPs follow a similar synthetic strategy as previous SERS probes, where the initial step of loading dye molecules onto the AuNPs gives rise to concentration- and dye-dependent inconsistencies[11] in the Raman signals that may lead to uncontrolled aggregation and ultimately result in low reproducibility.[12,13]

In the present study, we combined a phospholipid with a chromophore to coat AuNPs, thereby both providing SERS detection capabilities and conferring structural stability and biocompatibility. We have previously reported synthesis of a porphyrin–lipid conjugate using a near-infrared (NIR) photosensitizer, pyropheophorbide-a,[14,15] linked to a single acyl chain phospholipid, 16:0 lysophosphatidylcholine, at the glycerol backbone. We have demonstrated that these conjugates (pyro-lipid or PL) can self-assemble into bilayer nanoparticles, yielding phototherapeutic and imaging functions.[16,17] Porphyrins have strong Raman scattering due to their heterocyclic pyrrole structure and can be enhanced by both electromagnetic and charge transfer to exhibit SERS spectra.[18] However, the Raman signal is usually overwhelmed by the endogenous fluorescence. Although metal-free or closed-shell metal-inserted porphyrins are fluorescent, chelation of open-shell metal ions (e.g., Cu^{2+} or Mn^{3+}) within the planar structure quenches the fluorescence. This ability to chelate divalent metallic ions on pyro-lipid was also previously demonstrated with Cu^{2+} loaded

Received: April 16, 2012
Revised: August 3, 2012
Published: August 9, 2012

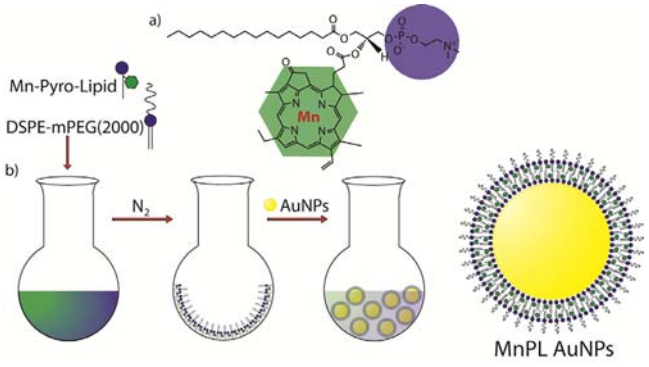
 © 2012 American Chemical Society

pyro-lipid, which maintained bilayer stacking assembly and could serve as positron emission tomography (PET) imaging contrast agents.[19] It is also known that chelation of Mn^{3+} can convert a porphyrin from a fluorescent sensor to an MRI contrast agent.[20] Hence, inserting suitable metal ions into porphyrins could eliminate fluorescent interference with the Raman signals, as well as introducing multimodal imaging functionality.

RESULTS AND DISCUSSION

Here, we report successful development of a porphyrin−lipid conjugate with quenched fluorescence by Mn^{3+} that confers biocompatibility to the AuNP surface and stabilizes the nanoparticles in various aqueous buffers, as well as acting as a Raman reporter. Unlike conventional methods where surface agents are used to encapsulate the pre-Raman dye adsorbed gold nanoparticle, we have simplified the synthesis of these SERS probes by using a phospholipid−chromophore conjugate acting both as the Raman reporter and protective surface coating. At the same time, we eliminate the necessity of selecting specific dyes only suitable for adsorption to AuNPs and provide a more reproducible strategy to obtain consistent Raman intensities for making SERS probes.

Scheme 1. Structure of Manganese Pyro-Lipid (MnPL) (a) and Three-Step Procedure for Creating SERS AuNPs with MnPL (b)



The conjugation of pyropheophorbide-a to 1-palmitoyl-2-hydroxy-*sn*-glycero-3-phosphocholine and the method of subsequent manganese chelation onto the pyro-lipid (MnPL) are described in detail elsewhere.[16] The resulting MnPL has quenched fluorescence, as expected (Supporting Information Figure 1). As shown in Scheme 1, MnPL is mixed with PEGylated phospholipids (1,2-distearoyl-*sn*-glycero-3-phosphoethanolamine-*N*-[methoxy(polyethylene glycol)-2000]) in a 1:1 ratio in chloroform and dried as a lipid film under N_2 gas in a round-bottom flask. The lipid film is directly hydrated with 60 nm AuNPs suspended in distilled H_2O. As for any energetically favorable conformation with phospholipids, direct hydration often creates multilamellar vesicles; thus, the MnPL-AuNP composites are further modified by vortexing, sonication, and subsequent rounds of centrifugation to ensure uniform phospholipid coating and that any free vesicles without any entrapped gold nanoparticles are removed. The resulting structure can be seen in Figure 1a, where the transmission electron microscopy (TEM) image shows a clear phospholipid coating of 4−7 nm.

To assess whether the MnPL coating also acts as a Raman reporter, we characterized the purified solution using a Raman spectrometer operating at 785 nm excitation (Figure 1b). Comparing this spectrum with Raman spectra from resonance Raman scattering of similar metallo-porphyrins,[21] each of the prominent peaks at 751 cm^{-1}, 986 cm^{-1}, 1138 cm^{-1}, 1228 cm^{-1}, 1327 cm^{-1}, and 1531 cm^{-1} were closely matched, confirming that the observed spectrum displayed the pyropheophorbide-a within the nanoparticle assembly. This clearly demonstrates that Mn^{3+} loaded pyropheophorbide-a situated within the lipid coating is detectable by Raman

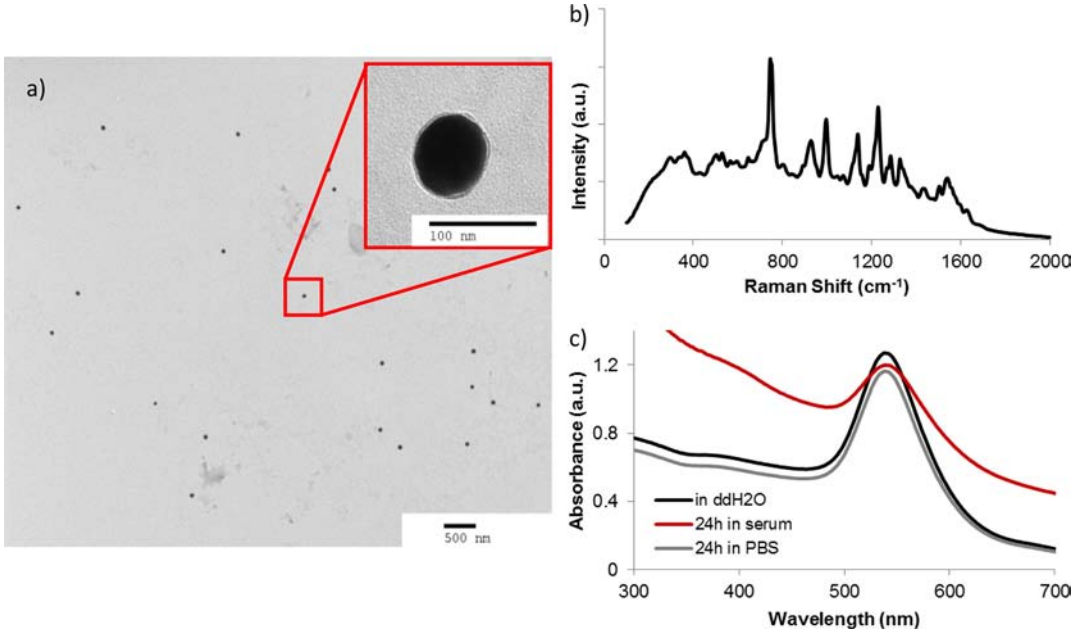


Figure 1. TEM image (a) of MnPL AuNP showing full coverage of pyro-lipid surrounding the AuNP surface with thickness of 4−7 nm. Surface enhanced Raman spectrum (b) of MnPL AuNPs with 785 nm laser (75 mW, 1 s). (c) UV−vis spectra of MnPL AuNPs after 24 h in differing buffers (distilled water (ddH_2O), serum, and phosphate buffered saline (PBS)) a 37 °C.

dx.doi.org/10.1021/bc300214z | *Bioconjugate Chem.* 2012, 23, 1726−1730

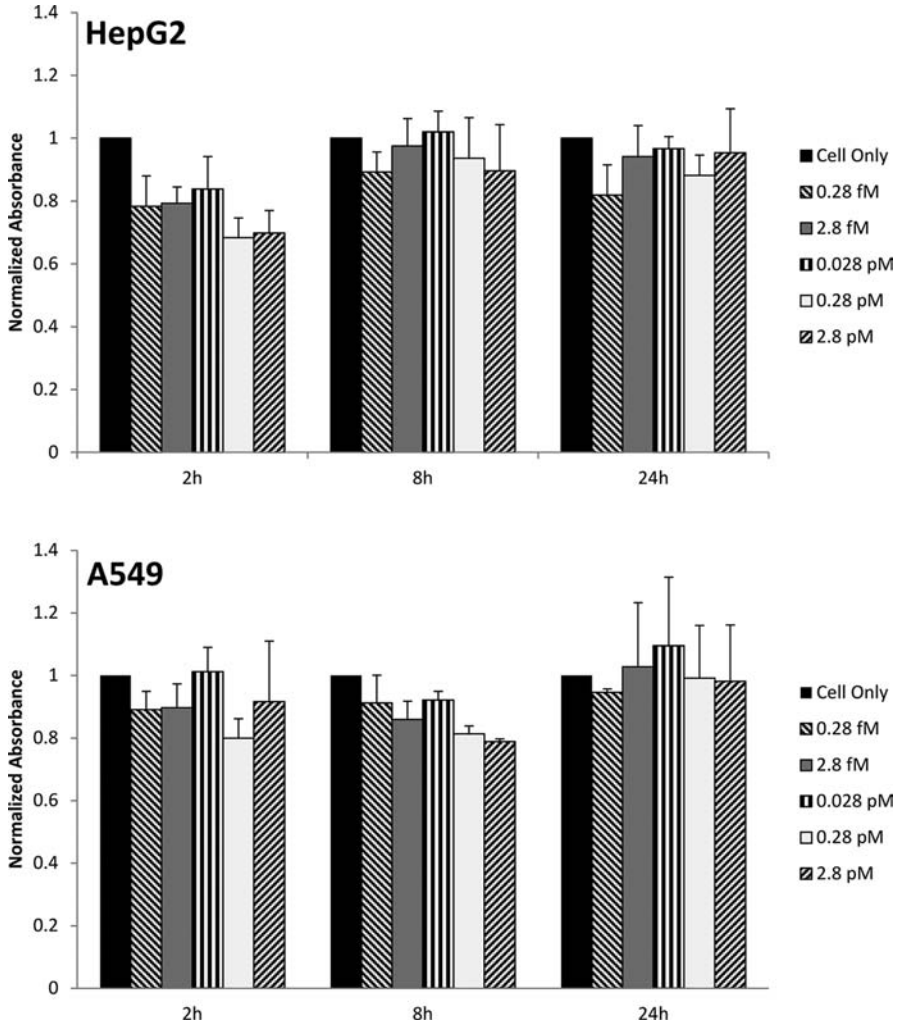


Figure 2. Cytotoxicty of MnPL AuNPs on HepG2 and A549 human cell lines determined by MTT assay. The relative cell viability was normalized to untreated cells for varying NP concentrations and incubation times. Error bars represent mean value ± standard deviation of three independent experiments, each performed in triplicate.

spectroscopy and that it does not require the Raman dye be adsorbed onto the AuNP surface. Moreover, we specifically identified this as a surface-enhancement effect from its interaction with the AuNP surface and not due any excessive free porphyrins or pyro-lipid in solution, since no Raman signal could be detected from MnPL in solution at over 1000× concentration in the absence of AuNPs (Supporting Information Figure 2).

As expected, the use of MnPL as surface coating conferred outstanding biocompatible stability, similar to that from phospholipid coating alone.[10] As seen in Figure 1c, there was no shift in the absorption maximum (λ_{max} = 542 nm) of MnPL AuNPs after 24 h in either phosphate buffered saline (PBS) or 50% fetal bovine serum (FBS) solution. The lack of any red shift of the absorption peak demonstrates that the MnPL is sufficient to prevent AuNP aggregation from serum proteins and at physiological ion concentrations. There is a broadening of the absorption peak for nanoparticles in serum, which is likely due to the protein corona expected to adhere on their surface.[22,23]

We investigate the effect of MnPL AuNPs on the viability of different human cell lines at doses that are believed to be in the range likely encountered in vivo, namely 1−100 gold nanoparticles per cell.[24] The cytotoxicity of MnPLAuNPs to different cell lines was assessed by using MTT assay. Human liver hepatocellular carcinoma HepG2 cell line was chosen to test the MnPL toxicity to liver cells since gold nanoparticles have high accumulation in the liver,[24] while the human non-small cell lung cancer A549 cell line was selected as the target cell line for SERS molecular imaging. As shown in Figure 2, no significant toxicity was observed in either HepG2 or A549 cells incubated with MnPL AuNPs at concentrations of 0.28 fM, 2.8 fM, 28 fM, 0.28 nM, 2.8 nM (1, 10, 100, 1000, 10000 NP/cell, respectively) for 2, 8, and 24 h. The low cytotoxicity of MnPL AuNP was also confirmed on two other cell lines (Supporting Information Figure 3).

We further analyzed the MnPL AuNPs as a SERS imaging probe by incubating MnPL AuNPs with A549 cells for 1 h at 37 °C and subsequently imaging by confocal Raman microscope. The AuNPs were removed and cells were washed repeatedly with PBS and fixed with 4% paraformaldehyde. Confocal Raman microscopy maps was taken with 785 nm excitation with an integration time of 250 ms at each 5 μm step. The pseudocolored image shows the signal intensity corresponding to the peak at 1239 cm^{-1} (Figure 3b). The differential interference contrast (DIC) image (Figure 3a) shows intracellular and extracellular clusters of AuNPs that coincide with regions of peak SERS intensity in the corresponding Raman

dx.doi.org/10.1021/bc300214z | Bioconjugate Chem. 2012, 23, 1726−1730

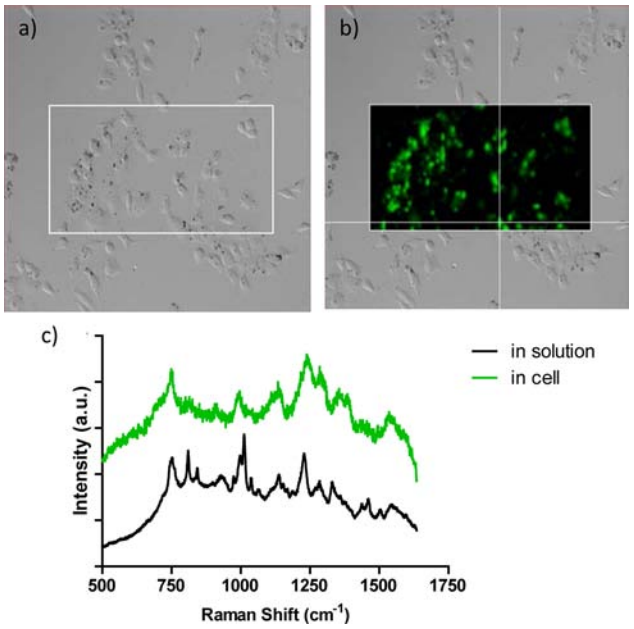


Figure 3. DIC (a) and Raman (b) microscopy images of A549 lung cancer cells showing MnPL AuNP used for cellular imaging. Images were captured using 785 nm laser illumination and displaying the intensity at 1239 cm^{-1}. Point spectrum measurements (c) of MnPL AuNPs in cells (green) at the crosshairs shown in (b) compared with MnPL AuNPs in solution (black) with 785 nm laser at 3 mW integrated for 250 ms.

map (Figure 3b). Although the MnPL AuNPs were incubated for a relatively short time, it is not surprising that they are detected both on the periphery and inside the cells, since A549 cells display active nonspecific endocytosis.[25] Comparing the spectrum between MnPL AuNPs in solution with that spectrum within the cells, there is both an increase in background intensity and a broadening of specific peaks (Figure 3c). The former is likely due to the fixation and mounting reagents used to preserve cell structure for microscopy, which have a weak fluorescence at 785 nm excitation. These additional molecules may also be within the SERS enhancement field, leading to smaller additional peaks and broadening of the existing peaks of the MnPL AuNPs. It cannot be ruled out that the broadening of the Raman peaks may be in part from molecular changes due to aggregation of pH-induced effects from endosomal uptake. Nevertheless, it is clear that, through the combination of porphyrin−lipid on AuNPs to create MnPL AuNPs, porphyrins do function as an effective Raman reporter for SERS imaging.

In summary, we have demonstrated a novel strategy to create SERS probes by combining a phospholipid surface coating with a chromophore. This will expand the selection of dyes that can be used for Raman multiplex detection, since they no longer require specific thiol groups for adsorption to the AuNP surface. In addition, this approach streamlines the synthesis, provides stability, and reduces the variability due to the uncontrollable amount of Raman dye needed to first adsorb to gold nanostructures prior to surface functionalization. To our knowledge, this is the first use of porphyrin as a Raman reporter molecule for SERS based molecular imaging. The use of Mn-based porphyrins not only eliminates the fluorescence background, but also creates unique intrinsic multimodal imaging (optical plus magnetic resonance) and therapeutic capabilities.

In the past decade, there has been increased interest in the clinical use of label-free Raman spectroscopy to delineate cancerous specimens in situ with remarkable specificity and sensitivity,[26,27] while an alternative strategy has been to introduce SERS nanoprobes that target cancer biomarkers as molecular imaging agents to confer diagnostic sensitivity and specificity in vivo. The unique spectral fingerprint of SERS nanoprobes allows for easy differentiation of SERS signal from background noise from the biological sample, as well as multiplexed imaging of multiple SERS contrast agents in vivo. Work done by Nie et al. has shown sensitivity of SERS contrast agents for detecting target cancer cells in mouse whole blood cells (WBC) at levels greater than 10^4:1 WBC to cancer cell.[28] This investigation prompted an institutionally approved clinical trial detecting circulating tumor cells in SCCHN patients. Furthermore, studies conducted by Gambhir et al. have shown the utility of SERS contrast agents to delineate tumor margins from healthy tissue in brain cancer bearing animal models.[29] This has shown the potential of SERS optical contrast agents to aid surgical resection and help reduce the recurrence of cancer resulting from remaining cancer cells. With improvements to the signal strength, biocompatibility, and development of new instrumentation, optical imaging using SERS contrast agents is showing promising and exciting utility for in vivo molecular imaging in the clinical setting.

■ ASSOCIATED CONTENT

Supporting Information

Detailed experimental methods, fluorescence quench of pyro-lipid by Mn chelation, demonstration of the lack of Raman signal from free MnPL at over 1000× concentration of that used in MnPL AuNP, and additional MTT assay results. This material is available free of charge via the Internet at http://pubs.acs.org

■ AUTHOR INFORMATION

Corresponding Author

*Correspondence to Dr. Gang Zheng, 101 College Street, TMDT 5-363, Toronto, Ontario M5G 1L7, Canada. Tel: 416-581-7666; Fax: 416-581-7667; E-mail:gang.zheng@uhnres.utoronto.ca.

Notes

The authors declare no competing financial interest.

■ ACKNOWLEDGMENTS

This work was supported by Natural Science and Engineering Research Council of Canada, Canadian Institute of Cancer Research, Canadian Foundation for Innovation, Princess Margaret Hospital Foundation and the Joey and Toby Tanenbaum/Brazilian Ball Chair in Prostate Cancer Research.

■ REFERENCES

(1) Kneipp, J., Kneipp, H., and Kneipp, K. (2008) SERS - a single-molecule and nanoscale tool for bioanalytics. *Chem. Soc. Rev. 37*, 1052−1060.

(2) Zavaleta, C. L., Smith, B. R., Walton, I., Doering, W., Davis, G., Shojaei, B., Natan, M. J., and Gambhir, S. S. (2009) Multiplexed imaging of surface enhanced Raman scattering nanotags in living mice using noninvasive Raman spectroscopy. *Proc. Natl. Acad. Sci. U. S. A. 106*, 13511−6.

(3) Qian, X., Peng, X. H., Ansari, D. O., Yin-Goen, Q., Chen, G. Z., Shin, D. M., Yang, L., Young, A. N., Wang, M. D., and Nie, S. (2008)

In vivo tumor targeting and spectroscopic detection with surface-enhanced Raman nanoparticle tags. *Nat. Biotechnol. 26*, 83−90.
(4) Thakor, A. S., Luong, R., Paulmurugan, R., Lin, F. I., Kempen, P., Zavaleta, C., Chu, P., Massoud, T. F., Sinclair, R., and Gambhir, S. S. (2011) The fate and toxicity of Raman-active silica-gold nanoparticles in mice. *Sci. Transl. Med. 3*, 79ra33.
(5) Jokerst, J. V., Miao, Z., Zavaleta, C., Cheng, Z., and Gambhir, S. S. (2011) Affibody-functionalized gold-silica nanoparticles for Raman molecular imaging of the epidermal growth factor receptor. *Small 7*, 625−33.
(6) Schlucker, S. (2009) SERS Microscopy: nanoparticle probes and biomedical applications. *ChemPhysChem 10*, 1344−1354.
(7) Flynn, N. T., Tran, T. N. T., Cima, M. J., and Langer, R. (2003) Long-term stability of self-assembled monolayers in biological media. *Langmuir 19*, 10909−10915.
(8) Love, J. C., Estroff, L. A., Kriebel, J. K., Nuzzo, R. G., and Whitesides, G. M. (2005) Self-assembled monolayers of thiolates on metals as a form of nanotechnology. *Chem. Rev. 105*, 1103−69.
(9) Zavaleta, C. L., Hartman, K. B., Miao, Z., James, M. L., Kempen, P., Thakor, A. S., Nielsen, C. H., Sinclair, R., Cheng, Z., and Gambhir, S. S. (2011) Preclinical evaluation of Raman nanoparticle biodistribution for their potential use in clinical endoscopy imaging. *Small 7*, 2232−40.
(10) Tam, N. C., Scott, B. M., Voicu, D., Wilson, B. C., and Zheng, G. (2010) Facile synthesis of Raman active phospholipid gold nanoparticles. *Bioconjugate Chem. 21*, 2178−82.
(11) Faulds, K., Littleford, R. E., Graham, D., Dent, G., and Smith, W. E. (2004) Comparison of surface-enhanced resonance Raman scattering from unaggregated and aggregated nanoparticles. *Anal. Chem. 76*, 592−8.
(12) Cialla, D., Marz, A., Bohme, R., Theil, F., Weber, K., Schmitt, M., and Popp, J. (2012) Surface-enhanced Raman spectroscopy (SERS): progress and trends. *Anal. Bioanal. Chem. 403*, 27−54.
(13) McLaughlin, C., Graham, D., and Smith, W. E. (2002) Comparison of resonant and non resonant conditions on the concentration dependence of surface enhanced Raman scattering from a dye adsorbed on silver colloid. *J. Phys. Chem. B 106*, 5408−5412.
(14) Zhang, M., Zhang, Z., Blessington, D., Li, H., Busch, T. M., Madrak, V., Miles, J., Chance, B., Glickson, J. D., and Zheng, G. (2003) Pyropheophorbide 2-deoxyglucosamide: a new photosensitizer targeting glucose transporters. *Bioconjugate Chem. 14*, 709−14.
(15) Lovell, J. F., Liu, T. W., Chen, J., and Zheng, G. (2010) Activatable photosensitizers for imaging and therapy. *Chem. Rev. 110*, 2839−57.
(16) Lovell, J. F., Jin, C. S., Huynh, E., Jin, H., Kim, C., Rubinstein, J. L., Chan, W. C., Cao, W., Wang, L. V., and Zheng, G. (2011) Porphysome nanovesicles generated by porphyrin bilayers for use as multimodal biophotonic contrast agents. *Nat. Mater. 10*, 324−32.
(17) Lovell, J. F., Jin, C. S., Huynh, E., Macdonald, T. D., Cao, W., and Zheng, G. (2012) Enzymatic regioselection for the synthesis and biodegradation of porphysome nanovesicles. *Angew. Chem., Int. Ed. Engl. 51*, 2429−33.
(18) Murphy, S., Huang, L., and Kamat, P. V. (2011) Charge-transfer complexation and excited-state interactions in porphyrin-silver nanoparticle hybrid structures. *J. Phys. Chem. C 115*, 22761−22769.
(19) Shi, J., Liu, T. W., Chen, J., Green, D., Jaffray, D., Wilson, B. C., Wang, F., and Zheng, G. (2011) Transforming a targeted porphyrin theranostic agent into a PET imaging probe for cancer. *Theranostics 1*, 363−70.
(20) Zhang, X. A., Lovejoy, K. S., Jasanoff, A., and Lippard, S. J. (2007) Water-soluble porphyrins as a dual-function molecular imaging platform for MRI and fluorescence zinc sensing. *Proc. Natl. Acad. Sci. U. S. A. 104*, 10780−5.
(21) Andersson, L. A., Loehr, T. M., Cotton, T. M., Simpson, D. J., and Smith, K. M. (1989) Spectroscopic analysis of chlorophyll model complexes: methyl ester ClFe(III)pheophorbides. *Biochim. Biophys. Acta 974*, 163−79.
(22) Lundqvist, M., Stigler, J., Elia, G., Lynch, I., Cedervall, T., and Dawson, K. A. (2008) Nanoparticle size and surface properties determine the protein corona with possible implications for biological impacts. *Proc. Natl. Acad. Sci. U. S. A. 105*, 14265−70.
(23) Cedervall, T., Lynch, I., Lindman, S., Berggard, T., Thulin, E., Nilsson, H., Dawson, K. A., and Linse, S. (2007) Understanding the nanoparticle-protein corona using methods to quantify exchange rates and affinities of proteins for nanoparticles. *Proc. Natl. Acad. Sci. U. S. A. 104*, 2050−5.
(24) Boisselier, E., and Astruc, D. (2009) Gold nanoparticles in nanomedicine: preparations, imaging, diagnostics, therapies and toxicity. *Chem. Soc. Rev. 38*, 1759−1782.
(25) Stearns, R. C., Paulauskis, J. D., and Godleski, J. J. (2001) Endocytosis of ultrafine particles by A549 cells. *Am. J. Respir. Cell Mol. Biol. 24*, 108−15.
(26) Molckovsky, A., Song, L.-M. W. K., Shim, M. G., Marcon, N. E., and Wilson, B. C. (2003) Diagnostic potential of near-infrared Raman spectroscopy in the colon: Differentiating adenomatous from hyperplastic polyps. *Gastrointestinal Endoscopy 57*, 396−402.
(27) Zavaleta, C. L., Kircher, M. F., and Gambhir, S. S. (2011) Raman's "effect" on molecular imaging. *J. Nucl. Med. 52*, 1839−1844.
(28) Wang, X., Qian, X., Beitler, J. J., Chen, Z. G., Khuri, F. R., Lewis, M. M., Shin, H. J. C., Nie, S., and Shin, D. M. (2011) Detection of circulating tumor cells in human peripheral blood using surface-enhanced Raman scattering nanoparticles. *Cancer Res. 71*, 1526−1532.
(29) Kircher, M. F., de la Zerda, A., Jokerst, J. V., Zavaleta, C. L., Kempen, P. J., Mittra, E., Pitter, K., Huang, R., Campos, C., Habte, F., Sinclair, R., Brennan, C. W., Mellinghoff, I. K., Holland, E. C., and Gambhir, S. S. (2012) A brain tumor molecular imaging strategy using a new triple-modality MRI-photoacoustic-Raman nanoparticle. *Nat. Med. 18*, 829−834.

Bioconjugate Chemistry

Article

pubs.acs.org/bc

Synthesis of Novel Mannoside Glycolipid Conjugates for Inhibition of HIV-1 *Trans*-Infection

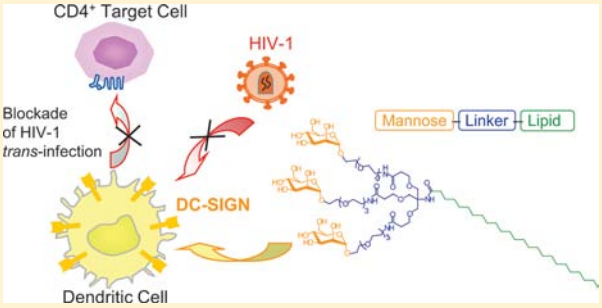
Laure Dehuyser,[†,§] Evelyne Schaeffer,[*,‡,§] Olivier Chaloin,[‡] Christopher G. Mueller,[‡] Rachid Baati,[*,†] and Alain Wagner[†]

[†]Laboratory of Functional Chemo Systems, CNRS-UdS UMR 7199, Faculté de Pharmacie, Université de Strasbourg, 74 route du Rhin, 67400 Illkirch, France

[‡]Laboratory of Immunology and Therapeutic Chemistry, CNRS UPR 9021, Institut de Biologie Moléculaire et Cellulaire, 15 rue René Descartes, 67000 Strasbourg, France

Supporting Information

ABSTRACT: Mannose-binding lectins, such as dendritic cell-specific ICAM-3-grabbing non-integrin (DC-SIGN), are expressed at the surface of human dendritic cells (DCs) that capture and transmit human immunodeficiency virus type-1 (HIV-1) to CD4$^+$ cells. With the goal of reducing viral *trans*-infection by targeting DC-SIGN, we have designed a new class of mannoside glycolipid conjugates. We report the synthesis of amphiphiles composed of a mannose head, a hydrophilic linker essential for solubility in aqueous media, and a lipid chain of variable length. These conjugates presented unusual properties based on a cooperation between the mannoside head and the lipid chain, which enhanced the affinity and decreased the need for multivalency. With an optimal lipid length, they exhibited strong binding affinity for DC-SIGN (K_d in the micromolar range) as assessed by surface plasmon resonance. The most active molecules were branched trimannoside conjugates, able to inhibit the interaction of the HIV-1 envelope with DCs, and to drastically reduce *trans*-infection of HIV-1 mediated by DCs (IC_{50s} in the low micromolar range). This new class of compounds may be of potential use for prevention of HIV-1 dissemination, and also of infection by other DC-SIGN-binding human pathogens.



INTRODUCTION

Since the beginning of the AIDS pandemia in the early 1980s, there are 32 antiretroviral drugs approved for therapy. They target different stages of the human immunodeficiency virus type-1 (HIV-1) life cycle, such as entry, reverse transcription, integration, and maturation.[1] Their drawbacks are virus-induced drug resistance and drug-induced side effects. A complementary approach is now dedicated to the search of inhibitors able to prevent mucosal infection and transmission, since the epidemic disease has been largely maintained by mucosal transmission.[2,3] After crossing the mucosal barrier, HIV-1 infects dendritic cells (DCs), macrophages, and T lymphocytes, residing underneath epithelial layers. DCs are one of the first cell types to be infected by HIV-1, mostly the R5 strain.[4−7] In addition, DCs contribute to early-stage viral dissemination and transmission by their ability to capture, transport virions, and mediate infection of new target cells.[8−10] This so-called *trans*-infection can occur by distinct pathways. The first mechanism implies the DC-specific intercellular adhesion molecule 3 [ICAM-3]-grabbing nonintegrin (DC-SIGN), a C-type lectin highly expressed at the surface of DCs.[11−13] DCs capture HIV-1 through DC-SIGN and transfer them to target CD4$^+$ cells through cell−cell junctions.[10] The vast majority of virions transmitted in *trans* originate from the cell plasma membrane rather than from intracellular vesicles.[14] Other studies found that DCs transmit HIV-1 through a DC-SIGN-independent exocytic pathway that involves HIV-associated exosomes.[15]

DC-SIGN is a type II membrane protein with a short amino-terminal cytoplasmic tail, a neck region, and a single C-terminus carbohydrate recognition domain (CRD). The extracellular CRD is a tetramer stabilized by an α-helical stalk, which specifically recognizes glycosylated proteins, and binds ligands bearing mannose and related sugars. The interaction of this domain with high-mannose structures of glycoproteins is multivalent and calcium-dependent.[16,17] It interacts with envelope glycoproteins from distinct viruses such as HIV-1, Ebola, Hepatitis C, and Dengue,[18−22] but also with mycobacteria,[23] fungi,[24] and parasites.[25] The HIV-1 envelope consists of the gp120 glycoprotein, exposed on the surface of the virion, and the transmembrane protein gp41. The highly glycosylated gp120 interacts with the mannose-binding domain of DC-SIGN at the surface of DCs.[26−28]

Previous studies aimed at preventing HIV transmission by targeting DC-SIGN have reported the synthesis of multivalent carbohydrate-containing molecules. Indeed, monovalent carbohydrates present weak millimolar binding constants for

Received: November 29, 2011
Revised: June 27, 2012
Published: August 7, 2012

 © 2012 American Chemical Society

protein−carbohydrate recognition. It has been well recognized that the multivalent effect improves binding affinities by orders of magnitude. DC-SIGN binds to Man(9)GlcNAc(2) oligosaccharide 130-fold more tightly than mannose.[17] Mannose dendritic polymers were found to interfere with the interaction between DC-SIGN and gp120 proteins.[29,30] Two recent reports have described that multivalent mannoside polymers inhibit HIV transmission mediated by cell lines engineered to express DC-SIGN. First, gold mannoglyco-nanoparticles were shown to inhibit HIV *trans*-infection mediated by Raji-DC-SIGN cells.[31] Second, mannosyl glycodendritic structures, based on second and third generations of Boltorn hyperbranched dendritic polymers functionalized with mannose, inhibited HIV *trans*-infection mediated by THP-1-DC-SIGN cells.[32]

Distinct studies have described that the interaction between C-type lectins and natural lipomannans, a complex of four-domain amphipathic molecules, is influenced by the presence of a lipid moiety. Indeed, the major cell-wall lipoglycans of *Mycobacterium tuberculosis* are high-molecular-weight mannosylated lipoarabinomannans (ManLAM) that strongly interact with DC-SIGN. Their lipid appendages, which are not directly linked to the mannose moieties, are thought to be involved in a supramolecular organization of the molecules by formation of micelles that increase ManLAM avidity for DC-SIGN.[33,34] These data highlight the crucial role of lipids for creating a multivalent mannose presentation via structure formation into dynamic micelles.

Therefore, with the goal of inhibiting HIV-1 *trans*-infection by blocking interactions with DC-SIGN, we decided to investigate the activity of low-molecular-weight mannose-based glycolipids. We designed a novel class of conjugates, formed by three building blocks that combine a polar mannose epitope moiety, a hydrophilic linker essential for water solubility, and a hydrophobic saturated lipid chain of variable length. Here, we describe their synthesis, their chemical and biological characteristics, namely, their affinity for DC-SIGN, their capacity to inhibit the binding of gp120 to DCs, and their ability to reduce HIV-1 *trans*-infection mediated by infected primary human immature DCs. Our findings revealed a branched trimannoside glycolipid conjugate able to drastically limit HIV-1 *trans*-infection.

■ EXPERIMENTAL PROCEDURES

Compounds synthesis and characterization are described in Supporting Information.

Critical Micelle Concentrations (CMC) and Dynamic Light Scattering (DLS). The CMC were measured using pyrene as an extrinsic fluorescent probe, as described.[35] Briefly, a range of glycolipid samples were dissolved in water (1 mL), with concentrations ranging from 1.0 to 0.001 mg/mL. A stock solution of pyrene (1 mM) in dimethyl sulfoxide was added to each sample. Fluorescent emission of pyrene was measured at 25 °C using a Fluorolog spectrofluorometer (Jobin Yvon, Horiba). The intensities of fluorescence emission were determined at 374 nm (I_{374}) and at 383 nm (I_{383}), with an excitation at a 339 nm wavelength. The ratios I_{374}/I_{383} were calculated and plotted against the glycolipid concentration. The CMC value was determined at the intersection of the two straight lines. The hydrodynamic diameters of micelles were measured in water by DLS measurements using a Zetasizer Nano ZS system (Malvern Instruments) as described.[36]

Surface Plasmon Resonance (SPR). SPR experiments were performed using a Biacore 3000. Immobilization of human DC-SIGN (Lys62-Ala404, from R&D Systems) on a CM5 sensor chip (GE-Healthcare, Uppsala, Sweden) was performed by injecting 70 μL of DC-SIGN (50 μg/mL in formate buffer, pH 4.3) onto the surface activated with *N*-ethyl-*N*′-dimethylaminopropyl carbodiimide (EDC)/*N*-hydroxysuccinimide (NHS), which gave a signal of approximately 8000 RU, followed by 20 μL of ethanolamine hydrochloride, pH 8.5, to saturate the free activated sites of the matrix. Biosensor assays were performed with HEPES-buffered-saline (10 mM HEPES, 150 mM sodium chloride, pH 7.4) containing 0.005% surfactant P20 and 5 mM $CaCl_2$, as running buffer. All binding experiments were carried out at 25 °C with a constant flow rate of 20 μL/min. The compounds dissolved in the running buffer (0.39 to 50 μM) were injected for 3 min, followed by a dissociation phase of 3 min. The sensor chip surface was regenerated after each experiment by injecting 10 μL of EDTA 0.5 M pH 8.0. A simple channel activated by EDC/NHS and deactivated with ethanolamine was used as control. The kinetic parameters were calculated using the *BIAeval 4.1* software. Analysis was performed using the simple Langmuir binding model with separate k_a/k_d (k_{on}/k_{off}). The specific binding profiles were obtained after subtracting the response signal from the control channel and from blank-buffer injection. The fitting to each model was judged by the χ^2 value and randomness of residue distribution compared to the theoretical model (Langmuir binding 1:1).

Cell Culture. MAGI-CCR5 cells are HeLa-CD4-LTR-LacZ cells expressing both CXCR4 and CCR5 coreceptors (received from NIH AIDS Research and Reference Program, from Dr. Julie Overbaugh[37]). HEK293T cells were used for HIV-1 production. MCF-7 cells were used for viability tests. All cell lines were cultured at 37 °C and 5% CO_2 in Dulbecco's modified Eagle's medium (DMEM) supplemented with gentamycin and 10% (v/v) heat-inactivated fetal bovine serum (FBS).

Generation of Human Monocyte-Derived Dendritic Cells. Elutriated human monocytes were obtained from the French Blood Bank (Etablissement Français du Sang, Strasbourg, France). To generate monocyte-derived dendritic cells, monocytes were cultured at 37 °C and 5% CO_2 in RPMI 1640 medium supplemented with 10% FBS, gentamycin, 50 ng/mL of recombinant human granulocyte macrophage colony stimulating factor (rhGM-CSF; ImmunoTools), and 10 ng/mL of recombinant human interleukin-4 (rhIL-4; ImmunoTools), with readdition of cytokines at day 3. Cells were harvested on day 5, and specific cell marker expression (CD1a, DC-SIGN) was characterized by flow cytometry on a FACS Calibur flow cytometer (Beckton-Dickinson) and analyzed with the *CellQuest Pro* software (BD Biosciences).

Flow Cytometry. Expression of cell markers (CD1a, DC-SIGN) was determined in FACS buffer (1% fetal bovine serum in PBS) at 4 °C for 20 min, using specific antibodies and their corresponding isotype controls (from BD-Pharmingen): CD1a-allophycocyanin (HI149), CD209/DC-SIGN-PerCP-Cy5.5 (DCN46).

Competition Assays between TriMan$_{C24}$ and HIV-1 gp120. Human DCs (1×10^5 in 100 μL) were aliquoted in a 96-well microtiter plate in RPMI 1640 medium (without FBS). To assess the binding of HIV-1 glycoprotein 120, FITC-conjugated recombinant gp120 HIV-1 IIIB (ImmunoDiagnostics Inc., Woburn, MA, USA) was added to the cells (final

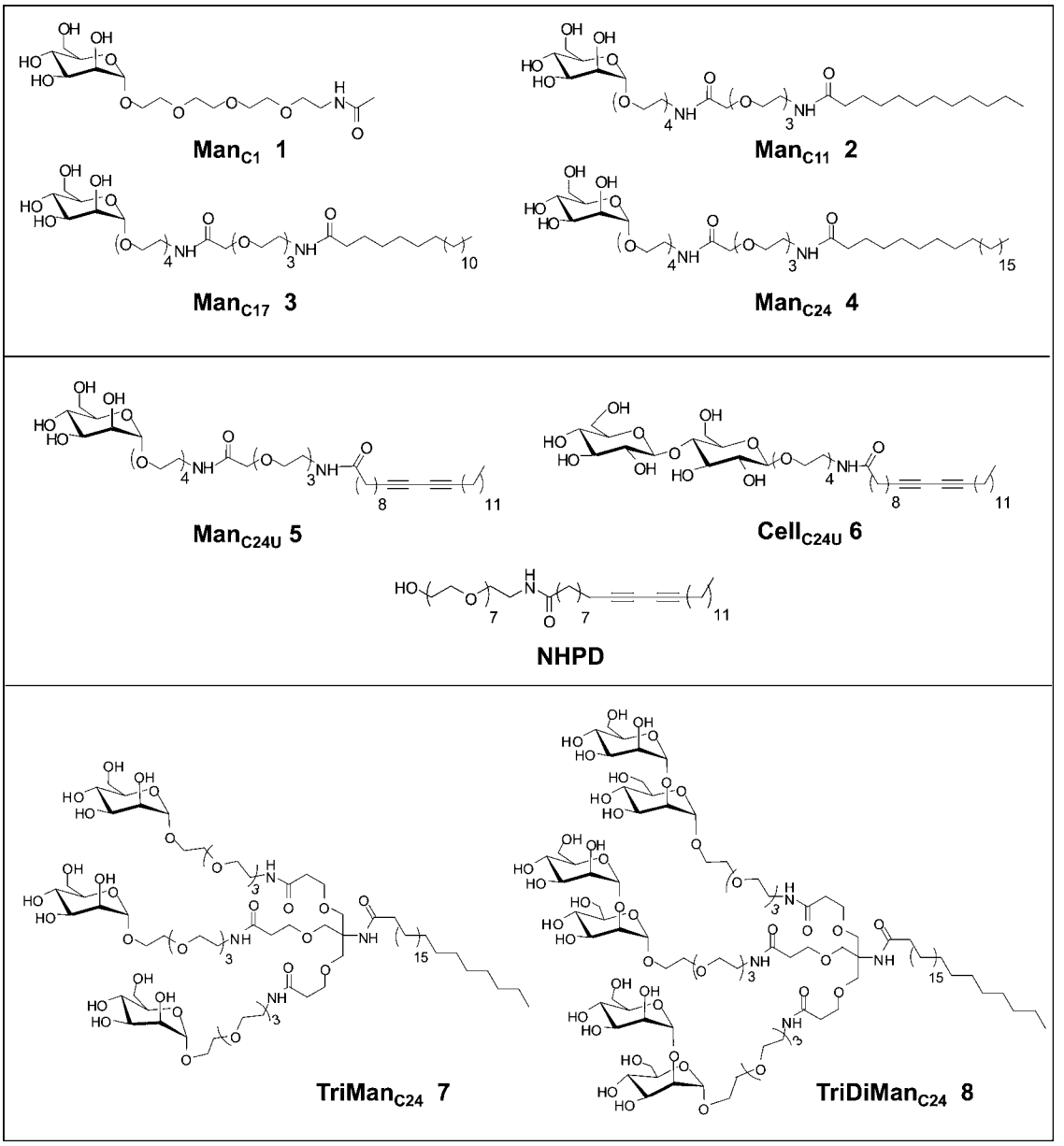


Figure 1. Structure of mannoside glycolipid conjugates **1**−**8**.

concentration of 5 μg/mL) and incubated for 45 min at 37 °C. For competition assays, cells were pretreated with either mannan (100 μg/mL final, corresponding to 620 μM of mannose units) or TriMan (100 μM) for 30 min at 37 °C, followed by incubation with gp120-FITC for 45 min at 37 °C. After washing with HBSS buffer (Lonza), expression of fluorescence intensity was analyzed on a FACS Calibur flow cytometer with the *CellQuest Pro* software.

HIV-1 Production. Molecular clones of HIV-1 NL4−3 (X4 strain) and an NL4−3 R5-tropic version[38] were transfected into HEK293T cells and viruses harvested from the supernatants 48 h later. All transfections were performed using calcium phosphate for precipitation of DNA. Viral stocks were normalized based on their p24 Gag content, measured in an enzyme-linked immunosorbent assay (ELISA) using the Innotest HIV antigen mAb kit (Innogenetics).

HIV-1 *Trans*-Infection. Mannoside glycolipids (1.0 or 0.5 mM stock solution in water) were serially diluted in water. Human DCs (1×10^5 in 200 μL) were pretreated with different concentrations of compounds, mannan (Sigma), or culture medium alone in RPMI 1640 medium containing 10% FBS for 45 min at 37 °C, prior to infection with HIV-1 (100 ng of p24Gag) for 3 h. Excess free virus and molecules were removed by three washes. DCs were then cocultured with MAGI-CCR5 cells (1×10^5) at 37 °C plated in a 48-well plate. After two days, viral infection of MAGI-CCR5 cells was quantitated following β-galactosidase assays and enumerating blue cells by light microscopy. The IC_{50}s were determined by serial dilution of each compound. The *trans*-infection assays were repeated a minimum of three times, and the IC_{50}s determined using *Kaleidagraph*.

RESULTS AND DISCUSSION

Synthesis of Monovalent Glycolipids Conjugates 1−4. Synthesis of the monosaccharide conjugates **1**−**4** (Figure 1) was achieved as depicted in Figure 2A. The linker between the mannose and the lipid chain was introduced for assuring

dx.doi.org/10.1021/bc200644d | *Bioconjugate Chem.* 2012, 23, 1731−1739

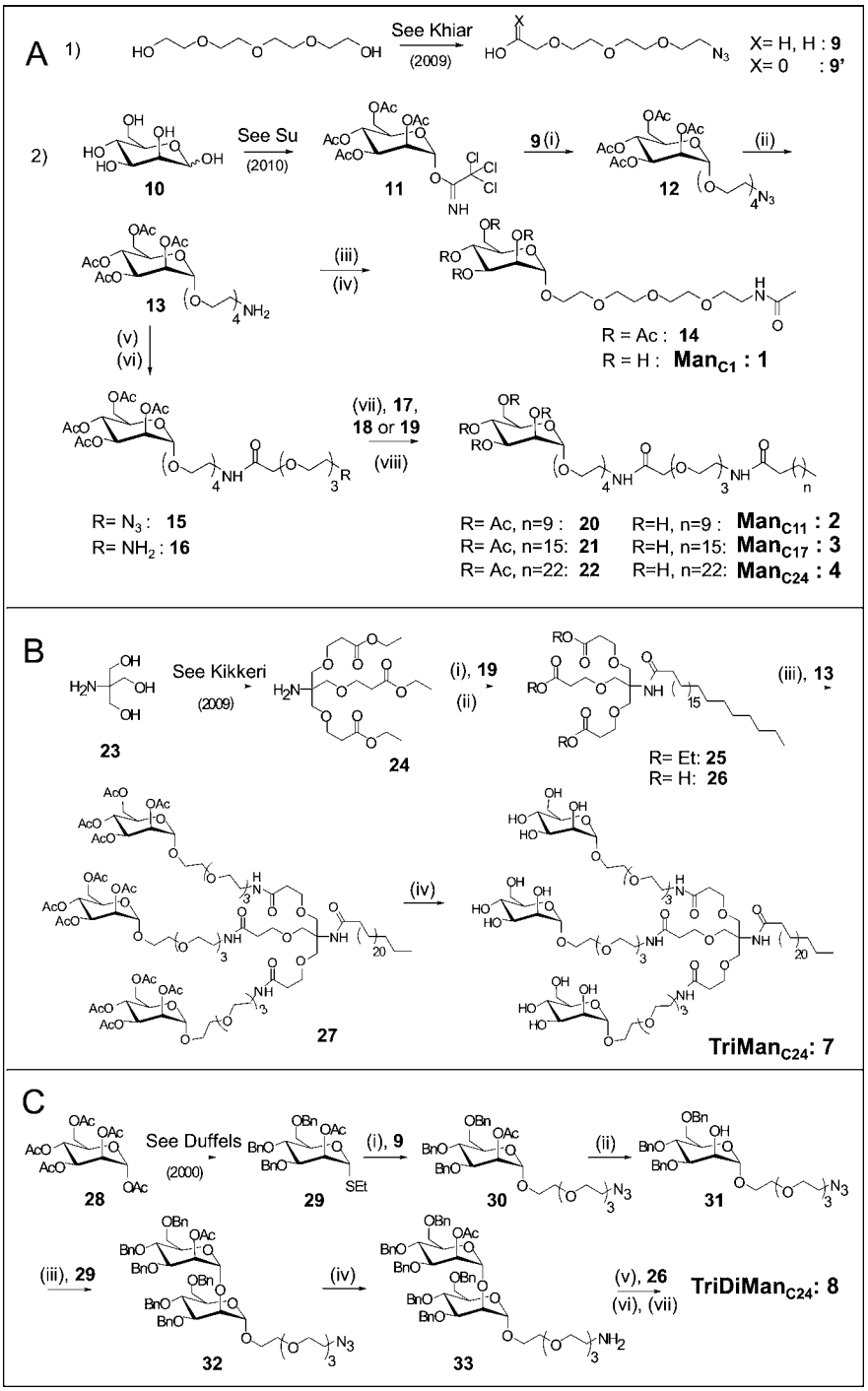


Figure 2. Synthesis of linear and ramified mannoside glycolipids. (A) Synthesis of mannosides **1**–**4**. Conditions: (i) TMSOTf, DCM, 0 °C to RT, overnight, 47%; (ii) PPh_3, THF, H_2O, RT, overnight, 81%; (iii) CH_3COCl, THF, 0 °C to RT, overnight, 25%; (iv) $NaOCH_3$, MeOH, RT, quantitative yield; (v) DCC, HOBT, THF, reflux, overnight, **9′**, (14%); (vi) PPh_3,THF, H_2O, RT, overnight, 49%; (vii) DCC, HOBT, THF, reflux, overnight; lauric acid **17** (98%), stearic acid **18** (78%), pentacosanoic acid **19** (88%); (viii) $NaOCH_3$, MeOH, RT, overnight, quantitative yield. (B) Synthesis of trivalent mannoside **7**. Conditions: (i) Pentacosanoic acid **19**, HOBt, DCC, THF, reflux, overnight, 77%; (ii) NaOH 4 N, THF/EtOH, RT, overnight, 94%; (iii) HOBt, HBTU, DIPEA, THF, reflux, overnight, 63%; (iv) $NaOCH_3$, MeOH, RT, overnight, quantitative yield. (C) Synthesis of trivalent dimannoside **8**. Conditions: (i) **9**, TMSOTf, NIS, MS 4A, DCM, RT, overnight, 76%; (ii) K_2CO_3 (cat), MeOH, RT, overnight, 96%; (iii) **29**, TMSOTf, NIS, MS 4A, DCM/Et_2O, RT, overnight, 58%; (iv) PPh_3, THF, H_2O, RT, overnight, 61%; (v) **26**, HOBt, HBTU, DIPEA, THF, reflux, overnight, 27%; (vi) K_2CO_3 (cat), MeOH, RT, overnight, quantitative yield; (vii) H_2, $Pd(OH)_2/C$, MeOH, RT, overnight, 97%.

solubility of the molecules in physiological media. The key intermediates PEG-azido linker **9′** and the glycosyl donor **11** were prepared from tetraethylene glycol and D-mannose **10**, respectively.[39,40] Briefly, glycosylation of **11** with alcohol **9**[41] followed by the reduction of the azido function of **12**[42] afforded the pivotal amine compound **13**, which upon acetylation conditions and Zemplen final deprotection gave Man_{C1} **1**. Alternatively, amide coupling of **13** with PEG-carboxylic acid **9′** yielded sugar **15**. After reduction of the azide function using Staudinger reduction to afford **16**, the product was engaged in

dx.doi.org/10.1021/bc200644d | *Bioconjugate Chem.* 2012, 23, 1731–1739

amide bond formation with lauric **17**, stearic **18**, or pentacosanoic **19** acids to give, respectively, Man_{C11} (**2**), Man_{C17} (**3**), and Man_{C24} (**4**) in good chemical isolated yields (Supporting Information).

Synthesis of the Multivalent Conjugate $TriMan_{C24}$ 7. Based on previous studies showing that multiple mannose units, such as dendron-formed structures, are necessary for an optimal interaction with DC-SIGN, we synthesized multivalent compounds. To obtain **7** (Figure 2B), the synthesis of the key branched amine connector **24** was achieved.[43] Treatment of **24** with pentacosanoic acid **19** and DCC yielded triester **25**, which was saponified to tricarboxylic acid **26**. Compound **26** was then reacted with sugar **13** under DCC/HOBt conditions to furnish trimannosylated product **27**, which was deprotected to afford $TriMan_{C24}$ **7**.

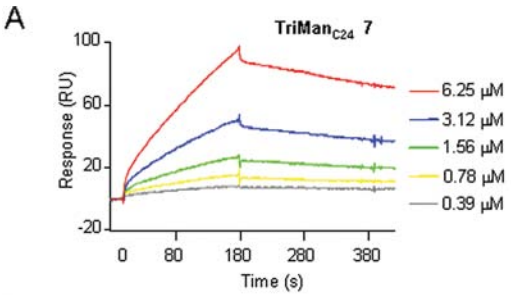
Synthesis of $TriDiMan_{C24}$ 8. To further enhance the multivalent mannose presentation, we produced $TriDiMan_{C24}$ **8** (Figure 2C). The glycosyl donor **29** was first synthesized.[44−46] After glycosylation with alcohol **9** affording **30**, the acetate function at C2 of **30** was selectively removed to yield the C2 free hydroxyl sugar acceptor **31**. Subsequent glycosylation with glycosyl donor **29** gave the expected disaccharide **32**. Selective reduction of the azido group using PPh_3/H_2O in standard conditions led to **33**. Further coupling to the tricarboxylic acid connector **26** afforded the expected fully protected $TriDiMan_{C24}$ molecule. Removal of the acetates and global deprotection of the benzyl groups afforded $TriDiMan_{C24}$ **8**.

Synthesis of Monovalent unsaturated Glycolipids Conjugates 5−6. To examine the importance of a saturated versus an unsaturated chain, we synthesized **Man_{C24U} 5**, containing two triple insaturations, by amide bond formation between intermediate **16** and 10,12-pentacosadiynoic acid. As a control for the role of the sugar head, $Cell_{C24U}$ **6** containing a cellobiose (or glucose−glucose) unit (Figure 1) was synthesized, as described in the Supporting Information.

Properties of Mannoside Glycolipid Conjugates. All conjugates **1**−**8** could be solubilized in water by simple stirring, thanks to the hydrophilic linker. The saturated molecules exhibited no noticeable cytotoxicity on cells, as shown by viability assays on a human cell line and by dead cell staining of human DCs. The unsaturated compounds **5** and **6** were noncytotoxic up to 250 μM (Supporting Information).

Micelles are dynamic systems that can spontaneously self-assemble above the critical micelle concentration (CMC), thus avoiding unnecessary construction steps to afford multivalent systems. Interestingly, when compounds were dissolved in water at 0.5 mg/mL, molecules Man_{C17} **3**, Man_{C24} **4**, and $TriMan_{C24}$ **7** were able to auto-organize in micelles, at a CMC of, respectively, 112, 97, and 109 μM. The hydrodynamic diameter of these micelles was determined by dynamic light scattering and was, respectively, 17, 17, and 39 nm. Unsaturated Man_{C24U} **5** had a lower CMC of 13 μM, and micelles had a hydrodynamic diameter of 11 nm. Molecules Man_{C1} **1**, Man_{C11} **2**, and $TriDiMan_{C24}$ **8** were unable to form micelles.

Affinities for DC-SIGN. Using surface plasmon resonance (SPR), we assessed the ability of our compounds to bind to the carbohydrate recognition domain (CRD) of DC-SIGN. A CM5 sensor chip was functionalized with the DC-SIGN CRD, and increasing concentrations of the various compounds, mannan as a positive control and octa(ethylene glycol) (OEG) as a negative control, were injected over the chip surface. By evaluation of the sensorgrams, we deduced the association (k_{on}) and dissociation (k_{off}) rate constants and the resulting dissociation equilibrium constant ($K_D = k_{off}/k_{on}$) (Figure 3). As expected, mannan efficiently bound to the surface, while



B

Compound	k_{on} ($M^{-1}s^{-1}$)	k_{off} (s^{-1})	K_D (μM)	R_{max} (RU)	Chi²
Man_{C1} **1**	N.b.		N.b.		
Man_{C11} **2**	N.b.		N.b.		
Man_{C17} **3**	Low.b	.	769		
Man_{C24} **4**	273	0.09 10^{-3}	0.32	589	0.228
Man_{C24U} **5**	538	1.38 10^{-3}	2.57	54	0.205
$Cell_{C24U}$ **6**	N.b.	N.b.	N.b.		
$TriMan_{C24}$ **7**	295	0.94 10^{-3}	3.19	305	0.331
$TriDiMan_{C24}$ **8**	369	1.20 10^{-3}	3.25	210	14.1

Figure 3. Direct binding by surface plasmon resonance (SPR) of mannoside glycolipid conjugates to DC-SIGN immobilized on a CM5 sensor chip. (A) Sensorgram of the binding of **7** to DC-SIGN (CRD) immobilized via amino groups. The binding response (in RU) was recorded as a function of time. (B) Kinetic parameters of interactions. k_{on}, kinetic association rate; k_{off}, kinetic dissociation rate; K_D, equilibrium dissociation constant; R_{max} (RU), maximal response expressed as resonance units; χ^2, chi square value. 1:1 Langmuir binding model was used for all compounds, except for compound **3**, for which steady-state affinity was used for calculation. With the control compound NHPD lacking mannose, no binding was detected at 100 μM. "N.b.": No binding until 50 μM.

OEG was unable to bind. We found that Man_{C1} **1** and Man_{C11} **2** were unable to bind, Man_{C17} **3** bound with a low affinity, while Man_{C24} **4** exhibited an optimal affinity in the submicromolar range. These data showed that the affinity of the linear molecules for DC-SIGN correlated with the length of the lipid chain, suggesting that the lipid moiety of the molecule—at an optimal size of 24 carbon atoms—enhanced the binding capacity of the mannose polar head in a cooperative manner.

One mannose unit in Man_{C24} **4** was sufficient for an effective interaction, with a K_D in the submicromolar range. $TriMan_{C24}$ **7** and $TriDiMan_{C24}$ **8** also efficiently bound to DC-SIGN, with the K_D in the low micromolar range, although they presented no improvement over Man_{C24} **4**. Similarly, Man_{C24U} **5** containing an unsaturated lipid chain exhibited a K_D in the low micromolar range, showing that these unsaturations did not improve the binding relative to a saturated chain. When the mannose head was replaced by a glucose unit (cellobiose), the binding was lost, which clearly revealed the importance of the mannose head. Similarly, when the sugar head was lacking, in NHPD composed of a linker conjugated to a 24-carbon lipid chain (see Figure 1), no binding was detected, which allowed us to rule out nonspecific binding. These results stressed the

dx.doi.org/10.1021/bc200644d | *Bioconjugate Chem.* 2012, 23, 1731−1739

importance of the mannose head, as well as of the 24-carbon saturated or unsaturated lipid chain.

Altogether, these data demonstrated that glycolipid conjugates, formed by a C24-lipid chain covalently linked to one, three, or six mannose units, bind to the CRD of DC-SIGN with a good affinity.

It is worth noting that Man_{C24} **4**, Man_{C24U} **5**, $TriMan_{C24}$ **7**, and $TriDiMan_{C24}$ **8** interacted with DC-SIGN at concentrations below their CMC; the binding was effective below 10 μM, as visualized on the sensorgram Figure 3A. Thus, although molecules **4**, **5**, and **7** are able to form micelles, while **8** is unable to form micelles, they could all bind to DC-SIGN as single molecules, and micelle formation was not required. This contrasts with mycobacterial mannosylated lipoarabinomannans (ManLAM), in which terminal mannose residues and the lipid moiety are critical for binding to the pulmonary surfactant protein A (SP-A). In this case, lipids are required for an aggregate/micellar organization of the lipoglycan, since interaction with SP-A is lost in the presence of a low concentration of mild detergent (0.0005% of Polysorbate 20).[47] In similar detergent conditions, binding of our $mannosylated_{C24}$ lipids to DC-SIGN was conserved, confirming that a process of supra-macromolecular structure formation is not required for binding to DC-SIGN.

Binding Competition with HIV-1 gp120. We examined the ability of our compounds to inhibit the interaction of HIV-1 gp120 with DC-SIGN expressed at the surface of DCs. Immature DCs were prepared by differentiation of human monocytes. The expression levels of DC-SIGN were controlled by flow cytometry. As expected, results showed a high level of expression on DCs but no expression on monocytes, as indicated by the mean fluorescence index (MFI) (Figure 4A). When cells were incubated with fluorescently labeled gp120, we observed a strong fluorescence for DCs but not for monocytes, demonstrating more gp120 binding to DCs (Figure 4B). Some binding to monocytes was observed, likely owing to interaction with other cell surface proteins.[48]

We then performed competition assays by preincubating DCs with either compound $TriMan_{C24}$ **7** or mannan followed by addition of fluorescently labeled gp120 (Figure 4C). Flow cytometry showed that **7** was able to compete with gp120-FITC for the binding to DCs. Although inhibition was not complete, 100 μM of $TriMan_{C24}$ **7** interfered better than mannan (620 μM of mannose units) with the binding of gp120 to DCs.

Inhibition of HIV-1 *trans*-Infection Mediated by DCs. To investigate the ability of our compounds to inhibit HIV-1 *trans*-infection, we chose to infect DCs to best mimic *in vivo* conditions of viral capture by mucosal DCs. The DCs were mixed with the different compounds for 45 min at 37 °C, before exposure to HIV-1. After a 3 h incubation, the cells were extensively washed to remove unbound virions and mannosides and then cocultured with MAGI-CCR5 cells. This procedure allows precise quantification of HIV-1 replication in reporter MAGI-CCR5 cells by detection of β-galactosidase activity, since these cells express an integrated copy of the HIV long terminal repeat (LTR) fused to the β-galactosidase reporter gene. MAGI-CCR5 express the CD4 receptor and CCR5 and CXCR4 coreceptors, required for entry of, respectively, HIV-1 R5 and X4.

We first exposed DCs to the HIV-1 R5 strain, mostly involved in mucosal infections,[7,49,50] in the presence of the linear glycolipids **1**–**6** (Figure 5A). While Man_{C1} **1** and Man_{C11} **2** did not present better inhibitory activity than mannan, Man_{C17} **3**, Man_{C24} **4**, and Man_{C24U} **5** clearly reduced *trans*-infection in a dose-dependent manner, more efficiently than mannan (0.6 and 1.5 mM of mannose units). This inhibition was in the high micromolar range with an IC_{50} of 120 μM. Interestingly, $Cell_{C24U}$ **6** was unable to affect *trans*-infection, which showed the importance of the mannose head in the inhibition process. Dose–response experiments were then performed to compare the inhibitory capacity of the linear Man_{C24} **4** and branched $TriMan_{C24}$ **7** and $TriDiMan_{C24}$ **8**. When compared with Man_{C24} **4**, $TriMan_{C24}$ **7** displayed a more potent inhibitory activity in the submicromolar range (IC_{50} of 0.5 μM). At the highest concentrations, *trans*-infection was drastically reduced, down to a residual level of 20% (Figure 5B). $TriDiMan_{C24}$ **8** exhibited a powerful inhibitory activity in the nanomolar range (IC_{50} of 38 nM), although, surprisingly, infection leveled off at 40% (Figure 5C). The residual level of *trans*-infection may be explained by the previously reported distinct mechanisms of viral transmission, besides the transfer mediated by DC-SIGN.

We further examined the effect of $TriMan_{C24}$ **7** on the HIV-1 X4 strain (Figure 5D). Similar to the effect on the R5 strain, it also inhibited HIV-1 X4 *trans*-infection down to a residual level of 15%, although with a higher IC_{50} (7 μM). These findings demonstrate that $TriMan_{C24}$ **7** is an active mannoside glycolipid

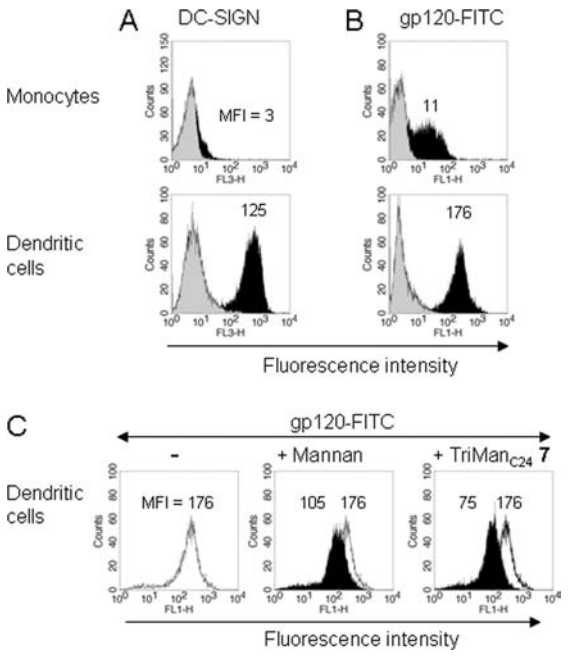


Figure 4. $TriMan_{C24}$ **7** competes with HIV gp120 binding to dendritic cells (DCs). (A) Cell surface expression of DC-SIGN on DCs and monocytes, analyzed by flow cytometry. Filled and gray histograms represent, respectively, antigen labeling and isotype controls. Values of mean fluorescence intensity (MFI) for antigen labeling are indicated. (B) Interaction of gp120-FITC with monocytes and DCs, after incubation for 45 min at 37 °C (filled histograms). Gray histograms represent untreated cells, in the presence of IgG1-FITC control. (C) DCs were exposed to $TriMan_{C24}$ **7** (100 μM) or mannan (100 mg/mL or 620 mM of mannose units) for 30 min or left untreated, followed by incubation with gp120-FITC for 45 min at 37 °C. Flow cytometry open and filled histograms correspond to cells binding gp120-FITC, respectively, in the absence and presence of pretreatment. Results are from one representative experiment repeated three times.

dx.doi.org/10.1021/bc200644d | *Bioconjugate Chem.* 2012, 23, 1731–1739

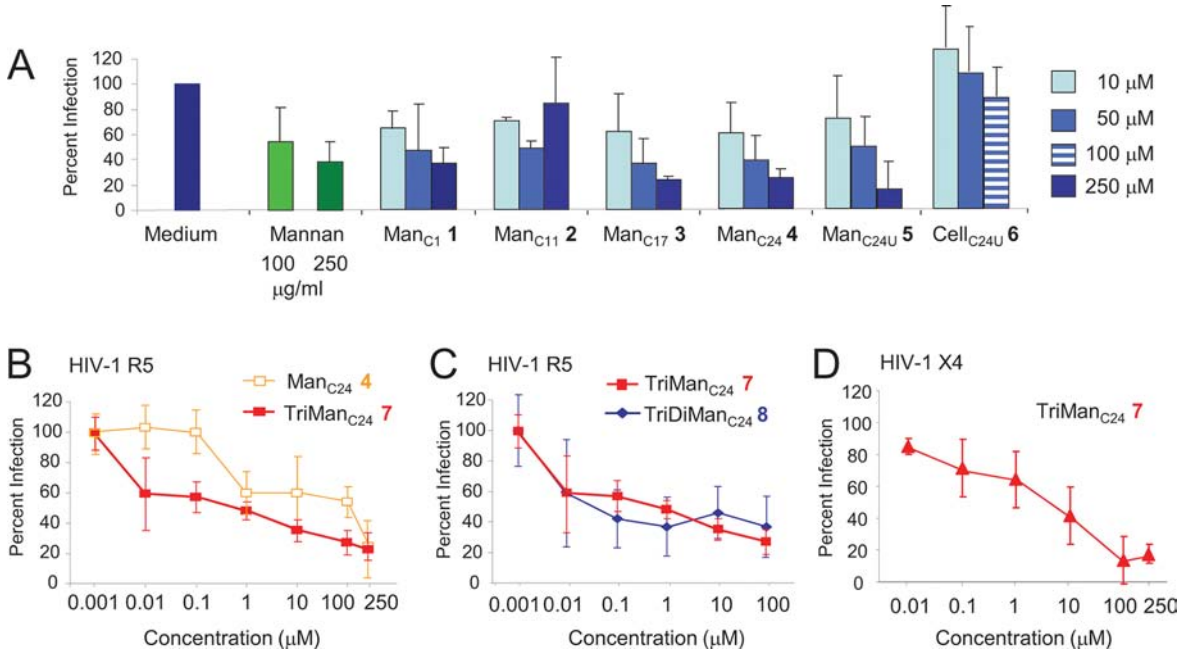


Figure 5. Inhibition of HIV-1 *trans*-infection by glycolipid conjugates. DCs were pretreated with the indicated compounds for 30 min at 37 °C, and then infected with HIV-1. After extensive washes, DCs were cocultured with MAGI-CCR5 cells for 2 days. Viral *trans*-infection was quantified. Values were normalized relative to 100% infection obtained with medium alone. Values are means ± SE from data obtained at least from three independent experiments. (A) Effect of the length of the carbon chain and of the sugar (either mannose or glucose). Mannan was included as a positive control. (B) Dose−response results for HIV-1 R5 exposed to mono- and trimannosides. (C) HIV-1 R5 exposed to tri- and tri-bis-mannosides. (D) HIV-1 X4 exposed to TriMan$_{C24}$ 7.

conjugate to reduce *trans*-infection of HIV-1 R5 and X4 mediated by DCs.

CONCLUSIONS

Our studies revealed the unexpected properties of a new class of glycolipid conjugates. These compounds are formed by three building blocks—a mannose head, a linker, and a C24 lipid chain—and are able to efficiently target DC-SIGN. Surprisingly, our data showed that a scaffold offering a multivalent mannose presentation, to mimic the high mannose structure occurring in glycoproteins, was not required for obtaining high binding affinity for DC-SIGN. Our SPR results demonstrated that the affinity of the mannose moiety for the extracellular domain of DC-SIGN could be greatly increased by coupling the mannose unit to a lipid chain of at least 17 carbons.

The activities of these conjugates—their affinity for DC-SIGN, their ability to compete for gp120 binding, and their inhibition of HIV-1 *trans*-infection—are based on the cooperation between the lipid chain and the linked mannose moiety. The lipid chain was originally synthesized for molecular structure formation into self-organized micelles, and thus afford a multivalent mannose presentation. Interestingly, we discovered that such a structure formation was not required, neither for binding to DC-SIGN nor for inhibiting HIV *trans*-infection, as revealed by Man$_{C24}$ **4**. Indeed, TriMan$_{C24}$ **7** and TriDiMan$_{C24}$ **8** inhibited viral *trans*-infection at an IC$_{50}$ of, respectively, 500 and 38 nM, well below their CMC, showing that they possess the property of being active not only as micelles, but also as individual molecules. It is likely that, in addition to the interaction of the mannose unit with the CRD, the lipid chain interacts with distinct amino acids of DC-SIGN, thus optimizing the binding. It could also be that the lipid chains of two molecules make hydrophobic interactions with each other while bound to the same or adjacent DC-SIGN molecules simulating a bivalent ligand that bridges binding sites. Such a chelating binding has been shown before to strongly increase binding affinity.[51,52] The precise role of the lipid chain in the molecular interactions between the compounds and DC-SIGN remains the subject of further studies. Our findings reveal that, thanks to this original cooperation, such conjugates are able to target DC-SIGN and inhibit HIV-1 *trans*-infection without the need for synthesis of previously reported complex mannosides structures.[31,32] Nevertheless, it is clear that the multivalent presentation of 6 and 3 mannoses helped improve the *trans*-infection ability.

The most likely hypothesis accounting for inhibition of HIV-1 *trans*-infection relies on the shield model: interaction of the compounds with DC-SIGN at the DC cell membrane prevents the attachment of HIV-1 to this receptor. In addition, partial down-regulation of DC-SIGN from the cell surface may also enhance the protective effect. One could also hypothesize a direct effect of the compounds on the virus particle. The molecule may disrupt the viral membrane by insertion of its lipid moiety, or interact via its mannose units with gp120 at the surface of the virus. Clearly, further studies are needed to shed more light on the precise inhibitory mechanism. Finally, the interest of this novel class of inhibitory molecules also lies in their potential ability to target other viruses and pathogens that use DC-SIGN or other C-type lectins for entry and infection.[18−25]

ASSOCIATED CONTENT

Supporting Information

Full synthetic and characterization details of the compounds including NMR spectra, and cell viability assays are provided.

dx.doi.org/10.1021/bc200644d | *Bioconjugate Chem.* 2012, 23, 1731−1739

This material is available free of charge via the Internet at http://pubs.acs.org.

AUTHOR INFORMATION

Corresponding Author

*E-mail: e.schaeffer@ibmc-cnrs.unistra.fr (E.S.); baati@bioorga.u-strasbg.fr (R.B.).

Author Contributions

[§]These authors contributed equally to this work.

Funding

This work was supported by the "Centre National de la Recherche Scientifique" (CNRS). The University of Strasbourg is acknowledged for a research grant to L.D.

Notes

The authors declare no competing financial interest.

ACKNOWLEDGMENTS

We are grateful to P. Pévet and S. Reibel-Foisset for the use of the A3/L3 platform of the Institut Fédératif de Recherches (IFR37), Strasbourg. We thank the AIDS Research and Reference Reagent Program, Division of AIDS, NIAID, NIH, for MAGI-CCR5 cells.

ABBREVIATIONS

DC-SIGN, dendritic cell-specific ICAM-3-grabbing nonintegrin; DCs, dendritic cells; HIV-1, human immunodeficiency virus type-1; CRD, carbohydrate recognition domain; CMC, critical micelle concentration; SPR, surface plasmon resonance

REFERENCES

(1) Flexner, C. (2007) HIV drug development: the next 25 years. *Nat. Rev. Drug Discovery 6*, 959−966.

(2) Hladik, F., and McElrath, M. J. (2008) Setting the stage: host invasion by HIV. *Nat. Rev. Immunol. 8*, 447−457.

(3) Haase, A. T. (2010) Targeting early infection to prevent HIV-1 mucosal transmission. *Nature 464*, 217−223.

(4) Hu, J., Gardner, M. B., and Miller, C. J. (2000) Simian immunodeficiency virus rapidly penetrates the cervicovaginal mucosa after intravaginal inoculation and infects intraepithelial dendritic cells. *J. Virol. 74*, 6087−6095.

(5) Gurney, K. B., Elliott, J., Nassanian, H., Song, C., Soilleux, E., McGowan, I., Anton, P. A., and Lee, B. (2005) Binding and transfer of human immunodeficiency virus by DC-SIGN+ cells in human rectal mucosa. *J. Virol. 79*, 5762−5773.

(6) Wilkinson, J., and Cunningham, A. L. (2006) Mucosal transmission of HIV-1: first stop dendritic cells. *Curr. Drug Targets 7*, 1563−1569.

(7) Yamamoto, T., Tsunetsugu-Yokota, Y., Mitsuki, Y. Y., Mizukoshi, F., Tsuchiya, T., Terahara, K., Inagaki, Y., Yamamoto, N., Kobayashi, K., and Inoue, J. (2009) Selective transmission of R5 HIV-1 over X4 HIV-1 at the dendritic cell-T cell infectious synapse is determined by the T cell activation state. *PLoS Pathog. 5*, e1000279.

(8) Geijtenbeek, T. B., Kwon, D. S., Torensma, R., van Vliet, S. J., van Duijnhoven, G. C., Middel, J., Cornelissen, I. L., Nottet, H. S., KewalRamani, V. N., Littman, D. R., Figdor, C. G., and van Kooyk, Y. (2000) DC-SIGN, a dendritic cell-specific HIV-1-binding protein that enhances trans-infection of T cells. *Cell 100*, 587−597.

(9) Piguet, V., and Steinman, R. M. (2007) The interaction of HIV with dendritic cells: outcomes and pathways. *Trends Immunol. 28*, 503−510.

(10) Wu, L., and KewalRamani, V. N. (2006) Dendritic-cell interactions with HIV: infection and viral dissemination. *Nat. Rev. Immunol. 6*, 859−868.

(11) Geijtenbeek, T. B., and van Kooyk, Y. (2003) DC-SIGN: a novel HIV receptor on DCs that mediates HIV-1 transmission. *Curr. Top. Microbiol. Immunol. 276*, 31−54.

(12) Arrighi, J. F., Pion, M., Wiznerowicz, M., Geijtenbeek, T. B., Garcia, E., Abraham, S., Leuba, F., Dutoit, V., Ducrey-Rundquist, O., van Kooyk, Y., Trono, D., and Piguet, V. (2004) Lentivirus-mediated RNA interference of DC-SIGN expression inhibits human immunodeficiency virus transmission from dendritic cells to T cells. *J. Virol. 78*, 10848−10855.

(13) Chung, N. P., Breun, S. K., Bashirova, A., Baumann, J. G., Martin, T. D., Karamchandani, J. M., Rausch, J. W., Le Grice, S. F., Wu, L., Carrington, M., and Kewalramani, V. N. (2010) HIV-1 transmission by dendritic cell-specific ICAM-3-grabbing nonintegrin (DC-SIGN) is regulated by determinants in the carbohydrate recognition domain that are absent in liver/lymph node-SIGN (L-SIGN). *J. Biol. Chem. 285*, 2100−2112.

(14) Cavrois, M., Neidleman, J., Kreisberg, J. F., and Greene, W. C. (2007) In vitro derived dendritic cells trans-infect CD4 T cells primarily with surface-bound HIV-1 virions. *PLoS Pathog. 3*, e4.

(15) Wiley, R. D., and Gummuluru, S. (2006) Immature dendritic cell-derived exosomes can mediate HIV-1 trans infection. *Proc. Natl. Acad. Sci. U.S.A. 103*, 738−743.

(16) Feinberg, H., Mitchell, D. A., Drickamer, K., and Weis, W. I. (2001) Structural basis for selective recognition of oligosaccharides by DC-SIGN and DC-SIGNR. *Science 294*, 2163−2166.

(17) Mitchell, D. A., Fadden, A. J., and Drickamer, K. (2001) A novel mechanism of carbohydrate recognition by the C-type lectins DC-SIGN and DC-SIGNR. Subunit organization and binding to multivalent ligands. *J. Biol. Chem. 276*, 28939−28945.

(18) Alvarez, C. P., Lasala, F., Carrillo, J., Muniz, O., Corbi, A. L., and Delgado, R. (2002) C-type lectins DC-SIGN and L-SIGN mediate cellular entry by Ebola virus in cis and in trans. *J. Virol. 76*, 6841−6844.

(19) Geijtenbeek, T. B., and van Kooyk, Y. (2003) Pathogens target DC-SIGN to influence their fate DC-SIGN functions as a pathogen receptor with broad specificity. *APMIS 111*, 698−714.

(20) Tassaneetrithep, B., Burgess, T. H., Granelli-Piperno, A., Trumpfheller, C., Finke, J., Sun, W., Eller, M. A., Pattanapanyasat, K., Sarasombath, S., Birx, D. L., Steinman, R. M., Schlesinger, S., and Marovich, M. A. (2003) DC-SIGN (CD209) mediates dengue virus infection of human dendritic cells. *J. Exp. Med. 197*, 823−829.

(21) Wang, Q. C., Feng, Z. H., Nie, Q. H., and Zhou, Y. X. (2004) DC-SIGN: binding receptors for hepatitis C virus. *Chin. Med. J. (Engl.) 117*, 1395−1400.

(22) Ludwig, I. S., Lekkerkerker, A. N., Depla, E., Bosman, F., Musters, R. J., Depraetere, S., van Kooyk, Y., and Geijtenbeek, T. B. (2004) Hepatitis C virus targets DC-SIGN and L-SIGN to escape lysosomal degradation. *J. Virol. 78*, 8322−8332.

(23) Geijtenbeek, T. B., Van Vliet, S. J., Koppel, E. A., Sanchez-Hernandez, M., Vandenbroucke-Grauls, C. M., Appelmelk, B., and Van Kooyk, Y. (2003) Mycobacteria target DC-SIGN to suppress dendritic cell function. *J. Exp. Med. 197*, 7−17.

(24) Cambi, A., Gijzen, K., de Vries, J. M., Torensma, R., Joosten, B., Adema, G. J., Netea, M. G., Kullberg, B. J., Romani, L., and Figdor, C. G. (2003) The C-type lectin DC-SIGN (CD209) is an antigen-uptake receptor for Candida albicans on dendritic cells. *Eur. J. Immunol. 33*, 532−538.

(25) Colmenares, M., Puig-Kroger, A., Pello, O. M., Corbi, A. L., and Rivas, L. (2002) Dendritic cell (DC)-specific intercellular adhesion molecule 3 (ICAM-3)-grabbing nonintegrin (DC-SIGN, CD209), a C-type surface lectin in human DCs, is a receptor for Leishmania amastigotes. *J. Biol. Chem. 277*, 36766−36769.

(26) Hong, P. W., Flummerfelt, K. B., de Parseval, A., Gurney, K., Elder, J. H., and Lee, B. (2002) Human immunodeficiency virus envelope (gp120) binding to DC-SIGN and primary dendritic cells is carbohydrate dependent but does not involve 2G12 or cyanovirin binding sites: implications for structural analyses of gp120-DC-SIGN binding. *J. Virol. 76*, 12855−12865.

(27) Su, S. V., Gurney, K. B., and Lee, B. (2003) Sugar and spice: viral envelope-DC-SIGN interactions in HIV pathogenesis. *Curr. HIV Res. 1*, 87−99.
(28) Feinberg, H., Castelli, R., Drickamer, K., Seeberger, P. H., and Weis, W. I. (2007) Multiple modes of binding enhance the affinity of DC-SIGN for high mannose N-linked glycans found on viral glycoproteins. *J. Biol. Chem. 282*, 4202−4209.
(29) Tabarani, G., Reina, J. J., Ebel, C., Vives, C., Lortat-Jacob, H., Rojo, J., and Fieschi, F. (2006) Mannose hyperbranched dendritic polymers interact with clustered organization of DC-SIGN and inhibit gp120 binding. *FEBS Lett. 580*, 2402−2408.
(30) Wang, S. K., Liang, P. H., Astronomo, R. D., Hsu, T. L., Hsieh, S. L., Burton, D. R., and Wong, C. H. (2008) Targeting the carbohydrates on HIV-1: Interaction of oligomannose dendrons with human monoclonal antibody 2G12 and DC-SIGN. *Proc. Natl. Acad. Sci. U.S.A. 105*, 3690−3695.
(31) Martinez-Avila, O., Hijazi, K., Marradi, M., Clavel, C., Campion, C., Kelly, C., and Penades, S. (2009) Gold manno-glyconanoparticles: multivalent systems to block HIV-1 gp120 binding to the lectin DC-SIGN. *Chem.—Eur. J. 15*, 9874−9888.
(32) Sattin, S., Daghetti, A., Thepaut, M., Berzi, A., Sanchez-Navarro, M., Tabarani, G., Rojo, J., Fieschi, F., Clerici, M., and Bernardi, A. (2010) Inhibition of DC-SIGN-mediated HIV infection by a linear trimannoside mimic in a tetravalent presentation. *ACS Chem. Biol. 5*, 301−312.
(33) Maeda, N., Nigou, J., Herrmann, J. L., Jackson, M., Amara, A., Lagrange, P. H., Puzo, G., Gicquel, B., and Neyrolles, O. (2003) The cell surface receptor DC-SIGN discriminates between Mycobacterium species through selective recognition of the mannose caps on lipoarabinomannan. *J. Biol. Chem. 278*, 5513−5516.
(34) Riviere, M., Moisand, A., Lopez, A., and Puzo, G. (2004) Highly ordered supra-molecular organization of the mycobacterial lipo-arabinomannans in solution. Evidence of a relationship between supra-molecular organization and biological activity. *J. Mol. Biol. 344*, 907−918.
(35) Perino, A., Klymchenko, A., Morere, A., Contal, E., Rameau, A., Guenet, J.-M., Mély, Y., and Wagner, A. (2011) Structure and behaviour of polydiacetylene-based micelles. *Macromol. Chem. Phys. 212*, 111−117.
(36) Morin, E., Nothisen, M., Wagner, A., and Remy, J.-S. (2011) Cationic polydiacetylene micelles for gene delivery. *Bioconjugate Chem. 22*, 1916−1923.
(37) Chackerian, B., Long, E. M., Luciw, P. A., and Overbaugh, J. (1997) Human immunodeficiency virus type 1 coreceptors participate in postentry stages in the virus replication cycle and function in simian immunodeficiency virus infection. *J. Virol. 71*, 3932−3939.
(38) Schaeffer, E., Soros, V. B., and Greene, W. C. (2004) Compensatory link between fusion and endocytosis of human immunodeficiency virus type 1 in human CD4 T lymphocytes. *J. Virol. 78*, 1375−1383.
(39) Khiar, N., Leal, M. P., Baati, R., Ruhlmann, C., Mioskowski, C., Schultz, P., and Fernandez, I. (2009) Tailoring carbon nanotube surfaces with glyconanorings: new bionanomaterials with specific lectin affinity. *Chem. Commun. 27*, 4121−4123.
(40) Su, Y., Xie, J., Wang, Y., Hu, X., and Lin, X. (2010) Synthesis and antitumor activity of new shikonin glycosides. *Eur. J. Med. Chem. 45*, 2713−2718.
(41) Tietze, L. F., Schmuck, K., Schuster, H. J., Muller, M., and Schuberth, I. (2011) Synthesis and biological evaluation of prodrugs based on the natural antibiotic duocarmycin for use in ADEPT and PMT. *Chem.—Eur. J. 17*, 1922−1929.
(42) Hatch, D. M., Weiss, A. A., Kale, R. R., and Iyer, S. S. (2008) Biotinylated bi- and tetra-antennary glycoconjugates for Escherichia coli detection. *ChemBioChem 9*, 2433−2442.
(43) Kikkeri, R., Garcia-Rubio, I., and Seeberger, P. H. (2009) Ru(II)-carbohydrate dendrimers as photoinduced electron transfer lectin biosensors. *Chem. Commun. 2*, 235−237.
(44) Floyd, N., Vijayakrishnan, B., Koeppe, J. R., and Davis, B. G. (2009) Thiyl glycosylation of olefinic proteins: S-linked glycoconjugate synthesis. *Angew. Chem. 48*, 7798−7802.
(45) Xue, J., Shao, N., and Guo, Z. (2003) First total synthesis of a GPI-anchored peptide. *J. Org. Chem. 68*, 4020−4029.
(46) Duffels, A., Green, L. G., Ley, S. V., and Miller, A. D. (2000) Synthesis of high-mannose type neoglycolipids: active targeting of liposomes to macrophages in gene therapy. *Chem.—Eur. J. 6*, 1416−1430.
(47) Sidobre, S., Puzo, G., and Riviere, M. (2002) Lipid-restricted recognition of mycobacterial lipoglycans by human pulmonary surfactant protein A: a surface-plasmon-resonance study. *Biochem. J. 365*, 89−97.
(48) Vives, R. R., Imberty, A., Sattentau, Q. J., and Lortat-Jacob, H. (2005) Heparan sulfate targets the HIV-1 envelope glycoprotein gp120 coreceptor binding site. *J. Biol. Chem. 280*, 21353−21357.
(49) David, S. A., Smith, M. S., Lopez, G. J., Adany, I., Mukherjee, S., Buch, S., Goodenow, M. M., and Narayan, O. (2001) Selective transmission of R5-tropic HIV type 1 from dendritic cells to resting CD4+ T cells. *AIDS Res. Hum. Retroviruses 17*, 59−68.
(50) Grivel, J. C., Shattock, R. J., and Margolis, L. B. (2011) Selective transmission of R5 HIV-1 variants: where is the gatekeeper? *J. Transl. Med. 9* (Suppl 1), S6.
(51) Kitov, P. I., Sadowska, J. M., Mulvey, G., Armstrong, G. D., Ling, H., Pannu, N. S., Read, R. J., and Bundle, D. R. (2000) Shiga-like toxins are neutralized by tailored multivalent carbohydrate ligands. *Nature 403*, 669−672.
(52) Schwefel, D., Maierhofer, C., Beck, J. G., Seeberger, S., Diederichs, K., Moller, H. M., Welte, W., and Wittmann, V. (2010) Structural basis of multivalent binding to wheat germ agglutinin. *J. Am. Chem. Soc. 132*, 8704−8719.

Bioconjugate Chemistry

Article

pubs.acs.org/bc

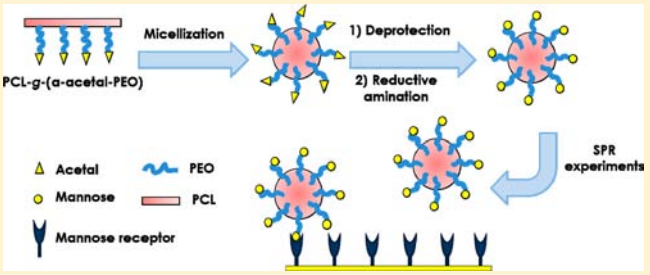
α-Acetal, ω-Alkyne Poly(ethylene oxide) as a Versatile Building Block for the Synthesis of Glycoconjugated Graft-Copolymers Suited for Targeted Drug Delivery

Hélène Freichels,[†,#] David Alaimo,[†] Rachel Auzély-Velty,[‡] and Christine Jérôme*[,†]

[†]Center for Education and Research on Macromolcules, University of Liège, B6a Sart-Tilman, 4000 Liège, Belgium

[‡]Centre de Recherches sur les Macromolécules Végétales (CERMAV-CNRS), BP53, 38041 Grenoble cedex 9, France (affiliated with Université Joseph Fourier, and member of the Institut de Chimie Moléculaire de Grenoble)

ABSTRACT: α-Acetal, ω-alkyne poly(ethylene oxide) was synthesized as building block of glycoconjugated poly(ε-caprolactone)-*graft*-poly(ethylene oxide) (PCL-*g*-PEO) copolymers. The alkyne group is indeed instrumental for the PEGylation of a poly(α-azido-ε-caprolactone-*co*-ε-caprolactone) copolymer by the Huisgen's 1,3 dipolar cycloaddition, i.e., a click reaction. Moreover, deprotection of the acetal end-group of the hydrophilic PEO grafts followed by reductive amination of the accordingly formed aldehyde with an aminated sugar is a valuable strategy of glycoconjugation of the graft copolymer, whose micelles are then potential. A model molecule (fluoresceinamine) was first considered in order to optimize the experimental conditions for the reductive amination. These conditions were then extended to the decoration of the graft copolymer micelles with mannose, which is a targeting agent of dendritic cells and macrophages. The bioavailability of the sugar units at the surface of micelles was investigated by surface plasmon resonance (SPR). The same question was addressed to nanoparticles stabilized by the graft copolymer. Enzyme linked lectin assay (ELLA) confirmed the availability of mannose at the nanoparticle surface.



INTRODUCTION

Biocompatible amphiphilic copolymers with well-defined architectures are one of the challenging and rewarding areas in polymer science, because they are able to form micelles in water with potential as drug delivery systems.[1−4] Indeed, the hydrophobic core of core−shell micelles can serve as a reservoir for hydrophobic drugs, which are accordingly protected from contact with the aqueous environment.[5,6] In this field, aliphatic polyesters, such as poly(ε-caprolactone) (PCL) and polylactide (PLA), are interesting hydrophobic candidates as a result of their degradability and biocompatibility. Moreover, poly(ethylene oxide) (PEO) is one of the most desired hydrophilic components because of nontoxicity, biocompatibility, lack of immunogenicity,[7] and protein repellency that confers stealthiness to micelles.[8−10]

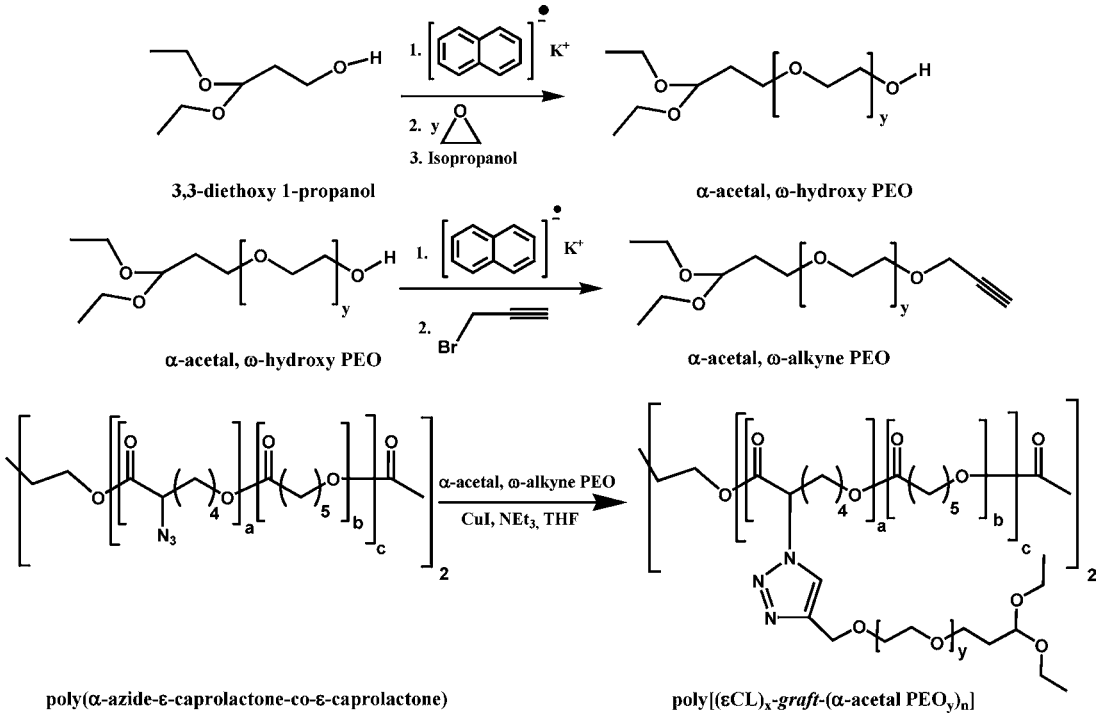
Last but not least, these amphiphilic copolymers can also be used as interfacial agents for the steric stabilization of polymeric nanoparticles.[11,12] In this context, previous works have emphasized the higher efficiency of graft copolymers over diblock copolymers of comparable hydrophilic−lipophilic balance (HLB) in stabilizing PLA nanoparticles and in repelling proteins.[13] Among the strategies reported in the scientific literature about the synthesis of amphiphilic PCL(PLA)-*g*-PEO copolymers, the grafting "onto" method has been widely studied, i.e., the grafting of functional PEO onto reactive aliphatic polyesters. Huisgens 1,3-dipolar cycloaddition,[8,14,15] atom transfer radical addition,[16] Michael addition,[17] and oxime formation[18,19] are the main grafting reactions used in this respect. Nevertheless, the lack of reactivity of the free α-end-group of the PEO grafts prevents any pilot molecule from being attached to these copolymers, which are then useless in active targeting. It is thus highly desirable to prepare nanocarriers decorated with ligands able to bind to receptor-expressing cells and to form ligand−particle complexes prone to internalization into the targeted cells by receptor-mediated endocytosis. The therapeutic activity of the entrapped drugs would thus be enhanced by the proper destination of the nanocarrier.[20]

In order to build up this type of intelligent nanocarrier with a graft architecture, α,ω-heterotelechelic PEO must be prepared. Tanigushi et al. reported a first strategy of grafting "onto" based on PEO end-capped with an α-aminooxy for further grafting onto a ketone-containing PCL and with an ω-hydroxyl group suited to the attachment of targeting molecules.[21,22] This heterotelechelic PEO was prepared in five steps, starting with an α,ω-hydroxyl PEO. One of the hydroxyl groups was protected by tetrahydropyranyl (THP), and the second hydroxyl group was tosylated before being reacted with *N*-hydroxyphthalimide. Finally, the protecting end-group was removed at low pH and the hydroxyl group was converted into an azide. However, the multistep synthesis of the difunctional

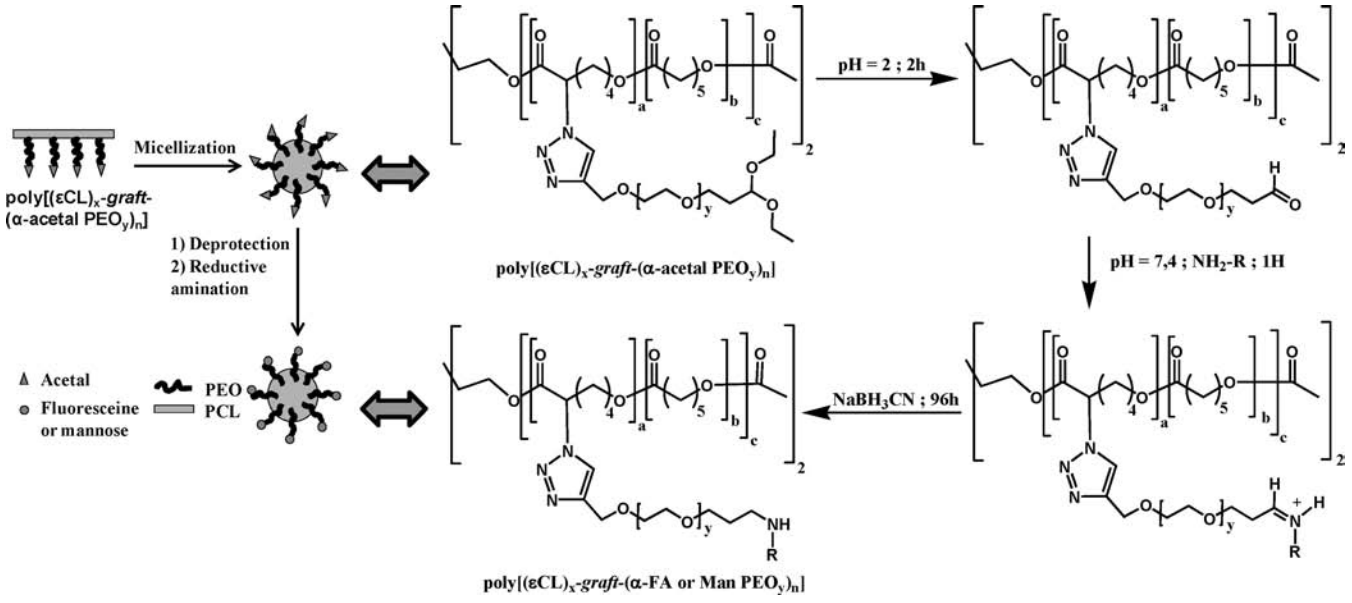
Received: December 19, 2011
Revised: July 3, 2012
Published: August 8, 2012

 © 2012 American Chemical Society dx.doi.org/10.1021/bc200650n | *Bioconjugate Chem.* 2012, 23, 1740−1752

Scheme 1. Strategy for the Preparation of Poly(εCL)-*graft*-(α-acetal PEO) Copolymers



Scheme 2. Decoration of Micelles by Reductive Amination of an Amino-Dye (when R = fluorescein) or Amino-Sugar (when R = mannose) with Reactive Poly[(εCL)-*graft*-(α-aldehyde PEO)] Micelles



PEO and the low yield are severe limitations for the preparation of the envisaged graft copolymers. There is thus a need for a much more straightforward synthesis of PCL-*g*-PEO copolymers.

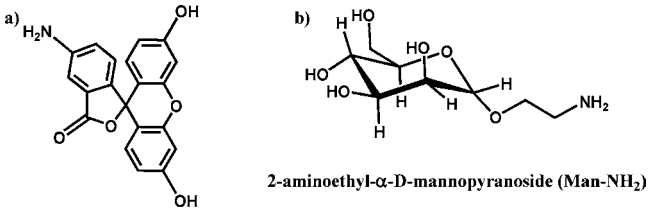
The purpose of this work is to synthesize a PCL-*graft*-α-acetal PEO copolymer in three steps. The first two steps were devoted to the synthesis of a heterotelechelic PEO: indeed, the anionic ring-opening polymerization of ethylene oxide by an alkoxide flanked by an acetal group. The ω-hydroxyl end-group of PEO was then converted into an alkyne (Scheme 1) reactive toward the azide pendant groups of PCL by the Huisgens 1,3 cycloaddition. This "click" reaction has the advantage of being tolerant to many functional groups and being carried out under mild conditions that may prevent PCL from being degraded[23−25] and was used by many research groups to prepare polymers, dendrimers, and hydrogels for drug delivery applications.[26] Moreover, Suksiriworapong et al. show the lack of toxicity for NPs decorated with nicotinic acid and *p*-aminobenzoic acid by click reaction even if copper was used during the synthesis.[27] Several copolymers were accordingly prepared, in which the number and length of the PEO grafts were changed in such a manner that the HLB was maintained close to 5. This low HLB close to 5 was chosen, on purpose for

dx.doi.org/10.1021/bc200650n | *Bioconjugate Chem.* 2012, 23, 1740−1752

the critical association concentration (cac) to be low, which is a requirement for biomedical application.[28]

The acetal end-group of the PEO grafts was hydrolyzed and the released aldehyde was reacted with an amino derivative by reductive amination. This coupling reaction was selected because it can occur in water, a good solvent for sugars, used as pilot molecules in drug targeting, and it is tolerant toward chemical functions of sugars, which does not impose additional protection/deprotection reactions. As illustrated in Scheme 2, a special effort will be devoted to the direct decoration of the micelles of the amphiphilic copolymer with an amine of interest. Fluoresceinamine (Scheme 3a) will be first studied as a model compound. This hydrosoluble fluorescent dye has the additional advantage of being easily localized by fluorescence, which allows learning about the fate of labeled micelles in cells or tissues.[29] Finally, mannose will be used as a potential targeting agent (Scheme 3b) of dendritic cells[30] and macrophages.[31]

Scheme 3. Structure of the Amino-Derivatives Coupled to Poly(εCL)-*graft*-(α-aldehyde-PEO) Micelles by Reductive Amination



The bioavailability of mannose at the surface of micelles will be studied by surface plasmon resonance (SPR). Indeed, the binding of mannosylated micelles to lectin-modified sensors can be directly probed by SPR. Two kinds of lectins (Concanavalin A (ConA) and *Burkholderia cepacia* complex lectin A (BclA)) will be immobilized on the sensorchips as models of mannose receptors at the surface of cells.

The final copolymers will be used as steric stabilizer of PLA nanoparticles. The targeting potential of these nanoparticles will be estimated by enzyme linked lectin assay (ELLA).

EXPERIMENTAL SECTION

Materials. Toluene (Chem-lab), THF (Chem-lab), diethyl ether (VWR), 2-propanol (VWR), *N*,*N*-dimethylformamide (DMF) (Aldrich), heptane (VWR), $CDCl_3$ (Aldrich), 3,3-diethoxy-1-propanol (Aldrich), copper iodide (Aldrich), triethylamine (Janssen Chimica), naphthalene (Aldrich), ethylene oxide (Messer), potassium (Fluka), propargyl benzoate (Aldrich), propargyl bromide (Aldrich), Sephadex G25 and G50 (Sigma-Aldrich), sodium cyanoborohydride (1 M THF solution, Aldrich), PLA (BioMérieux, M_n = 32 650 g/mol, $M_w/M_n \sim 1.5$), dithranol (Aldrich, 97%), phenol (Sigma, 99%), sulfuric acid (JT Baker), bovine serum albumin (BSA, Sigma), glycine (Aldrich), tris(hydroxymethyl)aminomethane (Tris) (Acros), manganese chloride (Sigma), calcium chloride (Riedel-de Haën), *N*-ethyl-*N*-[3-dimethylaminopropyl]-carbodi-imide (EDC, Fluka), *N*-hydroxysuccinimide (NHS, Acros), and Concanavalin A (ConA, Sigma-Aldrich) were used as received. 2,2-Dibutyl-2-stanna-1,3-dioxepane (DSDOP) was prepared as reported by Kricheldorf et al.[32] Synthesis of α-chloro-ε-caprolactone (αClεCL)[33] and of 2-aminoethyl-α-D-mannopyroside (Man-NH_2)[34] was also reported elsewhere. ε-Caprolactone (ε-CL) (Aldrich, 99%) was dried over calcium hydride under stirring at room temperature for 48 h and purified by vacuum distillation just before use. Milli-Q water was used in all the experiments. The lectin BclA was prepared as previously reported.[35]

Characterization Techniques. ^{1}H NMR spectra were recorded in $CDCl_3$ at 400 MHz in the FT mode with a Bruker AN 400 apparatus at 25 °C. Chemical shifts were given in ppm using tetramethylsilane (TMS) as an internal reference.

The number-average molecular weight (M_n) and polydispersity (M_w/M_n) were determined by size exclusion chromatography (SEC) at 45 °C. The chromatograph was equipped with a UV−visible detector, a refractive index detector, and two polystyrene gel columns (columns HP PL gel 5 μm, porosity: 10^2, 10^3, 10^4, and 10^5 Å, Polymer Laboratories) that were eluted by THF at a flow rate of 1 mL/min. The columns were calibrated with polystyrene and poly(ethylene oxide) standards, respectively (Polymer Laboratories).

The hydrodynamic diameter and the particle size distribution (PDI) of the nanoparticles were determined by quasi-elastic light scattering measurements at 25 °C using the cumulant method and a Malvern Zetasizer NanoZS from Malvern instruments (U.K.). Each value was the average of at least five measurements.

The UV−visible spectra were recorded on spectrophotometer Hitachi U3300.

MALDI-TOF mass spectrometry was carried out with a Bruker Reflex III equipped with a 337 nm N_2 laser in the reflector mode at a 20 kV acceleration voltage. Dithranol was used as the matrix. Sodium or potassium trifluoroacetate was added for ion formation. Samples were prepared by mixing matrix (20 mg/mL), sample (10 mg/mL), and salt (10 mg/mL) in a 10:1:1 ratio. The number-average molecular weight (M_n) of polymers was determined in the linear mode.

Surface plasmon resonance-based biosensors (SPR) experiments were conducted with a Biacore X instrument at 25 °C.

Synthesis. *α-Acetal-ω-Hydroxy Poly(ethylene oxide) (α-acetal-ω-hydroxy PEO).* In a flame-dried and argon-purged flask, 1.2 mL of 3,3-diethoxy-1-propanol (1.13 g; 7.6 mmol) in 200 mL of anhydrous THF was titrated with potassium naphthalenide in a THF solution (0.72 M) under argon. After vigorous stirring at room temperature for 15 min, the mixture was added into a 500 mL Parr reactor followed by 15 g of ethylene oxide (340 mmol). After 19 h of polymerization at 30 °C, 2-propanol was added, and the polymer was precipitated in an excess of diethyl ether and vacuum-dried at 30 °C. M_n of the recovered α-acetal-ω-hydroxy PEO was 2000 g/mol as determined by SEC. The amounts of the reactants were adapted to obtain polymers of other molar masses.^{1}H NMR ($CDCl_3$, 400 MHz) δ (ppm): 1.17 (t, 6H, C$\underline{H}_3$-CH_2-O), 1.88 (q, 2H, CH-C$\underline{H}_2$-CH_2), 3.4 (q, 4H, CH_3-C$\underline{H}_2$-O), 3.46 (t, 2H, CH_2-C$\underline{H}_2$-OH), 3.6 (s, 4H × DP_{EO}, O-C$\underline{H}_2$-C$\underline{H}_2$-O), 4.6 (t, 1H, C$\underline{H}$-CH_2); recovered yield: 90%.

α-Acetal-ω-Alkyne Poly(ethylene oxide) (α-acetal-ω-alkyne PEO). Three grams of α-acetal-ω-hydroxy poly(ethylene oxide) (2000 g/mol) were dried by repeated (three times) azeotropic distillations of toluene before dissolution in dry THF. Then, 0.75 equiv of potassium naphthalenide in THF (0.72 M) and 0.75 equiv of propargyl bromide were added to the polymer solution, which was stirred at room temperature overnight. The polymer was precipitated in ether at −20 °C, filtered, and dried at reduced pressure at room temperature. ^{1}H

dx.doi.org/10.1021/bc200650n | *Bioconjugate Chem.* 2012, 23, 1740−1752

NMR ($CDCl_3$, 400 MHz) δ (ppm): 1.17 (t, 6H, C$\underline{H}_3$-CH_2), 1.88 (q, 2H, CH-C$\underline{H}_2$-CH_2), 2.42 (t, 1H, C≡C$\underline{H}$), 3.4 (q, 4H, CH_3-C$\underline{H}_2$-O), 3.6 (s, 4H × DP_{EO}, O-C$\underline{H}_2$-C$\underline{H}_2$-O), 4.18 (d, 2H, O-C$\underline{H}_2$-C≡), 4.6 (t, 1H, O-C$\underline{H}$-CH_2); recovered yield: 90%.

Poly(α-azido-ε-caprolactone-co-ε-caprolactone) (Poly-(αN$_3$εCL-co-εCL)). This copolymer was prepared according to a reported procedure.[33] Briefly, α-chloro-ε-caprolactone (0.996 mg) was dried by repeated (three times) azeotropic distillations of toluene just before polymerization. Then, 19 mL of εCL and 80 mL of toluene were added to the reactor. When the solution was homogeneous, DSDOP (2.6 mL of a 0.52 M solution in toluene) was added and the polymerization allowed to proceed at 70 °C. After 140 min, 3.9 mL of pyridine and 3 mL of acetyl chloride were added. After overnight reaction at room temperature, the copolymer was purified by precipitation in heptane. A copolymer with 5 units of αClεCL and 144 units of εCL was recovered by precipitation in heptane and dried in vacuo at room temperature.

The chloride functions were converted into azide by reacting 8 g of poly(αClεCL-*co*-εCL) (dissolved in 80 mL of DMF) with 1.5 g of NaN_3 (10 equiv in respect to the chloride function). The mixture was stirred overnight at room temperature. After elimination of DMF at reduced pressure, 50 mL of toluene was added, and the insoluble salt was removed by centrifugation (5000 rpm at 25 °C for 15 min). A copolymer with 5 units of αN_3-ε-CL and 144 units of ε-CL was recovered by precipitation in heptane and dried in vacuo at room temperature. The amounts of reactants were adapted for getting copolymers of another azide content.

^{1}H NMR ($CDCl_3$, 400 MHz) δ (ppm): 1.38 (m, 2H × ($DP_{\varepsilon CL}$ + $DP_{\alpha N3\alpha CL}$), O-((CH_2)$_2$-C$\underline{H}_2$-(CH_2)$_2$-CH(N_3 or H)-C=O), 1.61−1.65 (m, 4H × $DP_{\varepsilon CL}$, O-CH_2-C$\underline{H}_2$-CH_2-C$\underline{H}_2$-CH_2-C=O and 2H × $DP_{\alpha N3\alpha CL}$, O-CHN_3-CH_2-CH_2-C$\underline{H}_2$-CH_2-C=O), 1.95−2.00 (m, 2H × $DP_{\alpha N3\alpha CL}$, CHN_3-C$\underline{H}_2$-CH_2), 2.05 (s, 6H, C$\underline{H}_3$C(O)O), 2.29 (t, 2H × $DP_{\varepsilon CL}$, O-(CH_2)$_4$-C$\underline{H}_2$-C=O), 3.83 (t, 1H × $DP_{\alpha N3\alpha CL}$, (CH_2)$_3$-C$\underline{H}N_3$-C=O), 4.05 (t, 2H × $DP_{\varepsilon CL}$, CH_2-C$\underline{H}_2$-O-C(=O)-CH_2), 4.15 (t, 2H × $DP_{\alpha N3\alpha CL}$, -C$\underline{H}_2$-O-C(=O)-CHN_3); recovered yield: 90%.

Poly(ε-caprolactone)-graft-(α-acetal poly(ethyleneoxide) (Poly[(εCL)$_x$-graft-(α-acetal PEO$_y$)$_n$]). One gram (0.17 mmol of azide function, 1 equiv) of Poly(αN$_3$εCL$_3$-*co*-PCL$_{145}$) and 449 mg (0.20 mmol, 1.2 equiv) of α-acetal, ω-alkyne PEO_{45} were transferred into a glass reactor containing 10 mL of THF. The solution was stirred until complete dissolution of the polymers. Then, 2 mg (0.02 mmol, 0.1 equiv) of NEt_3 and 3.8 mg (0.02 mmol, 0.1 equiv) of CuI were added into the reactor. The solution was stirred at 35 °C until the IR absorption of the azide at 2104 cm^{-1} disappeared completely, which occurred after 10 h.

Then, 30 μL of propargyl benzoate was added with a new amount of CuI and NEt_3. After 2 h of reaction, the graft copolymer was recovered by precipitation in diethyl ether. In order to remove the nongrafted PEO chains which coprecipitated with the graft copolymer, the micelles of the polymer mixture were eluted through a Sephadex column (mixture 1/1 of G25 and G50) and recovered by lyophilization for further characterization.

From ^{1}H NMR analysis, a composition poly[(εCL)$_{148}$-*graft*-(α-acetal PEO_{45})$_3$] was determined for the recovered graft copolymer. These conditions were adapted in the preparation of other graft copolymers.

^{1}H NMR ($CDCl_3$, 400 MHz) δ (ppm): 1.17 (t, 6H × $DP_{\alpha N3\alpha CL}$, C$\underline{H}_3$-CH_2), 1.38 (m, 2H × ($DP_{\varepsilon CL}$ + $DP_{\alpha N3\alpha CL}$), O-(CH_2)$_2$-C$\underline{H}_2$-(CH_2)$_2$-C=O), 1.61−1.65 (m, 4H × $DP_{\varepsilon CL}$, O-CH_2-C$\underline{H}_2$-CH_2-C$\underline{H}_2$-CH_2-C=O and 2H × $DP_{\alpha N3\alpha CL}$, O-CHN_3-CH_2-CH_2-C$\underline{H}_2$-CH_2-C=O), 1.88 (q, 2H × $DP_{\alpha N3\alpha CL}$, CH-C$\underline{H}_2$-CH_2), 2.05 (s, 6H, C$\underline{H}_3$C(O)O), 2.29 (t, 2H × $DP_{\varepsilon CL}$, O-(CH_2)$_4$-C$\underline{H}_2$-C=O), 3.4 (q, 4H × $DP_{\alpha N3\alpha CL}$, CH_3-C$\underline{H}_2$-O), 3.62 (s, 4H × DP_{EO} × $DP_{\alpha N3\alpha CL}$, O-C$\underline{H}_2$-C$\underline{H}_2$-O), 4.05 (t, 2H × ($DP_{\varepsilon CL}$ + $DP_{\alpha N3\alpha CL}$), CH_2-C$\underline{H}_2$-O-C=O), 4.6 (t, 1H × $DP_{\alpha N3\alpha CL}$, CH_2-C$\underline{H}$-($O)_2$), 4.7 (s, 2H × $DP_{\alpha N3\alpha CL}$, C-C$\underline{H}_2$-O), 5.0 (t, 1H × $DP_{\alpha N3\alpha CL}$ (C(O)-C$\underline{H}$-N), 7.80 (s, 1H × $DP_{\alpha N3\alpha CL}$, N-C$\underline{H}$-C); recovered yield: 75%.

Fluorescein and Mannose Coupling to Poly(εCL)-graft-(α-acetal PEO) Micelles. After complete dissolution of 100 mg of a poly(εCL)-*graft*-(α-acetal PEO) copolymer in 1 mL THF, the solution was added dropwise to 10 mL Milli-Q water. The pH was then adjusted very slowly at 2 with diluted chlorohydric acid (0.1 M). After 2 h, the pH was slowly raised to 7.4 with a phosphate buffer (500 mM, pH 8), and then, 2 equiv of the amino derivative was added. After 1 h, a 10-fold excess of $NaBH_3CN$ solution (43 μL, 0.043 mmol, 1 M solution in THF) was added. After 96 h of reaction, the reaction mixture was purified by dialysis (SpectraPor, cutoff of 6000−8000) against water for 3 days, by changing water 4 times/day. The copolymer was recovered by lyophilization for further characterization. Recovered yield: 98%.

Quantification of Grafted Man-NH_2 by Colorimetric Assay. To an aqueous solution of copolymer, 1 mL of a 5% aqueous phenol solution and 5 mL of concentrated sulfuric acid were rapidly added. The tube was allowed to stand 10 min at room temperature, before it was vigorously shaken and placed in a water bath at room temperature for 20 min before reading the absorbance at 486 nm. The amount of sugar was determined by reference to a standard curve of 2-aminoethyl-α-D-mannopyranoside.

Preparation of Micellar Solutions. Micelles were prepared by a nanoprecipitation procedure as technique described.[36] Briefly, 50 mg of copolymer were dissolved in 2.5 mL of THF. The mixture was stirred until complete dissolution of the copolymer. It was then added dropwise to 1.775 mL of Tris buffer (0.1 M Tris, 0.03 mM $CaCl_2$, 0.03 mM $MnCl_2$, pH = 7.4) under moderate stirring. THF was removed by dialysis again (Tris buffer and the solutions stored at 6 °C).

Preparation of Nanoparticles (NPs). Nanoparticles of PLA were prepared by a nanoprecipitation procedure as previously described.[12,36] Briefly, 35.2 mg of copolymer and 50 mg of PLA were dissolved in 2.5 mL of acetone. The mixture was stirred until the complete dissolution of the polymers, then added dropwise to 1.775 mL of Tris buffer (0.1 M Tris, 0.03 mM $CaCl_2$, 0.03 mM $MnCl_2$, pH = 7.4) under moderate stirring. Acetone was removed by evaporation under vacuum at room temperature and the solutions stored at 6 °C.

SPR Experiments. *Lectin Immobilization.* CM5 sensorchip (carboxymethylated dextran covalently attached to a gold surface) was used in each experiment. All the buffers were filtered through a 0.45 μm PTFE filter (Millipore). The lectins, ConA and BclA, were immobilized by the following procedure[35,37] at flow rate of 10 μL/min: the chip was activated with 70 μL EDC (75 mg/mL)/NHS (12 mg/mL) solution. Then, ConA in 0.1 M phosphate buffer (pH 7.4), or BclA in 10 mM acetate buffer (pH 4.5), was injected only into the sample channel. The volume was adapted depending on the required amount of bound proteins. Finally, the reactive groups

of the sensor surface were blocked with 1 M ethanolamine adjusted at pH 8.5 with HCl (70 μL). The reference channel was treated similarly, except for the lectin injection. 0.1 M Tris buffer (pH 7.4) containing 0.03 mM $CaCl_2$ and 0.03 mM $MnCl_2$ was used in all the recognition experiments.

SPR Measurements. After equilibration of the system by Tris buffer, thus until a stable baseline was observed, the solutions were injected in the reference and sample channels at a flow rate of 30 μL/min. The kinetic titration method[38−40] was used for each experiment, i.e., within a single binding cycle. Micellar solutions of increasing concentrations (90 μL) and Tris buffer (4 min) were alternatively injected. The sensorgrams were recorded as a succession of association and dissociation phases without regeneration between each injection of the micellar solution. All the data were then plotted after subtraction of the reference channel signal to remove any adverse contribution from refractive index noise due to the bulk contribution of the sample injection.

Biological Lectin Recognition Assay. This assay was realized as previously reported.[12,41]

RESULTS AND DISCUSSION

Synthesis of α-Acetal, ω-Alkyne Poly(ethylene oxide). The α-acetal, ω-alkyne poly(ethylene oxide) (α-acetal, ω-alkyne PEO) was synthesized in two steps (Scheme 1). The anionic ring-opening polymerization of ethylene oxide was first initiated by potassium 3,3-diethoxy-1-propoxide, thus an initiator that contains a protected aldehyde as previously reported by Nagasaki et al.[42] In a second step, the α-hydroxyl end-group of PEO was converted into an alkoxide by reaction with potassium naphthalenide, followed by a substitution reaction with propargyl bromide. Three α-acetal-ω-alkyne PEO's of different M_n were prepared by changing the monomer to initiator molar ratio (Table 1). ^{1}H NMR spectroscopy (Figure 1) showed the characteristic peaks of the acetal end-group at 1.18 ppm (methyl group), 4.62 ppm (acetal methine protons), and 1.88 ppm (methylene groups) which confirms the effective initiation of ethylene oxide by the functional initiator. The M_n of PEO was determined by integration of the characteristic peaks of the end-groups, and the peak at 3.6 corresponding to the methylene protons of PEO (Table 1). SEC analysis showed a monomodal elution peak (Figure 2a) and a low polydispersity (Table 1). Calibration of SEC was performed with PEO standards and allowed for the M_n to be determined (Table 1). Values for M_n from SEC were lower than the values of M_n established by ^{1}H NMR. Matrix-assisted laser desorption ionization time-of-flight mass spectrometry (MALDI-TOF) elucidated the polymer composition. As exemplified for the α-acetal-ω-alkyne PEO_{25}, the MALDI-TOF spectrum (Figure 3) showed three distributions that correspond to PEO chains centered around 1100 g/mol. The two main distributions correspond to the targeted α-acetal, ω-alkyne PEO associated with a K^+ or a Na^+ cation, respectively. The third small distribution corresponds to α,ω-alkyne PEO associated with Na^+ (∼8.2%). Water trace during the anionic polymerization of EO is a possible explanation for the formation of PEO end-capped with two hydroxyl groups and by two alkyne groups at the end of the second step. Water would actually contribute to the initiation of the EO polymerization. Even in a low amount, these chains are able to trigger cross-linking when used in the grafting "onto" reaction and thus to the gelation of the reaction medium. In order to avoid this side-reaction, α-acetal, ω-hydroxy PEO was purposely reacted with less than the stoichiometric amount of bromo-propyne. PEO was accordingly end-functionalized with 66% (α-acetal, ω-alkyne PEO_{66}), 72% (α-acetal, ω-alkyne PEO_{45}), and 71% (α-acetal, ω-alkyne PEO_{25}) of alkyne end-group, respectively.

Table 1. Characteristics of the Different α-Acetal-ω-alkyne PEO

#	sample[a]	M_n (SEC)[b]	M_w/M_n[b]	M_n (^{1}H NMR)[c]	M_n (MALDI-TOF)
1	α-acetal-ω-alkyne PEO_{25}	1100 g/mol	1.06	1200 g/mol	1100 g/mol
2	α-acetal-ω-alkyne PEO_{45}	2000 g/mol	1.05	2200 g/mol	n. d.[d]
3	α-acetal-ω-alkyne PEO_{66}	2900 g/mol	1.03	3200 g/mol	2950 g/mol

[a]The subscript numbers are the degree of polymerization (DP) of PEO. [b]Estimated by SEC (THF) with poly(ethylene oxide) calibration. [c]Determined by ^{1}H NMR ($CDCl_3$). The integrations (I) of the peak characteristic of PEO δ = 3.6 ppm and the acetal end-group at δ = 1.2, δ = 1.9, and δ = 4.6 ppm were used in the following relationship: M_n (PEO, ^{1}H RMN) = 44 × $(I_{3.6}/4)/[(I_{1.2}/6) + (I_{1.9}/2) + I_{4.6}]$. [d]Not determined.

Synthesis of Poly(εCL)-*graft*-(α-acetal PEO). Synthesis of the graft copolymers by the grafting "onto" strategy relies on the availability of azide pendent groups along the PCL backbone reactive toward with the alkyne end-group of the PEO chains. For this purpose, poly(α-azido-ε-caprolactone-*co*-ε-caprolactone) poly($\alpha N_3\varepsilon$CL-*co*-εCL) random copolymers were synthesized by ring-opening copolymerization of α-chloro-ε-caprolatone and ε-caprolactone in the presence of DSDOP followed by substitution of the chloride by an azide, as previously reported.[15,33] Nevertheless, it must be mentioned that the protection of the hydroxyl end-groups of the PCL backbone by reaction with acetyl chloride and pyridine was required to prevent backbiting reactions and the copolyester degradation during further derivatization. In order to keep the HLB of the graft copolymers produced by the coupling of PEO chains of various lengths constant, three poly(α-azido-ε-caprolactone-*co*-ε-caprolactone) (poly($\alpha N_3\varepsilon$CL-*co*-εCL)) of constant polymerization degree (M_n ∼ 17 000 g/mol) but different $\alpha N_3\varepsilon$CL contents were synthesized. The $\alpha N_3\varepsilon$CL contents were kept at 1.3, 2.0, and 3.4 mol % of polymer, produced by addition of azido-comonomer. Again, ^{1}H NMR allowed the composition of the azido-PCL backbones to be determined (Table 2).

Poly(εCL)-*graft*-(α-acetal PEO) copolymers were prepared by the Huisgens alkyne−azide cycloaddition reaction, thus by reaction of α-acetal, ω-alkyne PEO with poly($\alpha N_3\varepsilon$CL-*co*-εCL) with CuI as a catalyst and triethylamine as a base. In each case, 1.2 equiv of alkyne was used with respect to the azide pendant groups. Although the reaction was complete with PEO grafts of low molecular weight as assessed by the complete disappearance of the IR absorption of the azide groups at 2104 cm^{-1}, no reaction was observed when the PEO_{66} (M_n = 2900 g/mol) was reacted with the poly($\alpha N_3\alpha CL_2$-*co*-εCL_{148}), even for as long reaction time as 15 h, at higher catalyst content (10 equiv) and for more concentrated polymer solutions. The coupling of PEO of the higher molecular weight and lower functionality was thus kinetically limited. In contrast, two graft copolymers **4** and **5** were successfully prepared with PEO_{25} and PEO_{45}, respectively, whose characteristics are summarized in Table 2.

dx.doi.org/10.1021/bc200650n | *Bioconjugate Chem.* 2012, 23, 1740−1752

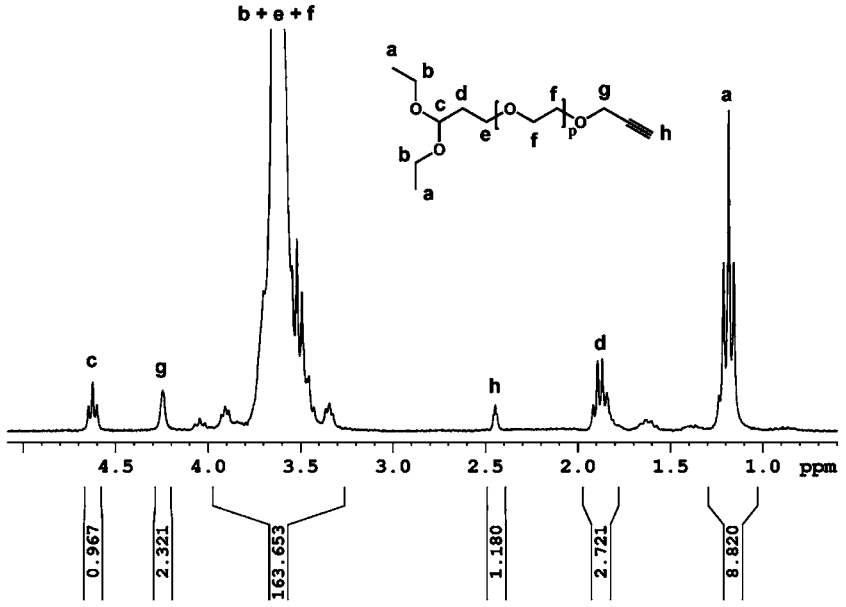


Figure 1. ^{1}H NMR of the α-acetal-ω-alkyne PEO ($M_{n(SEC)}$ 1100 g/mol) in $CDCl_3$.

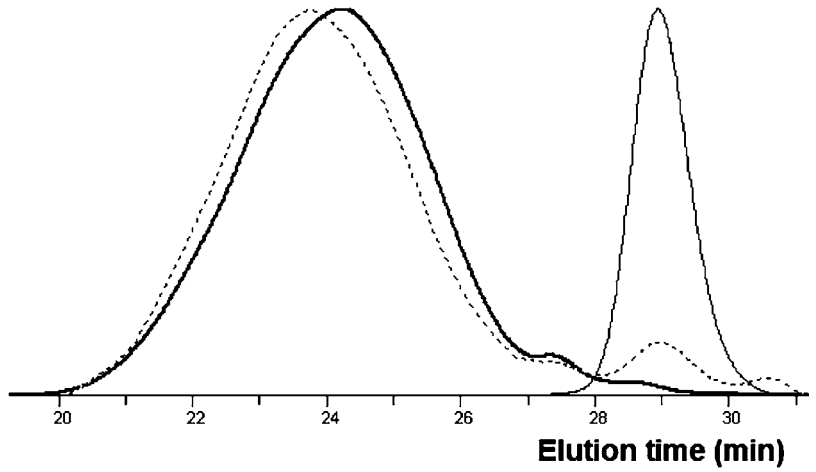


Figure 2. SEC traces in THF for (a) α-acetal, ω-alkyne PEO_{25} (regular line) and (b) poly(εCL)$_{149}$-*graft*-(α-acetal-PEO_{25})$_5$ before (dotted line) and after purification on a Sephadex column (bold line).

The excess of PEO used in the grafting reaction was separated from the amphiphilic copolymer. Purification of α-acetal-ω-alkyne PEO of low M_n (1100 g/mol) was straightforward by the selective precipitation of the graft copolymer in diethyl ether. This technique was, however, not relevant for α-acetal-ω-alkyne PEO of higher M_n (2000 g/mol), because of the coprecipitation of PEO and the graft copolymer. Nevertheless, the copolymer was purified in water, in which the copolymer formed micelles in contrast to unreacted PEO that remained highly soluble. This solution was eluted through a column of cross-linked dextran gel (Sephadex) used for gel filtration chromatography. The collected fractions were characterized by SEC (Figure 2), which confirmed the successful separation of PEO from the graft copolymer. ^{1}H NMR analysis of the pure copolymers (Figure 4) confirmed the quantitative grafting of PEO onto the PCL backbone as supported by the integration of the peaks characteristic of PEO (methylene at 3.6 ppm) and the polyester backbone (4.2 ppm). This spectrum also confirmed that the α-acetal end-group capping of the PEO grafts was maintained during the grafting "onto" reaction. As reported in Table 2, two copolymers with a similar HLB but a different number of grafts were made available.

Functionalization of the Graft-Copolymer Micelles in Aqueous Media. The second purpose of this work was to decorate the micelles formed by the graft copolymers in water by a sugar selected as a targeting unit. Because of the low HLB of the graft copolymers, the assistance of a water-miscible cosolvent (THF) was needed to prepare micellar solutions. THF is indeed a good solvent for both the PEO and PCL components. It was easily eliminated when the copolymer is completely dissolved, which results in the copolymer micellization. [36] Micelles were collected with an average diameter of about 80 nm for the copolymer **4** and 85 nm for the copolymer **5** as determined by DLS.

An amino-functional derivative of the targeting unit was then reacted with the deprotected aldehyde end-group of the PEO grafts, based on the hypothesis that these groups would be exposed at the surface of the micelles. The validity of this assumption was corroborated by using an amino-dye, i.e.,

dx.doi.org/10.1021/bc200650n | *Bioconjugate Chem.* 2012, 23, 1740−1752

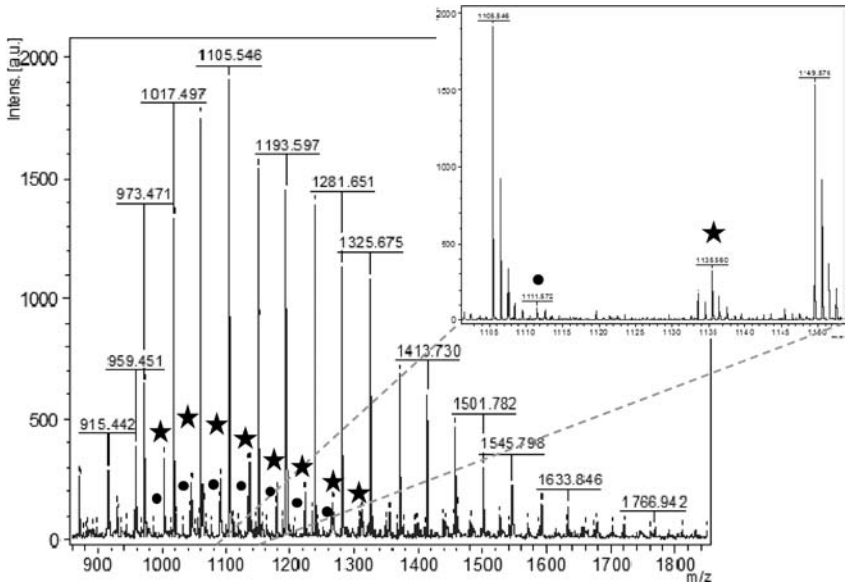


Figure 3. MALDI-TOF spectrum in water for the α-acetal, ω-alkyne PEO ($M_{n(SEC)}$ 1100 g/mol). Three populations are shown: (1) figures: α-acetal, ω-alkyne PEO ionized with K^+; (2) circles: α-acetal, ω-alkyne PEO ionized with Na^+; (3) stars: α,ω-alkyne PEO ionized with Na^+.

Table 2. Synthesis of Poly[(εCL)$_x$-*graft*-(α-acetal-PEO$_y$)$_n$] Prepared by Click Reaction

copolymer (#)	composition of the starting azido-PCL backbone[a]	DP of the starting α-acetal, ω-alkyne PEO[b]	number of PEO segments per copolymer chain[b]	M_w/M_n[c]	HLB[d]
poly[(εCL)$_{149}$-g-(α-acetal-PEO$_{25}$)$_5$] (**4**)	poly(αN$_3\varepsilon$CL$_5$-*co*-εCL$_{144}$)	25 (**1**)	5	1.6	4.9
poly[(εCL)$_{148}$-g-(α-acetal-PEO$_{45}$)$_3$] (**5**)	poly(αN$_3\varepsilon$CL$_3$-*co*-εCL$_{145}$)	45 (**2**)	3	1.6	5.2
poly[(εCL)$_{150}$-g-(α-acetal-PEO$_{66}$)$_2$] (**6**)	poly(αN$_3\varepsilon$CL$_2$-*co*-εCL$_{148}$)	66 (**3**)	n.d.[e]	n.d.[e]	5.2

[a]Determined by ^{1}H NMR in $CDCl_3$. [b]From Table 1. [c]Determined by SEC (THF) with a poly(ethylene oxide) calibration. [d]Determined with the Griffin's relationship: HLB = 20x{1 − [M_n(PCL)]/([M_n(PCL) + M_n(PEO)])}.[55] [e]Not determined.

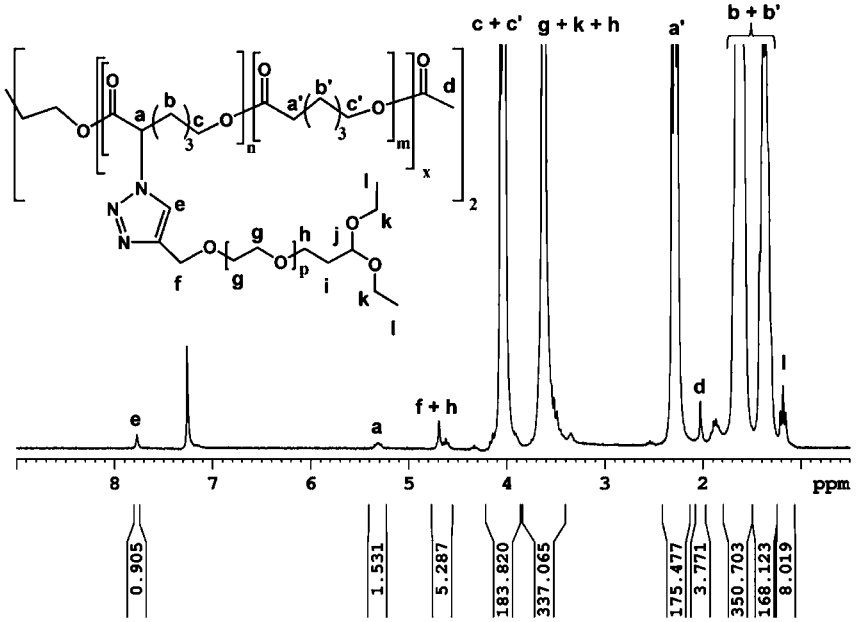


Figure 4. ^{1}H NMR ($CDCl_3$) of poly[(εCL)$_{148}$-*graft*-(α-acetal PEO$_{45}$)$_3$] (**5**) after purification.

aminofluorescein, easily detectable by UV, instead of aminomannose (Scheme 3). The coupling reaction occurred in three steps but in one pot as illustrated by Scheme 2. First, the acetal groups on the copolymer micelles were converted into aldehydes under mild acid conditions, i.e., at pH 2 for 2 h.[43] Then, the pH was increased up to 7.4 with a phosphate buffer and 2 equiv of aminofluorescein was added in order to form the Schiff base. After one hour, the Schiff base was reduced by

dx.doi.org/10.1021/bc200650n | *Bioconjugate Chem.* 2012, 23, 1740−1752

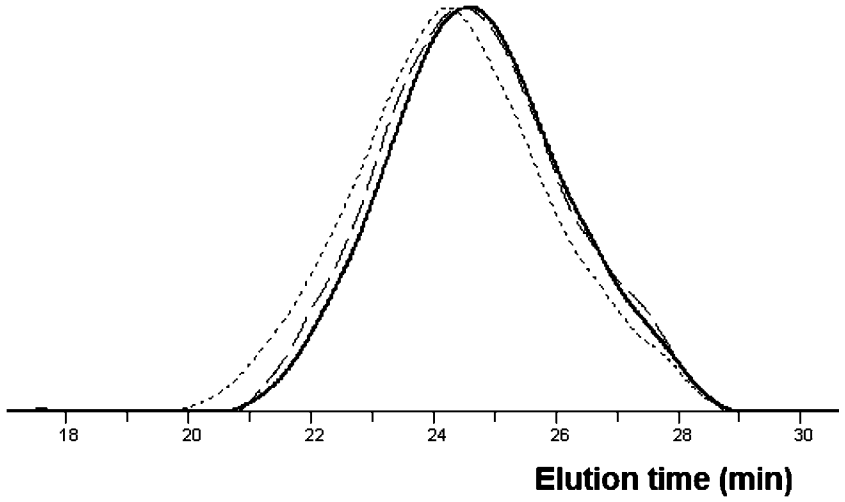


Figure 5. SEC chromatogram (RI detector in THF) of the graft copolymer **2** before (dotted line) and after (bold line) addition of fluoresceinamine onto the PEO chain ends by reductive amination. The dashed line is the chromatogram in THF with a UV detector at 274 nm.

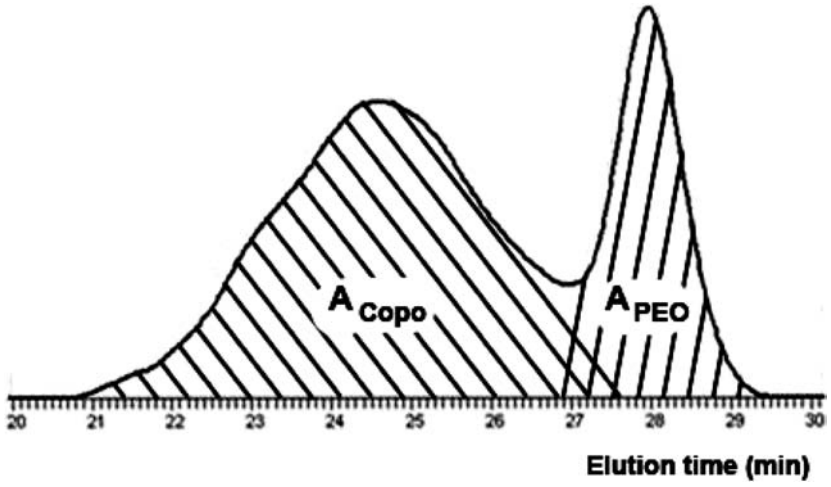


Figure 6. SEC analysis (THF and UV detector at 274 nm) of a mixture of the graft copolymer **4** poly[$(\varepsilon CL)_{149}$-*graft*-(α-FA $PEO_{25})_5$] (A_{Copo}) and standard PEO (M_n = 2900 g/mol) (A_{PEO}). M_{copo} = 27 mg and m_{PEO} = 3 mg.

addition of a 10-fold excess of sodium cyanoborohydride ($NaBH_3CN$) for 96 h. The control of the pH was critical in order to avoid the hydrolytic degradation of the copolymer, particularly during the aldehyde deprotection. After reaction, the micelles were purified by dialysis against water and recovered by lyophilization. Unexpectedly, the copolymers were not soluble in THF anymore. A possible explanation was that a few azide groups left on the polyester backbone were reduced in amines reactive toward the aldehyde end-group of the PEO grafts, so leading to cross-linking. This reduction reaction was previously reported in methanol in the presence of copper(II) and $NaBH_4$ at 5 °C.[44] In this work, the copper added during the click reaction could catalyze the azide reduction. Even though the content of these azide functions was below the detection limit of ^{1}H NMR, 5% might be enough to induce the copolymer cross-linking. In order to avoid this side reaction, a small molecule with an alkyne function (propargyl benzoate) was added to the reaction medium after the coupling of α-acetal-ω-alkyne PEO onto poly($\alpha N_3 \alpha$CL-*co*-εCL) in order to consume any residual azide groups. As a result of this additional step, the undesired cross-linking reaction was no longer observed during reductive amination such that the copolymers remained soluble in THF and could be characterized further.

The FA end-capped copolymers were analyzed by SEC in THF by using a UV-detector at a wavelength of strong absorption by fluorescein (274 nm). The chromatogram for the poly[$(\varepsilon CL)_{149}$-*graft*-(α-acetal $PEO_{25})_5$] copolymer superposed quite well to the SEC traces recorded by a classical refractive index detector for the same copolymer before and after reductive amination (Figure 5). Clearly, the copolymer absorbed at 274 nm after reductive amination which confirmed the successful coupling of FA. Moreover, the elution peak remained monomodal and symmetrical after reaction consistent with the absence of copolymer degradation. Moreover, the yield of the coupling reaction could be calculated from the area under the SEC_{UV} trace, which is actually proportional to the number of chromophores as exposed by eq 1[45]

$$A_{UV} = k \times n \quad (1)$$

where A_{UV} is the area under the SEC_{UV} trace, k is the specific UV response, which includes the instrumental constant and the specific absorption for a given chromophore, and n is the number of chromophores. The need for an internal probe was

dx.doi.org/10.1021/bc200650n | *Bioconjugate Chem.* 2012, 23, 1740−1752

met by adding the copolymer with a known amount of PEO chains end-capped by FA by the same recipe as the copolymer (M_n = 2900 g/mol; 44.6% of FA end-groups as determined by ^{1}H NMR). The relative area under the two elution peaks of the chromatogram was used to estimate the reaction yield provided that the molecular weight of the copolymer and the PEO standard was taken into account and their weight in the eluted sample. The average number of FA per standard PEO chain and PEO grafts per copolymer must also be considered (eq 2).

Figure 6 is a typical chromatogram for the poly[$(\varepsilon CL)_{149}$-*graft*-(α-FA PEO_{25})$_5$] copolymer. According to this method, 20% of the PEO grafts were end-capped by FA (Table 3).

$$\text{Yield}_{copo} = \frac{\text{Mn}_{copo} m_{PEO} 0.446}{2900 m_{copo} N} \frac{A_{copo}}{A_{PEO}} \quad (2)$$

Table 3. Coupling Yields for the Reductive Amination of Fluorescein Amine (FA) and 2-Aminoethyl-α-D-mannopyroside (Man-NH_2), Respectively, with the Aldehyde End-Group of the Graft or Block Copolymers

#	copolymer	amino-derivative	coupling yield[a] (mol %)
7	poly[$(\varepsilon CL)_{149}$-*g*-(α-acetal-PEO_{25})$_5$] (**4**)	FA	22[b]
8	poly[$(\varepsilon CL)_{148}$-*g*-(α-acetal-PEO_{45})$_3$] (**5**)	FA	18[b]
9	α-acetal-PEO_{114}-*b*-PCL_{149}[c]	FA	20[b]
10	poly[$(\varepsilon CL)_{149}$-*g*-(α-acetal-PEO_{25})$_5$] (**4**)	Man-NH_2	28[d]
11	poly[$(\varepsilon CL)_{148}$-*g*-(α-acetal-PEO_{45})$_3$] (**5**)	Man-NH_2	29[d]
12	α-acetal-PEO_{114}-*b*-PCL_{149}[c]	Man-NH_2	30[d]

[a]mol % of amino-derivative coupled per acetal function. [b]Determined by SEC-UV (THF) at 274 nm with the FA conjugated PEO internal probe. [c]Copolymer of linear architecture whose synthesis was reported in ref 47. [d]Determined by the colorimetric phenol/acid sulfuric method.

where A_{copo} and A_{PEO} are the areas under the SEC curves for the graft copolymer and the PEO, respectively, N is the number of starting acetal groups per polymer chain, 0.446 is the average number of FA end-groups coupled per PEO chain, and 2900 is the M_n of the PEO standard.

For sake of comparison, the yield of the reaction conducted with micelles of the PCL_{148}-*b*-PEO_{135} diblock copolymer was also 20%, which suggests that the copolymer architecture and the number of PEO chain per copolymer do not affect the coupling reaction that occurs at the surface of micelles in aqueous media. The advantage of the direct tagging of the micelles by a sugar in water is that additional steps of protection/deprotection of this sugar is not needed for making it soluble in organic media.

The experimental conditions used for the coupling of FA were extended to the amino-mannose shown in Scheme 3b. Since mannose cannot be detected by UV−visible spectroscopy, the coupling yield was determined by reaction of the copolymer with phenol and sulfuric acid following the formation of a colored compound that absorbs at 486 nm.[46] This colorimetric test specific to sugar concluded to a coupling yield close to 30% for both graft copolymers (Table 3), in line with data reported for the diblock copolymer of same molecular weight and composition.[47] The better coupling yield for the amino-mannose compared to FA more likely comes from the higher nucleophilicity of the aliphatic primary amine of mannose compared to the aromatic amine of FA.

Interaction of the Mannosylated Graft Copolymers with Lectins. Even though the functionalization yield of the copolymer was only 30%, the targeting ability of these micelles was investigated. For this purpose, the bioavailability of mannose at the surface of the poly(εCL)-*graft*-(α-Man PEO) copolymer micelles was assessed by surface plasmon resonance (SPR). The micelles had a hydrodynamic diameter of 87 nm for the poly[$(\varepsilon CL)_{149}$-*graft*-(α-Man PEO_{25})$_5$] **10** with PDI of 0.2 and a hydrodynamic diameter of 90 nm for the poly[$(\varepsilon CL)_{148}$-*graft*-(α-Man PEO_{45})$_3$] **11** with PDI of 0.25 (determined by DLS). In order to monitor the real-time interaction between the mannosylated micelles and a lectin, the concanavalin A (ConA), a protein able to form a complex with mannose, was immobilized onto the surface of a SPR sensorchip by a process described elsewhere.[37] ConA is a legume lectin from the jack-bean *Canavalia ensiformis* and a member of the C-type lectins that requires calcium and manganese cations for complexing mannose. Its monomeric weight is of 25.5 kDa, and the lectin is a dimer at pH < 6 and a tetramer at pH > 7. The binding site of ConA is specific to mannoside and glucoside residues.[48,49] In this study, increasing concentrations of mannosylated micelles were injected over the lectin modified SPR sensor, without regenerating the sensor between the injections. This method, which was previously reported for other types of complexes and named kinetic titration,[38] does not require having the SPR sensorship regenerated by a compound able to destroy the complexes but not the bioactivity of the receptor.[39,40] The recorded sensorgrams for the real-time interaction of the mannosylated micelles of the graft copolymers poly[$(\varepsilon CL)_{149}$-*graft*-(α-Man PEO_{25})$_5$] (**10**) and poly[$(\varepsilon CL)_{148}$-*graft*-(α-Man PEO_{45})$_3$] (**11**) with immobilized ConA are shown in Figure 7. 90 μL aliquots of micellar solutions of increasing concentrations from 0.005 to 2 mg/mL were injected over a period of 3 min at a flow rate of 30 μL/min (association phase) followed by flowing pure buffer

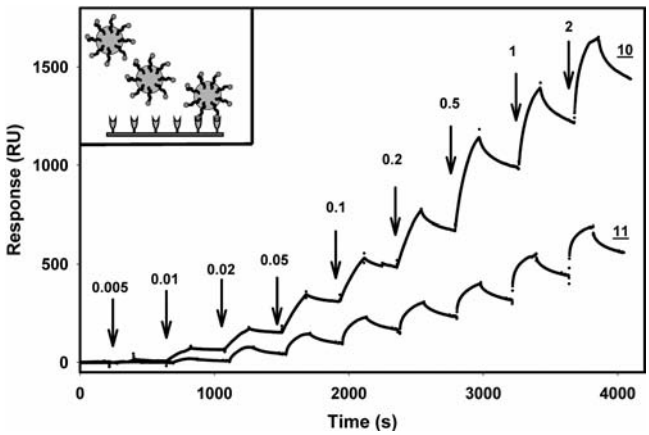


Figure 7. Real-time monitoring of the SPR signal for the interaction of micelles of poly[$(\varepsilon CL)_{149}$-*graft*-(α-Man-PEO_{25})$_5$] **10** (top curve) and poly[$(\varepsilon CL)_{148}$-*graft*-(α-Man-PEO_{45})$_3$] **11** (down curve) copolymers with ConA immobilized on the sensorchip (immobilized amount of lectin: 6300 RU). The kinetic titration method was used. Each step is indicated by an arrow that corresponds to the injection of 90 μL at a flow rate of 30 μL/min of micellar solution followed by 4 min flow of buffer. Values above the arrows indicate the sample concentration expressed in mg/mL. The inset is a representation of the interaction of micelles with the SPR surface modified lectins.

dx.doi.org/10.1021/bc200650n | *Bioconjugate Chem.* 2012, 23, 1740−1752

for 4 min (dissociation phase) between each injection. A considerable increase of the SPR signal was observed during the association phase for both the graft copolymers as result of the complexation of mannosylated micelles by the lectin ConA receptors immobilized to the surface of the sensor. The lowest concentration responsible for a detectable signal was 0.01 and 0.02 mg/mL for copolymer **10** and **11**, respectively. This difference might be the result of the higher density of mannose at the surface of the micelles formed by the copolymer **10**. Indeed, the copolymer **10** contains more PEO grafts and thus more mannose ligands than the copolymer **11** of similar HLB and sugar residue per PEO. Whatever the concentration, the complexation signal measured for the graft copolymer **10** was systematically higher than for the copolymer **11**. This observation confirms the more extensive complexation of the copolymer **10** micelles. A closer look at the SPR sensorgrams shows that the curve during the association phase is steeper for copolymer **10** than for copolymer **11**. Furthermore, the response curve during the association phases of copolymer **11** approached equilibrium at the end of the injection. This observation suggests that the complexation progresses more rapidly for copolymer **11** than for copolymer **10**. This difference in the complexation kinetics can be connected to the difference in flexibility of the copolymers. Indeed, the length of the PEO grafts in the two copolymers is not the same, and their mobility in the micellar shell must decrease as the length is shorter.

During the dissociation phase, the signal decreases in both cases, which suggests a partial decomplexation of mannose from the lectin layer. These data usually give access to the association and dissociation rate constants, and to the dissociation-binding equilibrium constant by using specific softwares, e.g., CLAMP[38] or MSK[40] custom-made, for fitting the kinetic titration curves. Nevertheless, the experimental data could not be fitted by these software, which may suggest a multivalent interaction between the mannosylated micelles and the lectin layer, which is beyond the scope of these software as already reported.[50]

In order to confirm the binding of the micelles by complexation with a potential receptor, *Burkholderia cepacia* lectin A (BclA) was immobilized onto a sensorchip. BclA is a dimeric bacterial lectin know for stronger binding to α-D-mannopyranosyl residue than ConA ($K_a = 3.6 \times 10^5$ M^{-1} [35] for BclA and $K_a = 8.2 \times 10^3$ M^{-1} for ConA [51]). With this BclA lectin, attention was paid to the effect of the density of the immobilized lectin on the SPR sensor surface, on the interaction with the mannosylated micelles of copolymer **11**. Sensors with different densities of BclA at the surface were prepared by changing the volume of the lectin solution. The quantity of immobilized lectins onto the sensor could be easily determined from the SPR signal variation before and after the lectin immobilization. Three sensors were thus modified by different amounts of BclA that corresponded to a SPR signal of 2560, 1140, and 740 response units (RU). Since 1 RU corresponds to 1 pg/mm^2 and the molecular weight of BclA is 28 000 g/mol, the distance between two lectins can be estimated at 4.26, 6.39, and 7.93 nm, respectively (Table 4). These figures are only rough estimates for two main reasons. First, all the binding sites of the immobilized lectins may not be available to interact with the micelles. Second, the immobilization process could also impair the structure of some binding sites. Therefore, the actual distance between near-neighbor active binding sites is most probably higher than the calculated one.

Table 4. Conversion of SPR Responses Unit (RU) into Distances between Near-Neighbor Lectins onto the Sensor Surface Based on 1 RU = 1 pg/mm2 and the Molar Mass of the BclA Lectin = 28 000 g/mol

amount of lectins (RU)	distance between lectins (nm)
2560	4.26
1140	6.39
740	7.93

Figure 8 shows the interaction of mannosylated micelles **11** with the three different sensors of decreasing BclA density. Similarly to Con A, clear association curves are recorded, with a slope which is however steeper and thus a progress of BclA/micelles interaction which is slower compared to ConA. During the buffer flow, no dissociation was observed with BclA which reflects a more stable complex in good agreement with the association constant of the ConA and BclA to α-D-mannopyranose. For the lowest lectin density, partial dissociation of the complex was observed during the buffer flow, meaning that the complex was then weaker. This might be explained by a decrease in the multivalency of the interactions between micelles and BclA. Of course, in the case of 740 RU, the distance between near-neighbor lectins on the surface might be higher than the distance between two mannose ligands at the surface of the micelles, so accounting for less multivalent interactions and/or a lower number of multiple interactions,[52−54] as schematized in Figure 9. Dissociation was also observed with ConA for similar reasons.

Steric Stabilization of PLA Nanoparticles Stabilized by Mannosylated Graft-Copolymers. Finally, the mannosylated graft copolymers were used to stabilize PLA nanoparticles (NPs) and to make them able to recognize lectins. The NPs were prepared by nanoprecipitation from an acetone solution (2.5 mL) containing 50 mg of PLA and 32.5 mg of copolymer.[12] The hydrodynamic diameter of the PLA NPs stabilized with the mannosylated graft copolymers **10** and **11** was around 365 nm with a PDI of 0.2. Recognition of BclA by the PLA NPs was tested by the enzyme linked lectin assay (ELLA). For this purpose, biotin-labeled BclA was incubated with the PLA NPs.[35] Biotinylated lectin on the surface of the PLA NPs was searched by using a streptavidine−peroxidase conjugate followed by the addition of the enzyme substrate. This multistep procedure allowed the lectin to be detected by UV−visible spectroscopy (Scheme 4). Figure 10 compares the absorbance of the PLA NPs stabilized by either each of the two mannosylated graft copolymers **10** and **11** or by a non-mannosylated copolymer **4** after interaction with biotin-labeled BclA. The absorbance was significantly higher for the mannosylated nanoparticles, which assesses for the availability of mannose residues to interacting with lectin. The positive response of the reference sample deprived of mannose might be explained by nonspecific adsorption of the lectin or the streptavidin−phosphatase conjugate.

CONCLUSION

Well-defined α-acetal, ω-alkyne poly(ethylene oxide)s were synthesized and used as building blocks for the synthesis of amphiphilic biodegradable PCL-*graft*-PEO copolymers, whose PEO grafts were end-capped by an acetal. The micelles of these copolymers were successfully labeled by a fluorescent dye by reductive amination in water. This strategy has the advantage of being implemented under mild aqueous conditions that

dx.doi.org/10.1021/bc200650n | *Bioconjugate Chem.* 2012, 23, 1740−1752

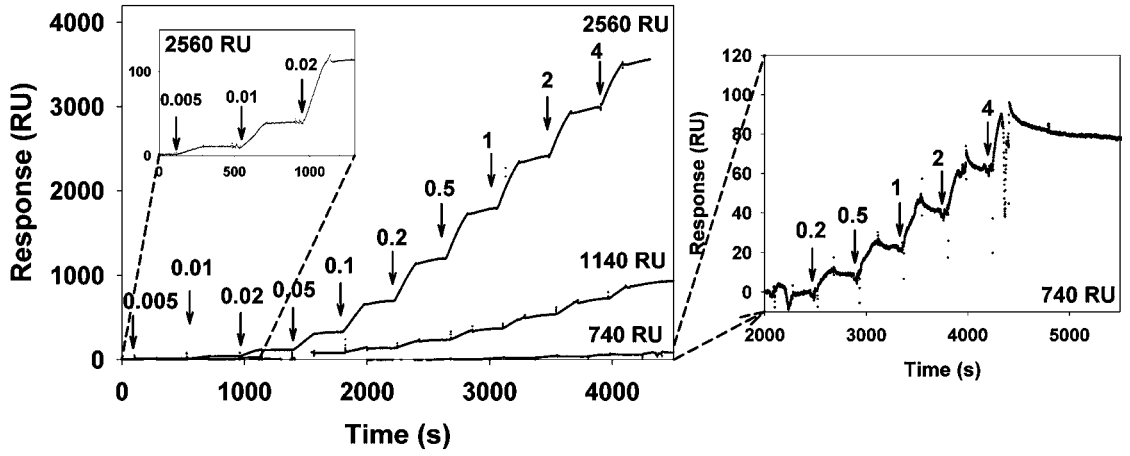


Figure 8. Sensograms recorded by kinetic titration of BclA with mannosylated micelles of copolymer poly[$(\varepsilon CL)_{148}$-*graft*-(α-Man-$PEO_{45})_3$] (**11**) (2560, 1140, and 740 RU of immobilized lectin). The curve on the right-hand side is a zoom in the case of 740 RU. The figure above the arrows indicates the micellar concentrations in mg/mL.

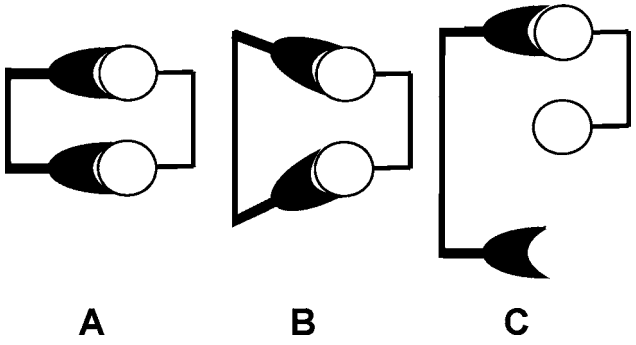


Figure 9. Possible cases for the divalent binding of a ligand to its receptor: (A) favorable case; (B) the linker molecule is shorter than the ideal length and the receptor conformation is deformed to allow a second binding; (C) the linker is too short for a divalent interaction to occur.

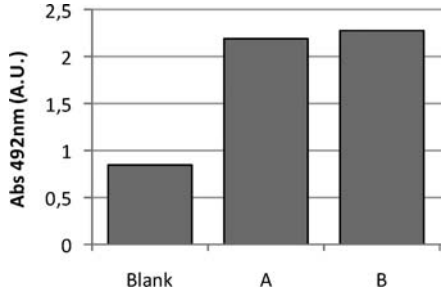


Figure 10. Absorbance at 492 nm of PLA nanoparticles stabilized by the mannosylated graft copolymer **10** (A) or **11** (B) and the non-mannosylated graft copolymer **4** (blank) after interaction with biotin labeled BclA.

preserve the copolymer from degradation and allows the labeling by aminated targeting agents. Indeed, mannose residues were successfully attached to the surface of micelles without the need of protection/deprotection steps of the sugar. The bioavailability of the sugar to complex appropriate receptors was unambiguously shows by surface plasmon resonance. Finally, the mannosylated graft copolymers were able to stabilize PLA nanoparticles for use in drug delivery systems. The ELLA test also confirmed the availability of the sugar at the NPs surface to bind with a specific lectin. The mannosylated PCL-*graft*-PEO copolymers are thus quite promising for the preparation of nanocarriers for site-specific drug delivery applications. The versatility of the strategy developed herein paves the way for preparation of labeled micelles with other types of amino-functional and hydrosoluble ligands, such as peptides.

AUTHOR INFORMATION

Corresponding Author

*E-mail: c.jerome@ulg.ac.be; Fax: +32 (0)43663497; Tel: +32 (0)43663461.

Present Address

[#]Max Planck Institute for Polymer Research, Ackermannweg 10, 55128 Mainz, Germany.

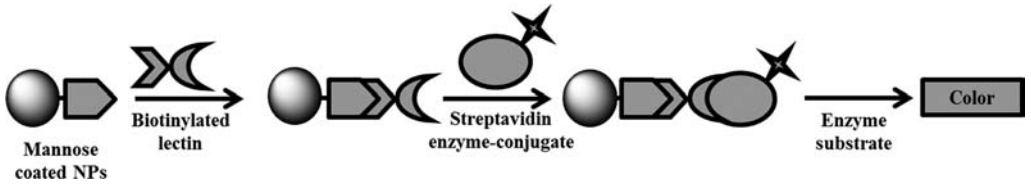
Notes

The authors declare no competing financial interest.

ACKNOWLEDGMENTS

H.F. and C.J. (CERM) are grateful to the "Interuniversity Attraction Poles Program (PAI 6/27) - Functional Supramolecular Systems", "Region Wallonne" in the framework of

Scheme 4. Scheme of the Multistep ELLA Test That Probes the Availability of Mannose Residues at the Surface of PLA Nanoparticles Stabilized by a Mannosylated Graft Copolymer



the project VACCINOR and "Grant F.R.S.-FNRS-Télévie" for financial support of this research. The authors are indebted to the CGRI-FNRS-CNRS program for financial support of this research in the framework of bilateral cooperation. We thank Anne Imberty for providing BclA lectin. The authors would like to thank Véronique Schmitz (CERM), Gabriel Mazzuccheli (CART), Catherine Gautier (CERMAV), and Claudine Fraipont (CIP) for their technical support. SPR data were obtained at the "Centre d'Ingenierie des Proteins" (CIP, University of Liège), which is supported by contract FRFC credit no 9.4519.98. The authors express gratitude to R. Riva and Ph. Lecomte for fruitful discussions.

REFERENCES

(1) Nishiyama, N., and Kataoka, K. (2006) Current state, achievements, and future prospects of polymeric micelles as nanocarriers for drug and gene delivery. *Pharmacol. Ther. 112*, 630−648.

(2) Wei, X., Gong, C., Gou, M., Fu, S., Guo, Q., Shi, S., Luo, F., Guo, G., Qiu, L., and Qian, Z. (2009) Biodegradable poly(ε-caprolactone)-poly(ethylene glycol) copolymers as drug delivery system. *Int. J. Pharm. 381*, 1−18.

(3) Blanco, E., Kessinger, C. W., Sumer, B. D., and Gao, J. (2009) Multifunctional micellar nanomedicine for cancer therapy. *Exp. Biol. Med. 234*, 123−131.

(4) Mahmud, A., Xiong, X.-B., Aliabadi Hamidreza, M., and Lavasanifar, A. (2007) Polymeric micelles for drug targeting. *J. Drug Target 15*, 553−84.

(5) Letchford, K., and Burt, H. (2007) A review of the formation and classification of amphiphilic block copolymer nanoparticulate structures: micelles, nanospheres, nanocapsules and polymersomes. *Eur. J. Pharm. Biopharm. 65*, 259−269.

(6) Jones, M.-C., and Leroux, J.-C. (1999) Polymeric micelles - a new generation of colloidal drug carriers. *Eur. J. Pharm. Biopharm. 48*, 101−111.

(7) Zalipsky, S., and Harris, J. M. (1997) Introduction to chemistry and biological applications of poly(ethylene glycol), in *Poly(Ethylene Glycol) - Chemistry and Biological Applications* (Harris, J. M., and Zalipsky, S., Eds.) pp 1−13, American Chemical Society, Washington, DC.

(8) Fuhrmann, K., Schulz, J. D., Gauthier, M. A., and Leroux, J.-C. (2012) PEG nanocages as non-sheddable stabilizers for drug nanocrystals. *ACS Nano 6*, 1667−1676.

(9) Owens, D. E., and Peppas, N. A. (2006) Opsonization, biodistribution, and pharmacokinetics of polymeric nanoparticles. *Int. J. Pharm. 307*, 93−102.

(10) Stolnik, S., Dunn, S. E., Garnett, M. C., Davies, M. C., Coombes, A. G. A., Taylor, D. C., Irving, M. P., Purkiss, S. C., Tadros, T. F., Davis, S. S., and Illum, L. (1994) Surface modification of poly(lactide-*co*-glycolide) nanospheres by biodegradable poly(lactide)-poly(ethylene glycol) copolymers. *Pharm. Res. 11*, 1800−1808.

(11) Garinot, M., Fievez, V., Pourcelle, V., Stoffelbach, F., des Rieux, A., Plapied, L., Theate, I., Freichels, H., Jerome, C., Marchand-Brynaert, J., Schneider, Y.-J., and Preat, V. (2007) PEGylated PLGA-based nanoparticles targeting M cells for oral vaccination. *J. Controlled Release 120*, 195−204.

(12) Rieger, J., Freichels, H., Imberty, A., Putaux, J.-L., Delair, T., Jerome, C., and Auzely-Velty, R. (2009) Polyester nanoparticles presenting mannose residues: toward the development of new vaccine delivery systems combining biodegradability and targeting properties. *Biomacromolecules 10*, 651−657.

(13) Rieger, J., Passirani, C., Benoit, J. P., Van Butsele, K., Jerome, R., and Jerome, C. (2006) Synthesis of amphiphilic copolymers of poly(ethylene oxide) and poly(ε-caprolactone) with different architectures, and their role in the preparation of stealthy nanoparticles. *Adv. Funct. Mater. 16*, 1506−1514.

(14) Parrish, B., Breitenkamp, R. B., and Emrick, T. (2005) PEG- and peptide-grafted aliphatic polyesters by click chemistry. *J. Am. Chem. Soc. 127*, 7404−7410.

(15) Riva, R., Schmeits, S., Jerome, C., Jerome, R., and Lecomte, P. (2007) Combination of ring-opening polymerization and "click chemistry": toward functionalization and grafting of poly(ε-caprolactone). *Macromolecules 40*, 796−803.

(16) Riva, R., Rieger, J., Jérôme, R., and Lecomte, P. (2006) Heterograft copolymers of poly(ε-caprolactone) prepared by combination of ATRA "grafting onto" and ATRP "grafting from" processes. *J. Polym. Sci., Part A: Polym. Chem. 44*, 6015−6024.

(17) Rieger, J., Van Butsele, K., Lecomte, P., Detrembleur, C., Jérôme, R., and Jérôme, C. (2005) Versatile functionalization and grafting of poly(ε-caprolactone) by Michael-type addition. *Chem. Commun.*, 274−276.

(18) Taniguchi, I., Mayes, A. M., Chan, E. W. L., and Griffith, L. G. (2005) A chemoselective approach to grafting biodegradable polyesters. *Macromolecules*, 216−219.

(19) Iha, R. K., Van Horn, B. A., and Wooley, K. L. (2010) Complex, degradable polyester materials via ketoxime ether-based functionalization: amphiphilic, multifunctional graft copolymers and their resulting solution-state aggregates. *J. Polym. Sci., Part A: Polym. Chem. 48*, 3553−3563.

(20) Sutton, D., Nasongkla, N., Blanco, E., and Gao, J. (2007) Functionalized micellar systems for cancer targeted drug delivery. *Pharm. Res. 24*, 1029−1046.

(21) Taniguchi, I., Kuhlman, W. A., Mayes, A. M., and Griffith, L. G. (2006) Functional modification of biodegradable polyesters through a chemoselective approach: application to biomaterial surfaces. *Polym. Int. 55*, 1385−1397.

(22) Taniguchi, I., Kuhlman, W. A., Griffith, L. G., and Mayes, A. M. (2006) Functional modification of biodegradable polyester for cell-specific biomaterial surfaces. *Polym. Prepr. 47*, 57−58.

(23) Lecomte, P., Riva, R., Jerome, C., and Jerome, R. (2008) Macromolecular engineering of biodegradable polyesters by ring-opening polymerization and 'Click' chemistry. *Macromol. Rapid Commun. 29*, 982−997.

(24) Evans, R. A. (2007) The rise of azide-alkyne 1,3-dipolar 'click' cycloaddition and its application to polymer science and surface modification. *Aust. J. Chem. 60*, 384−395.

(25) Rostovtsev, V. V., Green, L. G., Fokin, V. V., and Sharpless, K. B. (2002) A stepwise Huisgen cycloaddition procces: copper(I)-catalized regioselecte "ligation" of azides and terminal alkynes. *Angew. Chem., Int. Ed. 41*, 2596−2599.

(26) Lallana, E., Fernandez-Trillo, F., Sousa-Herves, A., Riguera, R., and Fernandez-Megia, E. (2012) Click chemistry with polymers, dendrimers, and hydrogels for drug delivery. *Pharm. Res. 29*, 902−921.

(27) Suksiriworapong, J., Sripha, K., Kreuter, J. r., and Junyaprasert, V. B. (2010) Investigation of polymer and nanoparticle properties with nicotinic acid and p-aminobenzoic acid grafted on poly(ε-caprolactone)-poly(ethylene glycol)-poly(ε-caprolactone) via click chemistry. *Bioconjugate Chem. 22*, 582−594.

(28) Nagy, M., Szöllösi, L., Kéki, S., and Zsuga, M. (2006) Self-assembly study of polydisperse ethylene oxide-based nonionic surfactants. *Langmuir 23*, 1014−1017.

(29) Luo, L. B., Tam, J., Maysinger, D., and Eisenberg, A. (2002) Cellular internalization of poly(ethylene oxide)-*b*-poly(ε-caprolactone) diblock copolymer micelles. *Bioconjugate Chem. 13*, 1259−1265.

(30) McGreal, E. P., Miller, J. L., and Gordon, S. (2005) Ligand recognition by antigen-presenting cell C-type lectin receptors. *Curr. Opin. Immunol. 17*, 18−24.

(31) Chellat, F., Merhi, Y., Moreau, A., and Yahia, L. H. (2005) Therapeutic potential of nanoparticulate systems for macrophage targeting. *Biomaterials 26*, 7260−7275.

(32) Kricheldorf, H. R., and Eggerstedt, S. (1998) Macrocycles. Part 2. Living macrocyclic polymerization of ε-caprolactone with 2,2-dibutyl-2-stanna-1,3-dioxepane as initiator. *Macromol. Chem. Phys. 199*, 283−290.

(33) Lenoir, S., Riva, R., Lou, X., Detrembleur, C., Jérôme, R., and Lecomte, P. (2004) Ring-opening polymerization of α-chloro-ε-caprolactone and chemical modification of poly(α-chloro-ε-caprolac-

tone) by atom transfer radical processes. *Macromolecules 37*, 4055−4061.
(34) Pourcelle, V., Freichels, H., Stoffelbach, F., Auzely-Velty, R., Jerome, C., and Marchand-Brynaert, J. (2009) Light induced functionalization of PCL-PEG block copolymers for the covalent immobilization of biomolecules. *Biomacromolecules 10*, 966−974.
(35) Lameignere, E., Malinovska, L., Slavikova, M., Duchaud, E., Mitchell, E. P., Varrot, A., Sedo, O., Imberty, A., and Wimmerova, M. (2008) Structural basis for mannose recognition by a lectin from opportunistic bacteria Burkholderia cenocepacia. *Biochem. J. 411*, 307−318.
(36) Vangeyte, P., Gautier, S., and Jérôme, R. (2004) About the methods of preparation of poly(ethylene oxide)-*b*-poly(ε-caprolactone) nanoparticles in water Analysis by dynamic light scattering. *Colloids Surf., A: Physiochem. Eng. Aspects 242*, 203−211.
(37) Murthy, B. N., Voelcker, N. H., and Jayaraman, N. (2006) Evaluation of a-D-mannopyranoside glycolipid micelles-lectin interaction by surface plasmon resonance method. *Glycobiology 16*, 822−832.
(38) Karlsson, R., Katsamba, P. S., Nordin, H., Pol, E., and Myszka, D. G. (2006) Analyzing a kinetic titration series using affinity biosensors. *Anal. Biochem. 349*, 136−147.
(39) Tang, Y., Mernaugh, R., and Zeng, X. (2006) Nonregeneration protocol for surface plasmon resonance: study of high-affinity interaction with high-density biosensors. *Anal. Chem. 78*, 1841−1848.
(40) Trutnau, H. H. (2006) New multi-step kinetics using common affinity biosensors saves time and sample at full access to kinetics and concentration. *J. Biotechnol. 124*, 191−195.
(41) Cade, D., Ramus, E., Rinaudo, M., Auzely-Velty, R., Delair, T., and Hamaide, T. (2004) Tailoring of bioresorbable polymers for elaboration of sugar-functionalized nanoparticles. *Biomacromolecules 5*, 922−927.
(42) Nagasaki, Y., Kutsuna, T., Iijima, M., Kato, M., and Kataoka, K. (1995) Formyl-ended heterobifunctional poly(ethylene oxide): synthesis of poly(ethylene oxide) with a formyl group at one end and a hydroxyl group at the other end. *Bioconjugate Chem. 6*, 231−233.
(43) Greene, T. W., and Wuts, P. G. M. (1999) *Protective Groups in Organic Synthesis*, 3rd ed., John Wiley & Sons, Inc.
(44) Rao, H. S. P., and Siva, P. (1994) Facile reduction of azides with sodium-borohydride copper (II) sulfate system. *Synth. Commun. 24*, 549−555.
(45) Fordor, Z., Fodor, A., and Kennedy, J. P. (1992) A GPC method to determine the composition of two component copolymers. *Polym. Bull. 29*, 689−696.
(46) Dubois, M., Gilles, K. A., Hamilton, J. K., Rebers, P. A., and Smith, F. (1956) Colorimetric method for determination of sugars and related substances. *Angew. Chem. 28*, 350−356.
(47) Freichels, H., Auzély-Velty, R., Lecomte, P., and Jérôme, C. (2012) Easy functionalization of amphiphilic poly(ethylene oxide)-b-poly(ε-caprolactone) copolymer micelles with unprotected sugar: synthesis and recognition by lectins. *Polym. Chem.*, DOI: 10.1039/c2py00572g.
(48) Ting, S. R. S., Chen, G., and Stenzel, M. H. (2010) Synthesis of glycopolymers and their multivalent recognitions with lectins. *Polym. Chem. 1*, 1392−1412.
(49) Olson, M. O. J., and Liener, I. E. (1967) Some physical and chemical properties of concanavalin A, the phytohemagglutinin of the jack bean. *Biochemistry 6*, 105−11.
(50) Jule, E., Nagasaki, Y., and Kataoka, K. (2003) Lactose-installed poly(ethylene glycol)-poly(D,L-lactide) block copolymer micelles exhibit fast-rate binding and high affinity toward a protein bed simulating a cell Surface. A surface plasmon resonance study. *Bioconjugate Chem. 14*, 177−186.
(51) Dam, T. K., and Brewer, C. F. (2002) Thermodynamic studies of lectin-carbohydrate interactions by isothermal titration calorimetry. *Chem. Rev. 102*, 387−429.
(52) Houseman, B. T., and Mrksich, M. (2002) Model systems for studying polyvalent carbohydrate binding interactions. *Host-Guest Chemistry 218*, 1−44.
(53) Mammen, M., Choi, S. K., and Whitesides, G. M. (1998) Polyvalent interactions in biological systems: Implications for design and use of multivalent ligands and inhibitors. *Angew. Chem., Int. Ed. 37*, 2755−2794.
(54) Reynolds, M., and Pérez, S. (2011) Thermodynamics and chemical characterization of protein-carbohydrate interactions: The multivalency issue. *C. R. Chim. 14*, 74−95.
(55) Becher, P., and Schick, M. J. (1987) Macroemulsions. *Surfactant Science Series 23*, 435−91.

Bioconjugate Chemistry

Article

pubs.acs.org/bc

PolyMPC–Doxorubicin Prodrugs

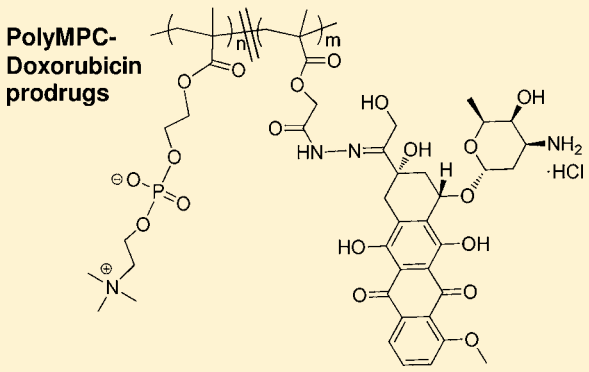
Xiangji Chen,[†] Sangram S. Parelkar,[†] Elizabeth Henchey,[‡] Sallie Schneider,[‡] and Todd Emrick*,[†]

[†]Polymer Science & Engineering Department, 120 Governors Drive, University of Massachusetts, Amherst, Massachusetts 01003, United States

[‡]Pioneer Valley Life Sciences Institute, 3601 Main Street, Springfield, Massachusetts 01199, United States

Supporting Information

ABSTRACT: We demonstrate the conjugation of the cancer drug doxorubicin (DOX) to poly(methacryloyloxyethyl phosphorylcholine) (polyMPC), linked by hydrazone groups, using (1) a one-pot ATRP/click sequence, and (2) a post-polymerization conjugation strategy. While the one-pot method gave polyMPC–DOX conjugates in a facile single step, post-polymerization conjugation gave higher-molecular-weight polymers with very high DOX loadings. DOX release from the polyMPC backbone was pH-dependent (faster at pH 5.0 than at pH 7.4) owing to the hydrazone linkage. Half-life values of DOX release ranged from 2 to 40 h at pH 5.0. Cell culture experiments showed that highly loaded polyMPC–DOX conjugates exhibited higher intracellular drug accumulation and lower half-maximal inhibitory concentration (IC_{50}) values, while a polymer with 30 wt % drug loading showed a maximum tolerated dose in the range of 30–50 mg/kg DOX equivalent weight in healthy mice.



INTRODUCTION

Polymer–drug conjugates as nanoscale therapeutics[1,2] are creating new opportunities for improved cancer therapy.[3−5] Conjugating anticancer drugs to water-soluble synthetic polymers improves drug solubility, prolongs *in vivo* circulation half-life ($t_{1/2}$), and reduces undesired side effects.[6,7] The large size of polymer molecules, relative to small molecule drugs, affords the drug with a large (several nanometers to tens-of-nanometers) hydrodynamic volume, which slows renal clearance and improves drug uptake into tumors (relative to healthy tissue) by the enhanced permeability and retention (EPR) effect.[8−10] The EPR effect benefits from the leaky vasculature and poor lymphatic drainage surrounding the growing neoplasms. As a result, polymer–drug conjugates have exhibited an increased therapeutic index (LD_{50}/ED_{50}) compared to free drugs. Numerous synthetic polymers have been conjugated covalently to different anticancer drugs to give structures that fall into the classification of polymer prodrugs.[11] Prominent examples of polymers used in cancer prodrug compositions include poly(ethylene glycol) (PEG),[12] poly-*N*-(2-hydroxypropyl)methacrylamide (HPMA),[13−15] poly(L-glutamic acid) (PG),[16,17] cyclodextrin-based polymers,[18,19] dextran,[20] and polyacetal poly(1-hydroxymethylethylene hydroxymethylformal) (PHF).[21]

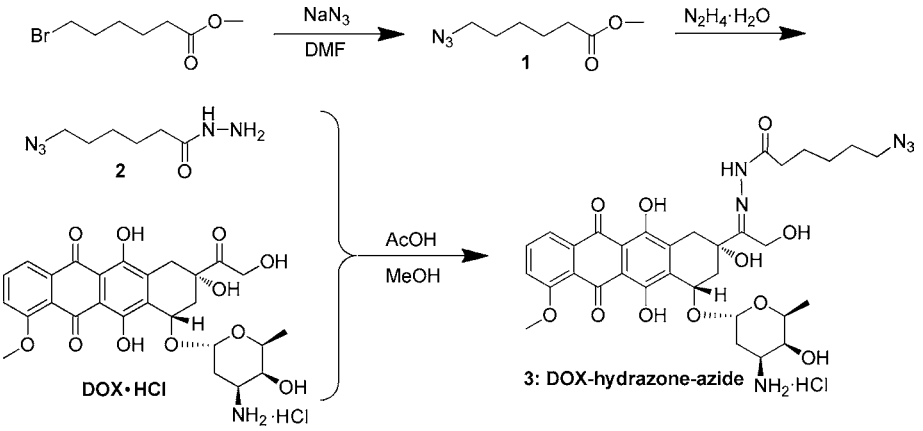
Effective polymer therapeutics requires the use of water-soluble, biocompatible polymers as starting materials. The water solubility and low toxicity and low immunogenicity of PEG have made it attractive for conjugation to numerous therapeutic proteins and peptide drugs to enhance therapeutic efficacy.[7] However, the zwitterionic water-soluble polymer, poly(methacryloyloxyethyl phosphorylcholine) (polyMPC),[22] has been used extensively in blood-contacting medical devices that require a high level of biocompatibility and resistance to protein adsorption.[22−28] PolyMPC has recently been considered as an alternative to PEG, and studied in conjugation chemistry with therapeutic proteins such as erythropoietin (EPO), granulocyte-colony stimulating factor (G-CSF), and interferon.[29,30] For example, 20 kDa PEG equivalent polyMPC–interferon was seen to have a longer pharmacokinetic (PK) profile (absorption $t_{1/2}$ = 7.3 h) than the 20 kDa disulfide PEGylated analogue (absorption $t_{1/2}$ = 3.3 h).[30] With regard to cancer therapeutics, we demonstrated the conjugation of camptothecin (CPT) to polyMPC using azide/alkyne click cycloaddition, in a one-pot polymerization/conjugation procedure of alkyne-substituted polyMPC with CPT-azide.[31] This approach provided polyMPC–CPT prodrugs with much higher drug loading than the PEGylation approach, due to the inherent restriction of PEG that limits drug conjugation only to the chain-ends.

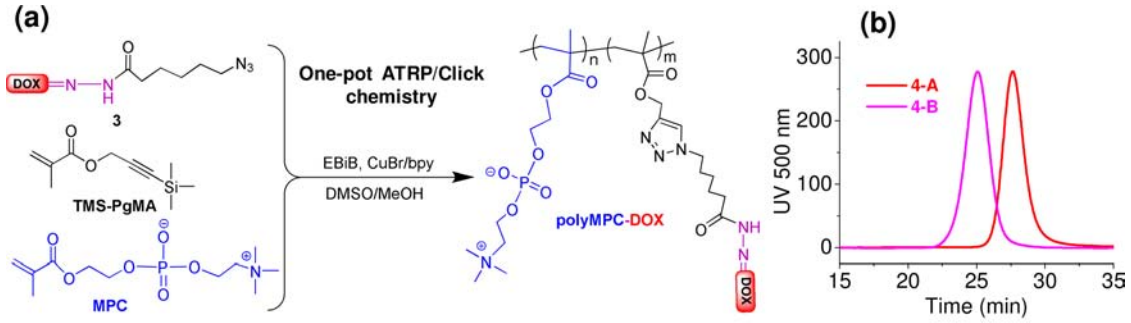
Doxorubicin (DOX) is a DNA intercalating drug with dose-dependent cytotoxicity affecting a broad range of DNA processes. DOX and its derivatives show pronounced anticancer activity that unfortunately is accompanied by undesirable side effects. Doxil, a PEGylated liposome encapsulant of DOX, shows favorable pharmacokinetics compared to free DOX, with significantly reduced dose-limiting

Received: December 20, 2011
Revised: July 17, 2012
Published: August 10, 2012

 © 2012 American Chemical Society dx.doi.org/10.1021/bc200667s | *Bioconjugate Chem.* 2012, 23, 1753–1763

Scheme 1





(c)

Conjugate	N_{MPC}	$N_{TMS\text{-}PgMA}$	$N_{DOX\text{-}N3}$	Conv. (%)	M_n(kDa)	PDI	DOX wt%	Target DOX wt%	Zeta potential (mV)
4-A	50	3	3	70	6.7	1.23	5.3	10	4.3
4-B	100	3	3	70	12.4	1.40	3.6	5.4	4.6

Figure 1. (a) One-pot ATRP/click cycloaddition synthesis of polyMPC–DOX; (b) aqueous GPC traces of conjugates **4-A** and **4-B**; (c) polyMPC–DOX conjugates prepared by one-pot ATRP/click method; N_{MPC}, $N_{TMS\text{-}PgMA}$, $N_{DOX\text{-}N3}$ are the molar equivalent to initiator EBiB; Conv (%) represents monomer conversion determined by ^{1}H NMR spectroscopy; DOX wt % is obtained by UV–vis spectroscopy at 488 nm.

toxicities associated with cardiomyopathy and myelosuppression.[32,33] However, Doxil has its own dose-limiting toxicities, including palmer-planter erythrodysesthesia (hand-foot syndrome) and mucositis/stomatitis[34−36] due to its accumulation in the skin.[37] Moreover, acquired cellular resistance to DOX from overexpression of P-glycoprotein encoded by the MDR1 (multidrug resistance 1) gene has been documented.[38,39]

Polymer–drug conjugation can alter the cellular internalization pathway of a drug, and circumvent P-glycoprotein associated multidrug resistance.[40,41] For example, DOX conjugation to a PEGylated dendrimer[42] at a drug loading of 10 wt % proved promising in preclinical studies. In this case, DOX was conjugated through its ketone group (at the 13 position carbon) by reaction with an acyl hydrazine of the dendrimer. HPMA,[43−45] poly(ethylene oxide)-*block*-poly(allyl glycidyl ether),[46] and degradable dendrimers[47] were also conjugated to DOX through hydrazones, showing improved efficacy in preclinical studies. The acid-sensitive hydrazone linker enables DOX release either extracellularly in the slightly acidic environment of tumor tissue[48,49] or intracellularly in the acidic environment of endosomal (pH ∼5.5–6.0) and lysosomal (pH ∼4.5–5.0) compartments.[50]

Here, we describe the preparation of polyMPC–DOX prodrugs that integrate the pH-responsive hydrazone linkages into the polyMPC structure. In one approach, DOX-azide **3** was synthesized and used for the preparation of polyMPC–DOX conjugates by a one-pot simultaneous ATRP polymerization and DOX grafting by azide–alkyne click chemistry. In a second approach, polyMPC with pendant acyl hydrazides was synthesized by copolymerization, and DOX was incorporated into the polymer by hydrazone formation. Using the latter method, high DOX loading on the polyMPC backbone was achieved (30 wt % and greater), as characterized by UV/vis spectroscopy. The pH dependence of DOX release from the polyMPC backbone was revealed using HPLC, and subcellular localization, intracellular abundance, and cytotoxicity profiles were determined in human breast and colon adenocarcinoma cells. The maximum tolerated dose (MTD) of polyMPC–DOX prodrug was also evaluated in normal mice.

RESULTS AND DISCUSSION

Synthesis of polyMPC–DOX by One-Pot Polymerization. The preparation of hydrazine-containing DOX-azide **3** is shown in Scheme 1, accomplished by first reacting methyl 6-bromohexanoate with sodium azide in DMF to give methyl 6-azidohexanoate **1** in 98% yield. Refluxing compound **1** in hydrazine monohydrate afforded the desired linker, compound **2**, in 60% yield after crystallization in methanol/ethyl ether

dx.doi.org/10.1021/bc200667s | *Bioconjugate Chem.* 2012, 23, 1753–1763

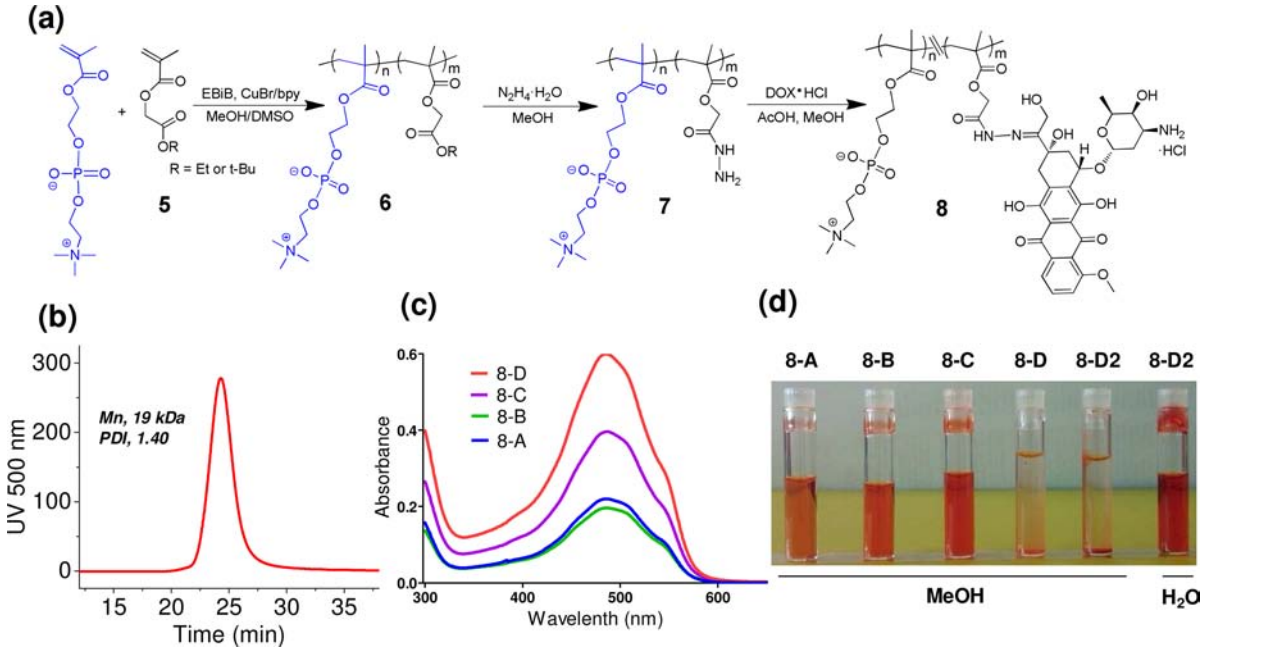


Figure 2. (a) ATRP copolymerization of MPC and TBOEMA, followed by acylhydrazine formation (**7**) and DOX conjugation (**8**). (b) Aqueous GPC trace of polyMPC–DOX conjugate **8-B**. (c) Overlay of UV/vis spectra of conjugates **8** in water at concentration of 0.1 mg/mL. (d) Conjugates **8-A**, **8-B**, and **8-C** are soluble in methanol and water, while **8-D** and **8-D2** are not soluble in methanol but are soluble in water.

Table 1. Poly(MPC-*co*-TBOEMA) (6) and the Corresponding Acyl Hydrazide Polymers (7)

polymer	target TBOEMA (mol %)[a]	conv (%)[b]	M_n (kDa)	PDI	TBOEMA (mol %)[c]	polymer	M_n (kDa)	PDI	hydrazine (mol %)[d]
6-A	10	90	16	1.54	10	**7-A**	16	1.56	9
6-B	10	70	25	1.32	12	**7-B**	25	1.34	13
6-C	20	50	28	1.43	19	**7-C**	29	1.49	21
6-D	40	53	22	1.50	38	**7-D**	31	1.45	37

[a]Based on monomer feed ratio. [b]Monomer conversion measured by ^{1}H NMR spectroscopy. [c]Estimated by ^{1}H NMR spectroscopy. [d]Estimated by ^{1}H NMR spectroscopy.

mixtures. Azide **2** was then coupled to DOX hydrochloride in methanol to give the desired DOX-azide **3**. FT-IR spectroscopy of **3** showed the expected azide signal at 2098 cm^{-1}, while ^{1}H NMR spectroscopy showed the alkyl chain (linker) signals from 1.1 to 1.3 ppm, and the phenyl protons of DOX at 7.95, 7.93, and 7.68 ppm. By ^{13}C NMR spectroscopy, the original DOX ketone carbon resonance at 214 ppm was absent, and a new resonance for the C═N of the hydrazone was seen at 187 ppm. High-resolution mass spectroscopy (HRMS) confirmed the successful isolation of DOX-azide **3** (Calcd: 697.2833; Found: *m*/*z* 697.2822 [M+H]).

One-Pot ATRP/Click Chemistry. DOX-azide **3** was introduced into the ATRP polymerization reaction with 1 molar equiv trimethylsilyl-protected propargyl methacrylate (TMS-PgMA), as shown in Figure 1. TMS-PgMA was copolymerized with MPC by ATRP, incorporating DOX into the structure by azide/alkyne cycloaddition as the polymerization proceeded. Monomer conversion of ~70% was achieved over a 20 h period, and the polyMPC–DOX conjugates were isolated in ~60% yield following precipitation into THF and column chromatography. The polyMPC–DOX conjugates were characterized by aqueous GPC (0.1 M $NaNO_3$, PEO standards) as shown in Figure 1. The PDI values of the conjugates resulting from this one-pot method were in the range 1.23–1.40, and the molecular weights obtained (6700–12 400 g/mol) confirm good compatibility of DOX with the click and ATRP conditions and mechanisms. The weight percentage of DOX in the conjugate was calculated based on its UV/vis absorption and the molar extinction coefficient of DOX·HCl (ε = 7654 L mol^{-1} cm^{-1} in water) at 488 nm. The drug loading was determined from the DOX-to-conjugate concentration, giving 3–5 wt % DOX by this one-pot method (Figure 1).

PolyMPC–DOX Synthesis by Post-Polymerization Conjugation. While the one-pot strategy represents a simple method for obtaining polyMPC–DOX conjugates, we turned to post-polymerization conjugation in an effort to optimize drug loading on the polyMPC platform. We found that copolymerization of MPC and monomer **5** gave copolymer **6** in excellent yield, and ester-to-acyl hydrazine conversion, using hydrazine hydrate, gave polyMPC-hydrazine **7**. Polymer **7** was then used for conjugation of DOX, again with DOX hydrochloride, as shown in the reaction sequence of Figure 2a. We note that the methyl and ethyl ester versions of monomer **5** were also employed successfully in polymerization and DOX-conjugation processes.

This two-step polymerization/conjugation approach proved straightforward and effective, and superior to the one-pot method with respect to obtaining high drug loading of the conjugates that was not achievable with the one-pot method. Monomer **5**, 2-*tert*-butoxy-2-oxoethyl methacrylate (TBOEMA), was synthesized according to the literature[51] with some modification. The sodium salt of methacrylic acid was esterified with *tert*-butyl bromoacetate in acetonitrile, using tetra-*n*-

butylammonium bromide as a phase transfer catalyst to give TBOEMA **5** as a colorless oil in 83% yield. MPC and TBOEMA were then copolymerized in DMSO/MeOH mixtures, using the CuBr/bipyridine (bpy) catalyst system, and the characteristics of the resulting polymers **6**-(**A** to **D**) are listed in Table 1. Copolymers having TBOEMA/MPC feed ratios in the range of 10:90 to 40:60 were targeted.

Conversion of MPC and monomer **5** to give copolymer **6** was monitored by ^{1}H NMR spectroscopy on aliquots taken from the polymerization mixture. Disappearance of MPC and TBOEMA was seen to occur over a similar time frame, giving 50−90% monomer conversion. Molar ratios of TBOEMA incorporated into copolymer **6** were in good agreement with targeted values, as judged by integration of ^{1}H NMR resonances at 3.58 ($-CH_2-N$ in MPC) and 1.39 ppm ($-(CH_3)_3$ in TBOEMA) (SI Figure S1). Number-average molecular weights (M_n) estimated by aqueous GPC (using PEO calibration standards) were in the range of 16−28 kDa, with PDI values ranging from 1.3 to 1.5. Copolymer **6** was converted to hydrazine-containing polyMPC **7**, with over 95% of the esters converted successfully as judged by disappearance of *tert*-butyl peak in the ^{1}H NMR spectrum (SI Figure S1). Purification by dialysis against water gave copolymer **7**, which was isolated by lyophilization, and characterized by GPC (SI Figure S2) and ^{1}H NMR spectroscopy. As shown in Table 1, M_n values of **7** changed little from their *tert*-butyl ester precursors, with the exception of **7-D**, having the highest hydrazine incorporation. Hydrazine content on polymer **7** estimated by ^{1}H NMR spectroscopy was in good agreement with TBOEMA incorporation of the precursor structures, and copolymer samples with hydrazine loadings ranging from 9 to 37 mol percent were carried on for attempted DOX conjugation.

DOX Conjugation to PolyMPC. Conjugation of DOX hydrochloride to copolymer **7** was performed in methanol to afford the desired polyMPC−DOX conjugates shown as **8**, containing multiple copies of DOX linked to the polyMPC backbone. PolyMPC−DOX **8** conjugates were purified by elution through a Sephadex LH-20 column (as a methanol solution), then a Sephadex G-25 column (as an aqueous solution). Following recovery of the solid material by freeze−drying, conjugate purity was examined by PD-10 (SI Figure S3) and SEC-HPLC, confirming the absence of unconjugated DOX. The targeted DOX loadings in Table 2 were calculated based on the hydrazine loadings in copolymer **7** in Table 1. The molecular weight of DOX hydrochloride conjugated at this level gives a theoretical DOX loading as high as 43 wt %. These values compared closely to the values obtained by UV−vis characterization, as given in Table 2. We recognize that these DOX loadings are high relative to other reported polymer−DOX prodrugs (typically ∼10−20 wt %).[42,46,52,53] Nonetheless, even with such high weight percent DOX, the conjugates maintained good solubility in water, owing to the extreme hydrophilicity of the polyMPC backbone. Such high drug loadings may represent an additional advantage of polyMPC−DOX for parenteral applications.

Table 2. Characterization of polyMPC−DOX Conjugates (8)

conjugate	target DOX (wt %)[a]	DOX (wt %)[b]	M_n (kDa)[c]	PDI[d]	est. M_n (kDa)[e]	D_h (nm)[f]	zeta (mV)[g]
8-A	16	17	11	1.68	19	7.4	6.9
8-B	23	15	19	1.40	29	11.0	8.1
8-C	39	30	ND[h]	ND	41	11.6	15.5
8-D	43	45	ND	ND	56	12.6	13.5
8-D2	43	30	ND	ND	44	15.5	18.5

[a]Calculated DOX loading based on the hydrazine content in corresponding parent polymer **7**. [b]Measured DOX loading from UV/vis absorption. [c]M_n from aqueous GPC calibrated with PEO standards. [d]Polydispersity index from aqueous GPC. [e]Estimated M_n based on corresponding parent polymer and DOX loading. [f]Hydrodynamic diameter measured in PBS by DLS. [g]Zeta potential measured in water by Zetasizer. [h]ND = not detected.

PolyMPC−DOX conjugates containing high DOX loadings presented interesting solubility properties. During the course of conjugation reaction, solubility in methanol was maintained. However, conjugates **8-D** and **8-D2** were found to be insoluble in methanol following purification and freeze-drying. Conjugates with lower DOX loading (<20 wt %) showed a slight tailing during elution by aqueous GPC (Figure 2), and conjugates with higher drug loadings were retained completely on the GPC columns (we note that DOX itself also did not elute under our conditions). As this elution behavior artificially lowers the GPC-estimated molecular weight, the M_n values given in Table 2 are based on the parent (i.e., hydrazine-containing) polymer. However, despite this observed insolubility in methanol, all of the polyMPC−DOX conjugates produced homogeneous solutions in water and injectable saline, allowing characterization of **8-C**, **8-D**, and **8-D2** by dynamic light scattering (DLS) to gauge their hydrodynamic diameter (Table 2). The measured diameters of these conjugates in phosphate-buffered saline (PBS) solution were in the range of 12−15 nm, marginally larger than the 7−11 nm values observed for the conjugates made from lower-molecular-weight polymers. Thus, in water and PBS, the polyMPC−DOX conjugates disperse well, with evidence for minor self-association, without the formation of large aggregate structures. In addition, zeta potential values of polyMPC−DOX recorded in pure water ranged from +7 to +19 mV, and increased with DOX loading. The HCl salt of DOX accounts for this charge and, as shown later, the charge of these conjugates appears to affect cell uptake.

DOX Release. The acyl hydrazone linkage connecting DOX to polyMPC is known for its stability at neutral pH and instability at low pH where the starting ketone and hydrazine are recovered. Drug release experiments were performed by dissolving the conjugate (2−5 mg/mL) in pH 7.4 and pH 5.0 buffers at 37 °C, taking aliquots for analysis after incubating at given time points. An apparent self-quenching of DOX fluorescence was noted in the polyMPC−DOX conjugate; this also has been reported by others.[54,55] However, the fluorescence intensity of DOX increased dramatically over a 24 h period at pH 5.0, as it was released from the conjugate, while the fluorescence intensity remained low at pH 7.4 even after 48 h (SI Figure S4). The percentage of DOX released from the polymer backbone was quantified by its UV/vis absorbance at 500 nm, following separation by size-exclusion HPLC. A representative HPLC chromatogram (SI Figure S5) showed polyMPC−DOX elution at 8 min, and free DOX at 19 min. The drug release profiles of conjugates **4-A** and **8-A**, made by one-pot and post-polymerization conjugation, respectively, are shown in Figure 3a,b. Both samples showed substantial DOX release at pH 5.0 and little release at pH 7.4, over a 24 h period. On the basis of these DOX releasing curves, the half-lives ($t_{1/2}$)

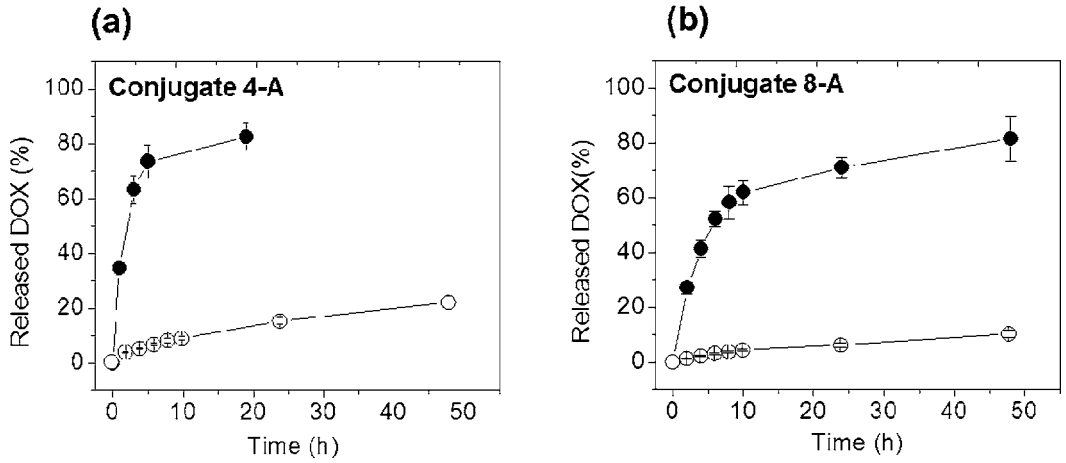


Figure 3. (a) DOX release profiles for conjugate **4-A** at pH 5.0 (filled) and pH 7.4 (open); (b) DOX release profiles for conjugate **8-A** at pH 5.0 (filled) and pH 7.4 (open). Error bars represent ± standard deviation (S.D.).

of the conjugates at pH 5.0 were calculated as 2.2 h for **4-A** and 5.8 h for **8-A**. Moreover, we note that the spectroscopic features of the released DOX are identical to those of the original free DOX, suggesting that DOX is not altered structurally during the course of the controlled polymerization.

Drug release curves for other conjugates are shown in SI Figure S6−10. The calculated half-lives of DOX-release at pH 5.0, and the percentage of DOX released from all of the conjugates over a 48 h period, are given in Table 3. All of the

Table 3. DOX Release from polyMPC−DOX Conjugates at pH 5.0 and 7.4

conjugate	4-A	4-B	8-A	8-B	8-C	8-D	8-D2
M_n (kDa)	7[a]	12[a]	11[a]	19[a]	41[b]	56[b]	44[b]
DOX (wt %)	5.3	3.6	17	15	30	45	30
$t_{1/2}$ at pH 5.0 (h)	2.2	2.4	5.8	8.5	22	40	38
release % at pH 7.4 in 48 h	22%	10%	10%	<5%	<5%	<3%	<5%

[a] M_n estimated from aqueous GPC calibrated with PEO standards. [b] M_n estimated based on corresponding parent polymer and DOX loading.

prodrugs released DOX relatively quickly at pH 5.0, with $t_{1/2}$ values ranging from 2 to 40 h, while only 2−20% of DOX was released over 48 h at pH 7.4. Conjugates **4-A** and **4-B** showed the shortest half-lives (2−3 h) of all the samples; these contain a longer DOX-to-polymer linkage, and have the lowest molecular weight and drug loading of the samples studied. Conjugates **8-C** and **8-D**, having higher molecular weight and higher drug loading, exhibited longer $t_{1/2}$ values; less drug was released at pH 7.4. Slower observed drug release for higher-molecular-weight conjugates has also been observed in HPMA-DOX prodrugs.[43,52]

Cell Uptake and Nuclear Localization. We tested polyMPC−DOX conjugates for their uptake into live cells and intracellular accumulation. Human breast adenocarcinoma (MCF7) cells were incubated with 5 μM DOX equivalent concentration of the prodrugs for 24 h, then counter-stained (in the nucleus) with 4,6-diamidino-2-phenylindole (DAPI), and imaged by fluorescence microscopy at a set camera exposure time. DOX and polyMPC−DOX conjugates exhibited efficient cellular uptake, entering essentially all of the MCF7 cells and the cell nuclei, as sampled from three randomly chosen microscopy fields. Conjugates **4-A** and **8-B**, having lower drug loadings, showed significantly less intracellular DOX fluorescence intensity relative to that observed from **8-D2** and **8-D** conjugates (Figure 4 and SI Figure S11). Following 24 h of incubation, none of the polyMPC−DOX conjugates showed any significant cytotoxicity, marked by the absence of floating dead cells and a nearly 95−100% cell density in the observed microscopy field demonstrating that conjugation of DOX to the polyMPC backbone initially masks the DOX cytotoxicity. On the other hand, cells incubated with free DOX for 24 h show high cytotoxicity, as expected, marked by the presence of floating dead cells and a significant decrease in cell density in the observed microscopy fields.

While Figure 4a−c and SI Figure S11a,b demonstrate polyMPC−DOX uptake by MCF7 cells, it is difficult to use this data quantitatively. Thus, we opted for an alternative technique in which DOX was isolated from the cells, apart from the polyMPC backbone, and characterized using a fluorescence plate reader. For this, MCF7 cells were grown in 10 cm cell culture dishes and when at 40% cell density were incubated with DOX equimolar concentrations (5 μM) of prodrugs for 12, 24, and 48 h. The total DOX fluorescence intensity, from the live cells, dead cells, and extracellular media, was then measured (separately) using a fluorescence plate reader, after releasing DOX from the polyMPC backbone by incubating in 0.5 M acetic acid. The fluorescence intensity values obtained were expressed as a percentage of DOX signal intensity measured from stock solutions. These DOX and polyMPC−DOX conjugate stock solutions were made by lyophilizing 10 mL of 5 μM DOX equivalent concentrations of DOX/**4-A**/**8-B**/**8-D**/**8-D2** in cell culture medium, then dissolving them in an equal volume of 0.5 M acetic acid. These values estimate, as best we are able, the percent DOX taken up and retained within the cells. Incubation of **8-D2**, **8-D**, and free DOX for 24 h results in about 20% accumulation in live cells, in contrast to **4-A** and **8-B** that show less than 5% DOX abundance. At 48 h incubation, about 28% of DOX from the total **8-D2** and **8-D** administered is present in the live cells, while free DOX resulted in high cytotoxicity as judged by the abundance of dead floating cells (Figure 5). Interestingly, conjugates **8-D2** and **8-D**, having higher drug loading and zeta potential values (Table 2), showed significantly greater intracellular accumulation over time, in contrast to **4-A** and **8-B** with their lower drug loading. We hypothesize that the higher zeta potential of

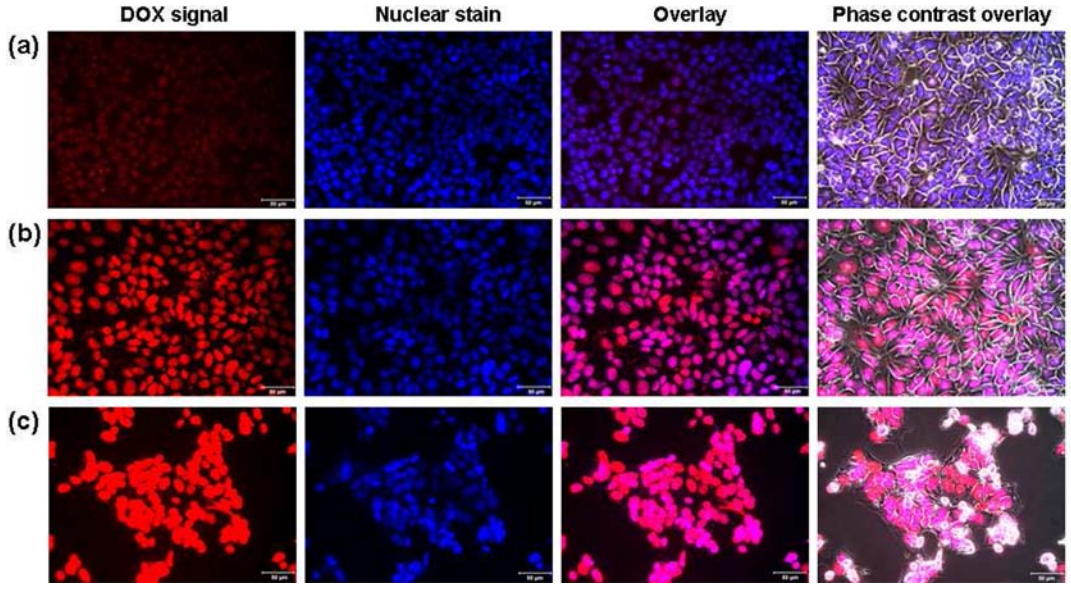


Figure 4. Fluorescence micrographs of human breast adenocarcinoma (MCF7) cells incubated for 24 h with DOX equivalent concentration of (a) **4-A**; (b) **8-D2**; and (c) free DOX. Images were obtained at a constant microscope camera exposure time. Scale bar = 50 μm.

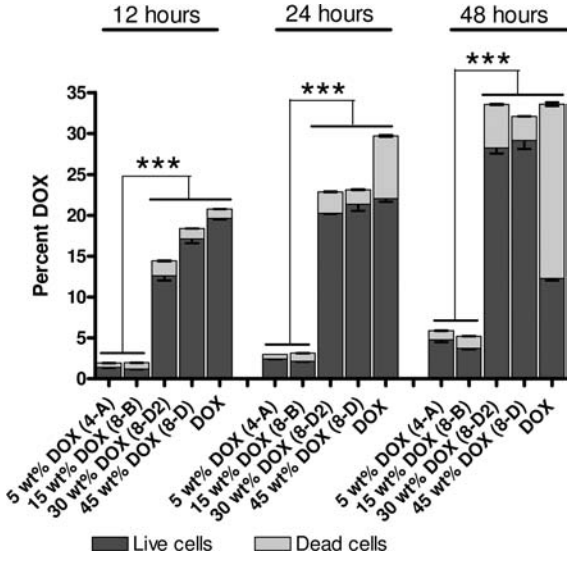


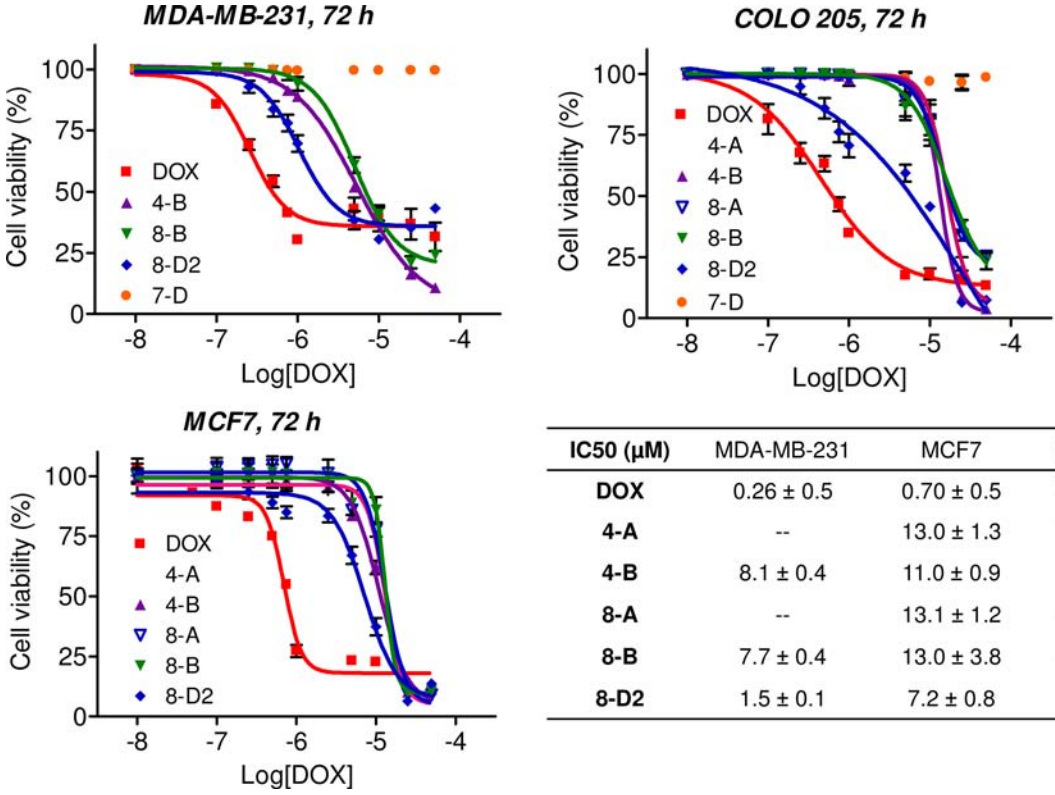
Figure 5. Intracellular abundance of DOX after 12, 24, and 48 h incubation of polyMPC-DOX conjugates **4-A**, **8-B**, **8-D2**, **8-D**, and free DOX at 5 μM DOX equivalent concentrations with MCF7 cells. Percent DOX on the *Y*-axis indicates the percentage of initially applied DOX (free or prodrug conjugated). *** indicates $p < 0.001$ for the percent DOX in live cells. Error bars represent ± SD.

8-D2 and **8-D** conjugates may enhance the association of these conjugates with the negatively charged cell membrane, thereby further enhancing cell entry by nonspecific endocytosis. Figure 5 graphs the dependence of cell uptake on DOX drug loading.

In Vitro Cytotoxicity of polyMPC–DOX Conjugates. The cytotoxicity of polyMPC–DOX structures was tested in the presence of different cancer cell lines, including human breast cancer (MCF-7 and MDA-MB-231) and colorectal (COLO 205) adenocarcinoma cells. This was done by incubating DOX-equivalent concentrations of polyMPC–DOX conjugates with these cells for 72 h, followed by cell viability measurements using a luminescence plate reader (see Experimental Section). Control experiments employed polyMPC itself in sterile distilled water. Dose response curves generated by Promega's CellTiter-Glo luminescent cell viability reagent showed that all conjugates were potent against the cancer cell lines tested here, and, importantly, the cytotoxicity arises from DOX only (after its release from the backbone) as the parent polyMPC-hydrazine itself (polymer **7-D**) exhibits no toxicity (Figure 6). The half-maximal inhibitory concentration (IC_{50}) values of the polyMPC–DOX prodrugs were in the range of 1.5–16 μM, as given in Figure 6 for a series of cancer cell lines. In general, the data show that polyMPC–DOX conjugates induce cytotoxicity at higher concentrations than does native DOX alone, as expected for polymer prodrugs. We note the following: (1) the MDA-MB-231 cancer cells were more sensitive to **8-D2** (IC_{50} 1.5 ± 0.1 μM) than were MCF7 (IC_{50} 7.2 ± 0.8 μM) and Colo205 (IC_{50} 8.4 ± 1.4 μM) cells; and (2) **8-D2** had lower IC_{50} values than did the other polyMPC–DOX conjugates. In general, given the favorable combination of DOX loading and cell culture data, we began to pursue *in vivo* testing of these structures, beginning with a maximum tolerated dose (MTD) study as described below.

Maximum Tolerated Dose (MTD) of polyMPC–DOX Conjugates. The maximum tolerated dose (MTD) of a drug describes its highest permissible and sublethal dose that produces limited toxicity when administered during the test study time frame. We examined the MTD of polyMPC–DOX conjugate **8-D2** in BALB/c athymic nude mice. Single doses of control (polyMPC only at 1 mg/50 μL concentration, or equivalent to the polyMPC concentration in the highest dose of polyMPC–DOX administered) and 10, 30, and 50 mg/kg DOX equivalent polyMPC–DOX were administered by tail vein injection. The MTD parameters were defined as the highest conjugate dose at which no animals died, and the body weight loss was not greater than 15% of the animal prior to treatment. Animal body weight and health were monitored each day for up to 30 days from conjugate administration. Control mice showed normal weight gain during the study period, demonstrating a good biocompatibility of the polyMPC backbone itself. Mice receiving 10 to 30 mg/kg DOX equivalent conjugates maintained good health and exhibited

dx.doi.org/10.1021/bc200667s | *Bioconjugate Chem.* 2012, 23, 1753–1763



IC50 (μM)	MDA-MB-231	MCF7	COLO 205
DOX	0.26 ± 0.5	0.70 ± 0.5	0.46 ± 0.7
4-A	--	13.0 ± 1.3	16.1 ± 2.1
4-B	8.1 ± 0.4	11.0 ± 0.9	13.4 ± 1.2
8-A	--	13.1 ± 1.2	14.5 ± 2.3
8-B	7.7 ± 0.4	13.0 ± 3.8	16.2 ± 1.1
8-D2	1.5 ± 0.1	7.2 ± 0.8	8.4 ± 1.4

Figure 6. Cytotoxicity of polyMPC−DOX conjugates in cell culture using human breast (MDA-MB-231 and MCF-7) and colon (COLO 205) adenocarcinoma cells. Error bars represent ± SD.

normal weight gain during the course of the 30 days (Figure 7). The 50 mg/kg group showed only 10% weight loss at 22 days,

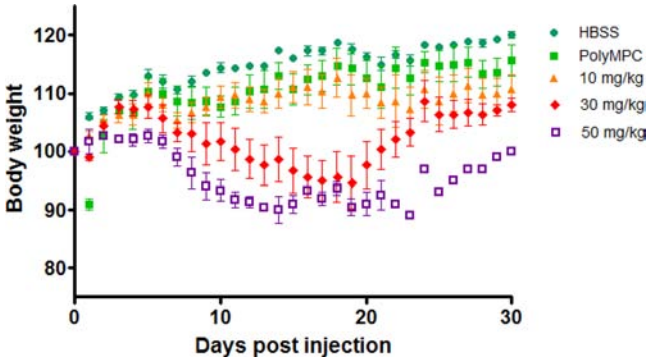


Figure 7. Maximum tolerated dose study of polyMPC−DOX in mice. Average mouse weights (n = 3) versus time. Error bars indicate ± SEM.

though we note that two of the mice were removed at that point due to necrosis in the tail caused at the injection site.

In summary, polyMPC−DOX conjugates linked through pH-responsive hydrazones groups were synthesized by two methods. The post-polymerization conjugation method allowed the prodrugs to be prepared with very high drug loading while maintaining water solubility. PolyMPC−Dox conjugates showed pH-responsive drug release profiles, with some additional dependence on molecular weight and drug loading. High drug loaded conjugates showed comparatively higher intracellular abundance in cancer cells, and lower IC_{50} values, and the maximum tolerated dose of polyMPC−DOX conjugates in mice was found to be several times that reported for free DOX. All these characteristics make polyMPC−DOX conjugates potentially advantageous for enabling a greater accumulation of the prodrugs in cancerous tissues, and reducing effects of nonspecific cytotoxicity associated with systemic administration. Such *in vivo* work will be reported subsequently for these and related polymer−drug conjugates.

EXPERIMENTAL SECTION

Materials. Sodium azide, copper(I) bromide, 2,2′-bipyridine (bpy), methyl 6-bromohexanoate, ethyl 2-bromoisobutyrate, *tert*-butyl bromoacetate, tetrabutylammonium bromide, hydrazine monohydrate, acetic acid, sodium sulfate, TFA, and anhydrous methanol were purchased from Aldrich. DOX was purchased from 21CEC. MPC and TMS-PgMA monomers were synthesized in-house according to the literature.[56,57] All other materials were used without additional purification. Spectra/Por 3 dialysis membrane was purchased from Spectrum Laboratories, Inc. The human colon (COLO 205) and breast (MCF7, MDA-MB-231) adenocarcinoma cells were purchased from American Type Culture Collection (ATCC), whereas RPMI 1640, DMEM, and MEM cell culture media were purchased from Invitrogen and Mediatech, respectively. Fetal bovine serum (FBS) was purchased from Atlanta biologicals and bovine insulin from Aldrich. Cell viability was measured using CellTiter-Glo luminescent cell viability assays (Promega). DNase I and RNase A were purchased from Aldrich, while Pronase was purchased from Roche.

Instrumentation. NMR spectra were recorded on Bruker DPX300 spectrometer ($\omega_{13C} = 0.25\omega_{1H}$). High-resolution mass spectral (HRMS) data were obtained on a JEOL JMS700 MStation. UV/vis absorbance measurements were taken on a Perkin-Elmer Lambda 25 UV/vis spectrometer. Fluorescence

dx.doi.org/10.1021/bc200667s | *Bioconjugate Chem.* 2012, 23, 1753−1763

spectra were recorded on a Perkin-Elmer LS55 fluorescence spectrometer. IR absorbance data were obtained on a Perkin-Elmer Spectrum One FT-IR spectrometer equipped with a universal ATR sampling accessory. Dynamic light scattering was performed on Malvern Zetasizer Nano-ZS. Molecular weights and polydispersity indices (PDIs) were estimated by gel permeation chromatography (GPC) in sodium nitrate (0.1 M with 0.02 wt % of NaN_3) aqueous solution against poly(ethylene oxide) standards, operating at 1.0 mL/min with an HP Series 1050 Pump, HP 1047A refractive index detector, and three Waters Ultrahydrogel Linear columns (300 × 7.8 mm). The HPLC system consisted of a Waters Alliance system with a 2996 photodiode array detector. A Shodex OH pack SB-804 HQ size exclusion column was used, eluting with 20% acetonitrile (0.05% formic acid) or 40% acetonitrile (0.1% TFA) at a flow rate of 1 mL/min.

One-Pot ATRP/Click Chemistry Synthesis of PolyMPC−DOX Conjugate. *Synthesis of Methyl 6-Azidohexanoate* ***1***. Methyl 6-bromohexanoate (6.0 g, 24 mmol) and sodium azide (4.7 g, 72 mmol) were stirred in DMF (20 mL). The reaction mixture was heated to 80 °C overnight, and salts were removed by filtration. The filtrate was poured into DCM (100 mL), and washed with 4 × 150 mL water. The organic phase was dried over $MgSO_4$ and concentrated by rotary evaporation. Compound **1** was obtained as a clear oil (4 g, 98%). IR: (cm^{-1}) 2099 (N_3), 1733 (C═O). ^1H NMR ($CDCl_3$, 300 MHz): δ 3.68 (s 3H), 3.38 (t, J = 6.8 Hz, 2H), 2.34 (t, J = 7.2 Hz, 2H), 1.64 (m, 4H), 1.43 (m, 2H). ^{13}C NMR ($CDCl_3$, 75 MHz): δ 173.9, 51.6, 51.2, 33.8, 28.5, 26.2, 24.4.

Synthesis of Compound ***2***. Compound **1** (3.0 g, 17.5 mmol) was stirred in hydrazine monohydrate (12 mL), and the mixture was heated at reflux for 30 min or until becoming homogeneous. Most of the solvent was removed by rotary evaporation, and the residue was crystallized in CH_2Cl_2/Et_2O to give compound **2** as white solid (1.8 g, 60% yield). IR: (cm^{-1}) 2101 (N_3), 1620 (C═O). ^1H NMR (DMSO, 300 MHz): δ 8.93 (s, 1H), 4.14 (s, 2H), 3.31 (t, J = 6.9 Hz, 2H), 2.00 (t, J = 7.1 Hz, 2H), 1.51 (m, 4H), 1.28 (m, 2H). ^{13}C NMR (DMSO, 75 MHz): δ 171.9, 51.0, 33.7, 28.4, 26.2, 25.2. HRMS-EI (m/z): $[M+H]^+$ calculated for $C_6H_{14}ON_5$: 172.1198, found: 172.1180.

Synthesis of DOX-azide ***3***. DOX hydrochloride (58 mg, 0.10 mmol) and compound **3** (51 mg, 0.30 mmol) were dissolved in dry methanol (15 mL). To this was added one drop of acetic acid and 50 mg of anhydrous sodium sulfate. The reaction mixture was stirred at room temperature for 12 h in the dark. The salt was removed by filtration, and the filtrate was concentrated by evaporation. Precipitation into dry acetonitrile gave compound **3** as a crude product, which was washed with dry acetonitrile three times to give a red solid (68 mg, 93%). IR: (cm^{-1}) 2098 (N_3). ^1H NMR (DMSO, 300 MHz): δ 10.32 (s, 1H), 7.93 (m, 2H), 7.68 (t, J = 4.6 Hz, 1H), 5.77 (s, 1H), 5.54 (s, 1H), 5.37 (m, 1H), 5.30 (m, 1H), 4.95 (t, J = 7.0 Hz, 1H), 4.40 (m, 2H), 3.99 (m, 4H), 3.54 (s, 1H), 3.14 (q, J = 6.8 Hz, 2H), 2.75 (d, J = 17.4 Hz, 1H), 2.21 (m, 2H), 2.11 (m, 2H), 1.87 (t, J = 11.4 Hz, 1H), 1.70 (d, J = 11.8 Hz, 1H), 1.53 (m, 1H), 1.33 (p, J = 7.1 Hz, 4H), 1.17 (d, J = 6.5 Hz, 3H), 1.09 (m, 2H). ^{13}C NMR (DMSO, 75 MHz): δ 186.9, 174.3, 161.3, 157.0, 154.7, 152.9, 137.1, 136.2, 135.2, 120.4, 120.2, 119.4, 111.0, 110.9, 99.5, 72.9, 72.5, 66.8, 66.6, 57.1, 56.4, 50.8, 47.0, 34.2, 31.5, 28.5, 26.4, 24.0, 17.3. HRMS-FAB (m/z): $[M+H]^+$ calculated for $C_{33}H_{41}O_{11}N_6$: 697.2833, found: 697.2822.

General One-Pot Procedure to Synthesize Polymer ***4***. The initiator EBiB (5.9 mg, 0.03 mmol) and MPC were combined, and DOX-azide **3** and TMS-PgMA were added in a 1:1 molar ratio. This solution was subjected to three vacuum/nitrogen cycles. DMSO (2 mL, previously purged with nitrogen gas) and MeOH (0.7 mL) were added using a degassed syringe. The reaction mixture was bubbled with nitrogen gas for 20 min. CuBr (8.6 mg, 0.06 mmol) and bipyridine (18.7 mg, 0.12 mmol) were added, quickly, as solids, under nitrogen atmosphere. The reaction mixture was purged with nitrogen gas for 20 min, then stirred at room temperature overnight. Monomer conversion was monitored by ^1H NMR spectroscopy, and the polymerization was terminated by precipitation into dry THF (100 mL). The crude product was isolated by filtration, and purified by column chromatography on silica gel to remove unreacted DOX-azide and MPC, giving polyMPC-DOX as reddish-purple solid. The product was purified further on a Sephadex G-25 column, washed with pure water, and the fractions containing polymer were freeze−dried to give polymer **4** as an orange−red solid.

*Synthesis of TBOEMA (****5****)*. The sodium salt of methacrylic acid (8.2 g, 80 mmol) was combined with *tert*-butyl bromoacetate (10.4 g, 52.0 mmol) in dry acetonitrile (50 mL). To this suspension was added *tetra-n*-butylammonium bromide (3.5 g). The reaction mixture was heated to reflux for 12 h, and residual salts were removed by filtration and solvent was removed by rotary evaporation. The residue was dissolved in DCM, and washed with water. The organic phase was dried over $MgSO_4$, and concentrated to give compound **5** as a light yellow oil (5.8 g, 58%). ^1H NMR ($CDCl_3$, 300 MHz): δ 6.23 (s, 1H), 5.65 (m, J = 1.5 Hz, 1H), 4.59 (s, 2H), 1.99 (s, 3H), 1.49 (s, 9H). ^{13}C NMR ($CDCl_3$, 75 MHz): δ 166.9, 166.7, 135.5, 126.6, 82.4, 61.4, 28.0, 18.3. MS-FAB (m/z): $[M+H]^+$ calculated for $C_{10}H_{16}O_4$: 201.11, found: 201.09.

General Procedure for Preparation of Copolymer ***6*** *by ATRP*. Initiator EBiB (5.9 mg, 0.03 mmol), MPC, and TBOEMA were combined and stirred in a round-bottom flask, and purged with three vacuum/nitrogen cycles. DMSO and MeOH were injected with a degassed syringe, and the mixture was purged with nitrogen gas for 20 min. CuBr (8.6 mg, 0.06 mmol) and bipyridine (18.7 mg, 0.12 mmol) were added, quickly, as solids under nitrogen atmosphere. Nitrogen gas was bubbled into the reaction mixture for 20 min, and the mixture was then stirred at room temperature, monitoring monomer conversion by ^1H NMR spectroscopy. The polymerization was terminated by introducing air to the mixture. Unreacted TBOEMA was removed by precipitation into dry THF (100 mL), and further washing with dry THF. The crude product was passed through a small column of silica gel to give copolymer **6** as white solid. Relative monomer ratios were determined by ^1H NMR spectroscopy, comparing signals at 3.75 ppm ($-CH_2-N$) and 1.39 ppm ($-(CH_3)_3$ in TBOEMA). ^1H NMR (D_2O, 400 MHz) δ = 0.8−1.2 (br, 3H), 1.39 (s, 9H), 1.8−2.2 (br, 2H), 3.2 (s, 9H), 3.75 (br, 2H), 4.1 (br, 2H), 4.25 (br, 2H), 4.4 (br, 2H), 4.55 (br, 2H) ppm; ^{13}C NMR (MeOD, 100 MHz): δ = 16.8, 18.5, 27.1, 44.7, 45.0, 53.4, 59.3, 61.7, 62.9, 64.8, 66.1, 82.1, 166.9, 176.8, 177.7 ppm.

Synthesis of Copolymer ***7***. Polymer **6** was dissolved in MeOH in the range of 100−200 mg/mL. Hydrazine monohydrate was added to the polymer solution to a final concentration of 25%, and the mixture was stirred at room temperature. When the reaction reached over 90% conversion, as monitored by ^1H NMR spectroscopy, the mixture was

diluted with water and purified by dialysis against water (MWCO 3500, 2 days) and filtered through a 0.45 μm membrane. Lyophilization gave polymer **7** as a white powder. Typical yields were about 60%, and the loading of the hydrazine group was calculated by comparing ^{1}H NMR signal intensities at 3.75 ppm ($-CH_2-$N in MPC) and 4.64 ppm ($-CH_2-$CONHNH$_2$). ^{1}H NMR (D_2O, 300 MHz): δ = 0.9−1.2 (br, 3H), 1.8−2.3 (br, 2H), 3.3 (s, 9H), 3.75 (br, 2H), 4.16 (br, 2H), 4.3 (br, 2H), 4.38 (br, 2H), 4.64 (br, 2H) ppm; ^{13}C NMR (MeOD, 100 MHz): δ = 16.8, 18.5, 44.7, 45.0, 53.4, 59.3, 62.2, 62.9, 64.8, 66.1, 167.1, 176.9, 178.1 ppm.

PolyMPC−Dox Conjugation. Conjugating DOX to polyMPC used similar methodology as for the synthesis compound **3**. PolyMPC−Dox **8-D** was prepared by combining polymer **7-D** (33 mg, 0.05 mmol hydrazine group) and DOX hydrochloride (29 mg, 0.05 mmol) in dry methanol (5 mL). To this solution was added 30 μL of acetic acid and 100 mg of anhydrous sodium sulfate. The reaction mixture was stirred at room temperature in the dark for 2 days. The conjugate was purified by elution with methanol through a Sephadex LH-20 column, then eluting with water through a Sephadex G-25 column. Lyophilization gave polyMPC−Dox conjugate **8-D** in 47% yield (29 mg). Higher yields were obtained for polyMPC−Dox samples having lower drug loadings.

Measurement of DOX Loading in polyMPC−Dox Conjugates. Dox-hydrochloride was dissolved in pure water at concentration of 0.01 mg/mL, and polymer−Dox conjugates were dissolved in pure water at concentrations ranging from 0.1 to 1 mg/mL. The DOX loading in each conjugate was calculated based on UV absorbance values at 488 nm.

Dynamic Light Scattering and Zeta Potential Measurements. DLS and zeta potential measurements were performed on a Malvern Zetasizer Nano-ZS (4 mW He−Ne laser, 633 nm). The size measurements were performed at a sample concentration of 2 mg/mL in PBS (pH 7.4), and optimum position and automatic attenuation selection were chosen to generate the optimum correlation curve. Zeta potential measurements were performed at 25 °C, at a concentration of 8 mg/mL conjugate in pure water. Each reported measurement represents the average value of three separate measurements.

DOX Release Experiments. Release of DOX from polyMPC−DOX conjugates at 37 °C was measured in buffer solutions. PolyMPC−DOX conjugates **4** and **8** were dissolved in two different buffers (pH 5.0, 100 mM acetate and pH 7.4, 100 mM phosphate) at concentrations from 2 to 5 mg/mL. The mixtures were incubated at 37 °C, and aliquots (100 μL) were removed at different time points. 20 μL aliquots were diluted in 2 mL PBS (pH 7.4) and their photoluminescence spectra recorded (excitation 470 nm). 50 μL aliquots were analyzed by SEC-HPLC, and the absorbance intensity at 500 nm determined the percent DOX released over the course of the experiment. SEC-HPLC conjugates **4-A**, **4-B**, **8-A**, and **8-B** utilized a mobile phase of 20% acetonitrile (0.05% formic acid) in water, while high DOX loading conjugates **8-C**, **8-D**, and **8-D2** required a mobile phase of 40% acetonitrile (0.1% TFA) in water.

Cell Culture. COLO 205 and MDA-MB-231 cancer cells were cultured in RPMI-1640 or DMEM medium supplemented with 10% fetal bovine serum (FBS), while MCF7 cells were cultured in MEM medium supplemented with 10% FBS and 0.01 mg/mL bovine insulin. All cells were grown in 5% CO_2 incubators at 37 °C.

Cell Assay. MCF7 cells seeded on sterile glass coverslips were taken to 80% cell density, and incubated for 24 h with 5 μM DOX equivalent concentration of polyMPC−DOX conjugates **4-A**, **8-B**, **8-D**, and **8-D2**, as well as free DOX. For fluorescence analysis, cells were washed with PBS, fixed in 2% paraformaldehyde for 20 min at room temperature (RT), and then washed in PBS (phosphate buffered saline). Cells were then permeabilized with 0.5% Triton-X 100 and nuclei counterstained with DAPI (4,6-diamidino-2-phenylindole) (1.5 μg/mL). Dox and DAPI was imaged at a constant exposure time of 13.8 and 16.2 s using the *MetaVue* Imaging Software. Phase contrast images were also obtained. MCF7 cells seeded in 10 cm cell culture dishes taken to 40% cell density were incubated for 12, 24, and 48 h with 5 μM DOX equivalent concentration of polyMPC−DOX conjugates or free DOX. At the respective time points, floating dead cells from the cell culture medium were collected by centrifugation, the supernatant cell culture medium was freeze−dried for 48 h, and the live cells were washed once with PBS and collected using a cell scraper. The collected samples were resuspended in PBS, then incubated with 0.5% SDS, DNase I (5 Units), Pronase (200 μg/mL), and RNase A (200 μg/mL) for 2 h at 37 °C. An equal volume of glacial acetic acid (0.5 M) was added, and incubation for 1 h gave complete release of DOX from the polymer backbone, as confirmed by SEC-HPLC. The final volume of the samples was adjusted to 1 mL with PBS. For measuring the percent DOX uptake by the cells, 10 mL of cell culture medium containing samples of 5 mM DOX concentration equivalent polymer−Dox conjugates (**4-A**/**8-B**/**8-D**/**8-D2**) were freeze−dried for 48 h, resuspended in PBS, and then incubated with 0.5% SDS, DNase I (5 units), Pronase (200 mg/mL), and RNase A (200 mg/mL) for 2 h at 37 °C. An equal volume of glacial acetic acid (0.5 M) was added, and the samples incubated for 1 h at 37 °C. The final volume of each sample was adjusted to 1 mL with PBS. Equal volumes of the samples were loaded into clear-bottom black-walled 96 well plates, and the DOX fluorescence from individual samples was measured at 485 nm/590 nm using the FLUOstar OPTIMA fluorescence detection plate reader (BMG LABTECH). The fluorescence intensities obtained were expressed as a percentage of DOX signal intensity measured from the respective polyMPC−DOX conjugate solutions (10 mL of 5 μM DOX equivalent **4-A**/**8-B**/**8-D**/**8-D2** in cell culture medium) applied to the cells. These values gave the percent DOX taken up and retained within the cells. Percent DOX accumulated was plotted using the *GraphPad Prism 4* statistical analysis software.

Cytotoxicity Assay. For *in vitro* cytotoxicity assays, cells were seeded in 96 well plates to ~40% cell density. The cells were then incubated for 72 h with varying doxorubicin equivalent concentrations of polymer−drug conjugates or polyMPC control. Cell viability post-treatment was measured using CellTiter-Glo luminescent cell viability assays from Promega (following manufacturer instructions) on a FLUOstar OPTIMA plate reader (BMG LABTECH). The percentage of DOX-mediated toxicity was calculated with respect to untreated cells, and graphed to give dose response curves. IC_{50} values for each treatment were calculated using *GraphPad Prism 4* software.

***In Vivo* Maximum Tolerated Dose.** Six-week-old athymic nude mice (Nu/J stock number 002019) were received from The Jackson Laboratory, Bar Harbor, ME, and handled and cared for in accordance with the Institutional Animal Care and Use Committee. Mice were randomly divided into 5 treatment

groups of 3 mice each, and injected with the appropriate treatment into the lateral tail vein using a 28 g, 1/2 in. needle. Control groups were injected with either 50 μL of Hank's Balanced Salt Solution (HBSS) or 2.1 mg polyMPC in 50 μL HBSS. Dose groups were injected with polyMPC−DOX (30% Dox by weight) dissolved in 50 μL of HBSS at a calculated Dox dosage of 10, 30, or 50 mg/kg based on an average mouse weight of 18 g. The mice were weighed prior to injection, and weighed daily and observed for toxicity for 30 days following injection. Toxicity was determined by either loss of greater than 15% body weight or presentation of stress symptoms such as scruffy appearance, abnormal respiration, huddled behavior, lethargy, weakness, or seizures. Average daily mouse weights were calculated for each treatment group.

■ ASSOCIATED CONTENT

Supporting Information

NMR spectra of polymers (**6-A**, **7-A**) and GPC chromatograms of the polymers (**7-A**,**B**,**C**,**D**), PD-10 column separation of conjugate **8-D2** and DOX, fluorescence spectra and HPLC chromatogram during the drug release studies, other drug release curves at pH 5.0, and fluorescence micrographs of MCF7 cells incubated with conjugates (**8-B** and **8-D**). This material is available free of charge via the Internet at http://pubs.acs.org.

■ AUTHOR INFORMATION

Corresponding Author

*E-mail: tsemrick@mail.pse.umass.edu.

Notes

The authors declare no competing financial interest.

■ ACKNOWLEDGMENTS

The authors acknowledge the financial support of the National Science Foundation Materials Research Science & Engineering Center (MRSEC) on Polymers (DMR-0820506), the NSF-supported Center for Hierarchical Manufacturing (DMI-0531171), SciDose, Inc, the Department of Energy (DE-SC0005166), the Rays of Hope Foundation, and the Center for Excellence in Apoptosis Research (CEAR) of the Pioneer Valley Life Sciences Institute (PVLSI).

■ REFERENCES

(1) Davis, M. E., Chen, Z., and Shin, D. M. (2008) Nanoparticle therapeutics: an emerging treatment modality for cancer. *Nat. Rev. Drug Discovery 7*, 771−782.

(2) Petros, R. A., and DeSimone, J. M. (2010) Strategies in the design of nanoparticles for therapeutic applications. *Nat. Rev. Drug Discovery 9*, 615−627.

(3) Vicent, M. J., and Duncan, R. (2006) Polymer conjugates: nanosized medicines for treating cancer. *Trends Biotechnol. 24*, 39−47.

(4) Duncan, R. (2006) Polymer conjugates as anticancer nanomedicines. *Nat. Rev. Cancer 6*, 688−701.

(5) Greco, F., and Vicent, M. J. (2009) Combination therapy: Opportunities and challenges for polymer-drug conjugates as anticancer nanomedicines. *Adv. Drug Delivery Rev. 61*, 1203−1213.

(6) Haag, R., and Kratz, F. (2006) Polymer therapeutics: Concepts and applications. *Angew. Chem., Int. Ed. 45*, 1198−1215.

(7) Pasut, G., and Veronese, F. M. (2009) PEG conjugates in clinical development or use as anticancer agents: An overview. *Adv. Drug Delivery Rev. 61*, 1177−1188.

(8) Matsumura, Y., and Maeda, H. (1986) A new concept for macromolecular therapeutics in cancer-chemotherapy - mechanism of tumoritropic accumulation of proteins and the antitumor agent smancs. *Cancer Res. 46*, 6387−6392.

(9) Maeda, H., and Matsumura, Y. (1989) Tumoritropic and lymphotropic principles of macromolecular drugs. *Crit. Rev. Ther. Drug Carr. Syst. 6*, 193−210.

(10) Maeda, H., Sawa, T., and Konno, T. (2001) Mechanism of tumor-targeted delivery of macromolecular drugs, including the EPR effect in solid tumor and clinical overview of the prototype polymeric drug SMANCS. *J. Controlled Release 74*, 47−61.

(11) Ringsdorf, H. (1975) Structure and properties of pharmacologically active polymers. *J. Polym. Sci., Part C: Polym. Symp.*, 135−153.

(12) Greenwald, R. B., Choe, Y. H., McGuire, J., and Conover, C. D. (2003) Effective drug delivery by PEGylated drug conjugates. *Adv. Drug Delivery Rev. 55*, 217−250.

(13) Thomson, A. H., Vasey, P. A., Murray, L. S., Cassidy, J., Fraier, D., Frigerio, E., and Twelves, C. (1999) Population pharmacokinetics in phase I drug development: a phase I study of PK1 in patients with solid tumours. *Br. J. Cancer 81*, 99−107.

(14) Seymour, L. W., Ferry, D. R., Kerr, D. J., Rea, D., Whitlock, M., Poyner, R., Boivin, C., Hesslewood, S., Twelves, C., Blackie, R., Schatzlein, A., Jodrell, D., Bissett, D., Calvert, H., Lind, M., Robbins, A., Burtles, S., Duncan, R., and Cassidy, J. (2009) Phase II studies of polymer-doxorubicin (PK1, FCE28068) in the treatment of breast, lung and colorectal cancer. *Int. J. Oncol. 34*, 1629−1636.

(15) Bissett, D., Cassidy, J., de Bono, J. S., Muirhead, F., Main, M., Robson, L., Fraier, D., Magne, M. L., Pellizzoni, C., Porro, M. G., Spinelli, R., Speed, W., and Twelves, C. (2004) Phase I and pharmacokinetic (PK) study of MAG-CPT (PNU 166148): a polymeric derivative of camptothecin (CPT). *Br. J. Cancer 91*, 50−55.

(16) Li, C., Yu, D. F., Newman, R. A., Cabral, F., Stephens, L. C., Hunter, N., Milas, L., and Wallace, S. (1998) Complete regression of well-established tumors using a novel water-soluble poly(L-glutamic acid) paclitaxel conjugate. *Cancer Res. 58*, 2404−2409.

(17) Bhatt, R. L., de Vries, P., Tulinsky, J., Bellamy, G., Baker, B., Singer, J. W., and Klein, P. (2003) Synthesis and in vivo antitumor activity of poly(L-glutamic acid) conjugates of 20(S)-camptothecin. *J. Med. Chem. 46*, 190−193.

(18) Schluep, T., Hwang, J., Cheng, J. J., Heidel, J. D., Bartlett, D. W., Hollister, B., and Davis, M. E. (2006) Preclinical efficacy of the camptothecin-polymer conjugate IT-101 in multiple cancer models. *Clin. Cancer Res. 12*, 1606−1614.

(19) Numbenjapon, T., Wang, J. Y., Colcher, D., Schluep, T., Davis, M. E., Duringer, J., Kretzner, L., Yen, Y., Forman, S. J., and Raubitschek, A. (2009) Preclinical results of camptothecin-polymer conjugate (IT-101) in multiple human lymphoma xenograft models. *Clin. Cancer Res. 15*, 4365−4373.

(20) Soepenberg, O., de Jonge, M. J. A., Sparreboom, A., de Bruin, P., Eskens, F., de Heus, G., Wanders, J., Cheverton, P., Ducharme, M. P., and Verweij, J. (2005) Phase I and pharmacokinetic study of DE-310 in patients with advanced solid tumors. *Clin. Cancer Res. 11*, 703−711.

(21) Yurkovetskiy, A. V., and Fram, R. J. (2009) XMT-1001, a novel polymeric camptothecin pro-drug in clinical development for patients with advanced cancer. *Adv. Drug Delivery Rev. 61*, 1193−1202.

(22) Lewis, A. L. (2000) Phosphorylcholine-based polymers and their use in the prevention of biofouling. *Colloid Surf., B: Biointerfaces 18*, 261−275.

(23) Ishihara, K., and Iwasaki, Y. (1998) Reduced protein adsorption on novel phospholipid polymers. *J. Biomater. Appl. 13*, 111−127.

(24) Ishihara, K., Nomura, H., Mihara, T., Kurita, K., Iwasaki, Y., and Nakabayashi, N. (1998) Why do phospholipid polymers reduce protein adsorption? *J. Biomed. Mater. Res. 39*, 323−330.

(25) Ishihara, K. (2000) New polymeric biomaterials: Phospholipid polymers with a biocompatible surface. *Front. Med. Biol. Eng. 10*, 83−95.

(26) Iwasaki, Y., and Ishihara, K. (2005) Phosphorylcholine-containing polymers for biomedical applications. *Anal. Bioanal. Chem. 381*, 534−546.

(27) Ishihara, K., and Takai, M. (2009) Bioinspired interface for nanobiodevices based on phospholipid polymer chemistry. *J. R. Soc. Interface 6*, S279−S291.
(28) Lewis, A. L., Hughes, P. D., Kirkwood, L. C., Leppard, S. W., Redman, R. P., Tolhurst, L. A., and Stratford, P. W. (2000) Synthesis and characterisation of phosphorylcholine-based polymers useful for coating blood filtration devices. *Biomaterials 21*, 1847−1859.
(29) Samanta, D., McRae, S., Cooper, B., Hu, Y. X., and Emrick, T. (2008) End-functionalized phosphorylcholine methacrylates and their use in protein conjugation. *Biomacromolecules 9*, 2891−2897.
(30) Lewis, A., Tang, Y. Q., Brocchini, S., Choi, J. W., and Godwin, A. (2008) Poly(2-methacryloyloxyethyl phosphorylcholine) for protein conjugation. *Bioconjugate Chem. 19*, 2144−2155.
(31) Chen, X. J., McRae, S., Parelkar, S., and Emrick, T. (2009) Polymeric phosphorylcholine-camptothecin conjugates prepared by controlled free radical polymerization and click chemistry. *Bioconjugate Chem. 20*, 2331−2341.
(32) Berry, G., Billingham, M., Alderman, E., Richardson, P., Torti, F., Lum, B., Patek, A., and Martin, F. J. (1998) The use of cardiac biopsy to demonstrate reduced cardiotoxicity in AIDS Kaposi's sarcoma patients treated with pegylated liposomal doxorubicin. *Ann. Oncol. 9*, 711−716.
(33) Safra, T., Muggia, F., Jeffers, S., Tsao-Wei, D. D., Groshen, S., Lyass, O., Henderson, R., Berry, G., and Gabizon, A. (2000) Pegylated liposomal doxorubicin (doxil): Reduced clinical cardiotoxicity in patients reaching or exceeding cumulative doses of 500 mg/m(2). *Ann. Oncol. 11*, 1029−1033.
(34) Lotem, M., Hubert, A., Lyass, O., Goldenhersh, M. A., Ingber, A., Peretz, T., and Gabizon, A. (2000) Skin toxic effects of polyethylene glycol-coated liposomal doxorubicin. *Arch. Dermatol. 136*, 1475−1480.
(35) Hamilton, A., Biganzoli, L., Coleman, R., Mauriac, L., Hennebert, P., Awada, A., Nooij, M., Beex, L., Piccart, M., Van Hoorebeeck, I., Bruning, P., and de Valeriola, D. (2002) EORTC 10968: a phase I clinical and pharmacokinetic study of polyethylene glycol liposomal doxorubicin (Caelyx (R), Doxil (R)) at a 6-week interval in patients with metastatic breast cancer. *Ann. Oncol. 13*, 910−918.
(36) Uziely, B., Jeffers, S., Isacson, R., Kutsch, K., Weitsao, D., Yehoshua, Z., Libson, E., Muggia, F. M., and Gabizon, A. (1995) Liposomal doxorubicin-antitumor-activity and unique toxicities during 2 complementary phase-I studies. *J. Clin. Oncol. 13*, 1777−1785.
(37) Elbayoumi, T. A., and Torchilin, V. P. (2008) Tumor-specific antibody-mediated targeted delivery of Doxil (R) reduces the manifestation of auricular erythema side effect in mice. *Int. J. Pharm. 357*, 272−279.
(38) Coley, H. M., Twentyman, P. R., and Workman, P. (1993) The efflux of anthracyclines in multidrug-resistant cell-lines. *Biochem. Pharmacol. 46*, 1317−1326.
(39) Harris, A. L., and Hochhauser, D. (1992) Mechanisms of multidrug resistance in cancer-treatment. *Acta Oncol. 31*, 205−213.
(40) Minko, T., Kopeckova, P., Pozharov, V., and Kopecek, J. (1998) HPMA copolymer bound adriamycin overcomes MDR1 gene encoded resistance in a human ovarian carcinoma cell line. *J. Controlled Release 54*, 223−233.
(41) Minko, T., Paranjpe, P. V., Qiu, B., Lalloo, A., Won, R., Stein, S., and Sinko, P. J. (2002) Enhancing the anticancer efficacy of camptothecin using biotinylated poly(ethyleneglycol) conjugates in sensitive and multidrug-resistant human ovarian carcinoma cells. *Cancer Chemother. Pharmacol. 50*, 143−150.
(42) Lee, C. C., Gillies, E. R., Fox, M. E., Guillaudeu, S. J., Frechet, J. M. J., Dy, E. E., and Szoka, F. C. (2006) A single dose of doxorubicin-functionalized bow-tie dendrimer cures mice bearing C-26 colon carcinomas. *Proc. Natl. Acad. Sci. U. S. A. 103*, 16649−16654.
(43) Etrych, T., Jelinkova, M., Rihova, B., and Ulbrich, K. (2001) New HPMA copolymers containing doxorubicin bound via pH-sensitive linkage: synthesis and preliminary in vitro and in vivo biological properties. *J. Controlled Release 73*, 89−102.
(44) Ulbrich, K., Etrych, T., Chytil, P., Jelinkova, M., and Rihova, B. (2003) HPMA copolymers with pH-controlled release of doxorubicin - In vitro cytotoxicity and in vivo antitumor activity. *J. Controlled Release 87*, 33−47.
(45) Mrkvan, T., Sirova, M., Etrych, T., Chytil, P., Strohalm, J., Plocova, D., Ulbrich, K., and Rihova, B. (2005) Chemotherapy based on HPMA copolymer conjugates with pH-controlled release of doxorubicin triggers anti-tumor immunity. *J. Controlled Release 110*, 119−129.
(46) Vetvicka, D., Hruby, M., Hovorka, O., Etrych, T., Vetrik, M., Kovar, L., Kovar, M., Ulbrich, K., and Rihova, B. (2009) Biological evaluation of polymeric micelles with covalently bound doxorubicin. *Bioconjugate Chem. 20*, 2090−2097.
(47) van der Poll, D. G., Kieler-Ferguson, H. M., Floyd, W. C., Guillaudeu, S. J., Jerger, K., Szoka, F. C., and Frechet, J. M. (2010) Design, synthesis, and biological evaluation of a robust, biodegradable dendrimer. *Bioconjugate Chem. 21*, 764−773.
(48) Tannock, I. F., and Rotin, D. (1989) Acid pH in tumors and its potential for therapeutic exploitation. *Cancer Res. 49*, 4373−4384.
(49) Engin, K., Leeper, D. B., Cater, J. R., Thistlethwaite, A. J., Tupchong, L., and McFarlane, J. D. (1995) Extracellular pH distribution in human tumors. *Int. J. Hyperthermia 11*, 211−216.
(50) Mellman, I., Fuchs, R., and Helenius, A. (1986) Acidification of the endocytic and exocytic pathways. *Annu. Rev. Biochem. 55*, 663−700.
(51) Curci, M., Mieloszynski, J. L., and Paquer, D. (1993) Synthesis of functionalized acrylates. *Org. Prep. Proc. Int. 25*, 649−657.
(52) Etrych, T., Chytil, P., Jelinkova, M., Rihova, B., and Ulbrich, K. (2002) Synthesis of HPMA copolymers containing doxorubicin bound via a hydrazone linkage. Effect of spacer on drug release and in vitro cytotoxicity. *Macromol. Biosci. 2*, 43−52.
(53) Prabaharan, M., Grailer, J. J., Pilla, S., Steeber, D. A., and Gong, S. Q. (2009) Amphiphilic multi-arm-block copolymer conjugated with doxorubicin via pH-sensitive hydrazone bond for tumor-targeted drug delivery. *Biomaterials 30*, 5757−5766.
(54) Kwon, G., Naito, M., Yokoyama, M., Okano, T., Sakurai, Y., and Kataoka, K. (1997) Block copolymer micelles for drug delivery: loading and release of doxorubicin. *J. Controlled Release 48*, 195−201.
(55) Lee, S. M., Chen, H. M., O'Halloran, T. V., and Nguyen, S. T. (2009) "Clickable" polymer-caged nanobins as a modular drug delivery platform. *J. Am. Chem. Soc. 131*, 9311−9320.
(56) Ishihara, K., Ueda, T., and Nakabayashi, N. (1990) Preparation of phospholipid polymers and their properties as polymer hydrogel membranes. *Polym. J. 22*, 355−360.
(57) Ladmiral, V., Mantovani, G., Clarkson, G. J., Cauet, S., Irwin, J. L., and Haddleton, D. M. (2006) Synthesis of neoglycopolymers by a combination of "click chemistry" and living radical polymerization. *J. Am. Chem. Soc. 128*, 4823−4830.

Bioconjugate Chemistry

Article

pubs.acs.org/bc

A Ruthenocene–PNA Bioconjugate — Synthesis, Characterization, Cytotoxicity, and AAS-Detected Cellular Uptake

Annika Gross,[#,†] Nina Hüsken,[#,†] Julia Schur,[‡] Łukasz Raszeja,[†] Ingo Ott,[‡] and Nils Metzler-Nolte*[,†]

[†]Inorganic Chemistry I, Bioinorganic Chemistry, Faculty of Chemistry and Biochemistry, Ruhr-University Bochum, Universitätsstrasse 150, D-44801 Bochum, Germany

[‡]Institute of Medicinal and Pharmaceutical Chemistry, Technical University Braunschweig, Beethovenstrasse 55, D-38106 Braunschweig, Germany

Supporting Information

ABSTRACT: Labeling of peptide nucleic acids (PNA) with metallocene complexes is explored herein for the modulation of the analytical characteristics, as well as biological properties of PNA. The synthesis of the first ruthenocene–PNA conjugate with a dodecamer, mixed-sequence PNA is described, and its properties are compared to a ferrocene-labeled analogue as well as an acetylated, metal-free derivative. The synthetic characteristics, chemical stability, analytical and thermodynamic properties, and the interaction with cDNA were investigated. Furthermore, the cytotoxicity of the PNA conjugates is determined on HeLa, HepG2, and PT45 cell lines. Finally, the cellular uptake of the metal-containing PNAs was quantified by high-resolution continuum source atomic absorption spectrometry (HR-CS AAS). An unexpectedly high cellular uptake to final concentrations of 4.2 mM was observed upon incubation with 50 μM solutions of the ruthenocene–PNA conjugate. The ruthenocene label was shown to be an excellent label in all respects, which is also more stable than its ferrocene analogue. Because of its high stability, low toxicity, and the lack of a natural background of ruthenium, it is an ideal choice for bioanalytical purposes and possible medicinal and biological applications like, e.g., the development of gene-targeted drugs.



INTRODUCTION

Peptide nucleic acids (PNA) are non-natural analogues of DNA and RNA with respect to their structure and hybridization properties. In PNA, the negatively charged (deoxy)ribose phosphodiester backbone of DNA/RNA is replaced by a neutral, pseudopeptide backbone of repeating *N*-(2-aminoethyl)glycine units.[1,2] Due to the noncharged backbone, PNA reveals outstanding hybridization properties, such as a thermodynamically and kinetically enhanced hybridization with DNA/RNA, and a high selectivity and excellent discrimination of single-nucleotide polymorphism (SNP). These features make PNA exceptionally attractive for analytical applications like the molecular recognition of nucleic acids.[3−7] Medicinal and biological applications such as in antigene/antisense therapy[8,9] or in drug discovery[10] additionally benefit from the high chemical stability and its resistance toward nucleases and proteases.[11] The main drawback of PNA regarding medicinal and biological applications is its poor intrinsic uptake, since unmodified PNA does not spontaneously enter the cell by passive diffusion through the cell membrane.[12] Several strategies for an enhanced cellular uptake have been reported like, e.g., microinjection, electroporation, or cell permeabilization.[13] Noninvasive methods usually use modified PNA oligomers with lipophilic moieties, negatively charged DNA complements, Trojan-peptides, and so forth, as trans membrane carriers.[13−17] An efficient uptake is observed for PNA oligomers labeled with cell-penetrating peptides (CPP) like penetratin, Tat-derived peptides, transportan, or poly-Arg sequences as trans membrane carriers.[18,19] A disadvantage of these peptide conjugates for in vivo applications is the often observed immunogeneity and the intrinsic toxicity of some of these peptides.[20]

In recent years, conjugates of metals or metal complexes and PNA oligomers have attracted great attention and were recently reviewed for the first time.[21−23] Several examples thereof were reported to modify the PNA properties to an increased cellular uptake. Our group found an improved cellular delivery of a PNA conjugate with a cobalt complex,[24] whereas Krämer et al. reported an enhanced uptake of Zn^{2+}-modified PNA oligomers.[25,26] The qualitative and quantitative detection of metal complex-conjugated biomolecules within the cell is greatly facilitated by the unique properties of the metal complexes. Specific examples include metalloimmunoassays,[27−29] atomic absorption spectrometry (AAS),[24] IR, fluorescence or optical spectroscopy,[30−34] as well as RAMAN- and IR-microscopy.[35−38] Thereby, especially an AAS-based quantification of the PNA uptake promises advantages over established biochemical methods due to its high sensitivity and metal-specificity.[39] The high sensitivity and metal-specificity of AAS bears the potential to overcome limitations inherent in other methods such as the measurement of luciferase activity which is sensitive toward cell parameters like the cell density or

Received: December 29, 2011
Revised: May 28, 2012
Published: July 24, 2012

ACS Publications © 2012 American Chemical Society

viability,[18] or the fluorescent-microscopic detection of fluorescent-labeled PNA, which is restricted due to the ability of fluorophores to change the distribution and uptake of the PNA conjugate as well as influencing the cell viability.[40−42]

Most frequently, organo-metal complex/PNA conjugates are prepared by solid-phase synthesis. Our group has presented different methods for the conjugation of metal complexes in the course of the solid-phase synthesis of PNA, using the peptide coupling of carboxylic acid derivatives of the metal-complexes or the Cu-catalyzed [2 + 3] cycloaddition between azides and terminal alkynes (click chemistry) as the key reaction.[43,44] The click chemistry approach enabled the introduction of one or even several (different) azido or alkynyl ferrocene derivatives to azide or alkyne functionalities at various positions within the PNA strand. With this chemistry, a target-oriented tuning of the properties of PNA could be realized.[45−47] Ferrocene conjugates of PNA oligomers and monomers have also been reported by Baldoli et al.[48−50] and Gasser et al.[51,52] The labeling of PNA monomers and oligomers with different metal complexes besides ferrocene has also been investigated by Maiorana et al., who presented PNA conjugates with organometallic complexes of chromium,[53,54] tungsten,[55] and rhenium, as well as the radioactive technetium isotope ^{99m}Tc.[56,57]

The aim of this work is to provide a new metal−organic label for PNA sequences, which obtains good cellular uptake properties and is analytically detectable in living cells. Furthermore, such a label should be synthetically easily accessible and chemically stable and should not negatively influence neither the DNA binding properties nor the cell viability. A label with such properties is of high importance for the design of, e.g., new anticancer therapeutics or diagnostics but can be furthermore highly valuable also for antigene/antisense agents in cell biology. As a promising organo-metallic complex regarding the desired properties, the ruthenium complex ruthenocene was chosen, which is the higher homologue of the well-studied ferrocene. Previously, our group presented a *tris*-(bipyridine)ruthenium(II) PNA conjugate, which shows interesting characteristics since the ruthenium complex is stable, undergoes reversible one-electron oxidation, and exhibits characteristic UV/vis absorption.[44] On the other hand, the bulkiness of this ruthenium complex might hinder the cellular uptake of the PNA conjugate, which could explain why related metal derivatives exhibited a moderate antiproliferative effect.[58] Therefore, although ruthenium has favorable properties *per se*, the *tris*(bipyridyl) complexes are far from ideal candidates as PNA labels for intracellular detection. In this paper, we report the facile solid-phase synthesis of a ruthenocenyl−PNA bioconjugate (Rc: ruthenocenyl, $CpRuC_5H_4$) *via* the peptide coupling of ruthenocenecarboxylic acid to the *N*-terminus of PNA. The Rc−PNA conjugate was comprehensively characterized by analytical techniques and the influence of the ruthenocene label onto the thermal stability of PNA•DNA duplexes was investigated in UV/vis-melting experiments. For possible medicinal or cell biological applications, the cellular uptake and the cytotoxicity of the Rc−PNA conjugate was studied. The experiments were additionally carried out with the analogue Fc−PNA conjugate (Fc: ferrocenyl, $CpFeC_5H_4$), as well as with an acetylated, metal-free PNA analogue.

EXPERIMENTAL SECTION

General Experimental Conditions. All reagents and HPLC-grade solvents were purchased from Acros (Geel, Belgium), Aldrich/Sigma/Fluka (Deisenhofen, Germany), E. Merck (Darmstadt, Germany), Novabiochem (Laufelfingen, Switzerland), and IRIS Biotech (Marktredwitz, Germany) and were used without further purification. The preloaded polystyrene resin was purchased from Rapp Polymers (Tübingen, Germany). Only L-amino acids were used throughout the synthesis. Fmoc/Bhoc-protected PNA monomers were purchased from Link Technologies (Lanarkshire, Scotland) and ASM (Hannover, Germany). All solutions were freshly prepared before use. HPLC fractions of all products were frozen in liquid nitrogen and lyophilized using a Christ Alpha 1−4 LD plus freeze−dryer. All aqueous solutions were prepared from Millipore water and filtered with a 0.22 μm syringe filter before use.

Mass Spectrometry. MALDI-TOF mass spectra were recorded on a Daltonics Autoflex instrument (Bruker, Karlsruhe, Germany) in linear mode with positive polarity using sinapic acid as the matrix (6 mg/mL in ACN/water (+ 0.1% TFA) = 2:1). ESI mass spectra were recorded on an Esquire 6000 instrument (Bruker, Karlsruhe, Germany) applying the following parameters: sputtering voltage 4 kV; nebulizer pressure 10−20 psi; drying gas 5−10 L/min, 300 °C; flow rate 240 μL/h. For all mass spectrometric measurements, the PNA samples were prepared as 1 mg/mL solutions in water (+ 0.1% TFA).

HPLC Analysis and Purification. HPLC analysis and purification were performed on a customized Knauer Smartline System (Knauer, Berlin, Germany), equipped with Knauer Smartline pumps 1000 and a Knauer Smartline UV detector 2550, using Reprosil-Pur C-18 reverse-phase columns (Dr. Maisch GmbH, Ammerbuch-Entringen, Germany) for analytical (250 × 4.6 mm) and preparative (250 × 10 mm) runs. Analytical (flow rate: 1.0 mL min^{-1}) and preparative (flow rate: 4.0 mL min^{-1}) runs were performed with a linear gradient of A (95% Millipore water, 5% ACN, 0.1% TFA (v/v/v)) and B (5% Millipore water, 95% ACN, 0.1% TFA (v/v/v)). Analytical runs: t = 0 min: 0% B; t = 18 min: 100% B; t = 22 min: 100% B; t = 30 min: 0% B. Preparative runs: t = 0 min: 0% B; t = 36 min: 100% B; t = 38 min: 100% B; t = 45 min: 0% B. All samples were filtered before injection using a 0.22 μm syringe filter. Spectra were recorded at 260 nm, and ambient temperature and retention times (t_R/[min]) were noted in each case.

Solid-Phase PNA Synthesis. SPPS was performed manually in 5 mL polypropylene one-way syringes as reaction vessels, which were equipped with a frit at the bottom. They were filled with 50 mg of polystyrene resin beads TentaGel R PHB Cys(Trt)Fmoc (0.18 mmol/g). The resin was swollen in DMF before use for 1 h. All reactions were performed on a mechanical shaker with 400 rpm, soaking approximately 3−4 mL of freshly prepared solutions into the syringe. Fmoc/Bhoc protected PNA monomers (5 equiv) were preactivated in Eppendorf tubes before every coupling step for 2 min with HATU (4.5 equiv) in DMF, adding DIPEA (0.2 M, 10 equiv), and 2,6-lutidine (0.3 M, 10 equiv) (A(Bhoc)-PNA-monomer: 5 min, C(Bhoc)-PNA-monomer: 7 min). The amino acids Fmoc-Ahx and Lys(Boc)Fmoc were preactivated in an analogous manner with TBTU and HOBt·H_2O (4.5 equiv each). For each coupling step, the resin beads were treated with the activated acid under vibration (50 °C, 20 min) and subsequently washed with DMF. Every coupling step was monitored by the Kaiser test. Twofold Fmoc deprotection was performed with piperidine (20%, v/v) in DMF (2 min + 10 min). The resin

beads were then washed successively with DMF, DCM, and DMF. The whole procedure (deprotection, coupling, monitoring) was repeated for every PNA monomer until the PNA sequence was completed. The synthesis of **AcPNA**, **FcPNA** and **RcPNA**, as described below, follows the Fmoc-deprotection of the last monomer of the completed PNA sequence. Final cleavage of the acetylated, ferrocenylated or ruthenocenylated PNA oligomer from the resin and the deprotection of all Bhoc, Boc, and Trt side chain protecting groups were simultaneously performed in TFA/TIS/phenol (85/5/10, v/v/v) (2 h + 1 h). Following the removal of TFA under reduced pressure, the crude product was precipitated with cold diethyl ether (−20 °C), washed twice with cold diethyl ether, and centrifuged each time (10 min, 8000 rpm). The obtained crude oligomer was lyophilized in acetonitrile/water, purified and analyzed with RP-HPLC, and finally characterized with MALDI-TOF and ESI mass spectrometry.

***N*-Terminally Acetylated PNA Oligomer (AcPNA).** **AcPNA** was synthesized on 50 mg (10 μmol) of the resin TentaGel R PHB, which was preloaded with the 12-mer PNA sequence H-t c t a c g a g a c t c Lys Ahx CysOH. Therefore, an *N*-terminal double acetylation was performed subsequent to the Fmoc deprotection of the last PNA monomer of this sequence by treating the resin with a solution of acetic hydride (5%, v/v) and DIPEA (6%, v/v) in DMF for 2 × 3 min under vibration. The resin was then successively washed with DMF, DCM, and MeOH and subsequently shrunk by treating the resin with MeOH under vibration (10 min, r.t.). After draining off the solvent and removal of solvent residues under reduced pressure, the cleavage from the resin following the general procedure yielded **AcPNA** as a white solid. **AcPNA** (M = 3614.5 g/mol): HPLC: t_R = 8.67 min, 100%. MALDI-TOF MS: m/z (%) = 3617.3 $[M+H]^+$ (100). ESI MS: m/z (%) = 1206.0 $[M+3H]^{3+}$ (25.5), 904.9 $[M+4H]^{4+}$ (100), 724.2 $[M+5H]^{5+}$ (17.3), 603.6 $[M+6H]^{6+}$ (4.1).

Ruthenocenoyl PNA Conjugate (RcPNA). The conjugation of ruthenocene via peptide coupling of ruthenocenecarboxylic acid was performed on 50 mg (10 μmol) of the resin TentaGel R PHB, which was preloaded with the 12-mer PNA sequence H-t c t a c g a g a c t c Lys Ahx CysOH, and follows the Fmoc deprotection of the last PNA monomer of this sequence. Ruthenocenecarboxylic acid (4 equiv) was preactivated for 3 min in an Eppendorf tube with HATU and HOBt·H_2O (4 equiv each) in NMP, containing DIPEA (0.2 M, 6 equiv). The resin was treated with the activated ruthenocenecarboxylic acid under vibration (3 h, r.t.). The resin was then successively washed with DMF, DCM, and MeOH and subsequently shrunk by treating the resin with MeOH under vibration (10 min, r.t.). After draining off the solvent and removal of solvent residues under reduced pressure, the cleavage from the resin following the general procedure yielded **RcPNA** as an off-white solid. **RcPNA** (M = 3830.4 g/mol): HPLC: t_R = 10.27 min, 100%. MALDI-TOF MS: m/z (%) = 3831.9 $[M+H]^+$ (100). ESI MS: m/z (%) = 1278.2 $[M+3H]^{3+}$ (74.9), 958.7 $[M+4H]^{4+}$ (100), 767.4 $[M+5H]^{5+}$ (24.5).

Ferrocenoyl PNA Conjugate (FcPNA). The conjugation of ferrocene via the peptide coupling of ferrocenecarboxylic acid was performed on 50 mg (10 μmol) of the resin TentaGel R PHB, which was preloaded with the 12-mer PNA sequence H-t c t a c g a g a c t c Lys Ahx CysOH, and follows the Fmoc deprotection of the last PNA monomer of this sequence. Ferrocenecarboxylic acid (5 equiv) was preactivated for 3 min in an Eppendorf tube with HATU and HOBt·H_2O (4.5 equiv each) in DMF, with DIPEA (0.2 M, 10 equiv) and 2,6-lutidine (0.3 M, 10 equiv). The resin was treated with the activated ferrocenecarboxylic acid under vibration (3 h, r.t.). The resin was then successively washed with DMF, DCM, and MeOH and subsequently shrunk by treating the resin with MeOH under vibration (10 min, r.t.). After draining off the solvent and removal of solvent residues under reduced pressure, the cleavage from the resin following the general procedure yielded **FcPNA** as a yellowish solid. **FcPNA** (M = 3784.5 g/mol): HPLC: t_R = 10.26 min, 100%. MALDI-TOF MS: m/z (%) = 3785.5 $[M+H]^+$ (100). ESI MS: m/z (%) = 1262.7 $[M+3H]^{3+}$ (35.2), 947.4 $[M+4H]^{4+}$ (100), 758.2 $[M+5H]^{5+}$ (17.0), 632.0 $[M+6H]^{6+}$ (2.9).

UV/vis Melting Studies. *Instrumentation.* UV/vis measurements were performed with the UV/vis spectrophotometer Varian Cary 100 Conc (Varian Inc., Palo Alto, CA, USA), equipped with a 6 × 6 multicell block and Peltier thermostat and running with the Cary Win UV/vis software with Cary Bio package. Quartz Suprasil QS cuvettes (4 × 10 mm; Hellma, Müllheim, Germany) were used and densely sealed with Teflon caps for all measurements to avoid solvent evaporation at higher temperatures. The multicell block was purged with nitrogen gas during all measurements at lower temperatures (T < 15 °C).

Determination of DNA and PNA Conjugate Concentrations. The UV/vis spectroscopic determination of the PNA conjugate concentration of the prepared stock solution (in 0.1 M PBS, pH 7.4) was performed from a diluted aliquot (1:10 dilution). The UV/vis spectrum (λ = 190−900 nm) was measured at 85 °C (after equilibration for 5 min to avoid PNA aggregation) versus a background of 0.1 M PBS (pH 7.4). The absorption A was read out at a wavelength of λ = 260 nm, to calculate the concentration c of the PNA solution according to the Beer−Lambert law $A = \varepsilon\, l\, c$ (ε: molar extinction coefficient; l: cuvette path length; c: concentration of the PNA conjugate). The determination of the exact DNA concentration of the purchased DNA sequence was performed at T = 25 °C, otherwise in an analogous manner to the determination of the PNA concentration.

Determination of the Molar Extinction Coefficient ε. The molar extinction coefficients ε of the PNA conjugates and DNA oligomers at λ = 260 nm were calculated from the incremental molar extinction coefficients ε_x of the nucleobases according to $\varepsilon = \sum_x n_x \varepsilon_x$ (x = A/a, G/g, T/t, C/c, Fc or Rc; n_x = number of monomer x in the oligomer). As proposed by Nielsen et al.,[59] the incremental molar absorption coefficient of fully unstacked DNA nucleosides (at T = 25 °C)[60] were taken as the incremental molar absorption coefficient of fully unstacked PNA nucleobases (requiring measurements at T > 80 °C), as reported in the literature (ε_a = 13 700 M^{-1} cm^{-1}, ε_t = 8600 M^{-1} cm^{-1}, ε_g = 11 700 M^{-1} cm^{-1}, ε_c = 6600 M^{-1} cm^{-1}, ε_{Fc} = 9500 M^{-1} cm^{-1}).[60,61] The incremental molar absorption coefficient of the ruthenocene moiety ε_{Rc} (λ = 260 nm, 0.1 M PBS, pH 7.4, T = 25 °C) was estimated using ruthenocenecarboxylic acid Rc-CO_2H as a model compound. UV/vis spectra (λ = 190−900 nm) of a concentration series in the range of c = 10−500 μM with increments of c = 50−100 μM were recorded. The absorption was read out at λ = 260 nm and plotted against the respective concentration of ruthenocenecarboxylic acid, to give a straight line with R^2 > 0.99995 (see Supporting Information). ε_{Rc} was calculated from the slope of these straight lines according to the Beer−Lambert law, to result in ε_{Rc} = 1310

(±181) M^{-1} cm^{-1} from three independent measurements. Based on this, the molar extinction coefficients were calculated to ε(**RcPNA**) = 118 010 M^{-1} cm^{-1}, ε(**FcPNA**) = 126 200 M^{-1} cm^{-1}, ε(**AcPNA**) = 116 700 M^{-1} cm^{-1}. The DNA concentration was calculated based on the following incremental molar absorption coefficients: ε_A = 15 300 M^{-1} cm^{-1}, ε_T = 8700 M^{-1} cm^{-1}, ε_G = 12 200 M^{-1} cm^{-1}, ε_C = 7600 M^{-1} cm^{-1}.[62]

UV/vis Melting Curves. For the measurement of PNA/DNA UV/vis melting curves, phosphate buffer solutions (0.1 M PBS, pH 7.4) of equimolar amounts of the single-stranded PNA conjugate **RcPNA**, **FcPNA**, or **AcPNA** and the single-stranded fully cDNA sequence G A G T C T C G T A G A with the final duplex concentration of c = 1.7 μM were prepared and filled into the quartz cuvettes. Multi-zeroing of the spectrophotometer was performed against cuvettes filled with phosphate buffer solution (0.1 M PBS, pH 7.4) at 25 °C. The controlled annealing of the PNA•DNA duplexes was performed by exposing the prepared PNA/DNA solutions to 85 °C for 5 min in the spectrophotometer and subsequently decreasing the temperature with a controlled cooling rate of 0.5 °C/min to a final temperature of 4 °C. Subsequently, the UV/vis melting curve was recorded at a wavelength of λ = 260 nm upon application of a temperature gradient ranging from T_0 = 4 °C to $T_{2.7\ h}$ = 85 °C with a heating rate of 0.5 °C/min. The collected raw data were saved as ASCII files and analyzed using the software *ORIGIN*. The obtained sigmoid-shaped melting curves were subjected to a polynomial data fit (9th order, 1000 data points) and subsequently differentiated (1st order). The melting point T_M is equal to the maximum of the first derivative.

Cell Culture. *General Procedure.* The human HepG2 cell line was obtained from "Deutsche Sammlung von Mikroorganismen und Zellkultur ACC 180". The cell lines HeLa and PT45 were provided by Prof. Hahn (Molekulare Onkologie, Ruhr-University Bochum, Bochum, Germany). Cells were grown in RPMI 1640 with 1% sodium pyruvate, 1% L-glutamine, 100 units/mL Pen Strep, and 10% fetal bovine serum. The cells were maintained at 37 °C in a humidified incubator under an atmosphere containing 5% CO_2. Wells used for HeLa cells were coated with 0.2% gelatin solution before use. HT-29 colon carcinoma cells were maintained in DMEM high glucose (PAA) supplemented with 50 mg/L gentamycin and 10% (v/v) fetal calf serum (FCS) prior to use.

Cytotoxicity Experiments. To determine the activity of **RcPNA** and **FcPNA** in comparison to **AcPNA**, two antiproliferative assays, resazurin and crystal violet, were performed. 6000 cells/well of HeLa, PT45, and HepG2 cells were incubated in 96-well plates at 37 °C and 5% CO_2 for 24 h. To determine the initial cell viability and biomass, a t_0-plate with HeLa, HepG2, and PT45 was additionally plated, and after 24 h incubation, the resazurin assay was performed. Subsequently, the cells were fixed with 0.2% glutardialdehyde solution, followed by the crystal violet assay. In the remaining plates the medium was replaced with medium containing **AcPNA**, **FcPNA**, or **RcPNA** with 0.5% DMSO added to improve the solubility of the compound. Concentrations between 1 and 200 μM were used and each concentration was tested six times in parallel. As a positive control, cisplatin was used, and as negative control, medium containing 0.5% DMSO. To determine the effect of metallocene carboxylic acid, ferrocene- and ruthenocenecarboxylic acid were tested up to a concentration of 1 mM under the same conditions as the metallocene–PNA conjugates. The incubation time of the compounds was 48 h. Then, the compound-containing medium was removed, the cells were washed with PBS, and the resazurin assay was performed.

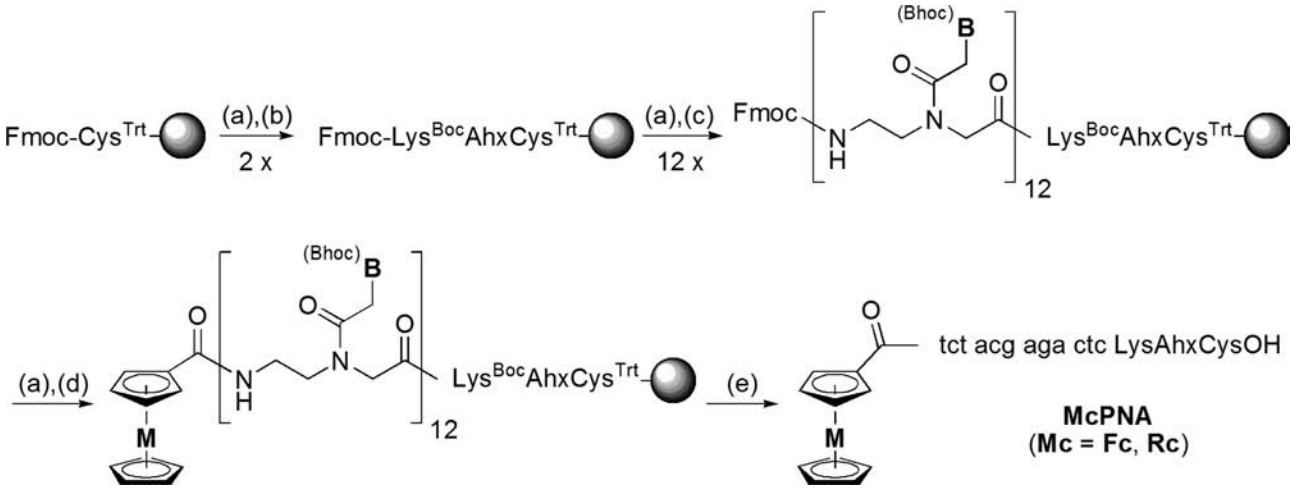
Resazurin Assay. 1 mL of resazurin solution per plate was diluted with 9 mL medium without phenol red. 100 μL of this solution was added per well and the plates were measured using a Tecan plate reader at 600 nm, using a reference wavelength of 690 nm. The plates were incubated for 2 h at 37 °C and 5% CO_2 and were measured again.

Crystal Violet Assay. To perform the crystal violet assay, the resazurin solution was removed and the cells were fixed using 0.2% glutardialdehyde for 25 min. The glutardialdehyde solution was removed and exchanged for 100 μL of 0.1% triton solution. After a short incubation, all liquids were removed and the fixed cells were stained with a 0.02 M crystal violet solution for 30 min. Afterward, the wells were washed intensely with H_2O and were filled with 100 μL of 96% ethanol, followed by shaking on a softly rocking rotary shaker for 3 h. The absorption of the ethanolic solution was measured using a microplate reader at 570 nm. The mean absorption of the initial cell plate (t_0-plate) for each cell line was subtracted from the absorption of each experiment and control. For both assays, the negative control was set to 100%.

Cellular Uptake. For cellular uptake studies, HT-29 colon carcinoma cells were grown until at least 70% confluency in 75 cm^2 cell culture flasks. Stock solutions of the metallocene–PNA conjugate, namely, **FcPNA** or **RcPNA**, in demineralized water were freshly prepared and diluted with cell culture medium to the desired concentration of 50 μM. The cell culture medium of the cell culture flasks was replaced with 10 mL of the cell culture medium solutions containing the metallocene–PNA conjugate and the flasks were incubated at 37 °C/5% CO_2 for 6 h. Subsequent to the incubation period, the culture medium was removed, and the cell layer washed with 10 mL PBS, treated with 2 mL trypsin solution (0.05% trypsin in PBS), and incubated for 2 min at 37 °C/5% CO_2 after removal of the trypsin solution. Cells were resuspended in 10 mL PBS and cell pellets were isolated by centrifugation (RT, 5400 rpm, 5 min). Cellular lysates were prepared by resuspending an isolated cell pellet in 1 mL demineralized water followed by ultrasonication. An aliquot was removed for the purpose of protein quantification by the method of Bradford.[63] The metal content of the samples was determined by high-resolution continuum source atomic absorption spectrometry (HR-CS AAS, see below). Results were calculated from the data of two independent experiments and are expressed as pmol of the metallocene–PNA conjugate per milligram of cellular protein. On the basis of the knowledge of the cellular diameter, the values were also estimated as intracellular molar metal concentrations.[64]

HR-CS AAS Measurements. A contrAA 700 high-resolution continuum source atomic absorption spectrometer (Analytik Jena AG) was used for the metal measurements. Iron was measured at a wavelength of 248.37 nm; ruthenium was quantified at a wavelength of 349.90 nm. Because of the high iron background level in biological material, matrix-matched calibration was used for iron quantification in the **FcPNA** samples. For this purpose, the protein levels of all samples and standards were adjusted to the same concentration by dilution with distilled water. For ruthenium measurements in the **RcPNA** samples, aqueous standards were used for calibration purpose. To 200 μL of all probes and standards each, 20 μL Triton X-100 (1%) and 20 μL nitric acid (13%) were added.

Scheme 1. Synthesis Scheme for the Solid-Phase Synthesis of Metallocene-PNA Conjugates FcPNA and RcPNA[a]



[a](a) Fmoc deprotection: piperidine/DMF (20%, v/v); (b) Coupling Fmoc-AA-OH (5 equiv): TBTU, HOBt·H_2O (4.5 equiv each), DIPEA, 2,6-lutidine (10 equiv each) in DMF; (c) coupling Fmoc-PNA(Bhoc)-OH (5 equiv): HATU (4.5 equiv), DIPEA, 2,6-lutidine (10 equiv each) in DMF; (d) coupling Fc-CO_2H (5 equiv): HATU, HOBt·H_2O (4.5 equiv each), DIPEA, 2,6-lutidine (10 equiv each) in DMF; coupling Rc-CO_2H (4 equiv): HATU, HOBt·H_2O (4 equiv each), DIPEA (6 equiv) in NMP; (e) Cleavage: TFA/TIS/phenol (85/5/10, v/v/v). See Experimental Section for further details.

Samples were injected at a volume of 25 μL into coated standard graphite tubes ("AAS IC-Standardrohr, beschichtet", Analytik Jena AG). The optimized temperature time program for iron in the graphite tube is given in the Supporting Information (Table S1). For ruthenium, a furnace program as described in the literature was used.[65] During the temperature program, the graphite tube was purged with a constant argon gas flow, which was only halted during the zeroing and atomization steps. The mean integrated absorbances of triple injections were used throughout the study.

RESULTS AND DISCUSSION

Synthesis, Characterization, and Chemical Stability. The 12-mer PNA sequence of the PNA conjugates **RcPNA**, **FcPNA**, and **AcPNA** was synthesized according to Scheme 1 by manual standard Fmoc solid-phase synthesis on a Fmoc-Cys(Trt) preloaded TentalGel R PHB resin using Fmoc/Bhoc-protected PNA monomers (see Experimental Section for details).[45] The chosen PNA sequence is a mixed sequence of all four nucleobases and targets a specific region in the central domain of the 16S rRNA of *E. coli*. A peptidic linker is bound to the PNA *C*-terminus, which contains a lysine residue for increased solubility and enhanced cellular uptake of the PNA conjugate.[16,45] The metallocene complex was conjugated to the PNA *N*-terminus, since an undesired decrease in PNA•DNA duplex stability was observed upon modification of internal strand positions of the PNA sequence.[66,67] Ferrocene and ruthenocene were conjugated to the deprotected *N*-terminus of the PNA oligomer on the solid support by performing peptide coupling with ferrocene carboxylic acid (Fc-CO_2H) and ruthenocene carboxylic acid (Rc-CO_2H), respectively, as the sequence-terminating coupling step.[45,68] The success of the coupling was monitored by the Kaiser test[69] and later proven by HPLC of the crude compound (Figure 1). For improved solubility of Rc-CO_2H, NMP was used instead of DMF. Cleavage from the resin and the removal of all protecting groups was performed with TFA/TIS/phenol 85:5:10 (v/v/v), and precipitation with diethyl ether followed by centrifugation gave the crude product of **RcPNA** as a white solid and of **FcPNA** as a yellowish solid. The *N*-terminally acetylated PNA oligomer **AcPNA** was synthesized as a metal-free analogue of **FcPNA** and **RcPNA**.

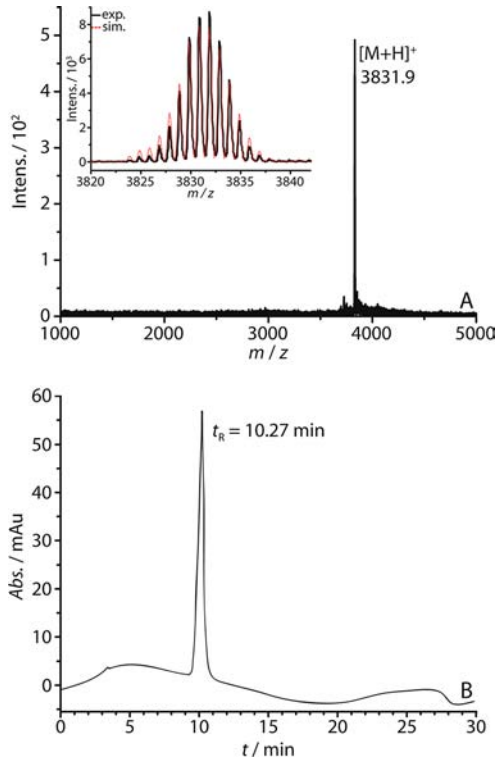


Figure 1. Analytical data of **RcPNA**. (A) MALDI-TOF spectrum; enlarged section shows the isotopic pattern of the base peak at m/z = 3831.9 (m/z-scale normalized to m/z of the base peak; continuous black line: measured pattern, dashed red line: isotope pattern simulated with the software Bruker Daltonics *DataAnalysis 3.4* (Bruker, Karlsruhe, Germany). (B) HPLC chromatogram detected at a wavelength of λ = 260 nm.

dx.doi.org/10.1021/bc200692g | *Bioconjugate Chem.* 2012, 23, 1764–1774

The crude products were purified by preparative HPLC (see Experimental Section). Analytical HPLC proved high purity of the three compounds and MALDI-TOF mass spectrometry showed only the respective $[M+H]^+$ peak for all compounds. In ESI-MS, all PNA conjugates showed the respective $[M+4H]^{4+}$ peak as the base peak with an excellent mass accuracy (deviation from theoretical value <0.26). All other peaks could be assigned to multiply charged species of the respective compounds, with a dominating presence of the respective $[M+5H]^{5+}$ and $[M+3H]^{3+}$ peaks. Comparison of the MALDI-TOF spectra as well as the analytical HPLC of the crude and the purified products revealed that the crude products of **RcPNA**, **FcPNA**, and **AcPNA** were already obtained with high purities of >98%. On the basis of HPLC and MS, it can be thus concluded that all solid-phase reaction steps during the synthesis of **RcPNA**, **FcPNA**, and **AcPNA** including the coupling of Rc-CO_2H and Fc-CO_2H occurred with nearly complete conversion. Magnification of the $[M+H]^+$ base peak in the MALDI-TOF spectra of **RcPNA** furthermore revealed a well-resolved isotope distribution (see Figure 1A), which is in good agreement with the calculated isotope pattern of **RcPNA** and hence is a distinct indicator for the presence of ruthenocene. The analytical characterization of the crude compounds furthermore indicates that both metallocene labels are completely stable to the fairly harsh TFA cleavage conditions. However, the ferrocene label turned out to be somewhat unstable upon extended storage even at −20 °C after HPLC purification, as shown by the MS detection of a molecular fragment resulting from the loss of the FeCp group (data not shown). The formation of this fragment can be explained by primary oxidation and subsequent degradation of ferrocene induced by nucleophilic agents, which is a well-known degradation pathway for ferrocene.[70] An analogous degradation was never observed for **RcPNA**. This observation is in line with the higher oxidation potential of ruthenocene vs ferrocene and indicates an improved stability in comparison to **FcPNA**. Analytical HPLC of the three conjugates furthermore shows similar retention times for the metal−PNA conjugates of t_R(**RcPNA**) = 10.27 min and t_R(**FcPNA**) = 10.26 min, whereas **AcPNA** exhibits a smaller value of t_R(**AcPNA**) = 8.67 min. Conjugation of ferrocene or ruthenocene to PNA oligomers thus induces an increase in the lipophilicity of the PNA oligomer.

DNA Binding. UV/vis melting experiments were performed in order to study the impact of the different *N*-terminally attached metallocene labels onto the thermodynamic stability of the corresponding fully complementary PNA•DNA duplexes. Melting experiments were performed by running a temperature profile from T = 5−85 °C with detection at a wavelength of λ = 260 nm (see Figure 2). The determined T_M values equal the maximum of the melting curves' first derivative. The PNA•DNA duplexes of **FcPNA** and **RcPNA** exhibit values of T_M(**FcPNA**•DNA) = 60.1 (±0.3) °C and T_M(**RcPNA**•DNA) = 60.5 (±0.2) °C, which are about 2.5 and 2.1 °C, respectively, lower than the value of T_M(**AcPNA**•DNA) = 62.6 (±0.3) °C determined for the acetylated analogue. The presence of the *N*-terminally bound metallocene complex hence slightly destabilizes the duplex structures. As a possible reason, an impediment of the nucleobase-pairing at the *N*-terminus under formation of a "frayed" strand-end is proposed, which has already been discussed for a *N*-terminally bound tris-(bipyridine)ruthenium-(II) complex and is furthermore documented for terminal single base pair mismatches.[44,71] This thermodynamic destabilization is underscored by differences in the related hypochromic effect during duplex formation. Whereas the **AcPNA**•DNA duplex exhibited a hypochromic effect of 12.3% upon duplex formation (comparing T = 80 and 5 °C), the metallocene PNA conjugates **FcPNA**•DNA and **RcPNA**•DNA show smaller values of 10.8% and 10.5%, respectively. Since the hypochromic effect is related to the extent of $\pi-\pi$ nucleobase stacking interactions, a smaller hypochromic effect supports the notion of metallocene-induced attenuation of the $\pi-\pi$ stacking.[44]

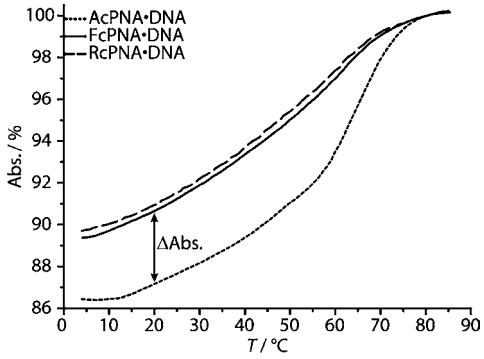


Figure 2. Overlay of UV/vis-melting curves of **RcPNA**, **FcPNA**, and **AcPNA** (absorbance is documented as the percentaged fraction of the absorbance of the fully unstacked, single-stranded species at T = 80 °C).

Antiproliferative Effect and Cellular Uptake Studies. The biological properties of the metallocene−PNA conjugates were examined as a basis for potential future applications as therapeutic or diagnostic agents, for instance, in cancer therapy. First, the cellular uptake of the metallocene−PNA conjugates was studied. To this end, the cellular metal concentrations were quantified by high-resolution continuum source atomic absorption spectrometry (HR-CS AAS), which is a novel AAS technology offering a simultaneous background correction besides a high specificity and low detection limits for metals.[39] Additionally, the cytotoxicity of all PNA conjugates was studied in order to determine a possible damage of the cell membrane due to apoptotic or necrotic effects, which would lead to artificially increased values for cellular uptake.

Cytotoxicity. The antiproliferative effects of **RcPNA** and **FcPNA** were studied in comparison to **AcPNA** using the resazurin assay and additionally the crystal violet assay. These two assays evaluate different cell parameters. While the resazurin assay determines the cell viability, the crystal violet assay gives information about the cell biomass. The commonly used human liver carcinoma cell line HepG2 and the cell line PT45, a pancreatic cancer cell line of high interest due to the profound resistance to treatment of pancreatic cancer, were chosen for comparative cytotoxicity measurements of all PNA conjugates. **RcPNA** was additionally tested on HeLa cells, a cervical cancer cell line which in general reveals the highest sensitivity of the studied cell lines. Both assays showed that none of the compounds had any cytotoxic effect after an incubation time of 48 h and up to a concentration of 200 μM (see Figure 3).

The absence of an antiproliferative effect of the metallocene-labeled conjugates **FcPNA** and **RcPNA** furthermore indicates that the metallocene groups do not increase the cytotoxicity of the PNA. This finding is supported by the absence of any

dx.doi.org/10.1021/bc200692g | *Bioconjugate Chem.* 2012, 23, 1764−1774

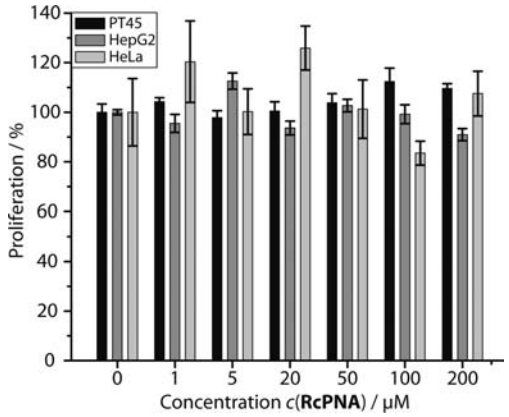


Figure 3. Proliferation of PT45, HepG2, and HeLa cells in the presence of varying concentrations of **RcPNA** (in medium with 0.5% DMSO), as determined by the crystal violet assay.

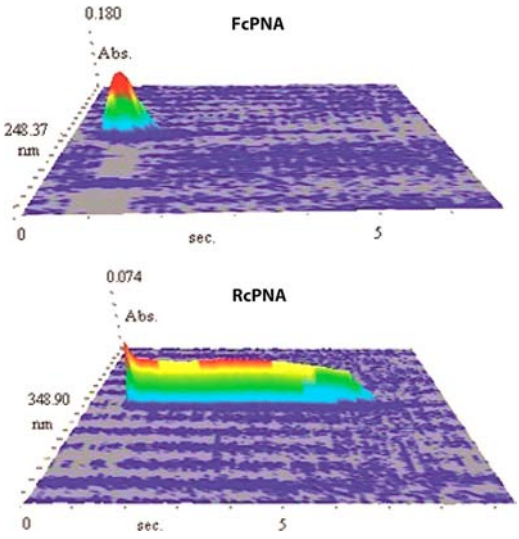


Figure 4. HR-CS AAS signal induced by **FcPNA** and **RcPNA**, respectively. The iron or ruthenium absorption signal can be measured at 248.37 nm (iron, **FcPNA**) or 349.90 nm (ruthenium, **RcPNA**) without background interferences. **RcPNA** shows a broad signal caused by its low volatility. In both cases, quantification was possible using the absorbances (correlation coefficient of standard curve >0.995).

cytotoxic activity of the free compounds ferrocene- and ruthenocenecarboxylic acid up to a concentration of 1 mM. While several ferrocene-containing compounds with strong antiproliferative activity are reported in the literature,[72,73] the cytotoxicity of compounds conjugated with a simple ferrocene amide moiety, as is present in **FcPNA**, is usually fairly low. The low toxicity of **RcPNA** is readily rationalized since ruthenocene is chemically and oxidative more stable than ferrocene,[74] limiting its possible interactions with biological material. This outcome is supported by our previous findings, which did not show any cytotoxic effect for ruthenocenecarboxylic acid or ruthenocene containing peptides.[75] Recently, Williams et al. reported ruthenocene analogues with a moderate to weak cytotoxicity. However, the cytotoxic effect of these derivatives appeared to be governed by the substituents of the ruthenocene rather than the metal complex itself.[76]

Cellular Uptake. The cellular uptake of the metallocene–PNA conjugates **FcPNA** and **RcPNA** was studied by incubating HT-29 colon carcinoma cells. The incubation was performed with 50 μM solutions of the respective conjugate in cell culture medium over a period of 6 h. The uptake of the metal compounds into the cells was quantified by determination of the iron and ruthenium content, respectively, by HR-CS AAS (see Figure 4). The cellular protein (CP) content of the same samples was measured simultaneously according to the method of Bradford.[63] Finally, the determined metal content was correlated to the cell protein content (pmol metal per μg CP).

The analysis revealed surprisingly high cellular uptake levels for the metallocene–PNA conjugates with a cellular iron concentration of 72 pmol/μg CP for **FcPNA** and a cellular ruthenium concentration of 21 pmol/μg CP for **RcPNA**. The determination of the cellular concentration of **FcPNA**, despite the high natural background of iron, was possible due to this exceptionally strong uptake of the iron-containing complex. On the basis of these values, the intracellular concentrations of **FcPNA** and **RcPNA** can be estimated on the basis of distinct cellular parameters (e.g., mean content of cellular protein, mean cell volume).[64] Both compounds revealed relatively high intracellular concentrations in the low millimolar range (14.2 mM for **FcPNA** and 4.2 mM for **RcPNA**, see Table 1). With this, the intracellular concentration of both PNA conjugates significantly exceeds the extracellular concentration of 50 μM, corresponding to a 284-fold accumulation for **FcPNA** compared to extracellular cell culture medium and an 83-fold cellular accumulation for **RcPNA**. This may indicate that the cellular uptake occurs according to an active uptake process rather than an unspecific diffusional process. This is an important finding regarding the fact that unmodified PNA is assumed to generally reveal a poor intrinsic uptake, and furthermore, no peptide modification according to classical noninvasive delivery strategies had been performed for the preparation of the compounds tested here. However, an increased intracellular concentration of a comparable octamer PNA sequence labeled with a cobalt complex ([Co(bpa)]-CH_2-(p-C_6H_4)-C(O)-Ahx-tgttatcc-Lys-NH_2) had been already reported by our group.[24] For this compound, a cellular uptake of ~0.18 pmol/μg CP with an intracellular concentrations of >70 μM was measured in comparison to the extracellular concentration of 50 μM (cell line: HT-29 colon carcinoma cells; incubation time: 6 h). The cellular uptake of the compounds presented here seems to be significantly improved to reach for **RcPNA** a 117-fold and for **FcPNA** a 400-fold accumulation if compared to the cobalt complex. Comparable high uptake values of 150-fold accumulation in the cell were presented by Ott et al. for Co-ASS (a cobalt carbonyl containing acetylsalicylic acid derivative) after 6 h incubation in MCF-7 cells.[77]

An important matter of discussion is the reason for the high cellular uptake of **FcPNA** and **RcPNA**. In comparison to previously reported PNA oligomers, a relatively good cellular uptake may be expected due to the short sequence length of just twelve oligonucleotides and most notably the positively charged lysine moiety, which was introduced into the peptide residue as an uptake enhancer. Moreover, the lipophilic metallocenes also seem to have a decisive effect on the cellular accumulation. Comparison between the cellular uptake values of **FcPNA** and **RcPNA** reveals a 3.4-fold larger value for **FcPNA**. While the overall structures of the two metallocenes are rather similar, ruthenocene has a larger volume than ferrocene (mean values for Fe–C distance: 2.048 Å, Ru–C distance: 2.208 Å).[78,79] Under the assumption of a more

Table 1. Experimental Data of AcPNA, FcPNA, and RcPNA

conjugate	T_M/°C[a]	ΔAbs/%[a]	t_R/min[b]	metal/protein/μg mg^{-1}[c]	cell concentration/mM[c]
AcPNA	62.6 (±0.3)	12.3 (±0.1)	8.67	–	–
FcPNA	60.1 (±0.3)	10.8 (±0.1)	10.26	4.05 ± 0.26	14.21 ± 0.91
RcPNA	60.5 (±0.2)	10.5 (±0.2)	10.27	2.15 ± 0.10	4.16 ± 0.18

[a]Analysis of the UV/vis melting experiments of the fully complementary PNA•DNA duplexes of the conjugates at λ = 260 nm. [b]Determined by HPLC. [c]Cellular uptake into HT-29 cells after 6 h incubation time determined by HR-CS AAS.

intricate and active uptake mechanism, a further impact could be attributed to the well-known differences in the chemical as well as electrochemical reactivity of ferrocene and ruthenocene.[80] In contrast, the impact of differences on the lipophilicity can be excluded based on the nearly identical HPLC retention times of t_R(**RcPNA**) = 10.27 min and t_R(**FcPNA**) = 10.26 min (see Table 1).

CONCLUSIONS

The first ruthenocene–PNA bioconjugate was synthesized and analyzed in this work in order to evaluate the suitability of ruthenocene–PNA conjugates for bioanalytical or medicinal applications like, e.g., as gene-targeted drugs or in antigene/antisense therapy. A comparative study with its ferrocene derivative, as well as nonmetallic acetylated analogue furnished the following results:

(1) The solid-phase synthesis of **RcPNA** proved to be fully comparable to the synthesis of **FcPNA** and **AcPNA** regarding conversion, purity and yield.

(2) The thermodynamic stability of **RcPNA** is comparable to that of the metal-free analogue **AcPNA** and superior to that of **FcPNA**, which can be explained by the different redox properties of the metal core.

(3) The thermal stability of the DNA duplex of **RcPNA** is comparable to that of the **FcPNA** analogue, and only slightly lower than that of the corresponding **AcPNA•DNA** duplex. This effect is ascribed to a steric hindrance by the metallocene complex.

The biological activity of the PNA conjugates was examined by studying their cytotoxicity and cellular uptake in different cell lines. All PNA conjugates were found to be nontoxic, indicating that the metallocene headgroup does not enhance the cytotoxicity of the nontoxic PNA sequence. Consequently, no cell damage distorts the results from the cellular uptake study. HR-CS AAS-quantification of the cellular uptake of **FcPNA** and **RcPNA** revealed cellular concentrations of both conjugates which are surprisingly high compared to literature values. Hence, a significant impact on the high uptake values can be ascribed to the presence of the metallocene group, with only minor differences between the two metal labels. However, further sequence characteristics have to be considered before a general pattern for the cellular uptake characteristics of both labels in bioconjugates can be derived.

Bioanalytical benefits of the ruthenocene–PNA conjugate in comparison to its ferrocene-labeled analogue are related to the absence of any natural background for ruthenium. A low natural background is especially important when using standard AAS- instead of HR-CS technology. Furthermore, potential detection and quantification by mass spectrometry is possible based on the metal's specific isotope pattern in all Ru-containing bioconjugates. All taken together, the favorable properties of ruthenocene-containing PNA bioconjugates as demonstrated herein make this class of compounds especially attractive for medicinal and biological applications.

ASSOCIATED CONTENT

Supporting Information

HPLC chromatograms, ESI- or MALDI-TOF spectra, and cytotoxicity assays (crystal violet and resazurin) for all PNA conjugates, UV-analysis for the determination of the extinction coefficient of Rc-CO_2H, UV-melting curves of the fully cDNA duplexes of all PNA conjugates. This material is available free of charge via the Internet at http://pubs.acs.org.

AUTHOR INFORMATION

Corresponding Author

*Fax: +49 (0)234 32 14378; Tel: +49 (0)234 32 28152; E-mail: Nils.Metzler-Nolte@ruhr-uni-bochum.de.

Author Contributions

#These authors have decided to publish this paper with shared first authorship and listing in alphabetical order.

Notes

The authors declare no competing financial interest.

ACKNOWLEDGMENTS

A.G. and N.H. thank the Ruhr-University Research School funded by Germany's Excellence Initiative [DFG GSC 98/1] for financial support. The authors thank Prof. Stephan Hahn and his co-workers for providing the HeLa, PT45, and HepG2 cells and cell laboratory facilities. Financial support from the German Science Foundation DFG (FOR 630) is also gratefully acknowledged.

ABBREVIATIONS

A, absorption; AAS, atomic absorption spectrometry; ACN, acetonitrile; Ahx, amino hexanoic acid; ASS, acetylsalicylic acid; bpa, 1,2-di(4-pyridyl)ethane; Bhoc, benzhydryl-oxycarbonyl; Boc, *tert*-butyl-oxycarbonyl; *c*, concentration; cp, cyclopentadiene; CP, cellular protein; DCM, dichloromethane; DIPEA, diisopropyl-ethylamine; DMF, *N*,*N*-dimethyl formamide; DMSO, dimethyl sulfoxide; ε, molar extinction coefficient; ESI, electrospray ionization; Fc, ferrocenyl ($C_5H_5FeC_5H_4$); FcH, ferrocene (dicyclopentadienyl iron, Cp_2Fe, $(C_5H_5)_2Fe$); Fmoc, fluorenylmethoxy-carbonyl; HATU, 2-(1*H*-7-azabenzotriazole-1-yl)-1,1,3,3-tetramethyluronium hexafluorophosphate; HOBt, 1-hydroxy-1*H*-benzotriazole; HPLC, high performance liquid chromatography; HR-CS, high-resolution continuum source; *l*, cuvette path length; MALDI-TOF, matrix assisted laser desorption/ionization - time-of-flight; MeOH, methanol; NMP, *N*-methyl-2-pyrrolidon; PBS, phosphate buffered saline; PHB, photochemical hole burning; Rc, ruthenocenyl ($C_5H_5RuC_5H_4$); RcH, ruthenocene; RP, reversed phase; rRNA, ribosomal RNA; PDA, photodiode array; PNA, peptide nucleic acids; SNP, single-nucleotide polymorphism; SPPS, solid phase peptide (or PNA) synthesis; TBTU, 2-(1*H*benzotriazole-1-yl)-1,1,3,3,-tetramethyluronium tetrafluoroborate; TFA, trifluoroacetic acid; TIS, triisopropyl silane; T_M, melting temperature value; t_R, retention time; The common three-letter

code for amino acids is used throughout. Only enantiomerically pure L amino acids were used. Nucleobases are denoted by their usual abbreviations in DNA; small letters, however, indicate PNA monomers

REFERENCES

(1) Nielsen, P. E., Egholm, M., Berg, R. H., and Buchardt, O. (1991) Sequence-selective recognition of DNA by strand displacement with a thymine-substituted polyamide. *Science 254*, 1497−1500.

(2) Egholm, M., Nielsen, P. E., Buchardt, O., and Berg, R. H. (1992) Recognition of guanine and adenine in DNA by cytosine and thymine containing peptide nucleic acids (PNA). *J. Am. Chem. Soc. 114*, 9677−9678.

(3) Wang, J., Paleček, E., Nielsen, P. E., Rivas, G., Cai, X., Shiraishi, H., Dontha, N., Luo, D., and Farias, P. A. M. (1996) Peptide nucleic acid probes for sequence-specific DNA biosensors. *J. Am. Chem. Soc. 118*, 7667−7670.

(4) Hüsken, N., Gębala, M., La Mantia, F., Schuhmann, W., and Metzler-Nolte, N. (2011) Mechanistic studies of Fc-PNA(•DNA) surface dynamics based on the kinetics of electron-transfer processes. *Chem. Eur. J. 17*, 9678−9690.

(5) Hüsken, N., Gębala, M., Battistel, A., La Mantia, F., Schuhmann, W., and Metzler-Nolte, N. (2011) Impact of single basepair mismatches on electron-transfer processes at Fc-PNA•DNA modified gold surfaces. *ChemPhysChem 13*, 131−139.

(6) Hüsken, N., Gębala, M., Schuhmann, W., and Metzler-Nolte, N. (2010) A single-electrode, dual-potential ferrocene−PNA biosensor for the detection of DNA. *ChemBioChem 11*, 1754−1761.

(7) Maurer, A., Kraatz, H.-B., and Metzler-Nolte, N. (2005) Synthesis and electrochemical characterization of metallocene-PNA oligomers. *Eur. J. Inorg. Chem.*, 3207−3210.

(8) Wang, G., and Xu, X. S. (2004) Peptide nucleic acid (PNA) binding-mediated gene regulation. *Cell Res. 14*, 111−116.

(9) Knudsen, H., and Nielsen, P. E. (1996) Antisense properties of duplex- and triplex-forming PNAs. *Nucleic Acids Res. 24*, 494−500.

(10) Good, L., and Nielsen, P. E. (1997) Progress in developing PNA as a gene-targeted drug. *Antisense Nucleic Acid Drug Dev. 7*, 431−437.

(11) Demidov, V. V., Potaman, V. N., Frank-Kamenetskii, M. D., Egholm, M., Buchardt, O., Sönnichsen, S. H., and Nielsen, P. E. (1994) Stability of peptide nucleic acids in human serum and cellular extracts. *Biochem. Pharmacol. 48*, 1310−1313.

(12) Wittung, P., Kajanus, J., Edwards, K., Nielsen, P., Norden, B., and Malström, B. G. (1995) Phospholipid membrane permeability of peptide nucleic acid. *FEBS Lett. 365*, 27−29.

(13) Koppelhus, U., and Nielsen, P. E. (2003) Cellular delivery of peptide nucleic acid (PNA). *Adv. Drug Delivery Rev. 55*, 267−280.

(14) Ljungstrøm, T., Knudsen, H., and Nielsen, P. E. (1999) Cellular uptake of adamantyl conjugated peptide nucleic acids. *Bioconjugate Chem. 10*, 965−972.

(15) Chinnery, P. F., Taylor, R. W., Diekert, K., Lill, R., Turnbull, D. M., and Lightowlers, R. N. (1999) Peptide nucleic acid delivery to human mitochondria. *Gene Ther. 6*, 1919−1928.

(16) Albertshofer, K., Siwkowski, A. M., Wancewicz, E. V., Esau, C. C., Watanabe, T., Nishihara, K. C., Kinberger, G. A., Malik, L., Eldrup, A. B., Manoharan, M., Geary, R. S., Monia, B. P., Swayze, E. E., Griffey, R. H., Bennett, C. F., and Maier, M. A. (2005) Structure-activity relationship study on a simple cationic peptide motif for cellular delivery of antisense peptide nucleic acid. *J. Med. Chem. 48*, 6741−6749.

(17) Marin, V. L., Roy, S., and Armitage, B. A. (2004) Recent advances in the development of peptide nucleic acid as a gene-targeted drug. *Expert Opin. Biol. Ther. 4*, 337−348.

(18) Bendifallah, N., Rasmussen, F. W., Zachar, V., Ebbesen, P., Nielsen, P. E., and Koppelhus, U. (2006) Evaluation of cell-penetrating peptides (CPPs) as vehicles for intracellular delivery of antisense peptide nucleic acid (PNA). *Bioconjugate Chem. 17*, 750−758.

(19) Koppelhus, U., Awasthi, S. K., Zachar, V., Holst, H. U., Ebbesen, P., and Nielsen, P. E. (2002) Cell-dependent differential cellular uptake of PNA, peptides, and PNA-peptide conjugates. *Antisense Nucleic Acid Drug Dev. 12*, 51−63.

(20) Jones, S. W., Christison, R., Bundell, K., Voyce, C. J., Brockbank, S. M. V., Newham, P., and Lindsay, M. A. (2005) Characterisation of cell-penetrating peptide-mediated peptide delivery. *Br. J. Pharmacol. 145*, 1093−1102.

(21) Gasser, G., Sosniak, A. M., and Metzler-Nolte, N. (2011) Metal-containing peptide nucleic acid conjugates. *Dalton Trans. 40*, 7061−7076.

(22) van Staveren, D. R., and Metzler-Nolte, N. (2004) Bioorganometallic chemistry of ferrocene. *Chem. Rev. 104*, 5931−5985.

(23) Salmain, M., and Metzler-Nolte, N. (2008) The bioorganometallic chemistry of ferrocene, in *Ferrocenes* (Stepnicka, P., Ed.) pp 499−639, John Wiley & Sons, Chichester, UK.

(24) Kirin, S. I., Ott, I., Gust, R., Mier, W., Weyhermueller, T., and Metzler-Nolte, N. (2008) Cellular uptake quantification of metalated peptide and peptide nucleic acid bioconjugates by atomic absorption spectroscopy. *Angew. Chem., Int. Ed. 47*, 955−959.

(25) Fuessl, A., Schleifenbaum, A., Goeritz, M., Riddell, A., Schultz, C., and Kraemer, R. (2006) Cellular uptake of PNA-terpyridine conjugates and its enhancement by Zn^{2+} ions. *J. Am. Chem. Soc. 128*, 5986−5987.

(26) Metzler-Nolte, N. (2006) Conjugates of peptides and PNA with organometallic complexes: syntheses and applications, in *Bioorganometallics* (Jaouen, G., Ed.) pp 125−179, Wiley-VCh, Weinheim, Germany.

(27) Cais, M., Slovin, E., and Snarsky, L. (1978) Metalloimmunoassay II. Iron-metallohaptens from estrogen steroids. *J. Organomet. Chem. 160*, 223−230.

(28) Cais, M., Dani, S., Eden, Y., Gandolfi, O., Horn, M., Isaacs, E. E., Josephy, Y., Saar, Y., Slovin, E., and Snarsky, L. (1977) Metalloimmunoassay. *Nature 270*, 535−536.

(29) Forrow, N. J., Foulds, N. C., Frew, J. E., and Law, J. T. (2004) Synthesis, characterization, and evaluation of ferrocene-theophylline conjugates for use in electrochemical enzyme immunoassay. *Bioconjugate Chem. 15*, 137−144.

(30) Vessières, A., Salmain, M., Brossier, P., and Jaouen, G. (1999) Carbonylmetallo immuno assay: a new application for Fourier transform infrared spectroscopy. *J. Pharm. Biomed. Anal. 21*, 625−633.

(31) Salmain, M., Vessières, A., Brossier, P., Butler, I. S., and Jaouen, G. (1992) Carbonylmetalloimmunoassay (CMIA) a new type of nonradioisotopic immunoassay. *J. Immunol. Methods 148*, 65−75.

(32) Guillena, G., Halkes, K. M., Rodriguez, G., Batema, G. D., van Koten, G., and Kamerling, J. P. (2003) Organoplatinum(II) complexes as a color biomarker in solid-phase peptide chemistry and screening. *Org. Lett. 5*, 2021−2024.

(33) Guillena, G., Rodriguez, G., Albrecht, M., and van Koten, G. (2002) Covalently bonded platinum(II) complexes of alpha-amino acids and peptides as a potential tool for protein labeling. *Chem. Eur. J. 8*, 5368−5376.

(34) Raszeja, L., Maghnouj, A., Hahn, S., and Metzler-Nolte, N. (2011) A novel organometallic Re(I) complex with favourable properties for bioimaging and applicability in solid-phase peptide synthesis. *ChemBioChem 12*, 371−376.

(35) Meister, K., Niesel, J., Schatzschneider, U., Metzler-Nolte, N., Schmidt, D. A., and Havenith, M. (2010) Label-free imaging of metal-carbonyl complexes in live cells by raman microspectroscopy. *Angew. Chem., Int. Ed. 49*, 3310−3312.

(36) Kong, K. V., Chew, W., Lim, L. H. K., Fan, W. Y., and Leong, W. K. (2007) Bioimaging in the mid-infrared using an organometallic carbonyl tag. *Bioconjugate Chem. 18*, 1370−1374.

(37) Yan, S. X., Seidel, M. T., Zhang, Z. Y., Leong, W. K., and Tan, H. S. (2011) Ultrafast vibrational relaxation dynamics of carbonyl stretching modes in $Os_3(CO)_{12}$. *J. Chem. Phys. 135*, 024501/1−024501/10.

(38) Li, C., and Leong, W. K. (2008) The deposition of osmium carbonyl clusters onto inorganic oxide surfaces: A ToF-SIMS and IR spectroscopic study of the surface species. *J. Colloid Interface Sci. 328*, 29−33.

(39) Welz, B., Becker-Ross, H., Florek, S., and Heitmann, U. (2005) *High-resolution continuum source AAS*, Wiley-VCH, Weinheim, Germany.
(40) Lundin, P., Johansson, H., Guterstam, P., Holm, T., Hansen, M., Langel, U., and El Andaloussi, S. (2008) Distinct uptake routes of cell-penetrating peptide conjugates. *Bioconjugate Chem. 19*, 2535−2542.
(41) Fischer, R., Waizenegger, T., Kohler, K., and Brock, R. (2002) A quantitative validation of fluorophore-labelled cell-permeable peptide conjugates: fluorophore and cargo dependence of import. *Biochim. Biophys. Acta, Biomembr. 1564*, 365−374.
(42) El-Andaloussi, S., Jaerver, P., Johansson, H. J., and Langel, U. (2007) Cargo-dependent cytotoxicity and delivery efficacy of cell-penetrating peptides: A comparative study. *Biochem. J. 407*, 285−292.
(43) Hess, A., and Metzler-Nolte, N. (1999) Transition metal labels on peptide nucleic acid (PNA) monomers. *Chem. Commun.*, 885−886.
(44) Verheijen, J. C., van der Marel, G. A., van Boom, J. H., and Metzler-Nolte, N. (2000) Transition metal derivatives of peptide nucleic acid (PNA) oligomers-synthesis, characterization, and DNA binding. *Bioconjugate Chem. 11*, 741−743.
(45) Hüsken, N., Gasser, G., Köster, S. D., and Metzler-Nolte, N. (2009) ″Four-potential″ ferrocene labeling of PNA oligomers via click chemistry. *Bioconjugate Chem. 20*, 1578−1586.
(46) Köster, S. D., Dittrich, J., Gasser, G., Hüsken, N., Henao Castañeda, I. C., Jios, J. L., Della Védova, C. O., and Metzler-Nolte, N. (2008) Spectroscopic and electrochemical studies of ferrocenyl triazole amino acid and peptide bioconjugates synthesized by click chemistry. *Organometallics 27*, 6326−6332.
(47) Gasser, G., Hüsken, N., Köster, S. D., and Metzler-Nolte, N. (2008) Synthesis of organometallic PNA oligomers by click chemistry. *Chem. Commun.*, 3675−3677.
(48) Baldoli, C., Falciola, L., Licandro, E., Maiorana, S., Mussini, P., Ramani, P., Rigamonti, C., and Zinzalla, G. (2004) A new ferrocene conjugate of a tyrosine PNA monomer: synthesis and electrochemical properties. *J. Organomet. Chem. 689*, 4791−4802.
(49) Baldoli, C., Licandro, E., Maiorana, S., Resemini, D., Rigamonti, C., Falciola, L., Longhi, M., and Mussini, P. R. (2005) Electrochemical activity of new ferrocene-labelled PNA monomers to be applied for DNA detection: Effects of the molecular structure and of the solvent. *J. Electroanal. Chem. 585*, 197−205.
(50) Baldoli, C., Rigamonti, C., Maiorana, S., Licandro, E., Falciola, L., and Mussini, P. R. (2006) A new triferrocenyl-tris(hydroxymethyl)-aminomethane derivative as a highly sensitive electrochemical marker of biomolecules: application to the labelling of PNA monomers and their electrochemical characterization. *Chem. Eur. J. 12*, 4091−4100.
(51) Gasser, G., and Spiccia, L. (2008) Synthesis of a ferrocenyl uracil PNA monomer for insertion into PNA sequences. *J. Org. Chem. 693*, 2478−2482.
(52) Gasser, G., Belousoff, M. J., Bond, A. M., and Spiccia, L. (2006) Facile synthesis and detailed characterization of a new ferrocenyl uracil peptide nucleic acid monomer. *J. Org. Chem. 71*, 7565−7573.
(53) Baldoli, C., Maiorana, S., Licandro, E., Zinzalla, G., and Perdicchia, D. (2002) Synthesis of chiral chromium tricarbonyl labeled thymine PNA monomers via the Ugi reaction. *Org. Lett. 4*, 4341−4344.
(54) Maiorana, S., Licandro, E., Perdicchia, D., Baldoli, C., Vandoni, B., Giannini, C., and Salmain, M. (2003) Synthesis of the first chiral PNA monomer labeled with a Fischer-type carbene complex. *J. Mol. Catal. A: Chem. 204−205*, 165−175.
(55) Salmain, M., Licandro, E., Baldoli, C., Maiorana, S., Tran-Huy, H., and Jaouen, G. (2001) Transition metal ('Fischer-type') carbene complexes as protein labelling reagents. *J. Organomet. Chem. 617−618*, 376−382.
(56) Xavier, C., Giannini, C., Gano, L., Maiorana, S., Alberto, R., and Santos, I. (2008) Synthesis, characterization, and evaluation of a novel 99mTc(CO)3 pyrazolyl conjugate of a peptide nucleic acid sequence. *J. Biol. Inorg. Chem. 13*, 1335−1344.
(57) Baldoli, C., Cerea, P., Giannini, C., Licandro, E., Rigamonti, C., and Maiorana, S. (2005) The metal-conjugated peptide nucleic acid challenge. *Synlett*, 1984−1994.
(58) Zava, O., Zakeeruddin, S. M., Danelon, C., Vogel, H., Grätzel, M., and Dyson, P. J. (2009) A cytotoxic ruthenium tris(bipyridyl) complex that accumulates at plasma membranes. *ChemBioChem 10*, 1796−1800.
(59) Nielsen, P. E., and Egholm, M. (1999) *Peptide Nucleic Acids - Protocols and Applications*, Horizon Scientific Press, Wymondham, UK.
(60) Dawson, R. M. C., Elliott, D. C., Elliott, W. H., and Jones, K. M. (1989) *Data for Biochemical Research*, 3rd ed., Oxford University Press, Oxford, UK.
(61) Anne, A., Bouchardon, A., and Moiroux, J. (2003) 3′-Ferrocene-labeled oligonucleotide chains end-tethered to gold electrode surfaces: Novel model systems for exploring flexibility of short DNA using cyclic voltammetry. *J. Am. Chem. Soc. 125*, 1112−1113.
(62) Puglisi, J. D., and Tinoco, J. I. (1989) Absorbance melting curves of RNA. *Methods Enzymol. 180*, 304−325.
(63) Bradford, M. M. (1976) A rapid and sensitive method for the quantification of microgram quantities of protein utilizing the principle of protein-dye binding. *Analyt. Biochem. 72*, 248−254.
(64) Ott, I., Scheffler, H., and Gust, R. (2007) Development of a method for the quantification of the molar gold concentration in tumour cells exposed to gold-containing drugs. *ChemMedChem 2*, 702−707.
(65) Schäfer, S., Ott, I., Gust, R., and Sheldrick, W. S. (2007) Influence of the polypyridyl (pp) ligand size on the DNA binding properties, cytotoxicity and cellular uptake of organoruthenium(II) complexes of the type $[(\eta 6\text{-}C_6Me_6)Ru(L)(pp)]^{n+}$ [L = Cl, n = 1; L = $(NH_2)_2CS$, n = 2]. *Eur. J. Inorg. Chem.*, 3034−3046.
(66) Kersebohm, T., Kirin, S. I., and Metzler-Nolte, N. (2006) Insertion of an internal dipeptide into PNA oligomers: Thermal melting studies and further functionalization. *Bioorg. Med. Chem. Lett. 16*, 2964−2968.
(67) Sosniak, A. M., Gasser, G., and Metzler-Nolte, N. (2009) Thermal melting studies of alkyne- and ferrocene-containing PNA bioconjugates. *Org. Biomol. Chem. 7*, 4992−5000.
(68) Gross, A., and Metzler-Nolte, N. (2009) Synthesis and characterisation of a ruthenocenoyl bioconjugate with the cyclic octapeptide octreotate. *J. Organomet. Chem. 694*, 1185−1188.
(69) Kaiser, E., Colescott, R. L., Bossinger, C. D., and Cook, P. I. (1970) Color test for detection of free terminal amino groups in the solid-phase synthesis of peptides. *Anal. Biochem. 34*, 595−598.
(70) Prins, R., Korswagen, A. R., and Kortbeek, A. G. T. G. (1972) Decomposition of the ferricenium cation by nucleophilic reagents. *J. Organomet. Chem. 39*, 335−344.
(71) Peyret, N., Seneviratne, P. A., Allawi, H. T., and SantaLucia, J., Jr. (1999) Nearest-neighbor thermodynamics and NMR of DNA sequences with internal A.A, C.C, G.G, and T.T mismatches. *Biochemistry 38*, 3468−3477.
(72) Vessières, A., Top, S., Pigeon, P., Hillard, E. A., Boubeker, L., Spera, D., and Jaouen, G. (2005) Modification of the estrogenic properties of diphenols by the incorporation of ferrocene. Generation of antiproliferative effects in vitro. *J. Med. Chem. 48*, 3937−3940.
(73) Plazuk, D., Vessières, A., Hillard, E. A., Buriez, O., Labbé, E., Pigeon, P., Plamont, M.-A., Amatore, C., Zakrzewski, J., and Jaouen, G. (2009) A [3]ferrocenophane polyphenol showing a remarkable antiproliferative activity on breast and prostate cancer cell lines. *J. Med. Chem. 52*, 4964−4967.
(74) Swarts, J. C., Nafady, A., Roudebush, J. H., Trupia, S., and Geiger, W. E. (2009) One-electron oxidation of ruthenocene: Reactions of the ruthenocenium ion in gentle electrolyte media. *Inorg. Chem. 48*, 2156−2165.
(75) Gross, A., Neukamm, M., and Metzler-Nolte, N. (2011) Synthesis and cytotoxicity of a bimetallic ruthenocene dicobalt-hexacarbonyl alkyne peptide bioconjugate. *Dalton Trans. 40*, 1382−1386.
(76) Micallef, L. S., Loughrey, B. T., Healy, P. C., Parsons, P. G., and Williams, M. L. (2011) Mono- and 1,1′-disubstituted organo-ruthenium cyclopentadiene complexes: synthesis, structural characterization, and antitumoral evaluation. *Organometallics 30*, 1395−1403.

(77) Ott, I., Schmidt, K., Kircher, B., Schumacher, P., Wiglenda, T., and Gust, R. (2005) Antitumor-active cobalt-alkyne complexes derived from acetylsalicylic acid: Studies on the mode of drug action. *J. Med. Chem. 48*, 622−629.
(78) Dunitz, J. D., Orgel, L. E., and Rich, A. (1956) The crystal structure of ferrocene. *Acta Crystallogr. 9*, 373−375.
(79) Hardgrove, G. L., and Templeton, D. H. (1959) The crystal structure of ruthenocene. *Acta Crystallogr. 12*, 28−32.
(80) Long, N. J. (1998) *Metallocenes: an introduction to sandwich complexes*, Blackwell Science, Oxford, UK.

Bioconjugate Chemistry

Article

pubs.acs.org/bc

Synthesis and Preclinical Evaluation of Bifunctional Ligands for Improved Chelation Chemistry of ^{90}Y and ^{177}Lu for Targeted Radioimmunotherapy

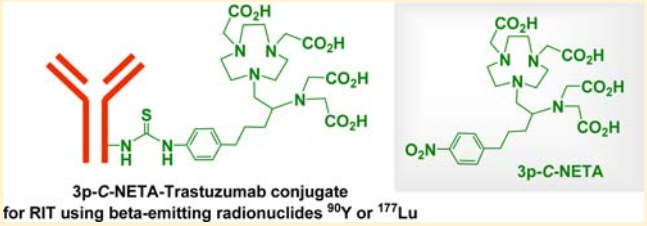
Chi Soo Kang,[†] Xiang Sun,[†] Fang Jia,[‡] Hyun A Song,[†] Yunwei Chen,[†] Michael Lewis,[‡] and Hyun-Soon Chong*,[†]

[†]Chemistry Division, Biological and Chemical Sciences Department, Illinois Institute of Technology, Chicago, Illinois, United States

[‡]Department of Veterinary Medicine and Surgery, Department of Radiology, Nuclear Science and Engineering Institute, University of Missouri-Columbia, Columbia, Missouri, United States

Supporting Information

ABSTRACT: We report a practical and high-yield synthesis of a bimodal bifunctional ligand 3p-*C*-NETA-NCS containing the isothiocyanate group for conjugation to a tumor targeting antibody. 3p-*C*-NETA-NCS was conjugated to a tumor-targeting antibody, trastuzumab, and the corresponding 3p-*C*-NETA-trastuzumab conjugate was evaluated and compared to trastuzumab conjugates of the known bifunctional ligands *C*-DOTA, *C*-DTPA, and 3p-*C*-DEPA for radiolabeling kinetics with ^{90}Y and ^{177}Lu. 3p-*C*-NETA-trastuzumab conjugate exhibited extremely rapid complexation kinetics with ^{90}Y and ^{177}Lu. ^{90}Y-3p-*C*-NETA-trastuzumab and ^{177}Lu-3p-*C*-NETA-trastuzumab conjugates were stable in human serum for 2 weeks. A pilot biodistribution study was conducted to evaluate *in vivo* stability and tumor targeting of ^{177}Lu-radiolabeled trastuzumab conjugate using nude mice bearing ZR-75-1 human breast cancer. ^{177}Lu-3p-*C*-NETA-trastuzumab conjugate displayed low radioactivity level at blood (1.6%), low organ uptake (<2.2%), and high tumor-to-blood ratio (6.4) at 120 h. 3p-*C*-NETA possesses favorable *in vitro* and *in vivo* profiles and is an excellent bifunctional chelator that can be used for targeted RIT applications using ^{90}Y and ^{177}Lu and has the potential to replace DOTA and DTPA analogues in current clinical use.



INTRODUCTION

Radioimmunotherapy (RIT) is a potent therapeutic technique applicable to numerous cancers.[1,2] Two RIT drugs, Zevalin and Bexxar, are clinically available for treatment of B-cell non-Hodgkin's lymphoma (NHL).[3−5] The RIT system generally consists of three components, a radionuclide, a tumor-targeting antibody or peptide, and a bifunctional ligand.[2,6] β-emitting radionuclides, ^{90}Y and ^{177}Lu, have been extensively explored for RIT. Highly energetic ^{90}Y ($t_{1/2}$ = 64.1 h, E_{max} = 2.3 MeV) has the advantage of relatively long-range tissue penetration and homogeneous dose distribution.[2,6] Less energetic ^{177}Lu ($t_{1/2}$ = 6.7 d, E_{max} = 0.5 MeV) has a shorter penetration range relative to ^{90}Y and is proposed to provide more selective tumor targeting and resultant lower normal tissue damage and better tolerance by patients.[2] Its longer half-life is sufficient for preparation and shipment of radioimmunoconjugate and allows for maximal delivery of dose to tumors.[2]

C-DOTA (Figure 1) forms a stable complex with lanthanides including ^{90}Y and ^{177}Lu.[7,8] The enhanced stability of the metal complexes of DOTA compared to acyclic ligand such as *C*-DTPA (Figure 1) is attributed to the macrocyclic effect and increased preorganization.[9,10] The therapeutic efficacy of ^{90}Y- or ^{177}Lu-labeled DOTA−antibody conjugates has been demonstrated in preclinical and clinical trials.[2,11,12] However, the slow formation kinetics and low radiolabeling efficiency of *C*-DOTA in binding ^{90}Y and ^{177}Lu remain limitations to broad RIT applications of the macrocyclic chelate.[12,13] Rapid radiolabeling kinetics of a bifunctional ligand conjugated to an antibody is required to minimize radiolytic damage to protein conjugates that can occur during radiolabeling of an antibody conjugate with high specific activity for therapeutic applications.[14] Development of superior chelation chemistry that allows for scale-up production of stable ^{90}Y- or ^{177}Lu-radiolabeled radioimmunoconjugates under mild and practical radiolabeling conditions is necessary for effective and safe RIT applications of ^{90}Y and ^{177}Lu.

We have synthesized the bimodal ligands in the series of NETA and DEPA (Figure 1) that possess both macrocyclic and acyclic moieties for cooperative metal binding.[15−18] The acyclic pendant donor groups in NETA or DEPA are proposed to rapidly initiate coordination to the metal, as in the case of DTPA, while the macrocyclic component, a partial NOTA (Figure 1) or DOTA backbone, is expected to tightly wrap around the metal ion trapped by the acyclic binding groups and

Received: December 31, 2011
Revised: June 7, 2012
Published: August 10, 2012

 © 2012 American Chemical Society dx.doi.org/10.1021/bc200696b | *Bioconjugate Chem.* 2012, 23, 1775−1782

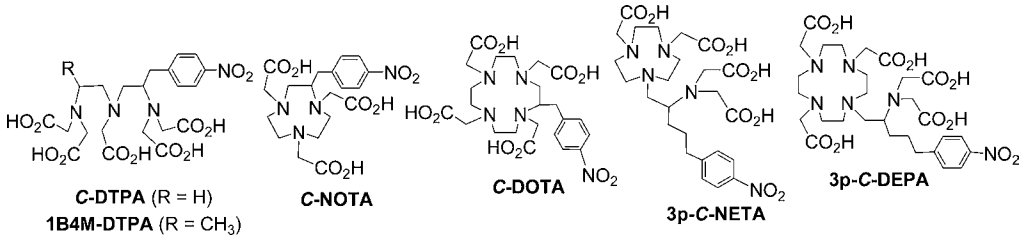


Figure 1. Bifunctional ligands in preclinical and clinical evaluation.

thereby achieve maximum complex stability by saturating the metal coordination sphere. The NETA- and DEPA-backboned chelators were shown to display favorable complexation kinetics and stability in binding ^{90}Y, ^{177}Lu, or $^{205/6}$Bi.[15−18]

Herein, we report an efficient synthesis of bifunctional ligand 3p-*C*-NETA-NCS containing the isothiocyanate group for conjugation to a tumor targeting antibody. 3p-*C*-NETA-NCS conjugated to trastuzumab was compared to trastuzumab conjugates of the known bifunctional ligands *C*-DOTA, *C*-DTPA, and 3p-*C*-DEPA for radiolabeling kinetics with ^{90}Y and ^{177}Lu. ^{90}Y-and ^{177}Lu-radiolabeled trastuzumab conjugates of 3p-*C*-NETA, 3p-*C*-DEPA, and *C*-DOTA were evaluated for *in vitro* serum stability. ^{177}Lu-3p-*C*-NETA-trastuzumab conjugate was also evaluated for *in vivo* biodistribution and tumor uptake study.

EXPERIMENTAL PROCEDURES

Instruments and Methods. ^{1}H, ^{13}C, and DEPT NMR spectra were obtained using a Bruker 300 instrument, and chemical shifts are reported in ppm on the δ scale relative to TMS. Electrospray ionization (ESI) high-resolution mass spectra (HRMS) were obtained on JEOL double sector JMS-AX505HA mass spectrometer (University of Notre Dame, IN). Size-exclusion HPLC (SE-HPLC) chromatograms were obtained on Agilent 1200 equipped with a diode array detector and an in-line IN/US γ-Ram Model 2 radiodetector (Tampa, FL) fitted with Bio-Silect SEC 250−5 column (Bio-Rad, Hercules, CA), TSK-G3000PW column (Tosoh bioscience, King of Prussia, PA), or a BioSep-SEC S 3000 column (Phenomenex, Torrance, CA).

Reagents. All reagents were purchased from Sigma-Aldrich (St. Louis, MO) and used as received unless otherwise noted. Trastuzumab (Herceptin; Genentech, South San Francisco, CA) was obtained through the Veterinary Resources Program (National Institutes of Health, Bethesda, MD) and provided by Dr. Martin Brechbiel (Radioimmune and Inorganic Chemistry Section, Radiation Oncology Branch, NIH). ^{90}Y (0.05 M HCl) and ^{177}Lu (0.05 M HCl) were purchased from Perkin-Elmer. *C*-DOTA was purchased from Macrocyclics (Dallas, TX).

Caution: ^{90}Y ($t_{1/2}$ = 64.1 h) is a β-emitting radionuclide. ^{177}Lu ($t_{1/2}$ = 6.7 days) is a β/γ-emitting radionuclide. Appropriate shielding and handling protocols should be in place when using the isotope.

***tert*-Butyl 2-{[2-(*tert*-Butoxy)-2-oxoethyl][2-iodo-5-(4-nitrophenyl)pentyl]amino} acetate (3).** To a solution of **1**[18] (100 mg, 0.221 mmol) and PPh_3 (69.5 mg, 0.265 mmol) in CH_2Cl_2 (2 mL) at 0 °C was added imidazole (18 mg, 0.265 mmol) and iodine (67.3 mg, 0.265 mmol) portionwise over 5 min. The reaction mixture was stirred for 4 h at 0 °C and RT for 1 h after which the reaction mixture was concentrated to dryness. The residue was purified by silica gel (60−230 mesh) column chromatography eluted with 10% ethyl acetate in hexanes to afford **3** (120 mg, 97%) as a brownish oil. ^{1}H NMR ($CDCl_3$, 300 MHz) δ 1.45 (s, 18H), 1.71−1.82 (m, 2H), 1.83−2.05 (m, 2H), 2.66−2.87 (m, 2H), 2.95 (dd, J = 8.6 Hz, J = 14.1 Hz, 1H), 3.29 (dd, J = 8.6 Hz, J = 14.1 Hz, 1H), 3.42 (dd, J = 17.3 Hz, J = 22.4 Hz, 4H), 4.10−4.18 (m, 1H), 7.35 (d, J = 8.6 Hz, 2H), 8.14 (d, J = 8.6 Hz, 2H). ^{13}C NMR ($CDCl_3$, 300 MHz) δ 28.2 (q), 30.8 (t), 34.9 (t), 36.0 (d), 36.3 (t), 56.9 (t), 64.1 (t), 81.2 (s), 123.6 (d), 129.2 (d), 146.4 (s), 149.9 (s), 170.4 (s). HRMS (Positive ion FAB) Calcd for $C_{23}H_{36}IN_2O_6$: $[M - I + OH]^+$ m/z 453.2601. Found: $[M - I + OH]^+$ m/z 453.2603.

***tert*-Butyl-2-[(1-{4,7-bis[2-(*tert*-butoxy)-2-oxoethyl]-1,4,7-triazonan-1-yl}-5-[4-(hydroxyl-nitro)phenyl]-pentan-2-yl)[2-(*tert*-butoxy)-2-oxoethyl]amino]acetate (7).** To a solution of **3** (50 mg, 0.089 mmol) in CH_3CN (1 mL) at 0 °C was added compound **5** (35.0 mg, 0.098 mmol) and DIPEA (34.5 mg, 0.267 mmol). The resulting mixture was stirred for 40 h at room temperature, while monitoring the reaction progress using TLC. The reaction mixture was concentrated to dryness. The residue was purified via column chromatography on silica gel (220−440 mesh) eluting with 3% CH_3OH in CH_2Cl_2 to provide product **7** (65 mg, 94%). ^{1}H and ^{13}C NMR data of **7** were identical to those as previously reported.[18]

***tert*-Butyl-2-[(1-{4,7-bis[2-(*tert*-butoxy)-2-oxoethyl]-1,4,7-triazonan-1-yl}-5-[4-(hydroxyl-nitro)phenyl]-pentan-2-yl)[2-(*tert*-butoxy)-2-oxoethyl]amino]acetate (7).** *Reaction of **2** with **5** in the Presence of $AgClO_4$.* To a solution of **2** (50 mg, 0.097 mmol) in CH_3CN (0.5 mL) at −5 °C was added $AgClO_4$ (20.1 mg, 0.097 mmol) and stirred for 10 min at the same temperature. Then, compound **5** (34.7 mg, 0.097 mmol) and DIPEA (37.6 mg, 0.291 mmol) in CH_3CN (0.5 mL) was sequentially added to the reaction mixture at −5 °C. The resulting mixture was warmed to room temperature and stirred for 24 h while monitoring the reaction progress using TLC. The residue was purified via column chromatography on silica gel (60−230 mesh) eluting with 3% CH_3OH in CH_2Cl_2 to provide the crude product **7** containing a tiny amount of the starting material **5** as an impurity. The crude product was treated with 0.1 M HCl solution (10 mL) and extracted with $CHCl_3$ (10 mL × 3). The combined organic layers were concentrated to dryness. The residue was treated with 0.1 M NaOH solution (10 mL) and extracted with $CHCl_3$ (10 mL × 3). The combined organic layers were dried over $MgSO_4$, filtered, and concentrated *in vacuo* to dryness to provide product **7** (66 mg, 86%) as a yellowish oil. ^{1}H and ^{13}C NMR data of **7** were identical to those previously reported.[18]

***tert*-Butyl-2-[(1-{4,7-bis[2-(*tert*-butoxy)-2-oxoethyl]-1,4,7-triazonan-1-yl}-5-[4-(hydroxyl-nitro)phenyl]-pentan-2-yl)[2-(*tert*-butoxy)-2-oxoethyl]amino]acetate (7).** *Reaction of **3** with **5** in the Presence of $AgClO_4$.* To a solution of **3** (50 mg, 0.089 mmol) in CH_3CN (0.5 mL) at −5

dx.doi.org/10.1021/bc200696b | *Bioconjugate Chem.* 2012, 23, 1775−1782

°C was added $AgClO_4$ (18.4 mg, 0.089 mmol) and stirred for 10 min at the same temperature. Then, compound **5** (31.8 mg, 0.089 mmol) and DIPEA (34.5 mg, 0.267 mmol) in CH_3CN (0.5 mL) was sequentially added to the reaction mixture at −5 °C. The resulting mixture was warmed to room temperature and stirred for 24 h while monitoring the reaction progress using TLC. The residue was purified via column chromatography on silica gel (60−230 mesh) eluting with 3% CH_3OH in CH_2Cl_2 to provide the crude product **7** containing a tiny amount of the starting material **5** as an impurity. The crude product was treated with 0.1 M HCl solution (10 mL) and extracted with $CHCl_3$ (10 mL × 3). The combined organic layers were concentrated to dryness. The residue was treated with 0.1 M NaOH solution (10 mL) and extracted with $CHCl_3$ (10 mL × 3). The combined organic layers were dried over $MgSO_4$, filtered, and concentrated *in vacuo* to dryness to provide product **7** (62 mg, 88%) as a yellowish oil. ^1H and ^{13}C NMR data of **7** were identical to those as previously reported.[18]

{4-[5-(4-Aminophenyl)-2-(bis-*tert*-butoxycarbonylmethylamino)pentyl]-7-*tert*-butoxycarbo-nylmethyl-[1,4,7]triazonan-1-yl}acetic Acid *tert*-Butyl Ester (8). To a solution of **7** (14.6 mg, 0.018 mmol) in ethanol (5 mL) at room temperature was added 10% Pd/C (3 mg) under Ar (g). The reaction mixture was placed under hydrogenation apparatus for 14 h. The resulting mixture was filtered via Celite bed and washed thoroughly with ethanol. The filtrate was concentrated to provide **8** (13.1 mg, 96%) as a yellowish solid. ^1H NMR ($CDCl_3$, 300 MHz) δ 1.45 (s, 36H), 1.50−1.70 (m, 4H), 1.92−2.05 (m, 1H), 2.18−2.32 (m, 1H), 2.38−2.90 (m, 15H), 3.08 (d, J = 16.6 Hz, 1H), 3.26 (d, J = 16.5 Hz, 1H), 3.34 (s, 2H), 3.44 (s, 4H), 6.60 (d, J = 8.3 Hz, 2H), 6.94 (d, J = 8.2 Hz, 2H); ^{13}C NMR ($CDCl_3$, 300 MHz) δ 27.8(t), 28.0(q), 28.1(t), 28.4(t), 29.6(t), 35.8(t), 51.3(t), 51.7(t), 53.5(t), 54.7(t), 55.9(t), 58.1(t), 58.5(t), 59.4(d), 81.2(s), 81.3(s), 82.2(s), 115.2(d), 119.1(d), 131.2(s), 145.5(s), 170.7(s), 170.9(s), 171.4(s). HRMS (Positive ion FAB) Calcd for $C_{41}H_{72}N_5O_8$: $[M + H]^+$ m/z 762.5381. Found: $[M + H]^+$ m/z 762.5364.

{4-[5-(4-Amino-phenyl)-2-(bis-carboxymethylamino)-pentyl]-7-carboxymethyl-[1,4,7]triazo-nan-1-yl}acetic Acid (9). To a flask containing compound **8** (8.5 mg, 0.011 mmol) at 0−5 °C was added dropwise 4 M HCl (g) in 1,4-dioxane (3 mL) over 20 min. The resulting mixture was gradually warmed to room temperature and continuously stirred for 18 h. Ether (20 mL) was added to the reaction mixture which was then stirred for 10 min. The resulting mixture was placed in the freezer for 1 h. The resulting precipitate was filtered and washed with ether. The solid product was quickly dissolved in deionized water. The aqueous solution was concentrated *in vacuo* to provide **9** (7.1 mg, 88%) as an off-white solid. ^1H NMR ($CDCl_3$, 300 MHz) δ 1.15−1.34 (m, 1H), 1.39−1.55 (m, 3H), 2.55 (t, J = 6.4 Hz, 2H), 3.00−3.20 (m, 2H), 3.20−3.73 (m, 17H), 3.87 (s, 4H), 7.18 (dd, J = 8.1 Hz, J = 20.3 Hz, 4H); ^{13}C NMR (D_2O, 300 MHz) δ 25.7 (t), 26.6 (t), 33.5 (t), 48.2 (t), 49.6 (t), 50.4 (t), 51.8 (t), 52.5 (t), 53.7 (t), 54.0 (t), 56.0 (t), 60.3 (d), 123.0 (d), 127.5 (s), 130.0 (d), 142.2 (s), 168.0 (s), 170.0 (s), 173.6 (s). HRMS (Positive ion FAB) Calcd for $C_{25}H_{40}N_5O_8$: $[M + H]^+$ m/z 538.2877. Found: $[M + H]^+$ m/z 538.2880.

{4-[2-(Bis-carboxymethylamino)-5-(4-isothiocyanatophenyl)pentyl]-7-carboxymethyl[1,4,7]-triazonan-1-yl}acetic Acid (3p-*C*-NETA-NCS, 10). To a solution of **9** (6.3 mg, 0.009 mmol) in water (0.15 mL) was added dropwise 1 M thiophosgene in $CHCl_3$ (11 μL, 0.011 mmol). The resulting mixture was stirred at room temperature for 3 h. The aqueous layer was concentrated *in vacuo* to provide pure **10** (6.0 mg, 95%) as a light yellowish solid. ^1H NMR (D_2O, 300 MHz) δ 1.31 (s, 1H), 1.57 (s, 3H), 2.95−3.28 (m, 5H), 3.29−3.53 (m, 12H), 3.60 (d, J = 17.3 Hz, 2H), 3.85 (s, 4H), 7.13 (s, 4H). HRMS (Positive ion FAB) Calcd for $C_{26}H_{38}N_5O_8S$: $[M + H]^+$ m/z 580.2441. Found: $[M + H]^+$ m/z 580.2439.

Conjugation of 3p-*C*-NETA-NCS to Trastuzumab. *C*-DTPA-NCS, 3p-*C*-DEPA-NCS, and *C*-DOTA-NCS were conjugated to trastuzumab as previously reported.[16] All absorbance measurements were obtained on an Agilent 8453 diode array spectrophotometer equipped with an 8-cell transport system (designed for 1 cm cells). Metal-free stock solutions of all buffers were prepared using Chelex-100 resin (200−400 mesh, Bio-Rad Lab, Hercules, CA, Cat# 142−2842). Chelex resin (1 g/100 mL) was added into the buffer solution and the mixture was shaken overnight in a shaker and filtered through a Corning filter system (Cat# 430513, pore size 0.2 μm). Disposable PD-10 Sephadex G-25 M columns (GE Healthcare, #17−0851−01) were rinsed with 25 mL of the conjugation buffer prior to addition of antibody. Amicon centricon C-50 (50 000 MWCO) centrifugal filter devices (Millipore, Bedford, MA, Cat# UFC805008) were used for purification of trastuzumab conjugate. The initial concentration of trastuzumab was determined by UV/vis spectroscopic method. Phosphate-buffered saline (PBS, 1×, 11.9 mM phosphates, 137 mM NaCl, and 2.7 mM KCl, pH 7.4) was purchased from Fisher Scientific and used as received. Conjugation buffer (50 mM HEPES, 150 mM NaCl, pH 8.6) was prepared as 1× solutions, chelexed, and filtered through the Corning filter. Trastuzumab (9.2 mg) was diluted to 2.5 mL using conjugation buffer, and the resulting solution was added to a PD-10 column. Conjugation buffer (6.0 mL) was added to the PD-10 column to exchange the buffer solution of the antibody and collected in a sterile test tube and checked for the presence of trastuzumab via analysis of the UV/vis spectrum at 280 nm. To a sterile test tube containing the recovered trastuzumab (7.0 mg) was added a 10-fold excess of 3p-*C*-NETA-NCS (45 μL, 10 mM). The resulting solution was gently agitated for 16 h at room temperature and placed on a Centricon C-50 membrane and spun down to reduce volume. PBS (3 × 2 mL) was added to the remaining solution of the 3p-*C*-NETA-trastuzumab conjugate followed by centrifugation to remove unreacted ligand. The volume of purified conjugate antibody was brought to 1.0 mL. To measure [trastuzumab] in the conjugates, a UV/vis spectrometer was zeroed against a cuvette filled with 2 mL of PBS with a window open from 190 to 1100 nm. A 50 μL portion of PBS was removed and discarded, 50 μL of the 3p-*C*-NETA-trastuzumab conjugate solution was added, and absorbance of the solution at 280 nm was noted. Beer's Law was used to calculate [trastuzumab] in the conjugate with molar absorptivity of 1.42. After centrifugation, 5.9 mg (4.06×10^{-5} M, 84%) of the trastuzumab remained.

Spectroscopic Determination of Ligand to Protein (L/P) Ratio. A stock solution of the Lu(III)-AAIII reagent was prepared in 0.15 M NH_4OAc (pH 7.0) by adding an aliquot of lutetium atomic absorption solution (5.79×10^{-3} M) into a 10 μM solution of AAIII to afford a 5 μM solution of Lu(III). This solution was stored in the dark to avoid degradation over time. A UV/vis spectrometer was zeroed against 8 well-dried blank

cuvettes with a window open from 190 to 1100 nm. A cuvette was filled with AAIII solution (2 mL), and the other 7 cuvettes with the Lu(III)-AAIII (2 mL). Lu(III)-AAIII (50 μL) in the 7 cuvettes was removed and discarded. Milli-Q water (50 μL) was added to the second cuvette, and one to five 10 μL additions of 3p-*C*-NETA (0.1 mM) were added to the 5 cuvettes to give a series of 5 different concentrations (2 mL total volume). The solutions in the third to the seventh cuvette were diluted to 2.0 mL by adding an aliquot of milli-Q water. Trastuzumab conjugate of 3p-*C*-NETA (50 μL) was added to the eighth cuvette containing Lu(III)-AAIII reagent (1950 μL). After addition of trastuzumab conjugate to the Lu(III)-AAIII solution, the resulting solution was equilibrated for 10 min. The absorbance of the resulting solution at 652 nm was monitored every 30 s over 6 min. The average of the absorbance of each solution was calculated, and the absorbance data from the Lu(III)-AAIII solution containing 6 different concentrations were used to construct a calibration plot of A_{652} versus [3p-*C*-NETA] by the equation, $Y = 0.1202 - (1.2138 \times 10^4)$[3p-*C*-NETA] ($R^2 = 0.9967$) wherein $Y = A_{652\ nm}$. The concentration of 3p-C-NETA in the trastuzumab conjugate was calculated (1.27×10^{-4}). The L/P ratio of 3p-*C*-NETA-trastuzumab conjugate ($[1.27 \times 10^{-4}$ M$]/[4.06 \times 10^{-5}$ M]) was measured to be 3.1.

Radiolabeling of Bifunctional Ligand−Trastuzumab Conjugates with ^{90}Y or ^{177}Lu. *C*-DTPA-trastuzumab, 3p-*C*-DEPA-trastuzumab, and *C*-DOTA-trastuzumab conjugates were prepared and purified as previously reported.[16] All HCl solutions were prepared from ultrapure HCl (Fisher Scientific, Cat# A466−500). For metal-free radiolabeling, plasticware including pipet tips, tubes, and caps was soaked in 0.1 M HCl overnight, washed thoroughly with Milli-Q (18.2 MΩ) water, and air-dried overnight. Ultra pure NH_4OAc (Aldrich, #372331) was used to prepare all NH_4OAc buffer solutions (0.25 M, pH 5.5). The buffer solutions were treated with Chelex-100 resin (Biorad, #142−2842, 1 g/100 mL buffer solution), shaken overnight at room temperature, and filtered through 0.22 μm filter (Corning, #430320) prior to use. To a buffer solution (30 μL, pH 5.5) in a capped microcentrifuge tube (1.5 mL, Fisher Scientific #05−408−129) was sequentially added a solution of bifunctional ligand−trastuzumab conjugate (30 μg) in PBS (5−10 μL) and ^{177}Lu (0.05 M HCl, 60 μCi, 2−3 μL). To a conjugate solution (15−27 μL, 30 μg) in a capped microcentrifuge tube (1.5 mL) was sequentially added a solution of 0.05 M HCl (6−15 μL) and ^{90}Y (0.05 M HCl, 60 μCi, 2−4 μL). The final volume of the resulting solution was around 40 μL, and the pH of the resulting reaction mixture was 5.5. The reaction mixture was agitated on the thermomixer (Eppendorf, #022670549) set at 1000 rpm at room temperature for 1 h. The labeling efficiency was determined by SE-HPLC (Bio-Silect SEC 250−5 column, PBS (pH 7.4) at a flow rate of 1 mL/min for method 1; BioSep-SEC S 3000, a solution of 0.05 M $NaSO_4$/0.02 M NaH_2PO_4/0.05% NaN_3 (pH 6.8) at a flow rate of 1 mL/min for method 2; or TSK-G3000 PW column, PBS (pH 7.4) at a flow rate of 1 mL/min for method 3) and ITLC (solvent: 20 mM EDTA/0.15 M NH_4OAc).

A solution of radiolabeled mixture (6 μL) was withdrawn at the designated time points (1 min, 5 min, 10 min, 20 min, 30 min, and 60 min), and DTPA solution (10 mM, 0.6 μL) was added to the mixture, and the resulting mixture was left for at least 20 min at RT. In ITLC analysis, peaks for bound and unbound radioisotope appeared around 30 mm and 50 mm from the origin, respectively. Bound and unbound radioisotope peaks appeared around 7.8 and 10.7 min (Method 1), 9.0 and 12.0 min (method 2), and 6.5 and 8.5 min (method 3), respectively.

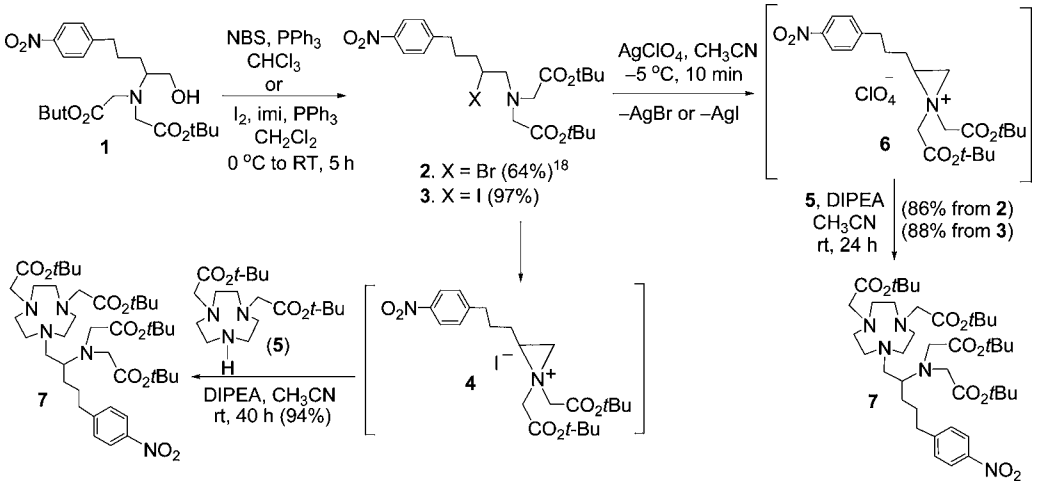
***In Vitro* Stability of ^{90}Y- and ^{177}Lu-Radiolabeled Trastuzumab Conjugate.** The radiolabeled trastuzumab conjugates were evaluated for stability in human serum (pH 7, 37 °C). ^{177}Lu-3p-*C*-NETA-trastuzumab, ^{177}Lu-*C*-DOTA-trastuzumab, or ^{177}Lu-3p-*C*-DEPA-trastuzumab was radiolabeled with ^{177}Lu at RT or 37 °C (0.25 M NH_4OAc, pH 5.5). The complex formed was purified by gel filtration chromatography using Biospin 6 column (Biorad, Cat# 732−6002) eluted with PBS (pH 7.4). The fraction containing ^{177}Lu-3p-*C*-NETA-trastuzumab (150 μL, ∼200 μCi), ^{177}Lu-*C*-DOTA-trastuzumab (30 μL, ∼100 μCi), or ^{177}Lu-3p-*C*-DEPA-trastuzumab (30 μL, ∼100 μCi) was added into human serum (1 mL, Gemini Bioproducts, #100110) in a microcentrifuge tube. The stability of the purified ^{177}Lu-3p-*C*-NETA-trastuzumab or ^{177}Lu-*C*-DOTA-trastuzumab in human serum (37 °C, pH 7) was evaluated for 14 days, and ^{177}Lu-3p-*C*-DEPA-trastuzumab in human serum (37 °C, pH 7) was evaluated for 2 days.

^{90}Y-3p-*C*-NETA-trastuzumab, ^{90}Y-*C*-DOTA-trastuzumab, or ^{90}Y-3p-*C*-DEPA-trastuzumab was radiolabeled with ^{90}Y at RT or 37 °C (0.25 M NH_4OAc, pH 5.5). The complex formed was purified by gel filtration chromatography using Biospin 6 column or PD-10 Sephadex G-25 M columns (GE Healthcare, #17−0851−01) eluted with PBS (pH 7.4). The fraction containing ^{90}Y-3p-*C*-NETA-trastuzumab (20 μL, ∼110 μCi), ^{90}Y-*C*-DOTA-trastuzumab (30 μL, ∼110 μCi), or ^{90}Y-3p-*C*-DEPA-trastuzumab (560 μL, 128 μCi) was added into human serum (1 mL, Gemini Bioproducts, #100110) in a microcentrifuge tube. The stability of the purified ^{90}Y-3p-*C*-NETA-trastuzumab or ^{90}Y-*C*-DOTA-trastuzumab in human serum (37 °C, pH 7) was evaluated for 14 days. The stability of ^{90}Y-3p-*C*-DEPA-trastuzumab in human serum (37 °C, pH 7) was evaluated for 7 days.

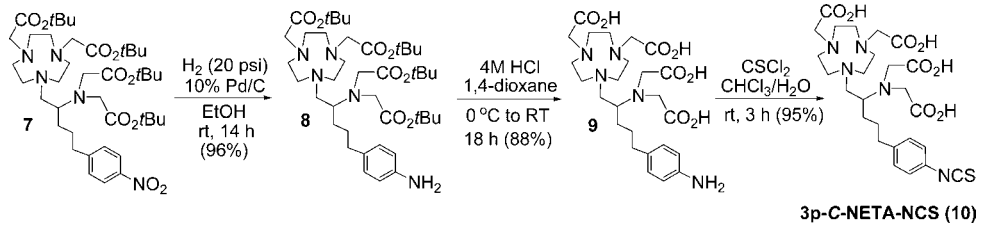
The serum stability of ^{90}Y- or ^{177}Lu-radiolabeled complex (37 °C, pH 7) was assessed by measuring the transfer of the radionuclide from the complex to serum proteins using SE-HPLC (Bio-Silect SEC 250-5 column, PBS (pH 7.4) at a flow rate of 1 mL/min for method 1 BioSep-SEC S 3000 column at a flow rate of 1 mL/min, eluent: 0.05 M $NaSO_4$/0.02 M NaH_2PO_4/0.05% NaN_3, pH 6.8 for method 2 or TSK-G3000PW column at a flow rate of 1 mL/min, eluent: PBS for method 3). A solution of the radiolabeled complex in serum (1−100 μL) was withdrawn at the designated time point, treated with DTPA (10 mM, 1−10 μL or 5 mM, 0.6 μL), incubated at room temperature for 20 min and then diluted with the HPLC eluent (160−200 μL) prior to SE-HPLC.

Radiolabeling with ^{177}Lu of Trastuzumab Conjugate for *in Vivo* Studies. 3p-*C*-NETA-trastuzumab was radiolabeled with ^{177}Lu for a trial biodistribution study. An aliquot of 0.25 M NH_4OAc (65.8 μL, pH = 5.0) was added to a solution of $^{177}LuCl_3$ (424 μCi, 2.3 μL) in 0.05 M HCl followed by 100 μg of 3p-*C*-NETA-trastuzumab in a solution of 0.25 M NH_4OAc (15.9 μL, pH = 7.0). The reaction mixture was incubated at room temperature for 15 min with mixing at 1000 rpm and quenched with 1 mM diethylenetriaminepentaacetic acid (DTPA) solution (pH = 6.0). The reaction mixture was allowed to stand for 15 min at room temperature, and then radiochemical purity and yield were determined using TLC (silica gel, Methanol/10% NH_4OAC = 1:1). The dose was then prepared for injection to mice without further purification.

Scheme 1. Optimized Synthesis of the Key Precursor Molecule 7



Scheme 2. Synthesis of Bifunctional Ligand 3p-*C*-NETA-NCS (10)



Biodistribution Study. All experiments were conducted in compliance with the guidelines established by the Animal Care and Use Committee of the University of Missouri-Columbia Animal Care Quality Assurance Office. Athymic nude mice were implanted subcutaneously (s.c.) in the hind flank with a suspension of 5×10^6 ZR-75−1 human breast cancer cells (0.15 mL) in Hank's Balanced Salt Solution. When tumors had grown to 100−400 mg (~30 days after tumor implantation), mice were injected intravenously (i.v.) via the tail vein with ^{177}Lu-3p-*C*-NETA-trastuzumab (27 μCi, 100 μL). The biodistributions were obtained at 24, 72, and 120 h post-injection. Tissues harvested included blood, liver, bone, and tumor. Tissues were drained of blood, weighed, and counted in a gamma counter with a standard of the injected dose, such that decay-corrected uptakes were calculated as percent injected dose per gram of tissue (% ID/g) and percent injected dose per organ (% ID/organ).

RESULTS AND DISCUSSION

The key step in the synthesis of 3p-*C*-NETA-NCS is the regiospecific ring-opening reaction of *N*,*N*-bisubstituted aziridinium ions **4** or **6** by bisubstituted 1,4,7-triazacyclononane (**5**) to generate the key precursor molecule **7** (Schemes 1 and 2). We recently reported the construction of **7** from the reaction of *N*,*N*-bisubstituted secondary β-amino bromide **2** with **5** based on the ring-opening strategy.[18] The intermediate compound **7** was efficiently prepared in 94% isolated yield, and no byproduct was formed during the ring-opening reaction. However, the reaction was very slow at room temperature and remained incomplete after 5 days. The mild reaction condition was required because an elevated temperature promoted the formation of an unwanted byproduct from intramolecular rearrangement of **2**.[18]

Inspired by high efficiency and regiospecificity of the ring-opening reaction of aziridinium ion, we sought optimization of the reaction conditions for the synthesis of **7**. We envisioned using secondary β-amino iodide **3** as the starting material based on the rationale that **3** containing iodine as an excellent leaving group would react significantly faster with the nucleophilic TACN analogue **5** and can be converted to **7** in higher isolated yield. We also investigated the use of a halo-sequestering agent $AgClO_4$ to see if the prompt formation of the azridinium ion can facilitate the nucleophilic attack of **5**. The optimization results are outlined in Scheme 1. Secondary β-amino iodide **3** was prepared using the efficient synthetic method that we developed. Iodination of **1**[18] using I_2, imidazole, and PPh_3 provided **3** in 97% isolated yield. Formation of aziridinium salt **4** from intramolecular rearrangement of **3** and subsequent regiospecific ring-opening of **4** by nucleophilic bisubstituted TACN **5** at the less hindered carbon provided the desired coupling product **7** in excellent isolated yield (94%). The effect of silver perchlorate on the formation of **7** was explored using secondary β-amino halides **2** and **3**. Treatment of **2** or **3** with silver perchlorate provided aziridinium perchlorate salt **6** which was further treated with **5** to provide the product **7** in 86% and 88% isolated yield, respectively. Our optimization strategy to prepare the key precursor **7** in an improved yield and at a shorter reaction time was found to be successful. The best result was obtained from the reaction of the secondary β-amino iodide **3** with **5** in the absence of silver perchlorate. It is noteworthy that both of the silver-promoted ring-opening reactions produced a small portion of the intramolecular rearrangement byproduct. Synthesis of the bifunctional ligand 3p-*C*-NETA-NCS (**10**) was accomplished as shown in Scheme 2. Compound **7** was hydrogenated using 10% Pd/C to afford compound **8** in 96% isolated yield. *tert*-butyl groups in **8** were

dx.doi.org/10.1021/bc200696b | *Bioconjugate Chem.* 2012, 23, 1775−1782

Table 1. Evaluation of Radiolabling Efficiency[a] (%) of Bifunctional Ligand−Trastuzumab Conjugates with ^{90}Y (RT, 0.25 M NH_4OAC, pH 5.5) Using ITLC[b] and HPLC[c] (parentheses)

time	3p-C-NETA-trastuzumab	3p-C-DEPA-trastuzumab	C-DTPA-trastuzumab	C-DOTA-trastuzumab
1 min	91.6 ± 3.1	30.6 ± 1.9	98.4 ± 0.4	23.1 ± 7.7
	(86.2 ± 3.5)	(29.3 ± 2.2)	(90.1 ± 1.2)	(24.1 ± 6.6)
5 min	99.6 ± 0.2	58.6 ± 1.6	98.7 ± 0.7	43.0 ± 9.9
	(94.4 ± 0.2)	(50.3 ± 1.8)	(89.9 ± 1.3)	(39.8 ± 8.3)
10 min	99.6 ± 0.3	66.3 ± 10.4	98.6 ± 0.8	56.5 ± 12.5
	(94.9 ± 1.4)	(58.2 ± 6.8)	(89.5 ± 0.8)	(50.9 ± 13.3)
20 min	99.6 ± 0.5	67.9 ± 7.2	98.7 ± 0.4	67.4 ± 12.2
	(93.1 ± 1.1)	(58.3 ± 7.1)	(89.3 ± 0.8)	(60.1 ± 15.2)
30 min	99.9 ± 0.1	67.50 ± 7.5	98.9 ± 0.3	69.7 ± 10.8
	(93.6 ± 0.9)	(57.4 ± 7.3)	(90.3 ± 0.6)	(62.7 ± 12.4)
60 min	99.8 ± 0.1	67.4 ± 9.0	99.2 ± 0.4	71.7 ± 8.9
	(93.4 ± 0.5)	(56.9 ± 5.3)	(90.0 ± 0.5)	(63.4 ± 11.3)

[a]Radiolabeling efficiency (mean ± standard deviation %) was measured in triplicate (n = 3). [b]ITLC eluent (20 mM EDTA/0.15 M NH_4OAc). [c]HPLC mobile phase (0.05 M $NaSO_4$/0.02 M NaH_2PO_4/0.05% NaN_3, pH 6.8 or PBS, pH 7.4).

Table 2. Evaluation of Radiolabling Efficiency[a] (%) of Bifunctional Ligand−Trastuzumab Conjugates with ^{177}Lu (RT, 0.25 M NH_4OAC, pH 5.5) Using ITLC[b] and HPLC[c] (parentheses)

time	3p-C-NETA-trastuzumab	3p-C-DEPA-trastuzumab	C-DTPA-trastuzumab	C-DOTA-trastuzumab
1 min	99.2 ± 0.2	35.9 ± 1.8	99.5 ± 0.3	29.7 ± 1.5
	(96.5 ± 1.2)	(29.8 ± 2.1)	(98.3 ± 0.6)	(28.1 ± 3.0)
5 min	99.9 ± 0.1	71.1 ± 2.2	99.4 ± 0.2	58.6 ± 1.3
	(97.7 ± 0.8)	(60.0 ± 1.9)	(98.3 ± 0.3)	(54.6 ± 1.5)
10 min	99.8 ± 0.1	85.3 ± 1.1	99.4 ± 0.4	75.5 ± 1.7
	(97.6 ± 1.3)	(75.2 ± 0.4)	(98.4 ± 0.7)	(70.1 ± 1.6)
20 min	99.9 ± 0.1	94.8 ± 0.4	99.6 ± 0.1	89.3 ± 0.1
	(97.6 ± 0.8)	(85.4 ± 1.0)	(98.3 ± 0.3)	(84.6 ± 1.4)
30 min	99.8 ± 0.1	97.9 ± 0.4	99.6 ± 0.2	94.2 ± 0.4
	(97.5 ± 0.3)	(87.3 ± 1.4)	(98.3 ± 0.3)	(90.1 ± 1.5)
60 min	99.9 ± 0.1	98.4 ± 0.8	99.4 ± 0.3	97.8 ± 0.3
	(97.4 ± 0.4)	(87.6 ± 1.3)	(98.1 ± 0.3)	(94.8 ± 1.3)

[a]Radiolabeling efficiency (mean ± standard deviation %) was measured in triplicate (n = 3). [b]ITLC eluent (20 mM EDTA/0.15 M NH_4OAc). [c]HPLC mobile phase (0.05 M $NaSO_4$/0.02 M NaH_2PO_4/0.05% NaN_3, pH 6.8 or PBS, pH 7.4).

removed by the treatment of **8** with 4 M HCl (g) in 1,4-dioxane. Reaction of **9** with thiophosgene in $CHCl_3/H_2O$ provided the desired 3p-*C*-NETA-NCS. The synthesis of 3p-*C*-NETA-NCS was achieved in 71% overall yield starting from the readily available compound **1**. The efficient synthetic method to **7** can be readily scaled up and applied to preparation of many other bifunctional chelates.

Trastuzumab is known to target HER2 (human epidermal growth factor receptor 2) overproduced in cancer cells and is a clinically available antibody for treatment of metastatic breast cancer.[19,20] 3p-*C*-NETA-NCS was conjugated with trastuzumab, and concentration of trastuzumab in the conjugate was quantified by the spectroscopic assay.[16] Ligand to protein ratio (L/P = 3.1) of 3p-*C*-NETA-trastuzumab conjugate was determined using Lu(III)-ArsenazoIII based UV−vis spectrophotometric assay.[16] Trastuzumab conjugates of other bifunctional ligands (*C*-DOTA, *C*-DTPA, and 3p-*C*-DEPA) were also prepared and evaluated for comparison. The purified trastuzumab conjugate (0.25 M NH_4OAc, pH 5.5) was labeled with ^{90}Y or ^{177}Lu at room temperature (RT).[18] During the reaction time (1 h), the components were analyzed using SE-HPLC after challenging the reaction mixture with 10 mM DTPA, and the radiolabeling efficiency (%) was determined using both ITLC and size exclusion (SE)-HPLC (Tables 1 and 2 and Supporting Information). The radiolabeling formation kinetics data indicate that 3p-*C*-NETA-trastuzumab conjugates were extremely rapid in binding ^{90}Y and ^{177}Lu and complexation was nearly complete in 1 min as determined by ITLC (91.6% for ^{90}Y and 99.2% for ^{177}Lu). Complexation kinetics of 3p-*C*-NETA-trastuzumab conjugate with ^{90}Y and ^{177}Lu was comparable to that of *C*-DTPA-trastuzumab conjugate. *C*-DOTA-trastuzumab displayed significantly slower complexation kinetics with ^{90}Y (71.7% at 1 h, Table 1), while the conjugate more rapidly bound to ^{177}Lu (>90% at 30 min, Table 2). 3p-*C*-DEPA-trastuzumab conjugate exhibited similar ^{90}Y- and ^{177}Lu-radiolabeling pattern to *C*-DOTA-trastuzumab, achieving the respective radiolabeling efficiency of ∼67% (1 h, Table 1) and >87% (30 min, Table 2) with ^{90}Y and ^{177}Lu. It appears that decadentate 3p-*C*-DEPA has too many donor groups to form a stable Y(III) or Lu(III) complex, and this may allow the formation of the Lu(III)- or Y(III)-3p-*C*-DEPA complex to be a reversible process. The results indicates that the tridentate pendant acyclic donors in 3p-*C*-NETA are essential in rapidly binding Y(III) and Lu(III) and improved complexation kinetics of NETA with the metals relative to DOTA is ascribed to cooperative and bimodal binding of acyclic and macrocyclic donors.

^{90}Y- or ^{177}Lu-radiolabeled trastuzumab conjugates of 3p-*C*-NETA, 3p-*C*-DEPA, and *C*-DOTA were further evaluated for *in vitro* serum stability (Supporting Information). Both ^{90}Y-3p-*C*-

dx.doi.org/10.1021/bc200696b | Bioconjugate Chem. 2012, 23, 1775−1782

NETA-trastuzumab and ^{177}Lu-3p-*C*-NETA-trastuzumab remained stable in human serum for 2 weeks as confirmed by radio-SE-HPLC analysis. However, a significant amount of the radioactivity was dissociated from ^{90}Y-3p-*C*-DEPA-trastuzumab (32%, 2 days) and ^{177}Lu-3p-*C*-DEPA trastuzumab (45%, 2 days). ^{90}Y-*C*-DOTA-trastuzumab and ^{177}Lu-*C*-DOTA-trastuzumab were quite stable releasing a minimal level of radioactivity over 2 weeks.

The *in vitro* result suggests that 3p-*C*-NETA was favorably compared to *C*-DOTA and displayed excellent complexation kinetics and stability with ^{90}Y and ^{177}Lu. 1B4M-DTPA[20] has been used as the chelator of ^{90}Y in Zevalin and was reported to exhibit rapid complexation kinetics with ^{90}Y. However, it should be noted that ^{90}Y-1B4M-DTPA-antibody conjugate was less stable than ^{90}Y-DOTA-antibody conjugate both *in vitro* and *in vivo*.[21]

The *in vivo* stability and tumor targeting of ^{177}Lu-3p-*C*-NETA-trastuzumab was evaluated by performing a pilot biodistribution study in ZR-75-1-bearing nude mice (Figure 2). The 3p-*C*-NETA-trastuzumab conjugate was radiolabeled

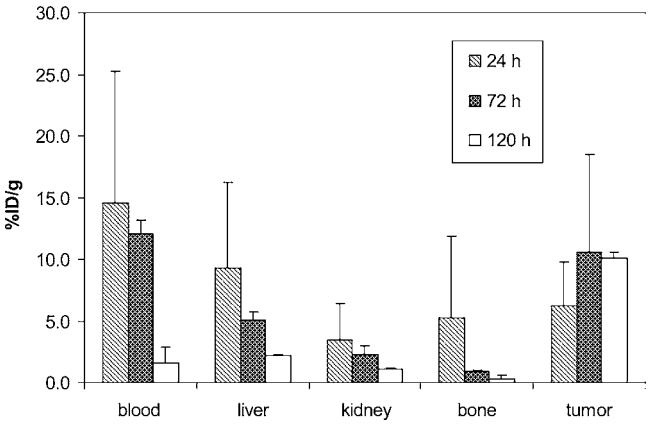


Figure 2. *In vivo* biodistribution of ^{177}Lu-3p-C-NETA-trastuzumab conjugate in ZR-75-1-bearing mice (% ID/g, n = 3, intravenous injection).

with ^{177}Lu at specific activity of 640 Ci/mmol and in 92.2% yield and radiochemical purity. The highest tumor uptake (10.55 ± 7.93%) of ^{177}Lu-3p-*C*-NETA-trastuzumab was observed at 72 h. ^{177}Lu-3p-*C*-NETA-trastuzumab exhibited the highest radioactivity level in the blood at 24 h (14.57 ± 10.63%), which was not significantly different than 72 h (12.09 ± 1.12%), but significantly decreased at 120 h (1.58 ± 1.30%). The ^{177}Lu-3p-*C*-NETA-trastuzumab conjugate resulted in a very low radioactivity level in the liver (2.20 ± 0.06%) and the kidneys (1.09 ± 0.12%) at 120 h. The radioimmunoconjugate displayed low bone uptake and a higher radioactivity level in the tumor, compared to the normal organs, over the course of the study and the highest tumor-to-blood ratio (6.39) at 120 h. The biodistribution data indicate that ^{177}Lu-3p-*C*-NETA remains stable *in vivo* and tumor targeting of ^{177}Lu-3p-*C*-NETA-trastuzumab can be improved by selecting an adequate HER2-positive tumor model.

CONCLUSION

Highly efficient and scalable synthetic route to the new bimodal bifunctional ligand 3p-*C*-NETA centered on the formation of *N,N*-bisubstituted β-amino iodide and nucleophilic ring-opening of an aziridinium ion was developed. The bimodal ligands, 3p-*C*-NETA and 3p-*C*-DEPA, and other known bifunctional ligands, *C*-DOTA and *C*-DTPA, were evaluated for a comparative ^{90}Y and ^{177}Lu-radiolabeleing kinetics study. 3p-*C*-NETA-trastuzumab conjugate instantly bound to ^{90}Y or ^{177}Lu with comparable radiolabeling kinetics to *C*-DTPA-trastuzumab conjugate, while 3p-*C*-DEPA- and *C*-DOTA-trastuzumab conjugates displayed similar and slow radiolabeling pattern in binding ^{90}Y and ^{177}Lu. Both ^{90}Y-3p-*C*-NETA-trastuzumab and ^{177}Lu-3p-*C*-NETA-trastuzumab were stable in human serum over 2 weeks. A significant amount of the radioactivity was released from both ^{90}Y-3p-*C*-DEPA-trastuzumab and ^{177}Lu-3p-*C*-DEPA-trastuzumab in serum over 24 h. ^{177}Lu-3p-*C*-NETA-trastuzumab conjugate produced a favorable biodistribution profile and exhibited low radioactivity level in organs and high tumor uptake. The results of the *in vitro* and *in vivo* studies indicate that bimodal and cooperative binding of the acyclic and macrocyclic moieties property in 3p-*C*-NETA led to fast complexation kinetics and high complex stability of the octadentate chelate in binding the lanthanides Y(III) and Lu(III). The bimodal ligand 3p-*C*-NETA has broad applications for RIT of various cancers using ^{90}Y and ^{177}Lu. On the basis of the favorable *in vitro* complexation and *in vivo* biodistribution data, 3p-C-NETA-NCS radiolabeled with ^{90}Y or ^{177}Lu will be further evaluated for comprehensive *in vivo* biodistribution, pharmacokinetics, and dosimetry using different antibodies and tumor models.

ASSOCIATED CONTENT

Supporting Information

HPLC and ITLC chromatograms for assessment of radiolabeling reaction kinetics and serum stability and *in vivo* biodistribution data. This material is available free of charge via the Internet at http://pubs.acs.org.

AUTHOR INFORMATION

Corresponding Author

*E-mail: Chong@iit.edu, Phone: 312-567-3235, Fax: 312-567-3494. Mailing address: 3101 S. Dearborn St, LS 182, Chemistry Division, Biological and Chemical Sciences Department, Illinois Institute of Technology, Chicago, IL, 60616.

Notes

The authors declare no competing financial interest.

ACKNOWLEDGMENTS

We acknowledge the financial support from the National Institutes of Health (R01CA112503 to H. S. Chong). We also acknowledge the Department of Veterans Affairs for providing resources and use of facilities at the Harry S. Truman Memorial Veterans' Hospital in Columbia, MO.

REFERENCES

(1) Knox, S. J., and Meredith, R. F. (2000) Clinical radioimmunotherapy. *Sem. Radiat. Oncol. 10*, 73−93.

(2) Milenic, D. E., Brady, E. D., and Brechbiel, M. W. (2004) Antibody-targeted radiation cancer therapy. *Nat. Rev. 3*, 488−98.

(3) Wiseman, G. A., White, C. A., Sparks, R. B., Erwin, W. D., Podoloff, D. A., Lamonica, D., Bartlett, N. L., Parker, J. A., Dunn, W. L., Spies, S. M., Belanger, R., Witzig, T. E., and Leigh, B. R. (2001) Biodistribution and dosimetry results from a phase III prospectively randomized controlled trial of Zevalin radioimmunotherapy for low-grade, follicular, or transformed B-cell non-Hodgkin's lymphoma. *Crit. Rev. Oncol. Hematol. 39*, 181−94.

(4) Vose, J. M. (2004) Bexxar: novel radioimmunotherapy for the treatment of low-grade and transformed low-grade non-Hodgkin's lymphoma. *Oncologist 9*, 160−72.
(5) Chinn, P., Braslawsky, G., White, C., and Hanna, N. (2003) Antibody therapy of non-Hodgkin's B-cell lymphoma. *Cancer Immunol. Immunother. 52*, 257−280.
(6) Srivastava, S., and Dadachova, E. (2001) Recent Advances in. Radionuclide Therapy. *Semin. Nucl. Med. 31*, 330−341.
(7) Cacheris, W. P., Nickle, S. K., and Sherry, A. D. (1987) Thermodynamic study of lanthanide complexes of 1,4,7-Triazacyclononane-N,N′,N″-triacetic Acid and 1,4,7,10-tetraazacyclododecane-N,N′,N″,N‴-tetraacetic acid. *Inorg. Chem. 26*, 958−960.
(8) Harrison, A., Walker, C. A., Parker, D., Jankowski, K. J., and Cox, J. P. (1991) The in vivo release of ^{90}Y from cyclic and acyclic ligand-antibody conjugates. *Nucl. Med. Biol. 18*, 469−476.
(9) Hinz, F. P., and Margerum, D. W. (1974) Ligand solvation and the macrocyclic effect. A study of Nickel(II)-Tertramine Complexes. *Inorg. Chem. 13*, 2941.
(10) Hancock, R. D, and Martell, A. E. (1989) Ligand design for selective complexation of metal ions in aqueous solution. *Chem. Rev. 89*, 1875−1914.
(11) Alvarez, R. D., Partridge, E. E, Khazaeli, M. B, Plott, G., Austin, M., Kilgore, L, Russell, C. D., Liu, T., Grizzle, W. E., Schlom, J., LoBuglio, A. F., and Meredith, R. F. (1997) Intraperitoneal radioimmuno-therapy of ovarian cancer with ^{177}Lu-CC49: a phase I/II study. *Gynecol. Oncol. 65*, 94−101.
(12) Chappell, L. L., Ma, D., Milenic, D. E., Garmasteni, K., Venditto, V., Beitzel, M. P., and Brechbiel, M. W. (2003) Synthesis and evaluation of novel bifunctional chelating agents based on 1,4,7,10-tetraazacyclododecane-*N*,*N*′,*N*″,*N*‴-tetraacetic acid for radiolabeling proteins. *Nucl. Med. Biol. 30*, 581−595.
(13) Stimmel, J. B., Stockstill, M. E., and Kull, F. C., Jr (1995) Yttrium-90 chelation properties of tetraazatetraacetic acid macrocyclices, diethylenetriaminepentaacetic acid analogues, and a novel terpyridine acyclic chelator. *Bioconjugate Chem. 6*, 219−225.
(14) Chakrabarti, M. C., Le, N, Paik, C. H., De Graff, W. G., and Carrasquillo, J. A. (1996) Prevention of radiolysis of monoclonal antibody during labeling. *J. Nucl. Med. 37*, 1384−1388.
(15) Chong, H. S., Lim, S., Baidoo, K. E., Milenic, D. E., Ma, X., Jia, F., Song, H. A., Brechbiel, M. W., and Lewis, M. R. (2008) Synthesis and biological evaluation of a novel decadentate ligand DEPA. *Bioorg. Med. Chem. Lett. 18*, 5792−5795.
(16) Song, H. A., Kang., C. S., Baidoo, K. E., Milenic, D. E., Chen, Y., Dai, A., Brechbiel, M. W., and Chong, H. S. (2011) Efficient Bifunctional Decadentate Ligand 3p-*C*-DEPA for Targeted Alpha Radioimmunotherapy Applications. *Bioconjugate Chem. 22*, 1128−1135.
(17) Chong, H. S., Garmestani, K., Millenic, D. E., and Brechbiel., M. W. (2002) Design, synthesis, and biological evaluation of novel macrocycles with pendant donor groups as radioimmunotherapy (RIT) agents. *J. Med. Chem. 45*, 3458−3464.
(18) Chong, H. S., Song, H. A., Kang, C. S., Le, T., Sun, X., Dadwal, M., Lee, H. B., Lan, X., Chen, Y., and Dai, A. (2011) A highly effective bifunctional ligand for radioimmunotherapy of cancer. *Chem. Commun. 47*, 5584−5586.
(19) Agus, D. B., Bunn, P. A., Jr., Franklin, W., Garcia, M., and Ozols, R. F. (2000) HER-2/neu as a therapeutic target in non-small cell lung cancer, prostate cancer, and ovarian cancer. *Semin. Oncol. 27*, 53−63.
(20) Baselga, J. (2001) Phase I and II clinical trials of trastuzumab. *Ann. Oncol. 12*, S49−55.
(21) Brechbiel, M. W., and Gansow, O. A. (1991) Backbone-substituted DTPA ligands for ^{90}Y radioimmunotherapy. *Bioconjugate Chem.*, 187−94.
(22) Camera, L., Kinuya, S., Garmestani, K., Wu, C., Brechbiel, M. W., Pai, L. H., McMurry, T. J., Gansow, O. A., Pastan, I., Paik, C. H., and Carrasquillo, J. A. (1994) Evaluation of the serum stability and in vivo biodistribution of CHX-DTPA and other ligands for yttrium labeling of monoclonal antibodies. *J. Nucl. Med. 35*, 882−9.

Bioconjugate Chemistry

Article

pubs.acs.org/bc

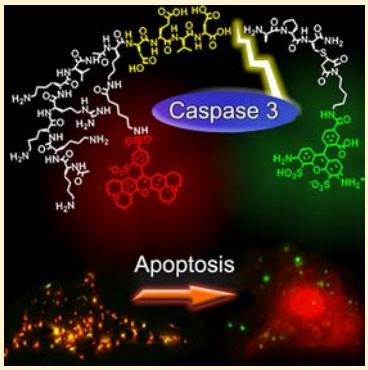
Caspase-Activated Cell-Penetrating Peptides Reveal Temporal Coupling Between Endosomal Release and Apoptosis in an RGC-5 Cell Model

James R. Johnson,[†] Brandon Kocher,[†] Edward M. Barnett,[‡] Jayne Marasa,[†] and David Piwnica-Worms*[,†]

[†]Molecular Imaging Center, Mallinckrodt Institute of Radiology, BRIGHT Institute, Departments of Cell Biology & Physiology, Developmental Biology, and [‡]Ophthalmology and Visual Sciences, Washington University School of Medicine, St. Louis, Missouri 63110, United States

Supporting Information

ABSTRACT: Caspase-activatable cell-penetrating peptide (CPP) probes, designed for efficient cell uptake and specificity via cleavable intramolecular quenched-fluorophore strategies, show promise for identifying and imaging retinal ganglion cell apoptosis *in vivo*. However, initial cell uptake and trafficking events cannot be visualized because the probes are designed to be optically quenched in the intact state. To visualize subcellular activation events in real-time during apoptosis, a new series of matched quenched and nonquenched CPP probes were synthesized. In both native and staurosporine-differentiated RGC-5 cells, probe uptake was time- and concentration-dependent through clathrine-, caveolin-, and pinocytosis-mediated endocytic mechanisms. During apoptosis, KcapTR488, a novel dual fluorophore CPP probe, revealed by multispectral imaging a temporal coupling of endosomal release and effector caspase activation in RGC-5 cells. The novel CPPs described herein provide new tools to study spatial and temporal regulation of endosomal permeability during apoptosis.



INTRODUCTION

Executioner caspases are central mediators of the apoptosis pathway, representing a final commitment to programmed cell death. Caspases are one of the most specific proteases, showing an absolute requirement for cleavage after aspartic acid[1] and at least four amino acids N-terminal to the cleavage site for efficient catalysis. The preferred recognition motif differs significantly between caspases, thereby contributing to their biologically diverse functions.[2] In addition to high specificity, caspases are also highly efficient, with k_{cat}/K_m values $>10^6$ M^{-1} s^{-1}.[3] When viewed from the perspective of a target for molecular imaging, these characteristics facilitate the rapid and specific detection of caspase activity *in vitro* and *in vivo*.

Previously, we reported the chemical and biochemical characterization of two cell-penetrating probes, TcapQ647 and KcapQ647 (**1**), designed for imaging effector caspases.[4−6] These probes are modular in design, consisting of a cell-penetrating peptide (CPP) sequence conjugated to an effector recognition sequence (DEVD) that is flanked by a fluorophore−quencher pair (Alexa Fluor 647 and QSY 21, respectively) rendering the intact probe optically silent. The cleavable domain of this probe, DEVD, is a specific substrate for effector caspases (**3** > **7**).[7,8] Upon recognition by effector caspases within cells, the probe is cleaved, separating the fluorophore from the quencher, thereby producing an intracellular fluorescent signal denoting activation of the apoptotic pathway (Figure 1). While the original probe, TcapQ647, showed promise both *in vivo* and *in vitro*,[5,9,10] the HIV Tat sequence has shown evidence of systemic toxicity at high doses,[11] prompting us to modify the cell-penetrating sequence. Replacement of the HIV-1 Tat sequence with the nuclear localization sequence of SV40 large T antigen (kkkrkv) yielded **1** (Figure 1).[6] This peptide sequence retains cell-penetrating capabilities without the systemic toxicity of the HIV-1 Tat sequence.[6]

Recently, we applied these caspase-activatable CPP probes to an *in vivo* rat model of retinal ganglion cell (RGC) degeneration as a demonstration of the potential for molecular imaging of RGC apoptosis in glaucoma.[10,11] Glaucoma is an optic neuropathy characterized by RGC death and axon loss, resulting in an excavated appearance to the optic nerve head and associated loss of vision. A wide array of specific triggers of RGC apoptosis are implicated in glaucoma, including blockage of axonal transport with neurotrophin deprivation, antibodies to heat shock proteins, ischemia and oxidative stress, vasoactive regulators such as endothelins and nitric oxide, and glutamate excitotoxicity.[12,13] Regardless of trigger, the apoptotic cascade results in cell suicide by invoking a series of cellular events leading to caspase activation, which is conserved in RGCs.[14,15] Using TcapQ647 and **1** directly applied into the vitreous humor, we previously reported the capacity to detect RGC apoptosis in models of RGC degeneration *in vivo*.[6,10]

While CPP probes of this class are activated upon exposure to caspase 3 *in vitro* and in live animals, details of the

Received: January 24, 2012
Revised: August 13, 2012
Published: August 19, 2012

ACS Publications © 2012 American Chemical Society

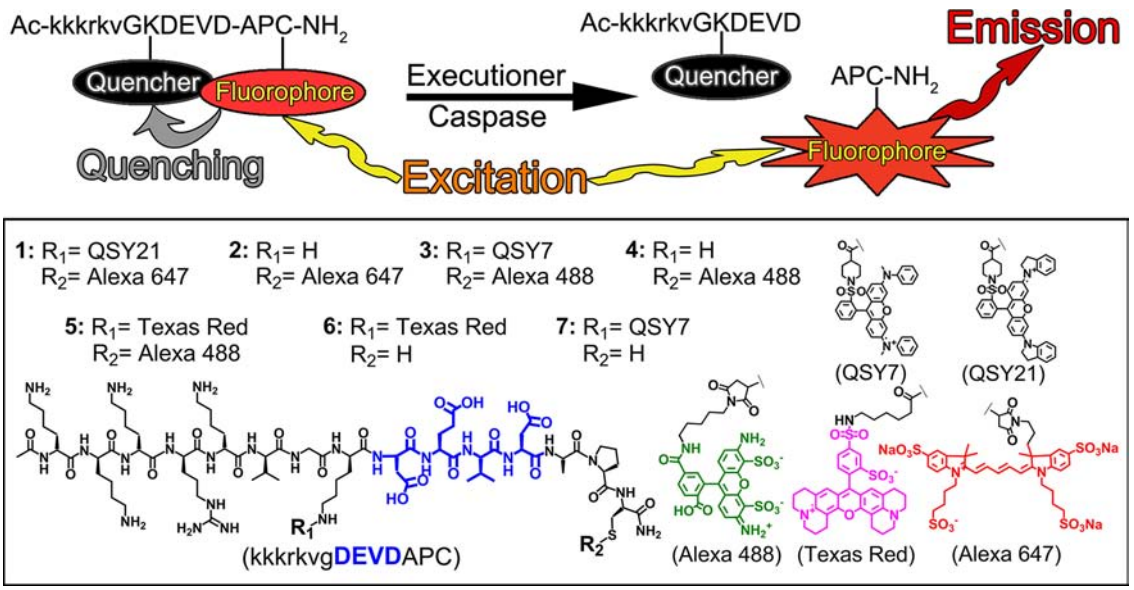


Figure 1. Schematic of caspase-mediated activation of CPP probes (top). Structures of CPP probes (bottom).

mechanisms of subcellular transport, access to active caspases, and the temporal relation to caspase activation remain unanswered. In particular, because it is not possible (by design) to visualize quenched probes prior to activation, the exact location and temporal events leading to intracellular activation of these and other quenched CPP probes are unresolved. Therefore, we synthesized a novel series of CPP probes based on this scaffold conjugated with either quenched fluorophore or nonquenched fluorophore combinations that afforded a variety of spectral properties. These probes enabled multispectral resolution of subcellular trafficking events in relation to probe activation both spatially and temporally in RGC-5 cells, a cell line highly relevant to the study of glaucomatous neurodegeneration.[16−19] Observing endosomal trafficking of these novel probes in healthy cells in relation to death-induced endosomal release and localization of caspase-cleaved probe fragments in dying cells provided direct evidence for temporal coupling of endosomal release and effector caspase activation in RGC-5 cells.

EXPERIMENTAL PROCEDURES

Probe Synthesis. Peptides were synthesized as previously reported with revisions to improve probe yield and simplify reaction conditions.[6] For **1**, standard solid-phase N-α-Fmoc chemistry was used to synthesize the peptide (Tufts University Peptide Synthesis Core, Boston, MA). Kcap, the core peptide, was composed of an all-D cell-penetrating peptide comprising the SV40 TAg nuclear localization signal (kkkrkv) linked to a cleavage sequence consisting of L-amino acids (KDEVDAPC). The N-terminus was acetylated and resin coupling afforded C-terminus amidation of the final product. For conjugation, in a small microwave reaction vial, 1 mL of 2% hydrazine in DMF was added to 25 mg of peptide on resin to selectively remove the single Dde group protecting the lysine N-terminal of the DEVD sequence. The reaction was stirred for 20 min at RT, the supernatant was then collected, and analyzed by UV−vis spectroscopy to confirm removal of the Dde protecting group. This step was repeated until complete removal of the Dde group was confirmed (5 repetitions). Deprotected peptide on resin was then rinsed with methanol followed by an ether rinse and dried via a stream of argon. To deprotected peptide on resin, 5 mg of QSY21 succimidyl ester (Invitrogen) in a minimal volume (<2 mL) of 2% *N*,*N*-diisopropyethylamine/DMF were added, and microwaved in a microwave reactor (CEM Discover) at 10 W for 10 min (max temp 65 °C). The reaction was allowed to continue overnight at room temperature. The resin was then transferred to a 10 mL peptide reaction vessel, rinsed with methanol, followed by ether, and dried via a stream of argon. Peptide was cleaved and deprotected from resin in 95% trifluoroacetic acid (TFA)/5% water for 2 h at RT followed by precipitation in cold ether (dry ice acetone bath) to yield the intermediate product **7**. **7** was then isolated by centrifuging the sample (2000 *g*) and the collected pellet dried under argon. One mg of Alexa Fluor 647 maleimide (Invitrogen) was dissolved in 1 mL of PBS buffer and added to 2 mL **7** in PBS. Conjugation to the C-terminal cysteine residue was allowed to proceed for 2 h. The final product, **1**, was purified using reverse-phase HPLC using a flow rate of 1 mL/min and a 5%/95% to 40%/60% acetonitrile/0.1% TFA/water/0.1% TFA gradient over 10 min followed by a 42%/58% acetonitrile/0.1% TFA/water/0.1% TFA gradient over 20 min (t_R = 17.2 min). **1** was collected by measuring absorbance at 214 and 605 nm (>98% purity) and characterized by MALDI mass spectrometry (**1**: *m*/*z* 3381.0 (**1** + 3Na$^+$); calc 3381.3).

3, **5**, and *D*-**5** were synthesized using the same procedure as **1**, except that QSY7 succimidyl ester (Invitrogen) (in **3**, **7**) or Texas Red succimidyl ester (Invitrogen) (in **5**, **6**) replaced QSY21, and Alexa Fluor 488 maleimide (Invitrogen) replaced Alexa Fluor 647 maleimide. **3** was collected during HPLC purification by measuring absorbance at 214 and 595 nm, while **5** was monitored at 495 and 595 nm. Constitutively active probes (**2** and **4**) were isolated during purification of **1** or **3** (t_R = 11.5 min **2**, t_R = 17.8 min for **3**, t_R = 12.2 min for **4**). **5**, **6**, and **7** were isolated at t_R = 17.7 min, t_R = 16.3 min, and t_R = 16.1 min, respectively. Tcap488 and Tcap647 were synthesized and isolated (t_R = 12.3 min Tcap488, t_R = 11.7 min for Tcap647) using the same procedures as **1**−**7**. Upon purification, probes were lyophilized and stored at −20 °C. All probes were characterized by MALDI mass spectrometry (**2**: *m*/*z* 2717.2 (**2**

dx.doi.org/10.1021/bc300036z | Bioconjugate Chem. 2012, 23, 1783−1793

+ $3Na^+$), calc 2717.1; **3**: *m/z* 3082.3, calc 3080.3; **4**: *m/z* 2441.4, calc 2440.1; **5**: *m/z* 3139.5, calc 3141.3; *D*-**5**: *m/z* 3139.9, calc 3141.3; **6**: *m/z* 2242.4, calc 2443.2; **7**: *m/z* 2382.4, calc 2382.2; Tcap488: *m/z* 2979.4, calc 2978.4; Tcap647: *m/z* 3266.0 (Tcap647 + KCl), calc 3264.4). **1**, **3**, and **5** were characterized by amino acid analysis (Texas A&M Peptide Chemistry Lab). Working solutions of each probe were prepared in DI water and the concentration standardized using molecular extinction coefficients (112 000 M^{-1} cm^{-1} at 605 nm for **1**; 239 000 M^{-1} cm^{-1} at 650 nm for **2** and Tcap647; 69 500 M^{-1} cm^{-1} at 496 nm for **3**; 71 000 M^{-1} cm^{-1} at 495 nm for **4** and Tcap488; 76 586 M^{-1} cm^{-1} at 595 nm for **5** and *D*-**5**; 89 000 M^{-1} cm^{-1} at 592 nm for **6**, 90 000 M^{-1} cm^{-1} at 565 nm for **7**).

Cell Culture. RGC-5 cells were obtained from the ATCC, cultured in phenol-free DMEM supplemented with 10% FBS, and incubated at 37 °C in a humidified, 5% CO_2 atmosphere. For high-throughput microscopy experiments, RGC-5 cells were plated onto 96-well clear bottom black-walled plates (Costar) and allowed to grow to ∼70% confluence. For high-resolution microscopy experiments, RGC-5 cells were plated onto #1.5 borosilicate 8-well chambered coverslips (Nunc) and allowed to grow to ∼70% confluence. For flow cytometry experiments, RGC-5 cells were plated onto 24-well clear plates and allowed to grow to ∼70% confluence. RGC-5 cells were differentiated by incubating in growth medium supplemented with 0.5 μM staurosporine (SS) for 1 h. Following SS exposure, growth media was removed and replaced with fresh media for experiments.

In Vitro Enzyme Assays. Caspase (human, recombinant from *E. coli*) assays were performed for caspases **2** (1.25 U; 8.3×10^{-5} mg), **3** (50 U; 1.4×10^{-6} mg), **6** (1.25 U; 9.6×10^{-5} mg), **7** (0.25 U; 1.0×10^{-5} mg), and **9** (1.25 U; 3.1×10^{-3} mg) (Calbiochem, La Jolla CA). All caspase assays were conducted in 50 mM HEPES, 1 mM EDTA, 100 mM NaCl, 10% glycerol, 0.1% CHAPS, pH 7.4 supplemented with 10 mM dithiothreitol (DTT) immediately prior to assay preparation. Granzyme B (human, recombinant from *E. coli*) and trypsin assays were conducted in TBS buffer (50 mM Tris, 100 mM NaCl, pH 7.5). Cathepsin L (human liver; Calbiochem, La Jolla CA) assays (0.06 mU; 5.0×10^{-5} mg) were conducted in 50 mM sodium acetate, 50 mM NaCl, 0.5 mM EDTA, pH 5.5 buffer supplemented with 10 mM DTT immediately prior to assay preparation. Enzymes were diluted in their respective assay buffer (50 μL final volume) and allowed to equilibrate at 37 °C for 10 min. Assays were conducted in 96 well clear-bottomed black-walled plates (Costar) and initiated by adding **1** or **3** (2 μM in 50 μL of enzyme buffer) to enzyme solutions. Assays were performed with 640 nm Ex and 680 nm Em filters for **1** or 485 nm Ex and 535 nm Em filters for **3** in a fluorometric plate reader (EnVision, Perkin-Elmer) at 37 °C for 30 min. Data were then background subtracted, normalized by enzyme mass (mg) and plotted against time (min). For initial cleavage rates (0−5 min), plots were fitted against a linear regression analysis to obtain the slope. K_m and k_{cat} values were determined using nonlinear regression analysis of probe cleavage rates.

Cell Viability Assays. Cell viability was determined via Alamar Blue assays using a plate reader (EnVision, Perkin-Elmer). Briefly, resazurin was added directly to cell culture wells (final concentration, 40 μM). Cells were incubated for 3 h at 37 °C in a humidified, 5% CO_2 atmosphere and subsequently assayed for resorufin fluorescence at 560 nm Ex and 590 nm Em. Viability of treated cells was expressed as a ratio by subtracting background signal from all values measured and normalizing against respective untreated cells.

Fluorescence Microscopy. High-resolution microscopy was conducted using a Nikon Ti-E PFS microscope equipped with a Nikon 40× 0.95 NA Plan APO objective, a Nikon 60× 1.4 NA Plan APO oil immersion objective, and Prior Lumen 200PRO illumination system with standard DAPI, FITC, Texas Red, and Cy5 filter sets. Images were acquired using a Photometrics CoolSNAP HQ^2 digital camera and images were processed and analyzed using the *Image J* software package (NIH). For colocalization experiments, the commercially available marker ER Tracker Green (Invitrogen) was used for the endoplasmic reticulum, Mito Tracker Green (Invitrogen) for mitochondria, C_6−NBD ceramide (Invitrogen) for the golgi apparatus, LysoTracker Red (Invitrogen) for lysosomes, and H33342 (Invitrogen) for nuclei.

High-throughput fluorescence microscopy was conducted using an InCell 1000 (GE Healthcare) equipped with DAPI, FITC, Cy3, and Cy5 filter sets using a Nikon 20× 0.45 NA S Plan Fluor objective. For time-lapse movies (Movies S1 and S2), a single representative field of view was selected and the time series acquisition option was utilized in the *InCell* software. All images were processed and analyzed using the *Image J* software package (NIH).

Immunohistochemistry. For immunohistochemistry, native and SS-treated RGC-5 cells were fixed using 4% paraformaldehyde solution in PBS buffer for 20 min. Cells were then rinsed 3 times with Tris-buffered saline (TBS; 100 mM Tris, 0.9% NaCl, pH 7.2). For Thy-1 antibody labeling, cells were blocked in a 5% normal goat serum in TBS for 30 min at room temperature. Cells were then exposed to a FITC-Thy-1 primary antibody (Santa Cruz, SC-18914FITC) in blocking buffer overnight at room temperature. For NMDAR1 antibody labeling, cells were blocked for 30 min using 5% normal goat serum solution in TBS. Cells were then exposed to 2.5 μg/mL NMDAR1 primary antibody (BD Biosciences clone 54.1) overnight at room temperature, rinsed with TBS buffer and exposed to a 10 μg/mL solution of goat antimouse secondary antibody conjugated to Alexa Fluor 594 for 45 min at room temperature. For NF70 antibody labeling, cells were blocked for 30 min using 5% normal goat serum solution in TBS. Cells were then exposed to 2 μg/mL NF-L primary antibody (Santa Cruz, SC-58559) for 45 min at room temperature. Following primary antibody labeling, cells were rinsed with TBS buffer and exposed to a 10 μg/mL solution of goat antimouse secondary antibody conjugated to Alexa Fluor 594 in a 1% normal goat serum solution for 45 min at room temperature. Following secondary antibody alone (control), labeled cells were rinsed 3 times with TBS buffer and immediately imaged using fluorescence microscopy.

Toxicity Models. For ionomycin toxicity, RGC-5 cells were exposed to 1, 3, 5, 10, or 20 μM ionomycin in cell growth media for up to 1 h. For SS overdose, cells were exposed to 5 μM SS in cell growth media for 3 h. Following toxin exposure, cells were coincubated with up to 10 μM **3**/Alexa Fluor 647-annexin V or **1**/FITC-annexin V for 30 min and exposed to 500 nM propidium iodide for 5 min. Cells were then gently rinsed 3 times with phenol-free cell growth media and imaged using fluorescence microscopy.

Flow Cytometry. Following treatments, RGC-5 cell cultures were prepared for analysis by removing media, rinsing with PBS buffer, and treating with trypsin (0.25% in PBS) to detach cells from culture wells. Flow cytometry (FACSCalibur,

dx.doi.org/10.1021/bc300036z | *Bioconjugate Chem.* 2012, 23, 1783−1793

BD Biosciences) was performed, and data were analyzed using the *Cell Quest* software package. Analysis was conducted for a minimum of 10 000 counting events and median values of histograms were used to quantify probe uptake.

Endocytosis Inhibition. To globally inhibit endocytosis, RGC-5 cells were incubated at 4 °C for 15 min, exposed to **4** (10 μM) in growth media, and incubated for another 3 h at 4 °C. Cells were then prepared for analysis by flow cytometry. To inhibit specific endocytosis mechanisms, cells were treated with chlorpromazine (30 μM), amiloride (3 mM), colchicine (10 μM), or genistein (200 μM) for 1 h prior to incubation with **4** in growth media. After incubation at 37 °C, 5% CO_2 for 3 h, cells were prepared for analysis by flow cytometry. Probe colocalization experiments with CF-dextran (3000 Da average molecular weight, Sigma-Aldrich) and CF-albumin (Sigma-Aldrich) were conducted under standard cell culture conditions.

RESULTS

Chemical and Biochemical Characterization of CPP Probes. This class of activatable CPP imaging probes is modular in design, comprising a CPP motif, a protease-cleavable peptide sequence, and a flanking quencher–fluorophore pair, each of which can be interchangeably mixed to yield the desired spectral properties.[4] Near-infrared probes with optical properties most favorable for whole body applications *in vivo* have been characterized previously,[5,6] but probes compatible with wavelengths of fluorophores commonly utilized in clinical imaging of the retina (e.g., fluorescein) have not been reported. For this study, the following CPPs were synthesized: KcapQ647 (**1**), Kcap647 (**2**), KcapQ488 (**3**), Kcap488 (**4**), L- and D-KcapTR488 (**5**), KcapTR (**6**), and KcapQ (**7**), (Figure 1). **1**[6] and **2**, a quenched/nonquenched probe pair, emit in the near-infrared window. The non-quenched analogue, **2**, lacks a quencher moiety, affording fluorescence regardless of caspase activity. **3** and **4**, a novel quenched/nonquenched probe pair that emit in the green optical window, incorporated a QSY7-Alexa Fluor 488 quencher–fluorophore pair instead of the QSY21-Alexa Fluor 647 pair. Alexa Fluor 488 is efficiently quenched when paired with QSY7. **4** was the nonquenched analogue of **3**. **5**, a novel dual fluorophore CPP, which contained Texas Red (TR) and Alexa Fluor 488, **6**, a nonquenched probe, which emitted in the red, and **7**, which contained only a quencher moiety, were synthesized using analogous synthetic strategies. All orthogonal conjugation reactions of fluorophores and quenchers with the peptide backbone were monitored by UV–vis spectroscopy, and confirmed by mass spectrometry and amino acid analysis.

For **3**, the quencher–fluorophore combination rendered a new probe potentially compatible with current clinical retinal imaging devices equipped for detection of fluorescent reporters in the visible spectrum of light, specifically bandwidths similar to carboxyfluorescein. The absorption spectrum of **3** revealed a substantial absorbance increase at 570 nm due to conjugation of QSY7 to the peptide backbone as compared to Alexa Fluor 488 alone conjugated to peptide (λ_{max} = 495 nm) (Figure 2A). The extinction coefficient at λ_{max} (496 nm) for **3** was 69 500 M^{-1} cm^{-1} via UV–vis spectroscopy coupled with amino acid analysis. The fluorescence quenching efficiency of **3** was high as determined by fluorometry following a 60 min incubation at 37 °C in either deionized water, PBS buffer, phenol-free DMEM media with 10% heat-inactivated fetal bovine serum, or 100% heat-inactivated fetal bovine serum (99%, 98%, 95%, and 95%,

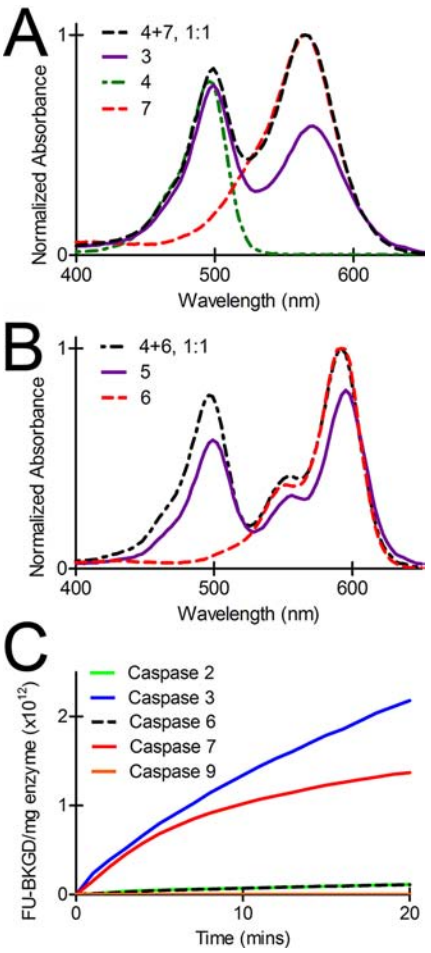


Figure 2. UV–vis absorption spectra of an eqimolar solution of **4** + **7** (black), **3** (purple), **4** (green), and **7** (red). (A). UV–vis absorption spectra of an equimolar solution of **4** + **6** (black), **5** (purple), and **6** (red). (B). Enzyme assays demonstrating the selectivity of **3** (1 μM) cleavage by recombinant caspases. Assays were normalized to mg of caspase for each enzyme (C).

respectively). **3** displayed a ratio of 1.3-fold between the absorbances at 496 and 570 nm, a significant blue-shift when compared to an equimolar solution of **4** and **7** wherein the ratio of the λ_{max} for the individual probes was 0.8 (Figure 2A), providing evidence for an H-dimer-mediated quenching mechanism.[20] The absorption spectrum of **5** revealed a substantial absorbance increase at 595 nm upon conjugation of Texas Red to the peptide backbone compared to Alexa Fluor 488 alone conjugated to peptide (Figure 2B). **5** displayed an extinction coefficient of 76 586 M^{-1} cm^{-1} at λ_{max} 595 nm with a ratio of 0.7-fold between the peak absorbances at 499 and 595 nm, compared to an equimolar solution of **4** and **6** wherein the ratio between the λ_{max} of **4** and **6** (592 nm) was observed to be 0.8. This shift in λ_{max} ratio and a 3 nm red shift in the absorbance spectra provided evidence for J-dimer formation between the Alexa Fluor 488 and Texas Red fluorophores of this intact probe.

Recombinant caspase assays were performed using continuous fluorometric analysis. To compare initial cleavage rates of **3** by each of the caspases 2, 3, 6, 7, and 9, results were normalized to mg of enzyme (Figure 2C) and rates of **3** cleavage determined by linear fit. Caspase 3 cleaved **3** with an initial cleavage rate of 2 × 10^{11} FU min^{-1} mg^{-1}, while caspases

dx.doi.org/10.1021/bc300036z | *Bioconjugate Chem.* 2012, 23, 1783–1793

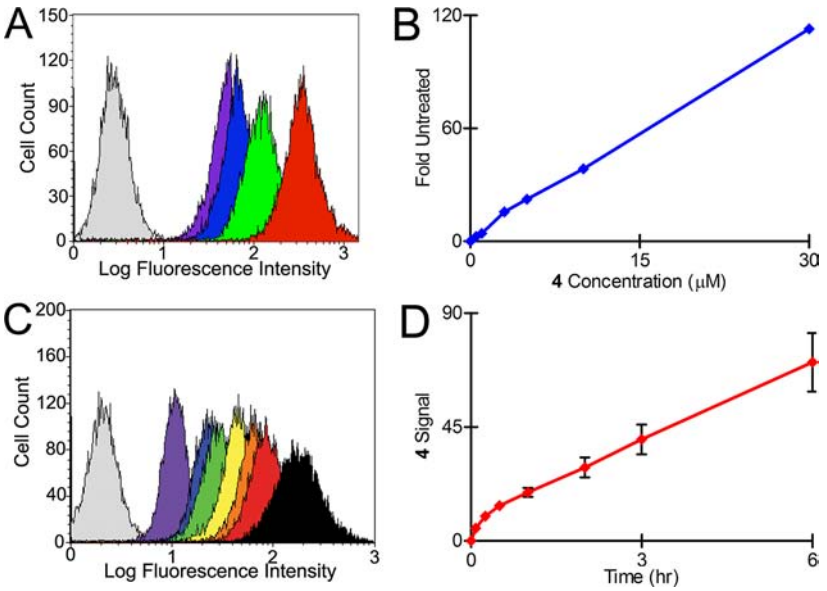


Figure 3. Flow cytometry histograms of native RGC-5 cells exposed to 0 (gray), 1 (purple), 5 (blue), 10 (green), and 30 (red) μM **4** for 3 h (A). Plot of **4** signal versus concentration in native RGC-5 cells (B). Flow cytometry histograms of native RGC-5 cells exposed to 10 μM **4** for 0 (gray), 0.08 (purple), 0.25 (blue), 0.5 (green), 1 (yellow), 2 (orange), 3 (red), and 6 (black) hours (C). Plot of **4** signal versus time in native RGC-5 cells (D).

7 and 6 cleaved **3** at 1×10^{11} FU min^{-1} mg^{-1} and 1×10^{10} FU min^{-1} mg^{-1}, respectively. Cleavage of **3** by initiator caspases 2 and 9 were 9×10^{9} FU min^{-1} mg^{-1} and 1×10^{7} FU min^{-1} mg^{-1}, respectively. Off-target proteases granzyme B (4×10^{5} FU min^{-1} mg^{-1}) and trypsin (1×10^{3} FU min^{-1} mg^{-1}) showed minimal fluorescence activation, providing further evidence of specificity. These data confirmed that **3** was specifically cleaved by effector caspases, preferentially caspase 3, similar to other probes of this class conjugated to different quencher–fluorophore pairs.[5,6]

Characterization and Differentiation of RGC-5 Cells. To determine the mechanism of cell penetration and subcellular localization kinetics, matched quenched/non-quenched probes were characterized in an *in cellulo* model of RGC neurodegeneration. RGC-5 cells are mouse retinal ganglion cells virally transformed by the ψ2 E1A virus for *in cellulo* experimental models of RGC degeneration.[21] These cells were characterized by RT-PCR and IHC analysis of various markers representative of retinal ganglion cells, and were originally reported to be sensitive to glutamate-induced excitotoxicity upon differentiation with succinyl concanavalin A.[22] Additionally, this cell line undergoes rapid differentiation into a more distinct neurite-like morphology with upregulation of neuronal markers upon low-dose treatment with the broad spectrum kinase inhibitor staurosporine (SS).[23] As use of the RGC-5 cell line increased, greater resistance to glutamate toxicity was reported over time.[24−26] To characterize the RGC-5 cells used for our studies, we subjected this cell line to an array of experiments to confirm differentiation upon SS exposure and to assess neuronal marker expression.

With 0.5 μM SS, changes in cell morphology consistent with differentiation were rapid, primarily occurring within 1 h at 37 °C. The distinct morphological alterations observed in RGC-5 cells, such as a change in soma from flat and polygonal to round and elevated as well as formation of multiple neurite projections from the soma, were consistent with previous findings.[23] Differentiation was easily monitored via serial imaging by bright field microscopy, enabling production of time lapse movies of the differentiation process (Figure S1 and Movie S1). Differentiation progressed less rapidly at room temperature as completion of morphological changes required approximately 2 h. Exposure to SS at concentrations exceeding 2 μM was toxic, causing blebbing and disruption of neurite morphology.

Immunohistochemistry documented the expression of several neuronal markers in native and SS-differentiated RGC-5 cells. Immunohistochemistry of NF70, Thy-1, and NMDAR1, markers of mature RGCs, was determined by fluorescence microscopy. NF70, Thy-1, and NMDAR1 antibody labeling in both native and SS-treated cells showed similar labeling intensity when judged qualitatively between cell states (Figures S2, S3). Semiquantitative ROI analysis with *Image J* software revealed approximately a 3-fold increase in fluorescence associated with NF70, 8-fold increase with Thy-1, and 2-fold with NMDAR1 for both cell states when compared to control cells (secondary antibody exposure alone for NF70 and NMDAR1; no antibody exposure for Thy1). Labeling patterns were diffuse throughout the cell body, consistent with previous findings.[23] Thus, we concluded that our RGC-5 cells retained a neuronal phenotype appropriate for further analysis.

Characterization of Probe Uptake in RGC-5 Cell Culture Models. The optimal concentration range of CPP probe for use in RGC-5 cells was determined by Alamar Blue assays to monitor cell viability after prolonged exposure to the quenched probe **1**. Increasing concentrations of **1** were added to a 96-well plate containing RGC-5 cells at 70% confluence. Under these conditions, **1** showed only a 7% loss of viability after a 24 h exposure at 19 μM and a 39% loss of cell viability at 19 μM after a 72 h exposure. For comparison, a first generation probe, TcapQ647, which differs only in the CPP sequence, was tested under similar conditions. Cells exposed to TcapQ647 showed a loss of 40% viability at 20 μM after 24 h, and >90% loss of viability at 10 μM after 72 h (Figure S4). Therefore, probes were typically used at 10 μM or less.

First, to investigate the trafficking pathways underlying probe uptake, we utilized nonquenched probes designed to be constantly fluorescent regardless of caspase activity. Flow

dx.doi.org/10.1021/bc300036z | *Bioconjugate Chem.* 2012, 23, 1783−1793

cytometry of RGC-5 cells exposed to nonquenched **4** (10 μM) showed a concentration-dependent increase in probe uptake (Figure 3A,B) as well as a time-dependent increase in probe uptake over a 6 h interval (Figure 3C,D). When compared to Tcap488, a nonquenched version of our previous generation of CPP probes, **4** showed a 25-fold lower uptake under equivalent conditions of exposure (10 μM for 3 h). Imaging by fluorescence microscopy under identical conditions confirmed localization of probe within punctate foci localized to the cytosol of RGC-5 cells. To further characterize CPP probes in RGC-5 cells, native and SS-differentiated RGC5 cells were exposed to the nonquenched probes **2** or **4** or coexposure of each, and examined by multispectral high-resolution fluorescence microscopy. Both native (Figure 4) and differentiated

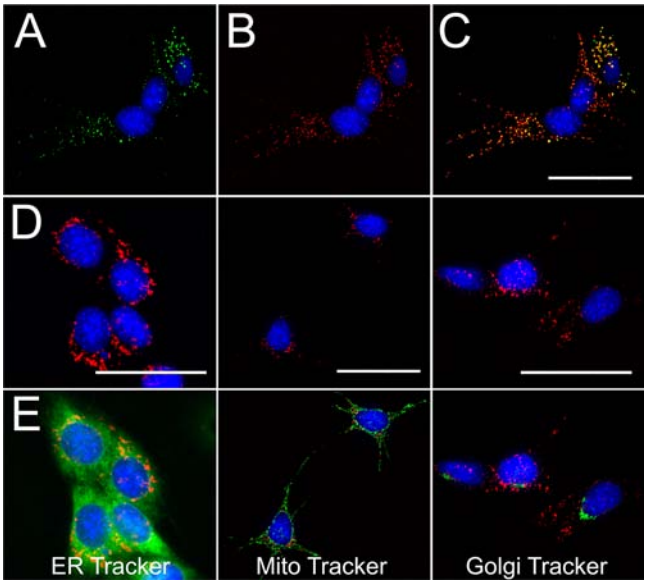


Figure 4. Fluorescence microscopy images of native RGC-5 cells following a 3 h coincubation with 10 μM **4** (A) and 10 μM **2** (B). Overlay of panels A and B (C) showing colocalization of each probe. Images of native RGC-5 cells following coexposure to **2** (10 μM, 3 h) (row D) and ER Tracker Green (1 μM, 30 min) (E, left), Mito Tracker Green (50 nM, 30 min) (E, middle), or C_6-ceramide-NBD (Golgi Tracker, 2.5 μM, 30 min) (E, right); overlay image of fluorescence fields (row E). Cells were counterstained with H33342 (pseudocolor blue) to show subcellular distribution relative to nuclei (50 μm scale bars).

RGC-5 cells demonstrated rapid and distinct probe uptake with a punctate distribution pattern. Cells simultaneously exposed to **2** and **4** displayed the identical subcellular localization pattern demonstrating that different fluorophores had no observable effect on the initial subcellular distribution of this class of CPP probes (Figure 4C). Similarly, cells simultaneously exposed to **4** and Tcap647 also displayed the same subcellular localization, providing evidence that these fluorophores, when appended to either the HIV-Tat cell penetrating sequence or the SV40 NLS, internalized into RGC-5 cells via the same trafficking pathways (Figure S5).

Colocalization experiments were then conducted with **2** and carboxyfluorescein (CF)-labeled albumin or dextran, markers of cell surface protein binding and fluid phase-mediated endocytosis, respectively.[27−29] High-resolution fluorescence microscopy of RGC-5 cells revealed strong colocalization of **2** with CF-albumin (Figure S6) and nearly identical colocalization with CF-dextran. High-thorughput fluorescence microscopy of RGC-5 cells cotreated with **2** and these endocytic markers followed by colocalization analysis via *Image J* produced Pearson's coefficients[30] of 0.732 and 0.873 for CF-dextran and CF-albumin, respectively, in native RGC-5 cells, while Pearson's coefficients of 0.639 and 0.831 were obtained for differentiated RGC-5 cells. In cells exposed to **2**, additional costaining experiments for endoplasmic reticulum, mitochondria, and golgi apparatus showed little if any colocalization of probe distribution with these subcellular organalles (Figure 4D,E). Similar results were obtained with SS-differentiated RGC-5 cells (Figure S7). Overall, these experiments provided evidence that the CPP probes were internalized into RGC-5 cells via endocytic mechanisms and retained in endosomal compartments.

The contribution of various endocytic pathways to probe uptake was further characterized by exposing RGC-5 cells to **4** in the presence of known inhibitors of endocytic processes[31] followed by quantification with flow cytometry (Table 1). The

Table 1. Relative Uptake of Kcap488 (4) into Native and SS-Differentiated RGC-5 Cells upon Treatment with Inhibitors of Endocytosis[a]

		RGC-5 cell state	
treatment	inhibition target	native	SS-differentiated
4 (10 μM) alone	-	1	1
4 °C incubation	general endocytosis	0.08 ± 0.03	-
Chloropromazine (30 μM)	clathrin-mediated	0.71 ± 0.05	0.74 ± 0.06
Amiloride (3 mM)	pinocytosis	0.58 ± 0.12	0.59 ± 0.12
Colchicine (10 μM)	pinocytosis	0.54 ± 0.05	0.55 ± 0.9
Genestein (200 μM)	caveolin-mediated	0.43 ± 0.03	0.65 ± 0.04

[a]Cells were incubated with inhibitors for 1 h prior to, and for the duration of probe exposure (10 μM **4** for 3 h), and probe uptake quantified by flow cytometry. Values are the median ± standard deviation obtained from three independent experiments normalized to **4** alone; n = 3 samples per treatment.

first method involved incubation of cell cultures at 4 °C, which blocked over 90% of the uptake of **4**. More detailed mechanistic insight was gained by exposing RGC-5 cells for 1 h to compounds that inhibit specific endocytic processes prior to addition of **4**. Chlorpromazine inhibits clathrin-mediated endocytosis, while genistein inhibits caveolin-mediated mechanisms.[32] Cells were also exposed to amiloride[33] and colchicine,[34] each an inhibitor of pinocytosis. All compounds showed partial inhibitory effects on uptake, but taken together, the data in Table 1 indicated that **4** was primarily transported by caveolin-mediated endocytosis in native cells, while probe uptake was more dependent on pinocytosis in SS-differentiated cells.

As would be expected for quenched probes prior to activation, imaging healthy RGC-5 cells by fluorescence microscopy following a 2 h exposure to **1** yielded no significant probe signal. However, nontarget activation of CPP-based probes has been previously reported with evidence of caspase-activatable probes undergoing lysosomal degradation via proteases such as cathepsins and legumains.[35−37] Degradation of the probe backbone could disrupt quencher−fluorophore interactions leading to nontarget probe signal. To evaluate potential lysosome-mediated degradation, fluorescence micros-

copy colocalization experiments after prolonged exposure of healthy RGC-5 cells to probe **1** (3 h) as well as biochemical characterization of cathepsin-mediated activation of **1** were conducted. High-resolution fluorescence microscopy of healthy native and SS-differentiated RGC-5 cells showed the delayed appearance of punctate signal with colocalization between LysoTracker-labeled compartments and activated **1** at 3 h (Pearson's coefficients of 0.566 and 0.612 for native and differentiated cells, respectively; Figure S8). To further characterize this delayed activation, cathepsin-mediated cleavage of **1** was studied using human cathepsin L and compared with cleavage via caspase 3 *in vitro*. Using nonlinear regression analysis of probe cleavage rates, K_m and k_{cat} values were determined (Table 2). These data confirmed that, while

Table 2. Kinetic Parameters of KcapQ647 (1) Cleavage

enzyme	K_m (nM)	k_{cat} (FU min^{-1} μM^{-1})	k_{cat}/K_m ((FU min^{-1} μM^{-1})/nM)
Caspase 3	2404	1 046 000	435
Cathepsin L	3872	375 000	97

executioner caspases were preferred for activation of our probes, compartmentalized nontarget signal was possible due to lysosomal degradation with prolonged probe exposure to healthy cells.

Characterization of Probe Activation in RGC-5 Cells. Excitotoxicity initiates apoptosis via excessive cellular calcium influx mediated by overstimulation of specific receptors, such as the NMDA or AMPA receptors.[38] Using the quenched probe, **1**-mediated detection of apoptosis was first attempted via NMDA and glutamate excitotoxicity models; however, both native and SS-differentiated RGC-5 cells displayed no loss in viability or probe activation at concentrations up to 5 mM and exposure times up to 48 h (data not shown). As an alternative to NMDA and glutamate excitotoxicity, we evaluated **1**- and **3**-mediated detection of apoptosis via an ionomycin toxicity model.[39] Ionomycin is a calcium ionophore commonly used to raise intracellular calcium levels and can be used to trigger cell death in a manner similar to excitotoxicity. Native and SS-differentiated RGC-5 cells were treated with 3 μM ionomycin followed by exposure to 10 μM **3** for 30 min. High-resolution fluorescence microscopy revealed distinct probe activation in dying cells within this time frame. CPP probe activation was confined to the cytosolic compartment and at no time after ionomycin treatment were endosomes observed (Figures 5 and SI Figure S9). Thus, quenched probe escaped from endosomes into the cytosol during the course of apoptosis rather than being activated within endosomes prior to escaping. Additionally, apoptosis was induced in RGC-5 cells by an extended exposure to SS. Herein, cells were incubated with SS for 3 h at 5 μM, exposed to **3** for 30 min and then imaged (Figure 6). Importantly, independent confirmation of apoptosis was obtained with annexin V costaining. Most cells displaying probe activation were also bound by Alexa Fluor 647-annexin V, with occasional cells showing only annexin V, a marker of phosphatidylserine externalization, an event generally found prior to effector caspase activation in the apoptotic cascade (Figure 5B). Identical results were obtained in this model with **1** and FITC-annexin V staining (data not shown). Notably, in both models of cell death, **1** and **3** were also activated in apoptotic bodies. These cell fragments were readily visualized using combined high-resolution fluorescence and bright field

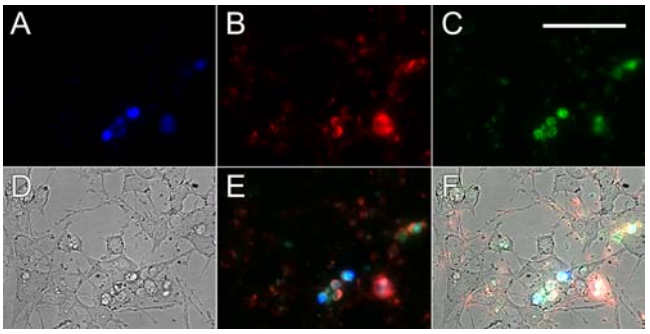


Figure 5. Fluorescence microscopy images of propidium iodide (500 nm) permeable (A) Alexa Fluor 647-annexin V-bound (B) and **3**-labeled (C) RGC-5 cells following a 1 h exposure to 10 μM ionomycin. Bright-field microscopy image of ionomycin-treated RGC-5 cells (D). Overlay of panels A–C showing KcapQ488 (pseudocolor green) activation and colocalization with propidium iodide (pseudocolor blue) and Alexa Fluor 647-annexin V (pseudocolor red) stained cells (E). Overlay of panels D and E (F) (50 μm scale bar).

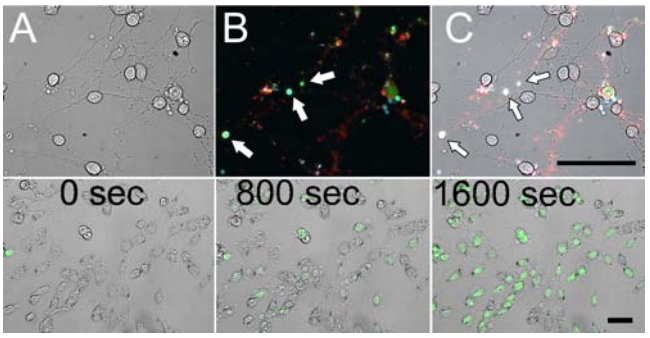


Figure 6. Transmitted light image of RGC-5 cells undergoing SS-induced apoptosis (5 μM SS, 3 h) (A). Overlay of fluorescence microscopy images of RGC-5 cells undergoing SS-induced apoptosis with concurrent propidium iodide staining (pseudocolor blue), **3** (10 μM) activation (pseudocolor green), and Alexa Fluor 647-annexin V staining (pseudocolor red) (B). Overlay of panels A and B (C). Arrows denote apoptotic bodies (B and C). Transmitted light and fluorescence microscopy overlay images taken from a time lapse movie of **3** (5 μM) activation in RGC-5 cells following exposure to ionomycin (20 μM) (bottom row). Times correspond to movie acquisition time (sec). Image acquisition began 1 min following ionomycin exposure (50 μm scale bars).

microscopy following costaining with fluorescent annexin V conjugates and propidium iodide (Figure 6). Furthermore, when cells were preloaded with **3** (5 μM) for 30 min and then, in the continued presence of quenched probe, treated with ionomycin (20 μM) and monitored for 1 h using real-time fluorescence microscopy, distinct intracellular activation of the probe was observed within the cytosol of individual cells starting at ~15 min. Sequential image acquisition enabled generation of time-lapse movies showing both morphological changes of the cells undergoing apoptosis and concurrent activation of **3** (Figure 6, bottom row and Movie S2).

Our data thus far demonstrate that CPP probes were internalized and retained in endocytic compartments within healthy cells. However, effector caspases are thought to reside entirely within the cytosol.[40−42] Thus, in the course of the apoptotic cascade, endosomal or endosomally associated release mechanisms[43−47] must enable probe access to the active pool of caspases. To temporally monitor CPP probe released into the cytosol, and the fate of CPP fragments after

dx.doi.org/10.1021/bc300036z | *Bioconjugate Chem.* 2012, 23, 1783−1793

cleavage, **5** was designed and synthesized to study probe trafficking in both healthy and apoptotic RGC-5 cells by multispectral fluorescence microscopy. This novel probe, which incorporated a Texas Red fluorophore in place of the QSY7 quencher, allowed concurrent multispectral tracking of the probe in both its intact and cleaved states. Live RGC-5 cells were exposed to **5** for 3 h, rinsed to remove exogenous probe, and examined. Healthy cells again displayed punctate, endosomal distribution patterns of the probe concurrently observable with both spectral windows, as expected for the intact probe and consistent with single channel analysis of RGC-5 cells exposed to either **2** or **4** alone (Figure 7, row A).

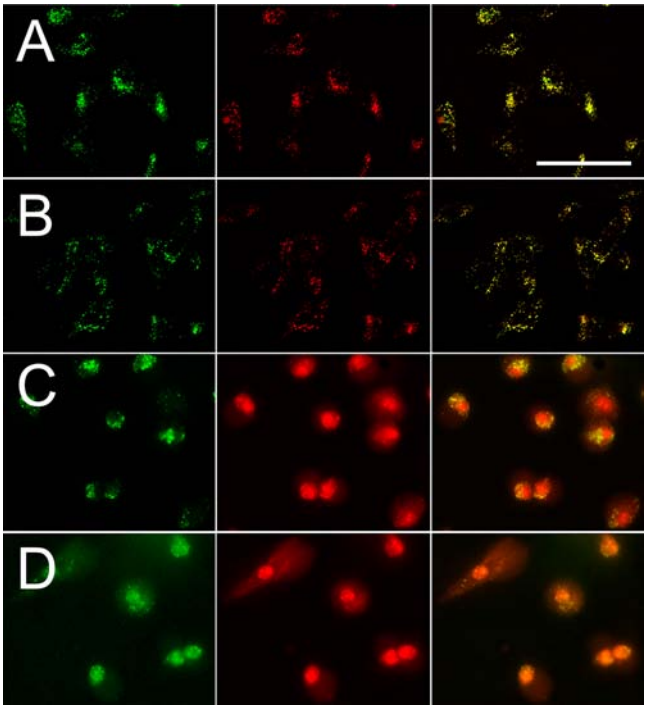


Figure 7. Fluorescence microscopy images of **5** (12 μM) distribution in native RGC-5 cells (row A); D-**5** (12 μM) distribution in native RGC-5 cells (row B); **5** (12 μM) distribution in ionomycin-treated (10 μM) native RGC-5 cells (row C); D-**5** (12 μM) distribution in ionomycin-treated (10 μM) native RGC-5 cells (row D). Left, fluorescence field for the Alexa Fluor 488-labeled C-terminus (pseudocolored green); middle, fluorescence for the Texas Red-labeled N-terminus (pseudocolored red); right, overlays of Alexa Fluor 488 and Texas Red images (50 μm scale bar).

Subsequently, cells were exposed to 10 μM ionomycin for 1 h. Examination by real-time fluorescence microscopy revealed a redistribution of **5** from endosomes to the cytosol wherein both C- and N-terminal fragments were observed. As expected by the conjugation design, the nucleus contained only the N-terminus with the progression of cell death (Figure 7, row C). Localization of the N-terminal fragment to the nucleus was expected as this fragment incorporated the SV40 large T antigen NLS. Importantly, there was no evidence for the asymmetric loss of fragments within endosomes, such as differential localization of probe signal between spectral windows, or transport into nonvesicular compartments prior to the appearance of cytosolic activation events during the apoptotic cascade (Figure 7, row C, right). Additionally, distribution of an all D-amino acid (cleavage resistant) peptide, D-**5**, displayed punctuate colocalization of signal in healthy cells (identical to **5**) with a cytosolic and concurrent nuclear distribution in both spectral windows in ionomycin-exposed cells (Figure 7, rows B,D). Following endosomal release, intact D-**5** was transported predominantly to the nucleus by the NLS. Similar results were obtained with SS-differentiated RGC-5 cells (Figure S10). Together, these data demonstrated that, during the cascade of apoptosis, CPP probes were first released from the endosomes to gain access to the cytosol and in turn were accessible to activated caspases as apoptosis progressed. Thus, endosomal release appears temporally coupled to effector caspase activation. Furthermore, the dual-label cleavable probe **5** also afforded a novel multispectral method to detect apoptosis by analysis of differential red/green ratios between the cytosol and nucleus.

DISCUSSION

These experiments provided validation of intramolecular-quenched, caspase-activatable optical imaging peptides as apoptosis biosensors for use in live cell models of RGC degeneration. Apoptosis assays are routinely used in cell biology research and in the drug discovery process. These typically sense key events in the apoptotic cascade, such as externalization of phosphatidylserine,[48−50] activation of caspases,[4,6,35−37,51] DNA fragmentation,[52] and depolarization of mitochondrial membrane potential.[53] While all of these methods have application in a variety of studies, each has its own limitations, such as cumbersome labeling conditions (annexin V), limited selectivity between necrotic and apoptotic cells (annexin V, depolarization probes, DNA fragmentation), limited access to active caspases within intact cells (non-permeant caspase substrates), or poor optical properties for analysis in real-time or *in vivo* (commercial caspase substrates, e.g., Ac-DEVD-AMC and Z-DEVD-R110). **1** and **3** facilitated detection of cells undergoing apoptosis in real-time using high-throughput imaging methods because the quenched probes could be introduced directly onto cells in cell culture media, readily internalized into cells, selectively activated by executioner caspases and imaged with minimal sample preparation.

Delivery of optically silent, activatable probes to the interior of living cells facilitated analysis by providing enhanced signal-to-noise and retention of the spatial distribution of probe signal. The strategy was scalable, enabling apoptosis detection in both population- and single-cell-based assays in real-time. The new quenched CPP probe, **3**, which incorporated a QSY7-Alexa Fluor 488 quencher−fluorophore pair, showed evidence of blue-shifted spectral changes similar to previously characterized probes containing QSY21-Alexa Fluor 647 pairs.[5,6] **3** also displayed quenching efficiencies of 99% in deionized water and 95% in 10% serum, while previously reported nucleotide-based probes incorporating QSY7-Alexa Fluor488 pairs optimized for FRET and static/contact-mediated quenching demonstrated 86% and 95% quenching efficiencies, respectively.[54] Overall, the blue-shifted spectral properties and high quenching efficiency observed with the QSY7-Alexa Fluor 488 pair in **3** are characteristic of an H-dimer mediated quenching mechanism.[54,55]

The data showing the preferential cleavage of **3** by caspase 3 > caspase 7 > caspase 6 ≫ initiator caspases, and the lack of activity in the presence of granzyme B or trypsin were consistent with previous probes of this class, indicating that the identity of the quencher−fluorophore pair did not impact biochemical specificity. We previously published that all D-

amino acid probes of this class as well as addition of caspase inhibitors blocked activation,[5,6] providing further evidence of specificity. Recent studies have demonstrated cleavage of activatable peptide probes via cathepsins and legumains,[35−37] as observed with the present CPP probes. While this can generate nontarget signal, short exposure times can circumvent undesired activation. Changes in probe architecture such as lysosomally inactivated fluorophores and alternative caspase cleavage sequences can be explored to further diminish nontarget signal. Additionally, whether nontarget-mediated activation of these CPP probes occurs *in vivo* remains to be explored.

Alexa Fluor 488 has similar excitation and emission profiles as carboxyfluorescein, and thus, **3**, **4**, and **5** are more compatible with instrumentation such as microscopes, plate readers, and flow cytometers that are not equipped with NIR optical systems. These wavelengths are also commonly utilized in clinical retinal imaging devices, an area of potential application of these probes. Broadly, the availability of a variety of caspase-activatable CPP probes in various emission windows may facilitate multispectral analysis when imaged in the presence of other reagents and labeled antibodies.

Live cell cytotoxicity assays demonstrated that **1** and **3** were specifically activated in cells undergoing apoptosis and enabled real-time fluorescence imaging of programmed cell death. Neuronal excitotoxicity models were attempted with NMDA and glutamate toxicity; however, RGC-5 cells were unresponsive to these treatments, consistent with literature reports of loss of sensitivity of RGC-5 cells to these compounds.[21] Additionally, NMDA and glutamate toxicity models (up to 5 mM each) were attempted with combinations of BSO (up to 200 μM),[26] D-serine (up to 100 mM),[56,57] and glycine (up to 100 mM)[58] with no significant loss in cell viability (data not shown). However, apoptosis and probe activation were readily observed upon treatment with ionomycin (Figures 5−7 and SI Figures S9 and S10), SS (Figure 6), or doxorubicin (data not shown). The capacity for this probe to detect apoptosis in single cells in real-time using a multiwell plate format will be useful for high-throughput assays, as probe activation is rapid and does not require rinse steps to remove exogenous or nonspecific signal. Additionally, our nonquenched probes **2**, **4**, and **5** allowed for detailed examination of probe behavior *in cellulo*. These probes were amenable to live cell studies, as they could be introduced directly into cell culture media without any special preparation, and performance was not hindered by media components, such as serum, simplifying experimental conditions and sample preparation.

The pharmacological inhibition of endocytic mechanisms which impacted accumulation levels of **4** lends further understanding of how these probes were internalized by cells, while ionomycin- and SS-induced apoptosis models with **5** demonstrated how CPP probes were released and gained access to active caspases during cell death processes. Mechanisms underlying endosomal permeability during the progression of apoptosis are not fully understood, but may involve several distinct mechanisms that are likely engaged in a death stimulus- and cell-type-dependent fashion as with other organelles.[43−47] Thus, the dual-labeled probe **5** may serve as a valuable tool for further investigations into mechanisms of endosomal release. The multispectral characteristics of **5** could be used in conjunction with other molecular markers and imaging methodologies to further characterize distinct steps of endosomal release associated with apoptosis during organ development and disease.

In summary, we have demonstrated the utility of caspase-activatable cell-penetrating optical imaging peptides using high-throughput and high-resolution live cell microscopy techniques. These probes can selectively identify cells undergoing apoptosis in real-time allowing for detailed examination of cell death processes *in cellulo*. Future experiments with this toolbox of probes will focus on further understanding endosomal permeability and trafficking behavior during cell death processes as well as optimization of probe use for monitoring apoptosis *in vivo*.

■ ASSOCIATED CONTENT

Supporting Information

Supplementary figures and movies further document RGC-5 cell line characterization, CPP probe colocalization, and caspase-activatable CPP probes in an ionomycin-induced cell death model. This material is available free of charge via the Internet at http://pubs.acs.org.

■ AUTHOR INFORMATION

Corresponding Author

*Tele: 314-362-9356. Fax: 314-362-0152. E-mail: piwnica-wormsd@mir.wustl.edu.

Notes

The authors declare no competing financial interest.

■ ACKNOWLEDGMENTS

Special thanks to Seth Gammon, Vijay Sharma, Jothilingam Sivapackiam, and Sundaram Guruswami for valuable discussions, as well as the High-Throughput Screening Core of the Molecular Imaging Center and Siteman Cancer Center at Washington University for microscopy use and support (P30 CA091842). This work was supported by NIH grants F32 EY20051-01 (J.R.J.), NIH R01 EY019587 (D.P.-W.), and P50 CA94056 (D.P.-W.). J.R.J., E.M.B., and D.P.-W. designed research; J.R.J., B.K., and J.M. performed research; J.R.J and D.P.-W. contributed new reagents/analytic tools; J.R.J., J.M., and D.P.-W. analyzed data; J.R.J. and D.P.-W. wrote the paper; and J.R.J., B.K., E.M.B., and D.P.-W. edited the paper.

■ ABBREVIATIONS

SS, Staurosporine; CPP, cell-penetrating peptide; RGC, retinal ganglion cell

■ REFERENCES

(1) Thornberry, N., and Lazebnik, Y. (1998) Caspases: enemies within. *Science 281*, 1312−1316.

(2) Talanian, R. V., Quinlan, C., Trautz, S., Hackett, M. C., Mankovich, J. A., Banach, D., Ghayur, T., Brady, K. D., and Wong, W. W. (1997) Substrate specificities of caspase family proteases. *J. Biol. Chem. 272*, 9677−9682.

(3) Salvesen, G. S., and Riedl, S. J. (2008) Caspase mechanisms, in: *Programmed Cell Death in Cancer Progression and Therapy*, Khosravi-Far, R., and White, E., Eds., pp 13−23, Springer, New York.

(4) Bullok, K., and Piwnica-Worms, D. (2005) Synthesis and characterization of a small, membrane-permeant, caspase-activatable far-red fluorescent peptide for imaging apoptosis. *J. Med. Chem. 48*, 5404−5407.

(5) Bullok, K. E., Maxwell, D., Kesarwala, A. H., Gammon, S., Prior, J. L., Snow, M., Stanley, S., and Piwnica-Worms, D. (2007) Biochemical and in vivo characterization of a small, membrane-permeant, caspase-

activatable far-red fluorescent peptide for imaging apoptosis. *Biochemistry 46*, 4055−4065.
(6) Maxwell, D., Chang, Q., Zhang, X., Barnett, E., and Piwnica-Worms, D. (2009) An improved cell-penetrating, caspase-activatable, near-infrared fluorescent peptide for apoptosis imaging. *Bioconjugate Chem 20*, 702−709.
(7) Thornberry, N. A., Rano, T. A., Peterson, E. P., Rasperi, D. M., Timkey, T., Garcia-Calvo, M., Houtzageri, V. M., Nordstromi, P. A., Royi, S., Vaillancourti, J. P., Chapman, K. T., and Nicholsoni, D. W. (1997) A combinatorial approach defines specificities of members of the caspase family and granzyme B: functional relationships established for key mediators of apoptosis. *J. Biol. Chem. 272*, 17907−17911.
(8) Lien, S., Pastor, R., Sutherlin, R., and Lowman, H. (2004) A substrate-phage approach for investigating caspase specificity. *Protein J. 23*, 413−425.
(9) Barnett, E. M., Elangovan, B., Bullok, K. E., and Piwnica-Worms, D. (2006) Selective cell uptake of modified Tat peptide-fluorophore conjugates in rat retina in ex vivo and in vivo models. *Invest. Ophthalmol. Vis. Sci. 47*, 2589−2595.
(10) Barnett, E., Zhang, X., Maxwell, D., Chang, Q., and Piwnica-Worms, D. (2009) Single-cell imaging of retinal ganglion cell apoptosis with a cell-penetrating, activatable peptide probe in an *in vivo* glaucoma model. *Proc. Natl. Acad. Sci. U.S.A. 106*, 9391−9396.
(11) McDunn, J., Muenzer, J., Dunne, B., Zhou, A., Yuan, K., Hoekzema, A., Hilliard, C., Chang, K., Davis, C., McDonough, J., Hunt, C., Grigsby, P., Piwnica-Worms, D., and Hotchkiss, R. (2009) An anti-apoptotic peptide improves survival in lethal total body irradiation. *Biochem. Biophys. Res. Commun.,*.
(12) McKinnon, S. J. (2003) Glaucoma: ocular Alzheimer's disease? *Front. Biosci. 8*, s1140−1156.
(13) Qu, J., Wang, D., and Grosskreutz, C. L. (2010) Mechanisms of retinal ganglion cell injury and defense in glaucoma. *Exp. Eye Res. 91*, 48−53.
(14) Garcia-Valenzuela, E., Shareef, S., Walsh, J., and Sharma, S. (1995) Programmed cell death of retinal ganglion cells during experimental glaucoma. *Exp. Eye Res. 61*, 33−44.
(15) Nickells, R. (1999) Apoptosis of retinal ganglion cells in glaucoma: an update of the molecular pathways involved in cell death. *Surv. Ophthalmol. 43*, S151−161.
(16) Kalapesi, F. B., Coroneo, M. T., and Hill, M. A. (2005) Human ganglion cells express the alpha-2 adrenergic receptor: relevance to neuroprotection. *Br. J. Ophthalmol. 89*, 758−63.
(17) Russo, R., Berliocchi, L., Adornetto, A., Varano, G. P., Cavaliere, F., Nucci, C., Rotiroti, D., Morrone, L. A., Bagetta, G., and Corasaniti, M. T. (2011) Calpain-mediated cleavage of Beclin-1 and autophagy deregulation following retinal ischemic injury in vivo. *Cell Death Dis. 2*, e144.
(18) Ju, W. K., Kim, K. Y., Duong-Polk, K. X., Lindsey, J. D., Ellisman, M. H., and Weinreb, R. N. (2010) Increased optic atrophy type 1 expression protects retinal ganglion cells in a mouse model of glaucoma. *Mol. Vis. 16*, 1331−42.
(19) Agar, A., Li, S., Agarwal, N., Coroneo, M. T., and Hill, M. A. (2006) Retinal ganglion cell line apoptosis induced by hydrostatic pressure. *Brain Res. 1086*, 191−200.
(20) Ogawa, M., Kosaka, N., Choyke, P. L., and Kobayashi, H. (2009) H-type dimer formation of fluorophores: a mechanism for activatable, in vivo optical molecular imaging. *ACS Chem. Biol. 4*, 535−46.
(21) Van Bergen, N. J., Wood, J. P., Chidlow, G., Trounce, I. A., Casson, R. J., Ju, W. K., Weinreb, R. N., and Crowston, J. G. (2009) Recharacterization of the RGC-5 retinal ganglion cell line. *Invest. Ophthalmol. Vis. Sci. 50*, 4267−72.
(22) Krishnamoorthy, R., Agarwal, P., Prasanna, G., Vopat, K., Lambert, W., Sheedlo, H., Pang, I., Shade, D., Wordinger, R., Yorio, T., Clark, A., and Agarwal, N. (2001) Characterization of a transformed rat retinal ganglion cell line. *Brain Res. Mol. Brain Res. 86*, 1−12.
(23) Frassetto, L., Schlieve, C., Lieven, C., Utter, A., Jones, M., Agarwal, N., and Levin, L. (2006) Kinase-dependent differentiation of a retinal ganglion cell precursor. *Invest. Ophthalmol. Vis. Sci. 47*, 427−438.
(24) Aoun, P., Simpkins, J. W., and Agarwal, N. (2003) Role of PPAR-gamma ligands in neuroprotection against glutamate-induced cytotoxicity in retinal ganglion cells. *Invest. Ophthalmol. Vis. Sci. 44*, 2999−3004.
(25) Fan, W., Agarwal, N., Kumar, M. D., and Cooper, N. G. (2005) Retinal ganglion cell death and neuroprotection: Involvement of the CaMKIIalpha gene. *Brain Res. Mol. Brain Res. 139*, 306−16.
(26) Maher, P., and Hanneken, A. (2005) The molecular basis of oxidative stress-induced cell death in an immortalized retinal ganglion cell line. *Invest. Ophthalmol. Vis. Sci. 46*, 749−57.
(27) Cheng, Z. J., Singh, R. D., Sharma, D. K., Holicky, E. L., Hanada, K., Marks, D. L., and Pagano, R. E. (2006) Distinct mechanisms of clathrin-independent endocytosis have unique sphingolipid requirements. *Mol. Biol. Cell 17*, 3197−210.
(28) Schnitzer, J. E., and Oh, P. (1994) Albondin-mediated capillary permeability to albumin. Differential role of receptors in endothelial transcytosis and endocytosis of native and modified albumins. *J. Biol. Chem. 269*, 6072−82.
(29) Sabharanjak, S., Sharma, P., Parton, R. G., and Mayor, S. (2002) GPI-anchored proteins are delivered to recycling endosomes via a distinct cdc42-regulated, clathrin-independent pinocytic pathway. *Dev. Cell 2*, 411−23.
(30) Manders, E. E. M., Verbeek, F. J., and Aten, J. A. (1993) Measurement of co-localisation of objects in dual-colour confocal images. *J. Microsc. 169*, 375−382.
(31) Ivanov, A. I. (2008) Pharmacological inhibition of endocytic pathways: is it specific enough to be useful? *Methods Mol. Biol. 440*, 15−33.
(32) Richard, J. P., Melikov, K., Brooks, H., Prevot, P., Lebleu, B., and Chernomordik, L. V. (2005) Cellular uptake of unconjugated TAT peptide involves clathrin-dependent endocytosis and heparan sulfate receptors. *J. Biol. Chem. 280*, 15300−6.
(33) Dharmawardhane, S., Schurmann, A., Sells, M. A., Chernoff, J., Schmid, S. L., and Bokoch, G. M. (2000) Regulation of macropinocytosis by p21-activated kinase-1. *Mol. Biol. Cell 11*, 3341−52.
(34) Krakauer, K. A., and Zurier, R. B. (1980) Pinocytosis in human synovial cells in vitro. Evidence for enhanced activity in rheumatoid arthritis. *J. Clin. Invest. 66*, 592−8.
(35) Edgington, L. E., Berger, A. B., Blum, G., Albrow, V. E., Paulick, M. G., Lineberry, N., and Bogyo, M. (2009) Noninvasive optical imaging of apoptosis by caspase-targeted activity-based probes. *Nat. Med. 15*, 967−73.
(36) Edgington, L. E., van Raam, B. J., Verdoes, M., Wierschem, C., Salvesen, G. S., and Bogyo, M. (2012) An optimized activity-based probe for the study of caspase-6 activation. *Chem. Biol. 19*, 340−52.
(37) Edgington, L. E., Verdoes, M., and Bogyo, M. (2011) Functional imaging of proteases: recent advances in the design and application of substrate-based and activity-based probes. *Curr. Opin. Chem. Biol. 15*, 798−805.
(38) Manev, H., Favaron, M., Guidotti, A., and Costa, E. (1989) Delayed increase of Ca2+ influx elicited by glutamate: role in neuronal death. *Mol. Pharmacol. 36*, 106−112.
(39) Trump, B. F., and Berezesky, I. K. (1995) Calcium-mediated cell injury and cell death. *FASEB J. 9*, 219−28.
(40) Chai, J., Wu, Q., Shiozaki, E., Srinivasula, S. M., Alnemri, E. S., and Shi, Y. (2001) Crystal structure of a procaspase-7 zymogen: mechanisms of activation and substrate binding. *Cell 107*, 399−407.
(41) Spencer, S. L., and Sorger, P. K. (2011) Measuring and modeling apoptosis in single cells. *Cell 144*, 926−39.
(42) Salvesen, G. S., and Riedl, S. J. (2008) Caspase mechanisms. *Adv. Exp. Med. Biol. 615*, 13−23.
(43) Repnik, U., and Turk, B. (2010) Lysosomal-mitochondrial cross-talk during cell death. *Mitochondrion 10*, 662−9.
(44) Matarrese, P., Manganelli, V., Garofalo, T., Tinari, A., Gambardella, L., Ndebele, K., Khosravi-Far, R., Sorice, M., Esposti, M. D., and Malorni, W. (2008) Endosomal compartment contributes

to the propagation of CD95/Fas-mediated signals in type II cells. *Biochem. J. 413*, 467−78.
(45) Ouasti, S., Matarrese, P., Paddon, R., Khosravi-Far, R., Sorice, M., Tinari, A., Malorni, W., and Degli Esposti, M. (2007) Death receptor ligation triggers membrane scrambling between Golgi and mitochondria. *Cell Death Differ. 14*, 453−61.
(46) Shiraishi, H., Okamoto, H., Yoshimura, A., and Yoshida, H. (2006) ER stress-induced apoptosis and caspase-12 activation occurs downstream of mitochondrial apoptosis involving Apaf-1. *J. Cell Sci. 119*, 3958−66.
(47) Johansson, A. C., Appelqvist, H., Nilsson, C., Kagedal, K., Roberg, K., and Ollinger, K. (2010) Regulation of apoptosis-associated lysosomal membrane permeabilization. *Apoptosis 15*, 527−40.
(48) Hanshaw, R. G., Lakshmi, C., Lambert, T. N., Johnson, J. R., and Smith, B. D. (2005) Fluorescent detection of apoptotic cells by using zinc coordination complexes with a selective affinity for membrane surfaces enriched with phosphatidylserine. *ChemBioChem 6*, 2214−20.
(49) Smith, B. A., Akers, W. J., Leevy, W. M., Lampkins, A. J., Xiao, S., Wolter, W., Suckow, M. A., Achilefu, S., and Smith, B. D. (2010) Optical imaging of mammary and prostate tumors in living animals using a synthetic near infrared zinc(II)-dipicolylamine probe for anionic cell surfaces. *J. Am. Chem. Soc. 132*, 67−9.
(50) Cordeiro, M., Guo, L., Luong, V., Harding, G., Wang, W., Jones, H., Moss, S., Sillito, A., and Fitzke, F. (2004) Real-time imaging of single nerve cell apoptosis in retinal neurodegeneration. *Proc. Natl. Acad. Sci. U.S.A. 101*, 13352−13356.
(51) Mizukami, S., Kikuchi, K., Higuchi, T., Urano, Y., Mashima, T., Tsuruo, T., and Nagano, T. (1999) Imaging of caspase-3 activation in HeLa cells stimulated with etoposide using a novel fluorescent probe. *FEBS Lett. 453*, 356−360.
(52) Negoescu, A., Lorimier, P., Labat-Moleur, F., Drouet, C., Robert, C., Guillermet, C., Brambilla, C., and Brambilla, E. (1996) In situ apoptotic cell labeling by the TUNEL method: improvement and evaluation on cell preparations. *J. Histochem. Cytochem. 44*, 959−68.
(53) Del Vecchio, S., Zannetti, A., Aloj, L., and Salvatore, M. (2003) MIBI as prognostic factor in breast cancer. *Q. J. Nucl. Med. 47*, 46−50.
(54) Marras, S., Kramer, F., and Tyagi, S. (1999) Efficiencies of fluorescence resonance energy transfer and contact-mediated quenching in oligonucleotide probes. *Nucleic Acids Res. 30*, e122.
(55) Johansson, M., Fidder, H., Dick, D., and Cook, R. (2002) Intramolecular dimers: a new strategy to fluorescence quenching in dual-labeled oligonucleotide probes. *J. Am. Chem. Soc. 124*, 6950−6956.
(56) Matsui, T., Sekiguchi, M., Hashimoto, A., Tomita, U., Nishikawa, T., and Wada, K. (1995) Functional comparison of D-serine and glycine in rodents: the effect on cloned NMDA receptors and the extracellular concentration. *J. Neurochem. 65*, 454−8.
(57) Stevens, E. R., Esguerra, M., Kim, P. M., Newman, E. A., Snyder, S. H., Zahs, K. R., and Miller, R. F. (2003) D-serine and serine racemase are present in the vertebrate retina and contribute to the physiological activation of NMDA receptors. *Proc. Natl. Acad. Sci. U. S. A. 100*, 6789−94.
(58) Johnson, J. W., and Ascher, P. (1987) Glycine potentiates the NMDA response in cultured mouse brain neurons. *Nature 325*, 529−31.

Bioconjugate Chemistry

Article

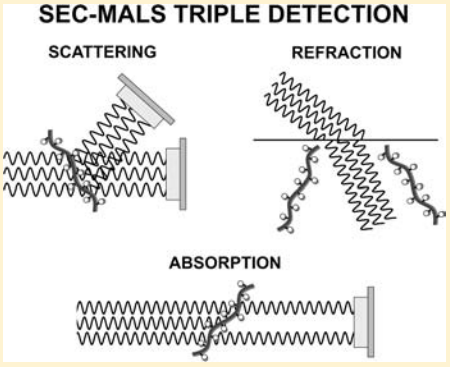
pubs.acs.org/bc

Molecular Characterization of Multivalent Bioconjugates by Size-Exclusion Chromatography with Multiangle Laser Light Scattering

Jacob F. Pollock,[†,∥] Randolph S. Ashton,[§] Nikhil A. Rode,[‡] David V. Schaffer,[§,∥] and Kevin E. Healy*[,†,‡,∥]

[†]Department of Bioengineering, [‡]Department of Materials Science and Engineering, [§]Department of Chemical Engineering, and [∥]UCSF/UCB Joint Graduate Group in Bioengineering, University of California at Berkeley, Berkeley, California, United States

ABSTRACT: The degree of substitution and valency of bioconjugate reaction products are often poorly judged or require multiple time- and product-consuming chemical characterization methods. These aspects become critical when analyzing and optimizing the potency of costly polyvalent bioactive conjugates. In this study, size-exclusion chromatography with multiangle laser light scattering was paired with refractive index detection and ultraviolet spectroscopy (SEC-MALS-RI-UV) to characterize the reaction efficiency, degree of substitution, and valency of the products of conjugation of either peptides or proteins to a biopolymer scaffold, i.e., hyaluronic acid (HyA). Molecular characterization was more complete compared to estimates from a protein quantification assay, and exploitation of this method led to more accurate deduction of the molecular structures of polymer bioconjugates. Information obtained using this technique can improve macromolecular engineering design principles and help to better understand multivalent macromolecular interactions in biological systems.



INTRODUCTION

Bioconjugation reaction methods have become increasingly important in biomaterial, biochemistry, pharmaceutical, and medical endeavors. They have been employed in diverse research fields for material synthesis,[1] macromolecular engineering,[2] biochemical modification,[3,4] and surface treatment.[5,6] A theme widely explored, for various medical applications, is the conjugation of a therapeutic biomolecule to either a synthetic or natural polymer or protein "scaffold" to create a decorated "carrier" for the bioactive agent. Knowing the true reaction efficiency, degree of substitution on the scaffold (i.e., the average number of ligands per potential reaction site on the molecular scaffold), conjugate valency (i.e., the average number of ligands per scaffold molecule), and macromolecule structure and size are crucial to understanding and controlling the chemical and biological performance of the conjugated scaffold.

Many extracellular proteins of mammalian tissue are multivalent and multifunctional, and this biochemical information directs cell behavior and tissue dynamics through receptor−ligand engagement and downstream signaling.[7,8] Therefore, multivalent bioactive conjugates have the potential to greatly improve pharmaceutical and biomaterial potency, and reduce the need for inefficient and potentially harmful doses of expensive therapeutics. They may also alter receptor−ligand dynamics (e.g., increased ligand localization and avidity, inhibited complex internalization and degradation), which could lead to improved potency of peptide and protein conjugates.[6,9] Furthermore, multivalent ligands have been known to increase activation of intracellular signaling when membrane-bound protein complexes are formed,[10,11] and natural physiological roles of soluble extracellular signaling aggregates have been recognized.[12] However, in many applications of bioconjugate reactions, the products are incompletely characterized in terms of molecular weight, degree of substitution, conjugate valency, and conjugate structure.

Conjugate valency is often poorly judged using common characterization techniques and can easily deviate from the expected. For example, for fixed weight concentrations of monomer and scaffold, the valency of a conjugate can vary considerably depending on the molecular weight of the scaffold. In addition, it is difficult to obtain information not only about the average valency, but the distribution of valencies within a preparation. Degradation, particularly of naturally derived or degradable polymer backbones (e.g., hyaluronic acid), can occur under the chemical conditions necessary for conjugation. Characterization of degrees of substitution and molecular weights therefore become critical when measuring the potency of various scaffolds, as well as in optimizing these multivalent biomimetic polymers for specific applications.[2,13]

Many chemical characterization techniques provide an incomplete picture of bioconjugate molecular structure, and therefore several are often used in conjunction.[14] Mass spectrometry is highly sensitive, but requires the ability to deconvolute molecular fragments and is more appropriate for lower molecular weight derivatized proteins and conjugates.[15−17] Protein quantification methods (e.g., bicinchoninic acid assay, Coomassie staining, ultraviolet light absorbance) can be used to estimate the average mass fraction of peptide or protein;[2] however, in the absence of accompanying measure-

Received: February 7, 2012
Revised: June 26, 2012
Published: July 16, 2012

ACS Publications © 2012 American Chemical Society

dx.doi.org/10.1021/bc3000595 | *Bioconjugate Chem.* 2012, 23, 1794−1801

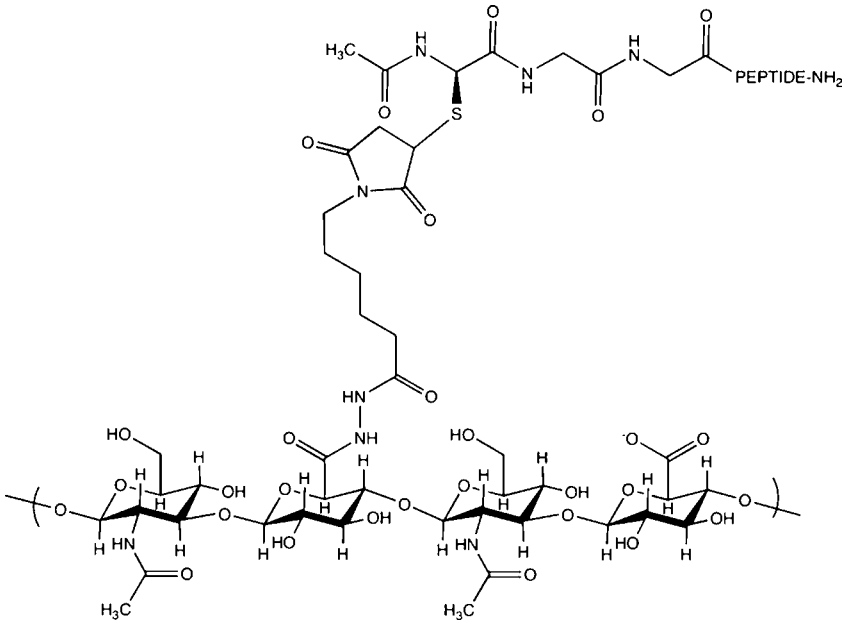


Figure 1. Hyaluronic acid–peptide conjugate chemical structure. A heterobifunctional linker was used to anchor peptide and protein via their terminal thiol-functional cysteine residues to the carboxylic acid groups of the linear hyaluronic acid polymer.

ments of scaffold concentration and molecular weight, these measurements do not provide direct information on the average or the distribution of conjugate valencies. Also, they generally require highly accurate protein standards that are difficult and time-consuming to prepare and validate. Fourier transform infrared spectroscopy (FTIR),[18] UV–vis spectroscopy,[19] and nuclear magnetic resonance (NMR)[20] provide molecular composition information, but end group identification or tagging is required for molecular weight characterization. These methods, along with biochemical, molecular biology, and fluorescence[18] assays, provide only an average ligand content or total molecular weight with no indication of their distribution. While traditional chromatographic methods can be used to obtain relative physicochemical properties and chemical composition,[16,17] light scattering methods can provide absolute molecular weight measurements without the use of standards.[21]

In this work, we sought to develop a technique and workflow that would characterize the distributions of molecular masses and ligand valencies of an entire macromolecule population within a conjugate reaction product, using a single measurement system with a reasonable sample size (<1.5 mg). An online three-detector method was used with continuous monitoring of differential refractive index (RI), ultraviolet light absorbance (UV), and multiangle laser light scattering (MALS) after size-exclusion chromatography (SEC).[22,23] We explored the natural biopolymer hyaluronic acid as a model scaffold, since it has been studied for numerous medical and pharmaceutical applications.[2,24−28] The reaction products of either peptides or proteins conjugated to a hyaluronic acid backbone were analyzed using this technique. The mass fractions and molecular weights determined were used to calculate valencies for comparison to those estimated using a standard protein quantification assay. We observed that reaction efficiency varied with the type and concentration of ligand conjugated. Furthermore, under some conditions the scaffold molecular weight decreased due to fragmentation of the backbone during the bioconjugation reaction. The triple detection method additionally provided novel information about ligand valency during this molecular weight change.

MATERIALS AND METHODS

Hyaluronic acid sodium salts (HyA) of 0.5 and 1.0 MDa MW served as the scaffolds for the conjugation reactions (Genzyme, Cambridge, MA). Conjugation reagents, including 1-ethyl-3-(3-dimethylaminopropyl) carbodiimide hydrochloride (EDC), *N*-hydroxysulfosuccinimide (sulfoNHS), and [*N*-ε-maleimidocaproic acid] hydrazide trifluoroacetic acid (EMCH), were purchased from Thermo Scientific Pierce. Tris(2-carboxyethyl) phosphine (TCEP), Dulbecco's phosphate buffered saline (DPBS), 2-(*N*-morpholino)ethanesulfonic acid (MES), and 10 kDa MW cutoff dialysis tubing (SnakeSkin) were also obtained from Pierce. All dry buffers were constituted in ultrapure ASTM type I reagent grade water (<18.2 MΩ·cm, pyrogen free, UPW). An Arg-Gly-Asp (RGD)-containing 15-mer peptide derived from bone sialoprotein (Ac-CGGNGEPRGDTYRAY-NH_2: **bsp-RGD(15)**)[29] was synthesized (American Peptide Co., Sunnyvale, CA) with two glycine spacer amino acids and an acylated cysteine amino-terminus for coupling via thiol reaction with maleimide groups of an activated HyA backbone. Recombinant modified Sonic hedgehog (**Shh**) protein was produced as described below. All reactions were performed under aseptic conditions using sterile-filtered solutions and autoclaved containers and instruments.

Coupling of Peptide to Hyaluronic Acid. Hyaluronic acid was first activated with maleimide groups by carbodiimide coupling of EMCH. Hyaluronic acid sodium salt 0.5 MDa (50 mg) was added to 8 mL of MES buffer (0.1 M, pH 6.5) and stirred under low shear until dissolved. Conjugation reagents (110 mg EDC, 30.8 mg sulfoNHS, and 13.2 mg EMCH) were dissolved in 2.2 mL MES buffer. Two mL of the conjugation reaction mixture was added through sterile-filter to the HyA solution and stirred. The final concentrations of each reagent for EMCH activation of HyA were as follows: 5 mg/mL HyA, 10 mg/mL EDC, 2.8 mg/mL sulfoNHS, and 1.2 mg/mL

dx.doi.org/10.1021/bc3000595 | *Bioconjugate Chem.* 2012, 23, 1794−1801

EMCH. The reaction was allowed to proceed for 2 h with stirring at room temperature in the dark. The solution was then thoroughly dialyzed through a 10 kDa MWCO membrane against MES buffer (0.1 M, pH 6.5) and transferred to another reaction vessel.

The peptide was then reduced and added to the activated HyA-EMCH solution for conjugation via reaction of the maleimide moieties with the thiol group of the peptide. In order to reduce any potential disulfide bonds formed by the peptide via spontaneous oxidation, 3 mg of NaOH and 5.7 mg of TCEP were added to 1 mL UPW. The bsp-RGD peptide (4.4 mg) was added to the alkaline reducing solution, allowed to react for 30 min at 4 °C, and added through a sterile-filter to the activated HyA-EMCH solution. The final solution was reacted overnight at 4 °C in the dark. The conjugate solution was then dialyzed three times for 2 h through a 10 kDa MWCO membrane against UPW. After dialysis, the solution was transferred to a 50 mL Steriflip tube (BD Bioscience) and lyophilized through the sterile-filter cap. The dry product was stored at −20 °C until characterization. The final chemical structure of the bioconjugate is depicted in Figure 1.

Recombinant Production of Modified Sonic Hedgehog Protein. A recombinant cysteine-modified N-terminal **Shh** was produced as previously described.[2,31] A sequence encoding a cysteine residue and a 6xHis tag were added via PCR to 3′ end of cDNA encoding the N-terminal signaling domain of rat Shh to allow for sulfhydryl-based reactions and protein purification, respectively. The conjugation site was chosen because it is distant from the active receptor-binding domain. In addition, valine and isoleucine residues were introduced to the N-terminus to increase potency by mimicking the hydrophobic palmitic acid modification of endogenous Shh. The modified Shh PCR product was inserted into a pBAD-HisA plasmid (Invitrogen), sequenced for confirmation, and expressed in BL21(DE3)pLysE *E. coli* upon arabinose induction. The cells were lysed, and the resulting expressed Shh was purified using NiNTA binding through the BioRad DuoFlow System and elution with imidazole. The isolated protein was dialyzed into pH 7.4 PBS containing 10% glycerol, 2 mM EDTA, and 50 μM $ZnSO_4$ and stored at −20 °C until conjugation.

Conjugation of Sonic Hedgehog Protein to Hyaluronic Acid. The modified Shh protein was conjugated to 1.0 MDa HyA through a similar two-step reaction process to the bsp-RGD (HyA-bsp-RGD(15)), using carbodiimide chemistry at the carboxylate group of the HyA and maleimide reaction at the protein C-terminal cysteine.[2] Hyaluronic acid was activated at 3 mg/mL in MES (0.1 M pH 5.0) with 3.9 mg/mL EDC, 1.1 mg/mL sulfoNHS, and 0.5 mg/mL EMCH. Activated HyA was purified by sequential dilution and centrifugation in 100 kDa MWCO centrifuge filters (Pall Gellman). The activated HyA-EMCH was reacted with the modified Shh at varying stoichiometric feed ratios to produce conjugates with different conjugate valency. The reaction was performed at 4 °C overnight in MES buffer (0.1 M pH 6.5) with 50 μM TCEP to maintain cysteine reduction. Following the reaction, the remaining maleimide groups were quenched by the addition of 0.5 mM dithiothreitol and incubation at 4 °C for 1 h. The HyA-Shh conjugation product was dialyzed into pH 7.4 PBS containing 2 mM EDTA and 50 μM ZnSO4 and stored at −20 °C until characterization.

SEC-MALS-RI-UV Analysis of Bioconjugates. The SEC-MALS-RI-UV setup consisted of an Agilent HPLC 1100 (including degasser, quaternary pump, autosampler, column holder, and UV−vis diode array detector) in line with a DAWN-EOS multiangle laser light scattering detector and Optilab-DSP relative refractive interferometer (Wyatt Technology, Santa Barbara, CA). Refractive index change was measured differentially with a GaAs laser at a wavelength of 690 nm, and UV absorbance was measured with the diode array detector at 280 nm. A PolySep-GFC-P Linear column was used for the HPLC (Phenomenex). HyA-peptide and HyA-protein conjugates were injected at 5 mg/mL and 3 mg/mL conjugate, respectively. The temperatures of the DSP and column holder were both maintained at 45 °C. Agilent software was used to control the HPLC, and Wyatt *Astra V* software was used for data collection and analysis. Normalization of the multiangle detectors was performed with 300 μL of 5 mg/mL bovine serum albumin (BSA) (Aldrich) in DPBS at a flow rate of 0.8 mL/min (used throughout unless otherwise noted) with DPBS as the mobile phase. Peak alignment and band broadening correction between the UV, MALS, and RI detectors were performed using *Astra* software algorithms. Analysis was restricted to detectors at moderate angles due to high noise at very low and very high angle detectors.

The specific refractive index values of the peptide, protein, HyA, and HyA-EMCH were confirmed by a 100% mass recovery method at a wavelength of 690 nm (the same as used in online detection). The UV absorbance coefficient values for each conjugate component were measured using an off-line UV−vis spectrophotometer at 280 nm wavelength. These values were confirmed using a 100% mass recovery method to corroborate UV and RI concentration source detectors. Zimm plots were created for 0.5 MDa HyA scaffold and a conjugate of 0.5 MDa HyA with bsp-RGD(15) at a 1 to 25 molar ratio (1:25, HyA:bsp-RGD(15)) using 200 μL injections of 1, 2, 3, and 4 mg/mL in DPBS at 45 °C with DPBS as the mobile phase.

RESULTS AND DISCUSSION

Online SEC-MALS-RI-UV Analysis of Hyaluronic Acid Bioconjugates. Measurement of RI, UV, and MALS signals allowed simultaneous online measurement of concentration, conjugate molar mass, and ligand mass fraction distribution among the modified polymer chains. Table 1 lists the physicochemical parameters of the conjugate components employed in this study. The weight-averaged molar mass (M_w) and z-averaged radius of gyration ($R_{G,z}$) were determined for each slice along the chromatogram (Figure 2a) using the Rayleigh-Gans-Debye equation

Table 1. Specific Refractive Indices ($\partial n/\partial c$) and 280 nm Absorbance Coefficients (ε_{abs}) for Hyaluronic Acid, EMCH-Activated Hyaluronic Acid, Peptide, and Proteins

component	$\partial n/\partial c$ (mL/g)	ε_{abs} (mL/g cm)	MW_w	sequence
HyA	0.167	22	0.5 and 1.0 MDa	
HyA-EMCH	0.167	22		
bspRGD	0.185	1840	1657	Ac-CGGNGEPRGDTYRAY-NH2
Shh	0.185	974	21 376	See reference (Wall et al. *Bioconjugate Chem*, 2008)

dx.doi.org/10.1021/bc3000595 | *Bioconjugate Chem.* 2012, 23, 1794−1801

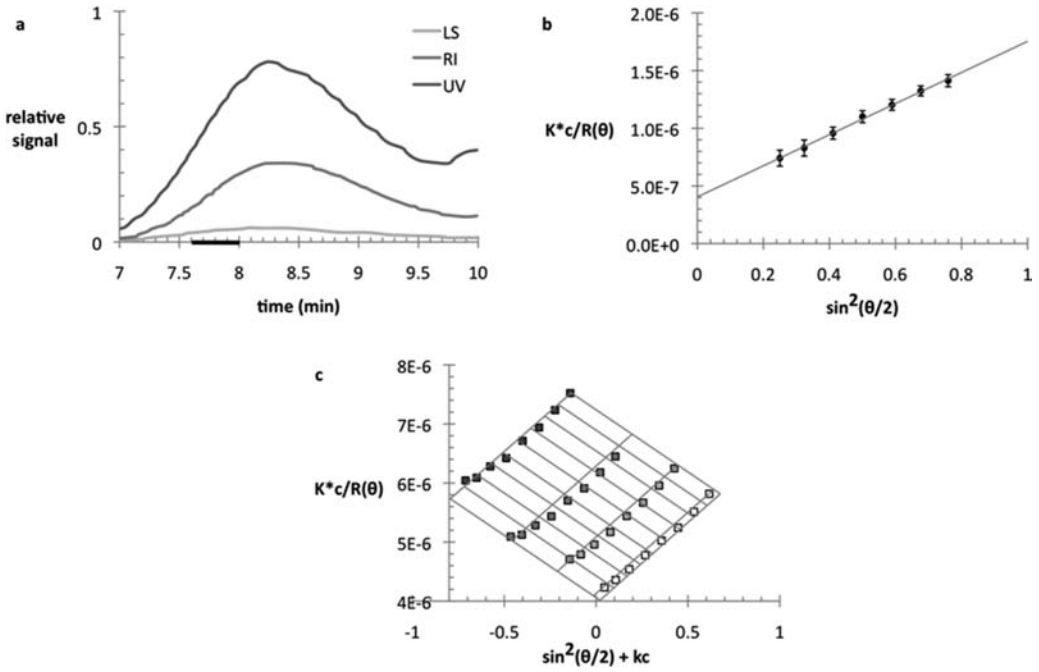


Figure 2. Representative chromatogram (a) with 90° light scattering (LS), refractive index (RI), and ultraviolet light absorbance (UV) signals and Debye plot (b) calculated from multi-angle laser light scattering (MALS) data at slices along the size-exclusion chromatogram for HyA-bsp-RGD(15) (1:25, HyA:bsp-RGD(15) molar reaction ratio). A Zimm plot (c) created from injectons of varying total conjugate mass for HyA-bsp-RGD(15) (1:25) used to calculate weight-averaged molecular mass (M_w), z-averaged radius of gyration, ($R_{G,z}$) and second virial coefficient (A_2).

$$\frac{K^*c}{R(\theta)} = \frac{1}{P(\theta)}\left(\frac{1}{M_w} + 2A_2c + 3A_3c^2 + \ldots\right)$$

$$K^* = \frac{4\pi^2 n_0{}^2\left(\frac{\partial n}{\partial c}\right)^2}{N_A\lambda_0^4}$$

$$\frac{1}{P(\theta)} = 1 + \frac{16\pi^2}{3\lambda^2}R_{G,z}^2\sin^2\left(\frac{\theta}{2}\right) + \ldots$$

where c is the concentration of polymer in solution, $R(\theta)$ is the excess Rayleigh scattering ratio, A_2 is the second virial coefficient, A_3 is the third virial coefficient, θ is the scattering angle, and $(\partial n)/(\partial c)$ is the specific refractive index increment of the macromolecule in solution. Debye plots ($K^*c/R(\theta)$ vs $\sin^2(\theta/2)$) were created for each slice along the chromatogram (Figure 2b). Zimm plots ($K^*c/R(\theta)$ vs $\sin^2(\theta/2) + kc$) were also constructed by injecting a series of concentrations through the SEC-MALS system, which gave the A_2, $R_{G,z}$, and M_w values of the backbone polymer and a representative conjugate (Figure 2c and Table 2).

The use of two concentration detectors (RI and UV) in combination with SEC-MALS allowed characterization of the molecular weight distribution and the relative composition of conjugated macromolecules. This was possible since the measured values of specific refractive index ($\partial n/\partial c$) and UV absorption coefficient (ε_{abs}) along the chromatogram are weight-averaged values for each component individually

$$\left(\frac{\partial n}{\partial c}\right)_t = \frac{m_1}{m_t}\left(\frac{\partial n}{\partial c}\right)_1 + \frac{m_2}{m_t}\left(\frac{\partial n}{\partial c}\right)_2 \quad \text{and}$$

$$(\varepsilon_{abs})_t = \frac{m_1}{m_t}(\varepsilon_{abs})_1 + \frac{m_2}{m_t}(\varepsilon_{abs})_2$$

Knowing $\partial n/\partial c$ and ε_{abs} for each component, these equations can be solved simultaneously to determine the mass fractions of each component of the conjugate. Valency information was obtained in this manner by dividing the total average ligand molar mass of the conjugate (mass protein or peptide per mole conjugate) by the individual ligand molecular weight.

Table 2. Weight-Averaged Molecular Mass (M_w), z-Averaged Radius of Gyration ($R_{G,z}$), and Second Virial Coefficient (A_2) for HyA and HyA-bsp-RGD(15) (1:25) as Determined by Zimm Plot Construction (as Measured at 45 °C in Phosphate Buffer)

sample	MW_w (10^5 g/mol)	$R_{G,z}$ (nm)	A_2 (10^{-3} mol mL/g^2)
HyA, 0.5 MDa	4.9 ± 0.24	55 ± 3.5	2.4 ± 0.76
HyA-RGD (1:25)	2.1 ± 0.74	70 ± 15.8	3 ± 1.6

Analysis of Hyaluronic Acid Conjugate Synthesis Products. Conjugates were made with HyA and Shh at several reaction ratios, and the products were characterized by SEC-MALS-RI-UV. Signals from the concentration detectors combined with MALS data were used to calculate the HyA and ligand molecular masses, as depicted in Figure 3 for HyA-Shh (1:40, HyA:Shh molar reaction ratio) conjugates made with 1.0 MDa HyA. These values for each conjugate were used to determine protein fraction distributions along the chromatograms, as presented in Figure 4. The quality of the data collected depended on the overall concentration of the conjugate as well as its degree of substitution. The cumulative and differential mass fractions were plotted against molar mass in Figure 5, depicting molecular weight distributions. The reaction and final ligand concentrations along with HyA and total ligand molecular weights of conjugate products are listed in Table 3 and Table 4.

The molecular weights of the HyA after Shh conjugation varied from batch to batch (Figure 6). It is known that HyA is

dx.doi.org/10.1021/bc3000595 | Bioconjugate Chem. 2012, 23, 1794−1801

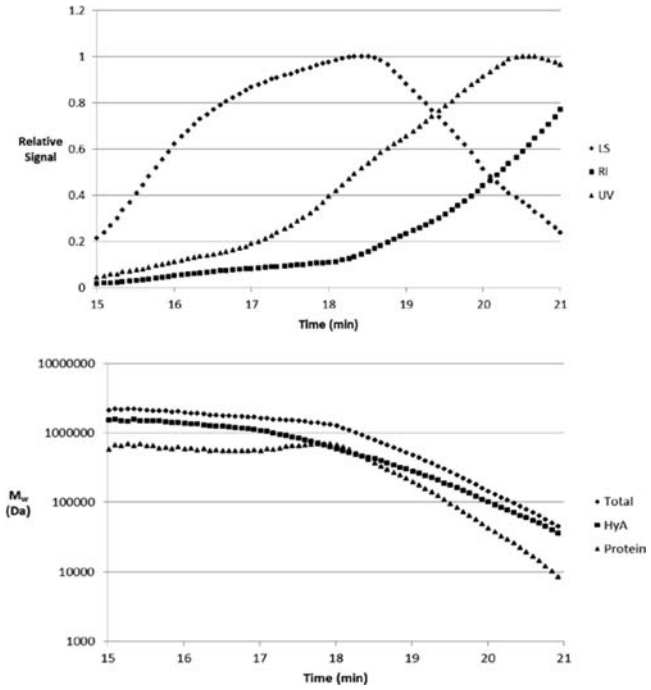


Figure 3. Detector signals (90° light scattering, LS, refractive index, RI, and ultraviolet light absorbance, UV) (a) collected during size-exclusion chromatography (SEC) combined with MALS data allowed calculation of hyaluronic acid and protein molecular weight distributions (b) of the HyA-Shh (1:40, HyA:Shh molar reaction ratio) conjugate.

susceptible to hydrolytic degradation, particularly under shear (e.g., in a stirred reaction, upon vortexing, or during sonication) or catalytic chemical conditions (e.g., acidic, alkaline, reductive, or oxidative). A reducing agent was used in the conjugation reaction, and the conjugate was exposed to shear in several steps of the reaction (stirring, pipetting). It is believed that the reducing conditions and shear led to molecular weight degradation of the HyA bioconjugates. The large variation in molecular weights is likely further due to differences in the way that the conjugates were handled, such as differences in stirring times or shear rates.

The input and output degrees of substitution (DS) for several HyA-Shh conjugates are plotted in Figure 7. Input and output DS were calculated according to

$$\mathrm{DS} = \frac{\#\mathrm{ligands/molecule}}{\#\mathrm{carboxylates/molecule}}$$

$$\text{input DS} = \frac{\mathrm{mols_{ligand}}}{\frac{\mathrm{MW_{w_{HyA}}}}{\mathrm{MW_{HyAdimer}}} \times \mathrm{mols_{HyA}}}$$

$$\mathrm{mols_{ligand}} = \frac{\mathrm{mass_{ligand,input}}}{\mathrm{MW'_{ligand}}}$$

$$\mathrm{mols_{HyA}} = \frac{\mathrm{mass_{HyA,input}}}{\mathrm{MW^{*}_{HyA}}}$$

$$\text{output DS} = \frac{\mathrm{MW_{w_{ligand}}}}{\mathrm{MW'_{ligand}}} \div \frac{\mathrm{MW_{w_{HyA}}}}{\mathrm{MW_{HyAdimer}}}$$

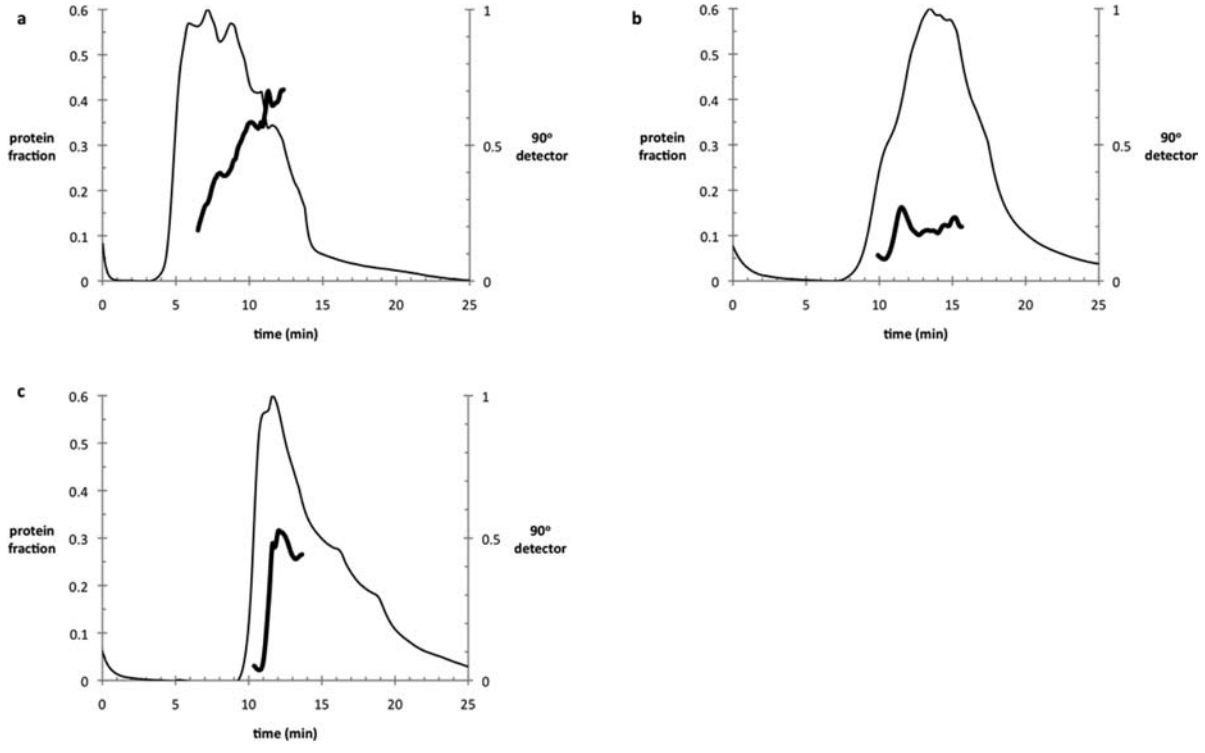


Figure 4. Protein fraction (dark line) and 90° light scattering intensity (light line) of (a) HyA-bsp-RGD(15) (1:25), (b) HyA-Shh (1:20), and (c) HyA-Shh (1:40) following size-exclusion chromatography. Light scattering instensity depends on concentration and total molar mass, with higher molar masses eluted first. Conjugation of bsp-RGD was more efficient than Shh, with smaller input reaction ratios achieving a higher final protein fraction due to the small size and ease of accessibility to the bsp-RGD reaction site when compared to Shh.

dx.doi.org/10.1021/bc3000595 | *Bioconjugate Chem.* 2012, 23, 1794–1801

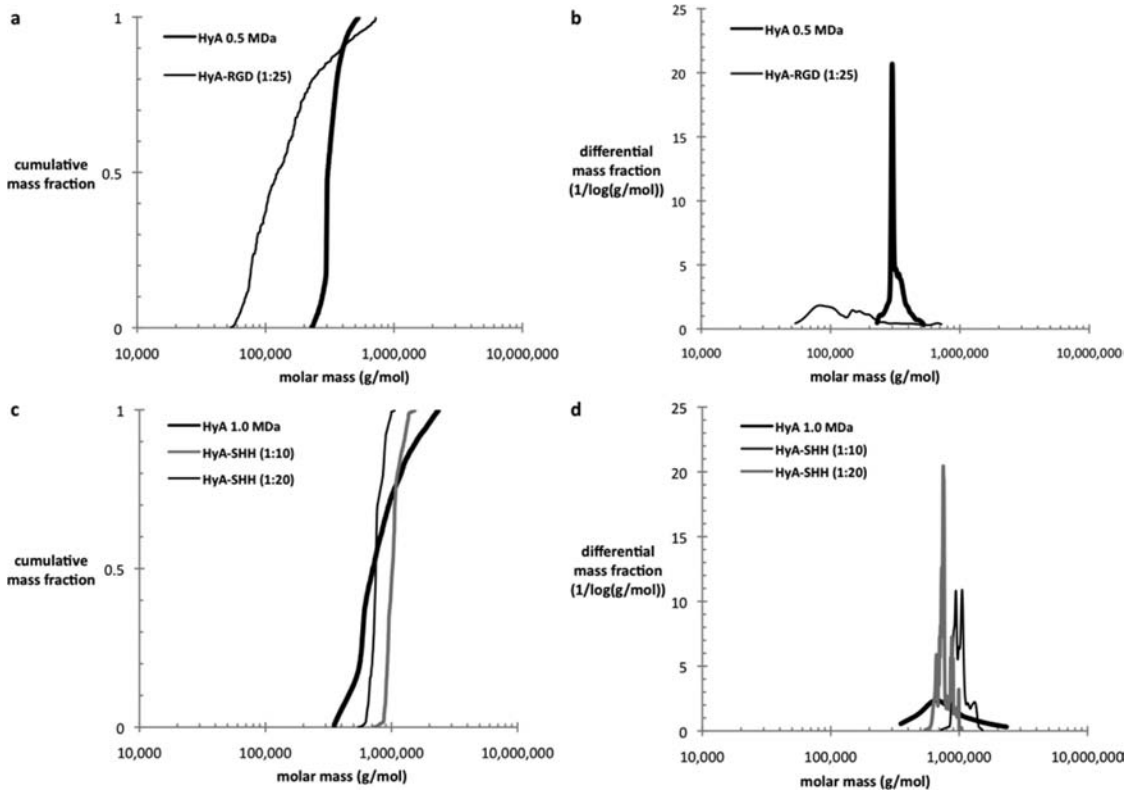


Figure 5. Cumulative (a,c) and differential (b,d) mass fractions versus molar mass of (a,b) 0.5 MDa HyA and HyA-bsp-RGD(15) (1:25) along with (c, d) 1.0 MDa HyA, HyA-Shh (1:20), and HyA-Shh (1:40).

Table 3. Bioconjugate Characterization of HyA-Peptide Products by SEC-MALS-RI-UV

	reaction molar ratio	reaction mass fraction	output ligand mass fraction	MW_w HyA (kDa)	MW_w ligand (kDa)	conjugate valency
HyA, 0.5 MDa				491		
HyA-bspRGD 1:10	10	0.04	0.09	413	19	11.5
HyA-bspRGD 1:25	25	0.11	0.33	141	72	43.4

*based on nominal HyA MW.

In these equations, primed quantities refer to the molecular weight of a single peptide or protein molecule. MW_w refers to the weight average molecular weight. Hyaluronic acid molecular weight was normalized by the dimer molecular weight as there is one reactive carboxylate group per dimer.

Differences in reaction efficiency between bsp-RGD(15) and Shh protein can be attributed to the higher molecular weight and steric hindrance of Shh protein. Higher conjugation efficiency of Shh to HyA was achieved when the reactions were performed at lower total reagent concentration (data not shown).

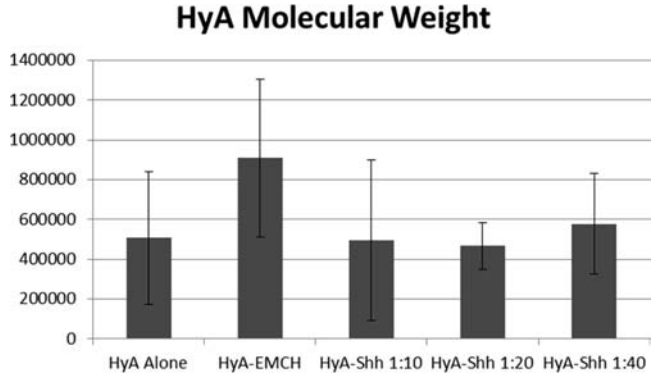


Figure 6. Weight-averaged molecular weights of hyaluronic acid in conjugates of varying reaction ratio. The error bars represent the standard deviation (N = 3).

Comparison of SEC-MALS-RI-UV Results with Input Ratios and BCA Results. Protein fractions measured by SEC-MALS-RI-UV corresponded well with results determined by

Table 4. Bioconjugate Characterization of HyA-Shh Products by SEC-MALS-RI-UV

	reaction molar ratio	reaction mass fraction	output ligand mass fraction	MW_w HyA (kDa)	MW_w ligand (kDa)	conjugate valency
HyA, 1.0 MDa				508 ± 335		
HyA-EMCH				909 ± 398	0	0.0
HyA-Shh 1:10	10	0.22	0.06 ± 0.01	496 ± 403	36 ± 22	1.7 ± 1.0
HyA-Shh 1:20	20	0.43	0.23 ± 0.04	468 ± 118	128 ± 49	6.0 ± 2.3
HyA-Shh 1:40	40	0.87	0.27 ± 0.10	578 ± 252	187 ± 33	8.7 ± 1.6

dx.doi.org/10.1021/bc3000595 | *Bioconjugate Chem.* 2012, 23, 1794−1801

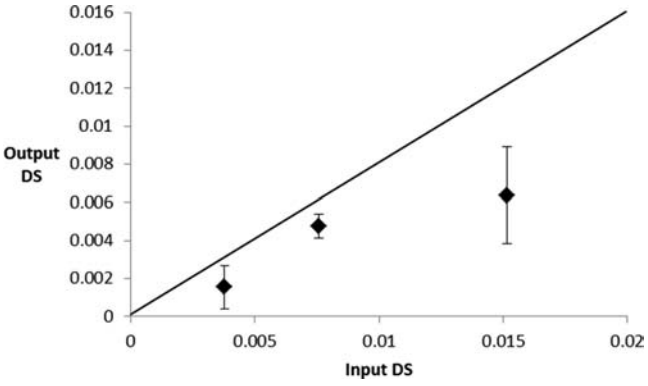


Figure 7. Input and output degrees of substitution (DS) values for HyA-Shh conjugates. The line represents correspondence of 1:1.

BCA protein measurements for a given batch of conjugate. The final conjugate valency differed from that calculated through the BCA assay, however (Figure 8). Differences in calculated

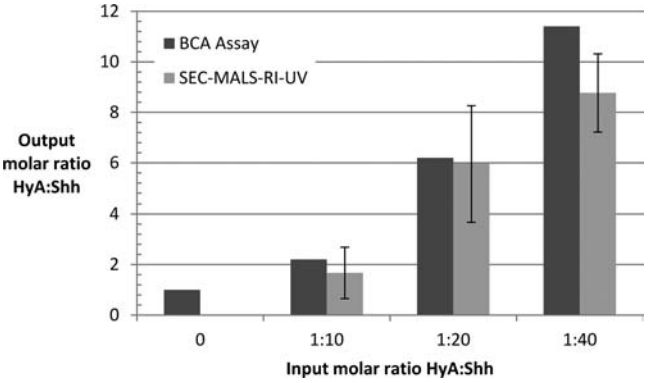


Figure 8. Comparison of input and output molar ratios as determined by SEC-MALS-RI-UV and BCA assay methods. Error bars represent the standard deviation (N = 3).

valency between SEC-MALS-RI-UV and BCA assay were due largely to fragmentation of the HyA backbone during the conjugate synthesis, and subsequently accounting for changes in the molecular weight. Valency determined by SEC-MALS-RI-UV was calculated based on the total weight-averaged ligand molecular weight in each conjugate divided by the molecular weight of the individual ligand, whereas in the BCA assay determination, the mass ratio of ligand to HyA was used to calculate the molar ratio based on the ligand and original HyA molecular weights. Using the valency data collected from the BCA measurements leads to a misinterpretation of multivalent macromolecular values, whereas that calculated using the SEC-MALS-RI-UV does not.

CONCLUSION

SEC-MALS with RI and UV detection is valuable for determining the molecular weight and protein fraction distributions of polymer bioconjugates. The amount of material needed for this method depends upon instrument sensitivity, molecular weight, and reagent physiochemical parameters, but is significantly less than standard methods (i.e., BCA). Accurate measurement of protein fraction requires that the bioconjugate components have differing refractive index increments and UV absorbance coefficients. These values can be determined using online or offline analysis of unconjugated reagents. SEC-MALS with triple detection (MALS, RI, UV) can also be used to accurately measure bioconjugation reaction efficiency and provide detailed molecular structural information along with precise distribution of substitution and valency data. In contrast, with the large variation in actual HyA molecular weight after the conjugation reaction, accurate measurement of the valency of the bioconjugates is impossible using more conventional batch techniques such as a BCA assay. Moreover, the capabilities of this method could be expanded by using the diode array detector (DAD) on a high-performance liquid chromatography (HPLC) instrument to measure UV absorbance at multiple wavelengths in order to simultaneously identify conjugate components with different absorbance spectra. In either case, more accurate deduction of the molecular structures of polymer bioconjugates can be used to improve macromolecular engineering design principles and better understand multivalent macromolecular interactions (e.g., receptor−ligand dynamics and enzyme kinetics). Furthermore, this analysis method can be used for quality assurance and to optimize reactor design and operations for large-scale production of designer bioconjugate products.

AUTHOR INFORMATION

Corresponding Author

*Fax: 510 642-5835. Tel: 510 642-3559. E-mail: kehealy@berkeley.edu.

Notes

The authors declare no competing financial interest.

ACKNOWLEDGMENTS

This work was supported in part by the American Heart Association #20082098, National Science Foundation (NSF Graduate Fellowship to JFP), the University of California at Berkeley (Berkeley Graduate Fellowship to JFP), the California Institute for Regenerative Medicine (Postdoctoral Fellowship to RSA), NIH R21EB007295, NIH NHLBI R01HL096525. The authors thank Melissa Velasquez for her assistance in HyA-peptide synthesis.

REFERENCES

(1) Elbert, D., and Hubbell, J. (2001) Conjugate addition reactions combined with free-radical cross-linking for the design of materials for tissue engineering. *Biomacromolecules 2*, 430−441.

(2) Wall, S. T., Saha, K., Ashton, R. S., Kam, K. R., Schaffer, D. V., and Healy, K. E. (2008) Multivalency of Sonic hedgehog conjugated to linear polymer chains modulates protein potency. *Bioconjugate Chem. 19*, 806−12.

(3) Drumheller, P., Elbert, D., and Hubbell, J. (1994) Multifunctional poly (ethylene glycol) semi-interpenetrating polymer networks as highly selective adhesive substrates for bioadhesive peptide grafting. *Biotechnol. Bioeng. 43*, 772−780.

(4) Stile, R. A., and Healy, K. E. (2001) Thermo-responsive peptide-modified hydrogels for tissue regeneration. *Biomacromolecules 2*, 185−94.

(5) Ho, M., Wang, D., Hsieh, H., Liu, H., Hsien, T., Lai, J., and Hou, L. (2005) Preparation and characterization of RGD-immobilized chitosan scaffolds. *Biomaterials 26*, 3197−3206.

(6) Ito, Y. (2008) Covalently immobilized biosignal molecule materials for tissue engineering. *Soft Matter 4*, 46−56.

(7) Sacchettini, J. C., Baum, L. G., and Brewer, C. F. (2001) Multivalent protein-carbohydrate interactions. A new paradigm for supermolecular assembly and signal transduction. *Biochemistry 40*, 3009−15.

(8) Kiessling, L. L., Gestwicki, J. E., and Strong, L. E. (2000) Synthetic multivalent ligands in the exploration of cell-surface interactions. *Curr. Opin. Chem. Biol. 4*, 696−703.
(9) Schamel, W. W. A., and Reth, M. (2008) Clustering models. *Adv. Exp. Med. Biol. 640*, 64−73.
(10) Geiger, B., Bershadsky, A., Pankov, R., and Yamada, K. M. (2001) Transmembrane crosstalk between the extracellular matrix–cytoskeleton crosstalk. *Nat. Rev. Mol. Cell Biol. 2*, 793−805.
(11) Huveneers, S., and Danen, E. H. J. (2009) Adhesion signaling - crosstalk between integrins, Src and Rho. *J. Cell Sci. 122*, 1059−69.
(12) McLellan, J. S., Zheng, X., Hauk, G., Ghirlando, R., Beachy, P. A., and Leahy, D. J. (2008) The mode of Hedgehog binding to Ihog homologues is not conserved across different phyla. *Nature 455*, 979−83.
(13) Saha, K., Pollock, J. F., Schaffer, D. V., and Healy, K. E. (2007) Designing synthetic materials to control stem cell phenotype. *Curr. Opin. Chem. Biol. 11*, 381−7.
(14) Bi, X., Shi, X., and Baker, J. R. (2008) Synthesis, characterization and stability of a luteinizing hormone-releasing hormone (LHRH)-functionalized poly(amidoamine) dendrimer conjugate. *J. Biomater. Sci., Polym. Ed. 19*, 131−42.
(15) Wang, L., Amphlett, G., Blättler, W. A., Lambert, J. M., and Zhang, W. (2005) Structural characterization of the maytansinoid-monoclonal antibody immunoconjugate, huN901-DM1, by mass spectrometry. *Protein Sci. 14*, 2436−46.
(16) Cheng, W., Satyanarayanajois, S., and Lim, L.-Y. (2007) Aqueous-soluble, non-reversible lipid conjugate of salmon calcitonin: synthesis, characterization and in vivo activity. *Pharm. Res. 24*, 99−110.
(17) Tzokova, N., Fernyhough, C. M., Butler, M. F., Armes, S. P., Ryan, A. J., Topham, P. D., and Adams, D. J. (2009) The effect of PEO length on the self-assembly of poly(ethylene oxide)-tetrapeptide conjugates prepared by "Click" chemistry. *Langmuir 25*, 11082−9.
(18) Mi, F.-L. (2005) Synthesis and characterization of a novel chitosan-gelatin bioconjugate with fluorescence emission. *Biomacromolecules 6*, 975−87.
(19) Demolliens, A., Boucher, C., Durocher, Y., Jolicoeur, M., Buschmann, M. D., and De Crescenzo, G. (2008) Tyrosinase-catalyzed synthesis of a universal coil-chitosan bioconjugate for protein immobilization. *Bioconjugate Chem. 19*, 1849−54.
(20) Oh, E. J., Park, K., Choi, J.-S., Joo, C.-K., and Hahn, S. K. (2009) Synthesis, characterization, and preliminary assessment of anti-Flt1 peptide-hyaluronate conjugate for the treatment of corneal neovascularization. *Biomaterials 30*, 6026−34.
(21) Wyatt, P. (1993) Light scattering and the absolute characterization of macromolecules. *Anal. Chim. Acta,*.
(22) Wen, J., Arakawa, T., and Philo, J. S. (1996) Size-exclusion chromatography with on-line light-scattering, absorbance, and refractive index detectors for studying proteins and their interactions. *Anal. Biochem. 240*, 155−66.
(23) Kendrick, B. S., Kerwin, B. A., Chang, B. S., and Philo, J. S. (2001) Online size-exclusion high-performance liquid chromatography light scattering and differential refractometry methods to determine degree of polymer conjugation to proteins and protein−protein or protein−ligand association states. *Anal. Biochem. 299*, 136−146.
(24) Ghosh, K., Shu, X. Z., Mou, R., Lombardi, J., Prestwich, G. D., Rafailovich, M. H., and Clark, R. A. (2005) Rheological characterization of in situ cross-linkable hyaluronan hydrogels. *Biomacromolecules 6*, 2857−65.
(25) Leach, J. B., Bivens, K. A., Collins, C. N., and Schmidt, C. E. (2004) Development of photocrosslinkable hyaluronic acid-polyethylene glycol-peptide composite hydrogels for soft tissue engineering. *J. Biomed. Mater. Res., Part A 70*, 74−82.
(26) Pouyani, T., and Prestwich, G. D. (1994) Functionalized derivatives of hyaluronic acid oligosaccharides: drug carriers and novel biomaterials. *Bioconjugate Chem. 5*, 339−47.
(27) Park, Y. D., Tirelli, N., and Hubbell, J. A. (2003) Photopolymerized hyaluronic acid-based hydrogels and interpenetrating networks. *Biomaterials 24*, 893−900.
(28) Peattie, R. A., Nayate, A. P., Firpo, M. A., Shelby, J., Fisher, R. J., and Prestwich, G. D. (2004) Stimulation of in vivo angiogenesis by cytokine-loaded hyaluronic acid hydrogel implants. *Biomaterials 25*, 2789−98.
(29) Rezania, A., and Healy, K. (2000) The effect of peptide surface density on mineralization of a matrix deposited by osteogenic cells. *J. Biomed. Mater. Res. 52*, 595−600.
(30) Nomizu, M., Kim, W., Yamamura, K., Utani, A., Song, S., Otaka, A., Roller, P., Kleinman, H., and Yamada, Y. (1995) Identification of cell binding sites in the laminin alpha1 chain carboxyl-terminal globular domain by systematic screening of synthetic peptides. *J. Biol. Chem. 270*, 20583−90.
(31) Ho, J., Chung, E., Wall, S., Schaffer, D., and Healy, K. (2007) *J. Biomed. Mater. Res., Part A 83*, 1200−1208.

Bioconjugate Chemistry

Article

pubs.acs.org/bc

Generation and Evaluation of Bispecific Affibody Molecules for Simultaneous Targeting of EGFR and HER2

Lina Ekerljung,[†,#] Helena Wållberg,[‡,#] Azita Sohrabian,[†] Karl Andersson,[†,§] Mikaela Friedman,[∥] Fredrik Y Frejd,[†,⊥] Stefan Ståhl,[*,‡] and Lars Gedda[†]

[†]Department of Radiology, Oncology and Radiation Sciences and [∥]Department of Genetics and Pathology, Uppsala University, Sweden

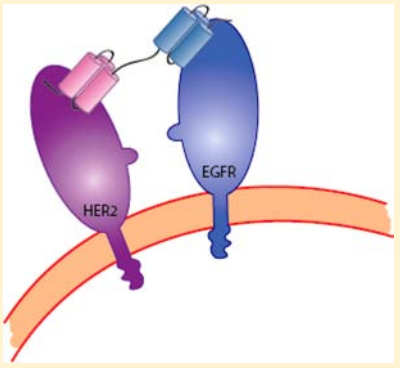
[‡]Division of Molecular Biotechnology, School of Biotechnology, KTH Royal Institute of Technology, Stockholm, Sweden

[§]Ridgeview Instruments AB, Uppsala, Sweden

[⊥]Affibody AB, Stockholm, Sweden

Supporting Information

ABSTRACT: Coexpression of several ErbB receptors has been found in many cancers and has been linked with increased aggressiveness of tumors and a worse patient prognosis. This makes the simultaneous targeting of two surface receptors by using bispecific constructs an increasingly appreciated strategy. Here, we have generated six such bispecific targeting proteins, each comprising two monomeric affibody molecules with specific binding to either of the two human epidermal growth factor receptors, EGFR and HER2, respectively. The bispecific constructs were designed with (i) alternative positioning (N- or C-terminal) of the different affibody molecules, (ii) two alternative peptide linkers $(Gly_4Ser)_3$ or $(Ser_4Gly)_3$, and (iii) affibody molecules with different affinity (nanomolar or picomolar) for HER2. Using both Biacore technology and cell binding assays, it was demonstrated that all six constructs could bind simultaneously to both their target proteins. N-terminal positioning of the inherent monomeric affibody molecules was favorable to promote the binding to the respective target. Interestingly, bispecific constructs containing the novel $(Ser_4Gly)_3$ linker displayed a higher affinity in cell binding, as compared to constructs containing the more conventional linker, $(Gly_4Ser)_3$. It could further be concluded that bispecific constructs (but not the monomeric affibody molecules) induced dimer formation and phosphorylation of EGFR in SKBR3 cells, which express fairly high levels of both receptors. It was also investigated whether the bispecific binding would influence cell growth or sensitize cells for ionizing radiation, but no such effects were observed.



INTRODUCTION

The EGFR-family consists of four members; EGFR, HER2, HER3, and HER4 (also known as ErbB1−4). The most extensively studied receptors are EGFR and HER2, while less is known about the other two. Abnormal expression and signaling of the receptors are associated with development and progression of several forms of cancer, and also associated with enhanced invasiveness and resistance to chemotherapy and radiation.[1,2] Activation of the receptors occurs through homo- or heterodimerization with another member of the EGFR family, resulting in trans-phosphorylation of tyrosine residues in the intracellular part of the receptor. These phosphorylation sites serve as initiation points for various signaling pathways leading to cellular processes such as proliferation, migration, and apoptosis. The effect on downstream signaling, and hence the biological outcome, depends on the composition of the receptor pair and the identity of the ligand.[3] HER2 is considered as the preferred dimerization partner for the other receptors,[4] and heterodimerization with HER2 leads to more potent signaling, for example, by decreased rate of ligand dissociation and receptor down-regulation.[3]

The EGFR family is a common target for both diagnostic and therapeutic applications. Several drugs have been developed with the intention to prevent oncogenic signaling by the receptors. Attempts have been made to interrupt dimerization and thus prevent "oncogenic effects" of the EGFRs. One such drug is the HER2-binding antibody pertuzumab (Omnitarg) which prevents HER2-dimerization.[5] Another possible approach is dual targeting of receptors where a binder that simultaneously targets two receptors could potentially prevent activating dimerization by steric interference.[6] Simultaneous targeting of two different receptors could also be used to improve the selective delivery of potent payloads to tumor lesions. Tuned bispecific binders could potentially be used to implicitly target receptors that are expressed also in normal tissue. By making a bispecific binder that binds moderately well

Received: February 9, 2012
Revised: August 7, 2012
Published: August 12, 2012

 © 2012 American Chemical Society

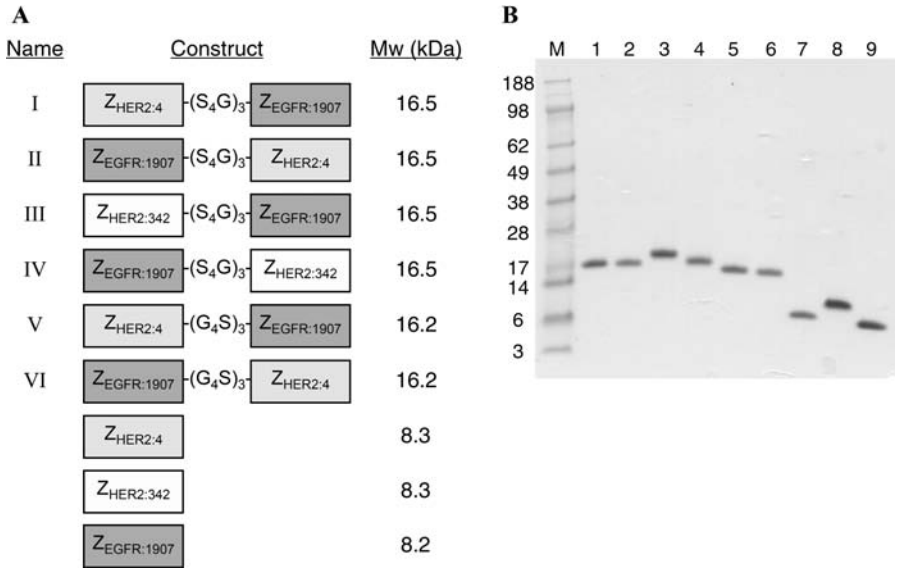


Figure 1. (A) Schematic overview of the six bispecific constructs designed and evaluated in this study, including their monomeric parent molecules. The bispecific binders are from now on denoted as constructs **I**–**VI**. The theoretical molecular weights are indicated to the right (kDa). (B) SDS-PAGE analysis of the IMAC-purified bispecific affibody molecules. Lanes I–VI: bispecific affibody molecules; lane 7, H_6-$Z_{HER2:4}$; lane 8, H_6-$Z_{HER2:342}$; lane 9, H_6-$Z_{EGFR:1907}$; lane M, marker proteins. Molecular weights are indicated in kDa.

to two different receptors, of which one is expressed also in normal tissue, the avidity effect will keep the bispecific binder bound mainly to cells expressing both receptors. The more a receptor is abundantly expressed in normal tissue, the weaker respective binder should be selected for the bispecific construct. This opens up the possibility to target EGFR positive tumors without excessive uptake in EGFR-expressing normal tissues. Coexpression of EGFR and HER2 has been reported in several cancers, and has been found as a prognostic marker in both NSCLC[7] and breast cancer.[8] This suggests that targeting both EGFR and HER2 may be of prognostic value and potentially advantageous in a treatment approach.

A first-generation bispecific affinity protein, generated from dimeric affibody molecules that target EGFR and HER2, has previously been generated and studied.[9] In the present study, we have generated bispecific affinity proteins based on monomeric EGFR and HER2 affibody molecules. The rational for this was that the very high affinity obtained by using dimeric affibody molecules, especially for the HER2-binder, would dominate the binding of the bifunctional construct as discussed in Friedman et al.[9] In the present study, we also investigate the influence of the linker and the positioning of the affibody molecules. Bispecific constructs were generated containing either of two different linkers, $(S_4G)_3$ or $(G_4S)_3$, and with the EGFR- and HER2-binding domains at either the N- or the C-terminus. The binding of the ligands, both in Biacore and to living cells, were studied together with their biological effects on receptor dimerization, phosphorylation, cellular growth, and survival after irradiation.

MATERIALS AND METHODS

Bacterial Strains and Vectors. The *Escherichia coli* (*E. coli*) bacterial strain RR1ΔM15[10] was used as host for all molecular cloning procedures and the *E. coli* strain BL21(DE3) was used for protein expression purposes. All bispecific constructs were subcloned into the expression vector pAY430, containing a multiple cloning site (the *Acc*I and *Pst*I restriction sites were employed here), a T7 promoter,[11] and a gene for Kanamycin (Km) resistance. In addition, pAY430 carries a gene sequence for an N-terminal hexahistidine tag (His_6-tag) and a C-terminal cysteine for purification purposes and site-specific labeling, respectively.

DNA Constructions. In order to construct affibody molecules with dual specificities, an EGFR-binding affibody molecule, $Z_{EGFR:1907}$,[12] and a HER2-binding affibody molecule, either the first generation binder $Z_{HER2:4}$[13] or the second generation binder $Z_{HER2:342}$,[14] displaying affinities toward HER2 of 50 nM and 22 pM, respectively, were recombinantly fused together head-to-tail. The resulting fusion proteins were separated by a 20-amino-acid-long linker sequence comprising either (SSSSG)-repeats or (GGGGS)-repeats for flexibility and separation of the binding domains. Moreover, variants of the bispecific construct where the EGFR- and HER2-binding arms were placed either at the N-terminus or the C-terminus were constructed. A schematic representation of the proteins can be seen in Figure 1A. The six bispecific binders are from now on denoted as constructs **I**–**VI**.

Each bispecific construct was assembled by amplification of the respective EGFR and HER2 affibody sequences (described in detail by Friedman et al.,[12] Wikman et al.,[13] and Orlova et al.[14]) in two separate PCR reactions and subsequent ligation of the resulting overlapping gene fragments. In a first reaction, the gene sequence of the affibody molecule to be placed at the N-terminus was PCR amplified using a forward primer introducing a *Pst*I restriction site and a reverse primer introducing the first part of the linker sequence and a *Sfi*I restriction site (Supporting Information). In a second reaction, the second part of the linker sequence, with a *Sfi*I restriction site, was introduced by the forward primer used to PCR amplify the affibody molecule to be placed at the C-terminus in the bispecific construct. Furthermore an *Acc*I restriction site was introduced by the reverse primer used in the second PCR reaction (Supporting Information). In addition, monomeric variants of $Z_{EGFR:1907}$, $Z_{HER2:4}$, and $Z_{HER2:342}$ were constructed as controls by amplification of the corresponding genes using forward and reverse primers with *Pst*I and *Acc*I restriction sites,

dx.doi.org/10.1021/bc3000645 | *Bioconjugate Chem.* 2012, 23, 1802–1811

respectively (Supporting Information). All PCR products were purified using a QIAquick PCR purification kit (QIAGEN) before digestion of the DNA fragments and the expression vector pAY430 (described above) with the appropriate restriction enzymes and subsequent ligation of inserts and vector. The resulting plasmids, encoding six different bispecific EGFR × HER2 constructs and three monomeric controls with an N-terminal His_6-tag and a C-terminal cysteine, were verified by sequencing before transformation into BL21(DE3) cells by heat chock for protein expression.

Protein Expression and Purification. The nine sequence confirmed affibody variants were expressed from pAY430 as His_6-tagged fusion proteins in the *E. coli* strain BL21(DE3). Transformed cells were grown overnight (ON) in 10 mL TSB + Y medium (30 g/L tryptic soy broth, 5 g/L yeast extract) supplemented with 50 μg/mL Km at 37 °C, 150 rpm. One milliliter of the ON culture was used for inoculation of 100 mL fresh medium (TSB + Y, 50 μg/mL Km) in shake flasks. The cells were grown at 37 °C, 200 rpm until $0.5 < OD_{600} < 1$, upon which gene expression was induced by addition of isopropyl-L-thio-β-D-galactopyranoside (IPTG) to a final concentration of 1 mM and protein expression was continued at 25 °C, 150 rpm ON. The cells were harvested by centrifugation, 2600 × *g*, 4 °C for 8 min, and the cell pellets stored at −20 °C until protein purification.

The nine His_6-tagged affibody variants were purified by immobilized metal ion chromatography (IMAC) under denaturing conditions. The cell pellets were dissolved in lysis buffer (7 M guanidine HCl, 47 mM Na_2HPO_4, 2.65 mM NaH_2PO_4, 10 mM Tris−HCl, 100 mM NaCl, and 20 mM β-mercaptoethanol, pH 8.0) and the cells lysed for 2 h at 37 °C under shaking before centrifugation, 30 000 × *g* for 20 min. The supernatants were passed through a 45 μm filter before loading on equilibrated (lysis buffer) HisPur Cobalt Resin (Thermo Fisher Scientific Inc., Rochester, NY, USA) columns. The bound proteins were washed with lysis buffer before elution with elution buffer (6 M urea, 50 mM NaH_2PO_4, 100 mM NaCl, 30 mM acetic acid, and 70 mM Na-acetate, pH 5.0) and subsequent buffer exchange of the purified proteins to PBS (2.68 mM KCl, 1.47 mM KH_2PO_4, 137 mM NaCl, and 8.1 mM Na_2HPO_4, pH 7.4) using PD-10 columns (GE Healthcare) according to the manufacturer's recommendations. The purity and identity of the recovered proteins were assessed by analyzing the proteins on SDS-PAGE, followed by Coomassie staining. Finally, in order to determine the concentration of the purified proteins, the absorbance at 280 nm was measured.

Conjugation with *N*-Ethylmaleimide. In order to prevent potential dimer formation due to the C-terminal cysteines and consequent interference with future experiments, the cysteines of the six bispecific and the three monomeric affibody molecules were capped by conjugation with *N*-ethylmaleimide (NEM). Approximately 2 mg of purified protein in 50 mM Tris-HCl, pH 8, was reduced with 30 mM dithiothreitol (DTT) for 30 min at 40 °C under shaking. Excess DTT was removed by passing the protein through a NAP-5 size exclusion chromatography (SEC) column (GE Healthcare) and the buffer was exchanged to 0.1 M NaAc, pH 6. A 5-fold excess of NEM was added to the reduced proteins and incubated at 40 °C for 1 h, after which unreacted NEM was removed by again passing the proteins over a SEC column and the buffer was exchanged to PBS. The efficiency of the conjugation with NEM was evaluated using mass spectrometry on an Agilent Technologies 6520 Accurate-Mass Q-TOF LC/MS system (Agilent) according to the manufacturer's recommendations. NEM-conjugated affibody molecules were used in all subsequent biosensor and cell studies.

Binding Analysis Using SPR. A Biacore 3000 instrument (GE Healthcare) was used to study the binding interaction between the six bispecific affibody molecules and the two targets EGFR and HER2. Recombinant human EGFR-Fc (hEGFR-Fc) and human HER2-Fc (hHER2-Fc) was immobilized on two of the flow-cell surfaces of a CM-5 sensor chip (GE Healthcare) according to the manufacturer's instructions. To a third flow-cell, a solution of equal amounts of EGFR-Fc and HER2-Fc was used to immobilize both targets on the same surface. One surface of the chip was activated and deactivated and used as a reference surface in all experiments.

In order to verify retained binding to EGFR and HER2 of the respective binding arms, the six NEM-capped, bispecific affibody molecules were diluted to 500 nM and 125 nM in HBS-EP buffer (10 mM Hepes, 150 mM NaCl, 3 mM EDTA, and 0.005% surfactant P20, pH 7.4) and subjected to kinetic analysis of their binding to EGFR and HER2. The proteins were injected over all surfaces at a flow rate of 30 μL/min for 3 min, followed by dissociation for 5 min. Monomeric $Z_{EGFR:1907}$, $Z_{HER2:4}$, and $Z_{HER2:342}$ were injected likewise as controls. All samples were run in duplicate.

In a second SPR biosensor experiment, the bispecific affibody molecules were investigated for their ability to bind EGFR and HER2 simultaneously in a sandwich-like setup. The bispecific proteins were diluted to 500 nM in HBS-EP buffer and injected over all surfaces at a flow rate of 30 μL/min. Following an association phase of 6 min, hEGFR-Fc or hHER2-Fc, diluted to a concentration of 100 nM in HBS-EP, was injected for an additional 4 min, followed by dissociation for 5.5 min.

After all injection cycles, the flow-cell surfaces were regenerated by injection of 15 μL 10 mM HCl. Data evaluation and estimation of the kinetic parameters k_a and k_d were performed using the software *TraceDrawer 1.1* (Ridgeview Instruments AB) assuming a one-to-one binding model.

Cell Lines. The human breast cancer cell line SKBR-3, the gastric carcinoma cell line NCI-N87, and the human squamous carcinoma cell line A-431 were purchased from ATCC (American Type Culture Collection). SKBR-3 cells express approximately 6×10^6 HER2 and 4×10^5 EGFR receptors per cell.[15] A-431 expresses 2×10^6 EGFR and 10^5 HER2.[15] We have not been able to detect HER2 by Western blot in A-431 cells without prior immunoprecipitation. NCI-N87 express relatively high levels of both receptors.[16] SKBR-3 and NCI-N87 cells were cultivated in RPMI1640, and A-431 cells in Ham's F-10. All cell culture media were supplemented with 10% fetal serum albumin (FBS), 2 mM L-glutamin, 100 IU/mL penicillin, and 100 μg/mL streptomycin.

LigandTracer Binding Assay. 20 MBq of ^{125}I was added to 5 μL of *N*-succinimidyl *p*-(trimethylstannyl)benzoate (SPMB) (1 mg/mL 5% acetic acid in methanol). Radiolabeling was initiated by adding 20 μL of chloramine-T (2 mg/mL, 5% acetic acid in MeOH) and mixed for 5 min. Labeling reaction was terminated by adding 40 μL sodium metabisulfite (NBS) (2 mg/mL in water). Reaction mixture evaporated to dryness with argon gas followed by addition of 40−60 μg of the bispecific affibody molecules (1 μg/μL in 0.1 M borate buffer pH 9). The coupling reactions continued for 1.5 h with continuous shaking. Reaction mixtures were separated on NAP-5 columns and the high-molecular-weight fractions containing

Table 1. Kinetic Data from the SPR Biosensor Analysis of the Bispecific Affibody Molecules

	EGFR[a]			HER2[a]			EGFR × HER2[a]		
	k_a (M^{-1} s^{-1})[b]	k_d (s^{-1})[b]	K_D (nM)[b]	k_a (M^{-1} s^{-1})[b]	k_d (s^{-1})[b]	K_D (nM)[b]	k_a (M^{-1} s^{-1})[b]	k_d (s^{-1})[b]	K_D (nM)[b]
I	1.1×10^4	5.3×10^{-4}	47	9.6×10^4	1.1×10^{-2}	115	*ND*	*ND*	*ND*
II	1.7×10^4	5.0×10^{-4}	29	9.8×10^4	1.7×10^{-2}	172	*ND*	*ND*	*ND*
III	6.8×10^3	5.9×10^{-4}	86	5.3×10^4	3.2×10^{-4}	6	4.7×10^4	1.7×10^{-4}	4
IV	1.1×10^4	6.1×10^{-4}	55	4.2×10^4	4.1×10^{-4}	10	3.9×10^4	1.3×10^{-5}	0.3
V	1.3×10^4	5.6×10^{-4}	43	1.1×10^5	1.3×10^{-2}	118	*ND*	*ND*	*ND*
VI	1.5×10^4	5.2×10^{-4}	35	8.7×10^4	1.9×10^{-2}	219	*ND*	*ND*	*ND*

[a]The analytes, bispecific affibody molecules, were injected over immobilized EGFR, HER2, and a mixed surface containing both EGFR and HER2. [b]Kinetic parameters were estimated using *TraceDrawer*. [c]*ND* = not determined

the ^{125}I-labeled proteins were eluted in 1 mL according to the manufacturer's recommendations.

SKBR-3 or A-431 cells were seeded on a local part of a cell dish (as described by Björke et al.[17]) and cultivated until the cell number was approximately 10^6. The ^{125}I-labeled bispecific affibody molecule was added to the cell dish and real-time ligand−cell interaction was monitored in room temperature with LigandTracer Grey (Ridgeview Instruments AB) by measurement of ^{125}I.[18,19] The concentration of ligand ranged from 20 to 210 nM depending on the calculated affinity for the receptors (data from SPR biosensor analysis, Table 1). Three experimental set-ups on both cell lines were used for all six binders: uptake at three different concentrations followed by retention, and two control experiments where one of the receptors was blocked by preincubation with 10-fold molar excess of a monovalent nonlabeled affibody molecule, $Z_{EGFR:1907}$, $Z_{HER2:4}$, or $Z_{HER2:342}$. Data evaluation and estimation of the equilibrium dissociation constant K_D were performed using the software *TraceDrawer 1.3* (Ridgeview Instruments AB) using a one-to-one binding model.

Receptor Phosphorylation and Dimerization Assays. Cell lysis and Western blotting was performed as previously described.[20] Antibodies specific for HER2 and phosphotyrosine (pY99) were from Santa Cruz Biotechnology. The anti-EGFR antibody was from Cell Signaling Technology. Antimouse and antirabbit antibodies linked with horseradish peroxidase were purchased from Invitrogen. The antibody directed to β-actin was from Sigma-Aldrich. All antibodies were used according to the manufacturer's instructions in PBS-T with 1% BSA and 0.1% NaAzide. For the dimerization study, the cells were washed with PBS and then incubated with 5 mM BS^3 (Bis(Sulfosuccinimidyl) suberate) (Thermo Fisher Scientific Inc.) for 30 min at room temperature. To end the cross-linking reaction, 1 M Tris-Cl was added to a final concentration of 20 mM and set on bench for 15 min. After this, the cells were lysed according to standard protocols and subjected to SDS-PAGE on NuPAGE 3−8% Tris-Acetate gels. DuoSet IC kit measuring phospho-EGFR and phospho-HER2 by ELISA were purchased from R&D Systems.

Clonogenic Assay. Subconfluent cultures of SKBR-3 cells were treated with 10 nM $Z_{HER2:342}$, construct **IV**, or left untreated for 2 h at 37 °C. Thereafter, the cells were irradiated with ^{137}Cs γ-ray photons at a dose rate of 1.034 Gy/min. The total dose was 4 or 8 Gy. Then, the cells were allowed to repair for about 16 h at 37 °C before trypsinized and reseeded at suitable concentrations. The cells were cultured for 3 weeks and then fixed in 97% ethanol and stained with hematoxylin. Colonies with more than 50 cells were counted.

Proliferation Assay. SKBR-3 and NCI-N87 cells were treated with 20 nM construct **II** or left untreated. The culture media and substances were replaced twice a week. Before the cells became confluent, they were trypsinized and counted. After this, a subpopulation was reseeded for further cultivation. The growth curves are calculated as if all cells were reseeded at each subcultivation. Three parallel culture flasks were kept for each experiment. The cell growth was monitored for 35 days in total.

Statistical Methods. Unpaired *t* tests were used to test for significant differences both in phosphorylation levels and survival. If $P < 0.05$, the difference was considered as significant.

RESULTS

Generation of Bispecific EGFR × HER2 Affibody Molecules. The six bispecific affibody molecules $Z_{HER2:4}$-$(S_4G)_3$-$Z_{EGFR:1907}$, $Z_{EGFR:1907}$-$(S_4G)_3$-$Z_{HER2:4}$, $Z_{HER2:342}$-$(S_4G)_3$-$Z_{EGFR:1907}$, $Z_{EGFR:1907}$-$(S_4G)_3$-$Z_{HER2:342}$, $Z_{HER2:4}$-$(G_4S)_3$-$Z_{EGFR:1907}$, and $Z_{EGFR:1907}$-$(G_4S)_3$-$Z_{HER2:4}$, hereafter named constructs **I**−**VI** (Figure 1A), and the three corresponding monomeric control proteins $Z_{HER2:4}$, $Z_{HER2:342}$, and $Z_{EGFR:1907}$ were expressed in *E. coli* as His_6-tagged fusion proteins. The His_6-tag was employed for purification of the affibody molecules by IMAC. Subsequent analysis of the purified proteins by SDS-PAGE revealed pure protein products of the approximate expected molecular weights (Figure 1B). The theoretical molecular weights of all proteins are indicated in Figure 1A. The slight differences in migration pattern are most likely due to the differences in amino acids recruited at the binding surface, since such variations have been observed previously. From $Abs_{280\ nm}$ measurements, the concentrations of all purified proteins could be determined, and the average yield was calculated to 120−170 mg purified protein per liter cultivation.

All proteins were produced with a C-terminal cysteine to provide means for site-specific modifications of the proteins (e.g., labeling with fluorophores or radioactive isotopes) should that be desired. However, for the initial characterization of the proteins by SPR biosensor analysis, capping of the free cysteines in order to prevent potential dimer formation of the proteins was advisible. Accordingly, the six bispecific affibody molecules and the monomeric control proteins were conjugated with *N*-ethylmaleimide. Subsequent MS analysis of the conjugated proteins revealed pure products with the correct molecular weight (data not shown).

Bispecific EGFR × HER2 Affibody Molecules Show Binding in SPR Analysis. In order to verify preserved functionality of the respective binding arms, the six bispecific affibody molecules were subjected to kinetic binding analysis to EGFR and HER2, using real-time biosensor analysis on a Biacore instrument. The bispecific proteins were injected at different concentrations over surfaces containing immobilized

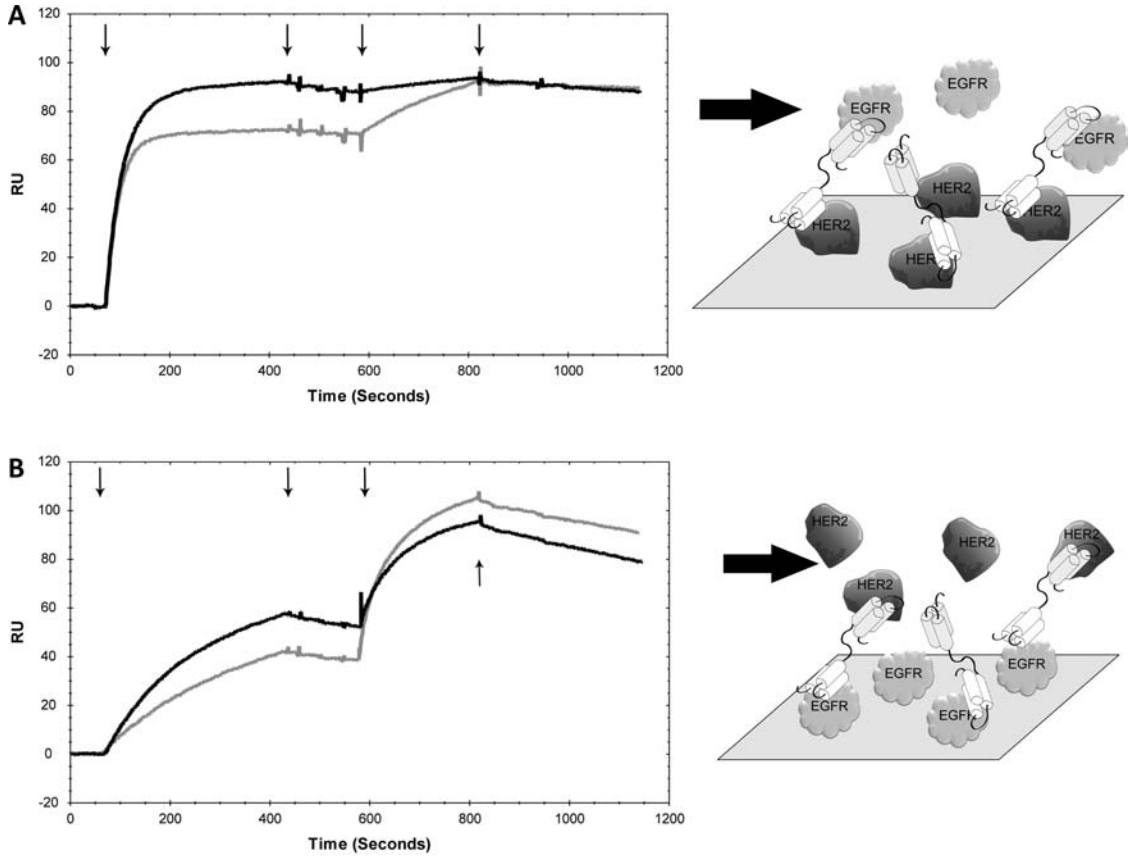


Figure 2. Sandwich analysis of the simultaneous binding to EGFR and HER2 measured in Biacore. Soluble EGFR or HER2 was injected after the bispecific affibody molecules **III** (Black) or **IV** (Gray) were allowed to bind to immobilized HER2 (A) or EGFR (B). In a second step, the bispecific affibody molecules could capture soluble EGFR or HER2 when already bound to their corresponding immobilized binding partner. Arrows indicate the start and end time points when substances were injected. To the right are schematic representations of the respective experimental setup in (A) and (B).

EGFR and HER2, respectively. Sensorgrams obtained from the biosensor analysis showed that both binding arms had preserved functionality and could bind to EGFR and HER2, respectively. Furthermore, it was shown that all bispecific affibody variants could bind to both EGFR and HER2 irrespective of the orientation of the binding domains (N- or C-terminus).

Using the binding-curve evaluation software *TraceDrawer*, the kinetic parameters, k_a and k_d as well as the dissociation equilibrium constant (K_D), for the EGFR and HER2 binding domains of the bispecific molecules interacting with their respective targets could be determined and are presented in Table 1. Since the constructs are bispecific the model used, assuming a 1:1 binding, is not ideal but will result in kinetic values of reasonable accuracy. All constructs displayed a slightly reduced affinity to their respective targets as compared to their monomeric parental molecules ($Z_{HER2:4}$, K_D = 50 nM and $Z_{HER2:342}$, K_D = 22 pM for HER2, and $Z_{EGFR:1907}$ K_D = 5 nM for EGFR).[12−14] The reduced affinity could largely be explained by a slower on-rate of the bispecific molecules. It was furthermore observed that the affinity to the target was increased when the binding domain was placed at the N-terminus. This observation was seen for both the EGFR- and HER2-binding affibody domains.

To a third surface of the Biacore chip, a mixture of EGFR and HER2 was immobilized and the simultaneous binding of the constructs to both targets was investigated. From the obtained sensorgrams, it was clear that, when allowed to interact with both receptors on the mixed target surface, all constructs displayed avidity effects and an increase in affinity in an additive manner, strongly suggesting that both binding arms of the bispecific constructs were simultaneously involved in the binding interaction. For constructs **III** and **IV**, containing the high-affinity anti-HER2 domain $Z_{HER2:342}$, the kinetic parameters and affinity for binding to the mixed surface could be determined. The affinity was shown to increase when both binding domains were recruited as compared to when binding to only one of the receptors with one arm (Table 1).

In a separate experiment, the simultaneous binding to both targets was investigated by a sandwich assay in which soluble EGFR and HER2 was injected after the bispecific affibody constructs **III** and **IV**, which in a first step had been allowed to bind to immobilized EGFR or HER2. The obtained sensorgrams showed that both bispecific variants could capture soluble EGFR and HER2 when already bound to their corresponding immobilized target (Figure 2). For construct **IV**, simultaneous binding to both targets was possible irrespective of whether the bispecific molecule was allowed to bind EGFR or HER2 first. For construct **III**, simultaneous binding to both targets was clearly possible when construct **III** was allowed to first interact with immobilized EGFR and thereafter capture HER2 in solution (Figure 2B). When first allowed to bind immobilized HER2, a weak increase in response when soluble EGFR was injected indicated that

dx.doi.org/10.1021/bc3000645 | *Bioconjugate Chem.* 2012, 23, 1802−1811

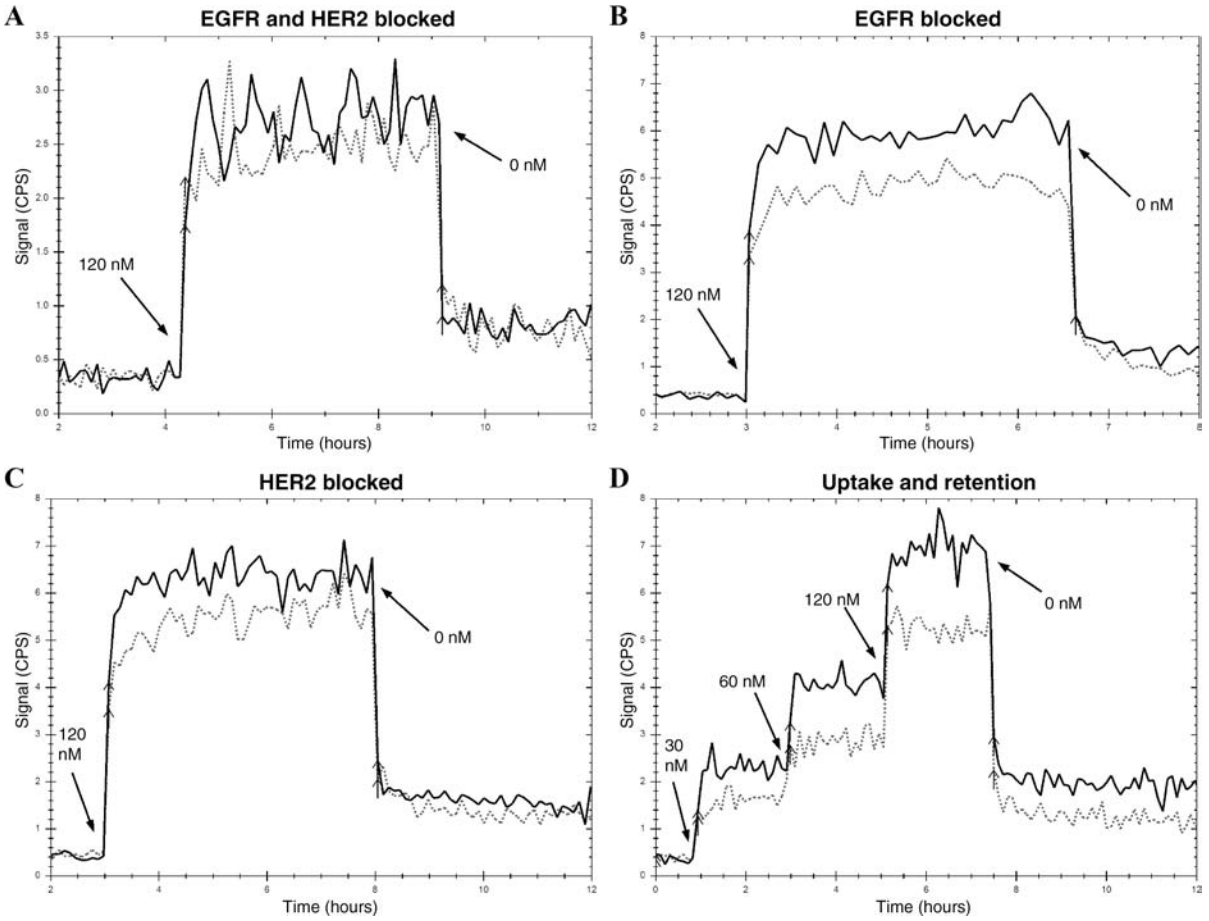


Figure 3. Binding curves of ^{125}I-labeled construct **I** to SKBR-3 cells measured in real time in *LigandTracer*. (A,B,C) ^{125}I-**I** was added at 120 nM to a cell dish which had already been incubated with 1.2 μM of unlabeled monomer ligand, $Z_{EGFR:1907}$ (B), $Z_{HER2:4}$ (C), or both (A). (A) After preblocking with both ligands, no binding could be monitored. (B,C) After preblocking with one of the ligands, some binding to the cells could be detected, most visible during the association phase. (D) ^{125}I-**I** was added to the cell dish in three concentrations, 30 nM, 60 nM, and 120 nM. After 7.5 h, the ligand was removed and the retention was followed. After 24 h, some binding could still be detected. Dotted line indicates the reference area were there were no cells, i.e., the background.

simultaneous binding was possible also in this situation, although less pronounced compared to construct **IV**. However, since both constructs could interact with both targets simultaneously in Biacore, binding studies using living cells were undertaken to further explore the interactions.

LigandTracer Cell Binding Assay. The interaction of the bispecific affibody molecules with living cells was analyzed by measuring the real-time binding of ^{125}I-labeled affibody constructs in LigandTracer. SKBR-3 cells, which express both EGFR and HER2 at relatively high levels, were used to investigate if the bispecific affibody ligands could bind both receptors. The second cell line, A-431, mainly express EGFR at high levels. All six binders were tested on both cell lines and for three experimental set-ups: cell binding at three different concentrations followed by retention, and two control experiments in which one of the receptors was blocked by preincubation of 10-fold molar excess of a monovalent nonlabeled affibody molecule, $Z_{EGFR:1907}$, $Z_{HER2:4}$, or $Z_{HER2:342}$. Preblocking of both receptors by adding both $Z_{EGFR:1907}$ and $Z_{HER2:4}$ was performed for construct **I**. Representative binding curves on SKBR-3 cells for ^{125}I-**I** are shown as an example in Figure 3. Data for all binders are summarized in Table 2 as estimated K_D calculated with *TraceDrawer* using a 1:1-binding model, or indicated as W when K_D could not be calculated due to weak binding (signal), or N when no binding was detected.

Table 2. Kinetic Data from the Binding Assay in Living Cells on *LigandTracer*

	binding to SKBR-3 cells K_D[a] (nM)			binding to A-431 cells K_D[a] (nM)		
	no block	preblock $Z_{HER2:4}/Z_{HER2:342}$	preblock $Z_{EGFR:1907}$	no block	preblock $Z_{HER2:4}/Z_{HER2:342}$	preblock $Z_{EGFR:1907}$
I	14	W	W	7	9	N
II	24	W	W	8	16	N
III	5	N	6.3	64	N	N
IV	2	N	2	0.3	2.7	N
V	370	N	W	120	W	N
VI	1000	N	N	28	17	N

[a]Kinetic parameters were estimated using *TraceDrawer* using a 1:1-binding model. W = weak binding, no kinetic parameters could be calculated. N = not detectable (no signal of binding was obtained).

As can be seen in Figure 3A, blocking both receptors suppressed binding of the bispecific affibody molecules completely, while blocking only one of the receptors resulted in weak but visible binding, notable during the association phase (Figure 3B,C). However, without any preblocking, a clear binding rate could be seen during both binding and retention

dx.doi.org/10.1021/bc3000645 | *Bioconjugate Chem.* 2012, 23, 1802−1811

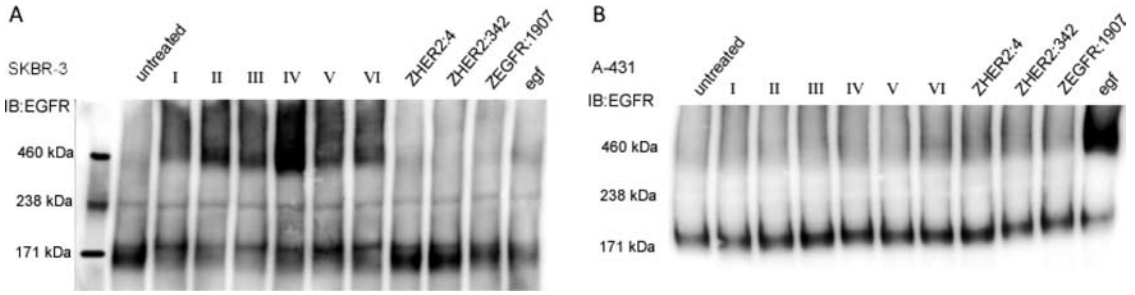


Figure 4. Dimerization assay of the bispecific binders. Monomeric affibody molecules and EGF were used as controls. After stimulation by 100 nM of each substance for 1 h at 37 °C, the chemical cross-linker BS^3 was added. EGF-treatment was only 5 min to minimize internalization. After cell lysis, the samples were subjected to SDS-PAGE, followed by transfer and Western blot. (A) SKBR-3 cells. (B) A-431 cells.

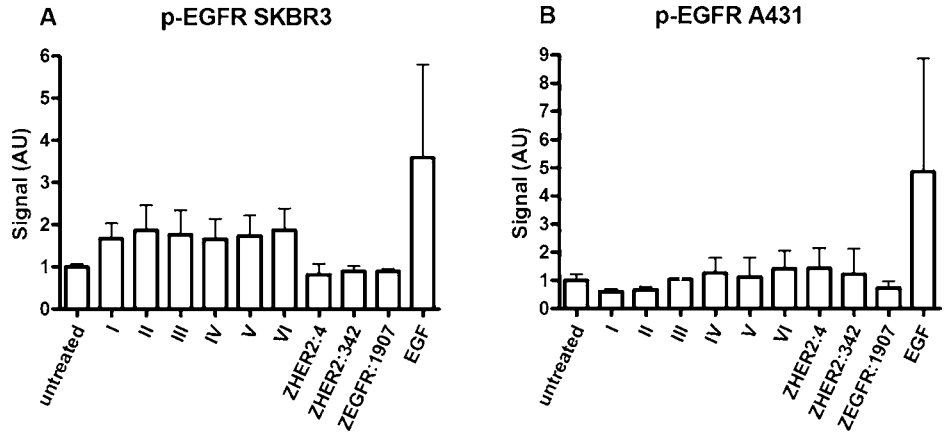


Figure 5. (A,B) Phosphorylation study of the EGFR receptor by ELISA. SKBR-3 cells (A) or A-431 cells (B) were stimulated by 100 nM of each substance for 1 h at 37 °C. EGF treatment was only 5 min to minimize internalization. To enable comparison between different experiments, the obtained values were normalized to its respective untreated control. The graphs show mean values from 4 experiments with standard deviations. Constructs **I**–**VI** and EGF significantly deviate from the untreated control in SKBR-3 cells, while the difference is significant only for EGF in A-431 cells (unpaired t test, $P < 0.05$).

phases (Figure 3D), indicating an avidity effect of construct **I**. Similar results were obtained also for construct **II**. On the other hand, neither of the constructs containing the affinity matured HER2-binder $Z_{HER2:342}$ (constructs **III** and **IV**) showed the same avidity effect on SKBR-3 cells as the constructs with $Z_{HER2:4}$. Binding to a cell surface where only HER2 was available (i.e., preblocking by $Z_{EGFR:1907}$ on SKBR-3 cells) resulted in the same apparent affinity as when EGFR was also available (Table 2).

Interestingly, the two constructs with the linker $(G_4S)_3$ (**V** and **VI**) demonstrated lower affinity than the corresponding constructs with the linker $(S_4G)_3$ (**I** and **II**). For **V** and **VI**, a difference in affinity depending on the orientation of $Z_{HER2:4}$ could also be seen, verifying the observation from the Biacore analysis that positioning at the N-terminus improves affinity. Construct **V** displayed higher affinity than **VI** to SKBR-3 cells (Table 2).

In the A-431 cell line, no binding could be seen when EGFR was blocked by $Z_{EGFR:1907}$, indicating that HER2 expression is too low to allow detection in LigandTracer. Constructs **II**–**V** showed improved binding to the cells when both receptors were present compared to when HER2 was blocked. It should be noted that, for construct **IV**, the K_D for A-431 is the same as when both receptors were present in the Biacore assay (0.3 nM). Both constructs **IV** and **VI**, which have higher affinity for the cells than **III** and **V**, respectively, shows that the affinity was favored by positioning of $Z_{EGFR:1907}$ at the N-terminus.

Receptor Phosphorylation and Dimerization. The effect of the bispecific affibody molecules on receptor phosphorylation and receptor dimerization were measured using Western blot and ELISA. As can be seen in Figure 4A, treatment by the bispecific constructs increased the levels of dimerized EGFR in SKBR-3 cells. The low level of dimerization shown after EGF treatment could be explained by rapid internalization and degradation of EGF-EGFR complexes. It should also be noticed that the assay cannot distinguish between homodimers and heterodimers. The levels of phosphorylated EGFR were also increased in SKBR3 cells when treated with constructs **I**–**VI** (Figure 5A). The control affibody molecules in monomeric forms, $Z_{EGFR:1907}$, $Z_{HER2:4}$, and $Z_{HER2:342}$, did not induce any dimerization or phosphorylation differing from the untreated cells. The phosphorylation results were confirmed by Western blot (data not shown). The levels of dimerized and phosphorylated HER2 were already high in unstimulated SKBR-3 cells. This can be explained by the high number of HER2 receptors, since overexpression is believed to lead to spontaneous dimerization and activation.[21,22] The six bispecific affibody molecules and EGF all had a tendency to increase the HER2 dimerization and phosphorylation in SKBR-3 cells, but due to the high background level, this was not significant (Supporting Information Figure S1).

In A-431 cells, none of the affibody molecules changed the receptor dimerization or phosphorylation (Figures 4B and 5B). The level of EGFR dimers was low in unstimulated A-431, but

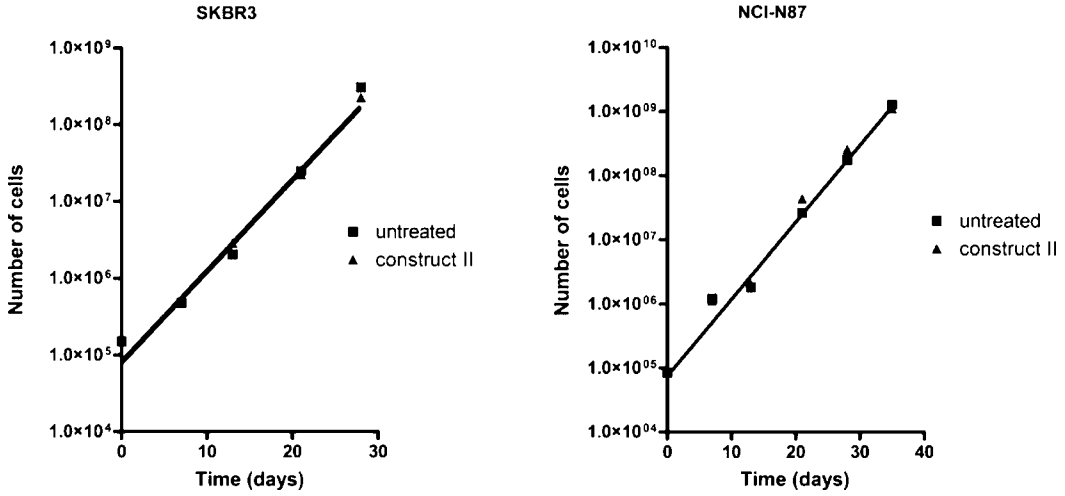


Figure 6. Proliferation assay. SKBR-3 and NCI-N87 cells were continuously treated with 20 nM of construct **II** or left untreated as a control. The cells were counted once a week, and a subpopulation was reseeded for further cultivation. No differences in growth rate were seen.

could be increased by treatment with EGF for 5 min (Figure 4B). Stimulation with EGF also resulted in increased phosphorylation levels of both EGFR (Figure 5B) and HER2; albeit, the level of HER2 was very low (data not shown).

Cell Proliferation Assay. To analyze if the bispecific affibody molecules could influence the proliferation of EGFR- and HER2-expressing cells, SKBR-3 and NCI-N87 cells were continuously treated with construct **II**. This binder was selected as the most interesting candidate of the six, since it showed avidity on SKBR-3 cells and that this orientation of the binding domains was preferable compared to construct **I**. As can be seen in Figure 6, construct **II** did not affect cell growth compared to untreated cells either in SKBR-3 or NCI-N87 cells.

Radiosensitizing Effects Analyzed by a Clonogenic Survival Assay. In order to further assess the biological effect of the bispecific affibody molecules and also compare with the previous bispecific binder from Friedman et al.,[9] $(Z_{HER2:342})_2$-$(G_4S)_3$-$(Z_{EGFR:1907})_2$, containing bivalent HER2- and EGFR-binding affibody molecules, a clonogenic survival assay on SKBR-3 cells was set up. Cells were analyzed after treatment with affibody molecules and ionizing radiation. Survival is shown in Figure 7. The four substances could be divided into two groups. Construct **IV** and monomeric $Z_{HER2:342}$, which both contain only one HER2-binding affibody moiety, did not differ from the untreated control. Interestingly, a dimeric HER2 binding construct $(Z_{HER2:342})_2$ and the previously studied bispecific $(Z_{HER2:342})_2$-$(G_4S)_3$-$(Z_{EGFR:1907})_2$ (denoted as **X** in Figure 7) significantly decreased survival ($P < 0.01$). Apparently, the valency of the HER2-binder is of importance for the effect of the ligand. Survival after 4 Gy of γ-irradiation did not differ between the two groups (data not shown).

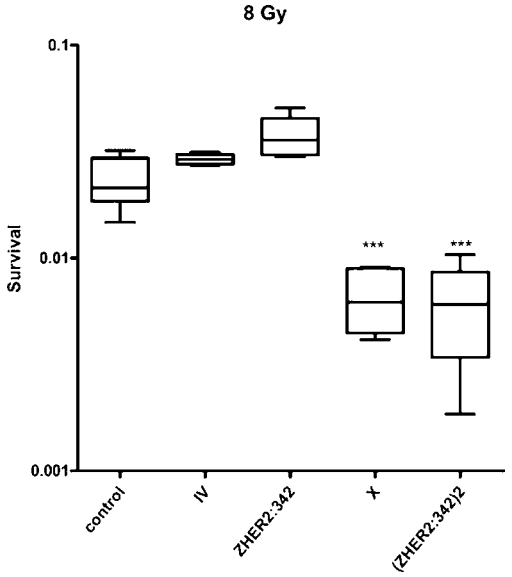


Figure 7. Clonogenic survival of SKBR-3 cells after irradiation by 8 Gy. Cells were treated with construct **IV**, $Z_{HER2:342}$, $(Z_{HER2:342})_2$-$(G_4S)_3$-$(Z_{EGFR:1907})_2$ (denoted as **X**), or $(Z_{HER2:342})_2$ for 2 h prior to irradiation and allowed to repair for 16 h before reseeding. After 3 weeks of cultivation, colonies containing more than 50 cells were counted and the survival fraction could be calculated. $(Z_{HER2:342})_2$ and the bispecific $(Z_{HER2:342})_2$-$(G_4S)_3$-$(Z_{EGFR:1907})_2$ significantly decreased survival ($P < 0.01$, unpaired t test), while treatment with $Z_{HER2:342}$ or construct **IV** did not differ from the irradiated control. Mean values and standard deviations are calculated on at least 3 replicates.

DISCUSSION

Six different bispecific affibody molecules with specificity to EGFR and HER2 were constructed by assembling gene sequences of previously described individual affibody molecules targeting EGFR or HER2.[12−14,23] The EGFR-binding affibody variant, $Z_{EGFR:1907}$, reported to bind to EGFR with an apparent affinity of 5 nM[12] was combined with two different variants of a HER2-binding affibody molecule, a first generation binder $Z_{HER2:4}$, binding to HER2 with an affinity of 50 nM,[13] and a second generation, affinity matured binder, $Z_{HER2:342}$, with an affinity to HER2 of 22 pM.[14] The two binding domains, directed at EGFR and HER2, were assembled head-to-tail, separated by a spacer sequence encoding a 20-amino-acid-long glycine- or serine-based linker, to facilitate flexibility and separation of the two binding arms. Furthermore, the influence of the N- or C-terminal positioning of the affibody molecules comprising the bispecific constructs was investigated.

Real-time biosensor analyses using Biacore showed that all bispecific constructs retained functionality in both binding arms and, furthermore, were capable of simultaneous interaction with

dx.doi.org/10.1021/bc3000645 | Bioconjugate Chem. 2012, 23, 1802−1811

both targets. Although the constructs displayed a reduced affinity to the targets compared to the monospecific control proteins, this was largely counteracted when the bispecific molecules were allowed to interact with both target proteins. Constructs **III** and especially **IV** showed increased affinity when binding to both EGFR and HER2, compared to when only one receptor was present. The Biacore data furthermore revealed a significant influence from the positioning of the binding domains. An N-terminal positioning was more favorable for the affinity to the respective targets. Also, LigandTracer analysis in living cells supported the observation that the affinity for each target was increased when the binder is placed at the N-terminus. This was most noticeable for constructs **V** and **VI**, which were the constructs with the overall lowest affinity. In SKBR-3 cells where the binding predominantly originates from the HER2-binding part, construct **V** had higher affinity than **VI**. In A-431 cells where binding is predominantly to EGFR, construct **VI** had higher affinity than **V** (Table 2). Interestingly, bispecific constructs containing the novel $(S_4G)_3$ linker displayed a higher affinity in cell binding, as compared to constructs containing the more conventional linker, $(G_4S)_3$.

Ligand binding to SKBR-3 cells showed that the constructs containing $Z_{HER2:4}$ and the linker $(S_4G)_3$ (**I** and **II**) displayed an avidity effect when both receptors were present (Figure 3 and Table 2), indicating that both binding arms of the bispecific constructs were involved in the binding interaction. In A-431 cells, constructs **II**–**V** showed increased binding when both receptors were present compared to when only EGFR was available. When EGFR was blocked, no binding could be detected in this cell line.

The differences in results between the binding data from the Biacore and the LigandTracer experiments (as well as between the two cell lines) can to a great extent be explained by the big differences in receptor numbers. In the Biacore setup, the EGFR and the HER2 receptor were present at approximately equal numbers, while in LigandTracer, it depended on the cell line. SKBR-3 cells have approximately 6×10^6 HER2 receptors but only 4×10^5 EGFR receptors.[15] Furthermore, in Biacore the binding is measured to recombinant proteins in an artificial environment, while the binding in LigandTracer is measured to functional receptors expressed on living cells.

The balance in receptor number as well as the difference in affinity for the two targets seems to have large impact on the binding characteristics of a bispecific binder. This can be exemplified by construct **IV**: In SKBR-3 cells, binding is predominantly originating from the high affinity HER2-binder $Z_{HER2:342}$ and no apparent contribution from the EGFR-binding part can be seen. In sharp contrast, in A-431 cells and to the mixed receptor surface in the Biacore, the construct shows avidity.

The Western blots after cross-linking with BS^3 clearly shows that all six bispecific affibody molecules induce EGFR dimerization when added to SKBR-3 cells. However, the assay cannot distinguish between fully functional receptor dimers and receptors that are merely present at the cell membrane in such proximity of each other that they can be cross-linked by BS^3. The phosphorylation results, which show a small significant increase in phosphorylated EGFR after treatment with bispecific binders, indicate that the EGFR is functionally dimerized. This is probably a heterodimer with HER2 since the monomeric $Z_{EGFR:1907}$ does not induce dimers or receptor phosphorylation (Figures 4 and 5). Why no significant HER2 dimerization and phosphorylation could be measured can be explained by the high background level of activated HER2 together with the known differences in receptor number of EGFR and HER2. The small increase of heterodimeric HER2 is probably masked by the large amount of HER2 dimers already existing and therefore cannot be quantified by our methods.

Dimerization of the EGFR family is known to be entirely receptor-mediated.[6] EGF simultaneously binds to both domain I and III on EGFR and is thereby believed to stabilize the receptor in its "open" configuration where the dimerization loop on domain II is exposed.[24] Whether the bispecific affibody molecules can induce functional receptor dimerization could be answered by the ability of the monomeric $Z_{EGFR:1907}$ to expose the dimerization arm. The HER2-binding part is of less importance since HER2 has its dimerization arm constitutively exposed. A previous study by Nordberg et al.[25] shows that $(Z_{EGFR:955})_2$ partly competes for the same epitope as EGF, and partly with the same epitope as Cetuximab (domain III). $Z_{EGFR:1907}$ is an affinity matured version of $Z_{EGFR:955}$ and should therefore bind the same epitope. Hence, $Z_{EGFR:1907}$ is likely to bind to domain III of EGFR.

To evaluate and compare the biological effect of the bispecific affibody molecules in this study, with the previous one described by Friedman et al.,[9] we analyzed the ability of the affibody molecules to sensitize for ionizing radiation in SKBR-3 cells. The HER2-binding part, $Z_{HER2:342}$ and $(Z_{HER2:342})_2$, of the constructs were used as control substances. Survival after 8 Gy γ-irradiation divided the substances into two groups; construct **IV** had no effect on the survival, similar to that of its HER2-binding part $Z_{HER2:342}$, while $(Z_{HER2:342})_2$ and $(Z_{HER2:342})_2$-$(G_4S)_3$-$(Z_{EGFR:1907})_2$ (denoted as **X** in Figure 7) significantly decreased survival compared to the irradiated control. Apparently, the valency of the binder in the bispecific construct is of importance, as speculated in our previous study.[9] Perhaps the "tetravalent" affinity protein $(Z_{HER2:342})_2$-$(G_4S)_3$-$(Z_{EGFR:1907})_2$ can bind two EGFR and two HER2 receptors, at least to some extent. Most likely, the receptor binding of $(Z_{HER2:342})_2$-$(G_4S)_3$-$(Z_{EGFR:1907})_2$ is dominated by the high-affinity ligand $(Z_{HER2:342})_2$. Furthermore, the proliferation assay showed that construct **II** had no effect on SKBR-3 or NCI-N87 cell growth.

To conclude, we have shown that using monomeric EGFR and HER2 for assembly of bispecific binders, rather than its dimeric equivalents, is more successful for making a functional bispecific affinity protein. Further, we have shown that all three monovalent binders are more functional when positioned at the N-terminal part of the construct and also that the linker $(S_4G)_3$ renders higher affinity of the bispecific binders compared to $(G_4S)_3$ on living cells. In this study, all six binders can simultaneously bind EGFR and HER2, without large effects on cells. Additional future studies should be conducted in vivo to further investigate the therapeutic effects of the bispecific constructs. This could furthermore advance our understanding of the effects from simultaneous targeting of EGFR and HER2.

■ ASSOCIATED CONTENT

Ⓢ Supporting Information

List of the sequences of all primers used for the construction of the bispeciffic affibody molecules. Figure S1 shows the Western blot analysis of phosphorylated EGFR in two different cell lines (SKBR-3 and A-431) after treatment with the bispecific affibody molecules. This material is available free of charge via the Internet at http://pubs.acs.org.

AUTHOR INFORMATION

Corresponding Author

*Phone: +46 8 5537 8329. Fax: +46 8 5537 8481. E-mail: stefan.stahl@biotech.kth.se.

Author Contributions

#Authors contributed equally.

Notes

The authors declare the following competing financial interest(s): One of the authors of this paper, Dr. Fredrik Y. Frejd, has an affiliation (employment) with Affibody AB. Affibody AB holds intellectual property rights and trademarks for affibody molecules. One of the authors of this paper, Dr. Karl Andersson, has an affiliation (employment and shareholder) with Ridgeview Instruments AB. Ridgeview Instruments AB holds intellectual property rights and trademarks for LigandTracer instruments and TraceDrawer software.

ACKNOWLEDGMENTS

This work was supported by grants from the Governmental Agency for Innovation Systems (VINNOVA), the Swedish Cancer Society (Cancerfonden), and the Swedish Research Council (Vetenskapsrådet). The authors are grateful for the technical assistance of Dr. Sebastian Grimm.

REFERENCES

(1) Chen, J. S., Lan, K., and Hung, M. C. (2003) Strategies to target HER2/neu overexpression for cancer therapy. *Drug Resistance Updates 6*, 129−136.

(2) Slamon, D. J., Clark, G. M., Wong, S. G., Levin, W. J., Ullrich, A., and McGuire, W. L. (1987) Human breast cancer: correlation of relapse and survival with amplification of the HER-2/neu oncogene. *Science 235*, 177−82.

(3) Marmor, M. D., Skaria, K. B., and Yarden, Y. (2004) Signal transduction and oncogenesis by ErbB/HER receptors. *Int. J. Radiat. Oncol. Biol. Phys. 58*, 903−913.

(4) Graus-Porta, D., Beerli, R. R., Daly, J. M., and Hynes, N. E. (1997) ErbB-2, the preferred heterodimerization partner of all ErbB receptors, is a mediator of lateral signaling. *EMBO J. 16*, 1647−55.

(5) Franklin, M. C., Carey, K. D., Vajdos, F. F., Leahy, D. J., de Vos, A. M., and Sliwkowski, M. X. (2004) Insights into ErbB signaling from the structure of the ErbB2-pertuzumab complex. *Cancer Cell 5*, 317−328.

(6) Garrett, T. P. J., McKern, N. M., Lou, M., Elleman, T. C., Adams, T. E., Lovrecz, G. O., Zhu, H.-J., Walker, F., Frenkel, M. J., Hoyne, P. A., Jorissen, R. N., Nice, E. C., Burgess, A. W., and Ward, C. W. (2002) Crystal structure of a truncated epidermal growth factor receptor extracellular domain bound to transforming growth factor ±. *Cell 110*, 763−773.

(7) Hirsch, F. R., Varella-Garcia, M., and Cappuzzo, F. (2009) Predictive value of EGFR and HER2 overexpression in advanced non-small-cell lung cancer. *Oncogene 28*, S32−S37.

(8) Tsutsui, S., Ohno, S., Murakami, S., Kataoka, A., Kinoshita, J., and Hachitanda, Y. (2003) Prognostic value of the combination of epidermal growth factor receptor and c-erbB-2 in breast cancer. *Surgery 133*, 219−221.

(9) Friedman, M., Lindström, S., Ekerljung, L., Andersson-Svahn, H., Carlsson, J., Brismar, H., Gedda, L., Frejd, F. Y., and Ståhl, S. (2009) Engineering and characterization of a bispecific HER2 × EGFR-binding affibody molecule. *Biotechnol. Appl. Biochem. 54*, 121−131.

(10) Rüther, U. (1982) pUR 250 allows rapid chemical sequencing of both DNA strands of its inserts. *Nucleic Acids Res. 10*, 5765−5772.

(11) Studier, W. F., Rosenberg, A. H., Dunn, J. J., and Dubendorff, J. W. (1990) Use of T7 RNA polymerase to direct expression of cloned genes, in *Methods Enzymol.* (David, V. G., Ed.) pp 60−89, Academic Press.

(12) Friedman, M., Orlova, A., Johansson, E., Eriksson, T. L. J., Höidén-Guthenberg, I., Tolmachev, V., Nilsson, F. Y., and Ståhl, S. (2008) Directed evolution to low nanomolar affinity of a tumor-targeting epidermal growth factor receptor-binding affibody molecule. *J. Mol. Biol. 376*, 1388−1402.

(13) Wikman, M., Steffen, A. C., Gunneriusson, E., Tolmachev, V., Adams, G. P., Carlsson, J., and Ståhl, S. (2004) Selection and characterization of HER2/neu-binding affibody ligands. *Protein Eng., Des. Sel. 17*, 455−462.

(14) Orlova, A., Magnusson, M., Eriksson, T. L. J., Nilsson, M., Larsson, B., Höiden-Guthenberg, I., Widström, C., Carlsson, J., Tolmachev, V., Ståhl, S., and Nilsson, F. Y. (2006) Tumor imaging using a picomolar affinity HER2 binding Affibody molecule. *Cancer Res. 66*, 4339−4348.

(15) Björkelund, H., Gedda, L., Barta, P., Malmqvist, M., and Andersson, K. (2011) Gefitinib induces epidermal growth factor receptor dimers which alters the interaction characteristics with ^{125}I-EGF. *PLoS ONE 6*, e24739.

(16) Schoeberl, B., Faber, A. C., Li, D., Liang, M. C., Crosby, K., Onsum, M., Burenkova, O., Pace, E., Walton, Z., Nie, L., Fulgham, A., Song, Y., Nielsen, U. B., Engelman, J. A., and Wong, K. K. (2010) An ErbB3 antibody, MM-121, is active in cancers with ligand-dependent activation. *Cancer Res. 70*, 2485−2494.

(17) Björke, H., and Andersson, K. (2006) Measuring the affinity of a radioligand with its receptor using a rotating cell dish with in situ reference area. *Appl. Radiat. Isotopes 64*, 32−37.

(18) Nestor, M., Andersson, K., and Lundqvist, H. (2008) Characterization of ^{111}In and ^{177}Lu-labeled antibodies binding to CD44v6 using a novel automated radioimmunoassay. *J. Mol. Recognit. 21*, 179−183.

(19) Barta, P., Malmberg, J., Melicharova, L., Strandgard, J., Orlova, A., Tolmachev, V., Laznicek, M., and Andersson, K. (2012) Protein interactions with HER-family receptors can have different characteristics depending on the hosting cell line. *Int. J. Oncol. 40*, 1677−1682.

(20) Ekerljung, L., Steffen, A. C., Carlsson, J., and Lennartsson, J. (2006) Effects of HER2-binding affibody molecules on intracellular signaling pathways. *Tumor Biol. 27*, 201−210.

(21) Penuel, E., Akita, R. W., and Sliwkowski, M. X. (2002) Identification of a region within the ErbB2/HER2 intracellular domain that is necessary for ligand-independent association. *J. Biol. Chem. 277*, 28468−28473.

(22) Ignatoski, K. M. W., LaPointe, A. J., Radany, E. H., and Ethier, S. P. (1999) erbB-2 overexpression in human mammary epithelial cells confers growth factor independence. *Endocrinology 140*, 3615−3622.

(23) Ekerljung, L., Lindborg, M., Gedda, L., Frejd, F. Y., Carlsson, J., and Lennartsson, J. (2008) Dimeric HER2-specific affibody molecules inhibit proliferation of the SKBR-3 breast cancer cell line. *Biochem. Biophys. Res. Commun. 377*, 489−94.

(24) Burgess, A. W., Cho, H. S., Eigenbrot, C., Ferguson, K. M., Garrett, T. P. J., Leahy, D. J., Lemmon, M. A., Sliwkowski, M. X., Ward, C. W., and Yokoyama, S. (2003) An open-and-shut case? Recent insights into the activation of EGF/ErbB receptors. *Mol. Cell 12*, 541−552.

(25) Nordberg, E., Friedman, M., Gostring, L., Adams, G. P., Brismar, H., Nilsson, F. Y., Stahl, S., Glimelius, B., and Carlsson, J. (2007) Cellular studies of binding, internalization and retention of a radiolabeled EGFR-binding affibody molecule. *Nucl. Med. Biol. 34*, 609−18.

Bioconjugate Chemistry

Article

pubs.acs.org/bc

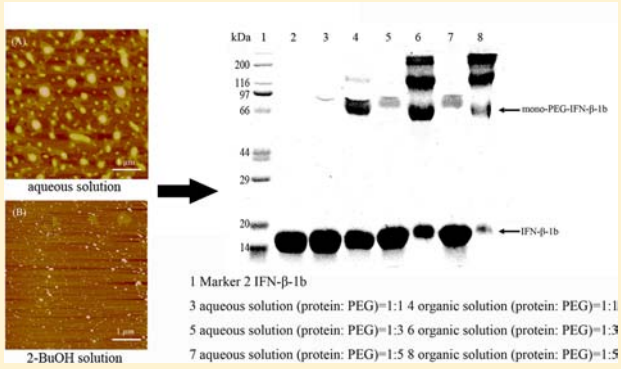
PEGylation of Proteins in Organic Solution: A Case Study for Interferon beta-1b

Fei Peng,[†,§,‡] Yinjue Wang,[†,‡] Lijing Sun,[†] Yongdong Liu,*[,†] Tao Hu,[†] Guifeng Zhang,[†] Guanghui Ma,[†] and Zhiguo Su*[,†]

[†]National Key Laboratory of Biochemical Engineering, Institute of Process Engineering, Chinese Academy of Sciences, Beijing 100190, China

[§]Graduate University of Chinese Academy of Sciences, Beijing 100049, China

ABSTRACT: Conventional protein PEGylation is carried out in aqueous solution. However, some hydrophobic proteins seem to be stable in organic solution. In this study, a novel approach of PEGylating IFN-β-1b in an organic solution of 2-butanol (2-BuOH) was investigated. Compared with protein PEGylation in aqueous solution, the overall modification yields increased more than 37%, while the yield of mono-PEGylated products could be increased by 36%. Furthermore, the PEGylated IFN-β-1b, which was obtained in organic solution, demonstrated 18% more antiviral potency than those derived from aqueous solution. The PEGylation step could be directly connected to the previous protein separation step for process integration. Dynamic light scattering (DLS) and atomic force microscope (AFM) analysis revealed that IFN-β-1b formed aggregates both in water and in 2-BuOH solutions. However, the aggregates were much smaller and more homogeneous in 2-BuOH than those in aqueous solution, thereby providing larger solvent accessible protein surfaces, which resulted in a more productive PEGylation process. In addition, the results of circular dichroism (CD), fluorescence spectra, and peptide mapping suggested that the increased bioactivity came from the difference in PEGylation site distribution due to solution environment that induced conformational discrepancy. The results of this study show that PEGylation of IFN-β-1b in organic solution is a facile and efficient process, which might find applications for other hydrophobic proteins.



INTRODUCTION

Conjugation of proteins with poly(ethylene glycol), known as PEGylation, has demonstrated advantages such as improved water solubility, extended circulation time in the body, and reduced possibility of degradation.[1,2] Conventionally, PEGylation of the protein is carried out in aqueous solution,[3−5] because most proteins maintain their native structure and activity in aqueous environment. However, some hydrophobic proteins, such as lipase and GFP-like fluorescent proteins, could be manipulated with organic solvent and still maintain their activity.[6,7] Furthermore, some enzymes have been found to be active in organic solution with different catalytic activities, and performing enzymatic reactions in the organic phase has attracted considerable interest over the past few years.[8−12]

Although PEG is soluble in water phase, it is also soluble in some organic solutions.[13] It is therefore interesting to investigate a PEGylation process in an organic solution. To do this, we select an interferon beta as a model protein for organic-phase PEGylation study. Interferon beta (IFN-β) belongs to a class of proteins known as interferons (IFNs) which are mainly secreted from leukocytes, fibroblasts, and T-lymphocytes.[14,15] Natural human IFN-β is a glycoprotein with an approximate molecular weight of 23 kDa, which has been associated with a variety of antiproliferative, immune-modulating, and antiviral activities.[16−18] Interferon beta-1b (IFN-β-1b) is a recombinant form of IFN-β which is expressed in *E. coli* without glycosylation consisting of 165 amino acids. It differs from natural IFN-β in that it lacks the N-terminal methionine and the Cysteine-17 was replaced by serine to improve its stability and activity.[19]

There are currently three marketed recombinant human IFN-β-1b, namely, Betaferon, Extavia, and Ziferon, which are mainly used to treat relapsing-remitting form of multiple sclerosis.[20,21] Though it has been a successful therapeutic protein, the special physicochemical properties of IFN-β-1b make the production process very complicated. IFN-β-1b is highly hydrophobic and easily aggregates or precipitates in aqueous solution. It was reported that IFN-β-1b is hardly soluble (<0.05 mg/mL) at physiological pH conditions on its own and requires surfactants, such as SDS or Laureth 12, to maintain its solubility.[22,23] Aggregations often occur during storage which could cause serious problem of neutralizing

Received: February 17, 2012
Revised: August 2, 2012
Published: August 9, 2012

ACS Publications © 2012 American Chemical Society

antibody. Moreover, IFN-β-1b has a very short terminal serum half-life (1.9 ± 0.43 h) following intravenous administration and needs frequent injections, which easily causes adverse effects such as injection site necrosis.[24,25] To solve these problems, one approach that is being explored is covalent attachment of poly(ethylene glycol) polymers to unstable proteins, i.e., PEGylation, which is a well-established and validated method to increase the stability, in vivo plasma retention time, and efficacy of protein pharmaceutics.[26−28] IFN-β-1b has been successfully PEGylated for this aim in aqueous solution.[29−32] However, PEGylation yield of IFN-β-1b was only around 20%, and a molar ratio as high as ten times PEG to protein had to be used.[29]

In spite of the poor solubility in aqueous solution, IFN-β-1b displayed reasonable solubility in 40−50% ethylene glycol in the presence of 0.5 to 1 M NaCl.[33,34] Research also demonstrated that IFN-β-1b could be extracted to 2-BuOH during purification and still maintain full activity after transfer into water solution.[35]

In this study, we exploited the possibility of PEGylation of IFN-β-1b in an organic solution. IFN-β-1b was extracted in 2-butanol (2-BuOH), followed by the addition of PEG Succinimidyl Carbonate (SC-PEG) to initiate the PEGylation reaction. Surprisingly, PEGylation yields of IFN-β-1b were found to be remarkably increased compared with the conventional aqueous solution reaction. Moreover, the in vitro bioactivity of the new process derived mono-PEGylated IFN-β-1b was 18% higher than those derived from aqueous solution. To probe into the reasons behind the higher efficiency of this organic solution based PEGylation approach, various characterization methods, including DLS, AFM, CD, fluorescence spectra, and peptide mapping assays were employed to compare the molecular size and conformation of IFN-β-1b in the two solution conditions. Finally, the native structure of the purified mono-PEGylated protein was confirmed and the PEG-IFN-β-1b conjugate demonstrated a significantly improved pharmaceutics profile compared with the unmodified protein.

EXPERIMENTAL PROCEDURES

Materials. *E. coli* with plasmid of recombinant human Interferon beta-1b (IFN-β-1b) was kindly supplied by Tianjin Pegylatt Biotechnology Co., Ltd. (China). The standard IFN-β-1b was purchased from R&D Systems Inc. (USA). All activated PEG polymers were purchased from Jenkem Technology Co., Ltd. (China). SDS, 2-BuOH, and β-mercaptoethanol were purchased from Sigma-Aldrich (USA). Prepacked HiLoad 16/60 Superdex 200 prep grade column and Sephadex G-25 column were purchased from GE Healthcare Bio-Sciences (Sweden). ELISA kits were purchased from R&D Systems (USA).

Expression and Solubilization of IFN-β-1b Inclusion Bodies. *E. coli* harboring plasmid of IFN-β-1b was first cultured at 37 °C in five shake-flasks each containing 500 mL LB medium supplemented with 100 μg/mL ampicillin and then inoculated in a BIOSTAT-C plus fermenter (Sartorius, Germany) when cell density reached OD600 of 0.8−1. Cells were continuously grown in 25 L fermentation medium (tryptone 10 g/L, yeast extract 10 g/L, glucose 10 g/L, Na_2HPO_4 2.8 g/L, K_2HPO_4 5.2 g/L, $MgSO_4$ 0.2 g/L, and $(NH_4)_2SO4$ 1.5 g/L) supplemented with 100 μg/mL ampicillin. IFN-β-1b expression was induced when cell growth reached midexponential phase with 1 mM isopropyl β-D-1-thiogalactopyranoside (IPTG). The cells were harvested by centrifugation at 4000 *g* for 10 min at 4 °C. The cell pellets were washed with TE (20 mM Tris−HCl, pH 8.0, 1 mM EDTA) buffer and resuspended in sonication buffer (20 mM Tris-HCl, pH 7.0). Mechanical disruption to release intracellular proteins was conducted using a sonicator (Sonics & Materials, USA). After sonication, the pellets were washed by 20 mM Tris-HCl, pH 7.0, 4 M urea, 1% Triton, 1 mM EDTA for three times, followed by extensive washing with double distilled water. The inclusion bodies (1 g wet weight) were completely dissolved with 15 mL of 20 mM sodium phosphate buffer, 0.6% SDS, pH 7.0, containing 10 mM β-mercaptoethanol.

Preparation of IFN-β-1b in 2-BuOH Solution for PEGylation. An equal volume of 2-BuOH was added to the solution of solubilized inclusion bodies and the mixture was gently agitated for 10 min. After standing for 1 h, the solution formed two layers and the upper layer containing 2-BuOH was acquired by centrifugation at 10 000 *g* for 15 min. All these operations were performed at room temperature.

Reducing SDS-PAGE was used to evaluate the purity of the extracted IFN-β-1b in 2-BuOH solution. Samples in 2-butanol were dried in an incubator at 60 °C and the dried material was dissolved in an equal volume of water for SDS-PAGE analysis. The polyacrylamide concentration of the stacking gel was 5% and the separating gel was 15%. The gel was stained using Coomassie brilliant blue dye. Protein concentration was determined using an A_{280} value of a 1 mg/mL solution as 1.5.[30] Mass values of IFN-β-1b were determined by matrix-assisted laser desorption ionization time-of-flight mass spectrometry (MALDI-TOF-MS, Bruker Daltronics, USA) using an internal standard with similar molecular weight on the R-cyano-4-hydroxycinnamic acid (CHCA) matrix.

Preparation of IFN-β-1b in Aqueous Solution for PEGylation. The above 2-BuOH solution containing IFN-β-1b was dried in an incubator at 60 °C, and the dried material was dissolved in an equal volume of water.

PEGylation of IFN-β-1b in 2-BuOH and Aqueous Solutions. IFN-β-1b (2 mg/mL) in both 2-BuOH and aqueous solutions were modified using 20 kDa SC-PEG, and different molar ratios of protein to PEG (1:1, 1:3, 1:5) were used. The PEGylation reactions were conducted at 25 °C for 4 h.

The mono-PEGylation yields and overall PEGylation yields were determined by SDS-PAGE analysis according to the following equations:

$$\text{mono-PEGylation yields} = \frac{\text{mono-PEGylated IFN-}\beta\text{-1b(mol)}}{\text{total IFN-}\beta\text{-1b for PEGylation(mol)}} \times 100\%$$

$$\text{overall PEGylation yields} = \frac{\text{all PEGylated IFN-}\beta\text{-1b(mol)}}{\text{total IFN-}\beta\text{-1b for PEGylation(mol)}} \times 100\%$$

Dynamic Light Scattering (DLS) Analysis. Protein samples (2 mg/mL) were subjected to particle size analysis using a Wyatt Dynapro Titan instrument (Wyatt Technology Corporation, USA), which employs a 832 nm laser and collects scattering intensity data at a fixed angle of 90°. Samples were examined in a dust-free quartz cuvette with 12 μL cell volume containing glass viewing windows for in situ scattering measurements at 20 °C. The acquisition time for each run

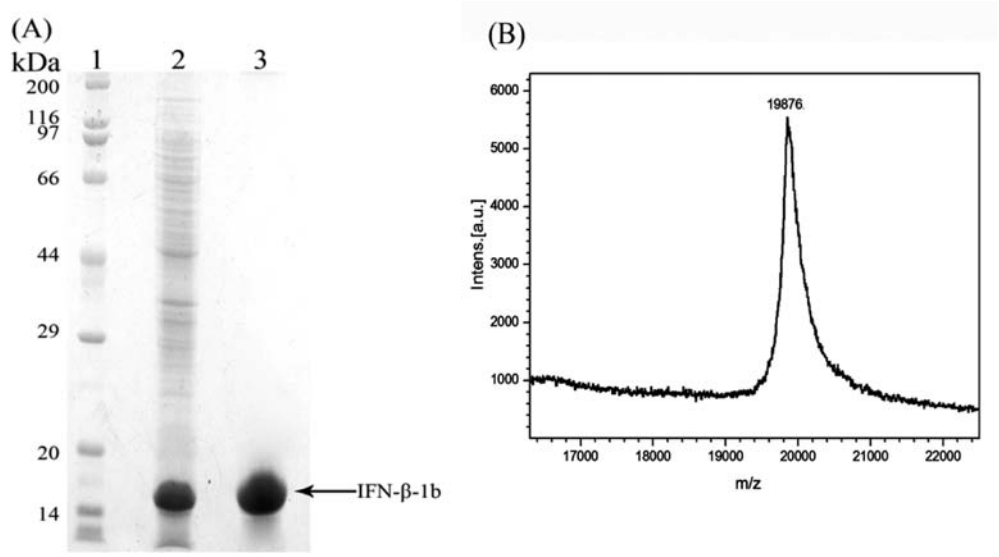


Figure 1. Analysis of the purified IFN-β-1b in 2-BuOH. (A) SDS-PAGE analysis of IFN-β-1b extracted in 2-BuOH. Molecular weight markers (lane 1), inclusion body (lane 2), and extracts in 2-BuOH (lane 3) were shown. (B) MALDI-TOF-MS analysis of IFN-β-1b. The sample was dissolved in water containing R-cyano-4-hydroxycinnamic acid as a matrix.

was 10 s and the experiment continued for more than 60 runs. The normalized intensity correlation functions were analyzed using *DynaPro Titan* software. Analysis of the correlation function of the whole experiment represents the statistically averaged and thermodynamically stable size distribution of the samples. The radius of hydration of IFN-β-1b in aqueous and 2-BuOH solutions were determined and then used to estimate molecular weights based on an empirical curve of globular proteins of known molecular weight vs radius of hydration.

Atomic Force Microscope (AFM) Analysis. AFM was used to visualize the surface micrographs of IFN-β-1b in both solutions. After cleaning the freshly cleaved mica with methanol and distilled water, a drop of protein solutions was applied and incubated for 5 min at room temperature, followed by immediate drying with EDC-650-15 Spin Processor (Laurell Technologies Corporation, USA) for analysis. Multimode VIII Bioscope Catalyst AFM (Veeco Instruments, USA) was used to monitor the location of the AFM cantilever over the mica surface through an optical microscope equipped with a CCD camera system. A DNP-10 silicon nitride (k = 0.06 nN/nm) cantilever was purchased from Veeco. Images were obtained with a Nanoscope 8.10 controller and 5 μm × 5 μm area was scanned using ScanAsyst mode at 1.0 Hz frequency. At least five high-quality images for each sample were captured and one image was selected from these for presentation.

Circular Dichroism (CD). Spectra of IFN-β-1b in aqueous and 2-BuOH solutions for PEGylation were collected using J-810 spectrometer (Jasco, Japan) in the wavelength range of 205−250 nm at 25 °C. The protein solutions were diluted by corresponding background buffers to 0.2 mg/mL for immediate analysis. The cuvette path length was 1 mm for far-UV region measurements. Each spectrum was scanned three times and the average spectrum was plotted.

Intrinsic Emission Fluorescence. Intrinsic emission fluorescence spectra of IFN-β-1b in aqueous and 2-BuOH solutions for PEGylation were analyzed using F-4500 fluorescence spectrophotometer (Hitachi, Japan). The protein solutions were diluted by corresponding buffers to 0.2 mg/mL for immediate analysis. Spectra were recorded on 1 cm path length cuvette with excitation slit width 5 nm and emission slit width 2.5 nm. The excitation wavelength was set as 295 nm for the specific excitation of tryptophan residues, and emission spectra were recorded from 310 to 400 nm at a constant slit of 1 nm.

Purification of Mono-PEGylated IFN-β-1b in 2-BuOH and Aqueous Solutions. IFN-β-1b (2 mg/mL) in aqueous and 2-BuOH solutions were both modified using 20 kDa SC-PEG, and a 1:1 molar ratio of protein to PEG was used. The PEGylation reaction was then conducted at 25 °C for 4 h. The PEGylation products in organic solvent were further dried in an incubator at 60 °C for 2 h, and the dried material was dissolved in 20 mM sodium phosphate, pH 7.0, 2% SDS. Then, both of the products derived from 2-BuOH and aqueous solutions were purified by size exclusion chromatography (SEC) on a prepacked HiLoad 16/60 Superdex 200 prep grade column with a running buffer of 20 mM sodium phosphate, pH 7.0, 2% SDS at a flow rate of 2 mL/min. The peak fractions containing mono-PEGylated IFN-β-1b (analyzed by SDS-PAGE) were collected. The purified mono-PEGylated protein was loaded onto a Sephadex G-25 column equilibrated with 20 mM sodium phosphate, 5% mannitol, pH 7.0, and the desalted peak was subsequently dialyzed against 20 mM sodium phosphate, 5% mannitol, pH 7.0, to remove residual SDS.

In Vitro Activity Assay. The in vitro antiviral activities of mono-PEGylated IFN-β-1b prepared in aqueous and 2-BuOH solutions were determined. WISH cells (3×10^5 cells/mL) in 0.1 mL of culture medium were distributed in 96-well microtiter plate and cultivated for 4−6 h. 0.1 mL of serially diluted protein samples and IFN-β-1b standard were then added to each well and incubated at 37 °C, 5% CO_2, for 24 h. The samples were poured out before vesicular stomatitis virus (50 μL) was added to each well. After another 24 h incubation at 37 °C, the supernatants were discarded and 100 μL of 3-(4,5-dimethylthiazol-2-yl)-2,5-diphenyltetrazolium bromide (MTT) at 5 mg/mL was added to each well and the plates were incubated for a further 2 h at 37 °C to measure the antiviral effects of IFN-β-1b using the MTT assay as previously described.[36] The plate was read at 570 nm by reference at

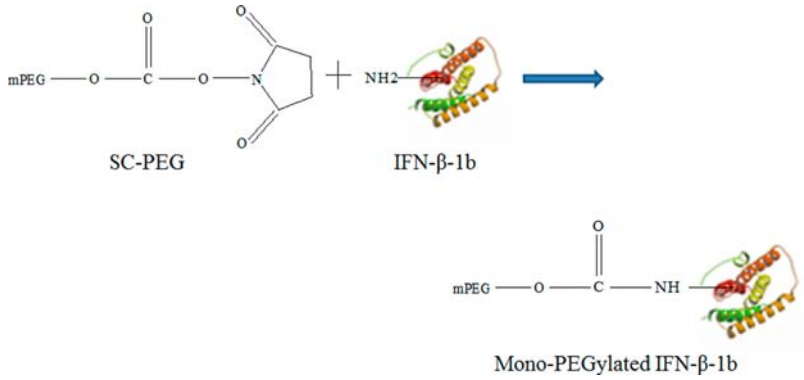


Figure 2. Reaction of SC-PEG with amine of protein to form a urethane linkage.

630 nm in a 96-well plate reader (Bio-Rad model 550, USA) to determine EC_{50} (the protein concentration supporting half-maximum cell proliferation response) values. All samples were analyzed in triplicate on each plate.

Peptide Mapping. Tryptic digestions of the mono-PEGylated IFN-β-1b prepared in aqueous and 2-BuOH solutions were performed in 50 mM NH_4HCO_3 containing 0.1% SDS (pH 8.3) at an enzyme to substrate ratio of 1:50 (w/w) for 16 h at 37 °C. The resulting peptides were separated by a Proteonavi C4 column (4.6 mm × 250 mm, SHISEIDO, Japan). The digested proteins were then subjected to the ion source of electrospray ionization mass spectrometer (LCQ DecaXP, Thermo Electron, USA). A spray voltage of 4.5 kV was employed and the heat capillary was kept at 275 °C. The mass spectrometer was scanned from m/z = 300 to 2000 in positive ion mode.

Pharmacokinetics Study. Groups of three male Sprague–Dawley rats (270–300 g) were injected subcutaneously with IFN-β-1b or mono-PEGylated conjugates at a dose of 100 μg/kg body weight. Sampling of blood (300 uL) was taken via the retro-orbital plexus into vials containing EDTA, at times prior to protein administration and at 2 min, 60 min, 2 h, 4 h, 8 h, 24 h, and daily for 3 additional days. The plasma was centrifuged and stored at −70 °C until analysis. Plasma levels of the test proteins were quantitated using ELISA kit (R&D systems Inc., USA). Pharmacokinetic parameters were calculated by Drug and Statistics for Windows (*DAS* v 1.0).

Data Analysis. Data are presented as means ± SDs. Statistical significances were determined using One-Way ANOVA, and P values of <0.05 were considered statistically significant.

RESULTS

Organic Extraction of IFN-β-1b. Organic solvent of 2-BuOH was used to extract INF-β-1b solubilized in 0.6% SDS. It was found that the concentration of dissolved inclusion body, the percentage of SDS in lysis buffer, and the ratio of aqueous to organic solvent were the key factors affecting the extraction efficiency. Under the optimized condition, IFN-β-1b with high purity (>90%) (Figure 1A) was obtained in 2-BuOH, ready for PEGylation without further purification. The molecular weight of the purified IFN-β-1b was determined to be 19 876 Da by MALDI-TOF (Figure 1B), which was identical to its theoretical value. The native disulfide bond was already formed, since no free sulfhydryl groups were detected in 2-BuOH solution measured by 4-PDS assay.[37] The water content of the IFN-β-1b extraction solution was 21% determined by Karl Fischer titration.[38] The SDS content was 0.2% detected by Methylene Blue method.[39] Therefore, the aqueous solution for PEGylation also contained 2 mg/mL protein and 0.2% SDS. The pH values of IFN-β-1b in 2-BuOH and aqueous solutions were both 7.0.

Comparison of PEGylation Yields of IFN-β-1b in Aqueous and 2-BuOH Solutions. The chemical conjugation reaction was shown in Figure 2. The results of IFN-β-1b PEGylated in aqueous and 2-BuOH solutions under the same conditions were analyzed and compared by SDS-PAGE analysis shown in Figure 3. The SDS-PAGE gel was scanned by Gel Doc 2000 (Bio-Rad, USA) and PEGylation yields were determined by the built-in *Quantity One* software (Table 1). The results showed that PEGylation in 2-BuOH solution remarkably increased the overall modification yields by a striking 37–81% under different PEG/protein ratios. More importantly, PEGylation of IFN-β-1b in 2-BuOH solution resulted in significantly increased yields of singly modified

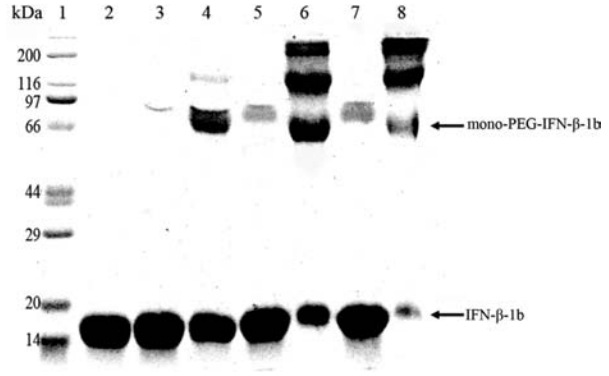


Figure 3. SDS-PAGE analysis of PEGylation yields. Molecular weight markers (lane 1), extracted IFN-β-1b (lane 2), and IFN-β-1b PEGylated in aqueous solution: protein/PEG = 1:1 (lane 3); 1:3 (lane 5); 1:5 (lane 7); IFN-β-1b PEGylated in 2-BuOH solution: protein/PEG = 1:1 (lane 4); 1:3 (lane 6); 1:5 (lane 8).

Table 1. Comparison of Modification Yields in Aqueous and 2-BuOH Solutions

	overall PEGylation yield (%)		Mono-PEGylation yield (%)	
protein:PEG	aqueous	2-BuOH	aqueous	2-BuOH
1:1	2	39	2	38
1:3	9	81	9	29
1:5	13	94	13	15

dx.doi.org/10.1021/bc300081f | *Bioconjugate Chem.* 2012, 23, 1812–1820

conjugates (PEG/protein ratios of 1:1 and 3:1), which are always the more desirable PEGylated species in the development of PEGylated biotherapeutics. It is notable that most of the IFN-β-1b proteins were converted into di- and multi-PEGylated conjugates in 2-BuOH solution when the PEG/protein ratio was raised to 5:1, resulting in a similar mono-PEGylation yield compared with the aqueous solution derived conjugates. These results demonstrated that PEGylation reaction of IFN-β-1b is greatly favored in the organic solution, which would lead to a considerable reduction in the amount of PEG reagents used, while still maintaining a fairly high PEGylation efficiency.

Comparisons of IFN-β-1b Aggregate Size in Aqueous and 2-BuOH Solutions. Our new IFN-β-1b PEGylation approach not only facilitated the integration of organic extraction and PEGylation reaction, but also markedly enhanced the product yield. It was reported that IFN-β-1b formed predominantly oligomeric aggregates through hydrophobic interaction in aqueous solution.[40] To investigate the molecular assembly of IFN-β-1b in 2-BuOH solution, particle size information of IFN-β-1b in aqueous and 2-BuOH solutions were detected by DLS (Table 2). The average hydrodynamic radius of IFN-β-1b in 2-BuOH solution was 4.0 nm, which was smaller than that in aqueous solution (5.2 nm). In addition, the polydispersities (Pd) of IFN-β-1b in 2-BuOH solution was 12.8%, which was lower than that in aqueous solution (23.1%), indicating a much narrower size distribution of IFN-β-1b aggregates in 2-BuOH solution. The estimated molecular weights based on hydrodynamic radius (MW-R) for IFN-β-1b in 2-BuOH and aqueous solution were 87 kDa and 160 kDa, respectively.

Table 2. Size Information of IFN-β-1b in Aqueous and 2-BuOH Solutions Determined by Dynamic Light Scattering[a]

	radius (nm)	Pd (%)	MW-R (kDa)	sum of squares
IFN-β-1b (aqueous solution)	5.2	23.1	160	0.445
IFN-β-1b (2-BuOH solution)	4.0	12.8	87	0.433

[a]The average hydrodynamic radius, polydispersity, and estimated molecular weights based on hydrodynamic radius (MW-R) were determined by DLS for IFN-β-1b (2 mg/mL) in aqueous and 2-BuOH solution. The statistical fit between measured and calculated data for radius is summarized in the sum of squares error value with values less than 1.0 considered to represent excellent fit.

IFN-β-1b particles were also observed by AFM (Figure 4). It can be seen that the average size of particles in 2-BuOH solution were remarkably smaller than those in aqueous solution. Central heights of the protein particles on the surface were also determined by statistical analysis of data using *Nanoscope 8.10* software. The mean height of IFN-β-1b in 2-BuOH solution was 5.19 ± 1.25 nm, significantly lower than that of the protein in aqueous solution (14.02 ± 5.03 nm).

Comparisons of IFN-β-1b Aggregate Conformation in Aqueous and 2-BuOH Solutions. CD analysis of the protein in aqueous and 2-BuOH solutions was presented in Figure 5. The CD profile of IFN-β-1b in aqueous solution was comparable with that of native structure,[33] with characteristic minima observed at 208 and 222 nm indicating the helix structure. However, the secondary structure of IFN-β-1b in 2-BuOH solution displayed a moderate conformational perturbation in comparison to the native structure.

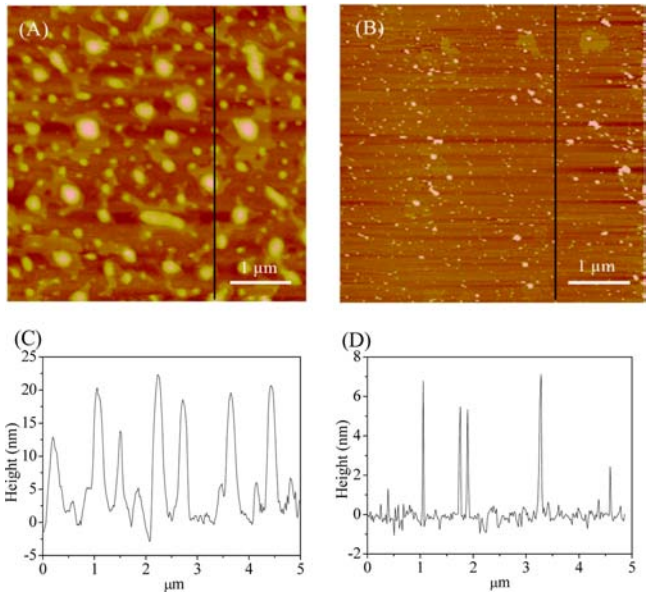


Figure 4. 5 μm × 5 μm topography of IFN-β-1b in aqueous solution (A) and 2-BuOH solution (B), and height magnification views (C and D) with corresponding cursor line profiles in A and B, respectively. Both graphs were captured under the same magnification.

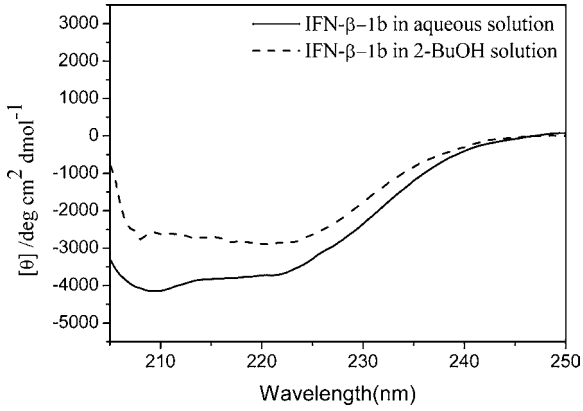


Figure 5. Circular dichroism analysis of IFN-β-1b in aqueous (solid line) and 2-BuOH (dashed line) solutions for PEGylation. IFN-β-1b was diluted by corresponding buffer to 0.2 mg/mL for immediate analysis.

Fluorescence spectra analysis of IFN-β-1b in aqueous and 2-BuOH solutions was shown in Figure 6. The maximum emission wavelength of IFN-β-1b in aqueous solution was 340 nm, an obvious blue-shift from that of free tryptophan (354 nm), and indicating compact packing of the protein structure in aqueous solution. In contrast, the maximum emission wavelength of IFN-β-1b and free tryptophan in 2-BuOH solution were 344 and 346 nm, respectively, indicating a less compact protein structure and the tryptophan residues of IFN-β-1b in 2-BuOH solution were largely solvent-exposed.

Characterization of the Mono-PEGylated IFN-β-1b Originated from PEGylation in Aqueous and 2-BuOH Solutions. After the desalting and dialysis step, SDS was undetectable determined by Methylene Blue method.[39] SDS-PAGE analysis (Figure 7A) demonstrated that the purity of mono-PEGylated IFN-β-1b from SEC was as high as 95%. CD

dx.doi.org/10.1021/bc300081f | *Bioconjugate Chem.* 2012, 23, 1812–1820

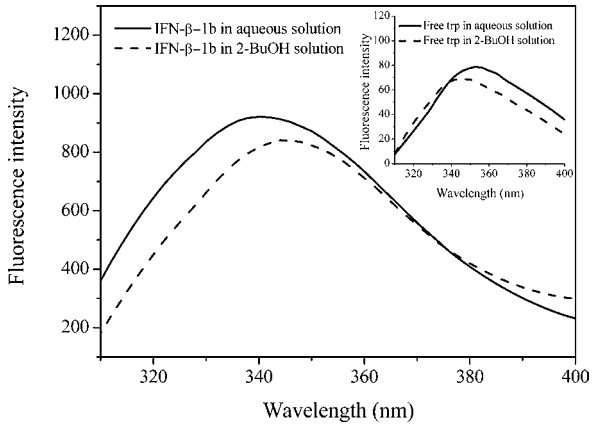


Figure 6. Intrinsic fluorescence spectra of IFN-β-1b in aqueous and 2-BuOH solutions for PEGylation. IFN-β-1b was diluted by corresponding buffer to 0.2 mg/mL for immediate analysis. Inset figure showed the tryptophan fluorescence analyzed in the respective solutions. The excitation wavelength was set as 295 nm for the specific excitation of tryptophan residues, and emission spectra were recorded from 310 to 400 nm.

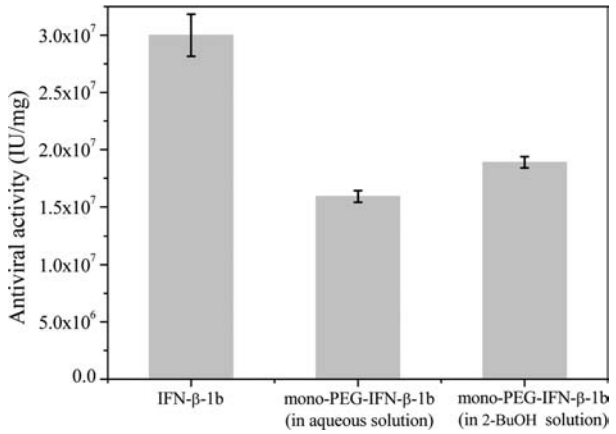


Figure 8. Antiviral activities of IFN-β-1b and mono-PEGylated IFN-β-1b. The antiviral activities of mono-PEGylated IFN-β-1b produced in aqueous and 2-BuOH solutions were calculated from EC_{50} values using a standard IFN-β-1b (3×10^7 IU/mg) as reference.

results (Figure 7B) confirmed the readjustment of the secondary structure of IFN-β-1b to the native one after being PEGylated and separated into the aqueous solution.

The antiviral activities of the mono-PEGylated proteins suffered moderate losses compared with that of the unmodified protein (Figure 8). The antiviral activity for the aqueous derived IFN-β-1b was $(3 \pm 0.2) \times 10^7$ IU/mg, which was consistent with the standard IFN-β-1b (3×10^7 IU/mg). The bioactivity of mono-PEGylated IFN-β-1b prepared in 2-BuOH solution was 1.89×10^7 IU/mg, 18% higher than that prepared in aqueous solution (1.59×10^7 IU/mg).

Peptide mappings demonstrated that the mono-PEGylated IFN-β-1b prepared by PEGylation in aqueous and 2-BuOH solutions both produced several positional isomers (Table 3). However, they differed significantly in the distribution of PEG conjugation sites. The 2-BuOH solution derived conjugates with PEG attached to K51, and K122 and K133 residues increased by 10% and 14%, respectively, while S1 plus K18 and K104 both decreased by 13%, compared with their counterparts derived from aqueous solution.

Table 3. Comparison of PEGylation Sites between Mono-PEGylated IFN-β-1b Prepared by PEGylation in Aqueous Solution and 2-BuOH Solution

	positional isomers (%)	
PEGylation sites	aqueous	2-BuOH
S1 plus K18	42	29
K104	18	5
K32	15	15
K122 and K133	17	31
K51	3	13
Other sites	5	7

Circulating levels of IFN-β-1b and mono-PEGylated IFN-β-1b prepared by PEGylation in aqueous and 2-BuOH solutions

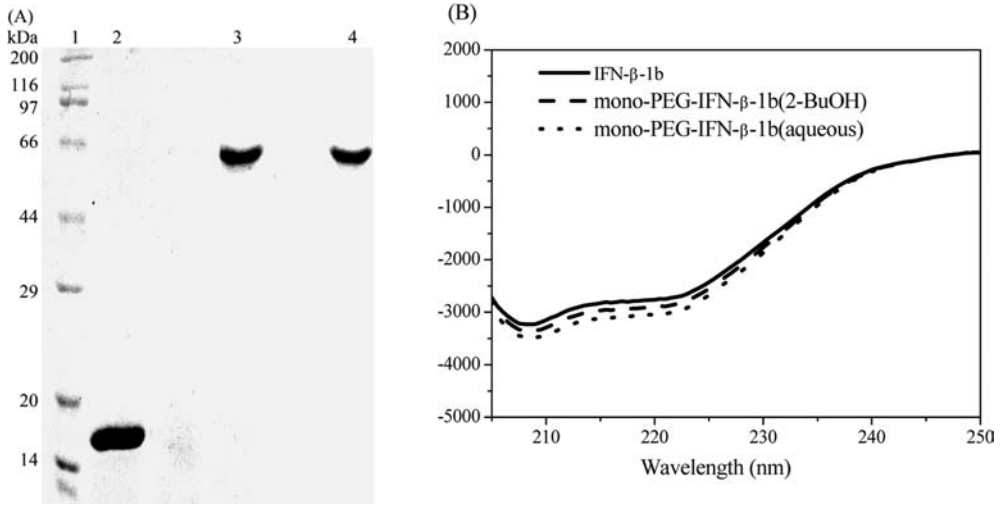


Figure 7. Purity and structural analysis of the purified mono-PEG-IFN-β-1b. (A) SDS-PAGE analysis. Molecular weight markers (lane 1), IFN-β-1b (lane 2), purified mono-SC-20K-PEG-IFN-β-1b derived from 2-BuOH solution (lane 3), and purified mono-SC-20K-PEG-IFN-β-1b derived from aqueous solution (lane 4) (B) Circular dichroism analysis of IFN-β-1b (solid line), purified mono-SC-20K-PEG-IFN-β-1b derived from aqueous solution (dotted line), and purified mono-SC-20K-PEG-IFN-β-1b derived from 2-BuOH solution (dashed line). Protein concentrations were 0.2 mg/mL in 20 mM sodium phosphate buffer, pH 7.0.

dx.doi.org/10.1021/bc300081f | *Bioconjugate Chem.* 2012, 23, 1812–1820

were measured by ELISA following subcutaneous injection. The mean serum concentration−time curves are shown in Figure 9 and the corresponding pharmacokinetic parameters

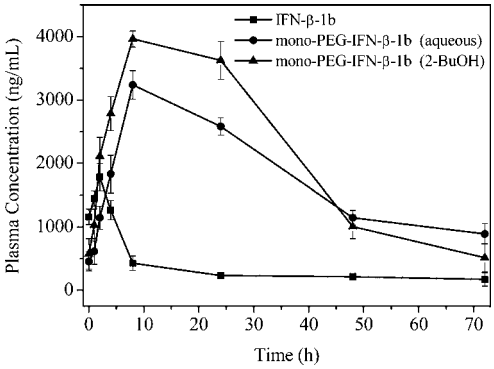


Figure 9. Pharmacokinetics profiles of IFN-β-1b and mono-SC-20K-PEG -IFN-β-1b. The rats were subject to subcutaneous administration at 0.1 mg protein/kg body weight. Plasma concentrations were measured at the indicated time points postadministration by ELISA.

Table 4. Summary of Pharmacokinetic Parameters of IFN-β-1b, Mono-PEGylated IFN-β-1b Following Subcutaneous Administration in Rats[a]

sample	dose (mg/kg)	AUC[b] (ng·h/mL)	half-life (h)
IFN-β-1b	0.1	24656 ± 5726	3.0 ± 0.5
mono-PEG-IFN-β-1b (aqueous)	0.1	125896 ± 15451	9.2 ± 0.6
mono-PEG-IFN-β-1b (2-BuOH)	0.1	155290 ± 16119	9.4 ± 1.0

[a]Values were expressed as the group mean ± SD. [b]Area under drug concentration versus time curve.

were shown in Table 4. The half-life of IFN-β-1b was 3 ± 0.5 h, while those of mono-PEGylated IFN-β-1b were both around 9 h. For AUC values, mono-PEGylated IFN-β-1bs both exhibited much greater plasma exposure than the unmodified molecule. These results showed that PEGylation significantly increased the plasma retention of IFN-β-1b, which may be translated into more therapeutic efficacy in clinical applications.

DISCUSSION

Organic solutions usually induce denaturation of proteins, i.e., they cause changes in tertiary structure of enzymes or proteins resulting in a loss of biological activity.[41,42] However, some hydrophobic proteins, such as IFN-β-1b, are stable in organic solutions. In the present study, a novel organic solution based PEGylation approach was developed, which leads to significantly increased product yields and simplification of the process procedures, compared with the conventional aqueous solution reaction.[29,30] The purification yield of the mono-PEGylated IFN-β-1b products derived from 2-BuOH solution could reach 64.8% compared to 60.5% achieved in aqueous solution. PEGylation of IFN-β-1b in organic solution was made possible by extraction of the protein into 2-BuOH, which resulted in a stable protein formulation with an IFN-β-1b purity over 90%. The following PEGylation process generated unexpectedly remarkably higher yields of conjugates relative to the aqueous solution reaction under the same conditions, which intrigued us to further probe into the reasons behind this phenomenon.

The instability of IFN-β-1b was featured by its formation of oligomeric aggregates in aqueous solution.[40] Therefore, it is interesting for us to examine the assembly characteristics of IFN-β-1b in 2-BuOH solution. According to the estimated mean molecular weights based on hydrodynamic radius data, IFN-β-1b existed in aqueous solution as an average octameric aggregate (160 kDa) at a concentration of 2 mg/mL, while it was downsized to a tetrameric aggregate (87 kDa) in 2-BuOH solution. In addition, the polydispersity values showed that the distribution of particle sizes of protein aggregates were more homogeneous in 2-BuOH solution. The visualized topography results by AFM analysis also corroborated the smaller size of IFN-β-1b in 2-BuOH solution. It is notable that the AFM data were obtained after drying of the sample on mica; therefore, the size information from the two experiments were not exactly in accordance with each other. However, these results clearly demonstrated that the protein particles in 2-BuOH solution were less aggregated and more uniformly distributed compared with those in aqueous solution. With regard to PEGylation of protein aggregates, it is reasonable to postulate that the constituent protein molecules which were buried inside the particle were more difficult to reach by the bulky PEG polymers. As a result, only those distributed on the surfaces of the aggregates could be modified. For larger protein aggregates, there were likely fewer overall surface exposed reactive sites for PEGylation, as a greater portion of the constituent proteins were inaccessible to the long coiled PEG reagents compared with smaller aggregates, which may account for why PEGylation of IFN-β-1b in 2-BuOH solution was more productive. Moreover, a more homogeneous protein aggregate in aqueous solution would be more beneficial to the reproducibility of the PEGylation reaction.

Mono-PEGylated proteins produced by random amine-directed chemistries commonly consisted of positional isomers, which are conjugate mixtures with single PEG attachments at different sites on the protein surface. Our modification of IFN-β-1b by 20 kDa SC-PEG resulted in a heterogeneous mixture of several positional isomers. Interestingly, the reaction solution environment seems to have a major impact on PEGylaton site distribution of the protein conjugates. CD characterization showed a moderate secondary structural loss for the 2-BuOH solution solubilized IFN-β-1b. In addition, the tryptophan residues of IFN-β-1b in 2-BuOH solution were determined to be more solvent exposed than those in aqueous solution by fluorescence analysis, implicating a conformational discrepancy between the two protein structures in terms of surface accessibility of certain amino acid residues. Therefore, the differences in PEGylation site distribution could be attributed to the varied reactive site exposure levels between the two structures of IFN-β-1b in aqueous and 2-BuOH solutions. Although IFN-β-1b was subject to some extent of denaturation in 2-BuOH solution, the protein could revert back to its native structure, avoiding the possible activity loss inflicted by the harsh organic solvent.

All of the known effects of the type I IFNs including IFN-β-1b are believed to be mediated through interaction with a common type I IFN receptor comprising two proteins, ifnar1 and ifnar2, and the binding energy from interaction of IFN-β with ifnar2 serves mainly to stabilize the bound IFN/receptor complex.[43−47] Among the identified PEGylation sites, S1 and K18 were located in A helix, which were involved in the binding

of IFN-β to ifnar2, while the other sites were not directly related to this interaction.[48] Therefore, PEGylation of these two functional residues could lead to greater loss of bioactivity due to more significant steric hindrance of the protein−receptor interaction, which may account for the higher bioactivity of mono-PEGylated IFN-β-1b obtained in 2-BuOH solution.

Finally, the remarkably improved pharmacokinetic profile of the 2-BuOH solution derived mono-PEGylated IFN-β-1b encouraged us to further develop more site-specific PEGylated IFN-β-1b therapeutics for in vivo pharmacological evaluation.

In conclusion, we developed a novel organic solution based protein PEGylation method for the development of a long-acting IFN-β-1b therapeutic. The size and conformation of the protein aggregates in 2-BuOH solution differed significantly from those in aqueous solution, which contributed to the markedly higher PEGylation yields and more potent antiviral activity of the 2-BuOH solution derived conjugates. Our PEGylation strategy for IFN-β-1b offers the opportunity for a practical and convenient approach for the development of long acting protein drugs with poor water solubility.

AUTHOR INFORMATION

Corresponding Author

*E-mail: zgsu@home.ipe.ac.cn, ydliu@home.ipe.ac.cn. Tel: +86-10-62561817. Fax: +86-10-62561813.

Author Contributions

‡Both authors contributed equally.

Notes

The authors declare no competing financial interest.

ACKNOWLEDGMENTS

This research was financially supported by the National Natural Science Foundation of China (Grant No. 20976178 and 20820102036).

REFERENCES

(1) Parrott, M. C., and DeSimone, J. M. (2012) Drug delivery: Relieving PEGylation. *Nat. Chem. 4*, 13−14.

(2) Kontermann, R. E. (2011) Strategies for extended serum half-life of protein therapeutics. *Curr. Opin. Biotechnol. 22*, 868−876.

(3) Bansal, R., Post, E., Proost, J. H., de Jager-Krikken, A., Poelstra, K., and Prakash, J. (2011) PEGylation improves pharmacokinetic profile, liver uptake and efficacy of Interferon gamma in liver fibrosis. *J. Controlled Release 154*, 233−240.

(4) Plesner, B., Fee, C. J., Westh, P., and Nielsen, A. D. (2011) Effects of PEG size on structure, function and stability of PEGylated BSA. *Eur. J. Pharm. Biopharm. 79*, 399−405.

(5) Wang, J., Hu, T., Liu, Y., Zhang, G., Ma, G., and Su, Z. (2011) Kinetic and stoichiometric analysis of the modification process for N-terminal PEGylation of staphylokinase. *Anal. Biochem. 412*, 114−116.

(6) Eltaweel, M. A., Abd Rahman, R. N. Z. R., Salleh, A. B., and Basri, M. (2005) An organic solvent-stable lipase from Bacillus sp.strain 42. *Ann. Microbiol. 55*, 187−192.

(7) Samarkina, O. N., Popova, A. G., Gvozdik, E. Y., Chkalina, A. V., Zvyagin, I. V., Rylova, Y. V., Rudenko, N. V., Lusta, K. A., Kelmanson, I. V., Gorokhovatsky, A. Y., and Vinokurov, L. M. (2009) Universal and rapid method for purification of GFP-like proteins by the ethanol extraction. *Protein Expression Purif. 65*, 108−113.

(8) Dhake, K. P., Deshmukh, K. M., Wagh, Y. S., Singhal, R. S., and Bhanage, B. M. (2012) Investigation of steapsin lipase for kinetic resolution of secondary alcohols and synthesis of valuable acetates in non-aqueous reaction medium. *J. Mol. Catal. B: Enzym. 77*, 15−23.

(9) Batistella, L., Lerin, L. A., Brugnerotto, P., Danielli, A. J., Trentin, C. M., Popiolski, A., Treichel, H., Oliveira, J. V., and de Oliveira, D. (2012) Ultrasound-assisted lipase-catalyzed transesterification of soybean oil in organic solvent system. *Ultrason. Sonochem. 19*, 452−458.

(10) Bridiau, N., and Maugard, T. (2012) Bacillus circulans β-galactosidase catalyses the synthesis of N-acetyl-lactosamine in a hydro-organic medium via a steady-state ordered Bi Bi reaction mechanism. *J. Mol. Catal. B: Enzym. 77*, 24−31.

(11) Wan, Y. Y., Miyakoshi, T., Du, Y. M., Chen, L. J., Hao, J. M., and Kennedy, J. F. (2012) Mechanism of monolignol biotransformation by Rhus laccases in water-miscible organic solutions. *Int. J. Biol. Macromol. 50*, 530−533.

(12) Hu, W., Guan, Z., Deng, X., and He, Y. H. (2012) Enzyme catalytic promiscuity: The papain-catalyzed Knoevenagel reaction. *Biochimie 94*, 656−661.

(13) Gehrhardt, H., and Mutter, M. (1987) Soluble polymers in organic chemistry. *Polym. Bull. 18*, 487−493.

(14) Fensterl, V., and Sen, G. C. (2009) Interferons and viral infections. *Biofactors 35*, 14−20.

(15) Theofilopoulos, A. N., Baccala, R., Beutler, B., and Kono, D. H. (2005) Type I interferons (alpha/beta) in immunity and autoimmunity. *Annu. Rev. Immunol. 23*, 307−36.

(16) Sun, Y., Qiao, L., Xia, H. H., Lin, M. C., Zou, B., Yuan, Y., Zhu, S., Gu, Q., Cheung, T. K., Kung, H. F., Yuen, M. F., Chan, A. O., and Wong, B. C. (2008) Regulation of XAF1 expression in human colon cancer cell by interferon beta: activation by the transcription regulator STAT1. *Cancer Lett. 260*, 62−71.

(17) Sternberg, Z., Chadha, K., Lieberman, A., Hojnacki, D., Drake, A., Zamboni, P., Rocco, P., Grazioli, E., Weinstock-Guttman, B., and Munschauer, F. (2008) Quercetin and interferon-beta modulate immune response(s) in peripheral blood mononuclear cells isolated from multiple sclerosis patients. *J. Neuroimmunol. 205*, 142−7.

(18) Smith, M. C., Bayless, A. M., Goddard, E. T., and Davido, D. J. (2011) CK2 inhibitors increase the sensitivity of HSV-1 to interferon-beta. *Antiviral Res. 91*, 259−66.

(19) Mark, D. F., Lu, S. D., Creasey, A. A., Yamamoto, R., and Lin, L. S. (1984) Site-specific mutagenesis of the human fibroblast interferon gene. *Proc. Natl. Acad. Sci. U. S. A. 81*, 5662−6.

(20) Conway, D., and Cohen, J. A. (2010) Combination therapy in multiple sclerosis. *Lancet Neurol. 9*, 299−308.

(21) Kappos, L., Freedman, M. S., Polman, C. H., Edan, G., Hartung, H. P., Miller, D. H., Montalban, X., Barkhof, F., Radu, E. W., Metzig, C., Bauer, L., Lanius, V., Sandbrink, R., and Pohl, C. (2009) Long-term effect of early treatment with interferon beta-1b after a first clinical event suggestive of multiple sclerosis: 5-year active treatment extension of the phase 3 BENEFIT trial. *Lancet Neurol. 8*, 987−97.

(22) Fernandes, P. M., and Taforo, T. (1991) Formulations for lipophilic IL-2 proteins. U.S. Patent 4,992,271.

(23) Hershenson, S., and Thomson, J. (1989) Isoelectric focusing of recombinant interferon-beta. *Appl. Theor. Electrophor. 1*, 123−5.

(24) Nikfar, S., Rahimi, R., and Abdollahi, M. (2010) A meta-analysis of the efficacy and tolerability of interferon-beta in multiple sclerosis, overall and by drug and disease type. *Clin. Ther. 32*, 1871−88.

(25) Burks, J. (2005) Interferon-beta1b for multiple sclerosis. *Expert Rev. Neurother. 5*, 153−64.

(26) Yu, P., Qin, D., Qin, G., Fan, B., Ma, G., and Su, Z. (2009) PEGylation of rhIL-1RA increased its solution stability at room temperature. *Process Biochem. 44*, 1340−1345.

(27) Pasut, G., and Veronese, F. M. (2011) State of the art in PEGylation: The great versatility achieved after forty years of research. *J. Controlled Release*, DOI: 10.1016/j.jconrel.2011.10.037.

(28) Bansal, R., Post, E., Proost, J. H., de Jager-Krikken, A., Poelstra, K., and Prakash, J. (2011) PEGylation improves pharmacokinetic profile, liver uptake and efficacy of Interferon gamma in liver fibrosis. *J. Controlled Release 154*, 233−40.

(29) Katre, N.; Knauf, M. J. (1990) Solubilization of immunotoxins for pharmaceutical compositions using polymer conjugation. U.S. Patent 4,917,888.

(30) Basu, A., Yang, K., Wang, M., Liu, S., Chintala, R., Palm, T., Zhao, H., Peng, P., Wu, D., Zhang, Z., Hua, J., Hsieh, M. C., Zhou, J., Petti, G., Li, X., Janjua, A., Mendez, M., Liu, J., Longley, C., Mehlig, M.,

Borowski, V., Viswanathan, M., and Filpula, D. (2006) Structure-function engineering of interferon-beta-1b for improving stability, solubility, potency, immunogenicity, and pharmacokinetic properties by site-selective mono-PEGylation. *Bioconjugate Chem. 17*, 618−30.
(31) Zhao, H., Yang, K., Martinez, A., Basu, A., Chintala, R., Liu, H. C., Janjua, A., Wang, M., and Filpula, D. (2006) Linear and branched bicin linkers for releasable PEGylation of macromolecules: controlled release in vivo and in vitro from mono- and multi-PEGylated proteins. *Bioconjugate Chem. 17*, 341−51.
(32) Thom, J., Anderson, D., McGregor, J., and Cotton, G. (2011) Recombinant protein hydrazides: application to site-specific protein PEGylation. *Bioconjugate Chem. 22*, 1017−20.
(33) Boublik, M., Moschera, J. A., Wei, C., and Kung, H. F. (1990) Conformation and activity of recombinant human fibroblast interferon-beta. *J. Interferon Res. 10*, 213−9.
(34) Utsumi, J., Yamazaki, S., Hosoi, K., Kimura, S., Hanada, K., Shimazu, T., and Shimizu, H. (1987) Characterization of E. coli-derived recombinant human interferon-beta as compared with fibroblast human interferon-beta. *J. Biochem. 101*, 1199−208.
(35) Lin, L. S., Yamamoto, R., and Drummond, R. J. (1986) Purification of recombinant human interferon beta expressed in Escherichia coli. *Methods Enzymol. 119*, 183−92.
(36) Mosmann, T. (1983) Rapid colorimetric assay for cellular growth and survival: application to proliferation and cytotoxicity assays. *J. Immunol. Methods 65*, 55−63.
(37) Tiso, M., Tejero, J., Basu, S., Azarov, I., Wang, X., Simplaceanu, V., Frizzell, S., Jayaraman, T., Geary, L., Shapiro, C., Ho, C., Shiva, S., Kim-Shapiro, D. B., and Gladwin, M. T. (2011) Human neuroglobin functions as a redox-regulated nitrite reductase. *J. Biol. Chem. 286*, 18277−89.
(38) De Caro, C. A., Aichert, A., and Walter, C. M. (2001) Efficient, precise and fast water determination by the Karl Fischer titration. *Food Control 12*, 431−436.
(39) Olkowska, E., Polkowska, Ż., and Namieśnik, J. Analytical procedures for the determination of surfactants in environmental samples. *Talanta* Doi:10.1016/j.talanta.2011.10.034.
(40) Utsumi, J., Yamazaki, S., Kawaguchi, K., Kimura, S., and Shimizu, H. (1989) Stability of human interferon-beta 1: oligomeric human interferon-beta 1 is inactive but is reactivated by monomerization. *Biochim. Biophys. Acta 998*, 167−72.
(41) Ghaouar, N., Elmissaoui, S., Aschi, A., and Gharbi, A. (2010) Concentration regimes and denaturation effects on the conformational changes of alpha-chymotrypsin by viscosity and dynamic light scattering measurements. *Int. J. Biol. Macromol. 47*, 425−430.
(42) Cardoso, T., Oliveira, C., Sarmento, A. C., Pereira, A., Nutley, M. A., Jess, T., Kelly, S. M., Cooper, A., Price, N. C., Pires, E., and Barros, M. (2009) Acetonitrile-induced unfolding of porcine pepsin A: A proposal for a critical role of hydration structures in conformational stability. *Int. J. Biol. Macromol. 45*, 213−220.
(43) Oliver-Martos, B., Orpez, T., Pinto-Medel, M. J., Mayorga, C., Garcia-Leon, J. A., Maldonado-Sanchez, R., Suardiaz, M., Guerrero, M., Luque, G., Leyva, L., and Fernandez, O. (2011) Gene expression in IFNss signalling pathway differs between monocytes, CD4 and CD8 T cells from MS patients. *J. Neuroimmunol. 230*, 153−9.
(44) de Weerd, N. A., Samarajiwa, S. A., and Hertzog, P. J. (2007) Type I interferon receptors: biochemistry and biological functions. *J. Biol. Chem. 282*, 20053−7.
(45) Novick, D., Cohen, B., and Rubinstein, M. (1994) The human interferon alpha/beta receptor: characterization and molecular cloning. *Cell 77*, 391−400.
(46) Domanski, P., Witte, M., Kellum, M., Rubinstein, M., Hackett, R., Pitha, P., and Colamonici, O. R. (1995) Cloning and expression of a long form of the beta subunit of the interferon alpha beta receptor that is required for signaling. *J. Biol. Chem. 270*, 21606−11.
(47) Lutfalla, G., Holland, S. J., Cinato, E., Monneron, D., Reboul, J., Rogers, N. C., Smith, J. M., Stark, G. R., Gardiner, K., Mogensen, K. E., et al. (1995) Mutant U5A cells are complemented by an interferon-alpha beta receptor subunit generated by alternative processing of a new member of a cytokine receptor gene cluster. *EMBO J. 14*, 5100−8.
(48) Runkel, L., deDios, C., Karpusas, M., Betzenhauser, M., Muldowney, C., Zafari, M., Benjamin, C. D., Miller, S., Hochman, P. S., and Whitty, A. (2000) Systematic mutational mapping of sites on human interferon-beta-1a that are important for receptor binding and functional activity. *Biochemistry 39*, 2538−51.

Bioconjugate Chemistry

Article

pubs.acs.org/bc

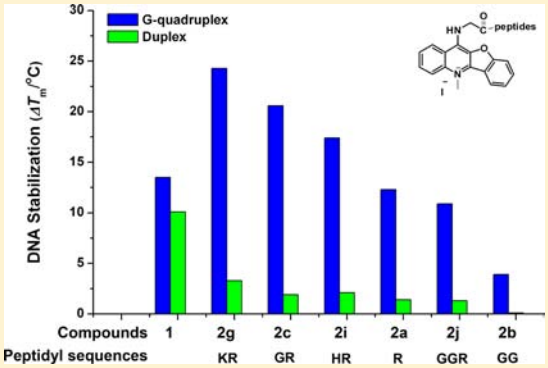
Benzofuroquinoline Derivatives Had Remarkable Improvement of their Selectivity for Telomeric G-Quadruplex DNA over Duplex DNA upon Introduction of Peptidyl Group

Yi Long, Zeng Li, Jia-Heng Tan, Tian-Miao Ou, Ding Li, Lian-Quan Gu, and Zhi-shu Huang*

School of Pharmaceutical Sciences, Sun Yat-sen University, Guangzhou 510006, People's Republic of China

Supporting Information

ABSTRACT: In order to improve the selectivity of 5-*N*-methyl quindoline (cryptolepine) derivatives as telomeric quadruplex binding ligands versus duplex DNA, a series of peptidyl-benzofuroquinoline (P-BFQ) conjugates (**2a**−**2n**) were designed and synthesized. Their interactions with telomeric quadruplex and duplex DNA were examined by using the fluorescence resonance energy transfer (FRET) melting assay, surface plasmon resonance (SPR), circular dichroism spectroscopy (CD), and molecular modeling studies. Introduction of a peptidyl group at 11-position of the aromatic benzofuroquinoline scaffold not only effectively increased its binding affinity, but also significantly improved its selectivity toward telomeric quadruplex versus duplex DNA. Combined with the data for their inhibitory effects on telomerase activity, their structure−activity relationships (SARs) studies showed that the types of amino acid residues and the length of the peptidyl side chains were important for the improvement of their interactions with the telomeric G-quadruplex. Long-term exposure of human cancer cells to **2c** showed a remarkable cessation in population growth and cellular senescence phenotype, and accompanied by a shortening of the telomere length.



INTRODUCTION

Cancer cells mostly maintain their indefinite telomere lengths via the synthesis of further telomeric DNA repeats using the telomerase enzyme, which will trigger cellular immortalization, a key step along the pathway to tumorigenesis.[1,2] Human telomeres comprise tandem repeats of the DNA motif (TTAGGG) together with associated telomeric proteins,[3,4] and the terminal 150−250 nucleotides at the extreme 3′-ends of telomeres are single-stranded, which could easily adopt G-quadruplex structures from stacked tetrads of hydrogen-bonded guanine bases.[5,6] Stabilization of telomeric G-quadruplexes by the binding of small molecules can lead to a range of biological effects,[7] including inhibition of the end-capping[8] and catalytic functions[9−11] of the telomerase enzyme. Thus, the design of drugs targeting at the telomeric G-quadruplex is an appropriate and promising approach for cancer chemotherapy. However, further efforts are still needed to improve the G-quadruplex selectivity over duplex DNA because ligand interaction with duplex DNA results in acute toxic and drastic side effects on normal tissues.[12]

In the past several years, a number of small molecules have been reported to bind with G-quadruplex DNA and effectively inhibit telomerase activity. Most of these molecules share a common feature of polycyclic aromatic cores that stack by $\pi-\pi$ interactions over the terminal planar G-tetrads of a quadruplex,[13] such as acridines,[14] anthraquinones,[15] indoloquinolines,[16] and porphyrins.[17] In addition, cationic side chains can interact with the negatively charged phosphate backbones in G-quadruplexes.[13] Our group has endeavored to explore potent and selective G-quadruplex ligands for several years. Indoloquinoline or benzofuroquinoline derivatives modified from cryptolepine are some among those ligands reported by us.[16,18] These ligands were capable of interacting with the telomeric G-quadruplex structure and showed inhibitory effect on telomerase; however, they also can intercalate into two base pairs of duplex DNA to a certain extent.[19] Thus, further efforts were undertaken for the purpose of improving selectivity of these compounds.

As is well-known, G-quadruplex DNA binding proteins are potentially useful for investigating the biologic role of G-quadruplex DNA. The specificity of recognition between G-quadruplex DNA binding proteins and G-quadruplex structures depends on the specific peptide sequences of those binding proteins.[20] For example, the specificity of G-quadruplex recognition depends on the guanidinium group of the arginine in the Arg-Gly-Gly repeat (RGG) domain in the C-terminal of Ewing's sarcoma protein (EWS).[21] In the meantime, it has also been reported that the combination of selected peptides to DNA binding scaffolds would greatly increase their selectivity to G-quadruplex versus duplex DNA.[22] Additionally, a

Received: March 13, 2012
Revised: July 21, 2012
Published: August 8, 2012

ACS Publications © 2012 American Chemical Society

significant role of ionic interactions has been confirmed, since *N*-terminal protonatable amino acids (Lys, Arg) largely incremented G-quadruplex binding.[23] Inspired by these findings, introduction of alkaline peptidyl side chains to classic benzofuroquinoline scaffold may be a feasible strategy through mimicking specific peptide sequences to improve its binding selectivity for telomeric G-quadruplex DNA.

On this basis, a series of 11-peptidyl benzofuroquinoline (P-BFQ) derivatives were designed for developing the ligands with better selective recognition and stabilizing ability of G-quadruplex. Peptidyl side chains mainly consist of alkaline and aromatic amino acid residues, such as Arg, Lys, His, and Phe. The peptidyl sequences are arranged as follows: Arg/Lys/His are located at the terminal of peptide chains, which can form alkaline positive center interacting with grooves and loops of G-quadruplex, Phe is located at the middle of peptide chains forming a certain steric conformation, and Gly played a joint role connecting with the scaffold. According to this principle of arrangement, a series of various peptidyl sequences were designed for this study, and some of these sequences just for control test purpose. We report here our research on the synthesis of P-BFQ conjugates, their interactions with telomeric G-quadruplex versus duplex DNA using biophysical and biochemical assays, and their inhibitory effects on telomerase activity by using TRAP-LIG assay, with compound **1** (reported earlier)[16] as reference compound. The ligand−quadruplex interactions were further explored by using molecular modeling studies, and cellular studies were performed to evaluate the cell senescence and telomere shortening effect induced by these P-BFQ derivatives.

EXPERIMENTAL PROCEDURES

Materials. The Fmoc protected amino acids, Rink amide AM resin, and others used for peptide synthesis were purchased from GL Biochem (Shanghai) Ltd. All oligomers/primers used in this study were purchased from Invitrogen and Sangon Biotech (China). All other chemicals or solvents were of analytical grade or better. Stock solutions of all the derivatives (10 mM) were made using DMSO (10%) or double-distilled deionized water.

Synthesis and Characterization of P-BFQ Conjugates. ^{1}H and ^{13}C NMR spectra were recorded using TMS as the internal standard in DMSO-d_6 with a Bruker BioSpin GmbH spectrometer at 400 MHz, mass spectra (MS) were recorded on a Shimadzu LCMS-2010A instrument with an ESI or ACPI mass selective detector, and high resolution mass spectra (HRMS) on Shimadzu LCMS-IT-TOF. Melting points (m.p.) were determined using a SRS-OptiMelt automated melting point instrument without correction. Flash column chromatography was performed with silica gel (200−300 mesh) purchased from Qingdao Haiyang Chemical Co. Ltd. The purification of all tested compounds was processed with preparative HPLC using a Varian Pro Star equipped with an UV−vis detector (BioRad) and a Phenomenex C18 (10.0 × 250 mm, 5 μm) column. The purities of all compounds were confirmed to be higher than 95% by using analytical HPLC with a dual pump Shimadzu LC-20AB system equipped with a Ultimate XB-C18 column (4.6 × 250 mm, 5 μm), and eluted with methanol/water (40:60 to 65:35) containing 0.1% TFA at a flow rate of 1 mL/min.

General Procedure for Preparation of Compounds 2a−2n. Peptidyl side chains were synthesized using solid-phase methodology by manual operation of a peptide synthesizer. The Fmoc protected various amino acids (4 equiv ratio excess to the resin) were coupled orderly to the Rink amide AM resin (500 mg) using DIC/HOBT (190 mg/200 mg) in DMF (4 mL) for 3 h, and the deprotection of the Fmoc group was carried out with piperidine/DMF 25% (2 mL) for 30 min. Then, intermediate compound **2** (322 mg) was mixed with deprotected peptidyl side chains using DIC/HOBT (475 mg/500 mg) in DMF (4 mL), with shaking for 12 h. After coupling with the compound **2**, the resin was treated with the cleavage reagent (95% TFA, 5% dd H_2O) for 2 h, washed with dry ether (30 mL), and then evaporated under vacuum. The crude products were purified by using preparative RP-HPLC with CH_3CN/H_2O (40:60) elution, and lyophilized to give compounds **2a−2n**.

11-(Carboxymethylamino)-5-methylbenzofuro[3,2-*b*]-quinolin-5-ium (II). Compound **1** was treated with glycin in 2-ethoxyethanol solution gave the intermediate compound **2** as a white solid with a yield of 41%. mp 217−219 °C. ^{1}H NMR (400 MHz, DMSO-d_6) δ 9.75 (t, J = 6.3 Hz, 1H), 8.67 (t, J = 8.4 Hz, 2H), 8.44 (d, J = 8.9 Hz, 1H), 8.17−8.07 (m, 1H), 7.96−7.87 (m, 2H), 7.84 (t, J = 7.5 Hz, 1H), 7.65 (t, J = 7.1 Hz, 1H), 4.80 (d, J = 6.3 Hz, 2H), 4.59 (s, 3H); HRMS (ESI+) m/z: Calc. for $C_{18}H_{15}N_2O_3^+$: 307.1077 $[M+H]^+$. Found 307.1087 $[M+H]^+$.

(*S*)-11-(2-(1-Amino-5-guanidino-1-oxopentan-2-ylamino)-2-oxoethylamino)-5-methylbenzofuro[3,2-*b*]-quinolin-5-ium (2a). Peptidyl coupling order is arginine, following the general procedure to give the desired compound **2a** as a straw yellow solid with a yield of 32%. mp 202−203 °C. ^{1}H NMR (400 MHz, DMSO-d_6) δ 9.71 (t, J = 6.4 Hz, 1H), 8.71 (d, J = 8.5 Hz, 1H), 8.63 (d, J = 8.2 Hz, 1H), 8.56 (d, J = 8.2 Hz, 1H), 8.43 (d, J = 9.0 Hz, 1H), 8.15−8.07 (m, 1H), 7.87 (ddd, J = 21.5, 15.3, 8.0 Hz, 3H), 7.64 (t, J = 7.4 Hz, 2H), 7.49 (s, 1H), 7.13 (s, 2H), 4.79 (d, J = 6.4 Hz, 2H), 4.58 (s, 3H), 4.25 (dd, J = 14.7, 7.0 Hz, 2H), 3.04 (dd, J = 13.1, 7.4 Hz, 2H), 1.73 (td, J = 10.5, 3.9 Hz, 1H), 1.63−1.28 (m, 4H); HRMS (ESI+) m/z: Calc. for $C_{24}H_{28}N_7O_3^+$: 462.2248 $[M+H]^+$. Found 462.2232 $[M+H]^+$.

11-(2-(2-(2-Amino-2-oxoethylamino)-2-oxoethylamino)-2-oxoethylamino)-5-methylbenzofuro[3,2-*b*]-quinolin-5-ium (2b). Peptidyl coupling order is glycine−glycine, following the general procedure to give the desired compound **2b** as a white solid with a yield of 29%. mp 200−212 °C. ^{1}H NMR (400 MHz, DMSO-d_6) δ 9.72 (t, J = 6.5 Hz, 1H), 8.70 (t, J = 8.4 Hz, 2H), 8.64 (d, J = 8.2 Hz, 1H), 8.44 (d, J = 8.9 Hz, 1H), 8.12 (dd, J = 9.8, 6.4 Hz, 2H), 7.93 (t, J = 5.9 Hz, 2H), 7.87−7.77 (m, 1H), 7.65 (ddd, J = 8.2, 5.8, 2.4 Hz, 1H), 7.23 (s, 1H), 7.02 (s, 1H), 4.78 (d, J = 6.4 Hz, 2H), 4.59 (s, 3H), 3.83 (d, J = 5.7 Hz, 2H), 3.60 (d, J = 5.8 Hz, 2H); HRMS (ESI+) m/z: Calc. for $C_{22}H_{22}N_5O_3^+$: 420.1666 $[M+H]^+$. Found 420.1658 $[M+H]^+$.

(*S*)-11-(2-(2-(1-Amino-5-guanidino-1-oxopentan-2-ylamino)-2-oxoethylamino)-2-oxoethylamino)-5-methylbenzofuro[3,2-*b*]quinolin-5-ium (2c). Peptidyl coupling order is arginine−glycine, following the general procedure to give the desired compound **2c** as a straw yellow solid with a yield of 28%. mp 195−196 °C. ^{1}H NMR (400 MHz, DMSO-d_6) δ 9.68 (t, J = 5.7 Hz, 1H), 8.66 (dd, J = 20.8, 8.5 Hz, 3H), 8.43 (d, J = 8.8 Hz, 1H), 8.17−8.09 (m, 1H), 8.03 (d, J = 8.1 Hz, 1H), 7.92 (s, 2H), 7.87−7.78 (m, 1H), 7.63 (dd, J = 13.2, 5.6 Hz, 2H), 7.35 (s, 1H), 7.05 (s, 1H), 4.77 (d, J = 5.6 Hz, 2H), 4.59 (s, 3H), 4.25−4.14 (m, 3H), 3.88−3.81 (m, 2H), 3.04 (d, J = 5.5 Hz, 2H), 1.72−1.63 (m, 1H), 1.58−1.27 (m,

4H); HRMS (ESI+) *m/z*: Calc. for $C_{26}H_{31}N_8O_4^+$: 519.2463 [M+H]$^+$. Found 519.2446 [M+H]$^+$.

(*S*)-11-(2-(2-(1-Amino-1-oxo-3-phenylpropan-2-ylamino)-2-oxoethylamino)-2-oxoethylamino)-5-methylbenzofuro[3,2-*b*]quinolin-5-ium (2d). Peptidyl coupling order is phenylalanine-glycine, following the general procedure to give the desired compound **2d** as a straw yellow solid with a yield of 27%. mp 200−202 °C. ^{1}H NMR (400 MHz, DMSO-d_6) δ 9.73 (t, J = 6.0 Hz, 1H), 8.71 (d, J = 8.5 Hz, 1H), 8.60 (dd, J = 13.1, 6.7 Hz, 2H), 8.42 (d, J = 8.9 Hz, 1H), 8.18−8.07 (m, 2H), 7.89 (d, J = 3.5 Hz, 2H), 7.82 (t, J = 7.6 Hz, 1H), 7.67−7.60 (m, 1H), 7.43 (s, 1H), 7.26−7.17 (m, 4H), 7.15 (d, J = 5.1 Hz, 1H), 7.07 (s, 1H), 4.74 (d, J = 5.9 Hz, 2H), 4.57 (s, 3H), 4.43 (dd, J = 13.0, 8.5 Hz, 1H), 3.85 (d, J = 21.8 Hz, 2H), 3.68 (d, J = 16.6 Hz, 2H); HRMS (ESI+) *m/z*: Calc. for $C_{29}H_{28}N_5O_4^+$: 510.2136 [M+H]$^+$. Found 510.2140 [M+H]$^+$.

11-(2-(2-((2*S*)-1-Amino-3-(4*H*-imidazol-4-yl)-1-oxopropan-2-ylamino)-2-oxoethylamino)-2-oxoethylamino)-5-methylbenzofuro[3,2-*b*]quinolin-5-ium (2e). Peptidyl coupling order is histidine-glycine, following the general procedure to give the desired compound **2e** as a straw yellow solid with a yield of 29%. mp 188−189 °C. ^{1}H NMR (400 MHz, DMSO-d_6) δ 9.90 (t, J = 6.1 Hz, 1H), 8.91 (s, 1H), 8.82−8.71 (m, 2H), 8.61 (d, J = 8.3 Hz, 1H), 8.41 (d, J = 9.0 Hz, 1H), 8.35 (d, J = 8.3 Hz, 1H), 8.12−8.05 (m, 1H), 7.91−7.85 (m, 2H), 7.83−7.78 (m, 1H), 7.62 (ddd, J = 8.1, 5.1, 3.0 Hz, 1H), 7.43 (s, 1H), 7.28 (s, 1H), 7.21 (s, 1H), 4.78 (d, J = 6.0 Hz, 2H), 4.57 (s, 3H), 4.53−4.45 (m, 2H), 3.87−3.77 (m, 2H), 3.13 (dd, J = 15.2, 4.5 Hz, 1H), 2.93 (dd, J = 15.2, 9.2 Hz, 1H); HRMS (ESI+) *m/z*: Calc. for $C_{26}H_{26}N_7O_4^+$: 500.2041 [M+H]$^+$. Found 500.2056 [M+H]$^+$.

(*S*)-11-(2-(2-(1,6-Diamino-1-oxohexan-2-ylamino)-2-oxoethylamino)-2-oxoethylamino)-5-methylbenzofuro-[3,2-*b*]quinolin-5-ium (2f). Peptidyl coupling order is lysine-glycine, following the general procedure to give the desired compound **2f** as a straw yellow solid with a yield of 26%. mp 201−202 °C. ^{1}H NMR (400 MHz, DMSO-d_6) δ 9.79 (t, J = 6.4 Hz, 1H), 8.75−8.67 (m, 2H), 8.63 (d, J = 8.2 Hz, 1H), 8.43 (d, J = 9.0 Hz, 1H), 8.13−8.09 (m, 1H), 8.03 (d, J = 8.1 Hz, 1H), 7.92 (dd, J = 7.0, 4.8 Hz, 2H), 7.84 (s, 1H), 7.64 (ddd, J = 8.2, 5.8, 2.5 Hz, 1H), 7.35 (s, 1H), 7.02 (s, 1H), 4.77 (d, J = 6.4 Hz, 2H), 4.58 (s, 3H), 4.20−4.11 (m, 2H), 3.85 (t, J = 5.5 Hz, 2H), 2.75−2.66 (m, 2H), 1.68−1.60 (m, 1H), 1.59−1.32 (m, 4H), 1.25 (dt, J = 16.3, 8.7 Hz, 2H); HRMS (ESI+) *m/z*: Calc. for $C_{26}H_{31}N_6O_4^+$: 491.2401 [M+H]$^+$. Found 491.2420 [M+H]$^+$.

11-(2-((*S*)-5-amino-6-((*S*)-1-amino-5-guanidino-1-oxopentan-2-ylamino)-6-oxohexylamino)-2-oxoethylamino)-5-methylbenzofuro[3,2-*b*]quinolin-5-ium (2g). Peptidyl coupling order is arginine-lysine, following the general procedure to give the desired compound **2g** as a yellow solid with a yield of 24%. mp 212−213 °C. ^{1}H NMR (400 MHz, DMSO-d_6) δ 9.80 (t, J = 12.5 Hz, 1H), 8.86 (s, 1H), 8.72 (d, J = 8.3 Hz, 1H), 8.61 (d, J = 8.1 Hz, 1H), 8.40 (d, J = 8.9 Hz, 1H), 8.21 (d, J = 6.4 Hz, 1H), 8.12−8.05 (m, 1H), 7.89 (t, J = 7.8 Hz, 2H), 7.79 (d, J = 7.2 Hz, 3H), 7.65−7.60 (m, 1H), 7.22 (s, 1H), 6.95 (s, 1H), 4.81 (d, J = 5.2 Hz, 2H), 4.55 (s, 3H), 4.26 (dd, J = 11.8, 5.6 Hz, 1H), 4.10 (dd, J = 12.8, 6.9 Hz, 1H), 3.09 (d, J = 5.6 Hz, 1H), 2.99 (s, 2H), 2.67 (s, 2H), 1.76−1.58 (m, 4H), 1.51 (dd, J = 14.3, 8.8 Hz, 4H), 1.43−1.19 (m, 5H); HRMS (ESI+) *m/z*: Calc. for $C_{30}H_{40}N_9O_4^+$: 590.3198 [M+H]$^+$. Found 590.3209 [M+H]$^+$.

11-(2-((*S*)-1-((*S*)-1-Amino-5-guanidino-1-oxopentan-2-ylamino)-1-oxo-3-phenylpropan-2-ylamino)-2-oxoethylamino)-5-methylbenzofuro[3,2-*b*]quinolin-5-ium (2h). Peptidyl coupling order is arginine-phenylalanine, following the general procedure to give the desired compound **2h** as a straw yellow solid with a yield of 26%. mp 204−205 °C; ^{1}H NMR (400 MHz, DMSO-d_6) δ 9.56 (t, J = 6.4 Hz, 1H), 8.71−8.59 (m, 3H), 8.43 (d, J = 9.0 Hz, 1H), 8.21 (d, J = 7.9 Hz, 1H), 8.15−8.09 (m, 1H), 7.89 (t, J = 7.8 Hz, 1H), 7.86−7.81 (m, 1H), 7.64 (t, J = 7.7 Hz, 1H), 7.51 (d, J = 8.4 Hz, 1H), 7.43−7.39 (m, 1H), 7.23 (dd, J = 7.3, 3.9 Hz, 5H), 7.11 (dd, J = 11.3, 8.2 Hz, 5H), 4.71 (dd, J = 17.3, 6.0 Hz, 2H), 4.59 (s, 3H), 4.18 (dd, J = 13.3, 7.3 Hz, 1H), 3.00 (ddd, J = 36.8, 13.2, 4.7 Hz, 4H), 1.61 (dd, J = 13.1, 6.8 Hz, 1H), 1.48−1.29 (m, 4H); HRMS (ESI+) *m/z*: Calc. for $C_{33}H_{37}N_8O_4^+$: 609.2932 [M+H]$^+$. Found 609.2932 [M+H]$^+$.

11-(2-((*S*)-1-((*S*)-1-Amino-5-guanidino-1-oxopentan-2-ylamino)-3-(1*H*-imidazol-4-yl)-1-oxopropan-2-ylamino)-2-oxoethylamino)-5-methylbenzofuro[3,2-*b*]quinolin-5-ium (2i). Peptidyl coupling order is arginine-histidine, following the general procedure to give the desired compound **2i** as a straw yellow solid with a yield of 28%. mp 193−194 °C. ^{1}H NMR (400 MHz, DMSO-d_6) δ 9.74 (t, J = 12.4 Hz, 1H), 8.90 (d, J = 8.0 Hz, 1H), 8.74 (s, 1H), 8.69 (d, J = 8.4 Hz, 1H), 8.60 (d, J = 8.2 Hz, 1H), 8.42 (d, J = 9.0 Hz, 1H), 8.31 (d, J = 7.2 Hz, 1H), 8.13−8.08 (m, 1H), 7.92−7.87 (m, 1H), 7.81 (t, J = 7.4 Hz, 2H), 7.73 (d, J = 8.4 Hz, 1H), 7.62 (t, J = 7.7 Hz, 1H), 7.50 (s, 1H), 7.26 (s, 1H), 7.13 (s, 1H), 4.97−4.63 (m, 4H), 4.57 (s, 3H), 4.13 (dd, J = 13.0, 7.9 Hz, 2H), 3.16 (dd, J = 14.8, 5.3 Hz, 2H), 3.01−2.90 (m, 3H), 1.68−1.60 (m, 1H), 1.58−1.43 (m, 2H), 1.40−1.33 (m, 2H); HRMS (ESI+) *m/z*: Calc. for $C_{30}H_{35}N_{10}O_4^+$: 599.2766 [M+H]$^+$. Found 599.2780 [M+H]$^+$.

(*S*)-11-(1-Amino-6-carbamoyl-1-imino-8,11,14-trioxo-2,7,10,13-tetraazapentadecan-15-ylamino)-5-methylbenzofuro[3,2-*b*]quinolin-5-ium (2j). Peptidyl coupling order is arginine-glycine-glycine, following the general procedure to give the desired compound **2j** as a straw yellow solid with a yield of 20%. mp 187−188 °C. ^{1}H NMR (400 MHz, DMSO-d_6) δ 9.74 (s, 1H), 8.78 (s, 1H), 8.71 (d, J = 8.1 Hz, 1H), 8.65 (d, J = 8.1 Hz, 1H), 8.43 (d, J = 8.9 Hz, 1H), 8.22 (s, 1H), 8.14−8.10 (m, 1H), 8.02 (d, J = 6.1 Hz, 1H), 7.96 (d, J = 8.1 Hz, 3H), 7.86−7.82 (m, 1H), 7.66 (s, 4H), 7.37 (s, 1H), 7.02 (s, 1H), 4.80 (d, J = 3.5 Hz, 2H), 4.60 (s, 3H), 4.21−4.15 (m, 4H), 3.10 (dd, J = 3.8, 1.6 Hz, 2H), 1.68 (dd, J = 2.6, 1.6 Hz, 1H), 1.52−1.48 (m, 4H); HRMS (ESI+) *m/z*: Calc. for $C_{28}H_{34}N_9O_5^+$: 576.2677 [M+H]$^+$. Found 576.2699 [M+H]$^+$.

11-((6*S*,9*S*)-1-Amino-9-benzyl-6-carbamoyl-1-imino-8,11,14-trioxo-2,7,10,13-tetraazapentadecan-15-ylamino)-5-methylbenzofuro[3,2-*b*]quinolin-5-ium (2k). Peptidyl coupling order is arginine-phenylalanine-glycine, following the general procedure to give the desired compound **2k** as a straw yellow solid with a yield of 22%. mp 215−217 °C. ^{1}H NMR (400 MHz, DMSO-d_6) δ 9.73−9.58 (m, 1H), 8.69 (d, J = 8.2 Hz, 1H), 8.64 (d, J = 8.1 Hz, 1H), 8.59 (s, 1H), 8.43 (d, J = 9.0 Hz, 1H), 8.29 (d, J = 4.5 Hz, 1H), 8.20 (d, J = 7.3 Hz, 1H), 8.15−8.09 (m, 1H), 7.90 (d, J = 4.5 Hz, 2H), 7.87−7.79 (m, 2H), 7.69 (s, 3H), 7.57 (s, 1H), 7.34 (d, J = 6.8 Hz, 1H), 7.21 (t, J = 8.4 Hz, 4H), 7.15−7.12 (m, 1H), 7.06 (s, 1H), 4.75 (d, J = 3.8 Hz, 2H), 4.59 (s, 3H), 4.24 (d, J = 5.2 Hz, 1H), 3.01 (d, J = 13.7 Hz, 2H), 2.73 (dd, J = 13.4, 6.9 Hz, 4H), 1.72−1.64 (m, 2H), 1.35−1.26 (m, 3H); HRMS (ESI+) *m/z*: Calc. for $C_{35}H_{40}N_9O_5^+$: 666.3147 [M+H]$^+$. Found 666.3132 [M+H]$^+$.

dx.doi.org/10.1021/bc300123m | *Bioconjugate Chem.* 2012, 23, 1821−1831

(*S*)-11-(1-Amino-6-carbamoyl-1-imino-8,11,14,17-tetraoxo-2,7,10,13,16-pentaazaoctadecan-18-ylamino)-5-methylbenzofuro[3,2-*b*]quinolin-5-ium (2l). Peptidyl coupling order is arginine-glycine-glycine-glycine, following the general procedure to give the desired compound **2l** as a straw yellow solid with a yield of 19%. mp 182−183 °C. ^{1}H NMR (400 MHz, DMSO-d_6) δ 9.82 (t, J = 6.4 Hz, 1H), 8.75 (d, J = 7.6 Hz, 2H), 8.63 (d, J = 8.2 Hz, 1H), 8.42 (d, J = 8.9 Hz, 1H), 8.29 (t, J = 5.6 Hz, 1H), 8.17 (t, J = 5.7 Hz, 1H), 8.13−8.08 (m, 1H), 7.96 (d, J = 8.1 Hz, 1H), 7.91 (dd, J = 9.2, 5.5 Hz, 2H), 7.81 (dd, J = 14.0, 6.8 Hz, 2H), 7.64 (ddd, J = 8.2, 5.9, 2.2 Hz, 1H), 7.37 (s, 1H), 7.09 (s, 1H), 4.80 (d, J = 6.3 Hz, 2H), 4.58 (s, 3H), 4.19 (dd, J = 13.2, 8.2 Hz, 3H), 3.85 (d, J = 5.6 Hz, 2H), 3.77−3.66 (m, 4H), 3.08 (dd, J = 12.2, 6.3 Hz, 2H), 1.76−1.68 (m, 1H), 1.59−1.36 (m, 4H); HRMS (ESI+) m/z: Calc. for $C_{30}H_{37}N_{10}O_6^+$: 633.2892 $[M+H]^+$. Found 633.2895 $[M+H]^+$.

11-((6*S*,9*S*,12*S*)-9-((4*H*-Imidazol-4-yl)methyl)-1-amino-12-benzyl-6-carbamoyl-1-imino-8,11,14,17-tetraoxo-2,7,10,13,16-pentaazaoctadecan-18-ylamino)-5-methylbenzofuro[3,2-*b*]quinolin-5-ium (2m). Peptidyl coupling order is arginine-histidine-phenylalanine-glycine, following the general procedure to give the desired compound **2m** as a straw yellow solid with a yield of 16%. mp 171−173 °C. ^{1}H NMR (400 MHz, DMSO-d_6) δ 14.17 (s, 2H), 9.66 (t, J = 5.5 Hz, 1H), 8.93 (s, 1H), 8.69 (d, J = 8.4 Hz, 1H), 8.63 (d, J = 8.2 Hz, 1H), 8.57 (t, J = 5.2 Hz, 1H), 8.42 (d, J = 9.0 Hz, 1H), 8.35 (d, J = 7.7 Hz, 1H), 8.20 (d, J = 7.8 Hz, 1H), 8.15−8.07 (m, 1H), 8.00 (d, J = 7.3 Hz, 1H), 7.96−7.74 (m, 3H), 7.71−7.57 (m, 2H), 7.50 (s, 1H), 7.33 (s, 1H), 7.16−7.12 (m, 1H), 4.78 (d, J = 5.4 Hz, 2H), 4.59 (s, 3H), 4.50 (d, J = 10.2 Hz, 1H), 4.18 (dd, J = 12.5, 7.2 Hz, 2H), 3.87−3.78 (m, 5H), 3.08 (dd, J = 13.8, 5.8 Hz, 3H), 2.97 (dd, J = 14.0, 5.0 Hz, 2H), 2.73 (dd, J = 13.6, 9.9 Hz, 1H), 1.77−1.65 (m, 1H), 1.64−1.34 (m, 3H); HRMS (ESI+) m/z: Calc. for $C_{41}H_{47}N_{12}O_6^+$: 402.1904 $[M+H]^{2+}$. Found 402.1902 $[M+H]^{2+}$.

11-((7*S*,10*S*,13*S*)-17-Amino-7-benzyl-13-carbamoyl-10-(3-guanidinopropyl)-2,5,8,11-tetraoxo-3,6,9,12-tetraazaheptadecylamino)-5-methylbenzofuro[3,2-*b*]-quinolin-5-ium (2n). Peptidyl coupling order is lysine-arginine-phenylalanine-glycine, following the general procedure to give the desired compound **2n** as a straw yellow solid with a yield of 17%. mp 177−179 °C. ^{1}H NMR (400 MHz, DMSO-d_6) δ 9.64 (s, 1H), 8.69 (d, J = 8.2 Hz, 1H), 8.64 (d, J = 8.2 Hz, 1H), 8.59 (s, 1H), 8.43 (d, J = 9.0 Hz, 1H), 8.30 (d, J = 6.1 Hz, 1H), 8.20 (d, J = 7.5 Hz, 1H), 8.15−8.09 (m, 1H), 7.86 (dt, J = 15.7, 6.0 Hz, 5H), 7.69 (s, 2H), 7.57 (s, 1H), 7.34 (d, J = 6.9 Hz, 1H), 7.20 (t, J = 12.1 Hz, 4H), 7.14 (d, J = 6.9 Hz, 1H), 7.06 (s, 1H), 4.75 (d, J = 5.0 Hz, 2H), 4.59 (s, 3H), 4.21−4.08 (m, 2H), 3.04 (dd, J = 25.8, 15.3 Hz, 4H), 2.75 (dd, J = 19.3, 6.2 Hz, 4H), 1.74−1.64 (m, 2H), 1.60−1.43 (m, 8H), 1.38−1.24 (m, 4H); HRMS (ESI+) m/z: Calc. for $C_{41}H_{52}N_{11}O_6^+$: 397.7085 $[M+H]^{2+}$. Found 397.7101 $[M+H]^{2+}$.

FRET Assays. FRET assay was carried out on a real-time PCR apparatus following previously published procedures.[24] The labeled oligonucleotides F21T: 5′-FAM-d(GGG-[TTAGGG]$_3$)-TAMRA-3′ and F10T: 5′-FAM-dTATAGCTA-TA-HEG-TATAGCTATA-TAMRA-3′ were used as the FRET probes. Fluorescence melting curves were determined with a Roche LightCycler 2 real-time PCR machine, using a total reaction volume of 20 μL, with 0.2 μM of labeled oligonucleotide in 10 mM Tris-HCl buffer, pH 7.2, containing 60 mM KCl. Fluorescence readings with excitation at 470 nm and detection at 530 nm were taken at intervals of 1 °C over the range 37−99 °C, with a constant temperature being maintained for 30 s prior to each reading to ensure a stable value. The melting of the G-quadruplex was monitored alone or in the presence of various concentrations of compounds and/or of double-stranded competitor ds26 (5′-CAATCGGATC-GAATTCGATCCGATTG-3′). Final analysis of the data was carried out using *Origin* 7.5 (OriginLab Corp.).

Surface Plasmon Resonance. SPR measurements were performed on a ProteOn XPR36 Protein Interaction Array system (Bio-Rad Laboratories, Hercules, CA) using a Neutravidin-coated GLH sensor chip. In a typical experiment, biotinylated HTG21 (5′-d(GGG[TTAGGG]$_3$)-3′) was folded in filtered and degassed running buffer (50 mM Tris-HCl, pH 7.2, 100 mM KCl). The DNA samples were then captured (∼1000 RU) in flow cell 1, leaving the fourth flow cell as a blank. Ligand solutions (at 4, 2, 1, 0.5, 0.25, 0.125 μM) were prepared with running buffer by serial dilutions from stock solution. Five concentrations were injected simultaneously at a flow rate of 100 μL/min for 150 s of association phase, followed with 300 s of dissociation phase at 25 °C. The GLH sensor chip was regenerated with short injection of 50 mM NaOH between consecutive measurements. The final graphs were obtained by subtracting blank sensorgrams from quadruplex sensorgrams. Data were analyzed with ProteOn manager software, using the Equilibrium method for fitting kinetic data.

CD Measurements. CD experiments were performed on a Chirascan circular dichroism spectrophotometer (Applied Photophysics). A quartz cuvette with 4 mm path length was used for the spectra recorded over a wavelength range of 230−450 at 1 nm bandwidth, 1 nm step size, and 0.5 s time per point. The oligomer HTG21 (5′-d(GGG[TTAGGG]$_3$)-3′) was diluted from stock to the required concentration (5 μM) in 10 mM Tris-HCl buffer, pH 7.2, 100 mM KCl, and then annealed by heating at 95 °C for 5 min, gradually cooled to room temperature, and incubated at 4 °C overnight. Then, CD titration was performed at a fixed HTG21 concentration (5 μM) with various concentrations (0−5 mol equiv) of the ligands in buffer containing 100 mM KCl at 25 °C. After each addition of ligand, the reaction was stirred and allowed to equilibrate for at least 10 min (until no elliptic changes were observed), and then a CD spectrum was collected. A buffer baseline was collected in the same cuvette, and subtracted from the sample spectra. Final analysis of the data was carried out using *Origin* 7.5 (OriginLab Corp.).

Molecular Modeling. The crystal structure of the parallel 22-mer telomeric G-quadruplex (PDB ID 1KF1)[25] was used as an initial model to study the interaction between the P-BFQ derivatives and telomeric DNA. For comparison with the DNA d(GGG[TTAGGG]$_3$) we used in the FRET and CD experiments, we removed the terminal 5′ adenine residue from the propeller-type structure and five adenines from each end of the hybrid-type structure to generate the 21-mer structure. Water molecules were removed from the PDB file, while the missing hydrogen atoms were added to the system using the Biopolymer module implemented in the *SYBYL7.3.5* molecular modeling software from Tripos Inc. (St. Louis, MO). Ligand structures were constructed by adopting the empirical Gasteiger-Huckel (GH) partial atomic charges, and then were optimized (Tripos force field) with a nonbond cutoff of 12 Å and a convergence of 0.01 kcal·mol^{-1}/Å over 10 000 steps using the Powell conjugate-gradient algorithm.

Docking studies were carried out using the *AUTODOCK 4.0* program.[26] By using ADT,[27] nonpolar hydrogens of telomeric G-quadruplex were merged to their corresponding carbons, and partial atomic charges were assigned. The nonpolar hydrogens of the ligands were merged, and rotatable bonds were assigned. The resulting G-quadruplex structure was used as an input for the *AUTOGRID* program. *AUTOGRID* gave a precalculated atomic affinity grid maps for each atom type in the ligand, plus an electrostatics map and a separate desolvation map present in the substrate molecule. The dimensions of the active site box, which was placed at the center of the G-quadruplex, were set to 60 Å × 60 Å × 60 Å with the grid points 0.375 Å apart. Docking calculations were carried out using the Lamarckian genetic algorithm (LGA). Initially, we used a population of random individuals (population size: 150), a maximum number of 25 000 000 energy evaluations, a maximum number of generations of 27 000, and a mutation rate of 0.02. One hundred independent docking runs were carried out for each ligand. The resulting positions were clustered according to a root-mean-square criterion of 0.5 Å.

TRAP-LIG Assay. The activity of P-BFQ conjugates to inhibit telomerase in a cell-free system was assessed with the TRAP-LIG assay following previously published procedures.[28] Protein extracts from exponentially growing A549 leukemia cells were used. Briefly, 0.1 μg of TS forward primer (5′-AATCCGTCGAGCAGAGTT-3′) was elongated by telomerase (500 ng protein extract) in TRAP buffer (20 mM Tris-HCl, pH 8.3, 68 mM KCl, 1.5 mM $MgCl_2$, 1 mM EGTA, and 0.05% Tween 20) containing 125 μM dNTPs and 0.05 μg BSA. The mixture was added to tubes containing freshly prepared ligand at various concentrations and to a negative control containing no ligand. The initial elongation step was carried out for 20 min at 30 °C, followed with 95 °C for 5 min, and a final maintenance of the mixture at 20 °C. To purify the elongated product and to remove the bound ligands, the quick nucleotide purification kit (Tiangen) was used according to the manufacturer's instructions. The purified extended samples were then subjected to PCR amplification. In this step, a second PCR master mix was prepared consisting of 1 μM ACX reverse primer (5′-GCGCGG[CTTACC]$_3$CTAACC-3′), 0.1 μg TS forward primer (5′-AATCCGTCGAGC-AGAGTT-3′), TRAP buffer, 5 μg BSA, 0.5 mM dNTPs, and 2 units of Taq polymerase. A 10 μL aliquot of the master mix was added to the purified telomerase-extended samples, and amplified for 35 cycles at 94 °C for 30 s, at 61 °C for 1 min, and at 72 °C for 1 min. Samples were separated on a 16% PAGE, and visualized with silver-staining. IC_{50} values were then calculated from the optical density quantitated from the *Quantity One* software.

Long-Term Cell Culture Experiments. Long-term proliferation experiments were carried out using the HL60 Human promyelocytic leukemia cells. Cells were grown in T80 tissue culture flasks at 1.0×10^5 per flask, and exposed to a subcytotoxic concentration of ligand or an equivalent volume of 0.1% DMSO every 4 days. The cells in control and drug-exposed flasks were counted and flasks reseeded with 1.0×10^5 cells. The remaining cells were collected and used for the measurements described below. This process was continued for 16 days.

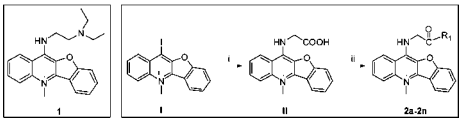
SA-β-Gal Assay. Cells treated with the ligand were incubated for 16 days. After the incubation, the growth medium was aspirated and the cells were fixed in 2% formaldehyde/0.2% glutaraldehyde for 15 min at room temperature. The fixing solution was removed, and the cells were gently washed twice with PBS, and then stained with the β-Gal staining solution containing 1 mg/mL of 5-bromo-4-chloro-3-indolyl-β-D-galactoside, followed with incubation overnight at 37 °C. The staining solution was removed, and the cells were washed three times with PBS. The cells were viewed under an optical microscope and photographed.

Telomere Length Assay. Cells treated with the ligand were incubated for 16 days. To measure the telomere length, genomic DNA was digested with Hinf1/Rsa1 restriction enzymes. The digested DNA fragments were separated on 0.8% agarose gel, transferred to a nylon membrane, and the transferred DNA was fixed on the wet blotting membrane by baking the membrane at 120 °C for 20 min. The membrane was hybridized with a DIG-labeled hybridization probe for telomeric repeats, and incubated with anti-DIG-alkaline phosphatase. TRF was performed through chemiluminescence detection.

RESULTS AND DISCUSSION

Chemistry. The synthesis of P-BFQ derivatives followed the general pathway as shown in Scheme 1. The key intermediate **I**

Scheme 1. Synthesis of P-BFQ Derivatives[a]



[a]Reagents: (i) glycine, 2-ethoxyethanol, 55 °C, 12 h; (ii) synthesized peptides, HOBT, DIC, DMF, RT 12 h.

of 11-iodo-5-methylbenzofuro [3,2-*b*]quinolin-5-ium was prepared following the procedure previously reported by Lu et al.[16,29,30] The substitution reaction of **I** mixed with glycin in 2-ethoxyethanol solution gave the intermediate **II**, which had a carboxyl group that can take condensation reaction with the amino terminal of peptidyl side chain.

All synthesized sequences of peptidyl side chain are shown in Table 1. The solid-phase synthesis of these short peptides was carried out manually using standard Fmoc strategy on a Rink Amide AM resin (4-(2′,4′-dimethoxyphenyl-Fmoc-aminomethyl)phe-noxyacetamido-norleucylaminomethyl resin).[31] The coupling procedure was performed with 4 equiv of *N*-Fmoc-protected amino acid, 4 equiv of DIC, and HOBt in DMF for 3 h. The coupling was monitored using standard Kaiser's test, and the Fmoc group was removed by incubation with 25% piperidine solution in DMF twice for about 30 min.

Then, 3 equiv of **II** were added into Fmoc deprotected peptidyl side chain with 10 equiv of DIC and HOBt in DMF for 12 h. The final cleavage of various P-BFQ conjugates (**2a**–**2n**) from the resin was carried out using a mixture of trifluoroacetic acid and water (95:5), and conjugates were purified by using preparative RP-HPLC. The compounds used in the biological activity tests were at least 95% pure according to the analytical HPLC. The structures of the synthesized compounds were confirmed by using HR MS/MS and NMR analysis.

Fluorescence Melting Assays. All synthesized compounds were evaluated for their thermodynamic stability and selectivity to telomeric G-quadruplex over duplex DNA through FRET melting experiments[24,32,33] with F21T and F10T, respectively, and the benzofuroquinoline derivative **1** previously reported by our group was used as a reference compound.

dx.doi.org/10.1021/bc300123m | *Bioconjugate Chem.* 2012, 23, 1821–1831

Table 1. G-Quadruplex Stabilization (ΔT_m) Potential Obtained from FRET-Melting, Equilibrium Binding Constants (K_D) Measured with SPR, and Telomerase Inhibition (IC_{50}) by P-BFQ Conjugates in Cell-Free Assay

		FRET (ΔT_m/°C)[b]		SPR (K_D/μM)			
compound	R_1[a]	F21T	F10T	G4	duplex	duplex/G4	telomerase inhibition (IC_{50}/ μM)
2a	R-NH_2	12.3 ± 0.3	1.4 ± 0.2	0.27	19.3	70.4	12.0
2b	GG-NH_2	3.9 ± 0.1	0.1 ± 0.0	2.29	12.6	5.5	>30
2c	GR-NH_2	20.6 ± 0.2	1.9 ± 0.3	0.65	45.2	69.0	7.4
2d	GF-NH_2	5.6 ± 0.6	0.1 ± 0.1	1.91	25.4	13.3	26.3
2e	GH-NH_2	7.7 ± 0.3	0.5 ± 0.2	0.32	21.8	67.9	>20
2f	GK-NH_2	14.8 ± 0.2	1.2 ± 0.1	0.66	86.6	130.2	13.8
2g	KR-NH_2	24.3 ± 0.8	3.3 ± 0.3	0.19	9.5	50.5	5.5
2h	FR-NH_2	13.1 ± 0.6	1.0 ± 0.1	0.42	23.4	55.0	14.6
2i	HR-NH_2	17.4 ± 0.6	2.1 ± 0.2	0.39	12.0	30.7	10.5
2j	GGR-NH_2	10.9 ± 0.3	1.3 ± 0.0	0.39	5.3	13.6	19.9
2k	GFR-NH_2	9.7 ± 0.5	1.2 ± 0.1	0.89	21.7	24.2	21.2
2l	GGGR-NH_2	9.6 ± 0.3	1.3 ± 0.1	0.76	11.8	15.5	22.7
2m	GFHR-NH_2	12.5 ± 0.2	0.6 ± 0.2	0.70	14.7	20.9	18.8
2n	GFRK-NH_2	11.2 ± 0.2	0.2 ± 0.0	0.62	13.3	21.2	20.4
1	--	13.5 ± 0.4	10.1 ± 0.1	0.76	1.82	2.4	13.3

[a] R_1 is the peptidyl sequences of these conjugates' side chains, starting from the terminal of scaffold. R, G, F, H, and K are abbreviations of Arginine, Glycine, Phenylalanine, Histidine, and Lysine, respectively. [b] $\Delta T_m = T_m$(DNA + ligand) − T_m (DNA). ΔT_m values of 0.2 μM F21T or F10T incubated with 1.0 μM compound in the presence of 60 mM KCl.

F21T (5′-FAM-d(GGG[TTAGGG]$_3$)-TAMRA-3′) represents the human telomeric DNA sequence, while F10T (5′-FAM-dTATAGCTATA-HEG-TATAGCTATA- TAMRA-3′) is a self-complementary duplex DNA hairpin.

The results of T_m values from the FRET melting experiments (Table 1 and SI Figure S1) indicated that the peptidyl-substituted benzofuroquinoline derivatives had a wide range of telomeric G-quadruplex DNA stabilizing activity with ΔT_m ranging from 3.9 to 24.3 °C, and the activity of some compounds (**2c**, **2f**, **2g**, and **2i**) are better than that of the reference compound **1**. The structure−activity relationships could be obtained from the stabilizing activity of the tested compounds toward telomeric G-quadruplex. In particular, it appeared that the introduction of arginine at a certain position of dipeptidyl side chain, such as compounds **2c**, **2g**, **2h**, and **2i**, remarkably increased their G-quadruplex stabilizing efficiency. This effect was weakened when amino acid residues changed from arginine (or lysine) to phenylalanine (**2d**), histidine (**2e**), or glycine (**2b**). This suggests that the positive charge and alkyl chain-length of the peptidyl side chain are important for its interaction with G-quadruplex. We compared ligands with different peptidyl length containing arginine, and the results showed that ligands **2c** and **2g** (ΔT_m values of 20.6 and 24.3 °C, respectively) with dipeptidyl side chain were better than other ligands with shorter or longer chain-length. From these data, we can determine that the distance between the scaffold and the positive charge of arginine must be moderate, which is essential to stabilize G-quadruplex DNA. This result was consistent with our molecular modeling studies shown below.

As shown in Table 1, all ligands had a rather weak effect on the thermal stability of the duplex DNA F10T, compared to reference compound **1**, suggesting their weak binding activity to the duplex DNA.[34,35] To further characterize the selectivity of these ligands for G-quadruplex DNA over duplex DNA, competitive FRET experiment was employed with a non-fluorescent duplex DNA competitor (ds26).[35,36] In these experiments, the labeled oligonucleotide F21T was melted in the presence of excess ds26 (15- and 50-fold excess). The result of competitive FRET melting assay was plotted in Figure 1.

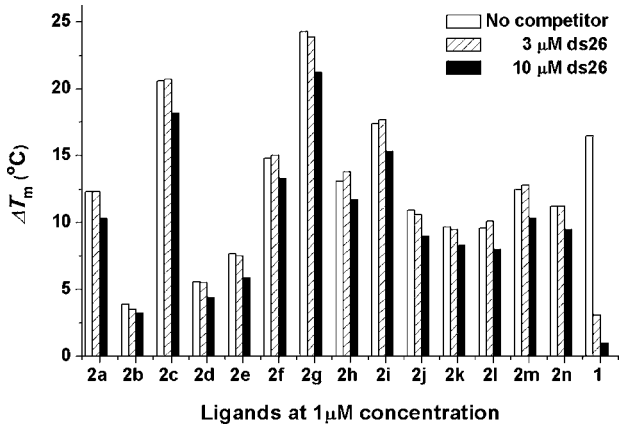


Figure 1. Competitive FRET results for P-BFQ ligands (**2a**−**2n**) and compound **1** (1 μM), without (blank) and with 15-fold (3 μM; grid) or 50-fold (10 μM, black) excess of duplex DNA competitor (ds26). The concentration of F21T was 0.2 μM.

The results clearly indicated a high level of stabilization of these ligands on telomeric G-quadruplex, which was only a little affected in the presence of 50-fold competitor ds26. Compared with reference compound **1**, selectivity of these compounds was highly improved. The results also showed that these compounds had high selectivity for G-quadruplex DNA over duplex DNA, which can be attributed to the introduction of the peptidyl side chain. Accordingly, the combined results of these assays demonstrated that peptidyl−benzofuroquinoline (P-BFQ) conjugates are a new class of potent and highly selective telomeric G-quadruplex binding ligands.

Surface Plasmon Resonance. In order to investigate the binding affinity of P-BFQ ligands for their quadruplex target and their level of specificity for quadruplex versus duplex DNA, the surface plasmon resonance (SPR) method was employed. The equilibrium constants for the binding of the ligands to DNA were determined using SPR with biotinylated DNA attached to a streptavidin-coated sensor chip.[37,38] A range of

dx.doi.org/10.1021/bc300123m | Bioconjugate Chem. 2012, 23, 1821−1831

concentrations of ligands were injected simultaneously to the immobilized various DNA and the blank reference.

The binding constants were determined using equilibrium analysis as shown in Table 1. The binding constants of the P-BFQ ligands to telomeric G-quadruplex and duplex DNA fell into a wide range (telomeric K_D, 0.19−2.29 μM; duplex K_D, 5.3−86.6 μM). All tested ligands were found to bind to the human telomeric G-quadruplex more tightly than their binding to duplex DNA. From these data, we can clearly see that introduction of peptidyl side chain onto the scaffold of BFQ induced, for most designed peptide sequences, gives a significant improvement of its specificity for quadruplex over duplex DNA compared with compound **1** [K_d(ds)/K_d(Htelo) = 2.4]. Compound **2b** had weak interaction with G-quadruplex based on FRET data, and was also found to have weak binding activity and specificity [K_d(ds)/K_d(Htelo) = 5.5]. Other compounds showed a discrimination of at least 10-fold for the G-quadruplex structure [K_d(ds)/K_d(Htelo) values ranging from 13.3 to 130.2]. For example, compound **2c**, which is a representative compound of these series, had excellent binding affinity and selectivity to telomeric G-quadruplex DNA as shown in Figure 2. All these results were approximately consistent with their ΔT_m values obtained from FRET melting.

Both FRET and SPR experimental results indicated that BFQ scaffold with introduced peptidyl side chain had greatly improved binding capability and selectivity to telomeric G-quadruplex DNA. Functional groups on side chain of amino acid residues are very important to their activity. Peptide sequences with arginine and lysine were optimal for their interactions with telomeric G-quadruplex DNA, while the introduction of glycine, phenylalalnine, or some other amino acid residues without positive charge on peptiyl side chain was unfavorable for their binding interactions and selectivity. Overall, SPR experiments indicated that P-BFQ conjugates had good selectivity for telomeric G-quadruplex, which were in agreement with our FRET data.

Circular Dichroism. Circular dichroism (CD) spectroscopy was used to determine the structural type of G-quadruplex DNA and the effect of ligand binding on quadruplex structures.[39] The interactions of synthesized conjugates with telomeric G-quadruplex DNA were further explored by using this method. The particular signature of the CD spectrum of the G-quadruplex is well-characterized. In the presence of 100 mM K^+, the CD spectrum of HTG21 in the absence of any compound showed a major positive band at 290 nm, a shoulder at around 270 nm, a small positive band at 250 nm, and a minor negative band near 234 nm. This indicated a mixture of antiparallel and parallel conformations, possibly including hybrid-types as well. As shown in Figure 3A, upon the addition of compound **2f** (5 mol equiv of HTG21) to the above solution, the CD spectrum significantly changed, with a

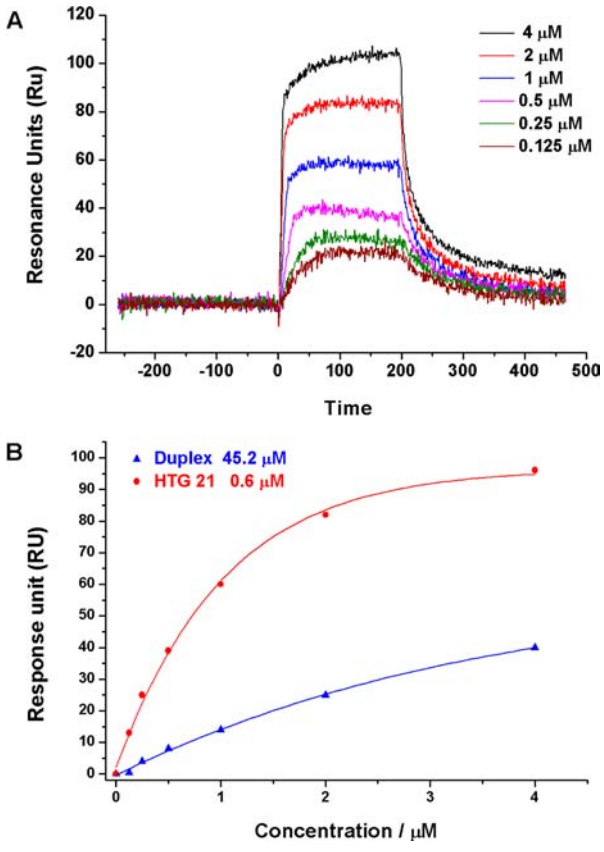


Figure 2. (A) SPR sensorgram overlay for binding of compound **2c** to telomeric quadruplex HTG21. Concentration range: 0.125, 0.25, 0.5, 1, 2, 4 μM from the bottom curve upward. (B) Binding plots used to determine the K_d value for **2c** with telomeric G-quadruplex and duplex DNAs, running buffer, 50 mM Tris-HCl, pH 7.2, 100 mM KCl.

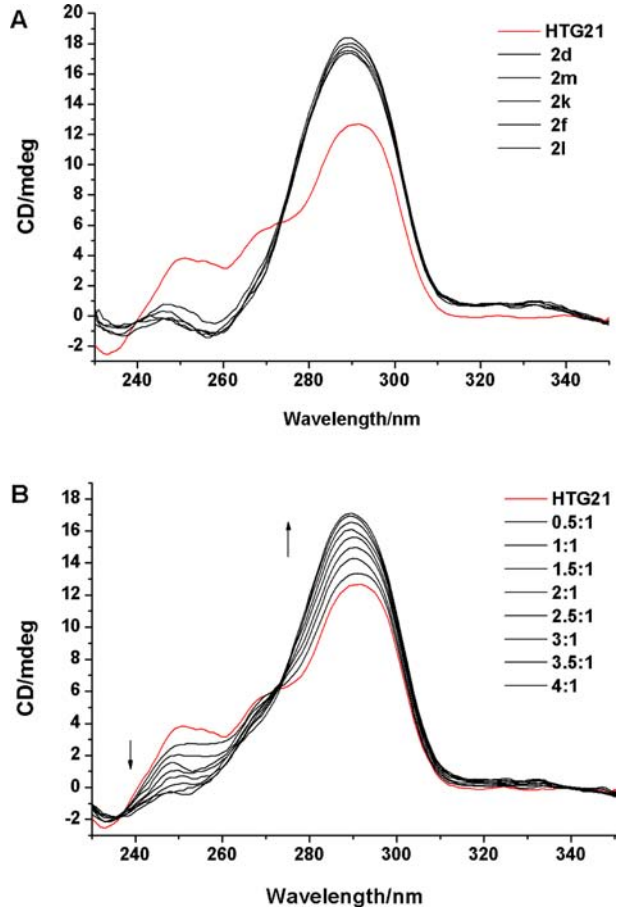


Figure 3. (A) CD spectra of HTG21 in 10 mM Tris-HCl buffer, pH 7.2, 100 mM KCl. CD spectra of HTG21 (dashed line), and HTG21 in the presence of 5 equiv of **2d**, **2f**, **2k**, **2l**, and **2m**, respectively. (B) CD titration spectra of HTG21 (5 μM) at increasing concentrations of **2c** (0−4 mol equiv; dashed line indicated HTG21 in the absence of **2c**).

dx.doi.org/10.1021/bc300123m | *Bioconjugate Chem.* 2012, 23, 1821−1831

dramatic increase of maximum band at 290 nm and the emergence of the shoulder at 270 nm, indicating the possible destruction of the parallel structure of the mixed G-quadruplex conformations; meanwhile, the small positive band at 250 nm disappeared, which led to the appearance of a positive band at 240 nm and a major negative band at 260 nm, suggesting the formation of an antiparallel structure. Similar results were also observed upon addition of other compounds (**2d**, **2k**, **2l**, **2m**) but with less significant changes.

In order to further study the binding interactions, CD spectra of HTG21 (5 μM) were also recorded in the presence of increasing concentrations of compound **2c** (2.5−20 μM, corresponding to 0.5−4 equiv of compound **2c**) (Figure 3B). The band with maximum at 291 nm significantly increased and shifted toward 288 nm, while the shoulder at 270 nm was also gradually enhanced and merged into the band at 288 nm. In the meantime, the small positive band at 250 nm gradually decreased. The changes of the CD spectra were notably concentration dependent, as shown in Figure 3B. All these CD studies illustrate that tested ligands might transform the preformed hybrid-type G-quadruplex structure into antiparallel G-quadruplex, which is consistent with the performances of the Quindoline derivatives we reported previously,[16] indicating manifest interactions of ligands with telomeric G-quadruplex DNA.

Molecular Modeling Studies. In order to understand the properties of the interactions between P-BFQ conjugates and the telomeric G-quadruplex DNA, molecular docking studies were performed. The crystal structure of the propeller telomeric G-quadruplex (d[$AG_3(T_2AG_3)_3$], PDB code: 1KF1) with potassium ion was used as a template for the modeling studies because it might be a more biologically relevant form.[40] Compound **2c** was selected for this study as one of the best binding ligands; meanwhile, **2b**, **2j**, and **2l** were also selected to study the effect of different peptide lengths on telomeric G-quadruplex. Our results from clustering analysis of molecular docking showed that compound **2c** could stack on both external G-quartet planes, and the peptidyl side chain with protonated amino group was just embedded into the grooves, and interacted with the phosphate diester backbone through hydrogen bonding and electrostatic interaction. Meanwhile, other tested compounds (**2b**, **2j**, **2l**) with longer or shorter side chains could not favorably interact with grooves (SI Figure S2). Therefore, the appropriate peptidyl side chain is critical in ligand−quadruplex interactions, which was confirmed by using biophysical and biochemical methods. Furthermore, **2c** had the same binding mode as reference compound **1**, and more hydrogen bonding interactions with grooves and loops might make **2c** have lower binding energy, as shown in Figure 4. In this experiment, 100 random starting structures were generated, and structures with lowest energy (average intermolecular binding energy, ΔG = −12.53 kcal/mol for **2c** and −9.87 kcal/mol for **1**) were obtained after the docking protocols were analyzed.

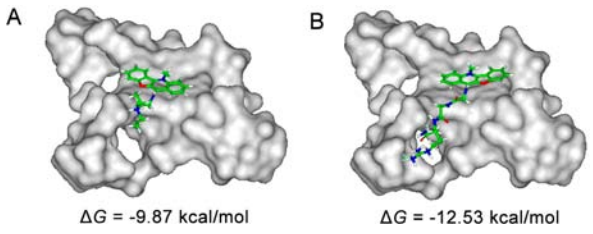


Figure 4. Side view of compound (a) **1** and (b) **2c** making stacking interactions with the 3′ G-quartet. The ligand side chain is lying in the grooves formed by the TTA loops. Pictures were generated by PyMOL.

Telomerase Inhibition. To determine the inhibitory ability of P-BFQ conjugates to human telomerase, a modified TRAP assay was adopted.[28] The TRAP-LIG assay provided quantitative measurement of telomerase inhibition by the small molecules, which is a reliable and reproducible approach to evaluate telomerase inhibitory effects without a separate Taq polymerase assay. Considering the compounds might interact with the extension reaction products thus interfering with the PCR step, the ligands were removed after incubation with the enzyme and prior to the amplification step. In the experiments, solutions of compounds were added to the telomerase reaction mixture containing extract from A549 leukemia cells, and their concentrations causing half enzyme inhibition ($^{Tel}IC_{50}$) were obtained as shown in Table 1.

The $^{Tel}IC_{50}$ values of these ligands ranged from 5.5 to 30 μM, which indicated that most of the tested compounds had remarkable inhibitory effects on telomerase activity. Thus, introduction of peptidyl side arms on BFQ scaffold could maintain or improve its inhibitory activity against telomerase. Compound **2g** with a dipeptide fragment of -Lys-Arg had the most potent inhibitory effect ($^{Tel}IC_{50}$ = 5.5 μM), while compounds (**2b**, **2d**, and **2e**) without arginine at their side chain had low inhibitory activity. Compared with reference compound **1** ($^{Tel}IC_{50}$ = 13.3 μM), reported telomerase inhibitor by our group previously,[16] some tested compounds with dipeptidyl side chain (contained argininyl/lysyl) had more potent inhibitory effects as shown in Table 1. In addition, compound **2g** also had an equivalent effect of inhibition relative to classical telomerase inhibitors such as BRACO-19 and TMPyP4 ($^{Tel}IC_{50}$ = 6.3 μM and 8.9 μM, respectively).[28] These results were consistent with those data obtained from previous experiments (FRET, SPR). Interestingly, the observed inhibition of telomerase elongation was well-related to G-quadruplex binding thermodynamics, as shown by the almost linear dependence of $^{Tel}IC_{50}$ for telomerase inhibition on $\Delta T_m/T_m$, where T_m is the melting temperature in the presence of 5 equiv of the compound (Figure 5).[41] The R^2 value of this linear equation reached 0.90, which indicated that the effect of a series of P-BFQ compounds had a good structure−activity relationship.

Cell Senescence Induced by Compound 2c. To examine the effect of representative compound **2c** on leukemia cell HL60, short-term cell viability was first determined in a 2-day cytotoxic assay (MTT assay). The results showed that **2c** had a moderate inhibitory effect, with an IC_{50} value of 45 μM for HL60 cells. This result prompted us to further investigate the long-term effect of this compound. To evaluate the long-term effect of **2c** on HL60, subcytotoxic concentrations (1.25 and 5 μM) of **2c** were adopted to avoid acute cytotoxicity and other nonspecific events that could lead to difficulty in result interpretation. Treatment of HL60 cells with 5 μM compound **2c** resulted in a significant inhibitory effect after 12 days. In the presence of even 1.25 μM compound **2c**, a discernible difference was observed between the control and treated cells (Figure 6A).

Morphologic examination of the cells during long-term studies showed an increased proportion of enlarged and flattened cells with phenotypic characteristics of senes-

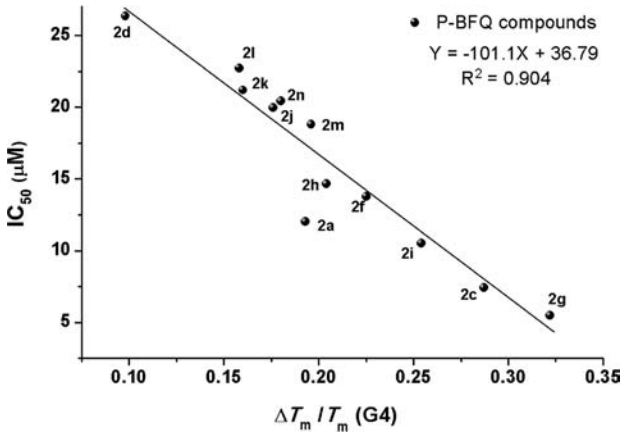


Figure 5. Correlation between telomerase elongation inhibition (IC_{50}) and thermal stabilization ($\Delta T_m/T_m$) of telomeric G-quadruplex measured for all tested ligands.

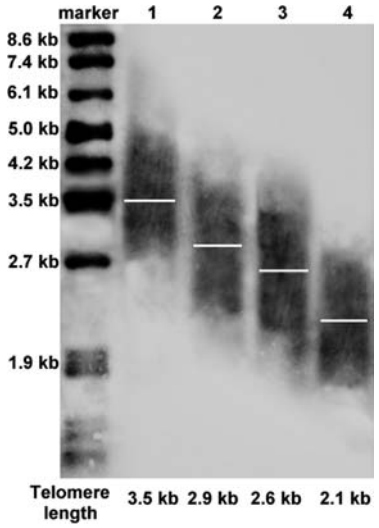


Figure 7. Effect of compound **2c** on telomere length. TRF analysis of HL60 cells treated with or without compound **2c** for 16 days. Lane 1, 0.1% DMSO; lane 2, 1.25 μM **2c**; lane 3, 2.5 μM **2c**; lane 4, 5 μM **2c**.

cence.[42,43] These flattened cells also stained positively for the senescence-associated β-galactosidase (SA-β-Gal) activity after continuous treatment by compound **2c** (Figure 6B,C). Results indicated that compound **2c** induced accelerated senescence of HL60 cancer cells.

Telomere Shortening by Compound 2c. Treatment of cancer cells with telomeric G-quadruplex ligands had been previously reported to disrupt telomere length maintenance and cause telomeres to erode.[44−46] To investigate whether **2c** could shorten telomeres, the telomere length was evaluated using the telomeric restriction fragment (TRF) length assay. The results showed that 5 μM compound **2c** triggered telomere shortening about 1.4 kb for HL60 cells, and telomere shortening was also observed after 2.5 μM and 1.25 μM of **2c** treatment (Figure 7). Dysfunctional telomere could activate p53 to initiate cellular senescence or apoptosis to suppress tumorigenesis[16] as reported, so the senescence induced by compound **2c** might result from this shortening of telomere length. This result is consistent with the activity expected for effective telomeric G-quadruplex ligand and telomerase inhibitor.[47]

CONCLUSIONS

The design of compounds targeting at the telomeric G-quadruplex DNA is a rational and promising strategy. Our previous work has confirmed that cryptolepine derivatives are powerful compounds for this target. On the basis of this result, a series of novel peptidyl derivatives were designed, synthesized, and evaluated as effective and selective G-quadruplex ligands. The present study showed that P-BFQ conjugates were a promising class of telomeric G-quadruplex binding ligands with significant selectivity against duplex DNA *in vitro*. The guanidine group of arginine could greatly contribute to the overall binding ability. Moreover, their cellular effects indicated that some potent compounds had more effective inhibitory activities than typical telomerase inhibitors, which were also consistent with the properties expected for potent telomeric G-quadruplex ligands and telomerase inhibitors. These results proved that introduction of peptidyl side chains is a novel approach for obtaining more efficient and selective telomeric G-quadruplex ligands.

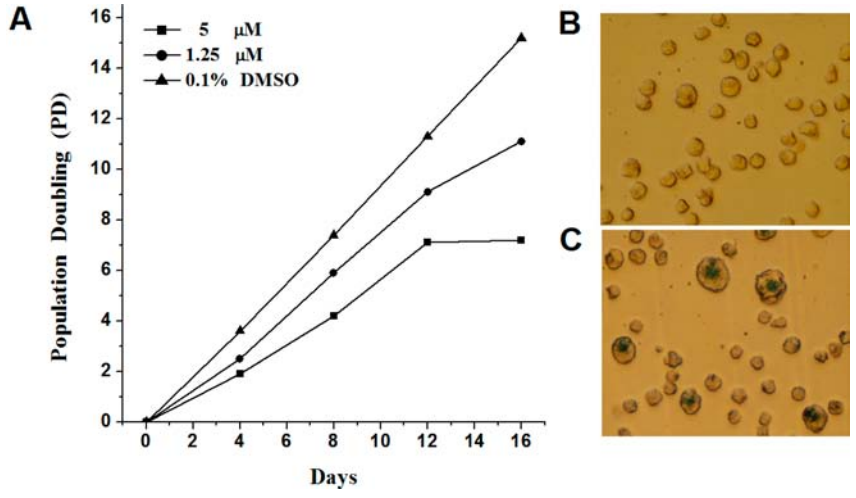


Figure 6. Senescence induced by compound **2c** on HL60 cells. (A) Long-term incubation of HL60 with compound **2c** at subcytotoxic concentrations. Expression of SA-β-Gal in HL60 cells after treatment with (B) 0.1% DMSO or (C) 5 μM compound **2c** continuously for 16 days.

dx.doi.org/10.1021/bc300123m | *Bioconjugate Chem.* 2012, 23, 1821−1831

■ ASSOCIATED CONTENT

Supporting Information

Figures S1−S3. This material is available free of charge via the Internet at http://pubs.acs.org.

■ AUTHOR INFORMATION

Corresponding Author

*Tel.: 8620-39943056; Fax: 8620-39943056; E-mail: ceshzs@mail.sysu.edu.cn.

Notes

The authors declare no competing financial interest.

■ ACKNOWLEDGMENTS

We thank the Natural Science Foundation of China (Grants U0832005, 21172272), the International S&T Cooperation Program of China (2010DFA34630), the Specialized Research Fund for the Doctoral Program of Higher Education (20110171110051), and the Science Foundation of Guangzhou (2009A1-E011-6) for financial support of this study.

■ REFERENCES

(1) Xu, L., and Blackburn, E. H. (2007) Human cancer cells harbor T-stumps, a distinct class of extremely short telomeres. *Mol. Cell 28*, 315−327.

(2) Campbell, N. H., Parkinson, G. N., Reszka, A. P., and Neidle, S. (2008) Structural basis of DNA quadruplex recognition by an acridine drug. *J. Am. Chem. Soc. 130*, 6722−6724.

(3) Moyzis, R. K., Buckingham, J. M., Cram, L. S., Dani, M., Deaven, L. L., Jones, M. D., Meyne, J., Ratliff, R. L., and Wu, J. R. (1988) A highly conserved repetitive DNA sequence, (TTAGGG)n, present at the telomeres of human chromosomes. *Proc. Natl. Acad. Sci. U.S.A. 85*, 6622−6626.

(4) Stewart, S. A., and Weinberg, R. A. (2006) Telomeres: cancer to human aging. *Annu. Rev. Cell. Dev. Biol. 22*, 531−557.

(5) Zaug, A. J., Podell, E. R., and Cech, T. R. (2005) Human POT1 disrupts telomeric G-quadruplexes allowing telomerase extension in vitro. *Proc. Natl. Acad. Sci. U.S.A. 102*, 10864−10869.

(6) Wright, W. E., Tesmer, V. M., Huffman, K. E., Levene, S. D., and Shay, J. W. (1997) Normal human chromosomes have long G-rich telomeric overhangs at one end. *Genes Dev. 11*, 2801.

(7) Neidle, S. (2010) Human telomeric G-quadruplex: the current status of telomeric G-quadruplexes as therapeutic targets in human cancer. *FEBS J. 277*, 1118−1125.

(8) Gomez, D., Wenner, T., Brassart, B., Douarre, C., O'Donohue, M. F., El Khoury, V., Shin-Ya, K., Morjani, H., Trentesaux, C., and Riou, J. F. (2006) Telomestatin-induced telomere uncapping is modulated by POT1 through G-overhang extension in HT1080 human tumor cells. *J. Biol. Chem. 281*, 38721−38729.

(9) Zahler, A. M., Williamson, J. R., Cech, T. R., and Prescott, D. M. (1991) Inhibition of telomerase by G-quartet DNA structures. *Nature 350*, 718−720.

(10) Sun, D., Thompson, B., Cathers, B. E., Salazar, M., Kerwin, S. M., Trent, J. O., Jenkins, T. C., Neidle, S., and Hurley, L. H. (1997) Inhibition of human telomerase by a G-quadruplex-interactive compound. *J. Med. Chem. 40*, 2113−2116.

(11) Read, M., Harrison, R. J., Romagnoli, B., Tanious, F. A., Gowan, S. H., Reszka, A. P., Wilson, W. D., Kelland, L. R., and Neidle, S. (2001) Structure-based design of selective and potent G quadruplex-mediated telomerase inhibitors. *Proc. Natl. Acad. Sci. U.S.A. 98*, 4844−4849.

(12) Tan, J. H., Gu, L. Q., and Wu, J. Y. (2008) Design of selective G-quadruplex ligands as potential anticancer agents. *Mini. Rev. Med. Chem. 8*, 1163−1178.

(13) Zagotto, G., Ricci, A., Vasquez, E., Sandoli, A., Benedetti, S., Palumbo, M., and Sissi, C. (2011) Tuning G-quadruplex vs double-stranded DNA recognition in regioisomeric lysyl-peptidyl- anthraquinone conjugates. *Bioconjugate Chem. 22*, 2126−2135.

(14) Moore, M. J., Schultes, C. M., Cuesta, J., Cuenca, F., Gunaratnam, M., Tanious, F. A., Wilson, W. D., and Neidle, S. (2006) Trisubstituted acridines as G-quadruplex telomere targeting agents. Effects of extensions of the 3,6- and 9-side chains on quadruplex binding, telomerase activity, and cell proliferation. *J. Med. Chem. 49*, 582−599.

(15) Huang, H. S., Chen, I. B., Huang, K. F., Lu, W. C., Shieh, F. Y., Huang, Y. Y., Huang, F. C., and Lin, J. J. (2007) Synthesis and human telomerase inhibition of a series of regioisomeric disubstituted amidoanthraquinones. *Chem. Pharm. Bull. (Tokyo) 55*, 284−292.

(16) Lu, Y. J., Ou, T. M., Tan, J. H., Hou, J. Q., Shao, W. Y., Peng, D., Sun, N., Wang, X. D., Wu, W. B., Bu, X. Z., Huang, Z. S., Ma, D. L., Wong, K. Y., and Gu, L. Q. (2008) 5-N-methylated quindoline derivatives as telomeric g-quadruplex stabilizing ligands: effects of 5-N positive charge on quadruplex binding affinity and cell proliferation. *J. Med. Chem. 51*, 6381−6392.

(17) Han, H., Langley, D. R., Rangan, A., and Hurley, L. H. (2001) Selective interactions of cationic porphyrins with G-quadruplex structures. *J. Am. Chem. Soc. 123*, 8902−8913.

(18) Zhou, J. L., Lu, Y. J., Ou, T. M., Zhou, J. M., Huang, Z. S., Zhu, X. F., Du, C. J., Bu, X. Z., Ma, L., Gu, L. Q., Li, Y. M., and Chan, A. S. (2005) Synthesis and evaluation of quindoline derivatives as G-quadruplex inducing and stabilizing ligands and potential inhibitors of telomerase. *J. Med. Chem. 48*, 7315−7321.

(19) Lisgarten, J. N., Coll, M., Portugal, J., Wright, C. W., and Aymami, J. (2002) The antimalarial and cytotoxic drug cryptolepine intercalates into DNA at cytosine-cytosine sites. *Nat. Struct. Biol. 9*, 57−60.

(20) Corbin-Lickfett, K. A., Chen, I. H., Cocco, M. J., and Sandri-Goldin, R. M. (2009) The HSV-1 ICP27 RGG box specifically binds flexible, GC-rich sequences but not G-quartet structures. *Nucleic Acids Res. 37*, 7290−7301.

(21) Takahama, K., Sugimoto, C., Arai, S., Kurokawa, R., and Oyoshi, T. (2011) Loop lengths of G-quadruplex structures affect the G-quadruplex DNA binding selectivity of the RGG motif in Ewing's sarcoma. *Biochemistry 50*, 5369−5378.

(22) Ladame, S., Schouten, J. A., Stuart, J., Roldan, J., Neidle, S., and Balasubramanian, S. (2004) Tetrapeptides induce selective recognition for G-quadruplexes when conjugated to a DNA-binding platform. *Org. Biomol. Chem. 2*, 2925−2931.

(23) Sissi, C., Gatto, B., and Palumbo, M. (2011) The evolving world of protein-G-quadruplex recognition: a medicinal chemist's perspective. *Biochimie 93*, 1219−1230.

(24) Rachwal, P. A., and Fox, K. R. (2007) Quadruplex melting. *Methods 43*, 291−301.

(25) Parkinson, G. N., Lee, M. P., and Neidle, S. (2002) Crystal structure of parallel quadruplexes from human telomeric DNA. *Nature 417*, 876−880.

(26) Morris, G. M., Goodsell, D. S., Halliday, R. S., Huey, R., Hart, W. E., Belew, R. K., and Olson, A. J. (1998) Automated docking using a Lamarckian genetic algorithm and an empirical binding free energy function. *J. Comput. Chem. 19*, 1639−1662.

(27) Sanner, M. F. (1999) Python: a programming language for software integration and development. *J. Mol. Graphics Mod. 17*, 57−61.

(28) Reed, J., Gunaratnam, M., Beltran, M., Reszka, A. P., Vilar, R., and Neidle, S. (2008) TRAP-LIG, a modified telomere repeat amplification protocol assay to quantitate telomerase inhibition by small molecules. *Anal. Biochem. 380*, 99−105.

(29) Fan, P. C., and Ablordeppey, S. Y. (1997) An alternative synthesis of 10H-indolo[3,2-*b*]quinoline and its selective N-alkylation. *J. Heterocyclic Chem. 34*, 1789−1794.

(30) Bierer, D. E., Dubenko, L. G., Zhang, P., Lu, Q., Imbach, P. A., Garofalo, A. W., Phuan, P. W., Fort, D. M., Litvak, J., Gerber, R. E., Sloan, B., Luo, J., Cooper, R., and Reaven, G. M. (1998) Antihyperglycemic activities of cryptolepine analogues: an ethno-

botanical lead structure isolated from Cryptolepis sanguinolenta. *J. Med. Chem. 41*, 2754−2764.
(31) Yamamoto, N., and Tamura, A. (2010) Designed low amphipathic peptides with alpha-helical propensity exhibiting antimicrobial activity via a lipid domain formation mechanism. *Peptides 31*, 794−805.
(32) Mergny, J. L., Lacroix, L., Teulade-Fichou, M. P., Hounsou, C., Guittat, L., Hoarau, M., Arimondo, P. B., Vigneron, J. P., Lehn, J. M., Riou, J. F., Garestier, T., and Helene, C. (2001) Telomerase inhibitors based on quadruplex ligands selected by a fluorescence assay. *Proc. Natl. Acad. Sci. U.S.A. 98*, 3062−3067.
(33) De Cian, A., Guittat, L., Kaiser, M., Sacca, B., Amrane, S., Bourdoncle, A., Alberti, P., Teulade-Fichou, M. P., Lacroix, L., and Mergny, J. L. (2007) Fluorescence-based melting assays for studying quadruplex ligands. *Methods 42*, 183−195.
(34) Dash, J., Shirude, P. S., Hsu, S. T., and Balasubramanian, S. (2008) Diarylethynyl amides that recognize the parallel conformation of genomic promoter DNA G-quadruplexes. *J. Am. Chem. Soc. 130*, 15950−15956.
(35) Moorhouse, A. D., Santos, A. M., Gunaratnam, M., Moore, M., Neidle, S., and Moses, J. E. (2006) Stabilization of G-quadruplex DNA by highly selective ligands via click chemistry. *J. Am. Chem. Soc. 128*, 15972−15973.
(36) De Cian, A., Delemos, E., Mergny, J. L., Teulade-Fichou, M. P., and Monchaud, D. (2007) Highly efficient G-quadruplex recognition by bisquinolinium compounds. *J. Am. Chem. Soc. 129*, 1856−1857.
(37) Teulade-Fichou, M. P., Carrasco, C., Guittat, L., Bailly, C., Alberti, P., Mergny, J. L., David, A., Lehn, J. M., and Wilson, W. D. (2003) Selective recognition of G-qQuadruplex telomeric DNA by a bis(quinacridine) macrocycle. *J. Am. Chem. Soc. 125*, 4732−4740.
(38) Rezler, E. M., Seenisamy, J., Bashyam, S., Kim, M. Y., White, E., Wilson, W. D., and Hurley, L. H. (2005) Telomestatin and diseleno sapphyrin bind selectively to two different forms of the human telomeric G-quadruplex structure. *J. Am. Chem. Soc. 127*, 9439−9447.
(39) Paramasivan, S., Rujan, I., and Bolton, P. H. (2007) Circular dichroism of quadruplex DNAs: applications to structure, cation effects and ligand binding. *Methods 43*, 324−331.
(40) Bates, P., Mergny, J. L., and Yang, D. (2007) Quartets in G-major. The First International Meeting on Quadruplex DNA. *EMBO Rep. 8*, 1003−1010.
(41) Zagotto, G., Sissi, C., Lucatello, L., Pivetta, C., Cadamuro, S. A., Fox, K. R., Neidle, S., and Palumbo, M. (2008) Aminoacyl-anthraquinone conjugates as telomerase inhibitors: synthesis, biophysical and biological evaluation. *J. Med. Chem. 51*, 5566−5574.
(42) Riou, J. F., Guittat, L., Mailliet, P., Laoui, A., Renou, E., Petitgenet, O., Megnin-Chanet, F., Helene, C., and Mergny, J. L. (2002) Cell senescence and telomere shortening induced by a new series of specific G-quadruplex DNA ligands. *Proc. Natl. Acad. Sci. U.S.A. 99*, 2672−2677.
(43) Hwang, E. S. (2002) Replicative senescence and senescence-like state induced in cancer-derived cells. *Mech. Aging Dev. 123*, 1681−1694.
(44) Sumi, M., Tauchi, T., Sashida, G., Nakajima, A., Gotoh, A., Shin-Ya, K., Ohyashiki, J. H., and Ohyashiki, K. (2004) A G-quadruplex-interactive agent, telomestatin (SOT-095), induces telomere shortening with apoptosis and enhances chemosensitivity in acute myeloid leukemia. *Int. J. Oncol. 24*, 1481−1487.
(45) Tauchi, T., Shin-ya, K., Sashida, G., Sumi, M., Okabe, S., Ohyashiki, J. H., and Ohyashiki, K. (2006) Telomerase inhibition with a novel G-quadruplex-interactive agent, telomestatin: in vitro and in vivo studies in acute leukemia. *Oncogene 25*, 5719−5725.
(46) Zhou, J. M., Zhu, X. F., Lu, Y. J., Deng, R., Huang, Z. S., Mei, Y. P., Wang, Y., Huang, W. L., Liu, Z. C., Gu, L. Q., and Zeng, Y. X. (2006) Senescence and telomere shortening induced by novel potent G-quadruplex interactive agents, quindoline derivatives, in human cancer cell lines. *Oncogene 25*, 503−511.
(47) Huang, F. C., Chang, C. C., Lou, P. J., Kuo, I. C., Chien, C. W., Chen, C. T., Shieh, F. Y., Chang, T. C., and Lin, J. J. (2008) G-quadruplex stabilizer 3,6-bis(1-methyl-4-vinylpyridinium)carbazole diiodide induces accelerated senescence and inhibits tumorigenic properties in cancer cells. *Mol. Cancer. Res. 6*, 955−964.

Bioconjugate Chemistry

Article

pubs.acs.org/bc

Metal-Free DNA Linearized Nuclease Based on PASP–Polyamine Conjugates

Chao Li,[†] Fangfang Zhao,[†] Yunan Huang,[†] Xueyuan Liu,[†] Yan Liu,[§] Renzhong Qiao,*[,†,‡] and Yufen Zhao[§]

[†]State Key Laboratory of Chemical Resource Engineering, Beijing University of Chemical Technology, Beijing, 100029, China

[‡]State Key Laboratory of Natural and Biomimetic Drugs School of Pharmaceutical Sciences, Peking University Health Science Center, Beijing, 100083, China

[§]Department of Chemistry, College of Chemistry and Chemical Engineering, Xiamen University, Xiamen 361005, China

Supporting Information

ABSTRACT: Genome manipulation controlled by small metal complexes has attracted extensive interest because of their potential application in the fields of molecular biotechnology and drug development. However, their medicinal application is still limited due to the distinct toxicity of the free radicals generated by partial metal complexes based on oxidative cleaving processes. Thus, it is still a challenge for us to use metal free agent to cleave DNA. In this work, we showed that a family of polyamine-grafted PASP (poly(aspartic acid)) conjugates is able to rapidly induce DNA cleavage in the absence of metal ions, and obtain a high-yield linearization product via a hydrolytic path. From the results of detailed control experiments, it was revealed that the formation of polyamine cation/phosphate anion pair and free ungrafted nucleophilic groups would be the key factors to improve DNA linearization. Constructing polyamine conjugates based on short peptide such as polyamine-grafted PASP, as achieved here, could provide an attractive strategy for developing mild and efficient artificial nucleases as well as researching catalytic mechanisms on DNA chemistry.



INTRODUCTION

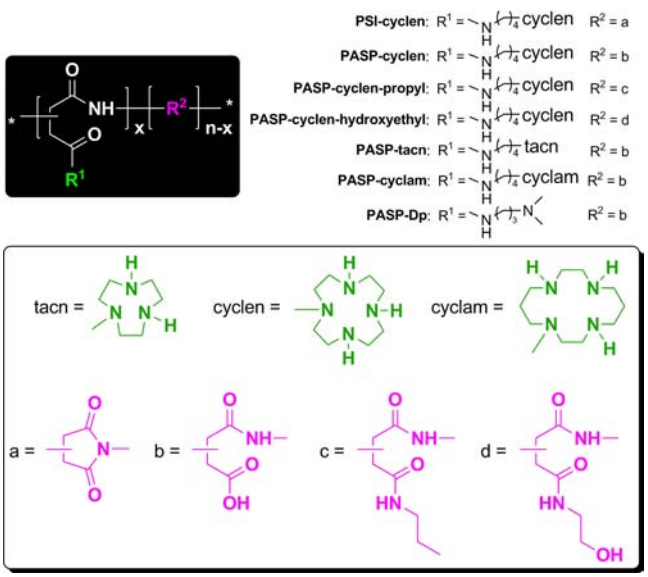
Artificial nucleases have attracted significant interest due to their abilities in accelerating DNA cleavage, which makes possible the DNA manipulations that are essential in biotechnology, medicine, and other fields.[1,2] Ligand-based hydrolytic DNA cleavage remains a challenge, as it is well-known that the half-life of DNA by spontaneous hydrolysis under physiological conditions is estimated as thousands to billions of years, which is primarily due to the repulsion between the negatively charged backbone and potential nucleophiles.[3] In the past few years, several research groups have been working on the design and evaluation of efficient DNA cleavage agents that are hydrolytic or oxidative in manner. Up to now, almost all of these obtained artificial agents need specific metal ions as cofactors for sequence-specific cleavage.[4,5] In spite of the successful results involving artificial metallonucleases, studies devoted to metal-free organic molecules as nucleic acid cleavage agents are not frequent.[6−8] Actually, the cleavage of DNA by metal-free compounds can be considered safer in the development of biotechnology, especially in gene therapy, since the absence of a redox active metal ion has the advantage of avoiding complications such as metal dissociation and uncontrolled redox chemistry reactions.[9,10]

Recently, metal-free DNA cleaving reagents have been pushed forward by some designs of efficient small organic molecules including guanidinium derivatives,[11,12] cyclodextrin derivatives,[13] and macrocyclic polyamine.[8] In addition, seryl-histidine as the shortest functional dipeptide reported in our previous works[14−17] exhibits high DNA cleavage activity, because the side chain hydroxyl of serine often serves as a nucleophile, while the side chain imidazole of histidine can serve as a proton donating or accepting group in enzymes. An important property of seryl-histidine is that it can induce efficient DNA hydrolysis in the absence of any metals. To explore its possible mechanism further in this work, we attempted to construct a longer peptide molecule than our previous work to evaluate whether it can maintain cleavage activity like dipeptide or superior properties. In the current work, we use PASP as a simple peptide to establish a new short peptide-based artificial nuclease, grafting polyamine (cyclen, tacn, and cyclam) to carboxyl groups of PASP (Scheme 1), and expect to have higher DNA binding affinity, since the excessive anionic carboxyl group in PASP will show electrostatic repulsion with the anionic phosphate backbone of DNA. The cleavage of DNA was investigated by agarose gel electrophoresis and atomic force microscopy (AFM). The interactions between DNA and PASP-polyamine were further studied by circular dichroism (CD) and fluorescence quenching. To further explore a possible mechanism and structure activity relationship of DNA cleavage induced by conjugates, a series of

Received: March 27, 2012
Revised: June 13, 2012
Published: August 8, 2012

 © 2012 American Chemical Society dx.doi.org/10.1021/bc300162g | *Bioconjugate Chem.* 2012, 23, 1832–1837

Scheme 1. Structures of PASP−Polyamine and Control Conjugates



ingenious control compounds were prepared and evaluated in comparison with the title compounds, as shown in Scheme 1.

EXPERIMENTAL PROCEDURES

General Information. MS (ESI) mass spectral data were recorded on a Finnigan LCQDECA mass spectrometer. ^{1}H NMR and ^{13}C NMR spectra were measured on a Bruker AV600 spectrometer, and chemical shifts in ppm are reported relative to internal Me_4Si ($CDCl_3$). All other chemicals and reagents were obtained commercially and used without further purification. Electrophoresis grade agarose and plasmid DNA (pUC18) were purchased from Promega Corporation. The molecular weight (MW) of the polymeric conjugate was measured by Maldi-Tof (Bruker Autoflex). Metal contents in deionized water and buffer solutions were measured by an Agilent 7500a inductively coupled plasma mass spectrometer (Agilent, Japan) system.

Maldi-Tof MS. Maldi-Tof MS was carried out on a Bruker Autoflex operating in reflected mode. 2-(4-Hydroxyphenylazo)-benzoic acid (HABA) was used as matrix, and NaCl or KCl was used as cationizing agent. Samples were dissolved in MeOH/H_2O (1:1) at a concentration of 1.0 μg·mL^{-1}. HABA was dissolved in dioxane at a concentration of 0.05 M. Sample (20 μL) and matrix (80 μL) solutions were mixed, and then, 80 μL of 0.02 M NaCl or KCl was added. Finally, 1 μL of the resulting mixture was placed on the Maldi plate.

Gel Electrophoresis Assay. Electrophoresis experiments were performed with plasmid DNA (pUC18). In a typical experiment, supercoiled pUC18 DNA (5 μL, 0.05 μg·μL^{-1}) in Tris−HCl buffer (40 mM, pH 7.4) was treated with different concentration catalyst, followed by dilution with the Tris−HCl buffer to a total volume of 80 μL. The samples were then incubated at different temperature and time, and loaded on a 1% agarose gel containing 1.0 μg·mL^{-1} ethidium bromide (EB). Electrophoresis apparatus consisted of a Biomeans Stack II-Electrophoresis system, PPSV-010. Electrophoresis was carried out at 85 V for 1 h in TAE buffer, and bands were visualized by UV light and photographed, recorded on an Olympus Grab-IT2.0 Annotating Image Computer System.

Fluorescence Quenching Assay. Fluorescence spectra were recorded on a Hitachi model F-4500 spectrofluorimeter, with excitation and emission band bass: 10 nm (λ_{ex} = 520, λ_{em} = 620 nm). A 10 mg·mL^{-1} solution of PASP−polyamine was titrated into the DNA-EB solution (60 μg·mL^{-1} calf thymus DNA solution including 0.1 mg·mL^{-1} EB) at pH 7.4 10 mM Tris−HCl buffer with 10 mM NaCl. Apparent binding constants (K_{app}) of the ligands with CT-DNA (calf thymus DNA, 60 μg·mL^{-1}) were estimated and compared by measuring the loss of EtBr fluorescence as a function of added ligand. The K_{app} values were calculated from: K_{EtBr}[EtBr] = K_{app}[Q], where [EtBr] and K_{EtBr} are the concentration and binding constant of EtBr, respectively, and [Q] is the concentration of quencher at 50% of maximal EtBr fluorescence. The binding constant of EtBr was taken to be 1 × 10^{7}.

Circular Dichroism (CD). All experiments were performed with a continuous flow of nitrogen purging the Jasco-810 spectropolarimeter with a path length cell of 1 cm at room temperature. A 10 mg·mL^{-1} solution of all samples was titrated into the DNA solutions (at pH 7.4, 10 mM Tris−HCl buffer with 10 mM NaCl) with a final concentration of 1.1 × 10^{-4} M. The standard scan parameters for all experiments used a wavelength range from 400 to 220 nm. Sensitivity was set at 100 mdeg and scan speed of 200 nm per minute. Three scans were made and the average value of them was calculated.

AFM Assay. Atomic force microscope (AFM) imaging was performed in tapping mode on a Digital Instruments multimode NanoScope III having a maximal lateral range of approximately 5 μm. All images were analyzed by tapping in air.

High-quality mica sheets (FluorMica) were cut with scissors into squares (1 cm × 1 cm) and attached with superglue to 15 mm round stainless steel sample disks (Ted Pella). Before each use, the mica was freshly cleaved by pulling off the top sheets with tape and then covered with 10 μL of autoclaved AFM buffer (10 mM Tris pH 7.5, 1 mM EDTA, 5 mM $MgCl_2$). The surface is precoated with Mg^{2+} to allow negatively charged DNA to bind. After 5 min, the buffer was rinsed thoroughly with 0.5 mL of distilled water, and the mica was briefly dried under a stream of N_2 (*g*).

The DNA sample was diluted with AFM buffer to 2.5 ng μL^{-1}, and then, 10 μL diluted sample was dropwise added to mica surface. After 5 min, the buffer was rinsed thoroughly with 0.5 mL of distilled water, and the mica was briefly dried under a stream of N_2 (*g*).

RESULTS AND DISCUSSION

Synthesis and Characterization of PASP−Polyamine and Their Control Derivatives. In this study, polyamine including tacn, cyclen, and cyclam is introduced to the carboxyl groups of PASP with a flexible linker; this process is realized by the typical hydrolysis reaction of poly(succinimide) (PSI) and polyamine containing the NH_2-terminal group. Initially, PSI as starting material for all compounds is prepared according to relative literature.[18,19] The remaining succinimide units after the grafting reaction are further hydrolyzed in the presence of NaOH, propylamine, ethanolamine, and *N*,*N*-dimethyl propylene diamine, thereby giving the title compounds, PASP-cyclen-propyl, PASP-cyclen-hydroxyethyl, and PASP-Dp, respectively. The route of synthesis and the NMR data are shown in SI Scheme S1 and Figures S1−S5, respectively.

To provide a credible control assay and present a convincing mechanism, PASP−polyamines with a similar degree of

dx.doi.org/10.1021/bc300162g | *Bioconjugate Chem.* 2012, 23, 1832−1837

polyamine substitute, such as PASP−cyclen (53.2%), PASP−tacn (48.9%), and PASP−cyclam (47.3%), are selected as candidates. The method of synthesis of control compounds endows them with the same degree of cyclen substitutes. The degree of substituted polyamines is calculated through the NMR data (see Supporting Information). The molecular weight range and TGA data of polyamine are given in SI Figure S6 and Table S2, respectively.

Electrophoresis Results of PASP−Cyclen Induced DNA Linearization. PASP−polyamine is found to mediate the rapid degradation of supercoiled (form I) plasmid DNA under mild conditions (pH 7.4, 37 °C). The DNA cleavage chemistry of PASP−polyamine is evaluated by concentration- and time-dependent assay. Importantly, linear (form III) DNA form prior to nicked (form II) under both time and concentration courses, suggesting excellent activity of DNA double-strand cleavage. In the case of PASP−cyclen, a mass of well-defined linear DNA is observed when the concentration is just 9.6 $\mu g \cdot mL^{-1}$. With the increase of the agent up to 38.2 $\mu g \cdot mL^{-1}$, plasmid DNA is almost linearized at 37 °C for 3 h. Linear DNA is gradually degraded into smears of progressively smaller fragments when the excessive PASP−cyclen is added into the reaction (Figure 1A). In time-dependent assay, quantitative production of linear DNA is observed within 30 min for PASP−cyclen. The profile for PASP−cyclen mediated reaction displays approximately pseudo-first-order kinetic behavior, with $k_{obs} \approx 0.585\ h^{-1}$ and $R^2 = 0.98$. The data after 6 h are omitted from Figure 1B since the DNA has already begun to smear as a result of multiple cleavage events. Subsequently, a standard statistical test for determining linearization with random or nonrandom DNA cleavage is applied. According to the Freifelder-Trumbo relationship,[20,21] the ratio of n_1/n_2 is just 1.24 ± 0.36 in our experiments, suggesting a nonrandom cleavage path by PASP−cyclen to efficiently form linear DNA. The cleavage behaviors of PASP−tacn and PASP−cyclam under the same conditions are similar to that of PASP−cyclen (SI Figure S7).

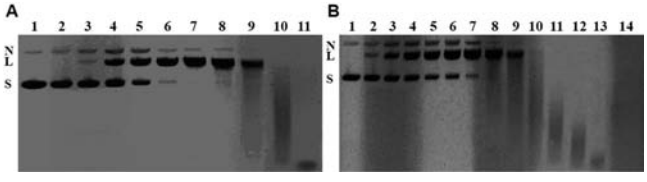


Figure 1. (A) Concentration dependence of pUC18 DNA (0.05 $\mu g \cdot \mu L^{-1}$) cleavage by PASP−cyclen in 40 mM pH 7.4 Tris−HCl buffer for 3 h at 37 °C. Lanes 1−11: 0, 2.4, 9.6, 16.8, 23.8, 31.0, 38.2, 45.4, 52.6, 79.6, and 86.8 $\mu g \cdot mL^{-1}$, respectively. (B) Time dependence of pUC18 DNA cleavage in the presence of 38.2 $\mu g \cdot mL^{-1}$ PASP−cyclen in 40 mM pH 7.4 Tris−HCl buffer at 37 °C. Lane 1, control; lanes 2−14: 0, 0.5, 1, 2, 4, 6, 8, 12, 16, 20, 24, 28, and 32 h. S: supercoiled DNA, N: nicked DNA, L: linear DNA.

A point worth emphasizing is that no extra metal ion is involved in the whole cleavage processes. The content of residual metals in cleavage reactions including Cu, Zn, Fe, and Co is measured by inductively coupled plasma-mass spectroscopy (ICP-MS). The data are listed in SI Table S1, indicating the content that is not enough to attack DNA with any pathways based on control trials.

Visual Presentation of DNA Linearization and Ligation−AFM Images. To get visible evidence about DNA cleavage mode and mechanism, AFM studies were performed. Without any treatment, the free DNA exists as supercoiled, and a little loose nicked forms (Figure 2A). After the addition of 38.2 $\mu g \cdot mL^{-1}$ or 79.6 $\mu g \cdot mL^{-1}$ PASP−cyclen, the mixtures are incubated in Tris−HCl buffer (pH 7.4) at 37 °C for 3 h, and the original supercoiled and nicked DNA turn into linear DNA (Figure 2B) or smaller fragments (Figure 2C), respectively. Subsequently, the extracted linear DNA generated from the reaction above are treated with T4 DNA ligase, and then, longer linear DNA are observed clearly in the AFM images (Figure 2D). This phenomenon shows DNA linkage in the presence of T4 DNA ligase, and it also proves that terminal groups of these fragments provided 3′-hydroxyls and 5′-phosphates, since DNA ligase requires them for ligation. The generation of these terminal groups is consistent with the

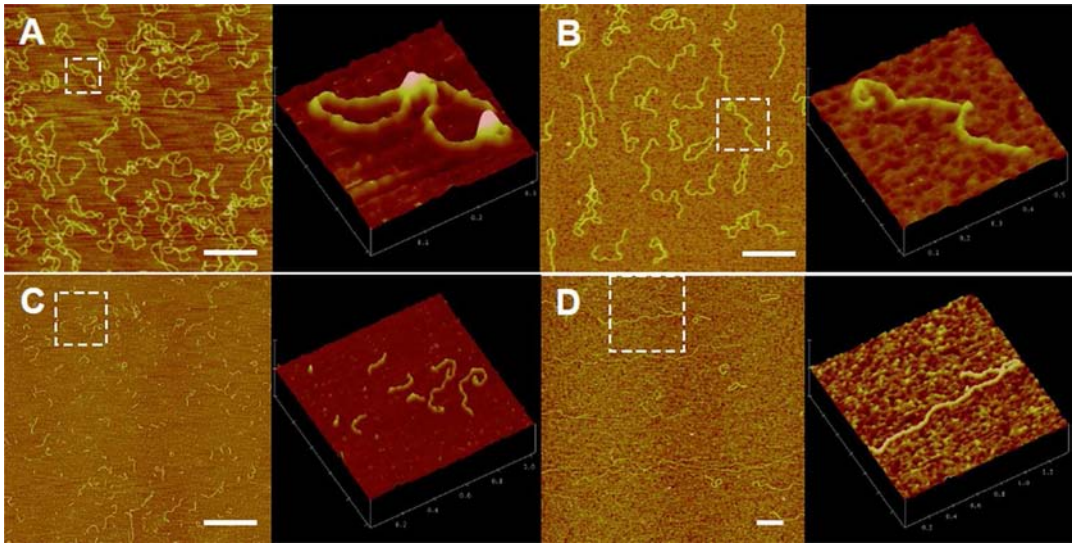


Figure 2. AFM images of pUC18 DNA molecules for different forms on mica in trap mode. (A) Supercoiled DNA without any treatment; (B) and (C) treated with PASP−cyclen (38.2 $\mu g \cdot mL^{-1}$ and 79.6 $\mu g \cdot mL^{-1}$) in Tris−HCl (pH 7.4) for 3 h at 37 °C, respectively; (D) recovered DNA with T4 DNA ligase for 12 h at 4 °C, respectively. Scale bar is 500 nm.

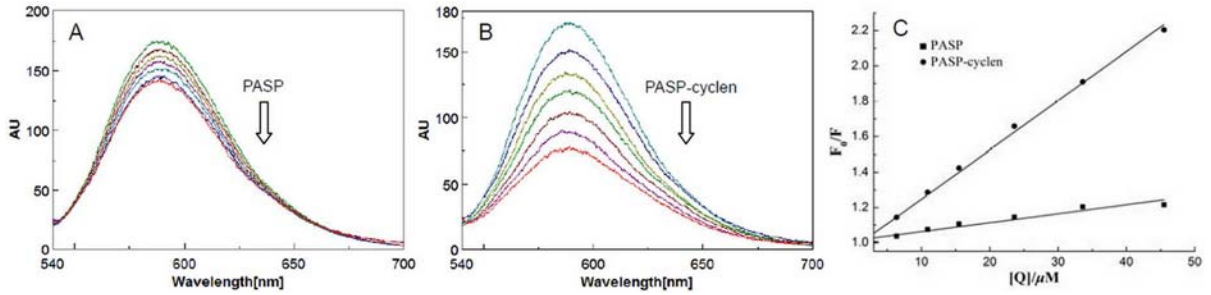


Figure 3. Fluorescence quenching by (A) PASP/CT-DNA and (B) PASP−cyclen/CT-DNA at pH 7.4 (10 mM Tris−HCl buffer with 10 mM NaCl) with quencher concentration of 0−90.0 $\mu g \cdot mL^{-1}$ (from top to bottom). (C) Plots of fluorescence quenching of CT-DNA by PASP (■) and PASP−cyclen (●).

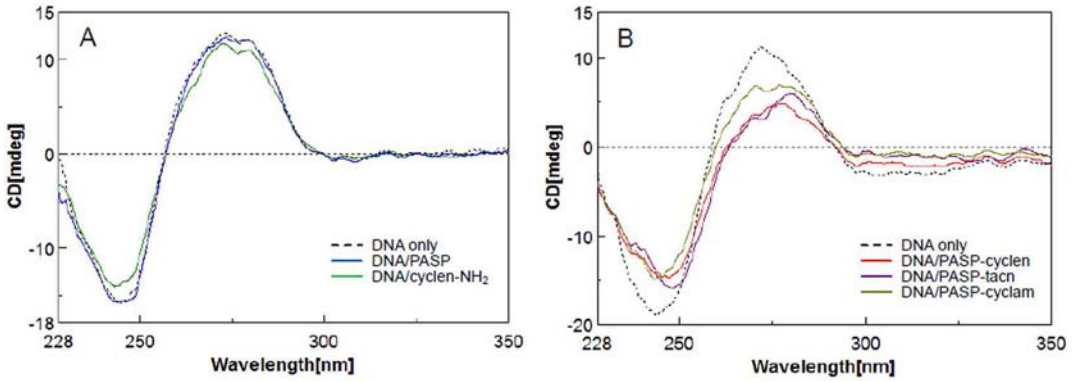


Figure 4. CD spectra of (A) DNA/control compounds (dash, DNA only; blue, DNA/PASP; green, DNA/cyclen-NH_2) and (B) DNA/PASP−polyamine with different ligands (dash, DNA only; red, DNA/PASP−cyclen; purple, DNA/PASP−tacn; desert tan, DNA/PASP−cyclam).

cleavage of phosphodiesters, and would be a characteristic of DNA hydrolysis cleavage.

Interaction between PASP−Polyamine and DNA. A competitive displacement assay using PASP and PASP−polyamine as quencher can characterize the affinity to DNA. To better demonstrate whether the PASP−cyclen conjugate possesses a better affinity to DNA compared with unmodified PASP, both fluorescence changes are recorded as shown in Figure 3. The fluorescence of PASP/DNA decreases by up to 17.8% with PASP concentration of 90.0 $\mu g \cdot mL^{-1}$ (Figure 3A). It can be seen that, with the increase in the amount of PASP, the intensity of fluorescence decreases, indicating that EB is replaced by the added PASP; that is, PASP selectively binds to DNA. The electrostatic interaction or hydrogen bond between PASP and DNA is enhanced, causing the release of more EB dye. However, addition of PASP−cyclen to DNA substantially induced fluorescence decease by up to 54.6% with the same concentration of quenching agent, obtaining C_{50} = 77.4 $\mu g \cdot mL^{-1}$ and K_{app} = 2.35 × 10^7 (Figure 3B). Subsequently, the data are plotted according to the Stern−Volmer equation[22] as shown in Figure 3C. DNA-EB is efficiently quenched by PASP−cyclen, resulting in a strict linear plot of a slope of 0.028, which is much larger than that of 0.005 by PASP. A large slope value corresponds to strong quenching and high binding ability to DNA. The result suggests that the interaction between quencher and DNA is enhanced due to the introduction of cyclen, resulting in the higher binding activity than that of PASP skeleton.

Conformational changes of DNA interacting with PASP−polyamine conjugates are further verified by CD experiments. All samples to be tested do not show any CD signal in the studied region studied. Positive and negative ellipticities centered around 245 and 275 nm arise from the DNA itself, revealing a double-stranded structure for the DNA (Figure 4, dashed line). Free DNA shows a typical CD spectrum for B-type. As control, addition of PASP or cyclen with NH_2-terminal linker to the DNA solution does not induce any CD signal change, as shown in Figure 4A, which suggests little or no interaction between DNA and ligands. Detectable changes in the CD spectra are, however, observed upon mixing DNA with PASP−cyclen under the same conditions. Both molar ellipticities of DNA at 245 and 275 nm are suppressed, accompanied with a certain quantity of red-shift (Figure 4B, red line). The result could be attributed to the weak interaction between DNA and PASP−cyclen, such as electronic charge and hydrogen bond. The absence of any detectable CD signals at 310−400 nm is the proof of the absence of minor groove binding between DNA and PASP−cyclen. The similar CD signal is observed under the same conditions when PASP−tacn (Figure 4B, purple line) and PASP−cyclam (desert tan line) are used as samples, respectively. These results are consistent with the affinity to DNA in the presence of PASP−polyamine, also shown by fluorescence quenching assay.

Control Assays for Exploring the Active Functional Group. In previous reports, no extraordinary activity of DNA double-strand cleavage was found in polyamine or PASP alone, especially to metal-free medium. However, simple polyamine grafted to PASP presents remarkable ability on the two breaks in this work, which could result from the synergy of polyamine-grafted and the remaining carboxyl in PASP. To further elucidate the possible process of DNA cleavage induced by PASP−polyamine, a series of ingenious control compounds

dx.doi.org/10.1021/bc300162g | Bioconjugate Chem. 2012, 23, 1832−1837

PSI−cyclen, PASP-cyclen-propyl, and PASP-cyclen-hydroxyethyl are designed and synthesized with the same degree of cyclen substitutes (from the same intermediate PSI−cyclen). The influence of the trace metal in medium and whether polyamine grafted to PASP on cleavage events are considered in detail. The corresponding assays are performed as shown in Figure 5. Initially, 38.2 $\mu g \cdot mL^{-1}$ of PASP, cyclen, and Zn(II) as

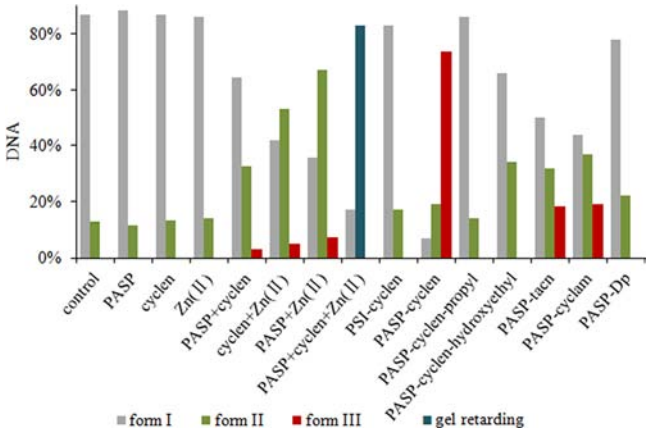


Figure 5. Quantitation of various DNA forms in control assays. pUC18 plasmid DNA is treated with various compounds (38.2 $\mu g \cdot mL^{-1}$) in Tris−HCl (pH 7.4) for 3 h at 37 °C.

independent control react with DNA, respectively, and little or no linearization of plasmid DNA is observed. The combination control of any two agents, such as PASP+cyclen, cyclen+Zn(II), and PASP+Zn(II), present good ability of DNA cleavage, but bad linearization. The remarkable behavior of gel retarding arises when the mixture of three components interacts with DNA, which is attributed to the existence of more electropositive constituents. Further, no detectable DNA cleavage appeared in the presence of PSI−cyclen or PASP-cyclen-propyl without free carboxyl under the same conditions, while PASP-cyclen-hydroxyethyl with hydroxyethyl retained the ability of DNA double-strand cleavage in spite of low effectivity, suggesting the necessity of "ungrafted" active moieties. Subsequently, the activity of PASP-Dp with tertiary amine as polyamine moiety is evaluated. From it, no positive result is obtained, which indicates that the multielectropositivity of protonated polyamine plays an important role in cleavage events.

Possible Mechanism of DNA Linearization Induced by PASP−Polyamine. Some possible processes of DNA cleavage induced by PASP−polyamine are speculated as shown in Figure 6: (i) the electropositivity of protonated polyamine contributes to the formation of polyamine cation/phosphate anion pair, which is connected via hydrogen bonds and electrostatic interactions. (ii) The electropositive phosphor is liable to be attacked by free ungrafted nucleophilic groups in the PASP skeleton. Phosphodiester linkage of DNA is cleaved by PASP−polyamine via transphosphorylation pathway. (iii) Compared with the free polyamine and nucleophilic group, the grafting mode based on a short peptide skeleton makes it more effective on DNA cleavage due to the accumulation of active groups.

Comparison with Analogous Research. A number of cleaving agents have been previously reported to linearize supercoiled DNA in the absence of metal ions. Kovalenko et al.[23] reported a type of lysine-enediyne conjugates which suggests a true double-strand DNA cleavage, and the length of

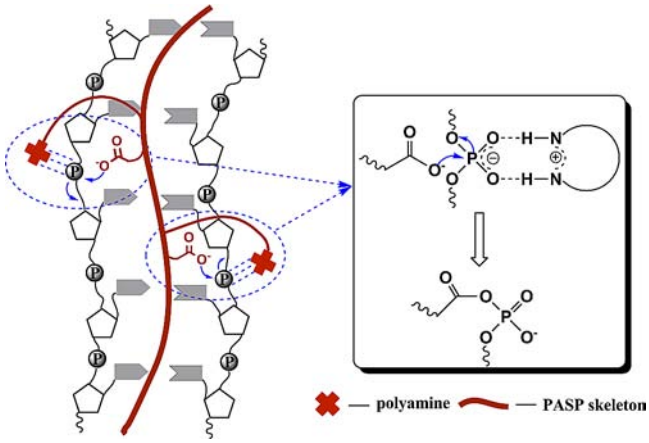


Figure 6. Possible process of DNA double-strand cleavage by PASP−polyamine.

linker plays an important role in randomicity of linearization. Compared with PASP−polyamine, although lysine−enediyne conjugates presented a good ability of linearization (n_1/n_2 10 for 32 min), it is worth pointing out that the whole process is achieved with the aid of irradiation.

Similar to our cleavage mechanism, the work of Sheng et al.[24] indicated DNA cleavage induced by tacn derivatives with guanidinium and hydroxyethyl side arms. The guanidinium group serves to bind and electrophilically activate the anionic phosphodiester through hydrogen bonding and electrostatic interaction, while the hydroxyl group works as a nucleophilic group in the transphosphorylation reaction. Kinetic data of DNA cleavage gave a good k_{max} of 0.160 h^{-1}, but it showed more randomness double-strand cleavage (n_1/n_2 from 8.16 to 43.76, calculated from Supporting Information of ref 24) than PASP−polyamine in optimum conditions. The excellent linearization may be attributed to the accumulated active groups on the short peptide skeleton, which provide a more efficient and deliberate attack on both strands.

■ CONCLUSIONS

In conclusion, we synthesized a new family of PASP grafted polyamine conjugates which could act as promising DNA cleavage agents, giving excellent double-strand cleavage ability toward plasmid DNA in the absence of metal ions. The ingenious control assay attempts to prove a possible process in which the free carboxyl groups in the PASP skeleton often serve as a nucleophile, while the polyamine can serve as a proton-donating or -accepting group to reduce electron density in phosphate, which is liable to breakage of the phosphodiester bond. Owing to these findings, these short peptides are expected to have exciting applications as mild metal-free catalytic tools in DNA chemistry. Studies are aimed at better understanding of the interaction between short modified peptides and nucleic acids, as well as providing a good strategy for developing novel effective artificial nucleases. The exploration of a definite mechanism and the design of new short peptide-based nucleases with improved DNA site selectivity are underway.

■ ASSOCIATED CONTENT

Ⓢ Supporting Information

Synthetic route of PASP−polyamine; characteristic via NMR; molecular range via Maldi-Tof MS; comparison of DNA

cleavage ability of different derivatives via gel; the content of metal ions in reaction; the TGA data of PASP−polyamine. This material is available free of charge via the Internet at http://pubs.acs.org.

AUTHOR INFORMATION

Corresponding Author

*Tel: (+86) 010 64413899, Fax: (+86) 010 82728926, E-mail: qiao_group@163.com.

Notes

The authors declare no competing financial interest.

ACKNOWLEDGMENTS

Support of this research by the National Nature Science Foundation of China is gratefully acknowledged (No. 20972014, No. 21202005, No. 21232005, and No. 21172016.). We thank Dr. Yanxia Jia from Institute of Biophysics, Chinese Academy of Sciences for AFM.

REFERENCES

(1) Cowan, J. A. (2001) Chemical nucleases. *Curr. Opin. Chem. Biol. 5*, 634−642.

(2) Mancin, F., Scrimin, P., Tecilla, P., and Tonellato, U. (2005) Artificial metallonucleases. *Chem. Commun. 5*, 2540−2548.

(3) Schroeder, G. K., Lad, C., Wyman, P., Williams, N. H., and Wolfenden, R. (2006) The time required for water attack at the phosphorus atom of simple phosphodiesters and of DNA. *Proc. Natl. Acad. Sci. U.S.A. 103*, 4052−4055.

(4) Niittymaki, T., and Lonnberg, H. (2006) Artificial ribonucleases. *Org. Biomol. Chem. 4*, 15−25.

(5) Morrow, J. R., and Iranzo, O. (2004) Synthetic metallonucleases for RNA cleavage. *Curr. Opin. Chem. Biol. 8*, 192−200.

(6) Schug, K. A., and Lindner, W. (2005) Noncovalent binding between guanidinium and anionic groups: focus on biological- and synthetic-based arginine/guanidinium interactions with phosph[on]ate and sulf[on]ate residues. *Chem. Rev. 105*, 67−113.

(7) Piatek, A. M., Gray, M., and Anslyn, E. V. (2004) Guanidinium groups act as general-acid catalysts in phosphoryl transfer reactions: a two-proton inventory on a model system. *J. Am. Chem. Soc. 126*, 9878−9879.

(8) Wan, S. H., Liang, F., Xiong, X. Q., Yang, L., Wu, X. J., Wang, P., Zhou, X., and Wu, C. T. (2006) DNA hydrolysis promoted by 1,7-dimethyl-1,4,7,10-tetraazacyclododecane. *Bioorg. Med. Chem. Lett. 16*, 2804−2806.

(9) Alkhader, S., Ezra, A., Kasparkova, J., Brabec, V., and Yavin, E. (2010) A metal-free DNA nuclease based on a cyclic peptide scaffold. *Bioconjugate Chem. 21*, 1425−1431.

(10) Li, Z. F., Chen, H. L., Zhang, L. J., and Lu, Z. L. (2012) Synthesis of [12]aneN_3-dipeptide conjugates as metal-free DNA nucleases. *Bioorg. Med. Chem. Lett. 22*, 2303−2307.

(11) Linton, B. R., Goodman, M. S., Fan, E., van Arman, S. A., and Hamilton, A. D. (2001) Thermodynamic aspects of dicarboxylate recognition by simple artificial receptors. *J. Org. Chem. 66*, 7313−7319.

(12) Shao, Y., Jia, Z. L., Ding, Y., Lu, X. M., Ke, Z. H., Xu, W. H., Liu, F., and Lu, G. Y. (2009) Synthesis and DNA cleavage activity of 2-hydrazinyl-1,4,5,6-tetrahydropyrimidine containing hydroxy group. *Bioorg. Med. Chem. 17*, 4274−4279.

(13) Nakanishi, I., Fukuzumi, S., Konishi, T., Oh kubo, K., Fujitsuka, M., Ito, O., and Miyata, N. (2002) DNA cleavage via superoxide anion formed in photoinduced electron transfer from NADH to γ-cyclodextrin-bicapped C_{60} in an oxygen-saturated aqueous solution. *J. Phys. Chem. B 106*, 2372−2380.

(14) Du, J. T., Li, Y. M., Wei, W., Wu, G. S., Zhao, Y. F., Kanazawa, K., Nemoto, T., and Nakanishi, H. (2005) Low-barrier hydrogen bond between phosphate and the amide group in phosphopeptide. *J. Am. Chem. Soc. 127*, 16350−16351.

(15) Feng, Y. P., Cao, S. L., Xiao, A. S., Xie, W. J., Li, Y. M., and Zhao, Y. F. (2006) Studies on cleavage of DNA by N-phosphoryl branched peptides. *Peptides 27*, 1554−1560.

(16) Sun, M., Ma, Y., Ji, S. H., Liu, H. A., and Zhao, Y. F. (2004) Molecular modeling on DNA cleavage activity of seryl - histidine and related dipeptide. *Bioorg. Med. Chem. Lett. 14*, 3711−3714.

(17) Chen, P. Y., Liu, Y., Gao, X., Xu, N. S, Niu, J., Liu, S. Y., and Zhao, Y. F. (2011) Evaluation of single-stranded oligonucleotide cleavage function of seryl-histidine dipeptide by electrospray ionization mass spectrometry. *Phosphorus, Sulfur Silicon Relat. Elem. 186*, 933−935.

(18) Nakato, T., Kusuno, A., and Kakuchi, T. (2000) Synthesis of poly(succinimide) by bulk polycondensation of L-aspartic acid with an acid catalyst. *J. Polym. Sci., Part A: Polym. Chem. 38*, 117−122.

(19) Tomida, M., and Nakato, T. (1997) Convenient synthesis of high molecular weight poly(succinimide) by acid-catalysed polycondensation of l-aspartic acid. *Polymer 38*, 4733−4736.

(20) Povirk, L. F., Wubker, W., Kohnlein, W., and Hutchinson, F. (1977) DNA double-strand breaks and alkali-labile bonds produced by bleomycin. *Nucleic Acids Res. 4*, 3573−3580.

(21) Freifelder, D., and Trumbo, B. (1969) Matching of single-strand breaks to form double-strand breaks in DNA. *Biopolymers 7*, 681−693.

(22) Cao, Y., and He, X. W. (1998) Studies of interaction between Safranine T and double helix DNA by spectral methods. *Spectrochim. Acta, Part A 54*, 883−892.

(23) Kovalenko, S. V., and Alabugin, I. V. (2005) Lysine-enediyne conjugates as photochemically triggered DNA double-strand cleavage agents. *Chem. Commun. 41*, 1444−1446.

(24) Sheng, X., Lu, X. M., Zhang, J. J., Chen, Y. T., Lu, G. Y., Shao, Y., Liu, F., and Xu, Q. (2007) Synthesis and DNA cleavage activity of artificial receptor 1,4,7-triazacyclononane containing guanidinoethyl and hydroxyethyl side arms. *J. Org. Chem. 72*, 1799−1802.

Bioconjugate Chemistry

Article

pubs.acs.org/bc

Somatostatin Subtype-2 Receptor-Targeted Metal-Based Anticancer Complexes

Flavia Barragán,[†,‡,#] Dolors Carrion-Salip,[§,#] Irene Gómez-Pinto,[⊥] Alejandro González-Cantó,[†,‡] Peter J. Sadler,[∥] Rafael de Llorens,[§] Virtudes Moreno,[‡] Carlos González,[⊥] Anna Massaguer,*[,§] and Vicente Marchán*[,†]

[†]Departament de Química Orgànica and IBUB and [‡]Departament de Química Inorgànica, Universitat de Barcelona, Martí i Franquès 1-11, E-08028 Barcelona, Spain

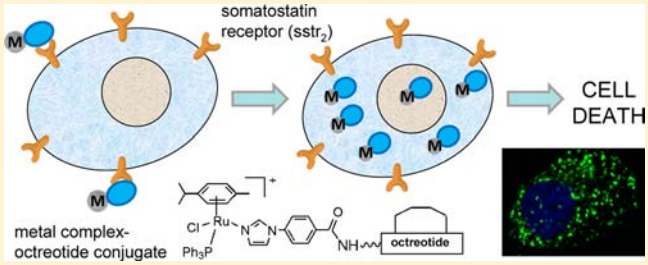
[§]Departament de Biologia, Universitat de Girona, Campus Montilivi, E-17071 Girona, Spain

[⊥]Instituto de Química-Física "Rocasolano", CSIC, Serrano 119, E-28006, Madrid, Spain

[∥]Department of Chemistry, University of Warwick, Coventry, CV4 7AL, United Kingdom

Supporting Information

ABSTRACT: Conjugates of a dicarba analogue of octreotide, a potent somatostatin agonist whose receptors are overexpressed on tumor cells, with [$PtCl_2$(dap)] (dap = 1-(carboxylic acid)-1,2-diaminoethane) (**3**), [(η^6-bip)Os(4-CO_2-pico)Cl] (bip = biphenyl, pico = picolinate) (**4**), [(η^6-*p*-cym)RuCl-(dap)]$^+$ (*p*-cym = *p*-cymene) (**5**), and [(η^6-*p*-cym)RuCl-(imidazole-CO_2H)(PPh_3)]$^+$ (**6**), were synthesized by using a solid-phase approach. Conjugates **3**–**5** readily underwent hydrolysis and DNA binding, whereas conjugate **6** was inert to ligand substitution. NMR spectroscopy and molecular dynamics calculations showed that conjugate formation does not perturb the overall peptide structure. Only **6** exhibited antiproliferative activity in human tumor cells (IC_{50} = 63 ± 2 μM in MCF-7 cells and IC_{50} = 26 ± 3 μM in DU-145 cells) with active participation of somatostatin receptors in cellular uptake. Similar cytotoxic activity was found in a normal cell line (IC_{50} = 45 ± 2.6 μM in CHO cells), which can be attributed to a similar level of expression of somatostatin subtype-2 receptor. These studies provide new insights into the effect of receptor-binding peptide conjugation on the activity of metal-based anticancer drugs, and demonstrate the potential of such hybrid compounds to target tumor cells specifically.



INTRODUCTION

The overexpression of the receptors for many regulatory peptides in human tumor cells in comparison to their expression in normal cells has prompted research on the use of such peptides in tumor targeting for both diagnostic and therapeutic purposes.[1−3] From the therapeutic point of view, a promising approach for the treatment of cancer consists of the attachment of a cytotoxic drug to a peptide moiety with the aim of improving its activity and bioavailability. This targeted anticancer strategy will result in therapeutic agents with increased tumor selectivity and decreased toxicity in normal tissues.

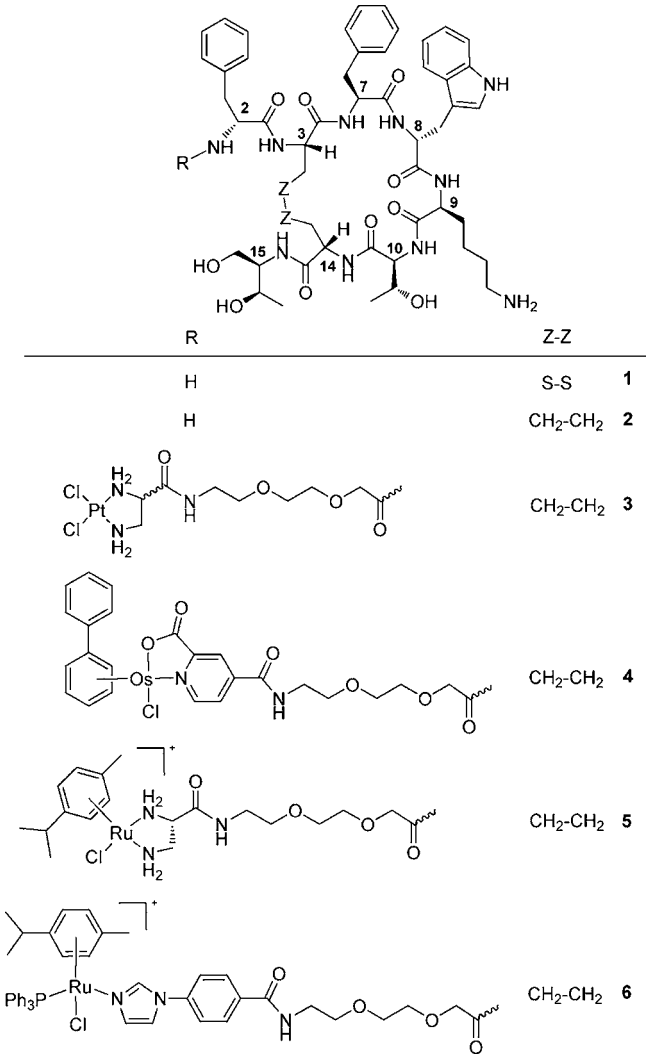
Among natural receptor-binding peptides, the neuroendocrine hormone somatostatin and its analogues have received much attention because of their high affinity against its five human receptors (sst_1−sst_5).[1,3,4] These receptors are overexpressed in various major tumor types, including lung, breast, prostate, adrenal, and neuroendocrine tumors in comparison with normal tissues.[5] The successful use of radiolabeled somatostatin for imaging and radionuclide therapy has prompted the development of new cyclic and acyclic analogues with better receptor affinity and higher stability under physiological conditions.[6]

Octreotide,[7] **1** (Chart 1), a metabolically stabilized cyclooctapeptide analogue of somatostatin that includes D-amino acids to enhance resistance to enzymatic degradation and a cystine bridge to stabilize the pharmacophore β-turn, is particularly interesting because of its high affinity and selectivity for the receptor sst_2,[6] which is the receptor subtype most frequently found on tumor cells. This selectivity has allowed the development of derivatives such as [^{111}In-DTPA]-octreotide and [^{90}Y-DOTA-Tyr^3]-octreotide which are used in the clinics for molecular imaging and therapy of neuroendocrine tumors, respectively.[8] Octreotide has also been conjugated to cytotoxic organic compounds such as doxorubicin, camptothecin, and paclitaxel, with promising results in some cases because of the reduced toxicity and the increased selectivity of the conjugates compared with that of the free drug.[4,9]

Received: March 30, 2012
Revised: August 6, 2012
Published: August 8, 2012

ACS Publications © 2012 American Chemical Society

Chart 1. Structure of the Conjugates Synthesized[a]



[a]Numbering of the amino acid residues follows that of native somatostatin.

Despite the successful history of cisplatin and its second-generation derivatives (carboplatin and oxaliplatin) in the treatment of some types of cancer,[10] the severe toxic side-effects and the acquired or intrinsic resistance of certain tumors has focused research on other metal-based complexes in an effort to develop improved chemotherapeutic agents.[11,12] Indeed, in addition to several platinum compounds, two ruthenium(III) coordination complexes, *trans*-[$RuCl_4$(DMSO)-(Im)]ImH (NAMI-A) and *trans*-[$RuCl_4(Ind)_2$]IndH (NKP-1339), are currently on clinical trials.[13,14]

In recent years, research on bioinorganic chemistry has also been focused on organometallic ruthenium(II) and osmium(II) arene complexes, since these compounds have shown promising *in vitro* and *in vivo* anticancer activities, including cell lines that have become resistant to cisplatin.[15−19] Ruthenium and its heavier congener osmium offer several advantages in comparison with platinum compounds, including the ability to bind to a wide variety of types of ligands, the availability of additional coordination sites in octahedral complexes, the possibility of controlling the shape of the complex, and the changes in the oxidation state. It is also particularly relevant that they have the capacity to undergo ligand exchange in a similar way to cisplatin, which makes them particularly attractive for developing new anticancer drugs. Unlike cisplatin, which has two reactive Pt−Cl coordination bonds, some active organometallic piano-stool complexes have only one reactive site (Ru/Os−Cl). The aquation of the chlorido complexes, mostly suppressed in extracellular fluids (chloride concentration ∼100 mM), is triggered inside the cell nucleus by the low chloride concentration (4 mM), allowing the interaction of the active aqua species with biomolecules such as DNA.[20−22]

On the basis of these precedents, a promising approach in the search of new metal-based anticancer drugs would consist of the conjugation of platinum and classical nonplatinum metal complexes (e.g., ruthenium and osmium) to carrier molecules such as receptor-binding peptides. Indeed, given the over-expression of selective receptors for these peptides on the membrane of tumoral cells, it is expected that the peptide sequences will have a positive effect on the therapeutic properties of the metal-based drug (e.g., reduction of the toxic side-effects) since they will act as a "tumour-targeting devices". With this idea in mind, we have synthesized conjugates between a dichloridoplatinum(II) complex and octreotide derivatives in which the disulfide bond had been replaced by CH_2—CH_2 or CH═CH linkages.[23] This chemical modification on the peptide does not substantially alter the binding affinity of the dicarba-octreotide analogues for the sst_2 receptor but increases the stability of the carrier biomolecule in the reductive cellular environment.[24] In addition, we have recently described the synthesis and DNA ruthenation under visible light irradiation of a photoactivated ruthenium(II) arene complex conjugated to a dicarba analogue of octreotide.[25] In recent years, several coordination or organometallic complexes have also been conjugated to carrier molecules such as receptor-binding peptides or known delivery peptides to improve both cellular uptake to cancer cells and cytotoxic activity of the metal-based drug.[26−33]

Herein, we report on the use of conjugates between octreotide and several metal complexes as new chemotherapeutic agents. In particular, the synthesis of hybrid compounds between the dicarba analogue of octreotide (**2**) and platinum(II), ruthenium(II), and osmium(II) metal complexes has been accomplished by efficient solid-phase procedures (compounds **3**−**6** in Chart 1). The influence of the attachment of the metal complex on the structure of octreotide has been studied by NMR spectroscopy and molecular dynamics, as well as the capacity of these conjugates to bind DNA. Finally, cellular uptake and cytotoxicity studies have been carried out in a normal cell line and two human tumoral cell lines.

EXPERIMENTAL PROCEDURES

Materials and Methods. Unless otherwise stated, common chemicals and solvents (HPLC-grade or reagent-grade quality) were purchased from commercial sources and used without further purification. Peptide-grade DMF was from Scharlau. Fmoc-protected amino acids, resins, and coupling reagents for solid-phase synthesis were obtained from Novabiochem, Bachem, or Iris Biotech. Fmoc-Hag-OH was purchased from Bachem. Fmoc-L-threoninol *p*-carboxyacetal was synthesized following previously reported procedures.[34] Solid-phase syntheses were performed manually in a polypropylene syringe fitted with a polyethylene disk. Second-generation Grubbs catalyst and Wilkinson's catalyst were purchased from Aldrich.

dx.doi.org/10.1021/bc300173h | *Bioconjugate Chem.* 2012, 23, 1838−1855

Milli-Q water was directly obtained from a Milli-Q system equipped with a 5000 Da ultrafiltration cartridge. Metal complexes (±)-[$PtCl_2$(dap)] (**7**),[23] (±)-[$PtCl_2$(Etdap)] (**15**),[35] [(η^6-bip)Os(4-CO_2-pico)Cl] (**8**),[36] [{(η^6-*p*-cym)Ru(μ-Cl)Cl}$_2$] (**9**), [(η^6-*p*-cym)$RuCl_2(PPh_3)$] (**10**),[37] and [(η^6-*p*-cym)$RuCl(PPh_3)_2][PF_6]$ (**11**)[38] were synthesized and characterized as previously described. L-2,3-Diaminopropionic acid methyl ester dihydrochloride[39] and N^{α},N^{β}-bis-(9-fluorenylmethyloxycarbonyl)-L-2,3-diaminopropionic acid[40] were synthesized as previously described. 5(6)-Carboxyfluorescein was purchased from Aldrich and octreotide acetate from Bachem. All the assayed compounds displayed a purity of ≥95%, determined by HPLC analysis.

The human breast cancer cell line MCF-7 and the human prostate carcinoma cell line DU-145 were obtained from the American Tissue Culture Collection (ATTC, Rockville, MD, USA). Chinese hamster ovary (CHO) cells were used as a nontumor cell line. The cells were maintained in Dulbecco's modified Eagle's medium supplemented with 10% fetal bovine serum and 1% penicillin−streptomycin (GIBCO BRL, Grand Island, NY) at 37 °C in a humidified atmosphere containing 5% CO_2. The cells were passaged two times per week.

NMR spectra were recorded at 25 °C on Varian Gemini 300 MHz and Varian Mercury 400 MHz spectrometers using deuterated solvents. Tetramethylsilane (TMS) was used as an internal reference (δ 0 ppm) for ^{1}H spectra recorded in $CDCl_3$ and the residual signal of the solvent (δ 77.16 ppm) for ^{13}C spectra. For CD_3OD, acetone-d_6, DMSO-d_6, or D_2O, the residual signal of the solvent was used as a reference.

High-resolution MALDI-TOF mass spectra were recorded on a 4800 Plus MALDI-TOF/TOF spectrometer (Applied Biosystems) in the positive-ion mode using 2,4-dihidroxybenzoic acid as a matrix. ESI mass spectra (ESI-MS) were recorded on a Micromass ZQ instrument with single quadrupole detector coupled to an HPLC. High-resolution electrospray mass spectra (HR ESI MS) were obtained on an Agilent 1100 LC/MS-TOF instrument.

Synthesis of Metal−Octreotide Conjugates (3−6 and 12) and Fluorescein-Labeled Peptides (13−14). Solid-phase peptide synthesis was performed on a Rink amide resin-*p*-MBHA (f = 0.34 mmol/g, 100−200 mesh) using standard Fmoc/tBu chemistry with the following side-chain protecting groups: Boc (N^i-*tert*-butoxicarbonyl, tryptophan, and N^e-*tert*-butoxicarbonyl, lysine), ^{t}Bu (*O*-*tert*-butyl, threonine), and Trt (*S*-trityl, cysteine). The assembly of the dicarba analogue of octreotide was performed as previously described.[23,24] Briefly, Fmoc-L-threoninol *p*-carboxyacetal (1.8 mol equiv) was first coupled using DIPC (1.8 mol equiv) and HOBt (1.8 mol equiv) in anhydrous DMF for 1 h. The following Fmoc-protected amino acids (2.4 mol equiv) were incorporated with HATU (2.3 mol equiv) and DIPEA (4.8 mol equiv) in anhydrous DMF for 1 h. Microwave-assisted ring-closing methatesis using second-generation Grubbs catalyst and hydrogenation reaction with Wilkinson's catalyst were carried out as previously described.[23] Finally, 8-(9-fluorenylmethyloxycarbonyl-amino)-3,6-dioxaoctanoic acid (3 mol equiv) or γ-aminoisobutyric acid (3 mol equiv) were coupled onto the cyclic dicarba analogue of octreotide **2** bound to resin with DIPC (3 mol equiv) and HOAt (3 mol equiv) in anhydrous DMF for 1 h. After removal of the Fmoc group (20% piperidine in DMF) from the Fmoc-protected linker-derivatized dicarba analogue of octreotide bound to resin, coupling or assembly of the metal complexes on the free *N*-terminal end was carried out as indicated for each metal. The reactor was protected from light by covering it with aluminum foil.

Side-chain deprotection and cleavage from the resin was performed simultaneously with TFA/TIS/H_2O 95:2.5:2.5 (peptides, fluorescein-labeled dicarba octreotide **13** and conjugate **4**), TFA/phenol/H_2O 95:2.5:2.5 (conjugates **3**, **5**, **6**, and **12**), or TFA/H_2O/TIS/EDT 94:2.5:2.5:1 (fluorescein-labeled octreotide **14**) for 1 h at room temperature. Most of the TFA was removed by bubbling N_2 into the solution, and the resulting residue was poured onto cold ether to precipitate the target compound.

Analytical reversed-phase HPLC analyses were carried out on a GraceSmart RP C_{18} column (250 × 4 mm, 5 μm, flow rate: 1 mL/min), using linear gradients of 0.045% TFA in H_2O (solvent A) and 0.036% TFA in ACN (solvent B). In some cases, small-scale purification was carried out using the same column. Large-scale purification was carried out on a Jupiter Proteo semipreparative column (250 × 10 mm, 10 μm, flow rate: 3−4 mL/min), using linear gradients of 0.1% TFA in H_2O (solvent A) and 0.1% TFA in ACN (solvent B). After several runs, pure fractions were combined and lyophilized.

Platinum−Octreotide Conjugate ***3***. [$PtCl_2$(dap)] (5 mol equiv) was coupled with DIPC (5 mol equiv) and NHS (10 mol equiv) in anhydrous DMF for 15 h at rt. Overall yield (synthesis + purification): 14%. Characterization: R_t = 14.2 min (analytical gradient: 20% to 60% in 30 min); HR ESI MS, positive mode: m/z 1479.5574 (calcd mass for $C_{60}H_{88}Cl_2N_{13}O_{14}Pt$ $[M+H]^+$: 1479.5598); HR MALDI-TOF MS, positive mode: m/z 1479.85 (calcd mass for $C_{60}H_{88}Cl_2N_{13}O_{14}Pt$ $[M+H]^+$: 1479.5598), m/z 1501.87 (calcd mass for $C_{60}H_{87}Cl_2N_{13}NaO_{14}Pt$ $[M+Na]^+$: 1501.5418).

Osmium−Octreotide Conjugate ***4***. [(η^6-bip)Os(4-CO_2-pico)Cl] (5 mol equiv) was coupled with DIPC (5 mol equiv) and HOAt (5 mol equiv) in anhydrous DMF for 3 h at rt. Overall yield (synthesis + purification): 16%. Characterization: R_t = 20.2 min (analytical gradient: 20% to 60% in 30 min); HR ESI MS, positive mode: m/z 1657.6621 (calcd mass for $C_{76}H_{94}ClN_{12}O_{16}Os$ $[M+H]^+$: 1657.6214); HR MALDI-TOF MS, positive mode: m/z 1679.60 (calcd mass for $C_{76}H_{92}ClN_{12}NaO_{16}Os$ $[M+Na]^+$: 1679.6034).

Ruthenium(dap)−Octreotide Conjugate ***5***. N^{α},N^{β}-Bis-(9-fluorenylmethyloxycarbonyl)-L-2,3-diaminopropionic acid (4 mol equiv) was coupled with HATU (3.9 mol equiv) in anhydrous DMF in the presence of DIPEA (8 mol equiv) for 1 h at rt. After removal of the Fmoc protecting groups, octreotide-bound resin was reacted with **9** (3 mol equiv) in the presence of LiCl (6.6 mol equiv) and NEt_3 (7.2 mol equiv) in a DMF/EtOH 9:1 mixture at 100 °C for 1 h under microwave irradiation (40 W). Overall yield (synthesis + purification): 10%. Characterization: R_t = 14.1 min (analytical gradient: 20% to 60% in 30 min); HR MALDI-TOF MS, positive mode: m/z 1448.40 (calcd mass for $C_{70}H_{100}N_{13}O_{14}Ru$ $[M-Cl-H]^+$: 1448.6556).

Ruthenium−Octreotide Conjugate ***6***. 4-(1*H*-Imidazol-1-yl)benzoic acid (10 mol equiv) was first coupled with DIPC (10 mol equiv) and HOBt (10 mol equiv) in anhydrous DMF for 1 h at rt. Then, imidazole-derivatized peptide-bound resin was reacted with **11** (3 mol equiv) in the presence of LiCl (3.3 mol equiv) and NEt_3 (20 mol equiv) in a DMF/EtOH 9:1 mixture for 8 h at 50 °C. Overall yield (synthesis + purification): 12%. Characterization: R_t = 14.6 min (analytical gradient: 30% to 100% in 30 min); HR ESI MS, positive mode: m/z 1830.7240 (calcd mass for $C_{95}H_{116}ClN_{13}O_{14}PRu$ $[M]^+$:

1830.7234), *m/z* 915.8672 (calcd mass for $C_{70}H_{102}ClN_{13}O_{14}Ru$ $[M+H]^{2+}$: 915.8656); HR MALDI-TOF MS, positive mode: *m/z* 1795.44 (calcd mass for $C_{95}H_{115}N_{13}O_{14}PRu$ $[M-Cl-H]^{+}$: 1794.7468).

Ruthenium–Octreotide Conjugate ***12***. Characterization: R_t = 17.7 min (analytical gradient: 30% to 100% in 30 min); HR ESI MS, positive mode: *m/z* 1768.6863 (calcd mass for $C_{93}H_{112}ClN_{13}O_{12}PRu$ $[M]^{+}$: 1768.6867), *m/z* 884.8481 (calcd mass for $C_{70}H_{102}ClN_{13}O_{14}Ru$ $[M+H]^{2+}$: 884.8478). The MS data correspond to the dicarba analogue of octreotide with CH=CH linkage.

Fluorescein-Labeled Dicarba Analogue of Octreotide ***13***. Resin-bound linker-derivatized dicarba analogue of octreotide was allowed to react with 5(6)-carboxyfluorescein (5 mol equiv), DIPC (5 mol equiv), and HOAt (5 mol equiv) in anhydrous DMF for 16 h, protected from light. After filtration and washing, peptide-bound resin was treated with 20% piperidine/DMF (2 × 45 min). Overall yield (synthesis + purification): 40%. Characterization: R_t = 23.3 min (analytical gradient: 20% to 60% in 30 min); HR ESI MS, positive mode: *m/z* 1486.6572 (calcd mass for $C_{78}H_{92}N_{11}O_{19}$ $[M+H]^{+}$: 1486.6571).

Fluorescein-Labeled Octreotide ***14***. Linear fluorescein-linker-derivatized octreotide was assembled on a Rink amide resin as described above with minor modifications: Fmoc-Hag-OH was replaced by Fmoc-Cys(Trt)-OH and all Fmoc-protected amino acids, Fmoc-linker-OH and 5(6)-carboxy-fluorescein (5 mol equiv) were coupled with DIPC (5 mol equiv) and HOAt (5 mol equiv) in anhydrous DMF. After treatment with 20% piperidine/DMF (2 × 45 min) and acidic cleavage and deprotection, the linear peptide was dissolved (final concentration *ca.* 1 mM) in an aqueous ammonium hydrogen carbonate solution (5%, pH 7.7) and stirred at room temperature for 72 h (some drops of DMSO and MeOH were added after 24 h to improve solubility as well as to increase the oxidation rate). Overall yield (synthesis + purification): 15%. Characterization: R_t = 23.5 min (analytical gradient: 20% to 60% in 30 min); HR-ESI MS, positive mode: *m/z* 1522.5673 (calcd mass for $C_{76}H_{88}N_{11}O_{19}S_2$ $[M+H]^{+}$: 1522.5699).

Synthesis of Metal Complexes. *[(η^6-p-cym)RuCl(dap)]-[PF_6]* ***(16)***. L-2,3-Diaminopropionic acid methyl ester dihydrochloride (0.068 g; 0.359 mmol) was reacted with complex **9** (0.1 g; 0.163 mmol) and NEt_3 (513 μL; 1.63 mmol) in MeOH (15 mL). The mixture was stirred at room temperature for 3 h. The resulting solution was filtered and the volume of the filtrate reduced (to *ca.* 7 mL) in a rotary evaporator. Solid NH_4PF_6 (10 mol equiv) was added to the solution and stirred at room temperature for 4 h. The resulting orange microcrystalline solid was filtered, washed with cold MeOH (10 mL), and dried *in vacuo* (68 mg, 40%). ^{1}H NMR (400 MHz, DMSO-d_6) δ (ppm): 1.22 (6H, d, *J* = 6.8 Hz), 2.15 (3H, s), 2.16–2.31 (2H, m); 2.7 (1H, sp, *J* = 6.8 Hz), 3.02 (1H, br s); 5.04–5.14 (2H, br m), 5.32 (1H, d, *J* = 5.6 Hz), 5.46 (1H, d, *J* = 6 Hz), 5.63 (1H, d, *J* = 6 Hz), 6.67 (1H, d, *J* = 5.6 Hz), 5.88–5.97 (2H, br m). $^{13}C\{^1H\}$ NMR (100 MHz, DMSO-d_6) δ (ppm): 18.0, 22.5, 30.4, 58.9, 78.6, 79.4, 80.8, 81.2, 95.7, 101.6, 176.8. HR ESI MS, positive mode: *m/z* 339.0650 (calcd mass for $C_{13}H_{21}N_2O_2Ru$ $[M-Cl-H]^{+}$: 339.0646). HR ESI MS, negative mode: *m/z* 373.0228 (calcd mass for $C_{13}H_{20}ClN_2O_2Ru$ $[M-2H]^{-}$: 373.0255).

[(η^6-p-cym)RuCl$_2$(Im-BzCOOMe)]. A suspension of **9** (200 mg, 0.33 mmol) in 10 mL of DCM was reacted with the methyl ester of the 4-(1*H*-Imidazol-1-yl)benzoic acid (1 mol equiv) and stirred at room temperature. Slowly, the suspension dissolved, and after 4 h, diethyl ether was added with stirring to the resulting orange solution until it became turbid. The separated red microcrystalline product was isolated by filtration, washed several times with ether, and dried under vacuo (165 mg, 50%). ^{1}H NMR (400 MHz, $CDCl_3$) δ (ppm): 1.31 (6H, d, *J* = 6.8 Hz), 2.24 (3H, s), 3.03 (1H, sp, *J* = 6.8 Hz), 3.95 (3H, s), 5.32 (2H. d, *J* = 5.4 Hz), 5.51 (2H. d, *J* = 5.4 Hz), 7.32 (1H, s), 7.43 (2H, d, *J* = 8.4 Hz), 7.53 (1H, s), 8.14 (2H, d, *J* = 8.4 Hz), 8.38 (s, 1H). $^{13}C\{^1H\}$ NMR (100 MHz, $CDCl_3$) δ (ppm): 20.1, 23.8, 32.2, 54.0, 83.0, 84.0, 100.0, 104.4, 119.9, 122.4, 131.6, 133.1, 135.0, 139.9, 140.9, 167.2.

[(η^6-p-cym)RuCl(Im-BzCOOMe)(PPh$_3$)][PF$_6$] ***(17)***. Complex [(η^6-*p*-cym)$RuCl_2$(Im-BzCOOMe)] (81 mg, 0.16 mmol) was reacted with PPh_3 (1 mol equiv) in methanol (5 mL) for 1 h under reflux. The resulting yellow solution was cooled to room temperature and ammonium hexafluorophosphate (1.1 mol equiv) dissolved in methanol (1 mL) was added. A yellow crystalline solid was filtered off and washed several times with methanol and diethyl ether (106 mg, 90%). ^{1}H NMR (400 MHz, acetone-d_6) δ (ppm): 1.19 (6H, dd, *J* = 7.2 Hz), 1.83 (3H, s), 2.60 (1H, sp, *J* = 7.2 Hz), 3.93 (3H, s), 5.36 (1H, dt, *J* = 6 Hz), 5.87 (1H, d, *J* = 6 Hz), 6.07 (1H, d, *J* = 6 Hz), 6.20 (1H, d, *J* = 6 Hz), 7.44–7.54 (17H, m), 7.65 (2H, dt, *J* = 10.4 Hz), 8.15 (2H, d, *J* = 8.8 Hz), 8.41 (1H, s). $^{31}P\{^1H\}$ NMR (acetone-d_6) δ (ppm): 36.51 (s). $^{13}C\{^1H\}$ NMR (100 MHz, acetone-d_6) δ (ppm): 19.1, 22.3, 24.2, 32.7, 53.9, 87.9, 90.2, 90.8, 95.7, 95.8, 105.0, 115.2, 115.3, 121.8, 123.1, 130.2, 130.3, 132.0, 132.1, 132.5, 132.9, 132.8, 133.0, 136.1, 136.2, 141.1, 141.3, 167.1. HR-ESI MS, positive mode: *m/z* 735.1488 (calcd mass for $C_{39}H_{39}ClN_2O_2PRu$ $[M]^{+}$: 735,1481), *m/z* 533.0729 (calcd mass for $C_{28}H_{29}ClPRu$ $[M-(Im-BzCOOMe)]^{+}$: 533.0739), *m/z* 497.0959 (calcd mass for $C_{28}H_{28}PRu$ $[M-(Im-BzCOOMe)-Cl-H]^{+}$: 497.0972).

DNA Binding Studies. Complexation reactions were carried out in H_2O (4 mM NaCl) at 37 °C. The required volume of an aqueous solution of the corresponding metal–octreotide conjugate was mixed with the required volume of an aqueous solution of 5′dCATGGCT (1–2 mol equiv). Regarding conjugate **5**, DNA binding studies were performed with the analogue with the CH=CH linkage isoster of octreotide (denoted as **5a**). In all cases, the solutions were 100 μM in the oligonucleotide. The evolution of the reactions was monitored by reversed-phase HPLC on Kromasil C_{18} columns (250 × 4.6 mm, 10 μm, flow rate: 1 mL/min), using linear gradients of aqueous triethylammonium acetate (0.05 M) (solvent A) and ACN (solvent B) or ACN/H_2O 1:1 (solvent B′). Metal adducts were isolated after several HPLC runs by using analytical separation conditions. HR MALDI-TOF MS analysis was carried out in the negative mode using 2,4,6-trihidroxyacetophenone matrix with ammonium citrate as an additive. Enzymatic digestions with 5′- and 3′-exonucleases (bovine spleen and snake venom phosphodiesterases, respectively) were performed as previously described.[41−43]

Adduct 5′dCATGGCT-conjugate ***3***. R_t = 11.0 min (gradient: 15% to 50% B in 30 min); HR MALDI-TOF MS, negative mode: *m/z* 3501.0 (calcd mass for $C_{128}H_{171}N_{38}O_{55}P_6Pt$ $[M-3H]^{-}$: 3500.95). MALDI-TOF MS after digestion with snake venom phosphodiesterase: *m/z* 2907.9 (-pCpT) (calcd mass for $C_{109}H_{146}N_{33}O_{42}P_4Pt$ $[M-3H]^{-}$: 2907.89). MALDI-TOF MS after digestion with bovine spleen phosphodiesterase: *m/z* 2594.8 (-CpApTp) (calcd mass for $C_{99}H_{134}N_{28}O_{37}P_3Pt$ [M-

3H]$^-$: 2594.83), *m/z* 2898.9 (-CpAp) (calcd mass for $C_{109}H_{147}N_{30}O_{44}P_4Pt$ [M-3H]$^-$: 2898.88).

Adduct 5′dCATGGCT-conjugate ***4***. R_t = 21.2 min (gradient: 5% to 90% B′ in 30 min); HR MALDI-TOF MS, negative mode: *m/z* 3715.8 (calcd mass for $C_{144}H_{178}N_{37}O_{57}OsP_6$ [M-2H]$^-$: 3715.02). MALDI-TOF MS after digestion with snake venom phosphodiesterase: *m/z* 2793.0 (-pGpCpT) (calcd mass for $C_{115}H_{141}N_{27}O_{38}OsP_3$ [M-2H]$^-$: 2792.88). MALDI-TOF MS after digestion with bovine spleen phosphodiesterase: *m/z* 2808.9 (-CpApTp) (calcd mass for $C_{115}H_{141}N_{27}O_{39}OsP_3$ [M-2H]$^-$: 2808.87), *m/z* 3113.9 (-CpAp) (calcd mass for $C_{125}H_{154}N_{29}O_{46}OsP_4$ [M-2H]$^-$: 3112.92).

Adduct 5′dCATGGCT-conjugate ***5a***. R_t = 20.5 min (gradient: 5% to 90% B′ in 30 min); HR MALDI-TOF MS, negative mode: *m/z* 3540.8 (calcd mass for $C_{138}H_{183}N_{38}O_{55}P_6Ru$ [M-3H]$^-$: 3540.02). MALDI-TOF MS after digestion with snake venom phosphodiesterase: *m/z* 2617.6 (-pGpCpT) (calcd mass for $C_{109}H_{146}N_{28}O_{36}P_3Ru$ [M-3H]$^-$: 2617.87). MALDI-TOF MS after digestion with bovine spleen phosphodiesterase: *m/z* 2633.7 (-CpApTp) (calcd mass for $C_{109}H_{146}N_{28}O_{37}P_3Ru$ [M-3H]$^-$: 2633.87), *m/z* 2937.7 (-CpAp) (calcd mass for $C_{119}H_{159}N_{30}O_{44}P_4Ru$ [M-3H]$^-$: 2937.91).

NMR Spectroscopy. The samples of the conjugates were prepared by dissolving the appropriate amount of compound in 500 μL of H_2O/DMSO-d_6 8:2 to give 0.8 mM solutions. NMR spectra were acquired on Bruker Avance spectrometers operating at 600 or 800 MHz, and processed with *Topspin* software. NOESY experiments were acquired with mixing times of 150 and 300 ms, and TOCSY spectra were recorded with standard MLEV-17 spin-lock sequence, and 80 ms mixing time. Water suppression in H_2O experiments was achieved by including a WATERGATE module in the pulse sequence prior to acquisition. NMR experiments were carried out at temperatures ranging from 0 to 25 °C. The spectral analysis program *Sparky*[44] was used for semiautomatic assignment of the NOESY cross-peaks and quantitative evaluation of the NOE intensities. Sequential assignment of the peptide moiety was carried out using standard ^{1}H NMR techniques.

Structural Modeling. Molecular dynamics calculations were carried out with the program *Sybyl X-1.3* (Tripos Inc.). Ten initial models for each conjugate were built from the dicarba analogue of octreotide **2** coordinates.[24] Metal complex coordinates were built from crystallographic structures of similar compounds.,[36,45] Each of the initial structures was minimized and then submitted to 300 ps of molecular dynamics simulations. Explicit solvent and periodic boundary conditions were included in the calculations. The last 50 ps of each run was averaged and energy-minimized. Backbone geometry of those peptide residues that do not exhibit significant chemical shift variations was loosely constrained by imposing dihedral angle restraints. Analysis of the representative structures was carried out with the programs *Sybyl* and *MOLMOL*.[46]

Immunocytochemistry. MCF-7 cells were seeded on fibronectin-coated coverslips and allowed to attach overnight. Then, the cells were incubated at 37 °C with medium containing 50 μM of **13** during 1, 3, and 6 h, or with medium alone as control. After that, the cells were washed with cold PBS (Gibco BRL) and fixed with 4% paraformaldehyde in PBS for 15 min at 4 °C. The cells nucleus were stained with 2 μg/mL Hoescht 33258 (excitation/emission: 352 nm/461 nm) during 15 min. After washing twice with cold PBS, the cells coverslips were mounted using a fluorescence mounting medium (Dako, Carpinteria, CA, USA) and examined using a Leica TCS-SP5 multiphoton and high-velocity spectral confocal microscope (Leica Microsystems, Nussloch, Germany).

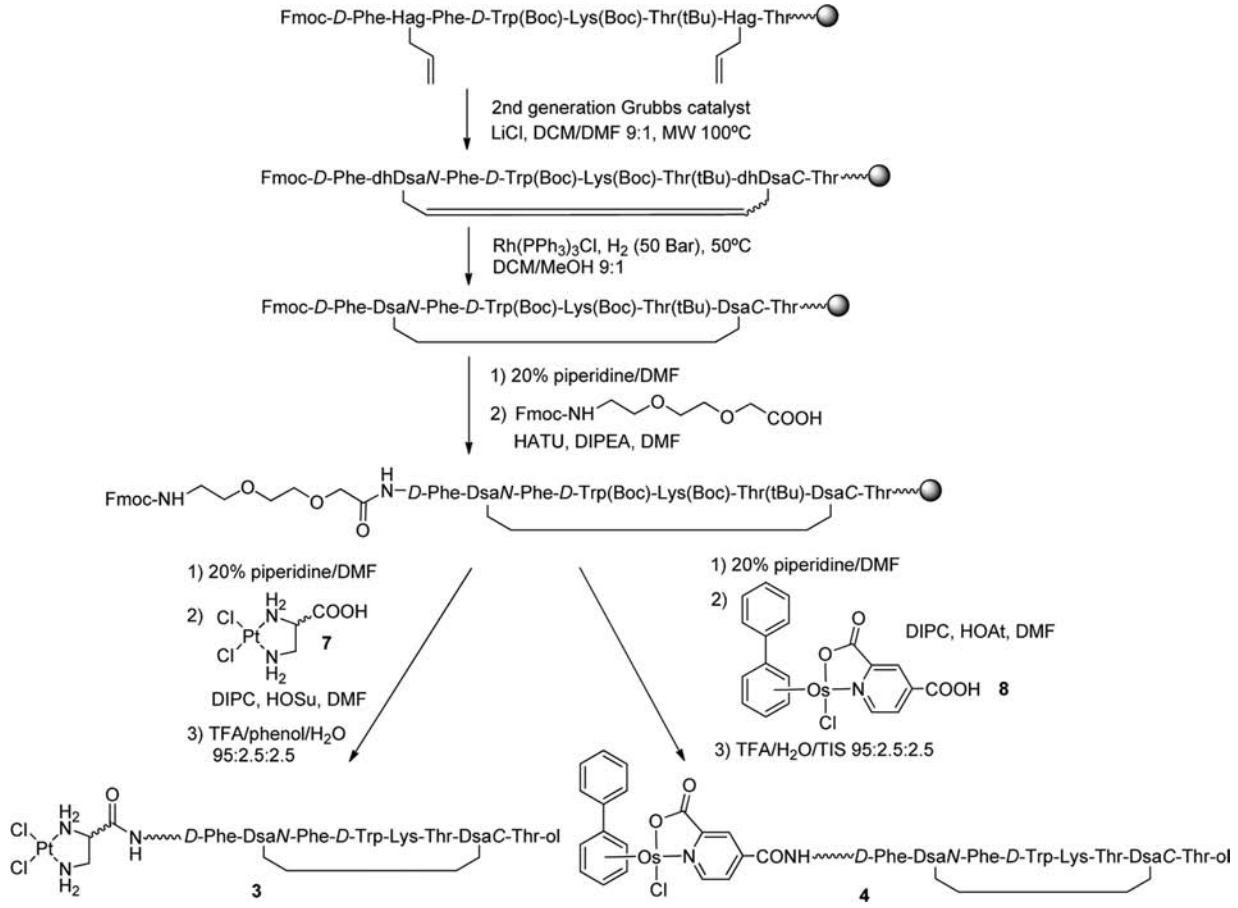
Internalization Experiments with 13 and 14. The uptake efficiency of **13** and **14** by the cells was quantified by flow cytometry. The cells were seeded onto 12-well plates and allowed to attach for 24 h. Next, the cells were treated at 37 °C with 50 μM of either **13** or **14** during 1, 3, and 6 h. After rinsing the cells three times with cold PBS, the cells were harvested by trypsinization and the fluorescence of the cells, corresponding to the uptake of the fluorescein-modified peptides, was analyzed using a FACSCalibur (Becton Dickinson Immunocytometry Systems, San Jose, CA) equipped with the *CellQuest* software (Becton Dickinson). Fluorescence intensity was represented on a 4 orders of magnitude log scale (1−10 000). Ten thousand cells were analyzed in each experiment.

Cytotoxicity Assays. The cytotoxicity of the conjugates and of the control complexes in MCF-7, DU-145, and CHO cells was determined by the MTT assay. Aliquots of 4000 DU-145 cells, 3500 MCF-7, or 2000 CHO cells were seeded onto flat-bottomed 96-well plates. Twenty-four hours later, the cells were treated for 72 h with the compounds at concentrations ranging from 0 μM to 250 μM. After removal of the treatment, the cells were washed with PBS and incubated for 3 additional hours with 100 μL of fresh culture medium together with 10 μL of MTT (Sigma-Aldrich). The medium was discarded and DMSO (Sigma-Aldrich) was added to each well to dissolve the purple formazan crystalls. Plates were agitated at room temperature for 10 min, and the absorbance of each well was determined on a Multiscan Plate Reader (ELX800, Biotek, Winooski, USA) at a wavelength of 570 nm. Three replicates were used in each experiment. For each treatment, the cell viability was determined as a percentage of the control untreated cells, by dividing the mean absorbance of each treatment by the mean absorbance of the untreated cells. The concentration that reduces by 50% the cell viability (IC_{50}) was established for each compound.

Ruthenium Accumulation in Cancer Cells. For ruthenium cellular uptake studies, 1.5 × 10^6 MCF-7 cells were plated in 100 mm Petri dishes and allowed to attach for 48 h. Next, the plates were exposed to the ruthenium−octreotide conjugate **6** or to the unconjugated ruthenium complex **17** at a concentration corresponding to a fifth of their IC_{50} (12.5 μM and 0.66 μM, respectively). Additional plates were incubated with medium alone as negative control. After 24 h of incubation, the cells were rinsed three times with cold PBS and harvested by trypsinization. The number of cells in each sample was counted manually in a hemocytometer using the Trypan blue dye exclusion test. Then, the cells were centrifuged to obtain the whole cell pellet for ICP-MS analysis. All experiments were conducted in triplicate.

ICP-MS Analysis. The whole cell pellets were dissolved in 300 μL of concentrated 72% v/v nitric acid, and the samples were then transferred into Wheaton v-vials (Sigma-Aldrich) and heated in an oven at 373 K for 18 h. The vials were then allowed to cool, and each cellular sample solution was transferred into a volumetric tube and combined with washings with Milli-Q water (1.7 mL). Digested samples were diluted 10 times with Milli-Q to obtain a final HNO_3 concentration of approximately 2.5% v/v. Ruthenium content was analyzed on an ICP-MS Perkin-Elmer Elan 6000 series machine at the Centres Científics I Tecnològics of the Universitat de Barcelona. The solvent used for all ICP-MS experiments was

Scheme 1. Schematic Representation of the Solid-Phase Approach Used for the Synthesis of Conjugates 3 and 4



Milli-Q water with 1% HNO_3. The ruthenium standard (High-Purity Standards, 1000 μg/mL ± 5 μg/mL in 2% HCl) was diluted with Milli-Q water to 100 ppb. Ruthenium standards were freshly prepared in Milli-Q water with 1% HNO_3 before each experiment. The concentrations used for the calibration curve were in all cases 0, 1, 2, 5, and 10 ppb. The isotope detected was ^{101}Ru and readings were made in triplicate. Rhodium was added as an internal standard at a concentration of 10 ppb in all samples.

SSTR2 Expression Analysis. SSTR2 expression on MCF-7, DU-145, and CHO cells surface was determined by double immunofluorescence. The cells were first fixed with PBS-1.5% formaldehyde and permeabilized with PBS-0.2%Tween 20 (Biorad). Then, the cells were incubated with a monoclonal antibody against human sst_2 receptor (R&D systems) during 30 min at 4 °C. After rinsing the cells with PBS, the cells were incubated 30 min at 4 °C in the presence of the Alexa-Fluor 488 conjugated goat antimouse IgG antibody (Invitrogen). Cells were washed again, and the fluorescence was analyzed using a flow cytometer (FACSCalibur, Becton Dickinson Immunocytometry Systems, San Jose, CA) equipped with the *CellQuest* software (Becton Dickinson). The fluorescence intensity of the cells was represented on a 4 orders of magnitude log scale (1−10 000). Ten thousand cells were analyzed in each experiment.

Statistical Analysis. The statistical analysis was performed with the *SPSS* statistical software for Windows (v 15.0; SPSS Inc., Chicago, IL, USA). Quantitative variables were expressed as mean and standard error (SE). The normality of the data was tested using the Kolmogorov−Smirnov test. The differences between data with normal distribution and homogeneous variances were analyzed using the parametric Student's *t* test. A value of $p < 0.05$ was considered significant.

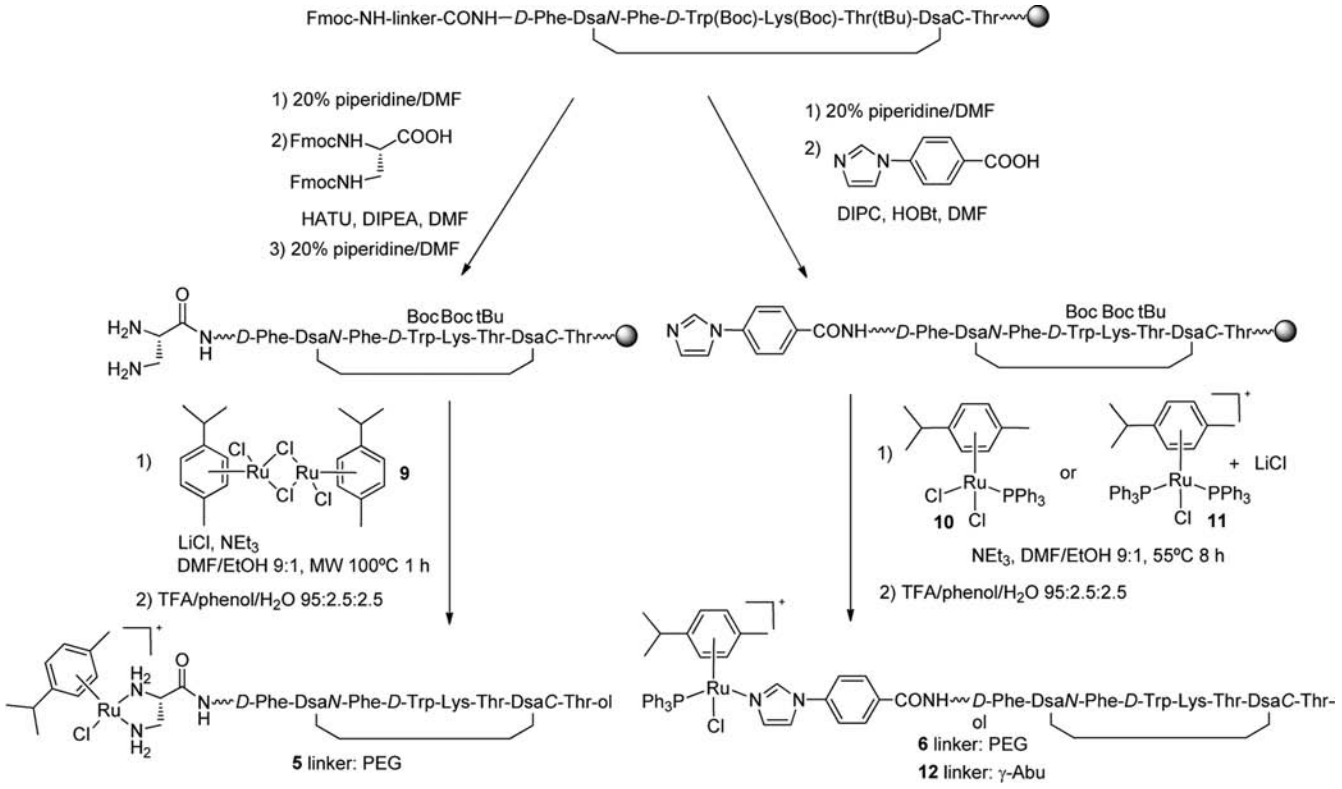
RESULTS AND DISCUSSION

Synthesis and Characterization of Conjugates between a Dicarba Analogue of Octreotide and Dichloridoplatinum(II) and Osmium(II) Complexes. In our previous work,[23] *cis*-dichlorido-(1-(carboxylic acid)-1,2-diaminoethane)platinum(II) complex, ([$PtCl_2$(dap)]), was chosen as a cisplatin analogue since it can form the expected intrachain Pt-*N*7/5′G,*N*7/3′G chelates upon reaction with DNA. The attachment of the platinum complex to the γ-aminoisobutyryl-derivatized dicarba analogue of octreotide (**2**) was carried out on a solid phase through the formation of an amide bond between its carboxylic function and the amine group of the spacer. Although the conjugate was able to bind to DNA in the same way as cisplatin, its low solubility in water precluded the evaluation of its biological activity. In order to improve the aqueous solubility for all the target conjugates, **3**−**6** (Chart 1), a poly(ethylene glycol) spacer has been introduced between the peptide sequence and the metal complex. This spacer is expected to be sufficiently long to keep the metal complex away from the pharmacophore sequence.

Following our previous results on the synthesis of platinum(II)−octreotide conjugates, a stepwise solid-phase strategy has been used for the preparation of conjugates **3**−**6**. This approach is particularly useful in this case, since it allows the

dx.doi.org/10.1021/bc300173h | *Bioconjugate Chem.* 2012, 23, 1838−1855

Scheme 2. Schematic Representation of the Solid-Phase Approach Used for the Synthesis of Conjugates 5, 6, and 12



regioselective introduction of the metal complex at the *N*-terminal end of the cyclic peptide. Otherwise, in a solution-phase approach the ε-NH_2 of the Lys residue would compete with the *N*-terminal amino group of octreotide. In order to increase the stability of the metal−octreotide conjugates, the CH_2−CH_2 linkage has been chosen as a disulfide isoster, since this modification keeps a higher selectivity for sst_2 somatostatin receptor than the CH═CH linkage.[24]

First, the linear peptide was synthesized manually on a Rink amide resin-*p*-MBHA using standard Fmoc-*t*Bu methodology (Scheme 1). All suitably protected Fmoc-amino acids were incorporated with HATU in the presence of DIPEA in anhydrous DMF as a solvent. As previously described,[23,24] Fmoc-protected threoninol functionalized as the *p*-carboxybenzaldehyde acetal was first anchored to the solid support. In addition, the two cysteine amino acids in octreotide were replaced by allyl glycine residues to perform the cyclization reaction. Once the linear peptide precursor had been assembled, on-resin microwave-assisted ring-closing metathesis was carried out with second-generation Grubbs catalyst for 1 h at 100 °C. Then, hydrogenation of the double bond using Wilkinson's catalyst afforded the protected cyclic saturated dicarba analogue of octreotide (**2**) bound to the resin. Finally, an Fmoc-protected poly(ethylene glycol) linker, 8-(9-fluorenylmethyloxycarbonyl-amino)-3,6-dioxaoctanoic acid, was incorporated at the *N*-terminal end using HATU as a coupling reagent.

The final step involved the removal of the Fmoc protecting group of the spacer (20% piperidine in DMF) and the incorporation of the required metal complex onto the free amino function of the linker. For the synthesis of conjugate **3**, $[PtCl_2(dap)]$ (**7**) was coupled using DIPC and NHS in anhydrous DMF (15 h at rt, protected from light).[23] Cleavage from the resin and removal of the protecting groups were carried out by treatment with a TFA/phenol/H_2O cocktail (95:2.5:2.5) for 1 h at rt. Reversed-phase HPLC analysis of the crude revealed a main double peak. Both peaks were isolated by semipreparative HPLC and characterized by HR MALDI-TOF and ESI MS and NMR as the expected diastereomeric dichloridoplatinum(II)−octreotide conjugates, **3**. The generation of both isomers is accounted from the use of a racemic platinum(II) complex.

Our next objective was focused on the conjugation of an organometallic osmium(II) complex to the dicarba analogue of octreotide. Among osmium complexes with anticancer activity, $[(\eta^6\text{-bip})Os(pico)Cl]$ is particularly interesting, since it exhibits promising activity in human ovarian cancer cells.[47,48] For this reason, we choose an analogue bearing a carboxylic function on the picolinate ligand, $[(\eta^6\text{-bip})Os(4\text{-}CO_2\text{-pico})Cl]$ (**8**), which would allow the attachment to octreotide. This complex has been very recently conjugated to polyarginines with different chain lengths using solid-phase procedures.[30] Hence, for the synthesis of conjugate **4**, $[(\eta^6\text{-bip})Os(4\text{-}CO_2\text{-pico})Cl]$ was coupled with either PyBOP or the more reactive HATU in the presence of DIPEA in anhydrous DMF (Scheme 1). After cleavage and deprotection with a TFA/TIS/H_2O cocktail (95:2.5:2.5; 1 h at rt, protected from light), reversed-phase HPLC analysis revealed a main peak (30−40%), which was isolated and characterized by HR MS and NMR as the target conjugate **4**. The conversion yield was substantially increased (90%) when coupling was performed with DIPC and HOAt in anhydrous DMF for 3 h. It is important to mention that, during HPLC analysis of conjugate **4**, a less retained peak was always observed, which was characterized by MS as the aqua conjugate (substitution of Cl by H_2O). This result reveals fast hydrolysis

kinetics for this osmium(II) complex in comparison with that of the platinum(II) complex (see below).

Synthesis and Characterization of Conjugates between a Dicarba Analogue of Octreotide and Ruthenium(II) Arene Complexes. Ruthenium−octreotide conjugates, **5** and **6**, were synthesized on a solid-phase following a different strategy than that used for platinum and osmium conjugates (Scheme 2). Thus, instead of synthesizing the required ruthenium complexes bearing a carboxylic function, we decided to incorporate the appropriate ligand at the *N*-terminal end of the linker-derivatized peptide, which would allow the assembly of the organometallic ruthenium(II) complex around it. This approach avoids some of the difficulties found during the synthesis of carboxylic acid containing ruthenium complexes, and it could be applied to the parallel synthesis of libraries of ruthenium−peptide conjugates.

First, we focused on mononuclear ruthenium(II) arene complexes of the type $[(\eta^6\text{-arene})RuCl(XY)]^+$, where XY is a *N,N*-chelating ligand such as ethylenediamine. These compounds show high cytotoxicities both *in vitro* and *in vivo*, with IC_{50} values comparable to carboplatin in human ovarian cancer cell lines (e.g., 9 μM for $[(\eta^6\text{-}p\text{-cym})RuCl(en)][PF_6]$).[49] In addition, they form monofunctional adducts at guanine nucleobases on DNA.

Attachment of $[(\eta^6\text{-}p\text{-cym})RuCl(en)]^+$ to octreotide was planned through the ethylenediamine ligand, as perfomed for the dichloridoplatinum(II) conjugate, which would lead to conjugate **5** (Chart 1). In order to incorporate 2,3-diaminopropionic acid into the *N*-terminal amino function of the linker-derivatized dicarba analogue of octreotide bound to the resin, the required N^{α},N^{β}-bis-(9-fluorenylmethyloxycarbonyl)-L-2,3-diaminopropionic acid was synthesized by reaction between L-2,3-diaminopropionic acid hydrochloride and 9-fluorenylmethyloxycarbonyl chloride. This Fmoc-protected chelating ligand was coupled with HATU in DMF in the presence of DIPEA for 1 h at rt (Scheme 2). After removal of the Fmoc protecting groups, the binding of the ruthenium arene to the chelating ligand was studied by reaction with the ruthenium dimer $[\{(\eta^6\text{-}p\text{-cym})Ru(\mu\text{-}Cl)Cl\}_2]$ (**9**). Optimized conditions required microwave irradiation at 100 °C for 1 h and the use of a slight excess of **9** (3 mol equiv) in the presence of LiCl (6.6 mol equiv) and NEt_3 (7.2 mol equiv) in a DCM/EtOH 9:1 mixture. The use of microwave irradiation in combination with this solvent was proven to be particularly important to achieve a good conversion yield. However, 30−40% conversion yields where obtained when DMF replaced DCM, and no irradiation was used (15 h heating at 60 °C). These results might be attributed to the instability of **9** at high temperatures during a prolonged time. Cleavage from the resin and deprotection was performed by treatment with a TFA/phenol/H_2O cocktail (95:2.5:2.5) for 1 h at rt. Reversed-phase HPLC analysis of the crude revealed a main peak (65%) which was isolated by semipreparative HPLC and characterized by HR MALDI-TOF and ESI MS as the expected ruthenium−octreotide conjugate, **5**.

Once we had synthesized conjugate **5**, we explored the possibility of assembling mononuclear ruthenium(II) arene complexes through a single monodentate ligand incorporated into the peptide fragment instead of using chelating ligands. On the basis of the excellent antitumor activities of some ruthenium(II) three-legged "piano stool" complexes containing planar *N*-heteroaromatic σ-bonded ligands and phosphine ligands,[50] with IC_{50} values lower than that of cisplatin, we focused on compounds of the type $[(\eta^6\text{-}p\text{-cym})RuCl(Im\text{-}Ph)(PPh_3)]^+$, where Im-Ph is 1-phenyl-imidazole. The conjugation of such triphenylphosphine-containing complexes to octreotide was planned through the phenyl ring linked to the imidazole ligand, which would allow the coordination of the ruthenium moiety. As in previous metal complexes, the hydrolysis of the Ru−Cl bond was expected to generate corresponding aqua species reactive toward DNA binding.

First, 4-(1*H*-imidazol-1-yl)benzoic acid was coupled onto two batches of linker-octreotide resin with DIPC and HOBt in anhydrous DMF for 1 h at rt, where linker refers to γ-aminoisobutyryl group or the poly(ethylene glycol) spacer (Scheme 2). The assembly of the metal complex was first explored with the γ-Abu linker-containing batch by using two ruthenium compounds, $[(\eta^6\text{-}p\text{-cym})RuCl_2(PPh_3)]$ (**10**) and $[(\eta^6\text{-}p\text{-cym})RuCl(PPh_3)_2]^+$ (**11**), since we hypothesized that the imidazole ligand could replace the more labile chlorido ligands. **10** was easily synthesized by refluxing dimer **9** with triphenylphosphine (2.3 mol equiv) in hexane for 15 h, whereas complex **11** was obtained from **10** by reaction with a slight excess of triphenylphosphine (2 mol equiv) in methanol at 35 °C for 2.5 h.[37,38]

Reaction of the imidazole-derivatized peptide-bound resin with complex **10** (4 mol equiv) was performed in the presence of NEt_3 (16 mol equiv) in a DMF/EtOH mixture (3:1) for 8 h at 55 °C. After treatment of the resin with a TFA/phenol/H_2O cocktail (95:2.5:2.5), the desired conjugate **12** was detected in the crude (18%) together with the imidazole-derivatized octreotide (20%), as inferred by HPLC and MS analysis (Figure 1A).

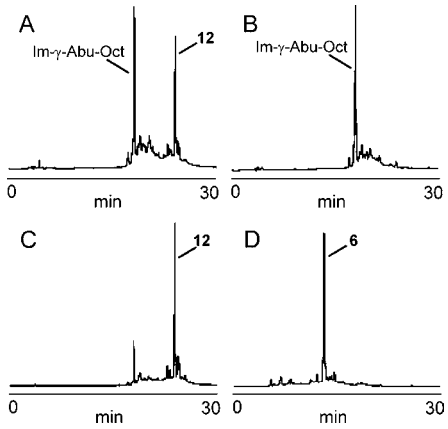


Figure 1. Reversed-phase HPLC traces of the reaction crudes for the synthesis of conjugate **12** by using complex **10** (A) or **11** (B) in the absence of LiCl or **11** in the presence of LiCl (C). Reaction crude for the synthesis of conjugate **6** when **11** was used in the presence of LiCl (D).

We next investigated the reaction of octreotide-bound resin with complex **11** under the same conditions. Unfortunately, reversed-HPLC analysis only revealed the presence of the imidazole-derivatized peptide, which indicates that imidazole was not able to substitute the chloride ligand in **11** (Figure 1B). This negative result might be attributed to the high steric hindrance around the metal because of the two bulky PPh_3 ligands. However, to our surprise, when the reaction of **11** (4 mol equiv) with the peptide was repeated in the presence of LiCl (4.4 mol equiv) and NEt_3 (16 mol equiv) in a DMF/EtOH 9:1 mixture for 8 h at 55 °C, HPLC analysis of the

dx.doi.org/10.1021/bc300173h | *Bioconjugate Chem.* 2012, 23, 1838−1855

cleaved, deprotected crude (TFA/phenol/H_2O 95:2.5:2.5, 1 h rt) showed the presence of a main peak (57%) which was isolated and characterized by MS as conjugate **12** (Figure 1C). Hence, imidazole is able to replace one of the two PPh_3 ligands in **11** instead of the Cl ligand, thereby allowing the conversion yield of conjugate **12** to be improved in comparison with that obtained when complex **10** is used. As shown in Figure 1D, the assembly of the ruthenium complex by using these optimized conditions was almost quantitative onto the imidazole-derivatized octreotide resin that contains the poly(ethylene glycol) linker, which allowed the target conjugate **6** to obtain with high yield (Scheme 2). This compound was isolated by semipreparative HPLC and fully characterized by HR MS and NMR.

In order to gain insight into the mechanism of this reaction, complex **11** was mixed with LiCl (1.4 mol equiv) and NEt_3 (1.9 mol equiv) in anhydrous DMF and heated at 55 °C. As shown in the ^{31}P NMR spectra (Figure 2), the single chemical shift

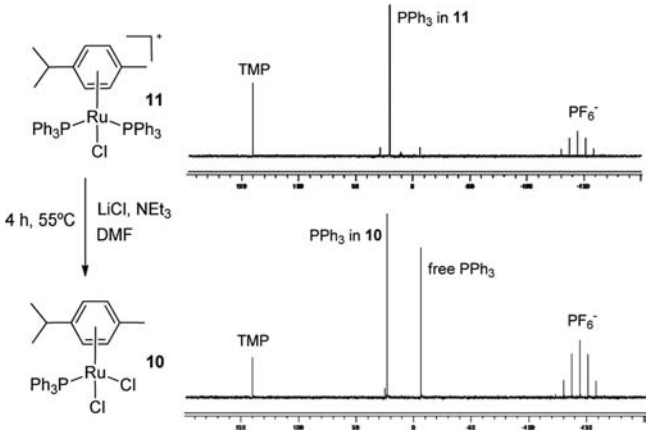


Figure 2. Schematic representation of the transformation of complex **11** to **10** (left) and ^{31}P NMR spectra of **11** (A) and of the reaction crude after heating **11** in the presence of LiCl and NEt_3 for 4 h at 55 °C (B).

corresponding to the two PPh_3 ligands in **11** (δ: 20.0 ppm) disappeared after 4 h. The two new signals (δ: 23.2 and −6.4 ppm) were assigned to the PPh_3 ligand in complex **10** and to the released PPh_3, respectively. These results demonstrate the *in situ* generation of complex **10** from **11** because of the presence of LiCl. This reaction might have future applications in the synthesis of new ruthenium complexes for catalysis or biomedical applications.

Activation of Metal−Octreotide Conjugates by Aqueous Hydrolysis. In general, the cytotoxic activity of metal-based anticancer drugs is intimately related with the processes that mediate their activation in aqueous media; these processes are known to facilitate the interaction of the metal, its ligands or the complex, or a fragment with the biological target (e.g., DNA, RNA, or proteins). In addition, aqueous stability is another fundamental prerequisite, since it might condition their success in clinical development. Cisplatin and its analogues can be considered prodrugs since their activation is produced through the dissociation of anionic ligands.[22,51] The resulting positively charged aqua species coordinate strongly to nuclear DNA while neutral complexes do not, which demonstrates that in these family of compounds the metal plays a functional role.[22] Organometallic complexes containing a labile group prone to substitution can also be activated inside the cells through hydrolysis. As previously stated, the activation of piano-stool organometallic ruthenium(II) complexes of the type $[(\eta^6\text{-arene})RuCl(XY)]^+$, where XY is a neutral chelating ligand, proceeds through the release of chloride ligand. The resulting aqua species is responsible for ruthenation of DNA by generating monofunctional adducts on guanine nucleobases. In a similar manner to cisplatin and related platinum(II) compounds, the high extracellular chloride concentration (100 mM) in comparison with that present in the nucleus and cytoplasm (4 and 22.7 mM, respectively)[52] ensures that the intact drug reaches its biological target before activation takes place. In addition, a close correlation between cancer cell cytotoxic activity and the capacity of some ruthenium(II) arene complexes to undergo hydrolysis of the Ru-halide bond has been established.[53] Osmium(II) arene complexes containing *N,N*-chelating ligands, such as ethylenediamine, experience much slower ligand exchange kinetics than ruthenium analogues.[54] The higher acidity of the water molecule bound to the osmium at physiological pH makes these compounds exist largely in their less reactive hydroxido form. These problems have been solved by using picolinate as chelating ligand since it increases both the hydrolysis rate and the basicity of the water molecule in the aqua species (e.g., $[(\eta^6\text{-arene})Os(pico)Cl]$) and, for instance, generates compounds with similar anticancer activity as ruthenium-arene analogues.[36,47]

On the basis to these precedents, we wanted to assess whether hydrolysis of the M-Cl bond occurs when Pt, Ru, and Os complexes are conjugated to octreotide. The stability of conjugates **3**−**6** (Chart 1) was investigated in aqueous solution at different chloride concentrations mimicking typical blood plasma, cell cytoplasm, and cell nucleus (100, 22.7, and 4 mM, respectively). In all cases, metal−octreotide conjugates (10 μM) were incubated at 37 °C for 24 h. In general, HPLC analysis showed that the peak of the parent chloride compound (e.g., R_t = 20.3 min for conjugate **4**) evolved into a new less retained peak (R_t = 16.9 min), which was isolated and characterized by ESI MS as the aqua conjugate (substitution of Cl by H_2O).

As previously found in some osmium(II) complexes,[48] the hydrolysis extent of conjugate **4** was highly dependent on the NaCl concentration. Almost 95% of the conjugate was hydrolyzed in the 4 mM NaCl solution, but the hydrolysis was substantially decreased in the more concentrated solutions of NaCl (Table 1). These results indicate that the covalent attachment of the peptide does not interfere with the hydrolysis properties of this osmium complex and,[48] more importantly, that the aqua species is not deactivated by reaction with amino

Table 1. Percentage of Aqua Adduct Formation in Water at Chloride Levels Typical of Blood Plasma (100 mM), Cell Cytoplasm (22.7 mM), and Cell Nucleus (4 mM), and Percentage of the Conjugate−DNA Adduct Formation in Aqueous 4 mM NaCl

	% aqua adduct			% DNA adduct
conjugate	4 mM NaCl	22.7 mM NaCl	100 mM NaCl	4 mM NaCl
3	16	7	3	42
4	95	35	12	49
5a[a]	97	83	74	37
6	0	0	0	0

[a]See the experimental section.

acids from the carrier peptide. Similar results were obtained for the ruthenium conjugate **5** at the 4 mM chloride concentration. However, the extent of hydrolysis of the Ru−Cl bond was substantially decreased at the higher NaCl concentrations (Table 1).

Regarding conjugate **3**, the hydrolysis of the Pt−Cl bond occurred to a lower extent than for conjugates **4** and **5** (only 16% after 24 h in 4 mM NaCl solution), and it was almost abolished at higher chloride concentration.

On basis to these results, it is expected that octreotide in conjugates **3** and **4** will have a positive effect on the delivery of the less reactive intact prodrug while outside the cell, but once in the cell cytoplasm and, particularly, in the cell nucleus, Pt and Os complexes will be selectively activated through hydrolysis to generate a species reactive toward DNA binding. However, hydrolysis of conjugate **5** in the blood plasma and in the cell cytoplasm might have important consequences for its biological activity since the metal complex could be deactivated by reaction with other potential ligands such as peptides or proteins.

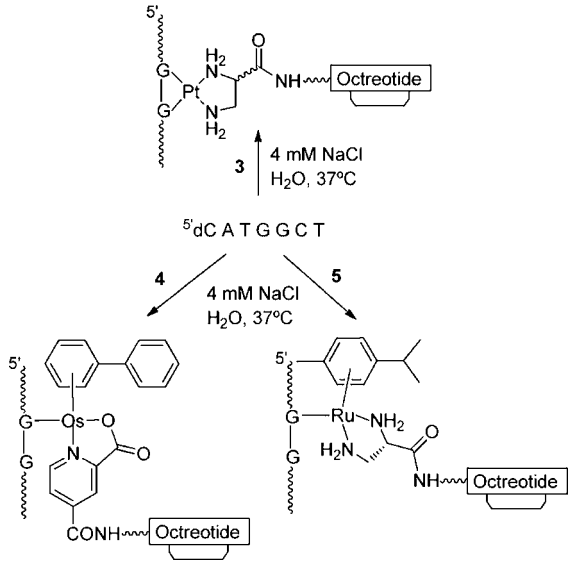
To our surprise, no hydrolysis occurred in the case of conjugate **6** upon incubation for 24 h at 37 °C, as inferred by HPLC analysis together with MS (see below).

DNA Binding Studies. In general, the chlorido species of Pt(II), Ru(II), and Os(II) complexes are relatively less reactive toward DNA nucleobases in comparison with the aqua adducts. The chloride concentration in the nucleus of cells (*ca.* 4 mM) is much less than that in the cytoplasm (*ca.* 22.7 mM) or outside cells (*ca.* 100 mM), which favors the formation of reactive aqua adducts in the vicinity of DNA. We incubated conjugates **3**−**6** in 4 mM NaCl at 37 °C with the short DNA oligonucleotide, 5′dCATGGCT. This oligonucleotide contains the target GG sequence of the anticancer drug cisplatin and is known to give the expected platinum 1,2-intrastrand GG chelates upon reaction with cisplatin, [Pt(en)Cl_2], or a dichloridoplatinum(II) conjugate of a dicarba analogue of octreotide.[23,41]

In the case of the platinum conjugate **3**, HPLC analysis showed the formation of a new peak with higher retention time than the parent oligonucleotide (42% after 24 h; see Table 1), attributable to the hydrophobicity of the platinum−peptide fragment. This new product was isolated and characterized by HR MALDI-TOF MS as an adduct between **3** and 5′dCATGGCT in which both chloride ligands had been lost. As expected from previous results,[23] MS analysis after enzymatic digestion with 5′- and 3′-exonucleases (bovine spleen and snake venom phosphodiesterases, respectively)[42,43] revealed the formation of a chelate between the platinum fragment of the conjugate and both guanines of the DNA chain (Scheme 3).

When osmium− and ruthenium(dap)−octreotide conjugates were incubated with 5′dCATGGCT, a major monofunctional adduct was formed between the metal fragment of the conjugate and the DNA chain. In both cases, the high metalation yield (49% for **4** and 37% for **5**) is in good agreement with the high degree of hydrolysis of the Os/Ru−Cl bonds. Enzymatic digestion in combination with MS revealed that in both cases metalation occurred at the guanine in the 5′ position (G4, see Scheme 3). This is a similar trend to that previously found with monofunctional platinum(II) complexes, such as $\{Pt(dien)\}^{2+}$, since they react exclusively with the 5′G nucleobase in the 5′dCATGGCT sequence.[41] The high affinity of similar ruthenium(II) arene complexes, such as [(η^6-*p*-cym)RuCl(en)]$^+$ or [(η^6-benzene)Ru(en)(OH_2)]$^{2+}$, for the *N*7 position of guanine over the other DNA nucleobases has been observed previously.[55−57] Regarding organometallic osmium(II) complexes with picolinate ligands, such as [(η^6-biphenyl)Os(picolinate)Cl]$^+$, rapid binding to calf thymus DNA has also been found.[58]

Scheme 3. Formation of Adducts between Conjugates 3−5 and the Oligonucleotide



Finally, the reaction of the ruthenium−octreotide conjugate **6** with DNA was studied. In good agreement with the absence of hydrolysis of the Ru−Cl bond in this compound, ruthenation of 5′dCATGGCT was not observed even after 48 h.

The overall results demonstrate that the activation of the M-Cl bond through hydrolysis in the Ru and Os conjugates seems to be very important for the binding to DNA, and there is a strong preference for the guanine nucleobases, especially those located at the 5′ end in GG sequences. However, in the case of the Pt(dap)-octreotide conjugate, platination is observed despite the slow kinetics for the hydrolysis of the Pt−Cl bond in the low chloride medium as found in the nucleus. The high thermodynamic stability of the *N*7,*N*7-GG intrastrand adduct might account for this result.

Efficiency of Intracellular Delivery of Dicarba Analogue of Octreotide (2). Compared to octreotide (**1**), the binding affinity of the dicarba analogue of octreotide (**2**) (Chart 1) is slightly reduced for sst_2, sst_4, and sst_5 receptors, although this reduction is smaller in the case of sst_2 receptor (about 23-fold for sst_2 vs 36- and 48-fold for sst_4 and sst_5, respectively).[6,24] However, as previously stated, this high affinity toward sst_2 receptor (44 nM) still makes **2** a suitable stabilized analogue of somatostatin to deliver cytotoxic metal complexes into cancer cells. In order to check the capacity of internalization of analogue **2** in our cell lines by confocal microscopy and flow cytometry, we labeled it with fluorescein. For the synthesis of the fluorescein-labeled dicarba analogue of octreotide (**13**), 5(6)-carboxyfluorescein was coupled on the linker derivatized peptide-bound resin by using DIPC and HOAt as coupling reagents. Washings with 20% piperidine/DMF before the final acidic treatment yielded a highly pure peptide.[59] As a control, fluorescein-labeled octreotide (**14**) was also synthesized using solid-phase procedures.

Next, the internalization capacity of analogue **2** was determined by confocal microscopy, after the incubation of

dx.doi.org/10.1021/bc300173h | *Bioconjugate Chem.* 2012, 23, 1838−1855

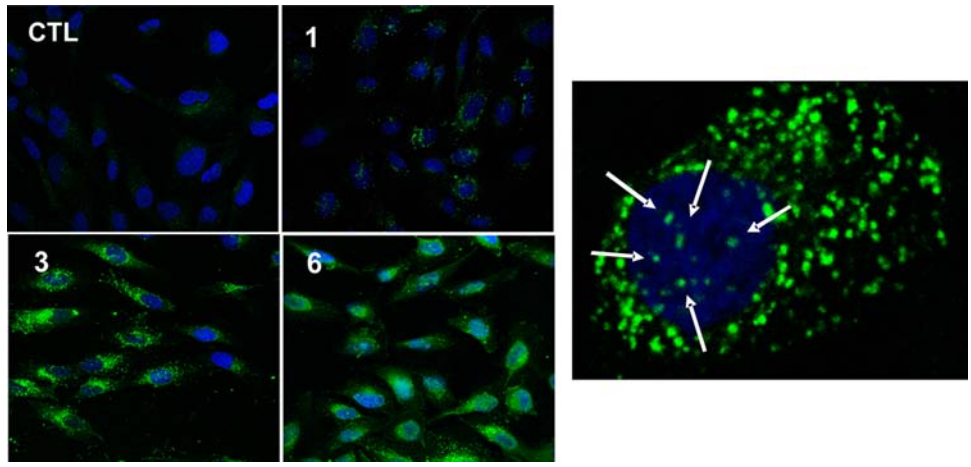


Figure 3. Confocal microscopic imaging of the internalization of the fluorescein-labeled dicarba analogue of octreotide (**13**) in MCF-7 cells. Left: MCF-7 cells incubated with 50 μM of **13** for 1, 3, and 6 h at 37 °C or medium alone as a control (CTL). The cell nuclei were stained with Hoechst (blue). The localization of **13** is indicated by the green fluorescence. Right: Higher-magnification image (1000×) of a MCF-7 cell incubated with 50 μM of **13** for 3 h at 37 °C. Arrows indicate the nuclear localization of **13**.

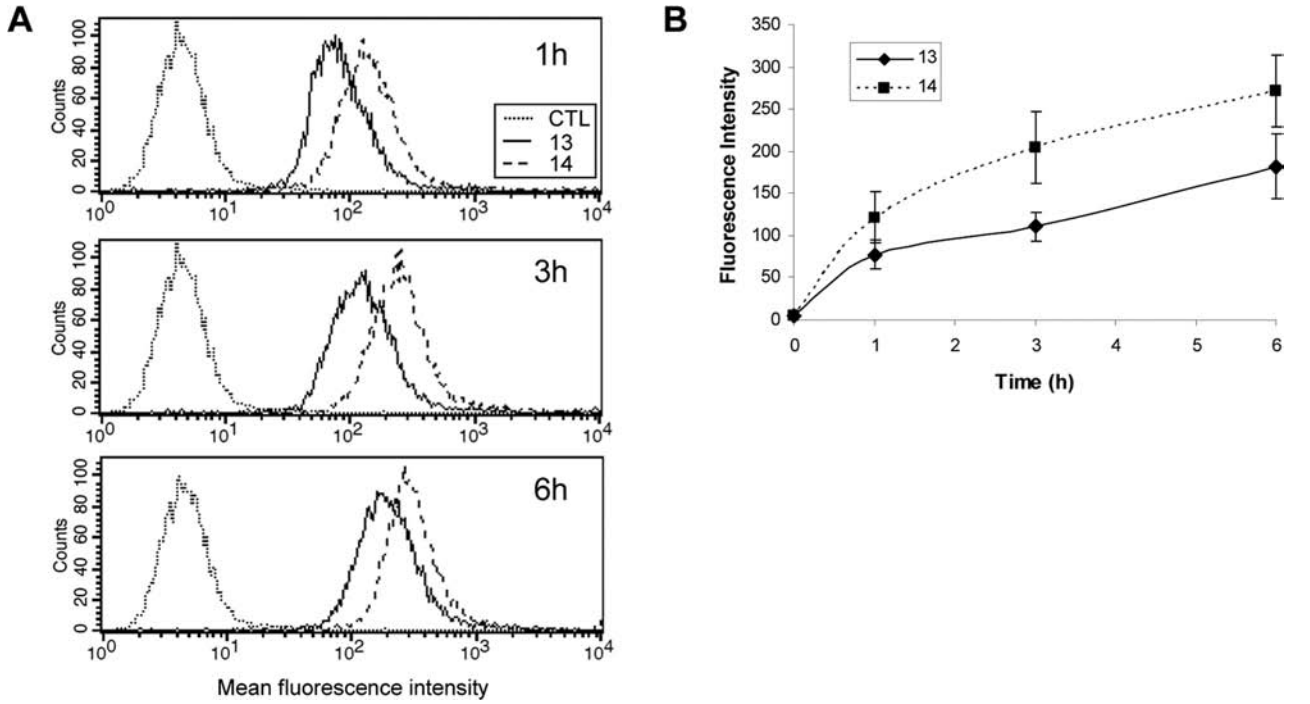


Figure 4. Intracellular delivery efficiencies of fluorescein-labeled dicarba analogue of octreotide (**13**) and of fluorescein-labeled octreotide (**14**) in MCF-7 cells. MCF-7 cells were incubated with the peptides for 1, 3, and 6 h at 37 °C or medium alone (CTL). The fluorescence intensity of the cells, corresponding to the intracellular uptake of the peptides, was determined by flow cytometry. (A) Flow cytometry histograms representing the fluorescence intensity of 10 000 cells on a four-decade log scale. Peptides **13** and **14** are depicted by solid and dashed lines, respectively. (B) Kinetics of the cellular uptake of **13** and **14**. Each point in the graphs represents the mean intracellular fluorescence intensity of three independent experiments ± SE.

$sstr_2$-expressing human breast cancer MCF-7 cells with 50 μM of the corresponding fluorescein-labeled peptide (**13**) for different times (1, 3, and 6 h). After 1 h of treatment, fluorescent vesicles, most likely endosomes, were visible in the cytoplasm of most of the examined cells, confirming the cellular uptake of the peptide (Figure 3). After 3 and 6 h, the number and the fluorescence density of the vesicles markedly increased, revealing an intense internalization of **13** during this period of time. At these time points, the vesicles were mainly clustered at the periphery of the cell nucleus. Higher-magnification (1000×) images from cells exposed to **13** for 3 h (Figure 3) revealed that, although the fluorescence vesicles were located mainly in the cell cytoplasm, a small proportion of the fluorescence was localized within the cell nucleus. Some authors have reported that somatostatin ligands may accumulate in the cell nucleus,[60,61] although the pathway for their nuclear localization remains to be elucidated.

The qualitative observations in confocal microscopy studies were confirmed with quantitative data obtained by flow cytometry. As represented in Figure 4A, the mean intracellular fluorescence intensity, corresponding to the internalization of **13**, increased over time. The intracellular fluorescence intensity

increased from 78 ± 16 at 1 h to 111 ± 17 at 3 h and 182 ± 39 at 6 h confirming an active cellular uptake of the peptide at these time points. In order to evaluate if **13** internalizes to a similar extent as native octreotide, MCF-7 cells were incubated in parallel with **14**. As expected from the higher affinity of octreotide for the somatostatin receptors,[6,24] the intracellular uptake of **14** was more elevated, by 40−57%, compared with that obtained in cells incubated with **13**. As shown in Figure 4B, the internalization kinetics was parallel for both peptides and it is also in good agreement with previous reports.[62,63] Despite the differences in the amount of internalized peptide, these results demonstrate that the dicarba analogue of octreotide (**2**) displays the internalization properties required to deliver the cytotoxic metal complexes into cancer cells.

Cancer Cell Cytotoxicity. To estimate the *in vitro* antitumor potential of the conjugates **3**, **4**, **5**, and **6**, their antiproliferative activity was determined in the MCF-7 cell line. The compounds were screened at a wide range of concentrations (from 0 to 250 μM) to determine the concentration that inhibits the cell growth by 50% (IC_{50}). The conjugates that did not inhibit cell growth by more than 50% at 250 μM were considered to be inactive. As shown in Table 2, only conjugate **6** displayed a measurable antiproliferative activity, and even that was only moderate (IC_{50} = 63.00 ± 1.53). On the basis of these results, we wondered whether the cytotoxic activity might be a consequence of the metal complex itself or of the conjugation to the peptide moiety. Hence, we tested the cytotoxicity of the parent metal complex alone, including the ligand attached to the peptide. The following complexes were synthesized and used as controls (Chart 2): $[PtCl_2(Etdap)]$ (**15**), $[(\eta^6\text{-}p\text{-cym})RuCl(dap)]^+$ (**16**), and $[(\eta^6\text{-}p\text{-cym})RuCl(Im\text{-}BzCOOMe)(PPh_3)]^+$ (**17**). Although we planned to mask the carboxylic function in all the complexes as a methyl or ethyl ester to avoid a negative charge that might hinder cell uptake and lower their biological activity, the complex $[(\eta^6\text{-}p\text{-cym})RuCl(Etdap)]^+$ spontaneously hydrolyzed to **16** during the workup of the reaction. Regarding the osmium complex $[(\eta^6\text{-bip})OsCl(4\text{-}CO_2Et\text{-pico})Cl)]^+$ (**18**), a moderate cytotoxic activity in the human ovarian A2780 and A2780cis cell lines (IC_{50} = 44 and 61 μM, respectively) has been recently reported in comparison with that of $[(\eta^6\text{-bip})OsCl(4\text{-Me-pico})Cl)]^+$ (IC_{50} = 4.4 and 7.6 μM in the A2780 and A2780cis cell lines, respectively).[36] Cytoxicity assays of the control complexes revealed that **17** was highly effective in MCF-7 cells, displaying an IC_{50} value (3.32 ± 0.54) comparable to that of cisplatin in this cell line (IC_{50} = 3.04 ± 0.25). In contrast, a moderate antiproliferative activity was obtained for complex **15** (IC_{50} = 67.00 ± 19.01) while complex **16** was noncytotoxic (Table 2).

Table 2. IC_{50} Values of Conjugates 3−6 and Control Complexes 15−17 in MCF-7 Cells[a]

	IC_{50} (μM)			
Conjugates	**3**	**4**	**5**	**6**
	>250	>250	>250	63.00 ± 1.53
Complexes	**15**	-	**16**	**17**
	67.00 ± 19.01	-	>250	3.32 ± 0.54

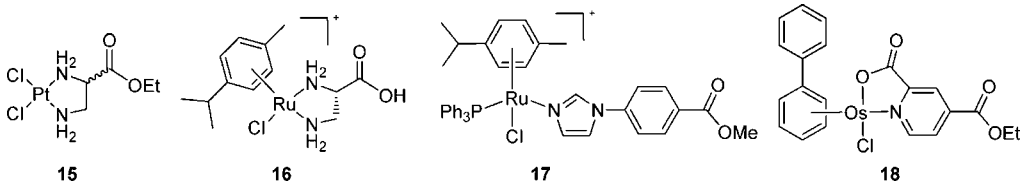
[a] IC_{50}: Inhibitory concentration that reduce by 50% the cell viability. The cytotoxicity was determined by the MTT assay after 72 h of drug exposure. Data represents the mean ± SE of at least three independent experiments.

Two important conclusions can be drawn from these results. First, high cytotoxic activity of the metal complex itself seems to be crucial for the efficacy of the conjugates as antitumoral agents. Second, conjugation of the complexes to the peptide moiety diminishes their cytotoxic capacity. For example, the cytotoxic activity of the ruthenium(II) arene complex $[(\eta^6\text{-}p\text{-cym})RuCl(Im\text{-}BzCOOMe)(PPh_3)]^+$ (**17**) is reduced about 19-fold when conjugated to the octreotide analogue (**6**), whereas complexes with moderate activity, such as $[PtCl_2(Etdap)]$ (**15**) or $[(\eta^6\text{-bip})OsCl(4\text{-}CO_2Et\text{-pico})Cl)]^+$ (**16**),[36] afford inactive peptide conjugates (**3** and **4**, respectively). On the other hand, the lack of activity for complex $[(\eta^6\text{-}p\text{-cym})RuCl(dap)]^+$ (**16**) or its octreotide conjugate (**5**) might be attributable to the high hydrolysis rate of the Ru−Cl bond, which would cause deactivation of the activated species by reaction with other biomolecules before it reaches nuclear DNA.

It is also interesting that the only conjugate that displays cytotoxic activity (**6**) does not interact with DNA, which can be attributed to the absence of hydrolysis of the Ru−Cl bond, even at a low chloride concentration (4 mM). This is also consistent with the fact that control complex **17** does not interact with double-stranded plasmid DNA after 48 h of incubation, as determined by electrophoretic mobility experiments (see Figure S-18 in the Supporting Information). Similarly to conjugate **6**, the aqua adduct of complex **17** was only formed after overnight incubation with a large excess of $AgNO_3$, as inferred by ^1H and ^{31}P NMR (see the Supporting Information). The overall results suggest that the cytotoxic activity of **6** and **17** might not be a consequence of their coordination to *N*-donor ligands from nucleic acids (DNA or RNA) or proteins. However, it cannot be rule out that their activation under physiological conditions occurs through coordination to sulfur-containing amino acids in peptides such as glutathione or in proteins.

In order to gain insight into the implication of somatostatin subtype-2 receptor on the cytotoxic activity of the ruthenium−octreotide conjugate **6**, the cellular uptake of this compound was compared with that of the unconjugated ruthenium complex **17**. Ruthenium accumulation (determined here as the net effect of influx and efflux of Ru) in the MCF-7 cancer cell line was determined by ICP-MS after a 24 h exposure to the compounds. Interestingly, the intracellular level of ruthenium after exposure to conjugate **6** (143.14 ± 16.6

Chart 2. Structures of the Control Metal Complexes



dx.doi.org/10.1021/bc300173h | *Bioconjugate Chem.* 2012, 23, 1838−1855

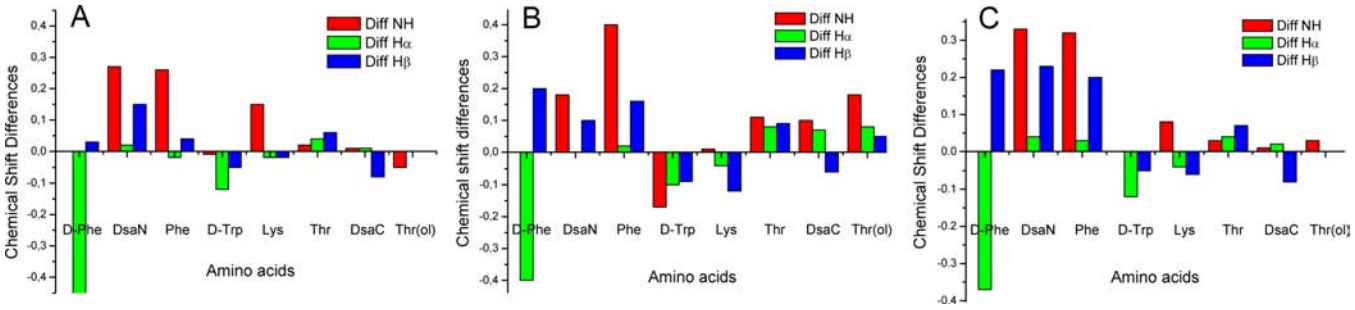


Figure 5. Chemical shift differences for NH, Hα, and Hβ protons between conjugates **3** (A), **4** (B), and **6** (C) and the dicarba analogue of octreotide (**2**).[24]

pmol Ru/10^6 cells) was higher than that of the parent complex **17** (68.01 ± 2.2 pmol Ru/10^6 cells). Such a significant difference between these compounds reveals that conjugation to the peptide moiety has a positive effect on the internalization of the ruthenium complex, thereby suggesting that the attachment of the metal complex to the peptide does not disturb its active conformation and hence its affinity toward somatostatin receptors is maintained (see below). Although the covalent attachment of a potential metal-based drug to a receptor-binding peptide such as octreotide is expected to increase the bioavailability, delivery, and accumulation of the complex to cancer cells, it must also be borne in mind that the peptide moiety might also inhibit or weaken the interaction of the metal fragment with the final biological target (e.g., DNA, RNA, or proteins), which would compromise its cytotoxic activity.[25] Release of the ruthenium fragment from the conjugate might be necessary to allow it to reach its target site. This might explain the apparently contradictory results from cytotoxicity and cellular uptake studies, since in this case, the covalent attachment of the ruthenium complex to the dicarba analogue of octreotide **2** increases uptake and accumulation of the drug in the cancer cell while the cytotoxic activity of the final conjugate is reduced.

Conformational Analysis by NMR Spectroscopy. It is well-known from NMR studies in water and in DMSO-d_6 solution that octreotide (**1**) adopts a predominant type II′ β-turn conformation across residues Phe^7-*D*-Trp^8-Lys^9-Thr^{10}.[64,65] The stability of this conformation together with the orientation of exocyclic residues (*D*-Phe^2 and Thr-ol^{15}) plays an important role in the binding of octreotide and its analogues to somatostatin receptors.[66,67] Regarding the dicarba analogue of octreotide used in this work (**2**), D′Addona et al. have recently described that replacement of cystine by a CH_2−CH_2 linkage does not substantially alter the secondary structure in the active region.[24] These NMR studies also suggest that there exists a conformational equilibrium between the antiparallel β-sheet structural cluster and a second conformational ensemble involving folded structures for the *C*-terminal residues. This hypothesis is in good agreement with previously reported findings for **1** that indicate that *C*-terminal amino acids fold into a 3_{10}-helix-like array or in a similar helical ensemble.[66] Furthermore, it is important to consider that the structure of **2** in the region of the *N*-terminal *D*-Phe^2 and *C*-terminal Thr(ol)^{15} is significantly different from that previously reported for **1**,[66] which might explain the differences in affinity for somatostatin receptors.[24] Given the implication of these amino acids both in the affinity and in the specificity for somatostatin receptors, we investigated whether the covalent attachment of metal complexes to the *N*-terminal end of **2** through a poly(ethylene glycol) linker might alter the active conformation of the peptide and, in particular, the structure around *D*-Phe^2 and Thr-ol^{15}.

In order to gain some insight into peptide conformation, conjugates **3**, **4**, and **6** were studied by 1D and 2D ^{1}H NMR spectroscopy. In all conjugates, significant line-broadening was observed at conjugate concentrations above 1 mM, suggesting that oligomerization takes place under these conditions. This effect is specially pronounced in the case of the osmium−octreotide conjugate (see the Supporting Information). To avoid oligomerization, 2D NMR spectra were recorded at a peptide concentration of 0.8 mM. Signals of the peptide were completely assigned using standard techniques (see Tables S1−3 in the Supporting Information). Resonances of the linker and of ligands in the metal fragments were also indentified, although not all of them could be unambiguously assigned to specific protons.

A comparison between the chemical shifts of the peptide fragment in the conjugates and the dicarba-analogue of octreotide (**2**)[24] indicates that residues *D*-Trp^8-Lys^9-Thr^{10}-DsaC^{14}-Thr(ol)^{15} have very similar chemical shifts, whereas significant differences are observed for protons of the amino acids *D*-Phe^2-DsaN^3-Phe^7 (Figure 5). This suggests that the peptide structure is only affected in the latter region. The chemical shift of Hα of *D*-Phe^2 is notably shifted downfield. This shift is attributed to the covalent attachment of the linker to the α-amino group of this amino acid through an amide bond. Interestingly, peaks for the NH protons of DsaN^3 and Phe^7 amino acids in all conjugates (and to a lesser extent for the Hβ signals) were shifted upfield.

Molecular dynamics calculations were carried out to gain further insight in the structural alterations induced in the peptide structure by the covalent attachment of the metal complex. The results are illustrated in Figure 6. The peptide backbone is not significantly altered with respect to the structure of the dicarba analogue of octreotide (**2**). In particular, the β-turn backbone geometry around residues *D*-Trp^8-Lys^9-Thr^{10}-DsaC^{14}-Thr(ol)^{15} is totally preserved. The main changes occur in residues *D*-Phe^2 and DsaN^3. Side chain conformations are less defined than in **2**. Linker and ligand fragments are mainly disordered. In some of the calculated conformers, the ligand or the linker exhibits contacts with aromatic residues *D*-Phe^2 and Phe^7 as well as with DsaN^3 (see Figure 6). These residues correspond to those that have changes in their ^{1}H NMR chemical shifts with respect to the unmodified peptide. This is also in good agreement with the fact that some NOEs were observed between the linker and *D*-Phe^2 (see Figure S-20 in the Supporting Information).

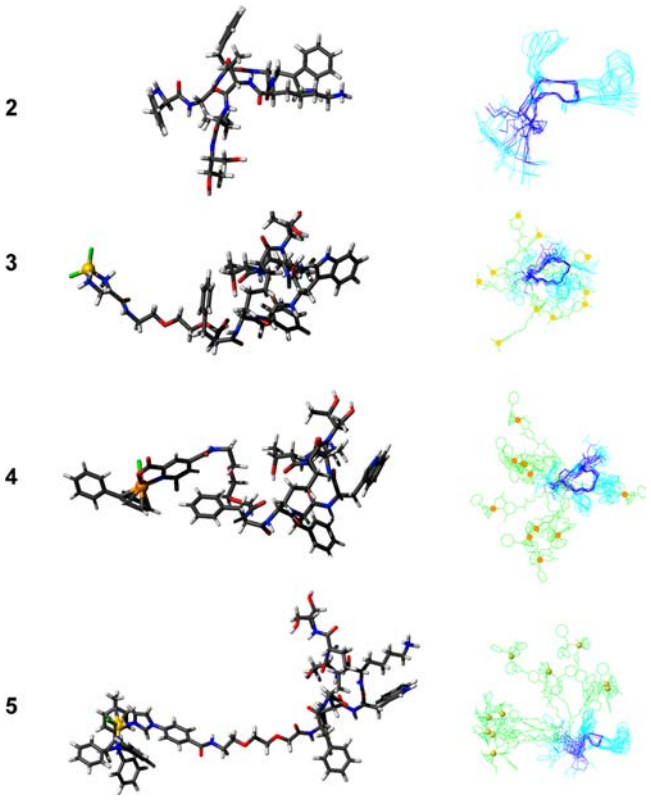


Figure 6. Model structures of the dicarba analogue of octreotide (**2**) and of conjugates **3**, **4**, and **6** (see Chart 1). Left: representative conformer. Right: ensemble with 10 conformers resulting from molecular dynamics calculations. Superposition was done by fitting the backbone peptide heavy atoms.

The NMR data and molecular dynamics calculations suggest that the covalent attachment of the metal complex does not substantially alter the global structure of the peptide. However, the aromatic ligands of the ruthenium and osmium complex in conjugates **4** and **6**, as well as the linker appear to have a tendency to interact with the aromatic residues located to their near side of the peptide sequence, which could be favored by the high flexibility of the poly(ethylene glycol) linker. This is particularly important in the case of the Phe^7 residue, since this amino acid is included in the so-called pharmacophore sequence of octreotide. These results support the hypothesis that the covalent attachment of both fragments might generate a significant population of peptide conformations with a decreased affinity for somatostatin receptors in comparison with that of the dicarba analogue of octreotide **2**. However, the dicarba analogue of octreotide **2** still retains the ability to internalize metal complexes upon conjugation, as demonstrated cellular uptake experiments with **6** and **17**.

Selectivity of the Ruthenium–Octreotide Conjugate (6). The main objective of a targeted strategy is the selective delivery of a cytotoxic drug to cancer cells in order to reduce toxicity to normal cells. Consequently, the reduction of the antiproliferative activity of a metal complex when conjugated with octreotide (Table 2) could be compensated by a selective and a more efficient delivery of the compound to the targeted cells. In order to corroborate this hypothesis, we determined whether the conjugation of the ruthenium(II) arene complex **17** to the octreotide analogue **2** (conjugate **6**) is correlated with its vehiculization to tumor cells overexpressing $sstr_2$, the most relevant receptor for octreotide internalization.[68] To this end, we further analyzed the cytotoxic activity of conjugate **6** in human prostate tumor DU-145 cells as well as and in the Chinese hamster ovary (CHO) cell line, in order to assess the selectivity of the ruthenium–octreotide conjugate for cancer cells with respect to normal cells (Table 3). As shown in Figure 7A, DU-145 cells were markedly more responsive to **6** than the MCF-7 and CHO cells, as the IC_{50} value (26.00 ± 3.46) was 2.4-fold lower than in MCF-7 cells and about 1.7-fold lower than in CHO cells (IC_{50}: 45.17 ± 2.61) (Table 3). This difference in the cytotoxic activity of conjugate **6** between the cell lines cannot be attributed to a different activity of the metal fragment in the different cells, as the control complex **17** cytotoxicity was higher in MCF-7 (IC_{50} = 3.32 ± 0.54) and

Table 3. IC_{50} Values of the Ruthenium–Octreotide Conjugate 6 and Control Complex 17 in Human Cancer Cell Lines (MCF-7 and DU-145) and in Normal Cells (CHO)[a]

	cell line, IC_{50} (μM)		
compound	MCF-7	DU-145	CHO
6	63.00 ± 1.53	26.00 ± 2.00	45.17 ± 2.61
17	3.32 ± 0.54	6.80 ± 0.99	5.8 ± 0.01

[a] IC_{50}: Inhibitory concentration that reduce by 50% the cell viability. The cytotoxicity was determined by the MTT assay after 72 h of drug exposure. Data represents the mean ± SE of at least three independent experiments.

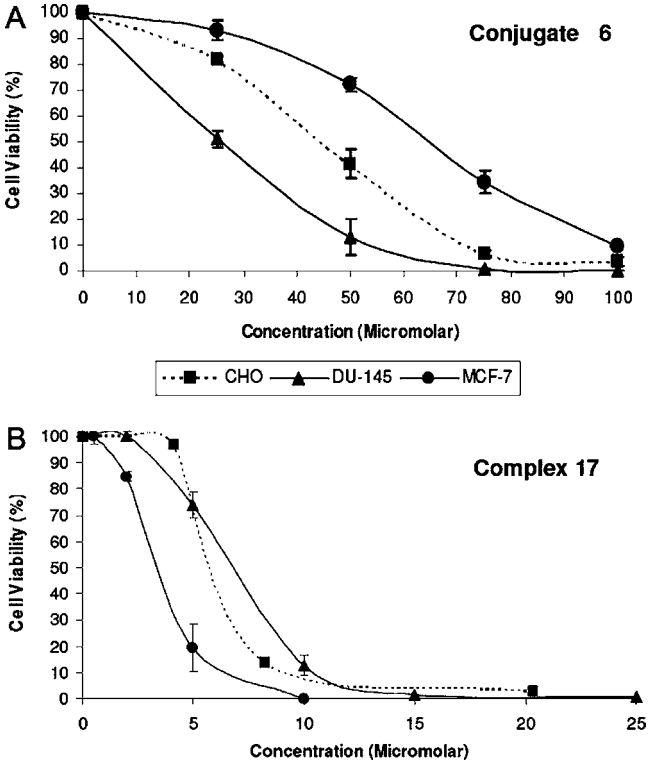


Figure 7. Cytotoxic effect of conjugate **6** (A) and complex **17** (B) in the MCF-7, DU-145, and CHO cell lines. Cells were treated for 72 h with the indicated concentrations of each compound. The cell viability was determined using the MTT assay. Each point in the graphs represents the mean of three independent experiments ± SE.

dx.doi.org/10.1021/bc300173h | *Bioconjugate Chem.* 2012, 23, 1838–1855

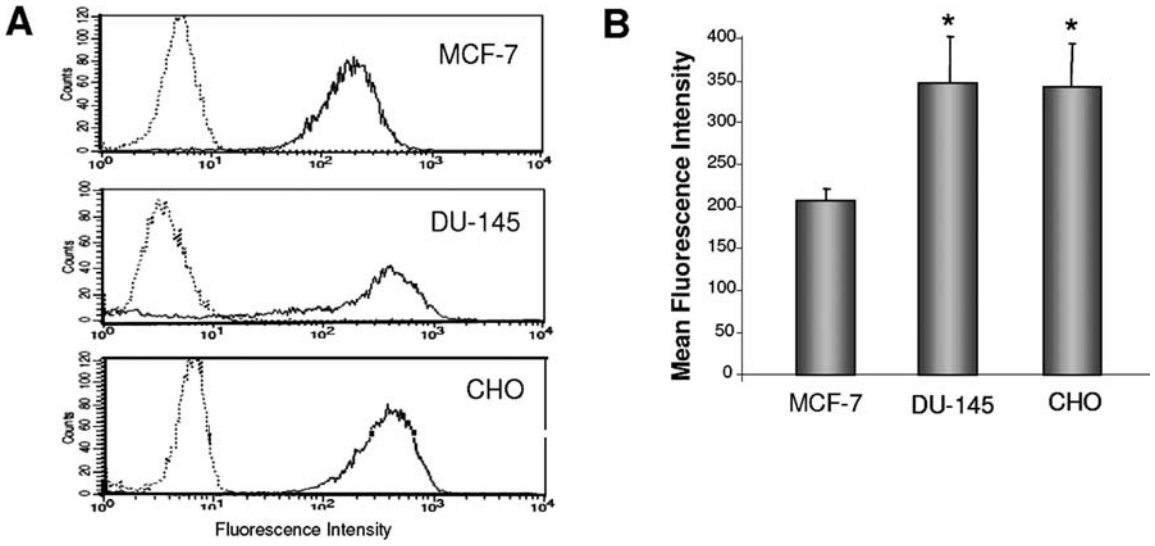


Figure 8. Expression of the sst_2 receptor on MCF-7, DU-145, and CHO cell lines. (A) Representative flow cytometry histograms obtained after the indirect immunofluorescence staining of the cells. Solid lines represent the fluorescence intensity of the cells after the incubation with an antibody against $sstr_2$ together with a control secondary antibody. Dotted lines indicate the background staining with the secondary antibody alone. (B) Each column in the graphs represents the mean fluorescence intensity of three independent experiments ± SE in MCF-7, DU-145, and CHO cells. *P < 0.05 vs MCF-7 cells.

more attenuated in DU-145 cells (IC_{50} = 6.80 ± 0.99) and CHO cells (5.8 ± 0,01) (Figure 7B) (Table 3).

In order to determine if the cytotoxic activity of **6** was related to the receptor expression on the cell surface, we next characterized the $sstr_2$ levels by flow cytometry. As shown in Figure 8A, $sstr_2$ expression was detected on the three cell lines. Notably, $sstr_2$ expression was significantly higher in the DU-145 and CHO cells than in MCF-7 cells (mean cell fluorescence intensity 347.5 ± 54.6, 344.0 ± 50.56, and 206.7 ± 14.27, respectively) (Figure 8B), which demonstrates that the cytotoxic activity of **6** is strongly correlated with $sstr_2$ expression levels, especially in the DU-145 and MCF7 cells. However, although the CHO cells displayed similar $sstr_2$ expression levels to DU-145, the toxicity of **6** was attenuated in these cells, suggesting some selective cytotoxic activity of the ruthenium−octreotide conjugate toward cancer cells with respect to normal cells.

As a very weak expression of $sstr_2$ has been previously reported in CHO cells,[69] the $sstr_2$ expression in this cell line was additionally examined according to their mRNA expression levels. PCR analyses confirmed $sstr_2$ gene expression in CHO cells, with similar mRNA levels than in MCF-7 cells (see the Supporting Information). Our results are in keeping with different studies describing that somatostatin receptors can also be identified in a broad panel of normal tissues, as well as in the human immune system.[70] As a consequence, new clinical applications for somatostatin analogues in several benign pathological diseases are emerging in addition to their role in malignant diseases.

All together, our results demonstrate a good correlation between the antitumor activity of the ruthenium−octreotide conjugate **6** and the expression of the sst_2 receptor on the cell surface and reveal the potential of conjugation with receptor-binding peptides such as octreotide to deliver metal-based anticancer drugs specifically to cells overexpressing somatostatin subtype-2 receptor.

■ CONCLUSIONS

In summary, in this work we have described a straightforward solid-phase methodology for the conjugation of a dichloridoplatinum(II) complex as well as three "piano-stool" organometallic ruthenium(II) and osmium(II) complexes to a dicarba analogue of octreotide, a potent somatostatin agonist whose receptors, particularly subtype 2, are overexpressed on the membrane of tumor cells. At nuclear Cl^- concentration (4 mM), platinum (**3**), osmium (**4**), and Ru(dap) (**5**) conjugates are activated through hydrolysis of the M-Cl, which correlates well with their DNA binding capacity, revealing in all cases a strong preference for guanine nucleobases. However, neither hydrolysis of the Ru−Cl nor interaction with DNA was observed in the case of the triphenylphosphine-containing ruthenium conjugate (**6**). Surprisingly, the latter conjugate displays antiproliferative activity, but the rest of the conjugates were noncytotoxic. Additional cytotoxic experiments with control metal complexes and cellular uptake experiments by ICP-MS, as well as conformational analysis of metal−octreotide conjugates by 2D NMR spectroscopy and molecular dynamics calculations, have allowed us to establish three general conclusions. First, a significant loss in the cytotoxic activity of the metal complex moiety always occurs when conjugated to the peptide sequence (e.g., IC_{50} = 3.32 ± 0.54 in MCF-7 cells and IC_{50} = 6.80 ± 0.99 in DU-145 cells for complex **17** vs IC_{50} = 63.00 ± 1.53 in MCF-7 cells and IC_{50} = 26.00 ± 2.00 in DU-145 cells for conjugate **6**); hence, it seems to be important to use metal complexes with high cytotoxic activity in order to develop peptide-conjugates with active biological properties. Second, despite the presence of some altered amino acids in the pharmacophore sequence of octreotide, particularly at the *N*-terminal end of the peptide, the overall structure is essentially maintained in the conjugate, which suggests that the affinity for somatostatin receptors would not be compromised upon conjugation to a metal complex; this observation is in good agreement with the higher accumulation of ruthenium in cancer cells upon exposure to the ruthenium−octreotide conjugate **6** in comparison with that of the parent complex **17**, which

demonstrates that the peptide has a positive effect on the internalization of the ruthenium complex. The choice of the spacer is also important, not only to improve aqueous solubility and to keep the metal complex away from the peptide, but also to reduce conformational freedom between both fragments in the conjugate. Third, the significantly higher expression of the sst_2 receptor on DU-145 cells compared to MCF-7 cells is in good agreement with IC_{50} values of conjugate **6** in both tumor cell lines. The fact that control complex **17** shows an attenuated cytotoxicity in DU-145 cells compared with MCF-7 cells supports that the antitumoral activity of the ruthenium–octreotide conjugate **6** is correlated with the overexpression of the sst_2 receptor on the cell surface. The cytotoxic activity of **6** in a nontumor cell line (CHO) was similar to that found in cancer cells, a result which can be attributed to a similar level of expression of somatostatin subtype-2 receptors.

The overall results of this work demonstrate the potential of conjugation between metal-based anticancer drugs and receptor-binding peptides such as octreotide to target tumoral cells through binding to specific receptors, including somatostatin subtype 2 receptor, overexpressed in their membranes. In the near future, this receptor-targeted anticancer strategy is expected to generate new antitumor drugs with reduced side-effects and reduced toxicity in normal cells. The potential of this strategy will be increased by using novel approaches to circumvent some of the limitations found in this work, particularly new biological vectors in combination with photoactivated metal complexes[25] or cleavable linkers[32] in the biological media. Work is in progress in this direction to generate more specific metal-based anticancer drugs.

■ ASSOCIATED CONTENT

Supporting Information

Selected MS spectra and HPLC traces of metal complex–octreotide conjugates and of DNA–conjugate adducts. NMR data of conjugates **3**, **4**, and **6**, and of control metal complexes. sstr2 mRNA expression in CHO and MCF-7 cells. This material is available free of charge via the Internet at http://pubs.acs.org.

■ AUTHOR INFORMATION

Corresponding Author

*Vicente Marchán: Phone +34 934021249, Fax +34 933397878, E-mail vmarchan@ub.edu. Anna Massaguer: Phone +34 972418370, Fax +34 972418150, E-mail anna.massaguer@udg.edu.

Author Contributions

[#]Both authors contributed equally to this work.

Notes

The authors declare no competing financial interest.

■ ACKNOWLEDGMENTS

This work was supported by funding from the Ministerio de Educación y Ciencia (CTQ2005-01834, CTQ2007-68014, CTQ2008-02064, and CTQ2010-21567), the Generalitat de Catalunya (2009SGR208 and Xarxa de Referència de Biotecnologia), Instituto de Salud Carlos III (grants RD06/0020/0041), the Programa d'Intensificació de la Recerca (UB) and the ERC (grant no 247450, to PJS). We thank Prof. Alfonso Carotenuto (University of Napoli) for providing the coordinates of the dicarba analogue of octreotide **2**, Dr. Sabine H. van Rijt (University of Warwick) for supplying the osmium complex **8**, and Dr. Isolda Romero (University of Warwick) and Dr. Antoni Padró (Centres Científics i Tecnològics, Universitat de Barcelona) for helpful assistance in the determination of ruthenium content by ICP-MS.

■ ABBREVIATIONS USED

Abu, aminoisobutyryl; ACN, acetonitrile; bip, biphenyl; cym, cymene (1-methyl-4-(1-methylethyl)benzene); dap, 1-(carboxylic acid)-1,2-diaminoethane; DCM, dichloromethane; dhDsa*C*, dehydrodiaminosuberic acid *C*-terminus; dhDsa*N*, dehydrodiaminosuberic acid *N*-terminus; DIPC, *N,N′*-diisopropylcarbodiimide; DIPEA, *N,N*-diisopropylethylamine; DMF, *N,N*-dimethylformamide; DMSO, dimethylsulfoxide; DTPA, diethylenetriamino-pentaacetic acid; DOTA, 1,4,7,10-tetraazacyclododecane-1,4,7,10-tetraacetic acid; Dsa*C*, diaminosuberic acid *C*-terminus; Dsa*N*, diaminosuberic acid *N*-terminus; ESI, electrospray ionization; Fluo, 5(6)-carboxyfluorescein; Fmoc, 9-fluorenylmethyloxycarbonyl; Hag, L-2-allylglycine; HATU, hexafluorophosphate salt of the (2-(7-aza-1*H*-benzotriazol-1-yl)-1,1,3,3-tetramethyluronium; HOAt, 1-hydroxy-7-azabenzotriazole; HOBt, 1-hydroxybenzotriazole; HR-ESI, high-resolution electrospray ionization; ICP-MS, inductively coupled plasma mass spectrometry; Im, imidazole; Ind, indazole; MALDI-TOF, matrix-assisted laser desorption ionization time-of-flight; MS, mass spectrometry or mass spectrum; MTT, 3-(4,5-dimethylthiazol-2-yl)-2,5-diphenyltetrazolium bromide; NHS, *N*-hydroxysuccinimide; NOE, nuclear Overhauser effect; NOESY, nuclear Overhauser enhanced spectroscopy; PBS, phosphate buffered saline; PEG, poly(ethylene glycol); pico, picolinate; sst, somatostatin; sstr, somatostatin receptor; TIS, triisopropylsilane; TMP, trimethylphosphite; TFA, trifluoroacetic acid

■ REFERENCES

(1) Reubi, J. C. (2003) Peptide receptors as molecular targets for cancer diagnosis and therapy. *Endocr. Rev. 24*, 389–427.

(2) Zaccaro, L., del Gatto, A., Pedone, C., and Saviano, M. (2009) Peptides for tumour therapy and diagnosis: Current status and future directions. *Curr. Med. Chem. 16*, 780–795.

(3) Okarvi, S. M. (2008) A comprehensive overview of peptide-based radiopharmaceuticals and cytotoxic conjugates, as well as their potential applications in cancer diagnosis and therapy. *Cancer Treat. Rev. 34*, 13–26.

(4) Mezo, G., and Manea, M. (2010) Receptor-mediated tumor targeting based on peptide hormones. *Expert Opin. Drug Delivery 7*, 79–96.

(5) Schaer, J. C., Waser, B., Mengod, G., and Reubi, J. C. (1997) Somatostatin receptor subtype expression in human pituitary, gastroentero-pancreatic and mammary tumors: comparison of mRNA analysis with receptor autoradiography. *Int. J. Cancer 70*, 530–537.

(6) Janecka, A., Zubrzycka, M., and Janecki, T. (2001) Somatostatin analogs. *J. Pept. Res. 58*, 91–107.

(7) Bauer, W., Briner, U., Dopfener, W., Haller, R., Huguenin, R., Marbach, P., Petcher, T. J., and Pless, J. (1982) SMS 201–995: a very potent and selective analogue of somatostatin with prolonged action. *Life Sci. 31*, 1133–1140.

(8) de Jong, M., Breeman, W. A. P., Kwekkeboom, D. J., Valkema, R., and Krenning, E. P. (2009) Tumor imaging and therapy using radiolabeled somatostatin analogues. *Acc. Chem. Res. 42*, 873–880.

(9) Sun, L.-C., and Coy, D. H. (2008) Cytotoxic conjugates of peptide hormones for cancer chemotherapy. *Drugs Future 33*, 217–223.

(10) Wheate, N. J., Walker, S., Craig, G. E., and Oun, R. (2010) The status of platinum anticancer drugs in the clinic and in clinical trials. *Dalton Trans. 39*, 8113−8127.
(11) Jakupec, M. A., Galanski, M., Arion, V. B., Hartinger, C. G., and Keppler, B. K. (2008) Antitumour metal compounds: more than theme and variations. *Dalton Trans.*, 183−194.
(12) van Rijt, S. H., and Sadler, P. J. (2009) Current applications and future potential for bioinorganic chemistry in the development of anticancer drugs. *Drug Discovery Today 14*, 1089−1097.
(13) Rademaker-Lakhai, J. M., Van den Bongard, D., Pluim, D., Beijnen, J. H., and Schellens, J. H. M. (2004) A phase I and pharmacological study with imidazolium-*trans*-DMSO-imidazole-tetrachlororuthenate, a novel ruthenium anticancer agent. *Clin. Cancer Res. 10*, 3717−3727.
(14) Jakupec, M. A., Arion, V. B., Kapitza, S., Reisner, E., Eichinger, A., Pongratz, M., Marian, B., Graf von Keyserlingk, N., and Keppler, B. K. (2005) KP1019 (FFC14A) from bench to bedside: preclinical and early clinical development - an overview. *Int. J. Clin. Pharmacol. Ther. 43*, 595−596.
(15) Peacock, A. F. A., and Sadler, P. J. (2008) Medicinal organometallic chemistry: Designing metal arene complexes as anticancer agents. *Chem. Asian J. 3*, 1890−1899.
(16) Levina, A., Mitra, A., and Lay, P. A. (2009) Recent developments in ruthenium anticancer drugs. *Metallomics 1*, 458−470.
(17) Casini, A., Hartinger, C. G., Nazarov, A., and Dyson, P. J. (2010) Organometallic antitumour agents with alternative modes of action. *Top. Organomet. Chem. 32*, 57−80.
(18) Gasser, G., Ott, I., and Metzler-Nolte, N. (2011) Organometallic anticancer compounds. *J. Med. Chem. 54*, 3−25.
(19) Süss-Fink, G. (2010) Arene ruthenium complexes as anticancer agents. *Dalton Trans. 39*, 1673−1688.
(20) Wang, F., Chen, H., Parsons, S., Oswald, I. D. H., Davidson, J. E., and Sadler, P. J. (2003) Kinetics of aquation and anation of ruthenium(II) arene anticancer complexes, acidity and X-ray structures of aqua adducts. *Chem.—Eur. J. 9*, 5810−5820.
(21) Kostrhunova, H., Florian, J., Novakova, O., Peacock, A. F. A., Sadler, P. J., and Brabec, V. (2008) DNA interactions of monofunctional organometallic osmium(II) antitumor complexes in cell-free media. *J. Med. Chem. 51*, 3635−3643.
(22) Pizarro, A. M., Habtemariam, A., and Sadler, P. J. (2010) Activation mechanisms for organometallic anticancer complexes. *Top. Organomet. Chem. 32*, 21−56.
(23) Barragán, F., Moreno, V., and Marchán, V. (2009) Solid-phase synthesis and DNA binding studies of dichloroplatinum(II) conjugates of dicarba analogues of octreotide as new anticancer drugs. *Chem. Commun.*, 4705−4707.
(24) D'Addona, D., Carotenuto, A., Novellino, E., Piccand, V., Reubi, J. C., Di Cianni, A., Gori, F., Papini, A. M., and Ginanneschi, M. (2008) Novel sst5-selective somatostatin dicarba-analogs: Synthesis and conformation-affinity relationships. *J. Med. Chem. 51*, 512−520.
(25) Barragán, F., López-Senín, P., Salassa, S., Betanzos-Lara, S., Habtemariam, A., Moreno, V., Sadler, P. J., and Marchán, V. (2011) Photocontrolled DNA binding of a receptor-targeted organometallic ruthenium(II) complex. *J. Am. Chem. Soc. 133*, 14098−14108.
(26) Dirscherl, G., and König, B. (2008) The use of solid-phase synthesis techniques for the preparation of peptide-metal complex conjugates. *Eur. J. Org. Chem.*, 597−634.
(27) Metzler-Nolte, N. (2010) Biomedical applications of organometal-peptide conjugates. *Top. Organomet. Chem. 32*, 195−217.
(28) Peindy N'Dongo, H. W., Ott, I., Gust, R., and Schatzschneider, U. (2009) Microwave-assisted solid-phase synthesis, cellular uptake, and cytotoxicity studies of cymantrene-peptide bioconjugates. *J. Organomet. Chem. 694*, 823−827.
(29) Gross, A., and Metzler-Nolte, N. (2009) Synthesis and characterization of a ruthenocenoyl bioconjugate with the cyclic octapeptide octreotate. *J. Organomet. Chem. 694*, 1185−1188.
(30) van Rijt, S. H., Kostrhunova, H., Brabec, V., and Sadler, P. J. (2011) Functionalization of osmium arene anticancer complexes with (Poly)arginine: effect on cellular uptake, internalization, and cytotoxicity. *Bioconjugate Chem. 22*, 218−226.
(31) Puckett, C. A., and Barton, J. K. (2010) Targeting a ruthenium complex to the nucleus with short peptides. *Bioorg. Med. Chem. 18*, 3564−3659.
(32) Splith, K., Hu, W., Schatzschneider, U., Gust, R., Ott, I., Onambele, L. A., Prokop, A., and Neundorf, I. (2010) Protease-activatable organometal-peptide bioconjugates with enhanced cytotoxicity on cancer cells. *Bioconjugate Chem. 21*, 1288−1296.
(33) Mukhopadhyay, S., Barnes, C. M., Haskel, A., Short, S. M., Barnes, K. R., and Lippard, S. J. (2008) Conjugated platinum(IV)-peptide complexes for targeting angiogenic tumor vasculature. *Bioconjugate Chem. 19*, 39−49.
(34) Hsieh, H.-P., Wu, Y.-T., Chen, S.-T., and Wang, K.-T. (1999) Direct solid-phase synthesis of octreotide conjugates: precursors for use as tumor-targeted radiopharmaceuticals. *Bioorg. Med. Chem. 7*, 1797−1803.
(35) Moradell, S., Lorenzo, J., Rovira, A., Robillard, M. S., Aviles, F. X., Moreno, V., de Llorens, R., Martinez, M. A., Reedijk, J., and Llobet, A. (2003) Platinum complexes of diaminocarboxylic acids and their ethyl ester derivatives: the effect of the chelate ring size on antitumor activity and interactions with GMP and DNA. *J. Inorg. Biochem. 96*, 493−502.
(36) van Rijt, S. H., Peacock, A. F. A., Johnstone, R. D. L., Parsons, S., and Sadler, P. J. (2009) Organometallic osmium(II) arene anticancer complexes containing picolinate derivatives. *Inorg. Chem. 48*, 1753−1762.
(37) Hodson, E., and Simpson, S. J. (2004) Synthesis and characterization of $[(\eta 6\text{-cymene})Ru(L)X_2]$ compounds: single crystal X-ray structure of $[(\eta 6\text{-cymene})Ru(P\{OPh\}_3)Cl_2]$ at 203 K. *Polyhedron 23*, 2695−2707.
(38) Chaplin, A. B., and Dyson, P. J. (2007) Catalytic activity of bis-phosphine ruthenium(II)-arene compounds: Structure-activity correlations. *Organometallics 26*, 2447−2455.
(39) Charvat, T. T., Lee, D. J., Robinson, W. E., and Chamberlin, A. R. (2006) Design, synthesis, and biological evaluation of chicoric acid analogs as inhibitors of HIV-1 integrase. *Bioorg. Med. Chem. 14*, 4552−4567.
(40) Gariepy, J., Remy, S., Zhang, X., Ballinger, J. R., Bolewska-Pedyczak, E., Rauth, M., and Bisland, K. (2002) A simple two-step approach for introducing a protected diaminedithiol chelator during solid-phase assembly of peptides. *Bioconjugate Chem. 13*, 679−684.
(41) Marchán, V., Moreno, V., Pedroso, E., and Grandas, A. (2001) Towards a better understanding of the cisplatin mode of action. *Chem.—Eur. J. 7*, 808−815.
(42) Marchán, V., Pedroso, E., and Grandas, A. (2004) Insights into the reaction of transplatin with DNA and proteins: Methionine-mediated formation of histidine-guanine trans-$Pt(NH_3)_2$ cross-links. *Chem.—Eur. J. 10*, 5369−5375.
(43) Algueró, B., López de la Osa, J., González, C., Pedroso, E., Marchán, V., and Grandas, A. (2006) Selective platination of modified oligonucleotides and duplex cross-links. *Angew. Chem., Int. Ed. 45*, 8194−8197.
(44) Goddard, D. T., and Kneller, G. *SPARKY*, University of California, San Francisco.
(45) Singh, S. K., Trivedi, M., Chandra, M., Sahay, A. N., and Pandey, D. S. (2004) Luminescent piano-stool complexes incorporating 1-(4-cyanophenyl)imidazole: Synthesis, spectral, and sructural studies. *Inorg. Chem. 43*, 8600−8608.
(46) Koradi, R., Billeter, M., and Wuthrich, K. (1996) MOLMOL: a program for display and analysis of macromolecular structures. *J. Mol. Graphics 14*, 29−32.
(47) Peacock, A. F. A., Parsons, S., and Sadler, P. J. (2007) Tuning the hydrolytic aqueous chemistry of osmium arene complexes with *N,O*-chelating ligands to achieve cancer cell cytotoxicity. *J. Am. Chem. Soc. 129*, 3348−3357.
(48) van Rijt, S. H., Mukherjee, A., Pizarro, A. M., and Sadler, P. J. (2010) Cytotoxicity, hydrophobicity, uptake, and distribution of

osmium(II) anticancer complexes in ovarian cancer cells. *J. Med. Chem. 53*, 840−849.
(49) Morris, R. E., Aird, R. E., Murdoch, P., del, S., Chen, H., Cummings, J., Hughes, N. D., Parsons, S., Parkin, A., Boyd, G., Jodrell, D. I., and Sadler, P. J. (2001) Inhibition of cancer cell growth by ruthenium(II) arene complexes. *J. Med. Chem. 44*, 3616−3621.
(50) Moreno, V., Font-Bardia, M., Calvet, T., Lorenzo, J., Aviles, F. X., Garcia, M. H., Morais, T. S., Valente, A., and Robalo, M. P. (2011) DNA interaction and cytotoxicity studies of new ruthenium(II) cyclopentadienyl derivative complexes containing heteroaromatic ligands. *J. Inorg. Biochem. 105*, 241−249.
(51) Gianferrara, T., Bratsos, I., and Alessio, E. (2009) A categorization of metal anticancer compounds based on their mode of action. *Dalton Trans. 37*, 7588−7598.
(52) Jennerwein, M., and Andrews, P. A. (1995) Effect of intracellular chloride on the cellular pharmacodynamics of cis-diamminedichloroplatinum(II). *Drug Metab. Dispos. 23*, 178−184.
(53) Wang, F., Habtemariam, A., van der Geer, E. P. L., Fernandez, R., Melchart, M., Deeth, R. J., Aird, R., Guichard, S., Fabbiani, F. P. A., Lozano-Casal, P., Oswald, I. D. H., Jodrell, D. I., Parsons, S., and Sadler, P. J. (2005) Controlling ligand substitution reactions of organometallic complexes: Tuning cancer cell cytotoxicity. *Proc. Natl. Acad. Sci. U.S.A. 102*, 18269−18274.
(54) Peacock, A. F. A., Habtemariam, A., Moggach, S. A., Prescimone, A., Parsons, S., and Sadler, P. J. (2007) Chloro half-sandwich osmium(II) complexes: influence of chelated *N,N*-ligands on hydrolysis, guanine binding, and cytotoxicity. *Inorg. Chem. 46*, 4049−4059.
(55) Novakova, O., Chen, H., Vrana, O., Rodger, A., Sadler, P. J., and Brabec, V. (2003) DNA Interactions of monofunctional organometallic ruthenium(II) antitumor complexes in cell-free media. *Biochemistry 42*, 11544−11554.
(56) Liu, H.-K., Wang, F., Parkinson, J. A., Bella, J., and Sadler, P. J. (2006) Ruthenation of duplex and single-stranded d(CGGCCG) by organometallic anticancer complexes. *Chem.—Eur. J. 12*, 6151−6165.
(57) Gossens, C., Tavernelli, I., and Rothlisberger, U. (2009) Binding of organometallic ruthenium(II) anticancer compounds to nucleobases: A computational study. *J. Phys. Chem. A 113*, 11888−11897.
(58) Kostrhunova, H., Florian, J., Novakova, O., Peacock, A. F. A., Sadler, P. J., and Brabec, V. (2008) DNA Interactions of monofunctional organometallic osmium(II) antitumor complexes in cell-free media. *J. Med. Chem. 51*, 3635−3643.
(59) Fischer, R., Mader, O., Jung, G., and Brock, R. (2003) Extending the applicability of carboxyfluorescein in solid-phase synthesis. *Bioconjugate Chem. 14*, 653−660.
(60) Watson, J. C., Balster, D. A., Gebhardt, B. M., O'Dorisio, T. M., O'Dorisio, M. S., Espenan, G. D., Drouant, G. J., and Woltering, E. A. (2001) Growing vascular endothelial cells express somatostatin subtype 2 receptors. *Br. J. Cancer 85*, 266−272.
(61) Hornick, C. A., Anthony, C. T., Hughey, S., Gebhardt, B. M., Espenan, G. D., and Woltering, E. A. (2000) Progressive nuclear translocation of somatostatin analogs. *J. Nucl. Med. 41*, 1256−1263.
(62) Zhang, Y., Wang, X., Wang, J., Zhang, X., and Zhang, Q. (2011) Octreotide-modified polymeric micelles as potential carriers for targeted docetaxel delivery to somatostatin receptor overexpressing tumor cells. *Pharm. Res. 28*, 1167−1178.
(63) Huang, C. M., Wu, Y. T., and Chen, S. T. (2000) Targeting delivery of paclitaxel into tumor cells via somatostatin receptor endocytosis. *Chem. Biol. 7*, 453−461.
(64) Wynants, C., Van Binst, G., and Loosli, H. R. (1985) SMS 201−995, a very potent analogue of somatostatin. Assignment of the 1H 500 MHz n.m.r. spectra and conformational analysis in aqueous solution. *Int. J. Pept. Protein Res. 25*, 608−614.
(65) Wynants, C., Van Binst, G., and Loosli, H. R. (1985) SMS 201−995, an octapeptide somatostatin analogue. Assignment of the 1H 500 MHz n.m.r. spectra and conformational analysis of SMS 201−995 in dimethylsulfoxide. *Int. J. Pept. Protein Res. 25*, 615−621.
(66) Melacini, G., Zhu, Q., and Goodman, M. (1997) Multiconformational NMR Analysis of sandostatin (octreotide): equilibrium between β-sheet and helical structures. *Biochemistry 36*, 1233−1241.
(67) Deshmukh, M. V., Voll, G., Kuehlewein, A., Maecke, H., Schmitt, J., Kessler, H., and Gemmecker, G. (2005) NMR studies reveal structural differences between the Gallium and Ytrium complexes of DOTA-D-Phe1-Tyr3-octreotide. *J. Med. Chem. 48*, 1506−1514.
(68) Reubi, J. C., Schar, J. C., Waser, B., Wenger, S., Heppeter, A., Schmitt, J. S., and Mäcke, H. R. (2000) Affinity profiles for human somatostatin receptor subtypes sstr1-sstr5 of somatostatin radiotracers selected for scintigraphic and radiotherapeutic use. *Eur. J. Nucl. Med. 27*, 273−282.
(69) Zhang, J., Jin, W., Wang, X., Wang, J., Zhang, X., and Zhang, Q. (2010) A novel octreotide modified lipid vesicle improved the anticancer efficacy of doxorubicin in somatostatin receptor 2 positive tumor models. *Mol. Pharm. 7*, 1159−1168.
(70) Cascini, G. L., Cuccurullo, V., and Mansi, L. (2010) The non tumour uptake of (111)In-octreotide creates new clinical indications in benign diseases, but also in oncology. *Q. J. Nucl. Med. Mol. Imaging 54*, 24−36.

Bioconjugate Chemistry

Article

pubs.acs.org/bc

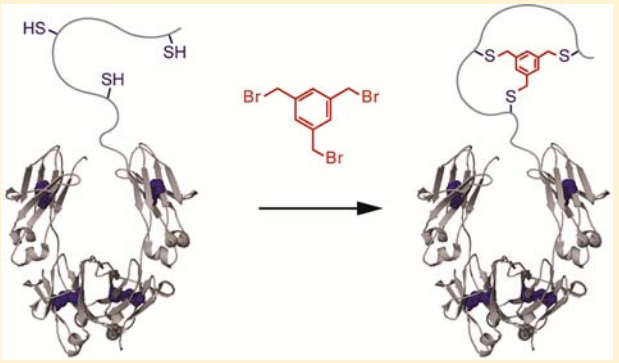
Chemical Macrocyclization of Peptides Fused to Antibody Fc Fragments

Alessandro Angelini,[†] Philippe Diderich, Julia Morales-Sanfrutos, Sarah Thurnheer, David Hacker, Laure Menin, and Christian Heinis*

Institute of Chemical Sciences and Engineering, Ecole Polytechnique Fédérale de Lausanne, CH-1015 Lausanne, Switzerland

Supporting Information

ABSTRACT: To extend the plasma half-life of a bicyclic peptide antagonist, we chose to link it to the Fc fragment of the long-lived serum protein IgG1. Instead of chemically conjugating the entire bicyclic peptide, we recombinantly expressed its peptide moiety as a fusion protein to an Fc fragment and subsequently cyclized the peptide by chemically reacting its three cysteine residues with tris-(bromomethyl)benzene. This reaction was efficient and selective, yielding completely modified peptide fusion protein and no side products. After optimization of the linker and the Fc fragment format, the bicyclic peptide was fully functional as an inhibitor (K_i = 76 nM) and showed an extended terminal half-life of 1.5 days in mice. The unexpectedly clean reaction makes chemical macrocyclization of peptide-Fc fusion proteins an attractive synthetic approach. Its good compatibility with the Fc fragment may lend the bromomethylbenzene-based chemistry also for the generation of antibody−drug conjugates.



INTRODUCTION

Bicyclic peptides with desired binding specificities can be isolated with moderate effort, time, and cost from large combinatorial libraries using phage display.[1−3] The libraries are generated by displaying linear peptides, containing two cysteines at both ends and one in the middle, on phage and by subsequently reacting the cysteine side chains with the trivalent thiol-reactive compound tris-(bromomethyl)benzene (TBMB).[1] TBMB efficiently and selectively reacts with three cysteine residues in peptides under mild conditions in aqueous solution.[4] Phage selections using this strategy had yielded bicyclic peptide inhibitors with nanomolar affinities for a range of disease targets including plasma kallikrein,[1,3] cathepsin G,[1] and a urokinase-type plasminogen activator.[2]

Depending on the clinical application, the bicyclic peptides need to circulate in the bloodstream at a minimal concentration for an extended time period to achieve good therapeutic effects. While bicyclic peptides were resistant to proteolysis when incubated in human plasma *ex vivo*,[1] they are expected to rapidly clear from the circulation through renal filtration. Cyclic peptides with similar size as the bicyclic peptides were found to have a terminal half-life of less than 30 min upon intravenous injection.[5−8] Various strategies had been applied to prolong the circulation time of peptides[8] or proteins,[9] the most common ones being conjugation or genetic fusion to long-lived serum proteins such as albumin or immunoglobulin, or linkage to large polymers such as poly(ethylene glycol).

In this work, we chose to conjugate a bicyclic peptide to the Fc fragment of human IgG1, which has a terminal half-life of multiple weeks in human. The half-lives of antibodies and antibody Fc fragments are particularly long because of their ability to be recycled in the endosomes through binding to neonatal receptor FcRn. Several protein- and one peptide-Fc fusion proteins are already in clinical use and their terminal half-lives are between 4 and 13 days.[10] While peptides and proteins can be expressed conveniently as genetic fusions with the Fc fragment, the chemical linkage of synthetic molecules has been more challenging. The molecules are preferentially tethered through activated chemical linkers to lysines on the immunoglobulin surface, to cysteines in the hinge regions, or to cysteines introduced at specific sites on the protein surface. The latter two cysteine-based strategies typically yield a higher degree of uniformity.[11−15]

Although bicyclic peptides might be synthetized and linked to Fc fragments using a standard chemical conjugation reaction, we tested in this work a new approach in which a peptide is expressed as Fc fusion and subsequently cyclized by a chemical reaction (Figure 1A). We reasoned that such a strategy involving one recombinant protein and a single chemical reaction would be more economical than an approach in which the peptide is first synthesized by solid-phase peptide synthesis, cyclized, activated with a chemical linker, and conjugated to an Fc fragment. As a model bicyclic peptide, we used a recently developed potent and selective inhibitor of human urokinase-type plasminogen

Received: April 4, 2012
Revised: June 18, 2012
Published: July 19, 2012

 © 2012 American Chemical Society dx.doi.org/10.1021/bc300184m | *Bioconjugate Chem.* 2012, 23, 1856−1863

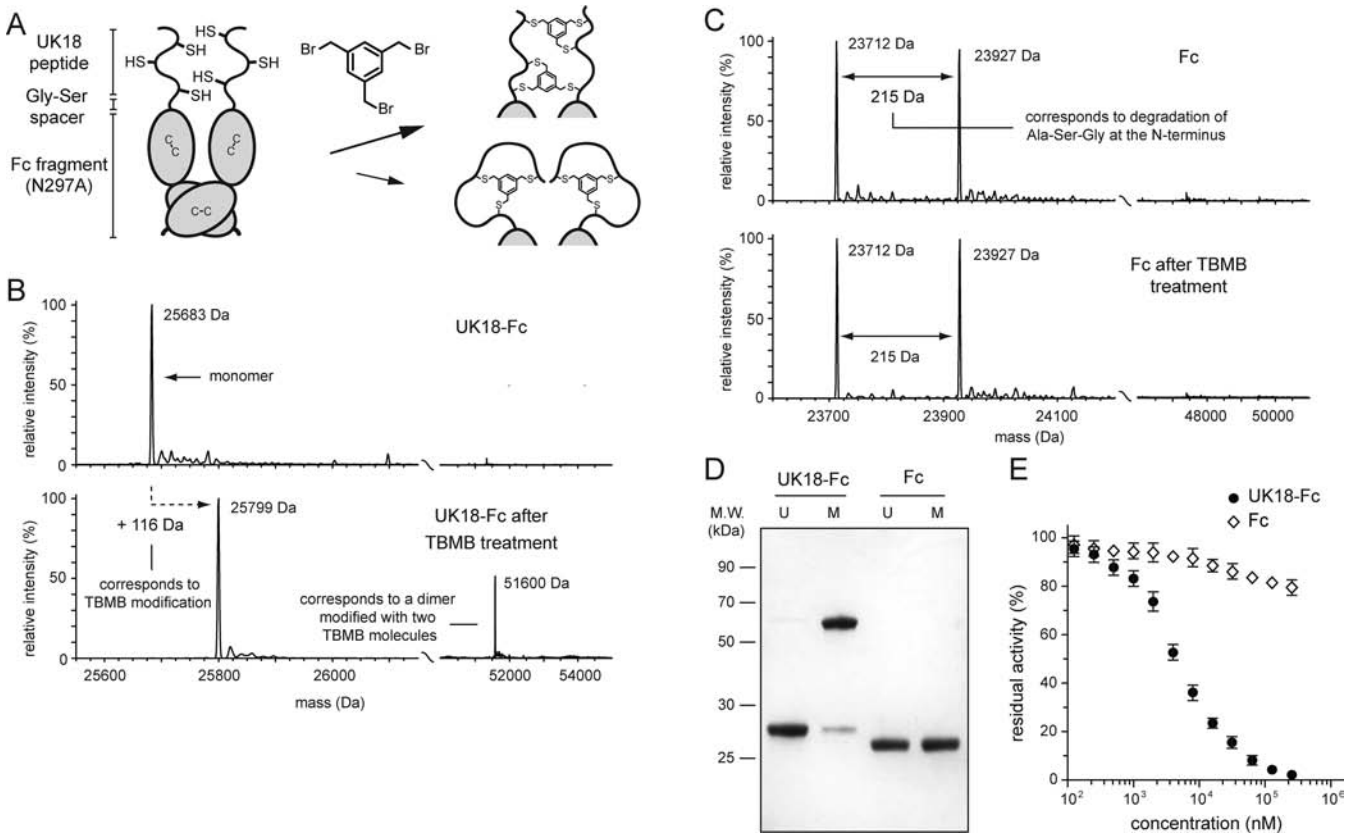


Figure 1. Chemical macrocyclization of homodimeric UK18-Fc fusion protein. (A) Schematic representation of the cyclization reaction based on sulfhydryl alkylation with TBMB. Two of the nine possible regioisomers are shown, including the desired one (lower right drawing). (B) Mass spectra of homodimeric UK18-Fc fusion protein before (upper panel) and after (lower panel) treatment with TBMB. Free cysteine residues in UK18-Fc fusion protein are quantitatively modified by TBMB adding to the monomer and dimer masses of 116 and 232 Da, respectively (see also SI Figure S3). (C) Mass spectra of Fc fragment alone before (upper panel) and after (lower panel) treatment with TBMB. In both spectra, two masses can be seen which correspond to entire Fc fragment and Fc fragment with a truncated N-terminus. No TBMB-modification was observed for Fc fragment (see also SI Figure S4). (D) Reducing SDS-PAGE with unmodified (U) and modified (M) homodimeric UK18-Fc fusion protein and Fc fragment. Covalently linked monomers run more slowly and the extent of cross-linking by TBMB can be seen. 1.5 μg aliquots of each unmodified (U) and modified (M) homodimer have been loaded per well. (E) Inhibition of human uPA by TBMB-modified homodimeric UK18-Fc fusion protein. Residual protease activity was determined with a fluorogenic substrate. The K_i values were calculated per UK18-Fc monomer unit (see also SI Figure S2A,B).

activator (uPA), termed UK18 (K_i = 53 nM; ^{N}ACSRYEVDCRGRGSACG^{C}).[2] Overexpression of the serine protease uPA is a feature of malignancy and is correlated with tumor progression and invasion.[16] Extension of the circulation time of UK18 inhibitor would allow testing of its therapeutic effect *in vivo*.

EXPERIMENTAL PROCEDURES

Cloning of Mammalian Expression Vectors. All mammalian expression vectors are based on pEXPR-IBA42 (IBA BioTAGnology GmbH, Göttingen, Germany) containing a CMV promoter and an ampicillin antibiotic resistance gene. Constructs for expression of UK18-hinge-Fc fusion protein with varying hinge regions were cloned by inserting *de novo* synthesized DNA (codon-optimized for expression in mammalian cells; GeneArt, Regensburg, Germany) into pEXPR-IBA42 (SI Figure S1A,B). The synthetic DNA is coding for the BM40 secretion signal (^{N}MRAWIFFLLCLAGRALA^{C}), UK18 peptide, a Gly-Ser dipeptide spacer, a variable hinge region, and an Fc fragment (based on the nucleotide sequence of human IgG1 heavy chain constant regions C_H2 and C_H3 with an Asn297Ala mutation; amino acids 236 to 446, Kabat numbering; accession number: AAL96263). The hinge regions are based on the human IgG1 hinge (amino acids 216 to 235, Kabat numbering; ^{N}EPKSCDKTHTCPPCPAPELL^{C}; underlined cysteine residues were replaced by serine) wherein one clone was produced without hinge and five clones with fractions of the discretely truncated hinge (3, 6, 12, 16, and 20 amino acids). All the synthetic genes contained the additional internal restriction sites *Apa*I and *Rsr*II to allow substitution of the DNA coding for the peptide. The DNA of the synthetic genes was provided in the bacterial vector pMK (GeneArt). Vector DNA was produced in *E. coli* DH5α (LB/kanamycin, 50 μg/mL) and subcloned into pEXPR-IBA42 via the restriction sites *Xba*I/*Hind*III. A vector for expression of the Fc fragment without any bicyclic peptide or hinge was generated by PCR-amplification of the UK18-Fc gene with the primers Hn-forw (5′-GAGAACCCACTGCTTACTGGC-3′) and Hn-stop-rev (5′-AAACTTAAGCTTATTATCACTAGCCCGGGCTCAGGCTCAGGCTTTTCTGG-3′; *Hind*III underlined) and inserted via the *Nhe*I and *Hind*III restriction sites into pEXPR-IBA42. All constructs were verified by DNA sequencing (Macrogen, Seoul, South Korea) and termed pEXPR-UK18-H0-Fc, pEXPR-UK18-H3-Fc, pEXPR-UK18-H6-Fc, pEXPR-UK18-H12-Fc, pEXPR-UK18-H16-Fc, pEXPR-UK18-H20-Fc, and pEXPR-Fc (see DNA sequences in Supporting Information). Vectors for expression of UK18-hinge-Fc-strep^{tag} fusion protein with varying hinge regions and Fc-

dx.doi.org/10.1021/bc300184m | *Bioconjugate Chem.* 2012, 23, 1856−1863

his_6^{tag} fusion protein for heterodimer production were cloned by inserting PCR-amplified DNA from the above-described constructs into pEXPR-IBA42 (Figure S1C). DNA coding for UK18-hinge-Fc-$strep^{tag}$ fusion protein with varying hinge regions was amplified from the above-described synthetic DNA in six separate PCR reactions using the primers Hn-forw (5′-GAGAACCCACTGCTTACTGGC-3′) and Hn-strepII-rev (5′-AAACTTAAGCTTATTATCACTATTTTTCGAACTGCGGGTGGCTCCAAGCCGAGCCCGGGCTCAGGCTCAGGCTTTTCTGG-3′; *Hind*III site underlined), the latter primer attaching a sequence encoding $strep^{tag}$ (^{N}WSHPQFEK^{C}) at the C-terminus of the Fc fragment. PCR products were inserted via *Xba*I and *Hind*III into pEXPR-IBA42. DNA coding for Fc-his_6^{tag} fusion protein was amplified from pEXPR-Fc using the primers Hn-forw and Hn-his6-rev (5′-AAACTTAAGCTTATTATCACTAGTGATGGTGATGGTGATGTCCCGAGCCCG GGCT CAGGCTCAGGCTTTTCTGG-3′; *Hind*III site underlined), the latter primer attaching a sequence encoding his_6^{tag} (^{N}HHHHHH^{C}) at the C-terminus of the Fc fragment. The PCR product was inserted via *Nhe*I and *Hind*III into pEXPR-IBA42. The correct sequences of the resulting plasmids pEXPR-UK18-H0-Fc-$strep^{tag}$, pEXPR-UK18-H3-Fc-$strep^{tag}$, pEXPR-UK18-H6-Fc-$strep^{tag}$, pEXPR-UK18-H12-Fc-$strep^{tag}$, pEXPR-UK18-H16-Fc-$strep^{tag}$, pEXPR-UK18-H20-Fc-$strep^{tag}$, and pEXPR-Fc-his_6^{tag} were confirmed by DNA sequencing (see DNA sequences in Supporting Information).

Expression and Purification of Fc Fusion Proteins. Fc fusion proteins were expressed in transiently transfected human embryonic kidney (HEK-293) cells (typically 100 mL cultures). Protocols used for cell culturing and transfection are described in detail in the Supporting Information. After 7 days of expression, cells were removed by centrifugation (2500 rpm for 15 min at 4 °C) and filtration (0.45 μm PES membranes filter) and the proteins in the supernatant purified as follows. The homodimeric UK18-hinge-Fc fusion proteins and the Fc fragment were purified by protein G affinity chromatography (1 mL HiTrap Protein G HP column; GE Healthcare, Uppsala, Sweden) and desalted on a Hiprep 26/10 desalting column (GE Healthcare) using buffer R (20 mM NH_4HCO_3, 150 mM NaCl, 5 mM EDTA, pH 8.0). The heterodimeric UK18-hinge-Fc-$strep^{tag}$/Fc-his_6^{tag} fusion proteins, expressed by cotransfection of two plasmids in equal quantities, were sequentially purified by protein G affinity chromatography, Ni-affinity chromatography (1 mL HisTrap FF column; GE Healthcare), streptavidin-based affinity chromatography (1 mL Strep-Tactin Superflow high capacity H-PR cartridge; IBA, BioTAGnology, GmbH) and desalted on a Hiprep 26/10 desalting column using buffer R. Detailed protocols with information on buffers and volumes are described in the Supporting Information.

Chemical Macrocyclization of Peptide Fused to Fc Fragment. Concentrated Fc fusion proteins (5 mL at 20−50 μM) were incubated with 1 mM TCEP (Sigma-Aldrich Chemie GmbH, Steinheim, Germany) in buffer R at 30 °C for 1 h to reduce cysteine side chains of the UK18 peptide. The reducing agent was removed by gel filtration using a Hiprep 26/10 desalting column (GE Healthcare) and buffer M (20 mM NH_4HCO_3, 5 mM EDTA, pH 8.0, 0.22 μm filtered and degassed). EDTA was used in buffer M to chelate divalent metal cations minimizing oxidation of sulfhydryl groups. Immediately after reduction and purification, the fusion proteins were reacted with 3-fold molar excess of TBMB as follows. To 4.5 mL of reduced homodimer (5 μM) or reduced heterodimeric Fc fusion protein (10 μM), 0.5 mL TBMB (300 μM in 100% v/v ACN) was added and incubated at 30 °C for 1 h. Excess of nonreacted TBMB was removed by gel filtration using a Hiprep 26/10 desalting column equilibrated with buffer Z (10 mM Tris-Cl, pH 7.4, 150 mM NaCl, 10 mM $MgCl_2$, 1 mM $CaCl_2$, 0.22 μm filtered and degassed). The TBMB-modified homo- and heterodimer Fc fusion protein samples were concentrated to 50−500 μM final concentration by using a 10 000 MWCO Vivaspin-20 ultrafiltration device (Sartorius-Stedim Biotech GmbH) at 3000 *g* and 4 °C.

SDS-PAGE and Analytical Gel Filtration. To investigate whether TBMB-treated peptide-Fc fusion proteins were composed of intermolecular or intramolecular covalently linked species, protein samples were analyzed by SDS-PAGE under denaturating and reducing conditions. Each Fc fusion protein, before and after TBMB-modification, was denaturated in ClearPAGE LDS sample buffer (CBS Scientific Company, San Diego, CA, USA) supplemented with 100 mM TCEP. Samples of 1.5 μg Fc fusion protein were treated for 5 min at 90 °C, loaded on a 12% SDS ClearPAGE gel in ClearPAGE SDS-reducing running buffer, and stained with Coomassie G-250 blue solution. Native size and oligomerization state of TBMB-modified peptide-Fc fusion proteins were analyzed by size-exclusion chromatography with a Superdex 75 10/300 GL column (GE Healthcare) connected to an AKTApurifier system and equilibrated with buffer Z. Samples of 100 μL Fc fusion protein (50 μM) were analyzed.

Mass Spectrometric Analysis. The molecular mass of Fc fusion proteins before and after modification with TBMB was determined with electrospray ionization mass spectrometry (ESI−MS) performed on a quadrupole time-of-flight mass spectrometer (Q−TOF) Ultima API (Waters, Millford, MA, USA) operated with the standard ESI source and in positive ionization mode. Protein samples were desalted before mass spectrometric analysis as described in the Supporting Information. The ESI-Q-TOF mass spectrometer was calibrated for a range of 500 to 2500 m/z. The mass accurancy was always better than 4 ppm, and it was monitored through continuous and automated reference mass introduction. Ten microliter desalted protein samples (5 μM) were injected for each measurement. Data were acquired, processed, and analyzed using the software *MassLynx* v 4.1 (Waters).

Protease Inhibition Assay. Inhibition of human uPA by the Fc fusion proteins was measured by incubating different concentrations of each Fc fusion protein (2-fold dilutions) with 1.5 nM human uPA (UPA-LMW, from human urine, 33 kDa; Molecular Innovations, Novi, MI, USA). The enzymatic assays were performed at 25 °C in 150 μL volume of buffer Z containing 10 mM Tris-Cl, pH 7.4, 150 mM NaCl, 10 mM $MgCl_2$, 1 mM $CaCl_2$, 0.1% w/v BSA, 0.01% v/v Triton-X100, and 5% v/v DMSO and using the fluorogenic substrate Z-Gly-Gly-Arg-AMC (50 μM; Bachem, Bubendorf, Switzerland). The initial velocities were monitored as changes in fluorescence intensity during 30 min on a Spectramax Gemini fluorescence plate reader (excitation at 355 nm, emission recording at 460 nm; Molecular Devices, Sunnyvale, CA, USA). K_i values were determined as described in the Supporting Information.

Determination of Pharmacokinetics in Mice. All animal studies were carried out according to Swiss regulations under a project license granted by the Service de la Consommation et des Affaires Vétérinaires Vaudois. Female BALB/c mice (Charles River, France) aged 7 to 9 weeks were intravenously injected with 100 μg heterodimeric UK18-H12-Fc-$strep^{tag}$/Fc-his_6^{tag} or

homodimeric Fc-his$_6^{tag}$ fusion protein. Blood samples (20 μL), collected 5 min, 6 h, and 12 h, as well as 1, 2, 4, and 8 days after injection, were kept at room temperature to coagulate; and serum was recovered after centrifugation at 6000 *g* for 10 min. UK18-Fc conjugate was quantified by an ELISA assay in which either human uPA or mouse anti-human Fc polyclonal antibody was immobilized on the bottom of a microtiter plate, the serum samples containing Fc protein added and captured protein detected with a goat anti-human-Fc antibody conjugated to HRP. A detailed protocol of the ELISA assay is provided in the Supporting Information.

RESULTS

Chemical Cyclization of Peptides Genetically Fused to an Fc Fragment. A fusion protein comprising an N-terminal 17-amino-acid peptide, a 2-amino-acid Gly-Ser spacer, and a C-terminal Fc fragment derived from human IgG1 was transiently expressed in mammalian cells and purified (Figure 1A and SI Figure S2A). From a 100 mL culture, 8−12 mg purified Fc fusion protein could be obtained. The hinge region, containing cysteine residues that form interchain disulfide bridges, was not included in the Fc fusion protein to prevent interference of the thiol groups with the peptide cyclization reaction. The single glycosylation site in the C_H2 domain of the Fc fragment was mutated (Asn297Ala) to facilitate monitoring of chemical modifications of the fusion protein by mass spectrometry. The 17-amino-acid peptide with the sequence ^{N}ACS-RYEVDCRGRGSACG^C is derived from the bicyclic peptide UK18 described above. The fusion protein of the peptide with human IgG Fc fragment is termed "UK18-Fc" in the following. UK18-Fc fusion protein was treated with the negatively charged reducing agent TCEP to favor reduction of cysteine residues in the solvent-exposed N-terminal peptide appendix over the less accessible intrachain disulfide bridges present in the C_H2 and C_H3 domains of Fc fragment. After TCEP removal, sulfhydryl groups were reacted with the cyclization reagent TBMB (Figure 1A). Mass spectrometric analysis revealed two products, the first one showing a mass of 25 799 Da, corresponding to UK18-Fc monomer modified with a single TBMB molecule (mass increase of 116 Da), and the second one showing a mass of 51 600 Da corresponding to homodimeric UK18-Fc fusion protein modified with two TBMB molecules (mass increase of 232 Da) (Figure 1B). A sequence-identical Fc fragment without any N-terminal peptide was expressed in parallel and used as a control to verify if any groups of Fc fragment are modified by TBMB. Expression of this Fc fragment yielded two products, one with the expected mass and one with a 215 Da smaller mass, corresponding to Fc fragment with a proteolytically truncated N-terminus (lacking Ala-Ser-Gly; Figure 1C). The homodimeric Fc fragment was not modified with TBMB, even at a 10-fold higher TBMB concentration (Figure 1C and SI Figure S5). In the mass spectrum, only Fc monomer can be seen, indicating that the two subunits of the homodimeric Fc fragment completely dissociate during mass spectrometric analysis. Following this observation, we wondered whether, in TBMB-modified homodimeric UK18-Fc fusion protein, the two monomers were covalently cross-linked as suggested by one of the mass peaks (Figure 1B). SDS-PAGE analysis of TBMB-modified homodimeric UK18-Fc fusion protein under reducing conditions showed two bands with the minor band having a molecular weight corresponding to a UK18-Fc monomer (~26 kDa) and the major band to a homodimeric UK18-Fc fusion protein (~52 kDa) (Figure 1D). The presence of a dimer under denaturing conditions showed that TBMB had indeed cross-linked two UK18-Fc monomers in a large fraction of the protein (SI Table S1). Most likely, the close spatial proximity of the two UK18 peptides in homodimeric UK18-Fc fusion protein had allowed reaction of one TBMB molecule with cysteines of both monomers. In a protease inhibition assay, the TBMB-modified homodimeric UK18-Fc fusion protein blocked human uPA with a K_i of 3 μM (Table 1).

Table 1. Inhibitory Activity of Homo- and Heterodimeric UK18-hinge-Fc Conjugates Towards Human uPA[a]

	$K_i \pm$ SE (nM)	
hinge	UK18-hinge-Fc homodimer	UK18-hinge-Fc heterodimer
H0	3079 ± 112	619 ± 39
H3	990 ± 24	202 ± 15
H6	310 ± 10	158 ± 14
H12	128 ± 6	76 ± 4
H16	149 ± 10	87 ± 1
H20	145 ± 9	83 ± 2

[a]The conjugates tested contain linkers of different lengths that are based on the amino acid sequence of the human IgG1 hinge (see the sequences in Figure 2A and SI Figure S1). The indicated name of the hinge reflects the number of amino acids in the linker. The K_i values of the Fc homo- and heterodimers were determined at 25 °C and physiological pH (7.4), using the fluorogenic Z-Gly-Gly-Arg-AMC substrate at a concentration of 50 μM. Averages from at least three measurements are indicated. S.E., standard error.

The K_i was calculated based on the concentration of an UK18-Fc monomer to facilitate a direct comparison with the activity of synthetic UK18. This activity is about 60-fold weaker than that of synthetic bicyclic peptide UK18 (K_i = 53 nM)[2] (Figure 1E).

Optimizing the Linker Length Between UK18 and Fc Fragment. Speculating that a longer linker between the peptide and the Fc fragment could reduce the cross-linking, we cloned and expressed UK18-Fc fusion proteins containing 3, 6, 12, 16, or 20 amino acids of the wild-type IgG1 hinge region in addition to the flexible Gly-Ser spacer (Figure 2A). The cysteine residues in these truncated hinges were replaced by serine to prevent undesired reactions with TBMB. SDS-PAGE analysis of the different Fc fusion proteins before and after modification with TBMB showed that the degree of cross-linking was gradually reduced with linker lengthening (Figure 2B). The monomer-to-dimer ratio of constructs with hinges of 12 or more amino acids was estimated to be around 3:1 (SI Table S1). Mass spectrometric analysis of the Fc fusion proteins showed *O*-glycosylation of constructs with linkers equal or longer than 12 amino acids (addition of 162, 203, and 291 Da; Figure 2C). Mass spectrometric analysis of the homodimeric UK18-hinge-Fc fusion proteins after TBMB-treatment showed that each of the monomers had reacted with one TBMB and the dimers with two TBMB. Similar to experiments with the initial UK18-Fc fusion protein, no incomplete or unspecific reaction could be detected. The inhibitory activities of the new constructs were found to improve significantly with linker lengthening (Figure 2D and Table 1). The fusion protein with a 12-amino-acid hinge was 20-fold more potent (K_i = 128 nM) than the initial construct having just a Gly-Ser spacer. Extending the hinge region to 16 or 20 amino acids did not further improve the inhibitory activity.

Generation of Fc Fragments with a Single Bicyclic Peptide. To completely prevent peptide cross-linking, we generated heterodimeric Fc fusion protein in which only one of the Fc monomers is displaying the UK18 peptide (Figure 3A).

dx.doi.org/10.1021/bc300184m | *Bioconjugate Chem.* 2012, 23, 1856−1863

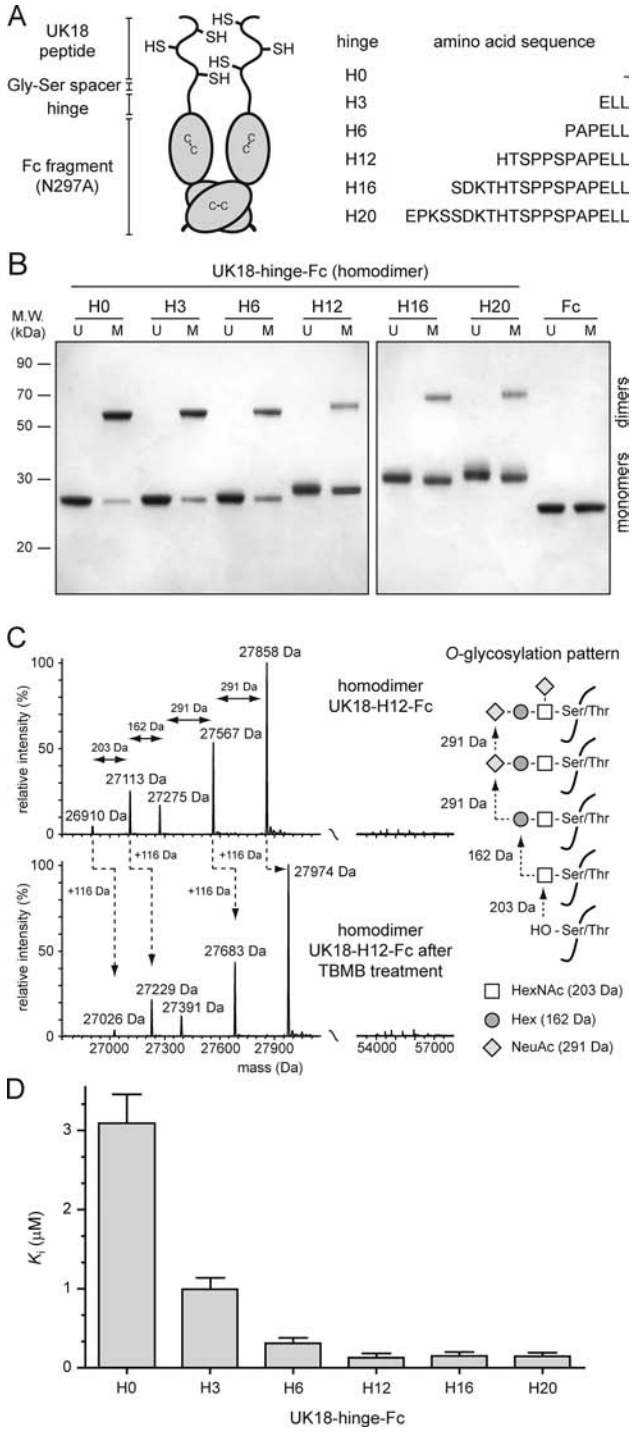


Figure 2. Fc fusion proteins with different peptidic linkers between the peptide and the Fc fragment. (A) Schematic representation of protein constructs. The peptidic linkers with different lengths are based on the amino acid sequence of the human IgG1 hinge region wherein cysteines were replaced by serines. The sequences are indicated as well as a name that reflects the number of amino acids (e.g., H3 contains 3 amino acids of the hinge) (see also SI Figure S1A,B). (B) Migration of homodimeric UK18-hinge-Fc fusion proteins with different linker lengths on a reducing SDS-PAGE. 1.5 μg of each unmodified and modified homodimeric Fc fusion proteins have been loaded per well. U = unmodified, M = TBMB-modified (see also SI Table S1). (C) Mass spectra of homodimeric UK18-hinge-Fc fusion protein with the H12 linker before (upper panel) and after (lower panel) modification with TBMB. Due to *O*-glycosylation of the hinge region, several molecular masses can be observed. All the masses are shifted by 116 Da, which corresponds to the mass change upon reaction with one TBMB molecule. NeuAc stands for *N*-acetylneuraminic acid (sialic acid), HexNAc for *N*-acetylhexosamine, and Hex for hexose (see also SI Figure S8). Mass spectra of constructs with different hinge lengths are shown in SI Figures S6, S7, S9, and S10. (D) Inhibitory activities of the homodimeric UK18-hinge-Fc fusion proteins after modification with TBMB. Residual activity of human uPA was measured at different protein concentrations and K_i values were determined (see Table 1). Averages from at least three measurements are indicated (see also SI Figure S2A,B).

We coexpressed a UK18-Fc fusion protein having a C-terminal strep-tag (strep^{tag}) and an Fc fragment without any peptide having a C-terminal polyhistidine tag (his$_6^{tag}$). The heterodimeric Fc fusion protein was extracted by sequential affinity purification on immobilized protein G, nickel, and streptavidin, respectively, and further purified by gel filtration. From a 100 mL culture, 1−2 mg of purified Fc fusion protein was obtained. A total of six different heterodimeric Fc fusion proteins were produced, each having a different hinge length. All the constructs were modified with TBMB and analyzed by SDS-PAGE and mass spectrometry (Figure 3B). Both the TBMB-modified and unmodified Fc fusion proteins migrated exclusively as monomers in a denaturing polyacrylamide gel, indicating that the two monomers were not cross-linked. This observation could be confirmed by mass spectrometry, showing that only the Fc fragment with the UK18 peptide was modified with TBMB (Figure 3C). The difference in mass was 116 Da, corresponding to the expected change due to the TBMB modification. Similar to what we had observed before with the Fc homodimers, the fusion proteins with longer linkers showed more potent inhibition (Figure 3D). This observation indicated that the activity of the initial UK18-Fc homodimer was impaired not only due to peptide cross-linking, but also due to a shorter linker which may sterically hinder binding of the bicyclic peptide to the target protein. The constructs with the best inhibitory activity were again those having hinge regions of 12, 16, and 20 amino acids (K_i of 76, 87, and 83 nM; Figure 3D and Table 1).

Plasma Half-Life and Stability of the Bicyclic Peptide-Fc Conjugate in Mice. The plasma half-life of the heterodimeric UK18-hinge-Fc fusion protein with the 12-amino-acid linker (UK18-H12-Fc-strep^{tag}/Fc-his$_6^{tag}$) showing the highest inhibitory activity was assessed in mice. UK18 inhibits mouse uPA around 1000-fold weaker than human uPA,[2] and this weak binding was expected not to influence the pharmacokinetics of the conjugate. 100 μg of Fc fusion protein was injected intravenously, and levels of the bicyclic peptide-Fc conjugate were quantified by ELISA after 5 min, 6 h, and 12 h as well as 1, 2, 4, and 8 days. Fc fusion protein in serum samples was captured in microtiter plates coated with human uPA and detected with an anti-human Fc antibody−peroxidase conjugate. This assay format assured that only Fc fusion protein with functional UK18 was quantified. The conjugate was cleared in two phases wherein the terminal half-life of the construct was 43 h (Figure 4). In a second ELISA assay, the concentration of human Fc fragment in the mouse blood samples was quantified by capturing the protein with a polyclonal anti-human Fc antibody and detecting with anti-human monoclonal antibody. In this assay format, any human Fc fragment was detected irrespective of the presence or absence of UK18. This experiment showed a similar clearance curve with a terminal half-life of 36 h

dx.doi.org/10.1021/bc300184m | *Bioconjugate Chem.* 2012, 23, 1856−1863

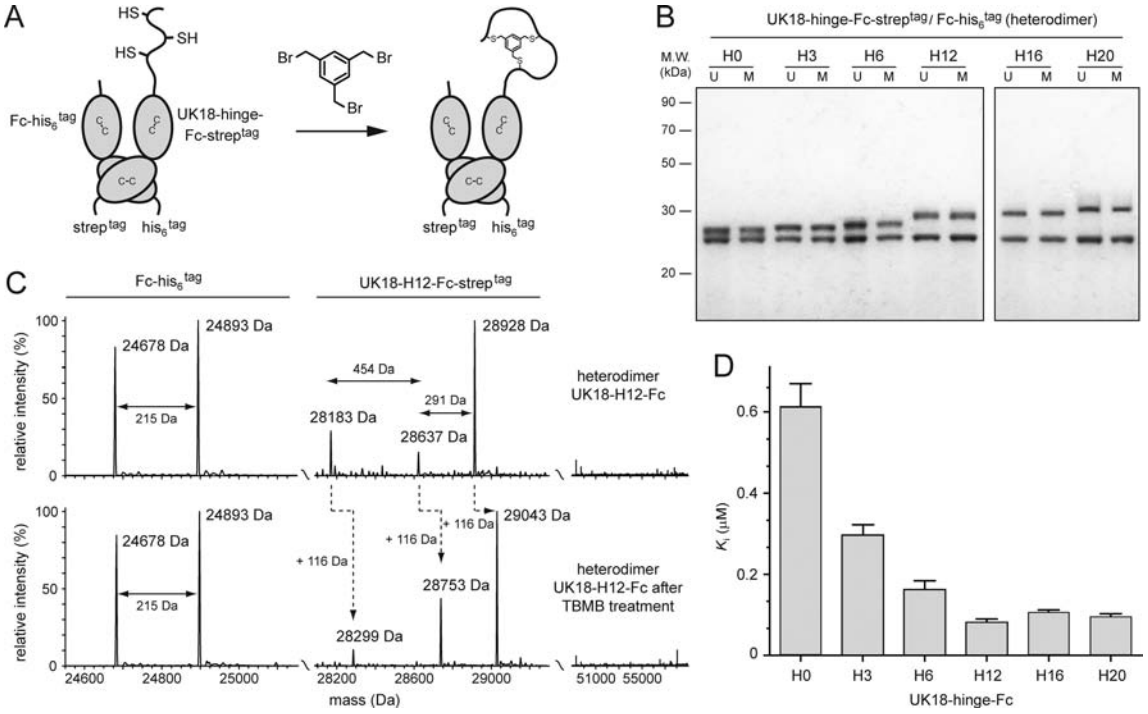


Figure 3. Macrocyclization of a single peptide fused to Fc fragment. (A) Schematic representation of UK18-hinge-Fc/Fc heterodimer and cyclization of the peptide with TBMB. The two different affinity tags polyhistidine-tag (his_6^{tag}) and streptavidin-tag ($strep^{tag}$) allowed the purification of heterodimer after coexpression of both Fc fusion proteins (see also SI Figure S1C). (B) Migration of the two subunits from the heterodimeric Fc fusion proteins on a reducing SDS-PAGE. The different hinge lengths of the fusion proteins are indicated. 1.5 μg of each unmodified (U) and modified (M) heterodimeric Fc fusion protein has been loaded per well. U = unmodified, M = TBMB-modified. (C) Mass spectra of UK18-hinge-Fc-$Strep^{tag}$/Fc-His_6^{tag} fusion protein before (upper panel) and after (lower panel) modification with TBMB. The analyzed Fc fusion protein contains a 12-amino-acid hinge region (H12) that was *O*-glycosylated. The mass of the Fc fusion protein after reaction with TBMB is shifted by 116 Da that corresponds to the mass change upon reaction with one TBMB molecule. The mass of this polyhistidine-tagged Fc fragment is unchanged (see also SI Figure S14). Mass spectra of constructs with different hinge lengths are shown in SI Figures S11, S12, S13, S15, S16, and S17. (D) Inhibitory activities of the heterodimeric Fc fusion proteins after modification with TBMB. Residual activity of human uPA was measured at different protein concentrations and K_i values were determined (see Table 1). Averages from at least three measurements are indicated (see also SI Figure S2C,D).

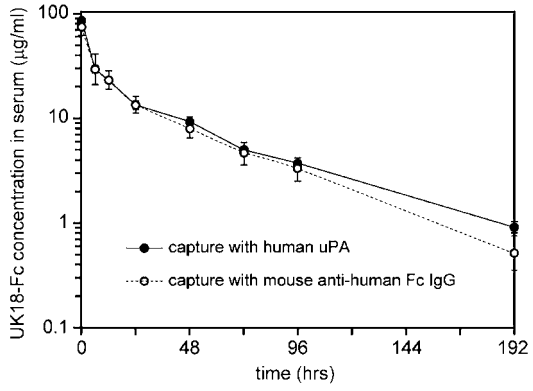


Figure 4. Pharmacokinetics of a bicyclic peptide UK18-H12-Fc-$strep^{tag}$/Fc-his_6^{tag} in female BALB/c mice. Serum concentrations of the heterodimer were measured with two different ELISA assays at the indicated time points. In the first assay, Fc fragment with functional UK18 was quantified by capturing the heterodimer with human uPA and detection with a monoclonal anti-human Fc antibody (●). In the second assay, all heterodimeric Fc fusion protein was quantified by capturing with a polyclonal anti-human Fc antibody and detection with a monoclonal anti-human Fc antibody (○). Averages obtained from experiments with 2 mice are shown. Standard deviations are indicated.

(Figure 4), suggesting that the bicyclic peptide UK18 linked to Fc fragment remained essentially functional for several days in circulation. Pharmacokinetic parameters including clearance and volume of distribution are indicated in Table 2. For comparison, the pharmacokinetics of an Fc fragment without bicyclic peptide was assessed. The homodimer of Fc-his_6^{tag} had a similar terminal half-life (33 h).

DISCUSSION

In contrast to the generation of disulfide-cyclized peptide-Fc fusion proteins, the formation of bicyclic peptide-Fc fusions posed a greater challenge since it involved (i) an intermolecular reaction between the peptide and the cyclization reagent, (ii)

Table 2. Pharmacokinetic Parameters of UK18-H12-Fc-$strep^{tag}$/Fc-his_6^{tag} after Intravenous Administration of 100 μg Protein (around 5.5 mg/kg) in Mice[a]

	UK18-H12-Fc-$strep^{tag}$/Fc-his_6^{tag}	
	with functional UK18	with Fc domains
C_{max} (μg/mL)	83.5	74.8
$t_{1/2}$ β (h)	43.3	36.5
$AUC_{0-8days}$ (h·μg/mL)	1873	1825
CL (mL/h)	0.064	0.07
V_d (mL)	4	3.7

[a]The plasma concentration of Fc fusion protein with functional K18 or of total Fc was quantified by EA. The fusion protein was captured on microtitre plates coated with human uPA or polyclonal anti-human Fc antibody. C_{max} was measured at 5 min.

dx.doi.org/10.1021/bc300184m | *Bioconjugate Chem.* 2012, 23, 1856−1863

three rather than one covalent bonds to be formed, and (iii) a reaction type which is less chemoselective than the oxidative coupling of thiols to disulfides. An additional challenge in the modification of sulfhydryl groups in peptides linked to Fc fragment was the presence of intradomain disulfide bridges in C_H2 and C_H3 that could potentially be reduced and modified. Despite this increased complexity, the modification of cysteines in peptide-Fc fusion proteins was surprisingly selective and efficient.

Initial problems resulting from cross-linking of spatially close peptides in UK18-Fc homodimers could be resolved by expressing a heterodimeric Fc fragment with only one subunit carrying a peptide. A number of elegant strategies have been developed to generate Fc heterodimers. Carter and co-workers had developed Fc heterodimers by introducing "knob-into-hole" mutations in the C_H3 domain.[17] Yan and co-workers had enhanced Fc heterodimer formation by placing complementary charges at the C_H3 domain interface.[18] Here, we chose a strategy based on differently tagged monomers that are sequentially purified by affinity chromatography. This approach gave smaller yields but guaranteed that all assembled Fc fragments were heterodimers. Peptides of these heterodimers were all correctly cyclized and a maximal inhibitory activity (K_i) of 76 nM could be observed which is comparable to the activity of chemically synthesized UK18 (53 nM). Coexpression of two different monomers may also allow the generation of Fc fragments with two bicyclic peptides, each one at a different end of the dimer to prevent cross-linking by TBMB. The bicyclic peptide could optionally have different sequences to generate bispecific ligands. The cross-linking of subunits by TBMB might alternatively be prevented by linking the peptides to the N-termini of a full-size IgG antibody. In this case, the Y-shape of immunoglobulin could be exploited to spatially separate the two peptides from each other.

A key parameter in the development of potent Fc-linked bicyclic peptide inhibitors was the length of the hinge region connecting the bicyclic peptide and the Fc fragment. Lengthening the hinge in homo- and heterodimeric UK18-Fc fusion protein significantly increased the inhibitory activity of the conjugates, indicating clearly that short linkers impair binding to uPA. Similar effects resulting from linker variation were previously reported for a number of peptide- or protein-Fc fusions.[19−21] In constructs with hinge regions equal to or longer than 12 amino acids, glycosylation occurred which was not anticipated. Mutation of the cysteine residues in the hinge of IgG1 (^{N}EPKSCDKTHTCPPCPAPELL^{C}) generates a sequence rich in proline and serine, which is known as a preferred *O*-glycosylation substrate.[22] The sequence with the cysteine to serine mutations is actually similar to the hinge sequence of IgA1 (^{N}PSTPPTPSPSTPPTPSPS^{C}) which is *O*-glycosylated.[23] Each of the glycosylated UK18-hinge-Fc fusion proteins was similarly modified having one, two, three, or four sugar units attached. On the basis of the mass spectrometric pattern, the glycosylation was composed of one *N*-acetylhexosamine, one hexose, and two *N*-acetylneuraminic acid units. On the basis of common *O*-glycosylation patterns in the IgA1 hinge and the mass spectrometry results, the units are most likely assembled in a branched structure as shown in Figure 2C with *N*-acetylhexosamine being *N*-acetylgalactosamine and hexose being galactose. The three conjugates that were glycosylated had the highest uPA inhibitory activity, but it is not clear if glycosylation had influenced the activity. It is more likely that their high activity results from the longer linkers.

The terminal half-life of the bicyclic peptide-Fc conjugate was 1.5 days and therefore around 100-fold longer than peptide macrocycles of the size of UK18. Compared to the non-glycosylated human IgG1 Fc fragment, having a terminal half-life of 2.5 days in mice,[24] the bicyclic peptide-Fc fusion was cleared more rapidly. The slightly shorter plasma half-life might result from a lower stability due to the lack of interdomain disulfide bridges. Human IgG1 Fc fragment glycosylated at Asn297 has a half-life of around 6 days, and it is likely that the circulation time of UK18-Fc could significantly be prolonged by using the glycosylated analogue.[24] The two ELISA formats that detected either Fc fragment with functional UK18 or Fc fragment irrespective of UK18 showed similar plasma half-lives. This finding indicated that the bicyclic peptide remained largely intact while circulating in the bloodstream of mice. This outcome was pleasing, since peptide macrocycles are not necessarily stable for extended time periods *in vivo*. For example, the cyclic atrial natriuretic peptide that was recently linked to the Fc fragment by native chemical ligation appeared to be degraded more rapidly than the Fc fragment was cleared from the circulation.[21] The long circulation time of the bicyclic peptide UK18 allows its testing in an animal tumor model. The 3-fold smaller molecular mass of the bicyclic peptide-Fc fusion protein compared to antibodies should allow it to penetrate better into tumors. Conjugates promising even better diffusion properties may be generated by fusing bicyclic peptides to recently developed monomeric Fc protein.[25]

The clean and efficient reaction of TBMB with Fc fragment suggests that bromomethyl-benzene groups can also be applied for other chemical modifications in antibodies or antibody fragments. For example, Fc fusions of phage-selected monocyclic peptides cyclized with bis-(bromomethyl)benzene linkers may be generated similarly to the bicyclic peptide fusions. Furthermore, antibody−drug conjugates that are increasingly being developed may be generated by linking chemically synthesized bromomethylbenzene-functionalized drugs to antibodies containing free cysteine residues. TBMB was proven to quantitatively modify peptides even if applied only at a small molar excess (e.g., at a ratio of peptide:TBMB = 1:1.2 at medium to high micromolar concentrations). This suggests that compounds functionalized with bromomethyl-benzene groups can be reacted with equimolar concentrations of antibody and compound, making the coupling economical.

In summary, we have shown that bicyclic peptide-Fc conjugates can be efficiently produced by post-translationally cyclizing a peptide-Fc fusion protein. The bicyclic peptide conjugated to Fc fragment having nearly the same activity as the synthetic bicyclic peptide and a terminal half-life of more than one day will allow testing its therapeutic effect in animal disease models. In addition, the chemical reaction might be applied to cyclize other formats of peptides fused to antibody fragments or to conjugate synthetic molecules to antibody Fc fragments or to entire antibodies.

■ ASSOCIATED CONTENT

Ⓢ Supporting Information

Detailed procedures for the expression, purification, and characterization of Fc fusion proteins. Supplementary analytical data such as gel filtration chromatograms and mass spectra are also provided. This material is available free of charge via the Internet at http://pubs.acs.org.

AUTHOR INFORMATION

Corresponding Author

*E-mail address: christian.heinis@epfl.ch.

Present Address

†David H. Koch Institute for Integrative Cancer Research, Massachusetts Institute of Technology, 77 Massachusetts Avenue, Cambridge MA, 02139, United States.

Notes

The authors declare no competing financial interest.

ACKNOWLEDGMENTS

We thank Dr. Christoph Rader for kindly providing a vector for the expression of IgG1 Fc fragment. The financial contributions from the Swiss National Science Foundation (SNSF Professorship PP00P3_123524/1 to C.H.), the National Competence Center for Biomolecular Imaging (NCCBI; PhD fellowship to P.D.), and Ministerio de Educacion del Gobierno de Espana (postdoc fellowship to J.M.S.) are gratefully acknowledged.

ABBREVIATIONS

TBMB, tris-(bromomethly)benzene; TCEP, tris-(carboxyethyl)-phosphine; uPA, urokinase-type plasminogen activator

REFERENCES

(1) Heinis, C., Rutherford, T., Freund, S., and Winter, G. (2009) Phage-encoded combinatorial chemical libraries based on bicyclic peptides. *Nat. Chem. Biol. 5*, 502−7.

(2) Angelini, A., Cendron, L., Chen, S., Touati, J., Winter, G., Zanotti, G., and Heinis, C. (2012) Bicyclic peptide inhibitor reveals large contact interface with a protease target. *ACS Chem. Biol. 7*, 817−21.

(3) Baeriswyl, V., Rapley, H., Stace, C., Pollaro, L., Teufel, D., Walker, E., Chen, S., Winter, G., Tite, J., and Heinis, C. (2012) Bicyclic peptides with optimized ring size inhibit human plasma kallikrein and its orthologs while sparing paralogous proteases. *ChemMedChem,*.

(4) Timmerman, P., Beld, J., Puijk, W. C., and Meloen, R. H. (2005) Rapid and quantitative cyclization of multiple peptide loops onto synthetic scaffolds for structural mimicry of protein surfaces. *ChemBioChem 6*, 821−4.

(5) Matzke, G. R., Zhanel, G. G., and Guay, D. R. (1986) Clinical pharmacokinetics of vancomycin. *Clinical Pharmacokinetics 11*, 257−82.

(6) Tan, A. C., Russel, F. G., Thien, T., and Benraad, T. J. (1993) Atrial natriuretic peptide. An overview of clinical pharmacology and pharmacokinetics. *Clinical Pharmacokinetics 24*, 28−45.

(7) Cockshott, I. D. (2000) Clinical pharmacokinetics of goserelin. *Clinical Pharmacokinetics 39*, 27−48.

(8) Pollaro, L., and Heinis, C. (2010) Strategies to prolong the plasma residence time of peptide drugs. *MedChemComm 1*, 319−324.

(9) Kontermann, R. E. (2011) Strategies for extended serum half-life of protein therapeutics. *Curr. Opin. Biotechnol. 22*, 868−76.

(10) Huang, C. (2009) Receptor-Fc fusion therapeutics, traps, and MIMETIBODY technology. *Curr. Opin. Biotechnol. 20*, 692−9.

(11) McDonagh, C. F., Turcott, E., Westendorf, L., Webster, J. B., Alley, S. C., Kim, K., Andreyka, J., Stone, I., Hamblett, K. J., Francisco, J. A., and Carter, P. (2006) Engineered antibody-drug conjugates with defined sites and stoichiometries of drug attachment. *Protein Eng., Des. Sel. 19*, 299−307.

(12) Carter, P. J., and Senter, P. D. (2008) Antibody-drug conjugates for cancer therapy. *Cancer j. 14*, 154−69.

(13) Senter, P. D. (2009) Potent antibody drug conjugates for cancer therapy. *Curr. Opin. Chem. Biol. 13*, 235−44.

(14) Alley, S. C., Okeley, N. M., and Senter, P. D. (2010) Antibody-drug conjugates: targeted drug delivery for cancer. *Curr. Opin. Chem. Biol. 14*, 529−37.

(15) Lyon, R. P., Meyer, D. L., Setter, J. R., and Senter, P. D. (2012) Conjugation of anticancer drugs through endogenous monoclonal antibody cysteine residues. *Methods Enzymol. 502*, 123−38.

(16) Andreasen, P. A., Egelund, R., and Petersen, H. H. (2000) The plasminogen activation system in tumor growth, invasion, and metastasis. *Cell. Mol. Life Sci. 57*, 25−40.

(17) Ridgway, J. B., Presta, L. G., and Carter, P. (1996) 'Knobs-into-holes' engineering of antibody CH3 domains for heavy chain heterodimerization. *Protein Eng. 9*, 617−21.

(18) Gunasekaran, K., Pentony, M., Shen, M., Garrett, L., Forte, C., Woodward, A., Ng, S. B., Born, T., Retter, M., Manchulenko, K., Sweet, H., Foltz, I. N., Wittekind, M., and Yan, W. (2010) Enhancing antibody Fc heterodimer formation through electrostatic steering effects: applications to bispecific molecules and monovalent IgG. *J. Biol. Chem. 285*, 19637−46.

(19) Bitonti, A. J., and Dumont, J. A. (2006) Pulmonary administration of therapeutic proteins using an immunoglobulin transport pathway. *Adv. Drug Delivery Rev. 58*, 1106−18.

(20) Dumont, J. A., Low, S. C., Peters, R. T., and Bitonti, A. J. (2006) Monomeric Fc fusions: impact on pharmacokinetic and biological activity of protein therapeutics. *BioDrugs 20*, 151−60.

(21) Mezo, A. R., McDonnell, K. A., Low, S. C., Song, J., Reidy, T. J., Lu, Q., Amari, J. V., Hoehn, T., Peters, R. T., Dumont, J., and Bitonti, A. J. (2012) Atrial natriuretic peptide-Fc, ANP-Fc, fusion proteins: semisynthesis, in vitro activity and pharmacokinetics in rats. *Bioconjugate Chem. 23*, 518−26.

(22) Gupta, R., and Brunak, S. (2002) Prediction of glycosylation across the human proteome and the correlation to protein function. *Pacific Symposium on Biocomputing*, 310−22.

(23) Yoo, E. M., and Morrison, S. L. (2005) IgA: an immune glycoprotein. *Clin. Immunol. 116*, 3−10.

(24) Kim, J. K., Firan, M., Radu, C. G., Kim, C. H., Ghetie, V., and Ward, E. S. (1999) Mapping the site on human IgG for binding of the MHC class I-related receptor, FcRn. *Eur. J. Immunol. 29*, 2819−25.

(25) Ying, T., Chen, W., Gong, R., Feng, Y., and Dimitrov, D. S. (2012) Soluble Monomeric IgG1 Fc. *J. Biol. Chem. 287*, 19399−408.

Bioconjugate Chemistry

Article

pubs.acs.org/bc

Therapeutic Anti-Methamphetamine Antibody Fragment-Nanoparticle Conjugates: Synthesis and *in Vitro* Characterization

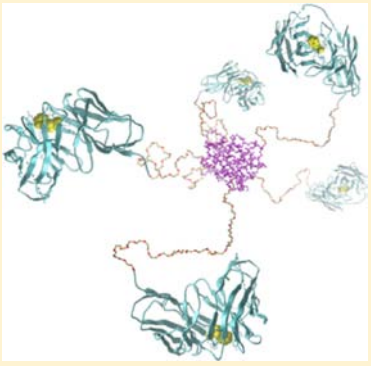
Nisha Nanaware-Kharade,[†] Guillermo A. Gonzalez, III,[†] Jackson O. Lay, Jr.,[‡] Howard P. Hendrickson,[§] and Eric C. Peterson*,[†]

[†]Department of Pharmacology and Toxicology, College of Medicine, University of Arkansas for Medical Sciences, 4301 West Markham Street, #611, Little Rock, Arkansas 72205, United States

[‡]Department of Chemistry and Biochemistry, University of Arkansas, Fayetteville, Arkansas 72701, United States

[§]Department of Pharmaceutical Sciences, College of Pharmacy, University of Arkansas for Medical Sciences, Little Rock, Arkansas 72205, United States

ABSTRACT: Treatments specific to the medical problems caused by methamphetamine (METH) abuse are greatly needed. Toward this goal, we are developing new multivalent anti-METH antibody fragment−nanoparticle conjugates with customizable pharmacokinetic properties. We have designed a novel anti-METH single chain antibody fragment with an engineered terminal cysteine (scFv6H4Cys). Generation 3 (G3) polyamidoamine dendrimer nanoparticles were chosen for conjugation due to their monodisperse properties and multiple amine functional groups. ScFv6H4Cys was conjugated to G3 dendrimers via a heterobifunctional PEG cross-linker that is reactive to a free amine on one end and a thiol group on the other. PEG modified dendrimers were synthesized by reacting the PEG cross-linker with dendrimers in a stoichiometric ratio of 11:1, which were further reacted with 3-fold molar excess of anti-METH scFv6H4Cys. This reaction resulted in a heterogeneous mix of G3-PEG-scFv6H4Cys conjugates (dendribodies) with three to six scFv6H4Cys conjugated to each dendrimer. The dendribodies were separated from the unreacted PEG modified dendrimers and scFv6H4Cys using affinity chromatography. A detailed *in vitro* characterization of the PEG modified dendrimers and the dendribodies was performed to determine size, purity, and METH binding function. The dendribodies were found to have affinity for METH identical to that of the unconjugated scFv6H4Cys in saturation binding assays, whereas the PEG modified dendrimers had no affinity for METH. These data suggest that an anti-METH scFv can be successfully conjugated to a PEG modified dendrimer nanoparticle with no adverse effects on METH binding properties. This study is a critical step toward preclinical characterization and development of a novel nanomedicine for the treatment of METH abuse.



INTRODUCTION

The socioeconomic impact of methamphetamine (METH) abuse is of great concern worldwide. Because of its multiple sites of action in the brain and other vital organs,[1] it is difficult to attenuate the detrimental effects of METH using a site specific receptor antagonist or agonist. Currently, there are no FDA approved medications to treat METH addiction. The available therapies are mainly supportive and involve behavior modification. METH specific antibody based medications that act as pharmacokinetic (PCKN) antagonist by reducing the concentration of METH in the brain and other crucial organs have shown promise as a potential therapeutic. Anti-METH monoclonal antibodies (mAb) alter the disposition of METH in the body and thus reduce the associated medical complications.[2] They significantly shorten the duration of METH induced locomotor activity[3] and also reduce or block METH self-administration in preclinical rat models.[4]

There are currently two forms of anti-METH mAbs in preclinical testing: a long-acting IgG and an extremely short-acting single chain variable fragment (scFv).[5] The prolonged serum half-life of IgG is largely attributed to the neonatal Fc receptor (FcRn) mediated recycling pathway.[6] In this, the interaction between the fragment crystallizable (Fc) region of IgG and the FcRn exposes IgGs to pH changes that could potentially alter critical molecular interactions in antigen binding sites. Indeed, *in vivo* inactivation of some anti-METH mAbs have been reported,[7] but whether this involves the FcRn pathway remains to be determined. Since anti-METH mAbs do not depend on Fc region interactions for complement binding, this domain could be removed with no loss of METH binding function. Thus, scFv6H4 without the FcRn binding domain was designed by joining the heavy and light chain variable domains of the parent anti-METH mAb6H4. This new antibody fragment was one-sixth the size of an intact IgG and capable of altering the *in vivo* disposition of METH within one minute of administration.[8] The scFv can be produced more economically, and the protein dose required to deliver the same number of anti-METH binding sites is one-third of the

Received: April 10, 2012
Revised: August 3, 2012
Published: August 9, 2012

ACS Publications © 2012 American Chemical Society

dx.doi.org/10.1021/bc300204n | *Bioconjugate Chem.* 2012, 23, 1864−1872

IgG. However, the small molecular size of monomeric scFv6H4 (~27 kDa) leads to its rapid clearance from the bloodstream. This PCKN property could be advantageous for treating acute drug overdose but not chronic METH abuse.

Numerous research groups in the field of oncology and neurology have reported conjugating drugs and proteins to nanoparticles as a way to improve efficacy, imaging, or targeting.[9−11] Nanotechnology provides a unique platform for customizing pharmacological properties like efficacy and PCKN. One particularly useful innovation in this field is a class of molecules called dendrimers.[12] In Greek, dendrimer means tree-like referring to the branched structure that increases in density with each round of synthesis, or generation (G1, G2, G3, etc.; Figure 1). Dendrimer particles are 1−10 nm

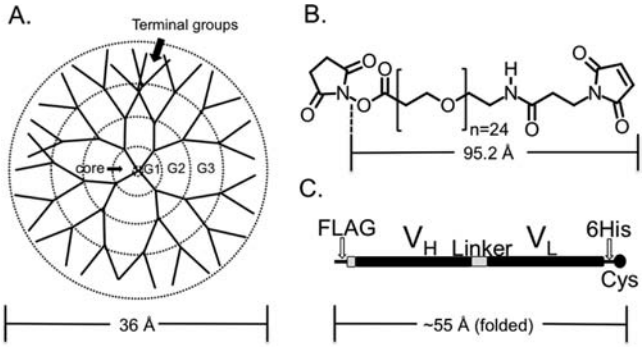


Figure 1. (A) Schematic of the polyamidoamine (PAMAM) dendrimer consisting of a core, three generations of synthesis, and terminal groups. (B) Structure representative of heterobifunctional polyethylene glycol (PEG) linker with *N*-hydroxysuccinimide (NHS) ester and maleimide groups with 24 ethylene oxide repeat units {succinimidyl-[(*N*-maleimidopropionamido)-tetracosaethyleneglycol] ester}. (C) Design schematic of scFv6H4Cys. V_H, variable heavy region; V_L, variable light region; linker, a 15 amino acid linking region; His6, 6-histidine tag for aiding purification; Cys, engineered cysteine residue for site-specific conjugation; FLAG, epitope for antibody recognition. Approximate dimensions of each dendribody component indicated to illustrate scale.

in diameter and have excellent monodispersity. They possess the potential to carry multiple functional groups that can be used for protein coupling, as well as a payload in the interior of the molecule.[13]

We envisioned that the PCKN of an anti-METH antibody fragment could be customized and optimally controlled by conjugating it to a dendrimer delivery system. The increase in molar mass of the nanoparticle could reduce the clearance of the conjugated antibody fragment from the body by reducing its potential for glomerular filtration (molecular weight cut off ~50 kDa) and restrict its volume of distribution to the vasculature. This novel prototype anti-METH antibody fragment conjugated to dendrimer nanoparticles (dendribodies) could also exhibit increased efficacy due to multivalency, improved residence time, and reduced antigenicity compared with the native antibody fragment. As a first step toward testing this hypothesis, in this article we describe the synthesis rationale, chemistry optimization, analysis of reaction intermediates, and *in vitro* functional analysis of a novel anti-METH scFv-dendrimer conjugate.

MATERIALS AND METHODS

Chemicals and Drugs. Enzymes and *Escherichia coli* strains were purchased from Invitrogen (Carlsbad, CA). [^3H]-*N*-Methyl-1-phenylpropane-2-amine (METH) (39 Ci/mmol) labeled at two metabolically stable sites on the aromatic ring structure was obtained from the National Institute on Drug Abuse (Bethesda, MD) after synthesis at the Research Triangle Institute (Research Triangle Park, NC). G3 PAMAM dendrimers were purchased from Dendritic Nanotechnologies, Inc. (Mt. Pleasant, MI). All other reagents were purchased from Sigma Aldrich (St. Louis, MO) unless otherwise noted.

Cloning and Large-Scale Expression of Anti-METH scFv6H4Cys. General molecular and genetic techniques for plasmid construction and transformation of scFv6H4Cys were performed as described in Sambrook and Russell.[14] A carboxyl terminus cysteine was engineered immediately following the hexa-histidine (His6) tag of scFv6H4 by DNA synthesis to create scFv6H4Cys in pUC57 vector (Genscript, Piscataway, NJ). The pUC57 scFv6H4Cys plasmid was transformed into *E. coli* strain DH5α (Invitrogen) for amplification and plasmid maintenance. The gene product was then restricted using *Eco*RI and XbaI, gel purified, and ligated into the matching sites in cloning vector pPICZαA (Invitrogen). Ampicillin resistant colonies containing pPICZαA were selected on plates containing LB agar and ampicillin. DNA was isolated, and the integrity of the transformed product was confirmed by restriction digestion and DNA sequencing (University of Arkansas for Medical Sciences DNA Core Sequencing Facility). After sequence confirmation, the plasmid was linearized with SacI and transformed into *Pichia pastoris* strain X33 by electroporation according to the manufacturer's instructions (Invitrogen).

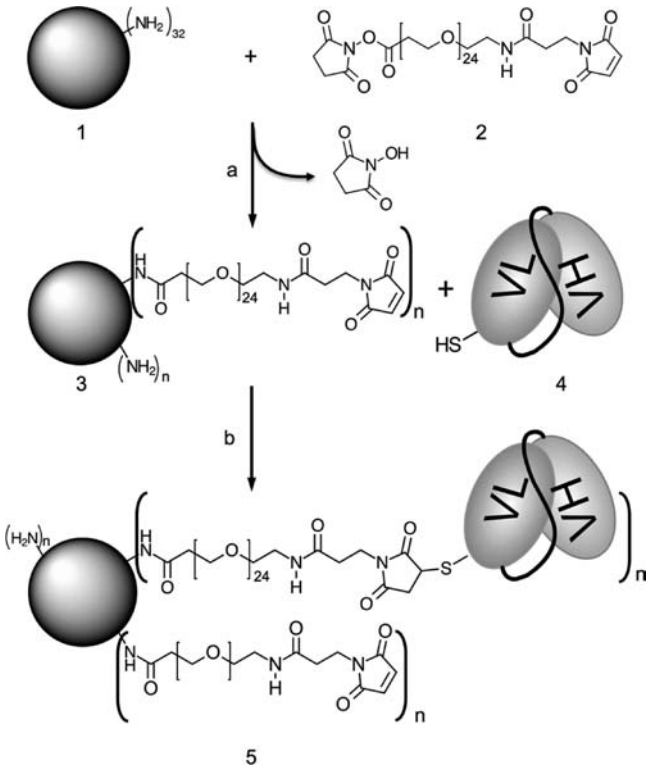
Zeocin-resistant colonies containing the scFv6H4Cys cDNA were selected on agar plates [1% (w/v) yeast extract, 2% (w/v) peptone, 2% (w/v) dextrose, 1 M sorbitol and 2% agar] containing 100 μg/mL Zeocin. Colonies that exhibited high Zeocin resistance were tested for scFv6H4Cys expression. In brief, colonies were picked from a freshly streaked plate and grown for 24 h in a 5 mL starter culture of BMGY [1% (w/v) yeast extract, 2% (w/v) peptone, 100 mM potassium phosphate, pH 6.0, 1.34% (w/v) yeast nitrogen base, 4 × 10^{-5}% biotin, and 1% (v/v) glycerol] at 30 °C. Then, 500 μL of this starter culture was inoculated in 50 mL of BMGY and cultured for an additional 18 h. The cells were harvested and resuspended in 500 mL of BMMY [BMGY with 0.5% methanol (w/v) substituted for glycerol] to induce protein expression. The cultures were grown at 30 °C with shaking overnight, and methanol was fed to a final concentration of 0.5% (w/v) at 24, 48, and 72 h. To harvest and analyze total scFv6H4Cys expression, the samples were centrifuged at 20,000 *g* for 10 min, and the supernatant was analyzed using SDS−PAGE and Coomassie dye G-250 based GelCode Blue staining (Pierce Thermo Scientific).

ScFv6H4Cys Purification and Formulation. The scFv6H4Cys expression product was purified as described for scFv6H4[15] using an AKTA explorer 100 fast protein liquid chromatography (FPLC) system and a nickel sepharose immobilized metal affinity chromatography (IMAC) HiPrep FF16/10 column (GE Healthcare, Piscataway, NJ). In brief, the column was equilibrated with 5 column volumes of binding/wash buffer (20 mM sodium phosphate buffer, pH 7.4, 500 mM NaCl, and 10 mM imidazole) and eluted in a single step with

the elution buffer (binding/wash buffer with 500 mM final concentration of imidazole). The fractions were collected, pooled, buffer exchanged, and concentrated into scFv administration buffer (15 mM sodium phosphate buffer and 150 mM NaCl, pH 7.5) using 7 or 20 mL Pierce concentrators with 9 kDa molecular weight cutoff (MWCO) (Pierce Thermo Scientific). The protein was characterized by SDS−PAGE, Western blot, and N-terminal sequencing (Midwest Analytical Inc., St. Louis, MO).

Synthesis of PEG_{24} Modified G3 PAMAM Dendrimers. A working stock of 0.1 mM G3 PAMAM dendrimers **1** (see Scheme 1) was prepared in phosphate buffered saline (PBS)

Scheme 1. Synthesis of Anti-METH scFv6H4Cys−Dendrimer Conjugates (Dendribodies)[a]



[a]G3 PAMAM dendrimer **1** is reacted with a heterobifunctional PEG_{24} crosslinker **2** to produce PEG modified dendrimer **3** along with the loss of NHS group. Compound **3** is then conjugated to reduced scFv6H4Cys **4**, via a thioether bond to produce the dendribody **5**. Reagents and conditions: (a) phosphate buffered saline, pH 7.4, 2 mM EDTA, room temperature (RT), dark, shaking, 2 h; (b) 50 mM sodium phosphate buffer, pH 6.4, 150 mM NaCl, 2 mM EDTA, RT, dark, shaking, 2 h.

(2.683 mM KCl, 1.47 mM KH_2PO_4, 136.893 mM NaCl, and 8.101 mM Na_2HPO_4) (MP Biomedicals LLC, Solon, OH) containing 1 mM EDTA. The heterobifunctional cross-linker with *N*-hydroxysuccinimide (NHS) ester and maleimide groups with PEG **2** spacer arms (NHS-PEG_{24}-Mal) was added in 5-, 10-, 15-, and 20-fold molar excess to the dendrimer working stock (e.g., 2 mM cross-linker to 0.1 mM dendrimer). The G3 dendrimer **1** and PEG_{24} **2** conjugation reactions were set up in stoichiometric ratios such that a single PEG_{24} molecule had 5, 11, 16, or 32 amine groups of dendrimer available for interaction. The reaction was incubated at room temperature (RT) for 2 h in the dark with gentle shaking. After incubation, excess of cross-linker and leaving NHS group were removed using protein desalting spin columns (Thermo Fisher Scientific) equilibrated with conjugation buffer (50 mM sodium phosphate buffer, pH 6.4, 150 mM NaCl, and 2 mM EDTA).

Characterization of PEG_{24} Modified G3 PAMAM Dendrimers. PEG_{24} modified G3 PAMAM dendrimers **3** were characterized using UV spectrometry, gel electrophoresis, and matrix-assisted laser desorption ionization−time-of-flight mass spectrometry (MALDI-TOF). A Nanodrop 1000 spectrophotometer (Thermo Fisher Scientific) was used to obtain UV spectra. Reducing SDS−PAGE analysis was conducted using 4−12% acrylamide Bis-Tris NuPage gels (Invitrogen) according to the manufacturer's instruction. Samples were heated with sample loading buffer containing dithiothreitol (DTT) at 70−80 °C for 10 min and were run at 200 V for 35 min. The gel was stained with Coomassie based GelCode Blue for 1 h at RT and destained overnight in water. For PEG-specific iodine staining, the gel was soaked in 5% barium chloride solution for 10 min and placed in 0.1 M iodine solution until a brown color developed.[16] MALDI-TOF mass spectra were obtained on a Bruker Ultraflex II TOF-TOF (Arkansas Statewide Mass Spectrophotometry Facility). A 1 M solution of 2,5-dihydroxybenzoic acid in 90% methanol with 0.1% formic acid (MALDI matrix) was mixed with the various reaction ratios of PEG_{24} modified dendrimer **3** samples in a 1:1 ratio (v/v), and 1 μL of the mixture was deposited onto the MALDI target. Mass spectra were acquired in the linear, positive ion mode and externally calibrated with a protein standard mixture.

Synthesis and Optimization of PEG_{24} Modified G3 PAMAM Dendrimer 3 and scFv6H4Cys 4 Conjugation Reactions. The individual parameters of the dendribody **5** reaction (i.e., reaction ratios of PEG modified dendrimers **3** to scFv6H4Cys **4**, type and concentration of reducing agent, pH, temperature, EDTA, and NaCl concentration) were optimized to obtain the maximum dendribody **5** yield. The reaction was performed in conjugation buffer at pH 6.2, 6.4, 6.6, 6.8, 7.0, and 7.2. The conjugation reaction was then set at 10, 25, and 37 °C to determine the optimum temperature. To ensure that the scFv6H4Cys's **5** thiol groups remained in their reduced state, various concentrations of two reducing agents TCEP (tris-2-carboxyethyl phosphine) and DTT were explored. The scFv6H4Cys was treated with freshly prepared 2, 4, 6, 8, and 10 mM DTT or TCEP equal to 2-, 5-, or 10-fold the protein concentration. These reduction reactions were allowed to proceed for 2 h at RT in the dark with shaking. DTT treated scFv6H4Cys **5** was desalted twice to ensure complete removal of DTT as confirmed by Ellman's assay (Thermo Fisher Scientific) using the Pierce desalting spin column into the conjugation buffer. The PEG_{24} modified dendrimers **3** were reacted with a three-fold excess of reduced scFv6H4Cys **4**. This reaction was allowed to proceed for 2 h at RT in the dark with shaking to produce dendribodies.

Characterization of PEG_{24} Modified G3 PAMAM Dendrimers and scFv6H4Cys Conjugates (Dendribodies). Dendribodies **5** were characterized using SDS−PAGE, SEC, and Western blot. Gel electrophoresis was performed as described for PEG_{24} modified dendrimers **3** and was used to assess the efficiency of cross-linking. Western blot was used to detect the presence of scFv6H4Cys **4** in the higher molecular weight dendribody **5** bands. The gel was electrophoretically transferred to a polyvinylidine fluoride membrane using a XCell *SureLock* Mini-Cell Western blotting kit (Invitrogen) as per the

manufacturer's instructions. The membranes were then blocked with 10% nonfat dry milk overnight at 4 °C and incubated for 2 h at RT with 1:5000 mouse monoclonal anti-FLAG M2-alkaline phosphatase antibody (Invitrogen) made in 0.2% w/v bovine serum albumin (Biorad Laboratories Inc., Hercules, CA). Following incubation, the membrane was washed with tris-buffered saline (+0.1% Tween-20, three times with 5 min per rinse). Bands were identified by exposing the membrane to 5-bromo-4-chloro-3-indolyl-phosphate in conjunction with nitro blue tetrazolium for colorimetric detection.

Purification of the Dendribodies 5 from the Unreacted PEG_{24} Modified G3 PAMAM Dendrimers 3 and scFv6H4Cys 4. Dendribodies **5** were purified by IMAC using an AKTA Explorer 100 FPLC and a 1 mL HiTrap IMAC FF column. In brief, the column was equilibrated with five column volumes of binding/wash buffer (containing 10 mM imidazole) at 1 mL/min. The dendribody reaction mixture containing the unreacted PEG_{24} modified dendrimers **3**, unconjugated scFv6H4Cys **4**, and dendribodies **5** was loaded onto the column. The dendribodies **5** were eluted from the column with the elution buffer (binding/wash buffer plus 470 mM imidazole, pH of 7.5) and collected as 0.5 mL fractions. The elution profile was monitored by UV absorbance at 220, 254, and 280 nm wavelengths. Fractions were analyzed by SDS–PAGE, and the fractions enriched in dendribodies **5** were pooled and concentrated into PBS using 3 kDa MWCO Vivaspin concentrators (GE Healthcare).

Saturation Binding Assay for Determination of K_D Values for METH. A rapid equilibrium dialysis (RED) (Pierce Thermo Scientific) device was used to perform the saturation binding assay. The Teflon base plate was washed in 20% v/v ethanol for 10 min. After ethanol removal, the base plate was thoroughly rinsed three times with water and allowed to dry. RED inserts with a nominal MWCO of 6–8 kDa were used. A concentration of scFv6H4Cys **4** or dendribodies **5** that was found to bind 20% of a 50,000 dpm [^{3}H]-METH solution was added to the sample chamber. This protein concentration was determined using a titration binding assay where serial dilutions of scFv6H4Cys **4** or dendribodies **5** were allowed to bind a constant concentration of [^{3}H]-METH. For total binding, 100 μL of PBS and 200 μL of increasing concentrations of [^{3}H]-METH were added into the buffer chamber. For nonspecific binding, 100 μL of PBS was replaced by 100 μL of 10 μM unlabeled METH as a competitor for [^{3}H]-METH. After loading, the plates were sealed with self-adhesive plastic sealing sheets to prevent evaporation and incubated overnight at RT on an orbital shaker with gentle shaking. After equilibrium was reached (18 h), a 50 μL aliquot from both the sample and buffer sides was added to 5 mL of scintillation fluid, vortexed, and was quantified using liquid scintillation spectrophotometry.

Data Analysis and Statistics. Data represent the mean ± standard error of the mean (SEM) of triplicate determinations. The saturation binding data was analyzed by nonlinear curve fitting using Graphpad PRISM 5.0d software.

RESULTS

Overall Design of Dendribody Synthesis. Generation 3 polyamidoamine (G3 PAMAM) dendrimers **1** consist of a diaminobutane core that has undergone three generations of synthesis, doubling the number of functional groups with each progressive generation. It was used as the supporting scaffold of dendribody **5** (Figure 1A) as it has a maximum number of 32 amine terminal groups, which can be utilized for conjugation with a variety of homo- and heterobifunctional cross-linking agents. We chose a heterobifunctional PEG cross-linker that is reactive to amines via an NHS ester at one terminus and to a free sulfhydryl group via a maleimide group at the opposite terminus. PEG chains of varying size (690, 856, 1270, 3400, and 5000 Da) were investigated for their ability to form dendribodies. However, only 1270 Da PEG with 24 ethylene oxide repeats (PEG_{24}) (Figure 1B) resulted in successful dendribody formation.

Sulfhydryl cross-linking was used to conjugate the anti-METH antibody fragment to dendrimers because it has been shown to be effective for site-specific coupling of proteins to nonprotein molecules, such as detection probes, PEG, and liposomes.[17−19] Our design goal was to utilize the selective reactivity of the cysteine to the maleimide group of a heterobifunctional PEG linker. The scFv inherently possess cysteines that form intrachain disulfide bonds in the variable light and heavy chains; however, conjugating to these internal cysteines could disrupt the structure of the antibody and ligand binding. Thus, we engineered an scFv with a cysteine at the carboxy-terminus of the DNA coding sequence to create scFv6H4Cys (Figure 1C).

The general steps to assemble the dendrimer-PEG-scFv6H4Cys conjugate are represented in Scheme 1. Briefly, the first step was to cross-link the NHS-moiety of the heterobifunctional PEG_{24} **2** to the amine terminal groups of the G3 PAMAM dendrimer **1**, followed by the removal of unreacted dendrimers and PEG_{24} by desalting chromatography (Scheme 1). Step two was to treat the carboxy-terminal cysteine of the scFv6H4Cys **4** with DTT reducing agent followed by a desalting step (Scheme 1). We found the later step to be important for two reasons. First, it reduces any disulfide mediated scFv dimerization or any potential disulfide interactions that occurred during scFv production in the presence of sulfhydryl-containing amino acids or peptides in the cell growth media. Second, the desalting step serves as a quick method of buffer exchange and removes the small adducts and DTT, both of which could compete and interfere with the maleimide reaction. Once the PEG_{24} modified dendrimer **3** and DTT treated scFv6H4Cys **4** were desalted and buffer exchanged, they were combined. This allowed the free sulfhydryl groups of the scFv6H4Cys to covalently link to the maleimide groups of the PEG modified dendrimer **3** forming the final dendribody **5** product. Scheme 1 represents a single scFv conjugated to the PEG modified dendrimer **3** for illustration purposes. However, higher order conjugates are possible, and this was the goal of the optimization experiments presented in this article.

PEG Modification of G3 PAMAM Dendrimers. In order to control the degree of PEG modification of the dendrimers, the cross-linking reaction of NHS-PEG-maleimide **2** to G3 PAMAM dendrimer **1** was performed with PEG_{24}:G3 stoichiometric ratios of 5:1, 11:1, 16:1, and 32:1. In this reaction, an amide bond is formed when the NHS-ester reacts with a terminal amine of the dendrimer, releasing a NHS cyclic group. Hydrolysis of the NHS-ester is a major competing reaction of the NHS-ester acylation reaction since a NHS group is released by both reacting with primary amines and by hydrolysis. Thus, the extent of NHS hydrolysis or reaction with primary amines in solution can be determined by measuring the absorbance of the NHS-ester group at 260 nm. Dendrimers and PEG_{24} do not exhibit UV absorption at this wavelength. This difference in spectral absorption allowed us to follow the

efficiency of PEG modification of dendrimers at increasing stoichiometric reaction ratios (Figure 2A) as well as during desalting. The NHS group and unreacted PEG_{24} **2** were removed to increase the efficiency of later steps of the dendribody **5** synthesis.

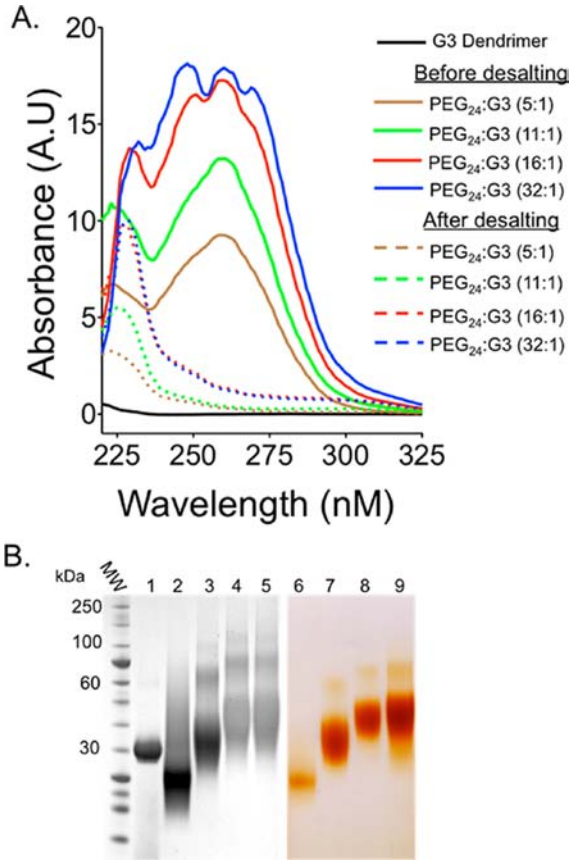


Figure 2. (A) UV spectroscopy monitoring of NHS cross-linking reaction. Representative UV wavelength scans from 220 to 325 nm of increasing reaction ratios of PEG_{24} to G3 PAMAM dendrimers before and after desalting. The solid and dotted lines represent the PEG_{24} modified dendrimers before and after desalting, respectively. (B) SDS–PAGE reducing gels loaded with reaction products of increasing ratios of PEG_{24} to G3 dendrimer: (lane 1) purified scFv6H4Cys, (lanes 2 and 6) 5:1, (lanes 3 and 7) 11:1, (lanes 4 and 8) 16:1, and (lanes 5 and 9) 32:1. The left gel panel is stained with Coomassie based GelCode Blue stain, and the right is stained with PEG-specific iodine stain.

Following desalting and spectrophotometric analysis, the degree of PEG modification of dendrimer was further analyzed by SDS–PAGE. The amine-terminated dendrimers **1** exhibit a net positive charge and do not migrate into standard polyacrylamide gels, even in the presence of SDS. However, they can be analyzed if the SDS–PAGE is conducted with reversed polarity.[20] We found that the PEG_{24} **2** alone migrated into SDS–PAGE gel, but it could not be detected with Coomassie-based stains. However, the new PEG modified dendrimer **3** migrated into SDS–PAGE gels and could be detected with a Coomassie-based stain (Figure 2B). As the ratio of PEG_{24}:G3 was increased, an apparent higher shift in the molecular weight of each band was observed suggesting increased functionalization of the dendrimers with saturation at higher PEG_{24} concentrations (Figure 2B, left panel). We confirmed that this molecular weight increase was due to the addition of the PEG_{24} cross-linker by staining a duplicate SDS–PAGE gel with PEG-specific iodine stain (Figure 2B, right panel).

MALDI-TOF Analysis of PEG Modified Dendrimers. While the SDS–PAGE analysis strongly indicated successful PEG_{24} **2** modification of the G3 PAMAM dendrimers **1**, we wanted to confirm this by MALDI-TOF analysis. This was a more accurate technique for analyzing the mass of G3 PAMAM dendrimers **1**, PEG_{24} cross-linker **2**, and the products of each PEG_{24}:G3 dendrimer reaction ratio. MALDI-TOF analysis suggested that the average mass of the G3 PAMAM dendrimers **1** and PEG_{24} **2** cross-linker alone was 6937 and 1280 Da, respectively, which closely agreed with the mass reported by the manufacturer (Table 1). Each of the PEG_{24}:G3 reactions showed increasing mass as the ratio of PEG_{24} to dendrimer was increased, confirming the SDS–PAGE results. The MALDI-TOF spectra showed a distribution of individual mass peaks. Figure 3A is a representative spectrum from the 5:1 PEG:G3 dendrimer reaction ratio. In addition to a broad peak that corresponds to the mass of the G3 dendrimer **1** alone, distribution of individual peaks were observed that iteratively increased by 1280 Da, corresponding to the theoretical mass addition of each PEG_{24} **2** cross-linker.

Table 1. Theoretical and Experimental Mass Additions of PEG_{24} to G3 PAMAM Dendrimers Corresponding to Each Reaction Ratio of the PEG_{24}:G3 Dendrimer[a]

PEG:dendrimer reaction ratio	Theoretical MW[b] Da	MALDI-TOF[c] m/z	PEG/dendrimer ratio
5:1	13324	13144	5
11:1	20998	29259	16
16:1	27393	34126	20
32:1	47857	34913	20

[a]The apparent molecular weights of PEG_{24} and the dendrimer are obtained from the manufacturers and calculated from MALDI-TOF spectra. [b]Theoretical mass addition by the dendrimer and PEG is 6929 and 1279 Da, respectively. [c]Experimental mass addition by the dendrimer and PEG is 6937 and 1280 Da, respectively.

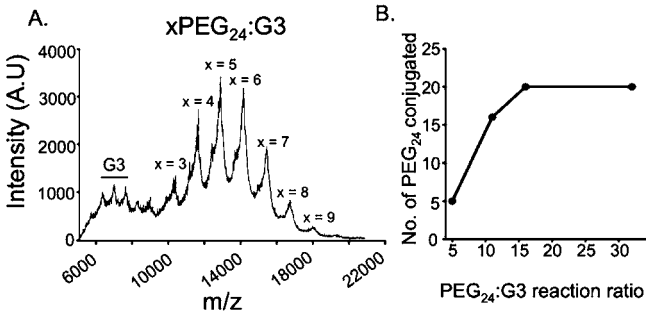


Figure 3. (A) Representative MALDI-TOF spectrum showing the peaks resolved from a 5:1 PEG_{24}:G3 dendrimer reaction. (B) Plot of the average number of PEG_{24} incorporated per dendrimer versus each reaction ratio as calculated from MALDI-TOF analysis.

As the PEG_{24}:G3 stoichiometric ratio increased, we observed an upward shift in the overall mass but reduced resolution of the individual mass peaks (data not shown). Thus, for the calculation of the average number of PEG_{24} **2** additions to G3 dendrimer **1**, we selected the mass of the highest peak or group of peaks. We are reporting the highest signal peak in Table 1

dx.doi.org/10.1021/bc300204n | Bioconjugate Chem. 2012, 23, 1864–1872

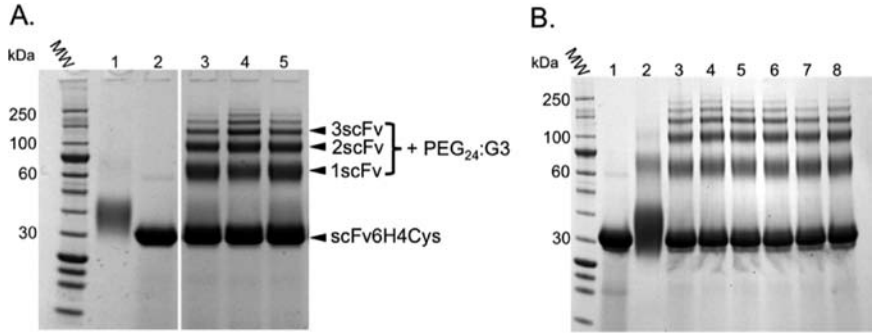


Figure 4. (A) SDS–PAGE reducing gel showing temperature optimization of the PEG_{24} modified dendrimer cross-linking to the scFv6H4Cys (dendribody) reaction: (lane 1) PEG_{24}:G3 dendrimer (reaction ratio 11:1); (lane 2) purified scFv6H4Cys; (lane 3) reaction incubated at 10 °C; (lane 4) 25 °C; and (lane 5) 37 °C. (B) SDS–PAGE reducing gel from the pH optimization study: (lane 1) purified scFv6H4Cys, (lane 2) PEG_{24}:G3 dendrimer (reaction ratio 11:1), dendribodies synthesized in conjugation buffer adjusted at pH 6.2 (lane 3), 6.4 (lane 4), 6.6 (lane 5), 6.8 (lane 6), 7.0 (lane 7) and 7.2 (lane 8).

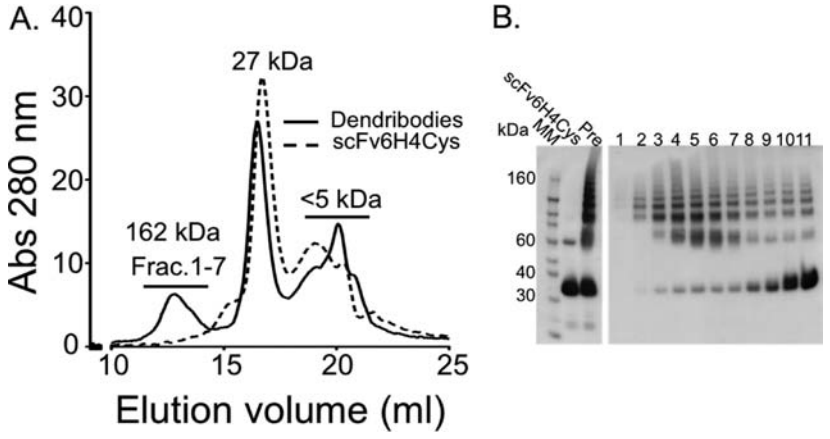


Figure 5. (A) SEC analysis of dendribodies before purification and DTT treated scFv6H4Cys. The solid and dotted lines represent the dendribodies and scFv6H4Cys, respectively. DTT treated scFv6H4Cys exists *in vitro* mainly as a monomer, shown by the prominent peak at 27 kDa. There is also a trace quantity of dimeric species eluting at approximately 15 mL. The dendribodies elute as a single peak of 162 kDa followed by the peak of unreacted scFv6H4Cys. (B) Western blot analysis showing (lane 1) purified scFv6H4Cys and (lane 2/Pre) dendribodies before purification, and (lanes 3–13) eluting fractions 1–11.

assuming that each reaction resulted in a Gaussian distribution of PEG_{24} molecules incorporated around this central peak.

The mass increase for the 5:1, 11:1, 16:1, and 32:1 PEG_{24}:G3 dendrimer reaction ratios corresponded to 5, 16, 20, and 20 PEG **2** additions, respectively (Figure 3B and Table 1). Surprisingly, we observed over 100% addition of the calculated PEG_{24} **2** to the dendrimers **1** for 5:1 and 11:1 reaction ratios. One explanation for this could be the differences in reported and actual concentrations of PEG_{24} **2** or G3 dendrimer **1** lots. Similar to the SDS–PAGE analysis, saturation between 16:1 to 32:1 PEG_{24} to G3 dendrimer reaction ratio was observed with a maximum addition of 20 PEG_{24} units per dendrimer. This suggested that after cross-linking, PEG_{24} occupied up to 63% of the available amines on the dendrimer (Figure 3B). We did not aim to saturate the dendrimers with PEG_{24} since excess unreacted PEG can be difficult to remove from the products. Therefore, we chose the 11:1 PEG_{24}:G3 dendrimer reaction ratio to synthesize the PEG modified dendrimer scaffold for dendribody production.

Cross-Linking Optimization of scFv6H4Cys to PEG Modified Dendrimers. After optimizing the PEG_{24}:G3 dendrimer reaction ratio, we began a series of experiments aimed at optimizing the addition of multiple scFv6H4Cys **4** molecules to the PEG_{24} modified dendrimer scaffold. These optimization experiments included varying numerous parameters known to affect the maleimide–thiol reaction efficiency including scFv to dendrimer stoichiometric ratio, ionic strength, EDTA concentration, temperature, and pH.[21]

The end point of the reaction efficiency was the number of scFv6H4Cys **4** molecules that could be linked to the PEG modified G3 dendrimer **3** core. We could determine the number of scFv6H4Cys **4** on each dendrimer since the reaction products formed distinct and well-resolved bands in an SDS–PAGE gel. We carefully examined both the maximum number of higher-order conjugates as well as the relative amounts of each species. To determine if temperature influenced the reaction efficiency, the dendribody conjugation was allowed to proceed at 10°, 25°, and 37 °C for 2 h and analyzed by SDS–PAGE (Figure 4A). The reaction temperature had a moderate effect on the efficiency of the reaction, with the 25 °C condition having a slightly higher efficiency in the number of scFv6H4Cys **4** molecules conjugated to PEG modified dendrimers. In our studies, NaCl and EDTA concentrations had negligible effects on the efficiency of the reaction (data not shown).

To determine how pH affected the cross-linking efficiency, we conducted six reactions ranging from pH 6.2 to 7.2. This range was selected based on the manufacturer's instructions and previous reports.[21] The optimal reaction was found to be pH

dx.doi.org/10.1021/bc300204n | *Bioconjugate Chem.* 2012, 23, 1864–1872

6.4 (Figure 4B). A Western blot (Figure 5B) probed with an anti-FLAG antibody further confirmed that the discrete banding pattern observed for the dendribodies **5** in the SDS−PAGE analysis was indeed from the addition of increasing numbers of scFv6H4Cys **4** to the PEG modified dendrimers **3**.

Purification of Dendribodies by Immobilized Metal Affinity Chromatography. For the functional assay, it was first necessary to separate the prototype dendribodies **5** from the unconjugated PEG modified dendrimers **3** and scFv6H4Cys **4**. We attempted several chromatographic purification techniques, including ion exchange (IEX, data not shown) and size exclusion chromatography (SEC). These two approaches were not suitable for dendribody purification due to either incomplete separation (IEX) or poor recovery of the product (SEC). However, SEC was a useful analytical tool for determining the native size of the dendribodies. On the basis of a standard curve of known molecular weight proteins, the calculated molecular weights of the predominant peaks of the dendribodies and unreacted scFv6H4Cys were determined to be 162 and 27 kDa, respectively (Figure 5A). The dendribodies eluted as a wide peak with molecular weight ranging from 90 to 305 kDa.

We were ultimately able to utilize the His6 tag of scFv6H4Cys **4** for purification of the dendribodies. The dendribody reaction mixture was applied to a Ni(II) affinity column and eluted with an imidazole gradient over 20 column volumes. The multiple dendribodies and reactants eluted at different concentrations in the imidazole gradient, presumably due to their relative strength of interaction with the immobilized nickel groups on the chromatography resin. The unreacted PEG modified dendrimer did not bind to the IMAC column and was detected in the flow through fractions (Figure 6A and B). Dendribodies with a lower number of scFv6H4Cys were eluted in the early fractions, whereas the higher-order dendribodies eluted later with increasing imidazole concentration. Unreacted scFv6H4Cys eluted from the column predominantly in the later fractions with a peak around 50% (235 mM) imidazole. The early elution fractions (Figure 6B, lanes 4 through 6) were pooled and concentrated (Figure 6C). The Western blot confirmed that this pooled fraction was enriched in lower order dendribodies. This confirmation was important since the lower order dendribodies migrate to a similar position on a gel as PEG_{24} modified dendrimers **3**.

Determination of *in Vitro* Activity of Dendribodies. To determine if the prototype dendribodies retained METH-binding function, a saturation binding equilibrium dialysis experiment was performed using a scFv6H4Cys and dendribody concentration capable of binding 20% of a 50,000 dpm ^{3}H-METH solution. An initial titration was performed to find a protein concentration that would provide a good signal-to-noise ^{3}H-METH binding ratio at low concentrations, while minimizing the effects of ligand depletion.[22] We compared the absolute affinities of the unreacted scFv6H4Cys **4** and the purified lower-order dendribodies **5** to ^{3}H-METH. The dissociation constant (K_D) of the dendribodies **5** and scFv6H4Cys **4** were 1.2 and 1.1 nM, respectively (Figure 7). The PEG modified dendrimers showed negligible nonspecific binding to ^{3}H-METH.

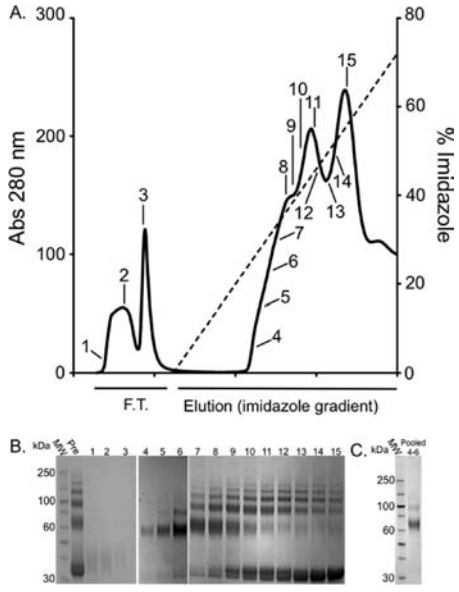


Figure 6. Purification of the dendribodies by immobilized metal affinity chromatography: (A) Separation profile of dendribodies from unreacted PEG_{24} modified dendrimers and scFv6H4Cys. Peak assignments: (1−3) unreacted PEG_{24} modified dendrimers, (4−6) dendribodies, and (7−15) a mixture of dendribodies and unreacted scFv6H4Cys. (B) SDS−PAGE analysis of the fractions eluted with imidazole gradient. (C) SDS−PAGE analysis of pooled and concentrated elution fractions 4−6.

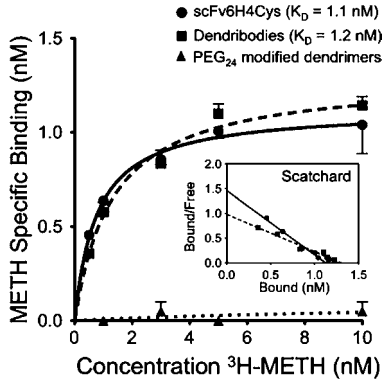


Figure 7. *In vitro* saturation binding assay: saturation data for specific binding of ^{3}H-METH to scFv6H4Cys, dendribodies, and PEG_{24} modified dendrimers with corresponding Scatchard plots (inset). ScFv6H4Cys retained affinity for ^{3}H-METH after conjugation to the dendrimers. Data points are the mean ± SEM of triplicate determinations.

■ DISCUSSION

The therapeutic application of the synthesis and testing of a novel anti-METH antibody fragment−dendrimer conjugate (dendribody) is to treat METH abuse and associated medical conditions. Site-specific sulfhydryl conjugation is becoming a common conjugation strategy to create bioconjugates. This strategy has several advantages over less selective conjugation strategies. First, site-specific conjugation distal to the METH binding site of the scFv6H4Cys **4** can lessen the likelihood of steric interference during METH interaction. Second, since the cysteine residue is located at the C-terminus of the protein, potential polymerization and unwanted side reactions could be avoided. Third, the heterobifunctional PEG-based linkers we

used are an important alternative to carbon-based spacers for protein−dendrimer conjugation because of their increased flexibility, solubility, decreased chance of aggregation, and reduced immunogenicity potential.[23−27] Thus, this elegant conjugation strategy could produce dendribodies with higher multivalency, solubility, and reduced risk of antigenicity.

It was critical to analyze each reaction product during dendribody development to allow optimal control of the stoichiometry of PEG_{24} **2** and scFv6H4Cys **4** additions to dendrimer **1**. We found the PEG_{24} modified dendrimers **3** separated well on a 4−12% gradient polyacrylamide gel and were detectable with a Coomassie-based stain (Figure 2B). This was interesting since neither G3 PAMAM dendrimers nor PEG_{24} alone take up this stain well. Additionally, we found that the intensity of Coomassie-based staining in gels decreased as the number of PEG_{24} additions to the G3 dendrimer increased. The reason for this is not clear but could be due to steric factors influencing entrapment of the dye or net charge changes to the molecule. The apparent size of the PEG_{24} modified dendrimers in an SDS−PAGE gel was larger than the size determined by MALDI-TOF. This could be attributed to an inherent property of PEG to increase the hydrodynamic volume of its conjugates.[28] We also observed high molecular weight bands in the PEG_{24} modified dendrimer lanes (Figure 2B), which were most likely due to their dimerization. These bands were not seen in the final dendribody reaction products.

The DTT treatment of scFv6H4Cys allowed the PEG_{24} maleimide group **2** to covalently link it to the G3 dendrimer. Since scFv6H4Cys **4** contains four internal cysteines that form two stabilizing disulfide bonds,[29] we were concerned that DTT treatment of the scFv6H4Cys would reduce these internal disulfide bridges and lead to loss of function; however, this was not the case. SDS−PAGE analysis confirmed that the maleimide−sulfhydryl reactions routinely produce dendribodies with a denatured size ranging from 50 to ∼200 kDa (Figure 4). However, SEC indicated a native size range for the dendribody peak of 90 to 305 kDa. This native size shift in the SEC analysis is most likely due to hydrodynamic volume changes induced by the PEG moiety, as the scFv6H4Cys peak was 27 kDa, agreeing with SDS−PAGE analysis. This change in apparent size might have important effects on *in vivo* PCKN parameters such as volume of distribution and clearance.

Despite the inclusion of excess molar amounts of PEG_{24} modified dendrimer **3** and scFv6H4Cys **4** in the reaction mixture in an attempt to achieve even higher order dendribodies, we rarely observed higher than six scFv per dendrimer. This was not entirely unexpected since our computer simulations based on the dimensions of each component (Figure 1) indicated that scFv6H4Cys molecules could cause steric inhibition at higher-order incorporations. It might be possible to create even higher order (higher multivalency) dendribodies by using a generation 4 or 5 dendrimer with 64 and 128 reactive amine groups, respectively. However, the potential for toxicity increases as the generation of PAMAM dendrimers increases.[30] The choice of a G3 PAMAM dendrimer **1** represented a compromised balance between the number of functional groups and safety.

The dendribody elution profile from the IMAC column was the result of two predominant factors: accessibility of the His6 tag to the Ni(II) groups and/or multivalency. The lower-order dendribody products with one scFv6H4Cys per dendrimer contain a single His6 affinity tag. The potential for His6−Ni(II) interaction could be hindered by the PEG modified dendrimer **3** and, most importantly, direct hindrance by the high PEG:His6 ratio in the lower order dendribodies. Higher order dendribodies with three to five scFv6H4Cys **4** groups (lower PEG:His6 ratio) eluted later, possibly due to the multiple His6 tags available to bind to the Ni(II) in an additive or synergistic fashion, similar to the cooperative avidity found with IgG or IgM interactions with multiple antigenic epitopes. Interestingly, we found that none of the dendribodies could be detected in Western blots by probing with an anti-His6 antibody (data not shown), suggesting that any degree of PEG modification was sufficient to block IgG access to the 6His tag but not the much smaller bead-chelated Ni(II). The His6 moiety of the unreacted scFv6H4Cys **4** was unhindered and eluted in the later, higher concentration imidazole fractions.

The affinity of scFv6H4Cys for METH (K_D = 1.1 nM) was determined by saturation binding equilibrium dialysis; however, a previously reported affinity for parent scFv6H4 (K_D = 10 nM) was established using a bead-based radioimmunoassay,[21] which, given the inherent discrepancies in the assays, could account for the differences in their affinities. Since the X-ray crystal structure of scFv6H4 indicated that METH binding occurs via a very deep pocket,[29] we were concerned that conjugation could affect METH interactions. Significant charge or steric changes even distal to the binding site of the antibody fragment have been shown to reduce affinity.[27] However, the scFv6H4Cys retained its affinity for METH in the conjugated form, indicating that the conjugation process had little or no effect on the binding pocket of the protein.

■ CONCLUSIONS

These studies describe initial steps in the development of a novel anti-METH scFv-based nanomedicine for METH abuse. We successfully conjugated multiple anti-METH scFvs to a dendrimer nanoparticle with no loss of affinity for METH. This is, to the best of our knowledge, the first description of conjugating an anti-drug of abuse antibody fragment to a nanoparticle with detailed characterization of reaction intermediates. We think that the dendribody design is a promising platform to customize PCKN parameters (size dependent extension of *in vivo* half-life) and improve the efficacy (multivalency) and safety of biotherapeutics.

■ AUTHOR INFORMATION

Corresponding Author

*Phone: 501-686-7335. E-mail: epeterson@uams.edu.

Notes

The authors declare no competing financial interest.

■ ACKNOWLEDGMENTS

This work was supported by the National Institute on Drug Abuse grant R01 DA026423 and the UAMS Pharmacology and Toxicology start-up funding to E.C.P. We thank Drs. S. Michael Owens, Prem Gupta, and Ms. Jennifer Gidden for consultation, manuscript review, and technical expertise.

■ ABBREVIATIONS

scFv, single-chain variable fragment; V_H, variable heavy region; V_L, variable light region; PCKN, pharmacokinetic; METH, (+)-methamphetamine; [^{3}H]-METH, (+)-2′,6′-$^3H(n)$ methamphetamine; SEC, size exclusion chromatography; PAGE, polyacrylamide gel electrophoresis; MALDI-TOF, matrix assisted laser desorption ionization−time-of-flight; BMGY,

buffered minimal glycerol-complex medium; G3, generation 3; PAMAM, polyamidoamine; PEG, polyethylene glycol

REFERENCES

(1) Segal, D. (1994) *Amphetamine and Its Analogs: Psychopharmacology, Toxicology, and Abuse*, pp 387−414, Academic Press, San Diego, CA.

(2) Laurenzana, E. M., Byrnes-Blake, K. A., Milesi-Hallé, A., Gentry, W. B., Williams, D. K., and Owens, S. M. (2003) Use of anti-(+)-methamphetamine monoclonal antibody to significantly alter (+)-methamphetamine and (+)-amphetamine disposition in rats. *Drug Metab. Dispos. 31*, 1320−1326.

(3) Byrnes-Blake, K. A., Laurenzana, E. M., Carroll, F. I., Abraham, P., Gentry, W. B., Landes, R. D., and Owens, S. M. (2003) Pharmacodynamic mechanisms of monoclonal antibody-based antagonism of (+)-methamphetamine in rats. *Eur. J. Pharmacol. 461*, 119−128.

(4) McMillan, D. E., Hardwick, W. C., Li, M., Gunnell, M. G., Carroll, F. I., Abraham, P., and Owens, S. M. (2004) Effects of murine-derived anti-methamphetamine monoclonal antibodies on (+)-methamphetamine self-administration in the rat. *J. Pharmacol. Exp. Ther. 309*, 1248−1255.

(5) Peterson, E. C., and Owens, S. M. (2009) Designing immunotherapies to thwart drug abuse. *Mol. Interventions 9*, 119−124.

(6) Roopenian, D. C., and Akilesh, S. (2007) FcRn: the neonatal Fc receptor comes of age. *Nat. Rev. Immunol. 7*, 715−725.

(7) Laurenzana, E. M., Hendrickson, H. P., Carpenter, D., Peterson, E. C., Gentry, W. B., West, M., Che, Y., Carroll, F. I., and Owens, S. M. (2009) Functional and biological determinants affecting the duration of action and efficacy of anti-(+)-methamphetamine monoclonal antibodies in rats. *Vaccine 27*, 7011−7020.

(8) Peterson, E. C., Gunnell, M., Che, Y., Goforth, R. L., Carroll, F. I., Henry, R., Liu, H., and Owens, S. M. (2007) Using hapten design to discover therapeutic monoclonal antibodies for treating methamphetamine abuse. *J. Pharmacol. Exp. Ther. 322*, 30−39.

(9) Peer, D., Karp, J. M., Hong, S., Farokhzad, O. C., Margalit, R., and Langer, R. (2007) Nanocarriers as an emerging platform for cancer therapy. *Nat. Nanotechnol. 2*, 751−760.

(10) Provenzale, J. M., and Silva, G. A. (2009) Uses of nanoparticles for central nervous system imaging and therapy. *Am. J. Neuroradiol. 30*, 1293−1301.

(11) Zhang, L., Gu, F., Chan, J., and Wang, A. (2008) Nanoparticles in medicine: therapeutic applications and developments. *Clin. Pharmacol. Ther. 85*, 761−769.

(12) Svenson, S., and Tomalia, D. A. (2005) Dendrimers in biomedical applications–reflections on the field. *Adv. Drug Delivery Rev. 57*, 2106−2129.

(13) Boas, U., and Heegaard, P. M. H. (2004) Dendrimers in drug research. *Chem. Soc. Rev. 33*, 43−63.

(14) Sambrook, J., and Russell, D. W. (2001) *Molecular Cloning: A Laboratory Manual*, Cold Spring Harbor Laboratory Press, Cold Spring Harbor, NY.

(15) Peterson, E. C., Laurenzana, E. M., Atchley, W. T., Hendrickson, H. P., and Owens, S. M. (2008) Development and preclinical testing of a high-affinity single-chain antibody against (+)-methamphetamine. *J. Pharmacol. Exp. Ther. 325*, 124−133.

(16) Kurfürst, M. M. (1992) Detection and molecular weight determination of polyethylene glycol-modified hirudin by staining after sodium dodecyl sulfate-polyacrylamide gel electrophoresis. *Anal. Biochem. 200*, 244−248.

(17) Baum, P., Müller, D., Rüger, R., and Kontermann, R. E. (2007) Single-chain Fv immunoliposomes for the targeting of fibroblast activation protein-expressing tumor stromal cells. *J. Drug Target 15*, 399−406.

(18) Thomas, J., Sherman, D. B., Amiss, T. J., Andaluz, S. A., and Pitner, J. B. (2007) Synthesis and biosensor performance of a near-IR thiol-reactive fluorophore based on benzothiazolium squaraine. *Bioconjugate Chem. 18*, 1841−1846.

(19) Brocchini, S., Godwin, A., Balan, S., Choi, J. W., Zloh, M., and Shaunak, S. (2008) Disulfide bridge based PEGylation of proteins. *Adv. Drug Delivery Rev. 60*, 3−12.

(20) Sharma, A., Desai, A., Ali, R., and Tomalia, D. (2005) Polyacrylamide gel electrophoresis separation and detection of polyamidoamine dendrimers possessing various cores and terminal groups. *J. Chromatogr., A 1081*, 238−244.

(21) Hermanson, G. (1996) *Hermanson: Bioconjugate Techniques*, Academic Press, San Diego, CA.

(22) Cheng, Y., and Prusoff, W. H. (1973) Relationship between the inhibition constant (K1) and the concentration of inhibitor which causes 50% inhibition (I50) of an enzymatic reaction. *Biochem. Pharmacol. 22*, 3099−3108.

(23) Lee, L. S., Conover, C., Shi, C., aWhitlow, M., and Filpula, D. (1999) Prolonged circulating lives of single-chain Fv proteins conjugated with polyethylene glycol: a comparison of conjugation chemistries and compounds. *Bioconjugate Chem. 10*, 973−981.

(24) Chapman, A. P. (2002) PEGylated antibodies and antibody fragments for improved therapy: a review. *Adv. Drug Delivery Rev. 54*, 531−545.

(25) Luo, D., Haverstick, K., Belcheva, N., Han, E., and Saltzman, W. M. (2002) Poly(ethylene glycol)-conjugated PAMAM dendrimer for biocompatible, high-efficiency DNA delivery. *Macromolecules 35*, 3456−3462.

(26) Yang, K., Basu, A., Wang, M., Chintala, R., Hsieh, M. C., Liu, S., Hua, J., Zhang, Z., Zhou, J., Li, M., Phyu, H., Petti, G., Mendez, M., Janjua, H., Peng, P., Longley, C., Borowski, V., Mehlig, M., and Filpula, D. (2003) Tailoring structure-function and pharmacokinetic properties of single-chain Fv proteins by site-specific PEGylation. *Protein Eng. 16*, 761−770.

(27) Kubetzko, S., Balic, E., Waibel, R., Zangemeister-Wittke, U., and Plückthun, A. (2006) PEGylation and multimerization of the anti-$p185^{HER-2}$ single chain Fv fragment 4D5: effects on tumor targeting. *J. Biol. Chem. 281*, 35186−35201.

(28) Plesner, B., Westh, P., Hvidt, S., and Nielsen, A. D. (2011) The molar hydrodynamic volume changes of factor VIIa due to GlycoPEGylation. *J. Pharm. Biomed. Anal. 55*, 597−602.

(29) Celikel, R., Peterson, E. C., Owens, S. M., and Varughese, K. I. (2009) Crystal structures of a therapeutic single chain antibody in complex with two drugs of abuse-methamphetamine and 3,4-methylenedioxymethamphetamine. *Protein Sci. 18*, 2336−2345.

(30) Malik, N., Wiwattanapatapee, R., Klopsch, R., Lorenz, K., Frey, H., Weener, J. W., Meijer, E. W., Paulus, W., and Duncan, R. (2000) Dendrimers: relationship between structure and biocompatibility in vitro, and preliminary studies on the biodistribution of ^{125}I-labelled polyamidoamine dendrimers in vivo. *J. Controlled Release 65*, 133−148.

Bioconjugate Chemistry

Article

pubs.acs.org/bc

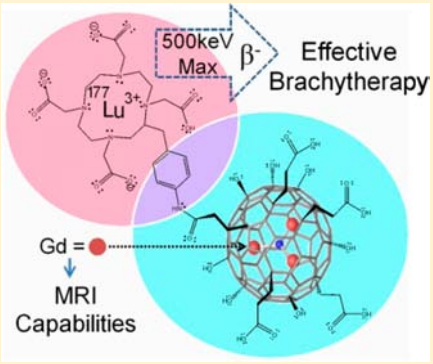
Metallofullerene-Nanoplatform-Delivered Interstitial Brachytherapy Improved Survival in a Murine Model of Glioblastoma Multiforme

John D. Wilson,[†] William C. Broaddus,[‡] Harry C. Dorn,[∥] Panos P. Fatouros,[†] Charles E. Chalfant,*[,§] and Michael D. Shultz*[,§]

[†]Departments of Radiology, [‡]Neurosurgery, and [§]Biochemistry and Molecular Biology, Virginia Commonwealth University, 1101 East Marshall Street, Richmond, Virginia 23298, United States

[∥]Department of Chemistry, Virginia Tech, 1109 Hahn Hall, Blacksburg, Virginia 24061, United States

ABSTRACT: Fullerenes are used across scientific disciplines because of their diverse properties gained by altering encapsulated or surface-bound components. In this study, the recently developed theranostic agent based on a radiolabeled functionalized metallofullerene (^{177}Lu-DOTA-f-Gd$_3$N@C$_{80}$) was synthesized with high radiochemical yield and purity. The efficacy of this agent was demonstrated in two orthotopic xenograft brain tumor models of glioblastoma multiforme (GBM). A dose-dependent improvement in survival was also shown. The *in vivo* stability of the agent was verified through dual label measurements of biological elimination from the tumor. Overall, these results provide evidence that nanomaterial platforms can be used to deliver effective interstitial brachytherapy.



INTRODUCTION

Glioblastoma multiforme (GBM) is a particularly difficult to treat and devastating disease. The prognosis for patients with newly diagnosed GBM carries a 1 year median survival, largely due to GBM resistance to current adjuvant therapies that often follow surgical resection, such as conventional radiation therapy and chemotherapy.[1,2] Residual cells at the margins of the resection frequently lead to tumor recurrence. Furthermore, a subpopulation of stem-like cells, known as GBM stem cells (GSCs), may be a major proponent of GBM recurrence due to higher chemo- and radioresistance, as well as having a higher tumorigenic potential and the ability to differentiate into several cell types.[3−8] These factors result in a high recurrence rate of these malignancies, and an inability to cure this difficult disease. Therefore, bringing novel nanomaterial based modalities to the clinician for treatment of high grade gliomas is of potential interest.

Nanomaterials offer promising solutions to the treatment of this serious disease because they present new strategies and have a size range capable of entering cells (1 to 1000 nm), a substantial multifunctional capability, and an inherently large surface-to-volume ratio. These characteristics of nanomaterials are critical, as recent literature has reported that doxorubicin delivered to cells via gold nanoparticles increased the rate of cellular drug uptake and was 20-fold more cytotoxic.[9] While the realm of nanomaterials is vast, the advancement and use of carbon based (carbonaceous) nanomaterials has continued to thrive since the discovery of the C$_{60}$ molecule in 1985 by Smalley, Kroto, Curl, and co-workers (Nobel Prize 1996).[10] Also known as "buckyballs" due to their resemblance to the geodesic domes of Richard Buckminster Fuller, fullerenes have shown potential for use in a multitude of medical fields due to their cage-like structure and diverse material properties. These multiple properties result from the encapsulation of various metals within the carbon cage[11−13] or decoration of the fullerene surface[14,15] with targeting,[12,16] diagnostic,[17,18] or biofunctional ligands.[19,20] The vision of nanomedicine has stimulated further fullerene advancements,[21,22] primarily due to the versatile functionality available in a single nanoplatform. There is increasing interest in the trimetallic nitride endohedral metallofullerenes A$_3$N@C$_{2n}$ (n = 34−50) because of their interesting electronic and structural properties.[23−25] In comparison with empty-cage fullerenes such as C$_{60}$, C$_{70}$, and C$_{84}$, these endohedral metallofullerenes have higher stability corresponding to lower chemical reactivity. Nevertheless, they exhibit sufficient chemical reactivity to accommodate a variety of different surface functionalization methods.[20,26−31] In particular, trigadolinium nitride C$_{80}$ endohedral metallofullerenes (Gd$_3$N@C$_{80}$) have shown great potential for application in biomedicine, especially as MRI contrast agents.[19,20,32−34]

In regard to cancers of the central nervous system (CNS), such as GBM, there is difficulty with treatment using conventional routes of administration due to the blood brain barrier (BBB). Advancements in clinical procedures have led to a method of drug delivery that circumvents the BBB and limits systemic toxicity known as convection-enhanced delivery (CED).[35,36] Also referred to as direct intraparenchymal infusion, CED is a procedural option that is less invasive than

Received: April 12, 2012
Revised: August 8, 2012
Published: August 10, 2012

ACS Publications © 2012 American Chemical Society

further tumor resection. It is often employed in cases when a patient has a region of tumor recurrence that is inoperable, or the physical burden of the surgery and recovery would be unwarranted or more detrimental to the patient's overall quality of life. In these and other situations, CED provides beneficial adjuvant therapy by the strategic placement of cannulae or catheters directly into target tissues through stereotactic methods and delivery of a therapeutic bolus. A positive pressure gradient slowly drives the agent through the interstitial space providing a more uniform and reproducible volume of distribution compared to intratumoral injection. This also allows for the delivery of large molecules and nanoparticles (<100 nm) that due to their size would not cross the BBB or diffuse effectively upon simple injection. Although CED is efficient for locally administering a high therapeutic dose with uniform distribution, other issues such as relatively rapid diffusion of therapeutic agents out of the brain has incited investigations using liposomes and nanomaterials to slow the biological decay of these agents from the tumor.[32,37]

Interstitial delivery of radioactive isotopes into tumors for therapeutic purposes (brachytherapy) has a long history of development and use for a variety of cancers. Such approaches are common for treatment of prostate and breast cancer, and there is a substantial history of use of a variety of isotopes for the treatment of malignant primary brain tumors.[38,39] Most techniques have involved stereotactic placement of catheters to be after-loaded with radioactive seeds for short-term high dose rate brachytherapy (after which the catheters are removed) or implantation of permanent seeds at the time of surgical resection of the tumor for low dose rate brachytherapy. A number of studies demonstrating promising results have been reported, although two prospective randomized trials using ^{125}I as the isotope in patients with newly diagnosed malignant gliomas did not demonstrate a benefit over conventional therapy with fractionated regional radiation treatments.[40,41] Nevertheless, significant interest in brachytherapy techniques remains for the treatment of primary brain tumors. These highly malignant tumors invariably recur after initial treatment with surgery, external beam radiation therapy, and chemotherapy. The recurrences are often identified on followup MR imaging while they are relatively discrete and small, making them excellent targets for therapy directed by image guidance. In some instances, the initial presentation of GBM is with a focal area of brain abnormality that is not amenable to surgical resection, making the possibility of needle biopsy followed by infusion of a brachytherapeutic isotope attractive. The ability to deliver an isotope by CED with high stereotactic precision and using ever more powerful neuro-imaging techniques promises improved targeting and coverage of the tumor cells. The possibility of using ^{177}Lu as the brachytherapy isotope for its advantageous path-length and half-life characteristics and the possibility of targeting tumor cells with affinity ligand-labeled radioactive nanoparticles[16] makes investigation of the efficacy of ^{177}Lu-DOTA-f-$Gd_3N@C_{80}$ on model human gliomas of great interest for advancing this approach to treating brain tumors.

In the presented study, the recently reported[32] theranostic agent ^{177}Lu-DOTA-f-$Gd_3N@C_{80}$ was infused by CED intratumorally to provide brachytherapy for orthotopic xenograft tumor-bearing mice. Since the imaging capabilities of this agent have previously been shown,[32] this work focused on demonstrating a therapeutic dose response and efficacy with *in vivo* models using two glioblastoma cell lines, U87MG and GBM12. Furthermore, modifications to previous synthetic methods are described that resulted in a higher yield and a more radiochemically pure material. Finally, two analytical methods were employed in determining the biological decay from the tumor and intracranial stability of the agent.

EXPERIMENTAL PROCEDURES

^{177}Lu-DOTA-f-$Gd_3N@C_{80}$ Theranostic Agent Synthesis. The $Gd_3N@C_{80}$ metallofullerenes were produced and surface functionalized for aqueous solubility and amide bond conjugation methods as previously reported to obtain f-$Gd_3N@C_{80}$.[20] Prior to activating the carboxyl groups on the f-$Gd_3N@C_{80}$ surface, 500 μL of f-$Gd_3N@C_{80}$ solution (0.27 mM - $Gd_3N@C_{80}$) was diluted with 500 μL of MES (2-[*N*-morpholino]ethanesulfonic acid; Sigma-Aldrich) buffer adjusted to pH 6.4 with Optima grade ammonium hydroxide (Fisher Scientific). The carboxyl groups were then activated for coupling reactions by addition of 100 μL of 1 M EDC (1-ethyl-3-[3-dimethylaminopropyl] carbodiimide; Thermo Scientific) and 100 μL of 1 M Sulfo-NHS (*N*-hydroxysulfosuccinimide; Thermo Scientific) and reacted at room temperature for 10 min. Immediately at 10 min, 2 μL of 2-mercaptoethanol (Sigma-Aldrich) was added to react excess EDC. Then, 2 mg of bifunctional *p*-NH_2-Bn-DOTA (DOTA) (2-(4-aminobenzyl)-1,4,7,10-tetraazacyclododecane-1,4,7,10-tetraacetic acid; Macrocyclics) was immediately combined with the activated f-$Gd_3N@C_{80}$ and reacted at room temperature for 2 h to couple the f-$Gd_3N@C_{80}$ to the primary amine on the bifunctional DOTA. Then, 100 μL of 0.275 M hydroxylamine was added to quench the reaction and convert nonreacted activated groups back to carboxyl groups. Purification at this step was be carried out by elution through a PD-10 Sephadex desalting column (GE Healthcare) using 0.25 mM ammonium acetate in Optima grade water (DI) (Fisher Scientific) as eluent.

For radioactive labeling, $^{177}LuCl_3$ was used as received from Perkin-Elmer (0.74 GBq, 15 μL) with the addition of DI water making a total volume of 50 μL. The 50 μL of $^{177}Lu^{3+}$ solution was then transferred into the purified DOTA labeled product (DOTA-f-$Gd_3N@C_{80}$) followed by the addition of 20 μL of Optima grade ammonium hydroxide. This shifted the pH to the basic buffering region of the ammonium acetate, which is more favorable for the ^{177}Lu-DOTA chelate formation. The reaction tube was then sealed and placed in a 40 °C oil bath for 12 h. Removal of free/unchelated $^{177}Lu^{3+}$ was accomplished using a cation exchange cartridge (Oasis MCX, 3 mL/60 mg, 60 μm; Waters). The cartridge was prewet with 3 mL of methanol (Fisher Scientific) and conditioned with DI water. Following this, the reaction solution was loaded onto the cartridge (gravity fed). Then, 1 mL of DI water was added to the cartridge and slowly extruded with a plunger to collect 1 mL of volume. Previous testing showed this methodology removed free $^{177}Lu^{3+}$ and eluted the fullerene nanoparticles.[32] Purification to obtain pure ^{177}Lu-DOTA-f-$Gd_3N@C_{80}$ for infusions was carried out by elution through a second PD-10 desalting column using sterile PBS as eluent. Samples were analyzed by high-performance liquid chromatography (HPLC) (Waters—isocratic, 90% 50 mM ammonium acetate/10% methanol) with UV—vis absorption and radioactive detectors (Bioscan) for radiopurity.

Dynamic light scattering (DLS) characterization (Malvern Instruments, Nano-ZS) was carried out on the functionalized metallofullerenes alone, f-$Gd_3N@C_{80}$, and a nonradiolabeled analogue of the theranostic agent, Lu-DOTA-f-$Gd_3N@C_{80}$. This "cold" form of the theranostic was synthesized by methods

identical to those described above with the exception of replacing the $^{177}LuCl_3$ solution with a $LuCl_3$ solution prepared to have a matching total Lu concentration.

Cell Culture. Human U87MG glioblastoma cells (American Type Culture Collection) and GBM12 cells (provided by Dr. C. David James - University of California, San Francisco, Department of Neurological Surgery) were grown in high-glucose DMEM supplemented with 10% FBS, 100 units/mL penicillin, and 100 units/mL of streptomycin (BioWhittaker Penicillin/Streptomycin, Cambrex Bio Science Walkersville, Inc.) at 37 °C in a 5% CO_2/95% air atmosphere. GBM12 cells were used from short-term cultures established from excised flank xenografts as previously described to promote invasive behavior.[42] To prepare cell inocula, cells were harvested from log phase cultures and resuspended in phosphate-buffered saline at a concentration of 5×10^4 cells/μL.

Tumor Implantation Procedures. All experiments involving the use of mice were carried out in accordance with protocols approved by the institutional animal care and use committee. Female Athymic Nude-Foxn1nu mice (Harlan Laboratories) were anesthetized with isoflurane (3% knock-down, 2% maintenance in oxygen) and placed in a stereotactic frame (David Kopf Instruments). Following a midline incision, a 0.7 mm burr hole was drilled in the skull 0.5 mm anterior to the bregma and 2 mm laterally to the right. A 25 μL Hamilton Syringe with a 28 gauge removable needle was used to inject 1×10^5 cells (U87MG or GBM12) in 2 μL of PBS at a depth of 4.0 mm from the surface of the skull and at a flow rate of 0.2 μL per minute using a microinjection pump (Bioanalytical Systems). The burr hole was sealed with sterile bone wax, the incision sutured, and animals were allowed to recover and subsequently placed in the vivarium.

Dose Preparations and Survival Studies. The radioactivity of the final ^{177}Lu-DOTA-f-$Gd_3N@C_{80}$ product in PBS was determined by gamma well counting and converted to units of megabecquerel (MBq). Since the focus of these studies was to determine a therapeutic dose response and efficacy, the mice were not imaged during the experiment because stress from imaging and anesthesia can alter survival outcome. As the survival studies would involve 48 mice requiring 3 consecutive days of 16 surgical procedures, each dose level was prepared in three separate vials. A combination of ^{177}Lu-DOTA-f-$Gd_3N@C_{80}$, f-$Gd_3N@C_{80}$, and PBS (all sterile or sterile filtered) were mixed in order to account for ^{177}Lu radioactive decay (half-life = 6.7 days) over the 3 day period, while maintaining a constant $Gd_3N@C_{80}$ concentration. This was important in order to keep the infused volume constant (10 μL). Survival studies were designed to assess a dose response (3 doses plus control) for the U87MG model and a single dose efficacy for the GBM12 model (high dose plus control). Thus, 36 mice (12 per day) were implanted orthotopically with U87MG cells as described above and 12 mice (4 per day) were implanted with GBM12 cells. Eight days post tumor cell inoculation, U87MG tumor-bearing mice were randomized into 4 groups of 9 mice each: a control group to receive only f-$Gd_3N@C_{80}$ and 3 treatment groups receiving 0.25, 0.75, or 1.35 MBq of ^{177}Lu-DOTA-f-$Gd_3N@C_{80}$ product. The GBM12 tumor-bearing mice were also randomized into 2 groups of 6 mice each: a control group (only f-$Gd_3N@C_{80}$) and a treatment group to receive 1.35 MBq of ^{177}Lu-DOTA-f-$Gd_3N@C_{80}$. Animals were anesthetized as before, incision made, and bone wax removed to reopen the burr hole. Centered stereotactically on the burr hole, the agents were delivered to the center of the tumor (depth, 4 mm) via CED at a rate of 0.2 μL/min for a total volume of 10 μL. The combination of the needle size (28-gauge), aqueous infusate medium, and slow infusion rate (0.2 μL/min) has been shown to provide efficient CED in rodent models.[37] A corresponding set of 1.5 mL agarose gels (0.6%) were infused with 10 μL of each dose under identical stereotactic conditions following surgical procedures. Activities of the gels were measured by gamma well counting and back-decayed to the time of infusion to obtain an accurate assessment of ^{177}Lu activity delivered. Animals were observed and weighed daily to follow the progression of disease. A 20% decrease in body weight relative to the treatment day was established as the primary criteria for euthanasia and the survival time was recorded as the number of days post tumor cell inoculation.

Tumor/Brain ^{177}Lu-DOTA-f-$Gd_3N@C_{80}$ Retention Studies. Inductively coupled plasma mass spectrometry (ICP-MS) (Varian 820-MS; Agilent Technologies) was used to determine the Gd concentration and radioactivity determined by gamma well counting in the tumor-bearing hemisphere over time. Twelve tumor-bearing mice were infused with 10 μL of ^{177}Lu-DOTA-f-$Gd_3N@C_{80}$ by CED as described earlier. The delivered ^{177}Lu activity was 0.571 ± 0.001 MBq and the total Gd delivered was 0.654 ± 0.045 μg determined from analysis of 4 gels infused under the stereotactic conditions. The animals were randomized into 4 groups of 3 mice, each group being euthanized at 4 different time points (immediately and 24, 48, and 168 h post infusion). Upon euthanasia, the brain of each mouse was excised and divided into the tumor-bearing hemisphere and the contralateral hemisphere. The two hemispheres were placed in 25 mL conical tubes, and frozen at −80 °C until all samples were obtained at the experimental time points. The samples were then thawed and sonicated vigorously in 1 mL of DI water for 30 s (sufficient time for complete tissue disruption). Then, 1 mL of Optima grade nitric acid (Fisher Scientific) was added to each sample, tubes subsequently sealed and incubated at 60 °C in an oven for 12 h (sufficient time for complete digestion of the tissue). The samples and a 1 mL wash with DI water were then filtered through a 0.45 μm polytetrafluoroethylene (PTFE) syringe filter (Whatman GD/XP, GE Healthcare, Princeton, NJ) into scintillation vials and incubated open at 80 °C until dry. Next, 375 μL (tumor-bearing hemispheres) or 200 μL (contralateral hemisphere) of Optima grade nitric acid was used to redissolve each sample, with the addition of DI water to bring the total volume to 1.5 and 0.8 mL, respectively. Then, 700 μL aliquots of each sample were subjected to gamma counting (for ^{177}Lu content) and ICP-MS (for Gd content). The percent infused dose was calculated by dividing each sample's Gd content or ^{177}Lu activity by the total amount of Gd or ^{177}Lu activity infused. Values were corrected for percent recovery from the digestion protocol as done previously.[32]

Statistical Analysis. All measured values are presented as mean ± standard error. Biological decay experiments involved three mice at each time point studied. The ICP-MS measurement of Gd content or gamma count of ^{177}Lu activity was expressed as a percentage of the gadolinium or ^{177}Lu activity relative to the infused dose (percent infused dose). For survival studies, statistical software (IBM *SPSS statistics 19.0*) was used to compute the mean survival time (±standard error) for the dose groups by using the Kaplan−Meier method. Survival curves were compared pairwise within each tumor model using the Mantel-Cox log rank test with $p < 0.05$ being considered significant.

RESULTS

Improved Synthetic Yield and Purity. The overall radioactive yield of the theranostic agent (^{177}Lu-DOTA-f-$Gd_3N@C_{80}$) from previous studies was reported to be <5% with radiochemical purity of 80%.[32] The starting $Gd_3N@C_{80}$ fullerene nanoparticle and ^{177}Lu-DOTA-f-$Gd_3N@C_{80}$ are illustrated in Figure 1 (top left and bottom respectively).

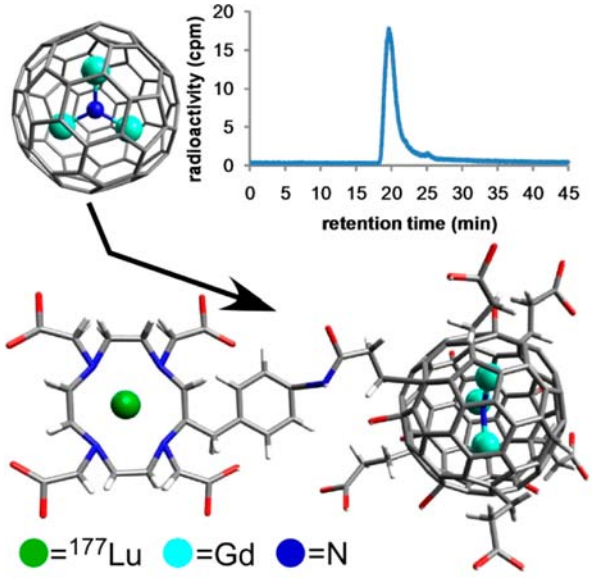


Figure 1. Illustration of the metallofullerene based therapeutic agent and improved yield and purity. (Top Left) Structures of the starting endohedral metallofullerene and (Bottom) final radiolabeled theranostic agent. (Top Right) HPLC analysis with radioactive detection showing the retention profile of the final purified product.

Using the methods outlined above in this work, the overall radioactive yield was improved to >50%. This was accomplished primarily by switching the order of the synthesis to link the DOTA on the f-$Gd_3N@C_{80}$ first, with a subsequent additional purification step to remove unconjugated DOTA. Analysis by HPLC with radioactive detection (Figure 1 − top right) showed the ^{177}Lu-DOTA-f-$Gd_3N@C_{80}$ product peak retention time around 20 min and the "free" or unbound ^{177}Lu-DOTA at 25 min. These two peaks integrate to give a value of 97% radiochemical purity. These results verify that the ^{177}Lu-DOTA-f-$Gd_3N@C_{80}$ can be produced with high yield and purity.

Further characterization by DLS was carried out to investigate the effect of the surface radiolabeling on functionalized metallofullerene cluster formation and size distribution. As seen in Figure 2, the f-$Gd_3N@C_{80}$ alone has a bimodal size distribution with peaks around 20.5 and 6.7 nm in terms of hydrodynamic diameter. The addition of the trivalent metal chelate, ^{177}Lu-DOTA, to the f-$Gd_3N@C_{80}$ surface resulted in a smaller size distribution centered at 1.4 nm. Therefore, the addition of the ^{177}Lu-DOTA disrupts the cluster formation and yields a hydrodynamic diameter more consistent with that of a single ^{177}Lu-DOTA-f-$Gd_3N@C_{80}$ particle.

Treatment of Murine Orthotopic Xenograft GBM Tumors with ^{177}Lu-DOTA-f-$Gd_3N@C_{80}$ Shows Improved Survival and Dose Response. Previous studies demonstrated therapeutic potential of this theranostic agent, providing prolonged survival above control out to 60 days at a single dose

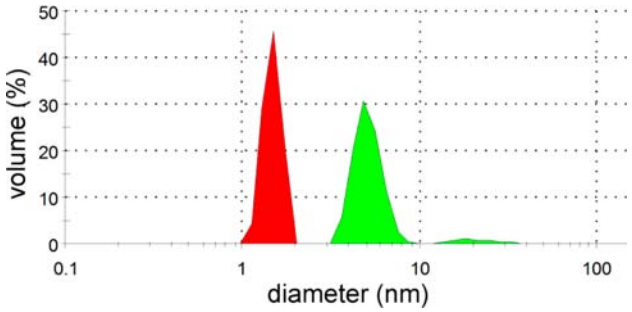


Figure 2. Dynamic light scattering analysis of clustering and size distribution of the f-Gd_3NC_{80} nanoplatform alone (green) and ^{177}Lu-DOTA-f-$Gd_3N@C_{80}$ (red).

of 1.11 MBq.[32] While these previous results were positive, they were limited in part due to the low overall radioactive yield. Now, with the improved synthetic methods and yield reported above, it was possible to investigate the necessary dose response of this agent. The therapeutic dose response of ^{177}Lu-DOTA-f-$Gd_3N@C_{80}$ was tested using the U87MG mouse model. To demonstrate translatability to another more invasive brain tumor cell line, a single dose therapeutic efficacy was tested using the GBM12 mouse model. Measurement results of the actual infused doses for each treatment group are as follows: U87MG model, 0.25 ± 0.01 MBq, 0.75 ± 0.04 MBq, and 1.35 ± 0.05 MBq; GBM12 model, 1.35 ± 0.05 MBq. During the survival studies, two of the U87MG tumor-bearing mice were euthanized due to complications unrelated to the experiment, and thus were removed from the study and not included in the following results. As seen in Figure 3 (top), the mean survival times post tumor cell inoculations for the U87MG tumor-bearing mice were 28.7 ± 1.2 days (20.7 days post treatment) for the control group and 48.7 ± 2.5 days (40.7 post treatment) for the 0.25 MBq group. Since the 0.75 MBq and 1.35 MBq groups both had censored events (mice still surviving at 100 days), only estimates of the mean survival could be made that are limited to the largest survival time. In the case of the 0.75 MBq group, the mean survival was 69.5 ± 8.3 days (61.5 post treatment) with 25% surviving at 100 days. In comparison, the 1.35 MBq group had 87.5% surviving at 100 days, euthanizing only 1 of 8 mice during the experimental period. These surviving mice were still thriving at day 100 as evidenced by their increasing/stable relative body weights (Figure 3 bottom). In regard to the GBM12 tumor-bearing mice, the control group survival was 38.3 ± 1.2 days (30.3 post treatment), while the 1.35 MBq group had 83.3% surviving at 100 days (euthanized 1 of 6 mice during experiment). Results of the pairwise comparisons between treatment groups within each tumor model revealed that all treatments were significantly different from their control ($p < 0.001$) and from each other ($p \leq 0.050$). These data verify efficacy of the ^{177}Lu-DOTA-f-$Gd_3N@C_{80}$ in two human GBM cell line models.

Biological Decay of the ^{177}Lu-DOTA-f-$Gd_3N@C_{80}$ from the Tumor Shows *in Vivo* Stability. The biological decay of the ^{177}Lu-DOTA-f-$Gd_3N@C_{80}$ out of the tumor was determined by tracking both the Gd and ^{177}Lu components of the agent. Figure 4 shows the percent of the infused dose (% ID) for the ^{177}Lu-DOTA-f-$Gd_3N@C_{80}$ in the tumor-bearing hemisphere as measured by ICP-MS (Gd) and gamma counting (^{177}Lu). If the covalent linkage between the fullerene cage and ^{177}Lu-DOTA were cleaved, the free ^{177}Lu-DOTA would be more rapidly cleared from the brain than the fullerene

dx.doi.org/10.1021/bc300206q | *Bioconjugate Chem.* 2012, 23, 1873−1880

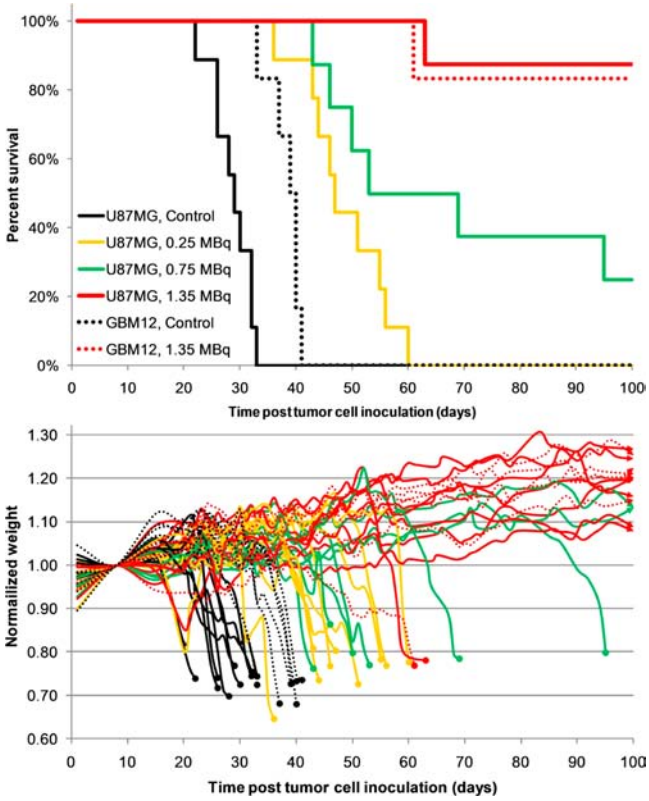


Figure 3. Survival studies with U87MG and GBM12 orthotopic tumor-bearing mice. (Top) Survival curves for the U87MG (solid lines) and GBM12 (dashed lines) tumor-bearing mice receiving either f-$Gd_3N@C_{80}$ as control (black, U87MG: n = 9, GBM12: n = 6) or a treatment of ^{177}Lu-DOTA-f-$Gd_3N@C_{80}$ at activities of 0.25 MBq (yellow, U87MG: n = 9), 0.75 MBq (green, U87MG: n = 8), or 1.35 MBq (red, U87MG: n = 8, GBM12: n = 6). (Bottom) Weights of the mice during the survival studies normalized to the day of treatment or control infusion (day 8).

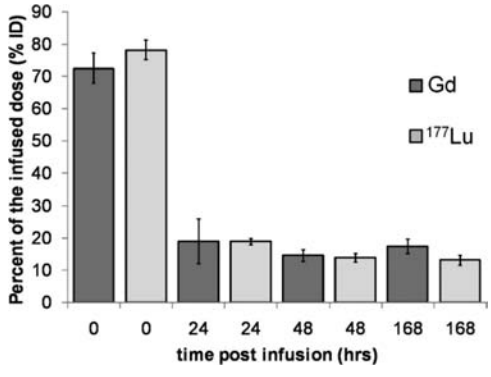


Figure 4. Tumor retention of ^{177}Lu-DOTA-f-$Gd_3N@C_{80}$. Measured values are plotted as the percent of the infused dose (%ID) determined by Gd measurement (dark gray) or ^{177}Lu measurement (light gray) at four time points of 0, 24, 48, and 168 h post infusion (n = 3 per time point).

nanoparticle as previously reported.[32] Therefore, the agreement between the %ID measurements at each time point gives indication that the ^{177}Lu-DOTA-f-$Gd_3N@C_{80}$ is not being significantly degraded over this period of time in the brain. Results for the contralateral brain hemisphere in terms of ^{177}Lu are as follows: 0 h = 1.90 ± 0.46% ID, 24 h = 0.54 ± 0.07% ID, 48 h = 0.47 ± 0.16% ID, and 168 h = 0.50 ± 0.05% ID.

DISCUSSION

Glioblastoma is highly malignant, usually occurring as a primary focus of tumor mass surrounded by a wide area of invasive tumor cells infiltrating the normal brain.[43] Peripheral metastases of GBM to other regions of the body are extremely rare, owing to the lack of predilection for metastasis of the cells and to the relatively short survival time of patients suffering from this disease. Most clinicians and investigators agree that improved control of locally invading tumor cells around the primary site of the tumor can provide significant improvements in the survival of these patients. Thus, GBM represents an ideal disease in which local delivery with wide distribution, such as is obtained with CED, can be expected to produce improvement in outcome. However, systemic delivery of targeted therapeutics brings with it additional considerations and concerns. For instance, even with small-molecule therapeutic agents that have good BBB penetration, the CNS delivery for a systemic dose is only in the 1% to 2% range. Particularly in the case of nanoparticle therapeutics and internal emitters for brachytherapy, effective therapeutic benefit in the brain from systemic delivery would require administration of a 2 orders of magnitude greater dose which poses significant concerns for peripheral toxicities. For these reasons, the investigations in this work were confined to local delivery by CED.

In regard to the improved survival and dose response, there are several factors that can be related to this positive outcome. First, the stability and retention of the ^{177}Lu-DOTA-f-$Gd_3N@C_{80}$ over the first 7 days is a critical parameter for delivering an absorbed radiation dose to the tumor. Also, the low levels of radioactivity found in the contralateral hemisphere as compared to the tumor-bearing hemisphere verify the benefits of local delivery by CED. Especially relevant to ^{177}Lu, this 7 day period corresponds to 1 half-life, during which 50% of the possible cumulative dose is delivered. Furthermore, the stability over this period would allow for the MRI contrast characteristics of the theranostic platform to be used for dosimetric analysis, which is essential for determining the absorbed radiation dose from the delivered activity. It is important to note here that our use of the term "theranostic" is defined as the modification of a diagnostic agent to provide therapy. In this case, the imaging aspect can be used to provide important information relevant to aforementioned dose calculations, monitoring for backflow during CED, and ensuring that the distribution of the agent adequately covers a prediagnosed treatment volume and area of interest. Concerning the biological decay, while a single C_{80} fullerene is <1 nm in diameter, once functionalized they exhibit a dynamic aggregation/disaggregation behavior which in part accounts for the high MRI relaxivity and tumor retention.[20,32] Whereas the ^{177}Lu-DOTA-f-$Gd_3N@C_{80}$ platform showed ∼13% remaining at 7 days (168 h), previous work with the f-$Gd_3N@C_{80}$ alone showed ∼45% remaining.[32] Reasoning for the differences in biological decay of the two platforms can be speculated using a simplistic model for escaping the brain/tumor. Figure 5 is an illustration of the possible routes the clustered or nonclustered fullerenes could be eliminated from the brain. While the BBB is complex in terms of its discrimination between compounds, it can be rationalized that the fullerene clusters that are closer to 20 nm in size are physically too large to cross the BBB or brain−cerebrospinal fluid−blood barrier (B-CSF-B). This then requires phagocytosis by immune responsive cells (e.g., macrophage, microglia, histiocyte, etc.) for clearance. A primary difference between the

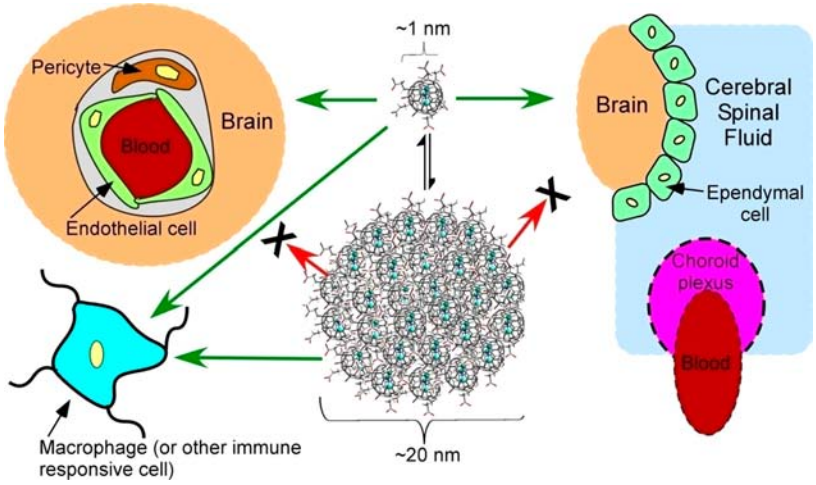


Figure 5. Illustration of biological elimination or decay from the brain/tumor. The dynamic clustering is illustrated (not to scale) with possible (green arrows) or improbable (red arrows) routes of elimination based on physical size alone.

f-$Gd_3N@C_{80}$ and ^{177}Lu-DOTA-f-$Gd_3N@C_{80}$ platforms delivered intratumorally is that the ^{177}Lu-DOTA-f-$Gd_3N@C_{80}$ is inducing radiation damage and apoptosis to the tumor cells,[32] thus resulting in a higher local immune response. This could partially account for the increased clearance rate. Also, as shown in the dynamic light scattering results in Figure 2, the attachment of the chelate containing the trivalent $^{177}Lu^{3+}$ disrupted the aggregation properties, which are primarily due to hydrogen bonding. This shifted the dynamics more toward the smaller size, thus opening the physical possibility of crossing the disrupted and less discriminative BBB or B-CSF-B barriers due to the presence of the tumor. Regardless, the biological decay of ^{177}Lu-DOTA-f-$Gd_3N@C_{80}$ was gradual enough to provide effective brachytherapy, as evidenced by the outcome of the survival studies.

Due to the positive dose response observed, it is plausible to relate the therapeutic benefit to the increasing amounts of ^{177}Lu activity delivered. The control comparison was specifically chosen to be the f-$Gd_3N@C_{80}$ alone, as reports have shown positive therapeutic effect linked to angiogenesis inhibition by clustering fullerenes.[44] Then, by keeping the total $Gd_3N@C_{80}$ constant, these studies isolated the effect to the delivery of brachytherapy. Recently, ^{177}Lu has emerged as a potential radioisotope of choice, due to its favorable nuclear characteristics: 6.67 day half-life, β-emitter at 497 keV max, γ-emitter at 208 keV (11%), 113 keV (6.4%).[45−47] These low energies provide localized dose delivery to the immediate cellular environment (0.7 mm tissue penetration), and thus following molecular targeting or direct intratumoral infusion, they irradiate primarily the malignant cells. Although this work focused on ^{177}Lu-radiolabeled fullerenes, other radionuclides (e.g., ^{90}Y) are expected to have similar biodistribution, exhibit complementary features, and can be used with the same methods presented. The β^- particles emitted by the ^{90}Y radionuclide have a path length of ∼4 mm in tissue and a half-life of 2.67 days. This could be an important isotope to investigate in optimizing the radiation dose with respect to the size of the tumor for translation into the clinic. Further long-term studies will be required to investigate biodistribution and radiotoxicity to peripheral organs, as these effects may be dose limiting.

In summary, this work demonstrated a dose-dependent increase in survival in a human GBM orthotopic tumor-bearing mouse model (U87MG) treated with the radiolabeled metallofullerene, ^{177}Lu-DOTA-f-$Gd_3N@C_{80}$, administered by CED. Efficacy was also shown in a second, more invasive tumor model (GBM12) at a single dose. Biological elimination from the brain and tumor measured by two independent methods verified that the platform was stable *in vivo* over a 7 day period allowing for the delivery of an efficacious brachytherapy dose. In addition, this nanoplatform has the potential to be further manipulated to concomitantly deliver radiosensitizing and other therapeutic agents. These cotreating agents can be selected to increase the tumor specificity of the therapy, thereby reducing the possibility of normal tissue damage. Also, when delivered by CED, all components would have identical intratumoral distribution which could be an important factor for maximizing the synergistic interactions between treatment modalities. Along with its MR imaging attributes, the nanoplatform presented may offer advantages to help overcome GBM resistance to current therapies.

AUTHOR INFORMATION

Corresponding Author

*Michael D. Shultz, Ph.D.: Phone 804-828-7943, Fax: 804-828-1473, E-mail: shultzmd@vcu.edu. Charles E. Chalfant, Ph.D.: Phone 804-828-9526, Fax 804-828-1473, E-mail: cechalfant@vcu.edu.

Notes

The authors declare no competing financial interest.

ACKNOWLEDGMENTS

This work was supported by research grants from the National Institutes of Health: CA119371 (J.D. Wilson), HL072925 (C.E. Chalfant), CA117950 (C.E. Chalfant), and CA154314 (C.E. Chalfant); and from the Veteran's Administration (VA Merit Review I (C.E. Chalfant) and a Research Career Scientist Award (C.E.Chalfant).

REFERENCES

(1) Butowski, N. A., Sneed, P. K., and Chang, S. M. (2006) Diagnosis and treatment of recurrent high-grade astrocytoma. *J. Clin. Oncol. 24*, 1273−1280.

(2) Grossman, S. A., Ye, X. B., Piantadosi, S., Desideri, S., Nabors, L. B., Rosenfeld, M., Fisher, J., and Consortium, N. C. (2010) Survival of patients with newly diagnosed glioblastoma treated with radiation and

temozolomide in research studies in the United States. *Clin. Cancer Res. 16*, 2443−2449.
(3) Dey, M., Ulasov, I. V., Tyler, M. A., Sonabend, A. M., and Lesniak, M. S. (2011) Cancer stem cells: the final frontier for glioma virotherapy. *Stem Cell Reviews 7*, 119−29.
(4) Gursel, D. B., Shin, B. J., Burkhardt, J. K., Kesavabhotla, K., Schlaff, C. D., and Boockvar, J. A. (2011) Glioblastoma stem-like cells-biology and therapeutic implications. *Cancers (Basel) 3*, 2655−2666.
(5) Huang, Z., Cheng, L., Guryanova, O. A., Wu, Q., and Bao, S. (2010) Cancer stem cells in glioblastoma−molecular signaling and therapeutic targeting. *Protein Cell 1*, 638−55.
(6) Bao, S. D., Wu, Q. L., McLendon, R. E., Hao, Y. L., Shi, Q., Hjelmeland, A. B., Dewhirst, M. W., Bigner, D. D., and Rich, J. N. (2006) Glioma stem cells promote radioresistance by preferential activation of the DNA damage response. *Nature 444*, 756−760.
(7) Yang, W. K., Cho, D. Y., Lin, S. Z., Hsu, D. M., Lin, H. L., Lee, H. C., Lee, W. Y., and Chiu, S. C. (2011) The role of cancer stem cells (CD133(+)) in malignant gliomas. *Cell Transplantation 20*, 121−125.
(8) Yang, Y. P., Chang, Y. L., Huang, P. I., Chiou, G. Y., Tseng, L. M., Chiou, S. H., Chen, M. H., Chen, M. T., Shih, Y. H., Chang, C. H., Hsu, C. C., Ma, H. I., Wang, C. T., Tsai, L. L., Yu, C. C., and Chang, C. J. (2011) Resveratrol suppresses tumorigenicity and enhances radiosensitivity in primary glioblastoma tumor initiating cells by inhibiting the STAT3 axis. *J Cell Physiol.,*.
(9) Zhang, X., Chibli, H., Mielke, R., and Nadeau, J. (2011) Ultrasmall gold−doxorubicin conjugates rapidly kill apoptosis-resistant cancer cells. *Bioconjugate Chem. 22*, 235−243.
(10) Kroto, H. W., Heath, J. R., Obrien, S. C., Curl, R. F., and Smalley, R. E. (1985) C-60 - Buckminsterfullerene. *Nature 318*, 162−163.
(11) Bethune, D. S., Johnson, R. D., Salem, J. R., Devries, M. S., and Yannoni, C. S. (1993) Atoms in carbon cages - the structure and properties of endohedral fullerenes. *Nature 366*, 123−128.
(12) Shultz, M. D., Duchamp, J. C., Wilson, J. D., Shu, C. Y., Ge, J. C., Zhang, J. Y., Gibson, H. W., Fillmore, H. L., Hirsch, J. I., Dorn, H. C., and Fatouros, P. P. (2010) Encapsulation of a radiolabeled cluster inside a fullerene cage, (LuxLu(3-x)N)-Lu-177@C-80: an interleukin-13-conjugated radiolabeled metallofullerene platform. *J. Am. Chem. Soc. 132*, 4980−4981.
(13) Stevenson, S., Rice, G., Glass, T., Harich, K., Cromer, F., Jordan, M. R., Craft, J., Hadju, E., Bible, R., Olmstead, M. M., Maitra, K., Fisher, A. J., Balch, A. L., and Dorn, H. C. (1999) Small-bandgap endohedral metallofullerenes in high yield and purity. *Nature 401*, 55−57.
(14) Diederich, F., and Thilgen, C. (1996) Covalent fullerene chemistry. *Science 271*, 317−323.
(15) Thompson, B. C., and Frechet, J. M. J. (2008) Organic photovoltaics - Polymer-fullerene composite solar cells. *Angew. Chem., Int. Ed. 47*, 58−77.
(16) Fillmore, H. L., Shultz, M. D., Henderson, S. C., Cooper, P., Broaddus, W. C., Chen, Z., Shu, C., Dorn, H. C., Corwin, F., Hirsch, J. I., Wilson, J. D., and Fatouros, P. P. (2011) Conjugation of functionalized gadolinium metallofullerenes with IL-13 peptides for targeting and imaging glial tumors. *Nanomedicine 6*, 449−458.
(17) Wharton, T., and Wilson, L. J. (2002) Toward fullerene-based X-ray contrast agents: design and synthesis of non-ionic, highly-iodinated derivatives of C-60. *Tetrahedron Lett. 43*, 561−564.
(18) Yuguo, L., Xiaodong, Z., Qingnuan, L., and Wenxin, L. (2001) Radioiodination of C60 derivative C60(OH)xOy. *Journal of Radio-analytical and Nuclear Chemistry 250*, 363−364.
(19) Fatouros, P., Corwin, F., Chen, Z.-J., Broaddus, W., Tatum, J., Kettenmann, B., Ge, Z., Gibson, H., Russ, J., Leonard, A., Duchamp, J., and Dorn, H. (2006) In vitro and in vivo imaging studies of a new endohedral metallofullerene nanoparticle. *Radiology 240*, 756−64.
(20) Shu, C., Corwin, F., Zhang, J., Chen, Z., Reid, J., Sun, M., Xu, W., Sim, J., Wang, C., Fatouros, P., Esker, A., Gibson, H., and Dorn, H. (2009) Facile preparation of a new gadofullerene-based magnetic resonance imaging contrast agent with high 1H relaxivity. *Bioconjugate Chem. 20*, 1186−1193.
(21) Chawla, P., Chawla, V., Maheshwari, R., Saraf, S. A., and Saraf, S. K. (2010) Fullerenes: from carbon to nanomedicine. *Mini-Rev. Med. Chem. 10*, 662−677.
(22) Partha, R., and Conyers, J. L. (2009) Biomedical applications of functionalized fullerene-based nanomaterials. *Int. J. Nanomed. 4*, 261−275.
(23) Chaur, M. N., Aparicio-Angles, X., Mercado, B. Q., Elliott, B., Rodriguez-Fortea, A., Clotet, A., Olmstead, M. M., Balch, A. L., Poblet, J. M., and Echegoyen, L. (2010) Structural and electrochemical property correlations of metallic nitride endohedral metallofullerenes. *J. Phys. Chem. C 114*, 13003−13009.
(24) Dunsch, L., and Yang, S. (2007) Metal nitride cluster fullerenes: Their current state and future prospects. *Small 3*, 1298−1320.
(25) Shinohara, H. (2000) Endohedral metallofullerenes. *Rep. Prog. Phys. 63*, 843−892.
(26) Cai, T., Ge, Z. X., Iezzi, E. B., Glass, T. E., Harich, K., Gibson, H. W., and Dorn, H. C. (2005) Synthesis and characterization of the first trimetallic nitride templated pyrrolidino endohedral metallofullerenes. *Chem. Commun.*, 3594−3596.
(27) Cai, T., Xu, L., Gibson, H. W., Dorn, H. C., Chancellor, C. J., Olmstead, M. M., and Balch, A. L. (2007) SC3N@C-78: Encapsulated cluster regiocontrol of adduct docking on an ellipsoidal metallofullerene sphere. *J. Am. Chem. Soc. 129*, 10795−10800.
(28) Cai, T., Xu, L., Shu, C., Champion, H. A., Reid, J. E., Anklin, C., Anderson, M. R., Gibson, H. W., and Dorn, H. C. (2008) Selective formation of a symmetric Sc3N@C-78 bisadduct: Adduct docking controlled by an internal trimetallic nitride cluster. *J. Am. Chem. Soc. 130*, 2136−2137.
(29) Cardona, C. M., Kitaygorodskiy, A., and Echegoyen, L. (2005) Trimetallic nitride endohedral metallofullerenes: Reactivity dictated by the encapsulated metal cluster. *J. Am. Chem. Soc. 127*, 10448−10453.
(30) Echegoyen, L., Chancellor, C. J., Cardona, C. M., Elliott, B., Rivera, J., Olmstead, M. M., and Balch, A. L. (2006) X-Ray crystallographic and EPR spectroscopic characterization of a pyrrolidine adduct of Y3N@C-80. *Chem. Commun.*, 2653−2655.
(31) Lukoyanova, O., Cardona, C. M., Rivera, J., Lugo-Morales, L. Z., Chancellor, C. J., Olmstead, M. M., Rodriguez-Fortea, A., Poblet, J. M., Balch, A. L., and Echegoyen, L. (2007) "Open rather than closed" malonate methano-fullerene derivatives. The formation of methano-fulleroid adducts of Y3N@C-80. *J. Am. Chem. Soc. 129*, 10423−10430.
(32) Shultz, M. D., Wilson, J. D., Fuller, C. E., Zhang, J., Dorn, H. C., and Fatouros, P. P. (2011) Metallofullerene-based nanoplatform for brain tumor brachytherapy and longitudinal imaging in a murine orthotopic xenograft model. *Radiology 261*, 136−143.
(33) Zhang, J. F., Fatouros, P. P., Shu, C. Y., Reid, J., Owens, L. S., Cai, T., Gibson, H. W., Long, G. L., Corwin, F. D., Chen, Z. J., and Dorn, H. C. (2010) High relaxivity trimetallic nitride (Gd3N) metallofullerene MRI contrast agents with optimized functionality. *Bioconjugate Chem. 21*, 610−615.
(34) Zhang, J. F., Ge, J. C., Shultz, M. D., Chung, E. N., Singh, G., Shu, C. Y., Fatouros, P. P., Henderson, S. C., Corwin, F. D., Geohegan, D. B., Puretzky, A. A., Rouleau, C. M., More, K., Rylander, C., Rylander, M. N., Gibson, H. W., and Dorn, H. C. (2010) In vitro and in vivo studies of single-walled carbon nanohorns with encapsulated metallofullerenes and exohedrally functionalized quantum dots. *Nano Lett. 10*, 2843−2848.
(35) Allard, E., Passirani, C., and Benoit, J. P. (2009) Convection-enhanced delivery of nanocarriers for the treatment of brain tumors. *Biomaterials 30*, 2302−2318.
(36) Vogelbaum, M. A. (2005) Convection enhanced delivery for the treatment of malignant gliomas: symposium review. *Journal of Neuro-Oncology 73*, 57−69.
(37) Pasha, S., and Gupta, K. (2010) Various drug delivery approaches to the central nervous system. *Exp. Opin. Drug Delivery 7*, 113−135.
(38) Gutin, P. H., Leibel, S. A., Wara, W. M., Choucair, A., Levin, V. A., Philips, T. L., Silver, P., DaSilva, V., Edwards, M. S. B., Davis, R. L., Weaver, K. A., and Lamb, S. (1987) Recurrent malignant gliomas:

survival following interstitial brachytherapy with high-activity iodine-125 sources. *J. Neurosurg. 67*, 864−873.
(39) McDermott, M. W., Berger, M. S., Kunwar, S., Parsa, A. T., Sneed, P. K., and Larson, D. A. (2004) Stereotactic radiosurgery and interstitial brachytherapy for glial neoplasms. *Neuro Oncol. 69*, 83−100.
(40) Laperriere, N. J., Leung, P. M. K., McKenzie, S., Milosevic, M., Wong, S., Glen, J., Pintilie, M., and Bernstein, M. (1998) Randomized study of brachytherapy in the initial management of patients with malignant astrocytoma. *Int. J. Radiation Oncology Biol. Phys. 41*, 1005−1011.
(41) Selker, R. G., Shapiro, W. R., Burger, P., Blackwood, M. S., Deutsch, M., Arena, V. C., Van Gilder, J. C., Wu, J., Malkin, M. G., Mealey, J., Jr., Neal, J. H., Olson, J., Robertson, J. T., Barnett, G. H., Bloomfield, S., Albright, R., Hochberg, F. H., Hiesiger, E., and Green, S. (2002) The brain tumor cooperative group NIH trial 87−01: A randomized comparison of surgery, external radiotherapy, and carmustine versus surgery, interstitial radiotherapy boost, external radiation therapy, and carmustine. *Neurosurgery 51*, 343−357.
(42) Giannini, C., Sarkaria, J. N., Saito, A., Uhm, J. H., Galanis, E., Carlson, B. L., Schroeder, M. A., and James, C. D. (2005) Patient tumor EGFR and PDGFRA gene amplifications retained in an invasive intracranial xenograft model of glioblastoma multiforme. *Neuro Oncol. 7*, 164−76.
(43) Quant, E. C., Drappatz, J., Wen, P. Y., and Norden, A. D. (2010) Recurrent high-grade glioma. *Current Treatment Options in Neurology 12*, 321−333.
(44) Meng, H., Xing, G. M., Sun, B. Y., Zhao, F., Lei, H., Li, W., Song, Y., Chen, Z., Yuan, H., Wang, X. X., Long, J., Chen, C. Y., Liang, X. J., Zhang, N., Chai, Z. F., and Zhao, Y. L. (2010) Potent angiogenesis inhibition by the particulate form of fullerene derivatives. *ACS Nano 4*, 2773−2783.
(45) Kocher, D. C. (1981) Radioactive Decay Tables. Springfield, National Technical Information Service, *DOE/TIC 11028*.
(46) Kolby, L., Bernhardt, P., Johanson, V., Schmitt, A., Ahlman, H., Forssell-Aronsson, E., Macke, H., and Nilsson, O. (2005) Successful receptor-mediated radiation therapy of xenografted human midgut carcinoid tumour. *Br. J. Cancer 93*, 1144−1151.
(47) Persson, M., Tolmachev, V., Andersson, K., Gedda, L., Sandstrom, M., and Carlsson, J. (2005) [Lu-177]pertuzumab: experimental studies on targeting of HER-2 positive tumour cells. *European Journal of Nuclear Medicine and Molecular Imaging 32*, 1457−1462.

Bioconjugate Chemistry

Article

pubs.acs.org/bc

Sugar and Heavy Atom Effects of Glycoconjugated Chlorin Palladium Complex on Photocytotoxicity

Shiho Hirohara,*[,†] Yuji Kawasaki,[‡] Ryota Funasako,[‡] Nobutaka Yasui,[‡] Masayasu Totani,[‡] Hiroki Alitomo,[§] Junpei Yuasa,[‡] Tuyoshi Kawai,[‡] Chio Oka,[∥] Masashi Kawaichi,[∥] Makoto Obata,*[,⊥] and Masao Tanihara[‡]

[†]Department of Chemical and Biological Engineering, Ube National College of Technology, 2-14-1 Tokiwadai, Ube 755-8555, Japan

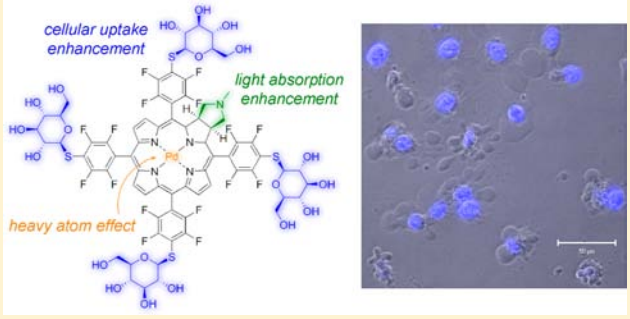
[‡]Graduate School of Materials Science and [∥]Graduate School of Biological Sciences, Nara Institute of Science and Technology, Takayama 8916-5, Ikoma, Nara 630-0192, Japan

[§]Department of Industrial Chemistry, Osaka Prefectural College of Technology, Osaka 572-8572, Japan

[⊥]Interdisciplinary Graduate School of Medicine and Engineering, University of Yamanashi, Kofu 400-8510, Japan

Supporting Information

ABSTRACT: Palladium(II) complexes of glycoconjugated porphyrin and pyrrolidine-fused chlorin were prepared to examine sugar and heavy atom effects on *in vitro* photocytotoxicity. Cellular uptake into HeLa cells was enhanced by introducing sugar units regardless of other features, such as the central ion (free base or palladium(II) ion) and the ring structure (porphyrin or chlorin). The palladium(II) complex of glycoconjugated pyrrolidine-fused chlorin (PdPC**2**) exerted an excellent degree of photocytotoxicity not only on HeLa cells, but also on metastatic B16-BL6 cells, weakly metastatic B16F1 cells, and metastatic 4T1 cells. However, free-base glycoconjugated pyrrolidine-fused chlorin (PC**2**) also exerted similar or much higher photocytotoxicity rather than PdPC**2**. Therefore, the palladium(II) ion did not improve the *in vitro* photocytotoxicity of PC**2**. The enhanced singlet oxygen generation of palladium(II) complexes (i.e., the heavy atom effect) was confirmed at least in O_2-saturated D_2O. In addition, the formation of hydrogen peroxide and hydroxyl radical were also detected in O_2-saturated phosphate buffered saline. However, the reactive oxygen species (ROS) generation efficiency, which is the product of the (relative) quantum yield of each ROS and the light absorbing ability, did not fit the trends of photocytotoxicity seen for the photosensitizers. In our glycoconjugated photosensitizers tested, the best indicator of the photocytotoxicity was found to be the light absorbing ability (namely, the oscillator strength in the wavelength region applied in the photocytotoxicity test). These results indicated that photochemical characteristics of glycoconjugated photosensitizers were notably susceptible to the microenvironment. The biological characteristics, such as the sugar effect, were a much more reliable approach to improving the photocytotoxicity of photosensitizers.



INTRODUCTION

Photodynamic therapy (PDT) is an anticancer therapy utilizing nontoxic photosensitizers and photoirradiation with visible light.[1−5] Upon photoirradiation, an administered photosensitizer generates reactive oxygen species (ROS) to kill malignant cells. The area of PDT action can be controlled by accumulation of photosensitizers and the area of photoirradiation. For successful PDT treatment, a photosensitizer must meet several conditions: (1) no cytotoxicity without photoirradiation, (2) reasonable cytotoxic ROS generation ability upon photoirradiation, (3) availability of longer-wavelength light, (4) reasonable water-solubility, and (5) selective accumulation to the tumor site.

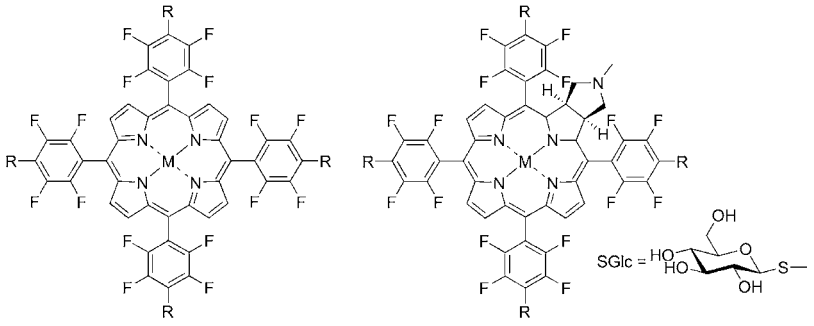
From a photochemical viewpoint, the lifetime of the photoexcited state of the photosensitizer is key for efficient generation of ROS. Therefore, intersystem crossing to triplet state is important because of its significantly longer lifetime. Introduction of heavy atom enhances the intersystem crossing to the excited triplet state, thereby resulting in an efficient generation of ROS. This phenomenon is the so-called "heavy atom effect". This strategy has been widely applied in a variety of photosensitizers, including porphyrin derivatives,[6−8] pentaphyrins,[9] texaphyrins,[10] boron dipyrromethene (BODIPY) derivatives,[11−13] and cationic chalcogenopyryliums.[14] While this effect is a physicochemically well-established phenomenon, very few examples clearly demonstrate an enhanced *in vitro* photocytotoxicity through the efficient ROS generation in cellular microenvironments, due to the heavy atom effect. For

Received: April 22, 2012
Revised: July 21, 2012
Published: September 4, 2012

ACS Publications © 2012 American Chemical Society

dx.doi.org/10.1021/bc300223j | *Bioconjugate Chem.* 2012, 23, 1881−1890

Chart 1. Structures of Glycoconjugated Photosensitizers



PP**2** (M = 2H, R = SGlc)
PdPP**2** (M = Pd, R = SGlc)

PdPC (M = Pd, R = F)
PtPC (M = Pt, R = F)
PC**2** (M = 2H, R = SGlc)
PdPC**2** (M = Pd, R = SGlc)

example, Gorman et al. reported the synthesis of a trifluoroboran complex of the azadipyrromethane having bromine atoms.[15] They demonstrated that the introduction of bromine atoms at the periphery of the azadipyrromethane ligand led to efficient $^1O_2$ generation in aqueous solution, as well as enhanced in HeLa cells and MRC5-SV40 transformed fibroblast cancer cells. As an example of porphyrin derivatives which are much more popular PDT photosensitizers, we also synthesized palladium(II) and platinum(II) complexes of pyrrolidine-fused chlorins (PdPC and PtPC, respectively, Chart1) and demonstrated significant heavy atom effect for the metal complex of chlorin not only in organic media, but also in the cellular microenvironment.[16]

From a biological viewpoint, an enhancement of cellular uptake of photosensitizers in malignant cells is of significant interest in improving photocytotoxicity.[17,18] Sibrian-Vazquez et al. synthesized a conjugate of phthalocyanine with a bifunctional peptide containing both a nuclear localization sequence and a cell-penetrating sequence.[19] These researchers found higher cellular uptake and photocytotoxicity for the phthalocyanine conjugates to HEp2 cells than for phthalocyanine bearing only quaternary ammonium groups. Folate receptor (FR), especially FR-α, is also an attractive target because it is overexpressed by many kinds of tumor cells including endometrial, colorectal, and brain metastases. Gravier et al. developed *meta*-tetra(hydroxyphenyl)chlorin, a well-known second-generation photosensitizer called Temoporfin or Foscan, conjugates with a folate.[20] These researchers demonstrated FR-dependent *in vivo* accumulation of the conjugate using mice bearing KB tumors (FR positive) and HT-29 tumors (FR negative). An enhanced uptake of glucose is a well-known feature of malignant cells and a key mechanism in tumor diagnosis by positron emission tomography using [2-^{18}F]2-deoxy-2-fluoroglucose ([^{18}F]FDG[21]). Many research groups including our laboratory have developed a wide variety of glycoconjugated photosensitizers to utilize this mechanism to enhance cellular uptake.[22−25] We systematically synthesized a number of tetraphenylporphyrin and tetrakis-(pentafluorophenyl)porphyrin-based photosensitizers bearing sugar moieties on the periphery, and we demonstrated that the introduction of sugar moieties into tetraphenylporphyrins or chlorins enhanced cellular uptake into HeLa cells relative to tetraphenylporphyrin tetrasulfonic acid (TPPS).[26,27]

To develop effective PDT photosensitizers, two approaches are available: introduction of heavy atoms to enhance intersystem crossing, and introduction of sugars to enhance cellular uptake by malignant cells. Here, an interesting question arose: do two separate effects, sugar and heavy atom, work additively, destructively, or synergistically? Recently, we reported the synthesis of glycoconjugated tetrakis-(tetrafluorophenyl)porphyrin and its zinc(II), palladium(II), and platinum(II) complexes.[28] The sugar effect was clearly confirmed by enhanced cellular uptake into HeLa cells. Unlike PdPC and PtPC,[16] however, the heavy atom effect was ambiguous in terms of *in vitro* photocytotoxicity. To answer this question, we prepared glycoconjugates of porphyrin and chlorin including PdPC and examined ROS generation ability of singlet oxygen ($^1O_2$), hydrogen peroxide (H_2O_2), and hydroxyl radicals (·OH) in aqueous media. The cellular uptake and photocytotoxicity in various malignant cells was also investigated. Because the *in vitro* heavy atom effect of PdPC was already well established,[16] the photocytotoxicity of the glycoconjugated PdPC validated the effectiveness of combining sugar and heavy atom effects.

EXPERIMENTAL SECTION

Materials and Methods. All chemicals were of analytical grade. TPPS and hematoporphyrin (HP) were purchased from Sigma-Aldrich Japan (Chiba, Japan). 4′,6-Diamidino-2-phenylindole dihydrochloride hydrate (DAPI) was purchased from Molecular Probes (Eugene, OR). Hydroxyphenyl fluorescein (HPF) was purchased from Sekisui Medical Co. Ltd. (Tokyo, Japan). The palladium(II) complex of chlorin (PdPC)[16] and the glycoconjugated photosensitizers PP**2**,[28] PC**2**,[29] and PdPP**2**[28] (Chart1) were prepared according to our previous papers. Acetyl 2,3,4,6-tetra-*O*-acetyl-1-thio-β-D-glucopyranoside (AcGlcSAc) was prepared according to previously published studies.[30] Preparative gel permeation chromatography (GPC) was performed on an LC-908 recycling preparative high-performance liquid chromatography (HPLC) system (Japan Analytical Industry Co., Ltd., Tokyo, Japan) equipped with two polystyrene columns (JAIGEL-2.5H and JAIGEL-2H) and using $CHCl_3$ as eluent. Preparative HPLC was carried out on octadecylsilyl-bound silica gel (Mightysil RP-18, 20 mmϕ × 250 mm, Kanto Chemical Co., Inc., Tokyo, Japan). Furthermore, ^{1}H, ^{13}C, and ^{19}F NMR spectra were recorded on JNM-EC600 (600 MHz, JEOL Ltd., Tokyo, Japan) and AVANCE 400 (400 MHz, Bruker Biospin K. K., Yokohama, Japan) instruments. UV−vis spectra were recorded on V-570 and V-550 spectrophotometers (JASCO Co., Ltd., Tokyo, Japan). Steady-state fluorescence (FL) spectra were recorded

on Jobin Yvon SPEX fluorolog3 instrument (HORIBA, Ltd., Kyoto, Japan). Elemental analyses were performed on a Perkin-Elmer 2400 series II CHNS/O elemental analyzer (Perkin-Elmer. Inc., Massachusetts, USA).

Stock solutions of photosensitizers were prepared by weighing the dried photosensitizers and dissolving them in dimethylsulfoxide (DMSO, Wako Pure Chemical Industries, Osaka, Japan). Stock solutions were kept in a freezer (−30 °C) until use. The absorbance and fluorescence intensity of each well were determined with a plate reader (Multiscan JX, Thermo Fisher Scientific Co., Yokohama, Japan and a SPECTRA Fluor Plus (TECAN Group Ltd., Seestrasse, Switzerland). Bright-field and fluorescence images of cells were taken using a confocal laser scanning microscope (CLSM, model LSM 510, Carl Zeiss, Jena, Germany).

Glycoconjugated Photosensitizer PdPC1. PdPC (110 mg, 96.8 μmol), AcGlcSAc (190 mg, 468 μmol), and diethylamine (3.0 mL) were dissolved in DMF (30 mL). The reaction mixture was stirred at room temperature for 24 h, diluted with $CHCl_3$ (30 mL), and washed with distilled water (30 mL × 5). The solution was dried over Na_2SO_4, and the solvent was removed under reduced pressure. The crude product was purified by column chromatography (silica gel, $CHCl_3$ to $CHCl_3$/EtOAc = 1/1 (v/v)) followed by preparative GPC to give PdPC**1** (150 mg, 66%) as a greenish red solid. Anal. Calcd. for $C_{103}H_{91}O_{36}N_5F_{16}S_4Pd + H_2O$: C, 48.87; H, 3.70; N, 2.77; Found: C, 49.02; H, 3.75; N, 2.44. ^{1}H NMR (600.07 MHz, $CDCl_3$, $Si(CH_3)_4$ = 0 ppm): δ (ppm) = 8.54 (2H, dd, ^3J = 5.8 Hz, ^3J = 9.9 Hz, 8,17-β-pyrrole*H*), 8.51 (2H, s, 12,13-β-pyrrole*H*), 8.26, 8.23 (2H, dd, ^3J = 5.0 Hz, ^3J = 4.8 Hz, 7,18-β-pyrrole*H*), 5.36−5.32 (4H, m, 3-Glc*H*), 5.34 (2H, m, 2,3-β-pyrrole*H*), 5.24−5.08 (12H, m, 1,2,4-Glc*H*), 4.33−4.23 (8H, m, 6-Glc*H*), 3.87 (4H, m, 5-Glc*H*), 3.18 (2H, brs, N−C*H*H), 2.56 (2H, brs, N−CH*H*), 2.25−2.06 (48H, s, CH_3). ^{13}C NMR ($CDCl_3$, 100.40 MHz, $CDCl_3$ = 77 ppm): δ (ppm) = 170.63, 170.19, 170.16, 169.44, 169.98, 169.35 (*C*═O), 156.04−155.83 (1,4,11,14-α-pyrrole*C*), 148.97−144.55 (2,6-Ph*C*, 3,5-Ph*C*), 138.46 (9,16-α-pyrrole*C*), 137.69 (6,19-α-pyrrole*C*), 131.92 (8,17-β-pyrrole*C*), 127.85 (12,13-β-pyrrole*C*), 127.34, 127.14 (7,18-β-pyrrole*C*), 121.44 (4-Ph*C*), 111.67 (1-Ph*C*), 109.49 (10,15-meso*C*), 98.22 (5,20-meso*C*), 84.55, 84.44 (1-Glc*C*), 76.40, 76.36 (5-Glc*C*), 73.87 (3-Glc*C*), 70.63, 70.60, 70.54 (2-Glc*C*), 68.08, 68.00 (4-Glc*C*), 63.60 (N-CH_2-), 61.81, 61.64 (6-Glc*C*), 50.74 (2,3-β-pyrrole*C*), 41.00 (N-CH_3), 20.62, 20.60, 20.58 (CH_3). ^{19}F NMR (376 MHz, $CDCl_3$, CF_3CO_2H = −76.50 ppm): δ (ppm) = −131.38 (1F, brs, 3,5-Ph*F*), −131.74, −131.97 (1F, m, 3,5-Ph*F*), −132.67 (2F, s, 3,5-Ph*F*), −135.31 (1F, brs, 2,6-Ph*F*), −137.26 (2F, m, 2,6-Ph*F*), −137.79, −137.83 (1F, m, 2,6-Ph*F*). UV−vis (*c* = 5.00 μM, DMSO, path length = 1 cm, 25 °C): λ/nm (ε × 10^{-4}/M^{-1} cm^{-1}) = 409 (14.6), 492 (0.83), 520 (0.36), 563 (1.01), 606 (5.31).

Glycoconjugated Photosensitizer PdPC2. PdPC**1** (150 mg, 60 μmol) was dissolved in CH_2Cl_2 (20 mL) and methanol (20 mL). Sodium methoxide was added to adjust the pH to 9. This mixture was refluxed for 1 h at 45−50 °C and was neutralized with acetic acid. After removal of the solvent, the crude product was purified by preparative reversed-phase HPLC (CH_3CN/H_2O = 1/1 (v/v)). The collected fraction was desalted by dialysis using a cellulose ester membrane (the molecular weight cutoff was 1000). Lyophilization of the desalted aqueous sample solution gave PdPC**2** (65 mg, 59%) as a dark red powder. Anal. Calcd. for $C_{71}H_{59}O_{20}N_5F_{16}S_4Pd + 6H_2O$: C, 43.75; H, 3.67; N, 3.59; Found: C, 43.80; H, 3.56; N, 3.62. ^{1}H NMR (600.07 MHz, CD_3OD, CHD_2OD = 3.30 ppm): δ (ppm) = 8.62 (2H, brs, 8,17-β-pyrrole*H*), 8.57 (2H, brs, 12,13-β-pyrrole*H*), 8.30 (2H, brs, 7,18-β-pyrrole*H*), 5.43 (2H, m, 2,3-β-pyrrole*H*), 5.04 (4H, m, 1-Glc*H*), 3.87 (4H, m, 6-Glc*H*), 3.65 (4H, m, 6-Glc*H*), 3.45−3.22 (12H, m, 2,3,4,5-Glc*H*), 2.90 (2H, brs, N−C*H*H), 2.31 (2H, brs, N−CH*H*), 2.25−2.06 (48H, s, CH_3). ^{13}C NMR (150.92 MHz, CD_3OD, CD_3OD = 49.0 ppm): δ (ppm) = 156.88 (1,4,11,14-α-pyrrole*C*), 149.41−146.44 (2,6-Ph*C*, 3,5-Ph*C*), 140.19 ((9,16-α-pyrrole*C*), 139.47 (6,19-α-pyrrole*C*), 133.42 (8,17-β-pyrrole*C*), 129.40 (12,13-β-pyrrole*C*), 128.74 (7,18-β-pyrrole*C*), 121.66−121.18 (4-Ph*C*), 115.31−114.96 (1-Ph*C*), 111.27 (10,15-meso*C*), 99.94 (5,20-meso*C*), 86.70, 86.51, 86.34 (1-Glc*C*), 82.79, 82.76, 82.72 (5-Glc*C*), 79.72, 79.70, 79.68 (3-Glc*C*), 76.04, 75.94 (2-Glc*C*), 71.68, 71.64 (4-Glc*C*), 64.26 (N-CH_2-), 63.04 (6-Glc*C*), 51.48 (2,3-β-pyrrole*C*), 40.84 (N-CH_3). ^{19}F NMR (376 MHz, CD_3OD, CF_3CO_2H = −76.50 ppm): δ (ppm) = −132.92 (1F, brs, 3,5-Ph*F*), −133.30, −133.58 (1F, m, 3,5-Ph*F*), −134.56 (2F, s, 3,5-Ph*F*), −138.04 (1F, brs, 3,5-Ph*F*), −140.52 (3F, s, 2,6-Ph*F*). UV−vis (*c* = 4.91 μM, DMSO, path length = 1 cm, 25 °C): λ/nm (ε × 10^{-4}/M^{-1} cm^{-1}) = 408 (16.2), 490 (0.88), 520 (0.37), 563 (1.08), 605 (6.10). FL (*c* = 4.91 μM, DMSO, path length = 1 cm, λ_{ex} = 408 nm, 25 °C, N_2): λ/nm = 614, 657, 719.

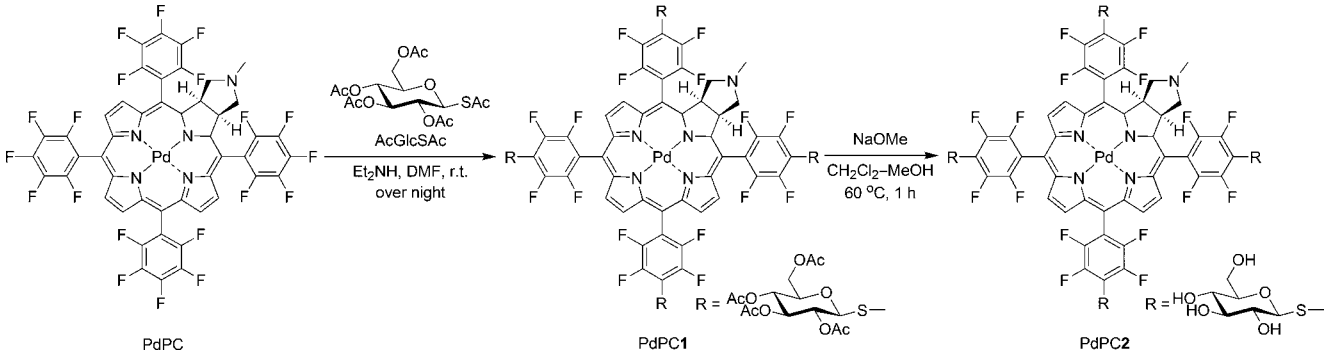
Quantum Yield of Singlet Oxygen (Φ_Δ). The photosensitizer was dissolved in D_2O (the absorbance of the solution was adjusted to 0.4 at 405 nm (TPPS), 393 nm (PdPP**2**), 387 nm (PdPC**2**), 432 nm (PP**2**), and 385.5 nm (PC**2**)) and was purged under oxygen for 5 min. Luminescence spectra of singlet oxygen sensitized by each photosensitizer solution was recorded using a spectrometer (Jobin Yvon SPEX fluorolog3, HORIBA, Ltd., Kyoto, Japan) equipped with a photomultiplier (NIR-PMT R5509−72, Hamamatsu Photonics K.K., Shizuoka, Japan) cooled to 193 K.

Relative Quantum Yield of Hydroxyl Radical ($\phi_{\bullet OH}$). Glycoconjugated photosensitizers PdPP**2**, PdPC**2**, PP**2**, PC**2**, HP (*c* = 1.00 μM), and HPF (*c* = 2 μM) were dissolved in PBS containing 1% DMSO and placed into a sample tube. Oxygen gas was introduced to the solution for 1 min after prior photoirradiation. Next, the solution was exposed to light from a 100 W halogen lamp (KBEX-102A, USHIO Inc., Tokyo, Japan) through a Y-50 cutoff filter (λ > 500 nm, Toshiba Co., Tokyo, Japan) at 37 °C. The initial rate of HPF-fluorescence intensity increments at 535 nm was monitored at the excitation wavelength of 485 nm. The rate constant was estimated from the first-order plot of HPF-fluorescence intensity increments against photoirradiation time. The relative quantum yield ($\phi_{\bullet OH}$) was evaluated by the initial increment rate of HPF-fluorescence intensity divided by the $f_{>500\ nm}$ value and was normalized to the value of HP.

Relative Quantum Yield of Hydrogen Peroxide (ϕ_{H2O2}). Glycoconjugated photosensitizers PdPP**2**, PdPC**2**, PP**2**, PC**2**, HP (*c* = 1.00 μM), and NaI (*c* = 200 mM) were dissolved in PBS containing 1% DMSO and placed into a sample tube. Oxygen gas was introduced to the solution for 1 min after prior photoirradiation. The solution was subsequently exposed to light from a 100 W halogen lamp through a Y-50 cutoff filter (λ > 500 nm) at 37 °C. The concentration of H_2O_2 was monitored by measuring the absorption at 365 nm (ε_{max} = 2.5 × 10^4 M^{-1} cm^{-1}). The rate constant was estimated from the first-order plot of the H_2O_2 concentration against the photoirradiation time. The relative quantum yield (ϕ_{H2O2})

dx.doi.org/10.1021/bc300223j | Bioconjugate Chem. 2012, 23, 1881−1890

Scheme 1



was evaluated by the initial increment rate of I_3^- formation divided by the $f_{>500\ nm}$ values and was normalized to the value for HP.

Cellular Uptake Measurement in HeLa Cells. HeLa cells (ATCC CCL-2) were obtained from Dainippon-Sumitomo Pharmaceutical (Osaka, Japan). Cells were grown in Dulbecco's modified Eagle's medium (DMEM) containing 10% fetal calf serum (FCS) (Hyclone Laboratories, Inc., Logan, UT). The cellular uptake of photosensitizers (PdPC, PdPP**2**, PdPC**2**, PP**2**, and PC**2**) by HeLa cells was examined as follows: HeLa cells (1×10^6 cells/well (a) and 2.5×10^6 cells/well (b)) in 1.5 mL of the culture medium were plated in a 6-well plate (Nalge Nunc International, Naperville, IL) and incubated for 24 h (37 °C, 5% CO_2). Next, 1.5 mL of 1.0 μM (a) and 0.2 μM (b) photosensitizer in culture medium and 2% DMSO was added to each well (two wells were used for each photosensitizer (b)) and the plate was incubated for 24 h. The final photosensitizer concentrations were 0.5 μM (a) and 0.1 μM (b) in the culture medium (final DMSO content was 1% in all cases). Next, the cells were washed twice with Dulbecco's phosphate-buffered saline (PBS). The cells of 1 well (a) and 2 wells (b) were lysed in 100 μL (a) and 200 μL (b) of DMSO (The cells in each well were lysed in 100 μL off DMSO and the extracts of the same two wells was combined and placed into a cuvette (b)). The absorbance (Soret band) of extracts was measured by UV–vis spectroscopy. The concentration of photosensitizers was calculated on the basis of calibration plots obtained for each photosensitizers in DMSO. The cellular uptake is given as the means of three (a) and four (b) replicate experiments.

Photocytotoxicity in HeLa Cells. The photocytotoxicity of the photosensitizers (PdPC, PdPP**2**, PdPC**2**, PP**2**, PC**2**, PdPP**2**, and PdPC**2**) in HeLa cells were examined as follows: HeLa cells (5×10^3 cells) in 100 μL of DMEM containing 10% FCS were plated in a 96-well plate (Nalge Nunc International) and were incubated for 24 h (37 °C, 5% CO_2). One hundred microliters of a photosensitizer in culture medium and 2% DMSO was added to each well. The plate was then incubated at 24 h in the presence of the photosensitizers. The photosensitizer concentration was varied from 0.05 to 0.5 μM (final DMSO content was 1% in all cases). The cells were washed twice with PBS, and 100 μL of the fresh culture medium was added. The cells were exposed to light from a 100 W halogen lamp equipped with a water jacket and a Y-50 cutoff filter. The light intensity was measured by using a UV–vis power meter (ORION/TH, Ophir Optronics Ltd., Jerusalem, Israel). The irradiation time was adjusted to obtain the desired light dose of 16 J·cm^{-2}. The mitochondrial activity of NADH dehydrogenase of the cells in each well was measured at 24 h after photoirradiation using WST-8 reagent (10 μL) from Cell Counting Kit-8 (Dojindo, Tokyo, Japan) according to the manufacturer's instructions. The absorbance at 450 nm was measured using a plate reader. The percentage of cell survival was calculated by normalization with respect to the value for no drug treatment.

Photocytotoxicity in B16F1, B16-BL6, and 4T1 Cells. Murine melanoma cell lines B16F1 and B16-BL6 were generously provided by Dr. Akihiko Itoh (Department of Pathology, Faculty of Medicine, Kinki University), and murine 4T1 breast cancer cells (ATCC CRL-2539) were generously provided by Dr. Hisataka Sabe (Department of Physiological Science, Graduate School of Medicine, Hokkaido University). Cells were grown in DMEM (Sigma-Aldrich Japan, Chiba, Japan) containing 10% FCS, 2 mM L-glutamine (Life Technologies Japan Ltd., Tokyo, Japan), and penicillin (Life Technologies Japan Ltd.)/streptomycin (Life Technologies Japan Ltd.). The photocytotoxicity of the photosensitizers (PC**2** and PdPC**2**) in B16F1 cells, B16-BL6 cells, and 4T1 cells were examined as follows: Cells (5×10^3 cells) in 100 μL of culture medium were plated in a 96-well plate and incubated for 24 h (37 °C, 5% CO_2). One hundred microliters of a photosensitizer in culture medium and 2% DMSO was added to each well. Next, the plate was incubated at 24 h in the presence of the photosensitizers. The photosensitizer concentration was varied from 0.05 to 0.5 μM (final DMSO content was 1% in all cases). The cells were washed twice with PBS, and 100 μL of the fresh culture medium was added. Each well was then photoirradiated under the same conditions as described previously.

Confocal Laser Scanning Microscopy (DAPI-Stained Cells). HeLa cells (1×10^4 cells) in 500 μL of DMEM containing 10% FCS were plated in 24-well plates (Nalge Nunc International), and incubated for 24 h (37 °C, 5% CO_2). Five hundred microliters of 1.0 μM PdPC**2** in culture medium and 2% DMSO was added to each well and were incubated for 24 h in the presence of the photosensitizer. The final concentration of photosensitizers was 0.5 μM (1% DMSO). Next, each well was photoirradiated under the same conditions as described in the photocytotoxicity test. Three hours after photoirradiation, the cells were stained with 0.3 μM DAPI in PBS for 5 min at room temperature and were washed twice with 500 μL of PBS. Next, 500 μL of Hank's balanced salt solution (HBSS) was added. Fluorescence images of DAPI-stained cells were taken with the CLSM using an excitation wavelength of 364 nm.

Confocal Laser Scanning Microscopy (HPF-Loaded Cells). HeLa cells (1×10^4 cells) in 500 μL of DMEM containing 10% FCS were plated in two 24-well plates, and

dx.doi.org/10.1021/bc300223j | Bioconjugate Chem. 2012, 23, 1881–1890

incubated for 24 h (37 °C, 5% CO_2). Five hundred microliters of 0.20 μM photosensitizer (PdPC**2** and PC**2**) in culture medium and 2% DMSO was added to each well and were incubated for 24 h in the presence of the photosensitizers. The final concentration of photosensitizers was 0.10 μM (1% DMSO). Twenty-four hours after incubation, the cells were washed twice with 500 μL of PBS and were incubated with 500 μL of 10 μM HPF in HBSS containing 0.2% DMF for 30 min (37 °C, 5% CO_2).[31] Next, each well was photoirradiated under the same conditions as described in the photocytotoxicity test. Ten minutes after photoirradiation, fluorescence images of HPF-loaded cells were taken with the CLSM using an excitation wavelength of 364 nm.

Statistical Analysis. All statistical evaluations were performed using Student's *t*-test. All values for photo and dark cytotoxicity are expressed as means ± standard deviation.

RESULTS AND DISCUSSION

Synthesis and Photophysical Properties. The palladium(II) complex of chlorin (PdPC)[16] and acetyl 2,3,4,6-tetra-*O*-acetyl-1-thio-β-D-glucopyranoside[30] were prepared according to previously published methods. The *S*-glycosylation of pentafluorophenyl groups of PdPC was performed in *N*,*N*-dimethylformamide (DMF) using diethylamine as a base at ambient temperature (Scheme 1). The crude product was purified by silica gel column chromatography followed by preparative GPC to give PdPC**1** as a greenish red solid in 66% yield. The removal of acetyl groups from PdPC**1** was performed by alkaline hydrolysis using sodium methoxide, and the crude product was purified by reverse-phase HPLC followed by dialysis and lyophilization to give PdPC**2** at a 59% yield. PdPC**1** and PdPC**2** were characterized by elemental analysis, NMR, and UV−vis spectroscopy. Figure 1 shows the

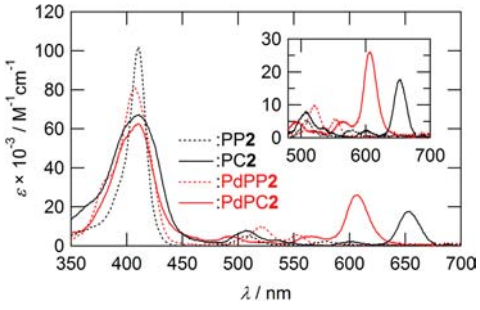


Figure 1. UV−vis spectra of PdPP**2**, PdPC**2**, PP**2**, and PC**2** in PBS containing 1% DMSO at 25 °C.

UV−vis spectra of PdPC and glycoconjugated photosensitizers PdPP**2**, PdPC**2**, PP**2**, and PC**2** recorded in PBS containing 1% DMSO. Spectral data in DMSO and PBS containing 1% DMSO are listed in Table 1. PdPC**1** and PdPC**2** had a major peak (Soret band) at ca. 410 nm and four vibronic peaks (Q bands) at ca. 490 (Q_{IV}), ca. 520 (Q_{III}), ca. 560 (Q_{II}), and ca. 610 nm (Q_I) (Figure 1). The Q_I peak of PdPC**2** was red-shifted by approximately 50 nm compared to that of the corresponding porphyrin PdPP**2**. In our photocytotoxicity test, the light in the wavelength region over 500 nm was used for excitation. The light-absorbing ability of photosensitizers was evaluated by the oscillator strength in wavelengths over 500 nm ($f_{>500\ nm}$). Table 1 lists the $f_{>500\ nm}$ values of PdPC and glycoconjugated photosensitizers PdPP**2**, PdPC**2**, PP**2**, and PC**2** in DMSO and PBS containing 1% DMSO. The $f_{>500\ nm}$ values of the chlorin derivatives PdPC**2** and PC**2** were almost 2 times greater than those of the corresponding porphyrin derivatives PdPP**2** and PP**2**. Whereas the introduction of palladium(II) ion led to significant blue shift of Q bands, the $f_{>500\ nm}$ values of the PdPP**2** and PdPC**2** was almost the same as those of the corresponding free-bases, PP**2** and PC**2**. Therefore, the introduction of palladium(II) ions did not affect the light-absorbing properties in our photocytotoxicity test.

Cellular Uptake. The cellular uptake of PdPC and glycoconjugated photosensitizers PdPP**2**, PdPC**2**, PP**2**, and PC**2** by HeLa cells was examined after 24 h of incubation at concentrations of 0.5 and 0.1 μM (Figure 2). The cellular uptake of all glycoconjugated photosensitizers was almost 4-fold higher than that of PdPC. However, no significant difference in cellular uptake was found regardless of chromophore (i.e., porphyrin ring or chlorin ring) or central metal ion at the concentration of 0.5 μM for of 0.1 μM. These concentrations were found to be sufficient for photocytotoxicity for the glycoconjugated photosensitizers tested (vide infra).

Photocytotoxicity. The cytotoxicity of PdPC and glycoconjugated photosensitizers PdPP**2**, PdPC**2**, PP**2**, and PC**2** was evaluated in HeLa cells at the photosensitizer concentration of 0.5 μM without photoirradiation and under photoirradiation from a 100 W halogen lamp (λ > 500 nm, 16 J·cm^{-2}). At 24 h post-photoirradiation, the cell survival rate was estimated in terms of the mitochondrial activity of NADH dehydrogenase using the WST-8 reagent from Cell Counting Kit-8 and normalized to that of no photosensitizer treatment. All photosensitizers showed no cytotoxicity in the dark (Figure 3a). The photocytotoxicity of PdPC (38.1%) was lower than those of all glycoconjugated photosensitizers (Figure 3b). Figure 4 shows bright field and fluorescence images of DAPI-stained HeLa cells at 3 h post-photoirradiation in the presence of PdPC**2**. HeLa cells treated with PdPC**2** and photoirradiation appeared shrunken, numerous apoptotic bodies were formed, and strong fluorescence from DAPI was observed, suggesting the formation of chromatin aggregates. The morphological changes in HeLa cells induced by PdPC**2** and photoirradiation were similar to free-base glycoconjugated photosensitizers PP**2**[25] and PC**2**.[29] The dose-dependent photocytotoxicity of PdPC and glycoconjugated photosensitizers PdPP**2**, PdPC**2**, PP**2**, and PC**2** was tested in HeLa cells in the concentration ranging from 0.5 to 0.05 μM (Figure 5). The drug concentrations inducing 50% cell death (EC_{50} values) decreased in the order of PdPC (5.0 μM) > PdPP**2** and PP**2** (0.15 μM) > PdPC**2** (0.1 μM) ≈ PC**2** (0.09 μM). As can be seen, the photocytotoxicity of all glycoconjugated photosensitizers was almost 40-fold greater than that of PdPC. In addition, the photocytotoxicity values of the chlorin derivatives (PdPC**2** and PC**2**) were approximately 1.5-fold greater than those of the corresponding porphyrin derivatives (PdPP**2** and PP**2**). The photocytotoxicity enhancement of the chlorin derivatives could be attributed to the increased photoexcitation probability, namely, the $f_{>500\ nm}$ value in PBS containing 1% DMSO. The glycoconjugated chlorins PC**2** and PdPC**2** were also examined for photocytotoxicity in highly B16-BL6 melanoma cells, weakly metastatic B16F1 cells and metastatic 4T1 breast cancer cells in the concentration ranged from 1.0 to 0.05 μM (Figure 6). Surprisingly, these photosensitizers showed excellent photocytotoxicity (EC_{50} = 0.5 μM) in the B16-BL6 melanoma cells.[32] The glycoconjugated free-base chlorin PC**2** exerted higher photocytotoxicity than the

dx.doi.org/10.1021/bc300223j | *Bioconjugate Chem.* 2012, 23, 1881−1890

Table 1. UV−vis Spectral Data for PdPP2, PdPC2, PP2, and PC2 in DMSO (upper row) and PBS Containing 1% DMSO (lower row) at 25 °C[a]

	λ_{max}/nm ($\varepsilon \times 10^{-3}$/M^{-1} cm^{-1})					
	Soret band	Q bands				$f_{>500\ nm}$[d]
PdPP**2**[b]	409 (287)	519 (27.3)	552 (16.8)			0.14
	406 (81)	522 (9.7)	547 (4.1)			0.06
PdPC**2**	408 (162)	490 (8.8)	520 (3.7)	563 (10.8)	605 (61.0)	0.23
	409 (62)	493 (4.9)	510 (2.2)	558 (4.5)	608 (26.1)	0.11
PP**2**[b]	415 (334)	507 (23.2)	539 (3.4)	581 (7.6)	636 (7.5)	0.11
	411 (102)	507 (5.2)	542 (0.8)	580 (2.5)	634 (0.8)	0.03
PC**2**[c]	412 (227)	506 (20.2)	537 (4.9)	598 (6.3)	652 (52.5)	0.20
	411 (67)	515 (6.1)	538 (2.9)	600 (2.3)	652 (17.6)	0.08

[a]In DMSO: [PdPP**2**] = 5.45 μM, [PdPC**2**] = 5.00 μM, [PP**2**] = 5.35 μM, [PC**2**] = 5.35 μM. In PBS containing 1% DMSO: [PdPP**2**] = [PdPC**2**] = [PP**2**] = [PC**2**] = 1.00 μM. [b]Spectral data in DMSO was cited from ref 28. [c]Spectral data in DMSO was cited from ref 29. [d]Oscillator strength in the range above 500 nm estimated as $4.32 \times 10^{-9} \int \varepsilon(\nu)\, d\nu$.

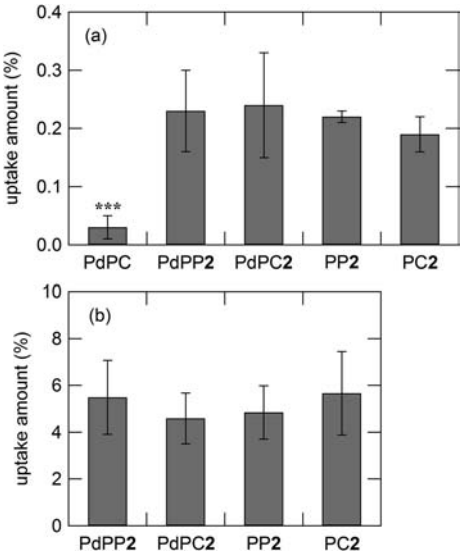


Figure 2. Relative cellular uptake of PdPC, PdPP**2**, PdPC**2**, PP**2**, and PC**2** by HeLa cells. The cellular uptake represents the percentage of the total amount of photosensitizer added. The concentration of photosensitizers was 0.5 μM (a) and 0.1 μM (b). HeLa cells: 1×10^6 cells/well (a) and 5×10^6 cells/well (b). Values are the means ± standard deviation of three replicate experiments. ***Significant difference ($p < 0.001$) in PdPC vs glycoconjugated photosensitizers.

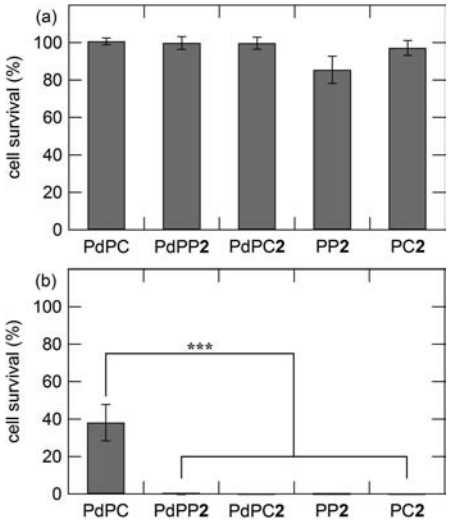


Figure 3. Dark cytotoxicity (a) and photocytotoxicity (b) of PdPC,[16] PdPP**2**,[28] PdPC**2**, PP**2**,[28] and PC**2**[29] in HeLa cells. The concentration of photosensitizers was 0.5 μM. The light dose was 16 J·cm^{-2} from a 100 W halogen lamp ($\lambda > 500$ nm). Values are the means ± standard deviation of six replicate experiments. ***Significant difference ($p < 0.001$) in PdPC vs glycoconjugated photosensitizers.

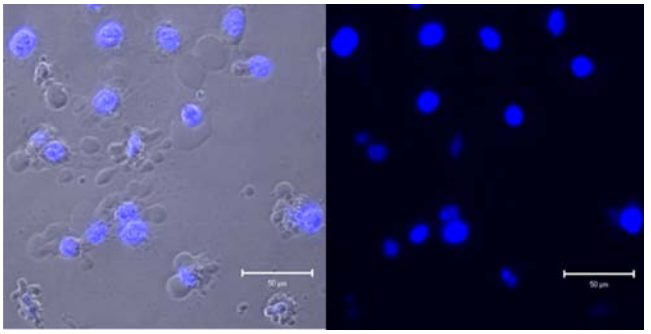


Figure 4. Bright field (left) and fluorescence (right) images of DAPI-stained HeLa cells treated with PdPC**2** 3 h after photoirradiation. The concentration of PdPC**2** was 0.5 μM. The excitation wavelength was 364 nm.

corresponding Pd(II) complex PdPC**2** in all cell lines examined.

ROS Study in Aqueous Media. The type of reactive oxygen species (ROS) generated depends on the photochemical reactions. Electron or proton transfer, so-called type I photoreaction, generates superoxide anion ($O_2^{\bullet -}$), hydrogen peroxide (H_2O_2), and hydroxyl radical ($^{\bullet}OH$), while energy transfer, so-called type II photoreactions, generate singlet oxygen ($^1O_2$). Generally $^1O_2$ is thought to be the dominant cytotoxic species in the photodynamic action of porphyrin derivatives. The quantum yield of $^1O_2$ production (Φ_Δ) was determined by detection of $^1O_2$ luminescence at 1270 nm in O_2-saturated D_2O containing 0.1% DMSO using TPPS (Φ_Δ = 0.72) as a standard.[33,34] As can be seen, the Φ_Δ values increased in the order of PC**2** (0.17) < PP**2** (0.25) < PdPC**2** (0.28) < PdPP**2** (0.52) (Table 2). The Φ_Δ values of the palladium(II) complexes were ca. 2-fold greater than those of the corresponding free-base compounds, thereby suggesting enhanced intersystem crossing due to the heavy atom effect. However, the Φ_Δ values of glycoconjugated photosensitizers PC**2** (0.17) and PdPC**2** (0.28) were small in comparison with the corresponding photosensitizers without sugar moieties PC (0.28) and PdPC (0.89) in C_6D_6.[16] These results suggested

dx.doi.org/10.1021/bc300223j | Bioconjugate Chem. 2012, 23, 1881−1890

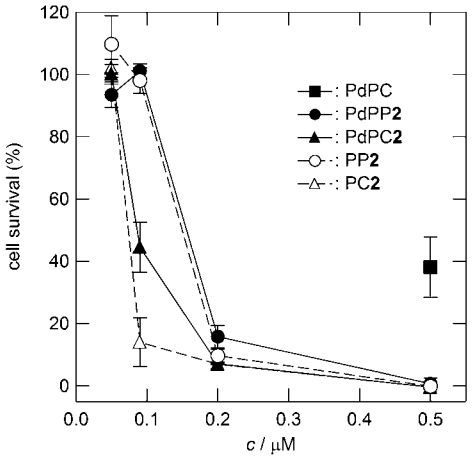


Figure 5. Cell survival (%) as a function of the concentration of PdPC,[16] PdPP**2**,[28] PdPC**2**, PP**2**,[28] and PC**2**[29] in HeLa cells. The light dose was 16 J·cm^{-2} from a 100 W halogen lamp (λ > 500 nm). Values are the means ± standard deviation of six replicate experiments.

that other deactivation processes, such as type I photoreaction and/or radiationless deactivation, were enhanced by *S*-glycosylation and/or the aqueous microenvironment. The productions of H_2O_2 and ·OH by type I photoreactions was detected by means of I_3^- formation[35] and the HPF fluorescence probe[31] upon photoirradiation (λ > 500 nm) in O_2-saturated PBS containing 1% DMSO. The relative quantum yield of H_2O_2 and ·OH production (ϕ_{H2O2} and $\phi_{\bullet OH}$) were evaluated by the initial rate of the formation of I_3^- and the initial increment rate of HPF-fluorescence intensity, respectively, divided by the $f_{>500\ nm}$ value, and normalized to the value for hematoporphyrin (HP) (Table 2). Both species were detected for all glycoconjugated photosensitizers. While no significant differences in the ϕ_{H2O2} values were found in the glycoconjugated photosensitizers, the $\phi_{\bullet OH}$ values dramatically increased in the order PC**2** < PP**2** < PdPC**2** < PdPP**2**. In general, the energy level of the occupied molecular orbital of the porphyrin ring was lower than that of the chlorin ring.[36] In addition, the palladium(II) ion lowered the energy level of the occupied molecular orbitals of porphyrin and chlorin rings.[37] Therefore, the order of the $\phi_{\bullet OH}$ values coincides with the order of occupied electronic energy levels of the macrocyclic ring. These results suggested that ·OH generation was triggered by the reduction of the photoexcited state of the glycoconjugated photosensitizers as in the case of cationic porphyrin reported by Mroz et al.[31] Even though the absolute

Table 2. Quantum Yield of Singlet Oxygen (Φ_Δ) and Relative Quantum Yield of Hydrogen Peroxide (ϕ_{H2O2}) and Hydroxyl Radical ($\phi_{\bullet OH}$) of the PdPP2, PdPC2, PP2, PC2, and Hematoporphyrin (HP)[a]

	Φ_Δ[b]	ϕ_{H2O2}[c]	$\phi_{\bullet OH}$[c]
PdPP**2**	0.52	2.7	14.6
PdPC**2**	0.28	1.8	6.3
PP**2**	0.25	2.5	1.2
PC**2**	0.17	1.9	0.9
HP		1	1

[a]The ϕ_{H2O2} and $\phi_{\bullet OH}$ values were evaluated by the initial rate of the formation of I_3^- and the initial increment rate of HPF-fluorescence intensity, respectively, divided by the $f_{>500\ nm}$ value, and normalized to the value for HP. [b]In O_2-saturated D_2O containing 0.1% DMSO. [c]In O_2-saturated PBS containing 1% DMSO.

quantum yield of ·OH production was not determined, no trade-off relationship between the Φ_Δ and $\phi_{\bullet OH}$ values suggested that the absolute quantum yield of ·OH was not large. The Φ_Δ, ϕ_{H2O2}, and $\phi_{\bullet OH}$ values of glycoconjugated photosensitizers PP**2**, PC**2**, PdPP**2**, and PdPC**2** afforded the simple estimation of the relative ROS generation amount by multiplying the $f_{>500\ nm}$ values. The estimated values, $\Phi_\Delta \cdot f_{>500\ nm}$, $\phi_{H2O2} \cdot f_{>500\ nm}$, and $\phi_{\bullet OH} \cdot f_{>500\ nm}$ could not explain the trend seen for photocytotoxicity.

DISCUSSION

Figure 7 summarizes the trend of photocytotoxicity (the reciprocal number of the EC_{50} value) and cellular uptake in HeLa cells, as well as the light-absorbing ability (the $f_{>500\ nm}$ value) and ROS generation of the glycoconjugated photosensitizers PdPP**2**, PdPC**2**, PP**2**, and PC**2** in aqueous solution. Unexpectedly, the photocytotoxicity of palladium(II) complexes PdPP**2** and PdPC**2** were almost the same as those of the corresponding free-bases PP**2** and PC**2**. In the case of the glycoconjugated photosensitizers PdPP**2** and PdPC**2**, the enhancement of photocytotoxicity by the heavy atom effect was weak in the cellular microenvironment. In our previous paper,[16] however, we clearly demonstrated an enhancement of ROS generation by the heavy atom effect for PdPC not only in organic media, but also in the cellular microenvironment. Therefore, the sugar moiety of PdPC**2** makes an effect to counterbalance the heavy atom effect of PdPC in the cellular microenvironment. The trend of photocytotoxicity was inconsistent with cellular uptake and ROS amount ($\Phi_\Delta \cdot f_{>500\ nm}$, $\phi_{H2O2} \cdot f_{>500\ nm}$, and $\phi_{\bullet OH} \cdot f_{>500\ nm}$ values). The trend for light

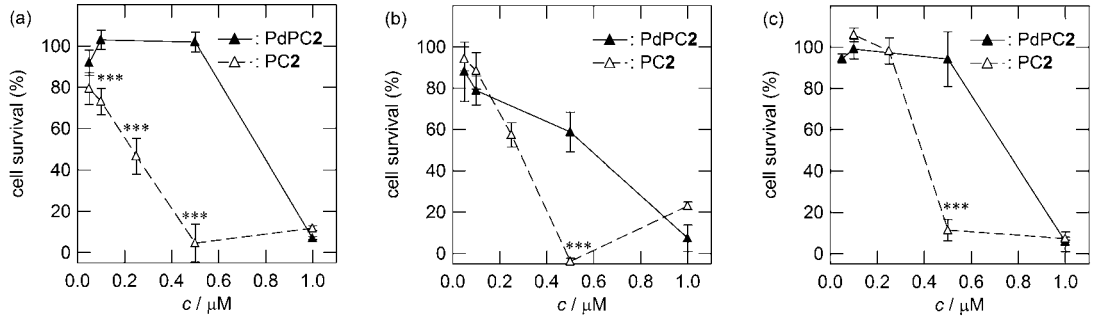


Figure 6. Cell survival (%) as a function of the concentration of PdPC**2** and PC**2** in B16F1 cells (a), B16-BL6 cells (b), and 4T1 cells (c). The light dose was 16 J·cm^{-2} from a 100 W halogen lamp (λ > 500 nm). Values are the means ± standard deviation of six replicate experiments. ***Significant difference (p < 0.001) in PdPC**2** vs PC**2**.

dx.doi.org/10.1021/bc300223j | *Bioconjugate Chem.* 2012, 23, 1881−1890

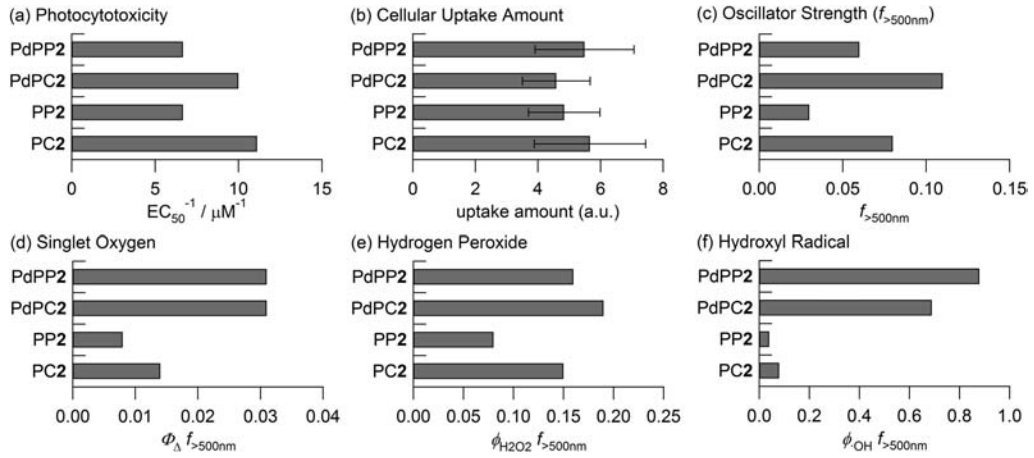


Figure 7. Summary of the trend of photocytotoxicity (the reciprocal number of the EC_{50} value) (a) and cellular uptake amount (b) in HeLa cells, the light absorbing ability (the $f_{>500\ nm}$ value) (c), and the ROS generation efficiency (d–f) of PdPP**2**, PdPC**2**, PP**2**, and PC**2** in aqueous solution.

absorbing probability, the $f_{>500\ nm}$ value, was relatively similar to that of photocytotoxicity. This result suggested that the quantum yield of ROS formation (Φ_Δ, f_{H2O2}, and $f_{\bullet OH}$) in the cellular microenvironment differed from those measured in aqueous media. As an example of such microenvironmental effects, Vakrat-Haglili et al. studied the microenvironmental effect on the photochemistry of the palladium(II) complex of bacteriopheorbide (Pd-Bpheid) in aqueous media.[38] These researchers showed that the palladium complex forms exclusively $^1O_2$ in organic media ($\Phi_\Delta \approx 1$ in acetone), but forms both $^1O_2$ and ·OH in micelles of TX-100/PBS (Φ_Δ value of 0.5 and absolute quantum yield of hydroxyl radical ($\Phi_{\bullet OH}$) of 0.001). An example of glycoconjugated photosensitizers, Yuying et al. reported the photochemical properties of glycoconjugated hypocrellin in aqueous media. Their ESR experiments clearly indicated that glycoconjugated hypocrellin generates $O_2\cdot^-$ and ·OH radicals in water. The Φ_Δ value of their glycoconjugated hypocrellin in water significantly decreased to 0.17, while the Φ_Δ value of hypocrellin B in chloroform was determined to be 0.76. These examples clearly demonstrate that photochemical properties of photosensitizers are notably sensitive to their microenvironment. In some cases, ROS generation diminished in aqueous media rather than organic media, possibly due to radiationless deactivation coupled with the microenvironment (and minor effects from type I photoreaction). The differences in the photochemical characteristics of the glycoconjugated photosensitizers seemed to be attenuated in the cellular microenvironment, and the photocytotoxicity simply depended on the light absorbing ability of the photosensitizers. Even though introducing a sugar moiety counterbalanced the heavy atom effect of PdPC in the cellular microenvironment, the photocytotoxicity of PdPC**2** was strikingly higher than that of PdPC owing to a dramatically improved cellular uptake. Therefore, the sugar effect was much more effective in improving PDT photosensitizers.

CONCLUSIONS

We have designed a novel PDT photosensitizer PdPC**2**, with three favorable features: (1) the chlorin ring absorbed longer wavelength light, (2) the palladium(II) ion enhanced ROS generation, and (3) the sugar moiety enhanced water-solubility and cellular uptake. The glycoconjugated photosensitizer PdPC**2** was successfully synthesized through *S*-glycosylation. Introduction of palladium(II) led to a blue shift of Q bands, which is a major drawback of this strategy. As expected, the quantum yield of $^1O_2$ formation in O_2-saturated D_2O for glycoconjugated porphyrin and chlorin increased upon complexation with palladium(II). However, the quantum yields were significantly lower than those without the sugar moiety. The glycoconjugated photosensitizers PdPC**2** and PC**2** exerted excellent photocytotoxicity in HeLa cells as well as highly metastatic B16-BL6 melanoma cells. Despite the enhanced $^1O_2$ quantum yield in O_2-saturated D_2O, the photocytotoxicity of the palladium(II) complexes PdPP**2** and PdPC**2** was almost the same as those of the corresponding free-bases PP**2** and PC**2**. The low $^1O_2$ quantum yield of glycoconjugated photosensitizers in aqueous media and the simple relationship between the trends of the EC_{50} values and the $f_{>500\ nm}$ values suggest that the photocytotoxicity of the glycoconjugated photosensitizers were negatively impacted by nonradiative deactivation in the cellular microenvironment. These findings suggested that the glycoconjugation of photosensitizers was better strategy than the introduction of heavy atoms to improve photocytotoxicity.

ASSOCIATED CONTENT

Supporting Information

^1H, ^{13}C, and ^{19}F NMR spectra of PdPC**1** and PdPC**2**, luminescence spectra of $^1O_2$, kinetic plots of H_2O_2 and ·OH detection experiments. These materials available free of charge via the Internet at http://pubs.acs.org.

AUTHOR INFORMATION

Corresponding Author

*Dr. Shiho Hirohara: Phone +81 836355609, Fax +81 836355469, E-mail hirohara@ube-k.ac.jp. Prof. Makoto Obata: Phone +81 552208549, Fax +81 552208549, E-mail mobata@yamanashi.ac.jp.

Notes

The authors declare no competing financial interest.

ACKNOWLEDGMENTS

This work was supported by the NAIST Presidential Special Fund, the Foundation "Hattori-Hokokai", the Izumi science and technology foundation, by the Adaptable and Seamless Technology Transfer Program through Target-driven R&D (A-STEP) of the Japan Science and Technology Agency (JST),

Sasagawa Scientific Research Grants from The Japan Science Society, grants from the Kao Foundation for Arts and Sciences, and Grants-in-Aid for Scientific Research and Priority Areas from the Ministry of Education, Culture, Sport, Science and Technology (MEXT) of the Japanese Government.

■ ABBREVIATIONS:

AcGlcSAc, acetyl 2,3,4,6-tetra-*O*-acetyl-1-thio-*β*-D-glucopyranoside; BODIPY, boron dipyrromethene; CLSM, confocal laser scanning microscope; DMF, *N*,*N*-dimethylformamide; DMEM, Dulbecco's modified Eagle's medium; DAPI, diamidino-2-phenylindole dihydrochloride hydrate; DMSO, dimethyl sulfoxide; FCS, fetal calf serum; [^{18}F]FDG, [2-^{18}F]2-deoxy-2-fluoroglucose; FR, folate receptor; PC**2**, free-base glycoconjugated pyrrolidine-fused chlorin; GPC, gel permeation chromatography; HBSS, Hank's balanced salt solution; HP, hematoporphyrin; HPLC, high-performance liquid chromatography; HPF, PBS, Dulbecco's phosphate-buffered saline; PDT, photodynamic therapy; ROS, reactive oxygen species; $^1O_2$, singlet oxygen; PdPC**2**, palladium(II) complex of glycoconjugated pyrrolidine-fused chlorin; FL, steady-state fluorescence; TPPS, tetraphenylporphyrin tetrasulfonic acid

■ REFERENCES

(1) Yano, S., Hirohara, S., Obata, M., Hagiya, Y., Ogura, S., Ikeda, A., Kataoka, H., Tanaka, M., and Joh, T. (2011) Current states and future views in photodynamic therapy. *J. Photochem. Photobiol. C: Photochem. Rev. 12*, 46−67.

(2) Detty, M. R., Gibson, S. L., and Wagner, S. J. (2004) Current clinical and preclinical photosensitizers for use in photodynamic therapy. *J. Med. Chem. 47*, 3897−3915.

(3) Kessel, D. (2004) Photodynamic therapy: from the beginning. *Photodiagn. Photodyn. Ther. 1*, 3−7.

(4) MacDonald, I. J., and Dougherty, T. (2001) Basic principles of photodynamic therapy. *J. Porphyrins Phthalocyanines 5*, 105−129.

(5) Pandey, R. K. (2000) Recent advances in photodynamic therapy. *J. Porphyrins Phthalocyanines 4*, 368−373.

(6) Krayer, M., Yang, E., Kim, H.-J., Kee, H. L., Deans, R. M., Sluder, C. E., Diers, J. R., Kirmaier, C., Bocian, D. F., Holten, D., and Lindsey, J. S. (2011) Synthesis and photophysical characterization of stable indium bacteriochlorins. *Inorg. Chem. 50*, 4607−4618.

(7) Kee, H. L., Bjaumik, J., Diers, J. R., Mroz, P., Hamblin, M. R., Bocian, D. F., Lindsey, J. S., and Holten, D. (2008) Photophysical characterization of imidazolium-substituted Pd(II), In(III), and Zn(II) porphyrins as photosensitizers for photodynamic therapy. *J. Photochem. Photobiol. A: Chem. 200*, 346−355.

(8) Serra, A. C., Pineiro, M., Gonsalves, A. M. d'A R., Abrantes, M., Laranjo, M., Santos, A. C., and Botelho, M. F. (2008) Halogen atom effect on photophysical and photodynamic characteristics of derivatives of 5,10,15,20-tetrakis(3-hydroxyphenyl)porphyrin. *J. Photochem. Photobiol. B: Biol. 92*, 59−65.

(9) Ballico, M., Rapozzi, V., Xodo, L. E., and Comuzzi, C. (2011) Metallation of pentaphyrin with Lu(III) dramatically increases reactive-oxygen species production and cell phototoxicity. *Eur. J. Med. Chem. 46*, 712−720.

(10) Guldi, D. M., Mody, T. D., Gerasimchuk, N. N., Magda, D., and Sessler, J. L. (2000) Influence of large metal cations on the photophysical properties of texaphyrin, a rigid aromatic chromophore. *J. Am. Chem. Soc. 122*, 8289−8298.

(11) He, H., Lo, P.-C., Yeung, S.-L., Fong, W.-P., and Ng, D. K. P. (2011) Synthesis and in vitro photodynamic activities of pegylated distyryl boron dipyrromethene derivatives. *J. Med. Chem. 54*, 3097−3102.

(12) Lim, S. H., Thivierge, C., Nowak-Sliwinska, P., Han, J., van der Bergh, H., Wagnières, G., Burgess, K., and Lee, H. B. (2010) In vitro and in vivo photocytotoxicity of boron dipyrromethene derivatives for photodynamic therapy. *J. Med. Chem. 53*, 2865−2874.

(13) Yogo, T., Urano, Y., Ishitsuka, Y., Maniwa, F., and Nagano, T. (2005) Highly efficient and photostable photosensitizer based on BODIPY. *J. Am. Chem. Soc. 127*, 12162−12163.

(14) Leonard, K. A., Hall, J. P., Nelen, M. I., Davies, S. R., Gollnick, S. O., Camacho, S., Oseroff, A. R., Gibson, S. L., Hilf, R., and Detty, M. R. (2000) A selenopyrylium photosensitizer for photodynamic therapy related in structure to the antitumor agent AA1 with potent in vivo activity and no long-term skin photosensitization. *J. Med. Chem. 43*, 4488−4498.

(15) Gorman, A., Killoran, J., O'Shea, C., Kenna, T., Gallagher, W. M., and O'Shea, D. F. (2004) In vitro demonstration of the heavy-atom effect for photodynamic therapy. *J. Am. Chem. Soc. 126*, 10619−10631.

(16) Obata, M., Hirohara, S., Tanaka, R., Kinoshita, I., Ohkubo, K., Fukuzumi, S., Tanihara, M., and Yano, S. (2009) In vitro heavy-atom effect of palladium(II) and platinum(II) complexes of pyrrolidine-fused chlorin in photodynamic therapy. *J. Med. Chem. 52*, 2747−2753.

(17) van Dongen, G. A. M. S., Visser, G. W. M., and Vrouenraets, M. B. (2004) Photosensitizer−antibody conjugates for detection and therapy of cancer. *Adv. Drug Delivery Rev. 56*, 31−52.

(18) Sharman, W. M., van Lier, J. E., and Allen, C. M. (2004) Targeted photodynamic therapy via receptor mediated delivery systems. *Adv. Drug Delivery Rev. 56*, 53−76.

(19) Sibrian-Vazquez, M., Ortiz, J., Nesterova, I. V., Fernández-Lázaro, F., Sastre-Santos, A., Soper, S. A., and Vicente, G. H. (2007) Synthesis and properties of cell-targeted Zn(II)−phthalocyanine−peptide conjugates. *Bioconjugate Chem. 18*, 410−420.

(20) Gravier, J., Schneider, R., Frochot, C., Bastogne, T., Schmitt, F., Didelon, J., Guillemin, F., and Barberi-Heyob, M. (2008) Improvement of *meta*-tetra(hydroxyphenyl)chlorin-like photosensitizer selectivity with folate-based targeted delivery. synthesis and in vivo delivery studies. *J. Med. Chem. 51*, 3867−3877.

(21) Waki, A., Fujibayashi, Y., and Yokoyama, A. (1998) Recent advances in the analyses of the characteristics of tumors on FDG uptake. *Nucl. Med. Biol. 25*, 589−592.

(22) Ballut, S., Naud-Martin, D., Loock, B., and Maillard, P. (2011) A strategy for the targeting of photosensitizers. synthesis, characterization, and photobiological property of porphyrins bearing glycodendrimeric moieties. *J. Org. Chem. 76*, 2010−2028.

(23) Singh, S., Aggarwal, A., Thompson, S., Tomé, J. P. C., Zhu, X., Samaroo, D., Vinodu, M., Gao, R., and Drain, C. M. (2010) Synthesis and photophysical properties of thioglycosylated chlorins, isobacteriochlorins, and bacteriochlorins for bioimaging and diagnostics. *Bioconjugate Chem. 21*, 2136−2146.

(24) Zheng, X., Morgan, J., Pandey, S. K., Chen, Y., Tracy, E., Baumann, H., Missert, J. R., Batt, C., Jackson, J., Bellnier, D. A., Henderson, B. W., and Pandey, R. K. (2009) Conjugation of 2-(10-hexyloxyethyl)-2-devinylpyropheophorbide-a (HPPH) to carbohydrates changes its subcellular distribution and enhances photodynamic activity in vivo. *J. Med. Chem. 52*, 4306−4318.

(25) Hirohara, S., Nishida, M., Sharyo, K., Obata, M., Ando, T., and Tanihara, M. (2010) Synthesis, photophysical properties and photocytotoxicity of mono-, di-, tri- and tetra-glucosylated fluorophenylporphyrins. *Bioorg. Med. Chem. 18*, 1526−1535.

(26) Hirohara, S., Obata, M., Saito, A., Ogata, S., Ohtsuki, C., Higashida, S., Ogura, S., Okura, I., Sugai, Y., Mikata, Y., Tanihara, M., and Yano, S. (2004) Cellular uptake and photocytotoxicity of glycoconjugated porphyrins in HeLa cells. *Photochem. Photobiol. 80*, 301−308.

(27) Hirohara, S., Obata, M., Ogata, S., Ohtsuki, C., Higashida, S., Ogura, S., Okura, I., Takenaka, M., Ono, H., Sugai, Y., Mikata, Y., Tanihara, M., and Yano, S. (2005) Cellular uptake and photocytotoxicity of glycoconjugated chlorins in HeLa cells. *J. Photochem. Photobiol. B: Biol. 78*, 7−15.

(28) Hirohara, S., Obata, M., Alitomo, H., Sharyo, K., Ando, T., Yano, S., and Tanihara, M. (2009) Synthesis and photocytotoxicity of S-glucosylated 5,10,15,20-tetrakis(tetrafluorophenyl)porphyrin metal

complexes as efficient $^1O_2$-generating glycoconjugates. *Bioconjugate Chem. 20*, 944−952.
(29) Hirohara, S., Obata, M., Alitomo, H., Sharyo, K., Ando, T., Tanihara, M., and Yano, S. (2009) Synthesis, photophysical properties and sugar-dependent in vitro photocytotoxicity of pyrrolidine-fused chlorins bearing S-glycosides. *J. Photchem. Photobiol. B: Biol. 97*, 22−33.
(30) Defaye, J., Driquez, H., Ohleyer, E., Orgeret, C., and Viet, C. (1984) Stereoselective synthesis of 1,2-trans-related 1-thioglycoses. *Carbohydr. Res. 130*, 317−321.
(31) Mroz, P., Bhaumik, J., Dogutan, D. K., Aly, Z., Kamal, Z., Khalid, L., Kee, H. L., Bocian, D. F., Holten, D., Lindsey, J. S., and Hamblin, M. R. (2009) Imidazole metalloporphyrins as photosensitizers for photodynamic therapy: role of molecular charge, central metal and hydroxyl radical production. *Cancer Lett. 282*, 63−76.
(32) Saiki, I., Murata, J., Yoneda., J., Kobayashi, H., and Azuma, I. (1994) Influence of fibroblasts on the invasion and migration of highly or weakly metastatic B16 melanoma cells. *Int. J. Cancer 56*, 867−873.
(33) Rodgers, Krasnovsky, Jr., A., A., M., A. J., Galpern, M. G. G., Rihter, B., Kenney, M. E., and Lukjanetz, E. A. (1992) Quenching of singlet molecular oxygen by phthalocyanines and naphthalocyanines. *Photochem. Phorobiol. 55*, 691−696.
(34) Redmond, R. W., and Gamlin, J. N. (1999) A Compilation of Singlet Oxygen Yields from Biologically Relevant Molecules. *Photochem. Photobiol. 70* (4), 391−475.
(35) Partovi-Nia, R., Su., B., Gros, F., Li, C. P., Barbe, J.-M., Samec, Z., and Girault, H. H. (2009) Proton Pump for O_2 Reduction Catalyzed by 5,10,15,20-Tetraphenylporphyrinatocobalt(II). *Chem.—Eur. J. 15*, 2335−2340.
(36) Ghosh, A. (1997) Theoretical comparative study of free base porphyrin, chlorin, bacteriochlorin, and isobacteriochlorin: evaluation of the potential roles of *ab Initio* Hartree-Fock and density functional theories in hydroporphyrin chemistry. *J. Phys. Chem. B 101*, 3290−3297.
(37) Felton, R. H. (1978) Primary redox reactions of metalloporphyrins. *The Porphyrins. Vol. V: Physical Chemistry, Part C* (Dolphin, D., Ed.) pp 53−125, Chapter 3, Academic Press, New York.
(38) Vakrat-Haglili, Y., Weiner, L., Brumfeld, V., Brandis, A., Salomon, Y., Mcllroy, B., Wilson, B. C., Pawlak, A., Rozanowska, M., Sarna, T., and Scherz, A. (2005) The microenvironment effect on the generation of reactive oxygen species by Pd-bacteriopheophorbide. *J. Am. Chem. Soc. 127*, 6487−6497.

Bioconjugate Chemistry

Article

pubs.acs.org/bc

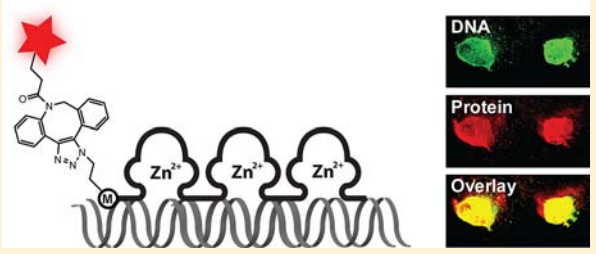
Specific Labeling of Zinc Finger Proteins using Noncanonical Amino Acids and Copper-Free Click Chemistry

Younghoon Kim,[†] Sung Hoon Kim,[‡] Dean Ferracane,[†] John A. Katzenellenbogen,[‡] and Charles M. Schroeder*[,†,§]

[†]Department of Chemical and Biomolecular Engineering, [‡]Department of Chemistry, and [§]Center for Biophysics and Computational Biology, University of Illinois at Urbana−Champaign, Urbana, Illinois 61801, United States

Supporting Information

ABSTRACT: Zinc finger proteins (ZFPs) play a key role in transcriptional regulation and serve as invaluable tools for gene modification and genetic engineering. Development of efficient strategies for labeling metalloproteins such as ZFPs is essential for understanding and controlling biological processes. In this work, we engineered ZFPs containing cysteine-histidine (Cys2-His2) motifs by metabolic incorporation of the unnatural amino acid azidohomoalanine (AHA), followed by specific protein labeling via click chemistry. We show that cyclooctyne promoted [3 + 2] dipolar cycloaddition with azides, known as copper-free click chemistry, provides rapid and specific labeling of ZFPs at high yields as determined by mass spectrometry analysis. We observe that the DNA-binding activity of ZFPs labeled by conventional copper-mediated click chemistry was completely abolished, whereas ZFPs labeled by copper-free click chemistry retain their sequence-specific DNA-binding activity under native conditions, as determined by electrophoretic mobility shift assays, protein microarrays, and kinetic binding assays based on Förster resonance energy transfer (FRET). Our work provides a general framework to label metalloproteins such as ZFPs by metabolic incorporation of unnatural amino acids followed by copper-free click chemistry.



INTRODUCTION

Zinc finger proteins (ZFPs) comprise a broad class of transcription factors in living organisms. ZFPs regulate gene expression by binding to target sites along chromosomal DNA with high specificity and moderate-to-high affinity.[1] Zinc fingers are classified based on amino acid residues coordinating zinc ions, with a major class containing a common structural element with two cysteine and two histidine residues complexed with a zinc ion (Cys2-His2 motif). Recent advances in ZFP engineering have enabled the design and construction of "programmable" transcription factors that target and bind to chromosomal DNA in a sequence-specific fashion, thereby enabling robust control of gene expression in live cells.[1−3] Synthetic ZFPs consist of tandem arrays of zinc finger modules assembled via molecular cloning. In addition, zinc finger nucleases (ZFNs) have been constructed by fusing zinc finger modules with the *Fok*I cleavage domain. ZFNs have been used for targeted manipulation of genomes in a variety of cell types, including human cell lines.[4−6] Using ZFNs, chromosomal DNA can be modified by producing double-stranded DNA breaks to induce site-specific homologous recombination, thereby allowing for direct modification of any desired genomic locus. Zinc finger technology has capitalized on the success of rapid construction methods for ZFPs, including a modular assembly method, combinatorial selection of engineered multifinger proteins (oligomerized pool engineering, OPEN), and context-dependent assembly methods (CoDA).[7−9]

Engineered ZFPs can be screened for sequence-specific DNA binding using powerful *in vivo* methods, including bacterial two-hybrid selection.[10] However, measurement of dynamic ZFP-DNA binding and binding kinetics is generally facilitated by *in vitro* methods or molecular-level biochemical tools.[11,12] Biochemical analysis can yield valuable mechanistic information regarding DNA site recognition by zinc finger modules. Fluorescence-based techniques such as Förster resonance energy transfer (FRET) allow for measurement of dynamic, nonequilibrium processes that are difficult to access using traditional electrophoretic mobility shift assays or immunoprecipitation methods. Characterization of DNA−protein interactions using fluorescence-based methods generally requires site-specific conjugation of fluorescent probes to minimize perturbations to protein structure and to retain protein activity.[13] A common strategy for protein labeling is conjugation of fluorescent tags at existing or engineered cysteine moieties on the protein backbone. However, this labeling strategy is generally not feasible if cysteine moieties are essential for protein function. In the context of zinc fingers, an intact and unmodified Cys2-His2 motif is required for competency in ZFP-based DNA recognition, and this presents a major challenge in labeling ZFPs using cysteine-based

Received: May 16, 2012
Revised: July 8, 2012
Published: August 8, 2012

ACS Publications © 2012 American Chemical Society

dx.doi.org/10.1021/bc300262h | *Bioconjugate Chem.* 2012, 23, 1891−1901

methods.[14,15] Targeted cysteine modification or nonspecific conjugation of fluorescent molecules to ZFPs tends to diminish or completely abolish the DNA-binding ability of ZFPs.[16] From this perspective, there is a strong need for development of new methods for specific labeling of ZFPs with fluorescent probes or chemical functional moieties to facilitate the study of DNA recognition, protein function, and dynamic binding of zinc finger modules.[12]

Development of new strategies for transcription factor labeling would enable fundamental research in gene network dynamics, transcriptional regulation, and genetic engineering. Metabolic labeling of ZFPs by direct incorporation of bioorthogonal moieties (e.g., azide) is a particularly attractive strategy to label proteins with fluorescent probes using click chemistry via copper-catalyzed azide−alkyne cycloaddition.[17] Click chemistry allows for rapid, robust, and specific chemical reactions, thereby serving as a practical and widely adopted labeling strategy.[18,19] Reaction conditions for click chemistry are generally robust, being insensitive to variations in salt concentration or the presence of additional functional groups such as primary amines. Copper (Cu) catalysts are commonly used to activate click reactions between an azide and a terminal alkyne to generate triazole moieties, and a triazole ligand is typically used to boost reaction yields and to enhance reaction rates in aqueous media.[19,20] Although a triazole ligand is not an absolute requirement for the azide−alkyne cycloaddition reaction, low reaction yields have been observed in the absence of the triazole ligand in typical aqueous buffers, and such low yields complicate quantitative studies of dynamic protein interactions.[21] In addition to copper-mediated azide−alkyne cycloaddition, copper-free strain-promoted cycloaddition can be used to avoid potentially toxic copper(I) (Cu^{1+}) ions for click reactions.[22] The conditions for copper-free click reactions are mild and biologically compatible, which facilitates bioorthogonal reactions and chemical conjugation in living cells.[23]

In this work, we report an efficient method for residue-specific labeling of ZFPs using direct metabolic incorporation of noncanonical amino acids followed by copper-free click chemistry. ZFPs consisting of tandem arrays of zinc finger modules are expressed by replacing natural methionine with azidohomoalanine (AHA) in cell cultures. In this way, noncanonical AHA amino acids are directly incorporated at targeted locations along the protein backbone to introduce reactive sites for click chemistry. Using this strategy, we compare both copper-mediated and copper-free strain-promoted [3 + 2] cycloaddition as labeling methods, and we assay the DNA binding properties of modified ZFPs using a solution-based FRET method and a microarray-based DNA hybridization imaging technique. Finally, we validate the metabolic labeling strategy for ZFPs by demonstrating competent DNA recognition and binding of target sequences with high specificity and affinity. Overall, we show that metabolic incorporation of unnatural amino acids, coupled with Cu-free click chemistry, is a powerful approach to study transcription factor binding using a wide variety of fluorescence-based techniques.

MATERIALS AND METHODS

Molecular Cloning. Standard protocols in molecular biology were used for molecular cloning, as described in the Supporting Information (SI).[24] Plasmid DNA was isolated from cell cultures using miniprep kits (Qiagen). Plasmid DNA was digested using restriction endonucleases (New England Biolabs), and gene inserts and linearized vectors were purified by agarose gel electrophoresis and gel extraction kits (Qiagen). All molecular subcloning was performed using *E. coli* strain DH5-alpha, pUC19 plasmid DNA, and a modified version of pcDNA 3.0 plasmid DNA (Invitrogen).

Design and Modular Assembly of ZFPs. The design and assembly of engineered zinc finger proteins was carried out as previously described.[25] Detailed procedures describing ZFP assembly are provided in SI.

Protein Expression and Purification. Engineered ZFPs were produced using *E. coli* protein expression host platforms (M15MA and B834) and purified using fast protein liquid chromatography (FPLC) by affinity-based and size exclusion methods, as described in SI.

Homology Modeling. Zif268 (pdb 1A1L_A) was used as a model protein for generating protein structures. Homology models were constructed using the Swiss Model server, and protein structures were rendered using VMD (Visual Molecular Dynamics, University of Illinois, Urbana−Champaign).[26]

Click Chemistry Reactions for Azide-Modified Proteins. For copper-mediated click chemistry reactions, purified protein (~μM concentration) was mixed with copper sulfate (final concentration of 100 μM), tris[(1-benzyl-*1H*-1,2,3-triazol-4yl)methyl] amine (TBTA) (200 μM), and ascorbic acid (0.5 mM), followed by the addition of Cy5-alkyne (~5−30× molar excess relative to protein). Ascorbic acid was freshly prepared for each batch reaction. For copper-free click chemistry reactions, fluorescein-dibenzylcyclooctyne (DBCO, Click Chemistry Tools, Scottsdale, AZ) or Cy5-DBCO was directly mixed with protein solutions. Cu-free click chemistry reactions were performed in protein elution buffer immediately following gel filtration (Superdex) or metal-ion affinity exchange chromatography (Ni-NTA), with the latter reaction containing 1 M imidazole. Reaction yields were independent of the buffer composition for reactions proceeding at room temperature (25 °C) in the presence of up to ~100× molar excess dye reactant. To monitor the reaction yield, mixtures were snap-frozen in ethanol/dry ice solution to stop the reaction. For MALDI-TOF mass spectrometry analysis, unreacted dye was removed by methanol/chloroform extraction. Labeled protein samples were analyzed by MALDI-TOF mass spectrometry, SDS-PAGE and fluorescence imaging using a Typhoon scanner (GE healthcare) for cyanine dye-labeled proteins, or a Storm scanner (GE healthcare) for fluorescein-labeled proteins.

Fluorescence Anisotropy. A 26-base oligonucleotide ("target1") encoding for a 9-base ZFP binding site and containing a fluorescein dye (6-FAM) at the 5′ terminus was obtained from Integrated DNA Technologies (Coralville, IA). The oligonucleotide sequence for "target1" was: 5′-6-FAM-TATGGAACTCATCAGCCTCATTTCTA-3′, where the ZFP binding site is shown as the underlined sequence. The "target1" oligo was converted to duplex DNA by hybridization with a complementary oligonucleotide, wherein the target and complementary strands were annealed by elevating the temperature to 95 °C for 5 min, followed by gradual cooling to room temperature. Fluorescence measurements were performed using a Cary Eclipse Fluorescence Spectrophotometer (Varian) equipped with excitation and emission polarizers, automated temperature control, and magnetic solution stirrers. ZFP-DNA binding was performed at 20 °C in the following reaction buffer: 20 mM Tris/Tris HCl (pH 7.9), 100 mM

Table 1. Summary of Engineered Zinc Finger Proteins Used in This Work[a]

ZFP	protein molecular weight (Da)	dissociation constant, K_d (nM)	number of zinc finger modules	fusion protein (post purification)	number of UAAs	location of UAAs
ZFP1	11040	158	3	None	1	N-terminus
ZFP2	38944	191	3	Cerulean (N-terminal fusion)	4	Cerulean FP domain
ZFP3	39505	167	3	mCherry (N-terminal fusion)	11	mCherry FP domain
ZFP4	39505	175	3	mCherry (C-terminal fusion)	11	mCherry FP domain
ZFP5	8716	~2000	2	None	1	N-terminus
ZFP6	12040	180	3	None	0	N/A

[a]Dissociation constants (K_d) were measured using fluorescence anisotropy (Materials and Methods). The 9-base DNA binding sequence for three-finger ZFPs (ZFP1-4 and ZFP6) was 5′-ATCAGCCTC-3′. Schematics of the protein constructs are shown in SI Scheme S1.

NaCl, 0.1 mM $ZnCl_2$, 1 mM TCEP, 20% glycerol, 0.05% Nonidet-40, 2 ng/mL dI-dC, and 50 μg/mL BSA. The optimal buffer composition for DNA binding was determined over the course of several control experiments. Fluorescence anisotropy was measured in solutions containing 20 nM 6-FAM labeled target1-dsDNA (duplex DNA) using bandwidths of 20 nm. Fluorescence anisotropy (r) was calculated by

$$r = \frac{I_{VV} - G \times I_{VH}}{I_{VV} + 2G \times I_{VH}} \qquad \text{with } G = \frac{I_{HV}}{I_{HH}} \tag{1}$$

where the instrument G factor is defined as the ratio of detection sensitivities for vertically and horizontally polarized light in the system, and H and V refer to the horizontal and vertical positions, respectively, of the excitation (first subscript) and emission (second subscript) polarizers.[27] For these measurements, the instrument G factor was carefully measured, and we observed that glycerol did not affect fluorescence measurements. For data analysis, a nonlinear regression method was used to fit the experimental data. In addition, anisotropy data was analyzed using a Hill equation to characterize the extent of cooperative protein binding.[28] Normalized anisotropy values were fit to a Hill equation

$$\theta = \frac{[\text{protein}]^n}{K_D + [\text{protein}]^n} \tag{2}$$

where θ is the fraction of occupied DNA bound to protein, K_D is the dissociation constant, and n is the Hill coefficient describing the extent of cooperative binding.

FRET Measurements. A 25-base oligonucleotide ("target2") encoding for a 9-base ZFP target DNA binding site and containing a Cy5 dye at the 5′ terminus was obtained from Integrated DNA Technologies. The oligo sequence for "target2" was 5′-Cy5-TATGGAACTCATCAGCCTCATTTCT-3′, where the ZFP binding site is shown as the underlined sequence. The "target2" oligo was converted to duplex DNA by hybridization with a complementary oligonucleotide. Fluorescence measurements were performed at 20 °C using a Cary Eclipse Fluorescence Spectrophotometer. For FRET measurements, the ZFP-DNA binding buffer was 20 mM Tris/Tris HCl (pH 7.9), 100 mM NaCl, 0.1 mM $ZnCl_2$, 1 mM TCEP, 20% glycerol, 0.05% Nonidet-40, 2 ng/mL dI-dC, and 50 μg/mL BSA. In addition, Cy3-DBCO-ZF2 protein was prepared in binding buffer at 600 nM, and "target2" Cy5-DNA was titrated to the desired final concentration. After incubating the reaction for 10 min at room temperature (25 °C), fluorescence spectra were measured. All samples were measured in triplicate, and disposable cuvettes were used to minimize residual fluorescence from previous measurements.

Electrophoretic Mobility Shift Assay (EMSA). Protein−DNA binding was assayed by EMSA using a protocol as previously described.[29] Briefly, an oligonucleotide ("target3") encoding for the ZFP binding sequence and containing a Cy3 dye at the 5′ terminus was used. The sequence for "target3" was 5′-Cy3-AATATGGAACTCATCAGCCTCATTTCTAAA-TATGAAGAGTT-AAGACGTAATG′. The "target3" oligonucleotide was converted to duplex DNA by hybridization with a complementary oligonucleotide. Alternatively, an amplicon (100 bp or 200 bp in length) containing the target binding sequence was obtained by PCR amplification using phage lambda DNA as a template in a standard PCR reaction (SI). Following PCR, amplicons were purified by PCR cleanup (Qiagen). For EMSA, protein and DNA were mixed in desired stoichiometric proportions and incubated in binding buffer at room temperature (25 °C) for 20 min. Following incubation, the mixture was supplemented with DNA loading dye for gel electrophoresis and run on an 8% polyacrylamide gel. Gels were imaged using ethidium bromide (EtBr) staining and UV illumination for PCR amplified DNA or a Typhoon scanner for cyanine dye-labeled DNA.

Microarray Measurements. PEGylated glass slides were prepared using PEG-biotin-NHS ester (MW 3500 g/mol) and mPEG-NHS ester (MW 5000 g/mol) as previously described.[30] PEGylated glass slides were treated with protein−DNA binding buffer, followed by incubation with neutravidin (0.5 mg/mL). Next, Cy3-biotin-DNA (1 μM in water), which has the same sequence as "target3" DNA, was printed as 1 nL spots on neutravidin treated PEGylated slides using a TeleChem Stealth SMP3 pin (Perkin-Elmer) as previously reported.[31] Briefly, the Cy3-biotin-DNA was diluted to a final concentration of 1 μM in deionized water, and the DNA solution was printed as spots on the functionalized glass slides in duplicate. After printing, slides were incubated with the DNA solution spots for 5 min. Glass slides were rinsed 4× with binding buffer to remove excess, unbound Cy3-DNA-biotin from the glass surface. Next, Cy5-ZFP (20 nM) in binding buffer solution was applied to Cy3-DNA surface array, followed by incubation for 5 min at a relative humidity of 55−60% at ambient temperature 25 °C. Glass slide arrays were rinsed with DNA−protein binding buffer to remove unbound Cy5-ZFP labeled proteins. DNA−protein complexes were imaged using a *GenePix Pro 6.5* double laser scanner at wavelengths of 535 and 635 nm (Axon Instruments). For imaging, the photomultiplier tube voltage was set to 550 V, and the gain was set to 30%. For display, pseudocolors were applied to Cy3 and Cy5 (green and

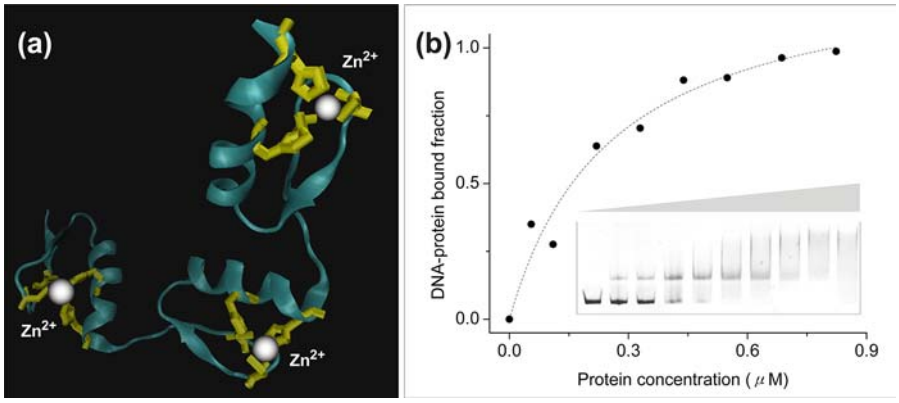


Figure 1. Engineered ZFPs bind target DNA in a sequence-specific fashion. (a) Homology model structure of a modular ZFP consisting of a tandem array of three repeating zinc finger modules, each containing a zinc ion in a Cys2-His2 complex (yellow). (b) Electrophoretic gel mobility shift assay (EMSA) shows that a three-finger ZFP (ZFP6) binds specifically to target DNA. The bound fraction was quantified to determine the equilibrium binding constant K_d. (inset) EMSA image shows that ZFP6 forms a specific complex with target DNA in the presence of nonspecific competitor DNA.

red, respectively), and pseudocolored images were merged using *Image J* (NIH) to show DNA–protein colocalization as overlapping colors in composite images.

RESULTS AND DISCUSSION

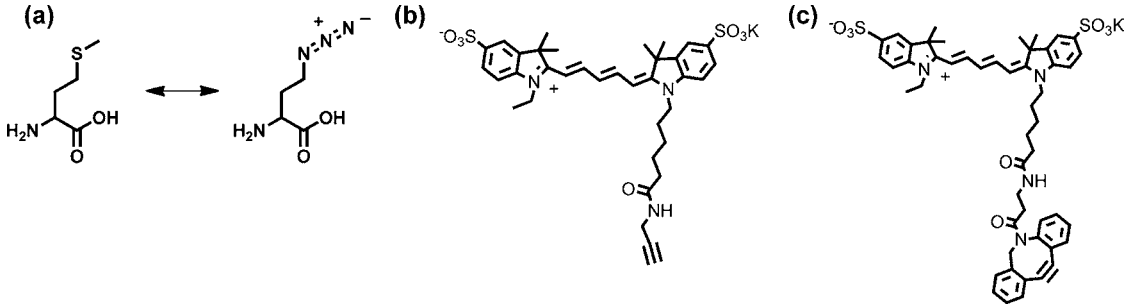
Engineering Zinc Finger Proteins for Specific DNA Binding. Recent advances in ZFP technology have enabled the design of chimeric ZFPs with the ability to bind to targeted DNA sequences. Individual zinc finger modules can be linked in tandem arrays, thereby enabling assembled ZFPs to bind to recognize DNA sequences of variable length. Using this approach, we cloned several multifinger ZFPs using a modular assembly method (Table 1).[7] A homology model structure for one of the engineered three-finger ZFPs (ZFP1) studied in this work is illustrated in Figure 1a, which shows that zinc fingers are stabilized by coordination of a zinc ion in a cysteine-histidine structural binding motif.

In an initial set of experiments, we expressed and purified several of the engineered ZFPs using natural amino acids. The DNA binding capacity for a three-finger ZFP (ZFP6) was characterized using an electrophoretic mobility shift assay (EMSA), as shown in Figure 1b. In this experiment, purified ZFP was mixed with equimolar amounts of DNA oligonucleotides encoding for the 9-base pair recognition sequence and nonspecific DNA without the target sequence. Electrophoretic shift assays clearly show that target DNA bands are up-shifted due to the formation of a specific protein–DNA complex (dissociation constant K_d = 180 nM), whereas nonspecific DNA did not yield a significant shift. As a control experiment, we determined that a single base pair mismatch in the target DNA recognition sequence prevents specific binding of ZFPs to target sequences (SI Figure S1). Based on these results, we concluded that chimeric ZFPs were capable of binding to target DNA with high affinity and specificity.

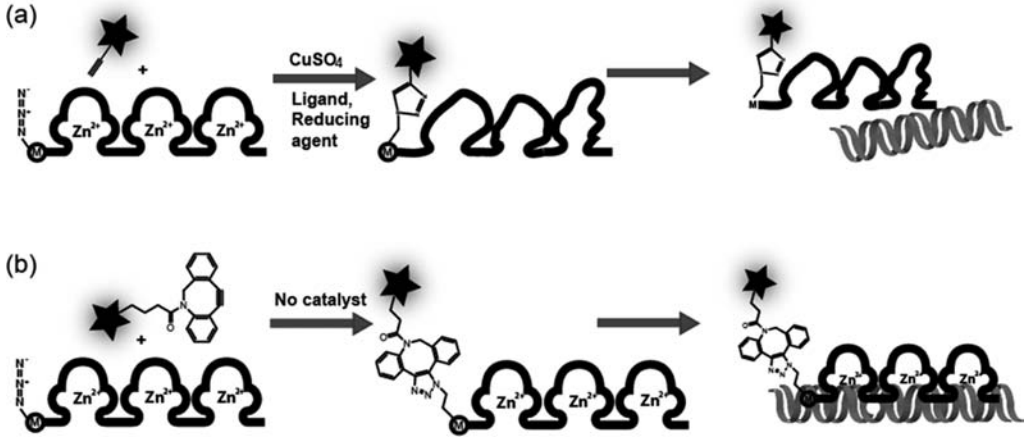
Residue Specific Noncanonical Amino Acid Incorporation. Specific labeling of ZFPs with fluorescent tags for quantitative binding assays presents several challenges. To specifically label ZFPs with fluorescent tags, we pursued three distinct approaches: (1) introduction of mutant cysteine residues as reactive sites, (2) labeling via fluorescent protein fusion domains, and (3) residue-specific substitution of amino acids. In the first approach, we engineered cysteine residues at the N- or C-terminus of a three-finger ZFP, followed by reaction with a maleimide-conjugated fluorescent dye. We observed that the DNA binding capacity for ZFPs labeled using this strategy was completely abolished, and we conjecture that the natural Cys2-His2 structural motif was perturbed due to cross-reactivity between the labeling probe and natural cysteine moieties using this strategy.[32] In a second approach, we generated N- or C-terminal fusions between ZFPs and mCherry or Cerulean fluorescent proteins. We found that the binding equilibrium of ZFP-fusion proteins is comparable to the parent ZFPs (SI Figure S2), and ZFPs with N- or C-terminal fusions exhibited similar specificity to target DNA compared to unlabeled ZFPs. In a series of control experiments, we verified that fluorescent proteins alone did not confer DNA-binding properties to ZFP-fusion proteins. However, in contrast to small molecule organic dyes, fluorescent proteins generally exhibit lower levels of brightness and photostability, which could potentially complicate quantitative fluorescence binding experiments or single molecule detection assays.

In a third approach, we pursued a bioorthogonal labeling strategy for ZFPs based on metabolic incorporation of unnatural amino acids (UAAs), followed by conjugation of organic dyes using azide–alkyne cycloaddition via click chemistry. For UAA incorporation into recombinant proteins, we adopted the method previously developed by the Tirrell group, wherein metabolic incorporation of UAAs is accomplished by universal replacement of one natural amino acid with a non-natural analogue.[17,33] In some cases, universal substitution of methionine can be used for protein labeling because the occurrence of methionine is low relative to other amino acids, yet most proteins have at least one methionine at the N-terminus. In *E. coli*, wild-type aminoacyl tRNA synthetases can charge cognate tRNAs with methionine analogues such as azidohomoalanine (AHA), and the ribosomal machinery universally incorporates the UAAs into growing protein chains during translation.[17,34] To ensure universal replacement of natural amino acids such as methionine with UAAs, methionine auxotroph strains of *E. coli* are often employed as protein expression platforms. Alternative strategies based on suppression of nonsense mutations at amber codons have also been developed for site-specific incorporation of UAAs into recombinant proteins.[35,36] In contrast to universal residue-specific replacement methods, site-specific incorporation methods can be used to introduce UAAs into specific target

Scheme 1. Chemical Structures of (a) Methionine (Met) and the Methionine Analogue Azidohomoalanine (AHA), (b) Cy5-Alkyne, and (c) Cy5-DBCO



Scheme 2. Schematic of Click Chemistry-Mediated Covalent Conjugation of Fluorescent Dyes to ZFPs Containing Metabolically-Incorporated Azide[a]



[a](a) Copper-mediated click chemistry was used to conjugate dyes containing linear alkynes with ZFPs; however, the ligand TBTA induced protein denaturation. (b) Copper-free click chemistry was used to conjugate dyes containing DBCO to ZFPs, thereby enabling ZFPs to retain sequence-specific DNA binding activity.

locations within proteins, which minimizes the potential for perturbations to natural protein structure. From this perspective, site-specific incorporation of UAAs is a versatile approach for protein modification. However, the residue-specific methionine replacement strategy can be pursued when the substituted residue is confined to a well-defined target site.[37]

The vast library of zinc finger modules provides ample flexibility to engineer ZFPs containing only a single methionine residue at the protein N-terminus, distal from the DNA binding region of the module. The modular assembly method allows for facile metabolic labeling of ZFPs with UAAs, because the library of zinc finger modules is degenerate for any given three-base sequence of DNA.[6,25] Therefore, we selected ZFP modules without methionine codons from the Zinc Finger Consortium library to exclude methionine residues from the DNA binding region, thereby preserving the DNA binding activity of the labeled protein. We used azidohomoalanine (AHA) as a methionine surrogate in *E. coli* methionine auxotroph strains (Scheme 1a), thereby replacing all methionine residues in recombinant proteins with AHA. Tandem arrays of zinc fingers were constructed consisting of two or three tandem modules to allow for specific binding to target DNA sequences (Table 1).

Metabolic incorporation of UAAs into ZFPs was carried out using the *E. coli* methionine auxotroph strain M15MA or B834 as a protein expression host. We observed that the methionine auxotroph strain M15MA efficiently incorporates AHA into expressed proteins in growth medium containing AHA, generally resulting in high levels of incorporation of AHA residues into recombinant proteins.[37] In the absence of methionine or AHA, *E. coli* cell cultures exhibited extremely poor cell growth over the course of several hours. Prior to inducing protein expression, basal expression was minimal due to the strong lacIq repressor module in the pQE80L expression plasmid. Following protein expression, ZFPs harboring metabolically incorporated UAAs were purified using metal-ion affinity chromatography (Ni-NTA resin), and protein samples were carried forward to click chemistry reactions.

In the absence of expression tags, three-finger ZFPs generally exhibited low expression yields in *E. coli* methionine auxotroph strains used in this work (B834, M15MA, or T7 Crystal). Without expression tags, the majority of three-finger ZFPs appeared in the insoluble fraction of cell cultures when expressed in methionine auxotroph strains. Moreover, we found that purification of ZFPs from the insoluble fraction of cell cultures was not feasible due to inefficient refolding of denatured ZFPs.[38] To enhance the expression yields of engineered ZFPs in methionine auxotroph strains, we used fluorescent proteins (FPs) as expression tags (Table 1), similar to previous studies using expression tags that do not interfere with DNA binding.[39,40] We observed substantial improvements in expression yields for ZFPs with N- or C-terminal FP fusions,

dx.doi.org/10.1021/bc300262h | *Bioconjugate Chem.* 2012, 23, 1891−1901

with a significant increase in the amount of expressed ZFP in the soluble fraction of cell cultures. In some cases, ZFP-FP fusion proteins were used for equilibrium DNA binding assays (SI Figure S2). However, for most three-finger ZFP constructs, we inserted a thrombin cleavage site between genes encoding for FPs and ZFP, thereby enabling the FP expression tags to be cleaved off of the ZFPs during purification after protein expression (SI Scheme S1). Using this approach, zinc finger modules can be cleaved from ZFP-FP constructs while the fusion protein is bound to the Ni-NTA affinity column, thereby generating high yields of three-finger ZFPs containing UAAs. We used biotinylated thrombin for the cleavage reaction, which enables facile removal of thrombin from ZFP samples using magnetic bead-based separation with streptavidin-coated microspheres. Purified ZFP was assayed using electrospray ionization mass spectrometry, which revealed highly purified protein at high yields (SI Figure S3).

The expression tag method described in this work provides several advantages for UAA incorporation using N-terminal methionine replacement. In prokaryotes, it is well-known that the N-terminal methionine is typically excised in the postexpression modification by methionine aminopeptidase (MetAP).[41] In a similar vein, MetAP can also remove N-terminal AHA, depending on the residue following the initial AHA.[37] Therefore, N-terminal expression tags intrinsically protect AHA residues from cleavage without the need for additional protein design or cloning steps.

Fluorescent Probe Conjugation using Click Chemistry with Linear Alkynes and Dibenzocyclooctyne. Following expression and purification, we labeled ZFPs with fluorescent dyes using two distinct strategies: Cu-mediated click chemistry using Cy5-conjugated with a propargyl group and Cu-free strain promoted [3 + 2] cycloaddition using Cy5-conjugated dibenzocycloocyne (DBCO), as denoted in Scheme 2. In the case of Cu-mediated click chemistry, we observed that addition of copper sulfate or the triazole ligand tris[(1-benzyl-1*H*-1,2,3-triazol-4yl)methyl] amine (TBTA), which is commonly used to accelerate Cu-mediated click cyclizations, resulted in protein precipitation and loss of protein function (SI Figure S7). Precipitated ZFPs showed a complete loss of DNA-binding activity (Figure 2), and precipitation of zinc finger proteins was

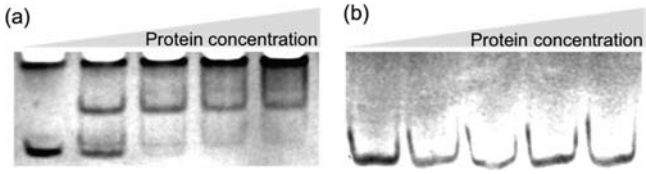


Figure 2. Gel electrophoretic mobility shift assay (EMSA) for a three-finger ZFP. (a) Under native conditions, ZFPs clearly form a specific complex with target DNA. (b) Upon addition of the triazole ligand TBTA and copper ions, ZFPs no longer form a specific complex with DNA, and the DNA binding activity is ablated.

irreversible. We attempted to resolubilize ZFPs using an excess amount of zinc ions in solution; however, the DNA binding activity of ZFP could not be recovered.

Zinc ion binding is a key requirement for efficient folding and activity of Cys2-His2 ZFPs because zinc finger modules possess $\beta\,\beta\,\alpha$ structures, which are stabilized by zinc chelation. Dissociation constants for zinc binding are typically in the range of 10^{-9} to 10^{-11} M, whereas ligands such as EDTA bind extremely tightly with dissociation constants of approximately 10^{-16} M.[42,43] Only a few minutes of exposure to strong chelating reagents such as EDTA will dissociate zinc ions from zinc finger proteins,[44] and loss of zinc ions induces structural perturbations. In zinc finger modules, consistent contacts are made between the DNA backbone and histidine residues. Specific contacts may be especially important in controlling docking arrangements, because they couple the structural core of the zinc finger directly to the sugar phosphate backbone of DNA. Furthermore, metal ion substitution can induce significant structural changes in ZFPs.[43,45] It is well-known that zinc finger modules can associate with Cu^{2+}, Ni^{2+}, or Co^{2+} ions, and the binding affinity is comparable to that of Zn^{2+}. However, the binding of divalent ions other than zinc can disrupt the $\beta\,\beta\,\alpha$ structure of zinc finger modules, and the DNA binding ability of ZFPs cannot be restored upon refolding.[46] Therefore, the addition of Cu^{2+} as a catalyst in Cu-mediated click reactions has the potential to induce structural perturbations in ZFPs.

Copper-mediated click chemistry requires a Cu chelating reagent to increase reaction rates and yields. TBTA has suitable chelating capacity for copper(II) and is widely used for copper-mediated click reactions. Upon addition of TBTA to a solution of copper(II), the faint blue color immediately turns to a darker blue, which indicates copper chelation (SI Figure S7). Moreover, we observed that TBTA can strongly chelate zinc(II), as well as copper(II), as evidenced by observing a color change (green to blue-green) that occurs when zinc ions are added to solutions containing TBTA and Cu^{2+} (SI Figure S7c). Under typical copper-mediated click reaction conditions involving ZFPs, zinc ions are present at relatively high concentrations (~mM), in vast excess relative to the ZFP in solution. Therefore, it is likely that addition of TBTA as a catalytic ligand for copper-mediated click reactions will be bound by free zinc ions, rather than copper, which will reduce the efficiency of TBTA on the copper-mediated click reactions. In addition, we observed that addition of copper sulfate to solutions containing ZFPs resulted in immediate protein precipitation (SI Figure S7a), which indicates that Cu^{2+} ions can interact with ZFPs in undesired ways. We further found that TBTA or copper ions, alone or together, can induce the precipitation of ZFPs (SI Figure S7b). We found that the precipitation of ZFPs was irreversible, because it could not be reversed by extensive dialysis against a zinc-rich solution.

Although ZFP recovery after denaturation has rarely been successful,[47] a limited number of wild-type ZFPs have been demonstrated to refold after denaturation and extensive purification. However, protein refolding is time-consuming, labor-intensive, and generally a low-yield process.[48] For "synthetic" or engineered proteins such as ZFPs constructed by modular assembly methods, the overall protein fold and corresponding energy minimization may be suboptimal due to the "cut and paste" assembly method of the individual zinc finger modules, thereby making it very challenging to efficiently refold zinc finger proteins into the native $\beta\,\beta\,\alpha$ protein architecture stabilized by coordination of a zinc ion. To overcome the problems associated with ZFP denaturation due to loss of zinc ions, we used Cu-free strain promoted [3 + 2] cycloaddition, which does not require catalysts or ligands for protein labeling.[49,50]

To demonstrate ZFP labeling using UAAs and Cu-free click chemistry, ZFPs were expressed and purified, and Cu-free click chemistry was used to label azide-modified ZFPs with fluorescein, Cy3, and Cy5-conjugated dibenzocyclooctyne

(DBCO).[51] Click reactions were monitored using MALDI-TOF and ESI (Q-TOF) mass spectrometry analysis and fluorescence-based gel imaging (Figure 3). More than 70% of

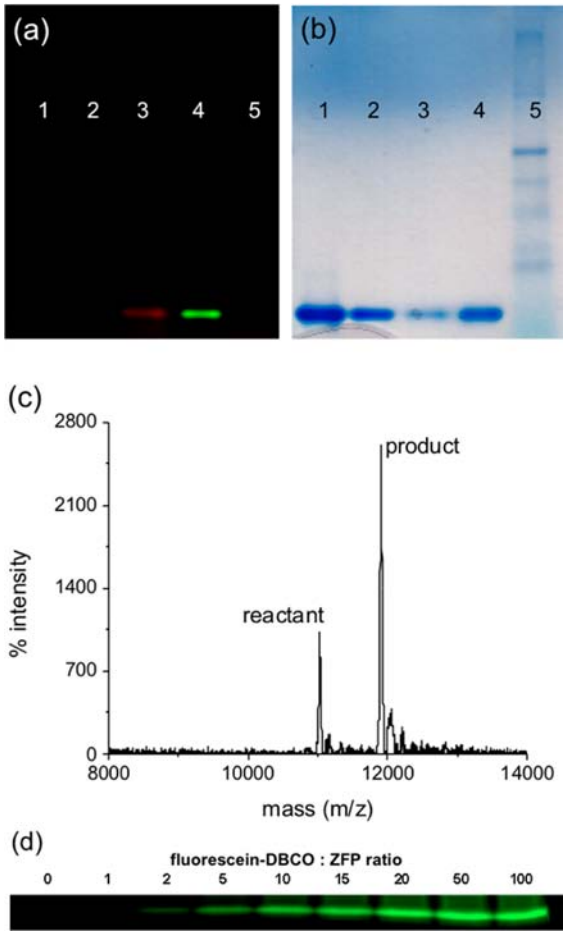


Figure 3. Copper-free click chemistry for specific labeling of ZFPs with fluorescent tags. (a) Fluorescent gel image and (b) SDS-PAGE analysis for a gel showing dye conjugation to three-finger ZFPs following copper-free click reactions. Lane 1, Met-ZFP1; Lane 2, AHA-ZFP1; Lane 3, Cy5-clicked-ZFP1; Lane 4, Cy3-clicked-ZFP1; Lane 5, protein MW ladder. (c) Protein mass spectrophotometric analysis (MALDI-TOF) of labeled ZFPs. AHA-ZFP1 (MW 11 035 Da) was reacted with Cy5-DBCO (MW 914 Da) using copper-free click chemistry, and the shift in mass confirms conjugation of a single Cy5 dye to ZFP1. Reaction yield calculated from the peak height is 72%. (d) Fluorescent gel showing that dye loading on ZFP5 increases upon increasing the stoichiometric ratio between fluorescein-DBCO and ZFP5 in the click reaction (1 h at 25 °C). An equal mass of protein was loaded in each lane.

the monofunctionalized three-finger ZFP was labeled with Cy5 using Cu-free click chemistry, as revealed by MALDI-TOF analysis (Figure 3c). The labeling reaction appeared to saturate in excess of 20:1 molar ratio of DBCO to ZFP following overnight reaction at 4 °C, as shown in Figure 3d. In addition, we observed no cross reactivity between natural amino acids and fluorescein−DBCO, according to MALDI-TOF analysis, even in the presence of ∼100× molar excess dye to protein in the reaction mixture, which is a clear advantage of bioorthogonal labeling chemistries. Bioorthogonal labeling strategies generally ensure highly specific labeling with minimal perturbations to protein structure, provided that the target labeling site is carefully selected based on protein structure/function considerations. In addition, Cu-free click chemistry also provided flexibility in reaction conditions for protein labeling. ZFPs labeled with fluorescein−DBCO at 4 °C overnight compared favorably with protein samples labeled 25 °C for two hours in terms of reaction yields, though higher temperatures generally showed slightly improved reaction yields, as shown in SI Figure S5. Over the course of two hours, reactions carried out at 55 °C resulted in ∼85% yield for ZFP5, whereas the reactions carried out at 25 °C resulted in ∼63% yield. Moreover, we observed Cu-free click labeling of ZFPs to proceed with high yields at 4 °C with overnight incubation, giving yields comparable to labeling reactions at two hours at 25 °C. In order to preserve the stability of purified transcription factor proteins such as ZFPs, it may be preferable to perform labeling reactions at 4 °C.

Binding Assays for ZFPs Labeled by Cu-Free Strain Promoted [3 + 2] Cycloaddition. We used fluorescence anisotropy to measure the binding isotherms of wild-type ZFP1 (Met-ZFP1), azide-labeled ZFP1 (AHA-ZFP1), and Cy5-DBCO-clicked ZFP1 (Cy5-ZFP1), as shown in Figure 4a. Metabolically labeled ZFP1 (AHA-ZFP1) and Cy5-DBCO-clicked ZFP (Cy5-ZFP1) exhibit nearly identical DNA binding properties compared to wild-type Met-ZFP1, as revealed by fluorescence anisotropy. The dissociation constants K_d calculated from fluorescence anisotropy experiments were as follows: 158 nM, 184 nM, and 123 nM for Met-ZFP1, AHA-ZFP1, and Cy5-ZFP1, respectively. Therefore, the dissociation constants were nearly the same for these three ZFP1 protein species, within experimental error, based on a Hill model fitting equation (Materials and Methods). The measured values of dissociation constants for engineered ZFPs are in agreement with previously published data for ZFPs.[40]

We also investigated the DNA binding properties of labeled ZFPs using gel electrophoretic mobility shift assays (EMSA). In these experiments, Cy5-clicked zinc finger proteins (Cy5-ZFP2) were bound to Cy3-labeled duplex DNA containing the 9-base "target2" DNA site for the three-finger tandem array of assembled ZFPs (Materials and Methods). EMSA revealed sequence-specific DNA binding of Cy5-ZFP2 to target Cy3-DNA in the presence of nonspecific competitor DNA (Figure 4b), which agrees with fluorescence anisotropy data for the same proteins (SI Figure S4). In these experiments, we used a fixed concentration of DNA (1 nM) and varied the concentration of labeled ZFP, which revealed the specific binding of ZFPs protein to target DNA. Unlike fluorescence anisotropy, EMSA is a quasi-steady-state method for assaying DNA binding; however, binding isotherms calculated from EMSA data were comparable to fluorescence anisotropy experiments, as shown in Figure S4. At a DNA:AHA-ZFP2 ratio of ∼1:60, nearly all DNA is bound to the zinc finger protein, as shown in Figure 4b. In addition, EMSA shows a distinct single band corresponding to the bound ZFP-DNA complex, which is suggestive of a well-defined protein−DNA complex in the bound state. Overall, these experiments demonstrate the utility of specific labeling of three-finger ZFPs with conserved DNA binding capacity of transcription factor proteins to target DNA sites.

Solution-Based FRET Binding Assays and Microarray Assays for Labeled ZFPs. To demonstrate the utility of labeling ZFPs using UAAs and Cu-free click chemistry for *in vitro* DNA binding assays or single molecule fluorescence experiments, we studied the binding between Cy3-clicked ZFP2

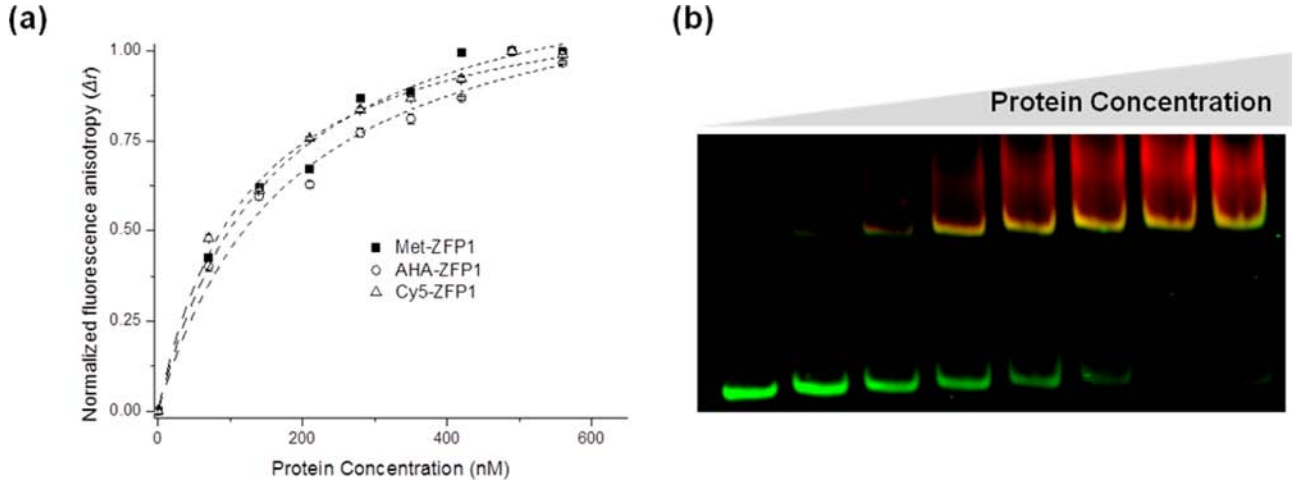


Figure 4. DNA binding assays for labeled ZFPs. (a) Fluorescence anisotropy shows that fluorophore-conjugated ZFPs are competent for sequence-specific DNA binding. Three-finger ZFPs were studied before and after click reactions, including the wild-type protein (Met-ZFP1, square), metabolically labeled azide containing protein (AHA-ZFP1, circle), and Cy5-clicked protein (Cy5-ZFP1, triangle). (b) Gel electrophoretic mobility shift assays (EMSA) show that labeled ZFPs effectively bind to target DNA in sequence-specific manner. Three-finger ZFPs (ZFP2) labeled with Cy5 (red) bind to Cy3-labeled DNA (green), and the protein–DNA complex (yellow) migrates through the gel with a clear mobility shift.

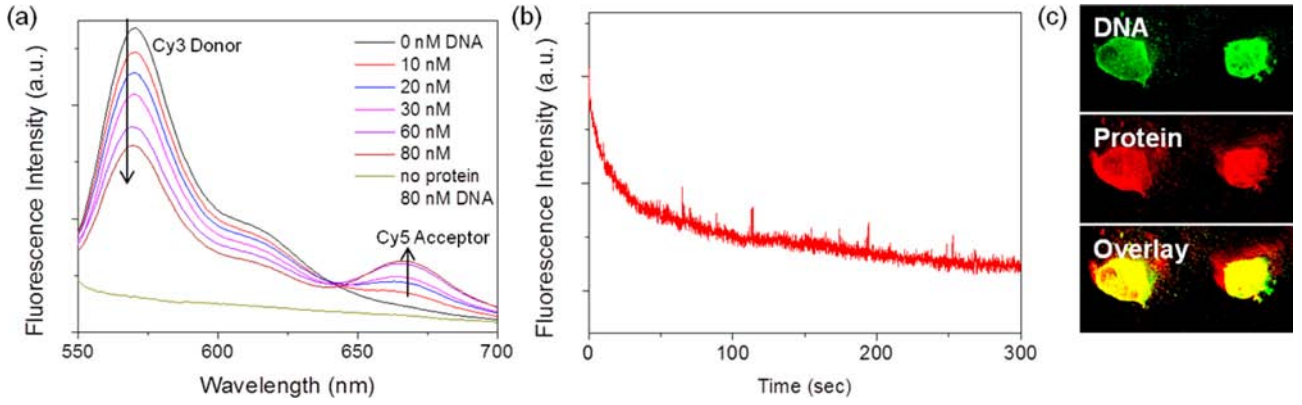


Figure 5. Solution-based FRET and surface-based DNA binding assays for labeled ZFPs. (a) Solution-based FRET reveals specific binding interactions between Cy3 dye labeled ZFPs and target Cy5-DNA. The concentration of Cy3-ZFP2 was maintained at 600 nM, and the Cy5-DNA concentration was varied. (b) Unbinding kinetics for a bound complex of Cy5-ZFP2 and Cy3-DNA measured by FRET. (c) Microarrays demonstrate colocalization between Cy5-labeled ZFP2 and surface-immobilized Cy3-DNA encoding for the target DNA binding sequence.

(Cy3-ZFP2) and Cy5-labeled target DNA (Cy5-DNA, "target2" DNA) using Förster resonance energy transfer (FRET). We designed a FRET dye pair using a Cy3-donor/Cy5-acceptor located on the labeled ZFP and target DNA, respectively. The binding site for DNA was designed to be located at a distance of 5 nm from DNA terminus containing the Cy5 dye molecule, which is within the Förster radius of 56 Å for a Cy3/Cy5 dye pair.[27] In these experiments, we used a fixed concentration of Cy3-ZFP2 in solution, and we varied the amount of Cy5-DNA while monitoring the FRET signal (Figure 5a). Samples were illuminated using an excitation wavelength of 520 nm to excite the Cy3 donor dye. Upon addition of Cy5-acceptor DNA to solution, we observed a decrease in Cy3 emission and a concomitant increase in Cy5 emission arising from FRET between the Cy3/Cy5 dye pair within the ZFP-DNA complex. FRET signals reached a maximum for solutions containing a 7.5:1 ratio of ZFP/DNA (600 nM Cy3-ZFP2 with 80 nM Cy5-DNA). As a control experiment, 80 nM Cy5-DNA alone did not show any considerable emission at 670 nm in the absence of Cy3-ZFP2. Overall, the FRET experiments reported here serve as proof-of-principle demonstration for studying dye-labeled transcription factors using fluorescence-based methods, which will enable kinetic binding experiments or transcription factor localization studies via bulk-phase or single molecule fluorescence imaging.

Inspired by equilibrium FRET measurements, we monitored the dynamic dissociation of ZFPs to target DNA, as shown in Figure 5b. Initially, an excess amount of unlabeled target DNA was added to a solution of Cy3-ZFP2 and Cy5-DNA, and the decrease in FRET was monitored over time. The fluorescence signal was fit to a single exponential decay, and we determined a characteristic time for dissociation as $t_{1/2}$ = 57 s. Kinetic binding/unbinding measurements typically require specialized equipment such as surface plasmon resonance (Biacore) or related techniques.[52] However, in our work, direct labeling of transcription factors allows for these measurements to be obtained using standard fluorescence spectrophotometers.

Several surface-based methods are available to study protein–DNA or protein–protein binding interactions, including label-free surface plasmon resonance, surface-based fluorescence detection using DNA microarrays and single

molecule fluorescence methods. Fluorescence-based single molecule techniques typically require surface passivation with PEG or polyelectrolyte multilayers, followed by immobilization of the target biomolecule to a glass surface. Here, we studied ZFP-DNA binding interactions on a glass surface passivated with poly(ethylene glycol) (PEG) using specific chemistry for biomolecule attachment (Figure 5c). In this way, we adapted DNA binding studies involving labeled ZFPs to assays involving solid supports, such as general microarray-based screening tools for proteomics or genomics. We used a microarray system for detection of ZFP-DNA binding that utilizes similar surface chemistry for surface-immobilized single molecule fluorescence experiments.

In this experiment, glass slides were first pretreated with PEG to minimize nonspecific protein binding. Next, Cy3-DNA (green) was printed on the PEGylated glass surface within a confined area, and Cy5-ZFP2 (red) was applied to the DNA-printed glass slide, incubated for 5 min, and copiously rinsed to remove unbound protein. Overlaid fluorescence images of Cy3-DNA-biotin and Cy5-ZFP2 show specific binding interactions between DNA and ZFP, as revealed by a distinctive yellow color. In particular, the ZFP binding pattern (red) precisely colocalizes with the DNA printing area (green), with the low background being the result of the hydrophilic PEG-treated surface.

CONCLUSIONS

ZFPs comprise a broad class of transcription factor (TF) proteins. TFs are fundamental elements of genetic control and play a key role in transcriptional regulation in living organisms. In this work, we developed an efficient method for specific labeling of ZFPs using metabolic incorporation of UAAs, followed by copper-free click chemistry. Modular ZFPs containing tandem arrays of three zinc fingers were successfully expressed using a universal amino acid replacement strategy by substituting azide-containing AHA for natural methionine in auxotroph strains. We demonstrate residue-specific labeling with dye-conjugated DBCO using copper-free click chemistry, generally achieving reaction yields in excess of ~70%. Moreover, the specific DNA binding activity was retained for ZFPs labeled via copper-free click chemistry. To our knowledge, this work represents an important advance in residue-specific labeling of ZFPs, which can be useful conducting *in vitro* screens for assembled ZFPs via solution-based FRET assays or microarray-based hybridization assays. Furthermore, this work will open new avenues for the molecular-level exploration of dynamic processes involving ZFP binding in solution-based assays and in surface-based fluorescence experiments using surface-immobilized protein strategies.

Bioorthogonal chemistries such as copper-catalyzed azide–alkyne cycloaddition broaden the toolset for investigation of protein–protein or protein–DNA interactions using solution-phase or surface-based assays. For microarrays or surface-based biosensing assays, biomolecules such as DNA or proteins are typically linked to surfaces using specific chemical attachment, and the binding partners are introduced in solution. Many surface-based assays rely on biotin–avidin linkage chemistry to immobilize biomolecules, which strongly motivates the need for additional orthogonal chemistries for fluorescent labeling of biomolecules. In the case of ZFPs, copper-mediated click chemistry completely abolishes the binding activity of zinc fingers to target DNA by disruption of the Cys2-His2 zinc ion complex caused by additives in the reaction, such as copper and chelating reagent. On the other hand, copper-free click chemistry provides an efficient strategy for residue-specific labeling of ZFP by incorporation of unnatural amino acids and copper-free click chemistry, which circumvents cross-reactivity with natural amino acid residues and retains protein function.

Overall, we anticipate that this labeling strategy will be useful in quantifying transcription factor dynamics using fluorescence-based methods, which will motivate new studies in gene network dynamics or regulation.[11] Until now, the study of transcription factor localization and dynamics has mainly relied on using fluorescent proteins as labeling probes. Using UAAs and copper-free click chemistry, ZFPs can be labeled with small molecule organic dyes for improved fluorescence brightness, which will enable quantitative studies of transcription factor binding kinetics.[53] Finally, the labeling method described in this work provides a general framework for labeling metalloproteins containing iron, zinc, or copper cofactors for mechanistic studies of protein function.

ASSOCIATED CONTENT

Supporting Information

Experimental data. This information is available free of charge via the Internet at http://pubs.acs.org/

AUTHOR INFORMATION

Corresponding Author

*E-mail: cms@illinois.edu.

Notes

The authors declare no competing financial interest.

ACKNOWLEDGMENTS

This work was supported by a Packard Fellowship from the David and Lucile Packard Foundation and an NIH Pathway to Independence Award (4R00HG004183-03 to C.M.S.) and an NIH MERIT Award (5R37DK-15556 to J.A.K.). We thank Professor A. J. Link (Princeton University) for generously providing *E. coli* auxotroph strain M15MA.

REFERENCES

(1) Urnov, F., Miller, J., Lee, Y., Beausejour, C., Rock, J., Augustus, S., Jamieson, A., Porteus, M., Gregory, P., and Holmes, M. (2005) Highly efficient endogenous human gene correction using designed zinc-finger nucleases. *Nature 435*, 646–651.

(2) Hockemeyer, D., Soldner, F., Beard, C., Gao, Q., Mitalipova, M., DeKelver, R., Katibah, G., Amora, R., Boydston, E., and Zeitler, B. (2009) Efficient targeting of expressed and silent genes in human ESCs and iPSCs using zinc-finger nucleases. *Nat. Biotechnol. 27*, 851–857.

(3) Rebar, E., and Pabo, C. (1994) Zinc finger phage: affinity selection of fingers with new DNA-binding specificities. *Science 263*, 671.

(4) Bibikova, M., Beumer, K., Trautman, J., and Carroll, D. (2003) Enhancing gene targeting with designed zinc finger nucleases. *Science 300*, 764.

(5) Hockemeyer, D., Soldner, F., Beard, C., Gao, Q., Mitalipova, M., DeKelver, R., Katibah, G., Amora, R., Boydston, E., and Zeitler, B. (2009) Efficient targeting of expressed and silent genes in human ESCs and iPSCs using zinc-finger nucleases. *Nat. Biotechnol. 27*, 851–857.

(6) Kim, H., Lee, H., Kim, H., Cho, S., and Kim, J. (2009) Targeted genome editing in human cells with zinc finger nucleases constructed via modular assembly. *Genome Res. 19*, 1279.

(7) Wright, D., Thibodeau-Beganny, S., Sander, J., Winfrey, R., Hirsh, A., Eichtinger, M., Fu, F., Porteus, M., Dobbs, D., and Voytas, D.

(2006) Standardized reagents and protocols for engineering zinc finger nucleases by modular assembly. *Nat. Protocols 1*, 1637−1652.
(8) Maeder, M. L., Thibodeau-Beganny, S., Sander, J. D., Voytas, D. F., and Joung, J. K. (2009) Oligomerized pool engineering (OPEN): an'open-source'protocol for making customized zinc-finger arrays. *Nat. Protocols 4*, 1471−1501.
(9) Sander, J. D., Dahlborg, E. J., Goodwin, M. J., Cade, L., Zhang, F., Cifuentes, D., Curtin, S. J., Blackburn, J. S., Thibodeau-Beganny, S., and Qi, Y. (2010) Selection-free zinc-finger-nuclease engineering by context-dependent assembly (CoDA). *Nat. Methods 8*, 67−69.
(10) Joung, J., Ramm, E., and Pabo, C. (2000) A bacterial two-hybrid selection system for studying protein DNA and protein-protein interactions. *Proc. Natl. Acad. Sci. U.S.A. 97*, 7382.
(11) Wang, Y., Guo, L., Golding, I., Cox, E. C., and Ong, N. (2009) Quantitative transcription factor binding kinetics at the single-molecule level. *Biophys. J. 96*, 609−620.
(12) Carroll, D., Morton, J., Beumer, K., and Segal, D. (2006) Design, construction and in vitro testing of zinc finger nucleases. *Nat. Protocols 1*, 1329−1341.
(13) Chen, I., and Ting, A. Y. (2005) Site-specific labeling of proteins with small molecules in live cells. *Curr. Opin. Biotechnol. 16*, 35−40.
(14) Lee, Y. M., and Lim, C. (2011) Factors controlling the reactivity of zinc finger cores. *J. Am. Chem. Soc.,*.
(15) Ahel, I., Ahel, D., Matsusaka, T., Clark, A. J., Pines, J., Boulton, S. J., and West, S. C. (2008) Poly (ADP-ribose)-binding zinc finger motifs in DNA repair/checkpoint proteins. *Nature 451*, 81−85.
(16) Aldovini, A., and Young, R. A. (1990) Mutations of RNA and protein sequences involved in human immunodeficiency virus type 1 packaging result in production of noninfectious virus. *J. Virol. 64*, 1920−1926.
(17) Link, A., and Tirrell, D. (2003) Cell surface labeling of Escherichia coli via copper (I)-catalyzed [3+ 2] cycloaddition. *J. Am. Chem. Soc. 125*, 11164−11165.
(18) Kolb, H., Finn, M., and Sharpless, K. (2001) Click chemistry: diverse chemical function from a few good reactions. *Angew. Chem., Int. Ed. 40*, 2004−2021.
(19) Meldal, M., and Tornoee, C. (2008) Cu-Catalyzed azide- alkyne cycloaddition. *Chem. Rev. 108*, 2952−3015.
(20) Kolb, H., Finn, M., and Sharpless, K. (2001) Click chemistry: diverse chemical function from a few good reactions. *Angew. Chem., Int. Ed. 40*, 2004−2021.
(21) Natarajan, A., Du, W., Xiong, C., DeNardo, G., DeNardo, S., and Gervay-Hague, J. (2007) Construction of di-scFv through a trivalent alkyne azide 1, 3-dipolar cycloaddition. *Chem. Commun. 2007*, 695−697.
(22) Baskin, J. M., Prescher, J. A., Laughlin, S. T., Agard, N. J., Chang, P. V., Miller, I. A., Lo, A., Codelli, J. A., and Bertozzi, C. R. (2007) Copper-free click chemistry for dynamic in vivo imaging. *Proc. Natl. Acad. Sci. U.S.A. 104*, 16793.
(23) Chang, P. V., Prescher, J. A., Sletten, E. M., Baskin, J. M., Miller, I. A., Agard, N. J., Lo, A., and Bertozzi, C. R. (2010) Copper-free click chemistry in living animals. *Proc. Natl. Acad. Sci. U.S.A. 107*, 1821−1826.
(24) Ausubel, F. M., Brent, R., Kingston, R., Moore, D. D., Seidman, J. G., Smith, J. A., Struhl, K. (2011) *Current Protocols in Molecular Biology*, Wiley.
(25) Wright, D., Thibodeau-Beganny, S., Sander, J., Winfrey, R., Hirsh, A., Eichtinger, M., Fu, F., Porteus, M., Dobbs, D., and Voytas, D. (2006) Standardized reagents and protocols for engineering zinc finger nucleases by modular assembly. *Nat. Protocols 1*, 1637−1652.
(26) Humphrey, W., Dalke, A., and Schulten, K. (1996) VMD: visual molecular dynamics. *J. Mol. Graphics 14*, 33−38.
(27) Lakowicz, J. R. (2006) *Principles of Fluorescence Spectroscopy*, 3rd ed., Springer, New York.
(28) Barbara, A. L., and Owen, C. T. M. (2009) Rapid method for measuring DNA binding to protein using fluorescence anisotropy. *Nat. Protocols,*.
(29) Hellman, L. M., and Fried, M. G. (2007) Electrophoretic mobility shift assay (EMSA) for detecting protein-nucleic acid interactions. *Nat. Protocols 2*, 1849−1861.
(30) Selvin, P., and Ha, T. (2008) *Single-molecule techniques: a laboratory manual*, Cold Spring Harbor Laboratory Press.
(31) Kim, S. H., Tamrazi, A., Carlson, K. E., Daniels, J. R., Lee, I. Y., and Katzenellenbogen, J. A. (2004) Estrogen receptor microarrays: subtype-selective ligand binding. *J. Am. Chem. Soc. 126*, 4754−5.
(32) Lee, Y. M., and Lim, C. (2011) Factors controlling the reactivity of zinc finger cores. *J. Am. Chem. Soc.,*.
(33) Kiick, K., Saxon, E., Tirrell, D., and Bertozzi, C. (2002) Incorporation of azides into recombinant proteins for chemoselective modification by the Staudinger ligation. *Proc. Natl. Acad. Sci. U.S.A. 99*, 19.
(34) Kiick, K., Saxon, E., Tirrell, D., and Bertozzi, C. (2002) Incorporation of azides into recombinant proteins for chemoselective modification by the Staudinger ligation. *Proc. Natl. Acad. Sci. U.S.A. 99*, 19.
(35) Chin, J. W., Cropp, T. A., Anderson, J. C., Mukherji, M., Zhang, Z., and Schultz, P. G. (2003) An expanded eukaryotic genetic code. *Science 301*, 964−967.
(36) Wang, L., Brock, A., Herberich, B., and Schultz, P. G. (2001) Expanding the genetic code of Escherichia coli. *Science 292*, 498−500.
(37) Wang, A., Winblade Nairn, N., Johnson, R. S., Tirrell, D. A., and Grabstein, K. (2008) Processing of N-Terminal Unnatural Amino Acids in Recombinant Human Interferon-β in Escherichia coli. *ChemBioChem 9*, 324−330.
(38) Rauscher, F. J., Morris, J. F., Tournay, O. E., Cook, D. M., and Curran, T. (1990) Binding of the Wilms' tumor locus zinc finger protein to the EGR-1 consensus sequence. *Science 250*, 1259.
(39) Kim, M. S., Stybayeva, G., Lee, J. Y., Revzin, A., and Segal, D. J. (2011) A zinc finger protein array for the visual detection of specific DNA sequences for diagnostic applications. *Nucleic Acids Res. 39*, e29−e29.
(40) Sander, J., Zaback, P., Joung, J., Voytas, D., and Dobbs, D. (2009) An affinity-based scoring scheme for predicting DNA-binding activities of modularly assembled zinc-finger proteins. *Nucleic Acids Res. 37*, 506.
(41) Ben-Bassat, A., Bauer, K., Chang, S. Y., Myambo, K., Boosman, A., and Chang, S. (1987) Processing of the initiation methionine from proteins: properties of the Escherichia coli methionine aminopeptidase and its gene structure. *J. Bacteriol. 169*, 751.
(42) Pabo, C. O., Peisach, E., and Grant, R. A. (2001) Design and selection of novel Cys2His2 zinc finger proteins. *Annu. Rev. Biochem. 70*, 313−340.
(43) Michael, S. F., Kilfoil, V. J., Schmidt, M. H., Amann, B. T., and Berg, J. M. (1992) Metal binding and folding properties of a minimalist Cys2His2 zinc finger peptide. *Proc. Natl. Acad. Sci. U.S.A. 89*, 4796.
(44) Nyborg, J. K., and Peersen, O. B. (2004) That zincing feeling: the effects of EDTA on the behaviour of zinc-binding transcriptional regulators. *Biochem. J. 381*.
(45) Hutchens, T. W., Allen, M. H., Li, C. M., and Yip, T. T. (1992) Occupancy of a C2-C2 type 'Zinc-finger'protein domain by copper Direct observation by electrospray ionization mass spectrometry. *FEBS Lett. 309*, 170−174.
(46) Predki, P. F., and Sarkar, B. (1994) Metal replacement in" zinc finger" and its effect on DNA binding. *Environ. Health Perspect. 102*, 195.
(47) Carroll, D., Morton, J., Beumer, K., and Segal, D. (2006) Design, construction and in vitro testing of zinc finger nucleases. *Nat. Protocols 1*, 1329−1341.
(48) Nurmemmedov, E., and Thunnissen, M. (2006) Expression, purification, and characterization of the 4 zinc finger region of human tumor suppressor WT1. *Protein Express. Purif. 46*, 379−389.
(49) Baskin, J. M., Prescher, J. A., Laughlin, S. T., Agard, N. J., Chang, P. V., Miller, I. A., Lo, A., Codelli, J. A., and Bertozzi, C. R. (2007) Copper-free click chemistry for dynamic in vivo imaging. *Proc. Natl. Acad. Sci. U.S.A. 104*, 16793.

(50) Lutz, J. F. (2008) Copper free azide-alkyne cycloadditions: new insights and perspectives. *Angew. Chem., Int. Ed. 47*, 2182−2184.
(51) Ning, X., Guo, J., Wolfert, M., and Boons, G. (2008) Visualizing metabolically labeled glycoconjugates of living cells by copper free and fast huisgen cycloadditions. *Angew. Chem. 120*, 2285−2287.
(52) Szabo, A., Stolz, L., and Granzow, R. (1995) Surface plasmon resonance and its use in biomolecular interaction analysis (BIA). *Curr. Opin. Struct. Biol. 5*, 699−705.
(53) Elf, J., Li, G. W., and Xie, X. S. (2007) Probing transcription factor dynamics at the single-molecule level in a living cell. *Science 316*, 1191.

Bioconjugate Chemistry

Article

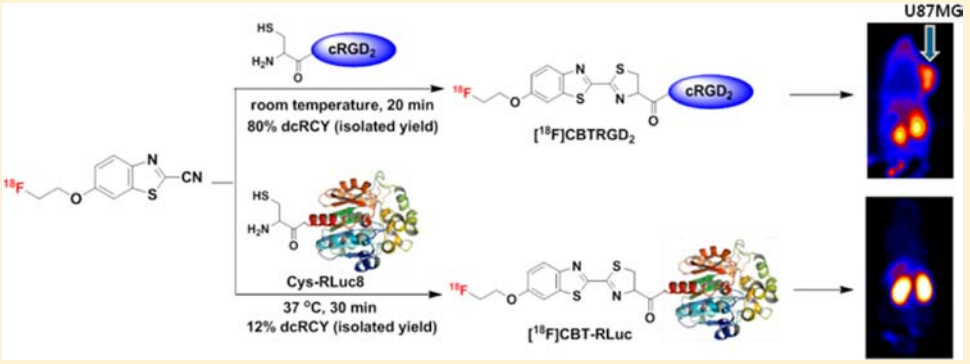
pubs.acs.org/bc

Efficient Method for Site-Specific ^{18}F-Labeling of Biomolecules Using the Rapid Condensation Reaction between 2-Cyanobenzothiazole and Cysteine

Jongho Jeon,‡ Bin Shen,‡ Liqin Xiong, Zheng Miao, Kyung Hyun Lee, Jianghong Rao,* and Frederick T. Chin*

Molecular Imaging Program at Stanford, Department of Radiology, Stanford University, 1201 Welch Road, Stanford, California 94305−5484, United States

Supporting Information



ABSTRACT: An efficient method based on a rapid condensation reaction between 2-cyanobenzothiazole (CBT) and cysteine has been developed for ^{18}F-labeling of N-terminal cysteine-bearing peptides and proteins. An ^{18}F-labeled dimeric cRGD ([^{18}F]CBTRGD$_2$) has been synthesized with an excellent radiochemical yield (92% based on radio-HPLC conversion, 80% decay-corrected, and isolated yield) and radiochemical purity (>99%) under mild conditions using ^{18}F-CBT, and shown good *in vivo* tumor targeting efficiency for PET imaging. The labeling strategy was also applied to the site-specific ^{18}F-labeling of a protein, *Renilla* lucifierase (RLuc8) with a cysteine residue at its N-terminus. The protein labeling was achieved with 12% of decay-corrected radiochemical yield and more than 99% radiochemical purity. This strategy should provide a general approach for efficient and site-specific ^{18}F-labeling of various peptides and proteins for *in vivo* molecular imaging applications.

INTRODUCTION

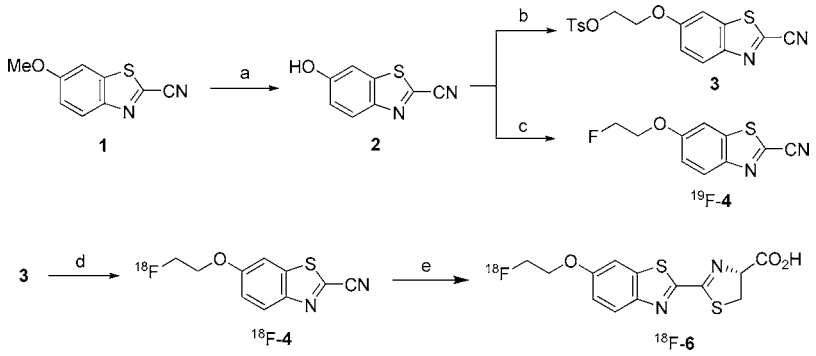
Positron emission tomography (PET) is a non-invasive molecular imaging technique with excellent sensitivity.[1] In the past two decades, various biomolecules have been radiolabeled for PET imaging studies of receptor activity in living subjects and for disease diagnostics including tumor detection.[2−5] As fluorine-18 (^{18}F) can be easily produced in high quantities on a medical cyclotron and has an ideal half-life of 110 min for imaging subjects, it is one of the commonly used radioisotopes for producing many PET tracers. Direct ^{18}F-fluorination, however, requires harsh reaction conditions such as high temperature, high pH, and harmful reagents (e.g., fluorine gas) that are not suitable for most biomolecules. Therefore, an indirect ^{18}F-labeling strategy is generally applied where the ^{18}F is first introduced into a small organic molecule (so-called ^{18}F-prosthetic group) followed by subsequent coupling to a specific functional group (i.e., $-NH_2$, $-CO_2H$, or $-SH$) in the biomolecules. Well-established ^{18}F prosthetic groups include the following: (1) ^{18}F-labeled benzaldehyde for labeling aminooxy groups via formation of an oxime bond;[6,7] (2) ^{18}F-labeled activated ester and maleimide for labeling amino and thiol groups, respectively;[8−11] (3) [^{18}F]fluoroazide and [^{18}F]-fluoroalkyne that can react with a biomolecule equipped with an alkyne and an azide group, respectively, through copper-catalyzed click chemistry.[12−16] In many cases, originally designed ^{18}F-prosthetic groups require lengthy synthetic procedures, relatively harsh reaction conditions, or difficult remote controls, which often result in poor radiochemical yield (RCY) and difficulty in purification. Recently, to overcome these problems, fast and specific ligation methods such as copper-free click reaction[17,18] and the [4 + 2] inverse electron demand Diels−Alder reaction between tetrazine structure and trans-cyclooctene[19−21] have been applied to the ^{18}F-labeling of biomolecules.

We have previously reported a versatile bioorthogonal conjugation using 2-cyanobenzothiazole (CBT) that can rapidly react with a cysteine moiety.[22,23] The observed second-order rate constant for this reaction was determined to be 9.19 M^{-1}

Received: May 23, 2012
Revised: July 23, 2012
Published: July 31, 2012

ACS Publications © 2012 American Chemical Society

Scheme 1. Synthesis of Tosylated CBT 3 and a Condensation Reaction between ^{18}F−4 and Free Cysteine[a]



[a]Reagents and conditions: (a) pyridine−HCl, 200 °C, 2 h, 75%; (b) ethylene glycol di-tosylate, K_2CO_3, DMF, room temperature, 8 h, 53%; (c) 2-fluoroethyl 4-methylbenzenesulfonate, K_2CO_3, DMF, room temperature, overnight, 70%; (d) K[^{18}F]F, 18-Crown-6, K_2CO_3, MeCN, 90 °C, 10 min, 20% (decay-corrected to end of bombardment, isolated yield); (e) L-cysteine, TCEP·HCl, $NaHCO_3$, MeOH/H_2O, room temperature, 1 min, 95%.

s^{-1}. This condensation reaction enables rapid and site-specific fluorescent labeling of target proteins *in vitro* and at the surface of live cells without the need of catalysts under ambient conditions. Its rapid reaction rate along with biocompatibility makes this CBT−cysteine condensation reaction attractive for radiolabeling of biomolecules such as peptides and proteins for PET imaging applications. Herein, we describe a facile and efficient ^{18}F-labeling method using ^{18}F-fluorinated-2-cyanobenzothiazole (^{18}F-CBT) as a novel prosthetic group and its application to radiolabeling of a dimeric cRGD peptide for *in vivo* cancer targeted PET imaging. We further demonstrated the site-specific ^{18}F-labeling of a cysteine-bearing protein using ^{18}F-CBT, and evaluated its biodistribution in a living mouse with PET imaging.

EXPERIMENTAL SECTION

^{18}F-Labeling of Tosylated CBT (3). [^{18}F]-Fluoride (1000 mCi) was prepared by proton bombardment of 2.5 mL [^{18}O] enriched water target via the ^{18}O(p,n)^{18}F nuclear reaction. The [^{18}F]-fluoride was then trapped onto a Sep−Pak QMA cartridge. 18-Crown-6/K_2CO_3 solution (1 mL, 15:1 MeCN/H_2O, 16.9 mg of 18-Crown-6, 4.4 mg of K_2CO_3) was used to elute the [^{18}F]-fluoride from QMA cartridge into a dried glass reactor. The resulting solution was azeotropically dried with sequential MeCN evaporations at 90 °C. A solution of compound **3** (2 mg in 1 mL of anhydrous MeCN) was added to the reactor and heated at 90 °C for 10 min. After cooling to 30 °C, 0.05 M HCl (2.5 mL) was added to quench the reaction mixture and prevented basic hydrolysis of the product ^{18}F−**4**. The crude mixture was then purified with a semipreparative HPLC (Phenomenex Gemini column: 10 × 250 mm, 5 μ, 3 mL/min, and eluent gradient: 0−3 min 40% (0.1% TFA containing MeCN in 0.1% TFA containing H_2O); 3−35 min 40−100% (0.1% TFA containing MeCN in 0.1% TFA containing H_2O), R_t = 21.0 min. The collected ^{18}F−**4** was diluted with H_2O (20 mL) and passed through a C18 cartridge. The trapped ^{18}F−**4** was eluted out with Et_2O (2.5 mL). The Et_2O was removed by helium stream and used for next reaction. The isolated radiochemical yield of ^{18}F−**4** was ca. 20% (140−150 mCi, decay-corrected to end of bombardment).

Radiosynthesis of [^{18}F]CBTRGD$_2$ (9). cRGD dimer **8** (1.2 mg) was dissolved in DMF (200 μL) containing 2 equiv of TCEP·HCl and 15 equiv of DIPEA. The resulting solution was added to ^{18}F−**4** (40 mCi) in DMF (200 μL) at room temperature. At different time points (1, 5, 10, and 20 min), the sample was taken from the crude mixture and the reaction was quenched with 10% AcOH aqueous solution. After 20 min, the conversion yield was 92% determined by analytical HPLC. The reaction was quenched by adding 10% AcOH aqueous solution and then the crude product was purified by a semipreparative HPLC to give [^{18}F]CBTRGD$_2$ **9** with 80% RCY (decay-corrected to the end of synthesis). [Phenomenex Gemini column: 10 × 250 mm, 5 μ, 5 mL/min, and eluent gradient: 0−50 min 10−50% (0.1% TFA containing MeCN in 0.1% TFA containing H_2O), R_t = 34.4 min.] The specific radioactivity was 1.3 ± 0.15 Ci/μmol.

Radiolabeling of Cys−RLuc8 (11). ^{18}F−**4** (10.7 mCi, 7.5 μL) in DMSO solution was added to a solution of Cys−RLuc **11** (5 nmol) in PBS buffer (150 μL, pH = 7.5 with 2 mM TECP), and stirred at 37 °C for 30 min. After the reaction, the crude mixture was diluted with PBS buffer until total volume was up to 1 mL. The crude mixture was directly loaded onto a NAP-10 column, which was pre-conditioned with elution buffer (PBS, pH = 7.4). The crude solution (1 mL) was allowed to enter into the column completely, and then, 1.5 mL of elution buffer (PBS, pH = 7.4) was added into the column to collect the product [^{18}F]CBT−RLuc **12** (12 ± 0.7%, n = 3, decay-corrected to end of synthesis, isolated yield). Overall reaction and purification steps were completed within 40 min. The specific radioactivity was 262 mCi/μmol.

microPET Imaging of U87MG Tumor Xenografts in Mice. Image analyses were carried out using a microPET R4 rodent model scanner (Siemens Medical Solutions). By tail-vein injection, each mouse was administered approximately 100 μCi of [^{18}F]CBTRGD$_2$ under isoflurane anesthesia. At 0.5, 1, and 2 h post-injection (n = 3 group), 5 min static PET scans were acquired. For the blocking experiments, the tumor-bearing mice were co-injected with 20 mg/kg mouse body weight of cRGD$_2$ **7** and [^{18}F]CBTRGD$_2$. PET images were acquired at 0.5, 1, and 2 h post-injection (n = 3 each group). For each scan, regions of interest (ROIs) were drawn over the tumor, liver, and kidney by using vendor software (*ASI Pro* 5.2.4.0; Simens Medical Solutions) on decay-corrected whole-body coronal images. The maximum radiochemistry concentration (accumulation) within a tumor or an organ was obtained from mean pixel values within the multiple ROI volume, which were converted to percent injected dose per gram (%ID/g).

dx.doi.org/10.1021/bc300273m | *Bioconjugate Chem.* 2012, 23, 1902−1908

RESULTS AND DISCUSSION

Synthesis of CBT Prosthetic Group and Its ^{18}F-Labeling Procedure. To carry out ^{18}F-labeling of the CBT structure, tosylated CBT **3** was prepared from commercially available 6-methoxy-CBT **1** (Scheme 1). The methyl group in compound **1** was removed using pyridine hydrochloride at 200 °C. The resulting hydroxyl−CBT derivative was converted to tosylate **3** by reacting with excess amount of ethylene glycol ditosylate. A ^{19}F-analogue, ^{19}F−**4**, was synthesized using 2-fluoroethyl 4-methylbenzenesulfonate as a reference for HPLC characterization of ^{18}F−**4**.

^{18}F-labeling of tosylate **3** was first performed with traditional phase transfer catalyst (PTC) Kryptofix 222 (K_{222}) (Figure 1);

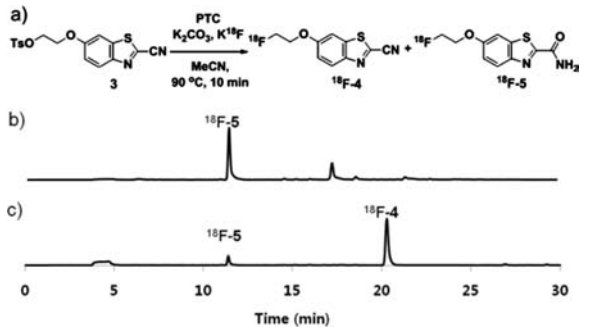
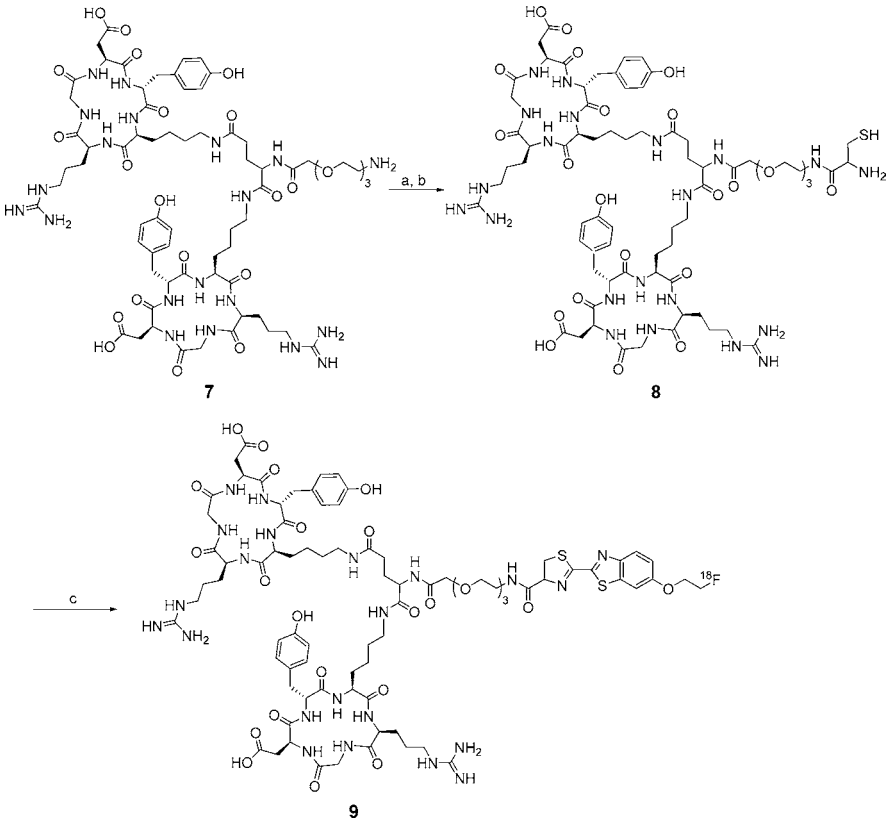


Figure 1. (a) ^{18}F-Fluorination reaction of tosylated CBT **3**. (b) Radiochromatography of the crude product using K_{222}. (c) Radiochromatography of the crude product using 18-crown-6.

however, an ^{18}F−byproduct was mainly observed on radio−HPLC chromatograph instead of the desired ^{18}F−**4** (Figure 1b), which might be due to the hydrolysis of the cyano group on CBT under this condition. Indeed, stability tests with tosylated CBT **3** and fluorinated CBT (^{19}F−CBT) showed that the CBT compounds were hydrolyzed under K_{222}/K_2CO_3 condition within 1 min and also unstable in the presence of Cs_2CO_3 or tetrabutylammonium bicarbonate (SI Figure S1). K_{222} contains nucleophilic nitrogen atoms that could attack the cyano group of **3** and cause facile hydrolysis under this common radiofluorination condition. To discover alternate ^{18}F-labeling conditions, we tested another PTC, and to our delight, the CBT precursor was stable for 10 min in the presence of 18-Crown-6/K^+ complex at 90 °C. Tosylated CBT **3** (2 mg) in MeCN was then added to the anhydrous 18-Crown-6/K^+/$[^{18}F]F^-$ complex, and the labeling reaction was carried out at 90 °C for 10 min. Radio−HPLC chromatograph indicated byproduct ^{18}F−**5** was suppressed under these conditions (Figure 1c). Automated syntheses have been accomplished with up to 1000 mCi of radioactivity, and the expected ^{18}F−**4** was obtained at a 20% RCY (decay-corrected to end of bombardment, isolated yield). Analytical HPLC revealed that the radiochemical/chemical purity of ^{18}F−**4** was more than 99%.

Condensation Reaction between ^{18}F−4 and Free L-Cysteine. The efficiency of condensation reaction between the prepared ^{18}F−**4** and free cysteine was subsequently investigated (Scheme 1). The reaction was carried out in MeOH/H_2O (1:1, 1 mL) at room temperature. TCEP·HCl (tris(2−carboxyethyl)-

Scheme 2. ^{18}F-Labeling of cRGD$_2$ Peptide Analogue Using ^{18}F−4[a]



[a]Reagents and conditions: (a) *N*-Boc-Cys(Trt) succinimidyl ester; (b) TFA, triisopropylsilane, DCM, 79% over 2 steps; (c) ^{18}F−**4**, DIPEA, TCEP·HCl, room temperature, 20 min, 80% (decay-corrected to end of synthesis, isolated yield).

dx.doi.org/10.1021/bc300273m | *Bioconjugate Chem.* 2012, 23, 1902−1908

phosphine hydrochloride, 2 equiv) was added to the reaction mixture for preventing undesired oxidation of the thiol group and pH was adjusted to 7.0−7.5 using aqueous $NaHCO_3$. The condensation reaction was quenched by adding 0.05 M aqueous HCl, and the conversion yield in the reaction was estimated by analytical HPLC. As shown in SI Figure S2, ^{18}F−**4** was converted to ^{18}F−**6** in more than 95% yield within 1 min. Given that ^{18}F−**4** was fully converted to ^{18}F−**6** in a few minutes at room temperature, the condensation reaction should be appropriate for ^{18}F-labeling of biomolecules.

^{18}F-Labeling of a Dimeric cRGD Peptide. We selected a dimeric cRGD peptide for our labeling because cRGD peptides have been shown to target $\alpha_v\beta_3$ integrin expression in tumors.[24,25] A number of ^{18}F prosthetic groups have been employed for labeling cRGD, some of which are currently in clinical trials such as [^{18}F]Galacto−RGD[26] and [^{18}F]-FPPRGD$_2$.[27,28] However, most of these ^{18}F labeling chemistries require multistep syntheses that resulted in low radiochemical yield and could be challenging to routinely produce for clinic use.[26−30] Since ^{18}F-CBT could be easily obtained by direct ^{18}F/tosylate substitution and the condensation reaction between ^{18}F-CBT and cRGD proceeds readily at room temperature, this novel ^{18}F-prosthetic group could provide more benefits over those previously reported. In detail, N-terminal cysteine was introduced to cRGD dimer **7** using N-Boc-Cys(Trt) succinimidyl ester in 2 steps (Scheme 2). cRGD derivative **8** was then reacted with ^{18}F−**4** in anhydrous DMF at room temperature. The conversion yield reached 92% after incubating 20 min with the ^{18}F-labeling agent at room temperature as determined by analytical radio-HPLC (SI Figure S3). After the labeling reaction was finished, the crude product was purified by semipreparative HPLC. The observed RCY of the ^{18}F-labeled product **9** was 80% (decay-corrected to end of synthesis), and the radiochemical purity was more than 99%. The final product [^{18}F]CBTRGD$_2$ **9** was obtained in an isolated overall yield of 7.5 ± 2.7% (decay-uncorrected) with a total synthesis time of 100 min (Table 1). Specific radioactivity

Table 1. Comparison of Radiochemical Procedure

	[^{18}F]FPPRGD$_2$	[^{18}F]CBTRGD$_2$
Radiosynthetic steps	4	2
Total synthesis time	180 min	100 min
RCY[a] (n = 3)	3.5 ± 1.8%	7.5 ± 2.7%
Specific radioactivity	0.97 ± 0.06 Ci /μmol	1.3 ± 0.15 Ci/μmol

[a]Decay-uncorrected, isolated yield.

of the final product was 1.3 ± 0.15 Ci/μmol. It is important to note that, during the HPLC purification of crude [^{18}F]-CBTRGD$_2$, all the impurity, reagent, and starting material have distinct retention time from the product (>10 min); and no other peaks appeared around the product peak on the HPLC chromatograph at UV 254 nm (SI Figure S4). In comparison to [^{18}F]FPPRGD$_2$ as previously reported in clinical studies, two impurities were identified to have retention times close to that of the final product (<1 min) and are difficult to remove.[27] Therefore, CBT-based ^{18}F labeling chemistry could offer the following advantages: (1) higher RCY; (2) fewer synthetic steps and shorter synthesis time; and (3) easier HPLC purification.

***In Vivo* Evaluation of [^{18}F]CBTRGD$_2$ with U87MG Tumor Xenograft Model.** Tumor targeting efficiency of [^{18}F]CBTRGD$_2$ **9** was evaluated in U87MG tumor bearing nude mice by static small animal imaging PET scans (Figure 2). PET imaging results showed that the tumor site was clearly

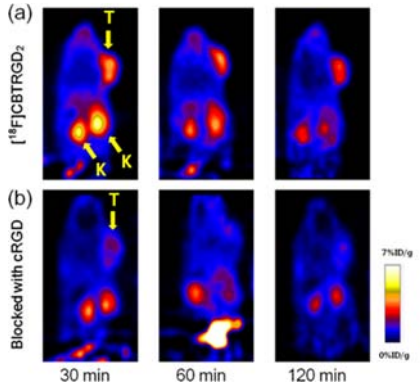


Figure 2. Representative small-animal PET images of U87MG tumor-bearing (right shoulder) mice. (a) Whole body coronal images at 30, 60, and 120 min after i.v. injection of [^{18}F]CBTRGD$_2$. (b) Whole body coronal images at 30, 60, and 120 min after co-injection of [^{18}F]CBTRGD$_2$ with cRGD$_2$ peptide (blocking). (T: U87MG tumor, K: kidney).

visualized with good tumor-to-background contrast within 30 min and the clearance of tracer uptake was observed at 120 min (Figure 2a). PET quantification results demonstrated that tumor-to-background (or muscle) ratios were 4.5 ± 0.83 (30 min), 5.4 ± 0.72 (60 min), and 6.3 ± 1.1 (120 min). The tumor uptake of [^{18}F]CBTRGD$_2$ was 5.62 ± 1.15%, 4.25 ± 0.82%, and 3.35 ± 0.71% at 30, 60, and 120 min, respectively (Table 2). A blocking experiment where the tracer was

Table 2. Uptake of [^{18}F]CBTRGD$_2$ in U87MG Tumor, Kidney, and Liver Derived from PET Quantification (%ID/g, n = 3)

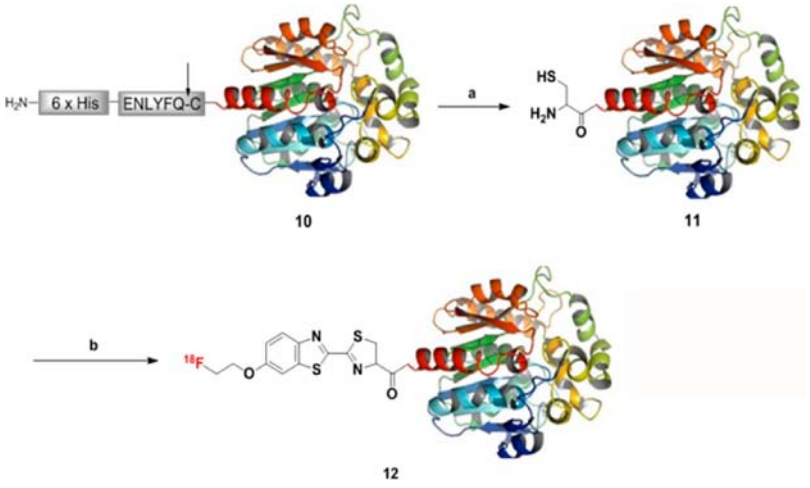
organ	time	[^{18}F]CBTRGD$_2$	blocked with cRGD$_2$
tumor	30 min	5.62 ± 1.15	1.62 ± 0.10
	60 min	4.25 ± 0.82	1.26 ± 0.13
	120 min	3.35 ± 0.71	0.49 ± 0.02
kidney	30 min	5.46 ± 1.10	2.76 ± 0.85
	60 min	3.99 ± 1.08	1.26 ± 0.23
	120 min	2.26 ± 0.67	0.81 ± 0.04
liver	30 min	3.64 ± 0.76	1.34 ± 0.06
	60 min	2.84 ± 0.76	0.70 ± 0.08
	120 min	2.15 ± 0.53	0.32 ± 0.01

coinjected with cRGD dimer (20 mg/kg) showed significantly reduced tumor uptake of the tracer (1.62 ± 0.10%, 1.26 ± 0.23%, and 0.81 ± 0.04% at 30, 60, and 120 min, respectively), suggesting that [^{18}F]CBTRGD$_2$ specifically bound integrin $\alpha_v\beta_3$ receptor (Figure 2b). We also carried out a comparison experiment with tracer **9** and [^{18}F]FPPRGD$_2$ in the same mice. PET imaging results showed that the specific tumor uptake of [^{18}F]CBTRGD$_2$ was 50% higher than that of [^{18}F]FPPRGD$_2$ at 30 min (SI Figure S5 and Table S1). [^{18}F]CBTRGD$_2$ also showed higher uptakes in organs such as liver and kidney than [^{18}F]FPPRGD$_2$, likely due to the increased lipophilicity from the aromatic structure in ^{18}F-CBT.

Recently, the [4 + 2] inverse electron demand Diels−Alder reaction was applied to ^{18}F-labeling of a cRGD peptide.[31] The rate of this conjugation method was faster than the other reactions described, but this ligation unfortunately created a

dx.doi.org/10.1021/bc300273m | Bioconjugate Chem. 2012, 23, 1902−1908

Scheme 3. ^{18}F−Labeling of Cys−RLuc8 11 Using ^{18}F−4[a]



[a]Reagents and conditions: (a) TEV protease (100 μg of protein/10 units of enzyme), 30 °C, 6 h; (b) ^{18}F−**4**, 37 °C, 30 min, 12 ± 0.7% (decay-corrected to end of synthesis, isolated yield).

mixture of isomers. Moreover, the ligation product from the reaction between tetrazine and *trans*-cyclooctene was large and hydrophobic, and thus, large amounts of radioactivity could be detected in normal organs. Considering that hydrophobic derivatization of isotope labeled tracers often spoils their desired *in vivo* pharmacokinetics properties, a relatively small hydrophobic part used in the CBT−cysteine reaction may have a less adverse effect on the biodistribution of the final tracer.

Site-Specific ^{18}F-Labeling of N-Terminal Cysteine Bearing RLuc8. We next investigated site-specific ^{18}F-labeling of a protein using ^{18}F−**4**. Several ^{18}F−prosthetic groups targeting lysine[8,9,32−34] and cysteine[35−37] residues have been applied to protein labeling by means of amidation, conjugate addition, and so on, but these methods normally result in a mixture of randomly labeled proteins. Moreover, non-site-specific labeling of proteins often resulted in decreased biological activity. For example, ^{18}F-labeled anti-carcinoembryonic agent diabody using *N*-succinimidyl-4-[^{18}F]-fluorobenzote ([^{18}F]SFB) showed lower immunoreactivity compared with nonlabeled protein.[33] Therefore, site-specific labeling of an amino acid residue away from the active site of the protein is highly desirable. Additionally, an efficient reaction under mild conditions is preferred for ^{18}F-labeling of protein.

For this study, the bioluminescent protein *Renilla* luciferase (RLuc8) was used as a model protein. The peptide substrate of tobacco etch virus (TEV) protease was fused at the N-terminus region of RLuc8 **10** to generate N-terminal cysteine (Scheme 3). TEV protease was added to the purified fusion protein to cleave the peptide substrate. After the reaction, it was purified with Ni−NTA agarose by using 6×His tag in front of the TEV protease sequence to provide the N-terminal cysteine RLuc (Cys−RLuc) **11**. During this procedure, uncleaved RLuc8 **10** and TEV protease with 6×His tag could be separated from the product. Cys−RLuc **11** was used in the next step without furthur purification. In the ^{18}F-labeling reaction, ^{18}F−**4** was added to Cys−RLuc **11** (5 nmol) in phosphate buffered saline (PBS, pH = 7.5 with 2 mM TECP), and then the labeling reaction proceeded at 37 °C for 30 min. The purification was accomplished by size exclusion chromatography (NAP−10 column) eluted with PBS (pH = 7.4) to afford [^{18}F]CBT−RLuc **12** with 262 mCi/μmol of specific activity. The observed RCY was 12 ± 0.7% (n = 3, decay-corrected to end of synthesis, isolated yield) and radiochemical purity was more than 99% as determined by radio−TLC analysis (SI Figure S6). In comparison, the same labeling reaction with RLuc8 **10**, which did not contain the required N-terminal cysteine group for coupling, provided no ^{18}F-labeled product. Therefore, we can conclude that ^{18}F-labeling of **11** with ^{18}F−**4** is site-specific. After the labeling reaction, the bioluminescent property of RLuc8 remained unchanged. The observed bioluminescent intensities of Cys−RLuc **11** and the purified product from the ^{18}F-labeling reaction were nearly the same (SI Figure S7).

To evaluate our new imaging probe in a living subject, we then carried out a PET imaging experiment by injecting [^{18}F]CBT−RLuc **12** (ca. 100 μCi) in non-tumor-bearing mice. PET images of different time points (20, 60, and 100 min) showed that primary radioactivity uptake was observed in the renal system within 20 min of injection and then subsequently cleared into bladder by 100 min (Figure 3). Based on PET

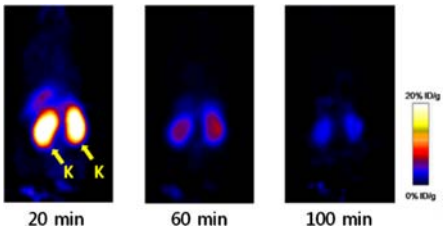


Figure 3. Whole body coronal images at 20, 60, and 100 min after i.v. injection of [^{18}F]CBT−RLuc8 (K: kidney).

quantification of the collected images, nonspecific liver accumulation was not observed (Table 3). These results were correlated well with a previous biodistribution study using ^{124}I−labeled RLuc8.[38]

Among various ^{18}F-precursors, ^{18}F-fluorobenzaldehyde ([^{18}F]FBA)[39,40] targeting an aminooxy group and ^{18}F-maleimide containing prosthetic groups[41,42] reacting with a thiol have been developed as site-specific labeling agents for proteins. They normally provided good ^{18}F-labeling results in terms of RCY and purity for each target protein. However, the labeling reaction using [^{18}F]FBA has to be done under aqueous

dx.doi.org/10.1021/bc300273m | *Bioconjugate Chem.* 2012, 23, 1902−1908

Table 3. Uptake of [^{18}F]CBT−RLuc8 in Kidney and Liver Derived from PET Quantification (%ID/g, n = 3)

organ	time	[^{18}F]CBT−RLuc8
kidney	20 min	17.3 ± 1.28
	60 min	7.94 ± 1.07
	100 min	2.98 ± 0.32
liver	20 min	7.18 ± 0.94
	60 min	3.15 ± 0.30
	100 min	1.61 ± 0.19
muscle	20 min	1.24 ± 0.03
	60 min	1.02 ± 0.02
	100 min	0.50 ± 0.04

acidic condition (pH < 4.5) that would potentially abolish the bioactivity of pH-sensitive enzymes or proteins. In the case of maleimide-containing prosthetic groups, their syntheses always require an additional coupling step because the maleimide structure is quite labile under the required basic ^{18}F-labeling conditions that often results in lengthy synthesis times and decreased RCYs. Moreover, these site-specific methods involved relatively complicated chemical ligation reactions or protein engineering procedures along with a couple of purification steps to generate a single reactive functional group on the protein. Compared with these methods, the N-terminal cysteine residue can be easily produced by a simple enzymatic cleavage with TEV protease and additional modification and purification steps are unnecessary for the ^{18}F-labeling reaction. Using this procedure, an N-terminal cysteine group can be readily prepared in a fusion protein. Therefore, our method has just three steps in total for protein labeling, (1) protein modification with TEV protease, (2) radiosynthesis of ^{18}F−**4**, and (3) a condensation reaction between ^{18}F−**4** and N-terminal cysteine protein under neutral condition; and it provides a useful and general protocol for efficient ^{18}F-labeling of various biomolecules.

CONCLUSIONS

This study demonstrated a highly efficient ^{18}F-labeling strategy of biomolecules such as peptide ligands and proteins based on a rapid condensation reaction of ^{18}F−**4**. The tosylated CBT derivative used for preparing ^{18}F−**4** can be easily synthesized from a commercially available precursor in two simple steps. The fast and specific reactivity of ^{18}F−**4** toward a free cysteine residue provides excellent RCYs under ambient temperature. The fast and specific reactivity of ^{18}F−**4** toward a free cysteine residue provides excellent RCYs under ambient temperature. Depending on the cysteine-containing molecules, the labeling can proceed efficiently in a number of different solvent systems, as demonstrated in DMF, MeOH/water, and PBS buffer solutions. An N-terminal cysteine could be introduced into the target molecules by chemical synthesis or enzymatic processing of specific peptide sequence fused to the target protein. Using this convenient labeling method, [^{18}F]CBTRGD$_2$ has been prepared in a much shorter synthesis time with a higher RCY compared to the PET tracer currently under clinical trial, [^{18}F]FPPRGD$_2$, and has shown better tumor targeting efficiency in mice than [^{18}F]FPPRGD$_2$ prepared by a different prosthetic group, 4-nitrophenyl 2-^{18}F-fluoropropionate (^{18}F−NFP). The increased accumulation of [^{18}F]CBTRGD$_2$ in livers may be due to the lipophilic structure of the CBT group, which should be ameliorated with modifications of the CBT structure that increase its hydrophilicity. On the other hand, when ^{18}F−**4** was used for site-specific ^{18}F-labeling of RLuc8, the ^{18}F-labeled protein showed little alteration in its biodistribution as revealed by PET imaging in healthy mice. We anticipate that this method could be generally applied to afford efficient and site-specific ^{18}F-labeling of peptides, proteins, or antibodies that contain an N-terminal cysteine.

ASSOCIATED CONTENT

Supporting Information

Synthesis and characterization of compounds, stability test of 2-cyanobenzothiazole (CBT) structures, radiochemical procedures for peptide and protein labeling and *in vivo* microPET imaging. This material is available free of charge via the Internet at http://pubs.acs.org.

AUTHOR INFORMATION

Corresponding Author

*E-mail addresses: jrao@stanford.edu, chinf@stanford.edu.

Author Contributions

‡These authors contributed equally.

Notes

The authors declare no competing financial interest.

ACKNOWLEDGMENTS

This work was supported in part by an IDEA award from Department of Defense Breast Cancer Research Program (W81XWH−09−1−0057) and the NCI ICMIC@Stanford (1P50CA114747−06).

REFERENCES

(1) Gambhir, S. S. (2002) Molecular imaging of cancer with positron emission tomography. *Nat. Rev. Cancer 2*, 683−693.

(2) Wester, H. J., Schottelius, M., Scheidhauer, K., Meisetschläger, G., Herz, M., Rau, F. C., Reubi, J. C., and Schwaiger, M. (2003) PET imaging of somatostatin receptors: design, synthesis and preclinical evaluation of a novel ^{18}F-labelled, carbohydrated analogue of octreotide. *Eur. J. Nucl. Med. Mol. Imaging 30*, 117−122.

(3) Stoeklin, G., and Wester, H. J. (1998) *Positron emission tomography: A critical assessment of recent trends*, pp 57−90, Kluwer Academic Publishers, Dordrecht, The Netherlands.

(4) Liu, S. (2006) Radiolabeled multimeric cyclic RGD peptides as integrin a_vb_3 targeted radiotracers for tumor imaging. *Mol. Pharmaceutics 3*, 472−487.

(5) Miller, P. W., Long, N. J., Vilar, R., and Gee, A. D. (2008) Synthesis of ^{11}C, ^{18}F, ^{15}O, and ^{13}N radiolabels for positron emission tomography. *Angew. Chem., Int. Ed. 47*, 8998−9033.

(6) Thumshirn, G., Hersel, U., Goodman, S. L., and Kessler, H. (2003) Multimeric cyclic RGD peptides as potential tools for tumor targeting: solid-phase peptide synthesis and chemoselective oxime ligation. *Chem.—Eur. J. 9*, 2717−2725.

(7) Poethko, T., Schottelius, M., Thumshirn, G., Hersel, U., Herz, M., Henriksen, G., Kessler, H., Schwaiger, M., and Wester, H. J. (2004) Two-step methodology for high-yield routine radiohalogenation of peptides: ^{18}F-labeled RGD and octreotide analogs. *J. Nucl. Med. 45*, 892−902.

(8) Wüst, F., Hultsch, C., Bergmann, R., Johannsen, B., and Henle, T. (2003) Radiolabelling of isopeptide N^{ε}-(γ-glutamyl)-L-lysine by conjugation with *N*-succinimidyl-4-[^{18}F]fluorobenzoate. *Appl. Radiat. Isot. 59*, 43−48.

(9) Wester, H. J., Hamacher, K., and Stöcklin, G. (1996) A comparative study of N.C.A. Fluorine-18 labeling of proteins via acylation and photochemical conjugation. *Nucl. Med. Biol. 23*, 365−372.

(10) Cai, W., Zhang, X., Wu, Y., and Chen, X. (2006) A thiol-reactive ^{18}F-labeling agent, *N*-[2-(4-^{18}F-fluorobenzamido) ethyl]maleimide,

and synthesis of RGD peptide-based tracer for PET imaging of a_vb_3 integrin expression. *J. Nucl. Med. 47*, 1172−1180.
(11) de Bruin, B., Kuhnast, B., Hinnen, F., Yaouancq, L., Amessou, M., Johannes, L., Samson, A., Boisgard, R., Tavitian, B., and Dollé, F. (2005) 1-[3-(2-[^{18}F]Fluoropyridin-3-yloxy)propyl]pyrrole-2,5-dione: design, synthesis, and radiosynthesis of a new [^{18}F]fluoropyridine-based maleimide reagent for the labeling of peptides and proteins. *Bioconjugate Chem. 16*, 406−420.
(12) Gill, H. S., and Marik, J. (2011) Preparation of ^{18}F-labeled peptides using the copper(I)-catalyzed azide-alkyne 1,3-dipolar cycloaddition. *Nat. Protoc. 6*, 1718−1725.
(13) Maschauer, S., Einsiedel, J., Haubner, R., Hocke, C., Ocker, M., Hübner, H., Kuwert, T., Gmeiner, P., and Prante, O. (2010) Labeling and glycosylation of peptides using Click chemistry: a general approach to 18F-glycopeptides as effective imaging probes for positron emission tomography. *Angew. Chem., Int. Ed. 49*, 976−979.
(14) Glaser, M., and Årstad, E. (2007) "Click labeling" with 2-[^{18}F]fluoroethylazide for positron emission tomography. *Bioconjugate Chem. 18*, 989−993.
(15) Li, Z. B., Wu, Z., Chen, K., Chin, F. T., and Chen, X. (2007) Click chemistry for 18F-labeling of RGD peptides and microPET imaging of tumor integrin a_vb_3 expression. *Bioconjugate Chem. 18*, 1987−1994.
(16) Marik, J., and Sutcliffe, J. L. (2006) Click for PET: rapid preparation of [^{18}F]fluoropeptides using Cu^I catalyzed 1,3-dipolar cycloaddition. *Tetrahedron Lett. 47*, 6681−6684.
(17) Campbell−Verduyn, L. S., Mirfeizi, L., Schoonen, A. K., Dierckx, R. A., Elsinga, P. H., and Feringa, B. L. (2011) Strain-promoted copper-free "Click" chemistry for ^{18}F radiolabeling of bombesin. *Angew. Chem., Int. Ed. 50*, 11117−11120.
(18) Evans, H. L., Slade, R. L., Carroll, L., Smith, G., Nguyen, Q., Iddon, L., Kamaly, N., Stöckmann, H., Leeper, F. J., Aboagye, E. O., and Spivey, A. C. (2012) Copper-free click−a promising tool for pre-targeted PET imaging. *Chem. Commun. 48*, 991−993.
(19) Li, Z. B., Cai, H., Hassink, M., Blackman, M. L., Brown, R. C. D., Conti, P. S., and Fox, J. M. (2010) Tetrazine-*trans*-cyclooctene ligation for the rapid construction of ^{18}F labeled probes. *Chem. Commun. 46*, 8043−8045.
(20) Keliher, E. J., Reiner, T., Turetsky, A., Hilderbrand, S. A., and Weissleder, R. (2011) High-yielding, two-step ^{18}F labeling strategy for ^{18}F-PARP1 inhibitors. *ChemMedChem 6*, 424−427.
(21) Reiner, T., Keliher, E. J., Earley, S., Marinelli, B., and Weissleder, R. (2011) Synthesis and in vivo imaging of a ^{18}F-labeled PARP1 inhibitor using a chemically orthogonal scavenger-assisted high-performance method. *Angew. Chem., Int. Ed. 50*, 1922−1925.
(22) Ren, H., Xiao, F., Zhan, K., Kim, Y. −P., Xie, H., Xia, Z., and Rao, J. (2009) A biocompatible condensation reaction for the labeling of terminal cysteine residues on proteins. *Angew. Chem., Int. Ed. 48*, 9658−9662.
(23) Liang, G., Ren, H., and Rao, J. (2010) A biocompatible condensation reaction for controlled assembly of nanostructures in living cells. *Nat. Chem. 2*, 54−60.
(24) Chen, X., Tohme, M., Park, R., Hou, Y., Bading, J. R., and Conti, P. S. (2004) Micro-PET imaging of a_vb_3-integrin expression with 18F-labeled dimeric RGD peptide. *Mol. Imaging 3*, 96−104.
(25) Xiong, J. P., Stehle, T., Zhang, R., Joachimiak, A., Frech, M., Goodman, S. L., and Arnaout, M. A. (2002) Crystal structure of the extracellular segment of integrin a_vb_3 in complex with an Arg-Gly-Asp ligand. *Science 296*, 151−155.
(26) Haubner, R., Kuhnast, B., Mang, C., Weber, W. A., Kessler, H., Wester, H. J., and Schwaiger, M. (2004) [^{18}F]Galacto-RGD: synthesis, radiolabeling, metabolic stability, and radiation dose estimates. *Bioconjugate Chem. 15*, 61−69.
(27) Chin, F. T., Shen, B., Liu, S., Berganos, R. A., Chang, E., Mittra, E., Chen, X., and Gambhir, S. S. (2012) First experience with clinical-grade [^{18}F]FPP(RGD)$_2$: an automated multi-step radiosynthesis for clinical PET studies. *Mol. Imaging Biol. 14*, 88−95.
(28) Mittra, E. S., Golis, M. L., Iagaru, A. H., Kardan, A., Burton, L., Berganos, R., Chang, E., Liu, S., Shen, B., Chin, F. T., Chen, X., and Gambihr, S. S. (2011) Pilot pharmacokinetic and dosimetric studies of ^{18}F-FPPRGD$_2$: a PET radiopharmaceutical agent for imaging a_vb_3 integrin levels. *Radiology 260*, 182−191.
(29) Poethko, T., Schottelius, M., Thumshirn, G., Herz, M., Haubner, R., Henriksen, G., Kessler, H., Schwaiger, M., and Wester, H. J. (2004) Chemoselective pre-conjugate radiohalogenation of unprotected mono- and multimeric peptides *via* oxime formation. *Radiochim. Acta 92*, 317−328.
(30) Liu, S., Liu, Z., Chen, K., Yan, Y., Watzlowik, P., Wester, H. J., Chin, F. T., and Chen, X. (2010) ^{18}F-labeled galacto and PEGylated RGD dimers for PET Imaging of a_vb_3 integrin expression. *Mol. Imaging Biol. 12*, 530−538.
(31) Selvaraj, R., Liu, S., Hassink, M., Huang, C., Yap, L., Park, R., Fox, J. M., Li, Z. B., and Conti, P. S. (2011) Tetrazine-trans-cyclooctene ligation for the rapid construction of integrin a_vb_3 targeted PET tracer based on a cyclic RGD peptide. *Bioorg. Med. Chem. Lett. 21*, 5011−5014.
(32) Kostikov, A. P., Chin, J., Orchowski, K., Niedermoser, S., Kovacevic, M. M., Aliaga, A., Jurkschat, K., Wängler, B., Wängler, C., Wester, H. J., and Schirrmacher, R. (2012) Oxalic acid supported Si−^{18}F-radiofluorination: one-step radiosynthesis of *N*-succinimidyl 3-(di-tert-butyl[^{18}F]fluorosilyl)benzoate ([^{18}F]SiFB) for protein labeling. *Bioconjugate Chem. 23*, 106−114.
(33) Cai, W., Olafsen, T., Zhang, X., Cao, Q., Gambhir, S. S., Williams, L. E., Wu, A. M., and Chen, X. (2007) PET imaging of colorectal cancer in xenograft-bearing mice by use of an ^{18}F-labeled T84.66 anti−carcinoembryonic antigen diabody. *J. Nucl. Med. 48*, 304−310.
(34) Grierson, J. R., Yagle, K. J., Eary, J. F., Tait, J. F., Gibson, D. F., Lewellen, B., Link, J. M., and Krohn, K. A. (2004) Production of [F-18]fluoroannexin for imaging apoptosis with PET. *Bioconjugate Chem. 15*, 373−379.
(35) Berndt, M., Pietzsch, J., and Wuest, F. (2007) Labeling of low-density lipoproteins using the ^{18}F-labeled thiol-reactive reagent *N*-[6-(4-[^{18}F]fluorobenzylidene)aminooxyhexyl]maleimide. *Nucl. Med. Biol. 34*, 5−15.
(36) Toyokuni, T., Walsh, J. C., Dominguez, A., Phelps, M. E., Barrio, J. R., Gambhir, S. S., and Satyamurthy, N. (2003) Synthesis of a new heterobifunctional linker, *N*-[4-(aminooxy)butyl]maleimide, for facile access to a thiol-reactive 18F-labeling agent. *Bioconjugate Chem. 14*, 1253−1259.
(37) Wuest, F., Berndt, M., Bergmann, R., van den Hoff, J., and Pietzsch, J. (2008) Synthesis and application of [^{18}F]FDG-maleimidehexyloxime ([^{18}F]FDG-MHO): a [^{18}F]FDG-based prosthetic group for the chemoselective ^{18}F-labeling of peptides and proteins. *Bioconjugate Chem. 19*, 1202−1210.
(38) Venisnik, K. M., Olafsen, T., Loening, A. M., Iyer, M., Gambhir, S. S., and Wu, A. M. (2006) Bifunctional antibody-Renilla luciferase fusion protein for in vivo optical detection of tumors. *Protein Eng. Des. Sel. 19*, 453−460.
(39) Flavell, R. R., Kothari, P., Bar−Dagan, M., Synan, M., Vallabhajosula, S., Friedman, J. M., Muir, T. W., and Ceccarini, G. (2008) Site-specific ^{18}F-labeling of the protein hormone leptin using a general two-Step ligation procedure. *J. Am. Chem. Soc. 130*, 9106−9112.
(40) Namavari, M., De Jesus, O. P., Cheng, Z., De, A., Kovacs, E., Levi, J., Zhang, R., Hoerner, J. K., Grade, H., Syud, F. A., and Gambhir, S. S. (2008) Direct site-specific radiolabeling of an affibody protein with 4-[^{18}F]fluorobenzaldehyde via oxime chemistry. *Mol. Imaging Biol. 10*, 177−181.
(41) Li, X., Link, J. M., Stekhova, S., Yagle, K. J., Smith, C., Krohn, K. A., and Tait, J. F. (2008) Site-specific labeling of Annexin V with F-18 for apoptosis imaging. *Bioconjugate Chem. 19*, 1684−1688.
(42) Gill, H. S., Tinianow, J. N., Ogasawara, A., Flores, J. E., Vanderbilt, A. N., Raab, H., Scheer, J. M., Vandlen, R., Williams, S., and Marik, J. (2009) A modular platform for the rapid site-specific radiolabeling of proteins with ^{18}F exemplified by quantitative positron emission tomography of human epidermal growth factor receptor 2. *J. Med. Chem. 52*, 5816−5825.

Bioconjugate Chemistry

Article

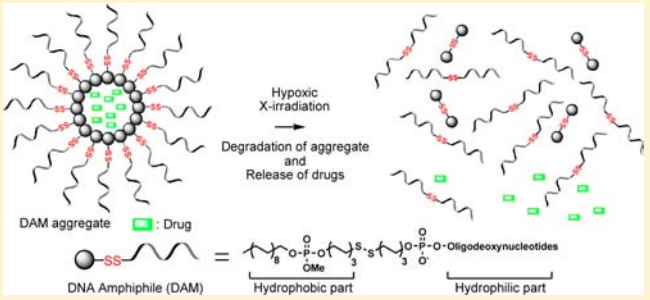
pubs.acs.org/bc

Radiolytic Reduction Characteristics of Drug-Encapsulating DNA Aggregates Possessing Disulfide Bond

Kazuhito Tanabe,* Takumi Asada, Takeo Ito, and Sei-ichi Nishimoto

Department of Energy and Hydrocarbon Chemistry, Graduate School of Engineering, Kyoto University, Katsura Campus, Nishikyo-ku, Kyoto 615-8510, Japan

ABSTRACT: Radiation-responsive aggregates consisting of artificial DNA were demonstrated. We prepared DNA amphiphiles (DAMs) consisting of oligodeoxynucleotides (ODNs) as the hydrophilic part and an alkyl chain as the hydrophobic part, which were linked by a radiation-sensitive disulfide bond. DAMs assembled to form nanosized aggregates in aqueous solution that encapsulated hydrophobic dyes and drugs. X-irradiation, which triggered selective reduction at the disulfide bond in the DAMs, induced an exchange reaction, resulting in dissociation of the aggregates and release of encapsulated dyes and drugs. Among the DAMs synthesized in this study, DAM 1 possessing 5 mer ODNs showed favorable properties as a nanocarrier; for example, the large amount of drug was encapsulated in the aggregates consisting of DAM 1, and the aggregates showed the high sensitivity to radiolytic reduction. Biological experiments using living A549 cells revealed that the aggregates smoothly penetrated into the cells without the need for transfection reagents, while the drugs inside the aggregates were inert because of the encapsulation. X-irradiation enhanced the cytotoxicity because of dissociation of the aggregates and concomitant release of drugs.



INTRODUCTION

Nanosized DNA architectures have attracted much attention as medical materials. Although exogenous oligonucleotides, which are applicable to antisense and siRNA, are prone to enzymatic degradation and showed low cell permeability due to their own negative charges, recent studies revealed that aggregates comprised of oligonucleotides had different properties from individual oligonucleotides, showing nuclease resistance and enhanced cellular uptake.[1−5] Therefore, aggregates of oligonucleotides are expected to be a new class of intelligent materials for gene targeting and manipulation without the need for conventional transfection reagents such as cationic polymers,[6,7] liposomes,[8] and viruses.[9]

Stimuli-responsive nanocarriers offer favorable properties for target-specific delivery of drugs.[10,11] The carriers keep the toxic drugs encapsulated in their hydrophobic core, while the drugs can be readily released and exhibit their original toxicity once appropriate stimuli are applied. Thus, the drugs can be delivered to target areas highly selectively to maximize their potential and minimize side effects. Several stimuli including pH,[12−14] temperature,[15−18] redox reaction,[19−21] and photoirradiation[22−24] have been employed to activate nanocarriers and release drugs; however, precise control of the function and drug efficacy still remain major issues.

Herein, we demonstrate a degradation of nanocarriers and release of drugs by means of hypoxic X-irradiation as an external stimulus. X-ray is an attractive trigger because the radiation reaction for activation of biomaterials can be regulated spatially and temporally without any additives. In addition, the high live-body permeability of X-ray is preferable for in vivo drug targeting. Recently, we identified that radiolytic reduction of a disulfide bond located in oligodeoxynucleotides (ODNs) induced an exchange reaction of the strand at the disulfide linkage in a hypoxia-selective manner.[25] Mechanistic studies revealed that reducing species such as hydrogen atoms and/or hydrated electrons (e_{aq}^-) generated from radiolysis of water molecules[26,27] are most likely to be a key active species for the exchange reaction and that a chain reaction proceeded to form exchanged products with multiple turnovers. This reaction has been applied to the interstrand ligation of two flanking ODNs[25] and intrastrand cyclization of stem-and-loop structured ODNs.[28]

These unique properties of DNA aggregates and the reaction of the disulfide bond motivated us to construct radiation-responsive drug carriers by means of ODNs possessing disulfide bond. We prepared nanocarriers consisting of DNA amphiphiles (DAMs), in which ODNs and an alkyl chain are employed as hydrophilic and hydrophobic parts, respectively, and these two parts were linked by a radiation-sensitive disulfide bond. In aqueous solution, DAMs self-assembled and formed nanosized aggregates which encapsulated hydrophobic dyes or antitumor drugs in their hydrophobic parts. The aggregates penetrated into living cells quite smoothly, and they did not show any significant cytotoxicity. The drugs in the aggregates were also inert because of the encapsulation. In contrast, aggregates containing drugs exhibited enhanced

Received: June 5, 2012
Revised: July 23, 2012
Published: August 22, 2012

ACS Publications © 2012 American Chemical Society

dx.doi.org/10.1021/bc3002985 | *Bioconjugate Chem.* 2012, 23, 1909−1914

cytotoxicity upon hypoxic X-irradiation due to degradation of the aggregates and release of the drugs.

EXPERIMENTAL PROCEDURES

General Procedures. All starting materials and reagents were purchased from Tokyo Kasei Kogyo (Tokyo, Japan), Wako (Tokyo, Japan), and Aldrich Chemical (Milwaukee, WI). All other solvents, purchased from Wako, were GR grade or dry grade and used without further purification. The ESI-MS spectra were recorded on a Exactive (Thermo) spectrometer. The organic reactions were carried out in oven-dried glassware under an argon atmosphere with magnetic stirring. Fluorescence spectra were recorded on a Shimadzu RF-5300PC spectrofluorophotometer with a 1 cm quartz cell. Hypoxic cell culture conditions were made by means of Russkin Invivo 400. DAMs were synthesized by automated DNA synthesis using Applied Biosystems model 3400 DNA/RNA synthesizer.

Syntheses of DAMs. Octadecanol (43.3 mg, 160 μM) was dissolved in dry CH_2Cl_2 (1 mL), and diisopropylethylamine (41.4 mg, 320 μmol) and *N,N′*-diisopropylmethylphosphonamidic chloride (39.5 mg, 200 μmol) were added to the solution. The resulting mixture was stirred at ambient temperature for 2 h. After the reaction, the mixture was filtered off and used for automated DNA synthesis without further purification. For the preparation of DAM 1−4, aqueous NH_3 solution was used for the cleavage of ODNs from support. On the other hand, K_2CO_3 in MeOH was used for the cleavage of DAM 5 from support. Synthesized DAMs were purified by reversed phase HPLC to give DAM 1−5. The purity and concentration of the DAMs were determined by complete digestion by AP, P1, and phosphodiesterase I at 37 °C for 12 h. Identities of synthesized ODNs were confirmed by ESI-TOF mass spectrometry (DAM 1: calcd 1065.30, found $[M - 2H]^{2-}$ 1065.31. DAM 2: calcd 1825.89, found $[M - 2H]^{2-}$ 1825.43. DAM 3: calcd 2230.56, found $[M - 3H]^{3-}$ 2230.11. DAM 4: calcd 1945.76, found $[M - 5H]^{5-}$ 1946.66. DAM 5: calcd 1058.31, found $[M - 2H]^{2-}$ 1058.26.

Measurement of Fluorescence Spectra. To form the aggregate, indicated concentrations of DAMs in phosphate buffer (100 mM, pH 7.0) were added to nile red or pyrene (10 μM) in acetonitrile. After the removal of the solvent in vacuo, the resulting mixture was dissolved in water to form the aggregate and measure the fluorescence spectra. We measured the fluorescence spectra by means of the excitation wavelength at 580 and 340 nm for nile red and pyrene, respectively.

Mesurement of Dynamic Light Scattering (DLS). The size distribution of aggregates was determined by Nano series Nano-ZS Zetasizer (Malvern Instrument). The aggregates (DAM 1, 60 μM; DAM 2, 30 μM; DAM 3, 30 μM; DAM 4, 30 μM) were prepared in aqueous solution containing phosphate Na buffer (100 mM, pH 7.0) as described above. After the filtration using 0.45 μm filter, the measurements of DLS were conducted at 25 °C.

Radiolytic Reduction of DAMs. To establish hypoxia, aqueous solutions of DAMs (30−60 μM) in 100 mM phosphate Na buffer (pH 7.0) containing 2-methyl-2-propanol (50 eq. to DAM) were purged with argon for 10 min and then irradiated in a sealed glass ampule at ambient temperature with an X-ray source (6.0 Gy min^{-1}). After the irradiation, the solution was immediately subjected to HPLC analysis.

Radiolytic Reduction of the Aggregates Encapsulating Pyrene Dye. Aggregates of DAM 1 (36 μM) encapsulating pyrene dye (10 μM) were formed in aqueous solution containing 2-methyl-2-propanol (1.8 mM) and phosphate Na buffer (100 mM, pH 7.0) as described above. The resulting solutions were purged with argon for 10 min and then irradiated in a sealed glass ampule at ambient temperature with an X-ray source (6.0 Gy min^{-1}). Before or after the irradiation, the solution was subjected to fluorescence measurements. Just before the measurements of fluorescence, the solutions were filtered through a 0.45 μm filter.

Assessment of Cytotoxicity toward A549 Cells. A549 cells were cultured in Dulbecco's Modified Eagle's Minimum Essential Medium (DMEM) containing 10% fetal bovine serum (FBS). The cells were seeded into 96-well plates (2000 cells/well) and cultured at 37 °C in a well-humidified incubator with 5% CO_2 and 95% air (aerobic condition) for 24 h. The cells were then incubated with the various concentrations of DAM 1 under aerobic conditions for 2 h. After the incubation, the medium containing DAM 1 was replaced by the fresh one, and the cells were further incubated for 48 h at 37 °C. After incubation, WST 8 was added to the cells and the cell viability assay was performed using a Microplate Reader (BIO-RAD).

Assessment of Cellular Penetration Using DAM 1 Aggregates Encapsulating Nile Red. To form the aggregate, DAM 1 (100 μM) in aqueous solution was added to nile red (1 μM) in acetonitrile. After the removal of the solvent in vacuo, the resulting mixture was dissolved in DMEM.

A549 cells were seeded into 96-well plates (10000 cells/well) and incubated at 37 °C for 24 h. The cells were then incubated with the DAM 1 aggregate encapsulating nile red under hypoxic conditions for 2 h. After the incubation, the medium containing DAM 1 was replaced by phosphate buffer and images were taken by microscope. (images under hypoxic conditions). The images were acquired with a microscope system (BZ-8000, KEYENCE) equipped with 560 nm excitation filter, 595 nm dichroic mirror, and 630 nm detection filter. A detector of the microscope was a CCD camera.

Radiation-Induced Cytotoxicity of DAM 1 Aggregate Encapsulating Camptothecin. To form the aggregate, DAM 1 (100 μM) in phosphate buffer (100 mM, pH 7.0) was added to camptothecin (200 nM) in acetonitrile. After the removal of the solvent in vacuo, the resulting mixture was dissolved in water to assess the radiation-induced cytotoxic effect.

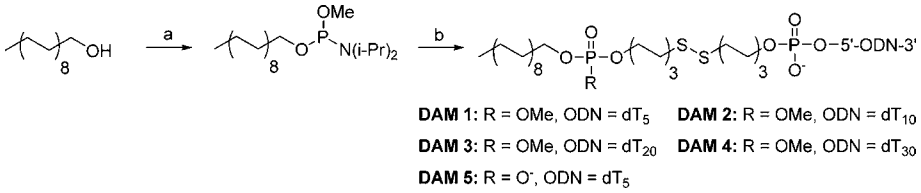
A549 cells were seeded into 96-well plates (2000 cells/well) and incubated at 37 °C for 24 h under hypoxic conditions (0.3% O_2). For the hypoxic treatment, the cells were treated in a hypoxic chamber, $Invivo_2$ 400 (Ruskinn). The cells were then incubated with the DAM 1 aggregate encapsulating camptothecin under hypoxic conditions for 2 h. After incubation, the medium containing DAM 1 was replaced by the fresh one, and the cells were X-irradiated at a dose of 6 and 9 Gy. When X-irradiation was conducted, the plates were kept under hypoxic conditions using an Anaeron pack system (Mitsubishi Gas Chemical Company Inc.). After irradiation, the cells were incubated for 48 h under aerobic conditions. Then, the cell viability assay was performed as described above.

RESULTS AND DISCUSSION

DAMs possessing various lengths of ODNs, and alkyl chains were prepared by automated DNA synthesis using the conventional phosphoramidite method. The crude DAMs were purified by reversed-phase HPLC, and incorporation of the alkyl chain into the ODN was confirmed by enzymatic digestion and ESI-TOF mass spectrometry. We employed simple oligothymidines as hydrophilic parts to avoid

dx.doi.org/10.1021/bc3002985 | *Bioconjugate Chem.* 2012, 23, 1909−1914

Scheme 1. Syntheses and Structures of DNA Amphiphiles (DAMs) Used in This Study[a]



DAM 1: R = OMe, ODN = dT_5 **DAM 2:** R = OMe, ODN = dT_{10}
DAM 3: R = OMe, ODN = dT_{20} **DAM 4:** R = OMe, ODN = dT_{30}
DAM 5: R = O^-, ODN = dT_5

[a]Reagents and conditions: (a) *N,N*-diisopropylmethylphosphonamidic chloride, diisopropylethylamine, CH_2Cl_2; (b) automated DNA synthesis.

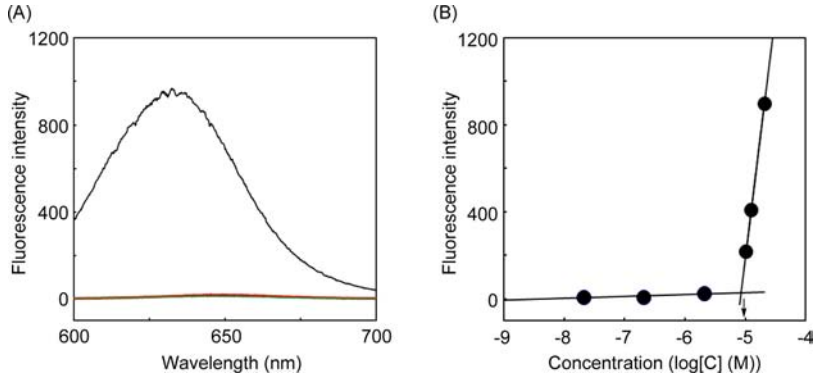


Figure 1. Formation of aggregates from DAM 1 and encapsulation of nile red. (A) Fluorescence spectra of nile red (10 μM) in aqueous solution containing phosphate Na buffer (100 mM, pH 7.0) in the presence of DAM 1 (20 μM, black), octadecane (20 μM, red), or oligodeoxynucleotides dT_5 (20 μM, green). The fluorescence spectra were measured at 580 nm excitation. (B) Plot of fluorescence intensity of nile red vs concentration of DAM 1 to determine critical aggregation concentration (CAC).

complicated function of other bases and base sequence in aggregate formation and radiolytic reduction. The DAMs used in this study are summarized in Scheme 1.

We initially measured the fluorescence emission of nile red in the presence of DAMs to characterize their aggregation properties in aqueous solution. Nile red is an intrinsically water-insoluble fluorescent dye, and therefore it shows no fluorescence in aqueous suspension. On the other hand, encapsulation of nile red into the aggregate consisting of amphiphilic molecules to dissolve the dyes results in a fluorescence emission even in aqueous solution.[11] Thus, we evaluated the aggregation of DAMs by monitoring the fluorescence emission. As shown in Figure 1, we observed strong fluorescence of nile red around 630 nm in the presence of DAM 1. The evidence that addition of corresponding ODN units (dT_5) or alkane (octadecane) to nile red did not enhance the fluorescence emission indicates that DAM 1 formed aggregates in aqueous solution to encapsulate hydrophilic nile red inside its hydrophobic part. All of the other DAMs showed similar behavior in the fluorescence emission. We next estimated the critical aggregation concentration (CAC) of DAMs by monitoring the fluorescence emission with increasing concentration of DAMs (Figure 1B). We observed a sudden increase in fluorescence intensity in the concentration range 2.3–8.4 μM, which was assigned as the CAC of each DAM. Among the DAMs possessing a phosphotriester group at hydrophobic parts (DAM 1–4), DAMs possessing a long ODN chain showed relatively small CAC values, while DAMs possessing a short ODN had high CAC values (Table 1). On the other hand, the CAC of DAM 5, which had phosphodiester group at a hydrophobic part, was estimated to be 33.8 μM. These results indicate that balance between hydrophilicity and hydrophobicity in DAMs is responsible for the formation of stable aggregates. We further verified the formation of

Table 1. Critical Aggregation Concentrations (CAC) of DAMs

	DAM 1	DAM 2	DAM 3	DAM 4	DAM 5
CAC (μM)	8.4	4.2	2.3	2.5	33.8

aggregates from DAMs 1–4 and measured their size in aqueous solution by means of dynamic light scattering (DLS). Figure 2 shows representative spectra of DAMs in 100 mM phosphate buffer (pH 7.0). The formation of two sizes of aggregate was observed for each DAM. The DAMs possessing shorter ODNs as a hydrophilic part predominantly formed

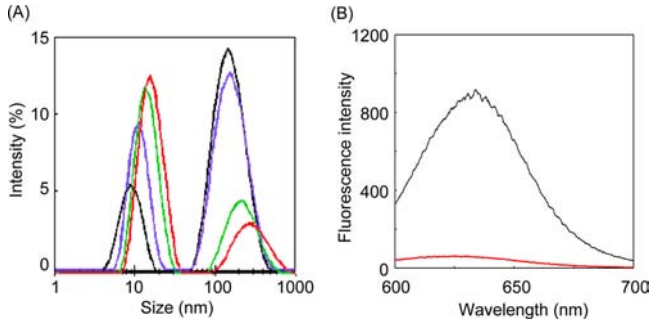


Figure 2. Size of aggregates consisted of DAMs and encapsulation of nile red by larger aggregates. (A) Size of aggregates consisting of DAM 1 (60 μM, black), DAM 2 (30 μM, blue), DAM 3 (30 μM, green), and DAM 4 (30 μM, red). DLS experiments were conducted using aqueous solution of DAMs containing phosphate Na buffer (100 mM, pH 7.0). (B) Fluorescence spectra of nile red (10 μM) in aqueous solution containing phosphate Na buffer (100 mM, pH 7.0) in the presence of DAM 1 (20 μM) before (black) or after (red) filtration using 100 nm filter. The fluorescence spectra were measured at 580 nm excitation.

dx.doi.org/10.1021/bc3002985 | *Bioconjugate Chem.* 2012, 23, 1909–1914

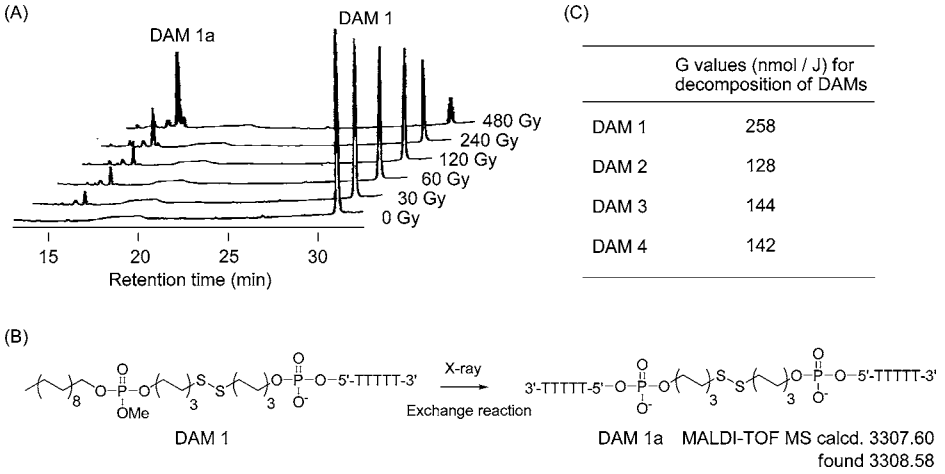


Figure 3. Radiolytic reduction of aqueous solution of DAMs under hypoxic conditions. (A) HPLC profiles for the reaction of DAM 1 (60 μM) in the hypoxic X-ray radiolysis of phosphate Na buffer solution (100 mM, pH 7.0) containing 2-methyl-2-propanol (3 mM) at ambient temperature. (B) X-ray irradiation of DAM 1 to form DAM 1a via strand exchange reaction. (C) *G* values for the decomposition of DAMs in the X-ray radiolysis.

large aggregates with a diameter of ca. 110 nm, while the main aggregates consisting of DAMs with long ODNs formed small aggregates with a diameter of ca. 15 nm. It is well-known that the sizes of the hydrophobic part and the hydrophilic part have potent influence on the size and shapes of the aggregates.[29] Although the correct forms of DAM aggregates are unclear at present, it is most likely that the chain length of ODNs significantly affects the size of the aggregates. To confirm which size of aggregate contributes to the encapsulation of nile red, we measured the fluorescence spectra of aggregates consisting of DAM 1 after filtration using a filter with 100 nm pore size. As shown in Figure 2B, a marked decrease in the fluorescence emission was observed for the filtered sample, indicating that encapsulation of nile red is attributed to the larger aggregates. We also confirmed that the amount of nile red encapsulated by DAM 1 and DAM 2 was larger than that for DAM 3 and DAM 4, which is consistent with the size of aggregates formed in the aqueous solution.

To characterize the reaction properties, we performed X-radiolytic reduction of DAMs 1−4 in argon-purged aqueous solutions containing 2-methyl-2-propanol. The scavenger 2-methyl-2-propanol was added to prevent possible side reactions derived by oxidizing hydroxyl radicals (OH•), which are one of the active species generated by the radiolysis of water.[26] Thus, reducing hydrated electrons (e_{aq}^-) and hydrogen atoms (H•) act as the major active species under these radiolysis conditions. Figure 3A shows a representative profile for the radiolytic reduction of DAM 1. Hypoxic irradiation of DAM 1 produced a single new product, DAM 1a, the yield of which increased as a function of increasing radiation dose. To identify the product, we purified DAM 1a and measured the mass spectrum. The molecular weight of the product was identical to the 10 mer ODNs possessing a disulfide bond, indicating that hypoxic X-irradiation of DAM 1 induced a change of chemical structure via intramolecular exchange of disulfide. The *G* values were estimated to be 258 nmol/J for the decomposition of DAM 1. Similar reductive exchange reactions upon hypoxic X-irradiation were confirmed for DAM 2, DAM 3, and DAM 4 with longer ODNs, although their reaction efficiencies were lower than that of DAM 1 because of the lower accessibility of reducing species to the target disulfides in DAMs 2−4, which showed increased electrostatic screening effects by negative charges on the ODN phosphate units (Figure 3C).

In this study, we developed a series of radiolytically degradable amphiphiles consisting of ODNs and alkyl chains. Of these, DAM 1 possessing 5 mer ODNs seems to have favorable properties for the construction of radiation-activated nanocarriers because DAM 1 formed the largest aggregate to encapsulate nile red as a phantom drug and showed the highest reaction efficiency upon hypoxic X-irradiation. In light of these observations, we next characterized the basic properties of DAM 1 aggregates against living cells and their ability to release drugs under irradiation conditions to apply DAM 1 aggregates as a radiation-activated drug carrier. We then evaluated the radiolytic reduction of DAM 1 aggregates, which encapsulated a fluorescent dye. We used pyrene as a phantom drug instead of nile red because nile red was unstable during hypoxic X-irradiation. As shown in Figure 4, strong fluorescence of pyrene was observed when DAM 1 was added to the aqueous solution. Thus, pyrene dye was encapsulated in the DAM 1 aggregates. In contrast, X-irradiation of the aggregates under hypoxic conditions led to a significant decrease in fluorescence, indicating that DAM 1 underwent an exchange reaction of disulfide to form DAM 1a, and thereby the encapsulated pyrene

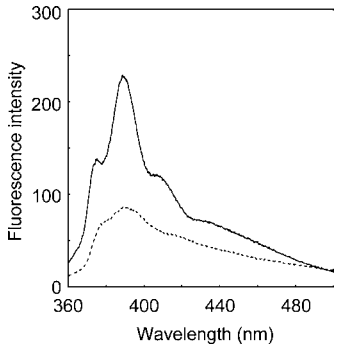


Figure 4. Radiolytic reduction of DAM 1 aggregate encapsulating pyrene. Fluorescence spectra of pyrene (10 μM) in the presence of DAM 1 (36 μM) in phosphate Na buffer solution (100 mM, pH 7.0) containing 2-methyl-2-propanol (1.5 mM). The spectra were measured after hypoxic X-irradiation (0 Gy, solid line; 360 Gy, dotted line).

dx.doi.org/10.1021/bc3002985 | *Bioconjugate Chem.* 2012, 23, 1909−1914

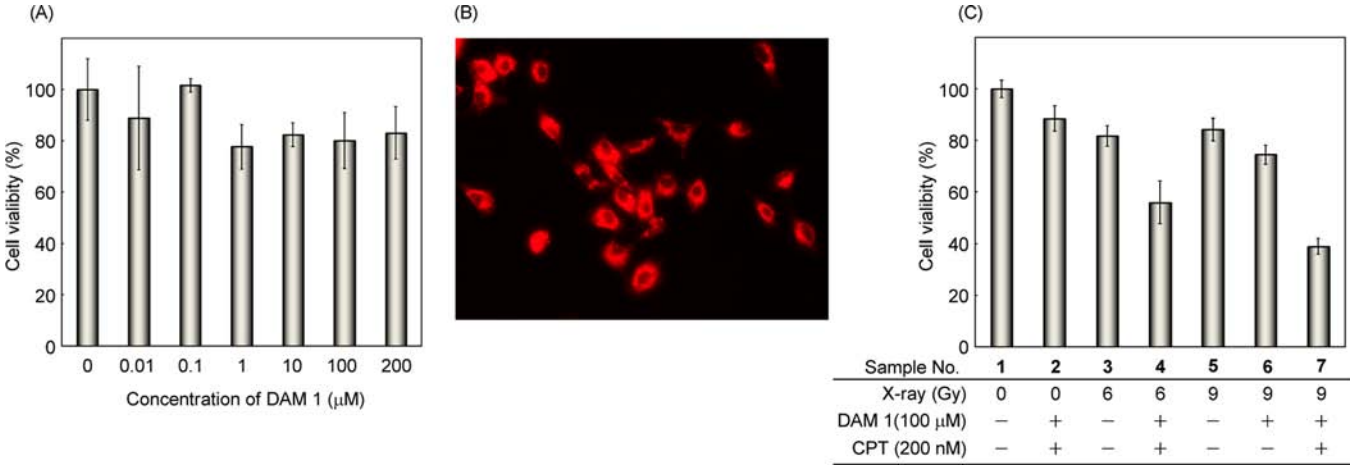


Figure 5. Biological experiments of DAM 1 aggregates encapsulating CPT using A549 cells. (A) Cytotoxicity of DAM 1 against A549 cells. A549 cells were incubated with indicated concentrations of DAM 1 under aerobic conditions for 48 h. To calculate the cell viability in each condition, WST 8 counts (OD_{450}) for each concentration of DAM 1 were compared to those in minimal concentration. Results are shown with the mean ± SD (n = 5). (B) Emission images of A549 cells as incubated with DAM 1 aggregates (100 μM) encapsulating nile red (1 μM). The cells were incubated with the aggregate for 2 h at 37 °C, and then the medium was replaced by PBS. After the replacement, the images were immediately taken by means of microscopy (excitation at 560 nm and emission at 630 nm). (C) Radiation-induced cytotoxicity of CPT encapsulated in DAM 1 aggregate against A549 cells under hypoxic conditions. A549 cells were cultured in the presence (+) or absence (−) of DAM 1 (100 μM) and CPT (200 nM) and treated with X-ray (0, 6, or 9 Gy) under hypoxic conditions. Results are shown with the mean ± SD (n = 4).

was released from the aggregates, the structure of which could not be maintained under radiation conditions. The amount of the released pyrene during X-irradiation up to 360 Gy was estimated to be 293 nM according to the relationships between fluorescence intensity and concentration of pyrene.

On the basis of the above reaction characteristics, an attempt was also made to demonstrate the radiolytic onset of drug potency using a human cell line of lung carcinoma A549 and an antitumor agent, camptothecin (CPT), as an encapsulated drug. Before an evaluating the radiolysis of the aggregates in living cells, we assessed the cytotoxic properties and cellular penetration of DAM 1. For the assessment of cytotoxicity, A549 cells were cultured for 48 h in the presence of various concentrations of DAM 1 and were subsequently subjected to a cell viability assay (Figure 5A). We confirmed that almost all of the cells had a high survival rate even in the presence of DAM 1 up to 200 μM, suggesting that DAM 1 had low cytotoxicity in this concentration range. The cellular penetration of DAM 1 aggregates containing nile red as a phantom drug was also evaluated. As shown in Figure 5B, clear fluorescence of nile red was observed from the cytoplasm of A549 cells when the cells were incubated with aggregates for 2 h. Thus, DAM 1 aggregate smoothly penetrated into the cells.

We subsequently investigated the radiation-dependent cytotoxic effect of drug-encapsulating DAM 1 aggregates. After administration of CPT-containing DAM 1 aggregates to A549 cells and incubation for 2 h to allow penetration into the cells, the medium was replaced with fresh medium to avoid undesirable activation of aggregates outside the cells. We then exposed A549 cells to X-radiolysis under hypoxic conditions. As shown in Figure 5C, a slight cytotoxic effect in the presence of 200 nM CPT, which was encapsulated in the aggregate, was observed under the conditions without X-irradiation (sample 2). However, given that the IC_{50} value of CPT against A549 cells is 59.4 nM, it is suggested that encapsulation of drugs by DAM 1 aggregates effectively suppressed the onset of the effect of CPT and that collapse of the aggregates to release CPT in reductive cytoplasm of the cells was negligible. It is striking that X-irradiation of the cells, to which CPT-encapsulating aggregates were administered, resulted in a significant decrease in cell viability, although A549 cells were practically resistant to 9 Gy radiation under hypoxic conditions in the presence of empty aggregates. We also confirmed that a lower dose of 6 Gy led to a decrease in cell survival rate (sample 4). These results strongly suggest that DAM 1 aggregates preferentially release toxic CPT via radiolytic reduction in hypoxic cells and thereby lead to enhanced cytotoxicity, consistent with the chemical reactivity upon X-irradiation. Thus, it is reasonably concluded that DAM 1 aggregates act as radiation-degradable drug carriers.

■ CONCLUSION

In conclusion, we have synthesized a series of DNA amphiphiles, DAMs, as radiation-activated drug carriers. The DAMs had an alkyl chain as the hydrophobic unit and ODNs as the hydrophilic unit, and these two functional units were connected by an X-ray-sensitive disulfide bond. The DAMs self-assembled to form nanosized aggregates, which encapsulated hydrophobic dyes and active drugs in their hydrophobic parts. Among the amphiphiles, DAM 1 possessing 5 mer ODNs showed good properties for drug encapsulation and radiolytic activation, and thereby we characterized the radiolytic release of an antitumor agent, camptothecin (CPT), which was encapsulated in the aggregates consisting of DAM 1. X-irradiation of A549 cells, to which DAM 1 aggregates with CPT were administered, resulted in an enhancement of cytotoxicity because of the radiolytic release of CPT from the aggregates. Thus, DAM 1 aggregates are promising as radiation-activated nanocarriers that are applicable to drug delivery and targeting. In vivo experiments to characterize the performance of the DAM 1 aggregates are in progress.

■ AUTHOR INFORMATION

Corresponding Author

*Phone: +81-75-383-2505. Fax: +81-75-383-2504. E-mail: tanabeka@scl.kyoto-u.ac.jp.

Notes

The authors declare no competing financial interest.

■ ACKNOWLEDGMENTS

This work was partly supported by the Strategic Promotion Program for Basic Nuclear Research from the Ministry of Education, Culture, Sports, Science and Technology (MEXT), Japan.

■ REFERENCES

(1) Cutler, J, I., Zhang, K., Zheng, D., Auyeung, E., Prigodich, A. E., and Mirkin, C. A. (2011) Polyvalent nucleic acid nanostructures. *J. Am. Chem. Soc. 133*, 9254−9257.

(2) Cobley, C. M., Chen, J., Cho, E. C., Wang, L. V., and Xia, Y. (2011) Gold nanostructures: a class of multifunctional materials for biomedical applications. *Chem. Soc. Rev. 40*, 44−56.

(3) Ryou, S.-M., Kim, S., Jang, H. H., Kim, J.-H., Yeom, J.-H., Eom, M. S., Bae, J., Han, M. S., and Lee, K. (2010) Delivery of shRNA using gold nanoparticle−DNA oligonucleotide conjugates as a universal carrier. *Biochem. Biophys. Res. Commun. 398*, 542−546.

(4) Giljohann, D. A., Seferos, D. S., Prigodich, A. E., Patel, R. E., and Mirkin, C. A. (2009) Gene regulation with polyvalent siRNA−nanoparticle conjugate. *J. Am. Chem. Soc. 131*, 2072−2073.

(5) Rosi, N. L., Giljohann, D. A., Thaxton, S., Lytton-Jean, A. K. R., Han, M. S., and Mirkin, C. A. (2006) Oligonucleotides-modified gold nanoparticles for intracellular gene regulation. *Science 312*, 1027−1030.

(6) Mintzer, M. A., and Simanek, E. E. (2009) Nonviral vectors for gene delivery. *Chem. Rev. 109*, 259−302.

(7) Zhang, K., Fang, H., Wang, Z., Li, Z., Tayler, J. −S. A., and Wooley, K. L. (2010) Structure−activity relationships of cationic shall-crosslinked knedel-like nanoparticles: shell composition and transfection efficiency/cytotoxicity. *Biomaterials 31*, 1805−1813.

(8) Huang, L., and Li, S. (1997) Loposomal gene delivery: a complex package. *Nature Biotechnol. 15*, 620−621.

(9) Young, L. S., Searly, P. F., Onion, D., and Mautner, V. (2006) Viral gene therapy strategies: from basic science to clinical application. *J. Pathol. 208*, 299−318.

(10) Ganta, S., Devalapally, H., Shahiwala, A., and Amiji, M. (2008) A review of stimuli-responsive nanocarriers for drug and gene delivery. *J. Controlled Release 126*, 187−204.

(11) Klaikherd, A., Nagamani, C., and Thayumanavan, S. (2009) Multi-stimuli sensitive amphiphilic block copolymer assemblies. *J. Am. Chem. Soc. 131*, 4830−4838.

(12) Chiu, H.-C., Lin, Y.-W., Huang, Y.-F., Chuang, C.-K., and Chern, C.-S. (2008) Polymer vesicles containing small vesicles within interior aqueous compartments and pH-responsive transmembrane channels. *Angew. Chem., Int. Ed. 47*, 1875−1878.

(13) Auguste, D. T., Furman, K., Wong, A., Fuller, J., Armes, S. P., Deming, T. J., and Langer, R. (2008) Triggered release of siRNA from poly(ethylene glycol)-protected, pH-dependent liposomes. *J. Controlled Release 130*, 266−274.

(14) Du, J., Tang, Y., Lewis, A. L., and Armes, S. P. (2005) pH-Sensitive vesicles based on a biocompatible zwitterionic diblock copolymer. *J. Am. Chem. Soc. 127*, 17982−17983.

(15) Sundararaman, A., Stephan, T., and Grubbs, R. B. (2008) Reversible restructuring of aqueous block copolymer assemblies through stimulus-induced changes in amphiphilicity. *J. Am. Chem. Soc. 130*, 12264−12265.

(16) Oupický, D., and You, Y. −Z. (2007) Synthesis of temperature-responsive heterobifunctional block copolymers of poly(ethylene glycol) and poly(*N*-isopropylacrylamide). *Biomacromolecules 8*, 98−105.

(17) Morishima, Y. (2007) Thermally responsive polymer vesicles. *Angew. Chem., Int. Ed. 46*, 1370−1372.

(18) Aathimanikandan, S. V., Savariar, E. N., and Thayumanavan, S. (2005) Temperature-sensitive dendritic micelles. *J. Am. Chem. Soc. 127*, 14922−14929.

(19) Takae, S., Miyata, K., Oba, M., Ishii, T., Nishiyama, N., Itaka, K., Yamasaki, Y., Koyama, H., and Kataoka, K. (2008) PEG-Detachable polyplex micelles based on disulfide-linked block catiomers as bioresponsive nonviral gene vectors. *J. Am. Chem. Soc. 130*, 6001−6009.

(20) Stevenson, M., Ramos-Perez, V., Singh, S., Soliman, M., Preece, J. A., Briggs, S. S., Read, M. L., and Seymour, L. W. (2008) Delivery of siRNA mediated by histidine-containing reducible polycations. *J. Controlled Release 130*, 46−56.

(21) Napoli, A., Valentini, M., Tirelli, N., Muller, M., and Hubbell, J. A. (2004) Oxidation-responsive polymeric vesicles. *Nature Mater. 3*, 183−189.

(22) Nishiyama, N., Iriyama, A., Jang, W.-D., Miyata, K., Itaka, K., Inoue, Y., Takahashi, H., Yanagi, Y., Tamaki, Y, Koyama, H., and Kataoka, K. (2005) Light-induced gene transfer from packaged DNA enveloped in a dendrimeric photosensitizer. *Nature Mater. 4*, 934−941.

(23) Goodwin, A. P., Mynar, J. L., Ma, Y., Fleming, G. R., and Fréchet, J. M. J. (2005) Synthetic micelle sensitive to IR light via a two-photon process. *J. Am. Chem. Soc. 127*, 9952−9953.

(24) Jiang, J., Tong, X., and Zhao, Y. (2005) A new design for light-breakable polymer micelles. *J. Am. Chem. Soc. 127*, 8290−8291.

(25) Tanabe, K., Kuraseko, E., Yamamoto, Y., and Nishimoto, S. (2008) One-electron reductive template-directed ligation of oligodeoxynucleotides possessing disulfide bond. *J. Am. Chem. Soc. 130*, 6302−6303.

(26) Buxton, G. V., Greenstock, C. L., Helman, W. P., and Ross, A. B. (1988) Critical review of rate constants for reactions of hydrated electrons, hydrogen atoms and hydroxyl radicals in aqueous solution. *J. Phys. Chem. Ref. Data 17*, 513−886.

(27) Spinks, J. W. T., Woods, R. J. (1990) *An Introduction to Radiation Chemistry*, Wiley-Interscience, New York.

(28) Tanabe, K., Matsumoto, E., Ito, T., and Nishimoto, S. (2010) Radiolytic cyclization of stem-and-loop structured oligodeoxynucleotide with neighboring arrangement of α,ω-bis-disulfides. *Org. Biomol. Chem. 8*, 4837−4842.

(29) van Hest, J. C. M., Delnoye, D. A. P., Baars, M. W. P. L., van Genderen, M. H. P., and Meijer, E. W. (1995) Polystyrene−Dendrimer amphiphilic block copolymers with a generation-dependent aggregation. *Science 268*, 1592−1595.

Bioconjugate Chemistry

Article

pubs.acs.org/bc

Alendronate-Conjugated Amphiphilic Hyperbranched Polymer Based on Boltorn H40 and Poly(ethylene glycol) for Bone-Targeted Drug Delivery

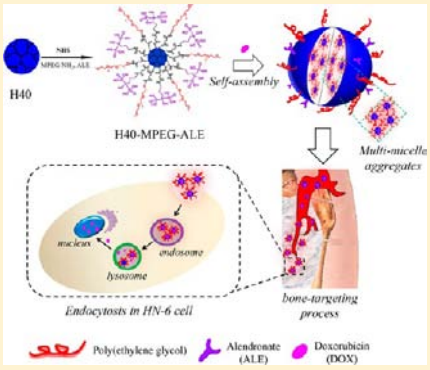
Hongying Chen,[†,#] Guolin Li,[†,#] Huirong Chi,[†] Dali Wang,[‡] Chunlai Tu,[‡] Lijie Pan,[§] Lijuan Zhu,[‡] Feng Qiu,[‡] Fulin Guo,*[,†] and Xinyuan Zhu*[,‡]

[†]Department of Oral and Maxillofacial Surgery and [§]Department of Preventive Oral Health, The First Affiliated Hospital of Harbin Medical University, 23 Youzheng Street, Nangang District, Harbin 150001, People's Republic of China

[‡]School of Chemistry and Chemical Engineering, State Key Laboratory of Metal Matrix Composites, Shanghai Jiao Tong University, 800 Dongchuan Road, Shanghai 200240, People's Republic of China

Supporting Information

ABSTRACT: A novel type of alendronate(ALE)-conjugated amphiphilic hyperbranched copolymer based on a hydrophobic hyperbranched Boltorn H40 (H40) core with ALE targeting moiety and many hydrophilic poly(ethylene glycol) (PEG) arms was synthesized as a carrier for bone-targeted drug delivery. The star copolymer H40-*star*-PEG/ALE was characterized using nuclear magnetic resonance (NMR), Fourier transformed infrared spectroscopy (FTIR), and gel permeation chromatography (GPC) analysis. Benefiting from its highly branched structure, H40-*star*-PEG/ALE could form micelles in aqueous solution, which was confirmed by transmission electron microscopy (TEM) and dynamic light scattering (DLS) techniques. The cytotoxicity and hemolysis of the H40-*star*-PEG/ALE micelles were evaluated via methylthiazoletetrazolium (MTT) assay against NIH/3T3 normal cells and red blood cell (RBC) lysis assay, respectively. As a model anticancer drug, doxorubicin (DOX) was encapsulated into the H40-*star*-PEG/ALE micelles. The anticancer activity of DOX-loaded micelles was evaluated by MTT assay against an HN-6 human head and neck carcinoma cell line. The strong affinity of H40-*star*-PEG/ALE micelles to bone was confirmed by the hydroxyapatite (HA) binding assay. These results indicate that the H40-*star*-PEG/ALE micelles are highly promising bone-targeted drug carriers for skeletal metastases.



INTRODUCTION

The skeleton is invariably metastasized or invaded by the malignancy at advanced stages.[1,2] In particular, the primary carcinomas of the breast, lung, kidney, and oral cavity have the powerful capacity of metastasis and/or invasion to the bone.[1−3] The bone metastasis or invasion is responsible for the disability (pathological fracture, hypercalcemia) and mortality.[1−4] During the past decades, the clinical therapies focus mainly on the surgical resection and the aggressive chemotherapy and radiotherapy.[5,6] For chemotherapy, the chemotherapeutic agents can inhibit the progression of cancers efficiently, but it is difficult to deliver drugs to the skeletal lesion sites because of the blood-bone barrier.[1,7] Futhermore, drugs themselves lack a desired selectivity to target the tumor tissue, leading to severe side effects including the toxicity of cardiac tissues and the inhibition of bone marrow.[1,8]

Recently, polymeric micelles formed by self-assembly of amphiphilic copolymers in aqueous solution have attracted tremendous attention as a drug delivery vehicle. These micelles can accumulate into tumor tissue because of the abnormal interstices of the vascular endothelium and the absence of lymphatic drainage system of some tumors, which is defined as the enhanced permeability and retention (ERP) effect.[1,9−11] In the literature, it is also frequently mentioned as passive targeting. However, the drug dose at carcinoma sites is usually low by the passive targeting, resulting in the poor efficacy for tumor inhibition.[12] To further improve the specific targeting and delivery efficiency, active targeting ability of the drug delivery systems is required. Active targeting can be achieved via functionalization of the micelle carriers with targeting ligands such as antibodies, peptides, and small molecules, which can recognize and bind to specific receptors that are unique to carcinoma cells or pathological tissues.[13,14] The drug bioavailability in the body is obviously enhanced and the adverse effects of chemotherapy drugs to normal tissues are enormously reduced.[1−5,15,16] It is well-known that bisphosphonates exhibit a high affinity for the bone mineral HA.[17,18] For the metastasized and/or invaded bone, the hydroxyapatite exposed in tumor surroundings can be used as the specific receptor for those bisphosphonate-functionalized drug carriers.

Received: June 12, 2012
Revised: August 20, 2012
Published: September 4, 2012

 © 2012 American Chemical Society dx.doi.org/10.1021/bc3003088 | *Bioconjugate Chem.* 2012, 23, 1915−1924

Miller et al. reported the *N*-(2-hydroxypropyl) methacrylamide copolymer−paclitaxel−alendronate conjugate as an effective bone-delivery system.[2,11,19] Salerno et al. prepared DOX-loaded bone-targeting nanoparticles based on the polymer of poly-(lactic-*co*-glycolide)−alendronate conjugate.[1,20] The linear polymers were employed as the backbone of the conjugates in the previous literature.[1,2,11,19,20] Comparing to the linear polymers of the same molecular weight and composition, the amphiphilic star-shaped block copolymers exhibit smaller hydrodynamic radius and lower melt and solution viscosities.[21] Due to the low critical micelle concentration (CMC) of amphiphilic star-shaped block copolymers, the self-assembled micelles have unique characteristics such as nanosize, high stability, and a core−shell architecture *in vivo*.[21] Thus, it can be imagined that if bisphosphonates are conjugated onto the surface of dendritic micelles, a bone-targeted drug delivery system with high stability might be developed.

In this work, a novel bone-targeting micelle with high stability was designed and successfully prepared from H40-*star*-PEG/ALE consisting of an aliphatic biodegradable polyester H40 inner core with alendronate bone-targeting moiety and many hydrophilic linear PEG arms. The biodegradable polyester H40 inner core served as the reservoir for hydrophobic drugs, while the hydrophilic PEG outer shell enhanced the micelle stability and prolonged the circulation time in the bloodstream. In the meantime, the conjugation of bisphosphonates provided strong affinity to the skeleton mineral hydroxyapatite, realizing the targeting of bone tissue. As a model anticancer drug, the hydrophobic DOX was encapsulated into the H40-*star*-PEG/ALE micelles, and the strong affinity of DOX-loaded H40-*star*-PEG/ALE micelles to bone tissue was validated by the hydroxyapatite binding assay.

MATERIALS AND METHODS

Materials. Triethylamine (TEA) and methylene dichloride (CH_2Cl_2) were dried over calcium hydride for 48 h and then distilled before used. Tetrahydrofuran (THF) was dried by refluxing with the fresh sodium-benzophenone complex (a thick purple color indicating a moisture- and oxygen-free solvent) and distilled just before used. H40 was obtained from Perstorp Polyols AB, Sweden. Aminopoly(ethylene glycol) monomethyl ether (PEG-NH_2) with M_n = 1 kDa was purchased from Jiaxing Biomatrix and Biotechnology limited company and used as received. ALE and 1,6-diphenyl-1,3,5-hexatriene (DPH) were used as received without further purification. Doxorubicin hydrochloride (DOX·HCl) was purchased from Beijing Huafeng United Technology Corporation and used as received. Clear polystyrene tissue culture treated 6-well, 12-well, and 96-well plates were obtained from Corning Coastar. Dulbecco's modified Eagle's medium (DMEM), fetal bovine serum (FBS), penicillin, and streptomycin were obtained from Biological Industries Ltd. *N*-Hydroxysuccinamide (NHS, Acros), polyethylenimine (PEI, water free, M_n = 10 kDa, Aldrich) were used as received. Dialysis tube (MWCO = 3.5 kDa) was purchased from Shanghai Lvniao Technology Corp. Dextran (M_n = 40 kDa) and all other chemical reagents of analytical grade were purchased from Shanghai Chemical Reagent Co. and used as received unless mentioned.

Synthesis of H40 with Carboxyl Terminal Group (H40-COOH). H40-COOH was prepared by reacting purified H40 with succinic anhydride.[22,23] In a typical procedure, 3.0 g (25.6 mmol hydroxyl groups) H40 was dissolved in 75 mL anhydrous THF in a 150 mL flask under moderate stirring for 30 min at room temperature. After completely dissolved, 3.84 g (38.4 mmol) succinic anhydride and 0.75 mL of TEA as the catalyst were quickly added into the flask under the equal reaction condition for 24 h. The crude product formed was precipitated in the cold diethyl ether twice and dried under the vacuum. The purified H40-COOH was obtained by employing the freeze−drying way after dialysis against deionized water using the membranous tube with the molecular weight cutoff 3.5 kDa for 48 h.

Synthesis of H40-CO-NHS. Briefly, 3.3 g (0.2 mmol) H40-COOH was dissolved in 20 mL anhydrous CH_2Cl_2. Then, 3.0 g (1.8 mL) sulfoxide chloride ($SOCl_2$) was to the 100 mL flask in an ice−water bath with stirring for 3 h, and the reaction was run in room temperature for another 24 h. The reaction solution was quickly evaporated under vacuum, and then 1.19 g (10.3 mmol) *N*-hydroxysuccinamide (NHS) with 20 mL fresh anhydrous CH_2Cl_2 was added to the flask in an ice−water bath with stirring for 24 h. Subsequently, the resulting mixture was poured into water, extracted with CH_2Cl_2, and dried by anhydrous $MgSO_4$. The solvent was concentrated by evaporation. At last, the concentrated solution was precipitated by cold diethyl ether, and product was dried under vacuum to a constant weight.

Synthesis of H40-*star*-PEG. Briefly, 0.9 g (0.045 mmol) H40-CO-NHS was dissolved in 20 mL anhydrous dioxane under moderate stirring at the room temperature. After completely dissolved, 2.88 g (2.88 mmol) PEG-NH_2 was quickly added to the flask under the same reaction conditions for 24 h. The crude product formed was precipitated with the cold diethyl ether and dried under the vacuum.

Synthesis of H40-*star*-PEG/ALE. Briefly, 0.5 g (0.012 mmol) H40-*star*-PEG was dissolved in 20 mL dioxane under moderate stirring at the room temperature. After completely dissolved, 0.123 g (0.378 mmol) ALE was quickly added into the flask. Then, 30.7 mg (0.77 mmol) NaOH was slowly added into the flask to regulate pH = 8.0 under the identical reaction condition for 24 h. The formed crude product was precipitated with dialysis against deionized water using the membranous tube with the molecular weight cutoff 3.5 kDa.

Preparation of H40-*star*-PEG/ALE Micelles and Their CMC. Typically, a total of 20 mg H40-*star*-PEG/ALE copolymer was dissolved in 2 mL DMF and stirred at room temperature for 3 h. Then, the 6 mL deionized water was slowly added into the copolymer solution under stirring for 2 h, and the solution was transferred into dialysis tubing (MWCO = 3.5 kDa) and dialyzed against the deionized water for 24 h. During the process, the water was renewed at appropriate intervals. To study the CMC of H40-*star*-PEG/ALE copolymer, DPH was employed as a UV−vis probe to monitor the absorbance at 313 nm. The H40-*star*-PEG/ALE copolymer solution with series of concentrations (from 5×10^{-6} to 0.5 mg/mL) was prepared, and then methanol solution of DPH was added. The DPH concentration was kept at a constant of 5.0×10^{-6} mol/L. The 313 nm wavelength absorbance of all solutions was recorded on Perkin-Elmer Lambda 20/2.0 UV−vis spectrophotometer.[24]

Characterization. ^{1}H NMR, ^{13}C NMR, and ^{31}P NMR spectra were recorded on Bruker AVANCEIII 400 spectrometer with DMSO-d_6, D_2O, and $CDCl_3$ as the solvents at 25 °C. Molecular weights and polydispersity index (PDI) of the synthesized samples were measured by GPC. GPC measurements were performed on a Perkin-Elmer series 200 system (10 μm PL gel 300 × 7.5 mm mixed-B and mixed-C column, linear poly(ethylene glycol) calibration equipped with a refractive index (RI) detector). $NaNO_3$ aqueous solution (0.05 M) was used as the mobile phase at a flow rate of 0.6 mL/min at 40 °C. FTIR spectra were recorded on a Paragon 1000 instrument by KBr sample holder method. DLS measurements were recorded on a Malvern Zetasizer Nano S device equipped with a 4.0 mW laser operating at λ = 633 nm. All samples of 0.5 mg/mL were tested with a scattering angle of 173° and at 37 °C. TEM studies were performed with a JEOL JEM-100CX-II instrument operated at 200 kV to observe the shape and size of the micelles. Samples were prepared by directly dropping the solution onto carbon-coated copper grids and then air-drying at room temperature overnight before measurement. The UV−vis spectra were measured on a Perkin-Elmer Lambda 20/2.0 UV−vis spectrophotometer. The calibration curve of absorbance measurements against a series of concentration of DOX was measured at 500 nm. The fluorescence spectra were recorded on a QM/TM/RM fluorescence spectrophotometer (Photon Technology International, Inc.) at room temperature.

Preparation of DOX-Loaded Micelles. DOX-loaded micelles were prepared via the encapsulation of hydrophobic DOX into the

amphiphilic H40-*star*-PEG/ALE. The details were as follows: 50 mg H40-*star*-PEG/ALE was dissolved in 4 mL DMF, followed by adding 5 mg DOX and the theoretical drug loading content was 10 wt %. Then, the mixture was added slowly to 6 mL of deionized water and stirred for another 3 h. Subsequently, the solution was dialyzed against deionized water for 24 h (MWCO = 3.5 kDa), and the deionized water was renewed every 4 h. The DOX-loaded nanoparticle solution was lyophilized and then dissolved in DMF. The DOX concentration was determined by the UV−vis measurements at absorbance wavelength of 500 nm.

Drug loading content (DLC) and drug loading efficiency (DLE) were calculated according to the following formula:

$$\text{DLC(wt\%)} = (\text{weight of loaded drug/weight of polymer}) \times 100\%$$

$$\text{DLE(\%)} = (\text{weight of loaded drug/weight of drug in feed}) \times 100\%$$

***In Vitro* Drug Release Assay.** The drug release assay was carried out in glass bottles at 37 °C in phosphate buffer (pH = 7.4) and acetate buffer (pH = 5.0) solutions. First, 4 mL DOX-loaded micelles were placed in a dialysis tube with a molecular weight cutoff of 3.5 kDa. Then, the dialysis bag was quickly immersed in 50 mL of the release medium in a laboratory shaker keeping the stirring (100 rpm) and a constant temperature (37 °C). At the predetermined intervals, 2 mL sample was withdrawn and the equal volume of fresh medium was replenished. The amount of released DOX was analyzed with the fluorescence measurements at 480 nm of excitation spectrum. The DOX-release studies were performed in triplicate, and the results were expressed as the average data with standard deviations.

Cell Culture. NIH/3T3 normal cells (a mouse embryonic fibroblast cell line) and HN-6 cancer cells were cultured in DMEM supplied with 10% FBS, and antibiotics (50 units/mL penicillin and 50 units/mL streptomycin) at 37 °C in a humidified atmosphere containing 5% CO_2.

Cytotoxicity Measurements of H40-*star*-PEG/ALE Micelles. The relative cytotoxicity of H40-*star*-PEG/ALE micelles against NIH/3T3 cells was estimated by MTT viability assay. In the MTT assay, NIH/3T3 cells were seeded into 96-well plates at a seeding density of 1.0×10^4 cells per well in 200 μL of complete medium. After 24 h of incubation, the culture medium was removed and replaced with 200 μL of a medium containing serial concentration of the H40-*star*-PEG/ALE micelles. The cells were grown for another 48 h. Then, 20 μL of 5 mg/mL MTT assay stock solution in PBS was added to each well. After incubating the cells for 4 h, the medium containing unreacted dye was removed carefully. The obtained blue formazan crystals were dissolved in 200 μL DMSO and the absorbance was measured with BioTek SynergyH4 at a wavelength of 490 nm.

Red Blood Cells (RBC) Lysis Assay. Ten mL of blood was obtained from the ear artery of a male New Zealand white rabbit. The 2% w/v RBC solution was acquired. Briefly, the blood was centrifuged at 2000 rpm for 10 min at 4 °C. Then, the supernatant was removed, and the erythrocytes were resuspended with ice-cold PBS (pH = 7.4). The cells were again centrifuged at the same condition. The process must be repeated more than four times to ensure the removal of any released hemoglobin. Finally, the supernatant was carefully removed, and the cells were resuspended in ice cold PBS to get RBC solution (2% w/v).[2,19,25] The copolymers and reference polymers (Dextran and PEI) were also prepared at serial concentration (0.02, 0.1, 0.2, 1, and 2 mg/mL) with PBS (pH = 7.4). Then, 2 mL of the H40-*star*-PEG/ALE copolymer and reference polymers (Dextran and PEI) were added to 2 mL of the 2% w/v RBC solution in 5 mL centrifuge tubes and incubated for 1 h at 37 °C. Dextran and PBS were used as negative controls, while PEI and 1% v/v solution TritonX-100 (100% lysis) were used as positive controls. After 1 h of incubation, the samples were centrifuged at 2000 rpm for 10 min, and the supernatants (200 μL) were transferred to 96-well plates. The absorbance of released hemoglobin was tested with a BioTek SynergyH4 at a wavelength of 545 nm.

Cellular Uptake of DOX-Loaded Micelles by HN-6 Cells. The experiments of intracellular drug release were performed on flow cytometry and confocal laser scanning microscopy (CLSM).

Flow Cytometry. HN-6 cells were seeded in 6-well plates at 5×10^5 cells per well in 1.5 mL of complete DMEM and cultured for 24 h. Then, the DOX-loaded H40-*star*-PEG/ALE micelles dissolved in DMEM culture medium at a final DOX concentration of 5 μg/mL were added to different wells and the cells were incubated at 37 °C for 5 min, 15 min, 0.5 h, and 3 h, respectively. Thereafter, the samples were prepared for flow cytometry analysis by removing the cell growth media, rinsing twice with ice-cold PBS, and treating with trypsin (150 μL). Then, 1 mL of ice-cold PBS was added to each culture well. Data for 1.0×10^4 gated events were collected and analysis was performed by means of a BD FACSCalibur flow cytometer and *CELLQuest* software.

CLSM. Cell uptake was further analyzed by CLSM studies. HN-6 cells were seeded into 6-well plates at 1×10^5 cells per well in 1 mL of complete DMEM and cultured for 24 h, followed by removing the complete medium and incubating with DOX-loaded H40-*star*-PEG/ALE micelles (1 mL of DMEM medium) at a final DOX concentration of 5 μg/mL. The cells were incubated at 37 °C for predetermined intervals. Subsequently, the cells were washed twice with ice-cold PBS and then fixed with 4% paraformaldehyde for 30 min at room temperature, and the slides were rinsed with ice-cold PBS for three times. Finally, the cells were stained with Hoechst 33342 for 7 min and the slides were rinsed with PBS three times. The slides were mounted and observed with a LSM 510 META.

Activity Analyses. The cytotoxicity of DOX-loaded H40-*star*-PEG/ALE micelles and free DOX against HN-6 cells was evaluated *in vitro* by MTT assay. HN-6 cells were seeded into 96-well plates with a density 8.0×10^3 cells per well in 200 μL of medium. After 24 h of incubation, the culture medium was removed and replaced with 200 μL of a medium containing serial dilutions of DOX-loaded micelles or free DOX. The cells were grown for another 48 h. Then, 20 μL of 5 mg/mL MTT assay stock solution in PBS was added to each well. After incubating the cells for 4 h, the medium containing unreacted MTT was removed carefully. The obtained blue formazan crystals were dissolved in 200 μL DMSO and the absorbance was measured in BioTek SynergyH4 at a wavelength of 490 nm.

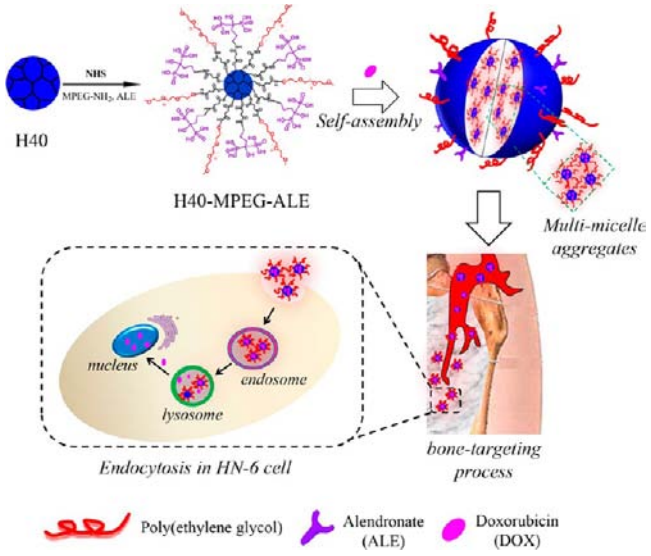
HA Binding Assay. First, the DOX-loaded H40-*star*-PEG/ALE and DOX-loaded H40-*star*-PEG micelles were counted to contain the equivalent quantity of DOX (1.0 mg). Then, the two samples were dissolved in PBS (pH = 7.4, 5 mg/mL). The solution (4 mL) was incubated with HA powder (270 mg), used to imitate the hard bone tissue, with 9 mL of PBS (pH = 7.4) at 37 °C in a 20 mL flask. As controls, both DOX-loaded H40-*star*-PEG/ALE and DOX-loaded H40-*star*-PEG were incubated at the same condition without HA powder. Then, the incubated samples were centrifuged at 5000 rpm for 5 min and a sample from the upper layer (2 mL) was collected after 0, 5, 15, 30, and 60 min, respectively. The UV−vis absorbance at 500 nm wavelength was employed to detect the unbound DOX-loaded micelles of the collected samples. The degree of HA binding (expressed as percent binding) was estimated as mean of three independent experiments according to the following formula:

$$[(\text{DOX-loaded micelles concentration without HA}) - (\text{DOX-loaded micelles concentration with HA})] / (\text{DOX-loaded micelles concentration without HA}) \times 100\%$$

RESULTS AND DISCUSSION

Synthesis and Characterizations of H40-*star*-PEG/ALE. Bisphosphonates such as ALE exhibit strong affinity to the skeleton mineral HA. If they are conjugated onto the surface of micelles, an efficient drug delivery system with high stability and active targeting ability could be obtained. The construction and application of such micelles for bone-targeting drug delivery are illustrated in Scheme 1. First, the amphiphilic

Scheme 1. Construction and Application of H40-*star*-PEG/ALE Micelles for Bone-Targeted Drug Delivery



hyperbranched copolymer H40-*star*-PEG/ALE was prepared through four-step reactions, the detailed synthetic route of the polymer is given in Scheme 2, and the chemical structural formula of H40 is also shown in Figure S1 in the Supporting Information. With the help of TEA catalyst, the carboxyl groups are introduced into the surface of H40 to produce H40-COOH via the reaction of H40 with the succinic anhydride.[24,25] After the reaction between H40-COOH and NHS, H40-CO-NHS is obtained. Based on the coupling reaction of H40-CO-NHS and PEG-NH_2, the hydrophilic PEG segments are grafted onto the hydrophobic H40 core to form H40-*star*-PEG. To accomplish the bone targeting property, ALE is further incorporated to H40-*star*-PEG via the reaction between the residual NHS groups of H40-*star*-PEG and the primary amine of ALE to obtain the final product H40-*star*-PEG/ALE. The ^{1}H NMR and ^{31}P NMR spectra of the copolymer H40-*star*-PEG/ALE are shown in Figure S2 and Figure S3 in the Supporting Information. As shown in Figure S2, the typical signals of H40-*star*-PEG/ALE can be detected at 3.57 (a), 3.25 (b), 3.06 (c), 2.54 (d), 2.43−2.46 (e), 2.23 (f), 1.79−1.85 (g), and 1.66 (h) ppm. Based on ^{1}H NMR of H40-*star*-PEG/ALE in Figure S2, about 22% of the −OH groups of H40 were functionalized by ALE and 31% of the −OH groups of H40 was grafted with PEG. The percentage of weight of ALE and PEG in the H40-*star*-PEG/ALE copolymer is 15% and 67%, respectively. The obvious shift of phosphate group of copolymer can be observed compared to the spectrum of ALE in Figure S3. The ^{13}C NMR spectra of H40 and H40-*star*-PEG/ALE are shown in Figure S4 in the Supporting Information. The typical signals of H40-*star*-PEG part can be observed at 33.2, 34.2, 38.9, 58.08, 65.35−71.00, and 181.3 ppm. The typical signals from the ALE moiety can be detected at 23.8, 32.4, 50.8, and 183.2 ppm. The appearance of these peaks confirms the successful conjugation. Hence, the given NMR data confirm that the H40-*star*-PEG/ALE is successfully synthesized.

The structures of all intermediates and H40-*star*-PEG/ALE were further analyzed by FTIR. The representative FTIR spectra are given in Figure S5 in the Supporting Information. In the spectra of H40 (Figure S5A) and H40-COOH (Figure S5B), the sharp peaks at 1733 cm^{-1} confirm the existence of carbonyl groups. After ligation with PEG-NH_2 and ALE, the FTIR spectrum of H40-*star*-PEG/ALE in Figure S5C differs obviously from that of H40 and H40-COOH. The peak at around 1733 cm^{-1} is weakened greatly, indicating that the terminal carboxyl groups have been coupled with the primary amines of PEG-NH_2 and ALE. In the meantime, the appearance of two strong bands at 1112 and 952 cm^{-1} can be attributed to the C−O−C and $-HPO_3$ stretching vibration of PEG and ALE, respectively. FTIR observation further supports the formation of H40-*star*-PEG/ALE.

The molecular weights and their polydispersities of the synthesized products were characterized by GPC, and the results are shown in Table 1. It can be found that the number-average molecular weight (M_n) of H40-*star*-PEG/ALE is 1.41 × 10^4 with a PDI of 1.30.

Scheme 2. Synthetic Route of H40-*star*-PEG/ALE

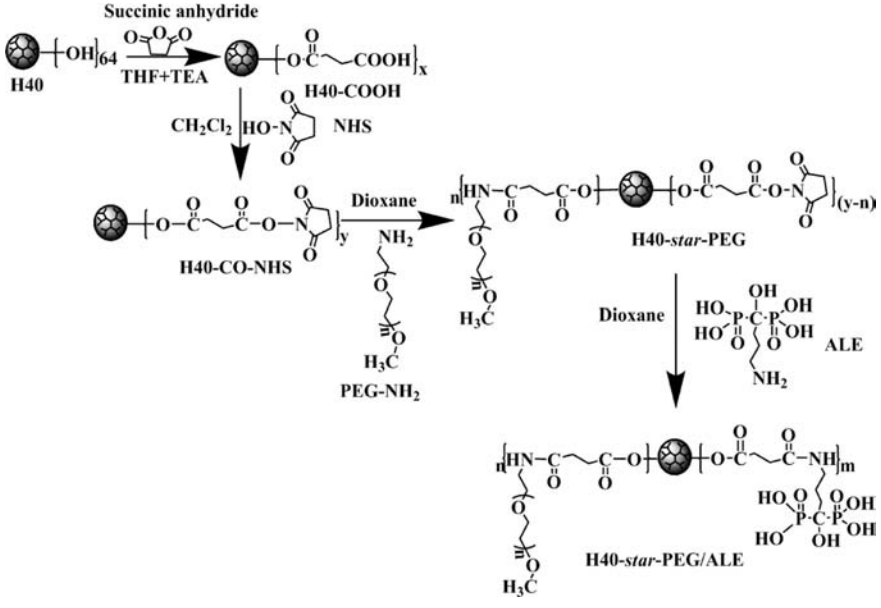


Table 1. GPC Results of H40, H40-COOH, and H40-*star*-PEG/ALE

sample	M_n	M_w	M_w/M_n
H40[a]	2800	5100	1.80
H40-COOH	6100	7800	1.28
H40-*star*-PEG/ALE	14100	18300	1.30

[a]From perstorp data sheet.

Characterization of Micelles. The size is an important parameter for micelles to be a drug delivery system, because the small-sized micelles (<200 nm) can avoid the uptake of the reticuloendothelial system (RES) and/or renal excretion, meanwhile enhancing passive targeting for tumor tissue.[26−28] To study the properties of the copolymer micelles, both DLS and TEM measurements were carried out. As shown in Figure 1A1, DLS results reveal that the average hydrodynamic diameter of the H40-*star*-PEG/ALE micelles is about 16 nm with a PDI of 0.263. The morphologies of the micelles were observed by the TEM. As shown in Figure 1B1, these micelles form uniform spherical structure in aqueous solution, and the average diameter is 14 nm, which is accordance with the results of DLS measurement. All the data indicate the micelles are suitable for being the drug delivery devices.

CMC Measurement of H40-*star*-PEG/ALE. As we know, CMC is one of the most important parameters for micelle formation. For the CMC value of H40-*star*-PEG/ALE star copolymer in aqueous solution, it is estimated by UV−vis technique using the 1,6-diphenyl-1,3,5-hexatriene (DPH) as a probe. As shown in Figure 2A, when the concentration of star copolymer is below the CMC value, the absorbance intensity of DPH is close to zero. As soon as the hydrophobic probe is encapsulated into the H40-*star*-PEG/ALE micelles, the absorbance intensity of DPH strengthens exponentially with the concentration. The two different states can be reflected by two fitting lines in Figure 2A. The intersection of the horizontal line and the rapidly rising line forms the turning point, which is the CMC value of the H40-*star*-PEG/ALE copolymer (0.002 35 mg/mL). The detected low CMC value confirms the formation of the H40-*star*-PEG/ALE micelles with high stability in aqueous solution. Meanwhile, H40-*star*-PEG/ALE micelles can remain stable *in vivo* because of the low CMC value.

Stability of H40-*star*-PEG/ALE Micelles in PBS (pH = 7.4) Buffer. The enhanced stability of star copolymer micelles were evaluated in PBS (pH = 7.4) at different time intervals by DLS. As shown in Figure 2B, the size variation of the micelles is very slight in 96 h, and the average diameter is around 16 nm. Therefore, the stability of prepared micelles offers the possibility for introduction to the body with the potential of therapeutics delivery.

***In Vitro* Cytotoxicity of H40-*star*-PEG/ALE Micelles.** The cytotoxicity of H40-*star*-PEG/ALE micelles was assessed *in vitro* by MTT assay against the NIH/3T3 normal cells. The MTT test is based on the capacity of a mitochondrial dehydrogenation enzyme in living cells to cleave the tetrazolium rings of the pale yellow MTT and form formazan crystals with dark-blue color.[29] Figure 3A gives the relative cell viability after 48 h incubation with the H40-*star*-PEG/ALE copolymers with a series of concentrations. The result illustrates that no distinct cytotoxicity against NIH/3T3 cells is observed even the concentration of copolymers is up to 1 mg/mL. Accordingly, these copolymers show low cytotoxicity to NIH/3T3 normal cells.

Hemolysis Experiment. The biocompatibility of H40-*star*-PEG/ALE copolymer under physiological conditions was

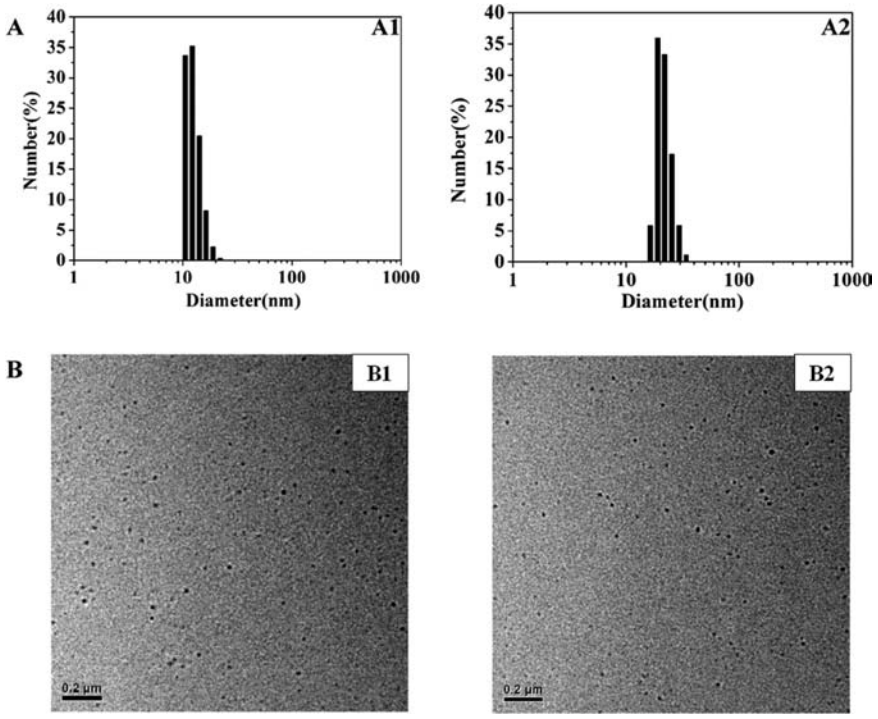


Figure 1. DLS and TEM measurements of the H40-*star*-PEG/ALE micelles and DOX-loaded micelles. (A) Size distribution of H40-*star*-PEG/ALE micelles by DLS: (A1) H40-*star*-PEG/ALE micelles and (A2) DOX-loaded micelles. (B) TEM images of the micelles: (B1) H40-*star*-PEG/ALE micelles and (B2) DOX-loaded micelles.

dx.doi.org/10.1021/bc3003088 | *Bioconjugate Chem.* 2012, 23, 1915−1924

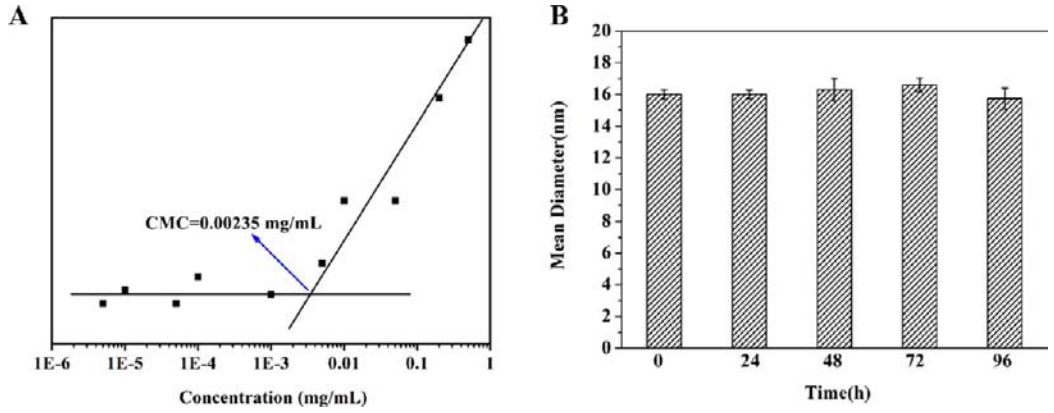


Figure 2. (A) Relationship of the absorbance intensity of DPH as a function of the star copolymer concentration of H40-*star*-PEG/ALE in aqueous solution at room temperature. (B) Size of H40-*star*-PEG/ALE micelles at different time intervals in PBS (pH = 7.4) determined by DLS. Data are presented as the average ± standard deviation (n = 3).

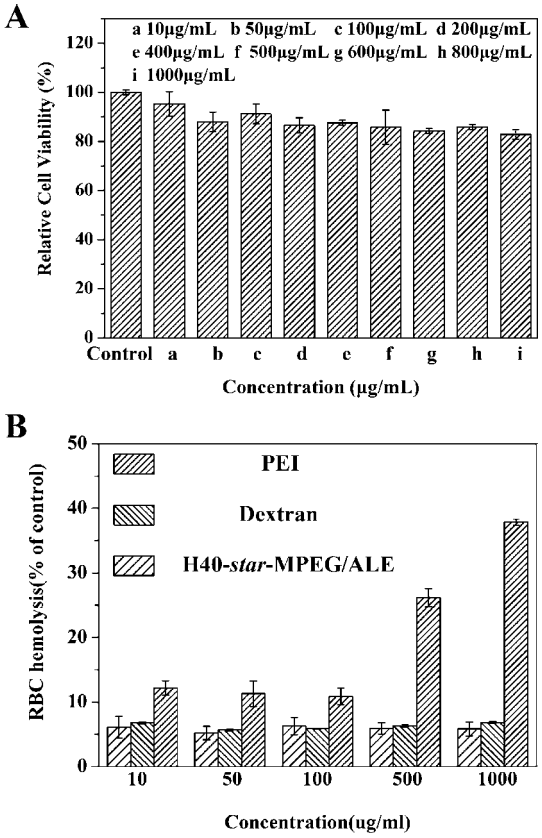


Figure 3. (A) Cell viability of H40-*star*-PEG/ALE copolymer against NIH/3T3 normal cells after cultured for 48 h with series of concentrations. NIH/3T3 cells incubated without polymers were used as the control. (B) Hemolysis assay of H40-*star*-PEG/ALE copolymer compared with PEI, and Dextran with 1 h. Triton X-100 (1% v/v) was used as a 100% hemolytic value. Data are presented as the average ± standard deviation (n = 3).

estimated via *in vitro* red blood cell hemolysis assay. We evaluated the red blood cells hemolysis via testing the amount of the hemoglobin released from RBC in the supernatant. Dextran and PEI were used as reference controls, and 1% v/v Triton X-100 was used as a 100% hemolysis value. As shown in Figure 3B, H40-*star*-PEG/ALE shows comparable hemoglobin release to dextran, which is significantly lower than the corresponding incubation time of PEI, even the concentrations up to 1 mg/mL. As incubated for 1 h, PEI causes approximately 8 times higher RBC hemolysis than the copolymers. The study exhibits inappreciable hemolytic activity of H40-*star*-PEG/ALE copolymer. Therefore, it is indicated that H40-*star*-PEG/ALE copolymers exhibit low cytotoxicity.

Drug Loading and Release. Hyperbranched polymers are promising candidates for drug delivery systems because of their intrinsic features, such as branching architecture, a large number of terminal functional groups, and good solubility. The abundantly branched architecture can induce the copolymer to form nanocavities, the condition of which determines their encapsulating and/or solubilizing profiles.[30] It is well-known that DOX is diffusely used to treat different types of malignant tumors in the clinic. Here, DOX was employed as a model anticancer drug to assess the drug loading capacity of H40-*star*-PEG/ALE micelles and release features. UV−vis spectroscopy was utilized to measure the drug-loading content and drug-loading efficiency of DOX in polymeric micelles. Based on the standard curve of the free DOX at 500 nm, the drug-loading efficiency was measured to be 68.8%. The theoretical drug-loading content was set to 10% and the final drug-loading content of H40-*star*-PEG/ALE micelles was 5%. The size and morphology of the DOX-loaded micelles in aqueous solution were measured by DLS and TEM techniques. As shown in Figure 1A2, the DOX-loaded micelles have an average size of 19 nm with a PDI of 0.382. The characteristic TEM picture in Figure 1B2 shows that the DOX-loaded micelles form spherical micelles of about 17 nm. It is noted that DOX-loaded H40-*star*-PEG/ALE micelles reveal a slight increase in the average size, compared to the blank micelles.

The *in vitro* release profile of DOX-loaded micelles was evaluated via dialysis in two buffer solutions with pH = 7.4 and 5.0 at 37 °C. Meanwhile, the feasibility and stability of H40-*star*-PEG/ALE micelles as a drug delivery system were investigated. As plotted in Figure 4, DOX is released quickly from the micelles in the first stage, and then released over a prolonged time. It is clearly found that the drug release from H40-*star*-PEG/ALE micelles at pH = 5.0 is much quicker than the release at pH = 7.4. At physiological conditions (pH = 7.4 and 37 °C), the cumulative release of DOX is low, less than 25% in 90 h. However, the amount of DOX released is more than 40% in a slightly acidic solution (pH = 5.0 and 37 °C) in 20 h. The fast release of DOX in acidic surroundings could be attributed to the protonation of the amino group of DOX and

dx.doi.org/10.1021/bc3003088 | *Bioconjugate Chem.* 2012, 23, 1915−1924

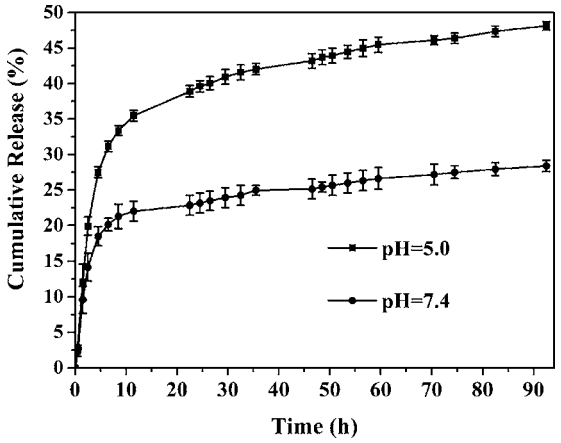


Figure 4. *In vitro* release profiles of DOX from the DOX-loaded H40-*star*-PEG/ALE micelles under neutral (pH = 7.4) and acidic (pH = 5.0) conditions at 37 °C. Data are presented as the average ± standard deviation (n = 3).

faster degradation of the micelle core at lower pH.[22,29] Hence, owing to the pH-dependent release feature, the bone-targeting micelles will be a promising drug delivery system to inhibit carcinoma cells in the bone resorption sites.

Cell Uptake. The cellular uptake of DOX-loaded H40-*star*-PEG/ALE micelles was evaluated by flow cytometry at the cellular level. DOX-loaded micelles with DOX concentration (5 μg/mL) were added to culture medium, and then the HN-6 cells were cultured at 37 °C for predetermined time intervals. In this experiment, DOX itself was used as a fluorescence marker.[31,32] The internalized DOX-loaded micelles were quantified by the fluorescence intensity. From Figure 5A, we can see that the fluorescence is found within 5 min and the fluorescence intensity increases with increasing time. When the incubation time increases to 180 min, the relative geometrical mean fluorescence intensity of HN-6 cells increases from 273 to 744 as shown in Figure 5B. The curves show that the gradually increasing intensity of fluorescence with increasing incubation time can be attributed to the cellular uptake of DOX-loaded micelles. We speculate that the efficient intracellular uptake of H40-*star*-PEG/ALE micelles can be attributed to the global molecular structure as well as the small hydrodynamic volume.[33]

CLSM was used to further evaluate the cellular uptake and intracellular release behavior of the DOX-loaded micelles by the HN-6 cells. The cells were cultured with DOX-loaded micelles (5 μg/mL of DOX concentration) at 37 °C for 5 min, 15 min, 0.5 h, and 3 h, respectively. The nucleus was stained with Hoechst 33342. Then, the pretreated cells were observed by CLSM. As shown in Figure 6, the red DOX fluorescence is observed principally in the cytoplasm of the cells when the cells are incubated with the DOX-loaded micelles for 5 min. The intensity of DOX fluorescence gradually increases when the incubation time increases from 5 min to 1 h. After incubation for 3 h, the red fluorescence is almost localized completely in the nucleus of the cells. This result indicates that DOX-loaded micelles may be taken up efficiently and then DOX is released from the micelles, thereby reaching the nucleus.[34,35] These results are in agreement with the flow cytometric analysis. The properties of H40-*star*-PEG/ALE micelles are important for use as an ideal drug delivery system.

***In Vitro* Anticancer Assay.** The tumor cell proliferation inhibitions of DOX-loaded H40-*star*-PEG/ALE micelles and free DOX were determined by MTT assay against HN-6 cancer cells *in vitro*. The HN-6 cells were incubated with DOX-loaded micelles and free DOX for 48 h at different DOX concentration from 0.02 to 0.6 μg/mL. The results of HN-6 cell relative viability are shown in Figure 7A. The loaded DOX concentration required for 50% cellular growth inhibition (IC_{50}) is about 0.1 μg/mL according to Figure 7A. The result reveals that DOX-loaded H40-*star*-PEG/ALE micelles can efficiently get into the carcinoma cells to produce the desired pharmacological effect. On the other hand, the IC_{50} of free DOX is about 0.05 μg/mL, which shows a better anticancer effect compared with DOX-loaded micelles. It is reported that the free DOX is more potent than the same dose of DOX-loaded micelles in cancer cell proliferation inhibition.[36] The lower cancer cell proliferation inhibition of DOX-loaded micelles may be due to the time-consuming DOX release from micelles and the delayed nuclear uptake in HN-6 cells. This phenomenon is in accord with the cellular uptake and DOX release assay by CLSM.

HA Binding of H40-*star*-PEG/ALE. For the metastasized or invaded bone tissue, the main constituent of skeleton HA was exposed in lysis sites. It is well-documented that the bisphosphonates exhibit a strong affinity to the bone mineral HA.[2,19,37−40] In particular, ALE has a strong affinity to bone

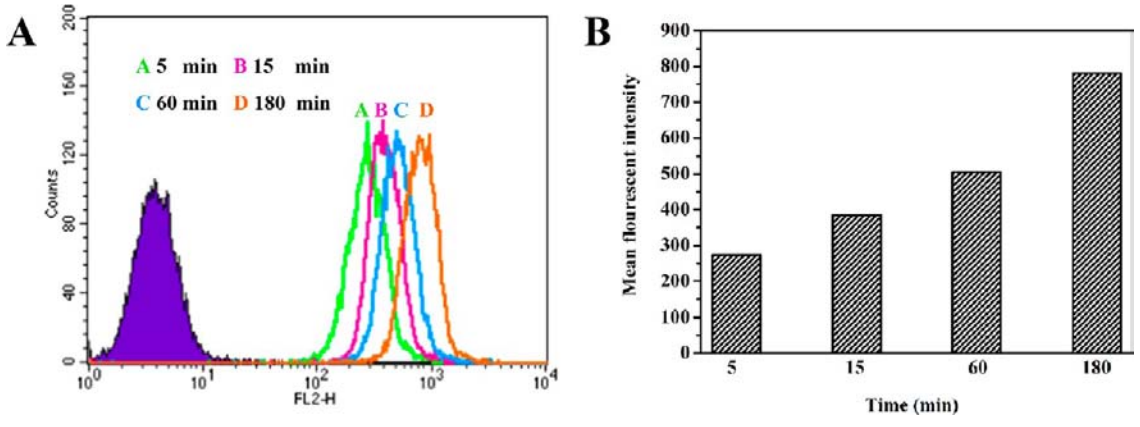


Figure 5. (A) Flow cytometry histogram profiles of HN-6 cells incubated with the DOX-loaded H40-*star*-PEG/ALE micelles at 37 °C for different time intervals. (B) Cellular uptake of the DOX-loaded H40-*star*-PEG/ALE micelles by HN-6 cells versus the time by flow cytometry analysis.

dx.doi.org/10.1021/bc3003088 | *Bioconjugate Chem.* 2012, 23, 1915−1924

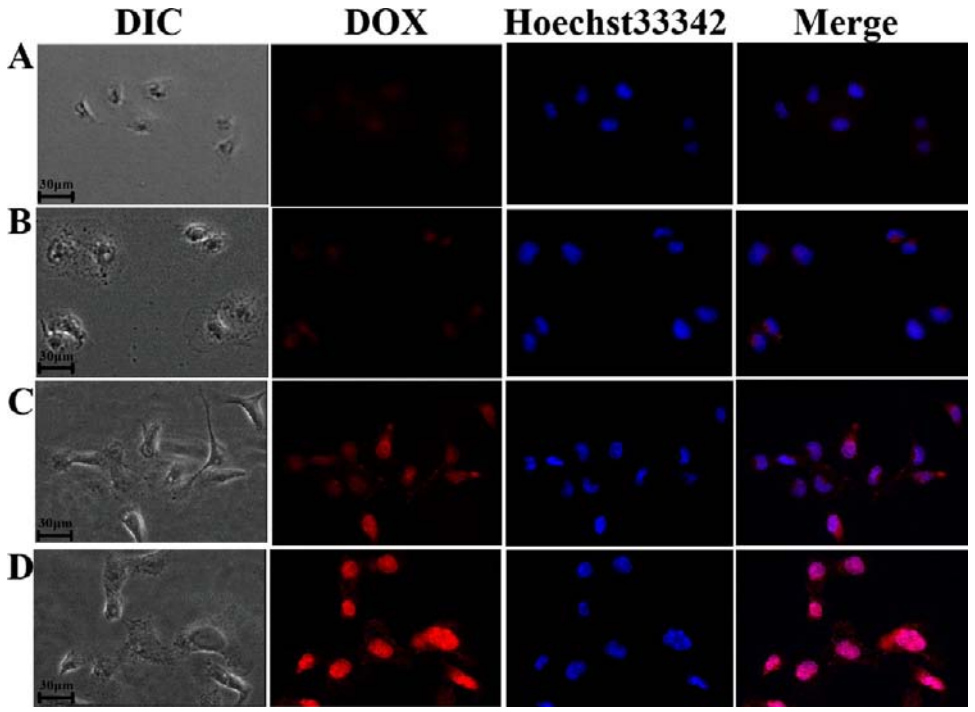


Figure 6. CLSM images of HN-6 cells incubated with DOX-loaded H40-*star*-PEG/ALE micelles for (A) 5 min, (B) 15 min, (C) 1 h, and (D) 3 h at 37 °C. (Red: DOX, Blue: Hoechst 33342.)

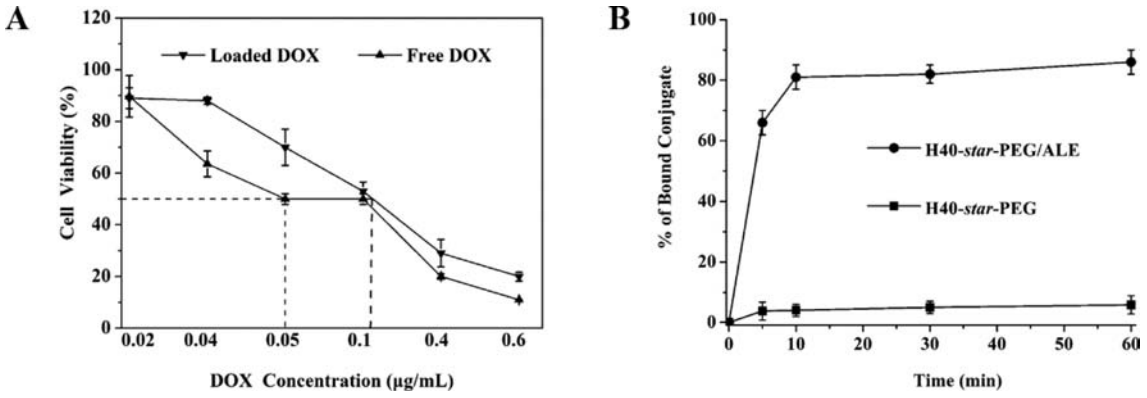


Figure 7. (A) Cell viability of HN-6 cells against DOX-loaded H40-*star*-PEG/ALE micelles and free DOX after incubating for 48 h with different DOX concentration. Data are presented as the average ± standard deviation (n = 6). (B) Binding kinetics of H40-*star*-PEG/ALE copolymer to the bone mineral HA. The copolymer was incubated with the bone mineral HA for 5, 10, 30, and 60 min. Data are presented as the average ± standard deviation (n = 3).

tissue, because of its phosphonate groups and hydroxyl group.[16,36] To estimate the binding capacity of ALE conjugated to H40-*star*-PEG micelles to bone tissue, a HA binding assay was carried out *in vitro*, using the DOX as a fluorescence marker. The binding kinetics of the DOX-loaded H40-*star*-PEG/ALE micelles and DOX-loaded H40-*star*-PEG micelles to HA is shown in Figure 7B. After 5 min of incubation, approximately 70% of H40-*star*-PEG/ALE micelles is bound to HA and reached the plateau within 10 min. In contrast, the nontargeted H40-*star*-PEG micelles hardly show any binding. This assay obviously proves the targeted capability of the H40-*star*-PEG/ALE micelles to bone. The results indicate that the H40-*star*-PEG/ALE micelles can precisely and quickly target the bone tissue lysis sites.

■ CONCLUSIONS

A well-defined ALE-conjugated amphiphilic hyperbranched copolymer H40-*star*-PEG/ALE was successfully prepared and characterized. The MTT experiment and hemolysis assay indicated that the H40-*star*-PEG/ALE had excellent biocompatibility. Flow cytometry and CLSM assay proved the efficient cell uptake of DOX-loaded H40-*star*-PEG/ALE micelles. *In vitro* proliferation inhibition of HN-6 cancer cells revealed that DOX-loaded H40-*star*-PEG/ALE micelles could kill cancer cells efficiently. Due to the strong affinity between ALE and HA, H40-*star*-PEG/ALE micelles can bind to HA in a short time. Therefore, this ALE-conjugated amphiphilic hyperbranched copolymer would serve as a potential bone-targeting drug delivery system.

dx.doi.org/10.1021/bc3003088 | *Bioconjugate Chem.* 2012, 23, 1915−1924

■ ASSOCIATED CONTENT

Supporting Information

Supplementary figures including the structural formula of H40, ^{1}H NMR, ^{31}P NMR, ^{13}C NMR, and FTIR spectra of intermediates, H40-*star*-PEG/ALE copolymer. This material is available free of charge via the Internet at http://pubs.acs.org.

■ AUTHOR INFORMATION

Corresponding Author

*E-mail: flguo1967@yahoo.com.cn (F. G.); xyzhu@sjtu.edu.cn (X. Z.). Tel.: +86-21-34205699; Fax: +86-21-34205722.

Notes

The authors declare no competing financial interest.

#These authors are joint first authors.

■ ACKNOWLEDGMENTS

This study was financially supported by Provincial Natural Science Foundation of Heilongjiang (D200848), the First Affiliated Hospital of Harbin Medical University Science Research Funds (2012B011), Provincial Youth Science Funds of Heilongjiang (QC2011C037), the First Affiliated Hospital of Harbin Medical University Science Research Funds (2011BS003), the National Natural Science Foundation of China (81272466), and China National Funds for Distinguished Young Scientists (21025417).

■ REFERENCES

(1) Salerno, M., Cenni, E., Fotia1, C., Avnet, S., Granchi, D., Castelli, F., Micieli, D., Pignatello, R., Capulli, M., Rucci, N., Angelucci, A., Del Fattore, A., Teti, A., Zini, N., Giunti, A., and Baldini, N. (2010) Bone-targeted doxorubicin-loaded nanoparticles as a tool for the treatment of skeletal metastases. *Curr. Cancer Drug Targets 10*, 649−659.

(2) Miller, K., Eldar-Boock, A., Polyak, D., Segal, E., Benayoun, L., Shaked, Y., and Satchi-Fainaro, R. (2011) Antiangiogenic antitumor activity of HPMA copolymer paclitaxel alendronate conjugate on breast cancer bone metastasis mouse model. *Mol. Pharm. 8*, 1052−1062.

(3) Guise, T. A. (2008) Antitumor effects of bisphosphonates: promising preclinical evidence. *Cancer Treatment Rev. 34*, S19−S24.

(4) Colleoni, M., O'Neill, A., Goldhirsch, A., Gelber, R. D., Bonetti, M., Thurlimann, B., Price, K. N., Castiglione-Gertsch, M., Coates, A. S., Lindtner, J., Collins, J., Senn, H. J., Cavalli, F., Forbes, J., Gudgeon, A., Simoncini, E., Cortes-Funes, H., Veronesi, A., Fey, M., and Rudenstam, C. M. (2000) Identifying breast cancer patients at high risk for bone metastases. *J. Clin. Oncol. 18*, 3925−3935.

(5) Segal, E., Pan, H., Benayoun, L., Kopečková, P., Shaked, Y., Kopeček, J., and Satchi-Fainaro, R. (2011) Enhanced anti-tumor activity and safety profile of targeted nano-scaled HPMA copolymer-alendronate-TNP-470 conjugate in the treatment of bone malignances. *Biomaterials 32*, 4450−4463.

(6) DuBois, S., and Demetri, G. (2007) Markers of angiogenesis and clinical features in patients with sarcoma. *Cancer 109*, 813−819.

(7) Shea, J. E., and Miller, S. C. (2005) Skeletal function and structure: implications for tissue-targeted therapeutics. *Adv. Drug Delivery Rev. 57*, 945−957.

(8) Richardson, D. S., and Johnson, S. A. (1977) Anthracyclines in hematology: preclinical studies, toxicity and delivery systems. *Blood Rev. 11*, 201−223.

(9) Chen, S., Zhang, X. Z., Cheng, S. X., Zhuo, R. X., and Gu, Z. W. (2008) Functionalized amphiphilic hyperbranched polymers for targeted drug delivery. *Biomacromolecules 9*, 2578−2585.

(10) Maedaa, H., Wua, J., Sawaa, T., Matsumurab, Y., and Horic, K. (2000) Tumor vascular permeability and the EPR effect in macromolecular therapeutics: a review. *J. Controlled Release 65*, 271−284.

(11) Miller, K., Erez, R., Segal, E., Shabat, D., and Satchi-Fainaro, R. (2009) Targeting bone metastases with a bispecific anticancer and antiangiogenic polymer-alendronate-taxane conjugate. *Angew. Chem., Int. Ed. 48*, 2949−2954.

(12) Brigger, I., Dubernet, C., and Couvreur, P. (2002) Nanoparticles in cancer therapy and diagnosis. *Adv. Drug Delivery Rev. 54*, 631−651.

(13) Prabaharan, M., Grailer, J. J., Pilla, S., Steeber, D. A., and Gong, S. Q. (2009) Folate-conjugated amphiphilic hyperbranched block copolymers based on Boltorn® H40, poly(L-lactide) and poly-(ethylene glycol) for tumor-targeted drug delivery. *Biomaterials 30*, 3009−3019.

(14) Yang, X. Q., Grailer, J., Pilla, S., Steeber, D. A., and Gong, S. Q. (2010) Tumor-targeting, pH-responsive, and stable unimolecular micelles as drug nanocarriers for targeted cancer therapy. *Bioconjugate Chem. 21*, 496−504.

(15) Choi, S. W., and Kim, J. H. (2007) Design of surface-modified poly(D,L-lactide-co-glycolide) nanoparticles for targeted drug delivery to bone. *J. Controlled Release 122*, 24−30.

(16) Yewle, J. N., Puleo, D. A., and Bachas, L. G. (2011) Enhanced affinity bifunctional bisphosphonates for targeted delivery of therapeutic agents to bone. *Bioconjugate Chem. 22*, 2496−2506.

(17) Wang, D., Miller, S., Sima, M., Kopeckova, P., and Kopecek, J. (2003) Synthesis and evaluation of water-soluble polymeric bone-targeted drug delivery systems. *Bioconjugate Chem. 14*, 853−859.

(18) Uludag, H. (2002) Bisphosphonates as a foundation of drug delivery to bone. *Curr. Pharm. Design 8*, 1929−1944.

(19) Clementi, C., Miller, K., Mero, A., Satchi-Fainaro, R., and Pasut, G. (2011) Dendritic poly(ethylene glycol) bearing paclitaxel and alendronate for targeting bone neoplasms. *Mol. Pharm. 8*, 1063−1072.

(20) Pignatello, R., Cenni, E., Micieli, D., Fotia, C., Salerno, M., Granchi, D., Avnet, S., Sarpietro, M. G., Castelli, F., and Baldini, N. (2009) A novel biomaterial for osteotropc drug nanocarriers: synthesis and biocompatiblity evaluation of a PLGA-ALE conjugate. *Nanomedicine 4*, 161−175.

(21) Tian, H. Y., Deng, C., Lin, H., Sun, J. R., Deng, M. X., Chen, X. S., and Jing, X. B. (2005) Biodegradable cationic PEG-PEI-PBLG hyperbranched block copolymer: synthesis and micelle characterization. *Biomaterials 26*, 4209−4217.

(22) Xiao, Y. L., Hong, H., Javadi, A., Engle, J. W., Xu, W. J., Yang, Y., Zhang, Y., Barnhart, T. E., Cai, W. B., and Gong, S. Q. (2012) Multifunctional unimolecular micelles for cancer-targeted drug delivery and positron emission tomography imaging. *Biomaterials 33*, 3071−3082.

(23) Shi, Z. Q., Zhou, Y. F., and Yan, D. Y. (2008) Facile fabrication of pH-responsive and size-controllable polymer vesicles from a commercially available hyperbranched polyester. *Macromol. Rapid Commun. 29*, 412−418.

(24) Jin, Y., Song, L., Su, Y., Zhu, L. J., Pang, Y., Qiu, F., Tong, G. S., Yan, D. Y., Zhu, B. S., and Zhu, X. Y. (2011) Oxime linkage: a robust tool for the design of pH-sensitive polymeric drug carriers. *Biomacromolecules 12*, 3460−3468.

(25) Li, G. L., Liu, J. Y., Pang, Y., Wang, R. B., Mao, L. M., Yan, D. Y., Zhu, X. Y., and Sun, J. (2011) Polymeric micelles with water-insoluble drug as hydrophobic moiety for drug delivery. *Biomacromolecules 12*, 2016−2026.

(26) Claesson, H., Malmström, E., Johansson, M., and Hult, A. (2002) Hyperbranched aliphatic polyesters and reactive diluents in thermally cured coil coatings. *Polymer 43*, 3511−3518.

(27) Schmalenberg, K. E., Frauchiger, L., Nikkhouy-Albers, L., and Uhrich, K. E. (2001) Cytotoxicity of a unimolecular polymeric micelle and its degradation products. *Biomacromolecules 2*, 851−855.

(28) Liu, J. Y., Pang, Y., Huang, W., Huang, X. H., Meng, L. L., Zhu, X. Y., Zhou, Y. F., and Yan, D. Y. (2011) Bioreducible micelles self-assembled from amphiphilic hyperbranched multiarm copolymer for glutathione-mediated intracellular drug delivery. *Biomacromolecules 12*, 1567−1577.

(29) Wang, D. L., Su, Y., Jin, C. Y., Zhu, B. S., Pang, Y., Zhu, L. J., Liu, J. Y., Tu, C. L., Yan, D. Y., and Zhu, X. Y. (2011) Supramolecular copolymer micelles based on the complementary multiple hydrogen

bonds of nucleobases for drug delivery. *Biomacromolecules 12*, 1370−1379.
(30) Pang, Y., Liu, J. Y., Su, Y., Wu, J. L., Zhu, L. J., Zhu, X. Y., Yan, D. Y., and Zhu, B. S. (2011) Design and synthesis of thermo-responsive hyperbranched poly(amine-ester)s as acid-sensitive drug carriers. *Polym. Chem. 2*, 1661−1670.
(31) Bae, Y., Fukushima, S., Harada, A., and Kataoka, K. (2003) Design of environment-sensitive supramolecular assemblies for intracellular drug delivery: polymeric micelles that are responsive to intracellular pH change. *Angew. Chem., Int. Ed. 42*, 4640−4643.
(32) Wartenberg, M., Hescheler, J., Acker, H., Diedershagen, H., and Sauer, H. (1998) Doxorubicin distribution in multicellular prostate cancer spheroids evaluated by confocal laser scanning microscopy and the "optical probe technique. *Cytometry 31*, 137−145.
(33) Pang, Y., Liu, J. Y., Wu, J. L., Li, G. L., Wang, R. B., Su, Y., He, P., Zhu, X. Y., Yan, D. Y., and Zhu, B. S. (2010) Synthesis, characterization, and *in vitro* evaluation of long-chain hyperbranched poly(ethylene glycol) as drug carrier. *Bioconjugate Chem. 21*, 2093−2102.
(34) Liu, J. Y., Huang, W., Pang, Y., Zhu, X. Y., Zhou, Y. F., and Yan, D. Y. (2010) Hyperbranched polyphosphates for drug delivery application: design, synthesis, and *in vitro* evaluation. *Biomacromolecules 11*, 1564−1570.
(35) Pang, Y., Zhu, Q., Liu, J. Y., Wu, J. L., Wang, R. B., Chen, S. Y., Zhu, X. Y., Yan, D. Y., Huang, W., and Zhu, B. S. (2010) Design and synthesis of cationic drug carriers based on hyperbranched poly-(amine-ester)s. *Biomacromolecules 11*, 575−582.
(36) Zhang, W. L., Li, Y. L., Liu, L. X., Sun, Q. Q., Shuai, X. T., Zhu, W., and Chen, Y. M. (2010) Amphiphilic toothbrushlike copolymers based on poly(ethylene glycol) and poly(ε-caprolactone) as drug carriers with enhanced properties. *Biomacromolecules 11*, 1331−1338.
(37) Hengst, V., Oussoren, C., Kissel, T., and Storm, G. (2007) Bone targeting potential of bisphosphonate-targeted liposomes: preparation, characterization and hydroxyapatite binding in vitro. *Int. J. Pharm. 331*, 224−227.
(38) Özcan, İ., Bouchemal, K., Segura-Sánchez, F., Özer, Ö., Güneri, T., and Ponchel, G. (2011) Synthesis and characterization of surface-modified PBLG nanoparticles for bone targeting: *in vitro* and *in vivo* evaluations. *J. Pharm. Sci. 100*, 4877−4887.
(39) Uludag, H., Kousiniors, N., Gao, T. J., and Kantoci, D. (2000) Bisphosphonate conjugation to proteins as a means to impart bone affinity. *Biotechnol. Prog. 16*, 258−267.
(40) de Rosales, R. T. M., Finucane, C., Mather, S. J., and Blower, P. J. (2009) Bifunctional bisphosphonate complexes for the diagnosis and therapy of bone metastases. *Chem. Commun. 32*, 4847−4849.

Bioconjugate Chemistry

Article

pubs.acs.org/bc

Biodegradable and Nontoxic Nanogels as Nonviral Gene Delivery Systems

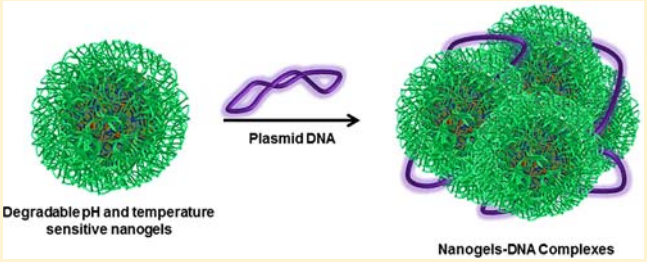
Rajesh Sunasee,[†] Phanphen Wattanaarsakit,[§] Marya Ahmed,[†] Farahnaz Begum Lollmahomed,[†] and Ravin Narain*,[†]

[†]Department of Chemical and Materials Engineering, University of Alberta, Edmonton, AB, T6G 2G6, Canada

[§]Department of Pharmaceutics and Industrial Pharmacy, Faculty of Pharmaceutical Sciences, Chulalongkorn University, Phyathai Road, Pathumwan, Bangkok, Thailand

Supporting Information

ABSTRACT: The development of polymeric systems with tailored properties as nonviral gene carriers continues to be a challenging and exciting field of research. We report here the synthesis and characterization of biodegradable, temperature- and pH-sensitive carbohydrate-based cationic nanogels as effective gene delivery carriers to Hep G2 cells. The temperature-sensitive property of the nanogels allows their facile complexation of DNA, while the pH-sensitive property allows the degradation of nanogels followed by the release of plasmid in the endosome. The nanogels are synthesized via reversible addition−fragmentation chain transfer polymerization (RAFT) technique and are evaluated for their DNA condensation efficacy. The gene delivery efficacies of these nanogels are subsequently studied and it is found that these cationic glyconanogels can serve as potent gene delivery vectors in hepatocytes. It is found that the gene delivery efficacies of this system are similar to that of branched poly(ethyleneimine), which is used as a positive control. Moreover, these nanogels show desirable properties for systemic applications including low toxicity and degradation in acidic environment.



INTRODUCTION

Transfer of genetic material into cells (both *in vitro* and *in vivo*) is crucial for studying gene function as well as conducting gene therapy. The past decade has seen significant progress in this area in order to establish the most desirable method for safe, effective, and target-specific gene delivery.[1,2] A variety of synthetic materials including cationic polymers, liposomes, and peptides have been investigated for their gene delivery potential.[1−9] Colloidal nanogel carriers have recently gained a lot of interest as novel therapeutic delivery agents in living cells and tissues. These cross-linked polymeric networks provide a core−shell structure, suitable for chemical engineering and for the encapsulation of materials in the core.[10−12] The use of nanogels as delivery carriers is desirable, due to their degradable nature, facile encapsulation of materials in the core, release of biomolecules upon an external stimuli, and low toxicity.[10−12] However, most of the studies focus on the loading of small molecules in nanogels, followed by their release in living cells, such as proteins, peptides, oligonucleotides, and siRNAs.[13−19] It has been shown that chemical cross-linking of cationic particles enables formation of polyplexes when mixed with nucleic acids to increase their stability and gene expression under physiological conditions.[19] Hence, cationic nanogels are synthesized and are studied for their gene expression. It has also been reported that encapsulation of large DNA molecules in nanogels leads to significant aggregation; in contrast, siRNA loading is successfully achieved using nanogel systems. However, these nanogels were not tested for their gene delivery efficacies *in vitro*.[20] The size of nanomaterials plays a critical role in their biological applications.[3,4] PEI-based nanogels of varying sizes have been prepared and studied for their gene expression. It is reported that transfection efficacies of these nanogels are dependent on their sizes, and nanogels ranging from 70 to 90 nm show optimum gene expression.[21,22] Recently, shell cross-linked kendel-like particles of 10 nm have been prepared to mimic histone-like properties. These nanoparticles containing hydrophobic core and cationic shell are found to efficiently deliver DNA and peptide nucleic acid (PNA) *in vitro*.[23] A variety of carbohydrate-based nanogels are synthesized and studied as gene or drug delivery carriers.[11,14,18,24,25] Carbohydrates are important structural and functional units of cell membranes. It has also been shown that incorporation of carbohydrate moieties in gene or drug delivery systems increases their cell viability and serum compatibility and decreases their toxicity.[7,8,11] Due to the limited control over the synthesis of polysaccharides-based nanogels, the core cross-linked particles are usually prepared by cross-linking the polysaccharide chains in the presence of DNA.[24]

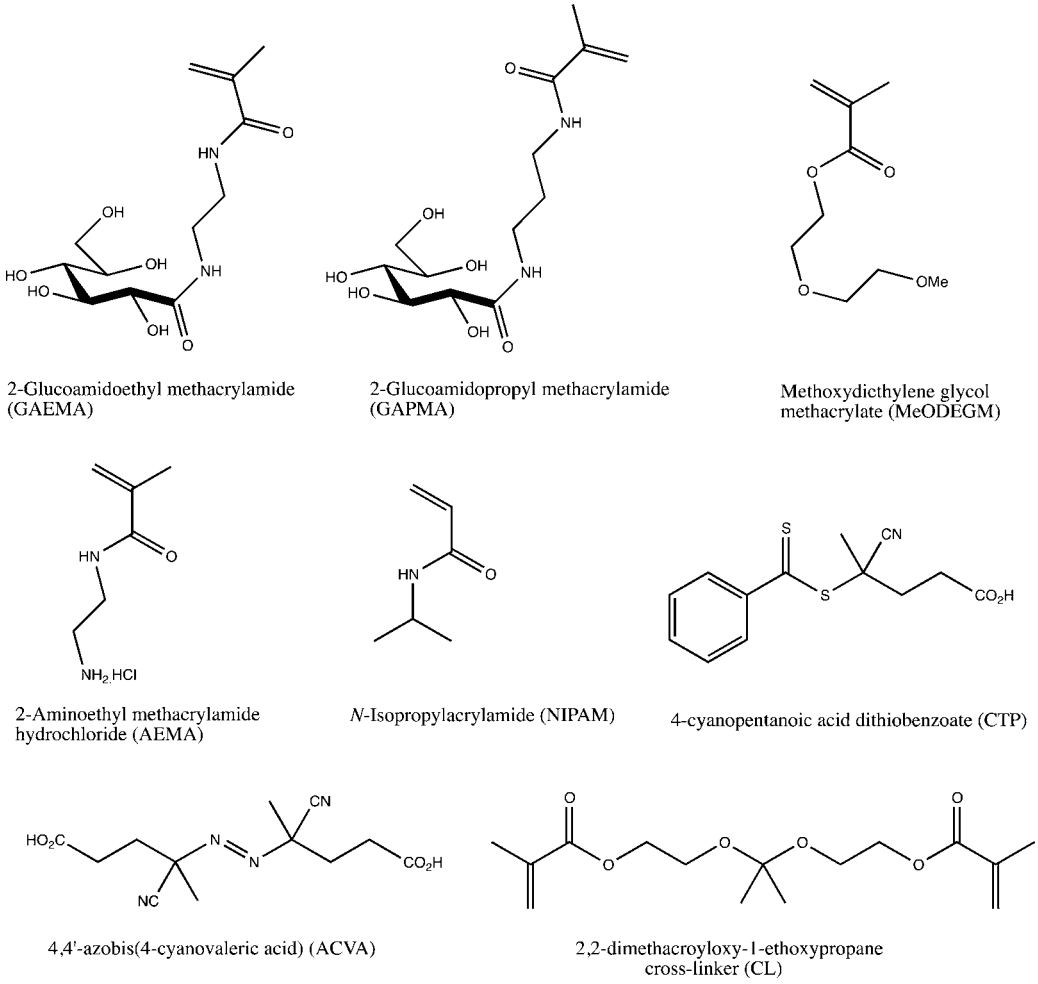
To obtain better control of the surface chemistry, size, and hence the gene expression of nanogel-based vectors, cationic

Received: June 14, 2012
Revised: August 10, 2012
Published: August 29, 2012

ACS Publications © 2012 American Chemical Society

dx.doi.org/10.1021/bc300314u | *Bioconjugate Chem.* 2012, 23, 1925−1933

Scheme 1. Chemical Structures of Monomers (GAEMA, GAPMA, MeODEGM, AEMA and NIPAM), Cross-Linker (CL), Chain Transfer Agent (CTP), and Initiator (ACVA) Used in This Study



nanogels with biocompatible moieties can be synthesized via the reversible addition−fragmentation chain transfer polymerization (RAFT) approach.[15,26] Earlier reports have shown the synthesis and use of a variety of cationic glycopolymers including diblock polymer, statistical polymers, and hyperbranched polymers for gene delivery applications.[7,8,27] Some of these polymers are shown to possess high gene expression along with low toxicity, but they are nondegradable vectors, which is an ideal requirement of a delivery vector for systemic applications. Herein, we report the synthesis and characterization of thermosensitive biodegradable cationic nanogels, as well as the study of their gene expression in Hep G2 cells. The small library of nanogels was characterized by dynamic light scattering (DLS), transmission electron microscopy (TEM), and scanning electron microscopy (SEM). The rational design of the nanogel systems was guided in part from our recently published work on the synthesis of degradable thermoresponsive poly(2-methacryloyloxyethyl phosphorylcholine), poly(MPC)-based nanogels for protein encapsulation and controlled release.[15] In this current system, we opt to have a cationic component in the core and a carbohydrate component on the surface of the nanogel in order to improve the biocompatibility and gene delivery efficacies of the nanogel-gene delivery system. The cationic temperature-sensitive core was employed to interact with anionic plasmid DNA at low temperatures (hydrophilic state), followed by the increase in temperature, which allowed the collapse of nanogels and entrapment of DNA between cationic cores of nanogels. The pH sensitive property of nanogels further allows the degradation of nanogels at acidic pH (endosomal pH), hence allowing the release of complexed DNA inside the cells. The transfection efficacies of nanogels are studied in Hep G2 cells, using β-galactosidase assay. The cellular uptake of selected nanogel samples are studied using Cy-3′-labeled plasmid. The toxicity post-transfection is obtained using MTT assay.

■ EXPERIMENTAL PROCEDURES

Materials and Methods. All chemicals were purchased from Sigma Aldrich (Canada) unless otherwise noted. Commercial grade reagents and solvents were used without further purification except as indicated below. Methoxydiethylene glycol methacrylate (MeODEGM, Scheme 1) was passed through a short pad of silica prior to use and *N*-isopropylacrylamide (NIPAM) was recrystallized three times from hexane. 3-Gluconamidopropyl methacrylamide (GAPMA) 2-gluconamidoethyl methacrylamide (GAEMA), 2-aminoethyl methacrylamide hydrochloride (AEMA), 2,2-dimethacroyloxy-1-ethoxypropane, as cross-linker, and 4-cyanopentanoic acid dithiobenzoate (CTP) were synthesized as described according to previous reports.[28−32] 2-Propanol, HPLC-grade water, acetone, *N,N*′-dimethylformamide (DMF), dioxane, and hexane were purchased from Caledon Laboratories (Canada).

dx.doi.org/10.1021/bc300314u | *Bioconjugate Chem.* 2012, 23, 1925−1933

Deionized water was obtained from in-house purification system. *O*-Nitrophenyl β-D-galactopyranoside (ONPG) (enzymatic), ethidium bromide, β-mercaptoethanol, MTT assay kit to determine cell viability, and 3-[(3-cholamidopropyl)-dimethylammonio]-1-propanesulfonate (CHAPS) were purchased from Sigma Aldrich. Branched PEI (M_w = 25 kDa) was purchased from Polysciences Inc. Cell Culture media Dulbecco's Modified Eagle Medium (DMEM; high glucose with L-glutamine and sodium pyruvate), penicillin (10 000 U/mL), streptomycin (10 mg/mL), 0.25% trypsin-EDTA, Dulbecco's modified Phosphate Buffer Saline (DPBS), and Fetal Bovine Serum (FBS) were from Invitrogen. Micro BCA assay kit was obtained from Fisher Scientific. Gwiz β-galactosidase plasmid was purchased from Sigma Aldrich. Cy-3′-DNA labeling kit was from Mirus Bio.

Synthesis of poly(GAPMA) and poly(GAEMA) macroCTA by RAFT Polymerization. GAPMA macroCTA was synthesized as previously reported.[31] A typical protocol is as follows: The polymerization was achieved at 70 °C, employing ACVA as the radical initiator and CTP as the RAFT CTA. In a 10mL Schlenk tube, GAPMA (1 g, 3.12 mmol) was dissolved in double-distilled deionized water (5 mL) before the addition of 1 mL of DMF solution containing CTP (9 mg, 0. 032 mmol) and ACVA (4 mg, 0.0097 mmol). The solution was degassed by purging nitrogen for 30 min and then placed with stirring in a preheated oil bath at a temperature of 70 °C. After 6 h, the reaction flask was placed in liquid nitrogen to stop the polymerization. The poly(GAPMA) homopolymer was precipitated out in acetone and the residual GAPMA monomer was removed by washing with an excess of methanol. The poly(GAPMA) macroCTA molecular weight (M_n) and molecular weight distribution (M_w/M_n) were found to be 9373 g/mol and 1.17, respectively, by gel permeation chromatography (GPC).

Synthesis of Cationic Nanogels by RAFT Polymerization. A typical procedure for the synthesis of poly($GAPMA_{29}$-*b*-(MeODEGM-*st*-CL-*st*-AEMA)$_{200}$) nanogel is as follows: The synthesis of the nanogel was achieved at 70 °C, employing ACVA as the radical initiator and poly$(GAPMA)_{29}$ as the macro-chain transfer agent. In a reaction test tube, poly$(GAPMA)_{29}$ macroCTA (0.078 g, 0.008 mmol) and AEMA (0.055 g, 0.33 mmol) were dissolved in double-distilled deionized water (3 mL), then MeODEGM (0.25 g, 1.32 mmol), 2,2-dimethacroyloxy-1-ethoxypropane10 as cross-linker (CL) (0.099 g, 0.33 mmol) (20 mol % with respect to total moles of MeODEGM and AEMA) and ACVA (1.2 mg, 0.004 mmol) were dissolved in 2 mL of 1,4-dioxane and added in the above solution. The solution was degassed by purging with nitrogen for 30 min and the reaction was carried out at 70 °C for 24 h. The reaction was then quenched in liquid nitrogen and by exposure to air. The product was purified by dialysis against distilled water for three days using dialysis membrane with a molecular weight cutoff of 12 000−14 000. The nanogel was obtained as a white powder after freeze−drying overnight and was stored in the refrigerator.

Nanogels and Plasmid DNA Binding Interaction. The binding ability of β-galactosidase plasmid to nanogels was evaluated by agarose gel electrophoresis. Gwiz-β-galactosidase plasmid (340 ng) was combined with increasing amounts of cationic nanogels (in water) and was incubated at 5 °C for 30 min followed by incubation at 37 °C for 30 min. The low incubation temperature (5 °C) hydrate the cationic core, hence allowing the complexation of DNA with cationic core. The elevated temperature (37 °C) then collapses the core and entraps the DNA between the cationic nanogels. Samples were then subjected to electrophoresis on a 1% agarose (135 mV) containing 1.0 μg/mL ethidium bromide in 1× Tris acetate/EDTA buffer for 25 min. The gels were visualized using UV trans-illuminator (Alpha Innotech; San Leandro, CA) at 300 nm.

Characterization of Nanogels. *Nuclear Magnetic Resonance.* MeODEGM shows thermoresponsive behavior and undergoes coil to globule transition at a lower critical solution temperature (LCST) of 24 °C. This transition was also studied at a molecular level by using variable temperature NMR spectroscopy technique in D_2O.

Gel Permeation Chromatography (GPC). The number average molecular weight (M_n) and polydispersity (M_w/M_n) of the macro CTAs were determined at room temperature using Viscotek conventional GPC connected to two Waters Ultrahydrogel linear WAT011545 columns (pore size: blend; exclusion limit = 7.0 × 10^6) and has a Viscotek model 250 dual detector. An acidic buffer of 0.50 M sodium acetate/0.50 M acetic acid was used as eluent. Calibration of GPC was done by six monodispersed poly(ethylene oxide) (PEO) standards (M_p − 1.01 × 10^3 − 1.01 × 10^5 g mol^{-1}).

Particle Sizes by Dynamic Light Scattering (DLS). Size of nanogels was analyzed using a Viscotek DLS 802 instrument, which is equipped with a He−Ne laser at a wavelength of 632 nm and a Peltier temperature controller. The aqueous nanogel solution was filtered through a 0.45 μm pore size Millipore membrane. Data were obtained at room temperature at an angle of 90° within the temperature range 25−50 °C. *Omni Size* software was used to record the DLS size data.

Particle Sizes and Morphology by Transmission Electron Microscopy (TEM) and Scanning Electron Microscopy (SEM). Size and morphology of nanogels at room temperature were analyzed by TEM on a Philips transmission electron microscope operated at 80 kV and fitted with a CCD camera. A droplet of a properly diluted nanogel solution (in water) was placed on the TEM carbon coated copper grid and allowed to air-dry before it was stained with phosphotungstic acid (2 wt % aqueous solution) for 1 min. The sample was then allowed to dry overnight prior to observation. SEM was performed using a scanning electron microscope FEI XL30 with accelerating voltage of 20 kV. Sample has been prepared by placing an aliquot of a dilute suspension of lyophilized nanogel on a copper grid coated with an amorphous carbon film and let the solvent evaporated. Then, sample was attached to a stub and sputter-coated with Au/Pd.

Cell Culture. Hep G2 cells were maintained in low glucose DMEM media supplemented with 10% FBS and 1% antibiotic, in a humidified atmosphere and 5% CO_2 at 37 °C. Upon 80% confluency, the cells were trypsinized with 0.25% trypsin with EDTA, were cultured twice a week, and were seeded in 24 well tissue culture plates.

Transfection. Hep G2 cells are seeded at the density of 60 000 cells per well, in 24 well tissue culture plates, and are incubated overnight. The media is removed and 100 μL of serum-free OMEM or serum-containing media is added followed by the addition of nanogel-DNA complexes prepared at varying mass ratios in OMEM media. The DNA dose (1.2 μg/well) is kept constant for all the experiments. The cells are incubated for 4 h and complexes containing media are replaced with fresh serum containing media. The cells are allowed to grow for 48 h before their lysis (CHAPS in Sodium Phosphate

lysis buffer) (pH = 7.5) followed by two freeze−thaw cycles. The activity of β-galactosidase is detected using β-galactosidase assay. Briefly, ONPG solution (150 μL of 4 mg/mL) is added to 50 μL of lysate volume in the presence of 4.5 μL 100× Mg solution (1.3 μL of β-mercaptoethanol in 400 μL of 0.1 M $MgCl_2$) in 96 well plates and plate is incubated at 37 °C. The yellow color developed is detected using a TECAN Genios Pro microplate reader at 420 nm after 4 h. The total protein content in cell lysate is detected using microBCA assay (Pierce). The development of purple color is read at 570 nm.

MTT Assay. The confluent Hep G2 cells are seeded in 24 well tissue culture plates at the density of 80 000 cells per well. The cells are allowed to adhere overnight, and fresh media at varying nanogel/DNA mass ratios (prepared in media, at constant DNA dose 1.2 μg/well) are added in duplicates. The cells are allowed to grow for four hours in the presence of nanogel complexes. The untreated cells and media alone are used as positive and negative controls, respectively. 125 μL MTT dye is then added per well, and plate is incubated for 2 h, followed by the addition of 500 μL of lysis buffer. The plate is read at 570 nm and percent cell viability is determined:

$$\%\text{cell viability} = (\text{treated cells} - \text{negative control}) / (\text{positive control} - \text{negative control}) \times 100$$

Confocal Microscopic Imaging of Cellular Uptake of Polyplexes. Hep G2 cells are seeded in 6 well tissue culture plates containing glass coverslips. The cells are allowed to adhere overnight. The media is changed and fresh serum containing media is added. The nanogels and Cy-3′-labeled DNA (1.2 μg) complexes formulated in OMEM at varying mass ratios are then added in different wells of 6 well plate. After two hours, cells are washed twice with DPBS, and are fixed with 3.7 wt % formalin in DPBS. The cells are rehydrated and are fixed on glass slides. The slides are imaged using Fluoview FV10i Olympus confocal microscope, and samples are excited at 512 nm and are detected at 570 nm, for Cy3′-labeled samples using 60× objective and 1.6× zoom.

RESULTS AND DISCUSSION

Nanogels are "smart" cargo-carrying nanomaterials, which have been used to deliver a variety of biomolecules both *in vitro* and *in vivo*.[1,2] Recently, cationic nanogels have been synthesized and are used for gene delivery.[23,33,34] The incorporation of nontoxic residues in gene delivery vectors is a well-established approach to reduce their toxicity.[3−9,11,15,24−26] Phosphorylcholine based nanogels have previously been synthesized by RAFT and are studied for their protein encapsulation and pH-dependent protein release.[15,26] In this study, well-defined carbohydrate-based cationic nanogels are synthesized by RAFT and are studied for their gene delivery potential. The nanogels bearing cationic thermosensitive core are cross-linked with acid-degradable cross-linker, while the shell of nanogels is fabricated with well-defined glycopolymers. The core of the nanogel consists of two main components, namely, poly(methoxydiethylene glycol methacrylate) (poly(MeODEGM), a well-known thermoresponsive polymer with an LCST of 24 °C,[35] and poly(2-aminoethyl methacrylamide hydrochloride) (poly(AEMA), a cationic component that can condense plasmid DNA. The shell of the nanogel consists of a carbohydrate-based component (GAEMA or GAPMA). GAPMA/GAEMA is chosen based on our previous results, which showed that both GAPMA and galactose bearing polymer (2-lactobionamidoethyl methacrylamide, LAEMA) are well taken up by hepatocytes.[8] GAPMA will be an ideal choice for the nanogels, as bulkiness of LAEMA moiety may hinder the interactions of DNA with cationic core, hence causing poor gene complexation and gene expression.

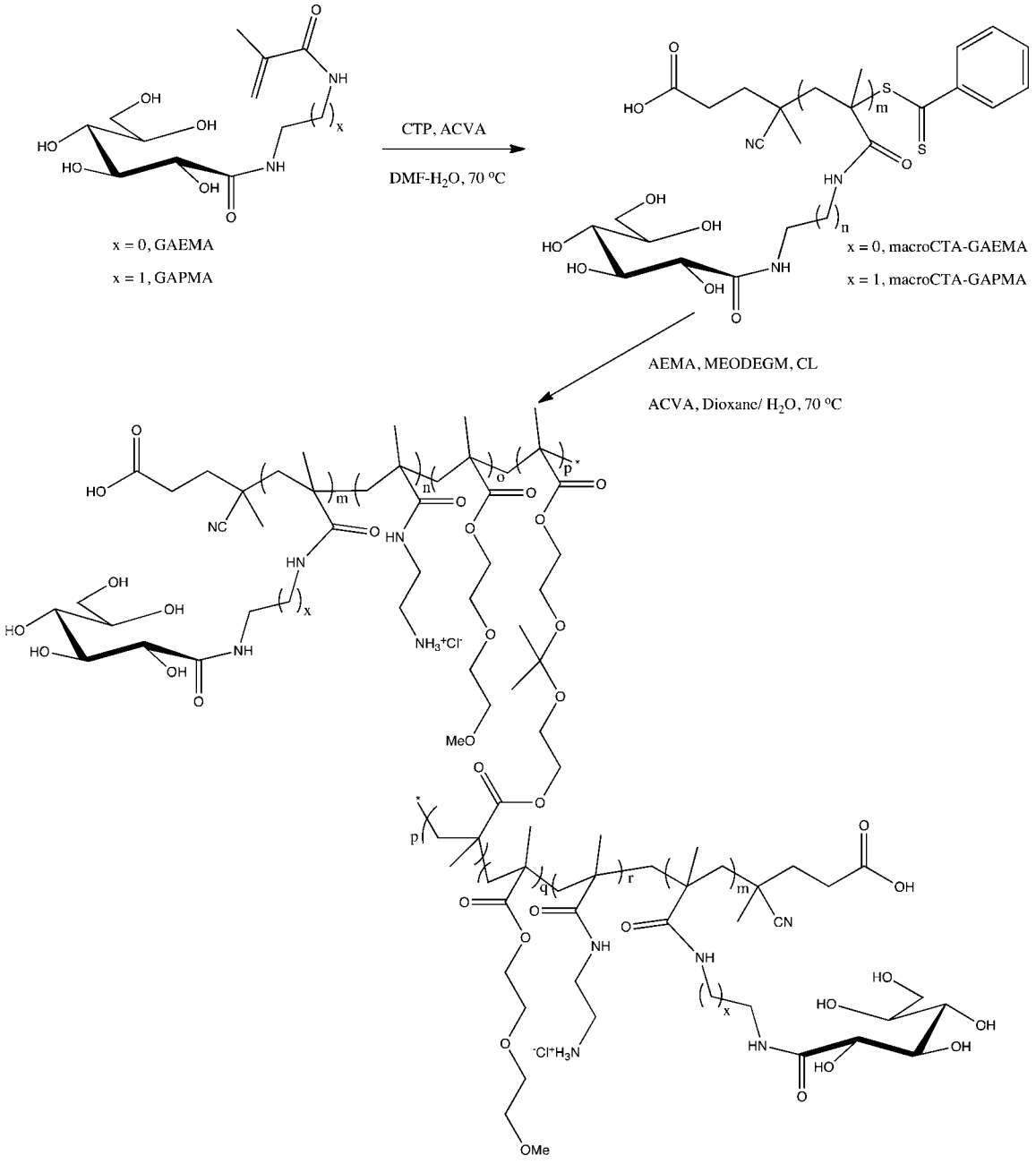
Nanogels Synthesis. Macro-CTAs of GAEMA and GAPMA were first synthesized with narrow molecular weight distributions and different degrees of polymerization via the RAFT process (Table 1 and Figure S2, Supporting Information Figure S1−S2). The macroCTAs were then used to copolymerize MeODEGM or NIPAM and AEMA in the presence of the acid-degradable cross-linker, 2,2-dimethacroyloxy-1-ethoxypropane, in water and dioxane using ACVA as initiator (Scheme 2, Supporting Information Figure S3). The nanogels (NGs) obtained by this one-pot protocol[15,36,37] were purified by dialysis and lyophilized. Different nanogel compositions were prepared at varying concentrations of cross-linker, and the hydrodynamic sizes were obtained by dynamic light scattering (DLS). It was observed that the sizes of these nanogels could be controlled accordingly (72−198 nm) by varying the cross-linker concentrations (10−20 mol %) and MeODEGM chain length (Table 2, Supporting Information Figure S3). The nanoparticles were characterized by both transmission electron microscopy (TEM) and scanning electron microscopy (SEM) as depicted in Figure 1 to determine the average particle size and morphology. All nanoparticles (NG-A3) were found to be well-defined spherical structures with diameters in the range of 190 to 193 nm in the dry state, which correlate well with the hydrodynamic size obtained by DLS result (198 nm). Furthermore, after freeze−drying, the nanogels could be redispersed in PBS and their sizes remained the same (Supporting Information Figure S4). The above tests indicate that the nanogels possess favorable stability for storage in both solution and solid forms. Poly(MeODEGM) shows thermoresponsive behavior and undergoes coil to globule transition at a lower critical solution temperature (LCST) of 24 °C. Temperature-dependent DLS studies indicated that nanoparticles shrunk from 116 nm at 15 °C to 54 nm at 50 °C (NG-A4) and 185 nm at 15 °C to 78 nm at 50 °C (NG-A2) as shown in Figure 2. The phase transition behavior of MeODEGM core was also studied at a molecular level using variable temperature ^{1}H NMR (VTNMR) spectroscopy. As expected, the ^{1}H NMR peak intensity peak at 3.4 ppm, which corresponds to a methylene group of poly(MEODEGM), collapsed with an increase in temperature (Supporting Information Figure S5). It should be noted that copolymerization of AEMA with MeODEGM during nanogel formation increased the LCST of the final product, due to the incorporation of hydrophilic moiety (AEMA).

Table 1. GPC Data of Macro-CTAs with Different Target Degrees of Polymerization

MacroCTA	$M_{n,GPC}$ (g/mol)	M_w/M_n
poly($GAEMA_{63}$)	19397	1.20
poly($GAEMA_{43}$)	13276	1.19
poly($GAPMA_{57}$)	18227	1.20
poly($GAPMA_{29}$)	9373	1.17

Nanogel−DNA Binding. An important requirement for an effective gene delivery system is the ability of the nanogels to

Scheme 2. Synthesis of Cationic Nanogels via RAFT



condense plasmid DNA as shown in Scheme 3. Polycationic materials with high molecular weights and charge densities can bind negatively charged DNA through electrostatic interactions.[23] The carbohydrate-based cationic nanogels synthesized were studied for their DNA condensation efficacies. Varying concentrations of nanogels were incubated with β-galactosidase plasmid and the DNA complexations were studied using agarose gel electrophoresis. It was found that low concentrations of nanogels (nanogel:DNA weight by weight ratio ranging from 4 to 20) could effectively complex DNA and produced cationic complexes retained in the well of agarose gels (Supporting Information Figure S6). Although the nanogels could complex DNA at very low w/w ratios, slightly higher amounts of nanogels were required to obtain optimum gene delivery efficacies. The nanogel−DNA complexes formulated were studied for their charge and sizes using zeta potential instrument and DLS (Figure 3). It is shown that NG-A1, NG-A2, NG-A3, and NG-A4 make stable complexes ranging from 100 to 600 nm in diameter at varying w/w ratios. However, NG-A5 produced micrometer-sized (4−5 μm) particles at high w/w ratio (100). The nanogel-DNA complexes are analyzed for their net positive charge in deionized water. It is found that all nanogels maintain net cationic character, when complexed with DNA at high w/w ratios. Though NG-A2 formulates 200 nm complexes with plasmid DNA, these complexes possess low zeta potential (close to 0) at w/w ratio of 60.

Gene Expression. The gene delivery efficacies of polysaccharide-based nanogels have been studied. For instance, cross-linked chitosan-based polyplexes were shown to enhance their stability in physiological conditions and hence have high gene expression.[24] Herein, carbohydrate-based cationic nano-

dx.doi.org/10.1021/bc300314u | Bioconjugate Chem. 2012, 23, 1925−1933

Table 2. Hydrodynamic Diameter of Nanogels with Varying Chain Length Compositions and Cross-Linker Concentrations

nanogel	nanogel composition	cross-linker (mol %)	hydrodynamic diameter (nm)	polydispersity
NG-A1	$GAEMA_{43}$-*b*-(MeODEGM-*st*-AEMA-*st*-$CL)_{200}$	20	139 ± 1.0	0.06
NG-A2	$GAEMA_{63}$-*b*-(MeODEGM-*st*-AEMA-*st*-$CL)_{100}$	10	174 ± 1.5	0.24
NG-A3	$GAPMA_{29}$-*b*-(MeODEGM-*st*-AEMA-*st*-$CL)_{200}$	20	198 ± 2.0	0.12
NG-A4	$GAPMA_{57}$-*b*-(NIPAM-*st*-AEMA-*st*-$CL)_{200}$	20	109 ± 1.1	0.25
NG-A5	$GAPMA_{57}$-*b*-(MeODEGM-*st*-AEMA-*st*-$CL)_{100}$	20	72 ± 0.8	0.14

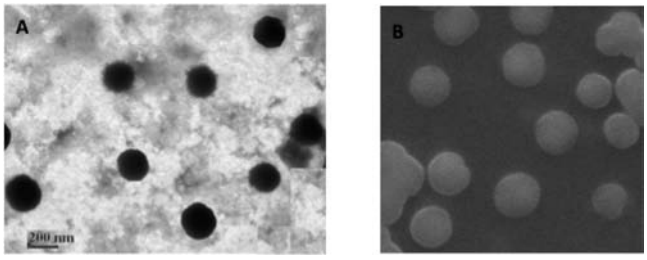


Figure 1. TEM (A) and SEM (B) images of cationic nanogels (NG-A3) synthesized via RAFT.

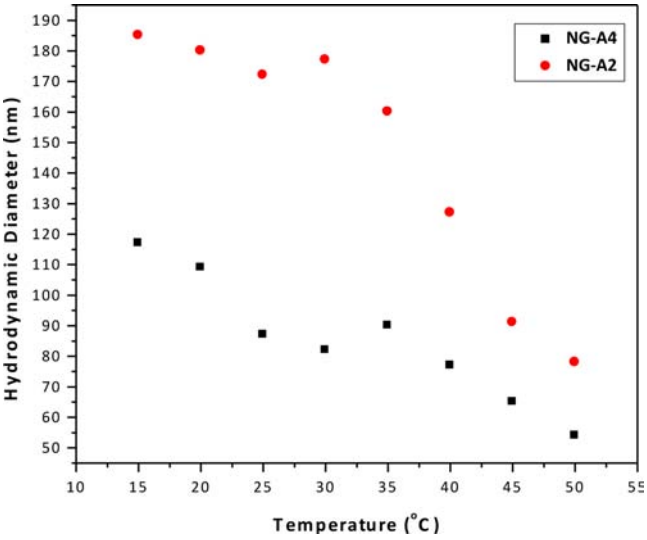
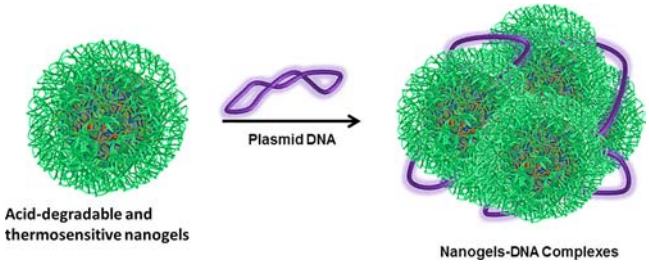


Figure 2. Hydrodynamic diameter of thermoresponsive cationic nanogels as a function of temperature.

gels of controlled architecture are produced via RAFT and are studied for their gene expression in the presence and absence of serum proteins. Although the complexation of nanogels with DNA occurred at low mass ratios as indicated by agarose gel electrophoresis, high mass ratios were required for gene expression. A series of varying mass ratios were titrated with nanogels to obtain the optimum gene expression. However, it should be noted that complexation of nanogels was done in water. Moreover, this trend is consistent with previous reports which show that high N/P ratio of polymers (sometimes as

Scheme 3. Complexation of pH and Temperature-Sensitive Nanogels with DNA



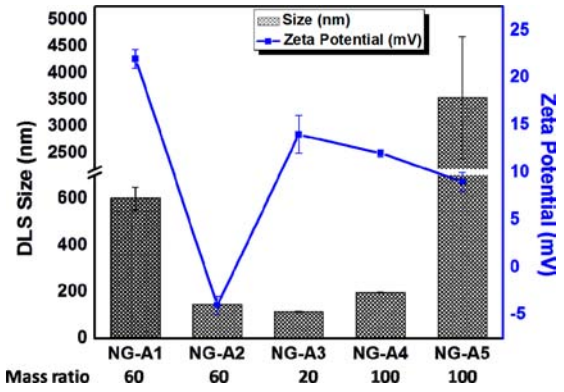


Figure 3. Size and net charge of polyplexes formed after incubation of cationic nanogels with β-galactosidase plasmid in deionized water.

high as 100 times) is required for gene expression than what is obtained for DNA complexation using agarose gel electrophoresis.[8] The DNA nanogel complexes were studied for their gene expression at varying mass ratios and constant DNA dose, in order to determine the optimum conditions for gene expression (Figure S7). It is found that NG-A1, NG-A2, and NG-A3 showed high gene delivery efficacies at varying w/w ratios (Figure 4). The gene delivery efficacies of NG-A1 and NG-A2 were high and comparable to those of branched PEI, in the presence and absence of serum proteins. NG-A3 showed slightly lower gene expression than NG-A2 and NG-A1. It should be noted that although NG-A2 produced neutral complexes as discussed above, these complexes showed high

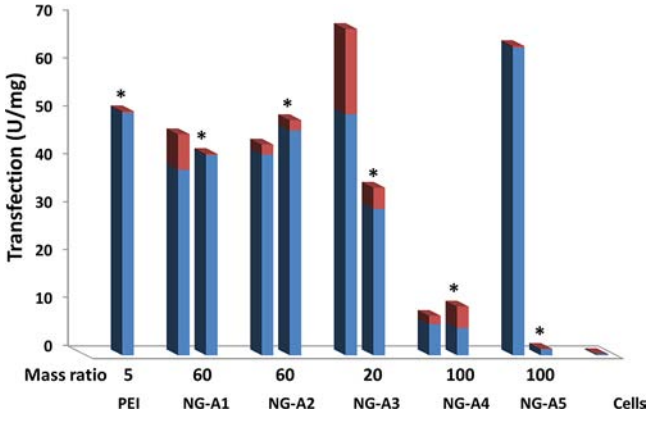


Figure 4. Transfection efficacies of nanogel−DNA complexes studied at constant DNA dose (of 1.2 μg/well) and of varying mass ratios of nanogels in the presence (*) and absence of serum, as determined using β-galactosidase assay. (the blue bars indicate the average transfection efficacies, while the red bar indicate standard deviations).

dx.doi.org/10.1021/bc300314u | *Bioconjugate Chem.* 2012, 23, 1925−1933

gene expression; in contrast, NG-A3 produced small particles with high zeta potential, but the transfection efficacy was slightly lower. This difference in gene expression of NG-A2 and NG-A3 might be due to stronger association of DNA with these nanogels, hence causing the slow release of plasmid and low gene expression in vitro. NG-A4 and NG-A5 showed poor gene expression in the presence of serum proteins. Although NG-A5 showed some gene expression in serum free media, it is thought that further aggregation and precipitation of these large complexes might be associated with their low gene expression in serum. NG-A4 showed poor gene expression in the presence and absence of serum proteins. NG-A4 showed efficient complexation of DNA as studied by agarose gel electrophoresis and DLS and zeta potential instruments; poor gene expression of these NIPAM-based nanogels is further investigated using toxicity assay and cellular uptake of complexes.

Toxicity Post-Transfection. The toxicity post-transfection of these nanogel–plasmid complexes is analyzed using MTT assay (Figure 5). It is shown that all these carbohydrate-based

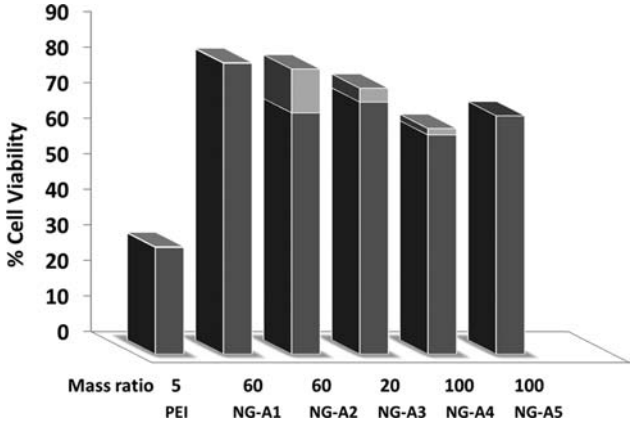


Figure 5. Toxicity post-transfection of nanogel–DNA complexes studied at varying mass ratios using MTT assay. (The black bars indicate % cell viabilities, while gray bars indicate standard standard deviations).

cationic nanogels are less toxic than PEI, regardless of mass ratio used for gene expression. Branched PEI showed low cell viability (30%) at low mass ratio (5). It should be noted that NG-A4, although showing poor gene expression, show high cell viability post-transfection, hence, low gene expression of this nanogel was not associated with the cytotoxicity of nanogel.

Cellular Uptake. We further studied the uptake of nanogel–DNA complexes in Hep G2 cells using confocal microscopy. To evaluate if the cellular uptake of nanogels was a critical factor in dictating their gene expression, nanogels with distinct physiochemical characteristics and gene profiles were compared. NG-A2 (which produced neutral complexes but showed high gene expression), NG-A4 (which produced small cationic complexes, but no gene expression), and NG-A5 (which produced micrometer-sized particles and showed poor gene expression in the serum containing media) are studied for the uptake of Cy-3′ DNA. Cy-3′ labeled DNA was complexed with nanogels at varying weight/weight ratios, and the uptake of complexes was studied after two hours of incubation with Hep G2 cells in the presence of serum proteins (Figure 6). It is shown that NG-A2 though produce large particles are well-uptaken and can accumulate in the nuclei of cells within 2 h of incubation. Moreover, diffused fluorescence in the nucleus

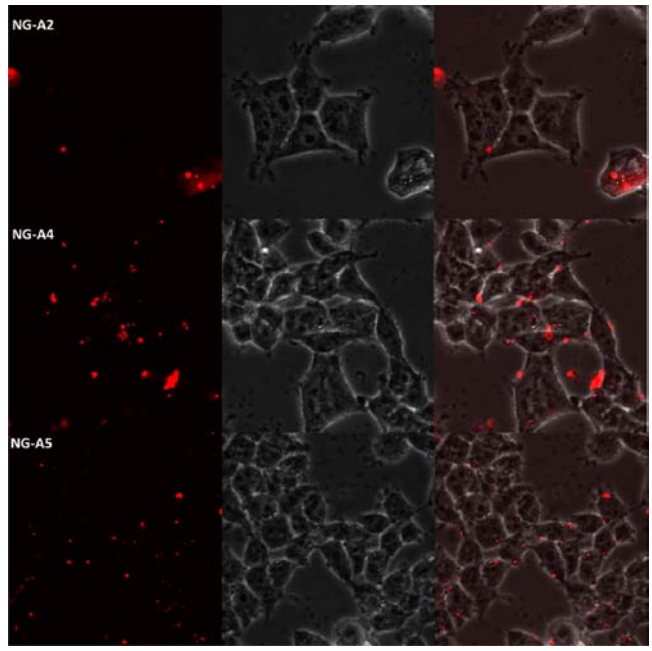


Figure 6. Confocal images of Cy-3′-labeled plasmid–nanogel complexes, after 2 h of incubation in Hep G2 in the presence of serum containing media.

indicates the rapid release of DNA in nucleus. NG-A4-based complexes showed poor cellular uptake. The presence of large particles associated with the periphery of cells indicates their aggregation on cell surface and complexes are not taken up even after 2 h of incubation, hence contributing toward their low gene expression. NG-A5 showed lower fluorescence than other nanogel-based complexes. The image shows the presence of small particles associated with the cells; however, these particles are mostly associated with the periphery and are not well internalized. Aggregation of NG-A5 in the presence of serum proteins may have affected their cellular uptake as seen by confocal images, and hence low gene expression was noted. Small particles produced remain associated with cell surface, which do not translate into significant gene expression as discussed above.

■ CONCLUSION

The study provides a detailed account on the synthesis of cationic nanogels *via* RAFT polymerization and their subsequent use as potent gene delivery carriers. Nanogels with a cationic temperature–pH-sensitive core and a permanently hydrophilic glycopolymer shell are fabricated. The nanogels produced are studied for their temperature-responsive behavior and are characterized using DLS, TEM, and SEM images. All of these cationic nanogels synthesized show high DNA complexation efficacies at relatively low weight/weight ratios, as revealed by agarose gel electrophoresis. The gene delivery efficacies of these carbohydrate-based cationic nanogels are studied. It is found that PEGMA based nanogels showed gene expression comparable to positive control (PEI), along with significantly low toxicities. Although all the nanogels produced show high cell viability, the low gene expression of NG-A4 and NG-A5 was associated with their low cellular uptake as determined from confocal images. The synthesis of biodegradable dual responsive nanogels, their low toxicities, and high gene expression present ideal properties

dx.doi.org/10.1021/bc300314u | *Bioconjugate Chem.* 2012, 23, 1925–1933

required for gene expression vectors. Further studies will be performed to determine the role of amine content, length of glycopolymer chains, and degree of cross-linking on the gene expression profile. Moreover, PEGylated sugar-based nanogels with varying PEG chain length will be prepared and will be studied for their gene expression *in vitro*.

■ ASSOCIATED CONTENT

Supporting Information

Synthesis of macro-CTAs, GPC data, synthesis of nanogels, VT-NMR spectra, temperature-dependent size change, and agarose gel electrophoresis. This material is available free of charge via the Internet at http://pubs.acs.org.

■ AUTHOR INFORMATION

Corresponding Author

*E-mail: narain@ualberta.ca, Telephone: 1-780-492-1736, Fax: 1-780-492-2881.

Notes

The authors declare no competing financial interest.

■ ACKNOWLEDGMENTS

The authors acknowledge support from Natural Sciences and Engineering Research Council of Canada (NSERC) for the funding of this work.

■ REFERENCES

(1) Kenya, K., Takeshi, S., Guisheng, Z., and Dexi., L. (2011) Advances in gene delivery systems. *Pharm. Med. 25*, 293−306.

(2) Mintzer, A. M., and Simanek, E. E. (2009) Nonviral vectors for gene delivery. *Chem. Rev. 109*, 259−302.

(3) Ahmed, M., Deng, Z., Liu, S., and Narain, R. (2009) Cationic glyconanoparticles: their complexation with DNA, cellular uptake, and transfection efficiencies. *Bioconjugate Chem. 20*, 2169−2176.

(4) Ahmed, M., Deng, Z., and Narain, R. (2009) Study of size dependent transfection efficiencies of gold nanoparticles in human cell line. *ACS Appl. Mater. Interfaces 1*, 1980−1987.

(5) Ahmed, M., Jiang, X., Deng, Z., and Narain, R. (2009) Cationic glyco-functionalized single walled carbon nanotubes as efficient gene delivery vehicles. *Bioconjugate Chem. 20*, 2017−2022.

(6) Ahmed, M., Bhuchar, N., and Narain, R. (2011) Well-controlled cationic water-soluble phospholipid polymer-DNA nanocomplexes for gene delivery. *Bioconjugate Chem. 22*, 1228−1238.

(7) Ahmed, M., and Narain, R. (2011) The effect of polymer architecture, composition, and molecular weight on the properties of glycopolymer-based non-viral gene delivery systems. *Biomaterials 32*, 5279−90.

(8) Ahmed, M., and Narain, R. (2012) The effect of molecular weight, compositions and lectin type on the properties of hyper-branched glycopolymers as non-viral gene delivery systems. *Biomaterials 33*, 3990−4001.

(9) Chen, J., Ahmed, M., and Narain, R. (2012) Synthesis of cationic magnetic nanoparticles and evaluation of their gene delivery efficacy in Hep G2 cells. *J. Biomed. Mater. Res. A,*.

(10) Kabanov, A. V., and Vinogradov, S. V. (2009) Nanogels as pharmaceutical carriers: finite networks of infinite capabilities. *Angew. Chem., Int. Ed. 48*, 5418−5429.

(11) Agnihotri, S. A., Mallikarjuna, N. N., and Aminabhavi, T. M. (2004) Recent advances on chitosan based micro- and nanoparticles in drug delivery. *J. Controlled Release 100*, 5−28.

(12) Du, F.-S., Wang, Y., Zhang, R., and Li, Z.-C. (2010) Intelligent nucleic acid delivery systems based on stimuli-responsive polymers. *Soft Matter 6*, 835−848.

(13) Deka, S. R., Quarta, A., Corato, R. D., Falqui, A., Manna, L., Cingolani, R., and Pellegrino, T. (2010) Acidic pH-responsive nanogels as smart cargo systems for the simultaneous loading and release of short oligonucleotides and magnetic nanoparticles. *Langmuir 26*, 10315−10324.

(14) Wu, W., Shen, J., Banerjee, P., and Zhou, S. (2010) Chitosan-based responsive hybrid nanogels for integration of optical pH-sensing, tumor cell imaging and controlled drug delivery. *Biomaterials 31*, 8371−8381.

(15) Bhuchar, N., Sunasee, R., Ishihara, K., Thundat, T., and Narain, R. (2012) Degradable thermo-responsive nanogels for proteins encapsulation and controlled release. *Bioconjugate Chem. 23*, 75−83.

(16) Lee, H., Mok, H., Lee, S., Oh, Y.-K., and Park, T. G. (2007) Target-specific intracellular delivery of siRNA using degradable hyaluronic acid nanogels. *J. Controlled Release 119*, 245−252.

(17) Blackburn, W. H., Dickerson, E. B., Smith, M. H., McDonald, J. F., and Lyon, L. A. (2009) Peptide-functionalized nanogels for targeted siRNA delivery. *Bioconjugate Chem. 20*, 960−968.

(18) Oh, J. K., Siegwart, D. J., and Matyjaszewski, K. (2007) Synthesis and biodegradation of nanogels as delivery carriers for carbohydrate based polymers. *Biomacromolecules 8*, 3326−3331.

(19) Vinogradov, V. S., Zeman, A. D., Batrakova, E., and VKabanov, A. V. (2005) Polyplex nanogel formulations for drug delivery of cytotoxic nucleoside analogs. *J. Controlled Release 107*, 143−157.

(20) McAllister, K., Sazani, P., Adam, M., Cho, M. J., Rubinstein, M., Samulski, R. J., and DeSimone, J. M. (2002) Polymeric nanogels produced *via* inverse microemulsion polymerization as potential gene and antisense delivery agents. *J. Am. Chem. Soc. 124*, 15198−15207.

(21) Goh, S. L., Murthy, N., Xu, M., and Frechet, J. M. J. (2004) Cross-linked microparticles as carriers for the delivery of plasmid DNA for vaccine development. *Bioconjugate Chem. 15*, 467−74.

(22) Raemdonck, K., Naeya, B., Buyens, K., Vandenbroucke, R. E., Hogset, A., Demeester, J., and De Smedt, S. C. (2009) Biodegradable dextran nanogels for RNA interference: Focusing on endosomal escape and intracellular siRNA delivery. *Adv. Funct. Mater. 19*, 1406−1415.

(23) Fang, H., Zhang, K., Shen, G., Wooley, K. L., and Taylor, J-S. A. (2009) Cationic shell-cross-linked kendel-like (cSCK) nanoparticles for highly efficient PNA delivery. *Mol. Pharmaceutics 6*, 615−626.

(24) Csaba, N., Koping-Hoggard, M., and Alonso, M. J. (2009) Ionically crosslinked chitosan/tripolyphosphate nanoparticles for oligonucleotide and plasmid DNA delivery. *Intl. J. Pharm. 382*, 205−214.

(25) Schmitt, F., Lagopoulos, L., Kauper, P., Rossi, N., Busso, N., Barge, J., Wagnieres, J., Laue, C., Wandrey, C., and Juillerat-Jeanneret, L. (2010) Chitosan-based nanogels for selective delivery of photo-sensitizers to macrophages and improved retention in and therapy of articular joints. *J. Controlled Release 144*, 242−250.

(26) Ahmed, M., and Narain, R. (2012) Intracellular delivery of DNA and enzyme in active form using degradable carbohydrate based nanogels. *Mol. Pharmaceutics*, under review.

(27) Smith, A. E., Sizovs, A., Grandinetti, G., Xue, L., and Reineke, T. M. (2011) Diblock glycopolymers promotes colloidal stability of polyplexes and effective pDNA and siRNA delivery under physiological salt and serum conditions. *Biomacromolecules 12*, 3015−3022.

(28) Narain, R., and Armes, S. P. (2002) Synthesis of low polydispersity, controlled-structure sugar methacrylate polymers under mild conditions without protecting group chemistry. *Chem. Commun. 23*, 2776−2777.

(29) Narain, R., and Armes, S. P. (2003) Direct synthesis and aqueous solution properties of well-defined cyclic sugar methacrylate polymers. *Macromolecules 36*, 4675−4678.

(30) Narain, R., and Armes, S. P. (2003) Synthesis and aqueous solution properties of novel sugar methacrylate-based homopolymers and block copolymers. *Biomacromolecules 4*, 1746−1758.

(31) Deng, Z., Ahmed, M., and Narain, R. (2009) Well-Defined Glycopolymers Synthesized via the Reversible Addition Fragmentation Chain Transfer Process in Aqueous Media. *J. Polym. Sci,: Part A: Polym. Chem. 47*, 614−627.

(32) Deng, Z., Bouchékif, H., Babooram, K., Housni, A., Choytun, N., and Narain, R. (2008) Facile synthesis of controlled-structure primary amine-based methacrylamide polymers via the reversible addition-

fragmentation chain transfer process. *J. Polym. Sci., Part A: Polym. Chem. 46*, 4984−4996.
(33) Xu, D.-M., Yao, S.-D., Liu, Y.-B., Sheng, K.-L., Hong, J., Gong, P.-J., and Dong, L. (2007) Size-dependent properties of M-PEIs nanogels for gene delivery in cancer cells. *Int. J. Pharm. 338*, 291−296.
(34) Dong, L., Xu, H., Liu, Y.-B., Lu, B., Xu, D.-M., Li, B.-H., Gao, J., Wu, M., Yao, S.-D., Zhao, J., and Guo, Y.-J. (2009) M-PEIs nanogels: potential nonviral vector for systemic plasmid delivery to tumor cells. *Cancer Gene Ther. 16*, 561−566.
(35) Lutz, J. F., Akdemir, O., and Hoth, A. (2006) Ion-Sensitive "Isothermal" Responsive Polymers Prepared in Water. *J. Am. Chem. Soc. 128*, 13046−13047.
(36) Zheng, G., Zheng, Q., and Pan, C. (2006) One-pot synthesis of micelles with a cross-linked poly(acrylic acid) core. *Macromol. Chem. Phys. 207*, 216−223.
(37) Jiang, X., Liu, S., and Narain, R. (2009) Degradable thermoresponsive core cross-linked micelles: fabrication, surface functionalization, and biorecognition. *Langmuir 25*, 13344−13350.
(38) De Smedt, S. C., Demeester, J., and Hennink, W. E. (2000) Cationic polymer based gene delivery systems. *Pharm. Res. 17*, 113−126.

Bioconjugate Chemistry

Article

pubs.acs.org/bc

A High-Affinity Gold-Binding Camel Antibody: Antibody Engineering for One-Pot Functionalization of Gold Nanoparticles as Biointerface Molecules

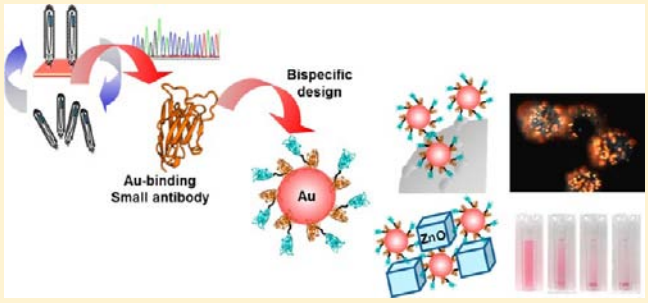
Takamitsu Hattori,[†] Mitsuo Umetsu,*[,†,‡] Takeshi Nakanishi,[†] Satoko Sawai,[†] Shinsuke Kikuchi,[†] Ryutaro Asano,[†] and Izumi Kumagai*[,†]

[†]Department of Biomolecular Engineering, Graduate School of Engineering, Tohoku University, Aoba 6-6-11, Aramaki, Aoba-ku, Sendai 980-8579, Japan

[‡]Center for Interdisciplinary Research, Tohoku University, Sendai, Aoba 6-3, Aramaki, Aoba-ku, Sendai 980-8578, Japan

Supporting Information

ABSTRACT: Antibodies, with their high affinity and specificity, are widely utilized in the field of protein engineering, medicinal chemistry, and nanotechnology applications, and our recent studies have demonstrated the recognition and binding of antibody for the surface on inorganic material. In this study, we generated a high-affinity gold-binding antibody fragment by a combination of peptide-grafting and phage-display techniques and showed the availability of the material-binding fragment for one-pot functionalization of nanoparticles as interface molecules. After a gold-binding peptide sequence was grafted into one of the complementarity determining regions of a single variable domain of a heavy-chain camel antibody, a combinatorial library approach raised by 20 times the affinity of the peptide-grafted fragment. The high-affinity gold-binding fragment (E32) spontaneously adsorbed on gold nanoparticles, and consequently the nanoparticles formed a stable dispersion in a high-ionic-strength solution. Multivalent and bispecific antibodies constructed on the E32 platform by means of fusion technology functionalized gold nanoparticles in one pot, and these functionalized nanoparticles could be used to obtain surface plasmon resonance scattering images of cancer cells and to spontaneously link two different nanomaterials. Here, we propose the bispecific antibodies as convenient interface molecules in the nanosized world.



INTRODUCTION

The downsizing of inorganic materials can impart unique electrical, photonic, and optical properties to the materials. Inorganic nanomaterials have been used as probes for biological sensing and imaging,[1,2] and they can also serve as building blocks in bottom-up construction of nanodevices.[3,4] For example, semiconductor nanomaterials called quantum dots exhibit size-dependent fluorescence and are widely used for cellular imaging,[5] and superparamagnetic iron oxide particles have been used for signal amplification in magnetic resonance imaging.[6] Homogeneous inorganic nanocrystals with defined shape and surface characteristics self-assemble into square and hexagonal packing,[7] and two types of nanoparticles with different sizes and shapes have been shown to assemble into a binary superlattice.[8] For both biological and nanotechnological applications, nanoparticles must form stable dispersions in solution and have surfaces designed to interact with targets such as proteins, cells, or nanoparticles. However, the methods for preparing nanoparticles with these two characteristics vary widely depending on the materials, and thus a trial and error process is required.

One method for preparing nanoparticles with the desired properties involves the use of material-binding peptides. During the past decade, several peptides with affinity for nonbiological materials, such as metals, metal oxides, and semiconductors, have been identified by means of combinatorial library approaches.[9,10] Such material-binding peptides have been used for bottom-up fabrication of bionanotechnology applications, such as patterning and assembly of proteins and nanomaterials,[11−13] biofunctionalization of nanoparticles,[14,15] and synthesis of crystalline metal nanoparticles.[16−18] However, the binding affinities of peptides are often not high enough for such applications.[19,20] Recently, we focused on antibodies as alternative material-binding molecules because they have higher affinities and specificities than peptides.[21,22] We prepared several antibody fragments with high affinity for the surface of inorganic nanomaterials;[20,23,24] the fragments strongly bind to the surface of specific inorganic nanoparticles, and the resulting

Received: June 15, 2012
Revised: August 5, 2012
Published: August 8, 2012

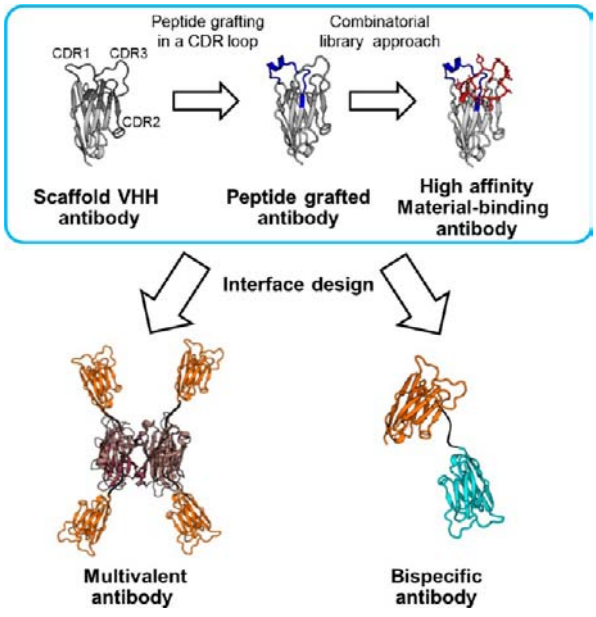
ACS Publications © 2012 American Chemical Society

dx.doi.org/10.1021/bc300316p | *Bioconjugate Chem.* 2012, 23, 1934−1944

nanoparticles can be as stably dispersed as proteins, even in high-salt buffer.[24]

In this study, we demonstrate the potential of material-binding antibodies as interface molecules that can stably disperse nanoparticles in high-ionic-strength solutions and simultaneously bind to targets. Gold nanomaterials are among the most well-studied nanomaterials. Gold nanostructures scatter and absorb visible and near-infrared light at a plasmon resonance wavelength that depends on the size and shape of the structure, and these characteristics have been used for biosensing,[25] imaging,[26] and optical nanocircuitry.[27] Here, we generated antibody fragments with high affinity and specificity for gold surfaces by means of a method we refer to as the "construction of antibodies by integrating grafting and evolution technology" (CAnIGET, Scheme 1),[20] in which the single variable domain of the heavy chain of a heavy chain camel antibody (VHH fragment) was functionalized by a combination of peptide grafting and in vitro selection. The generated high-affinity gold-binding VHH fragment (designated E32) strongly adsorbed on gold nanoparticles, which could then be stably dispersed in a high-ionic-strength solution. In addition, we designed and constructed two bispecific antibodies by joining two different VHH fragments. A bispecific antibody comprising a VHH fragment with affinity for gold nanoparticles and a VHH fragment with affinity for the epidermal growth factor receptor (EGFR) on cancer cells enabled us to obtain surface plasmon resonance (SPR) scattering images of the cells; and a bispecific antibody constructed from gold-binding and ZnO-binding VHH fragments allowed us to spontaneously link two different nanomaterials. Here, we propose a new methodology for stable dispersion of nanoparticles together with functionalization in one pot by using high-affinity material-binding antibody fragments.

Scheme 1. Construction of High-Affinity Material-Binding Antibody Fragments and Multivalent and Bispecific Antibody Fragments



EXPERIMENTAL PROCEDURES

Construction of the Expression Vector for VHH Fragments with a Gold-Binding Peptide in Complementarity Determining Regions (CDRs). The DNA sequence coding VHH_{GBP1}, a VHH fragment with a previously reported gold-binding peptide (GBP: LKAHLPPSRLPS)[28] in the CDR 1 loop, was synthesized by means of overlap extension PCR from a pRA-wtVHH-FLAG plasmid.[20] The gene fragments were inserted into *Nco*I−*Sac*II restriction sites of pRA-FLAG vectors to produce the pRA-VHH_{GBP1}-FLAG plasmid.

Construction of a Phage Library and Selection of VHH Fragments with High Affinity for Gold Surfaces. Construction of phage library and selection of VHH fragments with high affinity for gold surfaces were performed by means of the CAnIGET method.[20] Briefly, a gene encoding the VHH_{GBP1} fragment with a randomized sequence in the CDR3 loop was amplified from the pRA-VHH_{GBP1}-FLAG plasmid and inserted into the phagemid vector pTZ-PsFv2.[29] For the selection of VHH fragments with high affinity for gold surfaces, approximately 10^9 phages were mixed with 1 mg of gold powder (particle size <10 μm, Sigma-Aldrich, Tokyo, Japan) in a 10 mM phosphate solution (pH 7.5) containing 200 mM NaCl and 0.05% Tween 20. After the powder was washed with the phosphate solution five times, residual phages bound to the gold surface were eluted with 500 mM phosphate solution (pH 7.5) containing 200 mM NaCl. This panning procedure was performed four times, during which the phosphate concentration of the washing solution was increased from 30 to 50 mM (second wash, 30 mM; third and fourth washes, 50 mM). The amino acid sequences of 100 randomly chosen clones were analyzed. The selected VHH genes were inserted into the *Nco*I−*Sac*II restriction sites in the pRA-FLAG vector for expression in *Escherichia* (E.) *coli*.

Construction of Expression Vectors for Biotinylated VHH and Bispecific VHH Dimers. To construct bispecific antibodies with affinity for gold and EGFR, and with affinity for gold and ZnO, the gene for E32 VHH was fused at the C-terminus of Ia1 VHH (which has affinity for EGFR[30]) or 4F2 VHH (which has affinity for ZnO[20]) via a llama IgG2 upper hinge-linker (EPKIPQPQPKPQPQPQPQPQPKPQPKPEP).[31] The genes of the dimeric VHH fragments (Ia1-E32 and 4F2-E32) were generated by means of overlap extension PCR with LA-Taq DNA polymerase, and the gene fragments were inserted into the *Nco*I−*Sac*II sites of pRA-FLAG vectors (pRA-Ia1VHH-LH-AuE32VHH-FLAG and pRA-4F2VHH-LH-AuE32VHH-FLAG).

The DNA sequence coding one of the selected VHH genes (E32 clone) with the IgA hinge linker (SPSTPPTPSPSTPP) and a biotin acceptor peptide (Avitag; GGLDNDIFEAGKIEWH) at the C-terminus of VHH in that order (as reported by Cloutier et al.[32]) was generated by overlap extension PCR from the pRA-FLAG vector containing the E32 VHH fragment (pRA-AuE32VHH-FLAG), and the amplified fragments were inserted into the *Nco*I−*Spe*I restriction sites of the pRA-FLAG vector (pRA-AuE32VHH-Avitag).

Expression and Purification of VHH Fragments. Transformed *E. coli* BL21 (DE3) cells harboring the expression plasmid encoding the VHH and dimeric VHH fragments were incubated in 2 × yeast extract tryptone medium containing 100 g/mL ampicillin at 28 °C, and expression of antibody fragments under the control of the T7 promoter was induced by adding 1 mM isopropyl β-D-thiogalactopyranoside. VHH fragments were

dx.doi.org/10.1021/bc300316p | *Bioconjugate Chem.* 2012, 23, 1934−1944

Table 1. Amino Acid Sequences of CDR Loops of GBP-Grafted VHH Fragments[b]

Fragment	CDR1	CDR2	CDR3
	26 35c	50 65	95 102
cAbBCII10	GGSEYS-YSTF SLG	AIASM--GGLTYYADSVK-G	VRGYFMRLPSSHNFRY
	1-1 1-18	50 65	95 102
VHH_{GBP1}	GGSLKAHLPPSRLPSSLG	AIASM--GGLTYYADSVK-G	VRGYFMRLPSSHNFRY
	1-1 1-18	50 65	3-1 3-16
Randomized VHH_{GBP1}[a]	GGSLKAHLPPSRLPSSLG	AIASM--GGLTYYADSVK-G	VRGαββαββαββαFRY

[a] α and β in CDR3 of randomized VHH_{GBP1} were randomized to R or H and R, G, L, or V, respectively. [b] The sequence of the GBP is underlined. The numbering of the amino acids of cAbBCII10 VHH follows the Kabat numbering system.[33] The amino acids of the GBP-grafted CDR1 and randomized CDR3 are numbered as 1-1 to 1-18 and 3-1 to 3-16, respectively.[20]

extracted from the periplasm of the harvested cells by osmotic shock and were purified by anion/cation exchange chromatography and gel filtration chromatography (Hi-Load 16/600 Superdex 75 size exclusion column, GE Healthcare, Little Chalfont, UK) after treatment with ammonium sulfate. The bispecific VHH dimers were first purified by means of affinity chromatography on an anti-FLAG M2 affinity gel column (Sigma, Tokyo, Japan) and then fractionated by gel filtration chromatography.

For the expression of biotinylated VHH fragments, *E. coli* BL21 (DE3) cells were transformed by the plasmid of pBIRAcm encoding biotin ligase (Avidity Inc., Aurora, CO, USA), and then the same cells were transformed by the plasmids of pRA-AuE32VHH-Avitag. The transformed *E. coli* cells were incubated in 2 × yeast extract tryptone medium containing 100 μg/mL ampicillin and 34 μg/mL chloramphenicol at 28 °C. Expression of biotinylated VHH and biotin ligase was induced by adding 1 mM isopropyl β-D-thiogalactopyranoside in the presence of 50 μM of D-biotin (Sigma, St. Louis, MO, USA). VHH fragments were extracted from the periplasm of the harvested cells by osmotic shock and purified by means of affinity chromatography on a SoftLink Soft Release Avidin Resin column (Promega, Madison, WI, USA) and gel filtration chromatography. The fractionated biotinylated VHH was collected after the presence of biotin was confirmed in the proteins by means of Western blotting using streptavidin−horseradish peroxidase (GE Healthcare).

Analysis of Binding Affinities and Specificity of VHH Fragments for Gold Surfaces. Gold powder (6 mg) was added to 300 μL of 10 mM phosphate solution (pH 7.5; 200 mM NaCl, 0.05% Tween 20) containing VHH, and the solution was incubated for 30 min at 4 °C. After the solution was centrifuged at 20000*g* for 10 min, the amount of unbound VHH in the supernatant was measured by means of the bicinchoninic acid method with a Micro BCA Protein Assay Reagent Kit (Pierce Biotechnology, Rockford, IL, USA). The amount of protein adsorbed on the gold powder was calculated by subtracting the amount of unbound protein from the total amount of VHH used.

For analysis of the specificity of the VHH fragments for gold surfaces, commercially available gold, platinum, palladium, and silver plates (Nilaco, Tokyo, Japan) were soaked for 30 min in 10 mM phosphate solution (pH 7.5; 200 mM NaCl, 0.1% Tween 20) containing the VHH fragments with a FLAG tag. The plates were washed three times with the same phosphate solution without VHH and then soaked in a solution of mouse anti-FLAG M2 antibody (pH 7.5; 10 mM phosphate, 200 mM NaCl, 0.1% Tween 20). The plates were washed again three times, and the chemiluminescence from peroxidase conjugated to the anti-mouse antibody was observed on the plates.

Suppression of Gold Nanoparticle Aggregation by Gold-Binding VHH Fragments. A solution of gold nanoparticles (size 20 nm; Sigma-Aldrich, Tokyo, Japan) was dialyzed against 10 mM phosphate solution (pH 7.5). To the gold nanoparticle solution, bovine serum albumin (BSA, Sigma-Aldrich) or E32 VHH was added such that the concentrations of the nanoparticles and the protein were 0.1 nM and 40 nM, respectively, at various NaCl concentrations. The absorption spectra of the gold nanoparticle solutions were measured with a U-3000 spectrophotometer (Hitachi, Tokyo, Japan) every 30 min for 360 min, and the difference between the molar extinction coefficients at 523 and 630 nm ($\Delta\varepsilon_{523-630}$) was traced.

SPR Scattering Imaging of Carcinoma Cells Overexpressing EGFR. Gold nanoparticle solutions (size 41.6 nm; Tanaka Kikinzoku Kogyo, Tokyo, Japan) were dialyzed against 10 mM phosphate solution (pH 7.5), and Ia1-E32 VHH dimers were added to the 0.2 nM solution of gold nanoparticles to bring the dimer concentration to 1 μM. The solution of the nanoparticles and dimers was added to 1.0 × 10^4 Chinese hamster ovary cells and A431 cancerous cells. The cells were incubated for 15 min and washed with 10 mM phosphate solution (pH 7.5). SPR scattering images of the washed cells were obtained with an inverted Olympus IX81 microscope (Olympus, Tokyo, Japan) with a dark field condenser (U-DCW). A UPLFLN 100×O2 objective lens was used to collect only the scattered light from the samples.

Assembly of Gold Nanoparticles from Gold-Binding VHH Tetramers. A 36 μM solution of the E32 VHH fragments with the biotin tag at the C-terminus was mixed with 9 μM streptavidin to form E32 VHH tetramers. The tetramerization of E32 VHH was confirmed by gel filtration chromatography (Superdex 200 10/300 size exclusion column, GE Healthcare, Little Chalfont, U.K.). VHH tetramers at various concentrations were mixed with 0.1 nM gold nanoparticles in a 10 mM phosphate solution (pH 7.5). The $\Delta\varepsilon_{523-630}$ values were measured every 30 min for 540 min to observe the aggregation of the gold nanoparticles.

Linkage of Gold and ZnO Nanoparticles via Bispecific VHH Dimers. A 10 mM phosphate solution (1 mL, pH 7.5;

Table 2. Sequences of VHH Fragments after Four Rounds of Selection against Gold Particles[a]

Fragment	CDR3	Number of clones among 100 colonies
	3-1 3-16	
E3 VHH	VRGRRVRGGRLLHFRY	4
E9 VHH	VRGRRVRGGHVLRFRY	4
E12 VHH	VRGRRVRGGRVLRFRY	3
E32 VHH	VRGRRVRGGHLLRFRY	3

[a]Selected sequences are underlined. The amino acids of CDR3 in the selected VHH fragments are numbered as 3-1 to 3-16.[20]

200 mM NaCl) containing 40 μg of ZnO particles (~100 nm; Hosokawa Micron Inc., Hirakata, Japan) was sonicated for 1 min. E32 VHH, 4F2 VHH, and 4F2-E32 dimers were added to the suspension at various concentrations, and then 20 nm gold nanoparticles were added at a final concentration of 0.2 nM. The solutions were centrifuged at 9500g for 5 s, and the absorption spectra of the supernatants were measured.

In addition, solutions of 40−400 μg/mL ZnO particles and 1 μM 4F2-E32 dimeric VHH fragments were allowed to stand for 3 h without centrifugation after the addition of 0.2 nM gold nanoparticles, for observation of spontaneous precipitation of gold and ZnO nanoparticles. In addition, after the gold nanoparticles were added, the solution was dried on collodion-coated 400 mesh copper grids for transmission electron microscopy with a LEO 912 AB OMEGA electron microscope (Carl Zeiss, Oberkochen, Germany) operating 100 kV.

RESULTS

Generation of High-Affinity Gold-Binding VHH Fragments. In CAnIGET method,[20] material-binding peptide is replaced with one of three CDRs in VHH fragment and another CDR was randomized to select high-affinity VHH fragment by means of phage display approach. To generate VHH fragments with high affinity for gold surfaces, we replaced the CDR1 sequence in the VHH fragment of camel anti-BcII β-lactamase antibody cAbBCII10[33] with the sequence of a previously reported gold-binding peptide (GBP) (Table 1).[28] The CDR3 loop in the resulting GBP-grafted VHH fragment (VHH_{GBP1}) was randomized with the $\alpha\beta\beta\alpha$ repeating sequence format, where the α and β residues were randomized to Arg or His and to Arg, Gly, Leu, or Val, respectively; and the randomized VHH fragments were displayed on filamentous bacteriophage M13. The phages were mixed with gold powder, and then the powder was washed with 50−200 mM phosphate solutions containing 0.05% Tween 20 to remove nonspecifically bound phages. Residual phages on the powder were eluted with a highly concentrated phosphate solution (500 mM), which inhibits protein adsorption on inorganic materials.[20,34] After four rounds of selection, we randomly picked 100 colonies and then compiled statistics for the frequency of amino acid residues at each position in CDR3 before selection and after four rounds of selection by analyzing the sequences of the chosen clones (Figure S1 in the Supporting Information). The statistical analysis showed the concentrations of specific amino acids at each position resulting from the molecular evolutional process. Several colonies had the same clones (E3, E9, E12, and E32), each of which had the same arginine-rich sequence (RRVRGG, Table 2). We attempted to estimate the gold-binding affinity of these four clones. However, only the E32

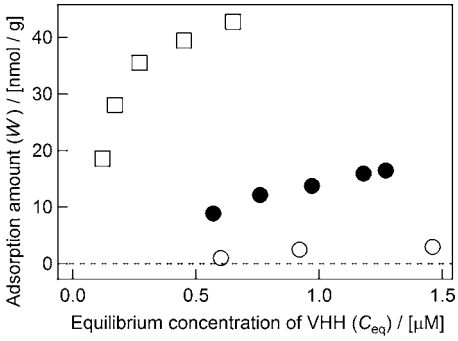


Figure 1. Adsorption isotherms for cAbBCII10 VHH (open circles), VHH_{GBP1} (filled circles), and E32 VHH (open squares) against 6 mg of gold particles in 10 mM phosphate solution (pH 7.5; 200 mM NaCl, 0.05% Tween 20).

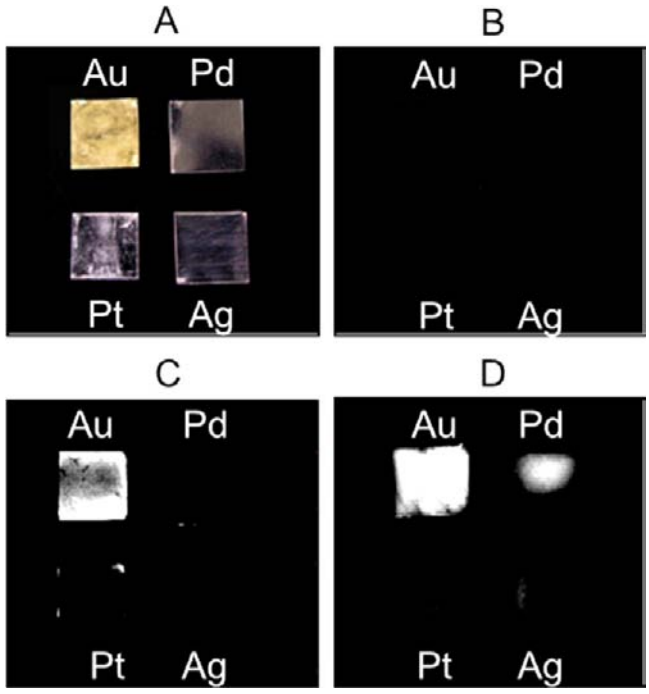


Figure 2. Specificity of VHH_{GBP1} and E32 VHH for material surfaces. Untreated gold, platinum, palladium, and silver plates (A) were soaked in a solution containing cAbBCII10 (B), VHH_{GBP1} (C), or E32 VHH (D), and then the residual VHH fragments with a FLAG tag at the C terminus on the plates were detected by the chemiluminescence from anti-mouse IgG antibody horseradish peroxidise.

dx.doi.org/10.1021/bc300316p | Bioconjugate Chem. 2012, 23, 1934−1944

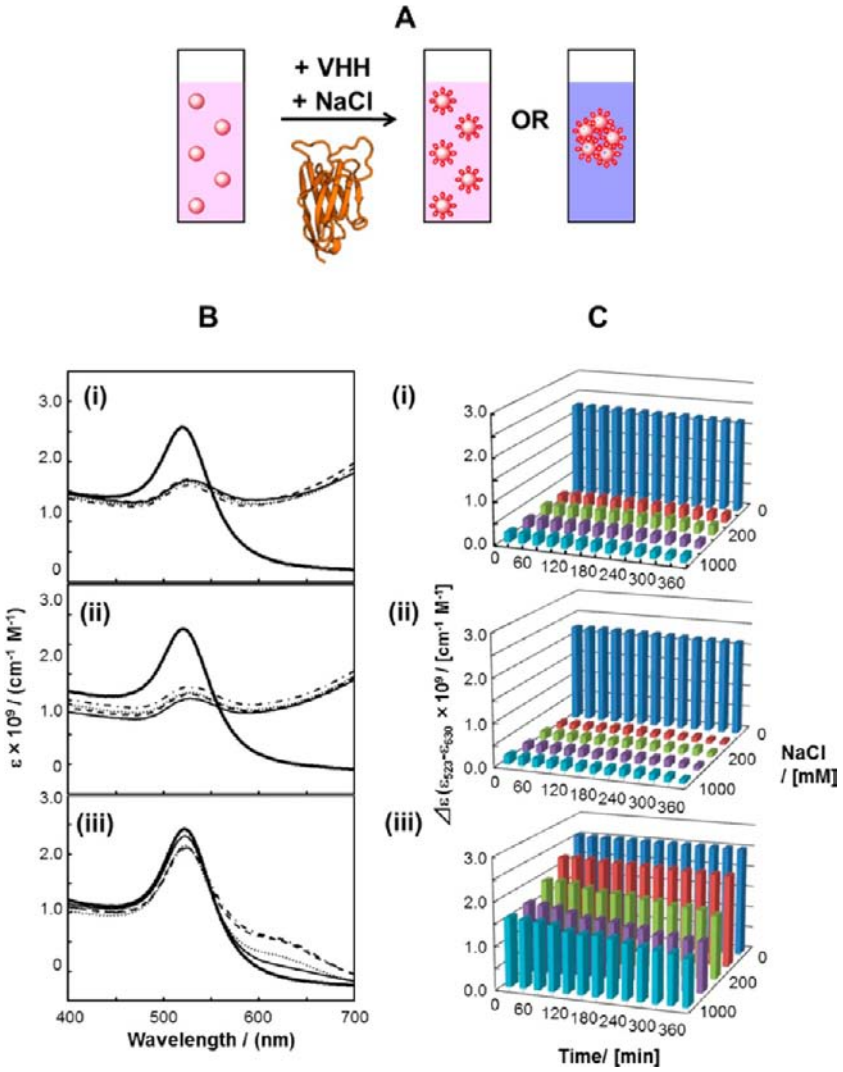


Figure 3. Suppression of gold nanoparticle aggregation by E32 VHH. (A) Experimental scheme for the analysis of aggregation suppression by VHH fragments. (B) Absorption spectra of 0.1 nM gold nanoparticles in 10 mM phosphate solution (pH 7.5) at NaCl concentrations of 0 M (bold solid line), 50 mM (solid line), 200 mM (dotted line), 500 mM (dashed line), and 1000 mM (dashed and dotted line), without protein (i), with 40 nM BSA (ii), and with 40 nM E32 VHH (iii). (C) Time dependence of the plasmon absorption at 520 nm from 0 to 360 min without protein (i), with 40 nM BSA (ii), and with 40 nM E32 VHH (iii) at NaCl concentrations of 0, 50, 200, 500, and 1000 mM.

clone was adequately expressed in *E. coli*, which was used for the binding assay; therefore, we measured the adsorption isotherms of the VHH_{GBP1} and E32 VHH fragments (Figure 1). Only small amounts of the cAbBCII10 VHH fragment were adsorbed on the gold particles (open circles in Figure 1), whereas the VHH_{GBP1} and E32 VHH fragments were bound with dissociation equilibrium constants (K_D) of 3 μM (close circles in Figure 1) and 150 nM (open squares in Figure 1), respectively: the affinity of E32 VHH was about 20 times that of VHH_{GBP1}. The grafting of material-binding peptide in CDR 1 functionalized the VHH fragment and the optimization of CDR3 sequence using phage display method promoted the affinity of the peptide-grafted VHH.

In addition, we also analyzed the affinity of VHH_{GBP1} and E32 VHH fragments for other inorganic materials. We soaked gold, palladium, platinum, and silver plates in a solution containing VHH fragments bearing a FLAG tag at the C termini. After washing the plates, we detected residual VHH fragments on the plates by measuring the chemiluminescence from horseradish peroxidase conjugated with anti-mouse Fc antibody via anti-FLAG M2 mouse antibody. Selective adsorption of the VHH_{GBP1} and E32 VHH fragments on the gold surface was clearly observed, although E32 VHH also bound weakly to palladium (Figure 2). These results indicate that the binding functionalities of VHH_{GBP1} and E32 VHH were selective for gold surfaces.

Suppression of Gold Nanoparticle Aggregation under High-Ionic-Strength Conditions by E32 VHH Fragments. We used the E32 VHH fragments to suppress gold nanoparticle aggregation in aqueous solution as follows. E32 VHH fragments (40 nM) were added to 10 mM phosphate (pH 7.5) solution containing 0.1 nM gold nanoparticles (size: 20 nm, Figure 3A). We chose the 1:400 molar ratio of gold nanoparticles to E32 VHH because at least 400 molecules of E32 VHH are required for complete coverage of the surface of 20 nm gold nanoparticles. A solution of 20 nm gold nanoparticles generally has a plasmon absorption at around 520 nm; however, the nanoparticles aggregate easily as the ionic strength is increased, and as a result, the plasmon absorption is red-shifted from the red to the purple region. Here, we

dx.doi.org/10.1021/bc300316p | *Bioconjugate Chem.* 2012, 23, 1934−1944

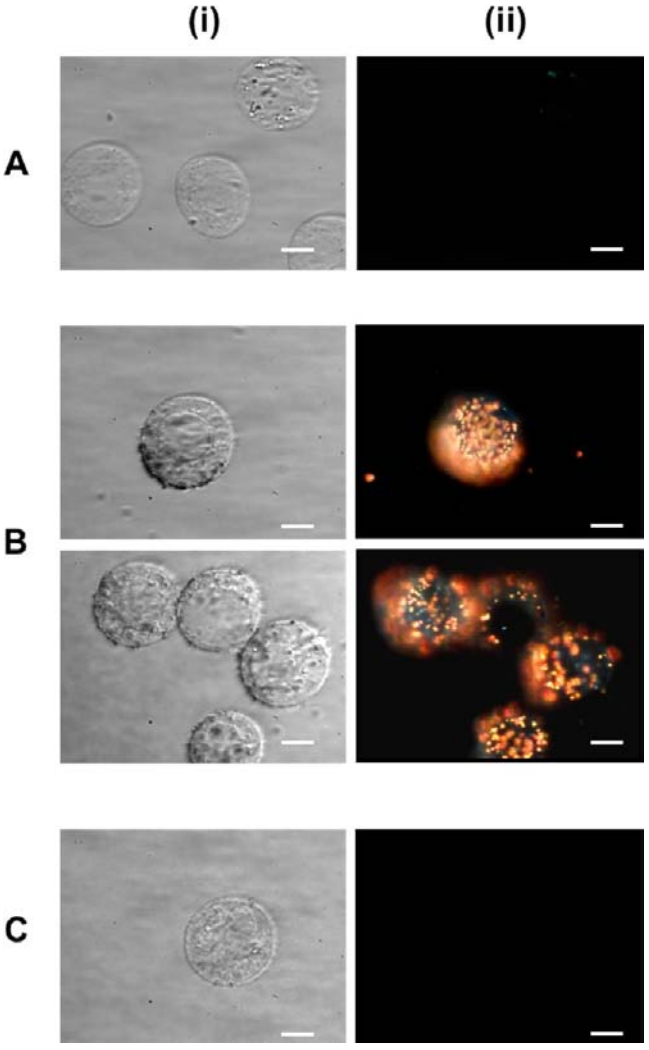


Figure 4. Micrograph (i) and surface plasmon resonance (SPR) scattering image (ii) of A431carcinoma cells with 0.2 nM gold nanoparticles (A), A431carcinoma cells with 1 μM VHH dimer and 0.2 nM gold nanoparticles (B), and CHO noncarcinoma cells with 1 μM VHH dimer and 0.2 nM gold nanoparticles (C). SPR scattering images were obtained by using a dark-field condenser. Gold color shows SPR scattering of gold particles. Scale bars = 10 μm.

observed that the plasmon absorption band of 0.1 nM gold nanoparticles in 10 mM NaCl (data not shown) was red-shifted relative to the band in the absence of NaCl, and the band disappeared when the NaCl concentration was increased to 50 mM in the absence of detergents (Figure 3Bi). Bovine serum albumin (BSA) is often used to inhibit nanoparticle aggregation,[35,36] and the molecular weight (BSA: ~60 kDa) is larger than that of VHH (~15 kDa); however, 40 nM BSA only slightly suppressed the aggregation of gold nanoparticles in 50 mM NaCl solution (Figure 3Bii). In contrast, the addition of 40 nM E32 VHH markedly suppressed aggregation even in 1000 mM NaCl solution (Figure 3Biii). Evaluation of the time dependence of the plasmon absorption at 520 nm at various NaCl concentrations indicated that E32 VHH suppressed the aggregation of gold nanoparticles for 6 h (Figure 3C). Although the plasmon absorption intensity decreased slightly with time at NaCl concentrations exceeding 200 mM even in the presence of E32 VHH, E32 VHH markedly suppressed gold nanoparticle aggregation at all the tested NaCl concentrations.

One-Pot Biofunctionalization of Gold Nanoparticles. Gold nanoparticles can resonantly scatter visible light when their surface plasmon oscillation is excited.[26] Here, we functionalized gold nanoparticles with bispecific VHH dimers with affinity for both EGFR and gold surfaces, for use in cellular imaging by means of SPR scattering. One advantage of working with antibodies is the ability to use various fusion technologies. E32 VHH was fused at the C-terminus of Ia1 VHH with affinity for EGFR[30] via a llama IgG2 upper hinge-linker,[31] and bispecific antibody with affinity for gold and EGFR (Ia1-E32 VHH) was constructed. In the absence of the Ia1-E32 VHH dimer, no SPR scattering was detected on A431 cancerous cells that overexpress EGFR (Figure 4A). In contrast, in the presence of the Ia1-E32 VHH dimer, clear SPR scattering by gold nanoparticles was detected on the cancerous cells (Figure 4B). In addition, we added gold nanoparticles functionalized with Ia1-E32 VHH dimers to Chinese hamster ovary cells on which no EGFRs were expressed; in this case, no SPR scattering from gold nanoparticles was observed even in the presence of the Ia1-E32 VHH dimer (Figure 4C). These results indicate that the dimer interlinked the gold nanoparticles and the EGFR-displaying cancerous cells. The dimer simultaneously stabilized and biofunctionalized the gold nanoparticles.

Construction of Biointerfaces between Nanomaterials. To demonstrate that material-binding camel antibody fragments could serve as biointerfaces between nanomaterials, we constructed E32 VHH tetramers by taking advantage of the biotin−avidin interaction (Figure 5A). E32 VHH fragments (36 μM) with the biotin acceptor peptide fused at the C-termini were mixed with 9 μM streptavidin, and the resulting E32 VHH tetramers were fractionated by size exclusion chromatography (Figure S2 in the Supporting Information). Then the tetramers were added at various concentrations to a 0.1 nM solution of gold nanoparticles in the absence of NaCl. When the tetramer concentration was <20 nM, the plasmon intensity at 520 nm decreased, but no red-shift was observed (Figure 5Bi,ii). However, when the tetramer concentration was >40 nM, the plasmon band was red-shifted (Figure 5Biii,iv), and the plasmon absorption intensity decreased rapidly with time (Figure 5C). These results indicate that the tetramers acted as interface molecules between the gold nanoparticles and that the nanoparticles spontaneously aggregated via the tetramers.

To use a material-binding VHH as a biointerface between different nanomaterials, we also designed bispecific VHH dimers from E32 VHH and a ZnO-binding VHH (4F2 VHH)[20] by fusing E32 VHH at the C-terminus of 4F2 VHH via a hinge-linker. When we centrifuged a suspension containing 0.2 nM gold nanoparticles (20 nm) and 40 μg/mL ZnO particles (~100 nm) with the E32 VHH or 4F2 VHH monomer, only ZnO particles precipitated; as a result, the supernatant had the same plasmon absorption intensity before centrifugation (open and closed circles in Figure 6). In contrast, when bispecific 4F2-E32 VHH dimers were added to the mixture of gold and ZnO particles, the plasmon absorption intensity decreased with increasing dimer concentration (open squares in Figure 6): the plasmon absorption intensity of the gold nanoparticles decreased at a dimer concentration of 40 nM, and complete precipitation of gold and ZnO nanoparticles was observed when the dimer concentration exceeded 500 nM. These results indicate that the 4F2-E32 VHH dimers linked the gold and ZnO particles and induced the precipitation of gold nanoparticles with ZnO.

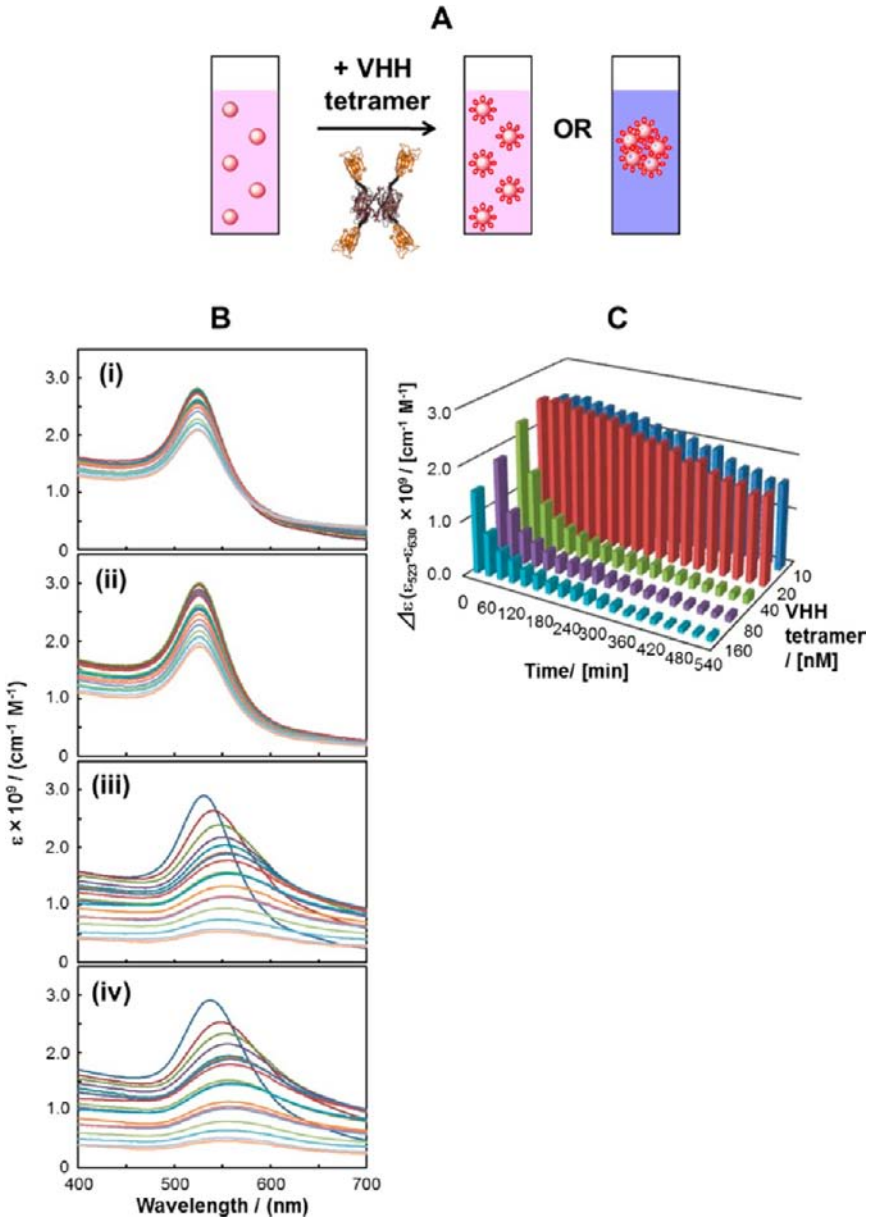


Figure 5. Functionalization of gold nanoparticles with a VHH tetramer. (A) Experimental scheme for functionalization by the VHH tetramer. (B) Time dependence of the absorption spectra of 0.1 nM gold nanoparticles in 10 mM phosphate (pH 7.5) in the presence of 10 nM (i), 20 nM (ii), 40 nM (iii), and 80 nM (iv) VHH tetramer in the absence of NaCl. The spectra were collected every 30 min for 540 min. (C) Aggregation behavior of gold nanoparticles upon addition of the VHH tetramer at various concentrations.

We also observed spontaneous precipitation of gold and ZnO particles in the presence of bispecific 4F2-E32 VHH dimers. We observed no change in a gold nanoparticle solution when ZnO particles were added in the absence of the bispecific dimers; whereas in the presence of dimers (1 μM), the addition of ZnO particles resulted in an immediate change in color of the solution from red to purple, and gold and ZnO particles spontaneously precipitated (Figure 7Ai). Spontaneous precipitation in the presence of bispecific VHH dimers was also observed when the amount of added ZnO particles was increased to 400 μg, and the particle aggregation rate was accelerated (Figure 7Aii).

The ZnO suspensions just after gold nanoparticles were added were dried on collodion-coated grids for transmission electron microscopy (Figure 7B). No gold nanoparticles were observed on the ZnO particles in the absence of the VHH dimer, whereas many gold nanoparticles were observed on the ZnO particles in the presence of the VHH dimer. These results indicate that the bispecific 4F2-E32 VHH dimers linked the ZnO and gold nanoparticles and induced spontaneous precipitation of both types of nanoparticles.

DISCUSSION

Generation of VHH Fragments with High Affinity and Specificity for Gold Surfaces. Antibodies are naturally occurring proteins with excellent molecular recognition in the immune system, and they have been widely used in medical, sensing, and imaging applications.[37,38] A few antibodies that can bind inorganic material surfaces have been identified,[24,39,40] but the number of material-binding antibodies is far lower than the number of material-binding peptides because of the low immunogenic potential of inorganic materials. Even when in

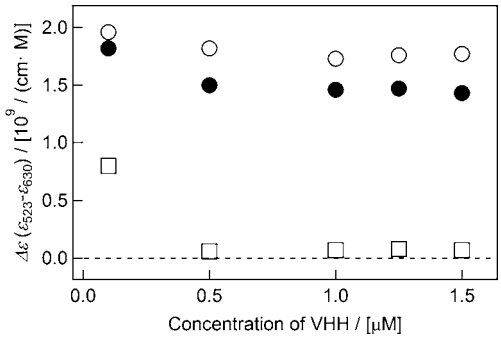


Figure 6. Absorption intensity of the plasmon band at 520 nm in the supernatant of a mixture of gold and ZnO nanoparticles at various concentrations (0.1, 0.5, 1.0, 1.25, and 1.5 μM) of E32 VHH (open circles), 4F2 VHH (filled circles), and VHH dimer (open squares) after centrifugation.

vitro selection methods are used, the fact that antibody fragments have higher molecular weights than peptides limits the library diversity. Previously, Barbas et al. generated the human antibody fragments with affinity for integrins by a combination of peptide grafting and in vitro selection: the sequence of the integrin-binding tripeptide (Arg-Gly-Asp) was grafted in a CDR, and the conformation of the grafted CDR was optimized by in vitro selection.[41] On the basis of their concept (a combination of peptide grafting and in vitro selection), we, recently, proposed the CAnIGET approach and conveniently generated the antibody fragments with high affinity for ZnO, CoO, and Al_2O_3 surfaces.[20,23] This method involves the application of the variable domain of a camel VHH, which is a simple single domain, as a scaffold for peptide grafting. The VHH domain is functionalized by replacing one CDR loop with a material-binding peptide and randomizing another CDR loop and selecting high-affinity fragments.

In this study, we grafted a previously reported gold-binding peptide sequence of GBP into the CDR1 loop of cAbBCII10 and selected high-affinity VHH fragments from a library in which the CDR3 loop of VHH_{GBP1} was randomized with an $\alpha\beta\beta\alpha$ motif (Arg or His at the α position, and Arg, Gly, Leu, or Val at the β position). After the selection of high-affinity clones, a specific amino acid was selected at each position. Interestingly, Arg was predominantly selected at the α positions (Figure S1 in the Supporting Information), and four clones (E3, E9, E12, and E32) found in several colonies among the 100 colonies that were chosen had the same Arg-rich alignment sequence (RRVRGG, Table 2). A His residue has been found in many previously reported material-binding peptides, but a study of the use of homopolypeptides for the adsorption on gold surfaces suggested that Arg and Thr residues have an affinity for gold surfaces.[42] This suggestion supports the preferred selection of Arg in CDR3 that we observed in this study.

Both VHH_{GBP1} and E32 VHH had specificity for gold surfaces (Figure 2C,D). This result supports our previous suggestion that the specificity of a selected VHH for inorganic materials depends on the peptide grafted into CDR1.[20] Recently, we identified a fragment of variable region (Fv) of a human antibody, A14P-b2, with affinity and specificity for gold surfaces from a phage-displayed library of a human antibody library.[24] The fragment was used for specific patterning of proteins and for an immunoassay on a gold-patterned substrate.[24] However, the fact that the human Fv is a heterodimer composed of the variable regions of the heavy chain (VH) and light chain (VL) complicates the design of bispecific molecules, such as diabodies and tandem single-chain Fvs (scFvs);[43] consequently, the preparation of bispecific antibodies in bacteria is often difficult. Previously, we used only the VH domain of A14P-b2 to generate a bispecific molecule by fusing the VH at the terminus of an antilysozyme scFv, and we demonstrated the use of the VH-scFv molecule for an immunoassay.[19,44] However, isolated VH domains tend to aggregate.[45] In the current study, we generated a gold-binding VHH fragment, which is a simple single domain and is stable even without the light chain fragment, and we expected that bispecific molecules generated with the VHH would be more stable.

One-Pot Functionalization of Gold Nanoparticles by Means of Gold-Binding VHH Fragments. Gold nanoparticles strongly absorb and scatter visible and near-infrared light by means of plasmon resonance.[2,25,26] The optical properties of nanoparticles depend on their size and colloidal stability, and they can be used as probes for sensing[25] and imaging[26] applications. The colloidal stability of gold nanoparticles is determined by the balance between van der Waals and electrostatic interactions.[46,47] Bare gold nanoparticles aggregate in response to small changes in ionic strength, owing to a decrease in electrostatic repulsion between particles that occurs upon binding of counterions to the particle surfaces. Surface modification with surfactants, polymers, or biomolecules can suppress the aggregation.[48]

Chemical coupling between gold and thiol groups has been often used to conjugate organic molecules to gold nanoparticle surfaces.[48] Proteins can be conjugated to the nanoparticles if the organic molecule linker has an appropriate functional group at the terminus opposite to the thiol group. However, the series of reactions required to generate such biofunctionalized gold nanoparticles is complicated, and it often reduces the activity of the immobilized proteins because the method cannot offer control of protein orientation at the surface and get around denaturation of proteins.[49] Here, we performed one-pot functionalization of gold nanoparticles by using the high-affinity, high-specificity interaction of material-binding antibody fragments with material surfaces. We obtained high-affinity E32 VHH fragments that spontaneously bound to gold nanoparticles and suppressed nanoparticle aggregation even in a high-ionic-strength solution. In addition, the simple single-domain structure of the VHH enabled us to design bispecific dimers by fusing different VHH fragments at the N-terminus of E32 VHH. For example, an anti-EGFR VHH was orientationally immobilized on gold nanoparticles in a single step.

In general, to obtain biofunctional nanoparticles for sensing and imaging, IgG-type antibodies with molecular weights of ~150 kDa (15 nm) are conjugated to gold nanoparticles. Conjugating several antibodies on a single nanoparticle is generally difficult. However, because the VHH dimers used in this study (~30 kDa) were much smaller than IgG type antibodies, the antigen-binding domains could be more efficiently and densely conjugated on the gold nanoparticles. The resulting functionalized nanoparticles can be expected to be useful for diagnostic applications such as gold labeling[50,51] and photothermal therapy involving gold nanorods.[52]

High-Affinity VHH Fragments as Interface Molecules. Although nanomaterials that have strictly controlled shapes and disperse completely in solution can self-assemble by means of two-dimensional crystallization,[7,8] interface linkers that act as a

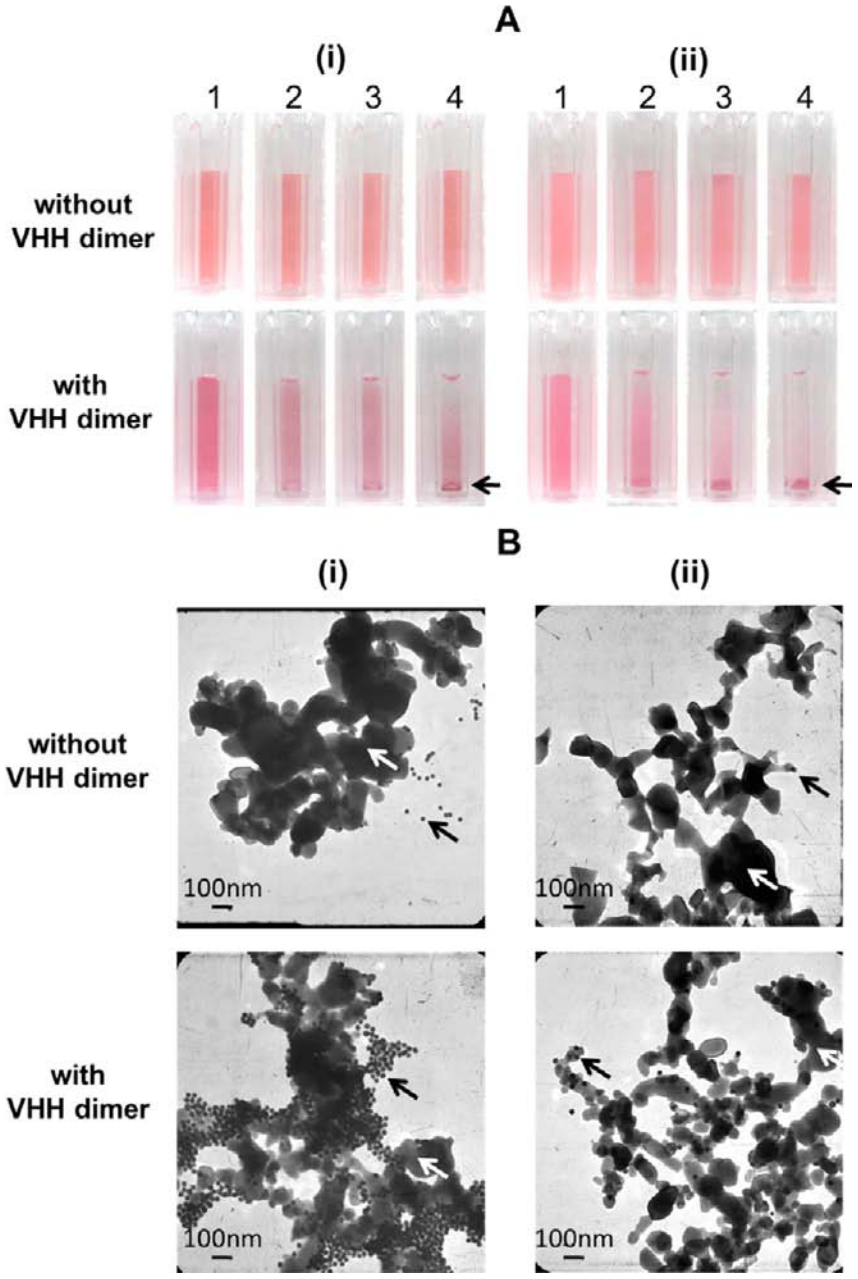


Figure 7. (A) Photographs showing spontaneous precipitation before the addition of 1 μM VHH dimer (1) and 60 min (2), 120 min (3), and 180 min (4) after addition of the dimer. (B) Transmission electron microscopy images of the mixture of gold nanoparticles (0.2 nM) and ZnO nanoparticles: 40 μg/mL (i) and 400 μg/mL (ii).

glue between different nanomaterials can facilitate complicated bottom-up assembly of nanodevices. Biomolecules such as nucleic acids and polypeptides are among the most attractive linkers because of their high specificity. For example, DNA–DNA,[53] biotin–avidin,[54,55] and antigen–antibody[56] interactions have been used to mediate self-assembly of nanomaterials by covalently conjugating the biomolecules on nanoparticles. In this study, we generated biomolecules with direct affinity for the surface of inorganic nanoparticles, which obviated the need for the fabrication of nanoparticle surfaces with specific functional groups for conjugating biomolecules. Many peptides with affinity for inorganic material surfaces have been identified by means of combinatorial approaches, and such peptides have been used for the patterning of nanoparticles and proteins on films.[13,57,58] However, there have been fewer reports on the use of material-binding peptides to link nanoparticles because the binding affinity of such peptides is not sufficient to overcome electrostatic interactions between nanoparticles or the Brownian motion of nanoparticles.[47,48] Here, we generated high-affinity gold-binding antibody fragments, and we used some previously reported structural formats of various multivalent and multispecific antibodies[43] to create tetravalent antibodies from gold-binding VHH fragments and bispecific VHH dimers by fusing a ZnO-binding VHH with a gold-binding VHH. These multivalent and multispecific antibody fragments spontaneously linked two different types of nanoparticles (gold–gold, gold–ZnO). Our results demonstrate the potential of high-affinity multivalent and bispecific antibodies to act as glues between nanomaterials.

In conclusion, we generated antibody fragments with high affinity and specificity for gold nanoparticle surfaces by a one-pot procedure involving integration of peptide-grafting and phage-display techniques. The resulting antibody fragment suppressed the aggregation of gold nanoparticles even in a high-ionic-strength solution, and multivalent and bispecific antibody fragments based on the gold-binding VHH could be used to selectively contact gold nanoparticles with cells displaying the EGFR receptor, as well as to spontaneously link two different nanomaterials (gold−gold, gold−ZnO). We describe the utilization of high affinitive material-binding antibody fragments for one-pot functionalization of gold nanoparticles.

■ ASSOCIATED CONTENT

Supporting Information

Additional figures for the frequencies of amino acids in randomized CDR3 loop of VHH_{GBP1} and the size-exclusion chromatography for E32 tetramer. This material is available free of charge via the Internet at http://pubs.acs.org.

■ AUTHOR INFORMATION

Corresponding Author

*Tel and fax: +81-22-795-7276. E-mail: mitsuo@kuma.che.tohoku.ac.jp.

Notes

The authors declare no competing financial interest.

■ ACKNOWLEDGMENTS

This work was supported by a Scientific Research Grant from the Ministry of Education, Science, Sports, and Culture of Japan (M.U. and I.K.), by Precursory Research for Embryonic Science and Technology from the Japan Science and Technology Agency (JST, M.U.), and JSPS research fellowships for young scientists (T.H.).

■ ABBREVIATIONS

BSA, bovine serum albumin; CAnIGET, construction of antibodies by integrating grafting and evolution technology; CDR, complementarity determining regions; EGFR, epidermal growth factor receptor; GBP, gold-binding peptide; SPR, surface plasmon resonance; VHH, variable domain of the heavy chain of a heavy chain camel antibody

■ REFERENCES

(1) Chan, W. C. W., and Nie, S. (1998) Quantum Dot Bioconjugates for Ultrasensitive Nonisotopic Detection. *Science 281*, 2016−2018.

(2) Cao, Y., Jin, R., and Mirkin, C. (2002) Nanoparticles with Raman spectroscopic fingerprints for DNA and RNA detection. *Science 297*, 1536−1540.

(3) Joo, S. H., Choi, S. J., Oh, I., Kwak, J., Liu, Z., Terasaki, O., and Ryoo, R. (2001) Ordered nanoporous arrays of carbon supporting high dispersions of platinum nanoparticles. *Nature 412*, 169−172.

(4) Caruso, F., Caruso, R. A., and Möhwald, H. (1998) Nano-engineering of inorganic and hybrid hollow spheres by colloidal templating. *Science 282*, 1111−1114.

(5) Gao, X., Cui, Y., Levenson, R. M., Chung, L. W. K., and Nie, S. (2004) In vivo cancer targeting and imaging with semiconductor quantum dots. *Nat. Biotechnol. 22*, 969−976.

(6) Mornet, S., Vasseur, S., Grasset, F., and Duguet, E. (2004) Magnetic nanoparticle design for medical diagnosis and therapy. *J. Mater. Chem. 14*, 2161−2175.

(7) Zhang, J., Ohara, S., Umetsu, M., Naka, T., Hatakeyama, Y., and Adschiri, T. (2007) Colloidal Ceria Nanocrystals: A Tailor-made Crystal Morphology in Supercritical Water. *Adv. Mater. 19*, 203−206.

(8) Shevchenko, E. V., Talapin, D. V., Kotov, N. A., O'Brien, S., and Murray, C. B. (2006) Structural diversity in binary nanoparticle superlattices. *Nature 439*, 55−59.

(9) Whaley, S. R., English, D. S., Hu, E. L., Barbara, P. E., and Belcher, A. M. (2000) Selection of peptides with semiconductor binding specificity for directed nanocrystal assembly. *Nature 405*, 665−668.

(10) Sarikaya, M., Tamerler, C., Jen, A. K-Y., Schulten, K., and Baneyx, F. (2003) Molecular biomimetics: nanotechnology through biology. *Nat. Mater. 2*, 577−585.

(11) Naik, R. R., Stringer, S. J., Agarwal, G., Jones, S. E., and Stone, M. O. (2002) Biomimetic synthesis and patterning of silver nanoparticles. *Nat. Mater. 1*, 169−172.

(12) Mao, C., Solis, D. J., Reiss, B. D., Kottmann, S. T., Sweeney, R. Y., Hayhurst, A., Georgiou, G., Iverson, B., and Belcher, A. M. (2004) Virus-based toolkit for the directed synthesis of magnetic and semiconducting nanowires. *Science 303*, 213−217.

(13) Shimada, Y., Suzuki, M., Sugiyama, M., Kumagai, I., and Umetsu, M. (2011) Bioassisted capture and release of nanoparticles on nano-lithographed ZnO films. *Nanotechnology 22*, 275302(1−6).

(14) Park, T. J., Lee, S. Y., Lee, S. J., Park, J. P., Yang, K. S., Lee, K. B., Ko, S., Park, J. B., Kim, T., Kim, S. K., Shin, Y. B., Chung, B. H., Ku, S. J., Kim do, H., and Choi, I. S. (2006) Protein nanopatterns and biosensors using gold binding polypeptide as a fusion partner. *Anal. Chem. 78*, 7197−7205.

(15) Zhou, W., Schwartz, D. T., and Baneyx, F. (2010) Single-pot biofabrication of zinc sulfide immuno-quantum dots. *J. Am. Chem. Soc. 132*, 4731−4738.

(16) Umetsu, M., Mizuta, M., Tsumoto, K., Ohara, S., Takami, S., Watanabe, H., Kumagai, I., and Adschiri, T. (2005) Bioassisted room-temperature immobilization and mineralization of zinc oxide - the structural ordering of ZnO nanoparticles into a flower-type morphology. *Adv. Mater. 17*, 2571−2575.

(17) Kramer, R. M., Li, C., Carter, D. C., Stone, M. O., and Naik, R. R. (2004) Engineered Protein Cages for Nanomaterial Synthesis. *J. Am. Chem. Soc. 126*, 13282−13286.

(18) Chiu, C.-Y., Li, Y., Ruan, L., Ye, X., Murray, C. B., and Huang, Y. (2011) Platinum nanocrystals selectively shaped using facet-specific peptide sequences. *Nat. Chem. 3*, 393−399.

(19) Ibii, T., Kaieda, M., Hatakeyama, S., Shiotuka, H., Kumagai, I., Watanabe, H., Umetsu, M., and Imamura, T. (2010) Direct immobilization of gold-binding antibody fragments for immunosensor applications. *Anal. Chem. 82*, 4229−4235.

(20) Hattori, T., Umetsu, M., Nakanishi, T., Togashi, T., Yokoo, N., Abe, H., Ohara, S., Adschiri, T., and Kumagai, I. (2010) High affinity anti-inorganic material antibody generation by integrating graft and evolution technologies. Potential of antibodies as biointerface molecules. *J. Biol. Chem. 285*, 7784−7793.

(21) Bogan, A. A., and Thorn, K. S. (1998) Anatomy of hot spots in protein interfaces. *J. Mol. Biol. 280*, 1−9.

(22) Li, Y., Li, H., Yang, F., Smith-Gill, S. J., and Mariuzza, R. A. (2003) X-ray snapshots of the maturation of an antibody response to a protein antigen. *Nat. Struct. Biol. 10*, 482−488.

(23) Hattori, T., Umetsu, M., Nakanishi, T., Tsumoto, K., Ohara, S., Abe, H., Naito, M., Asano, R., Adschiri, T., and Kumagai, I. (2008) Grafting of material-binding function into antibodies: functionalization by peptide grafting. *Biochem. Biophys. Res. Commun. 365*, 751−757.

(24) Watanabe, H., Nakanishi, T., Umetsu, M., and Kumagai, I. (2008) Human anti-gold antibodies: Biofunctionalization of gold nanoparticles and surfaces with anti-gold antibodies. *J. Biol. Chem. 283*, 36031−38.

(25) Mirkin, C. A., Letsinger, R. L., Mucic, R. C., and Storhoff, J. J. (1996) A DNA-based method for rationally assembling nanoparticles into macroscopic materials. *Nature 382*, 607−609.

(26) El-Sayed, I. H., Huang, X., and El-Sayed, M. A. (2005) Surface plasmon resonance scattering and absorption of anti-EGFR antibody conjugated gold nanoparticles in cancer diagnostics: applications in oral cancer. *Nano Lett. 5*, 829−834.

(27) Huang, J.-S., Callegari, V., Geisler, P., Brüning, C., JKern, J., Prangsma, J. C., Wu., X., Feichtner, T., Ziegler, J., Weinmann, P., Kamp, M., Forchel, A., Biagioni, P., Sennhauser, U., and Hecht, B. (2010) Atomically flat single-crystalline gold nanostructures for plasmonic nanocircuitry. *Nat. Commun. 1*, 150(1−8).
(28) Nam, K. T., Kim, D. W., Yoo, P. J., Chiang, C. Y., Meethong, N., Hammond, P. T., Chiang, Y. M., and Belcher, A. M. (2006) Virus-enabled synthesis and assembly of nanowires for lithium ion battery electrodes. *Science 312*, 885−888.
(29) Maenaka, K., Furuta, M., Tsumoto, K., Watanabe, K., Ueda, Y., and Kumagai, I. (1996) A stable phage-display system using a phagemid vector: phage display of hen egg-white lysozyme (HEL), Escherichia coli alkaline, phosphatase, and anti-HEL monoclonal antibody, HyHEL10. *Biochem. Biophys. Res. Commun. 218*, 682−687.
(30) Roovers, R. C., Laeremans, T., Huang, L., De Taeye, S., Verkleij, A. J., Revets, H., De Haard, H. J., and Van Bergen En Henegouwen, P. M. P. (2007) Efficient inhibition of EGFR signalling and of tumour growth by antagonistic anti-EGFR nanobodies. *Cancer Immunol. Immunother. 56*, 303−317.
(31) Conrath, K., Lauwereys, M., Wyns, L., and Muyldermans, S. (2001) Camel single-domain antibodies as modular building units in bispecific and bivalent antibody constructs. *J. Biol. Chem. 276*, 7346−7350.
(32) Cloutier, S. M., Couty, S., Terskikh, A., Marguerat, L., Crivelli, V., Pugnières, M., Mani, J., Leisinger, H., Mach, J., and Deperthes, D. (2000) Streptabody, a high avidity molecule made by tetramerization of in vivo biotinylated, phage display-selected scFv fragments on streptavidin. *Mol. Immunol. 37*, 1067−1077.
(33) Saerens, D., Pellis, M., Loris, R., Pardon, E., Dumoulin, M., Matagne, A., Wyns, L., Muyldermans, S., and Conrath, K. (2005) Identification of a universal VHH framework to graft non-canonical antigen-binding loops of camel single-domain antibodies. *J. Mol. Biol. 352*, 597−607.
(34) Yokoo, N., Togashi, T., Umetsu, M., Tsumoto, K., Hattori, T., Nakanishi, T., Ohara, S., Takami, S., Naka, T., Abe, H., Kumagai, I., and Adschiri, T. (2010) Direct and selective immobilization of proteins by means of an inorganic material-binding peptide: discussion on functionalization in the elongation to material-binding peptide. *J. Phys. Chem. B 114*, 480−486.
(35) Krämer, S., Xie, H., Gaff, J., Williamson, J. R., Tkachenko, A. G., Nouri, N., Feldheim, D. A., and Feldheim, D. L. (2004) Preparation of protein gradients through the controlled deposition of protein-nanoparticle conjugates onto functionalized surfaces. *J. Am. Chem. Soc. 126*, 5388−5395.
(36) Burt, J. L., Gutiérrez-Wing, C., Miki-Yoshida, M., and José-Yacamán, M. (2004) Noble-metal nanoparticles directly conjugated to globular proteins. *Langmuir 20*, 11778−11783.
(37) Adams, G. P., and Weiner, L. M. (2005) Monoclonal antibody therapy of cancer. *Nat. Biotechnol. 23*, 1147−1157.
(38) Sharkey, R. M., Cardillo, T. M., Rossi, E. A., Chang, C. H., Karacay, H., McBride, W. J., Hansen, H. J., Horak, I. D., and Goldenberg, D. M. (2005) Signal amplification in molecular imaging by pretargeting a multivalent, bispecific antibody. *Nat. Med. 11*, 1250−1255.
(39) Barbas, C. F., Rosenblum, J., and Lerner, R. (1993) Direct selection of antibodies that coordinate metals from semisynthetic combinatorial libraries. *Proc. Natl. Acad. Sci. U.S.A. 90*, 6385−6389.
(40) Schnirman, A. A., Zahavi, E., Yeger, H., Rosenfeld, R., Benhar, I., Reiter, Y., and Sivan, U. (2006) Antibody molecules discriminate between crystalline facets of a gallium arsenide semiconductor. *Nano Lett. 6*, 1870−1874.
(41) Barbas, C. F., Languino, L. R., and Smith, J. W. (1993) High-affinity self-reactive human antibodies by design and selection: Targeting the integrin ligand binding site. *Proc. Natl. Acad. Sci. U.S.A. 90*, 10003−10007.
(42) Peelle, B. R., Krauland, E. M., Wittrup, K. D., and Belcher, A. M. (2005) Design criteria for engineering inorganic material-specific peptides. *Langmuir 21*, 6929−6933.
(43) Holliger, P., and Hudson, P. J. (2005) Engineered antibody fragments and the rise of single domains. *Nat. Biotechnol. 23*, 1126−1136.
(44) Watanabe, H., Kanazaki, K., Nakanishi, T., Shiotsuka, H., Hatakeyama, S., Kaieda, M., Imamura, T., Umetsu, M., and Kumagai, I. (2011) Biomimetic engineering of modular bispecific antibodies for biomolecule immobilization. *Langmuir 27*, 9656−9661.
(45) Ward, E. S., Güssow, D., Griffiths, A. D., Jones, P. T., and Winter, G. (1989) Binding activities of a repertoire of single immunoglobulin variable domains secreted from Escherichia coli. *Nature 341*, 544−546.
(46) Derjaguin, B. V., and Landau, L. (1941) Theory of the stability of strongly charged lyophobic sols and of the adhesion of strongly charged particles in solutions of electrolytes. *Acta Physicochim. URSS 14*, 633−662.
(47) Verwey, E. J. W. (1947) Theory of the stability of lyophobic colloids. *J. Phys. Colloid Chem. 51*, 631−636.
(48) Daniel, M. C., and Astruc, D. (2004) Gold nanoparticles: assembly, supramolecular chemistry, quantum-size-related properties, and applications toward biology, catalysis, and nanotechnology. *Chem. Rev. 104*, 293−346.
(49) Norde, W. (1986) Adsorption of proteins from solution at the solid-liquid interface. *Adv. Colloid Interface Sci. 25*, 267−340.
(50) Lucocq, J. (1994) Quantitation of gold labelling and antigens in immunolabelled ultrathin sections. *J. Anat. 184*, 1−13.
(51) Mayhew, T. M., Muhlfeld, C., Vanhecke, D., and Ochs, M. (2009) A review of recent methods for efficiently quantifying immunogold and other nanoparticles using TEM sections through cells, tissues and organs. *Ann. Anat. 191*, 153−170.
(52) El-Sayed, I. H., Huang, X., and El-Sayed, M. A. (2006) Selective laser photo-thermal therapy of epithelial carcinoma using anti-EGFR antibody conjugated gold nanoparticles. *Cancer Lett. 239*, 129−135.
(53) Jones, M. R., Macfarlane, R. J., Lee, B., Zhang, J., Young, K. L., Senesi, A. J., and Mirkin, C. A. (2010) DNA-nanoparticle superlattices formed from anisotropic building blocks. *Nat. Mater. 9*, 913−917.
(54) Connolly, S., Fitzmaurice, D. S., and Connolly, D. (1999) Fitzmaurice, Programmed assembly of gold nanocrystals in aqueous solution. *Adv. Mater. 11*, 1202−1205.
(55) Dimitrijevic, N. M., Saponjic, Z. V., Rabatic, B. M., and Rajh, T. (2005) Assembly and charge transfer in hybrid TiO_2 architectures using biotin-avidin as a connector. *J. Am. Chem. Soc. 127*, 1344−1345.
(56) Shenton, W., Davis, S. A., and Mann, S. (1999) Directed self-assembly of nanoparticles into macroscopic materials using antibody−antigen recognition. *Adv. Mater. 11*, 449−452.
(57) Kacar, T., Ray, J., Gungormus, M., Oren, E. E., Tamerler, C., and Sarikaya, M. (2009) Quartz binding peptides as molecular linkers towards fabricating multifunctional micropatterned substrates. *Adv. Mater. 21*, 295−299.
(58) Wei, J. H., Kacar, T., Tamerler, C., Sarikaya, M., David, S., and Ginger, D. S. (2009) Nanopatterning peptides as bifunctional inks for templated assembly. *Small 5*, 689−693.

Bioconjugate Chemistry

Article

pubs.acs.org/bc

Optochemogenetics (OCG) Allows More Precise Control of Genetic Engineering in Mice with CreER regulators

Xin Lu,[†,‡,§,¶] Sarit S. Agasti,[⊥,¶] Claudio Vinegoni,[⊥] Peter Waterman,[⊥] Ronald A. DePinho,*[,†,‡,§] and Ralph Weissleder*[,⊥,∥]

[†]Department of Genomic Medicine, UT MD Anderson Cancer Center, Houston, Texas 77054, United States

[⊥]Center for Systems Biology, Massachusetts General Hospital/Harvard Medical School, Boston, Massachusetts 02114, United States

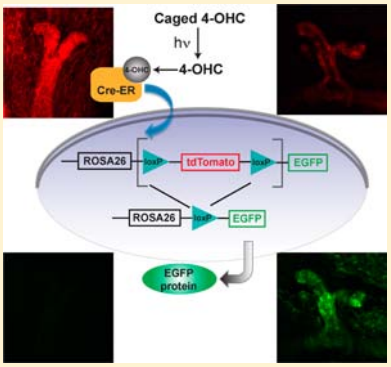
[∥]Department of Systems Biology, Harvard Medical School, Boston, Massachusetts 02114, United States

[‡]Department of Medical Oncology, Dana-Farber Cancer Institute, Boston, Massachusetts 02115, United States

[§]Department of Genetics and Department of Medicine, Harvard Medical School, Boston, Massachusetts 02115, United States

Supporting Information

ABSTRACT: New approaches that allow precise spatiotemporal control of gene expression in model organisms at the single cell level are necessary to better dissect the role of specific genes and cell populations in development, disease, and therapy. Here, we describe a new optochemogenetic switch (OCG switch) to control CreER/loxP-mediated recombination via photoactivatable ("caged") tamoxifen analogues in individual cells in cell culture, organoid culture, and *in vivo* in adult mice. This approach opens opportunities to more fully exploit existing CreER transgenic mouse strains to achieve more precise temporal- and location-specific regulation of genetic events and gene expression.



INTRODUCTION

Site-specific recombination mediated by Cre recombinase is a powerful genetic tool to manipulate genetic elements in model organisms.[1] When placed under the control of a tissue-specific promoter, Cre/LoxP-mediated recombination allows tissue-specific investigation of gene functions.[1] Fusing Cre with a mutant form of the estrogen receptor (ER) ligand binding domain further enables temporal control of recombination.[1] While this conditional CreER system allows for temporal control, the spatial control through tissue-specific promoters is limited by relatively broad activation in all target cells, nonspecificity of many of such cell type-"specific" promoters and/or the lack of validated promoters in certain cell types. We argue that, to better dissect the roles of different cell populations within tissues and organs, it would be highly desirable to develop methods that allow cell rather than tissue specific gene activation.

The prerequisite for selectively modulating biological function at a cellular level is the use of activation tools that can be confined to a cellular or even subcellular volume. Light can be used as an external orthogonal stimulus to activate biological functions in a spatiotemporally controlled fashion.[2,3] Light can furthermore be manipulated in a very precise manner to achieve activation of groups of cells or even individual cells in spatially defined regions of interest. Photochemical control of protein functions has been achieved through a variety of approaches, including caged small molecules, installation of caging groups or photoswitchable groups on the proteins, or fusion with photoactivatable protein domains.[4] A general method for creating photoactivatable caging systems is to first mask the activity of the biologically active substance through attachment of a photolabile protecting group, termed "caging group". Light then can be used to remove this caging group to activate and restore the native biological activity of the parent compound.[5−7] This approach has been applied to address various biological questions regarding cellular signaling pathways and neurological processes.[6,8−10]

Several approaches have been developed to render Cre-mediated recombination inducible by light. One study showed that Cre activity can be photoregulated by caging the critical residue Tyr324 in the protein structure.[11] However, the *in vivo* application of the method would require the generation of new Cre mutant animals. Alternatively, certain small molecule ER antagonists (tamoxifen and its derivatives) can be caged and photoreleased to control CreER activity. The feasibility of these approaches has been demonstrated in cell culture systems and the zebrafish model.[12−15] However, it is currently unknown whether caged tamoxifen analogues would work reliably in CreER transgenic mice where pharmacokinetics of caged drugs, delivery barriers, and complex light/tissue interactions are

Received: June 15, 2012
Revised: July 16, 2012
Published: August 23, 2012

ACS Publications © 2012 American Chemical Society

dx.doi.org/10.1021/bc300319c | *Bioconjugate Chem.* 2012, 23, 1945−1951

formidable obstacles. To address this question, we synthesized a caged tamoxifen analogue and applied the compound to a series of *in vitro* and *in vivo* photoactivation experiments to investigate whether it could reliably induce efficient light-dependent Cre-mediated recombination in mice. We confirmed the activity of this photochemogenetic (OCG) switch and suggest its application may significantly improve the current methods of modeling human diseases in mice where the CreER technology is employed.

EXPERIMENTAL PROCEDURES

Reagents and Instruments. Unless otherwise stated, all the reagents for the synthesis of caged 4-hydroxycyclofen (4-OHC) were obtained from Sigma-Aldrich (St. Louis, Missouri, USA) and used as received. ^{1}H NMR spectra were recorded on a Varian 400 MHz spectrometer. High-performance liquid chromatography−mass spectrometry (HPLC-MS) analysis was performed on a Waters (Milford, MA) LC-MS system. In the LC-MS system, electrospray ionization (ESI) was used to obtain mass spectrometry. A Waters XTerra C18 5 μm column was used for HPLC-MS analysis (eluents: 0.1% trifluoroacetic acid (v/v) in water and acetonitrile; gradient: 0−9.5 min, 5−100% B; 9.5−10.0 min 100% B). The chromatograms were processed using *MassLynx* software (from Waters). UV−vis spectra were recorded in a TECAN microplate reader. A 6 W hand-held UV lamp (UVP, LLC) was used for uncaging the caged 4-OHC both *in vitro* and *in vivo*.

Mice. All animal studies were approved by the Institutional Animal Care Committee. Homozygous *Rosa26CreER^{T2}*, *mT/mG*, and *R26R* mice in C57BL/6 background were obtained from Jackson Laboratory (Stock Number: 8463, 7676 and 3474, respectively). Heterozygous *Rosa26CreER^{T2};mT/mG*, and *Rosa26CreER^{T2};R26R* mice were generated by crossing the homozygous mice and were then used throughout the study.

Synthesis of Caged 4-OHC. The DMNPE caging group and 4-OHC were synthesized by following a previously described procedure.[14,27] 1-(4,5-Dimethoxy-2-nitrophenyl)-ethyl (DMNPE) moiety was conjugated to 4-OHC under Mitsonobu coupling conditions. Briefly, in a 25 mL round-bottom flask, DMNPE (0.014 g, 0.063 mmol), 4-OHC (0.020 g, 0.057 mmol), and triphenyl phosphine (PPh_3, 0.016 g, 0.063 mmol) were mixed together in 0.5 mL of tetrahydrofuran (THF) under an argon atmosphere. After stirring the solution at room temperature (RT) for ∼5 min, diisopropyl azodicarboxylate (DIAD, 0.012 mL, 0.063 mmol) was added dropwise to the reaction mixture. The reaction mixture was allowed to stir at RT for ∼2.5 h. The crude product was directly charged to a SiO_2 column for purification (eluent: 100% dichloromethane to 10% methanol in dichloromethane v/v). Caged 4-OHC was isolated as a yellow solid. Yield = 31%. ^{1}H NMR (400 MHz, $CDCl_3$): 7.65 (s, 1H), 7.20 (s, 1H), 6.93 (m, 4H), 6.79 (d, ^2J = 8.8 Hz, 2H), 6.67 (d, ^2J = 8.8 Hz, 2H), 6.10 (q, ^4J = 6.13 Hz, 1H), 4.03 (t, ^3J = 5.8 Hz, 2H), 3.94 (s, 3H), 3.89 (s, 3H), 2.72 (t, ^3J = 5.8 Hz, 2H), 2.35 (s, 6H), 2.18 (m, 4H), 1.67 (d, ^2J = 6 Hz, 3H), 1.56 (m, 6H). MS (electrospray ionization mass spectrometry: ESI-MS) calculated: 560.29, found: 561.40 $[M+H]^+$.

UV−vis and HPLC-MS Characterization of the Photocleavage of Caged 4-OHC. A 0.25 mM solution of caged 4-OHC in 1:1 (v/v) water/acetonitrile was used for the UV−vis spectroscopic characterization of the photocleavage reaction. The solution of the caged 4-OHC was placed in a 96 well black, clear-bottom microplate. The solution was then irradiated at ∼365 nm using a hand-held UV lamp. After light exposure, UV−vis spectra of the solution were recorded in a TECAN microplate reader. Time course of the photocleavage reaction was monitored by exposing the caged 4-OHC solution to light for different durations, and subsequently recording the UV−vis spectra of the solution. A 2.0 mM solution of caged 4-OHC in 1:1 (v/v) water/acetonitrile was used for the HPLC-MS study. The solution of the caged 4-OHC was placed in a glass vial and irradiated at ∼365 nm using a hand-held UV lamp. Aliquots were taken at different time intervals and injected to the HPLC-MS machine for analysis. *Prism* 5 (GraphPad, La Jolla, CA) for Mac was used to plot the data.

MEF Isolation and Photoactivation Procedure. Mouse embryonic fibroblasts were isolated from embryos of the cross between homozygous *Rosa26CreER^{T2}* and homozygous *mT/mG* (or *R26R*) following previously described protocol[28] and grown in DMEM with 10% FBS. To illuminate UV light on the cells, the cells were first grown in 60 mm dish overnight to become nearly confluent. Next day, the medium was replaced with medium containing caged 4-OHC at 5 μM and incubated for 30 min. The cells were washed twice quickly with warm PBS and covered with fresh medium. The dish was placed on the UV emission surface of a hand-held 6 W long-wavelength UV lamp (UVP, LLC), and UV light was kept on for a designated period of time. The cells were returned to the incubator to culture for 48−72 h before live imaging or flow cytometric analysis.

Mammary 3D Culture and Photoactivation Procedure. Mouse mammary epithelial cells were isolated from 6- to 8-week-old female *Rosa26CreER^{T2};mT/mG* mice as previously described.[29] Briefly, mammary glands were excised, minced using scalpels, and digested for 1 h in 300 U/mL type 1A collagenase (Sigma) and 100 U/mL hyaluronidase (Sigma). Cells were then treated with 0.25% trypsin/EDTA, Dispase (Invitrogen)/DNase (Sigma), and ACK lysing buffer (Invitrogen) in succession. Between each treatment, cells were rinsed in MEGM (1:1 DMEM/F12 Ham supplemented with 5 mg/mL insulin, 500 ng/mL hydrocortisone, 10 ng/mL EGF, 20 ng/mL cholera toxin, 5% bovine calf serum, and 1× penicillin/streptomycin). Afterward, cells were filtered twice through 40 mm nylon cell strainers and seeded in 35 μm dishes that contained a layer of Growth factor Reduced Matrigel (BD Biosciences) measuring approximately 1−2 mm thickness. Acini usually formed in 4−8 days. During photoactivation, the acini were incubated with MEGM containing 5 μM caged 4-OHC for 1 h. The cells were washed twice quickly with warm PBS and covered with fresh medium. The dish was placed on the UV emission surface of a hand-held 6 W long-wavelength UV lamp (UVP, LLC, exposure time: 1 min) or above the 60× objective of an inverted epifluorescent microscope equipped with a standard DAPI filter set. The cells were returned to the incubator to culture for >48 h before live cell imaging using an upright Zeiss 710 laser scanning confocal microscope equipped with 20× and 40× water immersion objectives.

Photoactivation Procedure in Mice. Female mice of 6−8 weeks old were clean-shaven on the dorsal and ventral sides. The caged 4-OHC was formulated in 1:1:8 N,N-dimethylacetamide/solutol/saline for *in vivo* delivery. The vehicle or 1 mg caged 4-OHC in vehicle was injected intraperitoneally. One hour later, the mice were anesthetized with isoflurane and exposed to UV light from the hand-held 6 W long-wavelength UV lamp (UVP, LLC) for 15 min. Alternatively, for mammary tissue illumination, the right inguinal (#4) mammary fat pad

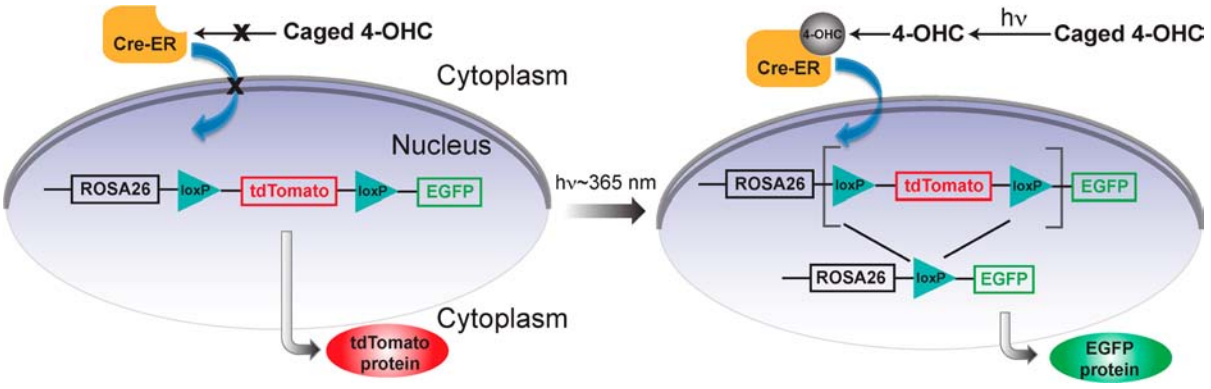


Figure 1. Schematics showing the photoactivation-dependent CreER/loxP system in the *Rosa26CreER^{T2};mT/mG* reporter mice. To produce a light-sensitive CreER/loxP system, 4-OHC was modified with a light-sensitive caging group to inhibit its ability to induce CreER-mediated recombination. Photoactivated release of 4-OHC induces EGFP gene expression in illuminated cells.

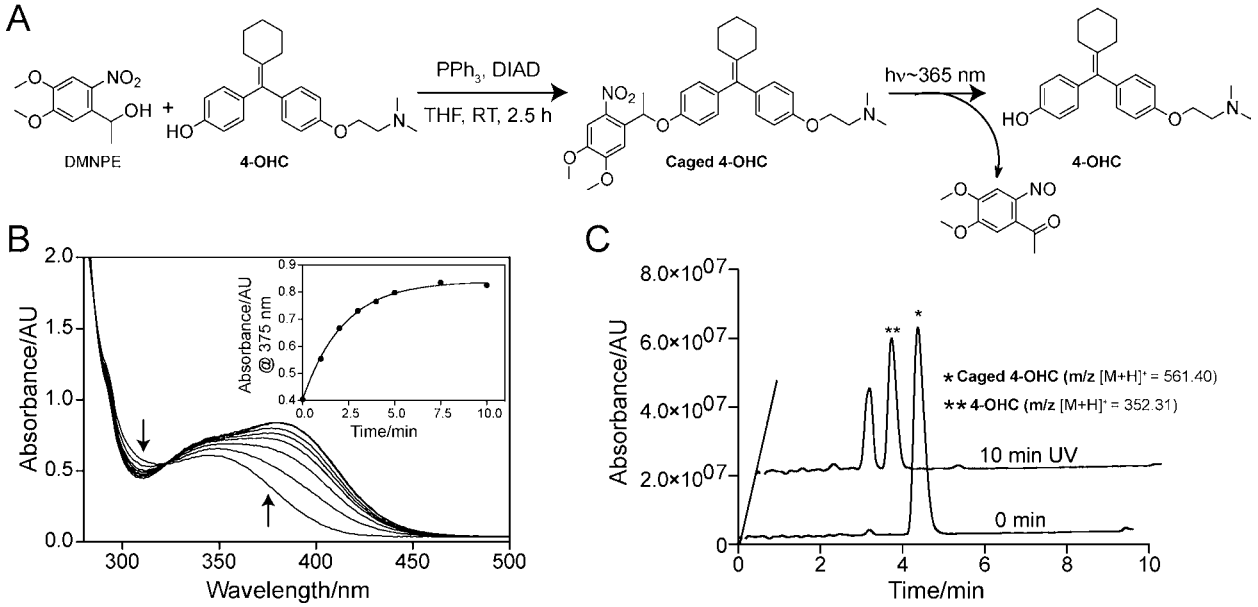


Figure 2. Synthesis of caged 4-OHC and photocleavage characterization. (A) Synthesis of caged 4-OHC under Mitsonobu reaction condition and activation (uncaging) of caged 4-OHC using 365 nm UV light. (B) Changes in UV−vis absorbance during the photocleavage of caged 4-OHC in water/acetonitrile (1:1 v/v). Inset shows the change in absorbance at 375 nm over UV irradiation time. Note that the photocleavage is complete within 10 min of irradiation. (C) HPLC-MS chromatograms showing the quantitative formation 4-OHC from caged 4-OHC upon UV irradiation. Caged 4-OHC solutions, before (0 min) and after light exposure (10 min UV), were analyzed by HPLC-MS. Formation of 4-OHC was identified by the appearance of molecular mass corresponding to 4-OHC (*m/z* 352.31 $[M+H]^+$). The peak other than the 4-OHC appeared in the 10 min UV chromatogram belongs to the cleaved caging group (see (A) for the photocleavage reaction).

was exposed by creating a small skin flap and illuminated with UV light for 15 min. For enhanced photoconversion, this procedure was repeated four times. On the seventh day, the mice were imaged with Olympus OV-110 epifluorescence imager to detect fluorescent signals emitted from the skin on the dorsal and ventral sides. Alternatively, the left and right mammary glands were dissected and immediately imaged using the intravital laser scanning microscope IV-110.

RESULTS

To design a biological system that can faithfully report on the induced activity of CreER, we took advantage of a recently developed double-fluorescent Cre reporter mouse, the *mT/mG* strain, [16] which expresses tdTomato prior to and EGFP following Cre-mediated recombination ubiquitously in tissues. The homozygous *mT/mG* mouse was crossed to the homozygous *Rosa26CreER^{T2}* strain,[17] and the progenies, *Rosa26CreER^{T2};mT/mG*, were heterozygous for both alleles. We reasoned that, by illuminating cells and tissues from these mice with UV light and looking for EGFP-expressed cells, we would be able to test the photoinduced activity of caged tamoxifen analogues (Figure 1).

We used the 4-hydroxytamoxifen (4-OHT) analogue, 4-hydroxycyclofen (4-OHC) as a small molecule agonist of the ER component of the fusion protein. Although 4-OHT and 4-OHC have similar binding affinity to the ER, 4-OHC is preferred over 4-OHT in view of its synthetic accessibility and better photostability.[14] As shown in Figure 2A, 4-OHC was caged by attaching a photolabile 1-(4,5-dimethoxy-2-nitrophenyl)ethyl (DMNPE) moiety to the free hydroxy group of 4-OHC using the Mitsonobu reaction.[14] Under ambient light, the DMNPE caging group is stable in physiological conditions. However, exposure to longwavelength UV irradiation (~350−410 nm with a peak at 365 nm) leads to

dx.doi.org/10.1021/bc300319c | *Bioconjugate Chem.* 2012, 23, 1945−1951

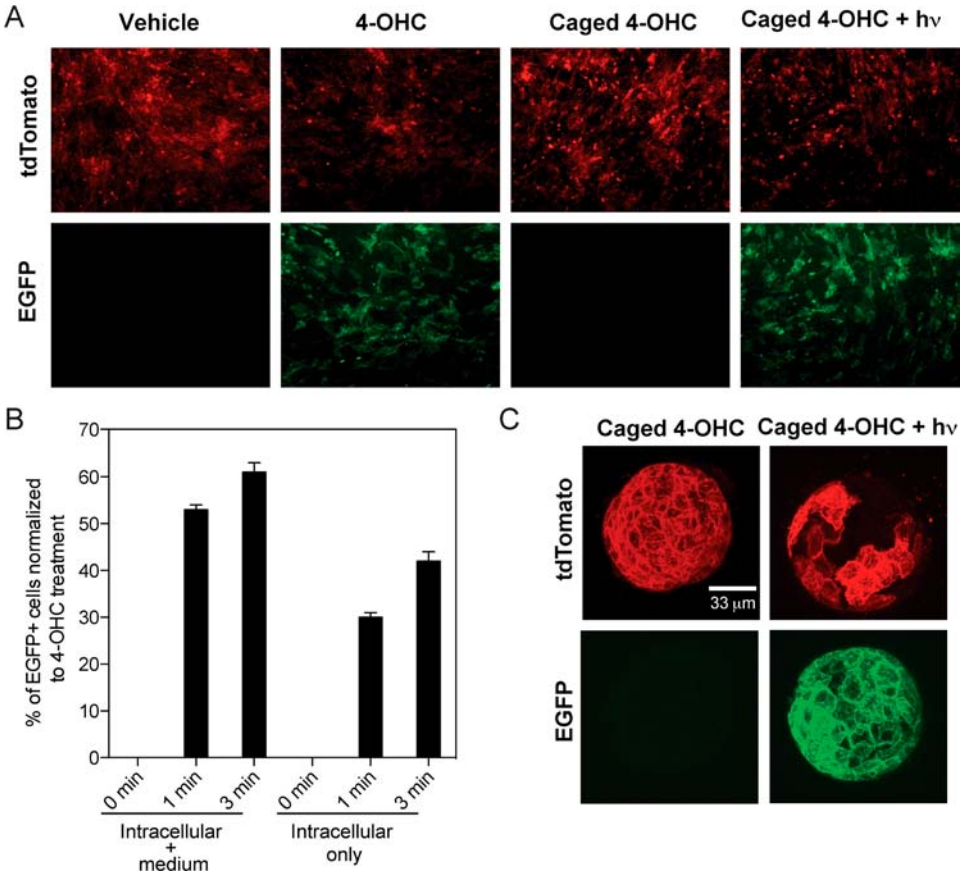


Figure 3. Photoactivation of caged 4-OHC *in vitro*. (A) Induction of EGFP expression by 365 nm UV activation of caged 4-OHC in MEFs isolated from *Rosa26CreER^{T2};mT/mG* embryos. (B) Flow cytometric quantification of EGFP^{+} MEF cells upon treatment with 4-OHC and caged 4-OHC under different durations of UV activation. The "intracellular + medium" group represents cell samples without PBS wash before UV irradiation, whereas the "intracellular only" group represents cell samples washed twice with PBS before UV irradiation. Data represent mean ± SD (*C*) EGFP expression induced by 365 nm UV activation of caged 4-OHC in mammary epithelial cells isolated from *Rosa26CreER^{T2};mT/mG* female mice and cultured to form acini on Matrigel. All acini grown on the dish were illuminated in a uniform manner to induce EGFP expression. Images shown are projections of the *Z*-stack confocal images.

photolytic cleavage, releasing 4-OHC (Figure 2A). The photocleavage reaction of the caged 4-OHC was monitored by UV−vis spectroscopy. A change in UV−vis absorption spectrum was observed when a solution of caged 4-OHC was exposed to a hand-held 365 nm UV lamp and was typical of the breakage of DMNPE caging group (Figure 2B). The photochemical reaction was complete within 10 min of exposure (inset of Figure 2B). High-performance liquid chromatography−mass spectrometry (HPLC-MS) verified the chemical identity of the photoreleased products and also confirmed quantitative, unidirectional conversion to 4-OHC (Figure 2C). Overall, these characterizations indicate that the caged 4-OHC undergoes efficient photocleavage at 365 nm UV light and releases 4-OHC.

To test the caged 4-OHC activity, we started with a simple biological system, the mouse embryonic fibroblasts (MEFs) isolated from the *Rosa26CreER^{T2};mT/mG* mice in cell culture conditions. *Rosa26CreER^{T2};mT/mG* MEFs were treated with either 4-OHC or caged 4-OHC and illuminated at 365 nm. As expected, photocleavage of the caged 4-OHC induced EGFP expression in a stringent fashion (Figure 3A,B). To provide an independent tester for the compound, we generated another reporter mouse, *Rosa26CreER^{T2};R26R* by crossing homozygous *Rosa26CreER^{T2}* with homozygous *Rosa26-loxP-STOP-loxP-lacZ* mice[18] (Figure S1A). Similar results were observed in the *Rosa26CreER^{T2};R26R* MEFs (Figure S1B). We did not observe any major phototoxicity or cell viability changes due to the UV irradiation in our experiments (energy density 1.6 mW/cm^2, photon energy 3.4 eV, number of photons per second per cm^2 2×10^{15}, up to 3 min exposure time), consistent with other reports.[5,19]

While a convenient system, the 2D cell culture cannot manifest all the biological responses of cells to external perturbations in a 3D environment. Therefore, we went on to test whether caged 4-OHC would enable light-dependent Cre-mediated recombination in a well-established organoid model, the mammary acinus culture.[20] Mammary epithelial cells from *Rosa26CreER^{T2};mT/mG* mice were isolated and overlaid on a basement membrane to allow polarized acinar structure development. The formed acini were subjected to caged 4-OHC treatment with or without subsequent brief UV illumination by the UV lamp (energy density 1.6 mW/cm^2, photon energy 3.4 eV, number of photons per second per cm^2 2×10^{15}, 1 min exposure time) (Figure 3C and Video S1−2) or the 60× objective of an inverted fluorescent microscope equipped with a standard DAPI filter set (Figure S2 and Video S3−4). Similar to 2D culture results, the caged 4-OHC allowed very tight control of EGFP expression in response to photoactivation.

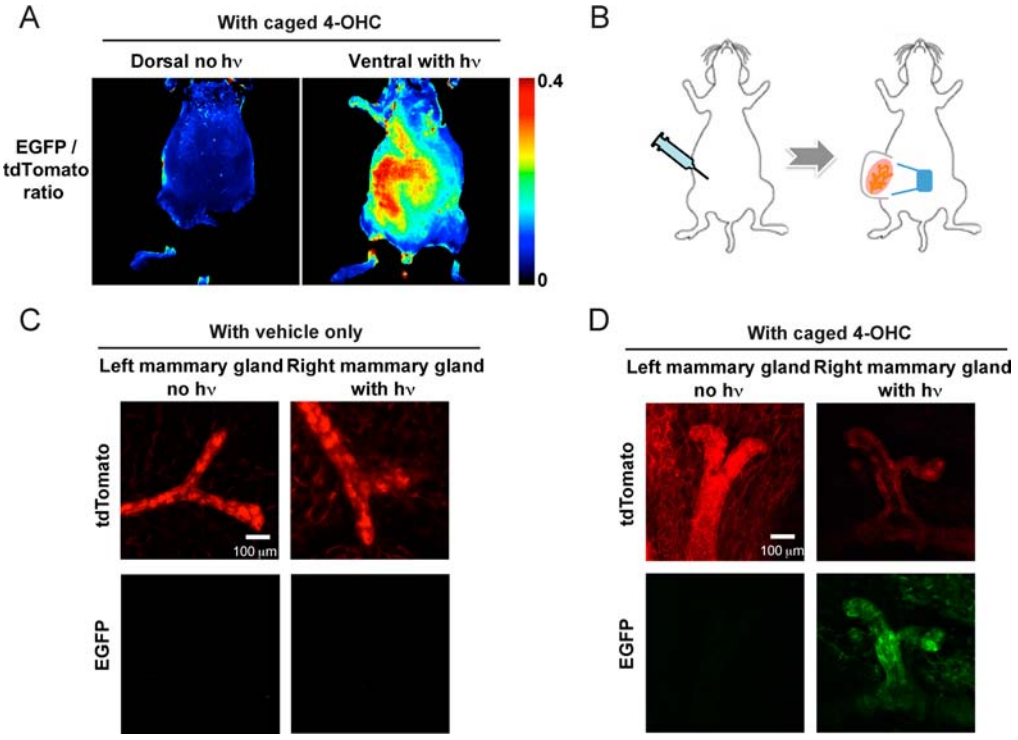


Figure 4. Photoactivation of caged 4-OHC *in vivo*. (A) Strong induction in EGFP expression on the ventral skin as a result of 365 nm UV illumination of the *Rosa26CreER^{T2};mT/mG* mice injected with caged 4-OHC. The dorsal skin was not illuminated and showed little EGFP signal. An increase in EGFP signal is followed by a decrease of tdTomato signal; low values of EGFP/tdTomato ratio correspond to low EGFP and high tdTomato, while high values of ratios correspond to high EGFP and low tdTomato. (B) Experimental design for intraperitoneal injection of vehicle or caged 4-OHC into the *Rosa26CreER^{T2};mT/mG* female mice and subsequent 365 nm illumination on the right inguinal (#4) mammary fat pad. (C,D) The results of experiments in (B) with mammary tissue *ex vivo* imaged with IV-110. Only the right illuminated mammary gland from the mouse injected with caged 4-OHC expressed EGFP.

Finally and most importantly, we demonstrated that caged 4-OHC was able to induce gene activation *in vivo* in mice upon photoactivation. We focused on two organs, skin and mammary glands, given their ease of imaging, accessibility to light and breadth of different cell populations. We used a custom-built broad illumination method for *in vivo* testing. We first monitored EGFP/tdTomato expression at the whole mouse level using the Olympus OV-110 epifluorescence imager.[21] Very low green autofluorescence was detected in *Rosa26-CreER^{T2};mT/mG* mice when treated with vehicle control and irradiated with 365 nm UV, and strong EGFP signal was detected when treated with 4-OHC (Figure S3). In the test experiment, *Rosa26CreER^{T2};mT/mG* mice were injected intraperitoneally with caged 4-OHC and subjected to UV illumination only on the ventral (but not dorsal) skin. Resultant EGFP signal was observed on the ventral skin but not on the dorsal skin (Figure 4A) with an average 2.5-fold increase in fluorescence intensity. Because the increase of the EGFP signal was concomitant with the decrease of the tdTomato signal, EGFP/tdTomato ratios were presented in Figure 4A for both ventral and dorsal skin.

We next tested the OCG switch on mammary glands of the female *Rosa26CreER^{T2};mT/mG* mice. The mice were injected with vehicle or caged 4-OHC, and only the right mammary gland was exposed to the 365 nm light, whereas the left was not (Figure 4B). Seven days later, the right and left mammary glands were resected for *ex vivo* imaging at a high spatial resolution using the Olympus Intravital Laser Scanning Microscope IV-110.[22] We first confirmed that 365 nm UV illumination of the mammary gland alone did not cause noticeable green autofluorescence increase or tissue morphological changes (Figure 4C). However, when caged 4-OHC was injected, the right, but not the left, mammary gland showed strong EGFP induction (Figure 4D). Taken together, the skin and mammary gland data clearly establish that the caged 4-OHC displayed superior *in vivo* inducibility by light and limited diffusion after uncaging to affect other organs.

■ DISCUSSION

In this study, we show that caged 4-OHC can efficiently regulate CreER-mediated recombination in a light-dependent manner not only in cell culture, but also in adult mice. While caged 4-OHT analogues were shown to control CreER-mediated gene expression in response to photoactivation in cell culture[12] and zebrafish,[14,15] our results demonstrate that this approach can indeed be applied to adult mice to induce localized gene activation as a function of light illumination.

Photoregulation of protein activity can be achieved through either photo-uncaging as shown in this study or using genetically engineered light-gated modules,[2] for example, split Cre recombinase fused to light-dependent dimerization partners CRY2 and CIBN.[23] One major advantage of using caged 4-OHC over other methods of making Cre activity photoregulatable is that one can seamlessly integrate the technology into numerous existing CreER mouse strains to achieve an additional level of stringent control, i.e., regional and cell-specific control of gene expression. This is of particular interest if the investigated biological questions require photoregulatable Cre activity in a mammalian model organism and can be studied based on existing CreER strains, because

dx.doi.org/10.1021/bc300319c | *Bioconjugate Chem.* 2012, 23, 1945−1951

constructing new mouse strains possessing the necessary light-gated modules will be a lengthy and costly process. For example, the villin-CreER^{T2} mouse allows efficient target gene recombination throughout the entire digestive epithelium in response to systemic tamoxifen treatment,[24] and by restricting light activation of caged 4-OHC to the colon, this mouse strain may become an excellent driver for spatiotemporal modeling of colorectal cancer in mice.

The application of the OCG switch is not confined to CreER; instead, it should provide photoregulation of a spectrum of ER-fusion proteins. These proteins were fused with ER to allow tamoxifen-dependent control of nuclear localization and protein activity.[25] For example, using the ER-fusion approach, we recently reported the marked reversal of systemic degenerative phenotypes in aged telomerase-deficient TERT-ER mice by tamoxifen treatment and telomerase reactivation.[26] It will be interesting to apply the OCG switch to this system to determine the contribution of each organ system to the phenotypic reversal.

In summary, we foresee the described OCG switch approach to find broad applications, especially in tumor and developmental biology, where localized and pattern-specific gene manipulation is of central importance to address many outstanding questions. We believe that this approach could likewise be applied to spatiotemporally controlled gene activation in internal organs by employing UV light guided through an optical fiber. Alternatively, two-photon activation can be used to somewhat increase the tissue penetration.

■ ASSOCIATED CONTENT

Supporting Information

Supporting figures and videos. This material is available free of charge via the Internet at http://pubs.acs.org.

■ AUTHOR INFORMATION

Corresponding Author

*E-mail: rdepinho@mdanderson.org, rweissleder@mgh.harvard.edu.

Author Contributions

¶These authors contributed equally to this work

Notes

The authors declare no competing financial interest.

■ ACKNOWLEDGMENTS

We are grateful to Rujuta Narurkar, Emma Labrot, Eliot Fletcher-Sananikone, Zhou Shan, and Shan Jiang for assistance in the animal facility. We thank Y. Alan Wang and other colleagues in our laboratories for helpful advice and discussion. We thank Joshua Dunham, Alex Zaltsman, and Lisa Cameron for help with imaging. This work was supported in part by grants PO1CA117969 (R.A.D.), U01CA141508 (R.A.D.), P50-CA86355 (R.W.), and U24CA092782 (R.W.). X.L. is supported by a postdoctoral fellowship from Jane Coffin Childs Memorial Fund. S.S.A. is supported by an NIH fellowship (HHSN268201000044C).

■ REFERENCES

(1) Nagy, A. (2000) Cre recombinase: the universal reagent for genome tailoring. *Genesis 26*, 99−109.

(2) Toettcher, J. E., Voigt, C. A., Weiner, O. D., and Lim, W. A. (2011) The promise of optogenetics in cell biology: interrogating molecular circuits in space and time. *Nat. Methods 8*, 35−38.

(3) Agasti, S. S., Chompoosor, A., You, C. C., Ghosh, P., Kim, C. K., and Rotello, V. M. (2009) Photoregulated release of caged anticancer drugs from gold nanoparticles. *J. Am. Chem. Soc. 131*, 5728−5729.

(4) Riggsbee, C. W., and Deiters, A. (2010) Recent advances in the photochemical control of protein function. *Trends Biotechnol. 28*, 468−475.

(5) Young, D. D., and Deiters, A. (2007) Photochemical control of biological processes. *Org. Biomol. Chem. 5*, 999−1005.

(6) Ellis-Davies, G. C. (2007) Caged compounds: photorelease technology for control of cellular chemistry and physiology. *Nat. Methods 4*, 619−628.

(7) Mayer, G., and Heckel, A. (2006) Biologically active molecules with a ″light switch. *Angew. Chem., Int. Ed. Engl. 45*, 4900−4921.

(8) Callaway, E. M., and Katz, L. C. (1993) Photostimulation using caged glutamate reveals functional circuitry in living brain slices. *Proc. Natl. Acad. Sci. U. S. A. 90*, 7661−7665.

(9) Ellis-Davies, G. C., and Kaplan, J. H. (1994) Nitrophenyl-EGTA, a photolabile chelator that selectively binds Ca2+ with high affinity and releases it rapidly upon photolysis. *Proc. Natl. Acad. Sci. U. S. A. 91*, 187−191.

(10) Ellis-Davies, G. C. (2008) Neurobiology with caged calcium. *Chem. Rev. 108*, 1603−1613.

(11) Edwards, W. F., Young, D. D., and Deiters, A. (2009) Light-activated Cre recombinase as a tool for the spatial and temporal control of gene function in mammalian cells. *ACS Chem. Biol. 4*, 441−445.

(12) Link, K. H., Shi, Y., and Koh, J. T. (2005) Light activated recombination. *J. Am. Chem. Soc. 127*, 13088−13089.

(13) Shi, Y., and Koh, J. T. (2004) Light-activated transcription and repression by using photocaged SERMs. *ChemBioChem 5*, 788−796.

(14) Sinha, D. K., Neveu, P., Gagey, N., Aujard, I., Benbrahim-Bouzidi, C., Le Saux, T., Rampon, C., Gauron, C., Goetz, B., Dubruille, S., Baaden, M., Volovitch, M., Bensimon, D., Vriz, S., and Jullien, L. (2010) Photocontrol of protein activity in cultured cells and zebrafish with one- and two-photon illumination. *ChemBioChem 11*, 653−663.

(15) Sinha, D. K., Neveu, P., Gagey, N., Aujard, I., Le Saux, T., Rampon, C., Gauron, C., Kawakami, K., Leucht, C., Bally-Cuif, L., Volovitch, M., Bensimon, D., Jullien, L., and Vriz, S. (2010) Photoactivation of the CreER T2 recombinase for conditional site-specific recombination with high spatiotemporal resolution. *Zebrafish 7*, 199−204.

(16) Muzumdar, M. D., Tasic, B., Miyamichi, K., Li, L., and Luo, L. (2007) A global double-fluorescent Cre reporter mouse. *Genesis 45*, 593−605.

(17) Ventura, A., Kirsch, D. G., McLaughlin, M. E., Tuveson, D. A., Grimm, J., Lintault, L., Newman, J., Reczek, E. E., Weissleder, R., and Jacks, T. (2007) Restoration of p53 function leads to tumour regression in vivo. *Nature 445*, 661−665.

(18) Soriano, P. (1999) Generalized lacZ expression with the ROSA26 Cre reporter strain. *Nat. Genet. 21*, 70−71.

(19) Cambridge, S. B., Geissler, D., Calegari, F., Anastassiadis, K., Hasan, M. T., Stewart, A. F., Huttner, W. B., Hagen, V., and Bonhoeffer, T. (2009) Doxycycline-dependent photoactivated gene expression in eukaryotic systems. *Nat. Methods 6*, 527−531.

(20) Debnath, J., Muthuswamy, S. K., and Brugge, J. S. (2003) Morphogenesis and oncogenesis of MCF-10A mammary epithelial acini grown in three-dimensional basement membrane cultures. *Methods 30*, 256−268.

(21) Thurber, G. M., Figueiredo, J. L., and Weissleder, R. (2009) Multicolor fluorescent intravital live microscopy (FILM) for surgical tumor resection in a mouse xenograft model. *PLoS One 4*, e8053.

(22) Kelly, K. A., Bardeesy, N., Anbazhagan, R., Gurumurthy, S., Berger, J., Alencar, H., Depinho, R. A., Mahmood, U., and Weissleder, R. (2008) Targeted nanoparticles for imaging incipient pancreatic ductal adenocarcinoma. *PLoS Med. 5*, e85.

(23) Kennedy, M. J., Hughes, R. M., Peteya, L. A., Schwartz, J. W., Ehlers, M. D., and Tucker, C. L. (2010) Rapid blue-light-mediated induction of protein interactions in living cells. *Nat. Methods 7*, 973−975.

(24) el Marjou, F., Janssen, K. P., Chang, B. H., Li, M., Hindie, V., Chan, L., Louvard, D., Chambon, P., Metzger, D., and Robine, S. (2004) Tissue-specific and inducible Cre-mediated recombination in the gut epithelium. *Genesis 39*, 186−193.
(25) Van Dyke, T., and Jacks, T. (2002) Cancer modeling in the modern era: progress and challenges. *Cell 108*, 135−144.
(26) Jaskelioff, M., Muller, F. L., Paik, J. H., Thomas, E., Jiang, S., Adams, A. C., Sahin, E., Kost-Alimova, M., Protopopov, A., Cadinanos, J., Horner, J. W., Maratos-Flier, E., and Depinho, R. A. (2011) Telomerase reactivation reverses tissue degeneration in aged telomerase-deficient mice. *Nature 469*, 102−106.
(27) Dyer, R. G., and Turnbull, K. D. (1999) Hydrolytic Stabilization of Protected p-Hydroxybenzyl Halides Designed as Latent Quinone Methide Precursors. *J. Org. Chem. 64*, 7988−7995.
(28) Sharpless, N. E., Ferguson, D. O., O'Hagan, R. C., Castrillon, D. H., Lee, C., Farazi, P. A., Alson, S., Fleming, J., Morton, C. C., Frank, K., Chin, L., Alt, F. W., and DePinho, R. A. (2001) Impaired nonhomologous end-joining provokes soft tissue sarcomas harboring chromosomal translocations, amplifications, and deletions. *Mol. Cell 8*, 1187−1196.
(29) Tiede, B. J., Owens, L. A., Li, F., DeCoste, C., and Kang, Y. (2009) A novel mouse model for non-invasive single marker tracking of mammary stem cells in vivo reveals stem cell dynamics throughout pregnancy. *PLoS One 4*, e8035.

Bioconjugate Chemistry

Article

pubs.acs.org/bc

Polyaminoquinoline Iron Chelators for Vectorization of Antiproliferative Agents: Design, Synthesis, and Validation

Vincent Corcé,[†,‡] Emmanuelle Morin,[†] Solène Guihéneuf,[†] Eric Renault,[†] Stéphanie Renaud,[‡] Isabelle Cannie,[‡] Raphaël Tripier,[§] Luís M. P. Lima,[§] Karine Julienne,[†] Sébastien G. Gouin,[†] Olivier Loréal,[‡] David Deniaud,*[,†] and François Gaboriau*[,‡]

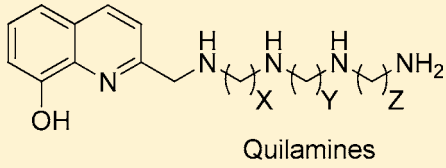
[†]LUNAM Université, CEISAM, Chimie Et Interdisciplinarité, Synthèse, Analyse, Modélisation, UMR CNRS 6230, UFR des Sciences et des Techniques, 2, rue de la Houssinière, BP 92208, 44322 NANTES Cedex 3, France

[‡]INSERM, UMR991, CHRU Pontchaillou, 35033 Rennes, France; Université de Rennes1, 35043 Rennes, France

[§]CNRS, UMR 6521, Université de Brest, Laboratoire de Chimie, Electrochimie Moléculaires et Chimie Analytique, 6 Avenue Victor Le Gorgeu, 29200 Brest, France

S *Supporting Information*

ABSTRACT: Iron chelation in tumoral cells has been reported as potentially useful during antitumoral treatment. Our aim was to develop new polyaminoquinoline iron chelators targeting tumoral cells. For this purpose, we designed, synthesized, and evaluated the biological activity of a new generation of iron chelators, which we named Quilamines, based on an 8-hydroxyquinoline (8-HQ) scaffold linked to linear polyamine vectors. These were designed to target tumor cells expressing an overactive polyamine transport system (PTS). A set of Quilamines bearing variable polyamine chains was designed and assessed for their ability to interact with iron. Quilamines were also screened for their cytostatic/cytotoxic effects and their selective uptake by the PTS in the CHO cell line. Our results show that both the 8-HQ moiety and the polyamine part participate in the iron coordination. **HQ1−44**, the most promising Quilamine identified, presents a homospermidine moiety and was shown to be highly taken up by the PTS and to display an efficient antiproliferative activity that occurred in the micromolar range. In addition, cytotoxicity was only observed at concentrations higher than 100 μM. We also demonstrated the high complexation capacity of **HQ1−44** with iron while much weaker complexes were formed with other cations, indicative of a high selectivity. We applied the density functional theory to study the binding energy and the electronic structure of prototypical iron(III)-Quilamine complexes. On the basis of these calculations, Quilamine **HQ1−44** is a strong tridentate ligand for iron(III) especially in the form of a 1:2 complex.



Quilamines

INTRODUCTION

Iron is an essential metal in many biological functions and an interesting and innovative target for anticancer therapy.[1] Growing tumor cells require large quantities of iron, expressed by an increase in the import proteins and a decrease in the export proteins of iron.[2,3] The activity and expression of ribonucleotide reductase (RR), the iron-dependent key enzyme regulating DNA synthesis and cell proliferation, are increased in tumor cells.[4] Previous studies have reported the relationship between body iron stores and the risk of cancers.[5,6] The iron load stimulates the proliferation of tumor cells *in vitro* and *in vivo*.[7] The need for iron during the cell cycle is illustrated by the overexpression of proliferating transferrin receptor cells on the plasma membrane, which allows transferrin-chelated iron to enter the cell.[8] In contrast, the underexpression of the cellular iron exporter, ferroportin, leads to an intracellular accumulation of iron, and is a biomarker for tumor growth in breast cancer.[9,10] Decreasing the exchangeable intracellular iron level with synthetic metal chelators is therefore an attractive method for limiting the proliferation of cancer cells.[11]

Iron chelators, like Deferoxamine initially developed for the treatment of primary iron overload, as well as Deferiprone[12,13] and Deferasirox,[14] more recently developed for the treatment of secondary overloads (thalassemias), inhibit the proliferation of tumor cells in culture. Their antiproliferative effects are modulated by their iron-chelating capacity and their cellular uptake. We recently showed that the antiproliferative effect of ICL670, a tridentate iron chelator with a hydroxyphenyltriazole skeleton (Deferasirox, Novartis Pharma), and O-Trensox resulted from the iron depletion induced in cells and the inhibitory action on the polyamine metabolism.[15,16] Deferoxamine inhibits the growth of melanoma and hepatoma cells *in vitro* and *in vivo*.[17] This chelator was effective in the treatment of leukemias and neuroblastomas in preliminary clinical trials.[18] The high antiproliferative activity observed with iron chelators derived from pyridoxal isonicotinoyl hydrazone, including aroylhydrazones and thiosemicarbazones, was assumed to involve both their iron-chelating efficiency and their ability to generate reactive oxygen species.[1] More recently, iron depletion induced by the iron chelators Deferoxamine and 2-hydroxyl-1-

Received: June 19, 2012
Revised: July 24, 2012
Published: August 8, 2012

ACS Publications © 2012 American Chemical Society

naphtylaldehyde isonicotinoyl hydrazone was shown to increase the expression of growth arrest and DNA damage genes.[19]

All these results suggest that, due to their antiproliferative and apoptotic properties, iron chelators could be used as an adjuvant in the treatment of cancers. The mechanism of action of cytotoxic antitumor agents, like Doxorubicin and Bleomycin, involves their iron-chelating ability to some extent. However, such therapy must target tumoral cells. In fact, conversely to what is observed in iron overload diseases, cells are not overloaded and the iron stores are not excessive. Therefore, uncontrolled iron depletion of normal cells may generate strong adverse effects. Despite the fact that tumoral cells require more iron, an antiproliferative therapeutic strategy based on iron deprivation of tumoral cells will benefit from a specific vectorization of the iron chelators to these cells.

Polyamine metabolism (biosynthesis and uptake), detrimental to cell proliferation, is also particularly amplified in tumor cells.[20] The Polyamine Transport System (PTS), which can deal with natural and synthetic polyamines, is increased in tumor cells.[21] This property is of potential interest to target antitumor agents.[22−24] Thus, various polyamine analogues have been grafted onto cytotoxic compounds like nitroimidazole,[25] chlorambucil,[26] acridine,[27] anthracene,[28] camptothecine,[29] naphthoquinone,[30] azepine, and benzazepine.[31] This concept of tumor vectorization by polyamines has also been developed to inhibit their own transporter,[32,33] to vectorize cytotoxic compounds such as dimethylsilane polyamine derivatives[34] or molecules carrying boron atoms for boronotherapy,[35,36] and finally to monitor the intracellular traffic of polyamines toward the cells by using fluorescent polyamine analogues.[28,37−39] More recently, F14512, a novel spermine epipodophyllotoxin conjugate, and inhibitor of DNA-topoisomerase II,[40] was selected for clinical development in AML phase I.

In order to generate iron chelator molecules targeting tumor cells, we planned to associate polyamine cargos with iron-chelating units to promote the uptake of the chelating motif by the overactive polyamine transport system of tumor cells.

For this purpose, we synthesized and evaluated a new generation of chelator-polyamine hybrids (Quilamines) which were designed to decrease the iron content in the iron complexes in cancerous cells, thus reducing tumor cell proliferation. The difference in PTS activation between healthy cells and tumor cells enables tumor cells to be targeted, whereas the strong dependence of these cells on iron ensures a secondary targeting.

Such a concept has been reported in previous studies on the synthesis and the biological properties of a chelating Deferiprone-type moiety linked to spermine.[41] In addition, other studies revealed that homospermidine−anthracene conjugates were more selectively recognized by the PTS than spermine derivatives.[38] Instead, we chose the hydroxyquinoline moiety, found in the iron chelator O-Trensox, which has a higher affinity for iron than Deferiprone.[42] The potential value of this structure in an anticancer strategy is illustrated by the example of Clioquinol (5-chloro-7-iodo-8-hydroxyquinoline). This antibiotic is also able to chelate metals, which results in an antiproliferative activity on tumor cells in culture and on grafted tumors in animals.[43,44] The structural requirement of the PTS for polyamine analogues has previously been demonstrated, showing its selectivity for a single CH_2 spacer between the heterocyclic part linked to a homospermidine moiety.[39,45]

In order to meet these objectives, we report here the synthesis of the first generation of Quilamines: a hydroxyquinoline moiety (HQ) linked by a single carbon atom (HQ1) to a linear polyamine chain of various types including the spermidine (HQ1-*XY*) and spermine (HQ1-*XYZ*) series (*X*, *Y*, and *Z* represent the alkyl chain length between the amino groups). In a cellular model, we screened the antiproliferative efficiency of these polyaminoquinolines (Quilamines) HQ1-*XYZ* as well as their specificity for the polyamine transport system. Finally, we evaluated the complexation properties of the most biologically efficient Quilamine **HQ1−44** toward iron(III) and competitive cations.

EXPERIMENTAL PROCEDURES

Chemistry. NMR spectra were recorded at room temperature with a Bruker Avance 300 Ultra Shield or Bruker Avance III 400 spectrometers. Chemical shifts are reported in parts per million (ppm); coupling constant are reported in units of Hertz [Hz]. Infrared (IR) spectra were recorded with a Bruker Vector 22 FTIR using KBr films or KBr pellets. Low-resolution mass spectra (MS) were recorded with a Thermo electron DSQ spectrometer. High-resolution mass spectra (HRMS) were recorded with a Thermofisher hybrid LTQ-orbitrap spectrometer (ESI^+) and with a Bruker Autoflex III SmartBeam spectrometer (MALDI). Microanalyses were performed on a Thermo Scientific FLASH 2000 Series CHNS/O Analyzers. Melting points were determined in open capillary tubes and are uncorrected. All reagents were purchased from Acros Organics or Aldrich and were used without further purification. Column chromatographies were conducted on silica gel Kieselgel SI60 (40−63 μm) from Merck. Reactions requiring anhydrous conditions were performed under argon. Dichloromethane was distilled from calcium hydride under nitrogen prior to use. Toluene and tetrahydrofuran were distilled from sodium/benzophenone under argon prior to use.

The compounds **1**−**5**, **8**−**20**, **24**, **25**, **28**, and **29** already have been described in the literature.

*Compound (**21**).* To solution of N^1,N^4-di-*tert*-butyloxycarbonylspermidine **3** (1 g, 2.9 mmol) in anhydrous acetonitrile (30 mL) was added potassium carbonate (1.41 g, 10.15 mmol), and the suspension was stirred at room temperature for 10 min under Ar. 4-Bromobutyronitrile (290 μL, 2.9 mmol) was added, and the resulting mixture was then stirred for 20 h at 50 °C. The mixture was filtered, the solvent was removed under reduced pressure, and the residue was purified by chromatography on silica gel ($CHCl_3$/MeOH/NH_4OH, 94:5:1) to give compound **21** as a colorless oil (850 mg, 71%).

*Compound (**21**).* Colorless oil (850 mg, 71%). IR (KBr): ν = 3349, 2974, 2932, 2866, 1693, 1515, 1478, 1454, 1418, 1390, 1365, 1273, 1250, 1168, 868, 774 cm^{-1}. ^1H NMR (400 MHz, [D_4]MeOD): δ = 1.39−1.64 (m, 22H, 2CH_2 3CH_3), 1.69 (q, 2H, CH_2, J = 7 Hz), 1.82 (q, 2H, CH_2, J = 7.24 Hz), 2.51 (t, 2H, CH_2, J = 7.16 Hz), 2.61 (dd, 2H, CH_2, J = 7.14 Hz, J = 7.44 Hz), 2.69 (dd, 2H, CH_2, J = 7.14 Hz, J = 7.44 Hz), 3.03 (t, 2H, CH_2, J = 6.78 Hz), 3.17−3.26 (m, 4H, 2CH_2) ppm. ^{13}C NMR (100 MHz, [D_4]MeOD): δ = 15.3, 26.3, 26.9, 27.7, 28.7 (tBu), 28.8 (tBu), 30.2, 38.9, 45.6, 48.1, 49.1, 50.3, 79.9, 80.9, 120.9, 137.5, 158.4. HRMS (MALDI): calcd. for $C_{21}H_{40}N_4O_4$ [M +H]$^+$ 413.3122; found 413.3118.

*General Procedure for the Preparation of Cyanopolyamines **22** and **23**.* To solution of di-*tert*-butyloxycarbonylhomospermidine **1** (0.2 g, 1.06 mmol) for **22** or di-*tert*-butyloxycarbonylspermidine **3** (0.2 g, 1.06 mmol) for **23** in methanol was added acrylonitrile (70.3 μL, 1.06 mmol) under Ar at 0 °C and stirred for 6 h, and the reaction mixture was

stirred at room temperature over a period of 12 h. The solvent was removed under reduced pressure and the residue was purified by chromatography on silica gel (chloroform/methanol/ammonia, 94:5:1).

*Compound (**22**).* Colorless oil (730 mg, 91%). IR (KBr): ν = 3347, 2974, 2932, 2863, 1688, 1521, 1478, 1454, 1418, 1390, 1365, 1251, 1171 cm^{-1}. ^1H NMR (400 MHz, [D_4]MeOD): δ = 1.43 (s, 9H, tBu), 1.46 (s, 9H, tBu), 1.46−1.63 (m, 8H, 4CH_2), 2.60 (t, 2H, CH_2, J = 6.85 Hz), 2.63 (dd, 2H, CH_2, J = 7.1 Hz), 2.87 (dd, 2H, CH_2, J = 6.76 Hz), 3.05 (t, 2H, CH_2, J = 6.8 Hz), 3.17−3.26 (m, 4H, 2CH_2) ppm. ^{13}C NMR (100 MHz, [D_4]MeOD): δ = 18.3, 26.5, 26.9, 27.8, 28.3, 28.7 (6C), 41.0, 45.9, 47.9 (2C), 49.7, 79.8, 80.8, 119.9, 157.4, 158.5. HRMS (MALDI): calcd. for $C_{21}H_{40}N_4O_4$ [M+Na]$^+$ 435.2942; found 435.2942.

*Compound (**23**).* Colorless oil (83%). IR (KBr): ν = 3582, 3341, 2976, 2932, 2863, 1683, 1520, 1479, 1418, 1390, 1365, 1251, 1164, 1081, 1040, 993, 869, 775 cm^{-1}. ^1H NMR (400 MHz, [D_4]MeOD): δ = 1.43 (s, 9H, 3CH_3), 1.46 (s, 9H, 3CH_3), 1.47−1.63 (m, 4H, 2CH_2), 1.69 (q, 2H, CH_2, J = 7 Hz), 2.60 (t, 2H, CH_2, J = 6.8 Hz), 2.63 (dd, 2H, CH_2, J = 7.1 Hz, J = 7.3 Hz), 2.86 (t, 2H, CH_2, J = 6.9 Hz), 3.03 (t, 2H, CH_2, J = 6.8 Hz), 3.17−3.27 (m, 4H, 2CH_2) ppm. ^{13}C NMR (100 MHz, [D_4]MeOD): δ = 18.3, 26.9, 27.8, 28.3, 28.7 (3C), 28.8 (3C), 41.0, 45.9, 47.9 (2C), 49.7, 79.9, 80.9, 119.9, 157.4, 158.4. HRMS (MALDI): calcd. for $C_{20}H_{38}N_4O_4$ [M+Na]$^+$ 421.2785; found 421.2774.

*General Procedure for the Preparation of Cyanopolyamines **26** and **27**.* A solution of di-*tert*-butyldicarbonate (2.5 equiv, 3.3 mmol) in anhydrous methanol was added dropwise to a stirring solution of **21** (1 equiv, 1.32 mmol) or **22** (1 equiv, 1.32 mmol) in solution of methanol and 10% of triethylamine (10 mL). After stirring for 24 h at room temperature, solvents were removed under reduced pressure to give a colorless oil, which was dissolved in dichloromethane, washed with saturated $NaHCO_3$ and then water. The organic layer was separated, dried over anhydrous Na_2SO_4, filtered, and concentrated under reduced pressure. The residue was purified by chromatography on silica gel (dichloromethane then dichloromethane/ethyl acetate: (8:2)).

*Compound (**26**).* Colorless oil (670 mg, 98%). IR (KBr): ν = 3360, 2975, 2932, 2868, 1698, 1519, 1479, 1455, 1417, 1390, 1366, 1249, 1163, 1077, 1040, 872, 773 cm^{-1}. ^1H NMR (400 MHz, [D_4]MeOD): δ = 1.43 (s, 9H, 3CH_3), 1.46 (s, 9H, 3CH_3), 1.47 (s, 9H, 3CH_3), 1.49−1.58 (m, 4H, 2CH_2), 1.69 (q, 2H, CH_2, J = 6.9 Hz), 1.87 (q, 2H, CH_2, J = 7 Hz), 2.44 (t, 2H, CH_2, J = 7 Hz), 3.03 (t, 2H, CH_2, J = 6.8 Hz), 3.17−3.27 (m, 6H, 3CH_2), 3.32 (t, 2H, CH_2, J = 7.1 Hz) ppm. ^{13}C NMR (100 MHz, [D_4]MeOD): δ = 14.9, 25.6, 26.6, 27.0, 28.75 (3C), 28.78 (3C), 28.8 (3C), 29.5, 30.3, 38.9, 45.9, 47.1, 47.8 (2C), 79.9, 80.9, 81.3, 120.8, 157.4, 158.4. HRMS (MALDI): calcd. for $C_{26}H_{48}N_4O_6$ [M+Na]$^+$ 535.3466; found 535.3463.

*Compound (**27**).* Colorless oil (395 mg, 99%). IR (KBr): ν = 3360, 2975, 2932, 2867, 1682, 1519, 1479, 1417, 1391, 1366, 1251, 1163, 1074, 871, 774 cm^{-1}. ^1H NMR (400 MHz, [D_4]MeOD): δ = 1.43 (s, 9H, 3CH_3), 1.46 (s, 9H, 3CH_3), 1.48 (s, 9H, 3CH_3), 1.50−1.61 (m, 8H, 4CH_2), 2.69 (t, 2H, CH_2, J = 6.6 Hz), 3.05 (t, 2H, CH_2, J = 6.8 Hz), 3.16−3.26 (m, 4H, 2CH_2), 3.29 (t, 2H, CH_2, J = 6.6 Hz), 3.50 (t, 2H, CH_2, J = 6.6 Hz) ppm. ^{13}C NMR (100 MHz, [D_4]MeOD): δ = 17.3 and 17.8 (rotamer), 26.8 (4C), 28.3 (3C), 28.6 (3C), 28.8 (3C), 41.0, 44.3, and 44.6 (rotamer), 48.1 (3C), 79.8, 80.8, 81.7, 119.5, 157.1, 157.4, 158.5. HRMS (MALDI): calcd. for $C_{26}H_{48}N_4O_6$ [M+Na]$^+$ 535.3466; found 535.3479.

*General Procedure for the Preparation of Homospermines **6** and **7**.* To a suspension of Raney Ni (2 g) in ethanol (10 mL) was added cyanopolyamines **26** or **27** (1 equiv, 1.4 mmol) and slowly NH_4OH (4 mL). The mixture was stirred under hydrogen (20 bar) at room temperature for 24 h. The Raney nickel was eliminated by filtration over a pad of Celite, and the filtrate was evaporated under reduce pressure. The resulting solid was dissolved in dichloromethane, washed with NaOH 2.5 M (2 times) and water, dried over anhydrous Na_2SO_4, filtered, and concentrated under reduced pressure to yield homospermine **6** or **7** as a colorless oil.

*Compound (**6**).* Colorless oil (99%). IR (KBr): ν = 3363, 2973, 2930, 2865, 1689, 1520, 1479, 1418, 1390, 1365, 1275, 1250, 1169, 875, 773 cm^{-1}. ^1H NMR (400 MHz, [D_4]MeOD): δ = 1.43 (s, 9H, 3CH_3), 1.45 (s, 9H, 3CH_3), 1.46 (s, 9H, 3CH_3), 1.48−1.63 (m, 8H, 4CH_2), 1.68 (q, 2H, CH_2, J = 6.8 Hz), 2.64 (dd, 2H, CH_2, J = 7.1 Hz), 3.03 (t, 2H, CH_2, J = 6.8 Hz), 3.16−3.27 (m, 8H, 4CH_2) ppm. ^{13}C NMR (100 MHz, [D_4]MeOD): δ = 26.7, 27.1, 28.8 (9C), 29.6, 30.2, 31.1, 38.9, 42.3, 48.1 (4C), 79.9, 80.8, 80.9, 157.4 (2C), 158.4. HRMS (MALDI): calcd. for $C_{26}H_{52}N_4O_6$ [M+Na]$^+$ 539.3779; found 539.3760.

*Compound (**7**).* Colorless oil (99%). IR (KBr): ν = 3362, 2974, 2931, 2866, 1683, 1520, 1479, 1455, 1418, 1390, 1365, 1251, 1170, 875, 773 cm^{-1}. ^1H NMR (400 MHz, [D_4]MeOD): δ = 1.43 (s, 9H, 3CH_3), 1.45 (s, 9H, 3CH_3), 1.46 (s, 9H, 3CH_3), 1.48−1.61 (m, 8H, 4CH_2), 1.68 (q, 2H, CH_2, J = 6.9 Hz), 2.62 (t, 2H, CH_2, J = 6.9 Hz), 3.04 (t, 2H, CH_2, J = 6.8 Hz), 3.15−3.29 (m, 8H, 4CH_2) ppm. ^{13}C NMR (100 MHz, [D_4]MeOD): δ = 26.5 (2C), 27.1 (2C), 28.3 (3C), 28.8 (6C), 32.1, 39.6, and 40.0 (rotamer), 41.0, 45.1, and 45.8 (rotamer), 47.9 (3C), 79.8, 80.8, 80.9, 157.4 (2C), 158.5. HRMS (MALDI): calcd. for $C_{26}H_{52}N_4O_6$ [M+Na]$^+$ 539.3779; found 539.3781.

*General Procedure for the Reductive Amination (**31**−**39**).* To a stirred solution of polyamines **1**−**9** (1.2 equiv, 0.72 mmol) in 1,2-dichloroethane (6 mL) at room temperature under argon was added 8-hydroxyquinoline-2-carbaldehyde **30** (1 equiv, 0.6 mmol). After 15 min, sodium triacetoxyborohydride (3 equiv, 1.8 mmol) was added and the mixture was stirred 2 to 4 h until aldehyde was consumed (monitored by TLC). The reaction mixture was quenched by adding 1 M NaOH, stirred 20 min, and the product was extracted three times with CH_2Cl_2, dried over anhydrous Na_2SO_4, filtered, and concentrated under reduced pressure. The residue was purified by chromatography on silica gel (chloroform/methanol/ammonia, 94:5:1 for **31**−**34**; and 95:4:1 for **35**−**39**).

*Compound (**31**).* Viscous yellow oil (705 mg, 91%). IR (KBr): ν = 3053, 2982, 2934, 1706, 1683, 1575, 1507, 1475, 1455, 1420, 1391, 1366, 1265, 1168, 1047 cm^{-1}. ^1H NMR (400 MHz, [D_4]MeOD): δ = 1.35−1.69 (m, 26H, 8CH_2 6CH_3), 2.77 (bs, 2H, CH_2), 3.03 (t, 2H, CH_2, J = 6.8 Hz), 3.13−3.26 (m, 4H, 2CH_2), 4.14 (s, 2H, CH_2), 7.10 (dd, H, J = 7.5 Hz, J = 1.3 Hz), 7.34 (dd, H, J = 8.3 Hz, J = 1.3 Hz), 7.41 (dd, H, J = 8.1 Hz, J = 7.6 Hz), 7.45 (d, H, J = 8.5 Hz), 8.20 (d, H, J = 8.5 Hz) ppm. ^{13}C NMR (100 MHz, [D_4]MeOD): δ = 26.5, 27.0, 27.2, 28.4, 28.7 (3C), 28.8 (3C), 40.9, 48.1, 49.9, 54.9, 79.8, 80.8, 112.2, 118.8, 122.1, 128.3, 129.4, 137.9, 139.2, 154.2, 157.4 (2C), 158.5. HRMS (MALDI): calcd. for $C_{28}H_{44}N_4O_5$ [M+H]$^+$ 517.3384; found 517.3386.

*Compound (**32**).* Viscous yellow oil (300 mg, 82%). IR (KBr): ν = 3341, 2974, 2933, 2824, 1689, 1595, 1573, 1508, 1476, 1420, 1391, 1366, 1274, 1230, 1169, 1088, 1034 cm^{-1}. ^1H NMR (400 MHz, [D_4]MeOD): δ = 1.36−1.48 (m, 18H, 9CH_3), 1.54−1.61 (m, 4H, 2CH_2), 1.66 (qt, 2H, CH_2, J = 6.8 Hz), 2.71 (t, 2H, CH_2, J = 6.8 Hz), 3.02 (t, 2H, CH_2, J = 6.8 Hz), 3.14−3.26 (m, 4H, 2CH_2), 4.07 (s, 2H, CH_2), 7.09 (dd, H, J = 7.5 Hz, J = 1.3 Hz), 7.32 (dd, H, J = 8.3 Hz, J = 1.3 Hz), 7.38 (dd, H, J = 7.6 Hz, J = 7.5 Hz), 7.42 (d, H, J = 8.5 Hz), 8.17 (d, H, J = 8.5 Hz) ppm. ^{13}C NMR (100 MHz, [D_4]MeOD): δ = 27.5 (2C), 28.7 (3C), 28.8 (3C), 29.4 and 30.2 (rotamer), 38.9, 45.6, and 46.1 (rotamer), 48.1, 50.1, 55.3, 79.9, 80.9, 112.1, 118.8, 122.1, 128.2, 129.4, 137.8, 139.3, 154.2, 157.4, 158.2, 158.4. HRMS (MALDI): calcd. for $C_{27}H_{42}N_4O_5$ $[M+H]^+$ 503.3228; found 503.3207.

*Compound (**33**).* Viscous yellow oil (280 mg, 90%). IR (KBr): ν = 3350.4, 2975, 2935, 2826, 1688, 1575−1250, 1171, 1033 cm^{-1}. ^1H NMR (400 MHz, [D_4]MeOD): δ = 1.32−1.61 (m, 22H, 2CH_2 6CH_3), 1.83 (qt, 2H, CH_2, J = 7.1 Hz), 2.72 (bt, 2H, CH_2), 3.03 (t, 2H, CH_2, J = 6.8 Hz), 3.17 (t, 2H, CH_2, J = 7.2 Hz), 3.22−3.38 (m, 2H, CH_2), 4.09 (s, 2H, CH_2), 7.10 (dd, H, J = 7.5 Hz, J = 1.3 Hz), 7.33 (dd, H, J = 8.3 Hz, J = 1.3 Hz), 7.39 (dd, H, J = 8.3 Hz, J = 7.6 Hz), 7.43 (d, H, J = 8.5 Hz), 8.18 (d, H, J = 8.5 Hz) ppm. ^{13}C NMR (100 MHz, [D_4]MeOD): δ = 26.9, 28.3, 28.7 (3C), 28.8 (3C), 29.6, 40.9, 45.3, 46.4, and 46.9 (rotamer), 47.8, 54.8, 79.8, 80.9, 112.1, 118.8, 122.1, 128.3, 129.4, 137.9, 139.2, 154.2, 157.5, 158.5 (2C). HRMS (MALDI): calcd. for $C_{27}H_{42}N_4O_5$ $[M+H]^+$ 503.3228; found 503.3215.

*Compound (**34**).* Viscous yellow oil (325 mg, 88%). IR (KBr): ν = 3357, 2976, 2935, 2827, 1689, 1600, 1574, 1509, 1477, 1422, 1392, 1367, 1251, 1170, 1089, 1033 cm^{-1}. ^1H NMR (400 MHz, [D_4]MeOD): δ = 1.42 (s, 18H, 6CH_3), 1.68 (qt, 2H, CH_2, J = 6.3 Hz), 1.83 (qt, 2H, CH_2, J = 7.1 Hz), 2.69 (t, 2H, CH_2, J = 7 Hz), 3.02 (t, 2H, CH_2, J = 6.8 Hz), 3.21 (t, 2H, CH_2, J = 7.2 Hz), 3.25−3.38 (m, 2H, CH_2), 4.08 (s, 2H, CH_2), 7.09 (dd, H, J = 7.5 Hz, J = 1.3 Hz), 7.33 (dd, H, J = 8.2 Hz, J = 1.2 Hz), 7.39 (dd, H, J = 8.1 Hz, J = 7.6 Hz), 7.44 (d, H, J = 8.5 Hz), 8.18 (d, H, J = 8.5 Hz) ppm. ^{13}C NMR (100 MHz, [D_4]MeOD): δ = 28.7 (3C), 28.8 (3C), 29.5, 30.1, 38.9, 45.8, 46.5, 49.8, 55.1, 79.9, 81.1, 112.1, 118.8, 122.1, 128.3, 129.4, 137.8, 139.2, 154.2, 157.5, 158.4 (2C). HRMS (MALDI): calcd. for $C_{26}H_{40}N_4O_5$ $[M+H]^+$ 489.3071; found 489.3048.

*Compound (**35**).* Viscous yellow oil (200 mg, 95%). IR (KBr): ν = 3351, 2974, 2932, 2865, 1699, 1601, 1573, 1506, 1472, 1418, 1366, 1250, 1173, 879, 836, 754 cm^{-1}. ^1H NMR (400 MHz, [D_4]MeOD): δ = 1.39−1.65 (m, 35H, 4CH_2 9CH_3), 2.72 (bt, 2H, CH_2), 3.03 (t, 2H, CH_2, J = 6.7 Hz), 3.13−3.24 (m, 8H, 4CH_2), 4.09 (s, 2H, CH_2), 7.09 (dd, H, J = 7.5 Hz, J = 1.3 Hz), 7.33 (dd, H, J = 8.2 Hz, J = 1.3 Hz), 7.39 (dd, H, J = 8.2 Hz, J = 7.5 Hz), 7.44 (d, H, J = 8.5 Hz), 8.19 (d, H, J = 8.5 Hz) ppm. ^{13}C NMR (100 MHz, [D_4]MeOD): δ = 26.6 (2C), 27.1 (2C), 27.6, 28.3, 28.8 (9C), 41.0, 48.0 (4C), 50.1, 55.3, 79.8, 80.8 (2C), 112.1, 118.8, 122.2, 128.3, 129.4, 137.8, 139.3, 154.2, 157.4 (2C), 158.2, 158.5. HRMS (MALDI): calcd. for $C_{37}H_{61}N_5O_7$ $[M+H]^+$ 688.4644; found 688.4672.

*Compound (**36**).* Viscous yellow oil (310 mg, 94%). IR (KBr): ν = 3360, 3051, 2972, 2929, 2864, 1695, 1616, 1558, 1520, 1506, 1495, 1472, 1464, 1456, 1363, 1248, 1164, 1090, 1044, 1005, 877, 835 cm^{-1}. ^1H NMR (400 MHz, [D_4]MeOD): δ = 1.34−1.61 (m, 35H, 4CH_2 9CH_3), 1.83 (qt, 2H, CH_2, J = 7.1 Hz), 2.70 (t, 2H, CH_2, J = 6.9 Hz), 3.04 (t, 2H, CH_2, J = 6.8 Hz), 3.13−3.25 (m, 6H, 3CH_2), 3.31 (m, 2H, CH_2), 4.08 (s, 2H, CH_2), 7.09 (dd, H, J = 7.4 Hz, J = 1.35 Hz), 7.34 (dd, H, J = 8.2 Hz, J = 1.35 Hz), 7.40 (dd, H, J = 8.2 Hz, J = 7.4 Hz), 7.45 (d, H, J = 8.5 Hz), 8.19 (d, H, J = 8.5 Hz) ppm. ^{13}C NMR (100 MHz, [D_4]MeOD): δ = 26.6 (2C), 27.0 (2C), 28.3, 28.7 (3C), 28.8 (6C), 41.0, 47.9 (4C), 49.8, 55.1, 79.8, 80.8, 80.9, 112.0, 118.8, 122.1, 128.3, 129.4, 137.8, 139.3, 154.2, 157.4 (2C), 157.5, 158.5. HRMS (MALDI): calcd. for $C_{36}H_{59}N_5O_7$ $[M+H]^+$ 674.4487; found 674.4492.

*Compound (**37**).* Viscous yellow oil (485 mg, 96%). IR (KBr): ν = 3357, 3052, 2975, 2931, 1683, 1600, 1573, 1505, 1471, 1418, 1390, 1366, 1248, 1164, 1086, 878, 835, 754, 703 cm^{-1}. ^1H NMR (400 MHz, [D_4]MeOD): δ = 1.35−1.53 (m, 33H, 3CH_2 9CH_3), 1.53−1.62 (m, 4H, 2CH_2), 2.70 (bt, 2H, CH_2), 3.02 (t, 2H, CH_2, J = 6.7 Hz), 3.21−3.26 (m, 8H, 4CH_2), 4.07 (s, 2H, CH_2), 7.08 (dd, H, J = 7.5 Hz, J = 1.3 Hz), 7.32 (dd, H, J = 8.2 Hz, J = 1.3 Hz), 7.39 (dd, H, J = 8.2 Hz, J = 7.5 Hz), 7.43 (d, H, J = 8.5 Hz), 8.17 (d, H, J = 8.5 Hz) ppm. ^{13}C NMR (100 MHz, [D_4] MeOD): δ = 26.6, 27.1, 27.7 (2C), 28.8 (9C), 29.5 and 30.2 (rotamer), 38.9, 45.7, 48.1 (3C), 50.1, 55.3, 79.9, 80.8, 80.9, 112.1, 118.7, 122.1, 128.2, 129.3, 137.8, 139.3, 154.2, 157.3 (2C), 158.3 (2C). HRMS (MALDI): calcd. for $C_{36}H_{59}N_5O_7$ $[M+H]^+$ 674.4487; found 674.4475.

*Compound (**38**).* Viscous yellow oil (290 mg, 96%). IR (KBr): ν = 3364, 3052, 2974, 2930, 1683, 1600, 1574, 1505, 1471, 1418, 1390, 1366, 1248, 1161, 1086, 871, 835 cm^{-1}. ^1H NMR (400 MHz, [D_4]MeOD): δ = 1.34−1.56 (m, 31H, 2CH_2 9CH_3), 1.68 (qt, 2H, CH_2, J = 6.8 Hz), 1.83 (qt, 2H, CH_2, J = 7.1 Hz), 2.70 (t, 2H, CH_2, J = 6.8 Hz), 3.03 (t, 2H, CH_2, J = 6.8 Hz), 3.14−3.25 (m, 6H, 3CH_2), 3.31 (m, 2H, CH_2), 4.08 (s, 2H, CH_2), 7.09 (dd, H, J = 7.5 Hz, J = 1.3 Hz), 7.34 (dd, H, J = 8.3 Hz, J = 1.3 Hz), 7.40 (dd, H, J = 8.3 Hz, J = 7.5 Hz), 7.45 (d, H, J = 8.5 Hz), 8.19 (d, H, J = 8.5 Hz) ppm. ^{13}C NMR (100 MHz, [D_4]MeOD): δ = 27.1 (2C), 28.6 (3C), 28.7 (3C), 28.8 (3C), 29.7 (2C), 38.9 and 45.4 (rotamer), 45.8, 47.1, 47.9 (2C), 49.8, 55.1, 79.9, 80.9, 81.0, 112.1, 118.8, 122.1, 128.3, 129.4, 137.9, 139.2, 154.2, 157.4 (2C), 158.1, 158.4. HRMS (MALDI): calcd. for $C_{35}H_{57}N_5O_7$ $[M+Na]^+$ 682.4150; found 682.4164.

*Compound (**39**).* Viscous yellow oil (240 mg, 89%). IR (KBr): ν = 3363, 3051, 2973, 2929, 1682, 1600, 1573, 1505, 1471, 1418, 1365, 1250, 1163, 1091, 982, 866, 835 cm^{-1}. ^1H NMR (400 MHz, [D_4]MeOD): δ = 1.42 (bs, 18H, 6CH_3), 1.44 (s, 9H, 3CH_3), 1.68 (qt, 2H, CH_2, J = 6.95 Hz), 1.75 (qt, 2H, CH_2, J = 7.1 Hz), 1.83 (qt, 2H, CH_2, J = 7.1 Hz), 2.69 (t, 2H, CH_2, J = 7.1 Hz), 3.03 (t, 2H, CH_2, J = 6.8 Hz), 3.13−3.25 (m, 6H, 3CH_2), 3.31 (m, 2H, CH_2), 4.07 (s, 2H, CH_2), 7.09 (dd, H, J = 7.5 Hz, J = 1.3 Hz), 7.33 (dd, H, J = 8.3 Hz, J = 1.3 Hz), 7.40 (dd, H, J = 8.3 Hz, J = 7.5 Hz), 7.44 (d, H, J = 8.5 Hz), 8.18 (d, H, J = 8.5 Hz) ppm. ^{13}C NMR (100 MHz, [D_4]MeOD): δ = 28.7 (6C), 28.8 (3C), 29.5 (3C), 38.9, 45.9 (3C), 47.1, 49.8, 55.1, 79.4, 79.9, 81.1, 112.0, 118.8, 122.1, 128.3, 129.3, 137.8, 139.2, 154.2, 157.3 (2C), 158.1, 158.40. HRMS (MALDI): calcd. for $C_{34}H_{55}N_5O_7$ $[M+H]^+$ 646.4174; found 646.4158.

General Procedure for Boc Removal (HQ1-XYZ). To a stirred solution of polyamines **31**−**39** (1 equiv, 0.5 mmol) dissolved in ethanol (3 mL) at 0 °C was added 6 M HCl (3 mL). After 18 h at room temperature, the solution was concentrated in vacuo, and the resulting solid was washed with cold ethanol, filtered, and dried in vacuo to afford Quilamine **40**−**48** as yellow solid, its hydrochloride salt.

*Compound HQ1-**44***. Yellow solid (73%). Mp sup 250 °C. IR (KBr): ν = 3384, 2957, 2798, 1642, 1606, 1551, 1513, 1461, 1420, 1398, 1344, 1302, 1252−1055, 841 cm^{-1}. UV−vis: λ_{max} (nm) ((ε M^{-1} cm^{-1} for pH 7.4), 272 (36300), 307 (2400). ^1H NMR (400 MHz, D_2O): δ = 1.76−2.04 (m, 8H, $4CH_2$), 3.06−3.22 (m, 6H, $3CH_2$), 3.38 (dd, 2H, J = 7.75 Hz, J = 7.45 Hz, CH_2), 4.78 (s, 2H, CH_2), 7.36 (dd, 1H, J = 7.45 Hz, J = 1.49 Hz, H_{7ar}), 7.60 (dd, 1H, J = 8.30 Hz, J = 1.49 Hz, H_{5ar}), 7.65 (dd, 1H, J = 8.30 Hz, J = 7.45 Hz, H_{6ar}), 7.76 (d, 1H, J = 8.60 Hz, H_{3ar}), 8.64 (d, 1H, J = 8.60 Hz, H_{4ar}) ppm. ^{13}C NMR (100 MHz, D_2O): δ = 22.7, 22.8 (2C), 24.0, 38.9, 46.9, 47.0, 47.3, 49.7, 114.1, 119.4, 121.1, 128.9, 129.3, 134.5, 141.8, 148.5, 149.5 ppm. HRMS (MALDI): calcd. for $C_{18}H_{29}N_4O$ [M+H-4HCl]$^+$ 317.2336; found 317.2348. Anal. Calcd for $C_{18}H_{32}Cl_4N_4O{\cdot}1.2\ H_2O$: C, 44.68; H, 7.17; N, 11.58. Found: C, 44.52; H, 6.97; N, 11.57.

*Compound HQ1-**34***. Yellow solid (80%). Mp sup 250 °C. IR (KBr): ν = 3493, 2957, 2770, 2528, 2403, 1599, 1515, 1480, 1458, 1420, 1398, 1304, 859 cm^{-1}. UV−vis: λ_{max} (nm) ((ε M^{-1} cm^{-1} for pH 7.4) 272 (32500), 307 (2100). ^1H NMR (400 MHz, D_2O): δ = 1.66−1.84 (m, 4H, $2CH_2$), 2.17−2.31 (m, 2H, CH_2), 2.97−3.06 (m, 2H, CH_2), 3.07−3.14 (m, 2H, CH_2), 3.15−3.24 (m, 2H, CH_2), 3.41 (m, 2H, CH_2), 4.68 (s, 2H, CH_2), 7.27 (dd, 1H, J = 6.61 Hz, J = 2.43 Hz, H_{7ar}), 7.49−7.57 (m, 2H, H_{5ar} and H_{6ar}), 7.61 (d, 1H, J = 8.50 Hz, H_{3ar}), 8.46 (d, 1H, J = 8.50 Hz, H_{4ar}) ppm. ^{13}C NMR (100 MHz, D_2O): δ = 22.7, 22.8, 23.9, 38.8, 44.5, 44.7, 47.1, 50.5, 113.2, 119.4, 120.8, 128.6, 128.7, 136.1, 139.9, 149.2, 105.4 ppm. HRMS (MALDI): calcd. for $C_{17}H_{27}N_4O$ [M+H-4HCl]$^+$ 303.2179; found 303.2183. Anal. Calcd for $C_{17}H_{30}C_{l4}N_4O{\cdot}0.4H_2O$: C, 41.89; H, 6.37; N, 11.47. Found: C, 42.15; H, 6.36; N, 11.16.

*Compound HQ1-**43***. Yellow solid (88%). Mp sup 250 °C. IR (KBr): ν = 3039, 2984, 2825, 1641, 1606, 1538, 1461, 1419, 1402, 1352, 1302, 842 cm^{-1}. UV−vis: λ_{max} (nm) ((ε M^{-1} cm^{-1} for pH 7.4) 272 (34500), 307 (2200). ^1H NMR (400 MHz, D_2O): δ = 1.84−2.05 (m, 4H, $2CH_2$), 2.11−2.22 (m, 2H, CH_2), 3.14−3.27 (m, 6H, $3CH_2$), 3.34−3.41 (m, 2H, CH_2), 4.75 (s, 2H, CH_2), 7.39 (dd, 1H, J = 6.5 Hz, J = 2.4 Hz, H_{7ar}), 7.62−7.70 (m, 2H, H_{5ar} and H_{6ar}), 7.71 (d, 1H, J = 8.5 Hz, H_{3ar}), 8.59 (d, 1H, J = 8.5 Hz, H_{4ar}) ppm. ^{13}C NMR (100 MHz, D_2O): δ = 22.8, 22.9, 23.8, 36.6, 44.6, 47.0, 47.1, 50.3, 113.3, 119.4, 120.9, 128.8 (2C), 135.8, 140.2, 149.3, 150.3 ppm. HRMS (MALDI): calcd. for $C_{17}H_{27}N_4O$ [M+H-4HCl]$^+$ 303.2179; found 303.2190. Anal. Calcd for $C_{17}H_{30}Cl_4N_4O{\cdot}1.1\ H_2O$: C, 43.62; H, 6.93; N, 11.97. Found: C, 43.4; H, 6.71; N, 12.19.

*Compound HQ1-**33***. Yellow solid (76%). Mp sup 250 °C. IR (KBr): ν = 3423, 2962, 2760, 2692, 1636, 1607, 1595, 1517, 1458, 1397, 1303, 1272, 1094, 842 cm^{-1}. UV−vis: λ_{max} (nm) ((ε $M^{-1}cm^{-1}$ for pH 7.4) 272 (36200), 307 (2200). ^1H NMR (400 MHz, D_2O): δ = 2.12−2.22 (m, 2H, CH_2), 2.28−2.39 (m, 2H, CH_2), 3.14−3.21 (m, 2H, CH_2), 3.22−3.34 (m, 4H, $2CH_2$), 3.42−3.49 (m, 2H, CH_2), 4.80 (s, 2H, CH_2), 7.37 (dd, 1H, J = 7.28 Hz, J = 1.46 Hz, H_{7ar}), 7.61 (dd, 1H, J = 8.37 Hz, J = 1.64 Hz, H_{5ar}), 7.66 (dd, 1H, J = 7.46 Hz, J = 7.28 Hz, H_{6ar}), 7.75 (d, 1H, J = 8.55 Hz, H_{3ar}), 8.63 (d, 1H, J = 8.55 Hz, H_{4ar}) ppm. ^{13}C NMR (100 MHz, D_2O): δ = 22.7, 23.7, 36.6, 44.7, 44.8, 44.9, 49.9, 114.0, 119.4, 121.1, 128.9, 129.2, 134.7, 141.6, 148.5, 149.7 ppm. HRMS (MALDI): calcd. for $C_{16}H_{25}N_4O$ [M+H-4HCl]$^+$ 289.2023; found 289.2034. Anal. Calcd for $C_{16}H_{28}Cl_4N_4O{\cdot}1.45\ H_2O$: C, 41.74; H, 6.77; N, 12.17. Found: C, 41.59; H, 6.58; N, 12.17.

*Compound HQ1-**444***. Yellow solid (95%). Mp sup 250 °C. IR (KBr): ν = 3426, 3038, 2956, 2874, 2799, 2758, 1642, 1606, 1598, 1449, 1302 cm^{-1}. UV−vis: λ_{max} (nm) ((ε M^{-1} cm^{-1} for pH 7.4) 272 (34500), 307 (2000). ^1H NMR (400 MHz, D_2O): δ = 1.75−2.03 (m, 12H, $6CH_2$), 3.06−3.22 (m, 10H, $5CH_2$), 3.34−3.41 (m, 2H, CH_2), 4.78 (s, 2H, CH_2), 7.39 (dd, 1H, J = 7.15 Hz, J = 1.79 Hz, H_{7ar}), 7.61−7.71 (m, 2H, H_{5ar} and H_{6ar}), 7.77 (d, 1H, J = 8.54 Hz, H_{3ar}), 8.65 (d, 1H, J = 8.54 Hz, H_{4ar}) ppm. ^{13}C NMR (100 MHz, D_2O): δ = 22.7, 22.8 (4C), 24.0, 38.9, 46.9 (3C), 47.0, 47.3, 49.8, 114.0, 119.4, 121.1, 128.9, 129.2, 134.8, 141.5, 148.7, 149.7 ppm. HRMS (MALDI): calcd. for $C_{22}H_{38}N_5O$ [M+H-5HCl]$^+$ 388.3071; found 388.3059. Anal. Calcd for $C_{22}H_{42}Cl_5N_5O$ 1.7 H_2O: C, 44; H, 7.62; N, 11.66. Found: C, 43.64; H, 7.45; N, 12.05.

*Compound HQ1-**443***. Yellow solid (91%). Mp sup 250 °C. IR (KBr): ν = 3441, 2951, 2777, 2577, 2421, 1641, 1597, 1515, 1477, 1451, 1418, 1401, 1352, 1301, 1247, 1232, 1209, 1168, 1092, 1056, 841 cm^{-1}. UV−vis: λ_{max} (nm) ((ε M^{-1} cm^{-1} for pH 7.4) 272 (35300), 307 (2000). ^1H NMR (400 MHz, D_2O): δ = 1.81−2.02 (m, 8H, $4CH_2$), 2.12−2.21 (m, 2H, CH_2), 3.12−3.27 (m, 10H, $5CH_2$), 3.35−3.39 (m, 2H, CH_2), 4.77 (s, 2H, CH_2), 7.39 (dd, 1H, J = 6.9 Hz, J = 2 Hz, H_{7ar}), 7.63−7.71 (m, 2H, H_{5ar} and H_{6ar}), 7.75 (d, 1H, J = 8.6 Hz, H_{3ar}), 8.63 (d, 1H, J = 8.6 Hz, H_{4ar}) ppm. ^{13}C NMR (100 MHz, D_2O): δ = 22.8 (2C), 22.9 (2C), 23.8, 36.6, 44.6, 46.9 (2C), 47.1, 47.2, 50.1, 113.7, 119.4, 121.1, 128.9, 129.1, 135.2, 141.0, 148.9, 149.9 ppm. HRMS (MALDI): calcd. for $C_{21}H_{36}N_5O$ [M+H-5HCl]$^+$ 374.2914; found 374.2927. Anal. Calcd for $C_{21}H_{40}Cl_5N_5O{\cdot}1.35\ H_2O$: C, 43.48; H, 7.42; N, 12.07. Found: C, 43.32; H, 7.25; N, 12.22.

*Compound HQ1-**344***. Yellow solid (92%). Mp sup 250 °C. IR (KBr): ν = 3416, 2954, 2770, 2441, 1631, 1602, 1512, 1456, 1412, 1351, 1312, 1249, 1168, 1095, 1056 cm^{-1}. UV−vis: λ_{max} (nm) ((ε M^{-1} cm^{-1} for pH 7.4) 272 (36900), 307 (2200). ^1H NMR (400 MHz, D_2O): δ = 1.77−1.92 (m, 8H, $4CH_2$), 2.28−2.39 (m, 2H, CH_2), 3.07−3.23 (m, 8H, $4CH_2$), 3.25−3.32 (m, 2H, CH_2), 3.41−3.47 (m, 2H, CH_2), 4.74 (s, 2H, CH_2), 7.35 (dd, 1H, J = 6.6 Hz, J = 2.3 Hz H_{3ar}), 7.60−7.66 (m, 3H,), 8.49 (d, 1H, J = 8.6 Hz) ppm. ^{13}C NMR (100 MHz, D_2O): δ = 22.7, 22.8 (3C), 23.9, 38.8, 44.5, 44.6, 46.8, 46.9, 47.1, 50.8, 112.7, 119.4, 120.6, 128.4, 128.6, 136.6, 139.1, 149.5, 150.7 ppm. HRMS (MALDI): calcd. for $C_{21}H_{36}N_5O$ [M+H-5HCl]$^+$ 374.2914; found 374.2905. Anal. Calcd for $C_{21}H_{40}Cl_5N_5O{\cdot}0.3\ H_2O$: C, 44.94; H, 7.29; N, 12.48. Found: C, 44.7; H, 7.15; N, 12.72.

*Compound HQ1-**343***. Yellow solid (92%). Mp sup 250 °C. IR (KBr): ν = 3386, 2957, 2776, 2425, 1642, 1606, 1312, 1461, 1413, 1348, 1303, 1252, 1111, 1093, 1058 cm^{-1}. UV−vis: λ_{max} (nm) ((ε M^{-1} cm^{-1} for pH 7.4) 272 (34500), 307 (2100). ^1H NMR (400 MHz, D_2O): δ = 1.81−1.91 (m, 4H, $2CH_2$), 2.12−2.22 (m, 2H, CH_2), 2.28−2.38 (m, 2H, CH_2), 3.13−3.32 (m, 10H, $5CH_2$), 3.41−3.48 (m, 2H, CH_2), 4.79 (s, 2H, CH_2), 7.38 (dd, 1H, J = 7 Hz, J = 1.93 Hz), 7.61−7.69 (m, 2H, CH_2), 7.74 (d, 1H, J = 8.6 Hz, H_{3ar}), 8.61 (d, 1H, J = 8.6 Hz, H_{4ar}) ppm. ^{13}C NMR (100 MHz, D_2O): δ = 22.7, 22.8 (2C), 23.8, 36.6, 44.5, 44.6 (2C), 44.8, 47.1, 50.2, 113.7, 119.4, 121.0, 128.9, 129.1, 135.3, 140.5, 148.8, 150.0 ppm. HRMS (MALDI): calcd. for $C_{20}H_{34}N_5O$ [M+H-5HCl]$^+$ 360.2758; found 360.2764. Anal. Calcd for $C_{20}H_{38}Cl_5N_5O{\cdot}0.7\ H_2O$: C, 43.33; H, 7.16; N, 12.63. Found: C, 43.05; H, 7.14; N, 12.97.

*Compound HQ1-**333***. Yellow solid (96%). Mp sup 250 °C. IR (KBr): ν = 3424, 2963, 2756, 2696, 2585, 2420, 1636, 1607, 1594, 1550, 1519, 1458, 1402, 1303, 1265, 1094 cm^{-1}. UV−vis:

λ_{max} (nm) ((ε M^{-1} cm^{-1} for pH 7.4) 272 (35400), 307 (2100). ^{1}H NMR (400 MHz, D_2O): δ = 2.12−2.26 (m, 4H, $2CH_2$), 2.29−2.39 (m, 2H, CH_2), 3.14−3.36 (m, 10H, $2CH_2NHCH_2$ and CH_2NH_2), 3.42−3.49 (m, 2H, NH CH_2), 4.79 (s, 2H, CH_2), 7.38 (dd, 1H, J = 6.8 Hz, J = 2 Hz, H_{7ar}), 7.61−7.69 (m, 2H, CH_2, H_{5ar} and H_{6ar}), 7.73 (d, 1H, J = 8.6 Hz, H_{3ar}), 8.61 (d, 1H, J = 8.6 Hz, H_{4ar}) ppm. ^{13}C NMR (100 MHz, D_2O): δ = 22.6, 22.7, 23.8, 36.6, 44.6, 44.7, 44.8 (3C), 50.3, 113.5, 119.4, 120.9, 128.8, 128.9, 135.5, 140.6, 148.6, 150.1 ppm. HRMS (MALDI): calcd. for $C_{19}H_{32}N_5O$ $[M+H-5HCl]^+$ 346.2601; found 346.2614. Anal. Calcd for $C_{19}H_{36}Cl_5N_5O{\cdot}0.85\ H_2O$: C, 42.02; H, 7; N, 12.9. Found: C, 42.13; H, 6.82; N, 12.73.

Study of the Acid−Base and Metal Complexation Properties of Quilamine HQ1-44. Potentiometric titrations were performed in a glass-jacketed titration cell thermostated at 25 ± 0.1 °C and closed under an inert gas atmosphere, using a Metrohm 702 SM Titrino titration stand connected to a Metrohm 6.0233.100 combined glass electrode and controlled by the *Metrohm Tinet 2.4* software. The titrant was a carbonate-free KOH solution at approximately 0.1 M prepared from a commercial ampule of analytical grade, and its exact concentration was obtained by titration of a standard HNO_3 solution. A stock solution of **HQ1−44** was prepared at ∼1.5 × 10^{-3} M. Stock solutions of iron(III), copper(II), zinc(II), and magnesium(II) cations were prepared at ∼0.05 M from the analytical grade salts $FeCl_3$, $CuCl_2$, $Zn(NO_3)_2$, and $MgSO_4$, and were standardized by complexometry against a standard EDTA (ethylenediaminetetraacetic acid) solution. Sample solutions contained ∼0.03 mmol of ligand in a total volume of 30 mL, with the ionic strength kept at 0.10 M using KNO_3 as background electrolyte. Complexation titrations were run by addition of approximately 0.5 or 1 equiv for iron(III) and copper(II), or 1 equiv for zinc(II) and magnesium(II). The $[H^+]$ of the solutions was determined by measurement of the electromotive force of the cell, $E = E^{\circ\prime} + Q \log[H^+] + E_j$. The term pH is defined as $-\log [H^+]$, and a value of K_w = $[H^+][OH^-]$ = $10^{-13.778}$ was taken from the literature for our experimental conditions. $E^{\circ\prime}$ and Q were determined by titrating a standard HNO_3 solution at the same ionic strength. The liquid-junction potential, E_j, was found to be negligible under the experimental conditions used. Each titration consisted of 150−200 equilibrium points in the range of pH 2.0−11.5, and at least two replicate titrations were performed for each individual system. The potentiometric data were refined with the *Hyperquad* software, and speciation diagrams were plotted using the *Hyss* software. The overall equilibrium (formation) constants β_i^H and β_{MmHhLl} are defined by $\beta_{MmHhLl=[MmHhLl]/[M]m[H]h[L]l}$ and $\beta_{MH-1\ L=}$ $\beta_{ML(OH)}$ × K_w, while stepwise equilibrium constants are given by $K_{MmHhLl=[MmHhLl]/[MmHh-1Ll][H]}$ and correspond to the difference in log units between overall constants of sequentially protonated (or hydroxide) species. The pM values for each metal complex were calculated from the full set of stability constants of each system at pH = 7.4 with c_L = 1.0 × 10^{-5} M and c_M = 1.0 × 10^{-6} M.

BIOLOGY

Chelator Solutions. All reagents, which were of the highest available grade, were obtained from Sigma-Aldrich Chimie (Saint Quentin Fallavier, France). All synthesized Quilamines were compared to the tridentate iron-chelator hydroxyphenyl-triazole ICL670 as a reference (Deferasirox, Exjade from Novartis Pharma) as well as to the 8-hydroxyquinoline. Stock solutions of each chelator (10 mM) were prepared in water. The high solubility of each derivative in culture medium in the concentration range 0−400 μM was preliminary verified by turbidimetry measurement. Three controls have been done for each experiment: one with the standard culture medium, and the other with culture medium. When chelator treatment was performed in the presence of exogenous iron, they have been iron saturated with 20 μM ferric iron ($FeCl_3$). Unbound iron was not removed from the medium. NTBI is classically used to induce iron overload in various cells because it represents the plasma iron species which is mainly responsible for creating parenchymal (especially hepatocyte) iron deposition in human chronic iron overload.

Comparison of Chelator Efficiency in Aqueous Phase, Competition with Calcein. Fluorescence emission (λ_{Exc} = 485 nm, λ_{Em} = 520 nm) of calcein (100 nM) in an HEPES buffer (20 mM HEPES, 150 mM NaCl, pH 7.3) was measured at room temperature in a microplate fluorescence reader (Packard, Fusion), equipped with an orbital stirring. Iron(III) (1 μM) slowly reacted with calcein and maximal quenching of its fluorescence was observed for time longer than 6 h. The fluorescence recovery was monitored after 4 h incubation in the presence of various chelator concentrations. In the absence of iron, various chelators slightly modulated the calcein fluorescence intensity. Results were expressed as a percentage of fluorescence recovery with respect to the free calcein fluorescence intensity measured in the absence of iron.

Cells Studies. The involvement of the PTS in the selective uptake of Quilamines was investigated by using Chinese hamster ovary cells (CHO) exhibiting high PTS activity[46] and the mutated derived-cell line CHO-MG cells, devoided of PTS (provided by Dr. W. Flintoff, University of Western Ontario). The CHO-MG cell was selected for growth resistance to methylglyoxalbis-(guanylhydrazone), using a single-step selection after mutagenesis with ethyl methanesulfonate. Therefore, highly selective PTS ligands should give high (CHO-MG/CHO) IC_{50} ratios.

The two cell lines were grown in RPMI 1640 medium, supplemented with 10% fetal calf serum (Eurobio, Les Ulis, France), 2 mM Glutamine (Bio Media, Boussens, France), 100 units/mL penicillin, and 50 μg/mL streptomycin, at 37 °C in 5% humidified CO_2. L-Proline (2 μg/mL) was added to the culture medium for CHO-MG cells.

Cell Treatment. For experiments, cells were harvested with trypsin and seeded 24 h before the polyamine treatment in 96-well microplates (Becton Dickinson, Oxnard, CA) at a density of 2000 cells per well. In these conditions, cells reached confluency in 5−6 days. Chelator exposure was performed one day after cell seeding in proliferating CHO and CHO-MG cells. The effect of Quilamines on cell viability was also tested in the presence of DFMO (1 mM), a selective inhibitor of ODC which induced a depletion of intracellular putrescine and spermidine and leads to an activation of the PTS. In this assay, the cells were seeded in the presence of the inhibitor. In other experiments, 50 μM spermidine was added to the culture medium to inhibit by a competitive inhibition, the active uptake of Quilamines from PTS. To prevent the oxidation of the exogenous polyamine by the serum amine oxidase present in the fetal calf serum, aminoguanidine (1 mM), an inhibitor of this enzyme, was added to the medium. The various derivatives were compared to the tridentate iron chelator hydroxyphenyl-triazole ICL670 (Deferasirox, Exjade) and to the bidentate 8-hydroxyquinoline.

Cytostatic and Cytotoxic Effects Measurements. Chelator exposure was performed one day after cell seeding in proliferating CHO and CHO-MG cells. After 72 h incubation at 37 °C, cell supernatants were collected for cytotoxicity measurement by measuring extracellular LDH activity (cytotoxicity detection kit − LDH, Roche, Penzberg, Germany). Extracellular LDH activity was measured as described by the manufacturer on a 20 μL aliquot of cell free medium obtained by centrifugation (2500 rpm/min during 5 min). LDH activities were detected by reading absorbance at 485 nm. They were reported as a percentage of extracellular LDH activity with respect to the control value.

Cell viability was determined by counting the cell nuclei after staining with the fluorescent DNA intercalating dye Hoechst 33342. The treated CHO and CHO-MG cells were washed twice with PBS (50 mM pH 7) and fixed with ethanol/acetic acid during 20 min at 4 °C. Cells were counterstained 10 min with Hoechst 33342 dye diluted by 1/1000 (5 μg/mL) in PBS and images were taken with an upright microscope (AxioImager M1, Zeiss, France). Images analysis and cell nuclei counting was performed with the simple *PCI* software (C Imaging Image Analysis System, Compix, USA). The number of cell nuclei was reported as a percentage of the control value. Parameters of the dose−response curves were deduced from a four-parameter curve fit according to Rodbard[47]

$$y = \frac{(A_{cmin} - A_{cmax})}{1 + \left(\frac{C}{C_{ip}}\right)P_{ip}} + A_{cmax}$$

in which y is the percentage of cell nuclei number with respect to the control, A_{Cmin} and A_{Cmax} are the y values observed for minimal and maximal chelator concentrations respectively, C is the chelator concentration (C_{ip} at the inflection point), and P_{ip} is the slope at inflection point of the sigmoid curve. Due to their biphasic feature, the dose−response curves were fitted as the sum of two sigmoids (double 4-parameter fit). Percentages of CHO and CHO-MG cells involved in each viability responses were deduced from the A_{Cmin}, A_{Cmax}, and IC_{50} values of each sigmoid, which were obtained from these fits.

Three independent replicates were performed for each experiment, which was repeated three times.

Computational Details. As its computational cost is in the same order of the Hartree−Fock (HF) method, DFT is applicable to much larger systems than the correlated *ab initio* methods. DFT theory has been used to obtain the structure and energy of all the compounds under study. We have selected for our calculations OPBE, one of the best performing exchange-correlation functional for the iron complexes,[48] which is the combination of Handy's optimized exchange (OPTX)[49] with the PBE correlation.[50] The 6-31G(d,p) basis set, a double-ζ Pople-type basis set for H,C N,O, and Cl atoms and the Lanl2DZ (Los Alamos National Laboratory 2 double-ζ) with effective core potentials (ECP) for Fe atom are employed in the present investigation.

The DFT calculations were carried out with the *Gaussian 09* software package.[51] All open-shell structures were calculated with unrestricted DFT method, whereas for closed-shell molecules, the restricted DFT method was employed. Calculations of iron complexes were performed for spin multiplicities 2, 4, and 6. The Fe(III) complexes were optimized, often using distinct geometries by placing the ligands in pseudo-octahedral orientation about the metal as starting points. These starting points have led to the most stable geometries presented below. The existence of local minima was checked by inspection of the Hessian matrix eigenvalues. For all iron complexes, the stability of the wave function was checked. Unscaled values were used for zero-point vibrational energy corrections for energy values. Thermal corrections were calculated for the evaluation of reaction enthalpies ΔH and Gibbs energies ΔG at 298.15 K, using standard statistical mechanic formulas in the independent mode, harmonic oscillator, and rigid rotor approximations.

RESULTS AND DISCUSSION

Chemistry. We first developed a synthetic protocol to tether 8-hydroxyquinoline-2-carbaldehyde to a set of linear polyamines by reductive amination (Figure 1).

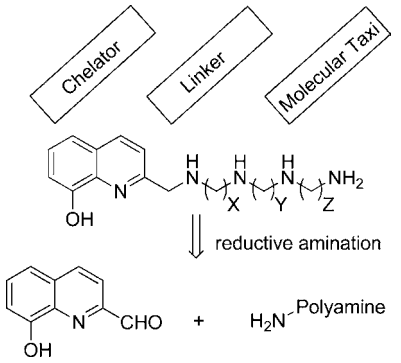
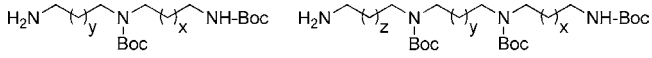


Figure 1. Quilamine **HQ1-*XYZ*** synthesis.

To optimize the efficiency of this novel family of Quilamines in terms of cytotoxicity and PTS selectivity, we studied the influence of the number of nitrogen atoms present in the polyamine chain and the distance between them. The synthesis of nine protected spermidine and spermine analogues described in Figure 2 was carried out. Diverse methodologies for the



x=2, y=2 : homospermidine **1**
x=2, y=1 : spermidine **2**
x=1, y=2 : spermidine **3**
x=1, y=1 : norspermidine **4**

x=2, y=2, z=2 : dihomospermine **5**
x=1, y=2, z=2 : homospermine **6**
x=2, y=2, z=1 : homospermine **7**
x=1, y=2, z=1 : spermine **8**
x=1, y=1, z=1 : norspermine **9**

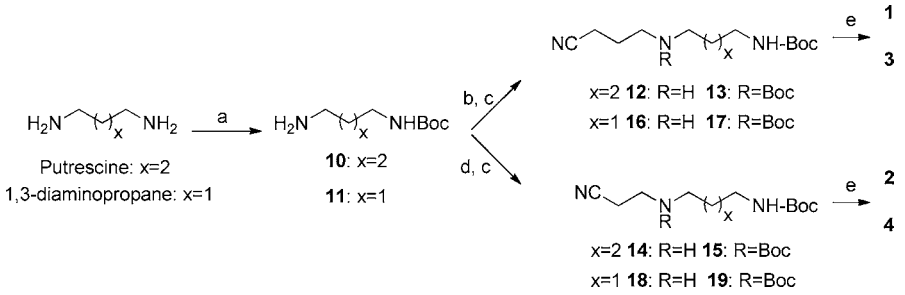
Figure 2. Structure of protected spermidine and spermine analogues **1**−**9**.

synthesis of polyamine have recently been reported in the literature.[52−54] We selected an iterative approach involving cyano-alkylation followed by nitrile reduction.[45,55,56]

The spermidine analogues **1**−**4** were prepared according to a modified four-step procedure providing good yields (Scheme 1).

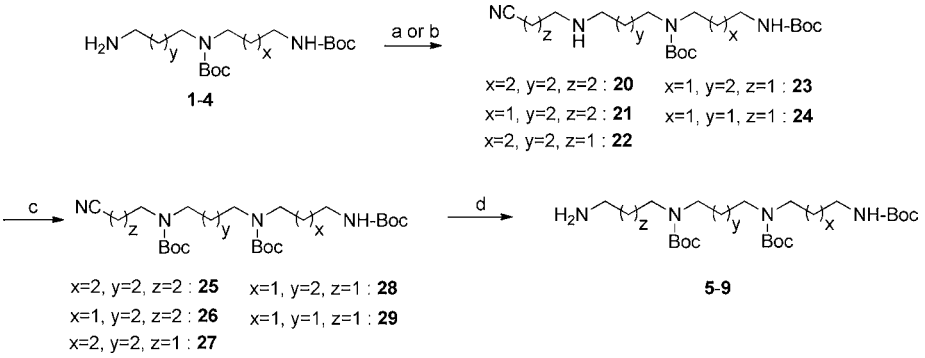
The first step consisted of reacting putrescine or 1,3-diaminopropane with di-*tert*-butyl dicarbonate (Boc_2O) leading to monoprotected diamines **10** and **11**, respectively. Amine **10** was reacted with 4-bromobutyronitrile to give secondary amine **12**, followed by quantitative Boc-protection giving rise to compound **13**. The nitrile was reduced by hydrogenation with Raney Ni to give masked homospermidine **1** with an overall yield of 63%. This procedure represents an improved yield compared to a previously described protocol (44% yield).[31,57]

Scheme 1. Synthesis of Spermidine Analogues 1−4[a]



[a]Reagents: (a) $(Boc)_2O$ (0.33 equiv), Et_3N, MeOH, 0 °C to r.t., 20 h; (b) 4-bromobutyronitrile (1 equiv), K_2CO_3, CH_3CN, 50 °C, 12 h; (c) $(Boc)_2O$ (2.5 equiv), Et_3N, MeOH, r.t., 20 h; (d) acrylonitrile (1 equiv), MeOH, 0 °C, 14 h; (e) H_2, Raney Ni, EtOH, NH_4OH, 20 atm, r.t., 12 h.

Scheme 2. Synthesis of Spermine Analogues 5−9[a]



[a]Reagents: (a) 4-bromobutyronitrile (1 equiv), K_2CO_3, CH_3CN, 50 °C, 12 h; (b) acrylonitrile (1 equiv), MeOH, 0 °C, 14 h; (c) $(Boc)_2O$ (2.5 equiv), Et_3N, MeOH, r.t., 20 h; (d) H_2, Raney Ni, EtOH, NH_4OH, 20 atm, r.t., 12 h.

N^4,N^8-Di-*tert*-butyloxycarbonylspermidine **2** was prepared, still from amine **10**, which was alkylated this time via a Michael-addition on acrylonitrile with a yield of 96%. Boc protection of the resultant secondary amine **14** provided nitrile **15**. Treatment with Raney Ni under 20 atm of hydrogen induced the expected nitrile reduction in quantitative yield with no further purification required. This method proved to be more suitable than that described by Paul M. O'Neill in 2010, which used $LiAlH_4$ as reagent and provided yields of no more than 24%.[58] With this protocol, di-Boc-spermidine **2** was obtained with a significantly higher overall yield than previously described (74% vs 32%).[59] N^1,N^4-Di-*tert*-butyloxycarbonylspermidine **3** and norspermidine **4** were prepared in the same manner from Boc-protected diamine **11** with an overall yield of 49% and 78%, respectively.

Dihomospermine **5**, homospermines **6** and **7**, spermine **8**, and norspermine **9** were designed as homologues of **1**−**4**, where the N^1-tether was sequentially lengthened. Compounds **5**−**9** were prepared similarly to the di-Boc spermidine analogues in three steps (Scheme 2). Spermine skeletons **1**−**4** were first alkylated with bromobutyronitrile or acrylonitrile to give compounds **20**−**24**. After protection of the secondary amino group with di-*tert*-butyl dicarbonate, compounds **25**−**29** were converted into the expected spermines **5**−**9** with excellent yields (84−95%).

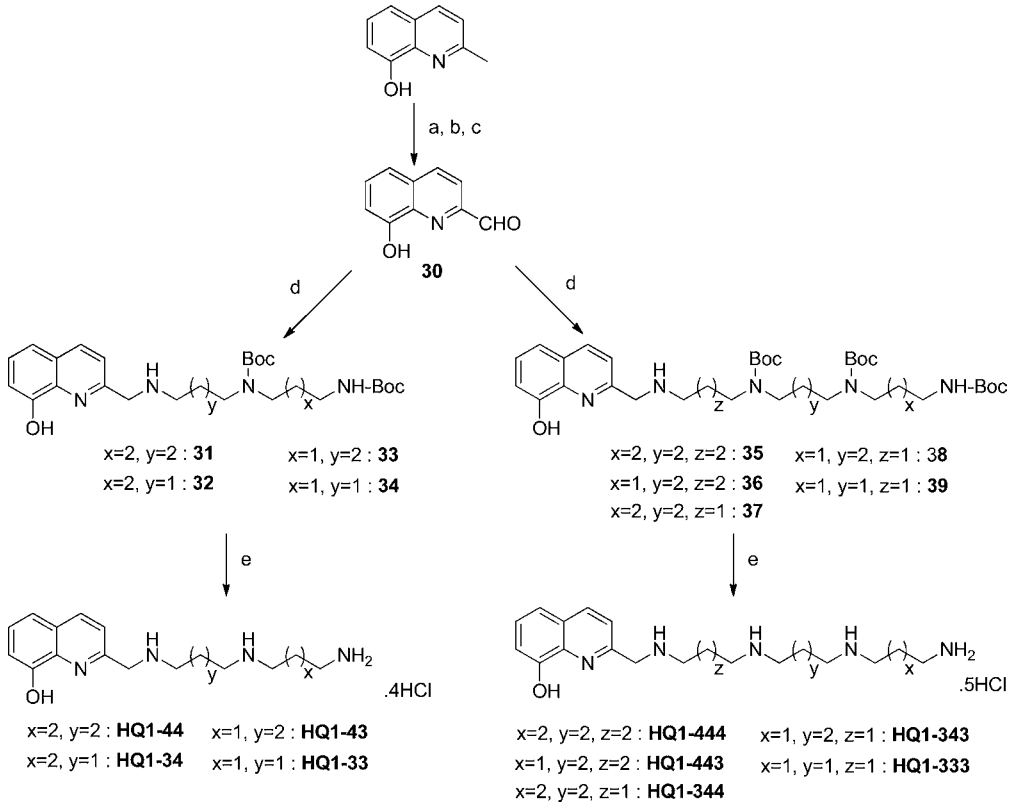
With protected polyamines **1**−**9** in hand, we decided to evaluate a reductive-amination protocol with 8-hydroxyquinoline-2-carbaldehyde to form the Quilamines **HQ1**-*XYZ*. 8-Hydroxyquinoline-2-carbaldehyde **30** was obtained in three steps according to methods previously described in the literature (Scheme 3).[60]

8-Hydroxyquinaldine was protected as the silylether by treatment with *tert*-butyldimethylsilyl chloride in the presence of imidazole, followed by an oxidation of the methyl group by selenium dioxide in 1,4-dioxane to yield the corresponding aldehyde in 90% yield. After deprotection of phenol by treatment with an excess of *tetra-n*-butylammonium fluoride in THF, the 8-hydroxyquinoline-2-carbaldehyde **30** was isolated with an overall yield of 66%. The reductive amination of this aldehyde with a range of polyamines **1**−**9** was achieved in one pot by using sodium triacetoxyborohydride for reduction of the imine generated *in situ*.[61] Protected intermediates **31**−**39** were isolated in good yields (82−96%). Removal of the Boc-protecting groups under acidic conditions at room temperature gave the polyaminoquinoline **HQ1**-*XYZ* as hydrochloride salts. These nine new Quilamines were fully characterized by a combination of the usual techniques (IR, UV−vis, MS, elemental analysis, ^{13}C and ^{1}H NMR) and fulfilled the purity required for the biological evaluations.

Biological Evaluations. *Cytostatic (Antiproliferative) and Cytotoxic Effects of Chelators.* Quilamines **HQ1**-*XYZ* were screened for their antiproliferative activity and cytotoxicity in CHO (Chinese Hamster Ovary) cells which exhibit high PTS activity[62] and the mutated derived-cell line CHO-MG cells, devoid of the PTS (provided by Dr. W. Flintoff, University of Western Ontario). CHO cells and the CHO-MG cell line were chosen to evaluate the potential role of the PTS as a selective transport system. We assessed the antiproliferative activity of the various compounds by measuring DNA content after Hoescht staining. The release of the cytoplasmic protein lactate dehydrogenase (LDH) into cell supernatants was used as a marker of cell membrane disruption correlated to cytotoxicity.

dx.doi.org/10.1021/bc300324c | *Bioconjugate Chem.* 2012, 23, 1952−1968

Scheme 3. Synthesis of Quilamines HQ1-*XYZ*[a]



[a]Reagents: (a) TBDMSCl (1.1 equiv), imidazole (1.1 equiv), CH_2Cl_2, r.t., 12 h; (b) selenium dioxide (1.2 equiv), 1,4-dioxane, 90 °C, 90 min; (c) TBAF (1.5 equiv), THF, r.t., 2 h; (d) polyamines **1**−**9**, $NaBH(OAc)_3$ (3 equiv), $C_2H_4Cl_2$, r.t., 12 h; (e) HCl 6 M, EtOH, r.t., 20 h.

The dose−response curves deduced from the counting of cell nuclei by Hoescht fluorescence in proliferating CHO cells were biphasic for the various Quilamines, including **HQ1**−**44** shown as an example in Figure 3A, except **HQ1**−**43**, **HQ1**−**343**, **HQ1**−**333**, and the reference chelator 8-hydroxyquinoline (8-HQ). They were fitted as a double four-parameter fit to calculate the percentage of cells involved in each viability component, the cytostatic (C1) and cytotoxic ones (C2), as well as their corresponding IC_{50} (Table 1). Dose−effect curves of the extracellular LDH released into the supernatant, expressed in relation to the untreated CHO and CHO-MG control cells, are reported in Figure 3B for **HQ1**−**44** and the two reference chelators (8-HQ and ICL670). The decrease in cell viability observed with 8-HQ (Figure 3A) was associated with a cytotoxic effect leading to LDH leakage (Figure 3B), while that observed with ICL670 and **HQ1**−**44** at concentrations lower than 10 μM corresponded to a cytostatic effect (no LDH release). LDH values for compound concentrations in the range of the cytostatic component **1** (10 μM) and the cytotoxic component **2** (100 μM) are also reported in Table 1.

The low concentration component 1 involved 80%, 55%, 35%, 60%, 30%, and 18% of CHO cells treated with **HQ1**−**44** (IC_{50-1} = 1.2 μM), **HQ1**−**444** (IC_{50-1} = 1.8 μM), **HQ1**−**443** (IC_{50-1} = 1.0 μM), **HQ1**−**33** (IC_{50-1} = 2.0 μM), **HQ1**−**34** (IC_{50-1} = 20.0 μM), and **HQ1**−**344** (IC_{50-1} = 2.0 μM), respectively; and only 20% of CHO cells treated by ICL670 (IC_{50-1} = 3.0 μM). As deduced from the absence of LDH leakage into supernatants, the chelator treatments at 10 μM were not cytotoxic and probably reflected the antiproliferative activity of the various compounds. In contrast, the second component of the dose−effect curves was associated with membrane damage and LDH release for a concentration of 100 μM and corresponded to the cytotoxicity of the various Quilamines and the reference chelators (8-HQ and ICL670). In nonproliferative CHO cells, treated with the various compounds at confluency (data not shown), the dose−response curves of cell viability were monophasic, with IC_{50} higher than 50−100 μM, and reflected only their cytotoxicity (LDH release).

The antiproliferative efficiency of the various Quilamines, deduced from the percentage of the low concentration component 1 (IC_{50-1} < 10 μM) was in the following order: **HQ1**−**44** (80%) > **HQ1**−**33** (60%) ∼ **HQ1**−**444** (55%) > **HQ1**−**443** (35%) > **HQ1**−**34** (30%) > **HQ1**−**344** (18%) > **HQ1**−**333** ∼ **HQ1**−**43** ∼ **HQ1**−**343**. The Quilamine **HQ1**−**44** exhibited the highest antiproliferative activity and the lowest cytotoxicity with respect to all the other compounds, including the reference chelator ICL670 (20%, IC_{50} = 3.0 μM).

*Selectivity for the Polyamine Transport System (**PTS**).* When cell viability was analyzed without multicomponent analysis, the dose−effect curves obtained with Quilamine **HQ1**−**44** showed overall IC_{50} values of 1.4 μM and 344 μM in the CHO and mutated PTS deficient CHO-MG cell line, respectively (Figure 3A and Table 2). The antiproliferative effect of this compound **HQ1**−**44** was observed in the micromolar range, while its cytotoxicity, which was detected by membrane damage (LDH release, Figure 3B), was observed only for concentrations higher than 100 μM in both CHO and CHO-MG cell lines.

dx.doi.org/10.1021/bc300324c | *Bioconjugate Chem.* 2012, 23, 1952−1968

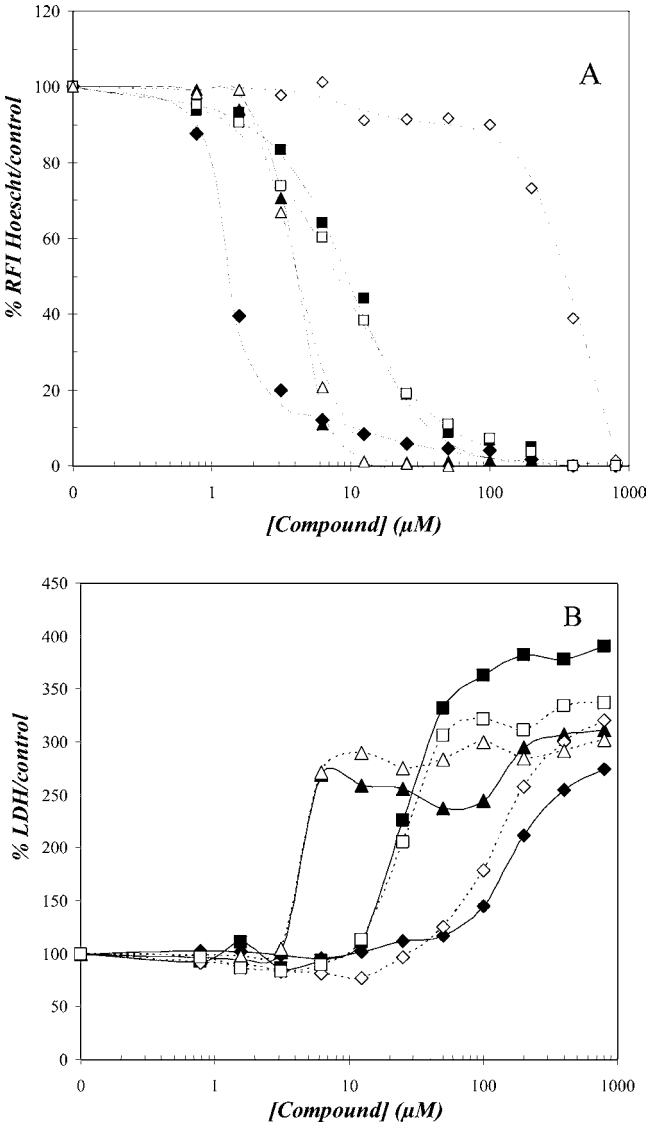


Figure 3. Cytostatic and cytotoxic effects of **HQ1−44**, 8-HQ, and ICL670 in the CHO (solid lines) and CHO-MG cell lines (dotted lines). The cytostatic effect was determined by measuring DNA content after Hoescht staining (A). The cytotoxic effect was evaluated by measuring LDH leakage into the culture medium (B). ◆ **HQ1−44** (CHO), ◇ **HQ1−44** (CHO-MG), ■ ICL670 (CHO), □ ICL670 (CHO-MG), ▲ 8-HQ 5CHO), Δ 8-HQ (CHO-MG) for A and B.

Due to the absence of a polyamine chain, the two reference chelators, 8-HQ and ICL670, were not imported by the PTS and showed an equivalent efficiency in the two cell lines with a CHO-MG/CHO IC_{50} ratio equal to 1. In contrast, a high value of this IC_{50} ratio was characteristic of a high PTS selectivity (Table 2). The Quilamine **HQ1−44**, which presents an exceptionally high CHO-MG/CHO IC_{50} ratio (249), was the one most efficiently imported into the CHO cells due to its strong selectivity of recognition by the PTS. Exogenous spermidine (50 μM), which induced a competitive inhibition of the **HQ1−44** uptake by the PTS, decreased the antiproliferative efficiency of this Quilamine in CHO cells (Figure S1, ESI). Conversely, the activation of the PTS induced by a DFMO pretreatment increased the cytostatic effect of **HQ1−44**. Both DFMO and exogenous spermidine treatments were ineffective at modulating the cytotoxic effect of **HQ1−44** on CHO-MG cells (data not shown). These results strongly suggest that the antiproliferative capacity of the various Quilamines depends mainly on their cell uptake by the PTS. Quilamines bearing a 44 polyamine chain (**HQ1−44**, **HQ1−444**) were more selectively recognized by the PTS than those bearing a 33 chain (**HQ1−33**, **HQ1−333**). The influence of the polyamine sequence on the selective uptake by the PTS in CHO cells was previously reported by using a collection (a set) of polyamine−anthracene conjugates.[28] Our results were in good agreement with this study showing the higher PTS selectivity of the 4,4-triamine analogues, its decrease after terminal amino-butylation such as in the 4,4,4-tetraamine and the lower PTS recognition of polyamine derivatives bearing a 3,3-triamine chain. In agreement with this previous study, 34 chains (**HQ1−34**, **HQ1−344**, **HQ1−343**) appeared to be poorly, or not, recognized by the PTS (Table 2). These similarities in the PTS targeting of our Quilamines and the polyamine−anthracene conjugates suggested the same cell uptake pathways for these two families of polyamine-analogues even if they could hit different cellular targets (DNA intercalation or iron depletion). The greater selectivity of the Quilamine **HQ1−44** for the PTS is in close agreement with previous works showing the higher cellular uptake of azepine−polyamine[31] and anthryl−polyamine[38] conjugates bearing a homospermidine chain.[44]

Complexation Properties of Quilamines toward Iron(III) and Competitive Cations. *Comparison of the Chelation Efficiency of Quilamines **HQ1-XYZ**, 8-HQ, ICL670, and O-Trensox.* The cellular labile iron pool (LIP) consists of chelatable and redox-active iron, which plays a key role as a crossroads of cell iron metabolism. The ability of iron chelators to mobilize this temporary iron pool bound to low-molecular-weight and low-iron-affinity chelators (citrate, ascorbate, phosphate, and adenosine triphosphate) is an essential factor influencing their biological efficiency. According to previous work, the calcein test can predict the iron-chelating efficiency of chelators.[63,64] Thus, an acellular calcein test was performed to compare the potential ability of Quilamines **HQ1-*XYZ***, ICL670, O-Trensox, and 8-HQ, iron chelators used as references, to chelate this labile iron pool at physiological pH. In solution, calcein, a fluoresceinated analogue of EDTA, binds iron(II) and, more slowly, iron(III).[65] The fluorescence of this metallosensor dye is quenched during its interaction with iron and, conversely, is restored if iron is removed from the [calcein-Iron] complex by a most efficient competitive iron chelator. The rate and extent of fluorescence recovery depend on the chelator concentration, the kinetics and stoichiometry of iron binding and the relative binding affinity. The calcein test is qualitative, but the concentration of the chelator for which 50% of the fluorescence is restored is indicative of the chelator affinity (RC_{50}).

Recovered calcein fluorescence was measured in aqueous medium 30 min after the addition of the competitive chelators and is reported as a function of their concentrations in Figure 4. As expected from their relative affinity for iron(III), the three reference chelators, 8-HQ, ICL670, and O-Trensox, exhibited RC_{50} values equal to 4, 1.4, and 0.9 μM, respectively (Table 3). Curves of calcein fluorescence recovery were monophasic for the three reference chelators, while they showed two distinct components for all Quilamines. The first component (C1) was observed in the micromolar range of concentrations and the second one for Quilamine concentrations higher than 10 μM (C2). These biphasic curves were fitted as a double four-

dx.doi.org/10.1021/bc300324c | *Bioconjugate Chem.* 2012, 23, 1952−1968

Table 1. Cytostatic/Cytotoxic Effects and IC_{50} of Quilamines HQ1-*XYZ*, 8-HQ, and ICL670 in the CHO Cell Line

	% component 1 (*Cytostatic*)[a]	IC_{50}-1 (μM)	%LDH/control (10 μM)	% component 2 (*Cytotoxic*)[b]	IC_{50}-2 (μM)	%LDH/control (100 μM)
HQ1−44	80	1.2	102	20	11	125
HQ1−444	55	1.8	105	45	65	204
HQ1−443	35	1	100	65	45	203
HQ1−33	60	2	102	40	45	378
HQ1−333	0	ND	111	100	15	124
HQ1−43	0	ND	97	100	30	228
HQ1−34	30	20	111	70	110	200
HQ1−344	18	2	101	82	70	160
HQ1−343	0	ND[c]	93	100	27	199
8-HQ	0	ND[c]	259	100	4	245
ICL670	20	3	108	80	11	402

[a]Cytostatic effect was determined by measuring DNA content after Hoescht staining. Dose−effect curves were fitted as a double four-parameter fit to calculate the percentage of cells involved in each viability component (cytostatic and cytotoxic) as well as their corresponding IC_{50}. [b]Cytotoxic effect was evaluated by measuring LDH leakage into the culture medium. [c]ND, not detectable.

Table 2. Selectivity of Quilamines for the PTS. Effect of Quilamines HQ1-*XYZ*, 8-HQ, and ICL670 in CHO and CHO-MG Cells

	IC_{50} (μM)		IC_{50} ratio[a]
compounds	CHO	CHO-MG	CHO-MG/CHO
HQ1−44	1.4	344.5	249
HQ1−444	6.3	239.5	38
HQ1−443	20.2	257.5	13
HQ1−33	5.7	117.9	21
HQ1−333	15.1	277.0	18
HQ1−43	31.3	163.5	5
HQ1−34	93.1	152.0	2
HQ1−344	55.9	207.1	4
HQ1−343	27.0	105.7	4
8-HQ	5.0	6.5	1
ICL670	9.2	8.0	1

[a]This denotes the (CHO/CHO-MG) IC_{50} ratio, a measurement of PTS selectivity.

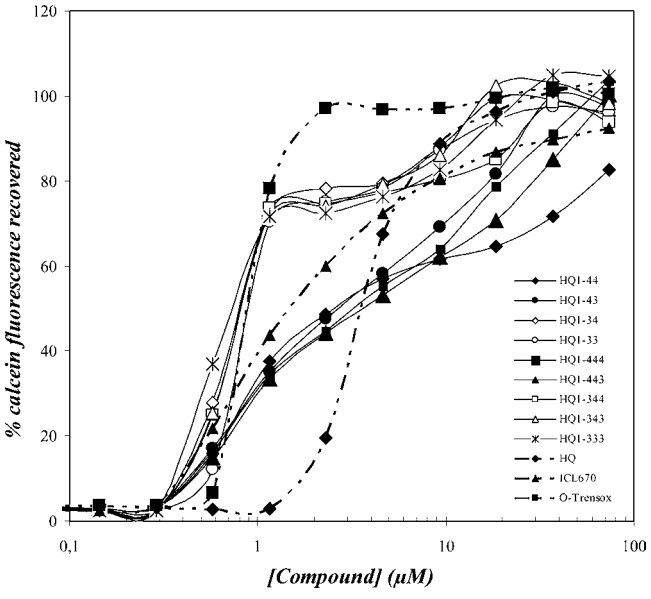


Figure 4. Comparison of the iron-chelating efficiency of Quilamines **HQ1-*XYZ*** with 8-HQ, ICL670, and O-Trensox, by calcein fluorescence measurements in a cell-free system.

Table 3. Percentage of Each Component and RC_{50} of HQ1-*XYZ*, 8-HQ, ICL670, and O-Trensox

compound	% component 1[a] (C1)	RC_{50}-1 (μM)	% component 2 (C2)	RC_{50}-2 (μM)
HQ1−44	58	1	42	57
HQ1−43	55	1	45	15
HQ1−444	53	1	47	18
HQ1−443	53	1	47	25
HQ1−34	78	0.7	22	10
HQ1−33	76	0.8	24	10
HQ1−344	74	0.65	26	20
HQ1−343	74	0.65	26	10
HQ1−333	72	0.6	28	12
8-HQ	100	4	0	0
ICL670	100	1.4	0	0
O-Trensox	100	0.9	0	0

[a]Biphasic curves (Figure 4) were fitted as a double four-parameter fit to calculate the percentage of each component as well as their corresponding concentration inducing half-fluorescence recovery (RC_{50}).

parameter fit to calculate the percentage of each component, as well as their corresponding concentration inducing half-fluorescence recovery (RC_{50}, Table 3). The first component C1 was greater with Quilamines **HQ1−3*YZ*** (72−78% with RC_{50} = 0.6−0.8 μM) than with Quilamines **HQ1−4*YZ*** (53−58% with RC_{50} = 1 μM). The ability of Quilamines to transchelate iron from calcein was between those of 8-hydroxyquinoline and O-Trensox. The shape of these curves (Figure 4) allowed two distinct groups of Quilamines to be discriminated: **HQ1−3*YZ*** (**HQ1−34**, **HQ1−33**, **HQ1−344**, **HQ1−343**, **HQ1−333**) and **HQ1−4*YZ*** (**HQ1−44**, **HQ1−43**, **HQ1−444**, **HQ1−443**) and suggested different modes of interaction with iron, probably modulated by the polyamine chain structure. Due to their amino groups, polyamines are able to chelate metallic cations.[66] The stability constants of these chelates increase with the number of amino groups and with the chain length of the polyamine.[67] Our results suggest the involvement of the amine group of the polyamine chain in the formation of iron complexes, as expected during the design and

synthesis of this Quilamine concept. The first secondary amine in Quilamines **HQ1** could be involved in iron coordination and probably the second one too, as deduced from the better iron-chelating efficiency of Quilamines **HQ1−3***YZ* compared to Quilamines **HQ1−4***YZ*.

*Complexation Properties of Quilamine **HQ1−44** toward Iron(III) and Competitive Cations.* To understand better the high iron affinity observed for the most promising chelator Quilamine **HQ1−44**, we assessed its complexation behavior toward iron(III) as well as other relevant cations such as copper(II), zinc(II), and magnesium(II), which may act as endogenous competitors of iron(III). This study was performed by potentiometric titrations in aqueous solutions at 25 °C. The ionic strength was adjusted to 0.10 M with potassium nitrate.

As a starting point, the acid−base properties of **HQ1−44** were first determined in the form of the protonation constants corresponding to its five basic centers located at the four amines and the single hydroxyl function. The calculated overall (log β) and stepwise (log K or pK_a) protonation constants are presented in Table 4. The four most basic centers were easily determined and have pK_a's in the range of 8−11, while the remaining center shows a much lower basicity with a pK_a that can just be estimated at around 1.3 as it is outside the accurate experimental range of the potentiometric technique used. The constants obtained can be understood in light of the known acid−base properties of the two functional moieties that constitute the ligand, 8-hydroxyquinoline[68] and homospermidine.[69] The highest pK_a of 10.83 must correspond to the protonation of the primary amine. The pK_a at 9.81 can easily be assigned to protonation of the hydroxyl group, as the yellow color of the ligand solution intensifies visibly around this pH value. The two remaining basic pK_a's of 9.05 and 7.98 belong to the two secondary amines, but it is not possible to assign the values individually. The acidic pK_a at 1.3 must be assigned to the protonation of the pyridine, as it is the least basic group in the chelator due to the close vicinity of the electron-withdrawing hydroxyl and secondary amine groups.

Table 4. Overall and Stepwise Protonation Constants for Compound HQ1-44 (25.0 °C, I = 0.10 M in KNO_3)

species[a]	log β	log K (pK_a)
HL	10.83	10.83
H_2L	20.64	9.81
H_3L	29.69	9.05
H_4L	37.67	7.98
H_5L	(39.0)[b]	(1.3)[b]

[a]HL = **HQ1−44**, and charges are omitted for the sake of clarity. [b]Values in brackets are approximate.

Next, we turned our attention to the complexation of iron(III). Since **HQ1−44** presents a total of 5 potential donor atoms for metal coordination, we performed potentiometric titrations with different amounts of metal in order to obtain a complete insight into the potential 1:2 and 1:1 metal-to-ligand complexation modes and the corresponding complex species. Thus, metal ratios of approximately 0.5 equiv and 1 equiv of iron(III) (relative to the ligand amount) were used during complexation titrations, and the titration curves obtained were used jointly to refine the complete model of stability constants for all the complex species. For both iron(III) ratios, species of 1:2 and 1:1 stoichiometry were present in equilibrium, with a predominance of 1:1 species for the higher amount of iron(III). There was an increasing tendency to form insoluble species above neutral pH, most likely hydroxocomplex species, with high amounts of iron(III). By refining together all the titrations performed, thermodynamic stability constants could be obtained accurately for only a limited set of complex species, mostly of 1:1 stoichiometry. This is due to some precipitation occurring at basic pH, which forced us to exclude the corresponding experimental results. However, as the amount of precipitate was small below pH = 9, we used the experimental data up to this pH in a separate refinement to obtain a rough approximation of the stability constants of the remaining species of 1:2 stoichiometry in order to gain an insight into the overall thermodynamic equilibria. A selection of calculated overall (log β) and stepwise (log K) stability constants is presented in Table 5 (a complete table showing the overall stability constants is available in ESI, Table S1).

Table 5. Overall and Stepwise Stability Constants for the Iron(III) Complexes of HQ1-44 (25.0 °C, I = 0.10 M in KNO_3)

species[a]	log β	log K
FeL	25.62	25.62
FeHL	32.13	6.51
FeH_2L	34.94	2.81
FeL_2	33.00	7.4
$FeHL_2$	42.20	9.2
FeH_2L_2	51.00	8.8
FeH_3L_2	59.10	8.1

[a]HL = **HQ1−44**, and charges are omitted for the sake of clarity.

Overall, we found that compound **HQ1−44** formed very strong iron(III) complexes. The thermodynamic stability of the complexes with 1:1 stoichiometry was very high, while that of complexes with 1:2 stoichiometry was more modest, as shown by the log K values of almost 26 for the former and below 8 for the latter. This clearly illustrates the preference of the ligand to form 1:1 complexes with adequate iron concentrations. However, the calculated overall log β values indicated that both 1:1 and 1:2 species were present successively in large amounts all along the pH scale: 1:1 species were formed between pH 2−6, while 1:2 species appeared above pH 6 with the largest amount occurring at around pH 7.5. This is demonstrated by the abundant presence of the three protonated species (log β around 60). This high thermodynamic stability also implies that a high complexation degree is attained at low pH values, with almost all of the iron(III) being chelated above pH = 3. This corresponds to a very small amount of free iron(III) present in solution at physiological pH (7.4), as indicated by a pFe^{3+} value of 19.4. It is thus clear that **HQ1−44** is a powerful chelator of iron(III).

We also studied the complexation of **HQ1−44** with competitive cations found *in vivo*. Titrations were performed in the presence of 0.5 equiv or 1 equiv of copper(II), and in the presence of 1 equiv of zinc(II) or magnesium(II). The calculated overall (log β) and stepwise (log K) stability constants are presented in Table S2 of the Supporting Information. The constant values show that strong complexes were formed with copper(II), with species of both 1:1 and 1:2 stoichiometries (pCu^{2+} = 12.6). The complexes of zinc(II) were only moderately stable, and also contained 1:1 and 1:2 species (pZn^{2+} = 7.8). With magnesium(II), only a few complex species of 1:1 stoichiometry were formed with an extremely low

stability (pMg^{2+} is insignificant). Distribution diagrams of the participating species for each metal are presented in ESI (SI Figures S2–S5). A competition diagram between Fe(III) and Zn(II) has been obtained from the values of all the stability constants with both metals; it clearly indicates the formation of a major amount of ternary species with Fe(III) all along the pH scale (in ESI SI Figure S6).

Taken together, these complexation studies prove that Quilamine **HQ1–44** forms very strong complexes with iron(III) and much weaker complexes with other endogenously relevant metal cations, indicative of a high selectivity for iron(III).

The preferential 1:2 [Fe/**HQ1–44**] stoichiometry of the ferric complex at pH = 7.4 was confirmed by the Job method of continuous variation (based on the MLCT (metal–ligand charge transfer) band) (Figure 5). The iron complex presents

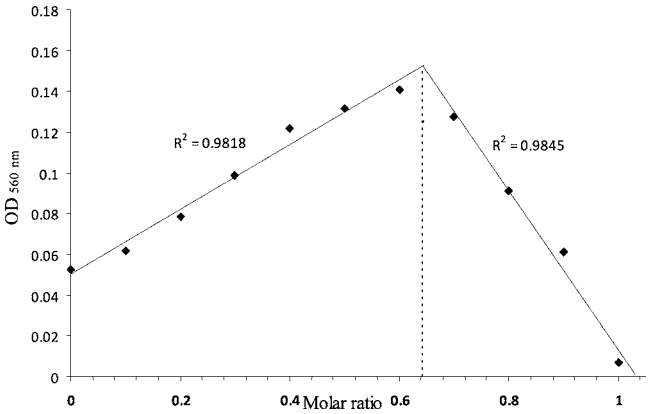


Figure 5. Job plot of **HQ1–44** at pH = 7.4 (λ_{max} = 560 nm). Solutions containing different ligand/Fe(III) ratios were prepared so that [ligand] + [Fe(III)] = 0.5 mM. The theoretical mole fraction maximum for a 2/1 ligand/Fe complex is 0.667; a linear intercept maximum of 0.65 was found.

colorimetric features (ε_{560} = 900 M^{-1} cm^{-1} for pH 7.4) and good stability properties (absorbance remains stable after several weeks). This clearly indicates that the homospermidine fragment of **HQ1–44** at pH = 7.4 alters the stoichiometry of the ferric complex. In fact, in the same conditions, hydroxyquinoline forms a 3:1 ligand/iron complex.

In view of this stoichiometry, it could be assumed that the iron complex [Fe/**HQ1–44**] forms three five-membered chelate rings in which the iron is probably coordinated by two vicinal *N*-atoms and a hydroxyl group (Figure 6). This

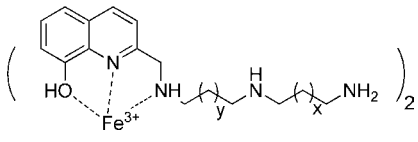


Figure 6. Hypothetical structure of **HQ1–44**/Fe complex with five-membered chelate rings.

stoichiometry was confirmed by elemental analysis, but unfortunately, repeated attempts to isolate X-ray quality crystals of the iron complex have so far been unsuccessful.

Due to the lack of the experimental electronic structure of metal complexes, the OPBE calculation was used to determine the energy and the structure of $[Fe\text{-}L_n]^{3+}$ (n = 1 or 2) complexes with a prototypical ligand **HQ1–1**.

Ab Initio Calculations. Density functional theory (DFT) calculations were carried out using the simplified model compound (**HQ1–1**) in which the polyamine moieties were replaced by a methylamine chain to render the calculations computationally tractable. All geometries reported in this paper are available in the Supporting Information. The ferric iron has 3d electrons and can thus adopt different spin configurations. The complexes were calculated in different spin states, but in all cases, the most stable Fe(III) complexes considered in this paper are high spin.

Despite the existence of a strong N_{qui}–HO hydrogen bond for the free ligand, which has been extensively studied by Shchavlev et al.,[70] iron(III) complexation is possible. The bonding in these complexes is expected to be dominated by ion–dipole electrostatic interactions although contributions arising from charge transfer, polarization, dispersion interactions, and exchange repulsive interactions at the equilibrium configuration of the complex are also likely to be present.

The geometries were compared with the bidentate ligand 8-HQ. The complexes were constructed by placing the ligands in pseudo-octahedral, but random, orientation about the metal under the C1 point group because we did not wish to presuppose any particular symmetry.

We modeled a highly stable complex like $[Fe(8\text{-}HQ)_n(H_2O)_{6-2n}]^{3+}$ (n = 1 or 2) to use as an energy reference and to consider reactions that correspond to an exchange of ligands (8-HQ and **HQ1–1**) as in eq 1.

$$[Fe(H_2O)_6]^{3+} + n\ 8\text{-HQ} \xrightleftharpoons{\beta_n(8\text{-HQ})} [Fe(8\text{-HQ})_n(H_2O)_{6-2n}]^{3+}$$
$$[Fe(H_2O)_6]^{3+} + n\ HQ1\text{-}1 \xrightleftharpoons{\beta_n(HQ1\text{-}1)} [Fe(HQ1\text{-}1)_n(H_2O)_{6-3n}]^{3+} \quad (1)$$
$$[Fe(8\text{-}HQ)_n(H_2O)_{6-2n}]^{3+} + n\ HQ1\text{-}1 \xrightleftharpoons{K_n exc} [Fe(HQ1\text{-}1)_n(H_2O)_{6-3n}]^{3+} + n\ 8\text{-HQ} + n\ H_2O$$

The equilibrium constant of the exchange reactions can be calculated from the computed standard free energy change of reaction [1] *in vacuo*. All free energy values were negative, so the chelation reaction was highly exothermic (Table 6). On the basis of the log $K_n$exc obtained, the $[Fe(\mathbf{HQ1–1})_n(H_2O)_{6-3n}]^{3+}$ were the most stable for the 1:1 and 1:2 species.

The $[Fe(HQ1–1H)_2]^{5+}$ complex is not presented here because it leads to the formation of a tetrahedral complex, due to the repulsion of the protonated amines. Figure 7 shows the minimum energy structures obtained for $[Fe(8\text{-}HQ)_1(H_2O)_4]^{3+}$, $[Fe(8\text{-}HQ)_2(H_2O)_2]^{3+}$, $[Fe(HQ1–1)_1(H_2O)_3]^{3+}$, and $[Fe(HQ1–1)_2]^{3+}$ complexes. All are distorted octahedrons. The successive replacement of H_2O by the methylamine chain for **HQ1–1** results in an increase in both the average metal–ligand bond distance and the stabilization energy of the complex. The most stable structure for the $[Fe(HQ1–1)_2]^{3+}$ complex is a distorted octahedron in which oxygen and nitrogen atoms from both **HQ1–1** neutral ligands are bound to the metal. The symmetry of this complex is very close to the C2 symmetry. The two 8-hydroxyquinoline groups are planar and form a five-membered chelate ring with iron, leading to the facial monomer. The bond lengths with iron are in narrow ranges: between 2.084 and 2.190 Å for Fe(III)–N bonds and 2.474 Å for Fe(III)–O bonds. The Fe(III)–O distances are much longer than observed with $[Fe(H_2O)_6]^{3+}$: 1.995 Å.[71] The Fe(III)–N distances are also significantly longer than those observed in triazamacrocyclic complexes (i.e., 2.23–2.33 Å).[72] The average five-membered chelate ring (N_{qui}FeO

dx.doi.org/10.1021/bc300324c | *Bioconjugate Chem.* 2012, 23, 1952–1968

Table 6. Log β_n, Log $K_n$exc, Selected Bond Distances (Å) and Angles (deg) of Octahedral Complexes Determined by Quantum Chemical UOPBE/6-31G(d,p) and (Fe Lanl2DZ) Calculations

complex	$[Fe(8\text{-}HQ)_1(H_2O)_4]^{3+}$	$[Fe(\mathbf{HQ1-1})_1(H_2O)_3]^{3+}$	$[Fe(8\text{-}HQ)_2(H_2O)_2]^{3+}$	$[Fe(\mathbf{HQ1-1})_2]^{3+}$
Logβ_n	58	75	82	111
Log$K_n$exc		17		29
FeO_{qui}[a]	2.498	2.547	2.360 and 2.360	2.474 and 2.474
FeO_w[a]	2.145 and 2.176 and 2.176	2.131 and 2.200 and 2.243	2.200 and 2.200	
FeN_{qui}[a]	2.172	2.117	2.117 and 2.117	2.084 and 2.084
FeN_{ma}[a]		2.161		2.190 and 2.190
FeO_w[a]	2.146		2.200 and 2.200	
$N_{qi}FeO_{qui}$[a]	68.85	68.37	72.18 and 72.18	70.34 and 70.34
$N_{qi}FeN_{am}$[a]		78.82		78.21 and 78.21
$N_{qi}FeO_w$[a]	93.92 and 93.92 and 102.65 and 150.77	94.16 and 97.77 and 157.95	97.29 and 97.29 and 99.97 and 99.97	
$N_{qi}FeO_{qui}$[a]				146.10 and 146.10
$O_{qi}FeO_{qui}$[a]			92.79	82.40
$N_{qi}FeN_{qui}$[a]			155.85	163.19
$N_{ma}FeN_{ma}$[a]				114.42
O_wFeO_w[a]	88.01 and 88.01 and 87.14 and 87.14 and 106.57 and 171.82	83.62 and 84.31 and 167.77	88.38	

[a] N_{qui}: N of quinoline, N_{ma}: N of methylamine, O_{qui}: O of quinoline, O_w: O of water.

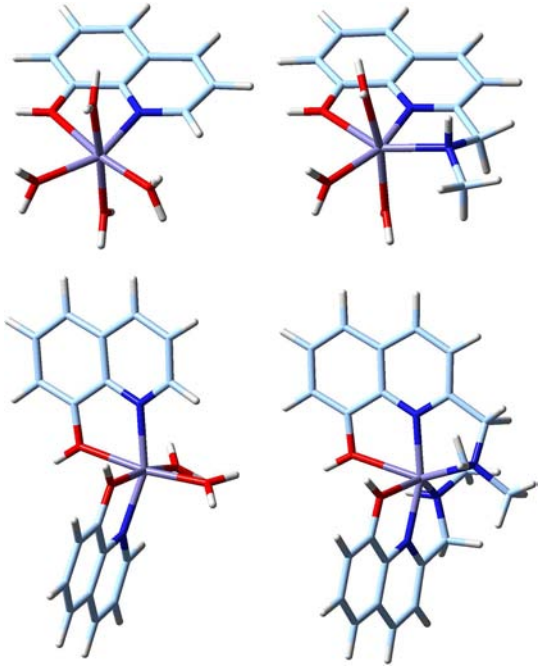


Figure 7. Minimum energy structures for $[Fe(8\text{-}HQ)_1(H_2O)_4]^{3+}$, $[Fe(\mathbf{HQ1-1})_1(H_2O)_3]^{3+}$, $[Fe(8\text{-}HQ)_2(H_2O)_2]^{3+}$, and $[Fe(\mathbf{HQ1-1})_2]^{3+}$ determined by quantum chemical UOPBE/6-31G(d,p) and (Fe Lanl2DZ) calculations.

and $N_{qui}FeN_{ma}$) is 74° (compared to 90° for an ideal octahedron). The apical angles ($N_{qui}FeO$ and $N_{ma}FeN_{ma}$) are 146.10°, 146.10°, and 163.19° (compared to 180° for an ideal octahedron). However, this distorted geometry does not impair the affinity of **HQ1−1** for iron as evidenced in the potentiometric assay.

CONCLUSION

We have developed a new type of iron chelator where an 8-hydroxyquinoline chelating subunit is grafted to polyamine vectors, in order to vectorize the iron chelator inside the cancerous cell with an overactive polyamine transport system (PTS). Nine Quilamines **HQ1-*XYZ***, differing in the nature of their polyamine chain, were synthesized in six or nine steps with good yields. The influence of the polyamine chain on the selective recognition of different Quilamines by the PTS was evidenced by comparing the antiproliferative activity obtained on a cell line displaying an efficient PTS (CHO) with that on a PTS-deficient mutant cell line (CHO-MG). This screening led us to choose the molecule **HQ1−44** from the synthesized Quilamines. The antiproliferative effect of **HQ1−44** occurred in the micromolar range, while a significant cytotoxicity was only observed at concentrations higher than 100 μM. We also demonstrated the high complexation capacity of **HQ1−44** with iron, while much weaker complexes were formed with other competitive cations. The ferric complex was shown to adopt preferentially a 1:2 [Fe/**HQ1−44**] stoichiometry at pH = 7.4. The binding energies and the equilibrium geometries of $[Fe\text{-}L_n]^{3+}$ (n = 1 or 2) complexes were assessed *in vacuo* from *ab initio* calculations. The stronger equilibrium constant of the exchange reactions between iron(III) and **HQ1−1** compared to 8-HQ was deduced from these calculations. The Quilamine is a tridentate ligand for iron(III) where both nitrogen and oxygen atoms form five-membered chelate rings.

In summary, Quilamines, and particularly **HQ1−44**, may be promising compounds for iron depletion in cancer therapies, due to their high affinity and selectivity for iron, their high antiproliferative activity associated with a low cytotoxicity, and their selective uptake by the PTS.

Further studies will evaluate the following: (i) the influence of modifying the length and the nature of the spacer between the chelating moiety and the homospermidine chain; (ii) the capacity to redox cycle and the generation of reactive oxygen species (ROS) (like the objective is an antitumor effect, the induction of oxidative stress may actually be a beneficial feature of an iron-chelator complex); (iii) the biological mechanisms of action of Quilamines, especially of **HQ1−44**; (iv) the antiproliferative efficiency of the Quilamine **HQ1−44** *in vitro* in various human tumor cell lines and *in vivo* in animal models.

dx.doi.org/10.1021/bc300324c | *Bioconjugate Chem.* 2012, 23, 1952−1968

■ ASSOCIATED CONTENT

Supporting Information

DFMO and exogenous spermidine treatments, stability constant data, and Cartesian coordinates of optimized structures. This material is available free of charge via the Internet at http://pubs.acs.org.

■ AUTHOR INFORMATION

Corresponding Author

* David Deniaud, Ph.D.: Phone 00-33-2-51125406, Fax 00-33-2-51125402, E-mail: david.deniaud@univ-nantes.fr. François Gaboriau, Ph.D.: Phone 00-33-2-23233861, Fax 00-33-2-99540137, E-mail: francois.gaboriau@univ-rennes1.fr.

Notes

The authors declare no competing financial interest.

■ ACKNOWLEDGMENTS

The authors are grateful to the Conseil Régional Pays de la Loire, to the French Ministry of Education, to the Ligue Nationale contre le Cancer (LNCC, Ille et Vilaine/Loire Atlantique), to the Association pour la Recherche sur le Cancer (ARC), and to the Centre National de la Recherche Scientifique (CNRS) for financial support. The geometry optimizations and the vibrational calculations reported in this paper were performed at CCIPL (Centre de Calcul Intensif des Pays de la Loire, Nantes, France) regional supercomputing center thanks to a dedicated CPU grant.

■ REFERENCES

(1) Richardson, D. R., Kalinowski, D. S., Lau, S., Jansson, P. J., and Lovejoy, D. B. (2009) Cancer cell iron metabolism and the development of potent iron chelators as anti-tumour agents. *Biochim. Biophys. Acta 1790*, 702−717.

(2) Kwok, J. C., and Richardson, D. R. (2002) The iron metabolism of neoplastic cells: alterations that facilitate proliferation? *Crit. Rev. Oncol. Hematol. 42*, 65−78.

(3) Brookes, M. J., Hughes, S., Turner, F. E., Reynolds, G., Sharma, N., Ismail, T., Berx, G., McKie, A. T., Hotchin, N., Anderson, G. J., Iqbal, T., and Tselepis, C. (2006) Modulation of iron transport proteins in human colorectal carcinogenesis. *Gut 55*, 1449−1460.

(4) Kolberg, M., Strand, K. R., Graff, P., and Andersson, K. K. (2004) Structure, function, and mechanism of ribonucleotide reductases. *Biochem. Biophys. Acta 1699*, 1−34.

(5) Ali, M. A., Akhmedkhanov, A., Zeleniuch-Jaquotte, A., Toniolo, P., Frenkel, K., and Huang, X. (2003) Reliability of serum iron, ferritin, nitrite, and association with risk of renal cancer in women. *Cancer Detect. Prev. 27*, 116−121.

(6) Huang, X. (2003) Iron overload and its association with cancer risk in humans: evidence for iron as a carcinogenic metal. *Mutat. Res. 533*, 153−171.

(7) Thompson, H. J., Kennedy, K., Witt, M., and Juzefyk, J. (1991) Effect of dietary iron deficiency or excess on the induction of mammary carcinogenenis by 1-methyl-1-nitrosourea. *Carcinogenesis 12*, 111−114.

(8) Daniels, T. R., Delgado, T., Rodriguez, J. A., Helguera, G., and Penichet, M. L. (2006) The transferrin receptor part I: Biology and targeting with cytotoxic antibodies for the treatment of cancer. *Clin. Immunol. 121*, 144−158.

(9) Pinnix, Z. K., Miller, L. D., Wang, W., D'Agostino, R., Jr., Kute, T., Willingham, M. C., Hatcher, H., Tesfay, L., Sui, G., Di, X., Torti, S. V., and Torti, F. M. (2010) Ferroportin and iron regulation in breast cancer progression and prognosis. *Sci. Transl. Med. 2*, 43−56.

(10) Pogribny, I. P. (2010) Ferroportin and hepcidin: a new hope in diagnosis, prognosis, and therapy for breast cancer. *Breast Cancer Res. 12*, 314−315.

(11) Richardson, D. R. (2002) Iron chelators as therapeutic agents for the treatment of cancer. *Crit. Rev. Oncol. Hematol. 42*, 267−281.

(12) Hoffbrand, A. V., Cohen, A., and Hershko, C. (2003) Role of deferiprone in chelation therapy for transfusional iron overload. *Blood*, 17−24.

(13) Maggio, A., D'Amico, G., Morabito, A., Capra, M., Ciaccio, C., Cianciulli, P., Di Gregorio, F., Garozzo, G., Malizia, R., Magnano, C., Mangiagli, A., Quarta, G., Rizzo, M., D'Ascola, D. G., Rizzo, A., and Midiri, M. (2002) Deferiprone versus deferoxamine in patients with thalassemia major: a randomized clinical trial. *Blood Cells, Molecules, and Diseases 28*, 196−208.

(14) Cappellini, M. D., Cohen, A., Piga, A., Bejaoui, M., Perrotta, S., Agaoglu, L., Aydinok, Y., Kattamis, A., Kilinc, Y., Porter, J., Capra, M., Galanello, R., Fattoum, S., Drelichman, G., Magnano, C., Verissimo, M., Athanassiou-Metaxa, M., Giardina, P., Kourakli-Symeonidis, A., Janka-Schaub, G., Coates, T., Vermylen, C., Olivieri, N., Thuret, I., Opitz, H., Ressayre-Djaffer, C., Marks, P., and Alberti, D. (2006) A phase 3 study of deferasirox (ICL670), a once-daily oral iron chelator, in patients with beta-thalassemia. *Blood 107*, 3455−3462.

(15) Chantrel-Groussard, K., Gaboriau, F., Pasdeloup, N., Havouis, R., Nick, H., Pierre, J. L., Brissot, P., and Lescoat, G. (2006) The new orally active iron chelator ICL670A exhibits a higher antiproliferative effect in human hepatocyte cultures than O-trensox. *Eur. J. Pharmacol. 541*, 129−137.

(16) Gaboriau, F., Laupen-Chassay, C., Pasdeloup, N., Pierre, J.-L., Brissot, P., and Lescoat, G. (2006) Modulation of cell proliferation and polyamine metabolism in rat liver cell cultures by the iron chelator O-trensox. *BioMetals 19*, 623−632.

(17) Richardson, D., Ponka, P., and Baker, E. (1994) The effect of the iron(III) chelator, desferrioxamine, on iron and transferrin uptake by the human malignant melanoma cell. *Cancer Res. 54*, 685−9.

(18) Donfrancesco, A., Deb, G., De Sio, L., Cozza, R., and Castellano, A. (1996) Role of deferoxamine in tumor therapy. *Acta Haematol. 95*, 66−69.

(19) Saletta, F., Rahmanto, Y. S., Siafakas, A. R., and Richardson, D. R. (2011) Cellular iron depletion and the mechanisms involved in the iron-dependent regulation of the growth arrest and DNA damage family of genes. *J. Biol. Chem. 286*, 35396−35406.

(20) Wallace, H. M., Fraser, A. V., and Hughes, A. (2003) A perspective of polyamine metabolism. *Biochem. J. 376*, 1−14.

(21) Grillo, M. A., and Colombatto, S. (1994) Polyamine transport in cells. *Biochem. Soc. Trans. 22*, 894−898.

(22) Palmer, A. J., and Wallace, H. M. (2010) The polyamine transport system as a target for anticancer drug development. *Amino Acids 38*, 415−422.

(23) Seiler, N. (2003) Thirty years of polyamine-related approaches to cancer therapy. Retrospect and prospect. Part 2. Structural analogues and derivatives. *Curr. Drug Targets 4*, 565−585.

(24) Seiler, N. (2003) Thirty years of polyamine-related approaches to cancer therapy. Retrospect and prospect. Part 1. Selective enzyme inhibitors. *Curr. Drug Targets 4*, 537−564.

(25) Holley, J., Mather, A., Cullis, P., Symons, M. R., Wardman, P., Watt, R. A., and Cohen, G. M. (1992) Uptake and cytotoxicity of novel nitroimidazole-polyamine conjugates in Ehrlich ascites tumour cells. *Biochem. Pharmacol. 43*, 763−769.

(26) Verschoyle, R. D., Carthew, P., Holley, J. L., Cullis, P., and Cohen, G. M. (1994) The comparative toxicity of chlorambucil and chlorambucil-spermidine conjugate to BALB/c mice. *Cancer Lett. 85*, 217−222.

(27) Delcros, J. G., Tomasi, S., Carrington, S., Martin, B., Renault, J., Blagbrough, I. S., and Uriac, P. (2002) Effect of spermine conjugation on the cytotoxicity and cellular transport of acridine. *J. Med. Chem. 45*, 5098−5111.

(28) Phanstiel, O., IV, Kaur, N., and Delcros, J. G. (2007) Structure-activity investigations of polyamine-anthracene conjugates and their uptake via the polyamine transporter. *Amino Acids 33*, 305−313.

(29) Dallavalle, S., Giannini, G., Alloatti, D., Casati, A., Marastoni, E., Musso, L., Merlini, L., Morini, G., Penco, S., Pisano, C., Tinelli, S., De Cesare, M., Beretta, G. L., and Zunino, F. (2006) Synthesis and

cytotoxic activity of polyamine analogues of camptothecin. *J. Med. Chem. 49*, 5177−86.
(30) Esteves-Souza, A., Lucio, K. A., Da Cunha, A. S., Da Cunha Pinto, A., Da Silva Lima, E. L., Camara, C. A., Vargas, M. D., and Gattass, C. R. (2008) Antitumoral activity of new polyamine-naphthoquinone conjugates. *Oncol. Rep. 20*, 225−231.
(31) Tomasi, S., Renault, J., Martin, B., Duhieu, S., Cerec, V., Le Roch, M., Uriac, P., and Delcros, J. G. (2010) Targeting the polyamine transport system with benzazepine- and azepine-polyamine conjugates. *J. Med. Chem. 53*, 7647−7663.
(32) Burns, M. R., Graminski, G. F., Weeks, R. S., Chen, Y., and O'Brien, T. G. (2009) Lipophilic lysine-spermine conjugates are potent polyamine transport inhibitors for use in combination with a polyamine biosynthesis inhibitor. *J. Med. Chem. 52*, 1983−1993.
(33) Covassin, L., Desjardins, M., Soulet, D., Charest-Gaudreault, R., Audette, M., and Poulin, R. (2003) Xylylated dimers of putrescine and polyamines: influence of the polyamine backbone on spermidine transport inhibition. *Bioorg. Med. Chem. Lett. 13*, 3267−3271.
(34) Delcros, J. G., Vaultier, M., Roch, N. L., Havouis, R., Moulinoux, J. P., and Seiler, N. (1997) Bis(7-amino-4-azaheptyl)dimethylsilane: a new tetramine with polyamine-like features. Effects on cell growth. *Anti-cancer Drug Design 12*, 35−48.
(35) Martin, B., Posseme, F., Le Barbier, C., Carreaux, F., Carboni, B., Seiler, N., Moulinoux, J. P., and Delcros, J. G. (2002) Z)-1,4-diamino-2-butene as a vector of boron, fluorine, or iodine for cancer therapy and imaging: synthesis and biological evaluation. *Bioorg. Med. Chem. 10*, 2863−2871.
(36) Zhuo, J. C., Cai, J., Soloway, A. H., Barth, R. F., Adams, D. M., Ji, W., and Tjarks, W. (1999) Synthesis and biological evaluation of boron-containing polyamines as potential agents for neutron capture therapy of brian tumors. *J. Med. Chem. 42*, 1282−1292.
(37) Annereau, J. P., Brel, V., Dumontet, C., Guminski, Y., Imbert, T., Broussas, M., Vispe, S., Breand, S., Guilbaud, N., Barret, J. M., and Bailly, C. (2010) A fluorescent biomarker of the polyamine transport system to select patients with AML for F14512 treatment. *Leuk. Res. 34*, 1383−1389.
(38) Wang, C., Delcros, J. G., Biggerstaff, J., and Phanstiel, O., IV (2003) Synthesis and biological evaluation of N1-(anthracen-9-ylmethyl)triamines as molecular recognition elements for the polyamine transporter. *J. Med. Chem. 46*, 2663−2671.
(39) Wang, C., Delcros, J.-G., Biggerstaff, J., and Phanstiel, O., IV (2003) Molecular requirements for targeting the polyamine transport system. synthesis and biological evaluation of polyamine anthracene conjugates. *J. Med. Chem. 46*, 2672−2682.
(40) Kruczynski, A., Vandenberghe, I., Pillon, A., Pesnel, S., Goetsch, L., Barret, J. M., Guminski, Y., Le Pape, A., Imbert, T., Bailly, C., and Guilbaud, N. (2011) Preclinical activity of F14512, designed to target tumors expressing an active polyamine transport system. *Invest. New Drugs 29*, 9−21.
(41) Bergeron, R. J., Singh, S., Bharti, N., and Jiang, Y. (2010) Design, synthesis, and testing of polyamine vectored iron chelators. *Synthesis*, 3631−3636.
(42) Baret, P., Béguin, C. G., Boukhalfa, H., Caris, C., Laulhere, J. P., Pierre, J. L., and Serratrice, G. (1995) O-TRENSOX: A promizing water-soluble iron chelator (both FeIII and FeII) potentially suitable for plant nutrition and iron chelation therapy. *J. Am. Chem. Soc. 117*, 9760−9761.
(43) Du, T., Filiz, G., Caragounis, A., Crouch, P. J., and White, A. R. (2008) Clioquinol promotes cancer cell toxicity through tumor necrosis factor alpha release from macrophages. *J. Pharmacol. Exp. Ther. 324*, 360−367.
(44) Ding, W. Q., Liu, B., Vaught, J. L., Palmiter, R. D., and Lind, S. E. (2006) Clioquinol and docosahexaenoic acid act synergistically to kill tumor cells. *Mol. Cancer Ther. 5*, 1864−1872.
(45) Wang, J., Xie, S., Li, Y., Guo, Y., Ma, Y., Zhao, J., Phanstiel, O., IV, and Wang, C. (2008) Synthesis and evaluation of unsymmetrical polyamine derivatives as antitumor agents. *Bioorg. Med. Chem. 16*, 7005−7012.
(46) Byers, T. L., and Pegg, A. E. (1989) Properties and physiological function of the polyamine transport system. *Am. J. Physiol. 257* (Cell. physiol. 26), C545−C553.
(47) Rodbard, D., and McClean, S. W. (1977) Automated computer analysis for enzyme-multiplied immunological techniques. *Clin. Chem. 23*, 112−115.
(48) Swart, M., Groenhof, A. R., Ehlers, A. W., and Lammertsma, K. (2004) Validation of exchange-correlation functionals for spin states of iron complexes. *J. Phys. Chem. A 25*, 5479−5483.
(49) Handy, A. J., and Cohen, N. C. (2001) Left-right correlation energy. *Mol. Phys.*, 403−412.
(50) Perdew, J. P., Burke, K., and M., E. (1997) Generalized gradient approximation made simple [phys. rev. lett. 77, 3865 (1996)]. *Phys. Rev. Lett. 7*, 1396−1398.
(51) Frisch, M. J., Trucks, G. W., Schlegel, H. B., Scuseria, G. E., Robb, M. A., Cheeseman, J. R., Scalmani, G., Barone, V., Mennucci, B., Petersson, G. A., Nakatsuji, H., Caricato, M., Li, X., Hratchian, H. P., Izmaylov, A. F., Bloino, J., Zheng, G., Sonnenberg, J. L., Hada, M., Ehara, M., Toyota, K., Fukuda, R., Hasegawa, J., Ishida, M., Nakajima, T., Honda, Y., Kitao, O., Nakai, H., Vreven, T., Montgomery, J., J. A., Peralta, J. E., Ogliaro, F., Bearpark, M., Heyd, J. J., Brothers, E., Kudin, K. N., Staroverov, V. N., Kobayashi, R., Normand, J., Raghavachari, K., Rendell, A., Burant, J. C., Iyengar, S. S., Tomasi, J., Cossi, M., Rega, N., Millam, J. M., Klene, M., Knox, J. E., Cross, J. B., Bakken, V., Adamo, C., Jaramillo, J., Gomperts, R., Stratmann, R. E., Yazyev, O., Austin, A. J., Cammi, R., Pomelli, C., Ochterski, J. W., Martin, R. L., Morokuma, K., Zakrzewski, V. G., Voth, G. A., Salvador, P., Dannenberg, J. J., Dapprich, S., Daniels, A. D., Farkas, O., Foresman, J. B., Ortiz, J. V., Cioslowski, J., and J., F. D. (2009) *Gaussian 09 Revision A.02*, Gaussian Inc., Wallingford, CT.
(52) Kuksa, V., Buchan, R., and Kong Thoo Lin, P. (2000) Synthesis of polyamines, their derivatives, analogues and conjugates. *Synthesis*, 1189−1207.
(53) Tian, Z.-y., Xie, S.-q., Mei, Z.-h., Zhao, J., Gao, W.-y., and Wang, C.-j. (2009) Conjugation of substituted naphthalimides to polyamines as cytotoxic agents targeting the Akt/mTOR signal pathway. *Org. Biomol. Chem. 7*, 4651−4660.
(54) Bergeron, R. J., Bharti, N., Wiegand, J., McManis, J. S., Yao, H., and Prokai, L. (2005) Polyamine-vectored iron chelators: the role of charge. *J. Med. Chem. 48*, 4120−4137.
(55) Kaur, N., Delcros, J.-G., Archer, J., Weagraff, N. Z., Martin, B. n. d., and Phanstiel, O., Iv (2008) Designing the polyamine pharmacophore: influence of N-substituents on the transport behavior of polyamine conjugates. *J. Med. Chem. 51*, 2551−2560.
(56) Gardner, R. A., Belting, M., Svensson, K., and Phanstiel. (2007) Synthesis and transfection efficiencies of new lipophilic polyamines. *J. Med. Chem. 50*, 308−318.
(57) Xie, S., Cheng, P., Liu, G., Ma, Y., Zhao, J., Chehtane, M., Khaled, A. R., Phanstiel, Iv, O., and Wang, C. (2007) Synthesis and bioevaluation of N-(arylalkyl)-homospermidine conjugates. *Bioorg. Med. Chem. Lett. 17*, 4471−4475.
(58) Chadwick, J., Jones, M., Mercer, A. E., Stocks, P. A., Ward, S. A., Park, B. K., and O'Neill, P. M. (2010) Design, synthesis and antimalarial/anticancer evaluation of spermidine linked artemisinin conjugates designed to exploit polyamine transporters in Plasmodium falciparum and HL-60 cancer cell lines. *Bioorg. Med. Chem. 18*, 2586−2597.
(59) de Medina, P., Paillasse, M. R., Payre, B., Silvente-Poirot, S., and Poirot, M. (2009) Synthesis of new alkylaminooxysterols with potent cell differentiating activities: identification of leads for the treatment of cancer and neurodegenerative diseases. *J. Med. Chem. 52*, 7765−7777.
(60) Jotterand, N., Pearce, D. A., and Imperiali, B. (2001) Asymmetric synthesis of a new 8-hydroxyquinoline-derived alpha-amino acid and its incorporation in a peptidylsensor for divalent zinc. *J. Org. Chem. 66*, 3224−3228.
(61) Abdel-Magid, A. F., Carson, K. G., Harris, B. D., Maryanoff, C. A., and Shah, R. D. (1996) Reductive amination of aldehydes and ketones with sodium triacetoxyborohydride. studies on direct and indirect reductive amination procedures. *J. Org. Chem. 61*, 3849−3862.

(62) Byers, T. L., Wechter, R., Nuttall, M. E., and Pegg, A. E. (1989) Expression of a human gene for polyamine transport in Chinese-hamster ovary cells. *Biochem. J. 263*, 745−752.
(63) Lescoat, G., Léonce, S., Pierré, A., Gouffier, L., and Gaboriau, F. (2012) Antiproliferative and iron chelating efficiency of the new bis-8-hydroxyquinoline benzylamine chelator S1 in hepatocyte cultures. *Chem.-Biol. Interact. 195*, 165−172.
(64) Rodriguez-Lucena, D., Gaboriau, F., Rivault, F., Schalk, I. J., Lescoat, G., and Mislin, G. L. A. (2010) Synthesis and biological properties of iron chelators based on a bis-2-(2-hydroxy-phenyl)-thiazole-4-carboxamide or -thiocarboxamide (BHPTC) scaffold. *Bioorg. Med. Chem. 18*, 689−695.
(65) Thomas, F., Serratrice, G., Béguin, C., Saint Aman, E., Pierre, J. L., Fontecave, M., and Laulhère, J. P. (1999) Calcein as a fluorescent probe for ferric iron. *J. Biol. Chem. 274*, 13375−13383.
(66) Lovaas, E. (1997) Antioxidative and metal-chelating effects of polyamines. *Adv. Pharmacol.*, 119−149.
(67) Palmer, B. N., and Powell, H. K. J. (1974) Polyamine complexes with seven-membered chelate rings: Complexe formation of 3-azaheptane-1,7-diamine, 4-azaoctane-1,8-diamine (spermidine), and 4,9-diazadodecane-1,12-diamine (spermine) with copper(II) and hydrogen ions in aqueous solution. *J. Chem. Soc., Dalton Trans.*, 2089−2092.
(68) Bardez, E., Devol, I., Larrey, B., and Valeur, B. (1997) Excited-state processes in 8-hydroxyquinoline: photoinduced tautomerization and solvation effects. *J. Phys. Chem. B 101*, 7786−7793.
(69) Kimberly, M. M., and Goldstein, J. H. (1981) Determination of pKa values and total proton distribution pattern of spermidine by carbon-13 nuclear magnetic resonance titrations. *Anal. Chem. 53*, 789−793.
(70) Shchavlev, A. E., Pankratov, A. N., and Shalabay, A. V. (2006) Dft computational studies on rotation barriers, tautomerism, intramolecular hydrogen bond, and solvent effects in 8-hydroxyquinoline. *Int. J. Quantum Chem. 4*, 876−886.
(71) Beattie, J. K., Best, S. P., Skelton, B. W., and White, A. H. (1981) Structural studies on the caesium alums, $CsMIII[SO_4]_2 \bullet 12H_2O$. *J. Chem. Soc., Dalton Trans.*, 2105−2111.
(72) Notni, J., Pohle, K., Peters, J. A., Görls, H., and Platas-Iglesias, C. (2009) Structural study of Ga(III), In(III), and Fe(III) complexes of triaza-macrocycle based ligands with N3S3 donor set. *Inorg. Chem. 7*, 3257−3267.

Bioconjugate Chemistry

Article

pubs.acs.org/bc

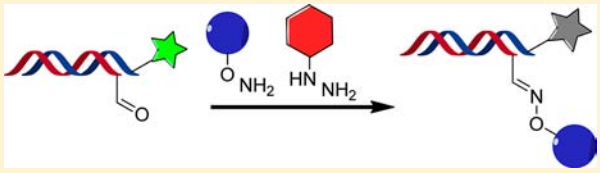
Fluorescence Quenchers for Hydrazone and Oxime Orthogonal Bioconjugation

Pete Crisalli, Armando R. Hernández, and Eric T. Kool*

Department of Chemistry, Stanford University, Stanford, California 94305-5080, United States

Supporting Information

ABSTRACT: We describe the synthesis and properties of new fluorescence quenchers containing aldehyde, hydrazine, and aminooxy groups, allowing convenient bioconjugation as oximes or hydrazones. Conjugation to oligonucleotides proceeded in high yield with aniline as catalyst. Kinetics studies of conjugation show that, under optimal conditions, a hydrazine or aminooxy quencher can react with aldehyde-modified DNA to form a stable hydrazone or oxime adduct in as little as five minutes. The resulting quencher-containing DNAs were assessed for their ability to quench the emission of fluorescein in labeled complements and compared to the commercially available dabcyl and Black Hole Quencher 2 (BHQ2), which were conjugated as phosphoramidites. Results show that the new quenchers possess slightly different absorbance properties compared to dabcyl and are as efficient as the commercial quenchers in quenching fluorescein emission. Hydrazone-based quenchers were further successfully incorporated into molecular beacons and shown to give high signal to background ratios in single nucleotide polymorphism detection *in vitro*. Finally, aminooxy and hydrazine quenchers were applied to quenching of an aldehyde-containing fluorophore associated with living cells, demonstrating cellular quenching within one hour.



INTRODUCTION

Fluorescence quenchers have garnered a wide variety of uses in assays for biomolecular detection and analysis.[1−11] Potent fluorescence quenching is often attained by placing the quencher molecule in close spatial proximity to the fluorophore to allow for contact quenching, where the fluorophore undergoes direct electronic interactions with the quencher moiety.[11−16] The resulting emission can be greatly reduced compared to the "on" state of the fluorophore separated from the quencher, which is important for lowering background signals. Many different fluorescence quenchers have been designed, including the widely used and commercially available Dabcyl (4-((4-(dimethylamino)phenyl)azo)benzoic acid), Black Hole Quenchers (BHQ),[17] the QSY series,[18] and BlackBerry Quenchers.[19] Other quenchers with broadened absorbance properties have been designed, based on such scaffolds as azaphthalocyanine,[20,21] azulene,[22] cyanine,[8] or napthalimide.[23]

Despite their broad use, however, these quenchers are limited by their chemistry of conjugation. Chemical attachment is nearly always done by one of two irreversible approaches: as a phosphodiester linkage via automated DNA synthesis, or as an amide link via reaction of carboxylate and amine. Development of new bioorthogonal means of attaching quencher molecules could allow for increased ease and speed of conjugation, enable conjugation of complex molecules with multiple functional groups, and provide greater freedom for design of multiplex assays.

Hydrazone and oxime chemistry has been advanced in recent years as a bioorthogonal means of attaching a variety of labels to molecules of interest, even in cellular conditions. Although the uncatalyzed condensations possess slow reaction kinetics, the development of aniline catalysis to greatly enhance reaction rate has allowed for a variety of useful applications.[24−26] Surprisingly, although these bond formations have been used to attach fluorophores to many molecules of interest,[25,27] we are aware of no reports of the use of oxime or hydrazone chemistry to attach a quencher to a fluorescently labeled molecule. Such an approach may be desirable for a variety of reasons. First, the mild chemistry allows conjugations in molecules that may have otherwise sensitive reactive groups. Second, this synthetic approach can allow for temporal control of when a quencher will be introduced into a system, yielding quenching after some fluorescence analysis has taken place. Further, if the reactive groups are placed in direct conjugation, formation of either oxime or hydrazone can result in direct electronic changes of the quencher itself (such as redshifting), which has been observed with hydrazone formation involving dyes.[28,29] Finally, since hydrazone/oxime chemistry can proceed intracellularly,[27,29] this offers the possibility of performing quenching experiments directly in cells.

Here, we report the preparation and properties of multiple new hydrazine, aminooxy, and aldehyde-containing fluorescence quenchers (Figure 1) that can easily be conjugated to aldehyde, aminooxy, or hydrazide modified molecules (such as DNA) (Figure 2) via the stable formation of oximes or hydrazones. The quenching efficiencies of these molecules are comparable to or slightly better than a commercially available

Received: June 27, 2012
Revised: August 20, 2012
Published: August 23, 2012

 © 2012 American Chemical Society

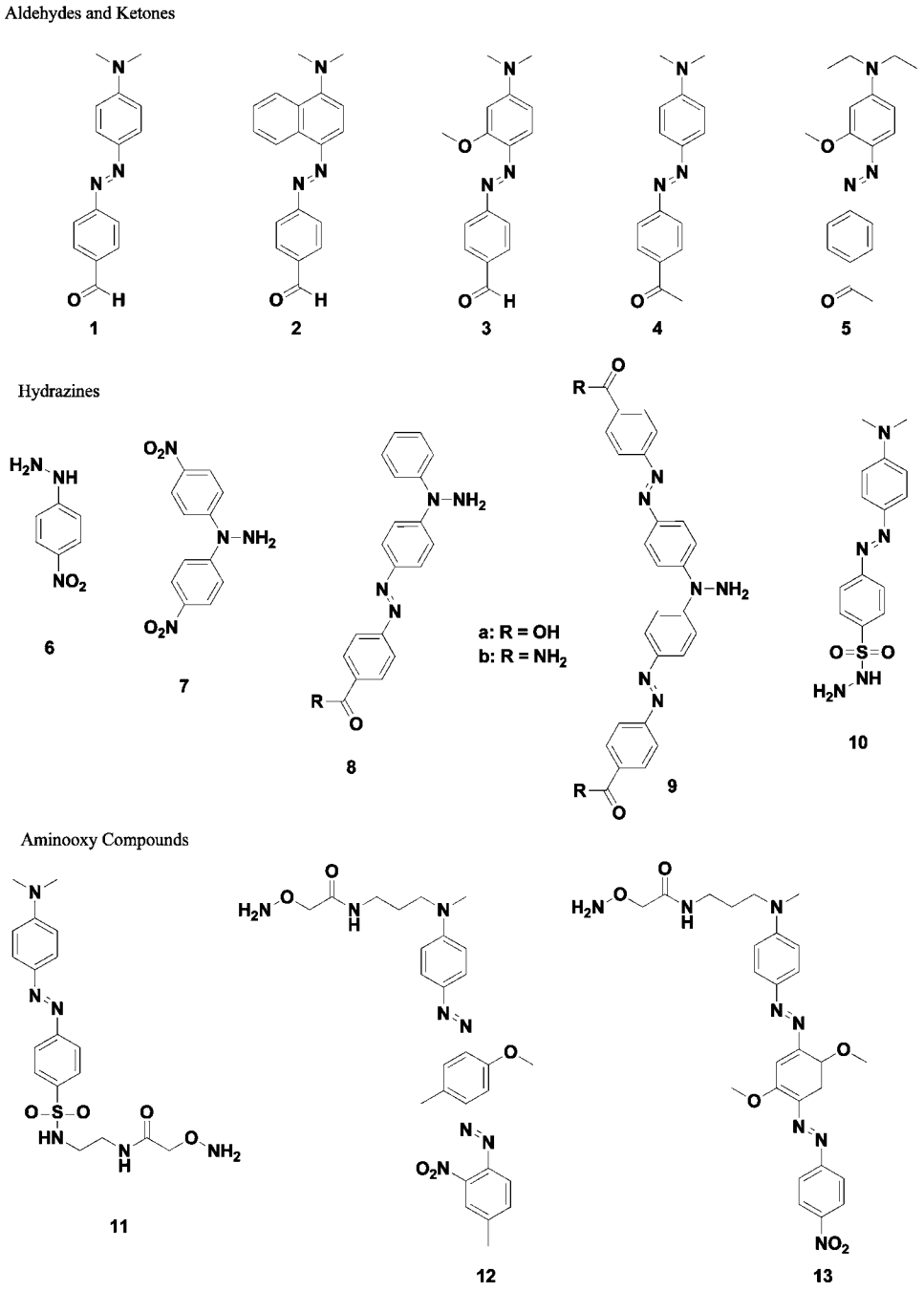


Figure 1. Aldehyde-, hydrazine-, and aminooxy-modified quenchers prepared for this study.

dabcyl quencher, but the new compounds offer a convenient bioorthogonal means of attaching the quencher moiety. We find that with aniline catalysis a quencher can form a stable DNA hydrazone adduct in high yield in as little as 5 min. Finally, we present preliminary experiments showing evidence of fluorescence quenching within living cells by cell-permeable quencher groups.

EXPERIMENTAL SECTION

Chemicals and Reagents. Chemicals were purchased from Sigma-Aldrich or TCI America and used without further purification. Solvents were purchased from Acros Organics and used as received. DNA phosphoramidites and solid supports were purchased from Glen Research. 5′-Dabcyl phosphoramidite, 3-formylindole phosphoramidite and 3′-Fluorescein CPG were purchased from Glen Research. 5′-BHQ2 phosphoramidite was purchased from Biosearch Technologies.

Instrumentation. ^{1}H and ^{13}C NMR spectra were recorded on a Varian 500 MHz NMR spectrometer and internally referenced to the residual solvent signal; *J* values are reported in Hz. Oligonucleotide sequences were synthesized on an ABI 394 DNA synthesizer using standard reagents and phosphoramidites. Analytical and semipreparative high-performance liquid chromatography was performed on a LC-CAD Shimadzu liquid chromatograph, equipped with a SPD-M10A VD diode array detector and a SCL 10A VP system controller using reverse-phase C18 columns (Grace ProSphere C18−300 10 μ for semipreparative scale HPLC, Alltech Platinum C18−100A 5 μ

dx.doi.org/10.1021/bc300344b | *Bioconjugate Chem.* 2012, 23, 1969−1980

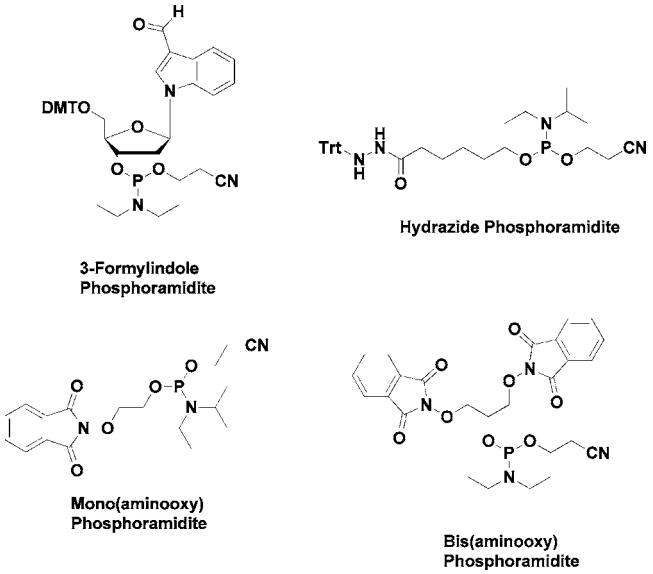


Figure 2. Aldehyde, hydrazide, and aminooxy phosphoramidites employed for oxime and hydrazone formation on DNA.

for analytical HPLC). DNA concentrations were determined on a Cary 100 Bio UV−visible spectrophotometer at 90 °C by measuring absorbance at 260 nm. Fluorescence measurements were performed on a Fluorolog 3 Jobin Yvon fluorescence spectrometer. ESI MS was determined by the Vincent Coates Foundation Mass Spectrometry Laboratory, Stanford University Mass Spectrometry. Oligonucleotide masses were determined by the Stanford University Protein and Nucleic Acid Facility using a Perspective Voyager-DE RP Biospectrometry MALDI-TOF mass-spectrometry instrument using a 3-hydroxypicolinic acid/diammonium hydrogen citrate matrix.

Synthetic Procedures. Compounds **1** and **10** were prepared according to published procedures.[30,31] Compound **6** is commercially available. Compounds **2**−**5** were prepared analogously to **1**, substituting the appropriate aniline for *N*,*N*-dimethylaniline in **2**, **3**, and **5** or using 4-aminoacetophenone in place of 4-aminobenzaldehyde for **4** and **5**. Representative reaction conditions and purification procedures are provided below. Hydrazide and aminooxy phosphoramidites were prepared according to published procedures.[32−34]

*Representative Conditions for Synthesis of **2**−**5**.* 0.454 g 4-aminobenzaldehyde or 0.507 g 4′-aminoacetophenone (3.75 mmol) was dissolved in 12 mL 1 M HCl and stirred at 0 °C. Separately, 0.272 g sodium nitrite (3.94 mmol, 1.05 equiv) was dissolved in 2 mL water and added dropwise. The resulting solution was stirred at 0 °C for 30 min. A solution of the corresponding aniline (3.94 mmol, 1.05 equiv) dissolved in 9 mL 1 M HCl was added followed by a solution of 2.15 g sodium acetate in 15 mL of water. The resulting red−orange suspension was stirred and allowed to warm to room temperature over a period of 1 h. The suspension was filtered, washed with water, and purified as described below to provide the desired aldehyde or ketone dye.

*4-((4-(Dimethylamino)naphthalen-1-yl)diazenyl)-benzaldehyde (**2**).* **2** was purified by column chromatography over silica gel eluting with chloroform to provide a red solid.

^{1}H NMR (500 MHz, $CDCl_3$): 3.05 (s, 6H), 7.07 (d, 1H, J = 8 Hz), 7.57 (dd, 1H, J = 7 Hz, 1.5 Hz), 7.65 (dd, 1H, J = 7 Hz, 1.5 Hz), 7.94 (d, 1H, J = 8.5 Hz), 8.02−8.04 (m, 2H), 8.08−8.11 (m, 2H), 8.22 (d, 1H, J = 8 Hz), 9.02 (d, 1H, J = 9 Hz), 10.09 (s, 1H). ^{13}C NMR (125 MHz, $CDCl_3$): 44.9, 113.0, 113.2, 123.3, 123.8, 124.8, 125.5, 127.2, 128.0, 130.8, 133.6, 136.8, 142.7, 155.6, 156.8, 191.8. ESI MS (Calc M+H = 304.14): 304.33.

*4-((4-(Dimethylamino)-2-methoxyphenyl)diazenyl)-benzaldehyde (**3**).* **3** was purified by column chromatography over silica gel eluting with dichloromethane to provide a dark red solid.

^{1}H NMR (500 MHz, $CDCl_3$): 3.13 (s, 6H), 4.04 (s, 3H), 6.19 (d, 1H, J = 2 Hz), 6.35 (dd, 1H, J = 9.5 Hz, 2 Hz), 7.84 (d, 1H, J = 9.5 Hz), 7.91−7.96 (m, 4H), 10.03 (s, 1H). ^{13}C NMR (125 MHz, $CDCl_3$): 40.4, 56.2, 94.3, 105.1, 118.4, 122.7, 130.8, 134.0, 135.8, 155.0, 157.6, 160.2, 191.9. ESI MS (Calc M+H = 284.14): 284.33.

*1-(4-((4-(Dimethylamino)phenyl)diazenyl)phenyl)-ethanone (**4**).* **4** was recrystallized from ethanol to provide a red solid.

^{1}H NMR (500 MHz, $CDCl_3$): 2.64 (s, 3H), 3.10 (s, 6H), 6.75 (d, 2H, J = 9 Hz), 7.87−7.91 (m, 4H), 8.06 (d, 2H, J = 8.5 Hz). ^{13}C NMR (125 MHz, $CDCl_3$): 26.9, 40.3, 111.5, 122.2, 125.6, 129.4, 136.9, 143.7, 153.0, 156.0, 197.7. ESI MS (Calc M +H = 268.14): 268.33.

*1-(4-((4-(Diethylamino)-2-methoxyphenyl)diazenyl)-phenyl)ethanone (**5**).* **5** was recrystallized from ethanol to provide a dark red solid.

^{1}H NMR (500 MHz, $CDCl_3$): 1.24 (t, 6H, J = 7 Hz), 2.62 (s, 3H), 3.45 (q, 4H, J = 7 Hz), 4.02 (s, 3H), 6.18 (d, 1H, J = 3 Hz), 6.31 (dd, 1H, J = 9.5 Hz, 3 Hz), 7.81−7.85 (m, 3H), 8.03 (d, 2H, J = 6.5 Hz). ^{13}C NMR (125 MHz, $CDCl_3$): 12.8, 26.8, 45.0, 56.2, 93.9, 104.9, 118.6, 122.2, 129.4, 133.5, 136.4, 152.7, 156.7, 160.3, 197.7. ESI MS (Calc M+H = 326.19): 326.33.

*tert-Butyl 2-(4-((4-(ethoxycarbonyl)phenyl)diazenyl)-phenyl)-2-phenylhydrazinecarboxylate (**14**).* 315 mg of *tert*-butyl 2-(4-nitrophenyl)-2-phenylhydrazinecarboxylate[35] was dissolved in 10 mL MeOH. A catalytic amount of 10% palladium on carbon was added and the solution stirred at room temperature overnight under a hydrogen atmosphere, after which TLC showed consumption of starting materials. The resulting solution was filtered through Celite and washed with methanol and the filtrate concentrated to afford the crude amino product. The crude amino product was dissolved in 7 mL toluene and treated with 256 mg ethyl 4-nitrosobenzoate[36] and 282 μL acetic acid. The resulting solution was stirred at 90 °C overnight under an argon atmosphere. TLC indicated the formation of a bright orange product. Volatiles were removed *in vacuo* and the crude material purified by silica column chromatography eluting with 5:2 Hexanes/EtOAc to afford 440 mg of a bright orange solid (quantitative). An analytically pure sample was obtained by recrystallization from methanol.

^{1}H NMR (500 MHz, $CDCl_3$): 1.33 (br s, 3H), 1.42 (t, 3H, J = 7 Hz), 1.51 (br s, 6H), 4.40 (q, 2H, J = 7 Hz), 7.11−7.19 (m, 3H), 7.31−7.40 (m, 4H), 7.88 (m, 4H), 8.16 (d, 2H, J = 8.5 Hz). ^{13}C NMR (125 MHz, $CDCl_3$): 14.4, 28.1, 28.3, 61.2, 81.8. 115.6, 115.9, 122.3, 122.5, 123.2, 124.9, 125.5, 129.5, 130.6, 131.3, 144.6, 147.0, 149.9, 154.7, 155.5, 166.3. ESI MS (Calc M +H = 461.22): 461.33.

*tert-Butyl 2,2-bis(4-nitrophenyl)hydrazinecarboxylate (**15**).* 300 mg of *tert*-butyl 2-(4-nitrophenyl)-diazenecarboxylate[35] was dissolved in 10 mL methanol. To this solution, 240 mg 4-nitrophenylboronic acid (1.2 equiv) and 18 mg (0.075 equiv) copper acetate monohydrate were added. The resulting solution was stirred overnight at 45 °C. Volatiles were removed *in vacuo* and the resulting solid purified by

column chromatography eluting with 3:1 hexanes/EtOAc → 2:1 hexanes/EtOAc to afford 390 mg (87%) of the desired product as a bright yellow solid.

^{1}H NMR (500 MHz, $CDCl_3$): 1.30 (br s, 3H), 1.51 (br s, 6H), 7.31 (d, 4H, J = 9 Hz), 8.22 (d, 4H, J = 9 Hz). ^{13}C NMR (125 MHz, $CDCl_3$): 28.0, 28.3, 83.3, 119.1, 125.7, 143.4, 149.5. ESI MS (Calc M+H = 375.13): 373.42.

*tert-Butyl 2-(4-((4-(ethoxycarbonyl)phenyl)diazenyl)-phenyl)-2-phenylhydrazinecarboxylate (**16**).* 300 mg of **15** was dissolved in 10 mL MeOH. A catalytic amount of 10% palladium on carbon was added and the solution stirred at room temperature overnight under a hydrogen atmosphere (balloon), after which TLC showed consumption of starting materials. The resulting solution was filtered through Celite and washed with methanol and the filtrate concentrated to afford the crude diamino product. The crude diamino product was dissolved in 7 mL toluene and treated with 515 mg ethyl 4-nitrosobenzoate[36] and 270 μL acetic acid. The resulting solution was stirred at 90 °C overnight under an argon atmosphere. TLC indicated the formation of a bright orange product. Volatiles were removed *in vacuo* and the crude material purified by column chromatography eluting with 3:1 hexanes/EtOAc → 2:1 hexanes/EtOAc to afford 297 mg (58%) of a bright red foam. An analytically pure sample was obtained by recrystallization from methanol.

^{1}H NMR (500 MHz, $CDCl_3$): 1.33 (br s, 3H), 1.43 (t, 6H, J = 7.5 Hz), 1.53 (br s, 6H), 4.41 (q, 4H, J = 7.5 Hz), 7.36 (d, 4H, J = 9 Hz), 7.91−7.96 (m, 8H), 8.18 (d, 4H, J = 8.5 Hz). ^{13}C NMR (125 MHz, $CDCl_3$): 14.4, 28.1, 28.4, 61.3, 82.4, 119.5, 122.5, 124.8, 130.6, 131.8, 148.1, 148.5, 155.3, 166.2. ESI MS (Calc M+H = 637.28): 637.42.

*tert-Butyl 2-((2-(4-((4-(dimethylamino)phenyl)diazenyl)-phenylsulfonamido)ethyl)amino)-2-oxoethoxycarbamate (**17**).* 113 mg of Boc(aminooxy)acetic acid was dissolved in 6 mL CH_2Cl_2. To this solution, 125 mg EDCI hydrochloride and 88 mg HOAt were added followed by 230 μL triethylamine. 188 mg of *N*-(2-aminoethyl)-4-((4-(dimethylamino)phenyl)-diazenyl) benzenesulfonamide[37] was added and the resulting suspension stirred overnight at room temperature. Solvents were eliminated and the crude solid was purified by column chromatography eluting with 3% MeOH in CH_2Cl_2 to afford 116 mg (38%) of a bright orange solid.

^{1}H NMR (500 MHz, $CDCl_3$): 1.48 (s, 9H), 3.12 (s, 6H), 3.19 (t, 2H, J = 5 Hz), 3.40 (t, 2H, J = 5 Hz), 4.28 (s, 2H), 5.71 (br s, 1H), 6.75 (d, 2H, J = 9.5 Hz), 7.74 (s, 1H), 7.88−7.90 (m, 4H), 7.95 (d, 2H, J = 7 Hz), 8.25 (br s, 1H). ^{13}C NMR (125 MHz, $CDCl_3$): 28.2, 38.5, 40.5, 43.6, 76.5, 83.8, 111.5, 122.7, 125.8, 128.0, 139.7, 143.6, 153.1, 155.6, 158.1, 169.8. ESI MS (Calc M-H = 519.20): 519.19.

*tert-Butyl 2-((3-(methyl(phenyl)amino)propyl)amino)-2-oxoethoxycarbamate (**18**).* 300 mg of Boc(aminooxy)acetic acid was dissolved in 10 mL CH_2Cl_2. To this solution, 451 mg of EDCI hydrochloride, 0.657 mL Et_3N, and 0.515 mL *N*-methyl-*N*-phenylpropane-1,3-diamine were added and the resulting solution stirred overnight at room temperature. The reaction was diluted with CH_2Cl_2, washed twice with water and once with brine. The organic layer was dried over $MgSO_4$, filtered, and concentrated, then purified by silica column chromatography eluting with 3:2 EtOAc/hexanes to afford 230 mg (43%) of a yellow oil.

^{1}H NMR (500 MHz, $CDCl_3$): 1.46 (s, 9H), 1.82−1.88 (m, 2H), 2.94 (s, 3H), 3.34−3.42 (m, 4H), 4.32 (s, 2H), 6.67−6.70 (m, 3H), 7.20−7.24 (m, 2H), 7.53 (s, 1H), 8.25 (br s, 1H). ^{13}C NMR (125 MHz, $CDCl_3$): 26.6, 28.1, 37.1, 38.5, 50.5, 76.5, 83.4, 112.4, 116.3, 129.3, 149.2, 158.0, 168.9. ESI MS (Calc M +H = 338.21): 338.27.

*Boc(aminooxy) BHQ1 (**19**).* 183 mg of **18** was dissolved in 10 mL tetrahydrofuran. 271 mg of Fast Corinth V salt was added followed by 2 mL MeOH to aid in solubility. The red−brown suspension was stirred at room temperature overnight and slowly became a dark red solution. Volatiles were removed and the crude material was purified by column chromatography eluting with 1:1 Hexanes/EtOAc → 1:3 Hexanes/EtOAc to afford 47 mg (13%) of a dark red solid.

^{1}H NMR (500 MHz, $CDCl_3$): 1.47 (s, 9H), 1.92 (m, 2H), 2.51 (s, 3H), 2.70 (s, 3H), 3.10 (s, 3H), 3.39 (m, 2H), 3.54 (t, 3H, J = 7.5 Hz), 4.01 (s, 3H), 4.35 (s, 2H), 6.75 (d, 2H, J = 9 Hz), 7.39 (s, 1H), 7.47 (d, 1H, J = 6.5 Hz), 7.57 (d, 2H, J = 8 Hz), 7.66 (d, 1H, J = 8 Hz), 7.70 (s, 1H), 7.91 (d, 2H, J = 9 Hz), 8.41 (br s, 1H). ^{13}C NMR (125 MHz, $CDCl_3$): 16.9, 21.4, 27.0, 28.2, 36.8, 38.8, 50.3, 56.4, 76.6, 83.6, 99.3, 111.4, 119.0, 119.1, 124.4, 126.0, 133.6, 133.6, 141.6, 149.5, 151.1, 169.0. ESI MS (Calc M+H = 649.31): 649.31.

*Boc(aminooxy) BHQ2 (**20**).* 230 mg of **18** was dissolved in 15 mL tetrahydrofuran. 854 mg of Fast Black K salt was added followed by 3 mL MeOH to aid in solubility. The red-brown suspension was stirred at room temperature for 2 h and slowly became a dark purple solution. Volatiles were removed and the crude material was purified by column chromatography eluting with 1:1 hexanes/EtOAc → EtOAc to afford 237 mg (53%) of a dark purple solid.

^{1}H NMR (500 MHz, $CDCl_3$): 1.47 (s, 9H), 1.93 (m, 2H), 3.11 (s, 3H), 3.40 (m, 2H), 3.55 (t, 3H, J = 7.5 Hz), 4.05 (s, 3H), 4.09 (s, 3H), 4.34 (s, 2H), 6.76 (dd, 2H, J = 7 Hz, 2 Hz), 7.46 (s, 1H), 7.50 (s, 1H), 7.64 (s, 1H), 7.93 (dd, 2H, J = 7 Hz, 2 Hz), 8.04 (dd, 2H, J = 7 Hz, 2 Hz), 8.37 (dd, 2H, J = 7 Hz, 2 Hz), 8.43 (br s, 1H). ^{13}C NMR (125 MHz, $CDCl_3$): 27.0, 28.2, 36.8, 38.9, 50.2, 56.8, 76.6, 83.5, 99.9, 101.0, 111.5, 123.8, 124.8, 126.3, 142.1, 144.5, 146.9, 148.4, 150.9, 152.0, 153.7, 156.5, 158.2, 169.1. ESI MS (Calc M+H = 651.29): 651.25.

DNA Conjugation. *Removal of Protecting Groups.* For aminooxy modified DNA, the phthalimide group was removed selectively with hydrazine as recommended in the literature.[34] For hydrazide modified DNA, the trityl group was removed on the DNA synthesizer using alternating 10 s cycles of deprotection reagent (3% trichloroacetic acid in dichloromethane) and dichloromethane washes for 3 min. Commercially available 3-formylindole utilizes no protection of the aldehyde. For compounds **7**−**9** and **11**−**13**, 20 mg of boc-protected precursor **14**−**17** or **19**−**20** was dissolved in 1 mL of 1:1 dichloromethane/trifluoroacetic acid and shaken at room temperature for 2 h to provide the free hydrazine or aminooxy compound for conjugation. Volatiles were removed *in vacuo* and the crude product was used for DNA labeling without further purification.

DNA Labeling. A solution of approximately 25 mM of desired label in 750 μL 9:1 dimethylformamide/water was added to the DNA CPG. 7.5 μL of aniline was added and the resulting solution was shaken at room temperature overnight. The CPG was rinsed 4 × 500 μL dimethylformamide and 4 × 500 μL acetonitrile. Labeled DNA was cleaved using standard deprotection conditions (concentrated aqueous ammonia, 55 °C, overnight) and purified by HPLC. Purity of the collected product was assessed by analytical HPLC.

Fluorescence Experiments. Fluorescence of the hybridization buffer (10 mM $MgCl_2$, 70 mM Tris·Borate, pH 7.55)

alone was first determined and subtracted from all subsequent fluorescence data. Fluorescein-labeled 20mer was added to the buffer solution to a final concentration of 30 nM. The fluorescence of the solution was measured in triplicate (excitation 494 nm and emission 517 nm, slits both 2 nm) and averaged, subtracting background buffer emission. A concentrated solution of quencher labeled DNA was added to bring the final volume of quencher strand to 150 nM. The oligonucleotides were allowed to hybridize until the fluorescence emission remained constant, then the fluorescence spectrum was taken in triplicate and averaged, subtracting background buffer emission. Quenching efficiency was calculated at the emission maxima by dividing the quenched fluorescence by the initial fluorescence, multiplying by 100, then subtracting from 100. All experiments were performed in triplicate and averaged.

Molecular beacon experiments were performed with the same hybridization buffer and a 100 nM concentration of molecular beacon. 200 nM of either the match, mismatch or deletion sequence were added and the change in fluorescence monitored. The beacon sequence was 5′-Quencher-(3-formylindole)-GCG-AGA-AGT-TAA-GAC-CTA-TGC-TCG-C-FAM-3′, where the underlined regions represent the stem region.[4] Match sequence (5′-CAT-AGT-TCT-TAA-CTT-3′), mismatch sequence (5′-CAT-AGT-T**G**T-TAA-CTT-3′), and deletion sequence (5′-CAT-AGT-T_T-TAA-CTT-3′) were purified by PolyPakII cartridges (Glen Research).[4]

Kinetics Experiments. A concentrated solution of 4-nitrophenylhydrazine in dimethylformamide (final concentration 200 μM) was added to a buffered solution (100 mM NH_4OAc, pH 4.5) containing 100 μM aldehyde modified DNA and either 0 mM or 100 mM aniline to a total volume of 200 μL. Twenty-five microliter samples were taken and immediately injected into an HPLC at 5 min, 80 min, 150 min, and 210 min. Yield was determined by dividing the integrated area of the product by the total integrated area of both the product and the starting material. The yield at time = 0 was assumed to be zero.

Cellular Experiments. CCL-2 HeLa cells (ATCC, Manassas, VA) were grown at 37 °C (5% CO_2) in Dulbecco's modified Eagles' medium (DMEM, GIBCO)—supplemented with 10% fetal bovine serum (FBS, GIBCO), 100 μg/mL streptomycin (GIBCO), and 100 U/mL penicillin (GIBCO)—until 60−80% confluency was reached. In preparation for *in vivo* experiments, cells were trypsinized, suspended in DMEM + 10% FBS, transferred to 8-chambered microscope slides (Lab-Tek II, 500 μL cell suspension containing *ca.* 10 000 cells per chamber), and incubated for 24 h. The following stock solution was prepared in DMEM (without phenol red indicator, GIBCO) supplemented with 100 mM sodium pyruvate: 10 μM 7-diethylamino-3-formylcoumarin. The following four stock solutions were prepared in Hanks' buffered saline solution (HBSS, GIBCO): 100 μM dabcyl, 100 μM dabcyl + 10 mM aniline, 100 μM **8** or **11**, and 100 μM **8** or **11** + 10 mM aniline.

To each 8-chambered microscope slide, media was removed, cells were washed with phosphate buffered saline (PBS, GIBCO) solution (2×), and fluorophore-containing media was added (500 μL). Each slide contained a control chamber with DMEM (without phenol indicator) only. After 1 h of incubation, media was removed, cells were washed with PBS (2×) buffer, and quencher-containing media was added (500 μL). The control chamber and an additional chamber in each slide contained HBSS only. Slides were incubated at 1, 2, or 3 h. After incubation period, media was removed, cells were washed with PBS (2×) buffer, removable chamber walls were detached, and the slide was prepared for fluorescence microscopy. Fluorescence microscopy was performed on a Nikon Eclipse E800 epifluorescence microscope equipped with a Spot RT Slider camera with an excitation filter of 400−440 nm and emission cutoff filter of greater than 470 nm. Camera and image settings were the same for all images.

RESULTS

Synthesis of Aldehyde, Hydrazine, and Aminooxy Quencher Derivatives. Both compounds **1** and **10** have been reported in the literature, but surprisingly have not been applied as fluorescence quenchers despite the obvious structural similarity to the commonly used quencher dabcyl.[30,31] Compound **10** has only sparsely been employed in detecting reducing sugars via hydrazone formation.[31] Synthetically, **2**−**5** were easily prepared using procedures analogous to that for the synthesis of **1** (Scheme S1).[30] Absorption properties of the free compounds in methanol are provided in Table 1.

Table 1. Absorption Properties of Free Aldehyde or Boc Protected Hydrazine Dyes in Methanol

dye	absorption maxima	ε_{max} (L mol^{-1} cm^{-1})	ε_{260} (L mol^{-1} cm^{-1})
1	449 nm	29 300	9000
2	451 nm	22 300	12 400
3	464 nm	42 100	11 300
4	443 nm	40 800	12 200
5	476 nm	41 400	9000
10	439 nm	40 200	14 000
14	412 nm	35 900	19 000
15	383 nm	28 800	7300
16	437 nm	55 600	24 500

Preparation of compounds **7**−**9** required a different approach (Scheme S2), particularly in the case of compounds **8** and **9** as no compounds containing both an aryl hydrazine and diazo bonds were found in a literature survey. However, the reported ability to cross-couple aryl boronic acids to asymmetric Boc-protected diazo compounds afforded a simple preparation of nitroarenes.[35] While the nitroarene precursor for preparation of **14** is known, preparation of dinitro compound **15** was realized by the analogous reaction of *tert*-butyl 2-(4-nitrophenyl)-diazenecarboxylate with 4-nitrophenylboronic acid in the presence of catalytic copper(II).[35] Reduction of the nitro group followed by reaction with ethyl 4-nitrosobenzoate[36] in the presence of acetic acid easily afforded the desired azo containing hydrazine precursors **14** and **16**. Absorption properties of the Boc-protected dyes in methanol can be found in Table 1.

Preparation of quenchers **11**−**13** required a different approach, particularly as no dye containing an aminooxy group attached directly to the aryl ring could be prepared. Consequently, Boc(aminooxy)acetic acid was attached via simple linkers to dabcyl and Black Hole Quencher 1 and 2 scaffolds, as shown in Scheme S3. As no changes in the chromophore were made by this synthetic approach, the photophysical properties of these molecules were assumed to be the same as the parent dyes.[17]

Based upon literature reports regarding possible problems with the stability of free hydrazines and, to a lesser extent, free aminooxy compounds,[25,38,39] we chose to store **7**−**9** and **11**−**13** as the Boc protected forms. The Boc group provides for a

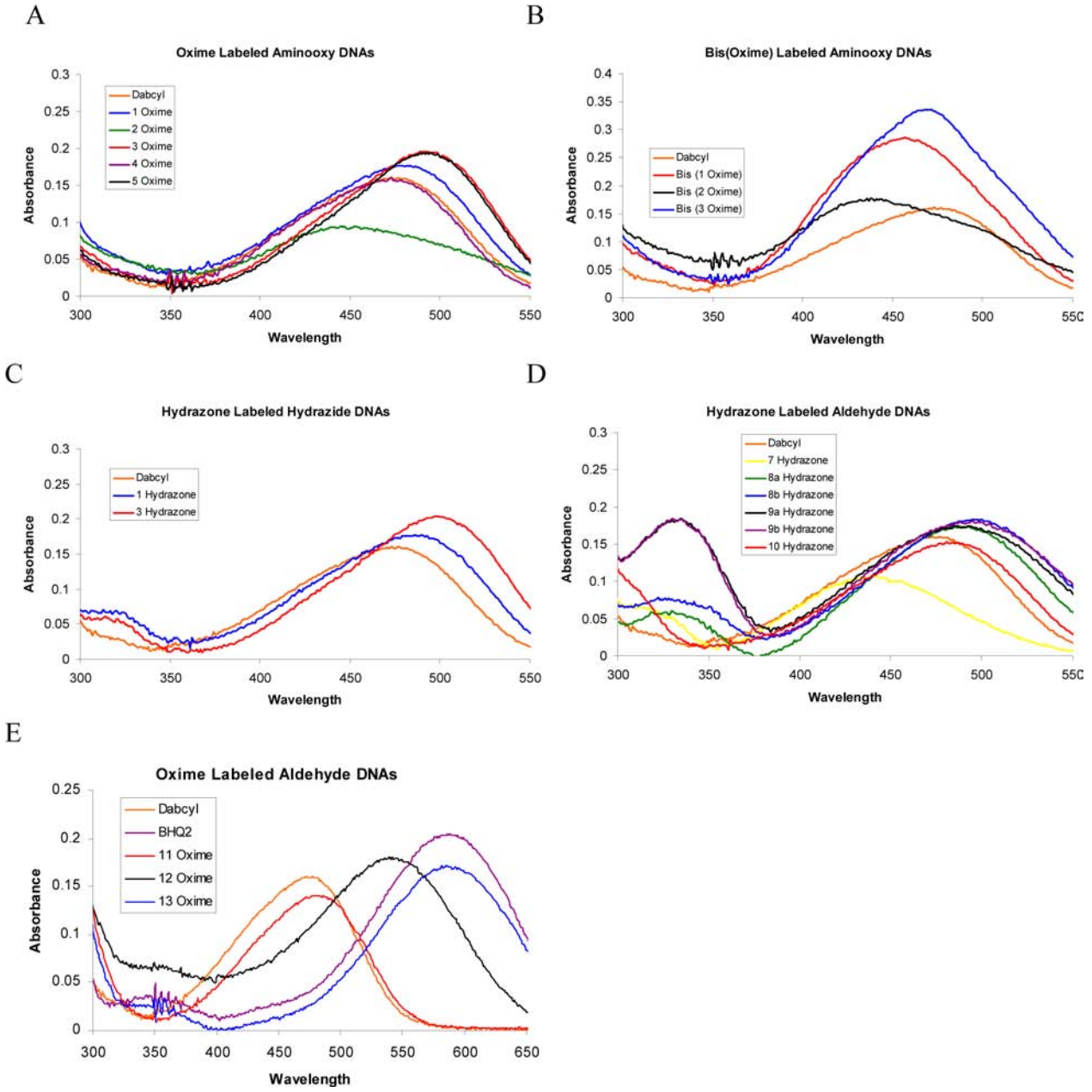


Figure 3. Absorption spectra of quenchers conjugated to DNA. (a) Oxime-labeled aminooxy DNA. (b) Bis(oxime)-labeled aminooxy DNA. (c) Hydrazone-labeled hydrazide DNA. (d) Hydrazone-labeled aldehyde DNA.

bench stable derivative and is easily cleaved with trifluoroacetic acid in dichloromethane to provide the free hydrazine or aminooxy compound for subsequent conjugation. MALDI-TOF data and spectral properties are consistent with the proper deprotection and labeling of DNA as the desired hydrazones or oximes.

Labeling of DNA. Conjugation experiments were performed by reaction of the dye with the modified DNA attached to the solid support in a DMF/water mixture in the presence of aniline at room temperature. Subsequent deprotection of the DNA was performed under standard aqueous ammonia conditions at 55 °C. Attachment of dyes to DNA via oxime formation (by reaction of aldehyde dyes with aminooxy DNA) was, qualitatively, higher yielding and provided more stable dyes than formation of hydrazone linkages, consistent with the greater stability of oximes versus hydrazones.[40] However, use of diphenylhydrazine derivatives **7**–**9** provided a higher yield of labeled DNA when compared to simple labeling with dabsyl hydrazide **10**, indicating that the diphenylhydrazine derivatives may be preferable to dabsyl hydrazide in terms of higher yield and stability. Oxime-labeled DNA was found to be stable for at least six months after storage at −80 °C, while dabsyl hydrazone labeled DNA did display a small degree of degradation and may require repurification after prolonged storage. Both hydrazones and oximes were stable at room temperature in biologically relevant pHs utilized for hybridization experiments and at pH 4.5 used for kinetics experiments.

Experiments showed that aldehyde derivatives of the quencher dyes provided much higher yields of the desired labeled DNA than did their methyl ketone counterparts. For example, attempted hydrazone formation with dyes **4** and **5** by

reaction with hydrazide modified DNA showed no observable product by HPLC, while only a low yield was obtained when forming an oxime with these dyes. Similarly, no bis(oximes) were obtained with the methyl ketone dyes. In contrast, formation of hydrazones or oximes with aldehyde dyes provided the desired DNA adduct as the major product (save for compound **2**, which did not form a stable hydrazone) as confirmed by the spectral properties and MALDI-TOF results. This is consistent with literature reports of the equilibrium constant for benzaldehyde-oxime and hydrazone formation being orders of magnitude higher than formation of the corresponding acetophenone oximes or hydrazones.[41]

Dyes **8** and **9** containing the ethyl ester protecting group provided a complication in labeling DNA, as the deprotection conditions employed (concentrated aqueous ammonia) resulted in two different products, one being the free carboxylic acid (**8a**, **9a**) and the other a primary amide (**8b**, **9b**). It is likely that using different deprotection conditions (e.g., 0.05 M K_2CO_3 in MeOH) would provide only the carboxylic acid product. However, as discussed below, the absorption and quenching properties of the dyes are sufficiently similar that the differences in the two products are relatively unimportant.

Absorption Properties of Labeled DNAs. *Hydrazones and Oximes of Aldehyde Quenchers.* Both hydrazones and oximes of aminooxy or hydrazide modified DNAs with **1** display similar properties to the commercially available amide-linked dabcyl quencher. Absorption maxima are only slightly red-shifted for the simple dabcyl derivative **1** (less than 10 nm) and display slightly higher extinction coefficients (Figure 3, Table 2). Comparison of the 1-(dimethylamino)-naphthalene moiety as in the oxime of **2** to dabcyl, however, shows a marked blue shift in the absorption maximum of approximately 30 nm with a decrease in the extinction coefficient, spectral properties that are generally not desirable in a fluorescence quencher. Introduction of a methoxy group into the dimethylaniline ring in the form of **3** provides for a red shift of approximately 25 nm and induces a greater increase in the extinction coefficient at the absorbance maximum, both desirable properties. Oximes of acetophenone dyes **4** and **5** provide similar spectral properties to their aldehyde counterparts **1** and **3**, with the DNA oxime of **4** possessing very similar properties to the commercially available dabcyl phosphoramidite. Absorption maxima and other spectral properties for these dye conjugates can be found in Table 2 and the spectra of the quenchers on DNA are provided in Figure 3.

Table 2. Absorption Properties of Oxime or Hydrazone Quenchers on DNA, Formed by Reaction of Carbonyl Based Dyes with Aminooxy or Hydrazide Modified DNA

dye	absorption maxima	$\Delta w_{\lambda\ 1/2\ max}$
Dabcyl	473 nm	406–519 nm (113 nm)
1 DNA Oxime	477 nm	408–526 nm (118 nm)
1 DNA Hydrazone	486 nm	417–532 nm (115 nm)
2 DNA Oxime	445 nm	392–527 nm (135 nm)
3 DNA Oxime	493 nm	428–536 nm (108 nm)
3 DNA Hydrazone	499 nm	432–535 nm (103 nm)
4 DNA Oxime	473 nm	405–516 nm (111 nm)
5 DNA Oxime	493 nm	428–536 nm (108 nm)
Bis (**1**) Oxime	457 nm	401 nm–513 nm (112 nm)
Bis (**2**) Oxime	438 nm	384–520 nm (136 nm)
Bis (**3**) Oxime	469 nm	411–523 nm (112 nm)

Interesting changes in the absorption spectrum are observed when two dyes are placed in close proximity via use of the bis(aminooxy) linker on DNA (Figure 3b, Table 2). In the case of two incorporations of **1**, the absorption maximum shifts to 457 nm, an approximately 20 nm blue shift relative to a single **1** DNA oxime. This is likely the result of a dye–dye interaction in the small linker. This shift is accompanied by the expected 2-fold increase in the molar extinction coefficient. Similar results are seen with the bis(**3**) oxime DNA, with a similar blue shift to 469 nm (versus 493 nm for the mono **3** oxime DNA) and increase in the absorbance. Interestingly, the bis(**2**) oxime displayed only a small blue shift in absorption maximum (from 445 nm for the mono-oxime to 438 nm for the bis-oxime).

Hydrazones of Hydrazine-Based Quencher Dyes. The hydrazine dyes reacting with aldehyde-modified DNA provided interesting changes in spectral properties (Figure 3d, Table 3).

Table 3. Absorption Properties of Hydrazone and Oxime Quenchers on DNA, Formed by Reaction of Hydrazine or Aminooxy Based Dyes with Aldehyde-Modified DNA

dye	absorption maxima	$\Delta w_{\lambda\ 1/2\ max}$
Dabcyl	473 nm	406–519 nm (113 nm)
BHQ2	589 nm	514–651 nm (137 nm)
6 DNA Hydrazone	464 nm	404–515 nm (111 nm)
7 DNA Hydrazone	441 nm	391–495 nm (104 nm)
8a DNA Hydrazone	493 nm	431–538 nm (107 nm)
8b DNA Hydrazone	495 nm	431–551 nm (120 nm)
9a DNA Hydrazone	484 nm	421–549 nm (128 nm)
9b DNA Hydrazone	495 nm	426–553 nm (127 nm)
10 DNA Hydrazone	481 nm	419–529 nm (110 nm)
11 DNA Oxime	482 nm	417–527 nm (110 nm)
12 DNA Oxime	542 nm	461–605 nm (144 nm)
13 DNA Oxime	586 nm	520–650 nm (130 nm)

Most valuably, we find that the formation of a hydrazone from the hydrazine dye results in increased conjugation and a general red shift in the optical absorption properties. Comparison of dye **10** with both products of dyes **8** and **9** shows that the latter dyes are red-shifted by approximately 15 nm, with absorption maxima of approximately 495 nm versus 481 nm for **10**. Moreover, comparison of the absorption of the Boc-protected dyes **14**–**16** in methanol to the labeled DNA also exhibits the red-shift upon conjugation (although some solvatochromicity likely explains part of the red-shift). While dye **14**, for example, absorbs maximally at 412 nm, attachment to DNA in the form of quencher conjugates **8a** and **8b** yield an absorption maximum of approximately 495 nm, an 80 nm red-shift. The color changes can be readily detected by the naked eye: while dye **15** is bright yellow as a free molecule in solution (absorbing maximally at 383 nm in MeOH), upon hydrazone formation with DNA an orange color is obtained, with an absorption maximum of 441 nm. Even simple 4-nitrophenylhydrazine reacts with aldehyde-modified DNA to shift the absorption maximum from below 400 to 461 nm upon hydrazone formation.

Surprising similarities are noted between the hydrazones of dyes **8** and **9** in labeled DNA, despite the fact that **9** is a dimeric chromophore while **8** is a monomer. In methanol, protected derivatives **14** and **16** display distinctly different absorption properties, with **14** having an absorption maximum of 412 nm and an extinction coefficient of 35 900, while **16** absorbs maximally at 437 nm with ε = 55 600. When attached to DNA

dx.doi.org/10.1021/bc300344b | *Bioconjugate Chem.* 2012, 23, 1969–1980

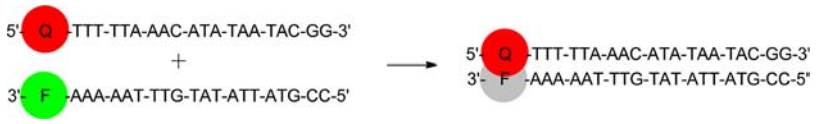


Figure 4. DNA-based assay used to assess fluorescence quenching.

as a hydrazone, however, all derivatives of **8** and **9** display approximately the same absorption spectra in the visible region (Figure 3d). This is likely due to steric crowding that shifts one of the aromatic rings in **9** out of conjugation.

The oxime-labeled DNA derivatives of aminooxy dabsyl (**11**), aminooxy BHQ1 (**12**), and aminooxy BHQ2 (**13**) provided, as expected, similar properties to their parent dyes, as linkers were used for attachment to DNA without any change in the dye scaffold proper (Figure 3e).

Quenching by Oxime and Hydrazone Dye Conjugates. Quenching experiments with the DNA–dye conjugates were performed using fluorescein-labeled DNA complements, monitoring the decrease in emission at 517 nm upon hybridization of the two DNA strands. The experimental duplexes were designed to yield contact quenching (by placing dye quencher and fluorophore together) as opposed to resonance energy transfer (RET), as the former is the mode of quenching most often employed in analytical experiments and provides greater quenching efficiency.[1−11,15] DNA sequences previously used in other quencher studies were employed here to allow for best comparison with published results and to provide for the simplest control of dye location via attachment to the 5′ end of one strand quenching a fluorophore on the 3′ end of the opposite strand (Figure 4).[15,23]

Quenching experiments confirmed that the new dyes are as efficient at quenching fluorescein as the commercially available dabcyl and BHQ 2 phosphoramidites (Table 4), confirming

Table 4. Quenching Efficiency (Fluorescein, λ_{em} = 517 nm) of Oxime or Hydrazone Labeled DNA Formed by Reaction of Carbonyl Based Quencher with Aminooxy or Hydrazide Modified DNA

dye	quenching efficiency
Dabcyl	96.7 ± 0.8%
1 DNA Oxime	97.0 ± 0.5%
1 DNA Hydrazone	96.3 ± 0.3%
2 DNA Oxime	95.0 ± 0.2%
3 DNA Oxime	96.8 ± 0.2%
3 DNA Hydrazone	97.1 ± 0.3%
4 DNA Oxime	96.3 ± 0.2%
5 DNA Oxime	94.9 ± 0.2%
Bis (**1**) Oxime	97.3 ± 0.2%
Bis (**2**) Oxime	96.1 ± 0.4%
Bis (**3**) Oxime	97.2 ± 0.2%

that attachment via this new approach retains the optical benefits of these quenchers. Hydrazone and oxime derivatives of **1** are, statistically speaking, as efficient at quenching fluorescein as the parent dabcyl with a general value of nearly 97%. Oximes or hydrazones of **3** provide a slight but not statistically significant increase in quenching efficiency. Two of the dyes do perform slightly worse than dabcyl (see data for **2** and **5**), indicating that these are not preferable for use as quenchers in future applications. Ground-state complexes of all dyes with fluorescein were observed and can be found in the Supporting Information (SI) file. As expected, the ground-state complexes between the hydrazone- and oxime-labeled quenchers and fluorescein are similar to the ground-state complex formed between dabcyl and fluorescein, indicative of the same contact quenching mechanism.

Consistent with their lack of spectral advantage (above), the bis(dye) oximes of **1**–**3** provided a negligible increase in quenching efficiency compared to the monodye labeled DNA derivatives despite having two chromophores. These results show that a second quencher moiety attached in this way does not provide a benefit in quenching efficiency versus a monomeric dye.

The hydrazones formed by reaction of a hydrazine dye with aldehyde-modified DNA again give similar quenching results as the commercially available dabcyl phosphoramidite (Table 5).

Table 5. Quenching Efficiency (Fluorescein, λ_{em} = 517 nm) of Hydrazone and Oxime Labeled DNA Formed by Reaction of Hydrazine or Aminooxy Quencher with Aldehyde Modified DNA

dye	quenching efficiency
Dabcyl	96.7 ± 0.8%
BHQ 2	96.6 ± 0.3%
6 DNA Hydrazone	95.6 ± 0.5%
7 DNA Hydrazone	96.6 ± 0.1%
8a DNA Hydrazone	96.5 ± 0.2%
8b DNA Hydrazone	96.7 ± 0.1%
9a DNA Hydrazone	93.5 ± 0.2%
9b DNA Hydrazone	96.3 ± 0.3%
10 DNA Hydrazone	96.7 ± 0.6%
11 DNA Oxime	96.1 ± 0.1%
12 DNA Oxime	96.4 ± 0.1%
13 DNA Oxime	96.5 ± 0.2%

Except for **9a** as a DNA hydrazone, all derivatives display quenching efficiencies of greater than 96%, statistically similar to the value for dabcyl. The nitroaryl quenchers as (**6** and **7**) also provide excellent quenching efficiencies of greater than 96% in each case.

Like the hydrazone conjugates, the oxime linkages (**11**–**13**) also showed similar quenching properties as the parent dyes. Statistically speaking, oximes **11** and **13** exhibited the same quenching efficiency as the parent dabcyl or BHQ2 quenchers (Table 5).

Testing Hydrazone-Linked Quenchers in Common Molecular Probes. The ability to easily synthesize aldehyde-modified DNA suggested the use of hydrazine quenchers in common fluorometric assays. As a proof of principle, a molecular beacon was prepared using commercial 3′-fluorescein and 5′-formylindole phosphoramidites, placing them in close proximity in the stem region of the beacon.[4] Hydrazone formation was easily achieved and two different molecular beacons created using dabsyl hydrazide **10** and the newly created dinitrodiphenylhydrazine **7**, which served as a surprisingly effective

dx.doi.org/10.1021/bc300344b | *Bioconjugate Chem.* 2012, 23, 1969–1980

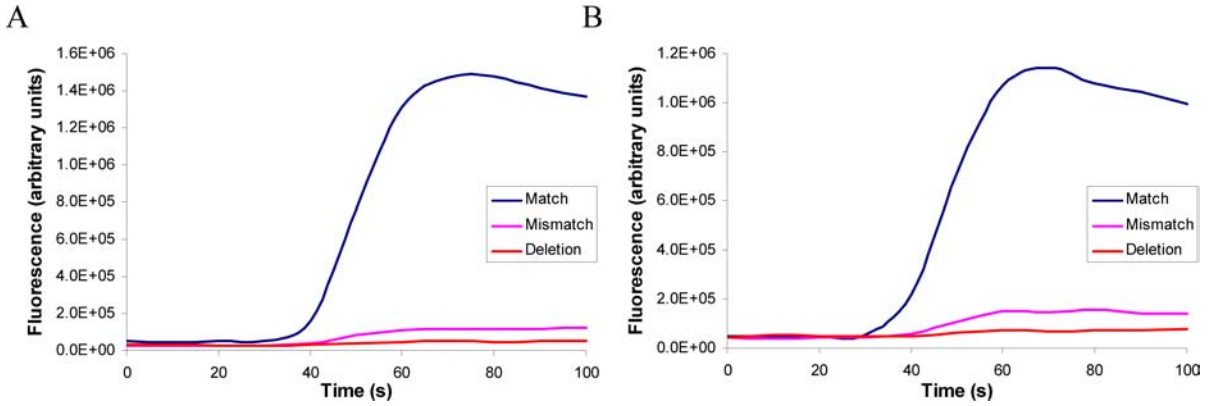


Figure 5. Performance of molecular beacons containing quenchers attached via hydrazone linkages upon exposure to matched, mismatched, and deletion target DNA sequences. (A) Beacon containing compound **7** as the quencher and (B) Beacon containing compound **10** as quencher.

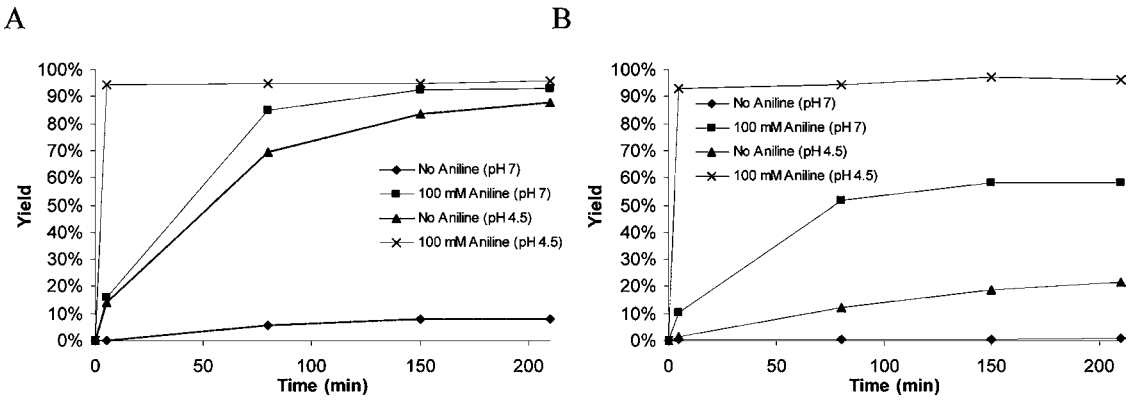


Figure 6. Kinetics of (a) hydrazone formation or (b) oxime formation between aldehyde modified DNA and **6** (hydrazone) or **11** (oxime) in the presence or absence of aniline at varying pH.

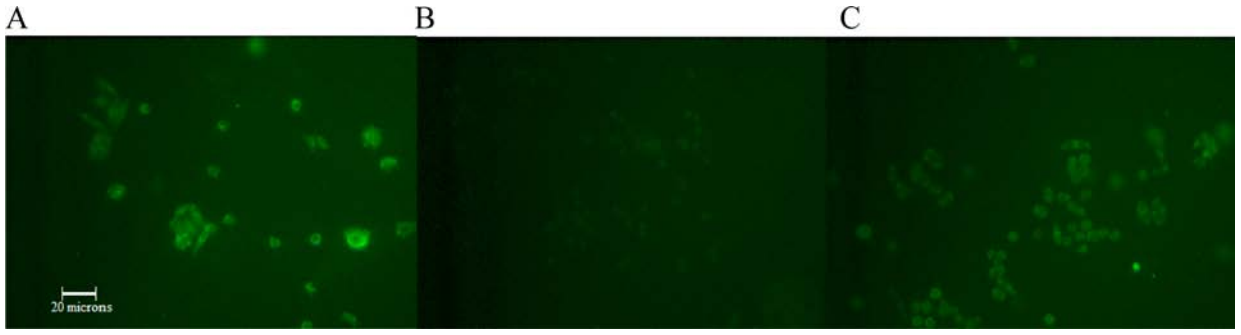


Figure 7. Treatment of HeLa cells with (a) 7-diethylamino-3-formylcoumarin alone, (b) aldehyde fluorophore, then 3 h incubation with quencher **11** and 10 mM aniline, (c) aldehyde fluorophore, then 3 h incubation with control dabcyl and 10 mM aniline.

quencher of fluorescein in the above DNA hybridization experiments.

Results showed that the molecular beacon containing quencher **10** increased fluorescence intensity by ca. 27-fold in the presence of the fully matched sequence, corresponding to a quenching efficiency of 96.2%, consistent with the DNA hybridization experiments (Figure 5). Little fluorescence activation was seen in the presence of a singly mismatched DNA or a DNA sequence containing a deletion. The hydrazone conjugate with dye **7** provided yet better results, displaying a >33-fold increase in fluorescence intensity upon hybridization with the fully matched sequence, indicative of a quenching efficiency of approximately 97%, slightly better than found in the DNA hybridization experiments.

Reaction Kinetics. While all hydrazones and oximes above were formed via attachment of the dye to DNA on solid support in a DMF/water mixture, application of quencher attachment directly in solution is often desirable. In this light, experiments were performed to assess oxime and hydrazone formation with dissolved DNAs at pH 4.5 or pH 7 in the presence or absence of aniline (Figure 6). Consistent with previous studies, pH 4.5 (100 mM NH_4OAc buffer) proved to be optimal for both hydrazone and oxime formation, while pH 7 (100 mM NaH_2PO_4) yielded a slower reaction.[24−26] Even in the absence of aniline as a catalyst, HPLC analysis indicated 88% conversion to hydrazone labeled DNA after 3.5 h of reaction at pH 4.5. In the presence of 100 mM aniline at pH 4.5, both the oxime and hydrazone products could be obtained

dx.doi.org/10.1021/bc300344b | *Bioconjugate Chem.* 2012, 23, 1969−1980



Figure 8. Treatment of HeLa cells with (a) 7-diethylamino-3-formylcoumarin alone, (b) aldehyde fluorophore, then 3 h incubation with quencher **8** and 10 mM aniline, (c) aldehyde fluorophore, then 3 h incubation with control 10 mM aniline.

in greater than 90% yield after only 5 min of reaction. As expected, both hydrazone and oxime formation at pH 7 showed considerably slower kinetics, with the uncatalyzed reaction showing less than 8% yield for hydrazone formation after 3.5 h and oxime formation being less than 1% after this time. Addition of aniline to the pH 7 buffer provided a strong increase in reaction rate, providing the hydrazone in over 90% yield after 3.5 h, while the oxime formation attained approximately 60% yield after this time.

Tests of Intracellular Quenching. To further test the efficiency and bioorthogonality of oxime and hydrazone formation in quenching of a fluorophore, HeLa cells were labeled by incubation with the aldehyde-containing fluorophore 7-diethylamino-3-formylcoumarin.[42] Hydrazone derivatives of this fluorophore have been used previously for intracellular detection of Cu(II)[43,44] and cysteine.[45] Without any quencher treatment, the bright fluorescence of the aldehyde fluorophore could easily be observed by epifluorescence microscopy (Figure 7a). However, upon treating the cells with aminooxy quencher **11** for 3 h in the presence of 10 mM aniline, considerable fluorescence quenching was observed (Figure 7b). Treatment of the cells with the parent non-aminooxy-containing quencher dabcyl and 10 mM aniline showed only a small degree of quenching (Figure 7c), confirming the necessity of the aminooxy group in **11** for oxime formation and fluorescence quenching. A similar experiment using a non-aldehyde-containing control fluorophore did not show strong fluorescence quenching by treatment of cells with **11**, again indicating the importance of oxime formation (Supporting Information).

Cellular quenching via the hydrazine quencher **8** with the same aldehyde fluorophore showed even stronger fluorescence quenching, as shown in Figure 8. After 3 h incubation, very little fluorescence was seen in the treated cells as compared to untreated cells or those exposed to aniline alone, while the presence of the cells was easily observed by brightfield microscopy (Supporting Information).

■ DISCUSSION

Our experiments establish compounds **1**−**13** as useful new scaffolds for reactive fluorescence quenchers, offering the convenience of conjugation via oxime or hydrazone formation. We find that dyes **2**, **4**, and **5** are less effective because of reduced quenching efficiency or poor oxime or hydrazone formation with DNA. However, dyes **1**, **3**, and **7**−**13** offer excellent properties as quenchers of fluorescein. Dye **3** also provides a new chromophore based on the dabcyl scaffold that has both a red-shift in the absorption maximum and an increase in extinction coefficient relative to the parent dye. Surprisingly, even the carboxylic acid derivative of this dye was apparently unknown in the literature. Incorporation of the methoxy group in the dimethylaniline ring of **3** provides for a moderate red-shift while also increasing the extinction coefficient for the dye in both methanol and on the DNA adducts. As quenching efficiency is slightly increased as well, this may be a desirable dabcyl derivative with improved spectral properties for quenching fluorescein and other dyes emitting in the same region.

To our knowledge, dyes **1** through **13** represent the first examples of aldehyde, ketone, aminooxy, or hydrazine based fluorescence quenchers that can be utilized for hydrazone formation with a molecule of interest. Significantly, the formation of the hydrazone results in a red-shift in the absorption of the dyes, and oxime or hydrazone formation also increases the extinction coefficients of the dye when conjugated to DNA. This is also the case for dyes **1**−**5**; for example, dye **1** shows a lower extinction coefficient than **4** in methanol, but clearly has a higher extinction coefficient when attached to DNA as a hydrazone or oxime. These results show the beneficial direct electronic interactions that occur upon formation of the dye oxime or hydrazone adducts.

This quencher conjugation approach offers clear advantages of mild reaction conditions, rapid reaction, and bioorthogonality of hydrazone formation. Standard postsynthetic labeling of amines with quenchers or other chromophores typically requires many hours to days of reaction and use of organic cosolvents to dissolve activated chromophores (typically NHS esters). In contrast, formation of the DNA hydrazone of 4-nitrophenylhydrazine (for example) proceeded rapidly in purely aqueous buffer without even the need for catalysis at pH 4.5, reaching 87% yield in less than 4 h. Addition of aniline as catalyst provided formation of either oximes or hydrazones in as little as 5 min.

The mild, rapid, and selective reaction may have utility beyond simple formation of biomolecular conjugates. For example, experiments in which a fluorescence signal needs to be removed prior to measuring a new signal had previously required photobleaching techniques which may damage cells or other analytes present.[46−49] The present experiments suggest a milder approach; rapid attachment of a quencher via bioorthogonal hydrazone or oxime formation might simplify such experiments and avoid high-intensity light exposure. In our preliminary experiments, aminooxy and hydrazine quenchers were shown to efficiently quench an aldehyde fluorophore in a cellular environment. Interestingly, this cellular quenching did not show the need for high amounts of aniline

catalysis to quickly attain significant fluorescence quenching at approximately neutral pH inside the cells. Future experiments will explore the generality and applications of this approach.

■ ASSOCIATED CONTENT

Supporting Information

NMR spectra of quencher dyes and intermediates, HPLC purity and MALDI-TOF of DNA strands, and additional spectral data. This material is available free of charge via the Internet at http://pubs.acs.org.

■ AUTHOR INFORMATION

Corresponding Author

*E-mail: kool@stanford.edu. Tel.: 650-724-4741. Fax: 650-725-0295.

Notes

The authors declare no competing financial interest.

■ ACKNOWLEDGMENTS

This work was supported by the National Institutes of Health (GM068122 and GM067201).

■ REFERENCES

(1) Kolpashchikov, D. M. (2010) Binary probes for nucleic acid analysis. *Chem. Rev. 110* (8), 4709−4723.
(2) Liu, J., Cao, Z., and Lu, Y. (2009) Functional nucleic acid sensors. *Chem. Rev. 109* (5), 1948−1998.
(3) Kobayashi, H., Ogawa, K., Alford, R., Choyke, P. L., and Urano, Y. (2010) New strategies for fluorescent probe design in medical diagnostic imaging. *Chem. Rev. 110* (5), 2620−2640.
(4) Tyagi, S., and Kramer, F. R. (1996) Molecular beacons: probes that fluoresce upon hybridization. *Nat. Biotechnol. 14* (3), 303−308.
(5) Franzini, R. M., and Kool, E. T. (2009) Efficient nucleic acid detection by templated reductive quencher release. *J. Am. Chem. Soc. 131* (44), 16021−16023.
(6) Nakayama, S., Yan, L., and Sintim, H .O. (2008) Junction probes − sequence specific detection of nucleic acids via template enhanced hybridization processes. *J. Am. Chem. Soc. 130* (38), 12560−12561.
(7) Li, J., Wang, F., Mamon, H., Kulke, M. H., Harris, L., Maher, E., Wang., L., and Makrigiorgos, G. M. (2006) Antiprimer quenching-based real-time PCR and its application to the analysis of clinical cancer samples. *Clin. Chem. 52* (4), 624−633.
(8) Peng, X., Chen, H., Draney, D. R., Volcheck, W., Schutz-Geschwender, A., and Olive, D. M. (2009) A nonfluorescent, broad-range quencher dye for Förster resonance energy transfer assays. *Anal. Biochem. 388*, 220−228.
(9) Blum, G., Mullins, S. R., Keren, K., Fonovic, M., Jedeszko, C., Rice, M. J., Sloane, B. F., and Bogyo, M. (2005) Dynamic imaging of protease activity with fluorescently quenched activity-based probes. *Nat. Chem. Biol. 1* (4), 203−209.
(10) Tung, C. (2004) Fluorescent peptide probes for in vivo diagnostic imaging. *Pept. Sci. 76* (5), 391−403.
(11) Tyagi, S., Bratu, D. P., and Kramer, F. R. (1998) Multicolor molecular beacons for allele discrimination. *Nat. Biotechnol. 16*, 49−53.
(12) Johansson, M. K., Fidder, H., Dick, D., and Cook, R. M. (2002) Intramolecular dimers: a new strategy to fluorescence quenching in dual-labeled oligonucleotide probes. *J. Am. Chem. Soc. 124* (24), 6950−6956.
(13) Lakowicz, J. R. (1999) *Principles of Fluorescence Spectroscopy*, Kluwer Academic/Plenum Publishers, New York.
(14) Bernacchi, S., and Mely, Y. (2001) Exciton interaction in molecular beacons: a sensitive sensor for short range modifications of the nucleic acid structure. *Nucleic Acids Res. 29*, e62.
(15) Marras, S. A. E., Kramer, F. R., and Tyagi, S. (2002) Efficiencies of fluorescence resonance energy transfer and contact-mediated quenching in oligonucleotide probes. *Nucleic Acids Res. 30*, e122.
(16) Johansson, M. K. (2006) Choosing reporter-quencher pairs for efficient quenching through formation of intramolecular dimers. In *Methods of Molecular Biology*, Vol 335, Fluorescent Energy Transfer Nucleic Acid Probes: Designs and Protocols, Didenko, V. V., Ed., Humana Press Inc., Totowa, NJ.
(17) Cook, R. M., Lyttle, M., and Dick, D. Dark quenchers for donor-acceptor energy transfer. U.S. Patent 7,019,129, March 28, 2006.
(18) Haugland, R. P., Singer, V. L., and Yue, S. L. Xanthene dyes and their application as luminescence quenching compounds. U.S. Patent 6,399,392, March 4, 2002.
(19) Berry, D. A., and Pearson, W. H. Dark quenchers, probes and other conjugates incorporating the same, and their use. U.S. Patent 7,879,986, February 3, 2006.
(20) Kopecky, K., Novakova, V., Miletin, M., Kučera, R., and Zimcik, P. (2010) Solid-phase synthesis of azaphthalocyanine-oligonucleotide conjugates and their evaluation as new dark quenchers of fluorescence. *Bioconjugate Chem. 21*, 1872−1879.
(21) Kopecky, K., Novakova, V., Miletin, M., Kučera, R., and Zimcik, P. (2011) Synthesis of new azaphthalocyanine dark quencher and evaluation of its quenching efficiency with different fluorophores. *Tetrahedron 67*, 5956−5963.
(22) Pham, W., Weissleder, R., and Tung., C. H. (2002) An azulene dimer as a near-infrared quencher. *Angew. Chem., Int. Ed. Engl. 41* (19), 3659−3662.
(23) Crisalli, P., and Kool, E. T. (2011) Multi-path quenchers: efficient quenching of common fluorophores. *Bioconjugate Chem. 22* (11), 2345−2354.
(24) Dirksen, A., Hackeng, T. M., and Dawson, P. E. (2006) Nucleophilic catalysis of oxime ligation. *Angew Chem., Int. Ed. 45* (45), 7581−7584.
(25) Dirksen, A., and Dawson, P. E. (2008) Rapid oxime and hydrazone ligations with aromatic aldehydes for biomolecular labeling. *Bioconjugate Chem. 19* (12), 2543−2548.
(26) Dirksen, A., Yegneswaran, S., and Dawson, P. E. (2010) Bisaryl hydrazones as exchangeable biocompatible linkers. *Angew. Chem., Int. Ed. 49* (11), 2023−2027.
(27) Key, J. A., Li, C., and Cairo, C. W. (2012) Detection of cellular sialic acid content using nitrobenzoxadiazole carbonyl-reactive chromophores. *Bioconjugate Chem. 23* (3), 363−371.
(28) Dilek, O., and Bane, S. L. (2011) Synthesis and spectroscopic characterization of fluorescent boron dipyrromethane-derived hydrazones. *J. Fluoresc. 21*, 347−354.
(29) Dilek, O., and Bane, S. L. (2008) Synthesis of boron dipyrromethane fluorescent probes for bioorthogonal labeling. *Tetrahedron Lett. 49* (8), 1413−1416.
(30) Mori, Y., Niwa, T., and Toyoshi, K. (1981) Carcinogenic azo dyes XVIII: Synthesis of azo dyes related to 3′-hydroxymethyl-4-(dimethylamino)azobenzene, a new potent hepatocarcinogen. *Chem. Pharm. Bull. 29* (5), 1439−1442.
(31) Muramoto, K., Gotto, R., and Kamiya, H. (1987) Analysis of reducing sugars as their chromophoric hydrazones by high-performance liquid chromatography. *Anal. Biochem. 162* (2), 435−442.
(32) Raddatz, S., Mueller-Ibeler, J., Kluge, J., Wäβ, L., Burdinski, G., Havens, J. R., Onofrey, T. J., Wang, D., and Schweitzer, M. (2002) Hydrazide oligonucleotides: new chemical modification for chip array attachment and conjugation. *Nucleic Acids Res. 30* (21), 4793−4802.
(33) Xu, Y., Suzuki, Y., Lönnberg, T., and Komiyama, M. (2009) Human telomeric DNA sequence-specific cleaving by G-quadruplex formation. *J. Am. Chem. Soc. 131* (8), 2871−2874.
(34) Lönnberg, T., Suzuki, Y., and Komiyama, M. (2008) Prompt site-selective DNA hydrolysis by Ce(IV)-EDTA using oligonucleotide multiphosphonate conjugates. *Org. Biomol. Chem. 6* (19), 3580−3587.
(35) Kisseljova, K., Tsubrik, O., Sillard, R., Mäeorg, S., and Mäeorg, U. (2006) Addition of arylboronic acids to symmetrical and unsymmetrical azo compounds. *Org. Lett. 8* (1), 43−45.
(36) Blackburn, O. A., Coe, B. J., and Helliwell, M. (2011) Tetrapalladium(II) bisazobenzene and azoazoxybenzene complexes: synthesis, electronic structures, and optical properties. *Organometallics 30* (18), 4910−4923.

(37) Li, S., Bowerman, D., Marthandan, N., Klyza, S., Luebke, K. J., Garner, H. R., and Kodadek, T. (2004) Photolithiographic synthesis of peptoides. *J. Am. Chem. Soc. 126* (13), 4088−4089.
(38) Schwartz, D. A., Abrams, M. J., Hauser, M. M., Gaul, F. E., Larsen, S. K., Rauh, D., and Zubieta, J. A. (1991) Preparation of hydrazino-modified proteins and their use for the synthesis of ^{99m}Tc-protein conjugates. *Bioconjugate Chem. 2*, 333−336.
(39) Mezo, G., Szabó, I., Kertész, I., Hegedüs, R., Orbán, E., Leurs, U., Bösze, S., Halmos, G., and Manea, M. (2011) Efficient synthesis of an (aminooxy) acetylated-somatostatin derivative using (aminooxy)-acetic acid as a 'carbonyl capture' reagent. *J. Pept. Sci. 17* (1), 39−46.
(40) Jencks, W. P. (1959) Studies on the mechanism of oxime and semicarbazone formation. *J. Am. Chem. Soc. 81* (2), 475−481.
(41) More O'Ferrall, R. A., O'Brien, D. M., and Murphy, D. G. (2000) Rate and equilibrium constants for formation and hydrolysis of 9-formylfluorene oxime: diffusion-controlled trapping of a protonated aldehyde by hydroxylamine. *Can. J. Chem. 78*, 1594−1612.
(42) Ray, D., and Bharadwaj, P. K. (2008) A coumarin-derived fluorescence probe selective for magnesium. *Inorg. Chem. 47*, 2252−2254.
(43) Huang, L., Cheng, J., Xie, K., Xi, P., Hou, F., Li, Z., Xie, G., Shi, Y., Liu, H., Bai, D., and Zeng, Z. (2011) Cu^{2+}-selective fluorescent chemosensor based on coumarin and its application in bioimaging. *Dalton Trans. 40*, 10815−10817.
(44) Ko, K. C., Wu, J.-S., Kim, H. J., Kown, P. S., Kim, J. W., Bartsch, R. A., Lee, J. Y., and Kim, J. S. (2011) Rationally designed fluorescence 'turn-on' sensor for Cu^2. *Chem. Commun. 47*, 3165−3167.
(45) Wu, J., Sheng, R., Liu, W., Wang, P., Ma, J., Zhong, H., and Zhuang, J. (2011) Reversible fluorescent probe for highly selective and sensitive detection of mercapto biomolecules. *Inorg. Chem. 50*, 6543−6551.
(46) Borejdo, J., Muthu, P., Talent, J., Gryczynski, Z., Calander, N., Akopova, I., Shtoyko, T., and Gryczynski, I. (2008) Reduction of photobleaching and photodamage in single molecule detection: observing single actin monomer in skeletal myofibrils. *J. Biomed. Optics 13* (3), 034021.
(47) Lepock, J. R., Thompson, J. E., Kruuv, J., and Wallach, D. F. H. (1978) Photoinduced crosslinking of membrane proteins by fluorescein isothiocyanate. *Biochem. Biophys. Res. Commun. 85*, 344−350.
(48) Bloom, J. A., and Webb, W. W. (1984) Photodamage to intact erythrocyte membranes at high laser intensities: methods of assay and suppression. *J. Histochem. Cytochem. 32*, 608−616.
(49) Wolf, D. E., Edidin, M., and Dragsten, P. R. (1980) Effect of bleaching light on measurements of lateral diffusion in cell membranes by the fluorescence photobleaching recovery method. *Proc. Natl. Acad. Sci. U.S.A. 77*, 2043−2045.

Bioconjugate Chemistry

Technical Note

pubs.acs.org/bc

Solid-Supported NOTA and DOTA Chelators Useful for the Synthesis of 3′-Radiometalated Oligonucleotides

Anu Kiviniemi,[†] Joonas Mäkelä,[†] Jussi Mäkilä,[§] Tiina Saanijoki,[‡] Heidi Liljenbäck,[‡] Päivi Poijärvi-Virta,[†] Harri Lönnberg,[†] Tiina Laitala-Leinonen,[§] Anne Roivainen,[‡,∥] and Pasi Virta*,[†]

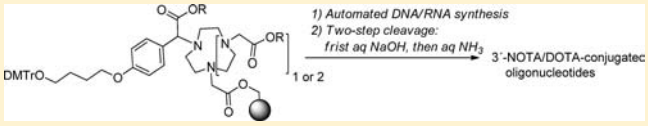
[†]Department of Chemistry, University of Turku, FI-20014 Turku, Finland

[§]Skeletal Biology Consortium, Department of Cell Biology and Anatomy, and [∥]Turku Center for Disease Modelling, University of Turku, FI-20520 Turku, Finland

[‡]Turku PET Centre, University of Turku and Turku University Hospital, FI-20521 Turku, Finland

Supporting Information

ABSTRACT: Esterified precursors of 1,4,7,10-tetraazacyclododecane-1,4,7,10-tetraacetic acid (DOTA; **18**) and 1,4,7-triazacyclononane-1,4,7-trisacetic acid (NOTA; **17**,**19**) ligands bearing a dimethoxytritylated hydroxyl side arm were prepared and immobilized via an ester linkage to long chain alkyl amine derivatized controlled pore glass (LCAA-CPG). Oligonucleotide chains were then assembled on the hydroxyl function and conjugates were released and deprotected by a two-step cleavage with aqueous alkali and ammonia. The 3′-DOTA and 3′-NOTA conjugated oligonucleotides were converted to ^{68}Ga chelates by a brief treatment with [^{68}Ga]Cl_3 at elevated temperature. Applicability of the conjugates for *in vivo* imaging with positron emission tomography (PET) was verified.



INTRODUCTION

Imaging by PET is an emerging technique for quantitative visualization of molecular binding *in vivo*.[1−3] The positron emitter may be introduced into the biomolecule of interest either covalently (e.g., ^{11}C, ^{18}F, ^{76}Br, ^{124}I) or by binding an appropriate radiometal (e.g., ^{89}Zr, ^{68}Ga, ^{64}Cu, ^{86}Y) to a chelating structure.[1−3] The latter approach usually involves two postsynthetic steps. An appropriate ligand precursor is first attached to the biomolecule, and then, the resulting conjugate is complexed with the radiometal. Sometimes this is carried out in reverse order, i.e., a prefabricated radiometal chelate is used for the conjugation.[4] The most extensively adopted precursors for the conjugation are *O*-succinimidyl ester and isothiocyanate derivatives of the complexing ligands [DOTA, NOTA, EDTA (ethylenediaminetetraacetic acid), DTPA (diethylenetriaminepentaacetic acid), and so forth],[2] which may be coupled to primary amino groups that naturally exist or may be synthetically introduced into the biomolecule. Excess of such reagents is needed to drive the reaction to completion. Although the conjugation itself may be carried out in a high yield, chromatographic behavior of the desired product may be difficult, owing to an insufficient difference in the chromatographic behavior between the conjugate and the parent biomolecule. This is the main shortcoming of the post synthetic bifunctional chelator (BFC) approach, in which the homogeneity of the isolated product may be way off the mark. The post synthetic conjugation is the only option for biologically produced biomolecules, but not necessary for synthetic peptides or oligonucleotides,[5−7] since a solid-phase conjugation may be applied as an integral part of the chain assembly. For example, DOTA has been coupled as tri-*tert*-butyl or triallyl esters to the amino terminus or ε-amino group of lysine residue in the Fmoc-based solid-phase peptide synthesis,[8−10] and a DOTA-derived phosphoramidite building block has been incorporated into an oligonucleotide chain in standard oligonucleotide synthesis.[11] Our interest is to conjugate other biomolecules to oligonucleotides[12−17] and to study their biodistribution *in vivo* by PET imaging. In many cases, the 5′-terminus of the oligonucleotide chain bears the desired biomolecule, and hence, the chelator should be introduced in the 3′-terminus. Construction of such biomolecular conjugates is not trivial and preliminary attempts to radiolabel them by post synthetic BFC approach have proven inefficient. The present study describes an efficient solid-supported technique for the introduction of 3′-terminal NOTA/DOTA-chelators, leaving the 5′-OH for further conjugation. Appropriate NOTA and DOTA precursors were immobilized to long chain alkyl amine derivatized controlled pore glass (LCAA-CPG) and automatic oligonucleotide chain elongation on these supports was carried out. A two-step cleavage (first 0.1 mol L^{-1} aq NaOH, then ammonolysis) released the desired 3′-NOTA and 3′-DOTA conjugated oligonucleotides. Apart from the synthesis of these universal supports, no profound synthetic skill is required. 3′-NOTA/DOTA-conjugated dT_6 and 2′-*O*-methyl oligoribonucleotide 5′-UGU AAA CCA UGA UGU GCU GCU A-3′(anti-miR15b) were synthesized. These conjugates were radiolabeled with

Received: May 14, 2012
Revised: July 2, 2012
Published: August 8, 2012

 © 2012 American Chemical Society

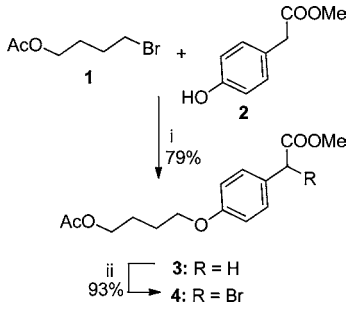
^{68}Ga and their applicability to *in vivo* imaging by PET was verified.

EXPERIMENTAL PROCEDURES

General Remarks. The NMR spectra were recorded at 500 MHz. The chemical shifts are given in ppm from internal TMS. The mass spectra were recorded using an ESI ionization method. RP HPLC analysis and purification of the oligonucleotide conjugates **20**–**25** were performed using a Thermo ODS Hypersil C18 (150 × 4.6 mm, 5 μm) analytical column with a gradient elution between 0.1 mol L^{-1} triethylammonium acetate in H_2O (A) and 0.1 mol L^{-1} triethylammonium acetate in 50% aqueous acetonitrile (B), flow rate 1.0 mL min^{-1}, λ = 260 nm. For radio-HPLC analyses, LaChrom Instruments (Hitachi; Merck, Darmstadt, Germany) with a Radiomatic 150TR radioisotope detector (Packard, Meriden, CT, USA) and a Jupiter C18 column (300 Å, 5 μm, 4.6 × 150 mm; Phenomenex, Torrance, CA, USA) with a gradient elution between 0.1 mol L^{-1} triethylammonium acetate in H_2O (A) and acetonitrile (C), flow rate 1.0 mL min^{-1}, λ = 260 nm were used. ^{68}Ga was obtained in the form of [^{68}Ga]Cl_3 from a ^{68}Ge/^{68}Ga generator (Eckert & Ziegler, California, USA). Among the compounds prepared, **4**, **7**–**11**, **13**–**19**, and their oligonucleotide conjugates are racemic mixtures. Resolution to enantiopure forms was not attempted.

Methyl 2-[4-(4-Acetoxybutoxy)phenyl]acetate (3). A mixture of methyl 4-hydroxyphenylacetate **2** (1.0 g, 6.0 mmol), 4-bromobutyl acetate **1** (1.2 mL, 7.8 mmol), and K_2CO_3 (0.83 g, 6.0 mmol) in DMF (5.0 mL) was stirred for 3 h at 100 °C and cooled down to room temperature (Scheme 1). Ice–water

Scheme 1[a]



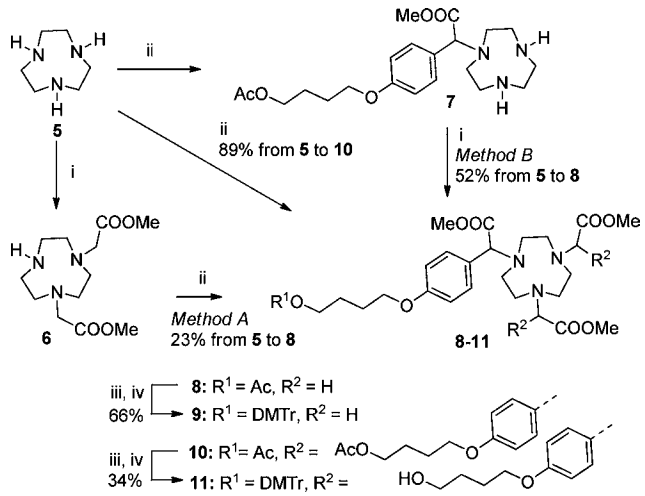
[a]Reagents and conditions: (i) K_2CO_3, DMF, 100 °C; (ii) 1,1′-azobis(cyclohexanecarbonitrile), NBS, CCl_4.

(50 mL) was added to the mixture and the product was extracted with diethyl ether (3 × 50 mL). The organic fractions were combined, washed with saturated $NaHCO_3$ and brine, dried with Na_2SO_4, filtered, and evaporated to dryness. The residue was purified by silica gel chromatography (1. EtOAc/petroleum ether, 4:6 v/v; 2. MeOH/CH_2Cl_2, 5:95, v/v) to yield 1.3 g (79%) of the product **3** as colorless oil. ^{1}H NMR (500 MHz, $CDCl_3$) δ 7.19 (d, 2H, J = 10.7 Hz), 6.85 (d, 2H, J = 10.8 Hz), 4.14 (t, 2H, J = 7.7 Hz), 3.98 (t, 2H, J = 7.3 Hz), 3.69 (s, 3H), 3.57 (s, 2H), 2.05 (s, 3H), 1.88–1.78 (m, 4H); ^{13}C NMR (125 MHz, $CDCl_3$) δ 172.5, 171.3, 130.3, 126.0, 114.4, 67.1, 64.2, 52.1, 40.3, 25.8, 25.4, 21.1; HRMS(ESI): [M+Na]$^+$ requires 303.1208, found 303.1195.

Methyl 2-[4-(4-Acetoxybutoxy)phenyl]-2-bromoacetate (4). Compound **3** (1.0 g, 2.8 mmol), *N*-bromosuccinimide (0.70 g, 3.1 mmol), and 1,1′-azobis(cyclohexanecarbonitrile) (44 mg, 0.14 mmol) in CCl_4 (20 mL) was refluxed for 5 h under nitrogen. Petroleum ether (20 mL) was added to the mixture, the resulted precipitate was filtered off, and the filtrate was evaporated to dryness. The residue was purified by silica gel chromatography (EtOAc/petroleum ether, 3:7, v/v) to yield 1.2 g (93%) of the product as colorless oil. ^{1}H NMR (500 MHz, $CDCl_3$) δ 7.48 (d, 2H, J = 6.8 Hz), 6.87 (d, 2H, J = 6.8 Hz), 5.36 (s, 1H), 4.14 (t, 2H, J = 6.3 Hz), 4.00 (t, 2H, J = 5.8 Hz), 3.79 (s, 3H), 2.06 (s, 3H), 1.88–1.81 (m, 4H); ^{13}C NMR (125 MHz, $CDCl_3$) δ 171.1, 168.9, 130.1, 127.7, 114.7, 67.4, 64.0, 53.3, 46.5, 25.8, 25.4, 21.0; HRMS (ESI): [M+Na]$^+$ requires 381.0314, found 381.0364.

Dimethyl 7-{1-[4-(4-Acetoxybutoxy)phenyl]-2-methoxy-2-oxoethyl}-1,4,7-triazacyclononane-1,4-diyl)-diacetate (8). *Method A*: Methyl 2-bromoacetate (0.38 mL, 4.0 mmol) was slowly added (during a period of 3 h) to a refluxing mixture of 1,4,7-triazacyclononane (**5**, 0.25 g, 1.9 mmol) and triethylamine (0.56 mL, 4.0 mmol) in methanol (2.0 mL) (Scheme 2). The mixture was refluxed for additional

Scheme 2[a]



[a]Reagents and conditions: (i) Methyl 2-bromoacetate, Et_3N, MeOH; (ii) **4**, Et_3N, MeCN; (iii) 0.1 mol L^{-1} NaOMe in MeOH; (iv) DMTrCl, pyridine.

4 h and evaporated to dryness.[18] The residue, triethylamine (0.29 mL, 2.1 mmol), and compound **4** (1.0 g, 2.9 mmol) were dissolved in acetonitrile (2.0 mL) and the mixture was stirred for 2 h at room temperature. Dichloromethane (80 mL) was added and the mixture was washed with saturated $NaHCO_3$ and brine. The organic layer was separated, dried over Na_2SO_4, filtered, and evaporated to dryness. The residue was purified by silica gel chromatography (Et_3N/MeOH/CH_2Cl_2, 1:5:94, v/v/v, twice) to yield 0.24 g (23%) of the product (**8**) as yellowish oil. *Method B*: A mixture of compound **4** (0.56 g, 1.6 mmol) in acetonitrile (0.50 mL) was slowly added to a mixture of 1,4,7-triazacyclononane (**5**, 0.20 g, 1.6 mmol) in methanol (0.50 mL). The mixture was stirred overnight at room temperature, and then triethylamine (0.86 mL, 6.4 mmol), methanol (0.50 mL), and methyl 2-bromoacetate (0.59 mL, 6.4 mmol) were added. The mixture was stirred overnight at ambient temperature, dissolved in dichloromethane, and washed with saturated $NaHCO_3$ and brine. The organic layer was separated, dried over Na_2SO_4, filtered, and evaporated to dryness. The residue was purified by silica gel chromatography (Et_3N/MeOH/

dx.doi.org/10.1021/bc300253t | *Bioconjugate Chem.* 2012, 23, 1981–1988

CH_2Cl_2, 1:5:94, v/v/v, twice) to yield 0.45 g (52%) of the product (**8**) as yellowish oil. ^{1}H NMR (500 MHz, $CDCl_3$) δ 7.27 (d, 2H, J = 8.6 Hz), 6.83 (d, 2H, J = 8.7 Hz), 4.50 (b, 1H), 4.13 (t, 2H, J = 6.0 Hz), 3.97 (t, 2H, J = 5.7 Hz), 3.70 (s, 3H), 3.67 (s, 6H), 3.40 (b, 4H), 3.01 (d, 2H, J = 11.3 Hz), 2.87 (d, 2H, J = 11.5 Hz), 2.84−2.79 (m, 8H), 2.04 (s, 3H), 1.86−1.78 (m, 4H); ^{13}C NMR (125 MHz, $CDCl_3$) δ 173.3, 172.5, 171.1, 130.1, 129.4, 116.4, 114.3, 71.4, 67.2, 64.1, 58.4, 55.3, 55.1, 53.2, 51.5, 51.3, 25.9, 25.4, 21.0; HRMS(ESI): $[M+H]^+$ requires 552.2921, found 552.2918.

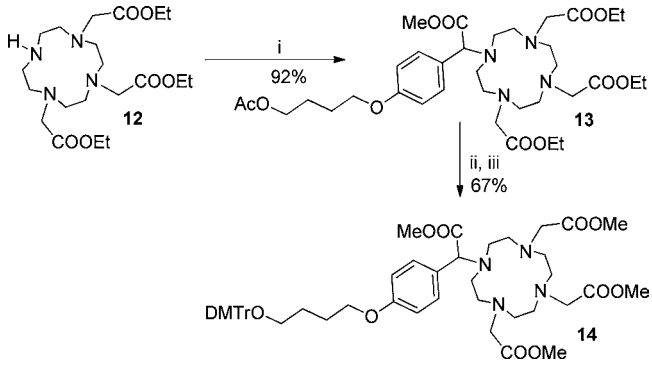
Dimethyl [7-(1-{4-[4-(4,4′-Dimethoxytrityloxy)-butoxy]phenyl}-2-methoxy-2-oxoethyl)-1,4,7-triazacyclononane-1,4-diyl]diacetate (9). Compound **8** (0.24 g, 0.44 mmol) was dissolved in 0.1 mol L^{-1} NaOMe/MeOH solution (4.0 mL) and the mixture stirred for 3 h at ambient temperature. Completion of acetyl removal was verified by MS(ESI). The mixture was neutralized by addition of pyridinium hydrochloride (50 mg, 0.43 mmol), stirred for 30 min, and evaporated to dryness. The residue was coevaporated with dry pyridine and dissolved in the same solvent (2.0 mL). 4,4′-Dimethoxytrityl chloride (0.22 g, 0.65 mmol) was added to the mixture and the reaction was stirred overnight at ambient temperature. Dichloromethane (100 mL) was added and the mixture was washed with saturated $NaHCO_3$ and brine. The organic layer was separated, dried over Na_2SO_4, filtered, and evaporated to dryness. The residue was purified by silica gel chromatography (Et_3N/MeOH/CH_2Cl_2, 1:5:94, v/v/v) to yield 0.23 g (66%) of the product **9** as yellowish oil. ^{1}H NMR (500 MHz, $CDCl_3$) δ 7.47 (m, 2H), 7.37−7.34 (m, 4H), 7.32−7.27 (m, 4H), 7.23−7.19 (m, 2H), 6.86−6.82 (m, 6H), 4.53 (b, 1H), 3.94 (t, 2H, J = 6.4 Hz), 3.80 (s, 6H), 3.73 (s, 3H), 3.69 (s, 6H), 3.42 (b, 4H), 3.15 (t, 2H, J = 6.3 Hz), 3.04 (d, 2H, J = 11.2 Hz), 2.89 (d, 2H, J = 11.3 Hz), 2.88−2.81 (m, 8H), 1.91 (m, 2H), 1.80 (m, 2H); ^{13}C NMR (125 MHz, $CDCl_3$) δ 173.4, 172.5, 158.8, 158.4, 145.3, 136.6, 130.2, 129.9, 129.2, 128.2, 127.7, 126.6, 116.4, 114.3, 112.8, 85.8, 71.5, 67.8, 62.9, 58.4, 55.4, 55.2, 55.0, 53.2, 51.5, 51.3, 26.7, 26.3; HRMS(ESI): $[M+H]^+$ requires 812.4122, found 812.4087.

Trimethyl (1,4,7-Triazacyclononane-1,4,7-triyl)tris{2-[4-(4-acetoxybutoxy)phenyl]acetate} (10). A mixture of **4** (1.1 g, 3.2 mmol) in acetonitrile (0.50 mL) was slowly added to a mixture of 1,4,7-triazacyclononane (0.10 g, 0.77 mmol) and Et_3N (0.32 mL, 2.3 mmol) in methanol (1.0 mL). The reaction was stirred overnight at ambient temperature, dichloromethane (30 mL) was added, and the mixture was washed with saturated $NaHCO_3$ and brine. The organic layer was separated, dried over Na_2SO_4, filtered, and evaporated to dryness. The residue was purified by silica gel chromatography (Et_3N/MeOH/CH_2Cl_2, 0.5:2.5:97, v/v/v) to yield 0.67 g (89%) of the product as colorless oil. ^{1}H NMR (500 MHz, $CDCl_3$) δ 7.27 and 7.21 (d and d, 6H, J = 8.6 Hz both), 6.86 and 6.83 (d and d, 6H, J = 8.8 and 8.7 Hz), 4.42 and 4.40 (s and s, 3H), 4.16 (t, 6H, J = 6.2 Hz), 3.99 (t, 3H, J = 6.0 Hz), 3.69 and 3.68 (s and s, 9H), 2.94−2.85 (m, 6H), 2.71−2.66 (m, 6H), 2.07 (s, 9H), 1.91−1.84 (m, 12H); ^{13}C NMR (125 MHz, $CDCl_3$) δ 173.5, 171.2, 158.5, 130.2, 129.4, 114.2, 71.3, 67.2, 64.1, 52.9, 52.7, 51.5, 25.9, 25.4, 21.0; HRMS(ESI): $[M+H]^+$ requires 964.4807, found 964.4813.

Dimethyl [7-(1-{4-[4-(4,4′-Dimethoxytrityloxy)-butoxy]phenyl}-2-methoxy-2-oxoethyl)-1,4,7-triazacyclononane-1,4-diyl]bis{2-[4-(4-hydroxybutoxy)phenyl]-acetate} (11). Compound **10** (0.67 g, 0.68 mmol) was dissolved in 0.1 mol L^{-1} NaOMe/MeOH solution (6.0 mL) and the mixture was stirred overnight at ambient temperature. The mixture was neutralized by addition of pyridinium hydrochloride (75 mg, 0.65 mmol), stirred for additional 30 min, and evaporated to dryness. The residue was coevaporated with dry pyridine and dissolved in the same solvent (2.0 mL). A mixture of 4,4′-dimethoxytritylchloride (0.23 g, 0.68 mmol) in dry pyridine (0.5 mL) was slowly added and the mixture was stirred for overnight. Dichloromethane (100 mL) was added and the mixture was washed with saturated $NaHCO_3$ and brine. The organic layer was separated, dried over Na_2SO_4, filtered, and evaporated to dryness. The residue was purified by silica gel chromatography (Et_3N/MeOH/CH_2Cl_2, 1:5:94, v/v/v, twice) to yield 0.27 g (34%) of the product **11** as yellowish oil. ^{1}H NMR (500 MHz, $CDCl_3$) δ 7.46 (m, 2H), 7.35 (m, 4H), 7.30−7.25 (m, 3H), 7.23−7.18 (m, 6H), 6.87−6.80 (m, 10H), 4.42−4.38 (m, 3H), 3.99 (t, 4H, J = 6.1 Hz), 3.93 (t, 2H, J = 5.9 Hz), 3.78 (s, 6H), 3.71−3.67 (m, 13H), 3.15 (t, 2H, J = 5.9 Hz), 2.98−2.80 (m, 6H), 2.78−2.62 (m, 6H), 1.92−1.83 (m, 6H), 1.83−1.72 (m, 6H); ^{13}C NMR (125 MHz, $CDCl_3$) δ 173.4, 158.7, 158.6, 158.3, 145.3, 136.6, 129.4, 129.2, 129.4, 128.1, 127.7, 126.6, 114.3, 113.0, 85.8, 71.9, 71.4, 67.8, 62.9, 62.3, 55.2, 52.9−52.7, 51.5, 29.4, 26.7, 26.3, 25.8; HRMS(ESI): $[M+H]^+$ requires 1140.5797, found 1140.5724.

Triethyl 2,2′,2″-(10-{1-[4-(4-Acetoxybutoxy)phenyl]-2-methoxy-2-oxoethyl}-1,4,7,10-tetraazacyclododecane-1,4,7-triyl)triacetate (13). Commercially available triethyl 2,2′,2″-(1,4,7,10-tetraazacyclododecane-1,4,7,-triyl)triacetate (**12**, 0.25 g, 0.58 mmol) was dissolved in a mixture of triethylamine (163 μL) and acetonitrile (2 mL) (Scheme 3).

Scheme 3[a]



[a]Reagents and conditions: (i) **4**, Et_3N, MeCN; (ii) 0.1 mol L^{-1} NaOMe in MeOH; (iii) DMTrCl, pyridine.

Compound **4** (0.31 g, 0.86 mmol) in acetonitrile (0.5 mL) was slowly added and the reaction mixture was stirred overnight at ambient temperature. The volatiles were evaporated and the residue was dissolved in dichloromethane and washed with saturated $NaHCO_3$ and brine. The organic layer was dried over Na_2SO_4, filtered, and evaporated to dryness. The residue was purified by silica gel chromatography (MeOH/Et_3N/CH_2Cl_2, a gradient from 5:1:94 to 10:1:89, v/v/v) to yield 0.38 g (92%) of the product **1** as colorless oil. ^{1}H NMR (500 MHz, $CDCl_3$) δ 6.69 (d, 2H, J = 7.5 Hz), 6.56 (d, 2H, J = 8.5 Hz), 4.36 (s, 1H), 4.03−3.91 (m, 3H), 3.90−3.76 (m, 5H), 3.67 (t, 2H, J = 5.5 Hz), 3.40 (s, 3H), 3.34 (m, 1H), 3.22−3.11 (m, 2H), 2.86−2.45 (m, 9H), 2.34−2.25 (m, 2H), 2.15−1.99 (m, 3H), 1.95−1.79 (m, 4H), 1.70 (s, 3H), 1.57−1.39 (m, 5H), 1.01−0.94 (m, 9H); ^{13}C NMR (125 MHz, $CDCl_3$) δ 175.0, 173.8, 173.5, 173.3, 170.7, 158.6, 131.1, 116.6, 114.0, 67.1, 64.5, 63.7, 61.2,

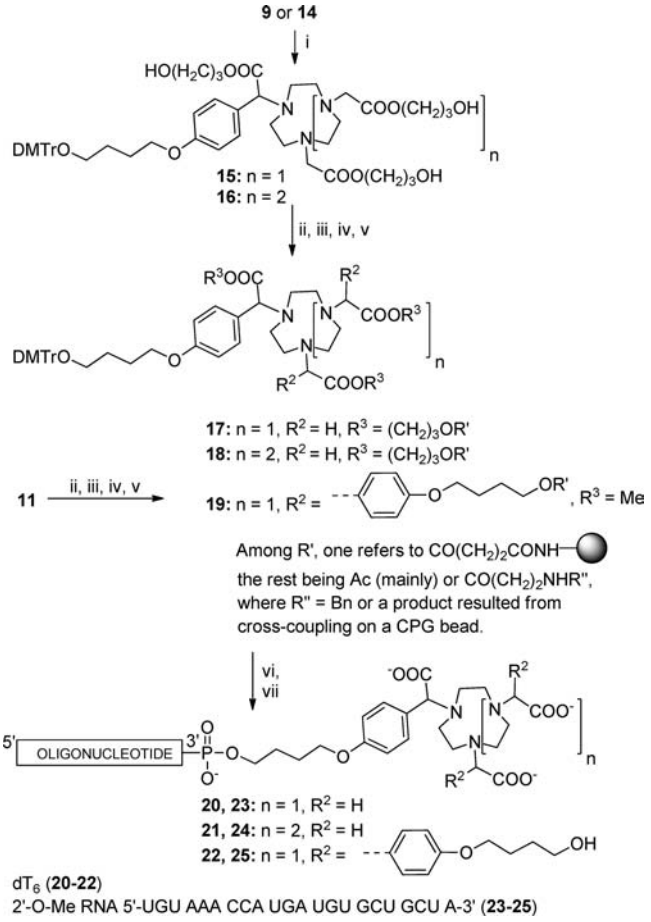
dx.doi.org/10.1021/bc300253t | Bioconjugate Chem. 2012, 23, 1981−1988

61.1, 61.1, 55.0, 54.9, 54.7, 52.6, 52.4, 52.2, 48.4, 48.0, 47.9, 44.4, 25.5, 25.0, 20.6, 13.9, 13.8, 13.8. ESI-MS: $[M+H]^+$ requires 709.4018, found 709.4019.

Triethyl 2,2′,2″-[10-(1-{4-[4-(4,4′-Dimethoxytrityloxy)-butoxy]phenyl}-2-methoxy-2-oxoethyl)-1,4,7,10-tetraazacyclododecane-1,4,7-triyl]triacetate (14). Compound **13** (0.33 g, 0.47 mmol) was dissolved in 0.1 mol L^{-1} NaOMe/MeOH solution (12 mL) and the mixture was stirred overnight at room temperature. The mixture was neutralized by addition of pyridinium chloride (0.20 g, 1.7 mmol) and the mixture was evaporated to dryness. The residue was dried by coevaporation with dry pyridine, dissolved in the same solvent (2.0 mL), and then 4,4′-dimethoxytrityl chloride (0.19 g, 0.56 mmol) was added. After overnight reaction, the mixture was concentrated to viscous, dissolved in CH_2Cl_2, and extracted with saturated $NaHCO_3$ and brine. The organic phase was dried over Na_2SO_4, filtered, and evaporated to dryness. The residue was purified by silica gel chromatography (MeOH/Et_3N/CH_2Cl_2, 10:0.5:89.5, v/v/v) to yield 0.29 g (67%) of the product **14** as a white solid. ^1H NMR (500 MHz, $CDCl_3$ + drops of CD_3OD) δ 7.47−7.42 (m, 2H), 7.37−7.30 (m, 4H), 7.30−7.25 (m, 2H), 7.20 (m, 1H), 7.00 (d, 2H, J = 7.0 Hz), 6.88 (d, 2H, J = 8.5 Hz), 6.85−6.80 (m, 4H), 4.71 (s, 1H), 3.96 (t, 2H, J = 6.3 Hz), 3.85−3.78 (m, 15H), 3.78 (s, 3H), 3.71 (m, 1H), 3.60−3.51 (m, 2H), 3.17−2.97 (m, 8H), 2.96−2.81 (m, 3H), 2.71−2.61 (m, 2H), 2.48−2.11 (m, 7H), 1.94−1.86 (m, 2H), 1.82−1.74 (m, 3H); ^{13}C NMR (125 MHz, $CDCl_3$) δ 175.4, 174.6, 174.4, 174.2, 159.1, 158.3, 145.2, 136.6, 131.3, 130.0, 128.1, 127.7, 126.6, 114.4, 113.0, 85.8, 67.8, 64.9, 62.9, 55.1, 54.9, 54.8, 52.9, 52.7, 52.6, 52.4, 52.3, 48.6, 48.2, 48.0, 44.6, 26.5, 26.2. ESI-MS: $[M+H]^+$ requires 927.4750, found 927.4743.

Preparation of Solid Supports (17−19). Compounds **9** and **14** (10 μmol) were converted to triols **15** and **16** by dissolving them to a mixture of 0.1 mol L^{-1} $NaO(CH_2)_3OH$ in 1,3-propanediol (0.50 mL) and acetonitrile (0.50 mL) ((i) in Scheme 4). The mixtures were stirred for 3 h at ambient temperature and neutralized by addition of a mixture of pyridinium chloride (20 mg, 0.17 mmol) in dry pyridine (0.1 mL). Dichloromethane (10 mL) was added and the mixtures were washed with saturated $NaHCO_3$ (5 mL × 3) and brine (5 mL). The organic layers were dried with Na_2SO_4, filtered, and evaporated to dryness. The completion of transesterification was verified by ESI(MS) in both cases. The residues of **15** and **16** and compound **11** (10 μmol) were dissolved in dry pyridine (0.50 mL) and succinanhydride (10 μmol) in dry pyridine (50 μL) and a catalytic amount of *N,N′*-dimethylaminopyridine (DMAP) were added ((ii) in Scheme 4). Mixtures were stirred overnight at ambient temperature and evaporated to dryness. According to MS(ESI) analysis, the main product in each case was monosuccinate, although di- and trisuccinates were observed. The residues were dissolved in dry DMF (0.50 mL) and suspended with LCAA-CPG support (200 mg). A mixture of HBTU [2-(1*H*-benzotriazole-1-yl)-1,1,3,3-tetramethyluronium hexafluorophosphate, 10 μmol) in dry DMF (0.50 mL) and DIEA (20 μmol) were added, the suspensions were shaken overnight at ambient temperature and the supports were then filtered, washed with DMF, CH_2Cl_2, and MeOH, and dried under vacuum ((iii) in Scheme 4). The potential unreacted carboxylic acid groups were capped by amide bond formation ((iv) in Scheme 4): Each batch of the supports was suspended in a mixture of HBTU (30 μmol), benzylamine (30 μmol), and DIEA (60 μmol) in DMF (1.0 mL); stirred overnight at ambient temperature; filtered and washed with DMF, CH_2Cl_2, and MeOH; and dried under vacuum. The unreacted hydroxyl groups of the solid-supported NOTA and DOTA ligands and the amino groups on the parent supports were then capped by acetylation ((v) in Scheme 4): Supports were suspended in a mixture of acetic anhydride, 2,6-lutidine, and *N*-methylimidazol in THF (5:5:8:82, v/v/v/v, for 15 min at 25 °C), filtered, washed with THF and CH_2Cl_2, and dried under vacuum. According to DMTr-cation assay of small support aliquots (**17−19**), loadings of 24−35 μmol g^{-1} were obtained without a marked difference between different ligands.

Scheme 4[a]



[a]Reagents and conditions: (i) $NaO(CH_2)_3OH$, 1,3-propanediol, MeCN; (ii) succinanhydride, DMAP, pyridine; (iii) LCAA-CPG, HBTU, DIEA, DMF; (iv) $BnNH_2$, HBTU, DIEA, DMF; (v) Ac_2O, 2,6-lutidine, *N*-methylimidazol, THF; (vi) standard automated oligonucleotide synthesis by the phosphoramidite chemistry; (vii) (1) 0.1 mol L^{-1} aq NaOH, (2) ammonolysis.

Synthesis of Conjugates 20−25. Columns loaded with supports **17−19** (0.5 μmol) were installed in an automated DNA/RNA synthesizer and oligodeoxyribonucleotide T_6 and 22-mer 2′-*O*-methyl oligoribonucleotide 5′-UGU AAA CCA UGA UGU GCU GCU A-3′(anti-miR15b) were assembled on each support **17−19**. Standard DNA and RNA protocols were followed using benzylthiotetrazol as an activator. According to the DMTr-cation assay, no deviations from the usual coupling yields were observed. Prior to ammonolysis of the conjugates (**20−25**), an alkaline aqueous treatment is needed to release the DOTA/NOTA moieties as carboxylates.[11] In order to optimize this base-catalyzed ester hydrolysis, solid-supported

dx.doi.org/10.1021/bc300253t | *Bioconjugate Chem.* 2012, 23, 1981−1988

conjugate **20** (8 mg sample of the support, 0.1 μmol) was first used as a test compound and subjected to various NaOH treatments (0.1 mol L^{-1} aq NaOH, 0.50 mL, 50 μmol, at 25 °C for 4 h[11] and at 55 °C for 1.5−3 h). The alkaline suspensions were neutralized by addition of 1.0 mol L^{-1} solution of ammonium chloride (50 μL, 50 μmol), and the deprotection was continued by subjecting the residues (with supports) to concentrated aqueous ammonia (overnight at 55 °C). In order to verify the importance of the aq NaOH pretreatment, ammonolysis alone was also used for the release. After ammonolysis, the crude product mixtures were subjected to RP HPLC (Figure 1) and the product peaks were characterized

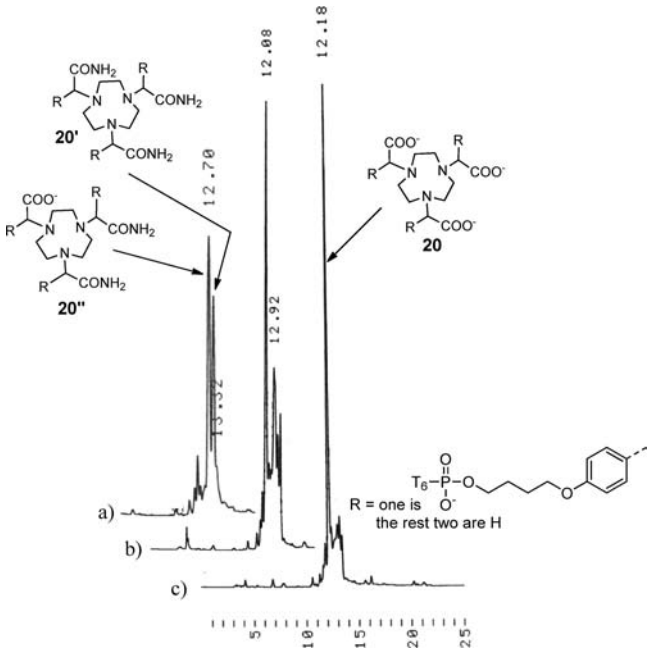


Figure 1. RP HPLC chromatograms of crude product (**20**) mixtures released from support using (a) ammonolysis overnight at 55 °C; (b) 1. 0.1 mol L^{-1} aq NaOH for 4 h at 25 °C, 2. ammonolysis overnight at 55 °C; (c) 1. 0.1 mol L^{-1} aq NaOH for 3 h at 55 °C, 2. ammonolysis overnight at 55 °C. RP HPLC conditions: from 10% to 25% MeCN in 0.1 mol L^{-1} aqueous triethylammonium acetate over 25 min, Thermo ODS Hypersil column (250 × 4.6 mm, 5 μm) at a flow rate of 1.0 mL min^{-1}.

by ESI(MS). It may be noted that monoisotopic exact mass of a carboxylate differs only 0.984 units from that of the corresponding carboxamide. They may, however, be reliably differentiated by an HRMS spectrometer using an internal mass standard and when the length of the oligonucleotide is relatively short (T_6). As seen in Figure 1a, mere ammonolysis gave a mixture in which the main components were the di and triamides (**20′**: $[(M-2H)/2]^{2-}$ requires 1143.266, found 1143.263, **20″**: $[(M-2H)/2]^{2-}$ requires 1143.758, found 1143.762). Aqueous 0.1 mol L^{-1} NaOH pretreatment at 25 °C for 4 h already gave the desired hydrolyzed conjugate **20** {$[(M-2H)]^{2-}$ requires 1144.742, found 1144.745}, but the amount of the side products was still remarkable (Figure 1b). Virtually complete ester hydrolysis took place, when the conjugate was treated with 0.1 mol L^{-1} aqueous NaOH at 55 °C for 3 h (Figure 1c). A prolonged reaction time (0.1 mol L^{-1} aq NaOH at 55 °C overnight) did not improve the yield. The two-step cleavage was similarly studied with solid supported **21** and **22**. In both cases, the same NaOH treatment (0.1 mol L^{-1} at 55 °C for 3 h) was sufficient to complete the ester hydrolysis. It is worth noting that exposure of the phosphodiester linkages and carboxylic acid groups consume a stoichiometric amount of NaOH, which should be taken account, when the length of the oligonucleotide increases. The volume of aq 0.1 mol L^{-1} NaOH should be respectively increased to compensate the effect of increased neutralization. Bearing this in mind, conjugates **23**−**25** were released following the optimized conditions and subjected to RP HPLC purification. Chromatograms of the crude products **23**−**25** are shown in Figure 2. Partial

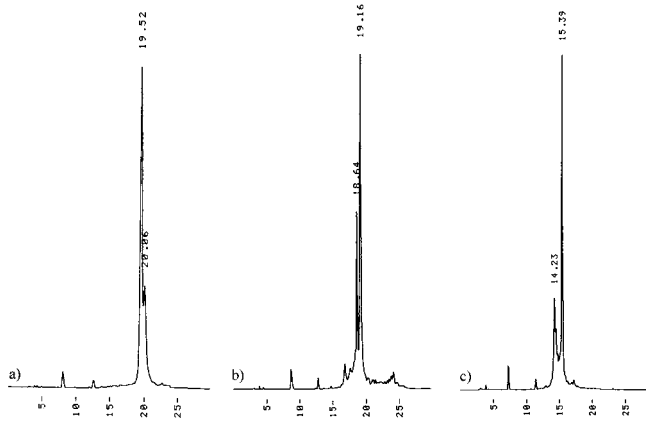


Figure 2. RP HPLC traces of crude product mixtures: (a) **23**, (b) **24**, and (c) **25**. Conditions: gradient elutions from 10% to 25% acetonitrile in 0.100 mol L^{-1} triethylammonium acetate over 25 min (a) and from 10% to 30% acetonitrile in 0.100 mol L^{-1} triethylammonium acetate over 25 min (b and c).

carboxamide formation could be observed [Figure 2a: 20.06 min (**23′**) and Figure 2c: 14.23 min (**25′**)], although the crude products [Figure 2a: 9.52 min (**23**), Figure 2b: 18.64 and 19.16 min (**24**), Figure 2c: 15.39 min (**25**)] were relatively pure. Interestingly, conjugate **24** appeared as two peaks in RP HPLC (Figure 2b: 18.64 and 19.16 min), which both gave the mass in ESI(MS) expected for the desired product. The extra peak was observed also in a chromatogram of **21**. In each product **20**−**25** mixtures, the main peak was isolated, lyophilized to dryness, and subjected to radiolabeling. The extra peaks related to **21** and **24** were discarded in spite of their potential authenticity. MS(ESI) data of the conjugates **20**−**25** are listed in Table 1.

Table 1. MS(ESI) Data of the Conjugates

conjugate	observed mass[a]	required mass
20	2291.5	2291.5
21	2619.7	2619.7
22	2392.6	2392.5
23	7837.6	7837.5
24	8165.6	8166.0
25	7937.8	7936.5

[a]Observed monoisotopic masses are calculated from $[M-nH]^{n-}$ or from $[M-nH+K]^{(n-1)-}$.

^{68}Ga Labeling of Conjugates. ^{68}Ga was obtained in the form of $[^{68}Ga]Cl_3$ from a ^{68}Ge/^{68}Ga generator (instrument details in general remarks) by elution with 0.1 mol L^{-1} HCl. Sodium acetate was then added to give a 0.4 mol L^{-1} solution with regard to sodium acetate. The pH was adjusted to 3.5 with HCl, NOTA/DOTA−conjugate (**20**−**25**, 5−12 nmol, as a 1

dx.doi.org/10.1021/bc300253t | Bioconjugate Chem. 2012, 23, 1981−1988

mM solution) was added, and the reaction mixture was incubated at 95 °C for 10−15 min. The radiochemical purity was determined by a RP radio-HPLC (see instrument details in general remarks) with gradient elutions C/A (v/v) from 10/90 to 30/70 in 13 min (**24** and **25**) and from 0/100 to 30/70 in 22 min (**20**−**23**). After each run, the column was washed by elution with 50 mmol L^{-1} aqueous phosphoric acid. An example (**24**) of radio-HPLC-chromatograms is shown in Figure 3.

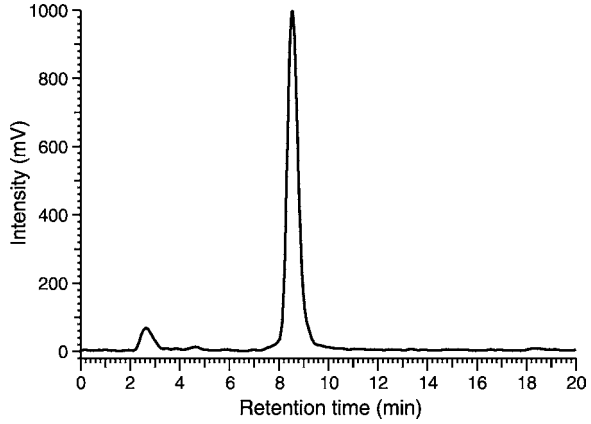


Figure 3. Example of radio-HPLC-chromatograms (^{68}Ga-DOTA-oligonucleotide **24**).

PET Imaging. The whole-body distribution of intravenously administered [^{68}Ga] chelates (17.5 ± 4.2 MBq, 4.2 ± 2.5 nmol) were evaluated in healthy Sprague−Dawley rats (n = 3−5 per tracer; weight 401 ± 99 g) using a high resolution research tomograph (Siemens Medical Solutions, Knoxville, TN, USA). Data acquired for 60 min were iteratively reconstructed with the ordered-subsets expectation maximization 3D algorithm (OSEM3D). Four additional rats (n = 1 per each tracer) were PET/computed tomography (CT) imaged by using Inveon Multimodality scanner (Siemens Medical Solutions, Knoxville, TN, USA).

RESULTS AND DISCUSSION

Synthesis of NOTA and DOTA Precursors 9, 11, and 14. 2-(4-Hydroxyphenyl)acetic acid was selected as a surrogate of one of the acetic acid ligands of NOTA and DOTA on constructing precursors for the solid-supported conjugation of these azacrown chelators. The 4-hydroxy function allowed attachment of a 4-(4,4′-dimethoxytrityloxybutyl) linker as a site for oligonucleotide chain assembly, while the original acetic acid structure is still essentially preserved. The 2-bromo derivative of this surrogate, viz., methyl 2-bromo-2-[4-(4-acetoxybutoxy)phenyl]acetate (**4**), was synthesized from commercially available methyl 2-(4-hydroxyphenyl)acetate (**2** in Scheme 1). S_N-2 displacement of the 4-bromo substituent from 4-bromobutylacetate by the phenoxide ion of **2**, followed by 1,1′-azoobis(cyclohexanecarbonitrile) initiated radical bromination gave **4** in 73% overall yield. Two methods (*Methods A and B*, in Scheme 2) were then evaluated for the selective alkylation of 1,4,7-triazanonane (**5**) to provide a precursor (**8**) for the desired chelator. In *Method A*, **5** was first carefully bisalkylated by methyl 2-bromoacetate (2.1 equiv) and the remaining secondary amine of the product (**6**)[18] was then alkylated with **4** (1.5 equiv). In *Method B*, alkylations were carried out in reverse order: **5** was first carefully reacted with 1 equiv of **4** to obtain **7** and the remaining two secondary amines were alkylated by methyl 2-bromoacetate (4.0 equiv), giving **8**. The formation of the intermediates **6** and **7** was verified by MS(ESI). In both methods, the bottleneck was purification. Although the yield by *Method A* (23%) was lower than by *Method B* (52%), the isolated product **8** was obtained in a purer form. **8** obtained by *Method B* may be used as a starting material for subsequent synthesis, but acceptably pure isolated product could not be obtained until two steps later, i.e., after introducing of the dimethoxytrityl group (**9**). Compound **8** was deacetylated by sodium methoxide catalyzed transesterification and the exposed hydroxyl group was dimethoxytritylated to give **9** in 66% yield.

For synthetic reasons, an alternative approach was applied for the synthesis of ligand precursor **11**. Problems concerning the selective methyl acetylation (*Methods A and B* above) could partially be avoided. Furthermore, this ligand precursor may be directly succinylated without any preceding transesterification step (cf. attachment of the NOTA/DOTA ligands **9** and **14** to LCAA CPG-support). Three spacers (4.0 equiv of **4**) were simultaneously introduced to **5**, which gave **10** in 89% yield. The acetyl groups were removed by sodium methoxide catalyzed transesterification as above, and then, one of the three hydroxyl groups was selectively dimethoxytritylated, giving **11** in 34% yield.

Commercially available triethyl 2,2′,2″-(1,4,7,10-tetraazacyclododecane-1,4,7-triyl)triacetate (**12**) was used as a starting material for the synthesis of DOTA precursor **14** (Scheme 3). **12** was alkylated by **4** (1.5 equiv) giving **13** in a high 92% yield and the acetyl group was replaced by dimethoxytrityl group as above to give **14** in 67% yield.

Attachment of the NOTA/DOTA-Derived Ligands to LCAA CPG-Support. Compounds **9**, **11**, and **14** were attached to LCAA-CPG support via conventional succinyl linker. Prior to succinylation, compounds **9** and **14** were converted to triols **15** and **16** by $NaO(CH_2)_3OH$ catalyzed transesterification ((i) in Scheme 4). Alcohols **11**, **15**, and **16** were then treated with succinanhydride ((ii) in Scheme 4), which gave mainly the desired monosuccinates, although formation of di- and trisuccinates was detected. Amide couplings to LCAA-CPG support were carried out using HBTU as an activator ((iii) in Scheme 4), which gave the desired CPG-supported NOTA and DOTA ligands **17**, **18**, and **19** with loadings of 24−35 μmol g^{-1}. The unreacted carboxyl, hydroxyl, and amino groups on the supports were capped by amide bond formation ((iv) in Scheme 4) and acetylation ((v) in Scheme 4) prior to oligonucleotide chain elongation.

Synthesis of the Conjugates 20−25. Oligodeoxyribonucleotide T_6 and 22-mer 2′-*O*-methyl oligoribonucleotide 5′-UGU AAA CCA UGA UGU GCU GCU A-3′(anti-miR15b) were assembled on resins **17**−**19** by the standard DNA and RNA protocol. After the chain elongation, the oligonucleotides were released by the optimized two-step procedure (see Experimental Section: first 0.1 mol L^{-1} aq NaOH, 3 h at 55 °C, followed be neutralization with 1.0 mol L^{-1} aq NH_4Cl and then standard ammonolysis). Examples of RP HPLC traces of the conjugates are shown in Figures 1 and 2. Conjugates **20**−**25** were homogeneous and their authenticity was verified by ESI(MS) (Table 1).

Applicability of the Conjugates for *in Vivo* Imaging with PET. Conjugates **20**−**25** were ^{68}Ga labeled as described before.[5,6] The radiochemical purity and the specific radioactivity of the conjugates ranged 86−97% and 2−12 MBq/

nmol, respectively. Applicability of the resulting ^{68}Ga chelates **20** and **23**−**25** for *in vivo* imaging with PET was then verified. The difference in biodistribution between **23** and **20** should show the significance of the oligonucleotide sequence (dT_6 vs anti-miR15b), while differences among **23**, **24**, and **25** are caused by the chelators. Conjugates **23**−**25** induced multifold radioactivity in kidneys, bone, and bone marrow, as compared with compound **20**. Conjugate **20** was excreted into urine, and also accumulated in small intestine and white adipose tissue in small quantities. Conjugates **23**−**25** had similar kinetics which were different from conjugate **20** in kidney, urinary bladder, and liver. Representative whole-body coronal PET/CT image of a rat intravenously injected with ^{68}Ga-DOTA-22mer **24** is shown in Figure 4.

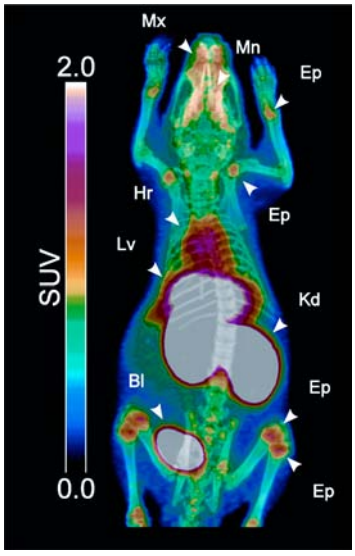


Figure 4. Representative whole-body coronal PET/CT image of a rat intravenously injected with ^{68}Ga-DOTA-22mer **24**. Image is a summation from 0 to 60 min after injection. Radioactivity accumulates in bone, kidneys (Kd), and liver (Lv). The bone accumulation is mainly observed in the epiphyses of long bones (Ep), in the maxilla (Mx), and in the mandibular (Mn) bones. Radioactive urine was observed in the bladder (Bl). In addition, the heart (Hr) was visible in the summed PET images, because of the high blood radioactivity in the first frames right after injection.

The larger molecular size of compounds **23**−**25** is probably causing the higher kidney uptake and lower urinary excretion compared with compound **20**. In order to clarify whether the bone accumulation is oligonucleotide sequence specific, comparative experiments with a scrambled sequence oligonucleotide should be performed.

CONCLUSIONS

Esterified DOTA and NOTA chelators bearing a dimethoxytritylated hydroxyl function have been successfully immobilized via an ester linkage to LCAA-CPG-supports. Such supports allow standard automated oligonucleotide synthesis by the phosphoramidite chemistry. A two-step cleavage, viz., alkaline hydrolysis followed by conventional ammonolysis, releases virtually pure 3′-DOTA/NOTA-conjugated oligonucleotides. ^{68}Ga may be introduced by a brief treatment with [^{68}Ga]Cl_3 at elevated temperature. ^{68}Ga labeling of the conjugates was straightforward. According to *in vivo* imaging with PET, differences in biodistribution were mainly caused by oligonucleotide sequence and/or length, and marginally by the chelators. Further studies are warranted to determine the role of sequence in bone accumulation.

ASSOCIATED CONTENT

Supporting Information

^{1}H NMR and ^{13}C NMR spectra of **3**, **4**, **8**−**11**, **13**, and **14**. This material is available free of charge via the Internet at http://pubs.acs.org.

AUTHOR INFORMATION

Corresponding Author

*E-mail: pamavi@utu.fi.

Notes

The authors declare no competing financial interest.

ACKNOWLEDGMENTS

The financial support from the Academy of Finland is gratefully acknowledged.

REFERENCES

(1) Tanaka, K., and Fukase, K. (2008) PET (positron emission tomography) imaging of biomolecules using metal-DOTA complexes: a new collaborative challenge by chemists, biologists, and physicians for future diagnistics and exploration of *in vivo* dynamics. *Org. Biomolec. Chem. 6*, 815−828.

(2) Wadas, T. J., Wong, E. H., Weisman, G. R., and Anderson, C. J. (2010) Coordination radiometals of copper, gallium, indium, yttrium, and zirconium for PET and SPECT imaging of disease. *Chem. Rev. 110*, 2858−2902.

(3) Zeglis, B. M., and Lewis, J. S. (2011) A practical guide to the construction of radiometallated bioconjugates for positron emission tomography. *Dalton Trans. 40*, 6168−6195.

(4) Tanaka, K., Masuyama, T., Hasegawa, K., Tahara, T., Mizuma, H., Wada, Y., Watanabe, Y., and Fukase, K. (2008) A submicrogram-scale protocol for biomolecule-based pet imaging by rapid 6π-azaelectrocyclization: visualization of sialic acid dependent circulatory residence of glycoproteins. *Angew. Chem., Int. Ed. 47*, 102−105.

(5) Roivainen, A., Tolvanen, T., Salomäki, S., Lendvai, G., Velikyan, I., Numminen, P., Välilä, M., Sipilä, H., Bergström, M., Härkönen, P., Lönnberg, H., and Långström, B. (2004) ^{68}Ga-labeled oligonucleotides for in vivo imaging with PET. *J. Nucl. Med. 45*, 347−355.

(6) Lendvai, G., Velikyan, I., Bergström, M., Estrada, S., Laryea, D., Välilä, M., Salomäki, S., Långström, B., and Roivainen, A. (2005) Biodistribution of ^{68}Ga-labelled phosphodiester, phosphorothioate, and 2′-O-methyl phosphodiester oligonucleotides in normal rats. *Eur. J. Pharm. Sci. 26*, 26−38.

(7) Schlesinger, J., Koezle, I., Bergmann, R., Tamburini, S., Bolzati, C., Tisato, F., Noll, B., Klussmann, S., Vonhoff, S., Wuest, F., Pietzsch, H.-J., and Steinbach, J. (2008) An ^{86}Y-labeled mirror-image oligonucleotide: influence of Y-DOTA isomers on the biodistribution in rats. *Bioconjugate Chem. 19*, 928−939.

(8) De Leon-Rodriguez, L. M., Kovacs, Z., Dieckmann, G. R., and Sherry, A. D. (2004) Solid-phase synthesis of DOTA-peptides. *Chem.—Eur. J. 10*, 1149−1155.

(9) Wängler, B., Beck, C., Wagner-Utermann, U., Schirrmacher, E., Bader, C., Rosch, F., Schirrmacher, R., and Eisenhut, M. (2006) Application of Tris-Allyl-DOTA in the preparation of DOTA-peptide conjugates. *Tetrahedron Lett. 47*, 5985−5988.

(10) Lewis, M. R., Jia, F., Gallazzi, F., Wang, Y., Zhang, J., Shenoy, N., Lever, S. Z., and Hannink, M. (2002) Radiometal-labeled peptide-PNA conjugates for targeting bcl-2 expression: preparation, characterization, and in vitro mRNA binding. *Bioconjugate Chem. 13*, 1176−1180.

(11) Jaakkola, L., Ylikoski, A., and Hovinen, J. (2006) Simple synthesis of a block for solid-phase labeling of oligonucleotides with

1,4,7,10-tetraazacyclododecane-1,4,7,10-tetraacetic acid (DOTA). *Bioconjugate Chem. 17*, 1105−1107.
(12) Katajisto, J., Virta, P., and Lönnberg, H. (2004) Solid-phase synthesis of multi-antennary oligonucleotide glycoconjugates utilizing on-support oximation. *Bioconjugate Chem. 15*, 890−896.
(13) Karskela, M., Virta, P., Malinen, M., Urtti, A., and Lönnberg, H. (2008) Synthesis and cellular uptake of fluorescent labeled multivalent hyaluronan disaccharide conjugates of oligonucleotide phosphorothioates. *Bioconjugate Chem. 19*, 2549−2558.
(14) Karskela, M., Helkearo, M., Virta, P., and Lönnberg, H. (2010) Synthesis of oligonucleotide glycoconjugates using sequential click and oxmation ligations. *Bioconjugate Chem. 21*, 748−755.
(15) Kiviniemi, A., Virta, P., and Lönnberg, H. (2008) Utilization of intrachain 4′-*C*-azidomethylthymidine for preparation of oligodeoxyribonucleotide conjugates by click chemistry in solution and on a solid support. *Bioconjugate Chem. 19*, 1726−1734.
(16) Kiviniemi, A., Virta, P., and Lönnberg, H. (2010) Solid-supported synthesis and click conjugation of 4′-*C*-alkyne functionalized oligodeoxyribonucleotides. *Bioconjugate Chem. 21*, 1890−1901.
(17) Kiviniemi, A., Virta, P., and Lönnberg, H. (2011) Solid-supported 2′-*O*-glycoconjugation of oligonucleotides by azidation and click reactions. *Bioconjugate Chem. 22*, 1249−1255.
(18) Ansari, M. H., Ahmada, M., and Dickeb, K. A. (1993) Synthesis of *N*-[3-(p-aminophenyl)-1-carboxypropyl]derivatives of 1,4,7-triazacyclononane-*N*,*N*′-diacetic acid and 1,4,7,10-tetraazacyclododecane-*N*,*N*′,*N*″-triacetic acid: macrocyclic bifunctional chelating agents useful for antibodies labelling. *Bioorg. Med. Chem. Lett. 3*, 1071−1072.